Recovery Act: Oxy-Combustion Technology Development for Industrial-Scale Boiler Applications

DOE/NETL Cooperative Agreement No. DE-NT0005290

Volume I – Executive Summary

Reporting Period
October 1, 2008 to April 30, 2014

Report Issued on July 29, 2014

Prepared for

U.S. Department of Energy
National Energy Technology Laboratory
Pittsburgh, Pennsylvania

Prepared by
Alstom Power Inc.
200 Great Pond Drive
Windsor, Connecticut 06095

Principal Investigator
Armand A. Levasseur

DISCLAIMER STATEMENT

This material is based upon work supported by the Department of Energy under Award Number DE-NT0005290.

This report was prepared as an account of work sponsored by an agency of the United States Government. Neither the United States Government nor any agency thereof, nor any of their employees, makes any warranty, express or implied, or assumes any legal liability or responsibility for the accuracy, completeness, or usefulness of any information, apparatus, product, or process disclosed, or represents that its use would not infringe privately owned rights. Reference herein to any specific commercial product, process, or service by trade name, trademark, manufacturer, or otherwise does not necessarily constitute or imply its endorsement, recommendation, or favoring by the United States Government or any agency thereof. The views and opinions of authors expressed herein do not necessarily state or reflect those of the United States Government or any agency thereof.

This report was prepared based on work conducted with support, in part, by grants made possible by the Illinois Department of Commerce and Economic Opportunity through the Office of Coal Development and the Illinois Clean Coal Institute as well as the Industrial Commission of North Dakota,. Neither the Illinois Department of Commerce and Economic Opportunity, Office of Coal Development, the Illinois Clean Coal Institute, nor the Industrial Commission of North Dakota, nor any person acting on behalf of either:

(A) Makes any warranty of representation, express or implied, with respect to the accuracy, completeness, or usefulness of the information contained in this report, or that the use of any information, apparatus, method, or process disclosed in this report may not infringe privately-owned rights; or

(B) Assumes any liabilities with respect to the use of, or for damages resulting from the use of, any information, apparatus, method or process disclosed in this report.

Information disclosed herein is furnished to the recipient solely for the use thereof as has been agreed upon with ALSTOM and all rights to such information are reserved by ALSTOM. The recipient of the information disclosed herein agrees, as a condition of its receipt of such information, that ALSTOM shall have no liability for any direct or indirect damages including special, punitive, incidental, or consequential damages caused by, or arising from, the recipient's use or non-use of the information.

Table of Contents

Table of Contents 3
Table of Figures 4
Table of Tables 5
1. Project Background 6
2. Basic oxy-combustion concept 8
3. Experimental Program – Volume II 11
3.1 15 MW_{th} Boiler Simulation Facility 11
3.2 Test Campaigns 13
3.2.1 Test campaign 1 – Powder River Basin subbituminous 14
3.2.2 Test campaign 2 – low sulfur bituminous 14
3.2.3 Test campaign 3 – high-sulfur Illinois bituminous 14
3.2.4 Test campaign 4 – North Dakota lignite 14
3.2.5 Test campaign 6 – Schwarze Pumpe lignite 15
3.2.6 Test campaign 5-1 – 2nd generation, low sulfur bituminous 15
3.2.7 Test campaign 5-2 – 2nd generation, PRB sub-bituminous 15
3.2.8 Test campaign 5-3 – 2nd generation, high sulfur bituminous 15
3.3 15 MW_{th} Test Results 15
3.3.1 Combustion Performance 15
3.3.2 NO_x Emissions 16
3.3.3 Sulfur Emissions 17
3.3.4 Trace Metals Emissions 17
3.3.5 Thermal Performance 17
3.3.6 Conclusions 20
4. Modeling and Validation – Volume III 21
4.1 Chapter 1: CFD Modeling of the 15 MW_{th} Boiler Simulation Facility 21
4.2 Chapter 2: CFD Modeling of 30 MW_{th} Schwarze Pumpe Oxy Pilot Plant 29
4.3 Chapter 3: CFD Modeling of the 500 kW IFK Facility 33
4.4 Chapter 4: Uncertainty Quantification 39
4.5 Chapter 5: Dynamic Process Modeling 44
5. Reference Oxy Boiler Designs – Volume IV 49
5.1 Oxy Boiler Design Cases 49
5.2 Performance 52
5.2.1 Power Output 52
5.2.2 Net Plant Efficiency 54
5.3 Cost Results 55
5.3.1 Total Overnight Cost 55
5.3.2 Cost of Electricity (COE) 58
5.3.3 Variable Cost of Generation 63

5.3.4 Cost of CO_2 Avoided/Captured 64
5.4 Environmental Performance 65
5.4.1 CO_2 Emissions 65
5.4.2 Non-CO_2 Emissions 66
5.5 Sensitivity Study of FGR Location 67
5.6 Summary 69

Table of Figures

Figure 2-1. Schematic of Oxy-Combustion Compared With Air Firing 9
Figure 2-2. Simplified Boiler Island Process Flow Diagram for Oxygen-fired PC Boiler 10
Figure 3-1. Boiler Simulation Facility 12
Figure 3-2. BSF process sketch 13
Figure 3-3. Effect of recirculation rate, Illinois high sulfur bituminous 18
Figure 3-4. Effect of varying oxygen distribution, Illinois high sulfur bituminous 19
Figure 3-5. Long-term temperature and heat flux profiles, ND lignite campaign 20
Figure 4-1. BSF CFD Model Geometry 22
Figure 4-2. BSF Wall Insulation and Test Plane Locations 23
Figure 4-3. BSF Predicted Temperatures for PRB Coal at Test Planes 25
Figure 4-4. Comparison of O_2 Concentrations on Test Planes 27
Figure 4-5. Comparison of Wall Incident Radiation at Plane 141 28
Figure 4-6. Comparison of Wall Incident Radiation at Plane 180 29
Figure 4-7. Oxy Pilot Plant Arrangement 30
Figure 4-8. CFD Geometry of the Oxy Pilot Plant 31
Figure 4-9. Contours of Temperature at Centerline Slices 32
Figure 4-10. Schematic of KSVA 500 kW Test Facility 34
Figure 4-11. Cold Flow Pitot Probe Predictions on Plane 1a 36
Figure 4-12. Temperature Distributions for Air and Oxy Firing 37
Figure 4-13. Oxygen Contour Plot Comparison (Mole %, Dry) 38
Figure 4-14. Gas Temperature Field in BSF Using ARCHES 41
Figure 4-15. Particle Number Density as a f(Particle Size) Using ARCHES 42
Figure 4-16. Load response to load ramp from 50% MCR to 100% MCR 45
Figure 4-17. Fuel/feedwater/oxidant/steam mass flow response to load ramp from 50% MCR to 100% MCR 45
Figure 4-18. Main/reheated steam temperature/pressure response to load ramp from 50% MCR to 100% MCR 46
Figure 4-19. Primary oxidant/secondary oxidant/supplementary O_2 flow response to FD fan trip 47
Figure 4-20. Fuel/feedwater/oxidant/steam mass flow response to FD fan trip 47
Figure 4-21. Main/reheated steam temperature/pressure response to FD fan trip 47
Figure 4-22. Furnace pressure response to FD fan trip 48
Figure 5-1. Simplified Process Flow Diagram for an Oxy-Fired Power Plant 49
Figure 5-2. Power Output Summary 53
Figure 5-3. Net Plant Efficiencies for all Air-Fired and Oxy-Fired Cases 55
Figure 5-4. Total Overnight Costs 58
Figure 5-5. COE and LCOE for All Cases 60
Figure 5-6. COE Breakdown by Cost Component 61
Figure 5-7. COE Sensitivity to CO_2 Allowance Price 62
Figure 5-8. COE Sensitivity to Coal Price 62
Figure 5-9. COE Sensitivity to Capacity Factor 63
Figure 5-10. Variable Cost of Generation vs. CO_2 Allowance Price 64

Figure 5-11. Cost of CO_2 Avoided and Captured 65
Figure 5-12. Summary of CO_2 Emissions for Air-Fired and Oxy-Fired Cases 66

Table of Tables

Table 3-1. BSF test campaigns 13
Table 5-1. Summary of Case Configurations.....50
Table 5-2. Summary of Thermal Performance and Auxiliary Loads 54
Table 5-3. Total Overnight and Total As Spent Capital Costs 57
Table 5-4. Summary of Emissions for all Air-Fired and Oxy-Fired Cases 67
Table 5-5. Cost Implications of FGR Location 68

1. Project Background

Alstom Power Inc. (Alstom), under U.S. DOE/NETL Cooperative Agreement No. DE-NT0005290, has conducted a development program to generate detailed technical information needed for application of oxy-combustion technology. The program is designed to provide the necessary information and understanding for the next step of large-scale commercial demonstration of oxy combustion in tangentially fired boilers and to accelerate the commercialization of this technology. The main project objectives include:

- Design and develop an innovative oxyfuel system for existing tangentially-fired boiler units that minimizes overall capital investment and operating costs.
- Evaluate performance of oxyfuel tangentially fired boiler systems in pilot scale tests at Alstom's 15 MW_{th} tangentially fired Boiler Simulation Facility (BSF).
- Address technical gaps for the design of oxyfuel commercial utility boilers by focused testing and improvement of engineering and simulation tools.
- Develop the design, performance and costs for a demonstration scale oxyfuel boiler and auxiliary systems.
- Develop the design and costs for both industrial and utility commercial scale reference oxyfuel boilers and auxiliary systems that are optimized for overall plant performance and cost.
- Define key design considerations and develop general guidelines for application of results to utility and different industrial applications.

The project was initiated in October 2008 and the scope extended in 2010 under an ARRA award. The completion date of the project was April 30, 2014. The work was divided into eight main tasks:

Task 1	Project Management
Task 2	Process and Firing System Design Screening
Task 3	Bench Scale Testing
Task 4	Large Pilot Scale Combustion Testing
Task 5	Data Analysis and Documentation
Task 6	Model Simulations
Task 7	Oxy Boiler Guidelines
Task 8	Demonstration Oxy Boiler Design, Performance and Costs
Task 9	Commercial Reference Oxy Boiler Design, Performance and Costs.

Central to the project was 15 MW_{th} testing in the BSF conducted under Tasks 4 and 5. This pilot-scale testing provided in-depth understanding of oxy-combustion under boiler conditions, detailed data for improvement of design tools, and key information for application to commercial scale oxy-fired boiler design. Significant improvement of CFD modeling tools for oxy-combustion application has been achieved, including comparison and validation against 15 MW_{th} experimental data. Additionally, dynamic modeling capabilities have been developed for oxy-combustion applications to assess key operation scenarios and support control system design. The testing results and design tools refined under the project were applied to develop detailed oxy-fired boiler designs for both utility and industrial applications. The design, performance and costs have been developed for a 450MW_e

demonstration-scale oxy-boiler, a 900MW_e large utility reference design and a 150MW_e equivalent industrial oxy-combustion retrofit.

To organize the documentation of the project work, the final report has been divided into four volumes.

Volume I - Executive Summary

Volume I is this document, which provides an overview of the project and a summary of key project results from all of the tasks.

Volume II - Experimental Program

Volume II provides details addressing 15 MW_{th} BSF testing including the test facility description and modifications for oxy-firing, test plan and testing procedures, characterization of test fuels including supplemental drop tube furnace testing, and discussion of test results.

Volume III - Modeling and Validation

Chapter 1 - CFD Modeling of the 15 MW_{th} Boiler Simulation Facility
Chapter 2 - CFD Modeling of the 30 MW_{th} Schwarze Pumpe Oxy Pilot Plant
Chapter 3 - CFD Modeling of the 500 kW IFK Facility
Chapter 4 - Uncertainty Quantification of CFD Simulations
Chapter 5 - Dynamic Process Modeling

Volume III addresses CFD combustion simulations and validation efforts as well as the dynamic process modeling work. Results are presented from CFD modeling studies for 15 MW_{th} BSF, the 30 MW_{th} Schwarze Pumpe Oxy Pilot Plant, and a 500 kW IFK combustor at the University of Stuttgart. The results of verification, validation and uncertainty quantification (V&V/UQ) work performed with the Institute of Clean and Secure Energy (ICSE) at the University of Utah are discussed. Work with the ICSE also included assessment of LES (large eddy simulation) modeling for oxy boiler application. Additionally, this volume addresses dynamic process model development for an oxy boiler system and presents simulation results of the dynamic response of key boiler operational parameters under various operating scenarios and abnormal operating events.

Volume IV - Reference Oxy Boiler Designs

Chapter 1 - Oxy Boiler Design Guidelines
Chapter 2 - Design, Performance, and Cost of 450MW_e Demonstration, 900MW_e Commercial, and Industrial Boilers
Chapter 3 - Oxy Boiler Island Advanced Process Control

Volume IV addresses the designs of the 450MW_e Demonstration Oxy Boiler, 900MW_e Reference Oxy Boiler, and Industrial Oxy Boiler Retrofit reference cases. Oxy boiler design guidelines and design considerations are discussed. The design details, performance and costing for each of the three oxy boiler cases are discussed. Oxy-fired CO_2 capture plant economic assessments based on DOE criteria are also presented.

2. Basic oxy-combustion concept

Oxy-combustion is a promising near-term technology for CO_2 capture and sequestration from coal-fired power plants. The basic concept of oxy-combustion (also referred to as 'oxyfuel' and 'oxy-firing') is illustrated in Figure 2-1.

The upper sketch in Figure 2-1 shows normal air firing of coal to produce a flue gas which contains mostly nitrogen from the air, approximately 15% CO_2 and about 3% oxygen. There are processes to remove the CO_2 from this flue gas for sequestration or use, but these processes have high energy consumption.

In oxy-combustion, the air is replaced by essentially pure oxygen from an air separation unit (ASU). With the nitrogen removed from the air, the combustion flue gas is now mostly CO_2 and moisture, and the volume of flue gas flow is reduced more than four-fold, as shown in the middle sketch in Figure 2-1. The advantage of oxy-firing is that it is easier to dry and purify this concentrated flue gas to produce a pure CO_2 stream for sequestration or use. The trade-off for the easier CO_2 processing is the additional energy and cost for the air separation step.

Burning the fuel with pure oxygen would produce flame temperatures too high for practical boiler materials and could also result in severe ash slagging and fouling. Therefore, most oxy-fired designs recycle a portion of the high-CO_2 concentration flue gas to dilute the oxygen and control the furnace temperature, as shown in the bottom sketch in Figure 2-1. Such an approach is mandatory for full dual air and oxy-fired operating capabilities or retrofit of an existing pulverized coal fired boiler.

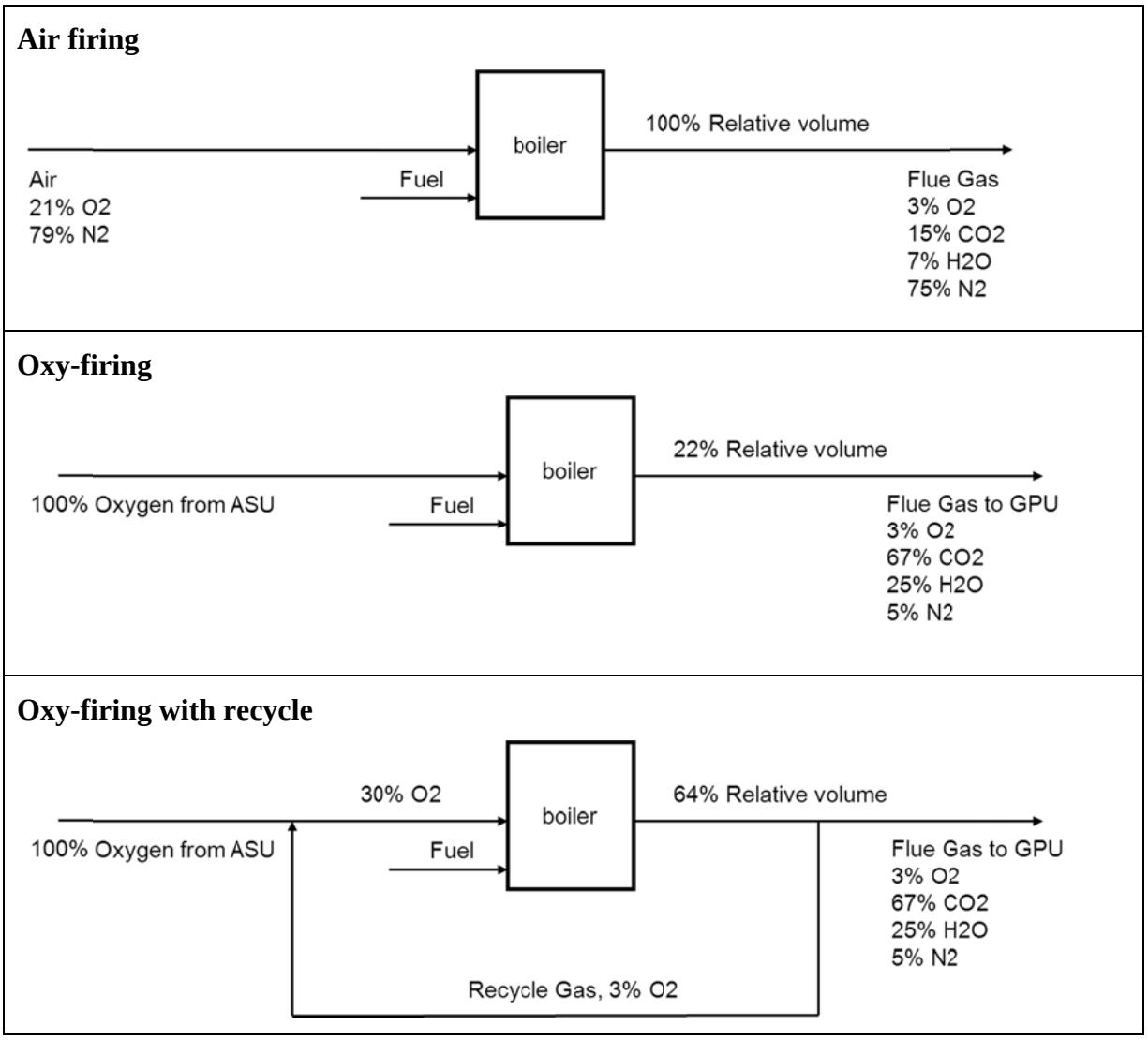

Figure 2-1. Schematic of Oxy-Combustion Compared With Air Firing

Figure 2-1 shows only the broad concepts of oxy-firing and flue gas recycle. Figure 2-2 is a more detailed schematic that shows some of the options for flue gas recycle take-off location.

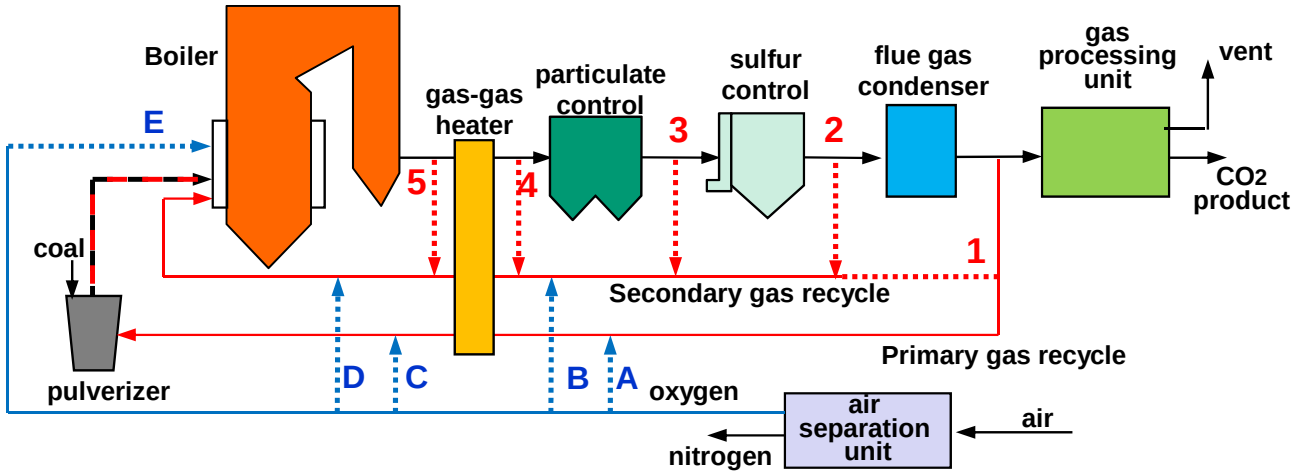

Figure 2-2. Simplified Boiler Island Process Flow Diagram for Oxygen-fired PC Boiler

Typically two main recycle streams are used by the boiler system:

1. Primary gas recycle to provide coal drying for pulverization and to transport the pulverized fuel to the burners, and
2. Secondary gas recycle to mix with oxygen to provide the main oxidant gas for combustion.

There are several options for the location to take flue gas for recirculation back to the boiler. Figure 2-2 identifies possible flue gas recycle take-off locations with dotted arrows numbered 1 through 5. The primary gas recycle is generally taken from after the flue gas condenser (FGC) (location 1), where it has been dried and is suitable for coal pulverization and transport. The moisture content of the dried flue gas might typically be in the range of 3 to 7%, depending on the temperature of available cooling water.

Secondary recirculation could be taken from any of the five locations in Figure 2-2. The secondary recycle stream represents the bulk of the total recycle flow and has a strong impact on the composition of gas in the boiler. For high sulfur coals, recycle would typically be taken after flue gas desulfurization (FGD) and before the FGC (location 2); this gas is wet (20-30% water) but otherwise relatively clean, with a high percentage of particulate and sulfur dioxide removed. For low sulfur coal, it may be advantageous to recirculate from before the FGD (location 3). Recirculation from after the air heater (location 4) or even after the economizer (location 5) will contain particulates as well as sulfur dioxide. In general, recirculation taken from nearer the boiler would result in more buildup of particulate, sulfur, chlorides, alkali, etc., in the recirculation loop; on the other hand, the size of the downstream equipment can be reduced.

The bottom sketch in Figure 2-1 shows a single oxidant stream with an oxidant concentration of 30%. Figure 2-2 shows that, in fact, there will be multiple streams, perhaps with different oxygen contents. It is convenient to calculate the average oxygen concentration of all the oxidant streams as if they were mixed. This is called the global O_2 value. The global O_2 is an indication of the overall amount of flue gas recirculation (FGR) – when more flue gas is recycled, the incoming nearly pure oxygen from the ASU is diluted to a lower value in the oxidant stream. The global O_2 value also depends on the amount of excess O_2 in the recycled flue gas.

3. Experimental Program – Volume II

Extensive 15 MW_{th} oxy-combustion testing in Alstom's Boiler Simulation Facility (BSF) and supporting bench scale testing were conducted under the experimental program. Eight comprehensive 15 MW_{th} oxy-fired test campaigns were performed with different coals, providing detailed data on combustion, emissions, and thermal behavior over a matrix of fuels, oxy-process variables and boiler design parameters. Details on the test facility, oxy-firing modifications, test plan and testing procedures, test fuel characterization, and test results are discussed in Volume II. An overview of this work is provided below.

3.1 15 MW_{th} Boiler Simulation Facility

Alstom's BSF is a tangentially-fired combustion test facility designed to replicate the time-temperature-stoichiometry history of a typical utility boiler. The BSF replicates all major attributes of a utility boiler including a "V" hopper, an arch, and appropriate (simulated) superheater, reheater, and economizer surfaces. The tangential firing system includes 3 levels of coal injection and two levels of separated overfire air. The typical firing capacity for pulverized coal operation is 15 MW_{th}. A photo of the BSF furnace with auxiliary equipment including oxygen supply systems is shown in Figure 3-1.

The furnace walls and heat transfer surfaces of the BSF are cooled by boiling water open to the atmosphere. Refractory lining inside the furnace walls restricts heat absorption to maintain an appropriate furnace gas temperature throughout the combustion chamber. The refractory lining is specifically designed to provide the desired furnace heat absorption and resulting furnace temperatures for the test. The same refractory lining is used during both air and oxy-combustion tests for each test campaign.

BSF testing has a long successful history of supporting development and commercialization of Alstom's combustion systems and other technologies.

Modifications for Oxy-Firing

Under this project, testing and facility requirements were established and modifications made to the BSF for oxy-fired testing. Modifications included:

- Installation of an oxygen supply and injection system;
- Installation of multiple gas recirculation systems;
- Installation of a new fabric filter for particulate removal;
- Installation of a new NID™ sulfur removal system; and
- Installation of new instrumentation and controls.

Modifications to provide oxy-fired operation and testing were completed in August 2009. Minor modifications were made between test programs to address issues identified during prior testing or prepare for specific tests.

A process schematic of the modified BSF is shown in Figure 3-2. The facility has the flexibility to operate under air or oxy-firing mode as well as different gas recycle configurations. The BSF includes major boiler island components including particulate and sulfur removal equipment and a flue gas condenser to dry primary recycle for coal transport.

Figure 3-1. Boiler Simulation Facility

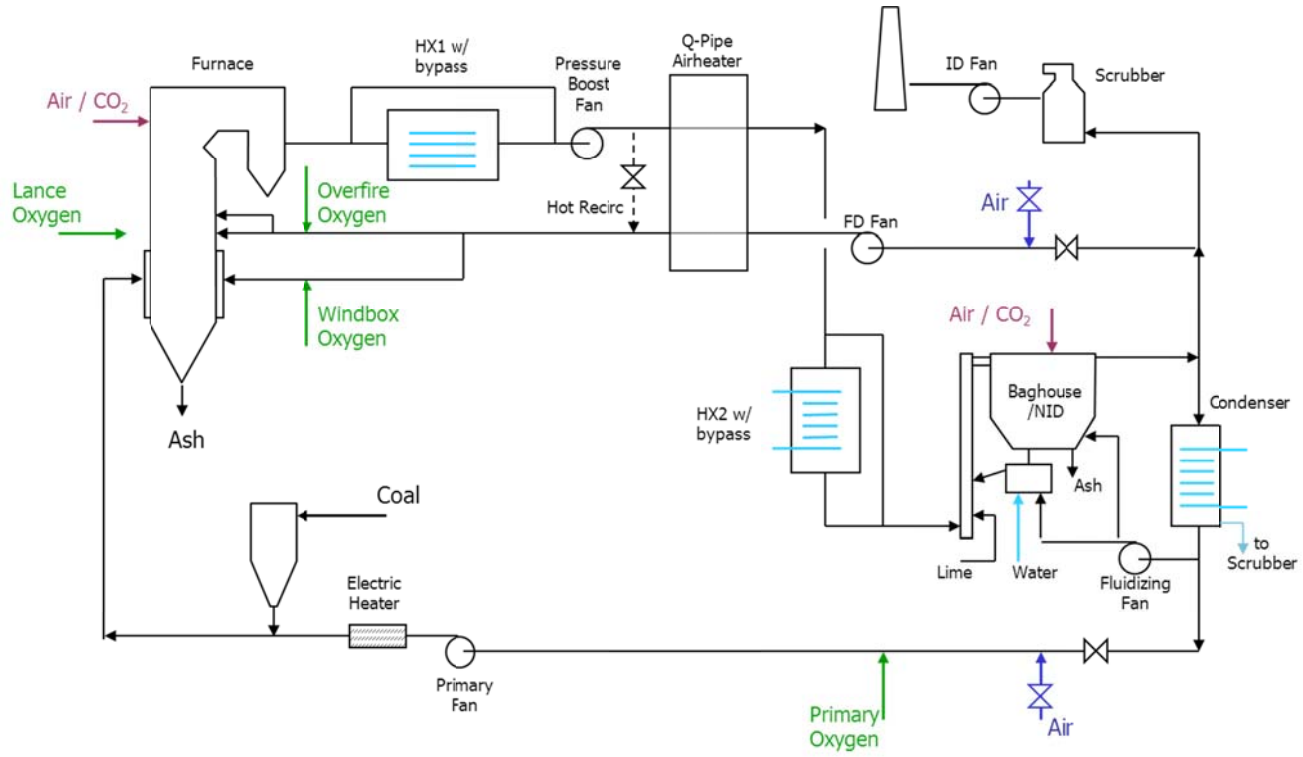

Figure 3-2. BSF process sketch

Oxygen can be added in several locations as shown in Figure 3-2. A supplemental oxygen injection system is used for more precise location of a portion of the oxygen.

3.2 Test Campaigns

From September 2009 through November 2012, eight oxy-combustion test campaigns were executed covering a broad range of fuels, process scenarios, and test conditions. Table 3-1 lists the test campaigns executed in the BSF. Test campaign 5 consisted of three separate campaigns which together constitute the second generation testing.

Table 3-1. BSF test campaigns

Campaign	Test Fuel	Mine	Test Date
1	PRB sub-bituminous	Black Thunder	September 3 to 12, 2009
2	Low sulfur bituminous	Fola	January 18 to February 4, 2010
3	High sulfur bit.	Prairie Eagle	April 25 to May 1, 2010
4	North Dakota lignite	Falkirk	October 4 to October 9, 2010
6 *	Schwarze Pumpe lignite	Lusation	July 11 to 18, 2011
5-1	Low sulfur bit.	Fola	December 7 to 16, 2011
5-2	PRB sub-bit.	Black Thunder	September 23 to 29, 2012
5-3	High sulfur, high chlorine bit.	Gallatia	October 31 to November 6, 2012

* Campaign 6 was moved up in the schedule to precede Campaigns 5, but the original numbering was retained.

The test fuels covered the range of lignite, sub-bituminous and bituminous coals including both high and low sulfur fuels. The test fuels also provided a range in ash properties.

The properties of the test coals were characterized using typical ASTM fuel and ash analyses including trace constituents. In addition, selected test coals were more thoroughly characterized in a bench scale

program utilizing Alstom's Drop Tube Furnace System (DTFS). The DTFS was used to generate char samples under both air and oxy-combustion conditions for subsequent surface area measurements and thermogravimetric reactivity testing as well as to generate ash samples for analysis with Computer Control Scanning Electron Microscopy (CCSEM) techniques. The DTFS was also used to evaluate high temperature devolatilization and gasification properties of these test fuels as well as evaluate combustion behavior under air and oxy-combustion conditions.

3.2.1 Test campaign 1 – Powder River Basin subbituminous

Test campaign 1 focused on testing the most promising oxy design concepts selected during preliminary studies. Baseline air-fired testing was initially conducted to establish comparative performance and emission data for the test coal. The selected design options were each tested in the BSF over a range of conditions with the objective of optimizing overall performance and emissions. Operating variables assessed included excess total oxygen, burner zone staging, and air in-leakage. Firing system design variables included FGR take-off location, FGR stream flow rates and injection locations, oxygen concentration in different input streams, fuel and oxidant injection parameters.

3.2.2 Test campaign 2 – low sulfur bituminous

Test campaign 2 focused on the most important operating and design parameters identified during the first test campaign and furnace measurements expanded to better understand the impacts. Operating variables assessed included excess total oxygen, burner zone staging, and recycle rate. Additional heat flux measurements around the furnace were taken. Like the first test campaign, baseline air-fired data was initially conducted to establish comparative performance and emission data for the test coal. The NID™ dry scrubbing system was shaken-down and tested in preparation for the following campaign 3.

3.2.3 Test campaign 3 – high-sulfur Illinois bituminous

This program, as originally proposed to the DOE, included assessment of very high sulfur levels by spiking sulfur to simulate high sulfur coal. With additional funding from the Illinois Clean Coal Institute (ICCI), test campaign 3 was added to the program to allow for actual testing with a high sulfur coal to provide realistic combustion conditions and improve the reliability of the data as well as greatly expand the amount of information that can be collected. Of particular interest were the SO_2 and SO_3 concentrations that built up due to the recycle of flue gas according to the level of sulfur capture. Like the first test campaign, baseline air-fired data was initially conducted to establish comparative performance and emission data for the test coal. The NID™ dry scrubbing system was utilized to capture sulfur in the recycle stream. Combustion testing during test campaign 3 focused on methods to adjust and control the heat flux profile during oxy-firing.

3.2.4 Test campaign 4 – North Dakota lignite

Test campaign 4 was also added to the original DOE program, with support of the North Dakota Industrial Commission, Lignite Research Council. Test campaign 4 focused on characterizing the oxy-combustion performance of North Dakota lignite. Particular focus was given to gaseous mercury concentrations that could build up during oxy-firing according to the level of mercury capture from the recycled flue gas in the baghouse. To understand the fate of SO_3 in the boiler, tests were conducted spiking SO_3 into the recycle stream. Like the first three test campaigns, baseline air-fired data was initially conducted to establish comparative performance and emission data for the test coal. The impact of operating and firing system design variables on thermal performance and emissions was assessed over a series of test points.

3.2.5 Test campaign 6 – Schwarze Pumpe lignite

Test campaign 6 focused on establishing a link between tests run at the tangentially-fired 15 MW_{th} oxy-fired BSF and the single burner down-fired 30 MW_{th} oxy-combustion pilot plant at Vattenfall's Schwarze Pumpe station. The Schwarze Pumpe oxy pilot is the world's first complete technology path for CO_2 capture, including an ASU and CO_2 processing plant. The experience from oxy combustion tests with the same fuel at the two facilities allows for a comparison between emissions, thermal data, and performance between the two facilities. Test data from the 15MW_{th} BSF and the 30MW_{th} oxy pilot plant has been used for refinement and validation of CFD codes under this project. Parameters varied during BSF testing include firing rate, recycle rate, staging, and excess oxygen. Tests were selected to match conditions from Schwarze Pumpe and from prior BSF tests.

3.2.6 Test campaign 5-1 – 2nd generation, low sulfur bituminous

Test campaign 5-1 was conducted with the same West Virginia low sulfur bituminous coal used during test campaign 2. Two close coupled recirculation systems were installed: 1) a single large ejector driving all the gas recirculation for the windbox secondary oxidant, and 2) four smaller ejectors driving recirculation utilizing a supplemental oxygen supply.

Test campaign 5-1 focused on three second generation concepts: close-coupled flue gas recirculation, use of oxygen driven ejectors to recirculate flue gas, and a compressed firing zone.

3.2.7 Test campaign 5-2 – 2nd generation, PRB sub-bituminous

Test campaign 5-2 was conducted with the same PRB sub-bituminous coal used during test campaign 1. A flue gas slip stream was installed to investigate the control of SO_3 and Hg in oxy-combustion flue gas. Inlet and outlet sampling systems were set up using an inertial separation probe (ISP) and a feed system was set up to add sorbents. Slip-stream testing was done to evaluate mercury control. Also tests were done with nitric oxide added to the flue gas recycle returning to the BSF burner/windbox and separated overfire ports to investigate NO_x reduction in the furnace.

3.2.8 Test campaign 5-3 – 2nd generation, high sulfur bituminous

Test campaign 5-3 was conducted with a high sulfur, high chlorine bituminous coal from Illinois (though not the same fuel used in test campaign 3). Slip-stream testing was done to evaluate acid-gas control and further nitric oxide injection tests were done. Other tests included increased firing rate, low excess O_2, and heat flux optimization on oxy-firing.

3.3 15 MW_{th} Test Results

3.3.1 Combustion Performance

For oxy-combustion, there is an economic advantage to reduce the excess oxygen supply and to reduce the amount of flue gas recycle. Reducing the excess oxygen reduces the amount of oxygen required from the ASU and reduces the purification costs for the CO_2 product gas. Reducing the amount of flue gas that is recirculated back to the boiler could reduce the size and cost of the boiler, the gas recirculation system and the downstream pollution control equipment, as well as reduce the parasitic power consumption.

Understanding the combustion impacts of reducing the amount of flue gas recycle and reducing the excess oxygen was an important objective of BSF testing. Reducing the amount of flue gas recycle impacts burner conditions/design parameters, furnace aerodynamics and combustion performance.

Combustion performance was assessed in parametric tests during each test campaign. Generally the carbon monoxide emissions when oxy-firing were as low as or lower than during comparable air-fired conditions. In general, the results indicate the dominating factors for CO emissions during air and oxy-firing are the same for a particular coal: complete mixing of the overfire oxidant before significant flue-gas cooling and final oxygen partial pressure, expressed as oxygen concentration in the flue gas. Carbon burnout was generally more complete during tests under oxy-fired operation than during air firing. For the oxy-fired tests, well less than 0.5% of the heat input was lost due to unburned carbon, even at the lowest excess O_2 levels. For all test fuels, it was possible to operate at less than 2% O_2 leaving the furnace without excessive CO emissions or unburned carbon loss during both air and oxy-firing.

3.3.2 NO_x Emissions

The emission of nitrogen oxides (NO_x) is an environmental concern in the design and operation of traditional air-fired combustion power plants. In the oxy-combustion process, environmental emissions of NO_x must still meet regulatory limits, and there is the additional consideration for the operation of the flue gas processing unit and the quality of the CO_2 product gas. Differences in combustion conditions and design flexibilities with the oxy-combustion process allow for new opportunities to control NO_x emissions. Understanding the impacts of firing system design and operation on NO_x emissions during oxy-combustion was a goal of this test program.

The formation of NO_x during combustion is a complex process, highly dependent upon the time-temperature-stoichiometric history inside the boiler as well as specific properties of the fuel being fired. Windbox stoichiometry is one of the key variables in a staged, low-NO_x firing system. For all BSF test campaigns, baseline air-fired testing was conducted to establish comparative performance and emissions data for the test coal. NO_x emissions measured during baseline air firing in the BSF were consistent with utility boiler experience. The net NO_x emissions on a mass (lb/hr) or thermal loading (lb/MMBtu) basis during oxy-firing were typically less than 50% of the NO_x levels during air firing at comparable firing conditions. The NO_x concentrations (ppm) during oxy-firing were typically higher than during air firing due to the absence of atmospheric nitrogen in the flue gas.

Air-combustion and oxy-combustion tests show a strong dependence of NO_x emissions on windbox stoichiometry. In general, it was possible to reduce the NO_x levels to a greater extent with bituminous coals under oxy-firing than air-firing. NO_x levels as low as 0.05 lb/MMBtu were obtained for all test coals under certain oxy-firing conditions in the BSF.

Air-firing shows a consistent decrease in NO_x emissions with decreasing outlet O_2. Oxy-combustion tests show little impact of excess oxygen on NO_x emissions. These results are consistent with an increase in thermal NO_x formation during air-combustion as the excess oxygen increases and minimal . thermal NO_x formation during oxy-combustion due to the depletion of nitrogen. The lower amount of NO_x emitted from the boiler loop during oxy-firing compared to air firing is influenced by several factors including reduced thermal NO_x, changes in the combustion gas composition impacting NO_x chemistry, and reburning of NO_x returned to the boiler with flue gas recycle. Varying the amount of flue gas recycle would be expected to change the amount of reburning, but the effects may be confounded by changes in furnace temperatures and residence times.

To more clearly see the effect of reburning, a series of tests injecting extra NO_x (as NO) into the recycled flue gas was done during the last two test campaigns:

PRB second generation with oxy-firing;
High sulfur bituminous with air and oxy-firing.

At normal windbox stoichiometries, most of the NO added to the windbox was destroyed in the furnace. Much more of the NO added only to the OFA region made it through to the furnace outlet. This is expected, due to the less intense substoichiometric conditions which can reduce the NO_x. At higher windbox stoichiometries, there is much less reduction of the injected NO added to the windbox or bulk flue gas. The result indicating nearly complete reburning of the recycled NO_x with deep windbox staging is important for extrapolation of the test results to commercial applications.

3.3.3 Sulfur Emissions

Under both air- and oxy-firing, nearly all of the sulfur in the coal will be released in the furnace. If the sulfur is not removed from the recycled flue gas, the concentration will be higher in oxy-firing due to the lack of nitrogen dilution. If sulfur is removed, then the concentration is diluted by the recycled flue gas. In both air- and oxy-firing, the rate of SO_2 leaving depends on the extent of removal in the flue gas scrubber.

As expected, without sulfur capture, SO_2 concentrations leaving the furnace were much higher during oxy-firing due to the lack of nitrogen dilution. The NID™ was very effective in removing SO_2 from the recycled flue gas, thereby reducing the SO_2 concentration leaving the furnace.

The SO_3 concentration was also reduced when the NID™ was operating. The net conversion to SO_3, expressed as the SO_3-to-SO_2 ratio, was similar for air and oxy-firing.

To investigate the fate of recycled SO_3, tests were done with SO_3 injected into the recycle stream. The results show the added SO_3 returning to the furnace did not contribute to an increased level at the furnace outlet. The SO_3 was reduced in the high temperature firing zone to SO_2 (possibly first to more reduced species such as H_2S).

During the second generation testing with high sulfur, high chlorine coal, SO_3 control by sorbent injection was tested on a slipstream of flue gas from the BSF. Four sorbents were tested: trona, hydrated lime, sodium bicarbonate and magnesium oxide. Significant capture rates of acid gases were achieved before the boiler gas-gas preheater, allowing lower exit temperatures and greater boiler efficiencies. There was little difference in the performance of these sorbents under air and oxy-fired conditions. Between 60 and 80% of the total SO_3 was captured by the sorbents.

3.3.4 Trace Metals Emissions

In most test campaigns, trace metal concentrations were measured at the furnace and baghouse outlets. Metals other than mercury were mostly removed in the baghouse.

Separate measurements on mercury speciation were done in Test campaign 4. Mercury leaving the furnace is mostly in elemental form, and most is oxidized after passing through the baghouse. In hot recycle tests (from location 5 in Figure 2-2), most of the mercury in the recycle stream had not yet oxidized.

In tests with powdered activated carbon (PAC), up to 70% mercury removal was achieved in oxy-firing consistent with the removal rates during air-firing under similar conditions.

3.3.5 Thermal Performance

In the oxy-combustion process, flue gas is recycled to the boiler to moderate the furnace temperatures and reduce peak heat flux. The quantity and distribution of recirculated flue gas and oxygen into the boiler will alter the heat release pattern in the combustor. Understanding and controlling this heat release pattern is an important goal of Alstom's oxy-combustion boiler development program.

The balance between furnace heat absorption and convection section heat absorption must be considered and the boiler designed appropriately. For retrofit applications, pressure part modifications could be minimized if existing furnace and convection section surfaces provide similar heat absorption during air and oxy-fired operation. For new applications, optimization of pressure part surfacing may be possible by further reducing gas recycle, but many factors must be considered that would limit this reduction. Some of the considerations associated with reducing gas recycle include higher peak heat fluxes requiring more cooling or use of high temperature materials, ash management and operational issues of the impact of higher temperatures on slagging and fouling behavior, and the impact of higher concentrations of corrosive constituents on fireside corrosion.

The furnace heat flux and heat absorption profiles can be controlled by a number of factors, including the gas recirculation rate, the distribution of recirculated gas, and the split of oxygen to the different windbox and overfire levels.

The left plot in Figure 3-3 shows the effect of varying recirculation rate on the vertical heat flux profile during Test campaign 3 with high sulfur bituminous. For these tests, the total oxygen input was held constant and the quantity of gas recycle was varied. Furnace heat flux increased as the mass flow through the boiler decreased.

The plot on the right of Figure 3-3 shows the percent of heat input absorbed in the furnace up to the outlet plane as the recycle rate changes. The heat absorbed decreases with higher recycle/lower global O_2. For this case with oxy-firing, a global O_2 of about 28% matches the heat absorbed of the air fired case for the high sulfur bituminous fuel. For other fuels, the percent heat absorbed in the furnace varies, but in each case oxy-firing with a global O_2 of between 26 and 30% gave the same percentage heat absorption as air firing.

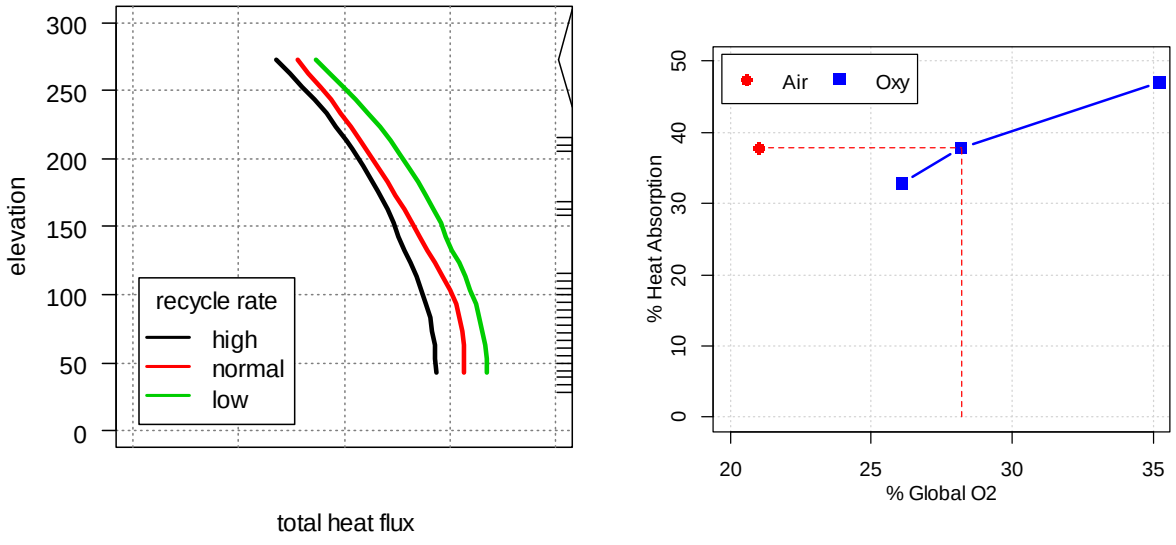

Figure 3-3. Effect of recirculation rate, Illinois high sulfur bituminous

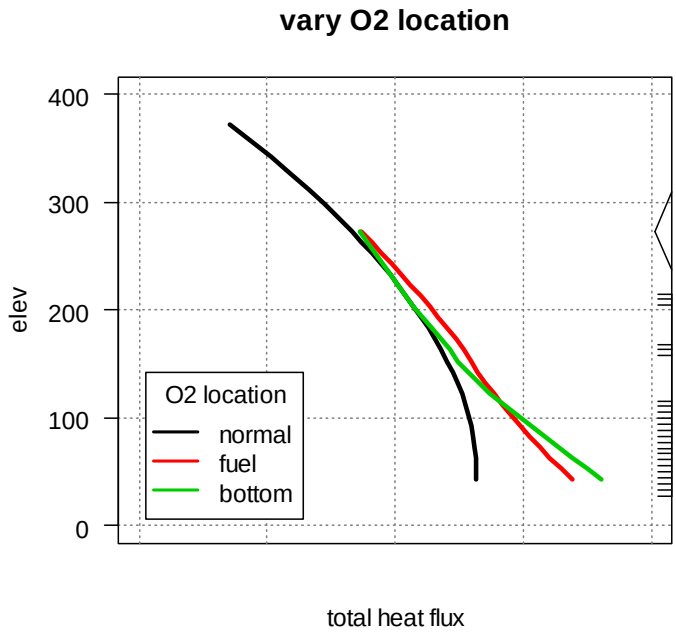

Figure 3-4. Effect of varying oxygen distribution, Illinois high sulfur bituminous

Impacts of local compartment enrichment were tested. Figure 3-4 shows the results of one variation during the Illinois bituminous test campaign. In the base test, oxygen was mixed normally with the flue gas recycle. In the next test, some oxygen was removed from the bulk oxygen addition and added to fuel compartments low in the windbox. Finally the oxygen was biased even more to the bottom compartments. In each case, the result is the same windbox stoichiometry, but with local oxygen enrichment. The heat flux in the lower furnace increased when oxygen input was shifted lower in the furnace and locally enriched in selected windbox compartments.

During each test campaign there was at least one long term test with air firing and oxy-firing. It was generally intended that the vertical heat flux profile of the oxy-fired long term test match that of the air fired test by adjusting the flue gas recycle and the distribution of flue gas and oxygen. Figure 3-5 shows an example of the matching heat flux profiles for the North Dakota lignite long-term tests.

These tests demonstrate that with the control of flue gas recycle and distribution of oxygen, furnace heat flux profiles can be adjusted during oxy-firing to match those with air firing.

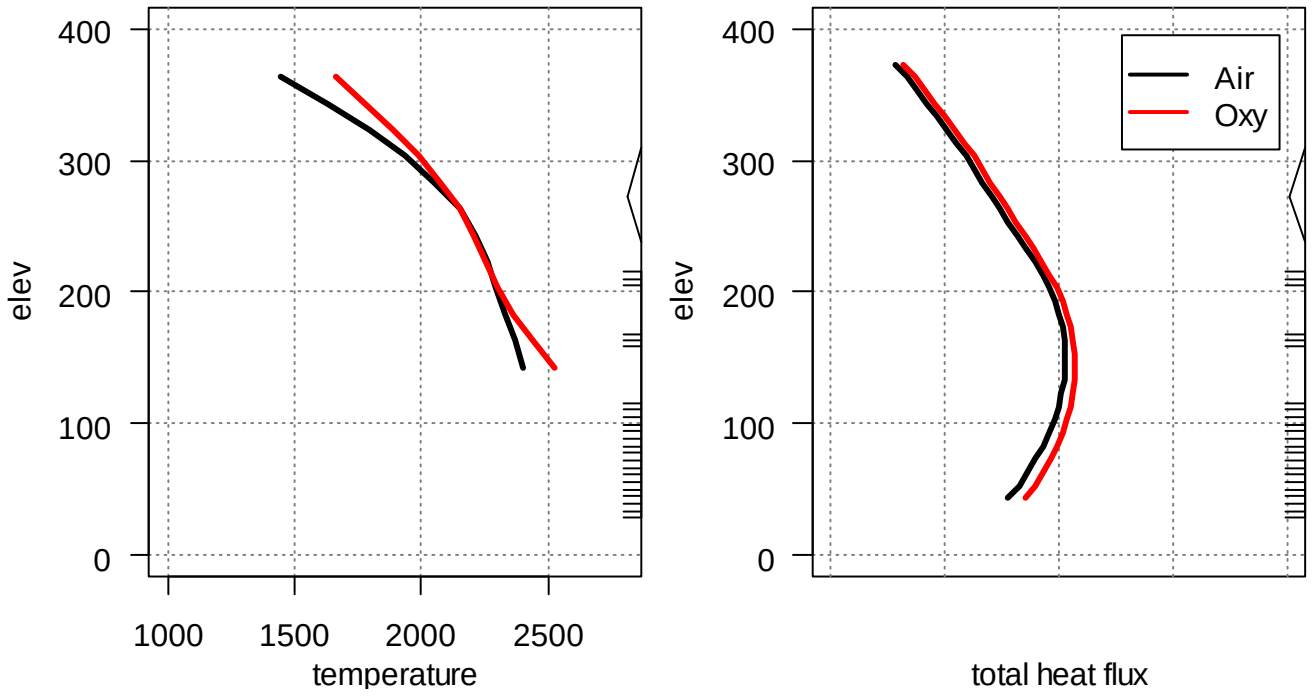

Figure 3-5. Long-term temperature and heat flux profiles, ND lignite campaign

3.3.6 Conclusions

The 15 MW_{th} test program achieved all major objectives. The BSF was modified to allow effective and comprehensive evaluation of oxy-combustion impacts over a range of representative oxy-process and boiler design conditions. The BSF provided stable operation and permitted testing over the full range of matrix parameters desired. Eight comprehensive test campaigns were completed providing a wealth of detailed information covering a range of coal types and boiler operating parameters.

Results of the 15 MWth testing demonstrate that there are no technical barriers restricting the continued development and commercialization of oxy-combustion from a boiler standpoint. Combustion performance, emissions, and thermal behavior (temperature, heat flux intensity, heat flux profile) can be controlled to similar levels as air firing. For a tangentially oxy-fired boiler, there are no major changes required to the current boiler design for oxy-firing. Boiler size and pressure part surfaces should only require minor modifications for oxy-fired retrofit applications. For new applications, additional control under oxy-firing may be used to an advantage with innovative design concepts to improve oxy-fired boiler performance and costs.

The data generated during the test program has proven extremely useful for the refinement and validation of engineering design tools, including CFD and dynamic modeling. The test results have also provided the basis for the development of procedures and guidelines for oxy-boiler design. The extensive database generated under this program is not only valuable for Alstom design, but can used by other researchers and organizations to support their development efforts.

The results of this test program provide a sound foundation for oxy-boiler design and commercial-scale demonstration. These results along with other large-scale oxy-combustion test programs conducted around the world confirm the technical viability of this technology and the readiness to proceed to the final development step of commercial-scale demonstration.

4. Modeling and Validation – Volume III

Along with the experimental work, the development of oxy-fuel combustion technology under this program included several modeling activities.

The modeling activities included a comprehensive set of CFD combustion simulations performed using the geometry for Alstom's 15-MW_{th}, tangentially-fired, Boiler Simulation Facility (BSF). The benefits of using CFD tools for the engineering scale-up of oxy-combustion systems from pilot-scale to commercial-scale plants include higher performance confidence, improved understanding of novel design features and optimization of design. In order to improve the confidence levels of the CFD tools, specific furnace configurations with well-defined operating conditions were modeled and the simulations were compared with detailed in-furnace mapping measurements. This linkage between comprehensive experimental testing and simulation activities was made through a number of modeling tasks that include simulation of the Alstom's 15-MW_{th}, tangentially-fired, BSF as well as other oxy-combustion geometries. The first four chapters of Volume III of this final project report include the details of the various CFD modeling activities.

The fifth chapter of Volume III discusses a dynamic modeling investigation of the transient responses of the oxy boiler island for various plant event scenarios.

4.1 Chapter 1: CFD Modeling of the 15 MW_{th} Boiler Simulation Facility

The bulk of the CFD modeling was associated with the BSF, where simulations were performed by experienced CFD modelers in Windsor using the ANSYS FLUENT® software. The test data used in the validation was collected for five (5) different test coals: a Powder River Basin (PRB) (Black Thunder) sub-bituminous coal, a West Virginia (Fola) eastern (low-sulfur) bituminous coal, an Illinois No. 6 (Prairie Eagle) eastern (high-sulfur) bituminous coal, a North Dakota (Falkirk) lignite and a Schwarze Pumpe (Lusation) lignite. The data was collected in intermittent test campaigns between the years 2009 and 2011. The data and the simulations include both air- and oxy-combustion.

In order to perform oxy-combustion calculations, the fundamental differences between air and oxy-fuel combustion were incorporated into the CFD calculations. Obvious differences such as the physical properties of the gas constituents certainly have a pronounced effect and were easily incorporated. Differences in density and nozzle velocities were also fundamental and required no significant modifications to the standard software. However, other submodels required attention and enhancements, such as the gas radiative properties. The FLUENT® default submodel for gas radiative properties that is used often in air-combustion simulations is the weighted-sum-of-grey-gas model (WSGGM). This model was found (at the time) to be inadequate for oxy-combustion cases. Consequently, Alstom developed a proprietary user-defined function (UDF) for use with FLUENT® to calculate the local gas-phase absorption coefficient. The UDF was based upon an Alstom implementation of the Edwards Wide-Band model, in which an interpolative table for the gas-phase absorption is constructed as a function of (a) the local, relative fraction of CO_2 in a composite mixture of CO_2 + H_2O, (b) the partial pressure of the composite CO_2 + H_2O mixture, (c) the local gas-phase temperature, and (d) a specific overall beam or path length for the system.

In addition, the default particle radiation properties in FLUENT®, based on an input emissivity and scattering factor, were replaced with a much more accurate UDF based on efficiencies. The UDF generates absorption and scattering efficiencies for weighted combinations of coal, char, and ash as a function of the local particle temperature and diameter. The efficiencies are calculated for a given refractive index from an Alstom-proprietary code based on Mie theory, and have been generated for

anthracite coal, bituminous coal, lignite coal, and ash. These additional particle absorption and scattering efficiencies were utilized in the present runs to enhance the overall radiation treatment.

Other than the above modifications, no additional UDFs, parameter adjustments, or significant property changes were made to accommodate the oxy-combustion system. An implicit assumption was made that the submodels for both the coal pyrolysis characteristics, and the wall heat transfer deposit thicknesses and resistances, were not a direct function of the type of combustion environment (whether air-combustion or oxy-combustion).

Alstom's 15-MW_{th}, tangentially-fired, BSF is part of the Alstom Power-Power Plant Laboratories' (Alstom) Combustion Research Complex located in Windsor, Connecticut. The firing system includes a burner belt with three elevations of coal nozzles, a number of secondary air nozzles, and two elevations of separated overfire air (SOFA) nozzles. The firing system in the BSF incorporates corner-fired burners that have been configured to generate a tangential firing pattern. The air nozzles are positioned at the same offset angles as the coal nozzles; however, the concentric firing system (CFS) nozzles are offset an additional 22 degrees from the normal firing angle.

The furnace geometry and computational mesh created for the BSF were generated using the ANSYS mesh program GAMBIT. The geometry and corresponding surface mesh for the BSF computational domain is pictured in Figure 4-1.

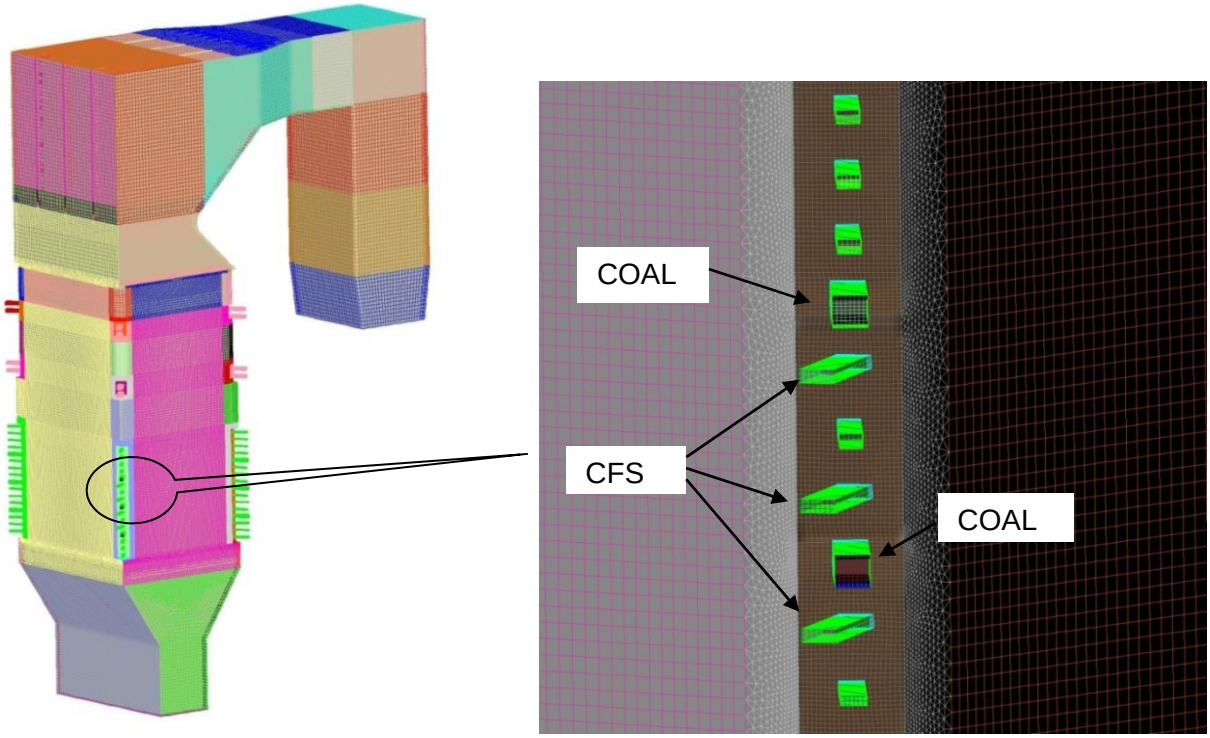

Figure 4-1. BSF CFD Model Geometry

The inlet boundary conditions for the feeds were prescribed from carefully analyzed and balance-checked experimental board data. The mass flow rates and overall stoichiometries are different for each test case. The inlet boundary conditions were prescribed as flow rates, temperatures, and species mass fractions for the primary air (PA), windbox combustion air, lower overfire air (LOFA), and upper overfire air (UOFA) sections, as well as for the coal feed rate. The stream compositions for the oxy

cases are different from those of the air cases due to the flue gas recycle strategy used in oxy combustion.

There are four (4) different wall-insulation zones as a function of vertical height in the BSF, with the upper furnace wall being un-insulated, bare steel, as shown in Figure 4-2. To model the effect of the insulation, a specified temperature boundary condition was used in conjunction with the FLUENT® code's thin-wall thermal resistance formulation. The specified temperature is on the far side of a thin wall, away from the adjacent fluid zone (and toward the waterside). The thermal resistance is the ratio of the parameters $\Delta x/k$, where Δx is the thickness of the resistance material(s), and k is the thermal conductivity.

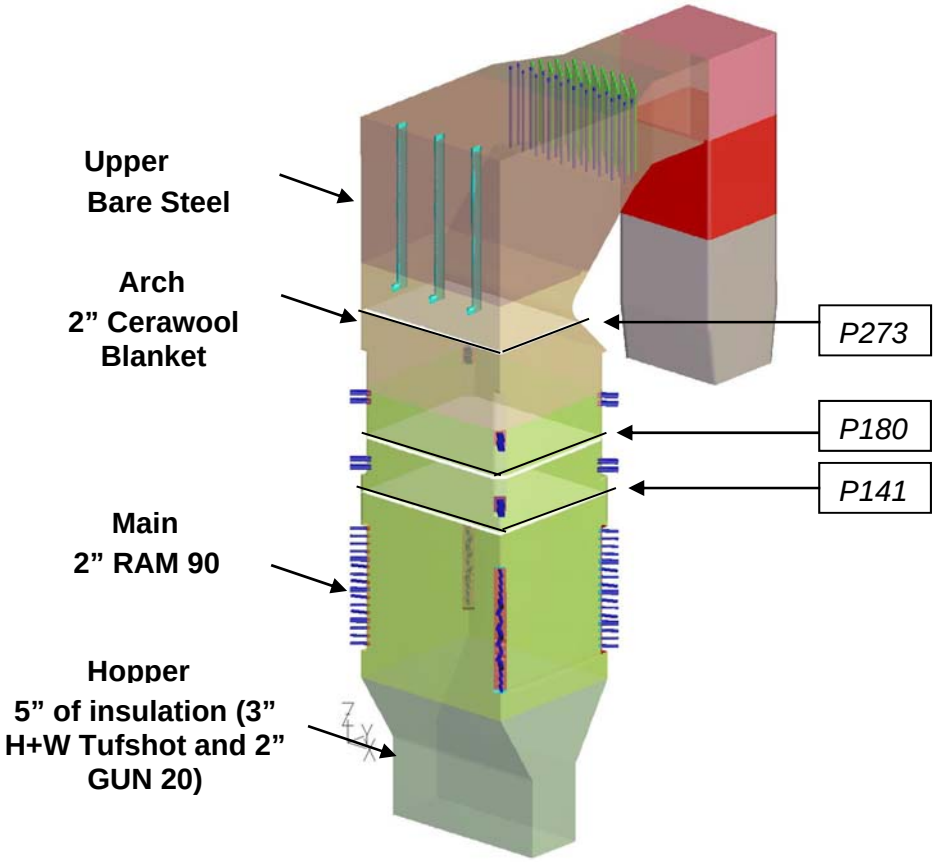

Figure 4-2. BSF Wall Insulation and Test Plane Locations

For each of the five (5) coals, the air-combustion case was run first in order to establish a baseline or reference point before moving to the more complex oxy-combustion case with the recycled flue gas and oxygen injection. For example, for the air-combustion case, the grid quality was assessed, the mass flow rates were checked against the desired flow rates, the heterogeneous reaction rates were tuned to any residual or unburned carbon constraints, and the wall thermal boundary conditions were calibrated to match the measured temperatures, all prior to transitioning the case to oxy conditions. The same property methods, reaction rates, and wall thermal boundary conditions were used in both the air and oxy cases; only the inlet boundary conditions changed.

To illustrate the predictive accuracy for gas temperature, a set of plots associated with the PRB coal Tests 11 and 12 are shown in Figure 4-3. For the air-combustion case, the main windbox oxygen-to-fuel stoichiometric ratio (i.e., 0.95) is higher than that of the oxy-combustion case (0.82). With this set

of conditions, the temperature in the vicinity of the main windbox would likely be higher in the air-combustion case than in the oxy-combustion case, all else being equal. The CFD simulations show that this is indeed the case. The higher H_2O and CO_2 concentrations, associated with the oxy-combustion case, also lower the temperature because of their higher gas emissivities (leading to higher wall heat flux) and higher specific heats. A visual survey of the experimental temperatures clearly shows a progression from hotter temperatures at Plane 141 to cooler temperatures at successively higher planes (Planes 180 and 273) as overfire air is added. The calculations show the same overall trend. Individual measurements may deviate 100 to 200 °F (55 K to 111 K) from the calculations, but this difference is considered reasonable and acceptable for suction pyrometer measurements, particularly in high-gradient regions. Broad differences at a particular plane indicate that deviations would be decreased by slightly adjusting the wall thermal boundary condition.

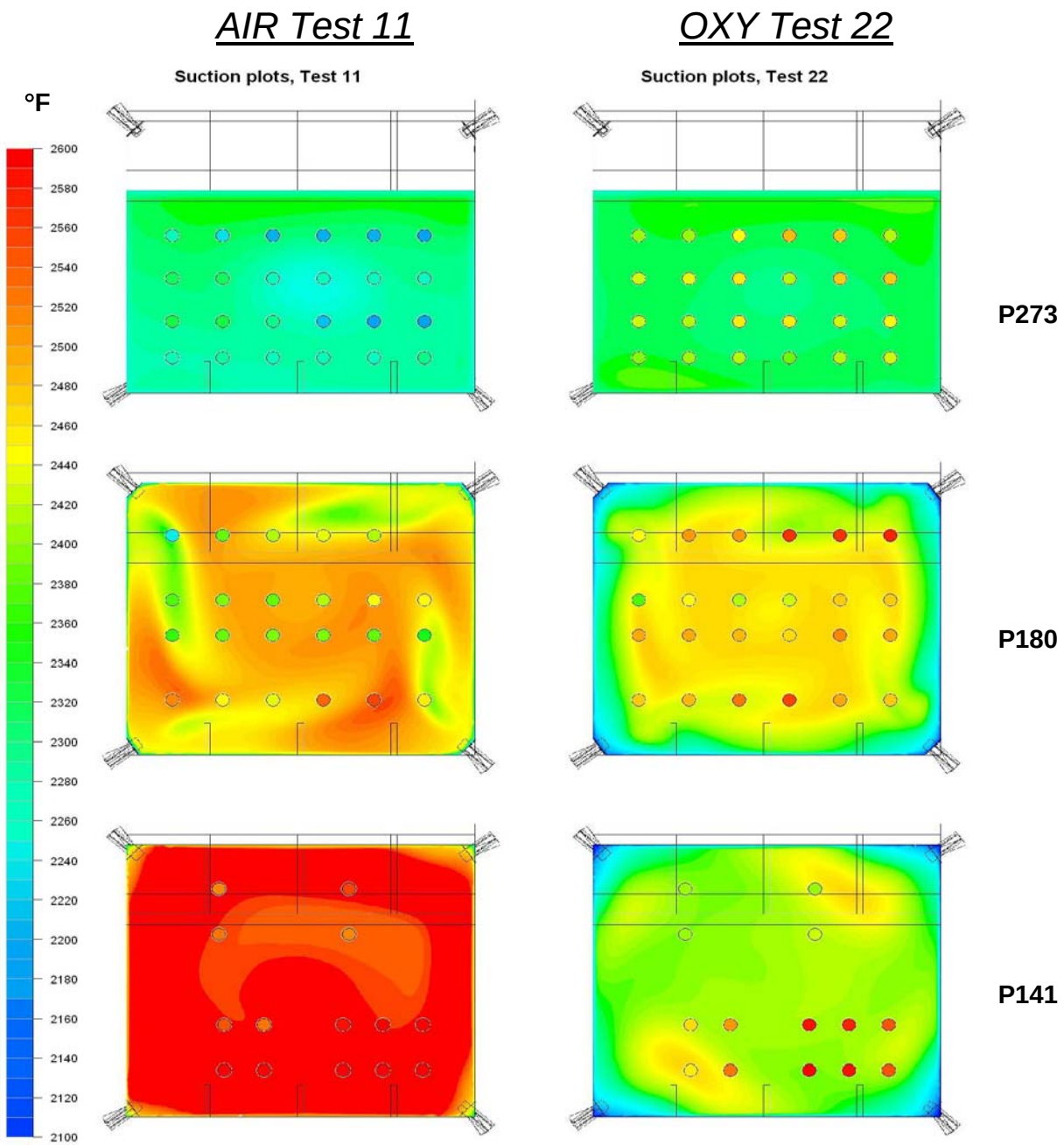

Figure 4-3. BSF Predicted Temperatures for PRB Coal at Test Planes

Some of the measurements indicate patterns that correspond with residual jets or core regions. For example, for the air case on Plane 141, some of the cooler temperatures are in the core region as indicated by both the calculated and measured temperatures. On Plane 180, some of the green dots are aligned with residual jets while the red and yellow dots are aligned with more intense combustion zones. At Plane 273, the temperatures are more uniform across the plane as the flow field becomes more homogenous due to mixing. Although there may be some local asymmetry and incongruities for individual data points, the overall agreement between the computations and experiments is considered

acceptable. An important conclusion is that the predictions for oxy-firing, given the uncertainties in the experimental data and boundary conditions, scale reasonably well from the air-combustion baseline. The oxy-firing predictions appear to capture the temperature data reasonably well. The temperature plots for the other coals are not too dissimilar from the ones shown above.

An illustration of the predictive accuracy for oxygen molar concentration is provided in Figure 4-4, showing predictions for Tests 39 and 50 with the Fola coal. As seen on the plot, the overall oxygen concentration appears to increase with increasing elevation, although locally high concentrations of oxygen indicate proximity to a feed stream. On Plane 180, the experimental data points appear to qualitatively follow the gross features of the computations. On Plane 273, for the air case, the imprints of the SOFA oxidant supply and swirl pattern are still visible at the horizontal furnace outlet plane, although significant asymmetry exists in both the experimental and computed values. On Plane 273, for the oxy case, the high, experimental O_2 concentrations appear to reside predominately on the right-hand side of the furnace, in a pattern that seems to be consistent with the CFD predictions. The scale is compressed and extends from 0 to 6%. Although local deviations between the predictions and the data may be significant for individual points, typical deviations are within a percentage point or two. This deviation is considered reasonable and acceptable given the uncertainties inherent in the experimental measurements, boundary conditions, and submodels. Again, it is important to recognize that the CFD calculations were able to reasonably capture the transition from the baseline air-fired case, at which the calibrations were performed, to the oxy-fired case, without any apparent deterioration of the prediction capability. A similar conclusion is appropriate for other species such as CO_2 and CO.

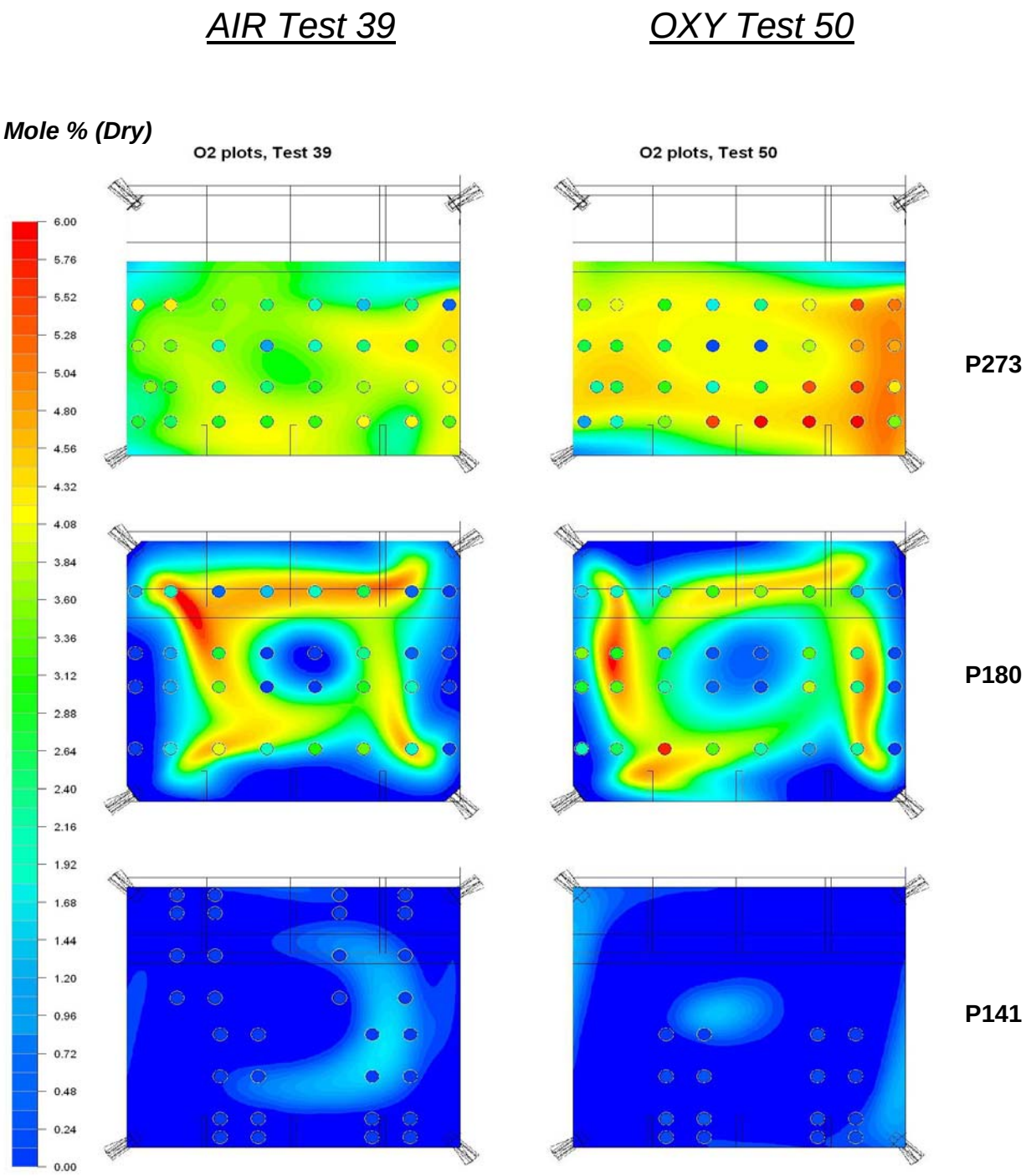

Figure 4-4. Comparison of O_2 Concentrations on Test Planes

An important parameter that was examined in great detail was the heat flux distribution. In general, the heat flux distribution both as a function of elevation and around the perimeter are important to the thermal design of the boiler. Understanding the fundamental differences between air and oxy combustion conditions and how the heat flux profiles change was of key interest. In addition, for oxy

firing the impacts of different staging conditions, local enrichment strategies, and other boundary conditions could be tested and simulated with CFD. An illustration of the predictions for the wall incident radiation as a function of elevation are shown in Figure 4-5 (Plane 141) and Figure 4-6 (Plane 180) for Tests 83 and 98, associated with the North Dakota lignite coal. On Plane 141, the incident radiation for the oxy case appears to be about 10% to 20% larger than that for the air case, for both the experimental data and the computations, depending upon the wall (e.g., right or left) at which the measurements are taken. On Plane 180, the incident radiation for the oxy case is about 10% larger than that for the air case, again for both the experimental data and the computations. Agreement with the data is good and is probably within 10% overall, when considering all of the planes. The uncertainty brackets on the heat flux probe measurements are tentatively projected to be within the range of 20% to 25%, and predictions within this range are considered to be reasonable and acceptable. Local predictions may deviate from the experimental heat flux values at certain elevations, but the overall absorption is not likely to exhibit significant error since the wall thermal boundary conditions were calibrated to some degree. It is important to note that the scaling between the air-combustion case and the oxy-combustion calculations appears to be consistent with the experimental data.

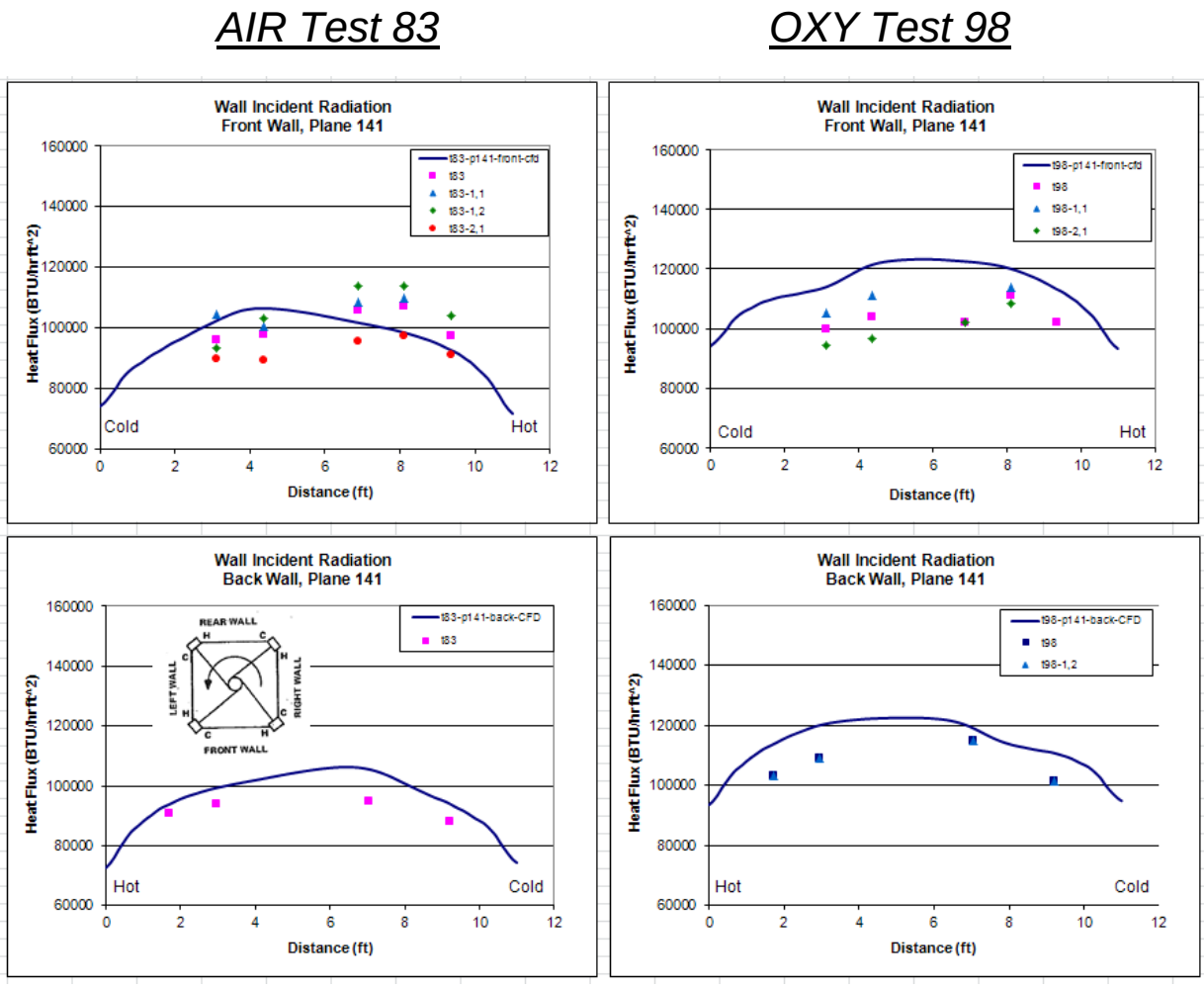

Figure 4-5. Comparison of Wall Incident Radiation at Plane 141

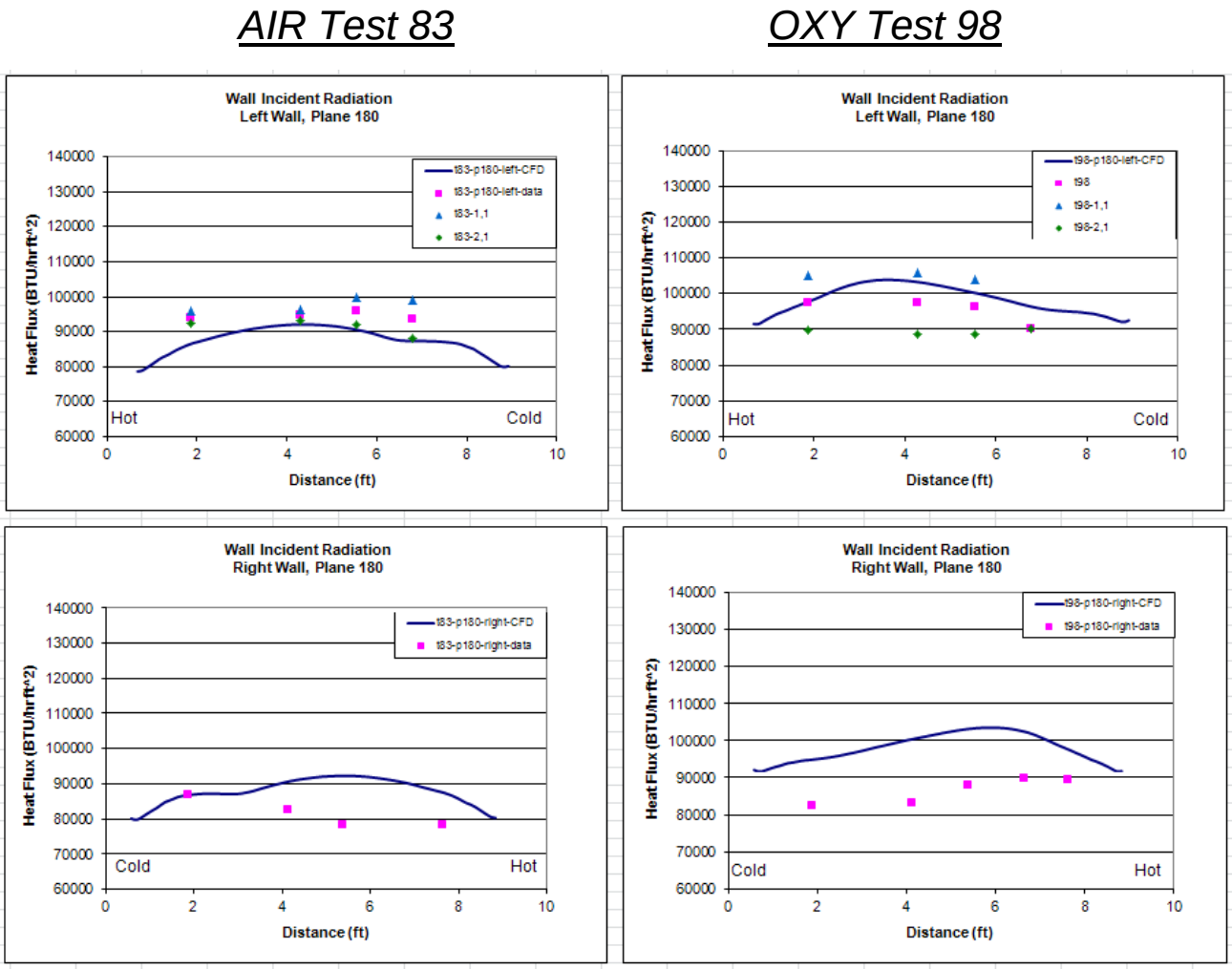

Figure 4-6. Comparison of Wall Incident Radiation at Plane 180

Given that expectation and understanding, and given that the baseline air-combustion cases were first tuned and calibrated before testing the predictive accuracy for the oxy cases, it can now be ascertained that the calculation of the oxy-combustion cases is also within reasonable and acceptable uncertainty bounds. In other words, the apparent predictive error associated with the oxy cases does not appear to be significantly increased or exacerbated relative to the overall predictive error exhibited by the baseline air cases. This leads to the overall conclusion that the FLUENT® code, in conjunction with the UDFs and modeling strategy, as implemented for the runs in question, includes the requisite physics to make the transition from air- to oxy-combustion CFD studies. This does not mean that enhancements could not be made to the boundary conditions or to the chemical-kinetic mechanisms or other submodels to improve the predictive accuracy for CFD in general, or oxy-combustion in particular. It simply means that the capability to study or design oxy-combustion systems, using FLUENT®, appears to be on par with the present capacity to study or design air-combustion systems.

4.2 Chapter 2: CFD Modeling of 30 MW_{th} Schwarze Pumpe Oxy Pilot Plant

In conjunction with internally funded development programs, Alstom has partnered with other entities to gather detailed probe measurements at the Schwarze-Pumpe Oxy Pilot Plant (OxyPP) facility. As

part of this DOE project, Alstom conducted CFD modeling tasks to model the various OxyPP facilities and to compare the calculations with the experimental data.

The 30 MW_{th} OxyPP arrangement is shown with an elevation and plan view in Figure 4-7**.** The furnace contains a single swirl burner mounted at the top firing downward. The burner arrangement used for the detailed testing included 3 concentric zones for the air or oxidant stream injection. The bulk of the testing and modeling effort was focused on the zone downstream of the burner. The waterwall shell of this furnace included a series of sample ports at various elevations as indicated. These ports were used to measure gas temperatures and species. The Alstom CFD model geometry of the furnace and burner used for the CFD simulations is provided in Figure 4-8Figure 4-8. Similar to the BSF modeling described in the previous section, the CFD model was created using the ANSYS/FLUENT® commercially-licensed software and includes approximately 4.5 million cells for the burner and the furnace, with the majority of the cells concentrated in the burner portion.

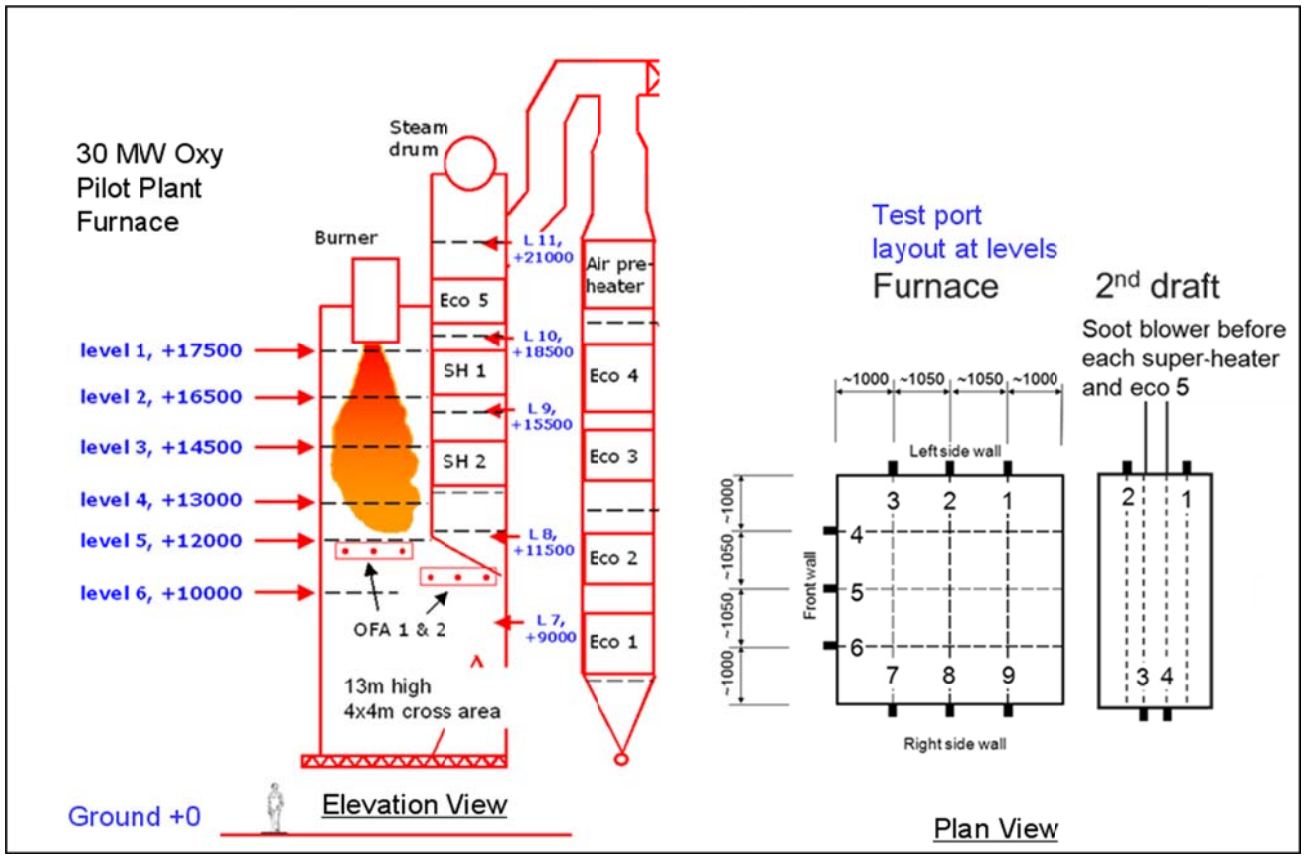

Figure 4-7. Oxy Pilot Plant Arrangement

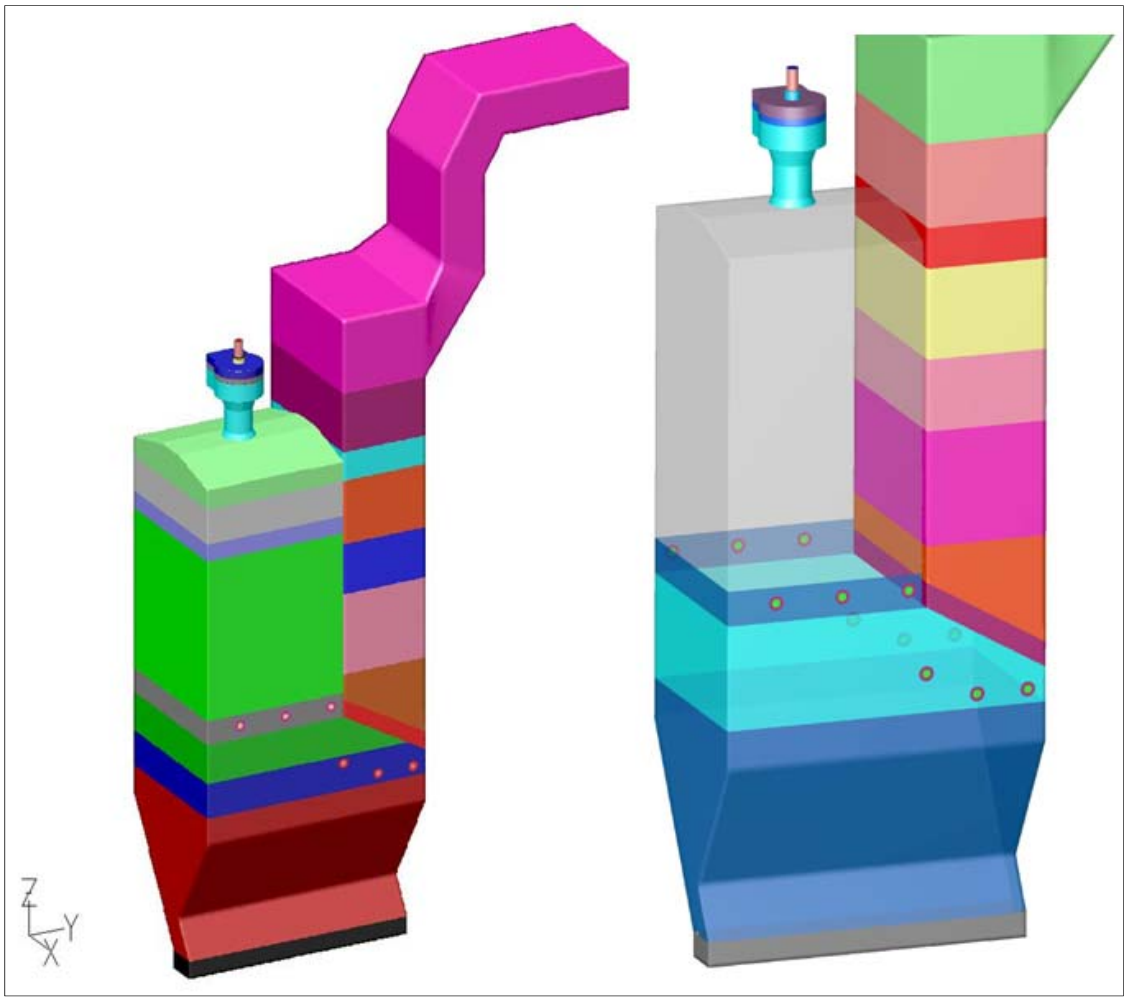

Figure 4-8. CFD Geometry of the Oxy Pilot Plant

Three cases were modeled with FLUENT® CFD software – an air-fired test (Air Test 332) and two oxy-fired tests (OF25 Test 333 and OF30 Test 334). The OF25 (Test 333) case has the highest main burner zone excess oxygen and overall excess oxygen of all of the three tests being examined, as well as the highest gas and coal flow rates. OF30 has the lowest overall excess oxygen ratio (1.052), as well as the lowest excess oxygen in the main burner zone itself (0.87), than the other two tests. The coal flow rate for OF30 is intermediate between the other two cases, but the total inlet gas mass flow rate is significantly less (by 14 to 18%) than the other two test cases.

Calculation results were obtained for both air and oxy firing tests. A pair of contour plots is provided in Figure 4-9 for Test OF25 to illustrate the temperature predictions, as a function of (a) turbulence model, and (b) the extent to which the full burner was modeled (as opposed to simply applying boundary conditions to inlet annuli). One can see from the near-burner flow fields that the Reynolds Stress Model (RSM) case manifests some instability effects, while the flow patterns in the k-ε case are much smoother. Despite the more diffusive nature typically associated with the k-ε model, the length of the flame zone in the k-ε case appears to be greater than that of the RSM. This longer flame length for the k-ε case also appears to induce a longer (absorbed) radiation wall heat flux zone and pushes the peak radiation wall heat flux value (not shown) downstream towards the OFA, relative to that of the

RSM case. The increased mixing of the RSM may in part be due to the stronger centerline reverse flow zones associated with the RSM.

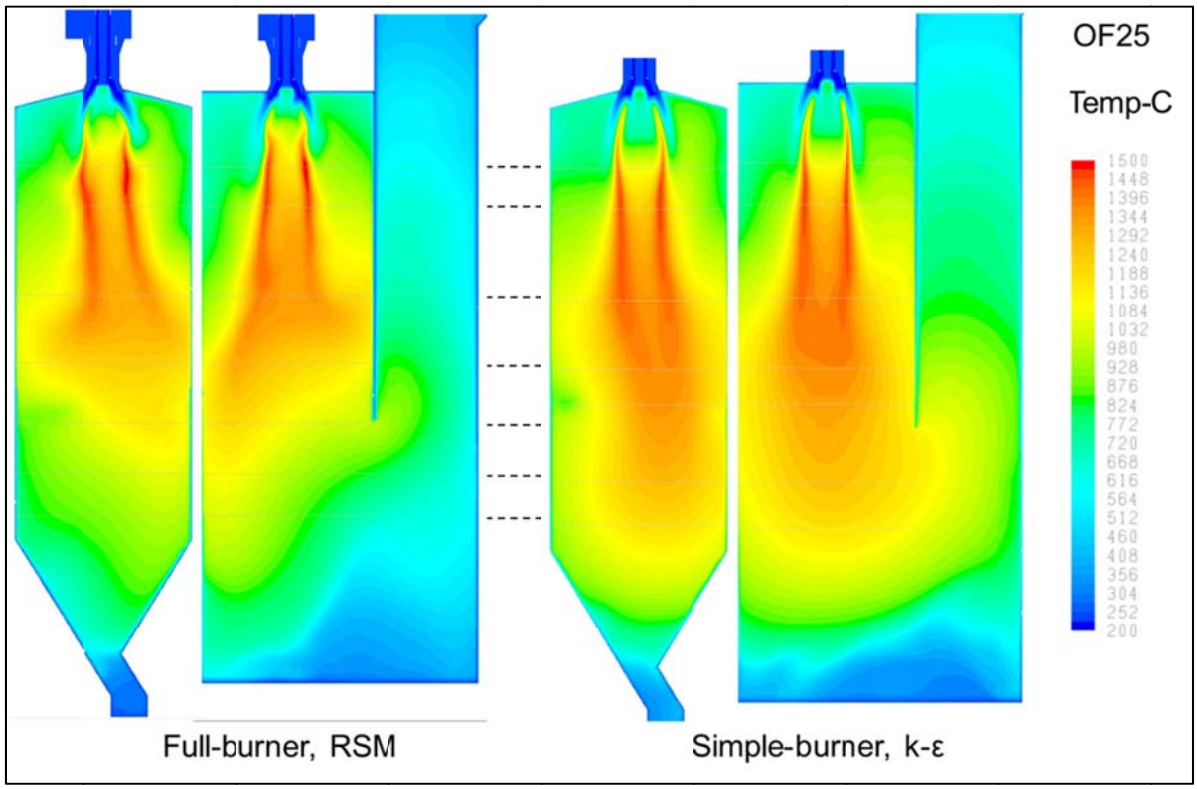

Figure 4-9. Contours of Temperature at Centerline Slices

Calculations of the three tests produced results and flame characteristics (in the form of contour plots) that could be reasonably explained based on the swirl levels, the excess air in the main furnace zone, and the overall stoichiometry.

A significant effort was made at the beginning of the project to ascertain the advantages and drawbacks of including the entire burner assembly in the computational domain, as opposed to applying circumferentially uniform inlet boundary conditions on a truncated burner. An assessment of other model selections, such as the Reynolds Stress Model versus the k-ε model, was also conducted. This report documents the results of those assessments. Alstom's stance is that its present CFD methodology, such as including the entire burner assembly as part of the computational domain, and utilizing the Reynolds Stress Model, are beneficial in more faithfully simulating the true physics of the actual experiments.

Calculation results were provided in the form of contour plots and longitudinal, planar-average profiles. In addition, detailed, two-dimensional line plots were prepared to compare the CFD calculations with the experimental data sets for three variables -- temperature, oxygen mole percent (wet) and CO mole percent (wet), along a single traverse at six (6) different elevations.

Conclusions with respect to the predictions of the experimental data may be itemized as follows:

- The temperature predictions, for the Air test and the OF25 test, are generally aligned either with the two available data sets, or they lie somewhere in between the two data sets. The predictive accuracy appears to be reasonable and acceptable. For the OF30 test, the predictions

were also acceptable, but the computations exhibited an excessive heat release in the upper furnace. This excessive computed heat release may be due to errors in the boundary conditions.

- For the Air test and the OF25 test, the calculations in the upper furnace exhibit an oxygen-starved core, near the burner symmetry axis, that is substantiated by the experimental data. The width of the core appears to be reasonably captured. However, the peak computed oxygen levels, on either side of the core, and extending to the walls, are higher than the experimental data. The calculated oxygen concentrations for OF30 Test 334 tend to underpredict the experimental oxygen concentrations in the main burner zone, which may be symptomatic of a feed stream boundary condition issue.
- The CO predictions for the Air test and the OF25 test are moderately good. The CO predictions for OF30 are somewhat excessive relative to the data in the upper furnace.
- The unburned carbon in the char appears to be reasonable.

From a comparison of the calculations with the data, it is apparent that the fidelity of the computations could always be enhanced for both air and oxy combustion simulations through both continued submodel development and a formalized uncertainty quantification process. Nevertheless, the predictions of the Air and OF OxyPP experimental data indicated that FLUENT®, given the model settings, the property databases, and the associated user-defined functions, was capable of adequately predicting both air and oxy combustion. The predictive accuracy for oxy firing appeared to be just as reliable as it was for the air-fired simulation. Based on these results, it is believed that oxy combustion calculations can be pursued at Alstom on the same basis as commensurate air combustion studies.

4.3 Chapter 3: CFD Modeling of the 500 kW IFK Facility

A third CFD modeling study was conducted on IFK's 500 kW combustion at the University of Stuttgart. The experimental data was collected at IFK on their 500 kW 0.8 m diameter cylindrical test furnace under a separately funded project. This included measurements from a series of air and oxy combustion firing tests using a down-fired lignite burner similar to that tested at Vattenfall AB's Schwarze-Pumpe 30 MW Oxy Combustion facility. The experimental tests conducted at IFK using the Vattenfall dried lignite included both staged and unstaged conditions. For the staged tests, a central OFA injection lance was used. Experimental measurements included probe traverses into the furnace at various elevations to measure gas temperatures, gas species and char burnout. The experimental data was collected by IFK ostensibly for the purpose of validating CFD models. To date, the validation has been performed separately by IFK, Vattenfall, and Alstom, using different codes. In an effort to be consistent with other oxy CFD studies reported under this DOE contract, tuning of the reaction models, rates and other factors were made consistent with the 30 MW pilot plant CFD modeling inputs described in a separate chapter of Volume III. Alstom's CFD modeling and validation of several different IFK test conditions are discussed in Chapter 3.

A schematic of the IFK facility and reactor are provided in Figure 4-10. The design of the IFK facility is based on the design of a conventional once-through pulverized fuel combustion boiler. The schematic depicts a "small-scale power plant" with a train of flue-gas cleaning unit operations, including a high-dust, selective catalytic reduction (SCR) unit, an electrostatic precipitator (ESP), and a bag-filter. Combustion air is provided by a forced draft (FD) fan, while an induced draft (ID) fan serves to transport the flue gases to the stack.

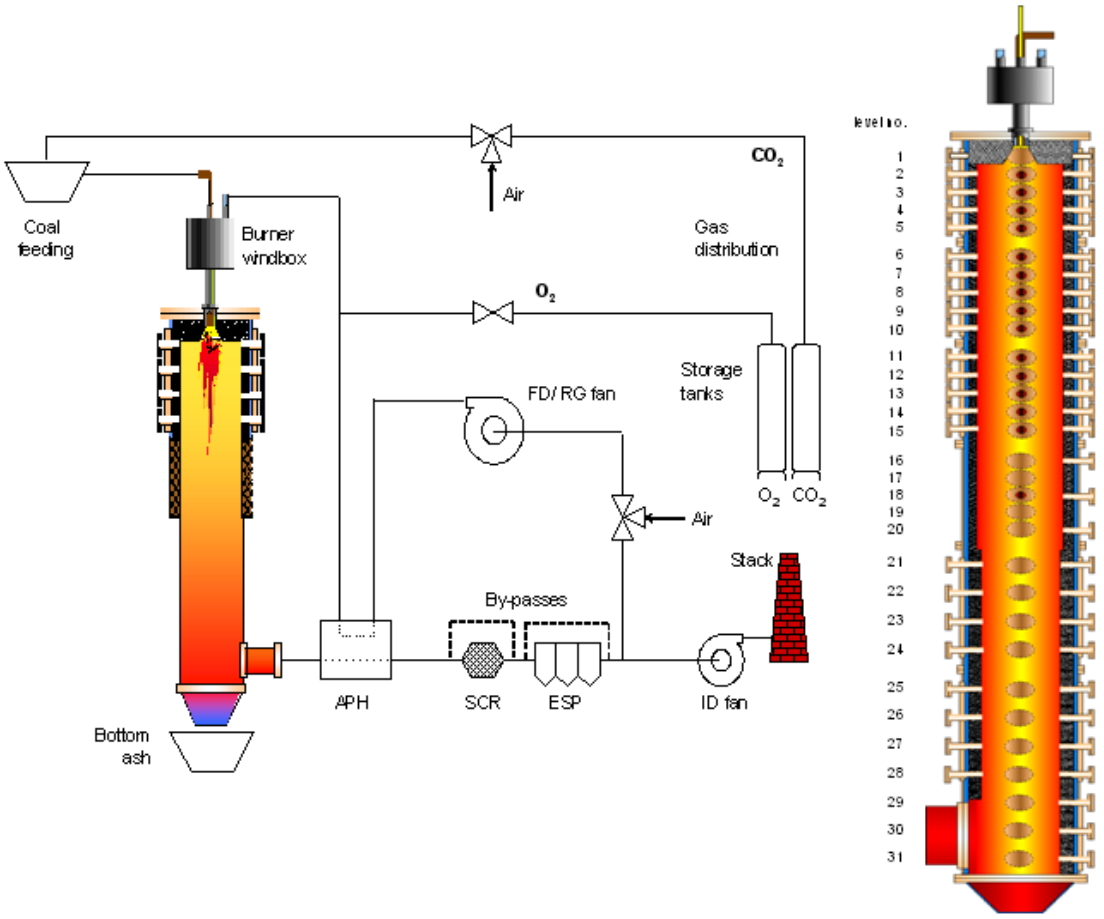

Figure 4-10. Schematic of KSVA 500 kW Test Facility

The reactor is a vertical, down-fired combustion chamber that consists of several cylindrical segments with a total length of about 7 m and an inner diameter of 750 mm. The amount of pulverized fuel fed is gravimetrically controlled by a dosing system, and then the fuel is conveyed pneumatically to the burner. Combustion air is fed to the burner through a secondary line and mixes with the fuel and gas in the primary line at the burner quarl. Swirl can be imparted to the secondary gas stream.

Measurement openings or sampling ports are integrated into the reactor wall. The ports allow measurements of gas emissions, temperatures, and/or ash in both vertical and horizontal direction by means of specially designed probes.

The final cases selected for modeling corresponded to two separate test campaigns segregated between the unstaged and staged firing modes. Two data sets were generated, in conjunction with the facility and burner modifications associated with the addition of downstream air/oxidant injection. In addition to the hot flow simulations, cold flow testing near the burner quarl was included to check the CFD predictions without the complexity of chemical reactions and heat transfer. These cold flow measurements were performed with a 5-hole, spherical, pitot probe. For the combustion test measurements, gas temperature and gas species sampling probes were taken along the height of the reactor. Total heat flux probes, as well as ellipsoidal radiometers (for total radiative heat flux measurements) were used at Levels 2 through 15, measuring fluxes close to the insulated wall.

Similar to the OxyPP and BSF simulations, the CFD modeling performed by Alstom was performed using FLUENT®. Meshing of the KSVA 500 kW Test Facility was accomplished by gridding the burner geometry as an integrated component with the reactor as part of a single computational domain using ANSYS Gambit® with about 2.7 million cells.

For the boundary condition specification, measured flow rates and compositions for the feed streams, as well as the experimental particle size distributions for the tests, were provided by IFK. To model the wall heat transfer in the hot cases, the reactor walls were given specified temperature boundary conditions. For the cold flow computational runs, specified inlet velocities and a constant fluid density were utilized.

Alstom used the Realizable k-ε submodel with standard wall functions for turbulence closure. User-defined functions (UDFs) were used for the gas absorption coefficient and for the particle absorption efficiency. The Discrete Ordinates (DO) model was used for the radiation calculations. Second-order discretization was used for the pressure, and second-order upwind numerics were specified for all of the other transport equations except for the species.

An example of some of the 5-hole pitot probe predictions at a single plane is shown in Figure 4-11. Profile plots along the x- and y-coordinate directions are compared with experimental, 5-hole pitot probe data for the axial velocity, radial velocity, and tangential velocity at Plane 1a, which is located inside the burner quarl. The burner corresponds to the Test Week 1 configuration.

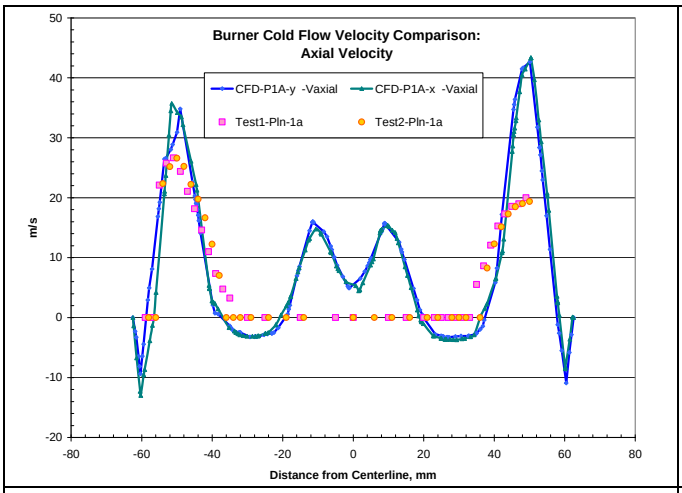

(a) Axial Velocity on Plane 1a

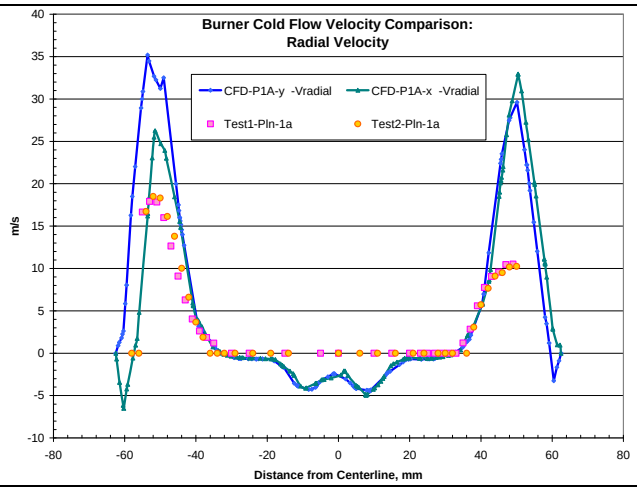

(b) Radial Velocity on Plane 1a

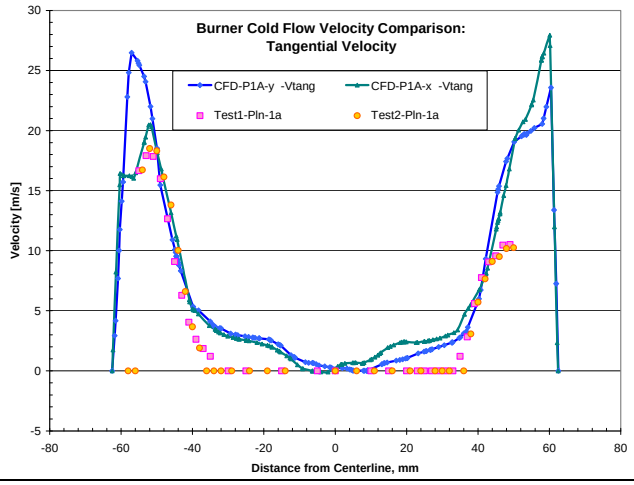

(c) Tangential Velocity on Plane 1a

Figure 4-11. Cold Flow Pitot Probe Predictions on Plane 1a

At Planes 1a and 1b, the external velocity component peaks near the quarl walls are reasonably captured, as they are at successive planes (shown in the body of the report). However, the experimental axial, radial and tangential velocities in the core region are all identically zero, indicating that rotation of the probe to pick up the velocity components in the opposite direction may have been required.

Some examples of predictions for temperature and oxygen concentration in reacting flow are also provided in the following two plots. Contour plots of temperature on an x-plane, bisecting the reactor, for the four cases, are shown in Figure 4-12. Each contour plot is overlaid with experimental data in the form of discrete, colored dots that are referenced to the same legend as the contour plot itself. Only elevations through Level 10 are shown in the truncated plots; the OFA lance injection plugs are in the vicinity of Level 11 and are therefore downstream of what is displayed.

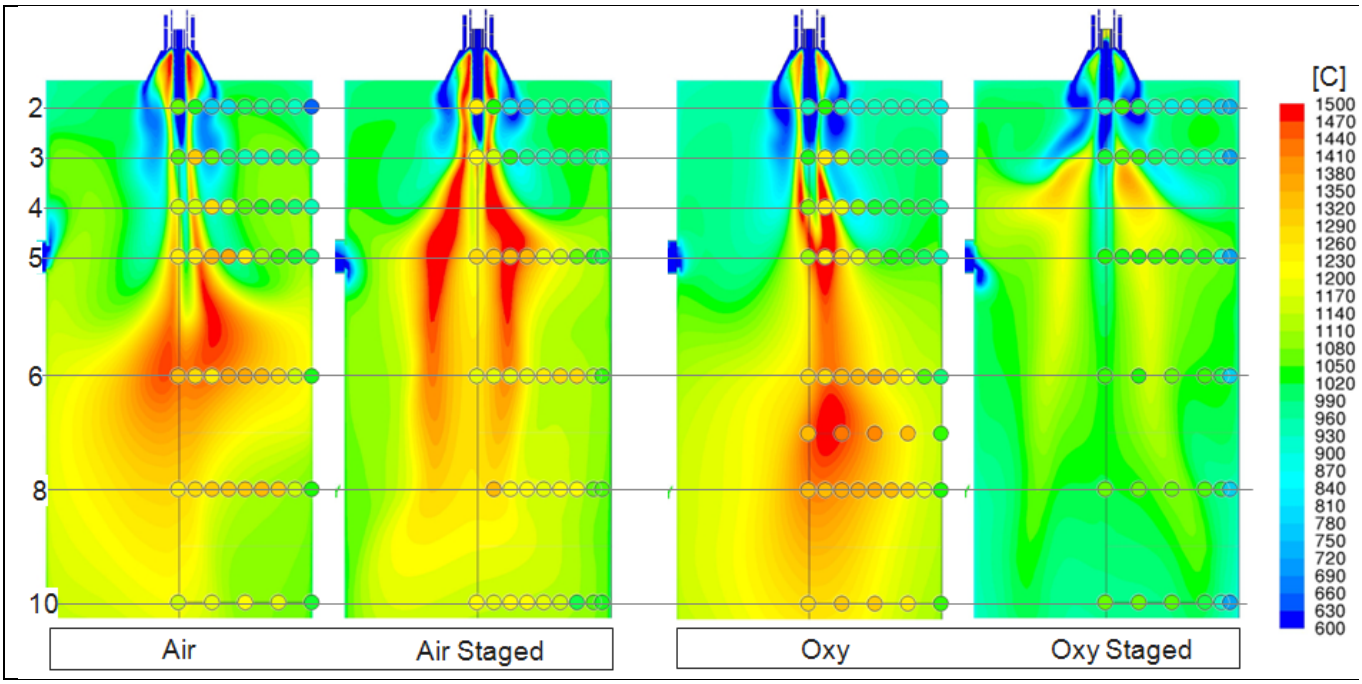

Figure 4-12. Temperature Distributions for Air and Oxy Firing

Significant differences exist between the computed contour plots. The unstaged cases appear to have corner recirculation zone reattachment points that are downstream of the Scan-2 port (the port on the left-hand side at Level 5), while the reattachment points in the staged cases appear to be positioned upstream of the Scan-2 port. This is probably due to the higher SA-2 swirl associated with the staged cases (i.e., higher swirl in TW-2 tests than in TW-1 tests), which helps to expand the flame beyond the quarl and mix out the flow field more rapidly than in the unstaged case.

The experimental temperature data tends to follow the computed contours fairly well. For the air-unstaged case at Levels 1 through 5, for example, the suction pyrometry data appears to indicate that lower temperatures are on the symmetry axis and then temperatures increase with an increase of radius until a peak temperature is reached, after which temperatures decrease to the wall. The peak experimental temperature location is located at a radius which is slightly larger than the radius of the peak computed temperature. The computational jet or flame does not seem to expand as rapidly as the rate indicated by the experimental data, although downstream of Level 5, both the experimental and computed flame zone flare out or balloon out in shape at approximately the same level. The experimental data does not achieve the peak values of 1500 °C exhibited by the calculations, and the experimental flame high-temperature region appears to be somewhat more diffuse and spread out. This may indicate the necessity of having more intermediate species in the computed flame zone and perhaps slower reaction rates. Nevertheless, given the uncertainty in the temperature measurements, particularly in the high-temperature and high-gradient regions, the predictions are very reasonable and encouraging.

Similar statements regarding comparison between the predictions and data may be made for the other air-staged and oxy cases. Even in the oxy-staged case, where the computed temperatures are depressed relative to the other cases, the experimental data appear to follow suit and scale down in a corresponding manner.

The transition from air (unstaged or staged) to oxy (unstaged or staged) also appears to be captured reasonably well, indicating that the necessary physics for oxy combustion are encompassed within the FLUENT® property packages and the UDFs. The accuracy of the computed oxy results appears to be within error bands that are similar to the prediction error bands associated with the air-combustion results.

Contour plots of oxygen concentration (in units of mole %, dry) on an x-plane, bisecting the reactor, for the four cases, are shown in Figure 4-13.

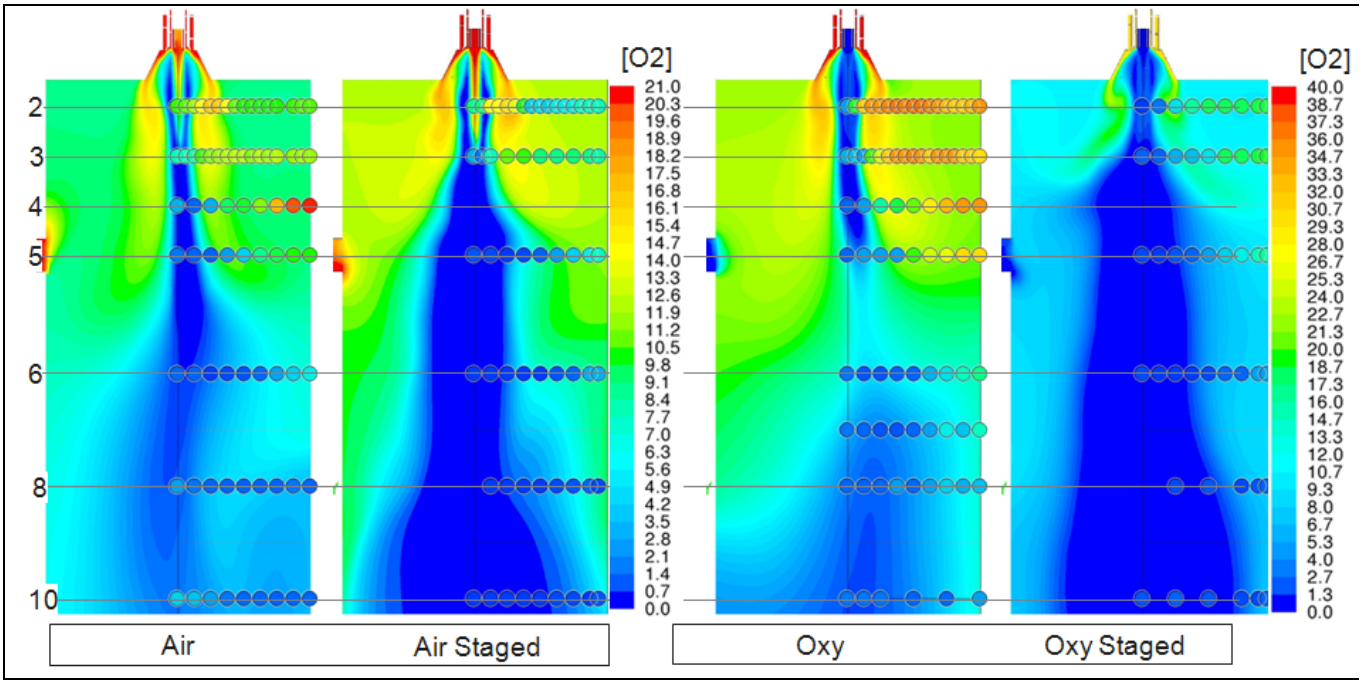

Figure 4-13. Oxygen Contour Plot Comparison (Mole %, Dry)

An oxygen-starved core is apparent in all of the computed contour plots. As expected, the staged cases exhibit a much larger or expanded oxygen-starved core than the unstaged cases (particularly since the OFA is introduced downstream at Level 11). The cases are qualitatively similar to each other in many respects, but they also have some quantitative differences.

Overall, the experimental data is generally similar to the computations. For the unstaged air case at Levels 2 and 3, the experimental data indicate a peak oxygen mole fraction in the flame at a radius similar to that shown by the data. At Level 4, the oxygen seems to increase to high inlet values near the wall. The high oxygen value near the wall must be due to the in-leakage from the Scan-2 port which is swept upstream (again indicative of the reattachment point lying downstream of the Scan-2 port). At Level 5, the data appears to coincide with the computed contours. The oxygen data at Levels 6 through 10 are relatively low in magnitude from the symmetry axis to the wall, in a manner that is in reasonable agreement with the computations. Interestingly, at Levels 8 and 10, the highest experimental data value is on the symmetry axis, which may indicate asymmetry in the actual flame.

For the air-staged case, the experimental data at Level 2 are at about 5 or 6% (mole %, dry) near the wall, while the computations are at probably twice that value. Alternatively, for the oxy-unstaged case at Level 2, the experimental data shows values around 30%, while the computations are at concentration magnitudes of around 20%. Therefore, the computation concentrations may depart from the data in the upstream corners of the reactor (and the departure may be positive or negative), but

overall, the predictions appear to capture much of the expansion of the oxygen-starved core and appear to follow the trends through each Level. Again, the predictions appear to be reasonable and acceptable over most of the domain.

General conclusions and observations may be itemized as follows:

- Overall, given the large uncertainty bands in the probe data, the temperature predictions are reasonable and acceptable. Furthermore, the transition from air-combustion to oxy-combustion is adequately addressed by the FLUENT® property databases, coupled with the UDFs. The predictive error inherent in the air-combustion calculations does not seem to be exacerbated by changing the boundary conditions and performing oxy-combustion predictions.

  At Levels 1 through 5, the computational flame profile (as indicated by temperature) does not seem to expand as rapidly as the rate indicated by the experimental data, although it is difficult to know how much of that apparent expansion is due to the probe suction-volume characteristics. Experimental peak temperatures remain significantly below the computed peak temperature of 1500 °C and the experimental peak flame values at Levels 6 through 10 appear to be more spread out or diffuse than the computed flame.

- Overall, the comparison of the experimental species data with the predictions is very encouraging. The overall flame shapes and flame expansions as a function of staging appear to simulate the data trends. Major species, such as oxygen and CO_2, are predicted reasonably well, although some quantitative differences are apparent in certain regions. For example, for some tests, the experimental mole fraction for O_2 and CO_2 may be ±10 percentage points different from the computations in the upper corner regions of the reactor.

- The rate of experimental CO production is much slower than the calculations in the near-nozzle region, never reaching the high CO concentrations exhibited by the calculations, but then the measured CO continues to be produced over a wide radius through Levels 6 and 8 while the computational CO rapidly depletes. The slow, but sustained, CO production in the actual flame may point to CO production from soot or char conversion rather than to rapid volatile combustion. An examination of minor species, such as CO, indicates that some speciation and reaction rate studies are necessary to surface the underlying reasons for the differences between the experimental data and the calculations.

- With the exception of some flawed total heat flux probe data (noted by IFK), the trends exhibited by the wall heat flux data or the ellipsoidal radiometer data, and the associated predictions, appear to match each other reasonably well, with the difference in peak magnitudes between the data and predictions varying between 15 to 30%. Qualitatively, the trends are fairly similar. The relative scaling or difference in magnitude between the air and oxy experimental data is also fairly consistent with the difference in magnitude between the calculated air and oxy cases.

4.4 Chapter 4: Uncertainty Quantification

In order to expand the simulation potential and better understand the confidence levels of CFD predictions, Alstom teamed with the University of Utah. Recognized as a key academic institution with decades of experience in coal combustion and more recently pioneering of large scale Large Eddy

Simulation (LES) work, the Windsor modelers teamed with Professor Phil Smith and his group at Utah's Institute of Clean and Secure Energy (ICSE). The collaboration was structured to allow both LES calculations to be extended to the BSF and also develop application skills associated with Verification and Uncertainty Quantification methods. A collaborative agreement between Alstom and the University of Utah was executed on August 30, 2011, and was designed to provide a more reliable computational tool and methodology through the validation and uncertainty quantification (V&UQ) process.

The ICSE program is an independent, DOE-sponsored program with the long-term objective of (a) expanding high-performance simulation tools to quantitatively predict the temperature and heat flux in oxy-coal burners for retrofitting power boilers and industrial furnaces for CO_2 capture, and (b) to perform verification, validation and uncertainty quantification (V&V/UQ) of the numerical and modeling error associated with this intended use of the simulation tool. The scope of the modeling tasks included steady-state FLUENT® based simulations of the BSF performed in Windsor, and companion transient coal combustion simulations of the BSF using the ARCHES code (containing the LES model), developed at the ICSE at the University of Utah.

The LES simulations of the BSF were performed with massive computing resources and supercomputers to advance coal combustion science to a higher level than could be achieved with steady-state FLUENT® models previously described in Volume I - Chapter 1. The LES simulation technique is very different fundamentally from Reynolds Averaged Navier Stokes (RANS) methods.

LES codes attempt to directly resolve a portion (e.g., 80%) of the turbulent kinetic energy spectrum, typically the larger length scales, and use modeling approximations to account for the smallest (dissipative) scales. The resolution of these turbulent eddies of varying spatial and temporal scales may be critical in correctly predicting the underlying physics that control boiler characteristics. Flame stability, particle drag effects, emissions, and other phenomena are strongly coupled to the turbulent eddies, which in turn, have an impact on the oxidant concentrations, local wall heat flux, etc. The LES codes are run in a time-accurate manner so that the majority of the turbulent kinetic energy spectrum is resolved, thus promoting much greater fidelity and predictive accuracy in the simulation than RANS computations.

An example of a volume-rendered gas temperature field at an arbitrary time step, using the ARCHES code, is provided in Figure 4-14. The impact of the turbulent eddies on the flame structure is evident.

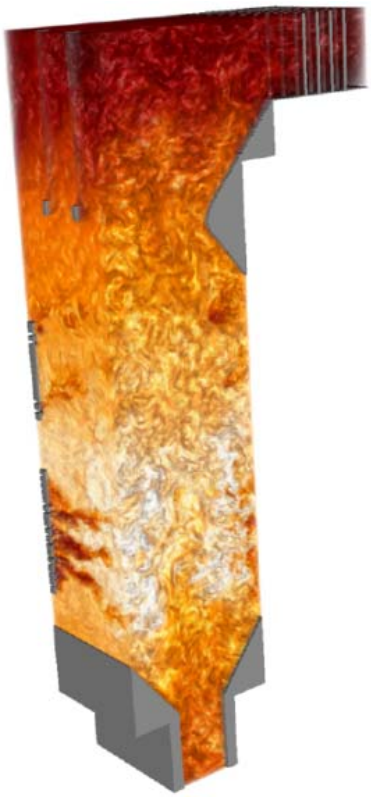

Figure 4-14. Gas Temperature Field in BSF Using ARCHES

Not all of the physics within the boiler are equally susceptible to the short time-scale phenomena. For example, the radiation flux to the walls responds instantaneously to the local temperatures, but since each ray must travel through a large volume of the domain, the integrated traces exhibit smoother results over time. The impact of the turbulent eddies on the particle number density depends on the particle size. This effect is shown in Figure 4-15. The particle number density is normalized to the inlet value, so that values greater than unity indicate local particle clustering.

As the particle size changes, the particle inertia will change. This makes the particles with different sizes respond differently to the local turbulent eddies. The small particles have very little inertia and will be entrained by the small scale turbulent eddies, which enhances their diffusion. Thus, in Panel (a) the small particles are more evenly distributed within the furnace. As particle size increases, the particle inertia increases by the particle diameter to a power of 3. Consequently, as shown in Panel (c), the small-scale turbulent eddies have little effect on the ballistic motion of these larger particles. The larger particles concentrate along the edges of coherent structures, and the clusters are more segregated.

These examples indicate the predictive potential inherent in LES codes; the enhanced resolution of the turbulent spatial and temporal scales does have a beneficial impact on the underlying physics, which should produce predictions that are more accurate and that have greater congruence with the experimental data. The RANS computations attempt to represent a wide range of length scales with modeled approximations (rather than resolved physics) using “mean” parameters.

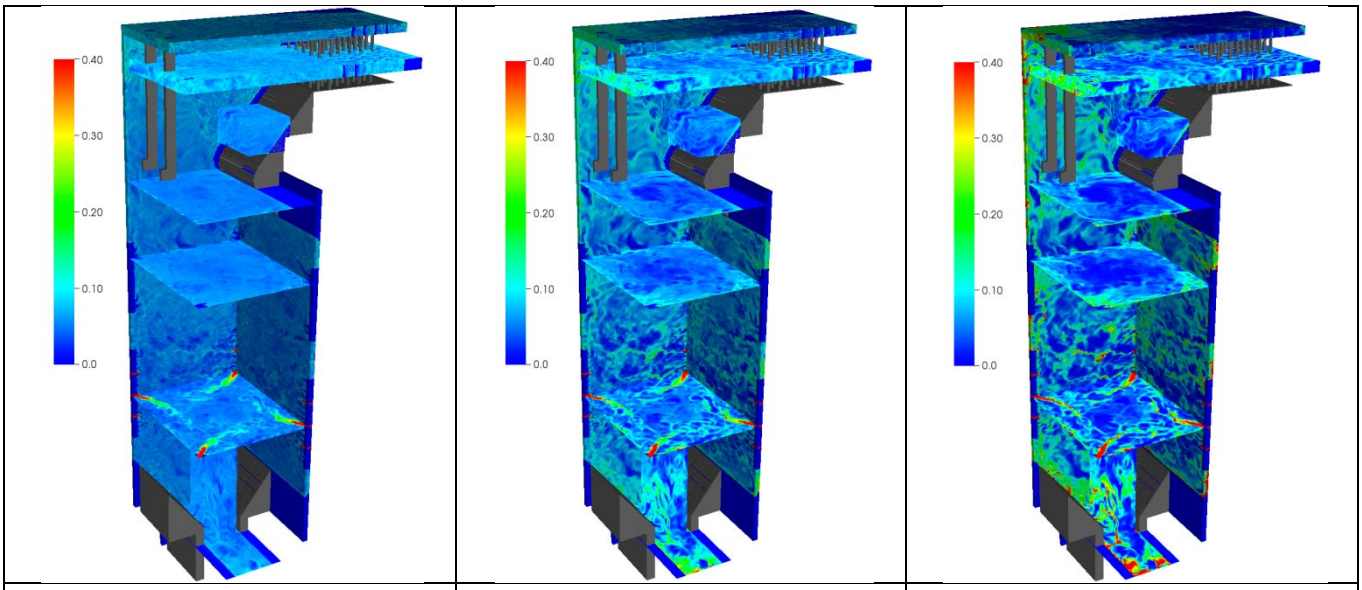

(a) d_p = 30 μm | (b) d_p = 60 μm | (c) d_p = 90 μm

Figure 4-15. Particle Number Density as a f(Particle Size) Using ARCHES

The computational study focused on the application of the V&UQ process for BSF Oxy Test 134, which used the Schwarze Pumpe lignite coal for fuel. The intent of the V&UQ analysis was to study the impact of various parameters on observables such as wall heat flux, gas temperature, and species. An input/uncertainty (I/U) map was created in which selected model parameters and boundary conditions were ranked or prioritized with respect to their projected impact on the temperature and wall heat flux, based initially on prior knowledge. Screening or scoping runs were made with CFD, in conjunction with the construction of the I/U map, to better assess the sensitivity of the observables to selected parameters, such as the wall thermal conductivity, and to assign uncertainty bounds to those parameters. Utilizing a simple "design of experiments" (DoE) scheme, an initial V&UQ run or case matrix was constructed, with 13 runs and 4 active variables – inlet coal mass flow rate, inlet gas mass flow rate, wall thermal conductivity (in the main furnace section only), and the devolatilization rate. The 13 CFD runs were completed by Alstom, the calculations were post-processed by Alstom, and the results were sent to ICSE for the V&UQ analysis. The results consisted of (a) the experimental data at each measurement point, and (b) the calculated value at each measurement point for each of the 13 CFD runs. ICSE has collected (and is in the process of collecting) similar calculation results from their LES runs (using essentially the same run matrix). However, at the time of this writing, ICSE is still working on completing the first seven (7) runs, due principally to the immense computational burden involved, as well as to case corrections and re-runs. Consequently, only the first 7 of the 13 runs completed by Alstom have been utilized in the V&UQ analysis. The V&UQ analysis is advancing in a progressive manner – from a more simplistic analysis (using only a few runs and a single independent variable) to a more complex analysis (involving several runs and multiple independent variables). Progressing from the simple to the more complex has been helpful in ensuring that the participants understand and digest both the methodology and the output from the analyses.

Three separate V&UQ analyses have been performed by ICSE:

- Consistency Analysis I. An initial V&UQ analysis was conducted with only three (3) of the computational cases (Cases 1, 4, and 5), in which a single active variable, the wall thermal conductivity was independently varied. This analysis was performed for both the LES and

RANS computations. The observables included only the mean temperature at three (3) planes and the heat flux data.

- Consistency Analysis II. An initial V&UQ analysis was conducted with only three (3) of the computational cases (Cases 1, 4, and 5), in which a single active variable, the wall thermal conductivity, was independently varied. This analysis was performed for both the LES and RANS computations. The difference between this analysis and the preceding analysis was that, in the present analysis, the number of observables was expanded to include all of the local point measurements of temperature, the heat flux data, and the oxygen concentrations.
- Consistency Analysis III. A second V&UQ analysis was conducted with seven (7) of the computational cases (Cases 1 through 7), in which three (3) active variables – the wall thermal conductivity, the coal mass flow rate, and the devolatilization rate – were independently varied. This analysis was performed only for the RANS computations (since the LES computations were not yet completed). The observables included all of the local point measurements of temperature, the heat flux data, and the oxygen concentrations.

The run matrix was limited to the oxy-fired case (Test 134), although the baseline run of the companion air-fired case (Test 109) was also run for comparison purposes. In the run matrix, the fuel and air flow rates were varied by ±1.5%, while the main furnace wall thermal conductivity was varied by ±25%. The devolatilization rate was increased and diminished by a factor of 5 from the baseline value.

The V&UQ analysis was performed with the Frenklach, et al. "data collaboration" and "consistency analysis" approach, and the resulting constrained optimization problem was solved utilizing a quadratic surrogate model and a Monte-Carlo type sampling procedure.

Results of Consistency Analysis II From the consistency analysis, the LES code is able to demonstrate slightly smaller error bars on temperature (+/- 85 K) and heat flux (+/- 2.0E+04 Btu/hr-ft^2) than the RANS calculations (+/- 100 K and +/- 3.0E+04 Btu/hr-ft^2, respectively), while the uncertainty on the oxygen concentration is somewhat larger for the LES code (+/- 3.0 mole % (wet)) than for the RANS code (+/- 2.5 mole % (wet)). However, the only statement of consistency that can be made, based on the application of the thermal conductivity as the single active variable, is that simultaneous consistency has been achieved for both the LES and RANS codes. One of ICSE's goals within their DOE project is to ultimately demonstrate the superiority of the LES code over RANS computations for some critical (as yet unidentified) facet of boiler physics. However, much more work needs to be done with the analysis before any conclusions about the superiority of a particular code or model can be claimed.

Results of Consistency Analysis III The consistency analysis was done only on the RANS results. Consistency was attained when the temperature error bars were expanded to +/- 125 K and the error bars on the oxygen concentration was limited to +/- 2 mole % (wet). The uncertainty bars on the wall heat flux varied as a function of the measurement port and took into account the replicates at each port. The error bars on temperature were adjusted to make the consistency region as narrow and small as possible. For the three active variables, the consistency region for the wall thermal conductivity ranged from 2.285 to 2.373 Btu/hr-ft-°F, and the consistency region for the coal flow rate ranged from 0.6046 to 0.6148 kg/s; the devolatilization rate multipliers appeared to have a very small impact on the results (even though the sampling ranged over an order of magnitude).

Simultaneous consistency has been achieved for both the LES and RANS codes. Differences in the upper and lower bounds of the observed variables between each code should not be used to infer that one code is more accurate than the other. Additional work needs to be done with the analysis before such a conclusion can be entertained: (a) First, the experimental uncertainties need to be determined for the active variables and observables, insofar as possible. This means that experimental uncertainties need to be determined for suction pyrometry, heat flux probes, sampling probes, and other instrumentation. The experimental uncertainty then becomes the "true" upper and lower bound to gauge the actual consistency region. (b) Secondly, additional active variables and observables (or parameters of interest) need to be brought into the analysis. The analysis of additional active variables, particularly scenario (i.e., boundary condition) parameters, will provide a more comprehensive view of the influence of those parameters on the simulations. Once those are understood, then the relative influence or accuracy of selected models, or even of entire codes, can be bracketed and properly assessed.

The aim of the modeling simulations will be to provide a more reliable computational tool and methodology which can ultimately be used to provide commercially attractive CO_2 capture solutions for both the retrofit of existing boilers and the installation of new boilers. The present task and report constitute only an initial foray into the realm of V&UQ analysis. A great deal more V&UQ work remains to be performed with the BSF data and the CFD models. This work will be carried out by ICSE (as they continue with their DOE funding). The V&UQ analysis is a formalized methodology which can highlight model or boundary condition weaknesses and inconsistencies; these weaknesses can then be subsequently addressed and improved, so that the goal of ultimately providing more reliable model predictions can be realized.

4.5 Chapter 5: Dynamic Process Modeling

The development of oxy boiler dynamic modeling capabilities to assess and refine the design of controls and operation systems for oxy boilers are addressed. Discussed are the results of a control and operability investigation of the transient responses of critical process variables in the oxy boiler island for various plant event scenarios. Before the dynamic analysis work was done, the oxy boiler island dynamic model simulation tool was validated and calibrated with reference to recent air-fired utility boiler design performance data at different load operating conditions to ensure the representativeness of the dynamic model. Process control loops for the oxy boiler island process have been refined and incorporated after the validation of the dynamic model.

The control and operability dynamic analysis mainly focuses on the transient responses of the process under various pre-defined operating scenarios. For the purpose of this dynamic simulation study, most of the boiler island transient analyses were in the oxy-firing mode. Two main types of control and operability simulation were conducted:

- Boiler Island normal operations
    - Transitions between air and oxy-mode operation
    - Load ramp up with different rates
    - Load step change
    - Oxy-mode minimum load operation (40-25%, including startup system)
    - Start-up from minimum load operation in air mode
- Boiler Island abnormal operations

- One mill trip (out of four)
- Fan trips (PA/FD/ID fan trips)
- Master fuel trip
- Interface subsystem trips

During daily operation, the unit load demand of the power plant is generated based on the requirements from the electricity market, which requires the steam plant/boiler island to be able to adjust the operating load in a timely manner. Plant operating flexibility is increasingly important as the percentage of intermittent renewable power increases. Two simulation scenarios for load ramping were designed to study the oxy boiler island under the fast load change requirement: load ramping from 35% MCR to 50% MCR at 3% MCR/min, and load ramping from 50% MCR to 100% MCR at 5% MCR/min. Figure 4-16 to Figure 4-18 illustrate the responses of selected operating parameters to load ramping from 50% MCR to 100% MCR at 5% MCR/min.

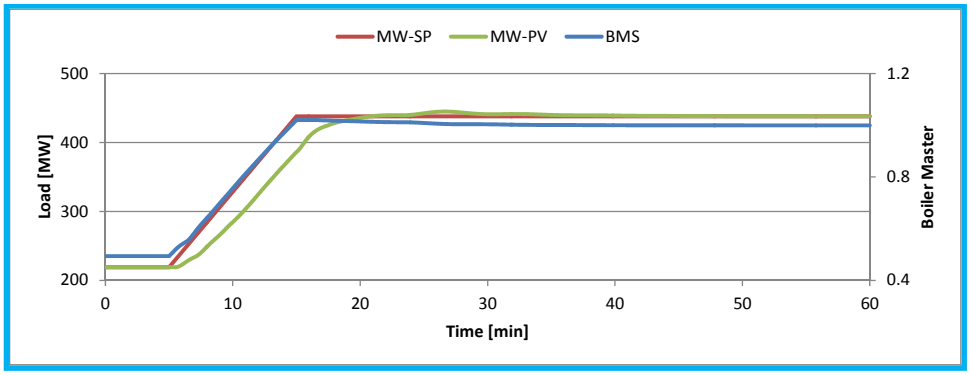

Figure 4-16. Load response to load ramp from 50% MCR to 100% MCR

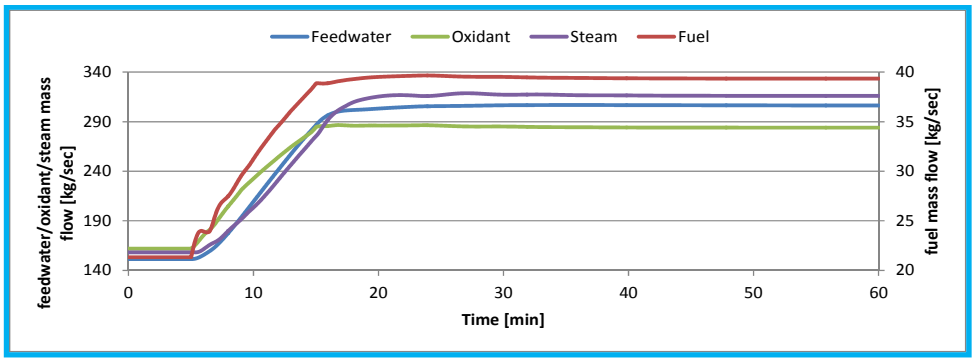

Figure 4-17. Fuel/feedwater/oxidant/steam mass flow response to load ramp from 50% MCR to 100% MCR

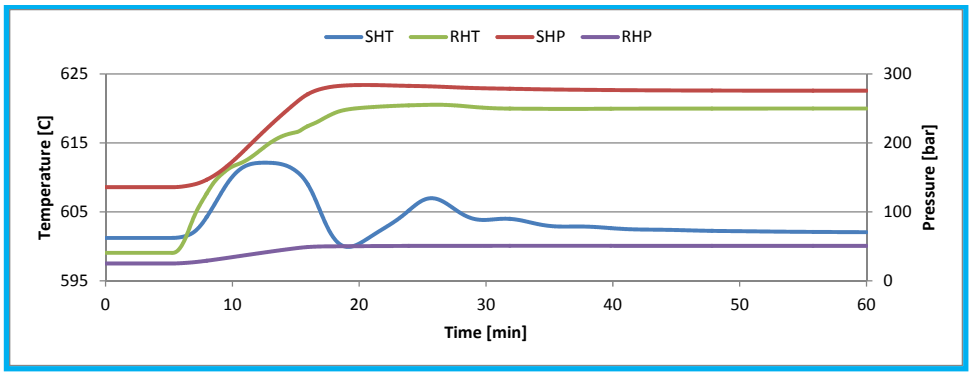

Figure 4-18. Main/reheated steam temperature/pressure response to load ramp from 50% MCR to 100% MCR

A 10% MCR load step change from 50% MCR to 60% MCR was also investigated. Additionally, the capability to run under a very low load (about 25% TMCR with no supporting oil) in oxy mode was assessed to address scenarios during high renewable generation and no additional grid demand, when all the generated power is consumed by the ASU and the GPU. The dynamic model was used to examine the feasibility and stability of the plant, and specifically the boiler unit, running at such a low load condition.

Abnormal operations, which refer to the unit's operations under unexpected disruptions, were also assessed. For the dual-fired pulverized coal boiler island process, typically these abnormal operating events require a fast and controlled response to various major equipment failures, including mill trips, fan trips, master fuel trip, as well as interface subsystem trips. In general, boiler island emergency operations under both air-firing mode and oxy-firing mode should be investigated. In this chapter, the emergency operations cases studied were limited and focused on oxy-mode operations. Responsive control actions for air-firing mode emergency operations can be designed based on conventional air-fired boiler operation procedures. The emergency operations studied in this chapter include mill trip, PA fan trip, FD fan trip, and ID fan trip.

The oxy-fired boiler island process is equipped with five coal mills, among which four are in use during normal full load operations with one coal mill as a spare. The mill trip will result in load run back to predetermined targets at specified run back rates. The oxy-fired boiler island process has one PA Fan, one ID Fan and one FD Fan. From the process design perspective, having a single fan may cost less compared to a pair of smaller fans; however, from the control and operation perspective, single fan design brings higher requirements of the fan performance for reliable plant control and operations, and any fan trip will cause the Master Fuel Trip (MFT) and the plant will go through an emergency plant shutdown sequence. The oxy boiler dynamic responses of selected boiler operating parameters to a trip of the forced draft fan resulting in a MFT are illustrated in Figure 4-18 to Figure 4-22.

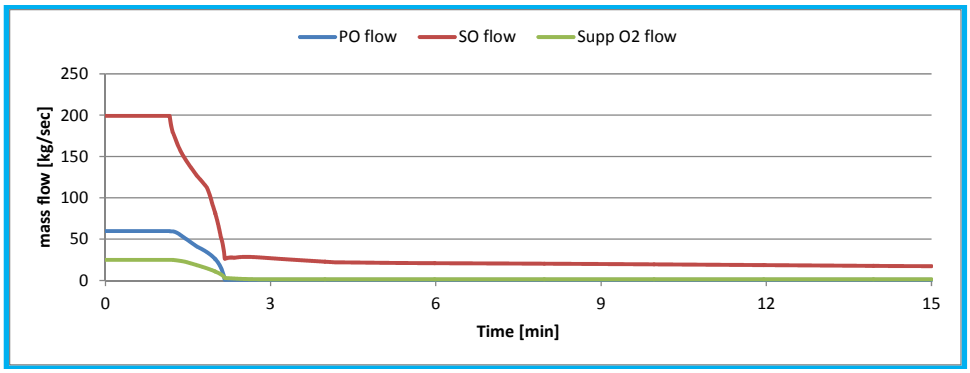

Figure 4-19. Primary oxidant/secondary oxidant/supplementary O_2 flow response to FD fan trip

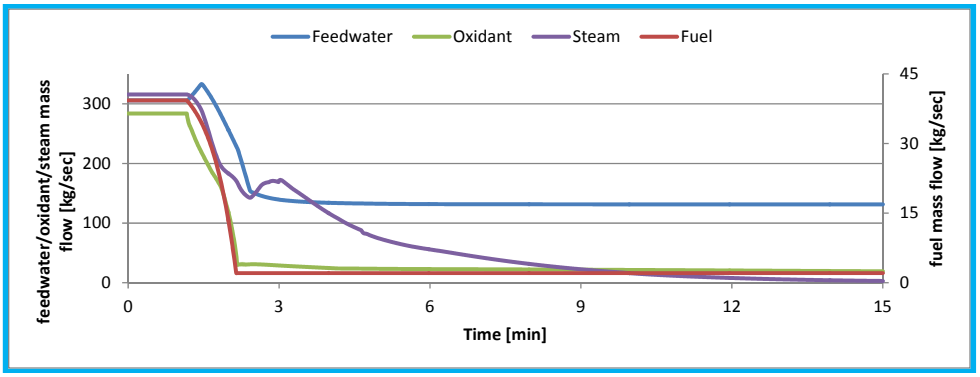

Figure 4-20. Fuel/feedwater/oxidant/steam mass flow response to FD fan trip

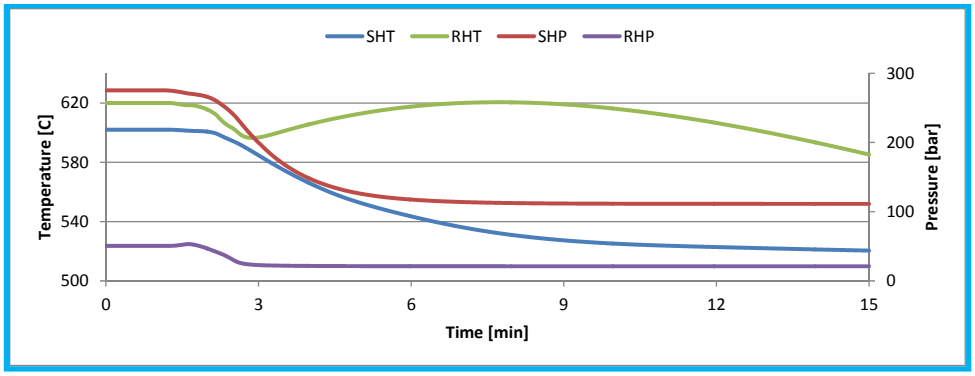

Figure 4-21. Main/reheated steam temperature/pressure response to FD fan trip

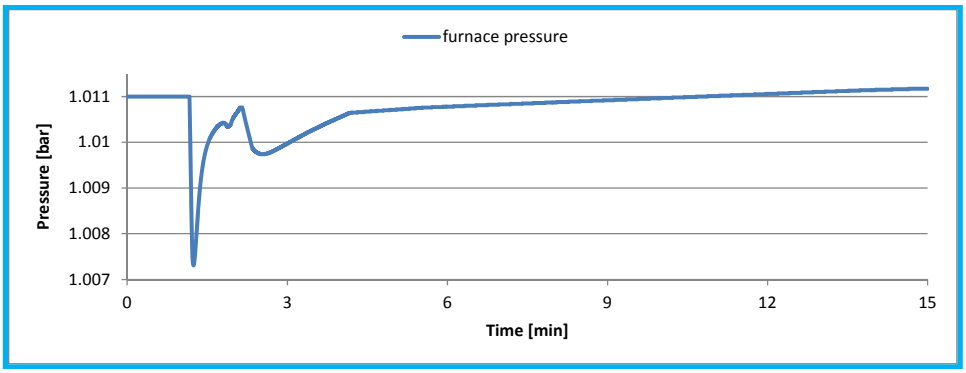

Figure 4-22. Furnace pressure response to FD fan trip

Overall, results of the transient analysis modeling for the oxy boiler island indicate that the dynamic response during normal operation such as load ramping during oxy-firing operation is generally similar to the behavior during traditional air-firing. The dynamic response of the oxy-boiler during abnormal events such as boiler equipment trips was also generally similar. The responses of the critical boiler process variables follow the same trends; however, magnitudes and/or settling time may vary somewhat due to the differences in the design and greater complexity of some of the oxy-boiler subsystems.

5. Reference Oxy Boiler Designs – Volume IV

There are significant differences between air-firing and oxy-firing with gas recycle that can impact the design and operation of the nearly all boiler systems. Combustion characteristics, gas properties, thermal characteristics and emission characteristics are different during air and oxy-firing. The general design guidelines and key considerations for oxy-firing have been developed for each of the major boiler systems. Many existing design procedures developed for air-firing can be applied for oxy-firing by taking into consideration the appropriate gas properties including changes in concentrations of trace constituents. Differences in combustion and thermal characteristics can be addressed by controlled gas recycle rate and firing system design. In general, it is not necessary to make major changes in the boiler design, its size and arrangement, and the heat transfer surfacing for oxy-firing.

Guidelines and key design considerations to address the application of oxy-combustion to pulverized coal boiler design and operation are presented in Volume IV of this final report and can be used assuming knowledge and understanding of air-fired boiler design.

5.1 Oxy Boiler Design Cases

The objective of this study was to assess the design modifications and costs associated with applying oxy-combustion technology to coal-fired utility-scale power plants and to an industrial scale coal-fired steam plant.

Four commercial scale power plants were designed and costs were developed for them in this study. A $450MW_{gross}$ oxy-fired SCPC plant was designed as representative of a demonstration plant for oxy-combustion technology. Figure 5-1 shows a simplified process flow diagram for the 450MW oxy-fired power plant. This was contrasted with a $450MW_{gross}$ air-fired SCPC plant. Similarly, a $900MW_{gross}$ oxy-fired SCPC plant was designed and costs were developed as representative of a first generation oxy-combustion commercial plant. A $900MW_{gross}$ air-fired plant was also included for comparison.

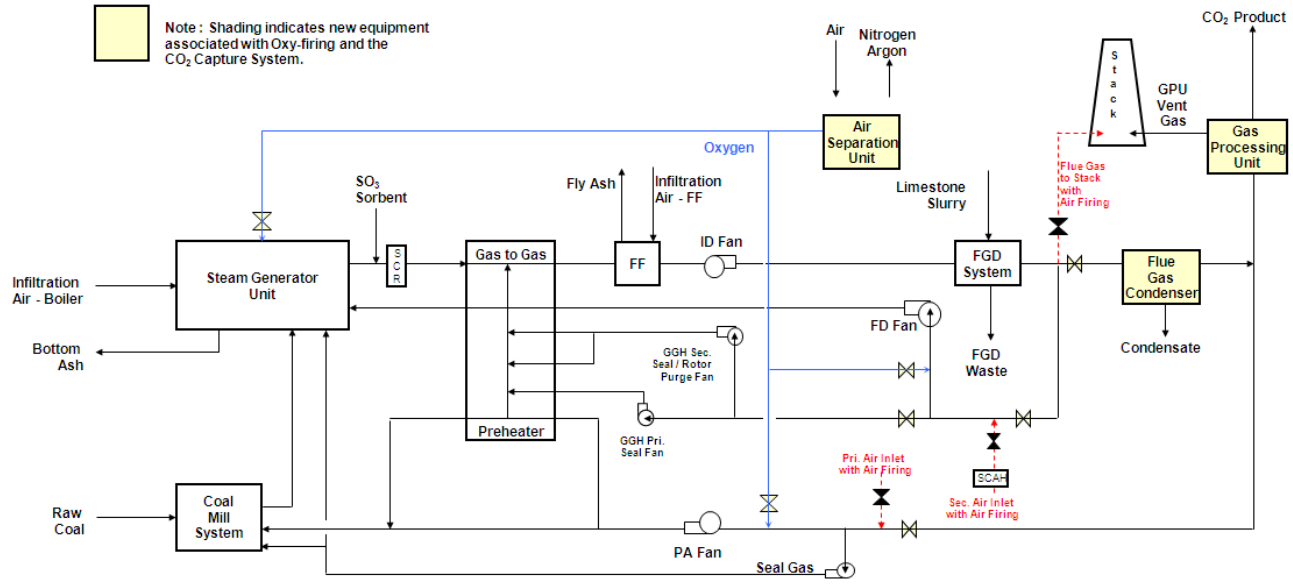

Figure 5-1. Simplified Process Flow Diagram for an Oxy-Fired Power Plant

Finally, this study included an evaluation of the design modifications and costs necessary to retrofit an existing air-fired industrial steam plant equivalent to $150MW_{gross}$ to oxy-combustion. The design study focused on the necessary boiler modifications for this conversion, although the major cost items associated with the addition of an Air Separation Unit (ASU) and Gas Processing Unit (GPU) for the final CO_2 purification and compression were also considered.

Table 5-1 summarizes the five case configurations considered in this study.

Table 5-1. Summary of Case Configurations

Unit Cycle	Steam Cycle, psig/°F/°F	Boiler Technology	Steam Flow Rate lb/hr	Sulfur Removal	CO_2 Separation
450MW Air-Fired PC w/o CCS	3930/1116/1148	2-Pass Supercritical PC	2,811,000	Wet FGD, Gypsum	N/A
450MW Oxy-Fired PC	3930/1116/1148	2-Pass Supercritical PC	2,811,000	Wet FGD, Gypsum	GPU
900MW Air-Fired PC w/o CCS	3930/1116/1148	Tower Supercritical PC	5,703,000	Wet FGD, Gypsum	N/A
900MW Oxy-Fired PC	3930/1116/1148	Tower Supercritical PC	5,703,000	Wet FGD, Gypsum	GPU
Oxy-Fired Industrial Boiler	1175/1000	Industrial Boiler	980,000	NID™	GPU

Legend:
PC - Pulverized Coal
CCS - Carbon Capture and Storage
FGD - Flue Gas Desulfurization
GPU - Gas Processing Unit
NID™ - Alstom Dry FGD System

A $450MW_{gross}$ oxy-fired SCPC plant was designed as representative of a demonstration plant for oxy-combustion technology. The boiler is designed for pulverized coal-firing with a nominal gross capacity of approximately 450 MW_e. It is designed for full load, dual firing capability using either air or oxygen as the oxidant for combustion of the fuel. The boiler is a sliding pressure supercritical (SPSC), once-through design, utilizing a TFS 2000™ firing system and SCR for NO_X control. It is a single reheat unit designed for variable pressure operation with a balanced draft furnace. The unit is capable of firing a range of pulverized coals, producing continuous steam flow to the turbine generator with nominal boiler maximum continuous rating (BMCR) outlet conditions of 2,550,680 lbm/hr (321.4 kg/s), 3,927 psig (270.8 bar), 1,117°F (602.5°C) at the superheater outlet, and 2,103,530 lbm/hr (265.0 kg/s), 726 psig (50.1 bar), 1,148°F (620.4°C) at the reheater outlet. Heavy fuel oil is used for start-up and as a support fuel during low load operation.

A $900MW_{gross}$ oxy-fired SCPC plant was designed and costs were developed as representative of a first generation oxy-combustion commercial plant. The boiler is a pulverized coal-fired unit, with a nominal capacity of approximately 900 $MW_{e\text{-}gross}$. It is designed for full load capability (100% TMCR) with oxygen firing and is limited to about 75% TMCR with air firing. It is a sliding pressure, supercritical, once-through design, utilizing a low-NO_x tangential firing system and SCR for NO_X control during air firing. It is a single reheat unit designed for variable pressure operation with a balanced draft furnace. The unit is capable of firing a range of pulverized coals and producing a continuous flow of steam to the turbine generator with nominal boiler outlet conditions of 5,174,600 lbm/hr (652 kg/s), 4,130 psig (284.8 bar), 1,117°F (603°C) at the superheater outlet, and 4,280,100 lbm/hr (539.4 kg/s), 863 psig (59.5 bar), 1,150°F (621°C) at the reheater outlet. Light fuel oil is used for start-up and as a support fuel for low load operation. A $900MW_{gross}$ air-fired plant designed for the same steam conditions was also included for comparison.

This study also included an evaluation of the design modifications and costs necessary to retrofit an existing air-fired industrial steam plant equivalent to $150MW_{gross}$ to oxy-combustion. The base case air-fired industrial boiler is a coal-fired unit, with a nominal capacity of about 980,000 lbm/hr of superheated steam flow. It was retrofitted to operate at full load capability using recirculated flue gas as the oxidant for combustion of the fuel. The retrofit unit operates with base case TFS (Tangential Firing System) system, SCR for NO_x control, NID™ dry scrubber system for SO_2 and fly ash control, and two gas-to-gas tubular heaters (GGH). The retrofit unit is capable of firing the design pulverized coal, producing continuous steam flow at nominal boiler outlet conditions of 123.6 kg/s (980,000 lbm/hr), 108.5 bar (1600 psig), 538°C (1,000°F) at the superheater outlet. Heavy fuel oil is used for start-up.

Oxygen Firing Process Considerations

The approach taken to design a boiler capable of oxy-firing combustion was essentially the same for all oxy-fired cases in this study. Oxy-fired combustion replaces combustion air with a mixture of nearly pure oxygen and recycled flue gas. The resulting flue gas, comprised of primarily CO_2 and H_2O vapor along with some N_2, O_2, and trace gases like SO_2 and NO_x, is then dried, compressed, and purified for sequestration, or used for enhanced oil or gas recovery.

The primary impacts of oxy-firing on the boiler design are associated with the potentially reduced combustion gas flow due to the removal of nitrogen (present with air firing) and the differences in the thermal and radiant properties of the flue gas. Burning coal with pure oxygen would result in excessive furnace temperatures causing ash slagging issues, corrosion issues, fine ash aerosols, and damage to boiler waterwalls if steam-side circulation is insufficient. Recycling a portion of the flue gas can compensate for these impacts. Thus, the furnace temperature can be maintained low enough to avoid ash slagging, fouling and corrosion, and the heat flux to furnace walls can be maintained within the limits imposed to prevent overheating of the tubes.

The location of the flue gas recirculation take-off can have a significant impact on the design and operation of the boiler and ancillary equipment. As gas recycle is taken closer to the boiler outlet, more of the downstream equipment can be reduced in size and cost. However, the concentration of impurities returned to the boiler increases as the gas recycle takeoff point approaches the boiler outlet, which impacts ash deposition, corrosion and pollutant levels, and must be addressed in the boiler design. Trade-offs between boiler impacts and downstream equipment savings are generally controlled by fuel characteristics and site-specific factors.

The basic concept entails:

- Use Oxygen instead of air for the combustion process in order to obtain a CO_2 rich flue gas mainly composed of CO_2 and H_2O (and some inert gases) “easily” cleaned and compressed
- Obtain the adequate purity of CO_2 in the flue gas in order to reach a composition suitable for transport under supercritical phase and then storage

This leads to the addition of two units to the conventional coal fired power plant:

- Air Separation Unit (ASU): An oxygen production unit
- Gas Processing Unit (GPU): A CO_2 purification unit to clean and compress under supercritical state the remaining CO_2 out of flue gas

In addition some modifications of the power plant itself are necessary, mainly:

- Partial recirculation of the flue gas in order to maintain appropriate temperature and heat absorption in the furnace and convection pass
- Removal of the water from the flue gas before treatment in the GPU: Flue Gas Condenser
- Minimization of leakage of air into the boiler
- Sizing of equipment, taking into account the additional needs of the ASU and GPU (mainly electrical energy, water…)
- Injection/mixing of oxygen in the flue gas path

The basic oxy-firing concept uses a mixture of oxygen and recirculated flue gas as an oxidant to replace combustion air. Oxy-coal combustion produces a flue gas stream comprising mainly CO_2 and water vapor with much smaller amounts of oxygen, nitrogen, argon, sulfur dioxide, etc. The flue gas leaving the boiler is cooled and cleaned of ash and sulfur compounds in traditional boiler island equipment. It is then dried, compressed, and purified into a CO_2 product stream in the GPU. It can then be available as a product for usage or for sequestration. Some of the flue gas produced is recirculated and mixed with relatively pure oxygen to form the oxidant streams for combustion of the coal.

5.2 Performance

5.2.1 Power Output

Figure 5-2 summarizes the net power and auxiliary power requirements for the air and oxy-fired cases at 450MW and 900MW. The gross plant outputs (sum of net power and auxiliary power) for the 450MW air and oxy-fired cases were kept identical to each other. The same approach was applied for the 900MW cases. The net power varied for each 450MW and 900MW depending upon the total auxiliary power requirements for each case. This is different from the approach used in the DOE Baseline Reports[1,2], where the SCPC w/o CCS and oxy-fired cases had a constant $550MW_{net}$ output, while the gross MW varied.

This difference in design approaches taken for the DOE cases required that the boiler size be increased for the oxy-fired case as the auxiliary power consumption increased considerably and the firing rate had to be increased. For the 450MW and 900MW cases under this study, the gross power output was fixed and the net power output was allowed to vary. Since the fuel firing rate remained constant, the boiler size remained essentially the same. Thus, the focus was on identifying the design changes and costs associated with redesigning an air-fired boiler for oxy-firing, rather than also accounting for an increased size boiler.

The auxiliary power requirements for all of the air-fired cases ranged from 5.0-5.2% of the gross power output. The auxiliary power requirement for the 450MW oxy-fired plant was 27.8% of the gross power output. This value decreased to 26.4% for the 900MW oxy-fired plant due to the improved thermal efficiency from integration of the ASU, GPU, and FGHR system. Although not shown here, the DOE Case 5C oxy-fired plant had an auxiliary power requirement of 30.2% of the gross power output. This is because this plant had a less efficient steam cycle than either the 450MW or 900MW plants in this study and did not have any integration.

Table 5-2 summarizes the performance results and auxiliary power requirements for the air and oxy-fired cases at 450MW and 900MW. The largest auxiliary power load for the oxy-fired cases was the

[1] Cost and Performance Baseline for Fossil Energy Plants Volume 1, DOE/NETL-2010/1397, November 2010
[2] Pulverized Coal Oxycombustion Power Plants Volume 1, DOE/NETL-2007/1291, August 2008

ASU, which was 64,550kW and 117,914kW for the 450MW and 900MW oxy-fired plants, respectively. The next largest auxiliary power load for the oxy-fired cases was the GPU CO_2 compressor, which was 37,683kW and 73,071kW for the 450MW and 900MW oxy-fired plants, respectively. In comparison, the boiler island auxiliary power decreased slightly to 22,647kW and 44,400kW for the 450MW and 900MW oxy-fired plants corresponding to a 3.7% and 0.5% decrease from air-firing. This is due to the higher gas density and lower volumetric gas flow rates in oxy-fired plants.

The largest impact of the air-fired industrial steam plant retrofit to oxy-fired capability was the addition of the power intensive ASU and GPU. The ASU requires an additional 24.3MW and the GPU adds 14.1MW of auxiliary power. Since it was assumed that the power necessary to drive this equipment would be taken off the grid, the industrial boiler was therefore able to maintain its steam capacity output. It was also assumed that changes in the auxiliary power requirements for the remaining boiler and steam plant equipment were minor and could be ignored.

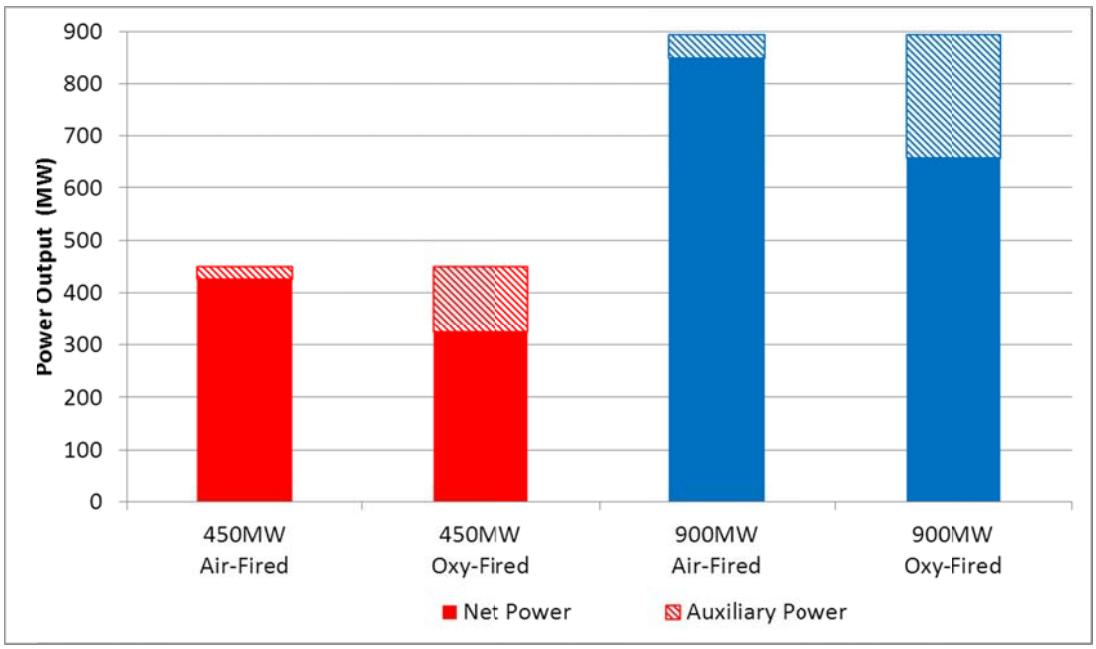

Figure 5-2. Power Output Summary

Table 5-2. Summary of Thermal Performance and Auxiliary Loads

		450MW	450MW	900MW	900MW
		Air-Fired	Oxy-Fired	Air-Fired	Oxy-Fired
Gross Power Output	MW	450.0	450.0	893.3	893.3
Net Power Output	MW	426.5	325.1	848.7	657.9
Coal Flow	lb/hr	295,086	296,543	598,606	601,529
Main Steam Flow	lb/hr	2,508,000	2,508,000	5,162,812	5,174,717
Fuel Heat Input (HHV)	MMBtu/	3,277	3,293	6,412	6,444
Net Plant Efficiency (HHV)	%	40.9%	31.5%	41.3%	32.5%
Boiler Efficiency	%	88.8%	88.8%	88.8%	88.8%

Auxiliary Load Summary

		450MW	450MW	900MW	900MW
		Air-Fired	Oxy-Fired	Air-Fired	Oxy-Fired
Coal Handling & Pulverizers	kW	2,319	2,331	4,705	4,728
Forced Draft Fans	kW	1,192	1,198	2,418	2,430
Primary Air Fans	kW	939	944	1,905	1,915
Induced Draft Fans	kW	5,423	4,413	11,001	10,811
SCR	kW	150	-	150	-
FF	kW	53	51	107	106
Wet FGD	kW	2,239	2,277	4,542	4,463
Power Plant Auxiliaries	kW	11,200	11,434	19,782	19,948
ASU Compressor/Auxiliaries	kW	-	64,550	-	117,914
GPU CO2 Compressor	kW	-	37,683	-	73,071
		-	-	-	-
Total Aux Power	kW	23,516	124,880	44,611	235,385
% Aux Power		5.2%	27.8%	5.0%	26.4%

5.2.2 Net Plant Efficiency

The net plant efficiency results in Table 5-2 are graphically presented in Figure 5-3. The net plant efficiency for the 450MW and 900MW air-fired cases are both about 41% HHV. This relatively high efficiency is attributed to the current state-of-the-art advanced steam conditions and efficient steam cycle arrangement. The net plant efficiency for the 450MW oxy-fired plant decreased by 9.4% points as compared to the 450MW air-fired case. This reduction is due to the increased auxiliary power requirements for the ASU and GPU. The net plant efficiency for the 900MW oxy-fired plant decreased by 8.8% points as compared to the 900MW air-fired case. The net plant efficiency for the 900MW oxy-fired plant was 0.6% points higher than the efficiency for the 450MW oxy-fired plant. This improvement is primarily due to the thermal integration of the ASU, GPU, and FGHR system. Further improvements can be expected in second generation oxy-fired plants with more thermal integration and advances in ASU and GPU designs that reduce their power requirements.

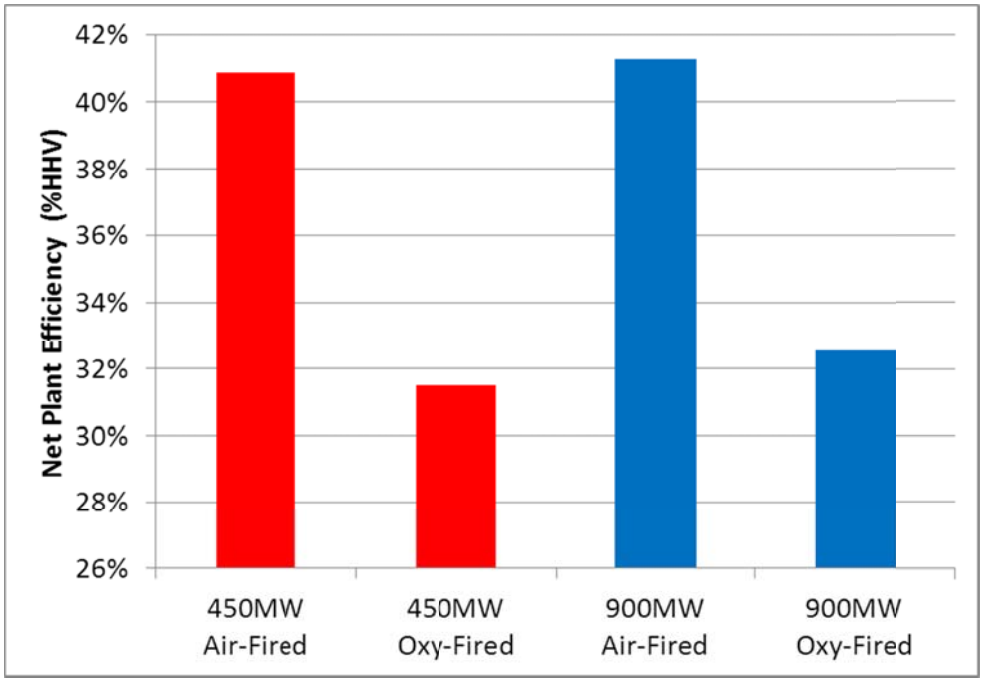

Figure 5-3. Net Plant Efficiencies for all Air-Fired and Oxy-Fired Cases

The energy penalty for the 450MW oxy-fired power plant (relative to the 450MW air-fired plant without CO_2 capture) is 23.0%. The energy penalty for the 900MW oxy-fired power plant (relative to the 900MW air-fired plant) decreased slightly to 21.3%. The Energy Penalty is defined here as:

$$\%\ \text{Energy Penalty} = \frac{-[\text{net plant efficiency(oxy-fired SCPC)} - \text{net plant efficiency(SCPC w/o CCS)}]}{\text{net plant efficiency(SCPC w/o CCS)}}$$

5.3 Cost Results

5.3.1 Total Overnight Cost

The capital costs for the 450MW and 900MW air-fired and oxy-fired plants and for the industrial steam plant retrofit to oxy-combustion were developed using the methodology described in the DOE's Cost Estimation Methodology guide.[3]

- Bare Erected Costs (BEC) were developed for all process equipment, facilities, and infrastructure – including materials and erection labor.
- Total Plant Costs (TPC) were developed by adding the cost of services by the engineering, procurement, and construction (EPC) contractor, along with process and project contingencies.
- The TPC is an overnight cost and is expressed in base year dollars (June 2011 dollars).
- Total Overnight Capital Cost (TOC) includes the TPC plus all other overnight costs, including owner's costs.

[3] Cost Estimation Methodology for NETL Assessments of Power Plant Performance, NETL Quality Guidelines for Energy System Studies, DOE/NETL-2-11/1455, April 2011

- The Total As-Spent Capital Costs (TASC) includes all capital expenditures during the capital expenditure period including their escalation and interest during construction. It is expressed in mixed, current-year dollars over the capital expenditure period.

Process contingencies were applied to selected capital cost estimates in the Total Plant Costs to compensate for performance uncertainties associated with the developmental status of the oxy-combustion technology. A 20% process contingency was applied to boiler island process area modifications associated with oxy-combustion that have not been demonstrated commercially and were thus designed using experimental data such as from Alstom's $15MW_{th}$ Boiler Simulation Facility. Process contingencies were applied to the following boiler equipment areas:

- Windbox and firing system modifications
- Ductwork modifications associated with oxy-firing
- Dampers and controls associated with oxy-firing

No process contingencies were taken for the ASU or GPU systems, consistent with the approach taken by the DOE for Case 5C and other DOE oxy-combustion cases.

The DOE developed detailed capital cost estimates of the Case 11 SCPC plant that are the basis for many of the cost estimates for equipment outside of the boiler island used for the 450MW and 900MW power plants in this study. The DOE subsequently updated the costs for this case to June 2011 dollars.[4] These updated costs were used in this study as a reference base and were adjusted by capacity factoring using the scaling parameters prescribed by the DOE[5] for those subsystems and components common to the 450MW and 900MW plants. Specifications for those components unique to these plants were based on heat and material balances. Costs were then developed by in-house cost-estimating, vendor quotes, or from quotes for similar equipment that were then adjusted for capacity and flow conditions. Costs for the major components included all items necessary to develop a complete cost, including items such as pressure parts, refractory, insulation, structural steel, casing, expansion joints, etc.

Table 5-3 summarizes the Total Overnight Costs (TOC) and the Total As Spent Capital Costs (TASC) for the 450MW and 900MW cases, without and with CCS. Also shown are the incremental capital costs to retrofit the $150MW_{gross}$ air-fired industrial steam plant to oxy-fired capability. All costs are based on June 2011 dollars. Figure 5-4 shows the Total Overnight Costs on a $/kW basis for the 450MW and 900MW cases. The following observations can be drawn from this study related to capital costs:

- The capital costs of these plants can't be compared directly since they are all designed with different net outputs. Normalizing the costs on a $/kW basis allows plants of different capacities to be fairly compared. On a $/kW basis, the total overnight capital cost for the 450MW oxy-fired plant increased by 78.1% relative to air-fired plant. The TOC cost increase for the 900MW oxy-fired plant was 78.5%. The added cost of integration of the ASU, GPU and FGHR for the 900MW offset some of specific cost decrease due to both scalability and technology maturity (commercial vs. demonstration plant).

[4] Updated Costs (June 2011 Basis) for Selection Bituminous Baseline Cases, DOE/NETL-341/082312, August 2012
[5] Capital Cost Scaling Methodology, Quality Guidelines for Energy System Studies, DOE/NETL-341/013113, January 2013

- Most of the capital cost increase for the oxy-fired plants and for the industrial steam plant retrofit is due to the addition of the ASU and GPU systems.
- The 450MW and 900MW boiler bare erected costs (materials and erection only) also increased by about 11% for the oxy-fired cases as compared to the air-fired cases. This increase accounts for the changes necessary to make the boiler oxy-capable, such as the addition of the flue gas recirculation system ducting, oxygen mixers, and windbox modifications.
- The TASC shown in Table 5-3 can be derived by multiplying the TOCs for the air-fired plants by a 1.134 factor (for low risk investor owned utilities) and by a 1.140 factor (for high risk investor owned utilities). The TASC includes all capital expenditures during the capital expenditure period including escalation and interest during construction. It is expressed in mixed, current-year dollars over the capital expenditure period.
- The incremental TOC to retrofit a $150MW_{gross}$ air-fired industrial boiler to oxy-fired capability is approximately $200 million. The costs of the boiler modifications are relatively modest at only 7% of the total capital cost. About 34% of the boiler cost is to modify the windbox assembly and firing system. Another 25% of the boiler cost is to modify the ductwork system (FGR ducts, duct insulation, O_2 mixers, supports, and hangers). The remaining 41% of the boiler cost covers the necessary dampers, control valves, O_2 analyzer, flow elements, and instrumentation. The majority of the retrofit capital cost is for the addition of the ASU and GPU. The ASU is 58% of the total retrofit cost while the GPU is 35% of the total retrofit cost.

Table 5-3. Total Overnight and Total As Spent Capital Costs

Case	Total Overnight Cost		Total As Spent Capital	
	1000$	$/kW	1000$	$/kW
450MW Air-Fired w/o Capt	1,330,385	3119	1,508,657	3537
450MW Oxy-Fired	1,806,428	5556	2,059,328	6334
900MW Air-Fired' w/o Capt	1,780,293	2098	2,018,853	2379
900MW Oxy-Fired	2,468,813	3745	2,808,747	4269
$150MW_{gross}$ Industrial Retrofit	201,524		229,272	

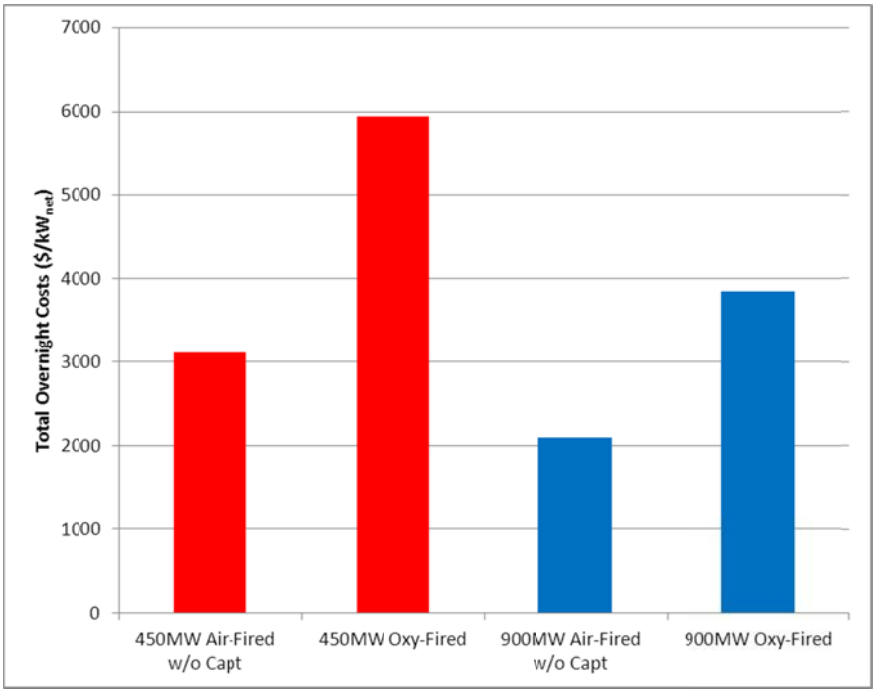

Figure 5-4. Total Overnight Costs

5.3.2 Cost of Electricity (COE)

The first year Cost of Electricity (COE) is the economic metric used in the analysis of the 450MW and 900MW power plant cases. It is the revenue received by the generator per net MWhr produced during the first year of operation assuming that the first year of operation COE escalates at a nominal annual rate equal to the general inflation rate (i.e. remains constant in real terms over the operational period of the plant). The levelized COE (LCOE) is the revenue received by the generator per net MWhr produced during the first year of operation assuming that the first year of operation COE escalates at a nominal annual rate of 0% (i.e. remains constant in nominal terms over the operation period of the plant).

The first year COE was developed using two different methodologies, consistent with the DOE guidelines.[6] The first method uses the NETL Power Systems Financial Model (PSFM). The model accepts all of the economic assumptions outlined in the DOE Cost Estimation Guidelines[7] along with specific information on the capital cost and fixed/variable O&M costs for each case. An alternative approach is to use the simplified capital charge factor method to calculate the cost of electricity. This alternate approach is described below. Both COE methodologies provide similar results and both were used for analysis of the cases in this study.

Simplified Capital Charge Factor Methodology

A simplified method of calculating the first year cost of electricity is also provided in the DOE Financial Model User's Guide.[8] The PSFM calculates a first year capital charge factor (CCF) that can be used to calculate the COE with the simplified equation shown below. Based on the economic

[6] Power Systems Financial Model Version 6.6 User's Guide, DOE/NETL-2011/1492, May 2011
[7] Cost Estimation Methodology for NETL Assessments of Power Plant Performance, DOE/NETL-2011/1455, April 2011
[8] Power Systems Financial Model Version 6.6 User's Guide, DOE/NETL-2011/1492, May 2011, pg. 14

factors specified by the DOE, the CCF for the 450MW and 900MW air-fired power plants is 0.116 based on a Low Risk Investor Owned Utility (IOU) and five year capital expenditure period. The CCF for all of the 450MW and 900MW oxy-fired power plants is 0.124 based on a High Risk Investor Owned Utility (IOU) and five year capital expenditure period.

The simplified COE is calculated by the following equation:

$$COE = \frac{(CCF)(TOC) + OC_{FIX} + (CF)\,OC_{VAR}}{(CF)\,(MWh)}$$

where:

COE = revenue received by the generator ($/MWh) during the air-fired or oxy-fired power plant's first year of operation (expressed in 2011 dollars), assuming that the COE escalates at a nominal annual rate equal to the general inflation rate, i.e., that it remains constant in real terms over the operational period of the power plant.
CCF = is the first year Capital Charge Factor that matches the applicable finance structure and capital expenditure period
TOC = Total Overnight Capital in 2011 dollars
OC_{FIX} = the sum of all fixed annual operating costs in 2011 dollars
OC_{VAR} = the sum of all variable annual operating costs, including fuel at 100% capacity factor, in 2011 dollars
CF = plant capacity factor, assumed to be constant over the operational period
MWh = annual net megawatt-hours of power generated at 100% capacity factor

Levelized COE

The Power Systems Financial Model provides the LCOE on a current dollar basis over a levelization period equal to the plants operational life – i.e., the LCOE is constant in current dollars over this period. The model provides a Levelization factor that can be multiplied by the COE to give the LCOE in base year dollars. The Levelization Factor for NETL defined economic inputs is 1.268.

Cost of CO_2 Transport and Storage

The cost of CO_2 transport and storage (T&S) needs to be included in the cost of electricity to derive the complete cost of capturing and storing CO_2. The updated DOE Baseline Report[9] specified the conditions and T&S costs to be used for DOE system studies. The costs are based on transporting high pressure (2200 psig) CO_2 from the 450MW or 900MW oxy-fired power plant through a 100km (62 mile) pipeline to the sequestration or EOR site. The CO_2 leaves the pipeline at a pressure of 1200 psig still in a supercritical state. For a Midwest plant location, the T&S value specified for DOE system studies is $10/tonne CO_2 in 2011 dollars. Note that the DOE's target of a COE Increase relative to the SCPC without CO_2 capture does not include T&S in the overall COE.

Summary of COE Results

Figure 5-5 compares the first year COE and the 30 year levelized LCOE for the 450MW and 900MW cases, without and with CCS. The COE (w/o T&S) for the 450MW oxy-fired plant increased by 72.9%

[9] Updated Costs (June 2011 Basis) for Selection Bituminous Baseline Cases, DOE/NETL-341/082312, August 2012, pg. 5-6

relative to the 450MW air-fired plant. The COE for the 900MW oxy-fired plant increased by 68.5% relative to the 900MW air-fired plant. The COE increase for both oxy-fired plants is well above the DOE COE increase target of 35%, which is not surprising as these plants are first generation CCS technologies. The 450MW oxy-fired plant is a demonstration plant capable of 100% air firing capacity and has not been optimized for oxy-firing, thus accounting for the higher COE than the 900MW oxy-fired commercial plant.

Further reductions in the COE can be expected in second generation oxy-fired plants from continued reductions in the capital cost and power requirements for the ASU and GPU, along with further optimization and integration of the overall power plant.

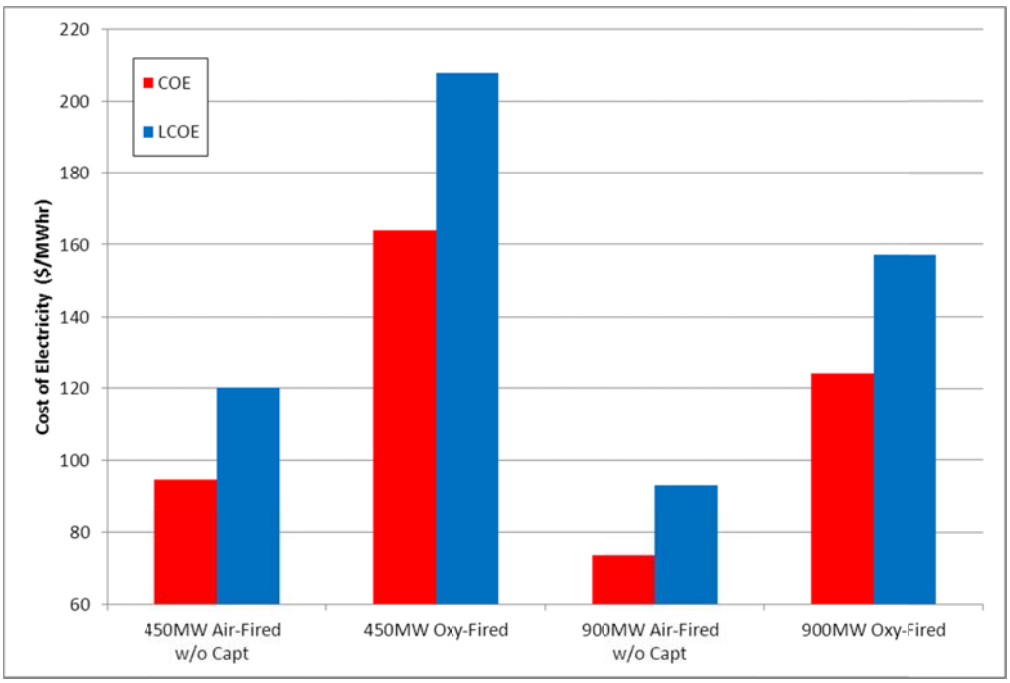

Figure 5-5. COE and LCOE for All Cases

Figure 5-6 again shows the COE for the 450MW and 900MW cases. The COE is broken down into its separate cost components of fuel, capital, fixed O&M, variable O&M, and T&S. The capital cost component shows the largest increase between the air-fired and oxy-fired cases due mostly to the additional ASU and GPU equipment. Fuel costs also increased due to the large parasitic power consumption of the ASU and GPU equipment.

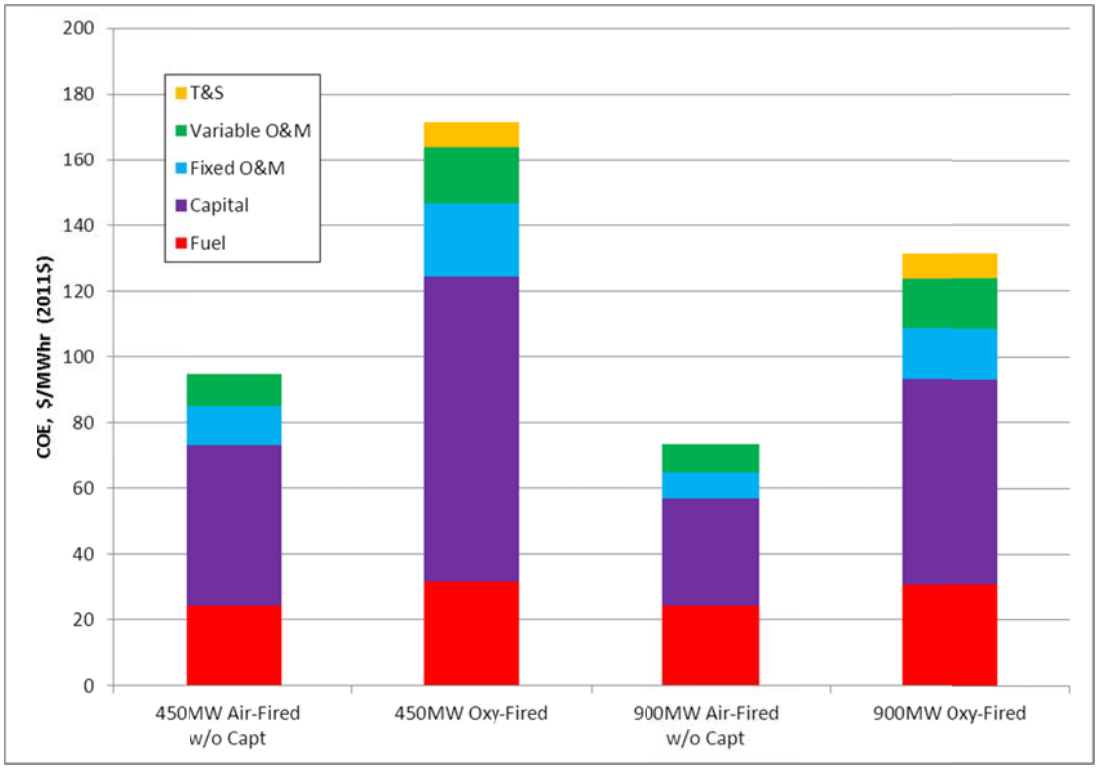

Figure 5-6. COE Breakdown by Cost Component

The economics of any technology can be heavily impacted by future legislation related to climate change. Figure 5-7 shows the COE sensitivity to a future CO_2 Allowance Price. The COE for the 450MW and 900MW oxy-fired cases show only modest COE increases since over 90% of the CO_2 is removed by the process. However, both air-fired plants without CO_2 capture show a significant increase in COE as the CO_2 Allowance Price is increased. The 900MW oxy-fired plant has economic parity (i.e. equal COEs) with the 900MW air-fired plant without CO_2 capture at a CO_2 allowance price 96 $/ton CO_2 before considering T&S costs. The 450MW oxy-fired plant has economic parity at a CO_2 allowance price of 120 $/ton CO_2.

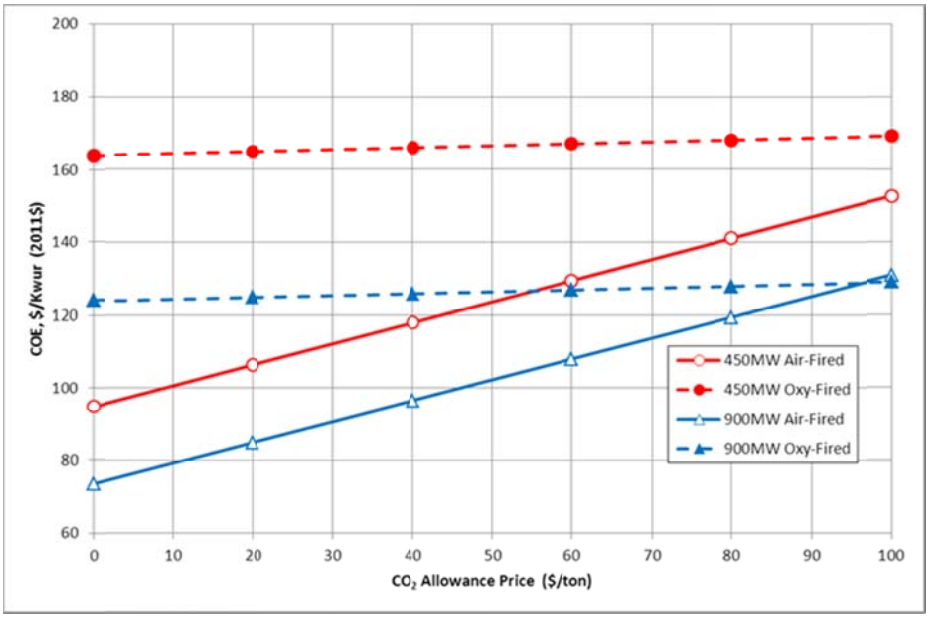

Figure 5-7. COE Sensitivity to CO_2 Allowance Price

Figure 5-8 shows the sensitivity of COE in $/MWh to coal price over the range from 1-5 $/MMBtu for the 450MW and 900MW plants. The CO_2 capture plants are shown without the cost of CO_2 T&S included. Increasing fuel costs has a greater impact on the oxy-fired plants than on the air-fired plants because of its lower net plant efficiency due to the increased auxiliary power requirements of the ASU and GPU.

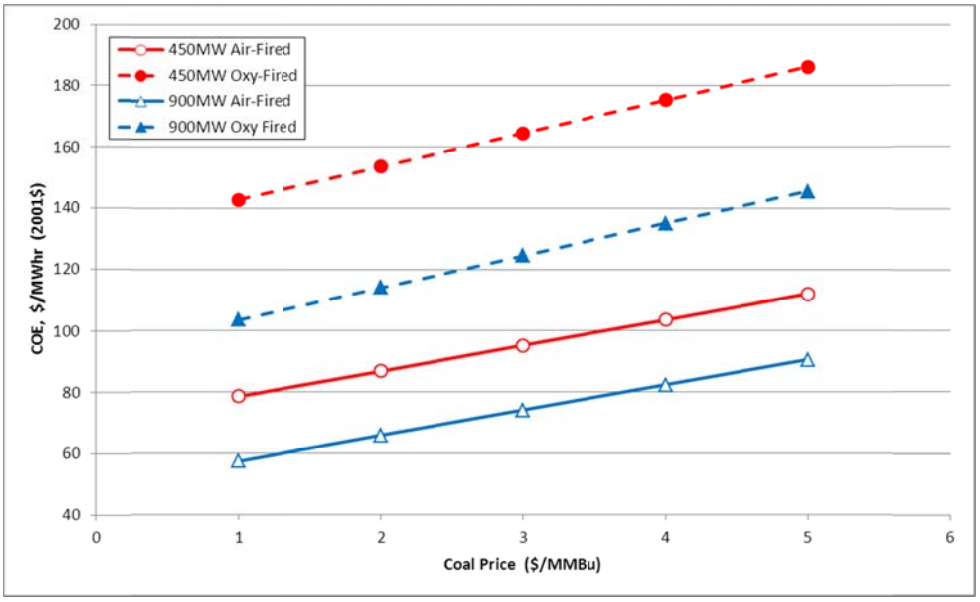

Figure 5-8. COE Sensitivity to Coal Price

Figure 5-9 shows the sensitivity of COE in $/MWh to capacity factor over the range from 30-90 percent for the 450MW and 900MW plants. The base capacity factor used in this study was 85 percent. All of the cases behave in a similar manner. As capacity factor is reduced, the COE increases exponentially. In general, for all of these plants as capacity factor is decreased from 90 percent to 30 percent, the COE is increased by about 250 percent.

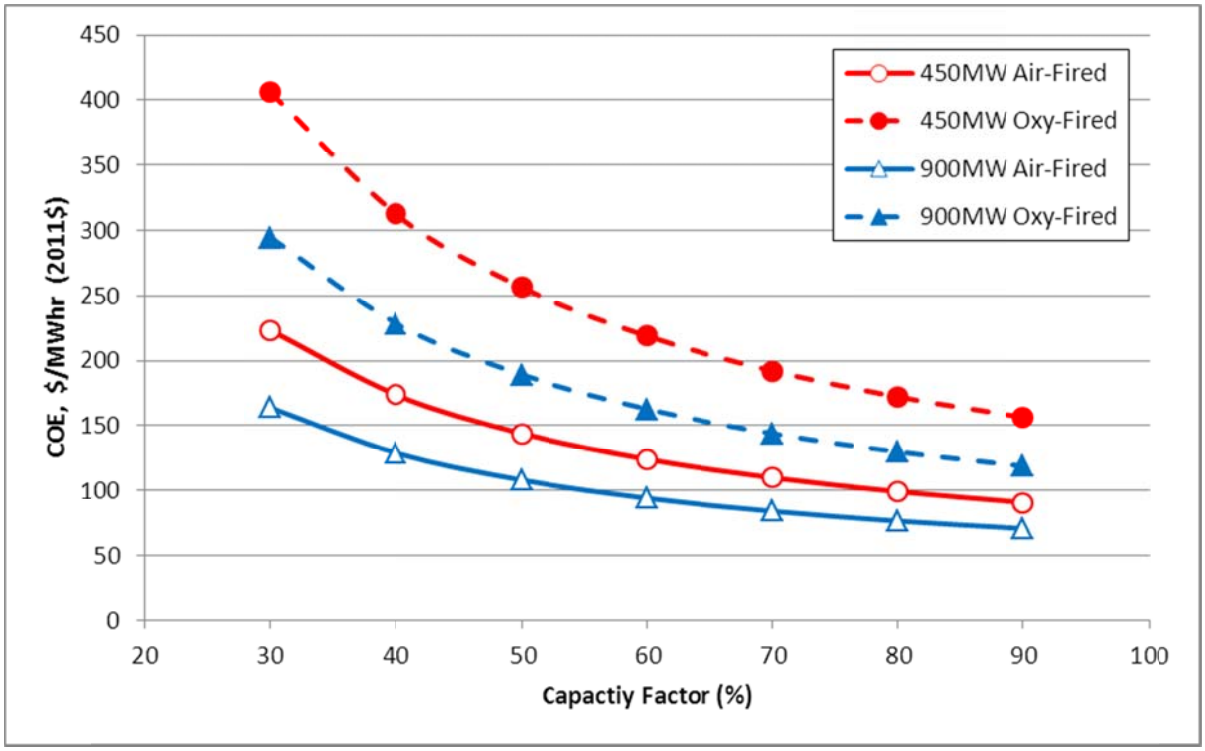

Figure 5-9. COE Sensitivity to Capacity Factor

5.3.3 Variable Cost of Generation

A key factor impacting the economics of a power generation technology is its variable cost of generation (or production cost). Technologies that have low variable costs of generation allow the units to dispatch to the highest capacity factors. It comprises those cost components that vary with the plants operation, including:

- Fuel
- Operating and maintenance
- CO_2 tax
- Transport and Storage

The fuel component depends on the cost of the fuel being consumed ($/10^6 Btu) and the efficiency of the plant (Btu/kWhr) utilizing the fuel. The operating and maintenance component includes the costs of all consumables and other variable costs, including water, sorbents, and ash disposal. The CO_2 tax component, which is not present in a non-carbon constrained world, depends on the tax level ($/Ton of CO_2 emitted), the carbon content of the fuel (lbm of carbon /10^6 Btu), and the fraction of CO_2 produced that is being captured. The transport and storage component depends upon the distance the CO_2 is being transported by pipeline and where it is being sequestered.

Figure 5-10 shows the variable cost of generation vs. the CO_2 Allowance Price for the 450MW and 900MW plants. The variable cost of generation includes all of the cost elements discussed above, including the T&S cost. With no CO_2 allowance price, the two air-fired plants without CCS (red and blue solid lines) would dispatch first. The 900MW oxy-fired plant will dispatch before the 900MW air-

fired plant at CO_2 Allowance Prices above 26 $/ton. The 450MW oxy-fired plant will dispatch before the 450MW air-fired plant at CO_2 Allowance Prices above 29 $/ton CO_2.

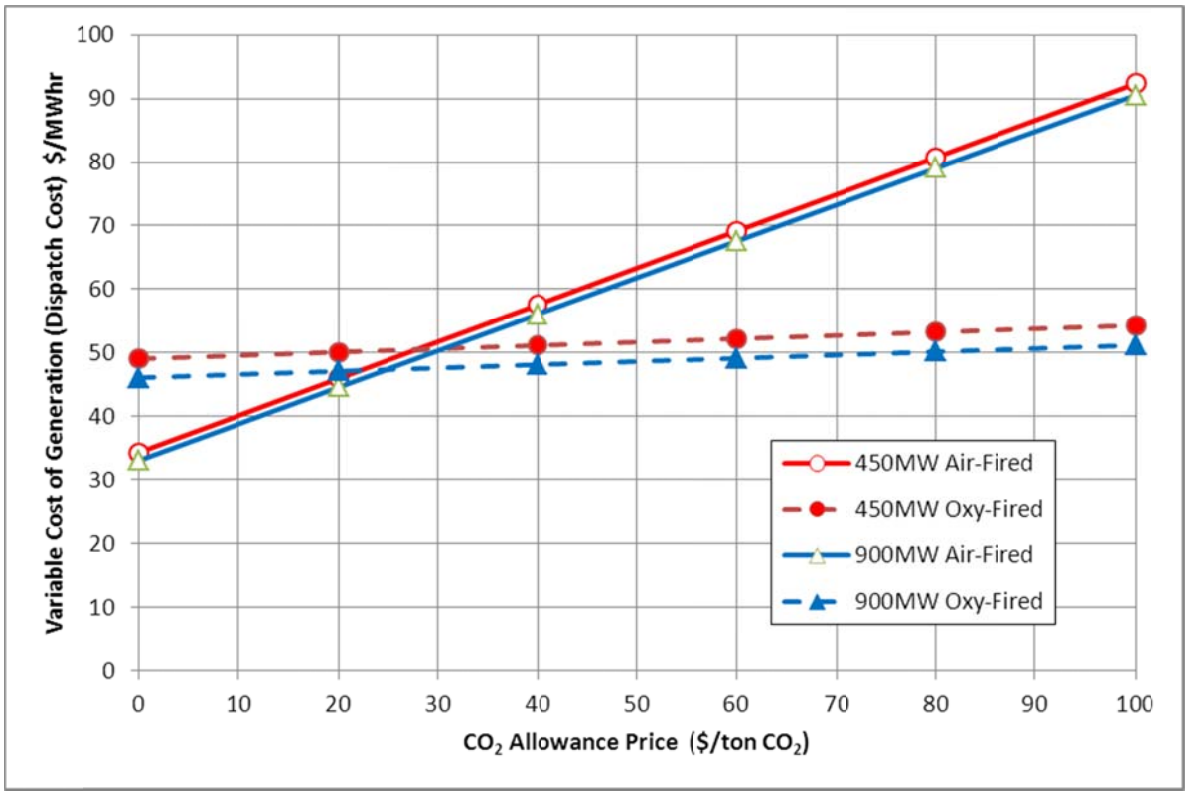

Figure 5-10. Variable Cost of Generation vs. CO_2 Allowance Price

5.3.4 Cost of CO_2 Avoided/Captured

The cost of CO_2 captured was calculated both from the standpoint of the cost of CO_2 removed and the cost of CO_2 avoided.

The Cost of CO_2 Captured or Removed is given by:

$$\text{Cost of } CO_2 \text{ Captured} = \frac{(\text{COE}_{\text{with removal}} - \text{COE}_{\text{w/o removal}})}{(CO_2 \text{ Captured})}$$

where

COE = cost of electricity ($/MWh$_{net}$)
CO_2 Captured = CO_2 captured for case (tonnes/MWh$_{net}$ or tons/MWh$_{net}$)

The equation used to calculate the Cost of CO_2 Avoided in $/tonnes or $/ton is as follows:

$$\text{Cost of } CO_2 \text{ Avoided} = \frac{(\text{COE}_{\text{with removal}} - \text{COE}_{\text{w/o removal}})}{(\text{Emissions}_{\text{w/o removal}} - \text{Emissions}_{\text{with removal}})}$$

where

COE = cost of electricity ($/MWhnet)
Emissions = CO_2 emissions for case (tonnes/MWhnet or tons/MWhnet)

Figure 5-11 shows the CO_2 mitigation costs for the 450MW and 900MW oxy-fired plants. The costs are relative to the 450MW and 900MW air-fired plants, respectively, and do not include T&S. Including T&S will increase the CO_2 mitigation costs by 8-12 $/ton CO_2. The CO_2 Avoided Cost was 131 $/ton for the 450MW oxy-fired plant and decreased to 96 $/ton for the 900MW oxy-fired plant. The CO_2 Captured Cost was 99 $/ton for the 450MW oxy-fired plant and decreased to 75 $/ton for the 900MW oxy-fired plant.

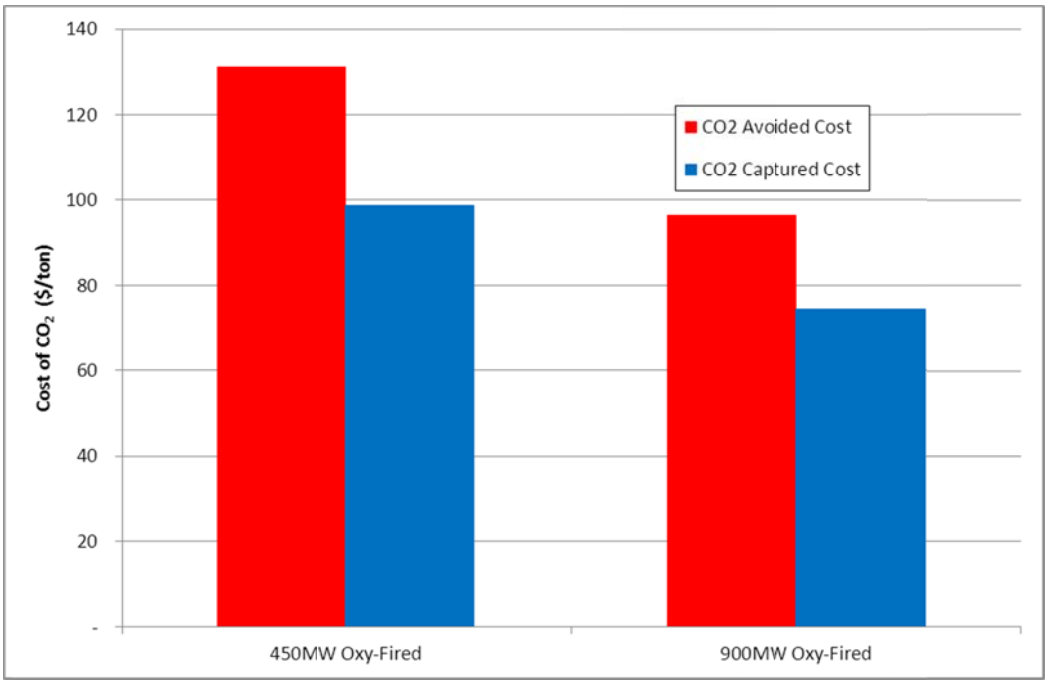

Figure 5-11. Cost of CO_2 Avoided and Captured

5.4 Environmental Performance

5.4.1 CO_2 Emissions

The carbon capture efficiency is a measure of the process effectiveness at capturing the carbon contained in the coal for sequestration or utilization. It is defined as:

$$\% \text{ Carbon Capture} = \frac{(CO_2\text{Coal} - CO_2\text{emitted})}{CO_2\text{Coal}}$$

The carbon capture efficiency for the oxy-fired 450MW Demonstration Plant, 900MW Commercial Plant, and Industrial Steam Plant was 93% for all cases. The carbon loss for each case was primarily from the GPU vent. The GPU design and performance for this techno-economic study was based on

the GPU used in Case 5C of the DOE Baseline Study.[10] Since the carbon capture is largely controlled by the GPU performance, the % carbon capture for all of these cases was essentially the same as for the DOE Case 5C.

Figure 5-12 shows the actual carbon emissions in lb CO_2/MMBtu for the air-fired and oxy-fired Demonstration Plant, Commercial Plant, and Industrial Steam Plant cases.

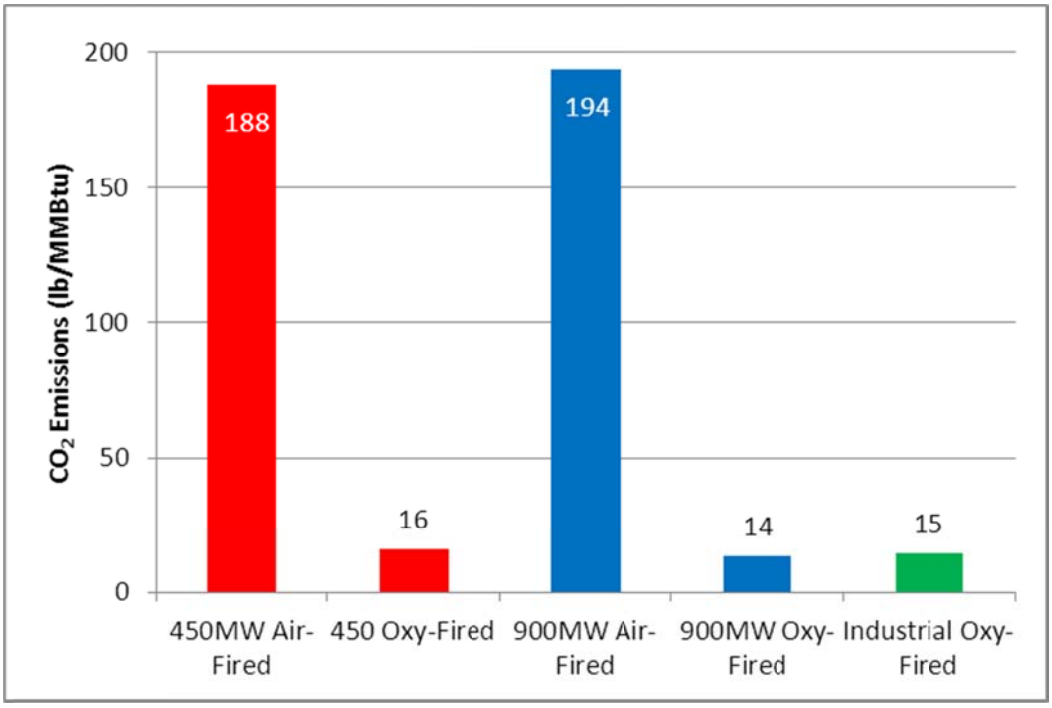

Figure 5-12. Summary of CO_2 Emissions for Air-Fired and Oxy-Fired Cases

5.4.2 Non-CO_2 Emissions

Table 5-4 summarizes the emissions from the air-fired and oxy-fired 450MW Demonstration Plant, 900MW Commercial Plant, and Industrial Steam Plant. The environmental targets selected for this study are identical to those chosen for the PC cases in the DOE Cost and Performance Baseline for Fossil Energy Plants[11] and are summarized in the first column of this table. This ensures that these cases can be compared fairly with plants evaluated in other DOE programs on a common basis. The targets established in the baseline report factored in existing environmental regulations and trends, recent permits, and the current BACT. This was compared with NSPS as of February 2006 which defined the minimum control level required for new fossil power plants. The BACT analysis was selected as the environmental target as shown in Table 5-4 since they exceeded the requirements for both NSPS and the average of recent permits.

The emissions for the air-fired cases shown in Table 5-4 match the environmental targets as the plants are designed and operated to meet these limits. NO_x emissions are controlled by the low NO_x firing system and SCR. SO_2 emissions are controlled by the WFGD for the 450MW and 900MW plants and by a NID™ for the industrial steam plant. Particulates are controlled by fabric filters for all cases. The

[10] Pulverized Coal Oxycombustion Power Plants Volume 1, DOE/NETL-2007/1291, August 2008

[11] Cost and Performance Baseline for Fossil Energy Plants Volume 1, DOE/NETL-2010/1397, November 2010

fabric filter for the industrial steam plant is an integral part of the NID™ system. The mercury emission limits are met by co-benefit capture from the combined effects of the SCR, fabric filter, and FGD. The SCR promotes the oxidation of elemental mercury. The oxidized mercury can then be more readily removed in the fabric filter and FGD. No activated carbon injection was necessary for these plants as the assumed 90% mercury co-benefit capture is sufficient to meet the mercury limits for this study.

The oxy-fired plants use the same environmental control equipment as for the air-fired plants. However, the emissions for the oxy-fired plants shown in Table 5-4 are significantly below emission targets used in this study. This is because additional removal takes place as the gas passes through the Flue Gas Condenser and GPU. A significant amount of the SO_2 remaining after the FGD is removed in the Flue Gas Condenser and then neutralized with NaOH. Most of the remaining SO_2 is further removed in the GPU. Similarly, most of the remaining NO_x is removed in the condensate when the flue gas is compressed in the GPU. A portion of the remaining NO_x is sequestered with the CO_2 product gas. Most of the oxidized mercury is removed in the FGD system and Flue Gas Condenser. The balance of the mercury is removed in an activated carbon bed in the GPU.

Table 5-4. Summary of Emissions for all Air-Fired and Oxy-Fired Cases

Power Plant Cases	Target	Air-Fired SCPC Power Plant 450MW	Oxy-Fired SCPC Power Plant 450MW	Air-Fired SCPC Power Plant 900MW	Oxy-Fired SCPC Power Plant 900MW	Oxy-Fired Steam Plant 150MW
SO_2 (lb/MMBtu)	0.085	0.085	< 0.01	0.085	< 0.01	< 0.01
NO_x (lb/MMBtu)	0.07	0.07	< 0.01	0.07	< 0.01	< 0.01
Particulates (lb/MMBtu)	0.013	0.013	< 0.01	0.013	< 0.01	< 0.01
Hg (lb/TBtu)	1.14	1.14	< 0.01	1.14	< 0.01	< 0.01
CO_2 (lb/MMBtu)		188	16	194	14	15

5.5 Sensitivity Study of FGR Location

A sensitivity study was conducted to evaluate the performance and cost impact of four different locations for the secondary flue gas recirculation duct take-off. The options considered included secondary FGR taken after the WFGD, before the WFGD, and before the Gas-Gas Heater. In this last scenario, an oxygen eductor is used to provide the motive force to convey the hot flue gas recycle back to the boiler. The last scenario had two options – one with the O_2 mixed directly with the secondary FGR and a second with the O_2 first preheated. The primary FGR ducts were taken after the Flue Gas Condenser for all cases to minimize the moisture concentration in the recirculation gas feeding the pulverizers. This study was focused on the performance and cost implications of the FGR location and did not consider the impact of increased SO_2 concentrations on the boiler design. However, the options that take recirculation gas before the WFGD would likely be limited to low sulfur fuels because of the potential impacts on boiler tube corrosion and additional costs associated with corrosion protection.

Model simulations showed that moving the secondary FGR duct before the WFGD slightly improved the boiler efficiency as compared to the base case with the secondary FGR after the WFGD. Moving the secondary FGR before the Gas-Gas Heater actually decreased the boiler efficiency by 0.7% points due to the lower temperature of the FGR entering the furnace after cold O_2 is mixed with it. However, preheating the O_2 before mixing it with the secondary FGR improved the boiler efficiency for the case with FGR ducts located before the Gas-Gas Heater by 1% point relative to the base case.

Table 5-5 summarizes the qualitative cost impacts for the different FGR locations as compared to Case 1. Moving the FGR location from after the WFGD (Case 1) to before the WFGD (Case 2) results in a slightly larger fabric filter (due to a higher gas temperature and volumetric flow leaving the Gas-Gas

Heater) and a smaller WFGD. Moving the FGR location before the Gas-Gas Heater (Cases 3 and 4) reduces the volumetric flow rate to all gas-touched equipment downstream of the boiler and before the Flue Gas Condenser, including the Gas-Gas Heater, fabric filter, and WFGD. Case 4 also requires the addition of an O_2 heater.

A simple cost analysis was conducted to capture the cost impacts on a 900MW oxy-fired plant for some of the major pieces of equipment impacted by the choice of FGR location. Table 5-5 shows that moving the FGR upstream of the WFGD can have significant cost benefits. Of course, there are other considerations, such as the impact of increased SO_2 concentration on the boiler materials that may override any advantages of moving the FGR location. There was little cost benefit to moving the FGR location from before the WFGD to before the Gas-Gas Heater if there is no O_2 preheat before mixing with the secondary FGR. Although Case 3 has a lower cost fabric filter than Case 2 due to reduced volumetric gas flow, this savings is offset by a lower boiler efficiency due to the reduced secondary FGR gas temperature entering the furnace. Preheating the O_2 before mixing with the secondary FGR (Case 4) results in improved boiler efficiency and greater capital cost reduction relative to Case 1.

Table 5-5. Cost Implications of FGR Location

	Case 1 After WFGD	Case 2 Before WFGD	Case 3 Before GGH	Case 4 Before GGH O_2 Preheat
Gas-Gas Heater	Base	Similar	Smaller	Smaller
Fabric Filter	Base	Larger	Smaller	Smaller
WFGD	Base	Smaller	Smaller	Smaller
O_2 AH	N/A	N/A	N/A	New
Δ Total Overnight Capital Cost ($M)	Base	-66	-67	-85
Δ Total Overnight Capital Cost ($/Kw)	Base	-101	-101	-130

There are other costs that were not considered in this simple cost analysis. Cost additions include an increased ASU capital cost and higher ASU power requirements for Case 4 as the oxygen needs to be delivered at a higher pressure for the oxygen eductor to provide the motive force necessary to convey the hot FGR back to the boiler. There may be some windbox modifications necessary for Cases 3 and 4 to deal with the hot, particulate laden FGR. Other costs may be necessary to cope with increase SO_2 concentrations in the boiler.

These cost adders are offset by various cost reductions that were not considered in this study. These include reduced capital costs for the ID Fan and gas ductwork, plus reduced auxiliary power requirements for the fabric filter, WFGD, and ID Fan. The impact on the flue gas heat exchanger (HEX) was also not considered, but the cost of this equipment would likely increase for Case 2 due to the increased sensible energy in the flue gas from the higher gas temperature. The HEX cost would likely decrease for Case 4 due to the significantly decreased volumetric flow rate relative to Case 1, which more than offsets an increase in flue gas temperature. The HEX cost for Case 3 would likely be just slightly less than for Case 1 as the increased flue gas temperature would almost offset the reduced volumetric flow rate.

Overall, the FGR location in Case 4 resulted in the most significant cost reduction as compared to the base case scenario. The capital cost reductions considered in this sensitivity study total 3.5% of the Total Overnight Costs of the 900MW oxy-fired plant that used the secondary FGR after the WFGD

(Case 1). The additional costs and savings not considered in this study are expected to increase the overall savings.

5.6 Summary

- Four utility scale power plants were designed and costs were developed for them in this study. A $450MW_{gross}$ oxy-fired SCPC plant was designed as representative of a demonstration plant for oxy-combustion. A $900MW_{gross}$ oxy-fired SCPC plant was designed and costs were developed as representative of a first generation oxy-combustion commercial plant. These plants were contrasted with a $450MW_{gross}$ and a $900MW_{gross}$ air-fired SCPC plant. This study also included an evaluation of the design modifications and costs necessary to retrofit an existing air-fired industrial steam plant equivalent to $150MW_{gross}$ to oxy-combustion.
- The net plant efficiency for the 450MW oxy-fired plant was 31.5% HHV, or 9.4% points less than the 450MW air-fired case. The net plant efficiency for the 900MW oxy-fired plant was 32.5% HHV, or 8.8% points less than the 900MW air-fired case. The reduction in net plant efficiency for the oxy-fired cases is primarily due to the increased auxiliary power requirements for the ASU and GPU.
- The net plant efficiency for the 900MW oxy-fired plant was 0.6% points higher than the efficiency for the 450MW oxy-fired plant. This improvement is primarily due to the thermal integration of the ASU, GPU, and FGHR system that was used for the 900MW oxy-fired plant design.
- The Total Overnight Capital cost for the 450MW oxy-fired plant increased by 78.1% relative to the air-fired plant. The Total Overnight Capital cost increase for the 900MW oxy-fired plant was 78.5% relative to the air-fired plant. The added cost of integration of the ASU, GPU, and FGHR for the 900MW offset some of the specific cost decrease due to both scalability and technology maturity (commercial vs. demonstration plant).
- Most of the capital cost increase for the oxy-fired utility plants is due to the addition of the ASU and GPU systems. The 450MW and 900MW boiler bare erected costs (materials and erection only) increased by about 11% for the oxy-fired cases as compared to the air-fired cases. This increase accounts for the changes necessary to make the boiler oxy-capable, such as the addition of the flue gas recirculation system ducting, oxygen mixers, and windbox modifications.
- The incremental Total Overnight Capital cost to retrofit the $150MW_{gross}$ air-fired industrial boiler to oxy-fired capability is approximately $200 million. The cost of the boiler modifications are only 7% of the total capital cost. The majority of the retrofit capital cost is for the addition of the ASU and GPU.
- The first year COE (w/o T&S) for the 450MW oxy-fired plant increased by 72.9% relative to the 450MW air-fired plant. The COE increase for the 900MW oxy-fired plant increased by 68.5% relative to the 900MW air-fired plant. The COE increase for both oxy-fired plants is well above the DOE COE increase target of 35%, which is not surprising as these plants are first generation CCS technologies. Further reductions in the COE can be expected in second generation oxy-fired plants from continued reductions in the capital cost and power requirements for the ASU and GPU, along with further optimization and integration of the overall power plant.
- The CO_2 Avoided Cost was 131 $/ton for the 450MW oxy-fired plant and decreased to 98 $/ton for the 900MW oxy-fired plant. The CO_2 Captured Cost was 99 $/ton for the 450MW oxy-fired plant and decreased to 75 $/ton for the 900MW oxy-fired plant.

- A sensitivity study evaluated the performance and cost impact of four different locations for the secondary flue gas recirculation duct take-off. Moving the FGR from after the WFGD to before the WFGD had little impact on the boiler efficiency. Moving the FGR before the Gas-Gas Heater actually decreased the boiler efficiency by 0.7% points due to the lower temperature of the FGR entering the furnace after cold O_2 is mixed with it. However, preheating the O_2 before mixing it with the secondary FGR improved the boiler efficiency for the case with FGR ducts located before the Gas-Gas Heater by 1% point relative to the case with the FGR location after the WFGD.
- A simple cost analysis identified the cost impacts on a 900MW oxy-fired plant for some of the major pieces of equipment impacted by the choice of FGR location. The results showed that moving the FGR upstream of the Gas-Gas Heater and preheating the O_2 before mixing with the secondary FGC can have significant cost benefits in terms of both boiler efficiency improvement and capital cost reduction. These benefits need to be weighed against other considerations, such as the impact of increased SO_2 concentration on boiler materials.

Recovery Act: Oxy-Combustion Technology Development for Industrial-Scale Boiler Applications

DOE/NETL Cooperative Agreement No. DE-NT0005290

Volume II – Experimental Program

Reporting Period
October 1, 2008 to April 30, 2014

Report Issued on July 29, 2014

Authors
Armand A. Levasseur
David G. Turek
Steven A. Unker

Prepared for
U.S. Department of Energy
National Energy Technology Laboratory
Pittsburgh, Pennsylvania

Prepared by
Alstom Power Inc.
200 Great Pond Drive
Windsor, Connecticut 06095

Principal Investigator
Armand A. Levasseur

DISCLAIMER STATEMENT

This material is based upon work supported by the Department of Energy under Award Number DE-NT0005290.

This report was prepared as an account of work sponsored by an agency of the United States Government. Neither the United States Government nor any agency thereof, nor any of their employees, makes any warranty, express or implied, or assumes any legal liability or responsibility for the accuracy, completeness, or usefulness of any information, apparatus, product, or process disclosed, or represents that its use would not infringe privately owned rights. Reference herein to any specific commercial product, process, or service by trade name, trademark, manufacturer, or otherwise does not necessarily constitute or imply its endorsement, recommendation, or favoring by the United States Government or any agency thereof. The views and opinions of authors expressed herein do not necessarily state or reflect those of the United States Government or any agency thereof.

This report was prepared based on work conducted with support, in part, by grants made possible by the Illinois Department of Commerce and Economic Opportunity through the Office of Coal Development and the Illinois Clean Coal Institute as well as the Industrial Commission of North Dakota,. Neither the Illinois Department of Commerce and Economic Opportunity, Office of Coal Development, the Illinois Clean Coal Institute, nor the Industrial Commission of North Dakota, nor any person acting on behalf of either:

(A) Makes any warranty of representation, express or implied, with respect to the accuracy, completeness, or usefulness of the information contained in this report, or that the use of any information, apparatus, method, or process disclosed in this report may not infringe privately-owned rights; or

(B) Assumes any liabilities with respect to the use of, or for damages resulting from the use of, any information, apparatus, method or process disclosed in this report.

Information disclosed herein is furnished to the recipient solely for the use thereof as has been agreed upon with ALSTOM and all rights to such information are reserved by ALSTOM. The recipient of the information disclosed herein agrees, as a condition of its receipt of such information, that ALSTOM shall have no liability for any direct or indirect damages including special, punitive, incidental, or consequential damages caused by, or arising from, the recipient's use or non-use of the information.

Table of Contents

Table of Contents iii
Table of Figures v
Table of Tables vii
Executive Summary viii
1. Introduction 1
1.1 Project background 1
1.2 Basic oxy-combustion concept 2
1.3 Oxy-firing configuration options 3
1.4 Global O_2 concentration to boiler 4
1.5 Stoichiometric oxygen requirement 4
2. Boiler Simulation Facility (BSF) 8
2.1 15 MW_{th} BSF 8
2.2 Modifications for Oxy-Firing 8
2.2.1 Windbox and firing system 12
2.2.2 Oxygen System 13
2.2.3 Fans and ducting 15
2.2.4 Baghouse / NID™ 16
2.2.5 Heat exchangers and condensers 17
2.2.6 Internal recirculation system 18
2.3 Data collection 21
2.3.1 Test measurements 21
2.3.2 Advant /LabView 22
2.3.3 Campbell data loggers 22
2.3.4 Board data 23
2.3.5 Other data 24
2.3.6 Deposition probes 25
3. Test campaigns 27
3.1 Test campaign 1 – Powder River Basin subbituminous 29
3.2 Test campaign 2 – low sulfur bituminous 30
3.3 Test campaign 3 – high-sulfur Illinois bituminous 32
3.4 Test campaign 4 – North Dakota lignite 33
3.5 Test campaign 6 – Schwarze Pumpe lignite 35
3.6 Test campaign 5-1 – 2nd generation, low sulfur bituminous 36
3.7 Test campaign 5-2 – 2nd generation, PRB sub-bituminous 38
3.8 Test campaign 5-3 – 2nd generation, high sulfur bituminous 40
4. Fuels Characterization 43
4.1 Experimental Procedures 44

4.1.1 Thermo-Gravimetric Analysis 44
4.1.2 Petrographic Analyses 45
4.1.3 Specific Surface Areas 45
4.1.4 Mini-Screen Analyses 45
4.1.5 Micro-Proximate Analyses 45
4.1.6 CCSEM Analyses 46
4.1.7 The Drop Tube Furnace System (DTFS) 46
4.1.8 Drop Tube Furnace Test Matrix 50
4.2 Fuel Characterization Results 51
4.2.1 Coal Analyses 51
4.2.2 CCSEM Ash Analyses 52
4.2.3 Char Characteristics 52
4.2.4 Petrographic Analysis 52
4.2.5 Thermo-Gravimetric Reactivities 53
4.2.6 Surface Area-Reactivity Relationships 56
4.2.7 Pyrolysis of Coals in DTFS 56
4.2.8 Gasification of Coals in DTFS 58
4.2.9 Combustion of Chars in DTFS 59
4.2.10 Gasification of Chars in DTFS 63
5. BSF results 65
5.1 Emission Considerations 65
5.2 Combustion 66
5.2.1 CO emissions 66
5.2.2 CO profiles along the furnace height 68
5.2.3 Unburned carbon 71
5.3 NO_x Emissions 73
5.3.1 NO_x injection tests 77
5.4 SO_2 81
5.5 SO_3 84
5.5.1 SO_3 control 87
5.6 Fly ash 88
5.6.1 Particle size and loading 88
5.6.2 Fly Ash analysis 90
5.7 Trace metals and mercury 92
5.7.1 Mercury removal 97
5.8 Ash Deposits and Corrosion 99
5.8.1 BSF Deposition/Corrosion Probes 99
5.8.2 Bench-Scale Corrosion Evaluation 102
5.9 Thermal Performance 103
5.9.1 Furnace heat flux profiles 103
5.9.2 Heat absorption in the furnace 110

6. Conclusions 113
7. Appendices 114
Appendix A. SO_3 sampling equipment and procedure 114
Appendix B. CCSEM Analysis 117
Appendix C. EERC Report on Mercury Emissions during Test Campaign 4 118
Appendix D. Deposition Probe Corrosion Report 119
Appendix E. Bench Scale High Temperature Corrosion Study 120
Appendix F. Bench Scale Waterwall Corrosion Study 121

Table of Figures

Figure ES- 1. Schematic of Oxy-Combustion Compared With Air Firing ix
Figure ES- 2. Simplified Boiler Island Process Flow Diagram for Oxygen-fired PC Boiler x
Figure ES- 3. Boiler Simulation Facility xi
Figure ES- 4. BSF process sketch xii
Figure ES- 5. Schematic of DTFS-1 xvi
Figure ES- 6. Char Combustion Efficiencies at 2650°F xviii
Figure ES- 7. Parent Coal Gasification Efficiencies by Ash Tracer xix
Figure ES- 8. Effect of recirculation rate, Illinois high sulfur bituminous xxiii
Figure ES- 9. Effect of varying oxygen distribution, Illinois high sulfur bituminous xxiii
Figure ES- 10. Long-term temperature and heat flux profiles, ND lignite campaign xxiv

Figure 1-1. Schematic of Oxy-Combustion Compared With Air Firing 2
Figure 1-2. Simplified Boiler Island Process Flow Diagram for Oxygen-fired PC Boiler 3
Figure 1-3. Typical Relationship Between Recycle Rate, Oxygen In Flue Gas, And Global O_2 5
Figure 1-4. Typical Furnace Stoichiometry Vs. Global O_2 6
Figure 2-1. Boiler Simulation Facility 8
Figure 2-2. BSF modification layout drawing 9
Figure 2-3. BSF process sketch 10
Figure 2-4. Photo of BSF with oxy modification, from north 11
Figure 2-5. Photo of BSF with oxy modifications, from south 11
Figure 2-6. Alstom TFS-2000® low-NOx tangential firing system 12
Figure 2-7. Windbox damper 13
Figure 2-8. Oxygen pad 14
Figure 2-9. BSF oxygen injection system and combustion ducting 14
Figure 2-10. Oxygen diffuser 15
Figure 2-11. BSF Flue Gas Recirculation and Boost Fans 15
Figure 2-12. BSF combustion air ductwork prior to insulation 16
Figure 2-13. NID™ desulfurization system 16
Figure 2-14. Photos of BSF fabric filter with NID™ system 17
Figure 2-15. BSF condenser and demisters 18
Figure 2-16. Close coupled recirculation system schematic 19
Figure 2-17. Close Coupled Recirculation System 19
Figure 2-18. Internal recirculation system heat exchanger 20
Figure 2-19. Oxygen ejectors delivered from supplier 21
Figure 2-20. BSF furnace probe measurement planes 22

Figure 2-21. Probe data logging computer 23
Figure 2-22. BSF Deposition Probes 26
Figure 3-1. Gantt chart of test campaign 1 (PRB sub-bituminous) 29
Figure 3-2. Gantt chart of test campaign 2 (low sulfur bituminous coal) 31
Figure 3-3. Gantt chart of test campaign 3 (high sulfur bituminous coal) 32
Figure 3-4. Gantt chart of test campaign 4 (North Dakota lignite) 34
Figure 3-5. Gantt chart of test campaign 6 (Schwarze Pumpe lignite) 35
Figure 3-6. Gantt chart of test campaign 5-1 (low sulfur bituminous coal) 37
Figure 3-7. Gantt chart of test campaign 5-2 (PRB sub-bituminous) 39
Figure 3-8. Gantt chart of test campaign 5-3 (high sulfur bituminous coal) 41
Figure 4-1. Schematic of DTFS-1 47
Figure 4-2. Ash Generation Procedure 48
Figure 4-3. Char Generation Procedure. 48
Figure 4-4. Coal Gasification Test Procedure 48
Figure 4-5. Char Gasification Test Procedure 49
Figure 4-6. Char Reactivity Test Procedure. 50
Figure 4-7. Non-Isothermal TGA's of 200x400 Parent Coals 54
Figure 4-8. TGA Peak Temperature vs. Vitrinite Reflectance (current fuels in red) 55
Figure 4-9. Isothermal TGA Combustion of 200x400 Chars in Air/N_2 at 700°C 55
Figure 4-10. Isothermal TGA Gasification of 200x400 Chars in CO_2/N_2 at 950°C 56
Figure 4-11. Size distribution of feed coals and generated chars in the DTFS 57
Figure 4-12. Parent Coal Gasification Efficiencies by Ash Tracer 59
Figure 4-13. Parent Coal Gasification Efficiencies by Carbon Monoxide Method 59
Figure 4-14. Char Combustion Efficiencies at 2650°F 60
Figure 4-15. Char Combustion Efficiencies at 2200 60
Figure 4-16. Char Combustion Efficiencies at 1800 61
Figure 4-17. Schwarze Pumpe Char Combustion Efficiencies 62
Figure 4-18. Black Thunder Char Combustion Efficiencies 62
Figure 4-19. Prairie Eagle Char Combustion Efficiencies 63
Figure 4-20. Char Gasification Efficiencies at 2650°F 64
Figure 5-1. BSF CO emissions *vs.* flue gas O_2 for air and oxy-firing 67
Figure 5-2. CO emissions during low excess oxygen tests, PRB sub-bit. testing 68
Figure 5-3. CO emissions during low excess oxygen tests, North Dakota lignite testing 68
Figure 5-4. Vertical O_2 and CO profiles 70
Figure 5-5. O_2 and CO profiles at three elevations, Test 22 71
Figure 5-6. Unburned carbon in flyash 72
Figure 5-7. Unburned carbon in fly ash and carbon heat loss 73
Figure 5-8. NO_x emissions versus windbox stoichiometric ratio, BSF and utility boilers 74
Figure 5-9. NO_x emissions *vs.* MBZ stoichiometry for air and oxy-firing (O_2 between 2.6 – 3%) 75
Figure 5-10. NO_x emissions *vs* MBZ stoichiometry at similar conditions 76
Figure 5-11. NO_x emissions *vs* outlet oxygen level at similar conditions 77
Figure 5-12. Addition of nitric oxide 79
Figure 5-13. Increase in NO_x at the furnace outlet with NO injection 80
Figure 5-14. Reduction of injected NO 81
Figure 5-15. Sulfur capture in the NID™, High Sulfur test 82
Figure 5-16. SO_2 emissions at the furnace and baghouse outlets 83
Figure 5-17. SO_3 measurement and injection locations 84
Figure 5-18. SO_2 and SO_3 (ppm, wet) at the economizer outlet 86
Figure 5-19. Results of SO_3 spiking tests 87
Figure 5-20. SO_3 control by sorbent injection 88
Figure 5-21. CARB Method 501 size distribution and loading at economizer outlet 89

Figure 5-22. Mercury and metals sampling locations 92
Figure 5-23. Trace metal mass ratio, furnace exit to fuel input (log scale) 95
Figure 5-24. Trace metal mass ratio, stack gas to fuel input 96
Figure 5-25. Summary of mercury levels 97
Figure 5-26. Mercury capture and sorbent utilization *vs.* PAC injection ratio 99
Figure 5-27. Deposition Probes with deposits after HiS IL Air (left) and Oxy (right) Tests 101
Figure 5-28. Deposition Probes with deposits after SPLIg Air (left) and Oxy (right) Tests 101
Figure 5-29. Effect of recirculation rate on vertical heat flux profile 105
Figure 5-30. Effect of varying oxygen distribution on vertical heat flux profile, high-sulfur fuel tests 106
Figure 5-31. Long-term temperature and heat flux profiles, PRB campaign 107
Figure 5-32. Long-term temperature and heat flux profiles, WVA Fola campaign 108
Figure 5-33. Long-term temperature and heat flux profiles, Ill Hi S campaign 108
Figure 5-34. Long-term temperature and heat flux profiles, ND lignite campaign 109
Figure 5-35. Long-term temperature and heat flux profiles, SP lignite campaign 110
Figure 5-36. Furnace heat absorption vs global O_2 111
Figure 5-37. Equivalent oxy-fired furnace heat absorption 112

Table of Tables

Table ES- 1. BSF test campaigns xii
Table ES- 2. Average coal analyses for each campaign xiii
Table ES- 3. Surface Area by BET xvii

Table 2-1. BSF firing system arrangement 13
Table 3-1. BSF test campaigns 27
Table 3-2. Average coal analyses for each campaign 28
Table 3-3. Test campaign 1 matrix (PRB sub-bituminous) 30
Table 3-4. Test campaign 2 matrix (low sulfur bituminous coal) 31
Table 3-5. Test campaign 3 matrix (high sulfur bituminous coal) 33
Table 3-6. Test campaign 4 matrix (North Dakota lignite) 34
Table 3-7. Test campaign 6 matrix (Schwarze Pumpe lignite) 36
Table 3-8. Test campaign 5-1 matrix (low sulfur bituminous coal) 38
Table 3-9. Test campaign 5-2 matrix (PRB sub-bituminous) 40
Table 3-10. Test campaign 5-3 matrix (high sulfur bituminous coal) 42
Table 4-1. Summary of feedstocks and tests 44
Table 4-2. Drop Tube Test Matrix 51
Table 4-3. Sized Coal and Char Analyses 52
Table 4-4. Petrographic Analysis of Parent Coals 53
Table 4-5. Surface Area by BET 56
Table 4-6. Q-Factors of 200x400 Parent Coals 58
Table 5-1. NO injection test conditions 78
Table 5-2. Ash oxide analyses 91
Table 5-3. Trace metal concentrations at the furnace outlet (µg per dry standard cubic meter) 93
Table 5-4. Trace metal concentrations at the baghouse outlet (µg per dry standard cubic meter) 94
Table 5-5. PAC injection for mercury removal 99
Table 5-6. Composition of Deposition Probe Ash Deposits 100
Table 5-7. High Temperature Corrosion Test Conditions 102
Table 5-8. Furnace Waterwall Tests Conditions 103
Table 5-9. Tests with varying recycle rate 104

Executive Summary

Project Background

Alstom Power Inc. (Alstom), under U.S. DOE/NETL Cooperative Agreement No. DE-NT0005290, is conducting a development program to generate detailed technical information needed for application of oxy-combustion technology. The program is designed to provide the necessary information and understanding for the next step of large-scale commercial demonstration of oxy combustion in tangentially fired boilers and to accelerate the commercialization of this technology. The main project objectives include:

- Design and develop an innovative oxyfuel system for existing tangentially-fired boiler units that minimizes overall capital investment and operating costs.
- Evaluate performance of oxyfuel tangentially fired boiler systems in pilot scale tests at Alstom's 15 MW_{th} tangentially fired Boiler Simulation Facility (BSF).
- Address technical gaps for the design of oxyfuel commercial utility boilers by focused testing and improvement of engineering and simulation tools.
- Develop the design, performance and costs for a demonstration scale oxyfuel boiler and auxiliary systems.
- Develop the design and costs for both industrial and utility commercial scale reference oxyfuel boilers and auxiliary systems that are optimized for overall plant performance and cost.
- Define key design considerations and develop general guidelines for application of results to utility and different industrial applications.

The project was initiated in October 2008 and the scope extended in 2010 under an ARRA award. The project completion date was April 30, 2014. Central to the project is 15 MW_{th} testing in the BSF, which provided in-depth understanding of oxy-combustion under boiler conditions, detailed data for improvement of design tools, and key information for application to commercial scale oxy-fired boiler design. Eight comprehensive 15 MW_{th} oxy-fired test campaigns were performed with different coals, providing detailed data on combustion, emissions, and thermal behavior over a matrix of fuels, oxy-process variables and boiler design parameters. Significant improvement of CFD modeling tools and validation against 15 MW_{th} experimental data has been completed. Oxy-boiler demonstration and large reference designs have been developed, supported with the information and knowledge gained from the 15 MW_{th} testing.

The results from the 15 MW_{th} testing in the BSF and complimentary bench-scale testing are addressed in this volume (Volume II) of the final report. The results of the modeling efforts (Volume III) and the oxy boiler design efforts (Volume IV) are reported in separate volumes.

Basic oxy-combustion concept

Oxy-combustion is a promising near-term technology for CO_2 capture and sequestration from coal-fired power plants. The basic concept of oxy-combustion (also referred to as 'oxyfuel' and 'oxy-firing') is illustrated in Figure ES- 1.

The upper sketch in Figure ES- 1 shows normal air firing of coal to produce a flue gas which contains mostly nitrogen from the air, approximately 15% CO_2 and about 3% oxygen. There are processes to

remove the CO_2 from this flue gas for sequestration or use, but these processes have high energy consumption.

In oxy-combustion, the air is replaced by essentially pure oxygen from an air separation unit (ASU). With the nitrogen removed from the air, the combustion flue gas is now mostly CO_2 and moisture, and the volume of flue gas flow is reduced more than four-fold, as shown in the middle sketch in Figure ES- 1. The advantage of oxy-firing is that it is easier to dry and purify this concentrated flue gas to produce a pure CO_2 stream for sequestration or use. The trade-off for the easier CO_2 processing is the additional energy and cost for the air separation step.

Burning the fuel with pure oxygen would produce flame temperatures too high for practical boiler materials and could also result in severe ash slagging and fouling. Therefore, most oxy-fired designs recycle a portion of the high-CO_2 concentration flue gas to dilute the oxygen and control the furnace temperature, as shown in the bottom sketch in Figure ES- 1. Such an approach is mandatory for full dual air and oxy-fired operating capabilities or retrofit of an existing pulverized coal fired boiler.

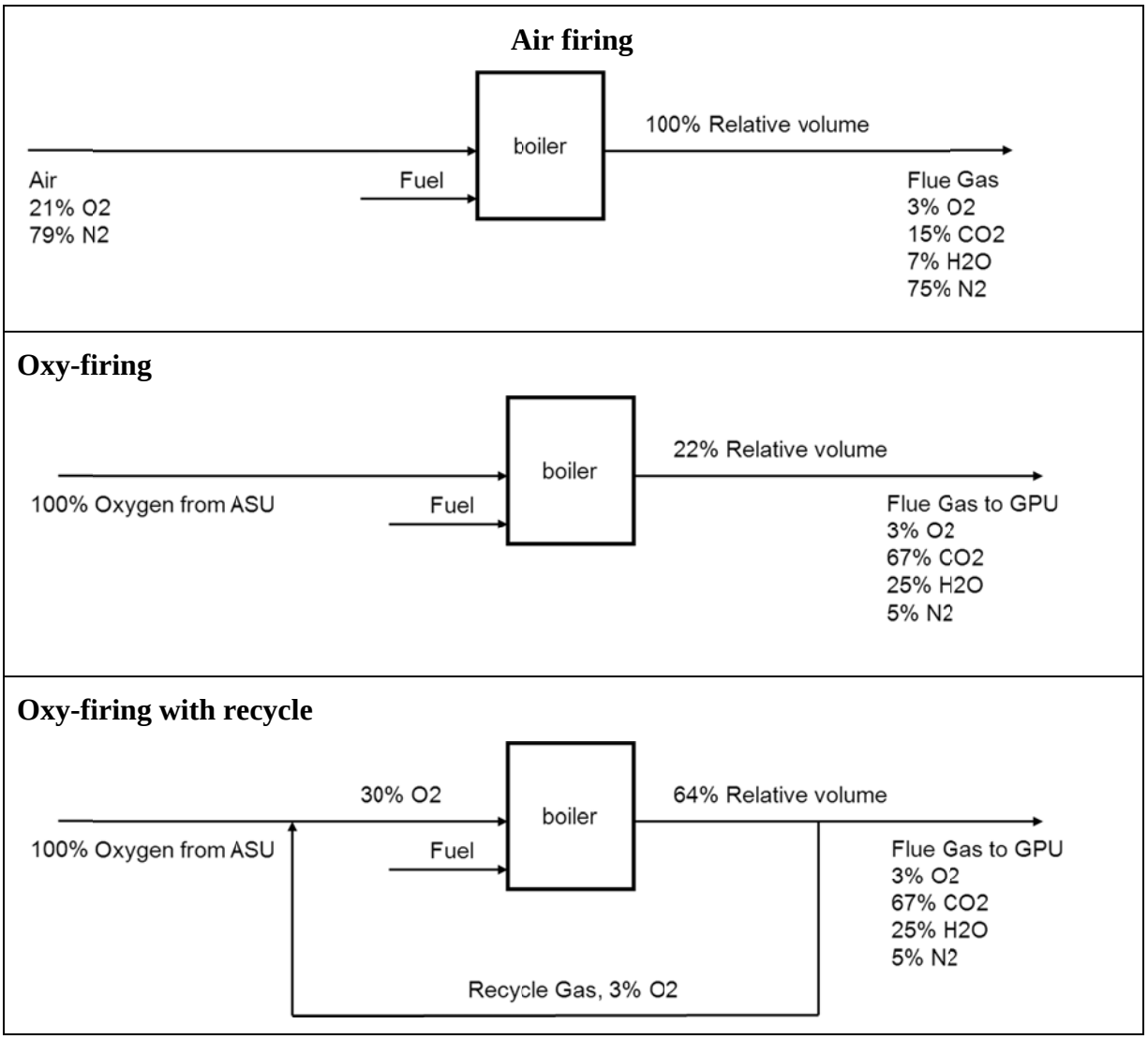

Figure ES- 1. Schematic of Oxy-Combustion Compared With Air Firing

Figure ES- 1 shows only the broad concepts of oxy-firing and flue gas recycle. Figure ES- 2 is a more detailed schematic that shows some of the options for flue gas recycle take-off location.

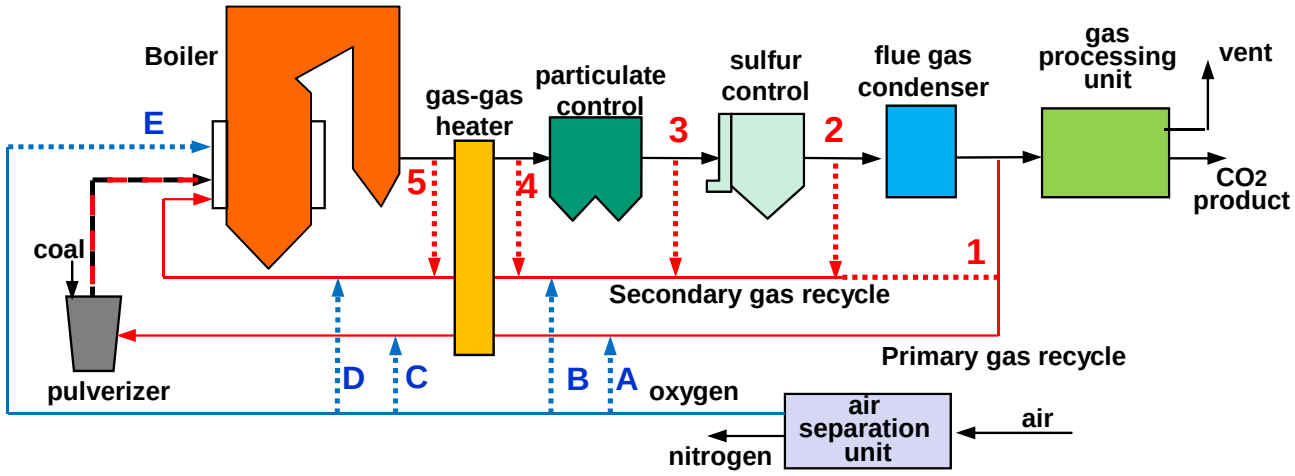

Figure ES- 2. Simplified Boiler Island Process Flow Diagram for Oxygen-fired PC Boiler

Typically two main recycle streams are used by the boiler system:

1. Primary gas recycle to provide coal drying for pulverization and to transport the pulverized fuel to the burners, and
2. Secondary gas recycle to mix with oxygen to provide the main oxidant gas for combustion.

There are several options for the location to take flue gas for recirculation back to the boiler. Figure ES- 2 identifies possible flue gas recycle take-off locations with dotted arrows numbered 1 through 5. The primary gas recycle is generally taken from after the flue gas condenser (FGC) (location 1), where it has been dried and is suitable for coal pulverization and transport. The moisture content of the dried flue gas might typically be in the range of 3 to 7%, depending on the temperature of available cooling water.

Secondary recirculation could be taken from any of the five locations in Figure ES- 2. The secondary recycle stream represents the bulk of the total recycle flow and has a strong impact on the composition of gas in the boiler. For high sulfur coals, recycle would typically be taken after flue gas desulfurization (FGD) and before the FGC (location 2); this gas is wet (20-30% water) but otherwise relatively clean, with a high percentage of particulate and sulfur dioxide removed. For low sulfur coal, it may be advantageous to recirculate from before the FGD (location 3). Recirculation from after the air heater (location 4) or even after the economizer (location 5) will contain particulates as well as sulfur dioxide. In general, recirculation taken from nearer the boiler would result in more buildup of particulate, sulfur, chlorides, alkali, etc., in the recirculation loop; on the other hand, the size of the downstream equipment can be reduced.

The bottom sketch in Figure ES- 1 shows a single oxidant stream with an oxidant concentration of 30%. Figure ES- 2 shows that, in fact, there will be multiple streams, perhaps with different oxygen contents. It is convenient to calculate the average oxygen concentration of all the oxidant streams if they were mixed. This is called the global O_2 value. The global O_2 is an indication of the overall amount of flue gas recirculation (FGR) – when more flue gas is recycled, the incoming nearly pure oxygen from the ASU is diluted to a lower value in the oxidant stream. The global O_2 value also depends on the amount of excess O_2 in the recycled flue gas.

Boiler Simulation Facility

Alstom's BSF is a tangentially-fired combustion test facility designed to replicate the time-temperature-stoichiometry history of a typical utility boiler. The BSF replicates all major attributes of a utility boiler including a "V" hopper, an arch, and appropriate (simulated) superheater, reheater, and economizer surfaces. The tangential firing system includes 3 levels of coal injection and two levels of separate overfire air. The typical firing capacity for pulverized coal operation is 15 MW_{th}. A photo of the BSF furnace with auxiliary equipment including oxygen supply systems is shown in Figure ES- 3.

The furnace walls and heat transfer surfaces of the BSF are cooled by boiling water open to the atmosphere. Refractory lining inside the furnace walls restricts heat absorption to maintain an appropriate furnace gas temperature throughout the combustion chamber. The refractory lining is specifically designed to provide the desired furnace heat absorption and resulting furnace temperatures for the test. The same refractory lining is used during both air and oxy-combustion tests for each test campaign.

BSF testing has a long successful history of supporting development and commercialization of Alstom's combustion systems and other technologies.

Modifications for Oxy-Firing

Under this project, testing and facility requirements were established and modifications made to the BSF for oxy-fired testing. Modifications included:

- Installation of an oxygen supply and injection system;
- Installation of multiple gas recirculation systems;
- Installation of a new fabric filter for particulate removal;
- Installation of a new NID™ sulfur removal system; and
- Installation of new instrumentation and controls.

Figure ES- 3. Boiler Simulation Facility

Modifications to provide oxy-fired operation and testing were completed in August 2009. Minor modifications were made between test programs to address issues identified during prior testing or prepare for specific tests

A process schematic of the modified BSF is shown in Figure ES- 4. The facility has the flexibility to operate under air or oxy-firing modes as well as different gas recycle configurations. The BSF includes major boiler island components including particulate and sulfur removal equipment and a flue gas condenser to dry primary recycle for coal transport.

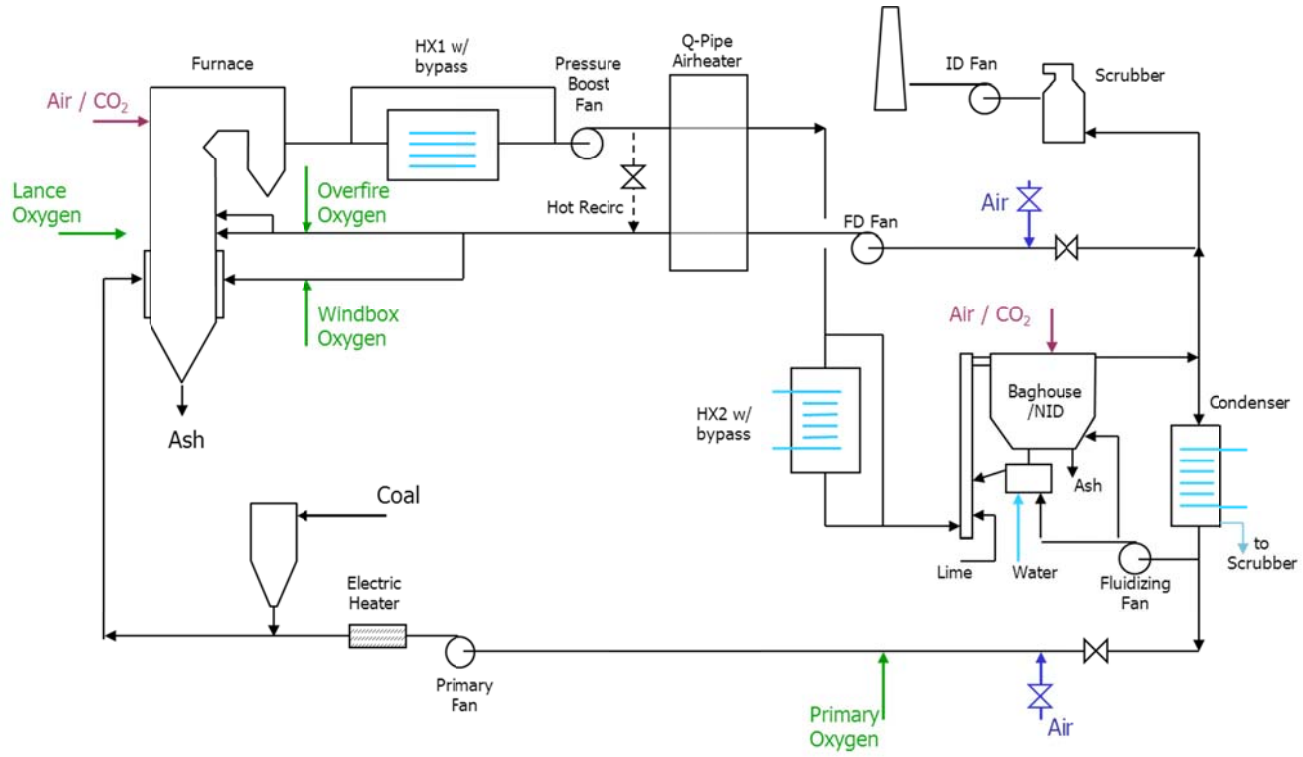

Figure ES- 4. BSF process sketch

Oxygen can be added in several locations as shown in Figure ES- 4. A supplemental oxygen injection system is used for more precise location of a portion of the oxygen.

Test Campaigns

From September 2009 through November 2012, eight oxy-combustion test campaigns were executed covering a broad range of fuels, process scenarios, and boiler design and operating conditions. Table ES- 1 lists the test campaigns executed in the BSF. Test campaign 5 consisted of three separate campaigns which together constitute the second generation testing.

Table ES- 1. BSF test campaigns

Campaign	Test Fuel	Mine	Test Date
1	PRB sub-bituminous	Black Thunder	September 3 to 12, 2009
2	Low sulfur bituminous	Fola	January 18 to February 4, 2010
3	High sulfur bit.	Prairie Eagle	April 25 to May 1, 2010
4	North Dakota lignite	Falkirk	October 4 to October 9, 2010
6 *	Schwarze Pumpe lignite	Lusation	July 11 to 18, 2011
5-1	Low sulfur bit.	Fola	December 7 to 16, 2011
5-2	PRB sub-bit.	Black Thunder	September 23 to 29, 2012
5-3	High sulfur, high chlorine bit.	Gallatia	October 31 to November 6, 2012

* Campaign 6 was moved up in the schedule to precede Campaigns 5, but the original numbering was retained.

Analyses of all as-fired coals are shown in Table ES- 2. These are averages of several analyses across the test series. Additional characterizations of some of the test fuels are described further below.

Table ES- 2. Average coal analyses for each campaign

Test campaign	1	2	3	4	6	5-1	5-2	5-3
Fuel	PRB	WV Fola	IL Hi S	ND Lignite	Schwarze Pumpe Lignite	WV Fola 2nd Gen	PRB 2nd Gen	Hi S 2nd Gen
Proximate analysis, wt % as fired								
Moisture	20.57	1.36	6.00	24.43	13.67	1.28	19.53	3.18
Ash	5.29	11.69	9.69	11.87	5.22	13.67	5.79	8.79
Volatiles	34.24	31.81	38.26	33.82	46.88	33.44	34.79	38.04
Fixed Carbon	39.91	55.29	46.05	29.87	34.23	51.61	39.89	50.00
SUM	100.00	100.14	100.00	100.00	100.00	100.00	100.00	100.00
HHV, BTU/lb	9364	13018	11873	7474	8998	12686	9675	12876
Ultimate analysis, wt % as fired								
Moisture	20.57	1.36	6.00	24.43	13.67	1.28	19.53	3.18
Hydrogen	3.74	4.85	4.47	3.01	4.02	4.76	3.76	4.76
Carbon	54.81	72.50	66.41	44.95	54.10	71.36	56.67	71.49
Sulfur	0.28	0.88	3.12	0.73	0.62	0.89	0.28	2.63
Nitrogen	0.79	1.46	1.33	0.81	0.63	1.49	0.47	1.47
Oxygen (diff)	14.52	7.26	8.98	14.20	21.74	7.67	13.50	7.68
Ash	5.29	11.69	9.69	11.87	5.22	13.67	5.79	8.79
SUM	100.00	100.00	100.00	100.00	100.00	101.10	100.00	100.00
Ash Oxide Analysis, wt % of ash								
SiO2	34.56	56.30	50.85	41.99	14.78	54.10	37.87	46.72
Al2O3	16.05	30.78	20.53	13.96	4.37	34.18	18.87	19.62
BaO	0.57	0.08	0.04	0.55	--	0.06	0.36	0.04
Fe2O3	6.16	5.58	15.56	6.47	23.00	4.07	5.94	16.48
TiO2	1.29	1.78	0.94	--	0.18	1.21	1.20	0.83
Mn3O4	0.03	0.02	0.04	0.08	0.29	0.01	0.03	0.05
CaO	19.72	0.84	3.52	14.84	25.89	0.99	17.86	4.84
MgO	4.23	0.82	0.96	4.50	9.59	0.72	3.79	0.96
Na2O	1.24	0.23	1.02	1.56	0.01	0.22	1.08	0.98
K2O	0.50	2.67	2.11	1.93	0.17	2.80	0.57	1.86
P2O5	0.81	0.15	0.52	0.18	0.08	0.13	0.84	0.09
SO3	11.67	0.71	2.81	11.99	18.29	0.74	8.50	5.58
SrO	0.31	0.07	0.03	0.31	--	0.04	0.28	0.03
Trace Metals, mg/kg dry coal								
Antimony	0.23	0.86	--	0.81	--	1.27	0.19	--
Arsenic	1.20	2.97	1.59	10.90	0.41	4.08	1.01	--
Barium	258.0	34.7	29.3	470.3	46.3	15.9	323.3	--
Beryllium	0.23	1.89	0.84	0.54	0.07	1.86	0.21	--
Cadmium	0.08	0.09	0.32	0.13	--	0.08	0.09	--
Chromium	4.33	23.35	18.53	9.23	1.09	24.93	3.80	--
Iron	2902	4578	9150	7127	8827	4180	2783	--
Lead	2.30	10.12	--	3.80	--	--	--	--
Mercury	0.06	0.12	0.07	0.09	0.05	0.13	0.06	0.06
Nickel	4.47	15.00	9.89	4.63	0.63	16.62	3.21	--
Silver	0.07	0.14	0.09	0.13	--	0.12	0.08	--
Strontium	176.46	64.65	20.03	417.50	128.67	13.27	165.67	--
Thallium	--	0.34	0.56	--	--	0.37	0.07	--
Titanium	519.5	1251.8	478.3	513.3	67.6	1168.3	433.0	--
Vanadium	13.73	36.75	27.60	18.20	1.55	46.17	12.35	--

Test campaign 1 – Powder River Basin subbituminous

Test campaign 1 focused on testing the most promising oxy design concepts selected during preliminary studies. Baseline air-fired testing was initially conducted to establish comparative

performance and emission data for the test coal. The selected design options were each tested in the BSF over a range of conditions with the objective of optimizing overall performance and emissions. Operating variables assessed included excess total oxygen, burner zone staging, and air in-leakage. Firing system design variables included FGR take-off location, FGR stream flow rates and injection locations, oxygen concentration in different input streams, fuel and oxidant injection parameters.

Test campaign 2 – low sulfur bituminous

Test campaign 2 focused on the most important operating and design parameters identified during the first test campaign and furnace measurements expanded to better understand the impacts. Operating variables assessed included excess total oxygen, burner zone staging, and recycle rate. Additional heat flux measurements around the furnace were taken. Like the first test campaign, baseline air-fired data was initially conducted to establish comparative performance and emission data for the test coal. The NID™ dry scrubbing system was shaken-down and tested in preparation for the following campaign 3.

Test campaign 3 – high-sulfur Illinois bituminous

This program, as originally proposed to the DOE, included assessment of very high sulfur levels by spiking sulfur to simulate high sulfur coal. With additional funding from the Illinois Clean Coal Institute (ICCI), test campaign 3 was added to the program to allow for actual testing with a high sulfur coal to provide realistic combustion conditions and improve the reliability of the data as well as greatly expand the amount of information that can be collected. Of particular interest were the SO_2 and SO_3 concentrations that built up due to the recycle of flue gas according to the level of sulfur capture. Like the first test campaign, baseline air-fired data was initially conducted to establish comparative performance and emission data for the test coal. The NID™ dry scrubbing system was utilized to capture sulfur in the recycle stream. Combustion testing during test campaign 3 focused on methods to adjust and control the heat flux profile during oxy-firing.

Test campaign 4 – North Dakota lignite

Test campaign 4 was also added to the original DOE program, with support of the North Dakota Industrial Commission, Lignite Research Council. Test campaign 4 focused on characterizing the oxy-combustion performance of North Dakota lignite. Particular focus was given to gaseous mercury concentrations that could build up during oxy-firing according to the level of mercury capture from the recycled flue gas in the baghouse. To understand the fate of SO_3 in the boiler, tests were conducted spiking SO_3 into the recycle stream. Like the first three test campaigns, baseline air-fired data was initially conducted to establish comparative performance and emission data for the test coal. The impact of operating and firing system design variables on thermal performance and emissions was assessed over a series of test points.

Test campaign 6 – Schwarze Pumpe lignite

Test campaign 6 focused on establishing a link between tests run at the tangentially-fired 15 MW_{th} oxy-fired BSF and the single burner down-fired 30 MW_{th} oxy-combustion pilot plant at Vattenfall's Schwarze Pumpe station. The Schwarze Pumpe oxy pilot is the world's first complete technology path for CO_2 capture, including an ASU and CO_2 processing plant. The experience from oxy combustion tests with the same fuel at the two facilities allows for a comparison between emissions, thermal data, and performance between the two facilities. Test data from the 15MW_{th} BSF and the 30MW_{th} oxy pilot plant has been used for refinement and validation of CFD codes under this project. Parameters

varied during BSF testing include firing rate, recycle rate, staging, and excess oxygen. Tests were selected to match conditions from Schwarze Pumpe and from prior BSF tests.

Test campaign 5-1 – 2nd generation, low sulfur bituminous

Test campaign 5-1 was conducted with the same West Virginia low sulfur bituminous coal used during test campaign 2. Two close coupled recirculation systems were installed: 1) a single large ejector driving all the gas recirculation for the windbox secondary oxidant, and 2) four smaller ejectors driving recirculation utilizing a supplemental oxygen supply.

Test campaign 5-1 focused on three second generation concepts: close-coupled flue gas recirculation, use of oxygen driven ejectors to recirculate flue gas, and a compressed firing zone.

Test campaign 5-2 – 2nd generation, PRB sub-bituminous

Test campaign 5-2 was conducted with the same PRB sub-bituminous coal used during test campaign 1. A flue gas slip stream was installed to investigate the control of SO_3 and Hg in oxy-combustion flue gas. Inlet and outlet sampling systems were set up using an inertial separation probe (ISP) and a feed system was set up to add sorbents. Slip-stream testing was done to evaluate mercury control. Also tests were done with nitric oxide added to the flue gas recycle returning to the BSF burner/windbox and separate overfire ports to investigate NO_x reduction in the furnace.

Test campaign 5-3 – 2nd generation, high sulfur bituminous

Test campaign 5-3 was conducted with a high sulfur, high chlorine bituminous coal from Illinois (though not the same fuel used in test campaign 3). Slip-stream testing was done to evaluate acid-gas control and further nitric oxide injection tests were done. Other tests included increased firing rate, low excess O_2, and heat flux optimization on oxy-firing.

Fuels Characterization

Four of the fuels fired in the BSF campaigns (Table ES- 2) were more thoroughly characterized in a bench scale program:

- Black Thunder Coal (BTC), the Powder River Basin (PRB) sub-bituminous coal from Campaign 1
- Fola Coal (WVC), the West Virginian bituminous coal from Campaign 2
- Prairie Eagle Coal (ILC), the high sulfur Illinois No. 6 bituminous coal from Campaign 3
- Schwarze Pumpe Coal (SPC), the German lignite from Campaign 6

The goal of the bench scale testing was to:

a) Characterize the combustion properties of BSF test fuels under both air, and oxy-combustion conditions.
b) Characterize the devolatilization and gasification properties of BSF test fuels.
c) Characterize ash from BSF test fuels under air and oxy-combustion conditions.

Drop Tube Furnace System

Alstom's Drop Tube Furnace System (DTFS) was used to support the bench scale characterization. The DTFS (Figure ES- 5) comprises a 1-inch diameter horizontal tube gas preheater and a 2-inch inner

diameter vertical tube test furnace for providing controlled temperature conditions. Both tubes are electrically heated with silicon carbide elements and are rated at 2800 °F. The DTFS is used to study pyrolysis, combustion, and gasification of coals and/or chars.

The principle operation of the DTFS is as follows. Size graded fuel is introduced with a small amount of carrier gas into the hot reaction zone of the test furnace through a water-cooled fuel injector. A preheated secondary gas stream is introduced around the primary stream. Injection of fuel particles into the hot gas stream results in a rapid heating of the particles to the prevailing gas temperature (at a rate of the order of 10^4 °C/sec). Following the rapid heating period, pyrolysis, gasification, and/or combustion of particles occur for a specific time. Then all reactions are rapidly quenched. Solid products are separated from the gaseous products in a filter housing, and an aliquot of the effluent gas sample is sent to a pre-calibrated Gas Analysis System.

The solid products collected at various locations along the axis of the DTFS reaction zone can be analyzed to determine solid conversion efficiencies.

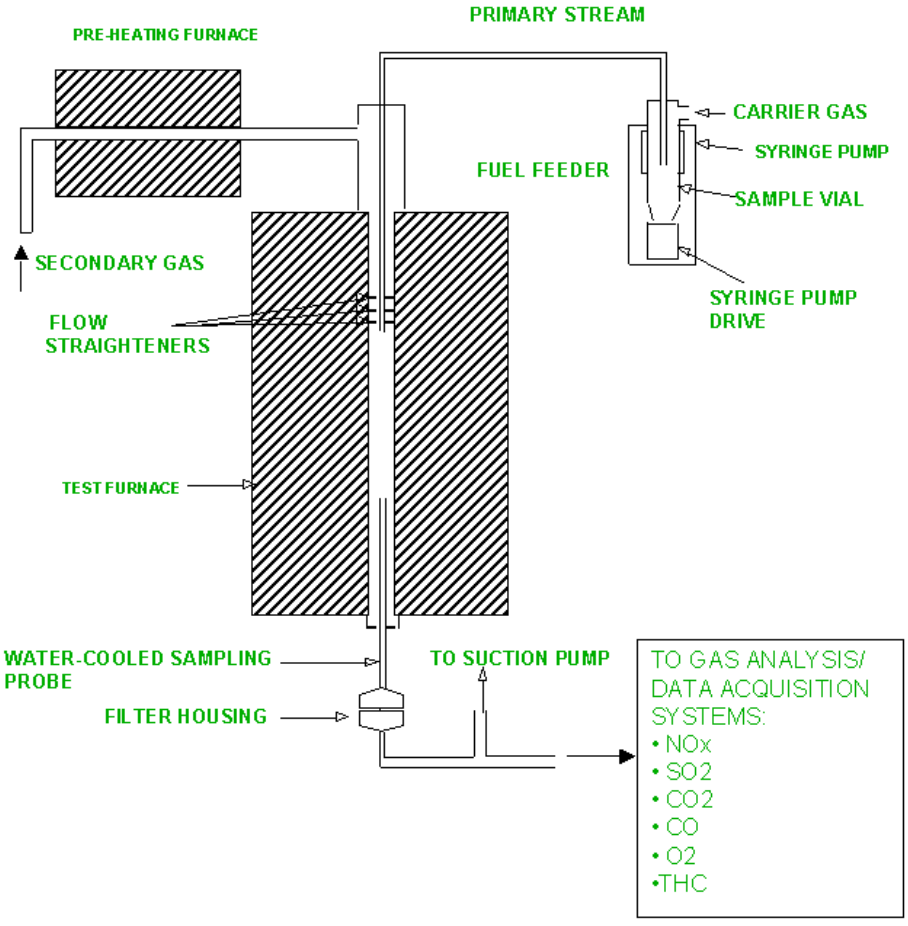

Figure ES- 5. Schematic of DTFS-1

In this program, the DTFS was used for 5 purposes:

1. Generate ash in air or simulated oxy conditions for further analysis.
2. Generate char in nitrogen or argon for further tests.
3. Gasify coal in CO_2.
4. Gasify char in CO_2 or 30% CO_2 / balance N_2.
5. Combust char in 3% O_2 / balance N_2 or CO_2.

The char samples for BET surface area and thermogravimetric analyses and the ash analyzed by CCSEM, discussed below were generated in the DTFS.

Surface Area-Reactivity Relationships

The principle of physical absorption of gases is used to determine specific surface areas of the solid fuels. BET surface areas of the parent coals and the chars generated in the DTFS are in Table ES- 3.

Table ES- 3. Surface Area by BET

Fuel	BET Surface Area (m^2/g)	
	coal	char
Schwarze Pumpe	1.8	295.8
Black Thunder PRB	3.6	127.4
Prairie Eagle	2.0	28.7
WV Fola	0.8	11.0

As expected, the chars have greater surface areas than the parent fuels and the Schwarze Pumpe lignite and the Black Thunder sub-bituminous chars have much greater surface areas than the bituminous chars.

Petrographic Analysis

Petrographic analysis can be used to describe coal's origin, structure, composition, changes and classification. For example, ISO currently uses vitrinite reflectance to rank coals from around the world. Coal petrography can also be used to evaluate the combustion kinetic behavior of coals. For instance, the Mean Max Vitrinite Reflectance measured for the four fuels are

Schwarze Pumpe	Black Thunder	Prairie Eagle	WV Fola
0.35	0.35	0.54	0.88

This ranking is broadly consistent with the BET surface area and other measures of coal reactivity.

Thermogravimetric Analysis

Several characterization tests were done in Alstom's TGA:

- non-isothermal combustion of parent coals in air heating at 10 °C/min to 700 °C,
- isothermal combustion of char in air at 700 °C,
- isothermal gasification of char in CO_2 at 900 °C.

The TGA combustion results on the test coals and chars are also generally consistent with BET surface area measurements and petrographic analysis. The same relative ranking of reactivity of the test fuels is indicated by all of these tests (Schwarze Pumpe most reactivity, then Black Thunder, Prairie Eagle,

and WV Fola the least reactivity.) TGA gasification results also show the same relative fuel reactivity ranking for gasification as was for measured for combustion reactivity.

DTFS Pyrolysis Efficiencies

The devolatilization yield from the high heat up rates in the drop tube is expected to differ from the standard ASTM volatile matter. The high temperature yield from the drop tube is typically greater than ASTM volatile matter and is more appropriate to use for modelling of combustion in a pulverized fuel furnace.

DTFS Combustion Efficiencies

The DTFS chars combustion rates were studied at three gas temperatures (1800, 2200, and 2650°F) in the presence of oxygen partial pressure of 0.03 atmosphere in both a nitrogen and carbon dioxide balance. The DTFS results show the same relative reactivity ranking between test fuels. Results show more rapid burnout rates under oxy-combustion conditions (O_2/CO_2 atmosphere) than in air (O_2/N_2 atmosphere). Figure ES- 6 is provides an example of the higher burnout rates with O_2/CO_2 at 2650°F furnace temperatures. Differences in combustion rates between air and oxy-combustion were greatest at 2650°F, the highest temperature studied. The higher rates during oxy-combustion may be attributed to gasification reactions between char and CO_2 and H_2O, which are at much higher concentration during oxy-combustion compared with air combustion.

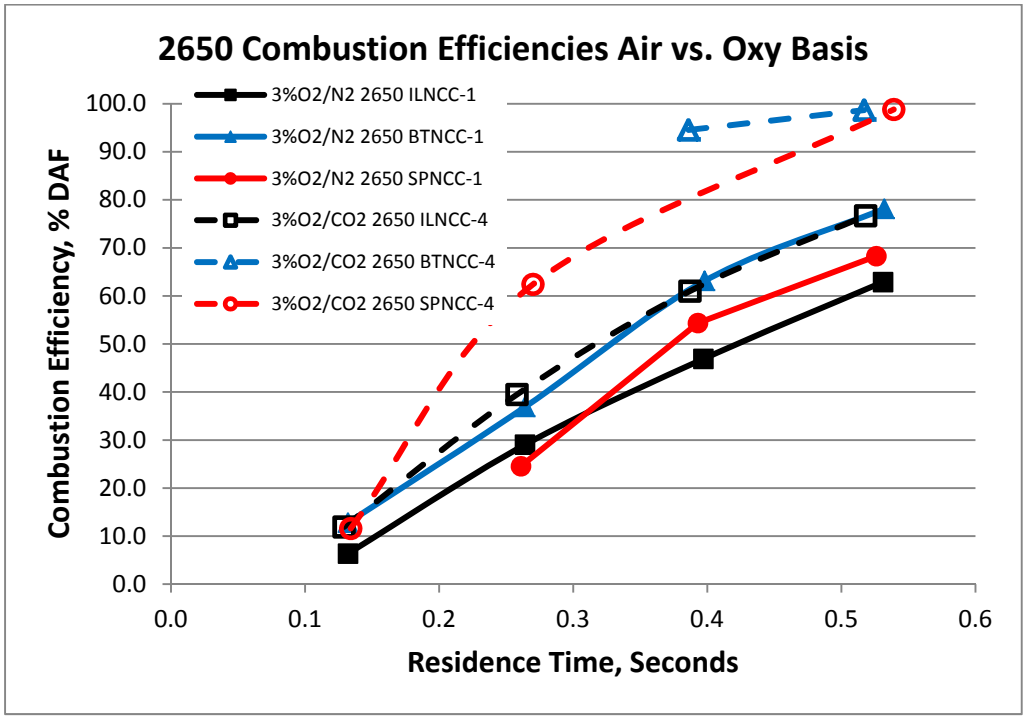

Figure ES- 6. Char Combustion Efficiencies at 2650°F

DTFS Gasification Efficiencies

The gasification of test coals was studied in 100% CO_2 at 2650°F gas temperature and used to calculate kinetic rates. Gasification efficiency results are plotted in Figure ES- 7. Gasification rates

for the test fuel follow the same relative ranking as observed in the DTFS combustion studies and other reactivity measures.

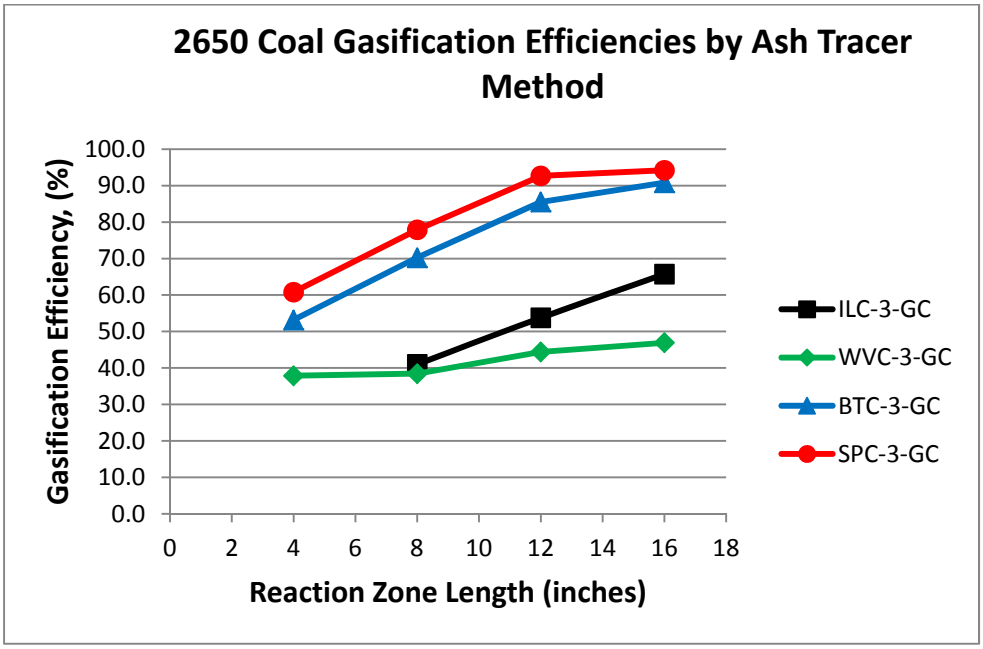

Figure ES- 7. Parent Coal Gasification Efficiencies by Ash Tracer

Computer Controlled Scanning Electron Microscopy (CCSEM)

CCSEM with backscattered electron imaging combined with automated particle recognition and chemical analysis was used to determine the composition, size and abundance of mineral types DTFS ash generated under air and oxy-fired conditions. The CCSEM method characterized approximately 3,000 ash particles. The compositional data was used to type the particles based on composition.

The CCSEM results revealed significant differences in the size distribution of the ashes generated by the four test coals as well as significant compositional difference between individual particles. This information is useful to assess ash deposition and erosion potential and was in general consistent with the performance observed during the 15 MW_{th} BSF testing. Although there were significant differences between coals, the ashes from the same coal were generally similar when produced under either air or oxy-fired conditions. This is again consistent with the similar ash slagging and fouling behavior observed during the 15 MW_{th} testing.

15 MW_{th} Test Results

Combustion Performance

For oxy-combustion, there is an economic advantage to reduce the excess oxygen supply and to reduce the amount of flue gas recycle. Reducing the excess oxygen reduces the amount of oxygen required

from the ASU and reduces the purification costs for the CO_2 product gas. Reducing the amount of flue gas that is recirculated back to the boiler could reduce the size and cost of the boiler, the gas recirculation system and the downstream pollution control equipment, as well as reduce the parasitic power consumption.

Understanding the combustion impacts of reducing the amount of flue gas recycle and reducing the excess oxygen was an important objective of BSF testing. Reducing the amount of flue gas recycle impacts burner conditions/design parameters, furnace aerodynamics and combustion performance.

- Reducing the amount of flue gas recycle to the boiler reduces the amount of oxygen returning to the boiler. At a constant outlet oxygen concentration, as the amount of recycled flue gas decreases, the stoichiometric ratio of oxygen to coal will decrease.
- Reducing the flue gas recycle to the boiler also reduces the volumetric flow to the boiler. At constant injection compartment sizing, as the amount of recycled flue gas decreases, the effective velocity and momentum will be reduced.

Combustion performance was assessed in parametric tests during each test campaign. Generally the carbon monoxide emissions when oxy-firing were as low as or lower than during comparable air-fired conditions. In general, the results indicate the dominating factors for CO emissions during air and oxy-firing are the same for a particular coal: complete mixing of the overfire oxidant before significant flue-gas cooling and final oxygen partial pressure, expressed as oxygen concentration in the flue gas.

For all test fuels, it was possible to operate at less than 2% O_2 leaving the furnace without excessive CO emissions or unburned carbon loss during both air and oxy-firing. For the oxy-fired tests, well less than 0.5% of the heat input was lost due to unburned carbon, even at the lowest excess O_2 levels.

NO_x Emissions

The emission of nitrogen oxides (NO_x) is an environmental concern in the design and operation of traditional air-fired combustion power plants. In the oxy-combustion process, environmental emissions of NO_x must still meet regulatory limits, and there is the additional consideration for the operation of the flue gas processing unit and the quality of sequestered gas. Combustion changes and design flexibilities with the oxy-combustion process allow for new opportunities to control NO_x emissions. Understanding the impacts of firing system design and operation on NO_x emissions during oxy-combustion is a goal of this test program.

The formation of NO_x during combustion is a complex process, highly dependent upon the time-temperature-stoichiometric history inside the boiler as well as specific properties of the fuel being fired. Windbox stoichiometry is one of the key variables in a staged, low-NO_x firing system. For a constant total oxygen input to the boiler, as more oxygen (or air) is shifted to the overfire locations, the stoichiometry in the windbox decreases. The typical pattern for air firing is that the NO_x emissions decrease as more air is shifted to the overfire locations. At some point, the emissions level off, and may even increase if the windbox stoichiometry decreases further.

For all BSF test campaigns, baseline air-fired testing was conducted to establish comparative performance and emissions data for the test coal.

NO_x emissions measured during baseline air firing in the BSF were consistent with utility boiler experience. The net NO_x emissions on a mass (lb/hr) or thermal loading (lb/MMBtu) basis during oxy-firing were typically less than 50% of the NO_x levels during air firing at comparable firing conditions.

The NO_x concentrations (ppm) during oxy-firing were typically higher than during air firing due to the absence of atmospheric nitrogen.

Air-combustion and oxy-combustion tests show a strong dependence of NO_x emissions on windbox stoichiometry. In general, it was possible to reduce the NO_x levels to a greater extent with bituminous coals under oxy-firing than air-firing. NO_x levels as low as 0.05 lb/ MMBtu were obtained for all test coals under certain oxy-firing conditions in the BSF.

Air-firing shows a consistent decrease in NO_x emissions with decreasing outlet O_2. Oxy-combustion tests show little impact of excess oxygen on NO_x emissions. These results are consistent with an increase in thermal NO_x formation during air-combustion as the excess oxygen increases and minimal thermal NO_x formation during oxy-combustion due to the depletion of nitrogen. The lower amount of NO_x emitted from the boiler loop during oxy-firing compared to air firing is influenced by several factors including reduced thermal NO_x, changes in the combustion gas composition impacting NO_x chemistry, and reburning of NO_x returned to the boiler with flue gas recycle. Varying the amount of flue gas recycle would be expected to change the amount of reburning, but the effects may be confounded by changes in furnace temperatures and residence times.

To more clearly see the effect of reburning, a series of tests injecting extra NO_x (as NO) into the recycled flue gas during a number of test campaigns. Results show that with strongly reducing conditions in the furnace windbox zone, most of the NO added through the windbox was destroyed in the furnace. Much more of the NO added only to the OFA region made it through to the furnace outlet. This is expected, due to the less intense reducing conditions in this region. At higher windbox stoichiometries, there was also much less reduction of the injected NO added through the windbox. The determination that nearly all the recycled NO_x is reburned when injected into the deeply staged burner zone is an important consideration for extrapolation of the test results to commercial applications.

Sulfur Emissions

Under both air- and oxy-firing, nearly all of the sulfur in the coal will be released in the furnace. If the sulfur is not removed from the recycled flue gas, the concentration will be higher in oxy-firing due to the lack of nitrogen dilution. If sulfur is removed, then the concentration is diluted by the recycled flue gas. In both air- and oxy-firing, the rate of SO_2 leaving the system to the stack or GPU depends on the extent of removal in the flue gas scrubber.

As expected, without sulfur capture, SO_2 concentrations leaving the furnace were much higher during oxy-firing due to the lack of nitrogen dilution. The NID™ dry scrubbing system was very effective in removing SO_2 from the recycled flue gas, thereby reducing the SO_2 concentration leaving the furnace. The SO_2 capture efficiencies were similar during both air and oxy-firing. Somewhat higher concentration of carbonates were measured in the solids removed from the scrubbing system, however the level of CO_2 capture by the calcium sorbent did not appear to impact SO_2 capture.

Measurements of SO_3 were taken during air and oxy-fired testing during all of the test campaigns. The SO_3 concentration was substantially reduced when the NID™ was operating. The net conversion to SO_3, expressed as the SO_3-to-SO_2 ratio, varies for the different test coals, but was generally similar during both air and oxy-firing.

To investigate the fate of recycled SO_3, tests were done with SO_3 injected into the recycle stream. The results show the added SO_3 returning to the furnace did not contribute to an increased level at the

furnace outlet. The SO_3 was reduced in the high temperature firing zone to SO_2 (possibly first to more reduced species such as H_2S in the sub-stoichiometric windbox zone).

During the second generation testing with high sulfur, high chlorine coal, SO_3 control by sorbent injection was tested on a slipstream of flue gas from the BSF. Four sorbents were tested: trona, hydrated lime, sodium bicarbonate and magnesium oxide. Significant capture rates of acid gases were achieved before the boiler gas-gas preheater, allowing lower exit temperatures and greater boiler efficiencies. There was little difference in the performance of these sorbents under air and oxy-fired conditions.

Trace Metals Emissions

In most test campaigns, trace metal concentrations were measured at the furnace and baghouse outlets. Metals other than mercury were mostly removed in the baghouse.

Separate measurements on mercury speciation were done in Test Campaign 4 with North Dakota lignite. Mercury leaving the furnace is mostly in elemental form, and most is oxidized after passing through the baghouse. In hot recycle tests (from location 5 in Figure ES- 2), most of the mercury in the recycle stream had not yet oxidized.

In tests with powdered activated carbon (PAC), similar mercury removal was achieved in oxy-firing as those during air-firing under similar conditions.

Thermal Performance

In the oxy-combustion process, flue gas is recycled to the boiler to moderate the furnace temperatures and reduce peak heat flux. The quantity and distribution of recirculated flue gas and oxygen into the boiler will alter the heat release pattern in the combustor. Understanding and controlling this heat release pattern is an important goal of Alstom's oxy-combustion boiler development program.

The balance between furnace heat absorption and convection section heat absorption must be considered and the boiler designed appropriately. For retrofit applications, pressure part modifications can be minimized if existing furnace and convection section surfaces provide similar heat absorption during air and oxy-fired operation. For new applications, optimization of pressure part surfacing may be possible by further reducing gas recycle, but many factors must be considered that would limit this reduction. Some of the considerations associated with reducing gas recycle include higher peak heat fluxes requiring more cooling or use of high temperature materials, ash management and operational issues associated with the impact of higher temperatures on slagging and fouling behavior, and the impact of higher concentrations of corrosive constituents on fireside corrosion.

The furnace heat flux and heat absorption profiles can be controlled by a number of factors, including the gas recirculation rate, the distribution of recirculated gas, and the split of oxygen to the different windbox and overfire levels.

The left plot in Figure ES- 8 shows the effect of varying recirculation rate on the vertical heat flux profile during Test campaign 3 with high sulfur bituminous. For these tests, the total oxygen input was held constant and the quantity of gas recycle was varied. Furnace heat flux increased as the mass flow through the boiler decreased.

The plot on the right of Figure ES- 8 shows the percent of heat input absorbed in the furnace up to the outlet plane as the recycle rate changes. The heat absorbed decreases with higher recycle/lower global O_2. For this case, a global O_2 of about 28% matches the heat absorbed of the air fired case for the high

sulfur bituminous test fuel. For other fuels, the percent heat absorbed in the furnace varies, but in each case oxy-firing with a global O_2 of between 26 and 30% gave the same percentage heat absorption as air firing.

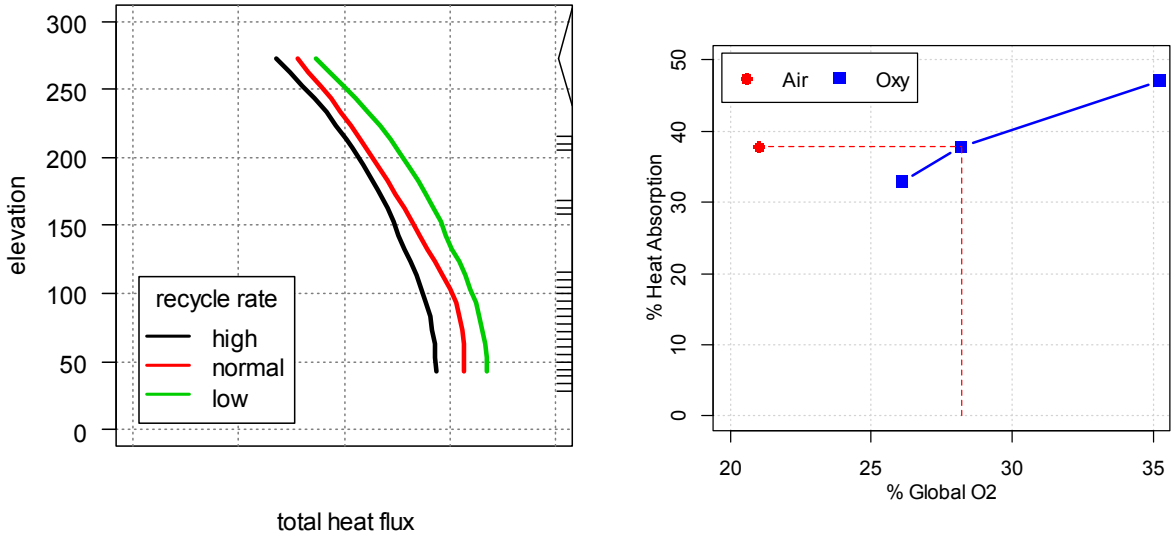

Figure ES- 8. Effect of recirculation rate, Illinois high sulfur bituminous

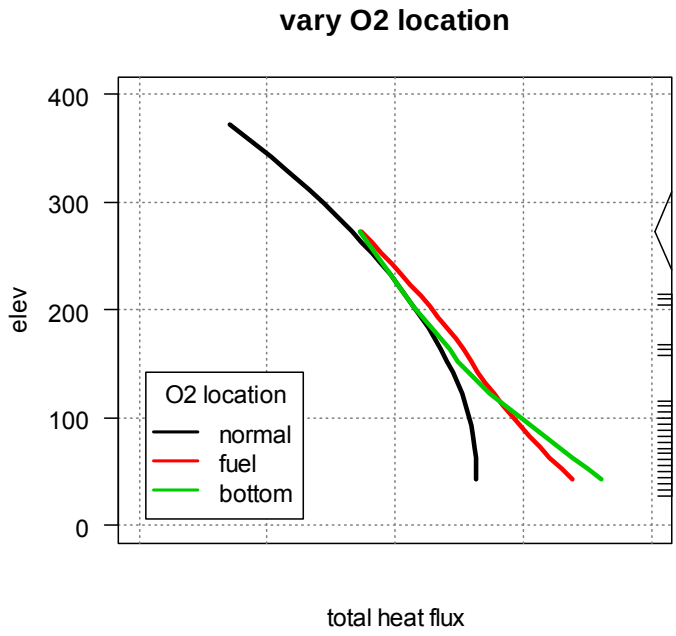

Figure ES- 9. Effect of varying oxygen distribution, Illinois high sulfur bituminous

Impacts of local compartment enrichment were also tested. Figure ES- 9 shows the results of one variation during the Illinois bituminous test campaign. In the "normal" test, oxygen was mixed in a specifically defined fashion with the flue gas recycle. In the next test, some oxygen was removed from the bulk oxygen addition and added to fuel compartments low in the windbox. Finally the oxygen was biased even more to the bottom compartments. In each case, the windbox stoichiometry was the same, but local oxygen enrichment was distributed differently. The heat flux in the lower furnace increased when oxygen input was shifted lower in the furnace and locally enriched in selected windbox compartments. Figure ES- 10 shows an example of the matching heat flux profiles for the North Dakota lignite long-term tests obtained by adjusting recycle rate and oxygen distribution into the furnace.

Results demonstrate that with the control of flue gas recycle and distribution of oxygen, furnace heat flux and boiler thermal performance during oxy-firing can be adjusted to match that for air firing.

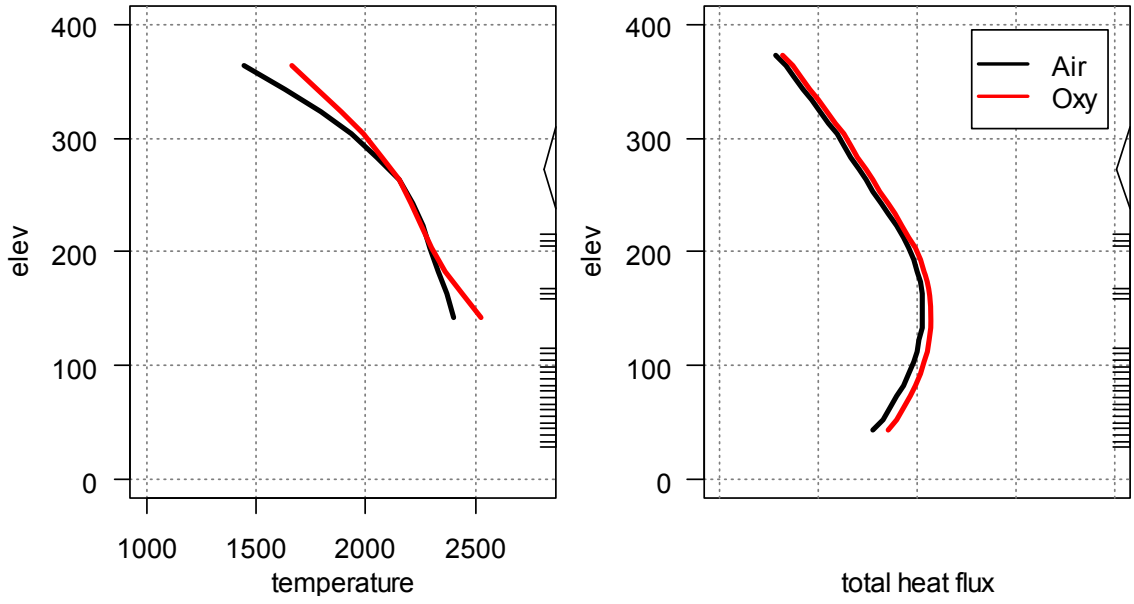

Figure ES- 10. Long-term temperature and heat flux profiles, ND lignite campaign

Conclusions

The 15 MW_{th} test program achieved all major objectives. The BSF was modified to allow effective and comprehensive evaluation of oxy-combustion impacts over a range of representative oxy-process and boiler design conditions. The BSF provided stable operation and permitted testing over the full range of matrix parameters desired. Eight comprehensive test campaigns were completed providing a wealth of detailed information covering a range of coal types and boiler operating parameters.

Results of the 15 MW_{th} testing demonstrate that there are no technical barriers restricting the continued development and commercialization of oxy-combustion from a boiler standpoint. Combustion performance, emissions, and thermal behavior (temperature, heat flux intensity, heat flux profile) can be controlled to similar levels as air firing. For a tangentially oxy-fired boiler, there are no major changes required to the current boiler design for oxy-firing. Boiler size and pressure part surfaces should only require minor modifications for oxy-fired retrofit applications. For new applications,

additional control under oxy-firing may be used to an advantage with innovative design concepts to improve oxy-fired boiler performance and costs.

The data generated during the test program has proven extremely useful for the refinement and validation of engineering design tools, including CFD and dynamic modeling. The test results have also provided the basis for the development of procedures and guidelines for oxy-boiler design. The extensive database generated under this program is not only valuable for Alstom design, but can used by other researchers and organizations to support their development efforts.

The results of this test program provide a sound foundation for oxy-boiler design and commercial-scale demonstration. These results along with other large-scale oxy-combustion test programs conducted around the world confirm the technical viability of this technology and the readiness to proceed to the final development step of commercial-scale demonstration.

1. Introduction

1.1 Project background

Alstom Power Inc. (Alstom), under U.S. DOE/NETL Cooperative Agreement No. DE-NT0005290, is conducting a development program to generate detailed technical information needed for application of oxy-combustion technology. The program is designed to provide the necessary information and understanding for the next step of large-scale commercial demonstration of oxy combustion in tangentially fired boilers and to accelerate the commercialization of this technology. The main project objectives include:

- Design and develop an innovative oxyfuel system for existing tangentially-fired boiler units that minimizes overall capital investment and operating costs.
- Evaluate performance of oxyfuel tangentially fired boiler systems in pilot scale tests at Alstom's 15 MW_{th} tangentially fired Boiler Simulation Facility (BSF).
- Address technical gaps for the design of oxyfuel commercial utility boilers by focused testing and improvement of engineering and simulation tools.
- Develop the design, performance and costs for a demonstration scale oxyfuel boiler and auxiliary systems.
- Develop the design and costs for both industrial and utility commercial scale reference oxyfuel boilers and auxiliary systems that are optimized for overall plant performance and cost.
- Define key design considerations and develop general guidelines for application of results to utility and different industrial applications.

To address these objectives, the project is structured into nine main tasks.

Task 1	Project Management
Task 2	Process and Firing System Design Screening
Task 3	Bench Scale Testing
Task 4	Large Pilot Scale Combustion Testing
Task 5	Data Analysis and Documentation
Task 6	Model Simulations
Task 7	Oxy Boiler Guidelines
Task 8	Demonstration of Oxy Boiler Design, Performance and Costs
Task 9	Commercial Reference Oxy Boiler Design, Performance and Costs

The project was initiated in October 2008 and the scope extended in 2010 under an ARRA award. The project completion date was April 30, 2014. Under Task 4, eight comprehensive 15 MW_{th} oxy-fired test campaigns were performed in Alstom's BSF with different coals, providing detailed data on combustion, emissions, and thermal behavior over a matrix of fuels, oxy-process variables and boiler design parameters. This work is central to the project, providing in-depth understanding of oxy-combustion, assessment of boiler performance impacts, detailed data for improvement of design tools, and key information for application to commercial scale oxy-fired boiler design. Significant improvement of CFD modeling tools and validation against 15 MW_{th} experimental data has been achieved. Oxy-boiler demonstration and large utility and industrial reference designs have also been developed.

This chapter of Volume 2 of the final report addresses the results from the 15 MW_{th} testing. Results of modeling efforts are reported separately in Volume 3, and the design, performance and costs of the demonstration and reference oxy-boiler systems are reported in Volume 4.

1.2 Basic oxy-combustion concept

Oxy-combustion is a promising near-term technology for CO_2 capture and sequestration from coal-fired power plants. The basic concept of oxy-combustion (also referred to as 'oxyfuel' and 'oxy-firing') is illustrated in Figure 1-1.

The upper sketch in Figure 1-1 shows normal air firing of coal to produce a flue gas which contains mostly nitrogen from the air, approximately 15% CO_2 and about 3% oxygen. There are processes to remove the CO_2 from this flue gas for sequestration or use, but these processes have high energy consumption.

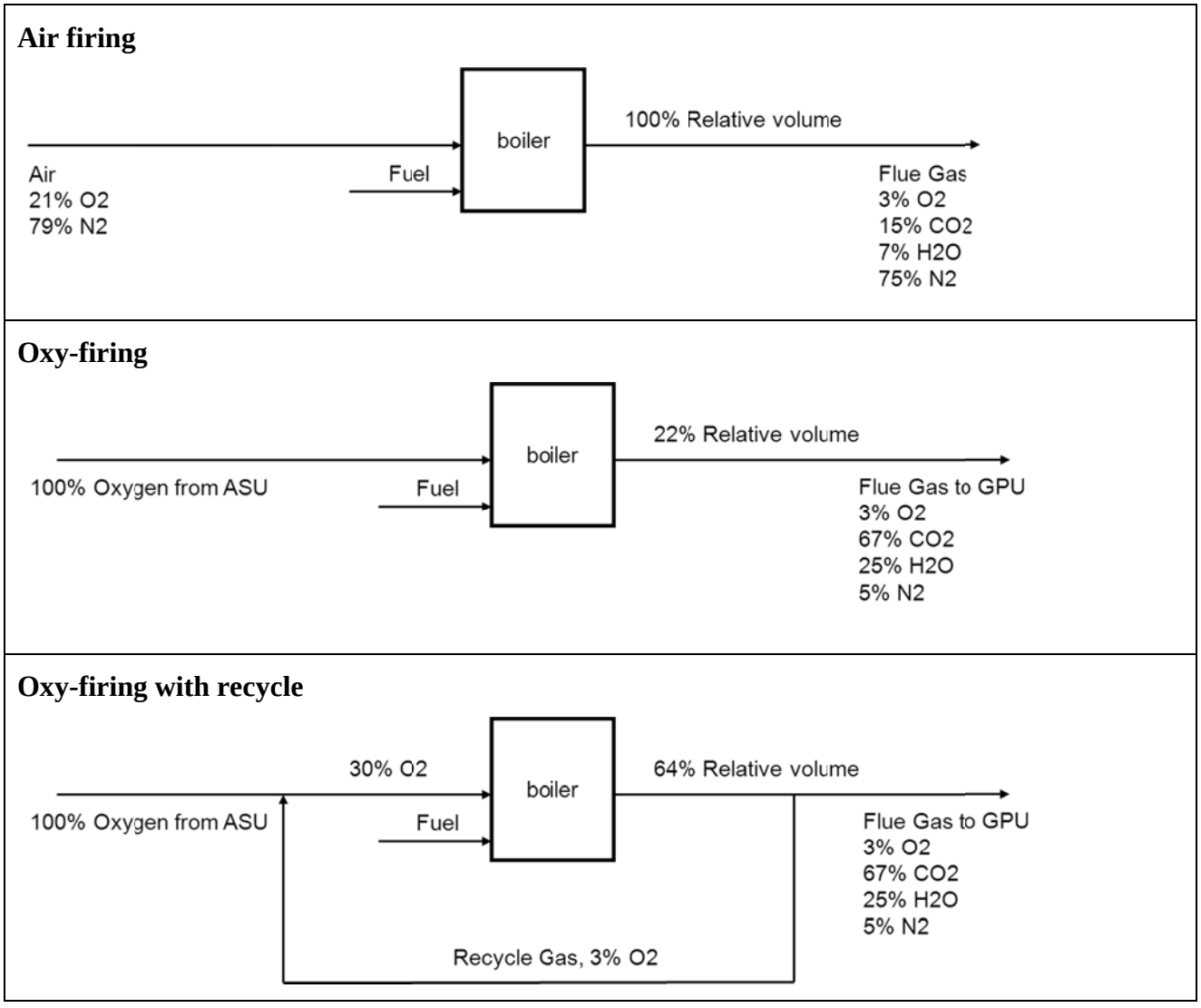

Figure 1-1. Schematic of Oxy-Combustion Compared With Air Firing

In oxy-combustion, the air is replaced by essentially pure oxygen from an air separation unit (ASU). With the nitrogen removed from the air, the combustion flue gas is now mostly CO_2 and moisture, and the volume of flue gas flow is reduced more than four-fold, as shown in the middle sketch in Figure 1-1. The advantage of oxy-firing is that it is easier to dry and purify this concentrated flue gas to produce a pure CO_2 stream for sequestration or use. The trade-off for the easier CO_2 processing is the additional energy and cost for the air separation step.

Burning the fuel with pure oxygen would produce flame temperatures too high for practical boiler materials and could also result in severe ash slagging and fouling. Therefore, most oxy-fired designs recycle a portion of the high-CO_2 concentration flue gas to dilute the oxygen and control the furnace temperature, as shown in the bottom sketch in Figure 1-1. Such an approach is mandatory for full dual air and oxy-fired operating capabilities or retrofit of an existing pulverized coal fired boiler.

1.3 Oxy-firing configuration options

Figure 1-1 shows only the broad concepts of oxy-firing and flue gas recycle. Figure 1-2 is a more detailed schematic that shows some of the options for flue gas recycle take-off location.

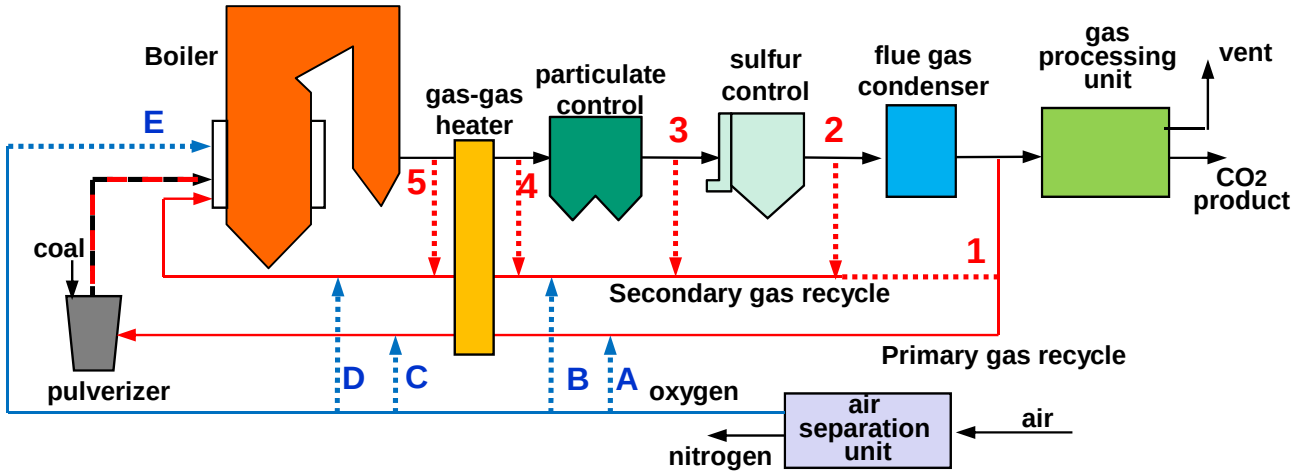

Figure 1-2. Simplified Boiler Island Process Flow Diagram for Oxygen-fired PC Boiler

Typically two main recycle streams are used by the boiler system:

1. Primary gas recycle to provide coal drying for pulverization and to transport the pulverized fuel to the burners, and
2. Secondary gas recycle to mix with oxygen to provide the main oxidant gas for combustion.

There are several options for the location to take flue gas for recirculation back to the boiler. Figure 1-2 identifies possible flue gas recycle take-off locations with dotted arrows numbered 1 through 5. The primary gas recycle is generally taken from after the flue gas condenser (FGC) (location 1), where it has been dried and is suitable for coal pulverization and transport. The moisture content of the dried flue gas might typically be in the range of 3 to 7%, depending on the temperature of available cooling water.

Secondary recirculation could be taken from any of the five locations in Figure 1-2. The secondary recycle stream represents the bulk of the total recycle flow and has a strong impact on the composition of gas in the boiler. For high sulfur coals, recycle would typically be taken after flue gas

desulfurization (FGD) and before the FGC (location 2); this gas is wet (20-30% water) but otherwise relatively clean, with a high percentage of particulate and sulfur dioxide removed. For low sulfur coal, it may be advantageous to recirculate from before the FGD (location 3). Recirculation from after the air heater (location 4) or even after the economizer (location 5) will contain particulates as well as sulfur dioxide. In general, recirculation taken from nearer the boiler would result in more buildup of particulate, sulfur, chlorides, alkali, etc., in the recirculation loop; on the other hand, the size of the downstream equipment can be reduced.

There are also several possibilities for adding the oxygen into the boiler system. Some or all of the oxygen can be mixed with the primary and/or secondary recycled flue gas. However, depending on the resultant oxygen concentration and the primary/secondary stream temperature, use of conventional materials such as carbon steel may not be suitable. Mixing a portion of the oxygen with the recycled flue gas before the gas-gas preheater provides an effective way of heating oxygen to improve boiler efficiency and also improve the performance of the gas-gas preheater.

1.4 Global O_2 concentration to boiler

The bottom sketch in Figure 1-1 shows a single oxidant stream with an oxidant concentration of 30%. Figure 1-2 shows that, in fact, there will be multiple streams, perhaps with different oxygen contents. It is convenient to calculate the average oxygen concentration of all the oxidant streams if they were mixed. This is called the global O_2 value. The global O_2 is an indication of the overall amount of flue gas recirculation (FGR) – when more flue gas is recycled, the incoming nearly pure oxygen from the ASU is diluted to a lower value in the oxidant stream. The global O_2 value also depends on the amount of excess O_2 in the recycled flue gas.

This relationship between recycle ratio, O_2 concentration in the flue gas and global O_2 is shown in Figure 1-3. The recycle rate can be expressed as the ratio of recycle flow to net flue gas flow (recirculation ratio) or the ratio of recycle flow to total flue gas flow (recirculation fraction). With fixed O_2 input and a desired O_2 concentration in the flue gas leaving the furnace (i.e., furnace stoichiometry), global O_2 level decreases as the recycle rate increases.

1.5 Stoichiometric oxygen requirement

For both air firing and oxy-firing, excess oxygen must be supplied to the furnace to ensure the burnout of the fuel. For air firing, the excess air might be in the range of 15 to 22% of the stoichiometric amount of air. This results in a flue gas containing about 3 to 4% O_2.

For oxy-combustion designs, it is typical to provide enough excess oxygen from the ASU (including any in-leakage to the furnace) to also produce a flue gas containing about the 3 to 4% O_2. Maintaining the same oxygen concentration in the flue gas provides similar oxygen availability for fuel burnout. This requires about 4 to 5% excess oxygen over the stoichiometric amount.

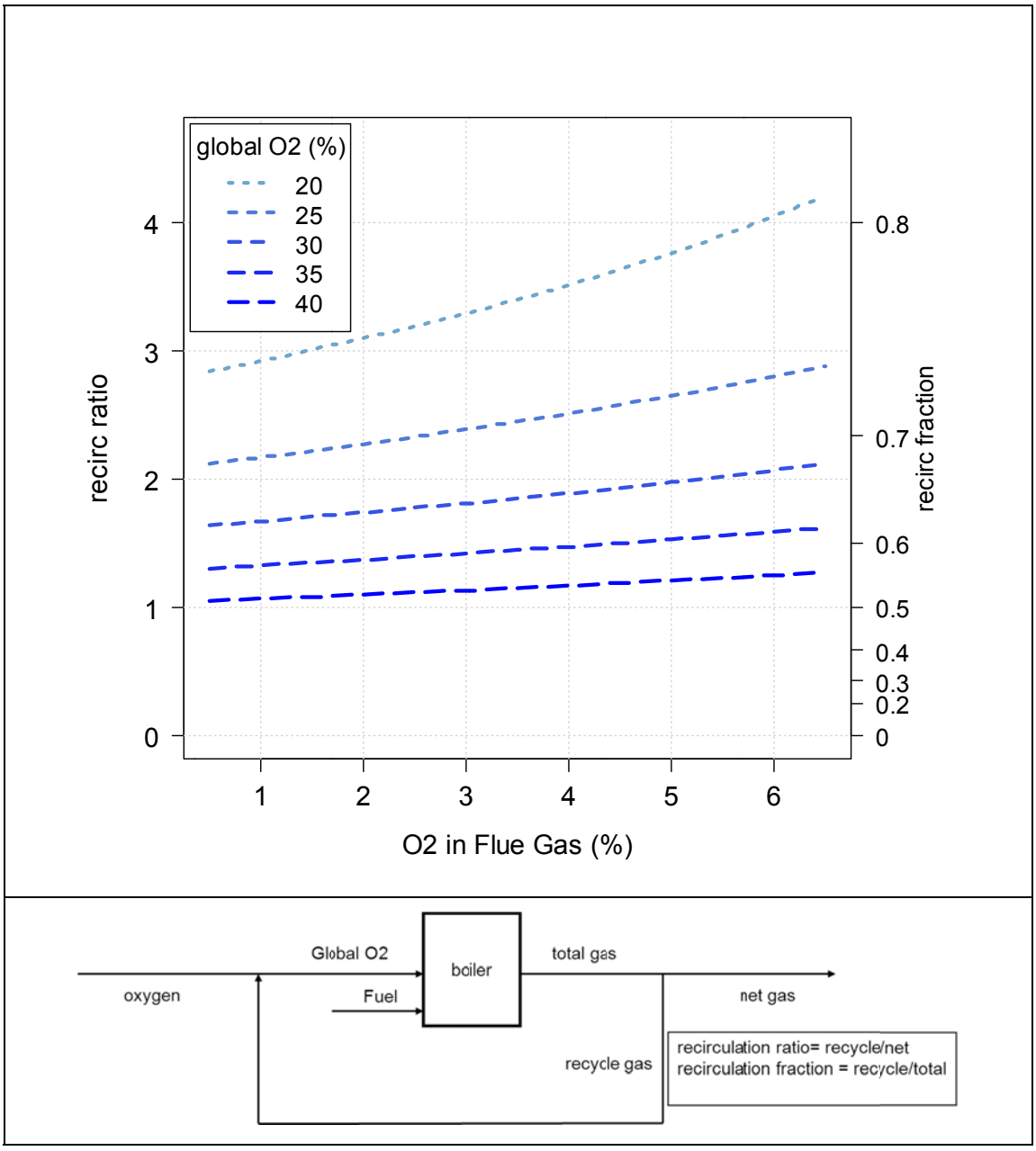

Figure 1-3. Typical Relationship Between Recycle Rate, Oxygen In Flue Gas, And Global O_2

Besides this excess oxygen requirement from the ASU, one can also consider the overall amount of oxygen entering the furnace, including the excess oxygen in the recycled flue gas. The upper sketch in Figure 1-4 shows an example with 3% excess O_2 in the flue gas and a global O_2 of 25%. The overall excess oxygen from the ASU is 4%, but by including the recirculated oxygen, the furnace stoichiometry is 1.15, or 15% excess oxygen.

The lower graph in Figure 1-4 shows the typical relationship between oxygen in flue gas, global O_2, and the furnace stoichiometry. As expected, the furnace stoichiometry increases with more excess oxygen in the flue gas and with more recycle (lower global O_2).

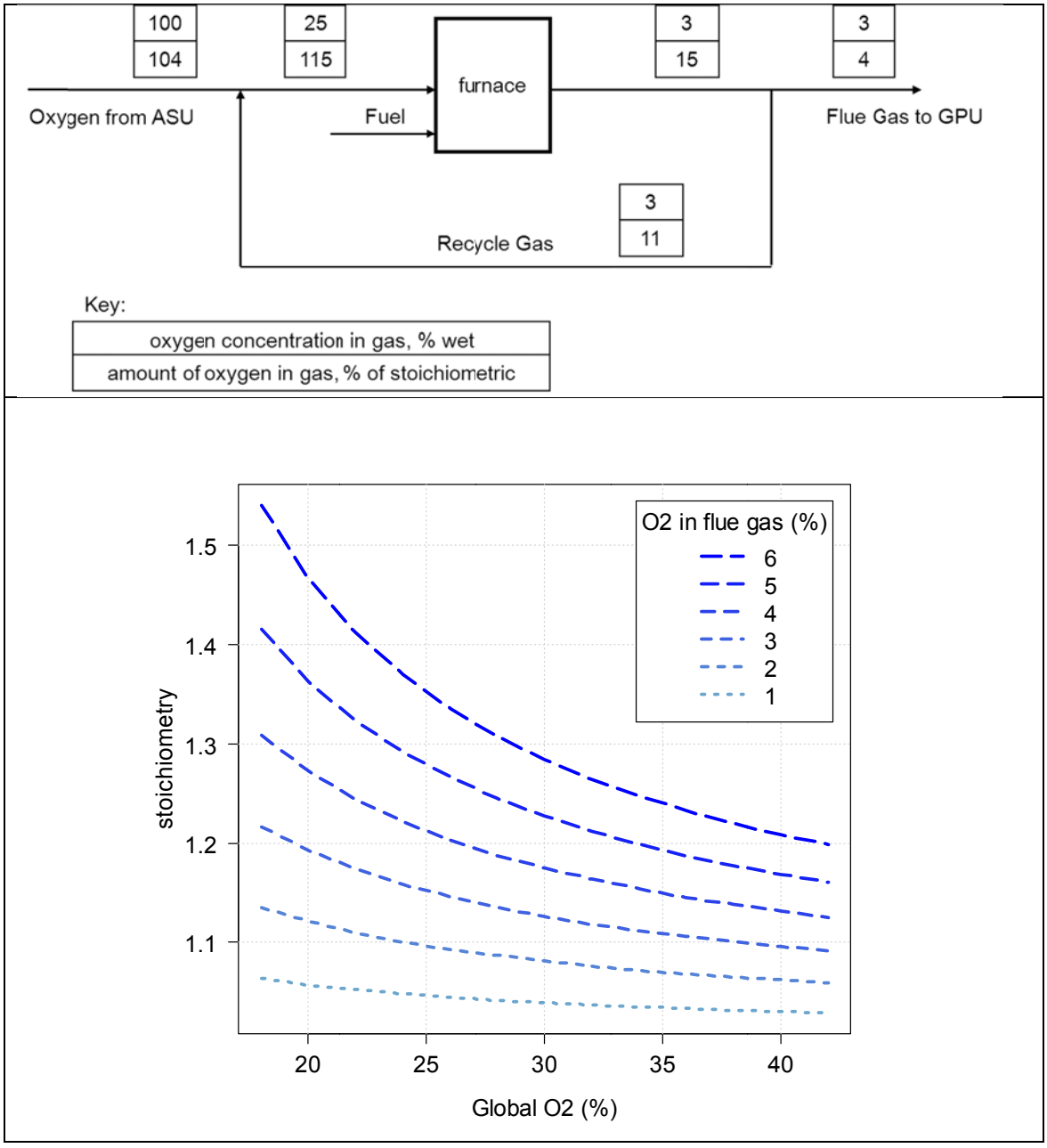

Figure 1-4. Typical Furnace Stoichiometry Vs. Global O_2

Under oxy-combustion, the carbon in the fuel burns to form mostly CO_2 and the hydrogen burns to form water. The main difference in the resulting flue gas is much less nitrogen. The molecular weight (and density) of the flue gas will be different than in air firing due to the change in composition. The relative concentrations of minor constituents in the flue gas, such as SO_2, NO_x, and CO also changes and can be significantly higher due to the absence of nitrogen. These different flue gas compositions have boiler performance and design implications can be very important. Key areas impacted include:

- combustion behavior,
- pollutant formation and emissions,
- heat transfer coefficients in the furnace, backpass, and preheater,
- radiant properties of gases in the furnace,
- gas density for flow calculations through heat transfer surface, ducts, and other components, and design of recirculation fans, and
- corrosion potential of many components including furnace waterwall, superheat and reheat heat transfer surfaces, low temperature convective surfaces and ducting.

The 15 MW_{th} test program in the BSF was designed and conducted to address these areas.

2. Boiler Simulation Facility (BSF)

2.1 15 MW_{th} BSF

Alstom's BSF is an atmospheric pressure water-cooled, balanced draft, combustion test facility designed to replicate the time-temperature-stoichiometry history of a typical utility boiler. Configurable in tangential or wall-fired modes, the BSF replicates all major attributes of a utility boiler including a "V" hopper, an arch, and appropriate (simulated) superheater, reheater, and economizer surfaces. The BSF furnace is shown in Figure 2-1.

Figure 2-1. Boiler Simulation Facility

The BSF has the capacity for firing solid, liquid and gaseous fuels. For pulverized coal firing, the BSF is typically fired at 40-60 million Btu/hr (13-18 MW_{th}). For oil or natural gas firing, the BSF is nominally rated at 90 million Btu/hr (26 MW_{th}). Actual firing rates are set on a case-by-case basis to appropriately match the desired time-temperature-stoichiometry history for combustion in the BSF with the expected field system design.

The furnace walls and heat transfer surfaces of the BSF are cooled by a surrounding water jacket open to the atmosphere. A refractory lining inside the furnace walls maintains an appropriate furnace gas temperature throughout the combustion chamber. The refractory lining is specifically designed to provide the desired furnace heat absorption and resulting furnace temperatures for the test. The same refractory lining is used during both air and oxy-combustion tests for each test campaign.

BSF testing has a long successful history of supporting development and commercialization of Alstom's combustion systems and other technologies.

2.2 Modifications for Oxy-Firing

Based on input from CFD modeling, testing and facility requirements were established and modifications were made to the BSF for oxy-fired testing. Modifications included:

- Installation of an oxygen supply and injection system;
- Installation of multiple gas recirculation systems;
- Installation of a new fabric filter for particulate removal;
- Installation of a new NID™ sulfur removal system; and
- Installation of new instrumentation and controls.

Modifications to provide oxy-fired operation and testing were completed in August 2009. Minor modifications were made between test programs to address issues identified during prior testing or prepare for specific tests. Subsequent modifications were completed to install equipment needed for second-generation concept testing. Major components installed for second-generation testing included:

- Windbox Oxidant Ejector System;
- Supplemental Oxygen Ejector; and
- Firing System modifications (center-wall ports)

Figure 2-2 shows a layout drawing of the BSF with the modifications for oxy-firing, with new components shown in blue. The facility modifications allow the flexibility to test under the base air-firing mode and three different oxy-fired process configurations. Secondary gas stream recycle can be returned to the furnace 1) before particulate and SO_2 removal, 2) after particulate removal, but without SO_2 scrubbing, and 3) after both particulate removal and SO_2 scrubbing.

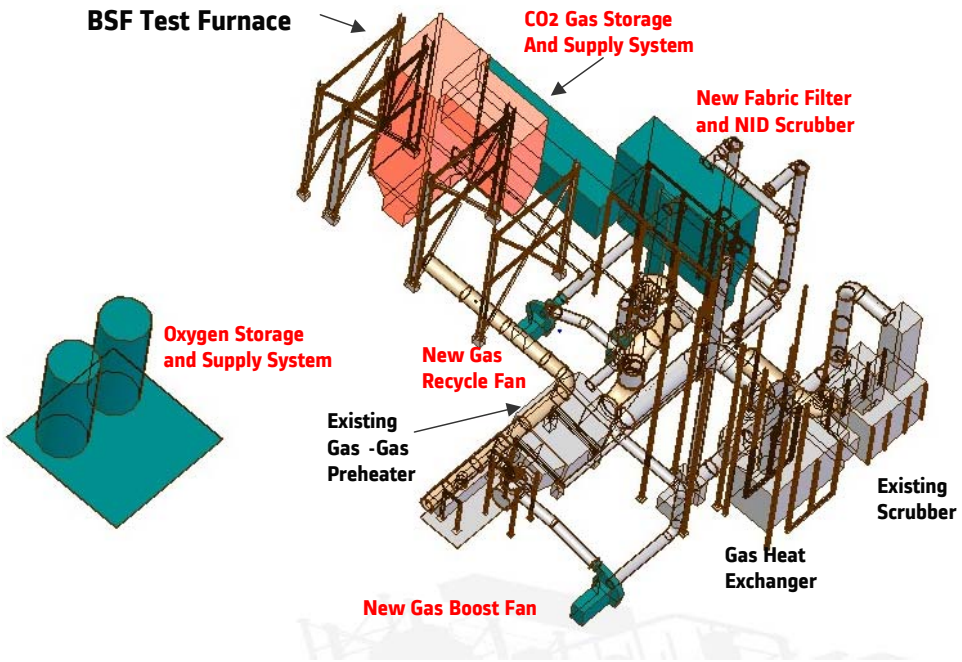

Figure 2-2. BSF modification layout drawing

A process schematic of the modified BSF is shown in Figure 2-3. For air firing, the primary and secondary air intake valves are open and the corresponding FGR valves are closed. Primary air transports the pulverized coal to the coal nozzles. Secondary air is heated in an air preheater, then distributed to the main windbox and to up to two separated overfire air elevations. The flue gas is cooled in water-cooled heat exchangers and the air preheater. A baghouse removes particulate matter, and also SO_2 when the NID™ system is operating. The NID™ system is an Alstom dry SO_2 scrubbing technology, based on the reaction between SO_2 and $Ca(OH)_2$ in humid conditions. The NID™ system is described in Section 2.2.4. A final scrubber is used to meet the site emission limits at all conditions.

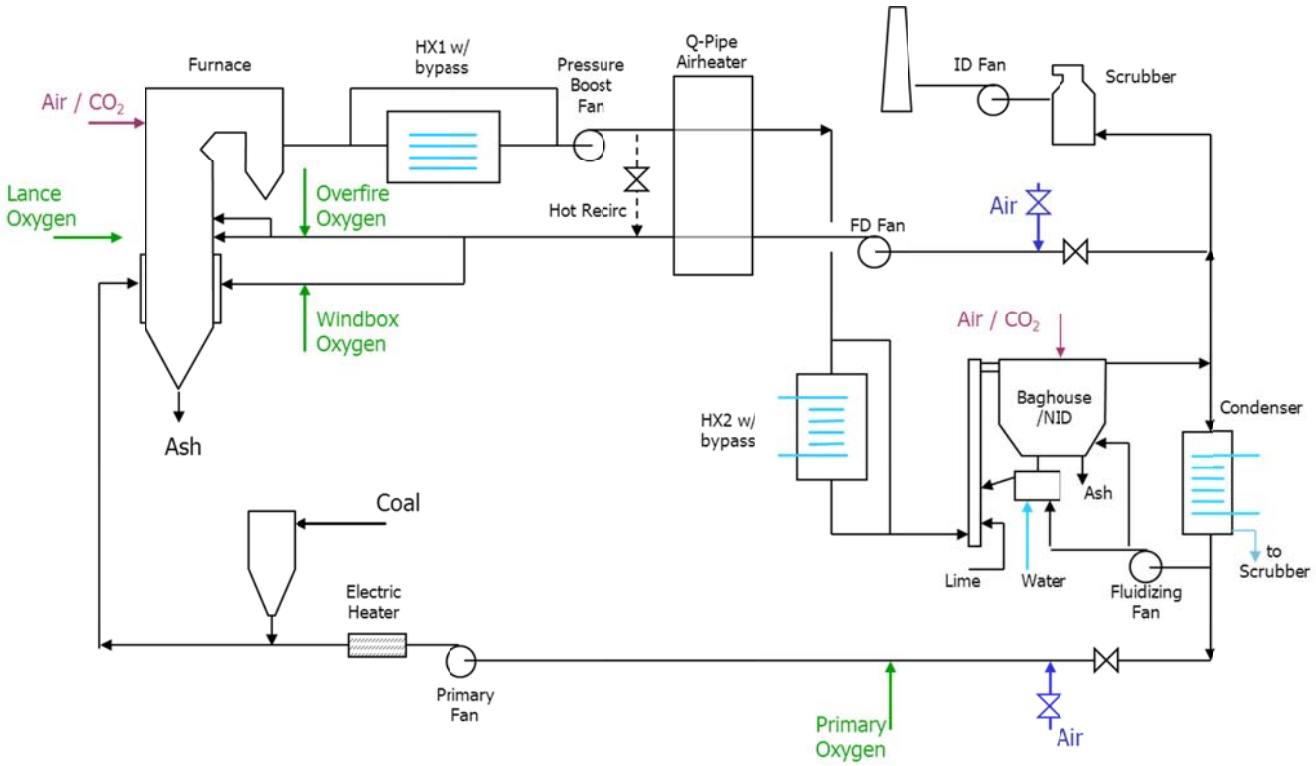

Figure 2-3. BSF process sketch

For oxy-combustion, the air in-take valves are closed and flue gas recycle valves are opened, and recycled flue gas replaces the air. Oxygen is added in several locations as shown in Figure 2-3. A supplemental oxygen injection system is used for more precise location of a portion of the oxygen. The primary recycle is dried in a condenser before transporting the coal. During oxy-combustion, CO_2 is used instead of air for purging cameras and viewports on the furnace and for pulsing the baghouse.

Figure 2-4 is a photo of the modified BSF with the newly installed oxygen storage system in the foreground. Figure 2-5 provides a view of the BSF showing the new fabric filter and the CO_2 gas storage and supply system. The CO_2 gas system is used to supply small purge gas flows to ports with on-line video cameras, thermal-imaging cameras, flame scanners, etc., as well as for fabric filter bag pulsing during the oxy-fired tests in order to minimize air addition.

Figure 2-4. Photo of BSF with oxy modification, from north

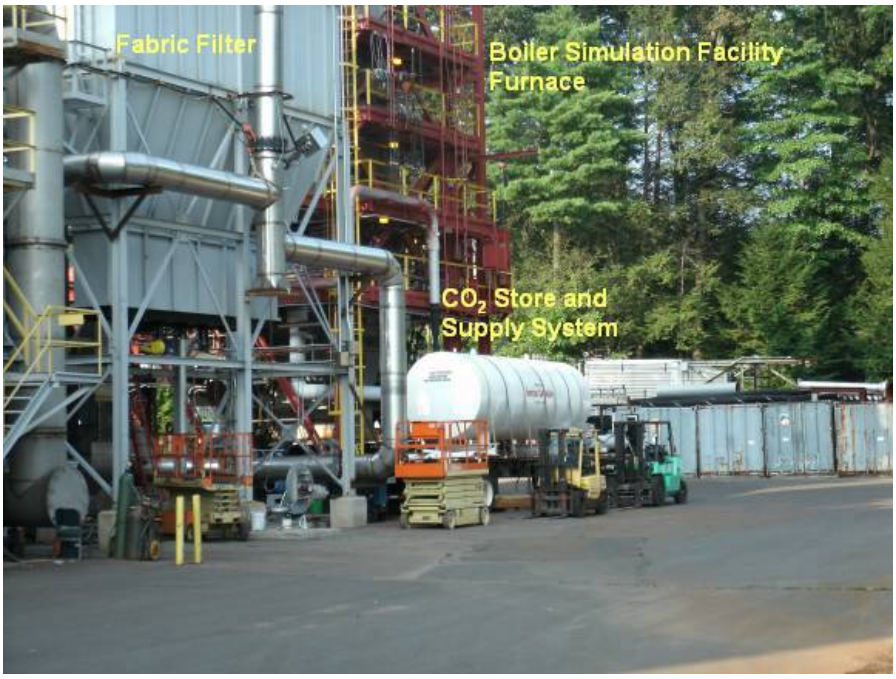

Figure 2-5. Photo of BSF with oxy modifications, from south

Further details on some of the major equipment sub-systems and modifications are given in the following sections.

2.2.1 Windbox and firing system

The BSF utilizes a flexible tangential firing system based around Alstom's TFS-2000® firing system, scaled for the 15MWt BSF. Table 2-1 presents the BSF firing system arrangement. Features include:

- Three Coal Elevations with LNCFS™-P2 Coal Nozzle (shown in Figure 2-6)
- Concentric Firing System (CFS™) Nozzles
- Close-Coupled Overfire Air (CCOFA)
- Multi-Level Separated Overfire Air (OFA)
- HP 323 mill equipped with Dynamic™ Classifiers
- Individual windbox dampers for partitioning of the air within the windbox (Figure 2-7)

The furnace is fired from four corners with three levels of coal injection and two levels of separated OFA, similar to the tangential firing system illustrated in Figure 2-6. In tangential firing systems, mixing of fuel and air (or oxygen) occurs throughout the furnace, whereas in wall-fired systems the mixing occurs primarily near the burner nozzle. Global furnace aerodynamics plays an important role for combustion, emissions and thermal behaviors.

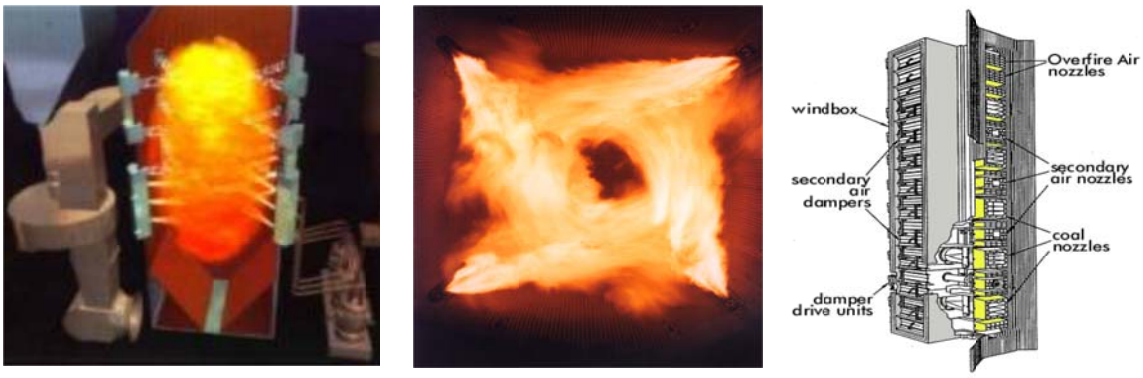

Figure 2-6. Alstom TFS-2000® low-NOx tangential firing system

Table 2-1. BSF firing system arrangement

Compartment	Description
USOFA	
USOFA	
LSOFA	
LSOFA	
CCOFA	Straight (Adj. Fixed)
CCOFA	Straight
CCOFA	Straight
Top End	Straight
Coal	P2
CFS	Angled 15°
Straight	Straight
CFS	Angled 15°
Coal	P2
CFS	Angled
Straight	Straight
CFS	Angled 15°
Coal	P2
Bottom End	Adjustable
Under Fire	Straight
Under Fire	Straight (Adj. Fixed)

Figure 2-7. Windbox damper

To allow for testing with higher oxygen temperatures and concentrations, new windboxes and OFA assemblies were constructed of 304SS. Nozzle tips were constructed of 309 and 310SS to withstand higher temperatures with little leakage oxidant. This design allowed for maximum control and flexibility of test conditions.

The design and location of the CCOFA and SOFA in the BSF were selected to provide residence times consistent with Alstom's recent commercial offerings. In general, oxy-combustion tests had longer residence times than air combustion tests. This is due to higher molecular weight and heat capacity of oxy-combustion flue gas relative to air combustion. These result in a lower volumetric flowrate and increased residence times.

2.2.2 Oxygen System

Oxygen supply for the BSF is provided by two 13,000 gallon vertical liquid oxygen tanks. Liquid oxygen is vaporized by a hot water bath vaporizer to supply oxygen at a rate up to 10,000 lb/hr. Hot water for vaporization comes from the BSF jacket. A picture of the oxygen pad with tanks and vaporizer units is shown in Figure 2-8.

Figure 2-8. Oxygen pad

Figure 2-9. BSF oxygen injection system and combustion ducting

Oxygen supply is regulated by two parallel flow control skids. Each flow control skid contains a block-and-bleed for isolation of the oxygen system during routine and emergency shut-downs, vortex shredding flowmeters, and flow control valves. The two flow control skids feed a common manifold which supplies oxygen to five different locations. Each oxygen flow location is independently measured by orifice flow meters and controlled by flow control valves. Oxygen flows can be independently controlled to the primary (fuel transport) FGR stream, the furnace windbox FGR stream, the separated overfire stream, the oxygen ejector, and a "lance" system which can feed oxygen locally to various firing system flow compartments entering the furnace. Figure 2-9 shows the oxygen flow control system.

Oxygen diffusers were used to mix the oxygen into the main flow stream. A total of three diffusers were installed, for the primary, windbox, and separated OFA. A picture of the oxygen diffusers is shown in Figure 2-10. Duct traverses of the windbox stream during second generation testing showed a good cross-sectional mixing by the diffusers. The diffusers are located up-stream of the oxygen monitors. Oxygen measurements were taken during testing downstream of the injection locations to determine the distribution of oxygen across ducting and confirm the level of mixing.

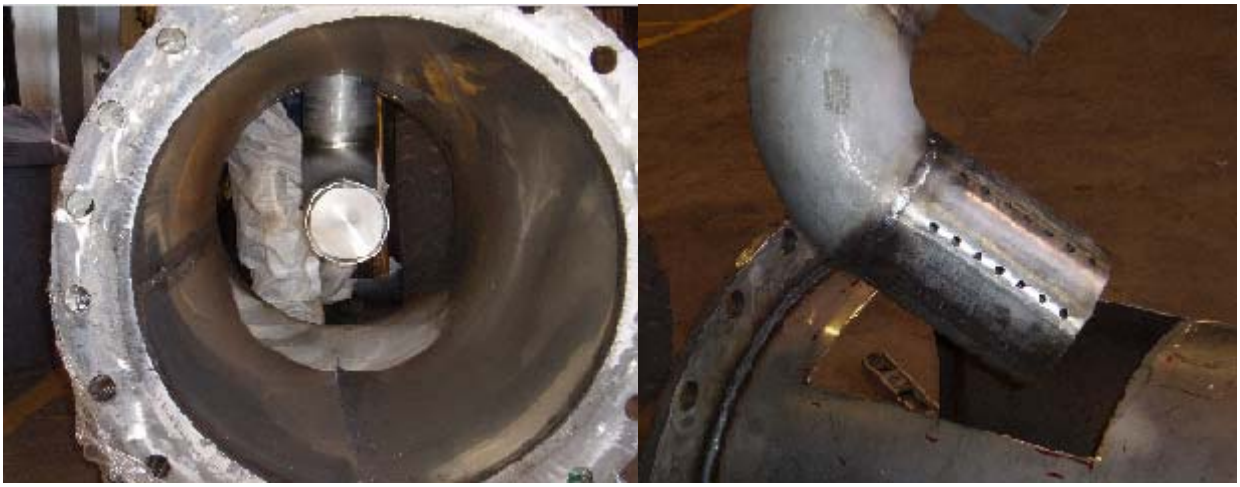

Figure 2-10. Oxygen diffuser

2.2.3 Fans and ducting

For flexibility and to minimize air infiltration to equipment downstream of the furnace (such as the fabric filter), a boost fan was added to the flue gas flow stream. The three fan system (FGR, gas boost, and induced draft fans) allows both the furnace and the fabric filter to operate close to atmospheric pressure. An existing primary air blower was used to transport coal to the furnace. Photos of the FGR and boost fans are shown in Figure 2-11. All fans were operated by variable frequency drives (VFD) to allow precise control over flow and pressures.

Figure 2-11. BSF Flue Gas Recirculation and Boost Fans

To allow for flexibilities in test conditions and operation, new combustion air ductwork was fabricated and installed. All secondary ductwork after oxygen injection was constructed to be compatible with oxygen enriched environments (> 23.5% oxygen). Ductwork was constructed of stainless steel with oxygen compatible gasket material and all welds were performed with an argon purge to prevent slag and scale build-up. A photo of new combustion air ductwork prior to insulation is shown in Figure 2-12.

Figure 2-12. BSF combustion air ductwork prior to insulation

2.2.4 Baghouse / NID™

For the purpose of the high-sulfur testing, a NID™ sulfur capture system was installed on the BSF baghouse. The NID™ system is an Alstom product based on dry SO_2 scrubbing technology. The NID™ system is a dry process based on the reaction between SO_2 and $Ca(OH)_2$ in humid conditions. The main features of the NID™ process are shown in Figure 2-13. Additional equipment needed to incorporate the NID™ test system in the BSF included a NID™ mixer/hydrator, additive feed system, NID™ reaction duct, modification of the flue gas ducting, and additional gas analyzers, instrumentation, and controls systems.

A unique feature of the NID™ technology is the fact that all recycled absorbent is being subject to wetting in the mixer, which maximizes the utilization of the recycled sorbent. Water is fed to the mixer to maintain a constant outlet flue gas temperature and desired humidity. After the drying/reaction step, the dried recycled dust is separated from the flue gas in the fabric filter and again fed to the mixer. Make-up hydrated lime is fed to the system to maintain the appropriate calcium-to-sulfur molar ratio and desired sulfur capture. A major advantage of the NID™ technology is that the sorbent is wetted and dispersed with aid from the flyash, allowing higher sorbent input and the capability to address much higher sulfur coal applications than conventional spray drying technologies.

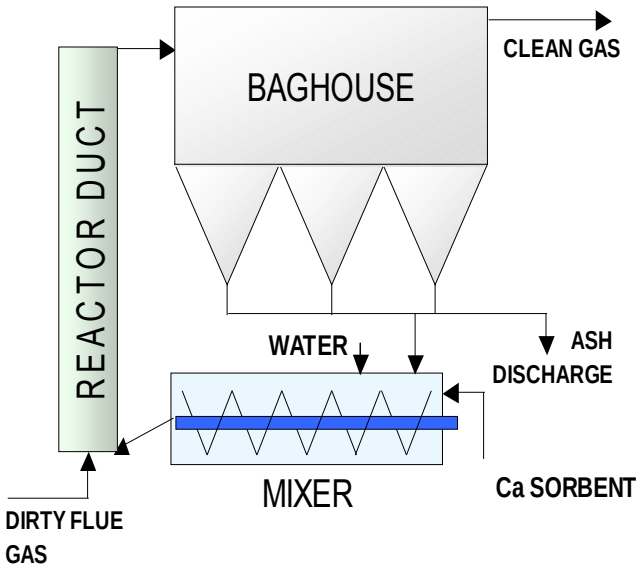

Figure 2-13. NID™ desulfurization system

Figure 2-14 provides a view of the BSF showing the fabric filter and NID™ dry scrubbing system. The pulse-jet fabric filter was constructed with a total cloth area of 7,020 ft^2. Filter bags, 480 in all,

were constructed of fiberglass with PTFE fill and designed for a maximum operating temperature of 400°F. The system was set up such that pulse gas could be either CO_2 or air.

Figure 2-14. Photos of BSF fabric filter with NID™ system

2.2.5 Heat exchangers and condensers

A counter-current shell-and-tube condenser was designed and constructed for BSF operation. The condenser dries the portion of the recycled flue gas used for coal transport and for fluidization in the baghouse/NID™ system. Figure 2-15 shows the BSF condenser and demisters. The condenser is designed with a series of cascading internal tube banks and a bottom sump to collect flue gas condensate. Flue gas condensate that collects in the sump is pumped to Alstom's waste-water holding tanks for subsequent disposal.

Figure 2-15. BSF condenser and demisters

Special care was taken in selection of materials of construction for the flue gas condenser. Alloys selected were constructed of super-ferritic stainless steel specially designed to resist chloride pitting and stress corrosion cracking. Tubes were constructed of Sea-Cure® while walls and tube sheets were constructed out of AL-6XN®. Initially, a type 304SS immersion sump pump was utilized to pump flue gas condensate, but this pump failed during the second BSF test campaign. The pump was replaced by an external flexible impeller pump with all wetted parts constructed of PTFE.

2.2.6 Internal recirculation system

In the fall of 2011, the BSF was modified with an internal recirculation system capable of testing close-coupled flue gas recirculation concepts. Figure 2-16 shows a layout drawing of the BSF with the close-coupled recirculation modifications, with new components shown in color. Close-coupled flue gas recirculation is driven by ejectors using oxygen as the motive gas to draw FGR from before the air heaters or pollution control systems. Two close coupled recirculation systems were installed: 1) a single large ejector driving all the gas recirculation for the windbox secondary oxidant, and 2) four smaller ejectors driving recirculation utilizing a supplemental oxygen supply. The supplemental oxygen supply is approximately 20% of stoichiometric oxygen that is added separately from the bulk oxidant streams in order to maintain the oxygen concentrations in primary and secondary recycle streams at a sufficiently low level and allow carbon steel fabrication of associated ductwork and process equipment.

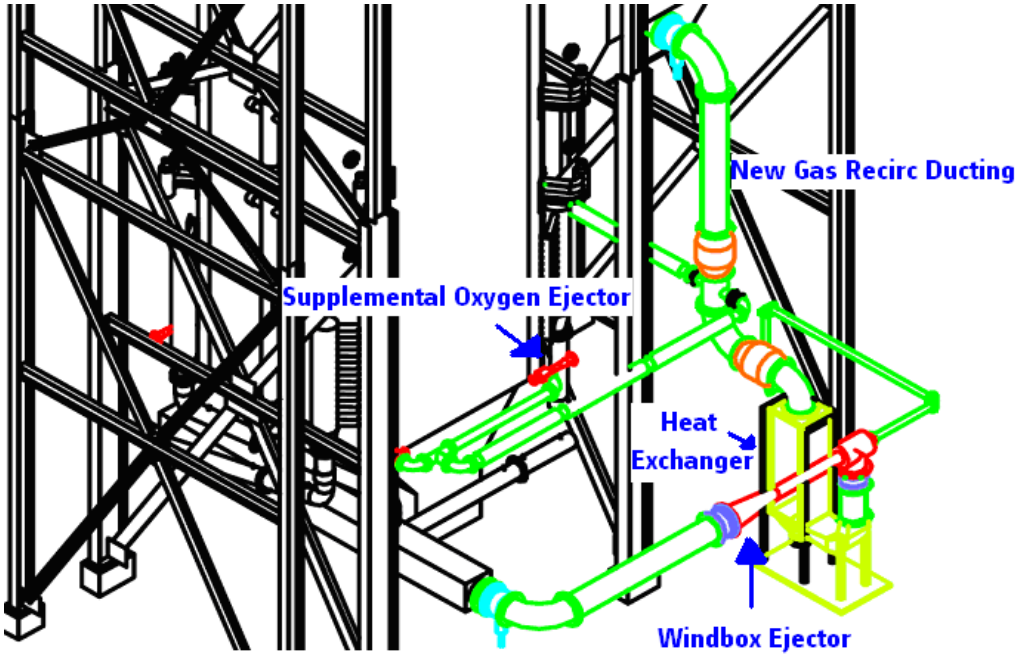

Figure 2-16. Close coupled recirculation system schematic

Figure 2-17. Close Coupled Recirculation System

Figure 2-17 shows a picture of the close-coupled recirculation system installed on the BSF. Close-coupled flue gas recirculation is driven by oxygen ejectors to draw flue gas recirculation. For the close-coupled recirculation system on the BSF, a supply nozzle was installed after the economizer into the gas exhaust duct.

The close-coupled recirculation system required the construction and installation of a heat exchanger, shown in Figure 2-18, to cool the gas to the temperature limitations of existing control valves on the BSF. Additional control valves were installed for the internal recirculation system to control ejector suction, discharge, and motive gas pressure, and to allow for safe transition between normal recirculation mode and recirculation with the ejector.

Figure 2-18. Internal recirculation system heat exchanger

Figure 2-19 shows the oxygen ejectors as received from the ejector supplier. A total of five ejectors were installed on the BSF. One large ejector was installed to supply all oxygen and recycled flue gas for the windbox secondary air, and four smaller ejectors were designed and installed to supply supplemental oxygen and flue gas for each windbox corner. The large ejector utilized oxygen at approximately 40-70 psig to supply the necessary motive force to all flue gas recycle for the windbox secondary oxidant. Supplemental ejectors were designed for lower oxygen pressure, approximately 3 to 5 psig, which was specified by prior reference plant designs from optimized Air Separation Units.

Figure 2-19. Oxygen ejectors delivered from supplier

2.3 Data collection

2.3.1 Test measurements

The BSF is instrumented to measure essentially all process flows, temperatures and pressures. Critical furnace operation and control information are measured, metered, and recorded by a state-of-the-art data acquisition and control system. Operational information such as combustion air and fuel input mass flow rates, air preheat temperatures, furnace exit gas temperatures, and fan speed settings, etc., are reduced, stored and displayed on-line for facility operation and post test data reduction use.

Four waterwall test panels are installed at three elevations in the furnace to continuously monitor heat absorption rate and observe the response to sootblowing. Six upper furnace test loops (called U-Tubes) are installed across the vertical furnace outlet plane to continuously measure upper furnace heat absorption rate and variations across the furnace.

In addition to the continuously logged data, probing and sampling is conducted at selected test conditions and furnace locations. Furnace and convection pass temperatures are measured using suction pyrometers. Heated gas extraction probes are used with a dedicated gas analysis system to measure in-furnace gas compositions. Incident heat fluxes to the furnace walls are measured using total heat flux probes and ellipsoidal radiometer probes which measure radiant heat flux. Typical measurement planes are shown in Figure 2-20.

Deposition/corrosion probes are installed at three furnace elevations to expose corrosion specimens and collect deposit samples – see Figure 2-20.

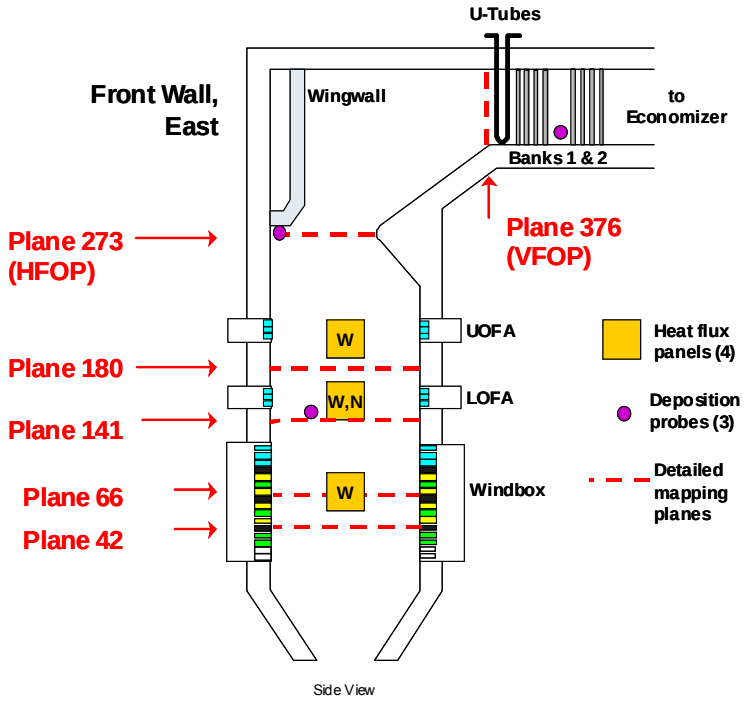

Figure 2-20. BSF furnace probe measurement planes

2.3.2 Advant /LabView

The Advant distributed control system (DCS) has the ability to log selected data into its Historian database. We have not found this to be convenient for inspecting and analyzing data during and after the tests, so we have set up a LabView program to acquire Advant data through an OPC server and make it available for trending and inspection during the test and archiving the data for later analysis.

A spreadsheet tag list of all the data to be logged is made for documentation. It contains the tag ID known to the DCS as well as a text description, the units of measurement, and the number of decimal places to be saved in the data files. This tag list defines the DCS data that is logged.

The DCS data is logged at two frequencies. Data is saved every one minute to text files on both the local hard drive and the network. Each data record is the current value from the DCS, not a one-minute average. This frequency is adequate for most of the data analyses.

Larger local and network text files are also saved with data every 5 seconds.

There is also the Advant Historian database for a further backup of the data.

2.3.3 Campbell data loggers

Several Campbell data loggers are used to record data not saved to the DCS.

Figure 2-21 shows the Campbell setup to log and monitor probe data from the in-furnace probes (except for the gas probe.) A series of umbilical (2 Type K Thermocouples, 1 Type B Thermocouple, and an Instrument Wires) run to various probing decks and walls to allow simple probing operation. The data is logged every 3 seconds.

Figure 2-21. Probe data logging computer

2.3.4 Board data

A great deal of important data is written down manually, rather than logged electronically. Some of this manual is typed up into electronic data files for subsequent analysis.

Test point start and stop times are written in the control room logbook. These are then typed up so our data analysis programs can read them.

Oxygen and carbon dioxide delivery times and quantities are noted on a written list. These can be entered into a spreadsheet to get a cumulative total to check against measured total feedrates.

Similarly, the **lime loading times and weights** are written down and can be used to get a cumulative rate.

Solids and liquid sampling times and locations are written down. This is typed up after the test and used to select samples to submit for analysis.

Gas analyzer calibrations are done every shift or so. During these times, the analyzers are set to zero and to span gas readings, sometimes more than once. The times are written into the gas system logbook and the operator's logbook as well. When calculating average gas compositions during test points, these times should be excluded. (We usually avoid calibrations during test points, but that is not always possible.)

Suction thermocouple probing times are written on data sheets along with the location of the probe (port number and depth) and an estimate of the average temperature during each test point. Periodically during the test week, this is typed up in Excel so the average temperatures can be plotted. These results are often used to set up subsequent test conditions as the test week goes along.

After the test week, the actual data is downloaded from the Campbell and each probing point is plotted to get a better look at the time for steady operation and a more accurate average temperature is calculated.

Similarly, the **heat flux probing times** are written down on data sheets along with the location of the probe (port number) and an estimate of the measured values (two temperatures for the total heat flux

probes and a voltage for the 2π radiant heat flux probe). As with the suction pyrometers, the board data values are typed up and used during the test and more accurate numbers are obtained after the test from the Campbell data.

In-furnace gas sampling probing times are written on data sheets along with the location of the probe (port number and depth). The data from the gas analyzers is logged by the Advant/LabView system. Generally the 5-second data files are used for analyzing the probing data because of the limited time the probe is at each point.

2.3.5 Other data

TRC

TRC Environmental Corporation (TRC) of Windsor, CT, was sub-contracted to collect samples at various locations during selected long-term test conditions for the following analyses:

Isokinetic dust sampling, EPA Method 5
Particle size, CARB Method 501
Particulate and metals concentration, EPA Method 29
Mercury concentration, EPA Method 30B
Particulate and HCl, EPA Methods 5/26A
SO_2 and sulfuric acid, NCASI/EPA Method 8A

Data from TRC, including all outside lab analysis, is provided in final reports and in Excel spreadsheets.

Mercury Evaluation

For the North Dakota lignite test campaign, the Energy & Environmental Research Center (EERC) measured gaseous mercury concentrations with two Continuous Mercury Monitors (CMMs) at the boiler outlet and in the flue gas recycle stream. EERC provided the data from the CMMs (including copies of the log books) after the test campaign in their final report. Data from the CMMs were also included in an Excel spreadsheet to allow easier plotting and averaging by Alstom.

For comparison with the continuous monitors, EERC also measured mercury emissions at selected times using sorbent traps (EPA Method 30B) and using the Ontario Hydro method. Each of the EERC measurements included information on the speciation of the mercury. Data from all sorbent traps were provided in EERC's final report to Alstom.

SO_3

The method used for SO_3 measurements during the oxy-fired Boiler Simulation Facility (BSF) testing is a modified version of ASTM Method 3226-73T, Controlled Condensation Method.

The basic steps of the standard method are:

- A measured volume flue gas sample is extracted using a heated glass-lined probe followed by a quartz filter controlled at 500°F.
- The sample passes through a filter to remove particulate
- The gas then goes through a glass coil condenser at a controlled temperature of 140-150°F .
- The condensed acid is collected and analyzed by titration.

Key modifications employed for the BSF SO_3 measurements are:

- Particulate is removed from the heated gas sample using an inertial separation probe (ISP) in place of the quartz filter. The ISP passes most of the gas axially through the probe, and a smaller, low velocity portion is withdrawn radially through the filter element wall for the sample. The axial gas velocity is high enough to prevent particle buildup on the filter wall, thus reducing the chance for acid vapor to react with the particles and not reaching the condenser. In other projects, a small ESP has also been successfully used instead of the inertial separation probe. The critical issue is that the sample gas is not drawn through a particulate covered filter, even if maintained at high temperature.
- The condenser temperature is maintained at a temperature where any SO_3 is condensed, but water vapor does not condense. This temperature is significantly higher for oxy-firing than for air-firing (~190°F) because of the higher moisture content of the gas.
- A glass wool plug is used at the end of the condenser to capture any H_2SO_4 aerosol which may have passed through the condenser.

More details are given in Appendix A.

Measured data for SO_3 sampling must be calculated and processed before a SO_3 concentration can be reported. The condensate sample collected during testing is diluted to 100 mL using de-ionized water and sent to a laboratory for measurement of sulfate (SO_4) concentration. Total dry gas flow passing through the condenser during the time period is calculated based on the recorded start and stop times of the sample, and the recorded temperature and pressure of the critical orifice located in the SO_3 sampling shed. Dry gas SO_3 concentration is calculated comparing the total amount of SO_4^{-2} collected to the dry gas flow. For the in-furnace SO_3 measurements, a dilution calculation by CO_2 concentration is used to determine what fraction of the dry gas flow was from flue gas.

Additional data is recorded on SO_3 sampling sheets by the SO_3 measurement team. This additional data includes heated zone temperatures, ISP probe flowrates, and leak check gas analysis readings.

2.3.6 Deposition probes

Three air-cooled deposition probes were constructed and installed in the BSF to collect deposits and probe metal specimens for further evaluation. Three probes are installed at locations shown in Figure 2-20. The first probe is located on the south wall of the lower furnace, halfway between the CCOFA and the Lower SOFA. The second probe is located on the east wall of the upper furnace, at the HFOP. The third probe is located in the back-pass, on the south wall between the first and second tube banks.

Figure 2-22 shows the three deposition probes used on the BSF. Probes 1 and 2 are of L-shape construction to mimic the orientation of boiler tubes in the lower furnace. Probe 3 is a straight probe and inserted perpendicular to the flow stream in the back-pass. All probes were designed with a removable coupon located on the end of the probe. These removable coupons are used as metal specimens for further evaluation. Probe coupon temperatures were monitored and controlled to the desired temperatures by modulating cooling air supply.

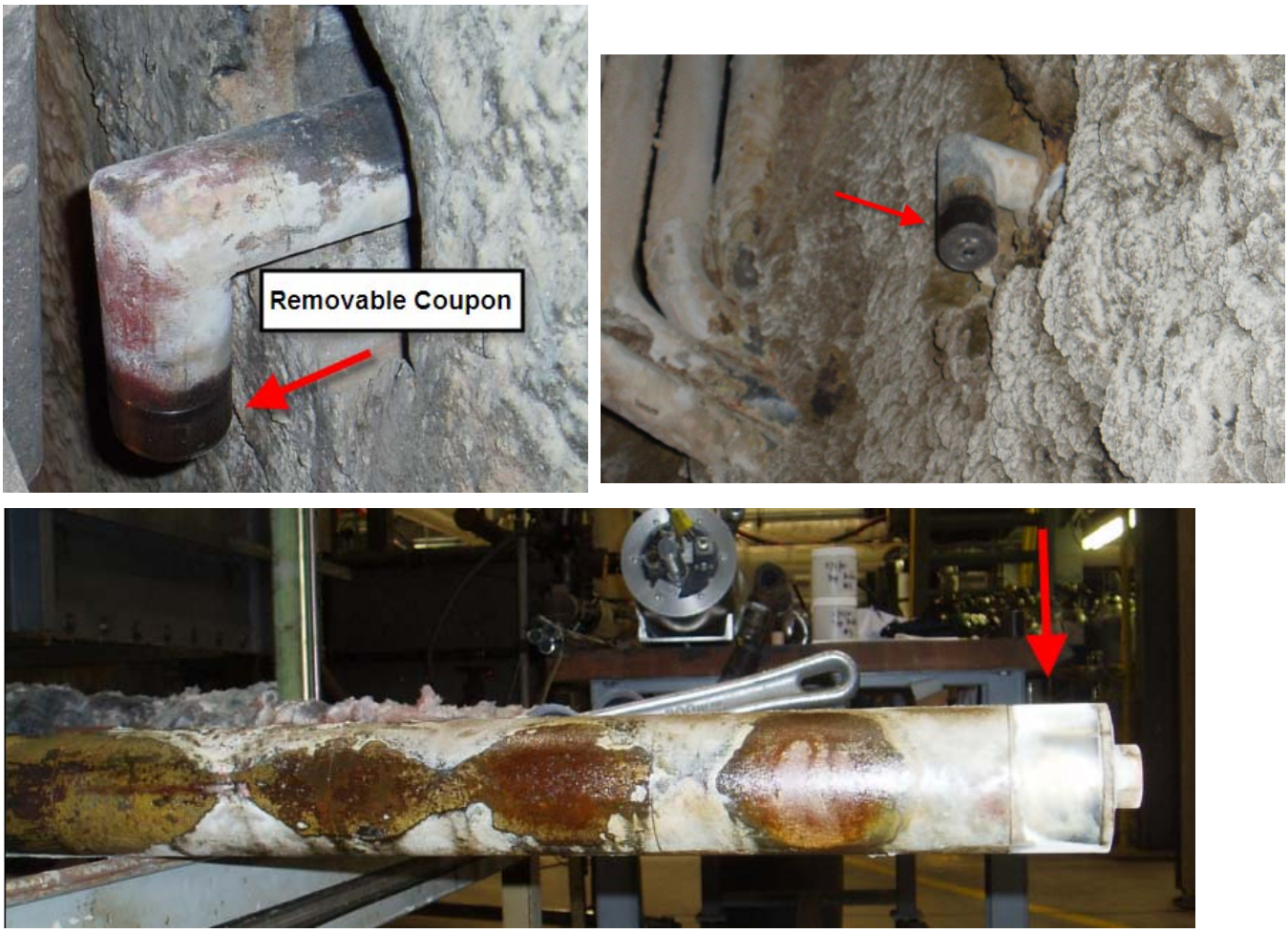

Figure 2-22. BSF Deposition Probes

3. Test campaigns

From September 2009 through November 2012, nine oxy-combustion test campaigns were executed covering a broad range of fuels, process scenarios, and test conditions. Table 3-1 lists the oxy-combustion test campaigns executed in the BSF. Test campaign 5 consisted of three separate campaigns which together constitute the second generation testing.

Table 3-1. BSF test campaigns

Campaign	Test Fuel	Mine	Test Date
1	PRB sub-bituminous	Black Thunder	September 3 to 12, 2009
2	Low sulfur bituminous	Fola	January 18 to February 4, 2010
3	High sulfur bit.	Prairie Eagle	April 25 to May 1, 2010
4	North Dakota lignite	Falkirk	October 4 to October 9, 2010
6 *	Schwarze Pumpe lignite	Lusation	July 11 to 18, 2011
5-1	Low sulfur bit.	Fola	December 7 to 16, 2011
5-2	PRB sub-bit.	Black Thunder	September 23 to 29, 2012
5-3	High sulfur, high chlorine bit.	Gallatia	October 31 to November 6, 2012

* Campaign 6 was moved up in the schedule to precede Campaigns 5, but the original numbering was retained.

Analyses of all as-fired coals are shown in Table 3-2. The BSF is not direct fired, so the moisture that is removed from the coal during the grinding process is lost. The analyses presented in Table 3-2 represent an average of several analyses across the test series.

Each of the campaigns is described in the following pages. The results of the tests are discussed below in Section 5. Detailed summaries of each of the test points are given in Appendix B of the Task 4 topical report[1]

[1] Topical Report: Task 4 –Testing in Alstom's 15 MWth Boiler Simulation Facility, submitted April 28, 2014

Table 3-2. Average coal analyses for each campaign

Test campaign	1	2	3	4	6	5-1	5-2	5-3
Fuel	PRB	WV Fola	IL Hi S	ND Lignite	Schwarze Pumpe Lignite	WV Fola 2nd Gen	PRB 2nd Gen	Hi S 2nd Gen
Proximate analysis, wt % as fired								
Moisture	20.57	1.36	6.00	24.43	13.67	1.28	19.53	3.18
Ash	5.29	11.69	9.69	11.87	5.22	13.67	5.79	8.79
Volatiles	34.24	31.81	38.26	33.82	46.88	33.44	34.79	38.04
Fixed Carbon	39.91	55.29	46.05	29.87	34.23	51.61	39.89	50.00
SUM	100.00	100.14	100.00	100.00	100.00	100.00	100.00	100.00
HHV, BTU/lb	9364	13018	11873	7474	8998	12686	9675	12876
Ultimate analysis, wt % as fired								
Moisture	20.57	1.36	6.00	24.43	13.67	1.28	19.53	3.18
Hydrogen	3.74	4.85	4.47	3.01	4.02	4.76	3.76	4.76
Carbon	54.81	72.50	66.41	44.95	54.10	71.36	56.67	71.49
Sulfur	0.28	0.88	3.12	0.73	0.62	0.89	0.28	2.63
Nitrogen	0.79	1.46	1.33	0.81	0.63	1.49	0.47	1.47
Oxygen (diff)	14.52	7.26	8.98	14.20	21.74	7.67	13.50	7.68
Ash	5.29	11.69	9.69	11.87	5.22	13.67	5.79	8.79
SUM	100.00	100.00	100.00	100.00	100.00	101.10	100.00	100.00
Ash Oxide Analysis, wt % of ash								
SiO2	34.56	56.30	50.85	41.99	14.78	54.10	37.87	46.72
Al2O3	16.05	30.78	20.53	13.96	4.37	34.18	18.87	19.62
BaO	0.57	0.08	0.04	0.55	--	0.06	0.36	0.04
Fe2O3	6.16	5.58	15.56	6.47	23.00	4.07	5.94	16.48
TiO2	1.29	1.78	0.94	--	0.18	1.21	1.20	0.83
Mn3O4	0.03	0.02	0.04	0.08	0.29	0.01	0.03	0.05
CaO	19.72	0.84	3.52	14.84	25.89	0.99	17.86	4.84
MgO	4.23	0.82	0.96	4.50	9.59	0.72	3.79	0.96
Na2O	1.24	0.23	1.02	1.56	0.01	0.22	1.08	0.98
K2O	0.50	2.67	2.11	1.93	0.17	2.80	0.57	1.86
P2O5	0.81	0.15	0.52	0.18	0.08	0.13	0.84	0.09
SO3	11.67	0.71	2.81	11.99	18.29	0.74	8.50	5.58
SrO	0.31	0.07	0.03	0.31	--	0.04	0.28	0.03
Trace Metals, mg/kg dry coal								
Antimony	0.23	0.86	--	0.81	--	1.27	0.19	--
Arsenic	1.20	2.97	1.59	10.90	0.41	4.08	1.01	--
Barium	258.0	34.7	29.3	470.3	46.3	15.9	323.3	--
Beryllium	0.23	1.89	0.84	0.54	0.07	1.86	0.21	--
Cadmium	0.08	0.09	0.32	0.13	--	0.08	0.09	--
Chromium	4.33	23.35	18.53	9.23	1.09	24.93	3.80	--
Iron	2902	4578	9150	7127	8827	4180	2783	--
Lead	2.30	10.12	--	3.80	--	--	--	--
Mercury	0.06	0.12	0.07	0.09	0.05	0.13	0.06	0.06
Nickel	4.47	15.00	9.89	4.63	0.63	16.62	3.21	--
Silver	0.07	0.14	0.09	0.13	--	0.12	0.08	--
Strontium	176.46	64.65	20.03	417.50	128.67	13.27	165.67	--
Thallium	--	0.34	0.56	--	--	0.37	0.07	--
Titanium	519.5	1251.8	478.3	513.3	67.6	1168.3	433.0	--
Vanadium	13.73	36.75	27.60	18.20	1.55	46.17	12.35	--

3.1 Test campaign 1 – Powder River Basin subbituminous

BSF Test campaign 1 was successfully conducted September 3 to 12, 2009, on a Powder River Basin sub-bituminous coal from the Black Thunder mine in Wyoming. A Powder River Basin (PRB) subbituminous coal was selected for this campaign due to the commercial significance in the US market. More than 500 tons of PRB coal was delivered from Amren's Newton generation station in Newton, IL. A Gantt chart of test campaign 1 is shown in Figure 3-1 and a test matrix is shown in Table 3-3.

Test preparations for BSF Test campaign 1 focused on modifying the BSF for oxy-firing and repairing existing equipment. More details on BSF modifications for oxy-firing are in Section 2.2. Prior to the test campaign there was a three-week shakedown period where new equipment was tried out and made operational. New fans were started up, the baghouse was tested, updated control logic and instrumentation was implemented, and the oxygen system was made operational. During shakedown, particular focus was given to inter-locks and logic between the oxygen skid and the BSF with trips and logic designed to prevent unsafe operation.

Test campaign 1 focused on testing the most promising oxy design concepts selected during process screening (Task 2 of the project). Baseline air-fired testing was initially conducted to establish comparative performance and emission data for the test coal. The selected design options were each tested in the BSF over a range of conditions with the objective of optimizing overall performance and emissions. Operating variables assessed included excess total oxygen, burner zone staging, and air in-leakage. Firing system design variables included FGR take-off location, FGR stream flow rates and injection locations, oxygen concentration in different input streams, fuel and oxidant injection parameters.

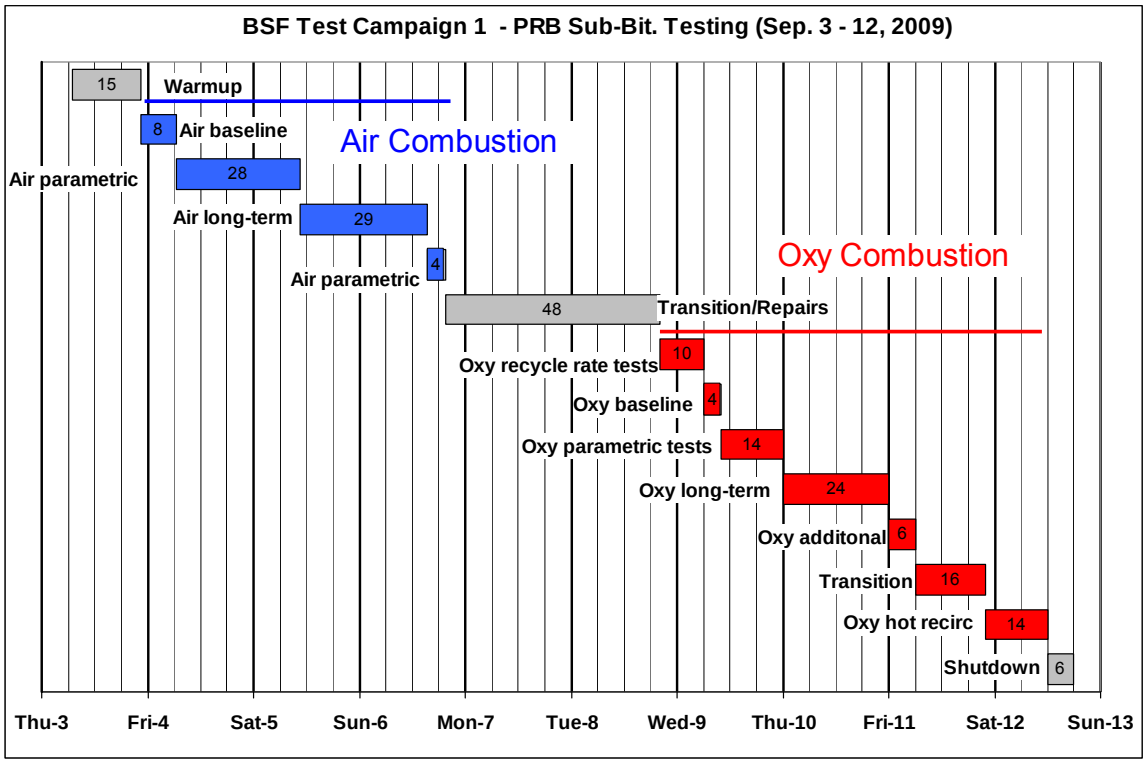

Figure 3-1. Gantt chart of test campaign 1 (PRB sub-bituminous)

Table 3-3. Test campaign 1 matrix (PRB sub-bituminous)

Test	Start	Duration	Description	Oxidant
1	9/3/09 22:30	7:40	PRB Baseline Conditions	Air
2	9/4/09 7:00	1:00	Less staging	Air
3	9/4/09 9:30	4:30	Deeper staging	Air
2A	9/5/09 0:47	1:19	Less staging repeat	Air
9	9/5/09 2:46	1:02	Low excess O2	Air
4A	9/5/09 4:15	0:49	High velocity windbox arrangement	Air
4B	9/5/09 5:30	0:30	Higher velocity windbox arrangement	Air
11	9/5/09 10:00	29:39	Air long-term testing	Air
6	9/6/09 16:04	1:46	Single SOFA upper elevation	Air
5	9/6/09 18:00	1:00	Single SOFA lower elevation	Air
12	9/8/09 20:00	4:16	High recycle	Oxy
13	9/9/09 1:33	2:02	Med recycle	Oxy
14	9/9/09 4:13	1:47	Low recycle	Oxy
15	9/9/09 9:30	0:30	Select recycle	Oxy
16	9/9/09 10:45	2:30	Match air-Fired velocity, enriched OFA	Oxy
22A	9/9/09 14:35	2:15	Match air-Fired velocity, enriched Windbox	Oxy
18	9/9/09 18:00	1:52	Single SOFA lower elevation	Oxy
19	9/9/09 20:10	1:18	Single SOFA upper elevation	Oxy
20	9/9/09 21:45	0:54	Single SOFA upper elevation, enrich windbox	Oxy
21	9/9/09 23:21	0:59	Single SOFA upper elevation, enrich OFA	Oxy
22	9/10/09 1:30	21:16	Oxy long-term testing	Oxy
23	9/11 00:30	0:40	Low excess O2	Oxy
24	9/11 01:55	0:25	Low primary O2 addition	Oxy
25	9/11/09 2:58	1:24	No primary O2 addition	Oxy
26	9/11/09 5:08	0:32	No primary O2 addition, enrich fuel air	Oxy
30	9/11/09 19:07	11:53	Baseline - oxy case 2 - hot FGR	Oxy
31	9/12/09 10:40	0:50	Oxy Case 2 - low excess O2	Oxy

3.2 Test campaign 2 – low sulfur bituminous

BSF Test Campaign 2 was successfully conducted January 18 to February 4, 2010, on a low-sulfur bituminous coal from the Fola mine in West Virginia. More than 250 tons of test coal was procured from the Fola mine in West Virginia. A Gantt chart of test campaign 2 is shown in Figure 3-2 and a test matrix is shown in Table 3-4.

Test preparations for the low sulfur bituminous coal focused on NID™ system installation, issues identified during Test Campaign 1, and preparations for cold weather testing. The entire probe water supply and drain system needed to be rebuilt for cold weather operation, insulating and heat tracing all exposed junctions and legs. Aspirators used for suction pyrometer testing were insulated and heat traced. Probe drain water lines were enlarged and rebuilt.

Test campaign 2 focused on the most important operating and design parameters identified during the first test campaign and furnace measurements expanded to better understand the impacts. Operating variables assessed included excess total oxygen, burner zone staging, and recycle rate. Additional heat flux measurements around the furnace were taken. Like the first test campaign, baseline air-fired data was initially conducted to establish comparative performance and emission data for the test coal. The NID™ dry scrubbing system was shaken-down and tested.

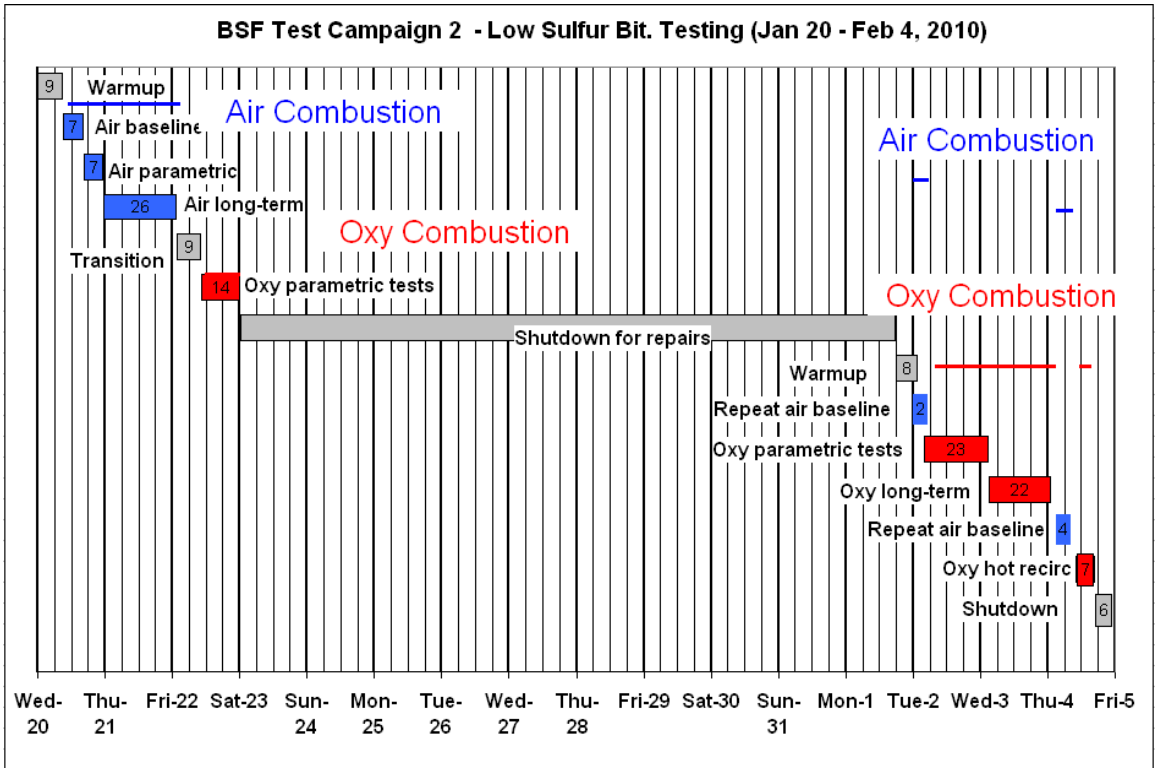

Figure 3-2. Gantt chart of test campaign 2 (low sulfur bituminous coal)

Table 3-4. Test campaign 2 matrix (low sulfur bituminous coal)

Test	Start	Duration	Description	Oxidant
36	1/20/10 9:00	7:20	Air fired baseline test, with restart	Air
37	1/20/10 16:50	1:10	Air fired low excess O2 test #1	Air
38	1/20/10 19:16	2:57	Air fired low excess O2 test #2	Air
39	1/20/10 23:30	2:25	Long term air fired test	Air
40	1/22/10 11:00	5:40	O2 distribution- Similar to PRB Staging	Oxy
41	1/22/10 17:20	2:31	O2 distribution- no UOFA	Oxy
42	1/22/10 20:12	2:03	O2 distribution- no OFA, open CCOFA	Oxy
43	1/22/10 23:47	0:39	O2 distribution - lance injection to fuel air	Oxy
44	2/2/10 1:45	1:45	Air Fired Baseline, Repeat of Test #39 Conditions	Air
45	2/2/10 10:05	2:47	Oxy Fired Low Excess O2 Test #1	Oxy
46	2/2/10 13:49	2:09	Oxy Fired Low Excess O2 Test #2	Oxy
45B	2/2/10 16:28	1:07	Oxy Fired Low Excess O2 Test #1 Repeat	Oxy
47	2/2/10 18:21	2:34	Oxy Fired Low Recycle with 2% outlet O2	Oxy
48	2/2/10 21:40	1:35	Oxy Fired Lower Recycle	Oxy
49	2/2/10 23:30	0:29	Oxy Lowest Recycle Rate	Oxy
50	2/3/10 2:55	22:25	Select Conditions for Long-Term Testing	Oxy
51	2/4/10 2:12	0:34	Low Load Oxy (70% Load)	Oxy
52	2/4/10 4:07	1:43	Repeat Air Long-Term Test	Air
53	2/4/10 6:51	0:43	Low Load Air	Air
54	2/4/10 10:10	6:50	Baseline - Oxy Case 2 - Hot FGR	Oxy

3.3 Test campaign 3 – high-sulfur Illinois bituminous

BSF Test Campaign 3 was successfully conducted April 25 to May 1, 2010 on a high-sulfur Illinois bituminous coal. More than 275 tons of test coal was procured from the Prairie Eagle mine in Illinois. A Gantt chart of test campaign 3 is shown in Figure 3-3 and a test matrix is shown in Table 3-5.

Test preparations for the Illinois campaign focused on routine cleaning, maintenance, measurement improvements, and instrument calibrations. The rebuilt primary air fan was installed and a new primary air electric heater was installed. The condensate pump purchased in February 2010 was installed with a containment system and skid enclosure. Ports in the lower windbox were modified to allow for heat flux probing. Problems related to cold weather operation were addressed, and some flue gas leaks were repaired. A NO_x analyzer was installed in the sample shed with the ability to sample from either the baghouse inlet, the baghouse outlet, or the in-furnace sampling system.

Test campaign 3 focused on characterizing the oxy-combustion performance of high sulfur Illinois coal. This program, as originally proposed to the DOE, included assessment of very high sulfur levels by spiking sulfur to simulate high sulfur coal. Test campaign 3, with additional funding from the Illinois Clean Coal Institute (ICCI), was added to the program to allow for actual testing with a high sulfur coal to provide realistic combustion conditions and improve the reliability of the data as well as greatly expand the amount of information that can be collected. Of particular interest were the SO_2 and SO_3 concentrations that built up due to the recycle of flue gas according to the level of sulfur capture. Like the first test campaign, baseline air-fired data was initially conducted to establish comparative performance and emission data for the test coal. The NID™ dry scrubbing system was utilized to capture sulfur in the recycle stream. Combustion testing during test campaign 3 focused on methods to adjust and control the heat flux profile during oxy-firing.

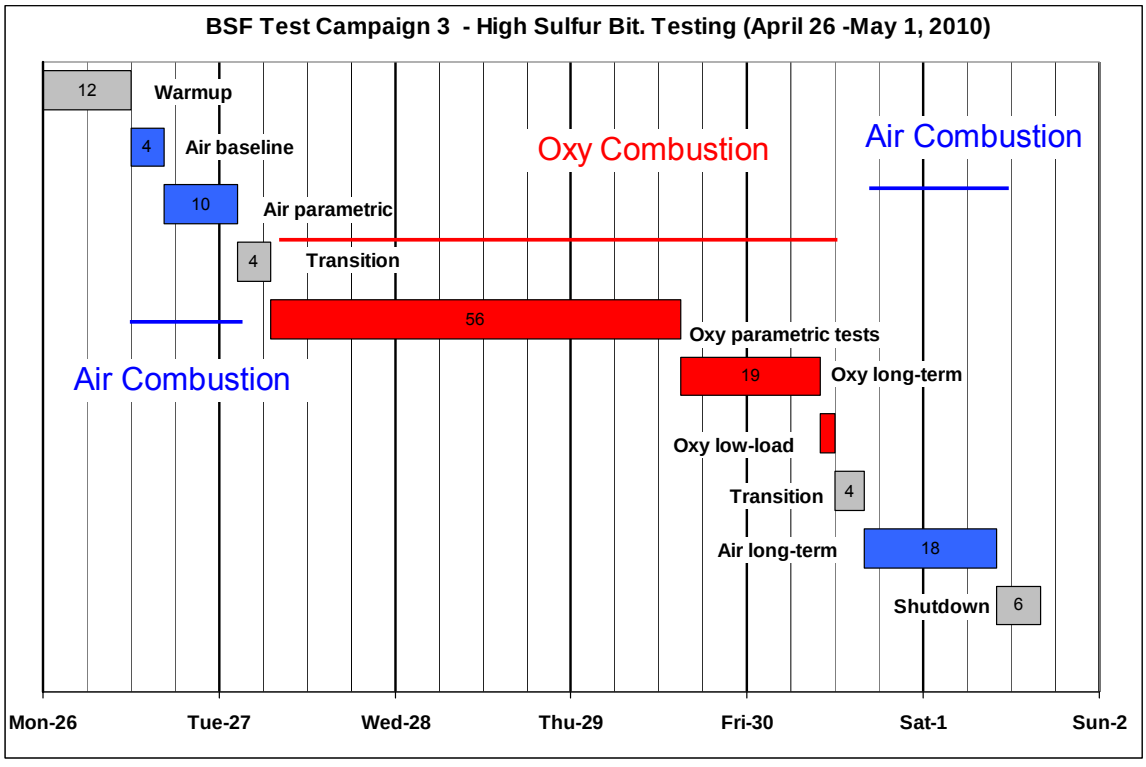

Figure 3-3. Gantt chart of test campaign 3 (high sulfur bituminous coal)

Table 3-5. Test campaign 3 matrix (high sulfur bituminous coal)

Test	Start	Duration	Description	Oxidant
55	4/26/10 12:30	3:50	High sulfur baseline conditions	Air
56	4/26/10 17:10	0:20	Air fired low excess O2 #1	Air
57	4/26/10 18:07	3:18	Air fired low excess O2 #2	Air
58	4/26/10 22:17	2:58	UOFA staging	Air
60	4/27/10 16:48	0:11	Busted test, TRIP	
61	4/27/10 21:25	1:32	Oxy fired recycle test #3 33% global O2	Oxy
62	4/28/10 0:00	2:18	Oxy fired recycle test #2 25% global O2	Oxy
63	4/28/10 4:20	1:40	Oxy fired recycle test #1 28% global O2	Oxy
64	4/28/10 6:50	0:27	28% global O2, low excess O2 #1	Oxy
65	4/28/10 8:15	2:03	28% global O2, low excess O2 #2	Oxy
66	4/28/10 12:27	1:07	Select recycle conditions, baseline testing	Oxy
72	4/28/10 15:20	1:10	No primary O2 addition, enrich windbox	Oxy
73	4/28/10 18:05	2:07	No primary O2 addition, fuel lance injection	Oxy
67	4/28/10 20:50	1:25	Fuel lance addition	Oxy
68	4/29/10 0:06	1:24	Bottom lance addition	Oxy
69	4/29/10 3:29	2:31	LOFA staging #1, lance injection to LOFA	Oxy
70	4/29/10 6:45	3:55	LOFA staging #2, LOFA only	Oxy
71	4/29/10 11:20	2:18	UOFA staging, no LOFA	Oxy
74	4/29/10 15:15	18:45	Oxy long-term test	Oxy
76	4/30/10 10:30	1:05	Low load oxy (70% load)	Oxy
75	4/30/10 15:45	16:32	Air long-term test	Air

3.4 Test campaign 4 – North Dakota lignite

BSF Test Campaign 4 was successfully conducted October 4 to October 9, 2010, on North Dakota lignite. More than 350 tons of test coal was procured from Great River Energy's Coal Creek Station in Underwood, North Dakota. A Gantt chart of test campaign 4 is shown in Figure 3-4 and a test matrix is shown in Table 3-6.

Test preparations for the North Dakota Lignite campaign focused on routine cleaning, maintenance, and calibrations. Problems discovered after test campaign 3 were addressed; main problems included burnt OFA units, broken Vaisala humidity probes, corroded sample port ball valves, and a plugged primary air heater. Ports were installed in the secondary recirculation system to measure mercury, and an SO_3 injection system was constructed. The dried lignite was taken from an intermediate point in the coal preparation system at Coal Creek Station and arrived with a lot of moisture, making coal unloading, storage and pulverization very challenging. The lignite was difficult to dry and grind to the desired fineness in the mill; agglomerated coal "balls" present in the pulverized coal supply caused operation problems.

Test campaign 4 focused on characterizing the oxy-combustion performance of North Dakota lignite. Test campaign 4 was added on to the original DOE program with support of the North Dakota Industrial Commission, Lignite Research Council. Particular focus was given to gaseous mercury concentrations that could build up during oxy-firing according to the level of mercury capture from the recycled flue gas in the baghouse. To understand the fate of SO_3 in the boiler, tests were conducted spiking SO_3 into the recycle stream. Like the first three test campaigns, baseline air-fired data was initially conducted to establish comparative performance and emission data for the test coal. The impact of operating and firing system design variables on thermal performance and emissions was assessed over a series of test points.

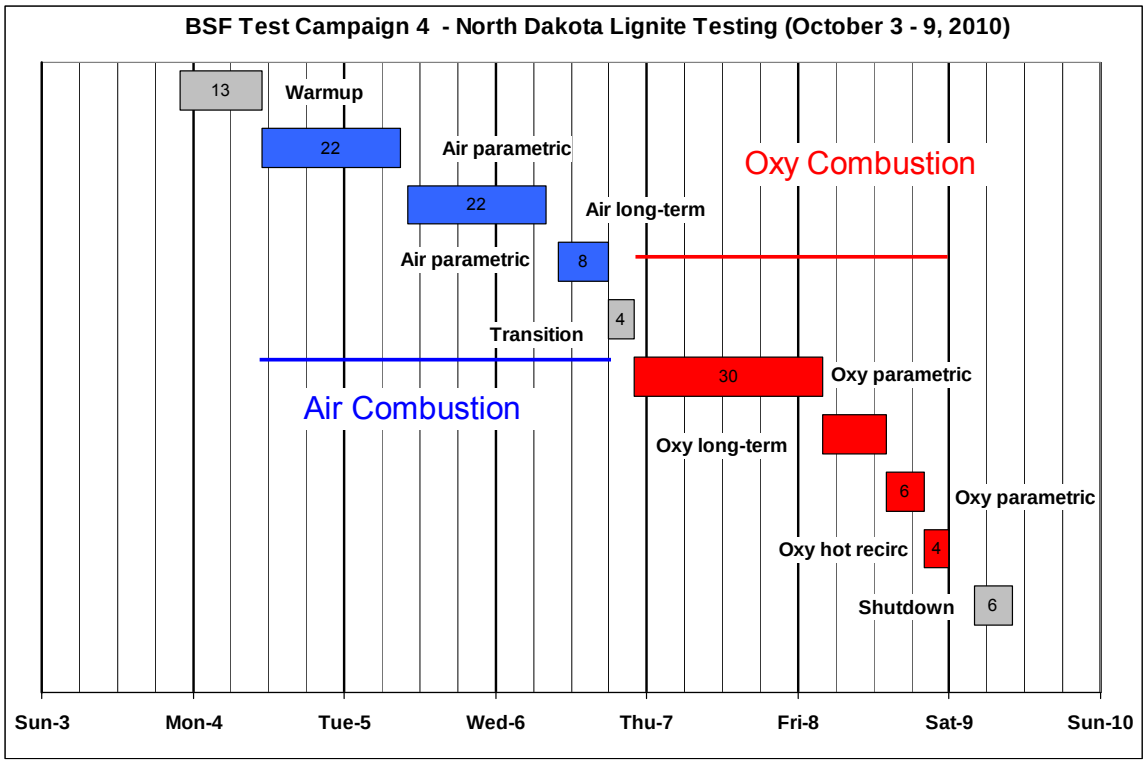

Figure 3-4. Gantt chart of test campaign 4 (North Dakota lignite)

Table 3-6. Test campaign 4 matrix (North Dakota lignite)

Test	Start	Duration	Description	Oxidant
77	10/4/10 11:11	1:40	Less Staged Conditions	Air
78	10/4/10 13:45	2:23	Baseline Conditions	Air
79	10/4/10 18:20	0:40	Air fired low excess O2 #1	Air
79A	10/4/10 19:10	1:20	Air fired low excess O2 Test #2	Air
80	10/4/10 21:00	1:55	Air fired low excess O2 Test #3	Air
81	10/4/10 23:47	1:14	Air fired deeply staged	Air
81B	10/5/10 1:10	0:39	Air fired deeply staged, higher windbox velocity	Air
82	10/5/10 7:00	0:15	Oxy fired baseline conditions	Oxy
83	10/5/10 10:21	22:09	Air long-term test	Air
84	10/6/10 9:50	0:26	Air fired low load #1 - 35 MMBTU	Air
85	10/6/10 10:48	0:35	Air fired low load #2 - 30 MMBTU	Air
86	10/6/10 16:25	0:55	Repeat air long-term test at higher velocity	Air
87	10/6/10 22:30	2:27	Oxy fired baseline conditions	Oxy
88	10/7/10 1:23	1:27	Oxy fired deeper staging	Oxy
89	10/7/10 3:30	2:57	Oxy fired less staging	Oxy
90	10/7/10 7:43	0:34	Oxy fired low excess O2 #1	Oxy
91	10/7/10 12:16	1:20	Oxy fired recycle test #1 25% global O2	Oxy
92	10/7/10 18:06	1:12	Oxy fired recycle test #2 28% global O2	Oxy
93	10/7/10 19:45	2:06	Oxy fired recycle test #3 33% global O2	Oxy
94	10/7/10 22:20	0:31	Low O2 #1 @ 33% global O2 test	Oxy
95	10/7/10 23:12	0:25	Low O2 #2 @ 33% global, higher velocity OFA	Oxy
96	10/8/10 0:15	1:18	Low O2 #3 @ 33% global O2 test	Oxy
97	10/8/10 2:25	0:55	Lance O2 injection to 1 CFS Level	Oxy
98	10/8/10 4:16	10:04	Long-term oxy	Oxy
99	10/8/10 15:00	3:49	Deeper staging for reduced sulfur testing	Oxy
100	10/8/10 18:50	1:24	Reduced sulfur testing with CFS enrichment	Oxy
101	10/9/10 0:29	2:58	Hot recirculation test	Oxy

3.5 Test campaign 6 – Schwarze Pumpe lignite

The original schedule called for this test to be the last campaign. The schedule changed and this test was done before the second generation testing, but the original numbering was retained. BSF Test Campaign 6 was successfully conducted July 11 to 18, 2011. More than 400 tons of pre-dried lignite burned at Vattenfall's Schwarze Pumpe pilot plant was supplied by Vattenfall. A Gantt chart of test campaign 6 is shown in Figure 3-5 and a test matrix is shown in Table 3-7.

Test preparations completed prior to the Schwarze Pumpe lignite (or Lusation lignite) included sealing of flue gas leaks and equipment repairs. Doors on top of the Q-Pipe were welded closed, a new skin was installed on the 5' duct, and a new skin was fitted to the exhaust gas from the facility to the scrubber. These repairs greatly reduced the sulfur smell around the test facility. The north igniter spark rod was repaired and a new main gas block-and-bleed was installed in the SE corner.

Test campaign 6 focused on establishing a link between tests run at the tangentially-fired 15 MW_{th} oxy-fired BSF and the single burner down-fired 30 MW_{th} oxy-combustion pilot plant at Vattenfall's Schwarze Pumpe station. The Schwarze Pumpe oxy pilot is the world's first complete technology path for CO_2 capture, including an ASU and CO_2 processing plant. The experience from oxy combustion tests with the same fuel at the two facilities allows for a comparison between emissions, thermal data, and performance between the two facilities. Test data from the 15MW_{th} BSF and the 30MW_{th} oxy pilot plant has been used for refinement and validation of CFD codes. Parameters varied during BSF testing include firing rate, recycle rate, staging, and excess oxygen. Tests were selected to match conditions and ranges experienced at Schwarze Pumpe and on prior BSF tests.

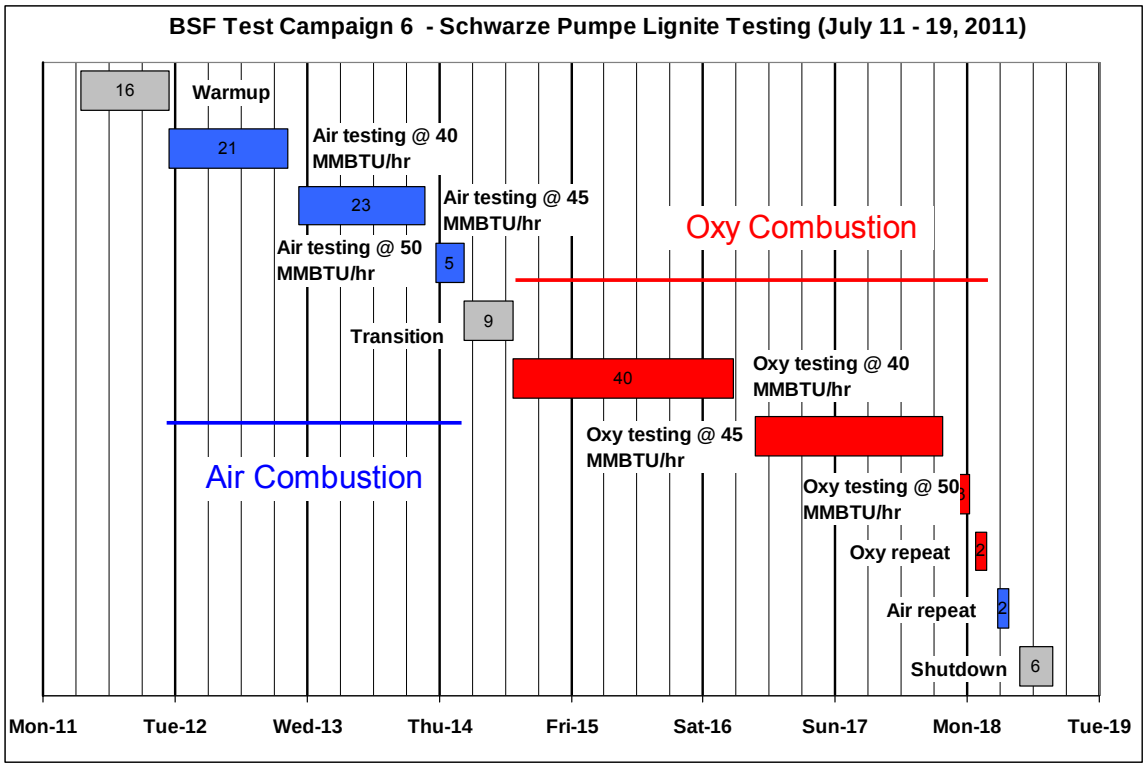

Figure 3-5. Gantt chart of test campaign 6 (Schwarze Pumpe lignite)

Table 3-7. Test campaign 6 matrix (Schwarze Pumpe lignite)

Test	Start	Duration	Description	Oxidant
102	07/11/11 23:15	4:00	40 MMBTU/hr match PRB/ND long term conditions	Air
103	07/12/11 04:52	11:15	40 MMBTU/hr match MR1 staging	Air
104	07/12/11 16:30	0:30	40 MMBTU/hr, excess stoichiometry test #1	Air
105	07/12/11 17:12	0:28	40 MMBTU/hr, excess stoichiometry test #2	Air
106	07/12/11 17:55	1:04	40 MMBTU/hr, excess stoichiometry test #3	Air
107	07/12/11 19:42	1:02	40 MMBTU/hr, excess stoichiometry test #4	Air
108	07/12/11 22:30	2:31	45 MMBTU/hr match MR1 staging	Air
109	07/13/11 02:00	13:02	45 MMBTU/hr match PRB/ND long term conditions	Air
110	07/13/11 15:25	1:46	45 MMBTU, less staging	Air
111	07/13/11 17:25	0:41	45 MMBTU, moderate staging	Air
112	07/13/11 18:17	0:46	45 MMBTU, deep staging	Air
113	07/13/11 19:47	0:48	45 MMBTU, excess stoichiometry test #2	Air
114	07/13/11 21:05	0:37	45 MMBTU, excess stoichiometry test #3	Air
115	07/13/11 23:45	3:41	50 MMBTU/hr match PRB/ND long term conditions	Air
116	07/14/11 04:25	0:22	PA/F #2 – lower PA/F	Air
117	07/14/11 13:35	2:33	40 MMBTU/hr match test #98	Oxy
118	07/14/11 17:25	0:30	40 MMBTU/hr, 23.5% Global, Low O2 #1	Oxy
120	07/14/11 19:39	0:50	40 MMBTU/hr, 23.5% Global, Low O2 #2	Oxy
121	07/14/11 22:51	0:40	40 MMBTU/hr, 28% Global, Low O2 #1	Oxy
122	07/15/11 00:09	0:37	40 MMBTU/hr, 28% Global, Low O2 #2	Oxy
123	07/15/11 01:55	0:46	40 MMBTU/hr, 28% Global, High O2 Test	Oxy
124	07/15/11 04:30	0:44	40 MMBTU/hr, 32.5% Global, Low O2 #1	Oxy
125	07/15/11 05:38	0:39	40 MMBTU/hr, 32.5% Global, Low O2 #2	Oxy
126	07/15/11 06:32	0:40	40 MMBTU/hr, 32.5% Global, increased OFA velocity	Oxy
127	07/15/11 08:54	8:53	40 MMBTU/hr match MR3 staging	Oxy
128	07/15/11 18:27	2:50	40 MMBTU/hr, no primary O2, enrich windbox	Oxy
129	07/15/11 22:47	3:08	40 MMBTU/hr, no primary O2, fuel lance enrichment	Oxy
130	07/16/11 02:47	2:09	40 MMBTU/hr, 32% Global O2	Oxy
131	07/16/11 09:20	3:41	45 MMBTU/hr, 23.5% Global O2 RR (Match MR3)	Oxy
132	07/16/11 14:00	2:25	45 MMBTU/hr, Staging Test #2	Oxy
133	07/16/11 16:55	2:25	45 MMBTU/hr, Staging Test #1	Oxy
134	07/16/11 21:10	14:20	45 MMBTU/hr, long-term testing	Oxy
135	07/17/11 15:30	4:19	45 MMBTU/hr, 32% global O2 RR test	Oxy
136	07/17/11 21:06	2:57	50 MMBTU/hr hr match PRB long term conditions	Oxy
137	07/18/11 01:34	2:14	Repeat test #127	Oxy
138	07/18/11 05:30	2:43	Repeat test #103	Air

3.6 Test campaign 5-1 – 2nd generation, low sulfur bituminous

BSF Test Campaign 5-1 was successfully conducted December 7 to 16, 2011. Testing was conducted with the same West Virginia low sulfur bituminous coal used during Test Campaign 2. Test fuel was selected to provide a link with Campaign 2 results and minimize baseline air and oxy-fired testing. More than 300 tons of test fuel were burned during 26 oxy-fired and 9 air-fired test conditions. A Gantt chart of test campaign 5-1 is shown in Figure 3-6 and a test matrix is shown in Table 3-8.

Test facility preparations completed prior to 2nd generation testing included design and installation of equipment needed for second-generation concept testing and general facility maintenance. The facility modifications allowed the flexibility to test close-coupled flue gas recirculation concepts. Close-coupled flue gas recirculation is driven by ejectors using oxygen as the motive gas to draw flue gas recirculation from before the air-heaters or pollution control systems. Two close coupled recirculation systems were installed: 1) a single large ejector driving all the gas recirculation for the windbox

secondary oxidant, and 2) four smaller ejectors driving recirculation utilizing a supplemental oxygen supply. Details of these systems can be found in section 2.2.6.

Test campaign 5-1 focused on evaluation of second-generation oxy boiler concepts that may improve oxy boiler and/or overall oxy plant performance and economics. Three main concepts were investigated: close-coupled flue gas recirculation, use of oxygen driven ejectors to recirculate flue gas, and a compressed firing zone. A series of tests were conducted under both air-firing and oxy-firing with flue gas recycle after the fabric filter to replicate prior test conditions and gather comparative information not measured during Test Campaign 2. To determine operating characteristics and stability of the ejector-driven system, a series of tests were conducted with the internal recirculation systems. Testing was also conducted using a compressed windbox arrangement to gain information on impacts on the heat flux profile and operating characteristics to guide future phases of Test Campaign 5.

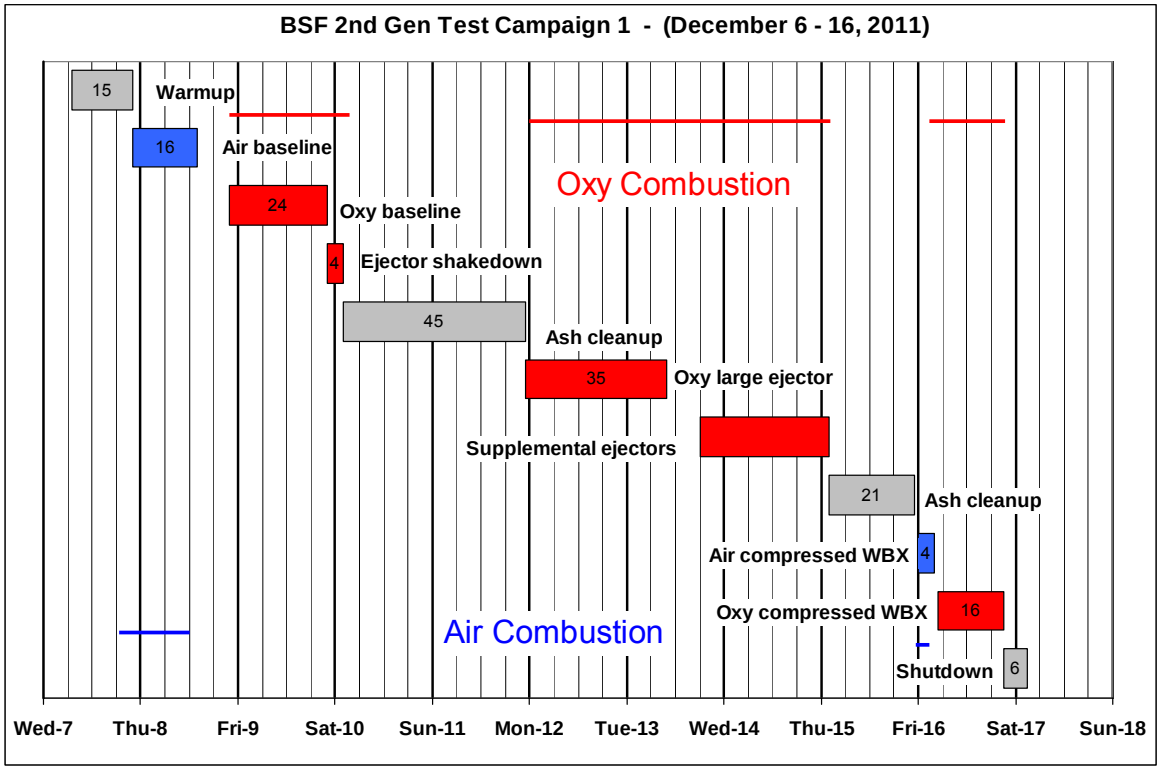

Figure 3-6. Gantt chart of test campaign 5-1 (low sulfur bituminous coal)

Table 3-8. Test campaign 5-1 matrix (low sulfur bituminous coal)

Test	Start	Duration	Description	Oxidant
140	12/7/2011 22:30	5:06	Air firing deeper furnace staging	Air
141	12/8/2011 4:10	0:30	Single SOFA - lower elevation only	Air
142	12/8/2011 4:45	0:30	Dual SOFA	Air
143	12/8/2011 5:30	0:27	Single SOFA - upper elevation only	Air
144	12/8/2011 6:20	0:31	Increased primary air velocity	Air
145	12/8/2011 7:06	6:53	Less furnace air staging - baseline testing	Air
146	12/8/2011 22:05	3:13	Windbox arrangement #1 – low vel.	Oxy
147	12/9/2011 1:48	3:19	Windbox arrangement #2 – matched vel.	Oxy
148	12/9/2011 9:00	4:39	Oxy-fired baseline testing	Oxy
149	12/9/2011 14:35	2:18	Oxy-fired deeper staging	Oxy
150	12/11/2011 22:35	7:32	Internal Recirc – baseline testing	Oxy
151	12/12/2011 6:44	7:56	Internal Recirc – deeper staging	Oxy
152	12/12/2011 15:40	5:21	Internal Recirc – deep staging	Oxy
153	12/12/2011 21:27	3:53	Internal Recirc – high suction rate	Oxy
154	12/12/2011 2:44	0:36	Internal Recirc – Low PA oxygen addition	Oxy
155	12/12/2011 4:22	1:00	Internal Recirc – No PA oxygen addition	Oxy
156	12/13/2011 5:45	4:20	Internal Recirc – baseline testing repeat	Oxy
157	12/13/2011 18:00	4:45	Small ejector – baseline staging, setup #1	Oxy
158	12/13/2011 23:10	2:53	Small ejector – baseline staging, setup #2	Oxy
159	12/14/2011 2:50	2:45	Small ejector – baseline staging, setup #3	Oxy
160	12/14/2011 6:15	3:45	Small ejector – deeper staging, setup #3	Oxy
161	12/14/2011 12:15	6:26	Small ejector – deeper staging, setup #2	Oxy
162	12/14/2011 19:00	3:38	Small ejector – deeper staging, setup #4	Oxy
163	12/14/2011 23:28	2:40	Small ejector – high suction, select setup	Oxy
164	12/16/2011 0:00	1:00	Compressed windbox baseline testing	Air
165	12/16/2011 1:30	0:30	Compressed windbox low O2 evaluation	Air
166	12/16/2011 2:53	0:38	Compressed windbox deeper staging	Air
167	12/16/2011 5:00	0:54	Compressed windbox, arrangement 1	Oxy
168	12/16/2011 6:20	0:35	Compressed windbox, arrangement 2	Oxy
169	12/16/2011 7:40	1:06	Select arrangement, deeper staging	Oxy
170	12/16/2011 9:10	0:32	Low excess O2 evaluation #1	Oxy
171	12/16/2011 10:20	0:55	Low excess O2 evaluation #2	Oxy
172	12/16/2011 11:35	0:35	Low excess O2 evaluation #3	Oxy
173	12/16/2011 13:00	2:10	Compressed windbox baseline testing	Oxy
174	12/16/2011 15:45	5:16	Long term test - detailed mapping	Oxy

3.7 Test campaign 5-2 – 2nd generation, PRB sub-bituminous

BSF Test Campaign 5-2 was successfully conducted September 23 to 29, 2012. Testing was conducted with the same PRB sub-bituminous coal used during Test Campaign 1. Test fuel was selected to provide a link with Campaign 1 results and minimize baseline air and oxy-fired testing. More than 290 tons of test fuel were burned during 26 oxy-fired and 9 air-fired test conditions. A Gantt chart of phase 2 testing is shown in Figure 3-7 and a test matrix is shown in Table 3-9.

Test facility preparations completed prior to 2nd generation - phase 2 testing included design and installation of a flue gas slip-stream. The flue gas slip stream was designed to cool 1,000 lb/hr of flue gas from 1000°F to 400°F in 1 second of residence time. This controlled time-temperature history was desired to understand the control of SO_3 and Hg in oxy-combustion flue gas. Inlet and outlet sampling systems were set up using an inertial separation probe (ISP) and a feed system was set up to add sorbents. Slip-stream testing was conducted on PRB coal to evaluate mercury control and with high sulfur, high chlorine coal in the following campaign to evaluate acid-gas control. A system was added

to spike nitric oxide into the flue gas recycle returning to the BSF burner/windbox and separate overfire ports to assess NO_x reduction.

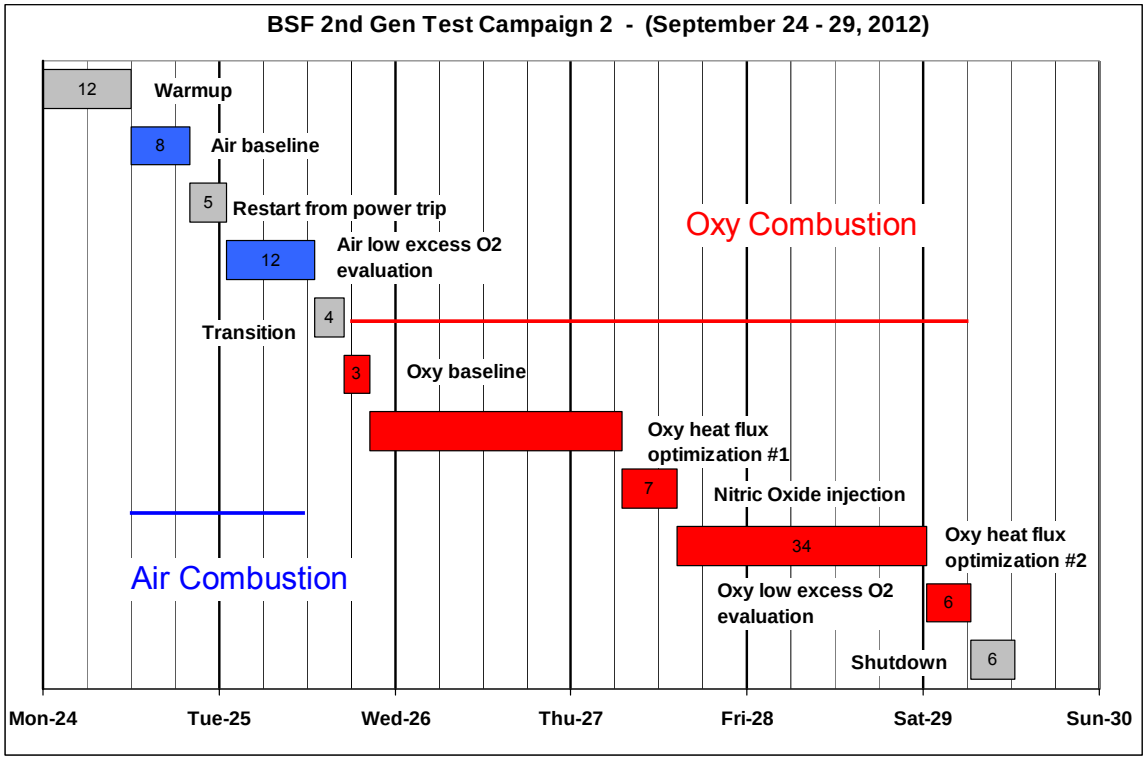

Figure 3-7. Gantt chart of test campaign 5-2 (PRB sub-bituminous)

Table 3-9. Test campaign 5-2 matrix (PRB sub-bituminous)

Test	Start	Duration	Description	Oxidant
201	9/24/12 11:37	0:48	Air fired baseline testing – deep staging	Air
202	9/24/12 12:45	2:00	Less furnace air staging #1	Air
203	9/24/12 15:24	1:20	Less furnace air staging #2	Air
204	9/24/12 18:12	1:40	Long term testing and Hg control stage #1	Air
205	9/25/12 1:06	0:44	Repeat Baseline Testing	Air
206	9/25/12 2:02	0:33	Low excess O2 evaluation #1	Air
207	9/25/12 3:10	0:48	Low excess O2 evaluation #2	Air
208	9/25/12 4:39	0:30	Low excess O2 evaluation #3	Air
209	9/25/12 6:00	7:00	Long term testing and Hg control stage #2	Air
210	9/25/12 17:55	1:00	Oxy fired baseline testing – deep staging	Oxy
211	9/25/12 19:15	1:00	Less furnace staging #1	Oxy
212	9/25/12 20:30	3:30	Less furnace staging #2 – enrich bulk	Oxy
213	9/26/12 0:00	3:08	Less furnace staging #2 – enrich windbox	Oxy
214	9/26/12 4:15	8:15	Long term testing and Hg control stage #1	Oxy
215	9/26/12 13:45	4:42	Heat flux optimization, local O2 enrich #1	Oxy
216	9/26/12 18:45	4:15	Heat flux optimization, local O2 enrich #2	Oxy
217	9/27/12 0:20	6:40	Heat flux optimization, local O2 enrich #3	Oxy
218	9/27/12 7:00	1:30	Nitric oxide – baseline, w/out injection	Oxy
219	9/27/12 8:32	0:30	Nitric oxide – secondary FGR injection #1	Oxy
220	9/27/12 9:05	0:46	Nitric oxide –secondary FGR injection #2	Oxy
221	9/27/12 10:13	1:12	Nitric oxide – windbox FGR injection	Oxy
222	9/27/12 11:47	0:30	Nitric oxide – OFA FGR injection #1	Oxy
223	9/27/12 12:18	0:20	Nitric oxide – OFA FGR injection #2	Oxy
224	9/27/12 13:15	0:34	Nitric oxide – Deep staging, w/out injection	Oxy
225	9/27/12 13:49	0:29	Nitric oxide – Deep staging, windbox FGR	Oxy
226	9/27/12 16:05	4:07	Heat flux optimization, local O2 enrich #4	Oxy
227	9/27/12 21:30	7:30	Heat flux optimization, local O2 enrich #5	Oxy
228	9/28/12 5:55	8:11	Heat flux optimization, local O2 enrich #6	Oxy
229	9/28/12 16:00	7:00	Heat flux optimization, local O2 enrich #7	Oxy
230	9/29/12 0:28	0:37	Low excess O2 eval #1 – 23.5% global O2	Oxy
231	9/29/12 1:35	0:30	Low excess O2 eval #2 – 28% global O2	Oxy
232	9/29/12 2:40	1:00	Low excess O2 eval #3 – 28% global O2	Oxy
233	9/29/12 4:05	0:35	Low excess O2 eval #4 – 28% global O2	Oxy
234	9/29/12 5:04	0:24	Low excess O2 eval #5 – 32% global O2	Oxy
235	9/29/12 6:17	0:34	Low excess O2 eval #6 – 32% global O2	Oxy

3.8 Test campaign 5-3 – 2nd generation, high sulfur bituminous

BSF Test Campaign 5-3 was successfully conducted October 31 to November 6, 2012. Testing was conducted with a high sulfur, high chlorine bituminous coal from the Galatia mine in southern Illinois (not the same fuel used in Campaign 3). More than 275 tons of test fuel were burned during 26 oxy-fired and 15 air-fired test conditions. A Gantt chart of phase 3 testing is shown in Figure 3-8 and a test matrix is shown in Table 3-10.

Slip-stream testing was done to evaluate acid-gas control and further nitric oxide injection tests were done. Other tests included increased firing rate, low excess O_2, and heat flux optimization on oxy-firing.

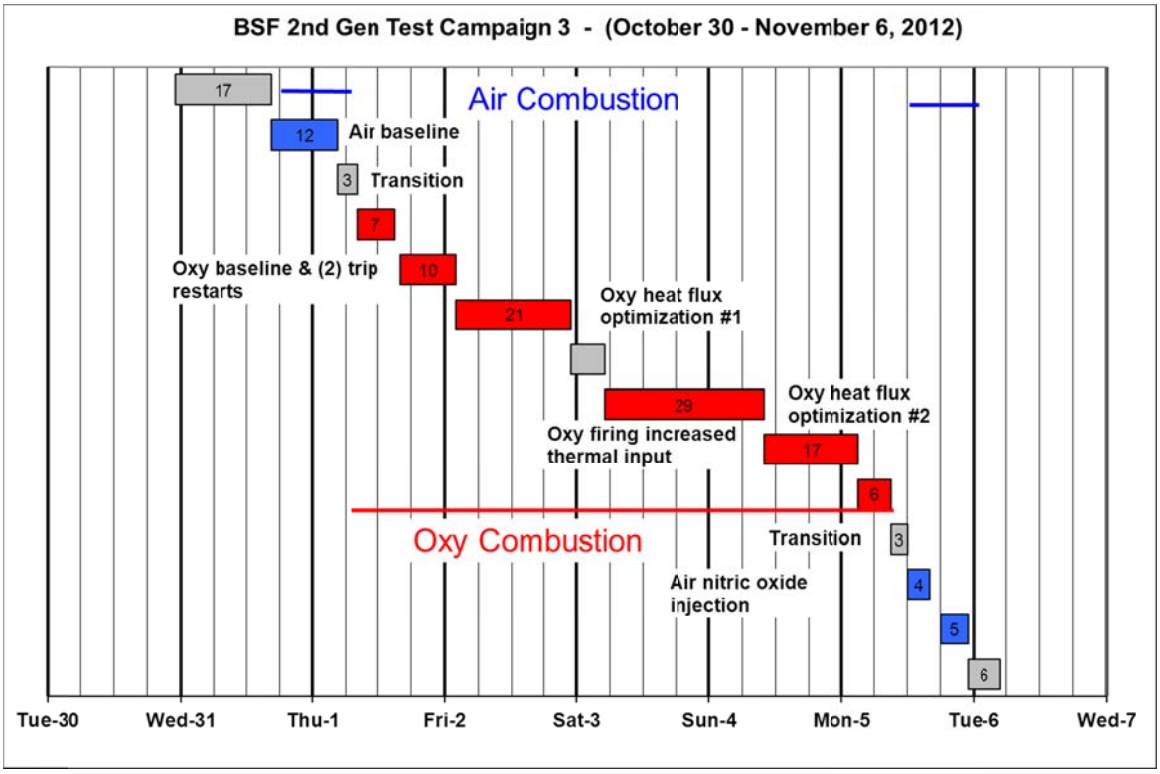

Figure 3-8. Gantt chart of test campaign 5-3 (high sulfur bituminous coal)

Table 3-10. Test campaign 5-3 matrix (high sulfur bituminous coal)

Test	Start	Duration	Description	Oxidant
236	10/31/12 16:30	1:25	Initial air fired baseline testing	Air
237	10/31/12 18:15	9:02	Deeper furnace air staging	Air
238	11/1/12 3:30	0:59	Less furnace air staging	Air
239	11/1/12 8:00	0:50	Oxy fired baseline testing – deep staging	Oxy
240	11/1/12 9:34	0:43	Nitric oxide – bulk secondary FGR #1	Oxy
241	11/1/12 10:19	0:32	Nitric oxide – bulk secondary FGR #2	Oxy
242	11/1/12 11:25	0:24	Nitric oxide – windbox FGR	Oxy
243	11/1/12 11:50	0:17	Nitric oxide – OFA FGR #1	Oxy
244	11/1/12 12:08	0:22	Nitric oxide – OFA FGR #2	Oxy
245	11/1/12 13:08	1:29	Nitric oxide – Less staging, w/out injection	Oxy
246	11/1/12 14:45	0:15	Nitric oxide – Less staging, windbox FGR	Oxy
247A	11/1/12 15:40	1:13	Heat flux optimization, select staging	Oxy
247B	11/1/12 18:25	3:35	Less furnace staging baseline testing	Oxy
248A	11/1/12 22:43	1:27	Heat flux optimization, local O2 enrichment	Oxy
248B	11/2/12 1:50	6:40	Heat flux optimization, local O2 enrichment	Oxy
249	11/2/12 8:55	3:45	Reduced recycle rate baseline testing	Oxy
250	11/2/12 14:25	8:35	32% global O2, local O2 enrichment	Oxy
251	11/3/12 5:45	2:15	23.5% global O2, deep staging	Oxy
252	11/3/12 9:00	8:18	28% global O2, deep staging, enrich WBX	Oxy
253	11/3/12 18:30	5:43	28% global O2, less staging, enrich WBX	Oxy
254	11/4/12 1:10	7:19	28% global O2 - local O2 enrichment	Oxy
255	11/4/12 10:55	3:50	High firing rate - local O2 enrichment #1	Oxy
256	11/4/12 15:25	3:33	High firing rate - local O2 enrichment #2	Oxy
257	11/4/12 20:30	6:30	High firing rate - local O2 enrichment #3	Oxy
258	11/5/12 4:50	0:30	Low excess O2 #1, 23.5% global O2	Oxy
259	11/5/12 5:30	0:30	Low excess O2 #2, 28% global O2	Oxy
260	11/5/12 6:21	0:39	Low excess O2 #3, 32% global O2	Oxy
261	11/5/12 7:20	0:25	Low excess O2 #4, 32% global O2	Oxy
262	11/5/12 8:11	0:24	Low excess O2 #5, 32% global O2	Oxy
263	11/5/12 11:47	1:45	Nitric oxide, baseline, w/out injection	Oxy
264	11/5/12 13:32	0:09	Nitric oxide – OFA	Air
265	11/5/12 13:41	0:09	Nitric oxide – Windbox	Air
266	11/5/12 13:53	0:10	Nitric oxide – Bulk secondary air	Air
267	11/5/12 14:40	0:12	Nitric oxide, less staging, w/out injection	Air
268	11/5/12 14:52	0:52	Nitric oxide, less staging, bulk secondary	Air
269	11/5/12 15:46	2:29	Repeat test #238	Air
270	11/5/12 19:05	0:30	Low excess O2 evaluation #1	Air
271	11/5/12 20:00	0:30	Low excess O2 evaluation #2	Air
272	11/5/12 20:45	0:45	Low excess O2 evaluation #3	Air
273	11/5/12 21:50	0:30	Low excess O2 evaluation #4	Air
274	11/5/12 23:00	0:23	Low excess O2 evaluation #5	Air

4. Fuels Characterization

Along with the fuel analyses shown in Table 3-2, four of the test fuels were more thoroughly characterized in a bench scale program. The goal was to

a) characterize the combustion properties of BSF test fuels under both air and oxy-combustion conditions, and
b) generate char kinetic data for BSF test fuels under oxy-firing conditions to support computational modeling efforts.

The four fuels selected were:

- Black Thunder Coal (BTC), the Powder River Basin (PRB) sub-bituminous coal from Campaign 1
- Fola Coal (WVC), the West Virginian bituminous coal from Campaign 2
- Prairie Eagle Coal (ILC), the high sulfur Illinois No. 6 bituminous coal from Campaign 3
- Schwarze Pumpe Coal (SPC), the German lignite from Campaign 6

The additional analyses were:

- BET surface area of char,
- Thermogravimetric analysis (TGA) of coal and char,
- Petrographic analysis of coal,
- Computer Controlled Scanning Electron Microscopy (CCSEM) of ash,
- Micro-proximate, micro-ultimate (H,C,N), and mini-screens for analysis of small sample quantities,
- Drop Tube Furnace System (DTFS) tests to measure the reactivity of coal and char under various envirionments,
- Processing of coal in the DTFS to produce the char and ash for the other analyses.

These are summarized in Table 4-1.

Table 4-1. Summary of feedstocks and tests

feedstock	analyses / tests		produced
Raw coal	analysis: proximate, ultimate, HV, ash comp., trace metals		
	petrographic analysis		
	dry, grind, and screen to 200x400 mesh	→	**Sized coal**
Sized coal	analysis: micro prox, ultimate, miniscreen		
	TGA – air burnoff		
	DTFS – coal gasification in 100% CO_2		
	DTFS in air or 21% O_2/79% CO_2	→	**Ash**
	DTFS in N_2	→	**Char**
Ash	analysis: micro prox, micro ult		
	CCSEM		
Char	analysis: microprox, ultimate, miniscreen		
	BET surface area		
	screen to 200x400 mesh	→	**Sized char**
Sized char	TGA – air combustion at 700°C		
	TGA – CO_2 gasification at 950°C		
	DTFS – combustion in 3% O_2 / balance N_2 (air fired)		
	DTFS – combustion in 3% O_2 / balance CO_2 (oxy fired)		
	DTFS – gasification in 100% CO_2 or 30/70 CO_2/N_2		

4.1 Experimental Procedures

The following American Society for Testing Materials (ASTM) techniques were used:

ASTM D3172-Standard Practice for Proximate Analysis of Coal and Coke.
ASTM D3176-Standard Practice for Ultimate Analysis of Coal and Coke.
ASTM D5865-Standard Test Method for Gross Calorific Value of Coal and Coke.
ASTM D6357-Test Methods for Determination of Trace Elements in Coal, Coke, & Combustion Residues from Coal Utilization Processes by Inductively Coupled Plasma Atomic Emission, Inductively Coupled Plasma Mass, & Graphite Furnace Atomic Absorption Spectrometry.
ASTM D6349-Standard Test Method for Determination of Major and Minor Elements in Coal, Coke, and Solid Residues from Combustion of Coal and Coke by Inductively Coupled Plasma – Atomic Emission Spectrometry.
ASTM D5373 Standard Test Methods for Determination of Carbon, Hydrogen and Nitrogen in Analysis Samples of Coal and Carbon in Analysis Samples of Coal and Coke.

The other tests and analyses are described in the following sections.

4.1.1 Thermo-Gravimetric Analysis

The Perkin Elmer Pyris-1 TGA at our Chattanooga Chemical Laboratory was used to determine char combustion and gasification reactivities under isothermal conditions. A 4-6 mg sample of char is placed in the TGA system and heated in the presence of nitrogen at 20°C/min to reactivity temperature

(700°C for combustion, and 950°C for gasification). After stabilization at this temperature, half of the gas is switched to reaction gas: air for combustion and carbon dioxide for gasification. (The other half is used as a purge and is always nitrogen.) The percent weight of the unburned or un-gasified char and the rate of weight loss are recorded on a strip chart as a function of time. These thermo-grams are used to determine the char combustion or gasification efficiency history and reactivity parameter (which indicates the maximum rate of weight loss per unit weight of the original sample in the TGA system).

The parent coals are characterized by a non-isothermal test to rank them in terms of reactivity. 4-6 mg of sample is placed in the TGA and heated in the presence of air/N_2 at 10°C/min until 700°C.

4.1.2 Petrographic Analyses

ALSTOM used Clark Testing Laboratories in Jefferson Hills Pennsylvania to perform the Petrographic analyses.

Petrography is, by definition, a branch of petrology that deals with the description and classification of rocks. Since coal is, in geo-chemical terms, an organic rock, it is appropriate to use petrographic analysis to describe its origin, structure, composition, changes and classification. There are two major classes of coal petrography: (1) reactive macerals, comprised principally of vitrinites, liptinites and 1/3 of semi-fusinites; and (2) inert macerals (inertinites), comprised principally of fusinites, and the remaining 2/3 of semi-fusinites. Work previously done by Power Plant Laboratories indicates that coal petrography may also be used to evaluate the combustion kinetic behavior of coals. ISO currently uses vitrinite reflectance to rank coals from around the world.[2]

4.1.3 Specific Surface Areas

The principle of physical absorption of gases is used to determine specific surface areas of the solid fuels. The Micromeritics TriStar II 3020 Physical Adsorption Analyzer at our Chattanooga Chemical Laboratory was utilized for the BET analysis[3].

4.1.4 Mini-Screen Analyses

Due to the limited quantity of coal, and coal char prepared for testing, the standard sieves used in ASTM D-4749 sieve analysis are too large. Therefore, mini-screens are utilized to determine the size fractions of the different test fuels. Standard mesh sizes 50, 100, 200, 230, 270, 325, and 400 are used in a similar manner to ASTM D-4749. Samples collected from the furnace are brushed off the collection filter, and are typically clumped together. Therefore, to break up any clumping (due to the filter-cake effect) samples are brushed through the 50 mesh screen prior to mini-screen analysis.

4.1.5 Micro-Proximate Analyses

The LECO TGA 701 in Alstom's Chattanooga Chemical Laboratory was used to determine the micro-proximate analyses of chars after it had been established that this apparatus yielded volatile matter results which were virtually indistinguishable from the corresponding ASTM proximate analyses. This method was used to save DTFS testing time since only milligrams, instead of one gram of sample is required to determine their proximate analyses.

In this test procedure, a sample (4-6 mg) is purged with nitrogen to remove oxygen traces. The moisture loss is obtained by heating in an inert atmosphere (nitrogen) to 105°C and holding for three minutes. Subsequently, the sample is heated at 100°C/min to 950°C and held at this temperature for

[2] ISO 11760:2005(E) Classification of Coals-International Standard
[3] Brunauer, S., Emmett, P. H., and Teller, E., "Adsorption of Gases in Multilayers," J. Am. Chem. Soc., 60, 309 (1938).

five minutes to obtain volatile matter. After this, the temperature is lowered to 750°C and a switching valve is used to introduce oxygen for the combustion of fixed carbon at this temperature. The residue represents ash content.

4.1.6 CCSEM Analyses

ALSTOM Power, Inc. contacted Microbeam Technologies, Inc. (MTI) to perform Computer Controlled Scanning Electron Microscopy (CCSEM) analysis of ash samples obtained from combustion in the drop tube furnace system.

CCSEM utilizes backscattered electron imaging combined with automated particle recognition and chemical analysis to determine the composition, size and abundance of mineral types in coal or ash. The CCSEM method is automated, allowing up to 3,000 mineral grains or ash particles to be characterized. The compositional data is used to type the particles based on composition. The particle typing is based on standard mineral compositions.

Ash samples are prepared for CCSEM using a dispersion mounting procedure where the ash material is dispersed in an alcohol medium and applied to a graphite pancetta faced with double stick carbon tape. The alcohol is allowed to evaporate leaving the ash particles dispersed on the carbon tape which allows for the detection and analysis of individual ash particles by the SEM. The sample mount is coated with carbon for improved conductivity in the SEM.

4.1.7 The Drop Tube Furnace System (DTFS)

The Drop Tube Furnace System (Figure 4-1) comprises a 1-inch diameter horizontal tube gas preheater and a 2-inch inner diameter vertical tube test furnace for providing controlled temperature conditions. Both tubes are electrically heated with silicon carbide elements (SiC) and are rated at 2800 °F. The DTFS is used to study pyrolysis, combustion, and gasification of coals and/or chars.

The principle operation of the DTFS is as follows. Size graded fuel is introduced with a small amount of carrier gas into the hot reaction zone of the test furnace through a water-cooled fuel injector. A preheated secondary gas stream is introduced around the primary stream. Injection of fuel particles into the hot gas stream results in a rapid heating of the particles to the prevailing gas temperature (at a rate of the order of 10^4 °C/sec). Following the rapid heating period, pyrolysis, gasification, and/or combustion of particles occur for a specific time. Then all reactions are rapidly quenched. Solid products are separated from the gaseous products in a small filter housing, and an aliquot of the effluent gas sample is sent to a pre-calibrated Gas Analysis System.

The solid products collected at various locations along the axis of the DTFS reaction zone can be analyzed to determine solid conversion efficiencies.

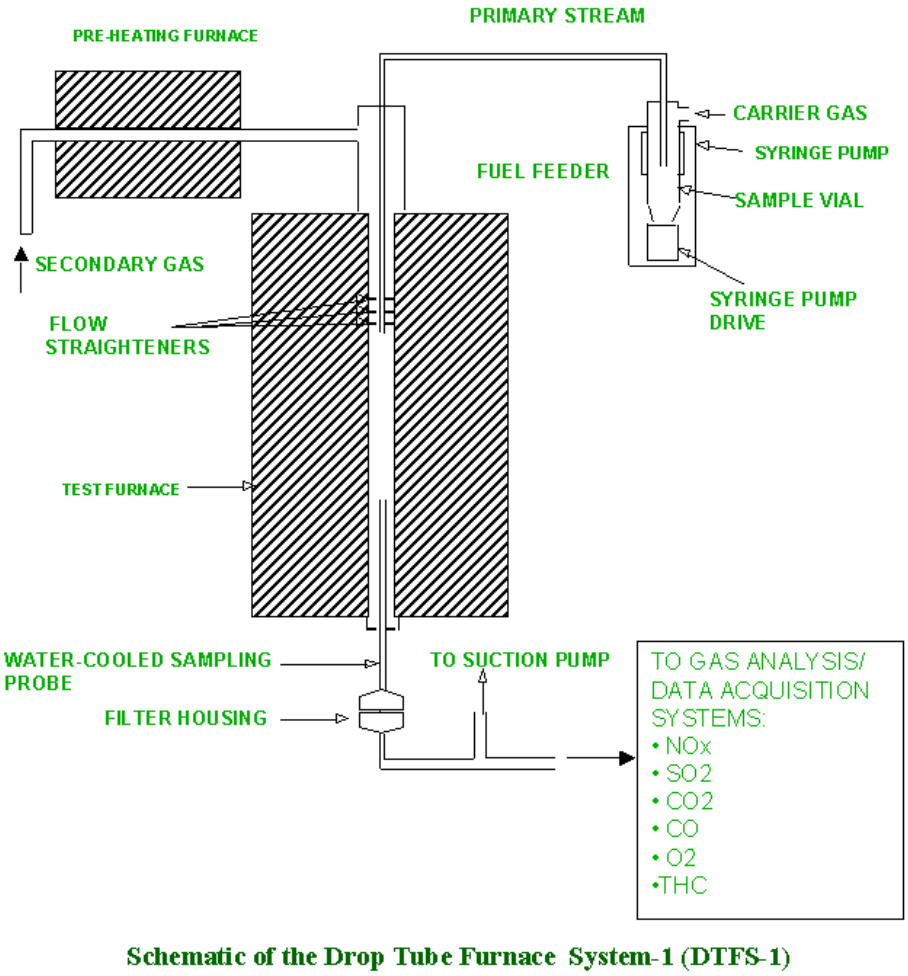

Figure 4-1. Schematic of DTFS-1

In this program, the DTFS was used for 5 purposes (refer to Table 4-1):

1. generate ash in air or simulated oxy conditions for further analysis,
2. generate char in nitrogen or argon for further tests,
3. gasify coal in CO_2,
4. gasify char in CO_2 or 30% CO_2 / balance N_2,
5. combust char in 3% O_2 / balance N_2 or CO_2.

These are described below.

4.1.7.1 Ash Generation

200x400 mesh coal was fed to the drop tube with a flow rate of 15 SLPM air at 2650°F to generate ash for CCSEM analysis. The ash was collected with the fixed probe positioned for a 24" reaction zone. Ash was generated in a similar manner with 21% oxygen 79% carbon dioxide reaction gas to simulate ash generated under oxy-firing conditions.

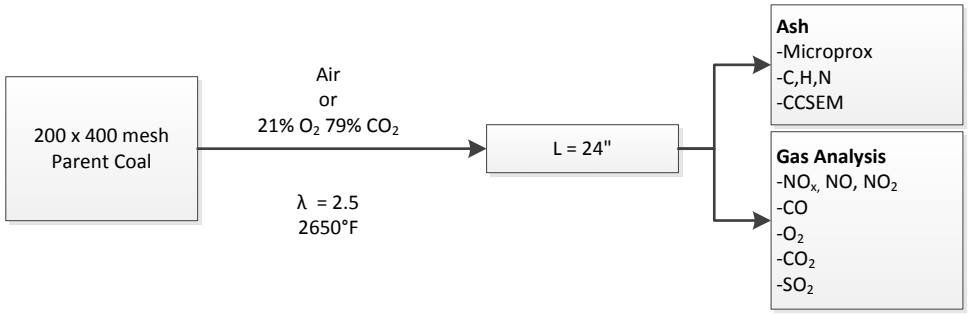

Figure 4-2. Ash Generation Procedure

4.1.7.2 Char Generation

All the coal chars were prepared in the DTFS under strictly similar conditions so that differences in their physical and chemical characteristics were due solely to differences in the nature of their parent coals. Nitrogen, and Argon chars were generated by feeding the 200x400 mesh feedstock at 0.18-0.22 g/min to the drop tube in 15 SLPM of 100% nitrogen, or argon at 2650°F with the fixed collection probe positioned for a 31" reaction zone. Raw chars were collected and further size graded to a 200x400 mesh cut. Short tests were run under similar conditions with different reaction zone lengths to look at de-volatilization rates, and swelling factors. The char generation procedure is summarized graphically in Figure 4-3.

Figure 4-3. Char Generation Procedure.

4.1.7.3 Coal Gasification

Gasification rates were taken for the parent coals at 2650°F. Sized coal particles were fed into a drop tube atmosphere of 100% carbon dioxide (flow rate 15 SLPM). Char particles were collected at four different reaction zone lengths to determine gasification efficiency as a function of residence time. The coal gasification procedure is summarized graphically in Figure 4-4.

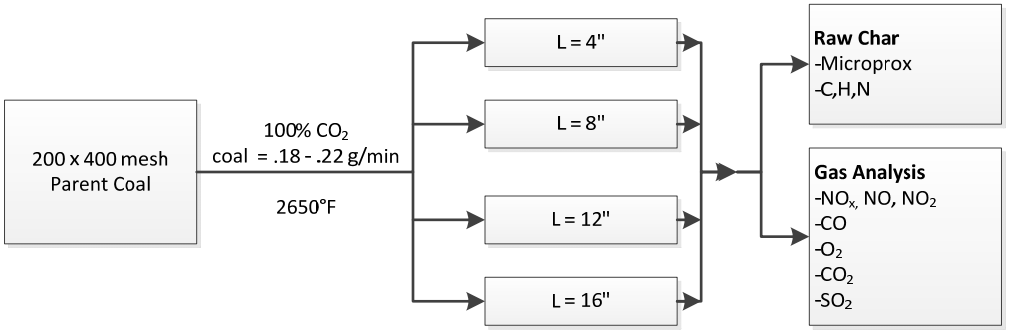

Figure 4-4. Coal Gasification Test Procedure

Char particles were collected from each reaction zone, and analyzed by micro-proximate procedures, and carbon, hydrogen, and nitrogen (CHN) mass percents were determined.

The gasification efficiency for parent coals was determined by the ash tracer technique, which assumes that the ash does not undergo appreciable changes during the gasification. The efficiency is calculated by

$$\eta = 100 * \left[1 - \left(\frac{A_0}{100 - A_0}\right) * \left(\frac{100 - A'}{A'}\right)\right]$$

where A_0 and A' are the percent ash contents (dry basis) of the feed sample and partially reacted char, respectively. and η is the gasification efficiency.

4.1.7.4 Char Gasification

Char gasification data was taken for Prairie Eagle nitrogen char, as well as Schwarze Pumpe nitrogen char. Sized nitrogen char particles were fed into the drop tube in an atmosphere of 100% carbon dioxide, or 30% CO_2 balance N_2 at 2200 and 2650°F (1800°F was too low for gasification reactions). Char particles were collected at four different reaction zone lengths to determine gasification efficiency as a function of temperature and residence time. See Figure 4-5.

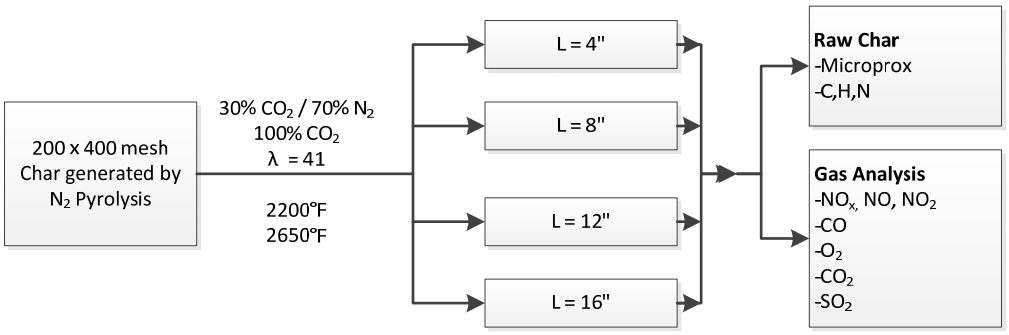

Figure 4-5. Char Gasification Test Procedure

Depending upon the experiment, gasification efficiencies for char could be very low compared to the gasification efficiencies for coal. There was often no significant difference between the ash content of the feed char and the partially gasified char. Therefore, gasification efficiency was calculated by using the values of CO concentrations in the exit gas by

$$\eta = \left(\frac{V}{V_0}\right) * \frac{\left(\frac{1}{2} * [CO]\right)}{\left(\dot{m} * \frac{[C]}{12}\right)}$$

where V is the volumetric flow rate of the reactant gas (corrected to STP), V_0 is the STP volume occupied by one mole of an ideal gas, $[CO]$ is the concentration in volume percent, $\dot{m}$ is the mass feed rate of the char, and $[C]$ is the percentage of carbon in the char.

4.1.7.5 Char Combustion

Sized nitrogen char particles were then fed to the drop tube at three different temperatures into an environment of 3% oxygen and 97% nitrogen (flow rate 15 SLPM) for baseline air char reactivities. Char/ash particles were collected at four different reaction zone lengths to determine carbon conversion efficiency as a function of temperature and residence time. This matrix of tests is summarized graphically in Figure 4-6.

Similarly, sized nitrogen char particles were fed to the drop tube at three different temperatures into an environment of 3% oxygen, and 97% carbon dioxide (flow rate 15 SLPM) for dry-oxy char

reactivities. Char/ash particles were collected at four different reaction zone lengths to determine carbon conversion efficiency as a function of temperature and residence time.

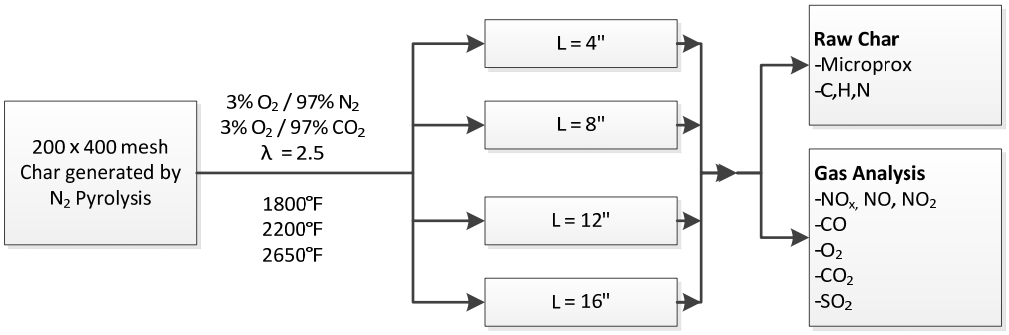

Figure 4-6. Char Reactivity Test Procedure.

For each char combustion test, approximately 1 gram of product material was collected and sent to the Alstom Chattanooga laboratory for micro-proximate and CHN analysis. Carbon conversion efficiency was calculated based on the ash tracer technique discussed earlier.

4.1.8 Drop Tube Furnace Test Matrix

The DTFS testing of four coals (Prairie Eagle from the Illinois No. 6 coal seam, Black Thunder from the Powder River Basin, Schwarze Pumpe Lignite from Germany, and Fola Mine West Virginia coal) and chars prepared therefrom was designed to study the effects of various operational parameters on their combustion, oxy-combustion, gasification, and pyrolysis characteristics. Prairie Eagle coal is abbreviated ILC, Black Thunder coal is abbreviated BTC, Schwarze Pumpe coal is abbreviated SPC, and Fola West Virginia coal is abbreviated WVC. The nitrogen generated chars are abbreviated as follows: Prairie Eagle nitrogen coal char is ILNCC, Black Thunder nitrogen coal char is BTNCC, Schwarze Pumpe nitrogen coal char is SPNCC.

Combustion was studied as a function of gas temperature, and reaction medium (air vs. oxy). Gasification was studied as a function of gas temperature, and carbon dioxide concentration. Pyrolysis was studied in nitrogen, and argon at 2650°F. Test conditions are summarized in Table 4-2.

Table 4-2. Drop Tube Test Matrix

Fuel	Test No.	Size Grades (Mesh)	Study	Reaction Medium (Vol. %)	Gas Temp. (F)
Illinois No 6 Coal (ILC)	ILC - 1	200 x 400	Pyrolysis/Char Gen	100% Nitrogen	2650
	ILC - 2	200 x 400	Pyrolysis/NOx/Char Gen	100% Argon	2650
	ILC - 3	200 x 400	Gasification	100 % Carbon Dioxide	2650
	ILC - 4	200 x 400	Ash Generation	21% O2 / 79% N2	2650
	ILC - 5	200 x 400	Ash Generation	21% O2 / 79% CO2	2650
Illinois No 6 Nitrogen Coal Char (ILNCC)	ILNCC - 1	200 x 400	Combustion	3% O2 / 97% N2	2650
	ILNCC - 2	200 x 400	Combustion	3% O2 / 97% N2	2200
	ILNCC - 3	200 x 400	Combustion	3% O2 / 97% N2	1800
	ILNCC - 4	200 x 400	Dry Oxy-Combustion	3% O2 / 97% CO2	2650
	ILNCC - 5	200 x 400	Dry Oxy-Combustion	3% O2 / 97% CO2	2200
	ILNCC - 6	200 x 400	Dry Oxy-Combustion	3% O2 / 97% CO2	1800
	ILNCC - 7	200 x 400	Gasification	100 % Carbon Dioxide	2650
	ILNCC - 8	200 x 400	Gasification	30% CO2 / 70% N2	2650
	ILNCC - 9	200 x 400	Gasification	100% Carbon Dioxide	2200
West Virginia Coal (WVC)	WVC - 1	200 x 400	Pyrolysis/Char Gen	100% Nitrogen	2650
	WVC - 2	200 x 400	Pyrolysis/NOx/Char Gen	100% Argon	2650
	WVC - 3	200 x 400	Gasification	100 % Carbon Dioxide	2650
	WVC - 4	200 x 400	Ash Generation	21% O2 / 79% N2	2650
	WVC - 5	200 x 400	Ash Generation	21% O2 / 79% CO2	2650
Black Thunder Coal (BTC)	BTC-1	200 x 400	Pyrolysis/Char Gen	100% Nitrogen	2650
	BTC-2	200 x 400	Pyrolysis/NOx/Char Gen	100% Argon	2650
	BTC-3	200 x 400	Gasification	100 % Carbon Dioxide	2650
	BTC-4	200 x 400	Ash Generation	21% O2 / 79% N2	2650
	BTC-5	200 x 400	Ash Generation	21% O2 / 79% CO2	2650
Black Thunder Nitrogen Coal Char (BTNCC)	BTNCC -1	200 x 400	Combustion	3% O2 / 97% N2	2650
	BTNCC -2	200 x 400	Combustion	3% O2 / 97% N2	2200
	BTNCC -3	200 x 400	Combustion	3% O2 / 97% N2	1800
	BTNCC -4	200 x 400	Dry Oxy-Combustion	3% O2 / 97% CO2	2650
	BTNCC -5	200 x 400	Dry Oxy-Combustion	3% O2 / 97% CO2	2200
	BTNCC -6	200 x 400	Dry Oxy-Combustion	3% O2 / 97% CO2	1800
Scwarze Pumpe Coal (SPC)	SPC-1	200 x 400	Pyrolysis/Char Gen	100% Nitrogen	2650
	SPC-2	200 x 400	Pyrolysis/NOx/Char Gen	100% Argon	2650
	SPC-3	200 x 400	Gasification	100 % Carbon Dioxide	2650
	SPC-4	200 x 400	Ash Generation	21% O2 / 79% N2	2650
	SPC-5	200 x 400	Ash Generation	21% O2 / 79% CO2	2650
Scwarze Pumpe Nitrogen Coal Char (SPNCC)	SPNCC - 1	200 x 400	Combustion	3% O2 / 97% N2	2650
	SPNCC - 2	200 x 400	Combustion	3% O2 / 97% N2	2200
	SPNCC - 3	200 x 400	Combustion	3% O2 / 97% N2	1800
	SPNCC - 4	200 x 400	Dry Oxy-Combustion	3% O2 / 97% CO2	2650
	SPNCC - 5	200 x 400	Dry Oxy-Combustion	3% O2 / 97% CO2	2200
	SPNCC - 6	200 x 400	Dry Oxy-Combustion	3% O2 / 97% CO2	1800
	SPNCC - 8	200 x 400	Gasification	100% Carbon Dioxide	2650

4.2 Fuel Characterization Results

4.2.1 Coal Analyses

Analyses and ranking of the as-received coal samples were shown in Table 3-2 The fuels ranged in rank from Schwarze Pumpe – a German lignite – to Fola Mine West Virginia high volatile bituminous A. Proximate analyses and higher heating values (HHV) are consistent with the rankings of these

fuels. Prairie Eagle is a high sulfur Illinois coal. Black Thunder is a mine located in the Powder River Basin (PRB) of Wyoming.

4.2.2 CCSEM Ash Analyses

Results of CCSEM analyses revealed significant differences in the size distribution of the ashes generated by the four test coals as well as significant compositional difference between individual particles. This information is useful to assess ash deposition and erosion potential and was in general consistent with the performance observed during the 15 MW_{th} BSF testing. Although there were significant differences between coals, the ashes from the same coal were generally similar when produced under either air or oxy-fired conditions. This is again consistent with the similar ash slagging and fouling behavior observed were the 15 MW_{th} testing. Detailed information on CCSEM results for each fuel ash is provided in the report from Microbeam Technologies, Inc., included as Appendix B.

4.2.3 Char Characteristics

Micro-Proximate, and Ultimate Analysis of sized coals, and chars is presented in Table 4-3. Sized coal analyses closely match the parent coal analysis listed in Table 3-2.

Table 4-3. Sized Coal and Char Analyses

	Schwarze Pumpe Lignite B		Black Thunder Sub A		Prairie Eagle hvBb		Fola hvAb	
Sample I.D.	200X400 Mesh Coal	200X400 Mesh Char	200x400 Mesh Coal	200x400 Mesh Char	200x400 Mesh Coal	200x400 Mesh Char	200x400 Mesh Coal	200x400 Mesh Char
Proximate, Wt. Percent								
Moisture	13.6	2.0	15.6	3.4	4.6	3.7	1.9	0.8
Volatile Matter	47.0	6.0	37.2	5.4	36.3	4.2	32.1	1.9
Fixed Carbon	34.1	77.1	41.5	77.1	51.2	76.4	54.9	77.9
Ash	5.3	14.9	5.7	14.2	7.9	15.7	11.1	19.4
Total	100.0	100.0	100.0	100.0	100.0	100.0	100.0	100.0
Ultimate, Wt. Percent								
Moisture	13.6	2.0	15.6	3.4	4.6	3.7	1.9	0.8
Hydrogen	4.0	0.0	4.0	0.0	4.8	0.0	4.9	0.0
Carbon	53.4	81.8	57.4	79.7	66.5	76.7	71.9	76.9
Sulfur	0.7	1.1	0.3	0.5	3.1	1.5	0.9	0.6
Nitrogen	0.7	0.5	0.8	0.6	1.3	0.8	1.4	0.9
Oxygen (difference)	22.3	-0.3	16.2	1.6	11.8	1.6	7.9	1.4
Ash	5.3	14.9	5.7	14.2	7.9	15.7	11.1	19.4
Total	100.0	100.0	100.0	100.0	100.0	100.0	100.0	100.0

4.2.4 Petrographic Analysis

Petrographic results are listed below in Table 4-4. ISO uses Mean Max Vitrinite Reflectance % to rank coals. Broad rank categories are separated as follows. Vitrinite reflectance greater than 6%

corresponds to either Meta-Anthracites, or Graphite. High rank coals (commonly known as anthracites) have a vitrinite reflectance greater than 2.0%, but less than 6.0%. Medium rank (bituminous) coals have vitrinite reflectance between 0.5% and 2.0%. Low rank (sub-bituminous, lignite, peat) coals have vitrinite reflectance less than 0.5%. High, medium, and low rank categories each have sub-categories such as sub-bituminous A, lignite B, etc. In the case of Schwarze Pumpe, and Black Thunder which are low rank coals with equal vitrinite reflectance, the method takes bed moisture percentage into account. Bed moisture percent greater than 35% corresponds to lignites or brown coals. Low rank coals with bed moisture less than 35% are considered sub-bituminous. The Schwarze Pumpe sample that was analyzed in this case was sent to the lab as a dried briquette. Schwarze Pumpe is a brown coal consisting of bed moisture well above 50%, however this coal represents the pre-dried fuel burned at the Vattenfall's oxy pilot plant and shipped to the U.S. as briquettes.

Table 4-4. Petrographic Analysis of Parent Coals

	Schwarze Pumpe Lignite B	Black Thunder Sub A	Illinois No. 6 hvBb	Fola Mine WV hvAb
Mean Max. Vitrinite Reflectance, %	0.35	0.35	0.54	0.88
Vitrinite, vol %	79.5	68.3	75.3	44.8
Exinite, vol %	12.7	6.4	4	10.4
Resinite, vol%	0	0.1	0	0
Semifusinite, vol %	3.4	12.7	2.9	7.3
Total Reactives	95.6	87.5	82.2	62.5
Inert Semifusinite, vol %	N/A	N/A	5.9	14.5
Micrinite, vol %	1.3	7.9	4.7	13
Fusinite, vol %	0.1	0.7	0.9	2.5
Mineral Matter, vol %	3	3.9	6.3	7.5
Total Inerts	4.4	12.5	17.8	37.5
Composition Balance Index	N/A	N/A	0.79	1.61
Rank Index	N/A	N/A	2.55	3.05
Calculated Stability Factor	N/A	N/A	19	28
Maceral Index (MI)[4]	58.27	19.39	6.60	0.74

Coal petrography can also be used to evaluate the combustion kinetic behavior of coals. For instance, the Mean Max Vitrinite Reflectance measured for the four fuels are

Schwarze Pumpe	Black Thunder	Prairie Eagle	WV Fola
0.35	0.35	0.54	0.88

This ranking is broadly consistent with the BET surface area and other measures of coal reactivity.

4.2.5 Thermo-Gravimetric Reactivities

Thermo-Gravimetric burn-off curves in air/N_2 (10°C/min ramp rate) for the four 200x400 mesh coals are shown in Figure 4-7 along with four reference fuels tested earlier.

Figure 4-7 displays the negative derivative of the raw TGA mass data – that is, the rate of weight loss. The peak temperature, where the rate is a maximum, gives an indication of the coal's reactivity. A more reactive fuel reaches its peak loss rate at a lower temperature.

[4] Su S., Pohl J.H., Holcombe D., Hart J.A.; *A proposed maceral index to predict combustion behavior of coal*. Fuel **80** pp. 699-706; 2001.

The Schwarze Pumpe lignite is the most reactive, followed by the Black Thunder PRB sub-bituminous A. The Jim Bridger sub-bituminous B is next. The Prairie Eagle Illinois coal is slightly more reactive than the 2 reference Illinois bituminous coals. The WV Fola coal is similar to the reference Pittsburgh No. 8.

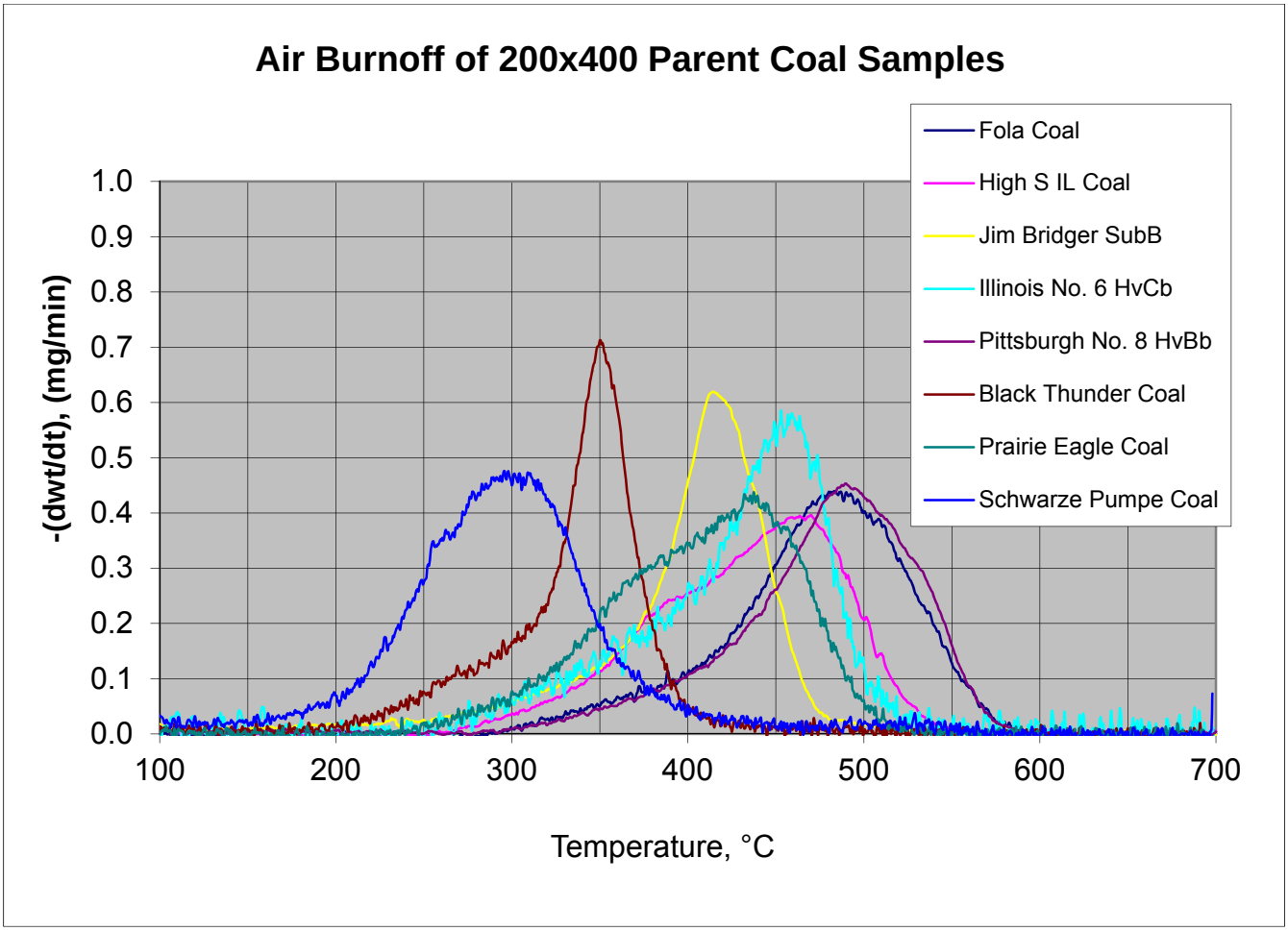

Figure 4-7. Non-Isothermal TGA's of 200x400 Parent Coals

These peak temperatures are plotted against the mean-max vitrinite reflectance of the parent coals in Figure 4-8. The coals in this study are plotted along with coals from previous studies (not the same reference fuels as in Figure 4-7).

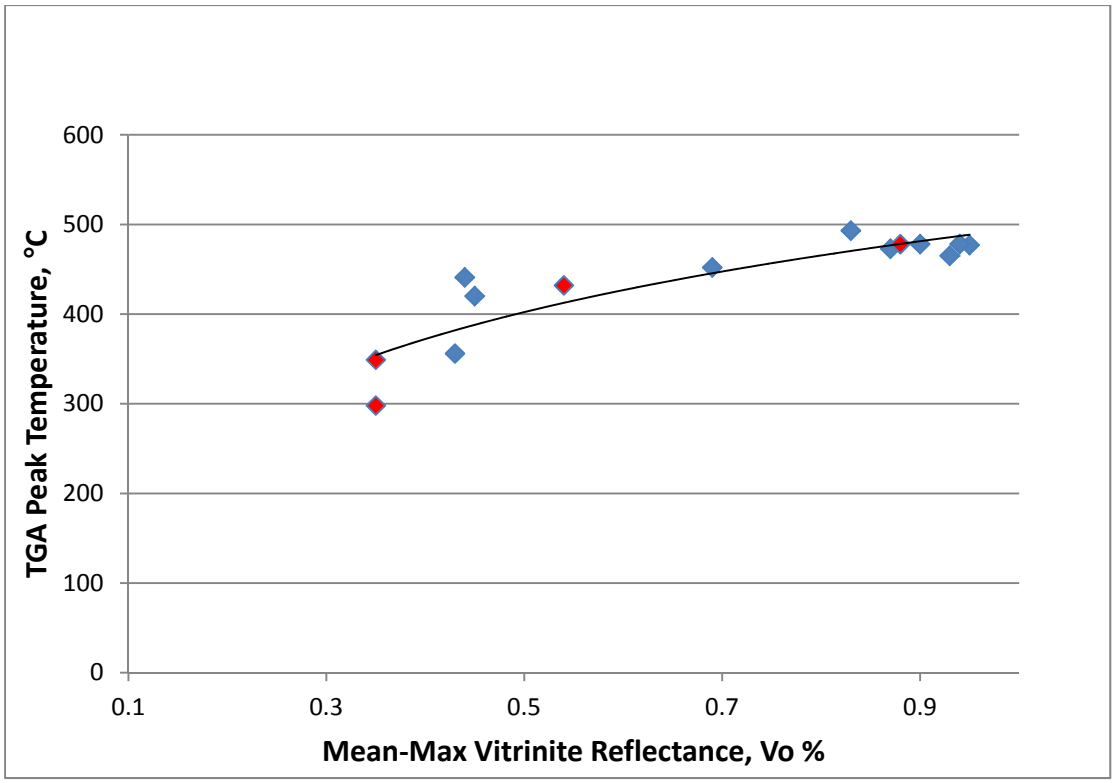

Figure 4-8. TGA Peak Temperature vs. Vitrinite Reflectance (current fuels in red)

The isothermal TGA char combustion results for each test fuel are shown in Figure 4-9. These char burnout curves all fell in a narrow band. However, the time required for complete burnout of the test fuels followed the same consistent trend with the TGA coal combustion results and the other measures of reactivity.

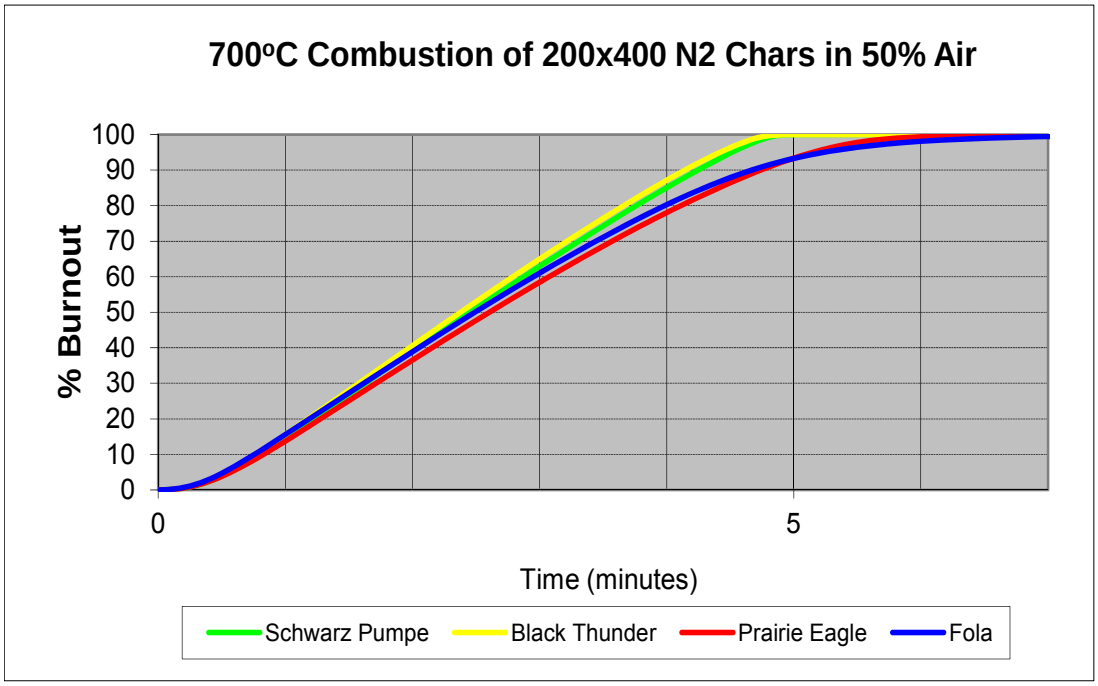

Figure 4-9. Isothermal TGA Combustion of 200x400 Chars in Air/N_2 at 700°C

Isothermal TGA gasification of drop tube generated chars was performed in a CO_2/N_2 atmosphere at 950°C. The gasification test results are presented in Figure 4-10 and show the same reactivity ranking as in the TGA combustion tests:

Schwarze Pumpe lignite > Black Thunder sub-bit> Prarie Eagle hvBb > Fola hvAb

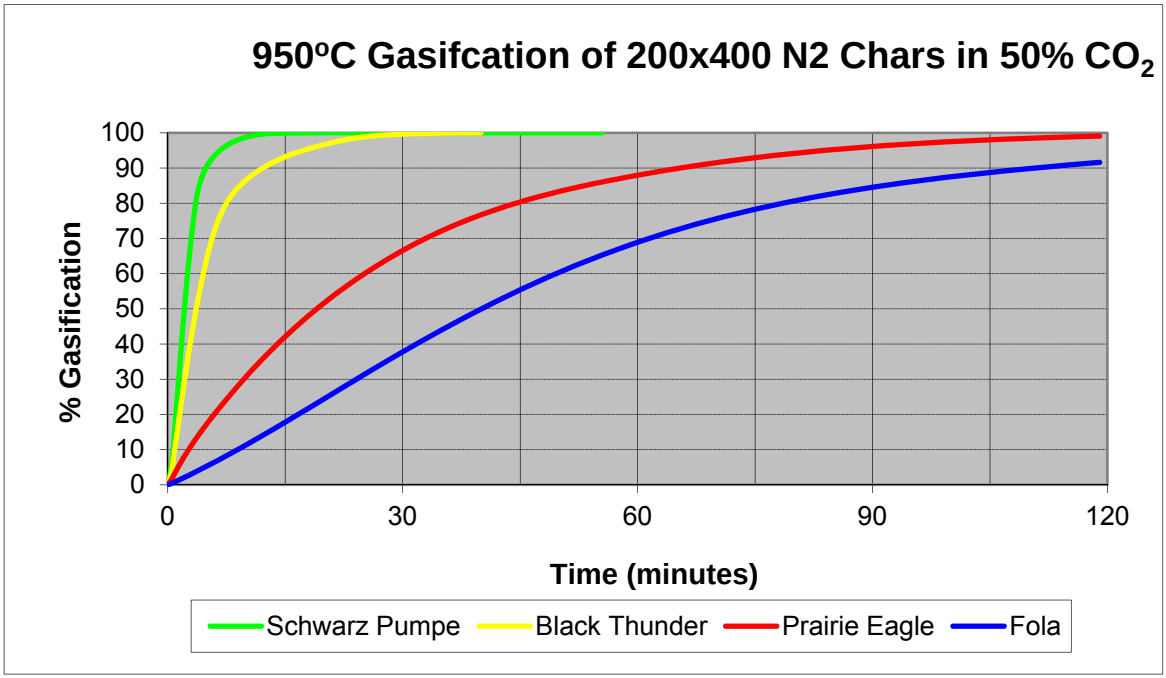

Figure 4-10. Isothermal TGA Gasification of 200x400 Chars in CO_2/N_2 at 950°C

4.2.6 Surface Area-Reactivity Relationships

BET surface areas of N_2 generated chars are displayed in Table 4-5.

Table 4-5. Surface Area by BET

Fuel	BET Surface Area (m^2/g)	
	coal	char
Schwarze Pumpe	1.8	295.8
Black Thunder PRB	3.6	127.4
Praire Eagle	2.0	28.7
WV Fola	0.8	11.0

BET surface areas of the DTFS chars follow the same relative order as the TGA reactivity results with the highest surface areas for the most reactive fuels.

4.2.7 Pyrolysis of Coals in DTFS

Pyrolysis, or devolatilization, of 200x400 mesh parent coal was done in the drop tube at 2650°F in nitrogen.

Char collected at the 31" reaction zone was used as the char feedstock for subsequent DTFS tests. Figure 4-11 shows the dry-screen particle size distributions (on a Rosin-Rammler scale) for the sized fuels and for the chars collected at 31". The Schwarze Pumpe lignite char was finer than the parent fuel. The lignite was received as briquettes, which were pulverized to reduce to individual particles. It is likely that the pulverization was incomplete, and the fuel fed to the drop tube further broke down during pyrolysis. The other fuels had much less change in size; in particular there is no evidence of significant swelling during pyrolysis.

The chars were re-screened to 200x400 mesh before using as feed in subsequent drop tube tests.

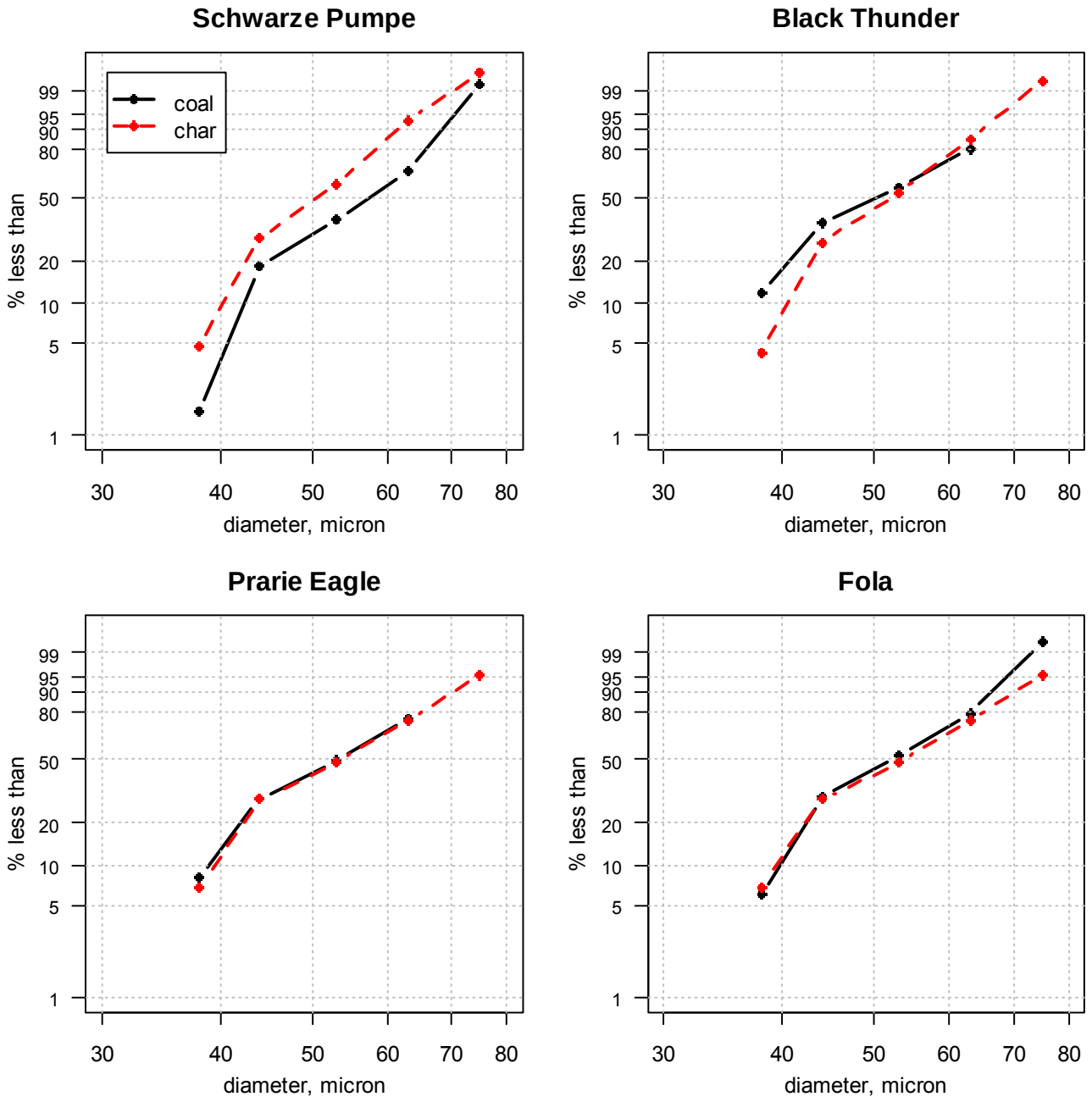

Figure 4-11. Size distribution of feed coals and generated chars in the DTFS

Char was also collected at 4", 8", and 16" for analysis, and the devolatilization efficiency, or yield, was calculated by the ash tracer method. The devolatilization yield from the high heat up rates in the drop tube is expected to differ from the standard ASTM volatile matter. The high temperature yield from the drop tube is typically higher than ASTM values and is more appropriate to use for modelling a pulverized fuel furnace. A Q-factor is defined as the volatile yield from the drop tube after 16" reaction zone relative to the ASTM volatile yield. Q-factors for the four fuels are shown in Table 4-6.

Table 4-6. Q-Factors of 200x400 Parent Coals

Coal	ASTM Volatile Matter of 200x400 Mesh Coal, VM_0, % Dry-Ash-Free Basis	DTFS Weight Loss at 16" Reaction Zone, VM_{16}, % Dry-Ash-Free Basis	Q-factor $Q = VM_{16}/VM_0$
Fola	36.9	42.8	1.16
Prairie Eagle	41.5	48.3	1.16
Black Thunder	47.2	52.0	1.10
Schwarze Pumpe	57.9	60.1	1.04

4.2.8 Gasification of Coals in DTFS

The gasification of 200x400 mesh size fractions of coals was studied in 100% CO_2 at 2650°F gas temperature. Gasification efficiency results plotted in Figure 4-12 and Figure 4-13 show the difference between calculating gasification efficiency based upon the ash tracer technique, and the CO concentration method respectively. Gasification efficiencies for BTC, SPC, and ILC exceeded 100% at times when using the CO concentration method. In those cases, the gasification efficiency was assumed to be 100%. But, calculation by ash tracer shows that the char collected at specifically the 12" and 16" reaction zones for BTC and SPC still contained gasifiable material where the CO method assumed 100% gasification. Therefore, for the gasification of the parent coals, the ash tracer technique was utilized to calculate reaction rates. Looking at Figure 4-12, the following trend is observed for data at each reaction zone length:

Schwarze Pumpe > Black Thunder > Prairie Eagle > Fola

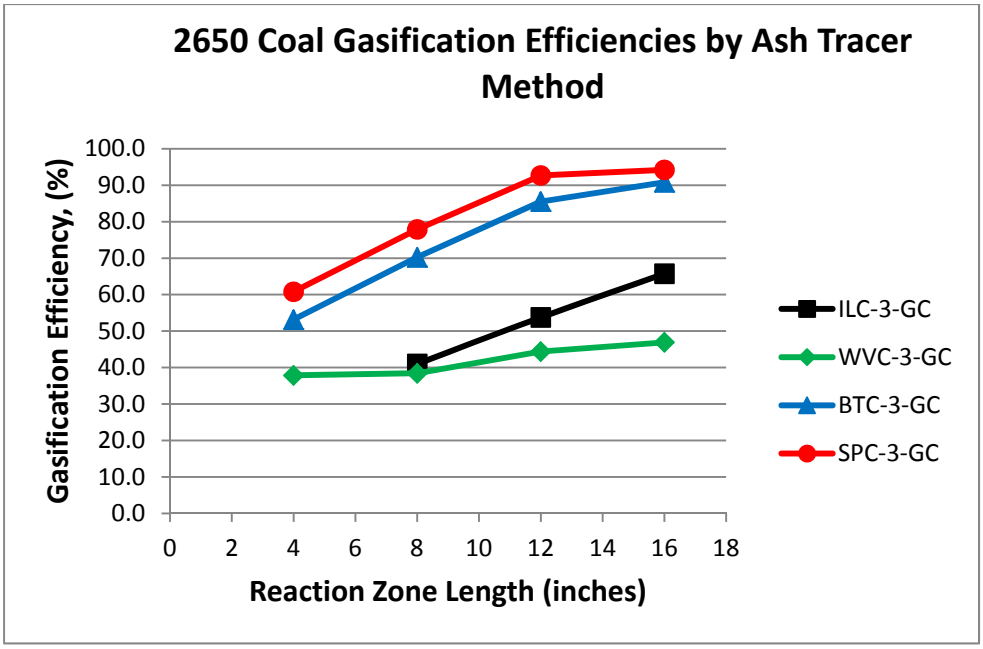

Figure 4-12. Parent Coal Gasification Efficiencies by Ash Tracer

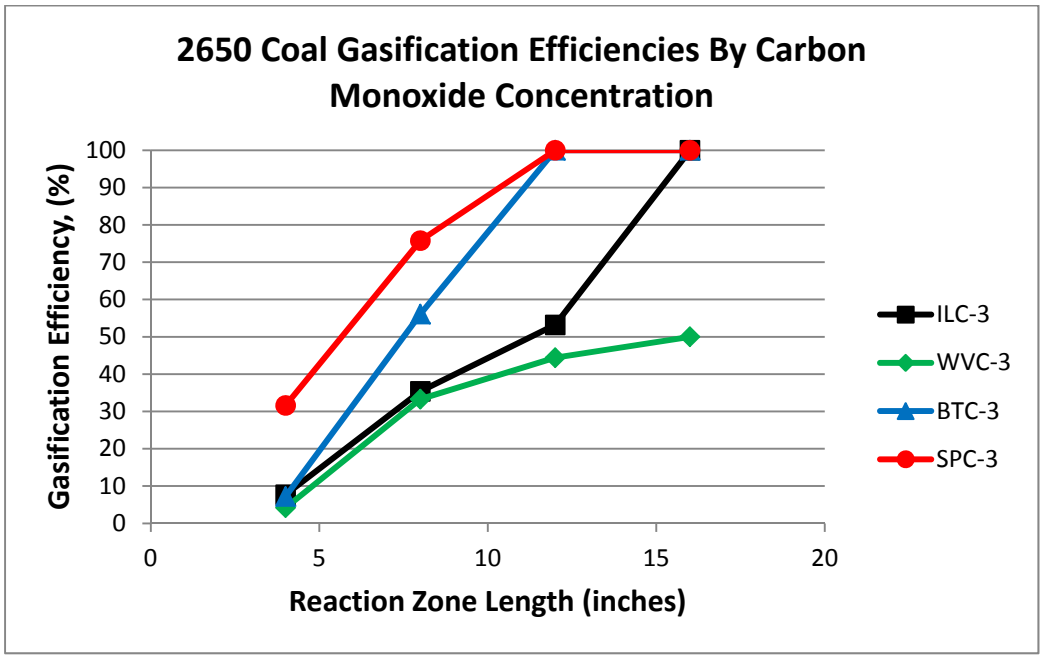

Figure 4-13. Parent Coal Gasification Efficiencies by Carbon Monoxide Method

4.2.9 Combustion of Chars in DTFS

The 200x400 mesh ILNCC, BTNCC, and SPNCC chars were studied at three gas temperatures (1800, 2200, and 2650°F) in the presence of oxygen partial pressure of 0.03 atmosphere in both a nitrogen and carbon dioxide balance. Results are given in Figure 4-14, Figure 4-15, and Figure 4-16 to represent the three reaction temperatures of 2650, 2200, and 1800°F respectively. Combustion efficiencies are plotted as a function of residence time. At each temperature the combustion efficiency is assumed to

start at zero where the reaction zone length, or residence time is equal to zero. As the particle travels further down the furnace, the combustion efficiency increases.

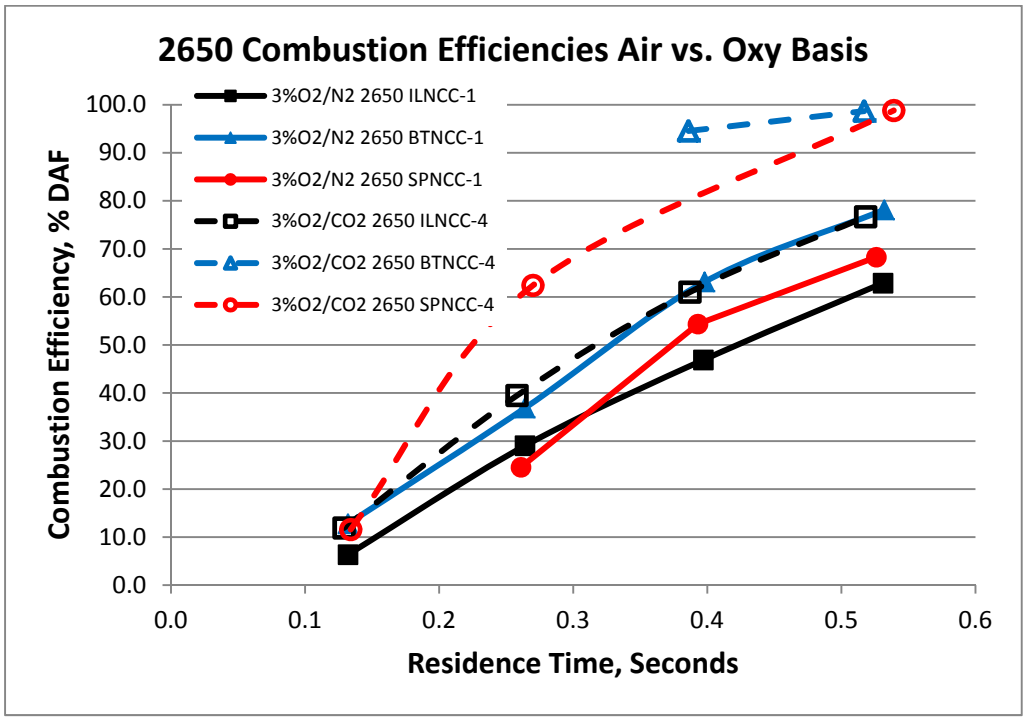

Figure 4-14. Char Combustion Efficiencies at 2650°F

At 2650°F the efficiencies are consistently higher for oxy-firing, and in each case, BT > SP > IL.

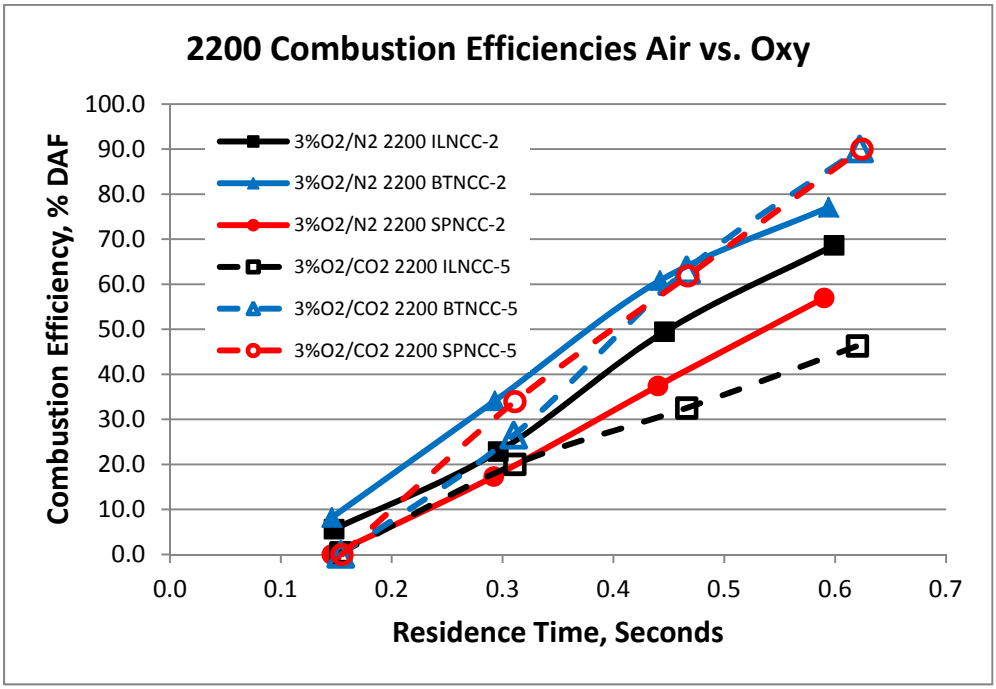

Figure 4-15. Char Combustion Efficiencies at 2200

At 2200°F the rankings are mixed:

Air Fired: BT > IL > SP

Oxy Fired: BT ≈ SP > IL

Compared to air firing, combustion in oxy firing is faster for SP, slower for IL, and mixed for BT. These differences are unexplained.

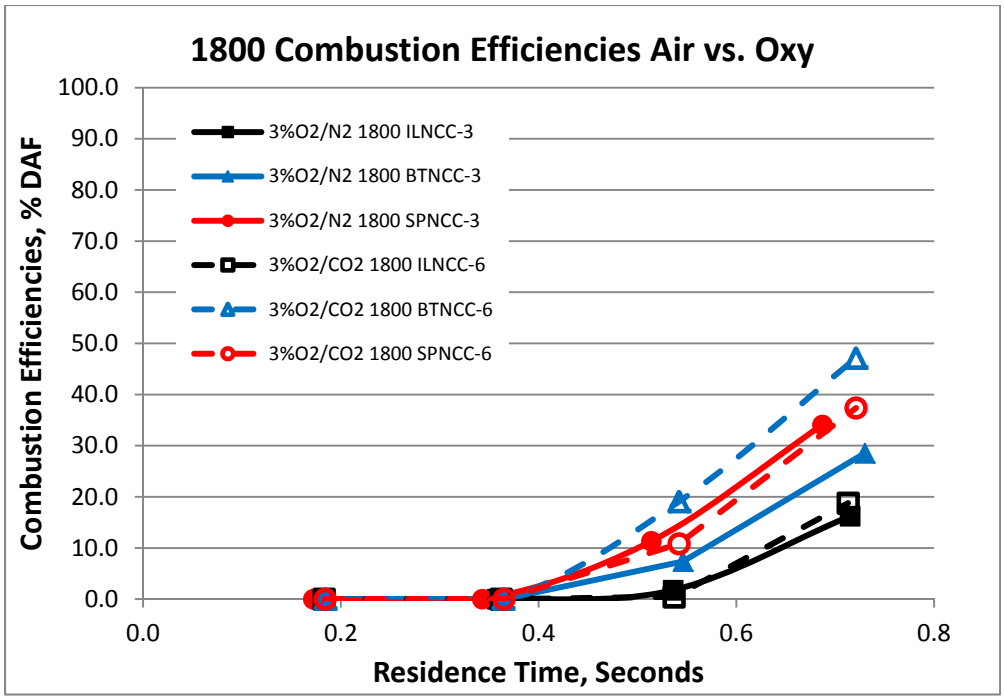

Figure 4-16. Char Combustion Efficiencies at 1800

At 1800°F the following trends are noticed:

Air Fired: SP > BT > IL

Oxy Fired: BT > SP > IL

The combustion is faster for oxy firing with the Black Thunder PRB, but similar to air firing for the other two fuels.

For another look at the effects of temperature, the data has been replotted by char type in Figure 4-17, Figure 4-18, and Figure 4-19.

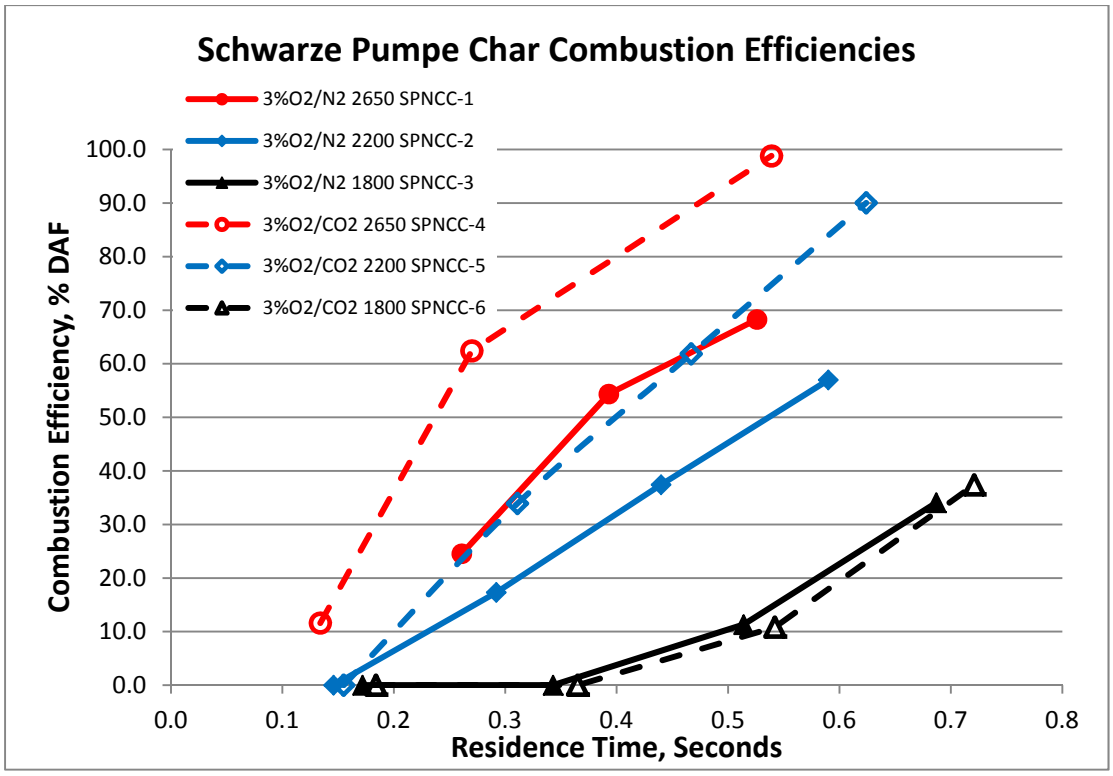

Figure 4-17. Schwarze Pumpe Char Combustion Efficiencies

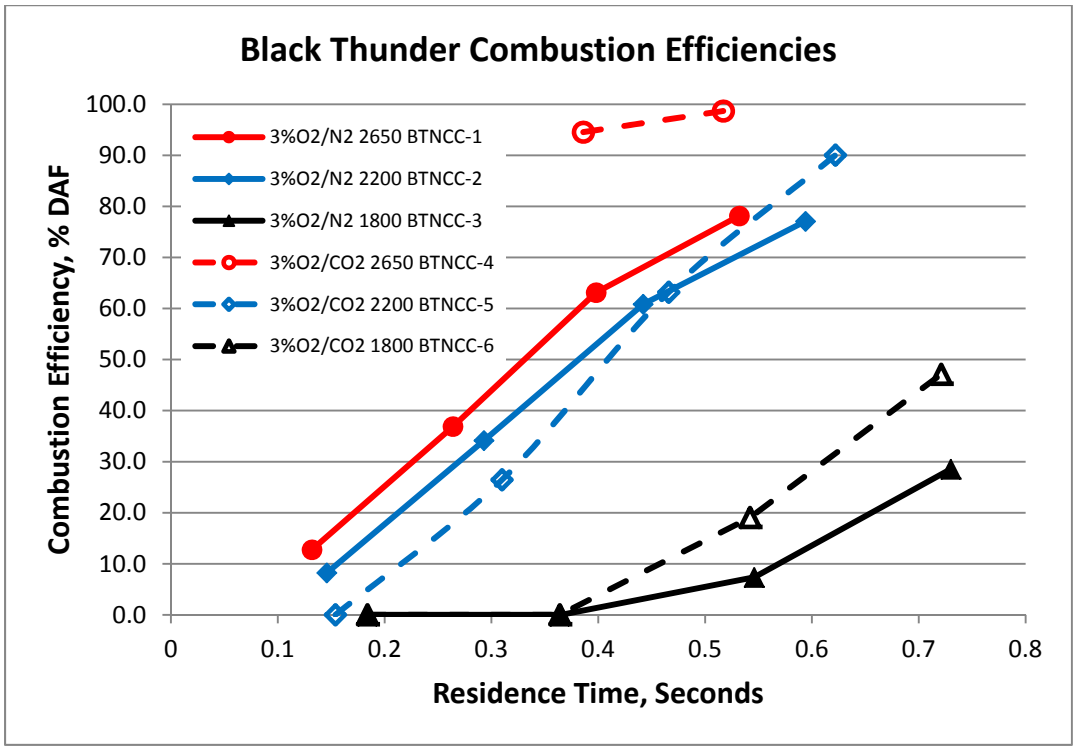

Figure 4-18. Black Thunder Char Combustion Efficiencies

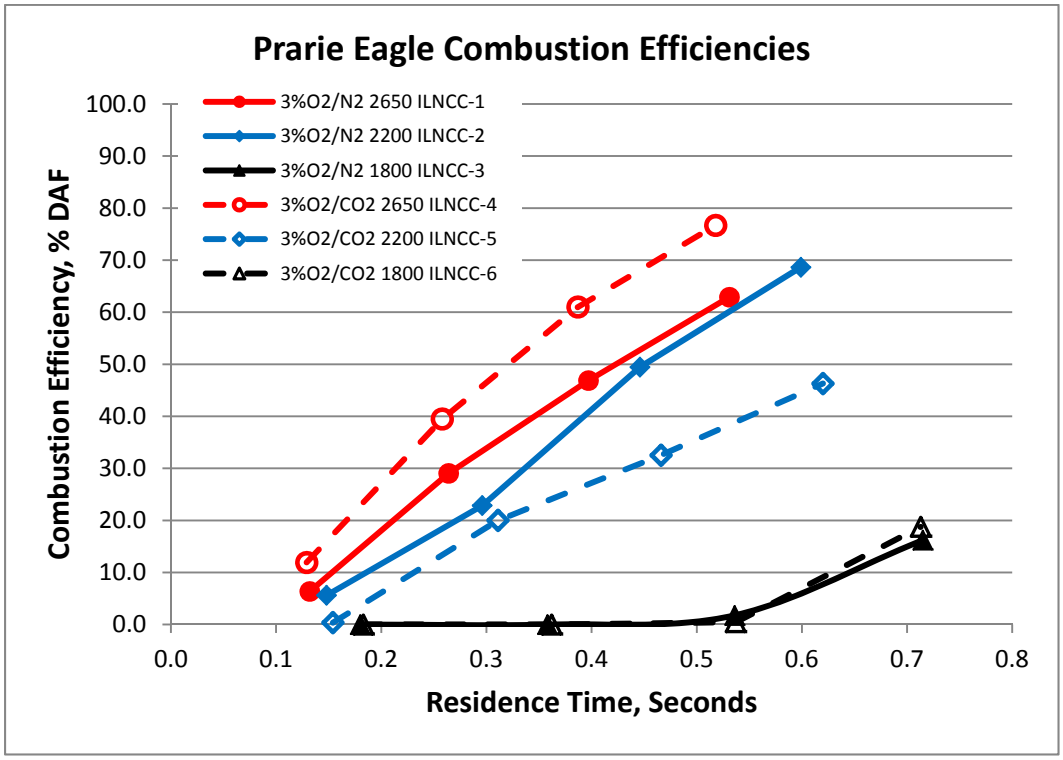

Figure 4-19. Prairie Eagle Char Combustion Efficiencies

4.2.10 Gasification of Chars in DTFS

Gasification efficiency for 200x400 nitrogen generated chars is plotted in Figure 4-20. Schwarze Pumpe char is seen to be more reactive than Prairie Eagle. The effect of CO_2 concentration 30% vs. 100% is also plotted.

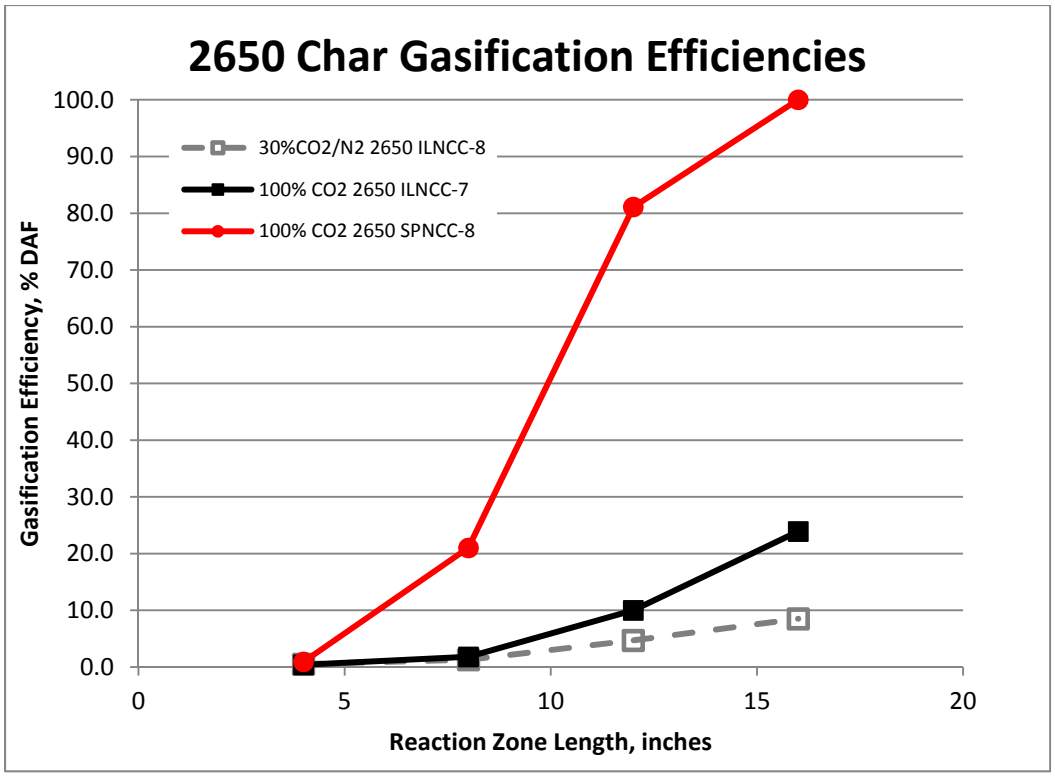

Figure 4-20. Char Gasification Efficiencies at 2650°F

5. BSF results

This section includes the results from the 6 BSF test campaigns. For convenience, many of the figures in this section use the following abbreviated labels for the test campaigns.

PRB Test campaign 1 with Powder River Basin subbituminous

WV Test Campaign 2 with Fola low-sulfur bituminous from West Virginia

HiS Test campaign 3 with Prairie Eagle high-sulfur bituminous from Illinois

NDlig Test campaign 4 with North Dakota lignite

SPlig Test campaign 6 with the Schwarze Pumpe dried lignite

WV.2g Test campaign 5-1 with Fola bituminous (same as Test campaign 2)

PRB.2g Test campaign 5-2 with Powder River Basin subbituminous (same as Test campaign 1)

HiS.2g Test campaign 5-3 with Galatia high-sulfur, high-chlorine bituminous from Illinois

5.1 Emission Considerations

This results section includes information on the emissions of particulate matter, CO, NO_x, SO_2, SO_3, mercury, and other trace metals. The relationship between emission rate and emission concentration is different for oxy-firing and air firing.

During air-firing, a certain level of each of these pollutants leaves the furnace, and may be further reduced – e.g., with a baghouse, scrubber, SCR – before entering the environment through the stack.

During oxy-firing, pollutants also leave the furnace and may be reduced in similar cleanup equipment. But from there, the flue gas is not just sent up the stack. A portion of the flue gas will be recycled to the furnace. Some of the pollutants will be removed in the GPU and some will be retained in the liquid CO_2 product and be sequestered. The vent gas from the GPU will be the main source of emissions. The amount of actual emissions to the atmosphere will depend on the required CO_2 product purity and the particular GPU design.

If coal were burned in pure oxygen and generated the same emission rate of a pollutant in lb/hr or lb/MMBtu fired as during air firing, the emission concentration would be higher due to the lack of nitrogen dilution. In oxy-firing with flue gas recycling, the pollutant concentration leaving the furnace depends on the concentration in the recycled flue gas. If the pollutant is removed in the recycled gas (for example, fly ash captured in a baghouse), the recycle gas dilutes the pollutant in the furnace and the concentration leaving the furnace may be similar to that in air firing. If the pollutant is not removed (for example, SO_2 if recycle is taken off before sulfur removal), the recycle gas is not a diluent and the concentration leaving the furnace may be as high as in pure oxy-firing.

The rate (e.g., in lb/MMBtu) is usually more appropriate for comparisons of pollutant emissions between air- and oxy-firing. In some cases, the concentration may be more relevant – for example, even though the amount of SO_2 and SO_3 in the flue gas is no greater during oxy-firing, a greater concentration may lead to more corrosion.

5.2 Combustion

For oxy-combustion, there is an economic advantage to reduce the excess oxygen supply and to reduce the amount of flue gas recycle. Reducing the excess oxygen reduces the amount of oxygen required from the ASU and reduces the purification costs for the CO_2 product gas. Reducing the amount of flue gas that is recirculated back to the boiler could reduce the size and cost of the boiler, the gas recirculation system and the downstream pollution control equipment, as well as reduce the parasitic power consumption.

Understanding the combustion impacts of reducing the amount of flue gas recycle and reducing the excess oxygen was an important objective of BSF testing. Reducing the amount of flue gas recycle impacts burner conditions/design parameters, furnace aerodynamics and combustion performance.

Reducing the amount of flue gas recycle to the boiler reduces the amount of oxygen returning to the boiler. At a constant outlet oxygen concentration, as the amount of recycled flue gas decreases, the stoichiometric ratio of oxygen to coal will decrease.

Reducing the flue gas recycle to the boiler also reduces the volumetric flow to the boiler. At constant injection compartment sizing, as the amount of recycled flue gas decreases, the effective velocity and momentum will be reduced.

5.2.1 CO emissions

It should be noted that the CO levels in the BSF are typically lower than at similar operating conditions in larger commercial units. This is mainly attributed to more complete mixing of overfire oxidant for the smaller cross-sectional area of the BSF. However, the minimum flue gas oxygen level to control CO was relatively low for both coals and was only slightly lower for air firing than for oxy-firing at the selected recirculation rate and staging conditions. In general, it was possible to operate the BSF at significantly less than 2% oxygen concentration in the flue gas at the furnace outlet before CO levels increased for all test coals under air and oxy conditions.

In general, the results indicate the dominating factors for CO emissions during air and oxy-firing are the same for a particular coal: complete mixing of the overfire oxidant before significant flue-gas cooling and final oxygen partial pressure, expressed as oxygen concentration in the flue gas.

Figure 5-1 shows the CO concentration (as ppm) and emission rate (as lb/MMBtu fired) at the economizer outlet for all the test points. The CO levels stay low down to an outlet O_2 level of about 1% (about 2.5% for the WV Fola test campaign).

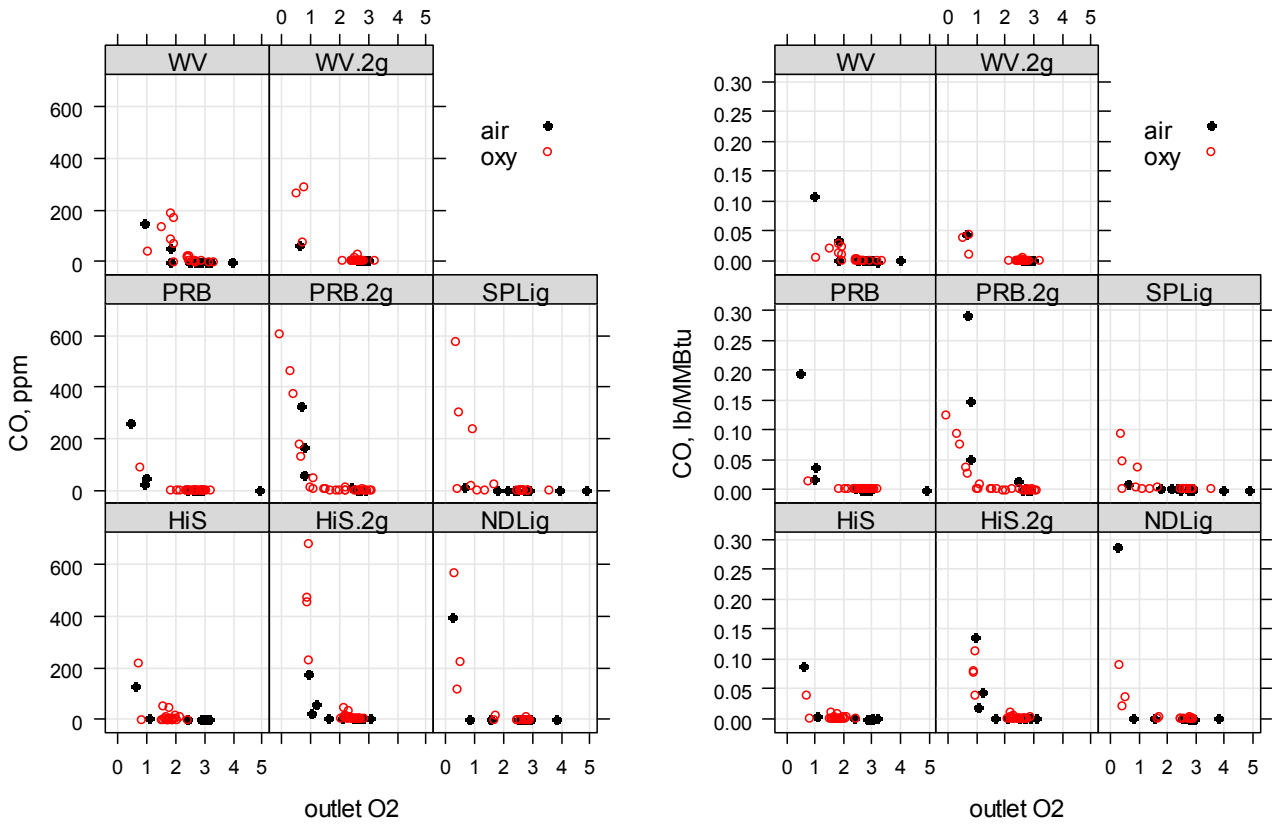

Figure 5-1. BSF CO emissions *vs.* flue gas O_2 for air and oxy-firing

Figure 5-1 shows the average CO and O_2 levels for each test point. In some tests, the excess O_2 level was decreased over a short period of time to see the point where the CO emissions rapidly increased.

For example, Figure 5-2 shows the results of tests with the PRB sub-bituminous coal. To normalize between air and oxy-firing, CO emissions are plotted on a lb/MMBTU basis. Air test #9 and oxy test #23 shown were operated at similar burner zone staging and over-fire air velocity. For the air and oxy-firing tests CO emissions exhibited the same trend, with rapid increase in CO emission below 1% O_2 in the flue gas.

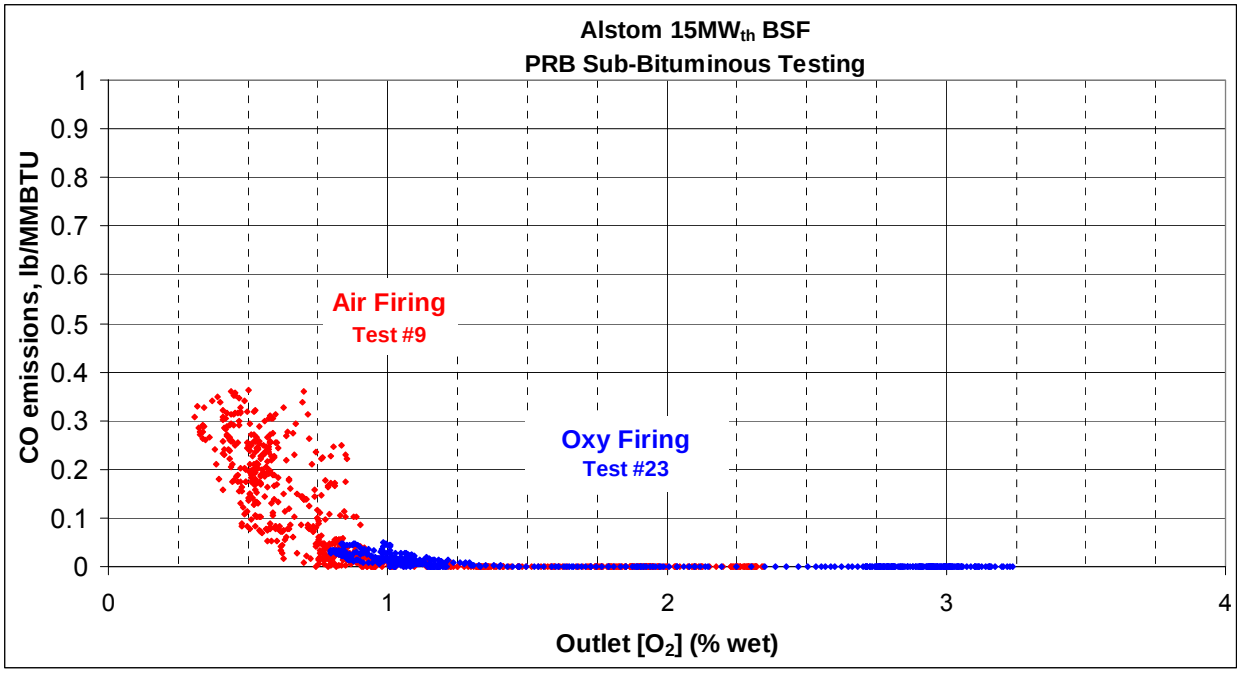

Figure 5-2. CO emissions during low excess oxygen tests, PRB sub-bit. testing

Figure 5-3 shows the results of tests with the North Dakota lignite. All tests exhibit a similar trend, with CO starting to increase below 1% O_2 and a rapid increase below 0.5% O_2 in the flue gas. There is little to distinguish between tests. Oxy test were operated over a range of global oxygen concentrations (from 24.8 to 30% global O_2) and there appeared to be no impact of the low global oxygen concentration on CO emissions.

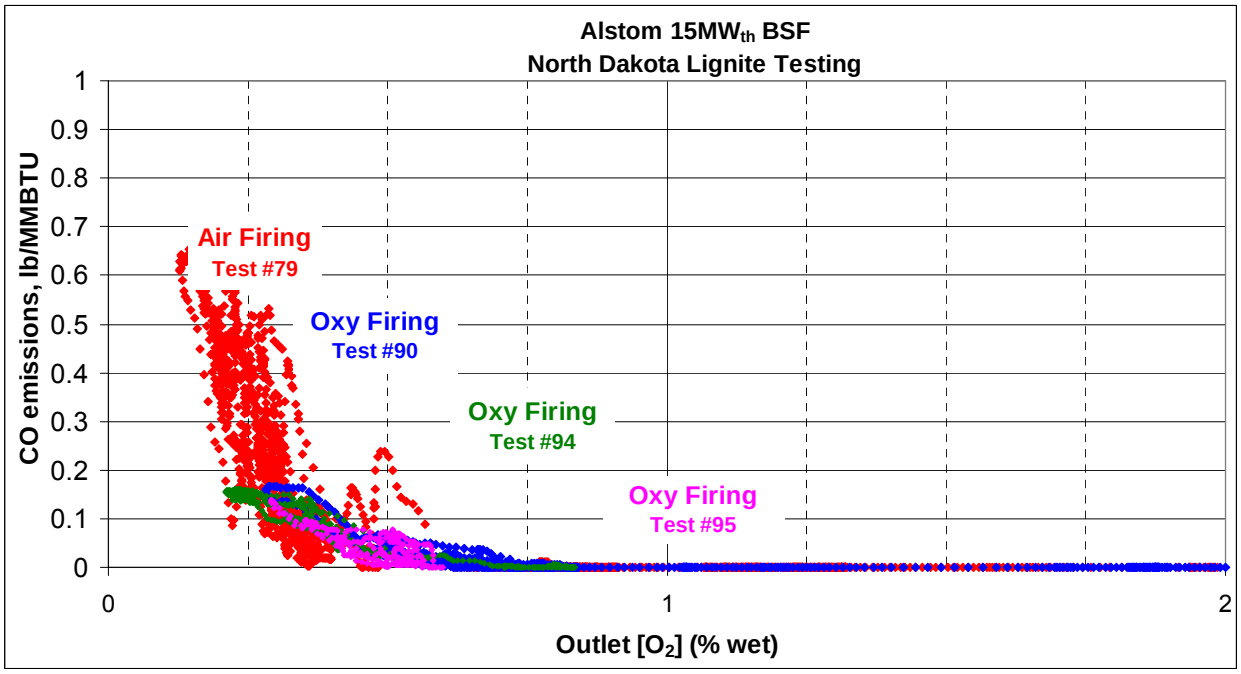

Figure 5-3. CO emissions during low excess oxygen tests, North Dakota lignite testing

5.2.2 CO profiles along the furnace height

During many of the long term tests, in-furnace gas samples were drawn along the furnace height – see Figure 2-20 for locations. CO and O_2 profiles for three test campaigns are shown in Figure 5-4.

Figure 5-4 and similar plots later in this report have markers on the right vertical axis indicating the elevations of the windbox, the upper and lower overfire compartments, and the arch at the horizontal furnace outlet plane – again, refer to Figure 2-20.

As expected, the O_2 increases and the CO decreases moving up from just above the windbox to the furnace outlet plane above the overfire air.

Figure 5-4 indicates the average concentration at each elevation. In many cases there is a considerable variation in O_2 and CO levels at any elevation. This too is expected – mixing of the added air or oxidant with the bulk gas is not immediate.

As an example, Figure 5-5 shows the variation in O_2 and CO concentrations for the oxy-fired Test 22. The three elevations shown are the same as in Figure 5-4:

elevation 141 above the windbox (bottom plot)
elevation 180 between the overfire airs
elevation 273 at the horizontal furnace outlet plane (top plot)

The measured O_2 and CO concentrations are represented by the dots according to the color scale (both are in % by volume, dry basis). The background picture is a prediction by a Fluent® CFD model with the same color scale.

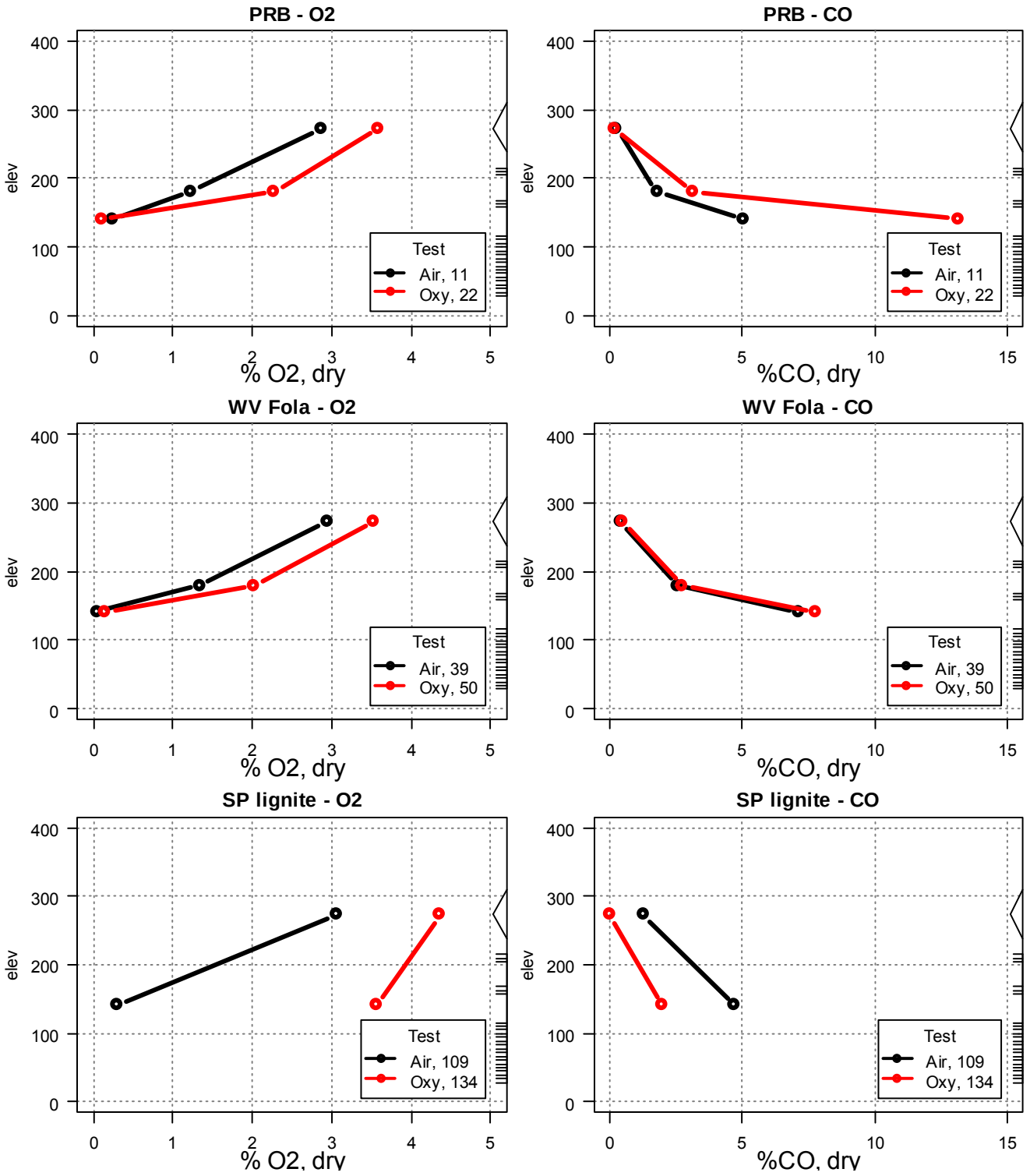

Figure 5-4. Vertical O_2 and CO profiles

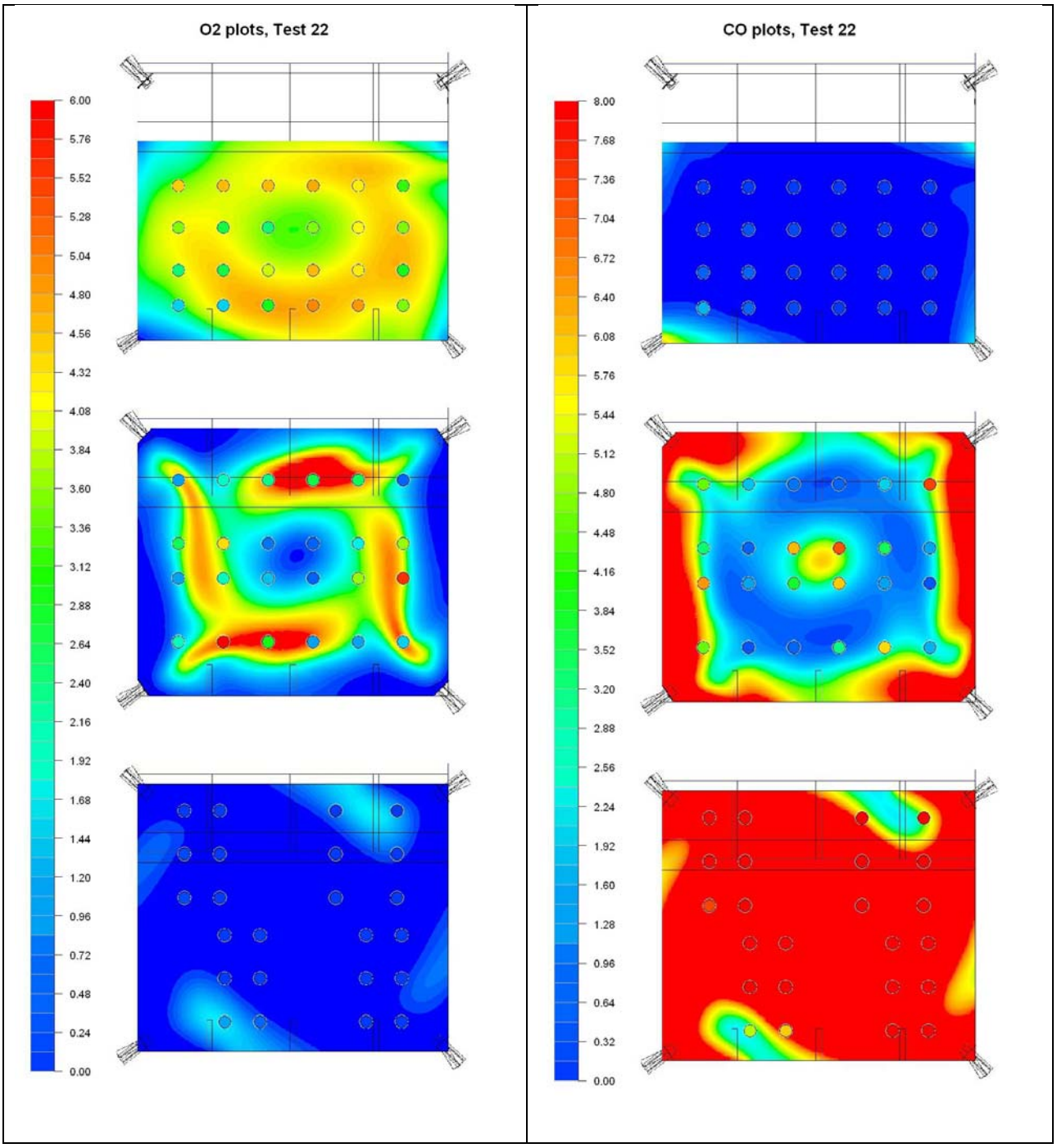

Figure 5-5. O_2 and CO profiles at three elevations, Test 22

5.2.3 Unburned carbon

For some of the test points, fly ash samples were taken at the economizer outlet. The sampling was not done isokinetically, but rather the sample was drawn at the average duct velocity at several locations across the duct in order to more quickly get a larger sample. The assumption is that this is a reasonable approximation of isokinetic conditions and that the fly ash sample composition and collection rate are

representative of the total fly ash. Note that isokinetic sampling was done for some tests; for example, the trace metals testing discussed in Section 5.7.

Figure 5-6 shows how the unburned carbon in the fly ash samples varied with oxygen level in the flue gas at the economizer outlet and with the main burner zone stoichiometry. Unburned carbon was low during all of these tests. In general, the unburned carbon decreases with higher O_2 in the flue gas and with increased main burner zone stoichiometry (less deep staging). The unburned carbon is lower for the oxy-combustion cases than air-combustion.

The low unburned carbon levels during oxy-fired tests are likely due to increased furnace residence time associated with lower volumetric gas flow rate and to carbon gasification reaction rates increasing with increasing CO_2 and H_2O in the recycled flue gas.

The tests points shown in Figure 5-6 do not include low load tests below 38 MMBtu/hr fired.

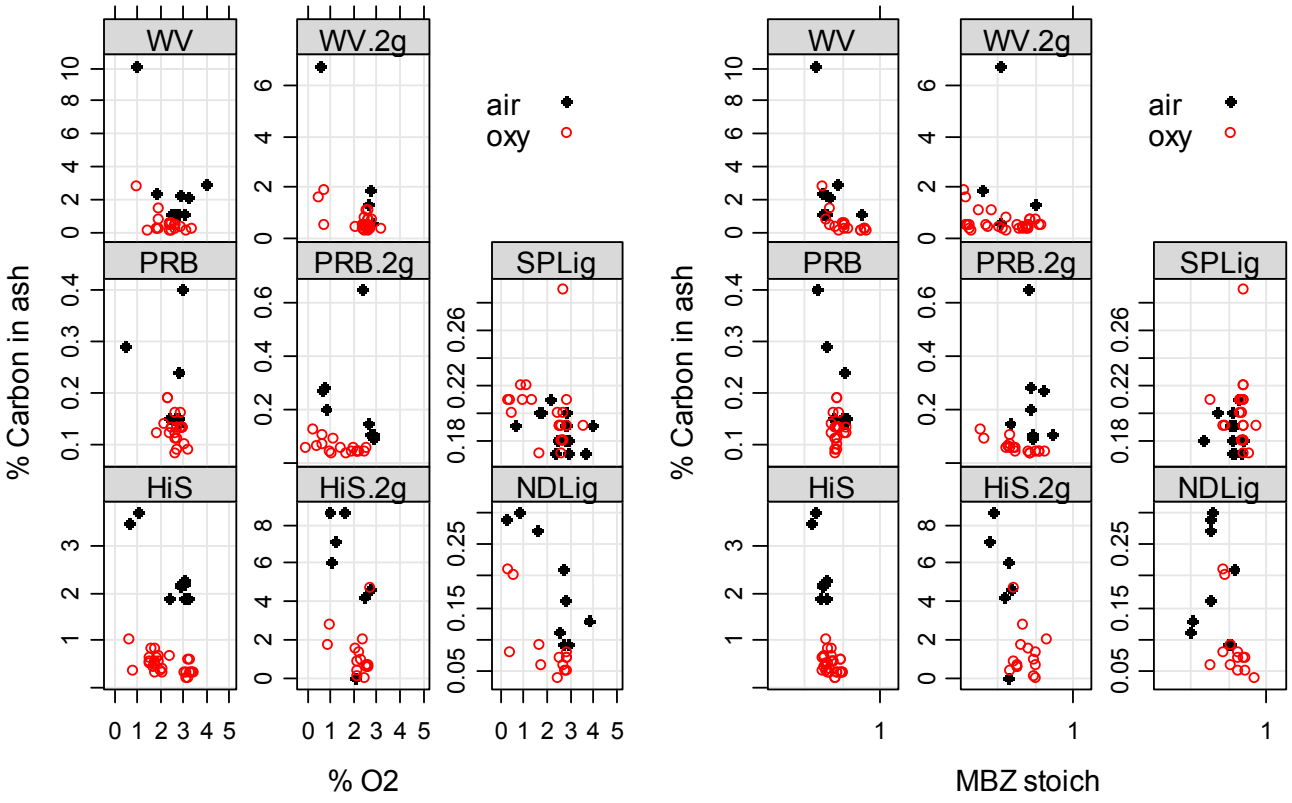

Figure 5-6. Unburned carbon in flyash

Note the variable scales in Figure 5-6 – the PRB subbituminous and the lignites had much lower carbon in the fly ash than the bituminous coals. This is clearly seen in Figure 5-7, where a common scale is used for all the fuels for the carbon in fly ash and the resulting carbon heat loss as a percent of the HHV firing rate. For the oxy-fired tests, well less than 0.5% of the heat input was lost due to unburned carbon.

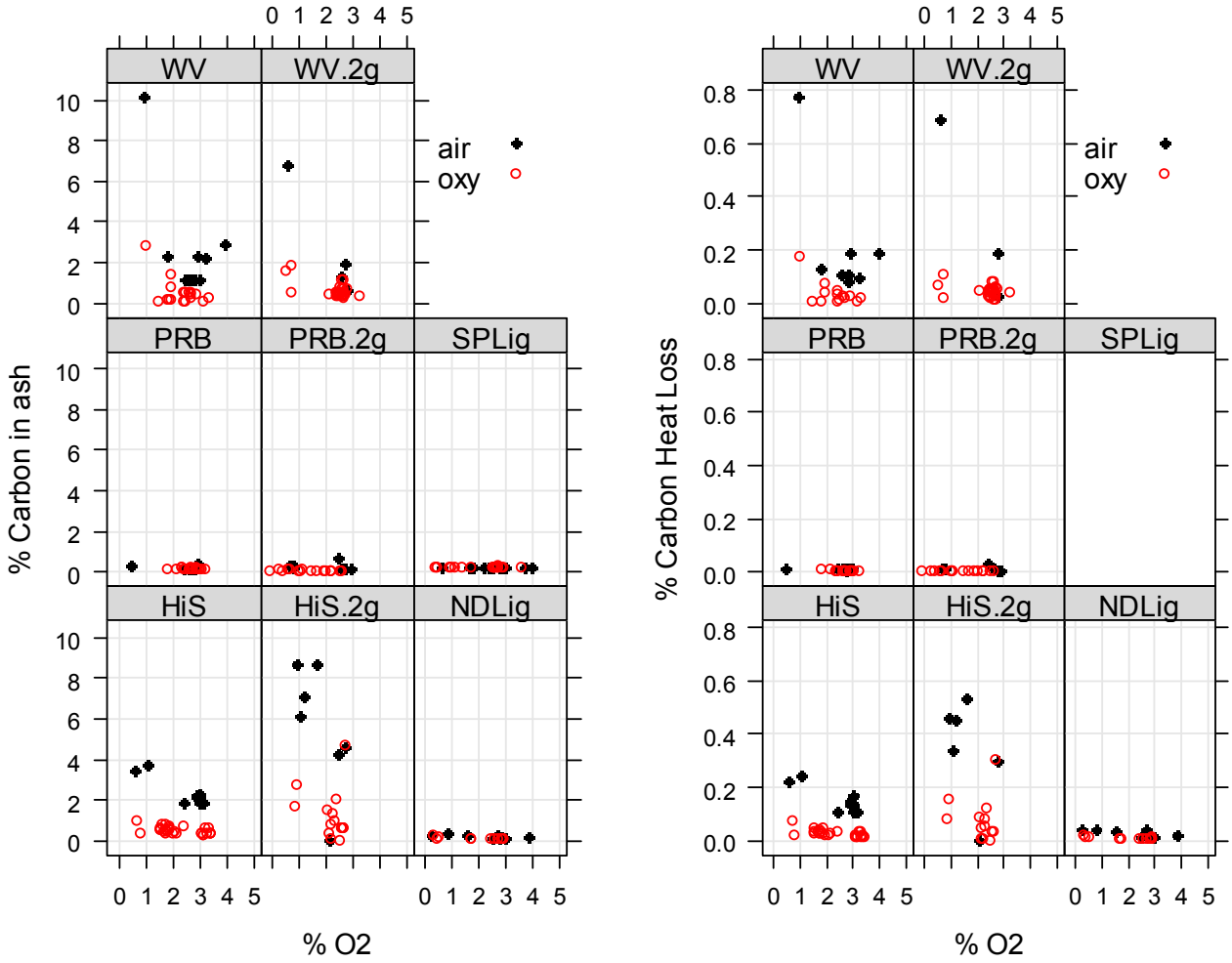

Figure 5-7. Unburned carbon in fly ash and carbon heat loss

5.3 NO_x Emissions

The emission of nitrogen oxides (NO_x) is an environmental concern in the design and operation of traditional air-fired combustion power plants. In the oxy-combustion process, environmental emissions of NO_x must still meet regulatory limits, and there is the additional consideration for the operation of the flue gas processing unit and the quality of sequestered gas. Combustion changes and design flexibilities with the oxy-combustion process allow for new opportunities to control NO_x emissions. Understanding the impacts of firing system design and operation on NO_x emissions during oxy-combustion is a goal of this test program.

The formation of NO_x during the combustion is a complex process, highly dependent upon the time-temperature-stoichiometric history inside the boiler as well as specific properties of the fuel being fired. Windbox stoichiometry is one of the key variables in a staged, low-NO_x firing system. For a constant total oxygen input to the boiler, as more oxygen (or air) is shifted to the overfire locations, the stoichiometry in the windbox decreases. The typical pattern for air firing is that the NO_x emissions decrease as more air is shifted to the overfire locations. At some point, the emissions level off, and may even increase if the windbox stoichiometry decreases further.

For all BSF test campaigns, baseline air-fired testing was conducted to establish comparative performance and emissions data for the test coal. Figure 5-8 shows the NO_x levels at the boiler outlet over a range of different windbox stoichiometries for the BSF and utility boilers. For a constant total oxygen input to the boiler, as more oxygen is shifted to the overfire locations, the stoichiometry in the windbox decreases. For each fuel, NO_x emissions measured during baseline air firing in the BSF were consistent with utility boiler experience and generally were low.

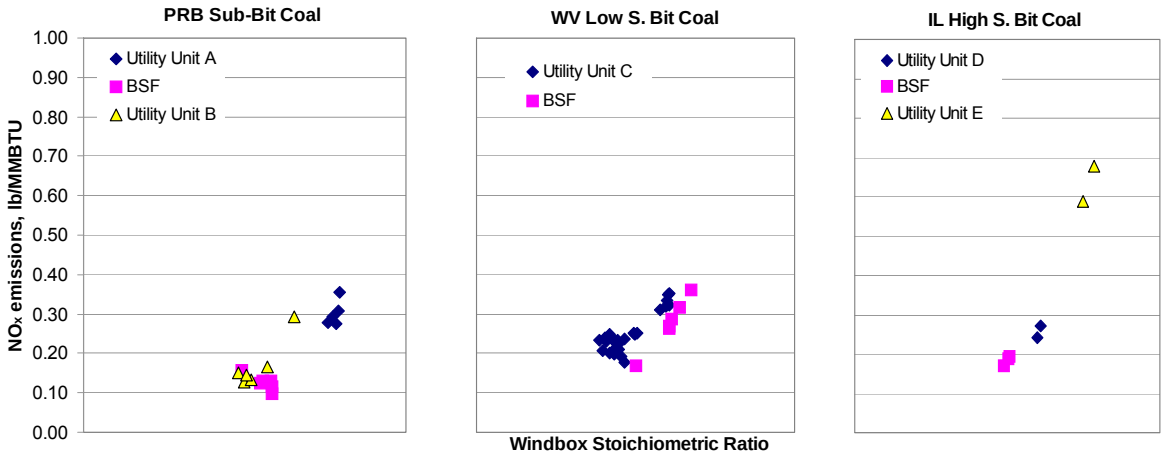

Figure 5-8. NO_x emissions versus windbox stoichiometric ratio, BSF and utility boilers

Figure 5-9 shows NO_x emission level varied with the degree of staging, shown as changing the stoichiometry in the main burner zone (MBZ), which is defined as the region below the close-coupled overfire air elevations (refer to Section 2.2.1). The NO_x is shown both as a concentration (ppm) and emission level (lb/MMBtu fired). The amount of NO_x produced (lb/MMBtu) is lower for oxy-firing, but due to the lack of nitrogen dilution, the concentration (ppm) is higher for oxy-firing.

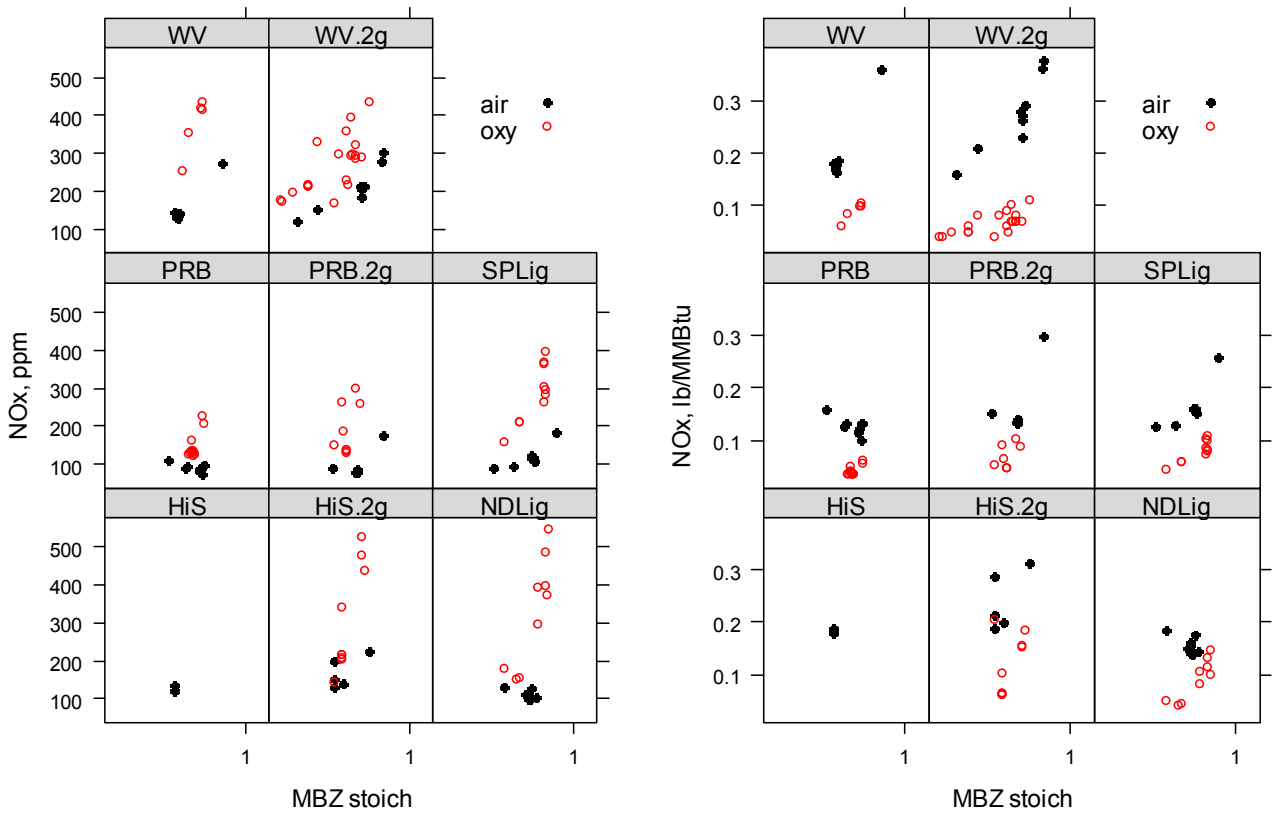

Figure 5-9. NO_x emissions *vs.* MBZ stoichiometry for air and oxy-firing (O_2 between 2.6 – 3%)

The data shown in Figure 5-9 is for all test points with the furnace outlet O_2 limited to between 2.6 and 3%. Figure 5-10 shows the impacts of MBZ stoichiometry for a more restricted subset with similar outlet O_2, furnace heat input, and recycle rate. Here the typical pattern is even clearer – including the increasing NO_x for some of the deepest staged air tests.

Air-combustion and oxy-combustion tests show a strong dependence of NO_x emissions on windbox stoichiometry. Oxy-combustion tests show a decrease in NO_x emissions through staging, and leveling off of NO_x emissions at deeper staging levels.

For similar staging conditions, the NO_x emissions during oxy-combustion are about 40 – 60% lower than with air firing.

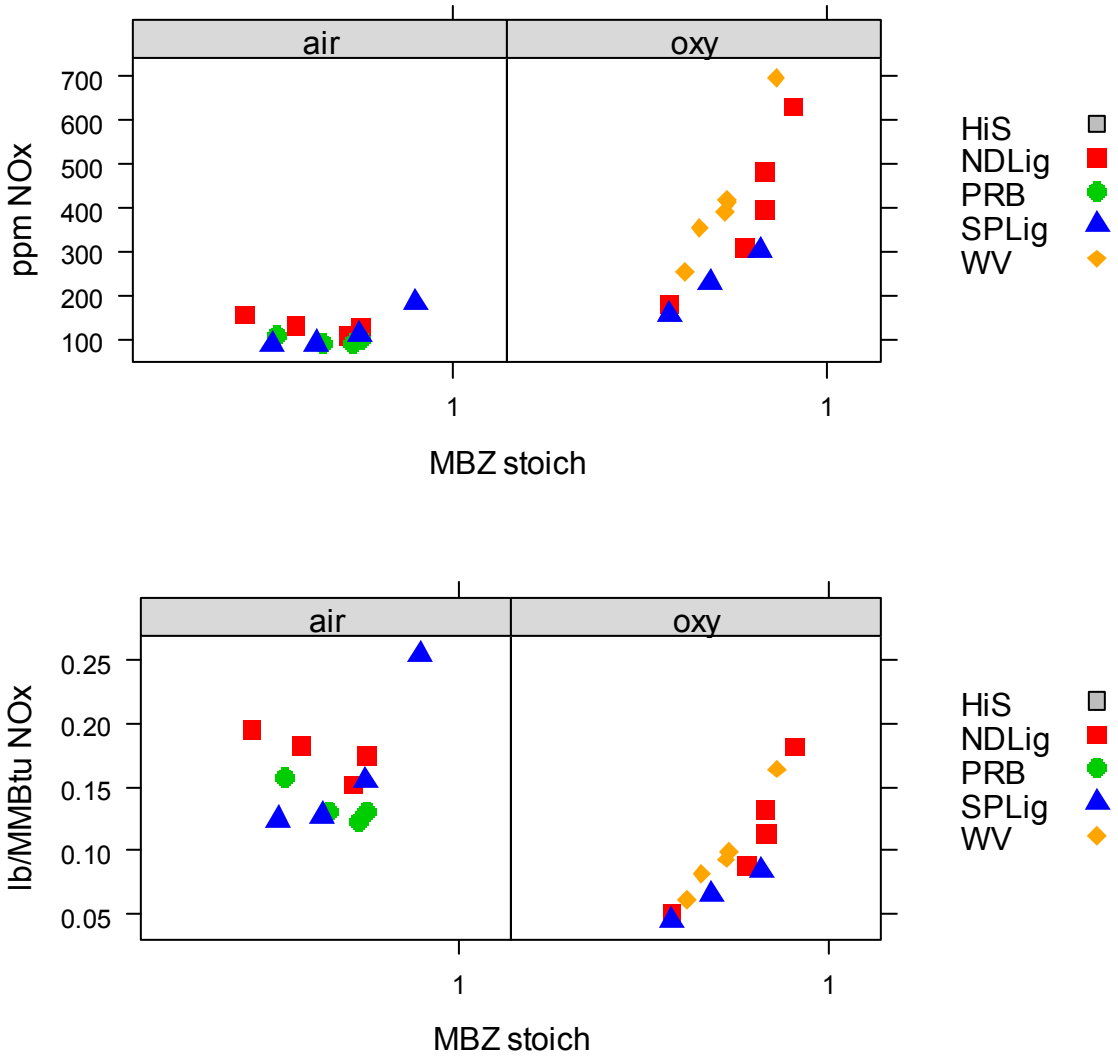

Figure 5-10. NO_x emissions *vs* MBZ stoichiometry at similar conditions

Figure 5-11 shows NO_x emissions versus the excess oxygen, shown as changing the oxygen concentration in the flue gas. The data points shown in Figure 5-11 represent combustion conditions selected to isolate the impacts of excess oxygen, i.e., similar windbox stoichiometry, furnace heat input, and recycle rate.

Over the range of conditions tested, air-firing shows a consistent decrease in NO_x emissions with decreasing outlet O_2. Oxy-combustion tests show little impact of excess oxygen on NO_x emissions. These results are consistent with an increase in thermal NO_x during air-combustion as the excess oxygen increases. Thermal NO_x results from the reaction of nitrogen and oxygen in a high-temperature combustion zone. With little nitrogen present during oxy-combustion, thermal NO_x is expected to be much lower during oxy-combustion.

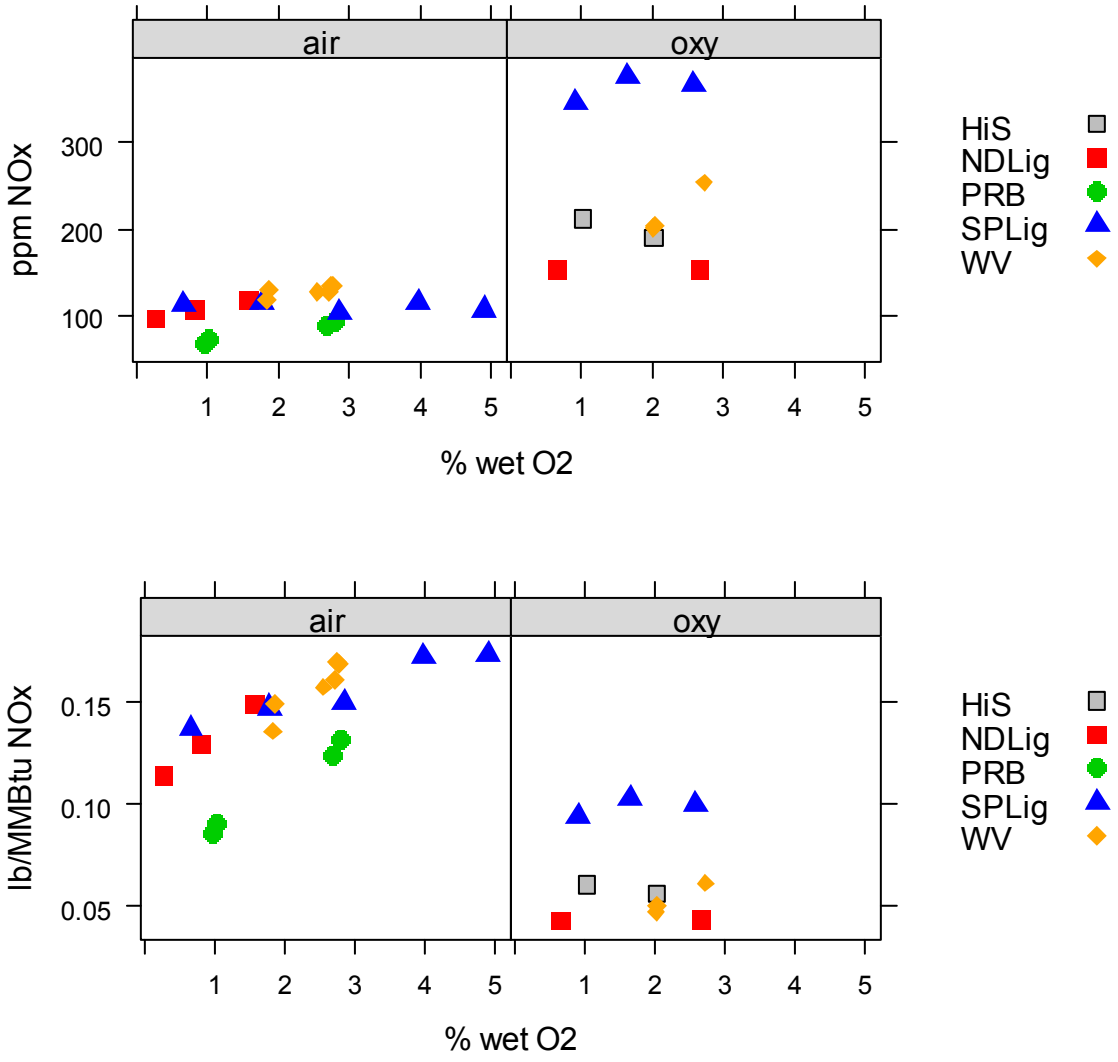

Figure 5-11. NO_x emissions *vs* outlet oxygen level at similar conditions

5.3.1 NO_x injection tests

The lower amount of NO_x emitted during oxy-firing compared to air firing is influenced by several factors including reduced thermal NO_x, changes in the combustion gas composition impacting NO_x chemistry, and reburning of NO_x returned to the boiler with flue gas recycle. Varying the amount of flue gas recycle would be expected to change the amount of reburning, but the effects may be confounded by changes in furnace temperatures and residence times.

To more clearly see the effect of reburning, a series of tests injecting extra NO_x (as NO) into the recycled flue gas was done in three series during the last two test campaigns:

PRB second generation with oxy-firing;
High sulfur bituminous with oxy-firing; and
High sulfur bituminous with air firing.

Nitric oxide was added to the flue gas recycle returning to the BSF in one of three locations: the windbox region, the overfire region, or the bulk flow before the flue gas splits going to both the windbox and overfire regions. Measurements of NO_x taken in the windbox inlet duct confirmed good mixing of the injected NO.

Figure 5-12 shows the traces of NO_x levels at the BSF outlet and the flow of added NO for each of the three test series. Details of the test conditions are shown in Table 5-1.

Following is a short narrative of the test conditions for the first series shown in the top plot of Figure 5-12. After establishing baseline conditions without injection, nitric oxide injection was started at 08:30, 9/27/2012, to the bulk secondary recycle gas with little to no change in outlet emissions. The injection rate was then increased to 50 SCFH with little to no impact on outlet emissions. At 10:00 the flow of nitric oxide began to drop off as the bottle contents were depleted. A fresh bottle was installed and injection began to the windbox recycle gas with little to no change in outlet NO_x emissions. At 11:45 injection began to the OFA recycle with a noticeable step-change in outlet NO_x emissions. At 12:15 the injection rate was increased with a further increase in outlet emissions.

At 12:45 furnace staging was changed – increasing the stoichiometry to the windbox region. The NO_x increased accordingly. The third bottle was run out, then a new baseline was established at this staging. Injection began at about 13:50 to the windbox with some moderate NO_x increase. In each plot of Figure 5-12, the vertical green line indicates the shift to the higher windbox stoichiometry.

Table 5-1. NO injection test conditions

Test	Campaign	Oxidant	Start	End	injection location	NO injection, SCFH	WBX stoich	%O2 wet	ppm NOx dry	ppm NO dry	NOx in, lb/hr	OFA NOx in, lb/hr	NOx out, lb/hr
218	PRB.2g	oxy	09/27 07:00	09/27 08:30	None	0.0	normal	2.7	130	130	3.3	0.7	4.7
219	PRB.2g	oxy	09/27 08:32	09/27 09:02	Bulk	22.9	normal	2.5	132	131	6.1	0.7	4.7
220	PRB.2g	oxy	09/27 09:05	09/27 09:51	Bulk	48.5	normal	2.4	138	137	9.3	0.8	4.9
221	PRB.2g	oxy	09/27 10:13	09/27 11:25	WBX	49.1	normal	2.6	131	131	9.2	0.7	4.7
222	PRB.2g	oxy	09/27 11:47	09/27 12:17	OFA	22.9	normal	2.2	185	183	7.3	1.0	6.6
223	PRB.2g	oxy	09/27 12:18	09/27 12:38	OFA	47.8	normal	2.2	261	257	12.2	1.4	9.3
224	PRB.2g	oxy	09/27 13:15	09/27 13:49	None	0.0	high	2.4	257	255	6.2	1.0	9.2
225	PRB.2g	oxy	09/27 13:49	09/27 14:18	WBX	47.4	high	2.5	300	290	13.1	1.1	10.8
239	HiS.2g	oxy	11/01 08:00	11/01 08:50	None	0.0	normal	2.7	200	198	5.4	1.2	7.6
240	HiS.2g	oxy	11/01 09:38	11/01 10:17	Bulk	25.0	normal	2.8	205	201	8.7	1.2	7.8
241	HiS.2g	oxy	11/01 10:19	11/01 10:51	Bulk	49.0	normal	2.8	214	214	11.8	1.3	8.1
242	HiS.2g	oxy	11/01 11:25	11/01 11:49	WBX	49.0	normal	2.8	213	216	11.7	1.3	8.0
243	HiS.2g	oxy	11/01 11:55	11/01 12:07	OFA	49.0	normal	2.8	341	334	15.3	2.0	12.9
244	HiS.2g	oxy	11/01 12:12	11/01 12:30	OFA	24.6	high	2.7	262	260	10.2	1.6	9.9
245	HiS.2g	oxy	11/01 14:30	11/01 14:37	None	0.0	high	2.8	433	424	11.4	1.7	15.8
246	HiS.2g	oxy	11/01 14:50	11/01 15:00	WBX	47.9	normal	3.0	523	518	19.7	2.0	19.3
263	HiS.2g	air	11/05 11:47	11/05 13:32	None	0.0	normal	2.7	142	140	0.0	0.0	9.0
264	HiS.2g	air	11/05 13:36	11/05 13:41	OFA	48.9	normal	2.7	200	200	5.9	0.0	12.6
265	HiS.2g	air	11/05 13:48	11/05 13:51	WBX	49.0	normal	2.7	151	149	5.9	0.0	9.4
266	HiS.2g	air	11/05 13:58	11/05 14:03	Bulk	49.0	normal	2.7	151	150	5.9	0.0	9.5
267	HiS.2g	air	11/05 14:40	11/05 14:52	None	0.0	high	2.5	243	241	0.0	0.0	14.7
268	HiS.2g	air	11/05 14:52	11/05 15:42	Bulk	46.0	high	2.5	257	256	5.6	0.0	15.6

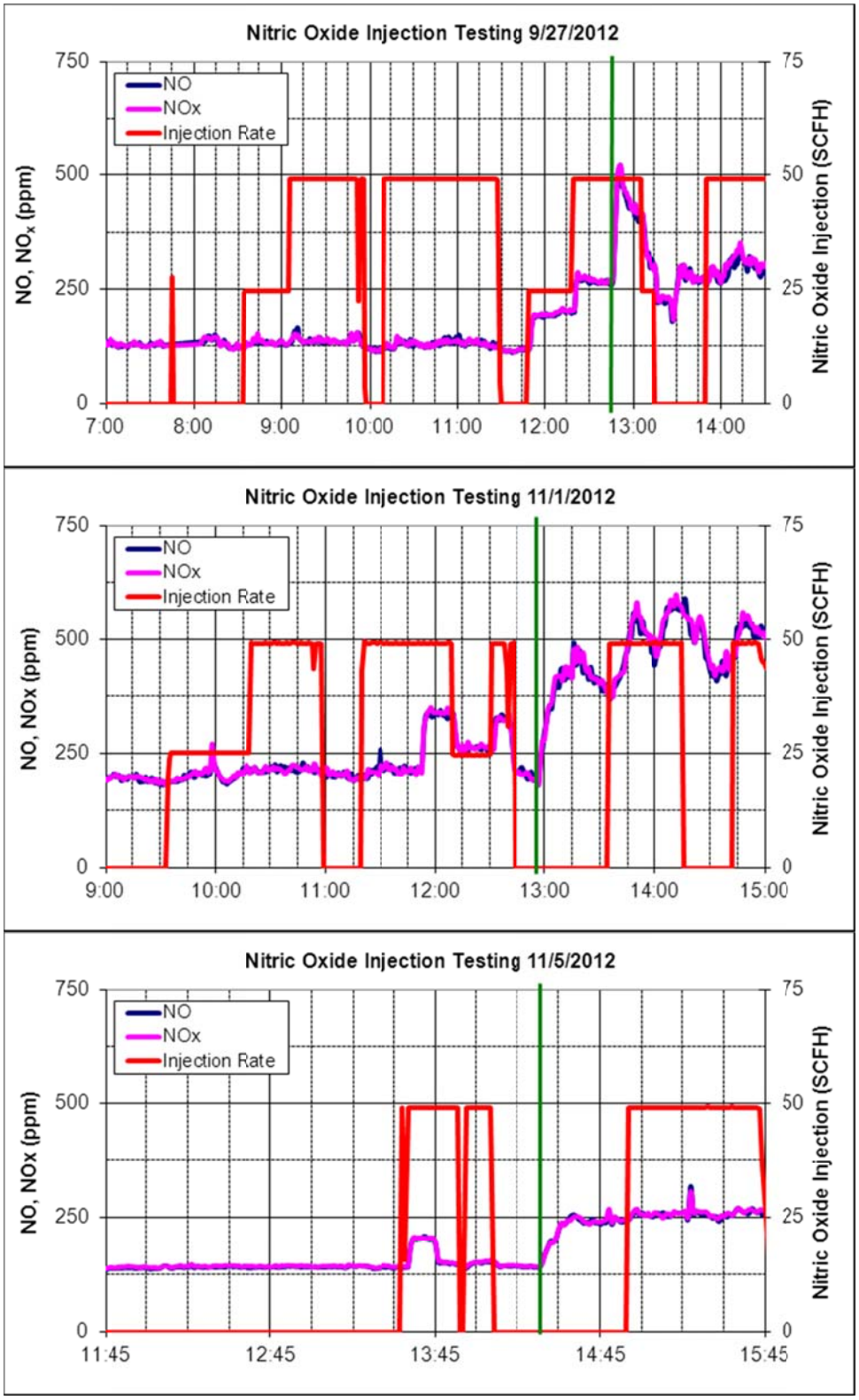

Figure 5-12. Addition of nitric oxide

Figure 5-13 shows the results as the amount of NO_x leaving the furnace compared to the amount entering – in each case relative to the corresponding test without NO injection. The NO_x entering

includes NO_x in the recycled flue gas (for oxy-firing) plus the injected NO. The dashed line indicates equal in and out.

At the normal windbox stoichiometries, shown in the top row, most of the NO added to the windbox or bulk flue gas was destroyed in the furnace. Much more of the NO added only to the OFA region made it through to the furnace outlet. This is expected, due to the less intense substoichiometric conditions which can reduce the NO_x.

At the higher windbox stoichiometries shown in the bottom row of Figure 5-13, there is much less reduction of the injected NO added to the windbox or bulk flue gas.

Figure 5-14 shows the results as the fractional reduction of the injected NO.

The result indicating nearly complete reburning of the recycled NO_x with deep windbox staging is important for extrapolation of the test results to commercial applications.

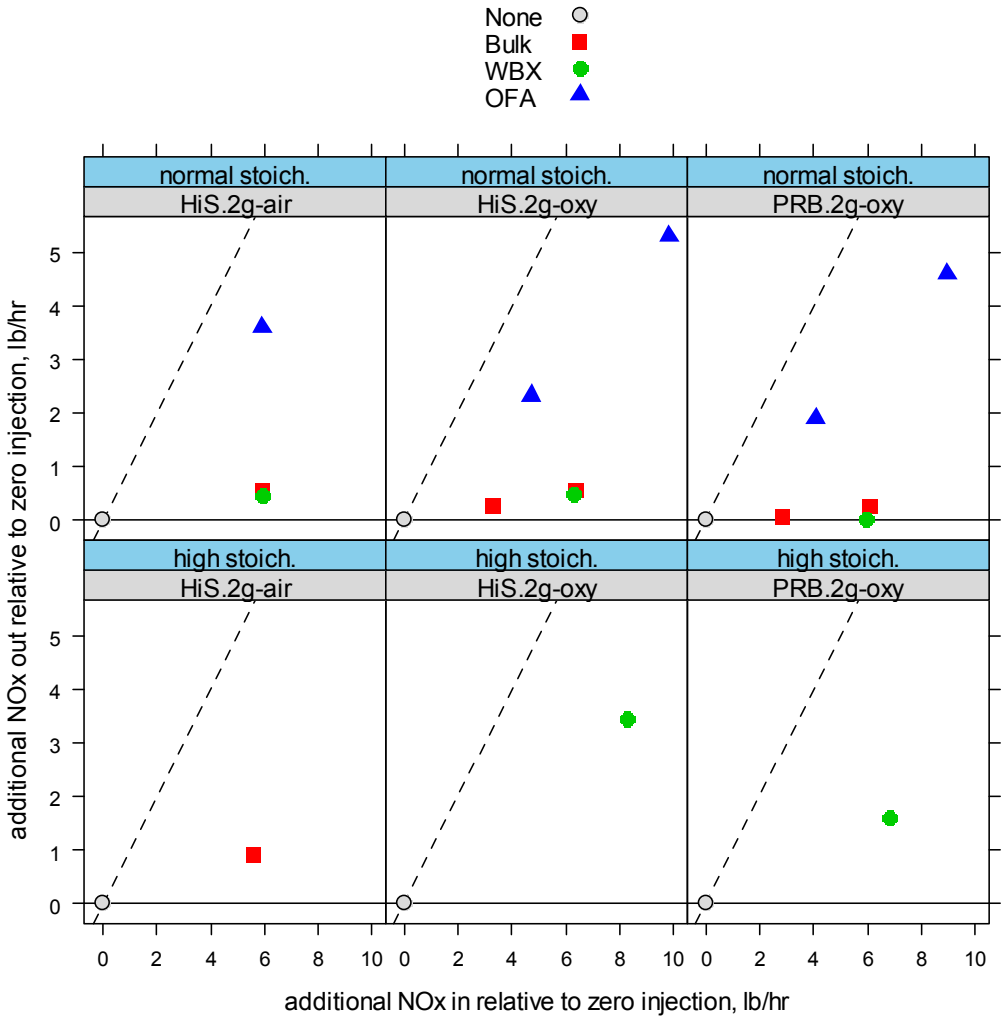

Figure 5-13. Increase in NO_x at the furnace outlet with NO injection

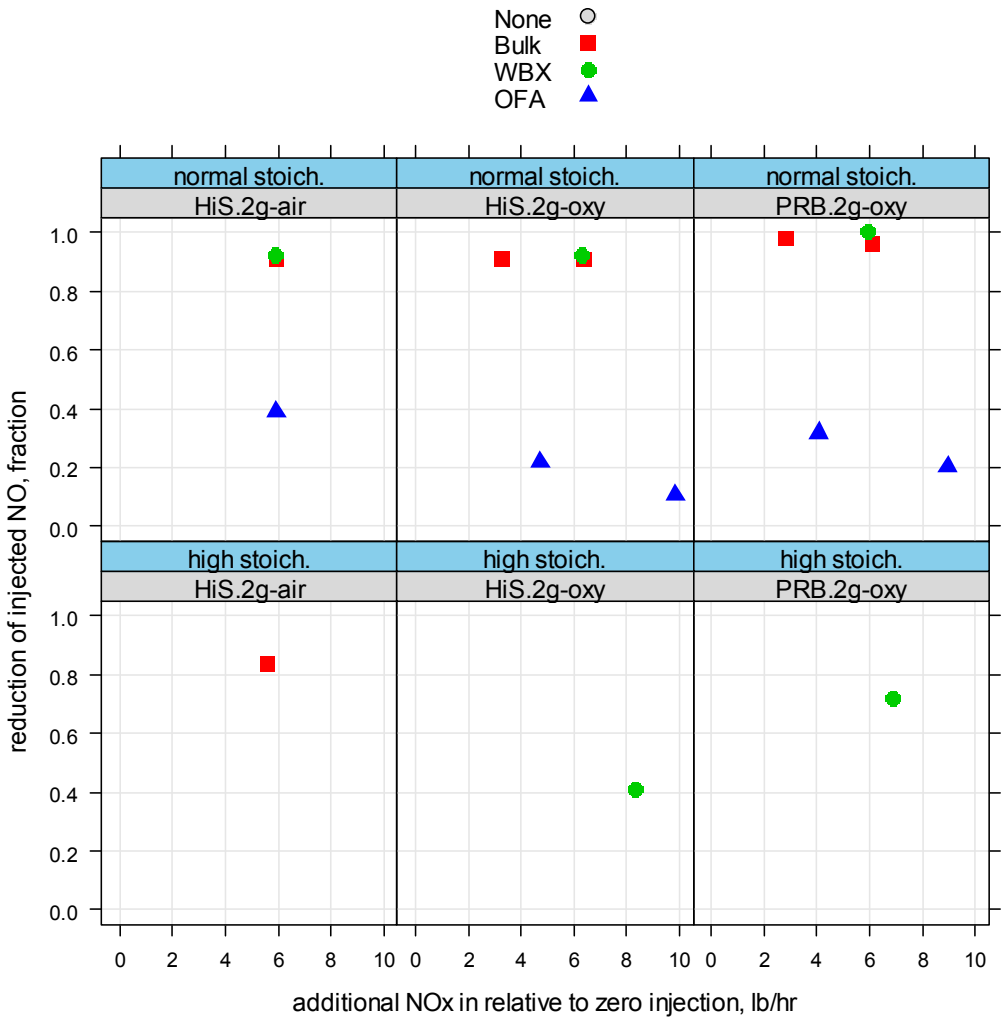

Figure 5-14. Reduction of injected NO

5.4 SO_2

Under both air- and oxy-firing, nearly all of the sulfur in the coal will be released in the furnace. If the sulfur is not removed from the recycled flue gas, the concentration will be higher in oxy-firing due to the lack of nitrogen dilution. If sulfur is removed, then the concentration is diluted by the recycled flue gas. In both air- and oxy-firing, the rate of SO_2 leaving depends on the extent of removal in the flue gas scrubber.

The NID™ system was installed and first tested during test campaign 2 firing the WV Fola low-sulfur bituminous coal.

During the third test campaign with Illinois high-sulfur bituminous coal, the NID™ system was operated for most of the test week. An overview of the NID™ system performance is shown in Figure 5-15.

The symbols represent the SO_2 concentration leaving the furnace (solid squares) and baghouse (open triangles) averaged over each test condition. At the first test point, on air firing with the NID™ system just starting operation, the SO_2 concentration leaving the baghouse is nearly the same as leaving the

furnace. It is slightly lower, as sulfur capture from the NID™ system started. As lime and water are added to the baghouse, the SO_2 leaving it drops to nearly zero. The SO_2 concentration leaving the furnace is unchanged, as expected.

Next the NID™ system was stopped and the transition to oxy-firing was made. The SO_2 concentration leaving the furnace increased by almost 5-fold as expected from the lack of nitrogen dilution in the flue gas. The SO_2 concentration at the baghouse exit should be nearly the same; however, the analyzer had a maximum range of 5000 ppm.

As shown in Figure 5-15, there were a few trips in the lime feeder when starting the NID™ system on oxy-firing, but after lime and water flow were established, the SO_2 leaving the baghouse dropped to about 500 ppm and then to under 100 ppm. In the oxy-fired case, the SO_2 level leaving the furnace also drops since SO_2 is removed from the recirculated flue gas.

The last oxy-fired test in Figure 5-15 was at 70% load. The flue gas recycle rate was kept high to maintain the gas velocity in the furnace. The relatively high recycle rate of clean flue gas (having gone through the NID™ system) dilutes the SO_2 level at the furnace outlet. This is similar to situation with air firing when a high excess air ratio is used at part load to maintain furnace velocities.

There was a transition back to air firing at the end of the week, with again very high sulfur capture from the NID™ system.

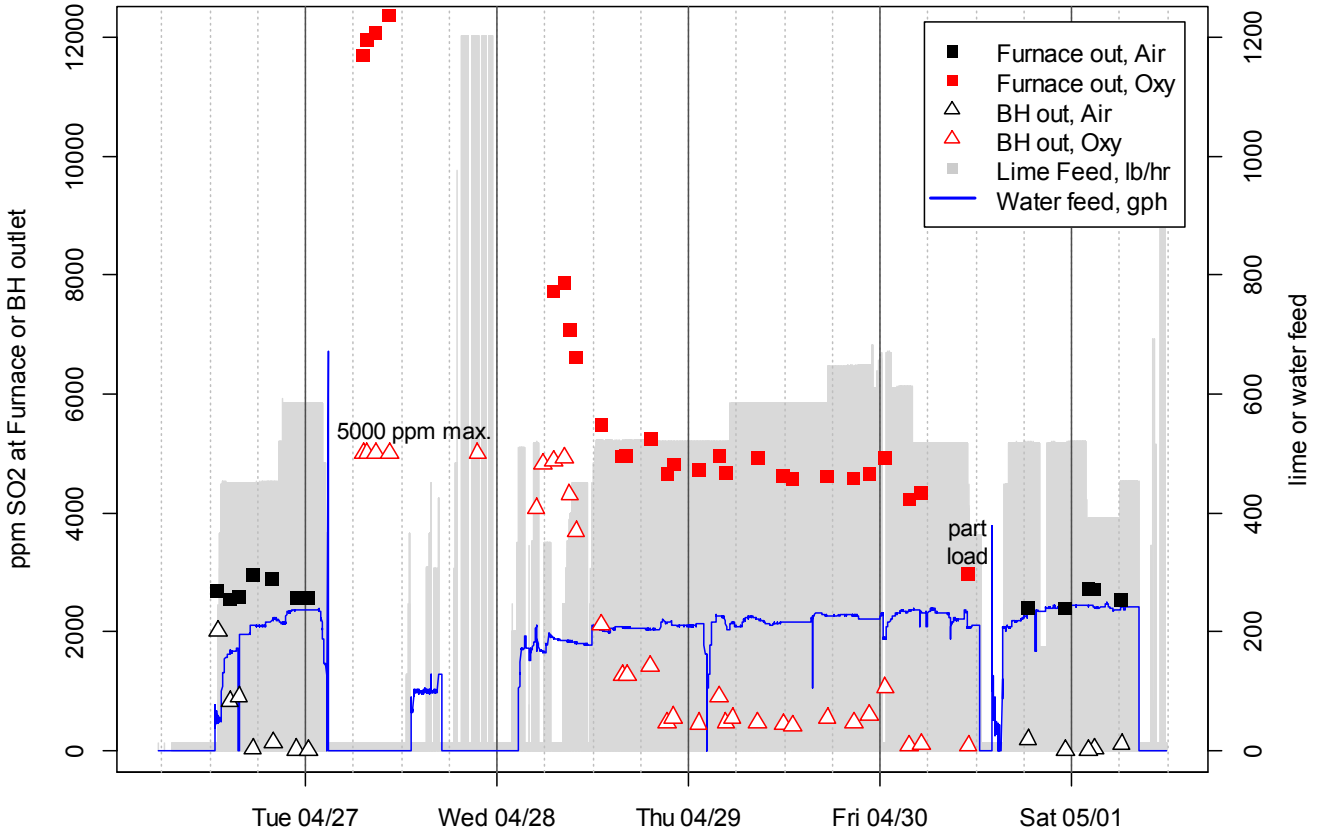

Figure 5-15. Sulfur capture in the NID™, High Sulfur test

Figure 5-16 shows a comparison of SO_2 concentration leaving the furnace and baghouse for all the test campaigns. The high sulfur test (HiS) shows the same features as discussed above:

the baghouse sulfur removal with constant furnace SO_2 on air firing;
the baghouse sulfur removal with dropping furnace SO_2 during oxy-firing; and
the 5000 ppm baghouse analyzer limit.

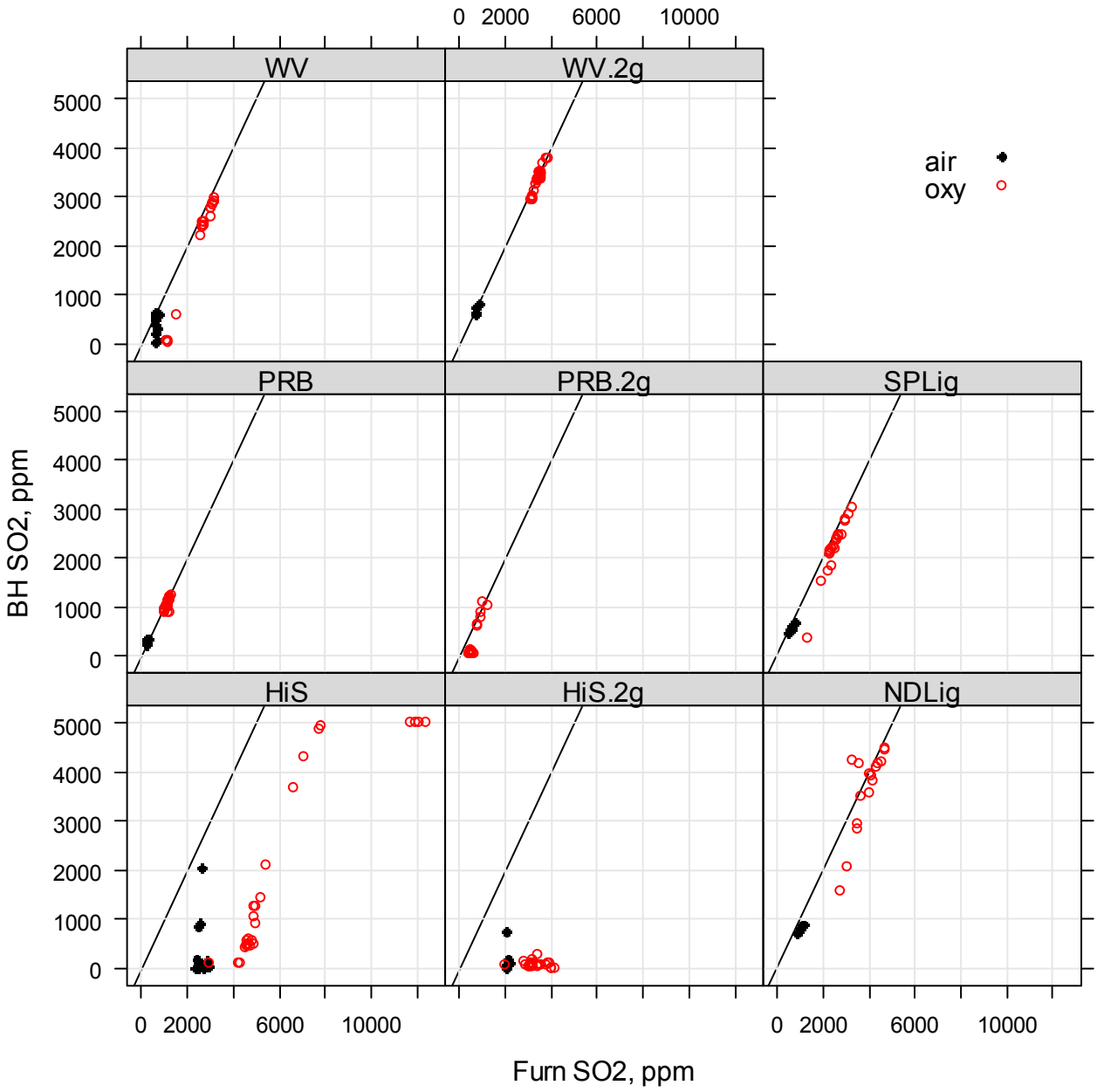

Figure 5-16. SO_2 emissions at the furnace and baghouse outlets

The WV Fola campaign shows a few similar test points during the initial testing of the NID™ system.

In the second generation hi sulfur campaign (HiS.2g), the NID™ system was operated constantly, so the baghouse SO_2 concentration is very low and the furnace concentration is also reduced.

The NID™ system operated during several of the second generation test points with low sulfur PRB fuel (PRB.2g). The SO_2 was reduced from over 1000 ppm to under 100 ppm.

In one oxy-fired test in the Schwarze Pumpe lignite test campaign (Test 134) the NID™ system operated, reducing the SO_2 to about 350 ppm.

In other cases, without the NID™ system operating, the SO_2 concentrations at both locations are the same.

5.5 SO_3

Measurements of SO_3 concentrations were made at four locations shown in Figure 5-17 under the following firing conditions:

- Air firing (Air);
- Oxy-firing without sulfur capture (Oxy);
- Oxy-firing with sulfur capture in the NID™ system (Oxy.SC);
- Hot recycle oxy-firing with secondary recycle from before the baghouse (Oxy.Hot);
- Oxy-firing with spiking of SO_3 in the recycle (Oxy.Spike); and
- Oxy-firing with close recycle with the ejector (Oxy.Educt).

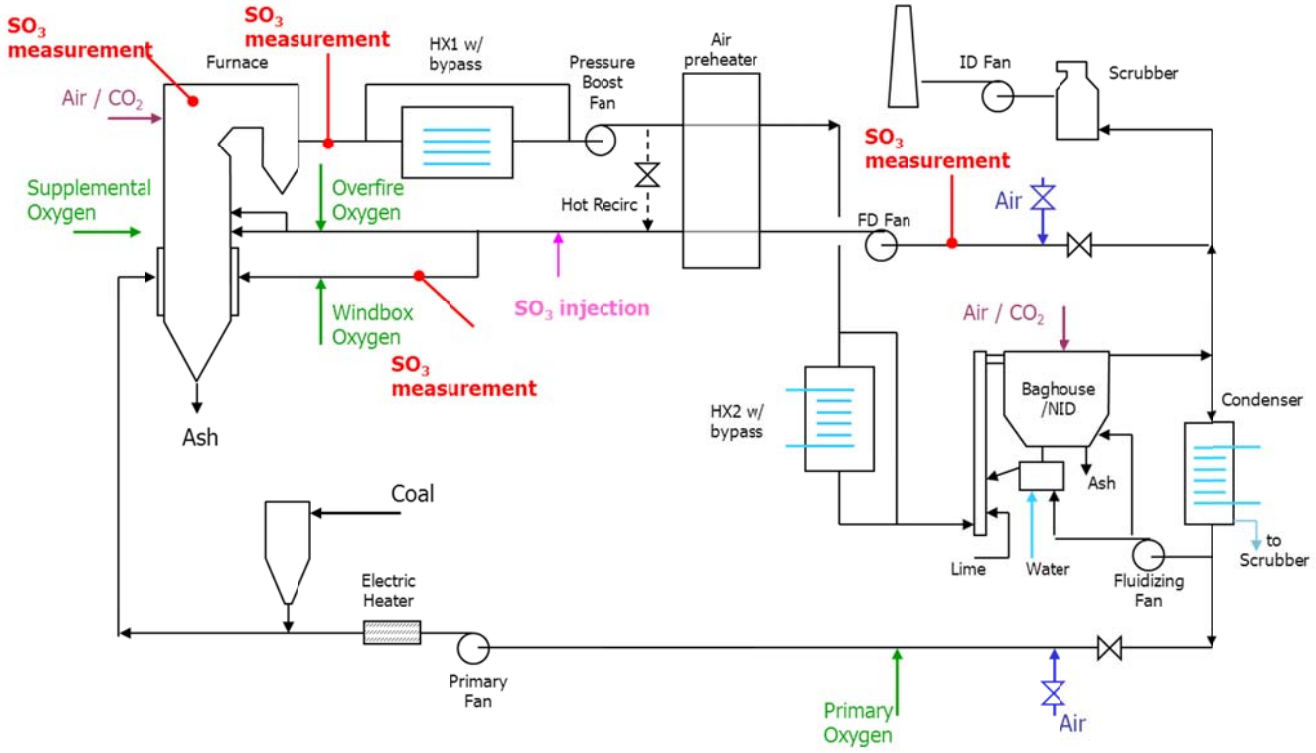

Figure 5-17. SO_3 measurement and injection locations

A description of the SO_3 measurement equipment and procedure is given in Section 2.3.5 and Appendix A.

The SO_2 and SO_3 concentrations measured over the range of conditions tested are plotted in Figure 5-18. The dashed lines in Figure 5-18 represent where the SO_3 level is 1, 2, and 3% of the SO_2 level – except for the Powder River Basin fuel, where they are lower by a factor of 10.

There were some problems with the SO_3 measurements during the WV Fola testing. On some test conditions the ISP had low gas flowrate which impacts inertial separation of the ash. This would result in a compromised SO_3 sample due to gas-ash interactions across the probe filter cake. Also the condensate bath temperature was set too low for oxy-combustion testing for which the flue gas has high water dewpoints. This would result in water condensing out in the condenser, possibly dissolving some flue gas SO_2 and biasing the SO_3 sample high. After noticing these errors in post-test analysis, procedures were modified to ensure desired conditions during the subsequent test campaigns.

As expected, higher SO_3 concentrations were measured during oxy-firing compared to air firing. The higher SO_3 concentrations are associated with higher SO_2 concentrations during oxy-firing. The net conversion rate of SO_2 to SO_3 appeared to be similar during both air and oxy-fired tests.

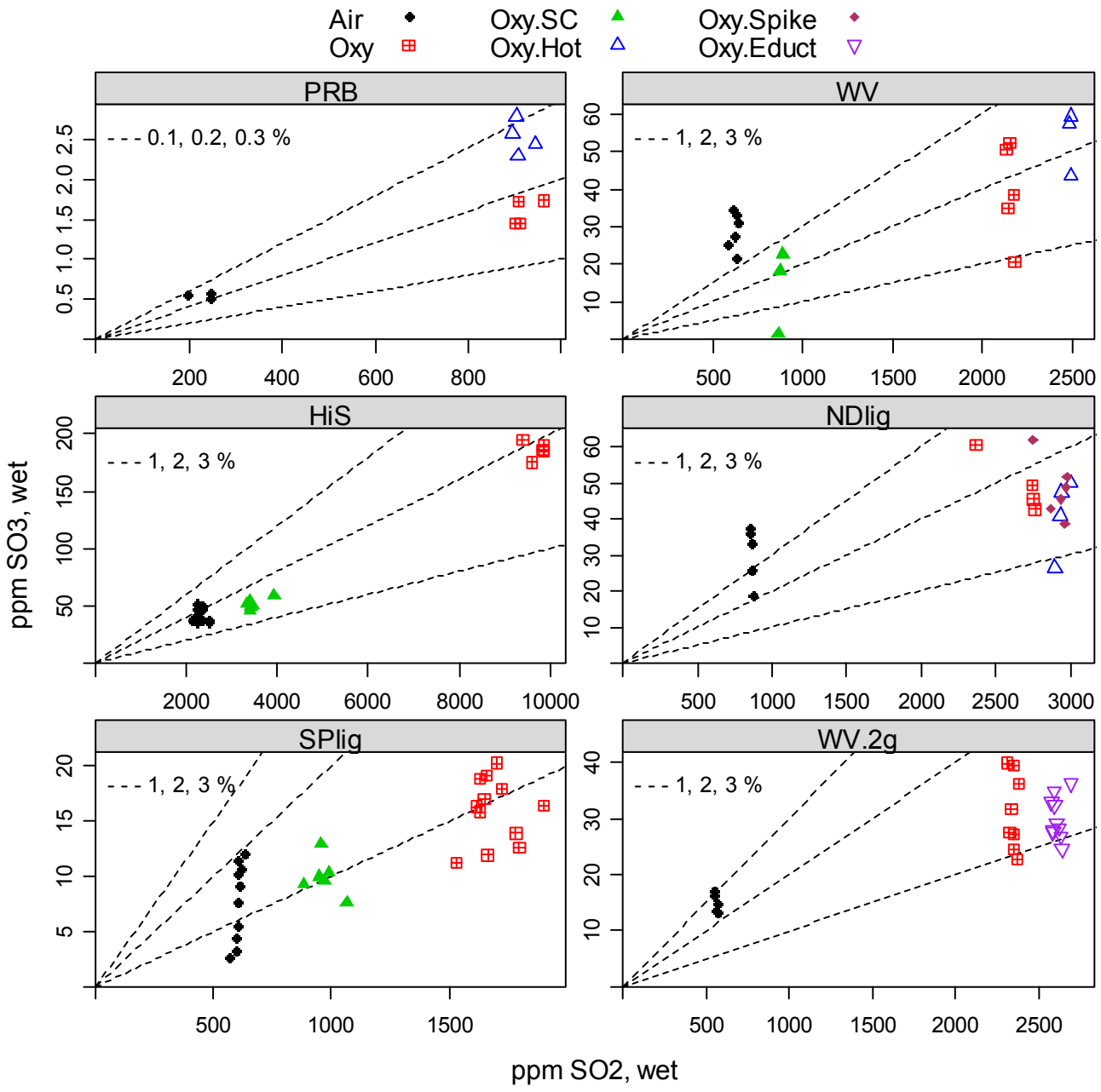

Figure 5-18. SO_2 and SO_3 (ppm, wet) at the economizer outlet

Even with hot recirculation, the SO_3 levels leaving the boiler did not increase significantly. The test facility configuration included a water-cooled heat exchanger, which condensed out some of the SO_3 before recycle. The design of a commercial system with hot recirculation would likely avoid this, and contain higher SO_3 levels in the recycle stream. This raises the question of whether the SO_3 in the recycle will be reduced in the furnace or will an even higher SO_3 content build up in the recycle loop, with the potential for high corrosion?

To simulate this, tests were done during the N.D. lignite campaign with SO_3 injected into the secondary gas recycle stream, after the air preheater and prior to oxygen addition (see Figure 5-17). The tests were done with secondary recycle through the baghouse without sulfur capture. A measured amount of sulfuric acid was vaporized and injected into the secondary ducting before the furnace and the concentration of SO_3 measured in the secondary recycle gas.

Figure 5-19 shows the results. The SO_3 concentration in the recycle stream is reduced to below 10 ppm. The concentration is 40 – 50 ppm leaving the furnace. When the SO_3 was spiked up to 80 – 160 ppm in the return gas, the level was still about 40-50 ppm at the boiler outlet. The SO_3 returning to the furnace does not contribute to an increased level at the furnace outlet. This is most likely due to the high temperature reduction of SO_3 in the furnace to SO_2 and possibly more reduced species such as H_2S. Thermodynamic analysis indicates that SO_2 is favored over $_{SO3}$ at a typical furnace temperature.

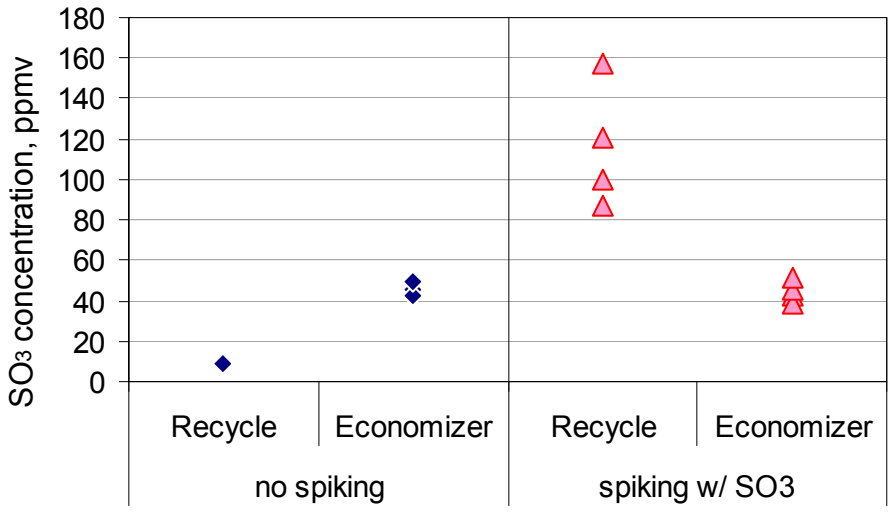

Figure 5-19. Results of SO_3 spiking tests

5.5.1 SO_3 control

During the second generation testing with high sulfur, high chlorine coal, SO_3 control by sorbent injection was tested on a slipstream of flue gas from the BSF. The slipstream of up to about 1000 lb/hr of flue gas was taken off before the gas-gas preheater. Inertial separation probes extracted gas samples for analysis both upstream and downstream of the sorbent injection location. The gas from the slipstream was not returned to the process (i. e., for oxy-firing it was not recycled to the furnace).

Figure 5-20 presents performance of the sorbents tested during air and oxy combustion testing. The four sorbents tested for the study were trona, hydrated lime, sodium bicarbonate and magnesium oxide. Results indicate that significant capture rates of acid gases are possible before the boiler gas-gas preheater, allowing lower exit temperatures and greater boiler efficiencies. There was little difference in the performance of these sorbents under air and oxy-fired conditions. Between 60 and 80% of the total SO_3 was captured by the sorbents.

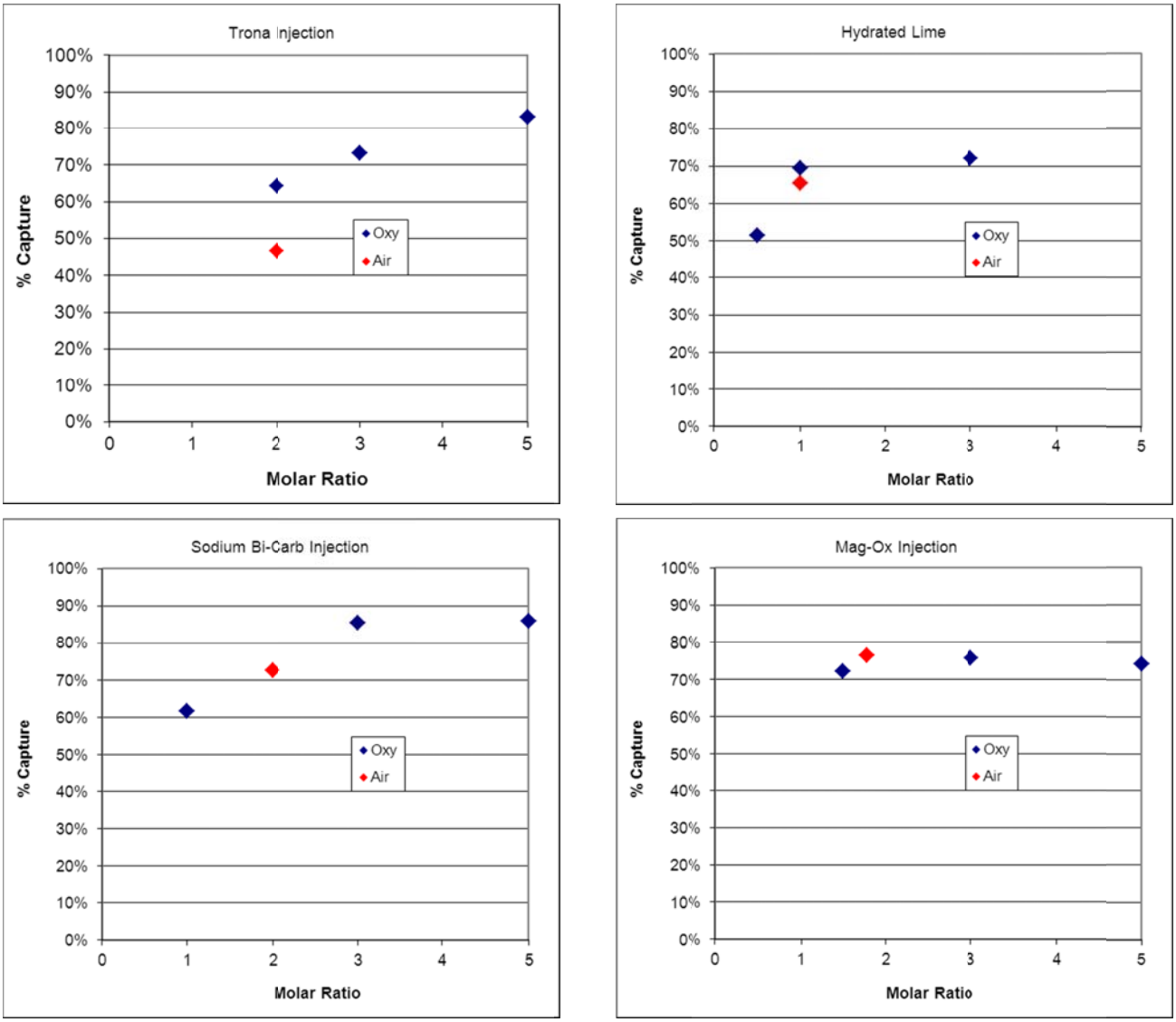

Figure 5-20. SO_3 control by sorbent injection

5.6 Fly ash

5.6.1 Particle size and loading

The curves in Figure 5-21 show the particle size at the economizer outlet measured by TRC using Method 501. They show the percentage of particles less than any particle size (up to 10 microns). The symbols in Figure 5-21 show the corresponding total dust concentration at the economizer outlet. (read the concentration in gm/m^3 on the y-axis – the horizontal placement is arbitrary.)

The dust loads are higher with recirculation, as some dust is returned to the furnace. Except for the WV coal, the size distribution is coarser with recirculation through the baghouse than with air firing.

For hot recycle (Hot) not through the baghouse, the size distribution is similar to air firing with a higher loading. This is what is expected.

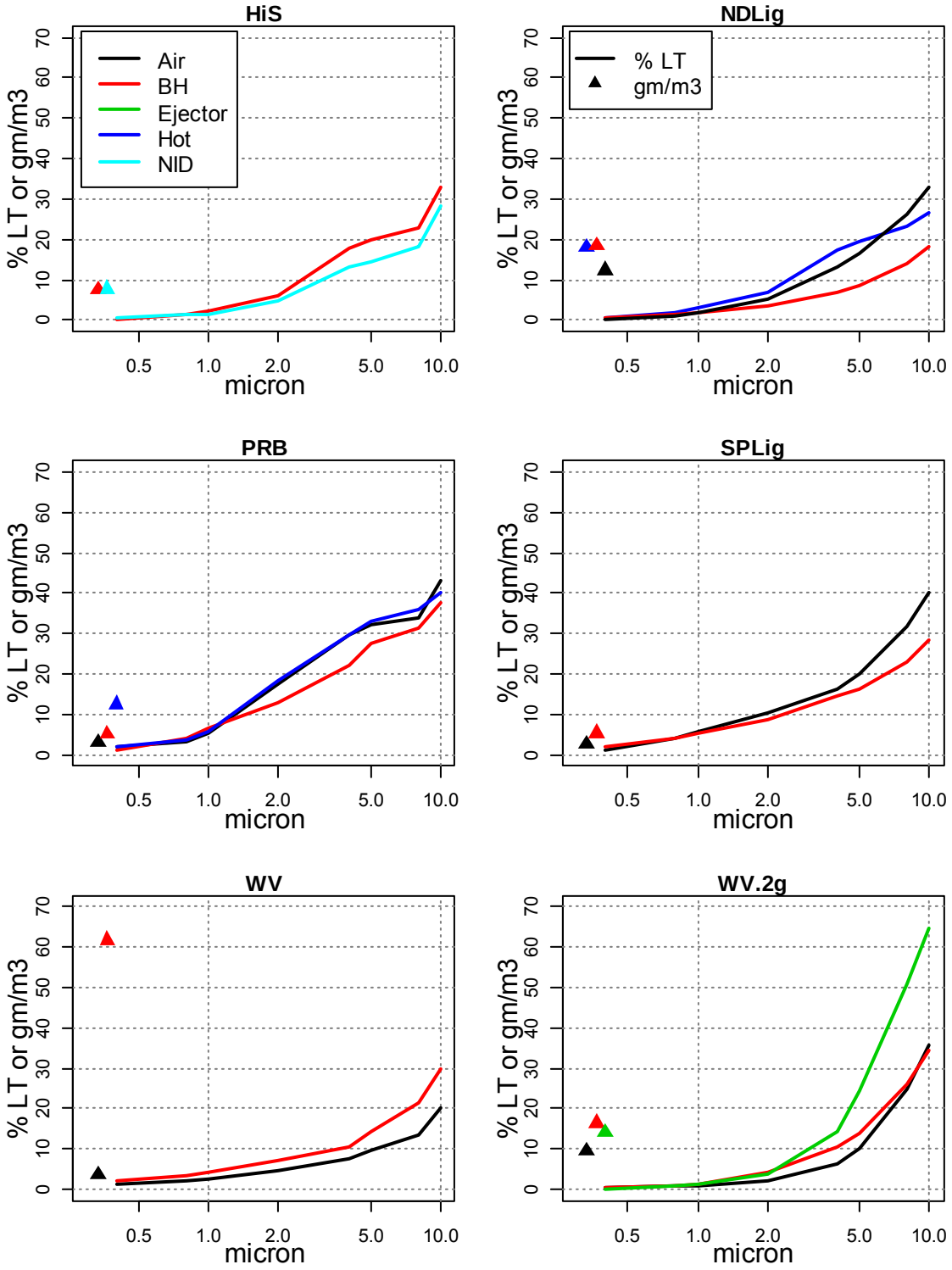

Figure 5-21. CARB Method 501 size distribution and loading at economizer outlet

5.6.2 Fly Ash analysis

The ash oxide analyses for fly ash samples taken at the furnace outlet and the baghouse are shown in Table 5-2. In general, the fly ash compositions were similar during air and oxy-fired tests reflecting the composition of the ash in the respective as-fired coal. The concentrations of carbonates in the fly ash collected at the furnace outlet (economizer) were very low during both air and oxy-firing as indicated by the CO_2 contents (less than 1%). The CO_2 contents in the ashes collected by the baghouse during oxy-firing were significantly higher (typically 15-30% CO_2 content) than the furnace outlet. Baghouse ash samples had higher CO_2 contents during NID operation under oxy-firing, reflecting the increased calcium content in the samples due to the addition of lime sorbent as well as the increased exposure time to the flue gas associated with ash recirculation around the baghouse for NID.

Table 5-2. Ash oxide analyses

Campaign	Time	Test	Oxidant	Loc	CO2	SiO2	Al2O3	BaO	Fe2O3	TiO2	Mn3O4	CaO	MgO	Na2O	K2O	P2O5	SO3	V2O5	SrO
PRB	09/05/2009 03:21	9	Air	Econ	0.056														
PRB	09/06/2009 13:05	11	Air	Econ		38.53	18.63	0.71	6.71	1.43	0.03	22.25	4.79	1.40	0.56	1.06	1.55		0.36
PRB	09/09/2009 01:43	13	Oxy	Econ		36.76	18.17	0.69	6.62	1.44	0.03	24.16	5.14	1.49	0.53	0.98	2.28		0.37
PRB	09/09/2009 18:29	18	Oxy	Econ	0.095														
PRB	09/11/2009 20:17	30	Oxy	Econ		37.53	20.88	0.75	6.41	1.44	0.03	21.10	4.44	1.57	0.63	1.02	1.93		0.34
PRB	09/12/2009 10:52	31	Oxy	Econ	0.07														
WV	01/21/2010 20:00	39	Air	Econ		54.79	34.56	0.08	4.02	1.91	0.01	1.12	0.74	0.28	2.08	0.19	0.27		0.07
WV	02/03/2010 14:07	50A	Oxy	Econ		54.78	34.60	0.07	4.01	1.97	0.01	1.02	0.71	0.25	2.12	0.17	0.18		0.07
WV	02/04/2010 15:12	54A	Oxy	Econ		54.32	34.45	0.08	3.97	2.00	0.01	1.02	0.71	0.28	2.30	0.53	0.27		0.07
HiS	04/27/2010 08:05	59	Air	Econ	0.14	51.86	21.46	0.04	13.60	1.02	0.04	3.20	0.97	1.13	2.23	0.61	1.67		0.03
HiS	04/30/2010 04:44	74	Oxy	Econ	0.15	52.63	20.68	0.04	14.01	0.97	0.04	3.10	1.02	1.04	2.14	0.47	0.79		0.03
HiS	05/01/2010 05:25	75	Air	Econ	<0.1	52.26	20.85	0.04	12.40	0.98	0.04	2.83	1.01	1.09	2.19	0.48	0.82		0.03
NDlig	10/05/2010 14:06	83	Air	Econ		48.09	16.41	0.59	6.57	0.60	0.08	15.33	5.01	1.81	2.30	0.17	0.25		0.34
NDlig	10/08/2010 12:05	98	Oxy	Econ		47.36	16.73	0.60	6.61	0.61	0.08	16.10	4.98	1.72	2.28	0.26	0.78		0.34
NDlig	10/09/2010 03:07	101	Oxy	Econ		46.49	16.22	0.35	6.64	0.61	0.08	16.32	5.03	1.87	2.30	0.33	1.07		0.33
SPlig	07/13/2011 07:42	109	Air	Econ	0.57	14.48	6.22		29.04	0.25	0.37	31.33	12.87	0.29	0.40	0.11	3.79		
SPlig	07/15/2011 09:19	127	Oxy	Econ	0.47	12.89	5.55		28.00	0.23	0.36	29.99	12.33	0.20	0.30	0.11	7.11		
SPlig	07/15/2011 18:27	133	Oxy	Econ	0.60	13.33	5.91		29.73	0.24	0.38	31.19	13.05	0.23	0.33	0.11	6.60		
SPlig	07/16/2011 09:04	134B	Oxy	Econ	0.53	12.14	5.73		29.21	0.24	0.36	30.49	12.57	0.23	0.32	0.11	5.56		
WV.2g	12/08/2011 17:11	145	Air	Econ	0.68	53.80	33.37	0.06	4.20	1.11	0.02	1.02	0.71	0.19	2.46	0.11	0.29	0.04	
WV.2g	12/09/2011 11:45	148	Oxy	Econ	0.59	53.10	33.86	0.06	4.04	1.30	0.01	1.12	0.62	0.26	2.51	0.13	0.52	0.04	
WV.2g	12/12/2011 04:33	155	Oxy	Econ	0.70	53.23	34.67	0.07	3.99	1.36	0.02	1.11	0.64	0.27	2.64	0.14	0.56	0.04	
WV.2g	12/12/2011 11:18	151	Oxy	Econ	0.58	53.27	34.22	0.06	3.92	1.28	0.01	1.12	0.65	0.34	2.53	0.12	0.51	0.04	
WV.2g	12/14/2011 13:41	161	Oxy	Econ	0.27	51.66	33.48	0.06	3.85	1.23	0.01	0.98	0.59	0.25	2.48	0.12	0.53	0.04	
WV.2g	12/16/2011 00:40	164	Air	Econ	0.45	52.37	33.15	0.06	4.50	1.22	0.02	1.27	0.83	0.19	2.58	0.13	0.48	0.04	
WV.2g	12/16/2011 13:10	173	Oxy	Econ	0.65	53.38	33.98	0.06	4.26	1.18	0.01	1.06	0.74	0.19	2.58	0.12	0.36	0.04	
WV.2g	12/16/2011 15:58	174	Oxy	Econ	0.46	52.15	33.83	0.06	4.21	1.27	0.02	1.08	0.62	0.26	2.53	0.14	0.92	0.04	
PRB.2g	09/24/2012 00:00	203	Air	Econ	0.65	40.60	20.65	0.59	6.04	1.37	0.03	20.61	4.43	1.26	0.67	0.76	1.43		0.31
PRB.2g	09/25/2012 09:48	209	Air	Econ	0.36	40.37	20.65	0.60	6.39	1.36	0.04	20.75	4.42	1.25	0.66	0.79	1.19		0.32
PRB.2g	09/26/2012 12:11	214A	Oxy	Econ	0.44	40.98	21.41	0.62	6.44	1.36	0.04	20.61	4.22	1.36	0.70	0.93	1.16		0.33
PRB.2g	09/26/2012 14:40	215	Oxy	BH	5.79	32.05	14.97	0.26	8.27	0.73	0.10	22.00	4.65	0.59	1.00	0.39	6.47		0.11
PRB.2g	09/28/2012 16:25	229	Oxy	BH	8.25	23.82	12.85	0.33	5.25	0.72	0.05	29.29	3.65	0.65	0.66	0.50	9.32		0.16
HiS.2g	10/31/2012 18:49	236	Air	Econ	0.38							4.84	0.99				1.45		
HiS.2g	10/31/2012 22:00	237	Air	BH	16.63							19.44	2.84				17.97		
HiS.2g	11/01/2012 11:53	242	Oxy	Econ	0.19							4.85	0.99				1.30		
HiS.2g	11/01/2012 13:15	245	Oxy	BH	27.05							33.12	1.99				24.66		
HiS.2g	11/01/2012 23:57	248A	Oxy	Econ	0.27							5.32	0.99				1.32		
HiS.2g	11/02/2012 14:54	250	Oxy	Econ	0.24							4.71	1.07				1.46		
HiS.2g	11/02/2012 17:00	250	Oxy	BH	32.07							34.81	1.47				32.47		
HiS.2g	11/02/2012 22:50	250	Oxy	BH	32.45							35.61	1.47				33.06		
HiS.2g	11/03/2012 10:07	252	Oxy	Econ	0.39							4.90	0.97				1.38		
HiS.2g	11/03/2012 12:30	252	Oxy	BH	29.96							32.12	1.40				26.84		
HiS.2g	11/03/2012 22:15	253	Oxy	BH	31.23							33.73	1.34				30.37		
HiS.2g	11/04/2012 11:25	255	Oxy	BH	31.49							33.29	1.38				30.00		
HiS.2g	11/04/2012 11:40	255	Oxy	Econ	0.17							5.23	1.02				1.51		
HiS.2g	11/04/2012 23:00	257	Oxy	BH	30.13	13.85	5.83	0.02	3.49	0.32	0.02	35.85	1.40	0.30	0.65	0.08	30.98		0.03
HiS.2g	11/05/2012 15:20	268	Air	BH	30.78							33.50	1.40				27.40		
HiS.2g	11/05/2012 15:41	268	Air	Econ	0.74	47.24	18.95	0.04	16.01	0.83	0.03	5.09	0.88	0.84	2.04	0.09	1.29		0.03

5.7 Trace metals and mercury

During each test campaign except the last (high sulfur second generation), trace metals were sampled and analyzed from the gas stream at the furnace outlet and after the baghouse isokinetically by EPA Method 29. The testing was done by TRC Environmental Corporation (TRC).

Figure 5-22 shows the locations of the metals sampling (along with the locations of separate mercury sampling during test campaign 4 discussed below).

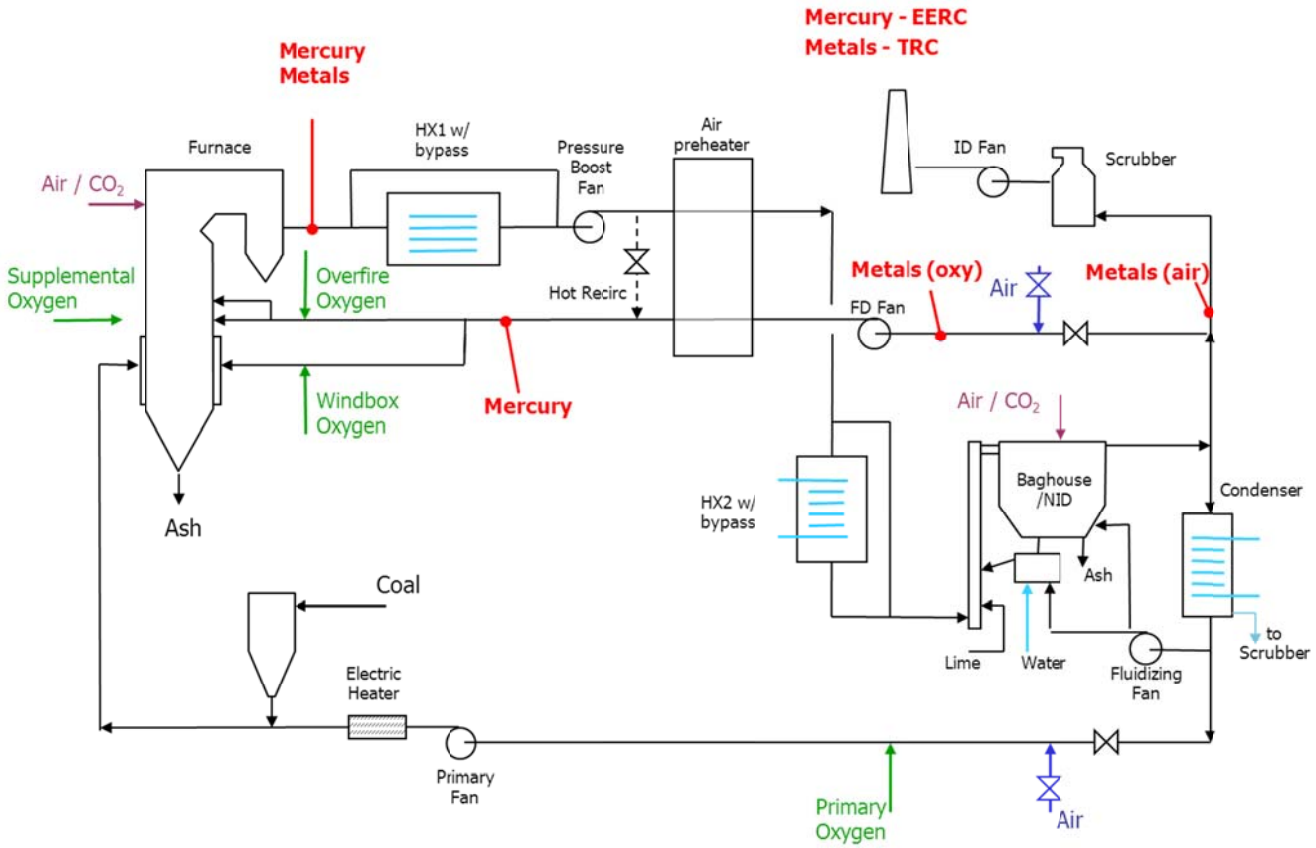

Figure 5-22. Mercury and metals sampling locations

Table 5-3 and Table 5-4 give the measured concentrations of 15 metals measured at the furnace outlet and baghouse outlet, respectively. Based on these concentrations and the fuel analyses given in Table 3-2, along with the flow rates, the mass flow ratio at the furnace outlet to the fuel input is shown in Figure 5-23. There is much variation in these calculated ratios. For example, there is much more barium and strontium leaving the furnace than in the fuel during the second generation campaign with WV Fola coal – even on the air fired tests without recycle. During the Schwarze Pumpe lignite and second generation PRB campaigns, much less barium and strontium was leaving the furnace.

During test campaign 2 with the low sulfur bituminous coal (WV), there is a consistent increase in the metals flow rates leaving the furnace when going to the hot recycle where the recycle did not go through the baghouse. This expected result was not so clear in the PRB and ND lignite campaigns.

Table 5-3. Trace metal concentrations at the furnace outlet (µg per dry standard cubic meter)

Test	Campaign	Condition	Sb	As	Ba	Be	Cd	Cr	Fe	Pb	Hg	Ni	Ag	Sr	Tl	Ti	V
11	PRB	Air	1.9E+1	1.3E+2	2.0E+4	2.2E+1	1.2E+1	4.1E+2	1.3E+5	1.7E+2	6.9E+0	3.9E+2	8.3E+0	1.3E+4	3.7E+0	4.5E+4	1.2E+3
22	PRB	Oxy	3.4E+1	1.9E+2	3.5E+4	3.4E+1	1.5E+1	5.6E+2	1.8E+5	3.0E+2	2.6E+1	6.2E+2	2.4E+1	1.2E+4	6.0E+0	6.9E+4	2.0E+3
30	PRB	Oxy.Hot	3.9E+1	2.5E+2	3.0E+4	3.5E+1	1.7E+1	4.5E+2	1.7E+5	3.6E+2	2.6E+1	6.8E+2	1.7E+1	1.8E+4	5.5E+0	4.3E+4	2.1E+3
39	WV	Air.NID	8.7E+1	2.9E+2	7.3E+3	2.2E+2	6.3E+0	2.2E+3	2.7E+5	1.3E+3	1.1E+1	1.3E+3	2.1E+1	6.0E+3	5.3E+1	1.1E+5	3.7E+3
40	WV	Oxy	1.3E+2	4.2E+2	1.0E+4	3.3E+2	1.5E+1	3.3E+3	3.8E+5	1.9E+3	2.2E+1	1.9E+3	3.1E+1	8.8E+3	7.7E+1	1.6E+5	5.6E+3
50	WV	Oxy.NID															
54	WV	Oxy.Hot	2.6E+2	6.8E+2	1.9E+4	6.1E+2	2.8E+1	6.3E+3	7.4E+5	3.9E+3	4.1E+1	3.4E+3	4.9E+1	1.7E+4	1.2E+2	3.3E+5	1.1E+4
65	HiS	Oxy	8.1E+1	2.6E+2	4.0E+3	1.6E+2	6.3E+1	2.1E+3	1.2E+6	7.9E+2	1.5E+1	1.5E+3	1.7E+1	2.9E+3	1.1E+2	8.1E+4	4.7E+3
74	HiS	Oxy.NID	5.7E+1	2.2E+2	3.1E+3	1.3E+2	5.1E+1	2.3E+3	1.0E+6	6.6E+2	1.2E+1	1.1E+3	1.1E+1	2.3E+3	1.1E+2	6.5E+4	3.7E+3
75	HiS	Air.NID	5.4E+1	1.9E+2	2.8E+3	1.3E+2	3.3E+1	2.3E+3	9.9E+5	6.0E+2	7.1E+0	1.2E+3	1.0E+1	2.2E+3	7.3E+1	6.3E+4	3.5E+3
101	NDlig	Oxy.Hot	1.9E+2	2.9E+3	1.2E+5	1.2E+2	2.8E+1	2.2E+3	1.1E+6	1.1E+3	4.7E+1	8.6E+2	5.5E+1	6.0E+4	1.4E+2	9.1E+4	3.9E+3
98	NDlig	Oxy	1.8E+2	2.5E+3	1.1E+5	1.0E+2	2.5E+1	2.1E+3	1.0E+6	1.0E+3	4.1E+1	8.1E+2	4.6E+1		1.2E+2	8.0E+4	3.4E+3
83	NDlig	Air	1.3E+2	1.6E+3	6.7E+4	7.0E+1	2.0E+1	1.3E+3	6.7E+5	7.0E+2	1.3E+1	4.9E+2	3.1E+1	3.7E+4	7.8E+1	5.3E+4	2.2E+3
109	SPlig	Air	2.9E+0	6.6E+1	1.1E+3	4.4E+0		8.0E+1	5.4E+5	4.4E+1	5.6E+0	7.4E+1		4.5E+3	2.7E+0	6.3E+3	2.6E+2
127	SPlig	Oxy	5.8E+0	7.9E+1	1.7E+3	6.9E+0	4.7E+0	8.8E+1	7.4E+5	5.2E+1	2.1E+1	7.0E+1	9.5E+0	6.1E+3		7.3E+3	1.4E+2
132	SPlig	Oxy	1.7E+1	1.1E+2	1.9E+3	7.8E+0	4.4E+0	1.4E+2	1.1E+6	7.1E+1	1.4E+1	9.1E+1	9.7E+0	9.6E+3		1.0E+4	1.9E+2
134	SPlig	Oxy.NID	1.0E+1	1.1E+2	3.0E+3	9.4E+0	5.9E+0	2.4E+2	1.2E+6	7.2E+1	1.8E+1	9.9E+1	8.2E+0	1.0E+4		1.1E+4	2.0E+2
145	WV.2g	Air	1.4E+2	3.6E+2	6.7E+3	2.0E+2	1.1E+1	2.2E+3	3.1E+5	1.7E+3	1.1E+1	1.5E+3	1.3E+1	4.5E+3	4.3E+1	9.0E+4	4.5E+3
148	WV.2g	Oxy	2.7E+2	7.8E+2	1.3E+4	4.0E+2	2.1E+1	5.1E+3	7.3E+5	3.2E+3	2.2E+1	3.1E+3	3.2E+1	8.6E+3	9.5E+1	2.0E+5	9.9E+3
151	WV.2g	Oxy.Hot	3.3E+2	9.3E+2	1.1E+4	4.5E+2	3.0E+1	5.6E+3	7.0E+5	3.7E+3	3.5E+1	3.2E+3	3.4E+1	7.4E+3	1.1E+2	2.1E+5	1.0E+4
156	WV.2g	Oxy.Hot	3.8E+2	9.3E+2	1.5E+4	5.1E+2	3.2E+1	5.4E+3	7.7E+5	4.4E+3	3.8E+1	3.7E+3	3.4E+1	9.8E+3	1.3E+2	2.3E+5	1.1E+4
209	PRB.2g	Air.NID		1.3E+2	2.1E+4			4.5E+2	1.8E+5	3.0E+2	1.3E+1	1.7E+2		1.2E+4		4.0E+4	1.3E+3
214	PRB.2g	Oxy.NID	4.1E+1	2.3E+2	2.5E+3	3.2E+1	1.1E+1	9.0E+2	3.2E+5	2.7E+2	2.0E+1	4.9E+2		2.1E+4		7.1E+4	2.4E+3

Empty rows: no sampling at furnace outlet for this test condition
Otherwise empty cells: below detection limits

Table 5-4. Trace metal concentrations at the baghouse outlet (µg per dry standard cubic meter)

Test	Campaign	Condition	Sb	As	Ba	Be	Cd	Cr	Fe	Pb	Hg	Ni	Ag	Sr	Tl	Ti	V
11	PRB	Air															
22	PRB	Oxy	1.7E+0	1.5E+0	5.6E+0	1.5E+0	1.6E+0	7.4E+0	9.3E+1	4.1E+0	1.7E+1	1.1E+1	3.1E+0	1.9E+0	1.5E+0	3.6E+0	5.0E+0
30	PRB	Oxy.Hot															
39	WV	Air.NID	1.2E+0	1.2E+0	9.4E+0	2.9E-1	3.2E-1	1.5E+0	8.6E+1	1.9E+0	1.0E-2	3.3E+0	5.7E-1	1.9E+0	1.4E+0	6.6E+0	8.6E-1
40	WV	Oxy															
50	WV	Oxy.NID	5.9E-1	1.2E+0	1.3E+1	1.3E-1	3.2E-1	5.0E+0	2.4E+2	2.6E+0	4.7E-1	7.4E+0	5.1E-1	7.3E+0	6.6E-1	7.1E+1	2.4E+0
54	WV	Oxy.Hot															
65	HiS	Oxy	1.5E+0	4.5E-1	6.1E+0	2.3E-1	3.1E+0	3.1E+0	1.1E+2	2.6E+0	1.3E+1	1.1E+1	1.6E+0	1.0E+0	1.4E-1	1.7E+1	7.8E+0
74	HiS	Oxy.NID	1.6E-1	4.0E-2	1.3E+0		4.0E-1	1.3E+1	7.3E+1	5.8E-1	3.8E+0	1.3E+1	1.0E-1	3.5E-1		3.9E+0	1.2E+0
75	HiS	Air.NID	9.0E-2	1.0E-1	1.9E+0		1.4E-1	9.0E+0	1.5E+2	5.1E-1	1.2E+0	9.9E+0	9.0E-2	5.2E-1	1.0E-2	5.3E+0	2.9E-1
101	NDlig	Oxy.Hot															
98	NDlig	Oxy								1.9E+1	3.1E+1						
83	NDlig	Air															
109	SPlig	Air	1.4E+0				1.2E+0	1.3E+0	6.7E+1	9.9E+0	7.2E+0			1.5E+0		5.9E+0	
127	SPlig	Oxy							7.8E+1	2.1E+0	2.5E+1						
132	SPlig	Oxy					5.4E+0	1.0E+1	1.4E+2	3.7E+0	4.1E+0	4.2E+0				3.4E+0	
134	SPlig	Oxy.NID					4.6E+0	7.1E+0	1.5E+2	6.0E+0	1.1E+1	4.8E+0		4.6E+1		4.9E+0	
145	WV.2g	Air															
148	WV.2g	Oxy															
151	WV.2g	Oxy.Hot															
156	WV.2g	Oxy.Hot															
209	PRB.2g	Air.NID						7.6E+0	2.3E+2	1.5E+1	6.0E-1	2.9E+1		1.3E+0		8.1E+0	
214	PRB.2g	Oxy.NID						3.9E+0		3.3E+0	8.1E+0	7.5E+0				5.8E+0	

Empty rows: no sampling at baghouse outlet for this test condition
Otherwise empty cells: below detection limits

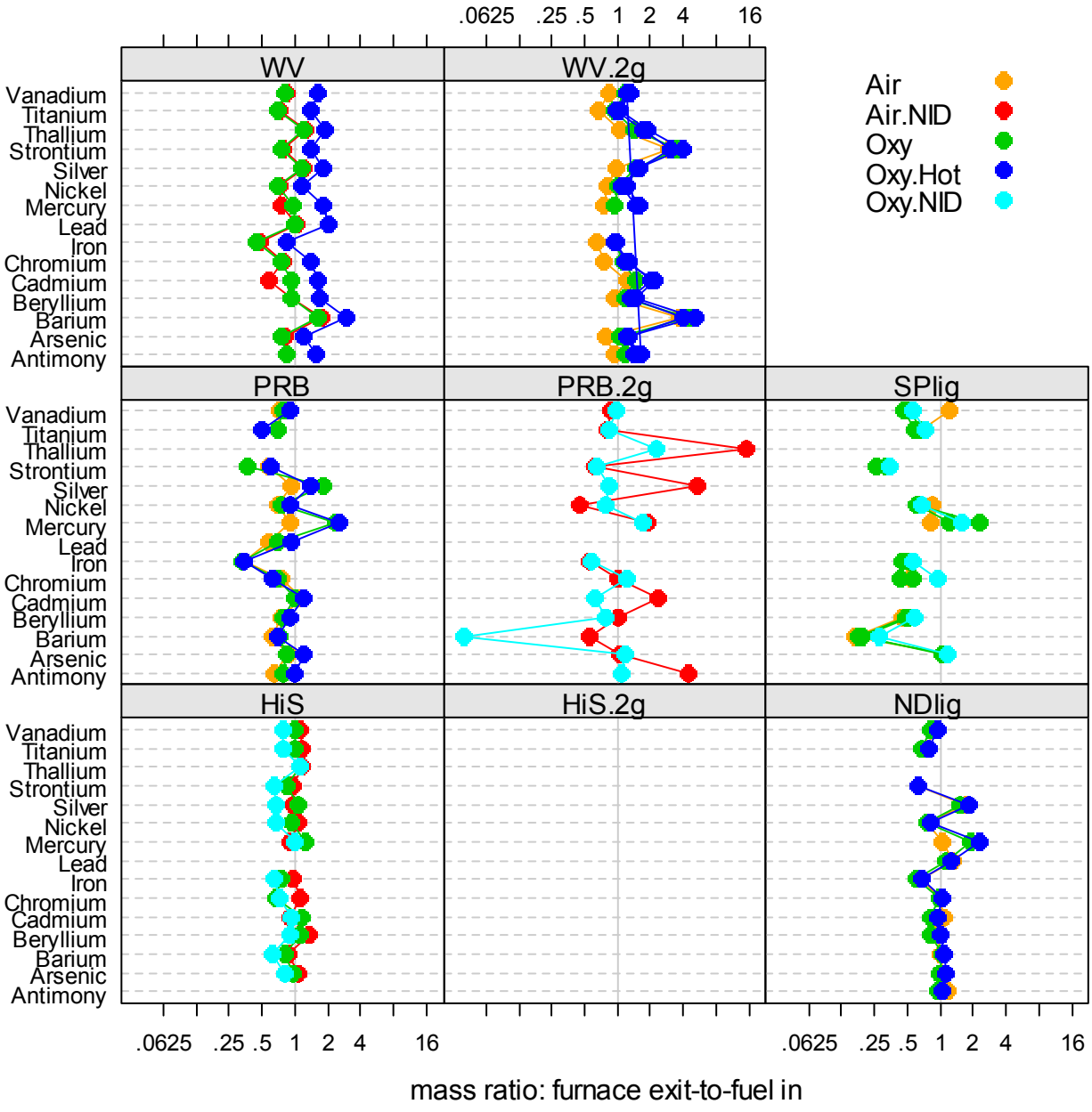

Figure 5-23. Trace metal mass ratio, furnace exit to fuel input (log scale)

The mass ratio of metals leaving the boiler system (recycle loop) compared to the fuel input is shown in Figure 5-24. Here it is clear that all metals other than mercury are mostly removed in the baghouse, although it appears that some small amount of antimony, cadmium, silver, and thallium escape the boiler island.

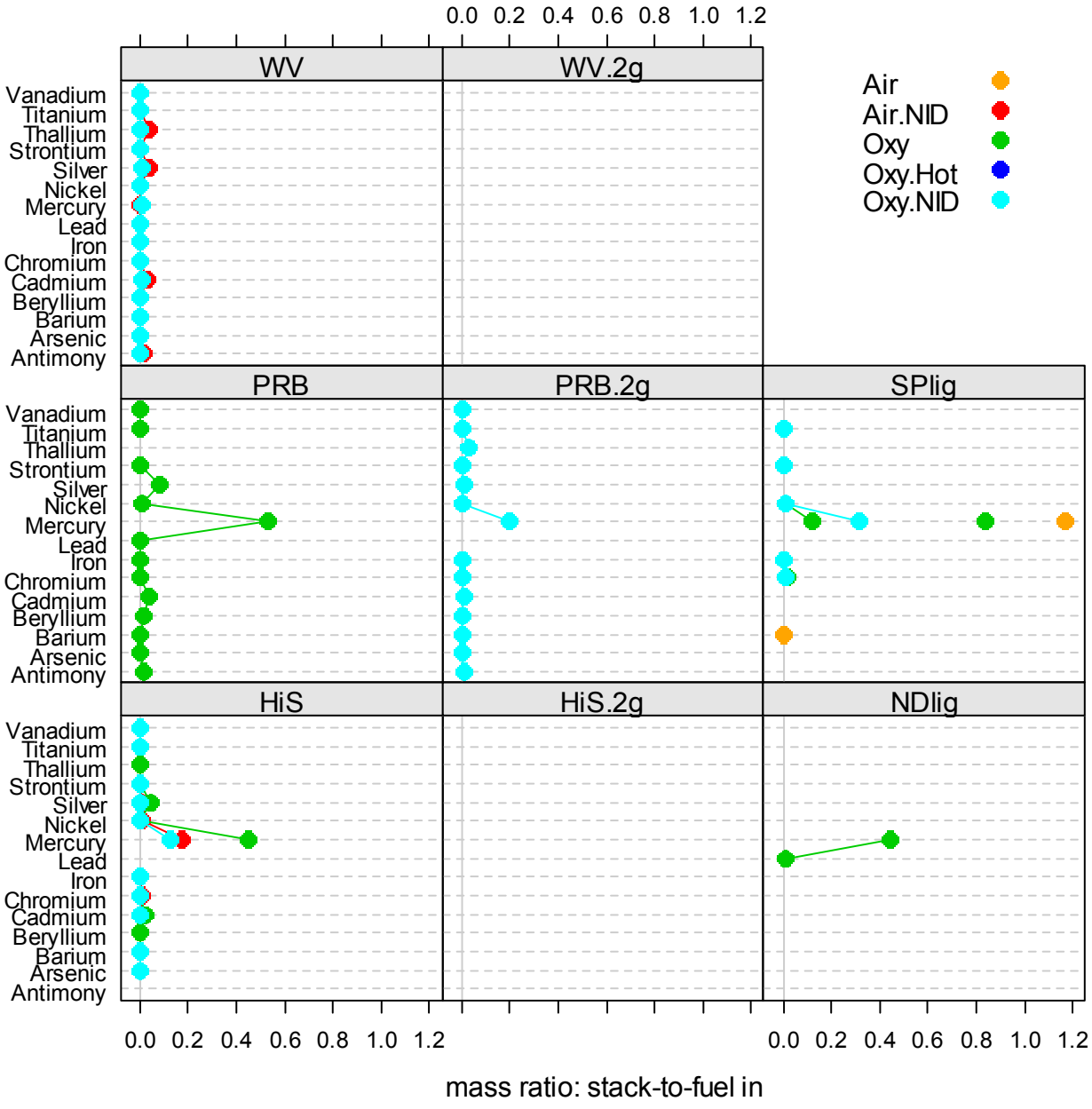

Figure 5-24. Trace metal mass ratio, stack gas to fuel input

During the North Dakota Lignite campaign, the Energy & Environmental Research Center (EERC) at the University of North Dakota measured mercury emissions using continuous mercury monitors (CMM). Mercury was measured at the economizer outlet throughout the test week and in the secondary recycle stream during the oxy-combustion tests. Sampling locations for EERC are also shown in Figure 5-22. The EERC report is included here as **Error! Reference source not found.**.

The mercury concentrations and flows are summarized in Figure 5-25 for the air and oxy-fired long-term baseline tests and the shorter hot recirculation test. The figure shows both the measured mercury concentrations (top chart) and the calculated mercury flow rates (bottom chart).

In each case, the mercury leaving the furnace is nearly all elemental mercury. For the air fired test, the mercury leaving the furnace is equal to the mercury in the fuel. For the oxy-fired tests, more mercury leaves the furnace than comes in with the fuel because of the mercury in the recycle gas. For the oxy-fired case with recycle through the baghouse (without the NID™ operating), most of the mercury in the recycled gas has been oxidized. For the hot recycle case which does not go through the baghouse, much less of the elemental mercury is oxidized.

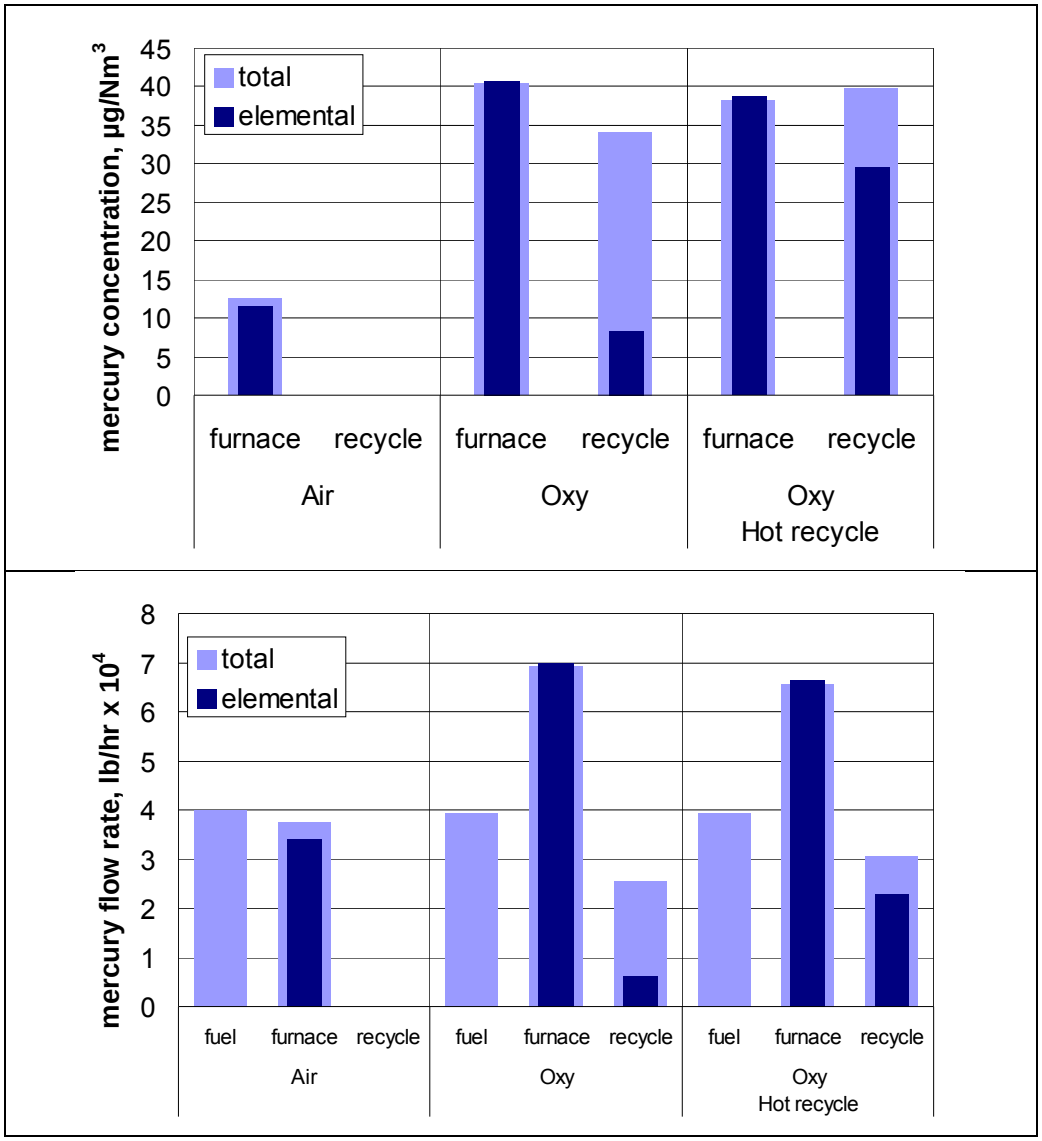

Figure 5-25. Summary of mercury levels

5.7.1 Mercury removal

In oxy-firing, mercury behaves the same way as in air firing. High concentrations of CO_2 in the flue gas in oxy-firing do not affect the mercury chemistry. In assessing the fate of mercury and its concentration in the flue gas, however, it is important to understand the effect of potentially higher concentrations of SO_x and other species as a result of the absence of nitrogen in the flue gas. The effect of air pollution control devices (e.g., SCRs, scrubbers, baghouses, ESPs, flue gas condensers) on

the fate of mercury needs to be properly assessed. In addition to these factors, flue gas recirculation scheme has to be taken into account.

SCRs would not be able to remove mercury but their catalysts oxidize a significant portion of the elemental mercury in the flue gas. Scrubbers, esp., wet scrubbers, if properly designed, absorb the majority of oxidized mercury, but may also reduce some of the oxidized mercury to elemental mercury ("re-emission"). Baghouses, in the presence of unburnt carbon or sorbent, are efficient in capturing the mercury. It is postulated that the carbon in the filter cake oxidizes elemental mercury, and then captures the oxidized mercury. ESPs are not as efficient as baghouses in oxidizing mercury or removing oxidized mercury. Finally, a properly designed FGC with sufficient contact between cooling liquid and flue gas is extremely effective in removing the oxidized mercury.

Consider an oxy-fired boiler configuration where the flue gas is taken off immediately downstream of the economizer (hot recycle). In this configuration, all of the oxidized mercury in the flue gas recycled into the furnace will be reduced back to elemental mercury. Immediately downstream of the flue gas take-off point, therefore, most of the mercury will be in elemental form. Mercury speciation and concentration can then be predicted by assessing the effect of each of the air pollution control devices downstream of the take-off point.

In the case of flue gas recirculation downstream of a scrubber, all of the mercury leaving the furnace will be in elemental form. Some of it will be oxidized and captured as it passes through the air heater, ESPs or baghouses. The majority of the oxidized mercury entering the scrubber will be captured in the scrubber. The level of mercury in the recycled flue gas may be less than that for the previous hot recycle case as some of it would have been captured in the scrubber. Most of the recycled mercury is, however, expected to be elemental mercury.

In oxy-firing, mercury in the flue gas leaving the boiler island has to be controlled to a very low level in order to avoid any corrosion of aluminum surfaces in the cold circuit of GPUs. The required level is on the order of a few ng/Nm^3. The control strategy in achieving this level is to oxidize mercury as much as possible so that it could be removed in the air pollution control devices and the FGC. This may require injection of halogen additives into the furnace; or sorbents designed for maximal oxidation of incoming mercury. The remainder will have to be removed in an activated carbon bed usually installed before, or as part of a GPU system.

During the second generation testing with Powder River Basin fuel, mercury removal with powdered activated carbon (PAC) was tested on a slipstream of flue gas from the BSF. The results for the six test points are shown in Table 5-5 and Figure 5-26. Oxy-firing conditions did not appear to have a significant impact on mercury capture. The performance of the PAC sorbent was similar at equivalent conditions under both air and oxy-firing.

The performance curve in Figure 5-26 shows that the PAC removal efficiency is the same for the air and oxy-firing. As expected, the mercury removal by the PAC increases with the injection rate and levels off at a higher injection rate.

Table 5-5. PAC injection for mercury removal

Start	End		Feed	Ratio	Removal	Utilization
9/24/2012 16:03	9/24/2012 16:33	Air	0.044	8.84	35	0.040
9/25/2012 07:12	9/25/2012 07:42	Air	0.088	19.85	63	0.032
9/25/2012 10:56	9/25/2012 11:26	Air	0.176	36.94	82	0.022
9/26/2012 07:45	9/26/2012 08:15	Oxy	0.044	6.16	34	0.055
9/26/2012 09:36	9/26/2012 10:06	Oxy	0.088	11.30	47	0.041
9/26/2012 10:47	9/26/2012 11:17	Oxy	0.176	25.22	70	0.028

Feed: PAC feed rate, lb/hr
Ratio: kg added PAC / gm Hg in flue gas
Removal: % mercury captured
Utilization: gm Hg captured / kg added PAC (= Removal / Ratio / 100)

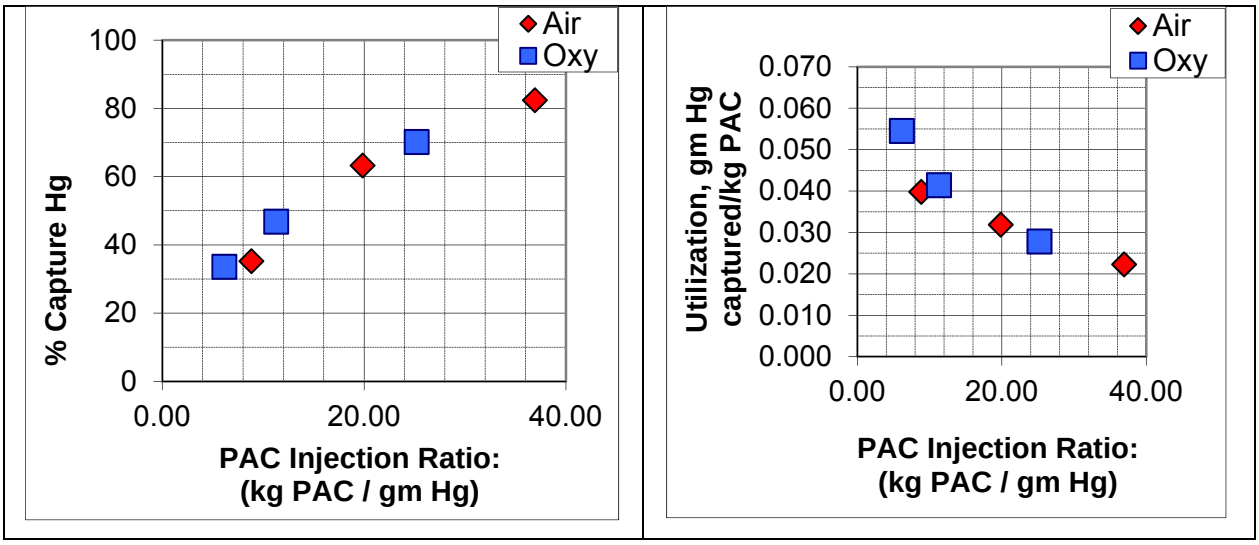

Figure 5-26. Mercury capture and sorbent utilization *vs.* PAC injection ratio

5.8 Ash Deposits and Corrosion

5.8.1 BSF Deposition/Corrosion Probes

As described in Section 2.3.6, temperature controlled deposition probes were installed in the BSF furnace convective section to evaluate ash deposit characteristics under air and oxy-fired conditions and to assess the corrosion attack during tests with each coal. Figure 2-20 shows the location of the probes: Probe 1 below the lower overfire air location, Probe 2 near the horizontal furnace outlet plane, and Probe 3 in the convective section.

5.8.1.1 Ash Deposition

Properties of ash deposits generated during testing were primarily dependent upon the properties of the coal fired and the local environment (gas temperature, incident heat flux, and oxidizing/reducing atmosphere). Differences in gas composition associated with oxy-combustion did not appear to have a strong impact on ash deposits (slagging or fouling) for the overall range of tests conducted. Comparable deposits formed from the same coal had generally similar compositions and physical

properties during both air and oxy-firing conditions. The elemental compositions (oxide basis) of ash deposits collected from the deposition probes under air and oxy-firing conditions are summarized in Table 5-6.

Table 5-6. Composition of Deposition Probe Ash Deposits

Campaign	WV Fola	WV Fola	WV Fola	WV Fola	WV Fola	WV Fola	HiS-IL	HiS-IL	HiS-IL	HiS-IL	HiS-IL	HiS-IL
Air/Oxy	Air	Air	Air	Oxy	Oxy	Oxy	Air	Air	Air	Oxy	Oxy	Oxy
	Probe #1	Probe #2	Probe #3	Probe #1	Probe #2	Probe #3	Probe #1	Probe #2	Probe #3	Probe #1	Probe #2	Probe #3
Probe Deposit Ash Composition												
%SiO2	43.4	48.8	45.4	47.1	48.4	39.8	33.2	20.8	10.8	17.5	49.1	19.9
%Al2O3	29.5	32.4	29.0	31.4	32.1	26.6	13.9	10.9	6.2	6.9	20.0	8.9
%Fe2O3	14.2	9.2	9.6	10.2	6.6	15.3	45.2	52.3	43.5	54.7	15.5	35.0
%CaO	1.7	1.7	3.0	1.3	1.5	2.6	2.3	2.0	1.6	2.0	3.0	1.8
%MgO	0.6	0.7	0.9	0.6	0.8	0.8	0.7	0.0	0.0	0.0	0.9	0.5
%Na2O	0.2	0.0	0.5	0.0	0.3	0.0	0.5	4.2	0.8	5.4	1.1	0.0
%K2O	3.1	2.5	2.5	2.7	2.6	2.0	1.5	2.8	0.5	3.1	2.7	1.1
%TiO2	2.6	2.8	3.6	2.8	3.0	2.3	0.7	0.5	0.0	0.4	1.4	0.7
%P2O5	1.2	0.0	0.8	1.1	0.8	0.6	0.0	0.3	0.0	0.0	0.0	0.0
%SO3	2.1	1.7	4.0	1.2	2.9	9.7	2.0	5.7	36.6	9.4	6.3	32.1
Total	98.5	99.8	99.2	98.4	99.1	99.6	100.0	99.5	100.0	99.5	100.0	100.0
Relative Enrichment Compared to Parent Coal Ash												
SiO2	0.77	0.87	0.81	0.84	0.86	0.71	0.65	0.41	0.21	0.34	0.97	0.39
Al2O3	0.96	1.05	0.94	1.02	1.04	0.86	0.68	0.53	0.30	0.34	0.97	0.43
Fe2O3	2.54	1.64	1.72	1.83	1.18	2.74	2.90	3.36	2.80	3.52	1.00	2.25
CaO	2.08	2.01	3.53	1.54	1.84	3.11	0.65	0.57	0.45	0.57	0.86	0.51
MgO	0.76	0.80	1.09	0.70	0.98	1.01	0.71	0.00	0.00	0.00	0.96	0.55
Na2O	0.89	0.00	2.22	0.00	1.42	0.00	0.50	4.14	0.80	5.31	1.05	0.00
K2O	1.16	0.95	0.93	1.01	0.99	0.74	0.71	1.33	0.24	1.48	1.30	0.51
TiO2	1.44	1.59	2.02	1.57	1.67	1.30	0.80	0.48	0.00	0.42	1.46	0.72
P2O5	7.80	0.00	5.27	7.60	5.47	4.07	0.00	0.50	0.00	0.00	0.00	0.00
SO3	2.92	2.45	5.66	1.76	4.07	13.74	0.71	2.03	13.04	3.34	2.23	11.43
Campaign	NDLig	NDLig	NDLig	NDLig	NDLig	NDLig	SPLig	SPLig	SPLig	SPLig	SPLig	SPLig
Air/Oxy	Air	Air	Air	Oxy	Oxy	Oxy	Air	Air	Air	Oxy	Oxy	Oxy
	Probe #1	Probe #2	Probe #3	Probe #1	Probe #2	Probe #3	Probe #1	Probe #2	Probe #3	Probe #1	Probe #2	Probe #3
Probe Deposit Ash Composition												
%SiO2	44.7	47.6	50.3	26.6	39.6	46.7	7.9	5.5	4.7	9.2	6.8	0.0
%Al2O3	12.9	12.8	13.9	8.5	11.6	14.0	2.3	2.5	3.6	2.8	2.8	3.8
%Fe2O3	11.7	7.8	8.5	40.5	6.9	8.5	24.6	24.8	33.3	26.6	26.4	38.9
%CaO	12.5	10.9	12.4	4.9	15.2	14.4	22.1	22.0	30.2	22.4	21.7	25.9
%MgO	2.9	2.4	3.0	2.3	3.2	3.4	6.0	5.8	8.4	5.6	5.7	7.9
%Na2O	2.8	2.3	2.1	2.8	2.1	2.4	1.9	0.6	0.7	2.0	0.7	
%K2O	3.6	3.6	3.2	1.9	2.9	3.0	2.6	2.0	0.7	3.0	1.5	0.8
%TiO2	1.1	1.3	1.5	0.4	0.7	1.2	0.0	0.0	0.0	0.0	0.0	0.4
%P2O5	0.0	0.0	0.0	0.0	0.0	0.0	0.0	0.0	0.0	0.0	0.0	0.0
%SO3	7.8	11.3	5.0	12.0	17.9	6.3	32.6	36.8	18.0	28.0	34.4	16.8
Total	100.0	100.0	100.0	100.0	100.0	100.0	100.0	100.0	99.6	99.7	100.0	94.5
Relative Enrichment Compared to Parent Coal Ash												
SiO2	1.06	1.13	1.20	0.63	0.94	1.11	0.54	0.37	0.32	0.62	0.46	0.00
Al2O3	0.93	0.92	0.99	0.61	0.83	1.00	0.52	0.58	0.83	0.65	0.63	0.86
Fe2O3	1.81	1.21	1.32	6.27	1.07	1.32	1.07	1.08	1.45	1.16	1.15	1.69
CaO	0.84	0.73	0.84	0.33	1.02	0.97	0.85	0.85	1.16	0.86	0.84	1.00
MgO	0.64	0.53	0.67	0.52	0.72	0.75	0.62	0.60	0.88	0.59	0.60	0.83
Na2O	1.77	1.49	1.33	1.80	1.33	1.57	10.45	3.50	3.64	11.11	3.81	0.00
K2O	1.87	1.88	1.67	0.99	1.50	1.57	15.39	11.82	4.30	17.75	8.72	4.47
TiO2	2.00	2.48	2.77	0.71	1.24	2.21	0.00	0.00	0.00	0.00	0.00	2.01
P2O5	0.00	0.00	0.00	0.00	0.00	0.00	0.00	0.00	0.00	0.00	0.00	0.00
SO3	0.65	0.94	0.42	1.00	1.49	0.52	1.78	2.01	0.98	1.53	1.88	0.92

Deposit compositions reflect the ash properties of the as-fired parent coal (see Table 3-2). The deposits generally showed enrichment of iron and alkali constituents compared to the parent coal ash, which is typical for coal-fired boiler ash deposits accumulating near tube surfaces. In general, probe deposits for these tests were thin (<1/8" thick), consisting of powder or friable scale material. Photos of Probe 1 deposits from the lower furnace region are shown in Figure 5-27 from tests with the high sulfur Illinois coal and in Figure 5-28 for the Schwarze Pumpe lignite. Probe 3 deposits from the convection region were typically powdery material, and generally contained higher concentrations of sulfur than furnace deposits.

Figure 5-27. Deposition Probes with deposits after HiS IL Air (left) and Oxy (right) Tests

Figure 5-28. Deposition Probes with deposits after SPLIg Air (left) and Oxy (right) Tests

5.8.1.2 Probe Corrosion Assessment

Specimens from the deposition probes were further analyzed to assess corrosive attack. The specimens with deposit were mounted in epoxy, sectioned and analyzed using optical and SEM techniques to measure corrosion products, metal loss and internal penetration of corrosive species. Due to the relatively short exposure period of the BSF tests (<100 hours), the amount corrosive attack was small (< 60 microns metal loss). However, for comparable samples (same coal fired and same exposure location), similar corrosive attack and metal loss was observed during both air and oxy-firing. More detailed discussion on the deposition probe corrosion measurements and results are provided in Appendix D.

5.8.2 Bench-Scale Corrosion Evaluation

Bench-scale corrosive tests were also conducted to provide additional information under longer exposure times under controlled environments. These tests were designed to separate the different parameters that influence corrosion behavior such as sulfur level, chlorine level, and temperature under air and oxy-firing atmospheres. One series of bench scale corrosion tests was conducted to address high temperature corrosion in the convection region (superheat and reheat tubes) of the boiler, and another series to address furnace waterwall corrosion.

5.8.2.1 High Temperature Corrosion Bench-Scale Tests

For the convection region high temperature corrosion tests, several power plant materials were tested in different air-firing and oxy-combustion environments at 600°C and 650°C. Six conditions were investigated with total corrosion exposure duration of 1000 and 3000 hours. Simulated US Eastern coal ash was applied to all material samples, ferritics (T23, T24, T92), austenitics (Super304H, HR3C) and Ni-base alloys (CCA617, Alloy 740). Additionally, simulated US Western ash was applied on samples of Super304H, HR3C, and Alloy 740. The ash was re-applied every 200 hours to insure a continuous supply of corrosive elements. The corrosion extent and morphology were evaluated after exposure by metallographic examination.

Table 5-7. High Temperature Corrosion Test Conditions

					Gas Composition, Vol%					
Condition	**Temp, C**	**Oxidant**	**Sulfur**	**Chlorine**	O_2	N_2	H_2O	CO_2	SO_2	HCl
1	650	oxy	M	M	3.0	7.59	25.0	64.0	0.2	0.02
2	650	air	M	M	3.6	71.29	10.0	15.0	0.2	0.02
3	600	air	L	H	3.6	71.29	10.0	15.0	0.08	0.03
4	600	oxy	H	M	3.0	7.59	25.0	64.0	0.4	0.02
5	600	oxy	L	L	3.0	7.59	25.0	64.0	0.08	0.01
6	600	air	M	L	3.6	71.29	10.0	15.0	0.2	0.01

Results show that the ferritic alloys exhibited significant metal loss of up to 400 microns after 3000 hours at 650°C. The oxide scale in all tests quickly developed and spalled several times within 1000 hour. The higher alloy materials exhibited good corrosion resistance under the given test conditions. The maximum metal loss after 3000 hours at 650°C was below 50 microns for austenitics and below 25 microns for the Ni-base alloys. The austenitic alloys showed mainly internal attack with thin external corrosion products.

Comparing behavior under the oxy-firing conditions with air-firing, the corrosion attack was generally similar for the same sulfur and chlorine levels. The effect of temperature seems to a have much stronger effect than the differences in CO_2 level and H_2O level (oxy vs. air). The level of corrosive elements (sulfur, chlorine) was the dominant factor for the metal loss of a specific alloy at a given temperature. More detailed discussion on the high temperature corrosion testing is provided in Appendix E.

5.8.2.2 Waterwall Corrosion Bench-Scale Tests

For the furnace waterwall corrosion tests, typical waterwall tubing materials (T11, T22, T23, and T24) were studied for corrosion behavior in simulated air-firing and oxy-firing conditions at 550°C for an exposure of 1000 hours. The materials were tested as either bare metal (no ash on surface) or coated with simulated Eastern coal ash. Tests were conducted under reducing conditions associated with low NO_x operation. A summary of the four test conditions investigated is shown in Table 5-8.

Table 5-8. Furnace Waterwall Tests Conditions

Air-Firing/ Condition - 1		Oxy-Firing/ Condition - 2		Air-Firing/ Condition - 3		Oxy-Firing/ Condition - 4	
Gases	Vol%	Gases	Vol%	Gases	Vol%	Gases	Vol%
N2	74.79	N2	14.79	N2	74.79	N2	14.57
CO2	12	CO2	54	CO2	12	CO2	54
H2O	10	H2O	25	H2O	10	H2O	25
SO2	0.18	SO2	0.18	SO2	0.36	SO2	0.36
H2S	0.02	H2S	0.02	H2S	0.04	H2S	0.04
HCl	0.01	HCl	0.01	HCl	0.03	HCl	0.03
CO	3	CO	6	CO	3	CO	6

Uniform corrosion was observed on each of the samples with negligible internal attack or pitting observed. The measured metal loss varied from 100 to 1000 microns over the range of alloys and test conditions. However, sample scale exfoliation produced during the testing resulted in scatter of the data for the scale thickness and weight gain measurements, raising uncertainty in metal loss values.

Results indicate corrosion behavior is strongly dependent on corrosive constituents in the gas and ash deposits at the material surface and does not appear to be negatively impacted by the CO_2-rich environment under oxy-firing conditions. The most aggressive metal loss occurred when the metal samples were coated in ash and exposed to air-fired simulated flue gas containing high sulfur and HCl levels. The lowest metal losses were under oxy-fired simulated flue gas with low sulfur and low HCl levels (with or without ash coating). More detailed discussion on the waterwall corrosion testing is provided in Appendix F.

5.9 Thermal Performance

5.9.1 Furnace heat flux profiles

In the oxy-combustion process, flue gas is recycled to the boiler to moderate the furnace temperatures and reduce peak heat flux. The quantity and distribution of recirculated flue gas and oxygen into the boiler will alter the heat release pattern in the combustor. Understanding and controlling this heat release pattern is an important goal of Alstom's oxy-combustion boiler development program.

The test results demonstrate that furnace heat flux profile can be controlled by a number of factors, including the gas recirculation rate, the distribution of recirculated gas, and the split of oxygen to the different windbox levels and to the overfire levels.

5.9.1.1 Effect of gas recirculation rate/global O_2

For each fuel, tests were done to vary the recirculation rate – and therefore the global O_2 content of the recycle. Three tests from each of the first four campaigns with high, medium, and low recycle rates are shown in Table 5-9.

Table 5-9. Tests with varying recycle rate

	PRB		Fola		Hi Sulfur		ND lignite	
	Test	Glob. O_2	Test	Glob. O_2	Test	Glob. O_2	Test	Glob. O_2
High recirc:	12	24	46	24	62	26	91	25
Medium recirc:	13	27	47	28	63	28	92	28
Low recirc:	14	30	48	33	61	33	93	33

A comparison of the vertical heat flux profiles for each test is shown in Figure 5-29. The points represent individual heat flux measurements; the lines are smooth fits through the points.

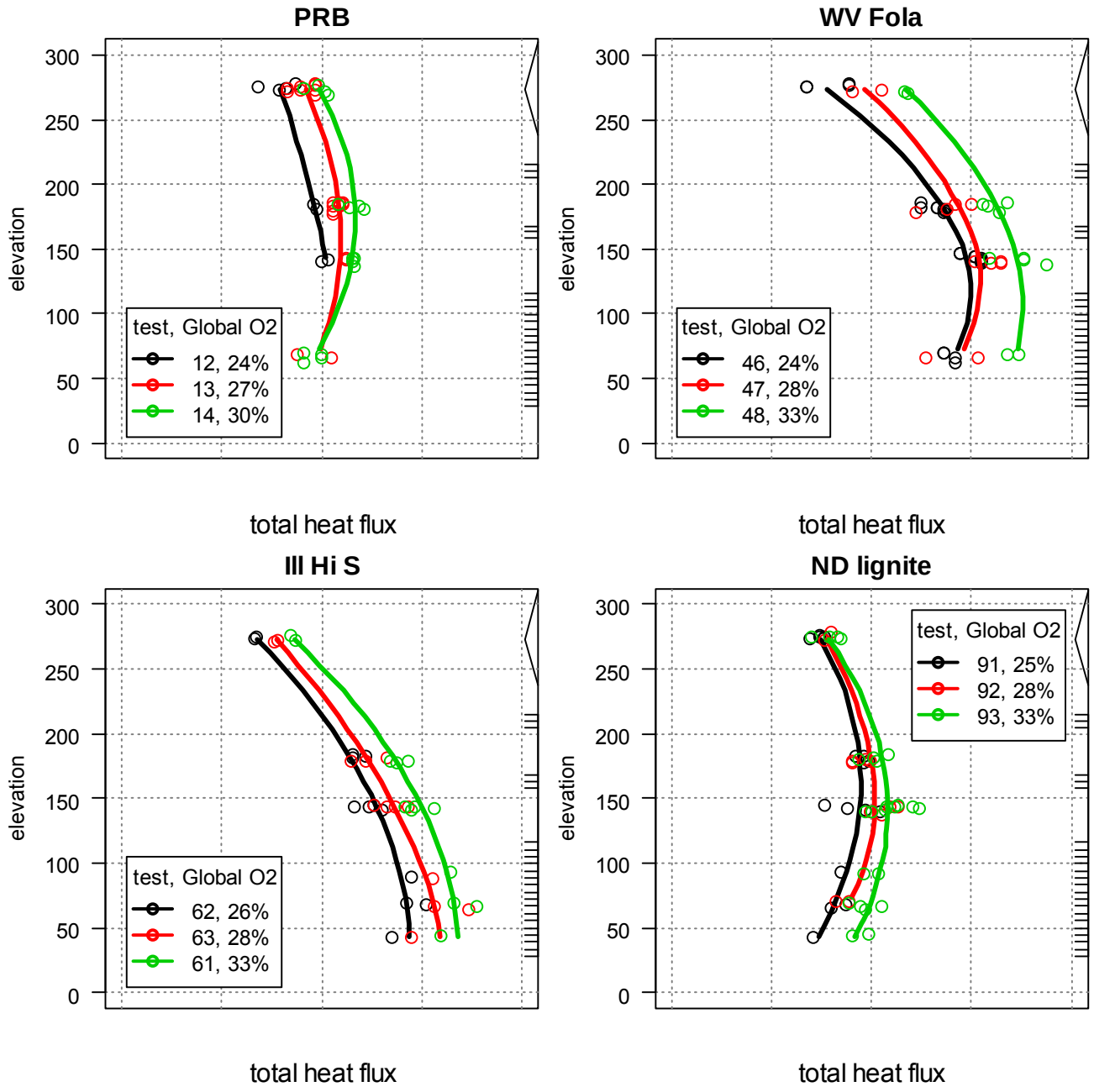

Figure 5-29. Effect of recirculation rate on vertical heat flux profile

For each test campaign, the total oxygen input was held constant and varying the quantity of gas recycle changed the global concentration. Furnace heat flux increased as the global oxygen concentration increased and the mass flow through the boiler decreased. As expected, the magnitude of heat flux change was different for each fuel tested, with the lower rank fuels (PRB and lignite) showing lower total heat flux and lower absolute change in heat flux between conditions.

5.9.1.2 Effect of varying oxygen location

Impacts of local compartment enrichment were tested during the Illinois bituminous test campaign. Figure 5-30 shows the results of one variation. In the base test, oxygen was mixed normally with the

flue gas recycle. In Test 67, some oxygen was removed from the bulk oxygen addition and added to fuel compartments low in the windbox. In Test 68 the oxygen was biased even more to the bottom compartments. In each case, the result is the same windbox stoichiometry, but local oxygen enrichment.

The heat flux in the lower furnace increased when oxygen input was shifted lower in the furnace and locally enriched in selected windbox compartments.

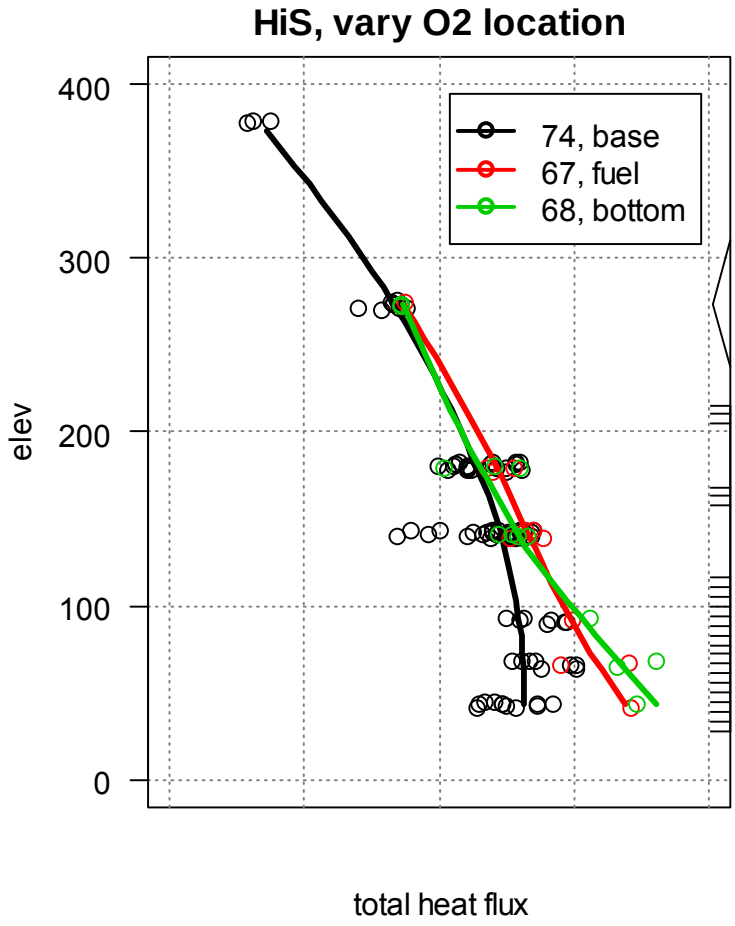

Figure 5-30. Effect of varying oxygen distribution on vertical heat flux profile, high-sulfur fuel tests

5.9.1.3 Long term heat flux profile

During each test campaign there was at least one long term test with air firing and oxy-firing. It was generally intended that the vertical heat flux profile of the oxy-fired long term test match that of the air fired test. The procedure generally was to run the long term air test first. Next came some shorter parametric oxy tests to guide the selection of the conditions for the long term oxy-fired conditions. Since it takes several hours to complete the mapping of the profile and raw measurements are not reduced until afterward, it is only after both tests are completed and analyzed, that we can see how well we matched the heat flux profiles.

The next five figures compare the air and oxy-fired profiles for the first five campaigns. In each figure, the plot on the left shows the temperatures measured by suction pyrometer. The right plot

shows the profile of total heat flux measured with the heat flux probes at one or more of the furnace walls.

Figure 5-31 shows the results for the PRB sub-bituminous test coal. The match between the air and oxy-fired cases in this first campaign is not very close. For these tests, the air and oxy-fired conditions were selected to provide equivalent firing rates, furnace gas mass flow rates, firing system staging, burner settings and excess oxygen in flue gas. The oxygen was maintain at 20-21% in the primary stream and remaining oxygen premixed in the secondary stream and uniformly distributed with the secondary flow to the burner and overfire injection locations. Results showed a delay in the initial heat release during oxy-firing. With more experience, the match was usually closer in subsequent campaigns as the appropriate amount of gas recycle and appropriate distribution of oxygen to the furnace were better understood.

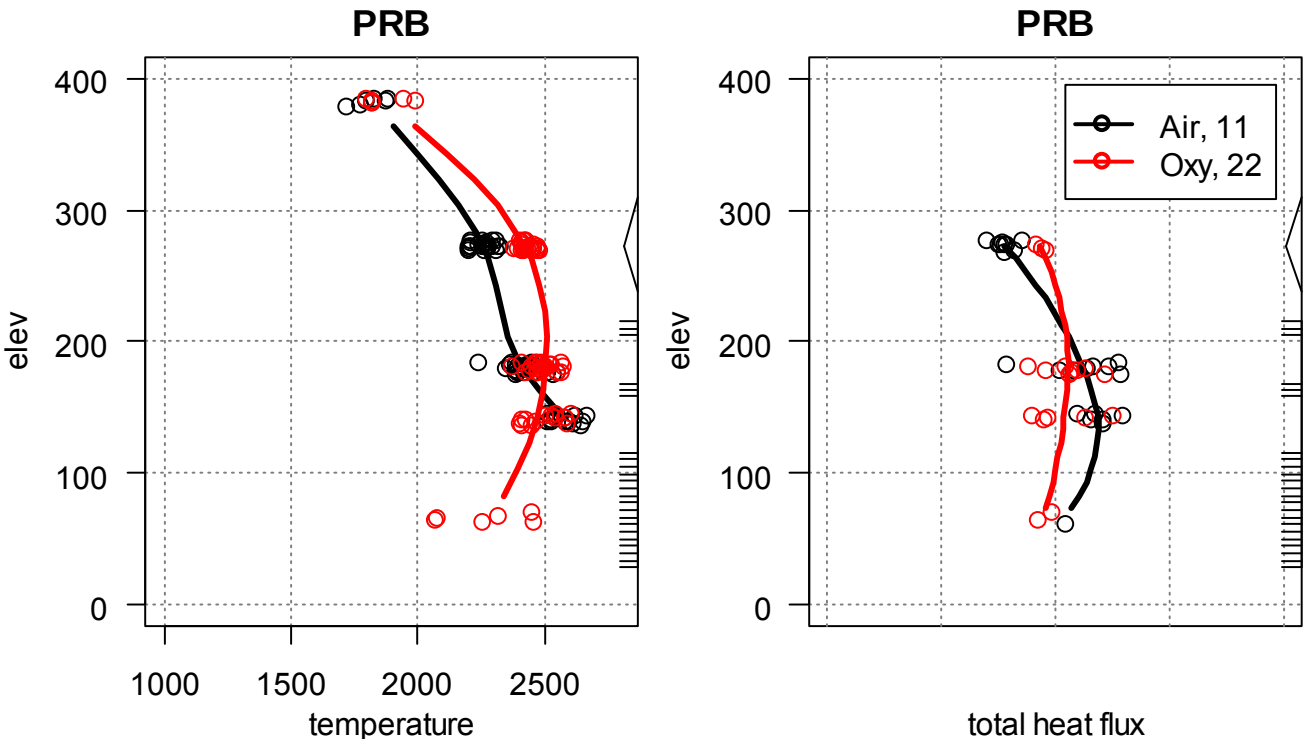

Figure 5-31. Long-term temperature and heat flux profiles, PRB campaign

Figure 5-32 shows a very good match for the WV Fola low-sulfur bituminous coal. Note that in this test only, we measured the temperature down in the furnace hopper below the windbox.

The heat flux in the windbox region was lower for the long-term oxy-fired test in the Illinois high sulfur campaign, as shown in Figure 5-33.

The match of the heat flux profile in the North Dakota lignite long-term tests was very good – see Figure 5-34.

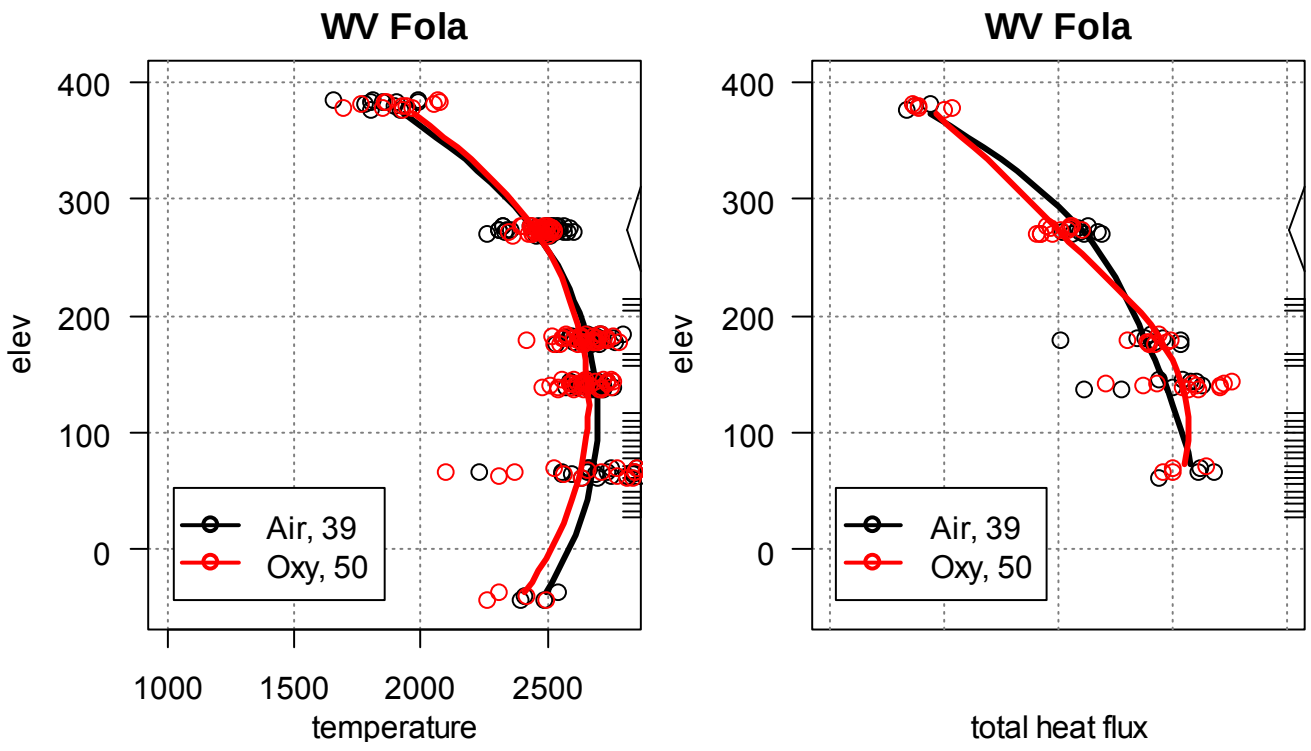

Figure 5-32. Long-term temperature and heat flux profiles, WVA Fola campaign

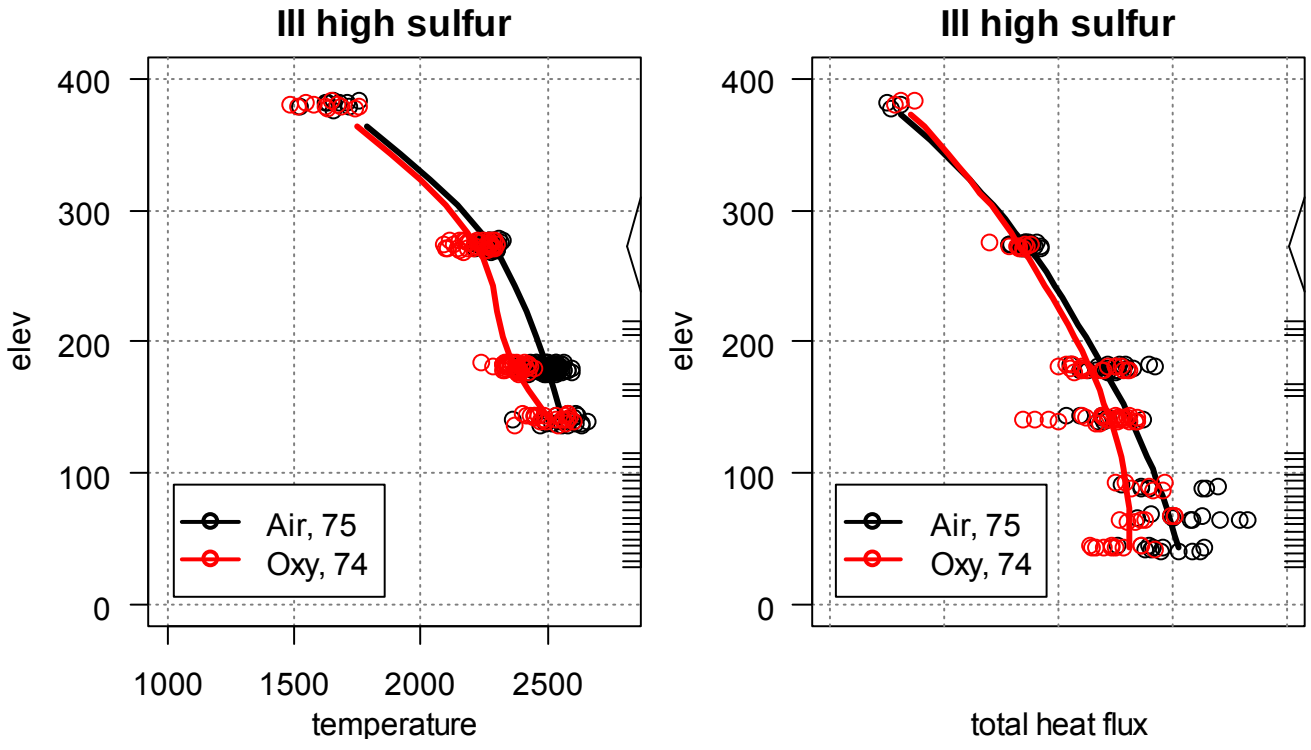

Figure 5-33. Long-term temperature and heat flux profiles, Ill Hi S campaign

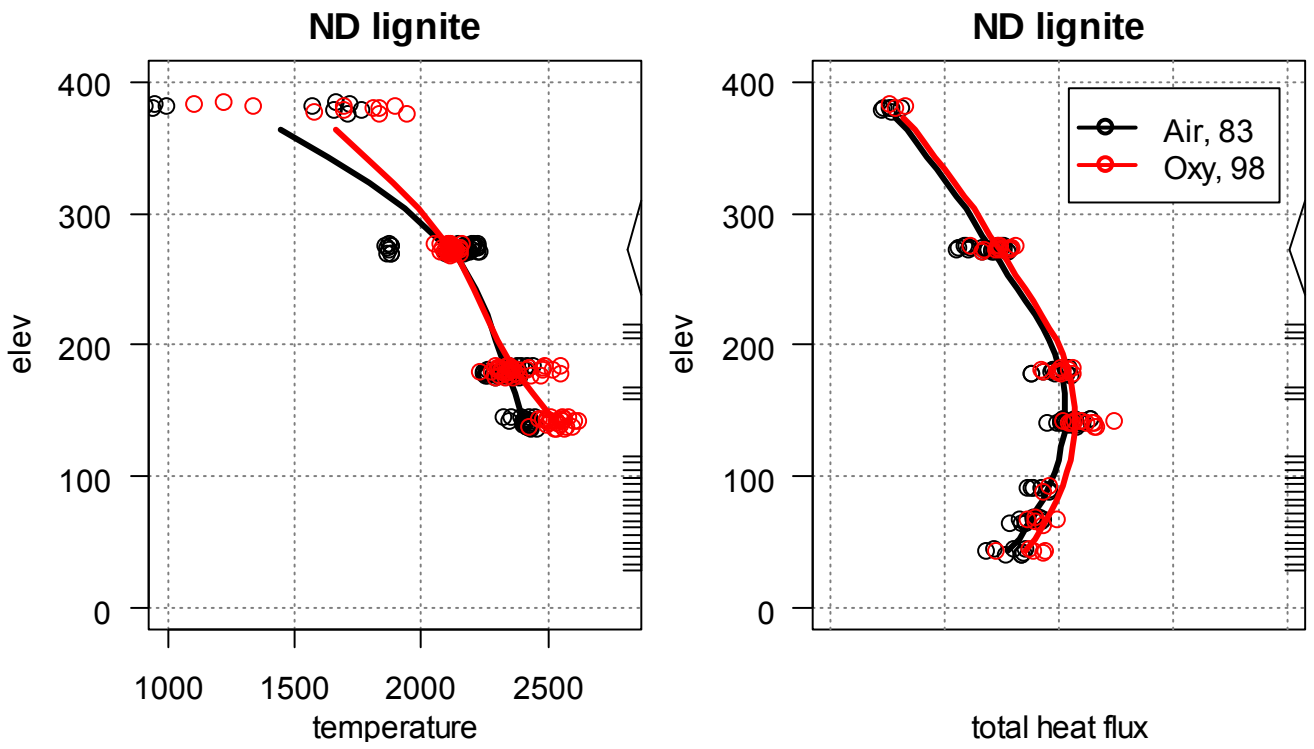

Figure 5-34. Long-term temperature and heat flux profiles, ND lignite campaign

Figure 5-35 shows the results from the Schwarze Pumpe lignite test campaign. The figure includes the normal load firing rate of 45 MMBtu/hr as well as a lower load at 40 MMBtu/hr.

The normal load cases show similar profiles with a higher peak flux in the oxy-fired case. The lower load case had a lower flux in the windbox region for the oxy-fired case.

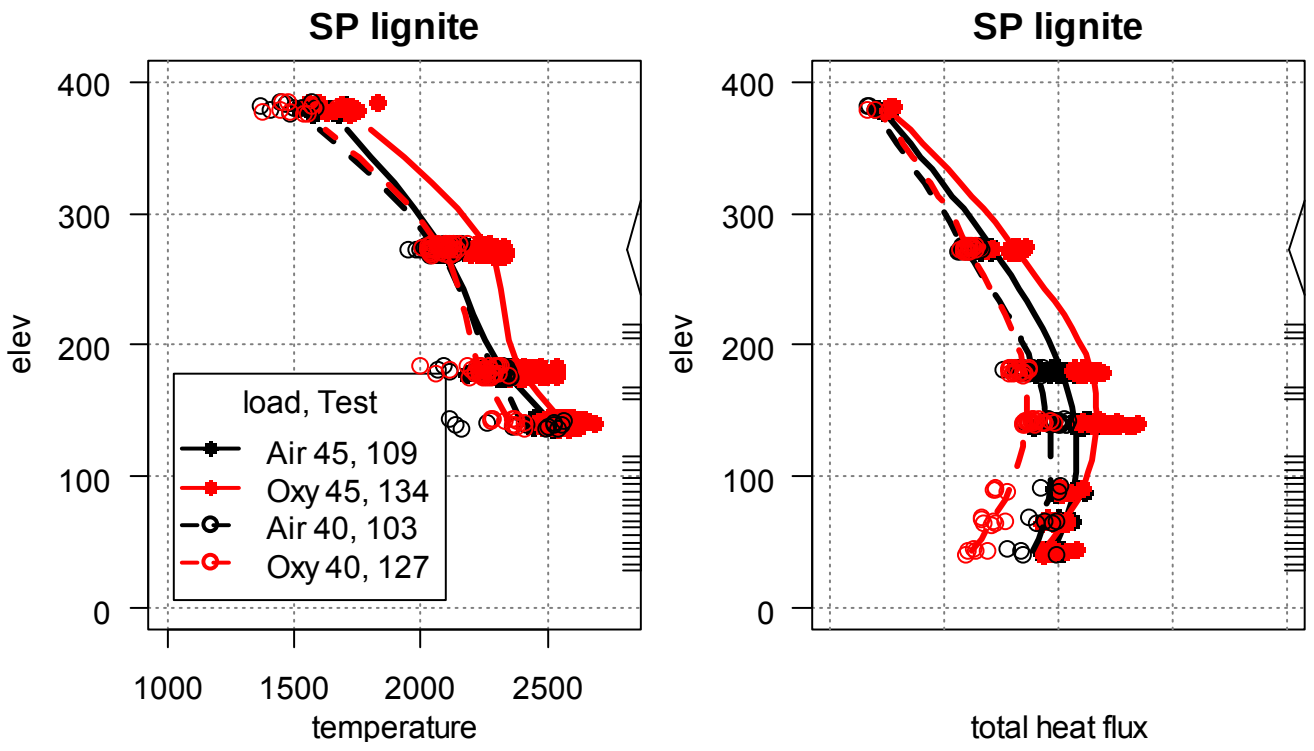

Figure 5-35. Long-term temperature and heat flux profiles, SP lignite campaign

These tests demonstrate that with the control of flue gas recycle and distribution of oxygen, the oxy-fired heat flux profiles can be adjusted to match those with air firing.

5.9.2 Heat absorption in the furnace

The balance between furnace heat absorption and convection section heat absorption must be considered and the boiler designed appropriately. For retrofit applications, pressure part modifications could be minimized if existing furnace and convection section surfaces provide similar heat absorption during air and oxy-fired operation. For new applications, optimization of pressure part surfacing may be possible by further reducing gas recycle, but many factors must be considered that would limit this reduction. Some of the considerations associated with reducing gas recycle include higher peak heat fluxes requiring more cooling or use of high temperature materials, ash management and operational issues as the impact of higher temperatures on slagging and fouling behavior, and the impact of higher concentrations of corrosive constituents on fireside corrosion.

As the recycle rate of flue gas increases (global O_2 decreases), the amount of heat absorbed in the furnace decreases. This is shown in Figure 5-36 for all test points where there was enough data to calculate the heat absorption.

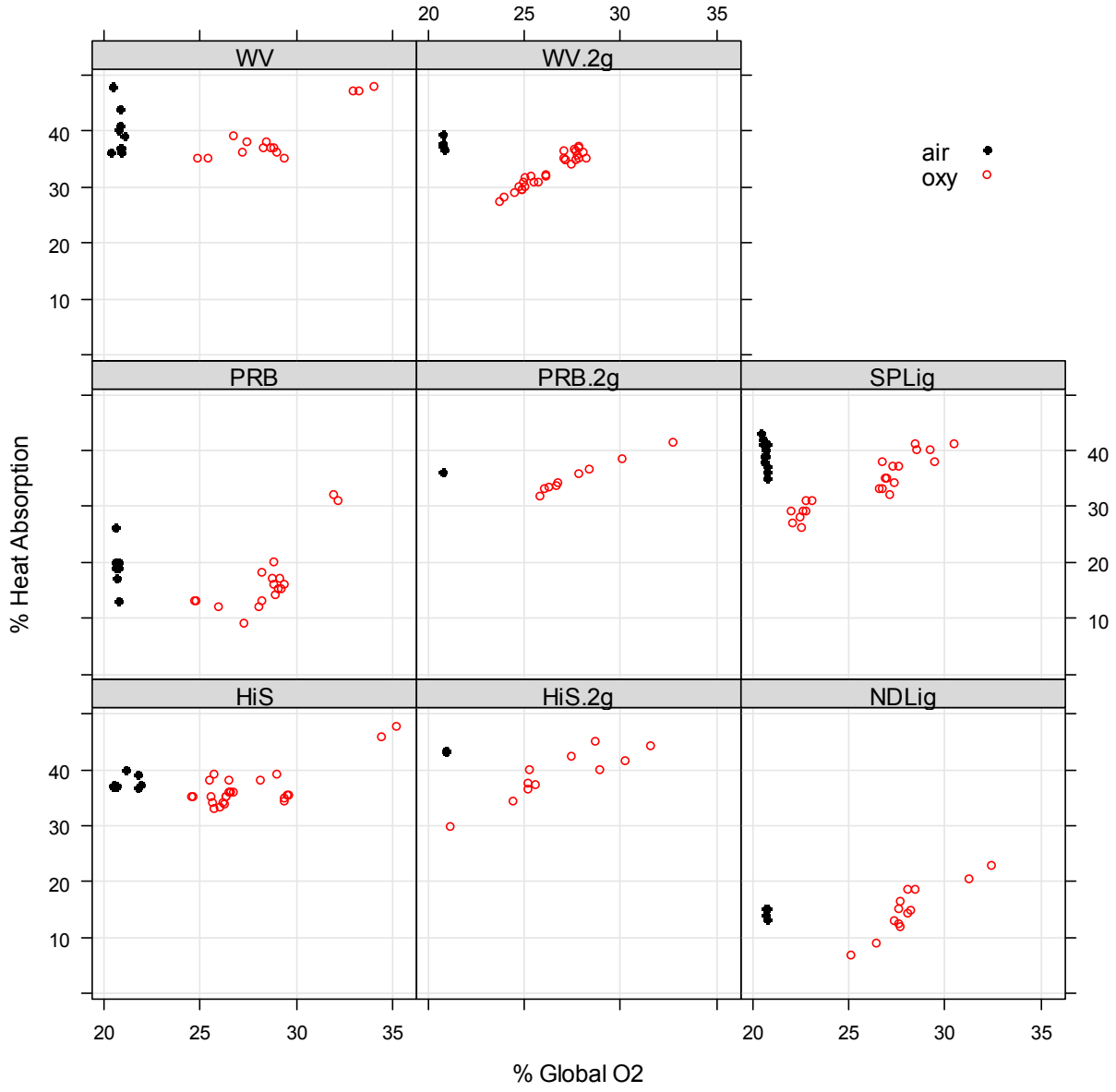

Figure 5-36. Furnace heat absorption vs global O_2

The air fired test points in Figure 5-36 – which are unaffected by flue gas recycle rates – show variations due to other factors such as windbox staging and load. These factors also affect the heat absorption in the oxy-fired tests, but it is clear that varying flue gas recycle is a major determinant of the furnace heat absorption.

Figure 5-37 shows the same data for a subset of tests in the first four campaigns where recycle rate was varied with other conditions held constant. The percentage heat absorbed in the furnace is different for each of the four fuels, but in each case oxy-firing with a global O_2 of between 26 and 30% gave the same percentage heat absorption as air firing.

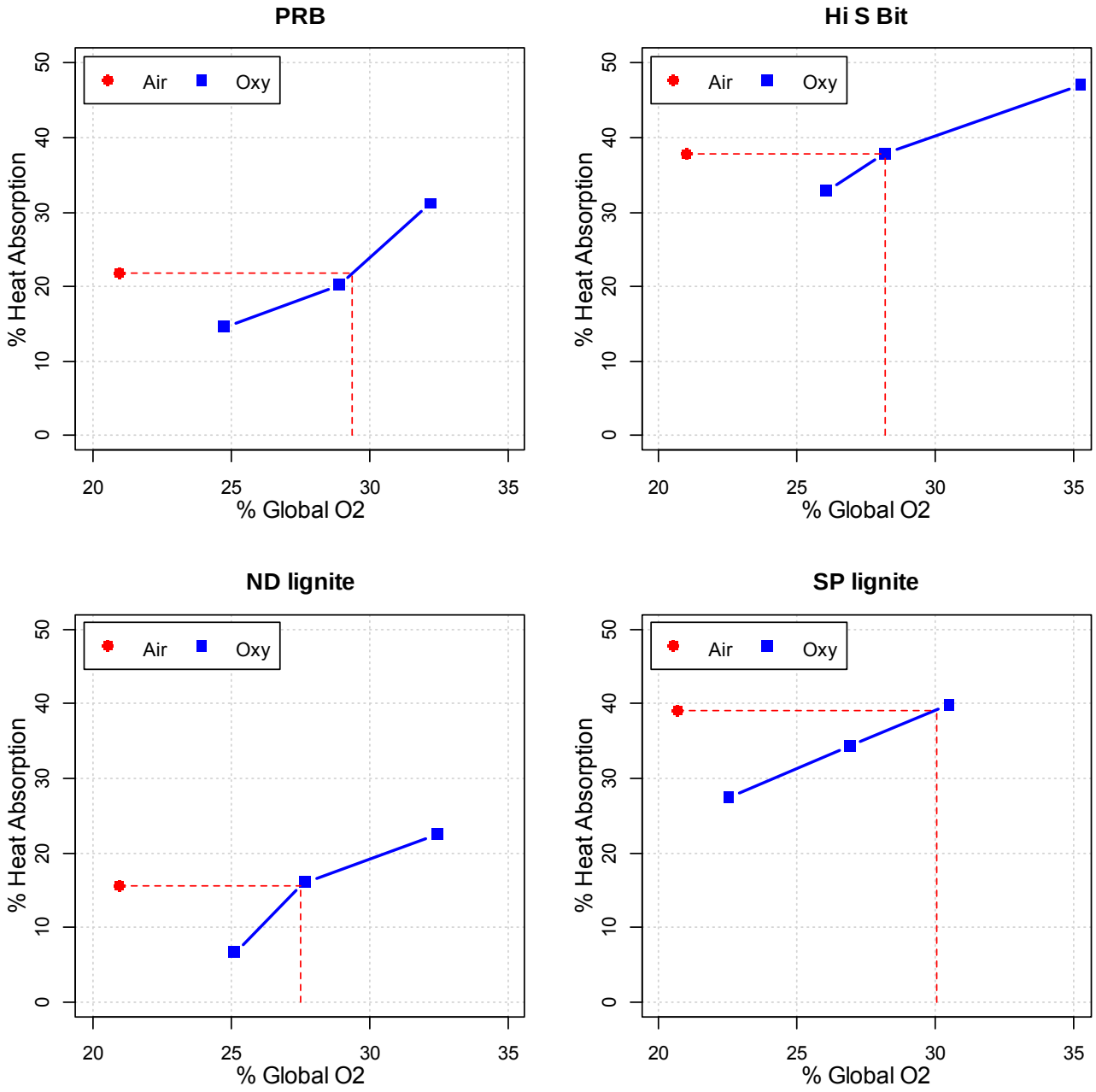

Figure 5-37. Equivalent oxy-fired furnace heat absorption

6. Conclusions

The 15 MW_{th} test program achieved all major objectives. The BSF was modified to allow effective and comprehensive evaluation of oxy-combustion impacts over a range of representative oxy-process and boiler design conditions. The BSF provided stable operation and permitted testing over the full range of matrix parameters desired. Eight comprehensive test campaigns were completed providing a wealth of detailed information covering a range of coal types and boiler operating parameters.

Results of the 15 MW_{th} testing demonstrate that there are no technical barriers restricting the continued development and commercialization of oxy-combustion from a boiler standpoint. Combustion performance, emissions, and thermal behavior (temperature, heat flux intensity, heat flux profile) can be controlled to similar levels as air firing. For a tangentially oxy-fired boiler, there are no major changes required to the current boiler design for oxy-firing. Boiler size and pressure part surfaces should only require minor modifications for oxy-fired retrofit applications. For new applications, additional control under oxy-firing may be used to an advantage with innovative design concepts to improve oxy-fired boiler performance and costs.

The data generated during the test program has proven extremely useful for the refinement and validation of engineering design tools, including CFD and dynamic modeling. The test results have also provided the basis for the development of procedures and guidelines for oxy-boiler design. The extensive database generated under this program is not only valuable for Alstom design, but can used by other researchers and organizations to support their development efforts.

The results of this test program provide a sound foundation for oxy-boiler design and commercial-scale demonstration. These results along with other large-scale oxy-combustion test programs conducted around the world confirm the technical viability of this technology and the readiness to proceed to the final development step of commercial-scale demonstration.

7. Appendices

Appendix A. SO_3 sampling equipment and procedure

Major Pieces of Equipment

- ISP – QSIS Model sold by Apogee Scientific
  - Includes Control Box Consisting of 2 Heated Zones, 4 Type K Thermocouple Inputs, 2 Pressure Gauges, and 1 Magnehelic differential pressure gauge
- Gas Analysis System – O_2 and CO_2 analyzer as a leak check method
  - In-duct Gas Species (O_2, CO_2, SO_2, CO, NO_x, H_2O) are monitored by a continuous gas analysis system
  - Gas composition (CO_2 and O_2) prior to the critical orifice is measured at the beginning and end of each test point and compared to the continuous gas analysis system as a leak check
- Graham Condenser – Of the jacket tube type, the jacket contains the coolant, and the condensation takes place inside the coil. This configuration maximizes collected condensate, since all the vapors must flow through the entire length of the coil, thus having prolonged contact with the coolant.
- Glass Wool Plug – Located at the outlet of the Graham condenser, collects any aerosol
- Heated Circulating Water Bath – Provides a constant temperature coolant to the Graham Condenser.
- Impinger Bucket – Anderson knockout impingers dry the sample gas after the sample has passed through the condenser
- Critical Orifice – Choked flow provides a steady and known sample flow
- Aspirator and Eductor – Provide driving force for the ISP flow and Condenser Sample

Pre-Testing Heated Zone Set Points and Checks

1. Ensure all zones are properly heated up and air is supplied to ISP Control Box
   a. Frit Heater is 232°C
   b. ISP Inlet Ball Valve Heated Rope at 232°C
   c. Condenser Connection Heated Rope at 232°C
2. Ensure Sample Collection Aspirator is in operation
3. Ensure Eductor Compressed Air Pressure at 60 psi (~4.1 bar gauge)
4. Ensure Heated Circulating Water Bath is Circulating Coolant at 90°C

ISP Operation Procedure

1. Open ISP Inlet Ball Valve
2. Open ISP Eductor/Aspirator Outlet Ball Valve (Dual action valve simultaneously opens the vent and supplies motive air to the Eductor – see Figure)
3. Adjust Eductor Compressed Air Supply to maintain 8 to 10 in H_2O of pressure drop (20 - 25 mbar) as measured by the Magnehelic differential pressure gauge. This pressure drop corresponds to approx. 100 ft/s (30 m/s) axial velocity, which is sufficient to ensure particle entrainment in the flue gas

4. Once flow through the ISP is stabilized, open the stopcock at the condenser outlet and begin condensing sample (the aspirator drawing the sample through the condenser is generally left running).
5. Check Critical Orifice pressures and temperatures to ensure flow through the condenser; adjust the aspirator as needed
6. Record sample collection process data
7. For a short time, also draw sample gas from the condenser to the O_2 and CO_2 analyzers for a leak check.
8. Once sample time is complete, close stopcock at condenser outlet
9. Close Eductor Outlet Dual Action Ball Valve
10. Close ISP Inlet Ball Valve
11. Remove condenser and collect samples

Sample Collection Procedure

1. Remove Glass Wool plug and rise plug in a separate sample for separate testing
2. Rinse a volumetric flask and funnel twice with de-ionized (DI) water before recovering each sample
3. Place condenser in glassware stand w/ SO_3 deposit down
4. Rinse w/ ~ 30 mL DI water catch through narrow funnel into volumetric flask (use higher flow DI bottle)
5. Turn condenser over in stand so SO_3 deposit is UP
6. Rinse w/ ~ 40 mL DI water. Catch as in step 3
7. Rinse interior of funnel cone into volumetric flask
8. Using low flow DI bottle, fill almost to 100 mL line, top off with pipette
9. Seal volumetric flask + invert 10 times to mix sample
10. If 100 mL was exceeded draw off excess w/ pipette, measure in a graduated cylinder, record on test sheet notes
11. Rinse sample container twice w/ small (~5mL) aliquot of sample
12. Transfer bulk of sample to sample container

Sample Analysis and Reporting Procedure

1. SO_4^{2-} concentration in the sample container is measured via Ion Chromatography and reported as mg/L
2. Total dry gas flow through the condenser is calculated based on the orifice rating and orifice pressures and temperature
3. SO_3 concentration is then calculated and results reported in ppmv, moisture free, corrected to 3% O_2 based on the continuous gas analysis system

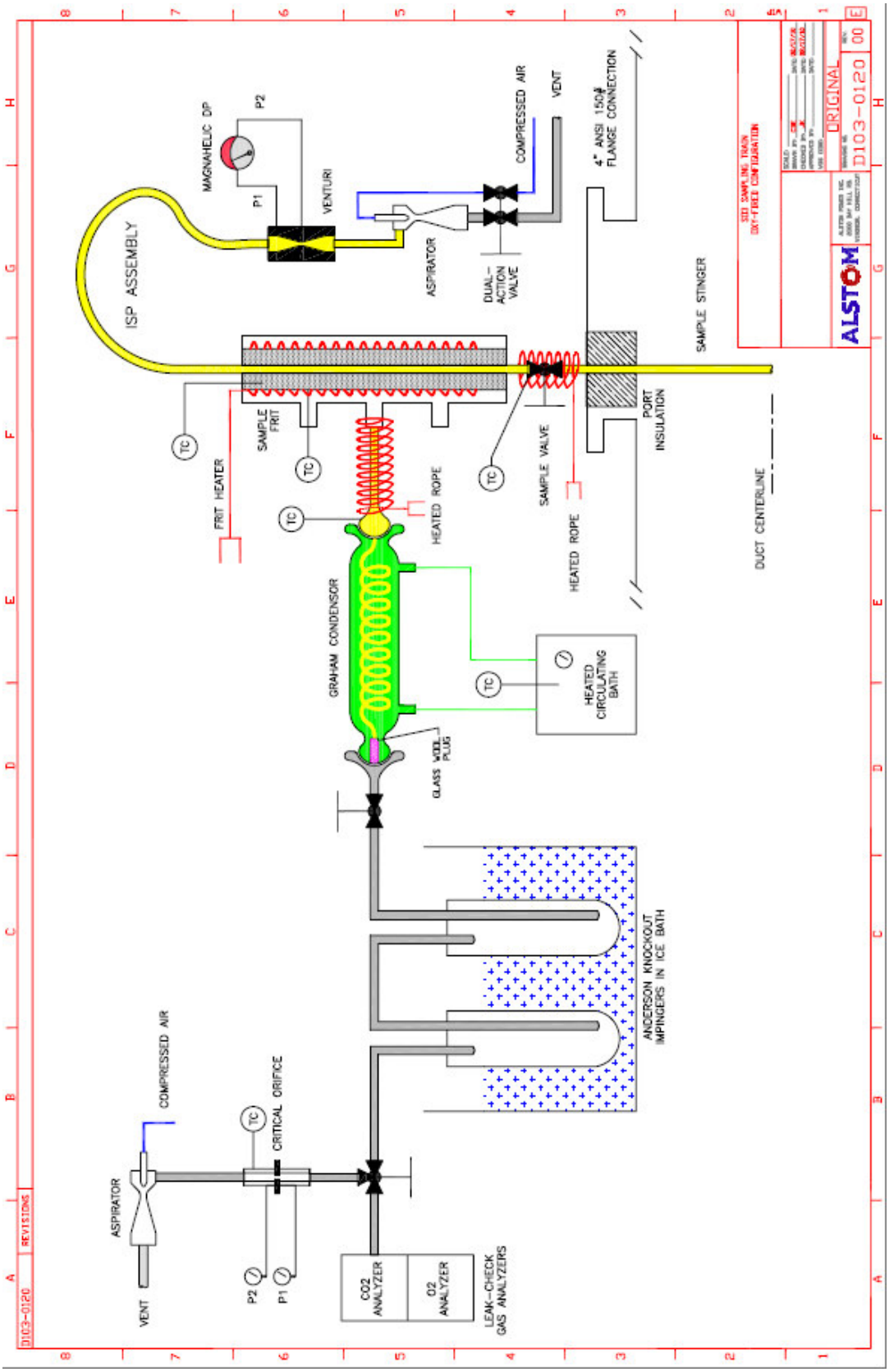

Diagram of Modified Controlled Condensation with ISP

Appendix B. CCSEM Analysis

This appendix contains the report from Microbeam Technologies, Inc. on the Computer Controlled Scanning Electron Microscopy (CCSEM) analysis of ash samples obtained from combustion in the drop tube furnace system.

CCSEM ANALYSIS OF DROP TUBE FURNACE ASH SAMPLES

Report prepared for:

Steven A. Unker, M.Sc.
Alstom Power Inc.
200 Great Pond Drive
Windsor, CT 06095

Report prepared by:
Steve Benson, President
Art Ruud, Research Scientist
Shuchita Patwardhen, Research Engineer
Microbeam Technologies, Inc.

November 22, 2013

MTI Report 1418

CCSEM ANALYSIS OF DROP TUBE FURNACE ASH SAMPLES

Introduction

Alstom Power Inc. contacted Microbeam Technologies, Inc. (MTI) to perform computer controlled scanning electron microscopy analysis of eight ash samples obtained from drop tube furnace testing conducted by Alstom Power. The ash samples are identified in Table 1.

Table 1. Sample identification.

MTI #	Description	Analysis Requested
MTI 13-160	BTC – 4 Ash	CCSEM
MTI 13-161	BTC – 5 Ash	CCSEM
MTI 13-162	ILC – 4 Ash	CCSEM
MTI 13-163	ILC – 5 Ash	CCSEM
MTI 13-164	SPC – 5 Ash	CCSEM
MTI 13-165	SPC – 4 Ash	CCSEM
MTI 13-166	WV6 – 5 Ash	CCSEM
MTI 13-167	WVC – 4 Ash	CCSEM

Methods and Materials

The eight ash samples were prepared for scanning electron microscopy analysis using a dispersion mounting procedure where the ash material was dispersed in an alcohol medium and applied to a graphite planchete faced with double stick carbon tape. The alcohol was allowed to evaporate leaving the ash particles dispersed on the carbon tape which allows for the detection and analysis of individual ash particles by the SEM. The sample mount was coated with carbon for improved conductivity in the SEM.

Computer Controlled Scanning Electron Microscopy (CCSEM) utilizes backscattered electron imaging combined with automated particle recognition and chemical analysis to determine the composition, size, and abundance of mineral types in coal or ash. The CCSEM method is automated, allowing up to 3,000 mineral grains or ash particles to be characterized. The compositional data is used to type the particles based on composition. The particle typing is based on standard mineral compositions. Note that for fly analysis some particles will be classified as a mineral but is likely not in the mineral form because it has went through the combustion process. The composition may match the mineral form. For example, the identification of kaolinite in fly ash means that the particle contains aluminum and silicon in the correct proportions that is consistent with kaolinite and does not contain the bound water. Microbeam utilizes this information to predict wear of system components, fireside slagging and fouling, bed agglomeration and clinkering, and the performance of air pollution control devices. The mineral or ash particle types considered are listed in the appendix.

Results and Discussion

The results of the CCSEM analysis of ash sample BTC-4 (MTI 13-160) is summarized in Tables 2 and 3. The analysis reveals that most of the ash particles (65.3%) do not fit into any of the known mineral classification and are therefore listed as unclassified. Of the mineral types identified, most were calcium-rich (8.3%), followed by mixed aluminosilicates (5.4%), calcium

aluminate (4.9%), calcium aluminosilicate (4.3%), and ankerite-derived oxide (4.1%). Several other particle types were found at levels less than 2 wt.%. The majority of the ash particles (81.1%) were 4.6 to 22 µm in size. The largest ash particle found was 83 µm in diameter. Figure 1 illustrates how the ash particles are distributed by size.

Table 2. CCSEM analysis results of BTC-4 Ash (MTI 13-160). Results expressed as weight percent on a mineral basis, normalized to 100%.

	Particle size, µm						
	1.0 to 2.2	2.2 to 4.6	4.6 to 10	10 to 22	22 to 46	46 to 400	TOTALS
QUARTZ	0	0	0	0.8	0.3	0.3	1.5
IRON OXIDE	0	0	0	0	0.1	0.2	0.3
PERICLASE	0	0	0	0	0	0	0
RUTILE	0	0	0	0	0	0	0
ALUMINA	0	0	0	0	0	0	0
CALCITE-DERIVED OXIDE	0	0.1	0.2	0.9	0.1	0	1.3
DOLOMITE-DERIVED OXIDE	0	0	0.1	0	0	0	0.1
ANKERITE-DERIVED OXIDE	0.2	0.5	1.2	2.1	0	0	4.1
KAOLINITE	0	0	0	0	0.2	0.1	0.3
MONTMORILLONITE	0	0	0	0	0.2	0.3	0.6
K AL-SILICATE	0	0	0	0	0	0	0
FE AL-SILICATE	0	0	0.1	0	0	0.1	0.2
CA AL-SILICATE	0	0	0.1	3.7	0.3	0.1	4.3
NA AL-SILICATE	0	0	0.1	0.2	0	0	0.3
ALUMINOSILICATE	0	0	0	0.4	0.5	0.1	0.9
MIXED AL-SILICATE	0	0	0.8	3.2	0.7	0.7	5.4
FE SILICATE	0	0	0	0	0	0	0
CA SILICATE	0	0	0	0.5	0.1	0	0.6
CA ALUMINATE	0	0.1	1.9	2.6	0.1	0.1	4.9
PYRITE	0	0	0	0	0	0	0
PYRRHOTITE	0	0	0	0	0	0	0
OXIDIZED PYRRHOTITE	0	0	0	0	0	0	0
GYPSUM	0	0	0	0	0	0	0
BARITE	0	0	0	0	0	0	0
APATITE	0	0	0	0	0	0	0
CA AL-P	0	0	0.1	0.3	0	0	0.4
KCL	0	0	0	0	0	0	0
GYPSUM/BARITE	0	0	0	0	0	0	0
GYPSUM/AL-SILICATE	0	0	0	0	0	0	0
SI-RICH	0	0	0.2	0.4	0.2	0.2	1.1
CA-RICH	0	0.2	1.5	6.4	0.1	0	8.3
CA-SI RICH	0	0	0.1	0.1	0.1	0	0.3
UNCLASSIFIED	1	5.3	17.3	35.7	3.3	2.6	65.3
TOTALS	1.2	6.5	23.7	57.4	6.4	4.8	100

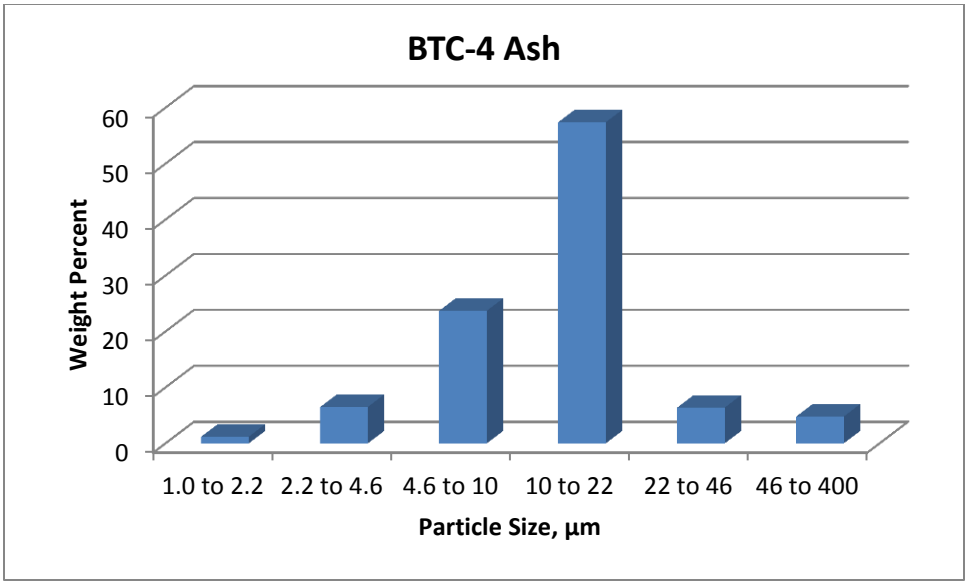

Figure 1. Distribution of the ash particles of BTC-4 Ash (MTI 13-160) by size.

Table 3 shows the elemental composition of the unclassified particles of BTC-4 ash as they are distributed throughout the size bins. Overall the unclassified particles consist mainly of calcium (32.6% as calcium oxide), aluminum (25.2% as aluminum oxide), silicon (12.8% as silicon dioxide), iron (9.1% as iron oxide), magnesium (8.4% as magnesium oxide) and phosphorus (5.2% as phosphorus pentoxide). The majority of the unclassified ash particles (89.2%) were less than 22 µm in size. The largest ash particle found in the unclassified material was 80.9 µm in diameter. Figure 2 illustrates how the unclassified ash particles are distributed by size.

Table 3. Elemental composition of the unclassified particles of BTC-4 ash. Results are expressed in weight percent equivalent oxide, normalized to 100%.

	Particle size, µm						
	1.0 to 2.2	2.2 to 4.6	4.6 to 10	10 to 22	22 to 46	46 to 400	Total
Na_2O	2.2	1.9	1.7	1.5	2.3	2.1	1.8
MgO	10.0	8.6	7.5	8.2	8.8	7.7	8.4
Al_2O_3	24.6	24.7	26.9	25.1	22.5	23.5	25.2
SiO_2	9.1	12.9	14.7	11.1	16.3	17.1	12.8
P_2O_5	6.0	5.5	5.0	4.7	4.9	5.0	5.2
SO_3	2.5	1.2	0.8	1.1	2.6	2.2	1.4
Cl	0.3	0.2	0.1	0.1	0.3	0.4	0.2
K_2O	0.4	0.3	0.2	0.2	0.3	0.3	0.3
CaO	29.3	31.4	33.0	37.2	31.2	31.8	32.6
Fe_2O_3	12.7	10.2	7.2	7.9	7.9	6.4	9.1
BaO	1.2	1.0	0.9	1.1	1.3	1.3	1.0
TiO_2	1.6	2.1	1.9	1.8	1.5	2.1	1.9
% of particles	16.5	25.5	27.7	19.5	8.2	2.6	100

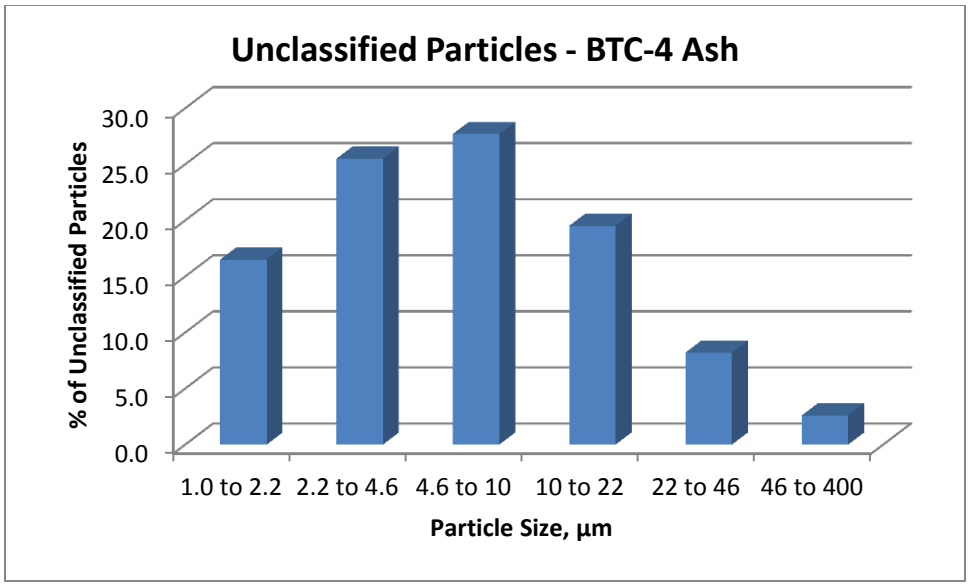

Figure 2. Distribution of the unclassified ash particles of BTC-4 Ash (MTI 13-160) by size.

CCSEM ANALYSIS OF DROP TUBE FURNACE ASH SAMPLES

The results of the CCSEM analysis of BTC-5 ash (MTI 13-161) are given in Tables 4 and 5. Most of the ash particles (62.1%) found in this analysis was unclassified. The identified particles included calcium aluminosilicate (8.9%), quartz (5.2%), mixed aluminosilicate (5.1%), calcium- rich particles (3.4%), and ankerite-derived oxide (2.6%). Numerous other particles were identified at concentrations less than 2 wt.%. Most of the ash particles (96.1%) were greater than 4.6 µm in size with 53.9% of the particles being 10 to 22 µm in size. The largest particle found was 239.2 µm in diameter. Figure 3 graphically shows the distribution of the ash particles by size.

Table 4. CCSEM analysis results of BTC-5 Ash (MTI 13-161). Results expressed as weight percent on a mineral basis, normalized to 100%.

	Particle size, µm						
	1.0 to 2.2	2.2 to 4.6	4.6 to 10	10 to 22	22 to 46	46 to 400	TOTALS
QUARTZ	0	0.1	0	0.3	0.5	4.2	5.2
IRON OXIDE	0	0	0	0.1	0.3	0.4	0.9
PERICLASE	0	0	0	0	0	0	0
RUTILE	0	0	0	0	0	0	0
ALUMINA	0	0	0	0	0	0	0
CALCITE-DERIVED OXIDE	0	0	0.2	0.2	0	0.1	0.5
DOLOMITE-DERIVED OXIDE	0	0	0.1	0.7	0	0	0.9
ANKERITE-DERIVED OXIDE	0.1	0.2	0.6	1.6	0.1	0	2.6
KAOLINITE	0	0	0	0	0.3	0.4	0.7
MONTMORILLONITE	0	0	0	0.1	0.3	0.4	0.8
K AL-SILICATE	0	0	0	0	0.4	1.1	1.6
FE AL-SILICATE	0	0	0	0	0	0.3	0.3
CA AL-SILICATE	0	0	0	4.9	3.3	0.6	8.9
NA AL-SILICATE	0	0	0	0.1	0.1	0	0.2
ALUMINOSILICATE	0	0	0	0	0.6	1.1	1.7
MIXED AL-SILICATE	0	0	0.1	0.1	2.5	2.4	5.1
FE SILICATE	0	0	0	0	0	0	0
CA SILICATE	0	0	0	0.7	0.6	0.2	1.5
CA ALUMINATE	0	0	0	0	0	0	0
PYRITE	0	0	0	0	0	0	0
PYRRHOTITE	0	0	0	0	0	0	0
OXIDIZED PYRRHOTITE	0	0	0	0	0	0	0
GYPSUM	0	0	0	0	0	0	0
BARITE	0	0	0	0	0	0	0
APATITE	0	0	0	0	0	0	0
CA AL-P	0	0.1	0.3	1.1	0.2	0	1.6
KCL	0	0	0	0	0	0	0
GYPSUM/BARITE	0	0	0	0	0	0	0
GYPSUM/AL-SILICATE	0	0	0	0	0	0	0
SI-RICH	0	0	0.1	0	0.7	0.8	1.6
CA-RICH	0	0.2	0.3	2.5	0.3	0.1	3.4
CA-SI RICH	0	0	0	0	0.3	0	0.3
UNCLASSIFIED	0.4	2.5	9.8	41.4	4.8	3.2	62.1
TOTALS	0.6	3.3	11.6	53.9	15.3	15.4	100

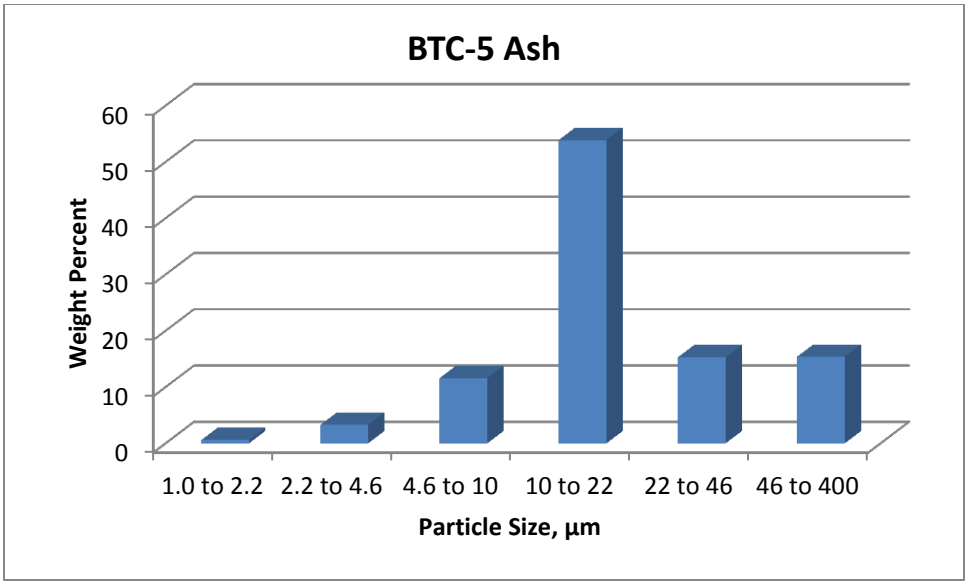

Figure 3. Distribution of the ash particles of BTC-5 Ash (MTI 13-161) by size.

Table 5 shows the elemental composition of the unclassified particles of BTC-5 ash as they are distributed throughout the size bins. The unclassified particles consist mainly of calcium (32.7% as calcium oxide), aluminum (24.6% as aluminum oxide), silicon (15.5% as silicon dioxide), magnesium (7.8% as magnesium oxide), iron (7.5% as iron oxide), and phosphorus (4.8% as phosphorus pentoxide). The majority of the unclassified ash particles are 2.2 to 46 µm in size. The largest unclassified particle found was 239.9 µm in diameter. Figure 4 illustrates how the unclassified ash particles are distributed by size.

Table 5. Elemental composition of the unclassified particles of BTC-5 ash. Results are expressed in weight percent equivalent oxide, normalized to 100%.

	Particle size, µm						
	1.0 to 2.2	2.2 to 4.6	4.6 to 10	10 to 22	22 to 46	46 to 400	Total
Na_2O	4.1	1.9	1.9	1.5	2.6	2.3	2.1
MgO	8.4	9.7	9.5	8.6	4.4	2.4	7.8
Al_2O_3	23.7	26.6	26.9	24.4	22.1	21.7	24.6
SiO_2	6.4	5.8	8.2	12.2	32.0	43.9	15.5
P_2O_5	6.3	5.7	4.9	4.2	4.4	4.9	4.8
SO_3	3.6	1.5	1.2	0.9	1.4	2.0	1.4
Cl	0.6	0.2	0.2	0.2	1.0	1.9	0.5
K_2O	0.8	0.2	0.2	0.1	1.2	2.6	0.5
CaO	33.7	37.0	36.3	37.9	22.5	10.5	32.7
Fe_2O_3	9.8	8.6	8.0	7.9	5.4	5.1	7.5
BaO	1.0	0.9	0.9	1.0	1.2	0.8	1.0
TiO_2	1.6	1.9	1.8	1.3	1.6	2.0	1.6
% of particles	8.1	14.5	21.7	31.2	21.6	2.9	100

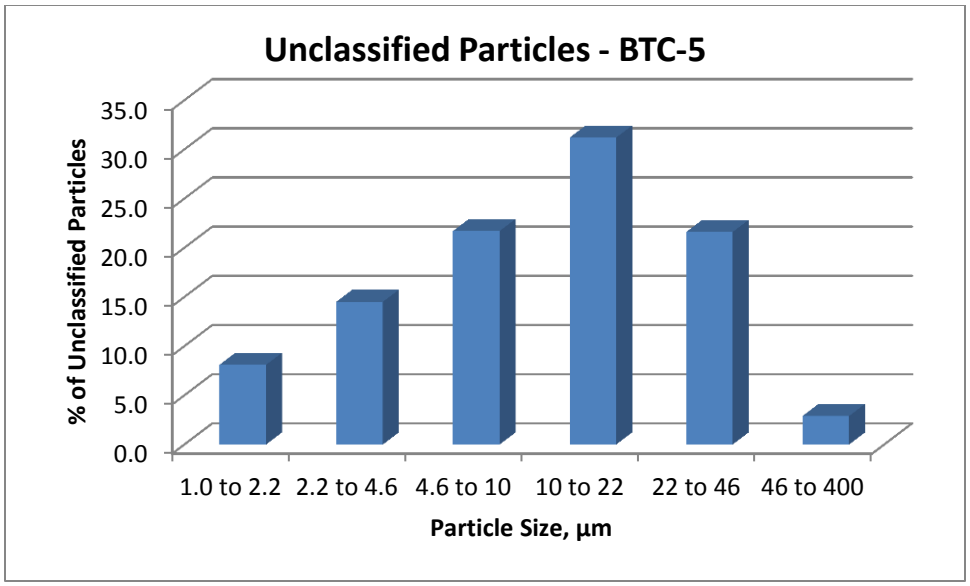

Figure 4. Distribution of the unclassified ash particles of BTC-5 Ash (MTI 13-161) by size.

CCSEM ANALYSIS OF DROP TUBE FURNACE ASH SAMPLES

The results of the CCSEM analysis of ILC-4 ash (MTI 13-162) is summarized in Tables 6 and 7. The major particle type identified by the analysis was iron aluminosilicate (23.9%) followed by mixed aluminosilicate (11.7%), potassium aluminosilicate (6.4%), iron oxide (6.3%), silicon-rich (4.7%), calcite-derived oxide (2.4%), and quartz (2.1%). Several other particle types were found at levels less than 2 wt.%. The unclassified particles accounted for 37.2% of the total. Most of the ash particles (97.3%) were greater than 4.6 µm in size with the largest particle being 224.2 µm in diameter. Figure 5 shows the distribution of the ash particles by size.

Table 6. CCSEM analysis results of ILC-4 Ash (MTI 13-162). Results expressed as weight percent on a mineral basis, normalized to 100%.

	Particle size, µm						
	1.0 to 2.2	2.2 to 4.6	4.6 to 10	10 to 22	22 to 46	46 to 400	TOTALS
QUARTZ	0	0	0.3	1.2	0.4	0.2	2.1
IRON OXIDE	0	0.1	1.5	2.9	1.1	0.7	6.3
PERICLASE	0	0	0	0	0	0	0
RUTILE	0	0	0	0	0	0	0
ALUMINA	0	0	0	0	0	0	0.1
CALCITE-DERIVED OXIDE	0	0	0.1	0.5	0.4	1.5	2.4
DOLOMITE-DERIVED OXIDE	0	0	0	0	0	0	0
ANKERITE-DERIVED OXIDE	0	0	0	0	0.1	0.6	0.8
KAOLINITE	0	0	0	0.4	0.6	0	1
MONTMORILLONITE	0	0	0	0.4	0.5	0.2	1.1
K AL-SILICATE	0	0	0.3	1.6	3.1	1.3	6.4
FE AL-SILICATE	0.1	0.7	3.4	11.5	5.8	2.5	23.9
CA AL-SILICATE	0	0	0	0	0	0	0
NA AL-SILICATE	0	0	0	0	0	0	0
ALUMINOSILICATE	0	0	0	0.4	0.7	0.4	1.4
MIXED AL-SILICATE	0	0	1.4	5.5	4	0.7	11.7
FE SILICATE	0	0	0	0.1	0.1	0	0.2
CA SILICATE	0	0	0	0	0	0	0
CA ALUMINATE	0	0	0	0	0	0	0
PYRITE	0	0	0	0	0	0	0
PYRRHOTITE	0	0	0	0	0	0	0
OXIDIZED PYRRHOTITE	0	0	0	0	0	0	0
GYPSUM	0	0	0	0	0	0	0
BARITE	0	0	0	0	0	0	0
APATITE	0	0	0	0	0	0	0
CA AL-P	0	0	0	0	0	0	0
KCL	0	0	0	0	0	0	0
GYPSUM/BARITE	0	0	0	0	0	0	0
GYPSUM/AL-SILICATE	0	0	0	0	0	0	0
SI-RICH	0	0.1	0.6	1.8	1.8	0.5	4.7
CA-RICH	0	0	0.1	0.1	0.1	0.2	0.5
CA-SI RICH	0	0	0	0	0	0	0
UNCLASSIFIED	0.3	1.4	3.9	7.2	10.1	14.3	37.2
TOTALS	0.4	2.3	11.6	33.6	28.9	23.2	100

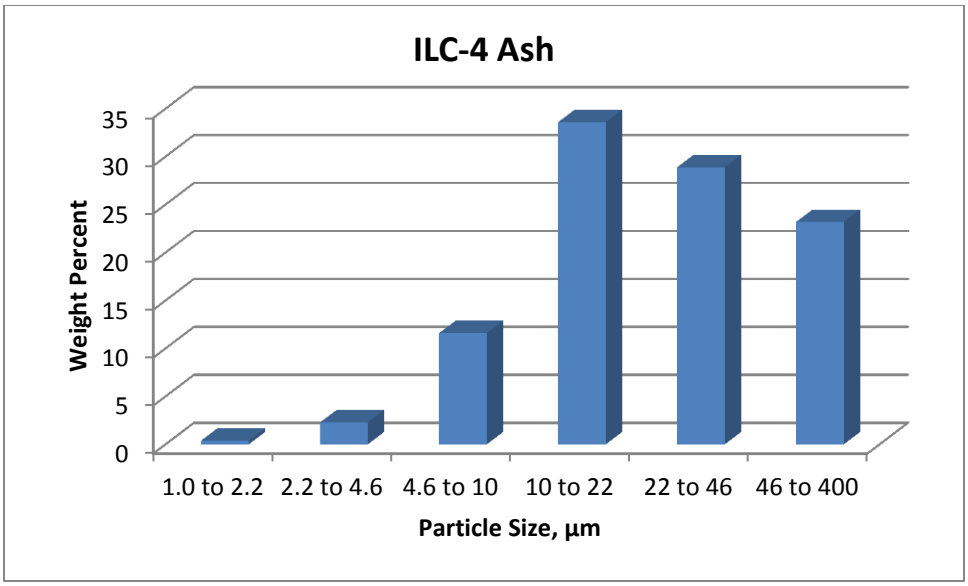

Figure 5. Distribution of the ash particles of ILC-4 Ash (MTI 13-162) by size.

Table 7 shows the elemental composition of the unclassified particles of ILC-4 ash as they are distributed throughout the size bins. The unclassified particles consist mainly of silicon (36.1% as silicon dioxide), aluminum (24.5% as aluminum oxide), iron (18.9% as iron oxide), calcium (4.1% as calcium oxide), phosphorus (4.0% as phosphorus pentoxide), and potassium (3.5% as potassium oxide). The unclassified particles ranged in size from 1.0 to 224.2 µm in diameter. Figure 6 illustrates how the unclassified ash particles are distributed by size.

Table 7. Elemental composition of the unclassified particles of ILC-4 ash. Results are expressed in weight percent equivalent oxide, normalized to 100%.

	Particle size, µm						
	1.0 to 2.2	2.2 to 4.6	4.6 to 10	10 to 22	22 to 46	46 to 400	Total
Na_2O	2.0	1.7	1.2	1.0	0.9	1.1	1.2
MgO	2.1	2.2	1.8	1.9	1.4	1.4	1.7
Al_2O_3	28.4	29.4	27.6	23.3	21.2	19.0	24.5
SiO_2	22.5	27.8	35.3	41.4	43.1	35.7	36.1
P_2O_5	3.7	4.7	4.6	4.2	3.7	2.9	4.0
SO_3	3.1	1.7	1.0	1.9	2.4	3.1	2.1
Cl	1.1	0.7	0.3	0.3	0.3	0.3	0.4
K_2O	2.3	2.2	3.0	3.6	4.4	4.7	3.5
CaO	6.3	5.5	4.0	3.4	2.8	4.4	4.1
Fe_2O_3	21.1	19.5	18.5	16.5	17.4	24.0	18.9
BaO	1.3	0.5	0.5	0.4	0.5	0.8	0.6
TiO_2	6.2	4.1	2.2	1.9	1.9	2.6	2.8
% of particles	11.3	12.2	23.5	13.1	29.0	10.9	100

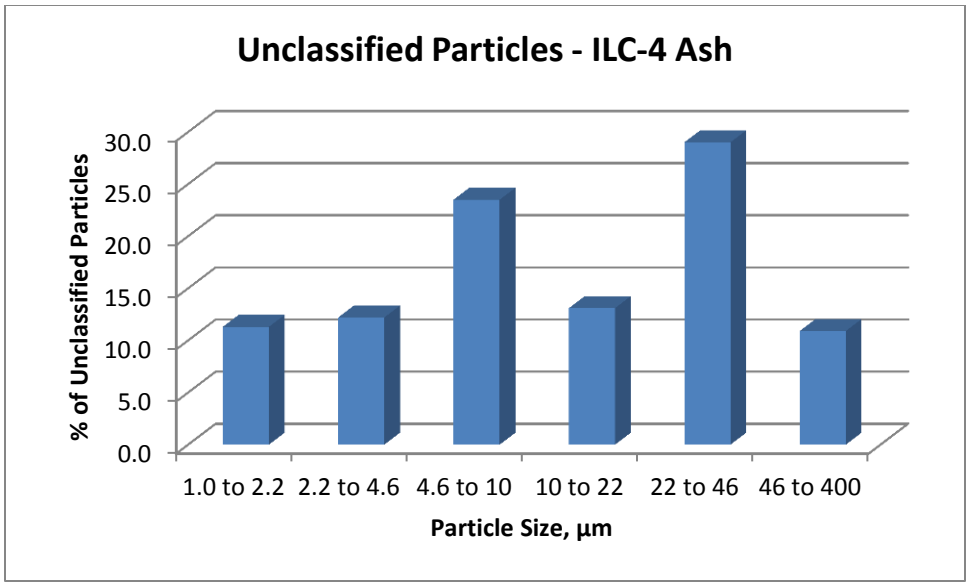

Figure 6. Distribution of the unclassified ash particles of ILC-4 Ash (MTI 13-162) by size.

CCSEM ANALYSIS OF DROP TUBE FURNACE ASH SAMPLES

The results of the CCSEM analysis of ILC-5 ash (MTI 13-163) are presented in Tables 8 and 9. The most abundant particle type identified by the analysis was iron aluminosilicate (22.4%) followed by mixed aluminosilicate (13.2%), iron oxide (10.2%), potassium aluminosilicate (7.2%), silicon-rich (4.4%), quartz (2.3%), and calcite-derived oxide (2.0%). Several other particle types were found at levels less than 2 wt.%. The unclassified particles accounted for 34.7% of the total. Most of the ash particles (96.9%) were greater than 4.6 µm in size with the 68% being 10 to 46 µm in size. The largest particle found was 245.5 µm in diameter. Figure 7 shows the size distribution of the ash particles.

Table 8. CCSEM analysis results of ILC-5 Ash (MTI 13-163). Results expressed as weight percent on a mineral basis, normalized to 100%.

	Particle size, µm						
	1.0 to 2.2	2.2 to 4.6	4.6 to 10	10 to 22	22 to 46	46 to 400	TOTALS
QUARTZ	0	0	0	1.4	0.4	0.4	2.3
IRON OXIDE	0.1	0.3	2.6	3.7	1.7	1.7	10.2
PERICLASE	0	0	0	0	0	0	0
RUTILE	0	0	0	0	0	0	0
ALUMINA	0	0	0	0	0	0	0
CALCITE-DERIVED OXIDE	0	0	0	0.3	0.5	1.1	2
DOLOMITE-DERIVED OXIDE	0	0	0	0	0	0	0
ANDERITE-DERIVED OXIDE	0	0	0	0	0	0	0.1
KAOLINITE	0	0	0	0	0.2	0	0.3
MONTMORILLONITE	0	0	0	0	0.4	0.3	0.7
K AL-SILICATE	0	0	0.2	1.5	3.8	1.8	7.2
FE AL-SILICATE	0	0.2	1.9	12.2	6	1.9	22.4
CA AL-SILICATE	0	0	0	0.1	0	0	0.1
NA AL-SILICATE	0	0	0	0	0	0	0
ALUMINOSILICATE	0	0	0	0.1	0.6	0.6	1.3
MIXED AL-SILICATE	0	0	0.4	4.9	6.1	1.6	13.2
FE SILICATE	0	0	0	0.1	0	0.5	0.6
CA SILICATE	0	0	0	0	0	0	0
CA ALUMINATE	0	0	0	0	0	0	0
PYRITE	0	0	0	0	0	0	0
PYRRHOTITE	0	0	0	0	0	0	0
OXIDIZED PYRRHOTITE	0	0	0	0	0	0	0
GYPSUM	0	0	0	0	0	0	0
BARITE	0	0	0	0	0	0	0
APATITE	0	0	0	0	0	0	0
CA AL-P	0	0	0	0	0	0	0
KCL	0	0	0	0	0	0	0
GYPSUM/BARITE	0	0	0	0	0	0	0
GYPSUM/AL-SILICATE	0	0	0	0	0	0	0
SI-RICH	0	0	0.4	1.8	1.4	0.8	4.4
CA-RICH	0	0	0	0.4	0	0.1	0.5
CA-SI RICH	0	0	0	0	0	0	0
UNCLASSIFIED	0.4	1.9	4	9.8	10.2	8.5	34.7
TOTALS	0.5	2.6	9.6	36.3	31.7	19.3	100

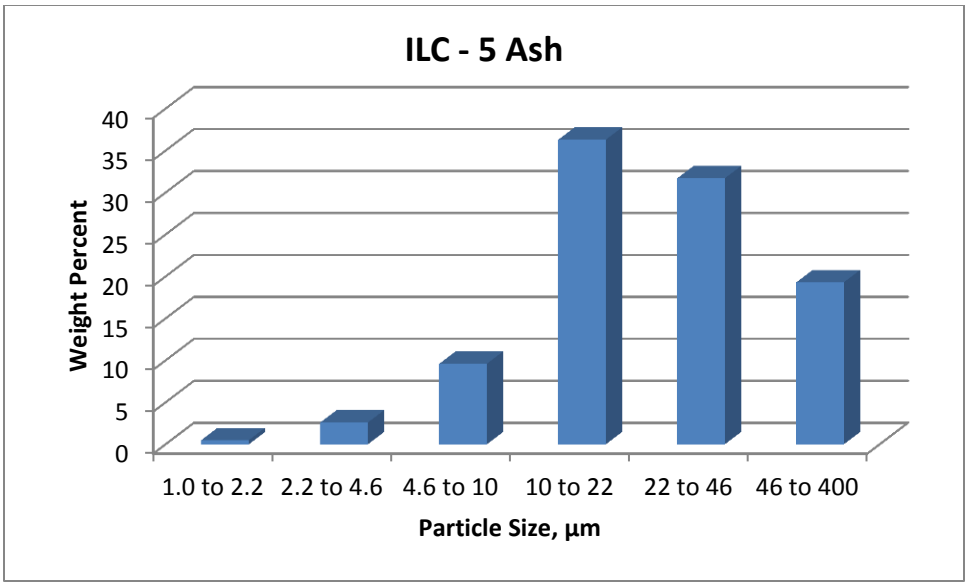

Figure 7. Distribution of the ash particles of ILC-5 Ash (MTI 13-163) by size.

Table 9 shows the elemental composition of the unclassified particles of ILC-5 ash as they are distributed throughout the size bins. The unclassified particles consist mainly of silicon (28.2% as silicon dioxide), iron (25.2% as iron oxide), aluminum (23.3% as aluminum oxide), calcium (4.6% as calcium oxide), phosphorus (3.6% as phosphorus pentoxide), sulfur (3.5% as sulfur trioxide), and potassium (3.1% as potassium oxide). The unclassified particles ranged from 1.0 to 245.2 µm in diameter. Figure 8 shows the size distribution of the unclassified ash particles.

Table 9. Elemental composition of the unclassified particles of ILC-5 ash. Results are expressed in weight percent equivalent oxide, normalized to 100%.

	Particle size, µm						
	1.0 to 2.2	2.2 to 4.6	4.6 to 10	10 to 22	22 to 46	46 to 400	Total
Na_2O	2.5	1.7	1.4	1.1	1.1	1.1	1.5
MgO	2.6	2.6	2.2	1.8	1.5	1.6	2.1
Al_2O_3	20.4	25.2	27.8	22.1	21.2	21.8	23.3
SiO_2	16.2	18.4	22.4	36.8	43.9	37.7	28.2
P_2O_5	3.0	3.3	4.0	3.7	3.8	3.7	3.6
SO_3	6.3	3.4	2.9	3.0	2.2	3.6	3.5
Cl	0.5	0.2	0.2	0.2	0.4	0.5	0.3
K_2O	2.3	1.8	2.3	3.6	4.8	5.2	3.1
CaO	5.9	7.0	5.9	2.9	1.7	2.5	4.6
Fe_2O_3	33.5	30.0	26.6	21.5	17.0	19.3	25.2
BaO	0.8	0.7	0.4	0.6	0.5	0.5	0.6
TiO_2	5.9	5.7	3.9	2.7	1.7	2.4	3.9
% of particles	16.8	26.5	16.5	9.8	23.6	6.9	100

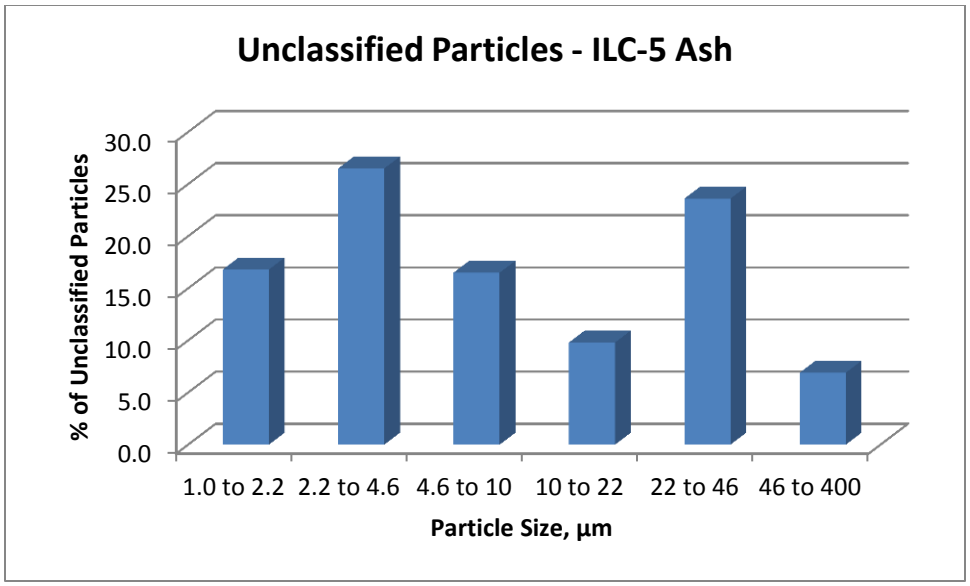

Figure 8. Distribution of the unclassified ash particles of ILC-5 Ash (MTI 13-163) by size.

CCSEM ANALYSIS OF DROP TUBE FURNACE ASH SAMPLES

The results of the CCSEM analysis of SPC-5 ash (MTI 13-164) is summarized in Tables 10 and 11. The most abundant particle type found was ankerite-derived oxide (oxide form of $[Ca,Mg,Fe]CO_3$) at 42.2% followed by quartz (2.8%) and dolomite-derived oxide (2.1%). Several other species were found at levels below 2 wt.%. The unclassified material accounted for 48% of the total. The majority of the ash particles were 4.6 to 22 µm in size with the largest particle found being 185.9 µm in diameter. Figure 9 shows the size distribution of the ash particles.

Table 10. CCSEM analysis results of SPC-5 Ash (MTI 13-164). Results expressed as weight percent on a mineral basis, normalized to 100%.

	Particle size, µm						
	1.0 to 2.2	2.2 to 4.6	4.6 to 10	10 to 22	22 to 46	46 to 400	TOTALS
QUARTZ	0	0	0	0.1	0.3	2.3	2.8
IRON OXIDE	0	0.1	0	0.1	0.3	0.2	0.7
PERICLASE	0	0	0	0	0	0	0
RUTILE	0	0	0	0	0	0	0
ALUMINA	0	0	0	0	0	0	0.1
CALCITE-DERIVED OXIDE	0	0	0	0	0.1	0	0.1
DOLOMITE-DERIVED OXIDE	0	0	0.3	1.5	0.3	0	2.1
ANKERITE-DERIVED OXIDE	0.3	3.2	12.9	18	6.1	1.6	42.2
KAOLINITE	0	0	0	0	0	0	0
MONTMORILLONITE	0	0	0	0	0	0	0
K AL-SILICATE	0	0	0	0.3	0.3	0.1	0.6
FE AL-SILICATE	0	0	0	0	0.1	0.1	0.1
CA AL-SILICATE	0	0	0	0	0	0	0
NA AL-SILICATE	0	0	0	0	0	0	0.1
ALUMINOSILICATE	0	0	0	0	0	0	0
MIXED AL-SILICATE	0	0	0	0	0.1	0.4	0.5
FE SILICATE	0	0	0	0	0	0.2	0.2
CA SILICATE	0	0	0	0	0.1	0	0.1
CA ALUMINATE	0	0	0	0	0	0	0
PYRITE	0	0	0	0	0	0	0
PYRRHOTITE	0	0	0	0	0	0	0
OXIDIZED PYRRHOTITE	0	0	0	0	0	0	0
GYPSUM	0	0	0	0	0	0	0.1
BARITE	0	0	0	0	0	0	0
APATITE	0	0	0	0	0	0	0
CA AL-P	0	0	0	0	0	0	0
KCL	0	0	0	0	0	0	0
GYPSUM/BARITE	0	0	0	0	0	0	0
GYPSUM/AL-SILICATE	0	0	0	0	0	0	0
SI-RICH	0	0	0	0.3	0.7	0.2	1.3
CA-RICH	0	0	0.2	0.1	0.1	0	0.4
CA-SI RICH	0	0	0	0.1	0	0	0.1
UNCLASSIFIED	0.2	1.2	10.9	26.2	7.4	2.5	48.5
TOTALS	0.5	4.6	24.5	46.7	16	7.7	100

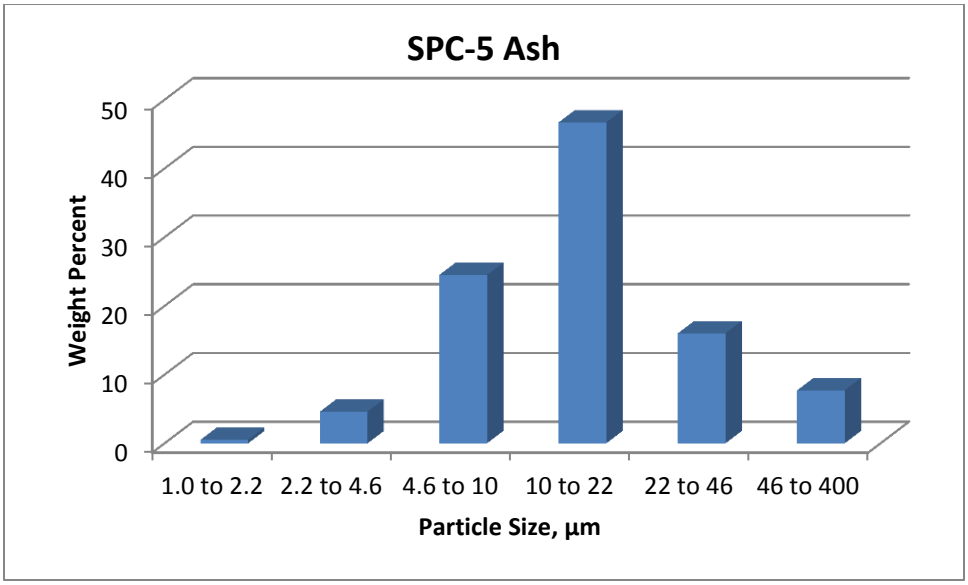

Figure 9. Distribution of the ash particles of SPC-5 Ash (MTI 13-164) by size.

Table 11 shows the elemental composition of the unclassified particles of SPC-5 ash as they are distributed throughout the size bins. The unclassified particles consist mainly of calcium (27.6% as calcium oxide), magnesium (26.0% as magnesium oxide), iron (18.3% as iron oxide), silicon (12.5% as silicon dioxide) and aluminum (9.9% as aluminum oxide). Most of the unclassified ash particles (88.2%) were 2.2 to 46 µm in size. The largest unclassified particle was 89.3 µm in diameter. The size distribution of the unclassified ash particles is shown in Figure 10.

Table 11. Elemental composition of the unclassified particles of SPC-5 ash. Results are expressed in weight percent equivalent oxide, normalized to 100%.

	Particle size, µm						
	1.0 to 2.2	2.2 to 4.6	4.6 to 10	10 to 22	22 to 46	46 to 400	Total
Na_2O	2.9	2.0	2.0	2.0	1.9	1.9	2.0
MgO	24.0	25.2	27.7	30.6	23.9	16.4	26.0
Al_2O_3	14.1	13.3	11.5	8.1	8.0	7.8	9.9
SiO_2	4.2	7.0	6.7	9.9	19.9	30.6	12.5
P_2O_5	1.3	1.0	1.0	0.6	1.0	1.2	0.9
SO_3	2.9	1.4	1.3	0.9	1.4	4.8	1.5
Cl	0.7	0.1	0.1	0.1	0.3	0.6	0.2
K_2O	0.6	0.2	0.1	0.0	0.3	1.2	0.2
CaO	28.8	29.6	29.8	28.7	25.5	19.5	27.6
Fe_2O_3	19.4	19.5	19.2	18.5	17.1	14.8	18.3
BaO	0.6	0.4	0.4	0.4	0.4	0.8	0.4
TiO_2	0.4	0.2	0.3	0.1	0.3	0.3	0.3
% of particles	7.2	12.1	23.7	21.7	30.7	4.6	100.0

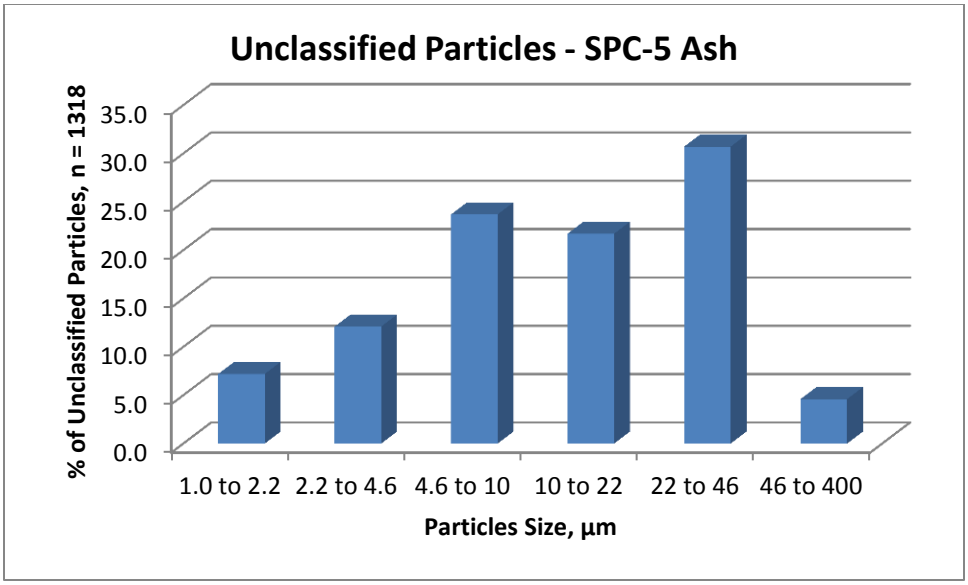

Figure 10. Distribution of the unclassified ash particles of SPC-5 Ash (MTI 13-164) by size.

CCSEM ANALYSIS OF DROP TUBE FURNACE ASH SAMPLES

The CCSEM analysis results for the SPC-4 ash (MTI 13-165) are given in Tables 12 and 13. The analysis reveals that 59.1% of the identified particles have a composition that is consistent with an ankerite derived oxide that is rich in calcium, magnesium and iron. Most of the remaining particles (32.4%) were unclassified. Several other particles were identified at concentrations less than 2 wt.%. The majority of the particles (66.2%) are 4.6 to 22 µm in size with 95% of all particles being greater than 4.6 µm. The largest ash particle found was 244.7 µm in diameter. The size distribution of the ash particles is shown in Figure 11.

Table 12. CCSEM analysis results of SPC-4 Ash (MTI 13-165). Results expressed as weight percent on a mineral basis, normalized to 100%.

	Particle size, µm						
	1.0 to 2.2	2.2 to 4.6	4.6 to 10	10 to 22	22 to 46	46 to 400	TOTALS
QUARTZ	0	0	0	0	0.2	0.6	0.9
IRON OXIDE	0	0	0.3	0.4	0.3	0.4	1.4
PERICLASE	0	0	0	0	0	0	0
RUTILE	0	0	0	0	0	0	0
ALUMINA	0	0	0	0	0	0	0
CALCITE-DERIVED OXIDE	0	0	0.1	0	0.1	0.1	0.2
DOLOMITE-DERIVED OXIDE	0	0	0.1	1.2	0	0	1.4
ANKERITE-DERIVED OXIDE	0.3	2.3	16.4	25.6	5.7	8.9	59.1
KAOLINITE	0	0	0	0	0	0	0
MONTMORILLONITE	0	0	0	0	0	0.1	0.1
K AL-SILICATE	0	0	0	0.1	0.1	0	0.2
FE AL-SILICATE	0	0	0.2	0.1	0.3	0	0.7
CA AL-SILICATE	0	0	0	0	0	0	0
NA AL-SILICATE	0	0	0	0	0	0	0
ALUMINOSILICATE	0	0	0	0	0	0	0
MIXED AL-SILICA	0	0	0	0.2	0.2	0	0.4
FE SILICATE	0	0	0.1	0	0	0.1	0.1
CA SILICATE	0	0	0	0	0	0	0
CA ALUMINATE	0	0	0.1	0.1	0	0	0.2
PYRITE	0	0	0	0	0	0	0
PYRRHOTITE	0	0	0	0	0	0	0
OXIDIZED PYRRHO	0	0	0	0	0	0	0
GYPSUM	0	0	0	0	0	0	0
BARITE	0	0	0	0	0	0	0
APATITE	0	0	0	0	0	0	0
CA AL-P	0	0	0	0	0	0	0
KCL	0	0	0	0	0	0	0
GYPSUM/BARITE	0	0	0	0	0	0	0
GYPSUM/AL-SILIC	0	0	0	0	0	0	0
SI-RICH	0	0	0.1	0.3	0.5	0.1	1
CA-RICH	0	0.1	0.3	1.2	0.2	0	1.8
CA-SI RICH	0	0	0.1	0	0	0	0.1
UNKNOWN	0.3	1	7.2	12.2	6.4	5.2	32.4
TOTALS	0.7	3.5	24.9	41.3	14.1	15.5	100

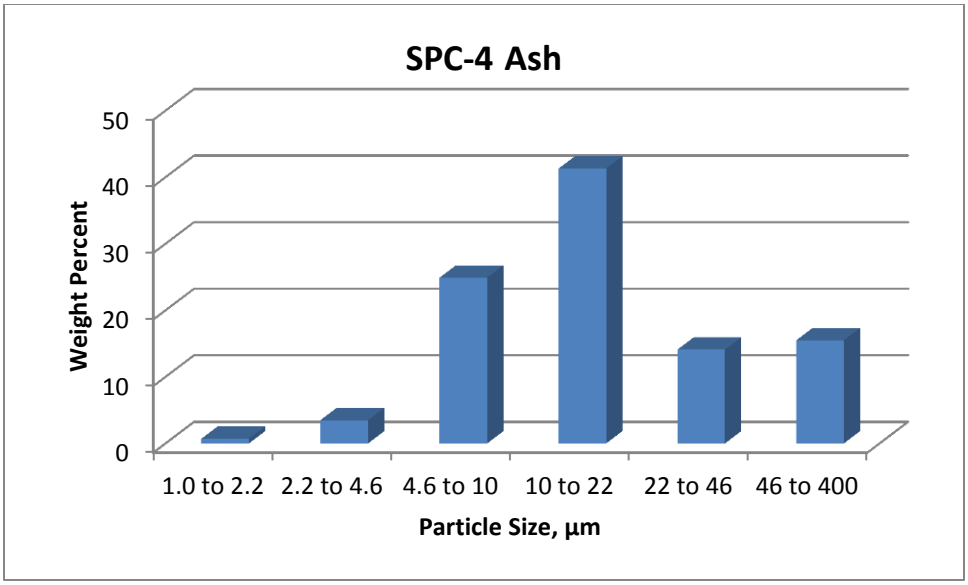

Figure 11. Distribution of the ash particles of SPC-4 Ash (MTI 13-165) by size.

Table 13 shows the elemental composition of the unclassified particles of SPC-4 ash as they are distributed throughout the size bins. The unclassified particles consist mainly of iron (25.4% as iron oxide), calcium (22.8% as calcium oxide), magnesium (21.1% as magnesium oxide), silicon (13.4% as silicon dioxide), aluminum (8.6% as aluminum oxide) and sulfur (4.2% as sulfur trioxide). Ash particles from 22 to 46 µm were the most abundant size (42.4%) with 74% of the unclassified ash particles ranging from 4.6 to 46 µm in size. The largest unclassified particle was 166.9 µm in diameter. Figure 12 shows the size distribution of the unclassified particles.

Table 13. Elemental composition of the unclassified particles of SPC-4 ash. Results are expressed in weight percent equivalent oxide, normalized to 100%.

	Particle size, µm						
	1.0 to2.2	2.2 to 4.6	4.6 to 10	10 to 22	22 to 46	46 to 400	Total
Na_2O	2.3	2.9	2.2	1.6	2.0	2.1	2.1
MgO	28.7	22.1	16.0	15.8	22.8	23.2	21.1
Al_2O_3	8.4	9.9	10.2	11.4	7.3	5.9	8.6
SiO_2	6.0	12.7	16.8	14.9	13.6	11.2	13.4
P_2O_5	0.8	0.9	0.9	1.0	0.8	0.6	0.8
SO_3	4.4	4.8	1.9	1.7	5.4	5.7	4.2
Cl	0.3	0.4	0.3	0.2	0.3	0.2	0.3
K_2O	0.2	0.4	0.1	0.2	0.6	0.6	0.4
CaO	18.2	20.6	31.4	33.9	18.4	17.0	22.8
Fe_2O_3	29.9	24.3	19.4	18.5	27.8	32.6	25.4
BaO	0.6	0.6	0.5	0.4	0.6	0.5	0.6
TiO_2	0.2	0.4	0.3	0.4	0.3	0.4	0.3
% of particles	8.9	8.3	19.4	12.2	42.4	8.8	100

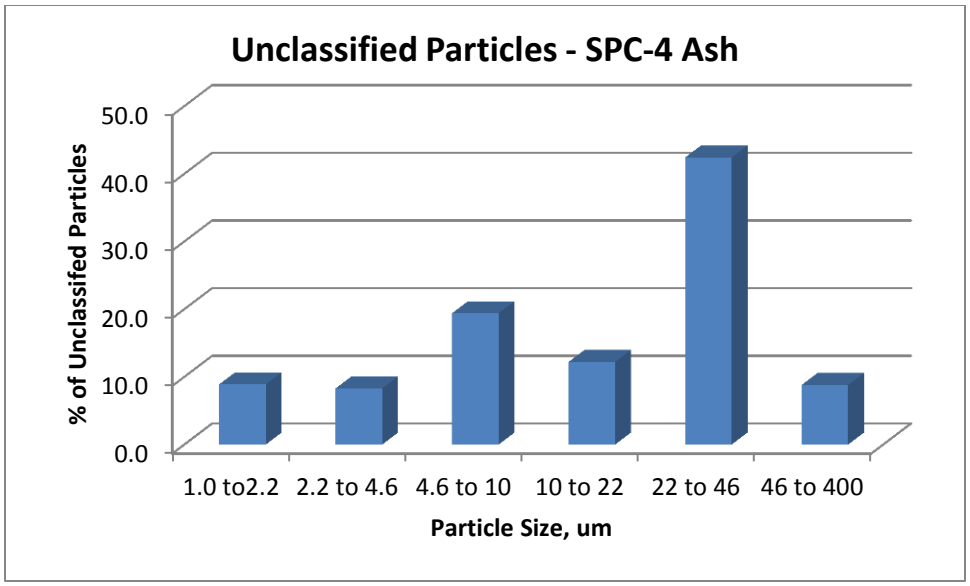

Figure 12. Distribution of the unclassified ash particles of SPC-4 Ash (MTI 13-165) by size.

CCSEM ANALYSIS OF DROP TUBE FURNACE ASH SAMPLES

The results of the CCSEM analysis of WV6-5 Ash (MTI 13-166) are presented in Tables 14 and 15. The analysis shows that the most abundant particle type found was mixed aluminosilicate at 26.0% followed by potassium aluminosilicate (16.1%), aluminosilicate (12.4%), ankerite-derived oxide (6.4%), kaolinite (6.2%), quartz (3.8%), iron aluminosilicate (3.1%) and silicon- rich particles (2.0%). Several other particle types were found at levels less than 2 wt.%. The unclassified particles accounted for 19.4% of the total. Most of the ash particles (89.8%) were greater than 10 µm in size with the largest particle found being 145.5 µm in diameter. The distribution of the ash particles by size is shown in Figure 13.

Table 14. CCSEM analysis results of WV6-5 Ash (MTI 13-166). Results expressed as weight percent on a mineral basis, normalized to 100%.

	Particle size, µm						
	1.0 to 2.2	2.2 to 4.6	4.6 to 10	10 to 22	22 to 46	46 to 400	TOTALS
QUARTZ	0	0.1	0.1	0.5	0.4	2.7	3.8
IRON OXIDE	0	0.1	0.1	0.1	0.2	0.5	1.1
PERICLASE	0	0	0	0	0	0	0
RUTILE	0	0	0	0	0	0	0
ALUMINA	0	0	0	0	0	0	0.1
CALCITE-DERIVED OXIDE	0	0.2	0	0.1	0	0.1	0.5
DOLOMITE-DERIVED OXIDE	0	0	0	0.3	0	0	0.3
ANKERITE-DERIVED OXIDE	0	0	0.5	4	0.9	1.1	6.4
KAOLINITE	0	0.1	0.4	1.5	2	2.3	6.2
MONTMORILLONITE	0	0	0.1	0.6	0.5	0.1	1.3
K AL-SILICATE	0	0.1	0.5	2.8	5.8	6.8	16.1
FE AL-SILICATE	0	0.1	0.3	1.3	0.8	0.5	3.1
CA AL-SILICATE	0	0	0.2	0.2	0.1	0.2	0.8
NA AL-SILICATE	0	0	0	0	0	0.1	0.1
ALUMINOSILICATE	0	0	0.6	2.6	4.2	4.9	12.4
MIXED AL-SILICATE	0.1	0.9	1.9	10.5	8.1	4.6	26
FE SILICATE	0	0	0	0	0	0	0
CA SILICATE	0	0	0	0	0	0	0
CA ALUMINATE	0	0	0	0	0	0	0
PYRITE	0	0	0	0	0	0	0
PYRRHOTITE	0	0	0	0	0	0	0
OXIDIZED PYRRHOTITE	0	0	0	0	0	0	0
GYPSUM	0	0.1	0	0	0	0	0.1
BARITE	0	0	0	0	0	0	0
APATITE	0	0	0	0	0	0	0
CA AL-P	0	0	0	0	0	0	0
KCL	0	0	0	0	0	0	0
GYPSUM/BARITE	0	0	0	0	0	0	0
GYPSUM/AL-SILICATE	0	0	0	0	0	0	0
SI-RICH	0	0	0.1	0.5	0.9	0.4	2
CA-RICH	0	0	0	0.1	0.1	0	0.3
CA-SI RICH	0	0	0	0	0	0	0
UNCLASSIFIED	0.2	1	1.8	4.3	5.5	6.6	19.4
TOTALS	0.6	2.9	6.7	29.2	29.6	31	100

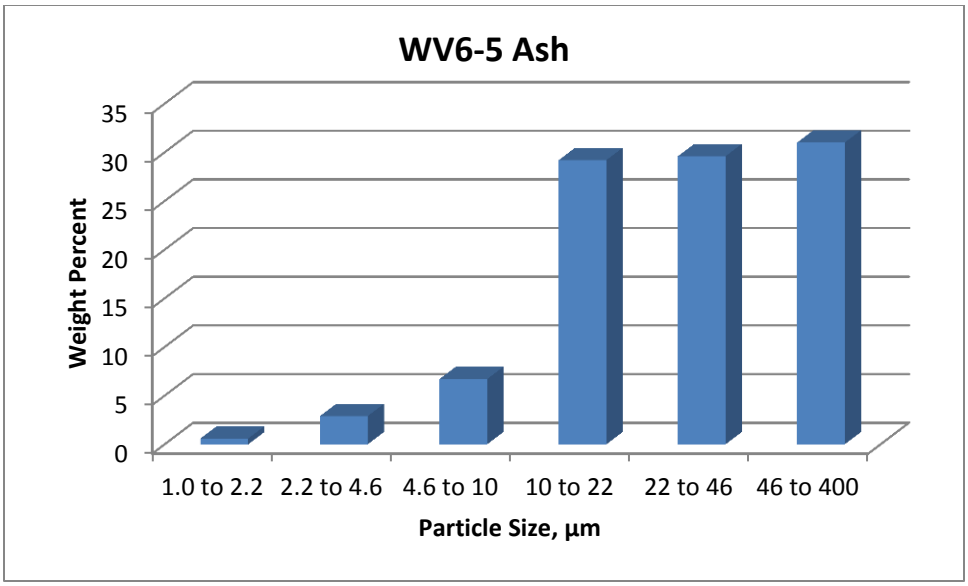

Figure 13. Distribution of the ash particles of WV6-5 Ash (MTI 13-166) by size.

Table 15 shows the elemental composition of the unclassified particles of WV6-5 ash as they are distributed throughout the size bins. The unclassified particles consist mainly of aluminum (30.1% as aluminum oxide), silicon (27.2% as silicon dioxide), calcium (9.9% as calcium oxide), iron (9.7% as iron oxide), phosphorus (5.7% as phosphorus pentoxide), titanium (5.4% as titanium dioxide) and magnesium (4.1% as magnesium oxide). The unclassified ash particles ranged from 1.0 to 129.8 µm in diameter with particles in the 22 to 46 µm size range as the most abundant. Figure 14 shows the distribution of the unclassified ash particles over the size ranges of the analysis.

Table 15. Elemental composition of the unclassified particles of WV6-5 ash. Results are expressed in weight percent equivalent oxide, normalized to 100%.

	Particle size, µm						
	1.0 to 2.2	2.2 to 4.6	4.6 to 10	10 to 22	22 to 46	46 to 400	Total
Na_2O	3.7	2.8	1.6	0.7	1.1	1.0	1.8
MgO	3.8	3.8	4.6	7.5	3.2	2.5	4.1
Al_2O_3	24.8	28.1	31.1	23.0	33.7	36.5	30.1
SiO_2	22.1	22.7	27.5	31.3	30.6	26.9	27.2
P_2O_5	5.1	6.5	5.8	4.3	5.8	6.2	5.7
SO_3	4.3	1.7	1.5	1.2	1.1	1.2	1.7
Cl	2.8	1.4	0.5	0.2	0.7	1.1	1.1
K_2O	2.3	1.4	1.9	1.1	3.7	4.2	2.5
CaO	14.2	13.8	10.2	16.2	4.6	4.8	9.9
Fe_2O_3	9.9	9.8	9.0	11.7	9.7	8.4	9.7
BaO	1.1	1.0	0.9	0.5	0.8	0.9	0.9
TiO_2	6.1	7.1	5.5	2.3	5.0	6.4	5.4
% of particles	13.3	17.9	18.3	12.4	26.7	11.4	100.0

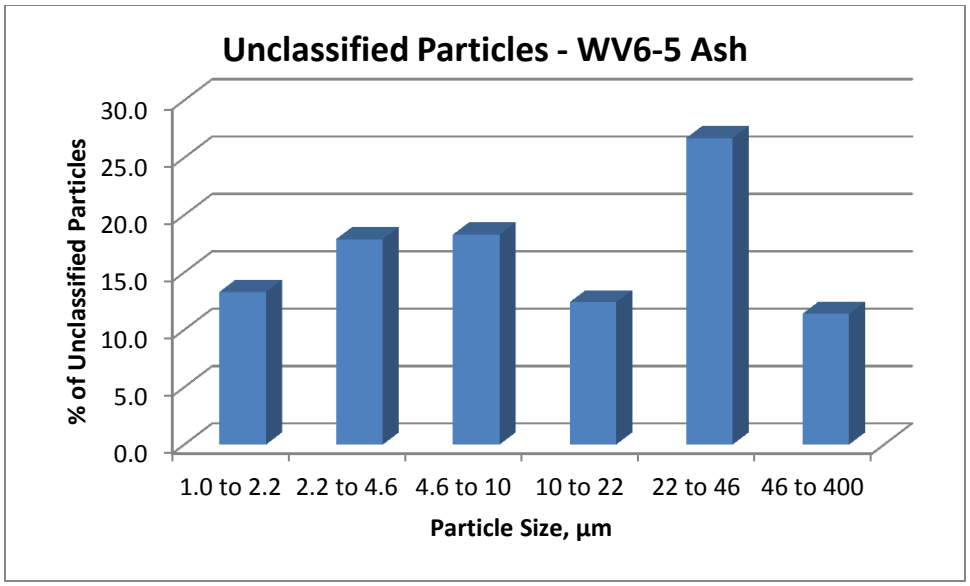

Figure 14. Distribution of the unclassified ash particles of WV6-5 Ash (MTI 13-166) by size.

CCSEM ANALYSIS OF DROP TUBE FURNACE ASH SAMPLES

The results of the CCSEM analysis of WVC-4 Ash (MTI 13-167) are found in Tables 16 and 17. The analysis shows that the most abundant particle type found was mixed aluminosilicate at 27.3% followed by potassium aluminosilicate (18.4%), aluminosilicate (13.2%), kaolinite (9.5%), silicon- rich particles (3.9%), montmorillonite (3.6%), iron aluminosilicate (3.2%) and quartz (2.8%). Other particles types were found at concentrations less than 2 wt.%. The unclassified particles made up 15.7% of the total. The majority of the ash particles were greater than 10 µm in size with the largest particle found being 129.9 µm in diameter. The size distribution of the ash particles is shown in Figure 15.

Table 16. CCSEM analysis results of WVC-4 Ash (MTI 13-167). Results expressed as weight percent on a mineral basis, normalized to 100%.

	Particle size, µm						
	1.0 to 2.2	2.2 to 4.6	4.6 to 10	10 to 22	22 to 46	46 to 400	TOTALS
QUARTZ	0	0	0	0.8	0.5	1.5	2.8
IRON OXIDE	0	0	0.1	0.3	0.4	0	0.9
PERICLASE	0	0	0	0	0	0	0
RUTILE	0	0	0	0	0	0.2	0.2
ALUMINA	0	0	0	0	0	0	0
CALCITE-DERIVED OXIDE	0	0	0	0	0	0	0
DOLOMITE-DERIVED OXIDE	0	0	0	0	0	0	0
ANKERITE-DERIVED OXIDE	0	0	0	0.5	0	0	0.5
KAOLINITE	0	0.1	0.7	3.7	3.1	1.9	9.5
MONTMORILLONITE	0	0	0.1	1.1	1.4	0.9	3.6
K AL-SILICATE	0	0.2	0.6	5.5	7.3	4.9	18.4
FE AL-SILICATE	0	0.1	0.5	1.4	0.8	0.4	3.2
CA AL-SILICATE	0	0	0.1	0.4	0.1	0	0.7
NA AL-SILICATE	0	0	0	0	0	0	0
ALUMINOSILICATE	0	0.1	1	6.1	3.9	2.1	13.2
MIXED AL-SILICATE	0.2	0.8	2.9	12	7.1	4.4	27.3
FE SILICATE	0	0	0	0	0	0	0
CA SILICATE	0	0	0	0	0	0	0
CA ALUMINATE	0	0	0	0	0	0	0
PYRITE	0	0	0	0	0	0	0
PYRRHOTITE	0	0	0	0	0	0	0
OXIDIZED PYRRHOTITE	0	0	0	0	0	0	0
GYPSUM	0	0	0	0	0	0	0
BARITE	0	0	0	0	0	0	0
APATITE	0	0	0	0	0	0	0
CA AL-P	0	0	0	0	0	0	0
KCL	0	0	0	0	0	0	0
GYPSUM/BARITE	0	0	0	0	0	0	0
GYPSUM/AL-SILICATE	0	0	0	0	0	0	0
SI-RICH	0	0	0.2	0.7	1.1	1.8	3.9
CA-RICH	0	0	0	0	0	0	0
CA-SI RICH	0	0	0	0	0	0	0
UNCLASSIFIED	0.2	0.7	1.1	3.5	4.8	5.3	15.7
TOTALS	0.5	2.3	7.3	36	30.6	23.3	100

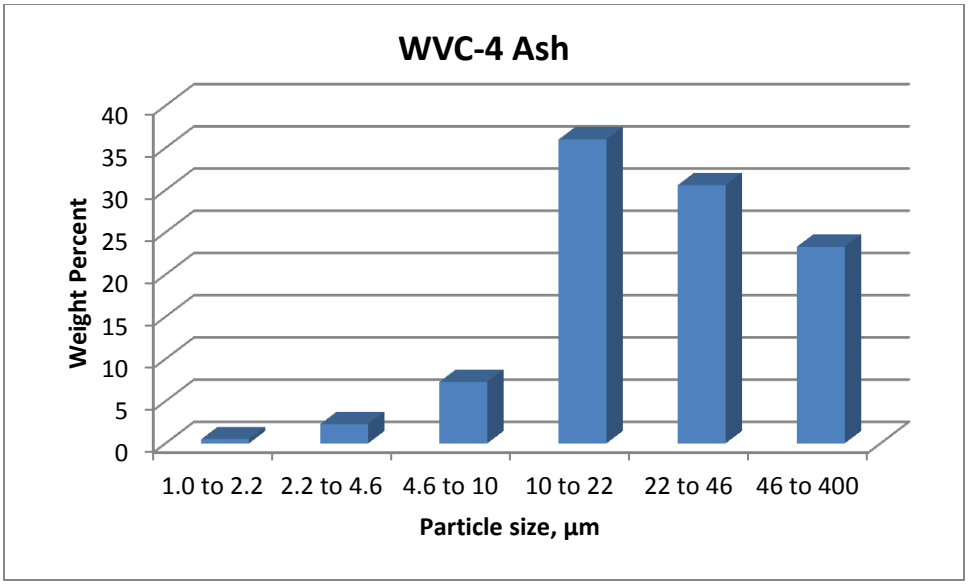

Figure 15. Distribution of the ash particles of WVC-4 Ash (MTI 13-167) by size.

Table 17 shows the elemental composition of the unclassified particles of WVC-4 ash as they are distributed throughout the size bins. Overall the unclassified particles consist of aluminum (35.2% as aluminum oxide), silicon (29.9% as silicon dioxide), titanium (7.7% as titanium dioxide), iron (6.5% as iron oxide), phosphorus (6.3% as phosphorus pentoxide), and calcium (5.6% as calcium oxide). The unclassified particles ranged from 1.1 to 108 µm in size with the 22 to 46 µm size as the most abundant. Figure 16 shows the distribution of the unclassified ash particles over the size ranges of the analysis.

Table 17. Elemental composition of the unclassified particles of WVC-4 ash. Results are expressed in weight percent equivalent oxide, normalized to 100%.

	Particle size, µm						
	1.0 to 2.2	2.2 to 4.6	4.6 to 10	10 to 22	22 to 46	46 to 400	Total
Na_2O	1.4	1.1	0.9	1.3	0.5	0.8	1.0
MgO	1.9	1.9	3.4	4.3	1.4	1.6	2.2
Al_2O_3	34.0	39.5	39.1	31.7	34.2	30.6	35.2
SiO_2	24.7	24.0	25.3	32.7	35.5	41.4	29.9
P_2O_5	5.9	7.0	7.0	6.0	5.9	5.8	6.3
SO_3	0.7	0.9	0.8	1.0	0.6	0.4	0.7
Cl	1.9	1.3	0.3	1.1	1.0	1.0	1.2
K_2O	1.7	1.8	2.0	2.9	4.2	3.6	2.7
CaO	7.6	8.1	5.8	5.1	3.1	3.1	5.6
Fe_2O_3	5.5	5.2	8.7	7.2	7.2	5.4	6.5
BaO	1.5	0.9	0.7	0.6	0.9	0.8	0.9
TiO_2	13.2	8.2	6.0	6.2	5.4	5.4	7.7
% of particles	20.7	20.7	12.8	11.5	24.9	9.5	100.0

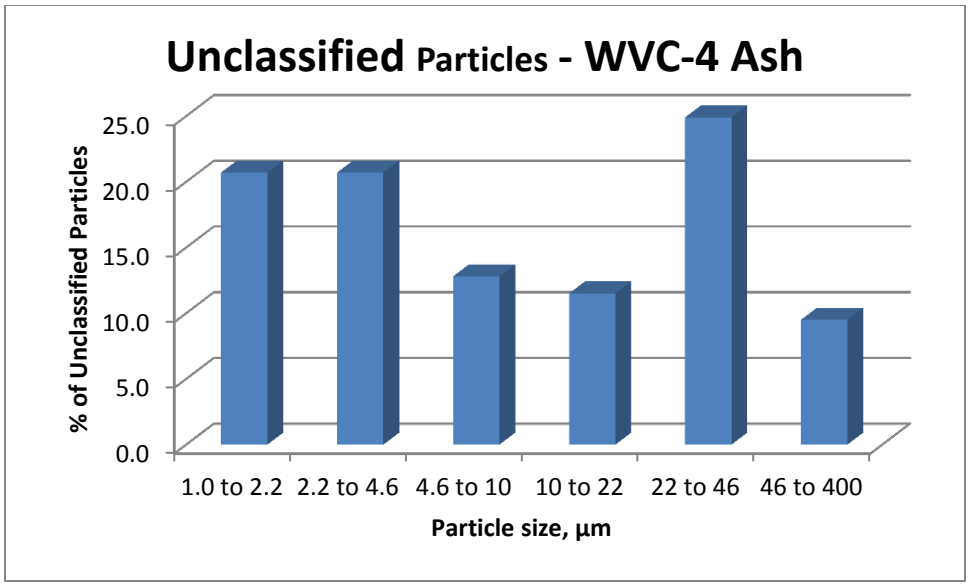

Figure 16. Distribution of the unclassified ash particles of WVC-4 Ash (MTI 13-167) by size.

APPENDIX

Table A-1. CCSEM mineral phases and chemical formulas.

MINERAL NAME	CHEMICAL FORMULA
QUARTZ	SiO_2
IRON OXIDE	FeO
PERICLASE	MgO
RUTILE	TiO_2
ALUMINA	Al_2O_3
CALCITE-DERIVED OXIDE	Oxide of $CaCO_3$
DOLOMITE-DERIVED OXIDE	Oxide of $(Ca,Mg)CO_3$
ANKERITE-DERIVED OXIDE	Oxide of $(Ca,Mg,Fe)CO_3$
KAOLINITE	$Al_2Si_2O_5(OH)_4$
MONTMORILLONITE	$(0.5Ca,Na)_{0.7}(Al,Mg,Fe)_4$-$(Si,Al)_8O_{20}(OH)_4$
K AL-SILICATE	$K_{1-1.5}Al_4Si_{7-6.5}Al_{1-1.5}O_{20}(OH)_4$
FE AL-SILICATE	
CA AL-SILICATE	
NA AL-SILICATE	
ALUMINOSILICATE	$Al_4Si_4O_{10}(OH)_8$
MIXED AL-SILICATE	
FE SILICATE	
CA SILICATE	$CaSiO_3$,Ca_2SiO_4
CA ALUMINATE	$Ca_3Al_2O_6$
PYRITE	FeS_2
PYRRHOTITE	$Fe_{1-x}S$
OXIDIZED PYRRHOTITE	
GYPSUM	$CaSO_4*2H_2O$
BARITE	$BaSO_4$
APATITE	$Ca_5F(PO_4)_3$
CA AL-P	
KCL	
GYPSUM/BARITE	
GYPSUM/AL-SILICATE	
SI-RICH	
CA-RICH	
CA-SI RICH	
UNCLASSIFIED	Does not fit within criteria for any above phase

Appendix C. EERC Report on Mercury Emissions during Test Campaign 4

This appendix contains the report (minus the lengthy appendices) from the Energy & Environmental Research Center on the mercury emissions sampling they did during the North Dakota Lignite test campaign 4.

DETERMINATION OF THE IMPACT OF A CO_2 MITIGATION TECHNOLOGY ON MERCURY EMISSIONS

Final Report

Prepared for:

Armand Levasseur

Alstom Power
2000 Day Hill Road
Windsor, CT 06095

Prepared by:

Dennis L. Laudal

Energy & Environmental Research Center
University of North Dakota
15 North 23rd Street, Stop 9018
Grand Forks, ND 58202-9018

2010-EERC-12-07 December 2010

EERC DISCLAIMER

LEGAL NOTICE This research report was prepared by the Energy & Environmental Research Center (EERC), an agency of the University of North Dakota, as an account of work sponsored by Alstom Power. Because of the research nature of the work performed, neither the EERC nor any of its employees makes any warranty, express or implied, or assumes any legal liability or responsibility for the accuracy, completeness, or usefulness of any information, apparatus, product, or process disclosed or represents that its use would not infringe privately owned rights. Reference herein to any specific commercial product, process, or service by trade name, trademark, manufacturer, or otherwise does not necessarily constitute or imply its endorsement or recommendation by the EERC.

TABLE OF CONTENTS

LIST OF FIGURES ii

LIST OF TABLES ii

1.0 INTRODUCTION 1

2.0 PROJECT OBJECTIVE 1

3.0 EQUIPMENT DESCRIPTION 2
- 3.1 Alstom Pilot Facilities 2
- 3.2 CMMs 2
- 3.3 Sampling Activities 3

4.0 RESULTS AND DISCUSSION 4

5.0 CONCLUSIONS 8

6.0 REFERENCE 8

PROJECT DATA ..... Appendix A
- CEM DATA FROM ALSTOM ..... Appendix A-1
- CMM DATA FROM EERC ..... Appendix A-2
- SORBENT TRAP AND OH DATA ..... Appendix A-3

EERC PROJECT LOG BOOKS ..... Appendix B

LIST OF FIGURES

1 Schematic of Alstom's BSF 2

2 CMM results at the combustion outlet location 6

3 CMM results at the secondary return air location 6

LIST OF TABLES

1 EERC Sampling Activities 4

2 Description of the Conditions That Occurred During the Test 4

3 Tests Conducted by Alstom 5

4 Major Downtimes for the CMMs 5

5 CMM Results for Each of the Alstom Tests 7

6 Sorbent Trap Results at the Combustor Outlet Sampling Location 10

7 Sorbent Trap Results at the Secondary Return Air Sampling Location 10

8 Comparison of Mercury Speciation Results for Speciating Sorbent Traps and CMMs 11

9 Ontario Hydro Mercury Sampling Results 11

DETERMINATION OF THE IMPACT OF A CO_2 MITIGATION TECHNOLOGY ON MERCURY EMISSIONS

1.0 INTRODUCTION

Oxycombustion is a promising near-term technology for CO_2 capture and sequestration from coal-fired power plants. Oxycombustion technology builds upon proven coal-based power generation and is an evolutionary development. The basic concept of oxycombustion ("oxyfuel") is to replace combustion air with a mixture of oxygen and recycled flue gas, thereby creating a high-CO_2-content flue gas stream that can be more simply processed for sequestration or high-purity product. The technology can be applied to both new and existing plants and has competitive economics with other CO_2 capture technologies.

Alstom Power Inc. (Alstom) is conducting tests at its tangentially fired 15-MW boiler simulation facility (BSF) at its Boiler Laboratories in Windsor, Connecticut, to develop and test oxyfuel tangentially fired technology for retrofit to existing boilers.

The overall objectives of the current Alstom project are to:

- Design and develop an innovative oxyfuel system for existing tangentially fired boiler units that minimizes overall capital investment and operating costs.

- Evaluate performance of oxyfuel boiler systems in pilot-scale tests at Alstom's 15-MW_{th} tangentially fired BSF.

- Address technical gaps for design of oxyfuel commercial utility boilers by focused testing in the BSF and improvement of engineering and CFD (computational fluid dynamics) tools.

However, a question that has been discussed is, What impact does oxycombustion have on mercury both in terms of speciation and total emissions? Therefore, Alstom and the Energy & Environmental Research Center (EERC) conducted tests at the BSF facility using continuous mercury monitors (CMMs), sorbent traps, and the Ontario Hydro (OH) mercury speciation method to measure both the total and speciated mercury across the system when a North Dakota lignite coal is fired.

2.0 PROJECT OBJECTIVE

The overall objective of the proposed work is to provide data as to mercury speciation and removal across a fabric filter when a test is being conducting using oxycombustion.

3.0 EQUIPMENT DESCRIPTION

3.1 Alstom Pilot Facilities

Alstom's 15-MW tangentially fired BSF at its Boiler Laboratories in Windsor has a long successful history of supporting development and commercialization of Alstom's firing systems and other combustion technologies. More detailed descriptions of these facilities have been previously presented (1). A schematic of system is shown in Figure 1. In general because of its scale and design, the BSF provides an excellent experimental tool to replicate tangential firing conditions in utility boilers and isolate variables to study behavior.

3.2 CMMs

Because the system was operated in an oxycombustion mode, it was not possible to use CMMs that utilize the standard wet conversion system (the NaOH removes CO_2). Therefore, the EERC installed monitors using dilution systems to minimize the effect of CO_2. Also, to compare results, both a dry thermal conversion system and a new type of wet conversion system were simultaneously operated at one of the sampling locations. All CMMs used for this test were manufactured by Tekran and measure mercury using cold-vapor atomic fluorescence spectroscopy. A complete description of the Tekran CMM can be found at Tekran's Web site at www.tekran.com. Therefore a detailed description will not be repeated in this report.

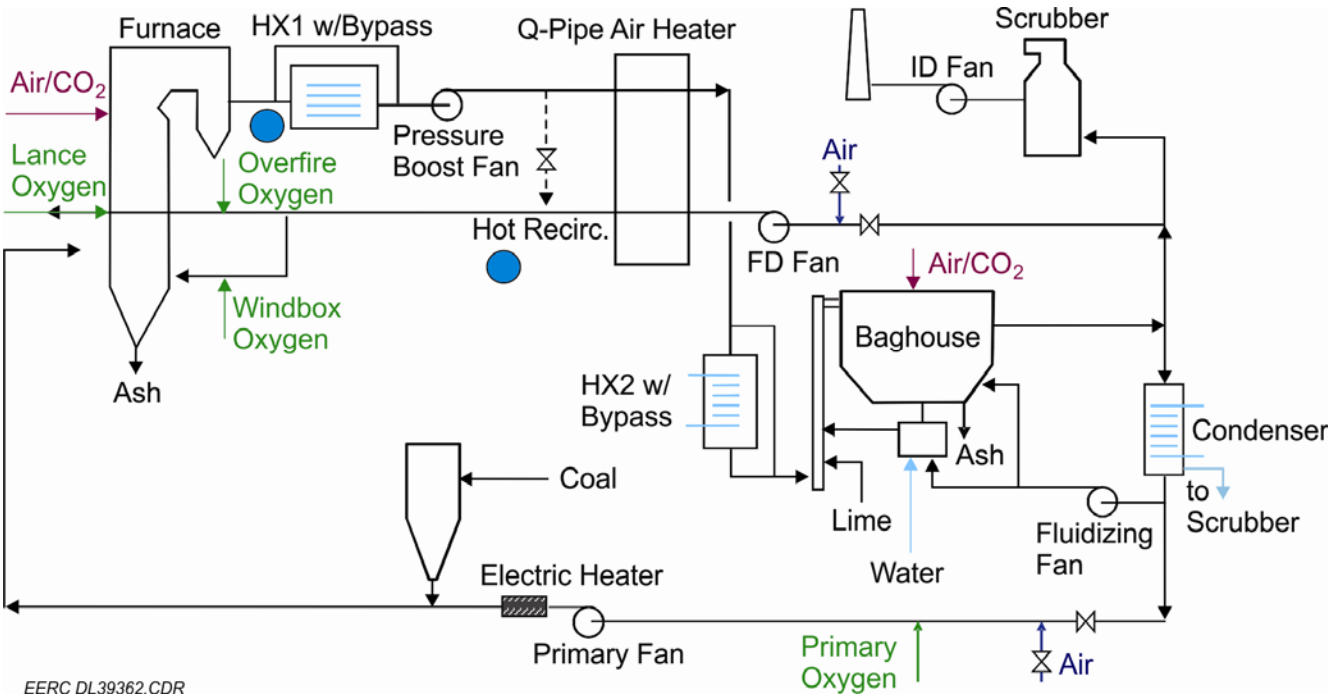

Figure 1. Schematic of Alstom's BSF (sampling locations are shown by the blue circles).

To use the CMMs for oxyfuel, we adjusted the data for the higher specific gravity of the flue gas. The orifice and mass flow controllers are designed for a specific gravity of 1.0, as is the case for the flue gas generated under standard air-fired combustion systems. An example of this calculation is shown below:

Assuming the following flue gas concentrations:

Gas	Flue Gas Conc., %	Spec. Grav. Gas	Flue Gas Spec. Grav.
O_2	2.92	1.1053	0.0323
CO_2	57.70	1.5300	0.8828
H_2O	30.15	0.6218	0.1875
SO_2	0.0040	2.2640	0.0001
NO_x	0.0003	1.0370	0.0000
N_2	9.23	0.9675	0.0893

The specific gravity of the flue gas is then 1.1919; the factor is then calculated by the equation:

$$F = \sqrt{\frac{1}{y_i G_i}} \qquad \text{[Eq. 1]}$$

For the example above, the F value is 0.9160. Because the volume of flue gas is lower than indicated by the CMM, the results are low by a factor of 0.9160.

3.3 Sampling Activities

Three different mercury-sampling methods were utilized for this test program, as there is a concern as to how accurately the various methods would measure mercury under oxyfuel combustion conditions. As was shown in Figure 1, all sampling was done at two locations: the first at the combustor outlet and the second at the secondary air return downstream of the baghouse. The secondary air return is only operated during oxycombustion.

At the combustion outlet location, the modified wet CMM was used, and multiple sorbent trap samples (1 was a speciation sorbent trap) were taken. In addition, three OH method samples were taken at this location. At the secondary return air location, two CMMs were installed. One had a dry thermal dilution conversion system and the other a modified wet system. At this location, two speciating sorbent trap samples and an OH method sample were taken as well. Table 1 shows the sampling activities for each location, and Tables 2 and 3 list the test conditions. The CMMs were operated continuously during the entire test period, with several exceptions as shown in Table 4.

Table 1. EERC Sampling Activities

Sorbent Traps					Ontario Hydro Sampling				
Date	Time	Duration	Sample Location	Test Cond.	Date	Time	Duration	Sample Location	Test Cond.
10/4/10	12:00	15	Comb. outlet	1	10/5/10	12:33	90	Comb. outlet	1
10/4/10	20:00	30	Comb. outlet	1	10/7/10	12:30	60	Sec. ret. air	1
10/5/10	7:21	16	Comb. outlet	2	10/8/10	7:25	60	Comb. outlet	1
10/6/10	11:59	15	Comb. outlet	4	10/8/10	14:15	60	Comb. outlet	1/2[1]
10/7/10	0:01	20	Comb. outlet	1					
10/7/10[2]	0:00	15	Sec. return air	1					
10/7/10[2]	0:35	15	Sec. return air	1					
10/7/10	0:41	15	Comb. outlet	1					
10/7/10	1:10	17	Comb. outlet	2					
10/7/10	9:50	20	Comb. outlet	2					
10/7/10	19:40	15	Sec. ret. air	2/1[3]					
10/7/10	21:42	20	Comb. outlet	1/2[4]					
10/8/10	9:02	20	Comb. outlet	1					
10/8/10	9:55	20	Comb. outlet	2					
10/8/10	13:00	25	Comb. outlet	1					
10/8/10	20:44	20	Comb. outlet	2					

[1] 7 min at Test Condition 1 and 43 min at Test Condition 2.
[2] Mercury speciation sorbent trap.
[3] 10 min at Test Condition 2 and 5 min at Test Condition 1.
[4] 9 min at Test Condition 2 and 11 min at Test Condition 1.

Table 2. Description of the Conditions That Occurred During the Test

Test Condition	Description
1	Times of steady-state boiler operation.
2	Times when the boiler was operating properly but conditions were being varied.
3	Times when the boiler was operating, but not operating properly because of equipment malfunctions.
4	Times when the boiler was operating on natural gas.
5	Times when the boiler was operating on gas/coal mixture.
6	Times when the boiler was not in operation.

4.0 RESULTS AND DISCUSSION

The CMM results are shown graphically in Figures 2 and 3. The CMM results for each of the Alstom tests are presented in Table 5. As can be seen in Table 5 the CMM results were very consistent for each test at both sampling locations. As expected, the mercury generated at the combustor outlet (~900°F) when a North Dakota lignite was fired was < 90% Hg^0 for all tests. This was true whether the combustor was air- or oxygen-fired. With the exception of one test (101), this changed quite dramatically at the secondary return air location (~200°F). Sampling

was only done at this location when oxyfuel tests were being conducted. The average % Hg^0 for

Table 3. Tests Conducted by Alstom

Test No.	Start	End	Oxidant	Fuel
077	10/4/10 11:20	10/4/10 12:48	Air-fired	ND lignite
078	10/4/10 14:40	10/4/10 16:08	Air-fired	ND lignite
079	10/4/10 18:20	10/4/10 19:00	Air-fired	ND lignite
79A	10/4/10 19:20	10/4/10 20:25	Air-fired	ND lignite
080	10/4/10 21:00	10/4/10 22:55	Air-fired	ND lignite
081	10/4/10 23:47	10/5/10 1:01	Air-fired	ND lignite
81B	10/5/10 1:21	10/5/10 1:49	Air-fired	ND lignite
	10/5/10 2:00	10/5/10 7:00	Transition	ND lignite
082	10/5/10 7:00	10/5/10 7:15	Oxy-fired	ND lignite
83A	10/5/10 10:30	10/5/10 15:10	Air-fired	ND lignite
83B	10/5/10 15:11	10/5/10 16:56	Air-fired	ND lignite
83C	10/5/10 22:25	10/6/10 1:00	Air-fired	ND lignite
83D	10/6/10 2:25	10/6/10 6:00	Air-fired	ND lignite
83E	10/6/10 7:05	10/6/10 8:30	Air-fired	ND lignite
084	10/6/10 9:58	10/6/10 10:16	Air-fired	ND lignite
085	10/6/10 10:48	10/6/10 11:23	Air-fired	ND lignite
086	10/6/10 17:15	10/6/10 17:20	Air-fired	ND lignite
087	10/6/10 22:40	10/7/10 0:57	Oxy-fired	ND lignite
088	10/7/10 1:28	10/7/10 2:50	Oxy-fired	ND lignite
089	10/7/10 3:50	10/7/10 6:20	Oxy-fired	ND lignite
090	10/7/10 7:43	10/7/10 8:17	Oxy-fired	ND lignite
091	10/7/10 12:20	10/7/10 13:30	Oxy-fired	ND lignite
092	10/7/10 18:23	10/7/10 19:18	Oxy-fired	ND lignite
093	10/7/10 19:50	10/7/10 21:51	Oxy-fired	ND lignite
094	10/7/10 22:25	10/7/10 22:45	Oxy-fired	ND lignite
095	10/7/10 23:12	10/7/10 23:37	Oxy-fired	ND lignite
096	10/8/10 0:15	10/8/10 1:33	Oxy-fired	ND lignite
097	10/8/10 2:25	10/8/10 3:20	Oxy-fired	ND lignite
98A	10/8/10 4:16	10/8/10 9:30	Oxy-fired	ND lignite
98B	10/8/10 11:00	10/8/10 14:20	Oxy-fired	ND lignite
099	10/8/10 16:50	10/8/10 18:09	Oxy-fired	ND lignite
100	10/8/10 18:50	10/8/10 20:14	Transition	ND lignite
101	10/9/10 0:29	10/9/10 3:27	Oxy-fired	ND lignite

Table 4. Major Downtimes for the CMMs

Secondary Return Air Location			Combustion Outlet Location		
Start	End	Reason	Start	End	Reason
10/4/10 10:30	10/4/10 16:00	No return air	10/4/10 10:30	10/5/10 11:00	Only measured elemental Hg (had to ship additional regents for conversion system to measure total Hg)
10/5/10 9:20	10/6/10 20:00	No return air	10/7/10 03:47	10/7/10 07:00	Air supply to the CMM has been shut off, shutting down the CMM vacuum pump.
10/7/10	10/7/10	BSF down	10/7/10	10/7/10	BSF down

14:00 18:00	14:00 18:00

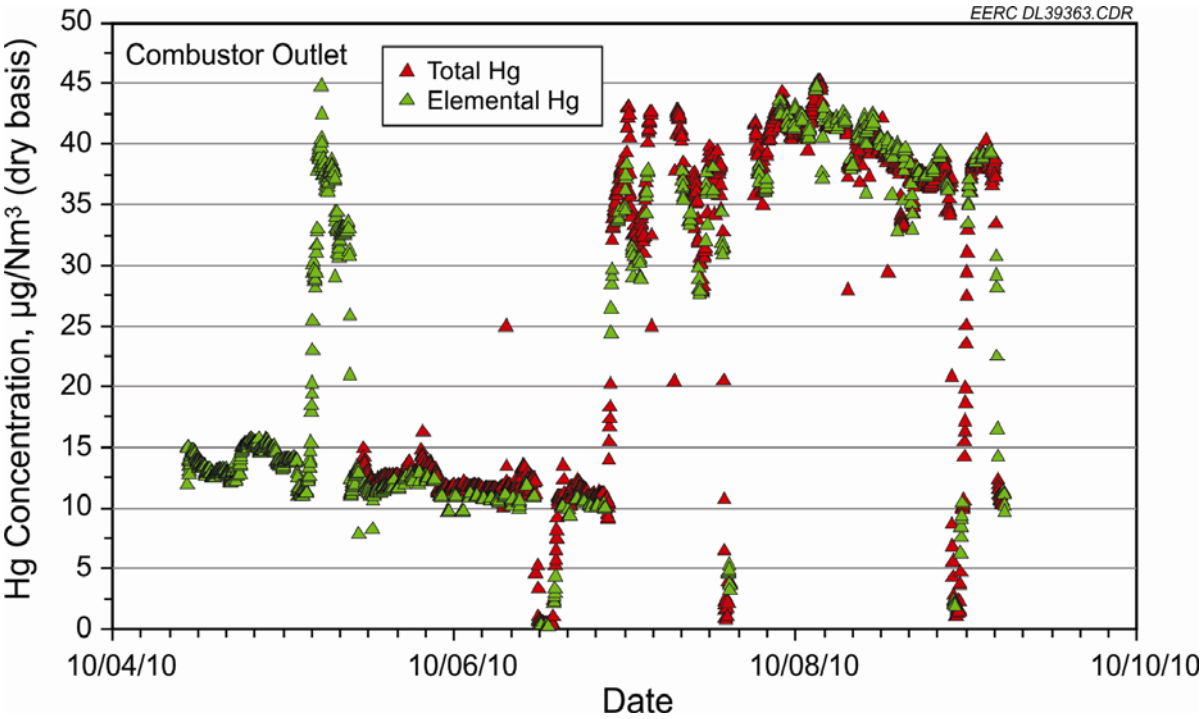

Figure 2. CMM results at the combustion outlet location.

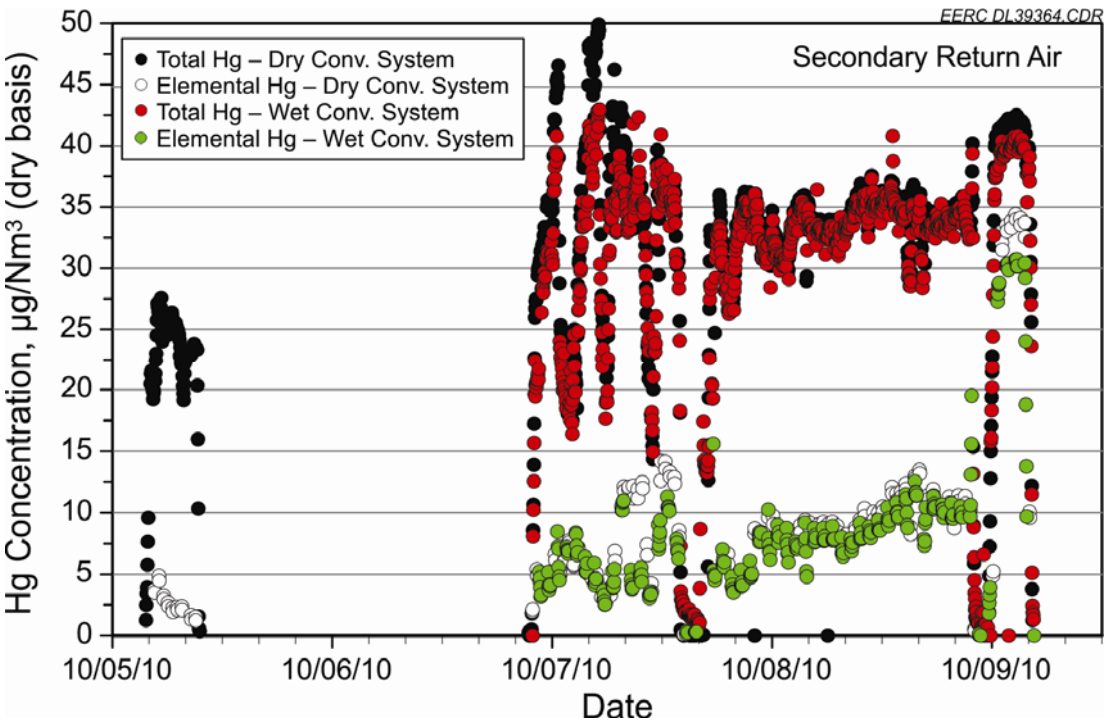

Figure 3. CMM results at the secondary return air location.

Table 5. CMM Results for Each of the Alstom Tests

	Combustion Outlet, µg/Nm^3				Secondary Return Air, µg/Nm^3			
Test No.	Hg (total)	Std. Dev. Hg (total)	Hg^0	Std. Dev. Hg^0	Hg (total)	Std. Dev. Hg (total)	Hg^0	Std. Dev. Hg^0
77	15.09*	–	13.82	0.40				
78	14.13*	–	12.94	0.13				
79	16.43*	–	15.04	0.12				
79A	16.70*	–	15.29	0.17				
80	16.24*	–	14.87	0.28				
81	15.03*	–	13.76	0.24				
81B	15.16*	–	13.88	0.14				
–	Transition							
82	40.94*	–	37.49	0.35	24.84	0.30	2.19	0.16
83A	12.63	0.59	11.40	0.84				
83B	12.47	0.11	11.70	0.20				
83C	11.63	0.10	10.27	0.65				
83D	11.54	0.14	10.77	0.12				
83E	11.69	0.50	10.66	0.38				
84	13.04	0.32	11.87	0.08				
85	11.90	0.47	10.89	0.08				
86	11.54	0.14	10.74	–				
87	37.65	2.66	35.14	1.64	33.69	5.49	4.98	1.28
88	32.60	1.23	29.90	0.73	20.42	2.52	7.00	0.73
89	–	–	–	–	35.69	9.85	4.00	1.04
90	40.64	1.10	36.40	0.84	36.82	2.41	11.42	0.58
91	37.68	1.10	36.71	1.18	35.85	1.32	11.83	1.50
92	38.85	1.62	37.62	0.44	29.64	2.15	6.17	0.51
93	41.57	1.06	40.18	3.43	33.80	2.14	4.70	0.56
94	42.49	0.46	41.48	–	33.05	0.68	8.00	0.33
95	40.97	0.39	–	–	31.36	0.73	9.03	1.07
96	41.07	0.33	42.28	0.22	31.17	0.67	8.21	0.44
97	44.15	0.85	44.65	0.19	34.72	0.72	7.68	0.65
98A	40.49	1.94	40.89	1.44	33.46	1.02	7.96	0.71
98B	40.32	7.08	40.87	6.38	35.60	0.87	9.81	0.95
99	37.34	0.35	37.65	0.22	33.77	0.56	10.93	0.56
100	Transition							
101	38.27	0.65	39.00	0.32	40.81	1.02	31.37	2.68

* Only Hg^0 was measured; Hg (total) is based on average % Hg^0 (92%) of later tests (see Table 4).

all the tests was 23.6%. The one exception was Test 101, where the Hg^0 was 76.9%. The reason

for this is unknown. The other obvious factor is that the mercury concentration at the combustor outlet is about 3 times greater than when oxyfuel is fired compared to air-fired.

As shown in Table 1, limited data were also taken using sorbent traps and the OH method. These results are shown in Tables 6–9. Although the comparison of the sorbent traps and OH methods to the CMM show some differences between the sampling methods, there is a reasonable agreement, and all methods show the same trends.

The complete results for all of the sampling methods are found in Appendix A, and a copy of the CMM log book is found in Appendix B. Both appendices can be found on the enclosed CD.

As was stated previously, two different CMMs were used at the secondary return air location. The first one used a modified wet conversion system, and the second was Tekran's standard dry dilution thermal convertor. There was very little difference between the total mercury concentrations between the two instruments. The average relative difference was only 3.75%. However, there was slight bias as the Tekran with the thermal dilution converter consistently gave values slightly higher than the instrument with the wet converter system. Although the speciation data were generated on a different time scale for the two instruments, there does not appear to be any significant difference in the measured Hg^0 concentrations between the two CMMs.

5.0 CONCLUSIONS

The following conclusions can be drawn from the data:

- The mercury speciation at the combustor outlet location was primarily Hg^0, as would be expected as this was North Dakota lignite and the temperature at this location was ~900°F. This was true whether the combustor was fired with air or oxygen.

- When the combustor was fired using the oxyfuel mode, the mercury concentration at the combustor outlet was much higher than when air-fired.

- The mercury speciation in the secondary return air was primarily oxidized mercury.

- The results using the CMM were very consistent throughout the test.

- Although there were some differences between the mercury measurement methods, the comparisons were within reason.

- There was very little difference in the mercury concentrations measured using the wet vs. the dry conversion systems.

6.0 REFERENCE

1. Richards, G.; Towle, D.; Lewis, R.; Connolly, K.; Hellewell, T. Development of an Enhanced Combustion Low-NO_x Pulverized Coal Burner. Presented at the 31st International Technical Conference on Coal Utilization & Fuel Systems, Clearwater, FL, May 21–25, 2006.

Table 6. Sorbent Trap Results at the Combustor Outlet Sampling Location

Date:	10/4/10	10/4/10	10/5/10	10/6/10	10/7/10	10/7/10	10/7/10	10/8/10	10/8/10	10/8/10*	10/8/10
Start Time:	12:00	20:00	7:21	11:59	1:10	0:41	21:42	9:02	9:55	13:00	20:44
Duration, min	15	30	16	15	17	15	20	20	20	25	20
Vm, liters, dry	12.000	30.000	16.000	7.500	8.650	7.500	20.375	10.050	10.000	10.275	10.300
P_b in Hg	30.06	30.00	29.95	29.41	29.47	29.47	29.65	29.72	29.72	29.47	29.68
Elev corr., ft	50	50	50	50	50	50	50	50	50	50	50
T_m, °F	73	86	71	62	60	71	66	62	76	97	73
Cm	0.9740	0.9740	0.9740	0.9740	0.9740	0.9740	0.9740	0.9740	0.9740	0.9740	0.9740
Hg Collected, ng	195.7	495.9	647.1	494	374.1	363.8	985.4	538.4	468.2	458.6	516.5
Vcorr, N liters, dry	11.613	28.285	15.486	7.251	8.412	7.142	19.708	9.818	9.514	9.328	9.842
Hg, µg/Nm^3, (dry)	16.85	17.53	41.79	68.13	44.47	50.94	50.00	54.84	49.21	49.16	52.48
CMM, µg/Nm^3, (dry)	14.87	16.56	33.52	–	32.63	35.63	42.43	41.00	40.47	39.14	37.79

* Speciating sorbent traps used.

Table 7. Sorbent Trap Results at the Secondary Return Air Sampling Location

Date:	10/7/10	10/7/10*	10/7/10*
Time:	0:00	0:35	19:40
Duration, min	15	15	15
Vm, liters, dry	16.000	15.500	16.000
P_b in Hg	29.47	29.47	29.62
Elev corr., ft	50	50	50
T_m, °F	72	80	66
Cm	0.9900	0.9900	0.9900
Hg Collected, ng	807.3	692.2	541.4
Vcorr,, N liters (dry)	15.458	14.753	15.714
Hg, µg/Nm^3 (dry)	52.22	46.92	34.45
CMM, µg/Nm^3 (dry)	36.08	39.49	37.30

* Speciating sorbent traps used.

Table 8. Comparison of Mercury Speciation Results for Speciating Sorbent Traps and CMMs

Sample Location:	Combustor Out		Secondary Return Air		Secondary Return Air	
Sample: Date/Time:	10/8/10 13:00		10/7/10 00:00		10/7/10 00:35	
Sampling Method:	Speciation Trap	CMM	Speciation Trap	CMM	Speciation Trap	CMM
Hg^0, µg/Nm^3	42.57	38.93	17.16	3.13	2.63	0.89
Hg^{2+}, µg/Nm^3	6.59	0.21	35.06	36.36	31.82	36.41
Total Hg, µg/Nm^3	49.16	39.14	46.92	39.49	34.45	37.30
Hg^0, %	86.6	99.5	32.9	7.9	7.6	2.3
Hg^{2+}, %	13.4	0.5	68.1	92.1	92.4	97.7

Table 9. Ontario Hydro Mercury Sampling Results

						Hg^P, µg/Nm^3	Hg^{2+}, µg/Nm^3			Hg^0, µg/Nm^3				
Date	Start Time	Sample Location	Duration, min	H_2O %	Dust Loading, grains/scf	Filter Conc.	Probe Conc.	KCl Conc.	Total Hg(2+)	H_2O_2 Conc.	$KMnO_4$ Conc.	Total Conc.	Total Hg Conc. µg/Nm^3	Hg^0, %
10/5/2010	12:33	Furnace Outlet	90	9.6	0.5396	0.006	0.74	2.88	3.63	0.25	4.29	4.53	8.17	52.47
10/7/2010	12:30	Sec. Return Air	60	29.8	0.0003	0.003	0.19	49.01	49.20	0.82	12.80	13.62	62.82	20.37
10/8/2010	7:25	Furnace Outlet	60	30.1	1.2741	0.015	0.20	7.60	7.80	2.62	37.66	40.28	48.08	78.32
10/8/2010	14:15	Furnace Outlet	60	29.7	1.0968	0.013	0.14	3.12	3.26	4.14	37.54	41.68	44.94	83.53

Appendix D. Deposition Probe Corrosion Report

This appendix contains a report by Alstom's Materials Testing Laboratory discussing the surface deposits and corrosion products from the deposition probes.

Technical Report

TTTM Materials Testing
1201 Riverfront Parkway
Chattanooga, TN 37402, USA
Tel.: (423) 826-1145
Fax: (423) 752-2825

Project Manager: Armand Levasseur

Project Name: DOE-Oxy fired Coupons

Document Title: OD Deposit Analysis of Oxy-fired Corrosion Probes

Lab. No.: 14F198

Date of Issue: 07/23/2014

Author(s): Leo Antony

Distribution: Kurt Johnson

Keywords: Oxy-fired coupons, OD deposits

Reviewed by: Kurt Johnson

1.0 INTRODUCTION

TTTM analyzed the surface deposits and corrosion products (if any) of selected samples from in-furnace probes exposed during oxy-fired testing in Alstom 15 MW Boiler Simulation Facility. The probes were identified in the laboratory as shown below:

Table 1. List of Probe Samples

	Sample ID		
DOE Oxy IL High S&Cl - BSF			
11/6/2012	Probe 1	Oxy-fired	Sample 4
11/6/2012	Probe 3	Oxy-fired	Sample 5
DOE Oxy Schwarze Pumpe - BSF			
7/14/2011	Probe 1	Air-fired	Sample 6
7/14/2011	Probe 3	Air-fired	Sample 7
7/18/2011	Probe 1	Oxy-fired	Sample 8
7/18/2011	Probe 3	Oxy-fired	Sample 9

The deposits were semi-quantitatively analyzed using a scanning electron microscope equipped with an energy dispersive spectroscope (EDS). Where sufficiently thick, the deposits were scraped from the probe surface and analyzed collectively. All the probe samples were mounted metallographically and then the OD corrosion products (if any) were analyzed and their thicknesses were measured. The results of the analyses are presented in Figures 1 through 12.

2.0 RESULTS

The maximum measured corrosion or the total metal loss observed on the OD surface of the probe samples are listed below in Table 2.

The total metal loss (µm) = Depth of internal attack/penetration (µm) + ½ Corrosion Product Thickness, µm (if any)

Table 2: Total Metal Loss for the Probe Samples

Sample ID			Total Metal Loss (TML), Micrometers
DOE Oxy IL High S&Cl - BSF			
11/6/2012	Probe 1	Sample 4	55
11/6/2012	Probe 3	Sample 5	12
DOE Oxy Schwarze Pumpe - BSF			
7/14/2011	Probe 1	Sample 6	40
7/14/2011	Probe 3	Sample 7	45
7/18/2011	Probe 1	Sample 8	36
7/18/2011	Probe 3	Sample 9	15

Superficial corrosion was detected in samples 5 and 9. Other samples showed corrosion attack in the range 36 to 55 micrometers.

The corrosion product for all the probe samples contained predominantly iron oxides with some sulfides.

Typically in all samples the OD deposits were representative of a fly ash and contained elements such as Na, Mg, Al, Si, K, Ca, Fe, and O_2 as seen in all samples.

Alstom Power, Inc.
TTT-M Materials Testing
1201 Riverfront Parkway
Chattanooga, TN 37402

Telephone: 423-826-1145
Fax: 423-752-2825
Email: leo.antony@power.alstom.com

Significant amounts of silica were present in the ash deposits of samples 4 and 5.

Sulfur presence in the deposits was detected in all probe samples.

.

Sample 4 showed the most total metal loss ~55 micrometers compared to other tested probe samples.

Alstom Power, Inc.
TTT-M Materials Testing
1201 Riverfront Parkway
Chattanooga, TN 37402

Telephone: 423-826-1145
Fax: 423-752-2825
Email: leo.antony@power.alstom.com

OD Deposit Analysis

Element	Weight %	Atomic %
O K	41.87	60.74
Na K	6.10	6.16
Mg K	0.33	0.32
Al K	6.04	5.20
Si K	12.03	9.94
S K	6.59	4.77
K K	6.25	3.71
Ca K	3.14	1.82
Ti K	0.35	0.17
Fe K	17.30	7.19

Wt%

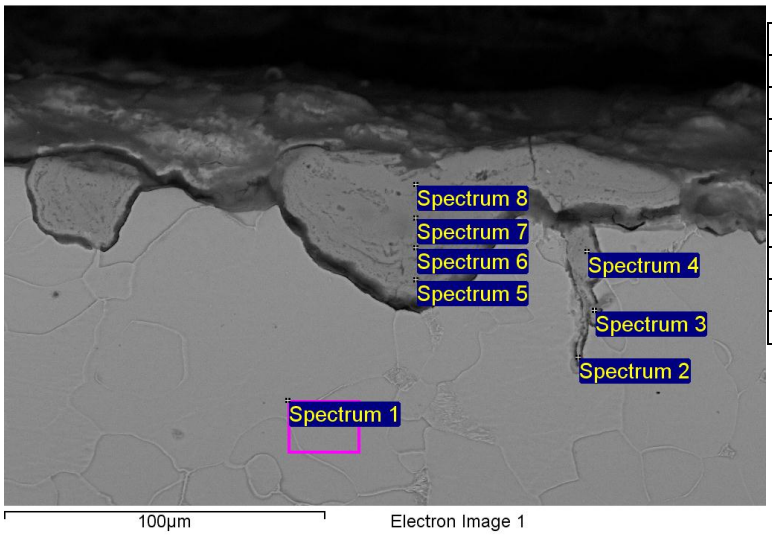

Spectrum	O	S	Mn	Fe
Spectrum 1				100.00
Spectrum 2	3.24			96.76
Spectrum 3	3.65	2.88		93.47
Spectrum 4	11.20	4.31		84.49
Spectrum 5	15.09	3.19		81.72
Spectrum 6	15.06	3.98	1.01	79.95
Spectrum 7	14.68	3.71		81.61
Spectrum 8	15.93	3.92		80.15

Figure 1. The semi-quantitative results of the SEM-EDS analysis made of the deposits on the probe (Top) and the OD corrosion product (Bottom) from Sample 4 identified as DOE Oxy IL High S&CI-BSF-11-6-2012-Probe#1 are shown.

Alstom Power, Inc.
TTT-M Materials Testing
1201 Riverfront Parkway
Chattanooga, TN 37402

Telephone: 423-826-1145
Fax: 423-752-2825
Email: leo.antony@power.alstom.com

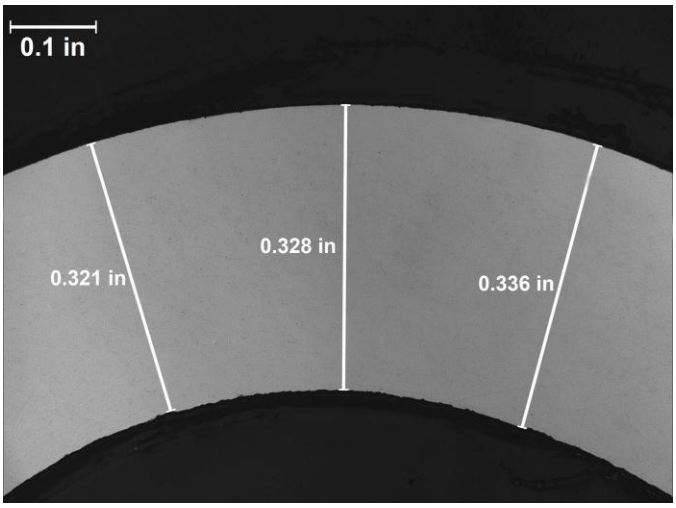

Sample 4

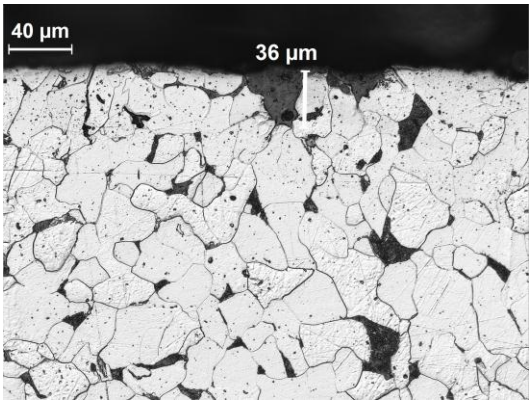

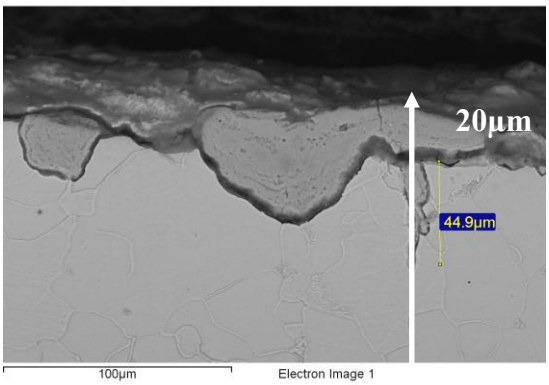

Sample 4

Figure 2. Documenting the typical thickness of the probe and the OD corrosion attack on sample 4 (DOE Oxy IL High S&CI-BSF-11-6-2012-Probe#1). Along the OD surface, corrosion product thickness of ~20 micrometers and a maximum internal penetration attack of ~45 micrometers were observed.

Alstom Power, Inc.
TTT-M Materials Testing
1201 Riverfront Parkway
Chattanooga, TN 37402

Telephone: 423-826-1145
Fax: 423-752-2825
Email: leo.antony@power.alstom.com

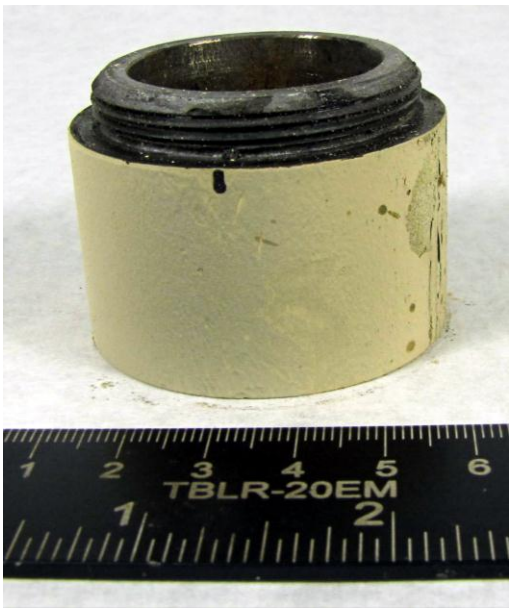

OD Deposit Analysis

Element	Weight %	Atomic %
O K	52.60	68.69
Na K	0.77	0.70
Mg K	0.61	0.53
Al K	9.78	7.58
Si K	18.66	13.88
S K	4.12	2.68
K K	1.65	0.88
Ca K	4.06	2.12
Ti K	0.79	0.34
Fe K	6.96	2.60

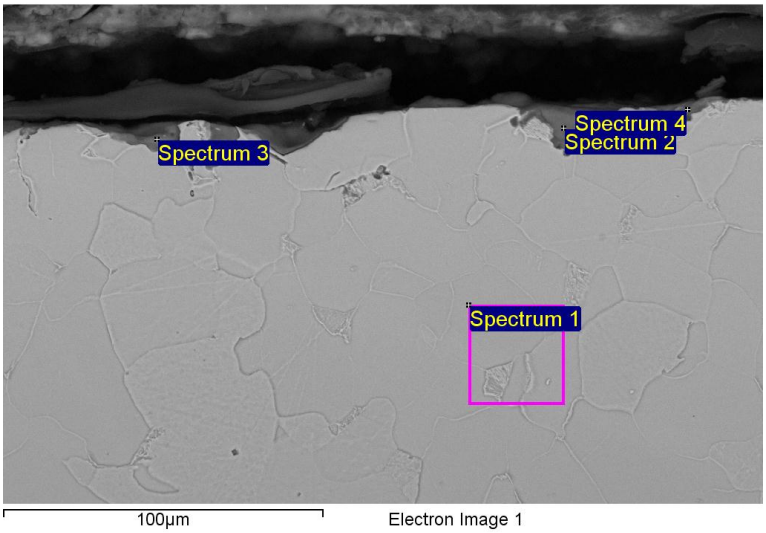

Wt%

Spectrum	O	S	Fe
Spectrum 1			100.00
Spectrum 2	25.04		74.96
Spectrum 3	29.36	2.12	68.52
Spectrum 4	23.72		76.28

Figure 3. The semi-quantitative results of the SEM-EDS analysis made of the deposits on the probe (Top) and the OD corrosion product (Bottom) from Sample 5 identified as (DOE Oxy IL High S&CI-BSF-11-6-2012-Probe#3) are shown.

Alstom Power, Inc.
TTT-M Materials Testing
1201 Riverfront Parkway
Chattanooga, TN 37402

Telephone: 423-826-1145
Fax: 423-752-2825
Email: leo.antony@power.alstom.com

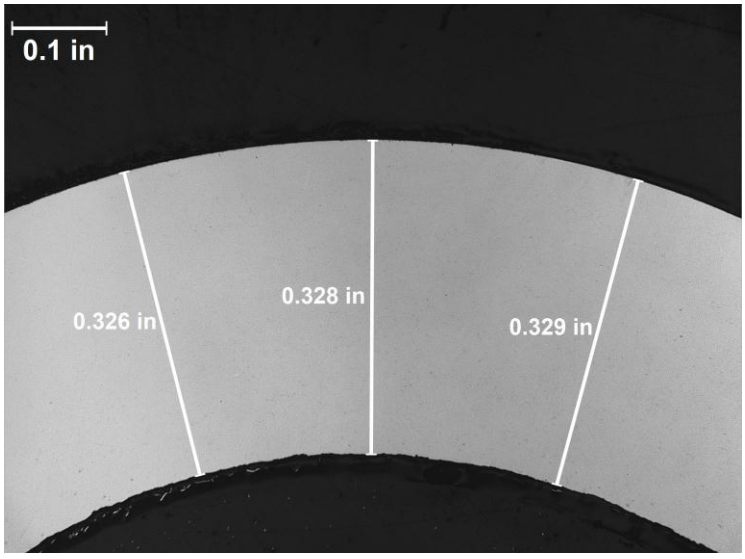

Sample 5

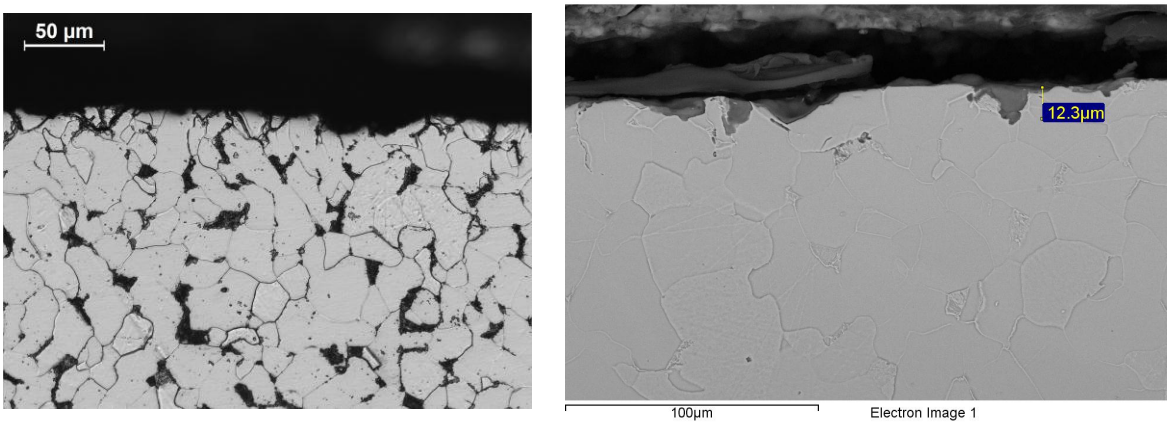

Sample 5

Figure 4. Documenting the typical thickness of the probe and the condition of the OD surface on sample 5 (DOE Oxy IL High S&CI-BSF-11-6-2012-Probe#3). Superficial corrosion (~12 micrometers) along the OD surface was seen.

Alstom Power, Inc.
TTT-M Materials Testing
1201 Riverfront Parkway
Chattanooga, TN 37402

Telephone: 423-826-1145
Fax: 423-752-2825
Email: leo.antony@power.alstom.com

OD Deposit Analysis

Element	Weight%	Atomic%
O K	43.24	64.24
Na K	1.37	1.41
Mg K	3.11	3.04
Al K	1.19	1.05
Si K	3.83	3.24
S K	13.01	9.65
K K	2.03	1.24
Ca K	14.41	8.55
Fe K	17.81	7.58

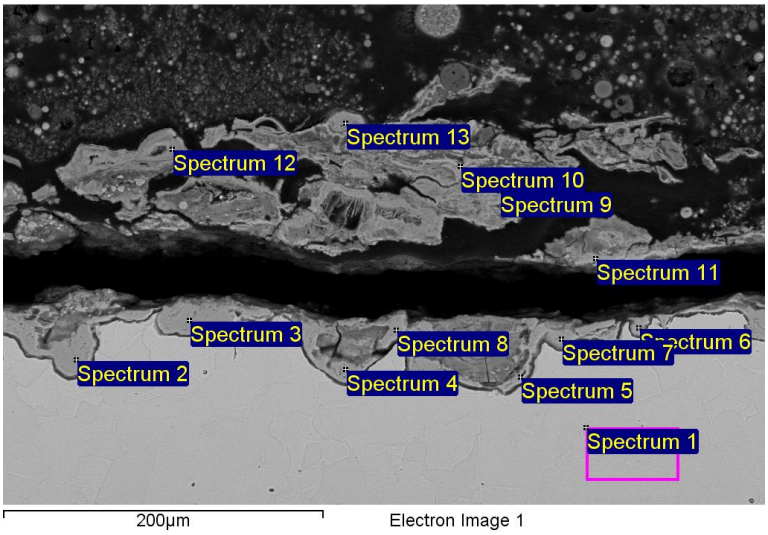

Wt%

Spectrum	O	S	Mn	Fe
Spectrum 1				100.00
Spectrum 2	16.12	8.10	0.67	75.11
Spectrum 3	18.21	5.32		76.47
Spectrum 4	17.82	5.99		76.19
Spectrum 5	8.60			91.40
Spectrum 6	10.29	3.13		86.58
Spectrum 7	16.17	4.54		79.29
Spectrum 8	14.09	5.64	0.68	79.60
Spectrum 9	19.95			80.05
Spectrum 10	21.35			78.65
Spectrum 11	18.45	3.29		78.26
Spectrum 12	19.23			80.77
Spectrum 13	21.44			78.56

Figure 5. The semi-quantitative results of the SEM-EDS analysis made of the deposits on the probe and the OD corrosion product from sample 6 identified as DOE Oxy Schwarze Pumpe-BSF-7-14-2011-Probe#1 are shown.

Alstom Power, Inc.
TTT-M Materials Testing
1201 Riverfront Parkway
Chattanooga, TN 37402
Telephone: 423-826-1145
Fax: 423-752-2825
Email: leo.antony@power.alstom.com

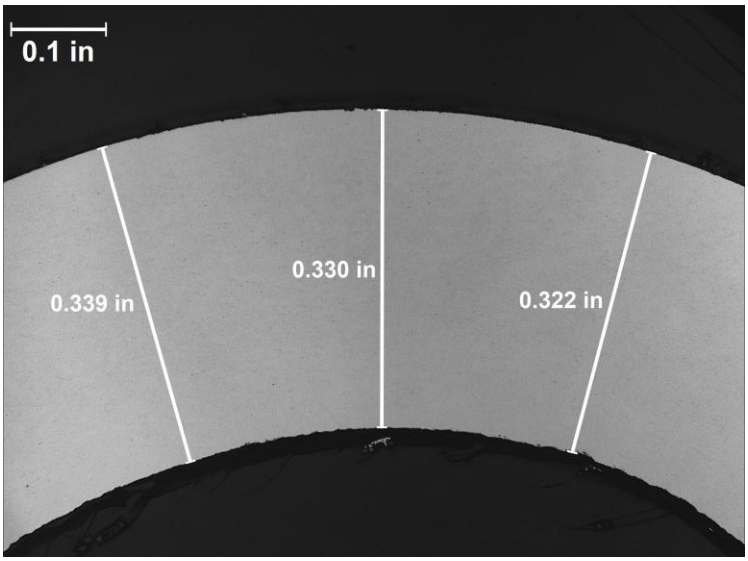

Sample 6

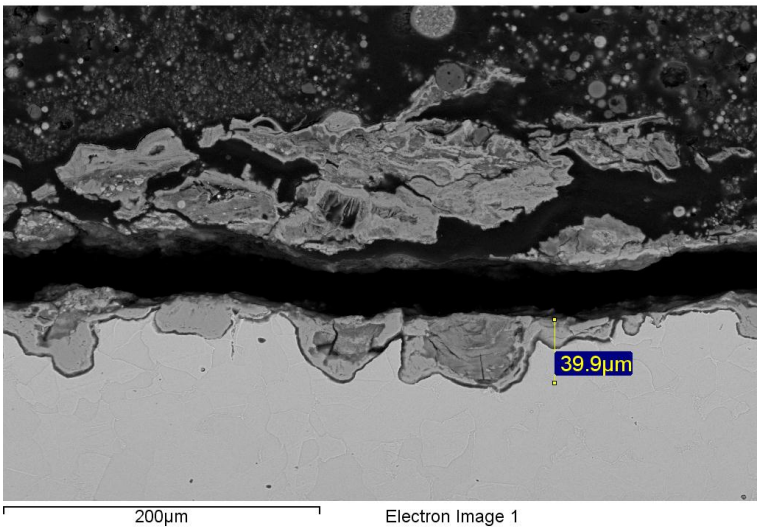

Sample 6

Figure 6. Documenting the typical thickness of the probe and the condition of the OD surface on sample 6 (DOE Oxy Schwarze Pumpe-BSF-7-14-2011-Probe#1). Along the OD surface, a maximum depth of internal penetration ~40 micrometers was observed.

Alstom Power, Inc.
TTT-M Materials Testing
1201 Riverfront Parkway
Chattanooga, TN 37402

Telephone: 423-826-1145
Fax: 423-752-2825
Email: leo.antony@power.alstom.com

OD Deposit Analysis

Element	Weight%	Atomic%
O K	40.59	62.70
Na K	0.46	0.50
Mg K	5.18	5.27
Al K	2.22	2.03
Si K	1.61	1.42
S K	7.24	5.58
K K	0.69	0.44
Ca K	20.00	12.33
Mn K	0.29	0.13
Fe K	21.70	9.60

Wt%

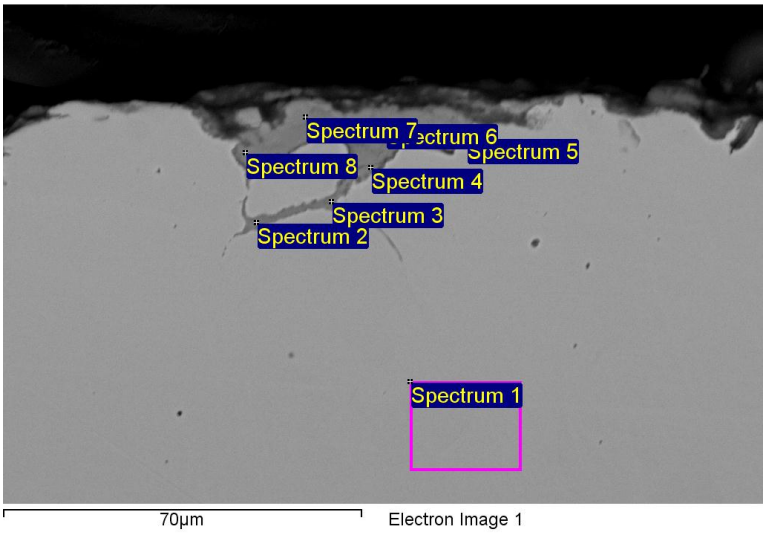

Spectrum	O	S	Mn	Fe
Spectrum 1				100.00
Spectrum 2	10.21			89.79
Spectrum 3	11.95			88.05
Spectrum 4	4.83		0.79	94.38
Spectrum 5	6.70	0.54		92.76
Spectrum 6	14.93	1.15		83.92
Spectrum 7	16.46	1.85		81.69
Spectrum 8	14.39	1.19		84.42

Figure 7. The semi-quantitative results of the SEM-EDS analyses made of the deposits on the probe and the OD corrosion product from Sample 7 identified as DOE Oxy Schwarze Pumpe-BSF-7-14-2011-Probe#3 are shown.

Alstom Power, Inc.
TTT-M Materials Testing
1201 Riverfront Parkway
Chattanooga, TN 37402

Telephone: 423-826-1145
Fax: 423-752-2825
Email: leo.antony@power.alstom.com

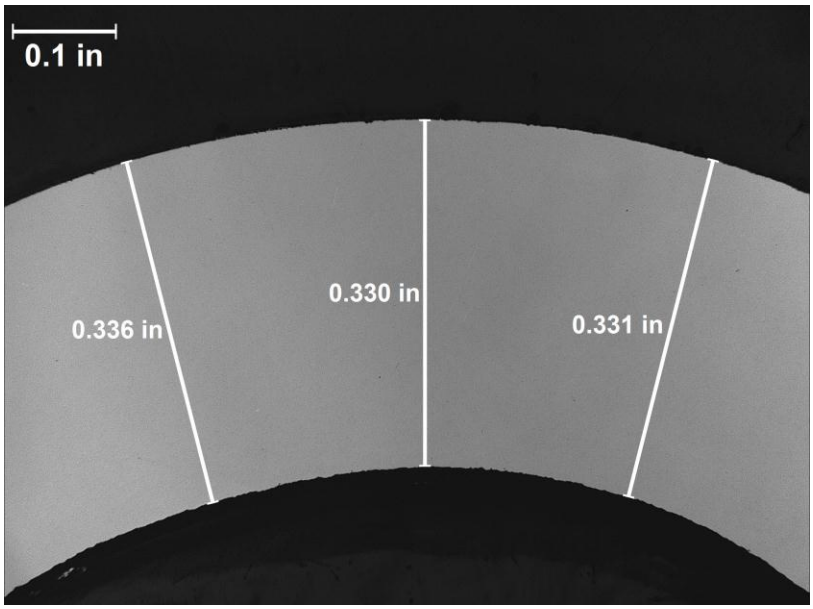

Sample 7

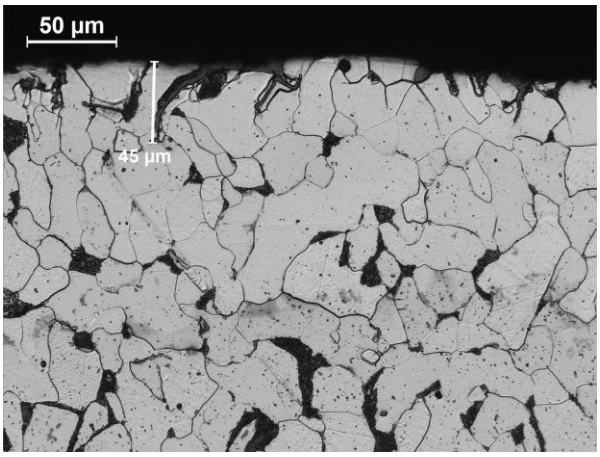

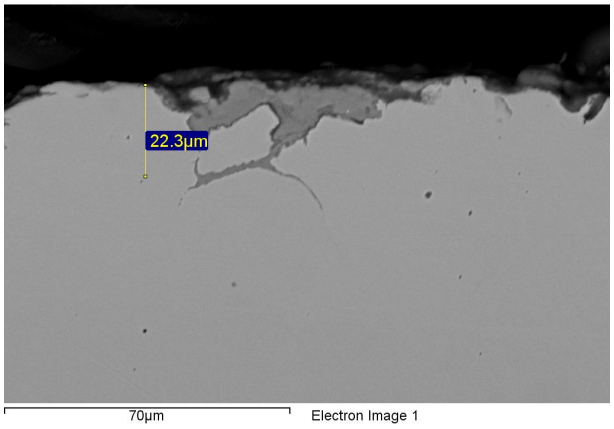

Sample 7

Figure 8. Documenting the typical thickness of the probe and the condition of the OD surface on sample 7 (DOE Oxy Schwarze Pumpe-BSF-7-14-2011-Probe#3). Along the OD surface, a maximum depth of internal penetration ~45 micrometers was observed.

Alstom Power, Inc.
TTT-M Materials Testing
1201 Riverfront Parkway
Chattanooga, TN 37402

Telephone: 423-826-1145
Fax: 423-752-2825
Email: leo.antony@power.alstom.com

OD Deposit Analysis

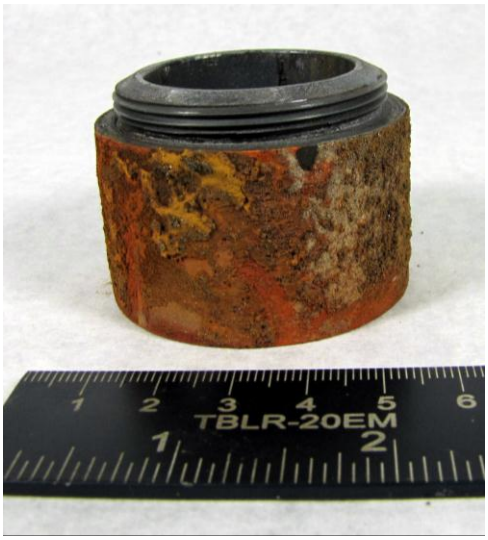

Element	Weight%	Atomic%
O K	46.06	65.95
Na K	2.11	2.10
Mg K	3.02	2.84
Al K	0.96	0.81
Si K	2.82	2.30
S K	15.66	11.18
K K	2.62	1.53
Ca K	14.27	8.16
Fe K	12.50	5.13

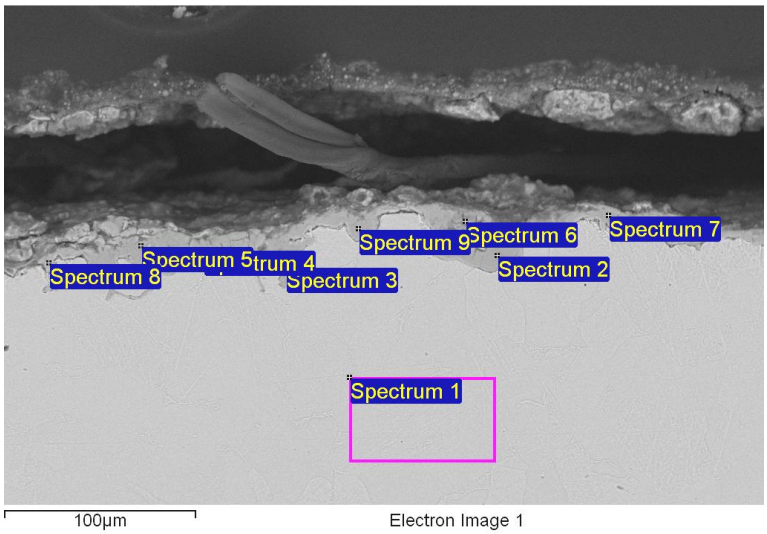

Wt%

Spectrum	O	S	Mn	Fe
Spectrum 1				100.00
Spectrum 2	13.76	5.49		80.75
Spectrum 3	16.71	2.47	0.63	80.19
Spectrum 4	17.45	0.81		81.74
Spectrum 5	16.66	2.15		81.19
Spectrum 6	21.51	1.24		77.25
Spectrum 7	14.89	5.78		79.33
Spectrum 8	14.62	5.12		80.26
Spectrum 9	14.70	4.59		80.72

Figure 9. The semi-quantitative results of the SEM-EDS analyses made of the deposits on the probe and the OD corrosion product from Sample 8 identified as DOE Oxy Schwarze Pumpe-BSF-7-18-2011-Probe#1 are shown.

Alstom Power, Inc.
TTT-M Materials Testing
1201 Riverfront Parkway
Chattanooga, TN 37402

Telephone: 423-826-1145
Fax: 423-752-2825
Email: leo.antony@power.alstom.com

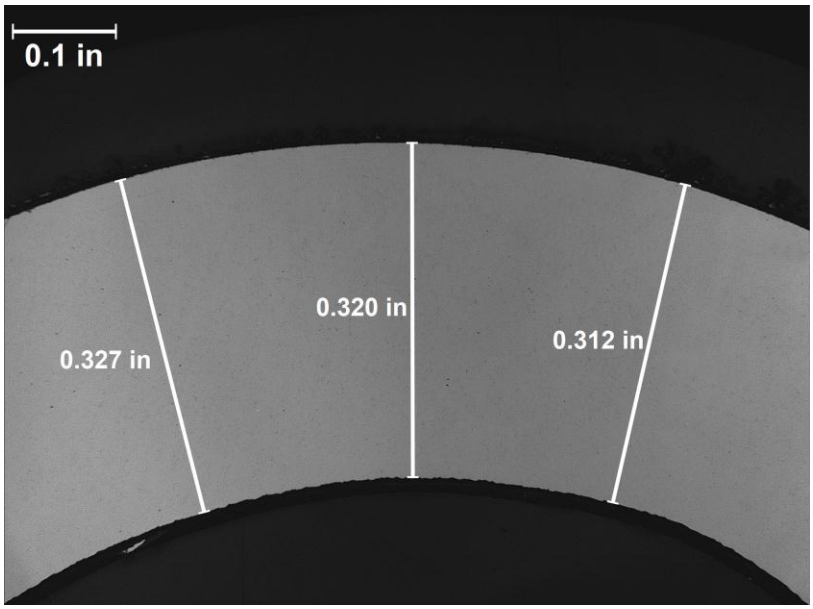

Sample 8

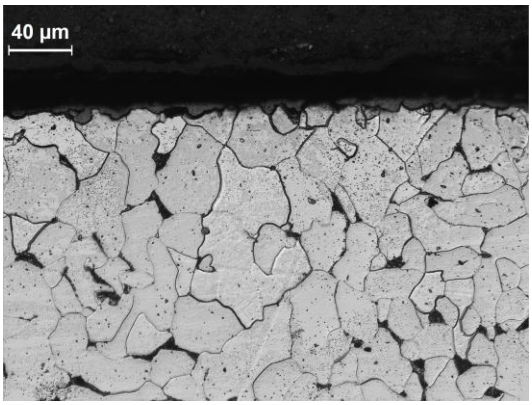

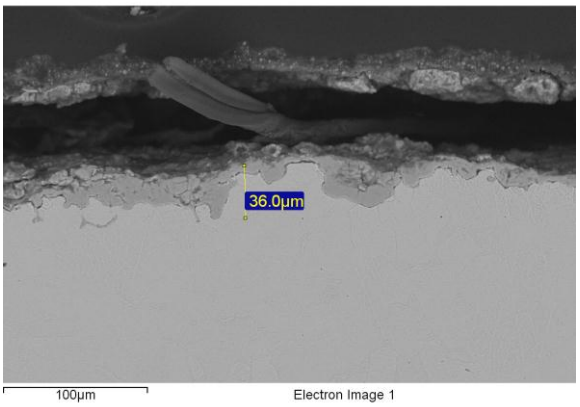

Sample 8

Figure 10. Documenting the typical thickness of the probe and the condition of the OD surface on sample 8 (DOE Oxy Schwarze Pumpe-BSF-7-18-2011-Probe#1). A maximum internal penetration of ~ 36 micrometers was observed along the OD surface.

Alstom Power, Inc.
TTT-M Materials Testing
1201 Riverfront Parkway
Chattanooga, TN 37402

Telephone: 423-826-1145
Fax: 423-752-2825
Email: leo.antony@power.alstom.com

OD Deposit Analysis

Element	Weight%	Atomic%
O K	39.72	61.85
Mg K	4.47	4.58
Al K	1.92	1.77
Si K	4.13	3.67
S K	6.69	5.20
K K	0.28	0.18
Ca K	20.73	12.89
Ti K	0.27	0.14
Fe K	21.78	9.72

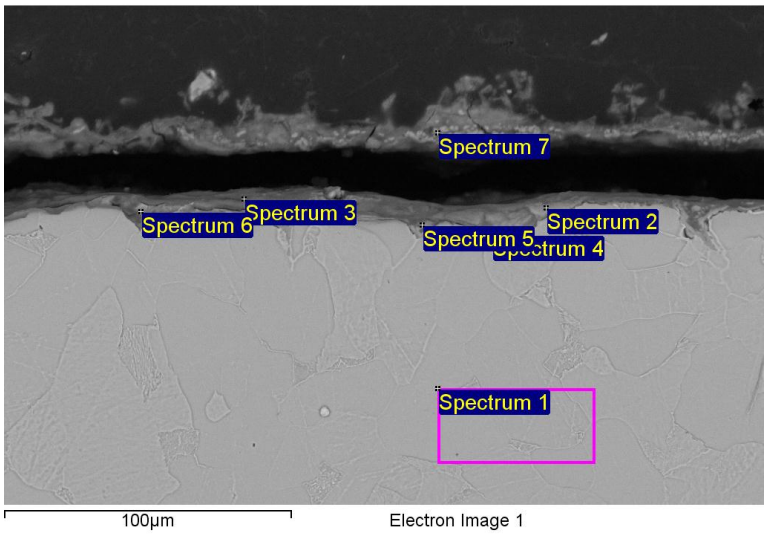

Wt%

Spectrum	O	S	Fe
Spectrum 1			100.00
Spectrum 2	18.43	0.77	80.80
Spectrum 3	26.28		73.72
Spectrum 4	10.11		89.89
Spectrum 5	16.38	0.94	82.69
Spectrum 6	19.12	1.04	79.84
Spectrum 7	20.66	0.56	78.78

Figure 11. The semi-quantitative results of the SEM-EDS analyses made of the deposits on the probe and the OD corrosion product from Sample 9 identified as DOE Oxy Schwarze Pumpe-BSF-7-18-2011-Probe#3 are shown.

Alstom Power, Inc.
TTT-M Materials Testing
1201 Riverfront Parkway
Chattanooga, TN 37402

Telephone: 423-826-1145
Fax: 423-752-2825
Email: leo.antony@power.alstom.com

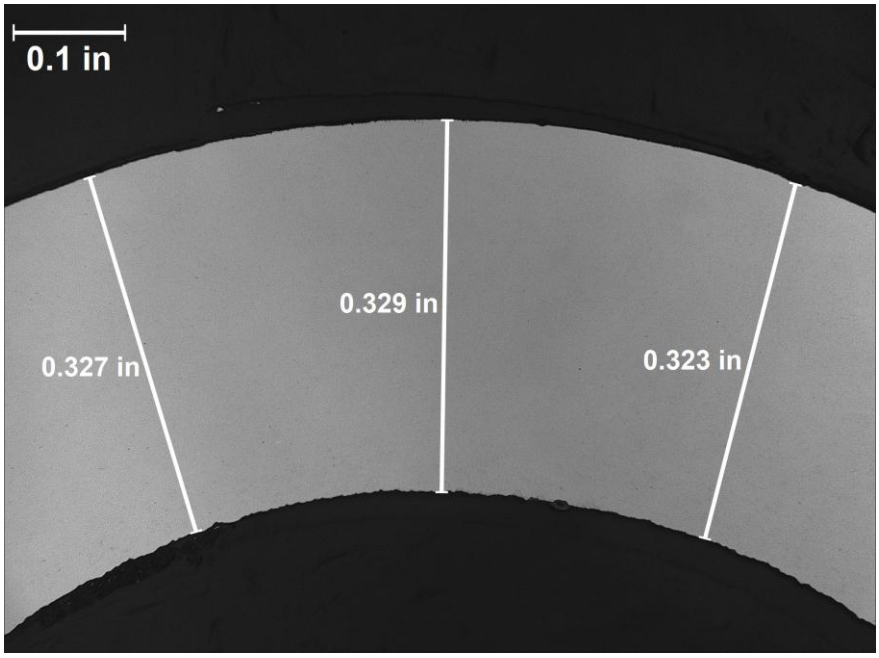

Sample 9

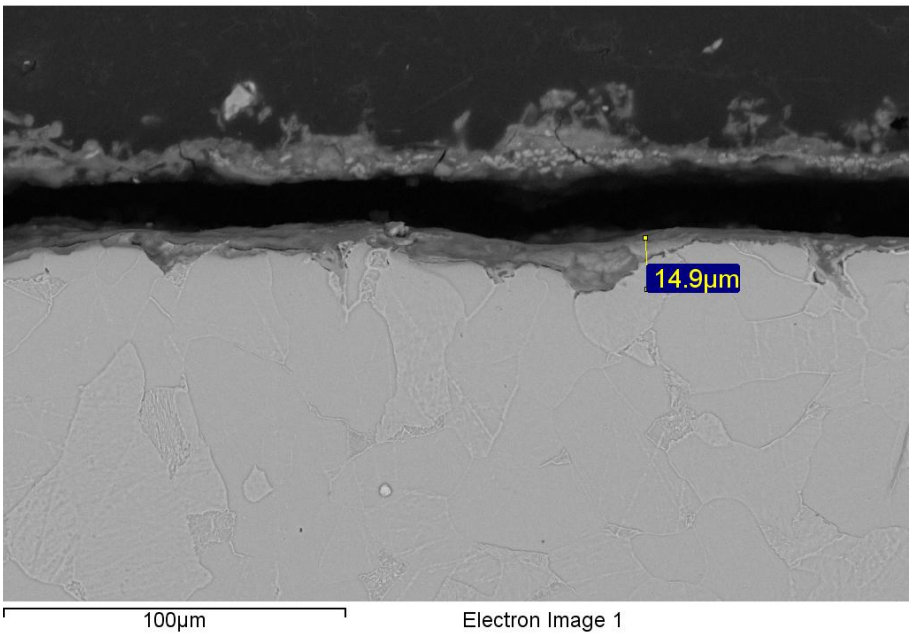

Sample 9

Figure 12. Documenting the typical thickness of the probe and the condition of the OD surface on sample 9 (DOE Oxy Schwarze Pumpe-BSF-7-18-2011-Probe#3). Along the OD surface, a maximum internal penetration of ~15 micrometers was observed.

Alstom Power, Inc.
TTT-M Materials Testing
1201 Riverfront Parkway
Chattanooga, TN 37402

Telephone: 423-826-1145
Fax: 423-752-2825
Email: leo.antony@power.alstom.com

Appendix E. Bench Scale High Temperature Corrosion Study

This appendix contains a report by Alstom's Materials Testing Laboratory discussing the results of bench scale corrosion testing at metal temperatures and environments simulating conditions in the convective pass.

ALSTOM

Technical Report

Project Leader: Bettina Bordenet

TTTM - Materials Technology Center
1201 Riverfront Parkway
Chattanooga, TN 37402, USA
Tel.: (423) 752-2845
Fax: (423) 752-2825

Document Title: DOE Oxy-Combustion High Temperature Corrosion Study.
Document Ref. No.: 12C077

Date of Issue: Nov 26, 2013

No. of pages: 142

Author(s): Leo Antony and Bettina Bordenet

Keywords: Corrosion Kinetics, Metal loss, Oxide Scale Growth, Oxy-Combustion, Air-firing, Oxidation, Sulfidation, Chlorination

Reviewed by: Rich Miller

Abstract:

T23, T24, T92, Super 304H, NF709R, HR3C, IN617, IN740, and alloy C263 materials were studied for corrosion behavior in a simulated oxy and air firing conditions at 600°C and 650°C for a maximum exposure of 3000 hours. All materials were tested as bare metal and coated with simulated eastern ash. In addition, Super304H, HR3C, and IN740 were tested with simulated western ash. After testing, the total metal loss for the alloys was measured and the nature of the corrosion attack was documented.

For ferritic materials, uniform corrosion was observed with negligible internal attack. In general, the application of ash did not enhance the metal loss. T23, T24 and T92 were severely attacked at 650°C for oxy and air firing conditions with the same sulfur and chlorine levels. Oxide spallation was evident on the test specimen after 1000 hours of exposure. The maximum metal loss was 0.016” for T23 and T24 and 0.008” for T92. T24 materials experienced similar corrosion attack when tested in both conditions. Furthermore, T23 and T92 exhibited slightly less metal loss in air-firing than in oxy firing. Specimens tested at 600°C with different levels of sulfur and chlorine experienced less metal loss (< 0.007” for T23 and T24, and <0.003” for T92) than at 650°C. Increasing the chlorine levels from (100ppm to 300ppm) resulted in higher metal loss (factor of 2 for T23 and T24 materials).

The austenitic stainless steels and nickel base materials, however, did not suffer any more than approximately 0.002” of metal loss. The corrosion morphology was characterized by both localized corrosion and internal attack (carburization/grain boundary attack). The nature of the internal attack for the austenitic steels was predominantly carburization. The depth of the carburization attack was measured by etching and was found to be shallow. The hardness of the carburized zone was slightly higher than that of the base material although it was still within specification except for HR3C. Internal attack of the nickel base alloys was less pronounced and was therefore the nature of the corrosion morphology was not characterized.

Corrosive attack for respective materials was strong dependent on metal temperature and on the concentration of corrosive species (sulfur, chlorine). The high CO2-rich environment of oxy-combustion did not appear to enhance corrosive attack.

---

1. Executive Summary

Oxy-fired technology is seen as one of the attractive options for carbon capture and storage. Here, the coal is burned with O2, coming from an air separation unit, instead of air. A major part (~2/3) of the CO2-rich exhaust gas is recycled back to the boiler to control the combustion temperature. The gas composition is significantly changed, when the combustion is changed from air-fired to oxy-fuel fired condition. The gas composition can vary in wide range for the different possible flue gas recycling schemes depending on wet / dry recycle or before or after sulphur removal.
The products of combustion in an oxy-fuel environment can a matter of concern for the boiler components (superheater and reheater), as the increased levels of CO2 and H2O can be coupled with potential increased levels of corrosive gases such as HCl and SO2 (up to ~4 times the levels found in conventional boilers using the same fuel, depending on the flue gas re-cycling configuration). The corrosion behavior needs to be re-evaluated for all the components in contact with the flue gas for oxidizing and reducing environments. The hottest zones of the convective heat exchanging surfaces are assumed to have the highest corrosion risk.
The aim of this test program was to separate the different parameters that influencing corrosion behavior such as, S-level, Cl-level, water content, air- / oxy-firing atmosphere and temperature. The high temperature corrosion of several power plant materials was tested in different air-firing and oxy-combustion environments at 600°C and 650°C Table 1). Six experiments were performed for total corrosion exposure duration of 1'000 and 3'000 hours. Simulated US Eastern coal ash was applied to all material samples, ferritics (T23, T24, T92), austenitics (Super304H, HR3C) and Ni-base alloys (CCA617, Alloy 740). Additionally, simulated US Western ash was applied on samples of Super304H, HR3C, and Alloy 740. The ash was re-applied every 200 hours to insure a continuous supply of corrosive elements. The corrosion extent and morphology were evaluated after exposure by metallographic examination.

					Gas Composition in [vol%]					
No.	**Temperature**	**Sulfur**	**Chlorine**	**Firing**	**O_2**	**N_2**	**H_2O**	**CO_2**	**SO_2**	**HCl**
1	650°C	medium	medium	oxy	3.0	7.59	25.0	64.0	0.2	0.02
2	650°C	medium	medium	air	3.6	71.29	10.0	15.0	0.2	0.02
3	600°C	low	high	air	3.6	71.29	10.0	15.0	0.08	0.03
4	600°C	high	medium	oxy	3.0	7.59	25.0	64.0	0.4	0.02
5	600°C	low	low	oxy	3.0	7.59	25.0	64.0	0.08	0.01
6	600°C	medium	low	air	3.6	71.29	10.0	15.0	0.2	0.01

Table 1: Overview of gas compositions and temperatures used in the present test program

The ferritic alloys are exhibiting significant metal loss of up to 16mils after 3'000h at 650°C. Their metal loss is a factor ~3 higher at 650°C, than at 600°C after 3'000 hours. The temperature seems to be one of the dominant parameters. At

600°C, the corrosion rate law appears to be more parabolic, whereas it seems to be more linear at 650°C for the ash-coated samples of the tested ferritic alloys. The oxide scale in all tests is spalling already several times until 1'000h. At 650°C, T23 and T92 are showing a slightly higher attack in the oxy-firing atmosphere than air-firing for the same sulfur- and chlorine-content. T24 instead, did exhibit a comparable metal loss in both atmospheres. In the test series at 600°C, the higher chlorine-level in the atmosphere did lead to higher metal loss, even if the sulfur-level was reduced.

The higher alloyed alloys exhibited a good corrosion resistance under the given boundary conditions. The maximum metal loss at 3'000h at 650°C was below 2mils for austenitics and below 1mil for the Ni-base alloys. The austenitic alloys showed mainly internal attack with thin external corrosion products. The internal attack is predominately carburization, but only with a small extent (determined by etching). The hardness of the caburized zone was only slightly higher than that of the base material. The corrosion morphology of the Ni-base alloys was mainly characterized by localized outer corrosion products with only minor internal attack (a few micrometers). No internal sulfidation could be noticed.

When comparing oxy-fuel condition with air-fired ones, the corrosion attack is generally similar for same S- and Cl-content. The effect of temperature seems to have a stronger effect than the differences in CO2-, H2O-levels (oxy vs. air). The level of corrosive elements (sulfur, chlorine) seems to be crucial for the metal loss. For comparable levels of corrosive elements (air-firing vs. oxy-firing with flue gas cleaning in the recirculation loop), the corrosion attack is expected to be only slightly worse than in air-firing based on the presented results. Hence, when oxy-firing will be run without flue gas cleaning in the recirculation loop, a deeper corrosion attack is anticipated due to higher levels in S, Cl compared to air-firing. These statements should be confirmed by long-term testing and investigation of steam loop samples.

2. Introduction

Oxy-fired technology is seen as one of the attractive options for carbon capture and storage. Here, the coal is burned with O2, coming from an air separation unit, instead of air. A major part (~2/3) of the CO2-rich exhaust gas is recycled back to the boiler to control the combustion temperature. The gas composition is significantly changed, when the combustion is changed from air-fired to oxy-fuel fired condition. The gas composition can vary in wide range for the different possible flue gas recycling schemes depending on wet / dry recycle or before or after sulphur removal.

The products of combustion in an oxy-fuel environment can a matter of concern for the boiler components (superheater and reheater), as the increased levels of CO2 and H2O can be coupled with potential increased levels of corrosive gases such as HCl and SO2 (up to ~4 times the levels found in conventional boilers using the same fuel, depending on the flue gas re-cycling configuration). The corrosion behavior needs to be re-evaluated for all the components in contact with the flue gas for oxidizing and reducing environments. The hottest zones of the convective heat exchanging surfaces are assumed to have the highest corrosion risk.

The aim of this test program was to separate the different parameters that influencing corrosion behavior such as, S-level, Cl-level, water content, air- / oxy-firing atmosphere and temperature. The high temperature corrosion of several power plant materials was tested in different air-firing and oxy-combustion environments at 600°C and 650°C. The materials selected for this research were T23, T24, T92, Super304H, IN617, NF709R, IN740, HR3C, and AlloyC263. The results of the testing predominately relate to superheater/reheater corrosion issues under oxy and air firing conditions. Testing to study waterwall corrosion issues were not included in this effort.

3. Experimental Procedures

The testing strategy and the chemical compositions of the simulated flue gases used in the study are listed in Tables 1a and b.

The boiler tube materials used in this study were chemically analyzed and the results reported in Tables 2, 3, and 4.

Ring sections were taken from the boiler tube materials in order to determine their OD and wall thicknesses. The measurements are presented in Tables 5 through 9.

The test specimens were arc sections taken from the boiler tube materials. The specimens were approximately 1” in axial length with an outside arc length of also approximately 1”. A hole was drilled into the center top of the specimens so that an alumina rod could be used to hold the specimens in ceramic fiberboard

boats. The cut surfaces of the specimens were wet-ground using 140 and 240 grit SiC papers. After grinding, the test specimens were ultrasonically cleaned in preparation for testing.

Prior to testing, the test specimens were weighed and their surface areas measured. The specimens were then arranged by material types, placed in ceramic boats (as shown in Figure 1), inserted into horizontal tube furnaces (see Figure 1) and heated to 600°C or 650°C. The furnaces were ramped up to a test temperature under an argon atmosphere and then the test atmosphere was established. Furnaces were cooled down under argon atmosphere. A schematic of the experimental set-up is shown in Figure 2. Once in the furnace, the test specimens were exposed to a simulated flue gases (see Table 1) that was fed into the furnaces at a constant rate under conditions of atmospheric pressure for a maximum of 3000 hours. Some of the test specimens of each material type were coated with ash prior to testing. Two different types of simulated ash (eastern bituminite, and western lignite) were used and their compositions are listed in Table 10. The dry ash was mixed with methyl cellulose and charcoal to obtain a slurry. The slurry was applied onto the inner and the outer surfaces of certain test specimens with a brush. The ash was reapplied to the specimens every 200 hours after the furnaces were cooled under an argon atmosphere and the old ash removed by brushing.

At the completion of the 1000 and 3000 hour test periods, the furnaces were cooled to room temperature and test specimens of each material type (both ashed and non ashed) were removed for metallographic evaluations.

The test specimens were evaluated as described below:

1) Metallographic analysis of test specimens by optical microscope and/or SEM (Scanning Electron Microscope):

    a. The test specimens were mounted (ideal orientation) using a Vacuum Impregnation method and clear epoxy.
    b. The mounted specimens were strategically sectioned with a diamond saw and prepared by standard metallographic practices.

2) Corrosion Product Measurement:

    a. The corrosion product was measured by Optical/SEM on metallographic cross-sections of the corroded test specimens and reported in inches or micrometers. The micrographs were documented.

3) Internal Penetration Attack:

a. The metallographic specimens were etched to reveal the microstructure and also to check for internal penetration attack if any.

4. Results and Discussion

The extent of corrosion (or metal loss) of the various alloys were determined from a combination of pre and post-test wall thickness measurements (using a stereo microscope), metallographic measurement of corrosion product scale thickness and the depth of any internal attack. The total metal loss (TML) represents corrosion on one side of the test specimen only. The TML is the sum of the external metal loss plus the internal attack (carburization, oxidation, and sulfidation). For uniform corrosion, the external metal loss was measured as half of the external corrosion product thickness where the external oxide scale was intact. In those cases where the scale spalled, wall thickness measurements were used to determine the metal loss. For localized corrosion, the maximum pit depth was measured and reported as external metal loss.

For ferritic materials, uniform corrosion was observed with negligible internal attack. Corrosion attack on the austenitic stainless steels and the nickel base materials was mainly characterized by internal attack. Localized corrosion was primarily observed in these alloys.

The micrographs of various alloys, when tested under conditions 1 to 6, are all listed in the addendum. The measured metal loss values for various alloys when tested under conditions 1 to 6 are listed in Tables 11 through 16.

The performances of various alloys when exposed to conditions 1 to 6 after 3000 hours of exposure are as follows:

Condition 1

The results showed that T23, T24 and T92, in general, were severely attacked in condition 1. T23 and T24 material (non-ashed) suffered maximum metal loss of approximately 12 and 14 mils after 3000 hours of exposure at 650°C for condition 1. There was no significant difference in the metal loss between the ashed and non-ashed samples of ferritic materials with the exception of T23 (which was coated with eastern ash). This test specimen showed a maximum metal loss of ~ 16 mils (0.016”). The corrosion product for ferritic materials was predominantly an oxidation product.

The austenitic stainless steels after 3000 hours of exposure at 650°C showed a metal loss of ~1 to 2 mils. Here, the metal loss was primarily due to internal penetration attack. Among the austenitic materials tested, Super304H (~ 19%

chromium) coated with western ash suffered a maximum metal loss of ~ 2 mils mostly from internal grain boundary attack. This attack is primarily due to higher sulphate levels in the western ash. Whereas HR3C material (~ 25% chromium) coated with western ash showed negligible attack, which indicates that the high chromium content is clearly beneficial in resisting corrosion attack. Carburization attack was also visible in these alloys (including NF709R).

The nickel base materials under this test condition performed well. IN740 material coated with western ash did not show any significant attack. The non-ashed samples showed ~1 mil metal loss in all the nickel base alloys tested with the exception of alloy C263 where both ashed and non-ashed showed ~1mil of metal loss.

Condition 2

In general, the ferritic materials were severely attacked in this condition. The T24 material showed the worst metal loss (measuring as much as 16 mils) in comparison to T23 and T92. T23 and T92 materials showed metal loss in the range 4 to 7 mils. The probable reason for this behavior could be attributed to the multilayering of oxidation product in the T24 material. The corrosion product for ferritic materials was predominantly an oxidation product.

Carburization damage along the OD surface was visible on all austenitic materials tested. HR3C material coated with eastern ash and super 304H materials (both ashed and non-ashed) showed ~ 2 mils metal loss, which are possibly attributed to carburization and subsequent grain boundary attack.

Among the various nickel base materials tested in this condition, IN740 performed the best with negligible corrosion attack on both ashed and non-ashed samples. IN617 and alloy C263 materials showed negligible attack when they were coated with eastern ash.

Condition 3

The metal loss values for ferritic materials were in the range 3 to 7 mils. T24 material showed a maximum metal loss of ~ 7 mils. There was no significant difference in the thickness of the corrosion product after 3000 hours of exposure between the ashed and non-ashed samples. The corrosion product appeared to be predominantly an oxidation product.

There was a difference in metal loss rate for the HR3C material between the ashed and the non-ashed samples. When coated with the eastern and the western ash, HR3C material showed a metal loss of ~ 2 mils. HR3C material showed negligible corrosion attack when it was non-ashed. Super304H materials

when coated with western ash showed ~ 2 mils of corrosion attack. NF709R material showed ~ 1 mil of corrosion attack between the ashed and non-ashed samples. The attack is predominantly carburization attack coupled with subsequent grain boundary attack.

Overall, nickel base alloys showed a negligible corrosion attack.

Condition 4

The metal loss values for ferritic materials were in the range 3 to 6 mils. T23 and T24 material under non-ashed condition showed a similar metal loss of ~ 6 mils. The corrosion product appeared to be predominantly an oxidation product.

Super304H and NF709R material showed a similar metal loss value between the ashed and non-ashed samples. HR3C performed well in this condition with a negligible corrosion attack. Again, the higher chromium content in this alloy is beneficial in resisting corrosion attack under higher sulfur test conditions.

IN617 and Alloy 263 materials showed a metal loss value of ~ 1 and 2 mils whereas IN740 had negligible attack and it performed very well. It is possible that the molybdenum content in the nickel base alloys (greater than 5%) may not be beneficial for high sulfur test conditions.

Conditions 5 & 6

The metal losses for all the ferritic materials were in the range 2 to 5 mils. The corrosion product formed on the external surface was predominantly an oxidation product.

Austenitic materials such as super304H material showed a metal loss of ~1 mil on both ashed and non-ashed samples for condition 5. Where as in condition 6, super304H coated with ash showed a metal loss of ~ 2 mils. The possible cause for this metal loss could be that condition 6 (on the ashed samples) contained more sulfur species.

Nickel base alloys performed well in conditions 5 and 6.

5. Summary/Conclusions

Fireside corrosion testing was performed in a simulated oxy and air firing conditions at 600°C and 650°C for an exposure period of 1000 and 3000 hours. Some of the test specimens were coated with the simulated eastern bituminous and the western lignite ashes. In this test campaign, a total of six tests were performed and the results are presented in this report. A range of typical and

proposed boiler tube alloys such as T23, T24, T92, Super304H, NF709R, HR3C, IN617, IN740 and alloy C263 materials were included in this test series.

In general results indicate that corrosive attack on respective alloys was strongly dependent metal temperature and the concentration of corrosive constituents (sulfur, chlorine). The higher CO2 and H2O concentrations associated with oxy-combustion conditions did not appear to have a strong impact on corrosive attack.

The test results are summarized as follows:

1. The metal losses for all the ferritic materials were predominantly calculated from the corrosion product thickness for all the conditions. The greatest wall loss measured was 16 mils. The corrosion product was predominantly an oxidation product.

2. The results showed that T23, T24 and T92, in general, were severely attacked in conditions 1 and 2 (at 650°C). T23 and T24 materials were significantly attacked in conditions 3 to 6. There was little difference in the thickness of the corrosion product after 3000 hours of exposure between the ashed with non-ashed samples that were exposed to conditions 1 through 6 for all materials with the exception of T23 and T24 for conditions 1 and 2. This could be attributed to possible flaking off corrosion product during ash re-coating.

3. T23 and T24 material suffered maximum metal loss of approximately 12 and 14 mils after 3000 hours of exposure at 650°C for condition 1. For condition 2, the T23 material had less metal loss than in condition 1. Infact, T23 suffered a metal loss of ~7 mils whereas T24 material suffered ~13 mils.

4. When comparing conditions 1 and 4, it is interesting to note that the temperature plays an important role in accelerating the corrosion rates of the ferritic materials.

5. No significant corrosion was seen on the austenitic stainless steels or various nickel-based alloys after 1,000 hours of exposure to each condition, 1 through 6. Whereas after 3000 hours of exposure at 650°C, the austenitic stainless steels showed negligible metal loss to ~2 mils for conditions 1 through 6. The attack on austenitic materials was predominantly due to carburization and subsequent grain boundary penetration attack.

6. It is interesting to note that the HR3C materials performed well under high sulfur condition (condition 4) where as it did not perform well when given an ash coating in high chlorine condition (condition 3). In fact, the material suffered a maximum metal loss of approximately 2 mils when coated with ashes (condition 3). It is clearly evident that the high chromium content in HR3C materials is beneficial in resisting sulfidation attack. Also ashed and non-ashed HR3C performed well under oxy firing conditions at 650°C (condition 1) as compared to air firing (condition 2).

7. In general, the nickel base materials performed well in all the test conditions (both ashed and non-ashed). The exception is alloy 263 in condition 4 showed a maximum metal loss of ~ 2 mils.

8. Also, it is noted that the IN617 and alloy C263 materials showed a metal loss value of ~ 1 and 2 mils whereas IN740 had negligible attack and it performed very well in condition 4. It is possible that the molybdenum content in the nickel base alloys (greater than 5%) may not be beneficial for high sulfur test conditions.

9. Carburization attack is characterized by the formation of internal carbides in the matrix of the material and at the grain boundaries. In order to determine the depth of the carburization attack, microhardness traverses were made across the thickness of the samples. The results were found to be consistent for super 304H and NF709R materials when compared with the pre-exposed sample hardness measurements and also when measuring the depth of the attack by examining etched metallographic sections at high magnifications. For HR3C materials, however, the hardness values were higher along the OD surfaces and also there was no hardness gradient observed, suggesting a lesser influence from carburization. The higher hardness values in the HR3C materials could possibly be due to a pre-existing cold-work layer which would be more susceptible to precipitation hardening than the base material when exposed to the test conditions.

5. References

1. Fireside Corrosion in Oxyfuel-Fired Boilers – Testing for the Oxycorr Program – Authors: Terry Totemeier and Bettina Bordenet.

2. Proposal for TTTM Activities in DOE Oxy-Combustion Boiler – Corrosion evaluation – Bettina Bordenet.

3. W.J. Quadakkers and H.Schuster, “Corrosion of High temperature Alloys in the Primary Circuit Helium of High Temperature Gas Cooled Reactors – Part-1: Theoretical background”, *Corrosion of High Temperature Alloys. Part-1*, Vol.36 (1985) pp141 – 150.

4. W.J. Quadakkers, “Corrosion of High temperature Alloys in the Primary Circuit Helium of High Temperature Gas Cooled Reactors – Part-2: Experimental Results”, *Corrosion of High Temperature Alloys. Part-2*, Vol.36 (1985) pp 335 – 347.

5. S. Sroda and S. Tuurna, “ Laboratory scale tests on corrosion behavior boiler materials in simulated combustion atmospheres – EU Project – OPTICORR”, Materials and Corrosion 2006, 57, No.3.

6. Flemming Jappe Frandsen, “Utilizing biomass and waste for power generation-a decade of contributing to the understanding, interpretation and analysis of deposits and corrosion products”, Fuel 2005, Volume 84, pg. 1277-1294.

6. Enclosures

The micrographs for various alloys when tested under conditions 1 through 6 and the hardness data for various austenitic materials are listed in the addendum. The first five hardness values for each material were measured from the OD surface, while the other values were measured from the midwall area.

Table 1a. Test Strategy

	No.	Run Order	Temperature	Sulfur	Chlorine	Firing
1st test series	1	1	650°C	medium	medium	oxy
	2	2	650°C	medium	medium	air
	3	3	600°C	low	high	air
	4	7	600°C	high	medium	oxy
	5	10	600°C	low	low	oxy
	6	11	600°C	medium	low	air

Table 1b. Flue Gas Compositions

	Condition 1	Condition 2	Condition 3	Condition 4	Condition 5	Condition 6
	Oxy firing	Air firing	Air firing	Oxy firing	Oxy firing	Air firing
Gases	Volume %	Volume %	Volume %	Volume %	Volume %	Volume %
O_2	3.00	3.60	3.60	3.00	3.00	3.6
HCl	0.02	0.02	0.03	0.02	0.01	0.01
N_2	7.78	71.18	71.29	7.58	7.79	71.19
H_2O	25.00	10.00	10.00	25.00	25.00	10.00
CO_2	64.00	15.00	15.00	64.00	64.00	15.00
SO_2	0.20	0.20	0.08	0.40	0.08	0.20

Table 2. Chemistry Results

Chemical Composition (Weight Percent)				
ELEMENT	**T23 Specimen**	**ASME Code Case 2199-4 (T23)**	**T24 Specimen**	
CARBON	0.05	0.04 - 0.10	0.090	
MANGANESE	0.44	0.10 - 0.60	0.56	
PHOSPHORUS	0.017	0.030 (max)	0.017	
SULFUR	0.002	0.010 (max)	0.003	
SILICON	0.24	0.50 (max)	0.27	
NICKEL	0.10	0.40 (max)	0.08	
CHROMIUM	2.34	1.90 - 2.60	2.45	
MOLYBDENUM	0.21	0.05 - 0.30	1.020	
VANADIUM	0.21	0.20 - 0.30	0.229	
COLUMBIUM	0.05	0.02 - 0.08	0.005	
TITANIUM	0.030	0.005 - 0.060	0.070	
COBALT	0.011	***	0.010	
COPPER	0.15	***	0.10	
ALUMINUM	0.03	0.030 (max)	0.012	
BORON	0.0009	0.0010 - 0.006	0.0046	
TUNGSTEN	1.53	1.45 - 1.75	0.01	
ANTIMONY		***	0.001	
ARSENIC	0.008	***	0.006	
TIN	0.011	***	0.007	
ZIRCONIUM	0.001	***	0.001	
LEAD	0.001	***	0.001	
IRON	Balance	***	Balance	
NITROGEN	0.01	0.015 (max)	0.006	
OXYGEN	0.020	***	***	
CALCIUM	***	***	***	

Table 3. Chemistry Results

Chemical Composition (Weight Percent)				
ELEMENT	**T92 Specimen**	**ASME Specification SA-213, T92**	**Super 304H Specimen**	**UNS No: S30432 (Super 304H)**
CARBON	0.110	0.07 - 0.13	0.08	0.07-0.13
MANGANESE	0.45	0.30 - 0.60	0.46	1.00 (max)
PHOSPHORUS	0.014	0.020 (max.)	0.017	0.040 (max)
SULFUR	0.004	0.010 (max.)	0.003	0.010 (max)
SILICON	0.35	0.50 (max.)	0.25	0.3 (max)
NICKEL	0.23	0.40 (max.)	9.19	7.5 – 10.5
CHROMIUM	9.02	8.50 - 9.50	19.0	17.0 – 19.0
MOLYBDENUM	0.378	0.30 - 0.60	0.156	***
VANADIUM	0.217	0.15 - 0.25	0.070	***
COLUMBIUM	0.065	0.04 - 0.09	0.500	0.30 – 0.6
TITANIUM	0.003	0.01 (max.)	0.002	***
COBALT	0.015	***	0.111	***
COPPER	0.09	***	2.74	2.5-3.5
ALUMINUM	0.013	0.02 (max.)	0.014	0.003-0.030
BORON	0.0010	0.001 - 0.006	0.0020	0.001-0.010
TUNGSTEN	1.97	1.50 - 2.00	0.03	***
ANTIMONY		***		***
ARSENIC	0.007	***	0.005	***
TIN	0.009	***	0.001	***
ZIRCONIUM	0.002	0.01 (max.)		***
LEAD	<0.001	***	0.001	***
IRON	Balance	Balance	Balance	Balance
NITROGEN	0.042	0.030- 0.070	0.104	0.05-0.12
OXYGEN	0.025	***		***

Table 4. Chemistry Results

	Chemical Composition (Weight Percent)							
ELEMENT	**IN617 Specimen**	**UNS no: NO6617 (IN617)**	**NF709R Specimen**	**ASME Code Case: 2581 (NF709R)**	**IN740 Specimen**	**HR3C Specimen**	**UNS No: S31042 (HR3C)**	**Alloy C263 Specimen**
CARBON	0.07	0.05 – 0.15	0.045	0.10 (max)	0.021	0.08	0.04 – 0.10	0.058
MANGANESE	0.04	1.0 (max)	0.009	1.50 (max)	0.24	1.11	2.00 (max)	0.12
PHOSPHORUS	0.004	0.004	0.024	0.030 (max)	0.004	0.014	0.045 (max)	0.004
SULFUR	0.006	0.015 (max)	0.002	0.030 (max)	0.006	0.002	0.030 (max)	0.005
SILICON	0.06	1.0 (max)	0.07	1.0 (max)	0.49	0.43	1.0 (max)	0.05
NICKEL	54.30	44.5 (min)	24.83	23.0 – 26.0	Balance	20.24	19.0 – 22.0	Balance
CHROMIUM	23.63	20.0 – 24.0	22.22	19.5 – 23.0	24.15	25.11	24.0 – 26.0	20.15
MOLYBDENUM	8.759	8.0 – 10.0	1.368	1.0 – 2.0	0.458	0.148	***	5.78
VANADIUM	0.021	***	0.063	***	0.025	0.053	***	0.032
NIOBIUM	0.02	***	0.07	0.10 – 0.40	1.82	0.45	0.20 – 0.60	0.03
TITANIUM	0.345	0.6 (max)	0.003	0.20 (max)	1.62	0.115	***	2.086
COBALT	11.15	10.0 – 15.0	0.144	***	19.21	0.04		19.535
COPPER	0.03	0.5 (max)	0.14	***	0.03	0.018		0.02
ALUMINUM	1.07	0.8 – 1.5	0.009	***	0.891	0.0033		0.434
BORON	0.0018	0.006 (max)	0.0030	0.002 – 0.010	0.0017	0.03		0.0017
TUNGSTEN	0.10		0.07	***	0.03			0.02
ANTIMONY				***		0.001		
ARSENIC			0.002	***		0.002		
TIN	<0.001		0.002	***	<0.001			<0.001
LEAD	0.004			***	0.001	<0.001		0.007
IRON	0.34	3.0 (max)	Balance	Balance	0.51	Balance	Balance	0.001
NITROGEN			0.14	0.10 – 0.25	0.51	0.22	0.15 – 0.35	0.19

Table 5. Dimensional Measurements of T23 and T24 Ring Sections

Sample #	T23											
Location	A-E	B-F	C-G	D-H						Min	Max	Average
OD, in.	1.757	1.756	1.753	1.750					OD, in.	1.750	1.757	1.754
ID, in.	1.382	1.370	1.393	1.390					ID, in.	1.370	1.393	1.384
	A	B	C	D	E	F	G	H				
Wall, in.	0.185	0.200	0.184	0.182	0.190	0.189	0.175	0.180	Wall, in.	0.175	0.200	0.186

Sample #	T24 tube											
Location	A-E	B-F	C-G	D-H						Min	Max	Average
OD, in.	2.006	2.010	2.010	2.011					OD, in.	2.006	2.011	2.009
ID, in.	1.500	1.520	1.505	1.517					ID, in.	1.500	1.520	1.511
	A	B	C	D	E	F	G	H				
Wall, in.	0.250	0.240	0.255	0.250	0.255	0.250	0.253	0.249	Wall, in.	0.240	0.255	0.250

Table 6. Dimensional Measurements of T24 (from the panel) and T92 Ring Sections

Sample #	T24 panel									
Location	A-E	B-F	D-H					Min	Max	Average
OD, in.	1.325	1.325	1.329				OD, in.	1.325	1.329	1.326
ID, in.	0.820	0.830	0.830				ID, in.	0.820	0.830	0.827
	.	B	D	E	F	H				
Wall, in.	0.250	0.250	0.250	0.256	0.250	0.245	Wall, in.	0.245	0.256	0.250

Sample #	**T92**											
Location	A-E	B-F	C-G	D-H						Min	Max	Average
OD, in.	1.062	1.065	1.064	1.060					OD, in.	1.060	1.065	1.063
ID, in.	0.728	0.727	0.720	0.721					ID, in.	0.720	0.728	0.724
	A	B	C	D	E	F	G	H				
Wall, in.	0.180	0.170	0.177	0.170	0.159	0.170	0.170	0.170	Wall, in.	0.159	0.180	0.171

Table 7. Dimensional Measurements of 304H and IN617 Ring Sections

Sample #	304H											
Location	A-E	B-F	C-G	D-H						Min	Max	Average
OD, in.	2.005	2.000	2.000	2.000					OD, in.	2.000	2.005	2.001
ID, in.	1.156	1.150	1.150	1.151					ID, in.	1.150	1.156	1.152
	A	B	C	D	E	F	G	H				
Wall, in.	0.420	0.419	0.420	0.428	0.431	0.434	0.430	0.420	Wall, in.	0.419	0.434	0.425

Sample #	IN617											
Location	A-E	B-F	C-G	D-H						Min	Max	Average
OD, in.	2.004	2.004	2.006	2.004					OD, in.	2.004	2.006	2.005
ID, in.	1.107	1.109	1.108	1.108					ID, in.	1.107	1.109	1.108
	A	B	C	D	E	F	G	H				
Wall, in.	0.449	0.450	0.455	0.453	0.450	0.450	0.444	0.445	Wall, in.	0.444	0.455	0.450

Table 8. Dimensional Measurements of NF709R and IN740 Ring Sections

Sample #	NF709R											
Location	A-E	B-F	C-G	D-H						Min	Max	Average
OD, in.	2.002	2.005	2.004	2.001					OD, in.	2.001	2.005	2.003
ID, in.	1.303	1.301	1.306	1.304					ID, in.	1.301	1.306	1.304
	A	B	C	D	E	F	G	H				
Wall, in.	0.350	0.360	0.369	0.360	0.350	0.340	0.331	0.340	Wall, in.	0.331	0.369	0.350

Sample #	Alloy 740											
Location	A-E	B-F	C-G	D-H						Min	Max	Average
OD, in.	2.000	1.995	2.000	2.000					OD, in.	1.995	2.000	1.999
ID, in.	1.200	1.200	1.200	1.200					ID, in.	1.200	1.200	1.200
	A	B	C	D	E	F	G	H				
Wall, in.	0.410	0.410	0.409	0.400	0.390	0.390	0.391	0.401	Wall, in.	0.390	0.410	0.400

Table 9. Dimensional Measurements of HR3C Ring Sections

Sample #	HR3C										
Location	A-E	B-F	C-G	D-H						Min	Max	Average
OD, in.	2.005	2.000	2.001	2.006					OD, in.	2.000	2.006	2.003
ID, in.	1.230	1.230	1.229	1.230					ID, in.	1.229	1.230	1.230
	A	B	C	D	E	F	G	H				
Wall, in.	0.392	0.390	0.380	0.381	0.380	0.390	0.395	0.400	Wall, in.	0.380	0.400	0.389

Table 10. Ash Composition

	Western US	Eastern US
Ash Elemental Composition	Wt,%	Wt, %
SiO2	45	45
Al2O3	14	20
Fe2O3	5	25
CaO	25	5
MgO	5	2
Na2O	1	1
K2O	1	1
TiO2		
P2O5		
SO3	6	1
% Mn3O4		
% Total	100	100
Grams/500 gms of ash Methyl Cellulose	8.30	16.60
Grams/500 gms of ash Charcoal	12.50	25.00
Base/Acid Ratio	0.649	0.523
Slagging Factor (Rs)		
Fouling Factor(Rf)	0.65	0.52
Ash Type	Lignite	Bituminous

Table 11. Total Metal Loss of Alloys for Condition 1

Exposure time, hours	Metal Loss of Alloys, mils					
	T23	T23 Eastern ash	T24	T24 Eastern ash	T92	T92 Eastern Ash
0	0	0	0	0	0	0
1000	6	5	6	7	4	3
3000	12	16	14	14	8	8

Exposure time, hours	Metal Loss of Alloys, µm							
	S304H	S304H Eastern ash	S304H Western ash	NF709R	NF709R Eastern ash	HR3C	HR3C Eastern ash	HR3C Western ash
3000	18	28	52	32	20	20	Negligible	Negligible

Exposure time, hours	Metal Loss of Alloys, µm						
	IN617	IN617 Eastern ash	IN740	IN740 Eastern Ash	IN740 Western ash	Alloy C263	Alloy C263 Eastern ash
3000	32	Negligible	23	Negligible	Negligible	47	25

1 mil = 0.001” = 25.4 Micrometers

Table 12. Total Metal Loss of Alloys for Condition 2

Exposure time, hours	Metal Loss of Alloys, mils					
	T23	T23 Eastern ash	T24	T24 Eastern ash	T92	T92 Eastern Ash
0	0	0	0	0	0	0
1000	4	5	7	5	2	2
3000	7	7	13	16	5	4

Exposure time, hours	Metal Loss of Alloys, µm							
	S304H	S304H Eastern ash	S304H Western ash	NF709R	NF709R Eastern ash	HR3C	HR3C Eastern ash	HR3C Western ash
3000	37	40	50	13	14	25	27	66

Exposure time, hours	Metal Loss of Alloys, µm						
	IN617	IN617 Eastern ash	IN740	IN740 Eastern Ash	IN740 Western ash	Alloy C263	Alloy C263 Eastern ash
3000	26	Negligible	Negligible	Negligible	Negligible	17	13

1 mil = 0.001” = 25.4 Micrometers

Table 13. Total Metal Loss of Alloys for Condition 3

Exposure time, hours	Metal Loss of Alloys, mils					
	T23	T23 Eastern ash	T24	T24 Eastern ash	T92	T92 Eastern Ash
0	0	0	0	0	0	0
1000	3	3	4	3	2	2
3000	6	6	7	6	3	3

Exposure time, hours	Metal Loss of Alloys, µm							
	S304H	S304H Eastern ash	S304H Western ash	NF709R	NF709R Eastern ash	HR3C	HR3C Eastern ash	HR3C Western ash
3000	27	27	49	27	21	Negligible	32	47

Exposure time, hours	Metal Loss of Alloys, µm						
	IN617	IN617 Eastern ash	IN740	IN740 Eastern Ash	IN740 Western ash	Alloy C263	Alloy C263 Eastern ash
3000	18	Negligible	Negligible	Negligible	Negligible	10	12

1 mil = 0.001” = 25.4 Micrometers

Table 14. Total Metal Loss of Alloys for Condition 4

Exposure time, hours	Metal Loss of Alloys, mils					
	T23	T23 Eastern ash	T24	T24 Eastern ash	T92	T92 Eastern Ash
0	0	0	0	0	0	0
1000	2	2	3	2	2	2
3000	6	4	6	5	3	3

Exposure time, hours	Metal Loss of Alloys, µm							
	S304H	S304H Eastern ash	S304H Western ash	NF709R	NF709R Eastern ash	HR3C	HR3C Eastern ash	HR3C Western ash
3000	26	26	20	33	27	Negligible	12	Negligible

Exposure time, hours	Metal Loss of Alloys, µm						
	IN617	IN617 Eastern ash	IN740	IN740 Eastern Ash	IN740 Western ash	Alloy C263	Alloy C263 Eastern ash
3000	22	32	Negligible	Negligible	Negligible	58	31

1 mil = 0.001” = 25.4 Micrometers

Table 15. Total Metal Loss of Alloys for Condition 5

Exposure time, hours	Metal Loss of Alloys, mils					
	T23	T23 Eastern ash	T24	T24 Eastern ash	T92	T92 Eastern Ash
0	0	0	0	0	0	0
1000	1	1	2	2	1	1
3000	2	3	4	5	2	2

Exposure time, hours	Metal Loss of Alloys, µm		
	S304H	S304H Eastern ash	S304H Western ash
3000	27	22	25

Exposure time, hours	Metal Loss of Alloys, µm	
	IN617	IN617 Eastern ash
3000	Negligible	Negligible

1 mil = 0.001” = 25.4 Micrometers

Table 16. Total Metal Loss of Alloys for Condition 6

Exposure time, hours	Metal Loss of Alloys, mils					
	T23	T23 Eastern ash	T24	T24 Eastern ash	T92	T92 Eastern Ash
0	0	0	0	0	0	0
1000	2	2	2	2	2	1
3000	4	3	4	4	3	2

Exposure time, hours	Metal Loss of Alloys, µm		
	S304H	S304H Eastern ash	S304H Western ash
3000	18	37	39

Exposure time, hours	Metal Loss of Alloys, µm	
	IN617	IN617 Eastern ash
3000	Negligible	Negligible

1 mil = 0.001” = 25.4 Micrometers

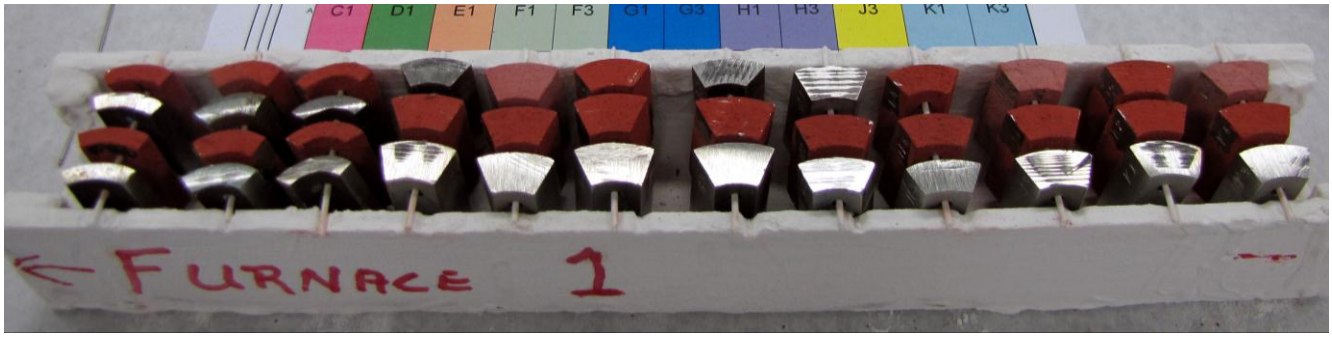

Figure 1. The top photo shows the tube furnaces that were used for the testing, while the bottom photo shows one of the ceramic boats with the test specimens (sample holder).

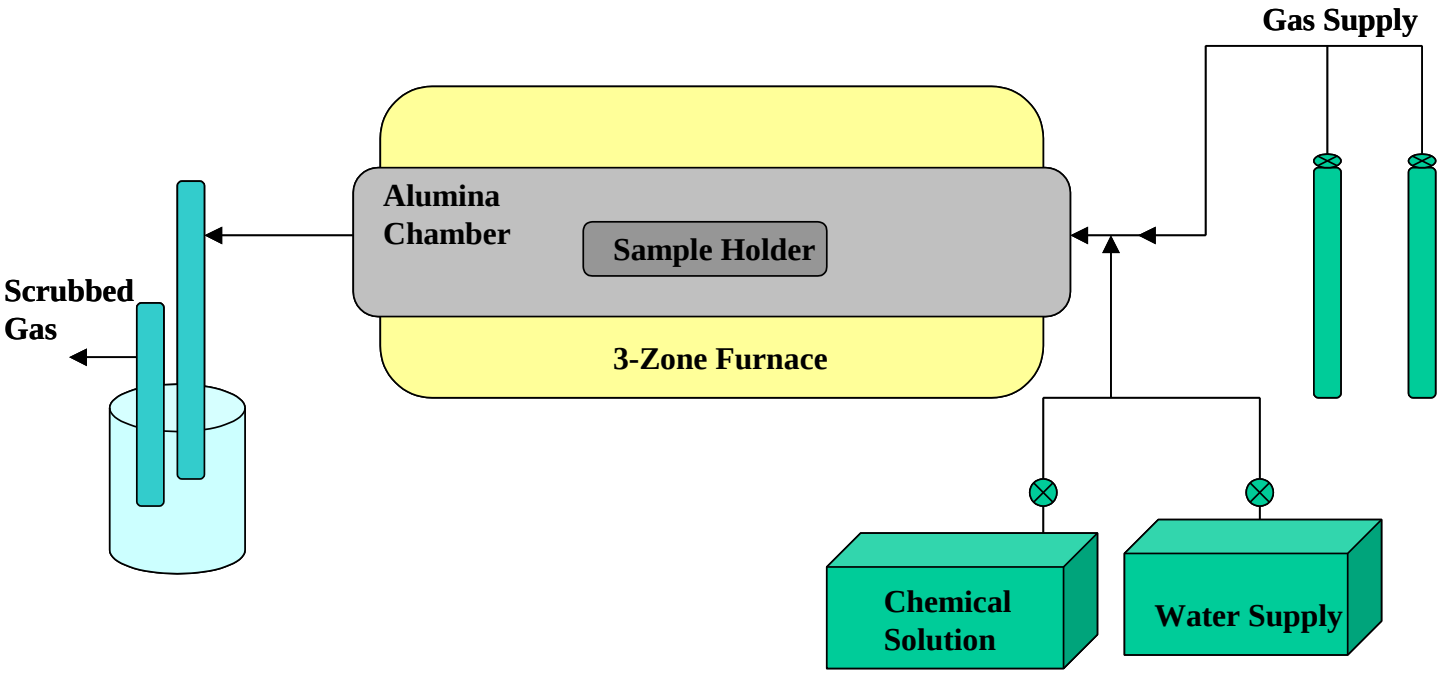

Figure 2. Shown is the schematic of the experimental set-up.

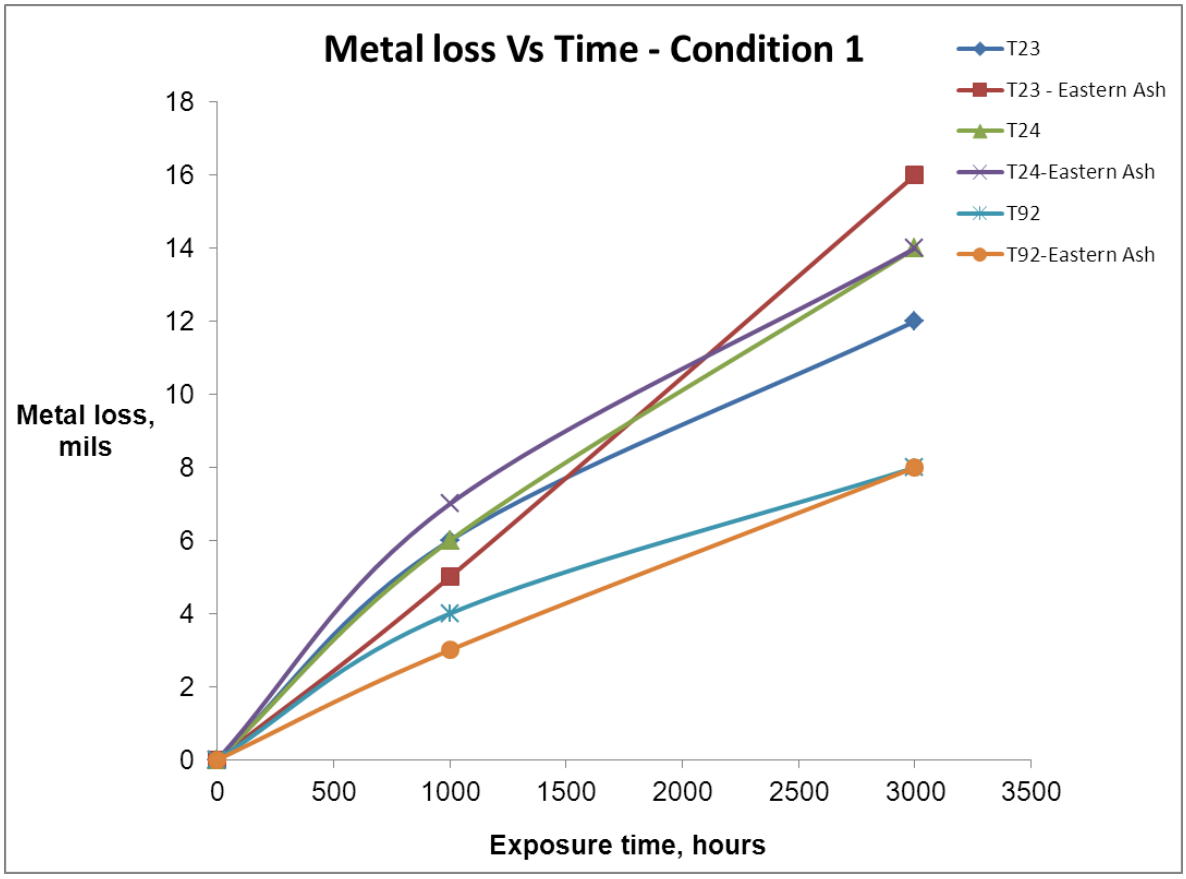

Figure 3. Documenting the metal loss vs. time plots for test condition 1 performed at 650°C.

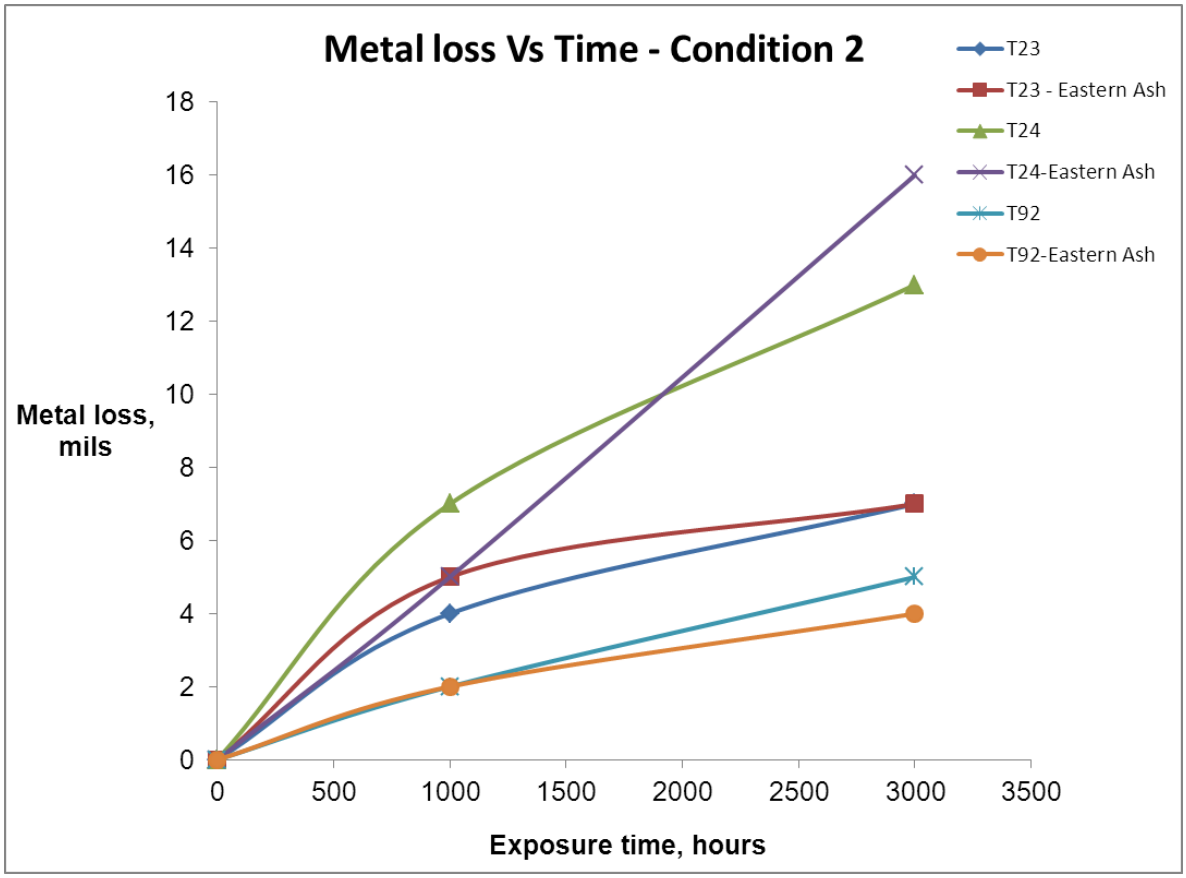

Figure 4. Documenting the metal loss vs. time plots for test condition 2 performed at 650°C.

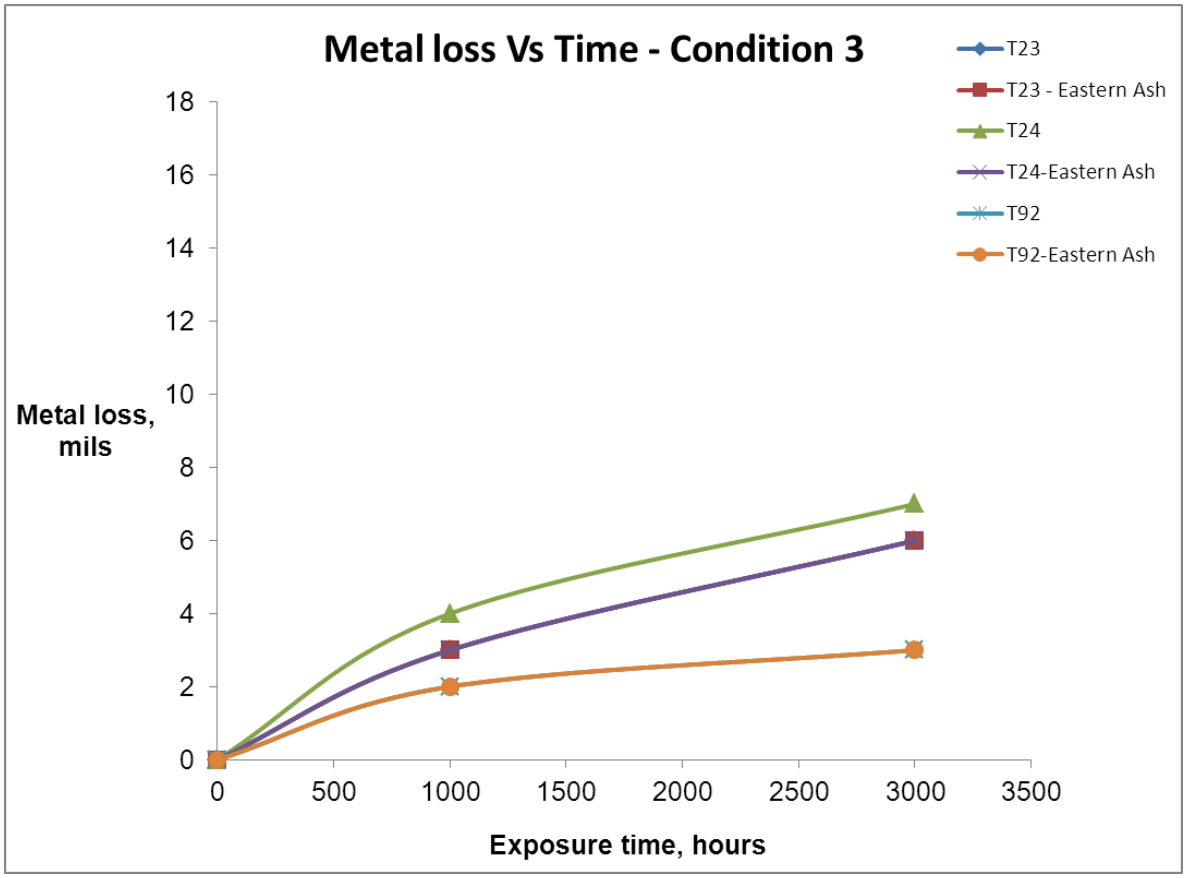

Figure 5. Documenting the metal loss vs. time plots for test condition 3 performed at 600°C.

.

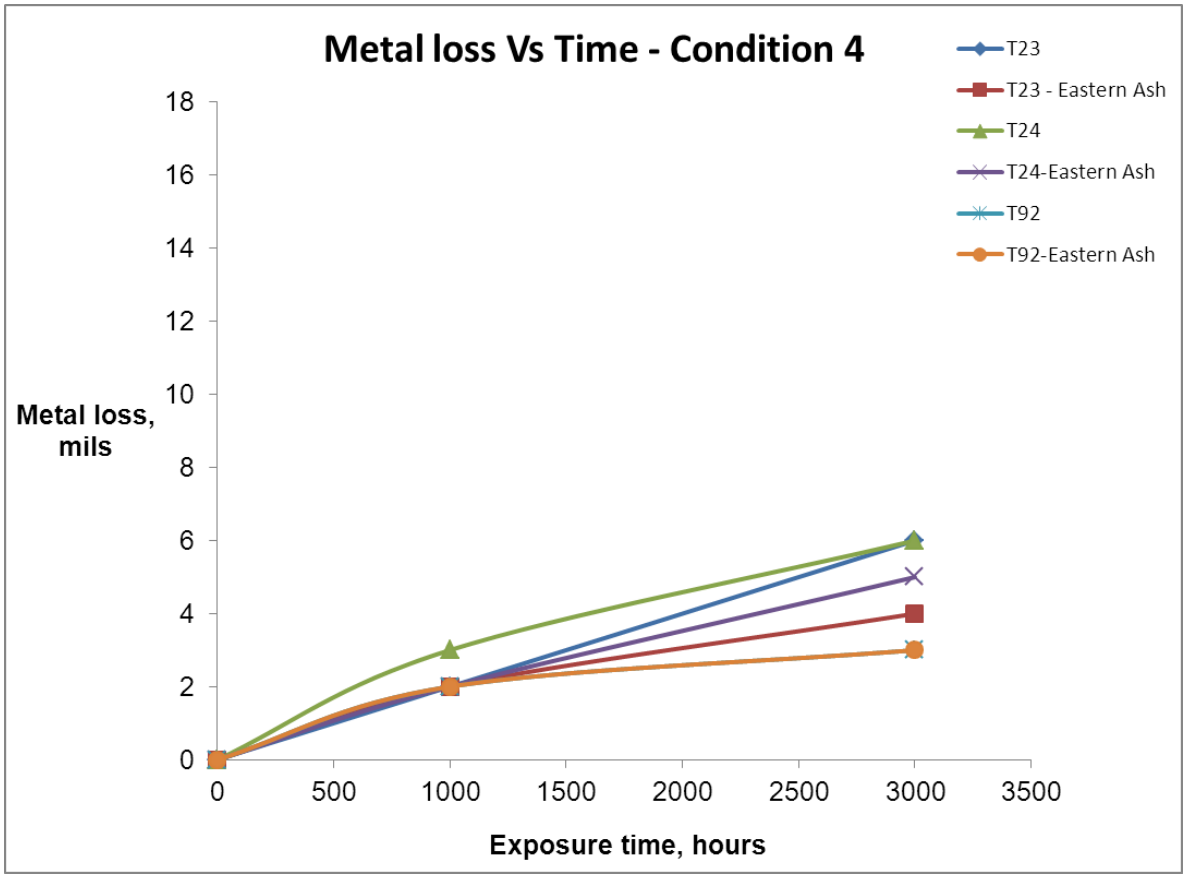

Figure 6. Documenting the metal loss vs. time plots for test condition 4 performed at 600°C.

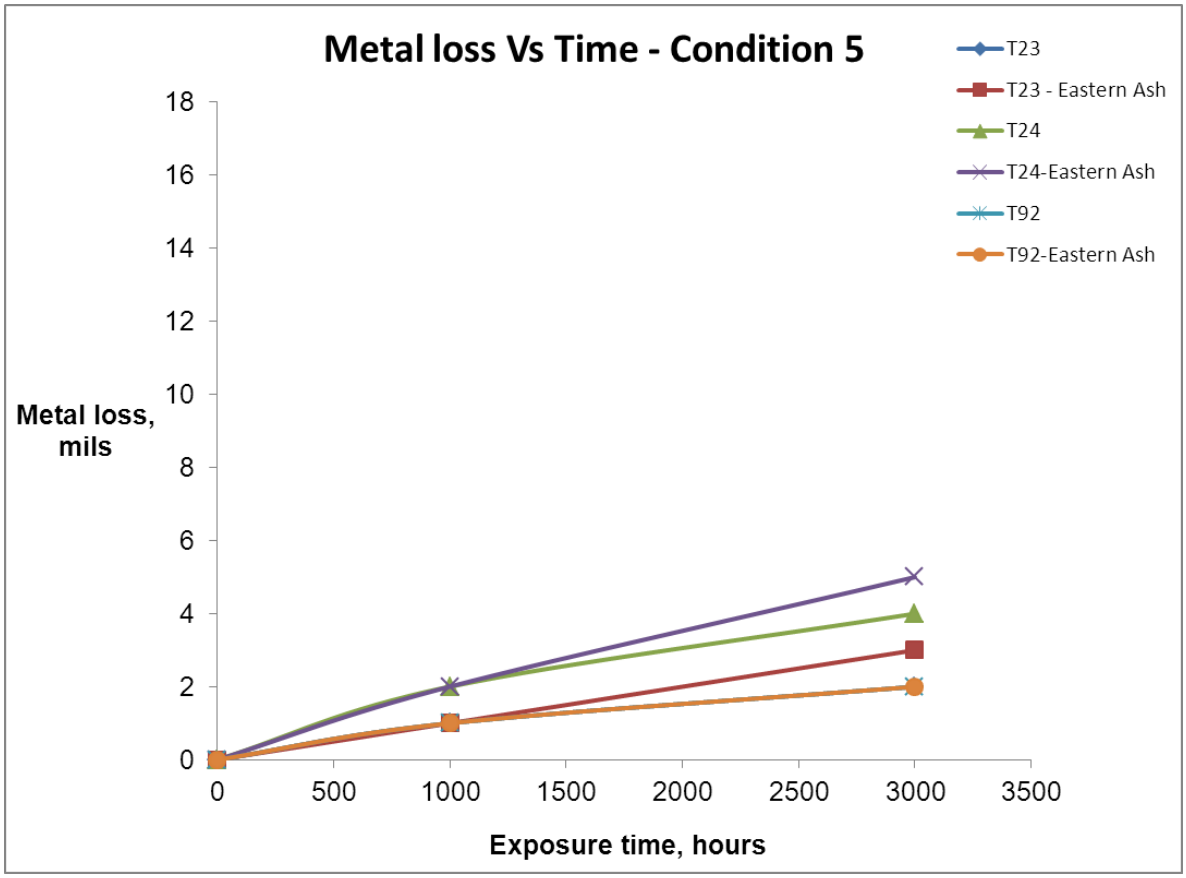

Figure 7. Documenting the metal loss vs. time plots for test condition 5 performed at 600°C.

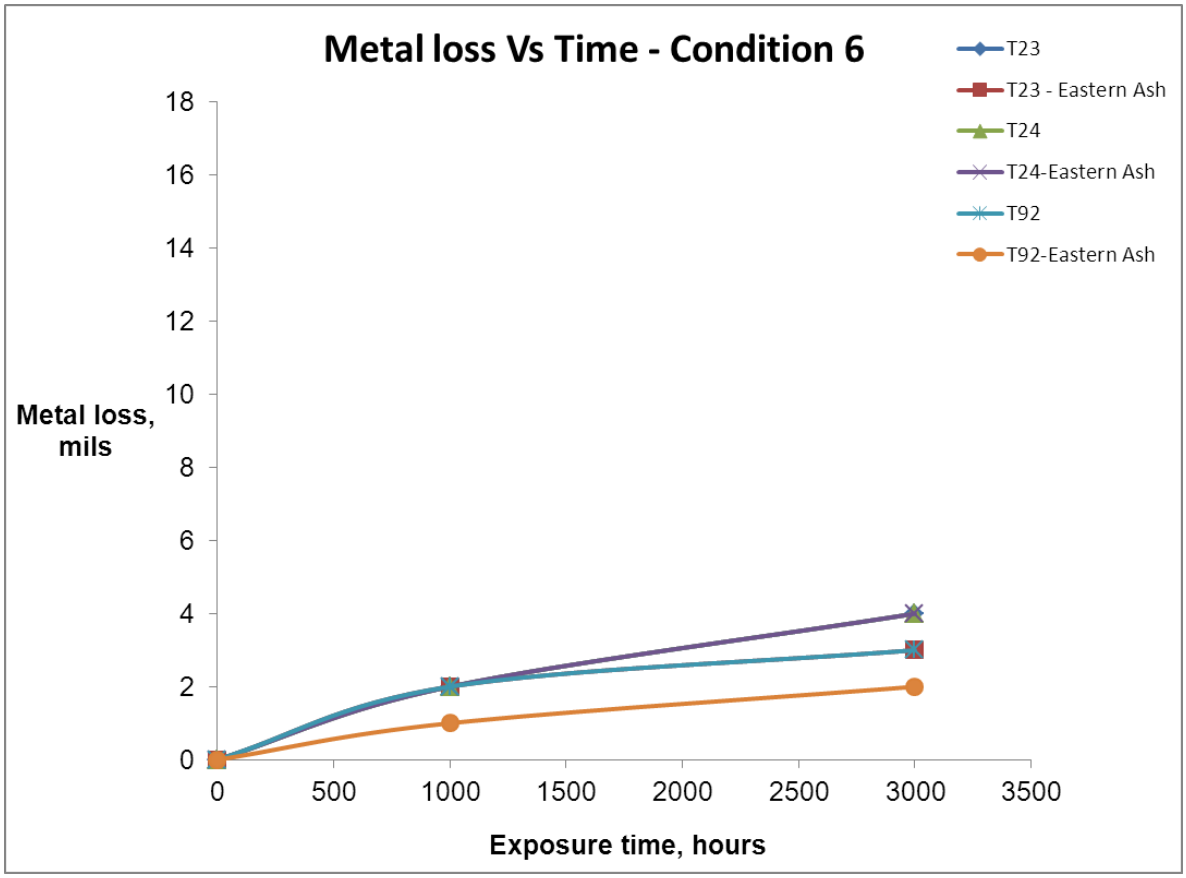

Figure 8. Documenting the metal loss vs. time plots for test condition 6 performed at 600°C.

Fireside Corrosion Conditions – Condition 1 Results – T23 Material

No Exposure	After 1000 hours	After 3000 hours
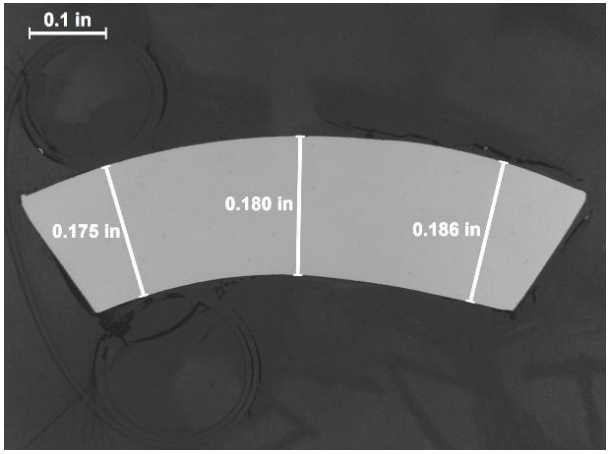	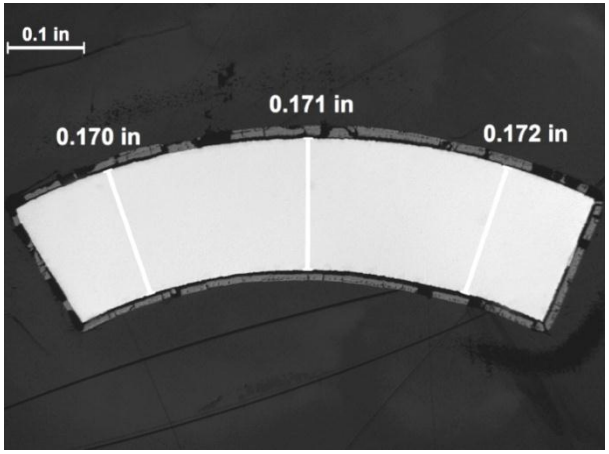	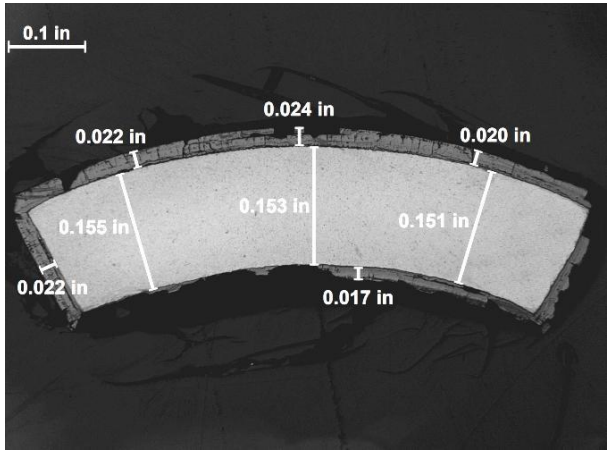
	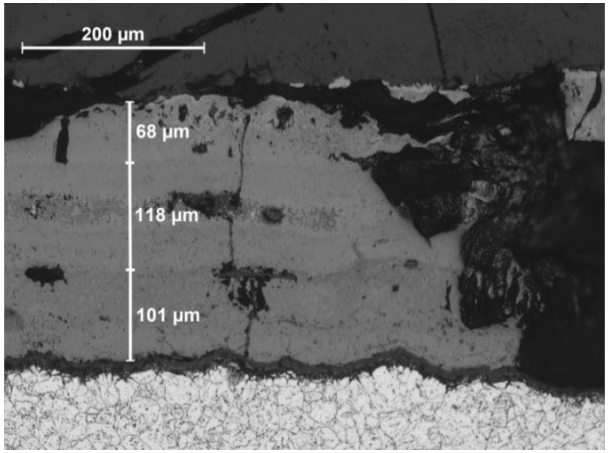	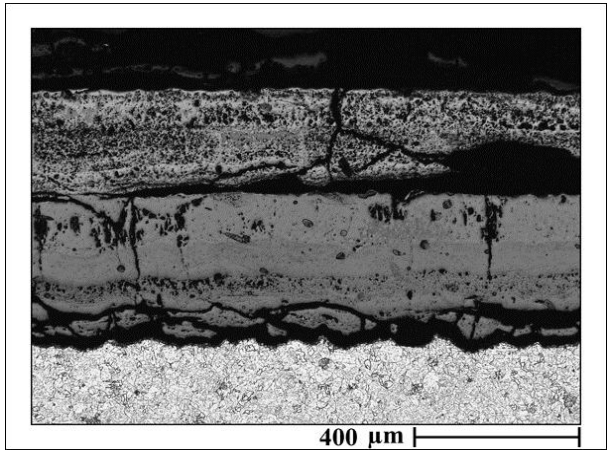

Fireside Corrosion Conditions – Condition 1 Results – T23 Material with Eastern Ash

No Exposure	After 1000 hours	After 3000 hours
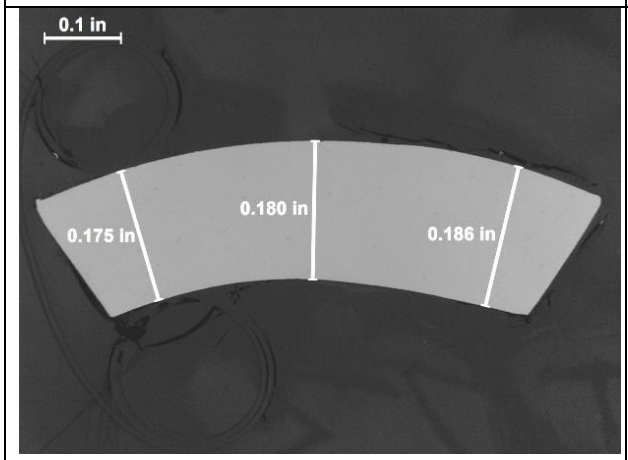	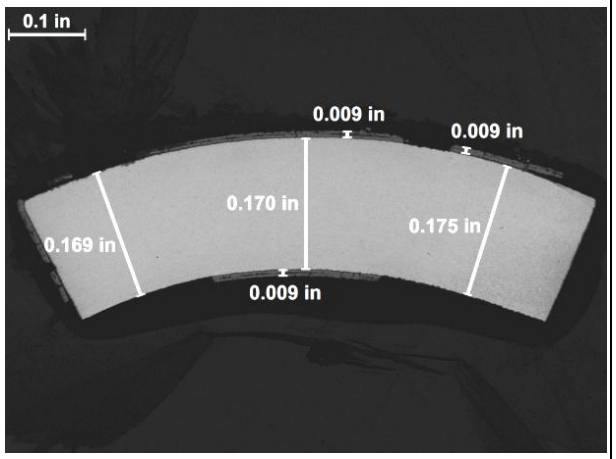	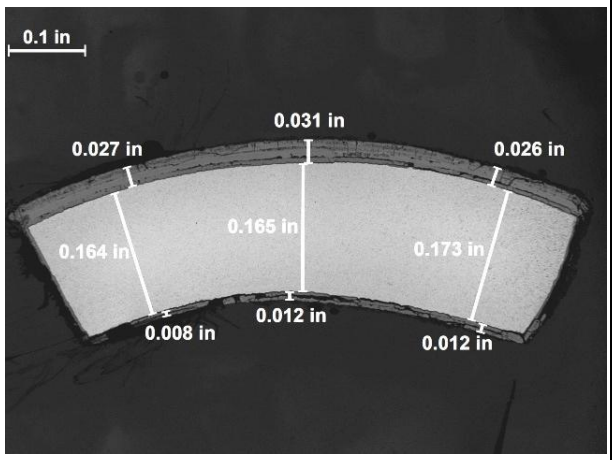
	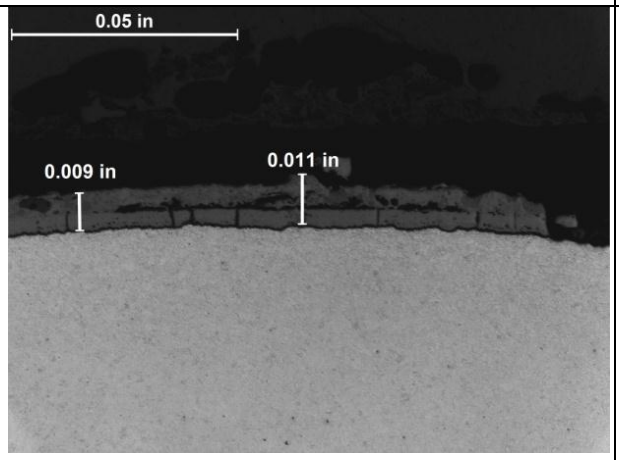	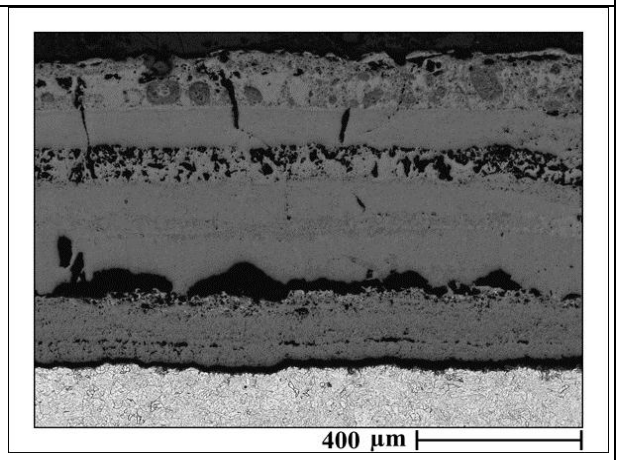

Fireside Corrosion Conditions – Condition 1 Results – T24 Material

No Exposure	After 1000 hours	After 3000 hours
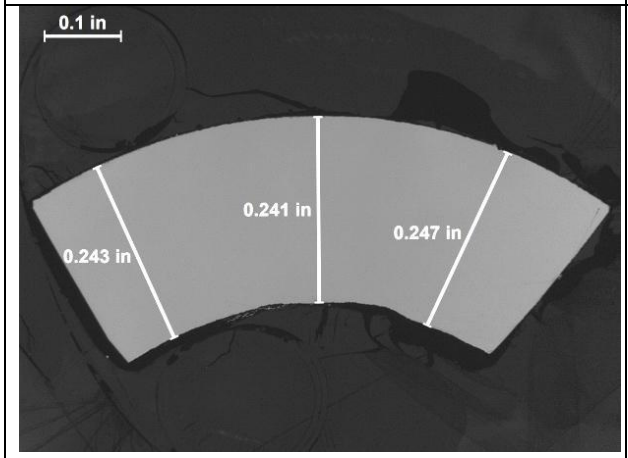	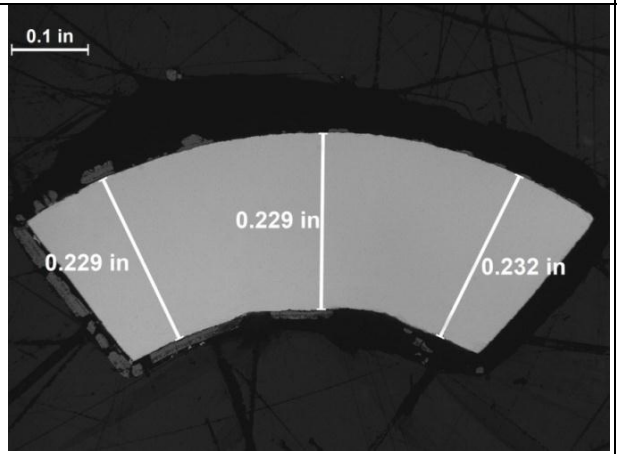	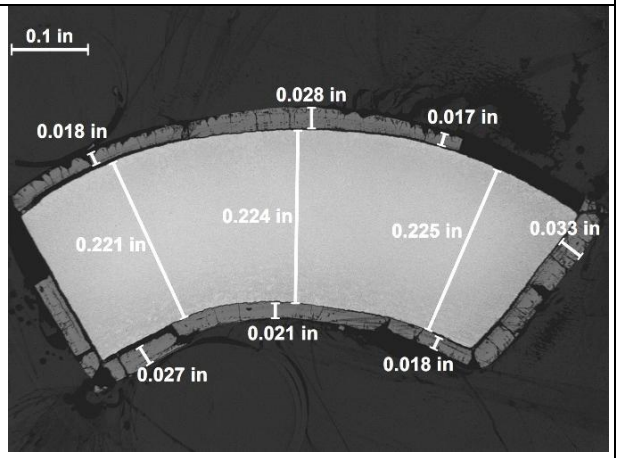
	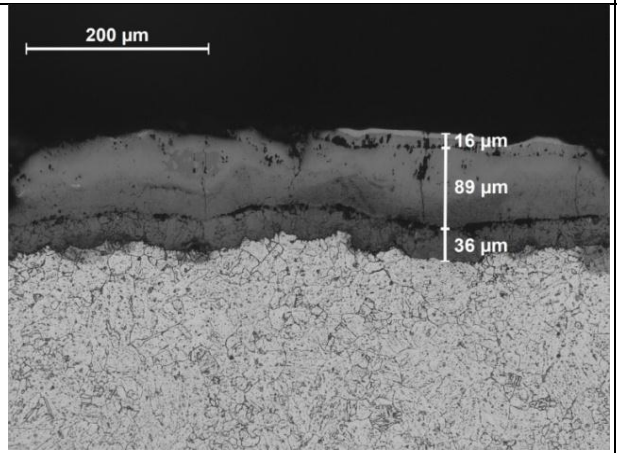	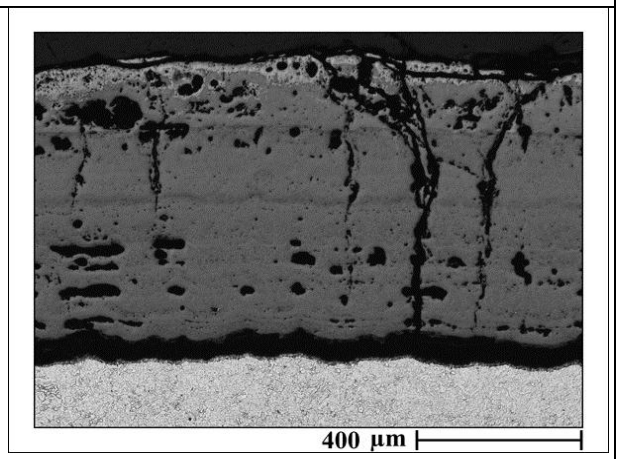

Fireside Corrosion Conditions – Condition 1 Results – T24 Material with Eastern Ash

No Exposure	After 1000 hours	After 3000 hours
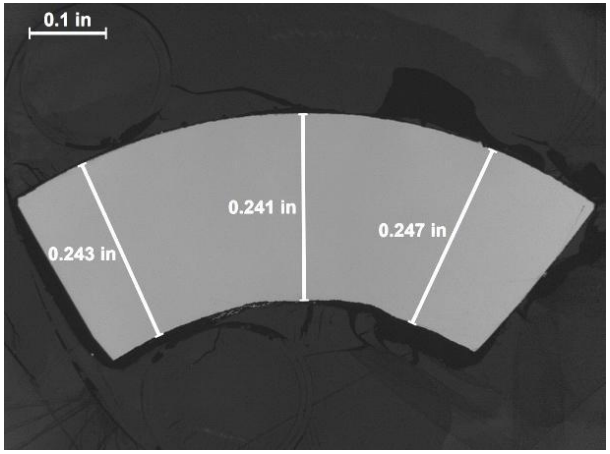	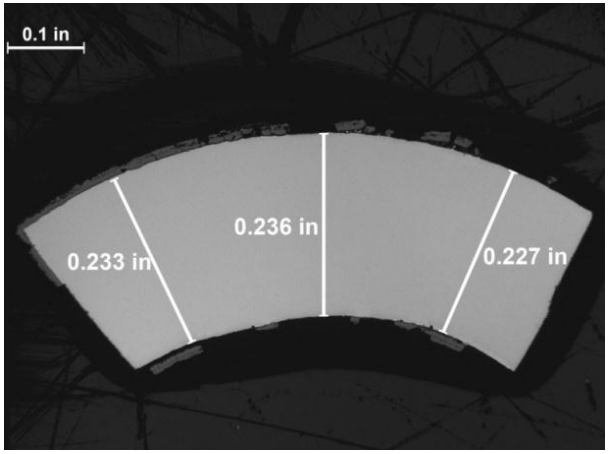	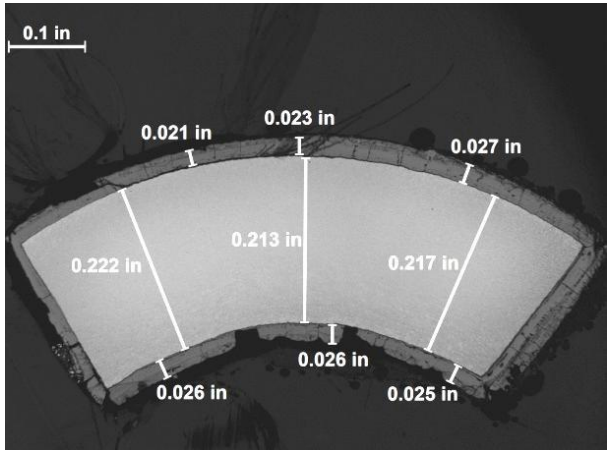
	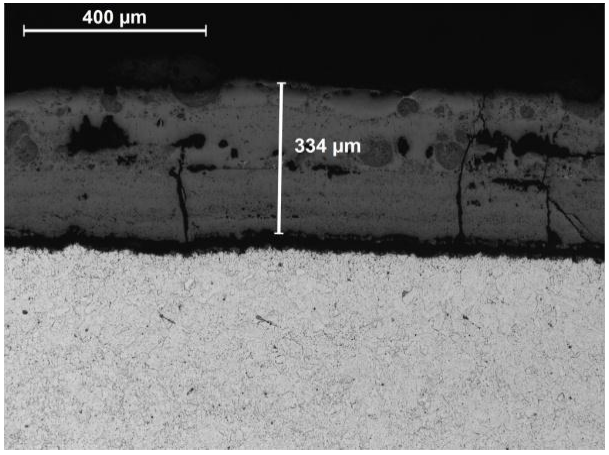	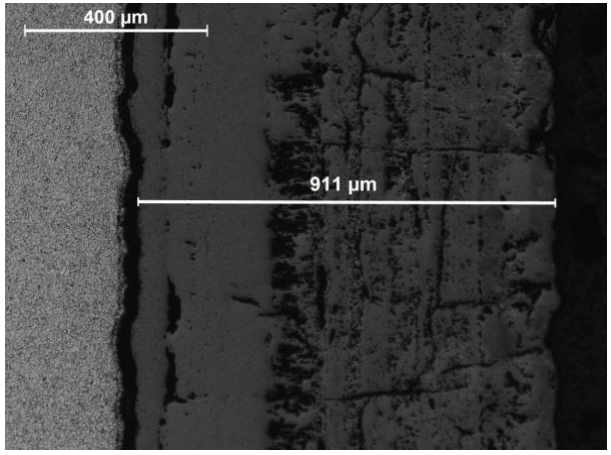

Fireside Corrosion Conditions – Condition 1 Results – T92 Material

No Exposure	After 1000 hours	After 3000 hours
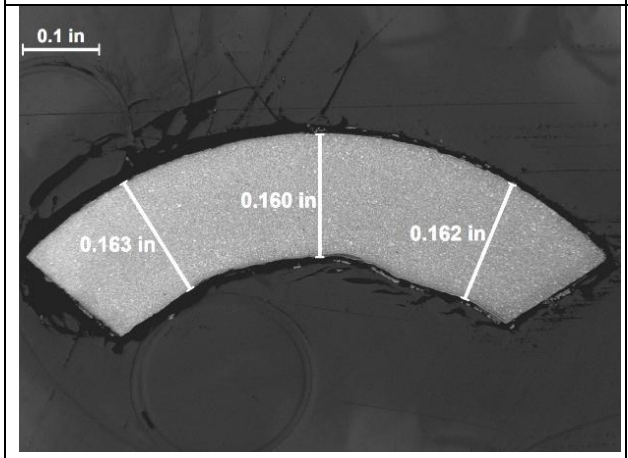	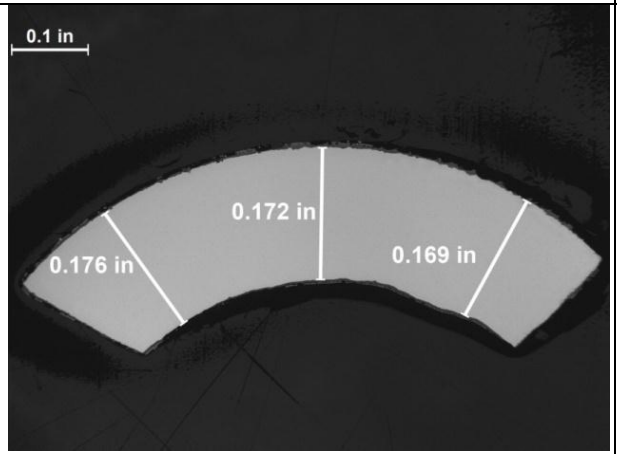	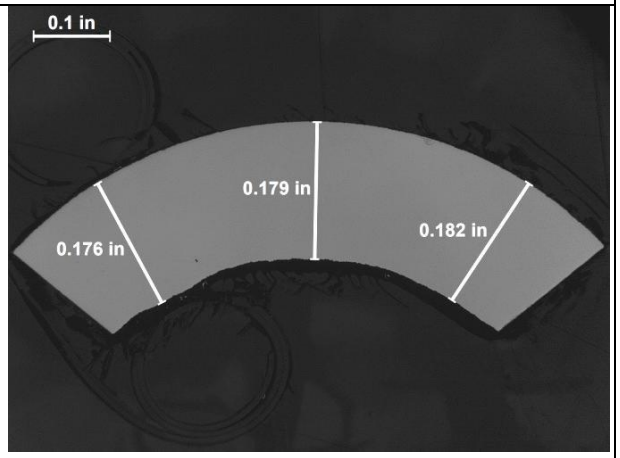
	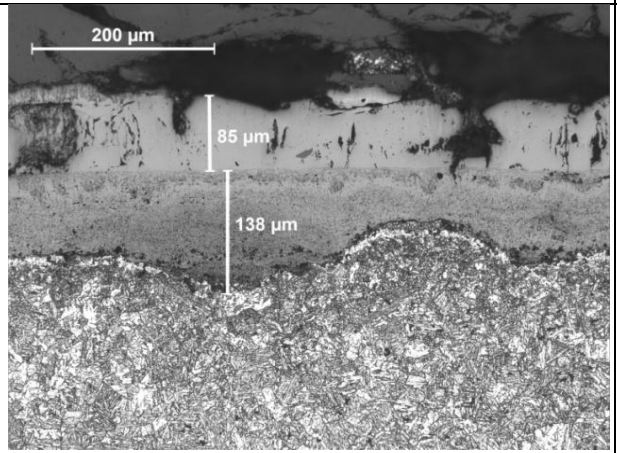	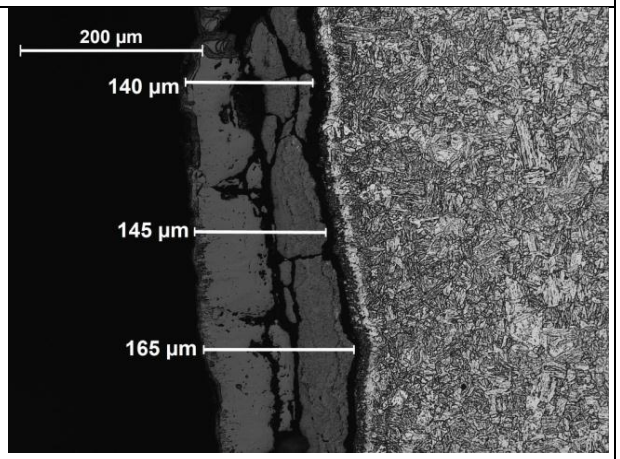

Fireside Corrosion Conditions – Condition 1 Results – T92 Material with Eastern Ash

No Exposure	After 1000 hours	After 3000 hours
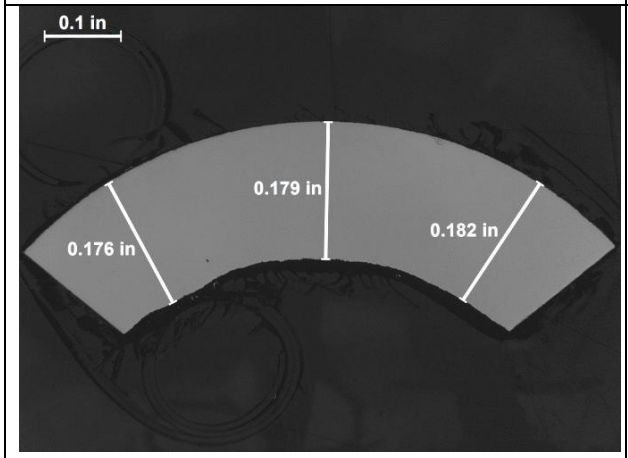	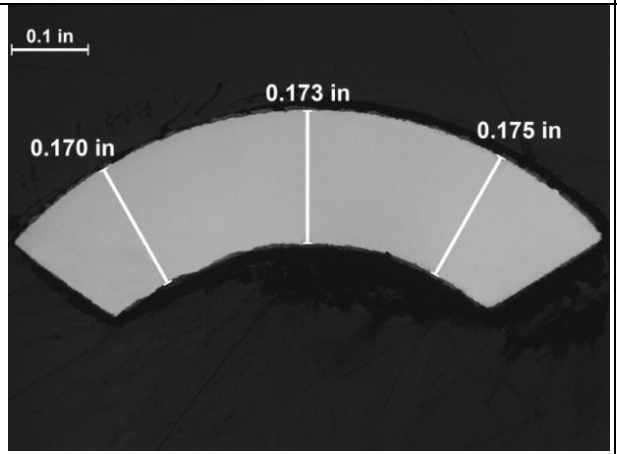	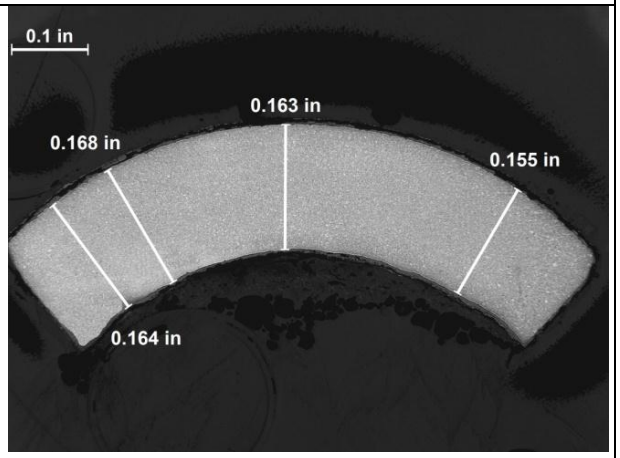
	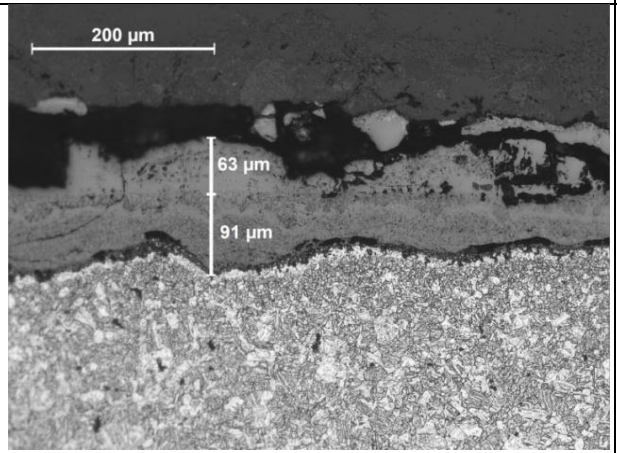	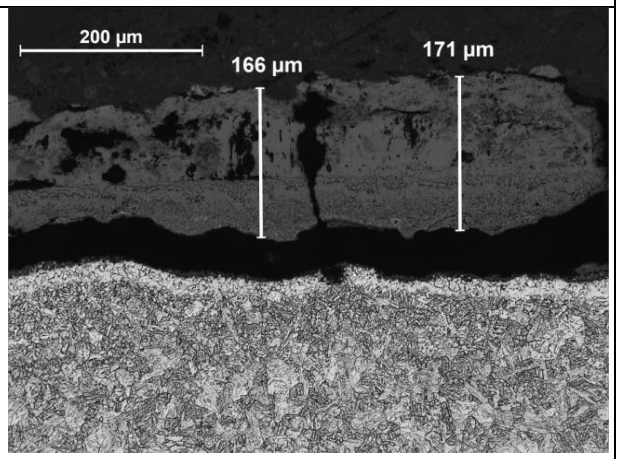

Fireside Corrosion Conditions – Condition 1 Results – Super304H Material

No Exposure	After 1000 hours	After 3000 hours
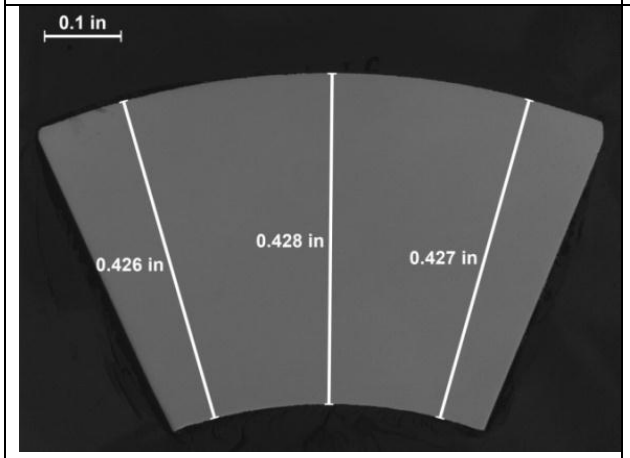	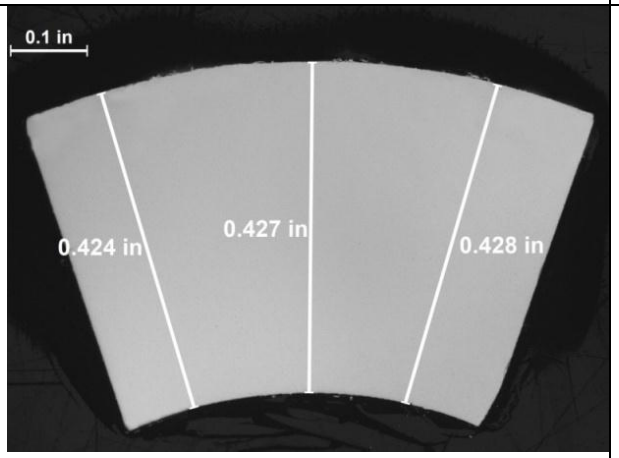	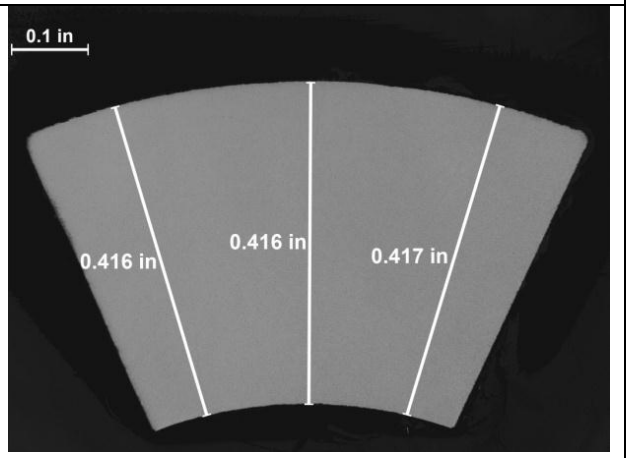
	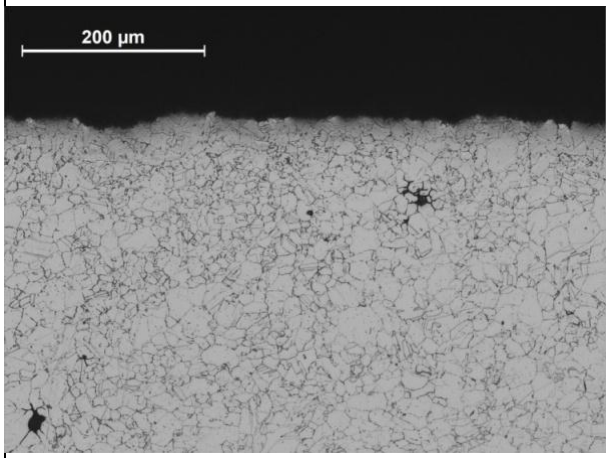	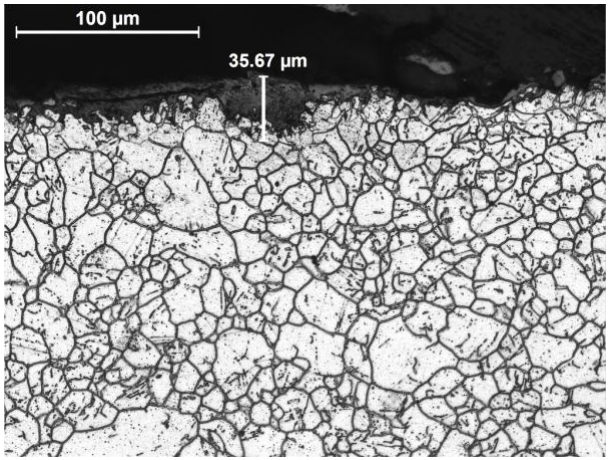

Fireside Corrosion Conditions – Condition 1 Results – Super304H Material with Eastern Ash

No Exposure	After 1000 hours	After 3000 hours
	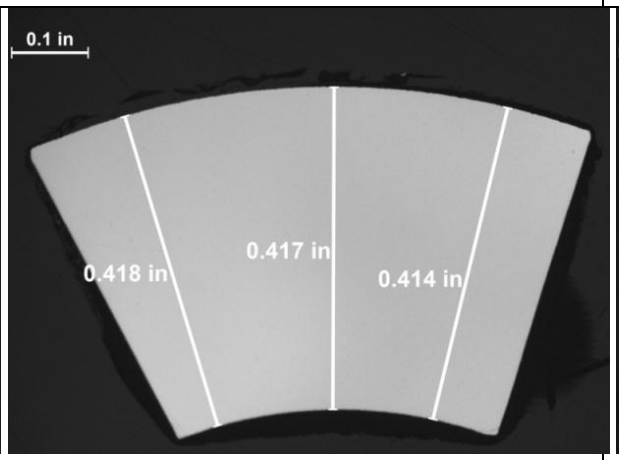	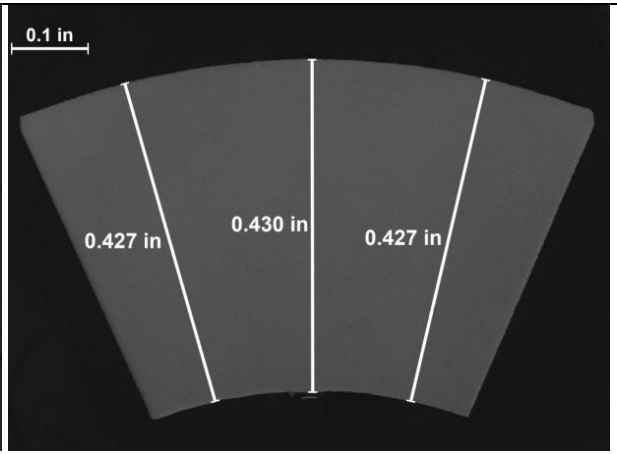
	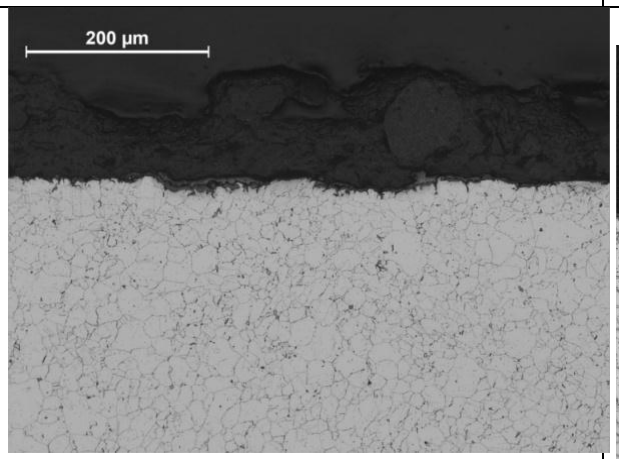	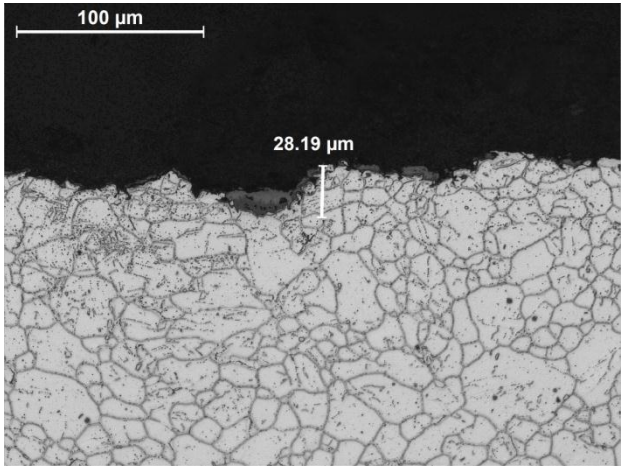

Fireside Corrosion Conditions – Condition 1 Results – Super304H Material with Western Ash

No Exposure	After 1000 hours	After 3000 hours
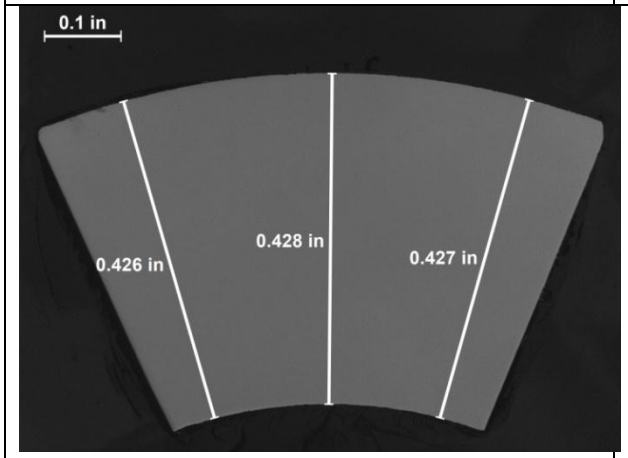	Not included in the test matrix	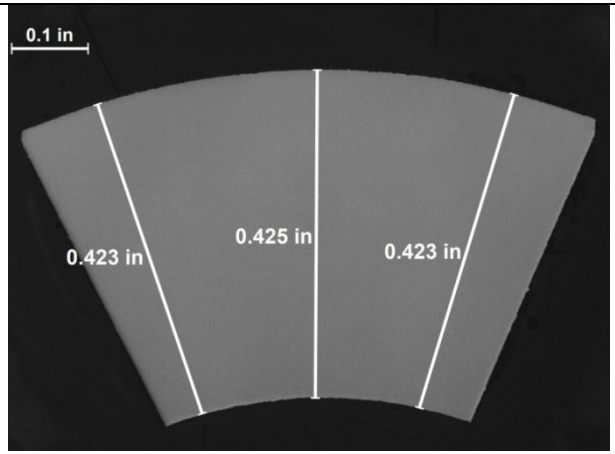
	Not included in the test matrix	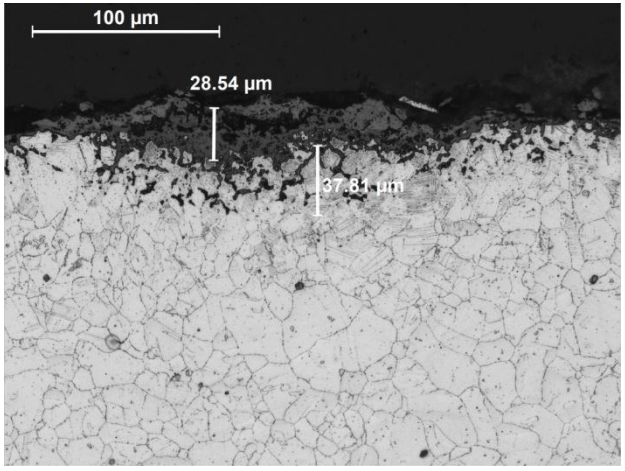

Fireside Corrosion Conditions – Condition 1 Results – IN617 Material

No Exposure	After 1000 hours	After 3000 hours
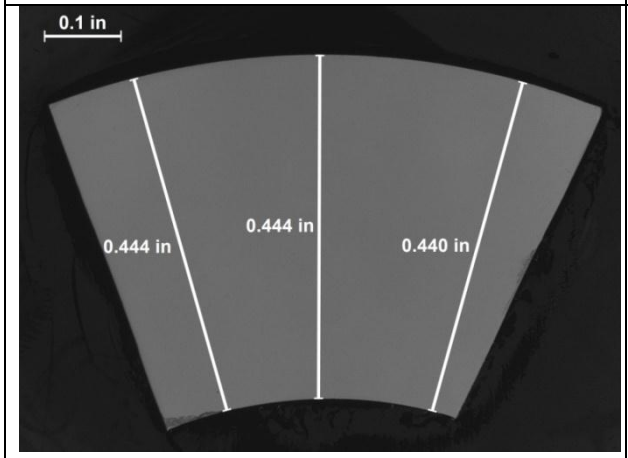	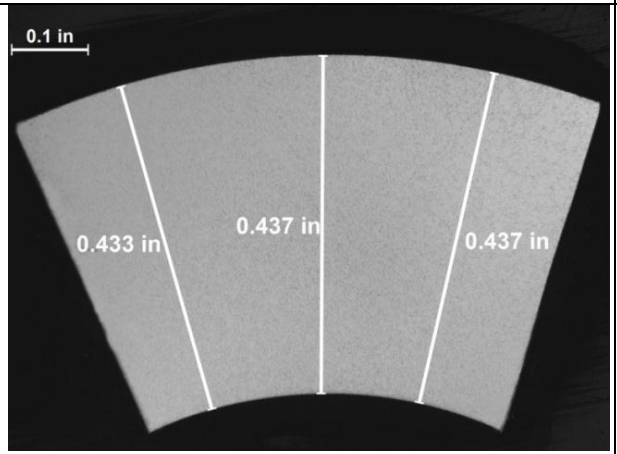	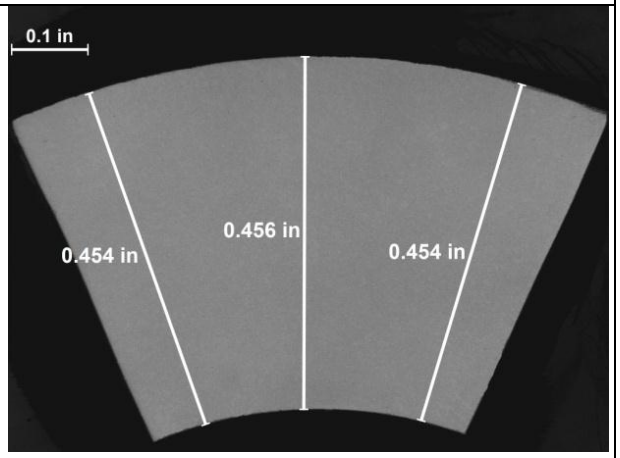
	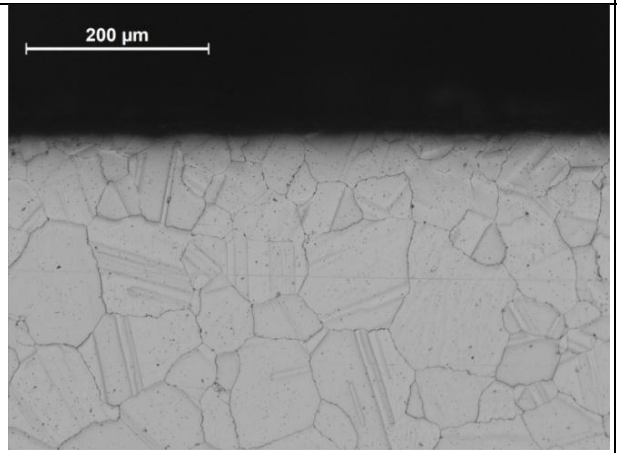	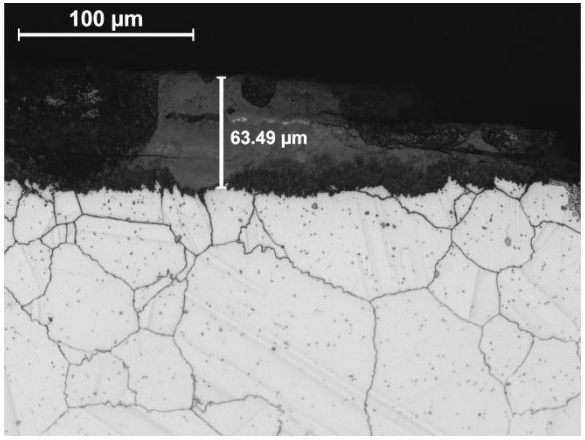

Fireside Corrosion Conditions – Condition 1 Results – IN617 Material with Eastern Ash

No Exposure	After 1000 hours	After 3000 hours
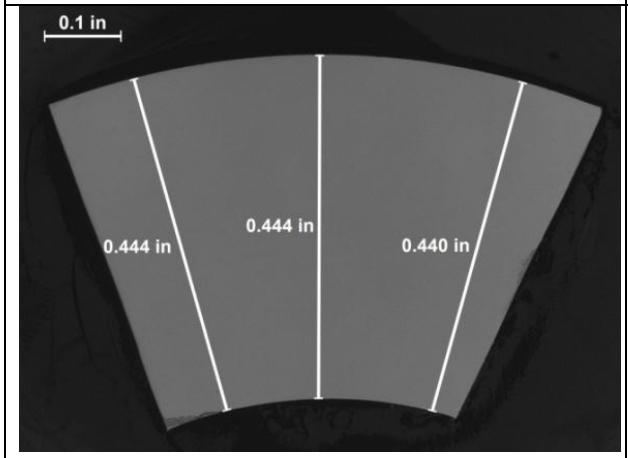	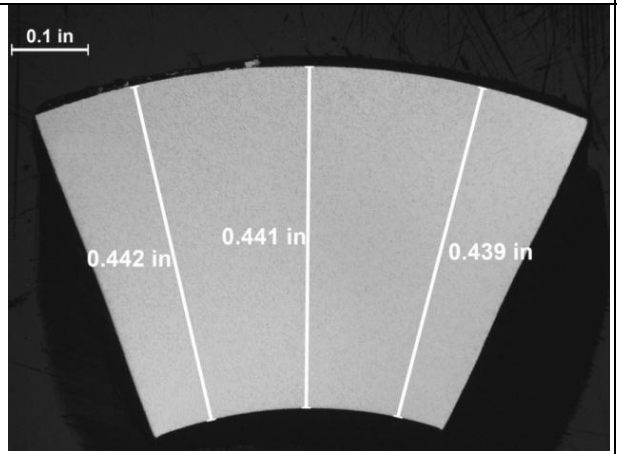	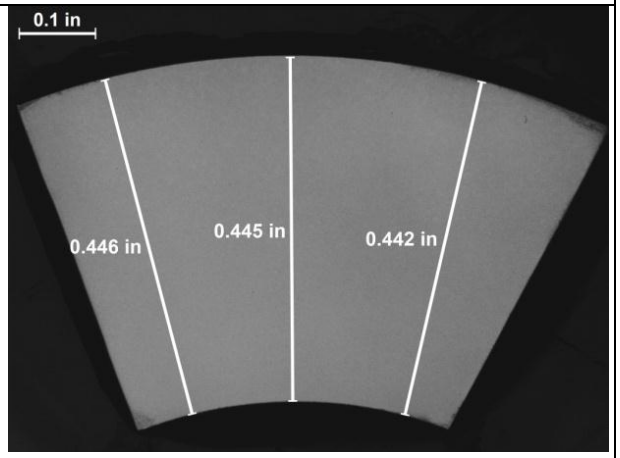
	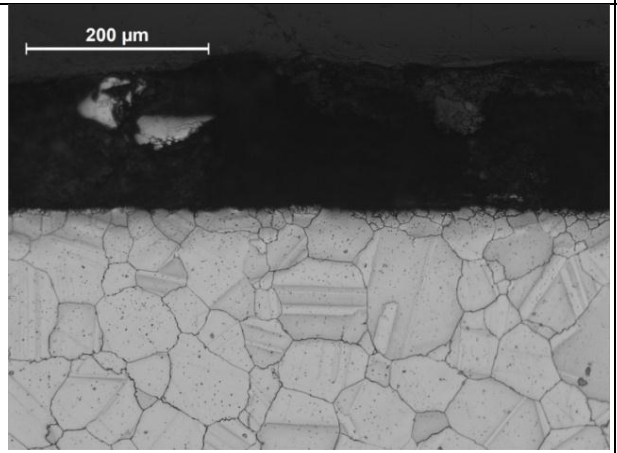	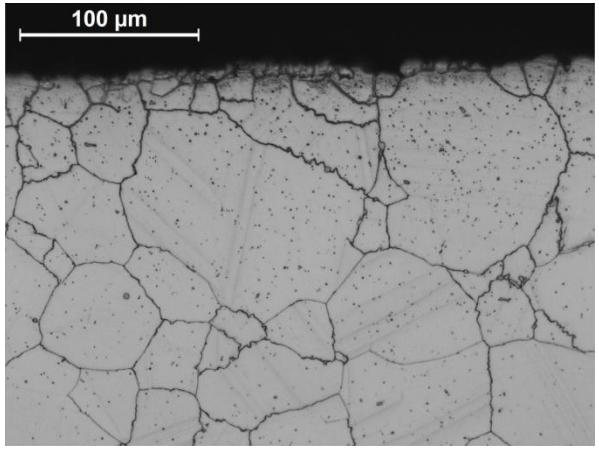

Fireside Corrosion Conditions – Condition 1 Results – NF709R Material

No Exposure	After 1000 hours	After 3000 hours
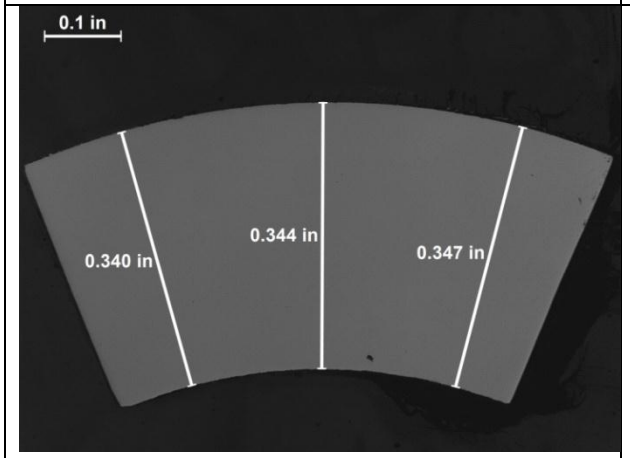	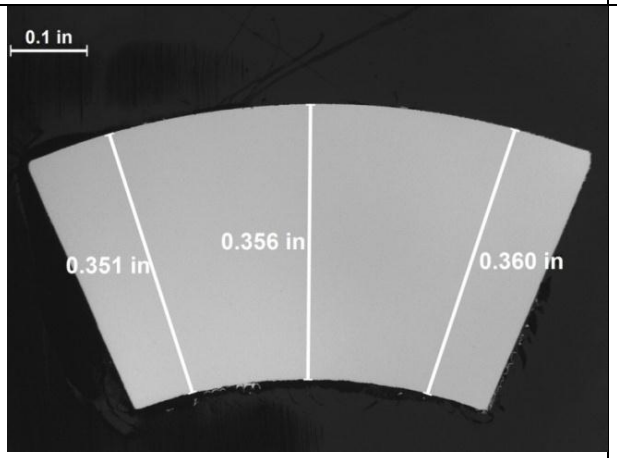	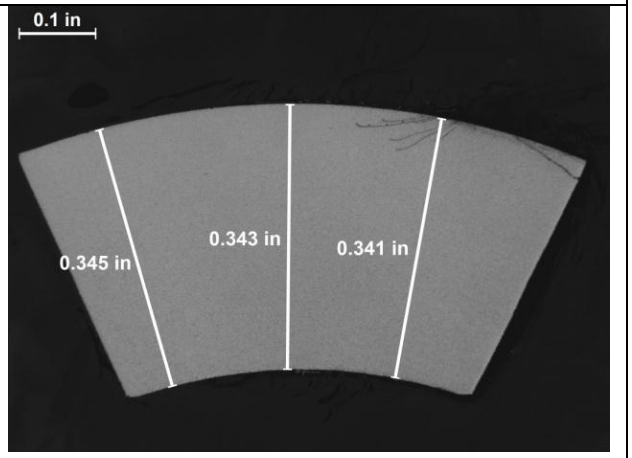
	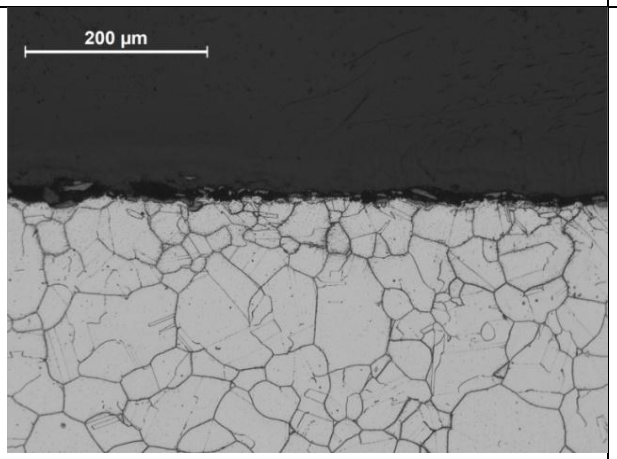	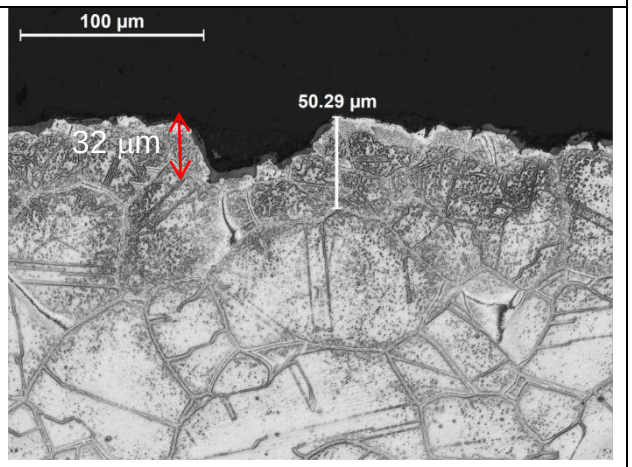

Fireside Corrosion Conditions – Condition 1 Results – NF709R Material with Eastern Ash

No Exposure	After 1000 hours	After 3000 hours
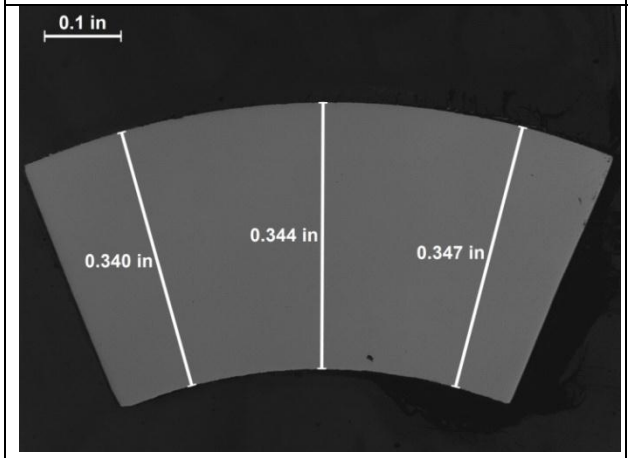	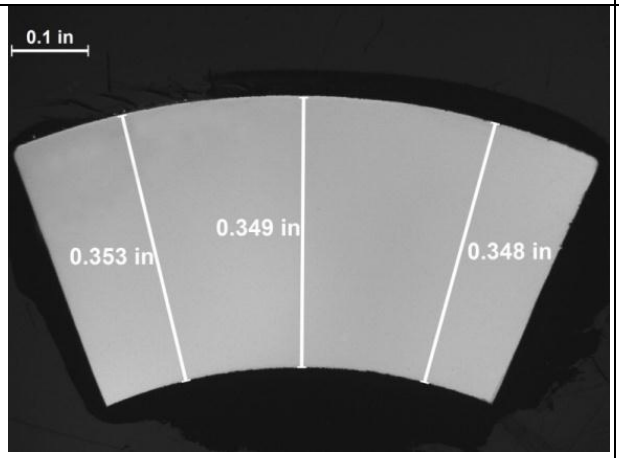	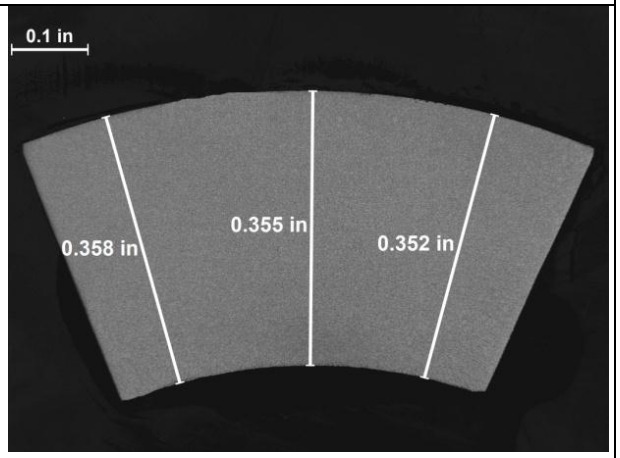
	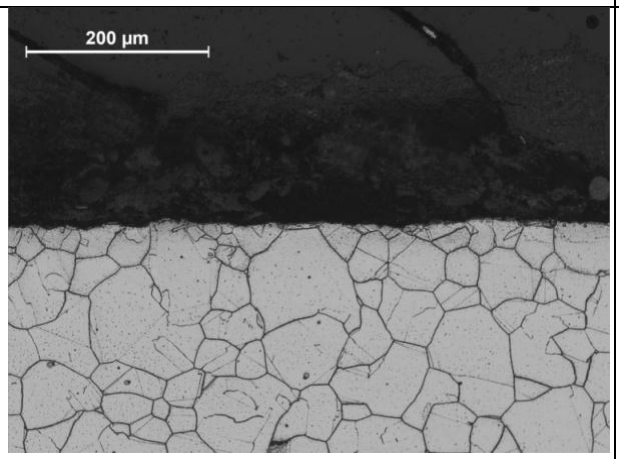	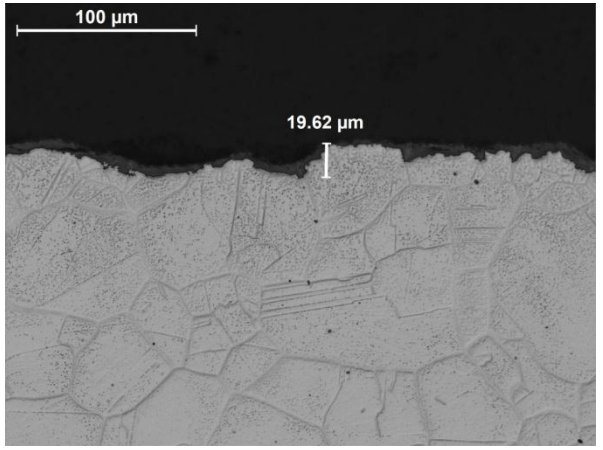

Fireside Corrosion Conditions – Condition 1 Results – Alloy 740 Material

No Exposure	After 1000 hours	After 3000 hours
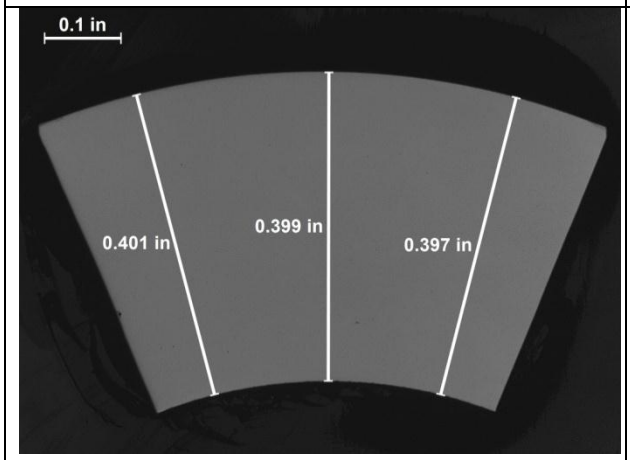	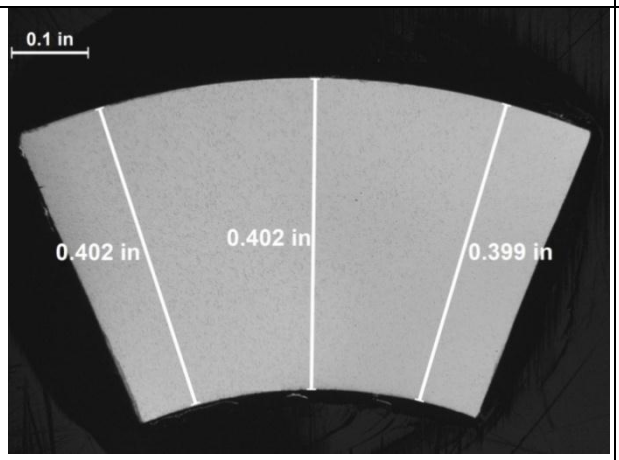	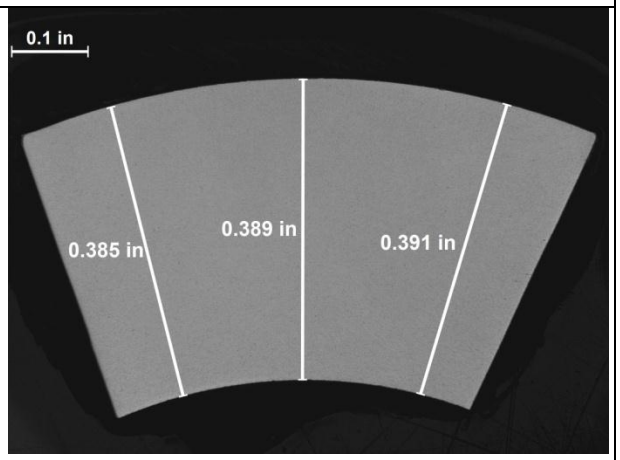
		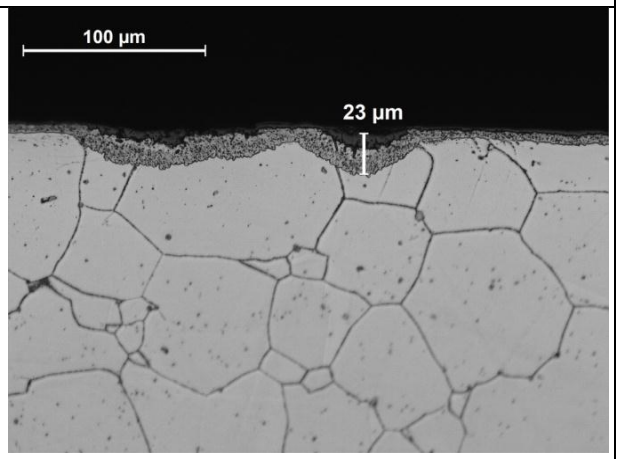

Fireside Corrosion Conditions – Condition 1 Results – Alloy 740 Material with Eastern Ash

No Exposure	After 1000 hours	After 3000 hours
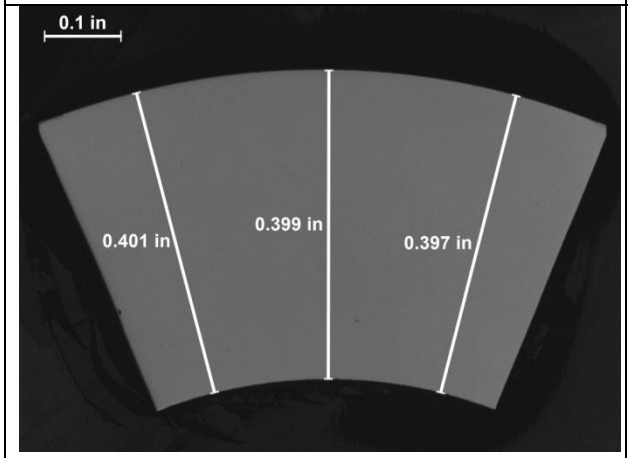	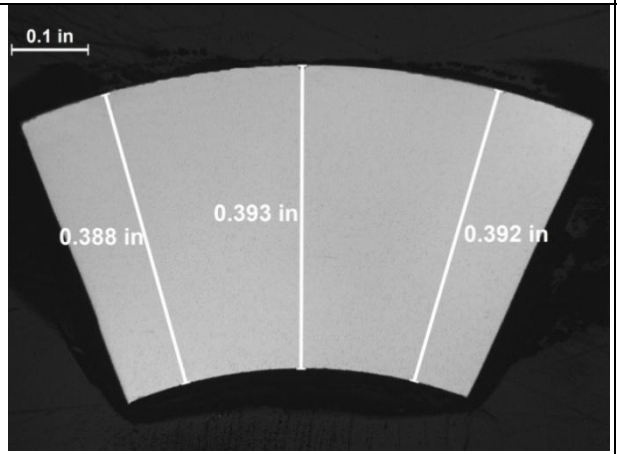	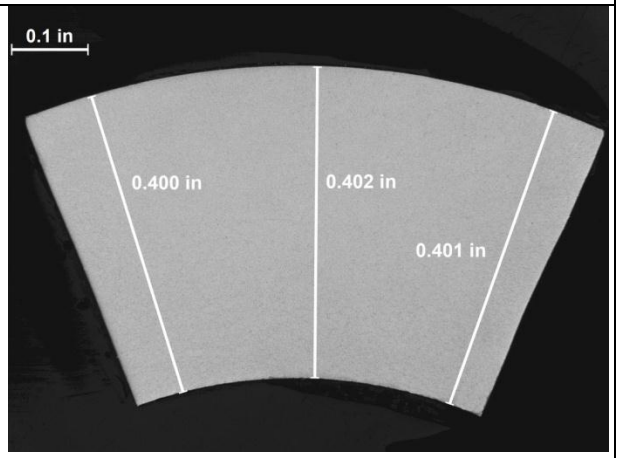
		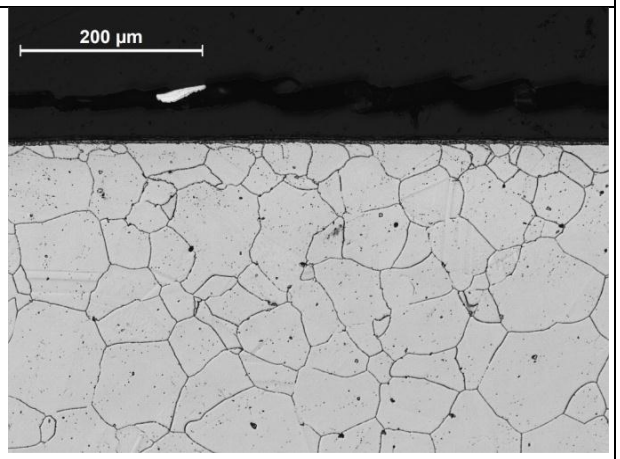

Fireside Corrosion Conditions – Condition 1 Results – Alloy 740 Material with Western Ash

No Exposure	After 1000 hours	After 3000 hours
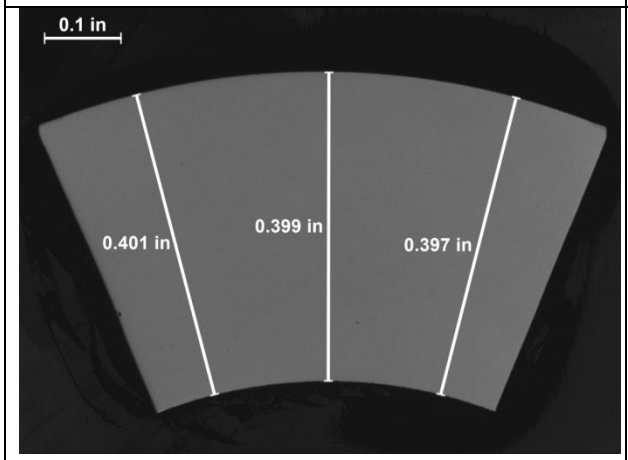	Not included in the test matrix	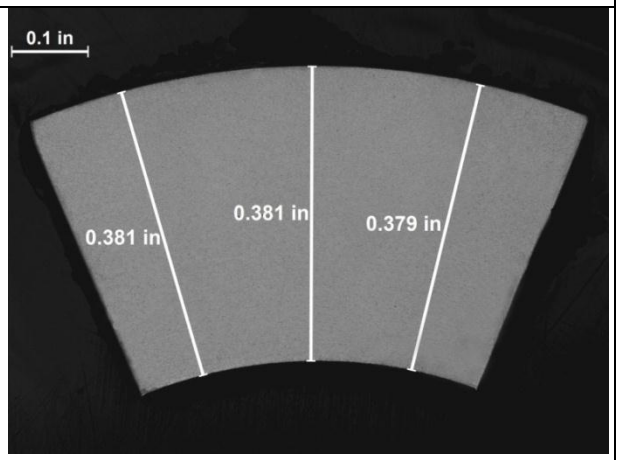
	Not included in the test matrix	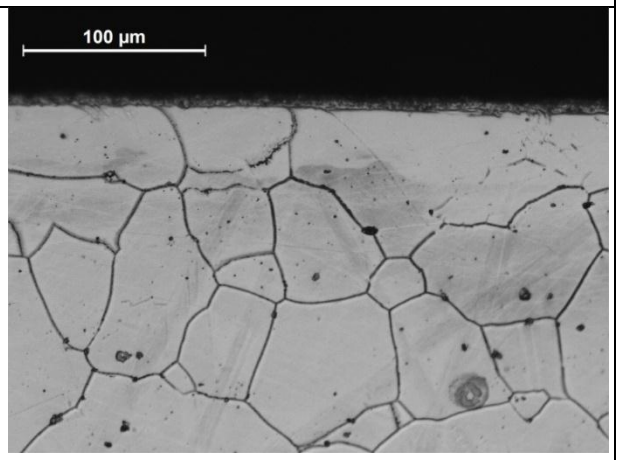

Fireside Corrosion Conditions – Condition 1 Results – HR3C Material

No Exposure	After 1000 hours	After 3000 hours
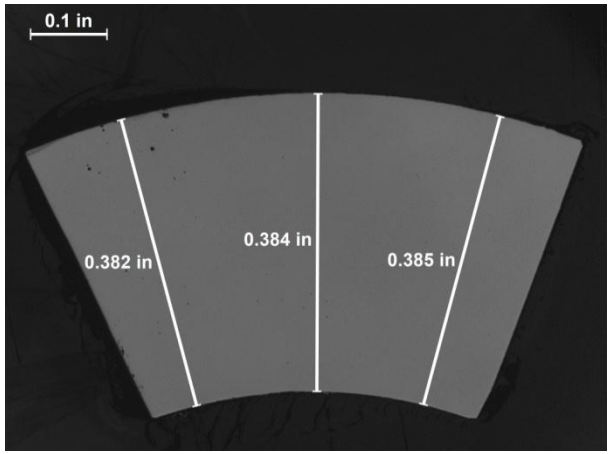	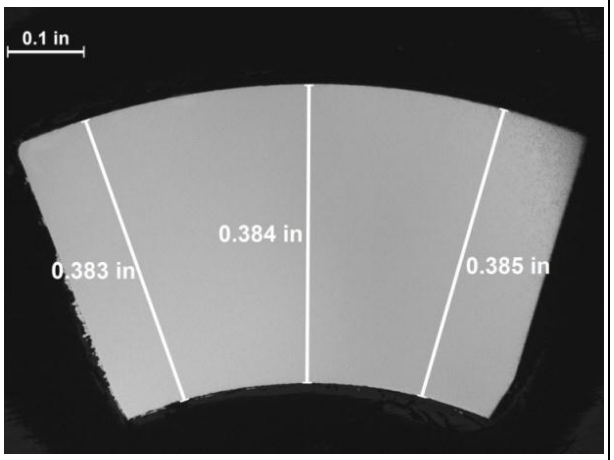	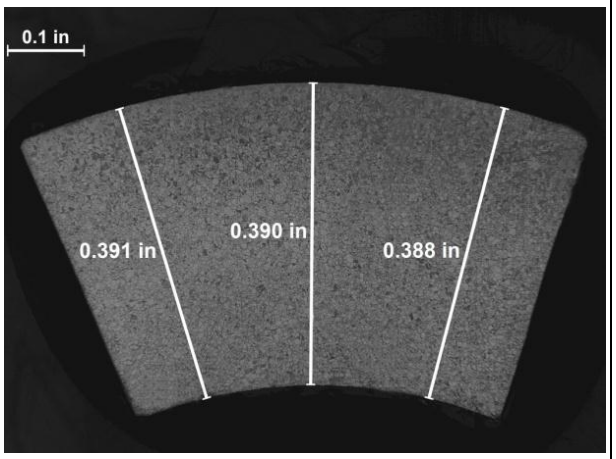
	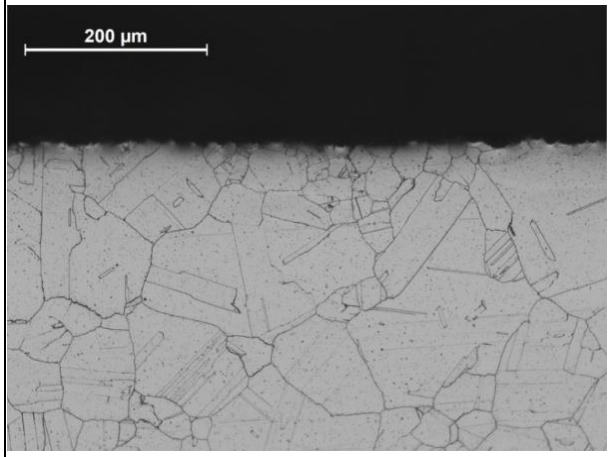	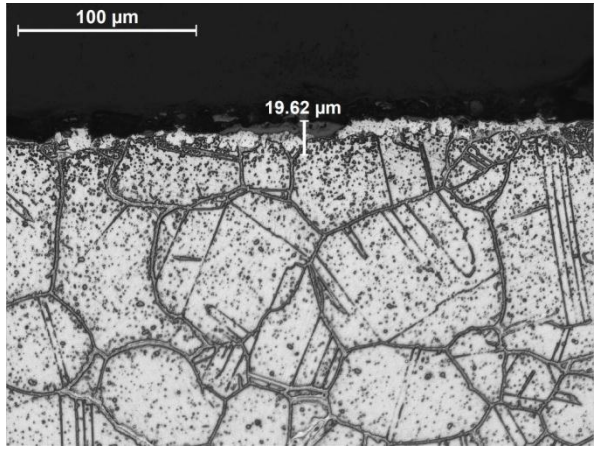

Fireside Corrosion Conditions – Condition 1 Results – HR3C Material with Eastern Ash

No Exposure	After 1000 hours	After 3000 hours
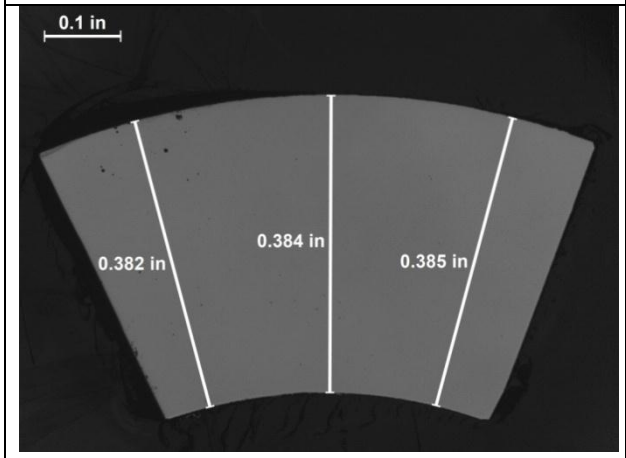	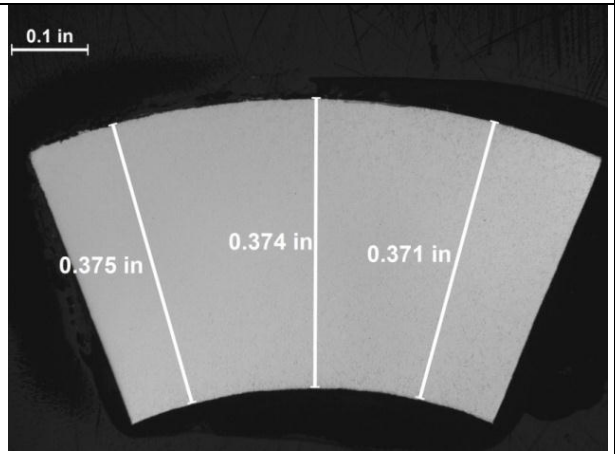	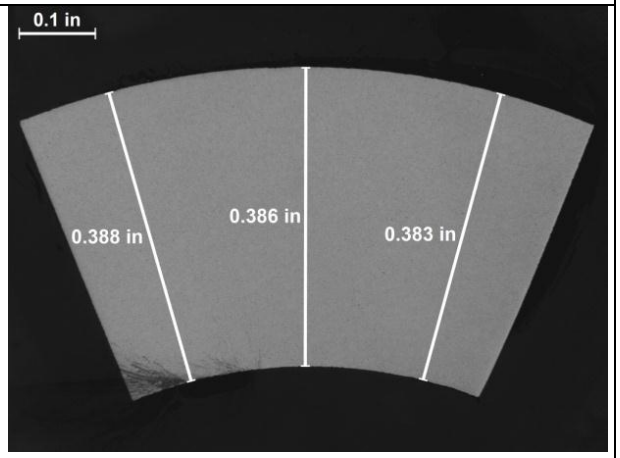
	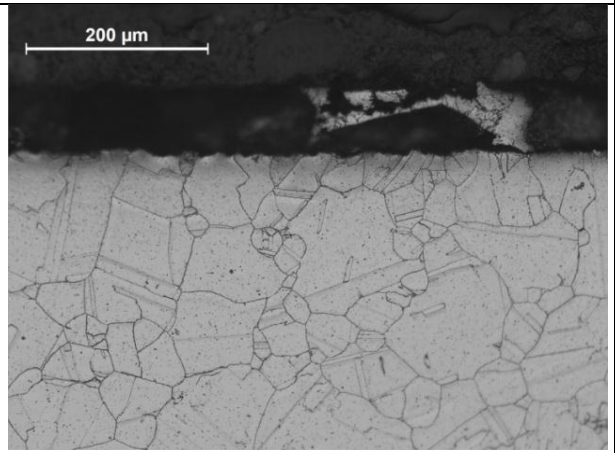	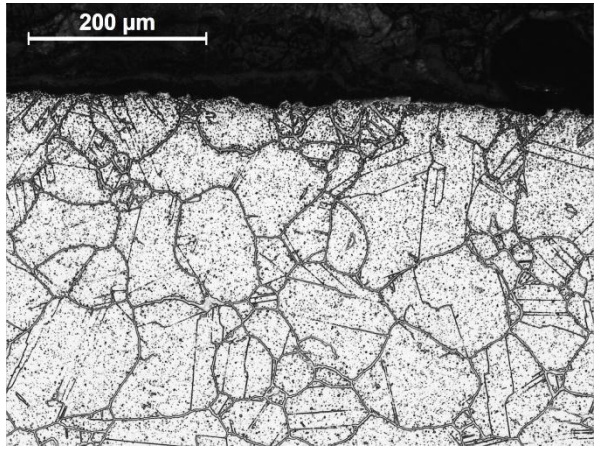

Fireside Corrosion Conditions – Condition 1 Results – HR3C Material with Western Ash

No Exposure	After 1000 hours	After 3000 hours
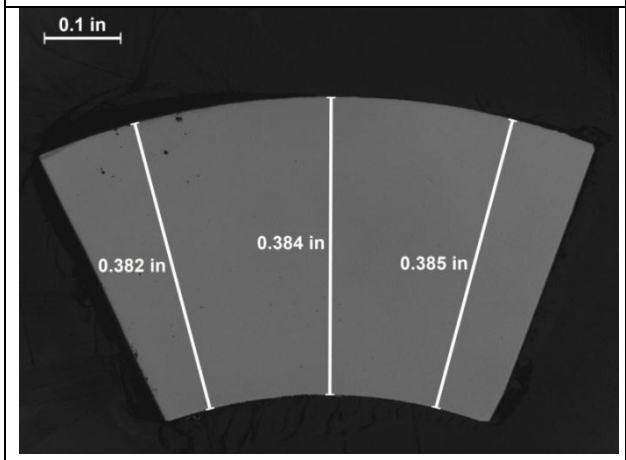	Not included in the test matrix	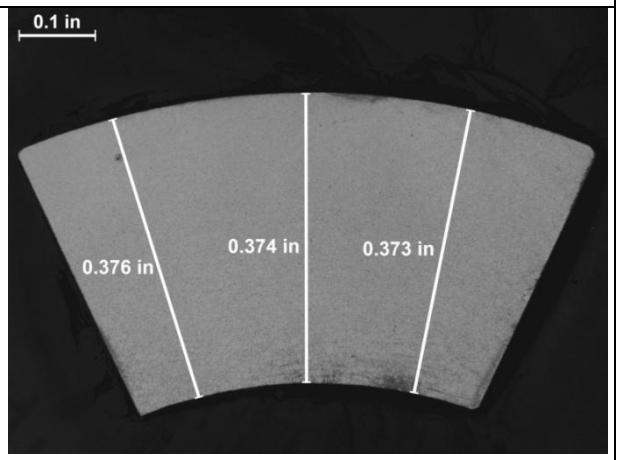
	Not included in the test matrix	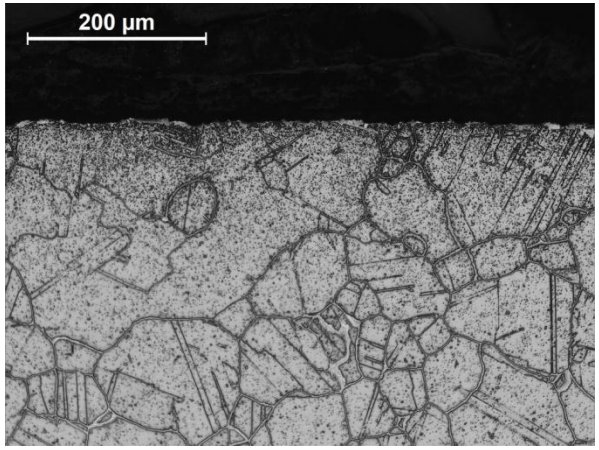

Fireside Corrosion Conditions – Condition 1 Results – C263 Material

No Exposure	After 1000 hours	After 3000 hours
	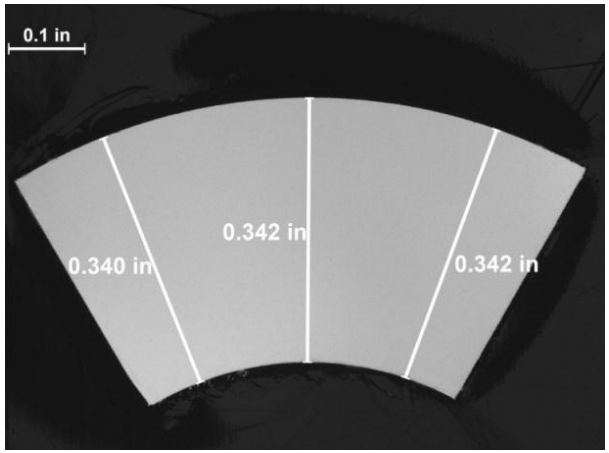	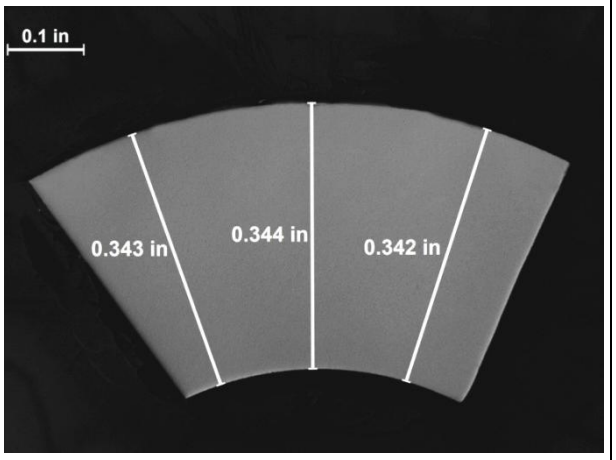
	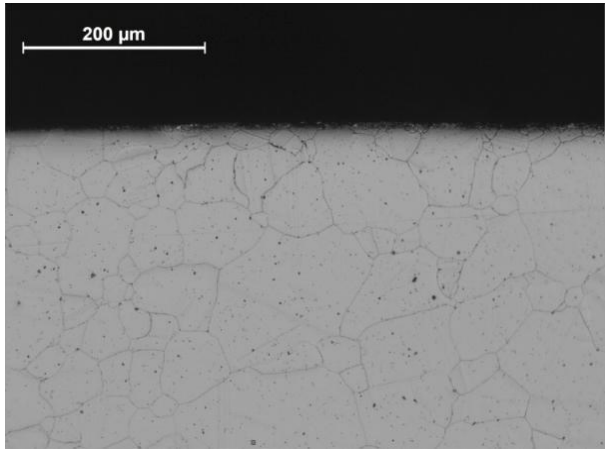	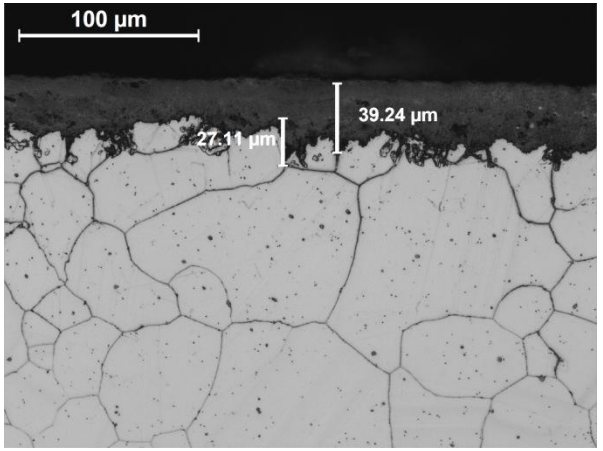

Fireside Corrosion Conditions – Condition 1 Results – C263 Material with Eastern Ash

No Exposure	After 1000 hours	After 3000 hours
	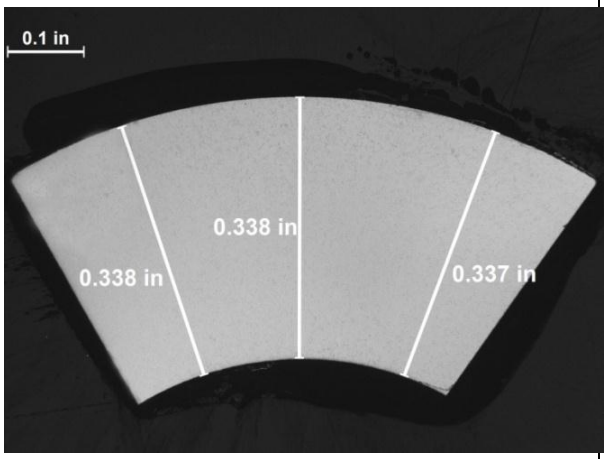	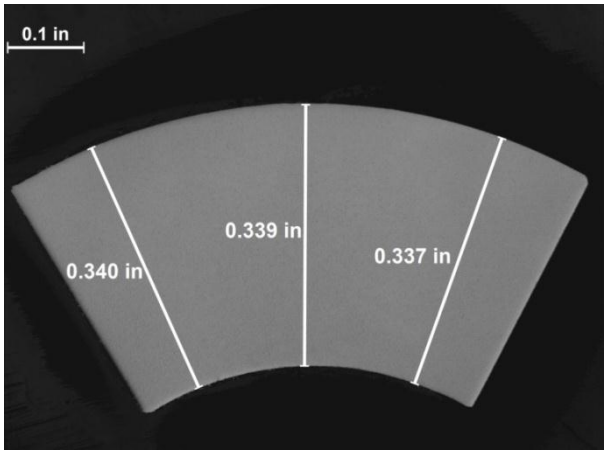
	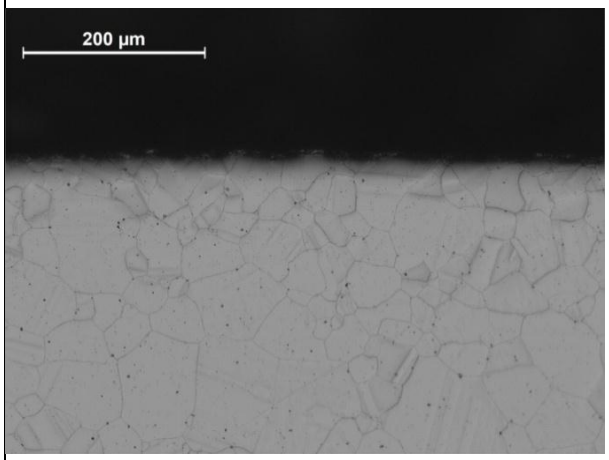	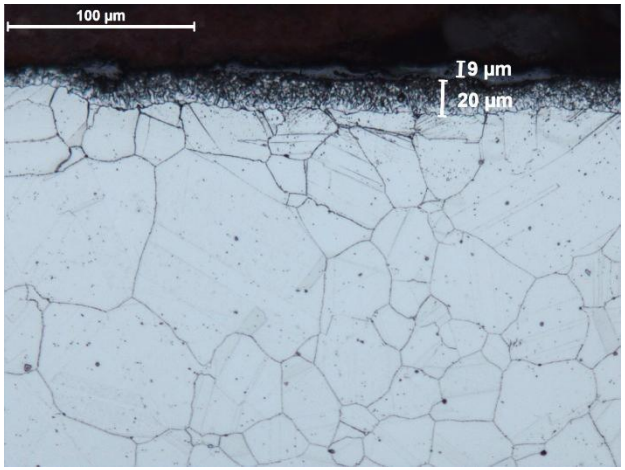

Fireside Corrosion Conditions – Condition 2 Results – T23 Material

No Exposure	After 1000 hours	After 3000 hours
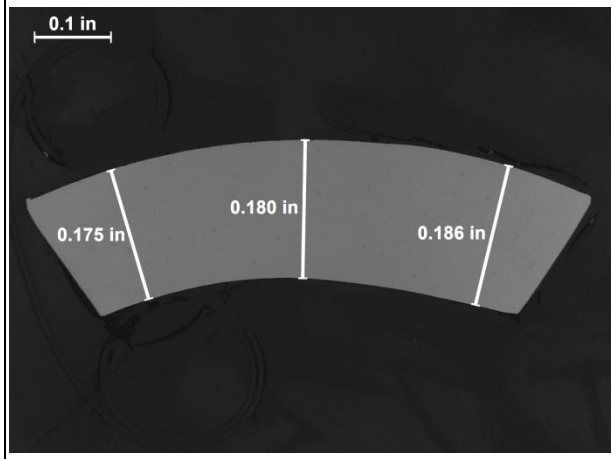	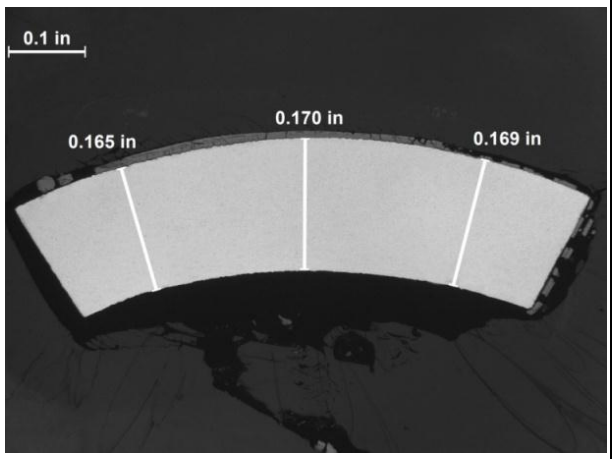	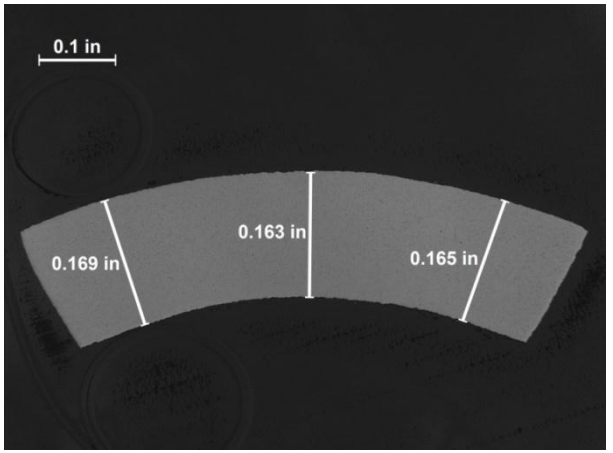
	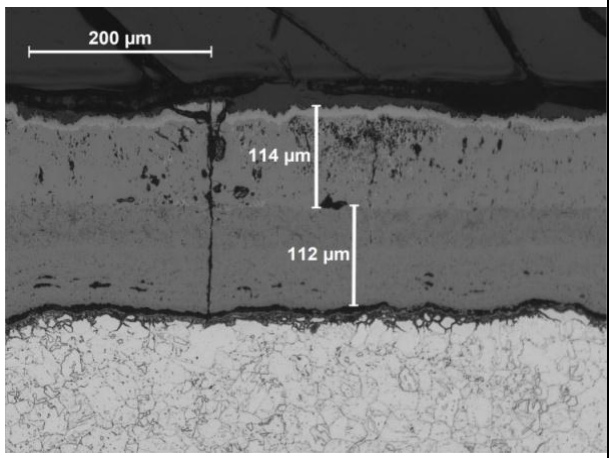	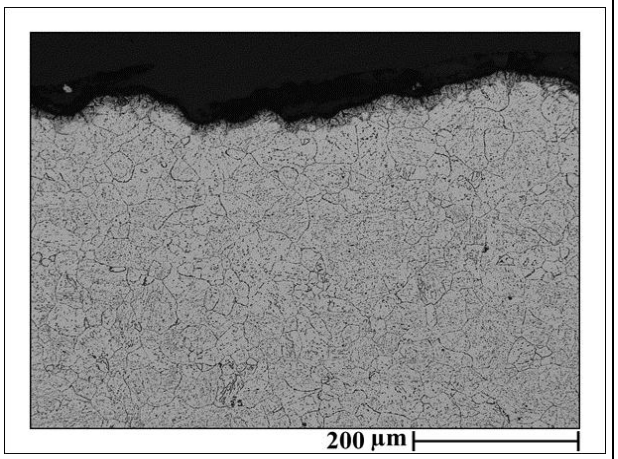

Fireside Corrosion Conditions – Condition 2 Results – T23 Material with Eastern Ash

No Exposure	After 1000 hours	After 3000 hours
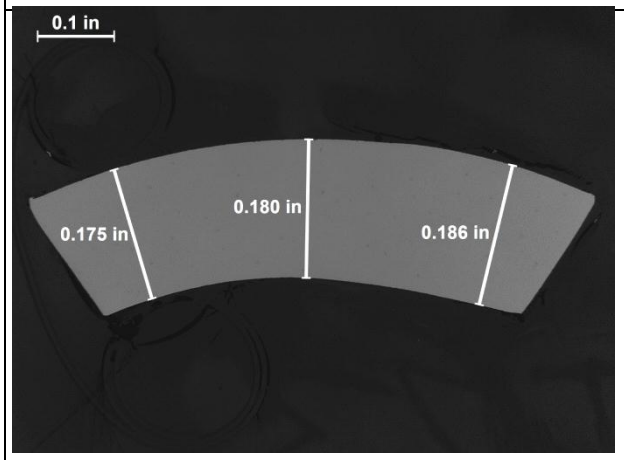	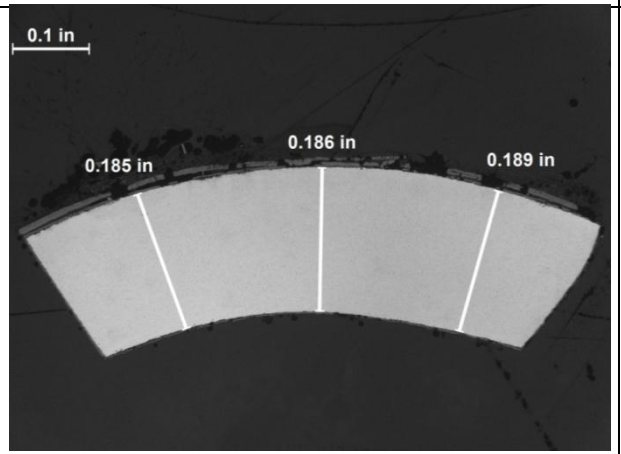	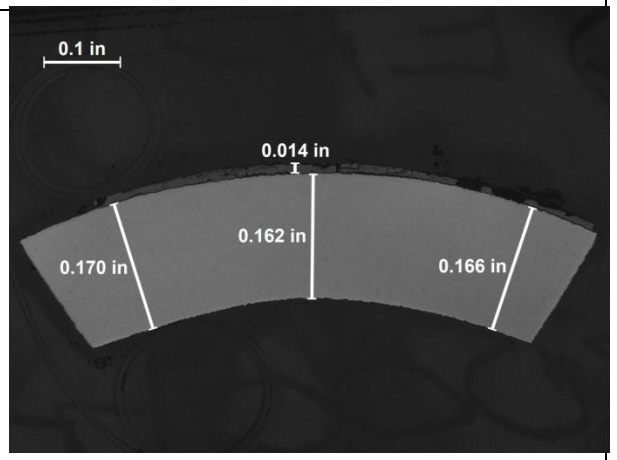
	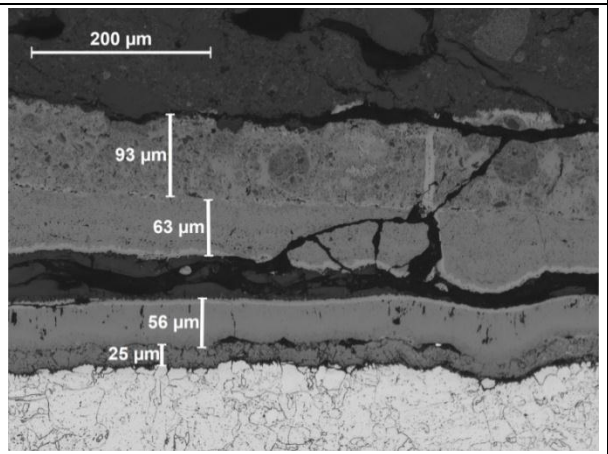	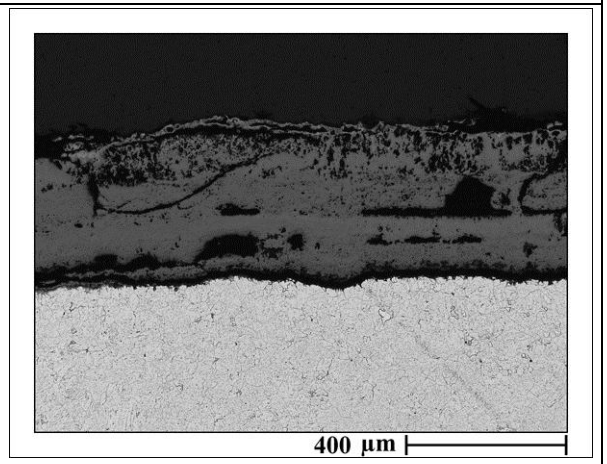

Fireside Corrosion Conditions – Condition 2 Results – T24 Material

No Exposure	After 1000 hours	After 3000 hours
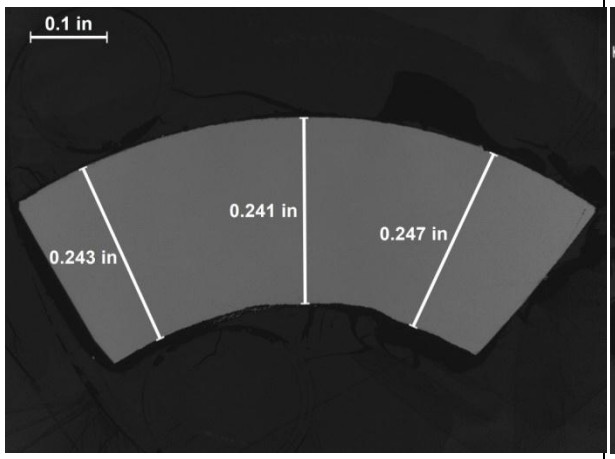	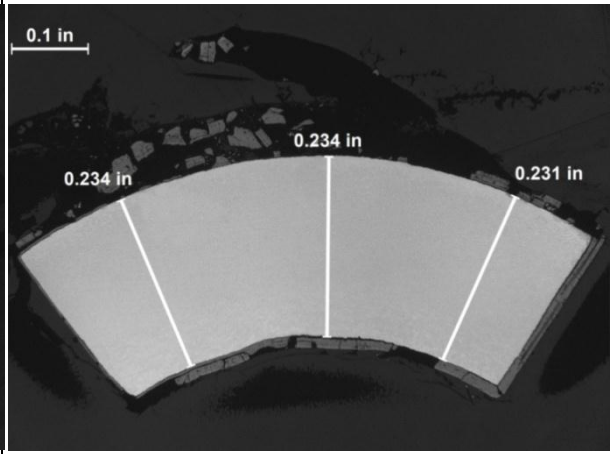	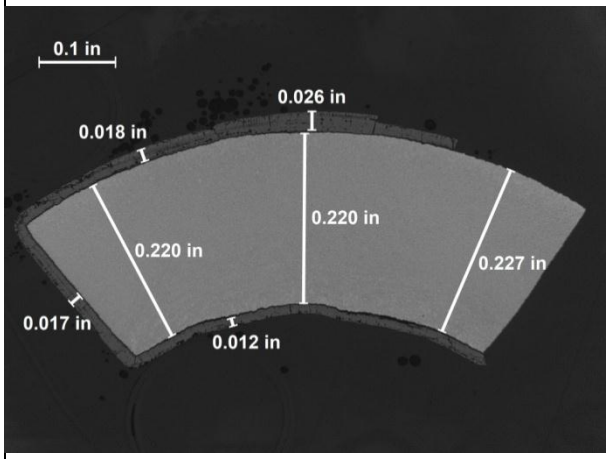
	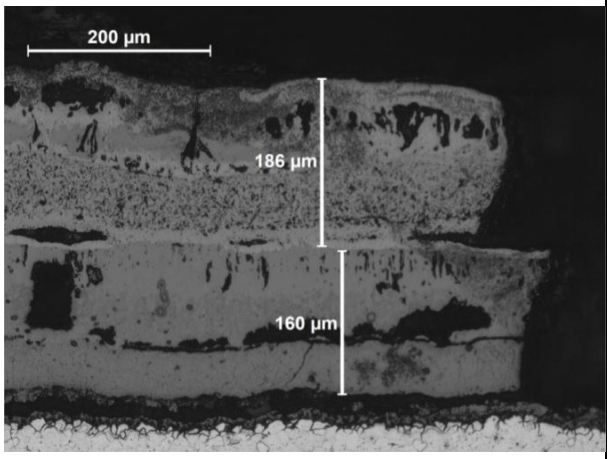	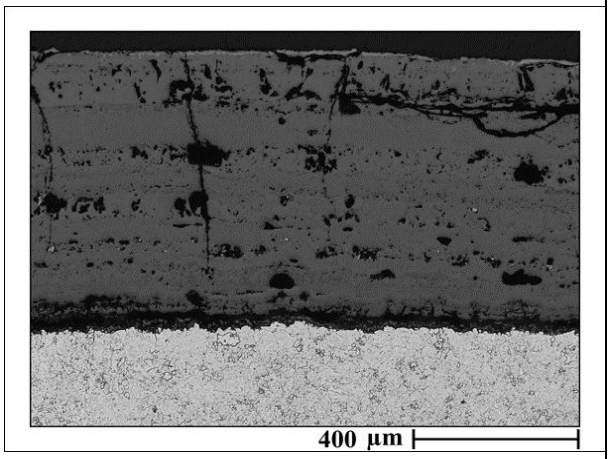

Fireside Corrosion Conditions – Condition 2 Results – T24 Material with Eastern Ash

No Exposure	After 1000 hours	After 3000 hours
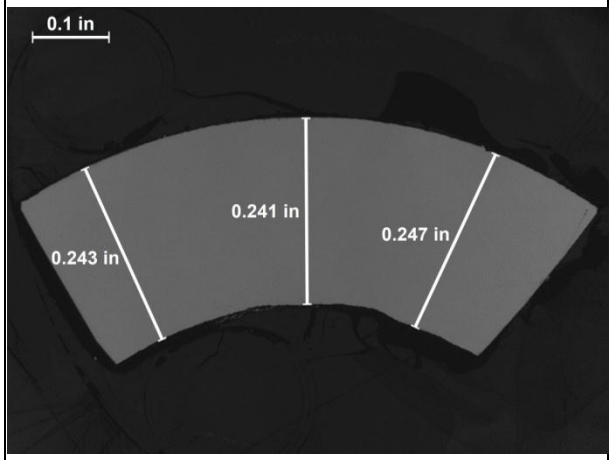	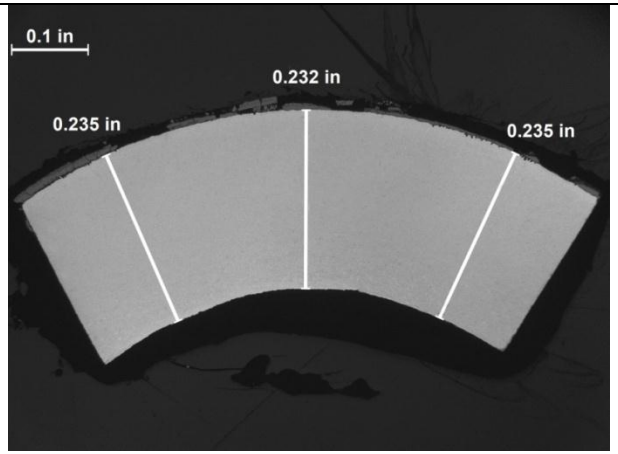	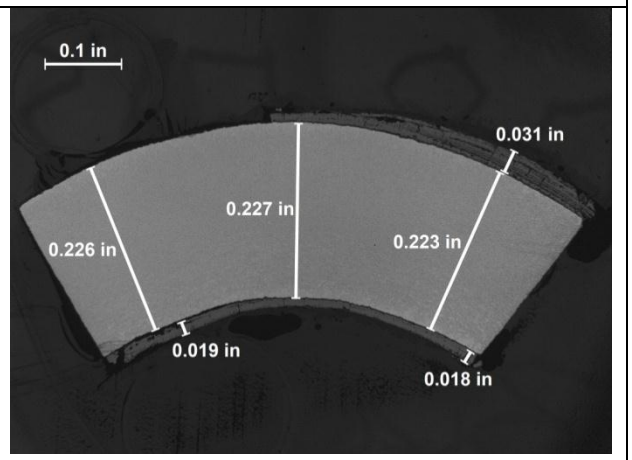
	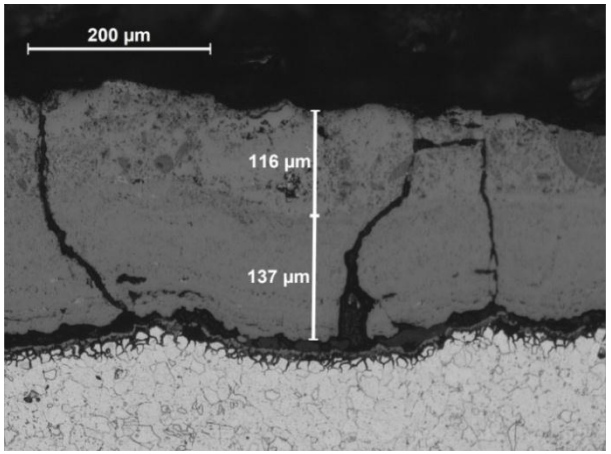	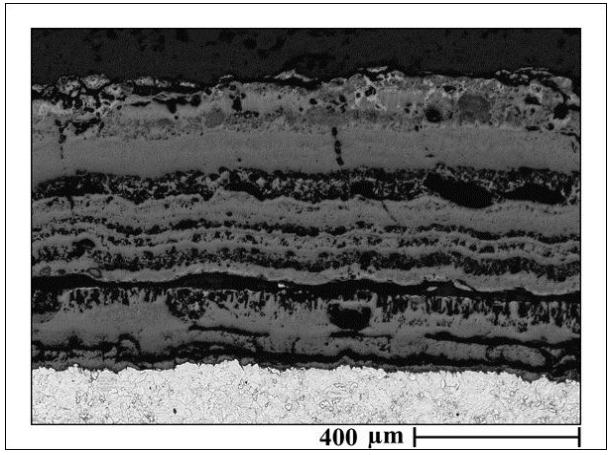

Fireside Corrosion Conditions – Condition 2 Results – T92 Material

No Exposure	After 1000 hours	After 3000 hours
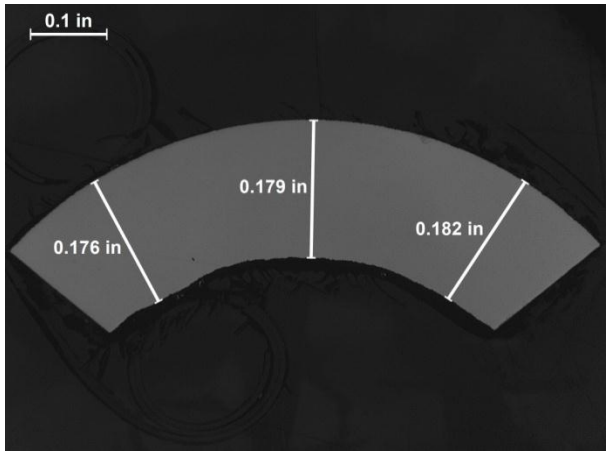	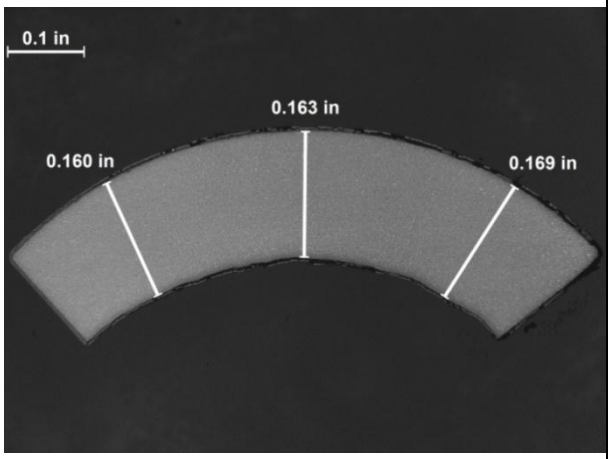	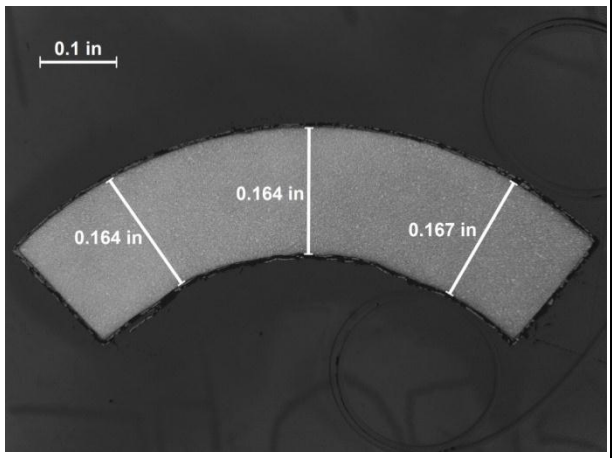
	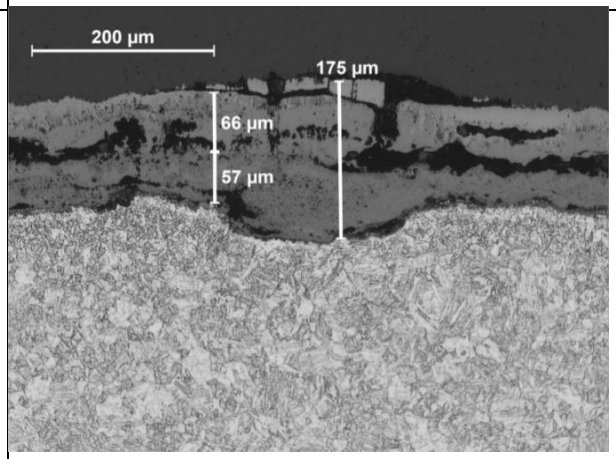	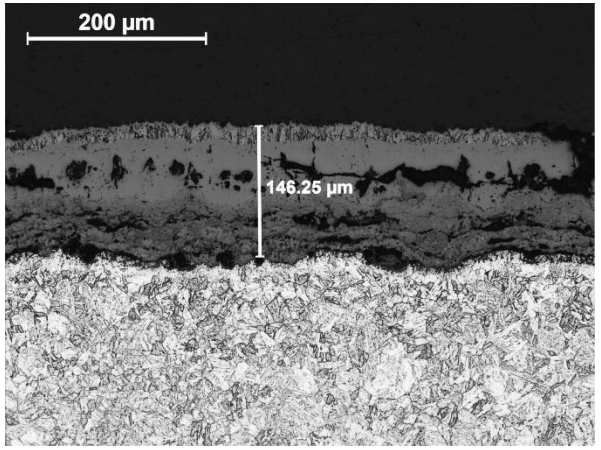

Fireside Corrosion Conditions – Condition 2 Results – T92 Material with Eastern Ash

No Exposure	After 1000 hours	After 3000 hours
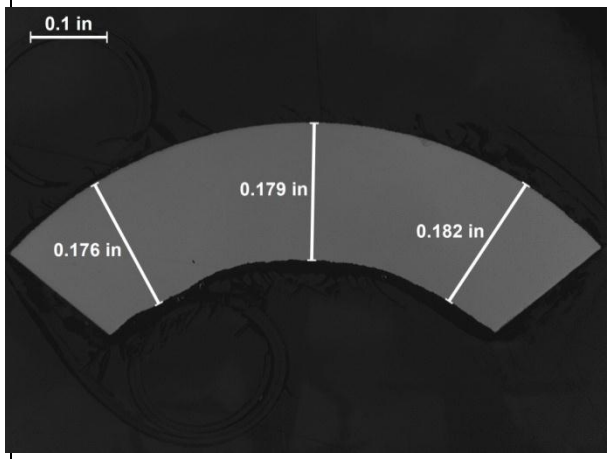	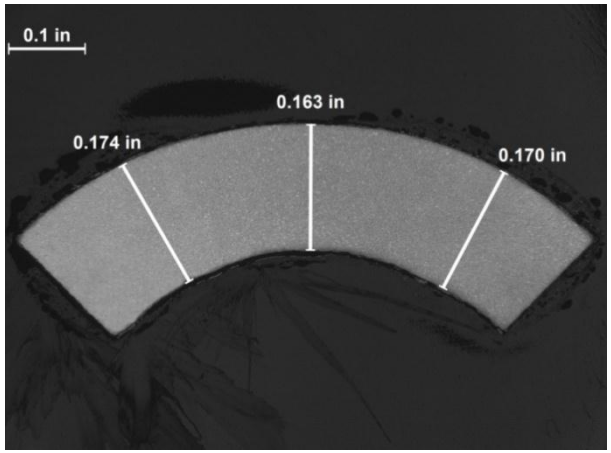	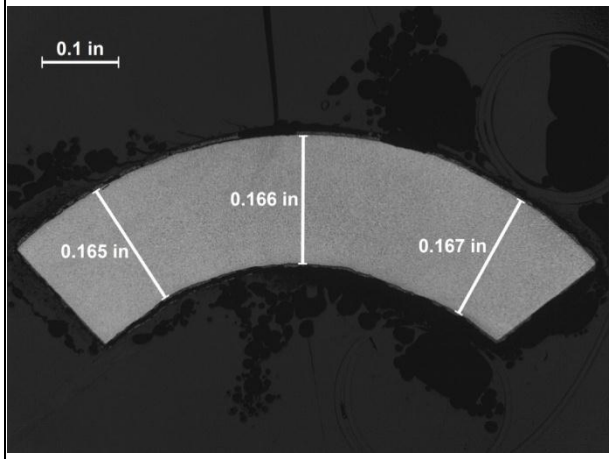
	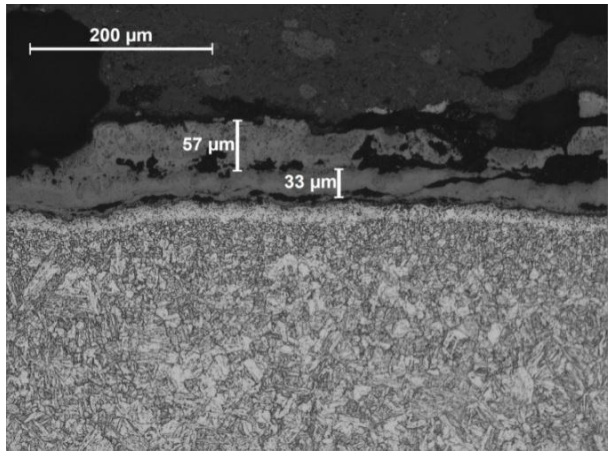	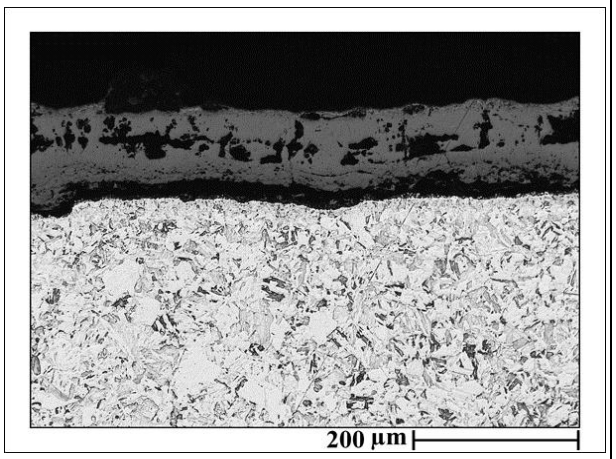

Fireside Corrosion Conditions – Condition 2 Results – Super304H Material

No Exposure	After 1000 hours	After 3000 hours
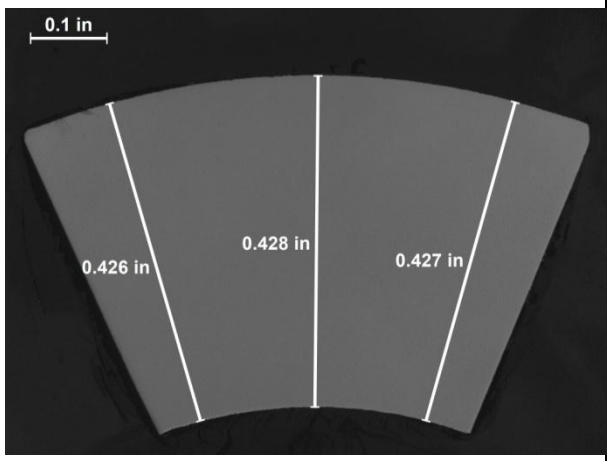	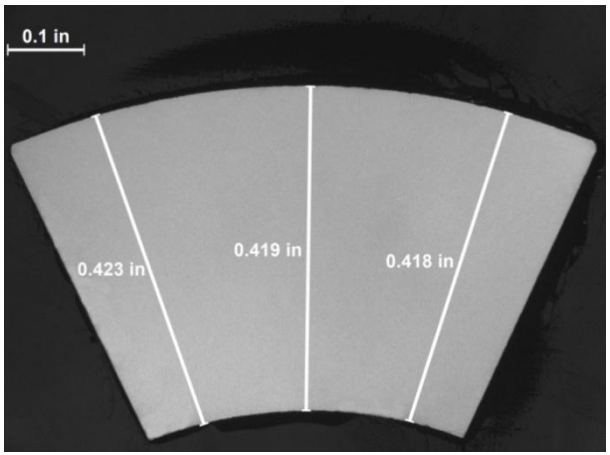	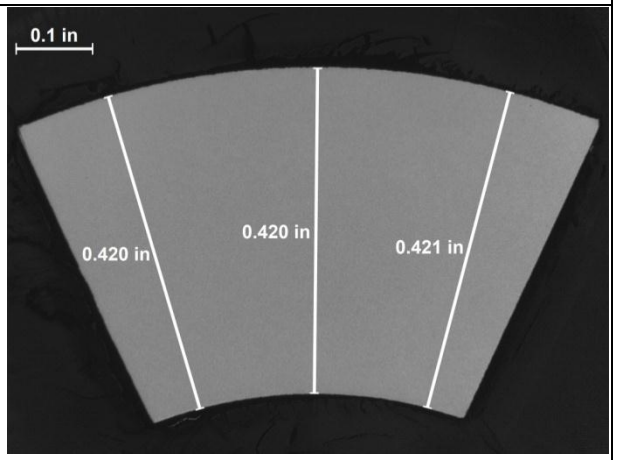
	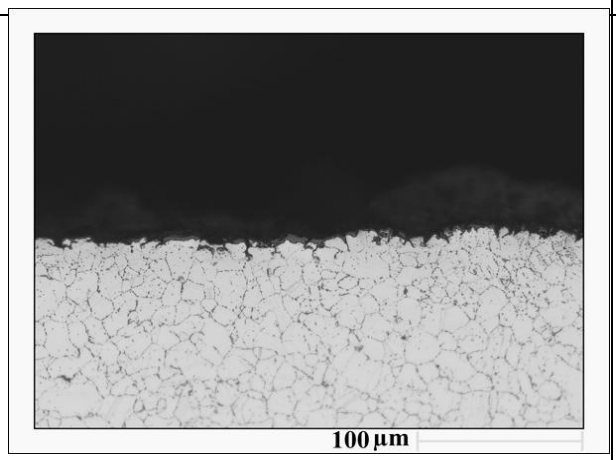	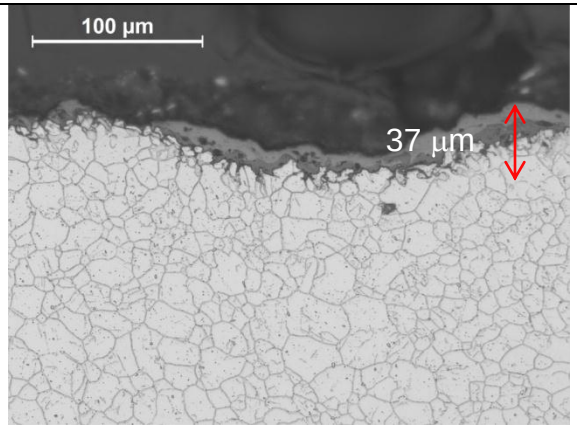

Fireside Corrosion Conditions – Condition 2 Results – Super304H Material with Eastern Ash

No Exposure	After 1000 hours	After 3000 hours
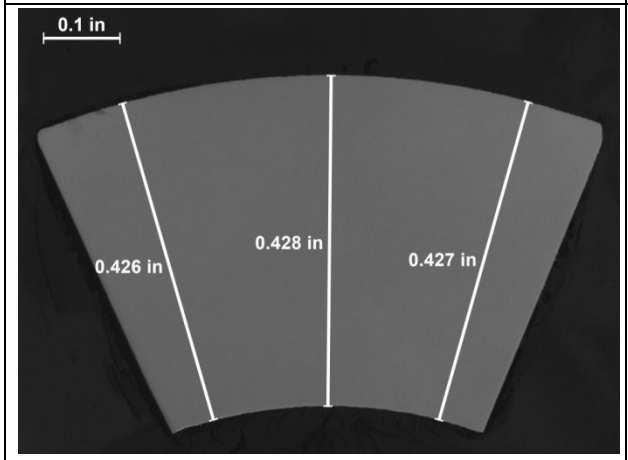	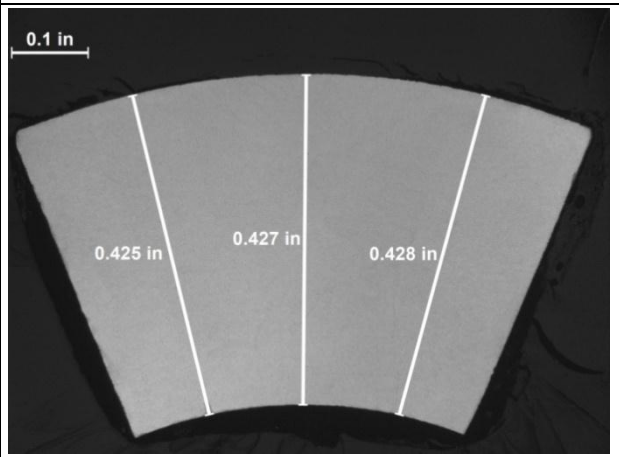	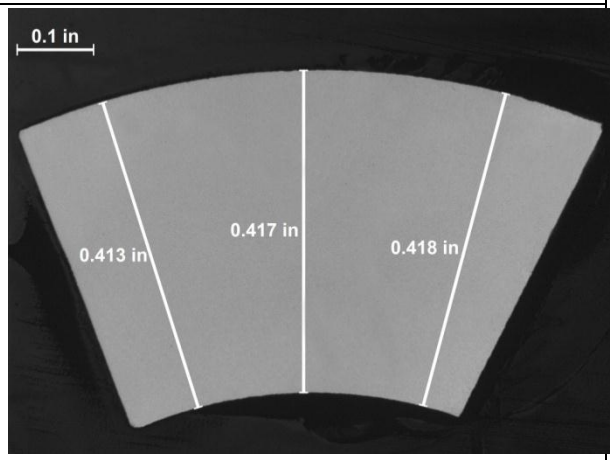
	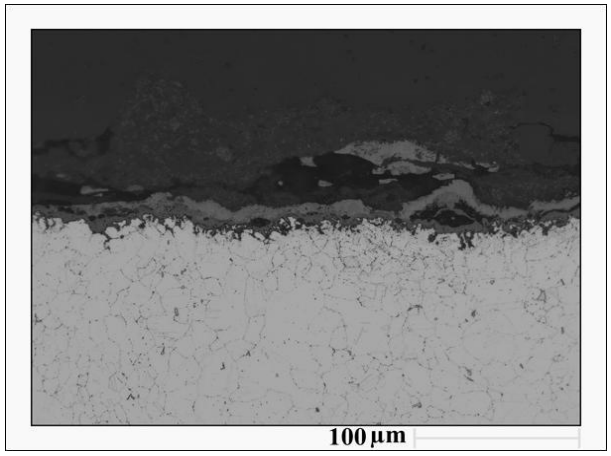	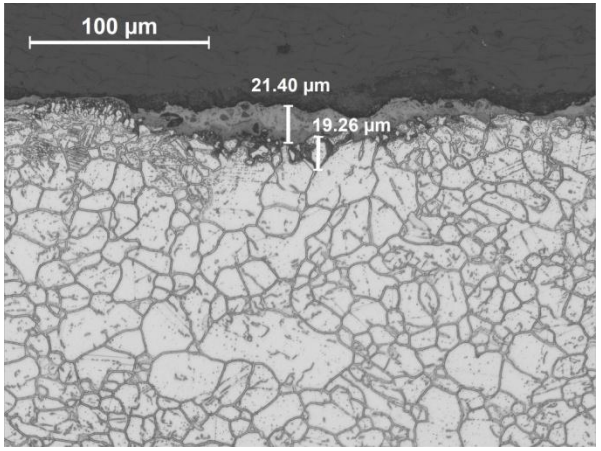

Fireside Corrosion Conditions – Condition 2 Results – Super304H Material with Western Ash

No Exposure	After 1000 hours	After 3000 hours
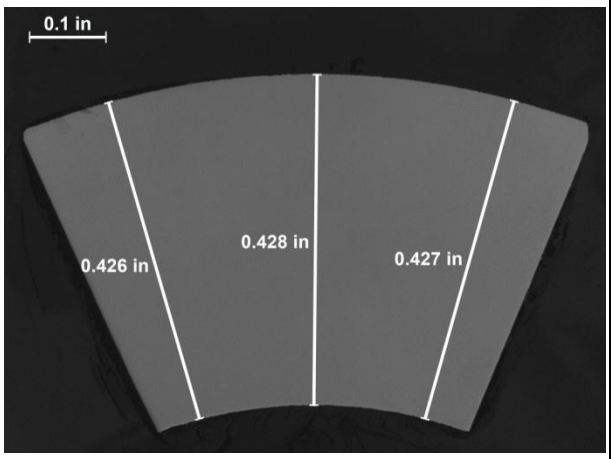	Not included in the test matrix	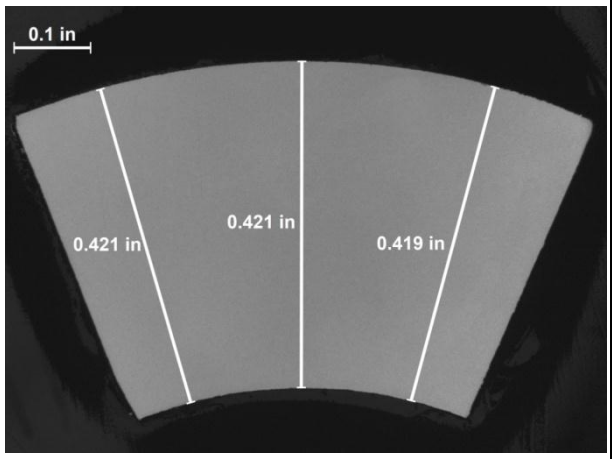
	Not included in the test matrix	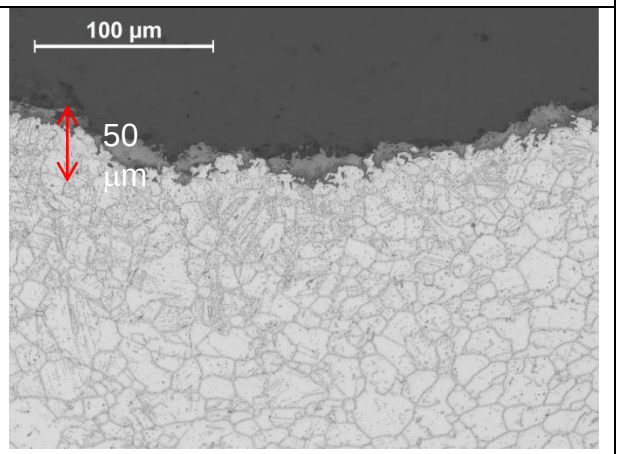

Fireside Corrosion Conditions – Condition 2 Results – IN617 Material

No Exposure	After 1000 hours	After 3000 hours
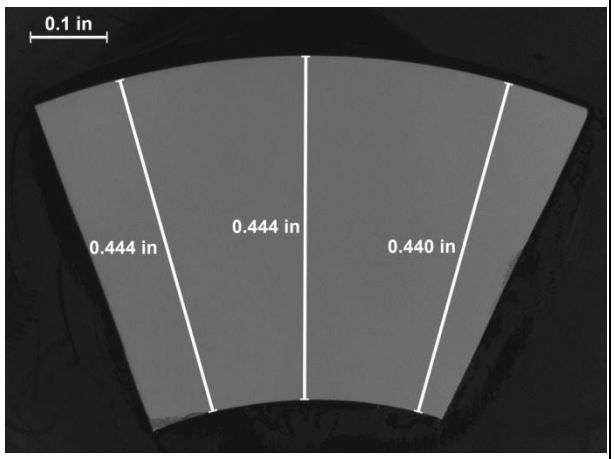	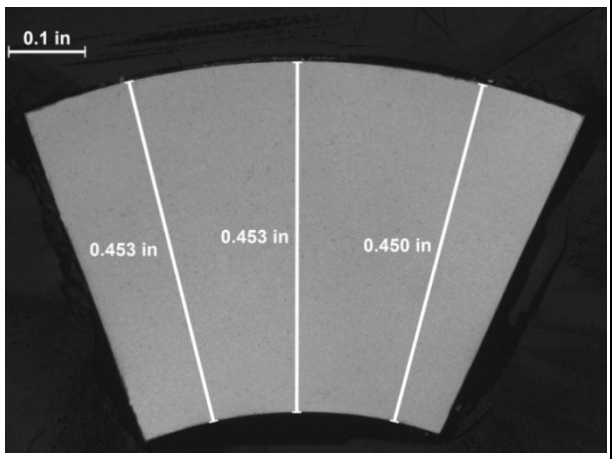	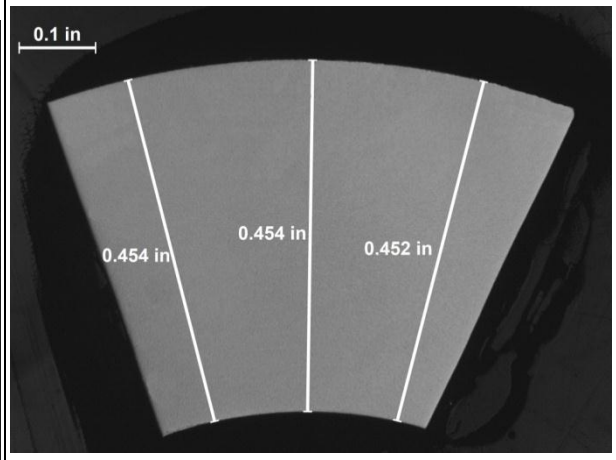
	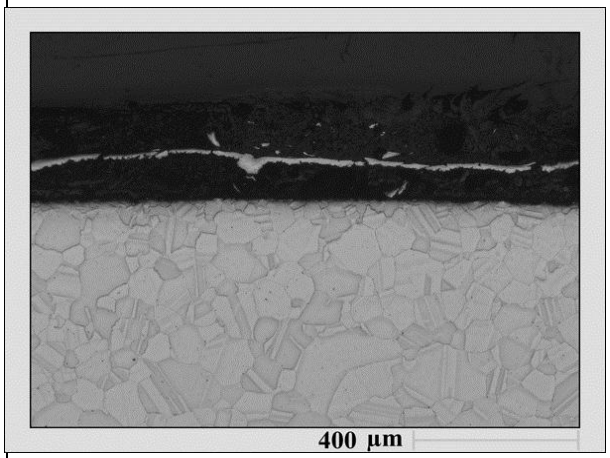	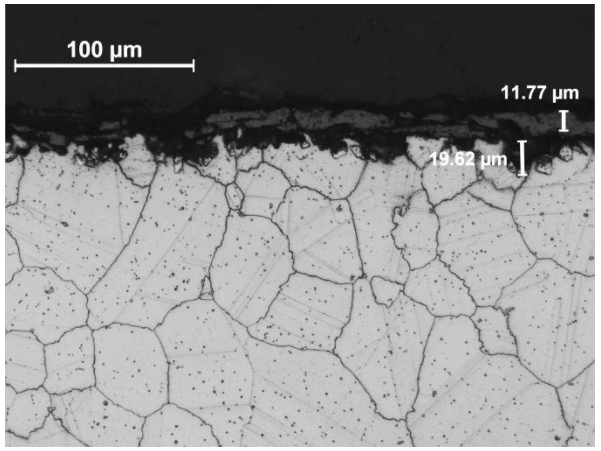

Fireside Corrosion Conditions – Condition 2 Results – IN617 Material with Eastern Ash

No Exposure	After 1000 hours	After 3000 hours
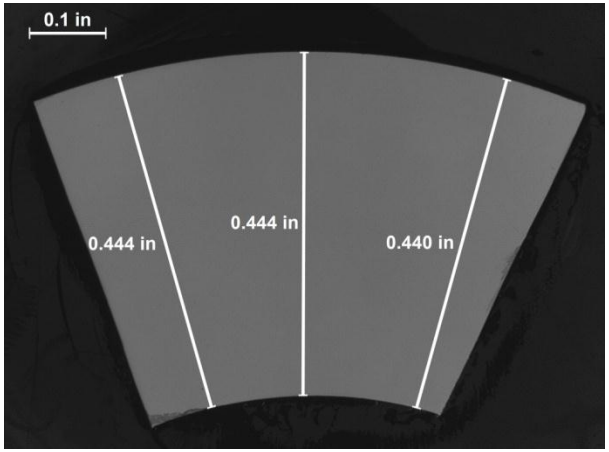	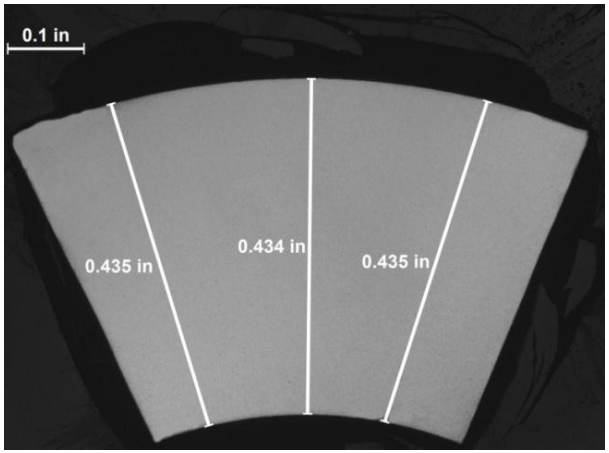	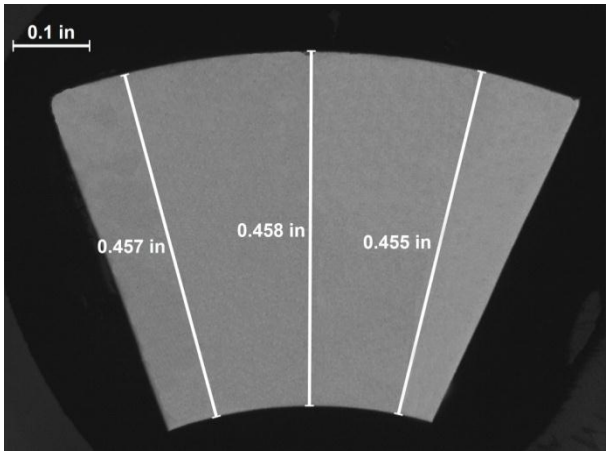
	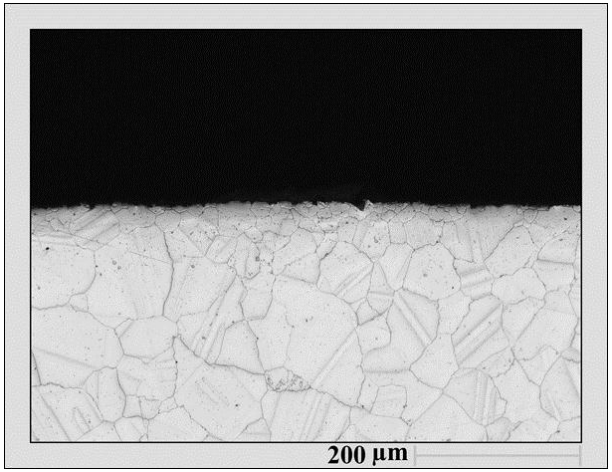	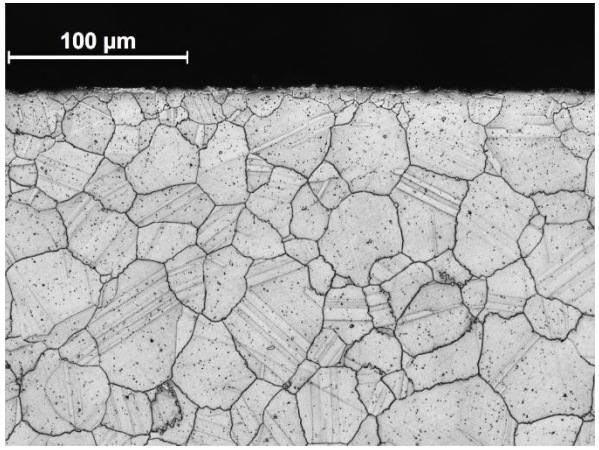

Fireside Corrosion Conditions – Condition 2 Results – NF709R Material

No Exposure	After 1000 hours	After 3000 hours
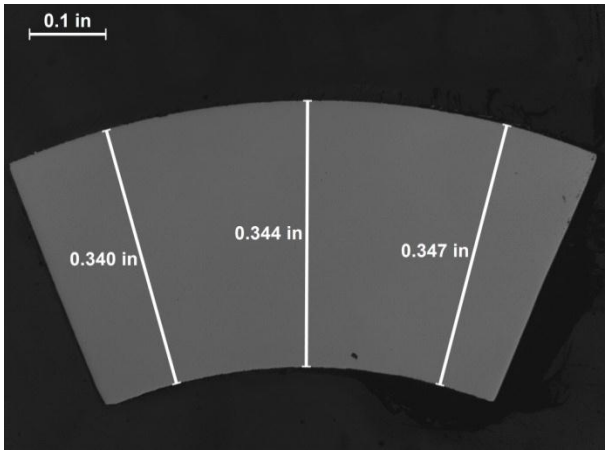	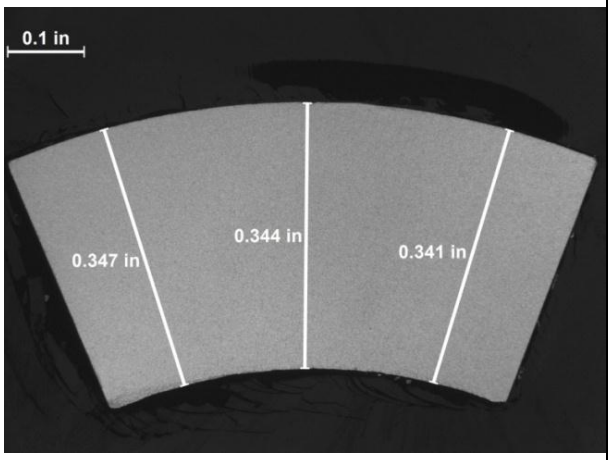	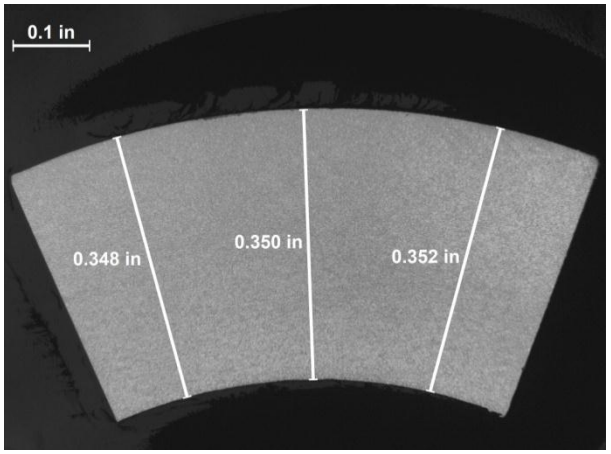
	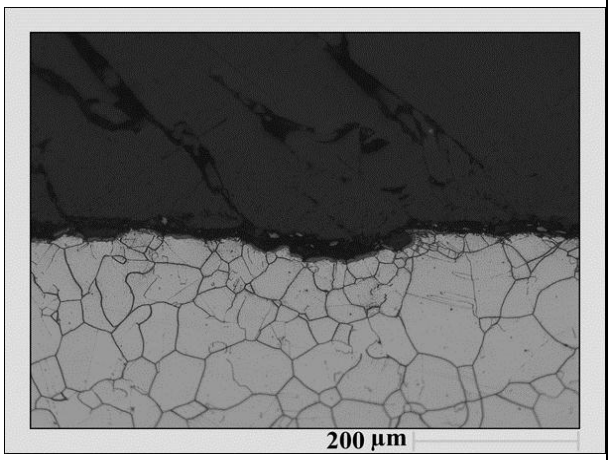	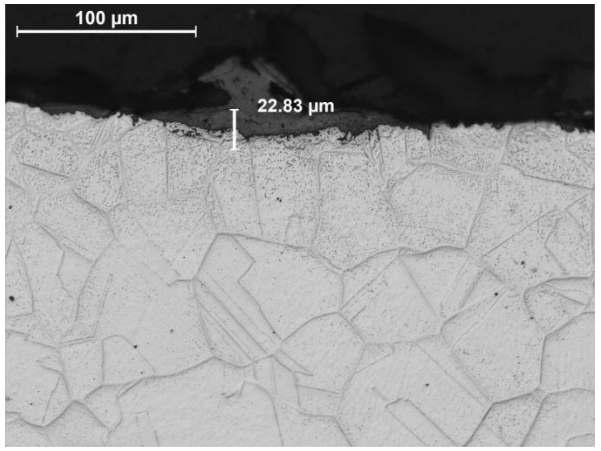

Fireside Corrosion Conditions – Condition 2 Results – NF709R Material with Eastern Ash

No Exposure	After 1000 hours	After 3000 hours
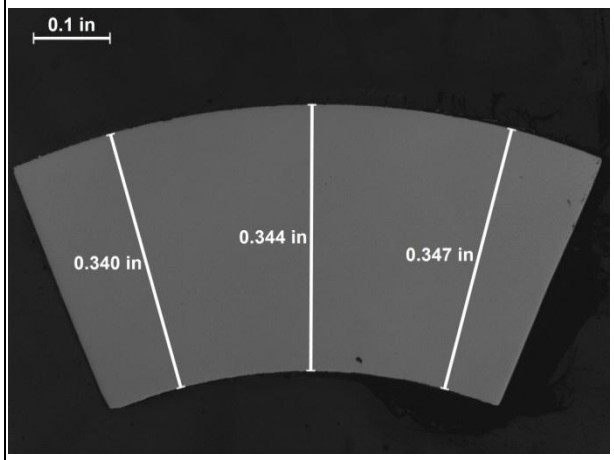	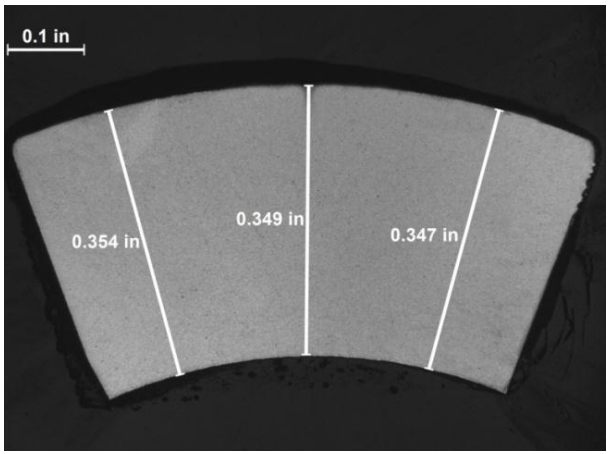	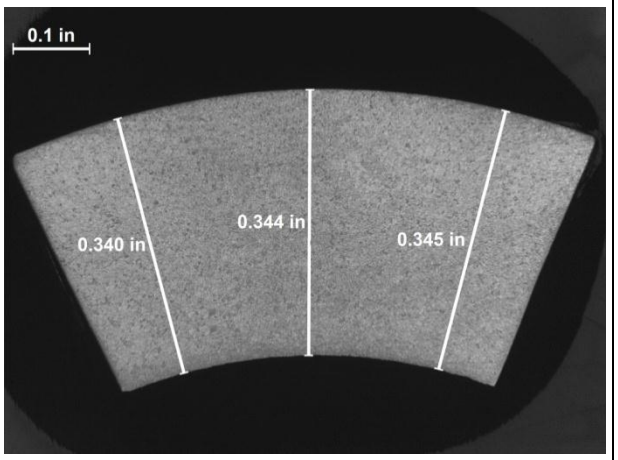
	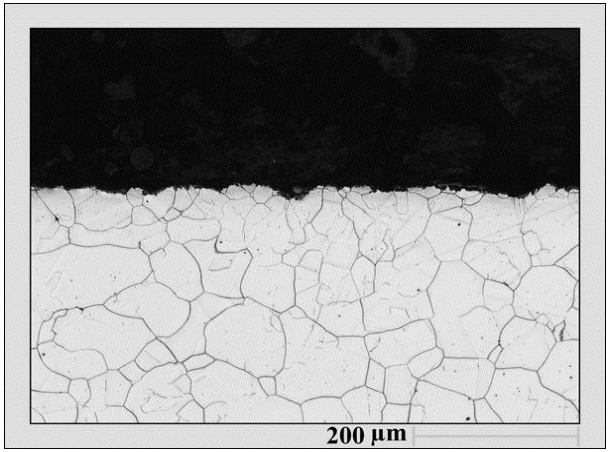	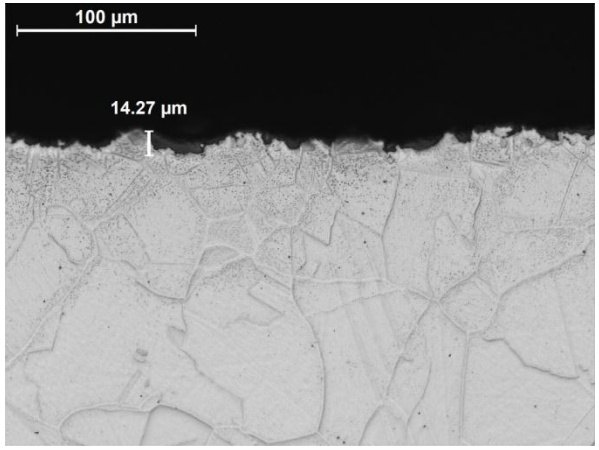

Fireside Corrosion Conditions – Condition 2 Results – Alloy 740 Material

No Exposure	After 1000 hours	After 3000 hours
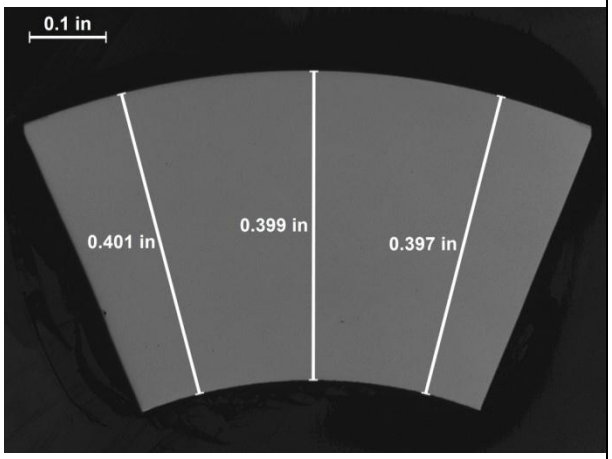	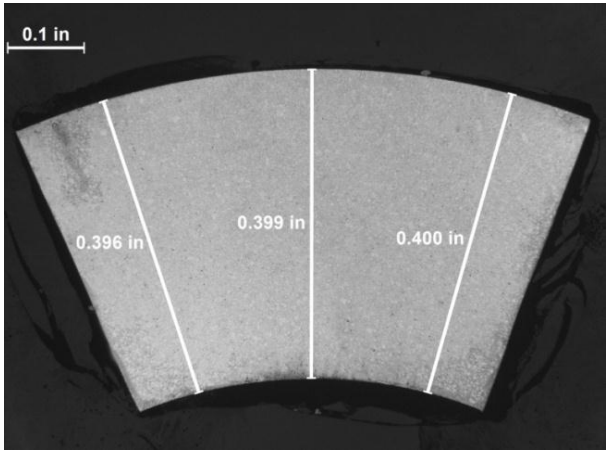	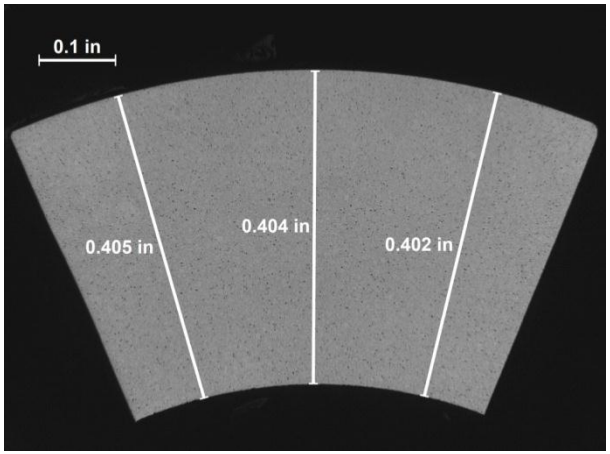
	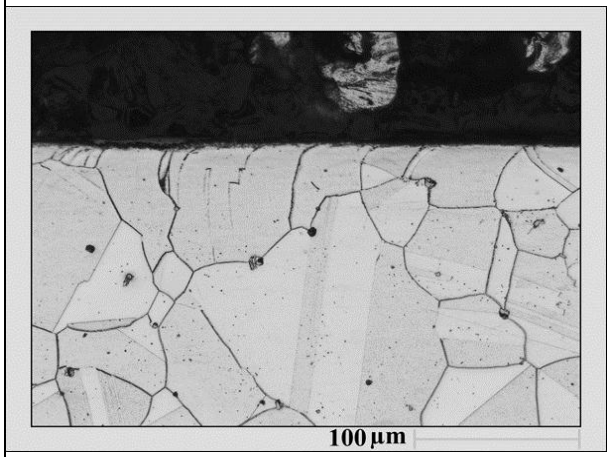	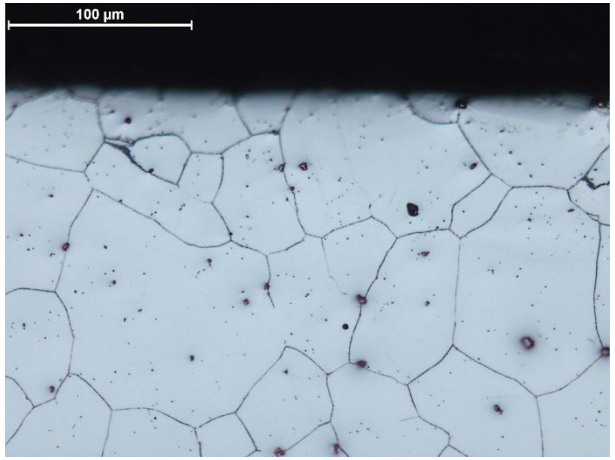

Fireside Corrosion Conditions – Condition 2 Results – Alloy 740 Material with Eastern Ash

No Exposure	After 1000 hours	After 3000 hours
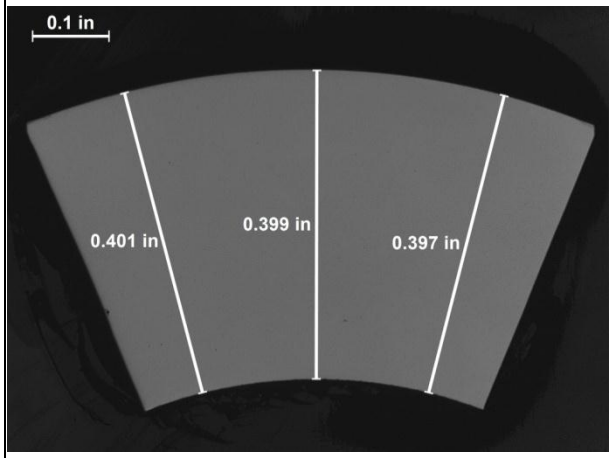	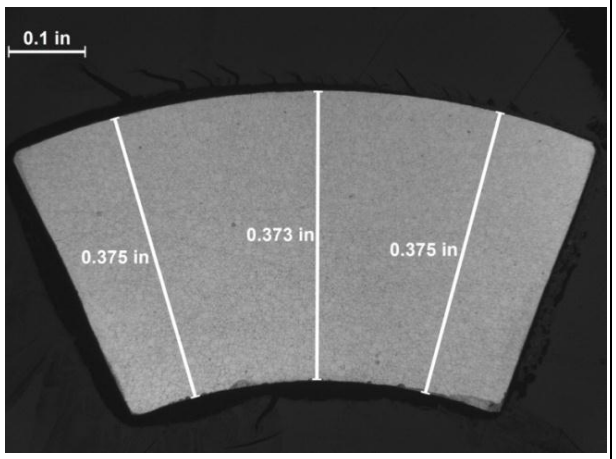	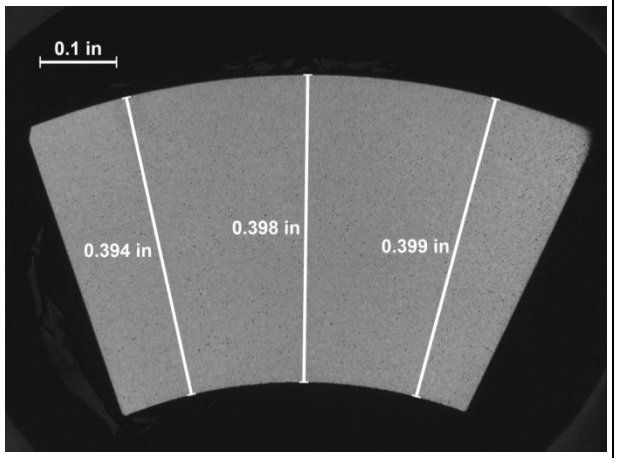
	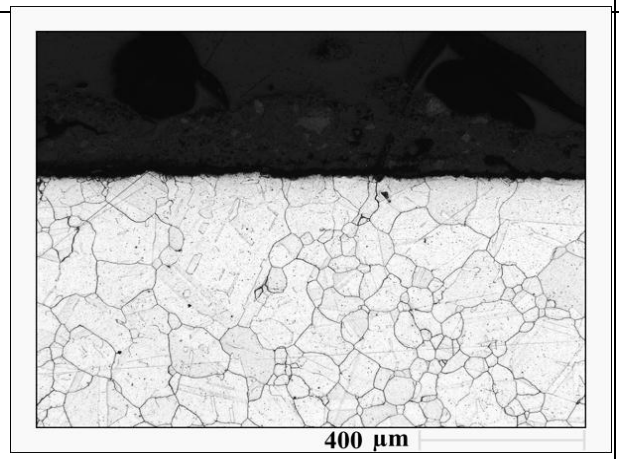	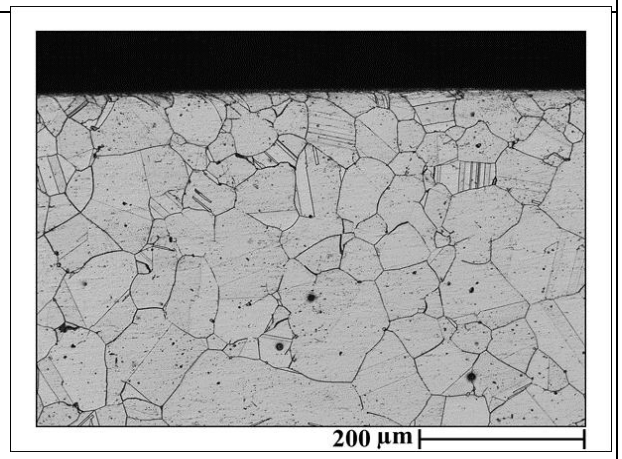

Fireside Corrosion Conditions – Condition 2 Results – Alloy 740 Material with Western Ash

No Exposure	After 1000 hours	After 3000 hours
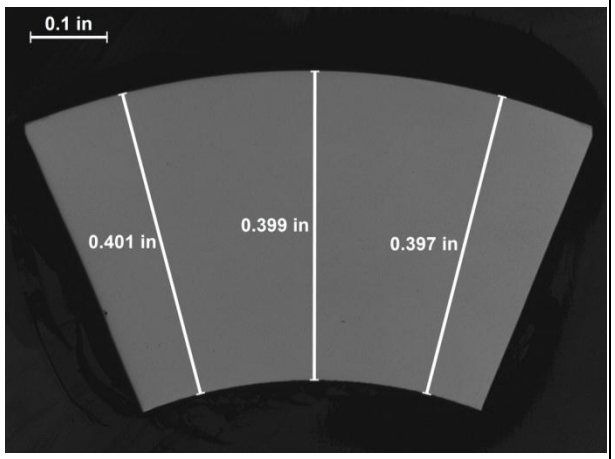	Not included in the test matrix	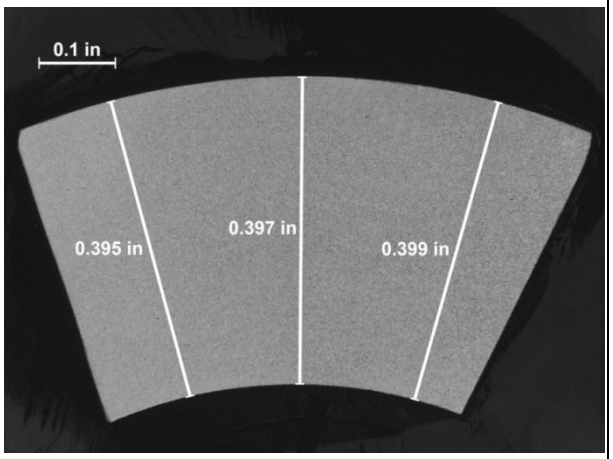
	Not included in the test matrix	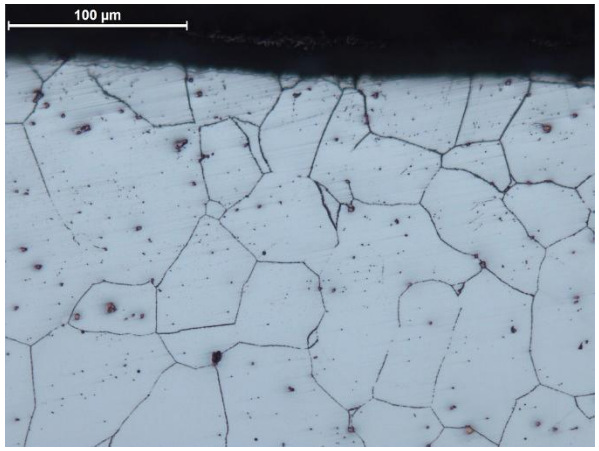

Fireside Corrosion Conditions – Condition 2 Results – HR3C Material

No Exposure	After 1000 hours	After 3000 hours
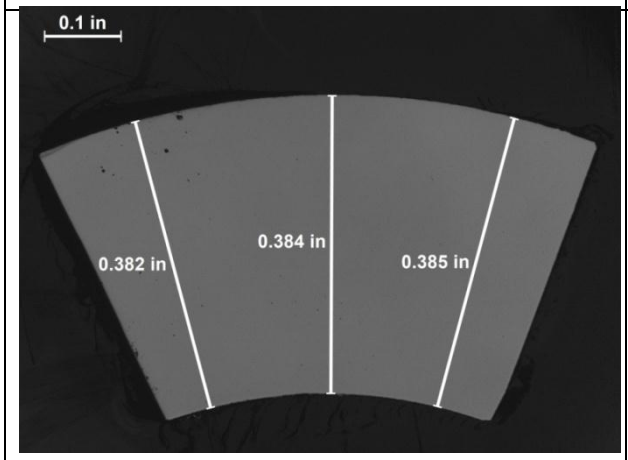	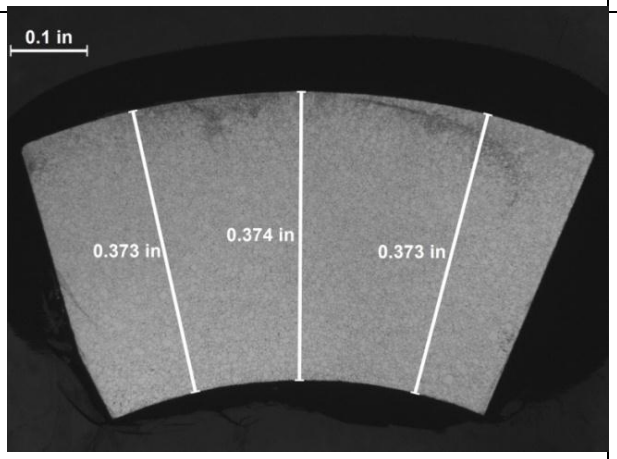	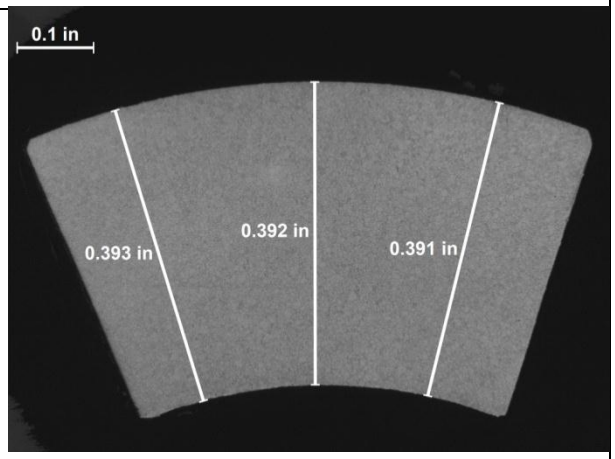
	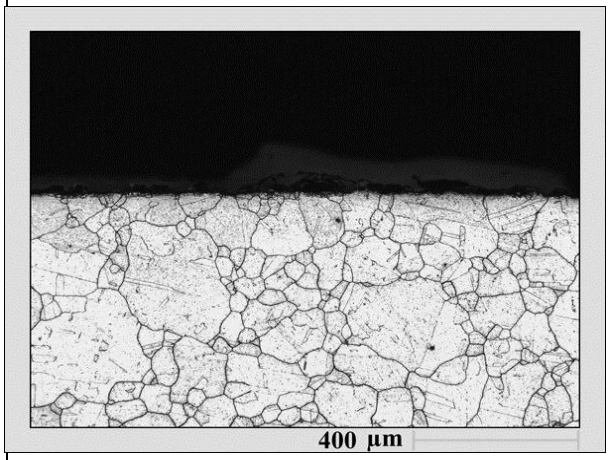	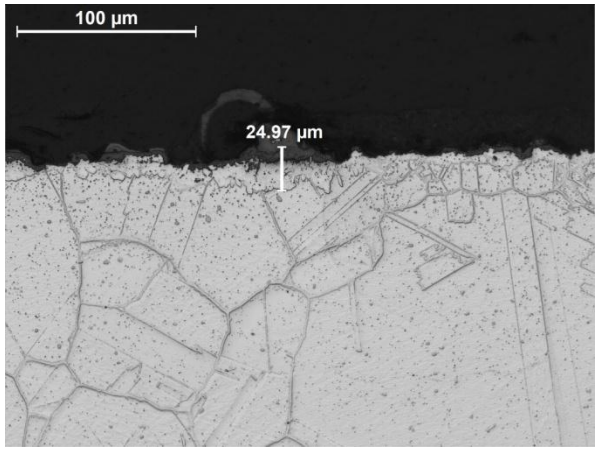

Fireside Corrosion Conditions – Condition 2 Results – HR3C Material with Eastern Ash

No Exposure	After 1000 hours	After 3000 hours
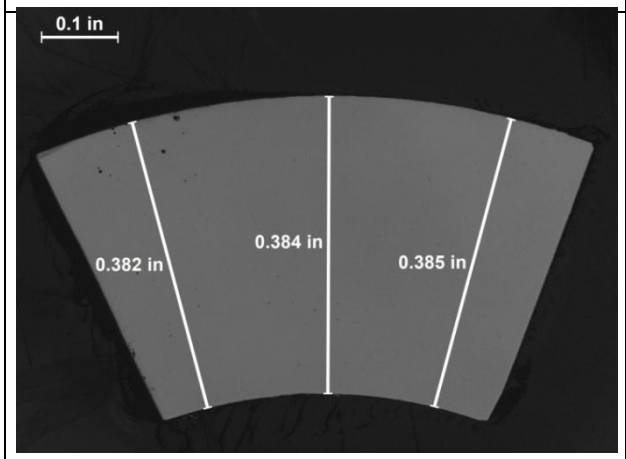	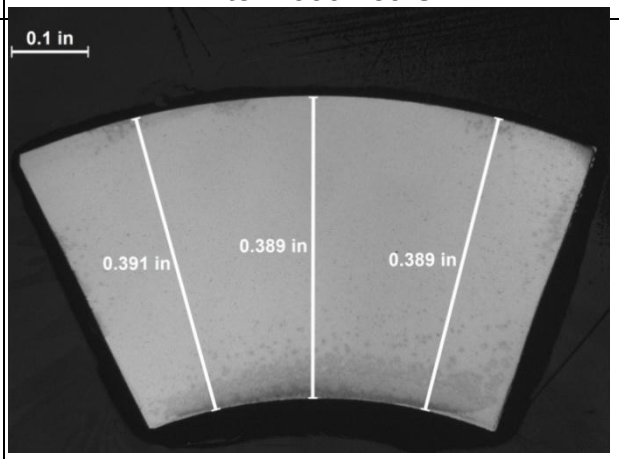	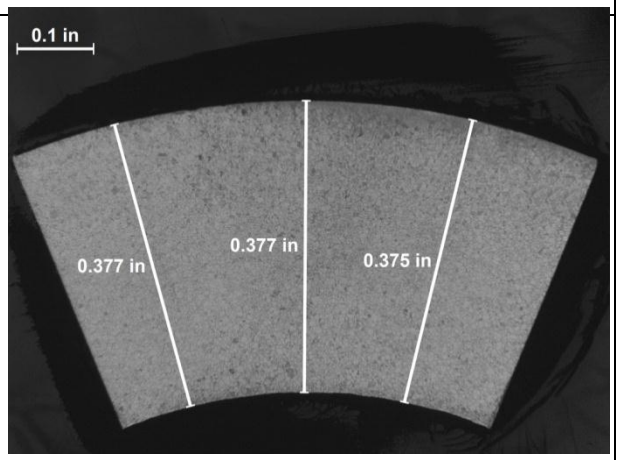
	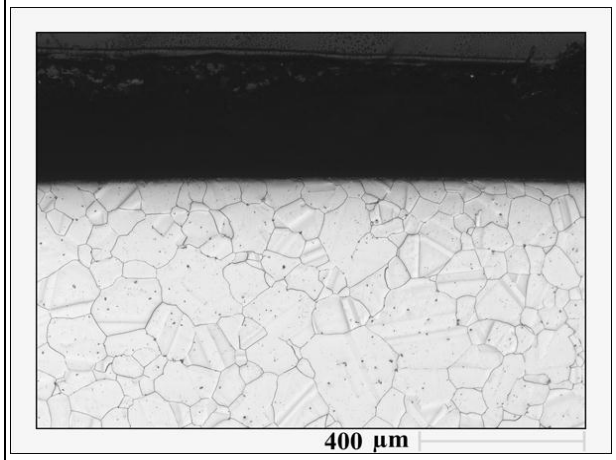	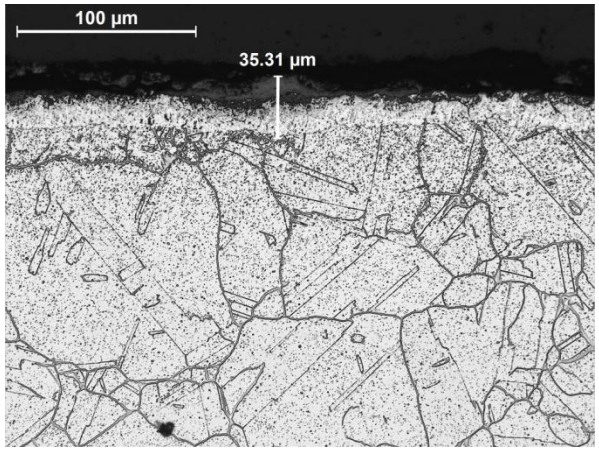

Fireside Corrosion Conditions – Condition 2 Results – HR3C Material with Western Ash

No Exposure	After 1000 hours	After 3000 hours
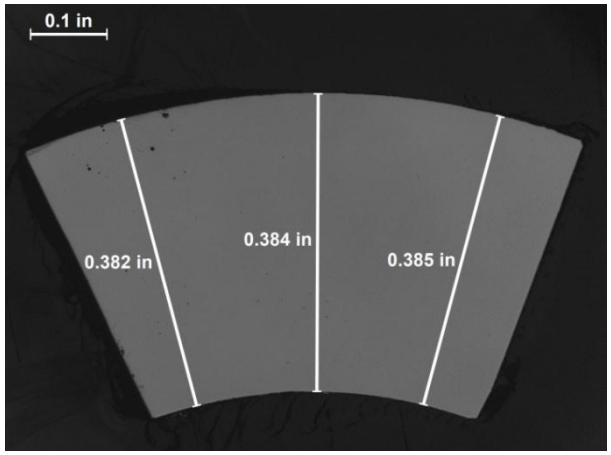	Not included in the test matrix	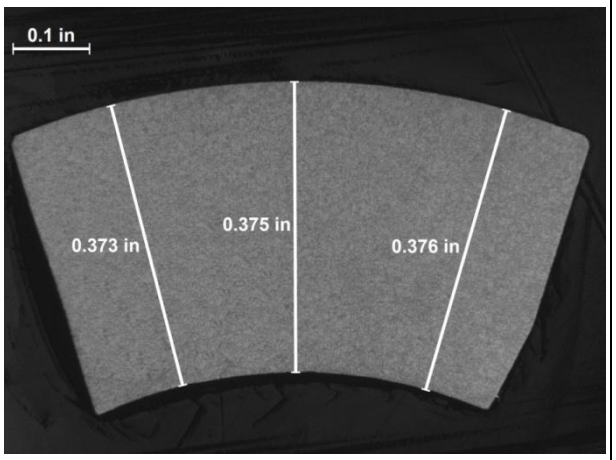
	Not included in the test matrix	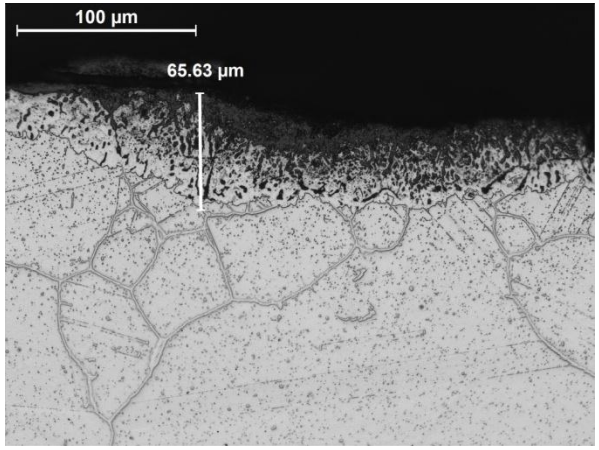

Fireside Corrosion Conditions – Condition 2 Results – C263 Material

No Exposure	After 1000 hours	After 3000 hours
	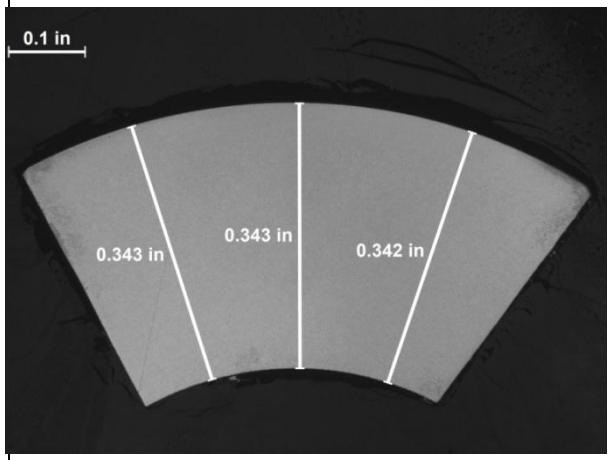	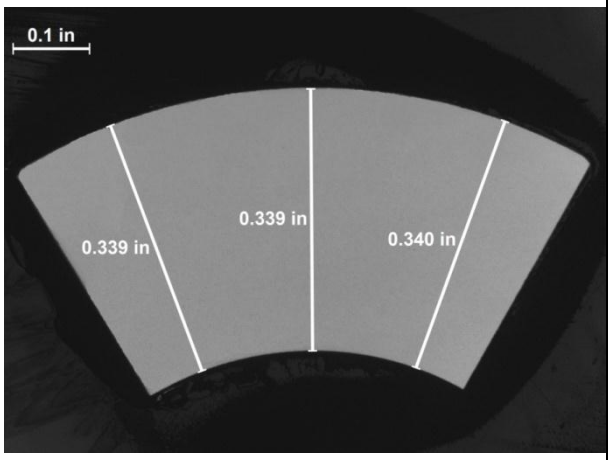
	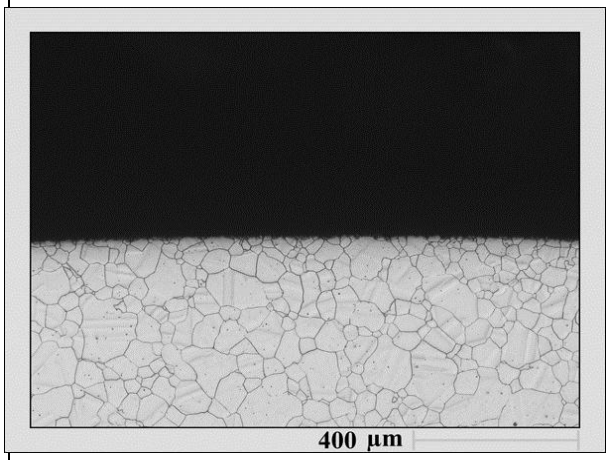	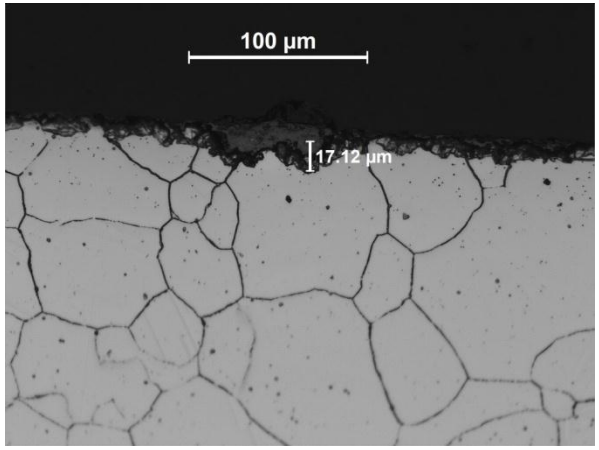

Fireside Corrosion Conditions – Condition 2 Results – C263 Material with Eastern Ash

No Exposure	After 1000 hours	After 3000 hours
	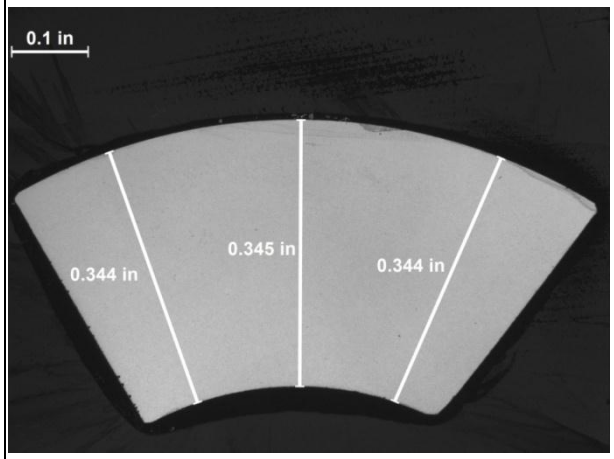	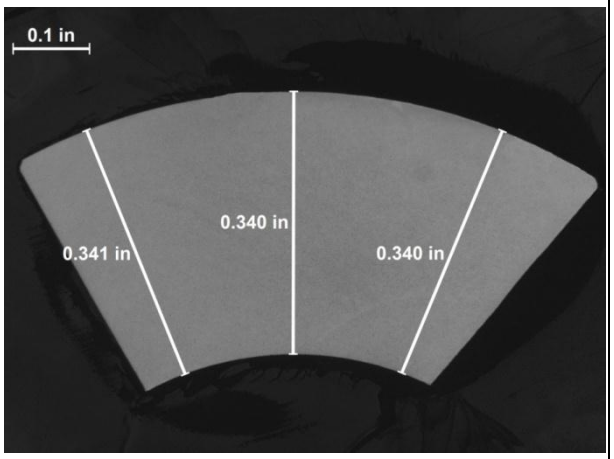
	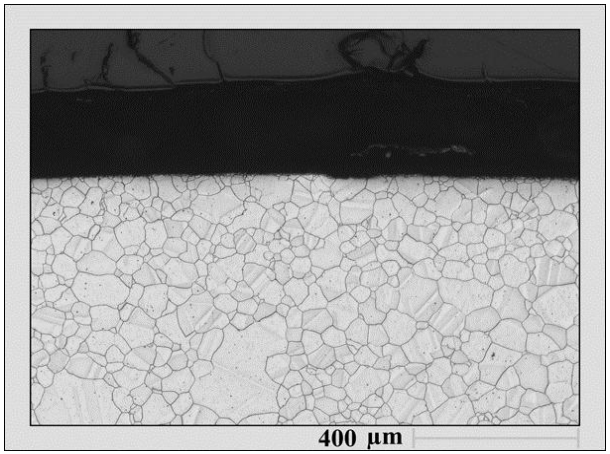	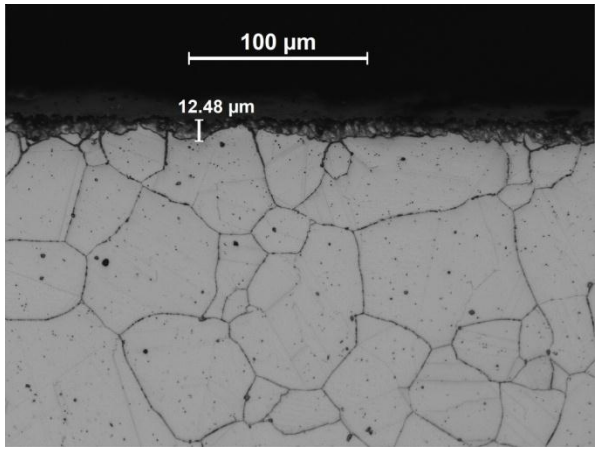

Fireside Corrosion Conditions – Condition 3 Results – T23 Material

No Exposure	After 1000 hours	After 3000 hours
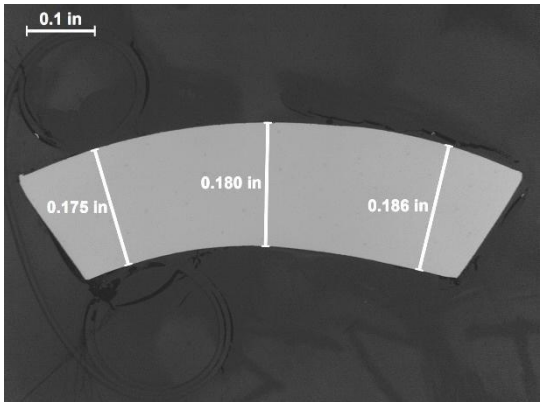	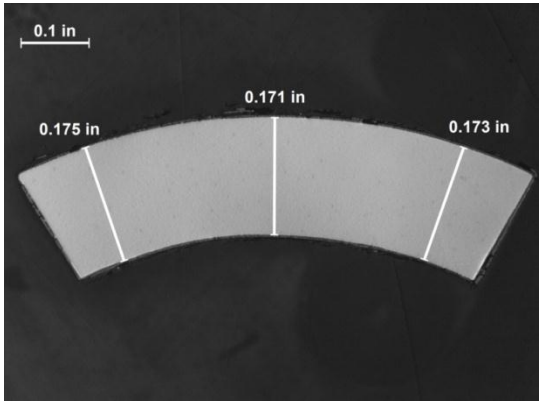	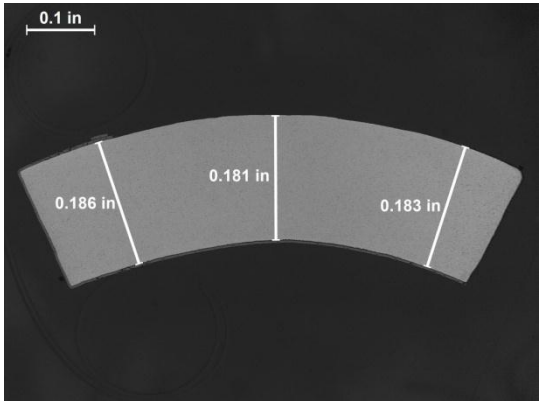
	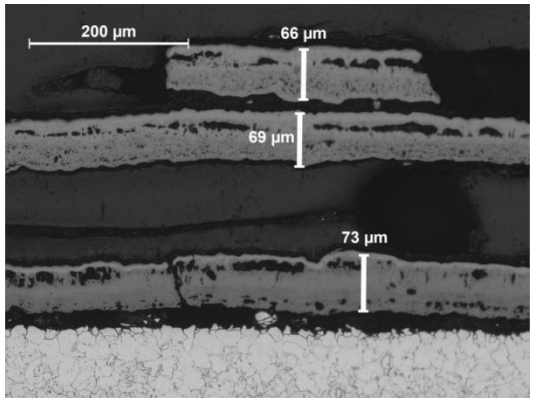	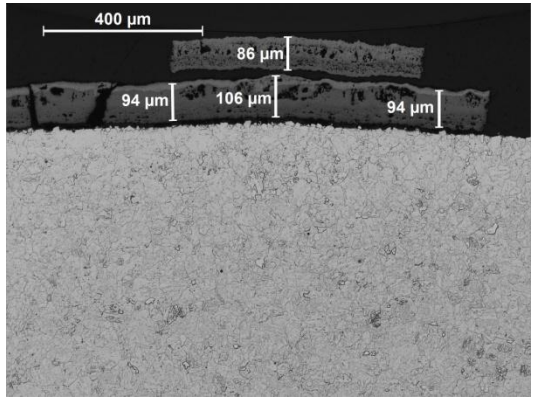

Fireside Corrosion Conditions – Condition 3 Results – T23 Material with Eastern Ash

No Exposure	After 1000 hours	After 3000 hours
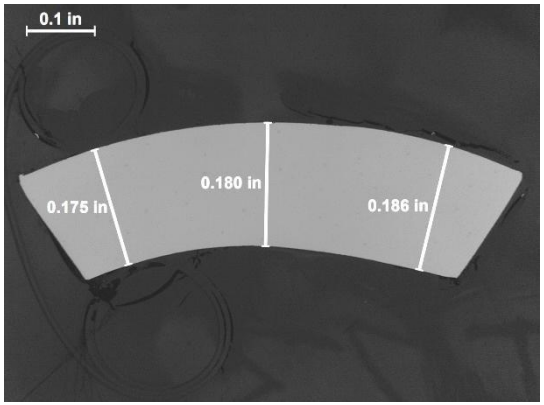	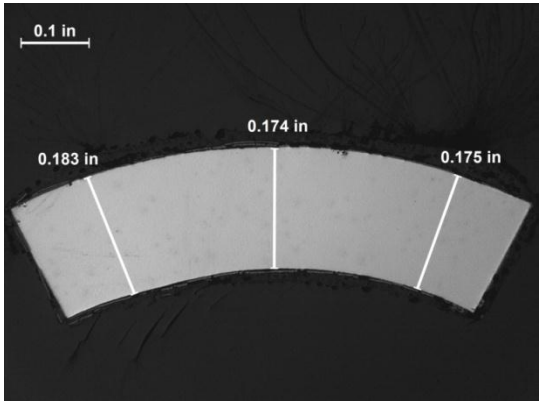	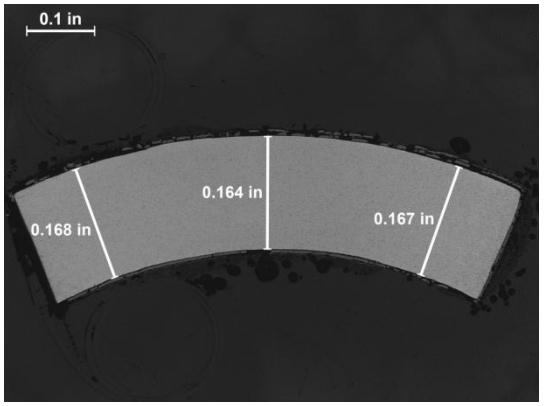
	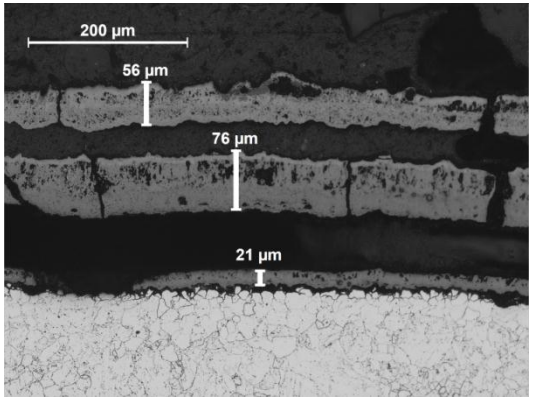	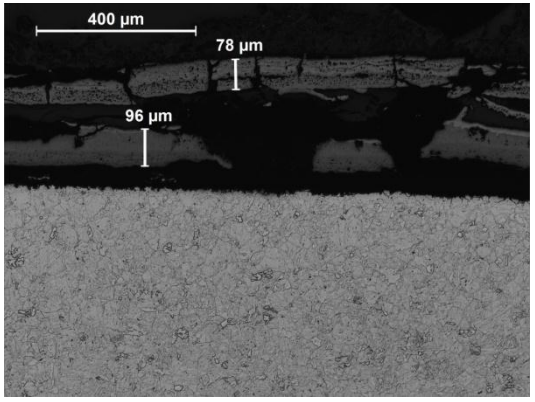

Fireside Corrosion Conditions – Condition 3 Results – T24 Material

No Exposure	After 1000 hours	After 3000 hours
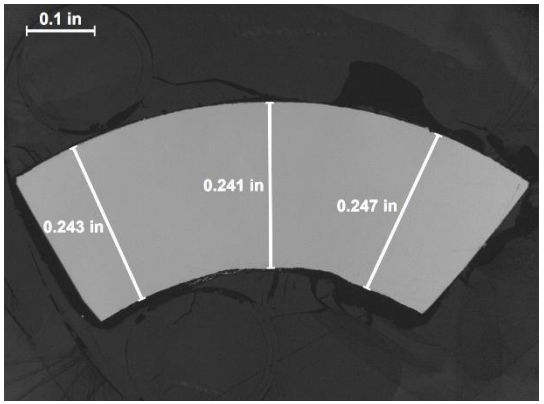	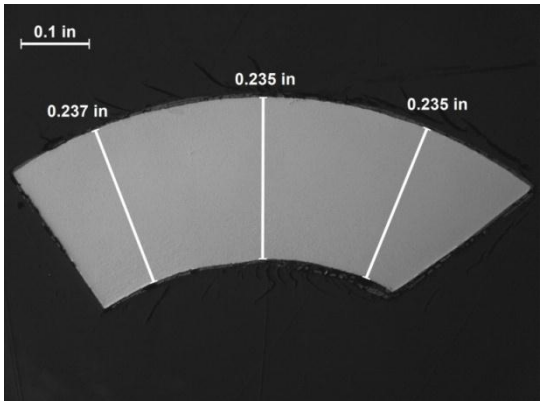	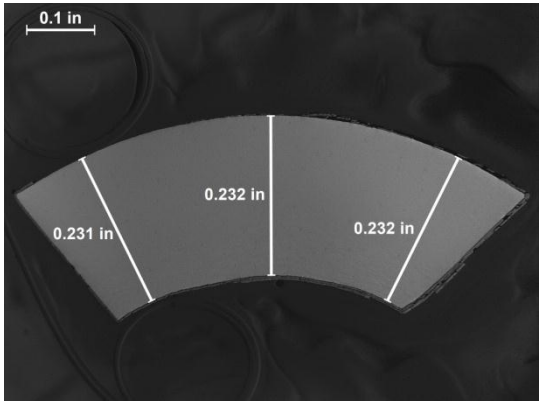
	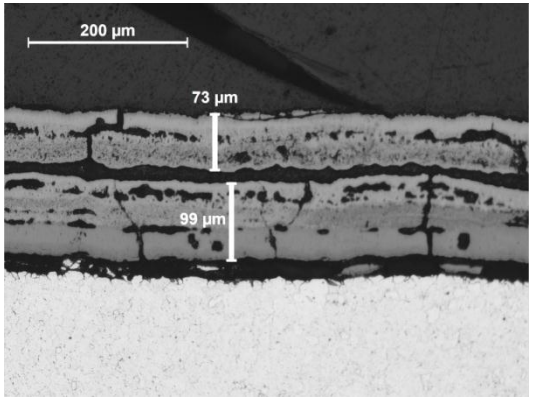	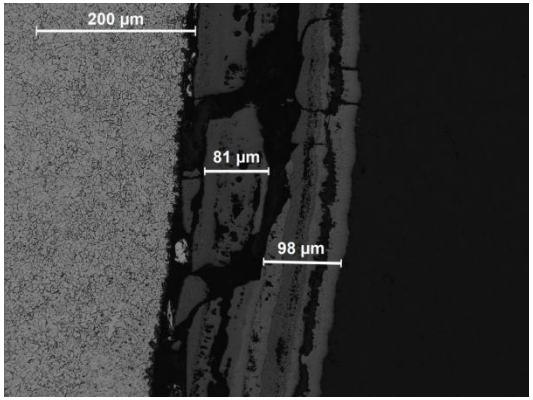

Fireside Corrosion Conditions – Condition 3 Results – T24 Material with Eastern Ash

No Exposure	After 1000 hours	After 3000 hours
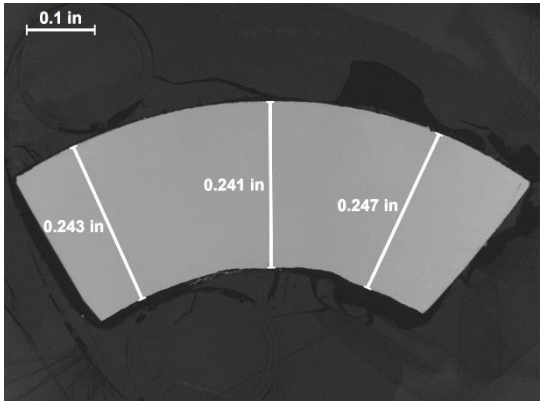	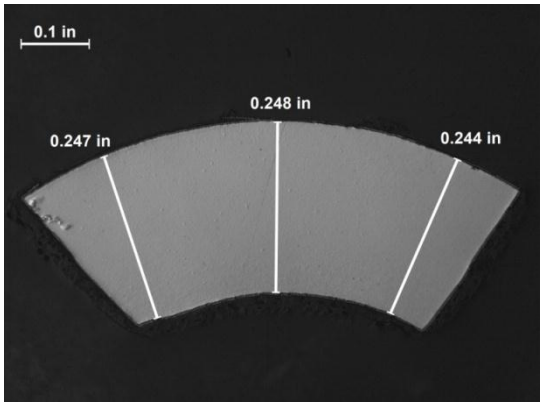	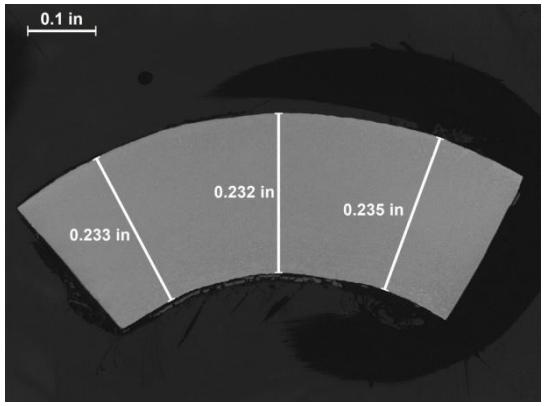
	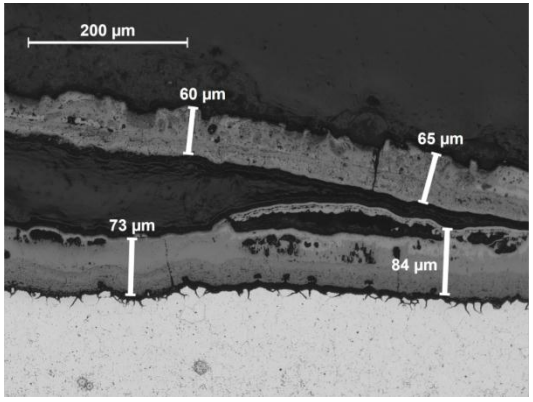	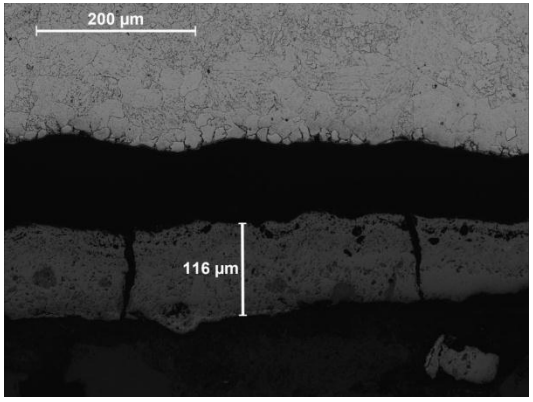

Fireside Corrosion Conditions – Condition 3 Results – T92 Material

No Exposure	After 1000 hours	After 3000 hours
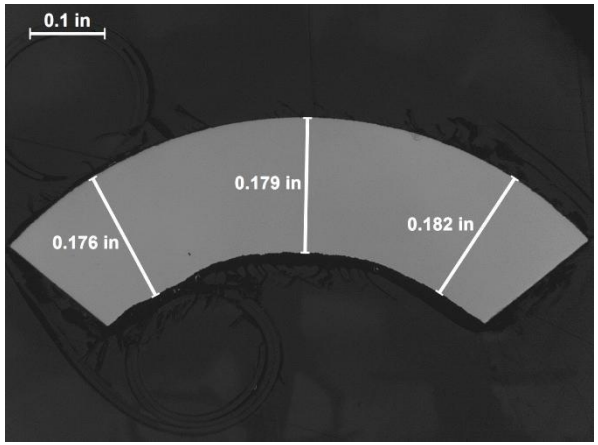	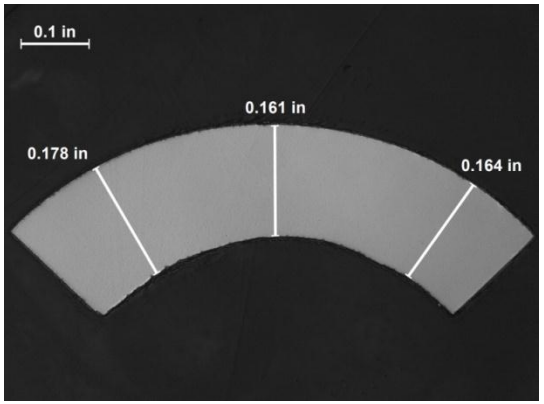	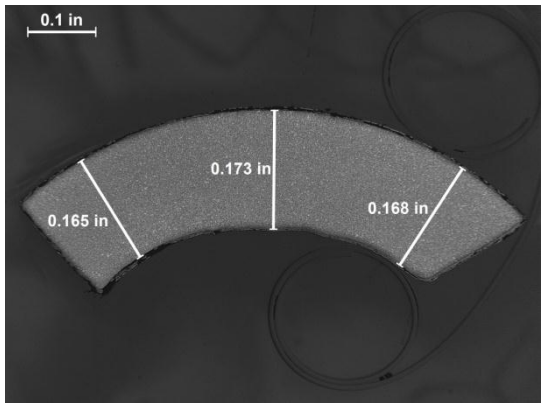
	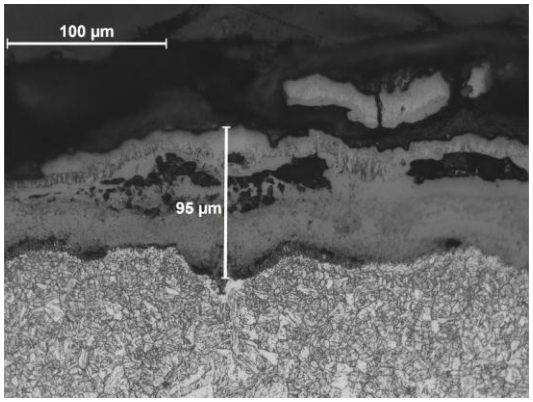	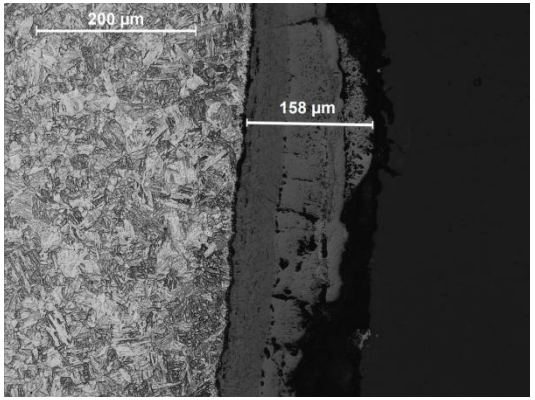

Fireside Corrosion Conditions – Condition 3 Results – T92 Material with Eastern Ash

No Exposure	After 1000 hours	After 3000 hours
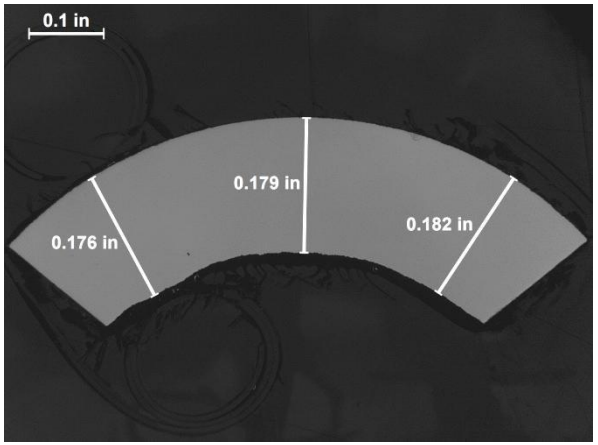	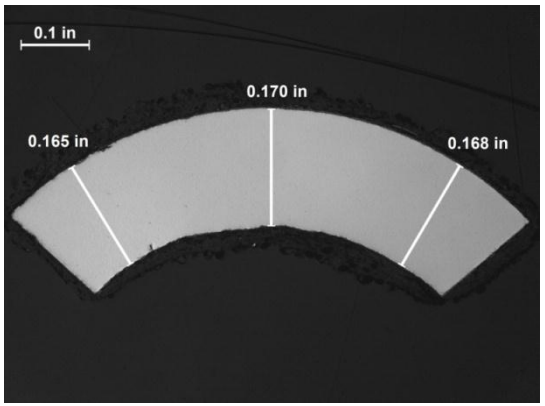	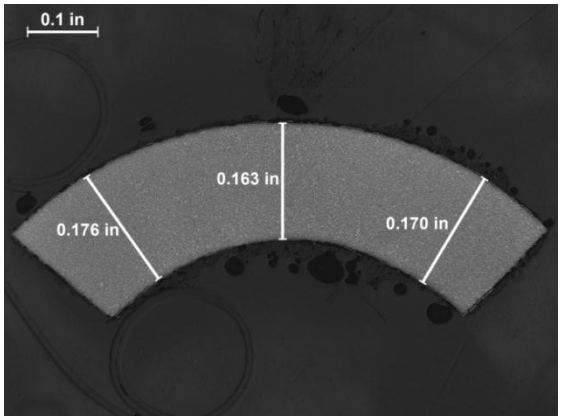
	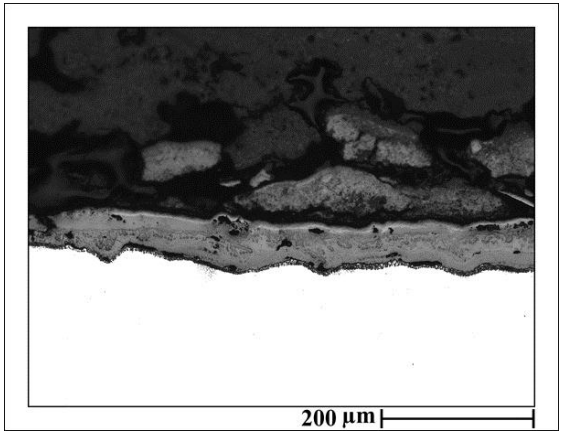	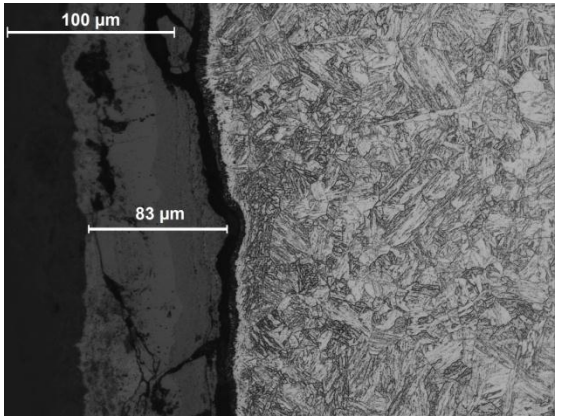

Fireside Corrosion Conditions – Condition 3 Results – Super304H Material

No Exposure	After 1000 hours	After 3000 hours
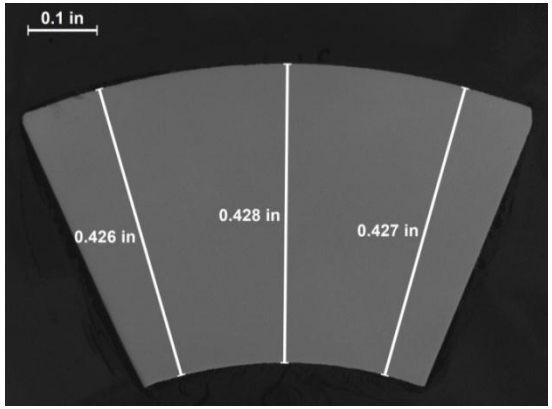	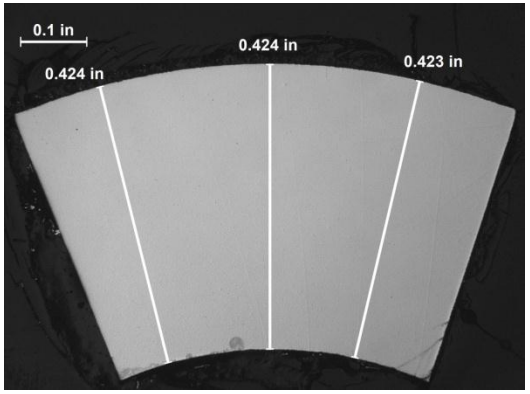	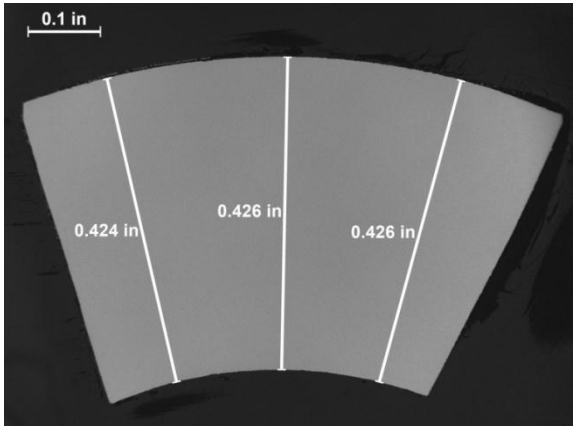
	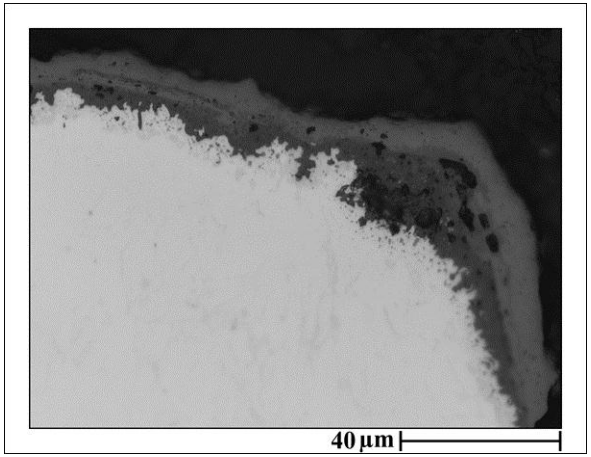	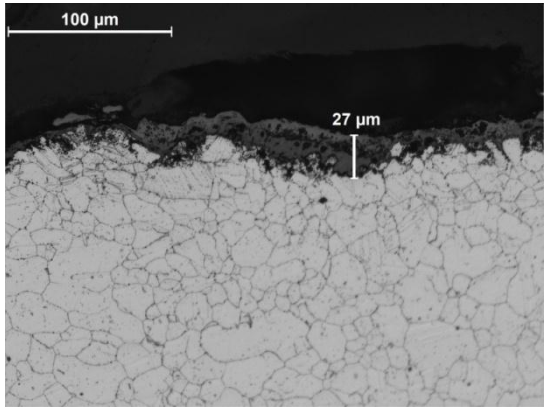

Fireside Corrosion Conditions – Condition 3 Results – Super304H Material with Eastern Ash

No Exposure	After 1000 hours	After 3000 hours
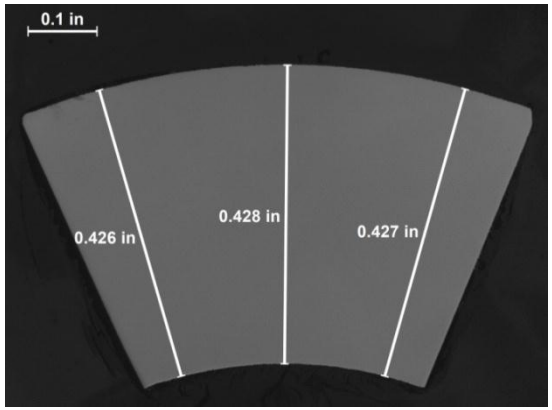	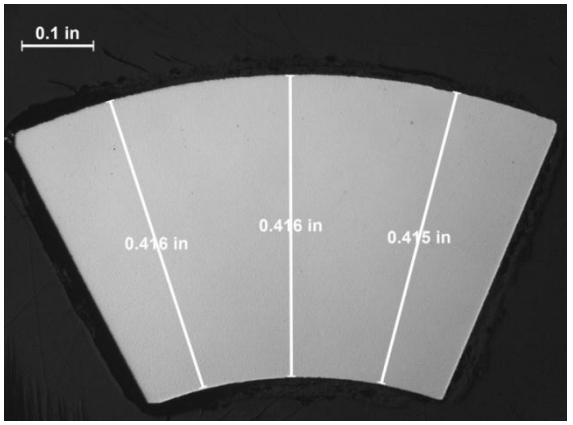	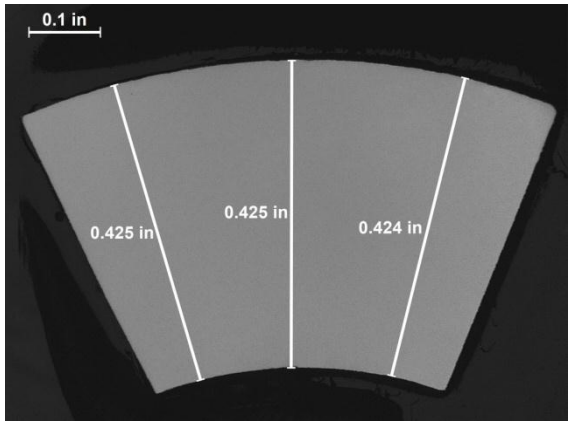
	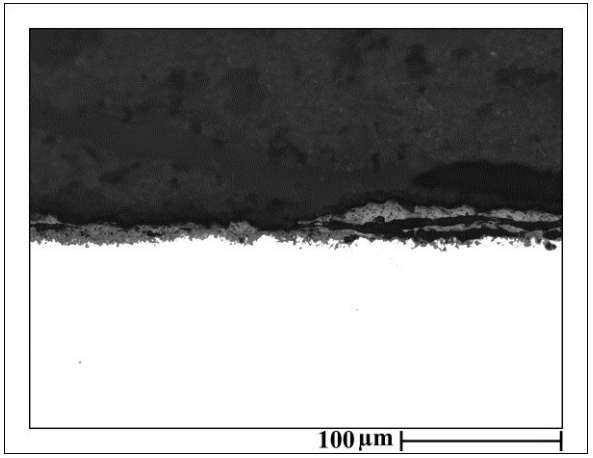	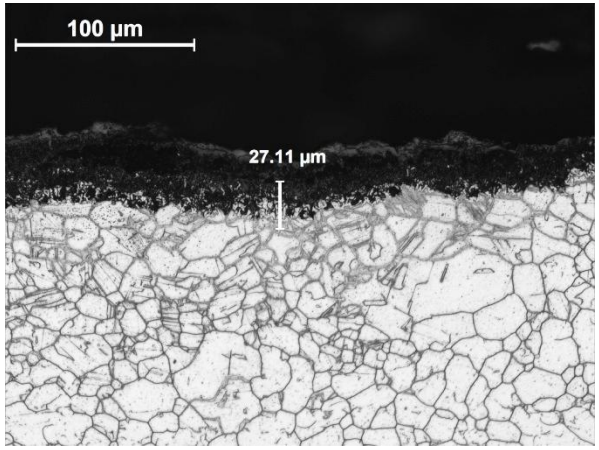

Fireside Corrosion Conditions – Condition 3 Results – Super304H Material with Western ash

No Exposure	After 1000 hours	After 3000 hours
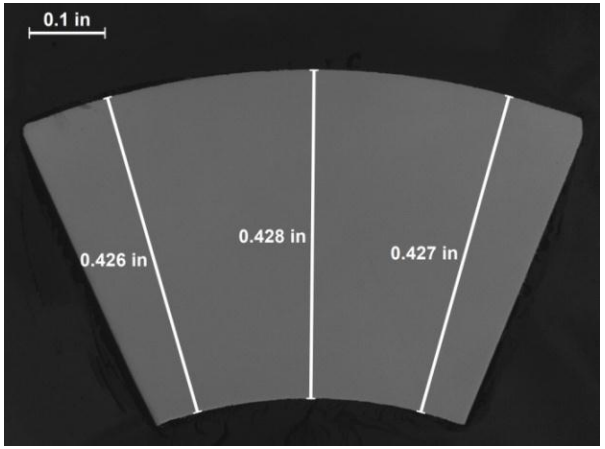		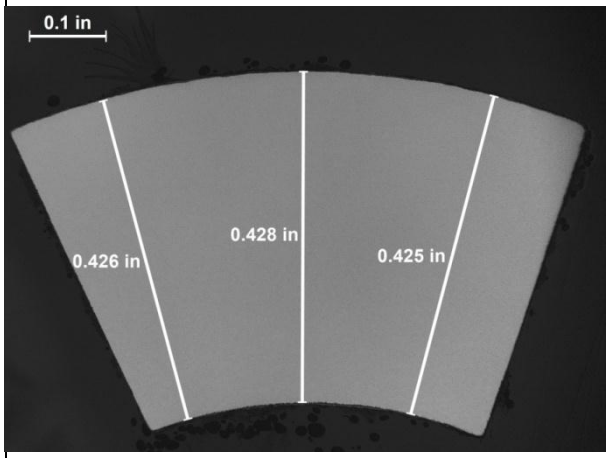
		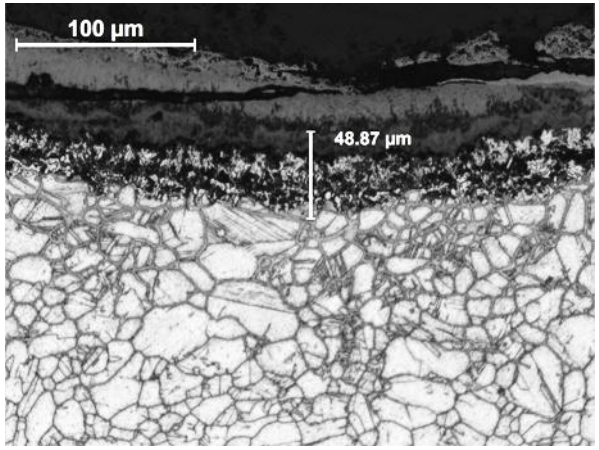

Fireside Corrosion Conditions – Condition 3 Results – IN617 Material

No Exposure	After 1000 hours	After 3000 hours
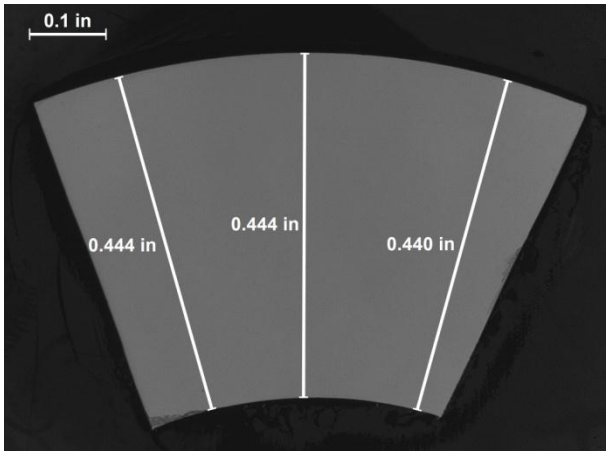	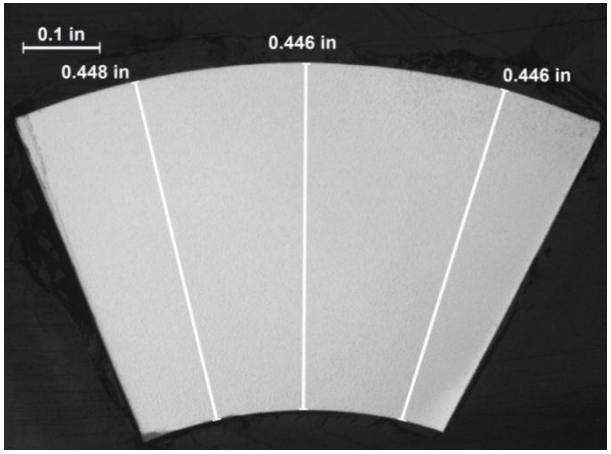	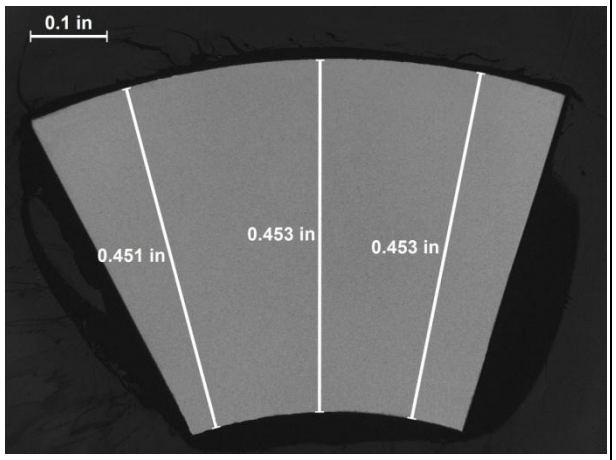
	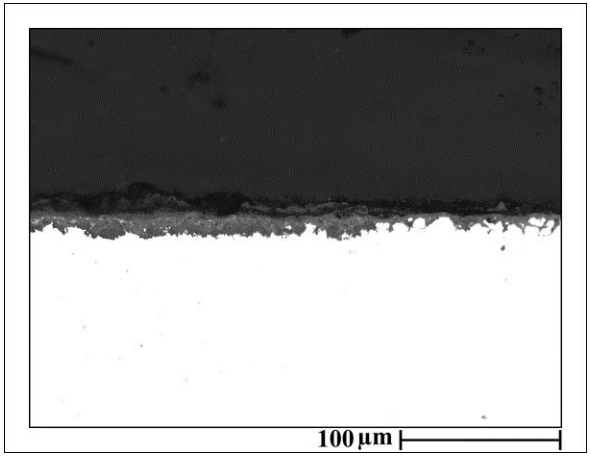	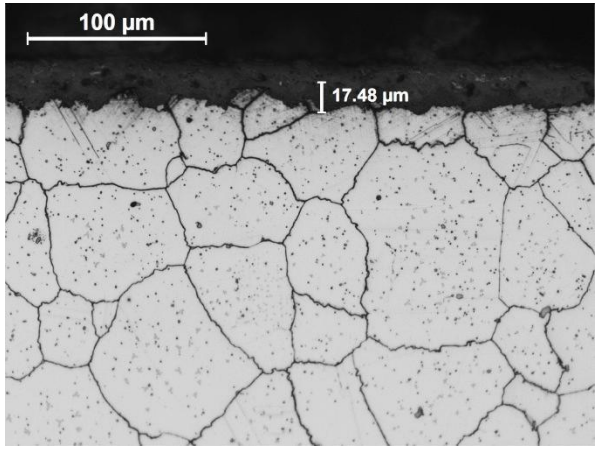

Fireside Corrosion Conditions – Condition 3 Results – IN617 Material with Eastern Ash

No Exposure	After 1000 hours	After 3000 hours
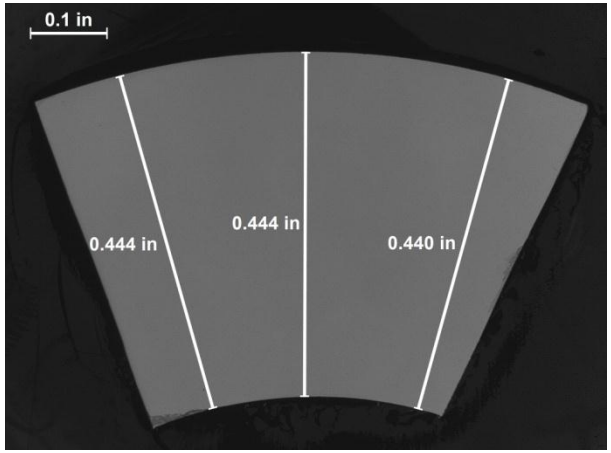	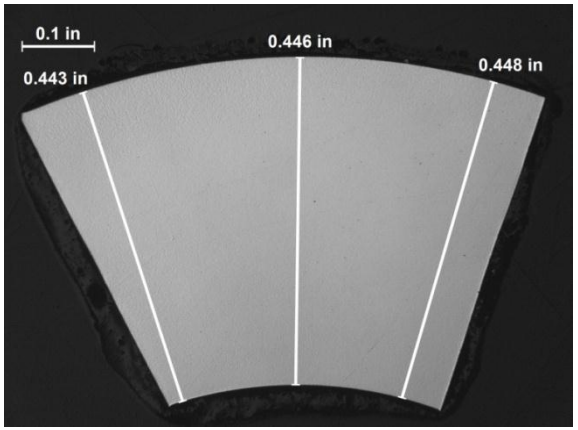	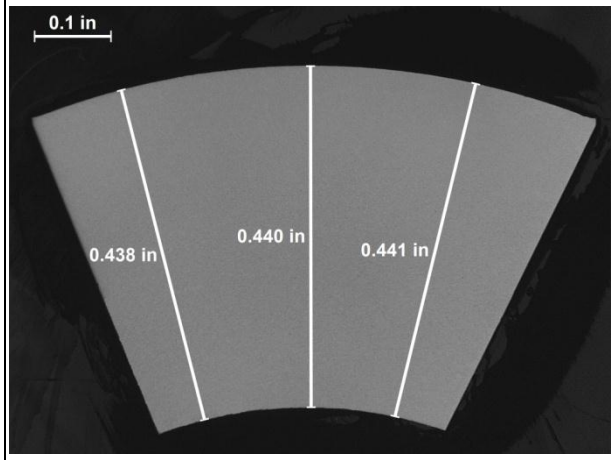
	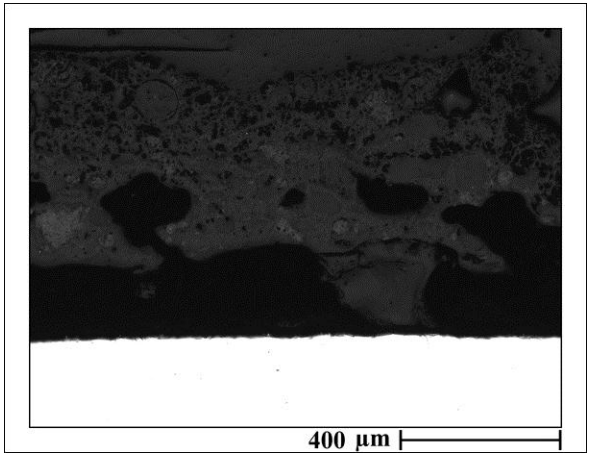	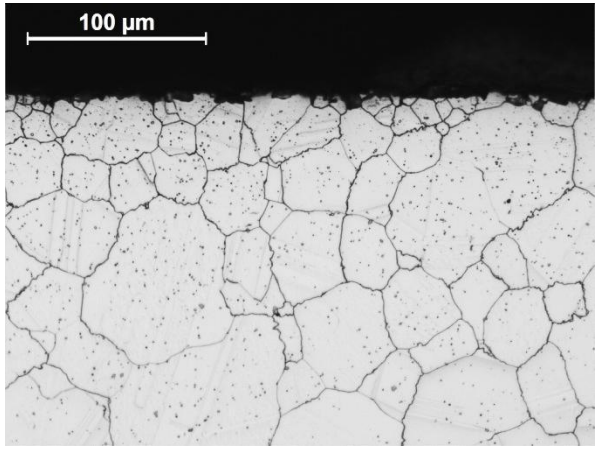

Fireside Corrosion Conditions – Condition 3 Results – NF709R Material

No Exposure	After 1000 hours	After 3000 hours
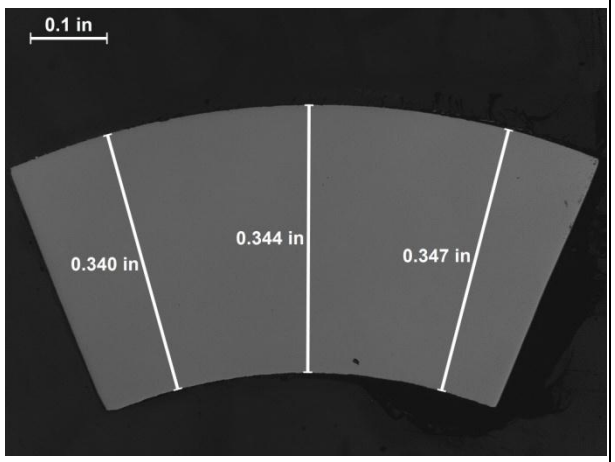	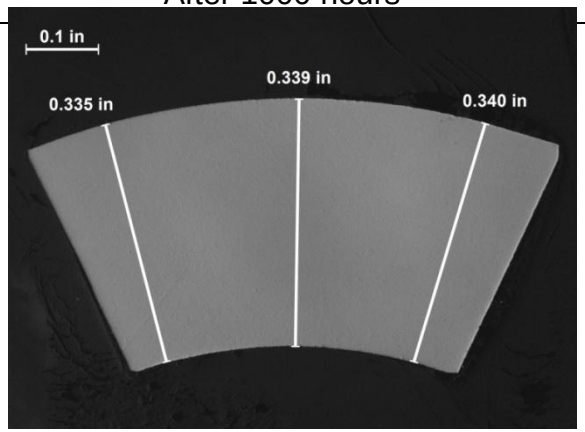	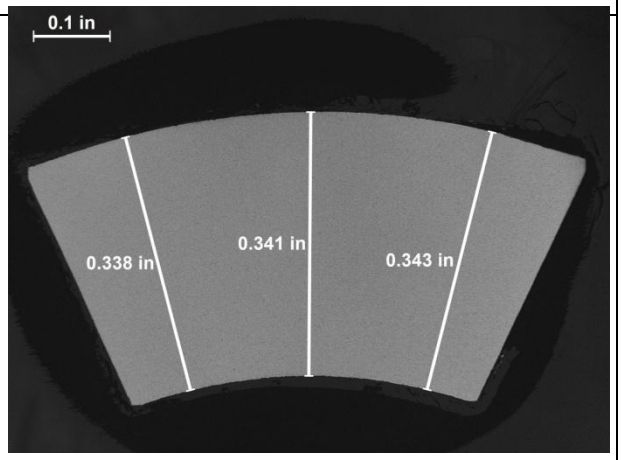
	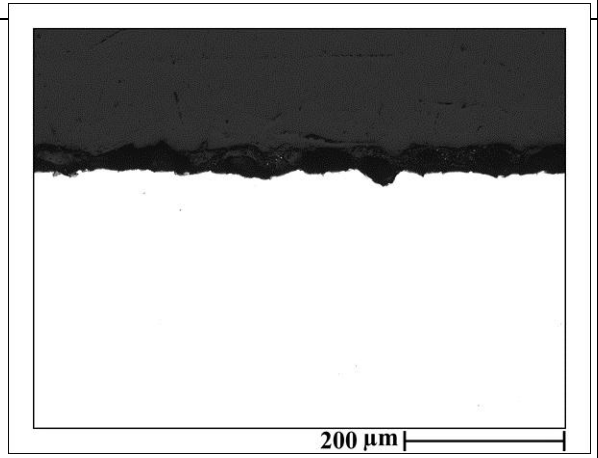	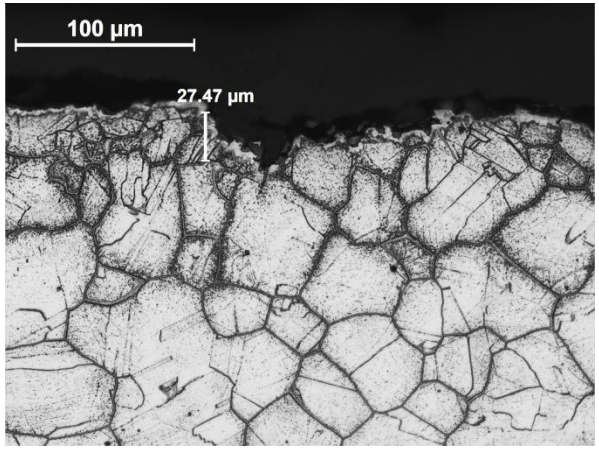

Fireside Corrosion Conditions – Condition 3 Results – NF709R Material with Eastern Ash

No Exposure	After 1000 hours	After 3000 hours
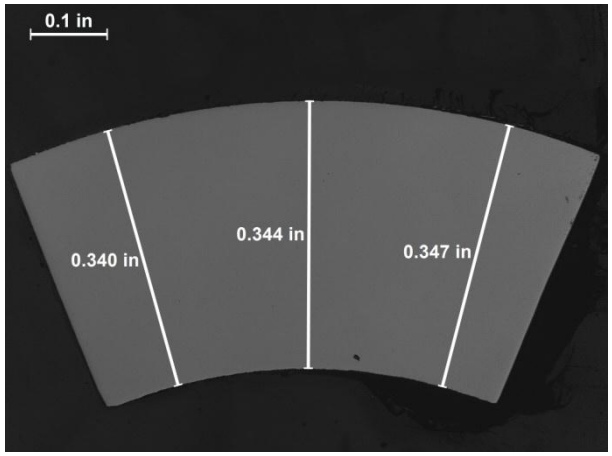	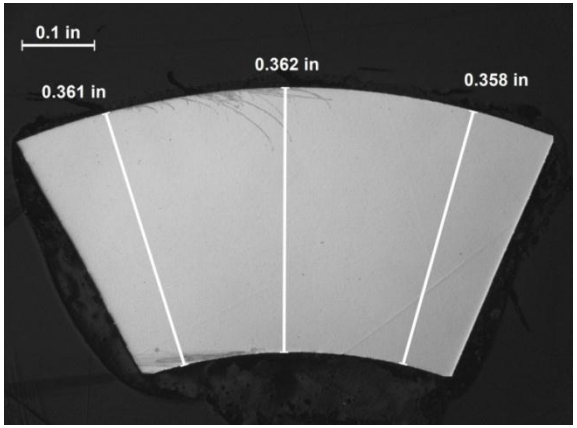	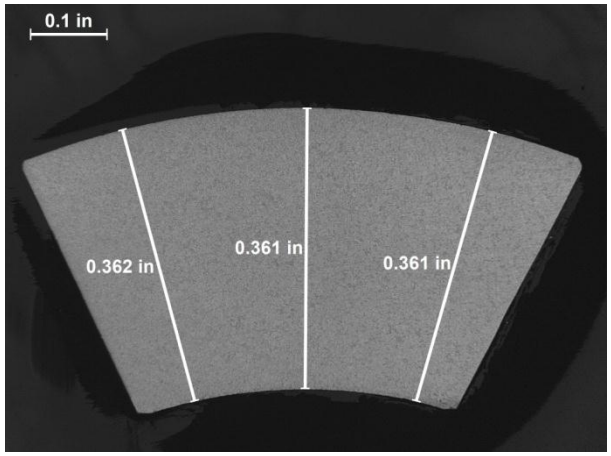
	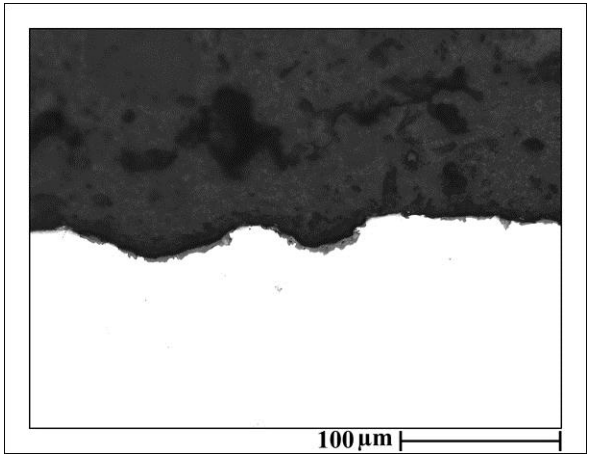	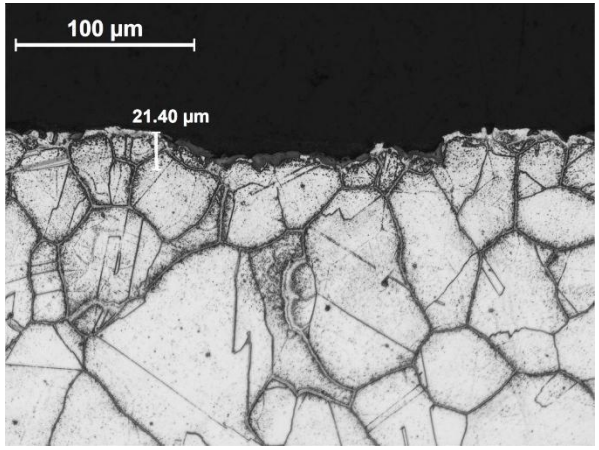

Fireside Corrosion Conditions – Condition 3 Results – Alloy 740 Material

No Exposure	After 1000 hours	After 3000 hours
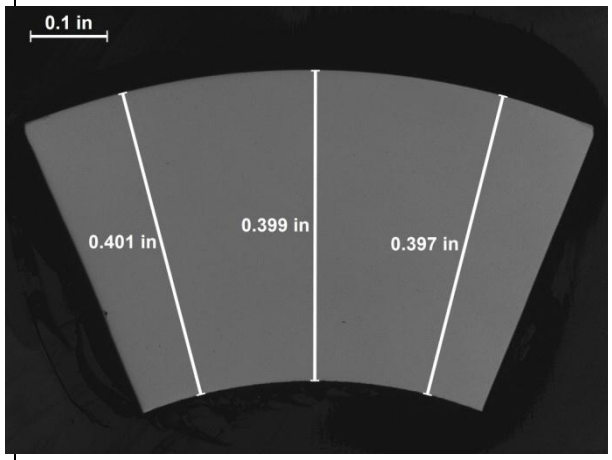	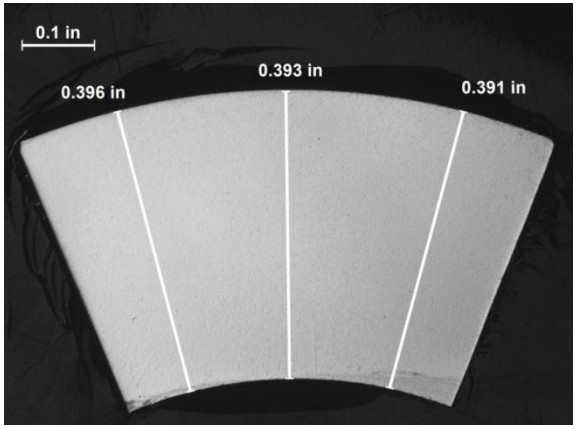	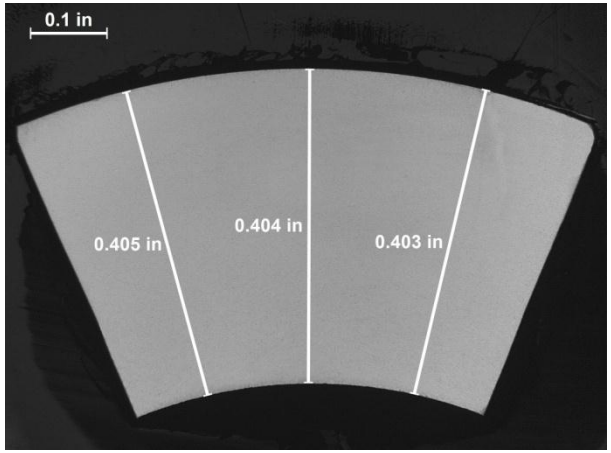
	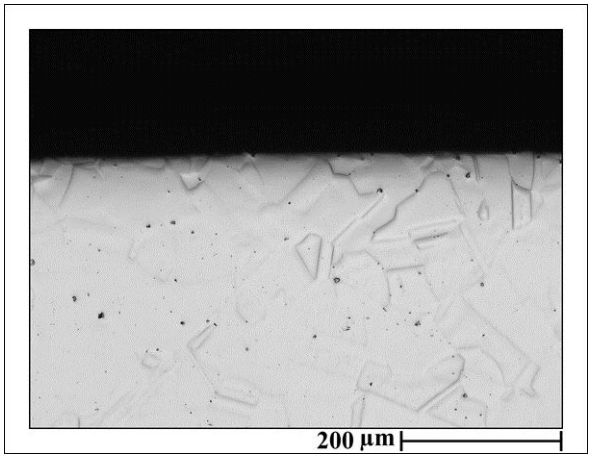	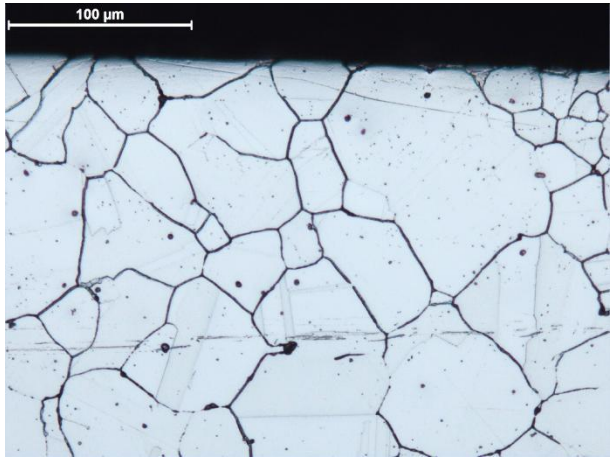

Fireside Corrosion Conditions – Condition 3 Results – Alloy 740 Material with Eastern Ash

No Exposure	After 1000 hours	After 3000 hours
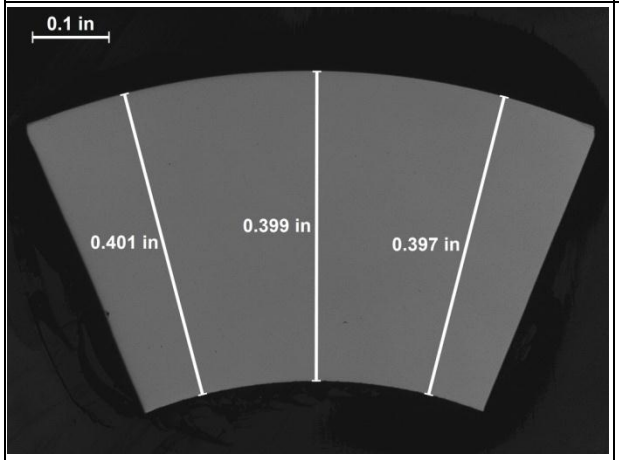	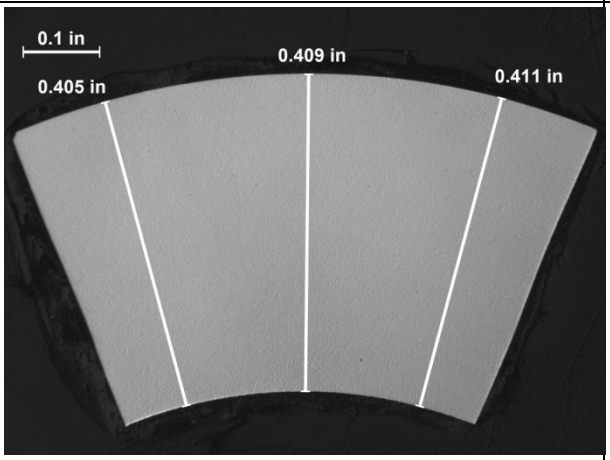	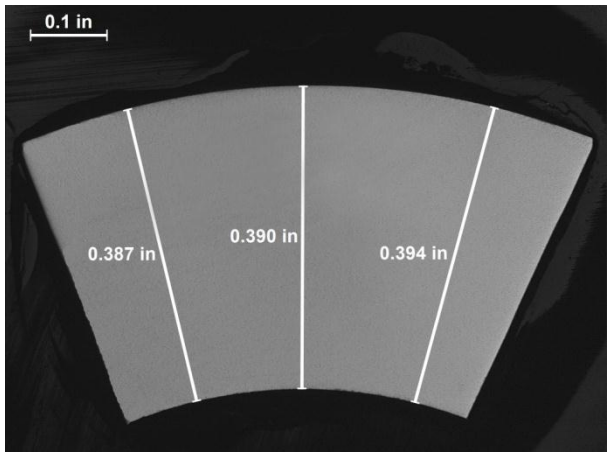
	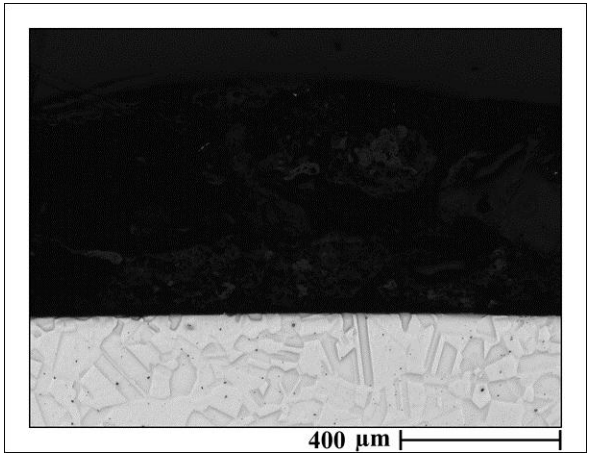	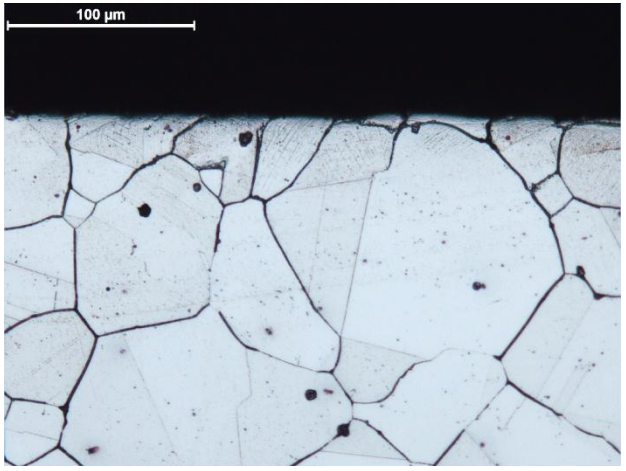

Fireside Corrosion Conditions – Condition 3 Results – Alloy 740 Material with Western Ash

No Exposure	After 1000 hours	After 3000 hours
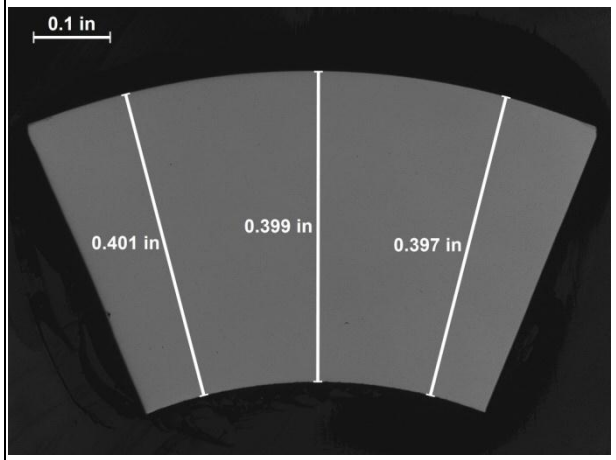	Not included in the test matrix	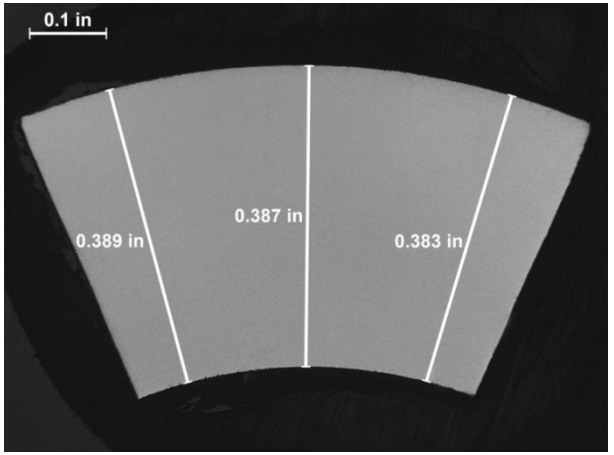
	Not included in the test matrix	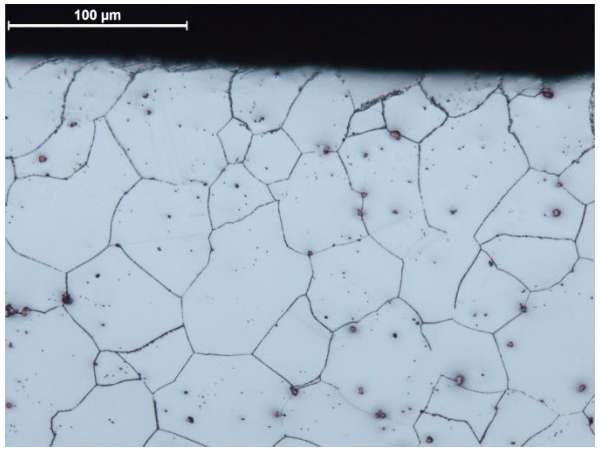

Fireside Corrosion Conditions – Condition 3 Results – HR3C Material

No Exposure	After 1000 hours	After 3000 hours
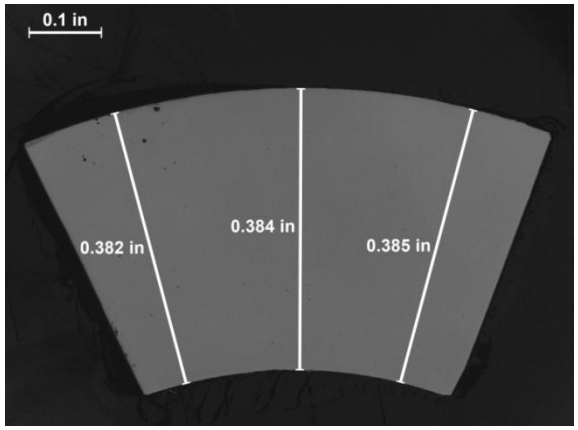	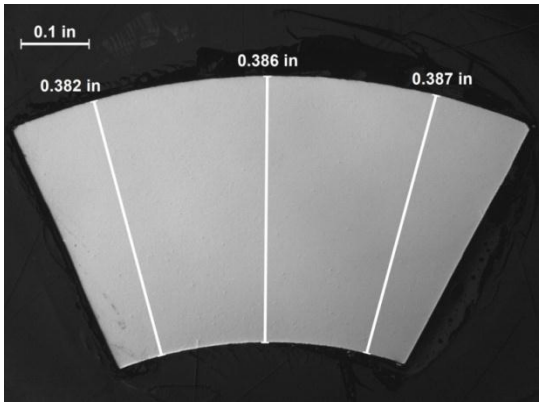	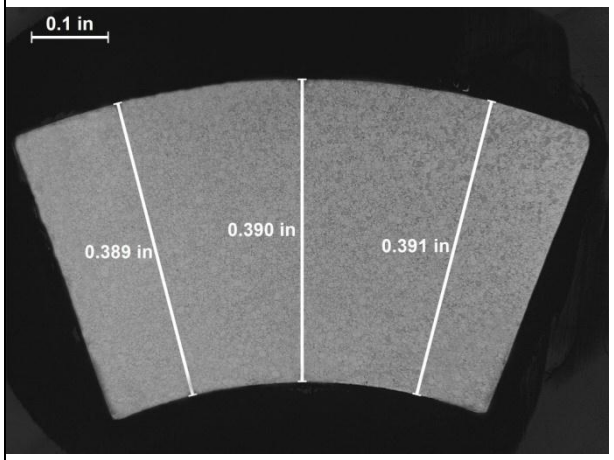
	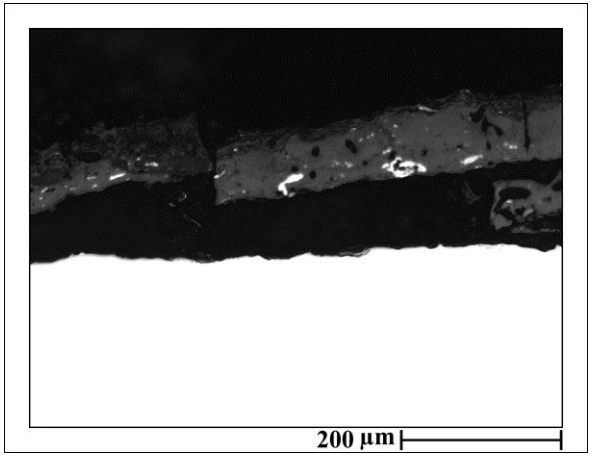	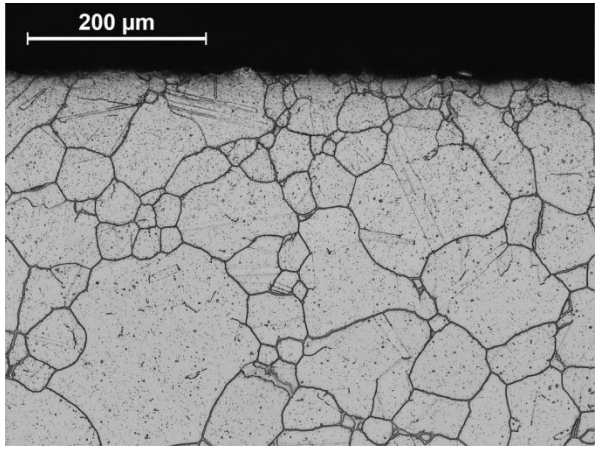

Fireside Corrosion Conditions – Condition 3 Results – HR3C Material with Eastern Ash

No Exposure	After 1000 hours	After 3000 hours
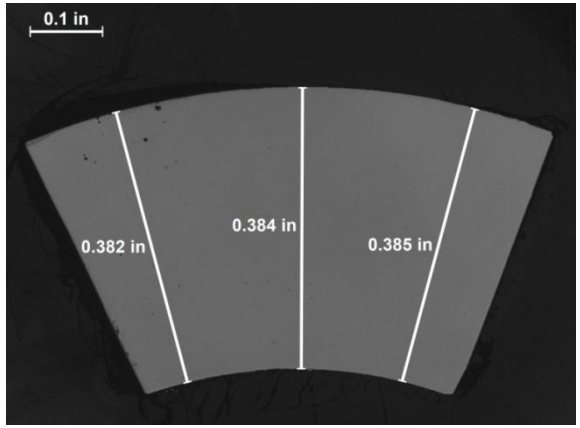	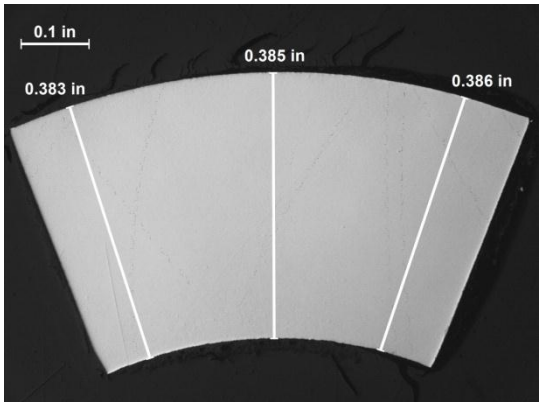	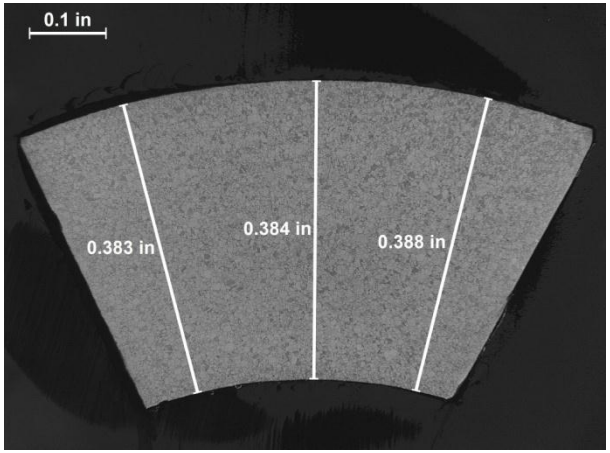
	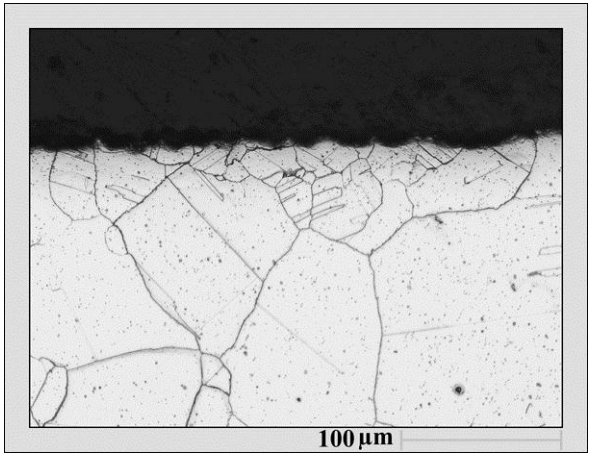	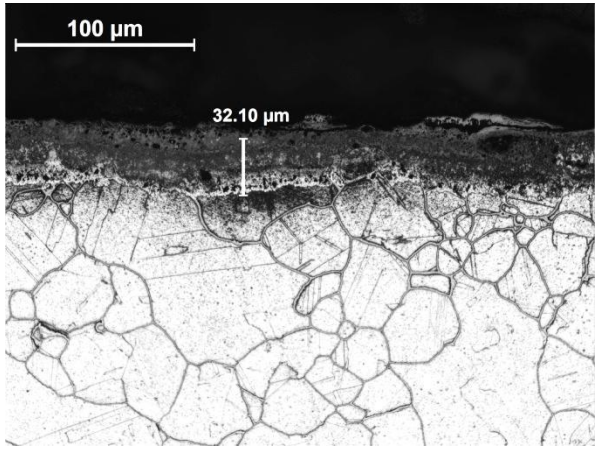

Fireside Corrosion Conditions – Condition 3 Results – HR3C Material with Western Ash

	After 1000 hours	After 3000 hours
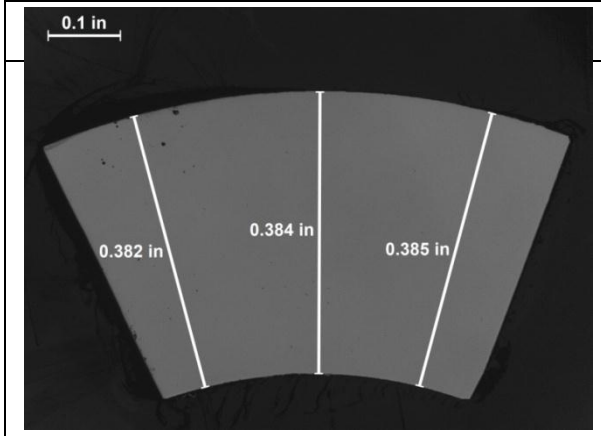	Not included in the test matrix	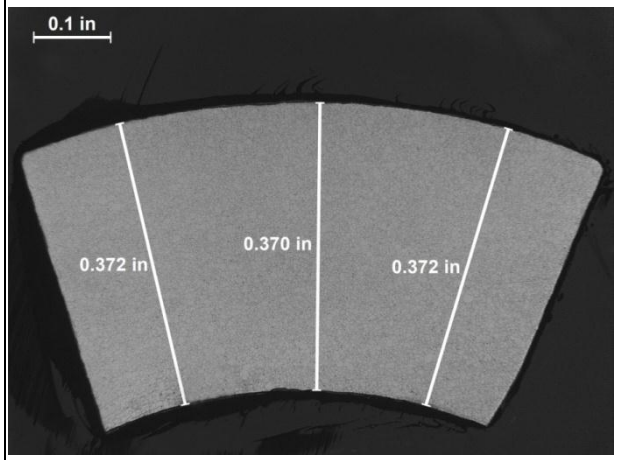
	Not included in the test matrix	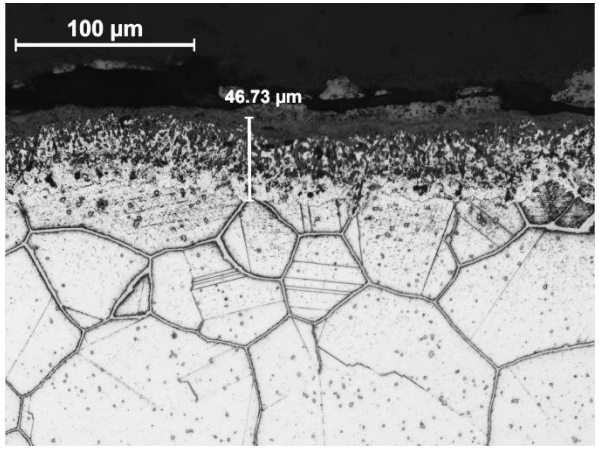

Fireside Corrosion Conditions – Condition 3 Results – C263 Material

No Exposure	After 1000 hours	After 3000 hours
	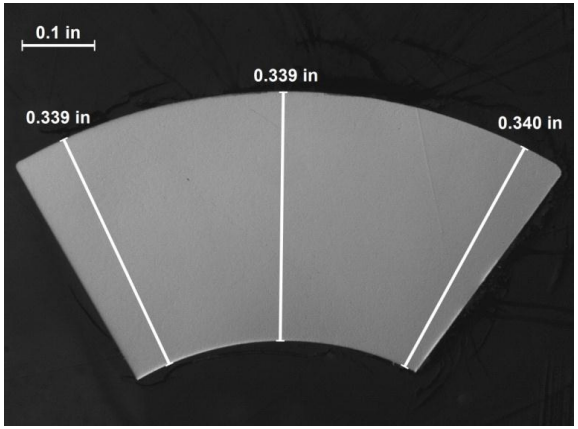	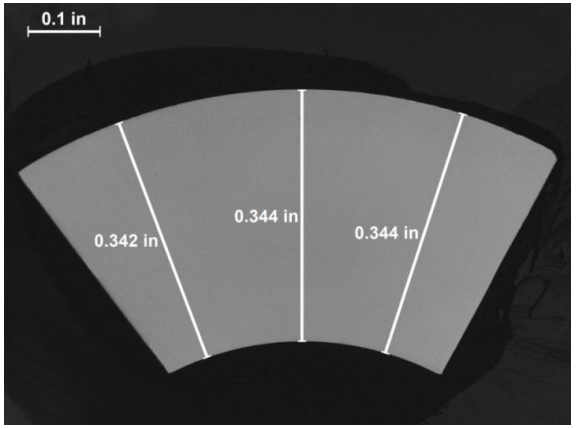
	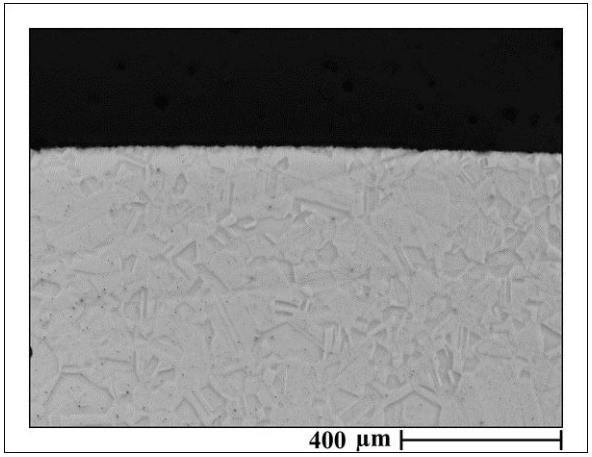	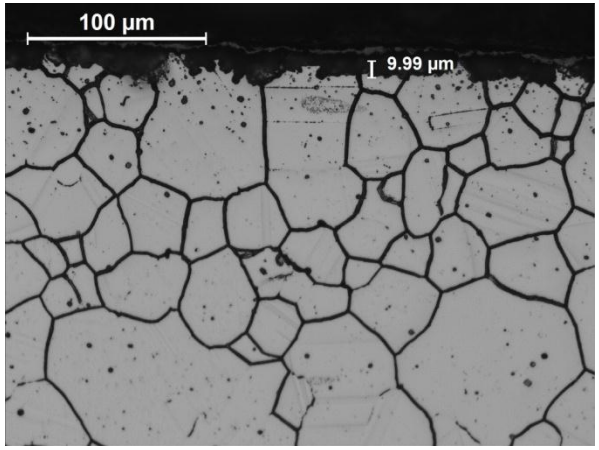

Fireside Corrosion Conditions – Condition 3 Results – C263 Material with Eastern Ash

No Exposure	After 1000 hours	After 3000 hours
	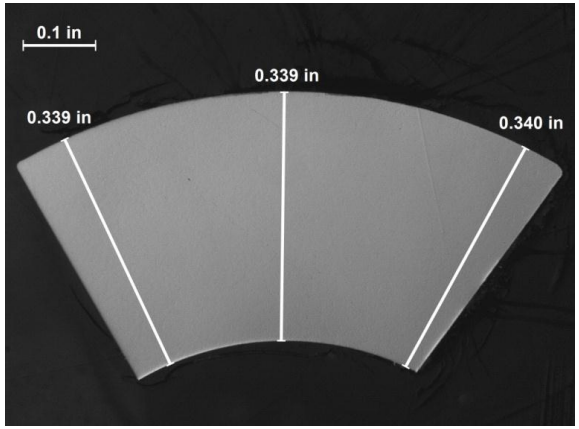	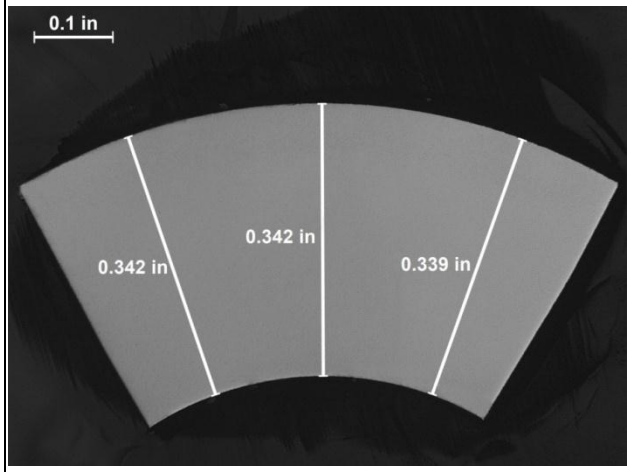
	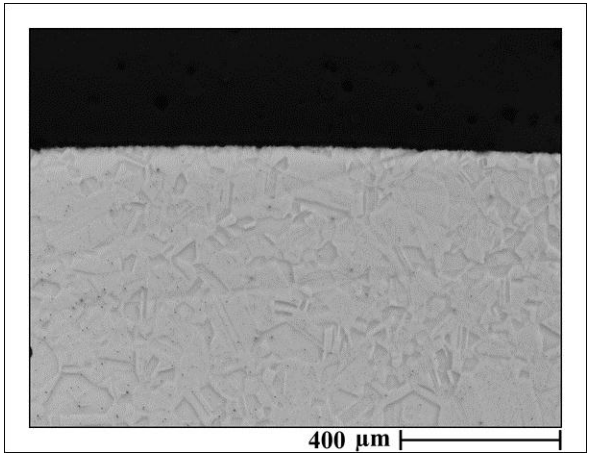	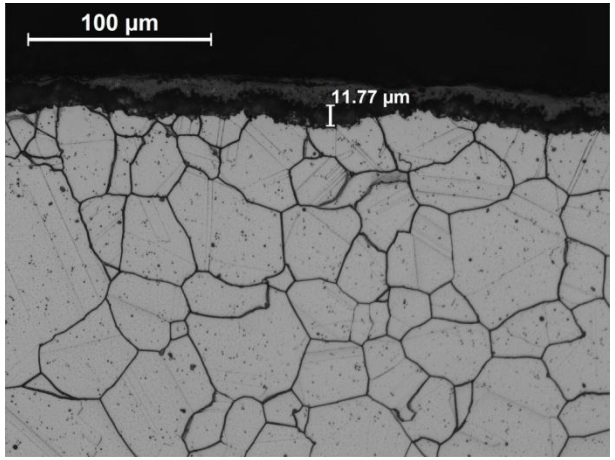

Fireside Corrosion Conditions – Condition 4 Results – T23 Material

No Exposure	After 1000 hours	After 3000 hours
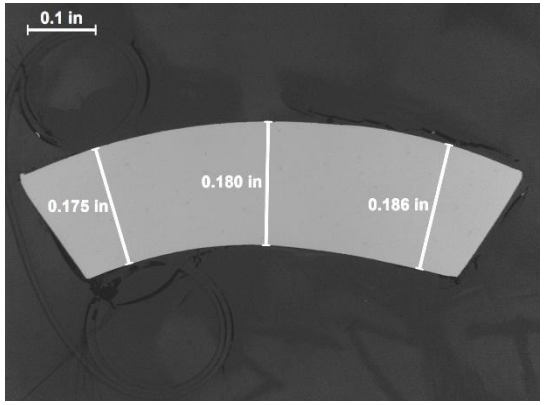	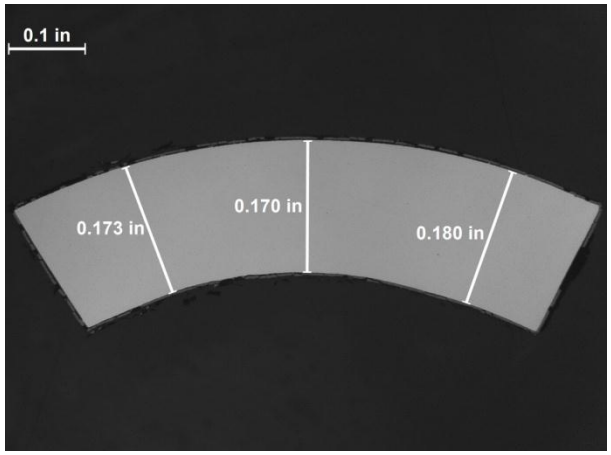	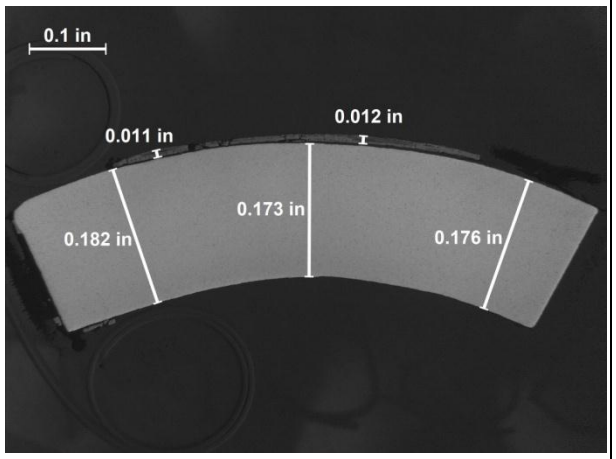
	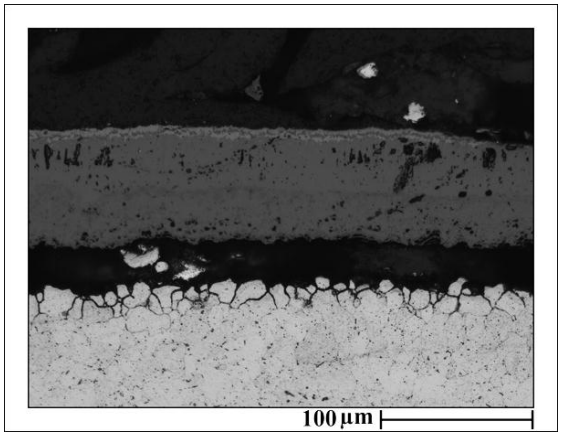	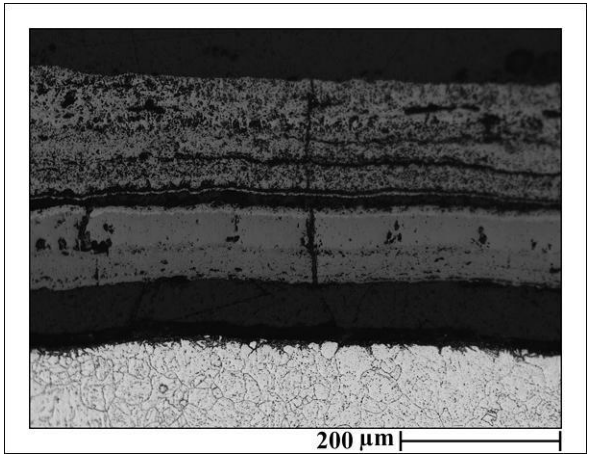

Fireside Corrosion Conditions – Condition 4 Results – T23 Material with Eastern Ash

No Exposure	After 1000 hours	After 3000 hours
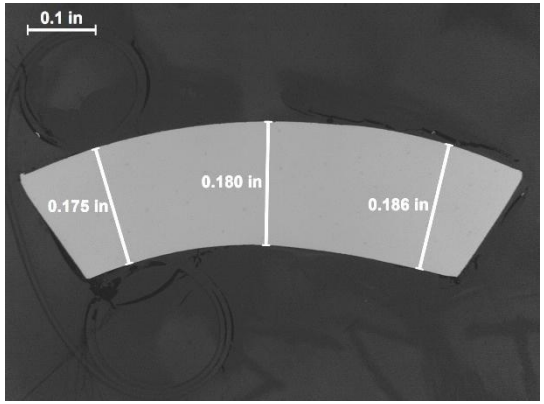	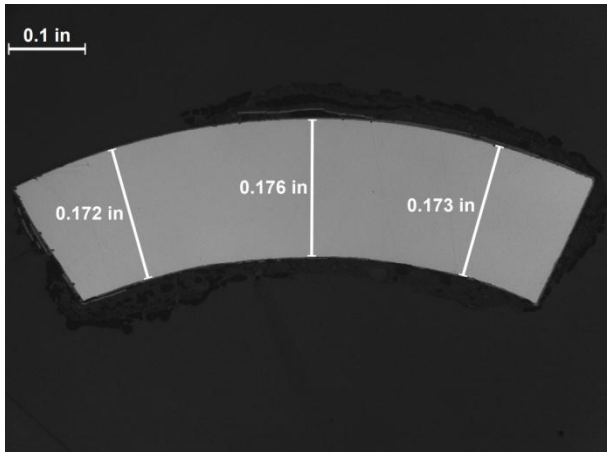	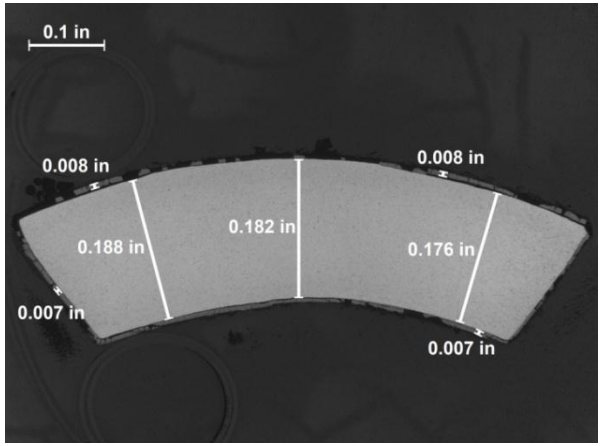
	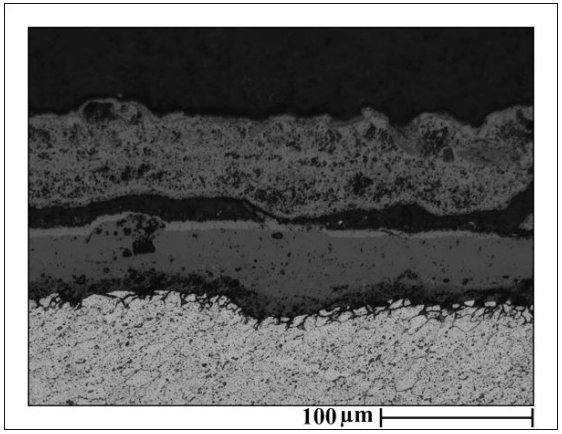	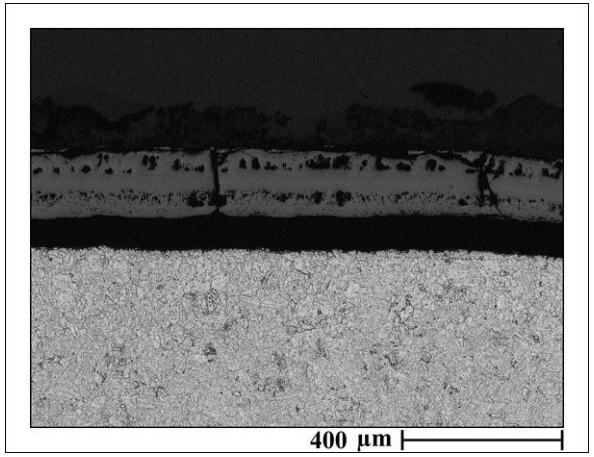

Fireside Corrosion Conditions – Condition 4 Results – T24 Material

No Exposure	After 1000 hours	After 3000 hours
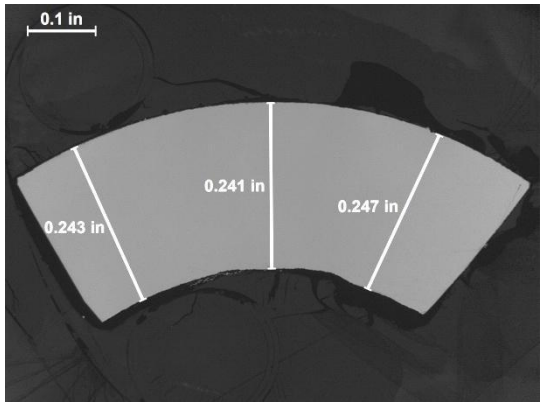	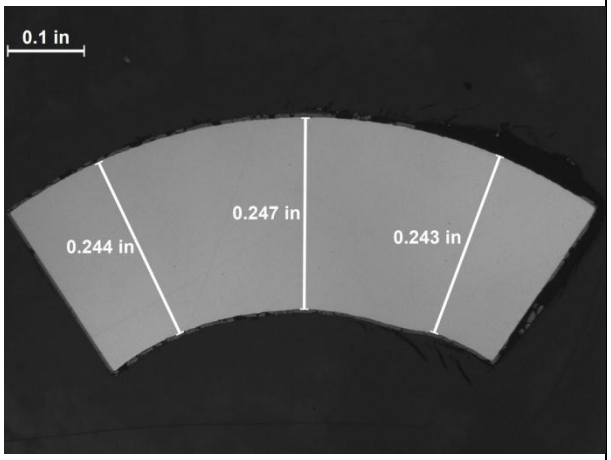	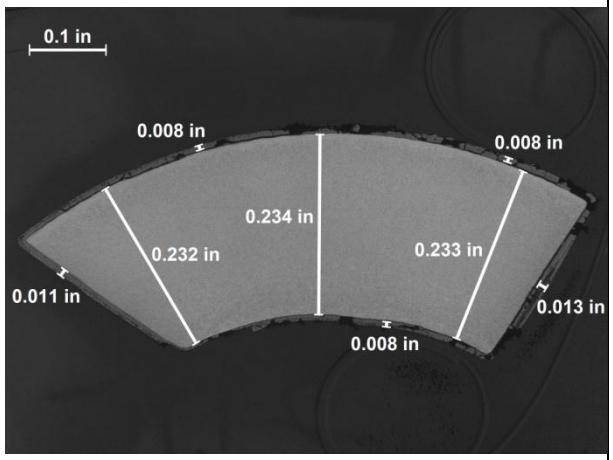
	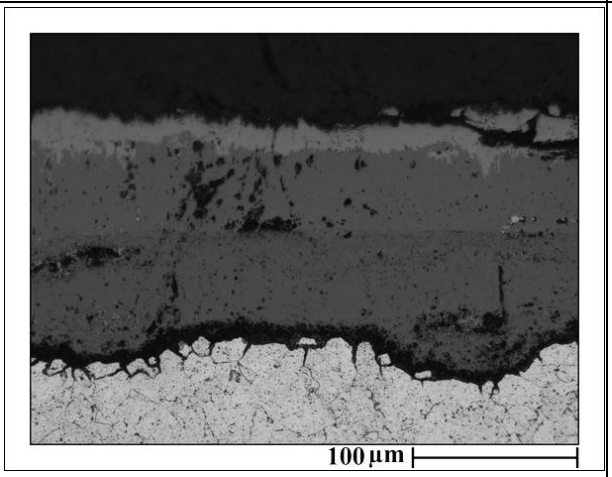	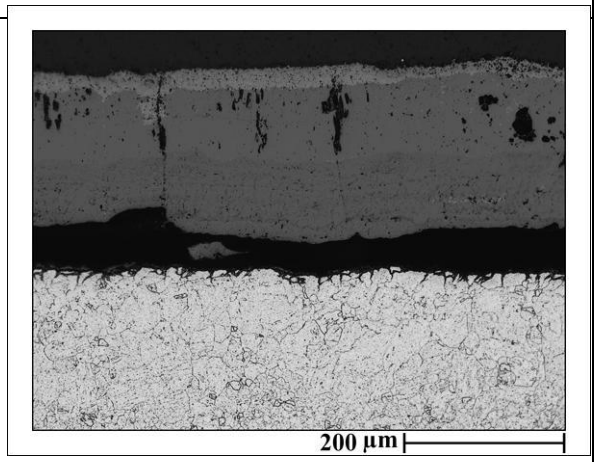

Fireside Corrosion Conditions – Condition 4 Results – T24 Material with Eastern Ash

No Exposure	After 1000 hours	After 3000 hours
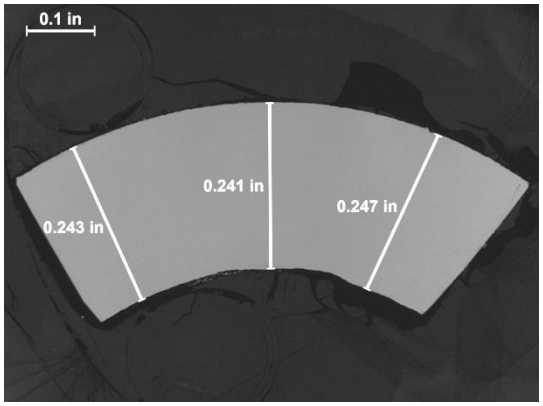	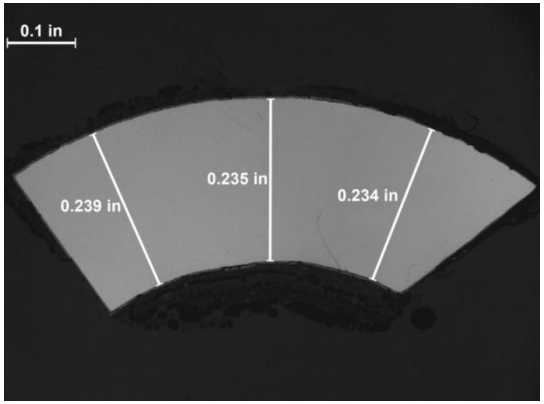	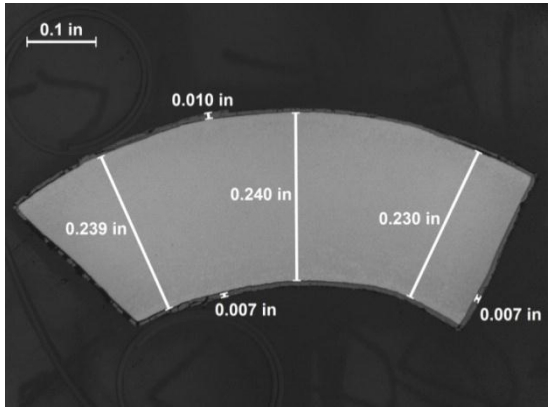
	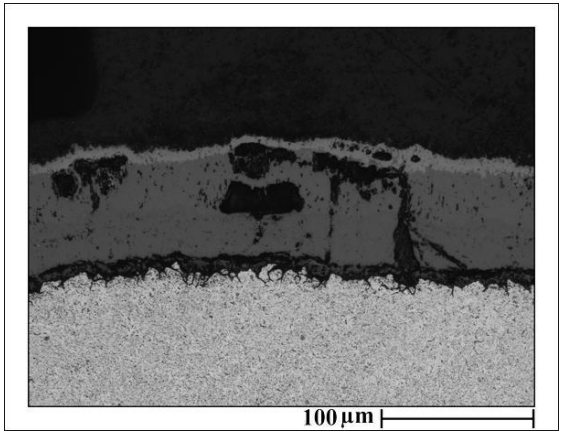	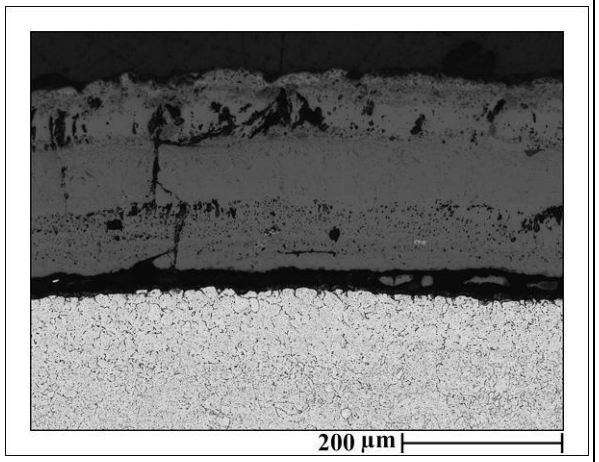

Fireside Corrosion Conditions – Condition 4 Results – T92 Material

No Exposure	After 1000 hours	After 3000 hours
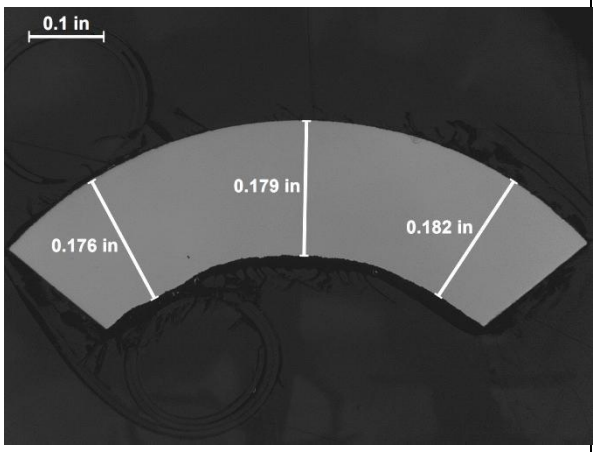	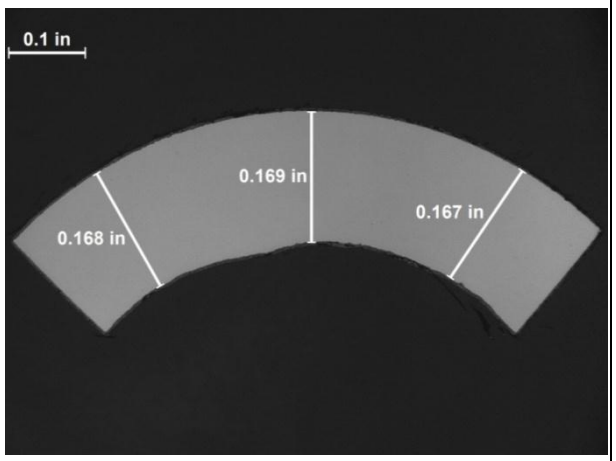	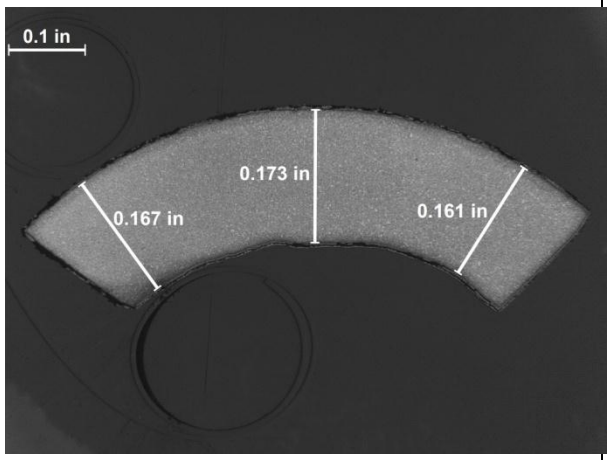
	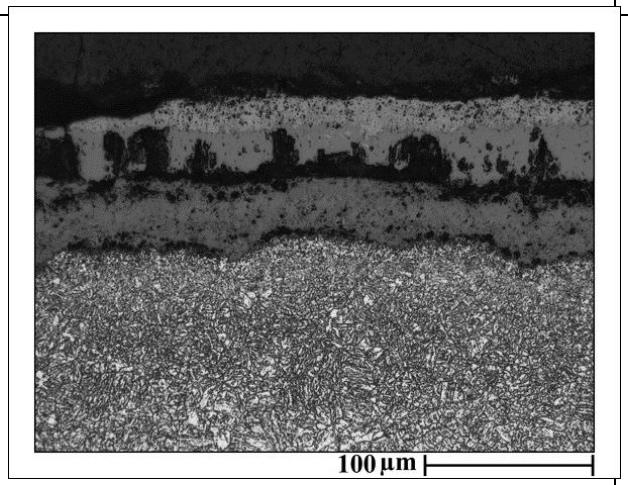	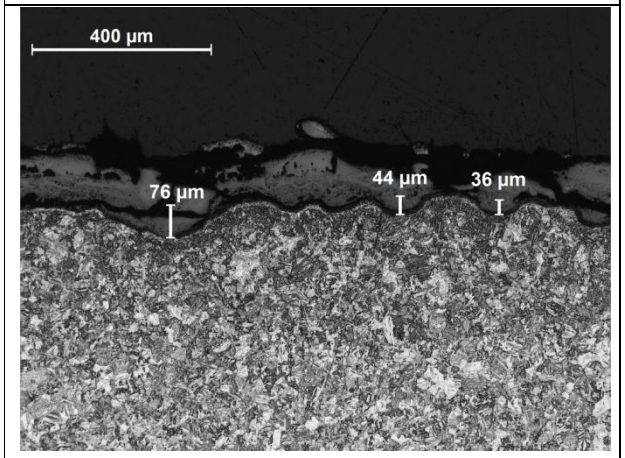

Fireside Corrosion Conditions – Condition 4 Results – T92 Material with Eastern Ash

No Exposure	After 1000 hours	After 3000 hours
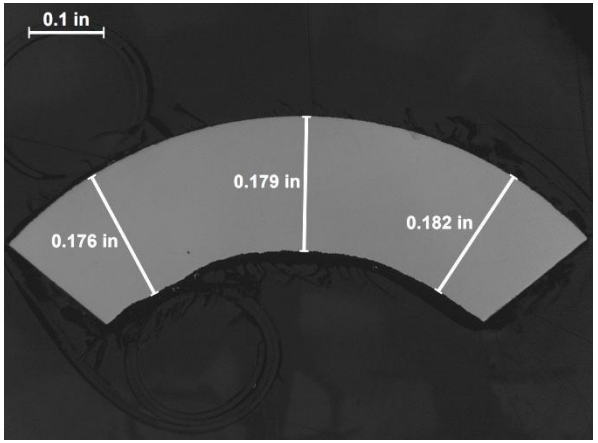	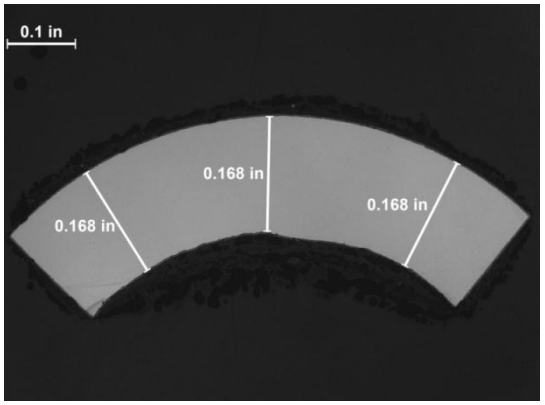	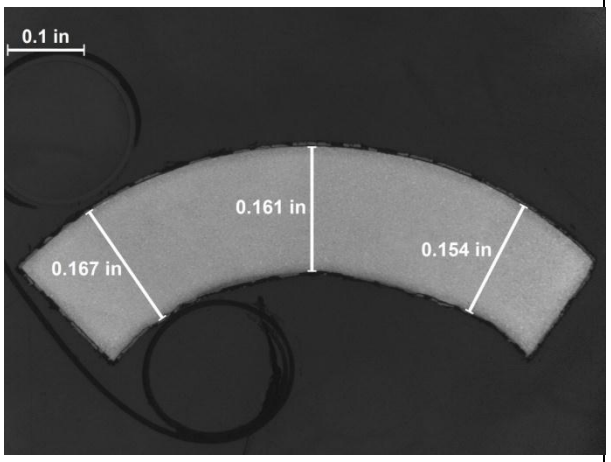
	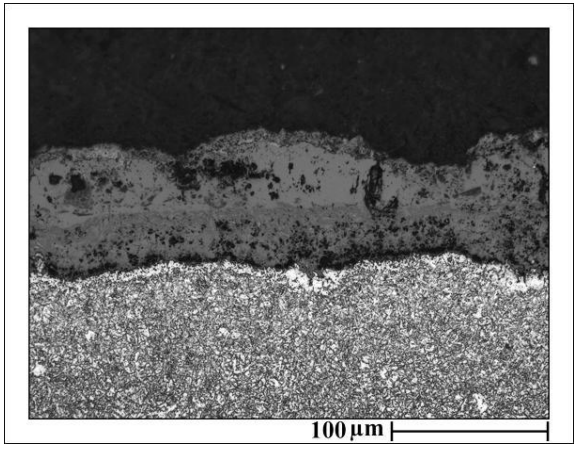	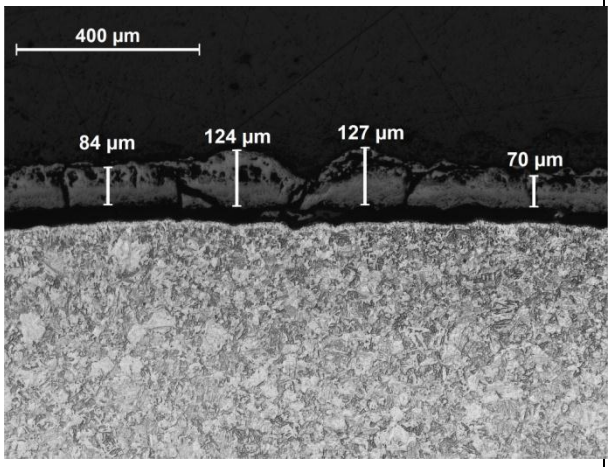

Fireside Corrosion Conditions – Condition 4 Results – Super304H Material

No Exposure	After 1000 hours	After 3000 hours
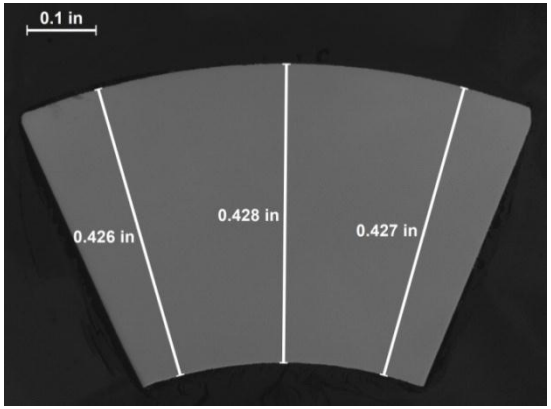	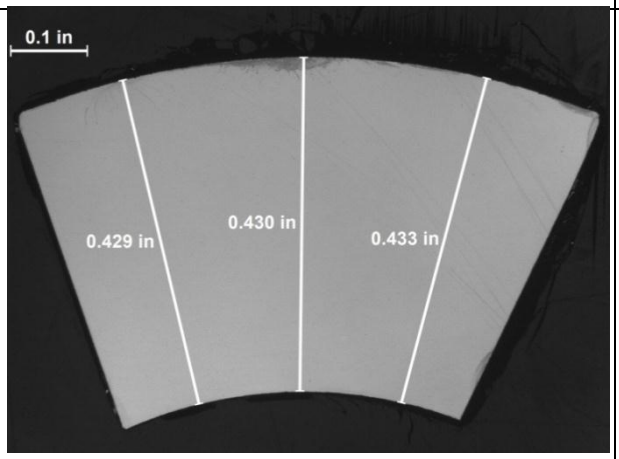	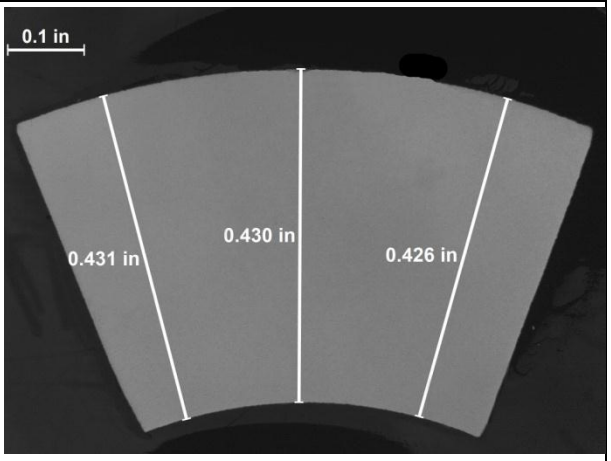
	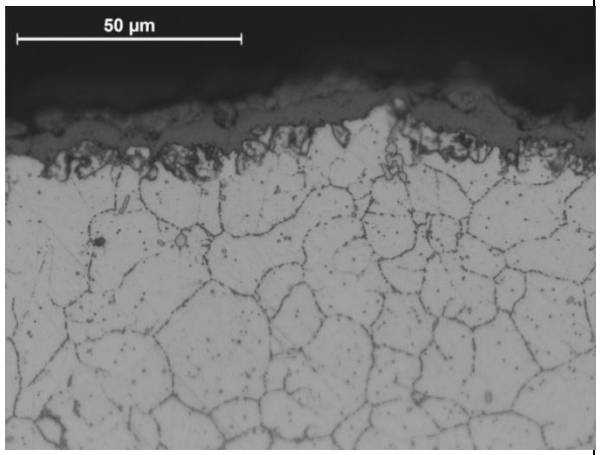	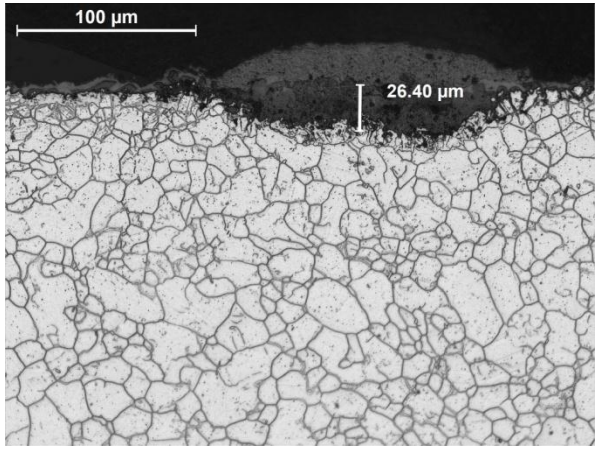

Fireside Corrosion Conditions – Condition4 Results – Super304H Material with Eastern Ash

No Exposure	After 1000 hours	After 3000 hours
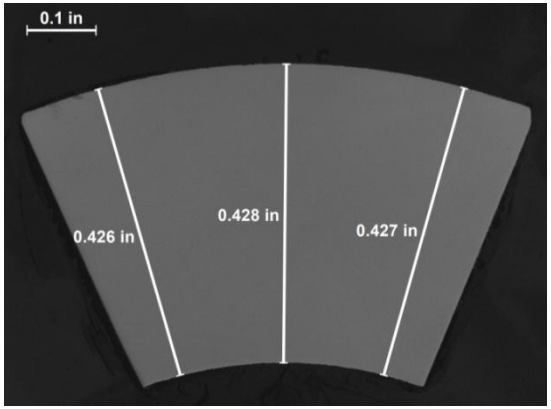	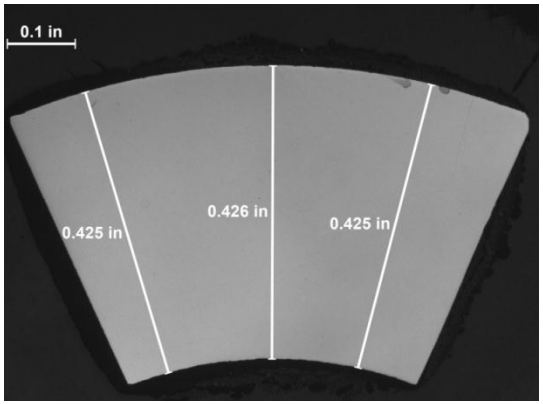	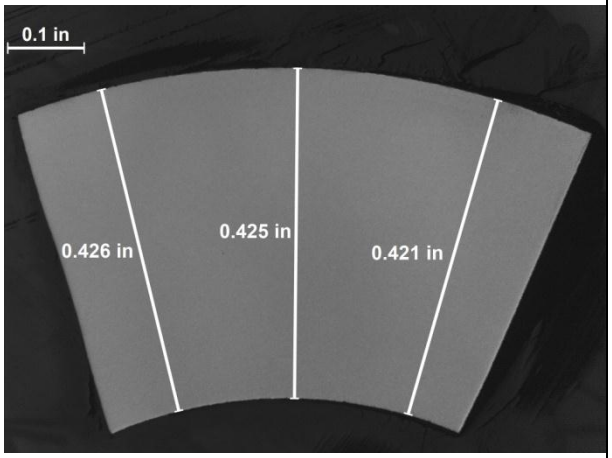
	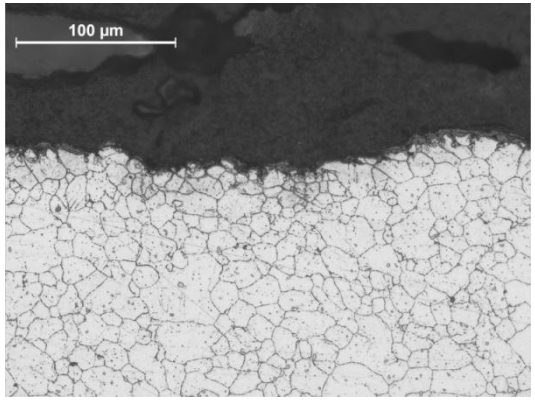	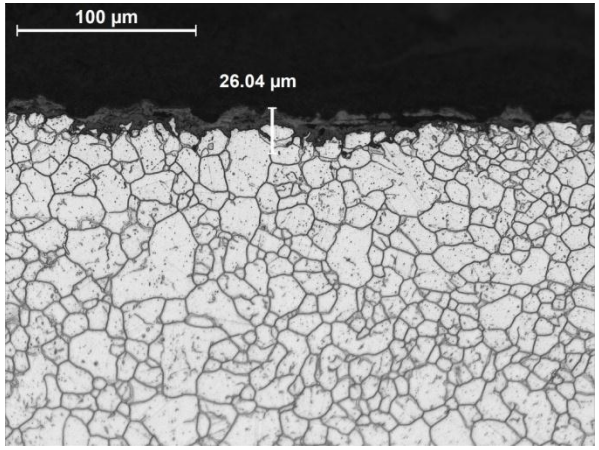

Fireside Corrosion Conditions – Condition4 Results – Super304H Material with Western Ash

No Exposure	After 1000 hours	After 3000 hours
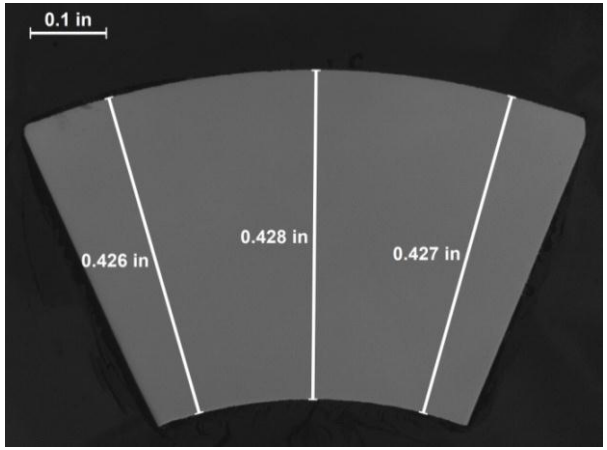	Not included in the test matrix	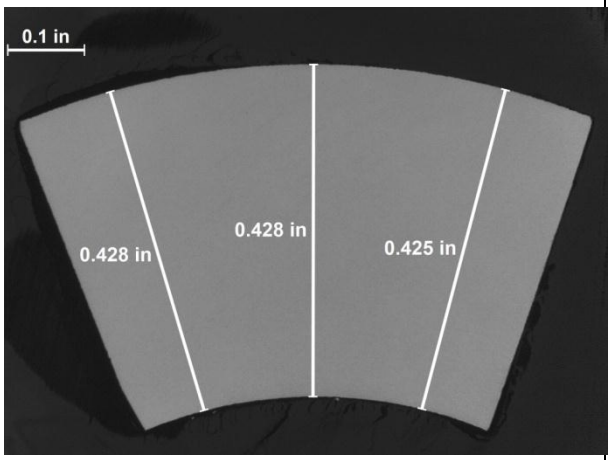
	Not included in the test matrix	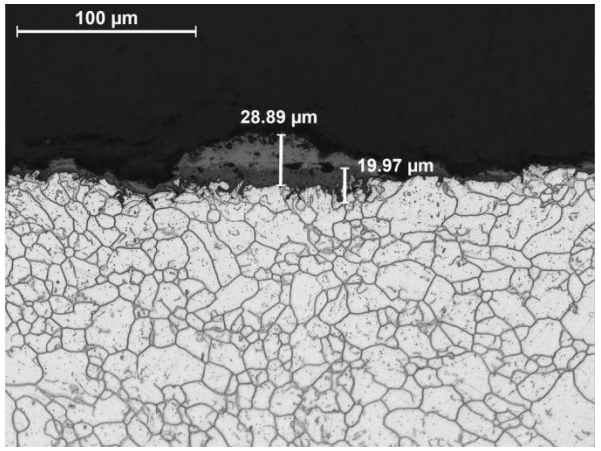

Fireside Corrosion Conditions – Condition 4 Results – IN617 Material

No Exposure	After 1000 hours	After 3000 hours
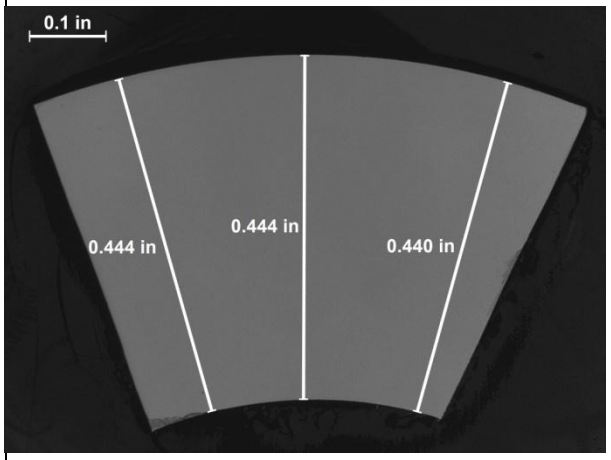	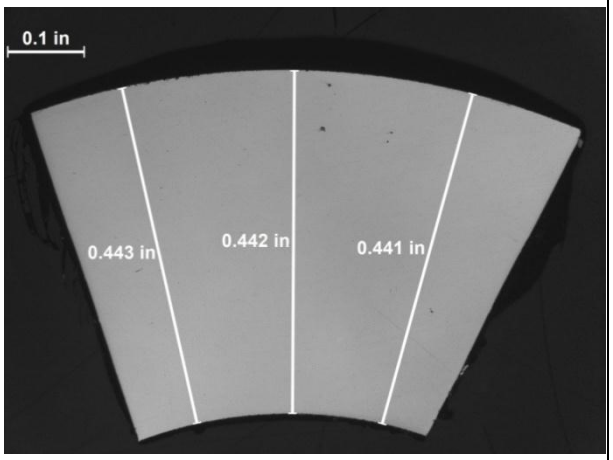	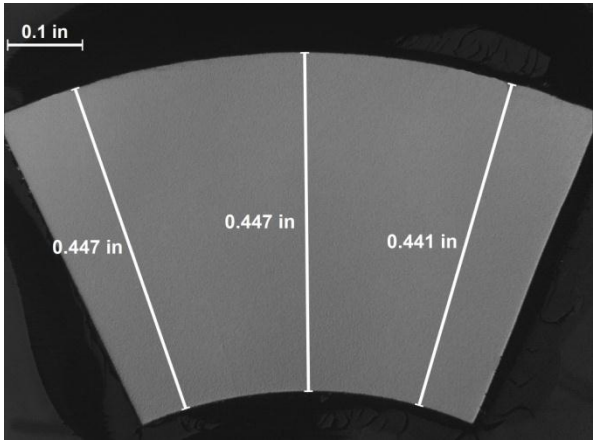
	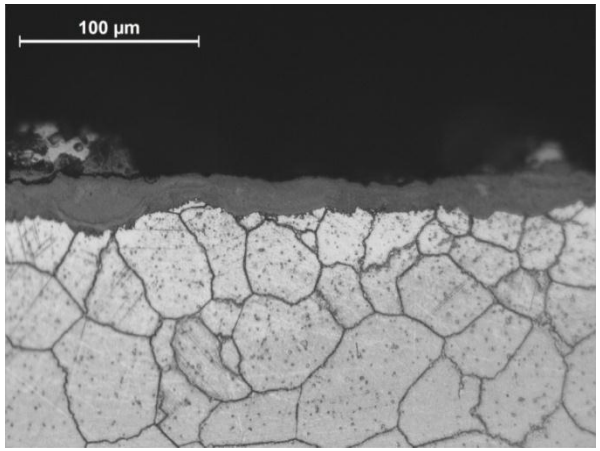	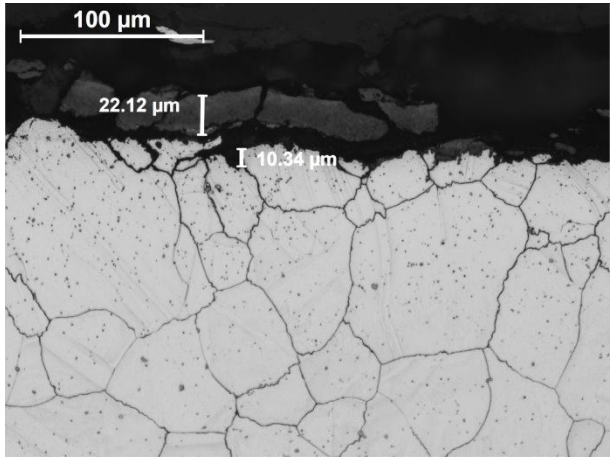

Fireside Corrosion Conditions – Condition 4 Results – IN617 Material with Eastern Ash

No Exposure	After 1000 hours	After 3000 hours
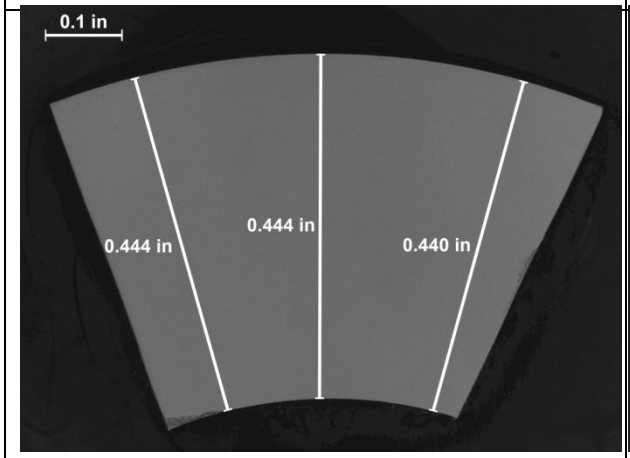	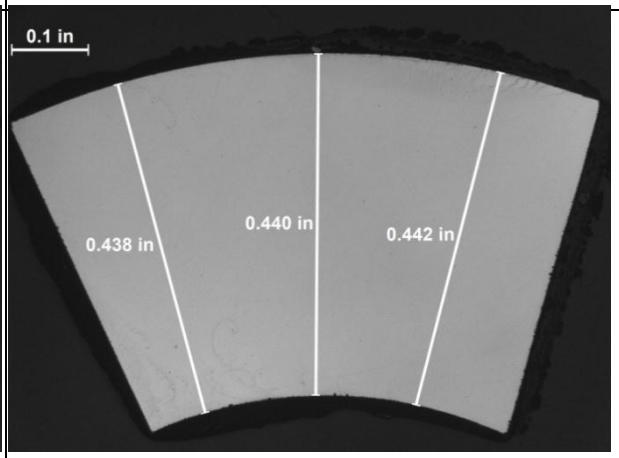	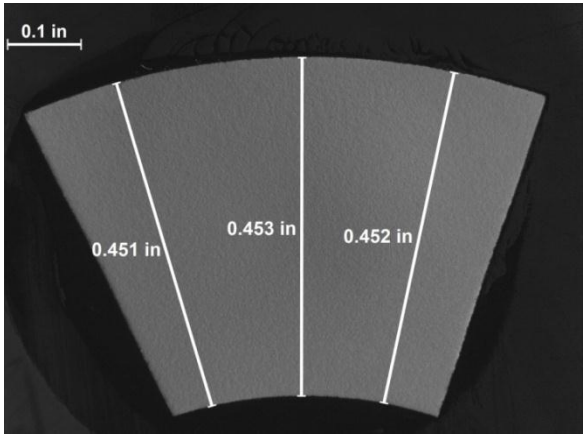
	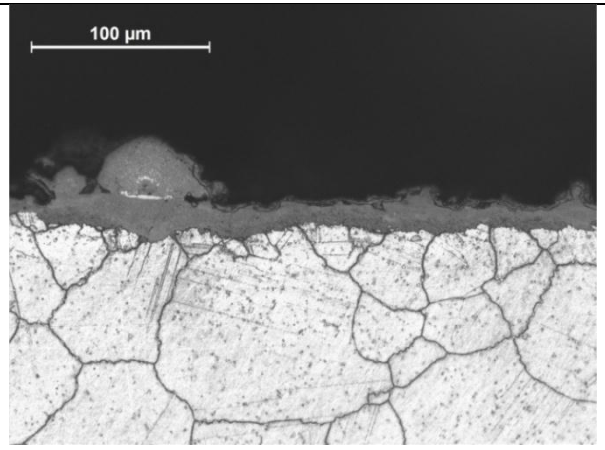	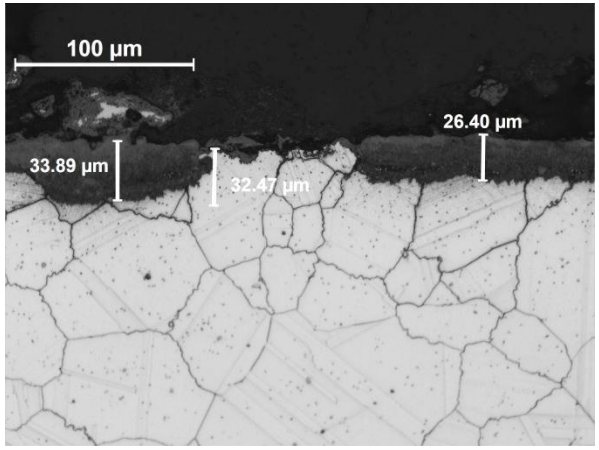

Fireside Corrosion Conditions – Condition 4 Results – NF709R Material

No Exposure	After 1000 hours	After 3000 hours
	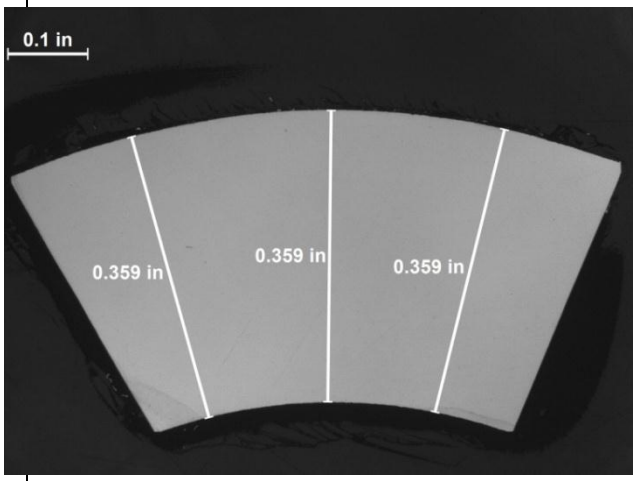	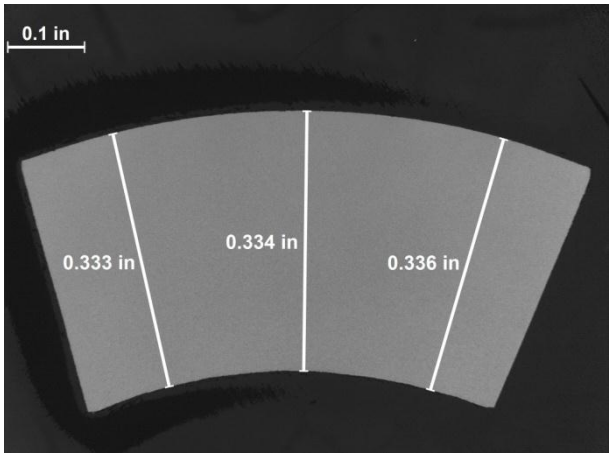
	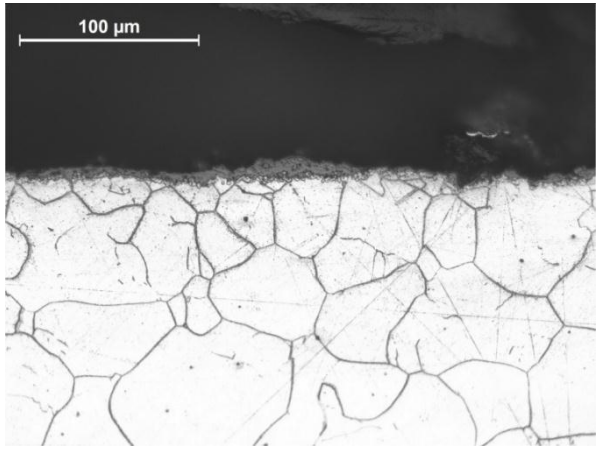	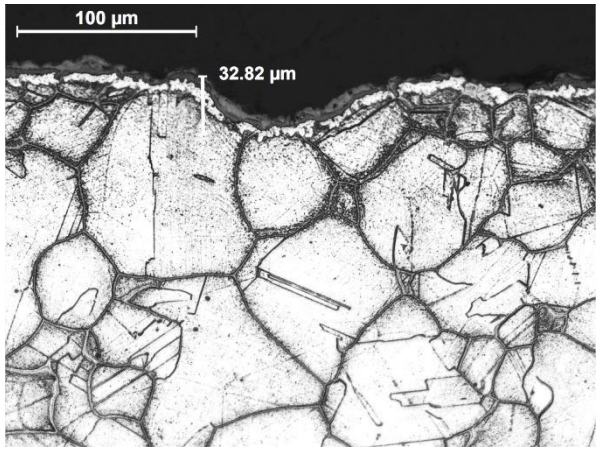

Fireside Corrosion Conditions – Condition 4 Results – NF709R Material with Eastern Ash

No Exposure	After 1000 hours	After 3000 hours
	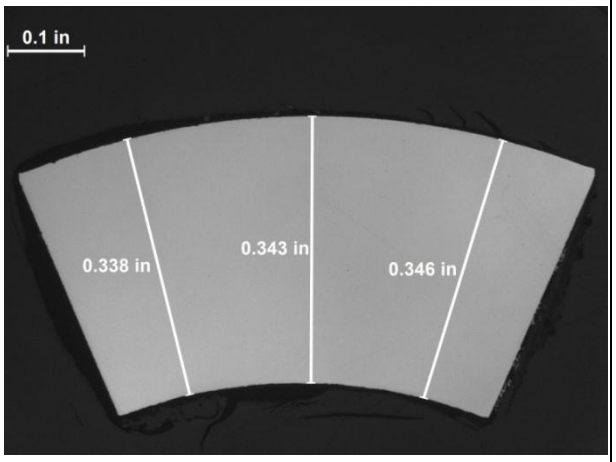	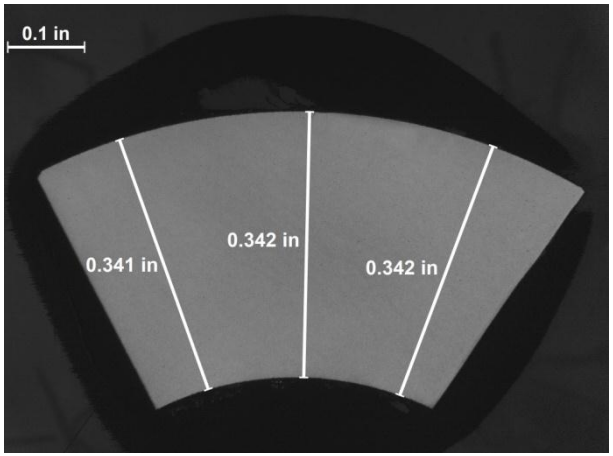
	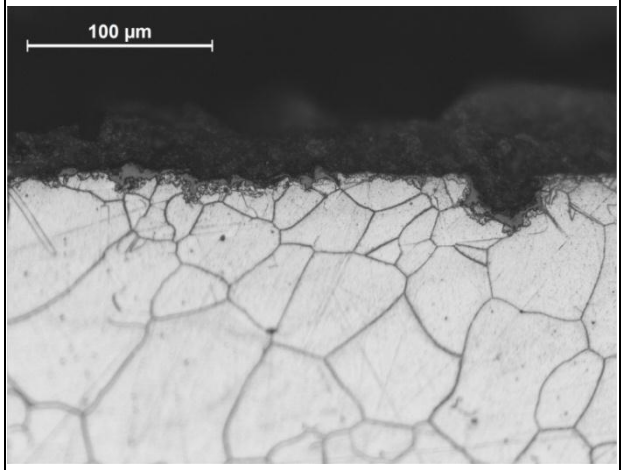	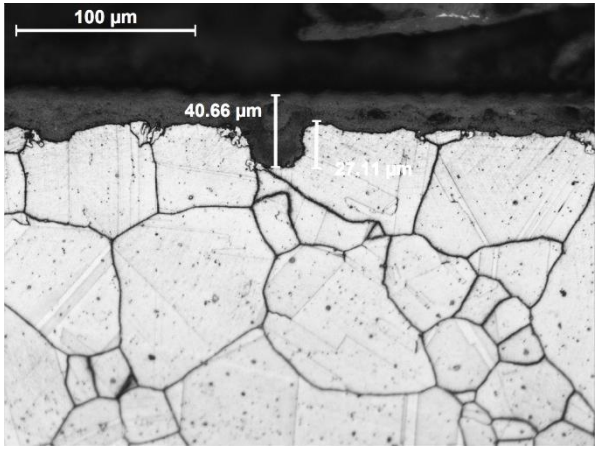

Fireside Corrosion Conditions – Condition 4 Results – Alloy 740 Material

No Exposure	After 1000 hours	After 3000 hours
	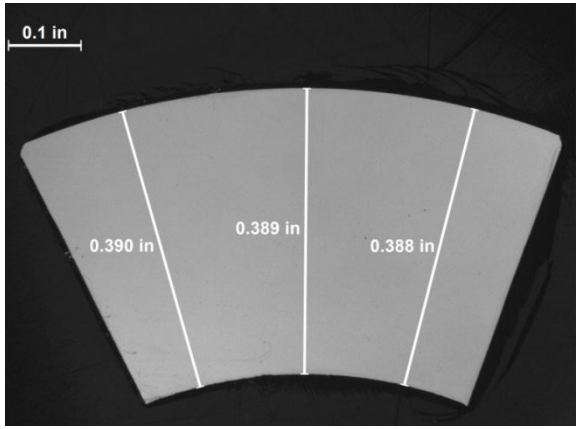	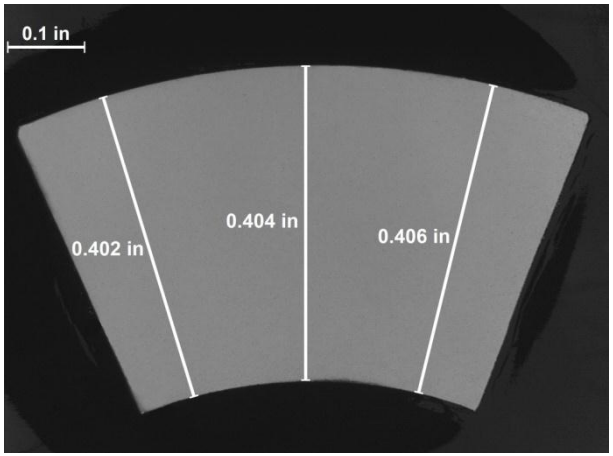
	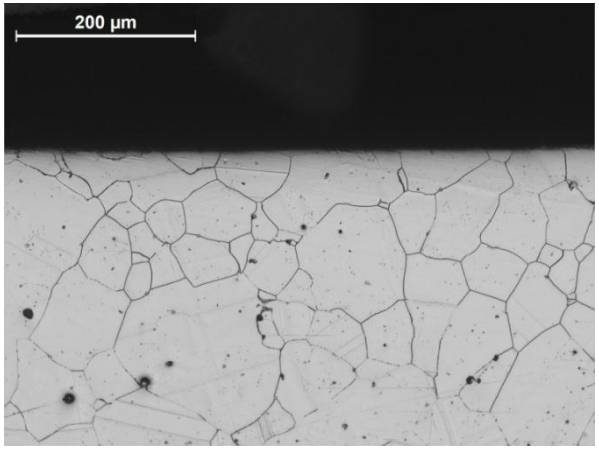	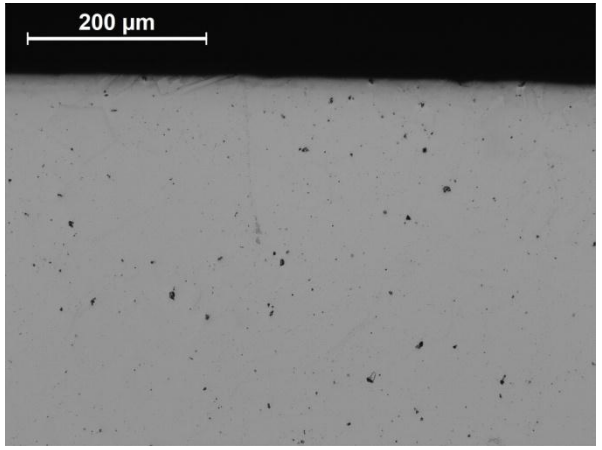

Fireside Corrosion Conditions – Condition 4 Results – Alloy 740 Material with Eastern Ash

No Exposure	After 1000 hours	After 3000 hours
	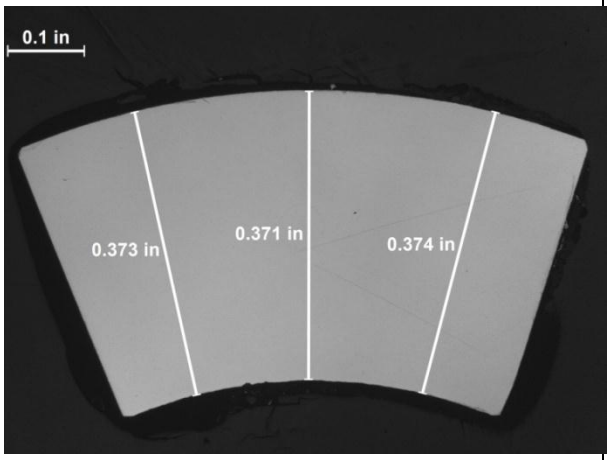	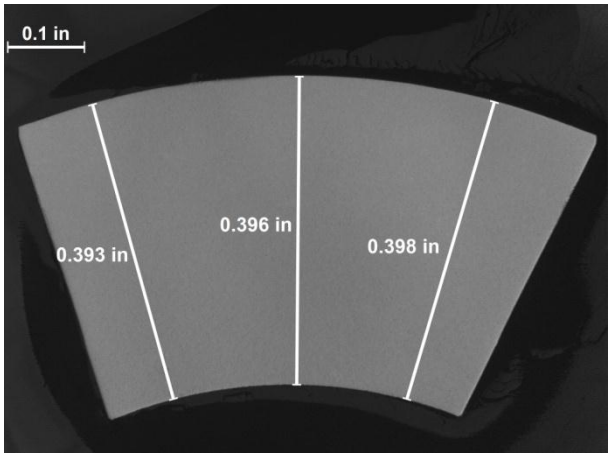
	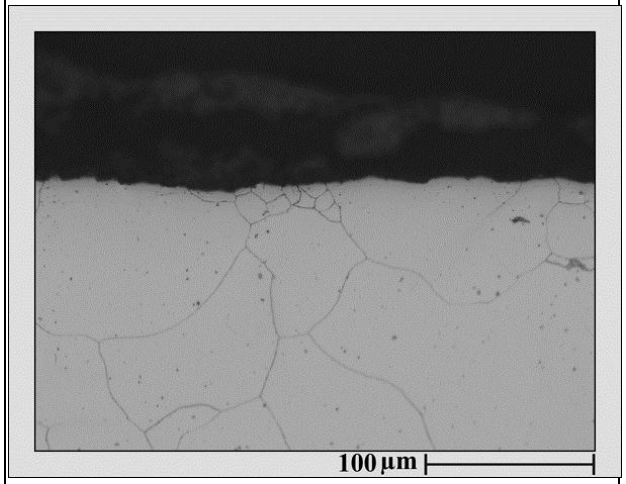	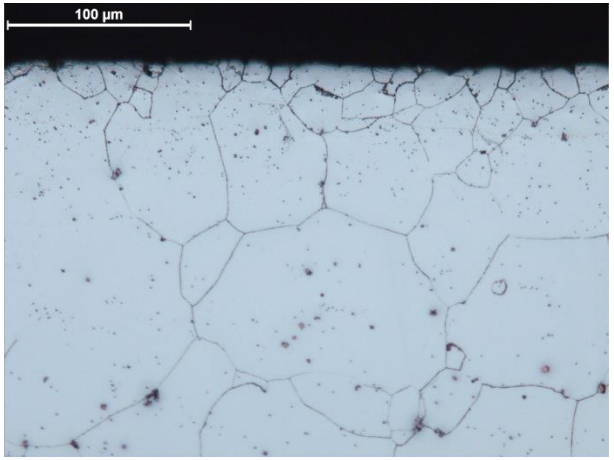

Fireside Corrosion Conditions – Condition 4 Results – HR3C Material

No Exposure	After 1000 hours	After 3000 hours
	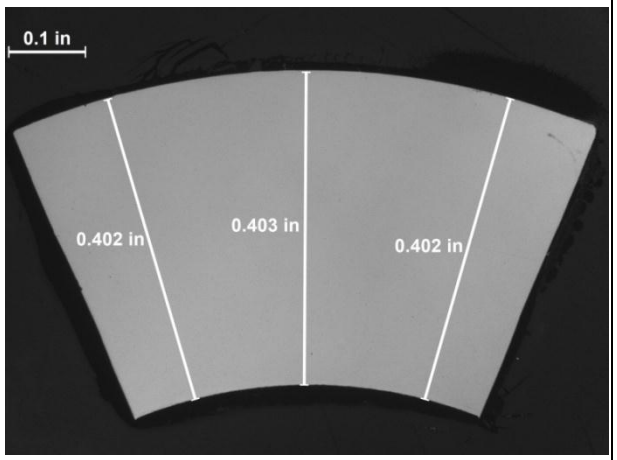	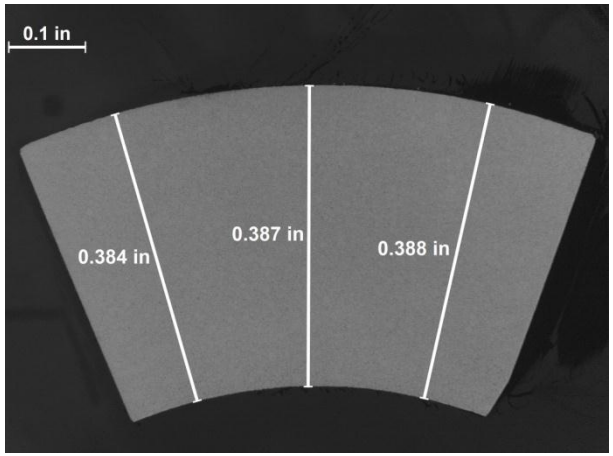
	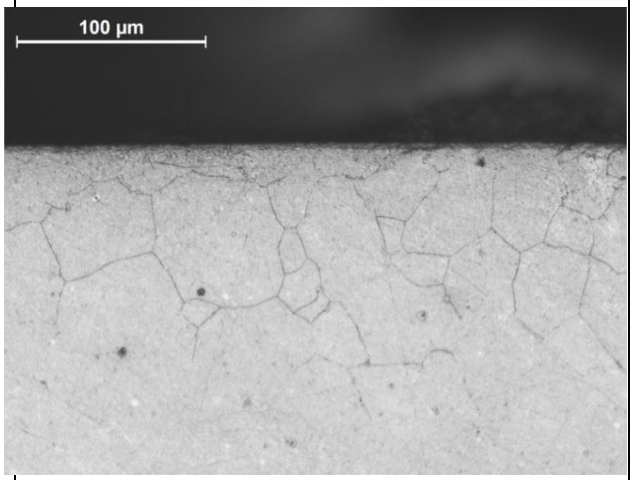	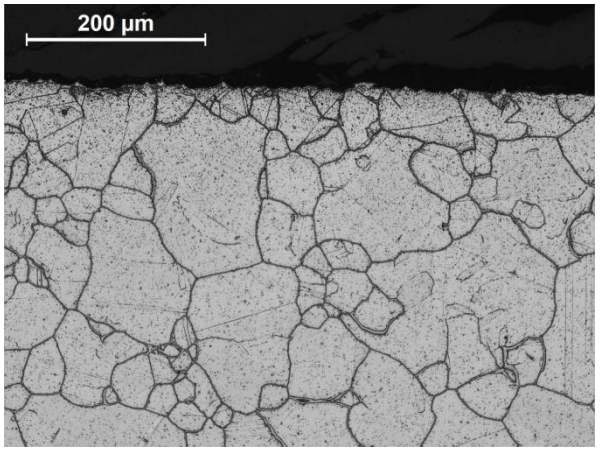

Fireside Corrosion Conditions – Condition 4 Results – HR3C Material with Eastern Ash

No Exposure	After 1000 hours	After 3000 hours
	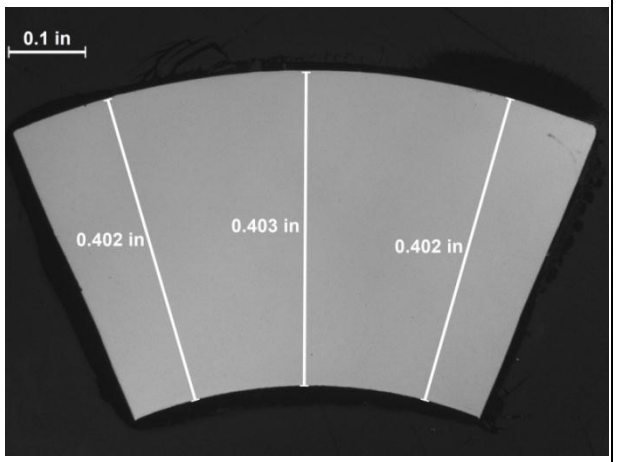	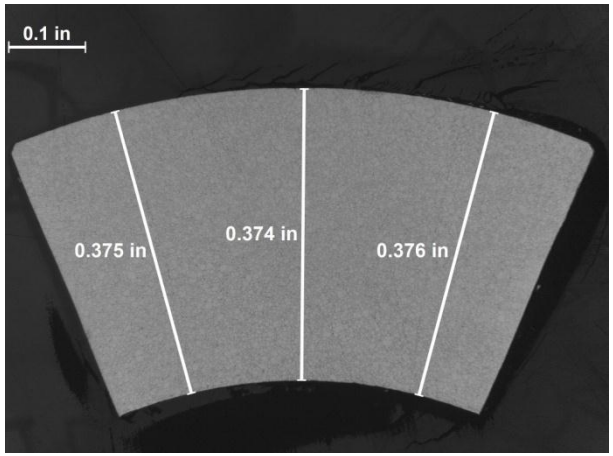
	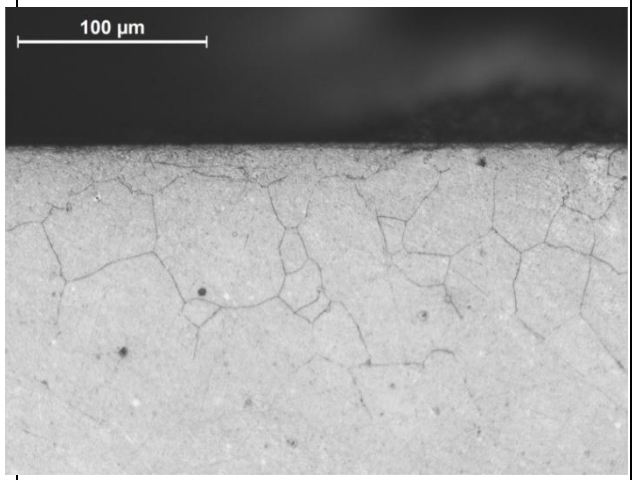	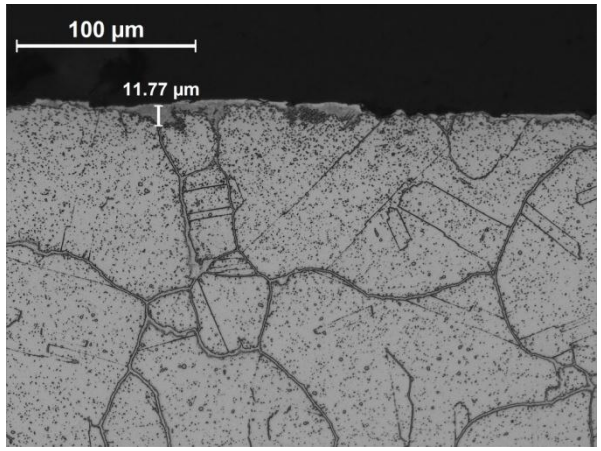

Fireside Corrosion Conditions – Condition 4 Results – HR3C Material with Western Ash

No Exposure	After 1000 hours	After 3000 hours
	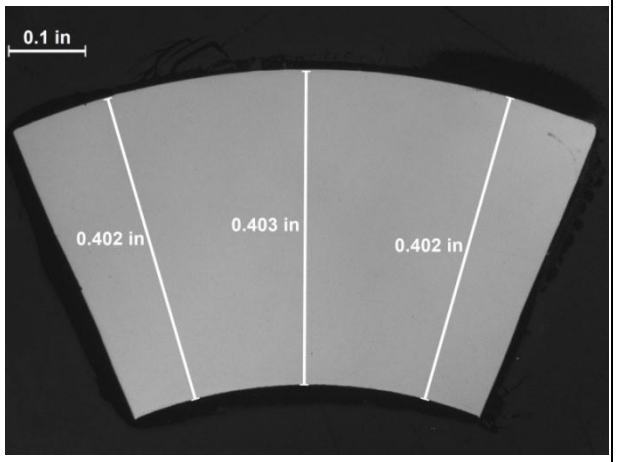	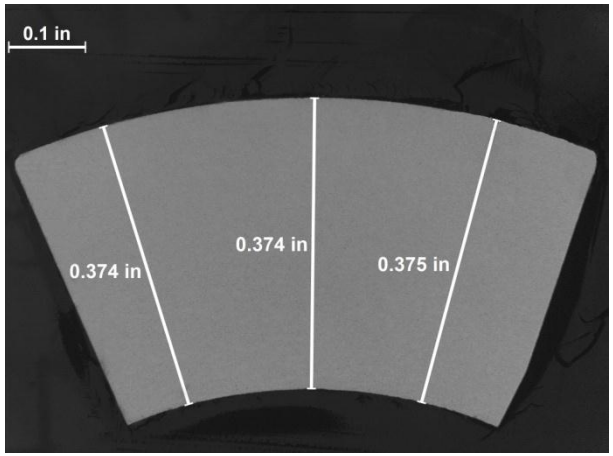
	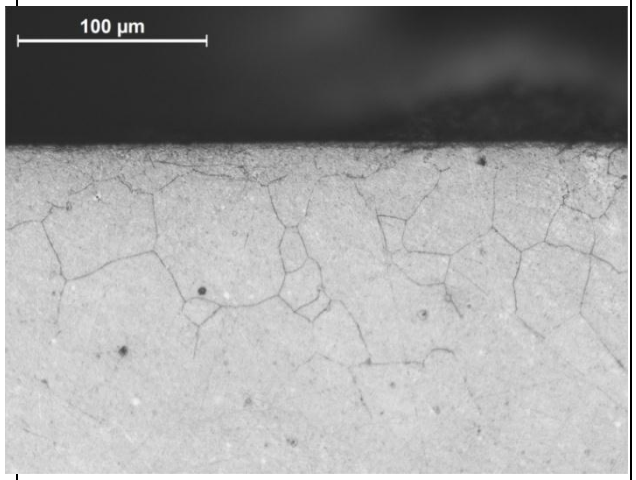	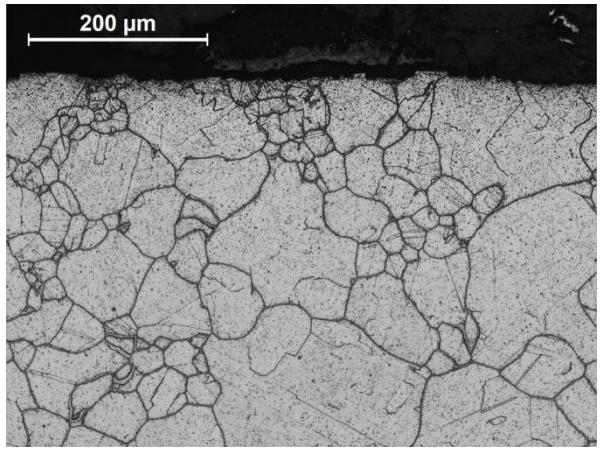

Fireside Corrosion Conditions – Condition 4 Results – C263 Material

No Exposure	After 1000 hours	After 3000 hours
	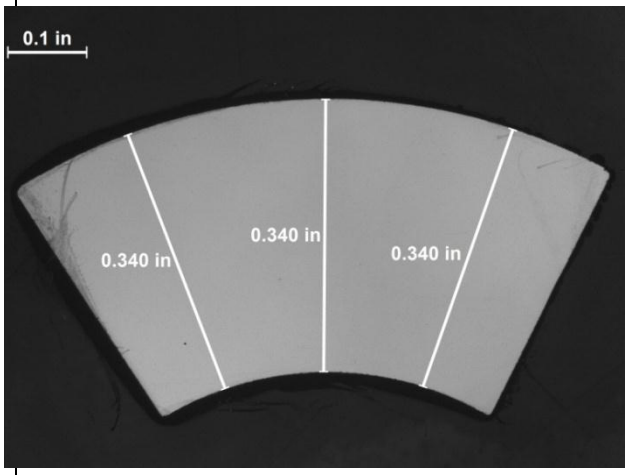	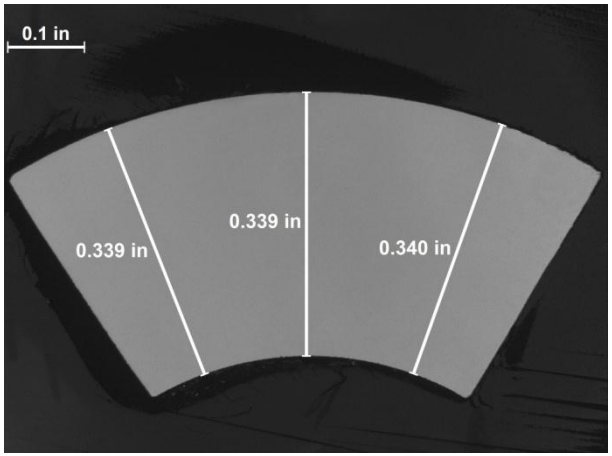
	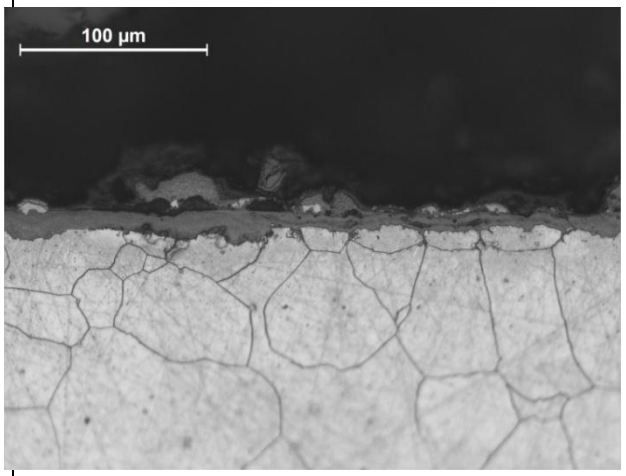	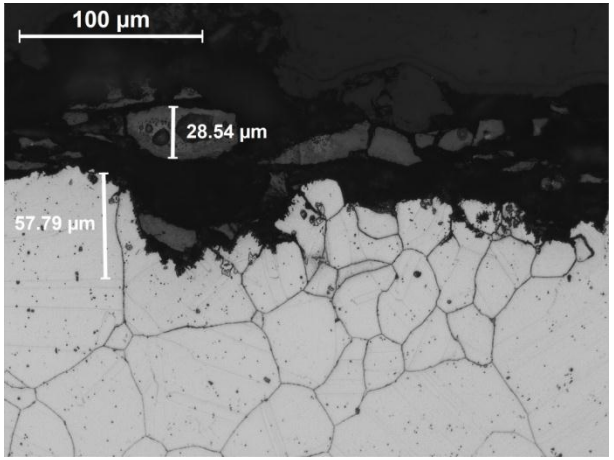

Fireside Corrosion Conditions – Condition 4 Results – C263 Material with Eastern Ash

No Exposure	After 1000 hours	After 3000 hours
	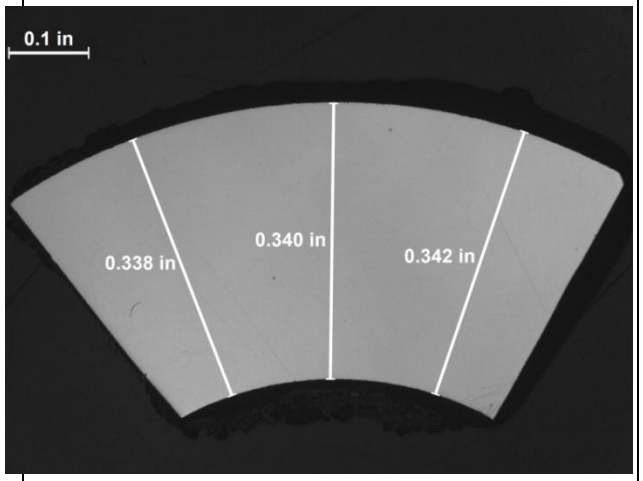	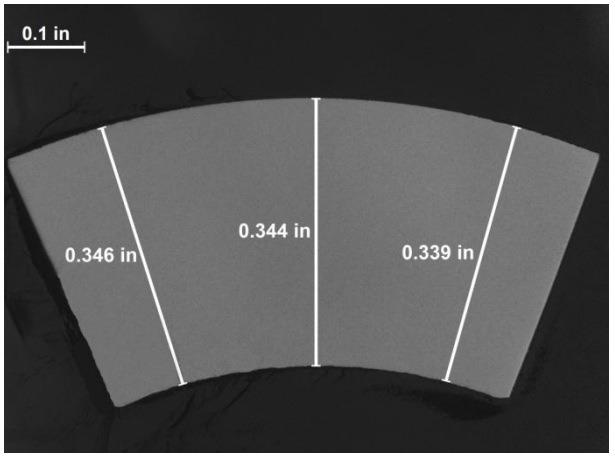
	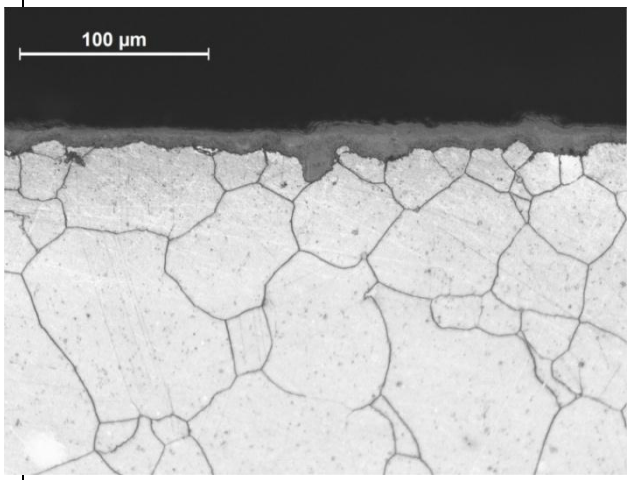	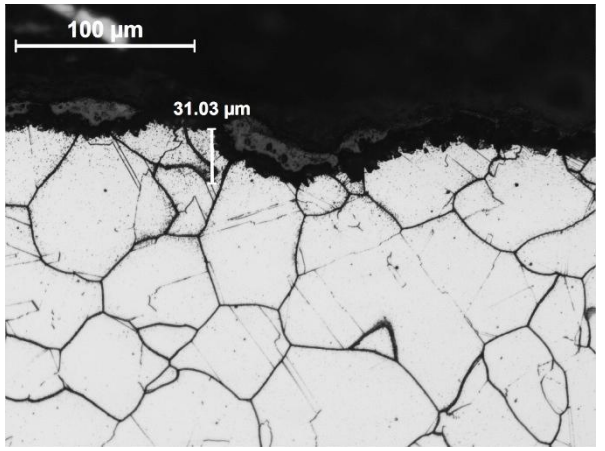

Fireside Corrosion Conditions – Condition 5 Results – T23 Material

No Exposure	After 1000 hours	After 3000 hours
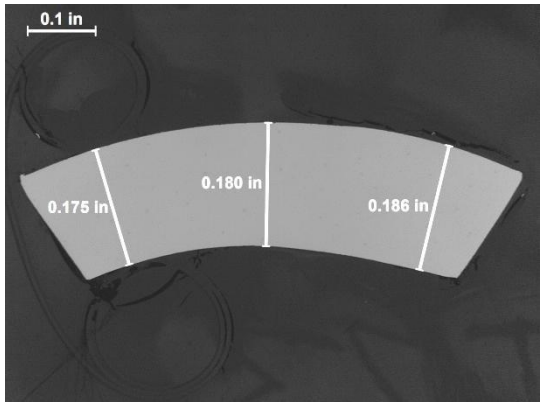	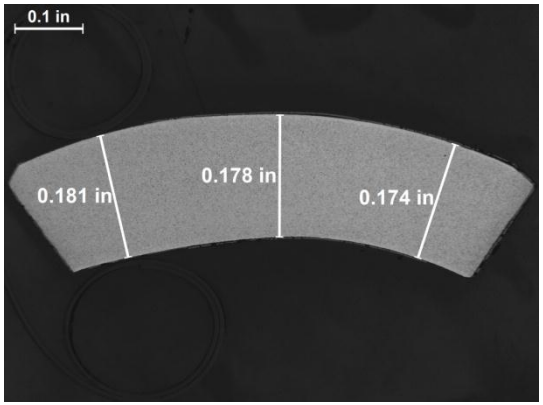	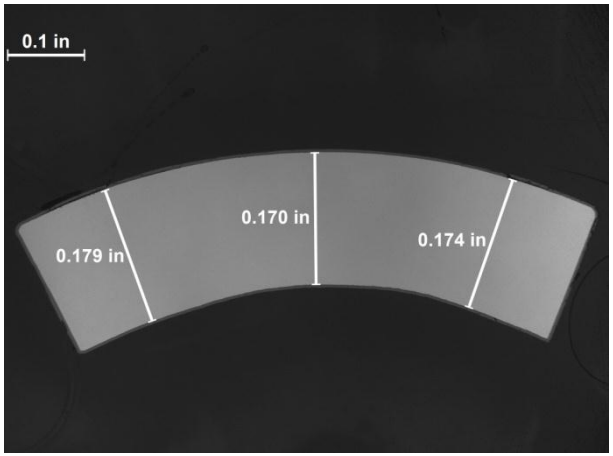
	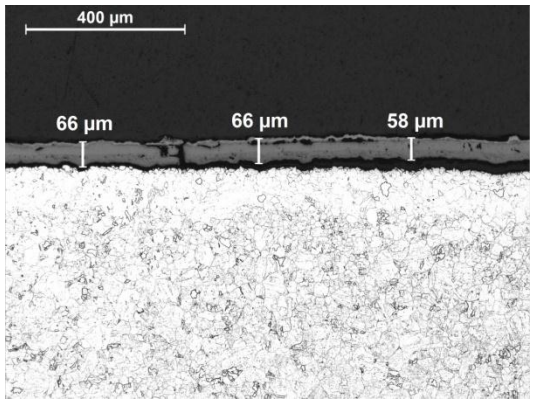	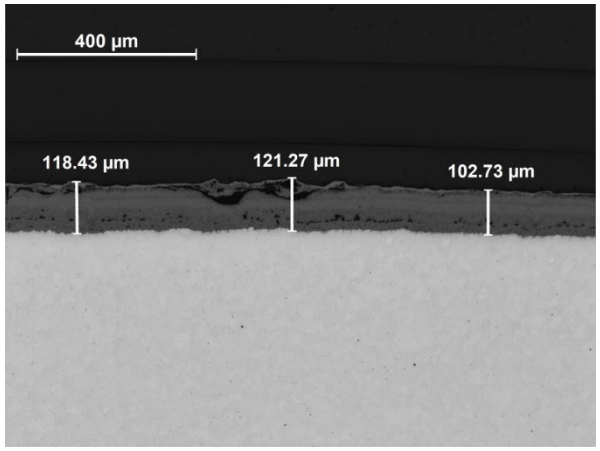

Fireside Corrosion Conditions – Condition 5 Results – T23 Material with Eastern Ash

No Exposure	After 1000 hours	After 3000 hours
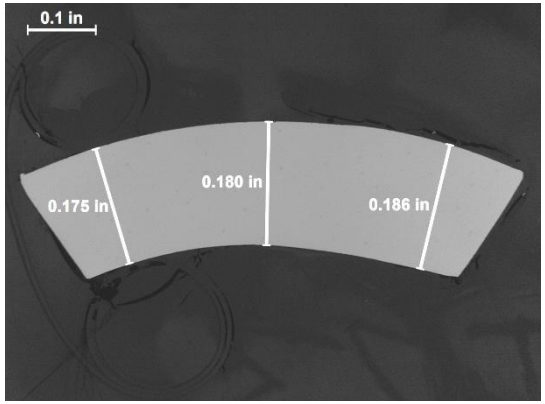	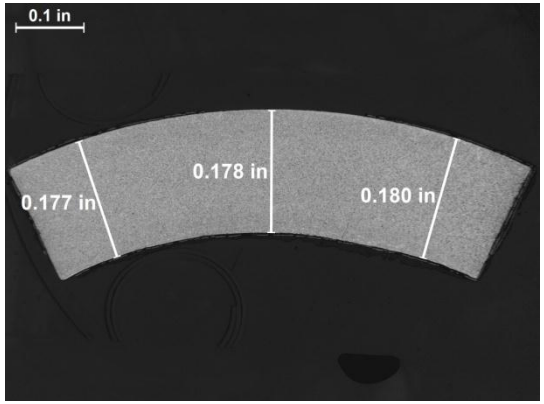	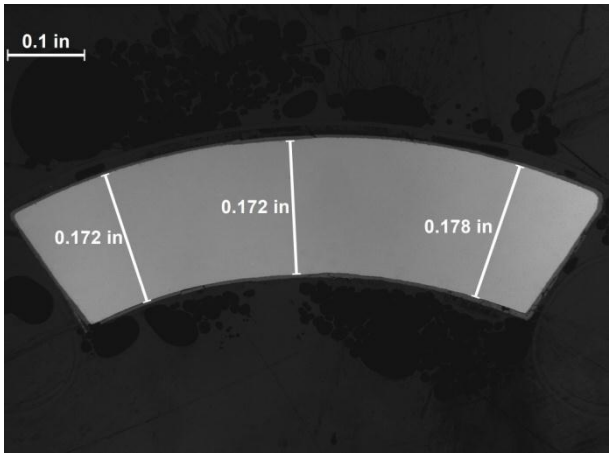
	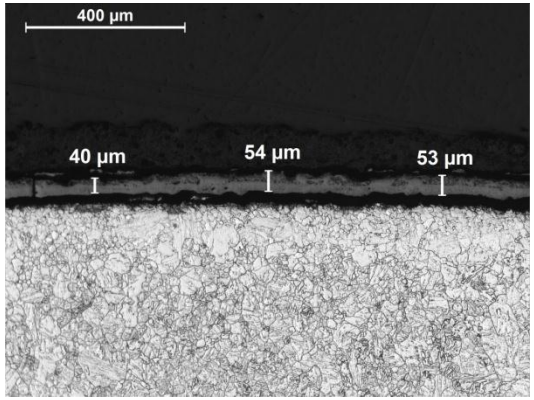	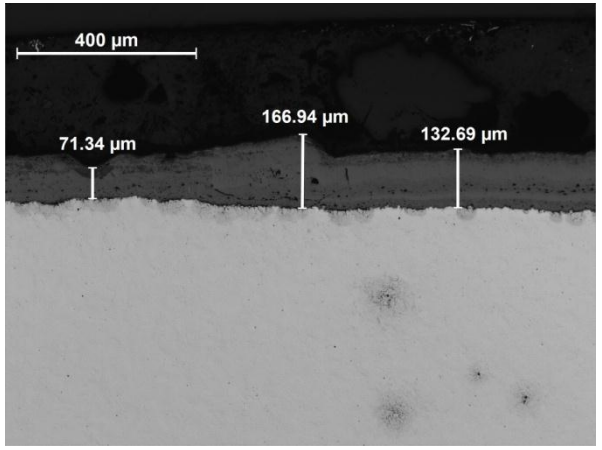

Fireside Corrosion Conditions – Condition 5 Results – T24 Material

No Exposure	After 1000 hours	After 3000 hours
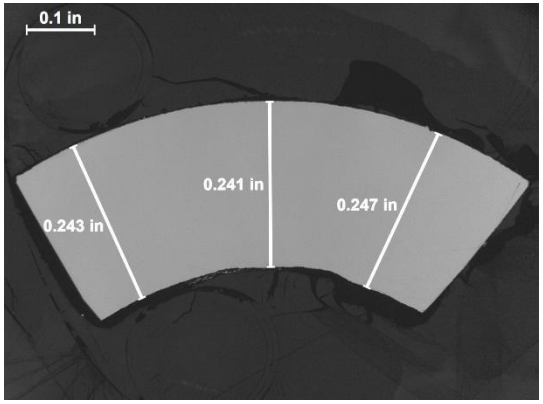	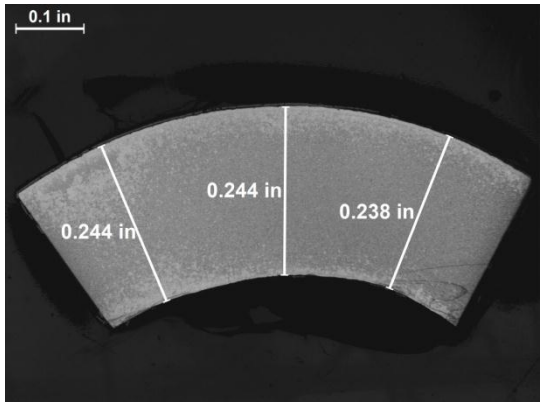	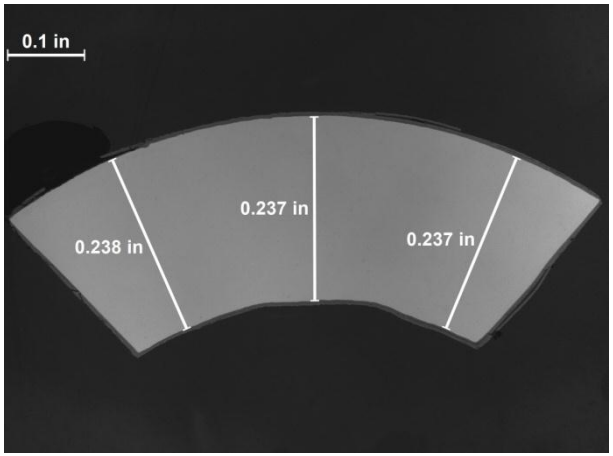
	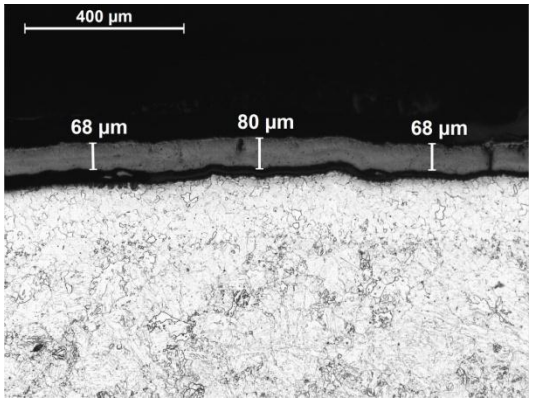	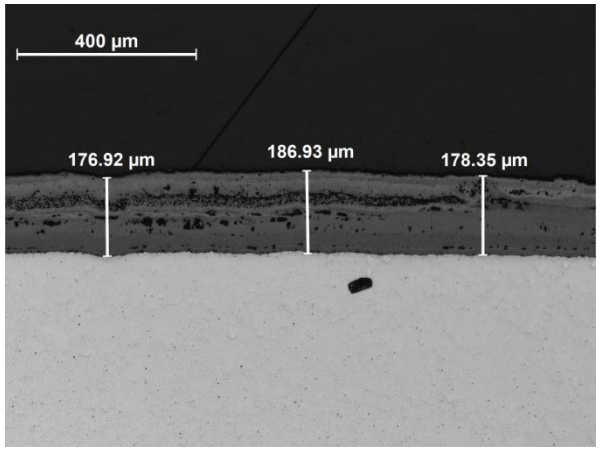

Fireside Corrosion Conditions – Condition 5 Results – T24 Material with Eastern Ash

No Exposure	After 1000 hours	After 3000 hours
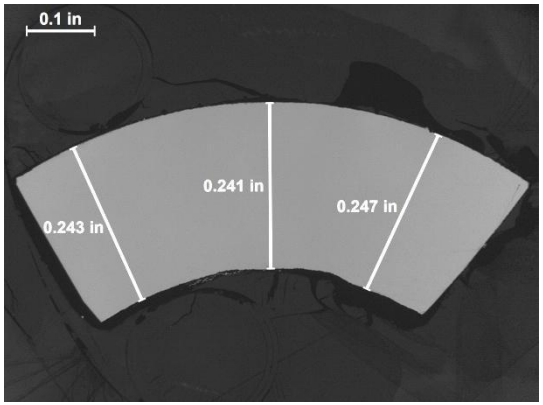	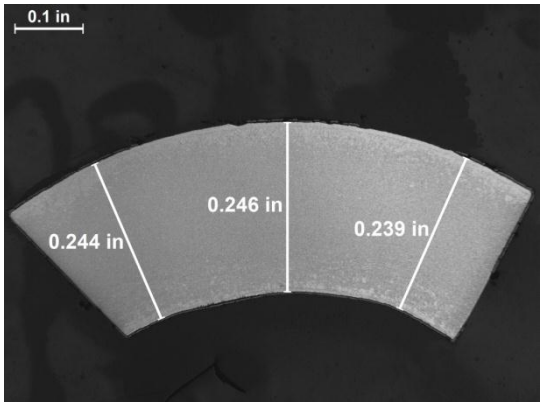	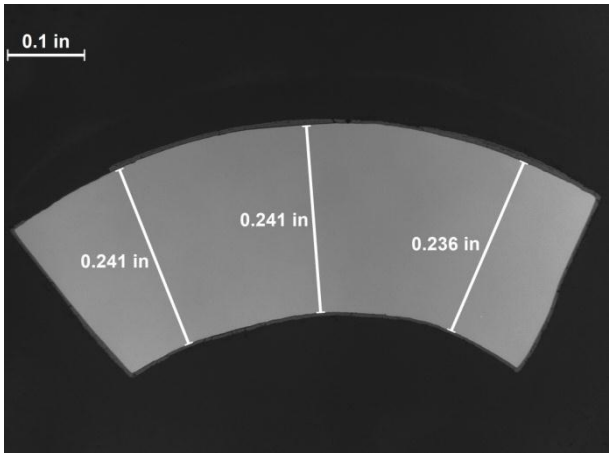
	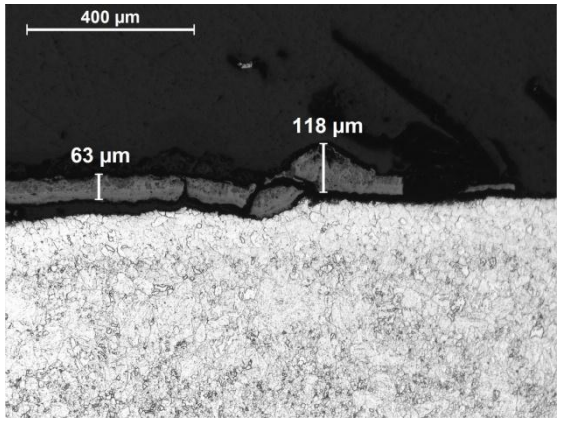	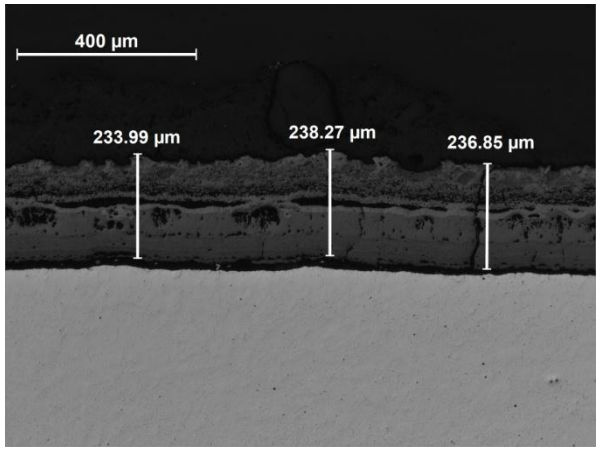

Fireside Corrosion Conditions – Condition 5 Results – T92 Material

No Exposure	After 1000 hours	After 3000 hours
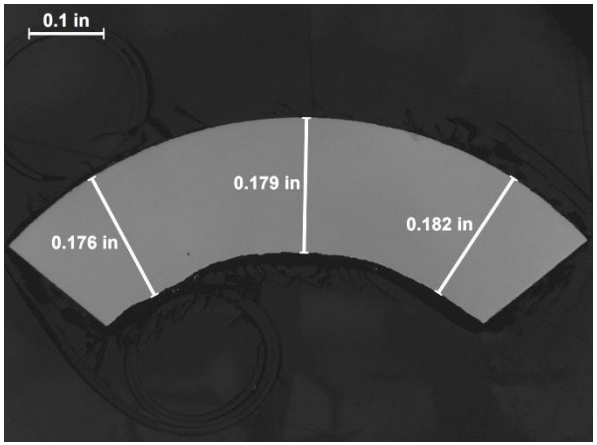	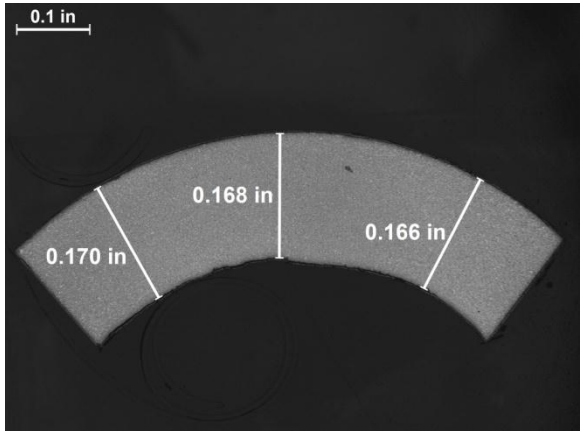	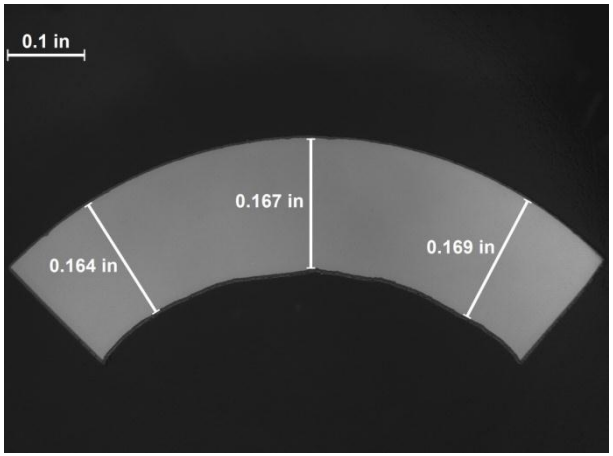
	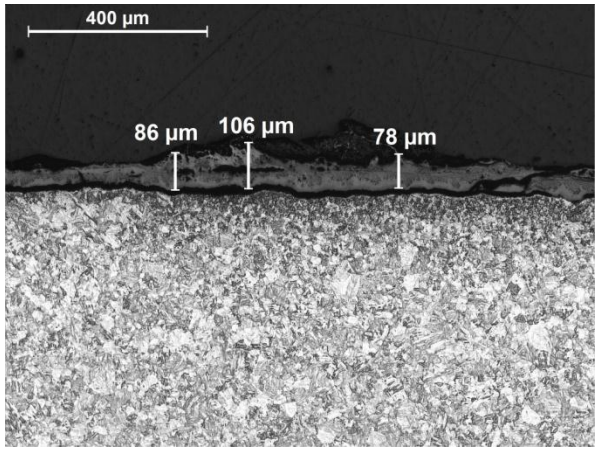	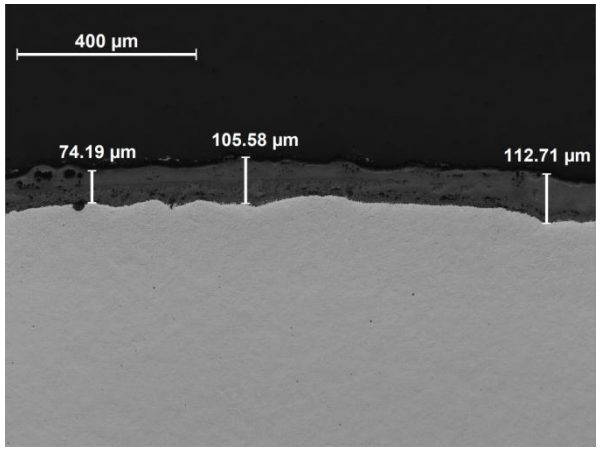

Fireside Corrosion Conditions – Condition 5 Results – T92 Material with Eastern Ash

No Exposure	After 1000 hours	After 3000 hours
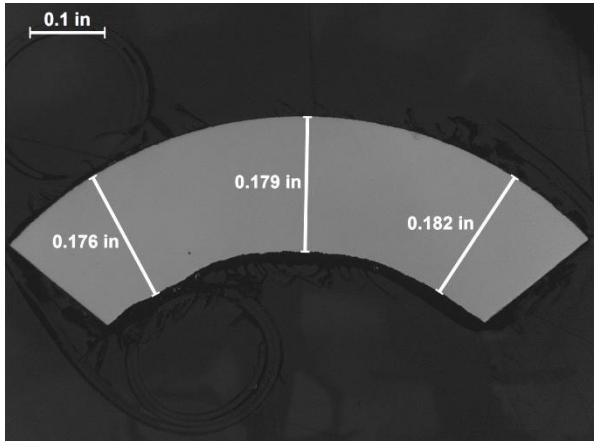	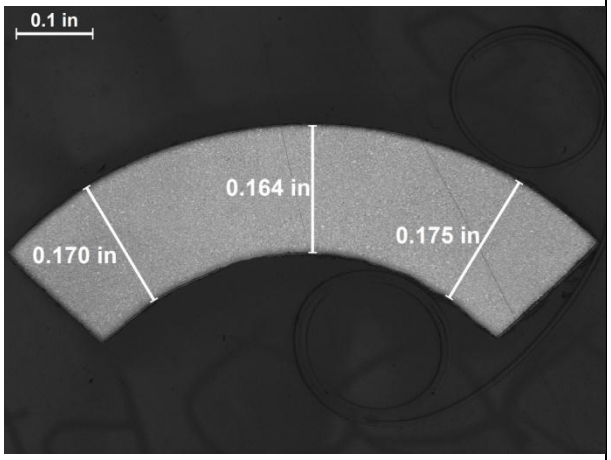	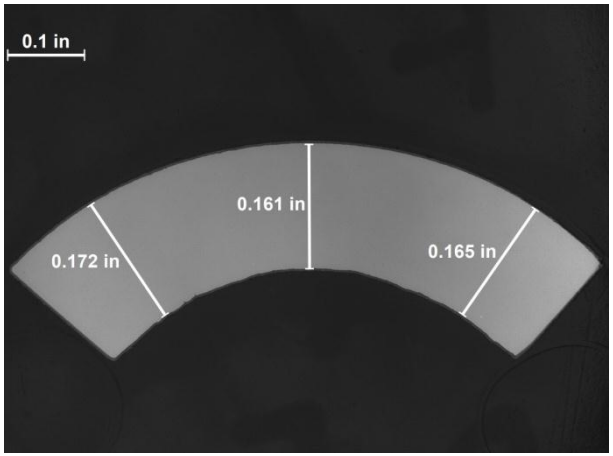
	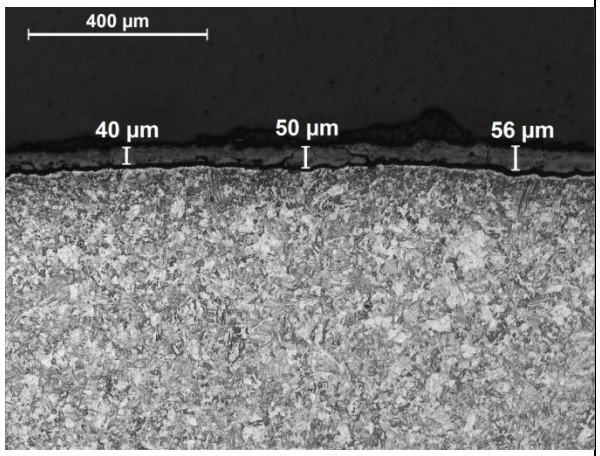	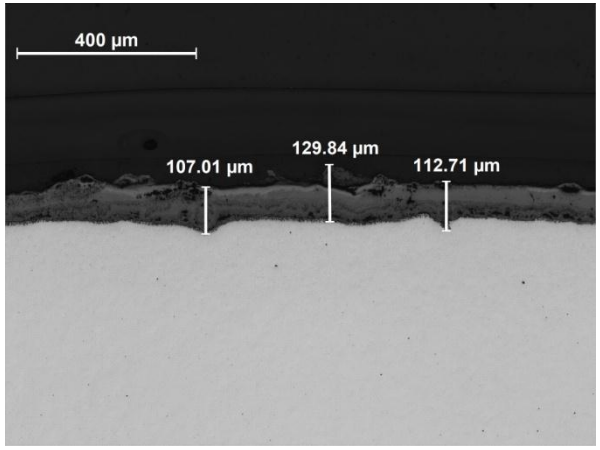

Fireside Corrosion Conditions – Condition 5 Results – 304H Material

No Exposure	After 1000 hours	After 3000 hours
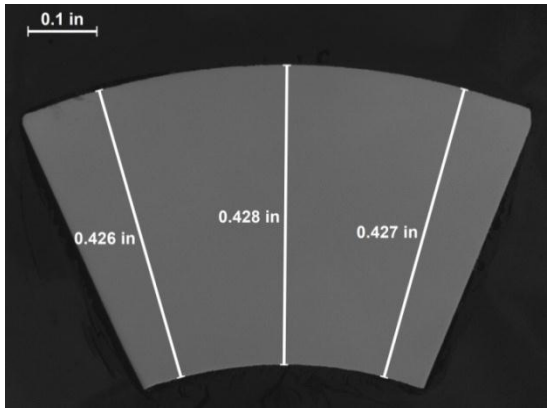	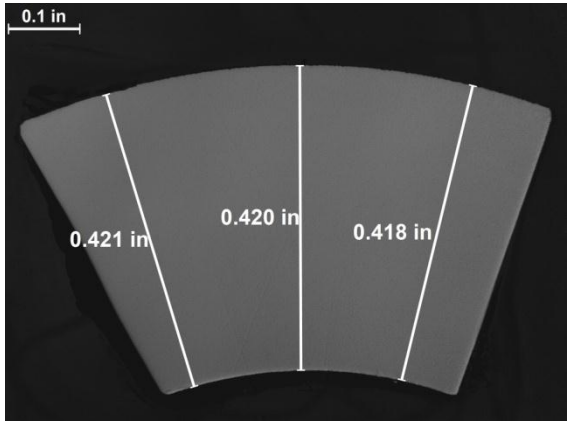	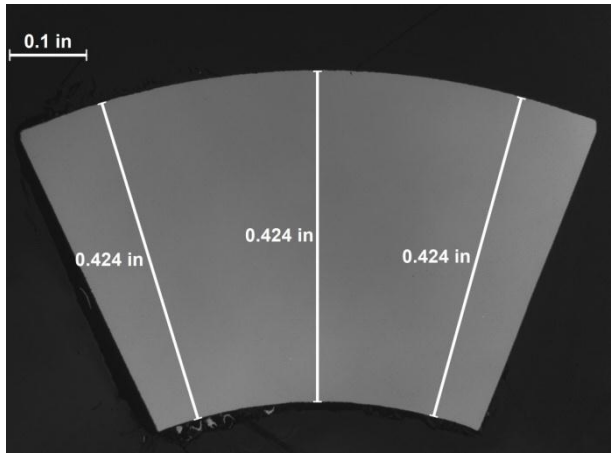
		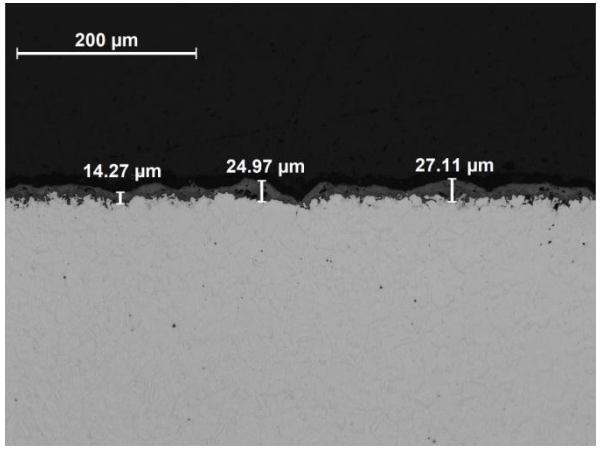

Fireside Corrosion Conditions – Condition 5 Results – 304H Material with Eastern Ash

No Exposure	After 1000 hours	After 3000 hours
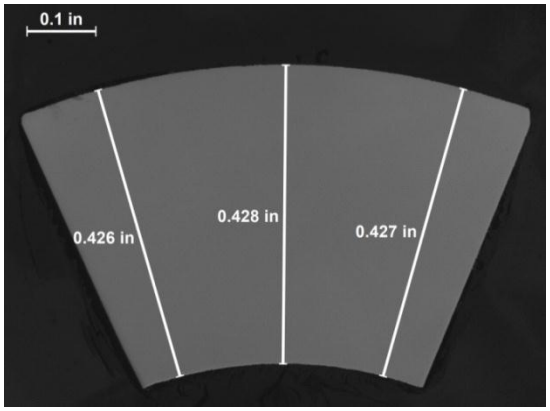	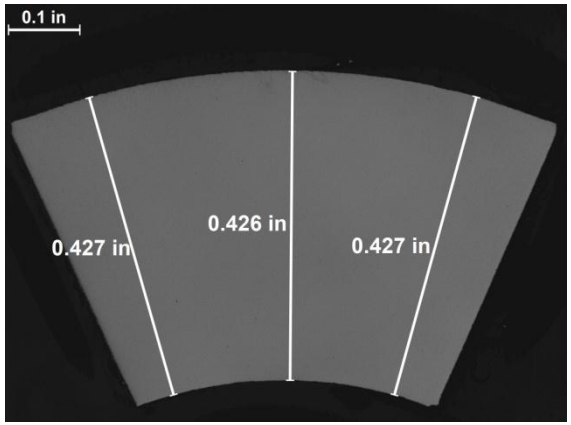	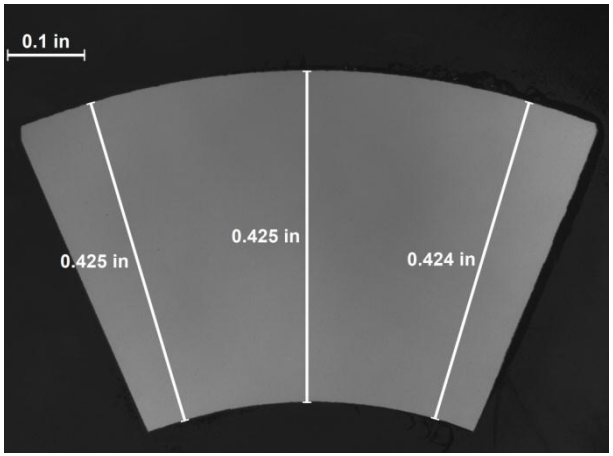
		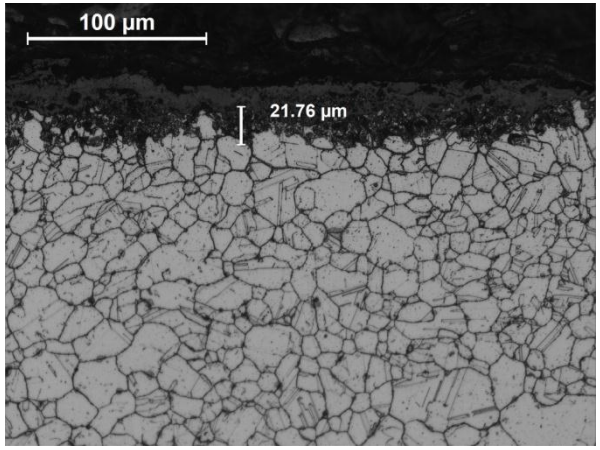

Fireside Corrosion Conditions – Condition5 Results – 304H Material with Western Ash

No Exposure	After 1000 hours	After 3000 hours
	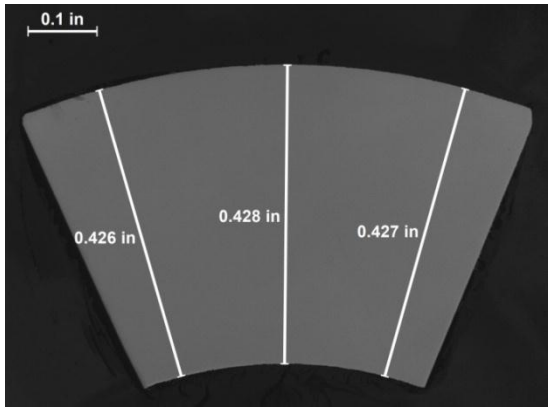	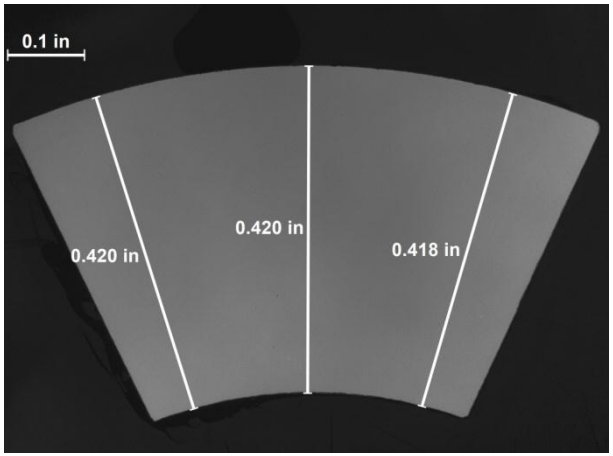
		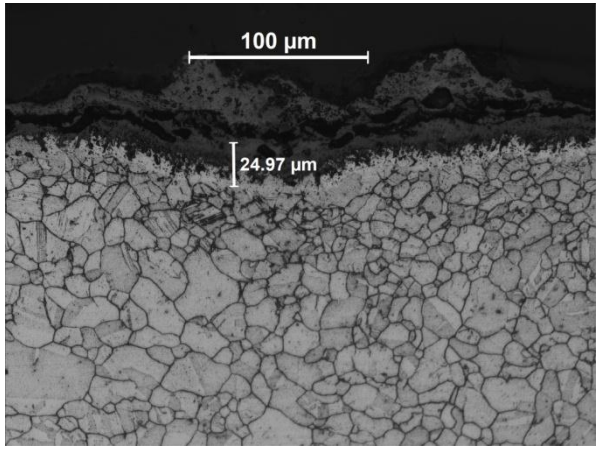

Fireside Corrosion Conditions – Condition 5 Results – IN617 Material

No Exposure	After 1000 hours	After 3000 hours
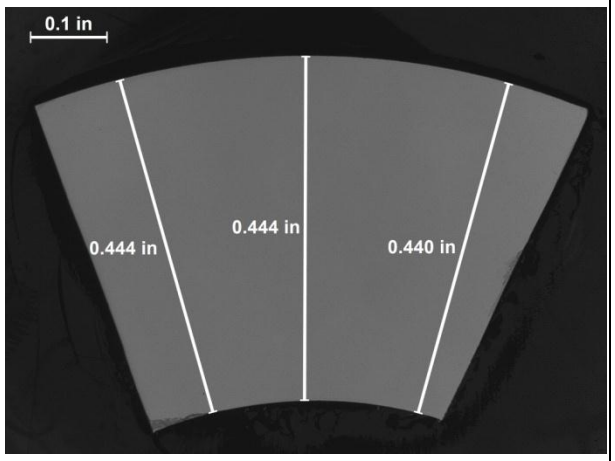	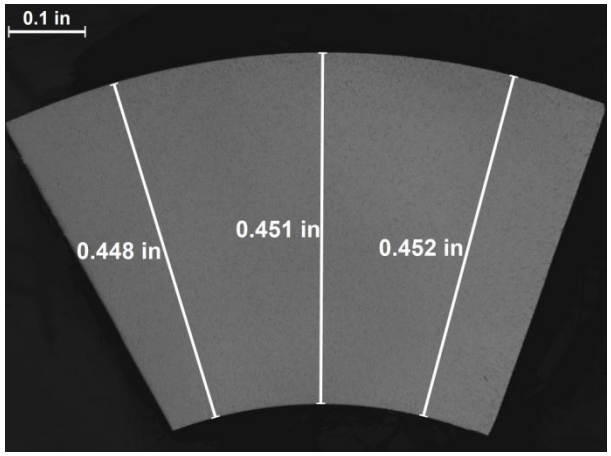	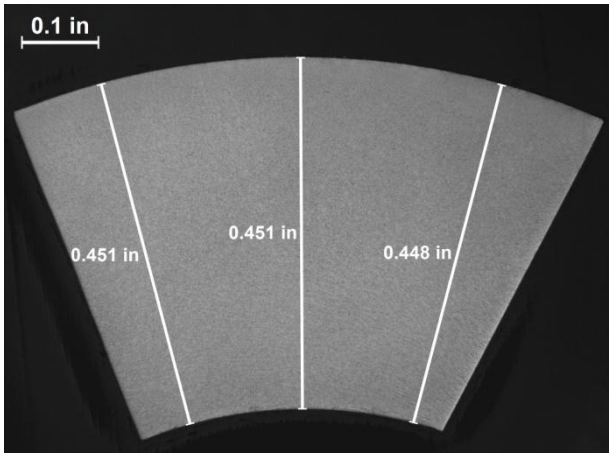
		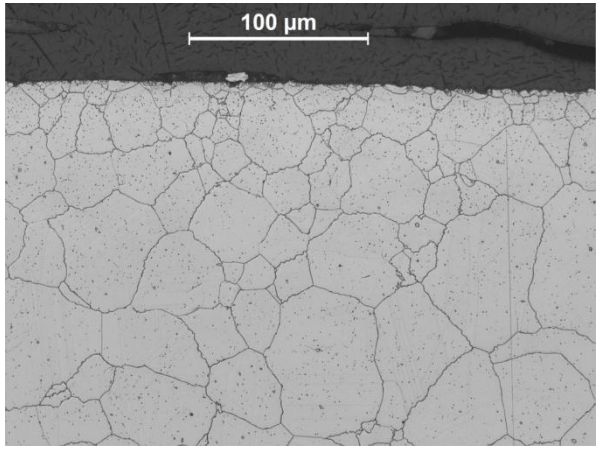

Fireside Corrosion Conditions – Condition 5 Results – IN617 Material with Eastern Ash

No Exposure	After 1000 hours	After 3000 hours
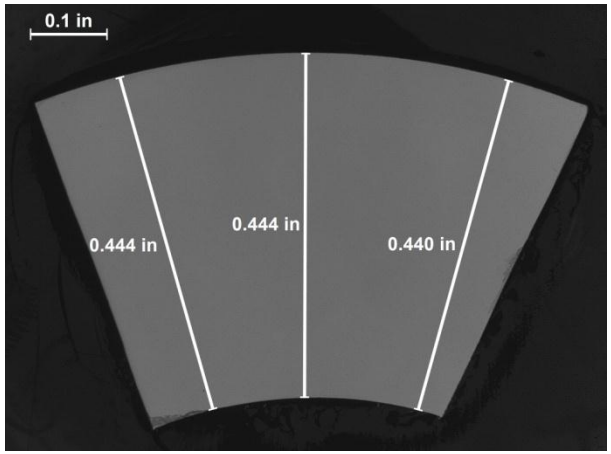	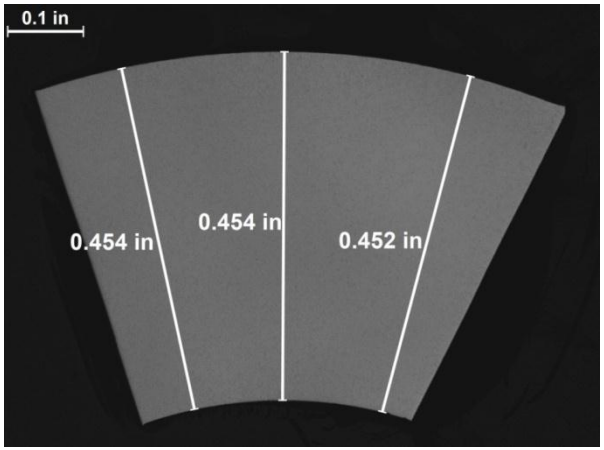	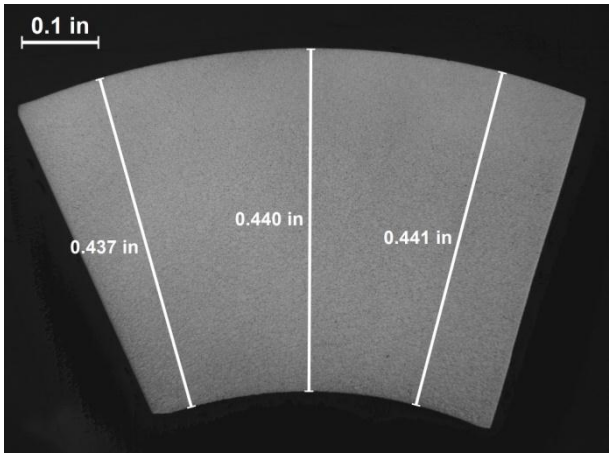
		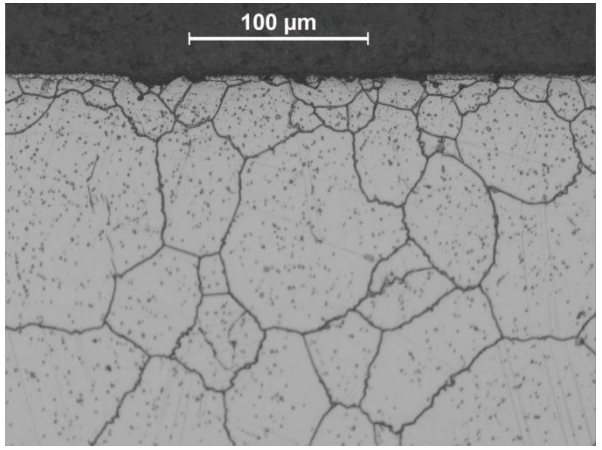

Fireside Corrosion Conditions – Condition 6 Results – T23 Material

No Exposure	After 1000 hours	After 3000 hours
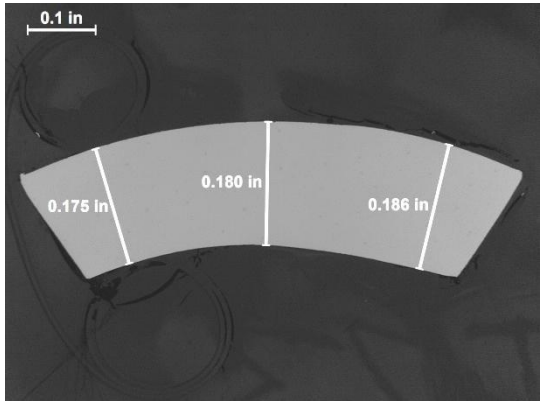	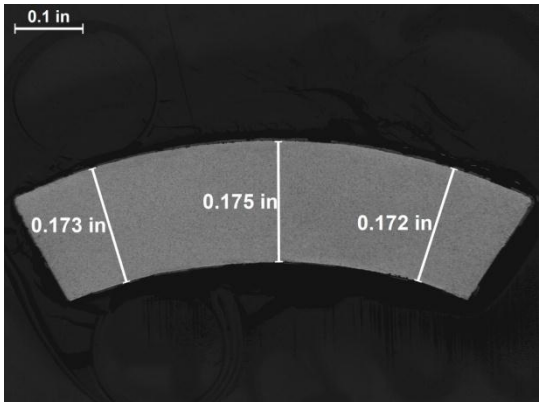	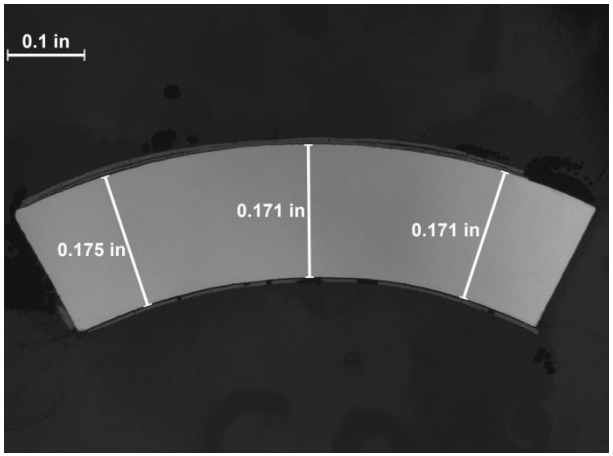
	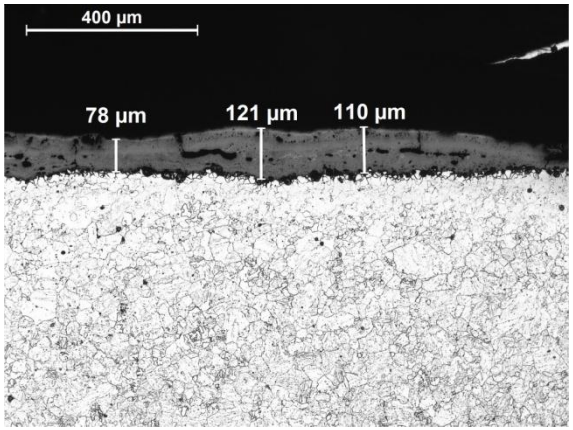	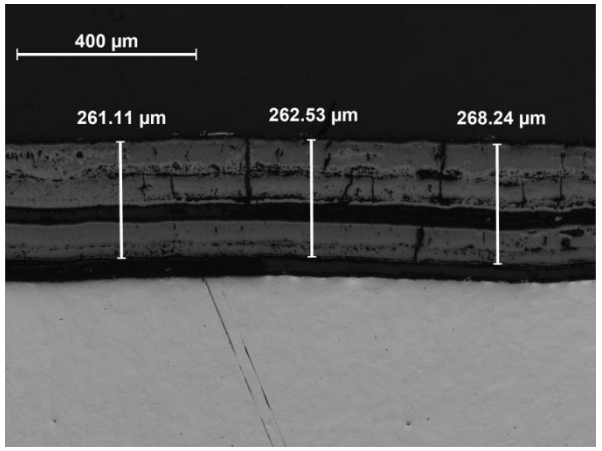

Fireside Corrosion Conditions – Condition 6 Results – T23 Material with Eastern Ash

No Exposure	After 1000 hours	After 3000 hours
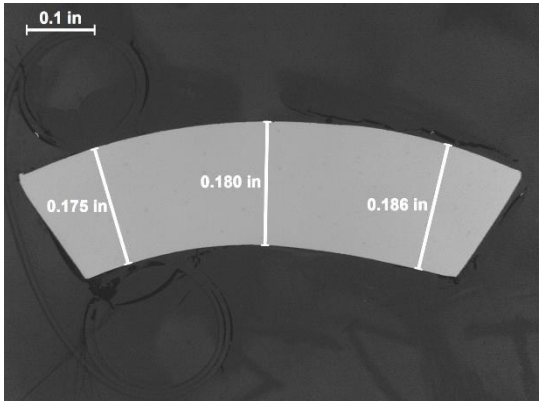	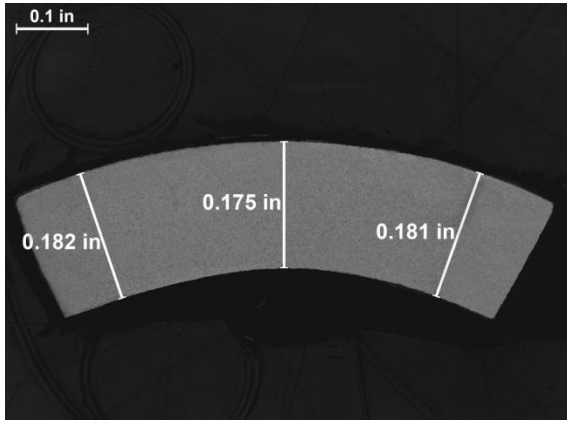	
	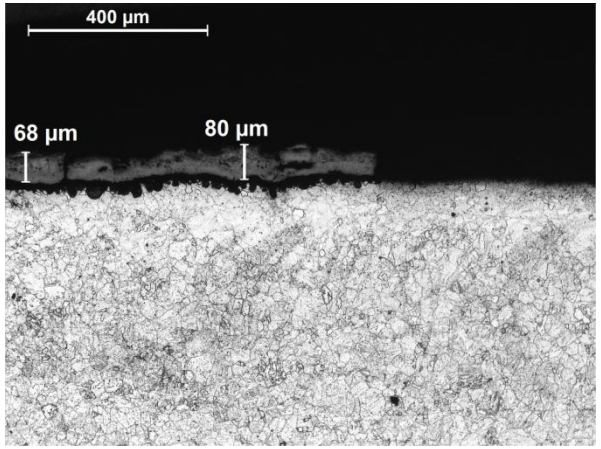	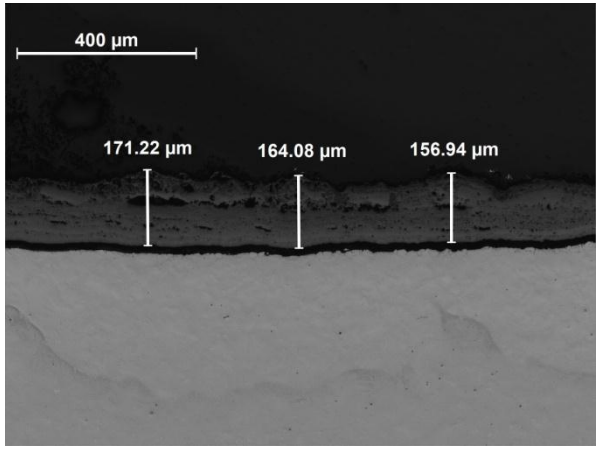

Fireside Corrosion Conditions – Condition 6 Results – T24 Material

No Exposure	After 1000 hours	After 3000 hours
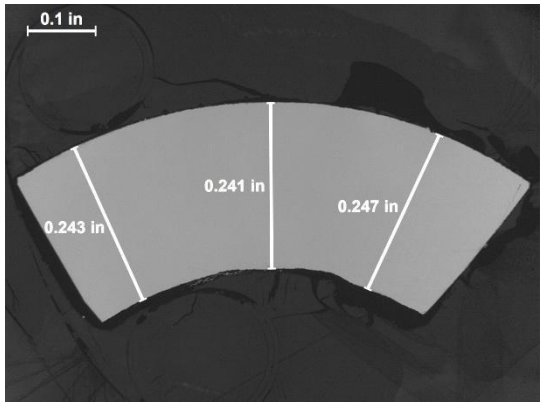	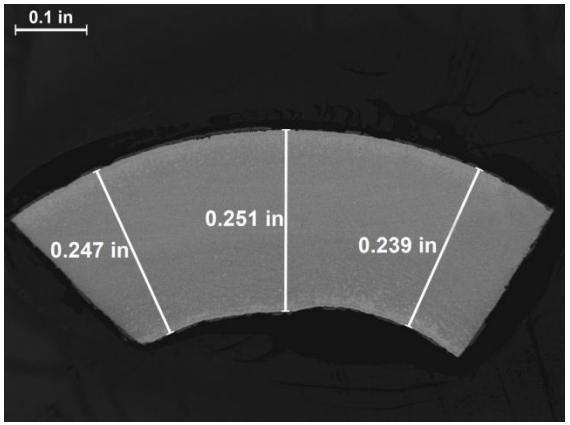	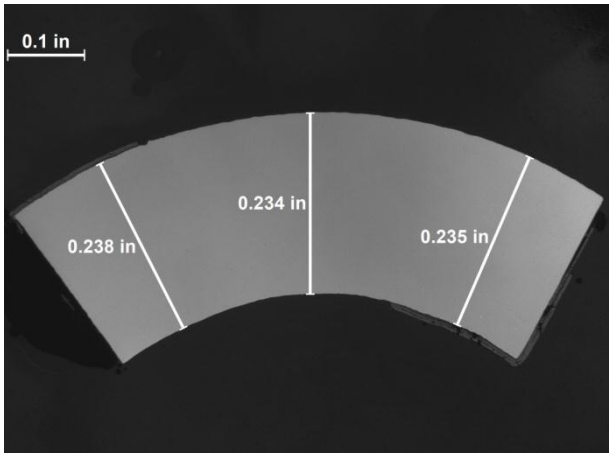
	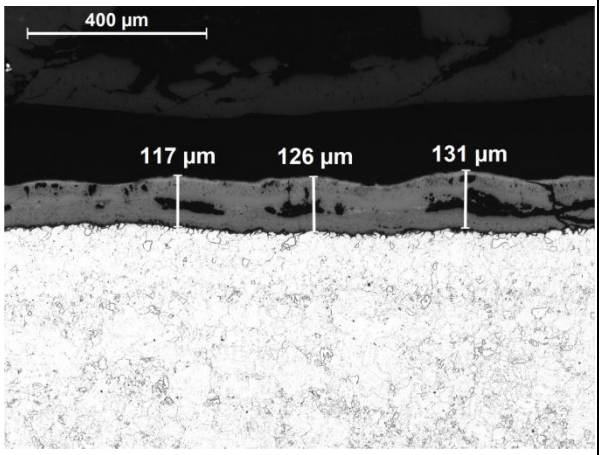	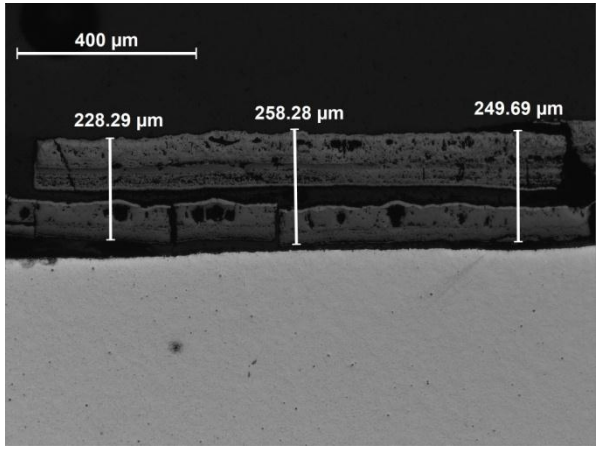

Fireside Corrosion Conditions – Condition 6 Results – T24 Material with Eastern Ash

No Exposure	After 1000 hours	After 3000 hours
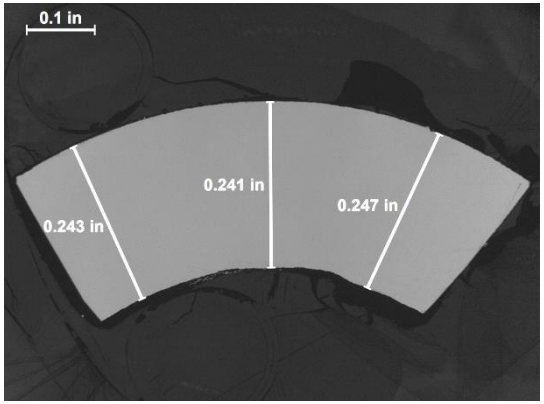	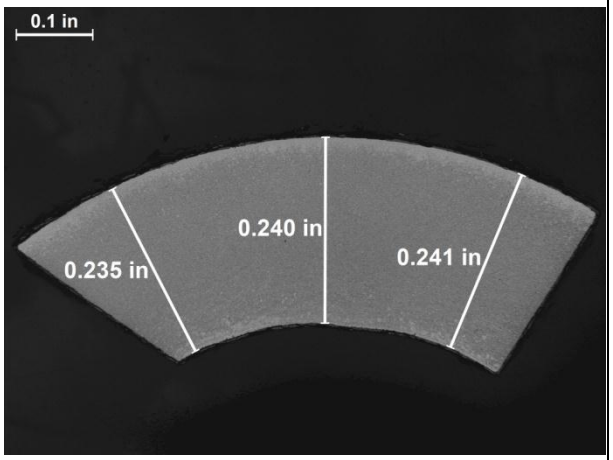	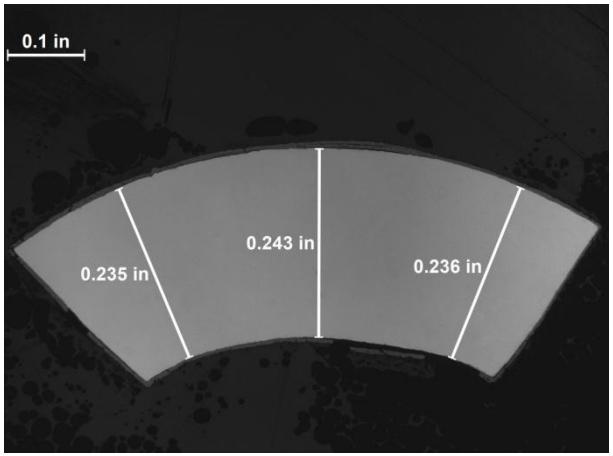
	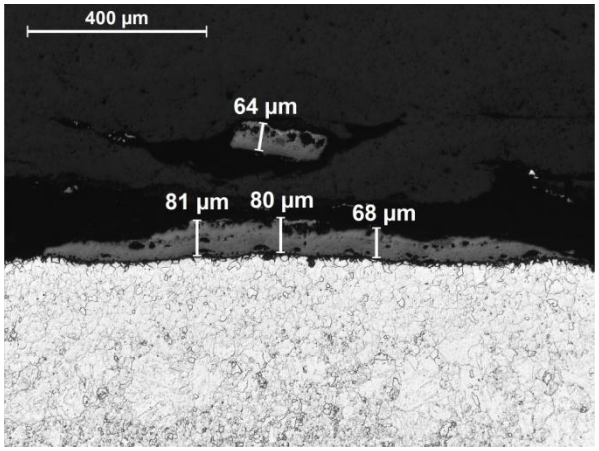	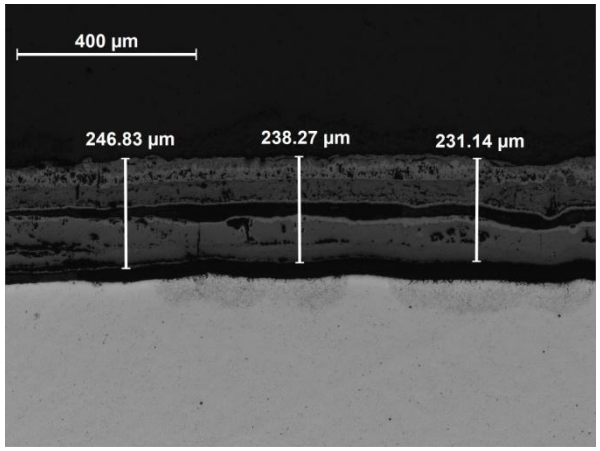

Fireside Corrosion Conditions – Condition 6 Results – T92 Material

No Exposure	After 1000 hours	After 3000 hours
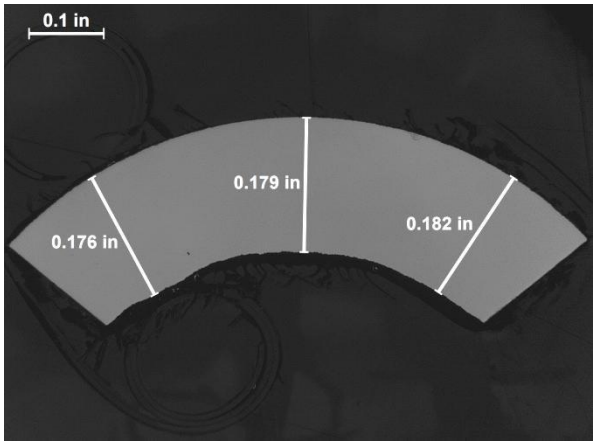	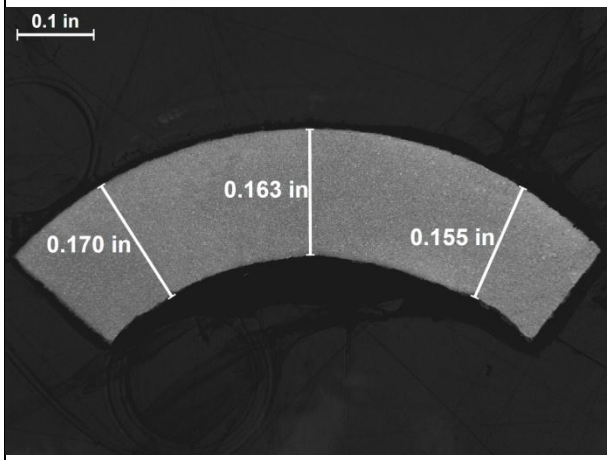	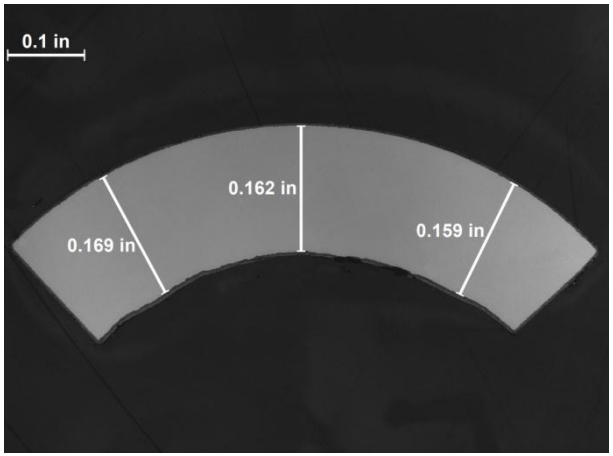
	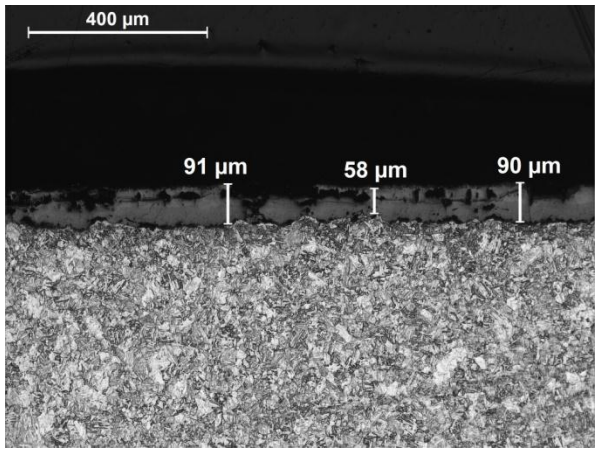	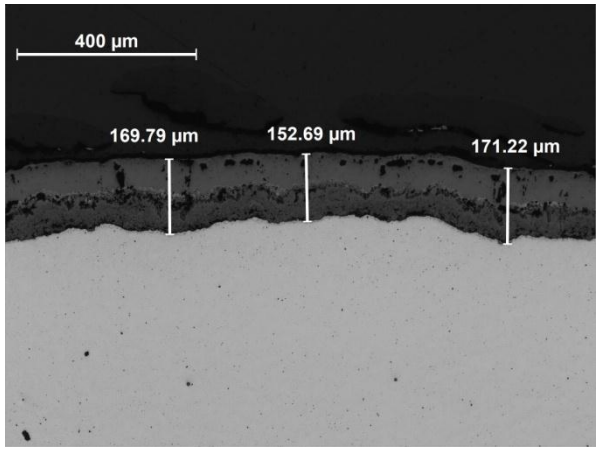

Fireside Corrosion Conditions – Condition 6 Results – T92 Material with Eastern Ash

No Exposure	After 1000 hours	After 3000 hours
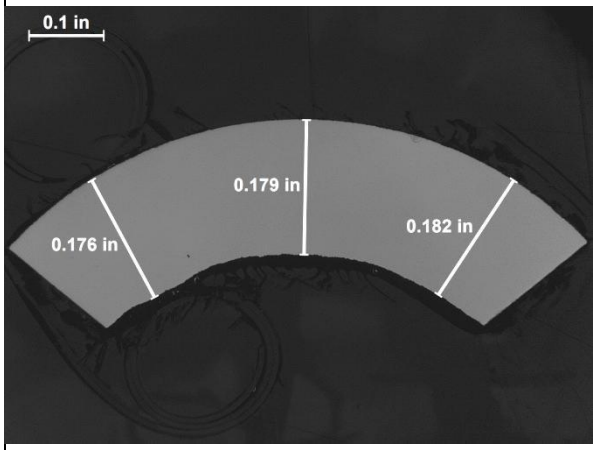	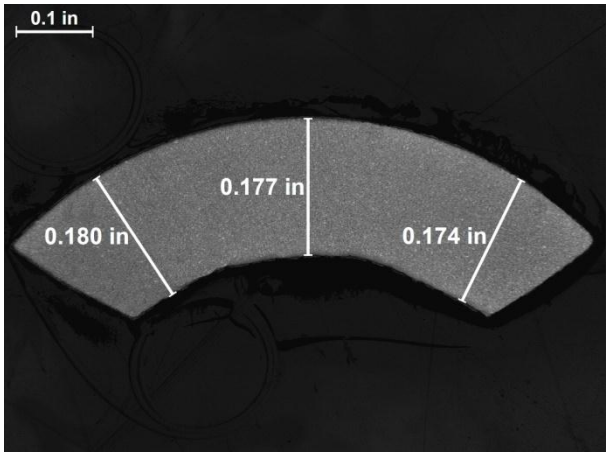	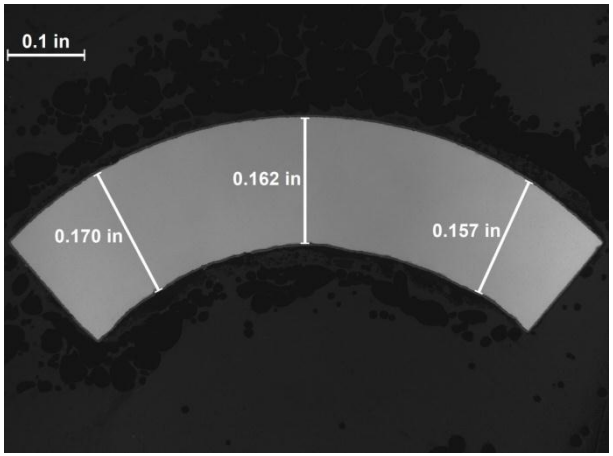
	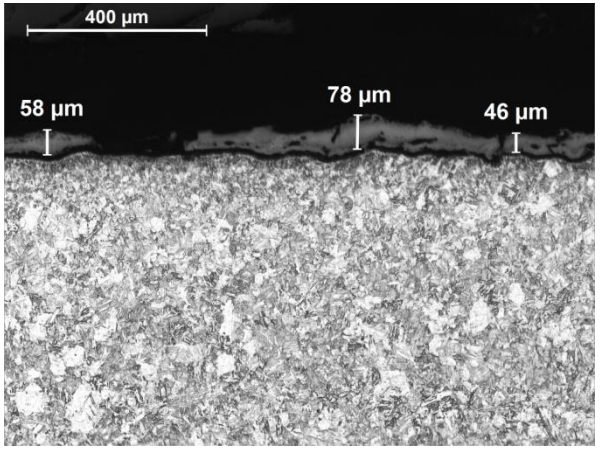	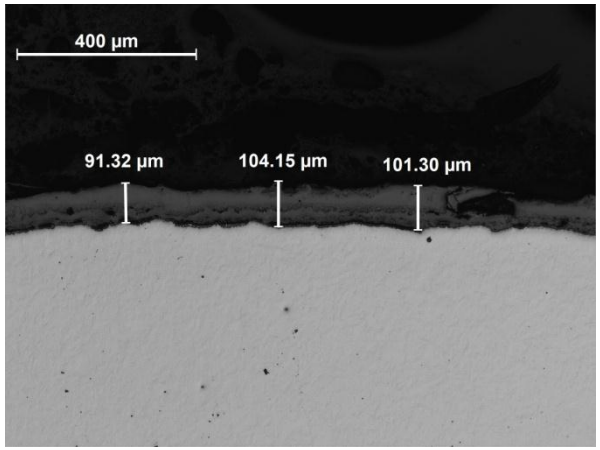

Fireside Corrosion Conditions – Condition 6 Results – 304H Material

No Exposure	After 1000 hours	After 3000 hours
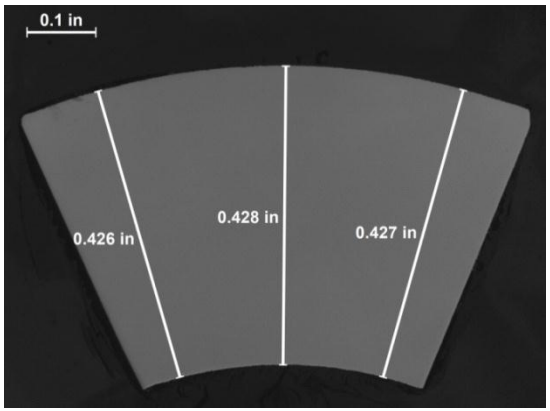	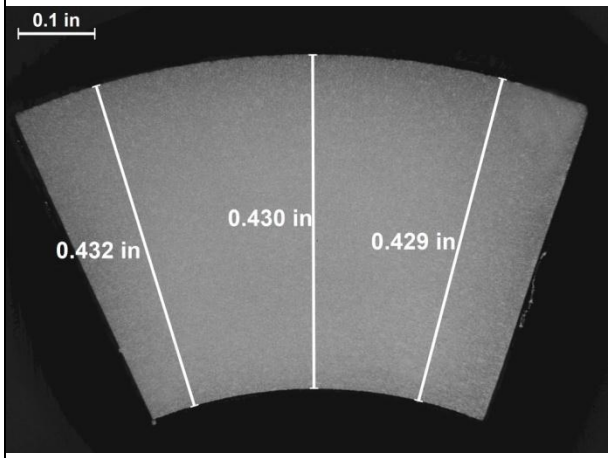	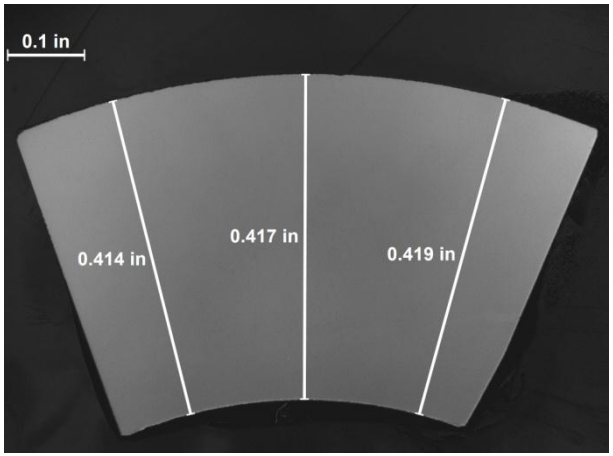
		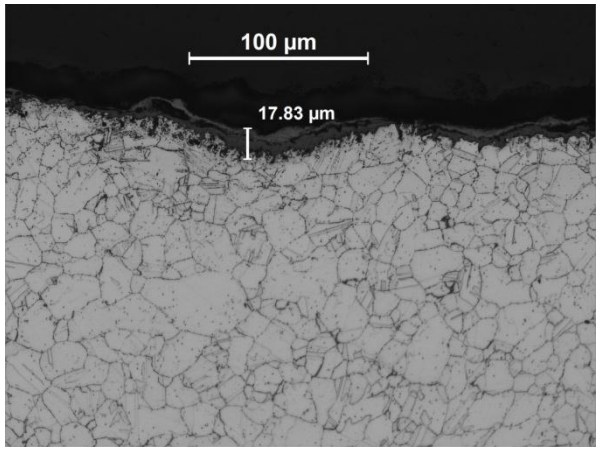

Fireside Corrosion Conditions – Condition 5 Results – 304H Material with Eastern Ash

No Exposure	After 1000 hours	After 3000 hours
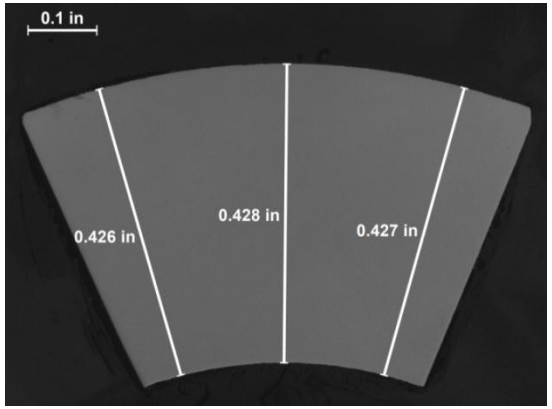	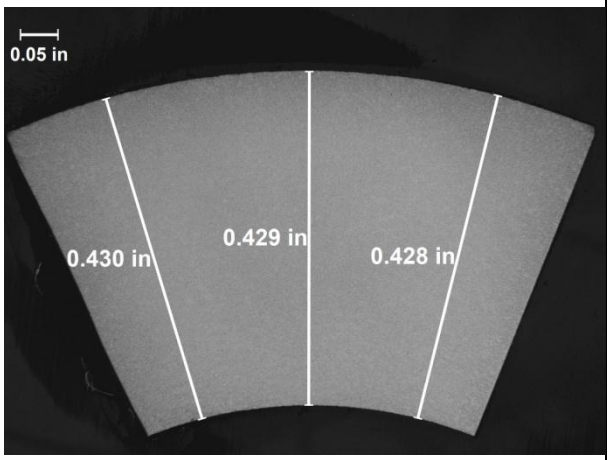	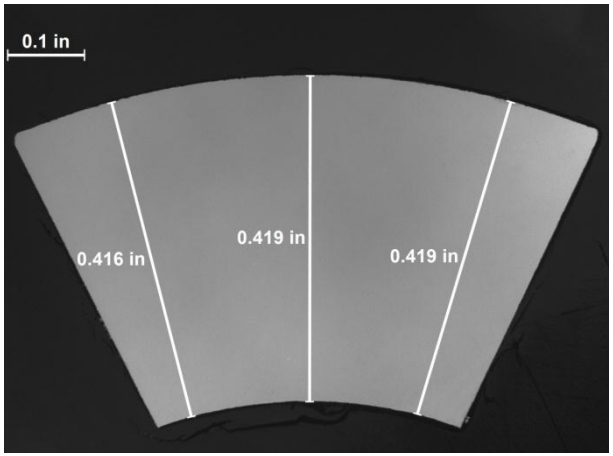
		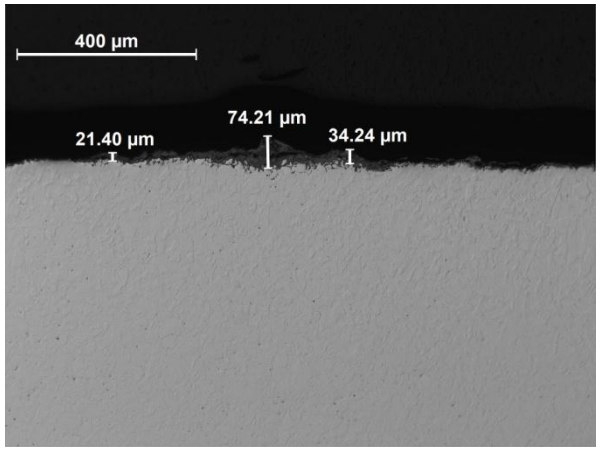

Fireside Corrosion Conditions – Condition 5 Results – 304H Material with Western Ash

No Exposure	After 1000 hours	After 3000 hours
		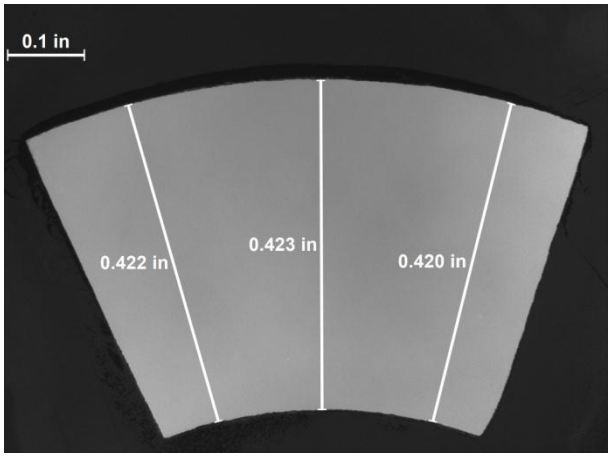
		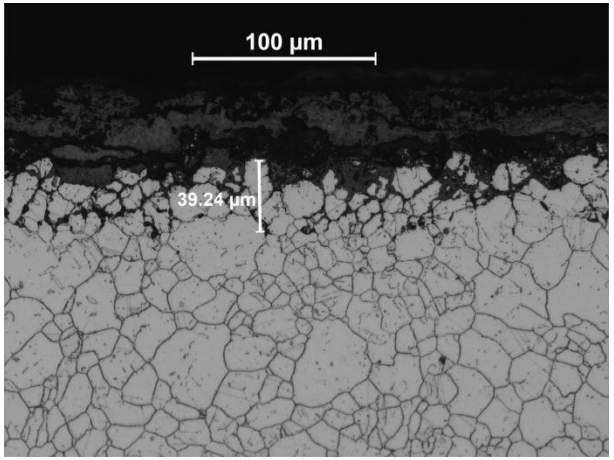

Fireside Corrosion Conditions – Condition 6 Results – IN617 Material

No Exposure	After 1000 hours	After 3000 hours
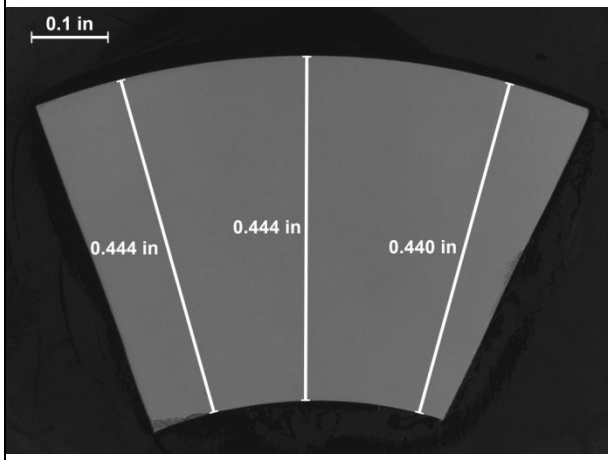	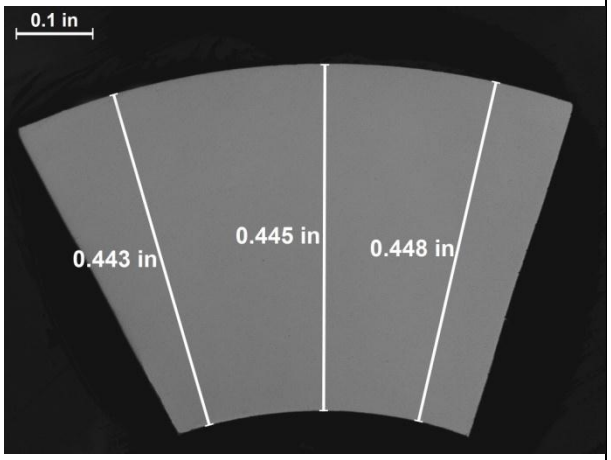	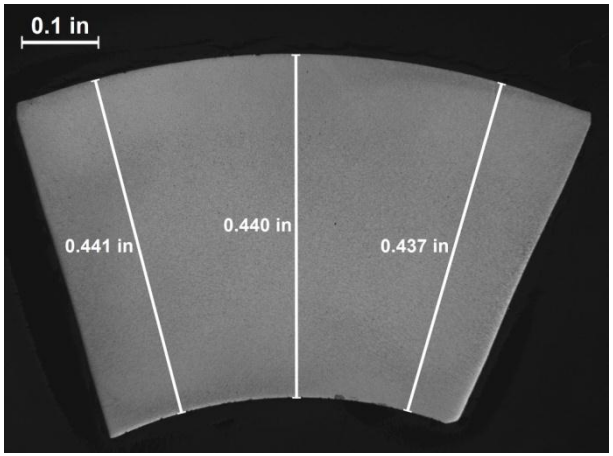
		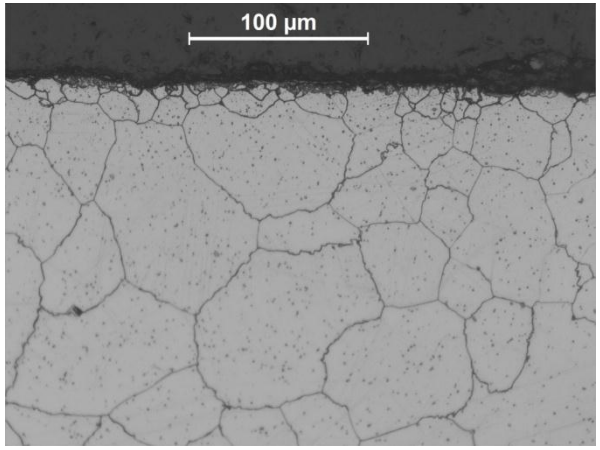

Fireside Corrosion Conditions – Condition 6 Results – IN617 Material with Eastern Ash

No Exposure	After 1000 hours	After 3000 hours
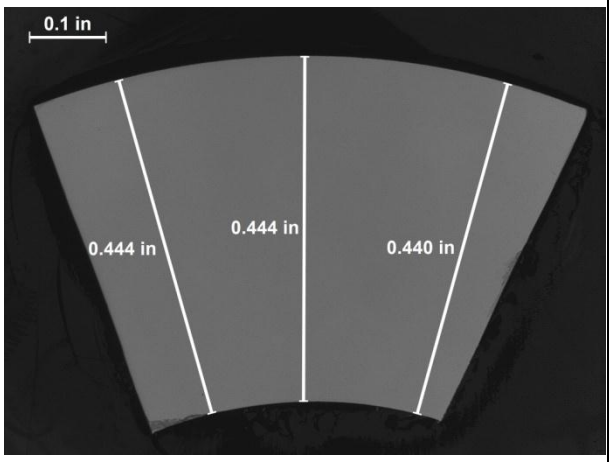	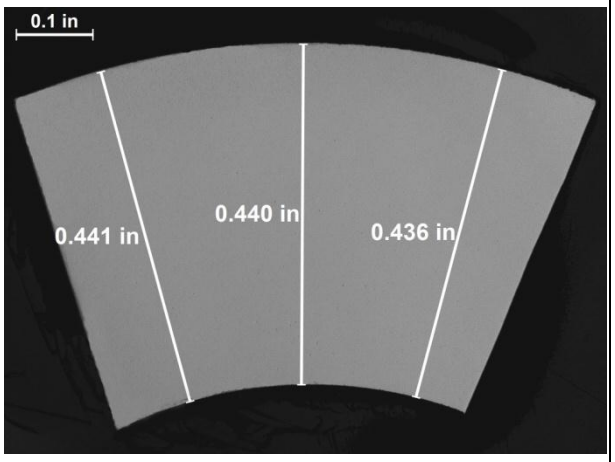	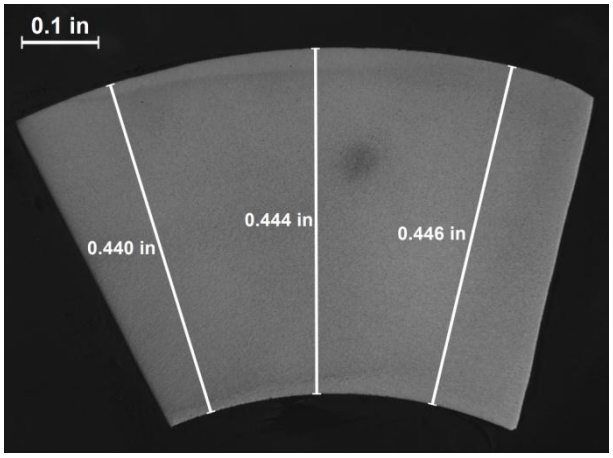
		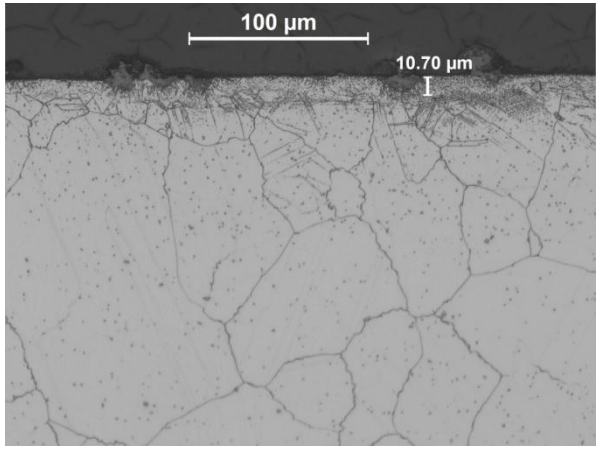

Condition 1 Test Results

268	Micro K3 - HR3C		206	Micro H4 - NF709R east
260			192	
273			183	
252			187	
268			182	
192			163	
189	midwall		181	midwall
279	Micro K5 west - HR3C		212	Micro H3 - NF709R
275			210	
264			199	
245			196	
252			202	
194			187	
214	midwall		180	midwall
267	Micro K4 east - HR3C			
268				
275				
271				
251				
231				
211	midwall			

Pre-exposed test results

HR3C-K42	239 HV 0.5		709R-H42	190 HV 0.5	S304H-F38 248 HV 0.5
	217 HV 0.5			185 HV 0.5	227 HV 0.5
	217 HV 0.5			174 HV 0.5	212 HV 0.5
	198 HV 0.5			182 HV 0.5	206 HV 0.5
	197 HV 0.5			178 HV 0.5	201 HV 0.5
	201 HV 0.5			178 HV 0.5	167 HV 0.5
	197 HV 0.5			195 HV 0.5	167 HV 0.5
	215 HV 0.5			163 HV 0.5	175 HV 0.5

Condition 2 Test Results

290	Micro K8	229	Micro F9 east	237	Micro H7 - NF709R
264	HR3C	206		205	
269		211		186	
256		216		201	
260		205		189	
208		194		154	
189	midwall	192	midwall	171	midwall
262	K9 east - HR3C	245	Micro F10 west		
255		230		231	H8 east -NF709R
243		234		221	
259		227		203	
251		227		196	
227		198		185	
229	midwall	196	midwall	180	
299	Micro K10 west			173	midwall
276		258	Micro F8		
267		237			
282		225			
280		220			
256		208			
245	midwall	189			
		185	midwall		

Pre-exposed test results

HR3C-K42	239 HV 0.5	709R-H42	190 HV 0.5	S304H-F38	248 HV 0.5
	217 HV 0.5		185 HV 0.5		227 HV 0.5
	217 HV 0.5		174 HV 0.5		212 HV 0.5
	198 HV 0.5		182 HV 0.5		206 HV 0.5
	197 HV 0.5		178 HV 0.5		201 HV 0.5
	201 HV 0.5		178 HV 0.5		167 HV 0.5
	197 HV 0.5		195 HV 0.5		167 HV 0.5
	215 HV 0.5		163 HV 0.5		175 HV 0.5

Condition 3 Test Results

	F3 600ºC 3000hr micro K13
267	
287	
249	
249	
254	
201	
191	midwall
	F3 600ºC 3000hr micro K14 east
280	
255	
237	
239	
227	
194	
202	midwall

	F3 600ºC 3000hr micro F14 east
237	
218	
221	
212	
213	
194	
191	midwall
	F3 600ºC 3000hr micro F15 west
279	
246	
219	
211	
219	
200	
197	midwall

204	F3 600ºC 3000hr micro H11 NF709R
185	
184	
199	
186	
176	
180	midwall
	F3 600ºC 3000hr micro H12 east
222	
209	
206	
204	
191	
170	
175	midwall

Pre-exposed test results

HR3C-K42	239 HV 0.5
	217 HV 0.5
	217 HV 0.5
	198 HV 0.5
	197 HV 0.5
	201 HV 0.5
	197 HV 0.5
	215 HV 0.5

709R-H42	190 HV 0.5
	185 HV 0.5
	174 HV 0.5
	182 HV 0.5
	178 HV 0.5
	178 HV 0.5
	195 HV 0.5
	163 HV 0.5

S304H-F38	248 HV 0.5
	227 HV 0.5
	212 HV 0.5
	206 HV 0.5
	201 HV 0.5
	167 HV 0.5
	167 HV 0.5
	175 HV 0.5

Condition 4 Test Results

299	F5 600ºC 3000hr micro K19 east
293	
266	
279	
260	
206	
198	midwall
258	F5 3000hr 600ºC micro K20 west
239	
264	
239	
231	
200	
202	midwall
280	F5 600ºC 3000hr micro K18
271	
289	
250	
254	
218	
208	midwall

222	F5 600ºC 3000hr micro H15
194	NF709R
205	
175	
184	
170	
190	midwall

Pre-exposed test results

HR3C-K42	239 HV 0.5
	217 HV 0.5
	217 HV 0.5
	198 HV 0.5
	197 HV 0.5
	201 HV 0.5
	197 HV 0.5
	215 HV 0.5

709R-H42	190 HV 0.5
	185 HV 0.5
	174 HV 0.5
	182 HV 0.5
	178 HV 0.5
	178 HV 0.5
	195 HV 0.5
	163 HV 0.5

S304H-F38	248 HV 0.5
	227 HV 0.5
	212 HV 0.5
	206 HV 0.5
	201 HV 0.5
	167 HV 0.5
	167 HV 0.5
	175 HV 0.5

Appendix F. Bench Scale Waterwall Corrosion Study

This appendix contains a report by Alstom's Materials Testing Laboratory discussing the results of bench scale corrosion testing at metal temperatures and environments simulating conditions in the waterwall region of the furnace.

ALSTOM

Technical Report

Project Leader: Bettina Bordenet

TTTM - Materials Technology Center
1201 Riverfront Parkway
Chattanooga, TN 37402, USA
Tel.: (423) 752-2845
Fax: (423) 752-2825

Document Title: DOE Oxy-Combustion Waterwall Corrosion Study – 1000 hour.

Document Ref. No.: 13G206

Date of Issue: Dec 19, 2013 **No. of pages**: 47

Authors: Jeff Mallat and Leo Antony

Reviewed by: Randy Wilson, Bettina Bordenet, Armand Levasseur

---

Summary:

Waterwall (WW) tubing materials T11, T22, T23, and T24 were studied for corrosion behavior in simulated air-firing and oxy-firing conditions at 550°C for an exposure of 1000 hours. The materials were tested as either bare metal (non-ashed) or coated with simulated eastern coal ash (ashed). After testing the total metal loss, scale thickness and weight change for the samples were measured. In addition, the nature of the corrosion attack was documented.

Uniform corrosion was observed on each of the samples, with negligible internal attack or pitting observed. Because scale exfoliation produced during the testing resulted in excessive scatter of the data for the scale thickness and weight gain measurements, metal loss during testing was used to draw the conclusions.

Results indicate corrosion behavior is strongly dependent on corrosive constituents in the gas and ash deposits at the material surface and does not appear to be negatively impacted by the CO_2-rich environment under oxy-firing conditions compared to the N_2-rich environment under conventional air-firing. Tests for air-firing, coated in ash, and with high sulfur and HCl in the simulated flue gas had the most aggressive metal loss. The oxy-fired test with low sulfur and low HCl (high CO & CO2) with ashed and non-ashed samples showed the least metal loss.

In general, each of the four alloy materials exhibited similar corrosion behavior under the respective test conditions.

---

1. Introduction

The overall objective of this research project was to study the WW corrosion of selected boiler materials T11, T22, T23, and T24 (ashed and non-ashed) and to determine the corrosion phenomena of these materials when exposed to simulated oxy-fired conditions and air-fired conditions at 550°C for a maximum exposure of 1000 hours. All results are reported in mm and grams. Follow-up testing to 3000 hours is expected at a future date.

2. Experimental Procedure

The testing strategy was to expose the four materials to both air-fired and oxy-fired conditions with both high and low sulfur + hydrochloric acid contents. This made four separate test atmosphere conditions as shown by the compositions and flow rates of the simulated flue gases listed in Table 1.

The four boiler tube materials used in this study were made to the requirements of ASME SA-213 for hot rolled tube. The composition of the materials was analyzed by optical emission spectroscopy and the results reported in Tables 2 and 3.

The test specimens were arc sections taken from the boiler tube materials. The specimens were approximately 25mm in axial length with an outside arc length of also approximately 25mm. A hole was drilled into the center top of the specimens so that an alumina rod could be used to hold the specimens in ceramic fiberboard boats. The cut surfaces of the specimens were wet-ground using 140 and 240 grit SiC papers. After grinding, the test specimens were cleaned in a 60°C solution of 6-v% HCL + 0.2-v% Rodine + deionized water for 1 hour prior to testing.

Prior to testing, the specimens were weighed and their surface areas measured. The specimens were then arranged for each condition and placed in ceramic boats, as shown in Figure 1. The boats were then inserted into horizontal tube furnaces, shown in Figure 2, and heated to 550°C. The furnaces were ramped up to test temperature under an argon atmosphere and then the testing atmosphere was established. After testing, the furnaces were cooled down under argon atmosphere. A schematic of the experimental set-up is shown in Figure 3.

Once in the furnace, the test specimens were exposed to the simulated flue gas that was fed into the furnace at a constant rate under conditions of just over atmospheric pressure for 1000 hours. One test specimen of each material type in each gas condition was coated with ash prior to testing, while one test specimen of each material type was tested bare. Simulated eastern U.S. coal ash (reducing) was used. The composition of this simulated ash is provided in Table 4. The dry ash was mixed with methyl cellulose and charcoal to make a slurry. About 1-mm, or about 0.3-g of the slurry was applied onto all surfaces of specific test specimens with a brush. The ash was reapplied to the specimens every 200 hours after the furnaces were cooled under an argon atmosphere and the old ash removed by brushing.

The exhaust flue gas was combusted with a propane flame to oxidize the H_2S before liberating to the atmosphere. The test system was rigged to shut down if the propane flame went out, and this occurred fourteen (14) times during testing. In total, there were eighteen (18) shut-downs during the testing duration; four (4) that were scheduled for the reapplication of the ash and fourteen (14) that were related to the propane flame-outs.

At the completion of the 1000 hour test period the furnaces were cooled to room temperature and all test specimens were removed for metallographic evaluation.

The test specimens were evaluated as described below:

1) Total Metal Loss (TML):
    a. TML was calculated as the starting wall thickness at the midpoint of the sample arc minus the remaining metal wall thickness at the midpoint of the sample arc minus any internal penetration attack.
    b. Dimensional measurements were taken of the pre-exposure test samples using calipers and recorded in millimeters.
    c. The post-exposure test samples were mounted (ideal orientation) using a vacuum impregnation method and clear epoxy.
    d. The mounted test samples were strategically sectioned with a diamond saw and prepared by standard metallographic practices.
    e. Dimensional measurements were taken of the remaining un-corroded metal at the midpoint of the sample arc of the mounted test samples using optical metallographic methods. The dimensional measurements were reported in millimeters.
    f. Internal Penetration Attack:
        i. The metallographic specimens were etched to reveal the microstructure and check for internal penetration attack, if present.
2) Scale Thickness (Corrosion Product) Measurement:
    a. The corrosion product was measured by optical methods on the cross-sections of the corroded test specimens and reported in millimeters.

3) Weight Change Measurement:
   a. Each test sample was weighed after testing for comparison with starting weight.

3. Results and Discussion

Uniform corrosion was observed on each of the specimens. Only a negligible amount of internal attack or pitting was seen.

Scale exfoliation produced during testing resulted in excessive scatter in data for scale thickness and weight gain measurements, therefore metal loss derived from dimensional measurements were used to draw conclusions. The micrographs of each of the alloys tested under conditions 1 to 4 are provided in the addendum.

The total metal loss values (TML) for all four alloys under each condition are given in Table 5. The ratio of ashed / non-ashed metal loss is also shown in Table 5. The TML, scale thickness and weight change are shown graphically in Charts 1-5. In general, all four alloys exhibited similar corrosion behavior under the respective test conditions.

The ratio of ashed to non-ashed TML in specimens under air-fired conditions ranged from 1.4 to 1.9. However, in oxy-fired conditions the ratio of TML for ashed to non-ashed specimens ranged from 0.6 to 2.7. Some of the oxy-fired tests exhibited ratios less than one (less TML *with* ash) and the oxy-fired tests typically exhibited a wider range of ratios with a larger standard deviation of ratios.

Condition 2 (oxy-fired, low S, low Cl, high CO & CO2) ashed and non-ashed showed the least TML. Still, the observed TML are significant for typical boiler environments.

4. Summary of Observations

1. Due to scale exfoliation and the resulting data scatter, scale thickness and weight change measurements were not used to analyze results. Total metal loss (TML) data taken from dimensional measurements was used to analyze results.

2. In general, all four alloys exhibited similar corrosion behavior under the respective test conditions.

3. No significant intergranular attack or pitting was observed on the surface of any sample after testing.

4. As expected, samples in high sulfur + HCl content exhibited greater TML.

5. Samples tested in air-fired conditions, generally, exhibited the greatest TML.

6. In all cases, the ashed samples exhibited greater TML than non-ashed samples under air-firing conditions.

7. The ashed samples exhibited greater TML than non-ashed samples under oxy-firing conditions.
    a. An exception to the above statement was observed for the T11 and T23 samples in condition 4 and the T24 sample in condition 2.

8. The variation in the test materials response to ashed and non-ashed conditions in oxy-fired conditions (condition 2 & 4) is noted and warrants further investigation in the future.

9. Condition 3 (air-fired, high S, high Cl, low CO & CO2) ashed and non-ashed showed the greatest TML.

10. Condition 2 (oxy-fired, low S, low Cl, high CO & CO2) ashed and non-ashed showed the least TML. It also showed the largest range in ratio of TML for ashed to non-ashed specimens; 0.9 to 2.7.

11. Although condition 2 (oxy-fired, low S, low Cl, high CO & CO2) ashed and non-ashed showed the least TML, the observed TML is significant for typical boiler environments.

12. This test was conducted for only 1000 hours, which is relatively short to capture long-term corrosion bevaior. Longer test times would impact the reliability of results

TABLE 1

Composition and Flow Rates of Simulated Flue Gas Test Atmospheres

Air-Firing/ Condition - 1			**Oxy-Firing/ Condition - 2**			**Air-Firing/ Condition - 3**			**Oxy-Firing/ Condition - 4**		
Gases		Vol%	Gases		Vol%	Gases		Vol%	Gases		Vol%
N2		74.79	N2		14.79	N2		74.79	N2		14.57
CO2		12	CO2		54	CO2		12	CO2		54
H2O		10	H2O		25	H2O		10	H2O		25
SO2		0.18	SO2		0.18	SO2		0.36	SO2		0.36
H2S		0.02	H2S		0.02	H2S		0.04	H2S		0.04
HCl		0.01	HCl		0.01	HCl		0.03	HCl		0.03
CO		3	CO		6	CO		3	CO		6
Total furnace flow, cc/min		275	Total furnace flow, cc/min		275	Total furnace flow, cc/min		275	Total furnace flow, cc/min		275
Test Gases	**Test Gas flow rate**	**Gas Consumption**	**Test Gases**	**Test Gas flow rate**	**Gas Consumption**	**Test Gases**	**Test Gas flow rate**	**Gas Consumption**	**Test Gases**	**Test Gas flow rate**	**Gas Consumption**
	cc/min	**ft^3/test**		cc/min	**ft^3/test**		cc/min	**ft^3/test**		cc/min	**ft^3/test**
N2 - SO2	50	106	N2 - SO2	25	53	N2 - SO2	100	212	N2 - SO2	25	106
N2-H2S	55	116	N2-H2S	16	34	N2-H2S	107	227	N2-H2S	16	116
CO2-CO	41.3	87	CO2-CO	165	349	CO2-CO	41	87	CO2-CO	165	87
N2	101.2	214									
Total	247.5	524	Total	206	436	Total	248	526	Total	206	310
Liquid feed: H20/HCl as Gas @ STP in cc/min		27.5000	**Liquid feed: H20/HCl as Gas @ STP in cc/min**		68.7500	**Liquid feed: H20/HCl as Gas @ STP in cc/min**		27.5000	**Liquid feed: H20/HCl as Gas @ STP in cc/min**		68.7500
Liquid feed: H20/HCl as liquid in cc/min		0.0221	**Liquid feed: H20/HCl as liquid in cc/min**		0.0552	**Liquid feed: H20/HCl as liquid in cc/min**		0.0221	**Liquid feed: H20/HCl as liquid in cc/min**		0.0552
Liquid feed: H20/HCl as liquid in cc/hour		1.3259	**Liquid feed: H20/HCl as liquid in cc/hour**		3.3147	**Liquid feed: H20/HCl as liquid in cc/hour**		1.3259	**Liquid feed: H20/HCl as liquid in cc/hour**		3.3147
HCl Feed as Gas @ STP in cc/min		0.0275	**HCl Feed as Gas @ STP in cc/min**		0.0275	**HCl Feed as Gas @ STP in cc/min**		0.0825	**HCl Feed as Gas @ STP in cc/min**		0.0825
HCl in H2O Concentration in moles/lliter		0.0556	**HCl in H2O Concentration in moles/lliter**		0.0222	**HCl in H2O Concentration in moles/lliter**		0.1667	**HCl in H2O Concentration in moles/lliter**		0.0667

TABLE 2
Base Metal Chemical Composition Analysis Results
(weight percent)

ELEMENT	T11 Specimen	ASME SA-213, T11	T22 Specimen	ASME SA-213, T22
CARBON	**0.08**	0.05 – 0.15	**0.11**	0.05 – 0.15
MANGANESE	**0.46**	0.30 – 0.60	**0.57**	0.30 – 0.60
PHOSPHORUS	**0.012**	0.025 max	**0.013**	0.025 max
SULFUR	**0.004**	0.025 max	**0.003**	0.025 max
SILICON	**0.57**	0.50 – 1.00	**0.24**	0.50 max
NICKEL	**0.14**	--	**0.16**	--
CHROMIUM	**1.15**	1.00 – 1.50	**2.10**	1.90 – 2.60
MOLYBDENUM	**0.52**	0.44 – 0.65	**0.94**	0.87 – 1.13
VANADIUM	**0.01**	--	**0.01**	--
COLUMBIUM	**<0.001**	--	**0.004**	--
TITANIUM	**0.031**	--	**0.002**	--
COBALT	**0.01**	--	**0.02**	--
COPPER	**0.18**	--	**0.15**	--
ALUMINUM	**0.01**	--	**0.018**	--
BORON	**0.0002**	--	**0.0003**	--
TUNGSTEN	**0.01**	--	**0.01**	--
ANTIMONY	**0.001**	--	**0.001**	--
ARSENIC	**0.012**	--	**0.009**	--
TIN	**0.009**	--	**0.008**	--
ZIRCONIUM	**0.001**	--	**0.002**	--
LEAD	**<0.001**	--	**0.001**	--
NITROGEN	**0.019**	--	**0.013**	--

TABLE 3
Base Metal Chemical Composition Analysis Results
(weight percent)

ELEMENT	T23 Specimen	ASME CC 2199-4, T23	T24 Specimen	ASME SA-213, T24
CARBON	**0.07**	0.04 - 0.10	**0.06**	0.05 – 0.10
MANGANESE	**0.43**	0.10 - 0.60	**0.61**	0.30 – 0.70
PHOSPHORUS	**0.019**	0.030 max	**0.018**	0.020 max
SULFUR	**0.002**	0.010 max	**0.002**	0.010 max
SILICON	**0.26**	0.50 max	**0.33**	0.15 – 0.45
NICKEL	**0.10**	0.40 max	**0.08**	--
CHROMIUM	**2.36**	1.90 - 2.60	**2.50**	2.20 – 2.60
MOLYBDENUM	**0.21**	0.05 - 0.30	**0.98**	0.90 – 1.10
VANADIUM	**0.20**	0.20 - 0.30	**0.24**	0.20 – 0.30
COLUMBIUM	**0.045**	0.02 - 0.08	**0.008**	--
TITANIUM	**0.030**	0.005 - 0.060	**0.067**	0.06 – 0.10
COBALT	**0.01**	--	**0.01**	--
COPPER	**0.15**	--	**0.10**	--
ALUMINUM	**0.028**	0.030 max	**0.019**	0.02 max
BORON	**0.0010**	0.0010 - 0.006	**0.0023**	0.0015 – 0.007
TUNGSTEN	**1.49**	1.45 - 1.75	**0.02**	--
ANTIMONY	**0.017**	--	**0.002**	--
ARSENIC	**0.009**	--	**0.007**	--
TIN	**0.011**	--	**0.007**	--
ZIRCONIUM	**0.003**	--	**0.003**	--
LEAD	**0.001**	--	**0.002**	--
NITROGEN	**0.016**	0.015 (max)	**0.009**	0.012 max

TABLE 4 Eastern U.S. Coal WW Reducing Ash Composition			
Element Oxide	**Ash Analysis Ignited Basis Weight %**	**Mat'l Used**	**g / 100g Ignited Mix**
SiO_2	45	Sea Sand SiO_2 Calcined Kaolin	21.43
Al_2O_3	20	$2SiO_2$-Al_2O_3 Calcined Kaolin	43.57
Fe_2O_3	25	40% ACS Grade Fe_3O_4 60% Pyrite (FeS_2)	9.67 22.54
CaO	5	ACS Grade CaO	5
MgO	2	ACS Grade MgO	2
Na_2O	1	ACS Grade Na_2CO_3	1.71
K_2O	1	ACS Grade K_2CO_3	1.77
TOTAL			107.69
Combustible Additives			
Carbon	5	Charcoal	5
Binder	1.5	Methyl Cellulose	1.5

TABLE 5 Total Metal Loss (mm)				
Sample	**Condition 1**	**Condition 2**	**Condition 3**	**Condition 4**
T11	0.34	0.11	0.54	0.57
T11 Ash	0.49	0.30	0.98	0.34
T22	0.33	0.15	0.52	0.30
T22 Ash	0.65	0.37	0.71	0.45
T23	0.26	0.20	0.50	0.39
T23 Ash	0.41	0.23	0.96	0.30
T24	0.38	0.27	0.47	0.32
T24 Ash	0.53	0.24	0.89	0.38
Ratio of Metal Loss for Material in Ashed to Non-Ashed				
T11 Ash **/** T11	1.4	2.7	1.8	0.6
T22 Ash **/** T22	1.9	2.5	1.4	1.5
T23 Ash **/** T23	1.6	1.2	1.9	0.8
T24 Ash **/** T24	1.4	0.9	1.9	1.2
Avg. Ratio	1.6	1.8	1.7	1.0
Std Dev	0.2	0.8	0.2	0.4

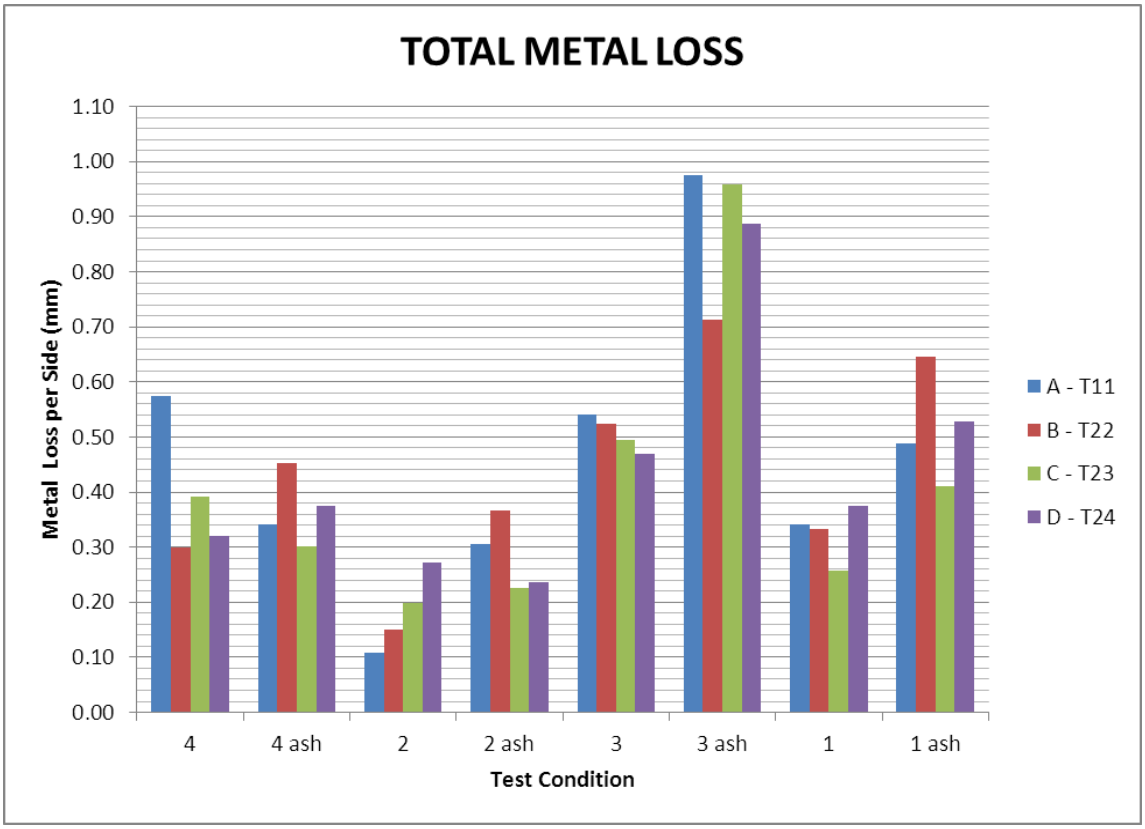

CHART 1: Metal loss per side in millimeters

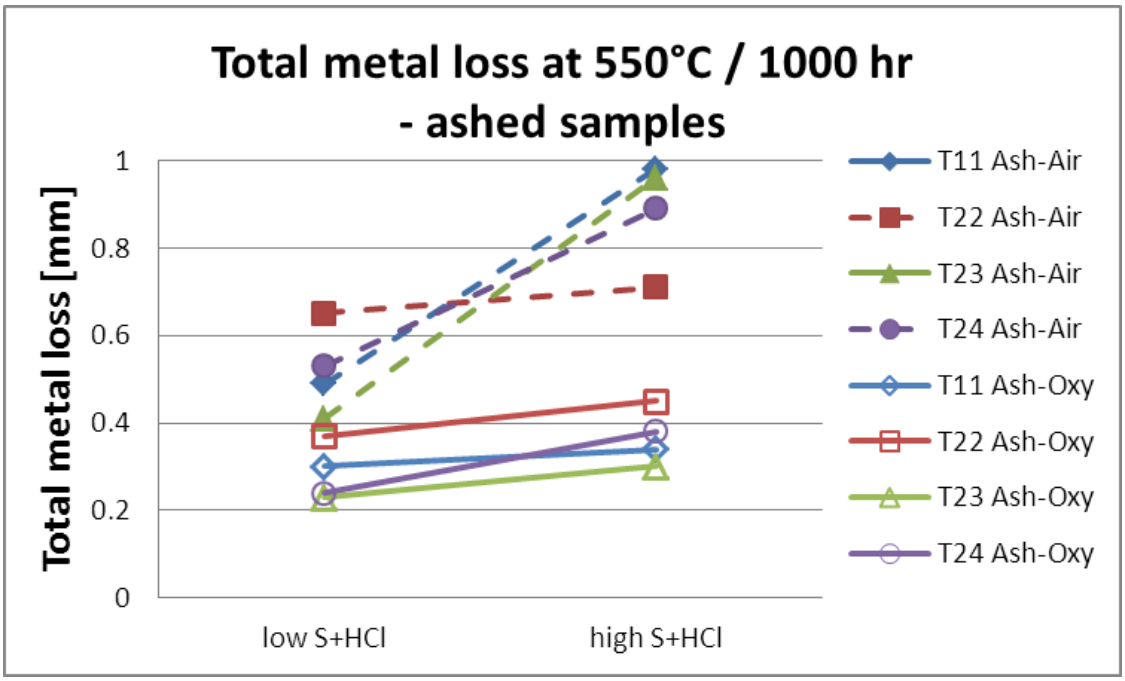

CHART 2: Metal loss of ashed samples in low versus high S+HCL.

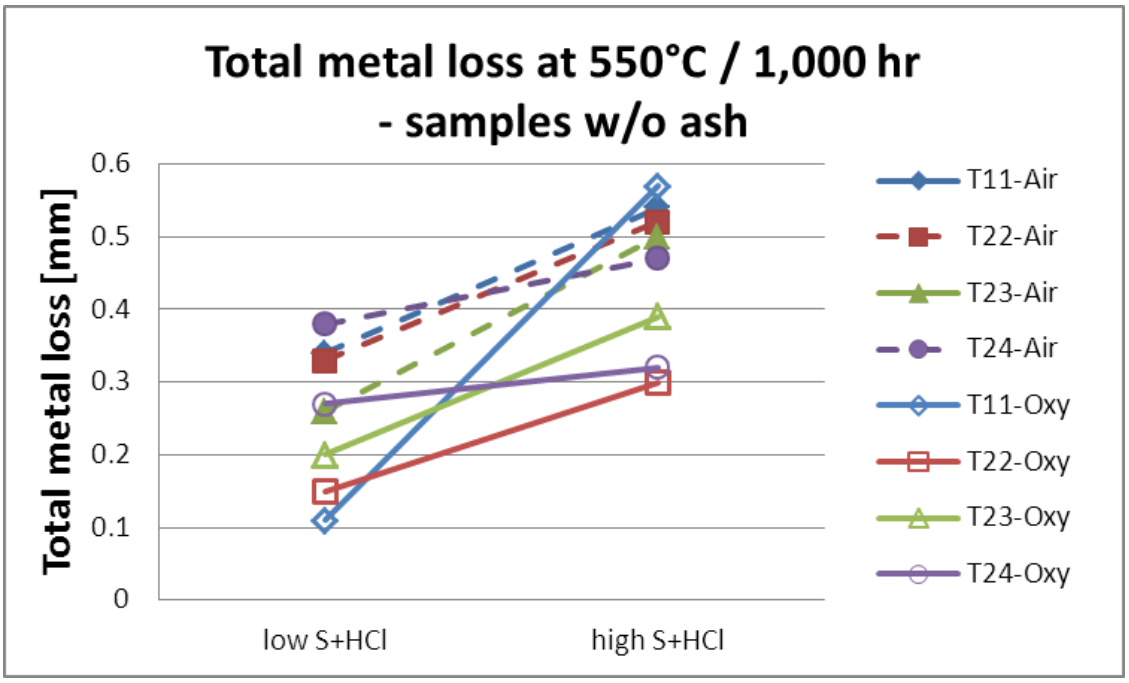

CHART 3: Metal loss of non-ashed samples in low versus high S+HCL.

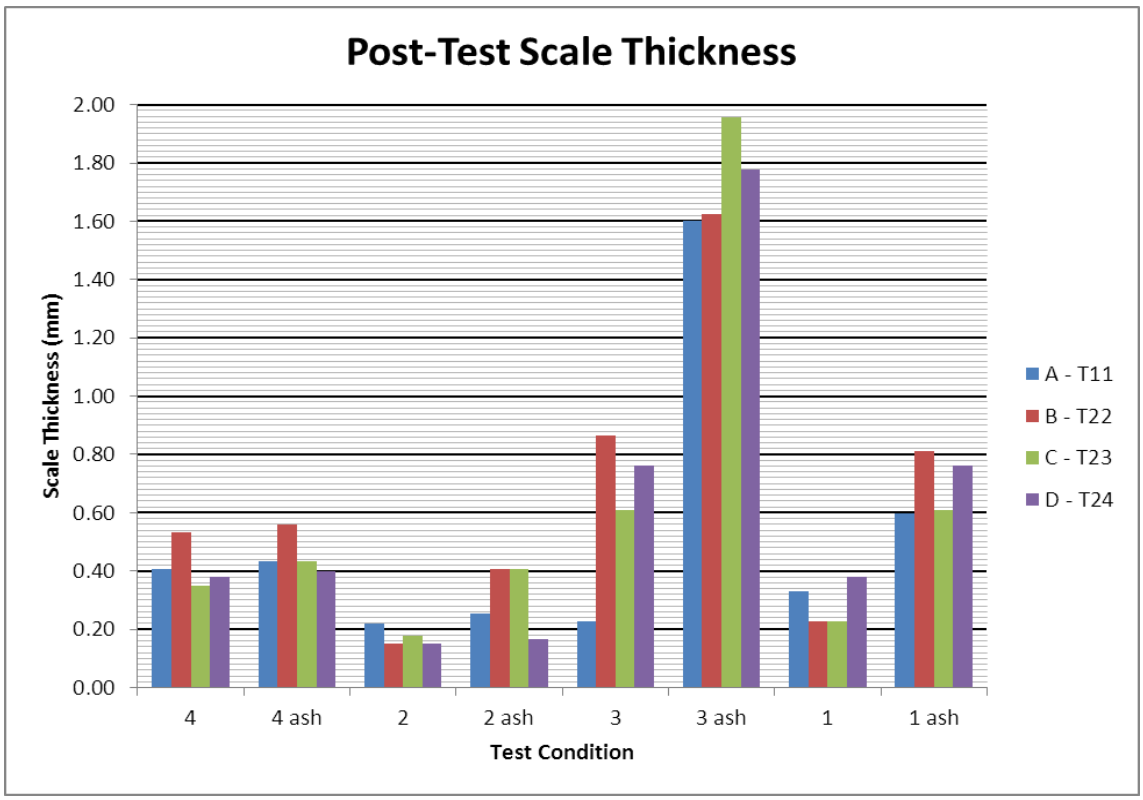

CHART 4: Post-test scale thickness in millimeters

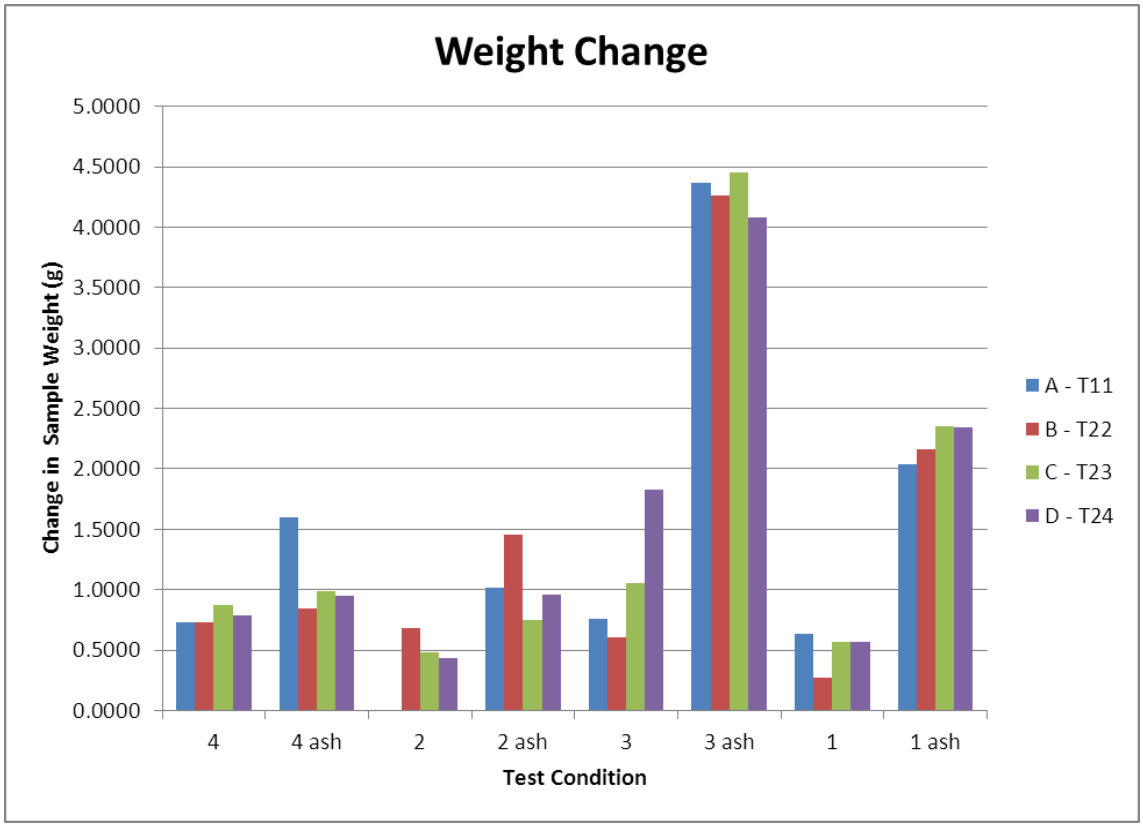

CHART 5: Change in sample weight after testing in grams.

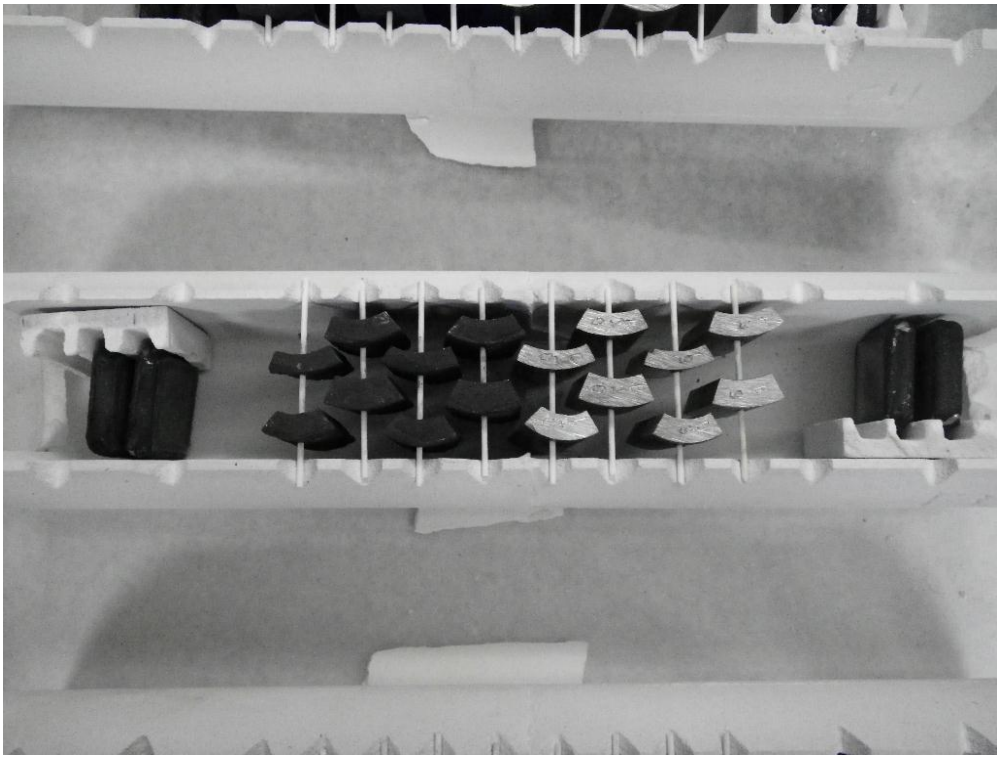

FIGURE 1: Photograph of a typical ceramic boat full of water wall corrosion test samples.

FIGURE 2: Photograph of the tube furnaces used for testing.

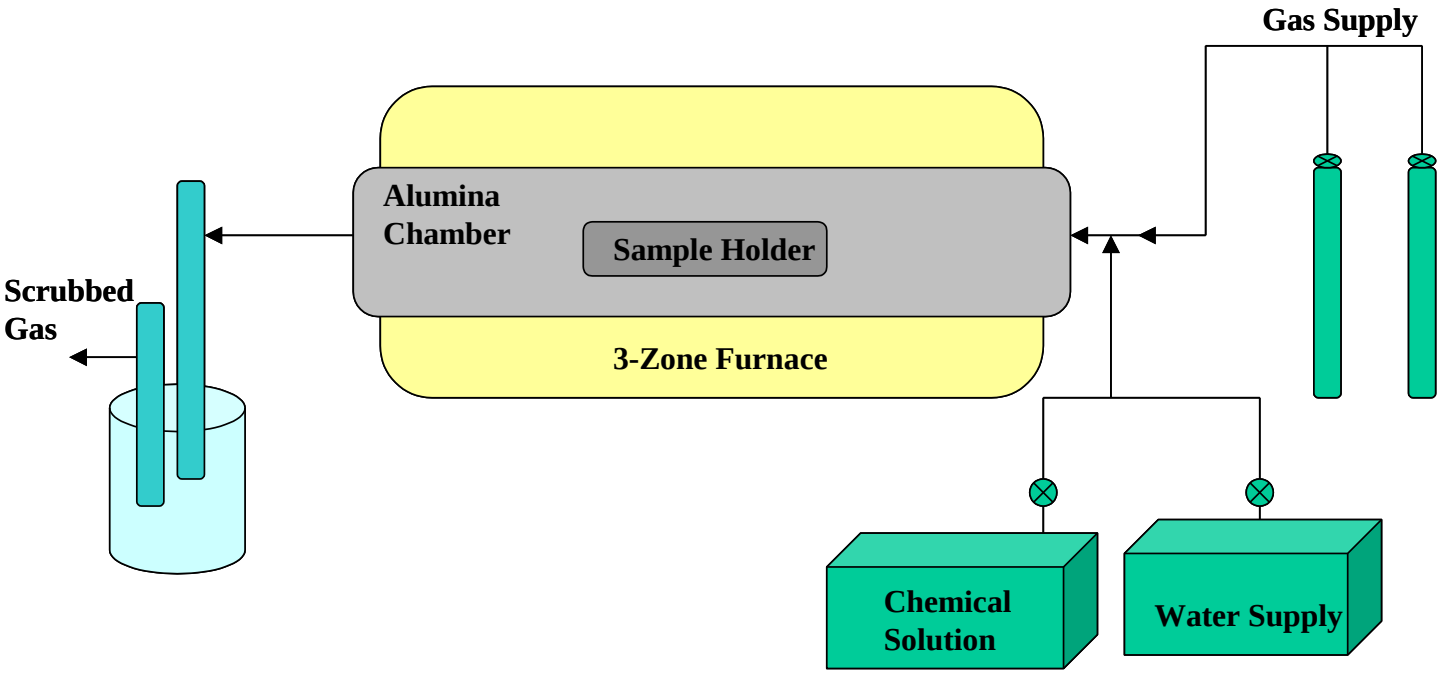

FIGURE 3: Shown is the schematic of the experimental set-up.

Fireside Corrosion Conditions – Starting Materials Before Exposure

T11	T22
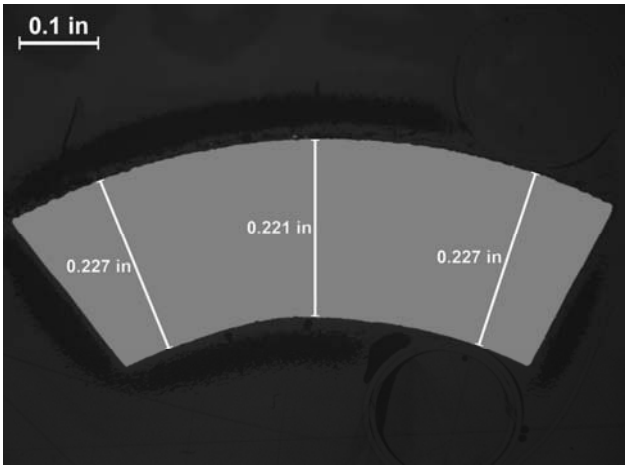	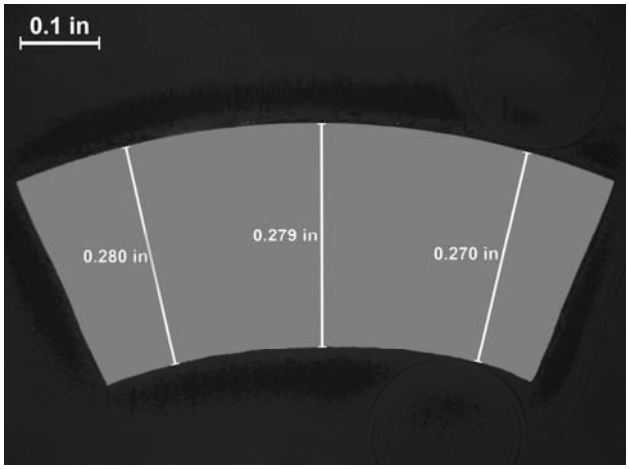
T23	**T24**
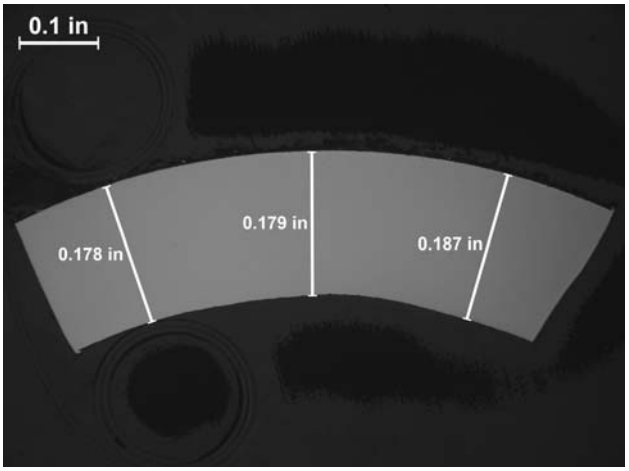	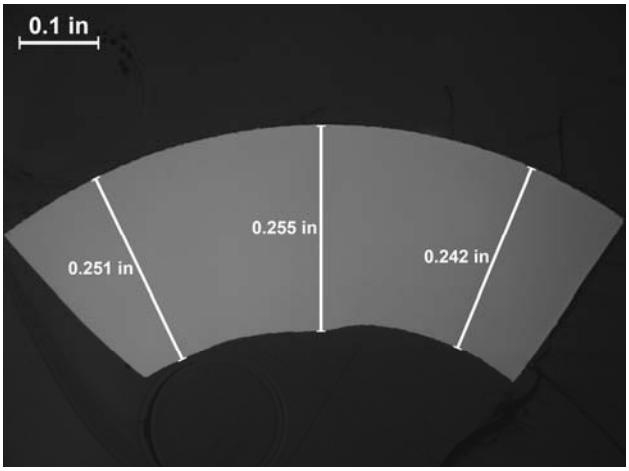

Fireside Corrosion Conditions – Condition 1 Results – T11 Material

A13 After 1000 hours

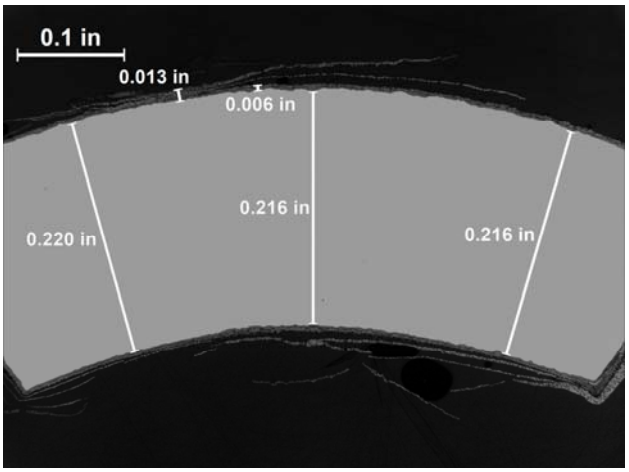

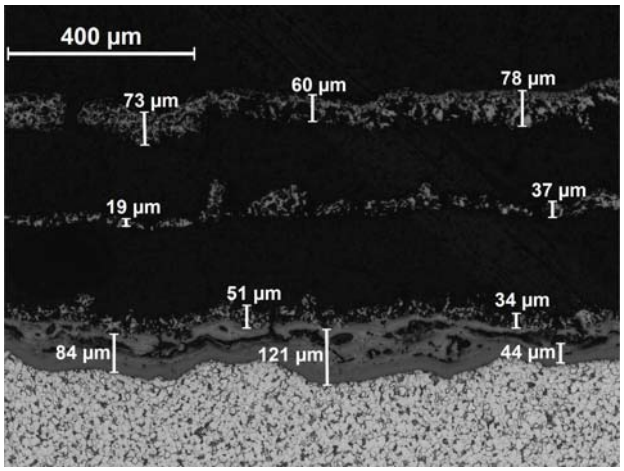

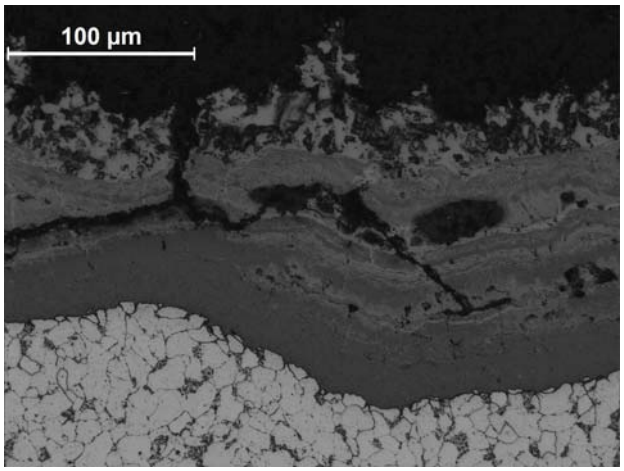

Fireside Corrosion Conditions – Condition 1 Results – T11 Material with Eastern Ash

A15 After 1000 hours

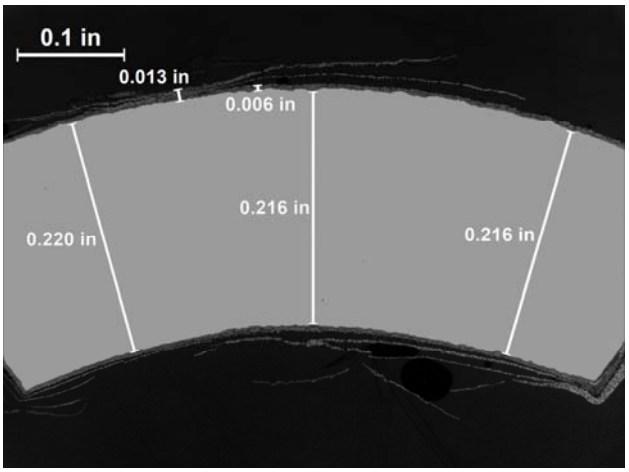

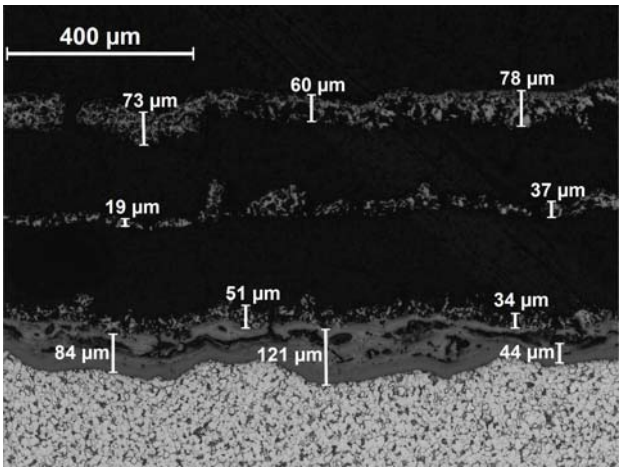

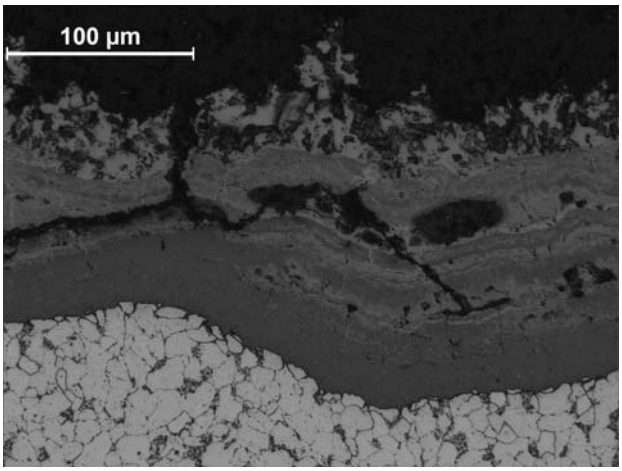

Fireside Corrosion Conditions – Condition 1 Results – T22 Material

B13 After 1000 hours

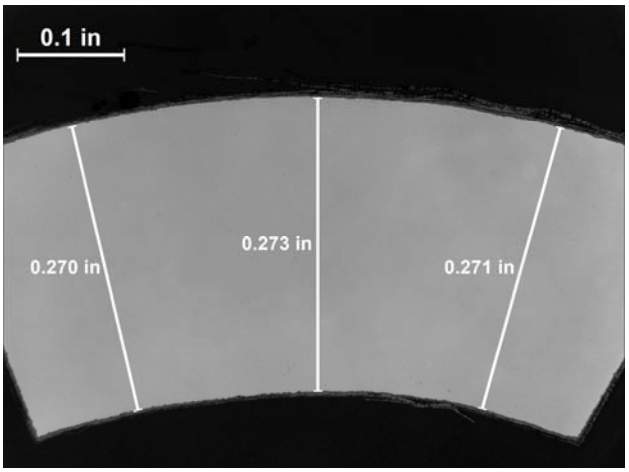

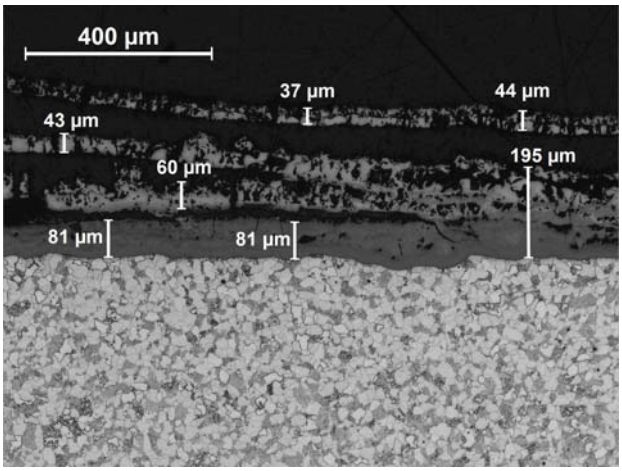

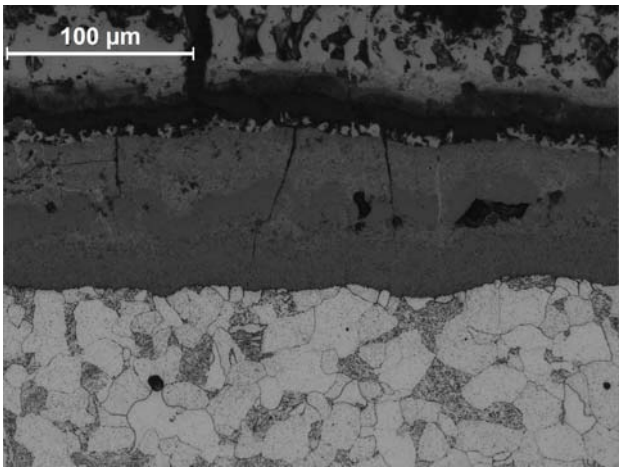

Fireside Corrosion Conditions – Condition 1 Results – T22 Material with Eastern Ash

B15 After 1000 hours

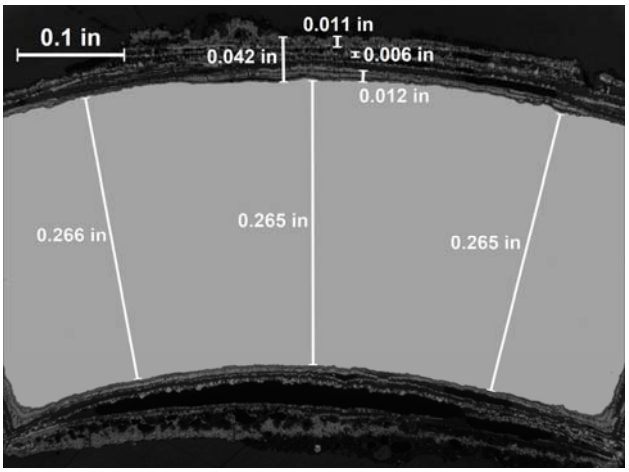

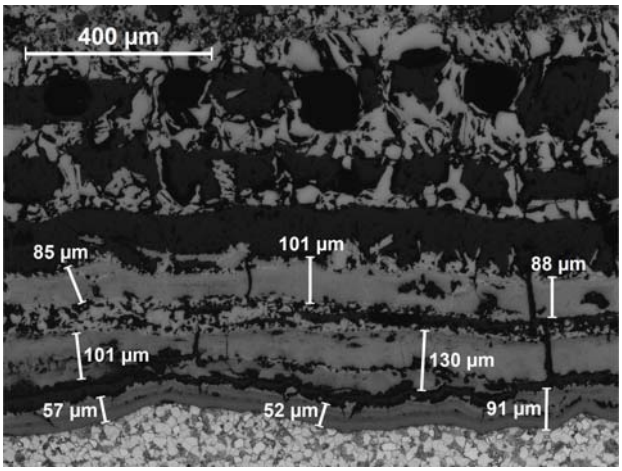

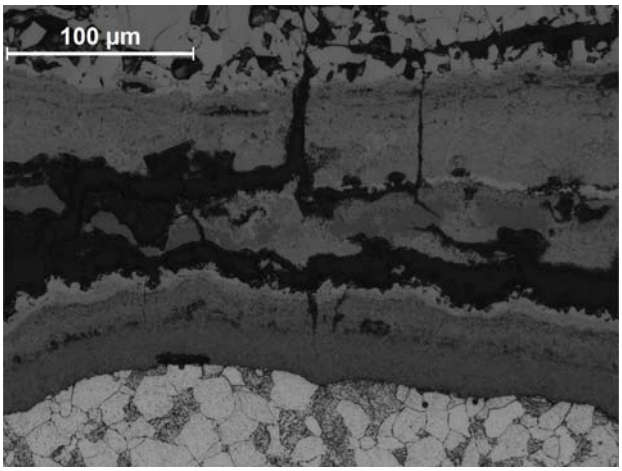

Fireside Corrosion Conditions – Condition 1 Results – T23 Material

C13 After 1000 hours

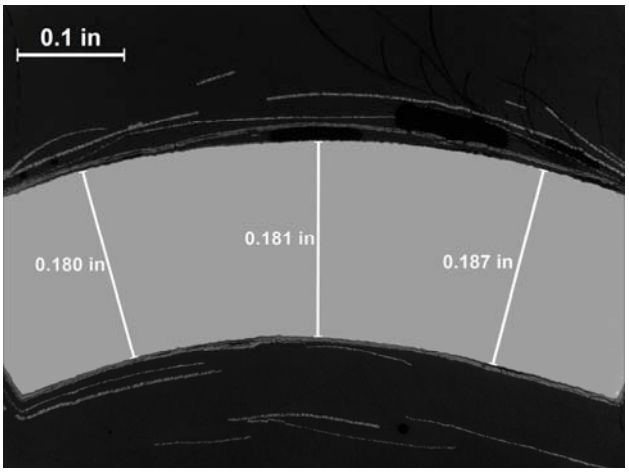

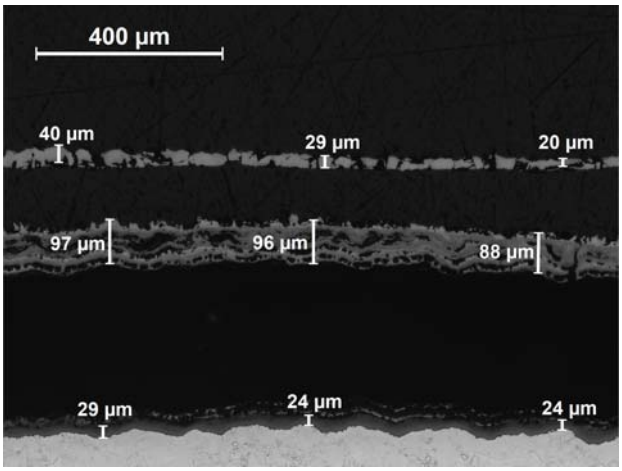

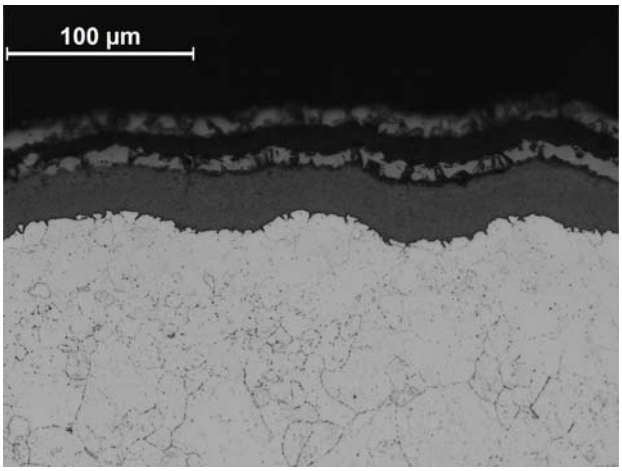

Fireside Corrosion Conditions – Condition 1 Results – T23 Material with Eastern Ash

C15 After 1000 hours

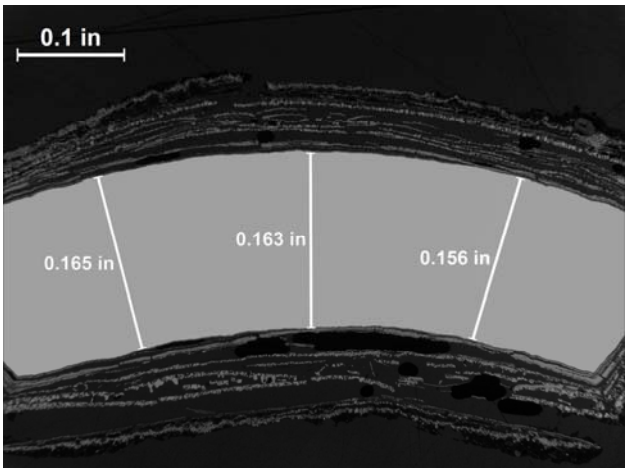

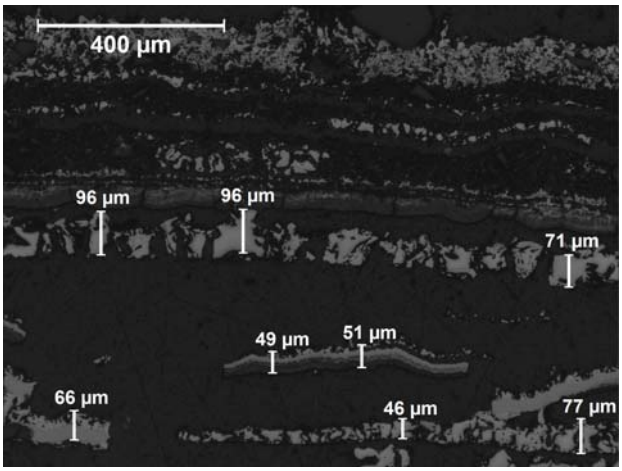

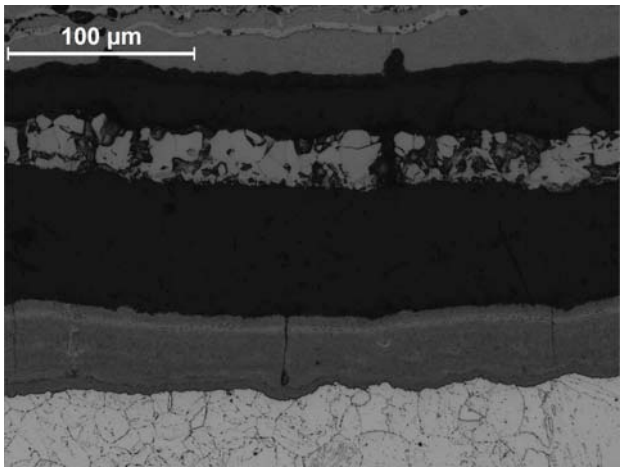

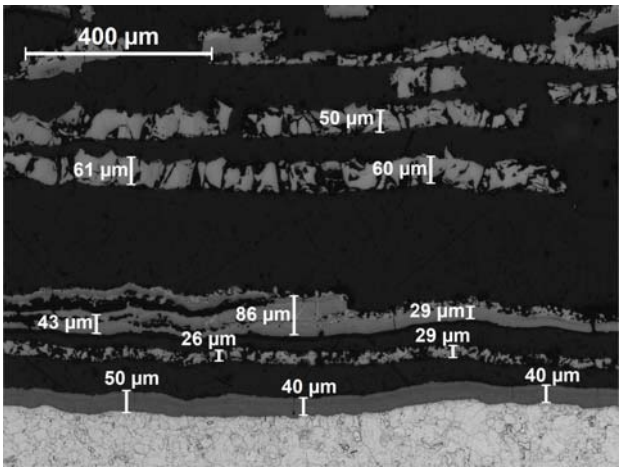

Fireside Corrosion Conditions – Condition 1 Results – T24 Material

D13 After 1000 hours

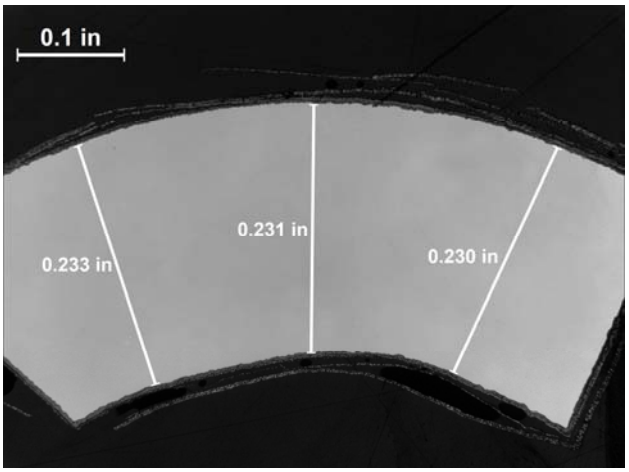

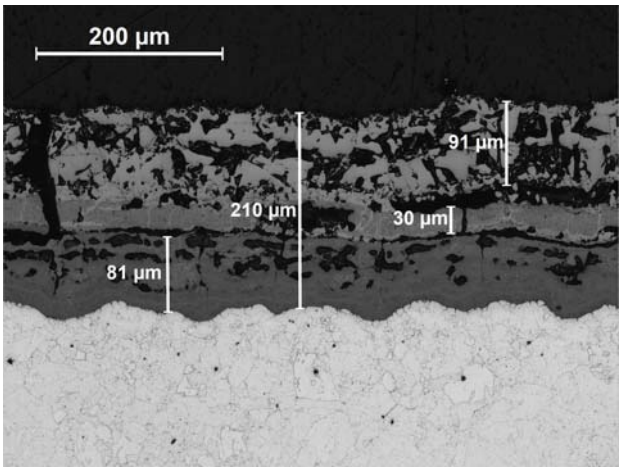

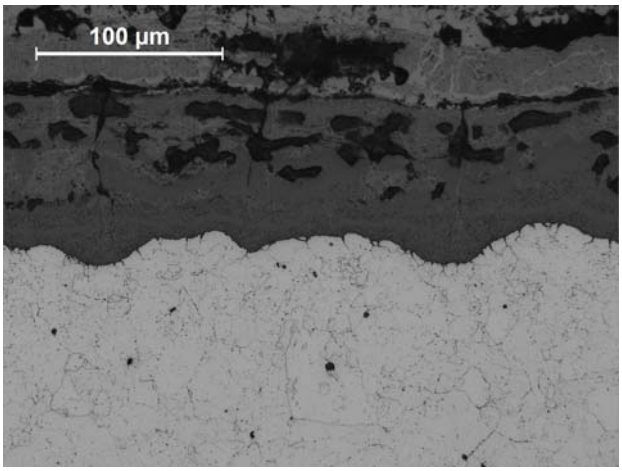

Fireside Corrosion Conditions – Condition 1 Results – T24 Material with Eastern Ash

D15 After 1000 hours

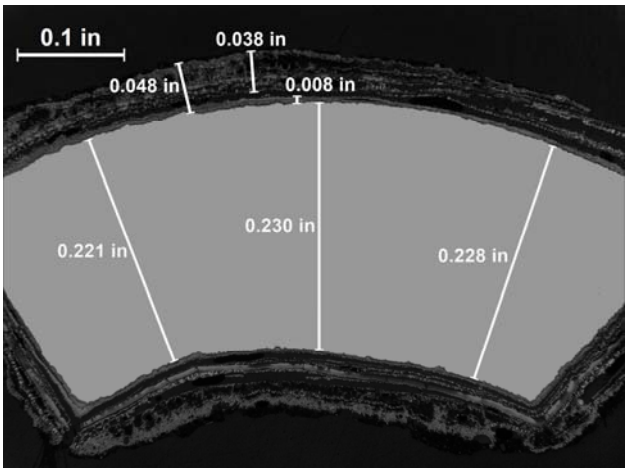

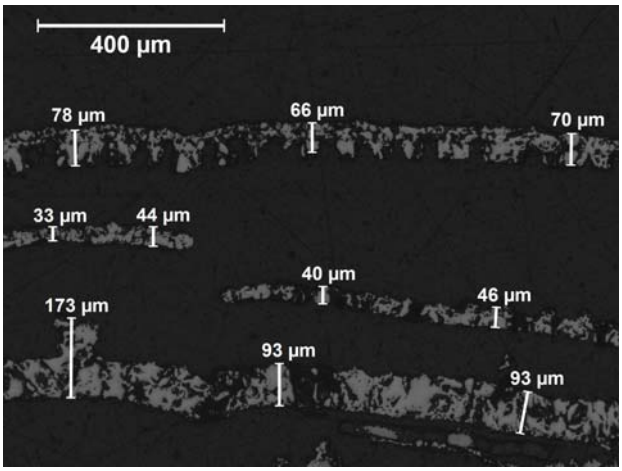

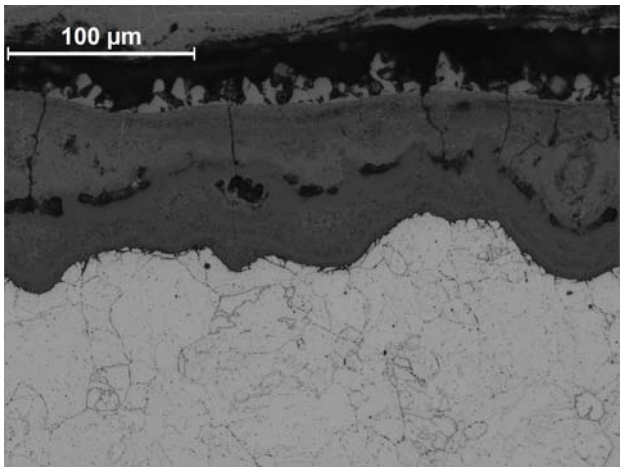

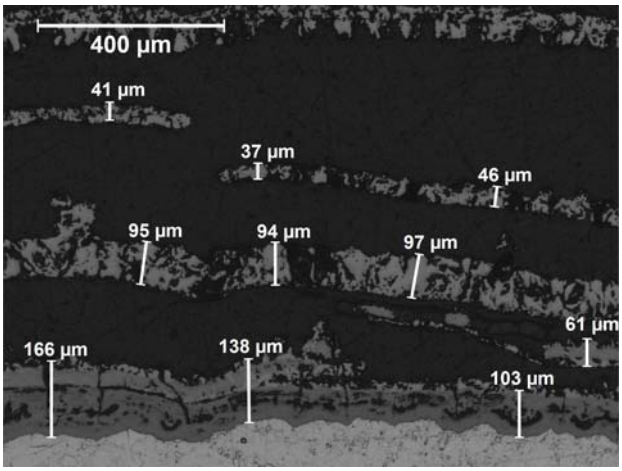

Fireside Corrosion Conditions – Condition 2 Results – T11 Material

A5 After 1000 hours

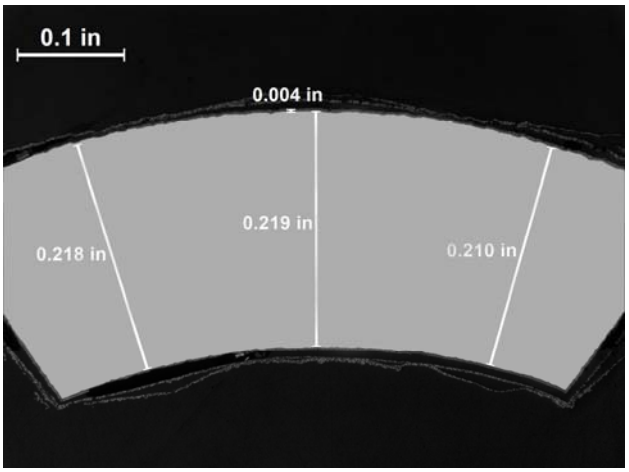

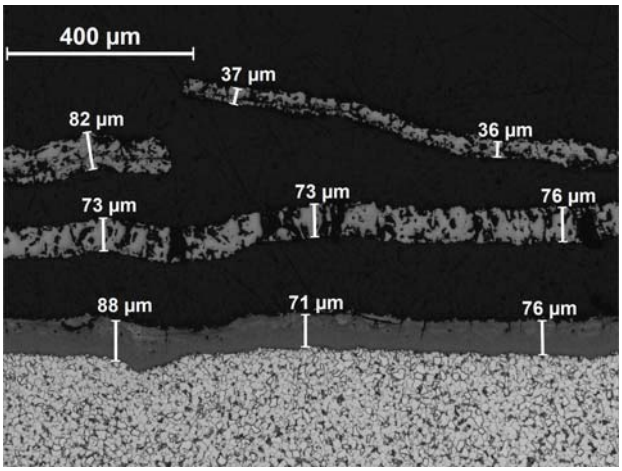

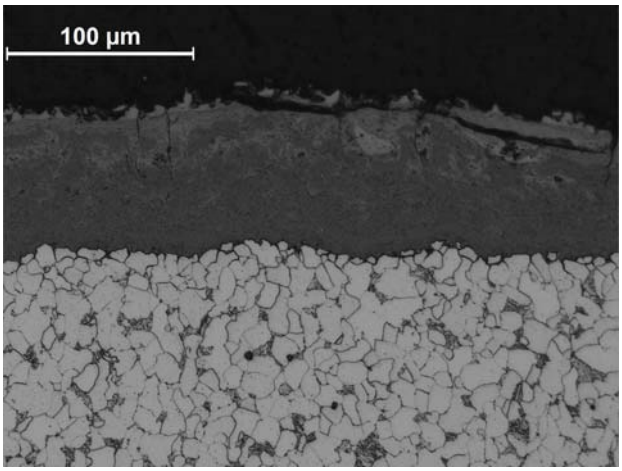

Fireside Corrosion Conditions – Condition 2 Results – T11 Material with Eastern Ash

A7 After 1000 hours

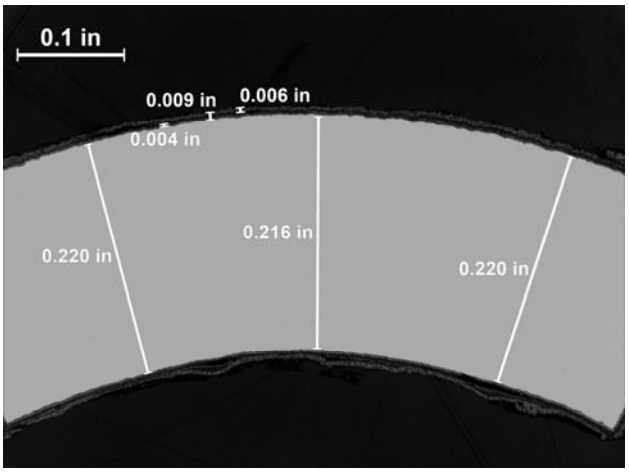

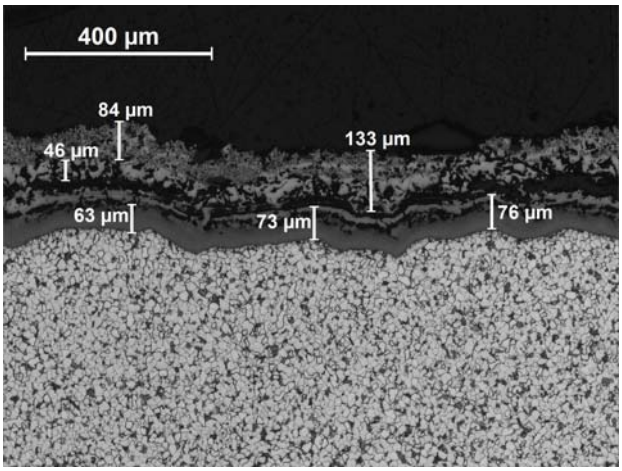

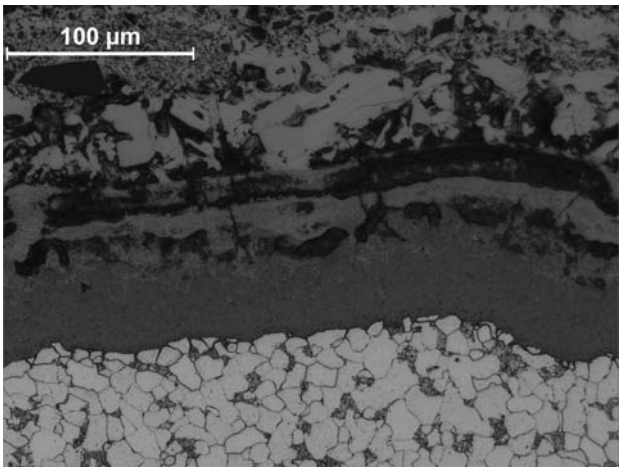

Fireside Corrosion Conditions – Condition 2 Results – T22 Material

B5 After 1000 hours

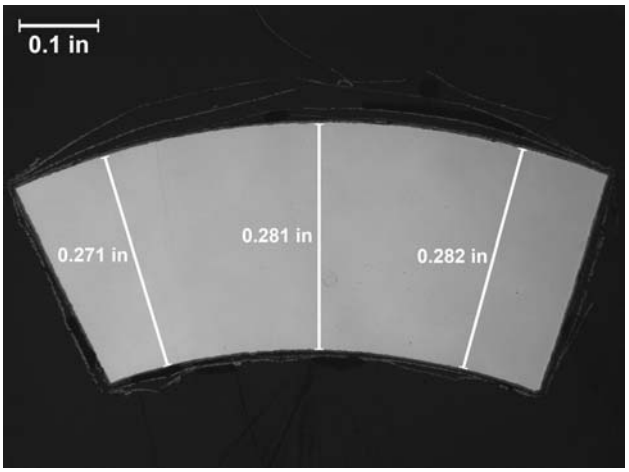

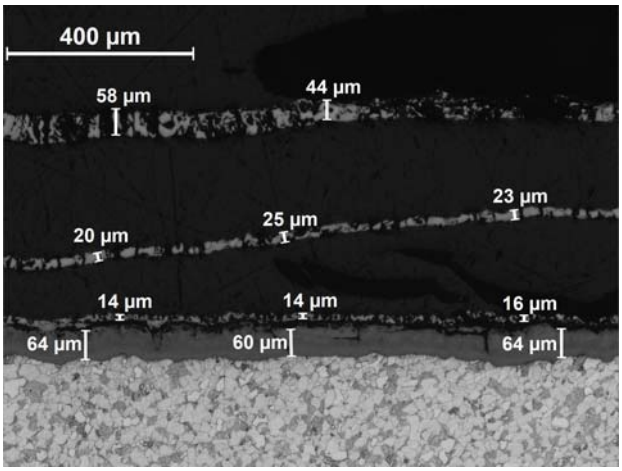

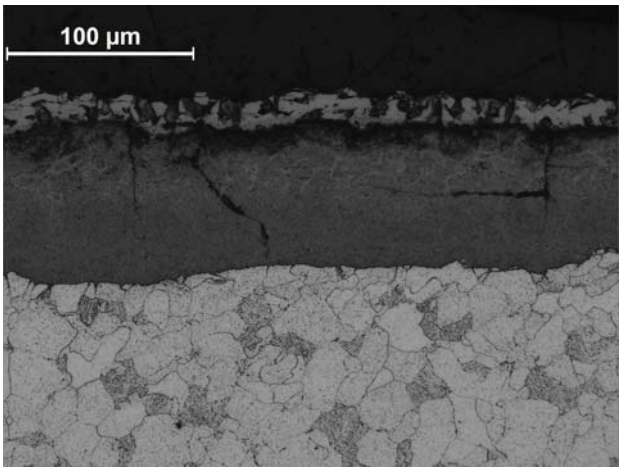

Fireside Corrosion Conditions – Condition 2 Results – T22 Material with Eastern Ash

B7 After 1000 hours

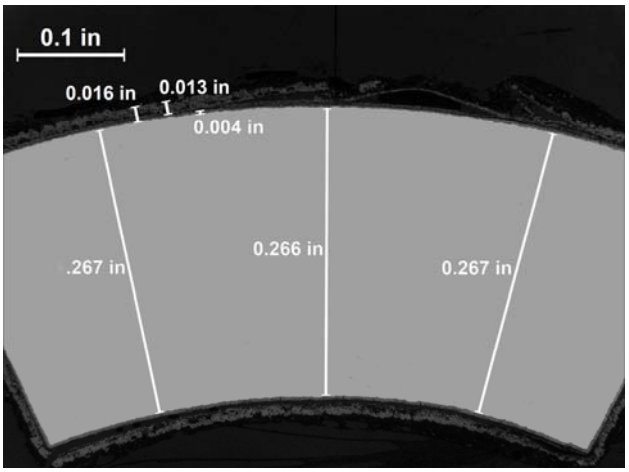

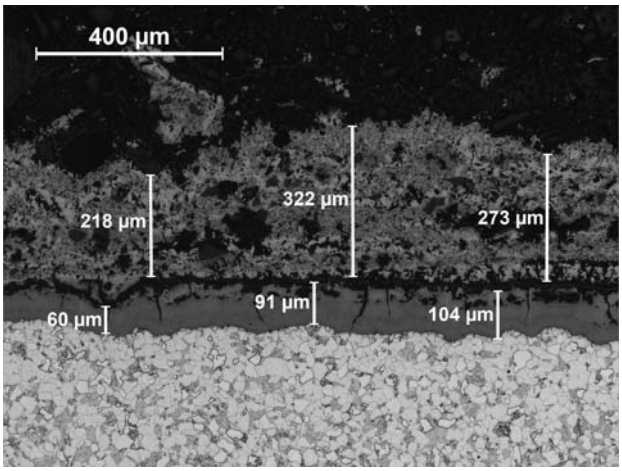

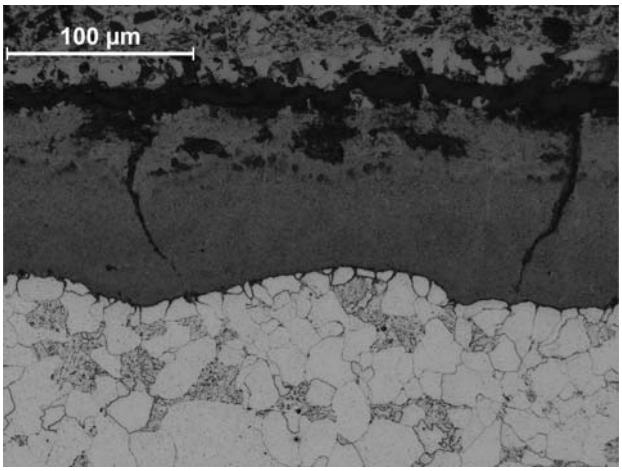

Fireside Corrosion Conditions – Condition 2 Results – T23 Material

C5 After 1000 hours

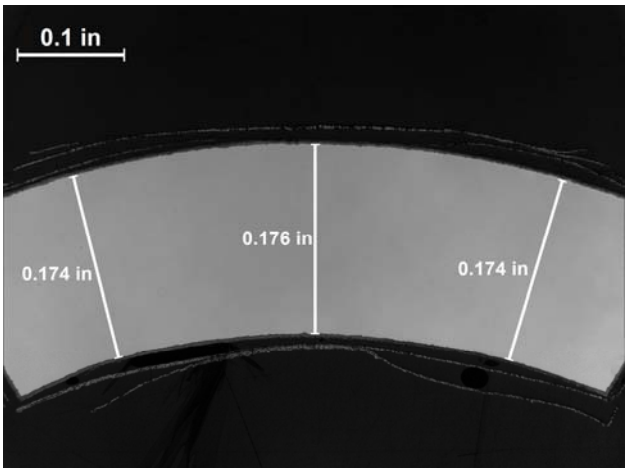

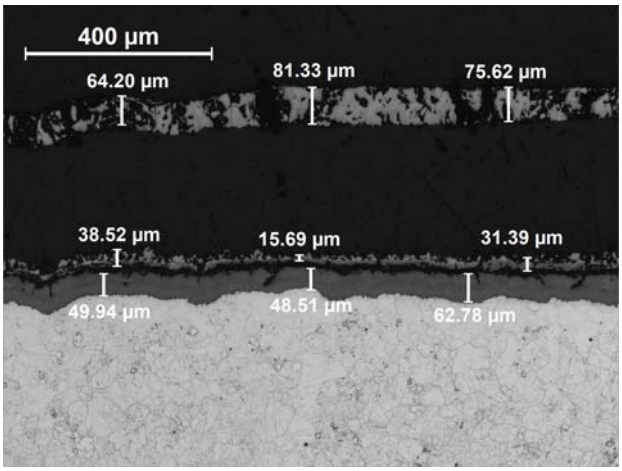

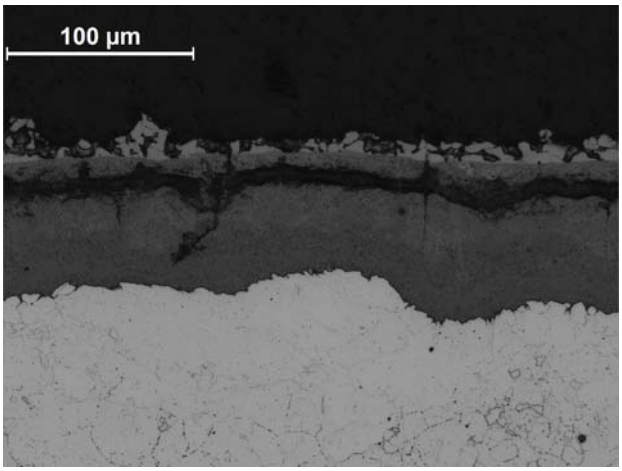

Fireside Corrosion Conditions – Condition 2 Results – T23 Material with Eastern Ash

C7 After 1000 hours

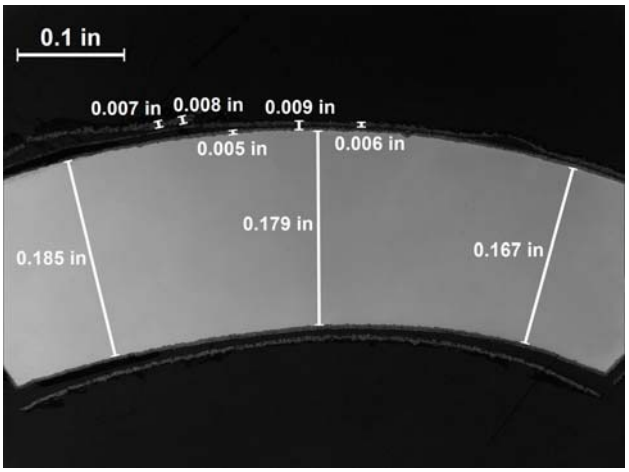

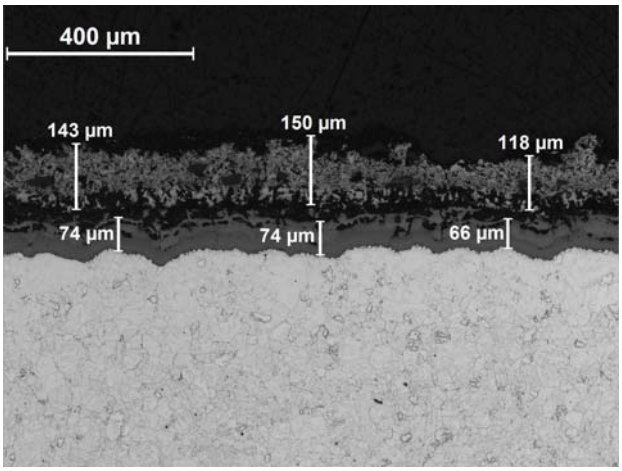

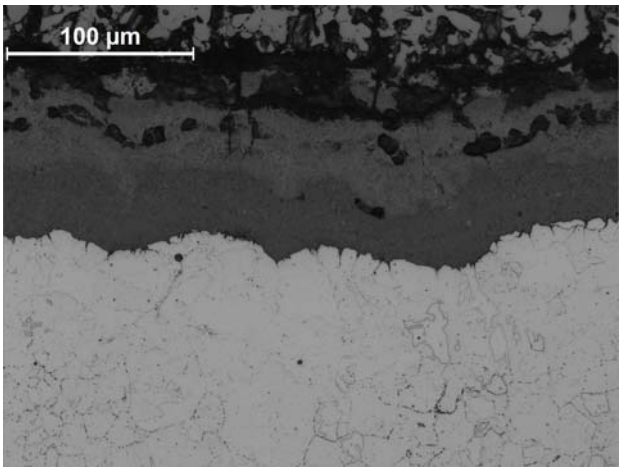

Fireside Corrosion Conditions – Condition 2 Results – T24 Material

D5 After 1000 hours

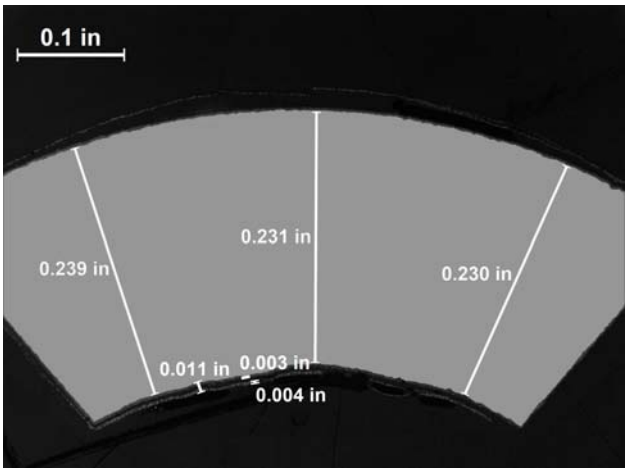

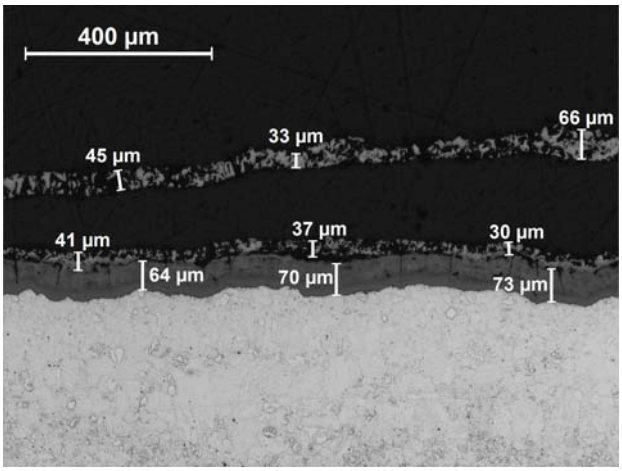

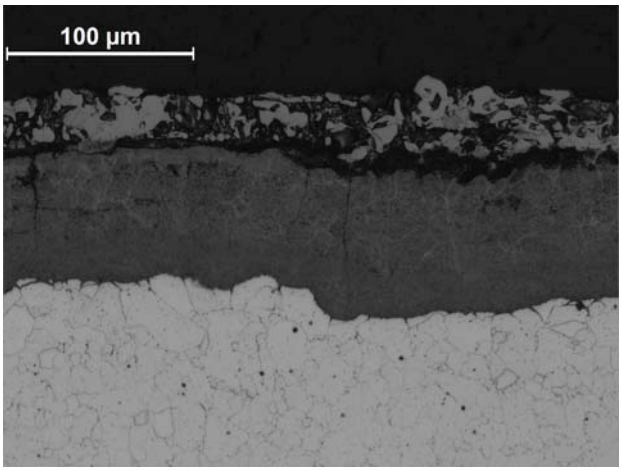

Fireside Corrosion Conditions – Condition 2 Results – T24 Material with Eastern Ash

D7 After 1000 hours

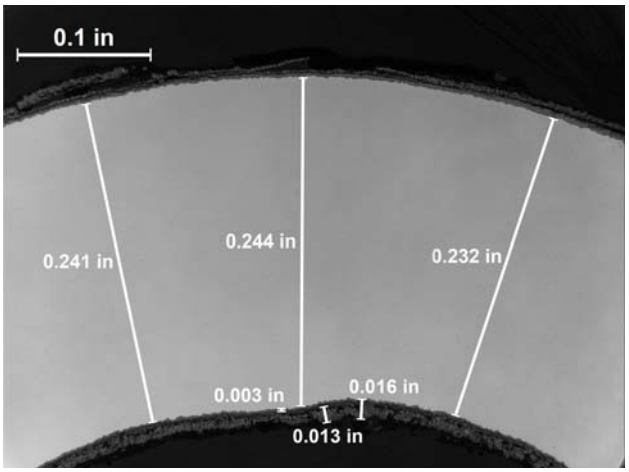

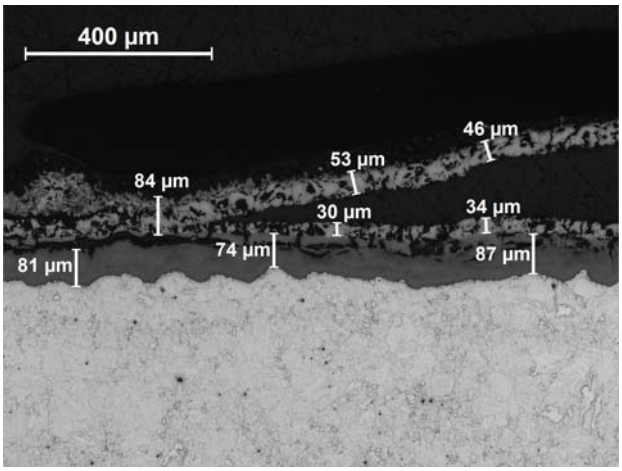

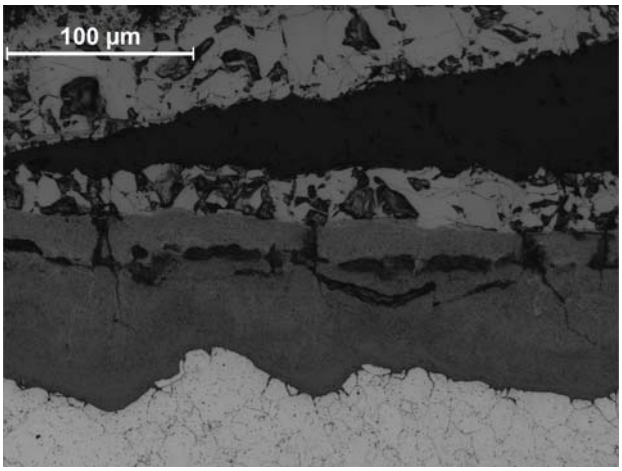

Fireside Corrosion Conditions – Condition 3 Results – T11 Material

A9 After 1000 hours

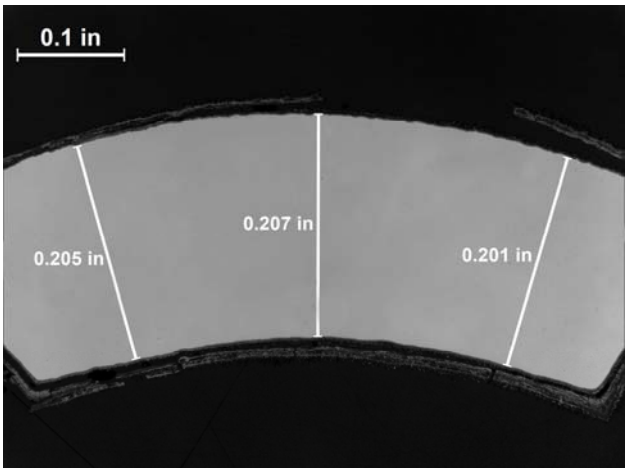

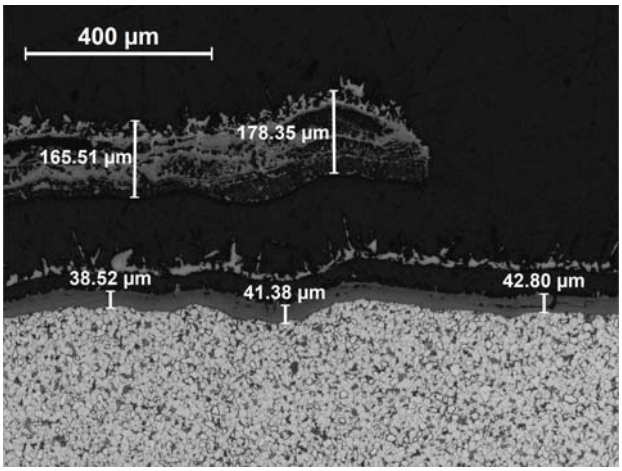

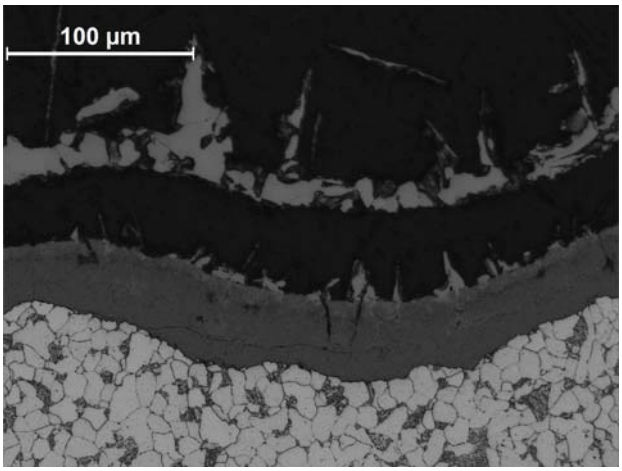

Fireside Corrosion Conditions – Condition 3 Results – T11 Material with Eastern Ash

A11 After 1000 hours

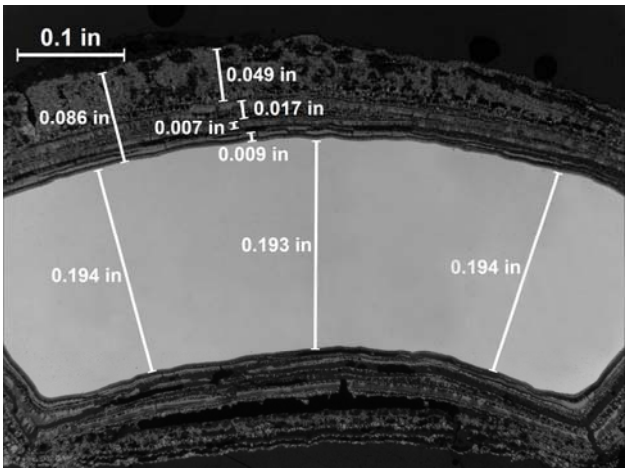

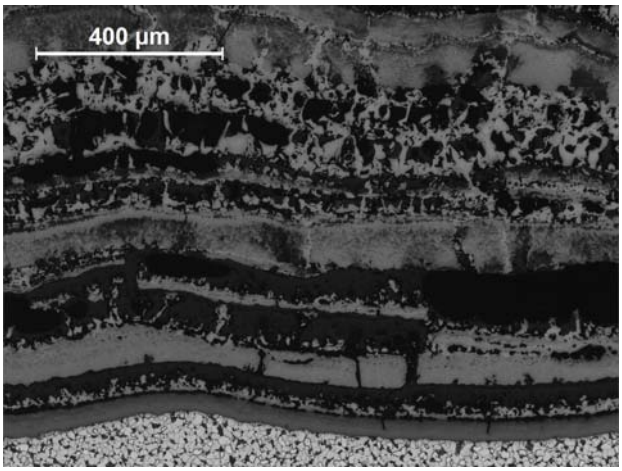

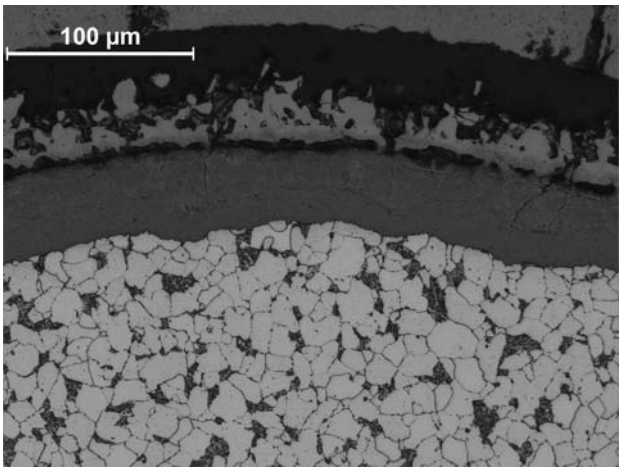

Fireside Corrosion Conditions – Condition 3 Results – T22 Material

B9 After 1000 hours

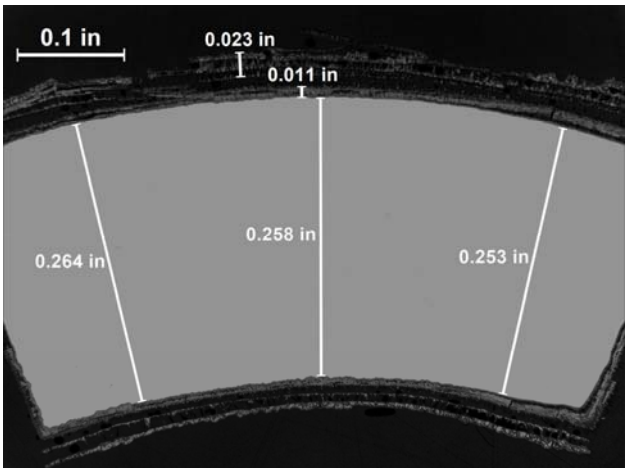

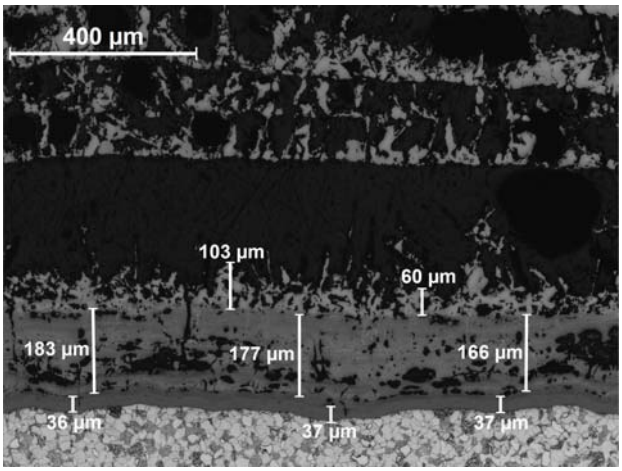

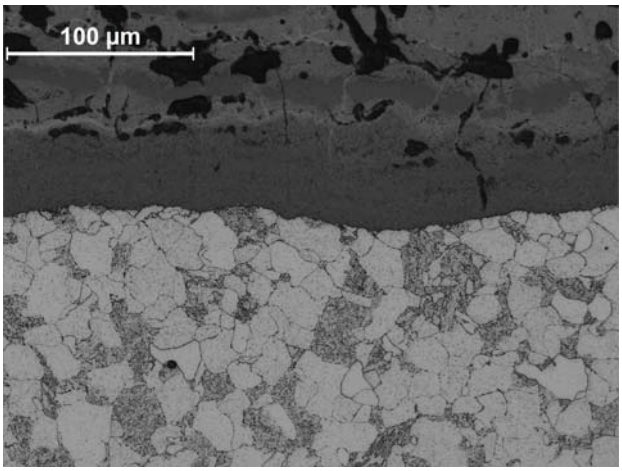

Fireside Corrosion Conditions – Condition 3 Results – T22 Material with Eastern Ash

B11 After 1000 hours

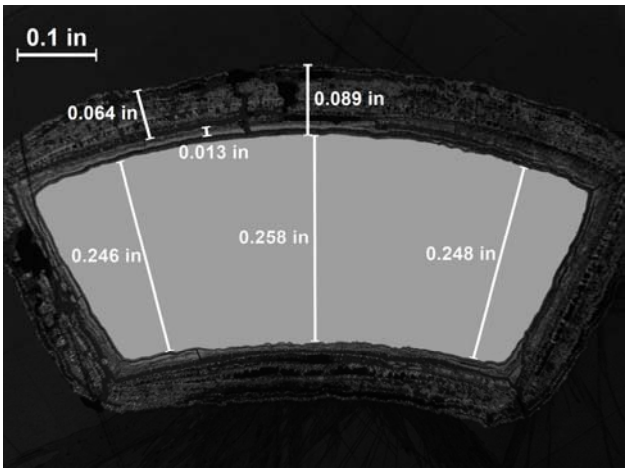

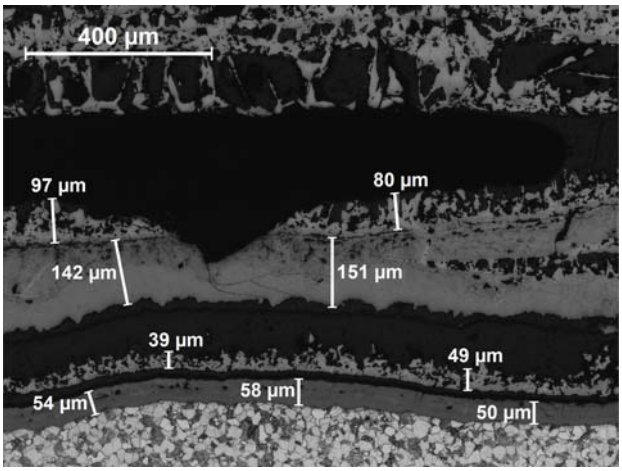

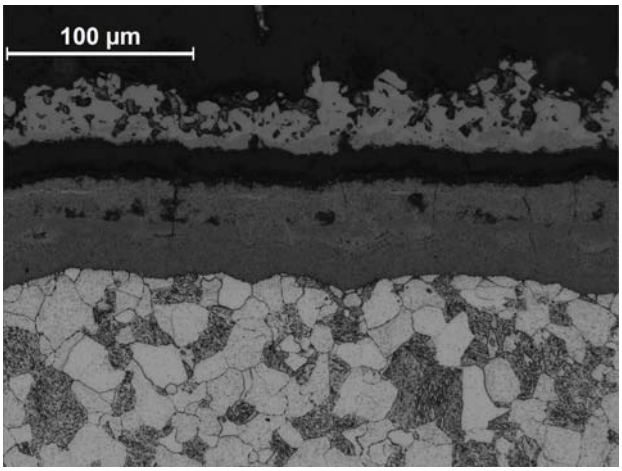

Fireside Corrosion Conditions – Condition 3 Results – T23 Material

C9 After 1000 hours

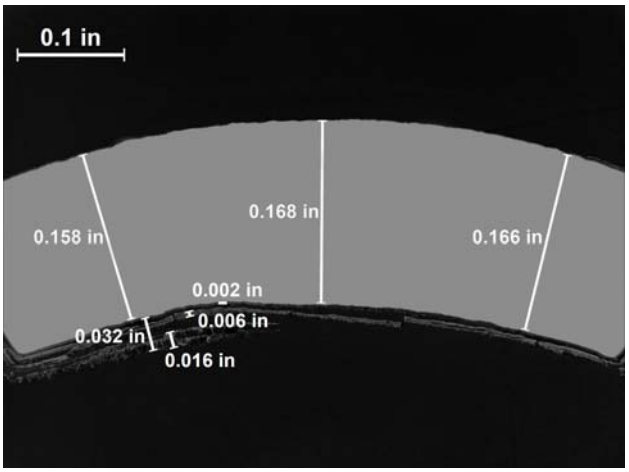

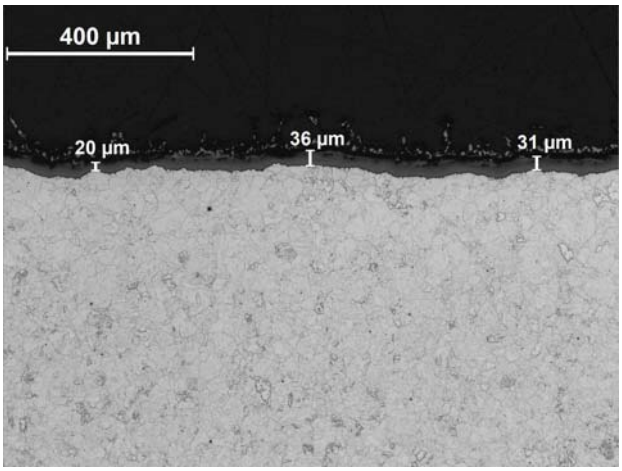

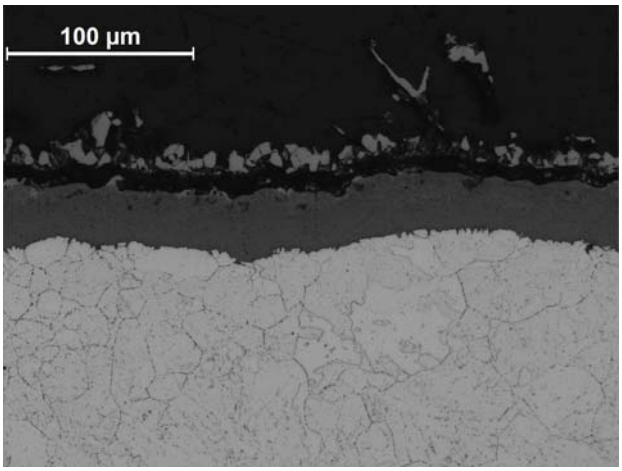

Fireside Corrosion Conditions – Condition 3 Results – T23 Material with Eastern Ash

C11 After 1000 hours

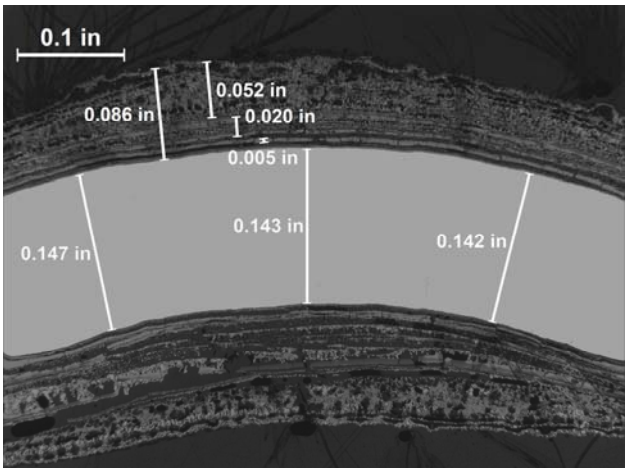

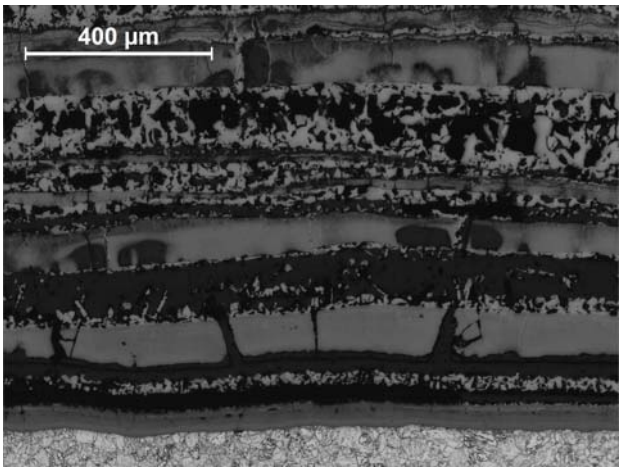

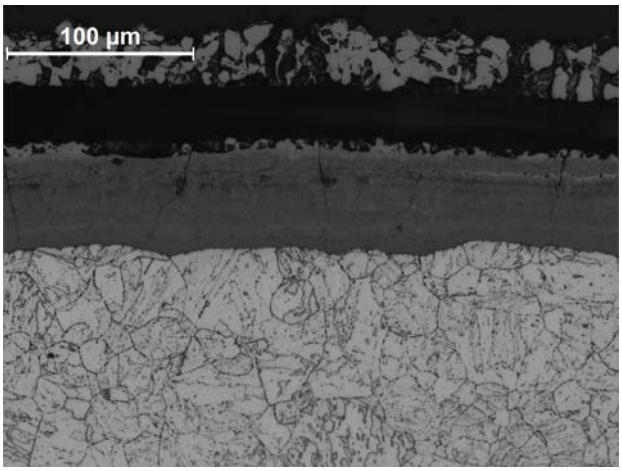

Fireside Corrosion Conditions – Condition 3 Results – T24 Material

D9 After 1000 hours

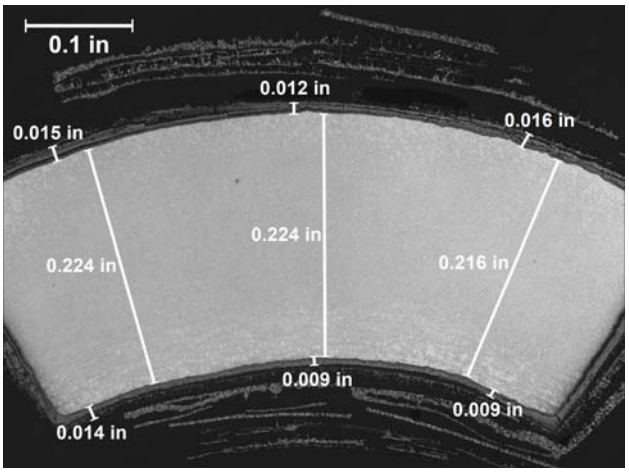

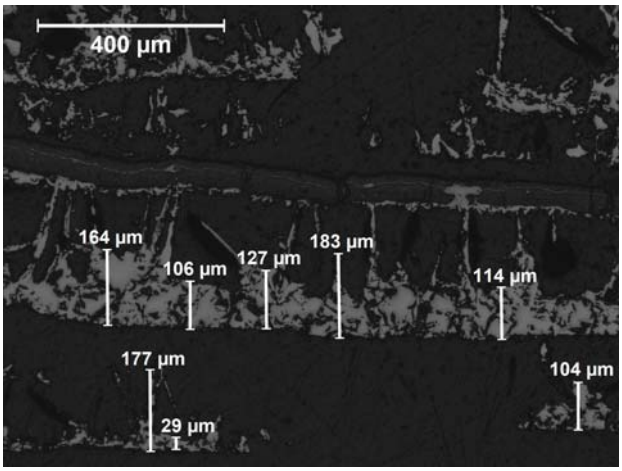

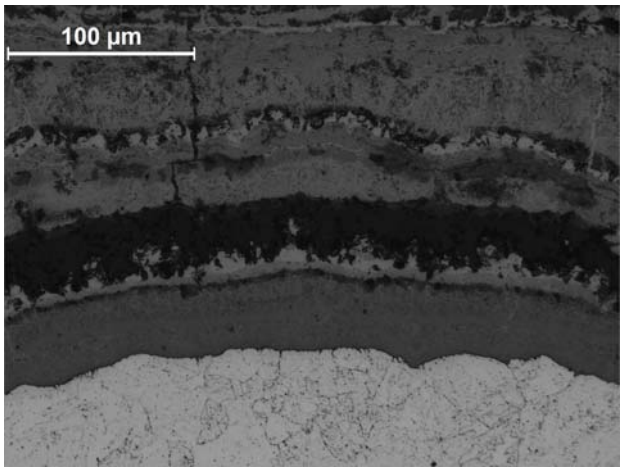

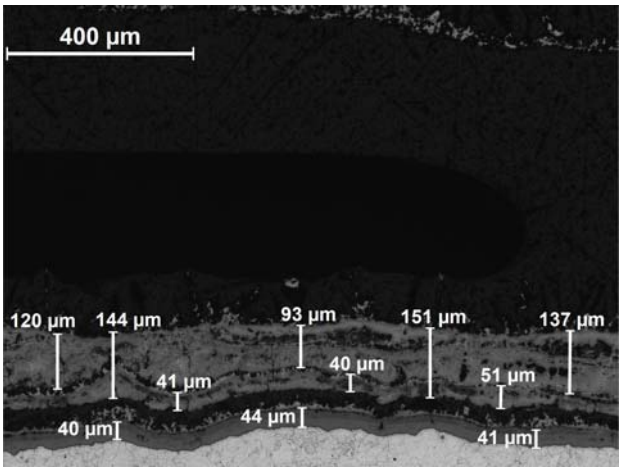

Fireside Corrosion Conditions – Condition 3 Results – T24 Material with Eastern Ash

D11 After 1000 hours

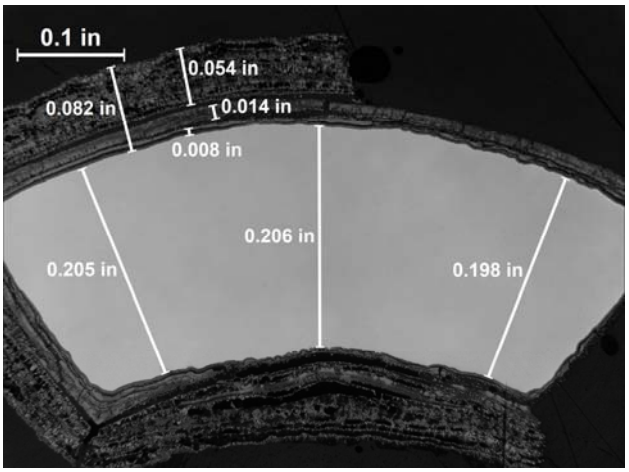

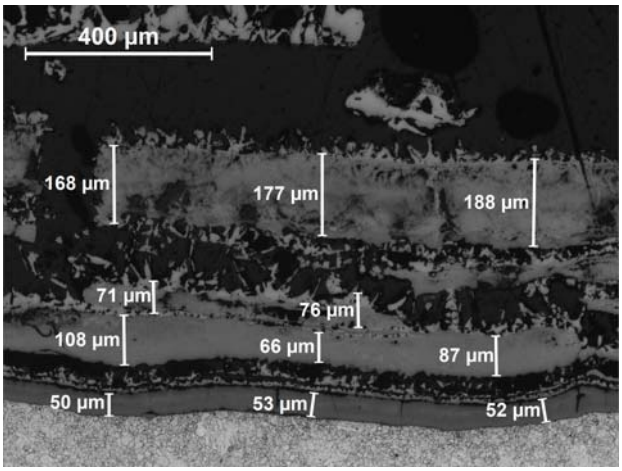

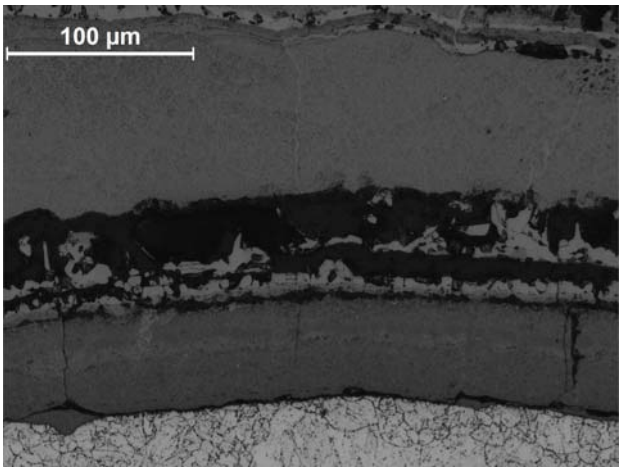

Fireside Corrosion Conditions – Condition 4 Results – T11 Material

A1 After 1000 hours

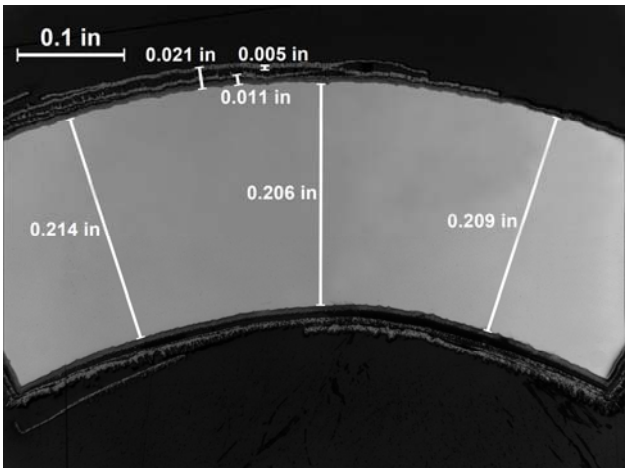

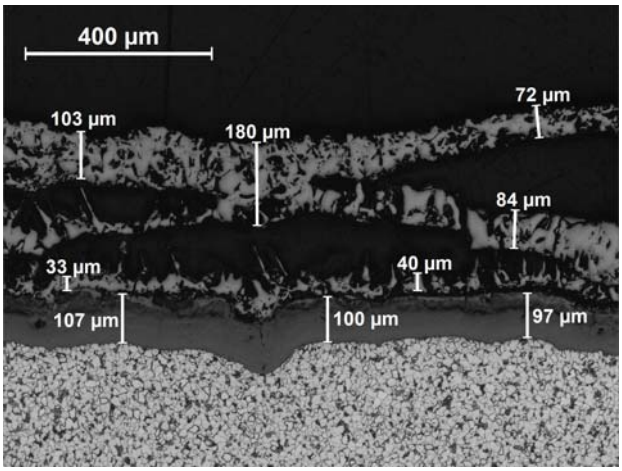

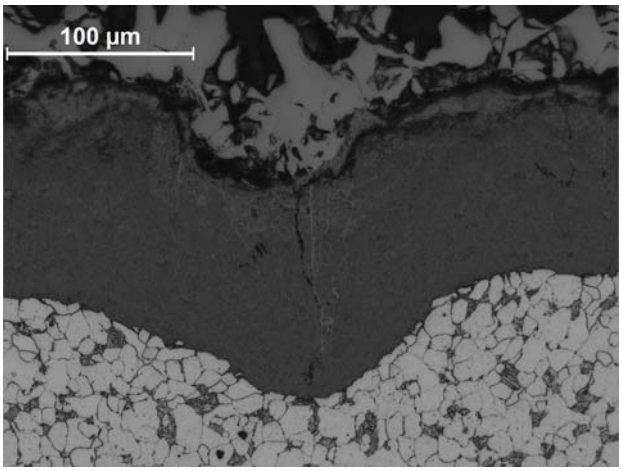

Fireside Corrosion Conditions – Condition 4 Results – T11 Material with Eastern Ash

A3 After 1000 hours

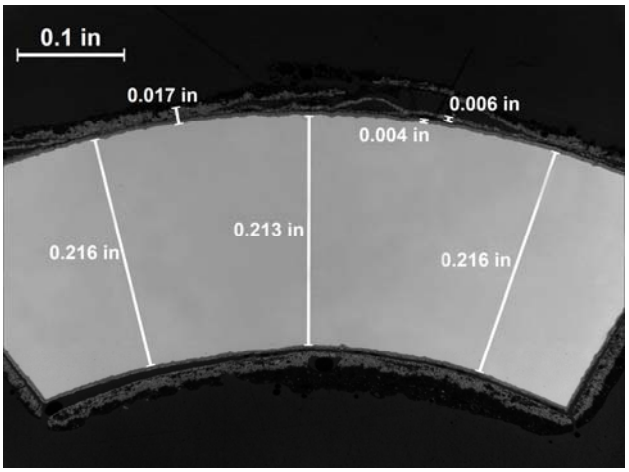

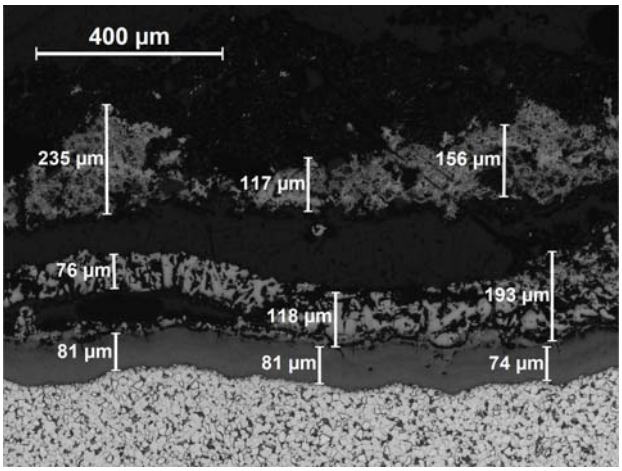

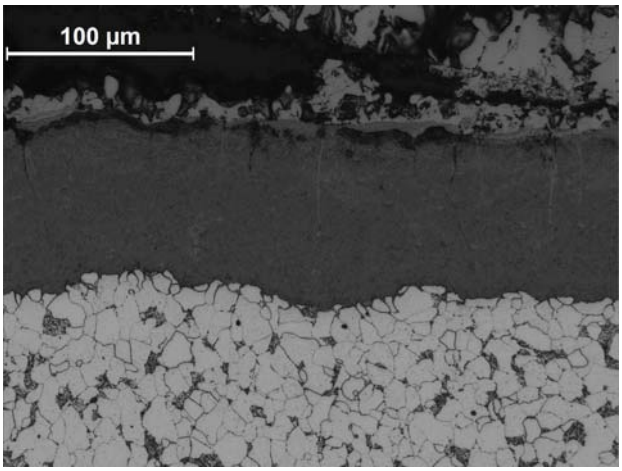

Fireside Corrosion Conditions – Condition 4 Results – T22 Material

B1 After 1000 hours

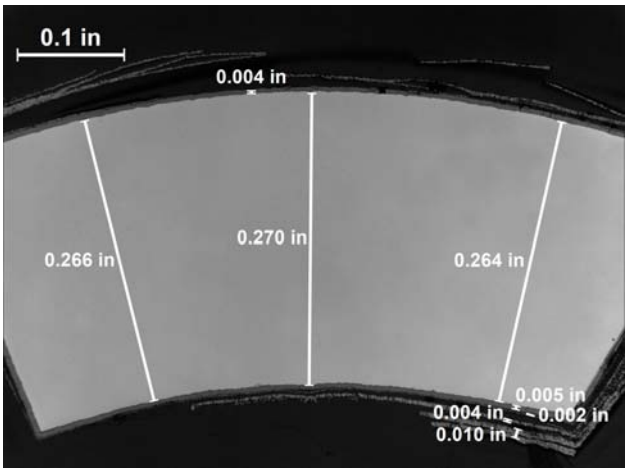

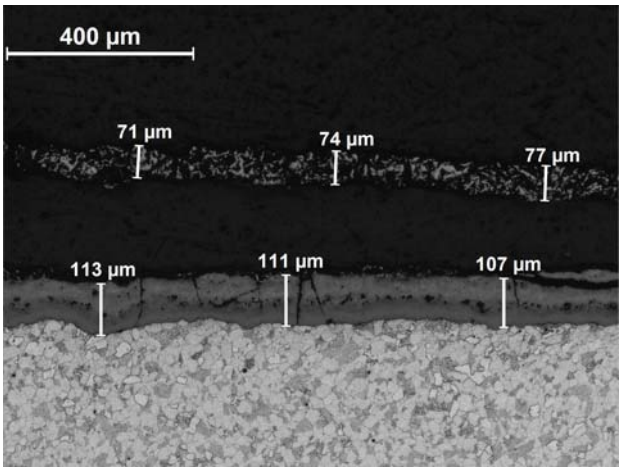

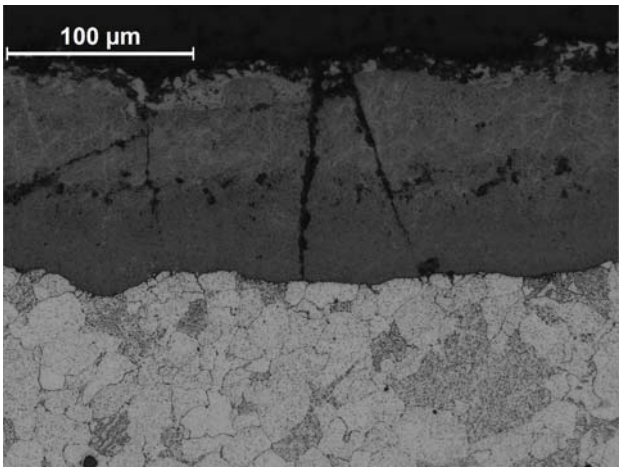

Fireside Corrosion Conditions – Condition 4 Results – T22 Material with Eastern Ash

B3 After 1000 hours

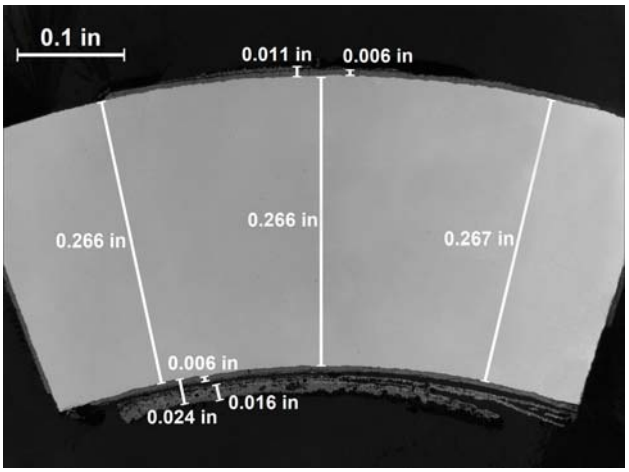

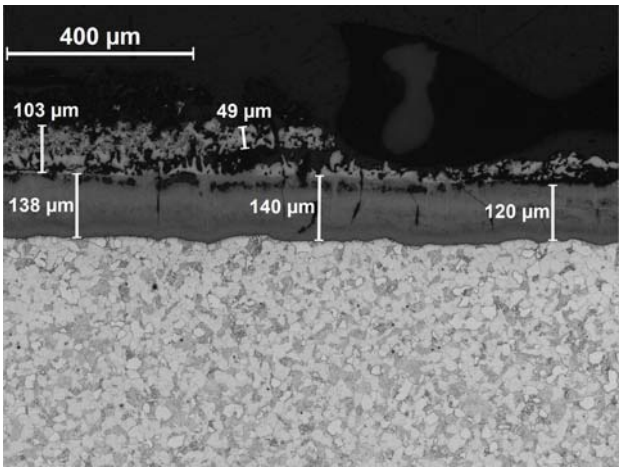

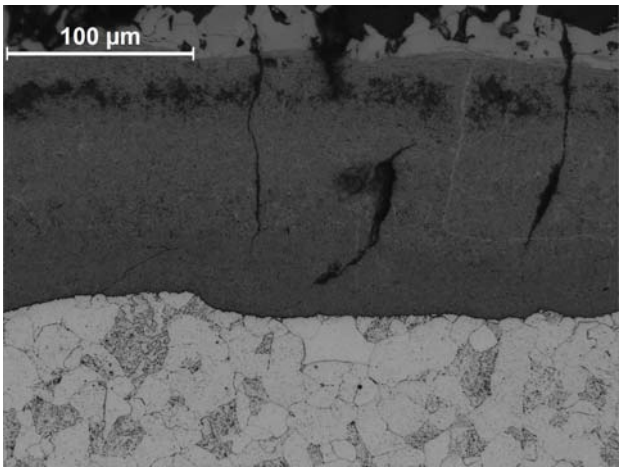

Fireside Corrosion Conditions – Condition 4 Results – T23 Material

C1 After 1000 hours

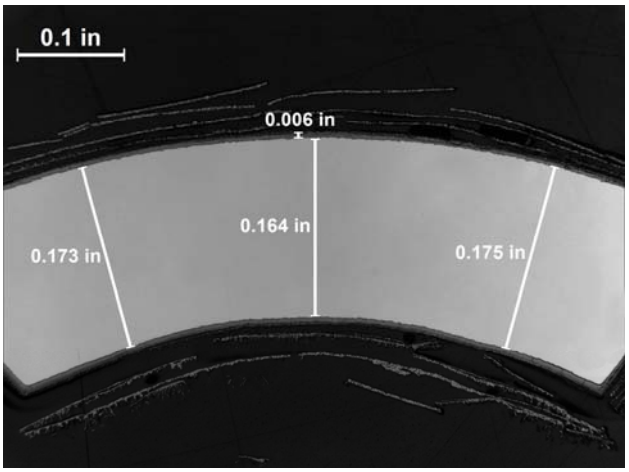

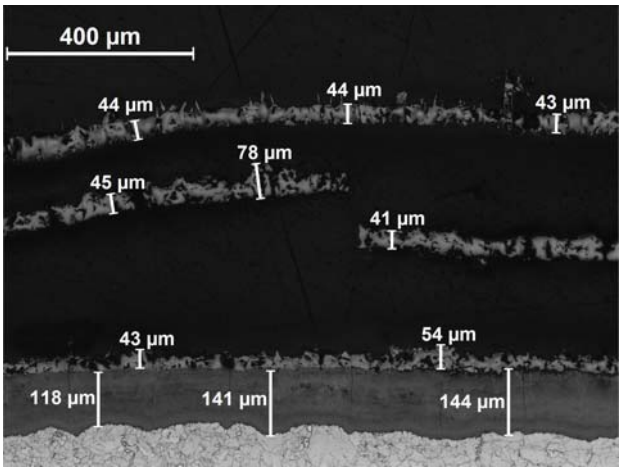

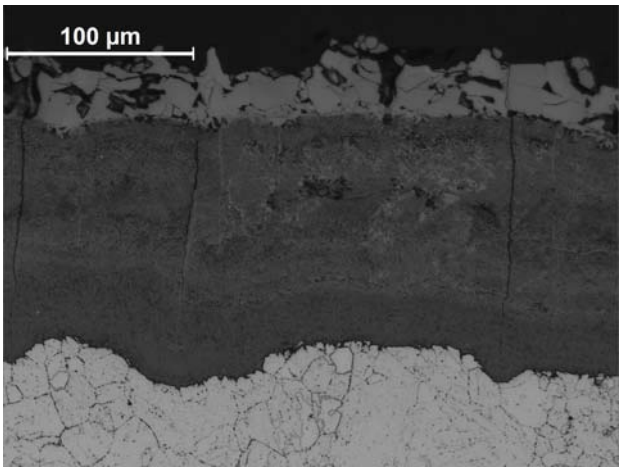

Fireside Corrosion Conditions – Condition 4 Results – T23 Material with Eastern Ash

C3 After 1000 hours

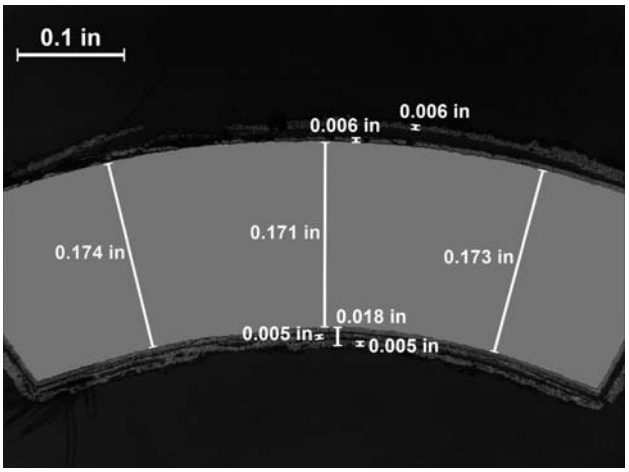

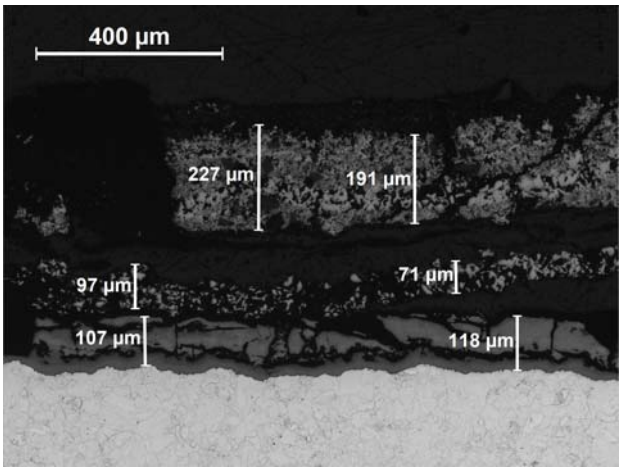

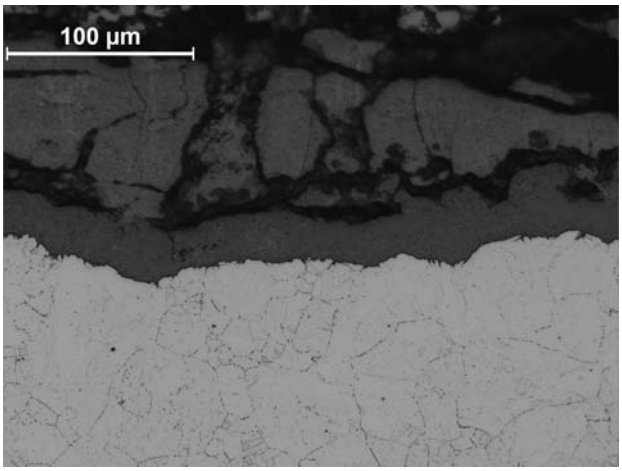

Fireside Corrosion Conditions – Condition 4 Results – T24 Material

D1 After 1000 hours

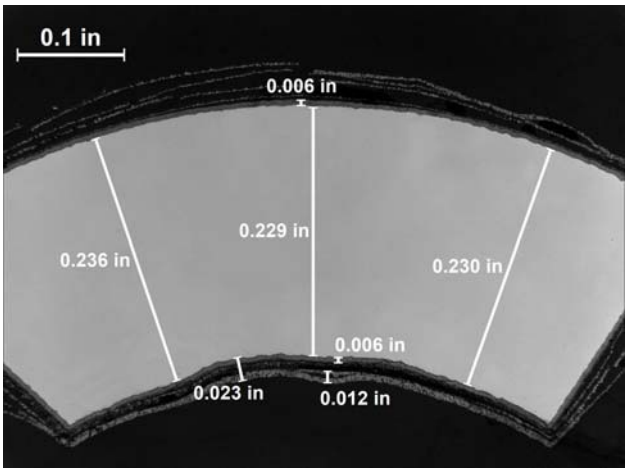

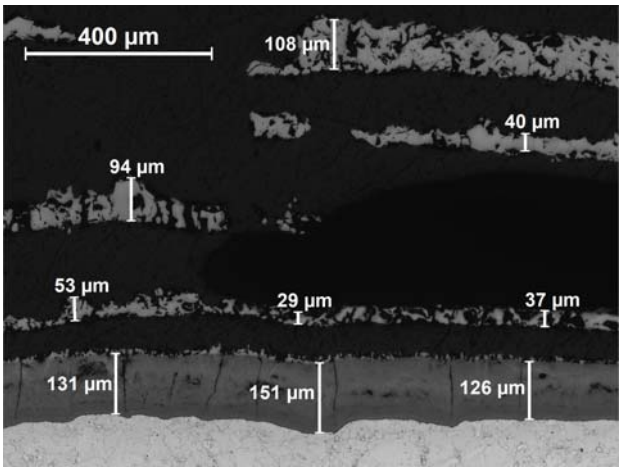

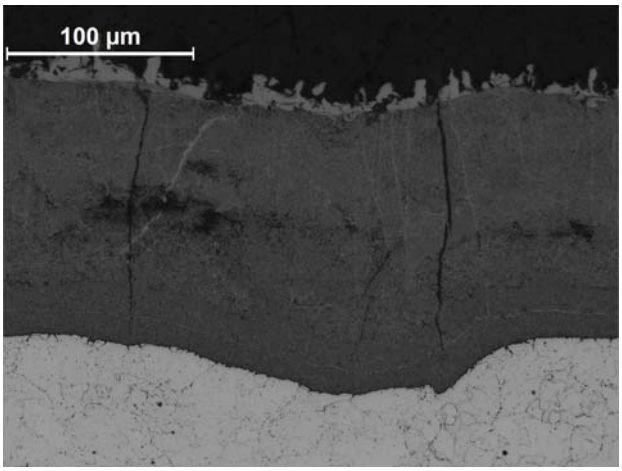

Fireside Corrosion Conditions – Condition 4 Results – T24 Material with Eastern Ash

D3 After 1000 hours

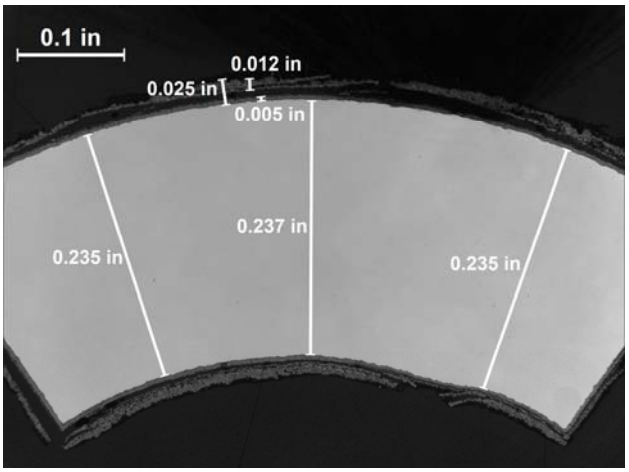

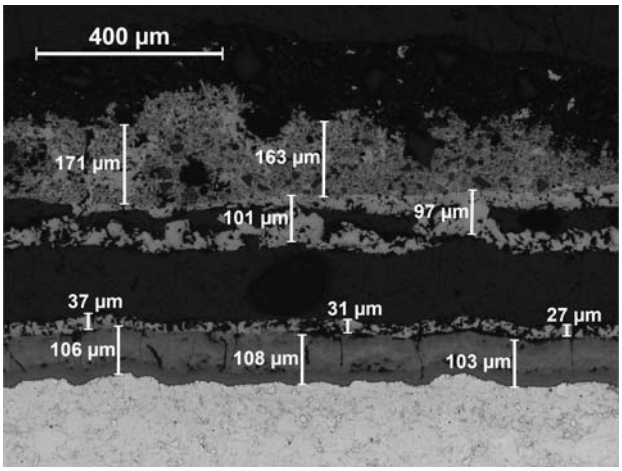

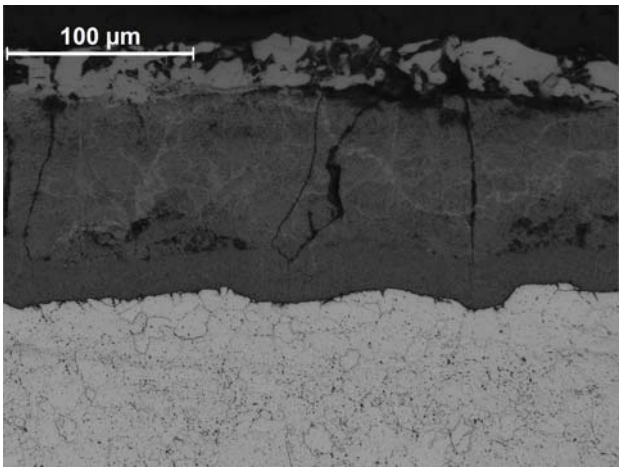

Recovery Act: Oxy-Combustion Technology Development for Industrial-Scale Boiler Applications

DOE/NETL Cooperative Agreement No. DE-NT0005290

Volume III – Modeling and Validation

Reporting Period
October 1, 2008 to April 30, 2014

Report Issued on July 29, 2014

Prepared for
U.S. Department of Energy
National Energy Technology Laboratory
Pittsburgh, Pennsylvania

Prepared by
Alstom Power Inc.
200 Great Pond Drive
Windsor, Connecticut 06095

Principal Investigator
Armand A. Levasseur

Chapter 1 CFD Modeling of the 15 MW_{th} Boiler Simulation Facility

Chapter 2 CFD Modeling of the 30 MW_{th} Schwarze Pumpe Oxy Pilot Plant

Chapter 3 CFD Modeling of the 500 kW IFK Facility

Chapter 4 Uncertainty Quantification of CFD Simulations

Chapter 5 Dynamic Process Modeling

DISCLAIMER STATEMENT

This material is based upon work supported by the Department of Energy under Award Number DE-NT0005290.

This report was prepared as an account of work sponsored by an agency of the United States Government. Neither the United States Government nor any agency thereof, nor any of their employees, makes any warranty, express or implied, or assumes any legal liability or responsibility for the accuracy, completeness, or usefulness of any information, apparatus, product, or process disclosed, or represents that its use would not infringe privately owned rights. Reference herein to any specific commercial product, process, or service by trade name, trademark, manufacturer, or otherwise does not necessarily constitute or imply its endorsement, recommendation, or favoring by the United States Government or any agency thereof. The views and opinions of authors expressed herein do not necessarily state or reflect those of the United States Government or any agency thereof.

This report was prepared based on work conducted with support, in part, by grants made possible by the Illinois Department of Commerce and Economic Opportunity through the Office of Coal Development and the Illinois Clean Coal Institute as well as the Industrial Commission of North Dakota,. Neither the Illinois Department of Commerce and Economic Opportunity, Office of Coal Development, the Illinois Clean Coal Institute, nor the Industrial Commission of North Dakota, nor any person acting on behalf of either:

(A) Makes any warranty of representation, express or implied, with respect to the accuracy, completeness, or usefulness of the information contained in this report, or that the use of any information, apparatus, method, or process disclosed in this report may not infringe privately-owned rights; or

(B) Assumes any liabilities with respect to the use of, or for damages resulting from the use of, any information, apparatus, method or process disclosed in this report.

Information disclosed herein is furnished to the recipient solely for the use thereof as has been agreed upon with ALSTOM and all rights to such information are reserved by ALSTOM. The recipient of the information disclosed herein agrees, as a condition of its receipt of such information, that ALSTOM shall have no liability for any direct or indirect damages including special, punitive, incidental, or consequential damages caused by, or arising from, the recipient's use or non-use of the information.

Recovery Act: Oxy-Combustion Technology Development for Industrial-Scale Boiler Applications

DOE/NETL Cooperative Agreement No. DE-NT0005290

Volume III – Modeling and Validation

Chapter 1 – CFD Modeling of the 15 MW_{th} Boiler Simulation Facility

Authors
Paul J. Chapman
David G. Sloan
Yen-Ming Chen

Table of Contents

1. Executive Summary 6
2. Objectives 17
3. Conclusions and Recommendations 18
4. Description of BSF 22
5. Technical Approach 25
   5.1 CFD Mesh 25
   5.2 Homogeneous and Heterogeneous Combustion Reaction Scheme 26
   5.3 Particle Combustion Model Description 29
   5.4 Boundary Conditions 32
   5.5 Convergence and Solution Considerations 36
6. Model Results for the Five Test Coals 38
   6.1 Black Thunder PRB Sub-Bituminous Coal 41
   6.2 West Virginia Fola Bituminous Coal 46
   6.3 Illinois No. 6 Bituminous Coal 50
   6.4 North Dakota Lignite Coal 53
   6.5 Schwarze Pumpe Lignite Coal 56
   6.6 Composite Comparisons of the Coal Tests 60
   6.7 Effect of Char Reaction Rates 61
   6.8 Results Summary 64
7. References 211

List of Figures

Figure 1-1. BSF CFD Mesh 9
Figure 1-2. BSF Wall Insulations and Test Planes 10
Figure 1-3. [AT-11:OT-22] Comparison of Temperature on Test Planes 12
Figure 1-4. [AT-39:OT-50] Comparison of O_2 Concentrations on Test Planes 14
Figure 1-5. [AT-83:OT-98] Comparison of Wall Incident Radiation at Plane 141 15
Figure 1-6. [AT-83:OT-98] Comparison of Wall Incident Radiation at Plane 180 16
Figure 4-1. Plan (or Top) View of Tangential Firing Pattern (Oil-Fired) in BSF 22
Figure 4-2. 15 MW Boiler Simulation Facility Model 23
Figure 4-3. Oxy Boiler Simulation Facility 24
Figure 5-1. BSF CFD Mesh 26
Figure 5-2. Coal Particle Size Distribution 31
Figure 5-3. Coal Combustion Laws or Stages 32
Figure 5-4. BSF Wall Insulations and Test Planes 35
Figure 5-5. Convergence History 37
Figure 6-1. [AT-11:OT-22] Contours of Temperature on X-Midplane 68
Figure 6-2. [AT-11:OT-22] Contours of Temperature on Test Planes 69
Figure 6-3. [AT-11:OT-22] Comparison of Temperature on Test Planes 70
Figure 6-4. [AT-11:OT-22] Contours of O_2 Concentrations on Test Planes 71
Figure 6-5. [AT-11:OT-22] Comparison of O_2 Concentrations on Test Planes 72
Figure 6-6. [AT-11:OT-22] Contours of CO_2 Concentrations on Test Planes 73
Figure 6-7. [AT-11:OT-22] Comparison of CO_2 Concentrations on Test Planes 74
Figure 6-8. [AT-11:OT-22] Contours of CO Concentrations on Test Planes 75
Figure 6-9. [AT-11:OT-22] Comparison of CO Concentrations on Test Planes 76
Figure 6-10. [AT-11:OT-22] Contours of H_2O Concentrations on Test Planes 77
Figure 6-11. [AT-11:OT-22] Comparison of H_2O Concentrations on Test Planes 78
Figure 6-12. [AT-11:OT-22] Contours of SO_2 Concentrations on Test Planes 79
Figure 6-13. [AT-11:OT-22] Comparison of SO_2 Concentrations on Test Planes 80
Figure 6-14. [AT-11:OT-22] Contours of Incident Radiation 81

Figure 6-15. [AT-11:OT-22] Comparison of Wall Incident Radiation at Plane 141 82
Figure 6-16. [AT-11:OT-22] Comparison of Wall Incident Radiation at Plane 180 83
Figure 6-17. [AT-11:OT-22] Comparison of Wall Incident Radiation at Plane 273 84
Figure 6-18. [AT-11:OT-22] Strip-Averaged Wall Incident Radiation 85
Figure 6-19. [AT-11:OT-22] Planar Averaged Temperature 86
Figure 6-20. [AT-11:OT-22] Planar Averaged O_2 87
Figure 6-21. [AT-11:OT-22] Planar Averaged CO_2 88
Figure 6-22. [AT-11:OT-22] Planar Averaged CO 89
Figure 6-23. [AT-11:OT-22] Planar Averaged SO_2 90
Figure 6-24. [AT-11:OT-22] Planar Averaged H_2O 91
Figure 6-25. [AT-39:OT-50] Contours of Temperature on X-Midplane 92
Figure 6-26. [AT-39:OT-50] Contours of Temperature on Test Planes 93
Figure 6-27. [AT-39:OT-50] Comparison of Temperature on Test Planes 94
Figure 6-28. [AT-39:OT-50] Contours of O_2 Concentrations on Test Planes 95
Figure 6-29. [AT-39:OT-50] Comparison of O_2 Concentrations on Test Planes 96
Figure 6-30. [AT-39:OT-50] Contours of CO_2 Concentrations on Test Planes 97
Figure 6-31. [AT-39:OT-50] Comparison of CO_2 Concentrations on Test Planes 98
Figure 6-32. [AT-39:OT-50] Contours of CO Concentrations on Test Planes 99
Figure 6-33. [AT-39:OT-50] Comparison of CO Concentrations on Test Planes 100
Figure 6-34. [AT-39:OT-50] Contours of H_2O Concentrations on Test Planes 101
Figure 6-35. [AT-39:OT-50] Comparison of H_2O Concentrations on Test Planes 102
Figure 6-36. [AT-39:OT-50] Contours of SO_2 Concentrations on Test Planes 103
Figure 6-37. [AT-39:OT-50] Comparison of SO_2 Concentrations on Test Planes 104
Figure 6-38. [AT-39:OT-50] Contours of Incident Radiation 105
Figure 6-39. [AT-39:OT-50] Comparison of Wall Incident Radiation at Plane 141 106
Figure 6-40. [AT-39:OT-50] Comparison of Wall Incident Radiation at Plane 180 107
Figure 6-41. [AT-39:OT-50] Comparison of Wall Incident Radiation at Plane 273 108
Figure 6-42. [AT-39:OT-50] Strip-Averaged Wall Incident Radiation 109
Figure 6-43. [AT-39:OT-50] Planar Averaged Temperature 110
Figure 6-44. [AT-39:OT-50] Planar Averaged O_2 111
Figure 6-45. [AT-39:OT-50] Planar Averaged CO_2 112
Figure 6-46. [AT-39:OT-50] Planar Averaged CO 113
Figure 6-47. [AT-39:OT-50] Planar Averaged SO_2 114
Figure 6-48. [AT-39:OT-50] Planar Averaged H_2O 115
Figure 6-49. [AT-75:OT-74] Contours of Temperature on X-Midplane 116
Figure 6-50. [AT-75:OT-74] Contours of Temperature on Test Planes 117
Figure 6-51. [AT-75:OT-74] Comparison of Temperature on Test Planes 118
Figure 6-52. [AT-75:OT-74] Contours of O_2 Concentrations on Test Planes 119
Figure 6-53. [AT-75:OT-74] Comparison of O_2 Concentrations on Test Planes 120
Figure 6-54. [AT-75:OT-74] Contours of CO_2 Concentrations on Test Planes 121
Figure 6-55. [AT-75:OT-74] Comparison of CO_2 Concentrations on Test Planes 122
Figure 6-56. [AT-75:OT-74] Contours of CO Concentrations on Test Planes 123
Figure 6-57. [AT-75:OT-74] Comparison of CO Concentrations on Test Planes 124
Figure 6-58. [AT-75:OT-74] Contours of H_2O Concentrations on Test Planes 125
Figure 6-59. [AT-75:OT-74] Comparison of H_2O Concentrations on Test Planes 126
Figure 6-60. [AT-75:OT-74] Contours of SO_2 Concentrations on Test Planes 127
Figure 6-61. [AT-75:OT-74] Comparison of SO_2 Concentrations on Test Planes 128
Figure 6-62. [AT-75:OT-74] Contours of Incident Radiation 129
Figure 6-63. [AT-75:OT-74] Comparison of Wall Incident Radiation at Plane 141 130
Figure 6-64. [AT-75:OT-74] Comparison of Wall Incident Radiation at Plane 180 131
Figure 6-65. [AT-75:OT-74] Comparison of Wall Incident Radiation at Plane 273 132
Figure 6-66. [AT-75:OT-74] Strip-Averaged Wall Incident Radiation 133

Figure 6-67. [AT-75:OT-74] Planar Averaged Temperature 134
Figure 6-68. [AT-75:OT-74] Planar Averaged O_2 135
Figure 6-69. [AT-75:OT-74] Planar Averaged CO_2 136
Figure 6-70. [AT-75:OT-74] Planar Averaged CO 137
Figure 6-71. [AT-75:OT-74] Planar Averaged SO_2 138
Figure 6-72. [AT-75:OT-74] Planar Averaged H_2O 139
Figure 6-73. [AT-83:OT-98] Contours of Temperature on X-Midplane 140
Figure 6-74. [AT-83:OT-98] Contours of Temperature on Test Planes 141
Figure 6-75. [AT-83:OT-98] Comparison of Temperature on Test Planes 142
Figure 6-76. [AT-83:OT-98] Contours of O_2 Concentrations on Test Planes 143
Figure 6-77. [AT-83:OT-98] Comparison of O_2 Concentrations on Test Planes 144
Figure 6-78. [AT-83:OT-98] Contours of CO_2 Concentrations on Test Planes 145
Figure 6-79. [AT-83:OT-98] Comparison of CO_2 Concentrations on Test Planes 146
Figure 6-80. [AT-83:OT-98] Contours of CO Concentrations on Test Planes 147
Figure 6-81. [AT-83:OT-98] Comparison of CO Concentrations on Test Planes 148
Figure 6-82. [AT-83:OT-98] Contours of H_2O Concentrations on Test Planes 149
Figure 6-83. [AT-83:OT-98] Comparison of H_2O Concentrations on Test Planes 150
Figure 6-84. [AT-83:OT-98] Contours of SO_2 Concentrations on Test Planes 151
Figure 6-85. [AT-83:OT-98] Comparison of SO_2 Concentrations on Test Planes 152
Figure 6-86. [AT-83:OT-98] Contours of Incident Radiation 153
Figure 6-87. [AT-83:OT-98] Comparison of Wall Incident Radiation at Plane 141 154
Figure 6-88. [AT-83:OT-98] Comparison of Wall Incident Radiation at Plane 180 155
Figure 6-89. [AT-83:OT-98] Comparison of Wall Incident Radiation at Plane 273 156
Figure 6-90. [AT-83:OT-98] Strip-Averaged Wall Incident Radiation 157
Figure 6-91. [AT-83:OT-98] Planar Averaged Temperature 158
Figure 6-92. [AT-83:OT-98] Planar Averaged O_2 159
Figure 6-93. [AT-83:OT-98] Planar Averaged CO_2 160
Figure 6-94. [AT-83:OT-98] Planar Averaged CO 161
Figure 6-95. [AT-83:OT-98] Planar Averaged SO_2 162
Figure 6-96. [AT-83:OT-98] Planar Averaged H_2O 163
Figure 6-97. [AT-109:OT-134] Contours of Temperature on X-Midplane 164
Figure 6-98. [AT-109:OT-134] Contours of Temperature on Test Planes 165
Figure 6-99. [AT-109:OT-134] Comparison of Temperature on Test Planes 166
Figure 6-100. [AT-109:OT-134] Contours of O_2 Concentrations on Test Planes 167
Figure 6-101. [AT-109:OT-134] Comparison of O_2 Concentrations on Test Planes 168
Figure 6-102. [AT-109:OT-134] Contours of CO_2 Concentrations on Test Planes 169
Figure 6-103. [AT-109:OT-134] Comparison of CO_2 Concentrations on Test Planes 170
Figure 6-104. [AT-109:OT-134] Contours of CO Concentrations on Test Planes 171
Figure 6-105. [AT-109:OT-134] Comparison of CO Concentrations on Test Planes 172
Figure 6-106. [AT-109:OT-134] Contours of H_2O Concentrations on Test Planes 173
Figure 6-107. [AT-109:OT-134] Comparison of H_2O Concentrations on Test Planes 174
Figure 6-108. [AT-109:OT-134] Contours of SO_2 Concentrations on Test Planes 175
Figure 6-109. [AT-109:OT-134] Comparison of SO_2 Concentrations on Test Planes 176
Figure 6-110. [AT-109:OT-134] Contours of Incident Radiation 177
Figure 6-111. [AT-109:OT-134] Comparison of Wall Incident Radiation at Plane 141 178
Figure 6-112. [AT-109:OT-134] Comparison of Wall Incident Radiation at Plane 180 179
Figure 6-113. [AT-109:OT-134] Comparison of Wall Incident Radiation at Plane 273 180
Figure 6-114. [AT-109:OT-134] Strip-Averaged Wall Incident Radiation 181
Figure 6-115. [AT-109:OT-134] Planar Averaged Temperature 182
Figure 6-116. [AT-109:OT-134] Planar Averaged O_2 183
Figure 6-117. [AT-109:OT-134] Planar Averaged CO_2 184
Figure 6-118. [AT-109:OT-134] Planar Averaged CO 185

Figure 6-119. [AT-109:OT-134] Planar Averaged SO_2 186
Figure 6-120. [AT-109:OT-134] Planar Averaged H_2O 187
Figure 6-121. Comparison of Planar Averaged Temperature for 5 Coal Tests (Line Plots) 188
Figure 6-122. Comparison of Planar Averaged Temperature for 5 Coal Tests (Bar Charts) 189
Figure 6-123. Comparison of Planar Averaged Oxygen for 5 Coal Tests (Line Plots) 190
Figure 6-124. Comparison of Planar Averaged CO for 5 Coal Tests (Line Plots) 191
Figure 6-125. Comparison of Carbon-in-Ash for 5 Coal Tests 192
Figure 6-126. Char Oxidation and Gasification Reaction Rates 193
Figure 6-127. [AT-75:OT-74: 2-Rates] Planar Averaged CO 194
Figure 6-128. [AT-75:OT-74: 2-Rates] Planar Averaged H_2O 195
Figure 6-129. [AT-75:OT-74: 2-Rates] Unburned Carbon at Boiler Outlet vs. Test Data 196
Figure 6-130. [AT-75:OT-74: 2-Rates] Planar Averaged O_2 197
Figure 6-131. [AT-75:OT-74: 2-Rates] Planar Averaged CO_2 198
Figure 6-132. [AT-75:OT-74: 2-Rates] Planar Averaged Temperature 199
Figure 6-133. [AT-75:OT-74: 2-Rates] Strip Averaged Incident Radiation 200
Figure 6-134. [AT-75:OT-74: 2-Rates] Contours of Temperature on X-Midplane 201
Figure 6-135. [AT-75:OT-74: 2-Rates] Contours of Temperature on Test Planes 202
Figure 6-136. [AT-75:OT-74: 2-Rates] Contours of CO on Test Planes 203
Figure 6-137. [AT-75:OT-74: 2-Rates] Contours of H_2O on Test Planes 204
Figure 6-138. [AT-75:OT-74: 2-Rates] Contours of O_2 on Test Planes 205
Figure 6-139. [AT-75:OT-74: 2-Rates] Contours of CO_2 on Test Planes 206
Figure 6-140. [AT-75:OT-74: 2-Rates] Contours of Incident Radiation 207
Figure 6-141. [AT-75:OT-74: 2-Rates] Comparison of Wall Incident Radiation at Plane 141 208
Figure 6-142. [AT-75:OT-74: 2-Rates] Comparison of Wall Incident Radiation at Plane 180 209
Figure 6-143. [AT-75:OT-74: 2-Rates] Comparison of Wall Incident Radiation at Plane 273 210

List of Tables

Table 5-1. Coal Analyses 28
Table 5-2. Stoichiometry of Volatile Decomposition Reaction for Various Coals 29
Table 5-3. FLUENT® Rosin-Rammler Parameters for the Five Test Coals 31
Table 5-4. Inlet Gas and Coal Flow Rates and Temperature for all Cases 33
Table 5-5. Windbox and Overfire Air Port Designations 34
Table 5-6. Wall (Specified Temperature) Boundary Conditions 36
Table 6-1. Post-processed and Outlet Boundary Condition Results 41

1. Executive Summary

Computational fluid dynamic (CFD) coal-combustion simulations of the Alstom's 15-MW_{th}, tangentially-fired, Boiler Simulation Facility (BSF) were conducted using the ANSYS FLUENT® software. The test data used in the validation was collected for five (5) different test coals: a Powder River Basin (PRB) (Black Thunder) sub-bituminous coal, a West Virginia (Fola) eastern (low-sulfur) bituminous coal, an Illinois No. 6 (Prairie Eagle) eastern (high-sulfur) bituminous coal, a North Dakota (Falkirk) lignite and a Schwarze Pumpe (Lusation) lignite. The data was collected in intermittent test campaigns between the years 2009 and 2011. The data and the simulations include both air- and oxy-combustion. These CFD simulations were performed as part of the Oxy Technology Development program, under the DOE Agreement DE-NT0005290, which began in September of 2008. This report provides a description of the modeling approach, test conditions, and results generated for the project, consistent with the project management plan and milestone log described in the Agreement.

The objective of the present computational work was to support a portion of Subtask 6.1 (see Volume I), specifically addressing the application and validation of the FLUENT® code with respect to the 15 MW_{th} BSF data. A detailed discussion of the grid generation process, reaction chemistry and coal particle injection approaches used in FLUENT are included within this report. The plotted results include contour plots and planar averages (as a function of elevation) of temperature, heat flux, and gas species distributions for both air-combustion and oxy-combustion cases.

In the oxy-fuel combustion process, pulverized coal is burned in a mixture of pure oxygen and recycled flue gas. The recycling of the flue gas, which is required to moderate flame temperature, produces a flame environment which has different properties than the usual coal-air flame environment. Some general comments can be made about some of the expected design considerations or differences between the air-combustion and oxy-combustion environments based on property considerations alone, and how those differences were addressed in the computational runs.

Oxy-Combustion Characteristic: Species Emissivity
• Species such as H_2O, CO_2, and CO have higher gas emissivities. Although particles, such as char and soot, tend to dominate (or have a much higher impact on) the radiative flux to the walls than the gases, the aforementioned gas species nevertheless make a significant contribution. Therefore, the recycled flue gas species H_2O and CO_2, associated with the oxy-combustion systems, would be expected to enhance the heat flux in those systems in the radiative section, resulting in a slightly lower gas temperature entering the convective section.
Treatment:
• The FLUENT default submodel for gas radiative properties that is used often in air-combustion simulations is the weighted-sum-of-grey-gas model (WSGGM). This model was found (at the time) to be inadequate for oxy-combustion cases. Consequently, Alstom developed a proprietary user-defined function (UDF) for use with FLUENT to calculate the local gas-phase absorption coefficient. The UDF was based upon an Alstom implementation of the Edwards Wide-Band model, in which an interpolative table for the gas-phase absorption is constructed as a function of (a) the local, relative fraction of CO_2 in a composite mixture of $CO_2 + H_2O$, (b) the partial pressure of the composite $CO_2 + H_2O$ mixture, (c) the local gas-phase temperature, and (d) a specific overall beam or path length for the system.

Oxy-Combustion Characteristic: Species Specific Heat
• The specific heat of H_2O is approximately a factor of 2 higher than that of N_2, and the specific heat of CO_2 exceeds that of N_2 by about 7%. Therefore, the extent of drying of the moisture in the recycle stream becomes a design factor, as well as the CO_2 concentration in the recycle stream. Due to the increased H_2O and CO_2 concentrations in the oxy-combustion systems, the oxy systems would be expected to exhibit delayed flame ignition and decreased flame propagation speeds, as well as a lower flame temperature for the same net heat input.
Treatment:
• The difference in specific heats between the air-combustion and oxy-combustion systems was automatically accounted for through the existing property databases in FLUENT.

Oxy-Combustion Characteristic: Species Molecular Weight
• The molecular weight of CO_2 (44 kg/kmol) is higher than the molecular weight of N_2 (28 kg/kmol) by a factor of 1.57. Therefore, for an equivalent mass displacement of N_2 by CO_2, as might occur in an oxy-combustion system, the density of the feed will be higher and the velocity will be lower by about 36%. This value may be mitigated somewhat depending upon the relative amount of H_2O (18 kg/kmol) in the system. Accordingly, the volumetric flow rate in an oxy-combustion system would be expected to decrease and the residence time would increase, relative to an air-combustion system.
Treatment:
• The difference in molecular weights between the air-combustion and oxy-combustion systems was automatically accounted for through the existing property databases in FLUENT.

Oxy-Combustion Characteristic: Species Diffusivity
• For char oxidation, the mass diffusion of O_2 in a high CO_2 environment is about 20% lower than the diffusion rate of O_2 in N_2 (at 1600 K). Consequently, the oxidation rate may become more mass-diffusion limited with high CO_2 (e.g., at the higher temperature, Zone III (film-diffusion-limited) conditions).
Treatment:
• A film diffusion coefficient that includes the pertinent diffusivity of the reactive gas (O_2, CO_2, or H_2O) in a particular background gas mixture, is already available in FLUENT as a user-input for each heterogeneous rate, and no additional user intervention is necessary to accommodate the differences in diffusivities between the air-combustion and oxy-combustion systems.

Oxy-Combustion Characteristic: Gasification Effects
• The high CO_2 or H_2O concentrations, associated with oxy-combustion systems, may promote char consumption by char-CO_2 or char-H_2O gasification, both of which are endothermic reactions.
Treatment:
• Both char oxidation and char gasification reactions (i.e., for CO_2 and H_2O) were specified for the heterogeneous reaction chemistry. Different coals were accorded different char oxidation and gasification rates, based on Alstom's experience base and calibrations.

Oxy-Combustion Characteristic: Particle Radiation Properties
• To more accurately differentiate between the gas-phase absorption and the particle absorption in an oxy-combustion environment, the default particle emissivity and scattering factor in FLUENT® were deemed inadequate.

Treatment:
• The default particle radiation properties in FLUENT®, based on an input emissivity and scattering factor, were replaced with a much more accurate UDF based on efficiencies. The UDF generates absorption and scattering efficiencies for weighted combinations of coal, char, and ash as a function of the local particle temperature and diameter. The efficiencies are calculated for a given refractive index from an Alstom-proprietary code based on Mie theory, and have been generated for anthracite coal, bituminous coal, lignite coal, and ash. These additional particle absorption and scattering efficiencies were utilized in the present runs to enhance the overall radiation treatment.

A soot model was also developed, but it was not developed in time to be used when these computational runs were generated. Instead, a surrogate (gas-phase) soot species (denoted C-gas) was used to represent the generation of soot. The C-gas species did not contribute to the radiation properties.

Other than the above modifications, no additional UDFs, parameter adjustments, or significant property changes were made to accommodate the oxy-combustion system. An implicit assumption was made that the submodels for both the coal pyrolysis characteristics, and the wall heat transfer deposit thicknesses and resistances, were not a direct function of the type of combustion environment (whether air-combustion or oxy-combustion).

A general description of the simulation approach will be provided in following paragraphs.

The gas-phase reaction mechanism was based upon four (4) single-step, irreversible, global reactions – volatile decomposition/reaction, CO oxidation, H_2 oxidation, and C-gas (surrogate soot species) oxidation. The global reaction mechanism includes nine (9) gaseous or volumetric species: volatile, O_2, CO_2, CO, H_2O, SO_2, H_2, C-gas, and N_2. The volatile species is a pseudo-species with a specific elemental formula that is derived from the portion of the coal mass that is assigned to the volatile off-gas. The high-temperature volatile yield value was estimated to be higher than the proximate yield value. Kobayashi-type (two-competing rates) and single rate expressions were used for the pyrolysis model. Species transport equations are converged for all of the species except for N_2, which is calculated by difference. For the main gas-phase combustion reactions, the turbulence-chemistry interaction was modeled using the composite Magnussen eddy-dissipation (mixing-limited / fast-chemistry) and Arrhenius rates (kinetically-limited) combustion submodel, in which the smaller of the two rates (eddy-dissipation or Arrhenius rates) takes local precedence. The turbulence model is the Realizable k-ε turbulence model, with standard wall functions.

The coal particle combustion model utilizes the Discrete Phase Model (DPM), which is a stochastic Lagrangian particle model. In the present cases, surface injection was used for the particles at 3 elevations of 4 corners each (for a total of 12 injection inlets). Particles, injected at the burner inlets, sequentially pass through a series of discrete “laws” or stages that include heating, water vaporization, devolatilization, char combustion, and finally, inert (ash) heating/cooling. The “wet combustion” model was used for the coal moisture. The char consists only of pure carbon (designated as C<s>), and ash. The heterogeneous reactions are composed of one (1) oxidation and two (2) gasification reactions, using the multi-surface reaction model. The char burning rate is a combination of a film-diffusion rate in series with a chemical reaction rate, where the apparent chemical reaction rate actually includes the composite effects of pore diffusion and interior particle reaction, expressed on an external surface area basis. The overall rate therefore uses a combination of an Arrhenius based kinetic rate, as well as a diffusion rate of the reactant species through the film to the surface of the char particle. The char can be oxidized or gasified

simultaneously. Initial rates were estimated based on in-house proprietary databases, experience in previous studies, and/or some calibration/tuning. In addition, the char burning process is limited to a constant-diameter, reducing-density model; when all of the char is consumed, the particle contains only residual ash. A Rosin-Rammler (logarithmic) distribution of 20 particle sizes was used to represent the pulverized coal particle size distribution.

Alstom's 15-MWth, tangentially-fired, Boiler Simulation Facility (BSF) is part of the Alstom Power-Power Plant Laboratories' (Alstom) Combustion Research Complex located in Windsor, Connecticut. The BSF is designed in such a way that it can be configurationally altered to test new design concepts, fire a wide variety of fuels, or to meet challenging project constraints stipulated by Alstom's clients. The firing system includes a burner belt with three elevations of coal nozzles, a number of secondary air nozzles, and two elevations of separated overfire air (SOFA) nozzles. The firing system in the BSF incorporates corner-fired burners that have been configured to generate a tangential firing pattern. The air nozzles are positioned at the same offset angles as the coal nozzles; however, the concentric firing system (CFS) nozzles are offset an additional 22 degrees from the normal firing angle.

The furnace geometry and computational mesh created for the BSF were generated using the ANSYS mesh program GAMBIT. An effort was made to generate a very high-quality mesh. For the corner regions, in the vicinity of the nozzles, care was taken to reduce the diffusive effects by concentrating more cells in the areas of high gradients, and, where possible, by aligning the mesh elements in the predominant direction of flow. Transitional volumes that included tetrahedral elements were used, as necessary, around the burner belt to connect the corner mesh with the interior mesh. The overall mesh contained over 4.135 million cells. The geometry and corresponding surface mesh for the BSF computational domain is pictured in Figure 1-1.

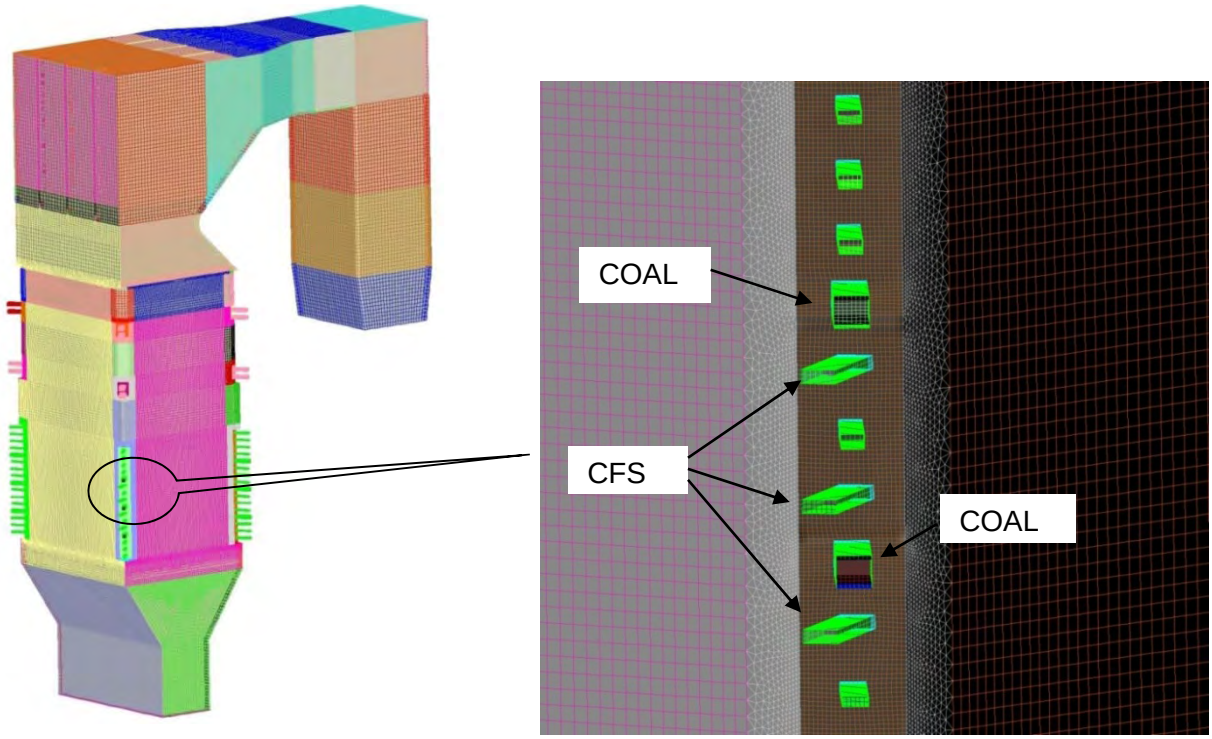

Figure 1-1. BSF CFD Mesh

The inlet boundary conditions for the feeds were prescribed from carefully analyzed and balance-checked experimental board data. The mass flow rates and overall stoichiometries are different for each test case. The inlet boundary conditions were prescribed as flow rates, temperatures, and species mass fractions (expressed as a percent) for the primary air (PA), windbox combustion air, lower overfire air (LOFA), and upper overfire air (UOFA) sections, as well as for the coal feed rate. The stream compositions for the oxy cases are different from those of the air cases due to the flue gas recycle strategy used in oxy combustion.

There are four (4) different wall-insulation zones as a function of vertical height in the BSF, with the upper furnace wall being un-insulated, bare steel, as shown in Figure 1-2. To model the effect of the insulation, a specified temperature boundary condition was used in conjunction with the FLUENT® code's thin-wall thermal resistance formulation. The specified temperature is on the far side of a thin wall, away from the adjacent fluid zone. The thermal resistance is the ratio of the parameters $\Delta x/k$, where Δx is the thickness of the resistance material(s), and k is the thermal conductivity. It was found necessary to adjust the thermal conductivity k of each zone (for a given inner surface temperature) to match the measured temperature data taken from Planes 141, 180, and 273 shown in Figure 1-2. This calibration procedure is necessary due to the lack of information about the degree and character of the fouling and slagging deposits on the wall surfaces in the different zones.

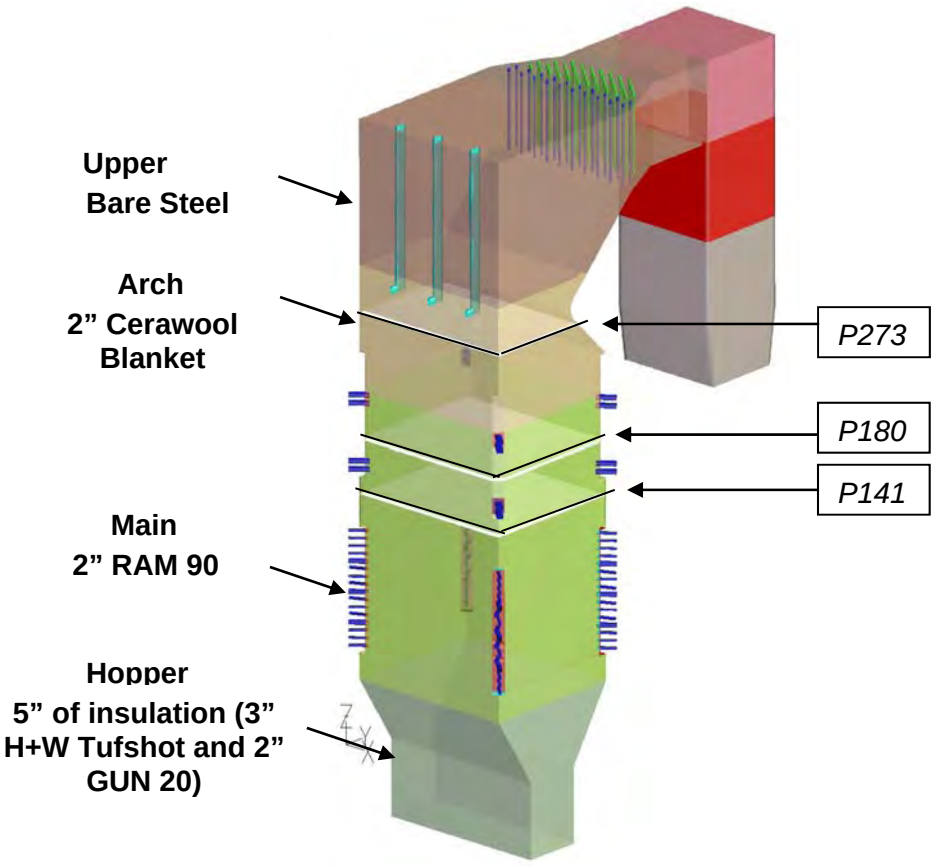

Figure 1-2. BSF Wall Insulations and Test Planes

For each of the five (5) coals, the air-combustion case was run first in order to establish a baseline or reference point before moving to the more complex oxy-combustion case with the recycled flue gas and oxygen injection. For example, for the air-combustion case, the grid quality was assessed, the mass flow rates were checked against the desired flow rates, the heterogeneous reaction rates were tuned to any residual or unburned carbon constraints, and the wall thermal boundary conditions were calibrated to match the measured temperatures, all prior to transitioning the case to oxy conditions. The same property methods, reaction rates, and wall thermal boundary conditions were used in both the air and oxy cases; only the inlet boundary conditions changed.

The predictions are available in a number of contour plots and line plots. Because of the large number of repetitive figure captions in the body of the report, an abbreviated notation for the test numbers was included in each caption, in the form of [AT-#:OT-#], where AT stands for air test and OT stands for oxy test, and # designates the actual test number.

To illustrate the predictive accuracy for gas temperature, a set of plots associated with Tests 11 and 12 for the Black Thunder PRB coal is shown in Figure 1-3. For the air-combustion case, the main windbox oxygen-to-fuel stoichiometric ratio (i.e., 0.95) is higher than that of the oxy-combustion case (0.82). Therefore, one might reasonably expect the temperature in the vicinity of the main windbox to be slightly higher in the air-combustion case than in the oxy-combustion case, all else being equal. This is indeed the case. The higher H_2O and CO_2 concentrations, associated with the oxy-combustion case, also helps to lower the temperature because of their higher gas emissivities (leading to higher wall heat flux) and higher specific heats. A visual survey of the experimental temperatures clearly shows a progression from hotter temperatures at Plane 141 to cooler temperatures at successively higher planes (Planes 180 and 273) as overfire air is added. The calculations show the same overall trend. Individual measurements may deviate 100 to 200 °F (55 K to 111 K) from the calculations, but this difference is considered reasonable and acceptable for suction pyrometry measurements, particularly in high-gradient regions. Broad differences at a particular plane indicate that deviations would be decreased by slightly adjusting the wall thermal boundary condition.

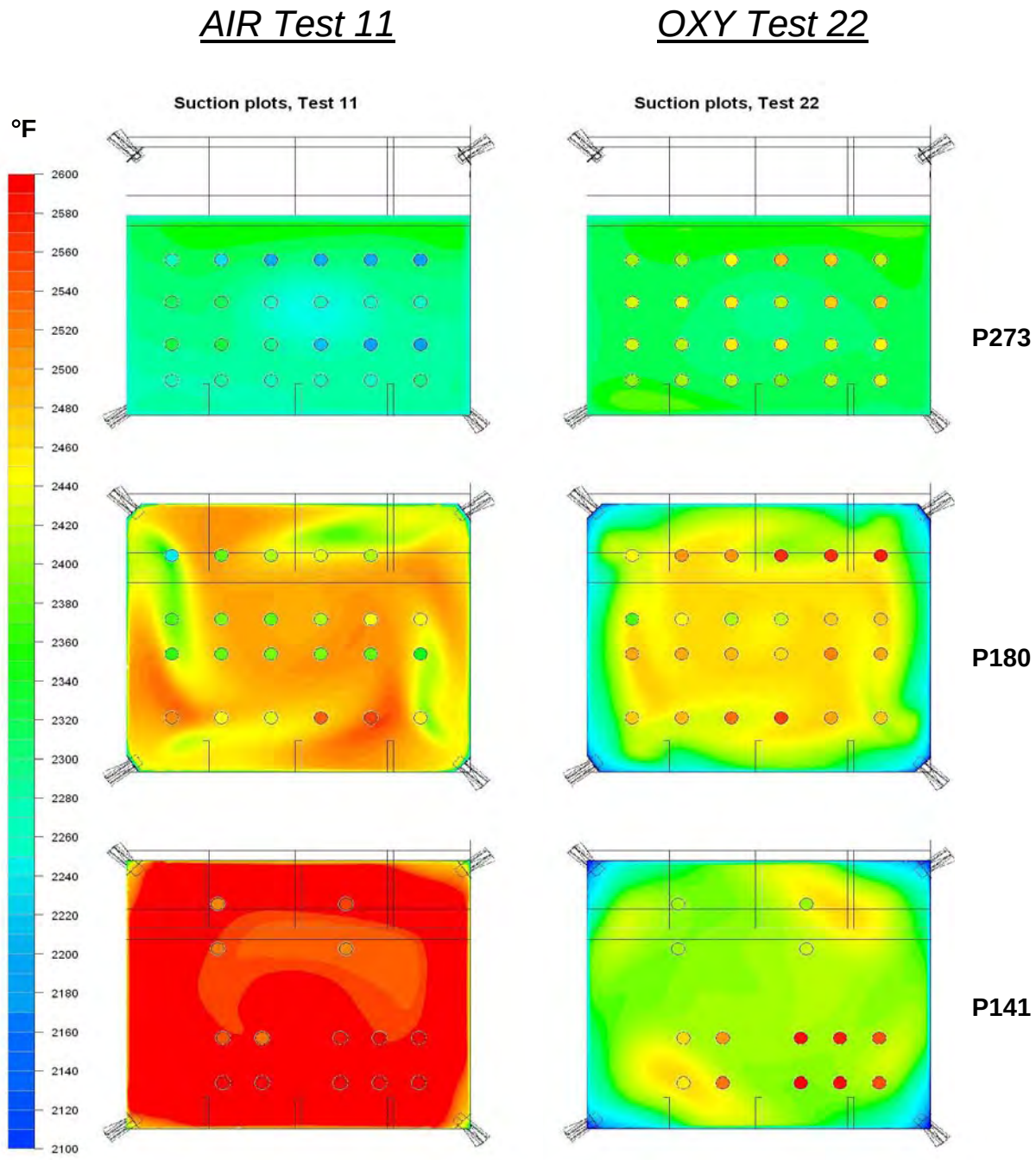

Figure 1-3. [AT-11:OT-22] Comparison of Temperature on Test Planes

Some of the measurements indicate patterns that correspond with residual jets or core regions. For example, for the air case on Plane 141, some of the cooler temperatures are in the core region as indicated by both the calculated and measured temperatures. On Plane 180, some of the green dots are aligned with residual jets while the red and yellow dots are aligned with more intense combustion zones. At Plane 273, the temperatures are more uniform across the plane as the flow field becomes more homogenous due to mixing. Although there may be some local asymmetry and incongruities for individual data points, the

overall agreement between the computations and experiments is considered acceptable. An important conclusion is that the predictions for oxy-firing, given the uncertainties in the experimental data and boundary conditions, scale reasonably well from the air-combustion baseline. The oxy-firing predictions appear to capture the temperature data reasonably well. The temperature plots for the other coals are not too dissimilar from the ones shown above.

An illustration of the predictive accuracy for oxygen molar concentration is provided in Figure 1-4, using Tests 39 and 50 for the Fola coal. As seen on the plot, the overall oxygen concentration appears to increase with increasing elevation, although locally high concentrations of oxygen indicate proximity to a feed stream. On Plane 180, the experimental data points appear to qualitatively follow the gross features of the computations -- the low oxygen regions around the periphery of the furnace, the higher oxygen concentrations in the jet regions, and the oxygen-starved core. On Plane 273, for the air case, the imprints of the SOFA oxidant supply and swirl pattern are still visible at the horizontal furnace outlet plane, although significant asymmetry exists in both the experimental and computed values. On Plane 273, for the oxy case, the high, experimental O_2 concentrations appear to reside predominately on the right-hand side of the furnace, in a pattern that seems to be congruent with the calculations. The scale is compressed and extends from 0 to 6%. Although local deviations between the predictions and the data may be significant for individual points, typical deviations are within a percentage point or two. This deviation is considered reasonable and acceptable given the uncertainties inherent in the experimental measurements, boundary conditions, and submodels. Again, it is important to recognize that the CFD calculations were able to reasonably capture the transition from the baseline air-fired case, at which the calibrations were performed, to the oxy-fired case, without any apparent deterioration of the prediction capability. A similar conclusion is appropriate for other species such as CO_2 and CO.

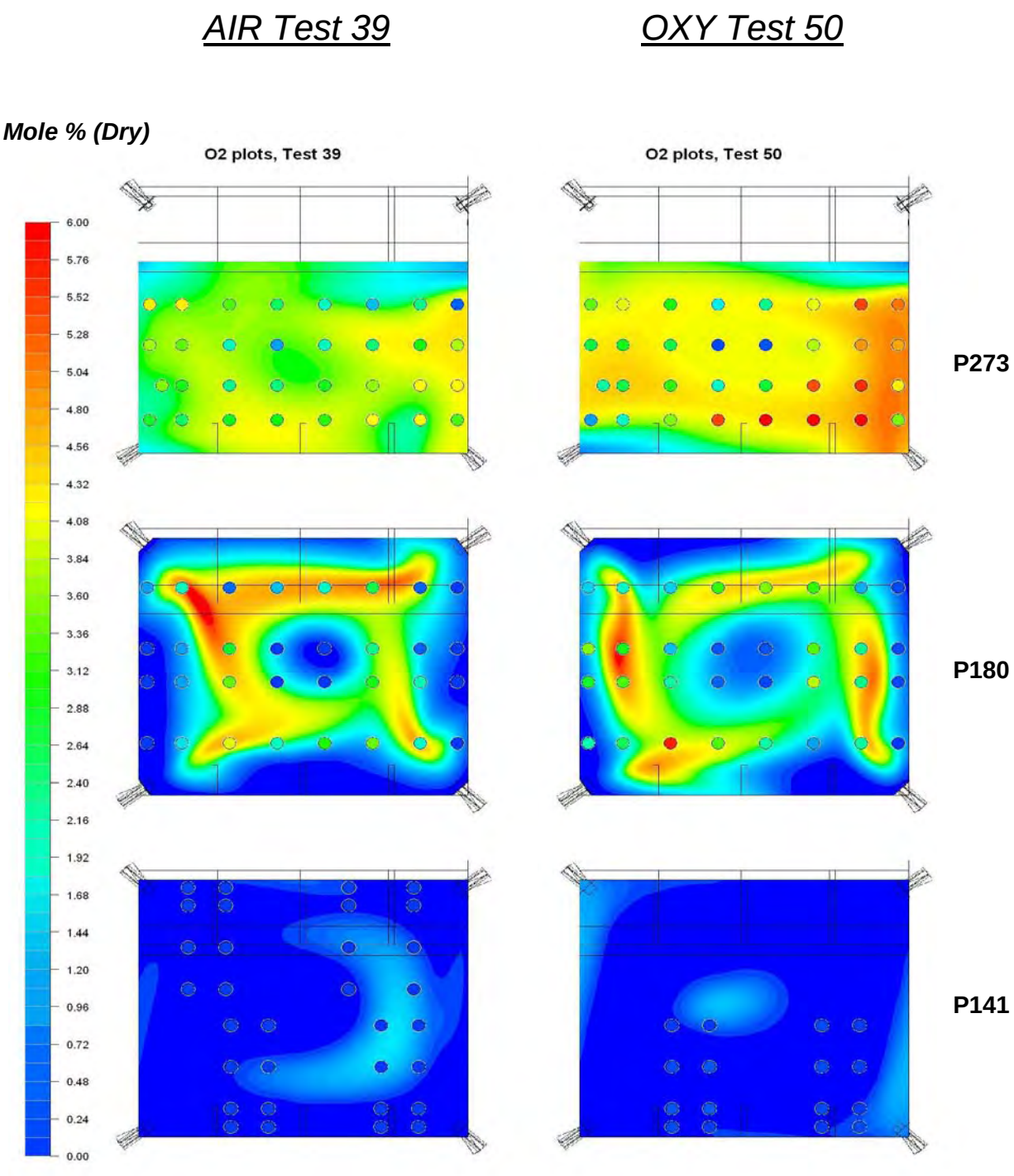

Figure 1-4. [AT-39:OT-50] Comparison of O_2 Concentrations on Test Planes

An illustration of the predictions for the wall incident radiation as a function of elevation are shown in Figure 1-5 (Plane 141) and Figure 1-6 (Plane 180) for Tests 83 and 98, associated with the North Dakota lignite coal. The "hot" and "cold" corner nomenclature is simply a device to help the reader orient himself to the geometry and walls of the furnace. The incident radiation to the walls qualitatively mirrors the

corresponding gas temperature profiles (not shown), which in turn becomes a function of the wall thermal conductivity calibration and the parameters and boundary conditions that impact local combustion. On Plane 141, the incident radiation for the oxy case appears to be about 10% to 20% larger than that for the air case, for both the experimental data and the computations, depending upon the wall (e.g., right or left) at which the measurements are taken. On Plane 180, the incident radiation for the oxy case is about 10% larger than that for the air case, again for both the experimental data and the computations. (Plane 273 is shown later in the report, but its predictions are similar). Agreement with the data is good and is probably within 10% overall, when considering all of the planes. The uncertainty brackets on the heat flux probe measurements are tentatively projected to be within the range of 20% to 25%, and predictions within this range are considered to be reasonable and acceptable. Local predictions may deviate from the experimental heat flux values at certain elevations, but the overall absorption is not likely to exhibit significant error since the wall thermal boundary conditions were calibrated to some degree. It is important to note that the scaling between the air-combustion case and the oxy-combustion calculations appears to be consistent with the experimental data.

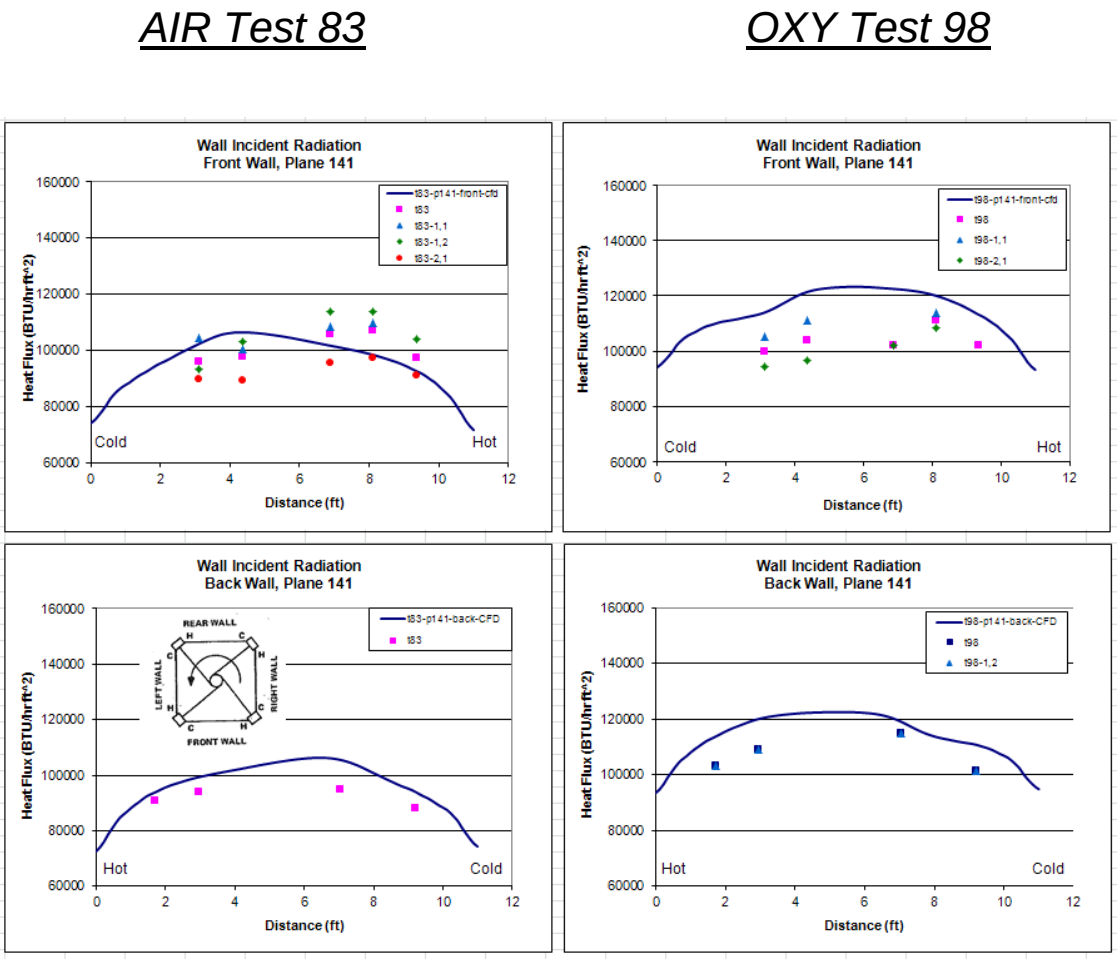

Figure 1-5. [AT-83:OT-98] Comparison of Wall Incident Radiation at Plane 141

AIR Test 83 *OXY Test 98*

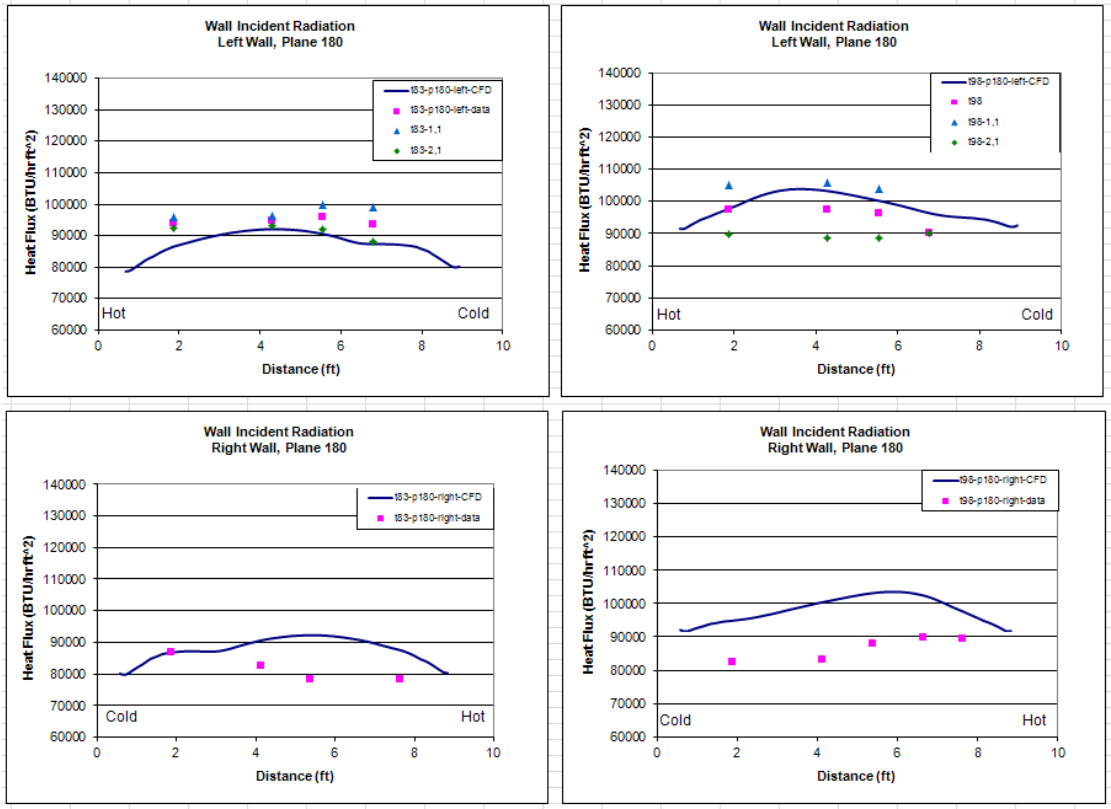

Figure 1-6. [AT-83:OT-98] Comparison of Wall Incident Radiation at Plane 180

The baseline air calculations are assumed to be within reasonable experimental uncertainty bounds for the types of probes utilized. (The uncertainty limits on the experimental data were delineated under a more formal uncertainty quantification discussed in Chapter 4.) Given that expectation and understanding, and given that the baseline air-combustion cases were first tuned and calibrated before testing the predictive accuracy for the oxy cases, it can now be ascertained that the calculation of the oxy-combustion cases is also within reasonable and acceptable uncertainty bounds. In other words, the apparent predictive error associated with the oxy cases does not appear to be significantly increased or exacerbated relative to the overall predictive error exhibited by the baseline air cases. This leads to the overall conclusion that the FLUENT® code, in conjunction with the UDFs and modeling strategy, as implemented for the runs in question, includes the requisite physics to make the transition from air- to oxy-combustion CFD studies. This does not mean that enhancements could not be made to the boundary conditions or to the chemical-kinetic mechanisms or other submodels to improve the predictive accuracy for CFD in general, or oxy-combustion in particular. It simply means that the capability to study or design oxy-combustion systems, using FLUENT®, appears to be on par with the present capacity to study or design air-combustion systems.

2. Objectives

This report summarizes computational fluid dynamics work that was done to support a portion of Subtask 6.1 (DOE/NETL Cooperative Agreement No. DE-NT0005290; see Ref. 1), which began in September of 2008, and which has a number of different components:

Subtask 6.1 – CFD Oxy-Combustion Model

- The ANSYS FLUENT® code, with improved submodels for combustion and radiation under oxy-combustion conditions, will continue to be applied and validated.
- Application of large-eddy simulation (LES) modeling for oxy-boiler application will be assessed and compared with simplified steady-state simulation approaches (specifically FLUENT®). More rigorous analysis of experimental and simulation data will also be conducted to statistically quantify uncertainty of modeling/prediction at both submodel and model levels. This will help improve prediction capability and accuracy of the modeling tools. This work will be conducted in collaboration with the Institute of Clean and Secure Energy (ICSE) at the University of Utah (Professor Phil Smith).
- Simulation results will then be compared with experimental validation data from small-scale facilities, the 15 MWth BSF and from the 30 MWth Schwarze Pumpe oxy pilot plant. The CFD code evaluation will include predictions for combustion, heat flux distribution, corrosion, and pollutant control.

The present report only addresses the application and validation of the FLUENT® code to the 15 MWth BSF data. The test data used in the validation was collected for five (5) different test coals in intermittent test campaigns between the years 2009 and 2011. The five (5) test coals are: a Powder River Basin (PRB) (Black Thunder) sub-bituminous coal, a West Virginia (Fola) eastern (low-sulfur) bituminous coal, an Illinois No. 6 (Prairie Eagle) eastern (high-sulfur) bituminous coal, a North Dakota (Falkirk) lignite and a Schwarze Pumpe (Lusation) lignite. Other reports or report sections will comprise the remaining workscope for the modeling task (Subtask 6.1).

The objective of this CFD modeling task was to simulate the performance of pilot-scale, oxy-combustion, tangentially-fired boiler tests in the BSF. The FLUENT® code was used to examine the differences between air- and oxy-firing for various coals. The CFD code was assessed and validated by comparing calculations with experimental data from the 2009-2011 BSF programs. The aim of the modeling simulations will be to provide a more reliable computational tool and methodology which can ultimately be used to provide commercially attractive CO_2 capture solutions for both the retrofit of existing boilers and the installation of new boilers. Indeed, the ultimate intent is to utilize the experimental test measurements and the simulation toolset to develop a basic design for a commercial-scale, oxy-boiler, demonstration project.

3. Conclusions and Recommendations

Alstom generated a high-quality CFD mesh for the 15 MWth BSF geometry and applied boundary conditions garnered from the experimental data. For the air-combustion case, the wall heat transfer boundary conditions in the cases were calibrated to the experimental temperature measurements. The heterogeneous oxidation rates were also calibrated to generate the proper unburned carbon at the exit of the computational domain. The air-combustion case was then used as the baseline run for the oxy-combustion case, in which only the inlet boundary conditions were changed. An air-combustion case and an oxy-combustion case were completed for each of the five (5) test coals. The cases were compared with the experimental data taken at three elevations – (a) a plane "midway" between the top of the main windbox and the lower SOFA (Plane 141), (b) a plane "midway" between the two SOFAs (Plane 180), and (c) a plane near the horizontal furnace outlet plane (HFOP) or arch (Plane 273). Alstom exercised diligence and care in performing a CFD analysis that (a) highlighted the differences between the air and oxy combustion computations for the five test coals, and (b) highlighted the differences between the computations and the experimental data.

Conclusions and recommendations may be itemized as follows:

- Comparison of the experimental data points with the calculated contours is encouraging. As a function of elevation (progressing from Plane 141 to Plane 180 to Plane 273), the calculation trends are aligned (on an overall, planar-averaged basis) with the trends exhibited by the data. Within each plane, the contours generally exhibit separate regions – a circumferential, near-wall region around the periphery, an interior ring composed of the remnants of the residual jets, and an inner core – that are oftentimes aligned with the patterns exhibited by the experimental data. These pattern matches indicate that the computations are able to mirror many of the underlying aerodynamic and physical features that are apparent in the data, at least qualitatively in many instances, and oftentimes, quantitatively.

- Based on comparison with experimental data, the apparent predictive error associated with the oxy cases does not appear to be significantly increased or exacerbated relative to the baseline air cases. This leads to the overall conclusion that the FLUENT® code, in conjunction with the UDFs and modeling strategy implemented, includes the requisite physics to make the transition from air- to oxy-combustion CFD studies. This does not mean that enhancements could not be made to the boundary conditions or to the chemical-kinetic mechanisms or other submodels to further improve the predictive accuracy for CFD in general, or oxy-combustion in particular. It simply means that the capability to study or design oxy-combustion systems, using FLUENT®, appears to be on par with the present capacity to study or design air-combustion systems.

- The wall heat transfer boundary conditions in the CFD runs were sectioned into four (4) segments, on the basis of the interior insulation adjacent to the waterwalls. As a function of elevation, the four segments are: (a) the hopper, (b) the main combustor (from the hopper to the top of the upper SOFA), (c) the arch region (top of the upper SOFA to a plane above the nose), and (d) the upper furnace. Except for the corners, the wall temperatures and resistances were circumferentially uniform. The wall heat transfer boundary condition is based on the "thin-wall" model and consists of an interior temperature, a wall emissivity, a wall thickness, and a material thermal conductivity. The thermal conductivity was typically adjusted (for the air cases only) until the averaged computational temperature matched the averaged temperature data at a particular elevation to

within an acceptable tolerance (typically less than +/- 100 °F). The wall emissivity was kept constant for all cases. The wall emissivity is a secondary factor that helps to fine-tune the heat transfer. Calibration of the wall boundary conditions revealed that applying a single thermal boundary condition to the main combustor region made it difficult to calibrate two of the measurement planes (Plane 141 and Plane 180) separately. More detailed considering of individual fouling and slagging patterns for each of the coals (both vertical and circumferential) should be considered in future modeling efforts.

- The temperature predictions, although a partial result of the thermal wall boundary condition calibration and the property UDFs, were very encouraging. The gas temperatures in the main windbox or fireball region appeared to be a strong function of the main windbox oxygen-to-fuel stoichiometric ratio. Given the main windbox stoichiometric ratios, and given the differences in feed conditions and firing rates between the air-combustion and oxy-combustion cases, it was ascertained that the overall measured and calculated temperature differences between the two cases were appropriate and in line with expectations.

  A visual survey of the experimental temperatures generally shows a progression from hotter temperatures at Plane 141 to cooler temperatures at successively higher planes (Planes 180 and 273) as overfire air is added. The calculations show the same overall trend in temperature decay. Some of the measurements at Planes 141 and 180 indicate patterns that correspond with the calculated residual jets or core regions. At Plane 273, the temperatures are more uniform across the plane as the flow field becomes more homogenous due to mixing. Although there may be some local asymmetry and incongruities for individual data points, and although there may be some displacement between the measured and calculated features, the overall agreement between the computations and experiments is considered acceptable. Individual measurements may deviate +/- 100 to 200 °F (55 K to 111 K) from the calculations, but this difference is considered reasonable for suction pyrometry measurements, particularly in high-gradient regions. The temperature predictions for oxy-firing, given the uncertainties in the experimental data and boundary conditions, scale reasonably well from the air-combustion baseline.

- Calculations of the surface incident radiation profiles at measurement ports on Planes 141, 180, and 273 were typically within +/- 10 to 20% of the measurements. Deviations larger than this are more likely a result of those factors that influence the heat release profile and the gas temperature profiles as a function of elevation, such as the calibration of the wall thermal boundary condition or the feed boundary condition, particle size distribution, etc.

  The computed (strip-averaged) incident radiation distribution is strongly linked to the gas temperatures, and the two variables appear to track each other qualitatively. For example, if the incident radiation profiles (as a function of elevation) for the air and oxy cases cross over each other, then the temperatures tend to do the same. The computations appear to reasonably capture the decay of the averaged incident radiation and temperature data from the top of the main windbox to the arch.

- The averaged oxygen concentration at Planes 141, 180, and 273 appears to be largely aligned with the data – the oxygen concentration is depleted above the windbox and is incremented in a step-wise fashion as the flow crosses each of the SOFA elevations. On Plane 141, the individual experimental points generally seem to be congruent with the computed contours. On Plane 180

(for the PRB and Fola tests), the measurement points indicate a strong oxygen-starved core, in agreement with the contours, and also provide some indication of the lower, residual SOFA jets. At Plane 273, the experimental data continue to demonstrate the persistence of a low-oxygen core, surrounded by a ring of higher O_2 concentration, and sometimes with low O_2 again around the periphery. In addition, on Plane 273, the experiments often indicate a higher O_2 region on the right-hand side of the furnace, which the computations also confirm in a number of instances.

- CO achieves its maximum values in the main windbox region, and then decays as additional oxygen is added through the SOFA regions. Within the simulations, the CO is calculated using single-step, user-specified kinetics (both heterogeneous and homogeneous). For such a simplistic CO mechanism, the computations do fairly well overall (predicting CO values within a factor of 2 of the experimental data) at Planes 141 and 180. On Plane 273, at the arch, the averaged computational CO goes to very low levels, while the averaged experimental values span a range from low CO values to about 1% (mole %, wet). Thus, the predicted CO appears to be consumed too rapidly, relative to the data. Interestingly, at the outlet of the domain, the computational CO ranges from 0 to a few hundred ppmv, while the experimental CO is essentially zero at the economizer outlet.

  The individual experimental data indicate that the high CO on Plane 180 is in a core region, as well as around the outer periphery of the furnace. This pattern is also shown by the computations. On Plane 273 the high experimental CO is found only in a persistent core region, whereas, as previously mentioned, the computational CO has already diminished to very low levels. In addition, the experimental oxygen concentrations tend to have lower core values on Plane 273, than do the computations, indicating that an underlying reason for the higher experimental CO values at the arch may be the persistence of a high-CO/low-O_2 core that is still limited by mixing. This may infer that a more sophisticated turbulence model should be used in the computations to try to simulate this persistent unmixedness of the core at the arch.

- The SO_2 data is somewhat ambiguous and difficult to understand. For two of the coal tests, the PRB and Fola coal tests, the averaged SO_2 monotonically increases as a function of elevation. The increase is greater for the oxy case than for the air case. For the high-sulfur bituminous coal, the sulfur monotonically increases for the oxy case and monotonically decreases for the air case. For the two lignite cases, the averaged SO_2 monotonically decreases.

  It is certainly reasonable that in fuel-rich regions of the main windbox, the sulfur species exists in forms other than SO_2, such as H_2S and CS_2. Sulfur is released as a volatile off-gas as H_2S, and any SO_2 fed into the system with the recirculated flue gas may be reduced to H_2S or a similar species in a locally fuel-rich region. However, it is difficult to understand why only the PRB, and the two bituminous coals would exhibit this monotonically-increasing trend characteristic, and not the lignite coals. The calculations cannot simulate a monotonically-increasing change of SO_2 with elevation, since all of the sulfur in the model is rapidly converted to SO_2 through volatile decomposition alone, and subsequent changes in SO_2 mole fraction with elevation are simply a function of the volumetric changes associated with other reactions and feed additions. For the present, it is believed that reduced sulfur species are playing a role in the staged zone, and perhaps at the outlet, but the extent of the role cannot be studied without implementing a more advanced sulfur mechanism. It is also noted that currently the model assumes that all of sulfur in the fuel is released as volatile matter. In reality, as much as half, if not more, of the total sulfur stays in the

char matrix and is released as the char burns out. The impact of this assumption on the overall sulfur profile also needs to be revisited.

- Direct comparisons between the experimental point measurements and the computed values at the same locations demonstrated success in qualitatively predicting the flow field features or patterns. Sometimes the qualitative agreement between the computed contours and the experimental data was very encouraging, but other times a pattern match was ambiguous or contradictory. Sometimes, the data points, on a given plane, exhibited some asymmetry not exhibited by the computations, or exhibited monotonic increases or decreases in magnitude that did not correspond to the contours. Some obvious reasons for these discrepancies include: (a) the computational jet trajectories, due to deficiencies in the Reynolds Averaged Navier-Stokes (RANS) model, do not precisely overlie the experimental aerodynamic patterns, (b) the particle dispersion is not modeled adequately, (c) the computational reaction kinetics are producing a different composition field, at a different rate, than the actual kinetic mechanisms, (d) the boundary conditions are not properly replicated, such as corner-to-corner imbalances in the coal or gas feed, or slag buildup on the walls and nozzles, (e) the variability and uncertainty in the measurements themselves, etc. For some variables like CO_2 or H_2O concentration at the arch, where "outlet" concentrations can be easily calculated on the basis of complete combustion, a mismatch of a few percentage points probably indicates an error in the feed rates or inlet compositions. For the oxy cases, since essentially all of the sulfur off-gas is ultimately oxidized to SO_2, errors in the final SO_2 concentration at the arch also probably indicate that the recycled SO_2 concentrations are not quite correct, relative to the data. Other variables, like the CO or H_2 concentration, are largely consumed by the time the gases reach the economizer outlet, and are principally a function of the user-specified homogeneous and heterogeneous kinetic rates.

- As part of this work, a sensitivity study was performed in which a case was run with both high and low heterogeneous kinetic rates. Although not fully quantified in the computations, gasification appears to play a role in the main windbox region, particularly for those coals that are more reactive. This was evidenced by the parametric study in which the higher (lignite) char oxidation and gasification rates were used to replace the slower (Illinois bituminous) rates. From the additional H_2 that was calculated from the enhanced rates (separately and apart from the H_2 produced from volatile decomposition alone), it became evident that gasification was indeed playing a role in the fuel-rich regions. It is surmised that gasification is probably enhanced by the higher CO_2 and H_2O concentrations that prevail in the oxy cases (due to flue gas recycle), and that the gasification that occurs does depress the temperature slightly in the main windbox region (due to its endothermic nature).

- Rigorous analysis of the uncertainty inherent in the experimental and simulation data is needed to understand the error bars on the data, as well as the contribution to the error by each of the models. The collaborative work with the University of Utah on "validation and verification/uncertainty quantification" (V&V/UQ), focusing on temperature and wall heat flux, is part of the ongoing effort to examine the prediction sensitivity to submodel parameters and to improve prediction capability and accuracy of the modeling tools. This effort is discussed in Chapter 4.

4. Description of BSF

The BSF is part of the Alstom Power-Power Plant Laboratories' (Alstom) Combustion Research Complex located in Windsor, Connecticut. This facility is an integral part of Alstom's worldwide corporate research network providing the key elements for successful power plant engineering and the development of new ideas and innovative designs for improved products and processes. The BSF is designed in such a way that it can be configurationally altered to test new design concepts, fire a wide variety of fuels, or to meet challenging project constraints stipulated by Alstom's clients.

The firing system includes a burner belt with three elevations of coal nozzles, a number of secondary air nozzles, and two elevations of separated overfire air (SOFA) nozzles. The firing system in the BSF incorporates corner-fired burners that have been configured to generate a tangential firing pattern, similar to that shown in the plan (or top) view provided in Figure 4-1. Considering a horizontal plane through an arbitrary nozzle, tangential firing is enabled by yawing the nozzle, in the direction of the fireball rotation, so that the firing angle of the nozzle is offset about 2.5 degrees from a hypothetical line connecting the corner with the center of the furnace. The air nozzles are positioned at the same offset angles as the coal nozzles; however, the concentric firing system (CFS) nozzles are offset an additional 22 degrees from the normal firing angle, as shown in Figure 4-2.

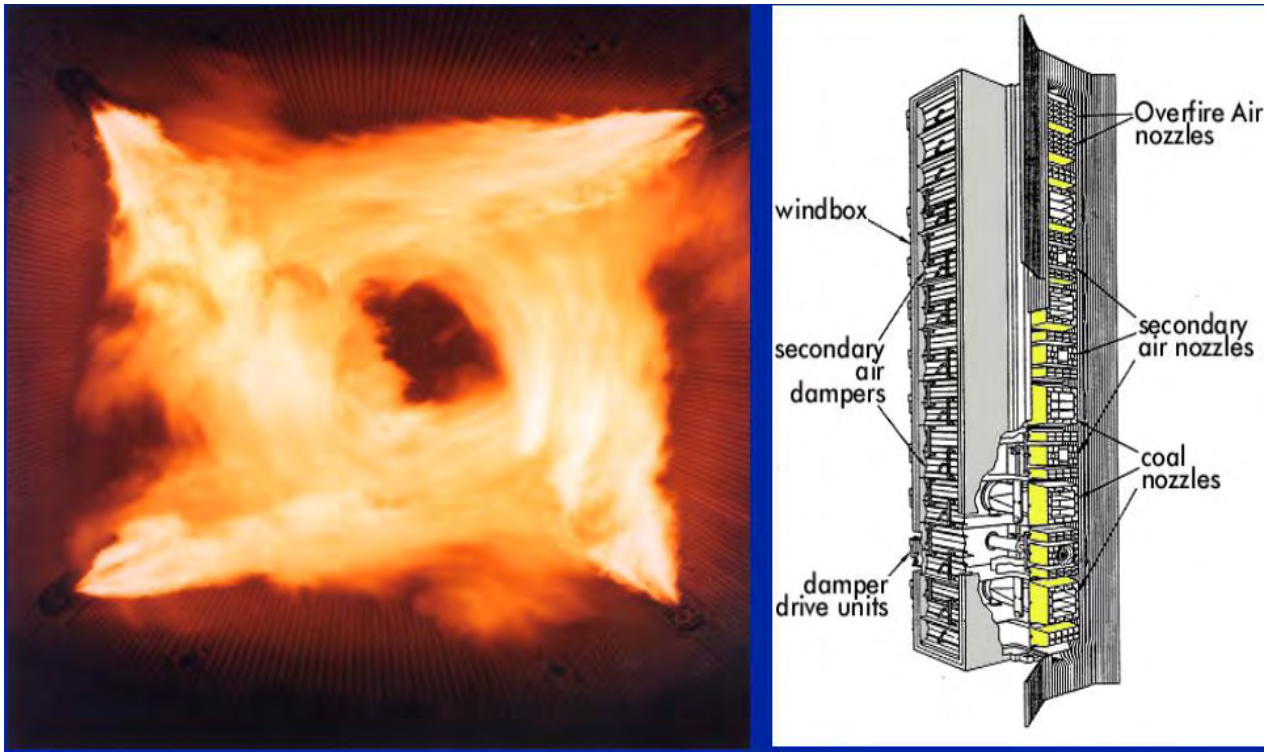

Top View **Windbox Elevation**

Figure 4-1. Plan (or Top) View of Tangential Firing Pattern (Oil-Fired) in BSF

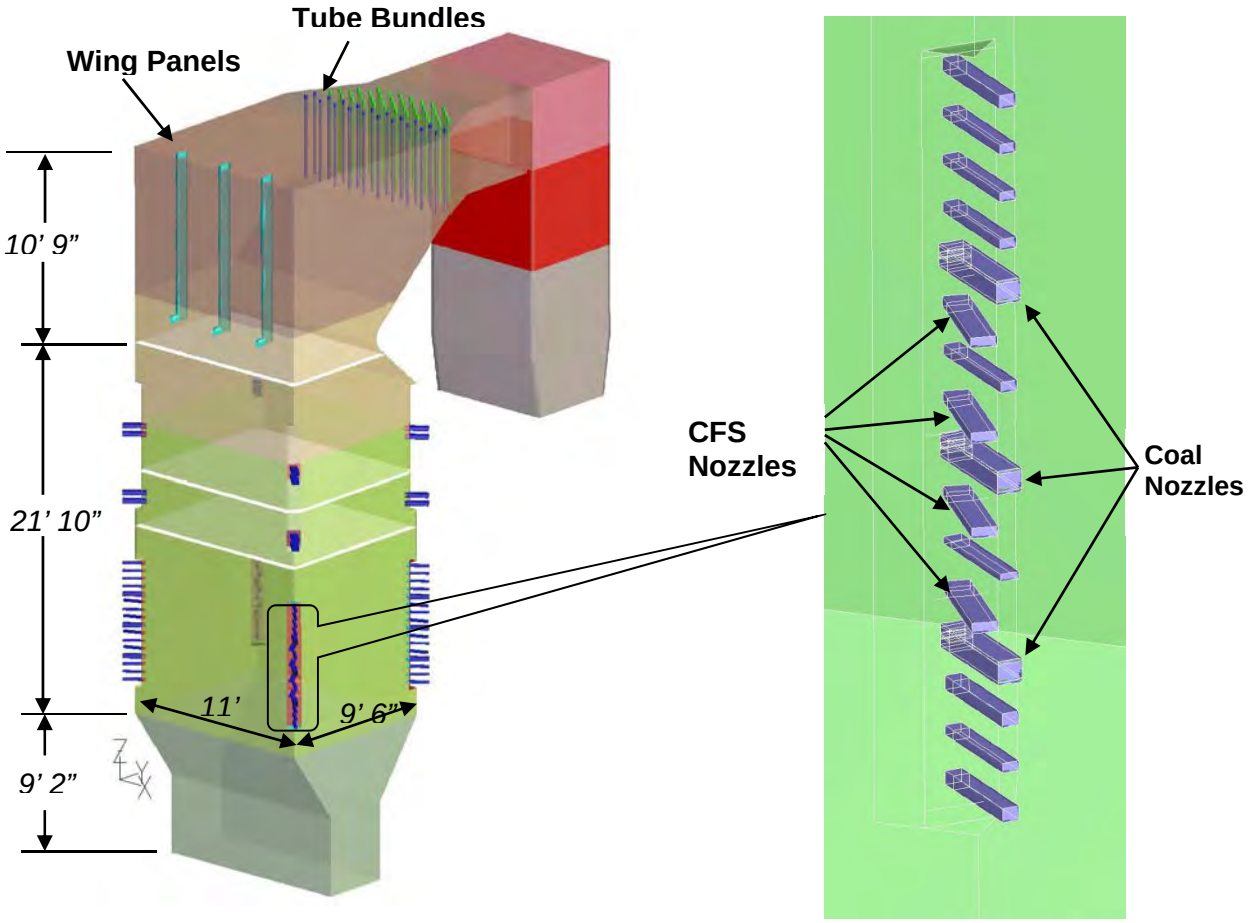

Figure 4-2. 15 MW Boiler Simulation Facility Model

The jacketed waterwalls and the interior insulation on the waterwalls are designed to provide the desired furnace absorption and furnace outlet temperatures. The wing panels and tube bundles, positioned in the upper furnace and convective pass, are intended to approximate additional superheat, reheat, or evaporative surface in a commercial furnace. The key dimensions of the BSF are shown in Figure 4-2.

To modify the BSF for oxy-combustion, several systems were added to the previously constructed air-fired facility, which include: oxygen supply tanks and injection system, flue gas recirculation ducting, dry scrubber fabric filter, and a CO_2 supply system, some of which are shown in Figure 4-3. Only the boiler itself was modeled with CFD. A number of test campaigns have been completed with the designated testing coals. The data collected are used to compare with the CFD predictions and to validate and refine the CFD sub-models. More detailed description of the BSF, and the 15 MWth testing performed, is provide in Volume II.

Figure 4-3. Oxy Boiler Simulation Facility

5. Technical Approach

A commercial CFD code, ANSYS FLUENT® Version 6.3.31, was used to model coal combustion in the 15 MW_{th}, tangentially-fired, Boiler Simulation Facility. Briefly, the code solves the conservation equations for mass, momentum and energy over the domain of interest by a finite volume method. The flow field is assumed to be incompressible, but the physical properties such as density and specific heat are allowed to vary with temperature. The computational domain of interest was decomposed and gridded using an ANSYS mesh generator. The desired cases were converged to a steady-state solution, and the velocity components, static pressure, temperature, species concentrations, and heat transfer quantities of interest were post-processed and compared with the experimental data for five (5) test coals from the 2009 through 2011 test campaigns. The five (5) test coals are: a Powder River Basin (PRB) (Black Thunder) sub-bituminous coal, a West Virginia (Fola) eastern (low-sulfur) bituminous coal, an Illinois No. 6 (Prairie Eagle) eastern (high-sulfur) bituminous coal, a North Dakota (Falkirk) lignite and a Schwarze Pumpe (Lusation) lignite. The bulk of the CFD work, consisting of the gridding and the running of the CFD cases, began in late 2009 and continued intermittently through mid-2012. Additional details concerning the gridding approach, the FLUENT® submodels utilized, and the post-processed results and data comparisons are discussed in the following subsections.

5.1 CFD Mesh

The furnace geometry and computational mesh created for the BSF were generated using the ANSYS mesh program GAMBIT Version 2.2.30.

An effort was made to generate a very high-quality mesh. A general maxim of grid generation is that grids that maximize the use of regular hexahedral (hex) elements are preferable, because hex elements are (a) more efficient on a volumetric efficiency basis, and (b) generally less diffusive compared to other types of elements (e.g., tetrahedral elements). Ultimately, however, the mesh construction for the BSF boiler geometry was dictated by the complexity of the nozzle tips in the corners, as well as the decomposition strategy required to connect the windbox/corner mesh to the interior core mesh and to the hopper and upper-furnace mesh blocks. As a first step, the geometry was subdivided (i.e., decomposed) into smaller blocks in order to construct the most efficient mesh, and to provide a reasonable connectivity and transference of mesh between the blocks, based on a strategy garnered through many years of gridding similar geometries. Secondly, the mesh was applied to the blocks. Topologically orthogonal regions of the furnace were meshed with hex elements, where possible. Certain transition regions, usually consisting of tetrahedral elements, were needed to bridge from a grid face with one cell pattern to an opposing or adjacent face with a very different grid pattern. This process of geometric decomposition and meshing was not automatic, but the time invested in developing a customized mesh was well worth the effort, since the final mesh resulted in (a) higher quality cells (better cell aspect ratios and less numerical diffusion), (b) greater cell concentration in regions of large gradients in flow and species, and (c) an overall reduced cell count (leading to faster convergence).

For the corner regions, in the vicinity of the nozzles, care was taken to reduce the diffusive effects by concentrating more cells in the areas of high gradients, and, where possible, by aligning the mesh elements in the predominant direction of flow. A small box “block” in the corner, oriented so that it was coaxial with the nozzle, while still encapsulating the end of the nozzles, was packed with relatively fine cells. A relatively fine mesh was used to model the tips and gaps around the nozzles so that entrainment and jet

dispersion were captured sufficiently. The mesh sizes for the passages inside the burner were on the order of 0.4 inch. This fine mesh was extruded out over many jet diameters in order to capture the jet penetration and dispersion. Outside of the corner (box) zone, the cell size was grown to match the larger cell elements elsewhere in the interior/core of the furnace. The challenge was to have sufficient resolution near the burner, but to still have a total mesh count that could be processed on the parallel-processing computer hardware. Transitional volumes, that included tetrahedral elements, were used, as necessary, around the burner belt to connect the corner mesh with the interior mesh. In addition, the triangular volumes in the corners (e.g., at the top and bottom of the windbox), that bring the cut-corners back to the square shape, were meshed with tetrahedral cells, and include a pair of non-conformal interface zones to minimize the skew in those regions.

The geometry and corresponding surface mesh for the BSF is pictured in Figure 5-1. The overall mesh contains over 4.135 million cells. The same mesh was used for all of the cases studied.

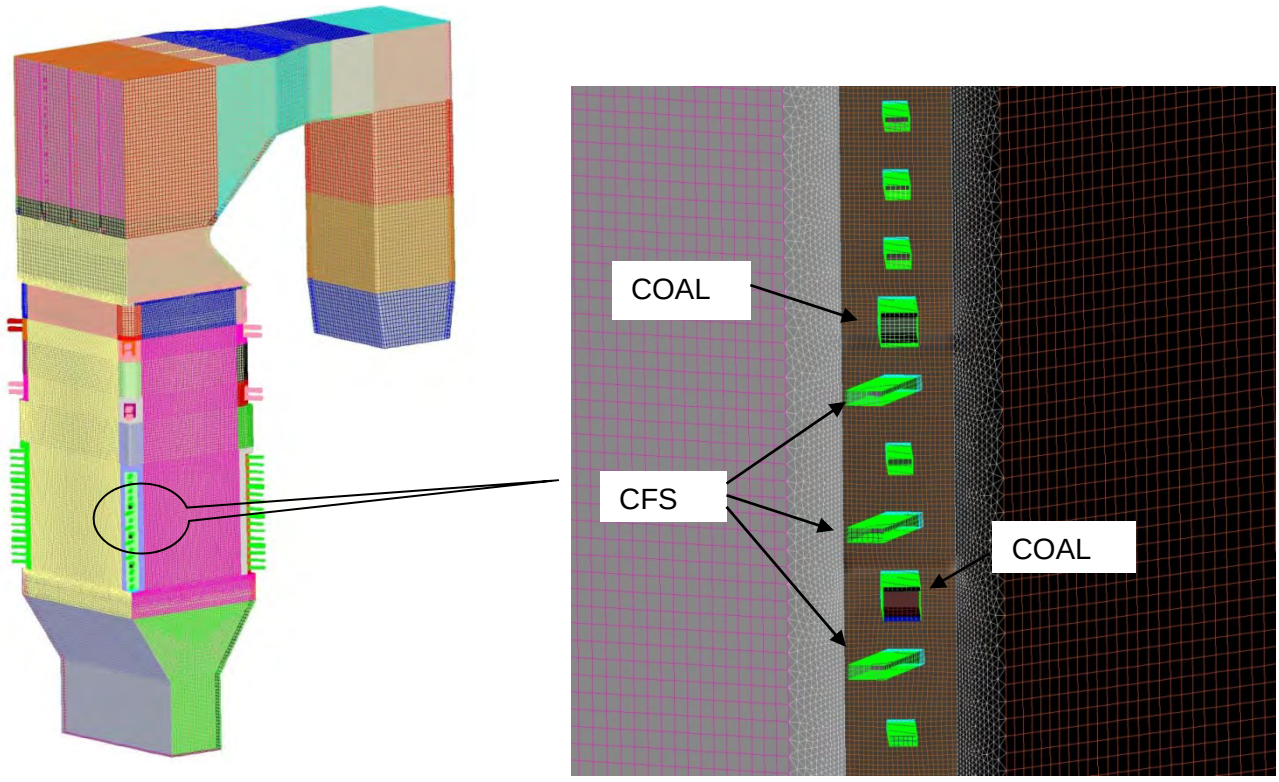

Figure 5-1. BSF CFD Mesh

5.2 Homogeneous and Heterogeneous Combustion Reaction Scheme

Within the computational domain of the furnace, the gas phase reactions and particle surface reactions are coupled, with the coal particles providing mass sources of water vapor and volatiles to the gas phase, as well as mass sources of combustion products from the char surface reactions. The gas-phase reactions must be considered in conjunction with the degree of turbulent mixing, which, in the present computations, is dictated by the Realizable k-ε turbulence model, with standard wall functions. For the main gas-phase combustion reactions, the turbulence-chemistry interaction was modeled using the

composite FLUENT® eddy-dissipation (mixing-limited / fast-chemistry) and Arrhenius rates (kinetically-limited) combustion submodel, in which the smaller of the two rates (eddy-dissipation or Arrhenius rates) takes local precedence. The Magnussen eddy-dissipation model is also commonly referred to as the "eddy-breakup" model in the open literature; over the years, this particular model has been used for almost all of the boiler computations at Alstom.

The gas-phase reaction mechanism was based upon four (4) single-step, irreversible, global reactions – volatile decomposition/reaction, CO oxidation, H_2 oxidation, and C-gas (surrogate soot species) oxidation. (Equilibrium constraints, such as the water-gas shift reaction, were not incorporated.) These same global rate expressions for the gas phase reactions (whether for oxy or air combustion), have been applied to other oxy-combustion systems that have been studied at Alstom. The global reaction mechanism includes nine (9) gaseous or volumetric species: volatile, O_2, CO_2, CO, H_2O, SO_2, H_2, C-gas, and N_2. Species transport equations are converged for all of the species except for N_2, which is calculated by difference using mass conservation principles.

The volatile species is a pseudo-species with a specific elemental formula that is derived from the portion of the coal mass that is assigned to the volatile off-gas. The volatile yield may be estimated, assigned from experiment, or calculated from commonly available software packages. The software packages rely solely on the fuel's proximate and ultimate analysis to generate a high-temperature volatile yield (HTVY) and speciation. In the present instance, the HTVY for each of the present BSF coals was estimated to be 30 to 43% higher than the proximate volatile matter. For the BSF cases and coals analyzed in the present study, the coal composition and yield analyses are shown in Table 5-1.

Table 5-1. Coal Analyses

	Black Thunder Powder River Basin (PRB)	West Virginia Fola	Illinois No. 6	North Dakota	Schwarze Pumpe
	Sub-bituminous	Bituminous	Bituminous	Lignite	Lignite
Proximate/Ultimate:	(AF, Mass, %)	(AF, Mass, %)	(AF, Mass, %)	(AF, Mass, %)	(AF, Mass, %)
Moisture	21.01	1.54	6.13	24.43	13.70
Volatile Matter	34.00	31.67	37.88	33.82	31.67
Fixed Carbon	39.79	55.63	46.06	29.87	49.42
Ash	5.20	11.16	9.93	11.87	5.21
C	54.71	68.25	66.24	44.95	53.96
H	3.73	4.57	4.45	3.01	3.9
O	14.26	12.19	8.58	14.2	22.01
N	0.81	1.43	1.31	0.81	0.6
S	0.28	0.86	3.35	0.73	0.62
Heating Value:					
HHV (Btu/lb, AF)	9,348	13,268	11,843	7,474	9,008
High-Temp Vol Yield:					
Ratio of HTVY to Proximate VY	1.386	1.386	1.436	1.3	1.386
HTVY (DAF)	63.87	50.29	64.81	69.02	54.14
Stoichiometric Mass of External O_2/ Mass AF Coal	1.6137	2.0676	2.0656	1.3016	1.5332
Stoichiometric Mass of External O2/ Unit Mass of AF Volatile	1.9170	2.0761	2.3505	1.7649	1.2356
AF	As-Fired Basis				
DAF	Dry, Ash-Free Basis				
HTVY	High-Temperature Volatile Yield				
PCCL	PC Coal Lab® Software				

During primary devolatilization, pyrolysis products include tar and light gases, such as CH_4, CO, CO_2, H_2S, etc. During secondary devolatilization, the distribution of the pyrolysis products changes somewhat and the tar is largely converted into soot. Computationally, the pyrolysis speciation was very much simplified, and the volatiles decomposition is presumed to form only N_2, SO_2, H_2, O_2, and C-gas. All of the carbon in the volatiles is relegated to the gaseous C-gas species, the C-gas is treated as a surrogate for the soot formed from the tars during secondary devolatilization. The C-gas is then allowed to oxidize to CO. The C-gas species is not coupled to the radiation model as a way to account for the impact of soot on radiation, but is simply treated as a direct carbon source, with a customized reaction rate that is different from that of the char particle. The concept of creating a C-gas species was suggested by ANSYS as a means of transferring some of the carbon constituents in the volatile to the gas phase without artificially giving it back to the char.

For these runs, the char consists only of pure carbon (designated as C<s>), and ash. The heterogeneous reactions are composed of one (1) oxidation and two (2) gasification reactions, using the multi-surface reaction model. The char burning rate is a combination of a film-diffusion rate in series with a chemical reaction rate. The apparent chemical reaction rate actually includes the composite effects of pore diffusion and interior particle reaction, expressed on an external surface area basis. The overall rate therefore uses a combination of an Arrhenius based kinetic rate, as well as a diffusion rate of the reactant species through the film to the surface of the char particle. The char can be oxidized or gasified simultaneously, depending upon the local concentration levels, although, usually, the magnitude of the rates are such that oxidation will dominate whenever oxygen is present. The addition of heterogeneous char gasification reactions provides a mechanism to convert the char to CO and H_2 in an oxygen deficient environment.

At Alstom, the char surface kinetic rates are typically estimated from a proprietary char oxidation kinetics database for a wide variety of coals, as well as from separate char oxidation and gasification measurements from previous Alstom drop-tube studies. Since there may be some uncertainty in such estimates, and since there is an inherent distribution of reactivities for different coal samples, even from the same mine or coal seam, a common practice in CFD studies is to calibrate some aspect of the coal/char reactivity for the boiler in question, at least when experimental data is available to do so. For some of the baseline air tests, Alstom elected to tune or adjust the pre-exponential factor in the char oxidation rate to the experimental carbon-in-ash value.

The CO_2 gasification Arrhenius rates are orders of magnitude less than the corresponding oxidation rates at low temperatures, but the gasification rates approach the oxidation rates at higher temperatures, in accordance with Goetz, et al. (Ref. 2). The large partial pressures of H_2O and CO_2 in oxy-combustion systems only increases the significance of gasification in fuel-rich regions. The H_2O gasification rate has been defined as being a factor of 2 higher than the CO_2 gasification rate.

The stoichiometric coefficients for Reaction 1 were obtained from the volatile yields and the elemental volatile composition, which varies from coal to coal, and are shown in Table 5-2.

Table 5-2. Stoichiometry of Volatile Decomposition Reaction for Various Coals

Black Thunder PRB	Volatile → C-gas + 0.792 H2 + 0.187 O2 + 0.037 SO2 + 0.012 N2
West Virginia Fola	Volatile → C-gas + 1.096 H2 + 0.171 O2 + 0.013 SO2 + 0.025 N2
Illinois No. 6	Volatile → C-gas + 0.722 H2 + 0.054 O2 + 0.034 SO2 + 0.015 N2
North Dakota	Volatile → C-gas + 0.711 H2 + 0.201 O2 + 0.011 SO2 + 0.014 N2
Schwarze Pumpe	Volatile → C-gas + 1.385 H2 + 0.478 O2 + 0.014 SO2 + 0.015 N2

5.3 Particle Combustion Model Description

The coal particle combustion model utilizes the Discrete Phase Model (DPM), which is a stochastic Lagrangian particle model. The model provides a means by which mass, momentum and energy, between the Lagrangian-based particle phase and the Eulerian-based gas phase, are coupled. In the present cases, surface injection was used for the particles at 3 elevations of 4 corners each (for a total of 12 injection inlets).

Particles, injected at the burner inlets, sequentially pass through a series of discrete "laws" or stages that include heating, water vaporization, devolatilization, char combustion, and finally, inert (ash) heating/cooling. The coal particles absorb heat from radiative and convective heat transfer mechanisms, as well as from a user-designated fraction of the surface heat of reaction. As the particles heat up, coal moisture is evaporated above a specified vaporization temperature (284 K) and further evolved at the boiling temperature (373 K) until all the assigned moisture is released to the surrounding gas. The volume fraction of moisture in the initial particle is specified in the "wet-combustion" model.

Following the moisture release, the particle continues to heat up until attaining the devolatilization temperature. FLUENT's default devolatilization models include both a Kobayashi-type (two-competing rates) pyrolysis model and a single rate expression, both of which are used often in CFD studies. During pyrolysis, the particle diameter swells to a new diameter dictated by the user-specified "swelling coefficient," which was set to 1.1 in the present runs. In the FLUENT code, all of the volatile fraction must be released before the char-burning can commence. In addition, the char burning process, based on the multi-surface model, is limited to a constant-diameter, reducing-density model. When all of the char is consumed, the particle contains only residual ash; the particle continues to be tracked until the maximum number of tracking steps is achieved or the particle leaves the domain.

A Rosin-Rammler (logarithmic) distribution of 20 particle sizes was used to represent the pulverized coal particle size distribution; the logarithmic diameter characterization resolves the smaller particles and enhances accuracy because of the sensitivity of the particle radiation to the ensemble surface area of the smaller particles. An example of a Rosin-Rammler fit, specifically for the Black Thunder PRB coal, is shown in Figure 5-2. A summary table of the Rosin-Rammler parameters used in FLUENT® for each test coal is provided in Table 5-3**.**

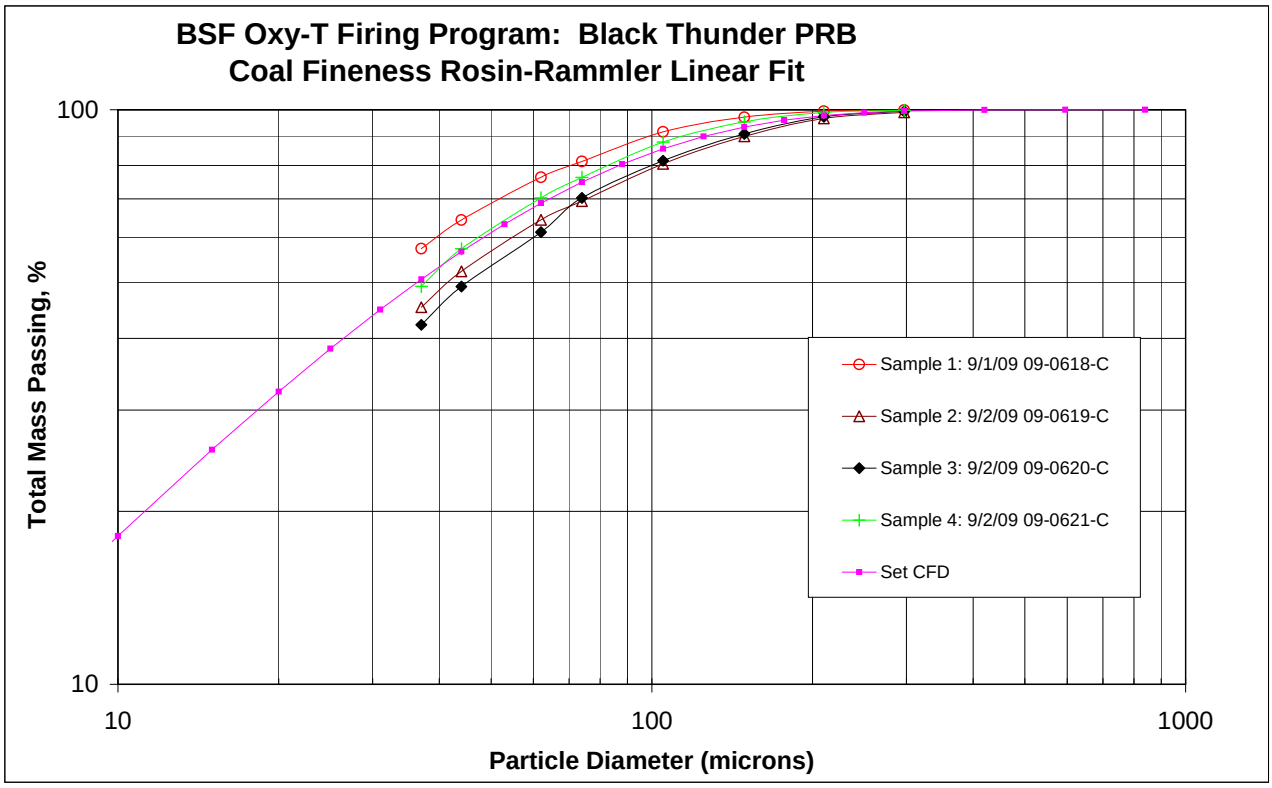

Figure 5-2. Coal Particle Size Distribution

Table 5-3. FLUENT® Rosin-Rammler Parameters for the Five Test Coals

	Black Thunder Powder River Basin (PRB)	West Virginia Fola	Illinois No. 6	North Dakota	Schwarze Pumpe
	Sub-bituminous	Bituminous	Bituminous	Lignite	Lignite
FLUENT® Rosin-Rammler Parameters					
Minimum Particle Size (microns)	1.5	1.5	3	3	3
Maximum Particle Size (microns)	200	200	200	200	200
Mean Particle Size (microns)	53	53	86	86	86
Slope (n) or Spread Parameter	0.965	0.965	0.98	0.98	0.98
Number of Diameters	20	20	20	20	20

Particle-radiation coupling was activated. A proprietary user-defined function (UDF) was used to calculate the particle absorption and scattering efficiencies, based upon parameters and values for bituminous coal. These same UDFs were used for all of the runs.

In the present set of runs, a single stochastic "try" was specified, which ultimately produced approximately 5,760 total particle injections. Turbulent particle dispersion utilized the "discrete random

walk" model; the "random eddy lifetime" option was not activated. Figure 5-3 illustrates some of the coal combustion "laws" described above – devolatilization, char consumption, and inert heating/cooling of ash – for the particle trajectories emanating from a single nozzle in the BSF. The overall residence time of the particles can range from a few seconds to many seconds, depending upon the particle injection location and the trajectory environment. In the present runs, very long residence times were encountered for some particles that spiraled or flowed downwards and settled on the hopper surface.

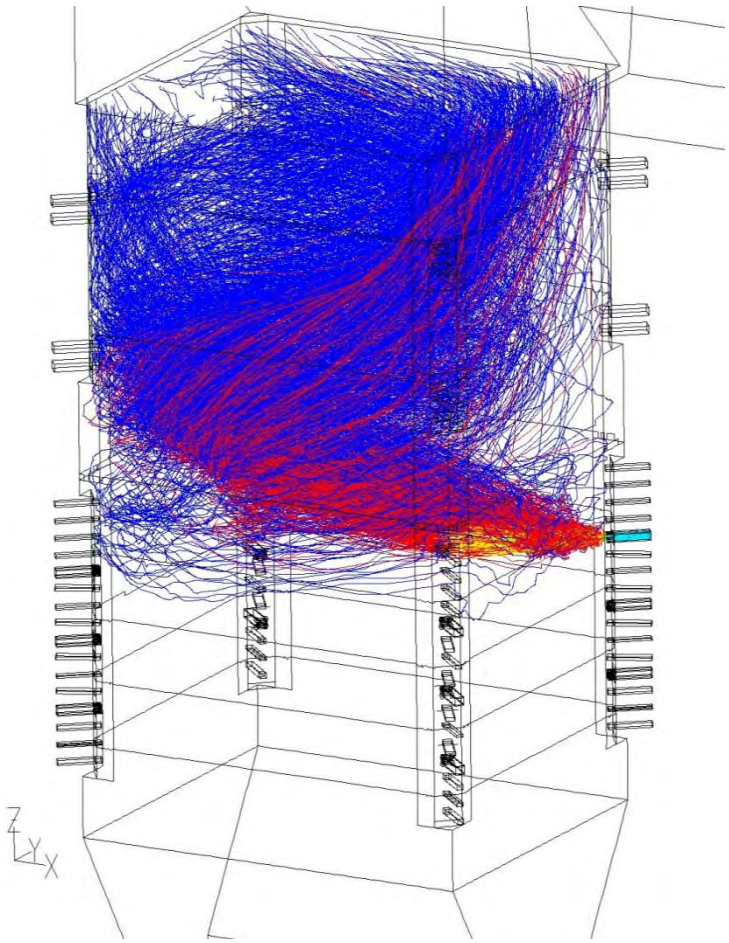

Figure 5-3. Coal Combustion Laws or Stages

5.4 Boundary Conditions

The inlet boundary conditions were prescribed through a mass-flow rate boundary specification for the Illinois, North Dakota, and Schwarze Pumpe coal cases; the inlet boundary conditions for the Fola and PRB coal cases utilize the velocity inlet specification. The inlet flow conditions for all of the air- and oxy-combustion simulation cases are shown in Table 5-4. This table includes the flow rates, temperatures, and species mass fractions (expressed as a percent) for the primary air (PA), windbox combustion air, lower

overfire air (LOFA), and upper overfire air (UOFA) sections, as well as the coal feed rate. The stream compositions for the oxy cases are different from those of the air cases due to the flue gas recycle strategy used in oxy combustion. The table also contains stoichiometric ratios and the relevant stoichiometries for both the main furnace zone and the overall domain.

Table 5-4. Inlet Gas and Coal Flow Rates and Temperature for all Cases

	Black Thunder PRB Sub-bituminous		West Virginia Fola Bituminous		Illinois No. 6 Bituminous		North Dakota Lignite		Schwarze Pumpe Liginte	
	Air Fired	Oxy Fired	Air Fired	Oxy Fired	Air Fired	Oxy Fired	Air Fired	Oxy Fired	Air Fired	Oxy Fired
Test #	11	22	39	50	75	74	83	98	109	134
PA Information										
Temperature [F]	140.0	140.0	140.0	188.5	140.3	153.0	108.3	132.5	106.9	137.5
O2 [mass, %]	22.96	15.51	23.22	17.10	23.19	17.53	23.40	16.99	23.08	13.51
CO2 [mass, %]	0.00	72.72	0.00	74.45	0.00	69.52	0.00	70.95	0.00	76.24
H2O [mass, %]	0.56	1.69	0.26	3.37	0.46	3.71	0.82	5.46	0.99	4.56
SO2 [mass, %]	0.00	0.12	0.00	0.00	0.00	0.07	0.00	0.13	0.00	0.08
N2 [mass, %]	76.48	9.97	76.52	5.08	76.36	9.16	75.79	6.47	75.93	5.61
Mass Flow Rate [lb/hr]	8,319	8,575	6,941	8,175	7,442	7,542	8,874	9,183	7,555	8,888
LOFA Information										
Temperature [F]	400.0	400.0	400.0	423.4	411.7	413.0	335.6	394.7	296.7	329.6
O2 [mass, %]	22.96	26.27	23.22	19.19	23.19	17.29	23.40	19.75	23.08	22.60
CO2 [mass, %]	0.00	61.37	0.00	70.22	0.00	65.97	0.00	63.58	0.00	60.72
H2O [mass, %]	0.56	8.42	0.26	5.59	0.46	9.97	0.82	10.85	0.99	12.99
SO2 [mass, %]	0.00	0.11	0.00	0.34	0.00	0.05	0.00	0.10	0.00	0.10
N2 [mass, %]	76.48	3.83	76.52	4.66	76.36	6.72	75.79	5.72	75.93	3.60
Mass Flow Rate [lb/hr]	4,619	4,466	7,351	4,976	6,819	5,244	5,216	3,081	4,596	3,129
UOFA Information										
Temperature [F]	400.0	400.0	400.0	422.3	407.9	412.0	332.8	385.7	290.6	320.3
O2 [mass, %]	22.96	26.27	23.22	19.19	23.19	19.83	23.40	19.75	23.08	22.60
CO2 [mass, %]	0.00	61.37	0.00	70.22	0.00	60.96	0.00	63.58	0.00	60.72
H2O [mass, %]	0.56	8.42	0.26	5.59	0.46	11.44	0.82	10.85	0.99	12.99
SO2 [mass, %]	0.00	0.11	0.00	0.34	0.00	0.06	0.00	0.10	0.00	0.10
N2 [mass, %]	76.48	3.83	76.52	4.66	76.36	7.71	75.79	5.72	75.93	3.60
Mass Flow Rate [lb/hr]	4,619	4,466	7,351	4,970	6,847	5,294	5,300	3,293	4,629	3,044
Windbox Information										
Temperature [F]	400.0	420.0	400.0	418.0	426.7	421.1	353.9	386.3	314.8	344.4
O2 [mass, %]	22.96	27.98	23.22	29.95	23.19	25.89	23.40	33.23	23.08	31.25
CO2 [mass, %]	0.00	59.32	0.00	60.89	0.00	55.95	0.00	52.82	0.00	53.58
H2O [mass, %]	0.56	8.66	0.26	4.83	0.46	10.81	0.82	9.01	0.99	11.47
SO2 [mass, %]	0.00	0.12	0.00	0.28	0.00	0.06	0.00	0.10	0.00	0.10
N2 [mass, %]	76.48	3.92	76.52	4.05	76.36	7.29	75.79	4.84	75.93	3.61
Mass Flow Rate [lb/hr]	23,505	18,821	21,472	20,170	20,312	22,054	20,014	18,034	21,430	19,470
Total Oxidant Flow [lb/hr]	41,062	36,328	43,116	38,290	41,419	40,134	39,404	33,591	38,210	34,530
Total O2 Flow [lb/hr]	9,428	8,942	10,011	9,347	9,603	8,989	9,221	8,812	8,819	8,680
Windbox+PA O2 Flow [lb/hr]	7,307	6,596	6,598	7,439	6,435	7,032	6,760	7,553	6,690	7,285
Coal Flow Rate [lb/hr]	4,762	4,972	4,159	4,106	3,955	3,972	5,883	5,878	4,862	4,964
Stoichiometric Mass of External O2 / Unit Mass of AF Coal	1.6137	1.6137	2.0676	2.0676	2.0656	2.0656	1.3016	1.3016	1.5332	1.5332
Windbox+PA O2/Coal Ratio	1.53	1.33	1.59	1.81	1.63	1.77	1.15	1.28	1.38	1.47
Total O2/Coal Ratio	1.980	1.799	2.407	2.277	2.428	2.263	1.567	1.499	1.814	1.748
Windbox+PA Stoichiometric Ratio [O2/Coal Basis]	0.951	0.822	0.767	0.876	0.788	0.857	0.883	0.987	0.897	0.957
Overall Stoichiometric Ratio [O2/Coal Basis]	1.227	1.115	1.164	1.101	1.176	1.096	1.204	1.152	1.183	1.140
HHV (Btu/lb, AF)	9,348	9,348	13,268	13,268	11,843	11,843	7,474	7,474	9,008	9,008
Firing Rate [Btu/hr]	4.452E+07	4.648E+07	5.518E+07	5.447E+07	4.683E+07	4.704E+07	4.397E+07	4.393E+07	4.380E+07	4.472E+07
Stoichiometric Mass of External O2/ Unit Mass of HTVY Volatile	1.9170	1.9170	2.0761	2.0761	2.3505	2.3505	1.7649	1.7649	1.2356	1.2356
Windbox+PA Stoichiometric Ratio [O2/ HTVY Volatile Basis]	1.698	1.468	1.741	1.988	1.273	1.385	1.481	1.656	2.536	2.705

The flow rates and compositions in the above table were extracted from data recorded by the BSF distributed control system. The data was post-processed to ensure that e.g., the correct mixture molecular

weight was used in the orifice plate calculations. A mass balance was done to more closely define the fuel feed rate and to approximate the air in-leakage. A more in-depth discussion of the data collection procedure and the methodology utilized to extract the values used for the BSF boundary conditions is provided in Volume II.

Table 5-5 shows a mapping of the sixteen levels of windbox air/coal ports plus the two levels each of the lower and upper overfire air ports. The port designations / names are also shown, as well as the port service status (i.e., in or out of service); "X" marks the ports with dampers in closed position. The flow rates through the air ports are proportional to the nozzle open area. A small amount of leakage air is allowed to pass through the small clearance (taken to be 0.5 square inches) of the closed ports. An EXCEL® spreadsheet is used to set up the inlet boundary conditions for all gas/fuel inlet ports.

Table 5-5. Windbox and Overfire Air Port Designations

	Black Thunder PRB Sub-bituminous		West Virginia Fola Bituminous		Illinois No. 6 Bituminous		North Dakota Lignite		Schwarze Pumpe Lignite	
	Air Fired	Oxy Fired	Air Fired	Oxy Fired	Air Fired	Oxy Fired	Air Fired	Oxy Fired	Air Fired	Oxy Fired
Test No.	11	22	39	50	75	74	83	98	109	134
Port 20	UOFA	UOFA	UOFA	UOFA	UOFA	UOFA	UOFA	UOFA	UOFA	UOFA
Port 19	UOFA	UOFA	UOFA	UOFA	UOFA	UOFA	UOFA	UOFA	UOFA	UOFA
Port 18	LOFA	LOFA	LOFA	LOFA	LOFA	LOFA	LOFA	LOFA	LOFA	LOFA
Port 17	LOFA	LOFA	LOFA	LOFA	LOFA	LOFA	LOFA	LOFA	LOFA	LOFA
Port 16	X	X	X	X	X	X	X	X	X	X
Port 15	CCOFA	CCOFA	CCOFA	CCOFA	CCOFA	CCOFA	CCOFA	CCOFA	CCOFA	CCOFA
Port 14	X	X	X	X	X	X	X	X	X	X
Port 13	Top End	Top End	Top End	Top End	Top End	Top End	Top End	Top End	Top End	Top End
Port 12	**Coal**	**Coal**	**Coal**	**Coal**	**Coal**	**Coal**	**Coal**	**Coal**	**Coal**	**Coal**
Port 11	CFS	CFS	CFS	CFS	CFS	CFS	CFS	CFS	CFS	CFS
Port 10	Straight	Straight	Straight	X	X	X	Straight	X	Straight	X
Port 9	CFS	CFS	CFS	CFS	CFS	CFS	CFS	CFS	CFS	CFS
Port 8	**Coal**	**Coal**	**Coal**	**Coal**	**Coal**	**Coal**	**Coal**	**Coal**	**Coal**	**Coal**
Port 7	CFS	CFS	CFS	CFS	X	X	CFS	X	CFS	CFS
Port 6	Straight	Straight	Straight	X	Straight	Straight	Straight	Straight	Straight	X
Port 5	CFS	CFS	CFS	CFS	CFS	CFS	CFS	CFS	CFS	CFS
Port 4	**Coal**	**Coal**	**Coal**	**Coal**	**Coal**	**Coal**	**Coal**	**Coal**	**Coal**	**Coal**
Port 3	Bottom End	Bottom End	Bottom End	Bottom End	Bottom End	Bottom End	Bottom End	Bottom End	Bottom End	Bottom End
Port 2	Under Fire	Under Fire	Under Fire	Under Fire	Under Fire	Under Fire	Under Fire	Under Fire	Under Fire	Under Fire
Port 1	X	X	X	X	X	X	X	X	X	X

There are four (4) different wall-insulation zones as a function of vertical height in the BSF, with the upper furnace wall being un-insulated, bare steel, as shown in Figure 5-4. To model the effect of the insulation, a specified temperature boundary condition was used in conjunction with the FLUENT® code's thin-wall thermal resistance formulation. The specified temperature is on the far side of a thin wall, away from adjacent fluid zone. The thermal resistance is the ratio of the parameters $\Delta x/k$, where Δx is the thickness of the resistance material(s), and k is the thermal conductivity. It was found necessary to adjust the thermal conductivity k of each zone (for a given inner surface temperature) to match the measured temperature data taken from Planes 141, 180, and 273 shown in Figure 5-4. This calibration procedure is necessary due to the lack of information about the degree and character of the fouling and slagging deposits on the wall surfaces in the different zones. Table 5-6 lists the k, Δx, and inner surface

temperature values used for all of the cases simulated. A few surfaces, such as the nozzles themselves and a portion of the corner plate through which the nozzles protrude, were prescribed with adiabatic thermal boundary conditions.

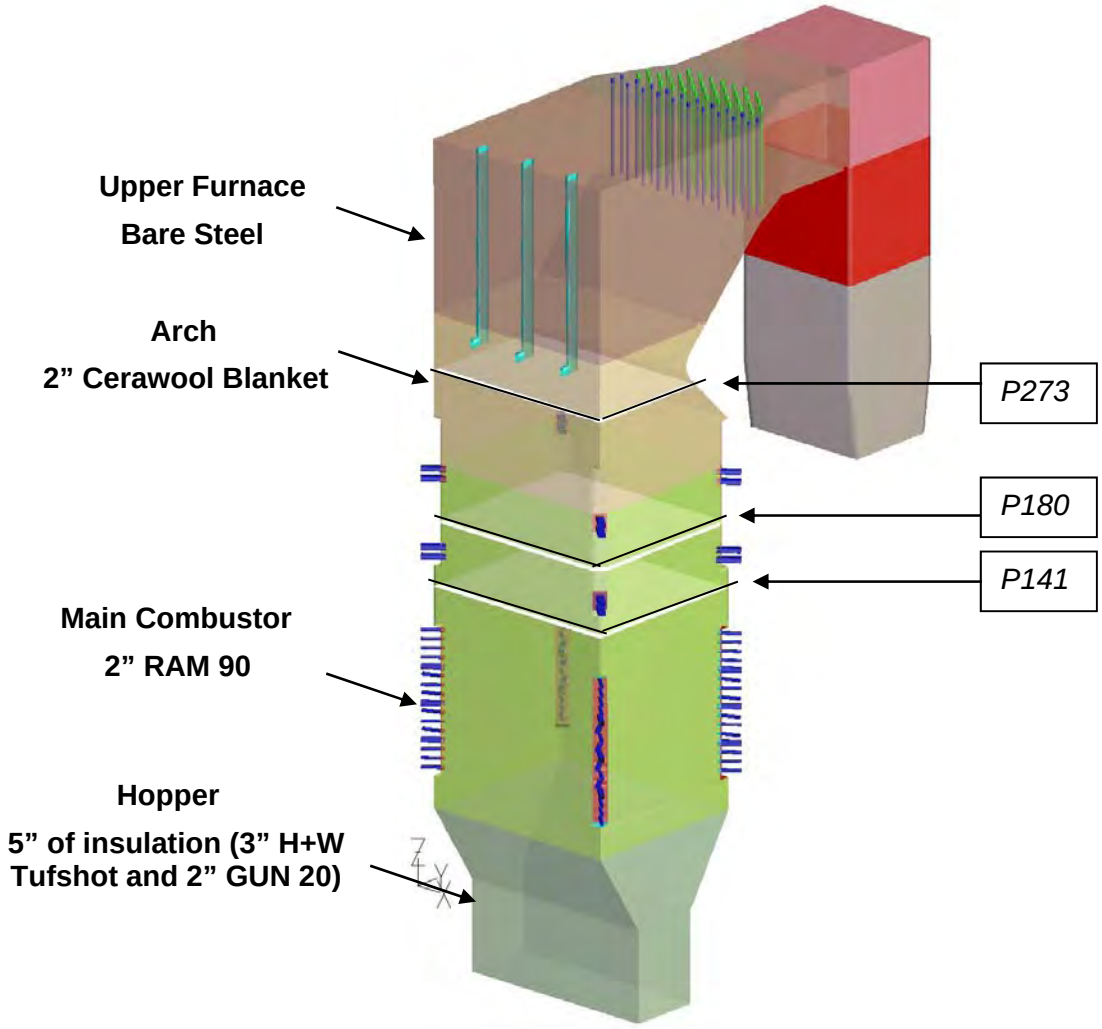

Figure 5-4. BSF Wall Insulations and Test Planes

Table 5-6. Wall (Specified Temperature) Boundary Conditions

	Black Thunder PRB	West Virginia Fola	Illinois No. 6	North Dakota	Schwarze Pumpe
Thermal Conductivity k of Wall Zones [W/m-°C (Btu/hr-ft-°F)]					
Upper Furnace	5.19 (3)	8.65 (5)	5.19 (3)	5.19 (3)	5.19 (3)
Arch	0.21 (0.12)	0.28 (0.16)	0.52 (0.3)	0.52 (0.3)	0.52 (0.3)
Main Combustor	2.86 (1.65)	4.33 (2.5)	3.46 (2)	3.46 (2)	3.46 (2)
Hopper	1.38 (0.8)	2.08 (1.2)	1.38 (0.8)	1.38 (0.8)	1.38 (0.8)
Wing Walls	2.86 (1.65)	4.33 (2.5)	3.46 (2)	3.46 (2)	3.46 (2)
Tube Banks	5.19 (3)	8.65 (5)	5.19 (3)	5.19 (3)	5.19 (3)
Upper Furnace	Bare Steel; Wall Thickness = 0.01278 m (0.5 in.); 533.33 K (500.33 °F)				
Arch	Cerawool Blanket; Wall Thickness = 0.0506 m (2.0 in.); 533.33 K (500.33 °F)				
Main Combustor	RAM 90; Wall Thickness = 0.0506 m (2.0 in.); 422.22 K (300.33 °F)				
Hopper	H+W Tufshot and GUN 20; Wall Thickness = 0.01270 m (5.0 in.); 422.22 K (300.33 °F)				
Wing Walls	Bare Steel; Wall Thickness = 0.06096 m (2.4 in.); 373.33 K (212.33 °F)				
Tube Banks	Bare Steel; Wall Thickness = 0.01280 m (0.5 in.); 373.33 K (212.33 °F)				
Note	Emissivity = 0.8 for all walls				

Other tube banks, such as the economizer tube bank in the backpass, were modeled as porous media, with a characteristic inertial resistance in each of the coordinate directions, and a specified volumetric energy extraction.

5.5 Convergence and Solution Considerations

The solution algorithm is based upon the SIMPLE pressure-correction algorithm with first-order upwind differencing. The radiation submodel was the Discrete Ordinates radiation model (solved every 10 gas-phase iterations), with the control angle parameters (theta divisions and phi divisions) set to a value of 2. A proprietary UDF was used to extract the local gas-phase absorption coefficient, rather than the default weighted-sum-of-gray-gas model in FLUENT®. Such a UDF was deemed to be more reliable for systems which have high CO_2 or H_2O partial pressure than the default model. The UDFs are compiled prior to run time.

The solution process within FLUENT® is usually performed in a segregated fashion, where the DPM sources are updated by an injection sequence, and then the Eulerian transport equations are sequentially updated for 25 to 50 gas-phase iterations, before a new sequence of injections is repeated. This process allows the solver to update and refine the particle momentum, energy and mass sources provided from the DPM injection. As the solution proceeds toward a final result, the impact of successive DPM injections, with proper under-relaxation, have progressively less impact on the gas phase. However, the stochastic particle tracking approach, and the associated random particle deflections, do tend to perturb the flow field, as indicated by the residual spikes in Figure 5-5. The degree of impact on the solution can be minimized by both under-relaxing the DPM results and by increasing the number of particles that are injected so that the individual variations within a cell have less of an impact. Although a small number of particles and a single stochastic try were used in the present computations, the cases converged well with a DPM under-relaxation factor of 0.1.

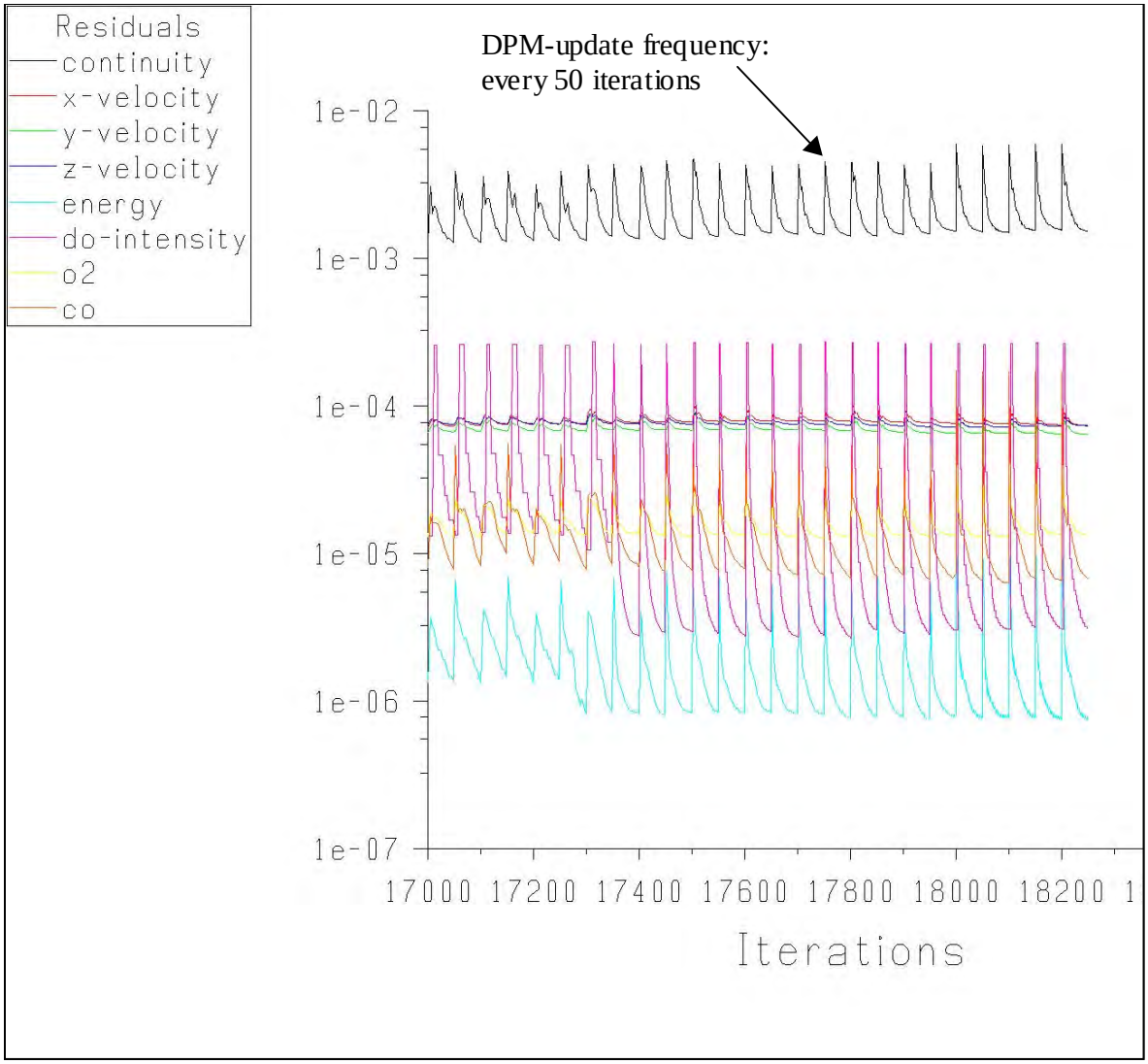

Figure 5-5. Convergence History

Although the residuals provide an indication of convergence, other FLUENT® metrics, such as the mass-weighted temperature at various planes, the outlet oxygen mole fraction, and other variables were routinely monitored to assess how much the flow field may continue to change as steady-state convergence is approached. In addition, overall energy and mass balances were intermittently checked by extracting data from FLUENT® and importing the data to EXCEL® spreadsheets. The integrity of the inlet boundary conditions, as well as the accuracy of the wall heat loss, temperatures, and species at various planes, were also checked against targets via EXCEL®.

6. Model Results for the Five Test Coals

For each coal, the air-combustion case was run first in order to establish a baseline or reference point before moving to the more complex oxy-combustion case with the recycled flue gas and oxygen injection. For example, for the air-combustion case, the grid quality was assessed, the mass flow rates were checked against the desired flow rates, the heterogeneous reaction rates were tuned to any residual or unburned carbon constraints, and the wall thermal boundary conditions were calibrated to match the measured temperatures, all prior to transitioning the case to oxy conditions. It should be stressed that the same property methods, reaction rates, and wall thermal boundary conditions were used in both the air and oxy cases; only the inlet boundary conditions changed. This implies that although in-furnace conditions change between air and oxy firing, (a) the property methods and kinetic rate expressions used in the CFD calculations remain fundamentally sound and valid and do not require modification, and (b) the degree of local fouling or slagging between the air and oxy tests (for a given coal) is not likely to change sufficiently to impact the tuned wall resistance. These assumptions are believed to be reasonable based on test observations and measurements.

The contour plot results for all of the cases are presented in a series of color plots for each test coal. Comparisons with test data are made primarily at three elevations, Planes 141, 180 and 273 (shown in Figure 5-4), where most of the data were collected. Due to the sparsity of the test data compared to the CFD mesh density, no meaningful contour plots of the experimental data can be generated to compare directly with the CFD contour plots. When available, the test data are shown on the CFD contour plots as discrete, colored dots. For earlier campaigns with PRB and Fola coals, where the data collection was not as exhaustive, some plots are presented without test data.

The experimental temperature measurements were derived from water-cooled, suction pyrometers, and the species measurements were collected using water-cooled, heated, gas extraction sampling probes. It should be noted that the species concentrations measured in the experiments are on the dry molar basis. Accordingly, custom field functions in FLUENT® were used to extract and present the CFD species concentration results on a dry molar basis in the pertinent contour plots. The SO_2 extracted in the suction probe and measured by the analytical array is the SO_2 species only (i.e., it is not a total sulfur measurement that is expressed in equivalent SO_2 terms).

Point measurements of the “total heat flux” at the wall were derived from the use of “total heat flux” probes at various sampling locations and elevations around the furnace. In the radiative section of the boiler, it is assumed that the probe measurements are equivalent to the incident surface radiative flux, since the probe tip is cold and clean, its re-radiation is insignificant, and radiation is the principal means of heat transfer at the planes of interest. The point measurements from the “total heat flux” probes were compared with computed (surface) incident radiant heat flux profiles across the span of each wall at those same elevations.

The span-wise profile plots of the computed (surface) incident radiative flux, along with the experimental data, have been oriented such that the distance on the abscissa always starts at zero. The abscissa is based upon the coordinate system for the geometry where the origin has been placed at the left-front corner, at the base of the geometry. Consequently, sometimes when the reader looks at a profile plot for a wall span, he will be looking from the outside of the boiler into the interior of the boiler (i.e., looking from the outside in), and sometimes the profile plot will be based upon an observer looking from the inside out. To help the reader orient himself to the viewing context associated with each graph, the notations “hot” or

"cold" have been added to the left and right sides of each profile plot, and a small schematic has been added to each figure with the "hot" and "cold" corner designations. It should be noted that the "hot" and "cold" corner designations are simply a viewing device intended to orient the reader; no physical or thermal significance should be attached to the walls or corners because of the notations.

The CFD predictions have presumed a uniform lateral deposit thickness all the way (circumferentially) around the furnace. Because of the refractory and insulation around the furnace, it is believed that local deposits will not change the gas temperature to the extent that the surface incident radiation will be impacted significantly. For the viewing convention adopted in the profile plots of the surface incident radiation, the "cold" corner is at 0% of the wall dimension and the "hot" corner is at 100% of the wall dimension. At Plane 141, many of the maxima are near the mid-span of the wall, but perhaps 70% of the plots at Plane 141 have maxima slightly on the hot–corner side. At Plane 180, all of the plots show that the maxima are skewed towards the hot corner. At Plane 273, the plots are flattened and more ambiguous; perhaps 60 to 75% of the plots may have the maxima skewed towards the hot corner. Again, no physical significance is attached to the "hot" and "cold" corners; the profile maxima will be a function of a number of different factors, including the direction of fireball rotation, the jet aerodynamics, the particle trajectories, the local radiative environment, etc.

Depending upon the range used for the color contour plots, some numerical values in the plots can be significantly higher than the range maximum, or significantly lower than the range minimum, indicated in the legends. Numerical values lying outside the color-key range will be regarded as "saturated" with the maximum or minimum color, as opposed to being merely clipped and assigned a white color. For example, cells or nodes in the plots with numerical values higher than the maximum in the color-key range will appear as a red color, while all cells or nodes with numerical values lower than the minimum in the color-map range will appear as a blue color. It should be noted that when the experimental data was superimposed on the contour plots as colored dots, the color of the dots was also subjected to this same "saturation" scheme at the color-map limits.

A post-processing UDF routine was used to extract planar averaged temperatures and species as a function of furnace elevation. The averaged planar data was extracted at height increments of 0.1 m. The routine extracts and exports all of the averaged species information on a wet molar basis. Rather than convert the averaged computed species values to a dry molar basis, it was decided to convert the test data to a wet molar basis on the planar averaged plots, using the experimentally determined water content. Consequently, although the species contour plots are on a dry molar basis, the profile plots for the species(as a function of elevation) are on a wet molar basis.

This same post-processing routine was also used to define horizontal (circumferential) wall strips, essentially stacked on top of each other from the bottom of the hopper to the roof. These wall strips were used to calculate the strip-averaged (i.e., circumferentially averaged) wall incident radiant heat flux as a function of elevation. The point measurements of the total (net) heat flux at the wall were averaged at prescribed elevations (e.g., planes P141, P180, and P273) and were included on the profile plots for comparison.

Some general comments can be made about some of the expected design considerations or differences between the air-combustion and oxy-combustion environments based on property considerations alone. These differences should be kept in mind as the coal test cases are discussed.

- Species such as H_2O, CO_2, and CO have higher gas emissivities. Although particles, such as char and soot, tend to dominate (or have a much higher impact) on the radiative flux to the walls than the gases, the aforementioned gas species nevertheless make a significant contribution. Therefore, the recycled flue gas species H_2O and CO_2, associated with the oxy-combustion systems, would be expected to enhance the heat flux in those systems in the radiative section, resulting in a slightly lower gas temperature entering the convective section.

- The specific heat of H_2O is approximately a factor of 2 higher than that of N_2, and the specific heat of CO_2 exceeds that of N_2 by about 7%. Therefore, the extent of drying of the moisture in the recycle stream becomes a design factor, as well as the CO_2 concentration in the recycle stream. Due to the increased H_2O and CO_2 concentrations in the oxy-combustion systems, the oxy systems would be expected to exhibit delayed flame ignition and decreased flame propagation speeds, as well as a lower flame temperature for the same net heat input.

- The molecular weight of CO_2 (44 kg/kmol) is higher than the molecular weight of N_2 (28 kg/kmol) by a factor of 1.57. Therefore, for an equivalent mass displacement of N_2 by CO_2, as might occur in an oxy-combustion system, the density of the feed will be higher and the velocity will be lower by about 36%. This value may be mitigated somewhat depending upon the relative amount of H_2O (18 kg/kmol) in the oxy-fired system. Accordingly, the volumetric flow rate in an oxy-combustion system would be expected to decrease and the residence time would increase, relative to an air-combustion system.

- For char oxidation, the mass diffusion of O_2 in a high CO_2 environment is about 20% lower than the diffusion rate of O_2 in N_2 (at 1600 K). Consequently, the oxidation rate may become more mass-diffusion limited with high CO_2 (e.g., at the higher temperature, Zone III (film-diffusion-limited) conditions). Perhaps more importantly, high CO_2 or H_2O concentrations, associated with oxy-combustion systems, may promote char consumption by char-CO_2 or char-H_2O gasification, both of which are endothermic reactions.

For reference purposes, a summary or roll up of some pertinent outlet parameters are shown in Table 6-1. The table contains the residual carbon-in-ash at the domain outlet, the temperature at the horizontal furnace outlet plane (Plane 273), the species compositions at the domain outlet, and calculated wall absorptions for various cumulative wall sections. The bituminous coal tests were the only tests which tended to have any significant residual carbon at the outlet. For each coal test, the outlet O_2 was roughly equivalent between the air case and the oxy case, except for the Illinois coal test, and to a lesser extent, the North Dakota lignite test. Among the coal tests, the Fola coal test had the highest heat absorption, followed by the Illinois coal test (in a manner congruent with their respective firing rates). The other three coal tests were somewhat similar and exhibited some overlap in both their absorptions and firing rates.

Table 6-1. Post-processed and Outlet Boundary Condition Results

	Black Thunder PRB Sub-bituminous		West Virginia Fola Bituminous		Illinois No. 6 Bituminous		North Dakota Lignite		Schwarze Pumpe Lignite	
	Air Fired	Oxy Fired	Air Fired	Oxy Fired	Air Fired	Oxy Fired	Air Fired	Oxy Fired	Air Fired	Oxy Fired
Test No.	11	22	39	50	75	74	83	98	109	134
Carbon in Ash (%, by Mass)										
Calculated	0.04	0.02	0.97	0.05	2.62	2.12	0.06	0.02	0.20	0.07
Experimental	0.15	0.13	1.16	0.51	2.17	0.77	0.09	0.07	0.02	0.04
HFOT [Plane 273] (°F)										
Calculated	2315	2335	2392	2329	2242	2193	2142	2109	2148	2183
Experimental	2257	2432	2477	2470	2277	2219	2107	2117	2088	2264
Domain Outlet Plane Species Composition (Mole %, Wet)										
O2	3.040	2.820	2.910	3.280	3.000	2.062	2.500	2.320	2.930	3.000
CO2	14.460	65.600	14.990	73.130	14.360	62.955	15.160	62.520	15.060	62.940
CO	0.003	0.015	0.032	0.005	0.029	0.027	0.005	0.000	0.002	0.000
SO2	0.027	0.095	0.071	0.226	0.274	0.369	0.092	0.179	0.065	0.131
H2O	10.100	25.160	6.650	17.660	7.380	25.502	11.770	28.870	10.490	29.240
N2	72.371	6.310	75.346	5.699	74.957	9.085	70.472	6.111	71.453	4.689
Total	100.000	100.000	100.000	100.000	100.000	100.000	100.000	100.000	100.000	100.000
Domain Outlet Plane Species Composition (Mole %, Dry)										
O2 (Mole %, Dry)	3.38	3.77	3.12	3.98	3.24	2.77	2.83	3.26	3.27	4.24
CO2 (Mole %, Dry)	16.08	87.65	16.06	88.81	15.50	84.51	17.18	87.90	16.82	88.95
CO (ppm, by Volume, Dry)	29	202	347	65	317	357	62	0	26	0
SO2 (ppm, by Volume, Dry)	298	1,271	763	2,745	2,958	4,953	1,045	2,517	724	1,851
N2 (Mole %, Dry)	80.50	8.43	80.71	6.92	80.93	12.19	79.87	8.59	79.83	6.63
Experimental Boiler Outlet Composition (Mole %, Dry)										
O2 (Mole %, Dry)	3.06	3.33	2.99	3.79	3.18	2.71	3.20	4.23	3.33	4.26
CO2 (Mole %, Dry)	16.49	89.35	15.70	88.31	14.93	84.47	16.27	84.74	16.87	89.74
CO (ppm, by Volume, Dry)	0	0	0	6	0	0	0	0	0	0
SO2 (ppm, by Volume, Dry)	277	1,219	677	1,606	------	------	951	4,052	685	1,316
Calculated External Wall Absorption (W) [Note 1]										
Absorption from Hopper Bottom to HFOP	-4.52E+06	-4.85E+06	-8.04E+06	-8.42E+06	-6.35E+06	-6.30E+06	-5.52E+06	-5.78E+06	-5.81E+06	-6.08E+06
Absorption from Hopper Bottom to Boiler Roof	-6.95E+06	-7.39E+06	-1.08E+07	-1.11E+07	-8.73E+06	-8.65E+06	-7.55E+06	-7.70E+06	-7.88E+06	-8.25E+06
Absorption for Entire Domain	-9.85E+06	-9.43E+06	-1.30E+07	-1.32E+07	-1.06E+07	-1.06E+07	-9.34E+06	-9.23E+06	-9.59E+06	-1.00E+07
Note 1	The wall absorption does not include volumetric heat extraction from porous media representing tube banks, etc.									
HFOP	Horizontal Furnace Outlet Plane [Plane P273]									
HFOT	Average gas temperature at the Horizontal Furnace Outlet Plane [Plane P273]									

Each coal section contains some redundancy in the discussion in order to allow each section to stand independently and alone. However, because many of the following figures are repetitive, an attempt was made to provide a majority of the commentary in the first section for the PRB coal, and to minimize the amount of commentary in subsequent sections, unless it was considered necessary to make or reinforce a point. Because of the large number of repetitive figure captions, an abbreviated notation for the test numbers was included in each caption, in the form of [AT-#:OT-#], where AT stands for air test and OT stands for oxy test, and # designates the actual test number.

6.1 Black Thunder PRB Sub-Bituminous Coal

This section addresses predictions for Air Test 11 and Oxy Test 22.

Figure 6-1 shows the temperature on a vertical (x-midplane or "symmetry") plane through the center of the furnace. The air-combustion case has a higher total oxidant flow rate and a lower coal flow rate than the oxy-combustion case. For the air-combustion case, the main windbox (i.e., defined herein as excluding the SOFAs) oxygen-to-fuel stoichiometric ratio (i.e., 0.95) is higher than that of the oxy-combustion case (0.82; see Table 5-4). Therefore, one might reasonably expect the temperature in the vicinity of the main windbox to be slightly higher in the air-combustion case than in the oxy-combustion case, all else being equal. This is indeed the case. As mentioned in the previous section, the higher H_2O and CO_2 concentrations, associated with the oxy-combustion cases, also help to lower the temperature because of their higher gas emissivities (leading to higher wall heat flux) and higher specific heats. Because of the higher CO_2 concentration in the oxy-combustion case, the extent of endothermic gasification and the associated decrease in temperature in the fuel-rich windbox region, may also be a factor, albeit perhaps a secondary or minor factor. The relative contribution of each of these factors to the temperature difference has not been quantified.

Figure 6-2 shows the temperature contours on Planes 141, 180 and 273 above the windbox. The oxy-combustion case has a higher (horizontal) furnace outlet temperature at Plane 273 due, in part, to a higher coal flow rate and lower total gas mass flow to heat up. Also, the coal combustion rate under oxy-combustion is slower due to the slower O_2 diffusion rate through CO_2 than through N_2 and higher specific heat of CO_2. The actual temperature at the arch will be a complex function of the overall stoichiometric ratio (oxygen basis), which is 1.227 for the air-combustion case, and 1.115 for the oxy-combustion case, and the relative amounts of diluent, as well the extent of combustion, the high-temperature speciation, and the specific heats.

Figure 6-3 shows the temperature on each of the three planes separately, with the test data superimposed for comparison purposes. The computations and data are shown on a constricted scale (only 2100 °F to 2600 °F) in order to emphasize differences. Although many of the experimental measurement points seem to compare well with the computations (e.g., air-fired, P141), other points appear to be systematically on the order of 100 to 200 °F off. Large deviations between an individual experimental data point and the calculated temperature may indicate that (a) the calculated jet aerodynamic patterns and reaction zones do not precisely overlie the experimental patterns, or (b) the calculated chemistry and kinetics are different from that occurring experimentally, or (c) some other (as yet undefined) systemic factor is impacting the predictions over the entire plane. At P180 and P273, for example, the measurements appear to be generally lower than the predictions for the air-fired case, while the opposite is true for the oxy-fired case. There certainly appears to be some asymmetry in the data (e.g., oxy-fired, P141) that cannot be readily explained or accounted for. Potential explanations for the asymmetry might include asymmetric wall slagging and partial blockage of nozzles due to slagging, imbalances in the coal or gas feeds, or uncertainties in the measurements themselves. The reader may attempt to visually average the data points to get an overall sense of the mean temperature, but to do so is quite challenging. In the planar-averaged profile comparisons, shown later, the data on a plane are collapsed to a single averaged data point; this may help to provide the reader with a more understandable qualitative indication as to how well the averaged predictions and data compare among all of the test cases. A discussion of the uncertainty and repeatability of the individual point measurements is provided in Section 5 (Volume III).

Figure 6-4 shows the oxygen concentrations on the test planes, with the test data superimposed on the predictions in Figure 6-5. At P141, the low oxygen reflects the staging oxidant-to-fuel ratios. At P180, the high oxygen gradients coincide with the temperature gradients around the jets. Regions of low oxygen concentration typically reflect regions of high CO_2 concentrations (shown later) and the corresponding

temperatures associated with the product species. Many of the experimental data points on this plane are indicative of, or manifest the presence of, the jet and core pattern, with lower oxygen concentration in the core and higher oxygen concentrations associated with the residual jets, in a manner somewhat substantiated by the calculations. However, some of the data points that cross, e.g., the rear-wall jet of the air-combustion case, indicate very low oxygen, seemingly contradicting the presence of the calculated high oxygen-containing jet. The imprints of the SOFA oxidant supply and swirl pattern are still visible at the horizontal furnace outlet plane (P273), with a ring of calculated high O_2 around the periphery and a lower O_2 concentration in the core; however, the experimental data on this plane are much more asymmetric and only partially validate a portion of the ring.

The jets on Plane 180 appear to penetrate much further in the oxy test than they do in the air test. One reason for this is that the total gas mass exiting the main windbox region and entering the SOFA zones is larger for the air case than for the oxy case, by at least 10% (see Table 5-4). Consequently, the jet-to-crossflow momentum ratio in the SOFA region is higher in the oxy case than in the air case, by about 40%, promoting greater jet penetration, despite the fact that this was offset somewhat by the lower velocity of the inlet jet for the oxy case (due to the higher molecular weight of the inlet gas stream).

Figure 6-6 shows the CO_2 concentrations on the test planes. Note that the color maps presented for the air- and oxy-combustion cases are necessarily different due to the high CO_2 concentration in the oxidant for the oxy-combustion case (about 88 mole % (dry) at the horizontal furnace outlet plane). While, for the air-combustion case, nitrogen is the major species in the flue gas, recycled CO_2 constitutes the majority of the flue gas in the oxy-combustion case. Figure 6-7 shows the contours of CO_2 on separate test planes with the test data superimposed. For the air case for P141, the experimental measurements appear to be higher around the periphery, in accordance with the predictions, although the experimental values do not indicate as much CO_2 in the core. The lower row of data points (dark blue points) at P180 represents a traverse line where the experimental data was not taken due to an instrumentation problem, and should be ignored. At P180 for the air case, the computational results indicate a CO_2 core that is only partially validated by the experimental data, with both higher and lower data points in the core region and in the jet trajectories. At Plane 273, for the air case, the experimental data does appear to indicate a core region of higher CO_2, surrounded by a region of lower CO_2. This observation is in rough accord with the calculations, although there is some asymmetry in the data. For the oxy case, at P180, the experimental data are qualitatively aligned with the computed contours, but at P273, the asymmetry in the experimental data is such that it is hard to see a good correlation with the calculations.

Figure 6-8 shows the CO concentrations on the test planes. The CO is produced from coal gasification and char/"C-gas" oxidation, and is plotted on the same scale for both the air and oxy calculations. Figure 6-9 shows the contours of CO concentrations on separate test planes with the test data superimposed. For the air case at P141, most of the computed CO is in an interior ring, attaining values of about 6 mole % (dry); the experimental data loosely validates this ring except for some asymmetry. For the oxy-combustion case at P141, the computed CO is globally high due to the windbox oxygen deficiency, coupled with gasification. Although the relative contributions are not known, it is suspected that gasification (arising from the large CO_2 and H_2O concentrations in the oxy case) plays a significant role. At P180, the experimental data seem to correlate fairly well with the calculations (with a few exceptions), indicating higher CO around the periphery, as well as in a small core region. At the horizontal furnace outlet plane (P273), almost all of the CO has been oxidized into CO_2, in a manner seemingly congruent with the data, although the data appear to have slightly higher values.

Figure 6-10 shows the H_2O concentrations on the test planes. Note that the color maps presented for the air- and oxy-combustion cases are different due to the higher H_2O concentration in the recycled flue gas fed to the oxy-combustion case. Figure 6-11 shows the contours of H_2O concentrations on separate test planes with the test data superimposed. The experimental data appear to be 1 to 3 percentage points lower than the computations at all planes. On P180, for the air case, the experimental data in the core does increase by a couple of percentage points, relative to the value in the jets, but the experimental core values do not achieve the same magnitude as the computations. The color-map scales are fairly constricted, thus overly emphasizing differences that may be due to uncertainties in the moisture or other hydrogen-containing species fed to the boiler.

Figure 6-12 shows the SO_2 concentrations on the test planes. Note that the color maps presented for the air- and oxy-combustion cases are different due to the higher SO_2 concentration in the recycled flue gas fed to the oxy-combustion case. Figure 6-13 shows the contours of SO_2 on separate test planes with the test data superimposed. The SO_2 extracted in the suction probe and measured by the analytical array is the SO_2 species only; it is not a total sulfur measurement that is expressed in equivalent SO_2 terms. The profile plot (Figure 6-14) shows that the averaged SO_2 concentration steadily increases as a function of elevation. For example, for the air case, the experimental SO_2 on P141 is about 100 ppm less than the average SO_2 values on P273. For the oxy case, the experimental SO_2 on P141 is about 200 ppm less than the average SO_2 values on P273. From this monotonic increase in SO_2 as a function of elevation, it is surmised that (1) the sulfur also exists in other forms in the fuel-rich windbox region (e.g., CS_2, H_2S, etc.), and then more fully converts, with the addition of oxygen from the SOFA ports, to SO_2, and (2) that some of the sulfur is retained in the char and evolves as the char is consumed. (Note that in the simulation, it was assumed that all of the fuel sulfur would be released from the coal along with volatile matter.) For the PRB coal, a negligible amount of the original sulfur in the coal is retained in the char (according to PC Coal Lab), but that retention value may be as high as 10% for other coals, if not more. Therefore, at least for the PRB coal, it is hypothesized that the monotonic increase is primarily due to the fact that the devolatilized sulfur exists initially as gaseous species other than SO_2. However, this pattern is only apparent in three (3) of the five (5) coal tests, and is not apparent in the lignite tests. Therefore, either lignite sulfur chemistry behaves differently than other coals, or the number of data points at the lower elevations is simply insufficient to provide a reliable average to establish a trend. At P141 for the air case, some of the higher point measurements are toward the periphery, in a manner similar to the computations, but there is not a strong pattern match. The same experimental pattern is displayed at P141 for the oxy case, but the computed values are all uniformly high. At P180, the computations indicate high SO_2 in the core, lower SO_2 in the vicinity of the jets, and then higher SO_2 near the walls. It is interesting that the experimental SO_2 is low in the oxygen-starved core and higher around the core where oxygen exists. This may again indicate that the sulfur may exist as a different species in oxygen-starved regions. The data are somewhat asymmetric, but similar reasoning can be put forward for the oxy case. At P273, it is difficult to say whether the subtle differences between the individual points indicate an overall pattern match with the computations, although, at least for the air case, perhaps it can be said that both the computations and the data indicate a slight, higher SO_2 core.

Figure 6-14 is a contour plot that shows the incident radiation for the air- and oxy-combustion cases. The incident radiation in the boiler is higher for the air-combustion case than for the oxy-combustion case primarily due to the higher furnace temperature in the air-combustion case. Figure 6-15 through Figure 6-17 show the incident radiation profile span-wise along the walls at the three test planes, with the measured data included (when available) for comparison. For the PRB air-combustion case, at Plane 141, the computed incident radiation on the wall appears generally to be about 15 to 30% higher than that

indicated by the experimental data. For the oxy-combustion case, at the same plane, the computed incident radiation appears to be closer to the measurements, but still somewhat high. At Plane 180, computations are closer to the data, but remain somewhat high overall. At Plane 273, predictions remain about 15 to 25% too high. In comparing the two cases, it appears evident that the magnitude of the radiation appears to qualitatively track the gas temperature, although it may be exacerbated by the T^4 radiation phenomenon. This may perhaps be more easily seen by examining the profile plots as a function of elevation for the incident radiation (Figure 6-18) and the gas temperature (Figure 6-19). The large over-prediction of the incident radiation is accompanied by an under-prediction of the temperature. A more rigorous calibration of the wall resistances to better match the arch temperature would have improved both the temperature predictions and the wall heat flux predictions.

Figure 6-18 shows the strip-averaged incident radiation distribution as a function of elevation for the air- and oxy-combustion cases, with the measured data included for comparison. It should be noted that the computation is an average of the incident flux for a given strip height, all the way around the periphery of the furnace (which allows different magnitudes on different walls), while the measurements are numerical averages of a few data points e.g., on two sides of the furnace only. The plot highlights the observation that the computed incident radiation for the air case is higher than that of the oxy case in the main furnace zone, but it becomes lower than the incident radiation for the oxy case as the horizontal furnace outlet plane (Plane 273) is approached. It should be noted that the gas temperature in **Figure 6-19. [AT-11:OT-22] Planar Averaged Temperature**Figure 6-19 exhibits a similar cross-over trend.

Qualitatively, the relative differences between the air and oxy cases, with respect to the incident radiation or the temperature, is mirrored by the data. Improvements to the quantitative accuracy may require additional study of a number of different factors. For example, particles in the core of the furnace emit radiation to the furnace walls; however, cooler particles near the wall can absorb the radiation from the core, and then emit radiation to the walls at a lower temperature, thus providing an insulative effect. Therefore, the particle trajectories and their proximity to the wall, as well as their temperature, have an important impact on the radiative flux to the walls. In addition, absorption and scattering efficiencies for bituminous coal were used for the PRB coal simulations (and all of the other coals tested.) It is not known to what extent the incident radiation might have been impacted if the actual absorption and scattering coefficients for the PRB (and each test) coal had been utilized instead of the generic bituminous coal values. Another factor may be the uncertainty in the wall emissivity. The wall deposit emissivity of for a PRB coal may vary substantially as a function of the interior wall temperature and the iron content in the deposit. Any uncertainty in the particle size distribution or particle reaction rates would help to mitigate somewhat the absence of proper experimental radiation properties, but some additional sensitivity runs to investigate the impact of these parameters might demonstrate how the predictions could be improved.

Figure 6-19 shows the planar averaged temperature as a function of elevation for the air- and oxy-combustion cases, with the measured data included for comparison. The computed temperature trends for both the air and oxy cases are qualitatively similar to the experimental values, although the calculations are about 100 °F lower than the data, demonstrating that additional calibration on the implicit wall heat transfer resistance could be performed to increase the predictive accuracy.

Figure 6-20 shows the planar averaged oxygen concentration (wet) as a function of elevation for the air- and oxy-combustion cases, with the measured data included for comparison. Oxygen concentrations in the hopper are a function of the local stoichiometry in that region, depending on the flow patterns and particle dynamics that carry coal and oxidant into the hopper. At Plane P141, between the windbox and

the lower SOFA, there appears to be some unused O_2 for the air-combustion case, while for the oxy-combustion case, the oxygen is essentially depleted. The oxygen concentration increases with successive SOFA additions, with the oxygen calculations at the arch leveling out at values slightly higher than the data. The computed oxygen concentrations at the arch are very similar to those at the exit of the domain, indicating that the PRB char has very low residual carbon and that any remaining reactions have very little effect on the oxygen levels between the arch and the domain exit.

Figure 6-21 shows the planar averaged CO_2 concentration (wet) as a function of elevation for the air- and oxy-combustion cases, with the measured data included for comparison. For the oxy-combustion case, the baseline CO_2 concentration is already high due to the CO_2 in the recycled flue gas feed. However, the CO_2 concentration continues to climb to even higher values as combustion progresses to completion, despite the dilution effect of the SOFA stages. The calculations appear to be reasonably aligned with the averaged experimental data.

Figure 6-22 shows the planar averaged CO concentration (wet) as a function of elevation for the air- and oxy-combustion cases, with the measured data included for comparison. CO is a minor species and is typically much more difficult to predict than a major product species; nevertheless, the CO concentrations are predicted reasonably well at all of the elevations for both cases. For the oxy-combustion case, the CO concentration is high within the hopper, due to negligible O_2 within the hopper region, while the opposite is true for the air case. (The air case has negligible CO in the hopper, due to excess O_2 in the same region.) As expected, the CO is high between the windbox and the SOFA, due to staging and depleted oxygen at that elevation, but the CO diminishes to hundreds or tens of ppm at the arch.

Figure 6-23 shows the planar averaged SO_2 concentration (wet) as a function of elevation for the air- and oxy-combustion cases, with the measured data included for comparison. As discussed previously, the baseline SO_2 level is higher for the oxy-combustion case than the air-combustion case, due to the SO_2 content in the recycled flue gas feed associated with the oxy case. The monotonic increase in the experimental SO_2 is postulated to infer that a portion of the sulfur exists in the fuel-rich region in forms other than SO_2 (e.g., H_2S, CS_2, etc.), and that with the introduction of additional oxygen, the various sulfur species gradually oxidize to SO_2. The calculations cannot simulate this change since all of the sulfur is rapidly converted to SO_2 through volatile decomposition alone, and subsequent changes in SO_2 mole fraction with elevation are simply a function of the volumetric changes associated with other reactions and feed additions. As an alternative explanation, the number of data points at the lower planes (e.g., Plane 141, etc.) may simply be too few in number to provide a reliable value with which to establish trends.

Figure 6-24 shows the planar averaged water concentration as a function of elevation for the air-and oxy-combustion cases, with the measured data included for comparison. Again, the water concentration is higher for the oxy-combustion case due to higher water concentration in the recycled flue gas. The predictions are 1 to 3 percentage points higher than the experimental data, but the predictions are probably reasonable given the uncertainties in the measured data, as well as the uncertainties in the feeds, coal composition, etc.

6.2 West Virginia Fola Bituminous Coal

This section addresses predictions for Air Test 39 and Oxy Test 50.

Figure 6-25 shows the temperature on a vertical plane through the center of the furnace. The oxy-combustion case has a higher windbox oxygen-to-fuel stoichiometric ratio (0.876; see Table 5-4) than that (0.767) of the air-combustion case. Consequently, the oxy-combustion case exhibits a higher main furnace temperature than the air-combustion case by perhaps 200 °F. The measurements, however, as will be shown later, indicate that the air case may be on the order of 50 °F hotter than the oxy case in the windbox region. This implies that an adjustment in boundary conditions may be warranted.

Figure 6-26 shows the temperature contours on Planes 141, 180 and 273 above the windbox. Figure 6-27 shows the temperature on these planes separately, with the test data superimposed for comparison purposes. Some of the colors are saturated and accurate differences are difficult to discern. However, on the average, at Plane 141, the experimental temperature for the air case is approximately 50 °F greater than that of the oxy case; at Plane 180, the two experimental temperatures are with 25 °F of each other, and at Plane 273, the average temperatures are practically coincident. The calculated temperature differences between the air and oxy cases are significantly greater. Again, the temperature predictions may have benefited by calibration or tuning adjustments to the wall heat transfer resistance.

Figure 6-28 shows the oxygen concentrations on the test planes, with the test data superimposed on Figure 6-29. On Plane P180, the experimental data points appear to qualitatively follow the gross features of the computations -- the low oxygen regions around the periphery of the furnace, the higher oxygen concentrations in the jet regions, and the oxygen-starved core. On Plane 273, for the air case, the imprints of the SOFA oxidant supply and swirl pattern are still visible at the horizontal furnace outlet plane, although significant asymmetry exists in both the experimental and computed values, and the experimental pattern only partially matches the computational pattern. On Plane 273, for the oxy case, the high, experimental O_2 concentrations do seem to reside predominately on the right-hand side of the furnace, in a pattern that seems to be congruent with the calculations.

Figure 6-30 shows the CO_2 concentrations on the test planes. Note that the color map scale for the oxy-combustion case is very different from that of the air-combustion case, due to the recycled flue gas feed stream. For the oxy-combustion case, the CO_2 concentration is around 89% (mole %, dry) at the horizontal furnace outlet (Plane 273). Figure 6-31 shows the contours of CO_2 on separate test planes with the test data superimposed for comparison purposes. It is difficult to see a strong pattern match between the data and the computations; the only statement that can be made is that the data and the computations do vary within the same maximum and minimum values. For the oxy-combustion case, the experimental data exhibit some apparent asymmetry, although the constricted color maps tend to artificially exaggerate the asymmetry (e.g., the difference between the green and the red colors is only 3 percentage points).

Figure 6-32 shows the CO concentrations on the test planes. The CO is largely produced from coal gasification, char oxidation, and “C-gas” oxidation and is plotted on the same scale for both the oxy and air cases. At the horizontal furnace outlet plane (P273), almost all the CO has been combusted into CO_2. Figure 6-33 shows the contours of CO concentrations on separate test planes with the test data superimposed. On Plane 141, CO values are globally higher, both computationally and experimentally, than at subsequent planes. At Plane 180, the experimental data tends to show some higher values of CO around the periphery of the furnace, as well as higher values in the core, seemingly in rough agreement with the computations. For the oxy case, the experimental core values are several percentage points higher than the computations. At Plane 273, the oxy case indicates the persistence of the core CO values, whereas the calculations indicate that the CO has been essentially consumed.

Figure 6-34 shows the H_2O concentrations on the test planes. Note that the color map scales presented for the air- and oxy-combustion cases are very different from each other, due to the higher H_2O concentration in the recycled flue gas for the oxy-combustion case. Figure 6-35 shows the contours of water concentrations on separate test planes with the test data superimposed. At Planes P180 and P141, the experimental H_2O concentrations for the air case appear to be uniformly lower than that of the computations, while for the oxy case, the data is uniformly higher than the computations. However, it should be noted that again the scales are quite constricted – limited to only 2 or 3 percentage points. Again, if species plots for species like CO_2 or H_2O exhibit pronounced differences between the predictions and the experimental data at the "outlet', ignoring any obvious errors in setting up the cases or performing the experiments, then the differences must be due to uncertainties in the feed rates and compositions, since the CFD computations are performing an overall element balance with essentially complete combustion.

Figure 6-36 shows the SO_2 concentrations on the test planes. Note that the color map scales presented for air- and oxy-combustions are different, due to the higher SO_2 content in the flue gas recycled to the oxy boiler.
Figure **6-37** shows the contours of SO_2 on separate test planes with the test data superimposed. Computationally, the sulfur species comes off with the volatile decomposition, and should be conserved at all elevations above the windbox. Experimentally, however, the concentration of the SO_2 tends to increase with elevation, implying that the sulfur may exist, at least partially, as other species besides SO_2 (e.g., H_2S, CS_2, etc.) down in the fuel-rich, main windbox zone. On Plane 180, for the air case, a slight qualitative pattern match may be discerned, with a single yellow (measured) dot in the high-concentration core region, surrounded by an annulus of lower-concentration green dots, with a few higher-concentration dots outside near the periphery. The calculations show a similar trend, although the change in magnitude from the peaks to the valleys are much greater for the computations. For the oxy case, although the colors are saturated, the bottom row increases (left to right) from 1750 ppmv to about 2800 ppmv. On the next two rows up, the core region is about 1400 ppmv, and it decreases toward each side, with a quick upswing near the wall, similar to the contours. On the top row, the values are about 1200 ppmv except for a slight increase near the walls. The magnitudes are different, but the annular (low-concentration) ring appears to be partially validated. At the arch (P273), for the air case, the calculations slightly overpredict the SO_2, but a core region of higher SO_2 may be observed in both the data (discerning between the green and blue dots) and computations. For the oxy case, experimental values (saturated colors) are about 3200 ppmv in the core and decrease to about 2900 ppmv away from the core. The calculations show an interior core value of about 2750 ppmv, while away from the core, values range from 2730 to 2700 ppmv; qualitatively the trend is the same, although the magnitudes are different.

Figure 6-38 shows the incident radiation for the air- and oxy-combustion cases. It should be noted that the scale for the radiation is much higher for the West Virginia Fola tests than for the other coal tests, because the firing rate in the Fola tests is about 20% or more higher than the other tests. The incident radiation is higher for the oxy-combustion case in the main furnace zone than in the air-combustion case, due to the higher main furnace temperature discussed previously. As mentioned earlier, the higher temperatures associated with the computed oxy-combustion case may indicate a boundary condition (feed) issue. The computed oxy case even has higher temperatures extending into the lower furnace, perhaps due to the 4% oxygen in the lower furnace, inducing more extensive combustion in the lower furnace.

Figure 6-39 to Figure 6-41 show the incident radiation along the walls on three test planes, with the measured data included for comparison. Experimentally, the oxy case does not appear to be too dissimilar from the air case. However, from the computational viewpoint, the computed incident radiation on the

wall for the oxy case appears generally to be at least 40% higher than that indicated by the experimental data at Plane 141, and perhaps 10 to 30% higher at Planes 180 and 273. For the air-combustion case, the computed incident radiation appears to be much closer to the measurements at Planes 141 and 180, while the predictions again diverge from the data at Plane 273, with the computations higher than the data by 10 to 15%. At Plane 273, the computations appear to flatten out more than the experimental data. The overall absorption from the bottom of the hopper to the HFOP is about 4.7% higher for the oxy case than the air case; the overall absorption from the bottom of the hopper to the roof is about 2.7% higher for the oxy case than for the air case. The computed HFOT for the oxy case is 2329 °F, which is lower than the corresponding air case (2392 °F). Therefore, it appears that the temperatures in the computed oxy case are higher in the windbox than in the corresponding windbox region of the computed air case, inducing a corresponding delta in the incident surface radiation between the two cases. In addition, a greater percentage of the total heat release for the computed oxy case is shifted towards the windbox and lower furnace regions, than for the air case; since the overall absorptions are similar, this causes the two incident radiation profiles to cross over each other.

Figure 6-42 shows the strip-averaged incident radiation distribution as a function of elevation for the air- and oxy-combustion cases, with the measured data included for comparison. The incident radiation is higher for the oxy case than for the air case in the main furnace zone, and then the incident radiation is higher for the air case than for the oxy case above the SOFA; this trend parallels a similar cross-over trend exhibited by the temperature profile. In terms of magnitude, the averaged predictions of the incident radiation at each plane appear to consistently over-predict the experimental data.

Figure 6-43 shows the planar averaged temperature as a function of elevation for the air- and oxy-combustion cases, with the measured data included for comparison. As mentioned above, the relative differences between the temperatures for the air and oxy cases is mirrored by a similar trend exhibited by the incident radiation. The profile computations over-predict the incident radiation, and largely under-predict the temperature.

Figure 6-44 shows the planar averaged oxygen concentration (wet) as a function of elevation for the air- and oxy-combustion cases, with the measured data included for comparison. In the hopper, the oxy case exhibits a larger concentration of unused O_2 than the air case, although the reason for this behavior is difficult to pin down. It appears to be simply a local phenomenon, based on the amount of fuel versus the amount of oxygen that is directed by the fluid dynamics and combustion processes into the hopper region. Experimental data in the hopper region would be very useful. The oxygen is largely depleted below the SOFA (at Plane 141), and then excess oxygen is incrementally added at each of the SOFA elevations until the arch (Plane 273) is reached. The predictions appear to track the experimental data fairly well.

Figure 6-45 shows the planar averaged CO_2 concentration (wet) as a function of elevation for the air- and oxy-combustion cases, with the measured data included for comparison. For the oxy-combustion case, the baseline CO_2 concentration from the recycled flue gas feeds is augmented by the additional CO_2 from the combustion. The CO_2 concentration is about 89% (mole %, dry) at the furnace outlet. Overall, the predictions appear reasonable overall, but are very good at the arch.

Figure 6-46 shows the planar averaged CO concentration (wet) as a function of elevation for the air- and oxy-combustion cases, with the measured data included for comparison. The CO is high in the main furnace zone due to staging. The oxy-combustion case has slightly less CO in the main furnace zone than the air case, due perhaps to the slightly higher oxygen-to-fuel stoichiometric ratio associated with the oxy

case. For both cases the computed CO rapidly drops off with the addition of SOFA, although the experimental CO appears to persist somewhat at Plane 273, perhaps due to continued CO release from the unburned carbon in the bituminous coal char. At Plane 273, the experimental data exhibits average values on the order of 0.005 mole fraction (wet), while the computed average values are much smaller; computationally, the oxy case still shows some significant CO values in the core, while the computations appear to be mostly mixed out. This indicates that the some residual mixing limitation may persist in the experimental data that is not reflected in the computations, or that CO is still being release from the bituminous coal char, or that, alternatively, the global, single-step kinetic rate used in the computations is too rapid, or some combination of these reasons. At the exit of the boiler domain (see Table 6-1), the computations exhibit 347 ppmv (dry) CO for the air case and 65 ppmv (dry) CO for the oxy case, while the experiments (economizer outlet) show 0 and 6 ppmv (dry), respectively.

Figure 6-47 shows the planar averaged SO_2 concentration (wet) as a function of elevation for the air- and oxy-combustion cases, with the measured data included for comparison. As mentioned above, the SO_2 level is higher for the oxy-combustion case than in the air-combustion case due to the SO_2 contained in the recycled flue gas feed. As mentioned previously, the almost monotonic increase in the SO_2 may indicate that sulfur may exist as other species in the oxygen-starved main furnace zone, that is only progressively converted to SO_2 as oxygen becomes available at higher elevations. This measured increase is much more apparent for the oxy case than it is for the air case. Again, this behavior is only true for the first 3 test coals; it is not true for the lignite coal tests.

Figure 6-48 shows the planar averaged H_2O concentration (wet) as a function of elevation for the air-and oxy-combustion cases, with the measured data included for comparison. Again, the H_2O concentration is higher for the oxy-combustion case than in the air case due to higher H_2O concentration in the recycled flue gas. The computed H_2O over-predicts the experimental H_2O at the arch by a couple of percentage points.

6.3 Illinois No. 6 Bituminous Coal

This section addresses predictions for Air Test 75 and Oxy Test 74.

Figure 6-49 shows temperature contours on a vertical plane through the center of the furnace. The temperatures in the lower furnace and windbox region for both the air-combustion case and the oxy-combustion case are practically equivalent, despite the fact that the oxy-combustion case has a slightly higher stoichiometric ratio in the windbox region and a slightly higher firing rate. In the SOFA region, the air-combustion case is only about 50 °F higher than the oxy-combustion case.

Figure 6-50 shows the temperature contours on Planes 141, 180 and 273 above the windbox. Figure 6-51 shows the temperature on these planes separately, with the test data superimposed for comparison purposes. For the air-combustion case, the averaged experimental data appear to be 75 °F (Plane 141) to 125 °F (Plane 180) higher than the computations, although locally, for certain data points, they may be on the order of 250 °F higher than the calculated contour value. The averaged measured temperatures for the air case are higher than the corresponding oxy case temperature at every plane. The experimental temperatures are much closer to the computations for the oxy case than for the air case, although there does not appear to be a strong pattern match between the experiments and the computations for either case. The slightly lower oxy-combustion case temperature, relative to the air case temperature, may be

caused by (a) a more pronounced gasification effect (endothermic) in the main windbox region, and (b) the highlighted differences in specific heats and gas emissivities associated with high CO_2 environments, discussed previously. Temperatures may also be impacted by the computed carbon-in-ash at the exhaust – the air case generated a value of 2.5% unburned carbon-in-ash (thus providing unused oxygen) and the oxy case produced 2% unburned carbon-in-ash, although this is probably a secondary effect, since this translates to > 99.98% carbon conversion.

Figure 6-52 shows the oxygen concentrations on the test planes, with the test data superimposed on Figure 6-53. At Plane 141, both the experimental and calculated values essentially show depleted oxygen. Unfortunately, experimental data was not available for Plane 180. At Planes 180 and 273, the computed oxygen levels are significantly greater for the air case than for the oxy case, due perhaps to a higher overall stoichiometric ratio for the air case. At Plane 273, the experimental data shows some very low O_2 values in the core with higher values in the annular (ring) region around the core, illustrating the persistence of an oxygen-starved core into the upper furnace, which the computations do not show to the same extent. The computations show a higher oxygen concentration skewed towards the right-hand side of the furnace. For the oxy case at Plane 273, the experimental data and the computations both seem to indicate a higher oxygen concentration at the front-right corner.

Figure 6-54 shows the CO_2 concentrations on the test planes. Note that the color map scales presented for the air- and oxy-combustion cases are necessarily different, due to the high CO_2 concentration in the flue gas recycled to the oxy boiler. For the oxy-combustion case, the CO_2 concentration is around 85% (mole %, dry) at the horizontal furnace outlet plane. Figure 6-55 shows the contours of CO_2 on separate test planes with the test data superimposed. In the air case, on Plane 273, the experimental CO_2 seems to be higher in the core, which concurs with the previous observation about the low experimental O_2 in the core. No strong pattern match between the data and the computations is readily apparent.

Figure 6-56 shows the CO concentrations on the test planes. Figure 6-57 shows the contours of CO concentration on separate test planes with the test data superimposed. At Plane 141, the figure shows higher experimental CO values in the main furnace/windbox zone than those exhibited by the computations. At the horizontal furnace outlet P273, almost all of the experimental CO has been combusted into CO_2, except for some residual CO in the core region, again indicating the presence of an oxygen-starved core that persists into the arch region. The computations indicate that the core essentially disappears as the upper elevations and arch are approached.

Figure 6-58 shows the H_2O concentrations on the test planes in an isometric view. Note that the color map scales presented for air- and oxy-combustions are different due to the higher H_2O concentration in the recycled flue gas for the oxy-combustion case**.** Figure 6-59 shows the contours of H_2O concentrations on separate test planes (plan view). Experimental values are not provided because no experimental H_2O values were tabulated for either test.

Figure 6-60 shows the SO_2 concentrations on the test planes. Note that the color map scales presented for air- and oxy-combustions are different due to the higher SO_2 concentration in the recycled flue gas for the oxy-combustion case.
Figure 6-61 shows the contours of SO_2 on separate test planes with the test data superimposed. At Plane 141, the averaged experimental SO_2 data for the air case is approximately a factor of 2 higher than that of the oxy case (see Figure 6-71), and at Plane 273, the reverse is true. The SO_2 in the air case appears to be monotonically decreasing with elevation (e.g., dilution effect) while the SO_2 in the oxy case appears to be

monotonically increasing with elevation (e.g., SO_2 progressively oxidized from other sulfur species), in spite of the SOFA dilution. The reason why the experimental SO_2 trend as a function of elevation in the oxy case is apparently opposite to that of the air case is not known. Both the experimental data and the computations for the oxy case on Plane 273 appear to indicate a core with slightly elevated values, as well as lower values on the right-hand side.

Figure 6-62 shows the incident radiation contours for the air- and oxy-combustion cases. Since the furnace temperatures are very similar for both cases, the incident radiation is also very similar for both cases. Figure 6-63 to Figure 6-65 show the incident radiation along the walls on three test planes, with the measured data included for comparison. Experimentally, at Plane 141, the oxy case does not appear to be too dissimilar from the air case. At Plane 180, the experimental incident radiation data for the air case appears to be about 10% larger than that for the oxy case. At Plane 273, the radiation data for the two cases become more equivalent. The computed incident radiation on Plane 141 tends to over-predict the data by 5 to 10%, but on the other hand, on Plane 180, the computed incident radiation tends to under-predict the data by 5 to 10%. In a manner similar to the other coal tests already discussed, the computations at Plane 273 tend to flatten out. The predictions at Plane 273 appear to be good.

Figure 6-66 shows the strip-averaged incident radiation distribution as a function of elevation for the air- and oxy-combustion cases, with the measured data included for comparison. Again, as far as the relative differences between the air-combustion case and the oxy-combustion case, the computed strip-averaged incident radiation tends to mimic the calculated temperature profile.

Figure 6-67 shows the planar averaged temperature as a function of elevation for the air- and oxy-combustion cases, with the measured data included for comparison. In the SOFA regions, the computed oxy-combustion case temperature is lower than that for the air-combustion case by about 50 °F, but otherwise the temperatures are very close. In a similar fashion, the experimental air-case temperature is larger than that of the oxy case, by perhaps 150 °F at Plane 180.

Figure 6-68 shows the planar averaged oxygen concentration (wet) as a function of elevation for the air- and oxy-combustion cases, with the measured data included for comparison. (Note: For this coal test only, since experimental H_2O data was not available, the computed H_2O was used to convert the experimental data to a wet basis.) At Plane 141, between the windbox and the lower SOFA, the oxygen essentially goes to near-zero, in agreement with the data. At the arch, the calculated oxygen profiles for the air and oxy cases diverge, with the air case yielding a higher arch value (at least 0.5 percentage points higher than the experimental value). The air-fired case has a somewhat higher overall stoichiometric ratio. On occasion, the unburned carbon-in-ash can be a significant factor -- air case: 2.5% predicted versus 2% experimental; oxy case: 2% calculated versus 0.75% measured, but the computed carbon conversion translates to > 99.98%. At the exit of the computational domain, the computed oxygen for the air case will decrease to 3.04% (mole %, wet), and the computed oxygen for the oxy case will decrease to 2.05%. The utilization of a larger heterogeneous rate (see Section 6.7) that burns out all of the carbon only reduces the computed average oxygen from 3.04% to 2.98%. One might ordinarily conclude that the inlet boundary conditions need to be adjusted to properly reflect the air-test measurement at the arch, but the experimental oxygen concentration at the economizer outlet (see Table 6-1) is also about 3%, thus leaving one to conclude that the averaged experimental value at the arch (2.5%) may be low.

Figure 6-69 shows the planar averaged CO_2 concentration (wet) as a function of elevation for the air- and oxy-combustion cases, with the measured data included for comparison. (Note: For this test only, since

experimental H_2O data was not available, the computed H_2O was used to convert the experimental data to a wet basis.) For the oxy-combustion case, the baseline CO_2 concentration is high due to the high CO_2 concentration levels in the flue gas recycled to the boiler. For both the air and the oxy cases, the computations appear to be reasonably aligned with the experimental data at Plane 273 (arch).

Figure 6-70 shows the planar averaged CO concentration (wet) as a function of elevation for the air- and oxy-combustion cases, with the measured data included for comparison. (Note: For this test only, since experimental H_2O data was not available, the computed H_2O was used to convert the experimental data to a wet basis.) At Plane 141, the difference between the experimental data points is larger than that between the computed profiles at the same elevation. Again this may be due to an insufficient number of points on that plane with which to make an accurate average. If the CO measurement is truly representative of the average, then the oxy case is generating significantly more CO, perhaps due to additional gasification. The fact that a significant amount of experimental CO still exists at the arch (Plane 273) in the oxy-combustion case is perhaps an indication that (a) the CO is merely decaying from a high initial peak caused by e.g., gasification, (b) significant CO off-gas from a slow burning carbon continues to track into the upper furnace, and/or (c) that the experimental CO consumption rate may be slower (due e.g., to mixing limitations) than that indicated by the calculations. The persistent high-CO/low-O_2 exhibited by the experimental data indicates that a mixing limitation may be the underlying reason for the higher CO at the arch, which may in turn point to a need for a more sophisticated turbulence model. Tuning of the homogeneous and heterogeneous char kinetics for the bituminous coal may be a secondary requirement.

Figure 6-71 shows the planar averaged SO_2 concentration (wet) as a function of elevation for the air- and oxy-combustion cases, with the measured data included for comparison. (Note: For this test only, since experimental H_2O data was not available, the computed H_2O was used to convert the experimental data to a wet basis.) As discussed above, the baseline SO_2 level is expected to be higher for the oxy-combustion case due to the SO_2 content in the recycled flue gas. For the oxy case, the monotonic increase in the experimental SO_2 as a function of elevation is apparent, signaling that perhaps the SO_2 exists as other reduced species in the lower (more fuel-rich) elevations. Figure 6-72 shows the planar averaged H_2O concentration (wet) as a function of elevation for the air-and oxy-combustion cases. Again, the baseline H_2O concentration is higher for the oxy-combustion case due to the higher H_2O concentration in the recycled flue gas. No experimental H_2O values were tabulated for either the air or oxy test, so the figure of the computations is provided only for reference.

6.4 North Dakota Lignite Coal

This section addresses predictions for Air Test 83 and Oxy Test 98.

Figure 6-73 shows the temperature on a vertical plane through the center of the furnace. The oxy-combustion case has a higher windbox oxygen-to-fuel stoichiometric ratio (0.987; see Table 5-4) than that (0.883) of the air-combustion case. Consequently, the oxy-combustion case exhibits a higher main furnace temperature than the air-combustion case.

Figure 6-74 shows the temperature contours on Planes 141, 180 and 273 above the windbox area. The swirling flow pattern inherent in the tangential firing design is clearly visible at P141 above the windbox, and at P180 between the overfire air levels, and persists to the horizontal furnace outlet (P273). Figure 6-75 shows the temperature on these planes separately, with the test data superimposed for comparison purposes. At Plane 141, the blue dots, near the front and rear walls, are presumably due to the ambient

cold air leaking through the measuring ports. There is a fairly encouraging pattern match on Plane 141, with the experimental temperatures exhibiting temperatures similar to those of the respective contour plots. On Plane 180, the magnitude of the measurements also scale reasonably well with the predictions, although for the oxy case, the experimental temperature measurements tend to show a hotter core with a cooler surrounding periphery, while the computations show a core that is cooler than the surrounding annulus by approximately 100 °F. Similarly, at Plane 273, for the air-combustion case, the computations exhibit a core that is cooler than the periphery, while the measurements show a core that is hotter than the periphery.

Figure 6-76 shows the oxygen concentrations (dry) on the test planes, with the test data superimposed on Figure 6-77. Experimental data are only available at Planes 141 and 273. For Plane 141, the data seems to scale in magnitude with the computations. For the oxy case on Plane 141, the oxygen levels appear to coincide with some computed, locally high, residual jet oxygen that has not yet fully mixed in. However, as shown in Figure 6-76**,** the average of such a limited number of high-oxygen data points will produce an abnormally high data point on the profile plot that is surely not representative of the true planar average. At Plane 273, there is some asymmetry in the data, but the data does tend to indicate the persistence of a slight oxygen-starved core. The computational imprints of the SOFA oxidant supply and swirl pattern are still visible at the horizontal furnace outlet plane.

Figure 6-78 shows the CO_2 concentrations on the test planes. Note that the color map scale for the oxy-combustion case is very different from that of the air-combustion case, due to the depletion of nitrogen. For the oxy-combustion case, the CO_2 concentration is around 89% (mole %, dry) at the horizontal furnace outlet. Figure 6-79 shows the contours of CO_2 on separate test planes with the test data superimposed for comparison purposes. At Plane 141, the experimental data appear to correspond fairly well (within a few percentage points) with the contour plots. At Plane 273, for the air case, the data seem to correspond to a pattern of a high CO_2 core, surrounded by a ring of diminished CO_2 concentration, surrounded yet again on the periphery (near the walls) with high CO_2 values. This pattern is qualitatively replicated by the simulations at that same plane. The oxy-combustion case exhibits a similar high-CO_2 core pattern that is manifested somewhat by both the measurements and the computations; the magnitudes do not match, but the difference between the magnitude of the core and the magnitude of the surrounding field (about 3 percentage points) does appear to be similar between the air and oxy cases.

Figure 6-80 shows the CO concentrations on the test planes**.** The CO is largely produced from coal gasification and char oxidation and is plotted on the same scale for both the oxy and air cases. At the horizontal furnace outlet plane (P273), almost all of the CO has been combusted into CO_2. Figure 6-81 shows the contours of CO concentrations on separate test planes with the test data superimposed. At Plane 141, there is some correspondence between the experiments and the computations, both with respect to the low CO in the residual jet regions and the higher CO in the broad core regions. At Plane 273, the experiments indicate a slight persistence of a higher CO core that is only barely predicted by the calculations.

Figure 6-82 shows the H_2O concentrations on the test planes. Note that the color map scales presented for the air- and oxy-combustion cases are very different from each other, due to the higher baseline H_2O content in the oxy case (due to nitrogen depletion). Figure 6-83 shows the contours of water concentrations on separate test planes with the test data superimposed. The scales are rather constricted, varying from 9 to 13% for the air-test scale and only from 28 to 30% for the oxy-test scale. The averaged measurements over the planes are within 1 to 2 percentage points of the averaged computed values over the planes (see

Figure 6-96). On Plane 273, for the air case, the experimental data indicate the presence of a small core where the values of H_2O are a couple of percentage points higher than the surrounding fluid. For the oxy case on Plane 273, the data also indicate a small core, although the computations exhibit slightly higher core values than the measurements.

Figure 6-84 shows the SO_2 concentrations on the test planes. Note that the color map scales presented for air- and oxy-combustion cases are different due to the higher SO_2 content in the flue gas recycled to the oxy boiler. Figure 6-85 shows the contours of SO_2 on separate test planes with the test data superimposed. There does not appear to be a pattern match on Plane 141. However, on Plane 273, the measurements do provide an indication of an SO_2 core, that is in qualitative agreement with the calculated contours. The SO_2 core pattern match is apparent for the air case at Plane 273. Although all of the experimental data points for the oxy case are saturated in color because they are larger in value than the color scale maximum, a written description of their values will be provided. The experimental core values for the oxy case at Plane 273 are about 4,700 ppmv (dry), and then they diminish to near-wall values that average about 500 ppm less. Quantitatively, the experimental peak values and gradient to the walls, for oxy-combustion, is substantially larger than that of the computations (by about a factor of 2), but the experimental confirmation of the presence of a core is gratifying.

Figure 6-86 shows the incident radiation contours for the air- and oxy-combustion cases. The incident radiation is higher for the oxy case in the main furnace walls due its correspondingly higher main furnace temperature (as discussed above). Figure 6-87 to Figure 6-89 show the incident radiation along the walls on three test planes, with the measured data included for comparison. On Plane 141, the incident radiation for the oxy case appears to be about 20% larger than that for the air case, for both the experimental data and the computations. On Plane 180, the incident radiation for the oxy case is about 10% larger than that for the air case, again for both the experimental data and the computations. However, at Plane 273, the calculated incident radiation for the oxy case becomes lower than that of the air case. This cross-over or switch in dominance between the air and oxy cases is also apparent in the temperature. Agreement with the data is good and is probably within 10% overall.

Figure 6-90 shows the strip-averaged incident radiation distribution as a function of elevation for the air- and oxy-combustion cases, with the measured data included for comparison. The incident radiation is higher for the oxy case than for the air case in the main furnace, but then the incident radiation for the oxy case drops below that of the air case in the vicinity of the upper SOFA. As mentioned previously, the air and oxy incident radiation profiles qualitatively mirror the corresponding temperature profiles. The trend exhibited by the averaged data appears to follow the computed trend within 10% or less.

Figure 6-91 shows the planar averaged temperature as a function of elevation for the air- and oxy-combustion cases, with the measured data included for comparison. As already discussed, the temperature is higher for the oxy-combustion case in the main burner zone due to its higher windbox stoichiometry, and the profiles are aligned with the incident radiation profiles. The data is also reasonably well matched by the predictions.

Figure 6-92 shows the planar averaged oxygen concentration (wet) as a function of elevation for the air- and oxy-combustion cases, with the measured data included for comparison. The oxy case has a main-burner zone stoichiometry of almost unity, and the computed profile indicates that the oxygen at Plane 141 never becomes as depleted as that of the air case. The experimental average of the oxygen concentration at Plane 141 shows a value near 3%, but that is probably due simply to an insufficient number of suction

data points across the plane. At Plane 273, for the air case, the calculated oxygen concentration at the arch matches that of the data, but the calculated oxygen concentration of the oxy case significantly under-predicts the experimental data point. Table 6-1 reveals that the computed outlet oxygen (at the domain outlet) is about 2.3% (mole %, wet), while the experimental outlet oxygen (at the economizer outlet) is about 3%. This indicates that the inlet feed conditions and flow rates used in the computations may need to be adjusted to match the outlet oxygen.

Figure 6-93 shows the planar averaged CO_2 concentration (wet) as a function of elevation for the air- and oxy-combustion cases, with the measured data included for comparison. The experimental data and the computations are in good agreement.

Figure 6-94 shows the planar averaged CO concentration (wet) as a function of elevation for the air- and oxy-combustion cases, with the measured data included for comparison. Both the computed oxy and air profiles appear to be roughly similar in magnitude in the main furnace zone, with the oxy profile magnitude being somewhat larger in the windbox region and lower in the hopper region. The addition of SOFA oxidant causes the computed CO to rapidly deplete to near zero at the arch (Plane 273), in partial agreement with the averaged experimental CO values. However, the averaged experimental CO for the oxy-combustion case is a somewhat larger than the air-combustion value at the arch, and may be dominated by a few higher core point values, where the measurements are higher than the surrounding field. The presence of an experimental high-CO/low-O_2 core at Plane 273 indicates that mixing may still be a limitation at this plane.

Figure 6-95 shows the planar averaged SO_2 concentration (wet) as a function of elevation for the air- and oxy-combustion cases, with the measured data included for comparison. As discussed above, the SO_2 level is higher for the oxy-combustion case, due to the baseline SO_2 content in the recycled flue gas fed to the oxy boiler. However, the SO_2 measurements for the oxy case are approximately 30% higher than that of the computations, possibly indicating that the SO_2 composition in the recycled flue gas and/or the sulfur content in the coal needs to be adjusted. Computationally, the sulfur species comes off with the volatile decomposition, and should be conserved at all elevations above the windbox. In the first three coal tests analyzed, the experimental concentration of the SO_2 tended to increase with elevation, implying that the sulfur may exist, at least partially, as other species besides SO_2 (e.g., H_2S, CS_2, etc.) down in the fuel-rich, main windbox zone. However, in the two lignite tests, including the present coal test, the SO_2 appears to be fully constituted by Plane 141 and then simply decreases with SOFA dilution. Certainly the average SO_2 value at Plane 141 is suspect, because the number of probe measurements at Plane 141 are insufficient to provide a reliable planar average. However, the postulate regarding the existence of reduced sulfur species in the main windbox needs to be tested, keeping in mind how the sulfur species evolve from both the volatile and the char (e.g., organic / pyrite / sulfate forms).

Figure 6-96 shows the planar averaged H_2O concentration (wet) as a function of elevation for the air-and oxy-combustion cases, with the measured data included for comparison. The planar-averaged measurements are within 1 to 3 percentage points of the computation.

6.5 Schwarze Pumpe Lignite Coal

This section comprises predictions for Air Test 109 and Oxy Test 134.

Figure 6-97 shows the temperature on a vertical plane through the center of the furnace. The oxy-combustion case has a higher windbox oxygen-to-fuel stoichiometric ratio (0.957; see Table 5-4) than that (0.897) of the air-combustion case. Consequently, the oxy-combustion case exhibits a higher main furnace temperature than the air-combustion case.

Figure 6-98 shows the temperature contours on Planes 141, 180 and 273 above the windbox area. The swirling flow pattern inherent in the tangential firing design is clearly visible at P141 (above the windbox), and at P180 (between the overfire air levels), and persists somewhat to the horizontal furnace outlet plane (P273). Figure 6-99 shows the temperature on these planes separately, with the test data superimposed for comparison purposes. Overall, the experimental temperatures appear to scale well with both (a) the change of temperature between elevations and (b) the change of temperature between the air and oxy cases. The oxy case appears to have a uniformly higher temperature than the air case, and both the calculations and the data reflect this difference. At Plane 141, the blue dots, near the front and rear walls, are presumably due to the ambient cold air leaking through the measuring ports. On Plane 141, although the averaged experimental temperatures follow the averaged computed temperatures, individual measurement points don't always seem to match individual contours; the high-temperature measurement points seem to be shifted away from the walls and more towards the interior of the furnace. Perhaps this implies that the computational jets are too near the walls and that the actual jets penetrate better. On Plane 180, the oxy case has a broad high-temperature core, and the experimental points seem to, at least in part, approximate that pattern, although again, adjacent measurement points may vary from 2350 to 2550 °F, all within a region that has a calculated temperature region that is uniformly about 2450 °F. On Plane 273, the experimental temperatures appear to exhibit a broader and slightly higher-temperature core, whereas the computations indicate a cooler core, in a manner similar to previous temperature comparisons. Alternatively, however, the reader may justifiably view Plane 273 and make the pronouncement that both the experimental temperature points and the computations are fairly homogeneous within some bounds (e.g., +/- 50 °F).

Figure 6-100 shows the oxygen concentrations on the test planes, with the test data superimposed on the planes in Figure 6-101. Experimental data are only available at Planes 141 and 273. For the air case on Plane 141, the data seems to correspond well with the computations. For the oxy case on Plane 141, the oxygen data levels appear to coincide with some computed, locally high, residual jet oxygen that has not yet fully mixed in. However, as shown in Figure 6-76**,** the average of such a limited number of high-oxygen data points will produce an abnormally high data point on the profile plot that is surely not representative of the true planar average. At Plane 273, the computational imprints of the SOFA oxidant supply and swirl pattern are still visible at the horizontal furnace outlet plane. Despite the individual variability between adjacent data points, the data at Plane 273 does tend to indicate the persistence of a slight oxygen-starved core, surrounded by a ring of higher oxygen concentrations, with an outer, near-wall periphery of lower oxygen concentrations. The computations appear to qualitatively mimic the same pattern.

Figure **6-102** shows the CO_2 concentrations on the test planes. Note that the color map scale for the oxy-combustion case is very different from that of the air-combustion case, due to the flue gas recycled to the oxy combustor. For the oxy-combustion case, the CO_2 concentration is around 90% (mole %, dry) at the horizontal furnace outlet. Figure 6-103 shows the contours of CO_2 on separate test planes with the test data superimposed for comparison purposes. At Plane 141, for the air case, the experimental data appear to correspond fairly well with the contour plots. The pattern for the oxy case shows a similar behavior, but

three of the experimental data points showing lower CO_2 near the core region may indicate that the experimental low CO_2 core or ring may be displaced radially relative to the computational low CO_2 ring. At Plane 273, the data appears generally to correspond to a pattern of a high CO_2 core, surrounded by a ring of diminished CO_2 concentration, surrounded yet again on the periphery (near the walls) with high CO_2 values (although there are individual points that do not seem to follow this pattern). This core-ring pattern is qualitatively replicated by both the air and oxy simulations at that same (arch) plane, and indeed, the maximum and minimum values for both the data and computations on that plane also seem to be in agreement.

Figure 6-104 shows the CO concentrations on the test planes**.** The CO is largely produced from coal gasification and char oxidation and is plotted on the same scale for both the oxy and air cases. At the horizontal furnace outlet plane (P273), almost all of the CO has been combusted into CO_2. Figure 6-105 shows the contours of CO concentrations on separate test planes with the test data superimposed. At Plane 141, there is some correspondence between the experiments and the computations, both with respect to the low CO in the residual jet regions (near the walls) and the higher CO in the broad core or core-annulus regions. At Plane 273, the experiments indicate a slight persistence of a higher CO core, but the computational CO core has visually disappeared at the arch elevation (at least based on the color map scale).

Figure **6-106** shows the H_2O concentrations on the test planes. Note that the color map scales presented for the air- and oxy-combustion cases are very different from each other, due to the higher baseline H_2O content in the oxy case (due to nitrogen depletion). Figure 6-107 shows the contours of H_2O concentrations on separate test planes with the test data superimposed. The scales are rather constricted, varying from 9 to 13% for the air-test scale and only from 28 to 30% for the oxy-test scale. The averaged measurements over the planes are within 1 to 3 percentage points of the averaged computed values over the planes (see Figure 6-120). On Plane 141 for the air case, there does not appear to be much of a pattern match; the data show less H_2O near the walls, with a monotonic increase toward the interior, while the computations indicate an annular ring of higher H_2O concentrations.. On Plane 273, for the air case, the experimental data indicate the presence of a small core, where the values of H_2O are about a percentage point higher than the surrounding fluid. For the oxy case, some of the experimental data points are saturated, so a written description of the data values will be given. At Plane 141, for the oxy case, the experimental values, ranging from 25 to 27 mole % (dry), follow the same trend as the computations – the near-wall values first increase slightly at the next point away from the wall, and then decrease in the vicinity of the low-H_2O ring by perhaps half a percentage point, and then increase in the core region by a small amount. At Plane 273, the values are about 27.5 to 28 mole % (dry) within the core region, and then the points decrease in value towards the wall by a percentage point or two, thus confirming the presence of a core, in accordance with the computations.

Figure 6-108 shows the SO_2 concentrations on the test planes. Note that the color map scales presented for air- and oxy-combustion cases are different due to the higher SO_2 content in the flue gas recycled to the oxy boiler. Figure 6-109 shows the contours of SO_2 on separate test planes with the test data superimposed. For the air case, there does not appear to be a strong pattern match on Plane 141, perhaps because the SO_2 has been reduced to other species. However, on Plane 273, for the air case, the measurements do provide a slight indication of an SO_2 core (interestingly through the presence of a single red dot and a few surrounding green dots). For the air case (at Plane 273), the values span from a core high of over 1000 ppmv to lower values of 600 to 500 ppmv. For the oxy case at Plane 141, the temperatures tend to increase from the near-wall values of 1200 to 1400 ppmv to interior points that are

200 to 300 ppmv higher (with some isolated exceptions), in accordance with the data. For the oxy case, the peak experimental value is at 2150 ppmv, other core values are about 1200 to 1300 ppmv, and surrounding values quickly diminish to 600 to 1000 ppmv near the wall. In both cases the computational gradients on Plane 273 are much less than the experimental gradients.

Figure 6-110 shows the incident radiation contours for the air- and oxy-combustion cases. The incident radiation is higher for the oxy case in the main furnace walls due its correspondingly higher main furnace temperature (as discussed above).

Figure 6-111 to Figure 6-113 show the incident radiation along the walls on three test planes, with the measured data included for comparison. The experimental data on Plane 141 appears to be about 20% larger for the oxy case than for the air case; for Planes 180 and 273, the oxy case data appears to be about 10% larger than that of the air case. The computations for the air case are approximately 5 to 10% higher than the experimental data. The computations for the oxy case are 10 to 20% higher on Plane 141 (perhaps enhanced by the higher computed oxygen in the lower furnace), but then the predictions are fairly similar to the measurements on Planes 180 and 273.

Figure 6-114 shows the strip-averaged incident radiation distribution as a function of elevation for the air- and oxy-combustion cases, with the measured data included for comparison. The incident radiation is higher for the oxy case than for the air case, not only in the main furnace region, but also up through the SOFA region. The air and oxy incident radiation profiles qualitatively mirror the corresponding temperature profiles. The decay of the averaged incident radiation data from the top of the windbox to the arch appears to follow the computed trend within 10% (except for one point).

Figure 6-115 shows the planar averaged temperature as a function of elevation for the air- and oxy-combustion cases, with the measured data included for comparison. The trend is the same as the incident radiation discussed above. The averaged experimental data are within 50 °F of the computations at Planes 141 and 180, and within 100 °F at the arch.

Figure 6-116 shows the planar averaged oxygen concentration (wet) as a function of elevation for the air- and oxy-combustion cases, with the measured data included for comparison. The computations for the oxy case exhibit large excess oxygen levels in the hopper region, while the air case shows completely depleted levels; no experimental data is available to validate the calculations in the lower furnace. The air and oxy case computations in the windbox and SOFA regions are very similar and track each other very well.

Figure 6-117 shows the planar averaged CO_2 concentration (wet) as a function of elevation for the air- and oxy-combustion cases, with the measured data included for comparison. The experimental data and the computations for the air case are in very good agreement; for the oxy case, the averaged experimental data are only a few percentage points higher than the computations. The CO_2 at the furnace arch translates to about 90% (mole %, dry).

Figure 6-118 shows the planar averaged CO concentration (wet) as a function of elevation for the air- and oxy-combustion cases, with the measured data included for comparison. In the hopper region, the CO concentration is high for the air case (because the O_2 is the same region is depleted), while the CO concentration for the oxy case is negligible (because the O_2 in the same region is high). Both the oxy and air computed profiles appear to be roughly similar in magnitude in the main furnace zone. The addition of

SOFA oxidant causes the computed CO to rapidly deplete to near zero at the arch (Plane 273). The averaged experimental CO data at the arch are both on the order of 1% (mole %, wet), while the computed values are indistinguishably close to the zero line. It is interesting that this level of experimental CO at the arch is similar to that of the bituminous coals. However, CO measurements at the boiler exit, downstream of the economizer, are essentially zero for all of the coal tests (see Table 6-1). Therefore, while significant unmixedness must prevail at the arch, there is sufficient residence time at high temperature to mix out and consume the CO prior to the gas reaching a quenching temperature downstream of the economizer. Both the computations and the data indicate a low O_2 core at the arch, with some experimental O_2 points less than 0.5% (mole %, dry), while the computational O_2 in the core is around 2%. Therefore, the experimental data at Plane 273 may indicate that the reactions at the arch are still limited somewhat by mixing, whereas the computations at the arch are seeing higher oxygen concentrations in the core (2%), having mixed out more rapidly than the experiments, with the result that the computational CO is burned out more readily. This implies that a more sophisticated turbulence model may be required in order to simulate the slower mixing exhibited by the experimental data and the persistence of the high-CO/low-O_2 core.

Figure 6-119 shows the planar averaged SO_2 concentration (wet) as a function of elevation for the air- and oxy-combustion cases, with the measured data included for comparison. As discussed above, the SO_2 level is higher for the oxy-combustion case, due to the baseline SO_2 content in the recycled flue gas fed to the oxy boiler. The SO_2 predictions for the air case seem reasonable. However, the SO_2 measurements for the oxy case at Plane 273 are approximately 600 ppm lower than that of the computations, possibly indicating that the SO_2 composition in the recycled flue gas needs to be adjusted. In the two lignite tests, including the present coal test, the SO_2 appears to be fully oxidized by Plane 141 and then simply decreases with SOFA dilution. The other coal test cases exhibit a monotonic increase in SO_2 as a function of elevation.

Figure 6-120 shows the planar averaged H_2O concentration (wet) as a function of elevation for the air-and oxy-combustion cases, with the measured data included for comparison. The planar-averaged measurements are within 1 to 3 percentage points of the computation.

6.6 Composite Comparisons of the Coal Tests

Figure 6-121 shows the temperature profile plots as a function of elevation for all of the coal tests on the same page (albeit on two different plots). The five air tests are shown in the top plot and the five oxy tests are shown in the bottom plot, within the same figure. This helps to provide a sense as to how the different tests differ from or compare with each other. Since wall resistance calibrations were performed in order to match the temperatures for each coal test, the calculation profiles are generally distributed from high to low temperature in the same sense as the data.

Figure 6-122 shows the deviation of the CFD predictions from the test data for the planar averaged temperature at the test planes, in the form of a bar chart. A negative deviation means the prediction is lower than measurement. Some of the deviations at certain planes can approach 100 to 150 °F, keeping in mind that the averaged temperature at Plane 141, and its deviation value, are more suspect because of the scarcity of experimental data points. It should be remembered that the wall resistance calibrations were performed for the air case first, and then those same wall boundary conditions were used without alteration for the oxy case. It can be seen that e.g., the air-PRB case could have been more rigorously calibrated, making the positive deviation a smaller (positive) number, but then the oxy-PRB case would

have had a larger negative deviation. Both of the air-bituminous cases could also have been calibrated better, which may have benefited the corresponding oxy cases. For the air-lignite cases, the deviations at the three planes may switch from positive to negative. The calibration scheme for this scenario is more challenging, and may indicate that there should be a wall resistance profile within the main windbox region, rather than a uniform resistance; however, this would require a wall resistance profile construction methodology based upon deposition and slagging maps (or deposition models), which was beyond the scope of the present program.

Figure 6-123 shows the oxygen concentration (wet) profile plots as a function of elevation for all of the coal tests, grouped separately on an air test plot and on an oxy test plot. The stoichiometric ratios in the windbox region vary from 0.767 to 0.951 for the air tests, and from 0.822 to 0.987 for the oxy tests (see Table 5-4). For the air test, the ordered windbox stoichiometric ratios are: Test 11 (0.951) > Test 109 (0.897) > Test 83 (0.883) > Test 75 (0.788) > Test 39 (0.767). The computed profiles in the vicinity of the windbox are grouped in a similar manner with Tests 11, 109, and 83 being the highest, and Tests 75 and 39 being the lowest. There is significant cross-over of the profiles, which should be expected because of differences in the char burning rates and the relative amounts of volatile off-gas, but the trend is still apparent. In addition, there are substantial differences in the excess oxygen in the hopper that may impact the windbox. For the oxy test, the ordered windbox stoichiometric ratios are: Test 98 (0.987) > Test 134 (0.957) > Test 50 (0.876) > Test 74 (0.857) > Test 22 (0.822). The computed profiles in the vicinity of the windbox are grouped in a similar manner with Tests 98 and 134 being the highest, and the remaining tests being the lowest. The values at the arch will be a function of the overall stoichiometric ratio, but may also be a strong function of the unburned carbon.

Figure 6-124 shows the CO concentration (wet) profile plots as a function of elevation for all of the coal tests, grouped separately on an air test plot (top plot in figure) and on an oxy test plot (bottom plot in figure). The CO in the hopper tends to be high for those cases in which the oxygen in the hopper is negligible, and vice-versa. In the windbox, the CO is a complex function of the amount of C-gas in the volatile and the oxidation/gasification rates of the char. Within the windbox and at Plane 141, some of the computations qualitatively follow the ordering of the data; with Test 39 being high for the air tests and Tests 83 and 109 being low. For the oxy tests, Test 22 exhibits a high value and Tests 98 and 134 show low values, again showing qualitative compliance between computations and the experiments. Test 75, however, with its large unburned carbon, has a high measured value at Plane 141, but a low to moderate predicted value. At the arch the computed CO generally appears to be lower than the measured values, indicating inadequate production of CO in the windbox and/or excessively rapid CO destruction kinetics in the presence of oxygen.

Figure 6-125 shows the carbon in ash for all of the cases simulated. As expected, the two bituminous cases exhibit the largest carbon-in-ash values. The CFD was roughly calibrated to the measured values for the air case, with the char rates remaining unchanged in the oxy cases. The agreement is generally good.

6.7 Effect of Char Reaction Rates

It is well known that the reaction rates for a given coal can differ substantially from seam to seam within the same mine. As part of the tuning procedure, it was therefore necessary to adjust the coal reaction rates used in the CFD simulation to match the unburned carbon-in-ash data. A systematic study of the effect of coal devolatilization and char oxidation/gasification rates is beyond the scope of this study. However, it

was deemed useful to perform a small sensitivity study with high and low heterogeneous rates to assess the impact on certain variables.

In this section, we report the CFD results for the air- and oxy-combustion cases at the same flow rate and boundary conditions as that specified for the Illinois bituminous coal cases, but with the char oxidation and gasification rates set at higher rates, identical to those used for lignite coal. The lignite reaction rates are higher than the Illinois bituminous coal over the relevant temperature range, as shown in Figure 6-126.

For the planar averaged, profile plots, the results for different reaction rates are shown on the same plot for both the air- and oxy-combustion cases. The contour plots are shown side by side, with the higher lignite rates on the left-hand side of the page and the Illinois bituminous rates on the right-hand side, for ease of comparison.

At the higher coal reaction rates (i.e., the lignite rates),
Figure **6-127** shows that there is a higher concentration of CO at and above the main windbox region due to the enhanced char oxidation and gasification rates. An effort has not been made to quantify how much of the change in CO concentration is due to enhanced oxidation and how much is due to gasification. The oxidation rates consume O_2 and produce CO; the gasification rates consume CO_2 and H_2O and produce CO and H_2/CO, respectively. When sufficient oxygen becomes available, the H_2 is, of course, transformed to H_2O, and the CO is transformed to CO_2, so that neither H_2 nor CO persist for long in excess-O_2 conditions at high temperature (at least with the present single-step rate formulations used in the CFD runs). H_2 is only produced through volatile decomposition and char gasification with the present mechanisms used in the CFD cases. To confirm whether gasification is occurring, H_2 plots (not shown) were also generated, along with those of CO. The plots clearly demonstrate that H_2 increases in the windbox region by perhaps a factor of 2 with the augmented gasification rates. Since H_2 can only be generated through volatile decomposition and gasification in the CFD runs, and since the amount of H_2 produced from volatile decomposition cannot change, the apparent increase in the H_2 demonstrates that gasification is a significant contributor to the differences exhibited in the present results. However, the relative degree to which char oxidation versus gasification dominates in a given zone was not quantified.

In Figure 6-128, the higher lignite rates cause the H_2O concentration to decrease in the windbox region, relative to the H_2O concentration profile associated with the bituminous rates, and then recover in the SOFA regions. Part of this decrease in the mole fraction can simply be attributed to the increase of the CO and H_2 mole fractions due to enhanced oxidation and gasification. It should be noted that in both oxidation to CO and in gasification, two moles of product gas species are produced for every mole of gas consumed. Consequently, the enhanced oxidation and gasification rates should cause the mole fractions of CO_2 and H_2O to decrease, which is what happens in the plots. As CO and H_2 are consumed in the SOFA regions, then one would expect the H_2O concentration to recover to the bituminous rate profile levels; this also occurs in agreement with expectations.

Figure 6-129 shows the amount of unburned carbon in ash at the exit of the CFD model domain for both the air- and oxy-combustion cases. At the higher lignite reaction rates, there is very little unburned carbon for both the air- and oxy-fired cases, while the bituminous coal rates agree much more closely with the experimental unburned carbon values. The amount of residual carbon in the ash has only a minor effect on the amount of excess oxygen available at the domain exit and within the boiler.

Figure 6-130 shows a slightly lower O_2 concentration in the windbox region than for the lower-rate profile, but there is very little discernible difference between the two rate lines for the oxy case in the same region. In the hopper region, the higher-rate profile shows significantly more O_2. One hypothesis may be that the higher heterogeneous rates consume more of the particle mass, which decreases the particle density and makes the particles less likely to gravitationally migrate towards the hopper, thus leaving a relative excess of oxygen in the hopper. At the arch (Plane 273), the bituminous rate exhibits a higher oxygen level, attributable to the higher unburned carbon associated with the bituminous char.

Figure 6-131 shows that, in the windbox region, the CO_2 concentration is lower for the higher lignite reaction rates, compared to the bituminous profile. Again this may be due to the increased number of moles of H_2 and CO created in the windbox region as a result of the enhanced char oxidation and gasification. At the horizontal furnace outlet plane (Plane 273), for the air case, the higher lignite rate produces a slight increase in the CO_2 concentration, simply due to lower unburned carbon. For the oxy case, the two profile curves at the arch are practically coincident.

Figure 6-132 shows that the temperature is slightly lower for the high lignite reaction rates in the vicinity of the windbox and hopper, relative to the bituminous profile. This is due to the endothermic nature of the coal gasification process. The higher gasification rate results in the lower temperature. At the overfire air levels and above, the situation is reversed. The higher lignite rate exhibits a slightly higher temperature than the bituminous profile, presumably because it generates less unburned carbon.

Figure 6-133 shows the strip averaged incident radiation which reflects the planar average temperature discussed above. The incident radiation profiles appear to qualitatively track the temperature profiles and trends.

Figure 6-134 shows the temperature contours on the vertical plane through the center of the furnace. Although it is difficult to see the relative differences in temperature with the large temperature scale used in this figure, the plots for the higher lignite rate should exhibit a slightly lower temperature in the windbox (due to the endothermic nature of gasification) and a higher temperature in the SOFA and upper furnace regions (due to greater carbon burnout).

Figure 6-135 shows the temperature contours on the test planes between and above the overfire air levels. In this figure, the scales are compressed and it is easier to see the higher temperature, associated with the lignite rates, in the SOFA and upper furnace regions.

Figure 6-136 shows the contours of CO on the test planes between and above the overfire air levels. The concentration of CO, at and above the windbox region, is higher for the case with the lignite rates than the case with the bituminous rates, due to the enhanced char oxidation and gasification rates associated with the lignite coal.

Figure 6-137 shows the contours of H_2O on the test planes between and above the overfire air levels. The higher lignite rates cause the H_2O concentration to decrease in the windbox region, relative to the H_2O concentration associated with the bituminous rates, and then recover in the SOFA regions. This decrease is due to the increase in the number of moles of H_2 and CO produced due to enhanced oxidation and gasification.

Figure 6-138 shows the contours of O_2 on the three test planes. The bituminous rate case exhibits a slightly higher oxygen level than the lignite rate case, which is attributable to the higher unburned carbon associated with the bituminous char.

Figure 6-139 shows the contours of CO_2 on the three test planes. In the windbox region, the CO_2 concentration is lower for the case with the lignite reaction rate, compared to the case with the bituminous rates. Again this may be due to the increased number of moles of H_2 and CO (as well as the increase in total moles) created in the windbox region as a result of the enhanced char oxidation and gasification. The CO_2 levels, between the two rate cases, become equivalent in the arch region as the CO and H_2 are consumed (due to the excess oxygen available above the SOFAs).

Figure 6-140 shows the incident radiation contours on the furnace walls. The incident radiation is lower at the main windbox level for the case with the higher lignite reaction rate than for the case with the bituminous rate. This is because the case with the higher lignite reaction rate exhibits a lower temperature in the lower furnace (due to increased gasification). In the upper furnace, the temperature and incident radiation associated with the lignite rate case are higher than that of the bituminous rate case, but the difference may be difficult to see on the contour plot.

Figure 6-141 to Figure 6-143 show the incident radiation span-wise along each of the walls on the three test planes, with the measured data included for comparison. (Note that the lignite rate is a pink line in the present plots, whereas previously it was a blue line in the other profile plots.) At Plane 141, there is a negligible difference between two cases with different reaction rates. At Planes 180 and 273 (SOFA region), the case with the lignite rate exhibits a higher incident flux (and temperature), due to enhanced carbon burnout.

6.8 Results Summary

For the five (5) test coals, the calculations have been rigorously compared with the experimental data. Contour plots and line plots have been used to good advantage to highlight the comparisons. Comparison of the experimental data points with the calculated contours is gratifying. As a function of elevation (progressing from Plane 141 to Plane 180 to Plane 273), the calculation trends are aligned (on an overall, planar-averaged basis) with the trends exhibited by the data. Within each plane, the contours generally exhibit separate regions – a circumferential, near-wall region around the periphery, an interior ring composed of the remnants of the residual jets, and an inner core – that are oftentimes aligned with the patterns exhibited by the experimental data. These pattern matches indicate that the computations are able to mirror many of the underlying aerodynamic and physical features that are apparent in the data, at least qualitatively in many instances, and oftentimes, quantitatively.

An overall summary is provided in the following bullet items:

- The gas temperatures in the main windbox or fireball region appeared to be a strong function of the main windbox oxygen-to-fuel stoichiometric ratio. Given the main windbox stoichiometric ratios, and given the differences in feed conditions and firing rates between the air-combustion and oxy-combustion cases, it is believed that the calculated scaling in temperatures between the two cases are consistent and appropriate.

A visual survey of the experimental planar-averaged temperatures generally shows a progression from hotter temperatures at Plane 141 to cooler temperatures at successively higher planes (Planes 180 and 273) as overfire air is added. The planar-averaged calculations show the same overall trend in temperature decay. Many of the measurements at Planes 141 and 180 indicate patterns that correspond with the calculated residual jets or core regions. At Plane 273, the temperatures are more uniform across the plane as the flow field becomes more homogenous due to mixing. Although there may be some local asymmetry and incongruities for individual data points, and although there may be some displacement between the measured and calculated features, the overall agreement between the computations and experiments is considered acceptable. Individual measurements may deviate +/- 100 to 200 °F (55 K to 111 K) from the calculations, but this difference is considered reasonable for suction pyrometry measurements, particularly in high-gradient regions. The temperature predictions for oxy-firing, given the uncertainties in the experimental data and boundary conditions, scale reasonably well from the air-combustion baseline.

- The averaged oxygen concentration at Planes 141, 180, and 273 appears to be largely aligned with the data – the oxygen concentration is depleted above the windbox and is incremented in a step-wise fashion as the flow crosses each of the SOFA elevations. On Plane 141, the individual experimental points generally seem to be congruent with the computed contours. On Plane 180 (for the PRB and Fola tests), the measurement points indicate a strong oxygen-starved core, in agreement with the contours, and also provide some indication of the lower, residual SOFA jets. At Plane 273, the experimental data continue to demonstrate the persistence of a low-oxygen core, surrounded by a ring of higher O_2 concentration, and sometimes with low O_2 again around the periphery. In addition, on Plane 273, the experiments often indicate a higher O_2 region on the right-hand side of the furnace, which the computations also confirm in a number of instances.

- CO achieves its maximum values in the main windbox region, and then decays as additional oxygen is added through the SOFA regions. Within the simulations, the CO is calculated using single-step, user-specified kinetics (both heterogeneous and homogeneous). For such a simplistic CO mechanism, the computations do fairly well overall (predicting CO values within a factor of 2 of the experimental data) at Planes 141 and 180. On Plane 273, at the arch, the averaged computational CO goes to very low levels, while the averaged experimental values span a range from low CO values to about 1% (mole %, wet). Thus, the predicted CO appears to be consumed too rapidly, relative to the data. Interestingly, at the outlet of the domain, the computational CO ranges from 0 to a few hundred ppmv, while the experimental CO is essentially zero at the economizer outlet.

  The individual experimental data indicate that the high CO on Plane 180 is in a core region, as well as around the outer periphery of the furnace. This pattern is also shown by the computations. On Plane 273 the high experimental CO is found only in a persistent core region, whereas, as previously mentioned, the computational CO has already diminished to very low levels. In addition, the experimental oxygen concentrations tend to have lower core values on Plane 273, than do the computations, indicating that an underlying reason for the higher experimental CO values at the arch may be the persistence of a high-CO/low-O_2 core that is still limited by mixing. This may infer that a more sophisticated turbulence model should be used in the computations to try to simulate this persistent unmixedness of the core at the arch.

- The SO_2 data is somewhat ambiguous and difficult to understand. For two of the coal tests, the PRB and Fola coal tests, the averaged SO_2 monotonically increases as a function of elevation. The increase is greater for the oxy case than for the air case. For the high-sulfur bituminous coal, the sulfur monotonically increases for the oxy case and monotonically decreases for the air case. For the two lignite cases, the averaged SO_2 monotonically decreases.

  It is certainly reasonable that in fuel-rich regions of the main windbox, the sulfur species exists in forms other than SO_2, such as H_2S and CS_2. Sulfur is released as a volatile off-gas as H_2S, and any SO_2 fed into the system with the recirculated flue gas may be reduced to H_2S or a similar species in a locally fuel-rich region. However, it is difficult to understand why only the PRB, and the two bituminous coals would exhibit this monotonically-increasing trend characteristic, and not the lignite coals. The calculations cannot simulate a monotonically-increasing change of SO_2 with elevation, since all of the sulfur in the model is rapidly converted to SO_2 through volatile decomposition alone, and subsequent changes in SO_2 mole fraction with elevation are simply a function of the volumetric changes associated with other reactions and feed additions. For the present, it is believed that reduced sulfur species are playing a role in the staged zone, and perhaps at the outlet, but the extent of the role cannot be studied without implementing a more advanced sulfur mechanism. It is also noted that currently the model assumes that all of sulfur in the fuel is released as volatile matter. In reality, as much as half, if not more, of the total sulfur stays in the char matrix and is released as the char burns out. The impact of this assumption on the overall sulfur profile also needs to be revisited.

- Calculations of the surface incident radiation profiles at measurement ports on Planes 141, 180, and 273 were typically within +/- 10 to 20% of the measurements. Deviations larger than this are more likely a result of those factors that influence the heat release profile and the gas temperature profiles as a function of elevation, such as the calibration of the wall thermal boundary condition or the feed boundary condition, particle size distribution, etc.

  The computed (strip-averaged) incident radiation distribution is strongly linked to the gas temperatures, and the two variables appear to track each other qualitatively. For example, if the incident radiation profiles (as a function of elevation) for the air and oxy cases cross over each other, then the temperatures tend to do the same. The computations appear to reasonably capture the decay of the averaged incident radiation and temperature data from the top of the main windbox to the arch.

- In this study, a small sensitivity study was performed in which a case was run with both high and low heterogeneous kinetic rates. Although not quantified in the computations, gasification does appear to play a role in the main windbox region, particularly for those coals that are more reactive. This was evidenced by the parametric study in which the higher (lignite) char oxidation and gasification rates were used to replace the slower (Illinois bituminous) rates. From the additional H_2 that was calculated from the enhanced rates (separately and apart from the H_2 produced from volatile decomposition alone), it became evident that gasification was indeed playing a role in the fuel-rich regions. It is surmised that gasification is probably enhanced by the higher CO_2 and H_2O concentrations that prevail in the oxy cases (due to flue gas recycle), and that the gasification that occurs does depress the temperature slightly in the main windbox region (due to its endothermic nature).

- Actual predictive accuracy, in the absence of a formal uncertainty analysis, is based on prior experience. Based on that experience, Alstom's has tentatively attempted to determine whether the calculations are, for the most part, within reasonable experimental uncertainties for the types of probes utilized. The baseline air-combustion cases were prepared and tuned, as required, to match implicit boundary conditions such as the outlet carbon-in-ash and the average temperatures at certain planes. Following that calibration, the oxy-combustion cases were prepared by changing the feed flow rates, temperatures, and compositions, and then the oxy-combustion cases were calculated and compared with the experimental data. Alstom's position is that the predictive accuracy associated with the oxy-combustion cases, is also within reasonable and acceptable uncertainty bounds. In other words, the apparent predictive error associated with the oxy cases does not appear to be significantly increased or exacerbated relative to the overall predictive error exhibited by the baseline air cases. This leads to the overall conclusion that the FLUENT® code, in conjunction with the UDFs and modeling strategy, as implemented for the runs in question, includes the requisite physics to make the transition from air- to oxy-combustion CFD studies. This does not mean that enhancements could not be made to the chemical-kinetic mechanisms or other submodels to improve the predictive accuracy; it simply means that Alstom's ability to study or design oxy-combustion systems, using FLUENT®, is roughly on par with its ability to study or design air-combustion systems.

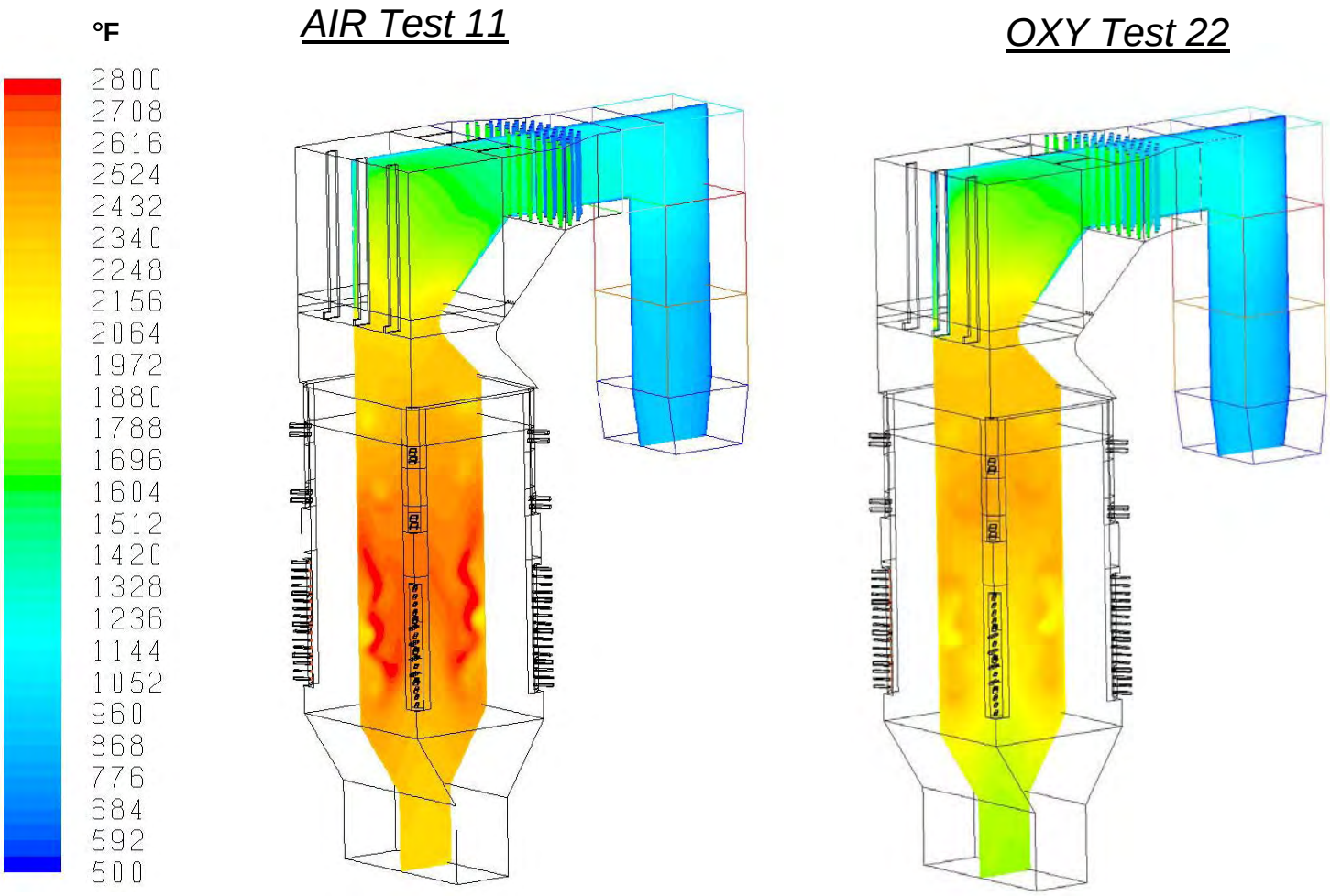

Figure 6-1. [AT-11:OT-22] Contours of Temperature on X-Midplane

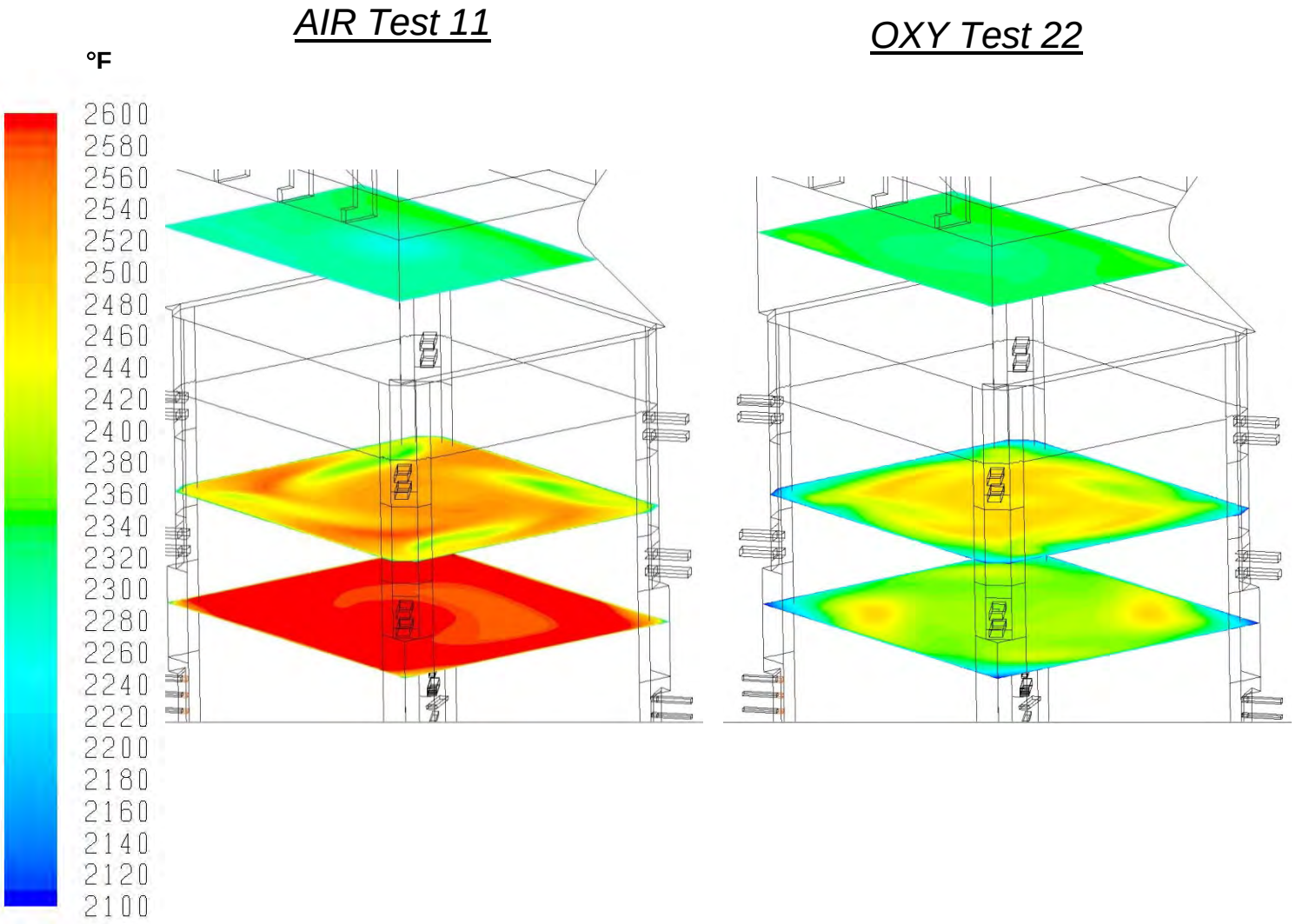

Figure 6-2. [AT-11:OT-22] Contours of Temperature on Test Planes

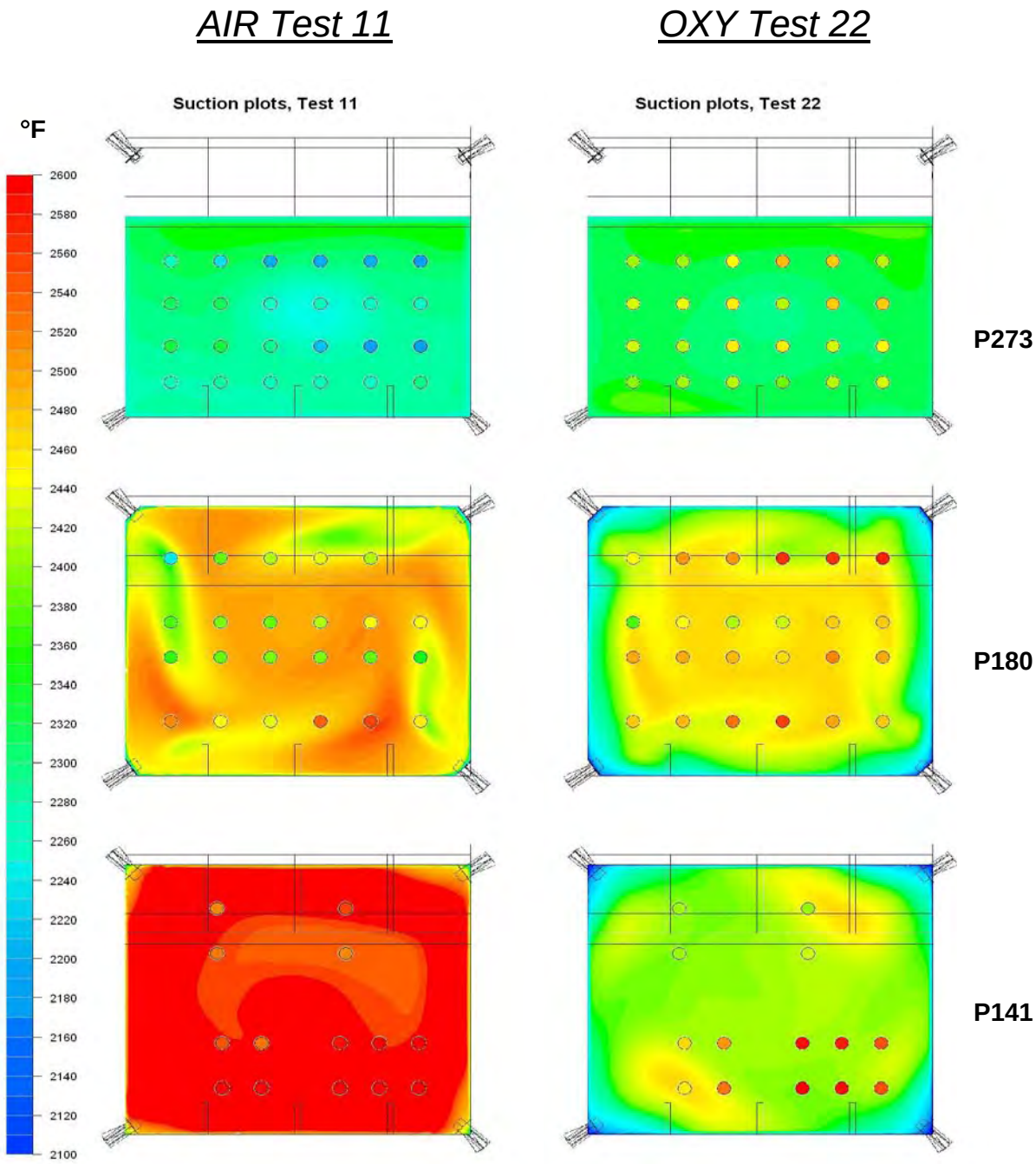

Figure 6-3. [AT-11:OT-22] Comparison of Temperature on Test Planes

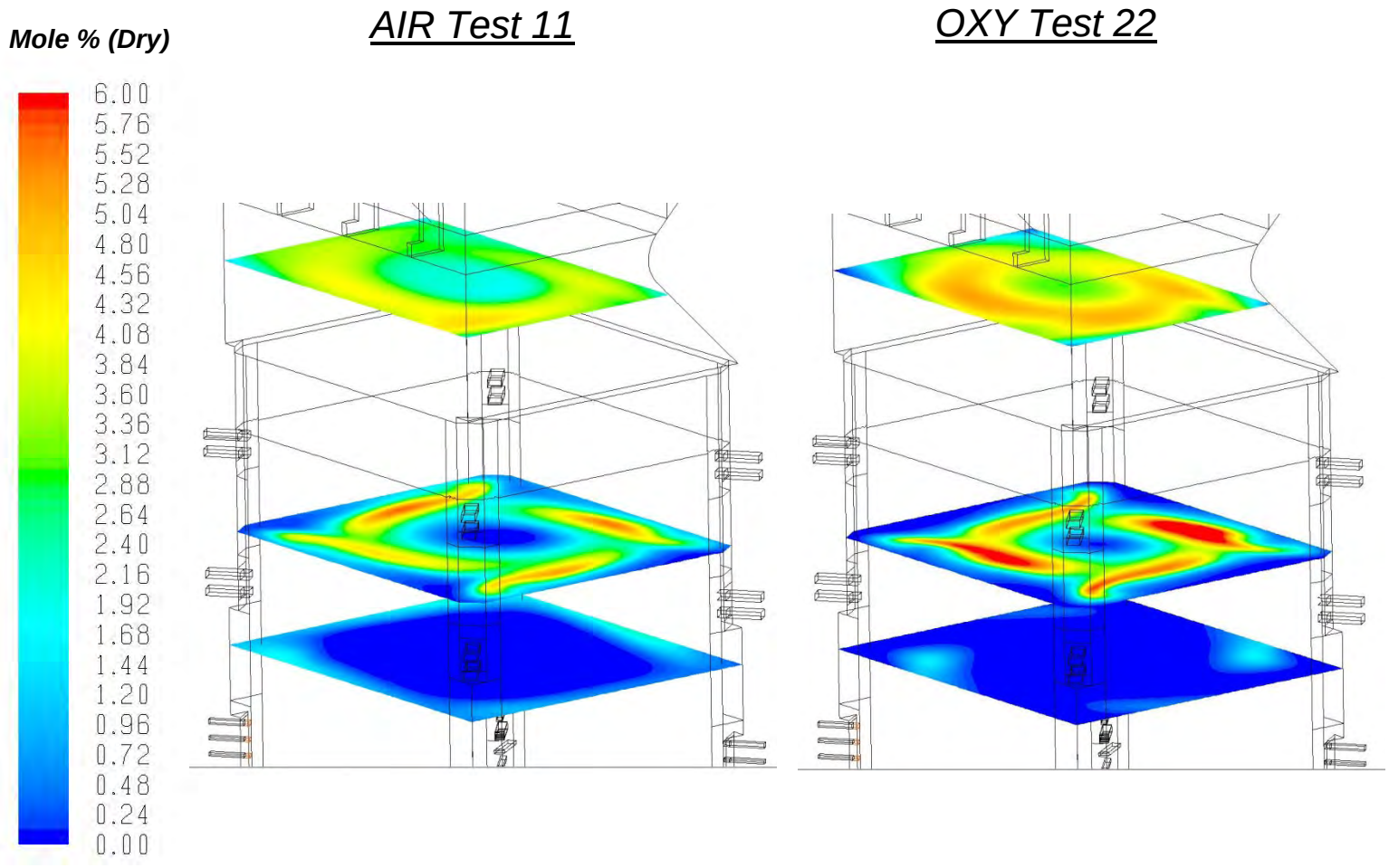

Figure 6-4. [AT-11:OT-22] Contours of O_2 Concentrations on Test Planes

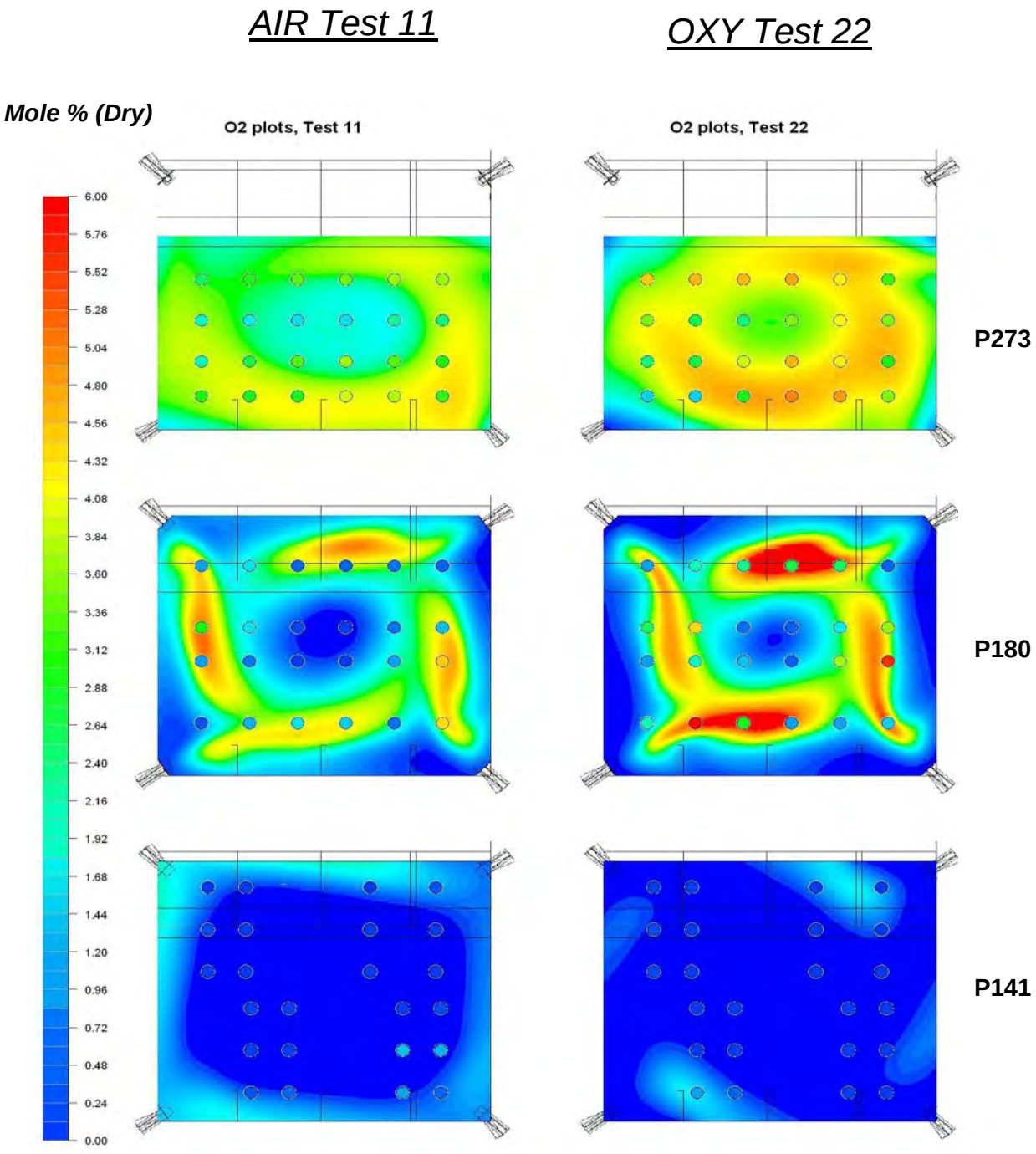

Figure 6-5. [AT-11:OT-22] Comparison of O_2 Concentrations on Test Planes

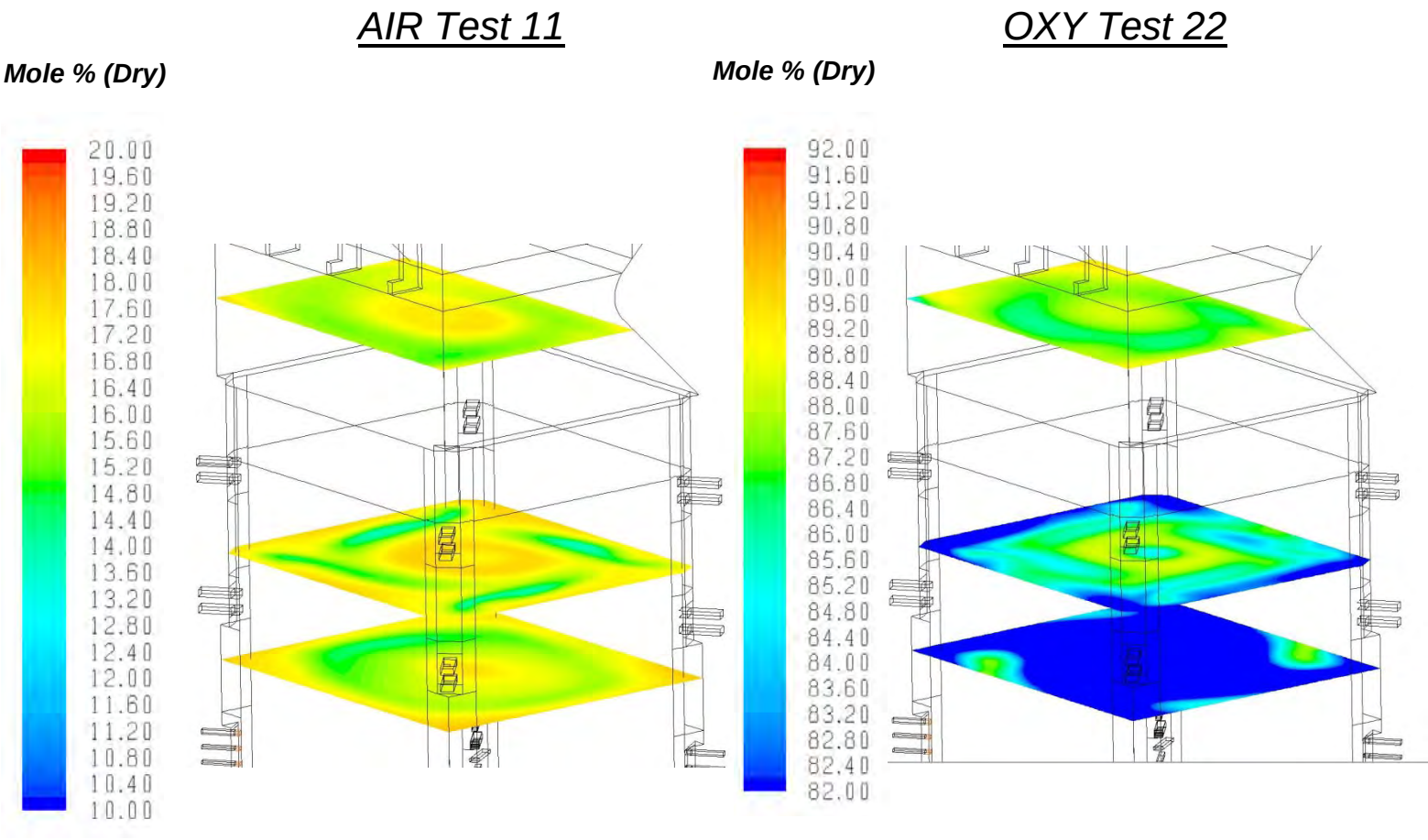

Figure 6-6. [AT-11:OT-22] Contours of CO_2 Concentrations on Test Planes

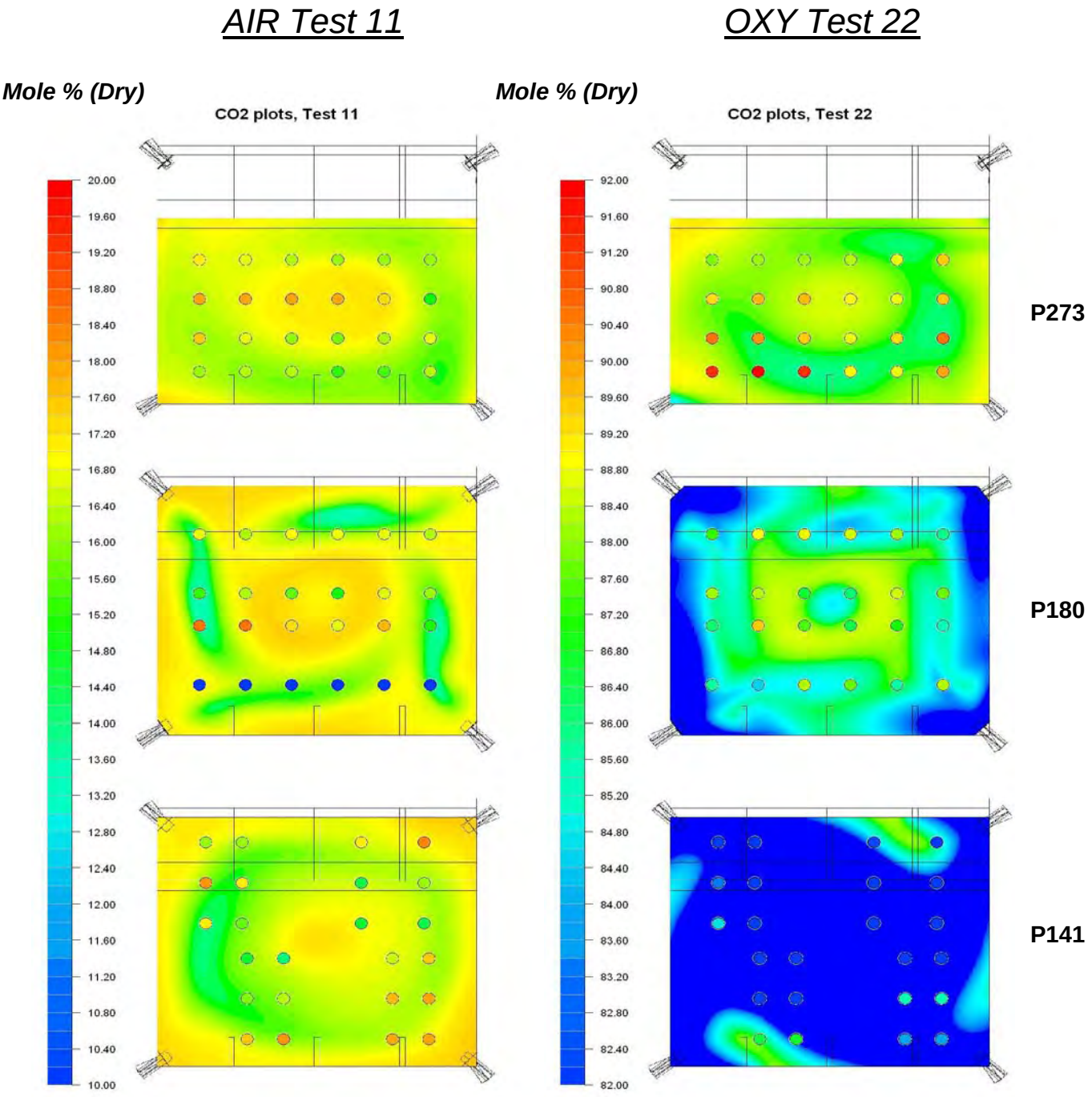

Figure 6-7. [AT-11:OT-22] Comparison of CO_2 Concentrations on Test Planes

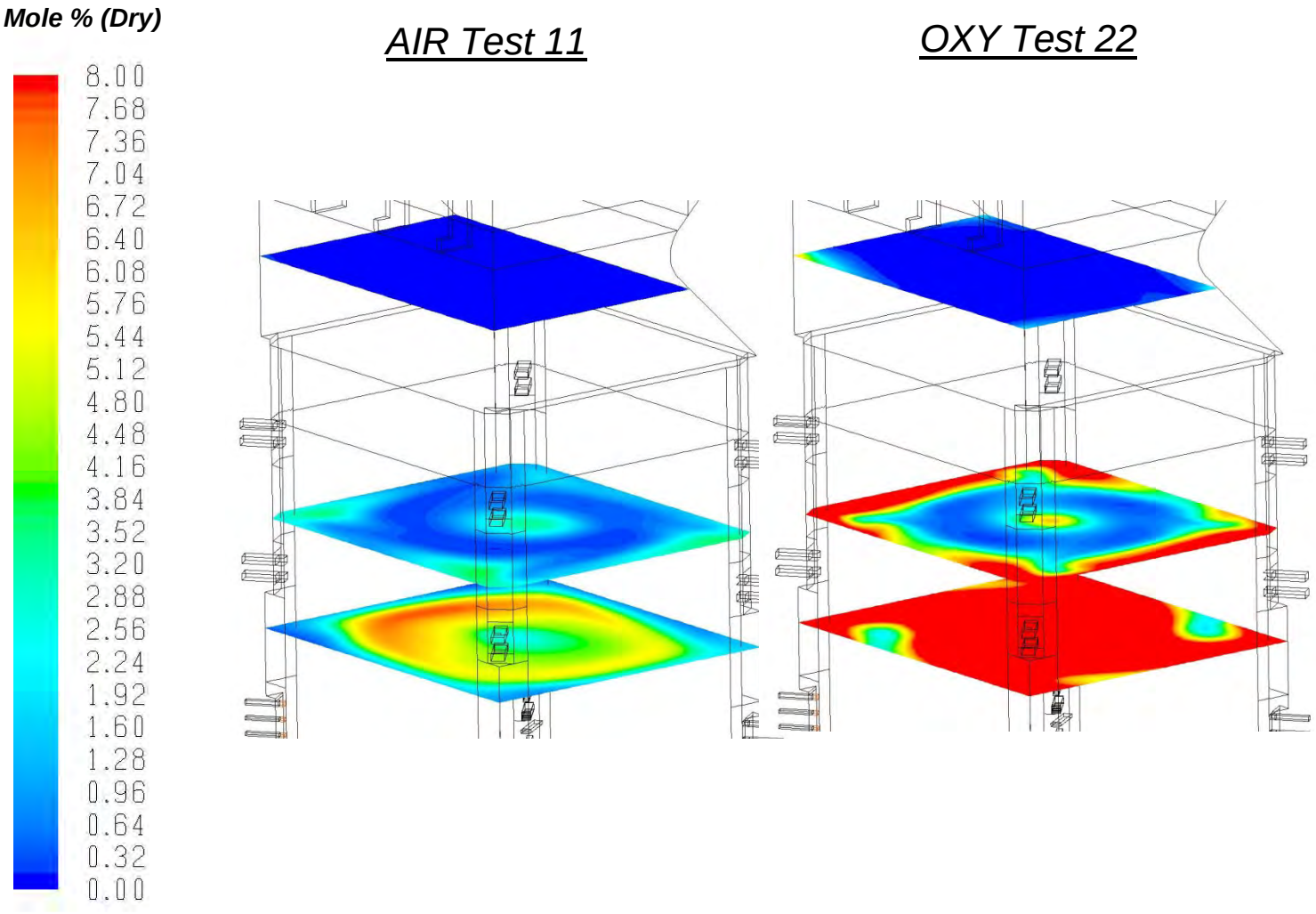

Figure 6-8. [AT-11:OT-22] Contours of CO Concentrations on Test Planes

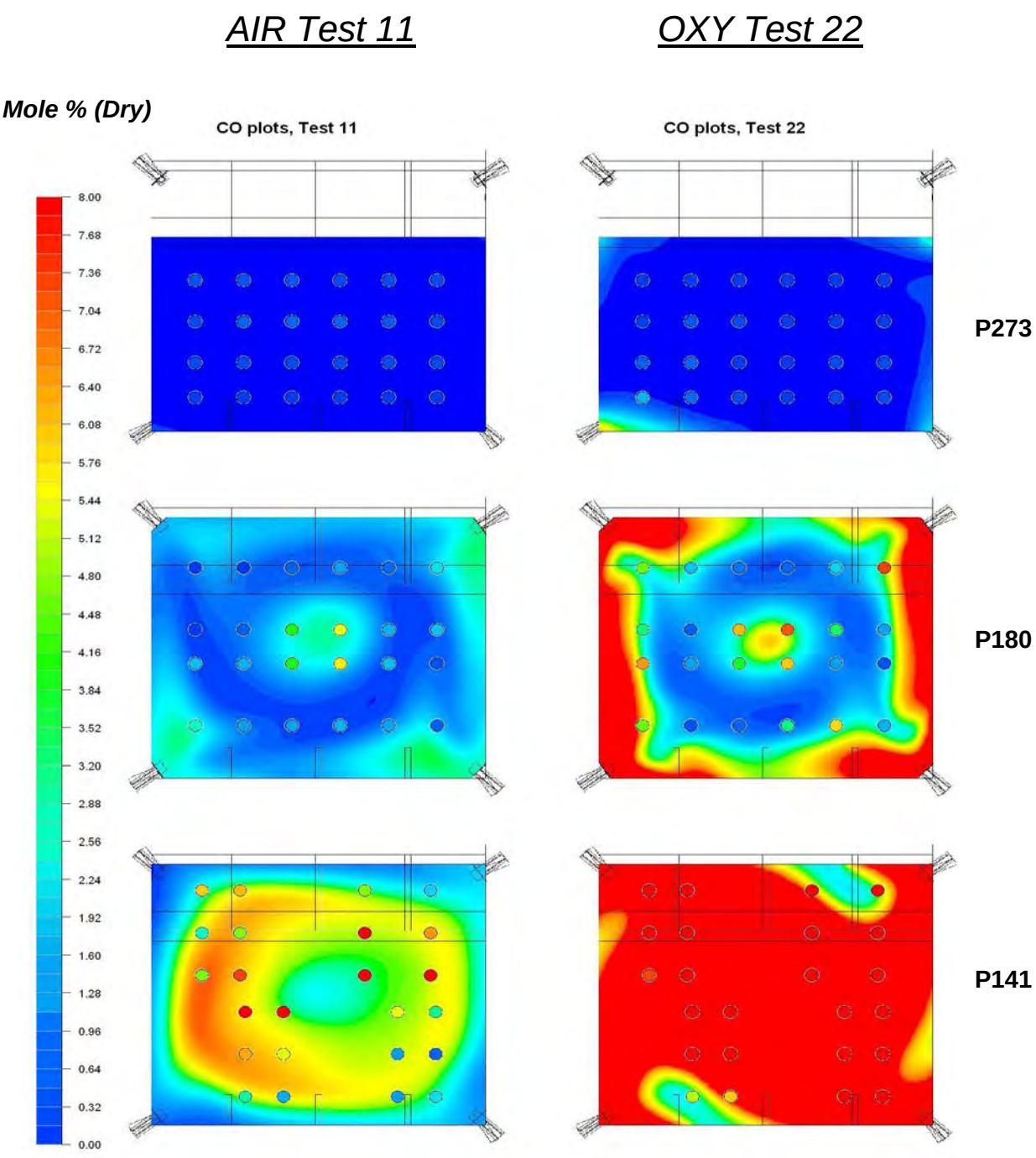

Figure 6-9. [AT-11:OT-22] Comparison of CO Concentrations on Test Planes

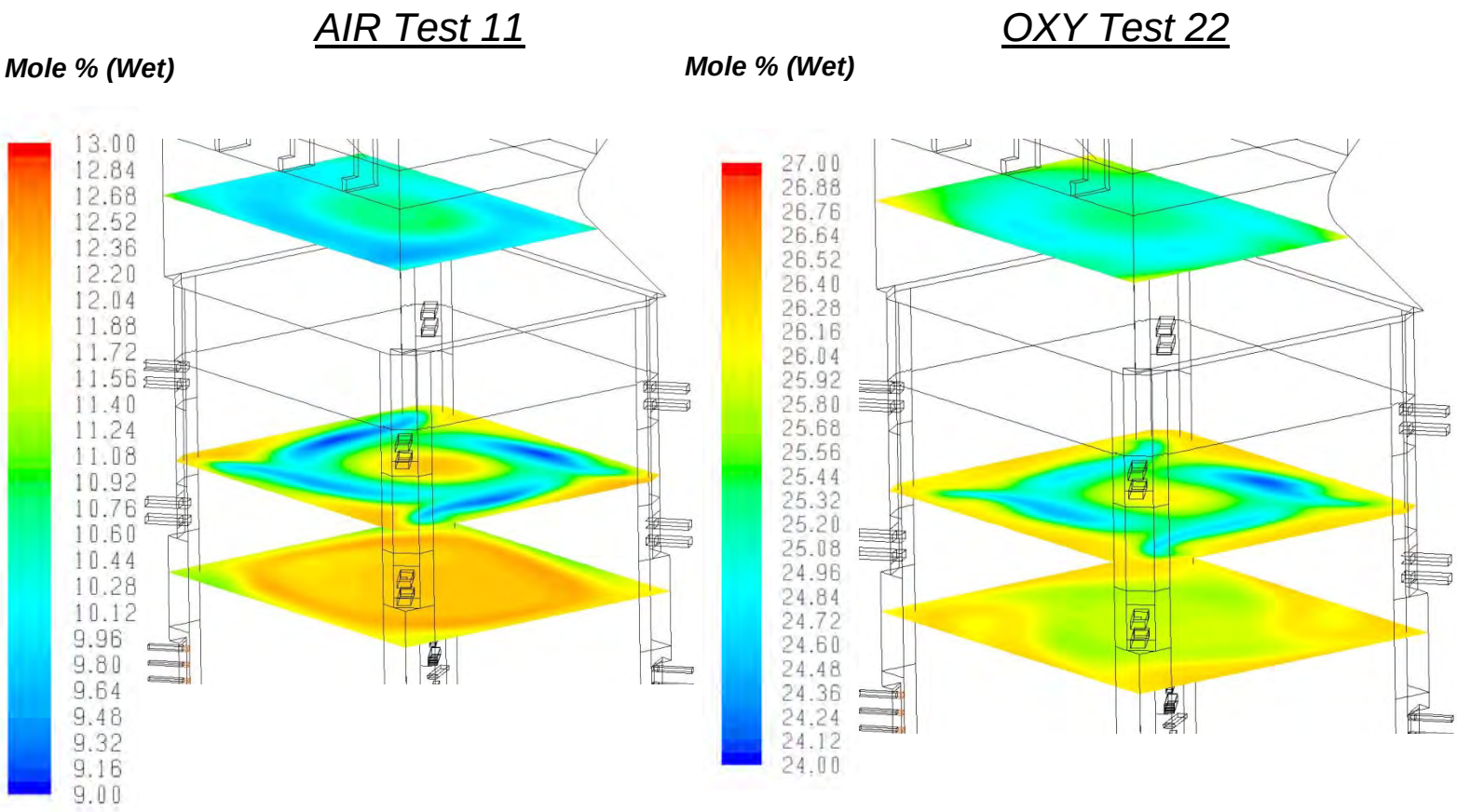

Figure 6-10. [AT-11:OT-22] Contours of H_2O Concentrations on Test Planes

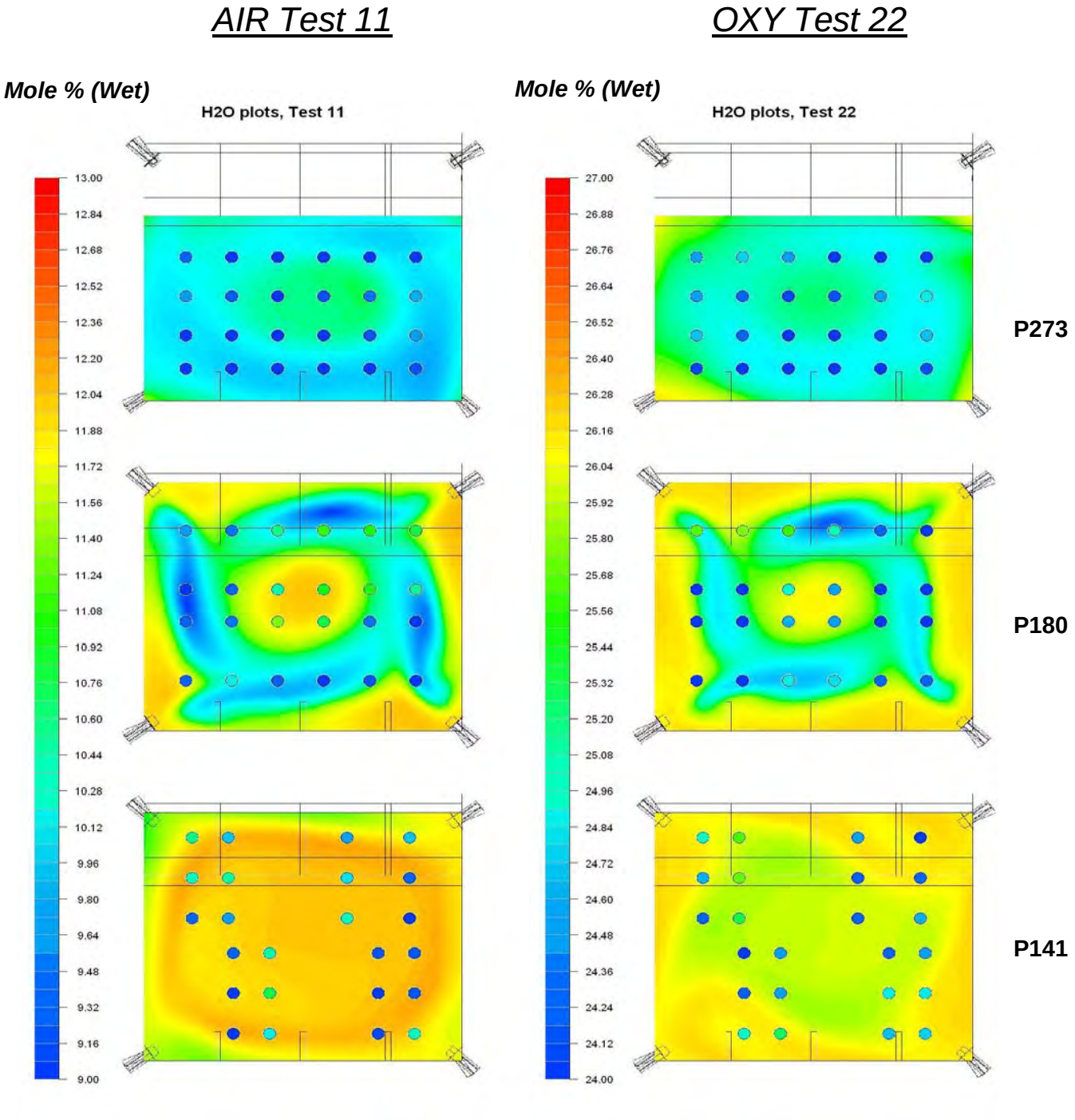

Figure 6-11. [AT-11:OT-22] Comparison of H_2O Concentrations on Test Planes

AIR Test 11 *OXY Test 22*

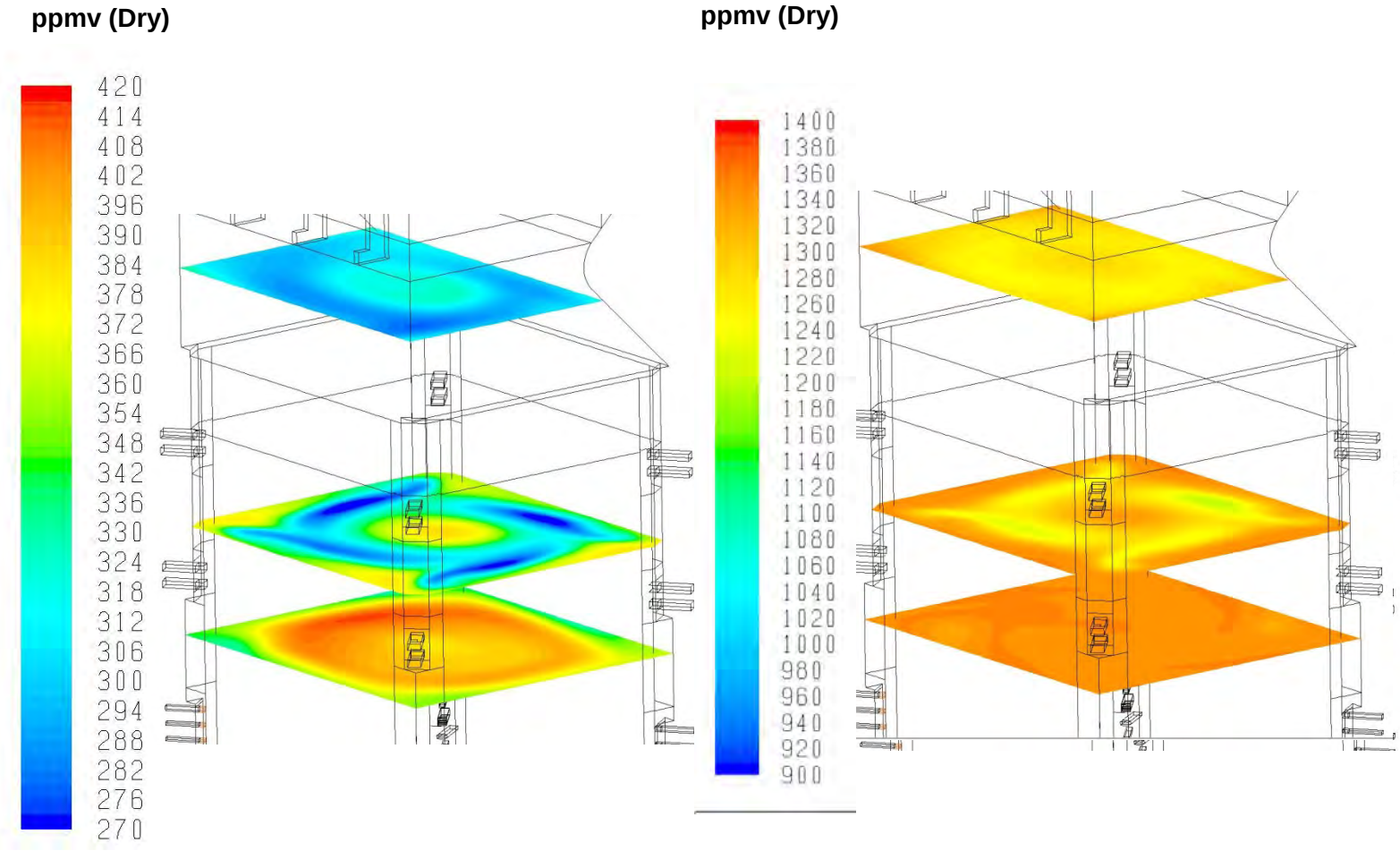

Figure 6-12. [AT-11:OT-22] Contours of SO_2 Concentrations on Test Planes

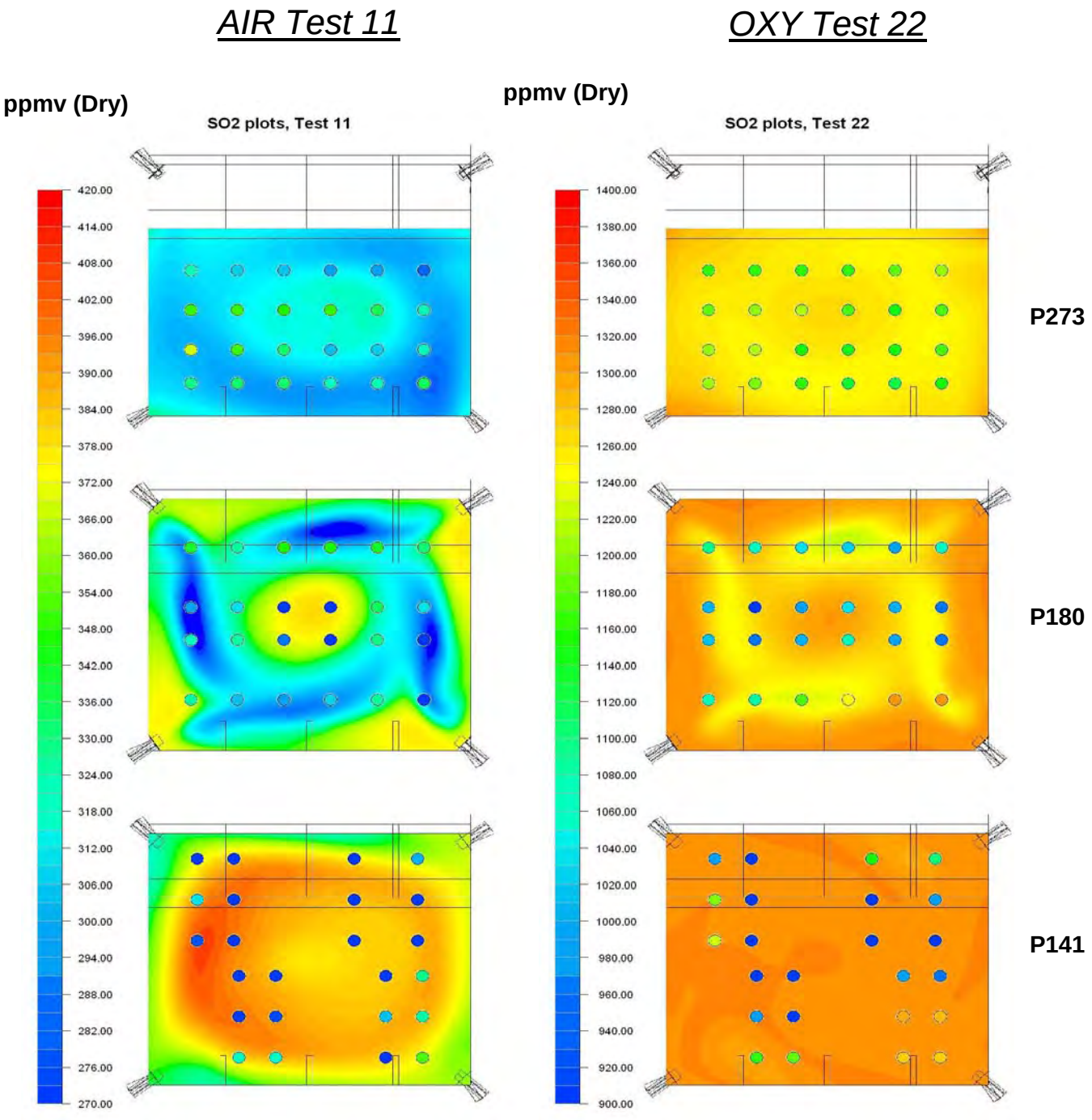

Figure 6-13. [AT-11:OT-22] Comparison of SO_2 Concentrations on Test Planes

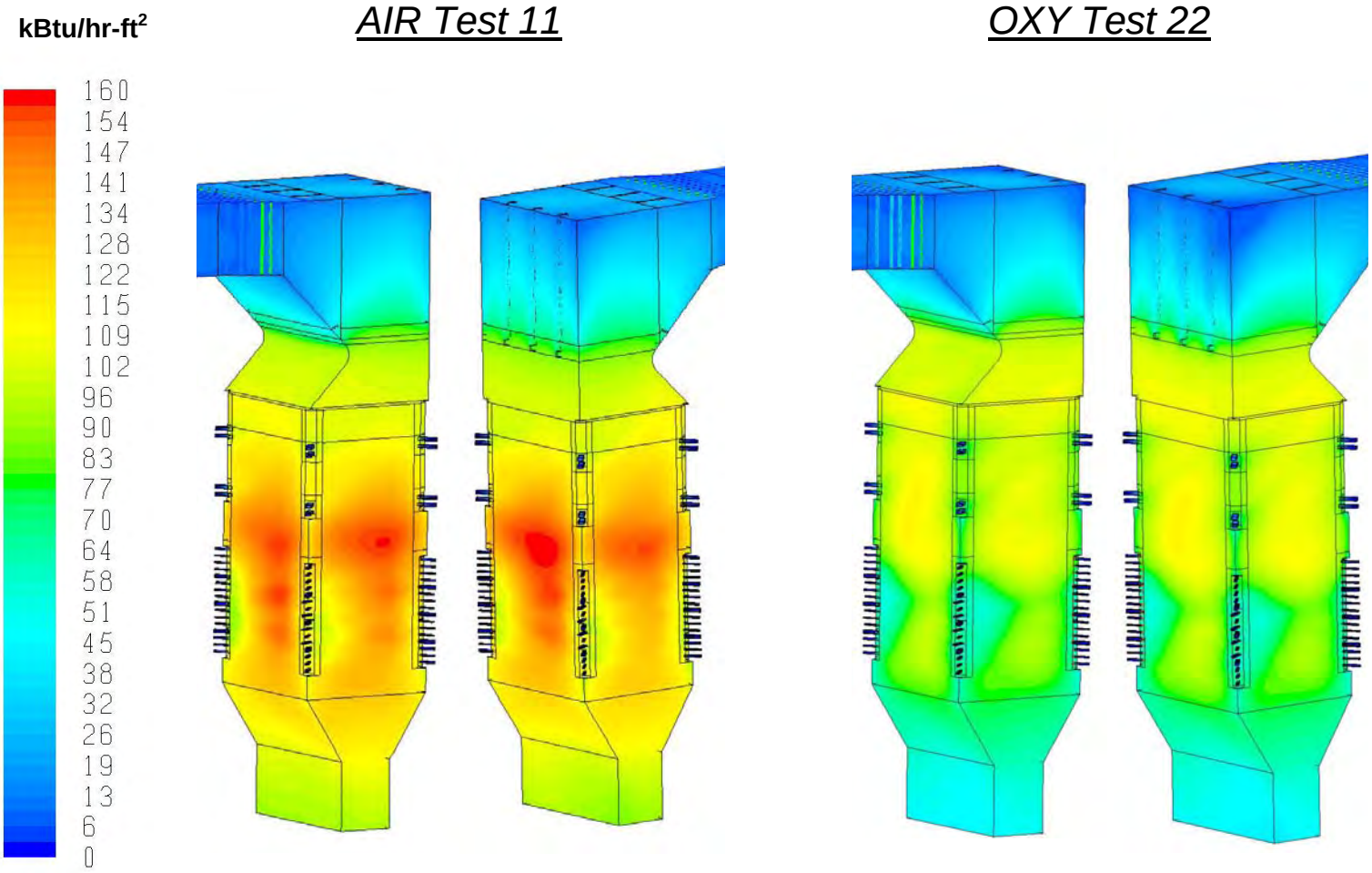

Figure 6-14. [AT-11:OT-22] Contours of Incident Radiation

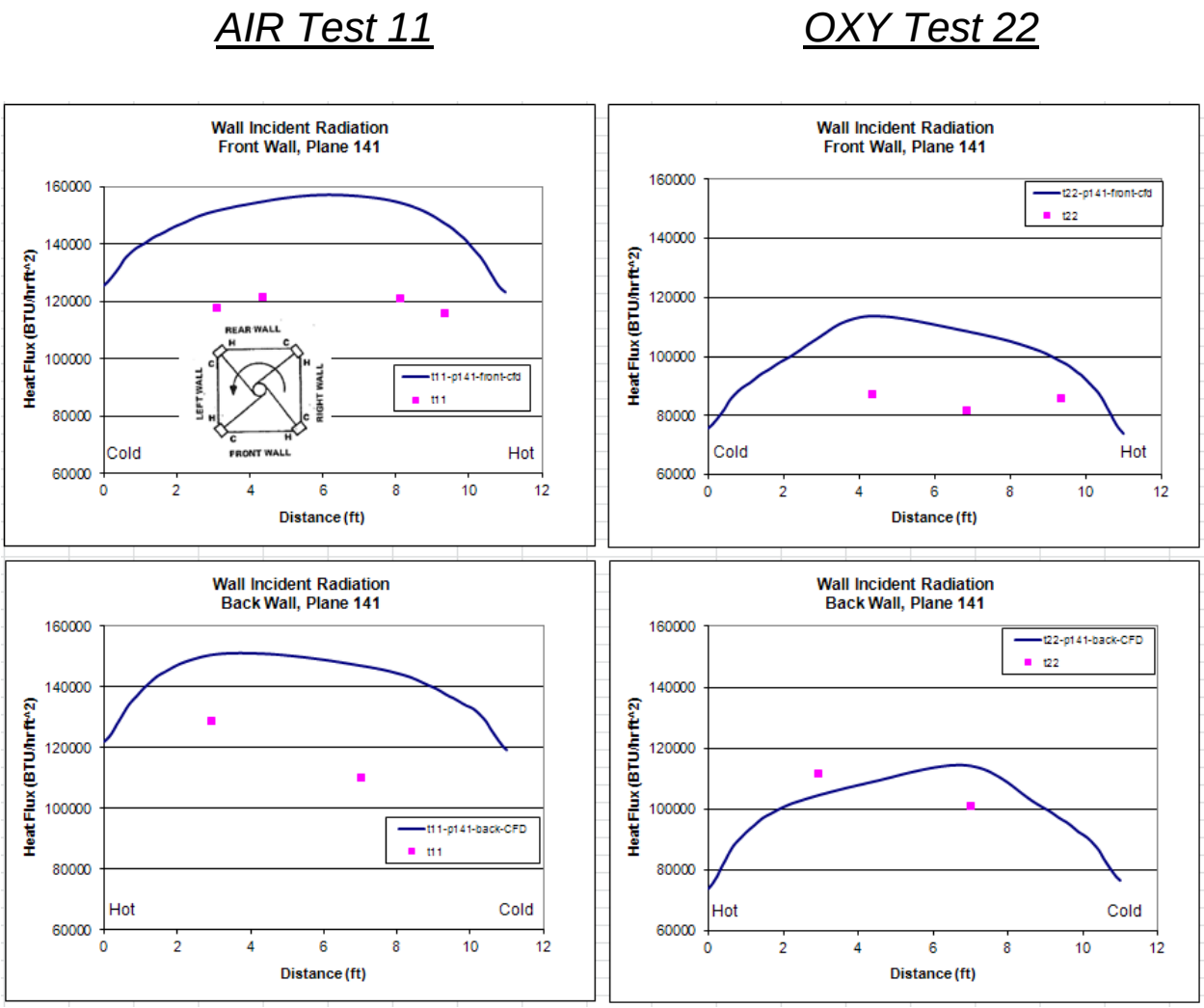

Figure 6-15. [AT-11:OT-22] Comparison of Wall Incident Radiation at Plane 141

AIR Test 11 *OXY Test 22*

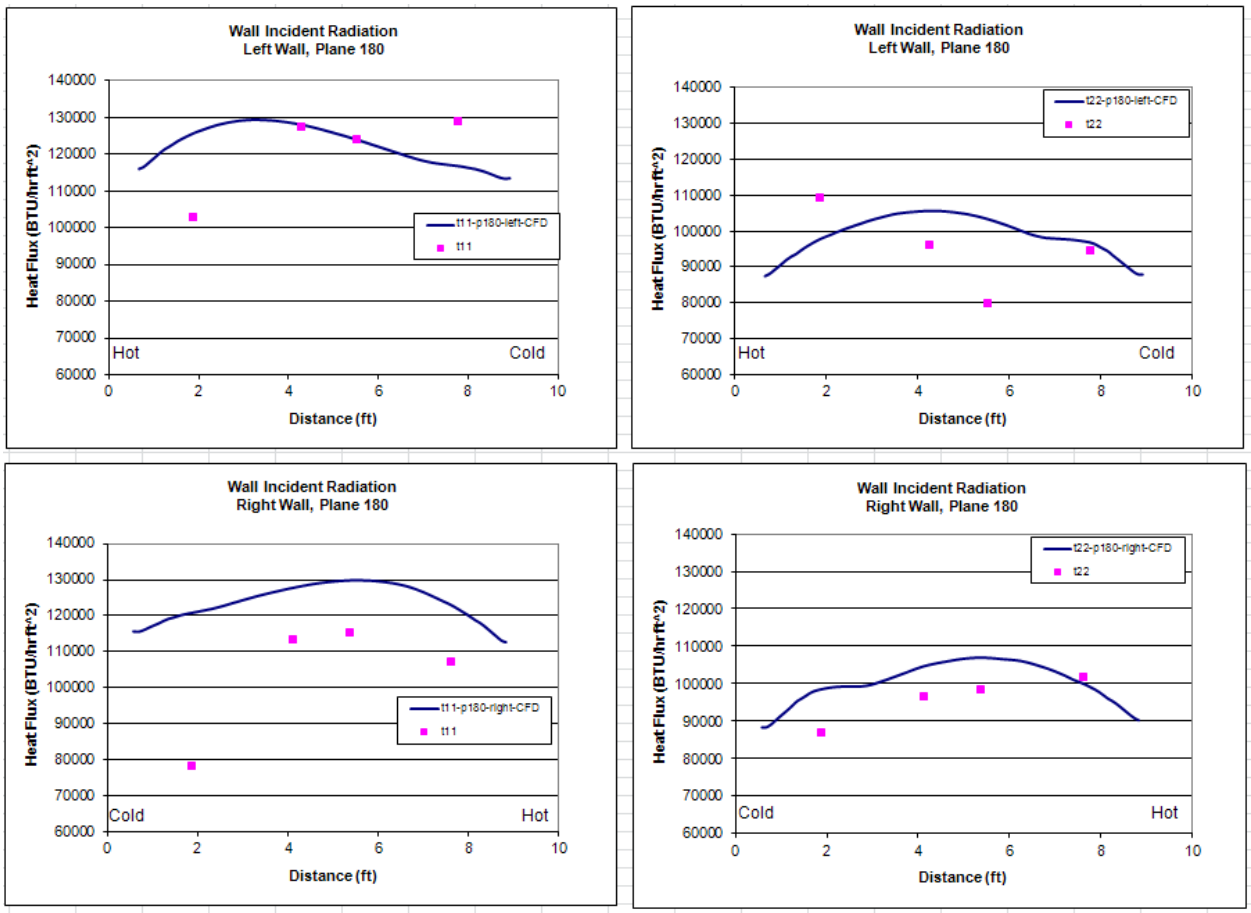

Figure 6-16. [AT-11:OT-22] Comparison of Wall Incident Radiation at Plane 180

AIR Test 11 *OXY Test 22*

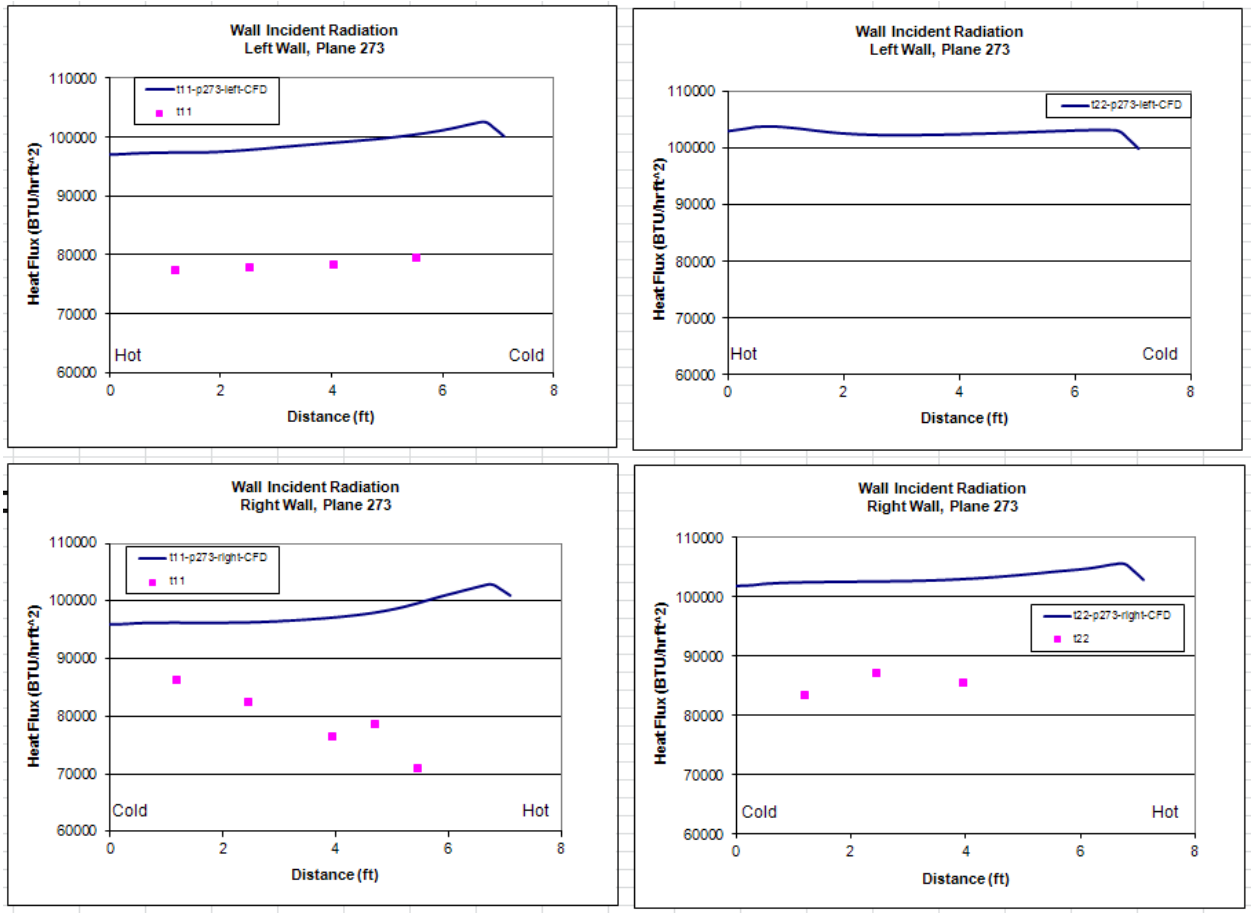

Figure 6-17. [AT-11:OT-22] Comparison of Wall Incident Radiation at Plane 273

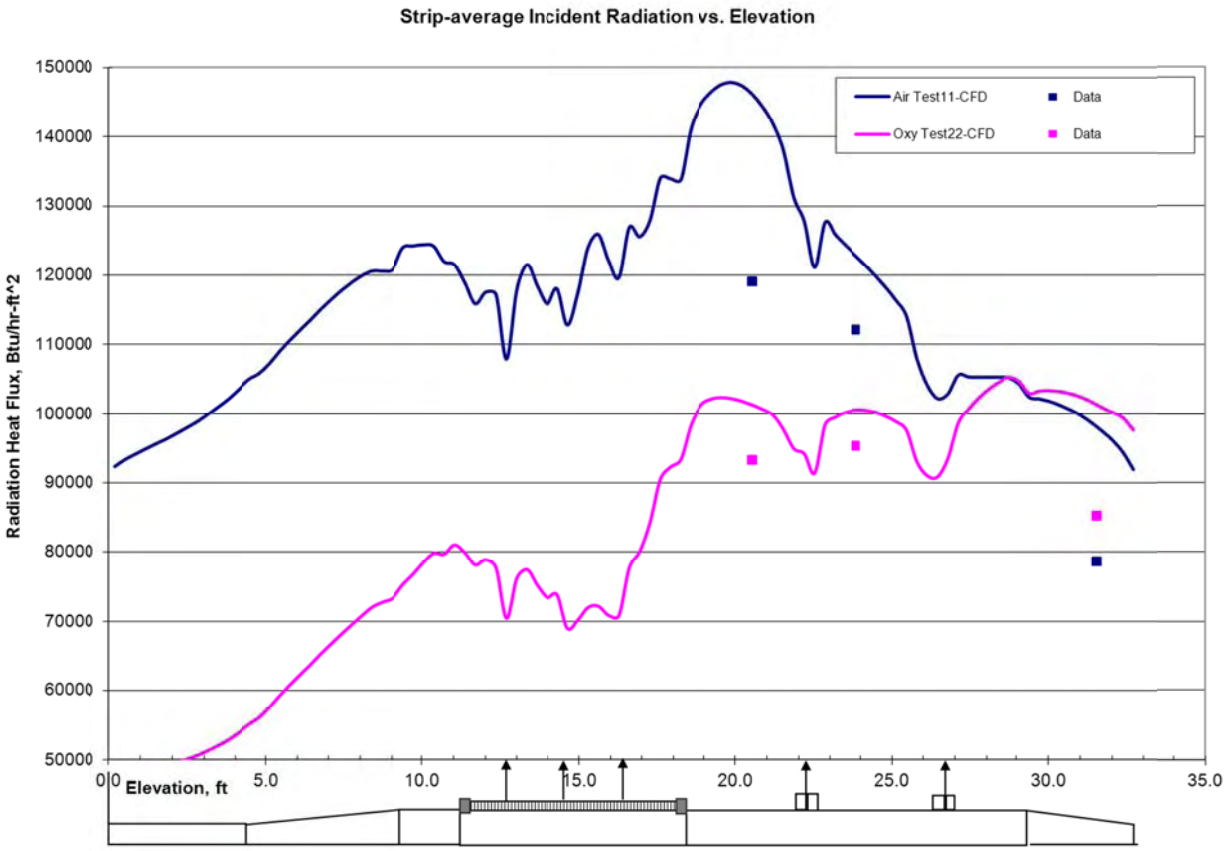

Figure 6-18. [AT-11:OT-22] Strip-Averaged Wall Incident Radiation

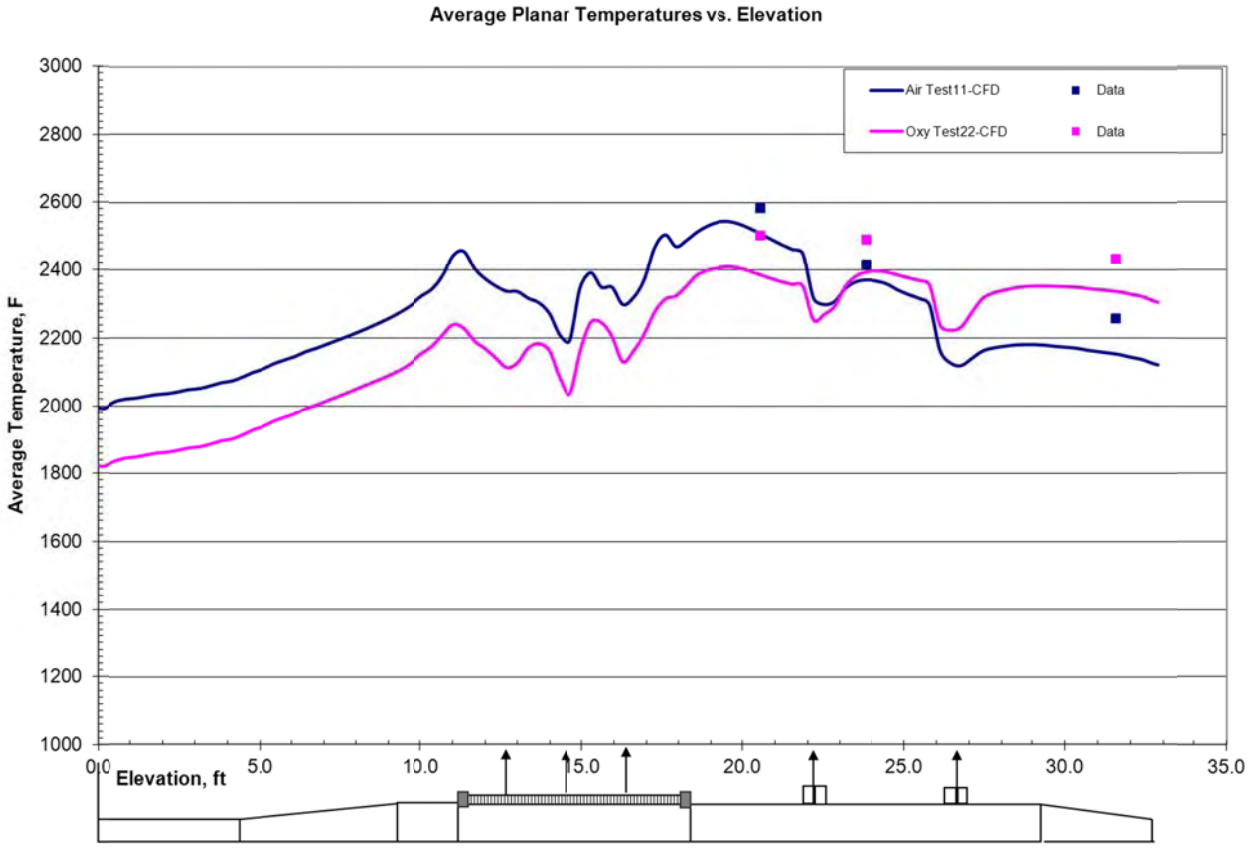

Figure 6-19. [AT-11:OT-22] Planar Averaged Temperature

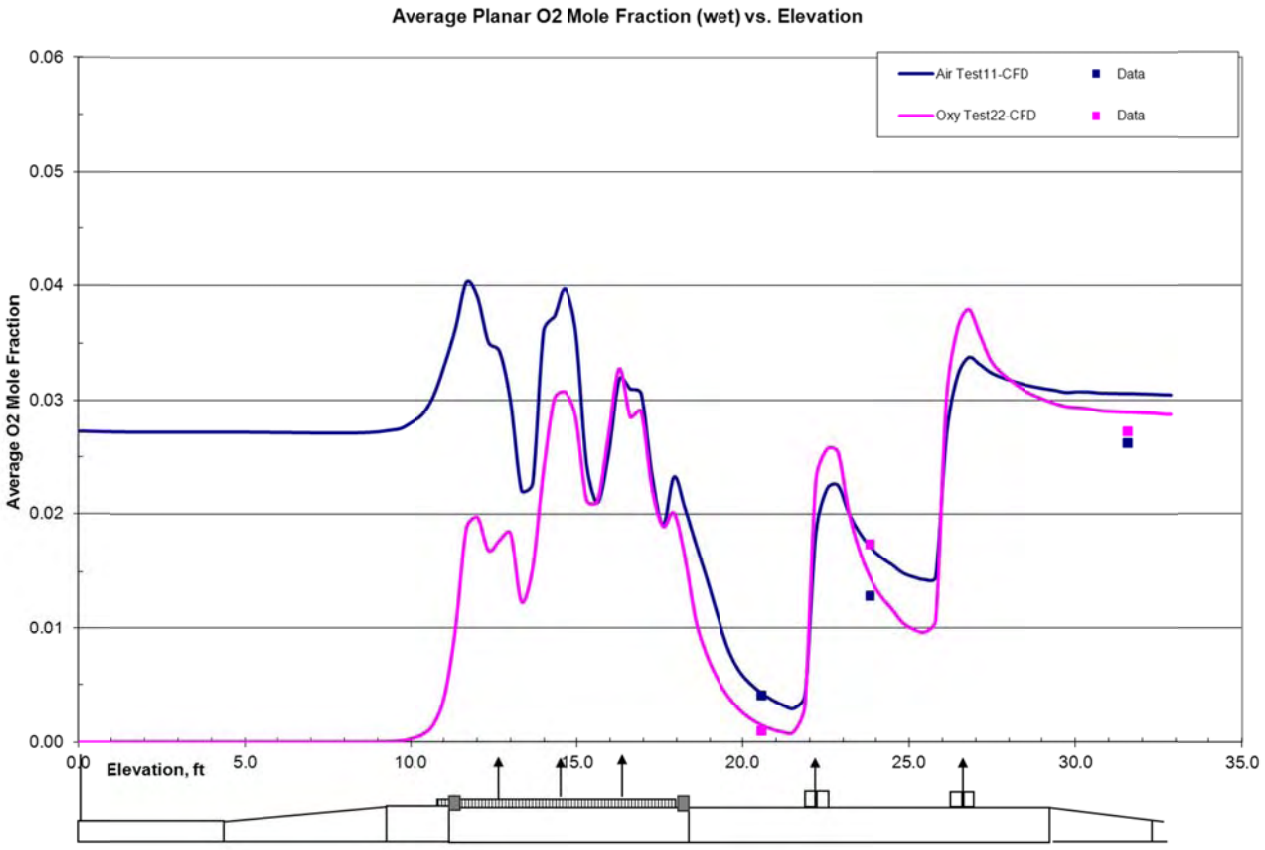

Figure 6-20. [AT-11:OT-22] Planar Averaged O_2

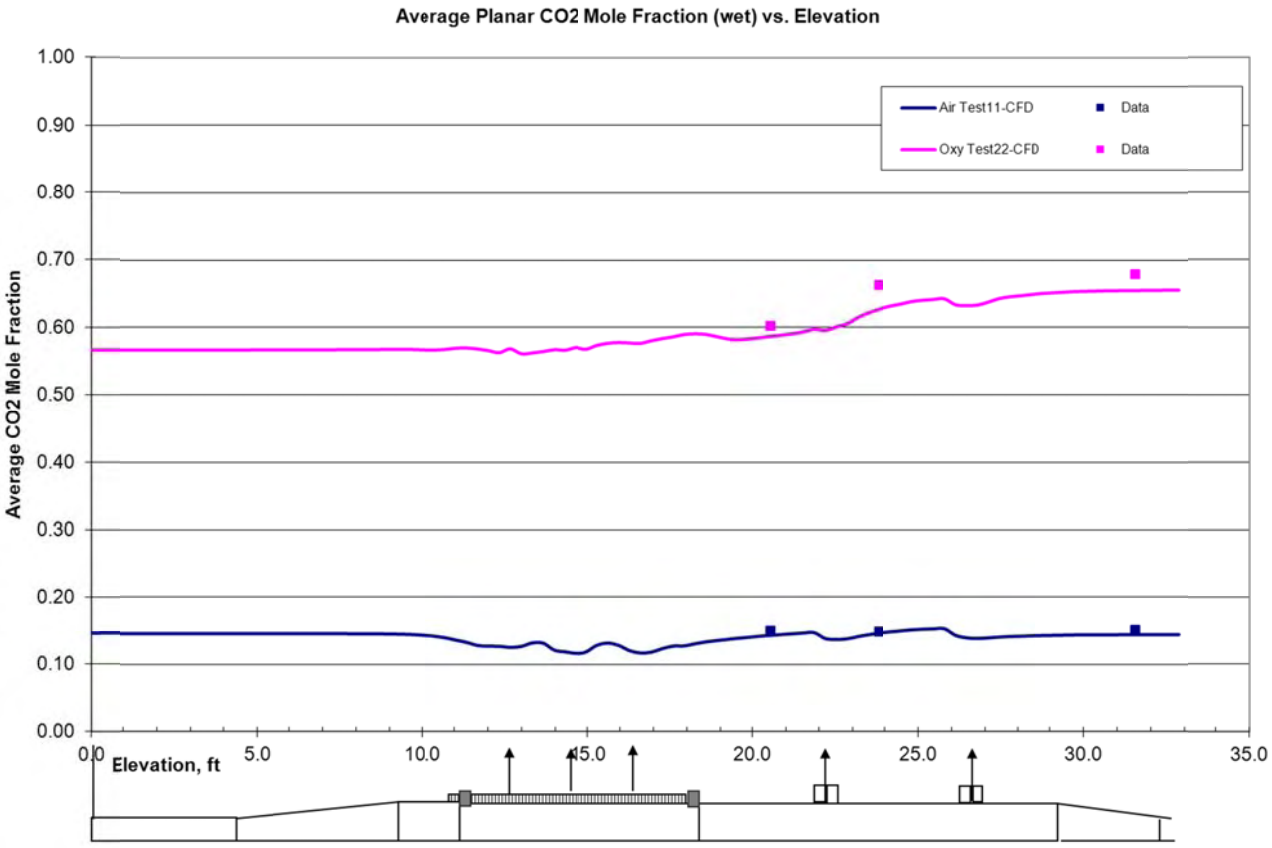

Figure 6-21. [AT-11:OT-22] Planar Averaged CO_2

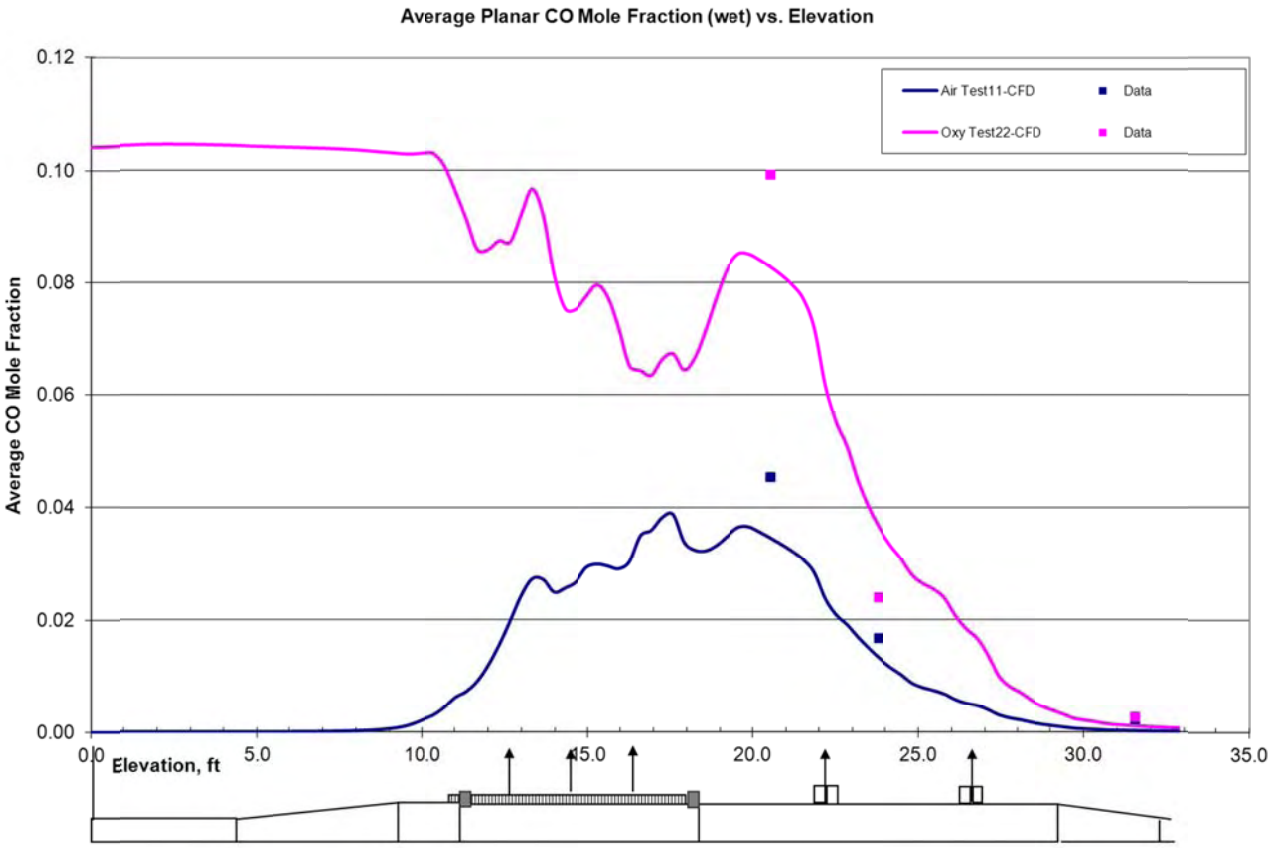

Figure 6-22. [AT-11:OT-22] Planar Averaged CO

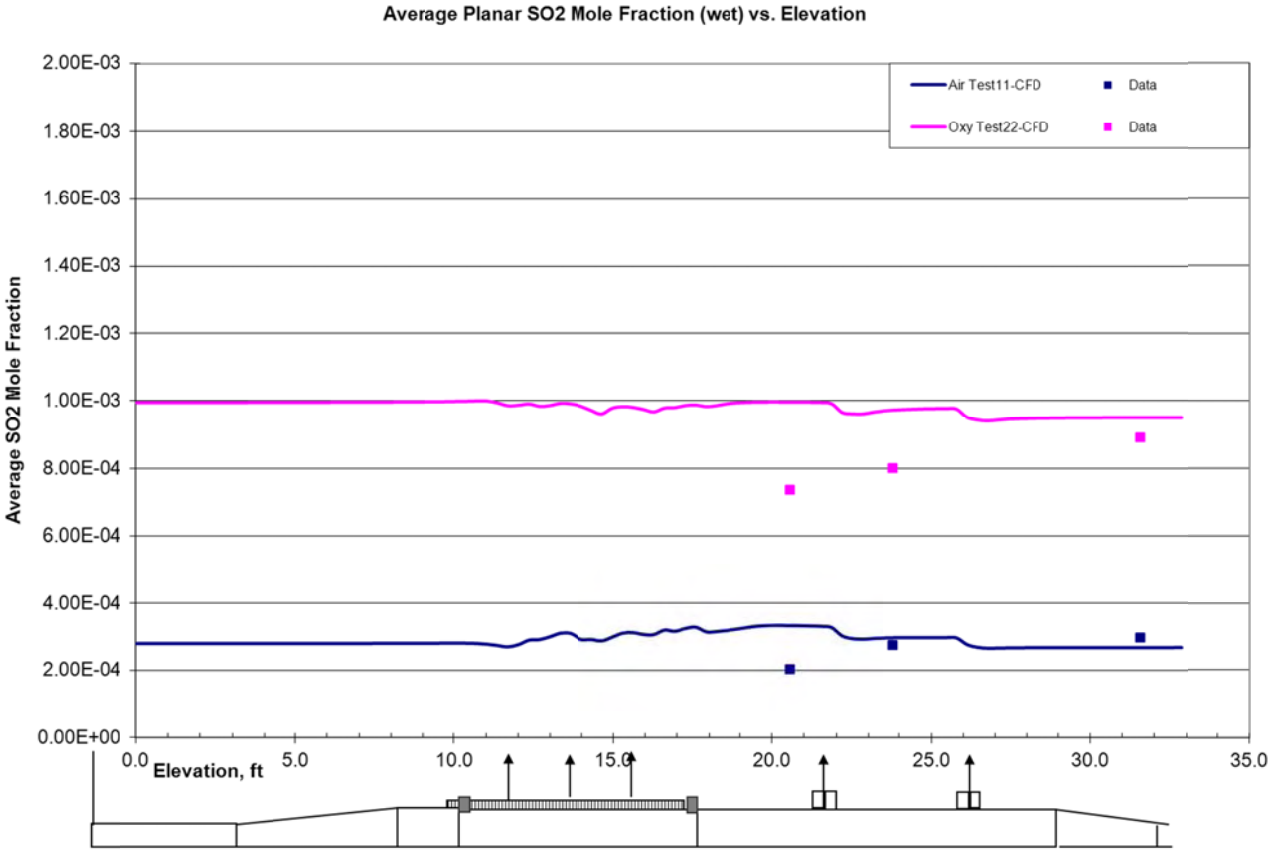

Figure 6-23. [AT-11:OT-22] Planar Averaged SO_2

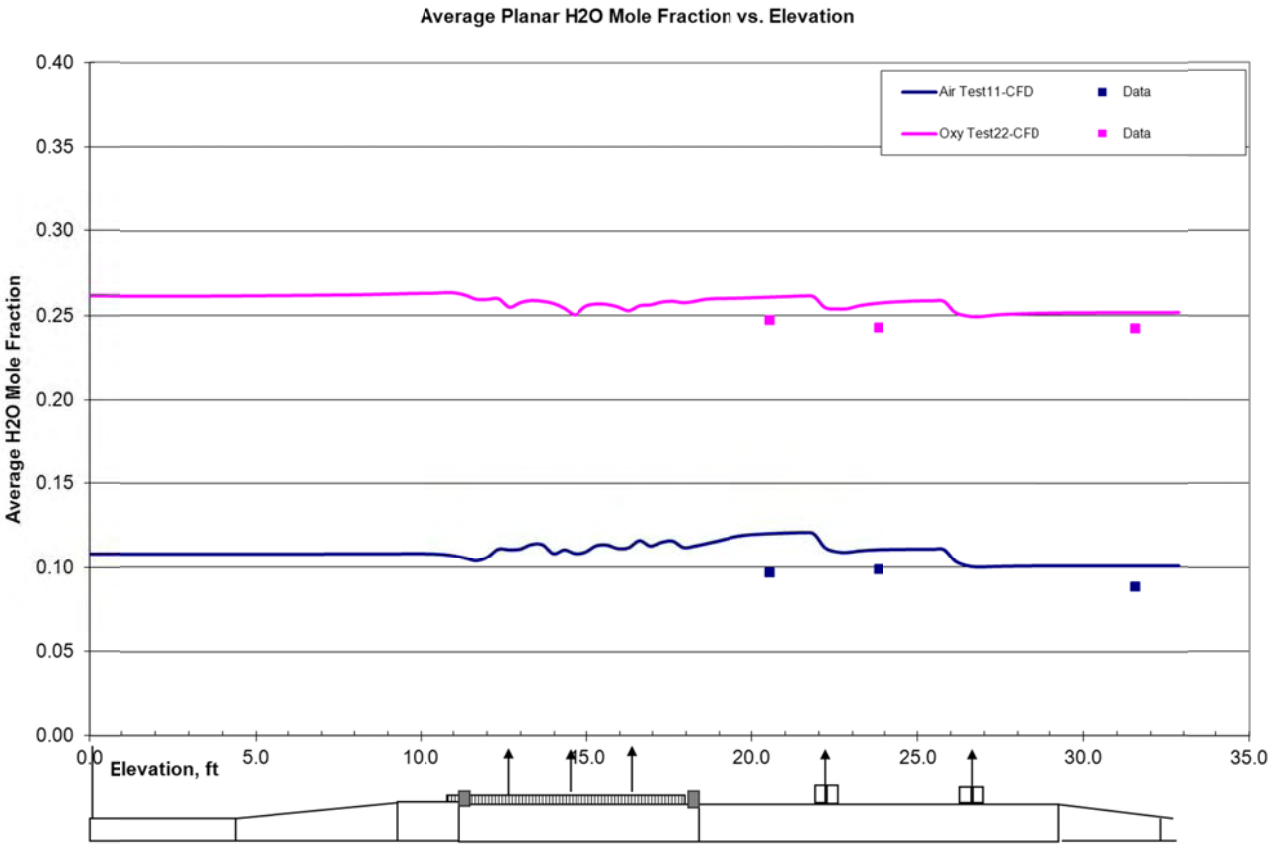

Figure 6-24. [AT-11:OT-22] Planar Averaged H_2O

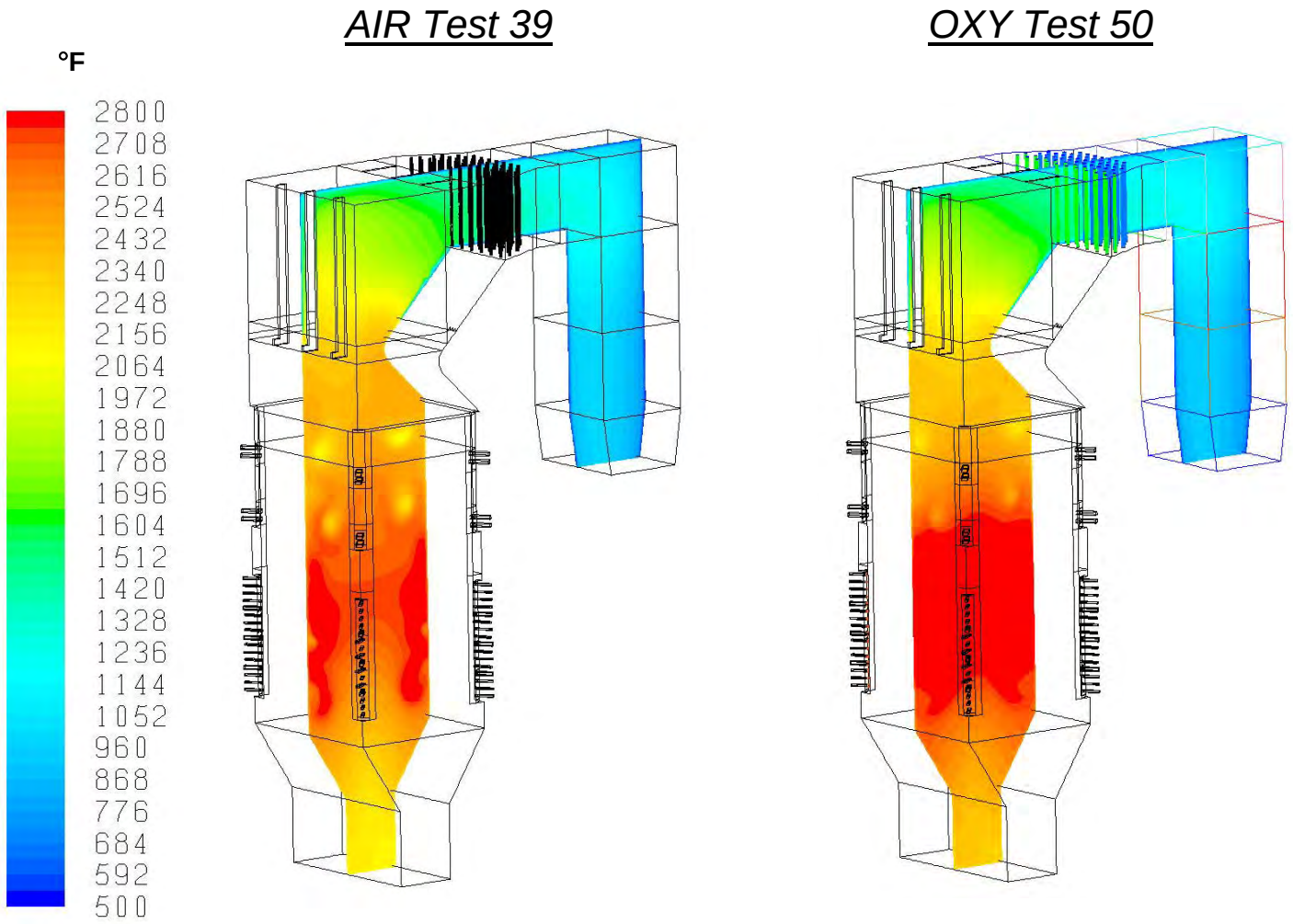

Figure 6-25. [AT-39:OT-50] Contours of Temperature on X-Midplane

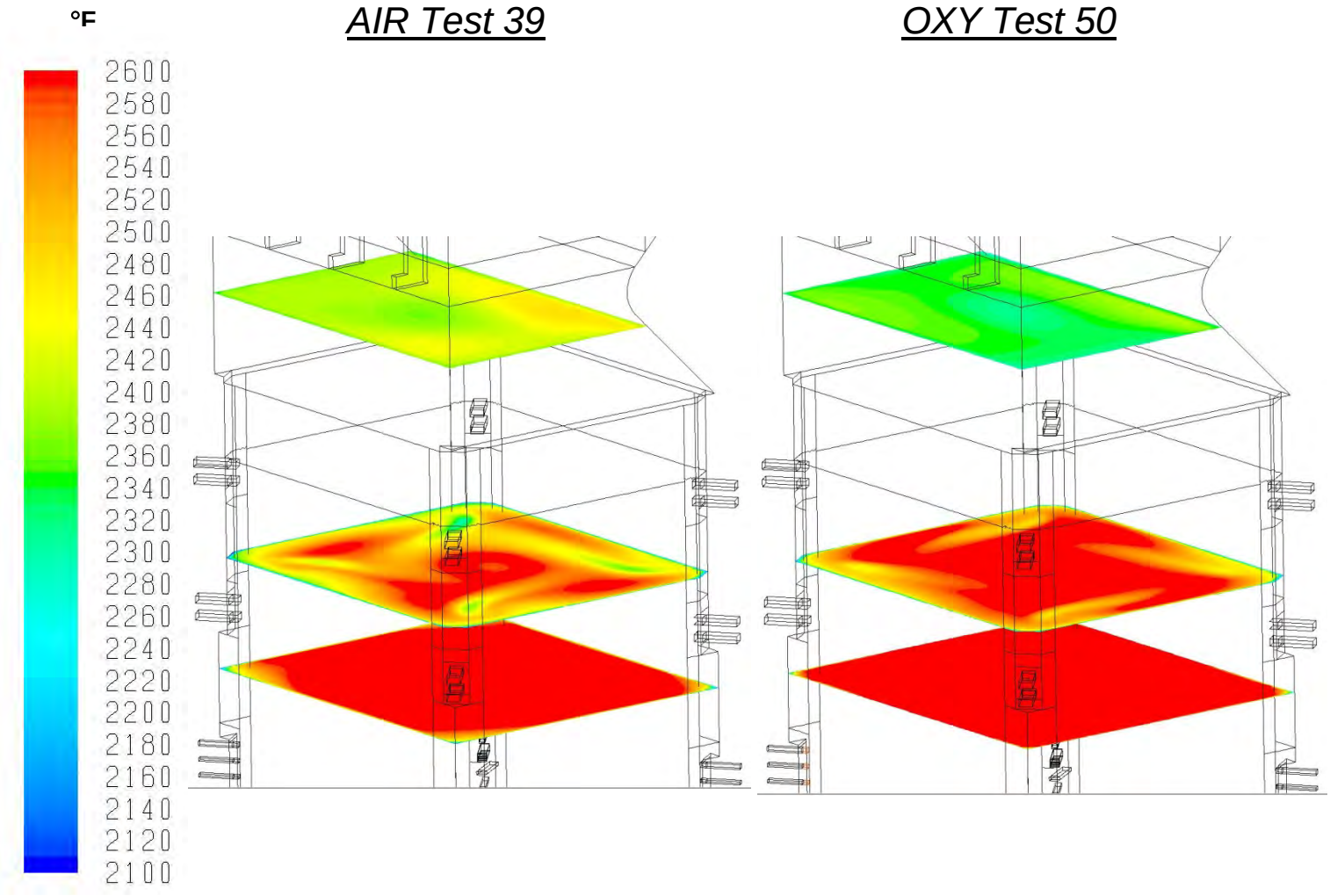

Figure 6-26. [AT-39:OT-50] Contours of Temperature on Test Planes

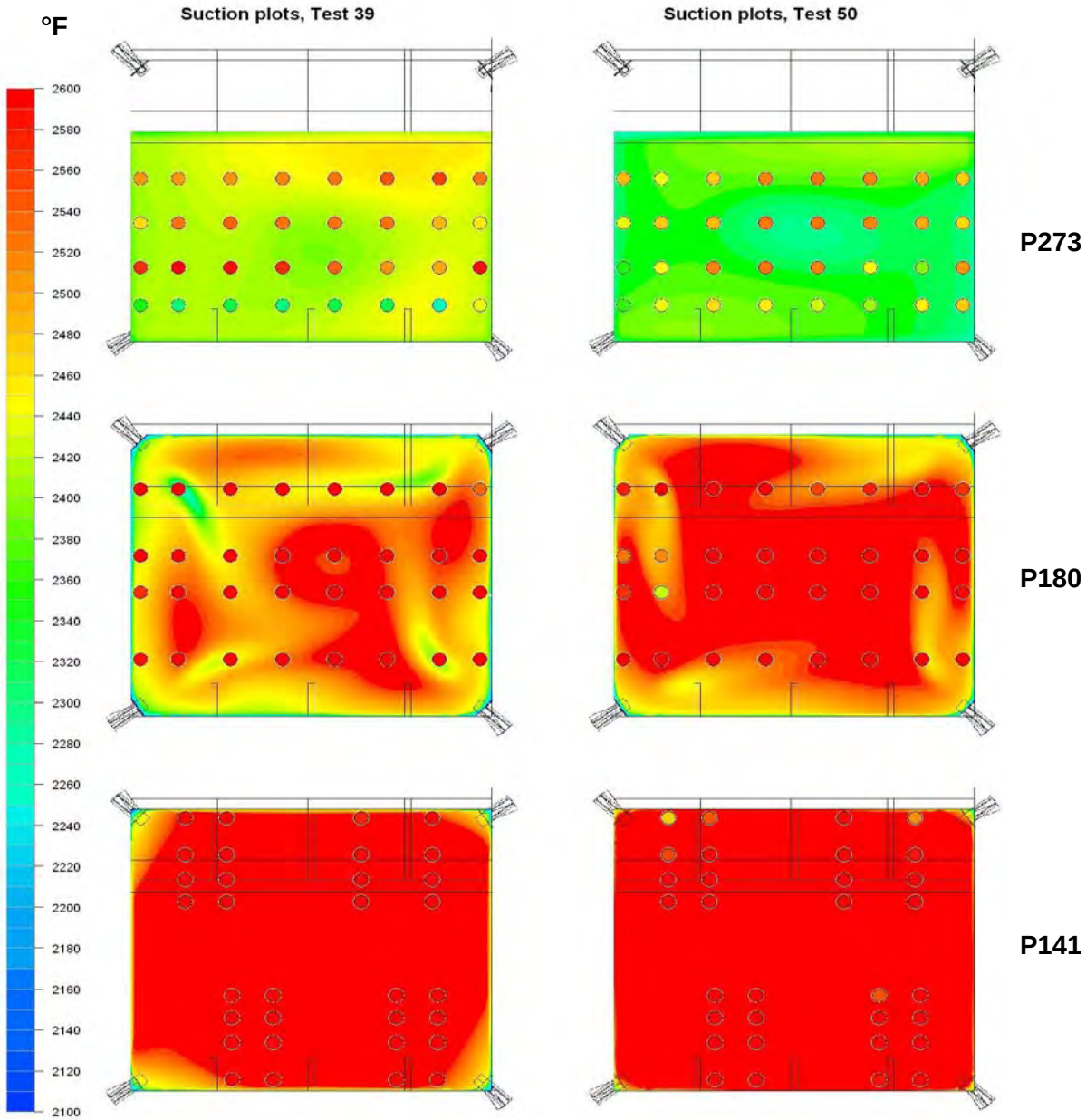

Figure 6-27. [AT-39:OT-50] Comparison of Temperature on Test Planes

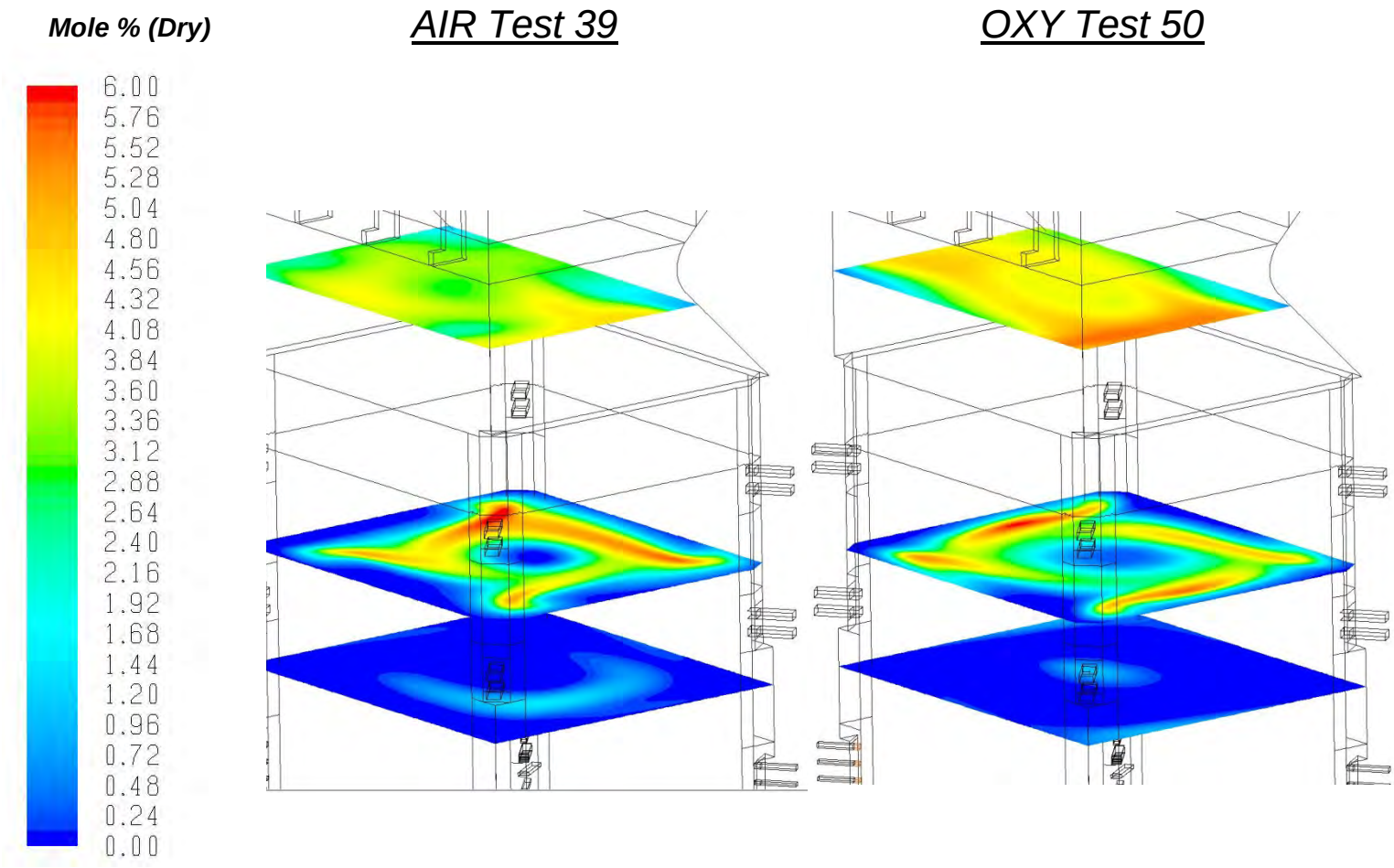

Figure 6-28. [AT-39:OT-50] Contours of O_2 Concentrations on Test Planes

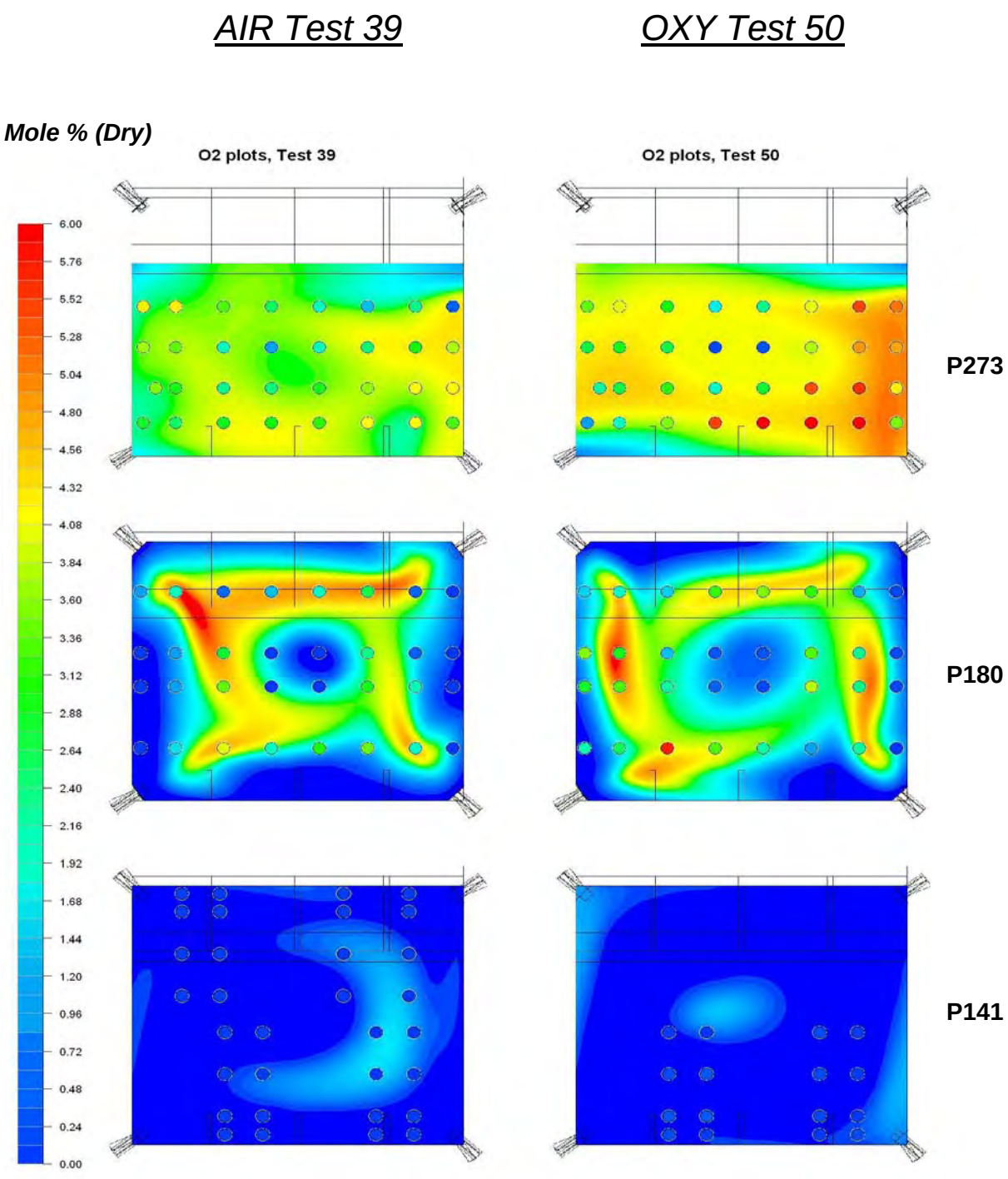

Figure 6-29. [AT-39:OT-50] Comparison of O_2 Concentrations on Test Planes

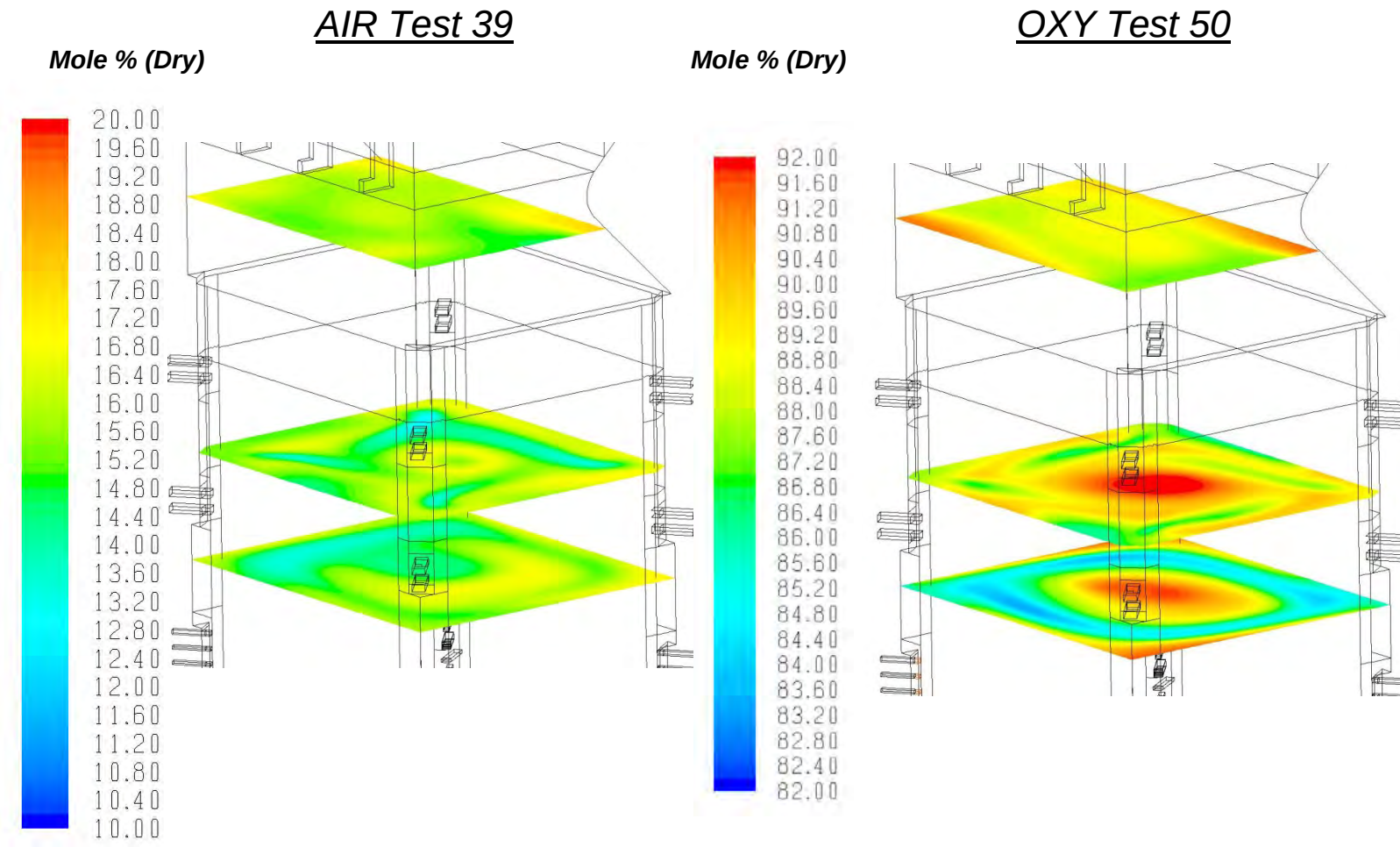

Figure 6-30. [AT-39:OT-50] Contours of CO_2 Concentrations on Test Planes

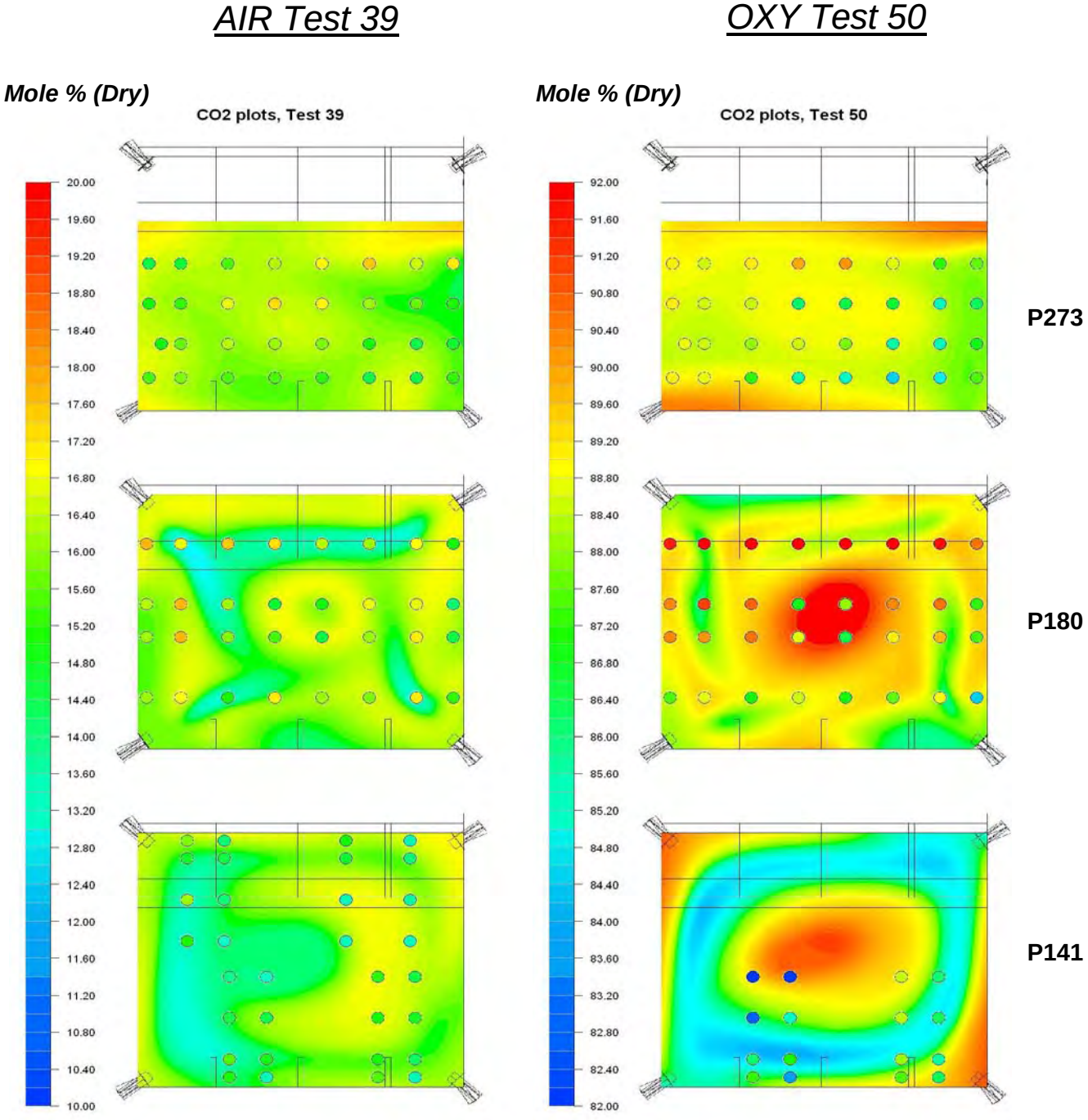

Figure 6-31. [AT-39:OT-50] Comparison of CO_2 Concentrations on Test Planes

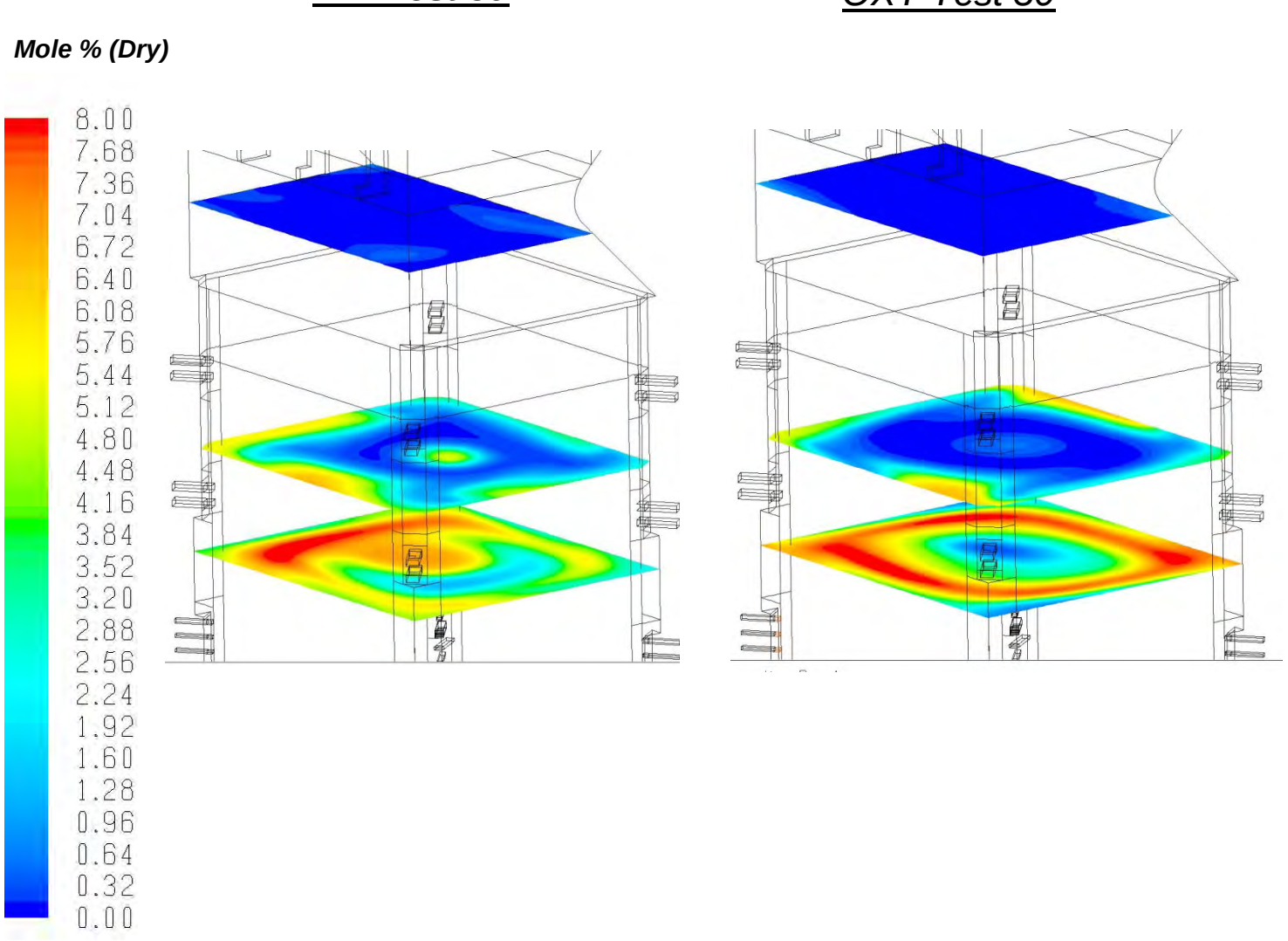

Figure 6-32. [AT-39:OT-50] Contours of CO Concentrations on Test Planes

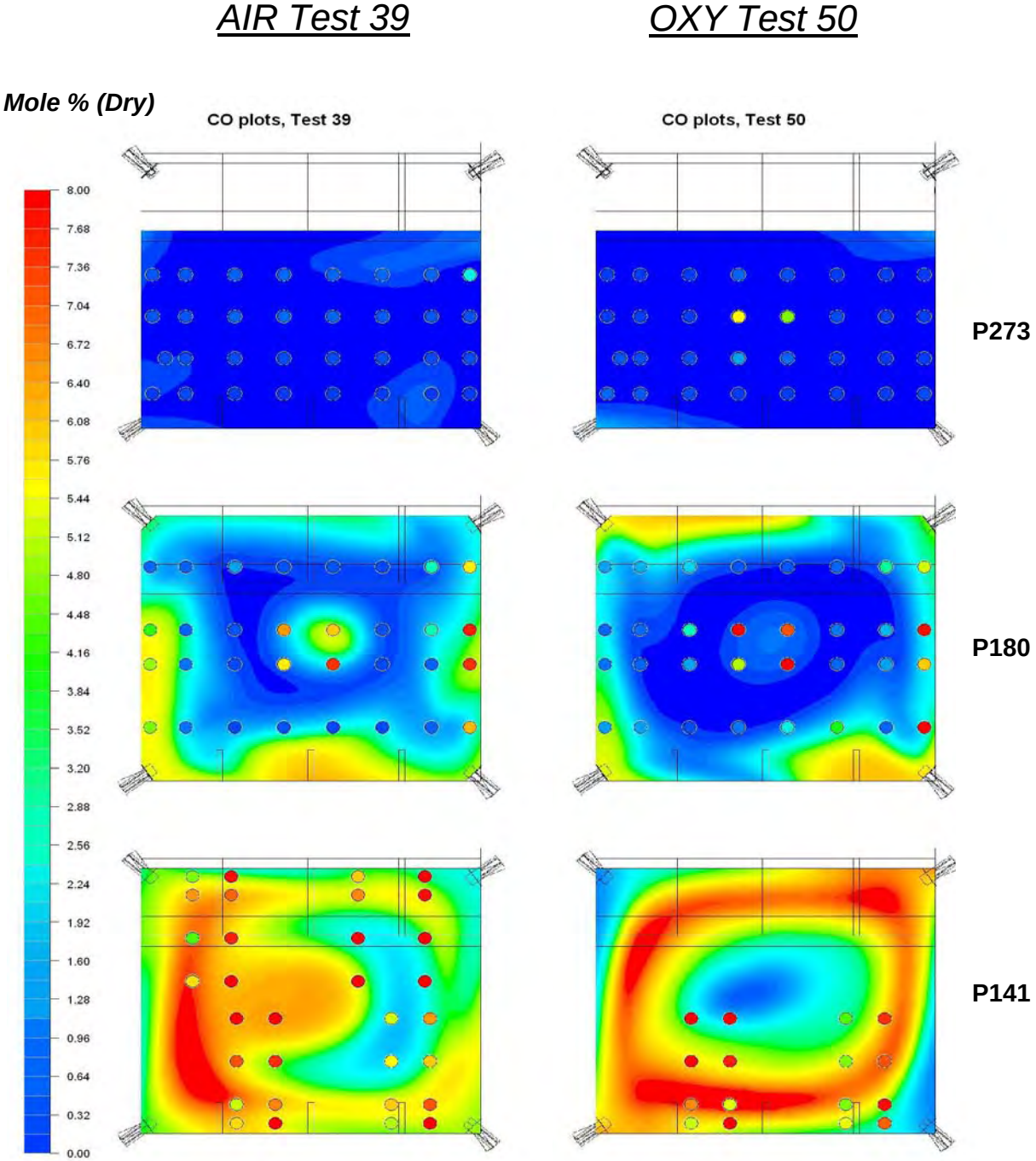

Figure 6-33. [AT-39:OT-50] Comparison of CO Concentrations on Test Planes

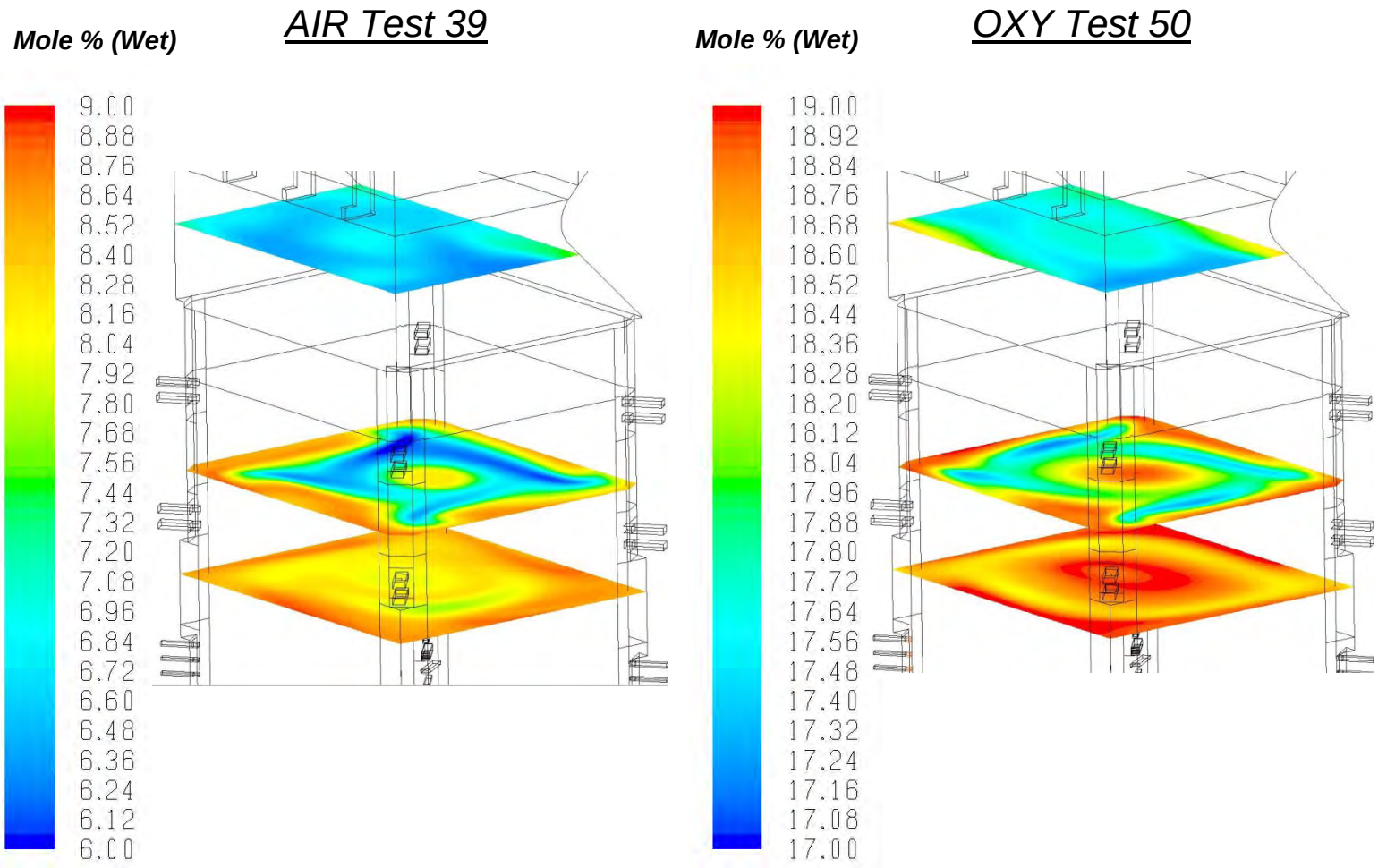

Figure 6-34. [AT-39:OT-50] Contours of H_2O Concentrations on Test Planes

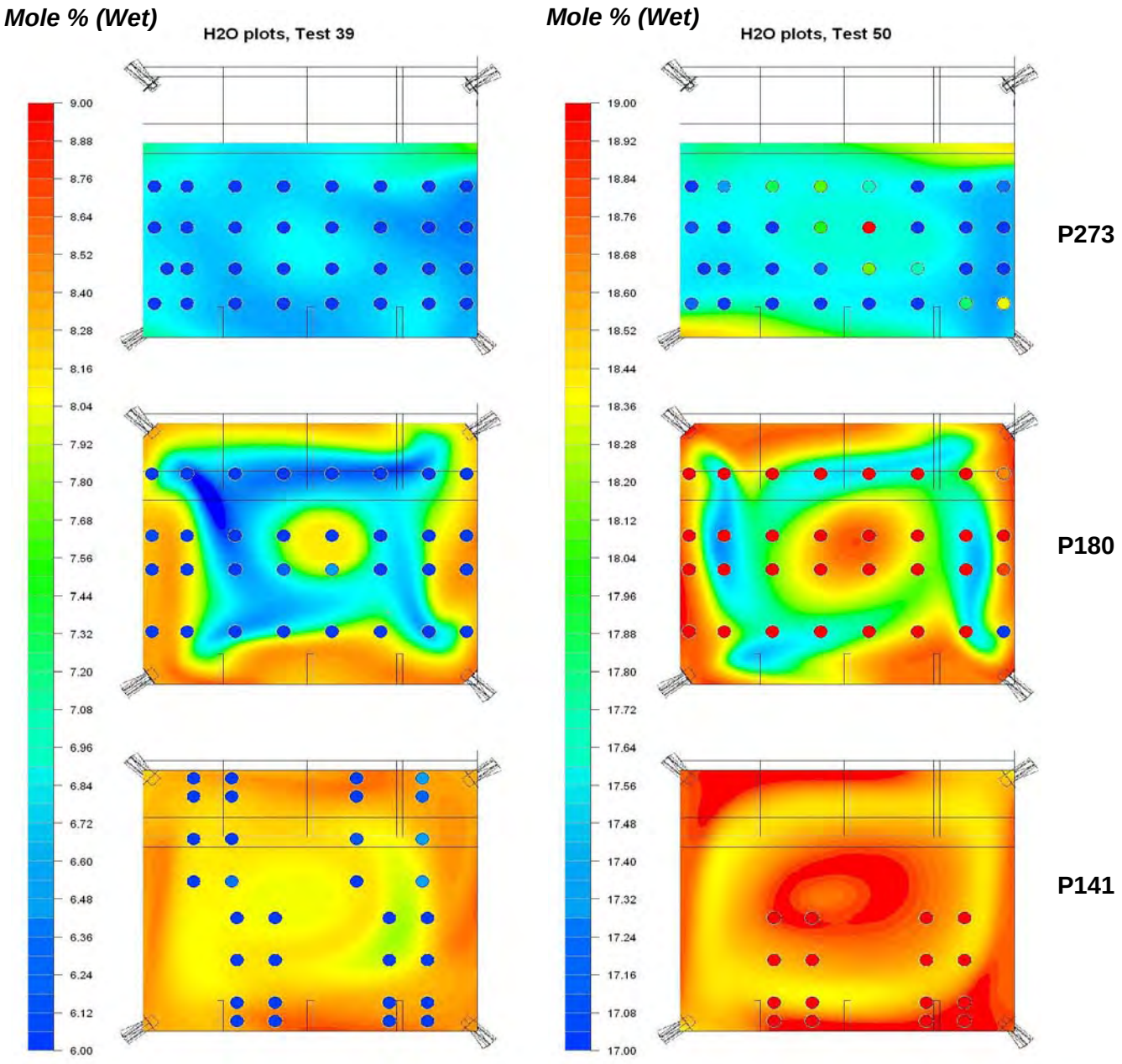

Figure 6-35. [AT-39:OT-50] Comparison of H_2O Concentrations on Test Planes

AIR Test 39 *OXY Test 50*

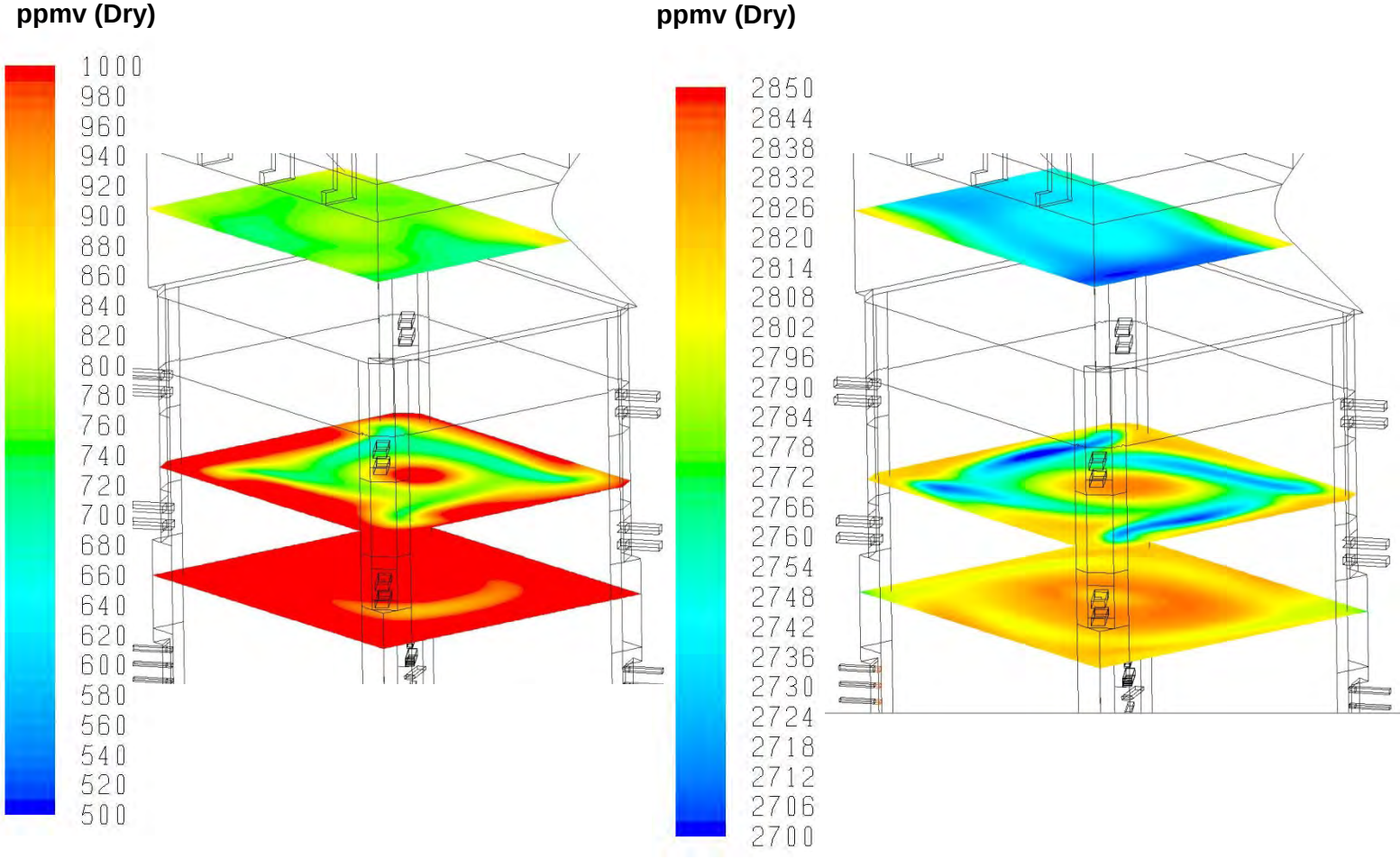

Figure 6-36. [AT-39:OT-50] Contours of SO_2 Concentrations on Test Planes

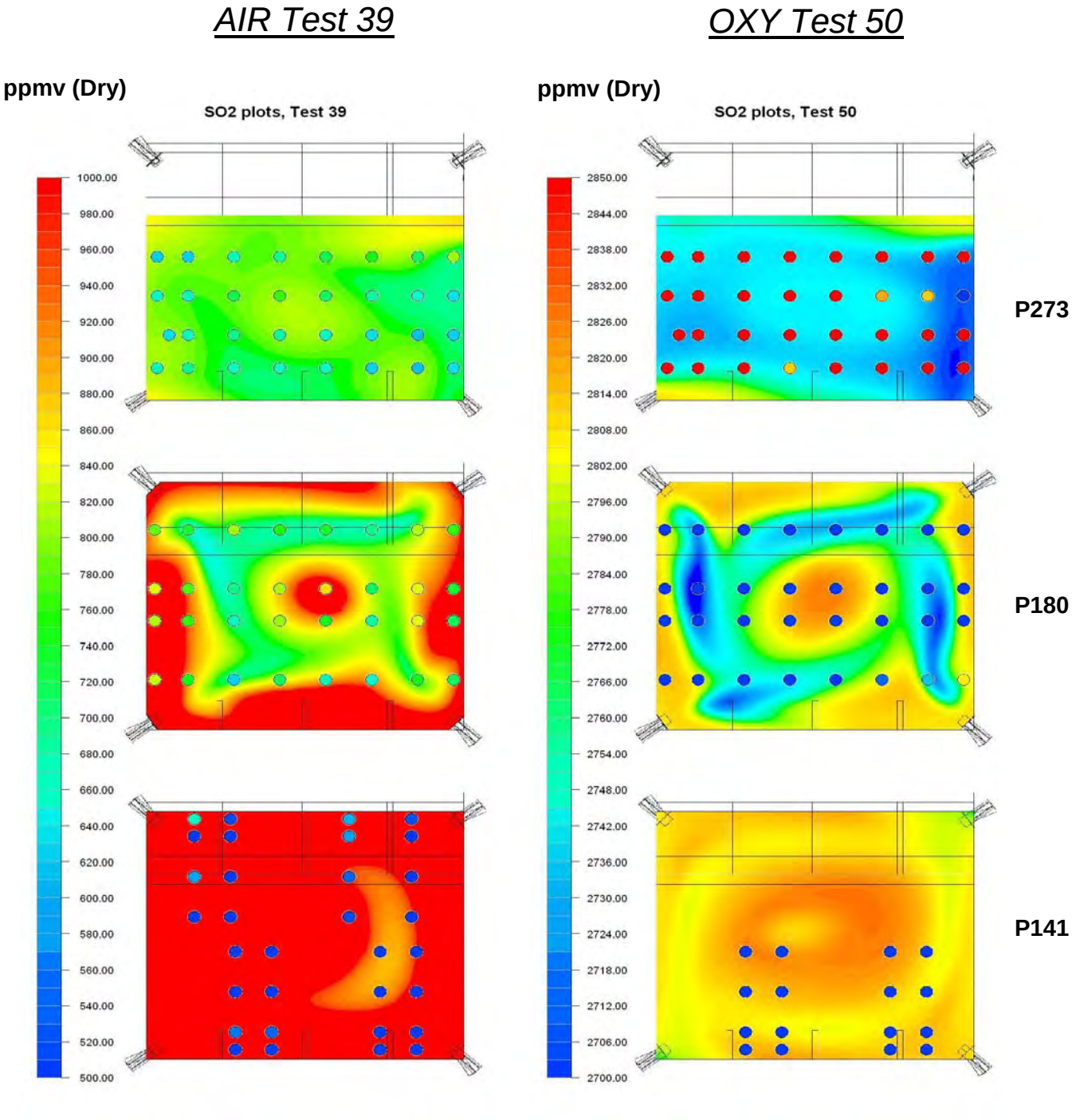

Figure 6-37. [AT-39:OT-50] Comparison of SO_2 Concentrations on Test Planes

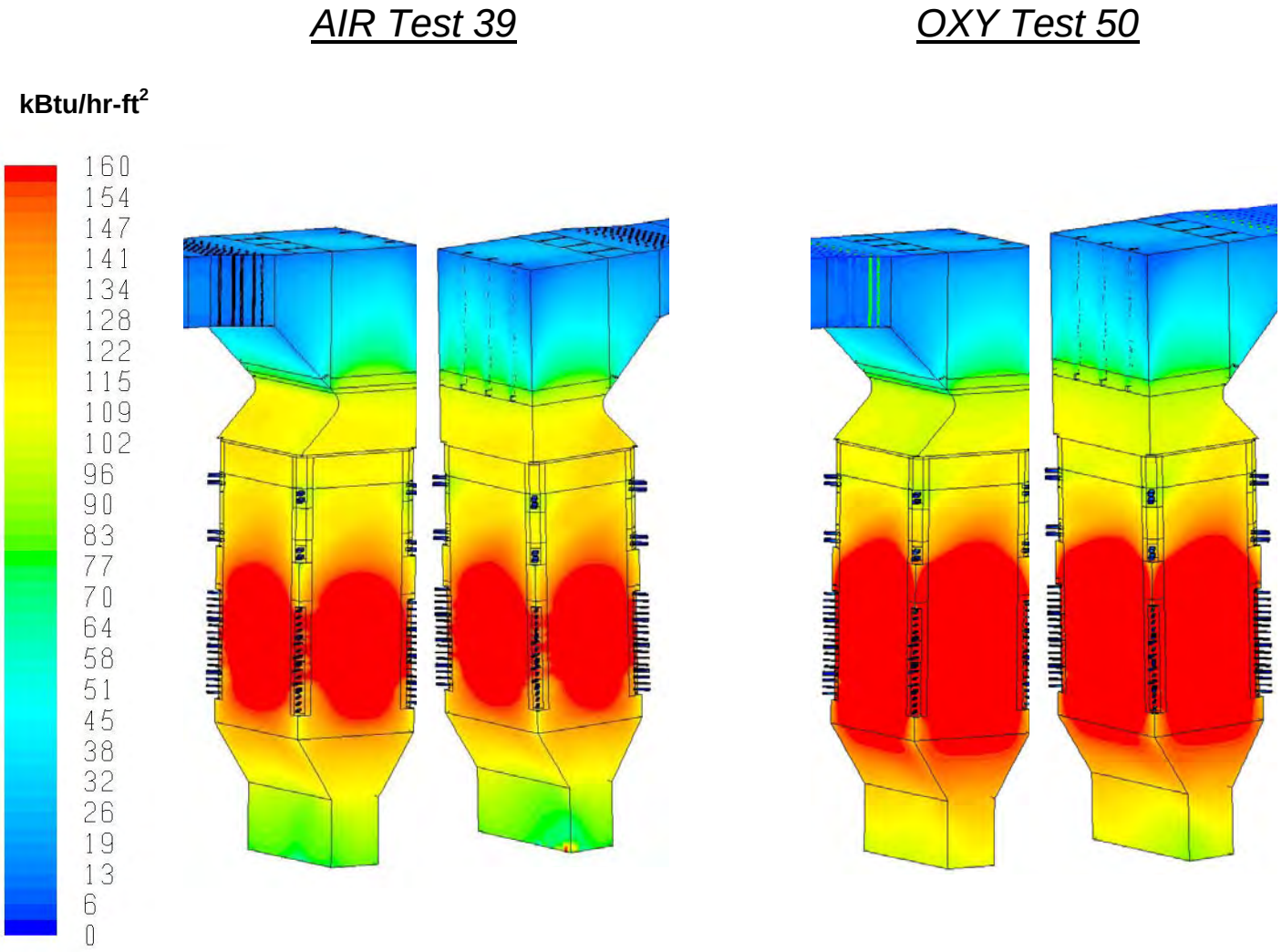

Figure 6-38. [AT-39:OT-50] Contours of Incident Radiation

AIR Test 39 *OXY Test 50*

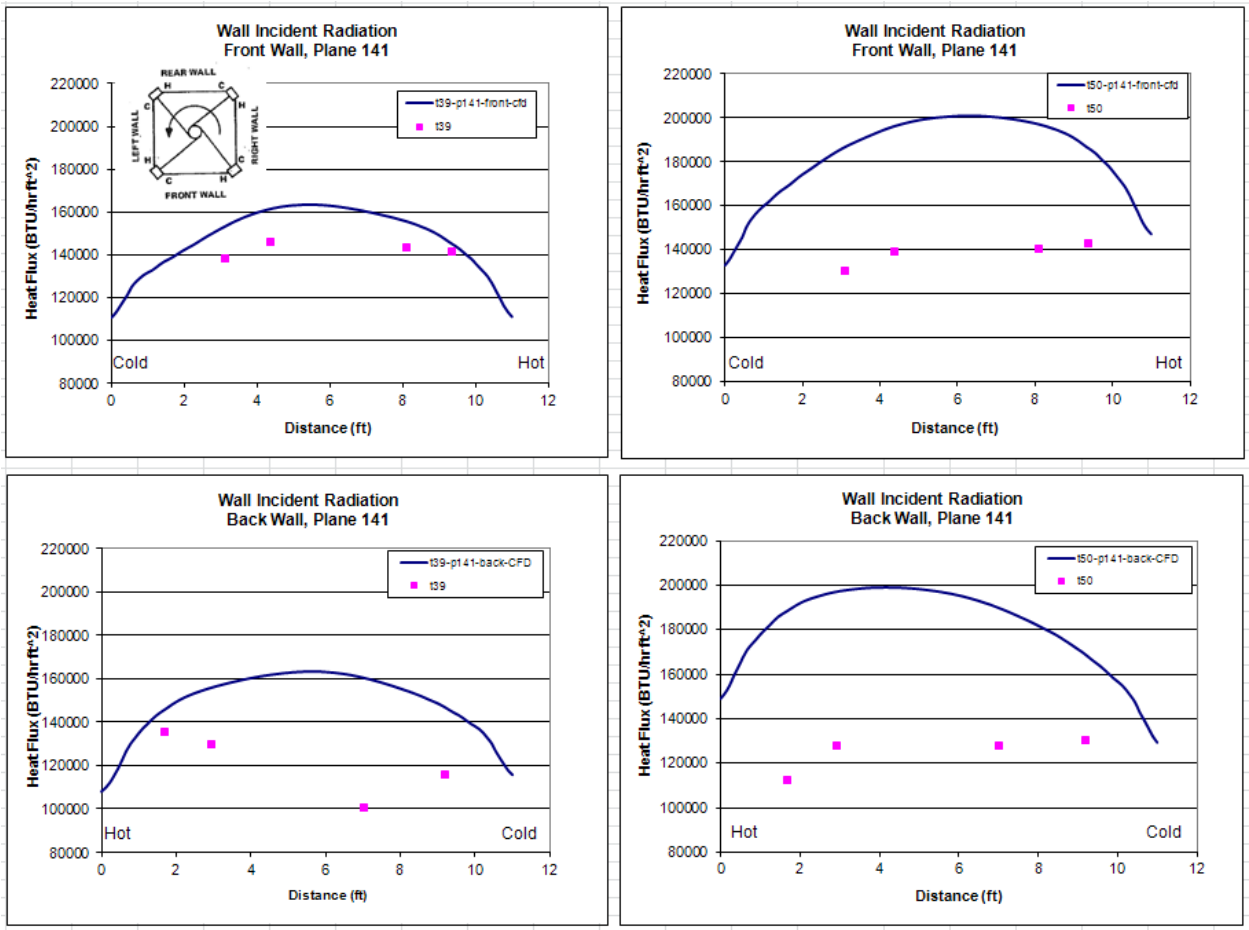

Figure 6-39. [AT-39:OT-50] Comparison of Wall Incident Radiation at Plane 141

AIR Test 39 *OXY Test 50*

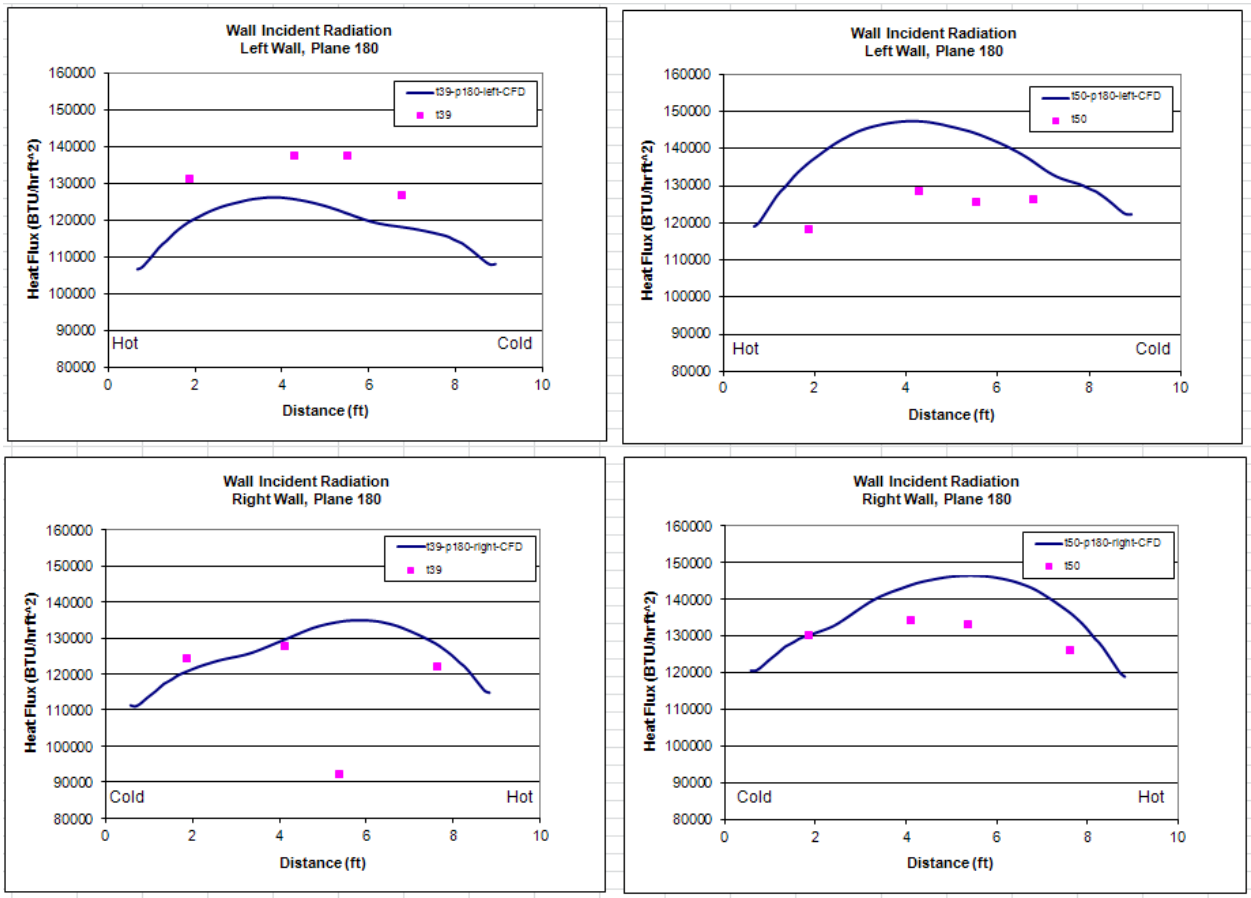

Figure 6-40. [AT-39:OT-50] Comparison of Wall Incident Radiation at Plane 180

AIR Test 39 *OXY Test 50*

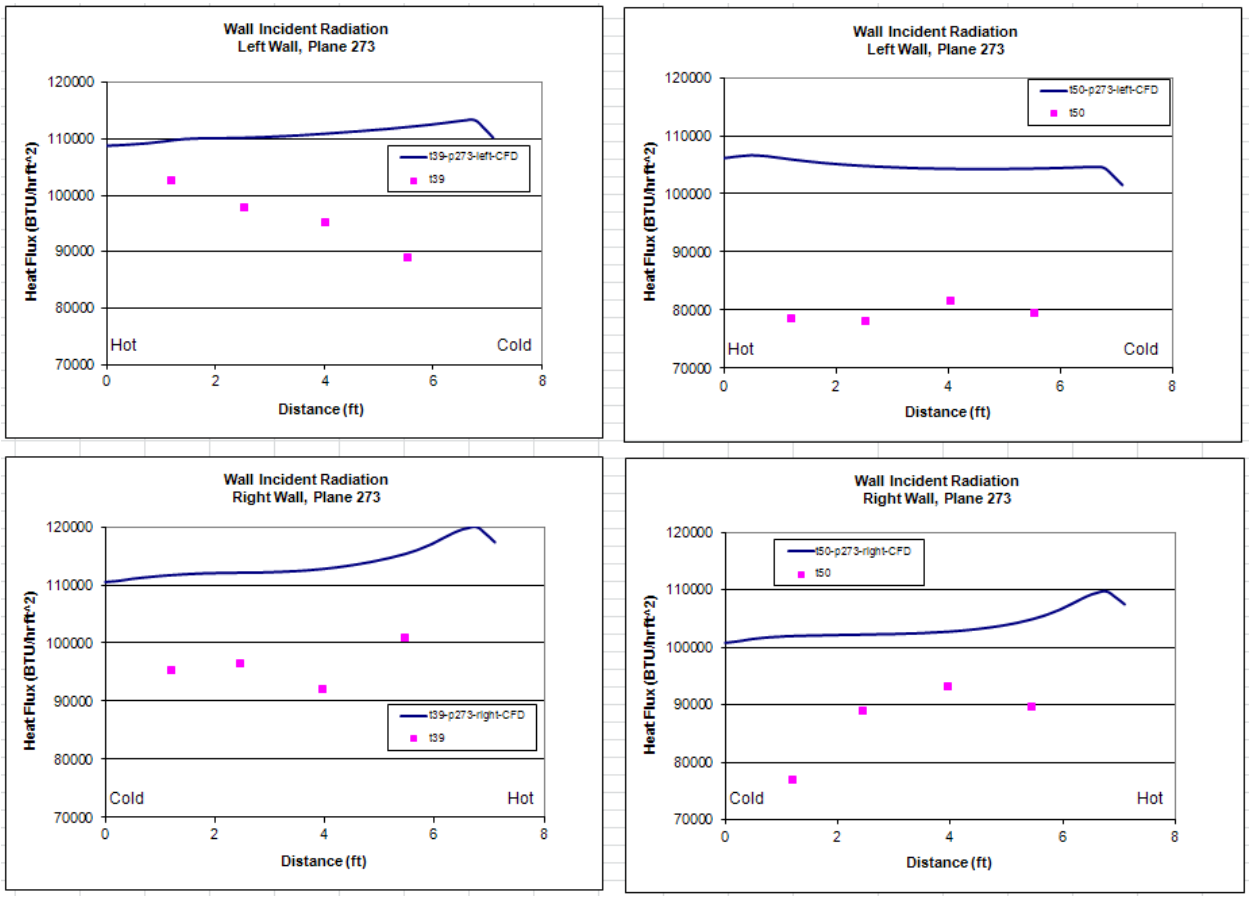

Figure 6-41. [AT-39:OT-50] Comparison of Wall Incident Radiation at Plane 273

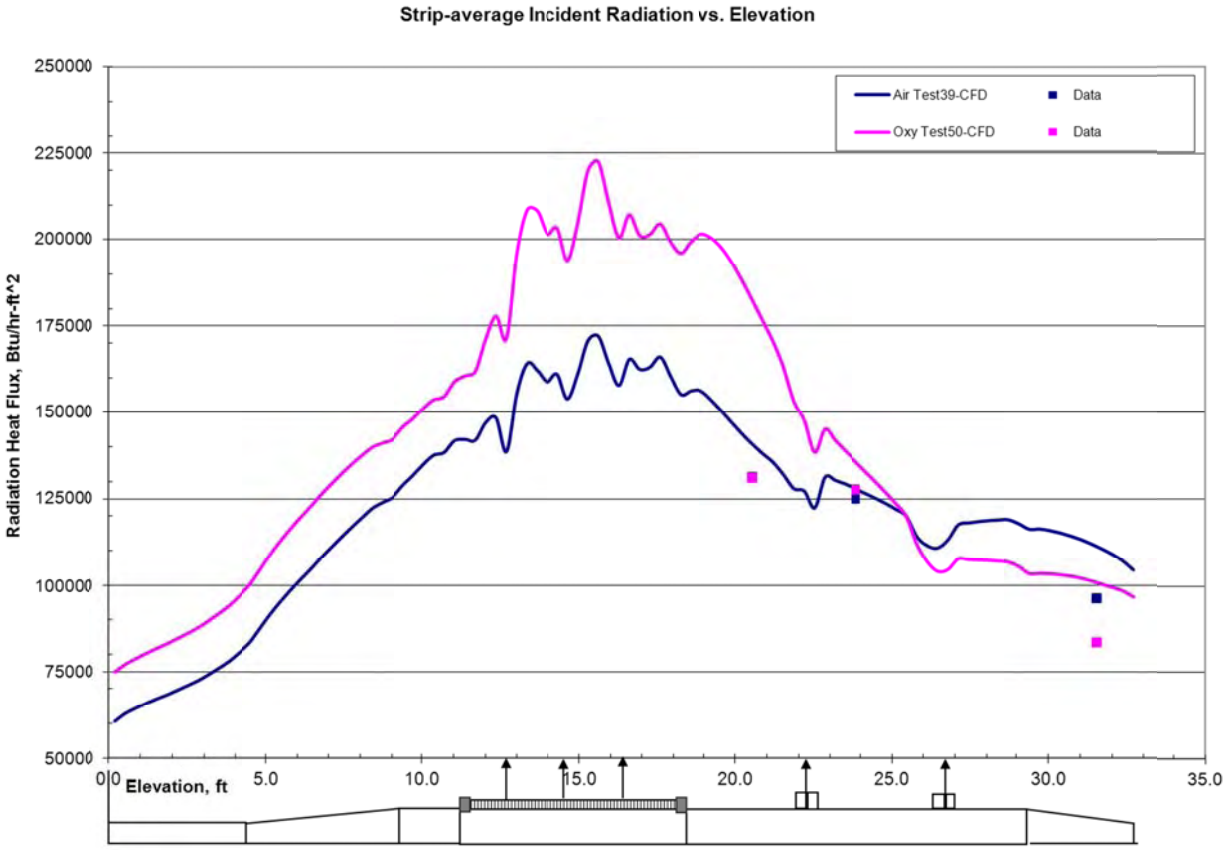

Figure 6-42. [AT-39:OT-50] Strip-Averaged Wall Incident Radiation

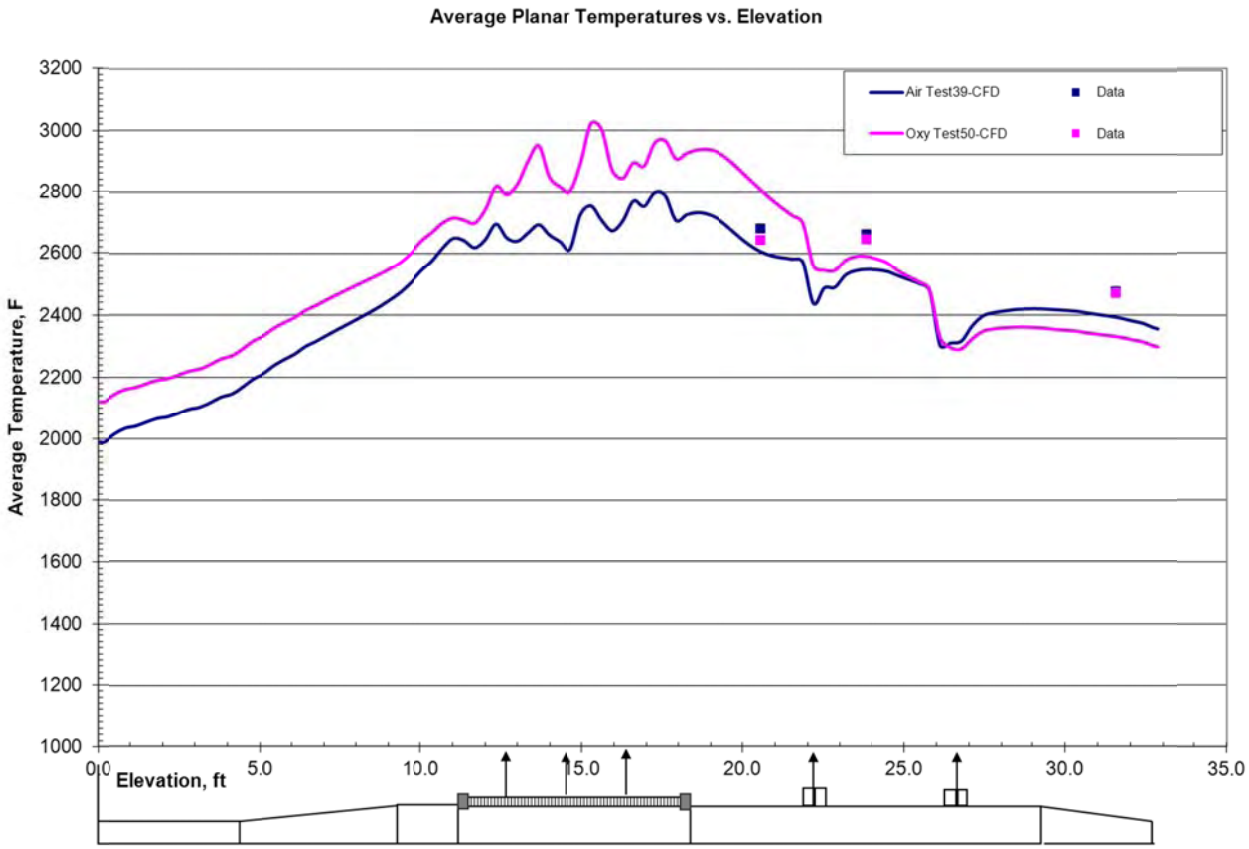

Figure 6-43. [AT-39:OT-50] Planar Averaged Temperature

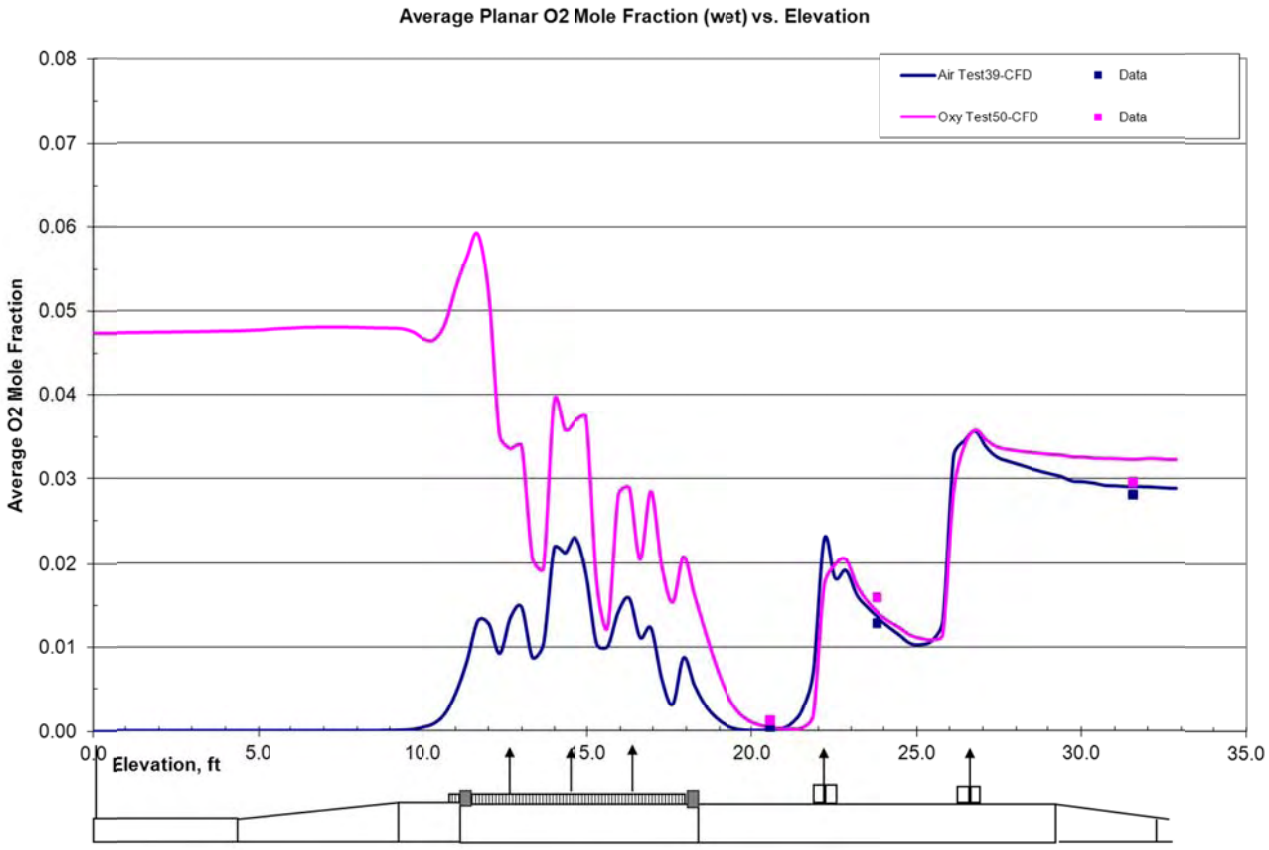

Figure 6-44. [AT-39:OT-50] Planar Averaged O_2

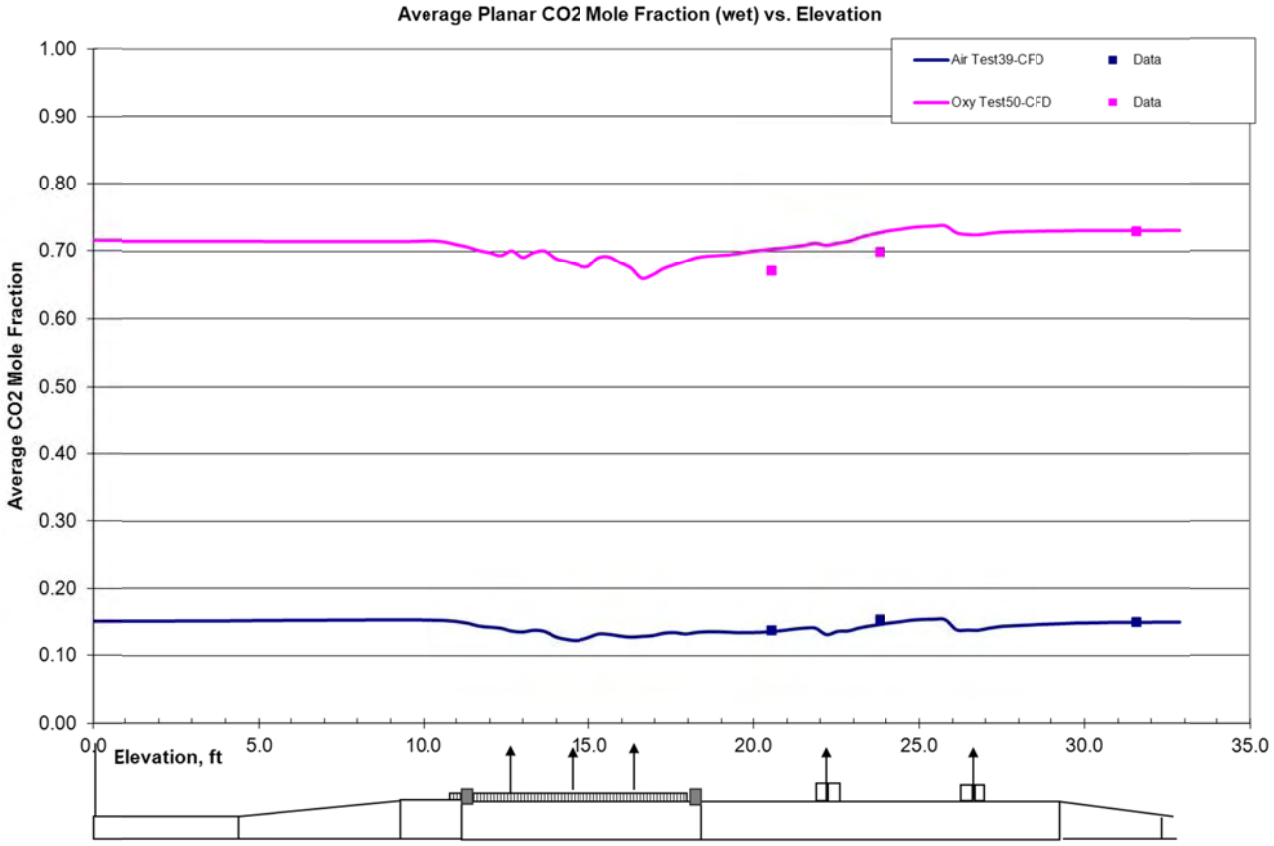

Figure 6-45. [AT-39:OT-50] Planar Averaged CO_2

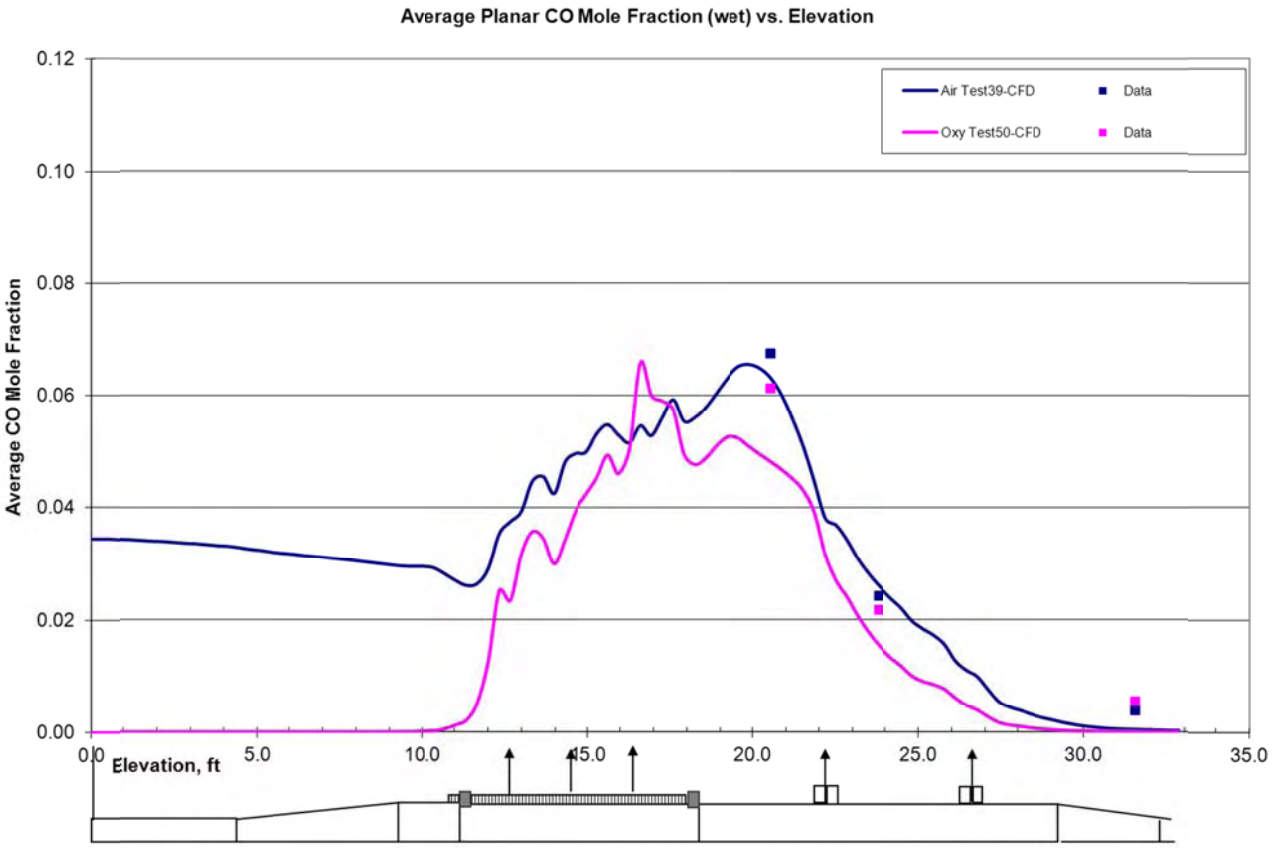

Figure 6-46. [AT-39:OT-50] Planar Averaged CO

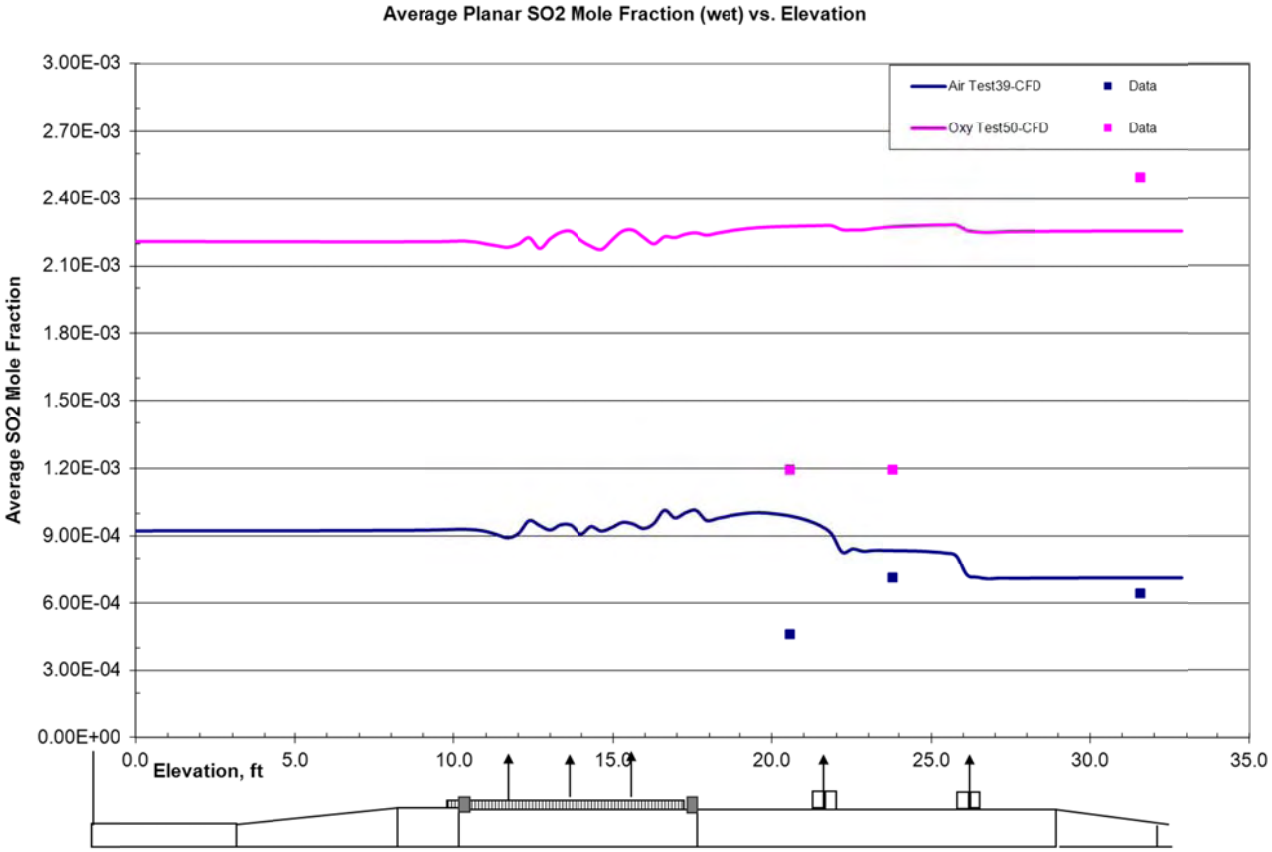

Figure 6-47. [AT-39:OT-50] Planar Averaged SO_2

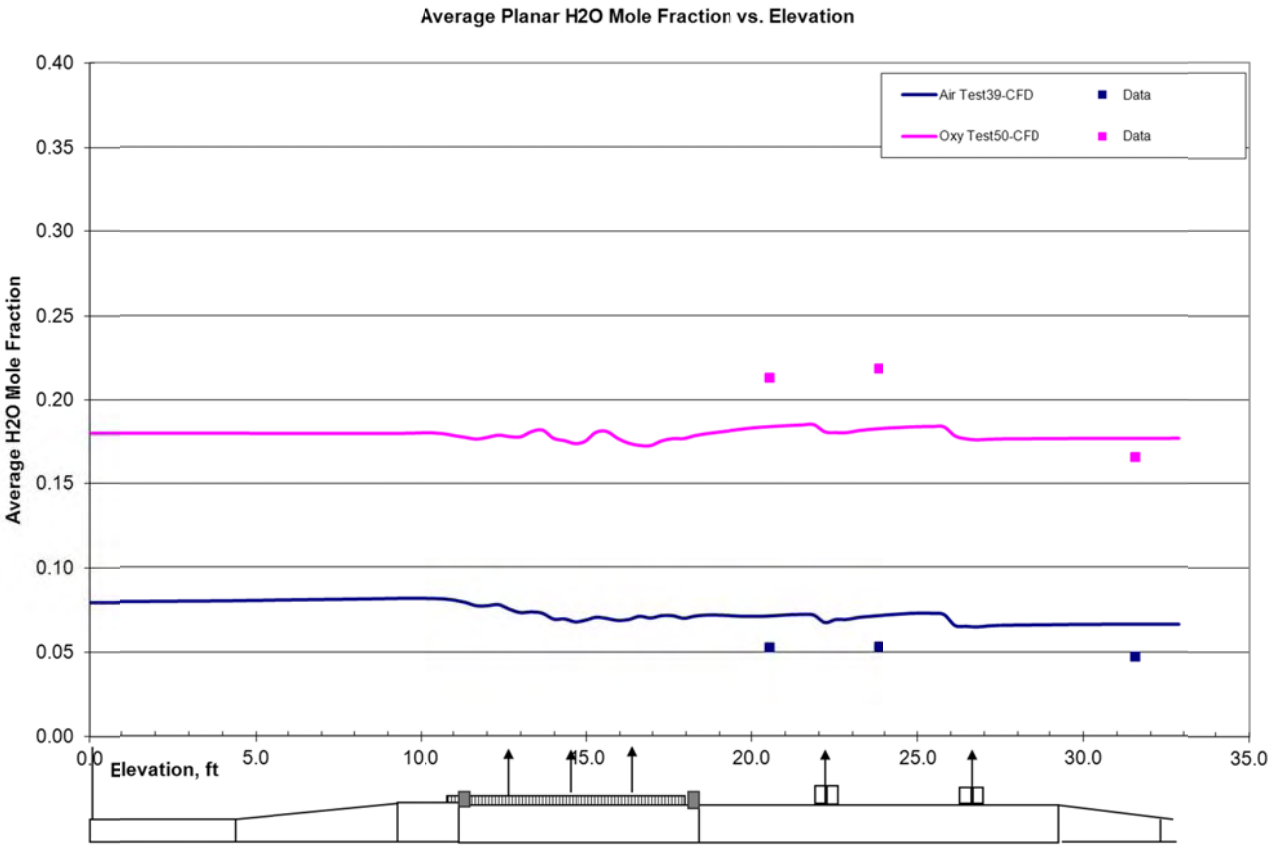

Figure 6-48. [AT-39:OT-50] Planar Averaged H_2O

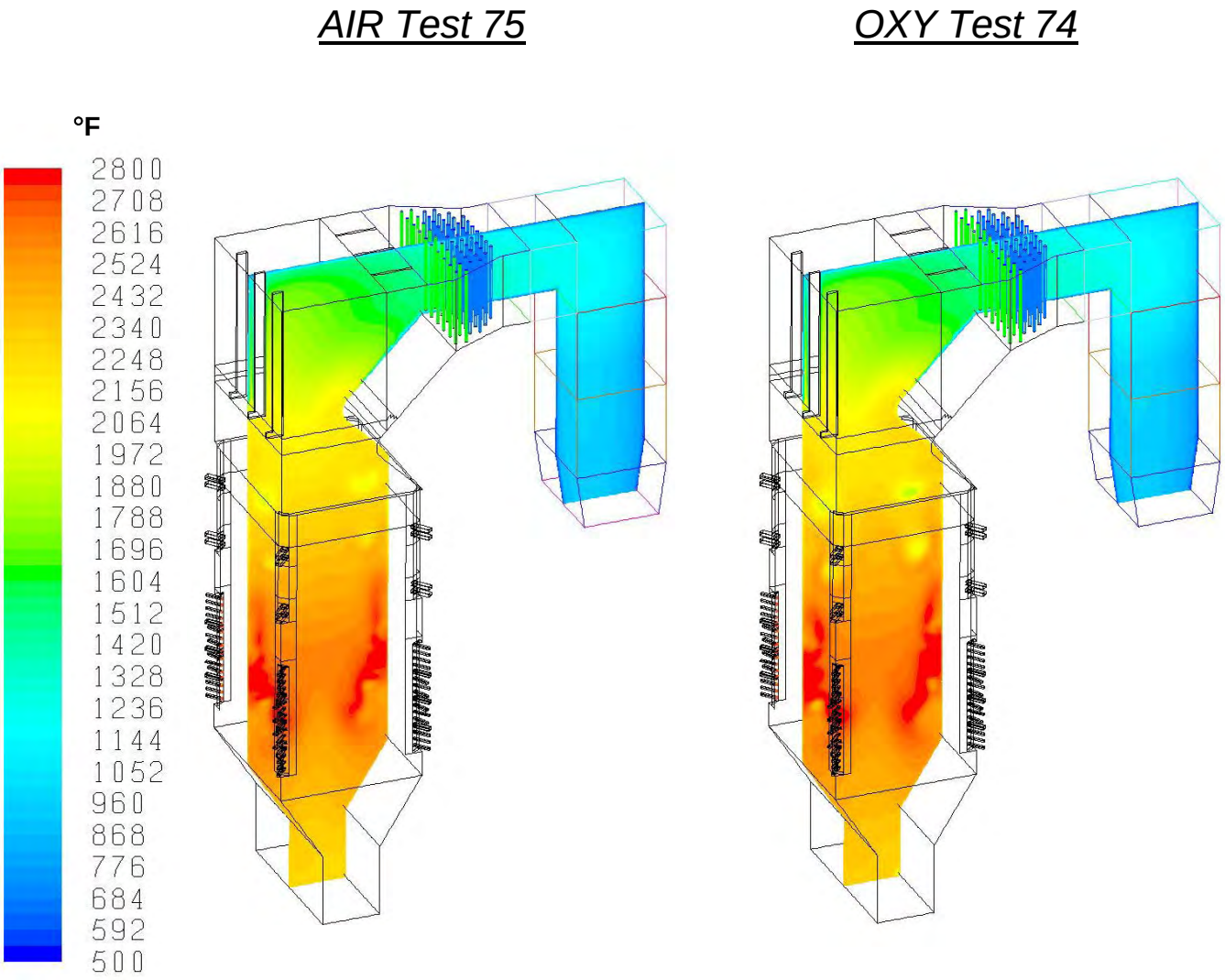

Figure 6-49. [AT-75:OT-74] Contours of Temperature on X-Midplane

AIR Test 75 *OXY Test 74*

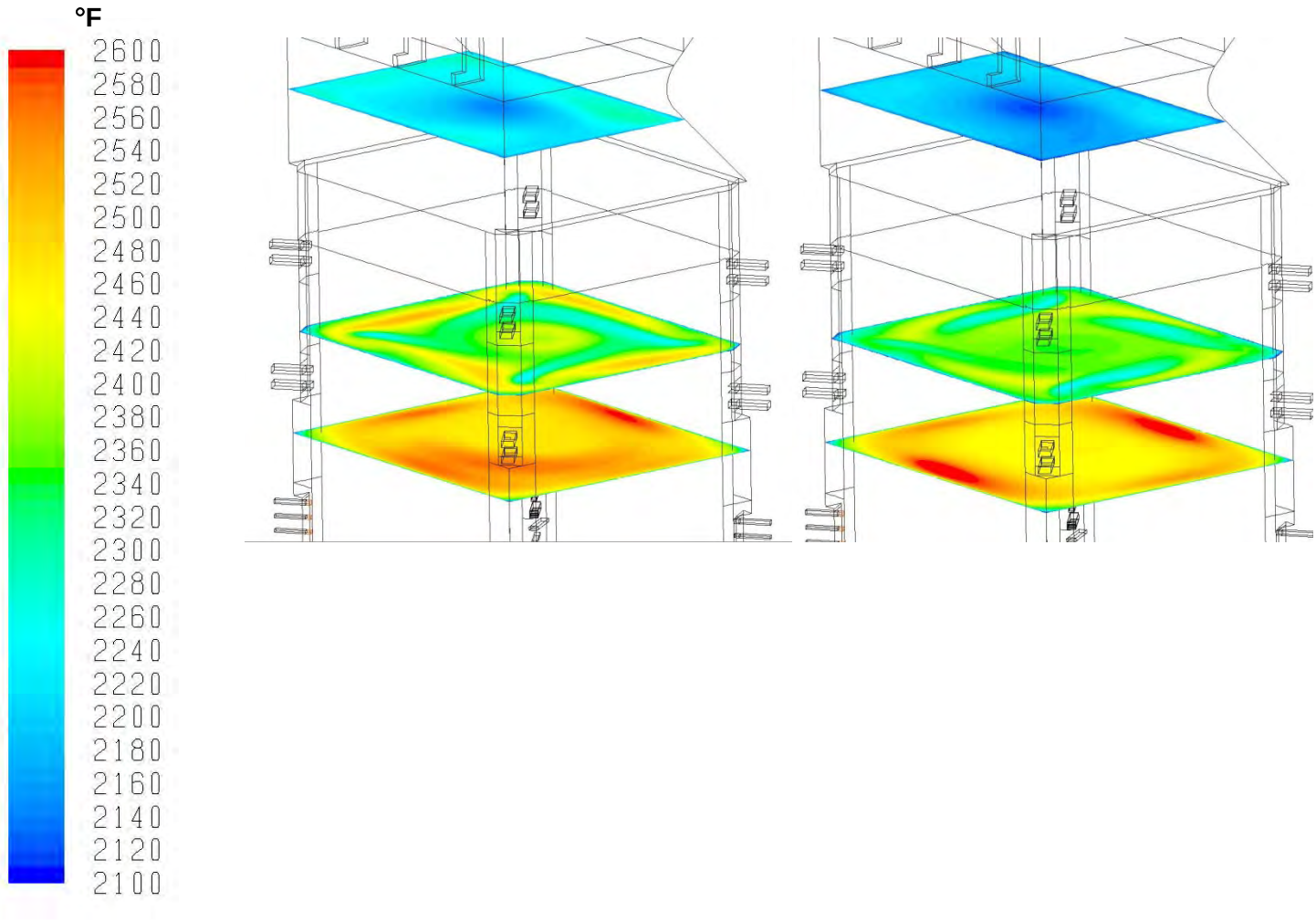

Figure 6-50. [AT-75:OT-74] Contours of Temperature on Test Planes

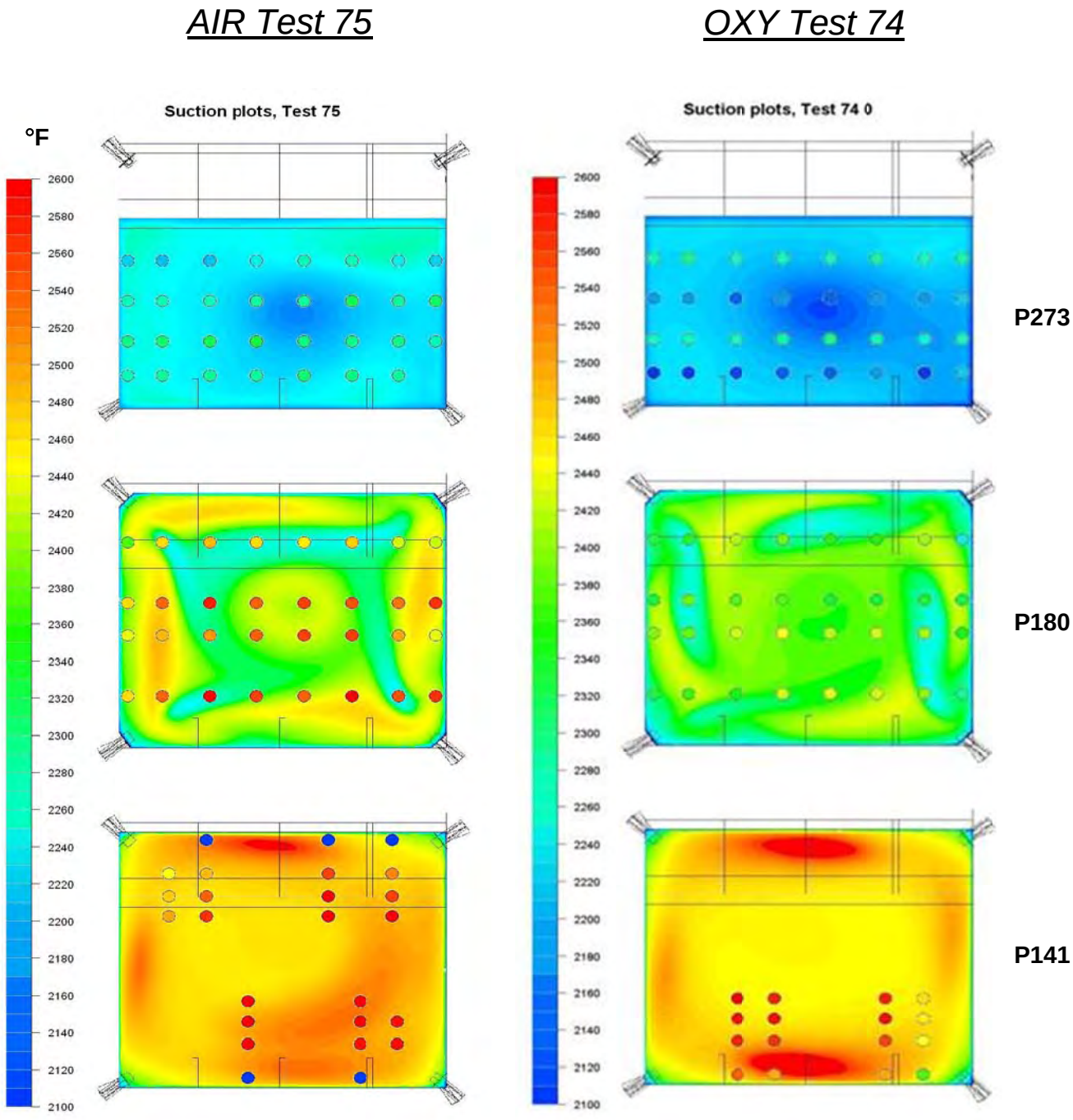

Figure 6-51. [AT-75:OT-74] Comparison of Temperature on Test Planes

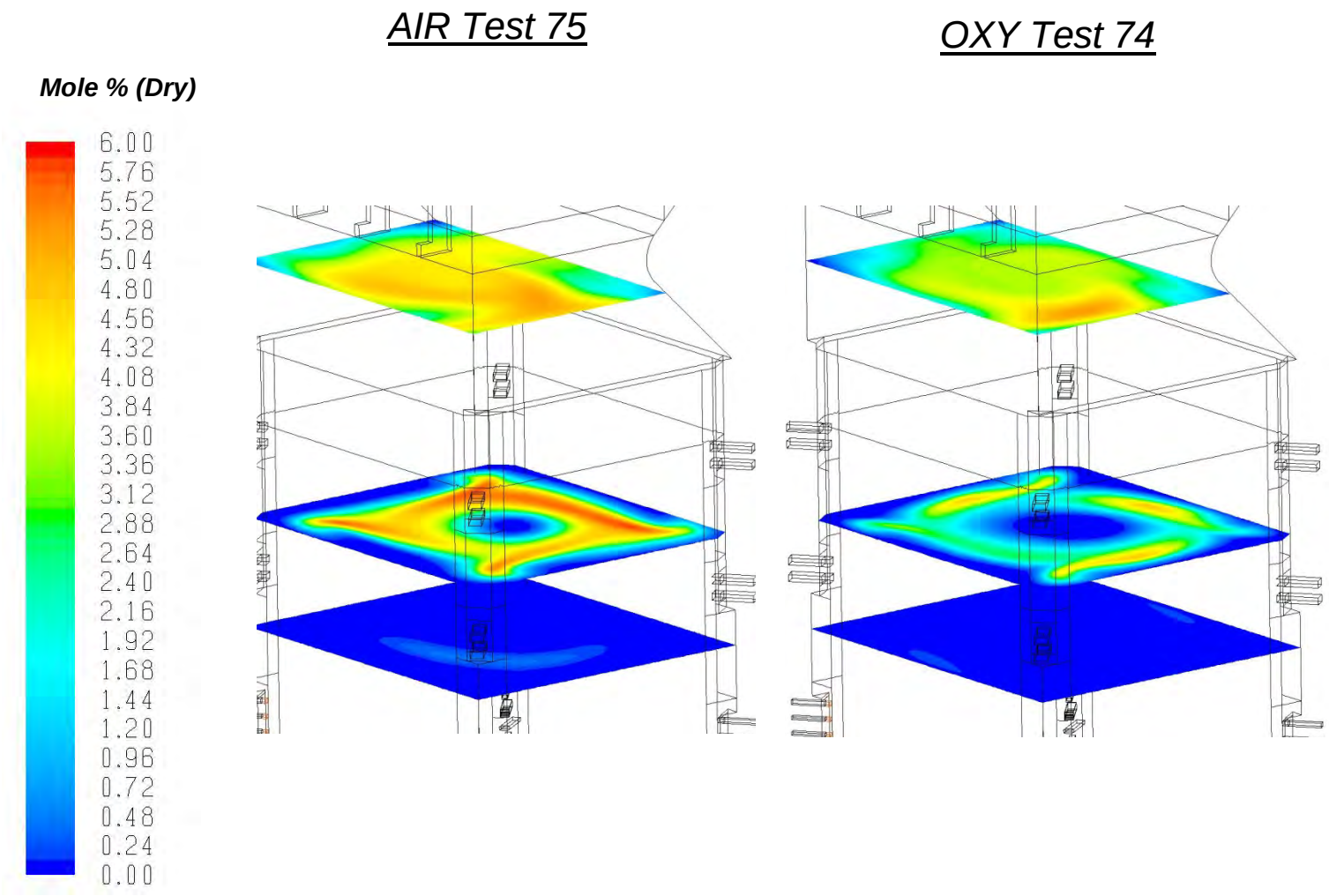

Figure 6-52. [AT-75:OT-74] Contours of O_2 Concentrations on Test Planes

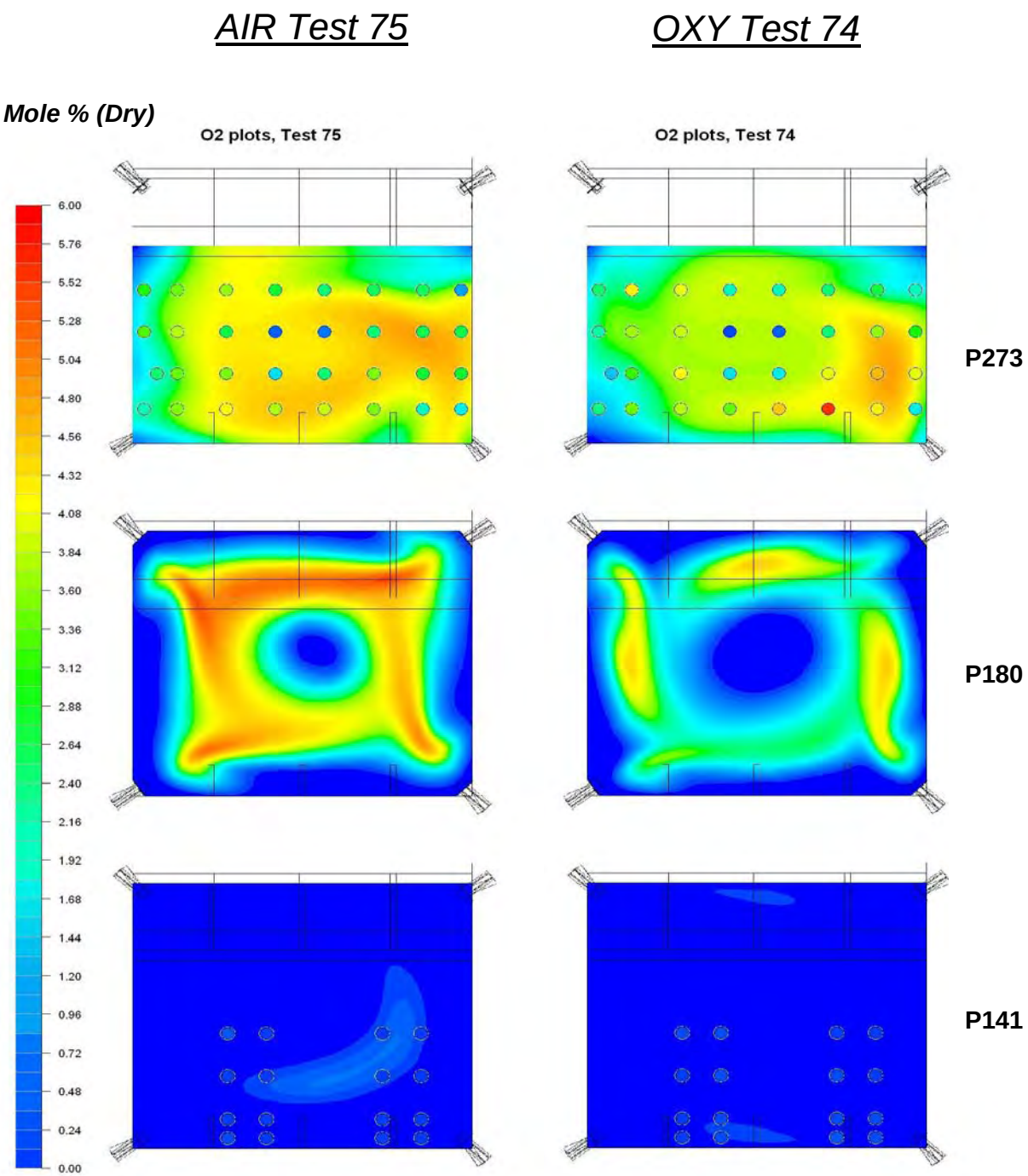

Figure 6-53. [AT-75:OT-74] Comparison of O_2 Concentrations on Test Planes

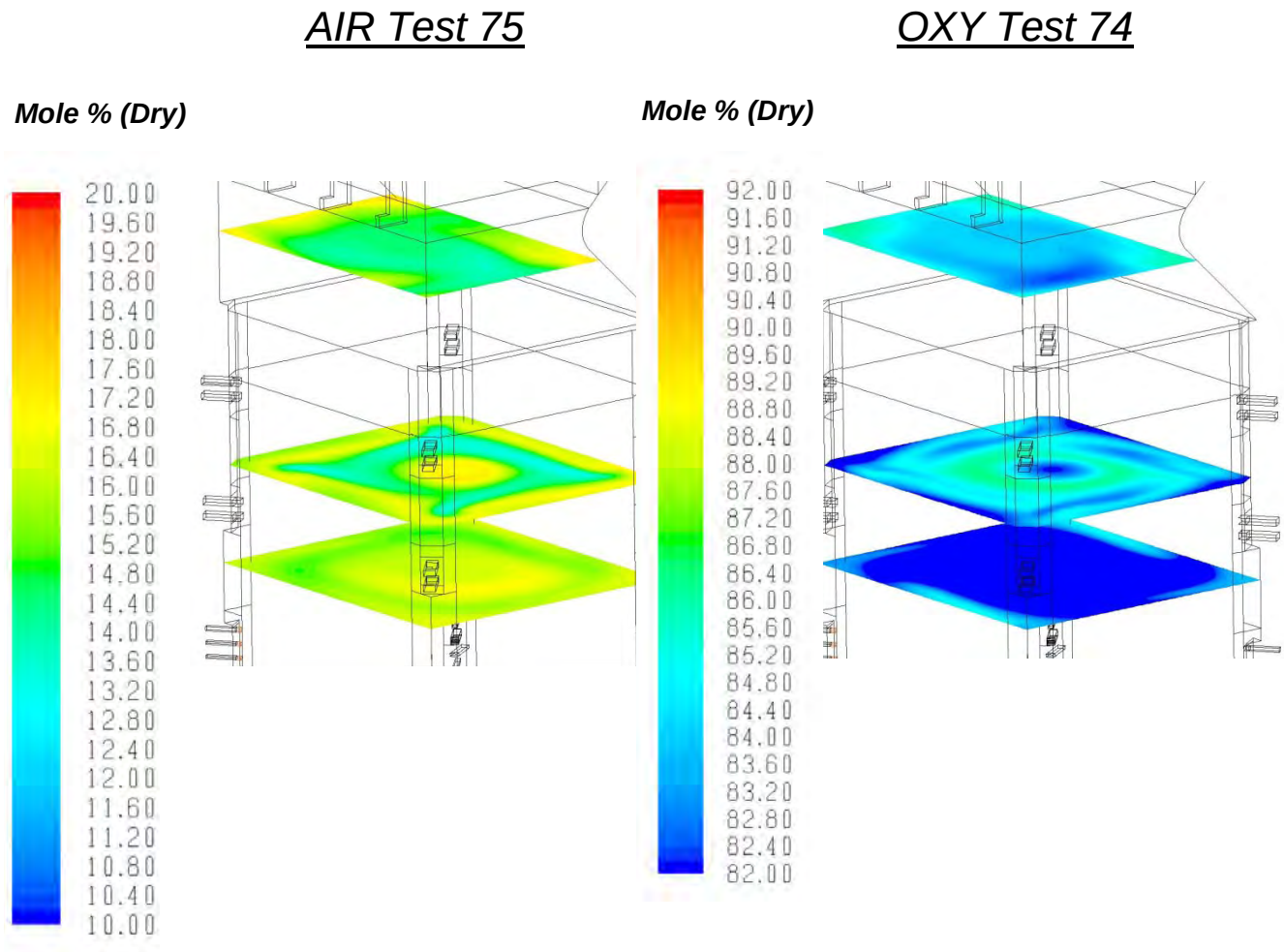

Figure 6-54. [AT-75:OT-74] Contours of CO_2 Concentrations on Test Planes

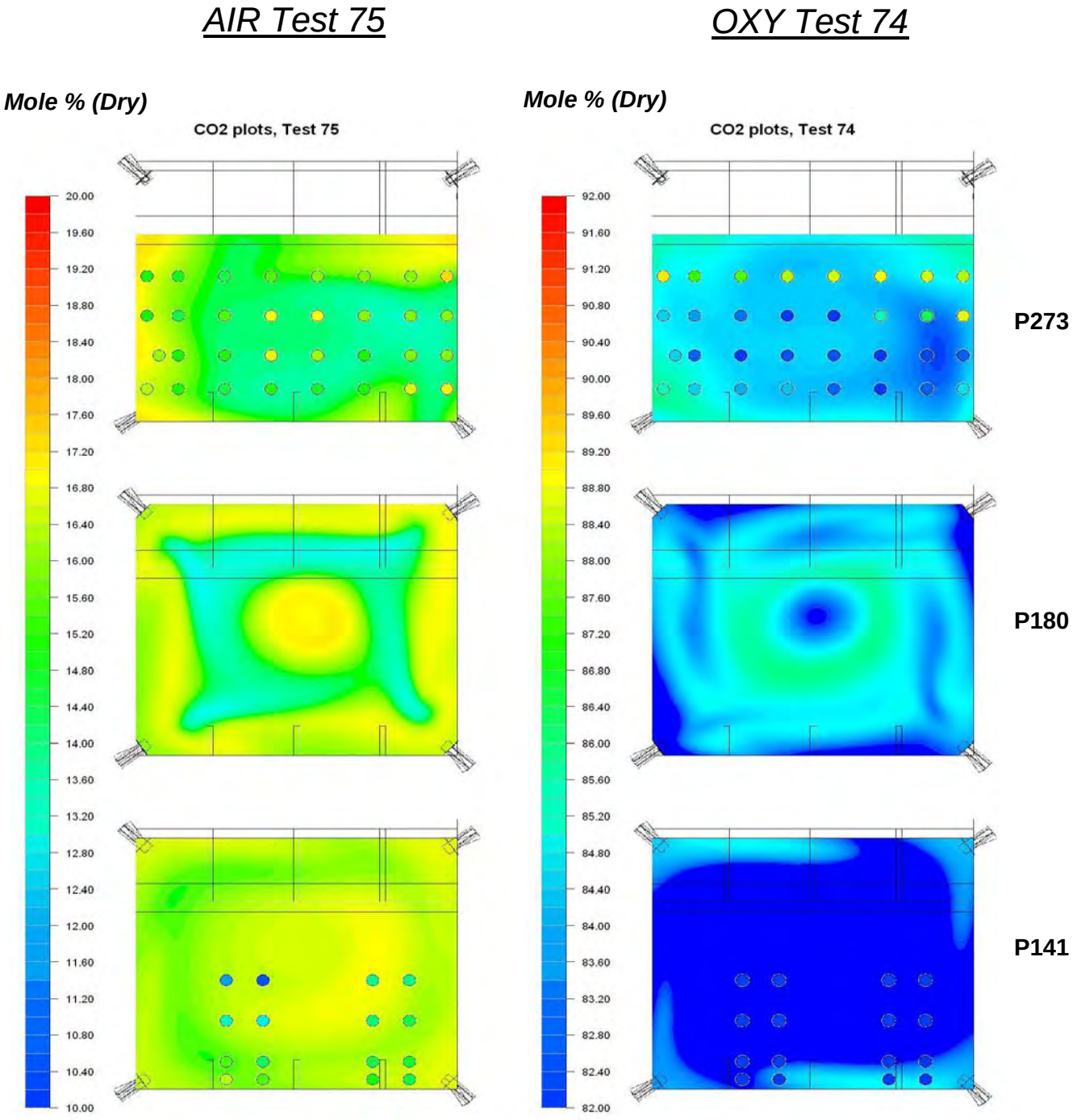

Figure 6-55. [AT-75:OT-74] Comparison of CO_2 Concentrations on Test Planes

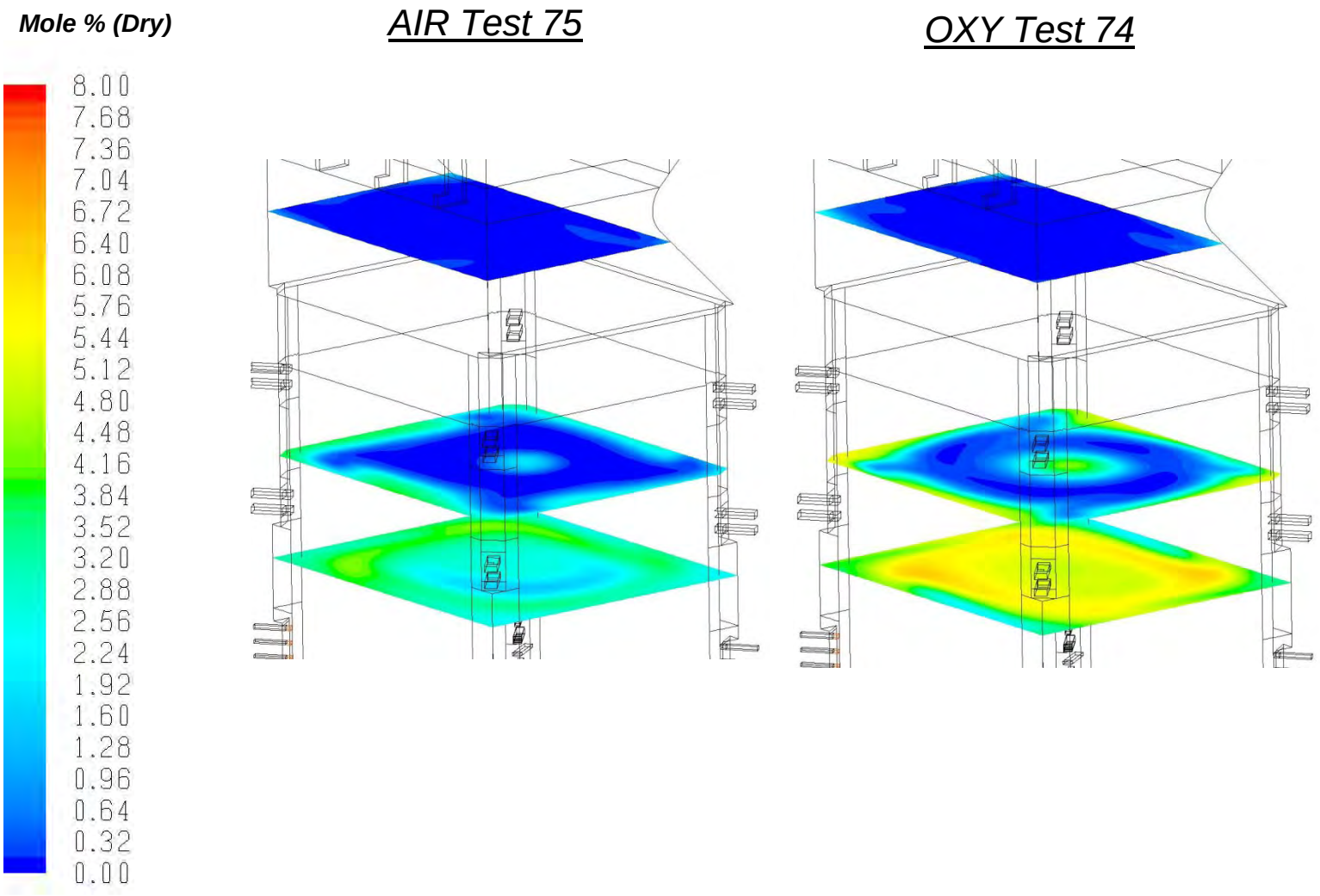

Figure 6-56. [AT-75:OT-74] Contours of CO Concentrations on Test Planes

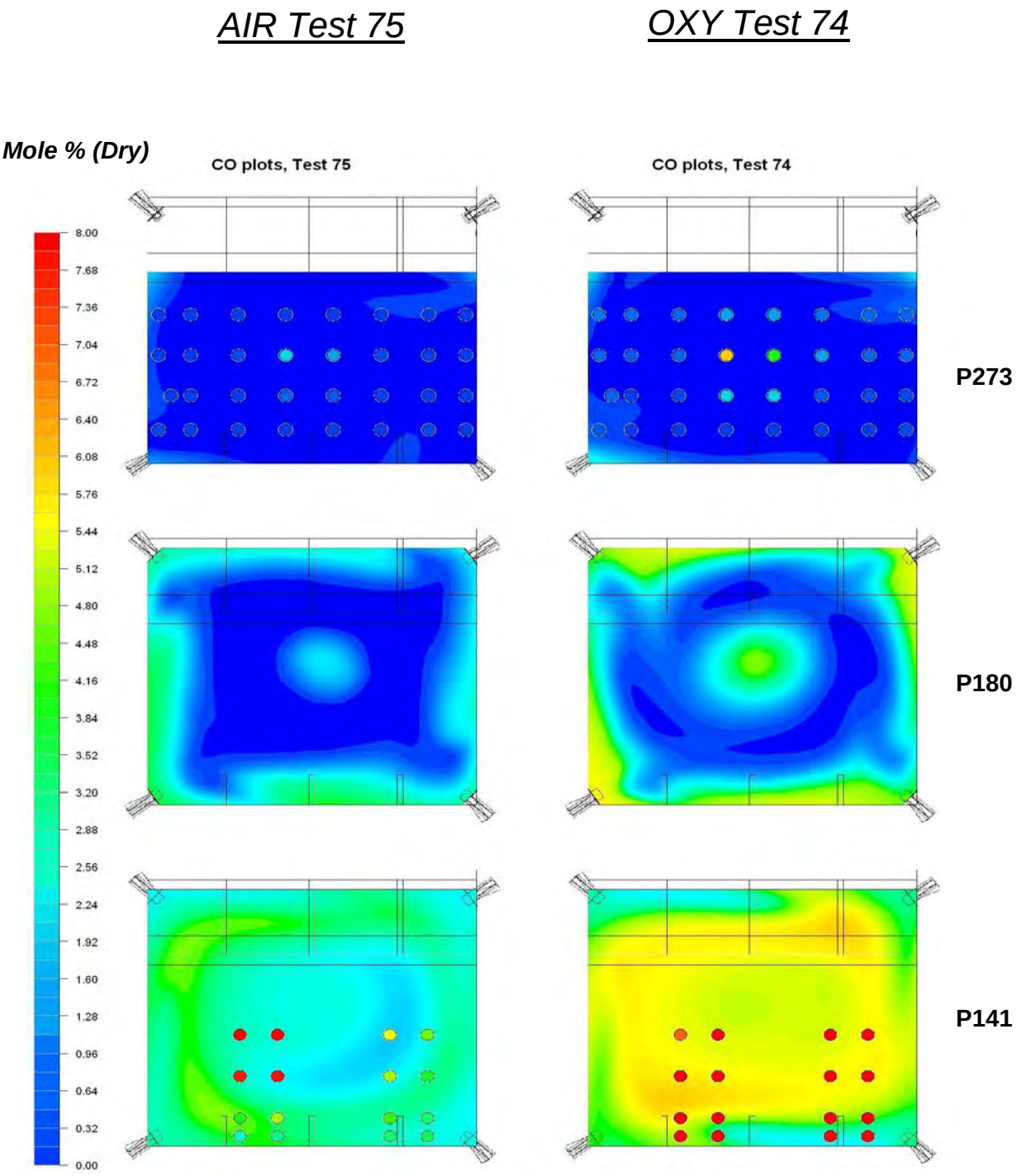

Figure 6-57. [AT-75:OT-74] Comparison of CO Concentrations on Test Planes

AIR Test 75

OXY Test 74

Mole % (Wet)

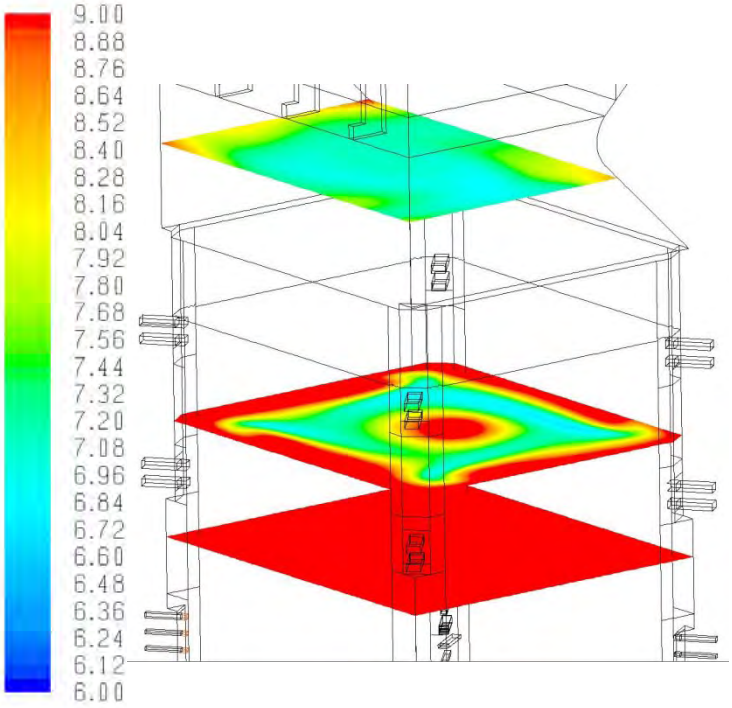

Mole % (Wet)

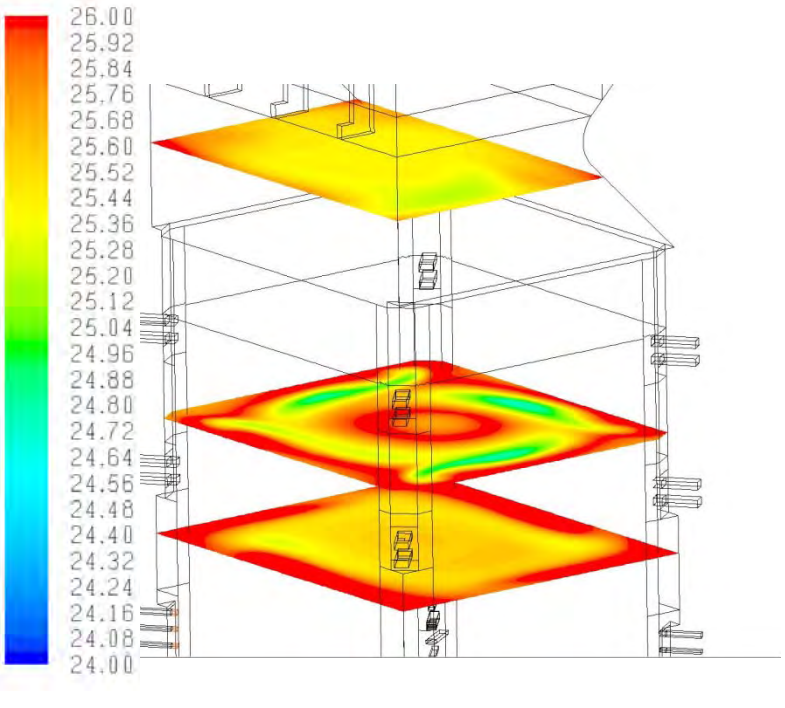

Figure 6-58. [AT-75:OT-74] Contours of H_2O Concentrations on Test Planes

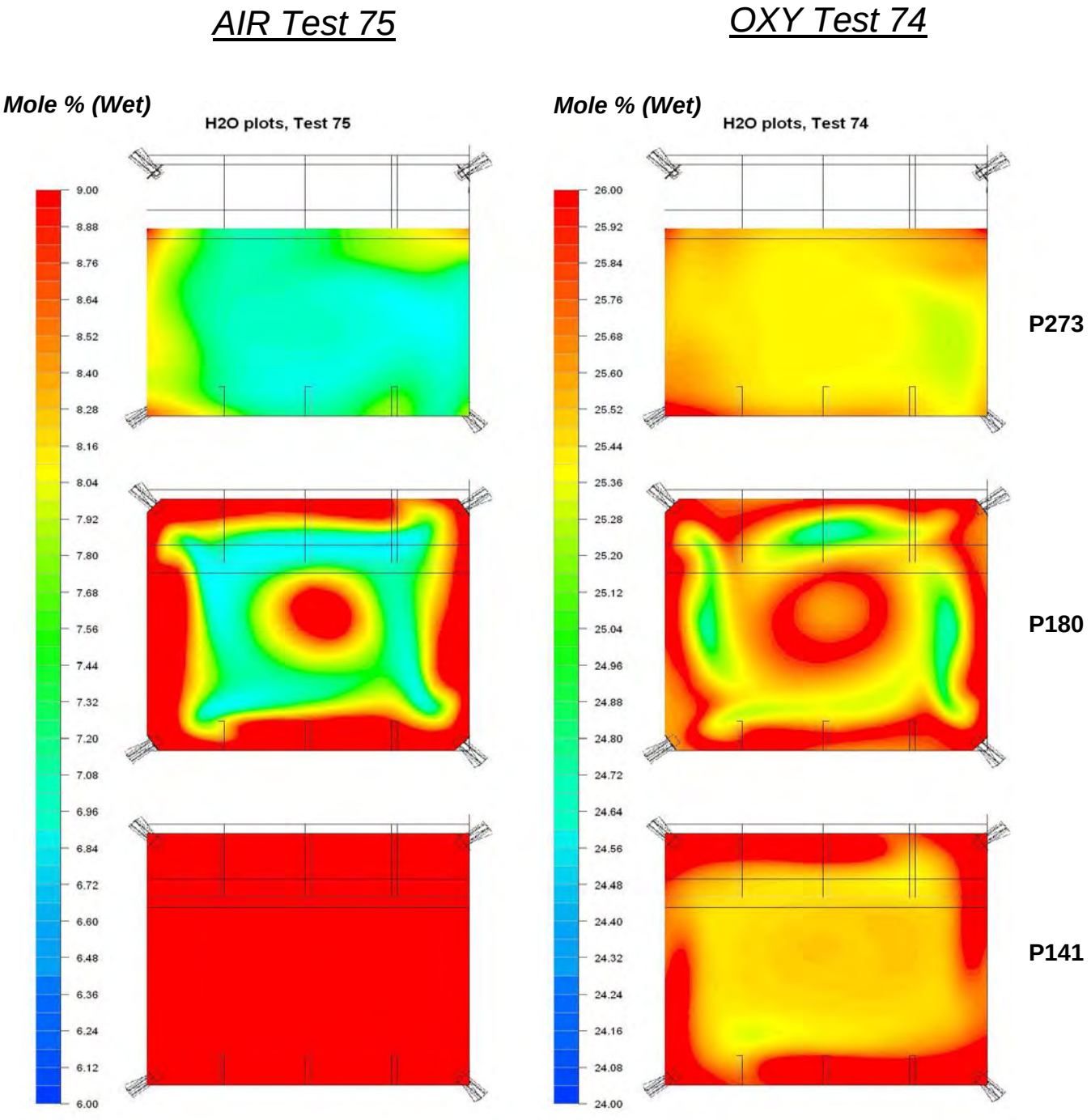

Figure 6-59. [AT-75:OT-74] Comparison of H_2O Concentrations on Test Planes

AIR Test 75

OXY Test 74

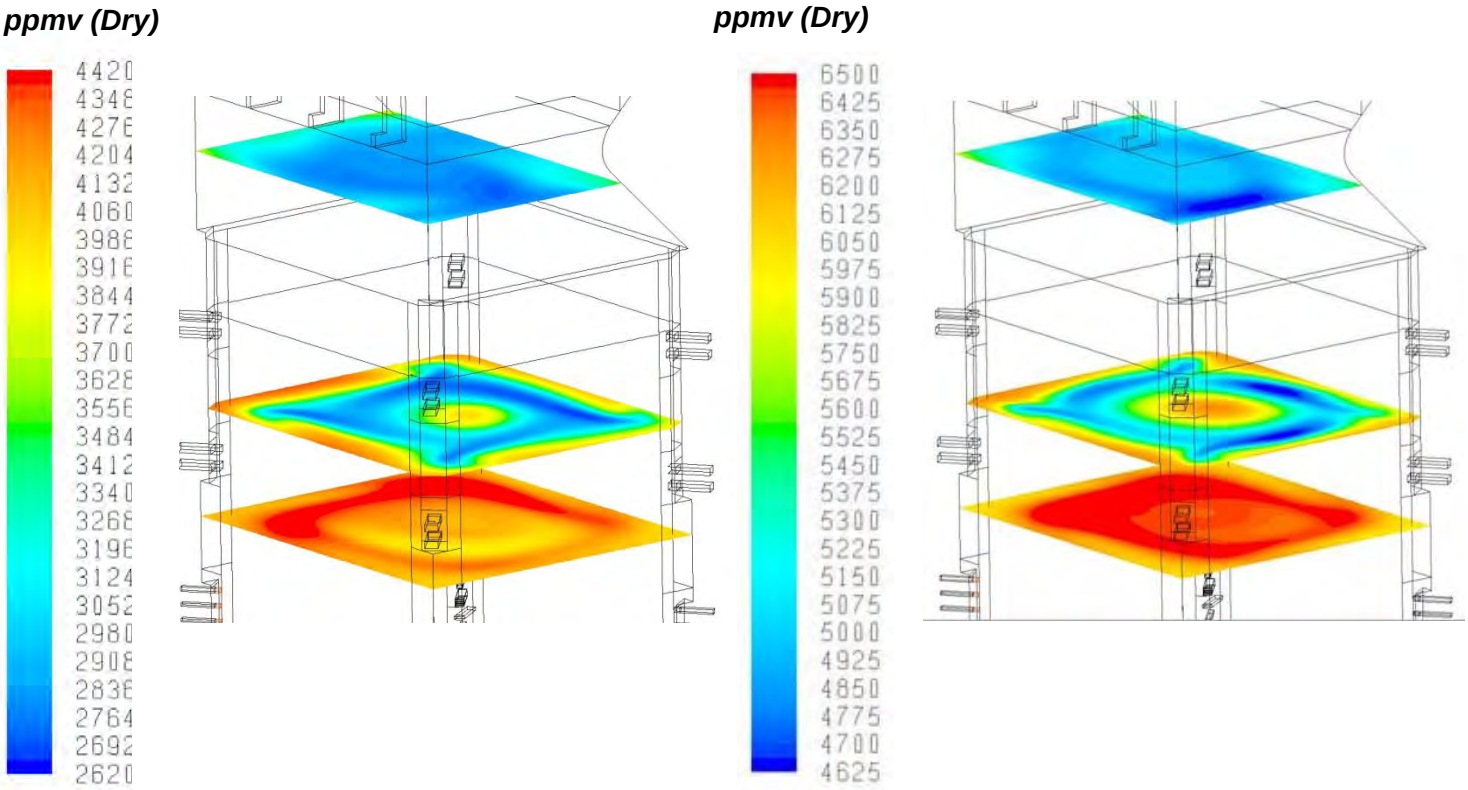

Figure 6-60. [AT-75:OT-74] Contours of SO_2 Concentrations on Test Planes

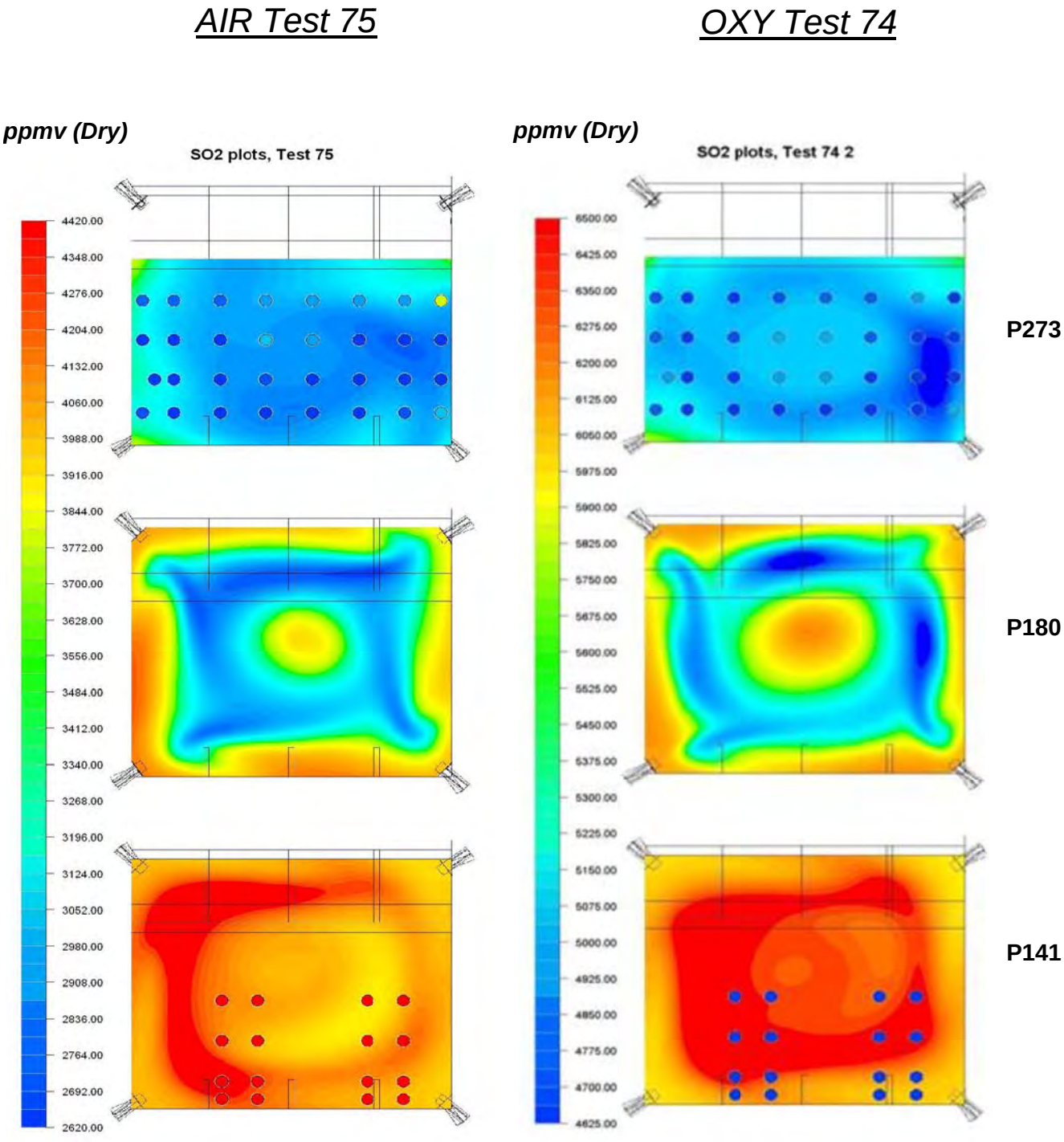

Figure 6-61. [AT-75:OT-74] Comparison of SO_2 Concentrations on Test Planes

AIR Test 75 *OXY Test 74*

kBtu/hr-ft^2

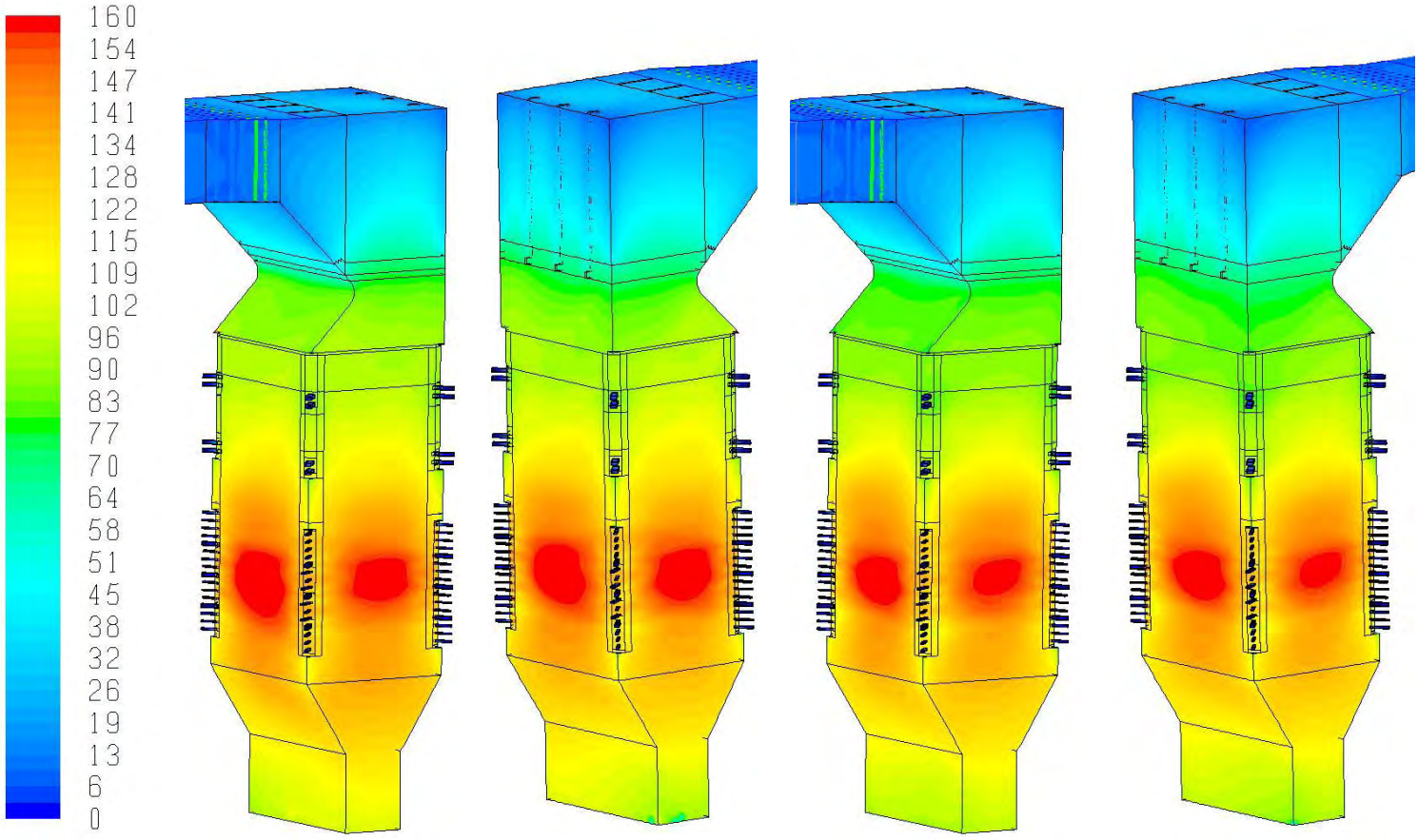

Figure 6-62. [AT-75:OT-74] Contours of Incident Radiation

AIR Test 75 *OXY Test 74*

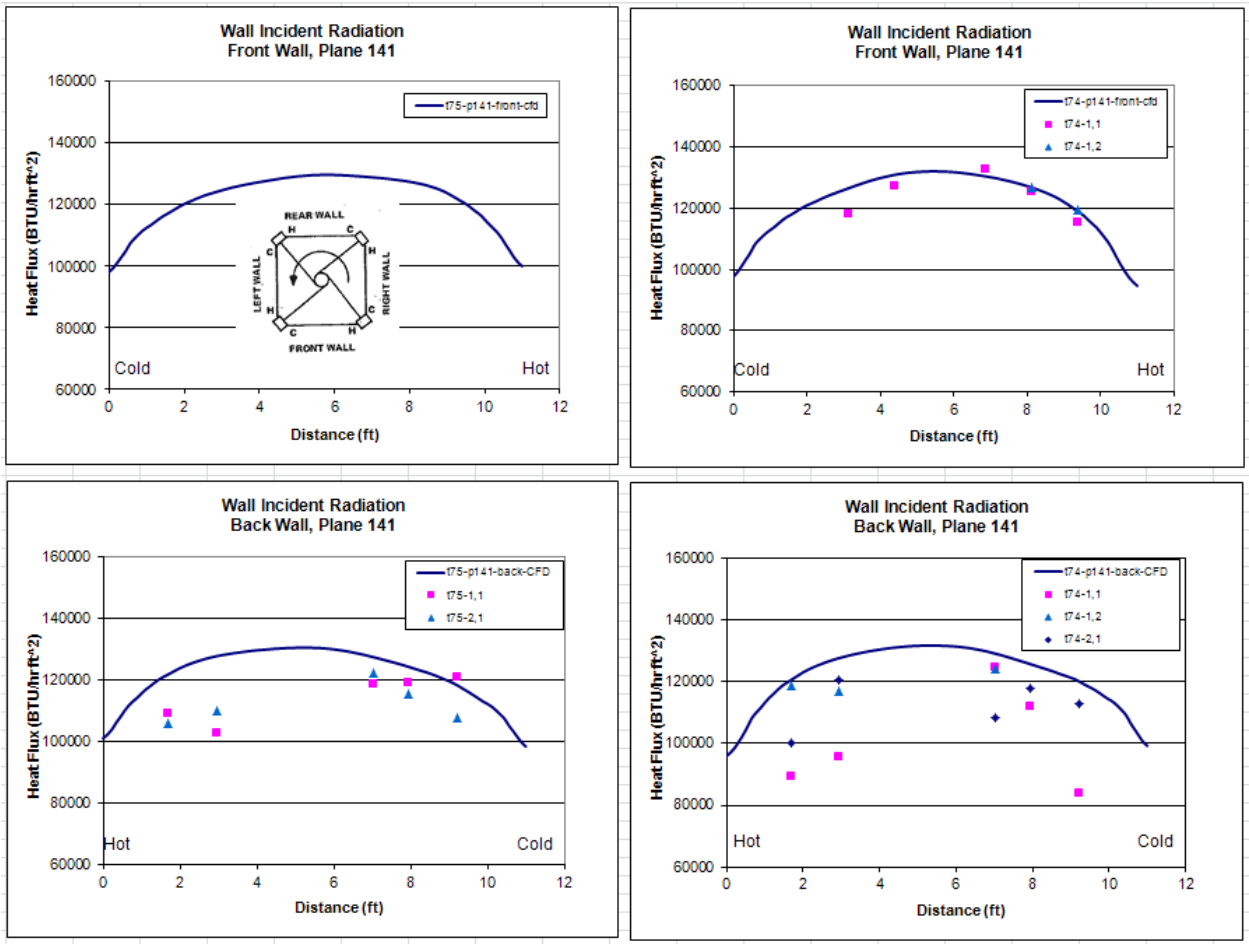

Figure 6-63. [AT-75:OT-74] Comparison of Wall Incident Radiation at Plane 141

AIR Test 75 *OXY Test 74*

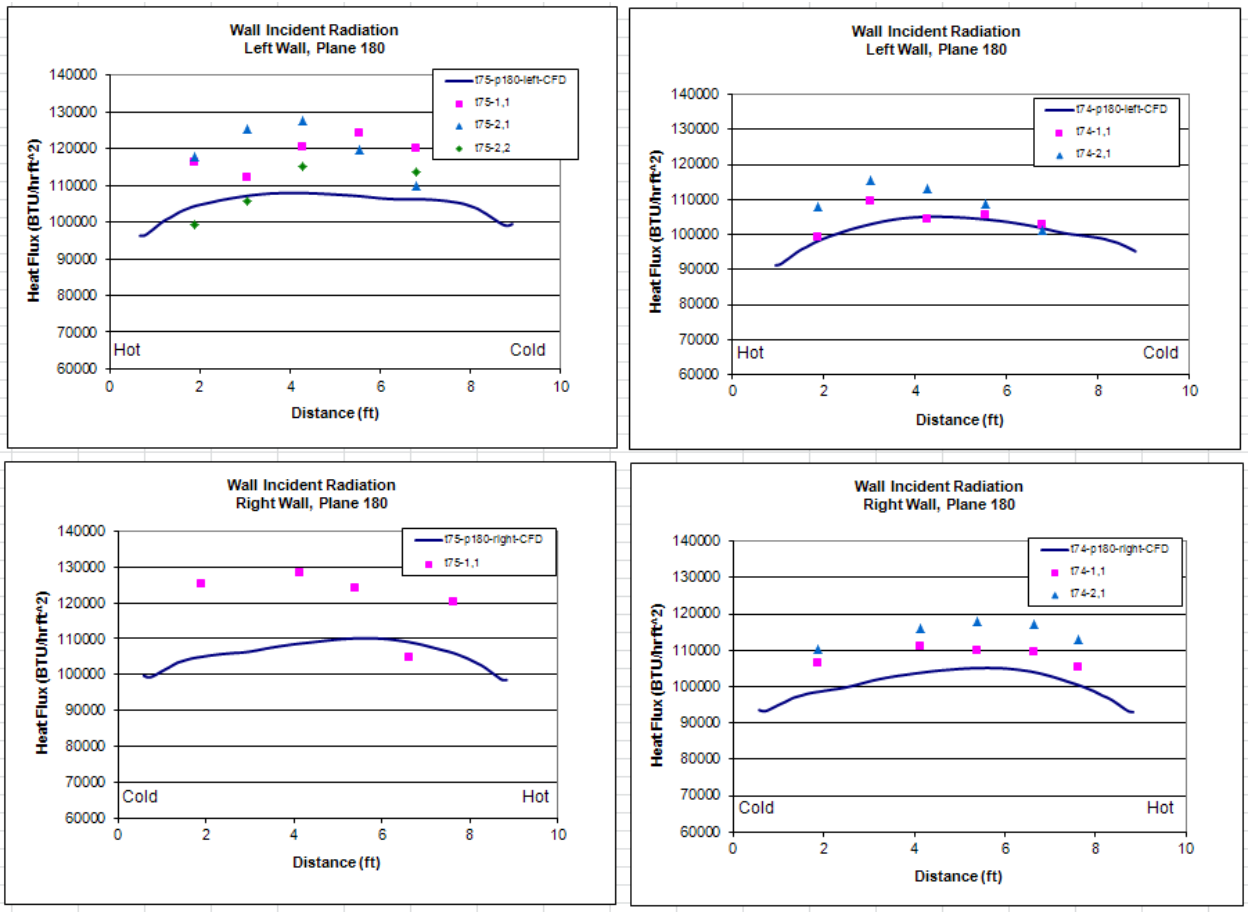

Figure 6-64. [AT-75:OT-74] Comparison of Wall Incident Radiation at Plane 180

AIR Test 75 *OXY Test 74*

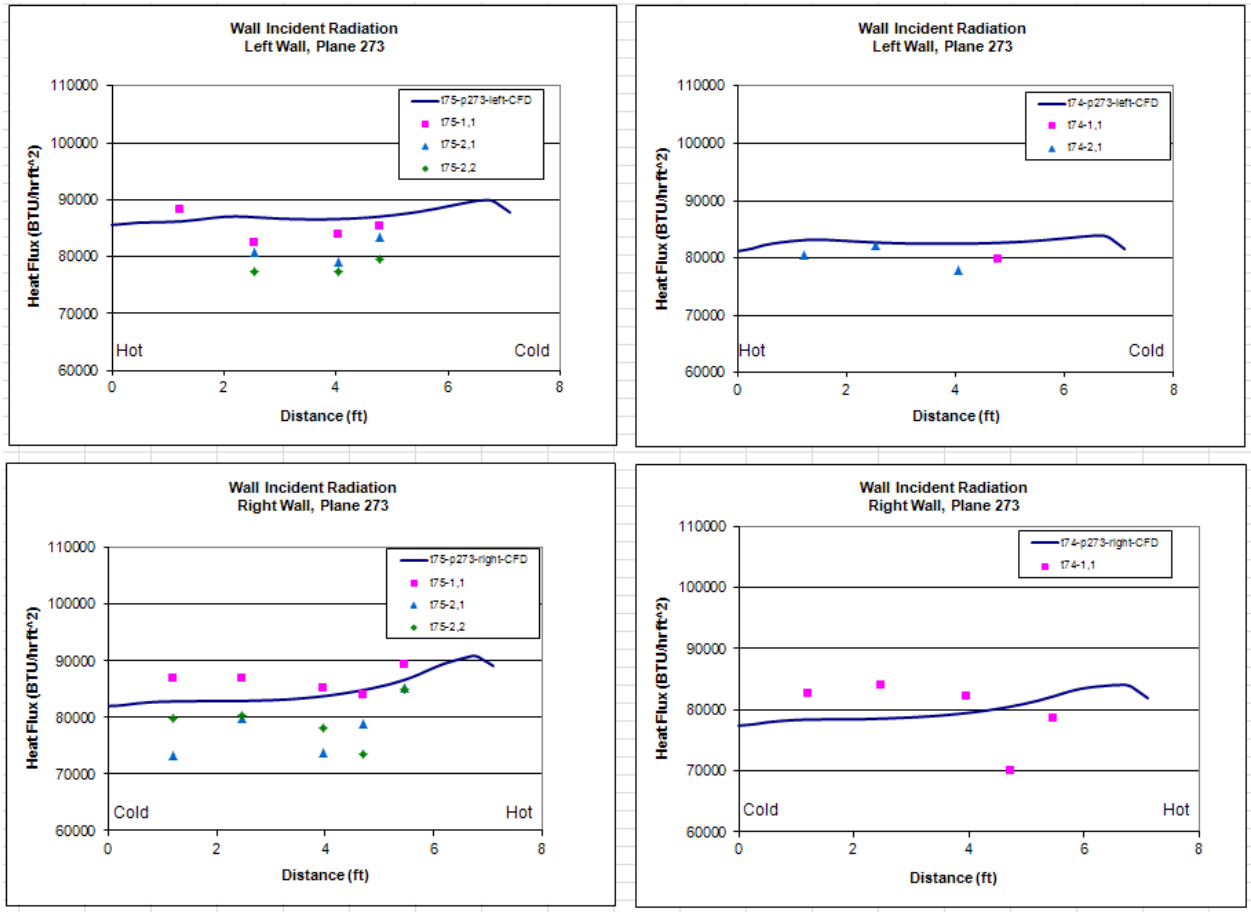

Figure 6-65. [AT-75:OT-74] Comparison of Wall Incident Radiation at Plane 273

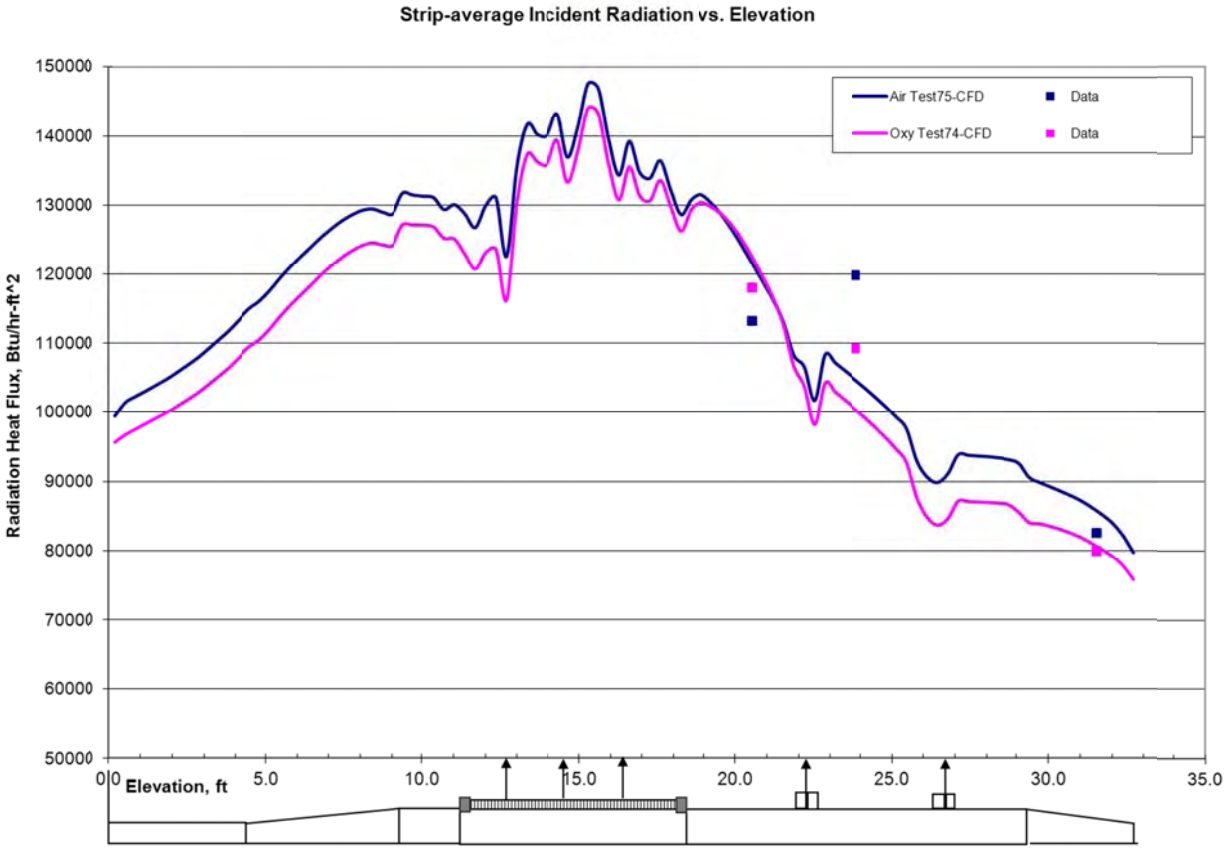

Figure 6-66. [AT-75:OT-74] Strip-Averaged Wall Incident Radiation

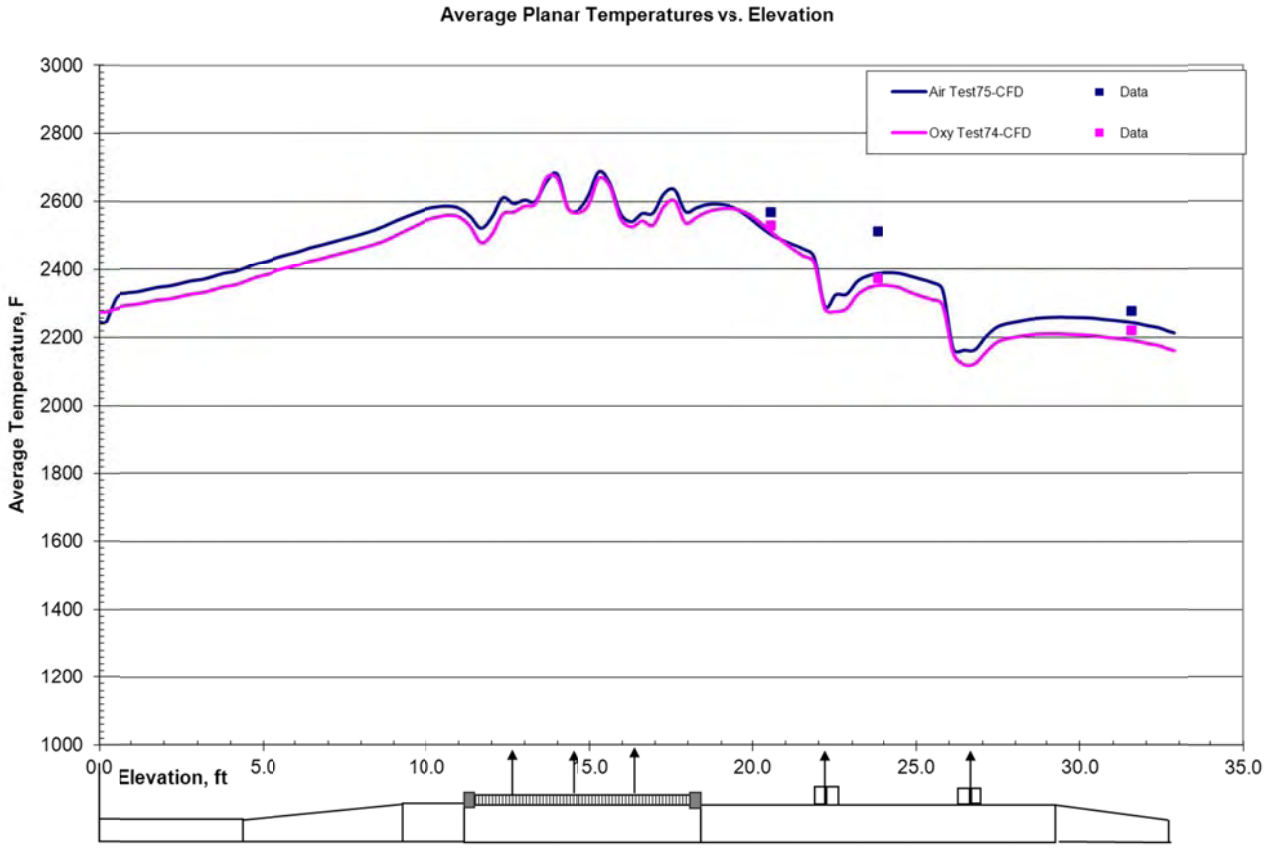

Figure 6-67. [AT-75:OT-74] Planar Averaged Temperature

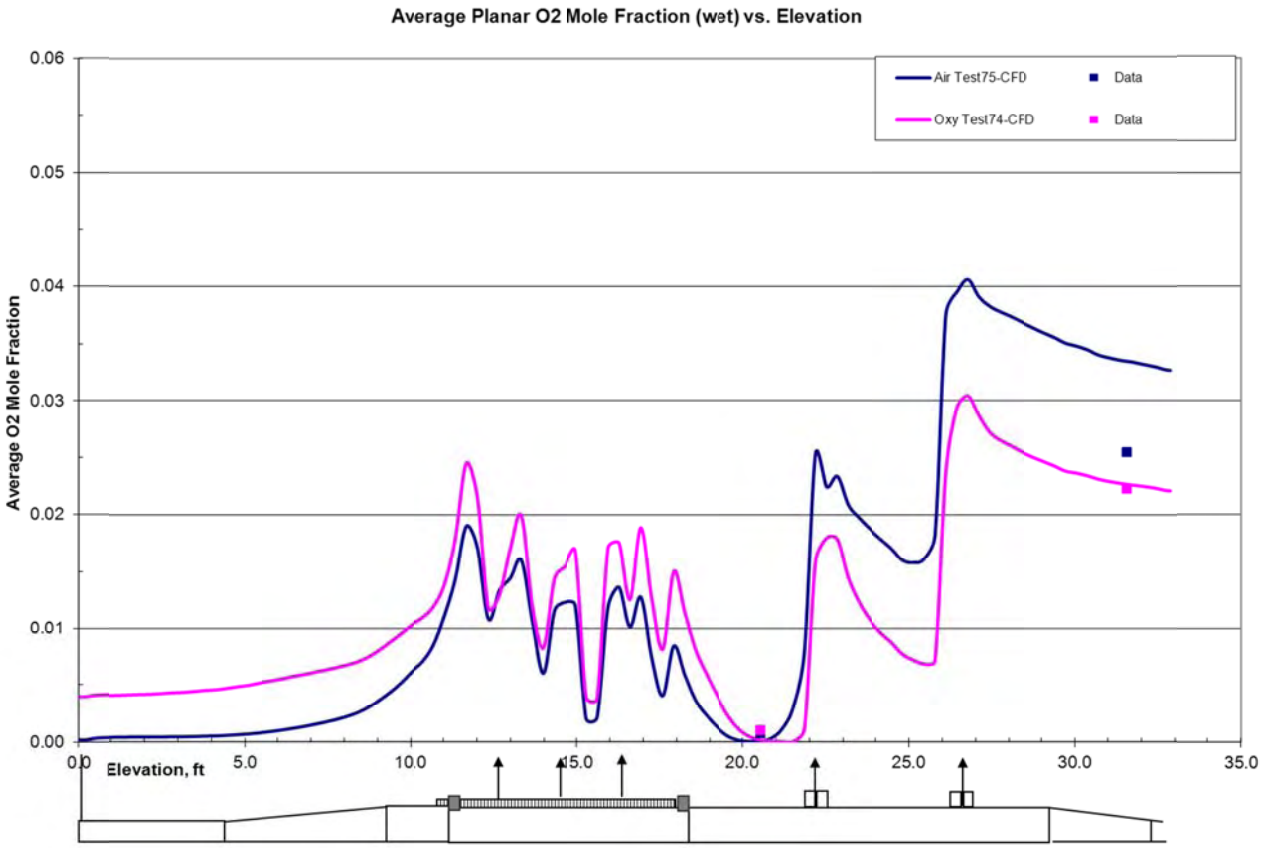

Figure 6-68. [AT-75:OT-74] Planar Averaged O_2

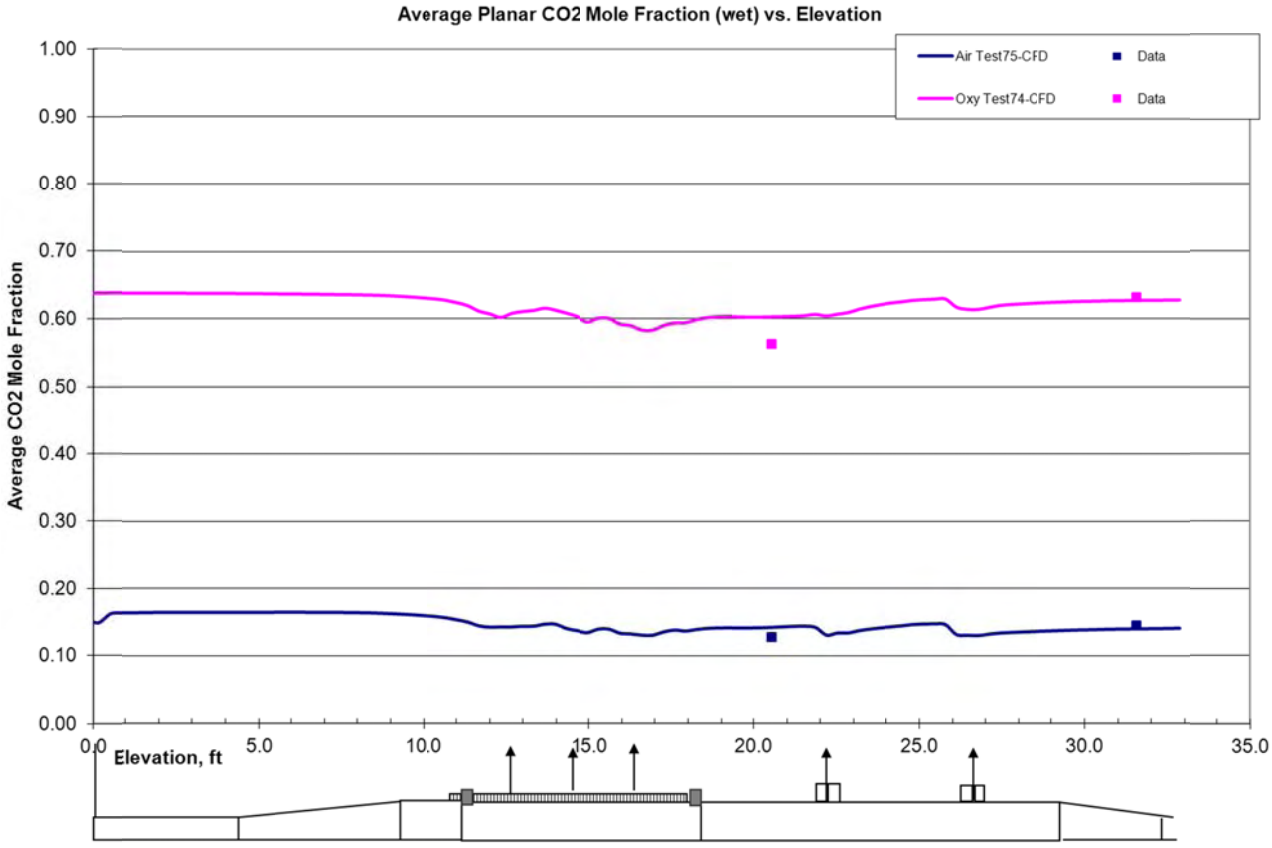

Figure 6-69. [AT-75:OT-74] Planar Averaged CO_2

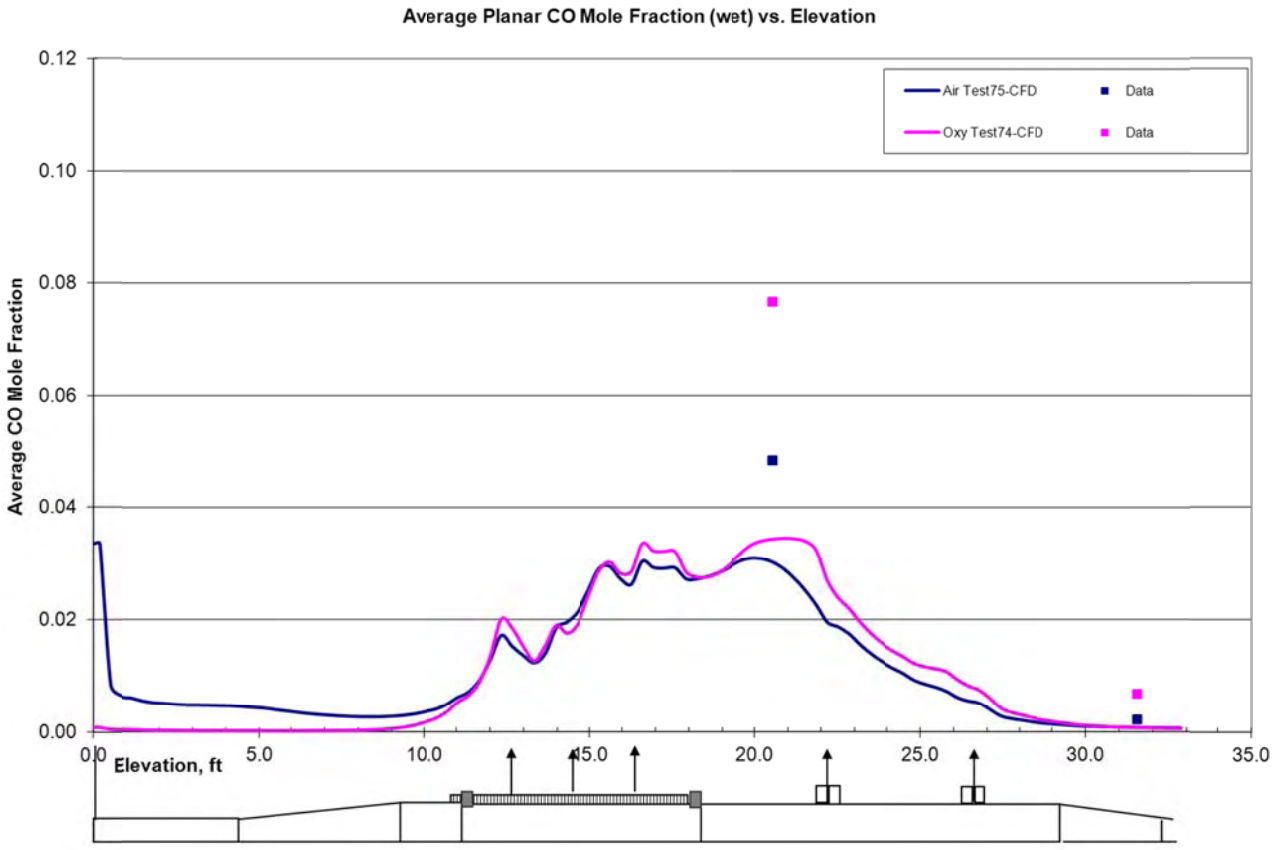

Figure 6-70. [AT-75:OT-74] Planar Averaged CO

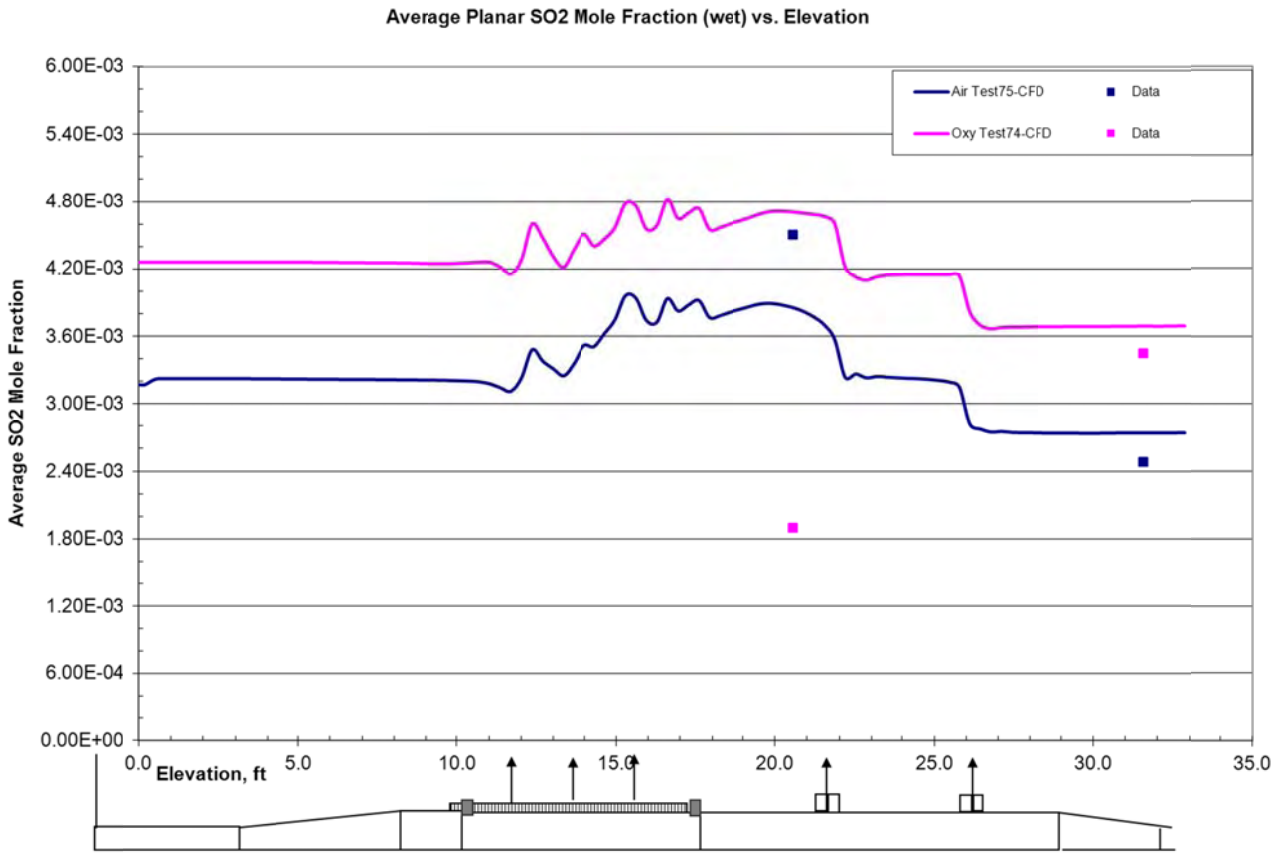

Figure 6-71. [AT-75:OT-74] Planar Averaged SO_2

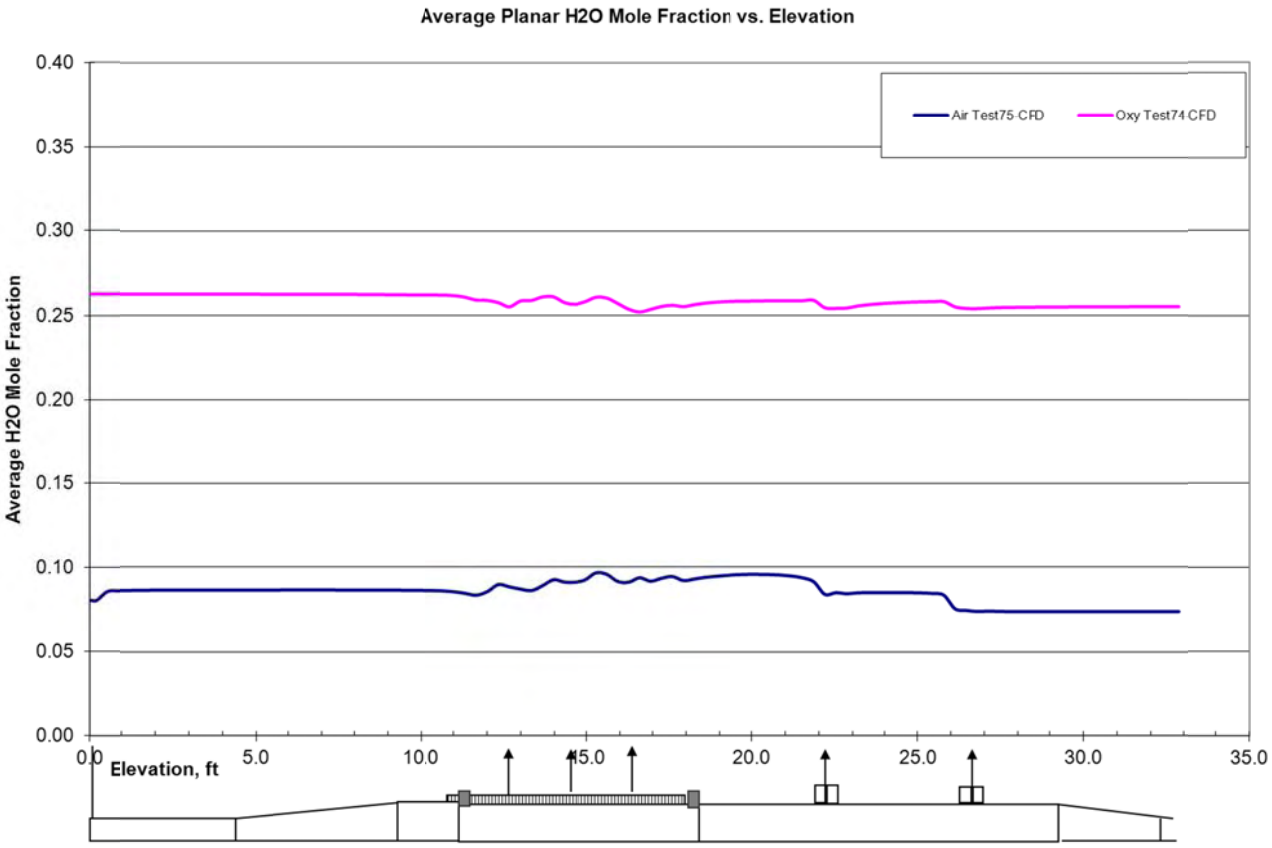

Figure 6-72. [AT-75:OT-74] Planar Averaged H_2O

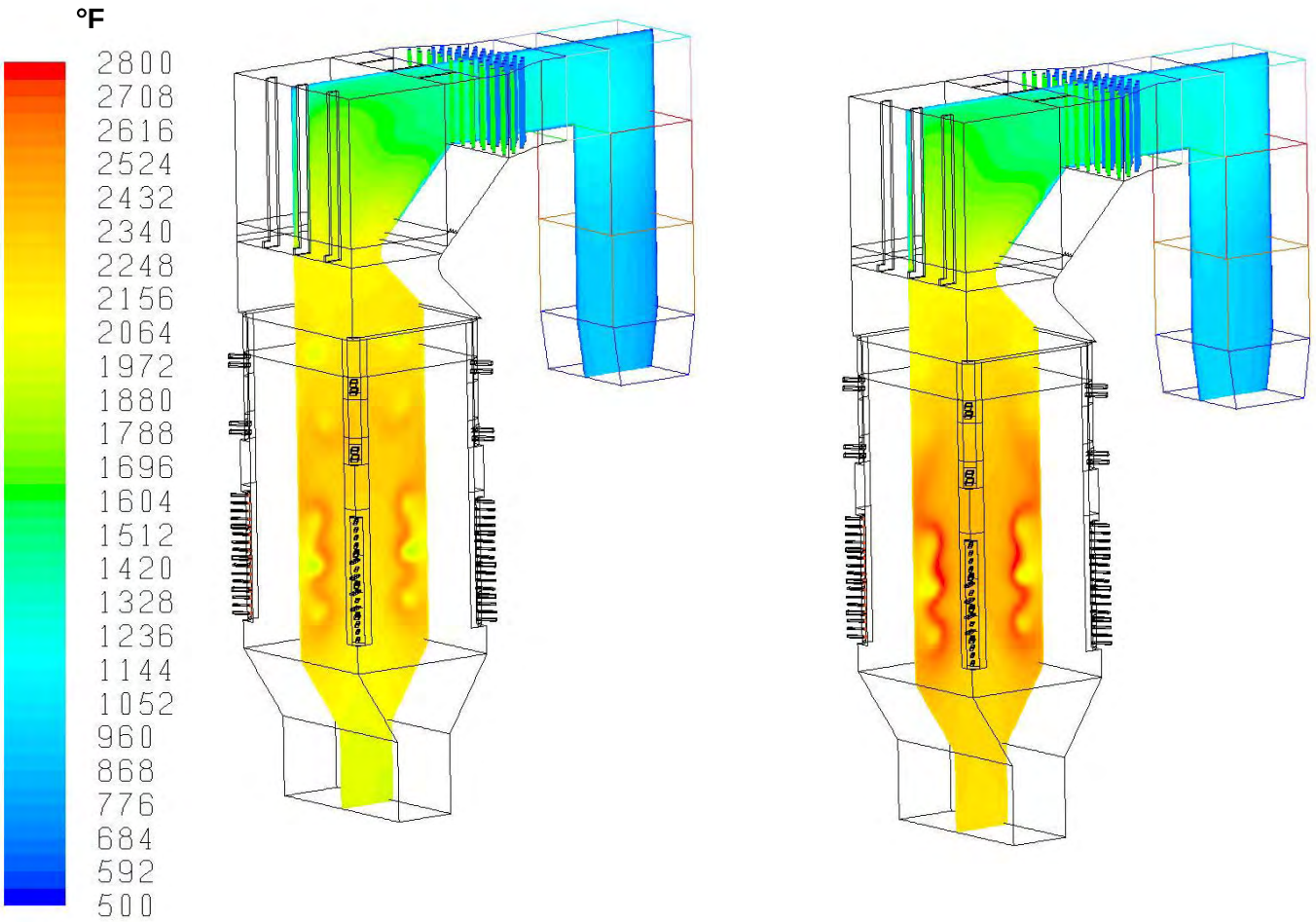

Figure 6-73. [AT-83:OT-98] Contours of Temperature on X-Midplane

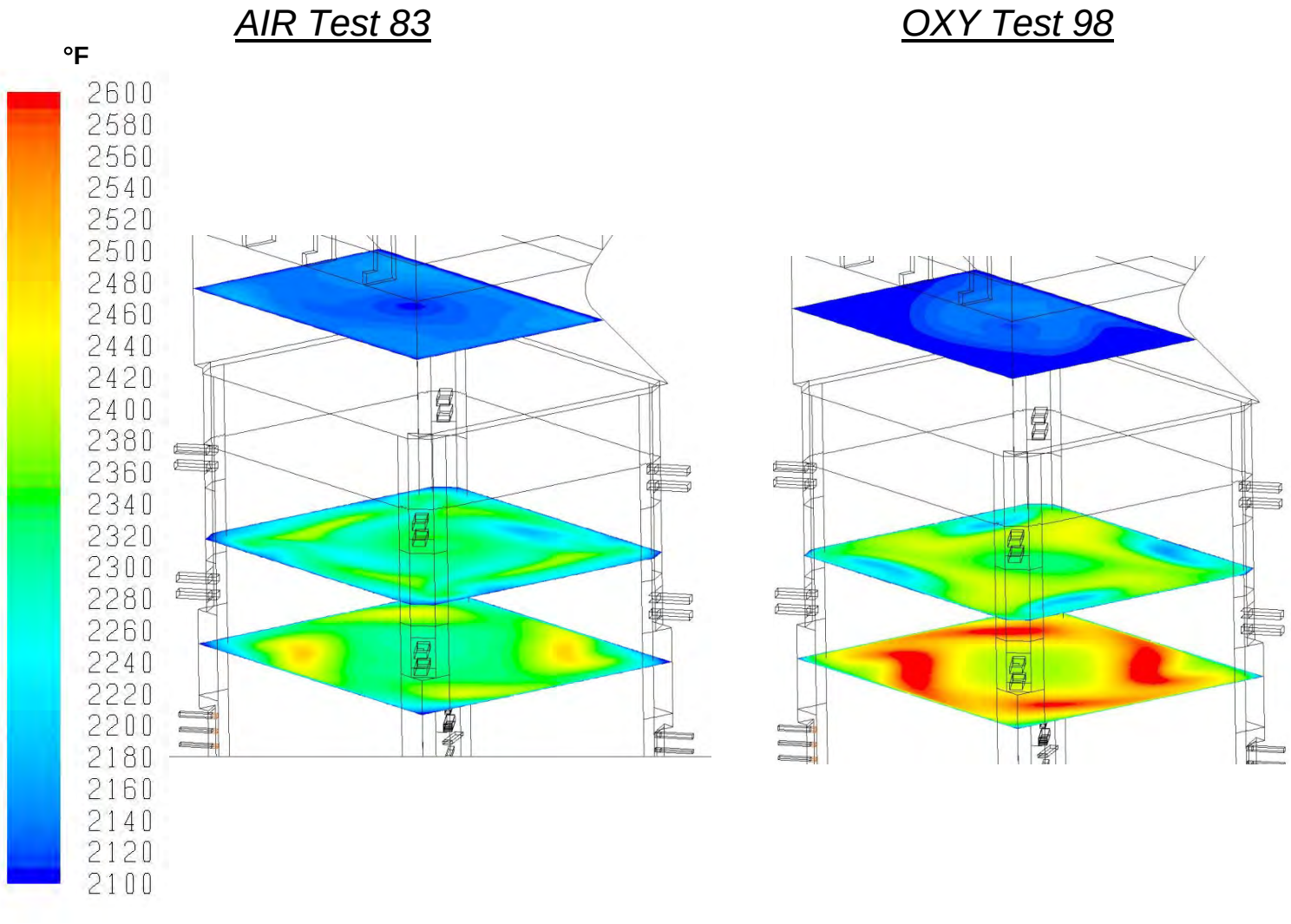

Figure 6-74. [AT-83:OT-98] Contours of Temperature on Test Planes

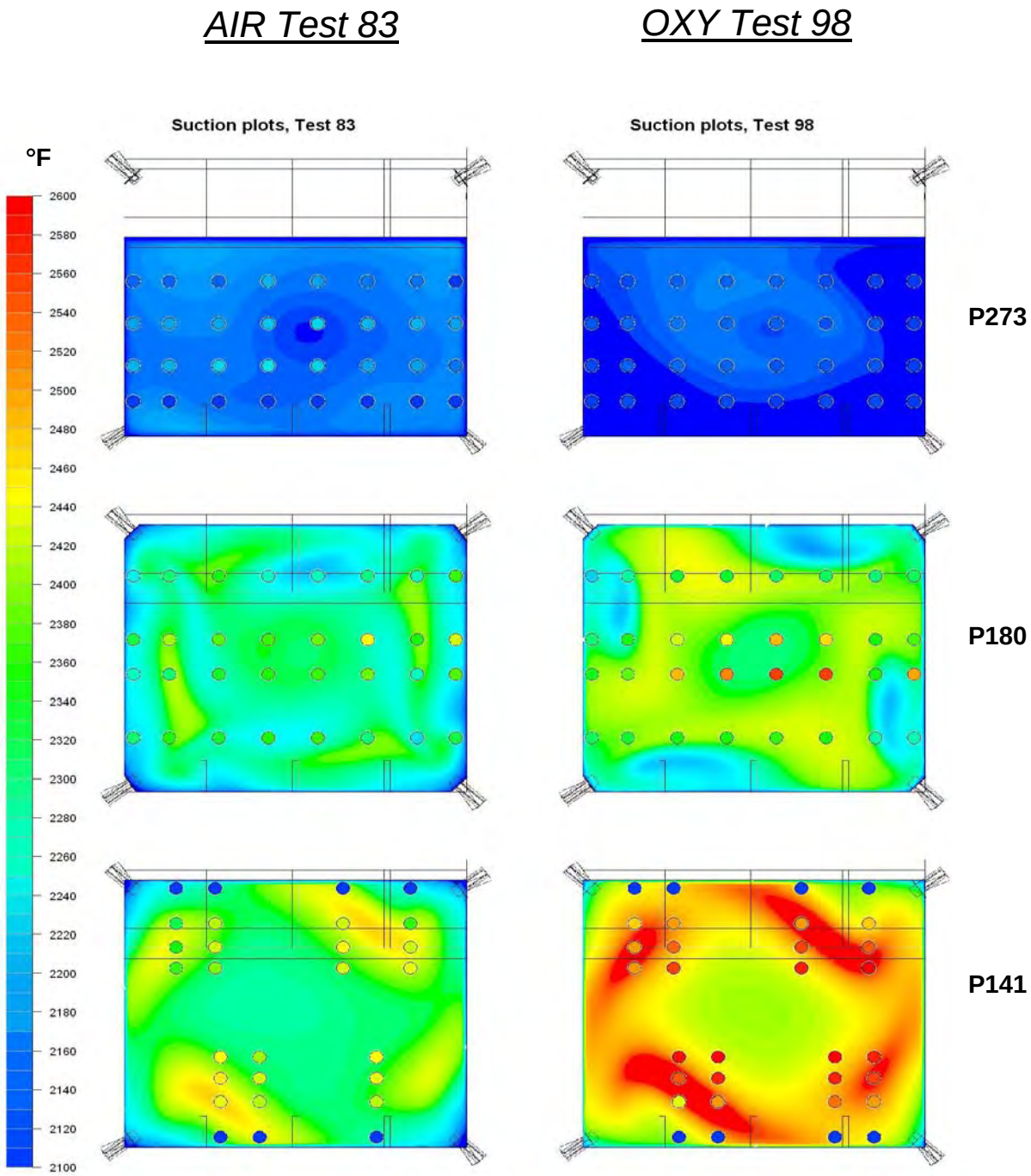

Figure 6-75. [AT-83:OT-98] Comparison of Temperature on Test Planes

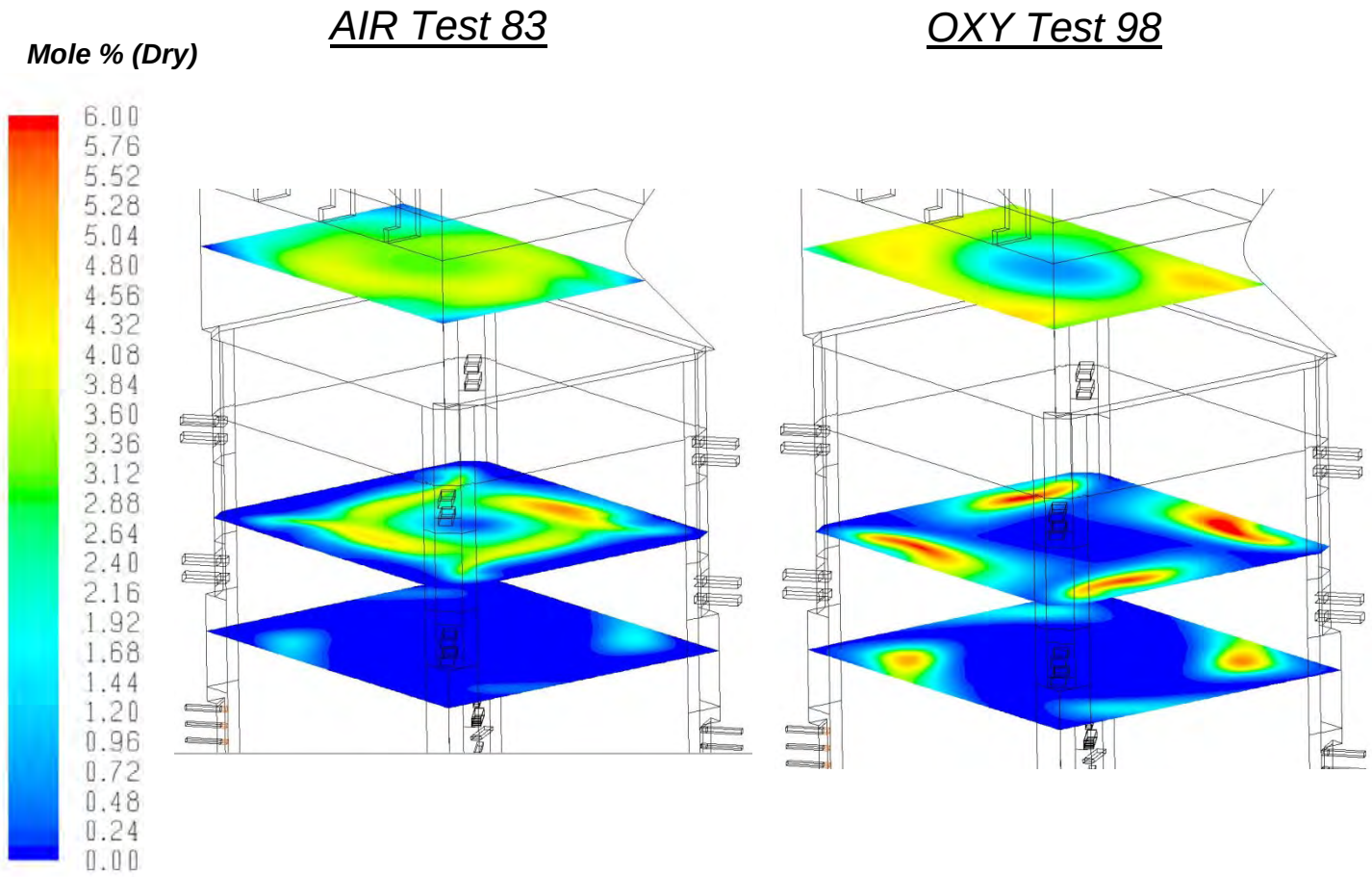

Figure 6-76. [AT-83:OT-98] Contours of O_2 Concentrations on Test Planes

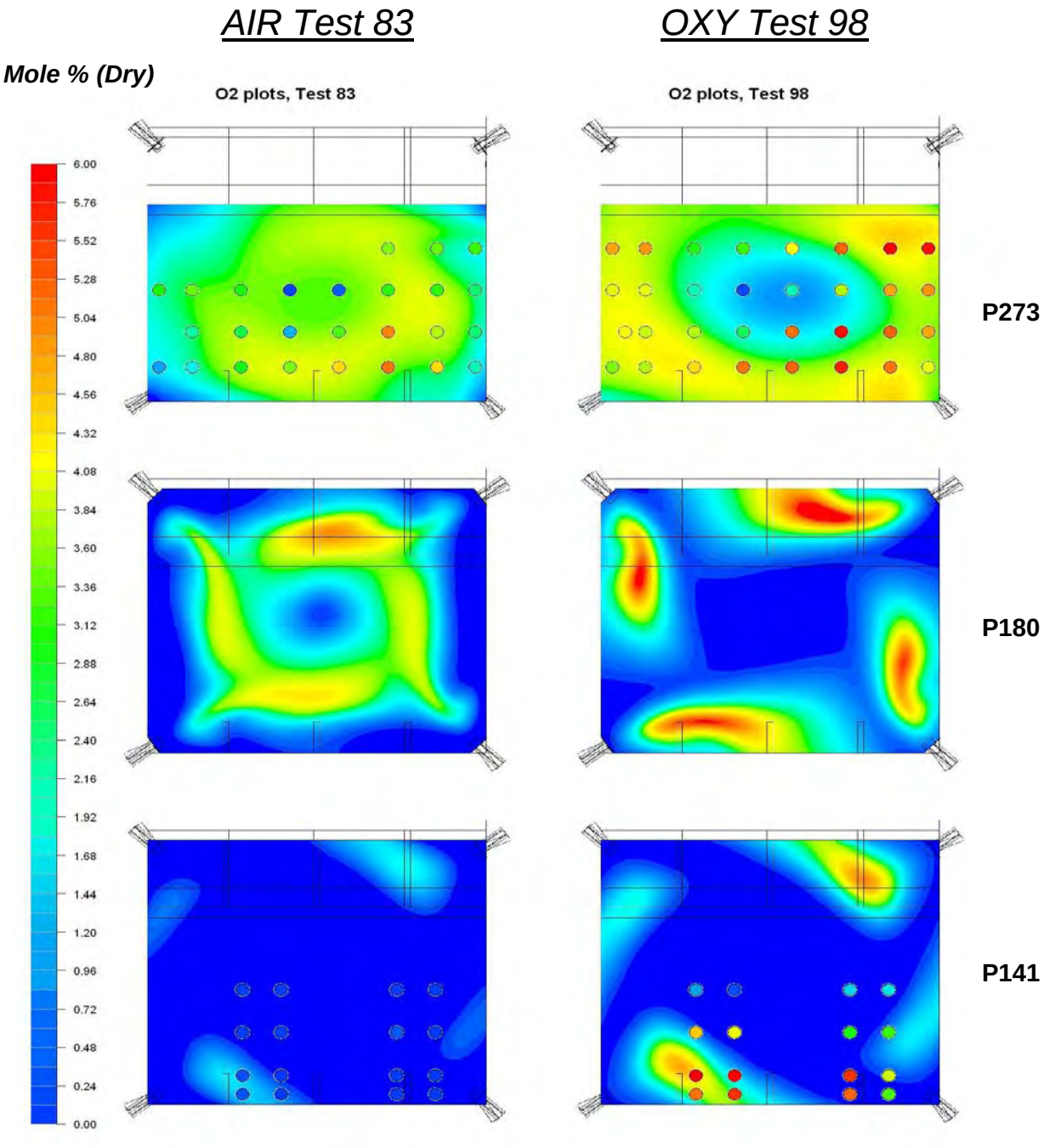

Figure 6-77. [AT-83:OT-98] Comparison of O_2 Concentrations on Test Planes

AIR Test 83

Mole % (Dry)

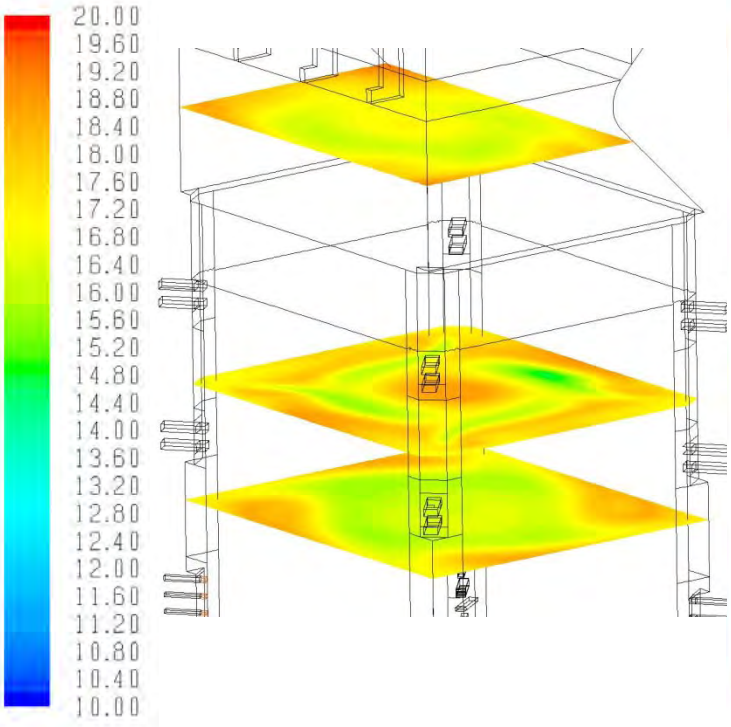

OXY Test 98

Mole % (Dry)

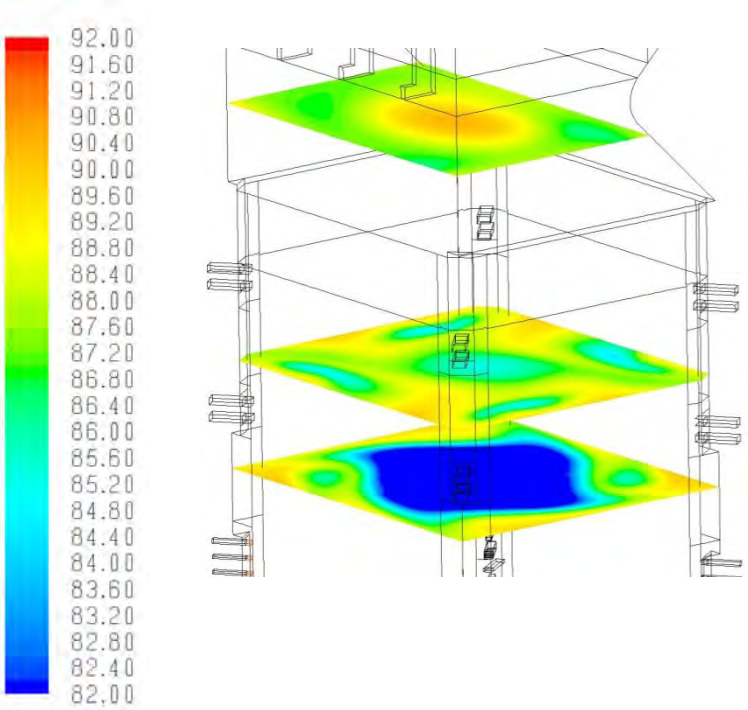

Figure 6-78. [AT-83:OT-98] Contours of CO_2 Concentrations on Test Planes

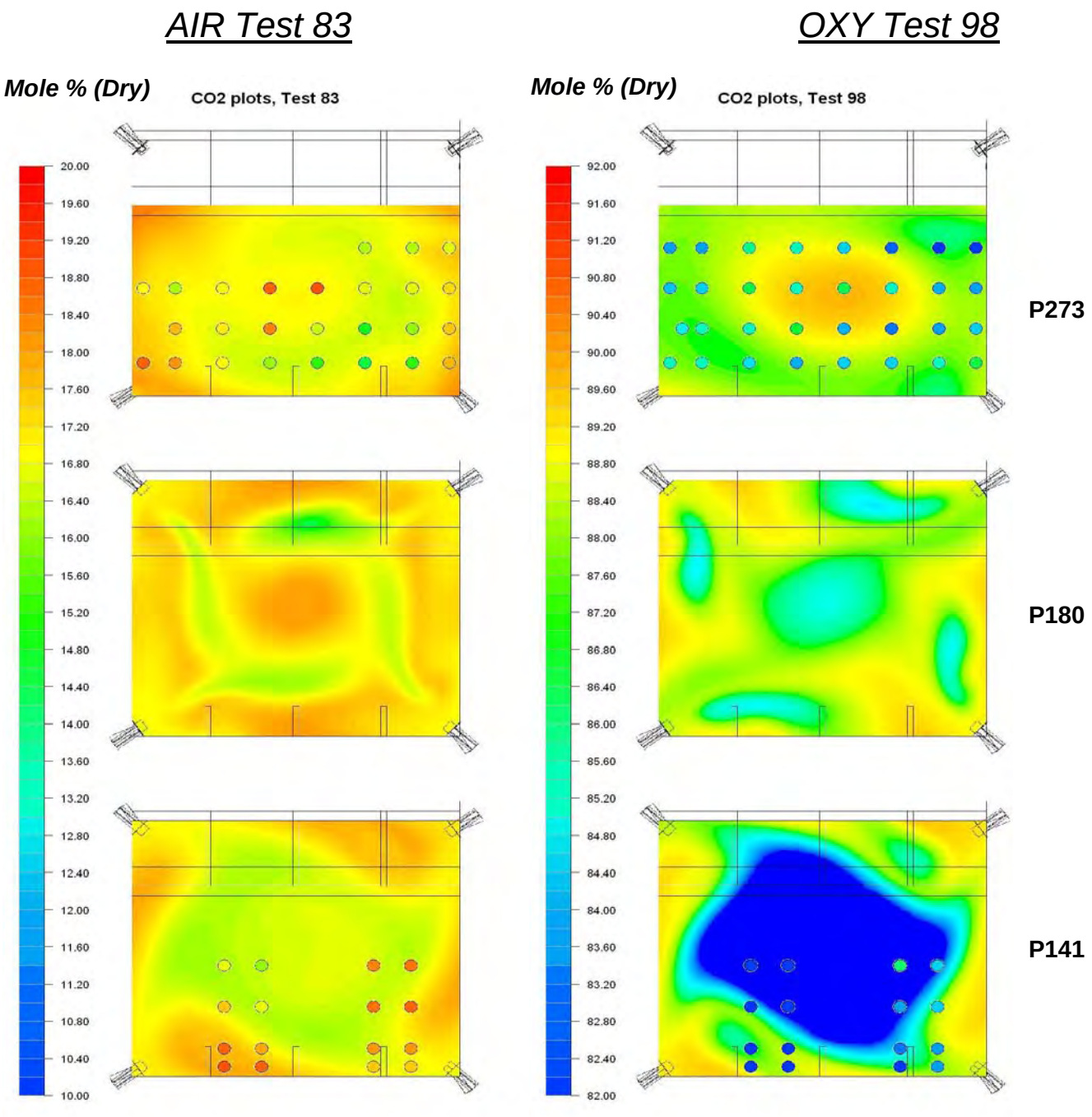

Figure 6-79. [AT-83:OT-98] Comparison of CO_2 Concentrations on Test Planes

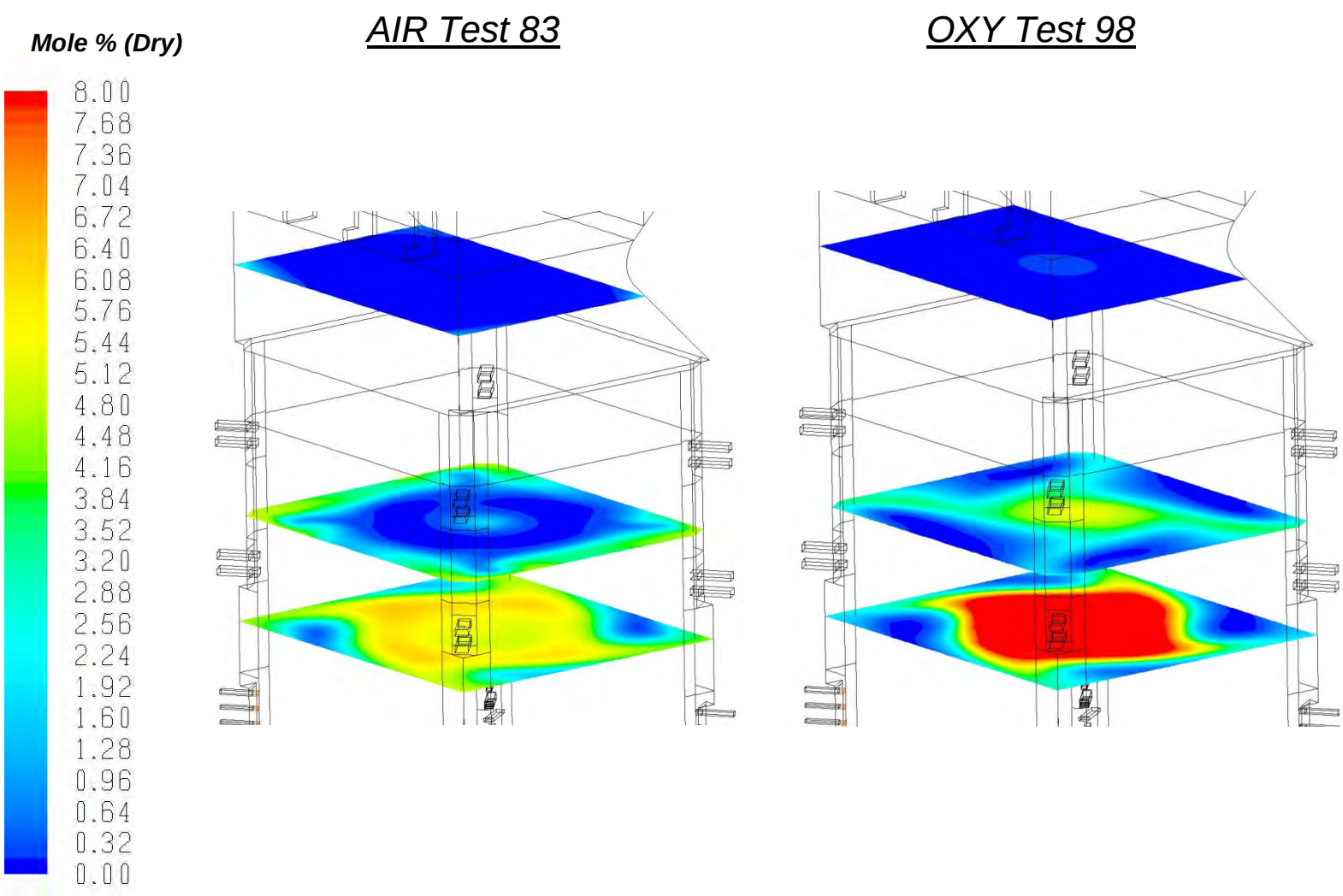

Figure 6-80. [AT-83:OT-98] Contours of CO Concentrations on Test Planes

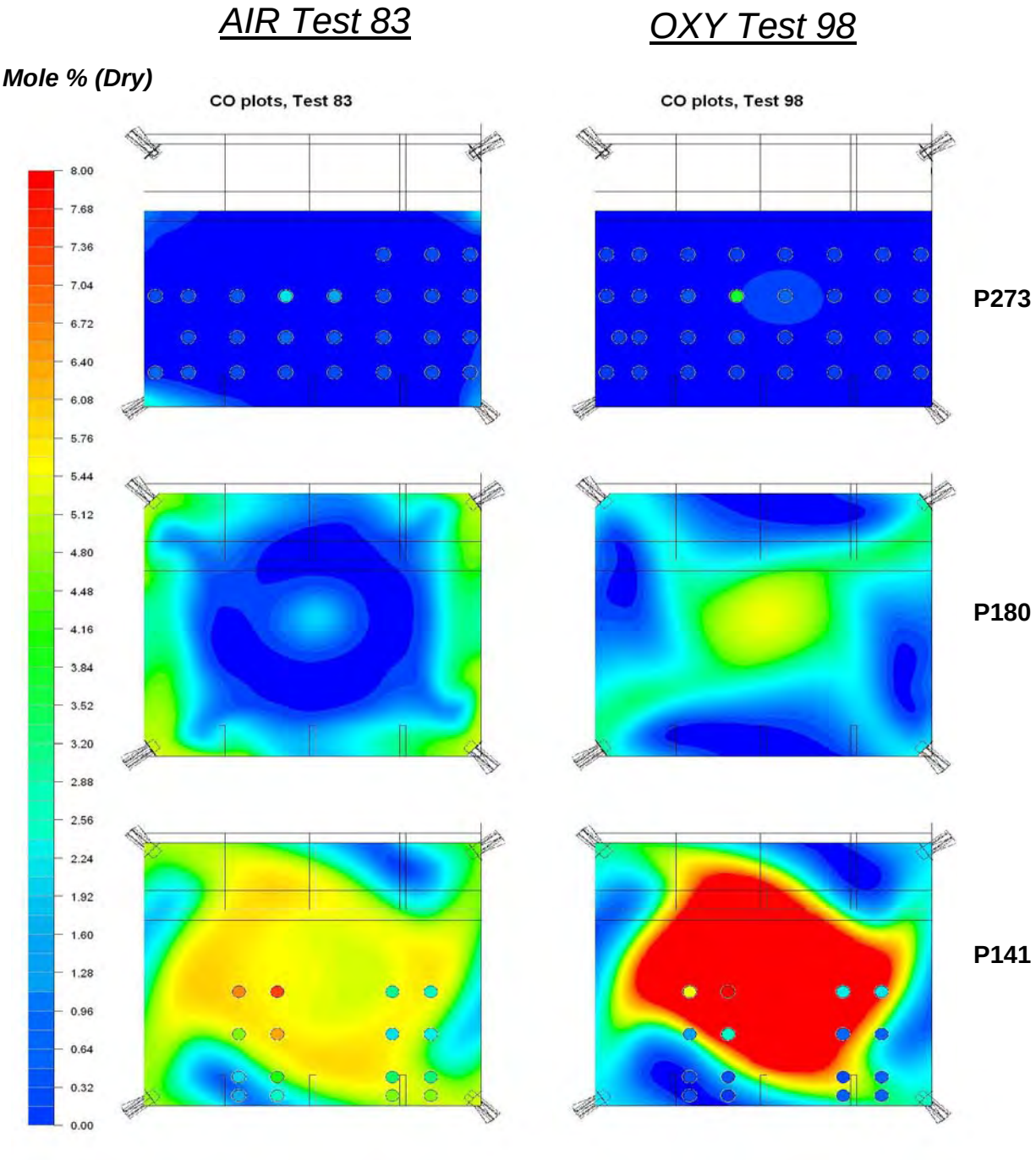

Figure 6-81. [AT-83:OT-98] Comparison of CO Concentrations on Test Planes

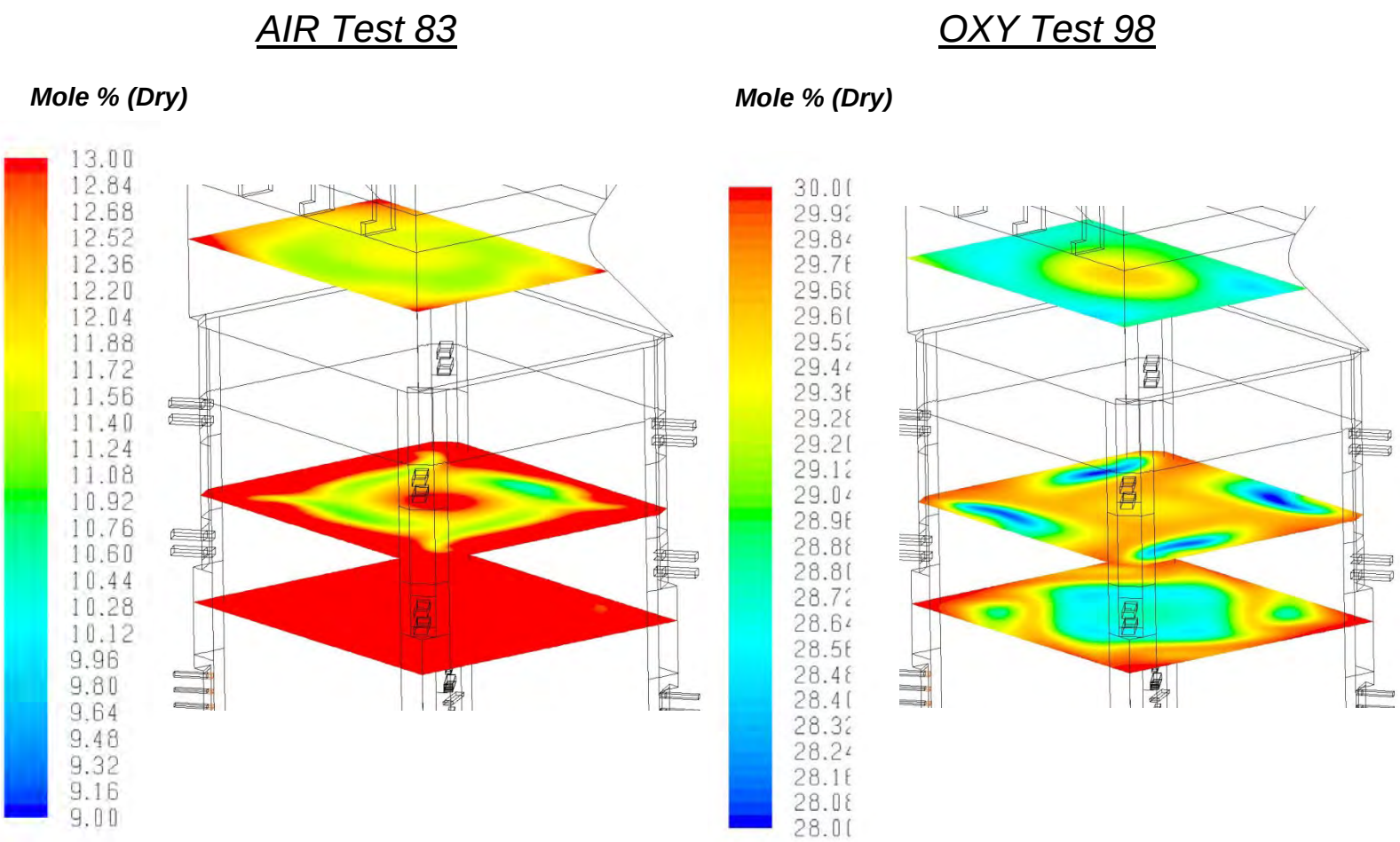

Figure 6-82. [AT-83:OT-98] Contours of H_2O Concentrations on Test Planes

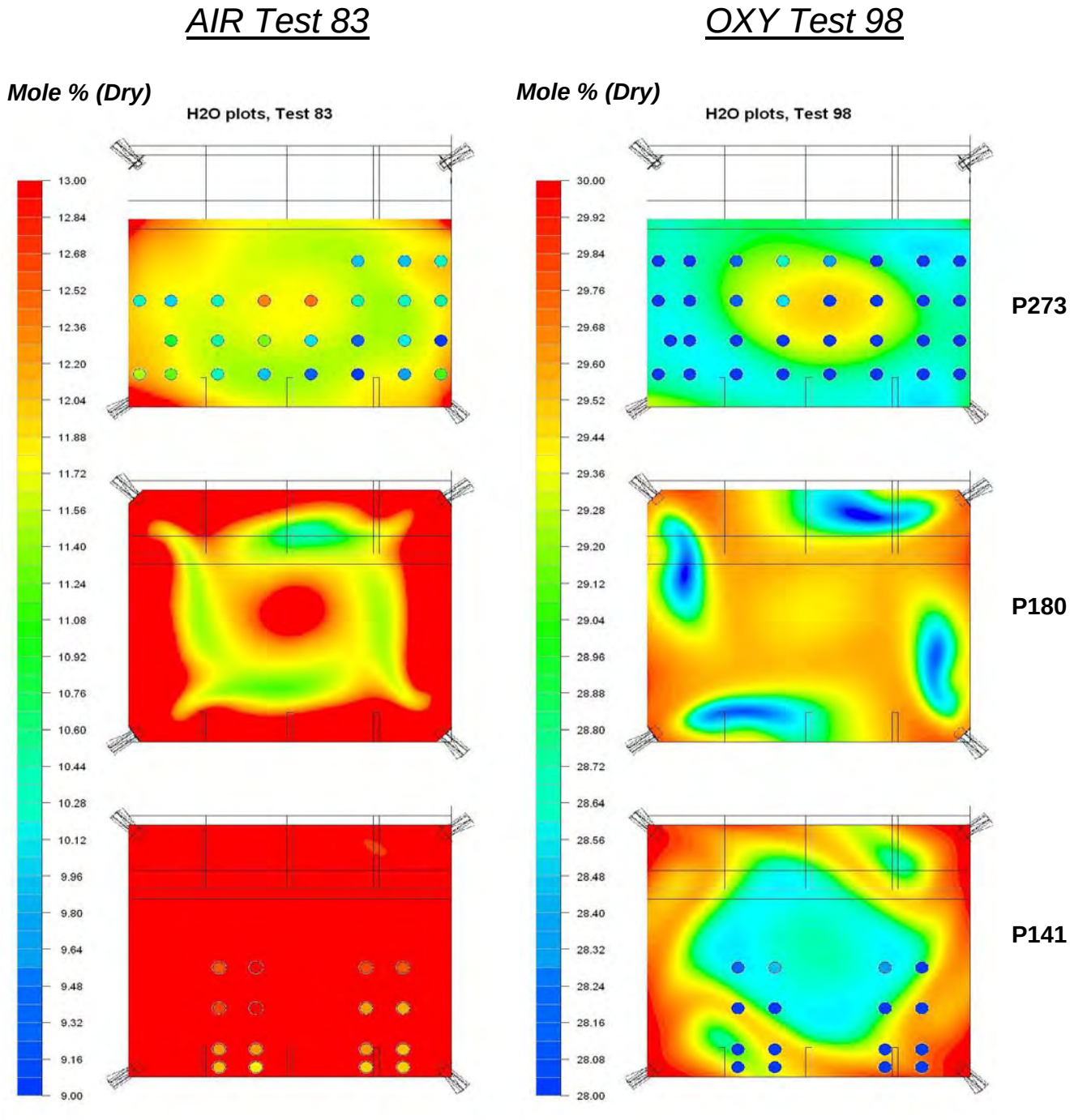

Figure 6-83. [AT-83:OT-98] Comparison of H_2O Concentrations on Test Planes

AIR Test 83 *OXY Test 98*

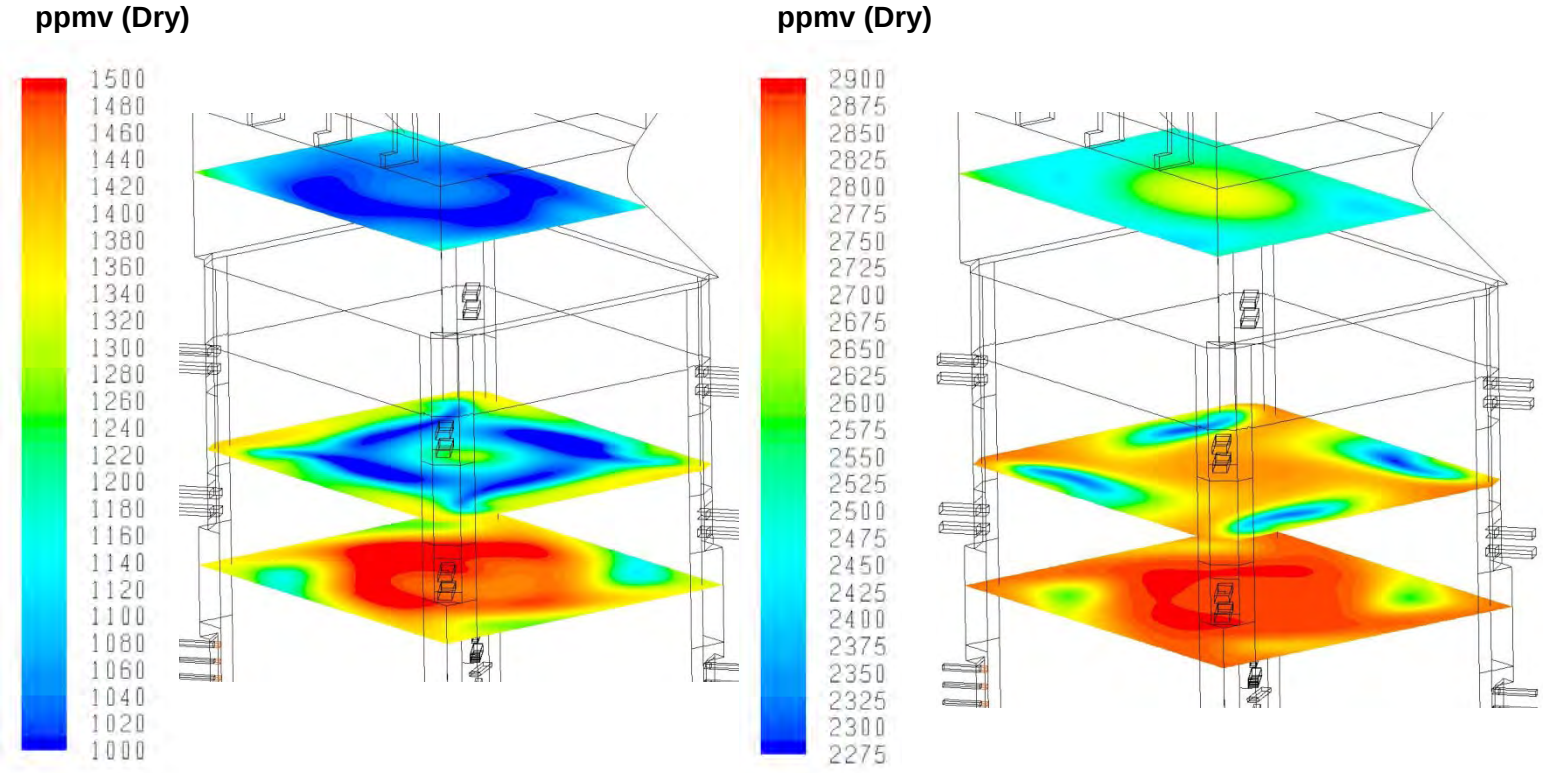

Figure 6-84. [AT-83:OT-98] Contours of SO_2 Concentrations on Test Planes

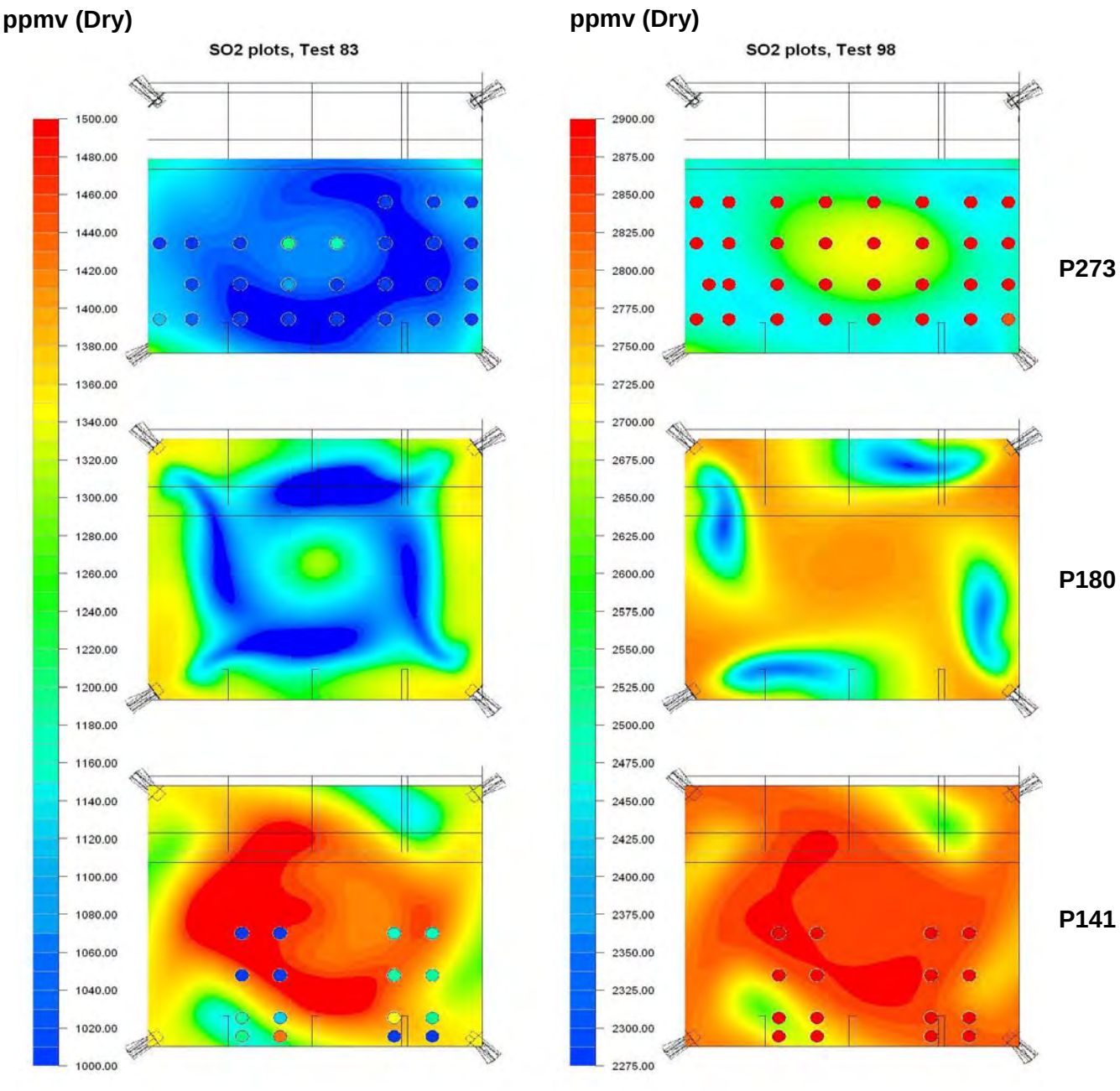

Figure 6-85. [AT-83:OT-98] Comparison of SO_2 Concentrations on Test Planes

AIR Test 83 *OXY Test 98*

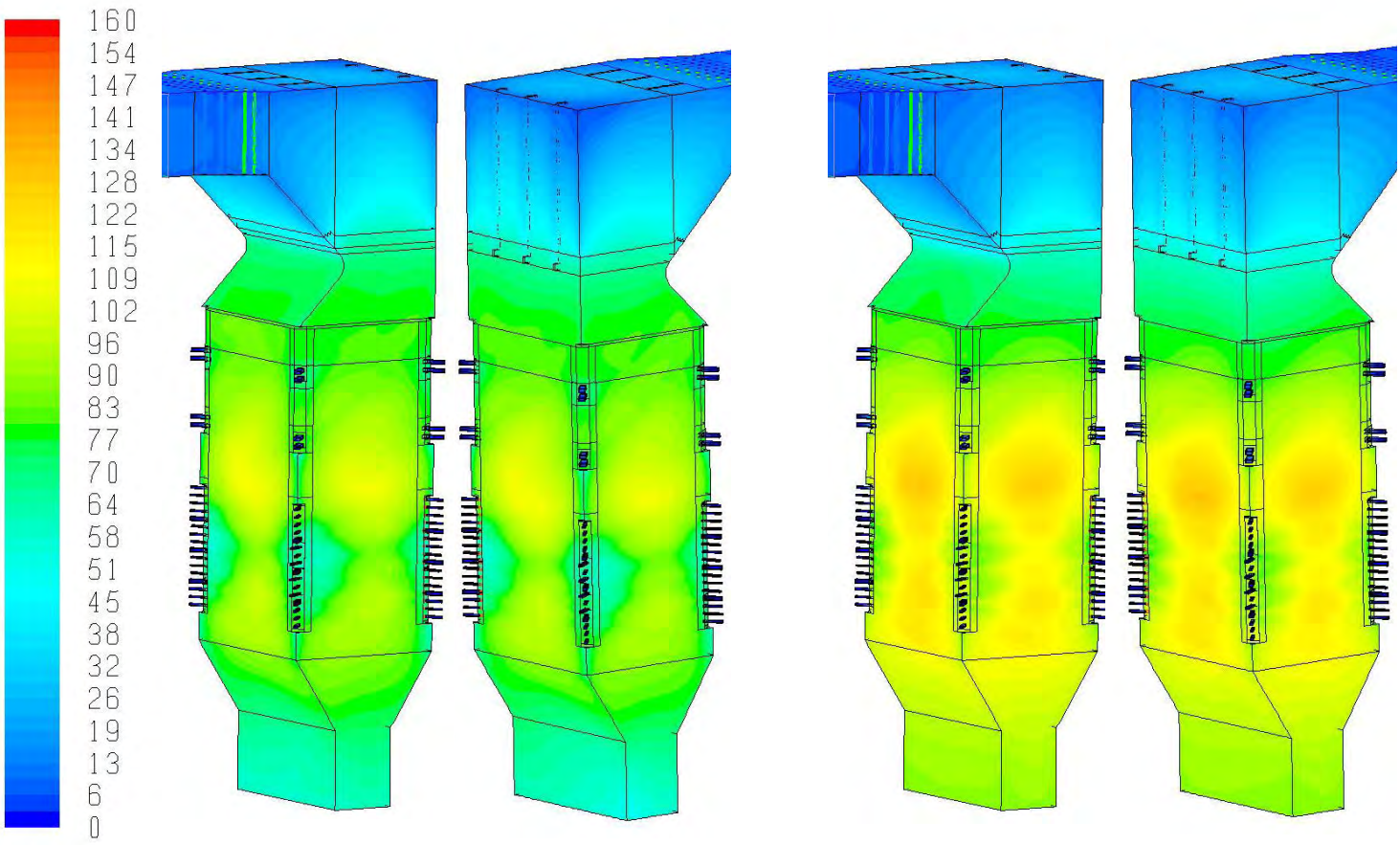

Figure 6-86. [AT-83:OT-98] Contours of Incident Radiation

AIR Test 83 *OXY Test 98*

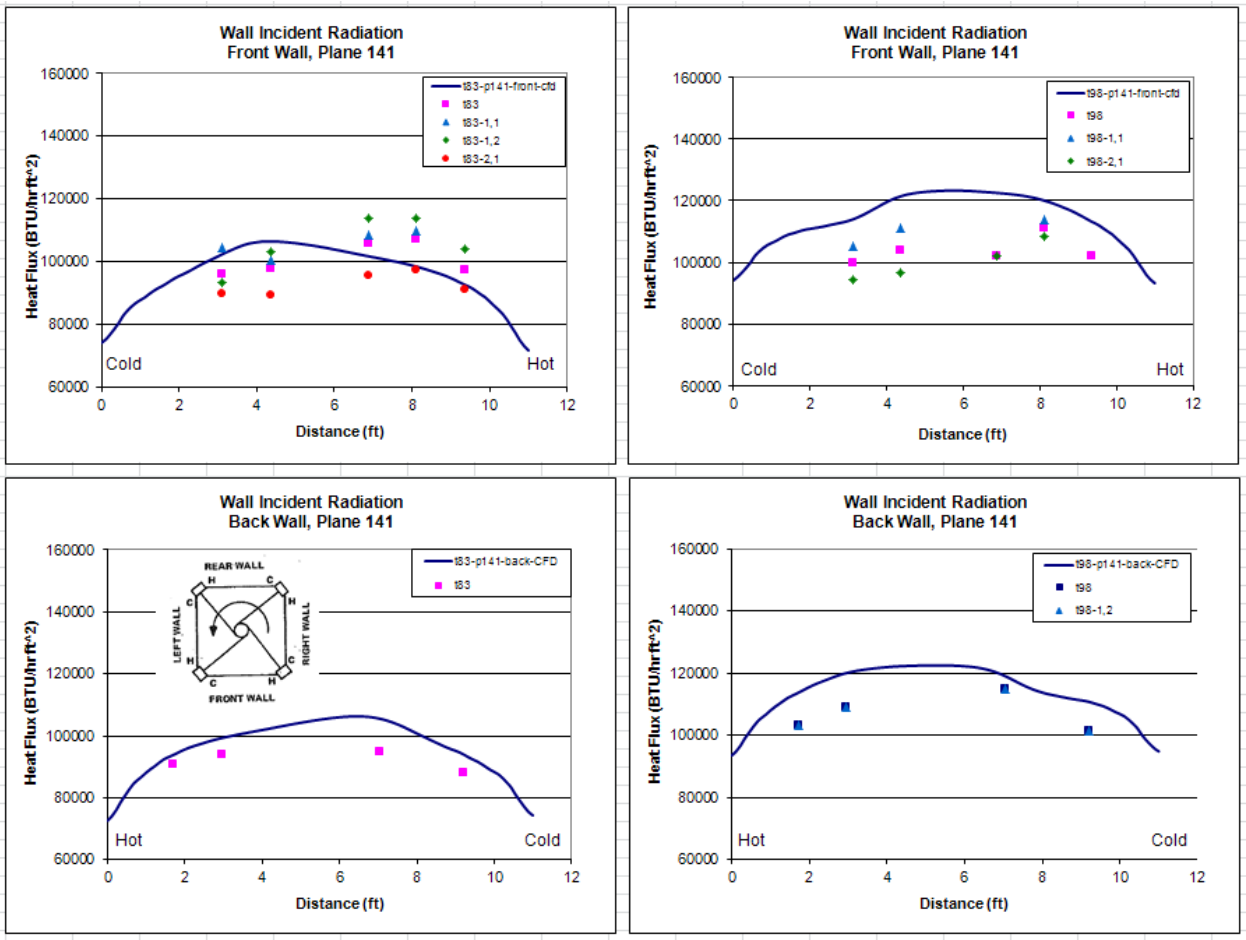

Figure 6-87. [AT-83:OT-98] Comparison of Wall Incident Radiation at Plane 141

AIR Test 83 *OXY Test 98*

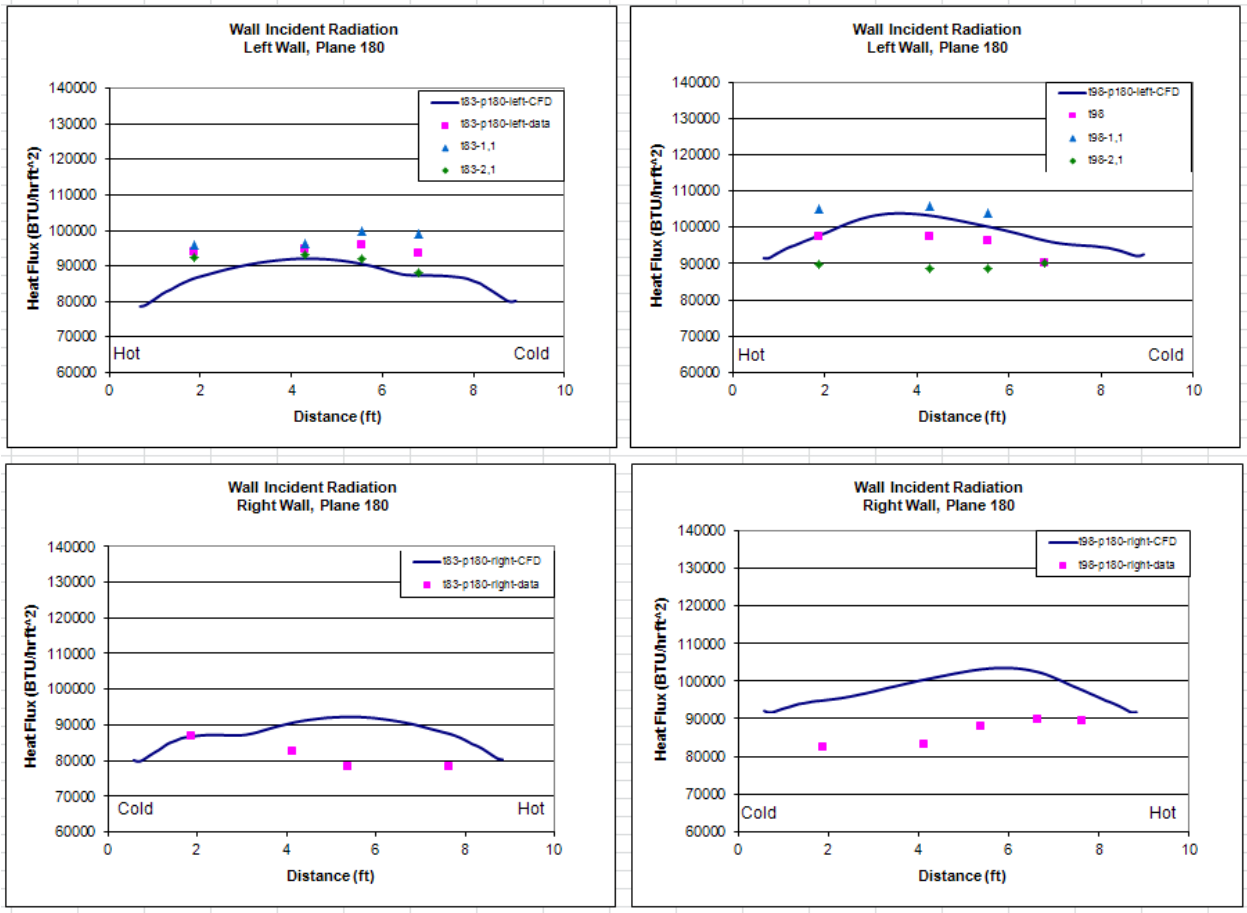

Figure 6-88. [AT-83:OT-98] Comparison of Wall Incident Radiation at Plane 180

AIR Test 83 *OXY Test 98*

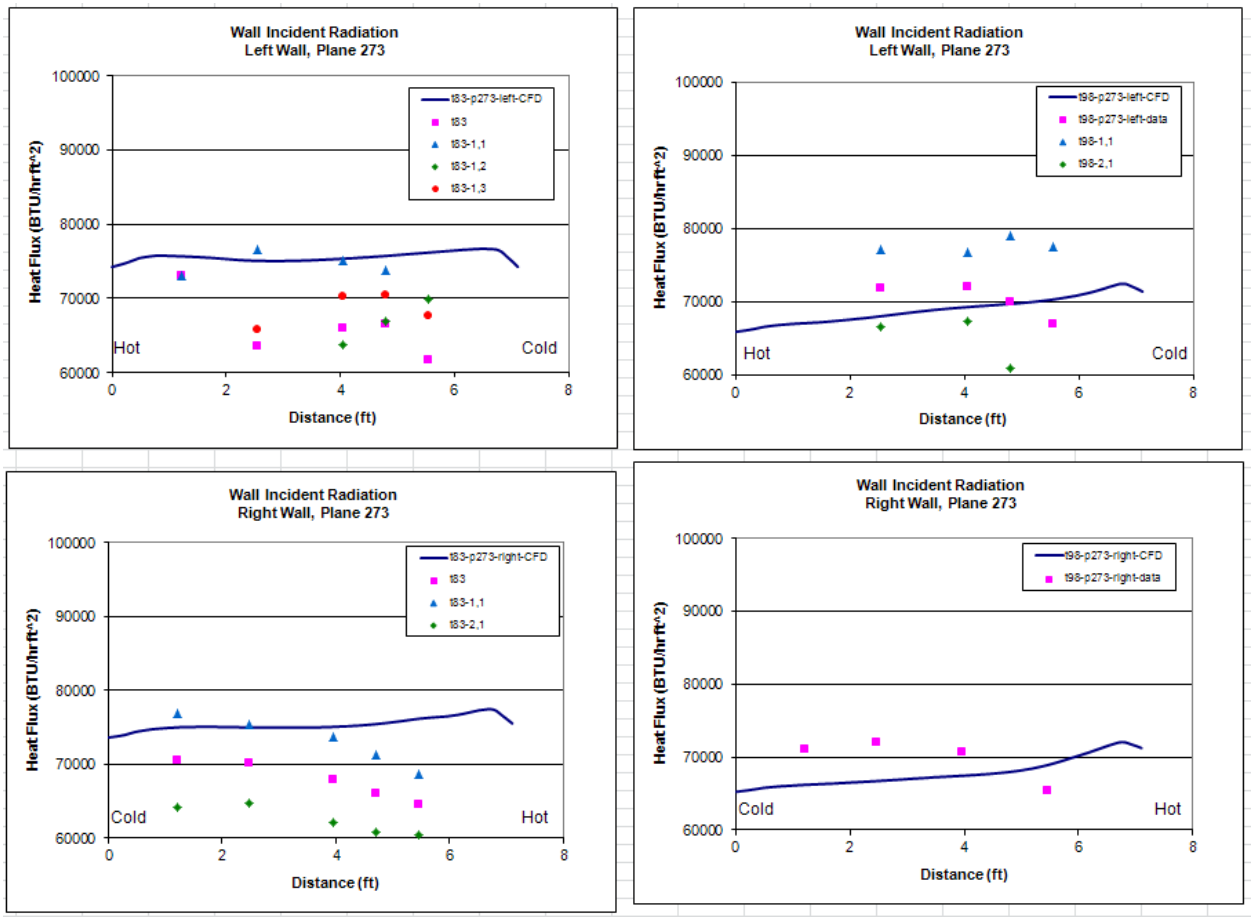

Figure 6-89. [AT-83:OT-98] Comparison of Wall Incident Radiation at Plane 273

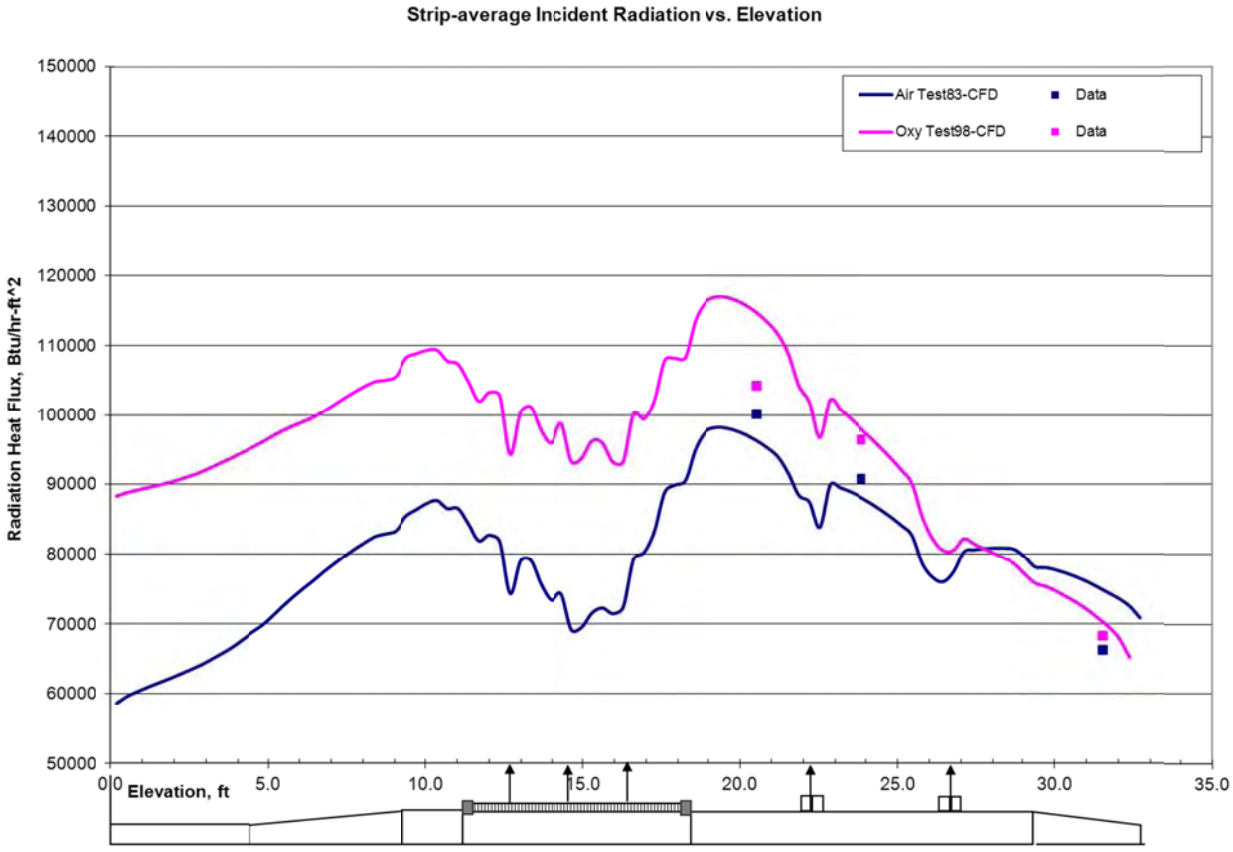

Figure 6-90. [AT-83:OT-98] Strip-Averaged Wall Incident Radiation

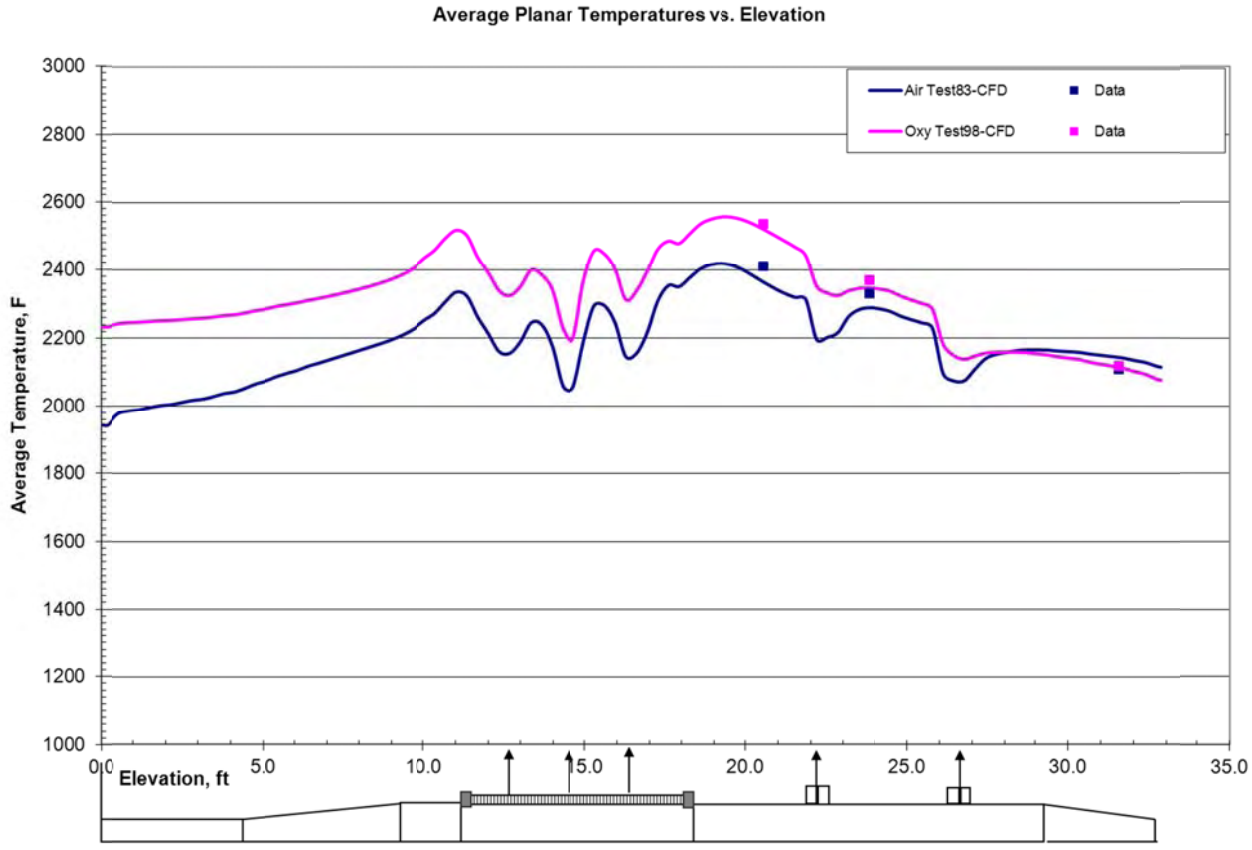

Figure 6-91. [AT-83:OT-98] Planar Averaged Temperature

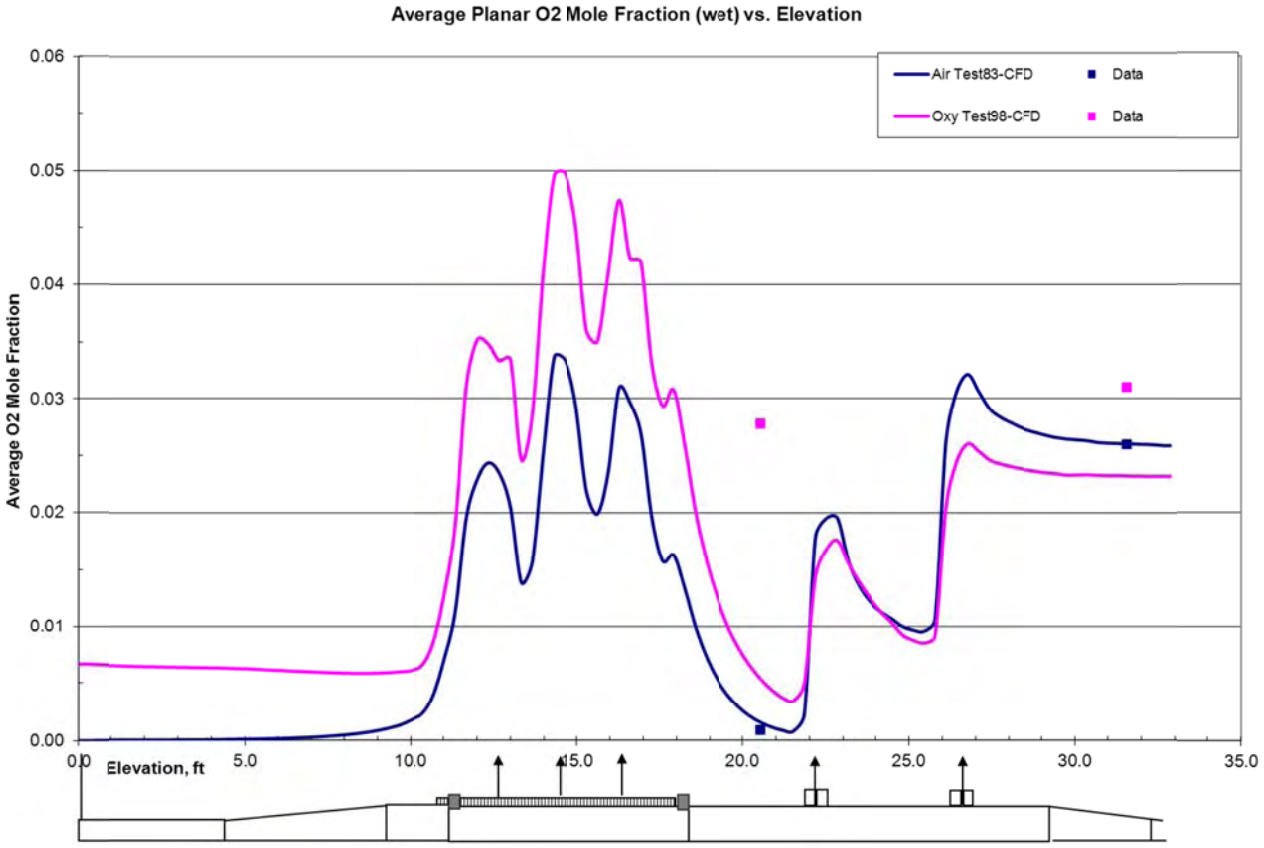

Figure 6-92. [AT-83:OT-98] Planar Averaged O_2

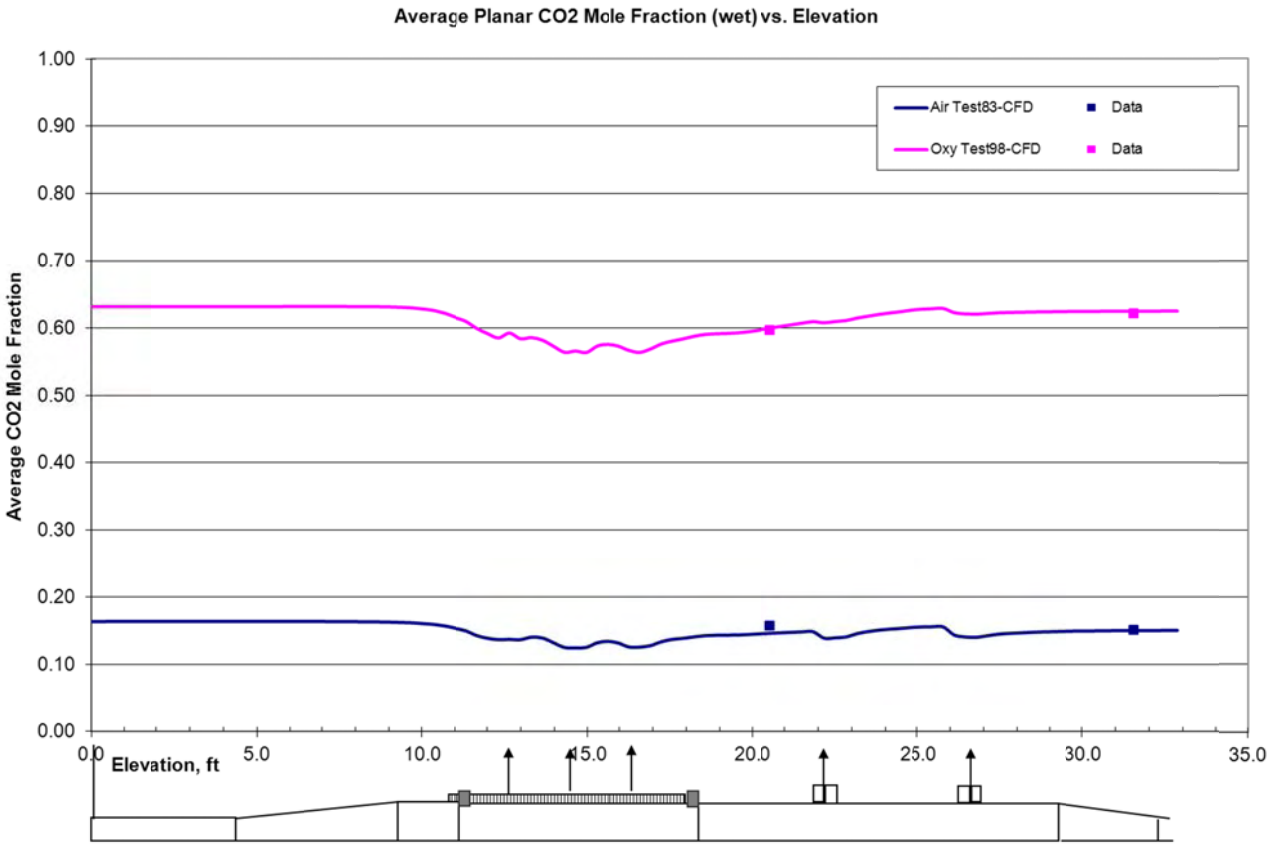

Figure 6-93. [AT-83:OT-98] Planar Averaged CO_2

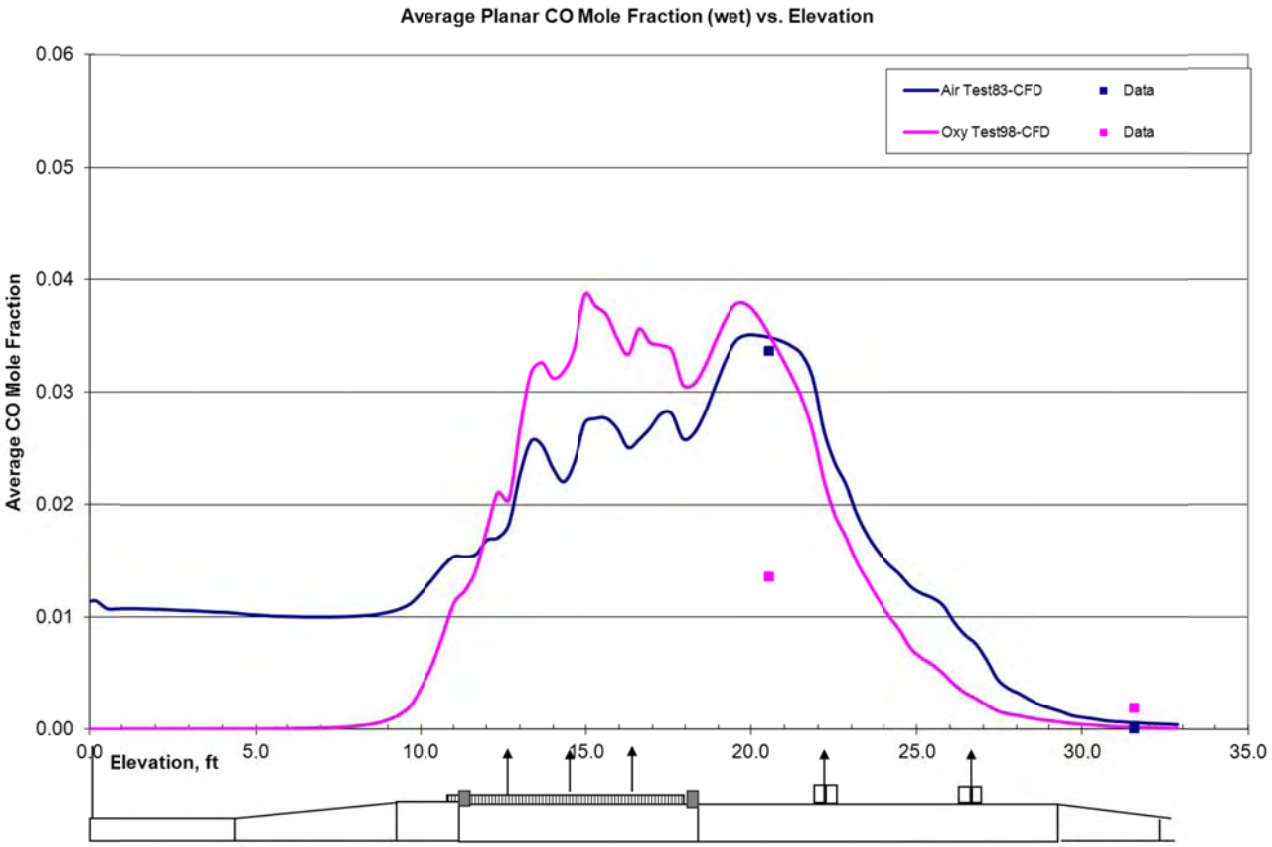

Figure 6-94. [AT-83:OT-98] Planar Averaged CO

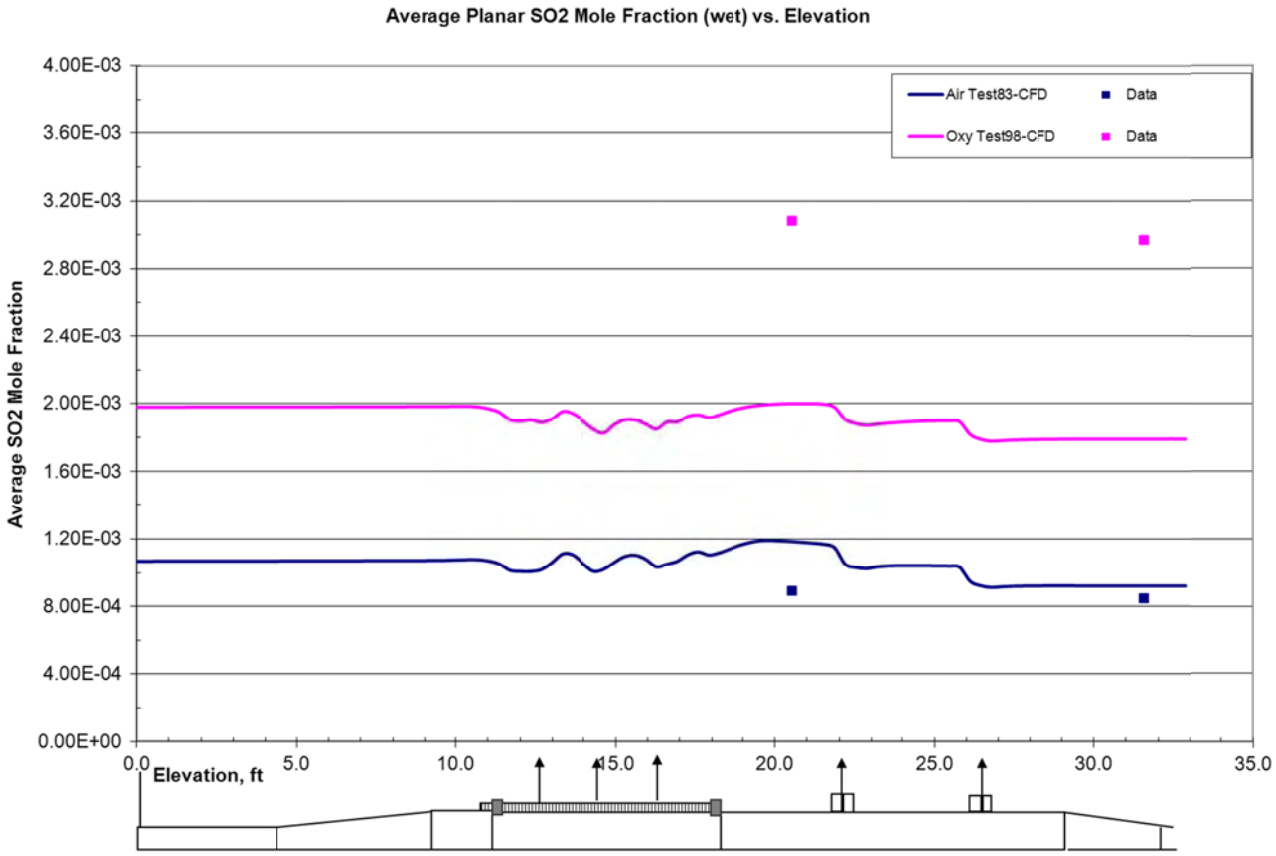

Figure 6-95. [AT-83:OT-98] Planar Averaged SO_2

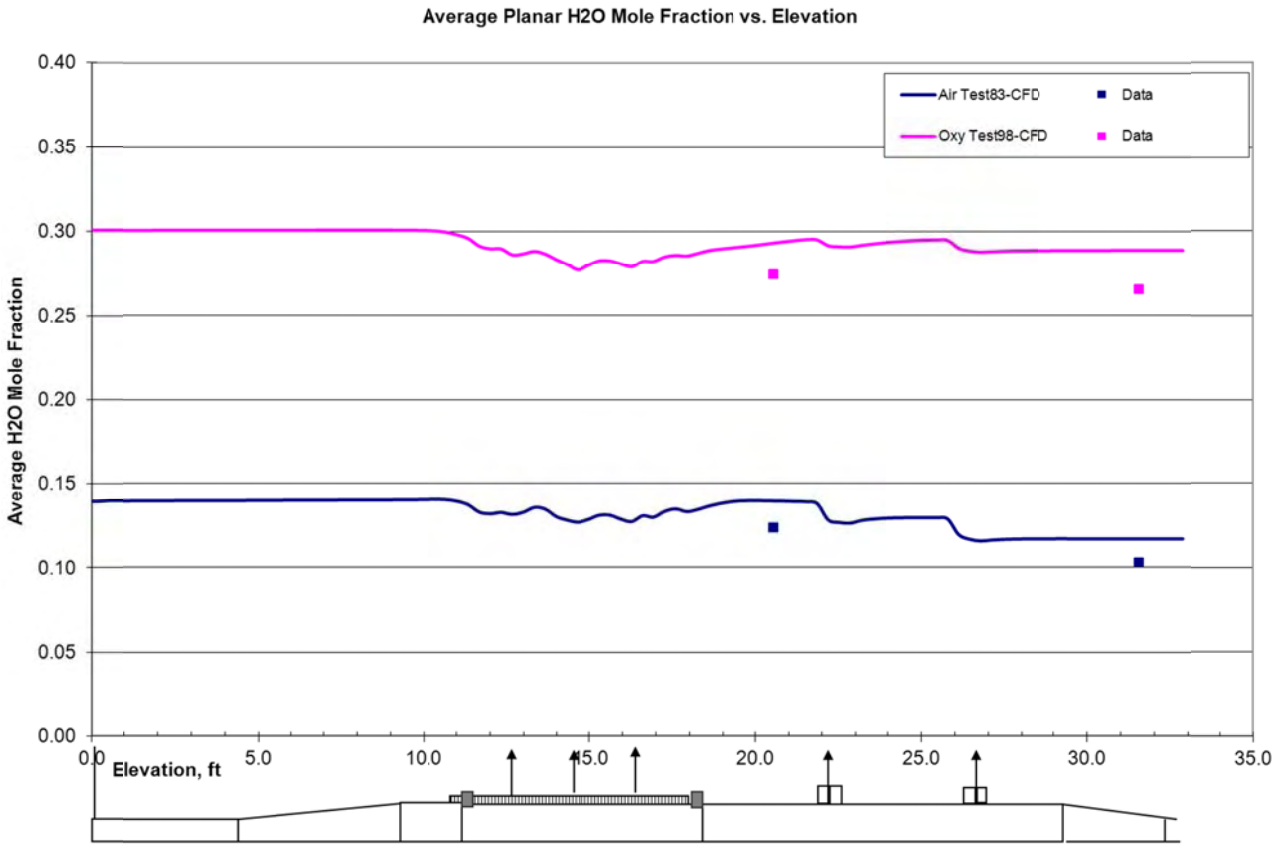

Figure 6-96. [AT-83:OT-98] Planar Averaged H_2O

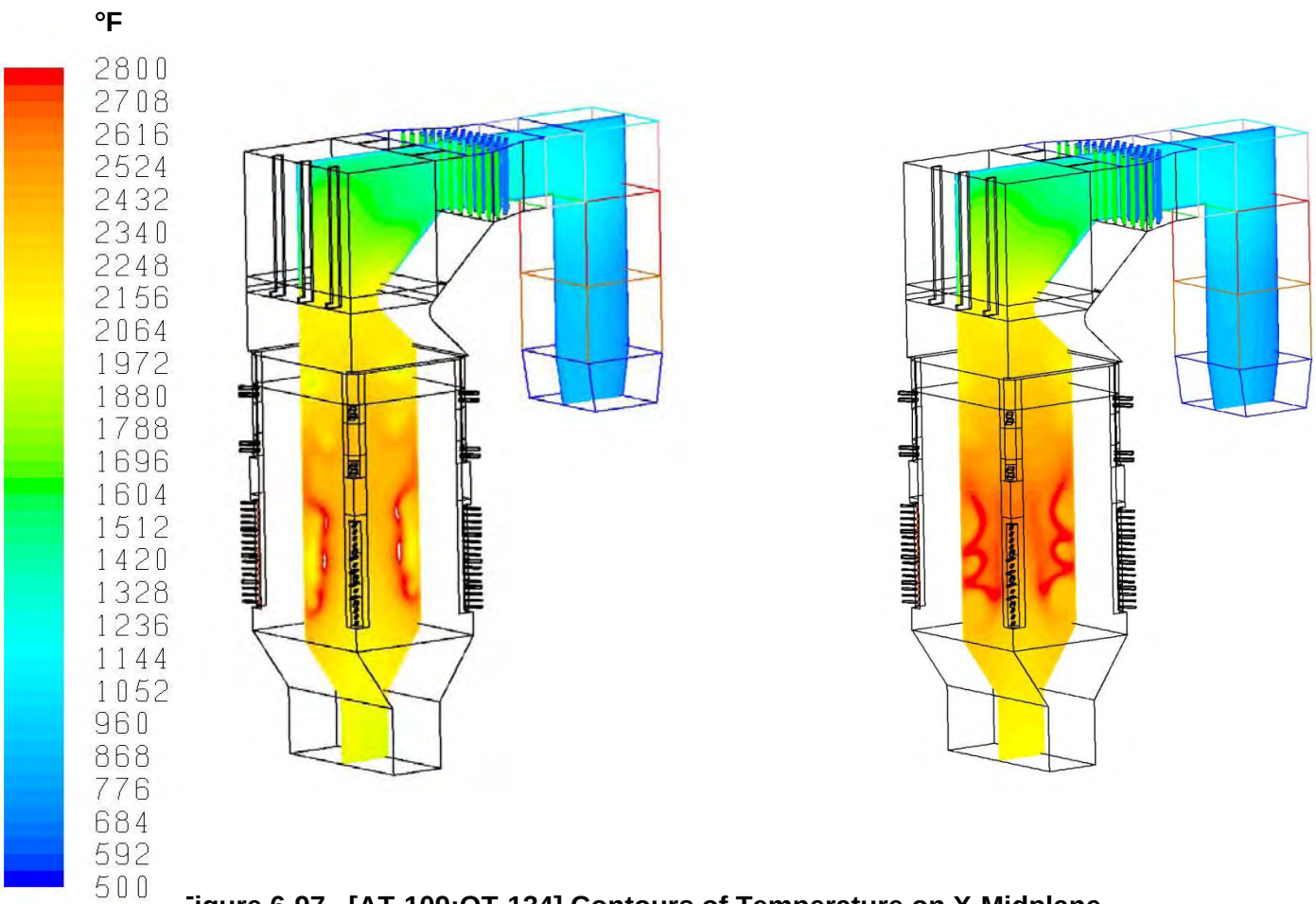

Figure 6-97. [AT-109:OT-134] Contours of Temperature on X-Midplane

AIR Test 109 *OXY Test 134*

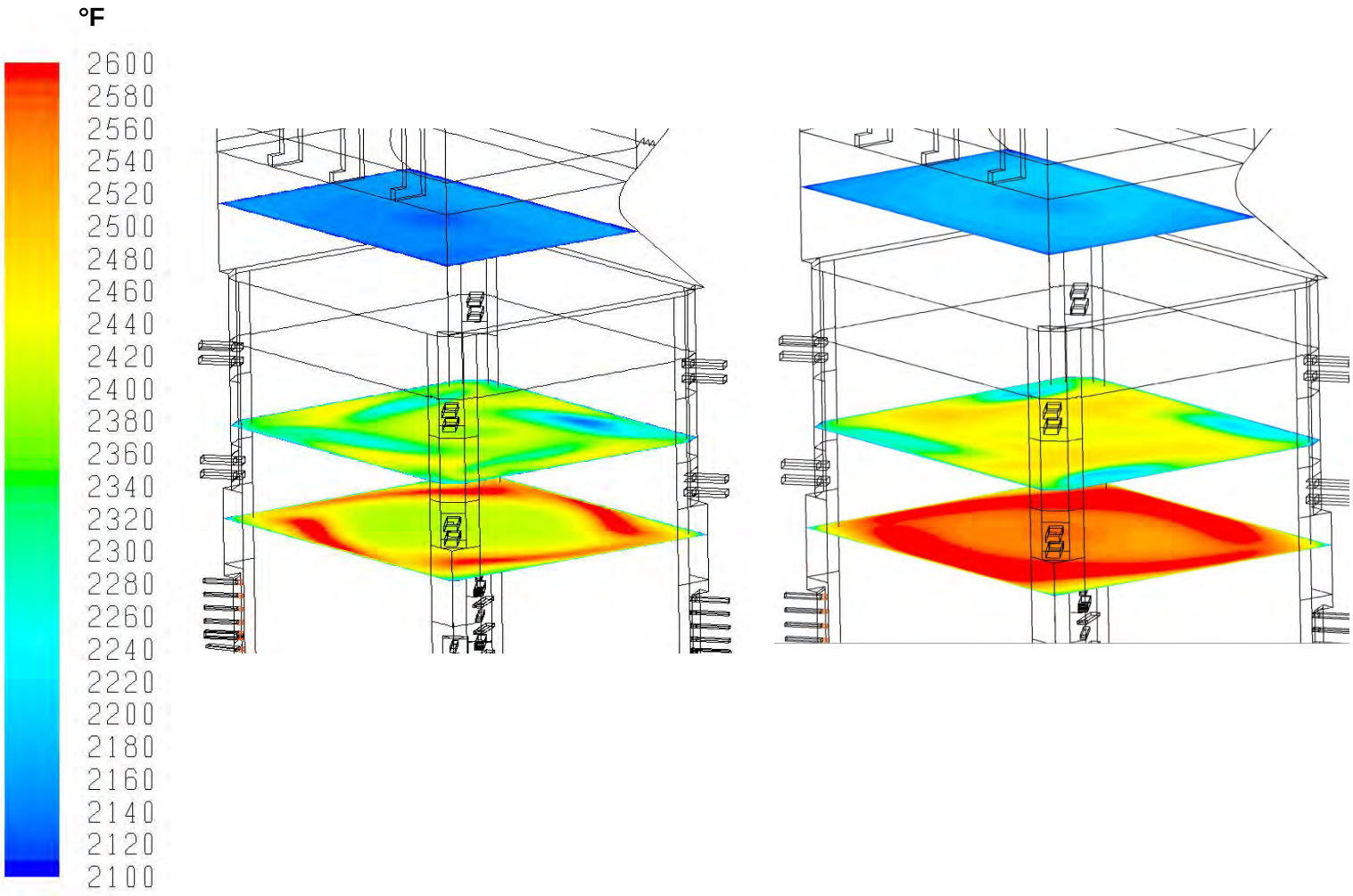

Figure 6-98. [AT-109:OT-134] Contours of Temperature on Test Planes

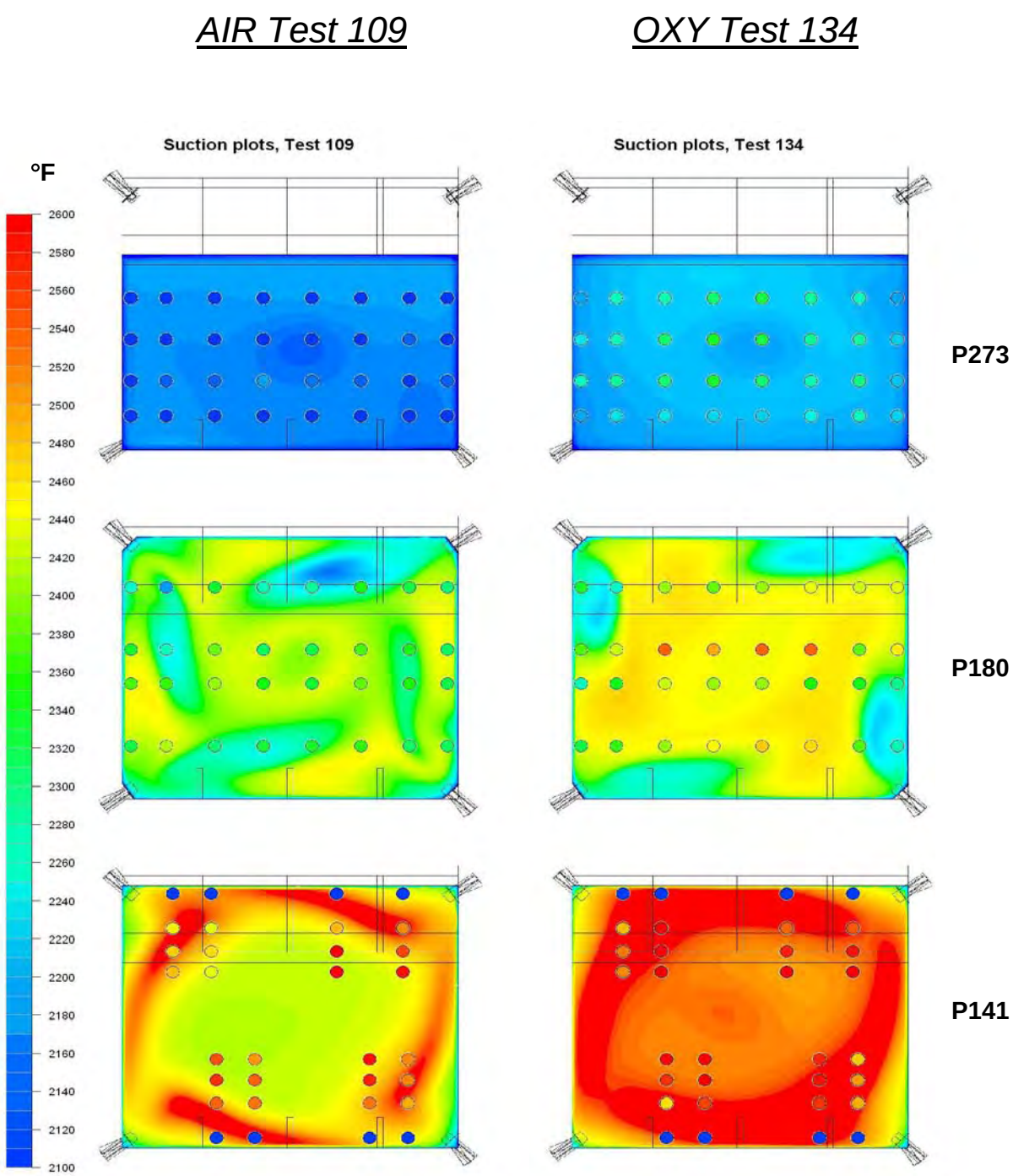

Figure 6-99. [AT-109:OT-134] Comparison of Temperature on Test Planes

AIR Test 109 *OXY Test 134*

Mole % (Dry)

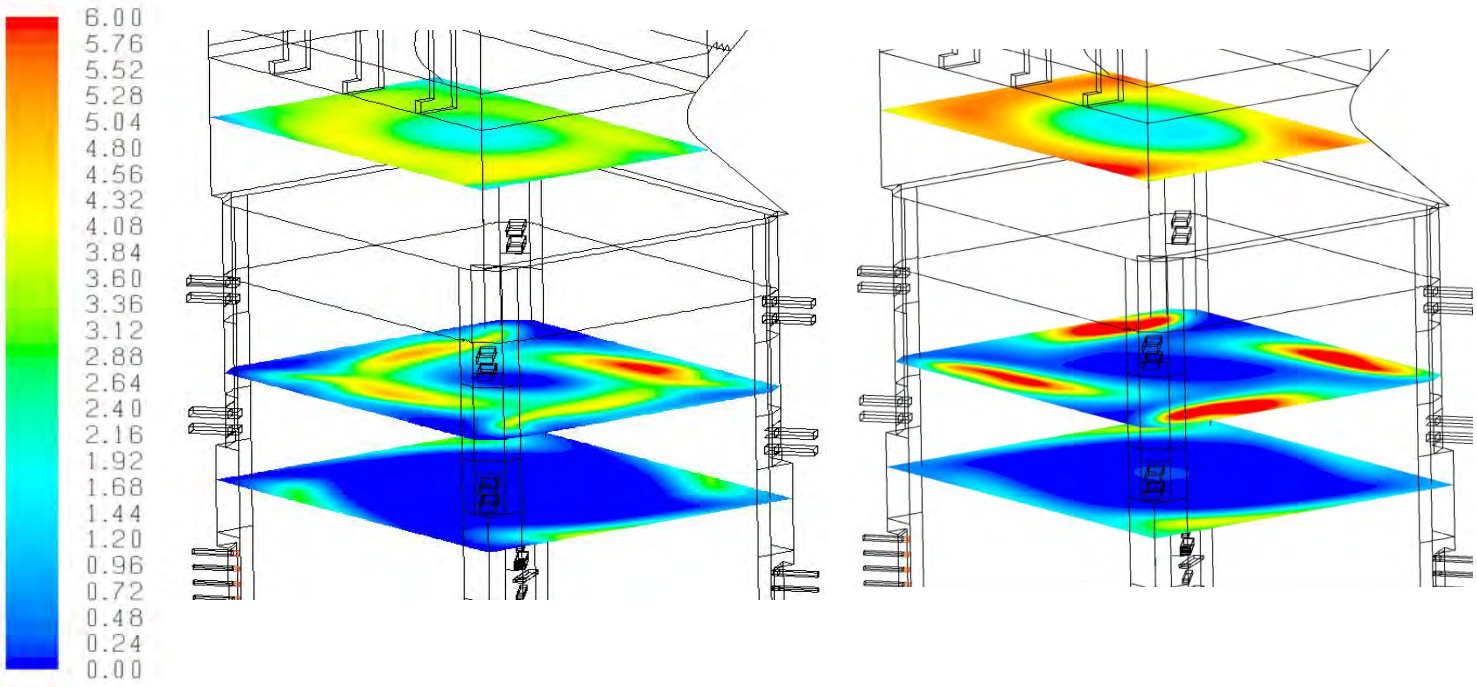

Figure 6-100. [AT-109:OT-134] Contours of O_2 Concentrations on Test Planes

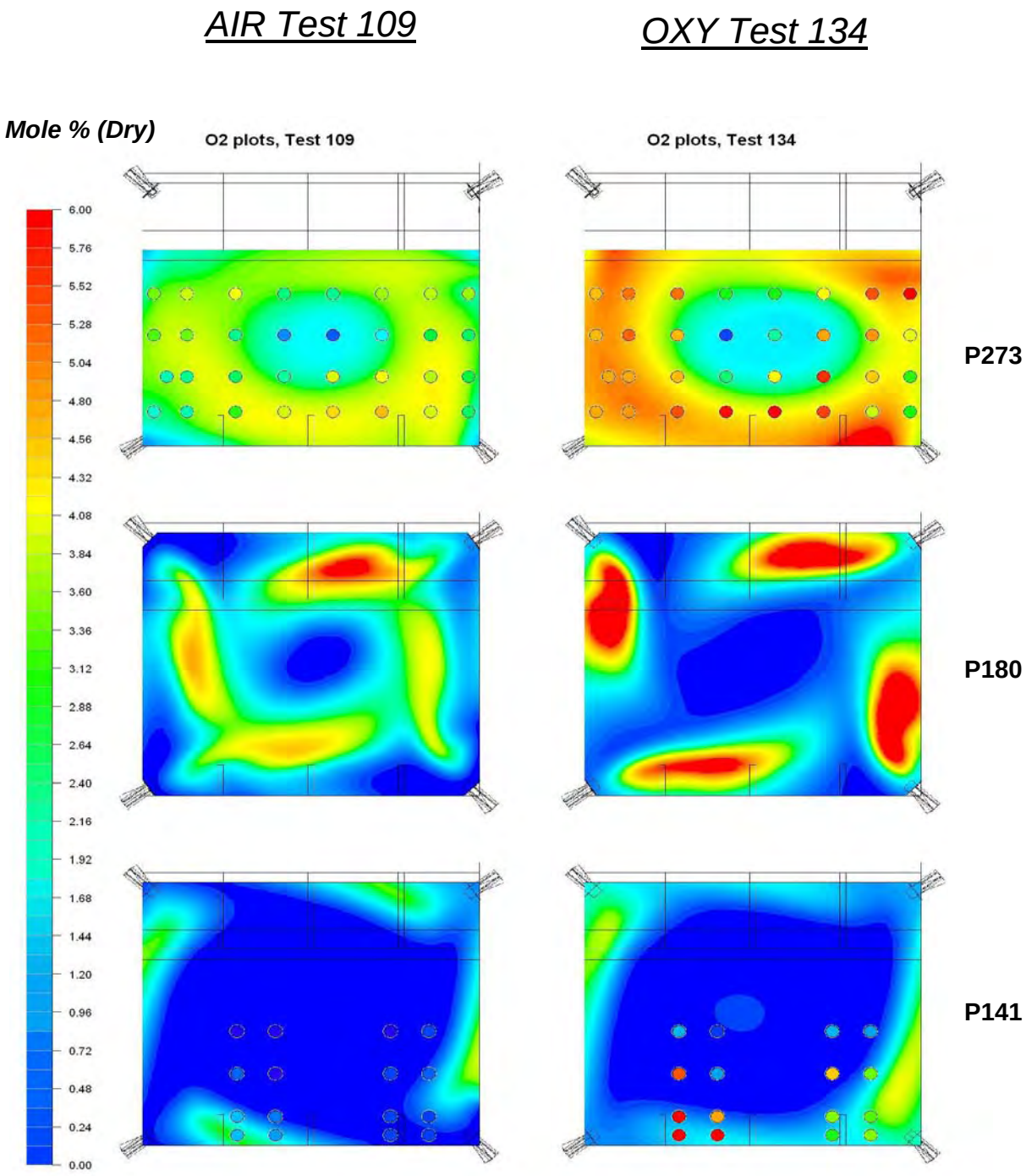

Figure 6-101. [AT-109:OT-134] Comparison of O_2 Concentrations on Test Planes

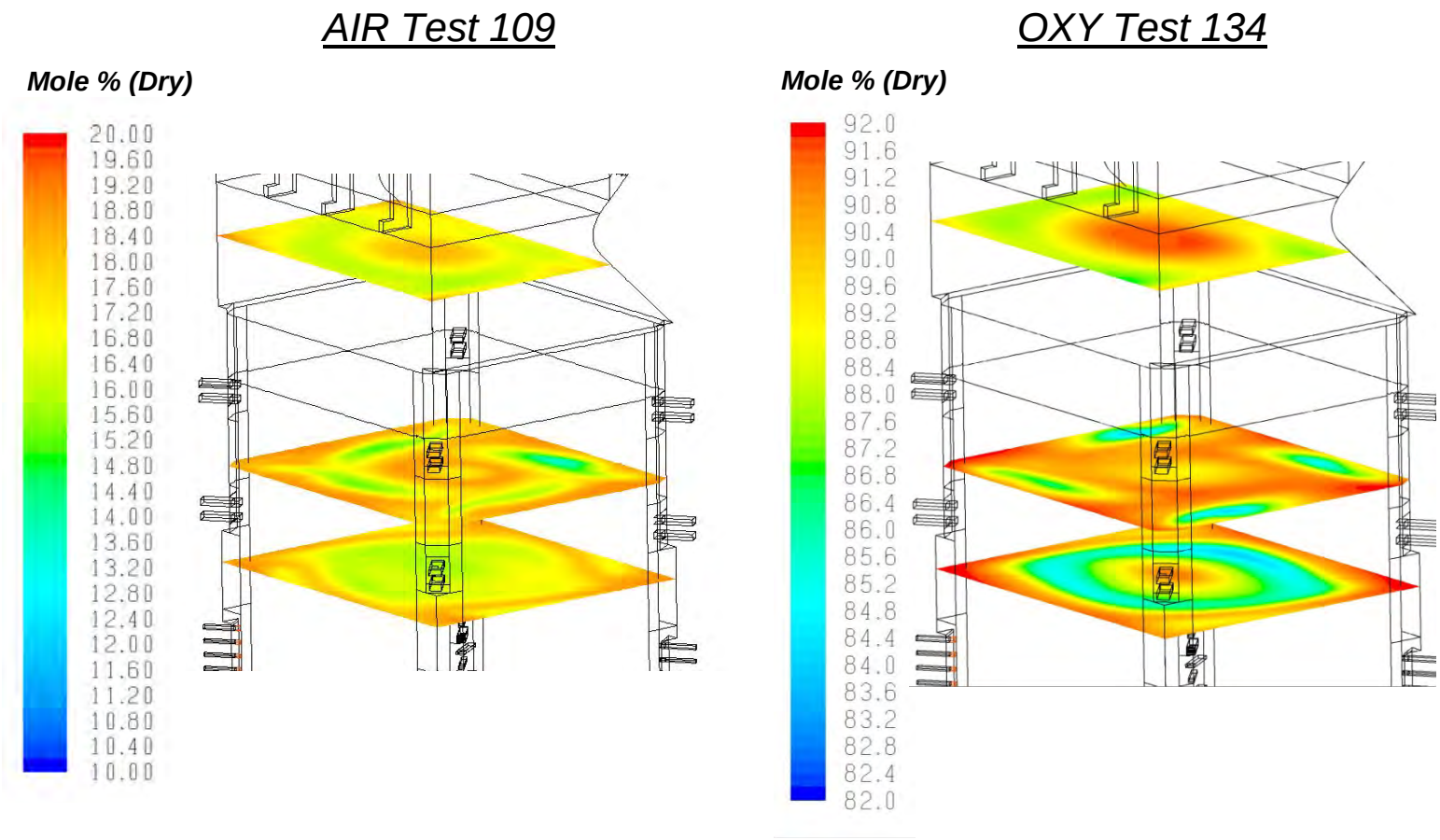

Figure 6-102. [AT-109:OT-134] Contours of CO_2 Concentrations on Test Planes

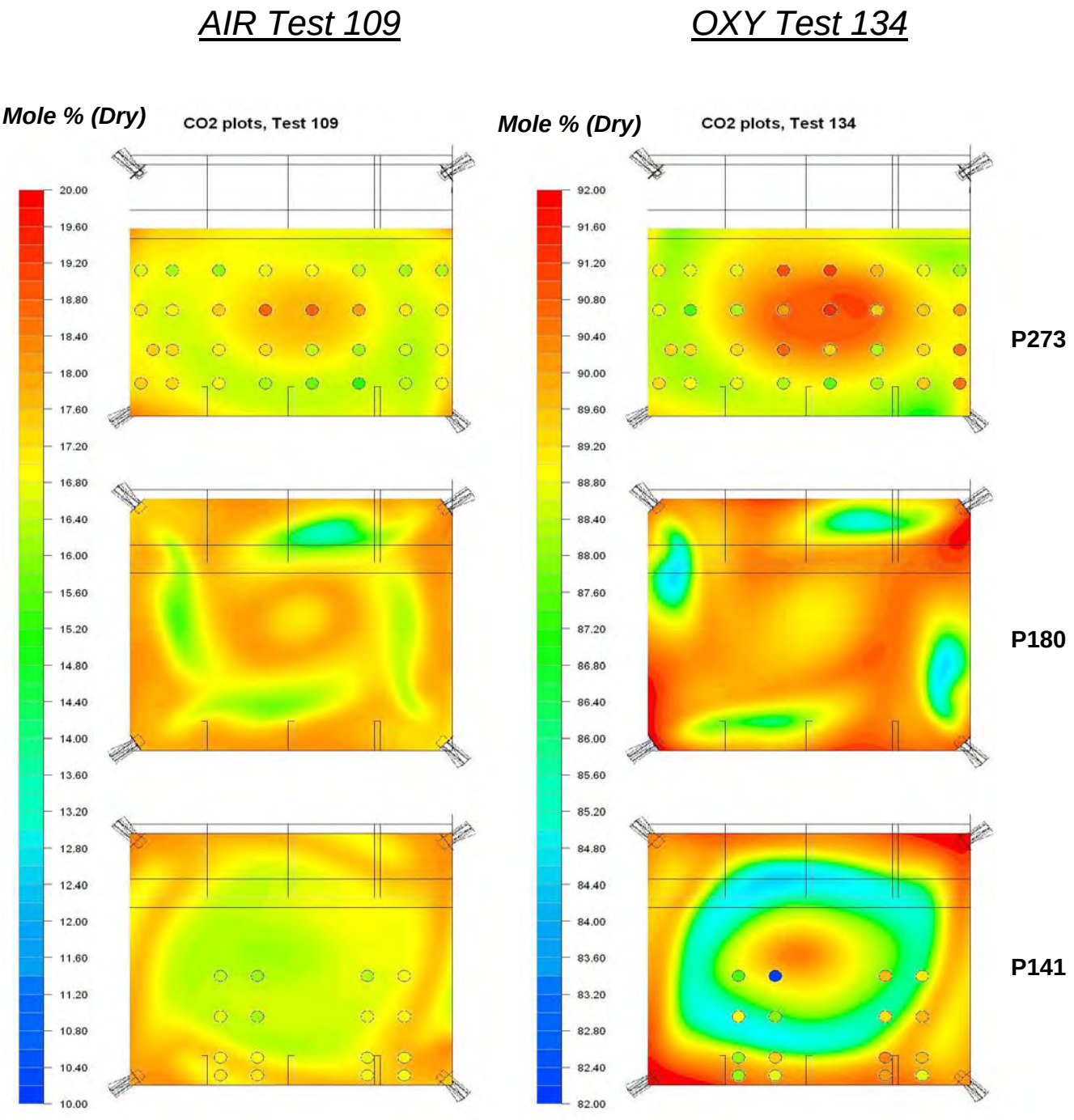

Figure 6-103. [AT-109:OT-134] Comparison of CO_2 Concentrations on Test Planes

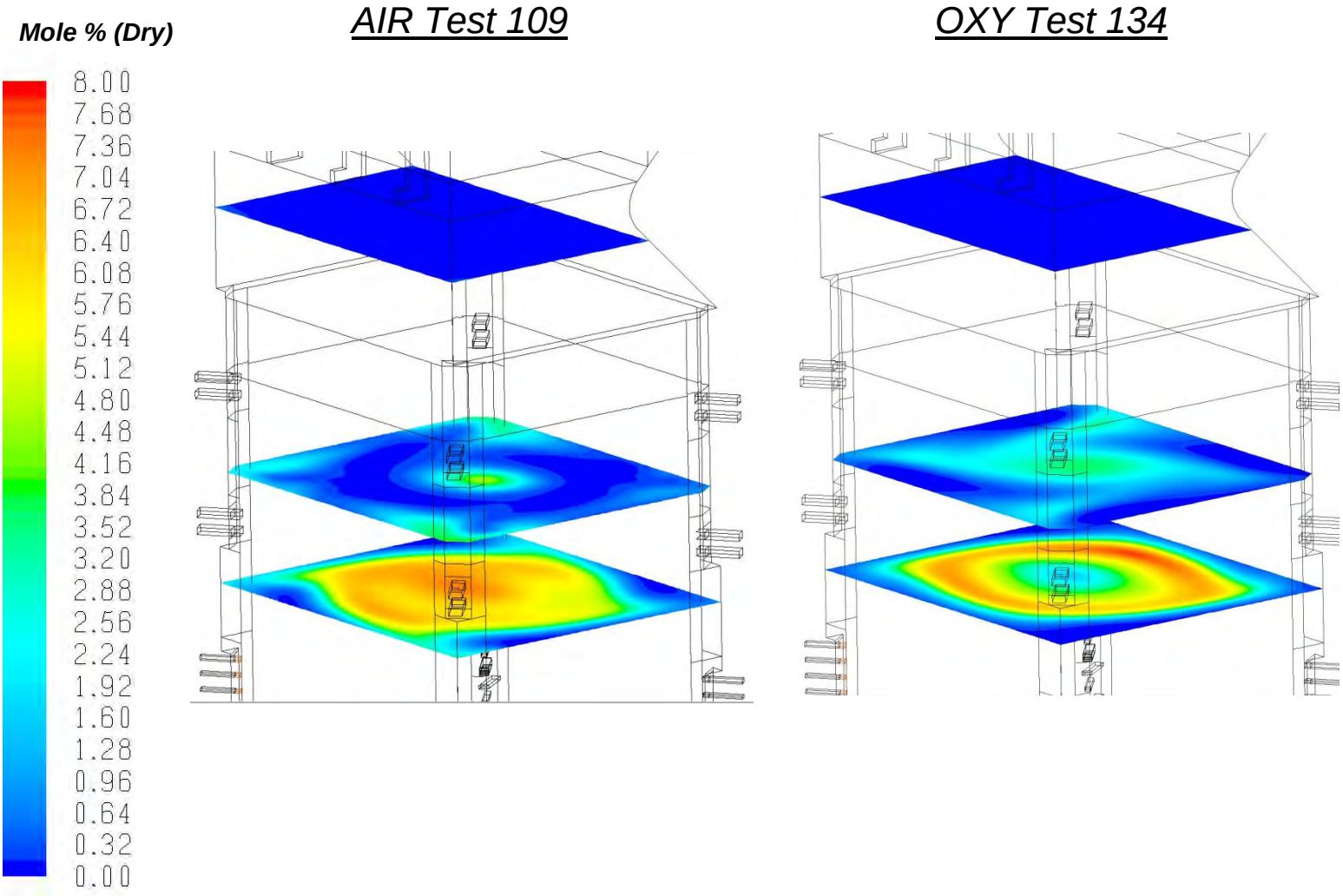

Figure 6-104. [AT-109:OT-134] Contours of CO Concentrations on Test Planes

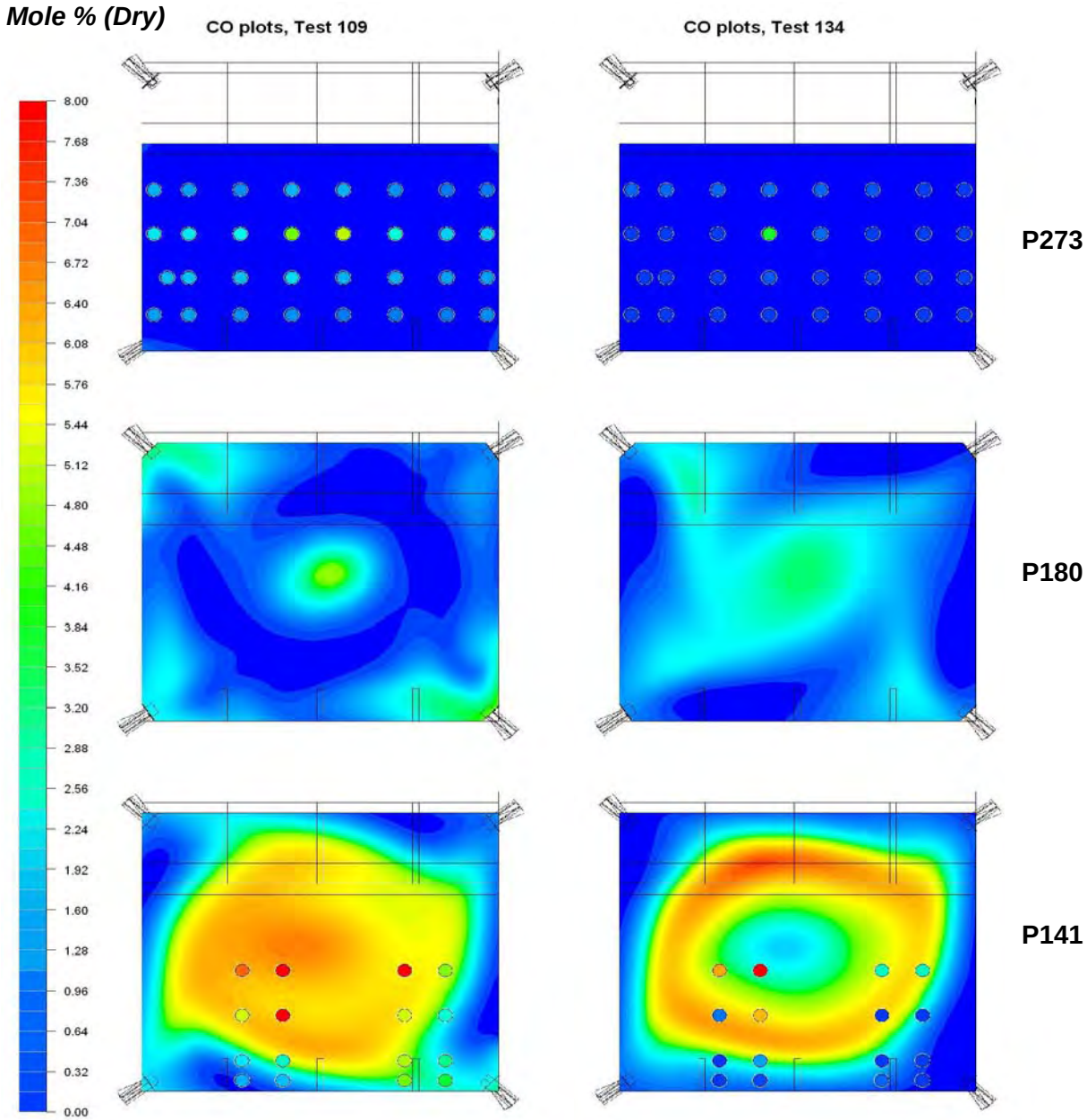

Figure 6-105. [AT-109:OT-134] Comparison of CO Concentrations on Test Planes

AIR Test 109

OXY Test 134

Mole % (Dry)

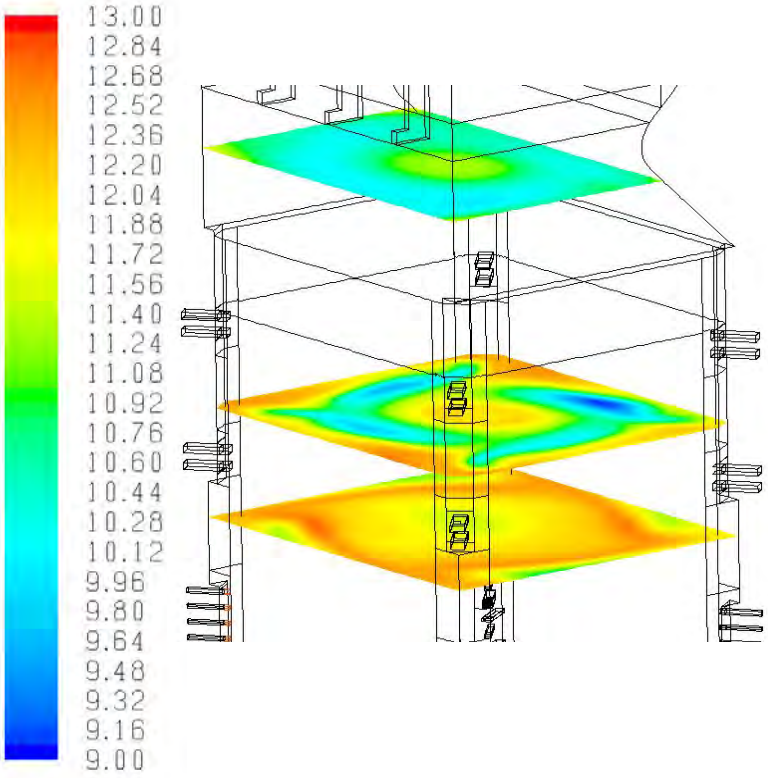

Mole % (Dry)

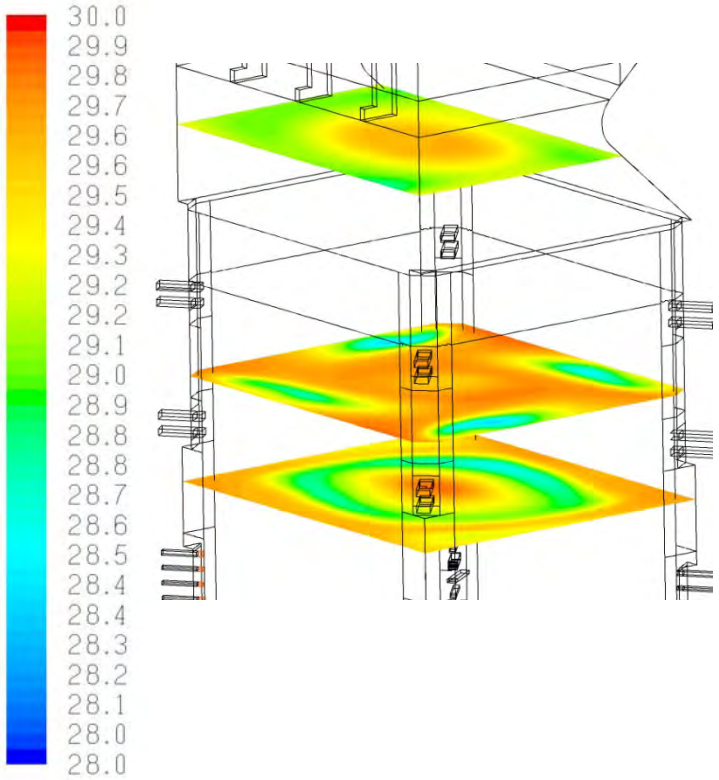

Figure 6-106. [AT-109:OT-134] Contours of H_2O Concentrations on Test Planes

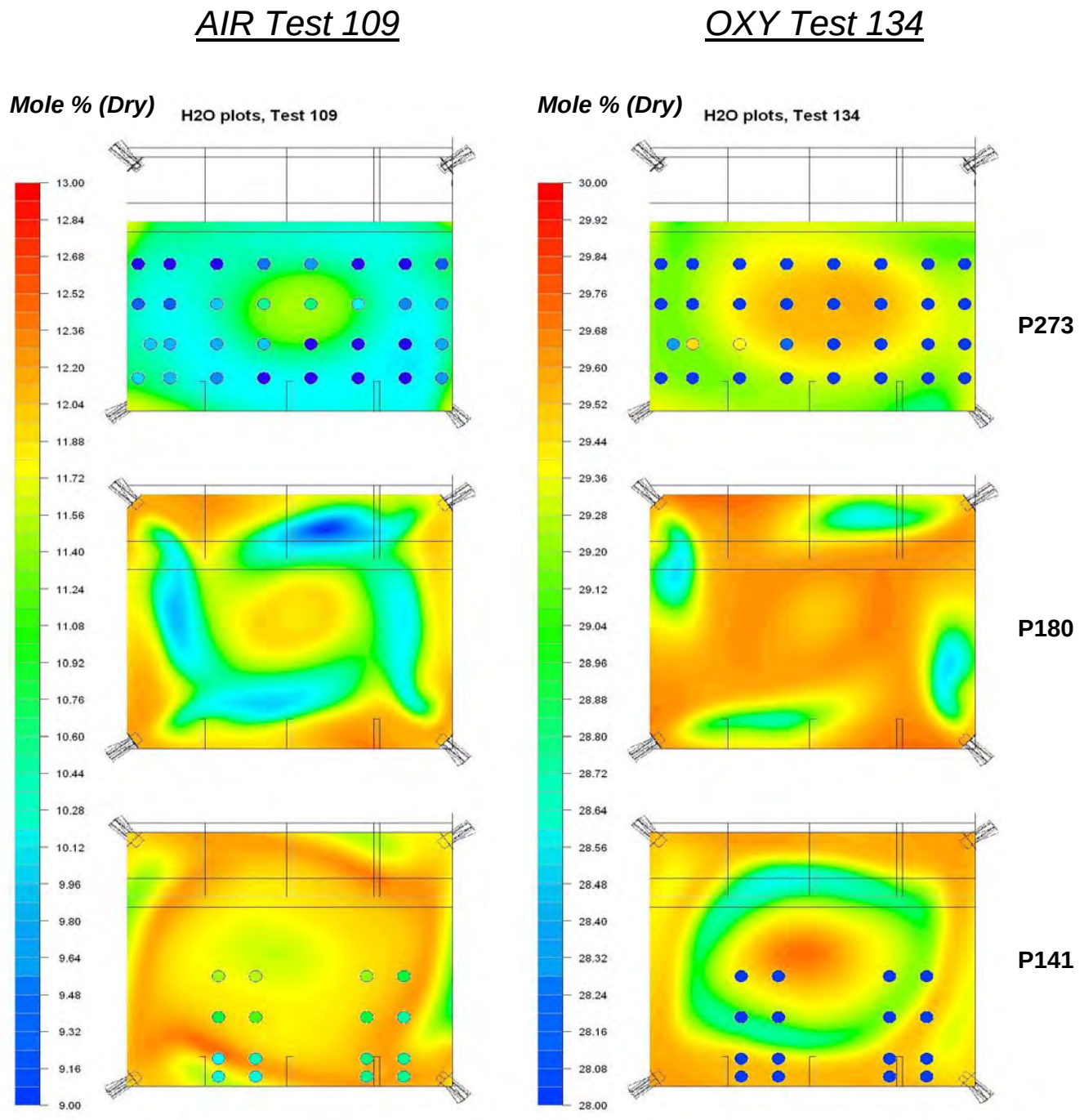

Figure 6-107. [AT-109:OT-134] Comparison of H_2O Concentrations on Test Planes

AIR Test 109 *OXY Test 134*

ppmv (Dry) **ppmv (Dry)**

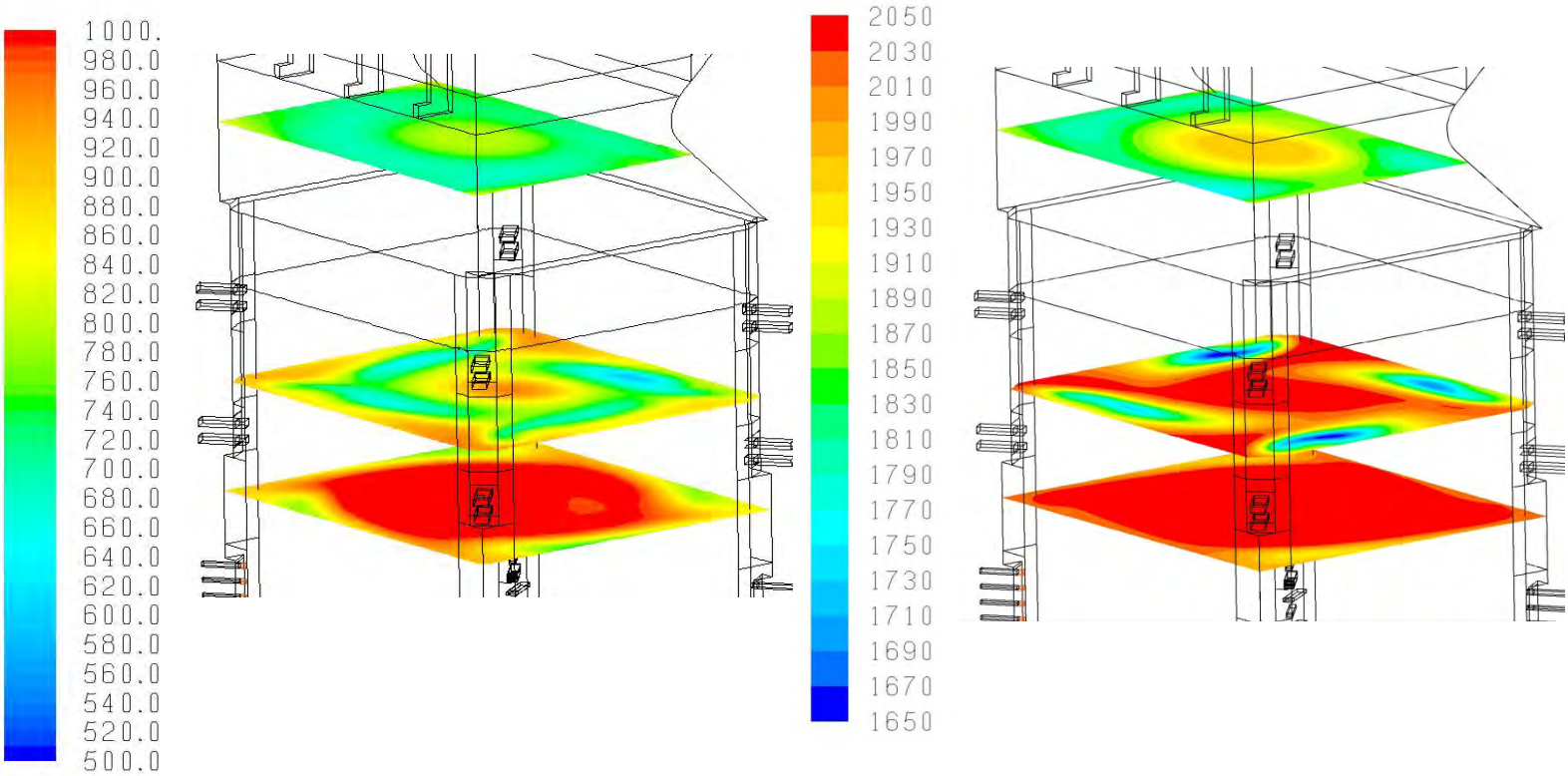

Figure 6-108. [AT-109:OT-134] Contours of SO_2 Concentrations on Test Planes

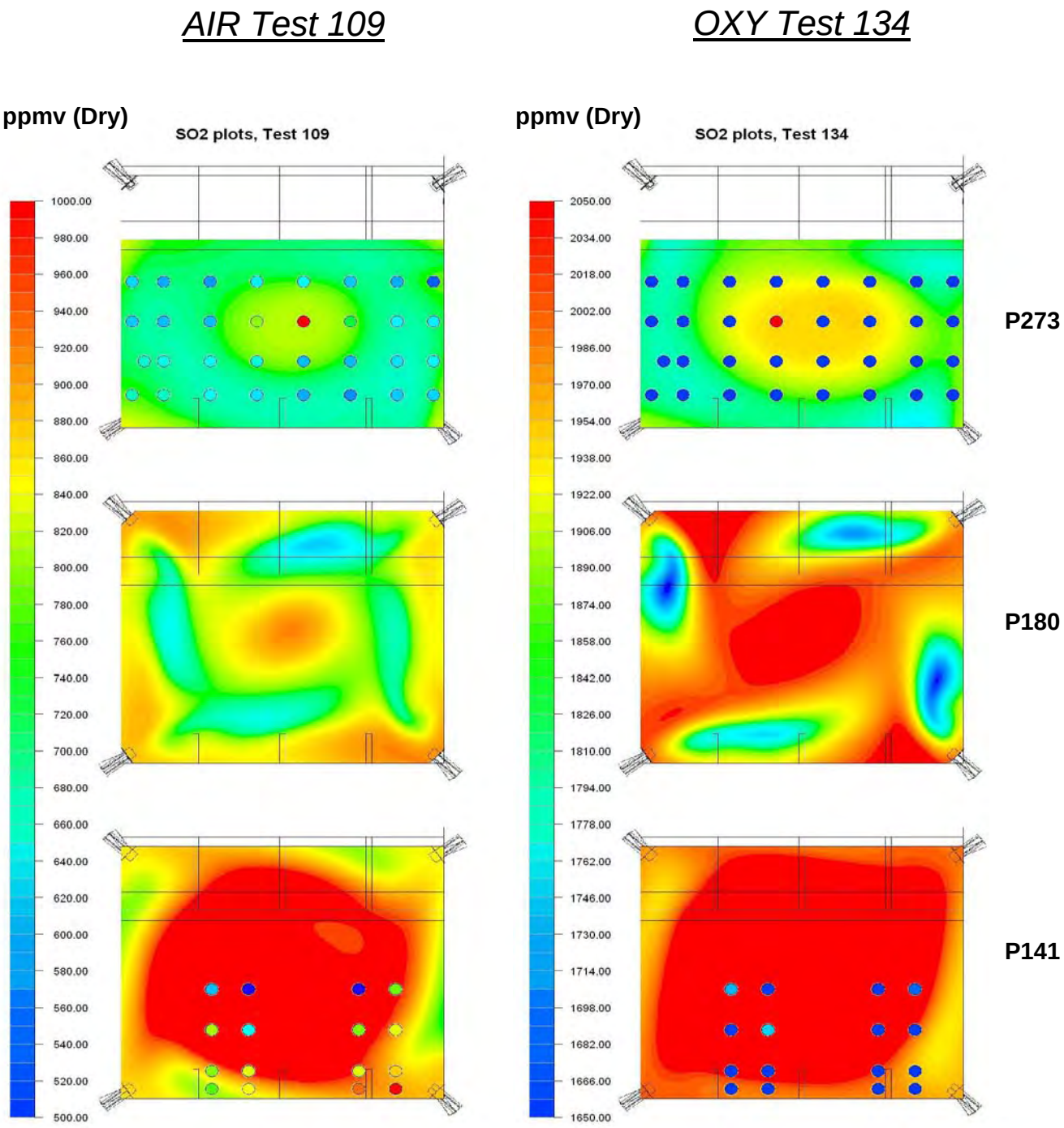

Figure 6-109. [AT-109:OT-134] Comparison of SO_2 Concentrations on Test Planes

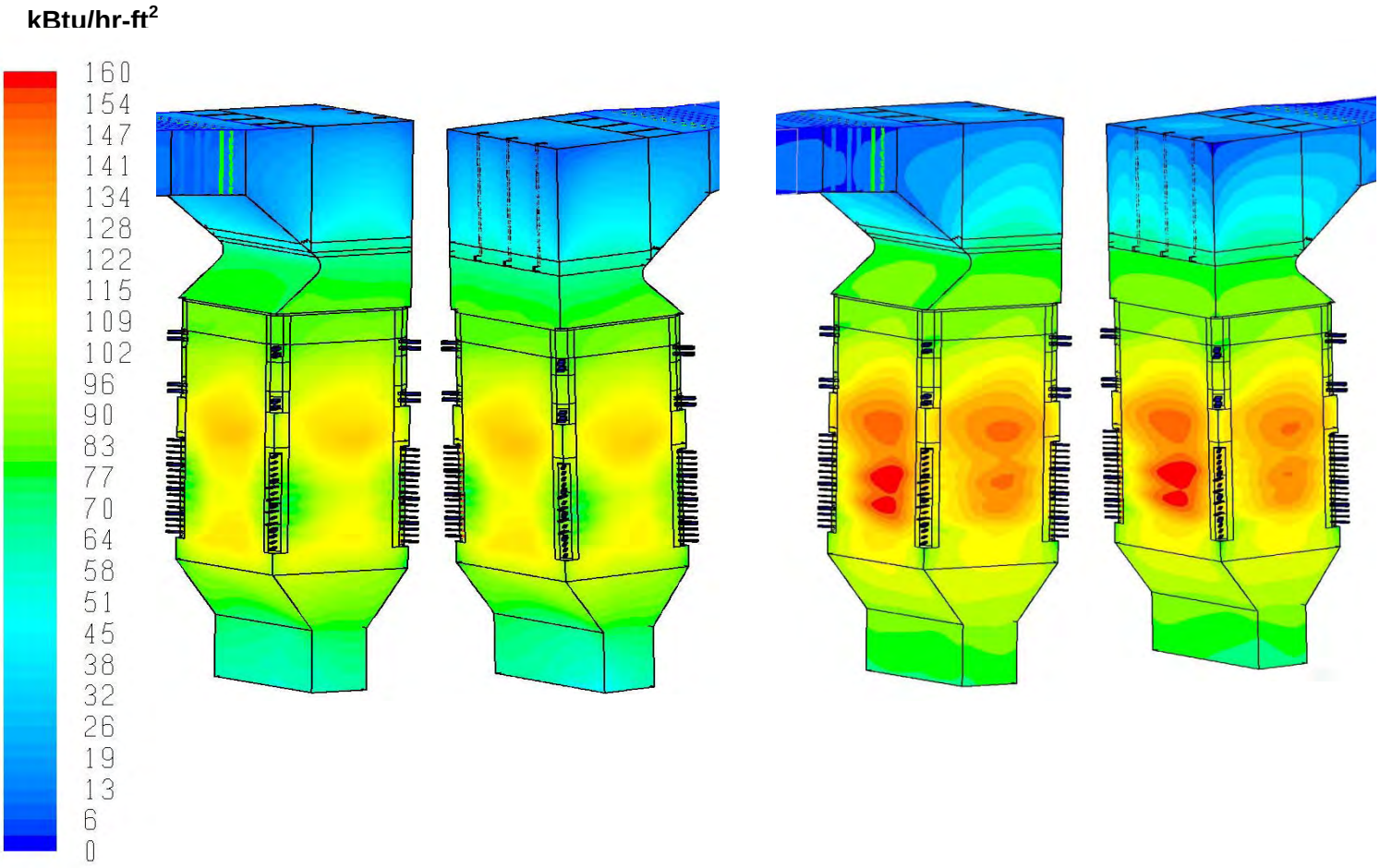

Figure 6-110. [AT-109:OT-134] Contours of Incident Radiation

AIR Test 109 *OXY Test 134*

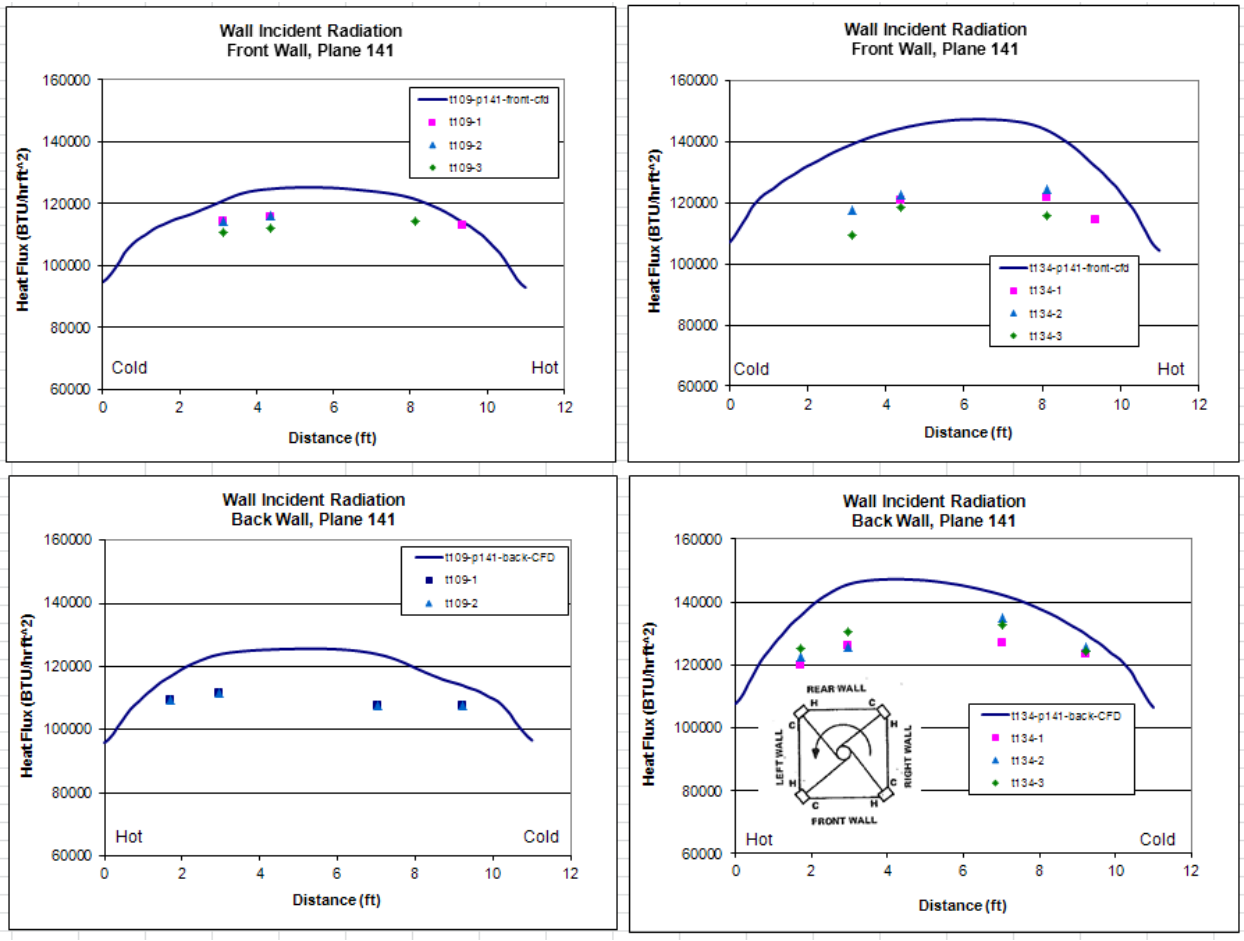

Figure 6-111. [AT-109:OT-134] Comparison of Wall Incident Radiation at Plane 141

AIR Test 109 *OXY Test 134*

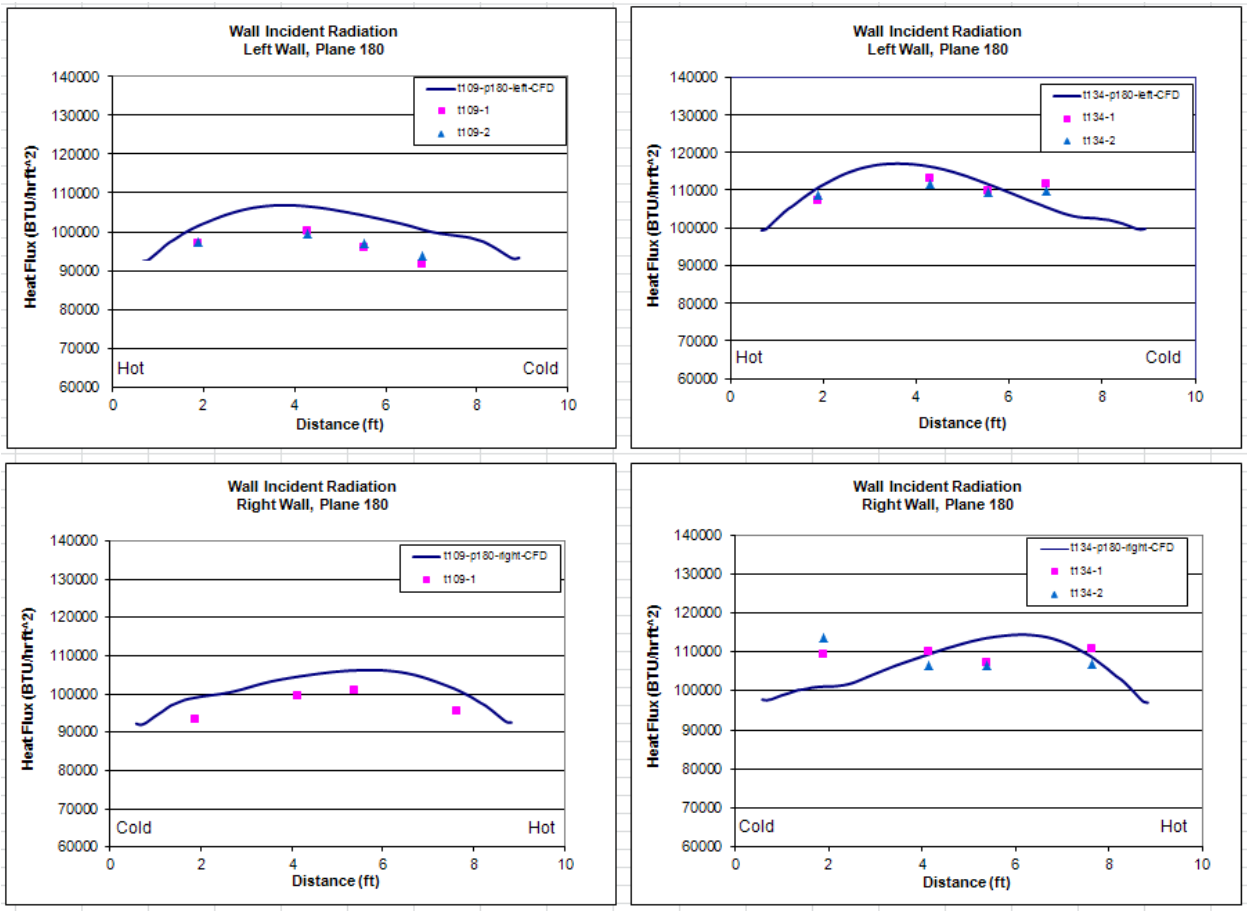

Figure 6-112. [AT-109:OT-134] Comparison of Wall Incident Radiation at Plane 180

AIR Test 109 *OXY Test 134*

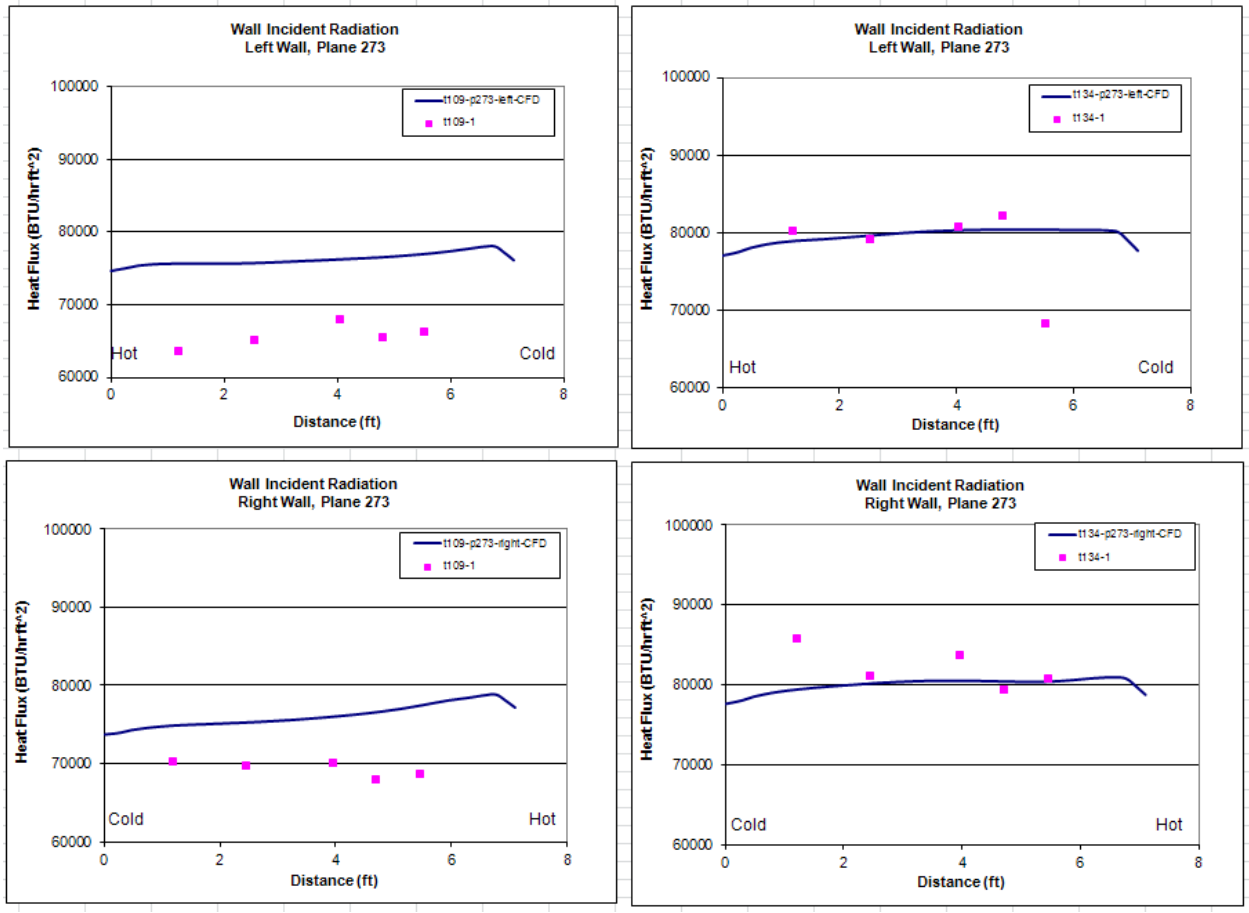

Figure 6-113. [AT-109:OT-134] Comparison of Wall Incident Radiation at Plane 273

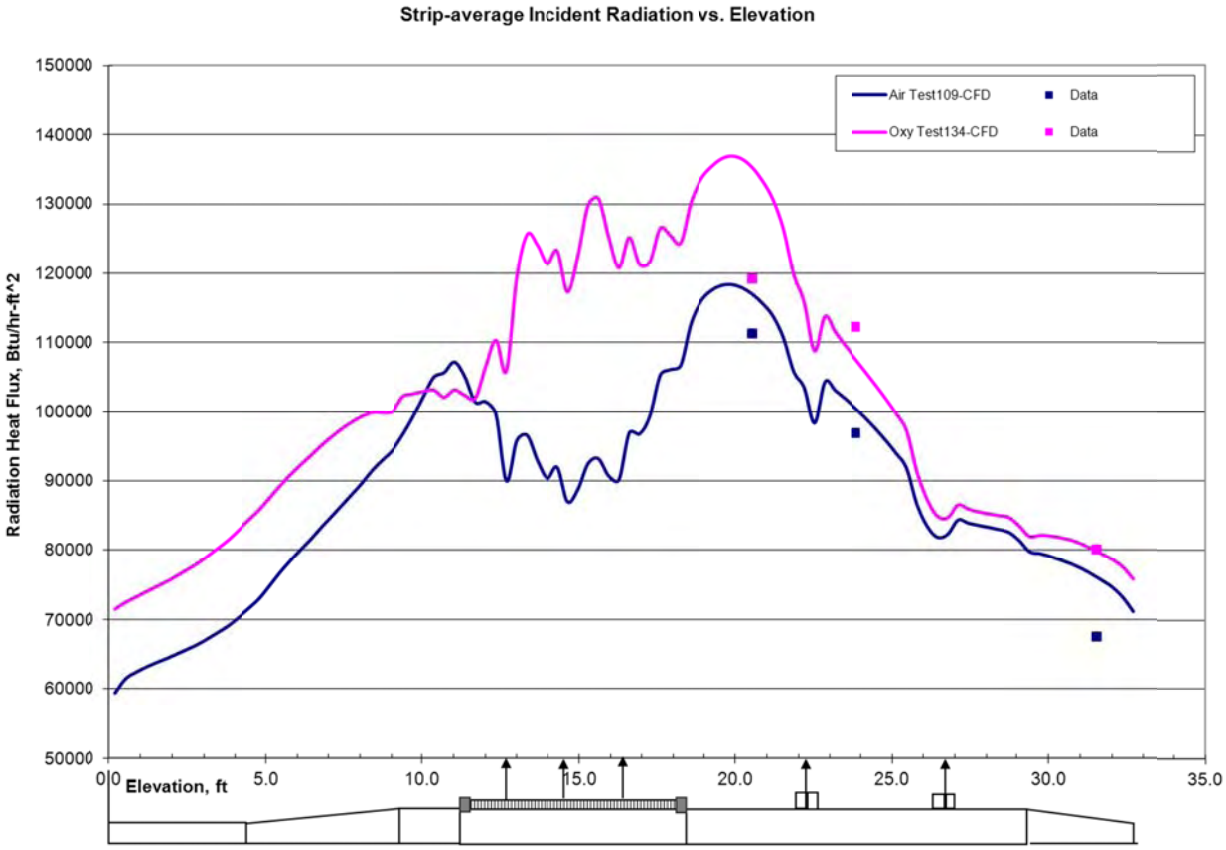

Figure 6-114. [AT-109:OT-134] Strip-Averaged Wall Incident Radiation

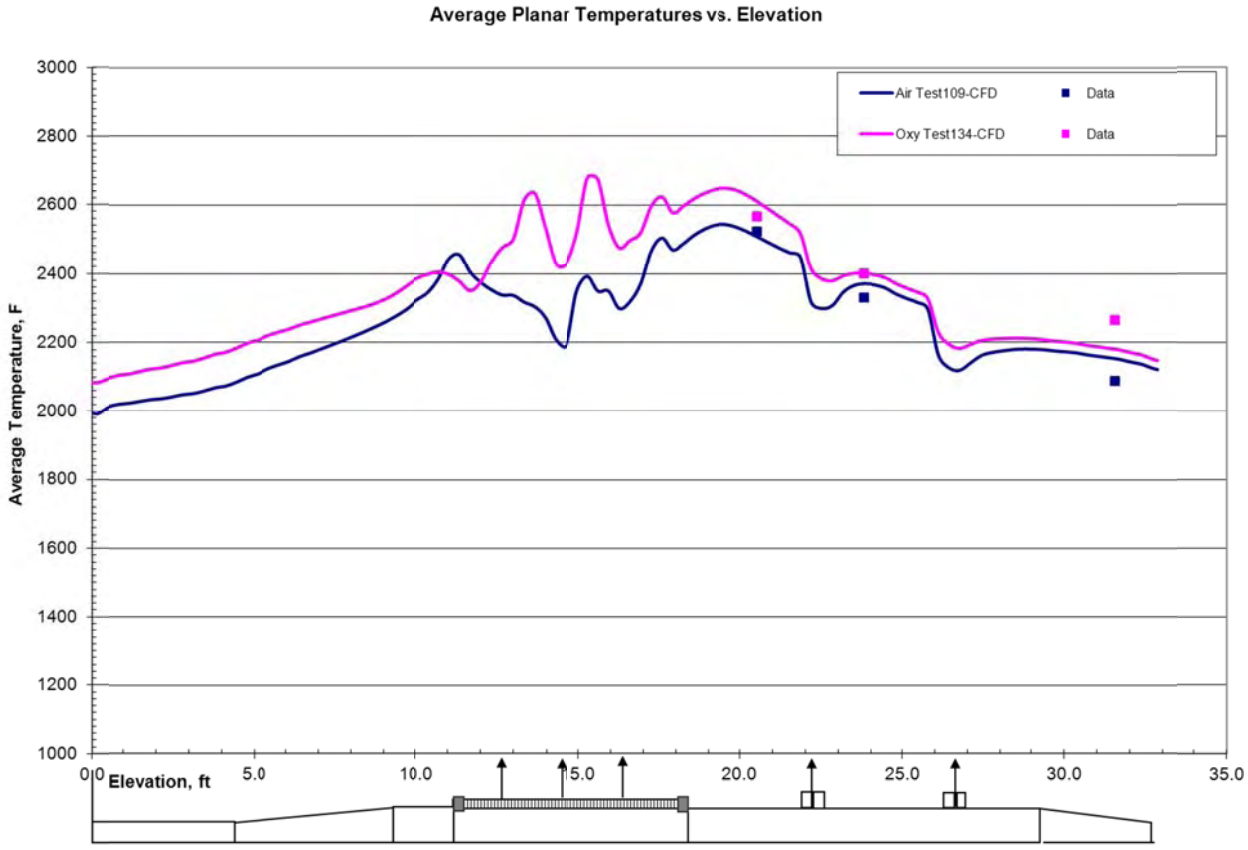

Figure 6-115. [AT-109:OT-134] Planar Averaged Temperature

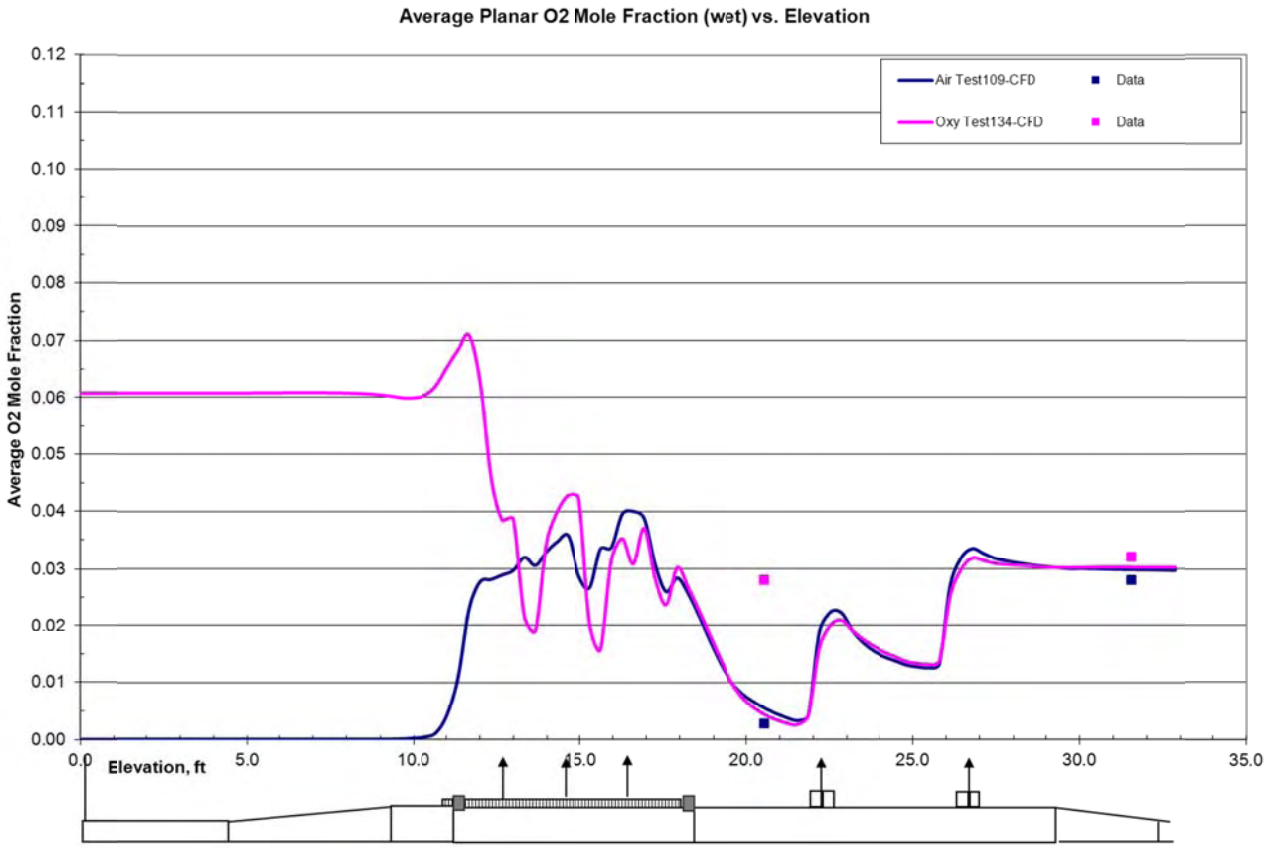

Figure 6-116. [AT-109:OT-134] Planar Averaged O_2

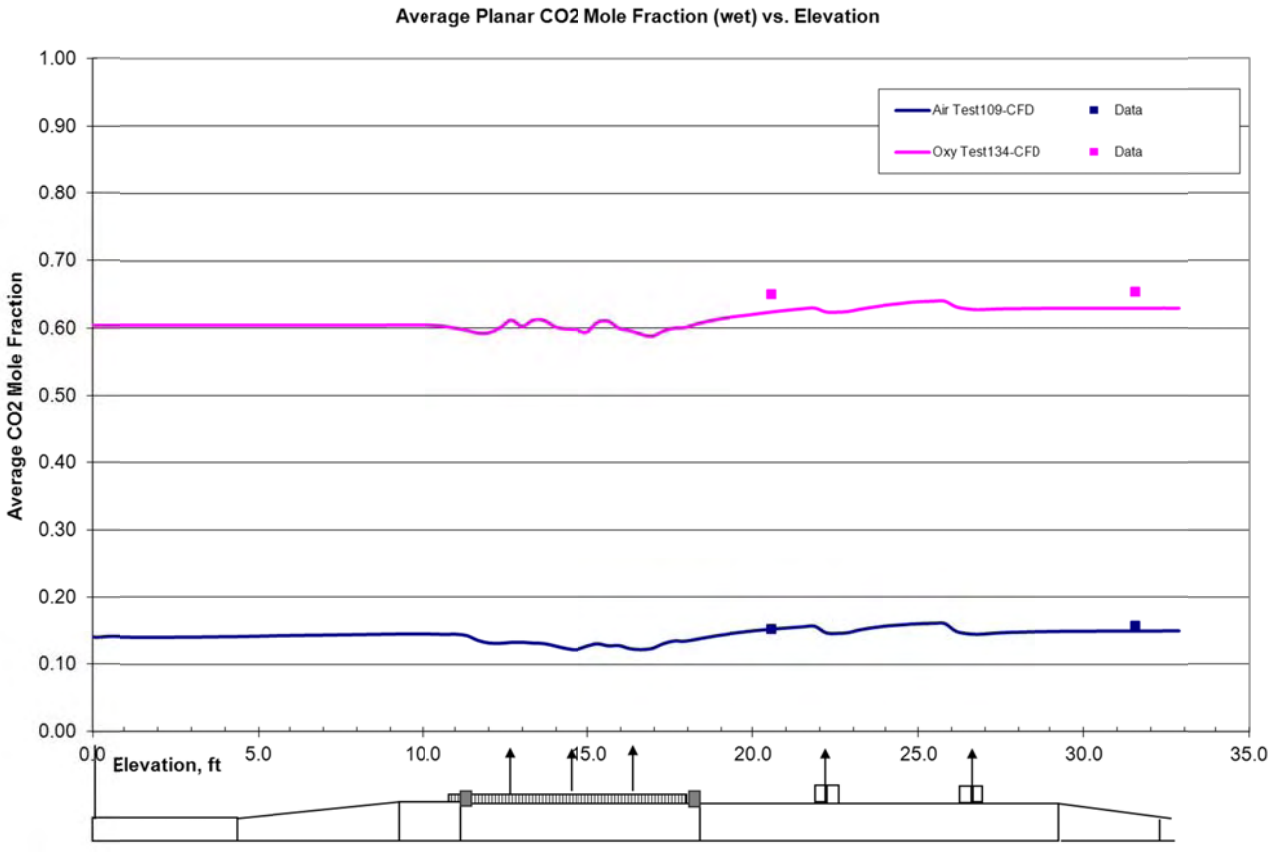

Figure 6-117. [AT-109:OT-134] Planar Averaged CO_2

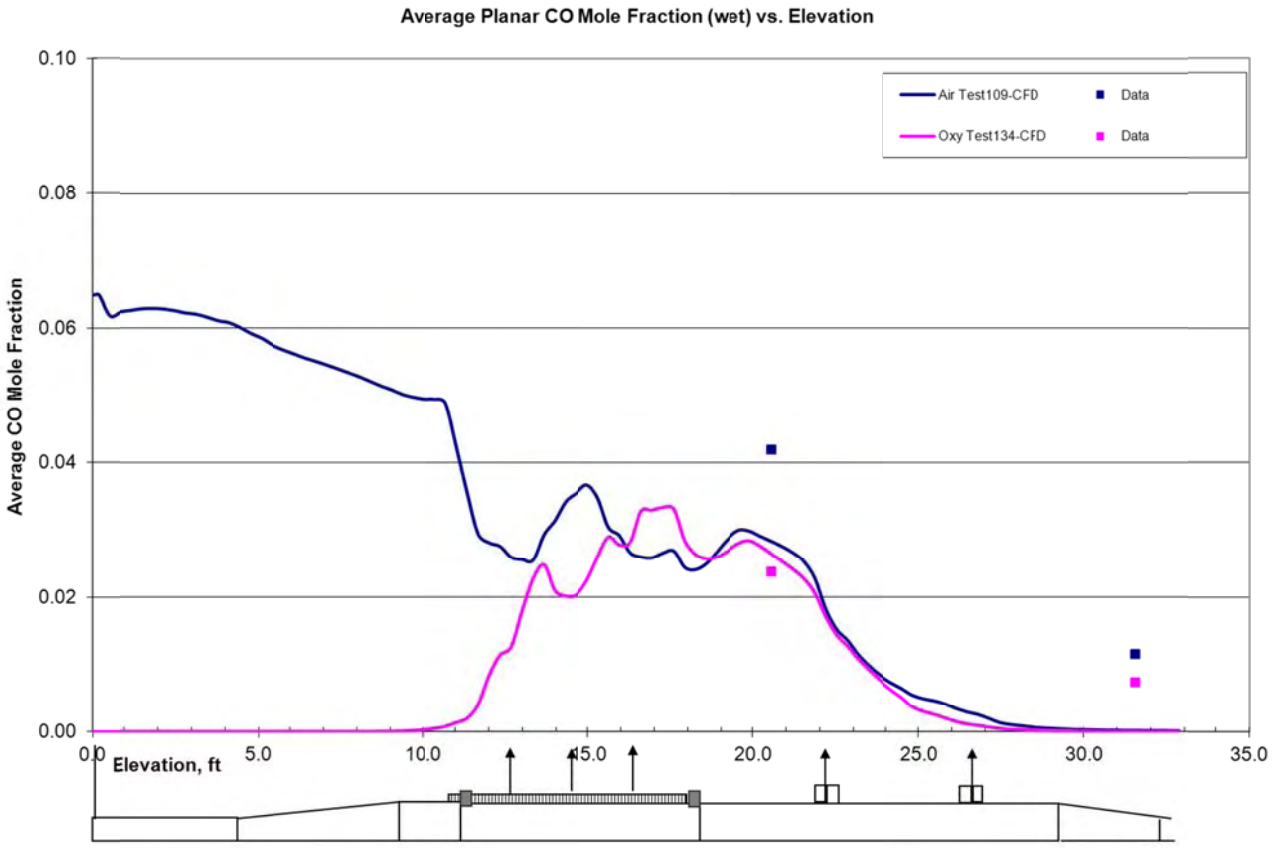

Figure 6-118. [AT-109:OT-134] Planar Averaged CO

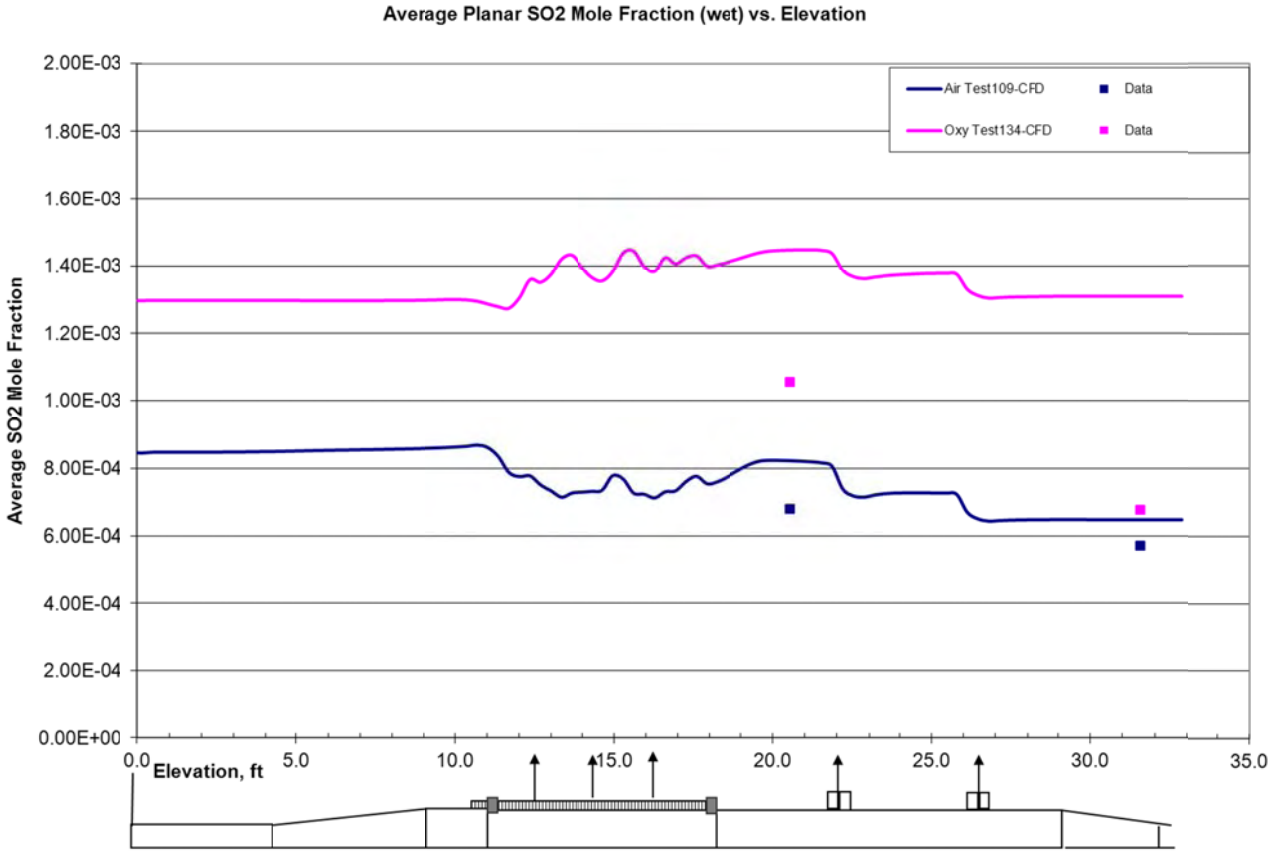

Figure 6-119. [AT-109:OT-134] Planar Averaged SO_2

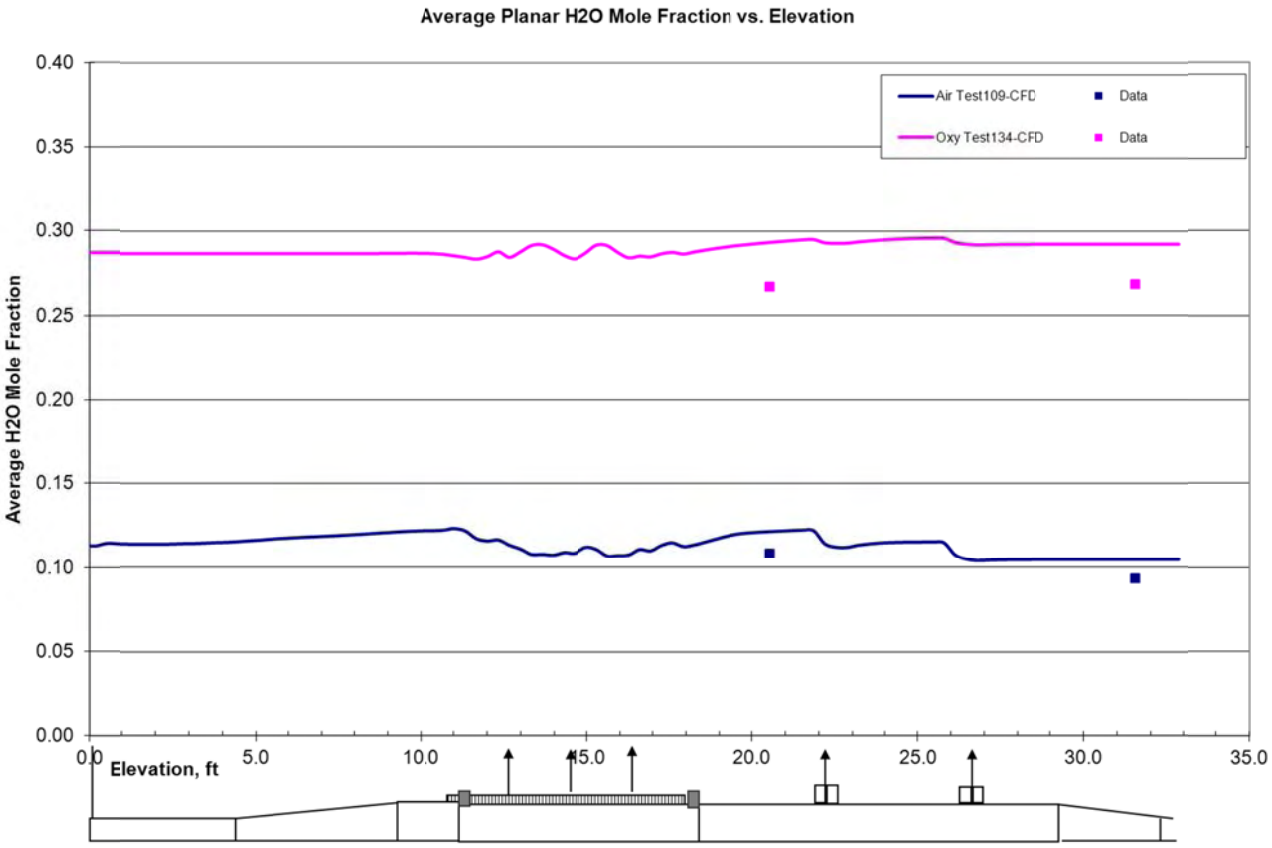

Figure 6-120. [AT-109:OT-134] Planar Averaged H_2O

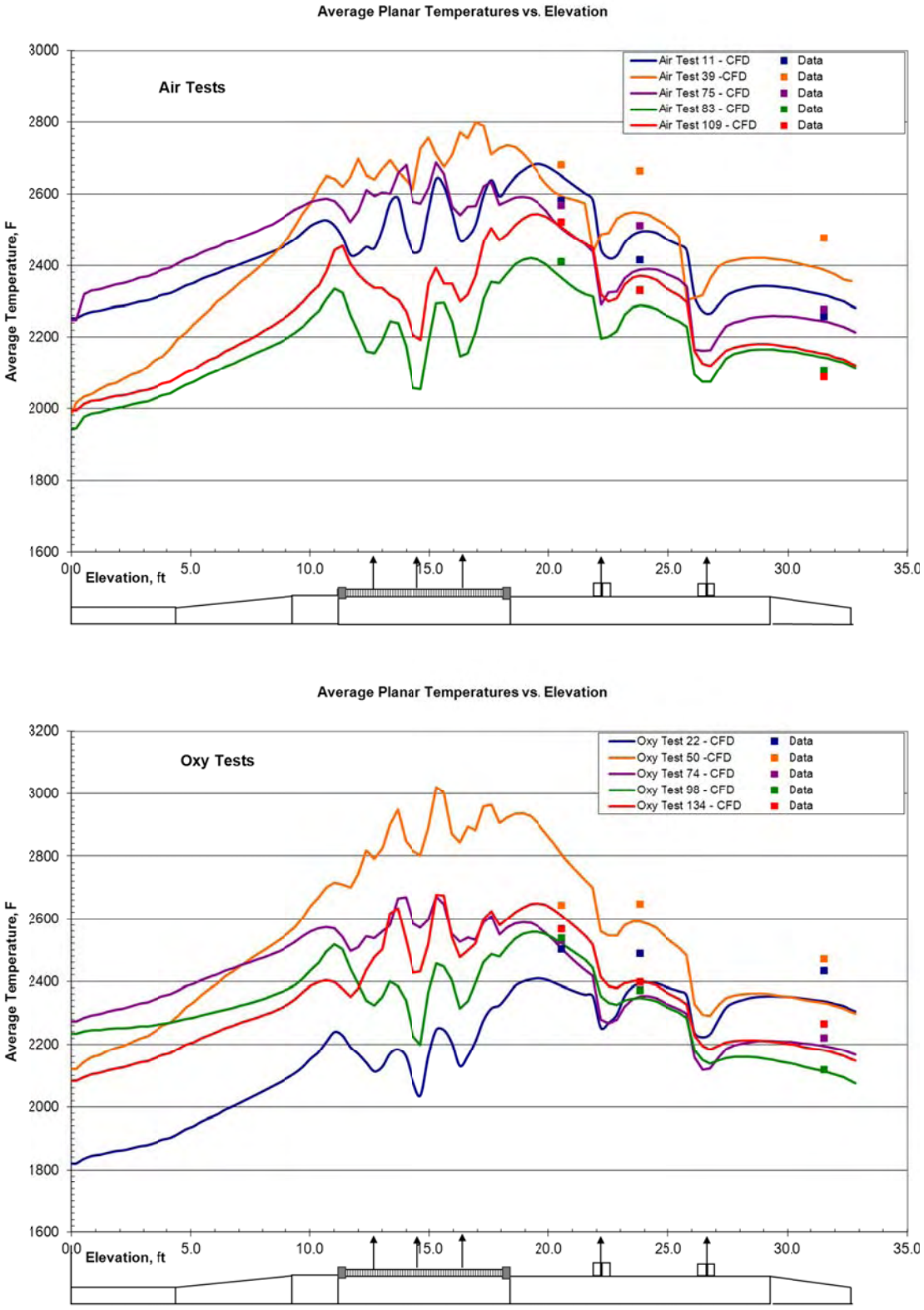

Figure 6-121. Comparison of Planar Averaged Temperature for 5 Coal Tests (Line Plots)

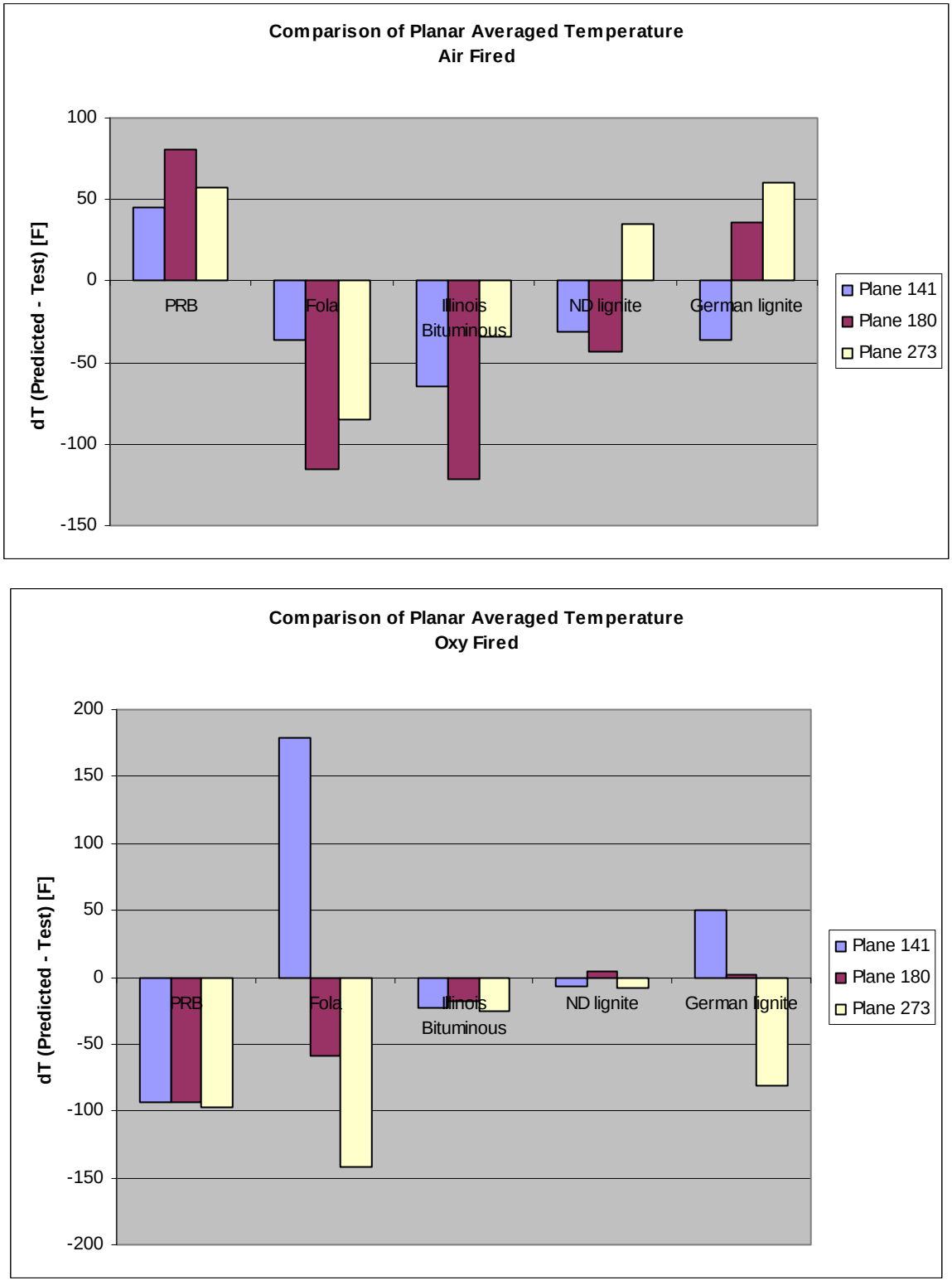

Figure 6-122. Comparison of Planar Averaged Temperature for 5 Coal Tests (Bar Charts)

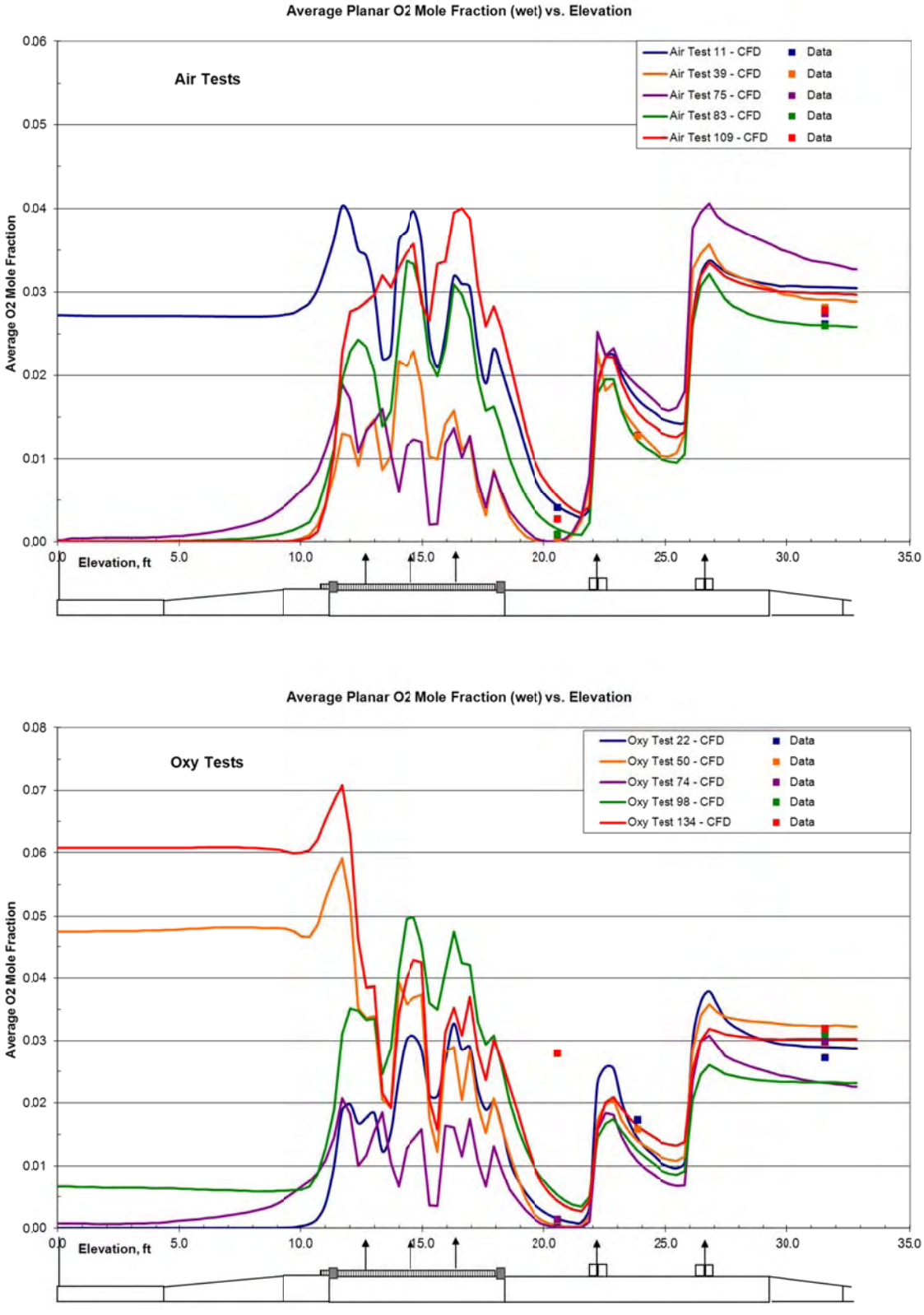

Figure 6-123. Comparison of Planar Averaged Oxygen for 5 Coal Tests (Line Plots)

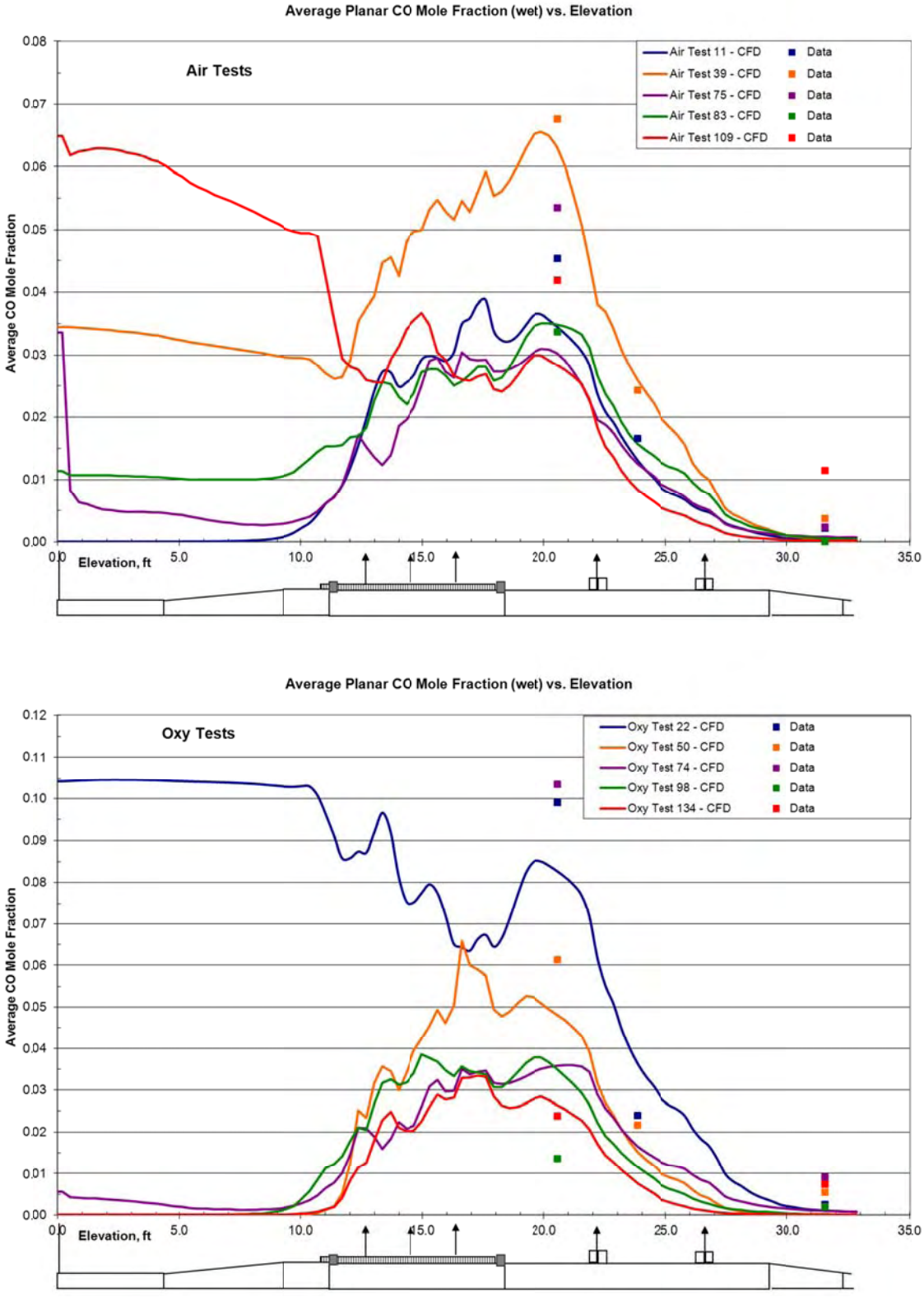

Figure 6-124. Comparison of Planar Averaged CO for 5 Coal Tests (Line Plots)

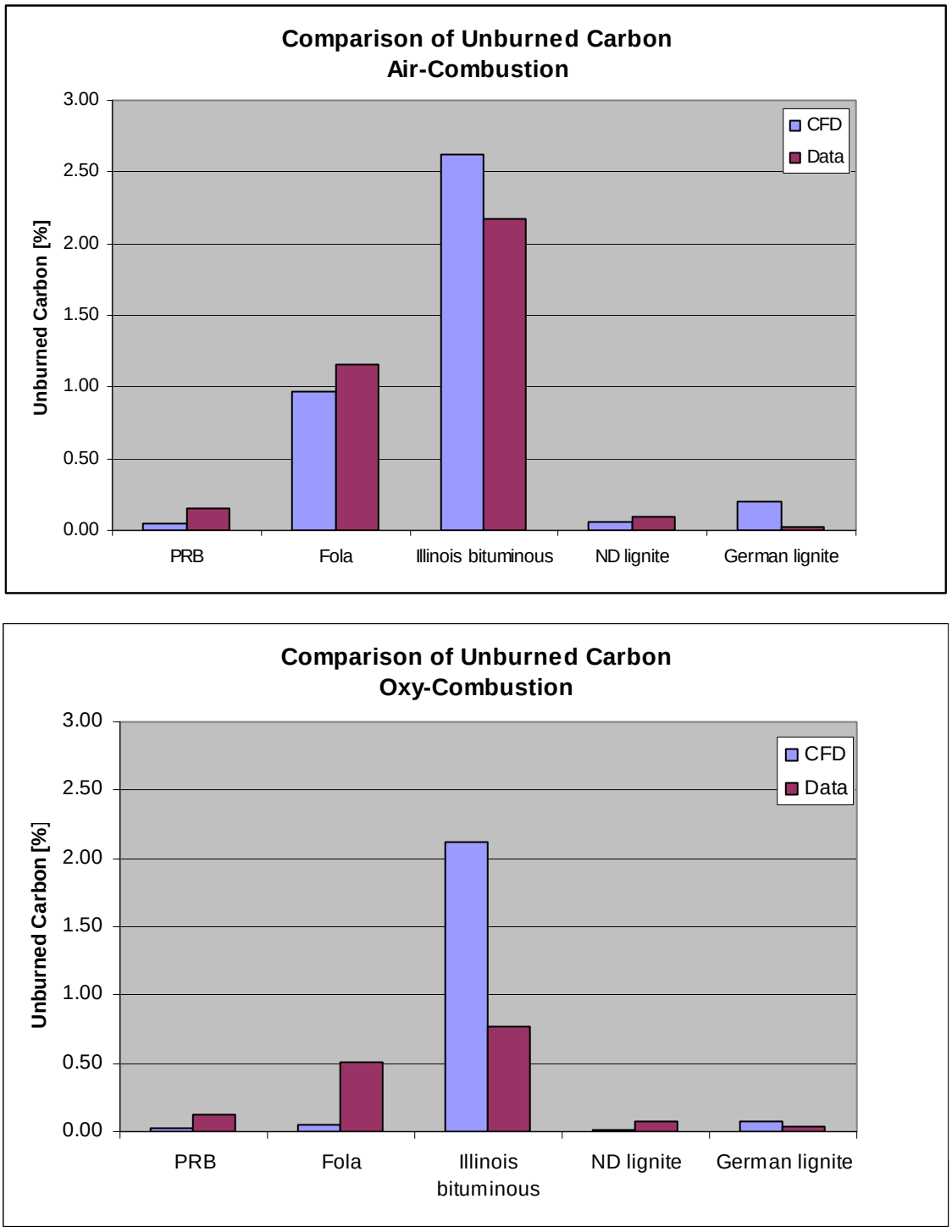

Figure 6-125. Comparison of Carbon-in-Ash for 5 Coal Tests

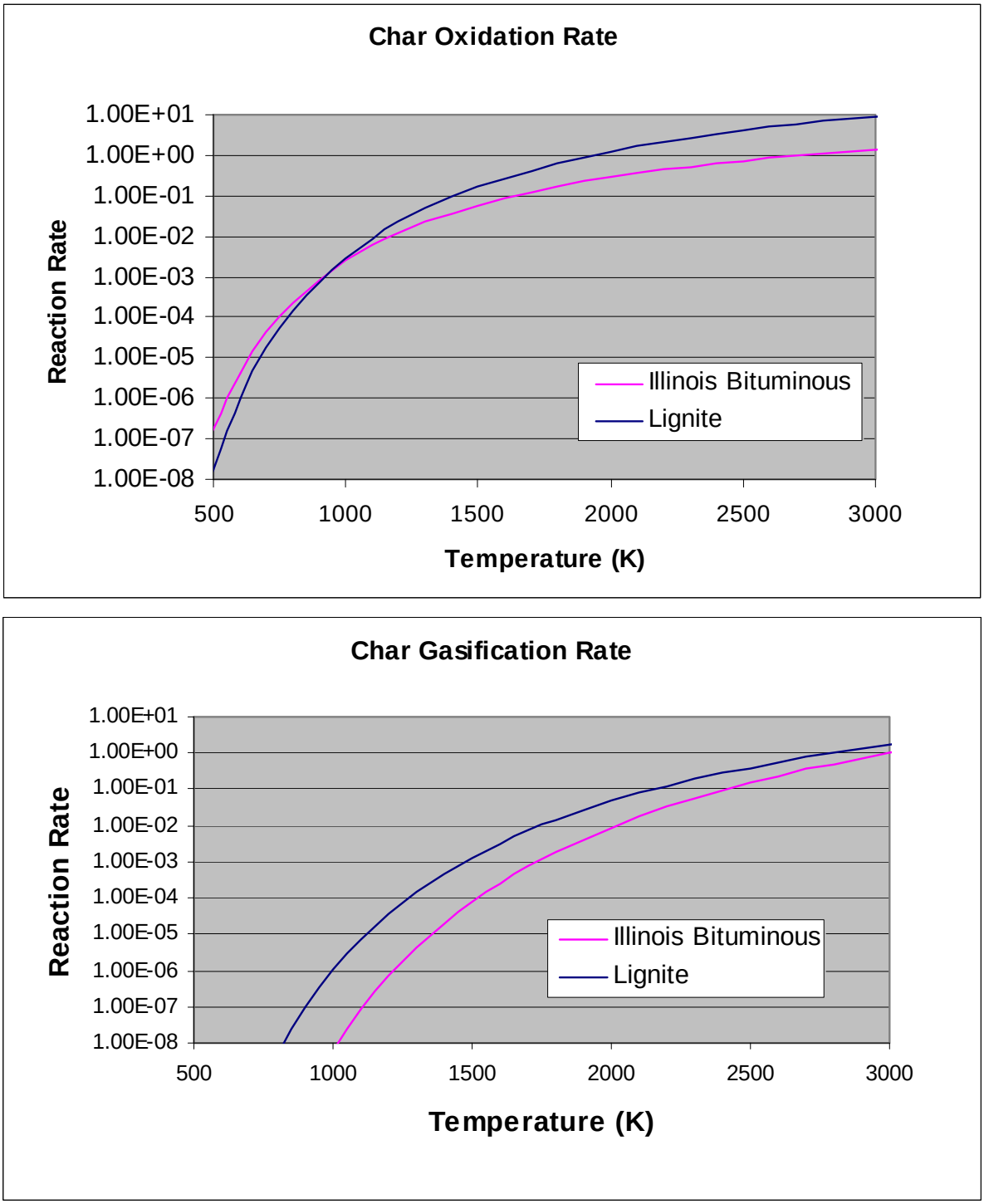

Figure 6-126. Char Oxidation and Gasification Reaction Rates

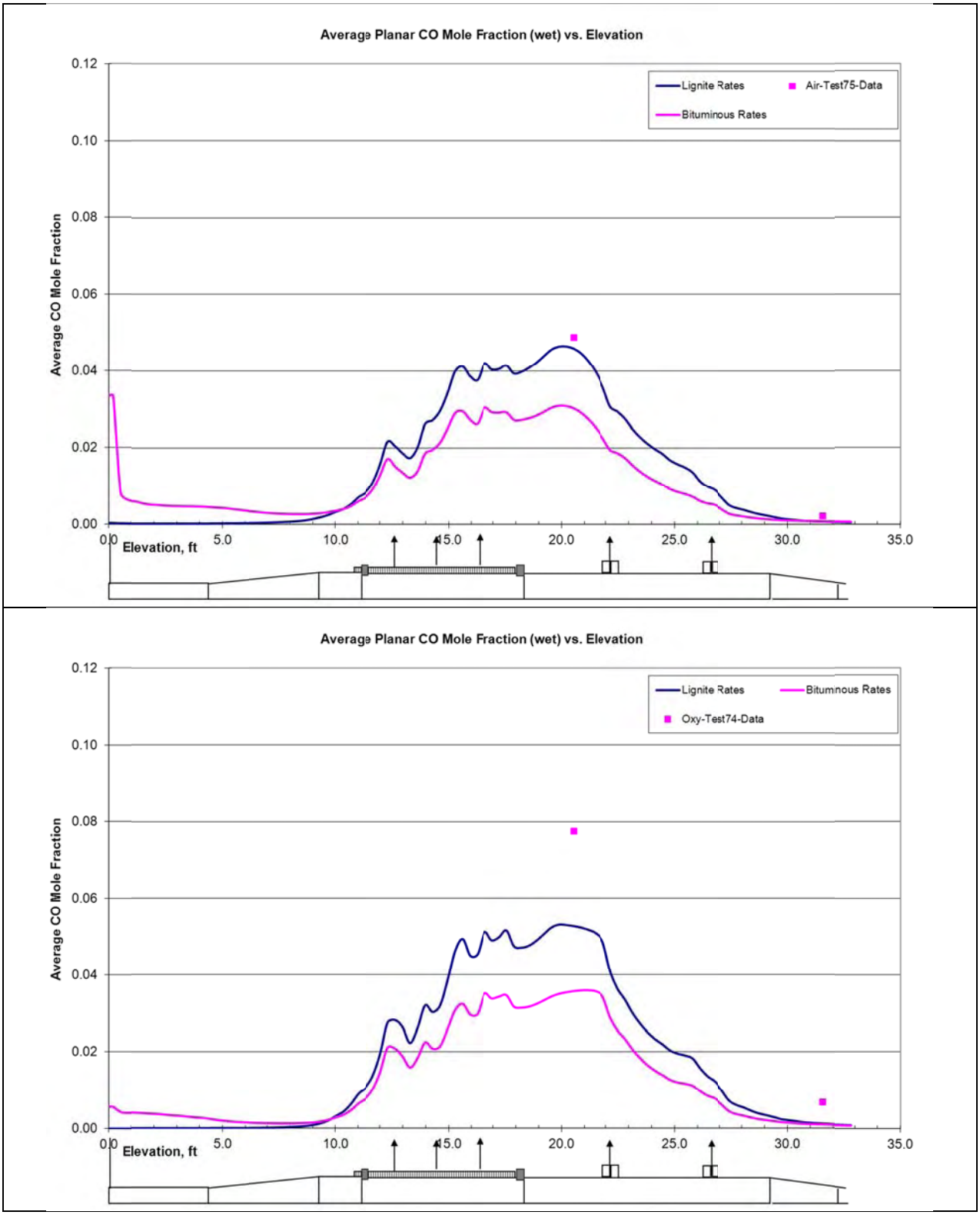

Figure 6-127. [AT-75:OT-74: 2-Rates] Planar Averaged CO

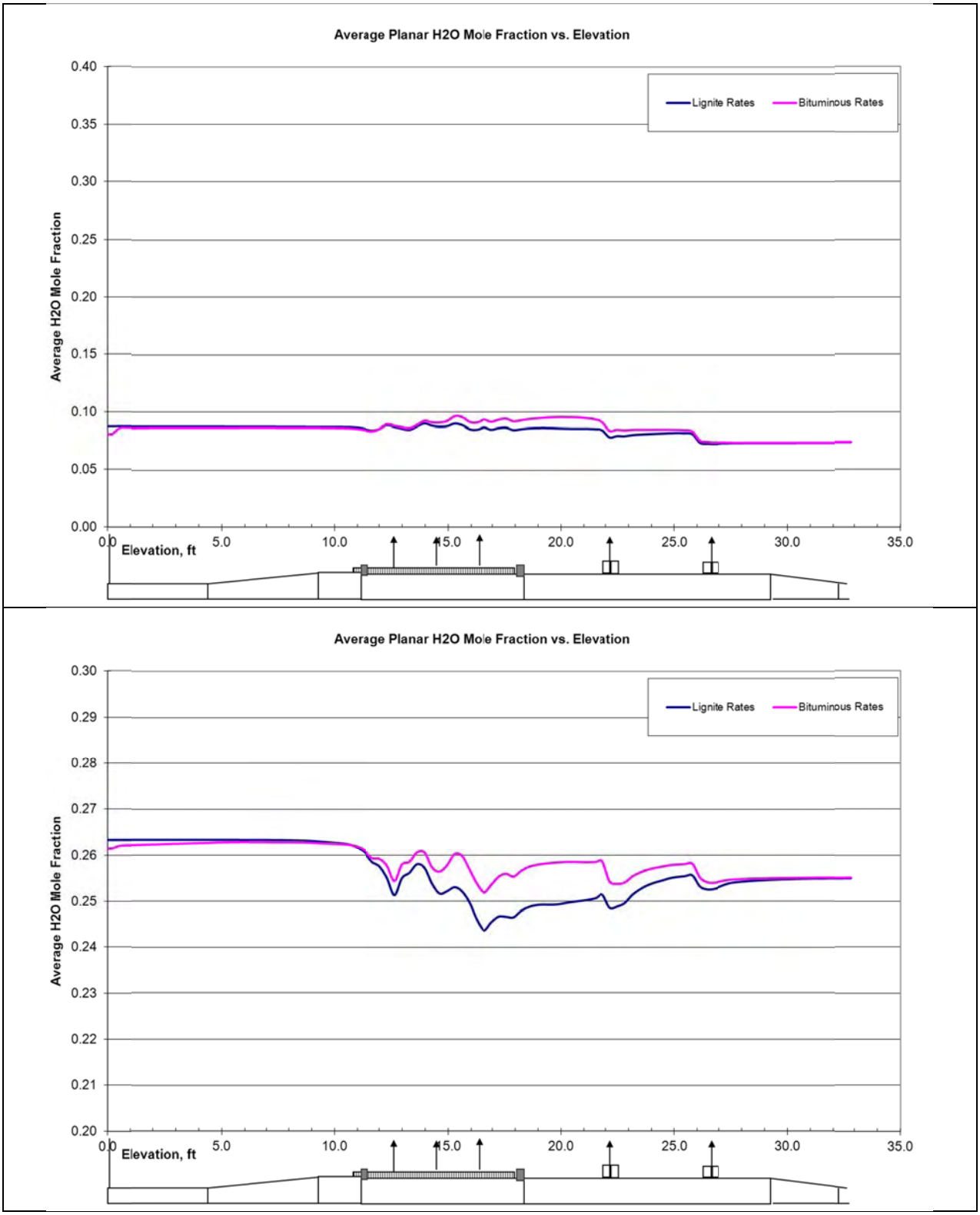

Figure 6-128. [AT-75:OT-74: 2-Rates] Planar Averaged H_2O

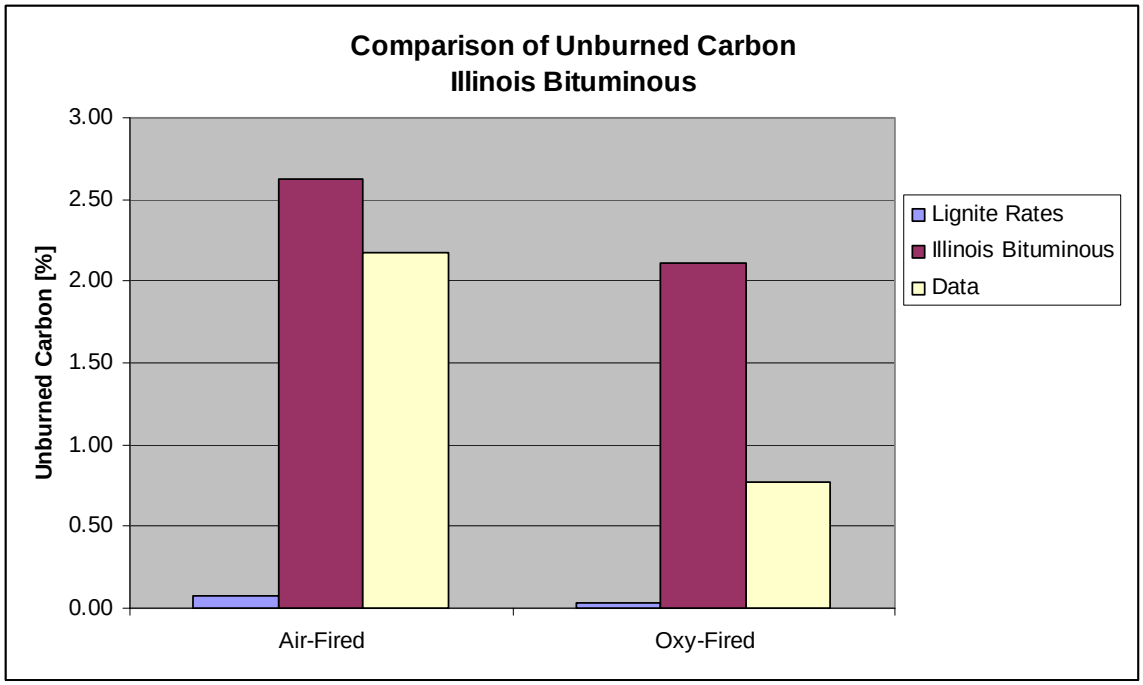

Figure 6-129. [AT-75:OT-74: 2-Rates] Unburned Carbon at Boiler Outlet vs. Test Data

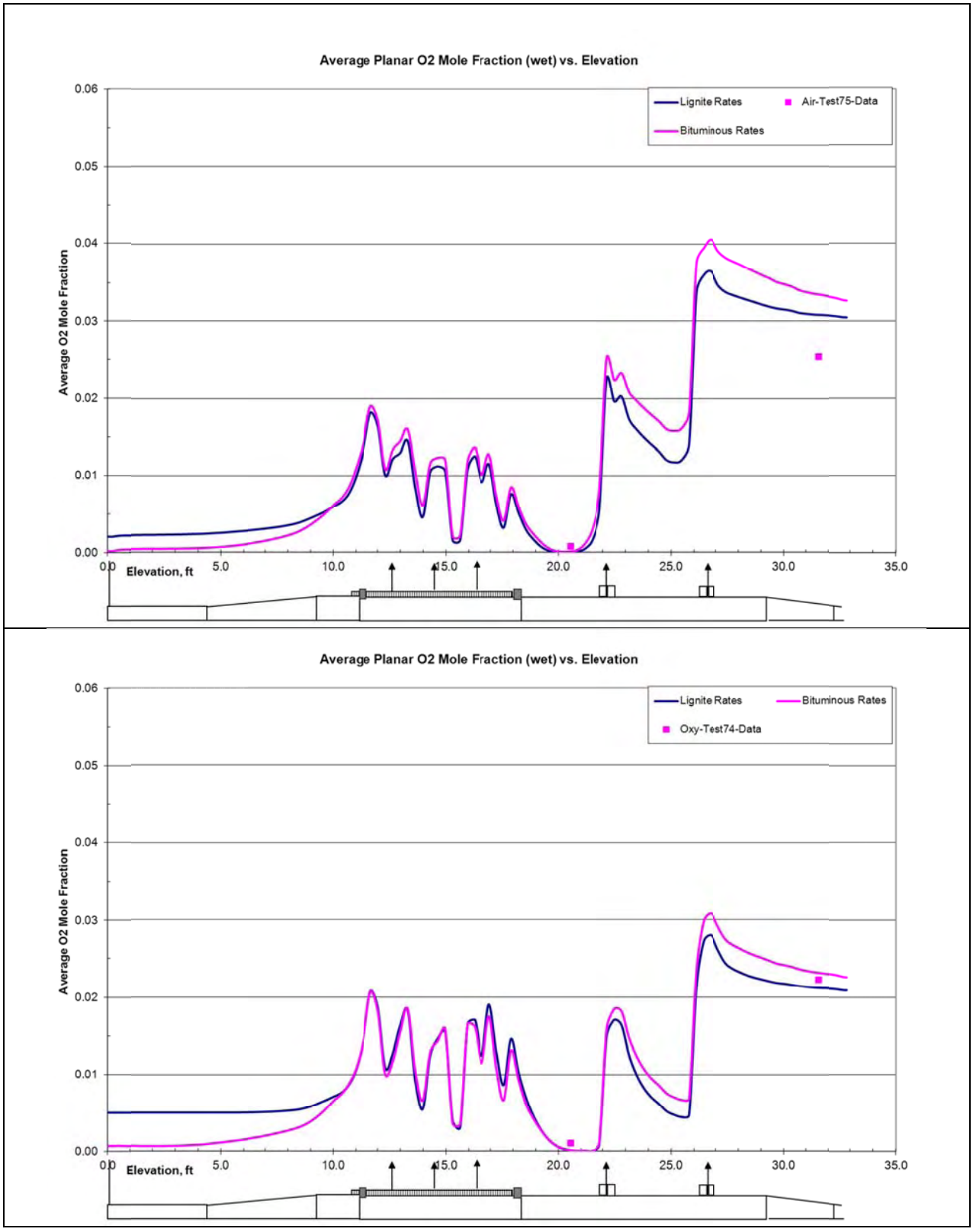

Figure 6-130. [AT-75:OT-74: 2-Rates] Planar Averaged O_2

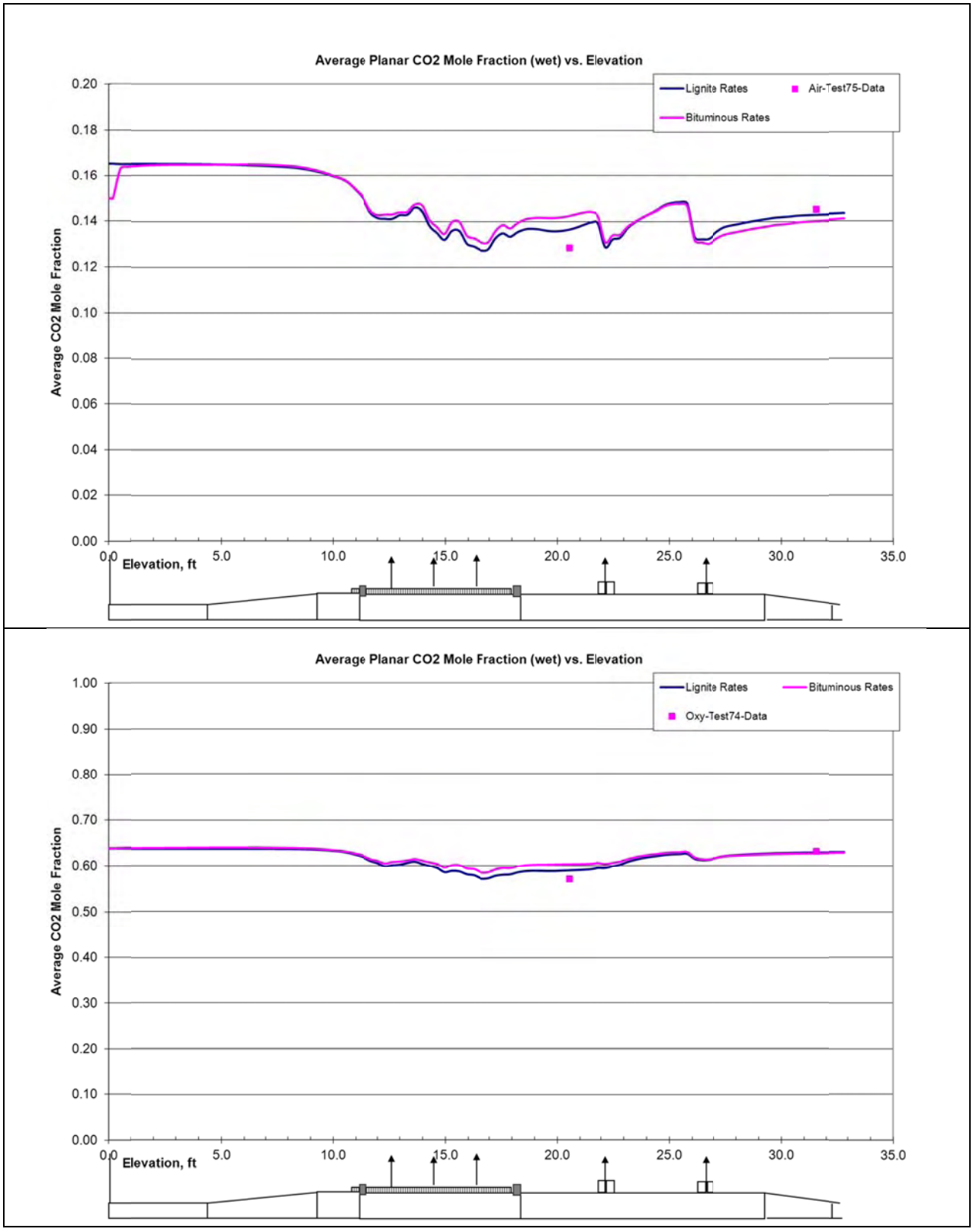

Figure 6-131. [AT-75:OT-74: 2-Rates] Planar Averaged CO_2

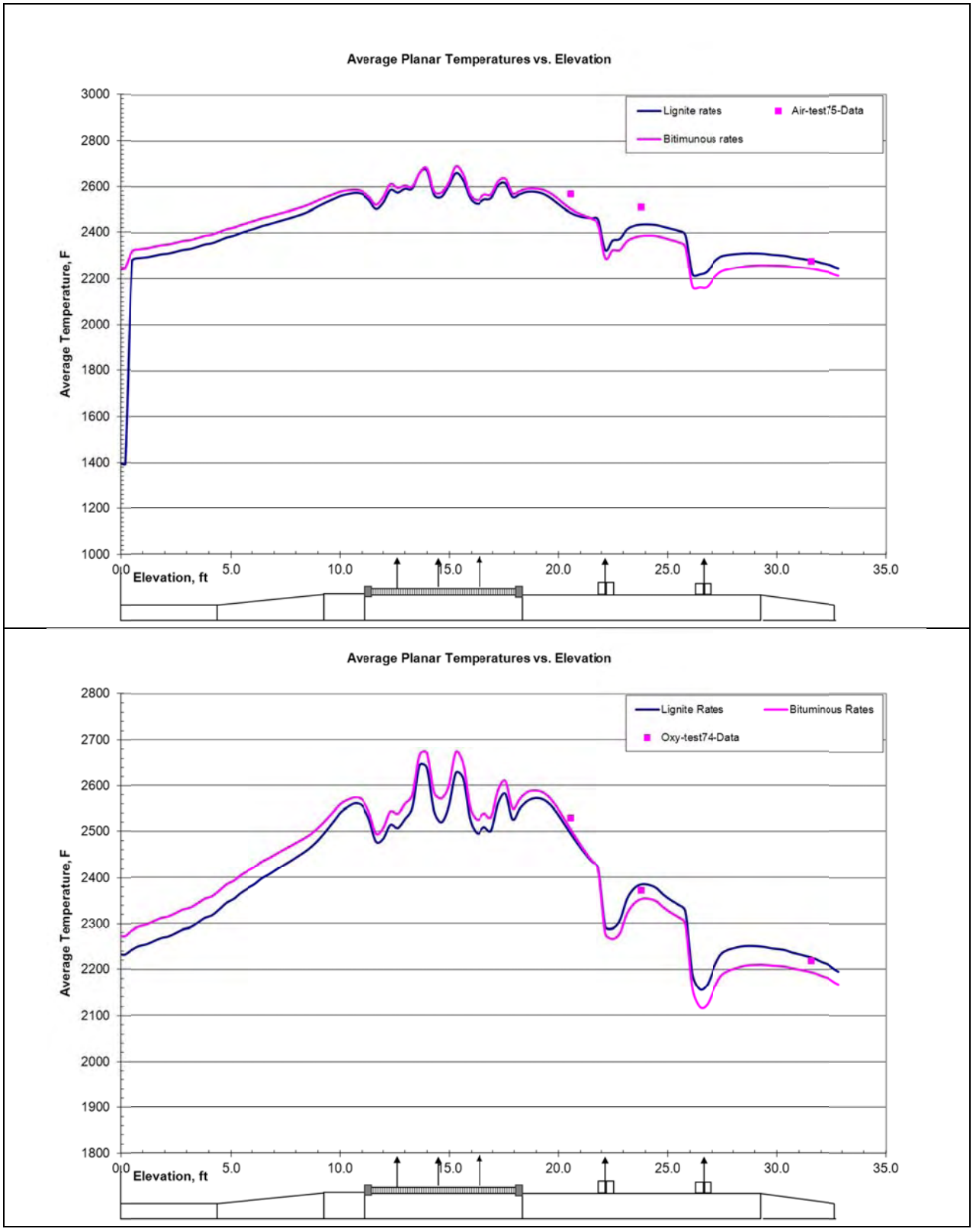

Figure 6-132. [AT-75:OT-74: 2-Rates] Planar Averaged Temperature

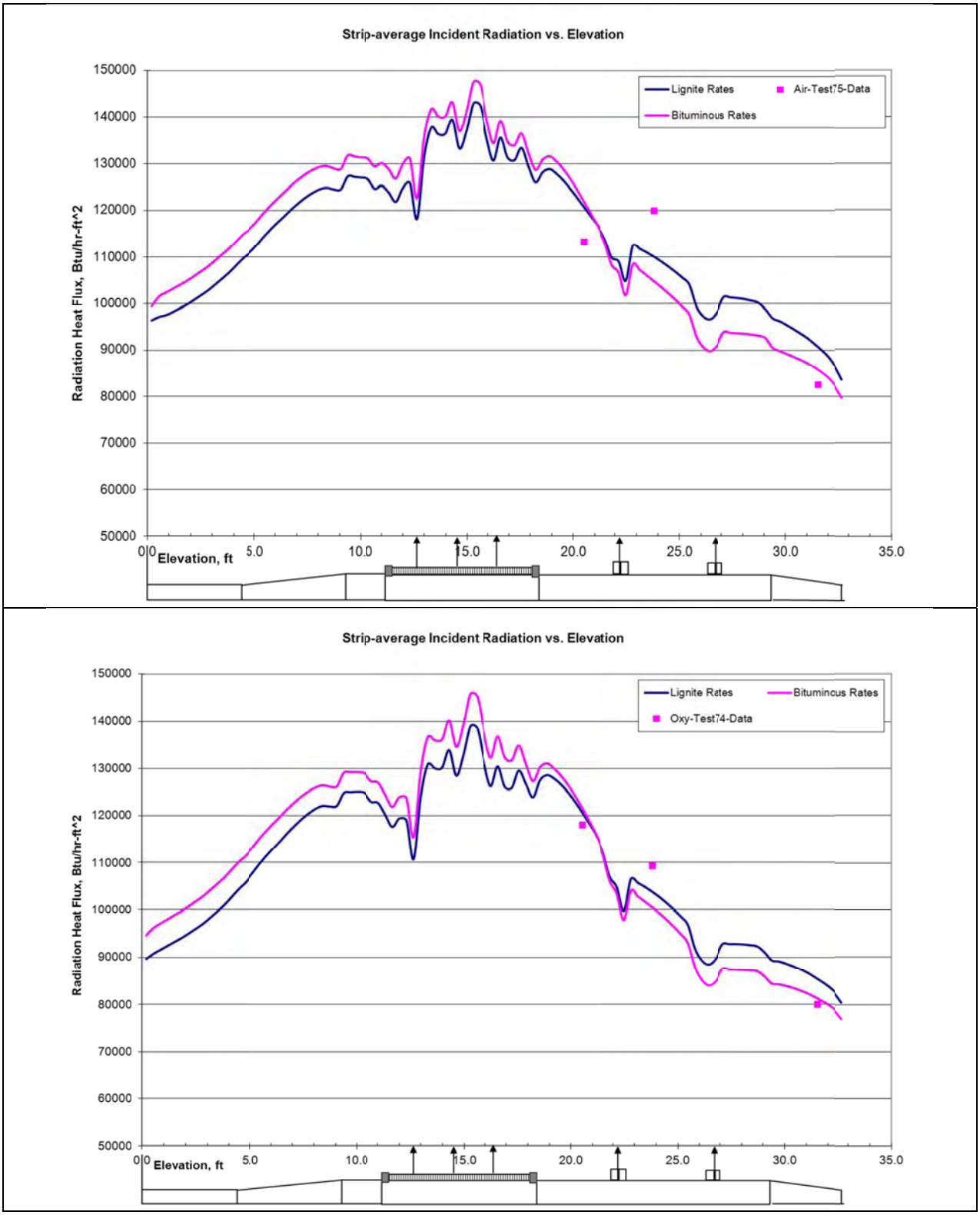

Figure 6-133. [AT-75:OT-74: 2-Rates] Strip Averaged Incident Radiation

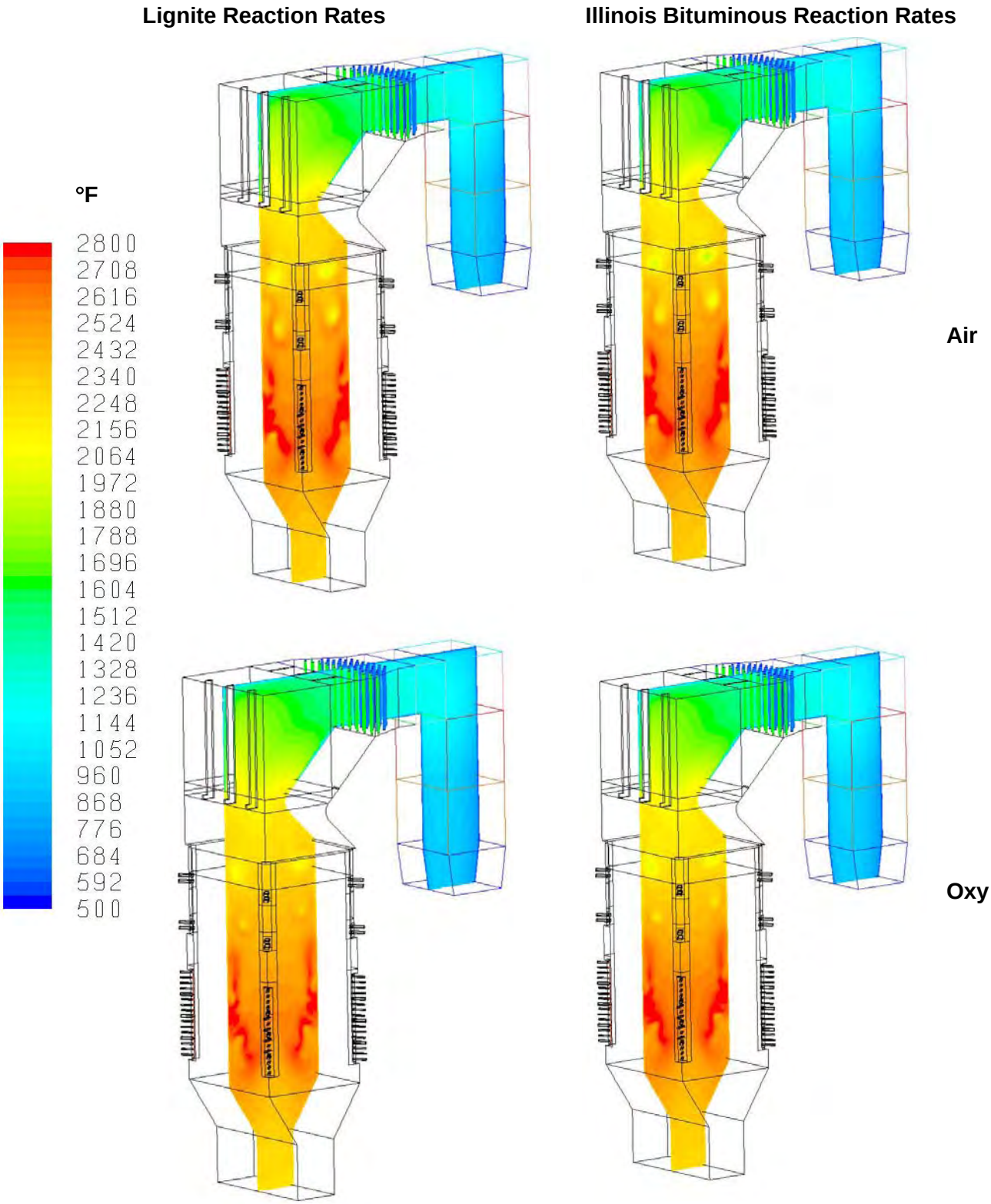

Figure 6-134. [AT-75:OT-74: 2-Rates] Contours of Temperature on X-Midplane

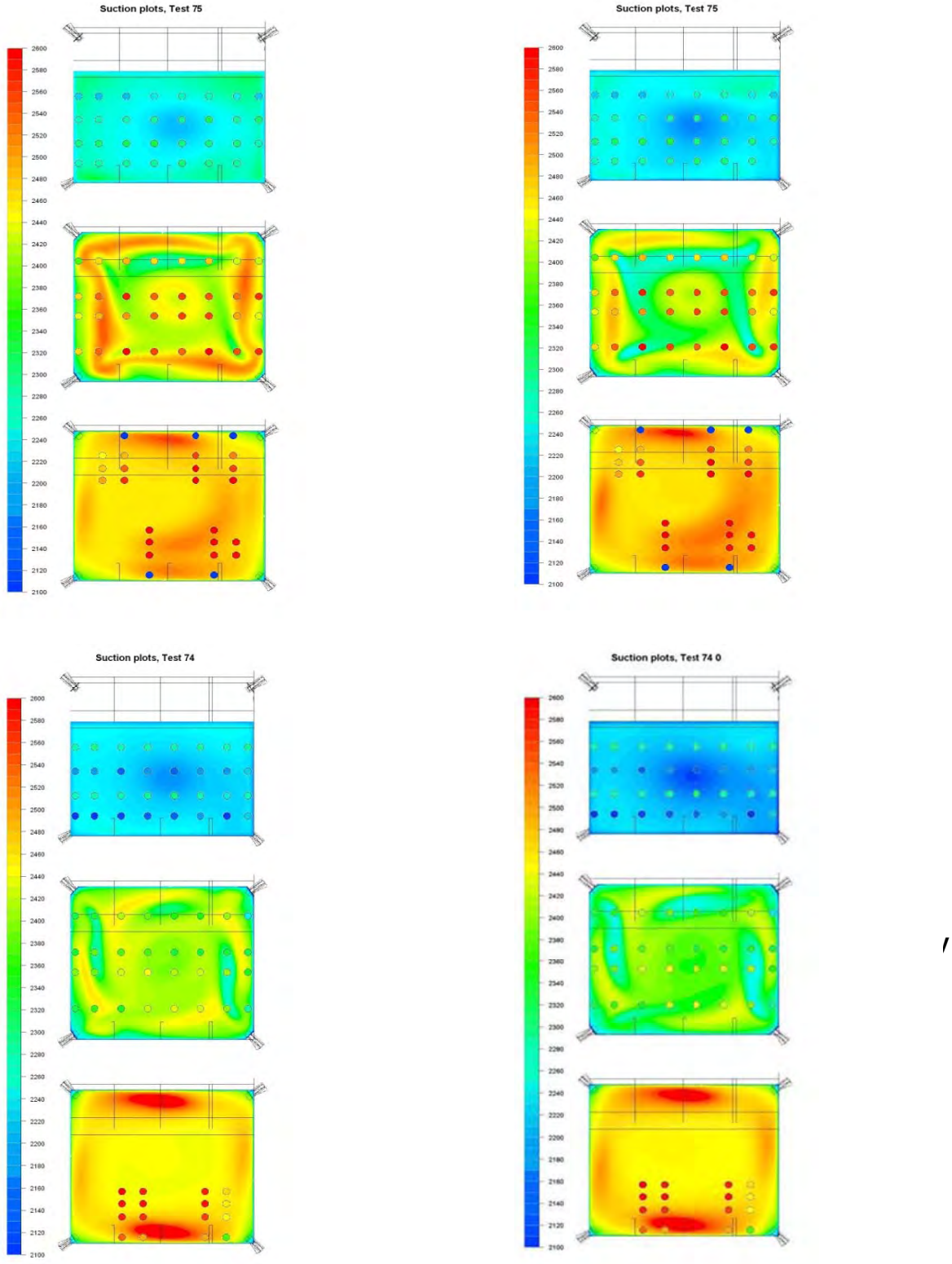

Figure 6-135. [AT-75:OT-74: 2-Rates] Contours of Temperature on Test Planes

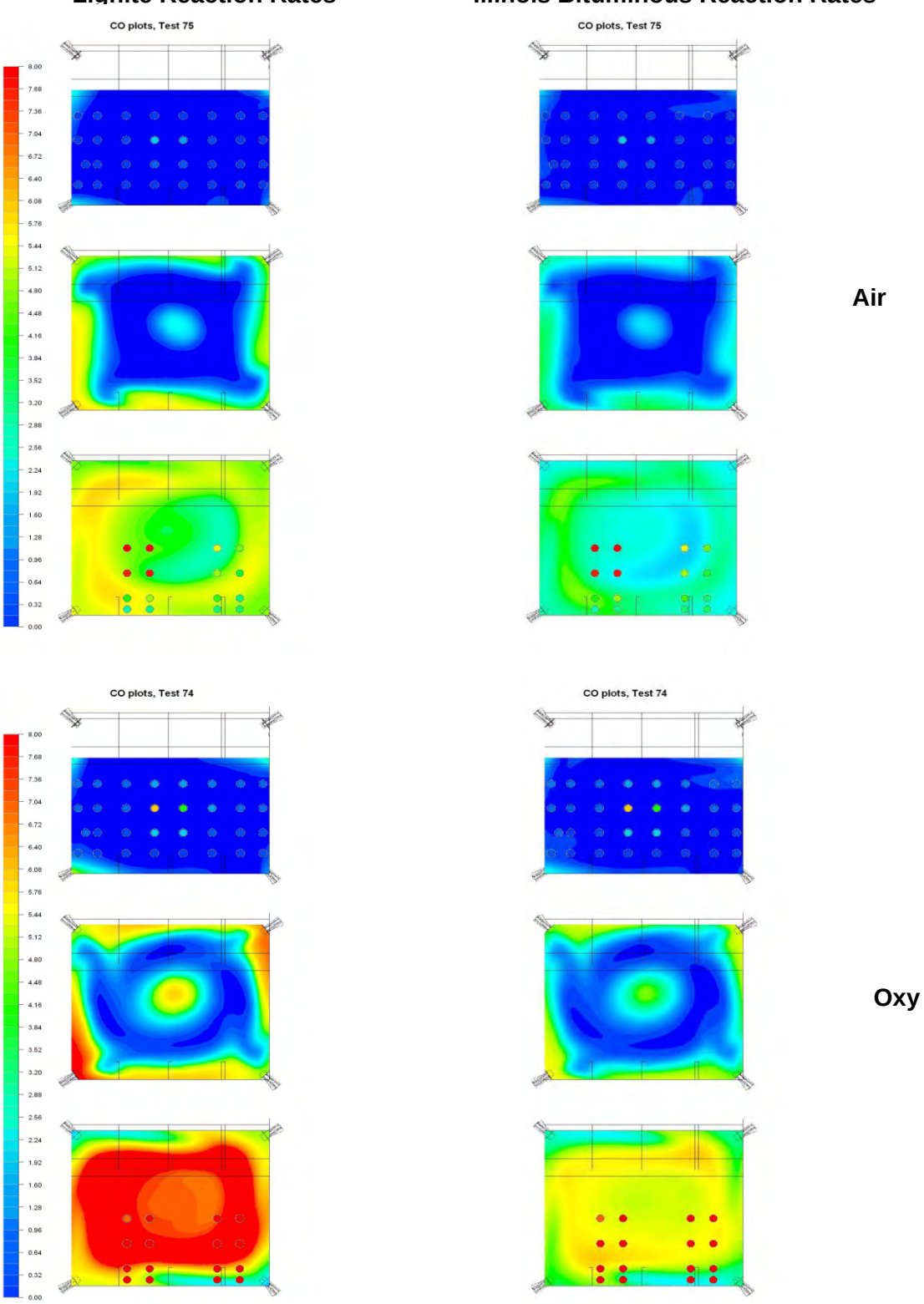

Figure 6-136. [AT-75:OT-74: 2-Rates] Contours of CO on Test Planes

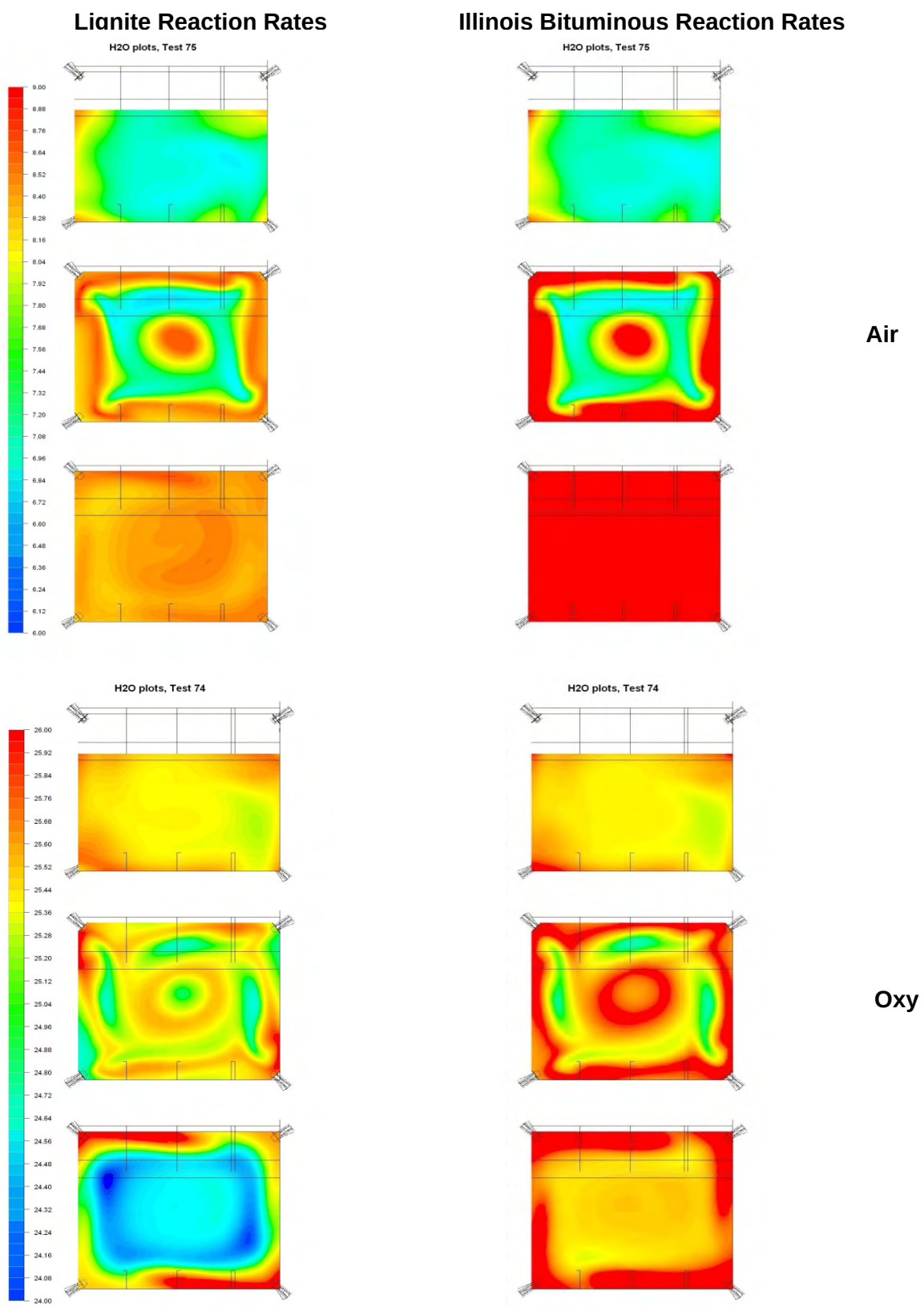

Figure 6-137. [AT-75:OT-74: 2-Rates] Contours of H_2O on Test Planes

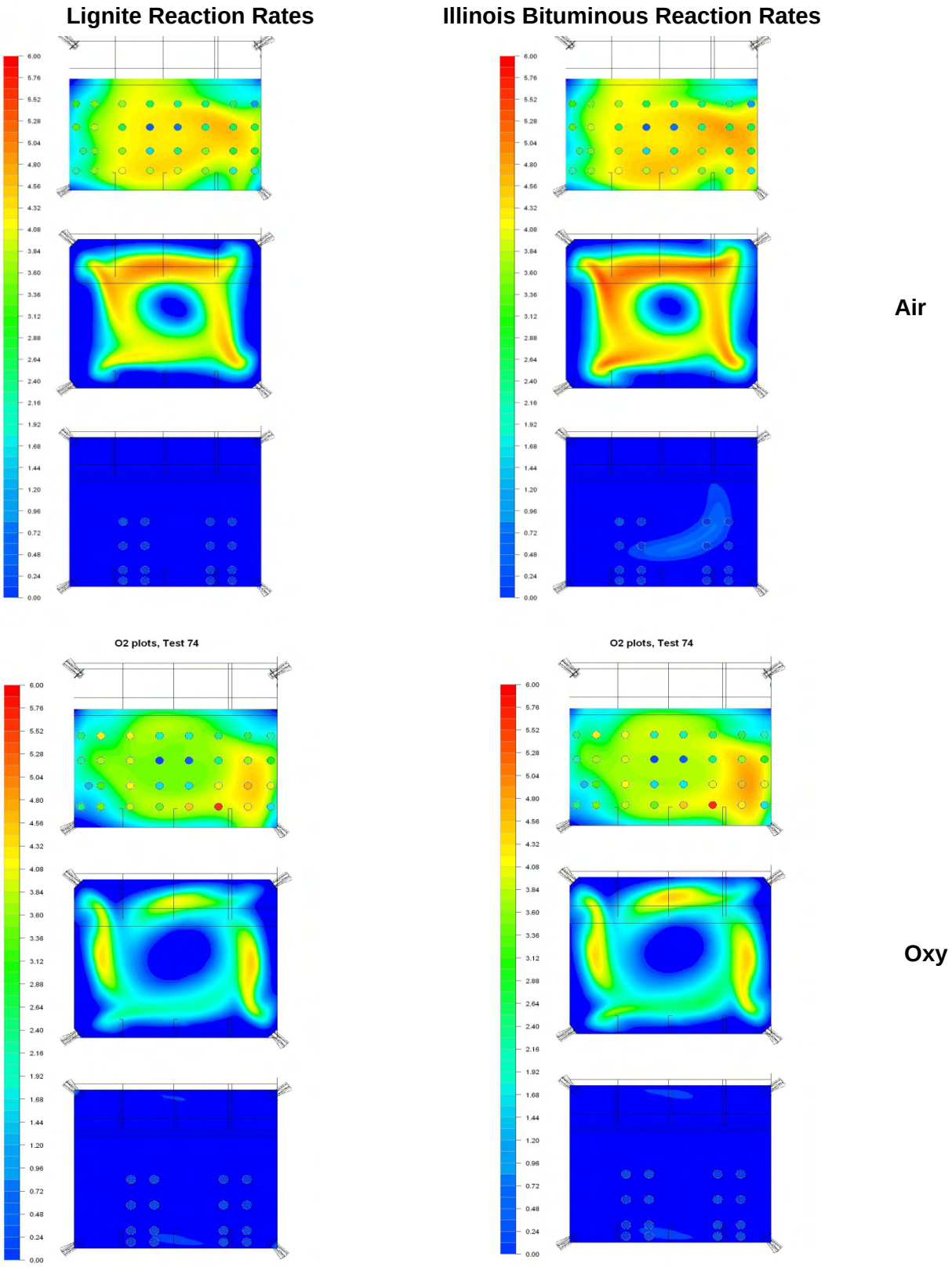

Figure 6-138. [AT-75:OT-74: 2-Rates] Contours of O_2 on Test Planes

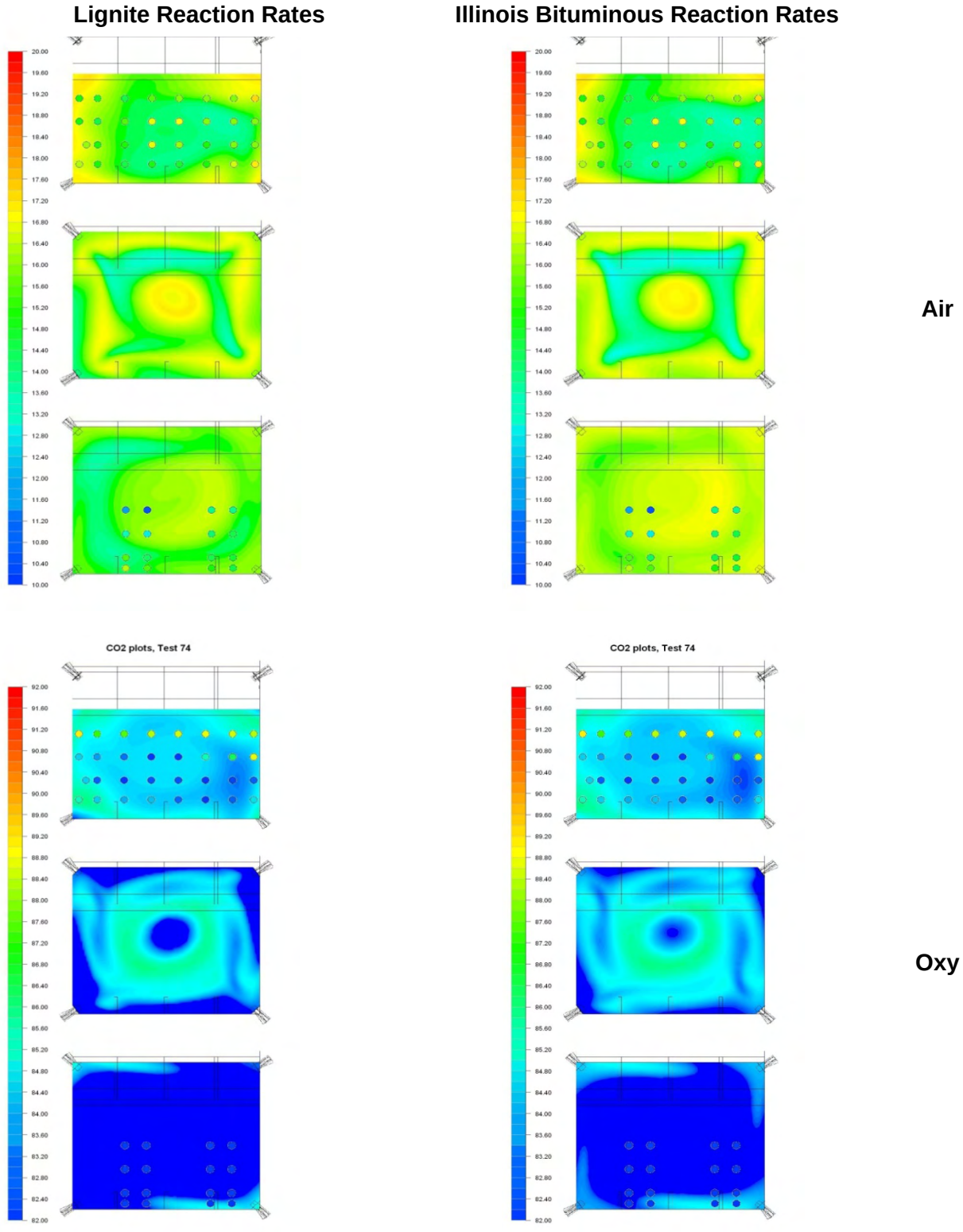

Figure 6-139. [AT-75:OT-74: 2-Rates] Contours of CO_2 on Test Planes

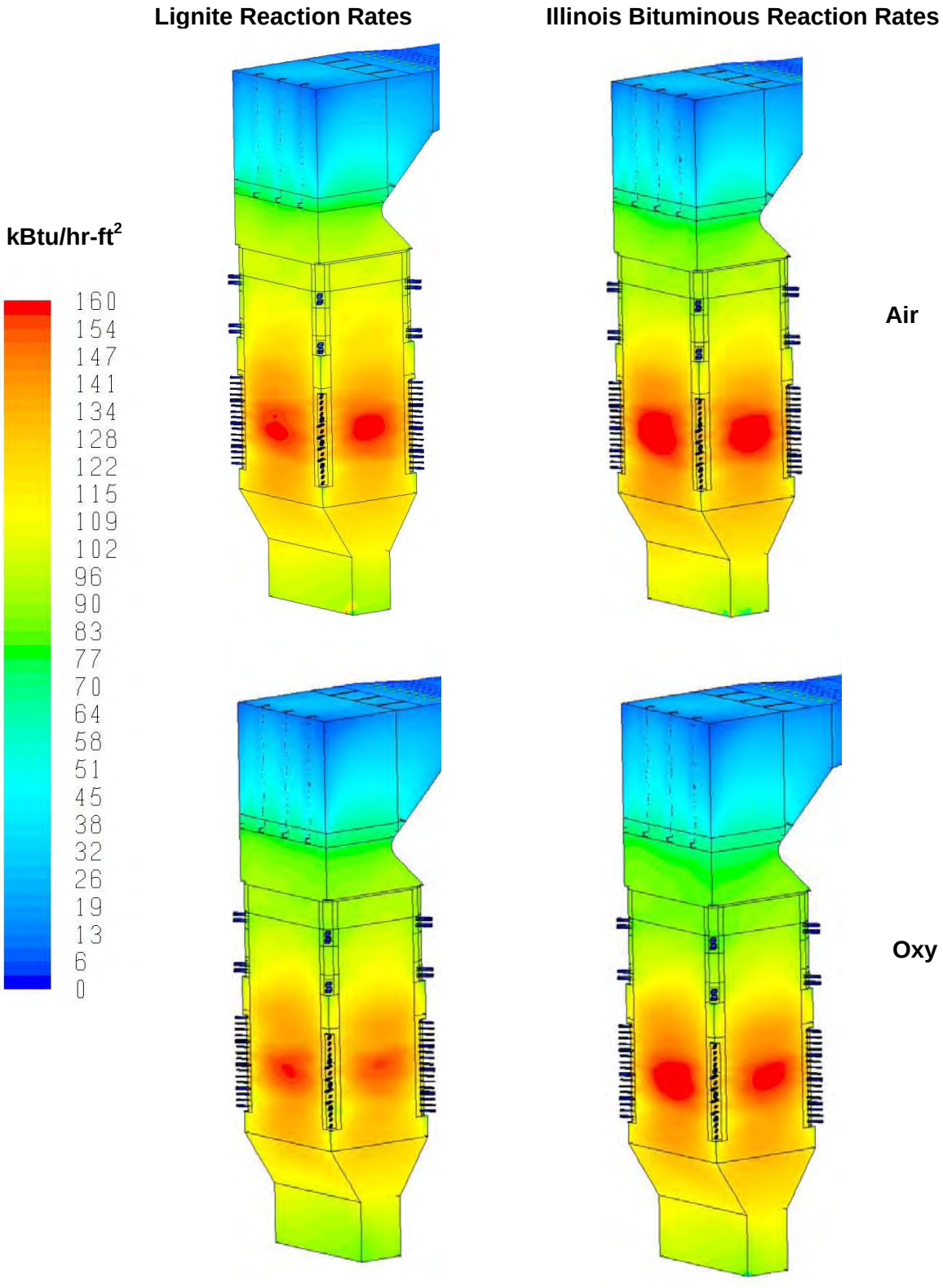

Figure 6-140. [AT-75:OT-74: 2-Rates] Contours of Incident Radiation

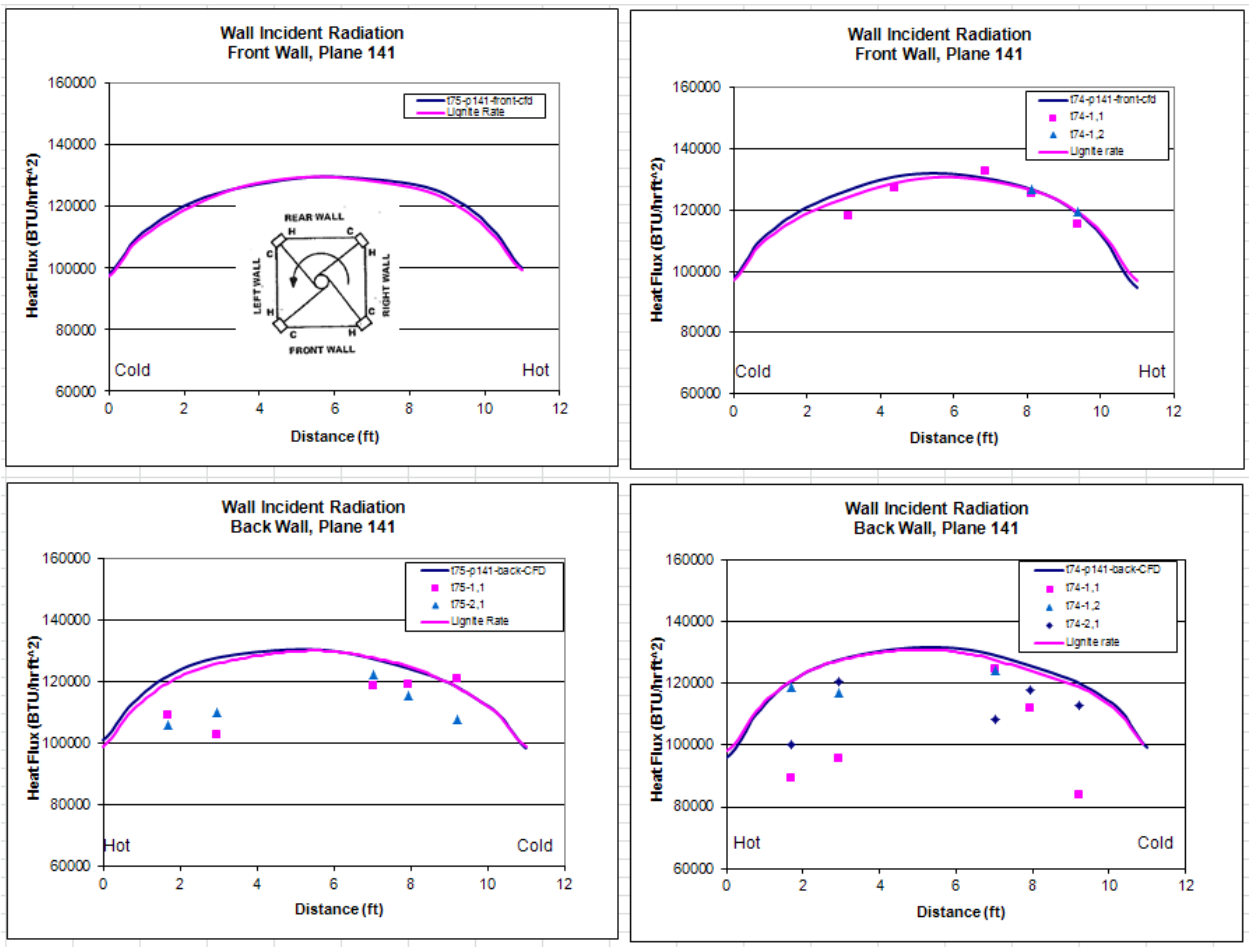

Figure 6-141. [AT-75:OT-74: 2-Rates] Comparison of Wall Incident Radiation at Plane 141

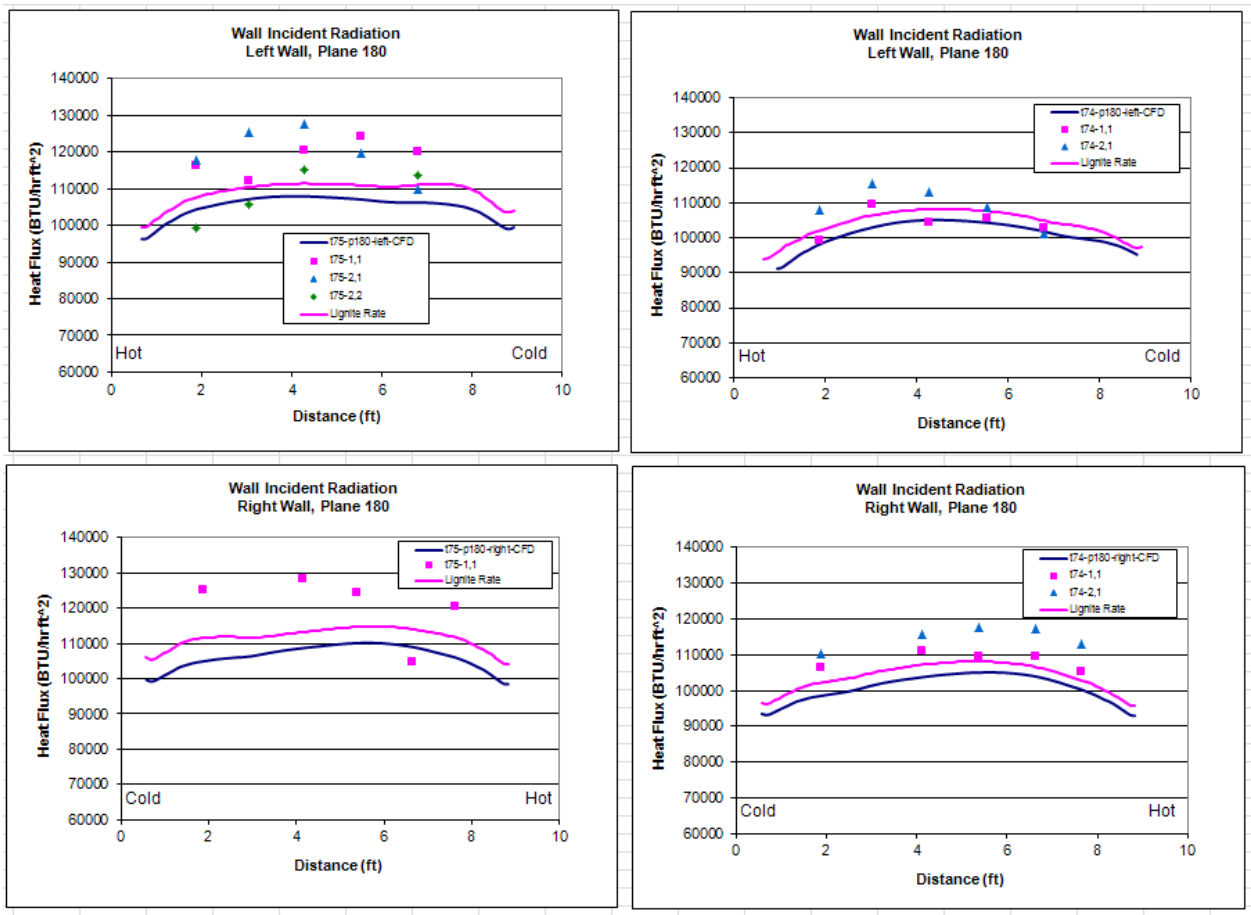

Figure 6-142. [AT-75:OT-74: 2-Rates] Comparison of Wall Incident Radiation at Plane 180

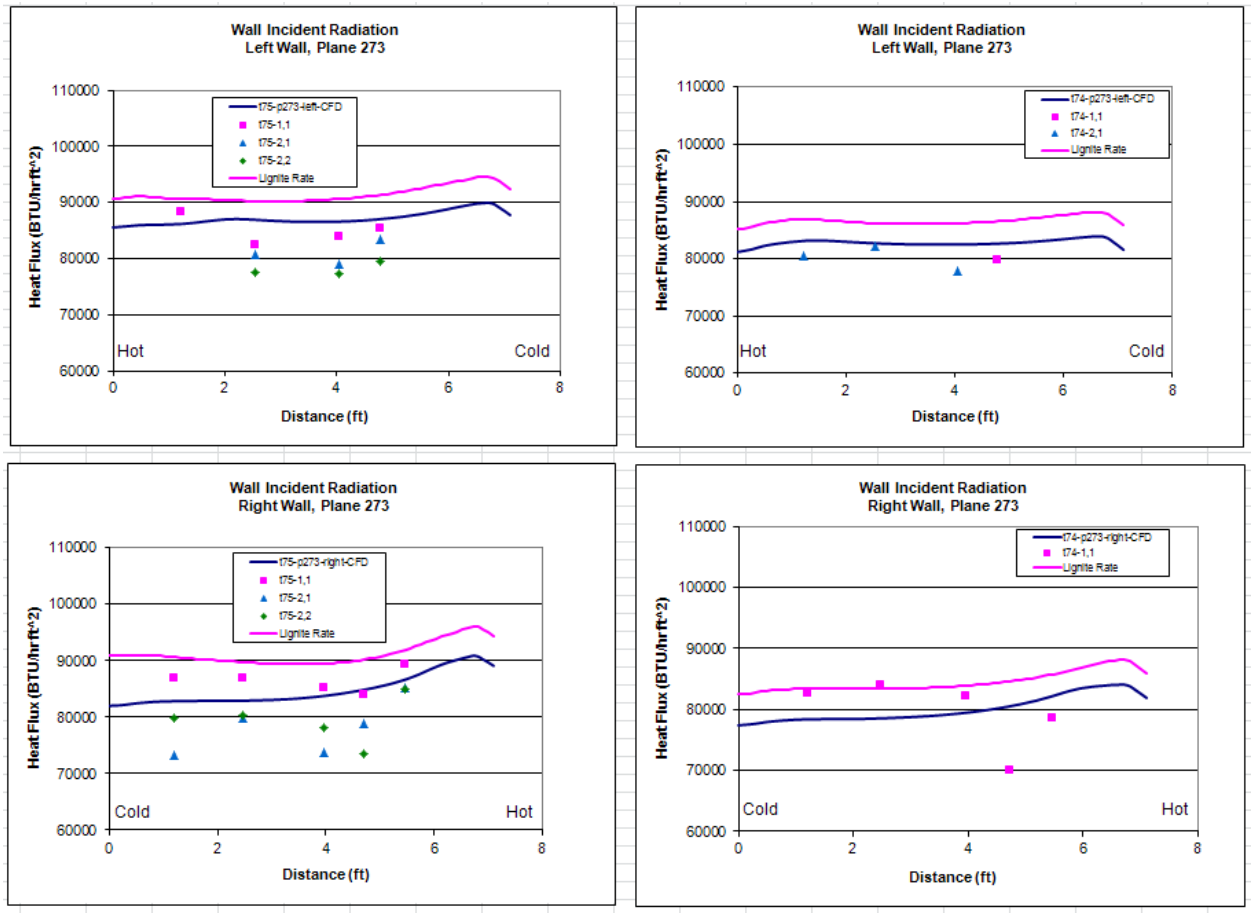

Figure 6-143. [AT-75:OT-74: 2-Rates] Comparison of Wall Incident Radiation at Plane 273

7. References

1. DOE/NETL Cooperative Agreement.No. DE-NT0005290, "Recovery Act: Oxy-Combustion Technology Development for Industrial-Scale Boiler Applications," performed by Alstom Power Inc. for U.S. DOE National Energy Technology Laboratory.

2. Goetz, G. J., N. Y. Nsakala, R. L. Patel, and G. H. Quentin, "Combustion and Gasification Kinetics of Chars from Four Commercially Significant Coals of Varying Rank," Presented at the International Conference on Coal Science, Pittsburgh, PA (August 15-19, 1983), C-E TIS-7290.

Recovery Act: Oxy-Combustion Technology Development for Industrial-Scale Boiler Applications

DOE/NETL Cooperative Agreement No. DE-NT0005290

Volume III – Modeling and Validation

Chapter 2 – CFD Modeling of the 30 MWth Schwarze Pumpe Oxy Pilot Plant

Authors
Paul J. Chapman
David G. Sloan

Table of Contents

1. Executive Summary 4
2. Objectives 9
3. Description of Schwarze Pumpe Pilot Plant 11
   3.1 Overall Geometric Description 11
4. Technical Approach 16
   4.1 Modeling Approach 16
   4.2 Development of the Model Geometry 16
   4.3 Computational Mesh 19
   4.4 Boundary Conditions 21
   4.5 Model Selections 25
   4.6 Burner Characteristics 27
   4.7 Impact of the Inlet Boundary Condition and Turbulence Model 31
   4.8 Contour Plots on the Burner Centerline Planes 36
   4.9 Planar Averaged Plots as a Function of Elevation 46
   4.10 Comparisons with Experimental Data 48
5. References 50

Table of Figures

Figure 1-1. Oxy Pilot Plant Arrangement 5
Figure 1-2. CFD Geometry of the Oxy Pilot Plant 6
Figure 1-3. Contours of Temperature at Centerline Slices 7
Figure 3-1. Burner Arrangement 11
Figure 3-2. Arrangement of the Oxy Pilot Plant 12
Figure 3-3. Furnace Probe Measurement Elevations or Levels 13
Figure 3-4. Sample Locations in the Furnace and Convective Section 15
Figure 4-1. Solid Geometry View of Burner 17
Figure 4-2. Cutaway View of Burner with Velocity Contours 18
Figure 4-3. Furnace Geometry and Wall Sections 19
Figure 4-4. Mesh at the Burner Centerline Slice 20
Figure 4-5. Mesh Distribution at Various Elevation Slices 21
Figure 4-6. Coal Fineness Distribution 24
Figure 4-7. Pathlines for Air and Oxy Simulations Released from the Burner Zones 28
Figure 4-8. Burner Velocity Contour Progression down the burner for OF-25 31
Figure 4-9. Designated Plane for Extraction of Inlet Velocity Profiles 32
Figure 4-10. Comparison of Fitted Profiles with Extracted Original 32
Figure 4-11. Temperature Distribution for Full and Truncated Burner Representations 33
Figure 4-12. Velocity Magnitude for Full and Truncated Burner Representations 33
Figure 4-13. X-Velocity Distribution for Full and Truncated Burner Representations 34
Figure 4-14. Vertical Velocity Distribution for Full and Truncated Burner Representations 34
Figure 4-15. Radiant Wall Flux Distribution for Full and Truncated Burner Representations 35
Figure 4-16. Contour Plots on Centerline Planes: Air Test 332 39
Figure 4-17. Contour Plots on Centerline Planes: OF25 Test 333 42
Figure 4-18. Contour Plots on Centerline Planes: OF30 Test 334 45
Figure 4-19. Planar Averaged Temperature vs. Elevation 47
Figure 4-20. Planar Averaged Oxygen Mole Percent vs. Elevation 47
Figure 4-21. Planar Averaged CO Mole Percent vs. Elevation 48

Table of Tables

Table 3-1. Furnace Wall Measurement Ports with Comments 14
Table 4-1. Summary of the Validation Conditions for Combustion in the OxyPP 22
Table 4-2. Inlet Boundary Conditions.....23

1. Executive Summary

Alstom has worked with various corporate entities and universities in a number of broad, internal development programs that have been dedicated to oxy-fuel combustion research. One of the purposes of the programs has been to access world-class experts from around the world, and to gather detailed experimental data at various combustion test facilities, where air and oxy combustion tests were performed under controlled conditions. An important aspect of those programs was to apply and enhance CFD modeling tools for prediction of combustion performance for scale-up from pilot scale to commercial equipment. In conjunction with that effort, Alstom conducted computational fluid dynamics (CFD) modeling tasks to model the various pilot test facilities and to compare the calculations with the experimental data.

The objective of the present computational work was to support a portion of Subtask 6.1 (DOE/NETL Cooperative Agreement No. DE-NT0005290; see Ref. 1), in which "simulation results will … be compared with experimental validation data from small-scale facilities." One of those facilities is Vattenfall's 30 MW_{th} Oxy Pilot Plant (OxyPP) at their Schwarze Pumpe station. Other small-scale facilities include the 15 MW_{th} Boiler Simulation Facility (BSF) and the KSVA 500 kWth test facility (University of Stuttgart), simulations of which have been reported in other chapters of this Volume III. This report specifically addresses the application and validation of the FLUENT® code with respect to the OxyPP data. The detailed experimental data from the OxyPP facility was previously collected in conjunction with a separately funded effort by Alstom and Vattenfall.

The 30 MW_{th} OxyPP arrangement is shown with an elevation and plan view in Figure 1-1. The furnace contains a single swirl burner mounted at the top firing downward. The burner arrangement used for the detailed testing included 3 concentric zones for the air or oxidant stream injection. The flows to each burner zone were measured individually. Pulverized lignite was transported pneumatically to the burner and injected into the center of the burner around a core air annulus used for gas start-up. The nominal 4.1 m^2 main furnace cross-section extends downward and then turns upward to enter superheater sections in the second pass. The bulk of the testing and modeling effort was focused on the zone downstream of the burner. The waterwall shell of this furnace included a series of sample ports at various elevations as indicated. These ports allowed sample probes to be inserted into the flame to measure gas temperatures and species. The Alstom CFD model geometry of the furnace and burner used for the CFD simulations is provided in Figure 1-2. The CFD model was created using the ANSYS/FLUENT® commercially-licensed software and includes approximately 4.5 million cells for the burner and the furnace, with the majority of the cells concentrated in the burner portion.

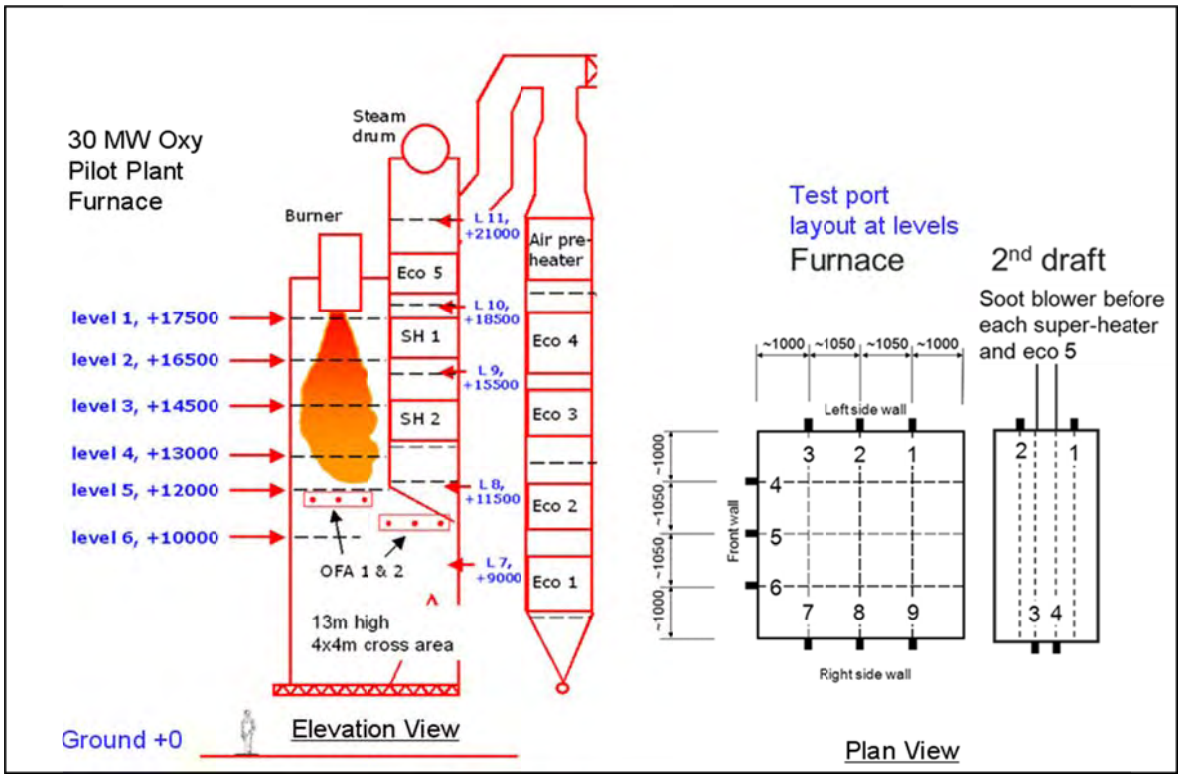

Figure 1-1. Oxy Pilot Plant Arrangement

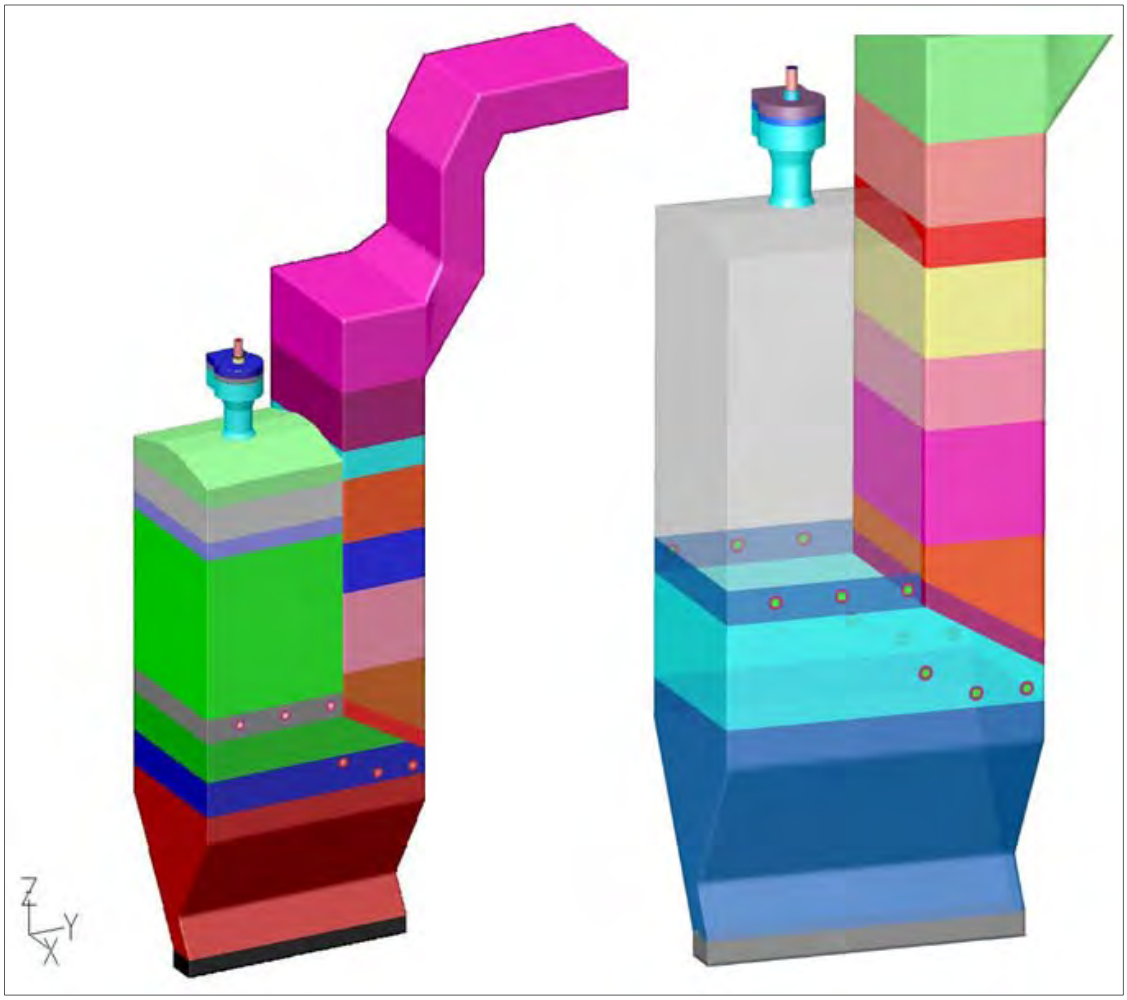

Figure 1-2. CFD Geometry of the Oxy Pilot Plant

Three cases were modeled with FLUENT CFD software – an air-fired test (Air Test 332) and two oxy-fired tests (OF25 Test 333 and OF30 Test 334). The OF25 (Test 333) case has the highest main burner zone excess oxygen and overall excess oxygen of all of the three tests being examined, as well as the highest gas and coal flow rates. OF30 has the lowest overall excess oxygen ratio (1.052), as well as the lowest excess oxygen in the main burner zone itself (0.87), than the other two tests. The coal flow rate for OF30 is intermediate between the other two cases, but the total inlet gas mass flow rate is significantly less (by 14 to 18%) than the other two test cases.

Calculation results were obtained for both air and oxy firing tests. A pair of contour plots is provided in Figure 1-3 for Test OF25 to illustrate the temperature predictions, as a function of (a) turbulence model, and (b) the extent to which the full burner was modeled (as opposed to simply applying boundary conditions to inlet annuli). One can see from the near-burner flow fields that the Reynolds Stress Model (RSM) case exhibits a more irregular shape compared to the k-ε results. Despite the more diffusive nature typically associated with the k-ε model, the length of the flame zone in the k-ε case appears to be greater than that of the RSM. This longer flame length for the k-ε case also appears to induce a longer (absorbed) radiation wall heat flux zone and pushes the peak radiation wall heat flux value (not shown)

downstream towards the OFA, relative to that of the RSM case. The increased mixing of the RSM may in part be due to the stronger centerline reverse flow zones associated with the RSM.

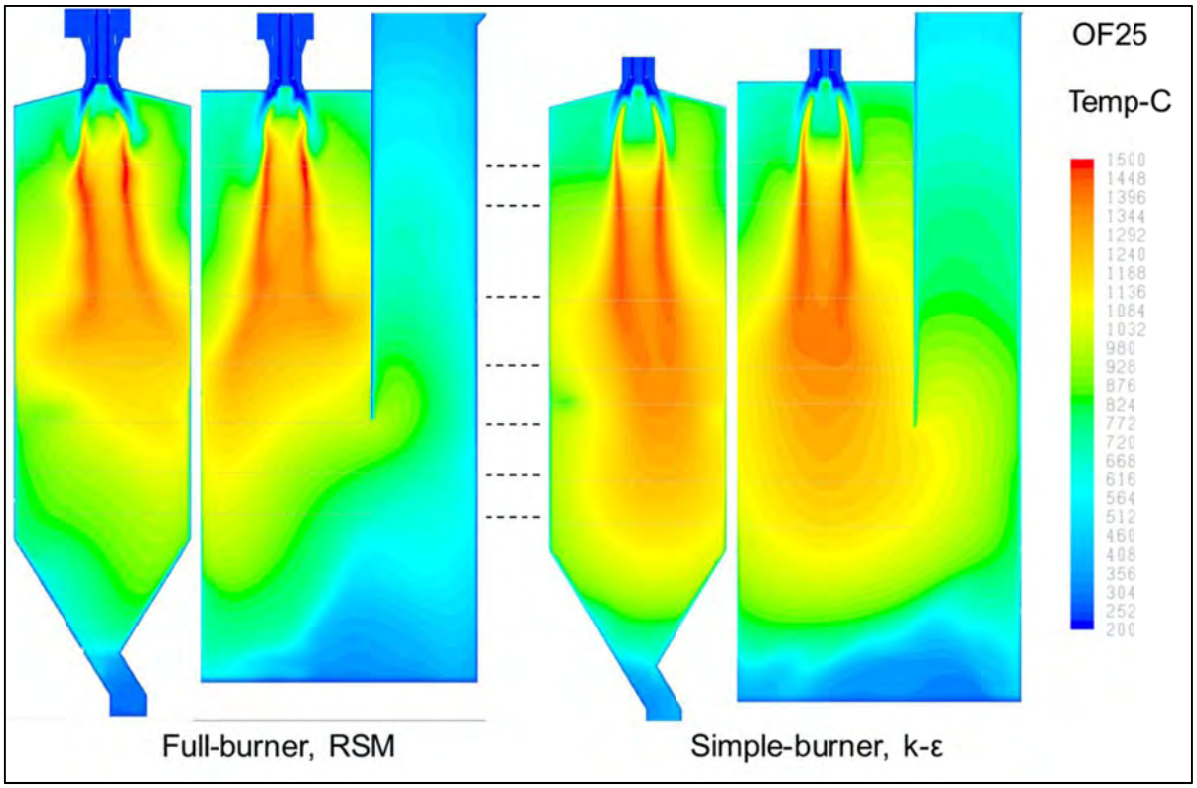

Figure 1-3. Contours of Temperature at Centerline Slices

Calculations of the three tests produced results and flame characteristics (in the form of contour plots) that could be reasonably explained based on the swirl levels, the excess air in the main furnace zone, and the overall stoichiometry.

A significant effort was made at the beginning of the project to ascertain the advantages and drawbacks of including the entire burner assembly in the computational domain, as opposed to applying circumferentially uniform inlet boundary conditions on a truncated burner. An assessment of other model selections, such as the Reynolds Stress Model versus the k-ε model, was also conducted. This report documents the results of those assessments. Alstom's present CFD methodology is to simulate as the burner internals within the computational domain where possible to capture irregularities. For these swirl flow burners, the Reynolds Stress Model was found to be more desirable in the early stages of the modeling of the OxyPP with the Burner-A configuration. In that initial phase, the RSM simulations were better able to capture stable combustion results without flame lift-off that was exhibited using the k-ε turbulence model selection.

Calculation results were provided in the form of contour plots and longitudinal, planar-average profiles. In addition, detailed, two-dimensional line plots were prepared to compare the CFD calculations with the experimental data sets for three variables -- temperature, oxygen mole percent (wet) and CO mole percent (wet), along a single traverse (connecting Ports 2 and 8) at six (6) different elevations.

Conclusions with respect to the predictions of the experimental data may be itemized as follows:

- The temperature predictions, for the Air test and the OF25 test, are generally aligned either with the separate data measurements taken using traditional suction pyrometers and optical probes. The predictive accuracy appears to be reasonable and acceptable. For the OF30 test, the predictions were also acceptable, but the computations exhibited an excessive heat release in the upper furnace. This excessive computed heat release may be due to errors in the boundary conditions.
- For the Air test and the OF25 test, the calculations in the upper furnace exhibit an oxygen-starved core, near the burner symmetry axis, that is substantiated by the experimental data. The width of the core appears to be reasonably captured. However, the peak computed oxygen levels, on either side of the core, and extending to the walls, are higher than the experimental data. The calculated oxygen concentrations for OF30 Test 334 tend to underpredict the experimental oxygen concentrations in the main burner zone, which may be symptomatic of a feed stream boundary condition issue.
- The CO predictions for the Air test and the OF25 test are moderately good. The CO predictions for OF30 are somewhat excessive relative to the data in the upper furnace.
- The unburned carbon in the char appears to be reasonable.

From a comparison of the calculations with the data, it is apparent that the fidelity of the computations could always be enhanced for both air and oxy combustion simulations, through both continued submodel development and a formalized uncertainty quantification process. Nevertheless, the predictions of the Air and OF OxyPP experimental data indicated that FLUENT®, given the model settings, the property databases, and the associated user-defined functions, was capable of adequately predicting both air and oxy combustion. The predictive accuracy for oxy firing appeared to be just as reliable as it was for the air-fired simulation. Based on these results, it is believed that oxy combustion calculations can be pursued at Alstom on the same basis as commensurate air combustion studies.

2. Objectives

Alstom has worked with various corporate entities and universities in a number of broad, internal development programs that have been dedicated to oxy-fuel combustion research. One of the purposes of the programs has been to access world-class experts from around the world, and to gather detailed experimental data at various combustion test facilities, where air and oxy combustion tests were performed under controlled conditions. An important aspect of those programs was to apply and enhance CFD modeling tools for prediction of combustion performance for scale-up from pilot scale to commercial equipment. In conjunction with that effort, Alstom conducted CFD modeling tasks to model the various pilot test facilities and to compare the calculations with the experimental data.

This report summarizes computational fluid dynamics work that was done, in part, to support a portion of Subtask 6.1 (DOE/NETL Cooperative Agreement No. DE-NT0005290; see Ref. 1). This program has a number of different objectives.

Subtask 6.1 – CFD Oxy-Combustion Model

- The ANSYS FLUENT® code, with improved submodels for combustion and radiation under oxy-combustion conditions, will continue to be applied and validated.
- Application of large-eddy simulation (LES) modeling for oxy-boiler application will be assessed and compared with simplified steady-state simulation approaches (specifically FLUENT®). More rigorous analysis of experimental and simulation data will also be conducted to statistically quantify uncertainty of modeling/prediction at both submodel and model levels. This will help improve prediction capability and accuracy of the modeling tools. This work will be conducted in collaboration with the Institute of Clean and Secure Energy (ICSE) at the University of Utah (Professor Phil Smith).
- Simulation results will then be compared with experimental validation data from small-scale facilities, the 15 MWth BSF and from the 30 MWth Schwarze Pumpe oxy pilot plant. The CFD code evaluation will include predictions for combustion, heat flux distribution, corrosion, and pollutant control.

This chapter only addresses the application and validation of the FLUENT® code to the third item – "Simulation results will then be compared with experimental validation data from small-scale facilities." – specifically the 30 MW_{th} Schwarze Pumpe oxy pilot plant. Simulations of the 15 MW_{th} BSF and the KSVA 500 kW_{th} test facility (University of Stuttgart) have been reported in other chapters of this Volume III.

The final cases selected for modeling corresponded to the air-fired test (Air Test 332), and the oxy-fired tests (OF25 Test 333 and OF30 Test 334). The OF25 and OF30 designations are indicative of the percent oxygen in the gas feeds (i.e., nominally 25% and 30% by mole) after oxygen was added to the recycle flue gas stream. The cases summarized are all fired with lignite coal.

The overall objective of this CFD modeling task was to simulate the performance of the oxy-fired, swirl-burner configuration tests in the Schwarze Pumpe pilot plant, and to use the simulations to validate the CFD code, submodels, and physical/chemical properties for oxy-combustion. This report describes the approach, boundary conditions, and prediction results for three (3) different Oxy Pilot Plant configurations. The FLUENT® code was used by Alstom to examine the apparent differences between air- and oxy-firing for a lignite coal. These CFD simulations were also used to investigate the impact of various submodel enhancements and model options. The overall goal was to develop a more accurate and

reliable computational tool and methodology for modeling oxy combustion to support the scale up from pilot scale to commercial scale for oxy-fired boilers.

3. Description of Schwarze Pumpe Pilot Plant

3.1 Overall Geometric Description

The main furnace has a centrally located single burner on the top of the main combustion section. The burner arrangement is shown in Figure 3-1. The burner inlet section is partitioned into 3 independently controllable flow zones. Burner swirl levels can be adjusted by means of controls on the top of the burner. The burner configuration was specially designed for the pilot plant, using design principles that could be adapted to full-scale burners.

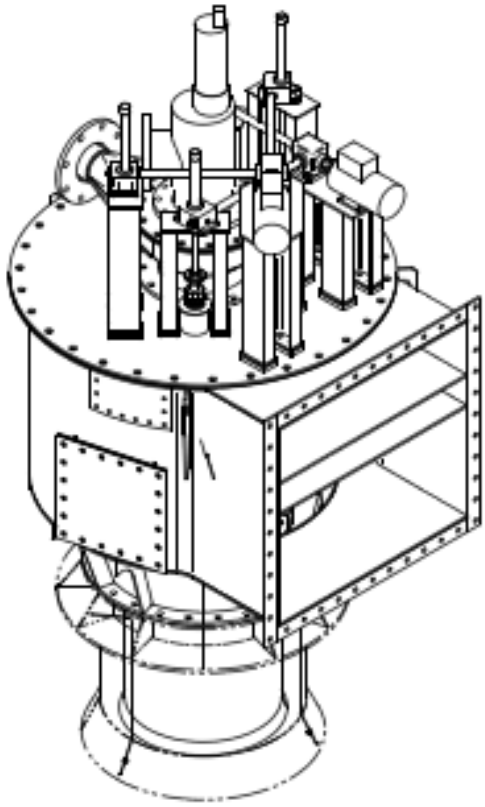

Figure 3-1. Burner Arrangement

The burner fires downward into the main furnace section that has a nearly square cross section measuring 4100 mm (width) x 4080 mm (depth). The adjacent convective section contains the superheater sections with cross sectional dimensions of 4100 mm (width) x 2400 mm (depth). The side and front views of the pilot plant, showing some of the port arrangements, are shown in Figure 3-2.

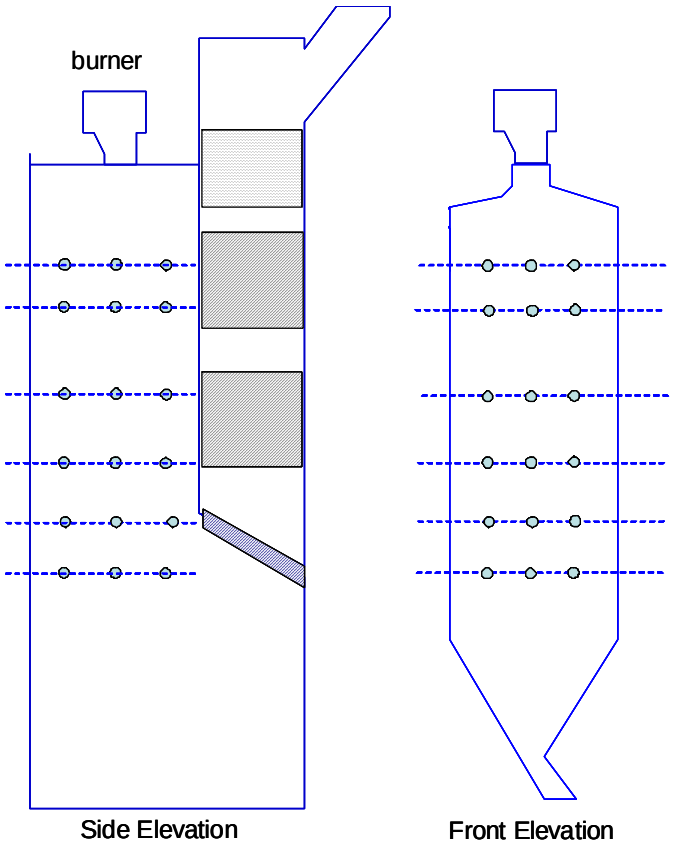

Figure 3-2. Arrangement of the Oxy Pilot Plant

The data measurements for each separate test, provided to Alstom, consisted of eight (8) measurement planes. The elevations in the furnace, at which experimental measurements were extracted, are denoted as Measurement Levels, indicated in units of millimeters from the reference ground level. Levels 1 through 8 correspond to the measurement plane data sets provided to Alstom for each test. The nominal or approximate elevations for the Measurement Levels are provided in Figure 3-3. Two levels of overfire air are also included, denoted as OFA-1 and OFA-2. The OFA-1 level includes two sets of opposing nozzles on both sides of the furnace. The OFA-2 level is similar, but shifted closer to the convective pass entrance. There is also an optional SCR system incorporated in the downstream sections of this unit.

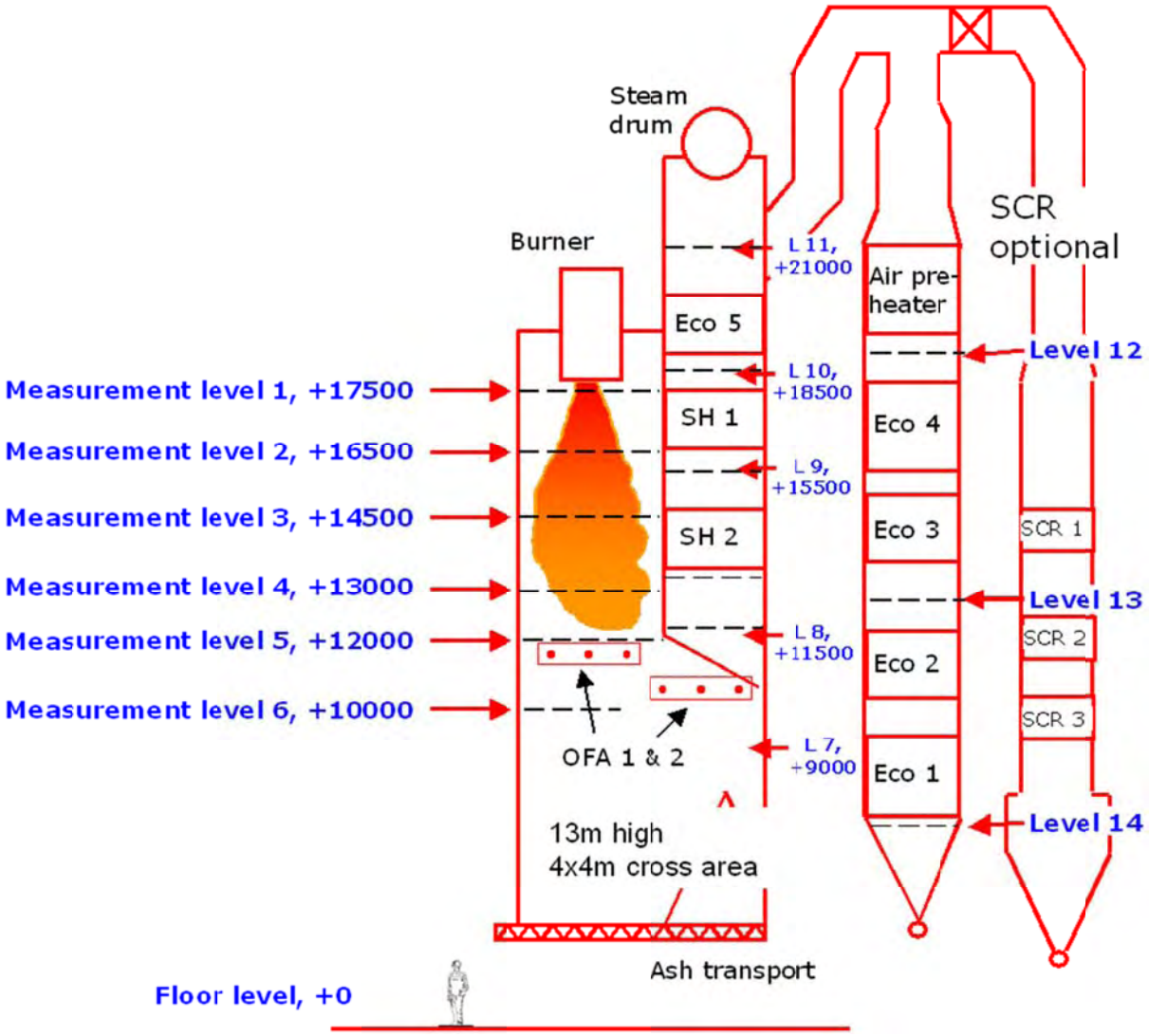

Figure 3-3. Furnace Probe Measurement Elevations or Levels

A synopsis of the port and measurement level elevations and nomenclature are provided in Table 3-1.

Table 3-1. Furnace Wall Measurement Ports with Comments

Front-Wall (FW) Elevation	Measurement Level (ML)	Comments
FW-1	ML-1	
FW-2	ML-2	
FW-3	[None]	
FW-4	ML-3	
FW-5	ML-4	
[None]	ML-5	Corresponds to the OFA-1 elevation.
FW-6	ML-8	ML-8 ports are in convective pass below Superheater-2 (SH-2) section, although there are also some side-wall ports in the main furnace region.
FW-7	ML-6	At elevation similar to that of OFA-2, although OFA-2 ports are situated in a span below the convective pass.
FW-8	ML-7	At elevation below OFA-2; measurement ports positioned below convective pass.

Each Measurement Level (ML) consists of a series of ports on different walls with access doors. Measurement Level 1 (ML-1) is closest to the burner, ML-5 corresponds to the OFA-1 port locations, and ML-6 is similar to the OFA-2 port elevation. The ML-7 ports are close to the hopper bend line and are situated primarily below the convective section and below the OFA-2 ports. The ML-8 port is located in the convective section above the OFA-2 elevation. At each level a series of samples was extracted from probes inserted from the outside of the furnace as indicated in Figure 3-4. Three (3) lateral ports were provided on each of three (3) walls – the front wall, the left side wall, and the right side wall of the main furnace.

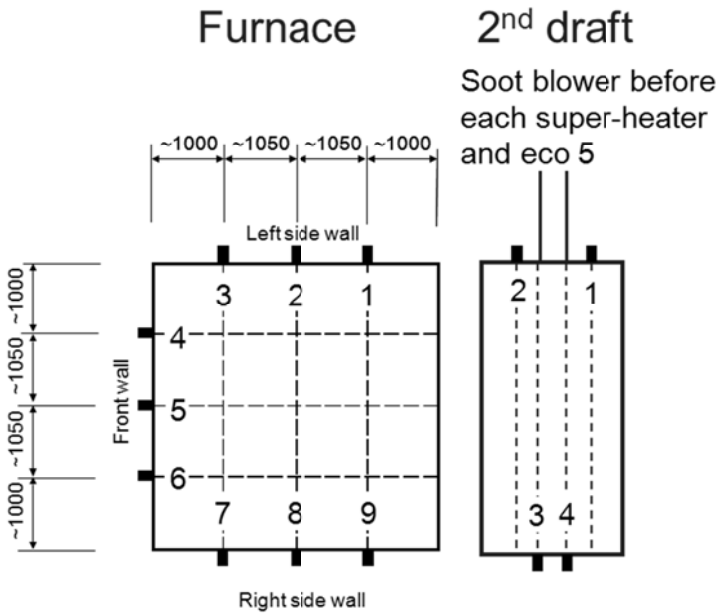

Figure 3-4. Sample Locations in the Furnace and Convective Section

These experimental measurement elevations or levels were used in conjunction with the test program to perform measurements of gas temperature and species concentrations. Gas species and temperature measurements were collected by Vattenfall Europe Power Consultant GmbH (VPC) with traditional gas sample probes and suction pyrometry, respectively. Additional gas species and temperature measurements were gathered by the Danish Technical University (DTU) team.

In addition to the sampling test ports at various locations on the front and side walls, a series of ports on the front wall (along two vertical lines) were devoted to the measurement of the local heat flux. The heat sensors are not removable probes, but rather left in place and are subject to deposits and slagging. According to the FLUENT definition, the surface incident heat flux at the sensor surface is equal to the sum of the absorbed, reflected, and transmitted heat fluxes at the control surface. The transmitted heat flux is zero (the probe is opaque), but due to slagging deposits, the reflectivity may be significant. Therefore, the absorbed radiation heat flux calculated by FLUENT (rather than the incident radiation) is used for comparison with the net radiation flux measured by the sensors.

4. Technical Approach

4.1 Modeling Approach

The approach to the modeling of the OxyPP at Schwarze Pumpe was to simulate the burner geometry with as much detail as possible, consistent with other round-burner modeling studies performed at Alstom. In previous modeling efforts of wall-burner furnaces, a detailed single burner model was constructed along with a full-furnace model that used a simplified representation of the many individual burners. For the full-scale furnace with rows of identical burners, a set of flow profiles derived from the single burner models could be prescribed and applied at a boundary plane in the burner upstream of the burner quarl, but downstream of the complicated vanes and windbox internals. This concept of using a detailed single burner to derive flow profiles that can be applied to a collection of burners is appealing, because it reduces the complexity of the full-furnace model to a mesh that both (a) comprises sufficient detail near the burners to capture the flame zone, and (b) leaves enough "room" in the mesh size for the mesh to be reasonably fine near the overfire air ports and other geometry features of importance. Such meshes can be constructed primarily from hexahedral (hex) mesh elements and a limited number of tetrahedral (tet) transition volumes. With this strategy, a furnace with, e.g., on the order of 24 to 48 burners could be meshed with about 3 to 5 million cells, which is within the computational resources and run times for a typical modeling study at Alstom.

For the Schwarze Pumpe modeling effort, the 30 MW Schwarze Pumpe furnace and burner were viewed in a fashion similar to the "detailed single burner," where the complex burner internals were meshed and merged with a relatively simple mesh of the downstream cavity. In this approach, where the entire furnace is treated as a detailed single burner model, it was not necessary to break the model into two separate models (i.e., a very detailed burner model with all the internals, and a furnace model where the burner is represented in a more crude fashion by a set of simplified 3-D velocity profiles applied to convenient inlet annuli).

4.2 Development of the Model Geometry

The geometry for the burner was provided previously in a series of dimensioned drawings. The drawings include multiple views of the burner housing, swirler hubs and swirler vanes. From these drawings, a 3-D geometry of the burner was created using ANSYS Gambit V2.4. An important feature of the Alstom dried-lignite burner (DLB) was the axial position of the swirler hubs. These hubs ride on rollers and shift vertically to partition the incoming air flow through the enclosed swirler hubs, or around the outside of the swirler hubs, where the air stream accelerates axially toward the burner throat. The position or swirler setting of the Umluft-1 (UML-1) and Umluft-2 (UML-2) hubs determines the degree of swirl inside the burner. The setting, expressed as a percent of full stroke, was oriented such that 100% corresponds to the swirler hub fully inserted into the tapered passage to channel all of the air in that zone through the swirler. Different values of the swirl settings required shifting the location of the hubs, which contained a set of fixed swirl vanes that were included in the model. Therefore different swirl settings required re-meshing of the burner, which resulted in slightly different furnace meshes for each setting. However, the impact of the swirl settings could be quantified at various locations downstream, and an initial appraisal of the results indicated that small changes could be made in the swirl setting without a significant downstream effect. Furthermore, while the test documentation appeared to indicate that for the various test conditions the burner swirl settings were different, the documentation was somewhat ambiguous or unclear on the matter, and a decision was made to use a single set of swirl settings for the 3 conditions studied. This

report describes the results for models generated using a single set of swirl settings: Umluft-1 = 65%, and Umluft-2 = 21%.

Solid views of the burner geometry are provided in Figure 4-1. The figure shows a pair of pictures, the left picture showing a transparent view of the two swirlers, and the picture on the right shows the encased swirlers and the partitioned inlet plenum. (The figures are illustrative only and do not necessarily correspond to the same swirl condition.) The coal and transport air/gas enter the "staub" through the annulus surrounding the "core air" cylinder (the yellow cylinder in the left picture). A "horn" plenum, that fed the annulus was modeled originally, but difficulties with coal ignition occurring in the stagnation regions inside the horn eventually induced Alstom to discard the horn in favor of a simple annular inlet boundary condition for the coal feed.

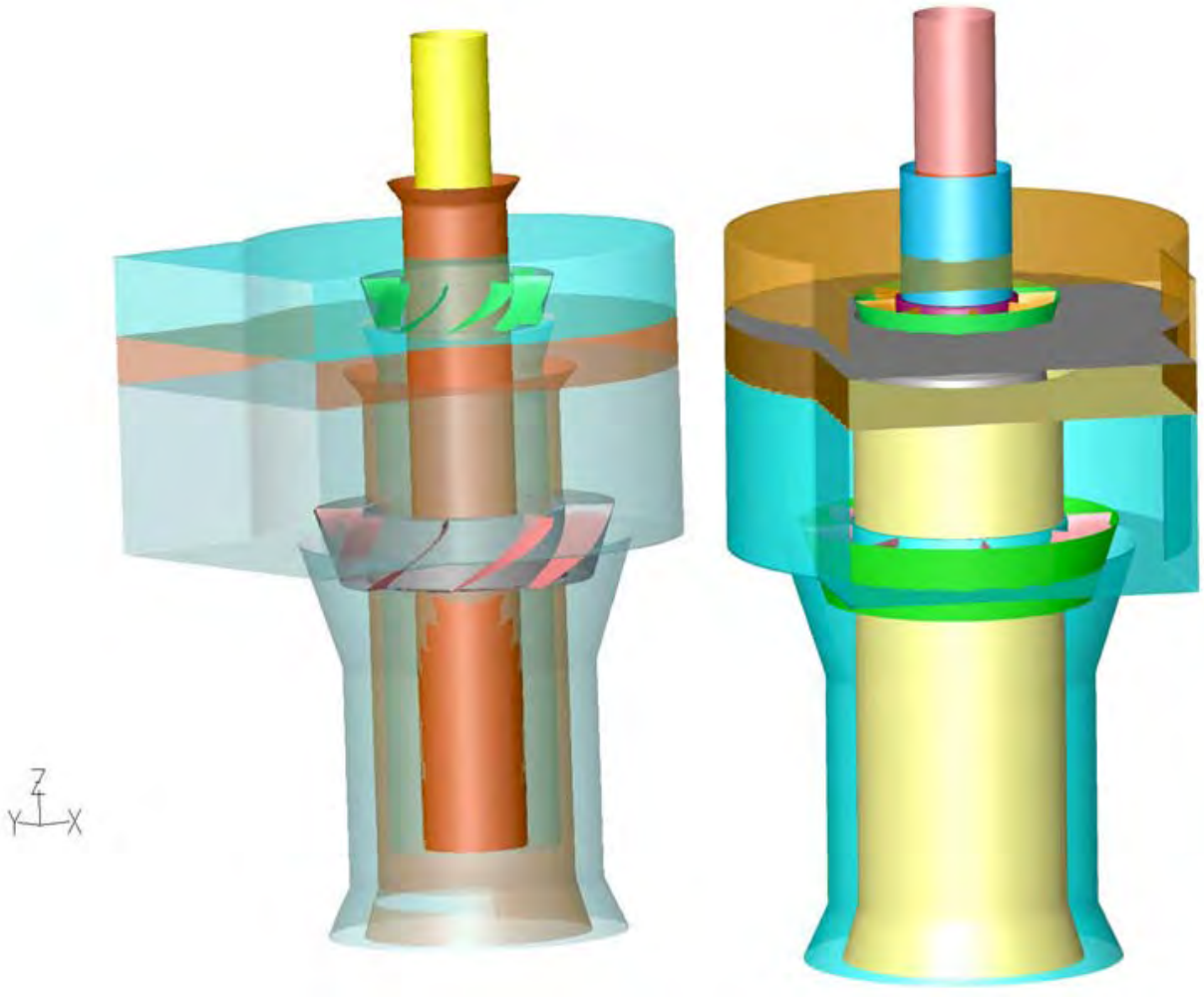

Figure 4-1. Solid Geometry View of Burner

The velocity distribution predicted for one of the cases is illustrated in a cutaway view with contours on the (Y-Z) mid-plane in Figure 4-2. The position of the lower swirler, relative to the surrounding converging section, clearly shows that hub insertion is not fully 100%, and that the resulting flow through the annulus and into the furnace, is a combination of axially-directed flow (from the portion of the flow that bypasses the swirler) and the portion of the flow that directly passes through the swirler.

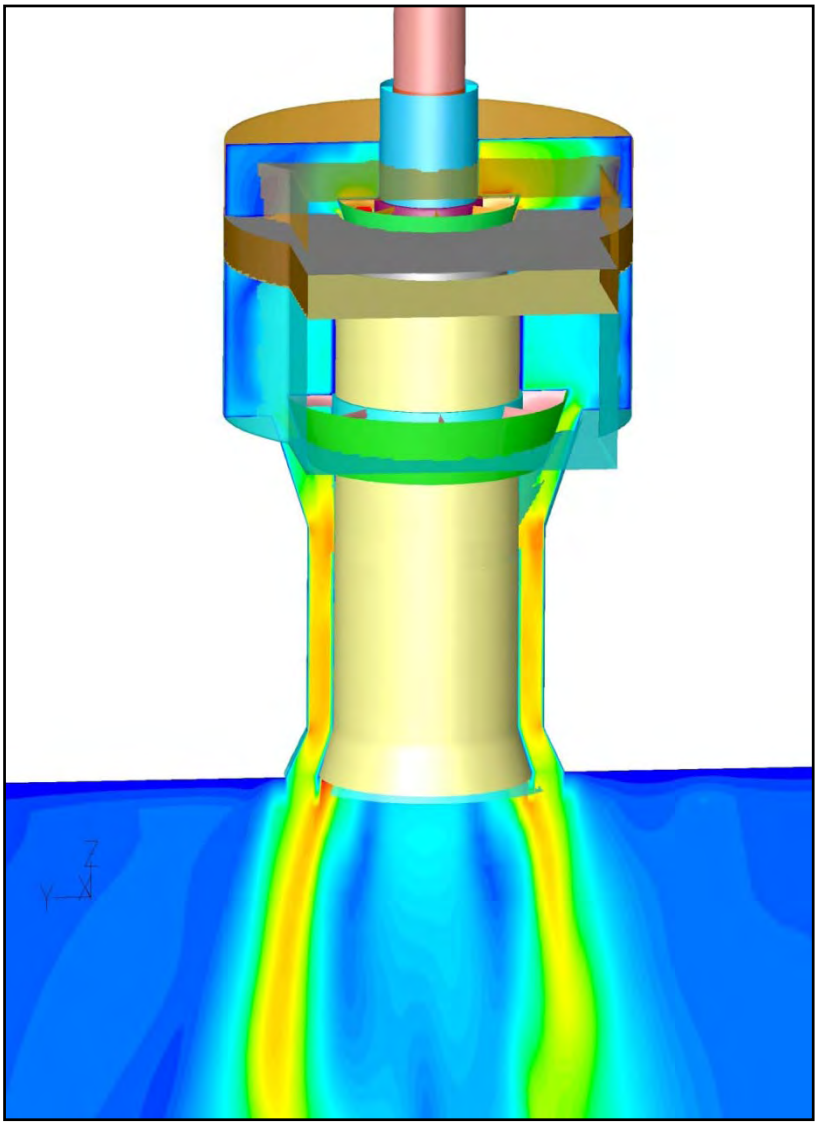

Figure 4-2. Cutaway View of Burner with Velocity Contours

The geometry of the remainder of the furnace was constructed from detailed drawings. A solid rendition of the burner and the furnace is provided in Figure 4-3. The modeled furnace zone extended from the burner inlet flange to the outlet of the second pass. The multicolored wall sections may represent distinct wall zones to which a separate wall thermal boundary conditions can be attached. They may also represent discrete volumes, such as those in the convective pass, in which a volume can encompass a superheater or economizer section, each with individualized pressure drops and volumetric energy extractions. The apparent "holes" on each of the side walls are the two sets of overfire air ports. It can be seen that the holes or jets for the top level of overfire air (OFA-1) are staggered relative to each other on opposite sides of the wall.

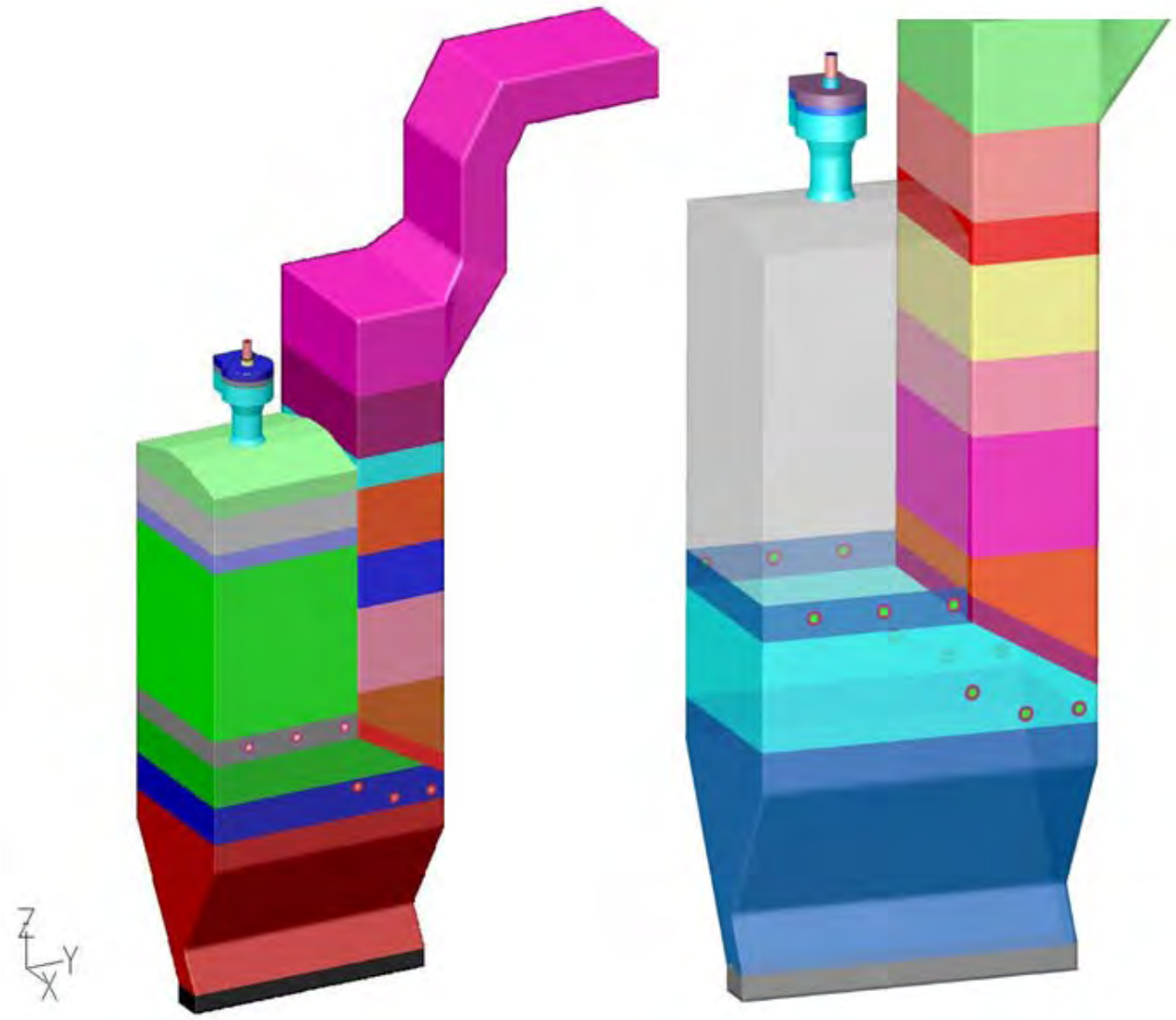

Figure 4-3. Furnace Geometry and Wall Sections

4.3 Computational Mesh

The computational mesh developed for this geometry includes both the burner and the entire furnace model from the burner inlet flange up to the outlet of the second pass. Alstom used its experience with Gambit to develop the 3-D geometry and the resulting computational mesh. The focus of the model simulations included the center or core zone, which encompasses the flame zone, the central recirculation zones, and the larger gradients downstream of the burners. The mesh consists of 4.5 million cells, with the detailed mesh extending from the burner to a location just upstream of the overfire air nozzles. Downstream of the overfire air nozzles, the hopper and backpass sections comprise a fairly coarse mesh and do not include geometric representation of the screen tubes, superheaters or other convective section surfaces. Instead, suitable draft loss and constant (volumetric) energy absorption rates were defined to yield reasonable predictions of the backpass temperature profile. A single mesh was used for all three test cases. The computational mesh at the centerline slice through the burner appears in Figure 4-4.

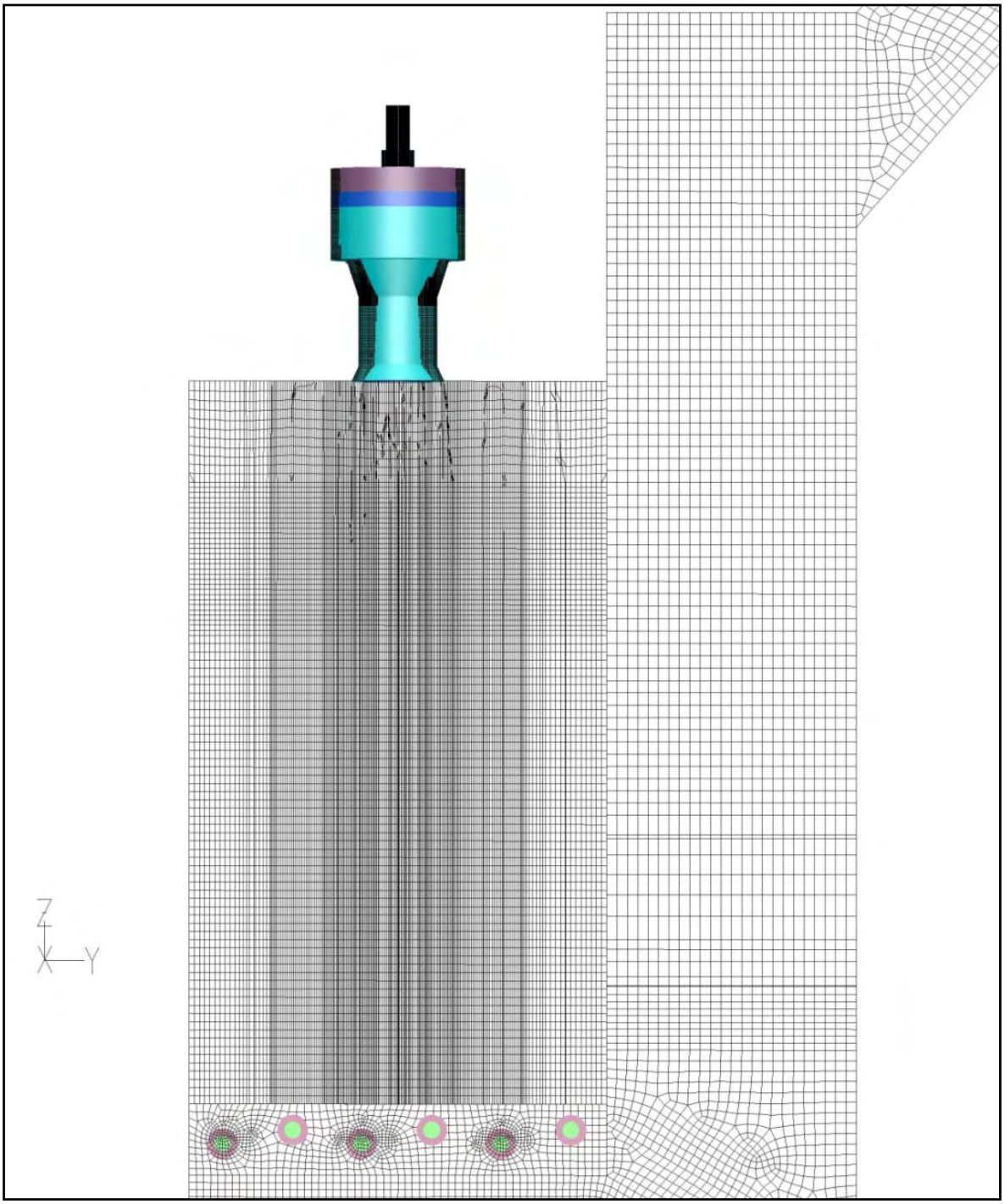

Figure 4-4. Mesh at the Burner Centerline Slice

The mesh distribution is concentrated in the center zone downstream of the burner. The cell distribution and topology of the mesh in the main furnace section is shown in a series of slices indicated in Figure 4-5.

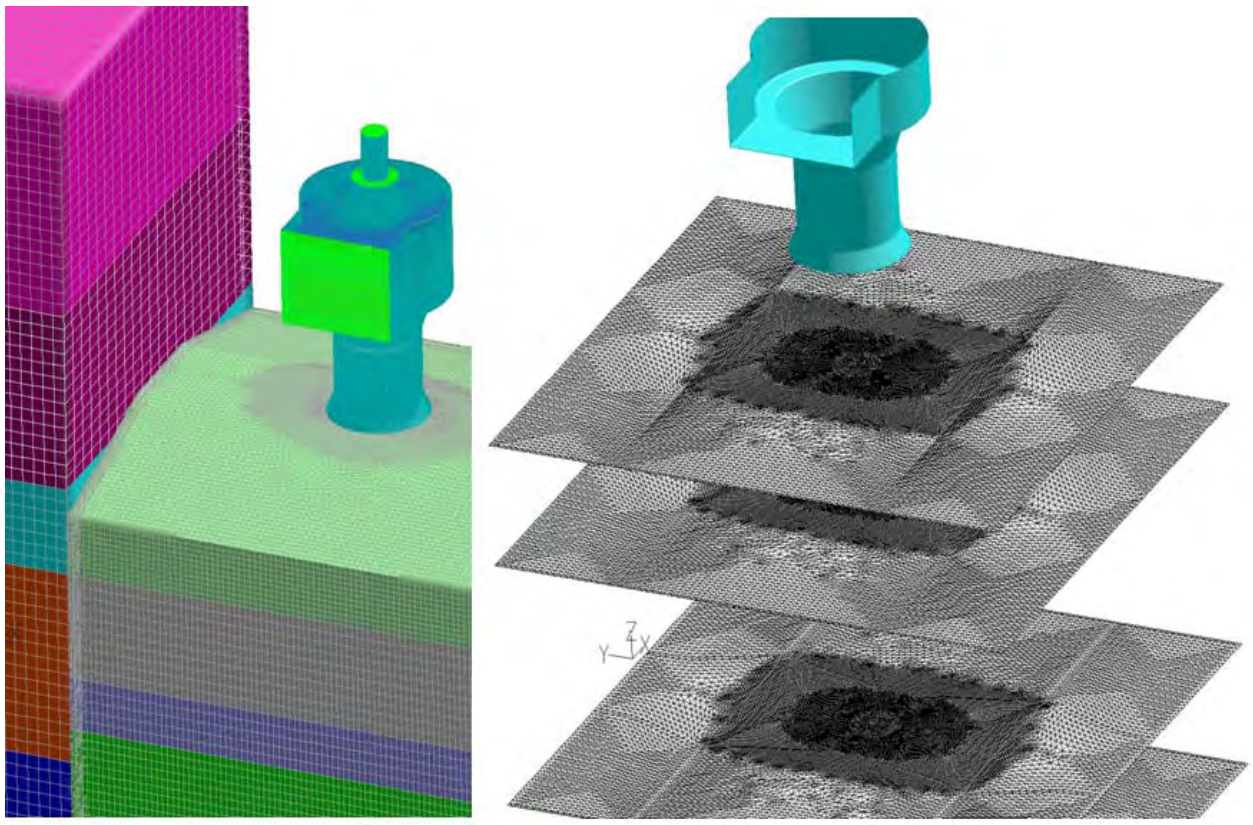

Figure 4-5. Mesh Distribution at Various Elevation Slices

4.4 Boundary Conditions

The boundary conditions for these models were formulated after discussions between Alstom and Vattenfall, which included a review of the data records and associated performance calculations to refine and check overall balances on the steam side during the test interval. Alstom provided these performance calculations on the steam-side checks, while other measurement records and data were captured and recorded by different Vattenfall groups, both in Germany and in Sweden. By using feedwater flows and temperatures, the performance predictions conducted by Alstom were sufficiently detailed to confirm that the operating conditions were consistent for the fuel firing rate. After a review of the steam-side calculations and experimental data was conducted by the teams at Alstom and Vattenfall, a recommended set of boundary condition specifications was generated. Alstom used this recommended set of flow boundary conditions and fuel analyses in its computations. Table 4-1 provides a summary of the coal composition, particle size distribution, and flow conditions used for the air-fired test (Air Test 332), and the oxy-fired tests (OF25 Test 333 and OF30 Test 334). The OF25 and OF30 designations are indicative of the percent oxygen in the gas feeds (i.e., nominally 25% and 30% by mole) after oxygen was added to the recycle flue gas stream. The tests summarized are all fired with lignite coal.

Table 4-1. Summary of the Validation Conditions for Combustion in the OxyPP

Fuel and transport gas

Ultimate analysis:

	Air case	OF25 case	OF30 case
C [mass%]	57.40	57.70	58.24
H [mass%]	4.36	4.41	4.45
O [mass%]	21.09	20.89	20.68
N [mass%]	0.73	0.71	0.62
S [mass%]	0.62	0.63	0.59
Moisture [mass%]	10.10	9.80	9.84
Ash [mass%]	5.70	5.86	5.58

Proximate analysis and heating value

	Air case	OF 25 case	OF30 case
Volatiles [mass%]	46.3	46.2	45.6
Fixed C [mass%]	37.9	38.1	39.0
Moisture [mass%]	10.1	9.80	9.8
Ash [mass%]	5.7	5.9	5.6
LHV [kJ/kg]	21412	21360	21496

Particle size distribution

	Air case	OF25 case	OF30case
R20 [mass %]	73.04	76.7	77.08
R40 [mass %]	56.18	61.3	59.8
R90 [mass %]	30.70	34.8	32.56
R200 [mass %]	7.01	7.58	7.19

Flows

	Air case	OF25 case	OF30 case
Fuel flow [kg/s]	1.277	1.296	1.288
Fuel temperature [°C]	25	25	25
Transport air + sealing gas [Nm^3/h]	1600	1421	1433

It was believed that the oxygen level in the stack measurements was corrupted somewhat because of air in-leakage, where the leakage was presumed to be somewhere in the convective section, backpass or in the cleanup equipment. Consequently, the flow rates were adjusted somewhat, based on measured oxygen concentrations at Measurement Levels 6, 7, and 8, to give calculated oxygen levels leaving the furnace that were believed to be more accurate. The inlet boundary conditions (mass flow rates, temperatures, and compositions) for the various inlets are provided in Table 4-2:

Table 4-2. Inlet Boundary Conditions

	Mass Flow Rate [kg/ s]	Mass Distribution [%]	Temperature [K]	O2 Mole Fraction [%]	CO2 Mole Fraction [%]	H2O Mole Fraction [%]	SO2 Mole Fraction [%]	N2 Mole Fraction [%]
Air Test 332								
Inlet Core (Kernluft)	0.535	5.03	523.00	20.71	0.03	1.12	0.00	78.14
Inlet OFA-1	0.636	5.98	523.00	20.71	0.03	1.12	0.00	78.14
Inlet OFA-2	0.636	5.98	523.00	20.71	0.03	1.12	0.00	78.14
Inlet Primary (Staub)	0.532	5.01	313.00	4.00	15.30	4.00	0.00	76.70
Inlet Umluft-1	3.080	28.97	523.00	20.71	0.03	1.12	0.00	78.14
Inlet Umluft-2	4.877	45.88	523.00	20.71	0.03	1.12	0.00	78.14
Inlet Umluft-3	0.333	3.13	523.00	20.71	0.03	1.12	0.00	78.14
Total Inlet Gas	10.630	100.00						
Coal Flow Rate	1.277							
Stoichiometric O2/ Coal Ratio	1.670							
Excess O2 Ratio	1.102							
MBZ Excess O2	0.96							
OF25 Test 333								
Inlet Core (Kernluft)	0.576	5.14	508.00	25.76	48.78	22.92	0.20	2.34
Inlet OFA-1	0.754	6.73	508.00	25.76	48.78	22.92	0.20	2.34
Inlet OFA-2	0.744	6.64	508.00	25.76	48.78	22.92	0.20	2.34
Inlet Primary (Staub)	0.726	6.48	313.00	4.30	84.20	4.30	0.00	7.20
Inlet Umluft-1	3.592	32.07	508.00	25.76	48.78	22.92	0.20	2.34
Inlet Umluft-2	4.430	39.56	508.00	25.76	48.78	22.92	0.20	2.34
Inlet Umluft-3	0.377	3.37	508.00	25.76	48.78	22.92	0.20	2.34
Total Inlet Gas	11.199	100.00						
Coal Flow Rate	1.296							
Stoichiometric O2/ Coal Ratio	1.685							
Excess O2 Ratio	1.153							
MBZ Excess O2	0.99							
OF30 Test 334								
Inlet Core (Kernluft)	0.597	6.53	486.00	29.22	45.79	21.44	0.17	3.38
Inlet OFA-1	0.799	8.74	486.00	29.22	45.79	21.44	0.17	3.38
Inlet OFA-2	0.706	7.72	486.00	29.22	45.79	21.44	0.17	3.38
Inlet Primary (Staub)	0.733	8.02	313.00	4.20	84.50	4.30	0.00	7.00
Inlet Umluft-1	3.657	40.01	486.00	29.22	45.79	21.44	0.17	3.38
Inlet Umluft-2	2.270	24.84	486.00	29.22	45.79	21.44	0.17	3.38
Inlet Umluft-3	0.378	4.14	486.00	29.22	45.79	21.44	0.17	3.38
Total Inlet Gas	9.140	100.00						
Coal Flow Rate	1.288							
Stoichiometric O2/ Coal Ratio	1.704							
Excess O2 Ratio	1.052							
MBZ Excess O2	0.87							

Note: MBZ = Main burner zone or burner zone upstream of the OFA

From the fuel and transport gas flow rates, inputs to FLUENT were calculated and assigned to the various burner zone inlets, with compositions and flows to match the required settings. To determine the relative partitioning of the lignite coal into its computational constituents, the ultimate and proximate analyses were processed to determine the moisture, volatile, and char inputs. Alstom assigned a high-temperature volatile yield factor based on a calculation using PC Coal Lab software. PC Coal Lab calculates the volatile high temperature yield, as well as the composition of the volatiles. The initial char fraction was

also determined by difference, and prescribed in the corresponding input sections of the FLUENT code. Because of the very similar composition of the fuel for the 3 test conditions, the same high-temperature volatile yield (multiplication) factor was used for all 3 cases, which produced a high-temperature volatile yield of 65.62 DAF % for the Air test, 65.37 DAF % for the OF25 test, and 64.34 DAF % for the OF30 test. Since the composition of the fuel was different for each run, an exact calculation of the products of combustion and excess oxidant levels was also determined for each run.

For the lignite fuel, the particle size distribution was fitted to a Rosin-Rammler function, with the specified minimum and maximum particle size, characteristic mean diameter, and calculated fitting exponent. These values were transferred to the cases as prescribed inputs. A plot of the typical particle size distribution curve for the fuel, for each case, appears in Figure 4-6.

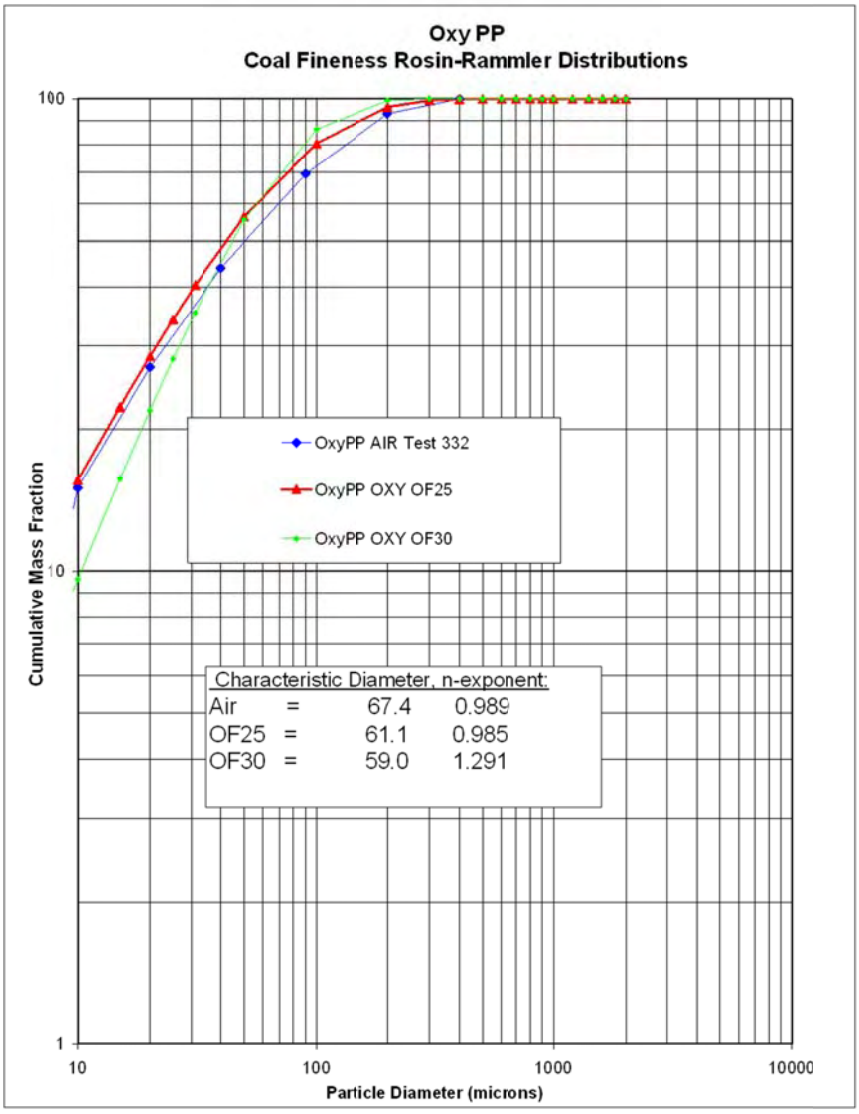

Figure 4-6. Coal Fineness Distribution

To model the wall heat transfer, a specified temperature boundary condition was used in conjunction with the FLUENT® code's thin-wall thermal resistance formulation. The specified temperature is on the far side of a thin wall, away from the adjacent fluid zone. The thermal resistance is the ratio of the parameters $\Delta x/k$, where Δx is the thickness of the resistance material(s), and k is the thermal conductivity.

It is usually necessary to adjust the thermal conductivity k of each zone (for a given inner surface temperature) to match the measured temperature data. For the present cases, the furnace walls were given a specified temperature of 500 K, a wall emissivity of 0.7, a thermal conductivity of 16 W/m-K (material denoted as "steel"), and a wall thickness equal to 0.002 m in the furnace zone and 0.005 m in the convective pass.

4.5 Model Selections

The majority of these OxyPP simulations were conducted using ANSYS FLUENT Version 6. Because Version 12 had just been issued during the period of time when the modeling effort had already been initiated, Version 6 continued to be used throughout the program. Similarly, when Version 14 was released, it was determined that the enhancements to the Version 14 software were not critical or necessary to the success of the modeling effort, and therefore no switch was made to the upgraded version. The models that were deployed in Version 6 had user-subroutines compiled for Version 6 as well. One reason for not switching over to the newer releases mid-stream is due to the customized post-processing utilities used to visualize the Fluent Version 6 results. For example, the filters that read the FLUENT case files do not work with Version 14.

For the main gas-phase combustion reactions, the turbulence-chemistry interaction was modeled using the composite Magnussen eddy-dissipation (mixing-limited / fast-chemistry) and Arrhenius rates (kinetically-limited) combustion submodel, in which the smaller of the two rates (eddy-dissipation or Arrhenius rates) takes local precedence. The Magnussen eddy-dissipation model is also commonly referred to as the "eddy-breakup" model in the open literature; over the years, this particular model has been used for almost all of the boiler computations at Alstom.

The gas-phase reaction mechanism was based upon four (4) single-step, irreversible, global reactions – volatile decomposition/reaction, CO oxidation, H_2 oxidation, and C-gas (surrogate soot species) oxidation. These same global rate expressions for the gas phase reactions (whether for oxy or air combustion), have been applied to other oxy-combustion systems that have been studied at Alstom. The global reaction mechanism includes nine (9) gaseous or volumetric species: volatile, O_2, CO_2, CO, H_2O, SO_2, H_2, C-gas, and N_2. Species transport equations are converged for all of the species except for N_2, which is calculated by difference using mass conservation principles.

All of the carbon in the volatiles is relegated to the gaseous C-gas species, and in a very approximate way, the C-gas is treated as a surrogate for the soot formed from the tars during secondary devolatilization. The C-gas is then allowed to oxidize to CO. The C-gas species is not coupled to the radiation model as a way to account for the impact of soot on radiation, but is simply treated as a direct carbon source, with a customized reaction rate that is different from that of the char particle. The concept of creating a C-gas species was suggested by ANSYS as a means of transferring some of the carbon constituents in the volatile to the gas phase without artificially giving it back to the char.

In the present runs, the char consists only of pure carbon (designated as C<s>), and ash. The heterogeneous reactions are composed of one (1) oxidation and two (2) gasification reactions, using the multi-surface reaction model. The char burning rate is a combination of a film-diffusion rate in series with a chemical reaction rate. The apparent chemical reaction rate actually includes the composite effects of pore diffusion and interior particle reaction, expressed on an external surface area basis. The overall rate therefore uses a combination of an Arrhenius based kinetic rate, as well as a diffusion rate of the reactant species through the film to the surface of the char particle. The char can be oxidized or gasified simultaneously, depending upon the local concentration levels, although, usually, the magnitude of the

rates are such that oxidation will dominate whenever oxygen is present. The addition of heterogeneous char gasification reactions provides a mechanism to convert the char to CO and H_2 in an oxygen deficient environment.

These same reaction rates were maintained for all of the OxyPP cases. The stoichiometric coefficients for the chemical reaction expressions were also maintained for all cases, except for the fuel-specific thermal breakdown of the volatile species into a set of oxidized or partially oxidized products. The changes impacted only the thermal decomposition reaction. Because the fuel composition was slightly different for each case, the composition of the volatile reaction products were also different. In the simple reaction mechanism used, the formation enthalpy of the "volatile" species was adjusted to balance the measured fuel heating value against the heat released from the combustion products dictated by the ultimate analysis. Depending upon the volatile composition and oxidation extent of the devolatilization reaction products, the reaction could be either exothermic or endothermic. It was important for ignition to make sure this first breakdown reaction was not endothermic which would delay the ignition progress using this simplistic reaction mechanism. The composition and oxidation extent of the products CO and H_2O products were adjusted so that this devolatilization reaction was neither endothermic nor exothermic. All other general reaction coefficients in the 7-reaction mechanism were the same for all of the cases.

It should be noted that Alstom's intent was to use the same kinetic parameters in both the OxyPP calculations and the IFK calculations (documented in a separate chapter of Volume III), since both experimental programs compared oxy- and air-fired scenarios, and both programs utilized the Schwarze Pumpe lignite.

Alstom used the higher-order Reynolds Stress Model (RSM) for turbulence closure. This model was selected to better capture the strength of the recirculation zones to maintain ignition and flame in the quarl, based on the difficulty that was observed in modeling the original burner configuration (Burner A). For that original burner geometry, the computational flame was observed to blow off in an unpredictable fashion, despite changes in reactivity to promote ignition. It was reasoned that using a model that was more suitable for capturing the swirl flow characteristics would improve the chances of maintaining the flame attachment. The revised Burner-B configuration was used for the majority of the operational tests at Schwarze Pumpe, including the period of time when the measurements of interest were taken. Therefore, the subsequent discussion and results apply to this revised Burner-B configuration and will be identified without the B designation. The use of the RSM turbulence model was retained for all of the modeling work associated with the burner configuration.

Twenty particle diameters were defined for the Rosin-Rammler (logarithmic) distribution, using one stochastic injection for each particle size group. Other particle model options simulations included the "discrete random walk" option, but not the "random eddy lifetime" option. The "wet combustion" model was also activated, to allow coal moisture to evaporate from the particle, prior to devolatilization. A single-rate model was used for devolatilization and the swelling factor was set to unity.

User-defined functions (UDFs) were used for the gas absorption coefficient and for the particle absorption efficiency. A constant value was input for the particle scattering factor and for the scattering coefficient (although the specification of a particle scattering factor is supposed to override the specification of the scattering coefficient in the FLUENT code).

The SIMPLE algorithm was used for the pressure-velocity coupling, second-order discretization was used for the pressure, and second-order upwind numerics were used for momentum, turbulent kinetic energy, and the turbulent dissipation rate. First-order discretization was used for all other transport equations, including the RSM.

Early in the program, two scoping studies were performed. First, Alstom demonstrated the impact on the downstream flow field based on how much of the burner was included in the model. This comparison showed predictions with the full burner, including the swirlers and lateral/side inlet, versus the predictions where the burner inlet profiles were applied downstream of the swirler vanes. Based on this comparison, the recommendation was made to utilize a grid in which the burner mesh was fully integrated with the furnace mesh. In the second scoping study, Alstom performed some additional screening or comparison runs to look at the impact of turbulence models. The comparison study included both RSM and k-ε turbulence model cases with the different inlet configurations. Based on this body of work, the RSM model was retained for all subsequent calculations. Some of the results from the scoping studies will be shown in a subsequent sub-section.

4.6 Burner Characteristics

The aerodynamics of the burner and the interaction of the various streams emerging from the burner downstream of the confluence plane are shown in Figure 4-7, in which the results from the Air case and the OF25 case are compared. The aerodynamics are displayed using pathlines which begin at various locations in the plenum. These runs were done with the RSM model, which tends to "laminarize" the flow field somewhat, making it more susceptible to the inherent physical instabilities that would exist in an actual transient, turbulent flow (as indicated by the "kinks" in the braid pattern). It can be seen that the core (or core air) flow, as well as the coal/transport gas (staub) flow diverge and expand downstream of the confluence plane due to the generation of a central reverse flow zone, as often occurs in systems with moderate to strong swirl. The tangential component imparted to UML-1 and UML-2 by the swirl vanes, as indicated by the twisting pathlines within the burner itself, have a significant entrainment effect upon adjacent annuli streams that are initially unswirled. No significant differences are discerned between the pathlines of the Air case and those of the OF25 case.

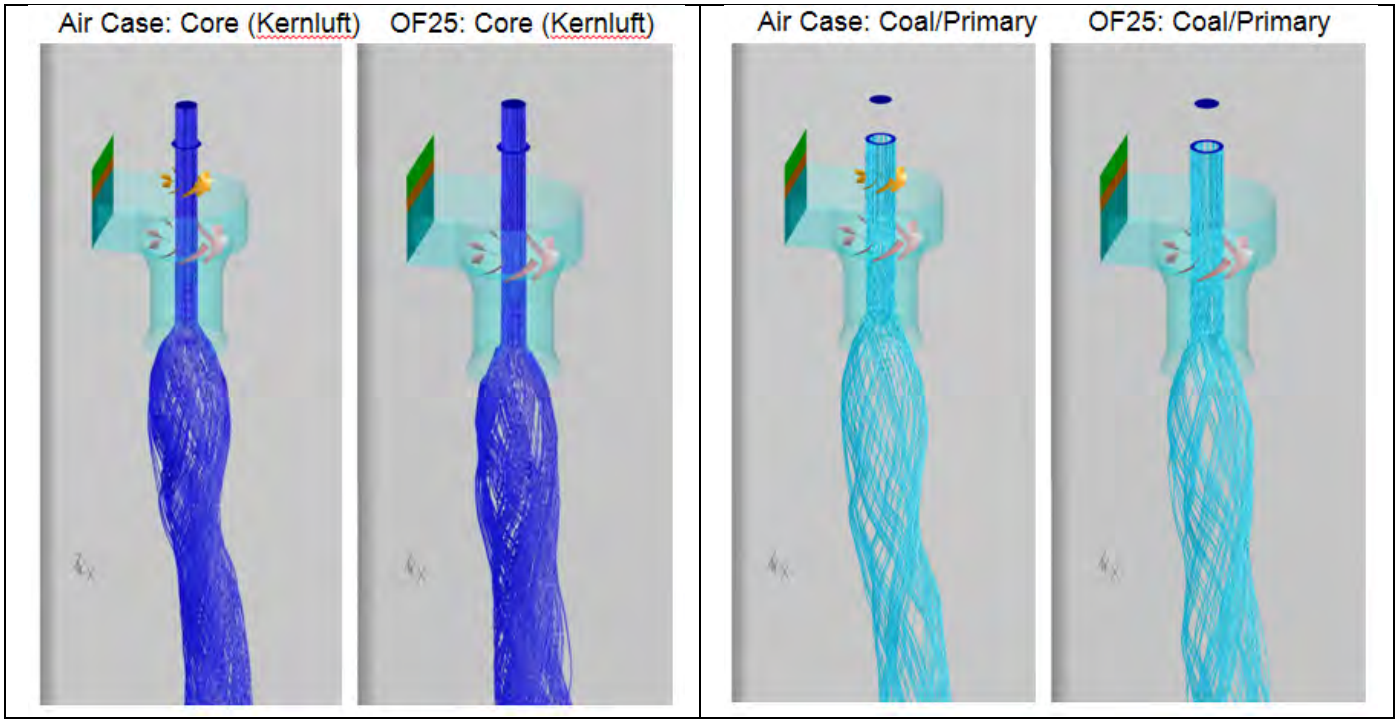

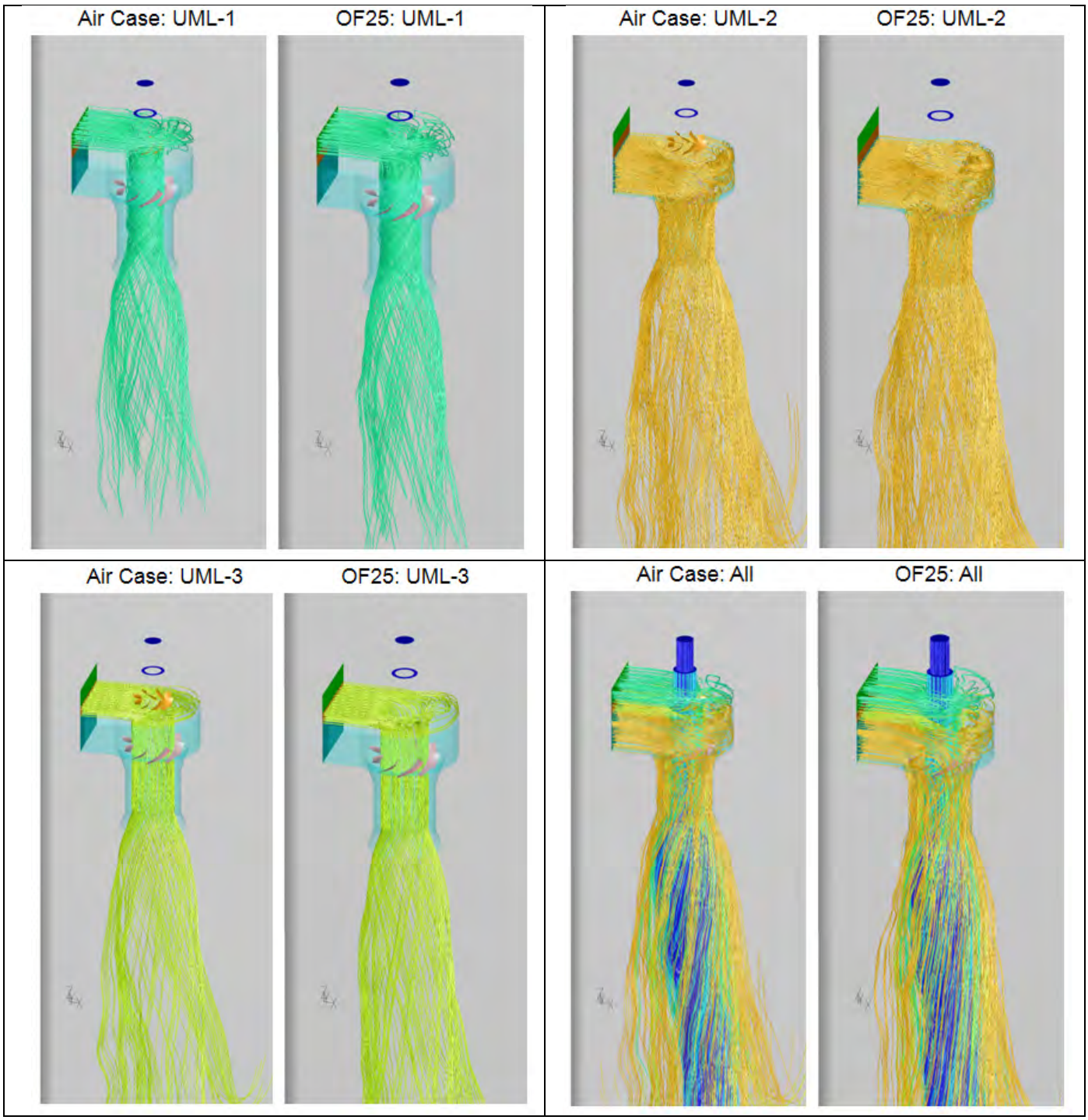

Figure 4-7. Pathlines for Air and Oxy Simulations Released from the Burner Zones

Flow entering the upper inlet plenum or chamber encounters (a) the central staub and core air cylinders, behind which transient separation and a wake may form, and (b) a rounded back wall, causing the pathlines, approaching each other from the two sides, to impact each other as opposed wall jets and to fill the space on the back side of the plenum through chaotic motion. This can induce a circumferential non-uniformity in the annular nozzle flows. The space between each pair of (stationary) swirl vanes acts to capture a (perhaps non-uniform) portion of the flow, and then redirects it to a different azimuthal position,

imparting a tangential velocity component to that portion of the flow. This non-uniformity in velocities, exhibited by the flow passing through the various annuli, is manifested in a progression of axial locations for the OF25 case.

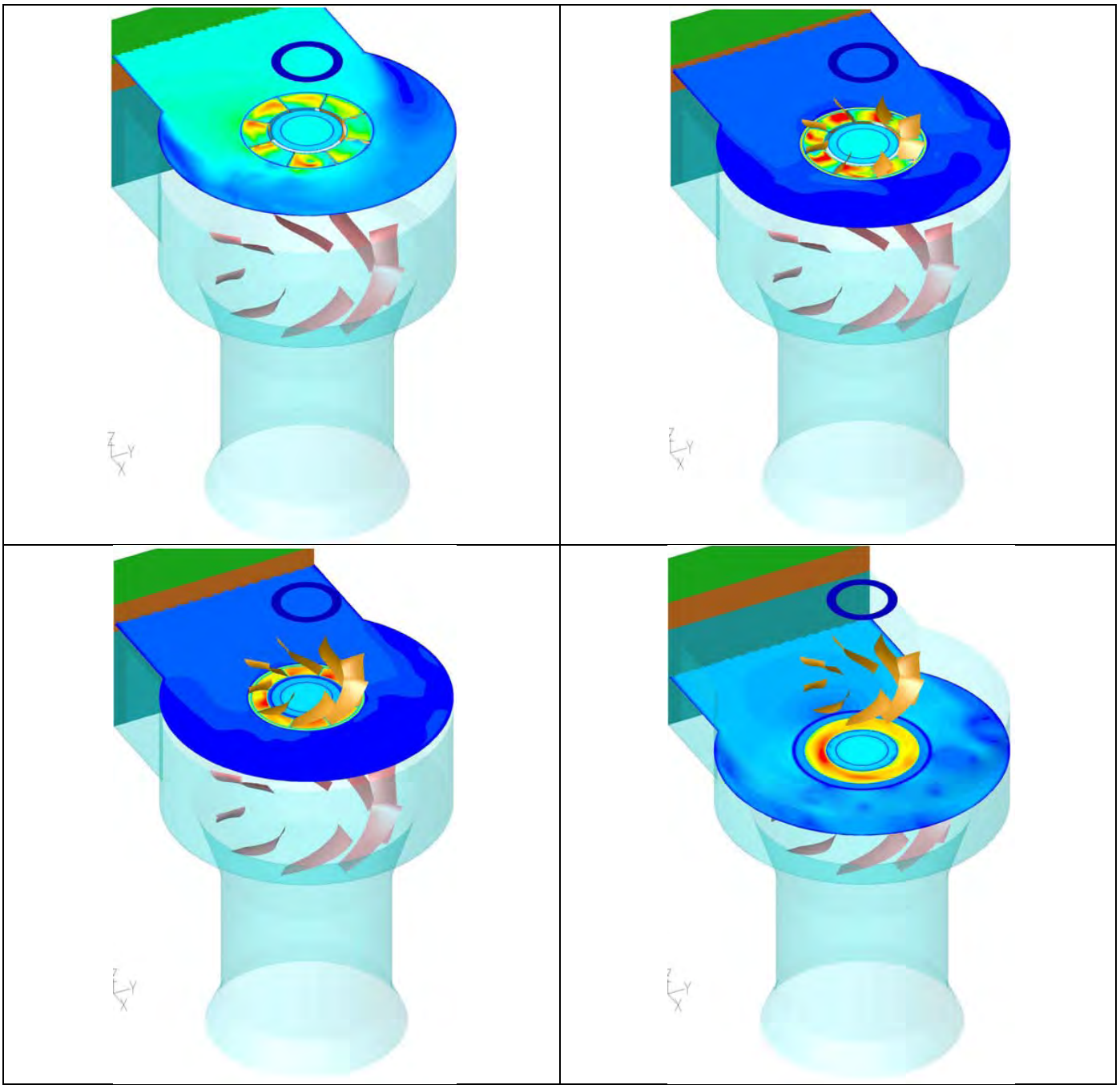

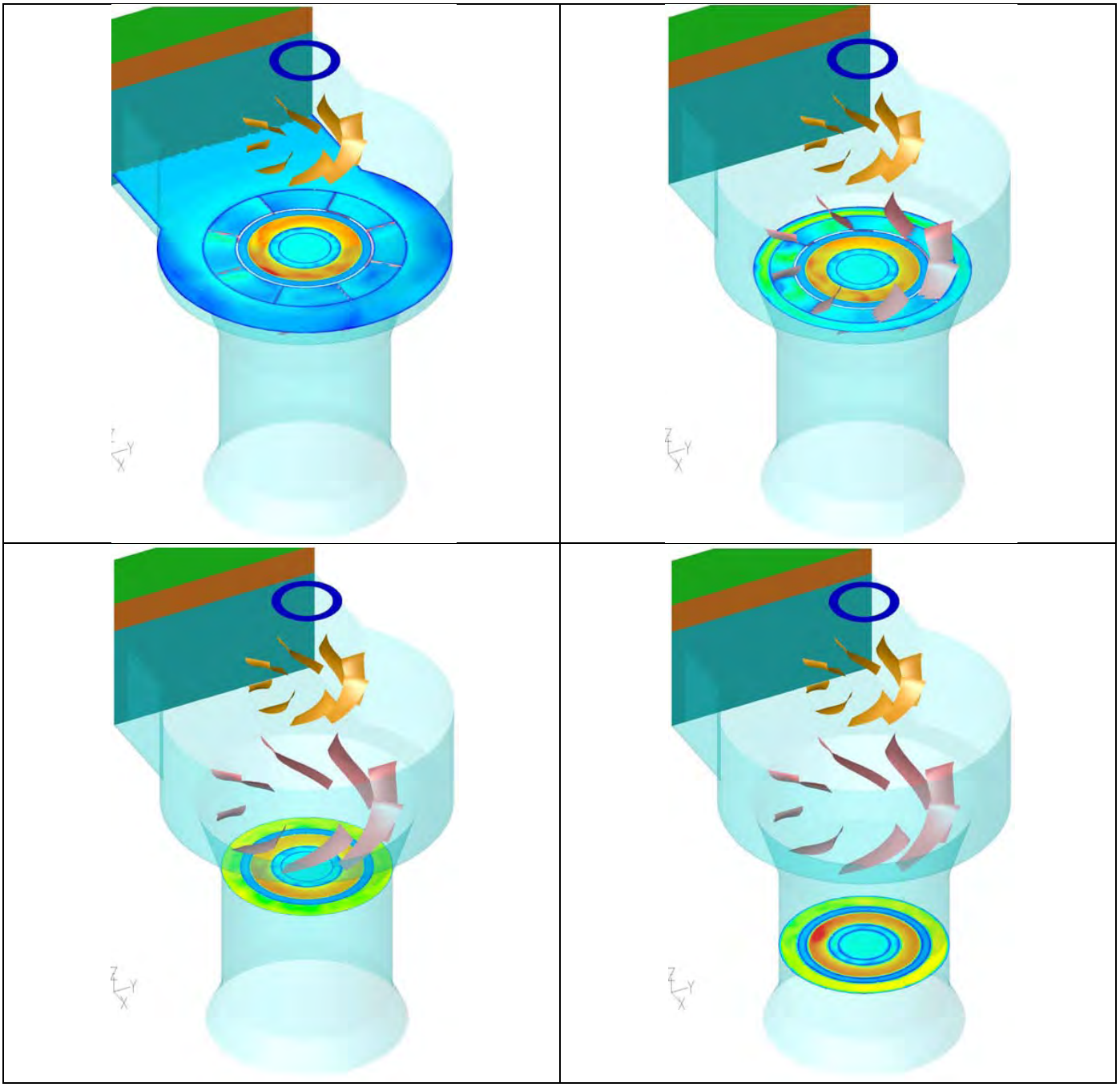

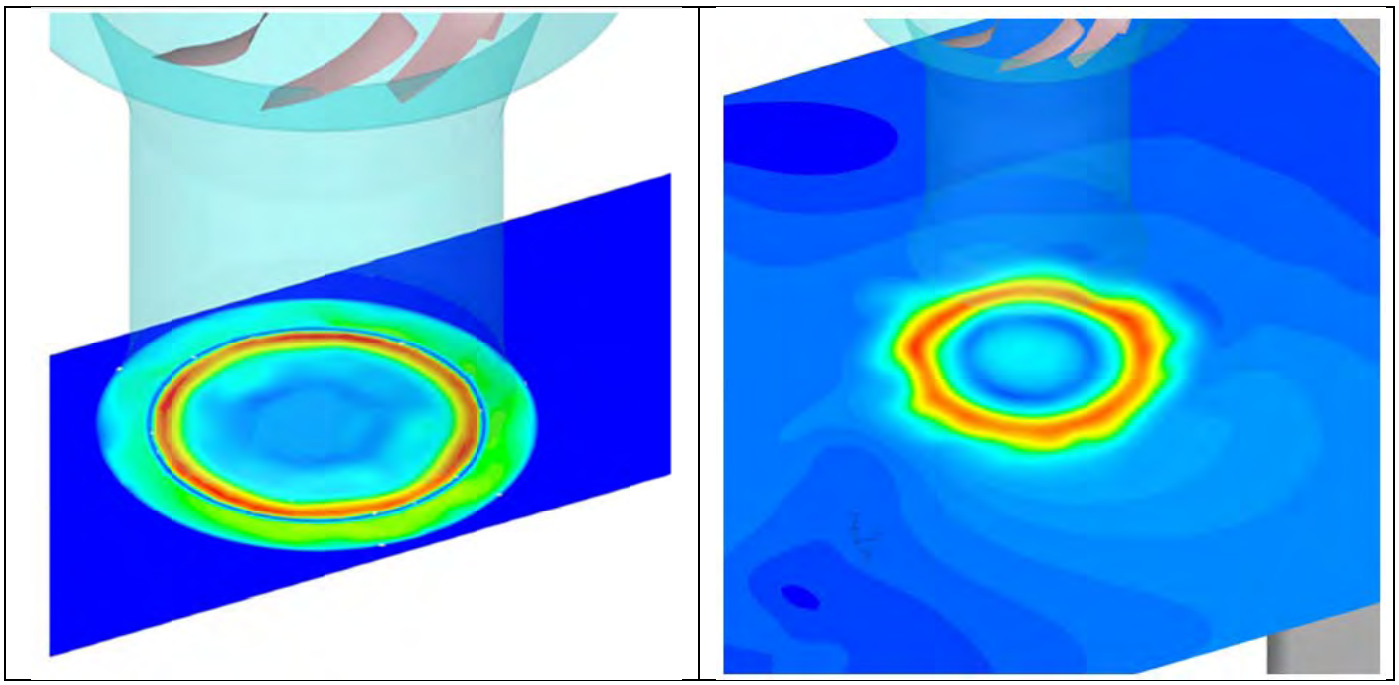

Figure 4-8. Burner Velocity Contour Progression down the burner for OF-25

The contours plotted are velocity magnitude. In the top-left picture, the maldistribution around the swirler vane assembly is apparent. By looking at the top swirling vanes in that picture, it can be seen that the pressure and flow distribution are not the same for each vane. The amount of flow entering each passage between the stationary vanes is a function of the approach streamline curvature and the pressure drop associated with each entry and vane channel. Thus each vane may experience different suction side and pressure side characteristics, depending on its azimuthal position around the swirler assembly, and the channel between each pair of vanes may capture a slightly different portion of the flow, and direct it to the trailing edge of the vanes.

A sequence of pictures show slices progressing down through the burner. After passing through the Umluft-1 swirler vanes, it can be seen that a high-velocity region is on one side of the annulus. Below the plenum, non-uniformity of the velocity is apparent in all of the annuli. The flow exhausting from the swirler (downstream of the confluence plane) also exhibits circumferential non-uniformity (with lobes).

4.7 Impact of the Inlet Boundary Condition and Turbulence Model

Alstom performed its CFD runs for the OxyPP with a full burner model (connected conformally to a furnace model) and with the RSM turbulence model. A small side study was performed to evaluate the impact of using the different approaches and models, all else remaining the same. Radial, axial, and tangential velocity profiles were extracted from the results of the full-burner model at a plane corresponding to the inlet of the truncated burner. The extraction plane is shown in Figure 4-9 and the fitted (smoothed) profiles, compared with the extracted original (full-burner) profiles, are provided in Figure 4-10. The contours show the velocity components Vx, Vy, and vertical Vz.

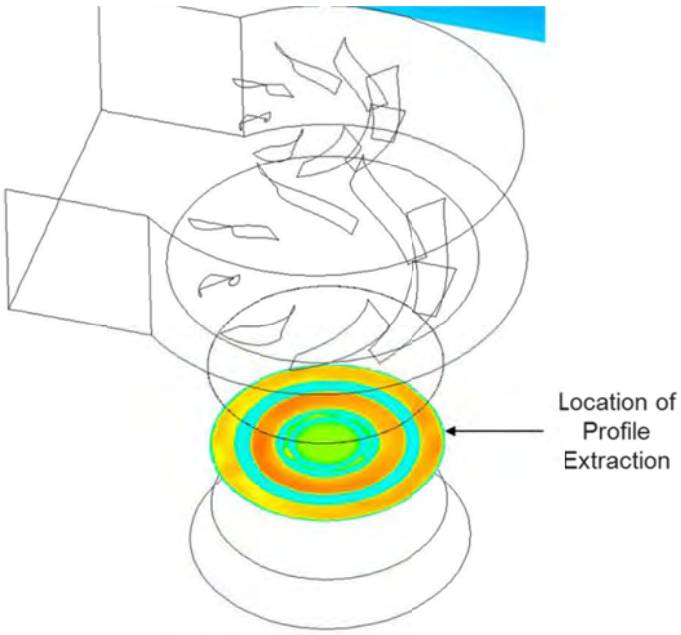

Figure 4-9. Designated Plane for Extraction of Inlet Velocity Profiles

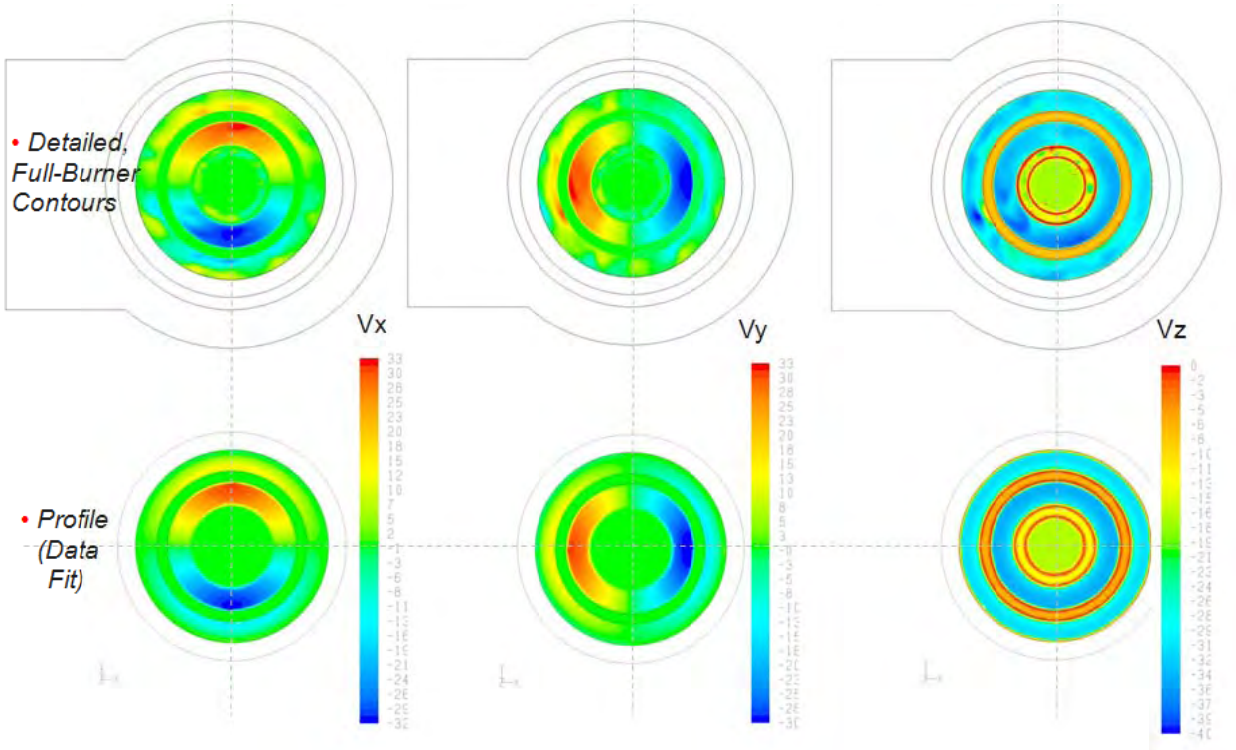

Figure 4-10. Comparison of Fitted Profiles with Extracted Original

The Realizable k-ε model with standard wall functions was utilized for the truncated burner models, along with the smoothed profiles for radial, axial, and tangential velocity distribution on the Umluft-1 and Umluft-2 inlets. A comparison of the full-burner, RSM results with the truncated-burner, k-ε model results are shown in the following series of comparison plots.

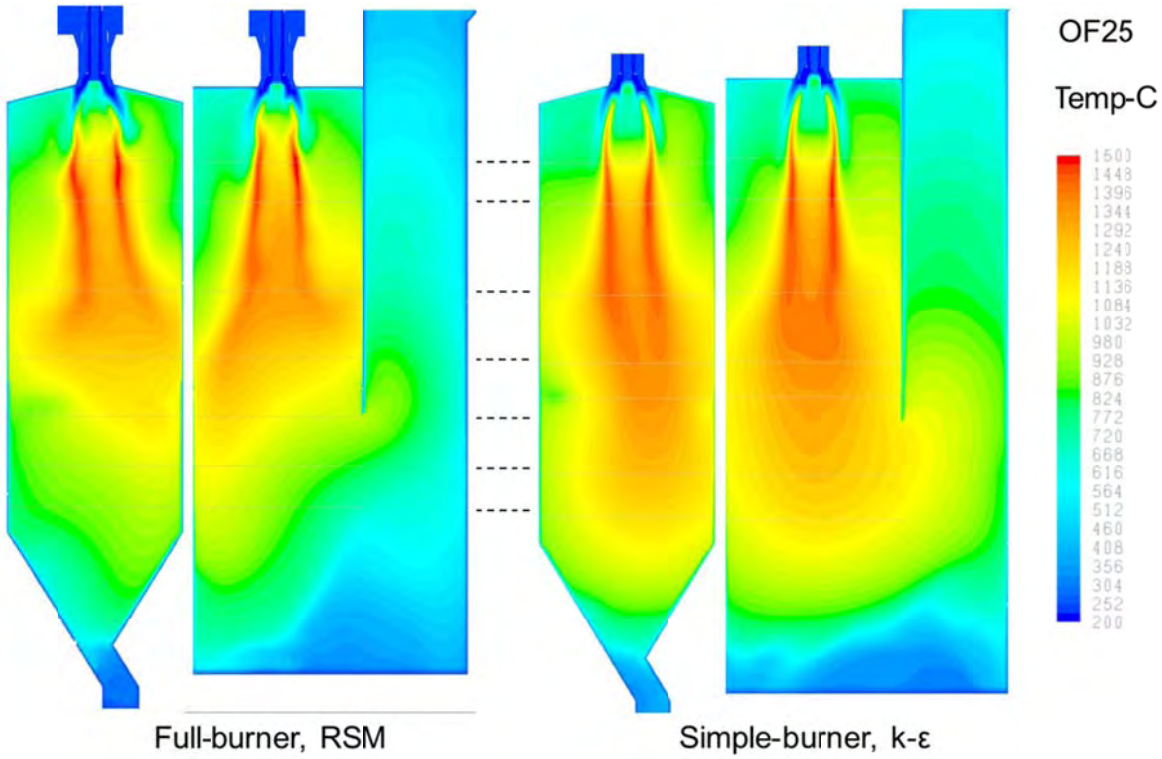

Figure 4-11. Temperature Distribution for Full and Truncated Burner Representations

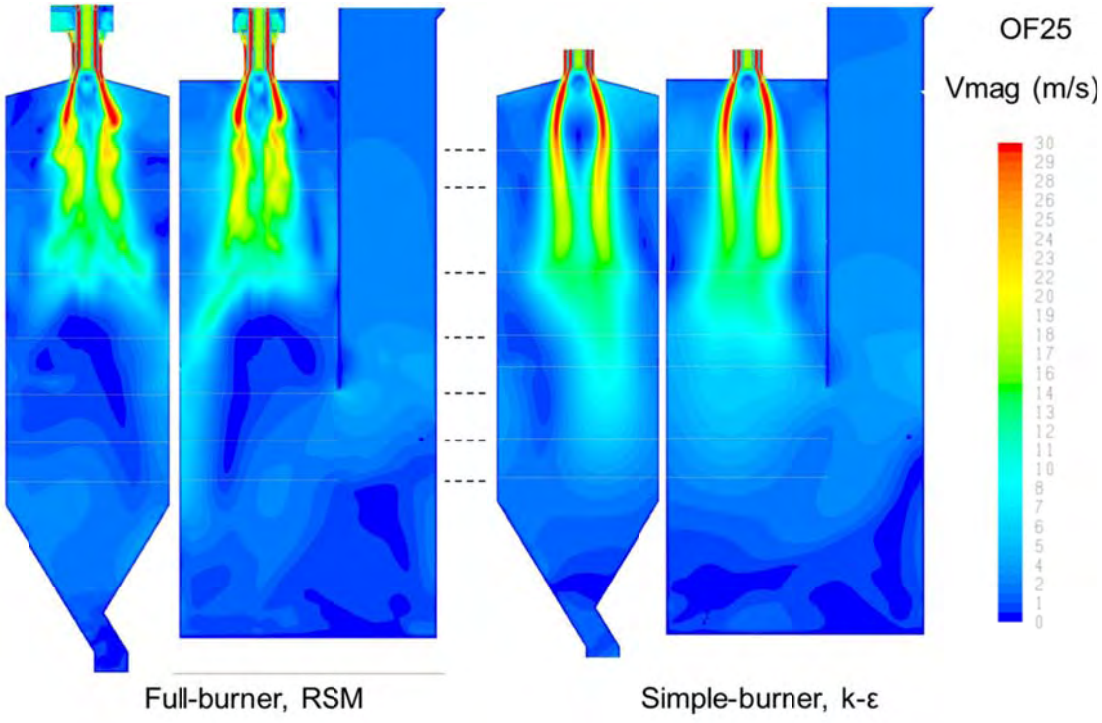

Figure 4-12. Velocity Magnitude for Full and Truncated Burner Representations

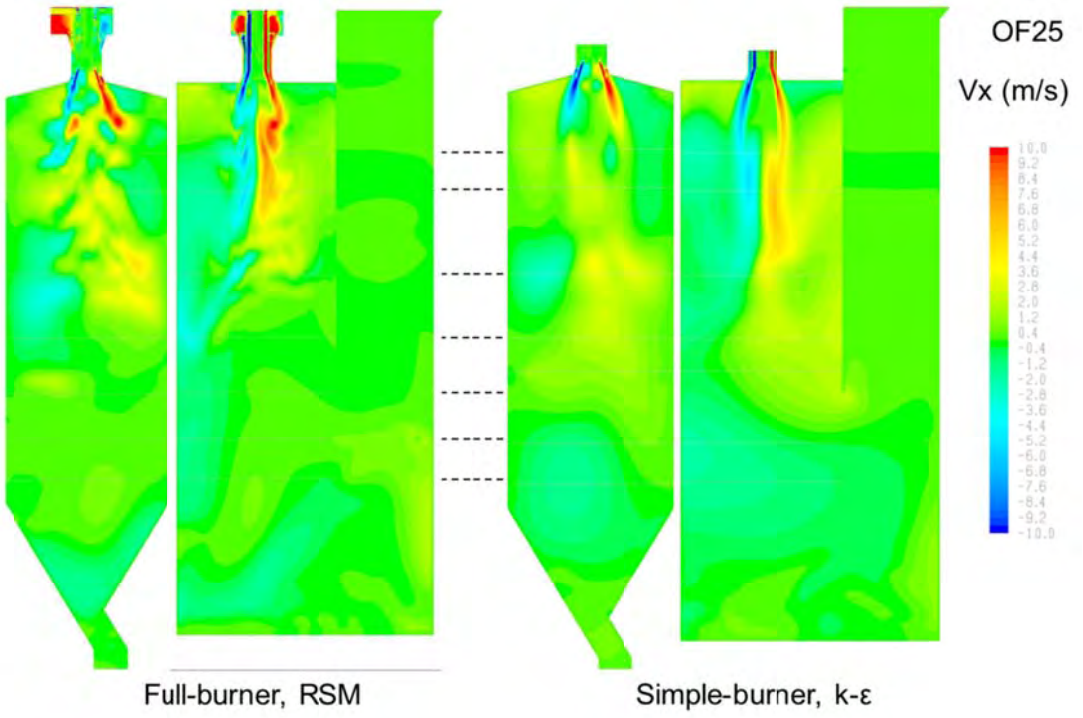

Figure 4-13. X-Velocity Distribution for Full and Truncated Burner Representations

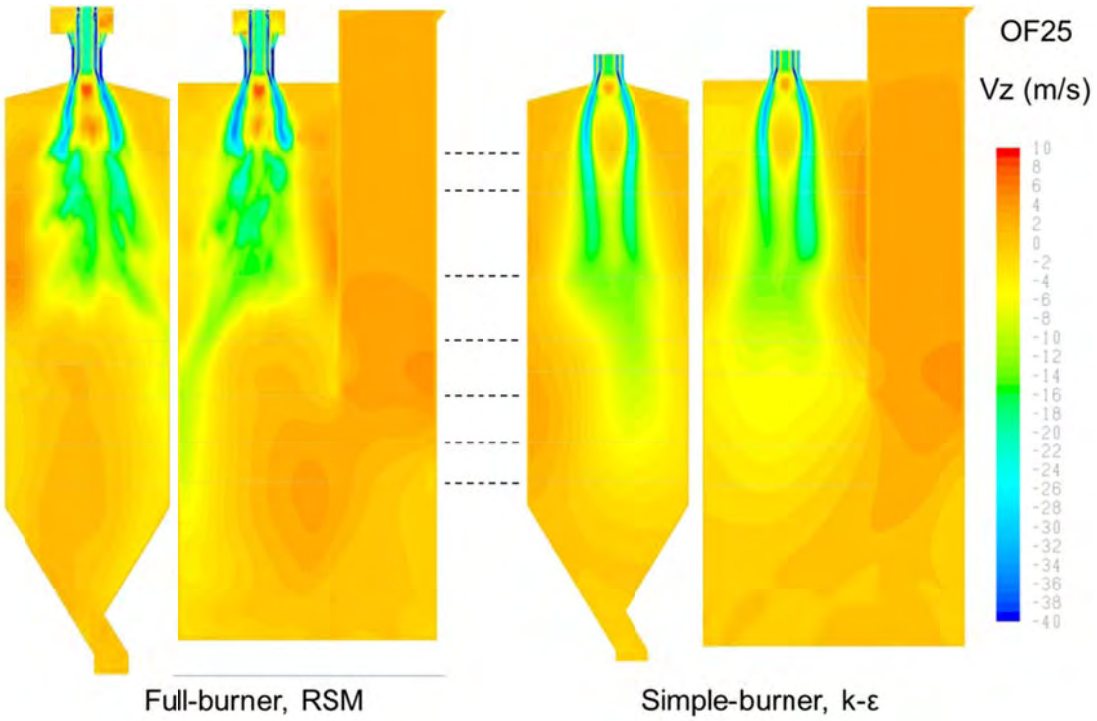

Figure 4-14. Vertical Velocity Distribution for Full and Truncated Burner Representations

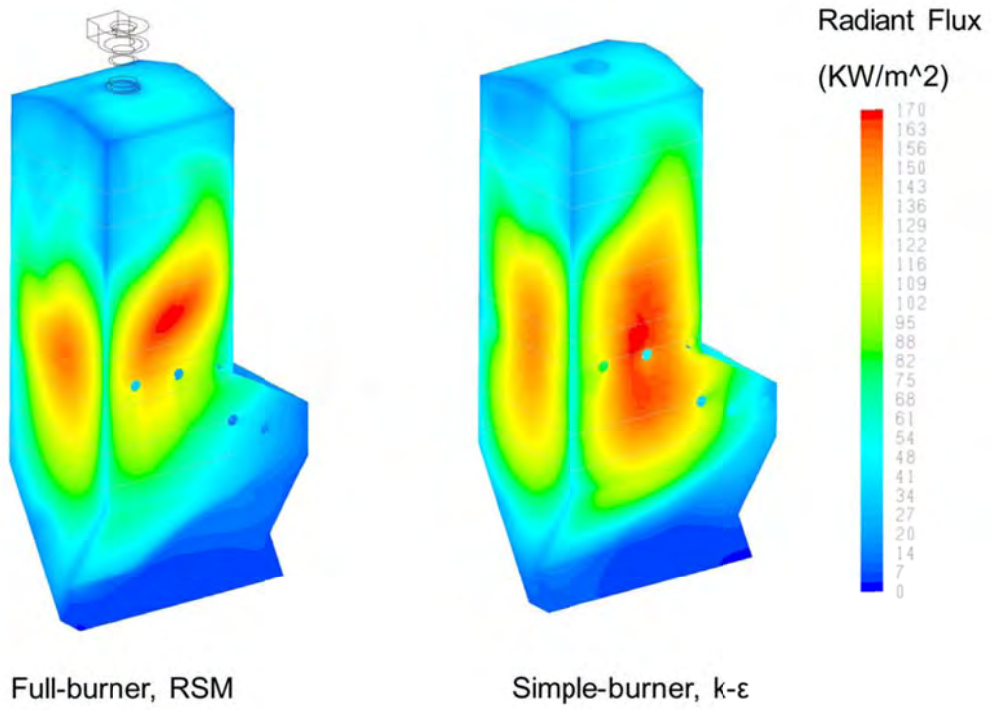

Figure 4-15. Radiant Wall Flux Distribution for Full and Truncated Burner Representations

. The left-hand plots in Figure 4-11 through Figure 4-15 portray the computational results with the full, attached burner and the RSM, while the right-hand pictures portray the results with a truncated burner, imposed inlet boundary conditions, and the k-ε turbulence model. As mentioned earlier, the imposed inlet boundary conditions are found by circumferentially averaging or smoothing the velocity components at the elevation where the burner is truncated or cut off. Each set of pictures contains two views – one view is aligned with the x-z center (y=0) plane, and the other view is aligned with the y-z center (x=0) plane, where the two view planes are referenced to a local coordinate system and symmetry line passing longitudinally through the center of the burner. The horizontal, dashed lines are indicative of the elevations for the several measurement levels (i.e., ML-1 through ML-7).

Figure 4-11 shows a comparison of the two scenarios for the gas temperature variable (expressed in °C). Figure 4-12 shows the velocity magnitude. Figure 4-13 shows the x-velocity (i.e., in and out of the page), to provide an indication of the tangential velocity, while Figure 4-14 shows the vertical or z-velocity, and the size and extent of the reverse flow zones. The final plot Figure 4-15 shows the absorbed radiation wall heat flux contribution for the two scenarios.

The full, attached burner will produce some circumferential non-uniformity in the velocity profiles at the confluence plane. The RSM is typically viewed as being more accurate than, and having less turbulent diffusion than, the k-ε model. In other words, the RSM is viewed as having a "laminarizing" effect upon the flow field, so that any underlying instabilities that might otherwise become apparent in a non-stationary flow field begin to surface or intrude in a sense, although such instabilities are not represented properly in a steady-state calculation. Consequently, it is expected that the k-ε model computations may exhibit more apparent diffusion, and that the aerodynamics and flame shape will be more symmetric or more smooth. The above figures largely confirm this expectation.

One can see from the near-burner flow fields that the RSM case manifests some significant instability effects, while the flow patterns in the k-ε case are much more smooth. Farther downstream, some

asymmetries begin to manifest themselves in both cases, as the flames try to attach to one of the walls, but the k-ε case still remains smoother and more symmetric. Despite the more diffusive nature typically associated with the k-ε model, the length of the flame zone in the k-ε case appears to be greater than that of the RSM. This longer flame length for the k-ε case also appears to induce a longer (absorbed) radiation wall heat flux zone and pushes the peak radiation wall heat flux value downstream towards the OFA, relative to that of the RSM case. The increased mixing of the RSM may in part be due to the stronger centerline reverse flow zones associated with the RSM. Two centerline reverse flow zones are apparent. The reverse flow zone nearest the nozzle reaches slightly upstream of the quarl effluence plane, and may be induced not only by the swirl, but also by the quarl expansion and the low velocity, large radius, centerline (core air) jet, which acts aerodynamically like a hub. The second reverse flow zone, positioned farther downstream (around Measurement Level 1), is due principally to the expansion induced by the swirl.

The objective of performing the above comparison was to illustrate how the calculation of inlet boundary conditions and selection of the turbulence model impact the results. The selection of imposed inlet boundary conditions and the k-ε model leads to results that appear to exhibit the qualitative behaviors (e.g., greater smoothness and symmetry) that characterize the CFD results provided by others modeling this geometry as part of the collaboration.

4.8 Contour Plots on the Burner Centerline Planes

This section provides contour plots for the three separate test cases – Air Test 332, Oxy-OF25 Test 333, and Oxy-OF30 Test 334. A collection of variables are plotted in contour format for each of these test conditions.

Air Test 332

Contour plots of temperature, species concentrations, and velocities are provided on the centerline planes (i.e., relative to the burner centerline) for Air Test 332 in Figure 4-16 It should be noted that temperature is in units of °C, species concentrations are in terms of mole % (wet), and velocities are in units of m/s. As noted previously, the underlying instabilities, so apparent in the RSM velocity contour plots, also produce kinks and lobes in the temperature and concentration contours.

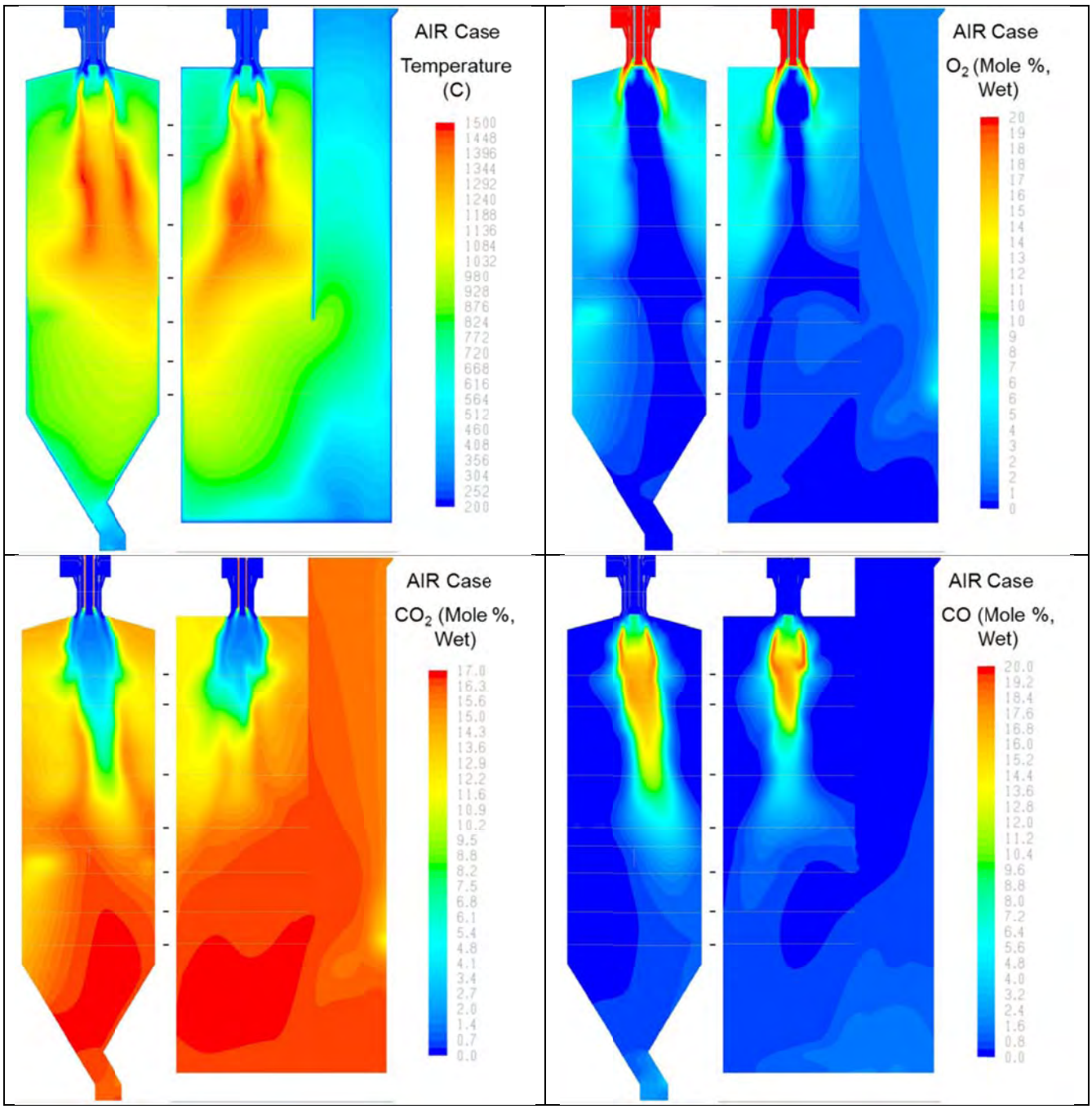
AIR Case
Temperature (C)
1500
1448
1396
1344
1292
1240
1188
1136
1084
1032
980
928
876
824
772
720
668
616
564
512
460
408
356
304
252
200
AIR Case
O2 (Mole %, Wet)
20
19
18
18
17
16
15
14
14
13
12
11
10
10
9
8
7
6
6
5
4
3
2
2
1
0
AIR Case
CO2 (Mole %, Wet)
17.0
16.3
15.6
15.0
14.3
13.6
12.9
12.2
11.6
10.9
10.2
9.5
8.8
8.2
7.5
6.8
6.1
5.4
4.8
4.1
3.4
2.7
2.0
1.4
0.7
0.0
AIR Case
CO (Mole %, Wet)
20.0
19.2
18.4
17.6
16.8
16.0
15.2
14.4
13.6
12.8
12.0
11.2
10.4
9.6
8.8
8.0
7.2
6.4
5.6
4.8
4.0
3.2
2.4
1.6
0.8
0.0

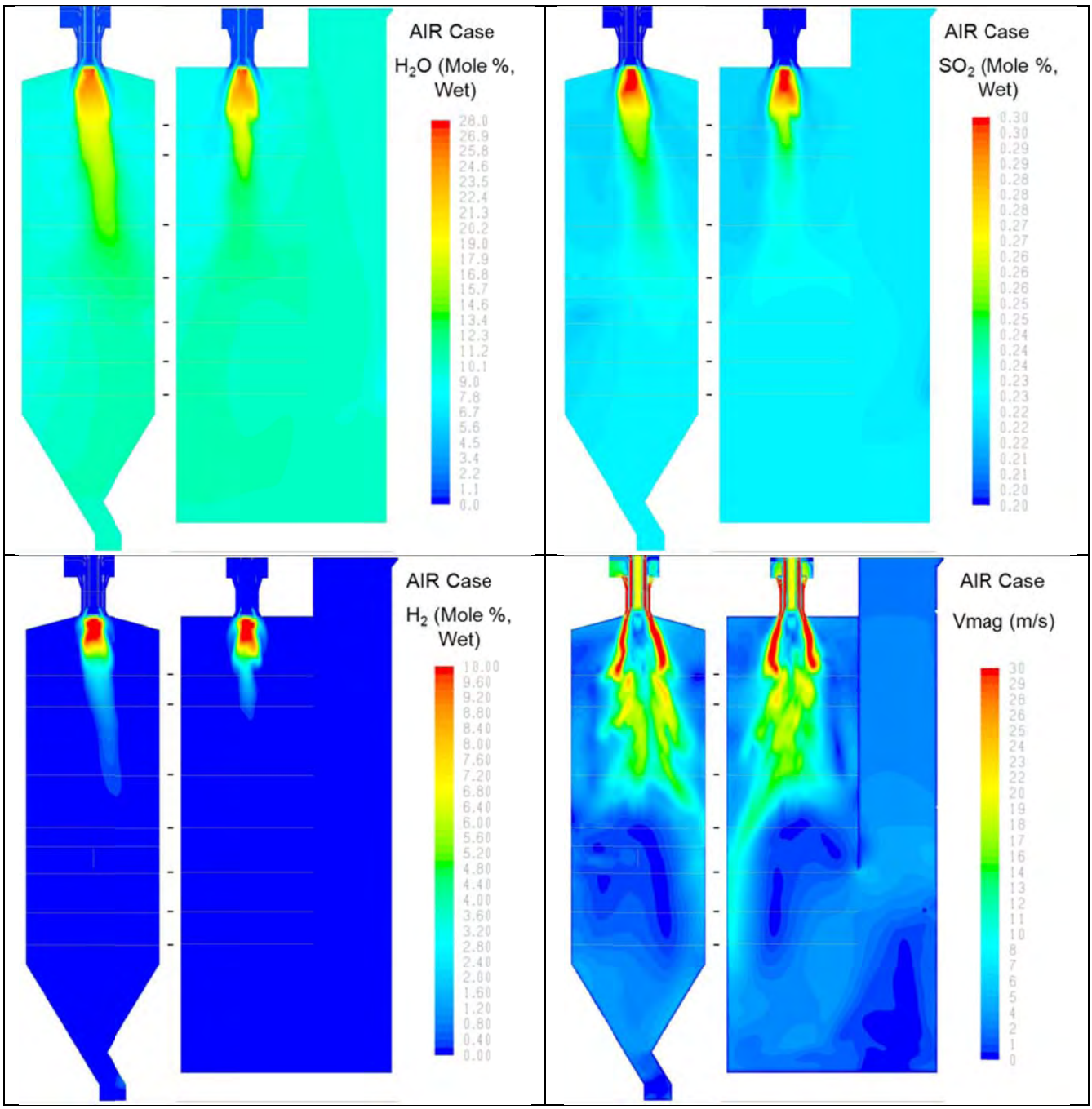
AIR Case
H2O (Mole %, Wet)
28.0
26.9
25.8
24.6
23.5
22.4
21.3
20.2
19.0
17.9
16.8
15.7
14.6
13.4
12.3
11.2
10.1
9.0
7.8
6.7
5.6
4.5
3.4
2.2
1.1
0.0
AIR Case
SO2 (Mole %, Wet)
0.30
0.30
0.29
0.29
0.28
0.28
0.28
0.27
0.27
0.26
0.26
0.26
0.25
0.25
0.24
0.24
0.24
0.23
0.23
0.22
0.22
0.22
0.21
0.21
0.20
0.20
AIR Case
H2 (Mole %, Wet)
10.00
9.60
9.20
8.80
8.40
8.00
7.60
7.20
6.80
6.40
6.00
5.60
5.20
4.80
4.40
4.00
3.60
3.20
2.80
2.40
2.00
1.60
1.20
0.80
0.40
0.00
AIR Case
Vmag (m/s)
30
29
28
26
25
24
23
22
20
19
18
17
16
14
13
12
11
10
8
7
6
5
4
2
1
0

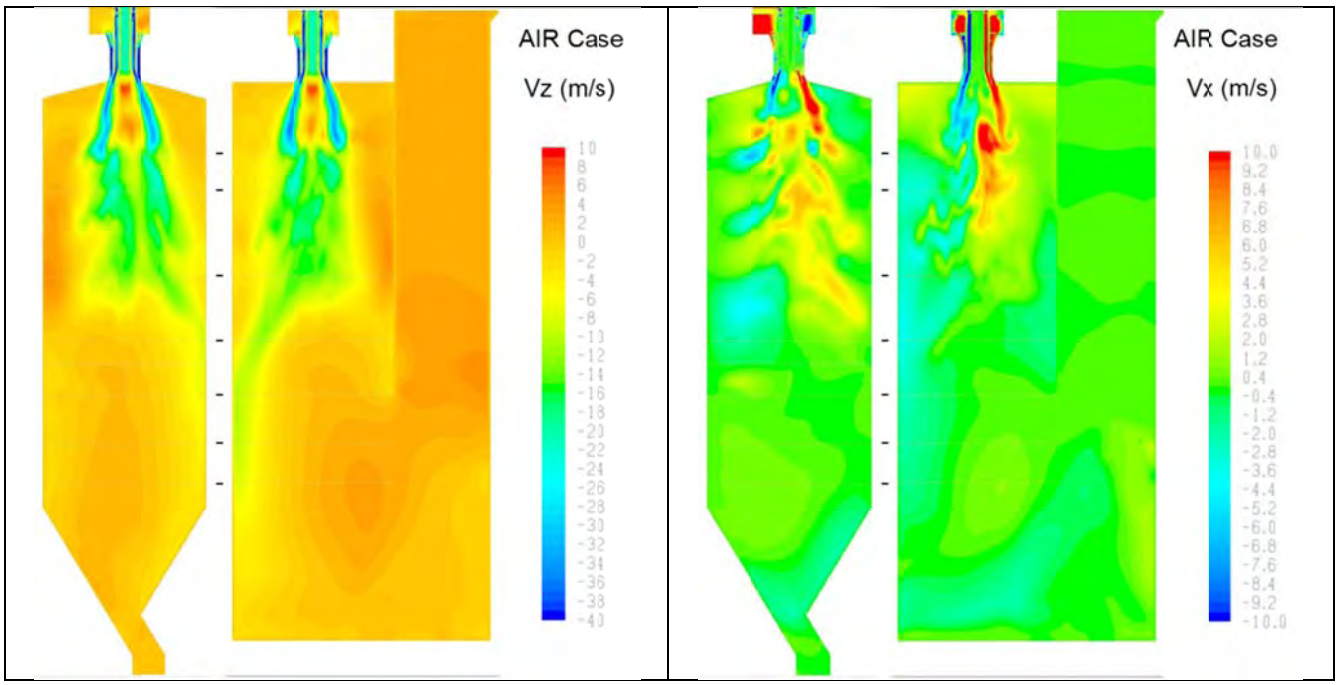

Figure 4-16. Contour Plots on Centerline Planes: Air Test 332

The flame appears to be attached well to the near-nozzle region. The primary flame attachment region appears to be on the burner symmetry axis, inside the quarl, in the vicinity of the core air. This centerline flame attachment region then stabilizes the coal-flame in the adjacent shear layers. As often occurs in confined furnaces, the downstream flame exhibits a tendency to migrate and to attach to an arbitrary wall. In the lower, right-hand corner of the plot, in the hopper region, the gas temperature decreases to about 700 K, probably because the majority of the fuel has been consumed, and the heat loss to the walls becomes greater than the residual heat release in that location.

The oxygen concentration is negligible within the flame zone, and a low oxygen concentration region also prevails in the hopper. The oxygen is replenished somewhat by the OFA jets before the flue gas exhausts up the convective pass. The CO is high in the near-flame region, but sufficient oxygen is available to burn out the CO in the convective pass (although quenching in the convective pass may freeze the CO at concentration levels higher than the model is predicting). There is a slight increase in CO in the hopper region, perhaps due to reaction of the residual char that is circulating in the hopper. H_2O gas originates from the coal moisture (as evidenced by H_2O concentrations in the near-nozzle region), volatile decomposition, and from complete combustion. The SO_2 species is also high in the near-nozzle region, since it appears as a volatile decomposition product in the present cases, and then quickly reaches a plateau (since it is thereafter neither created nor destroyed). The H_2 species is similarly created via volatile decomposition, but then reacts quickly (typically faster than the other gas-phase or heterogeneous-phase reactions) with the available oxygen and becomes ultimately completely consumed.

The highest velocity magnitudes and swirl velocities emanate from the burner annuli, and persist for at almost three (3) nozzle diameters. The longitudinal velocity (V_z) exhibits two sequential reverse flow zones along the burner centerline, one that penetrates upstream of the quarl effluence plane and the other that is positioned downstream. Incipient instabilities are evident for another 3 to 4 nozzle diameters downstream beyond the first three.

OF25 Test 333

A corresponding set of plots for OF25 is provided in Figure 4-17. The color scales for the plots of the 3 tests are identical, except that the scales for CO_2 and H_2O are increased in the oxy-fired cases to accommodate the flue gas recycle concentrations (i.e., 0 - 17 mole % (wet) range increased to 20 - 80 for CO_2, and 0 - 28 mole % (wet) range changed to 10 - 35 for H_2O). The OF25 (Test 333) case has the highest main burner zone excess oxygen and overall excess oxygen of all of the three tests being examined, as well as the highest gas and coal flow rates.

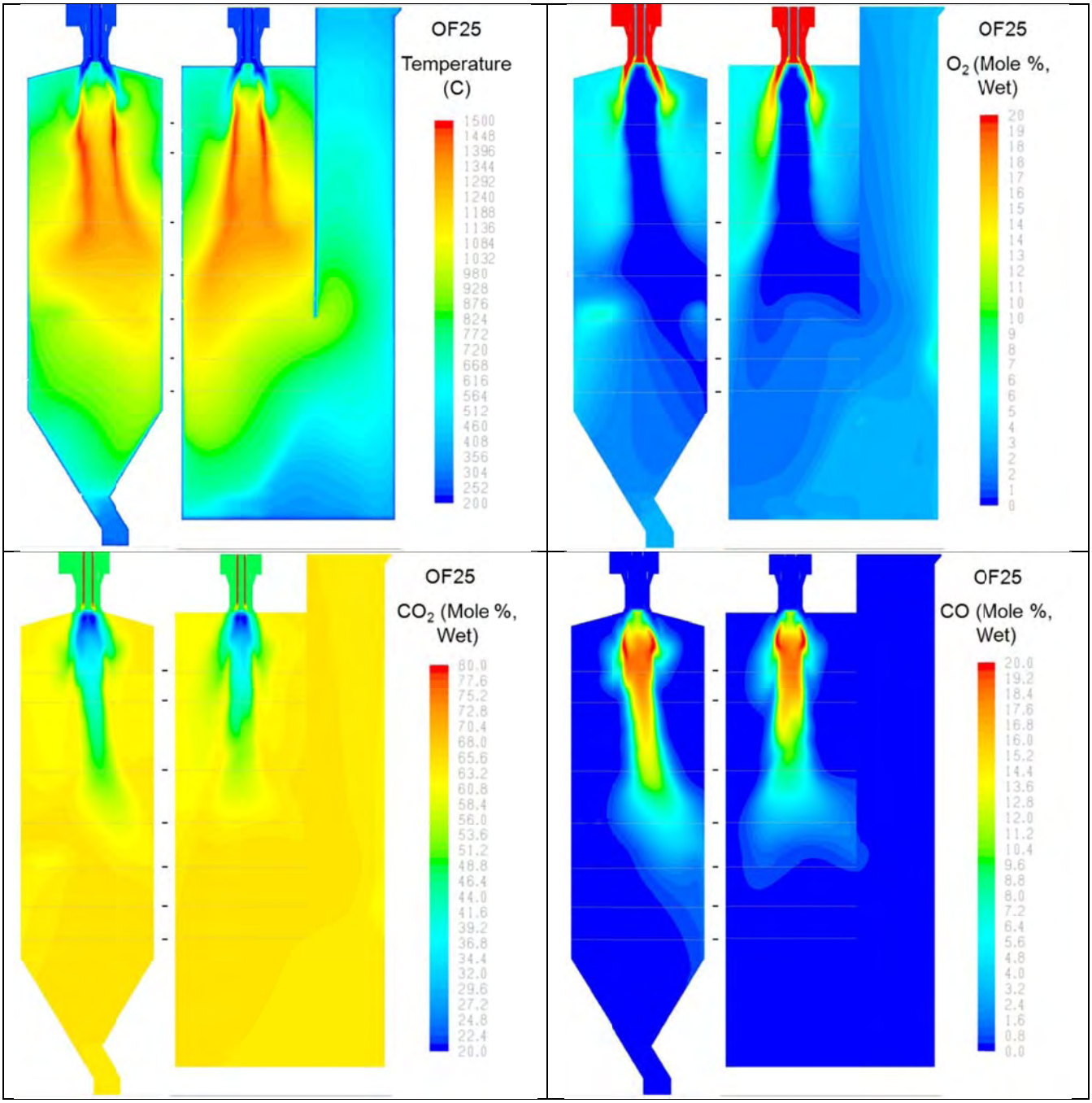

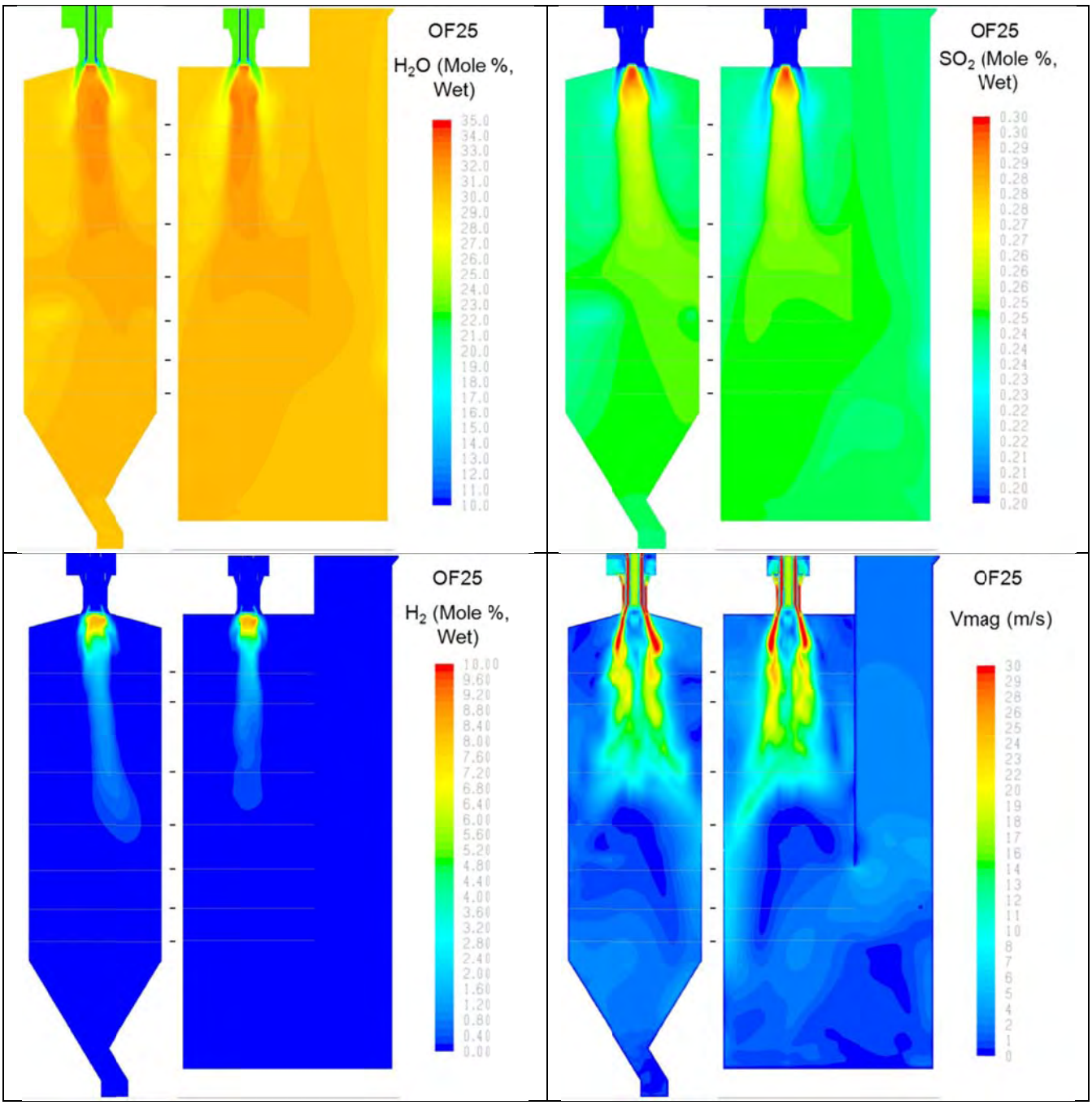
OF25
H2O (Mole %, Wet)
35.0
34.0
33.0
32.0
31.0
30.0
29.0
28.0
27.0
26.0
25.0
24.0
23.0
22.0
21.0
20.0
19.0
18.0
17.0
16.0
15.0
14.0
13.0
12.0
11.0
10.0
OF25
SO2 (Mole %, Wet)
0.30
0.30
0.29
0.29
0.28
0.28
0.28
0.27
0.27
0.26
0.26
0.26
0.25
0.25
0.24
0.24
0.24
0.23
0.23
0.22
0.22
0.22
0.21
0.21
0.20
0.20
OF25
H2 (Mole %, Wet)
10.00
9.60
9.20
8.80
8.40
8.00
7.60
7.20
6.80
6.40
6.00
5.60
5.20
4.80
4.40
4.00
3.60
3.20
2.80
2.40
2.00
1.60
1.20
0.80
0.40
0.00
OF25
Vmag (m/s)
30
29
28
26
25
24
23
22
20
19
18
17
16
14
13
12
11
10
8
7
6
5
4
2
1
0

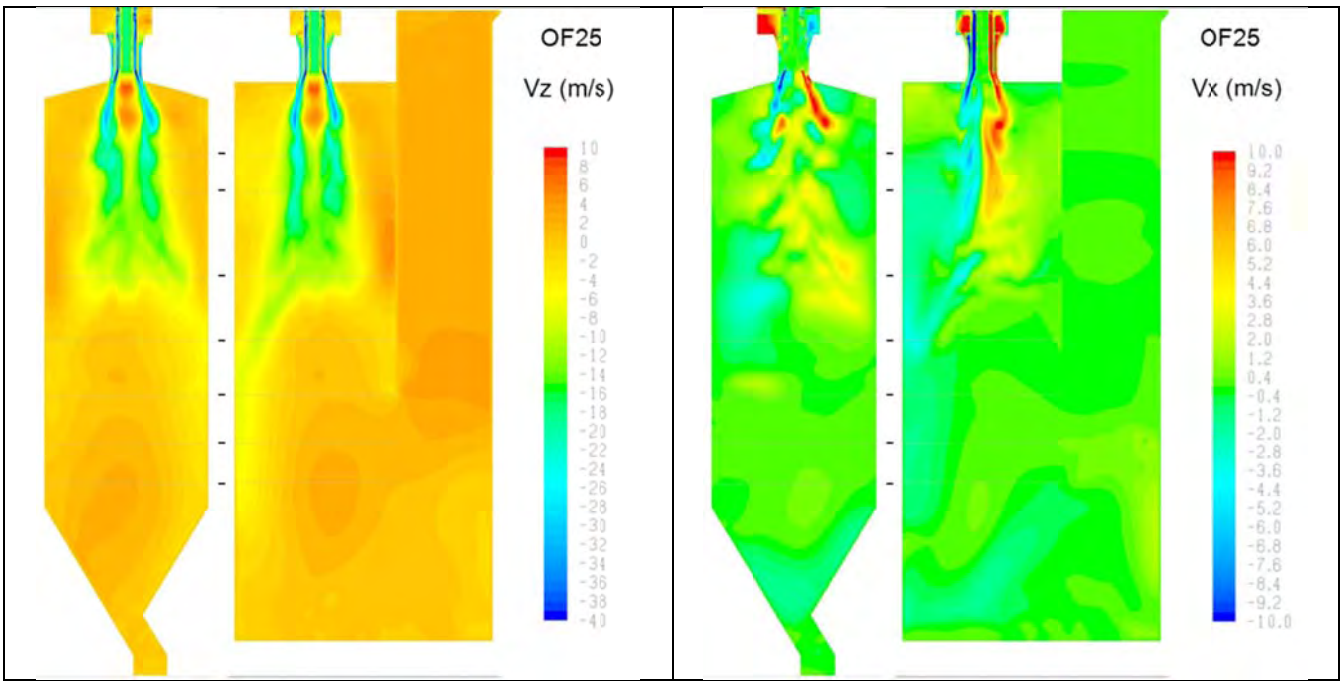

Figure 4-17. Contour Plots on Centerline Planes: OF25 Test 333

The temperature contours for the OF25 case appear to be similar to those of the air case, although the flame structure is a little more smooth and symmetric in the OF25 case. It is not known how much the computed flow field may be changing as a function of the number of iterations (if at all), but part of the flame structure may meander slightly because of the underlying physical and convergence instabilities associated with the RSM. Convergence metrics used for these simulations included tracking the outlet temperature and species concentrations until no changes were observed. In addition, energy balances were generated to be sure that the radiation, species and mass balances were within acceptable tolerances. All three (3) of these cases were run for a number of weeks, normally with a set of 3 quad-core machines to develop the final results included in this report.

The OF25 case has slightly more excess oxygen than the Air case, which is reflected in the exit values, as well as in the hopper region. However, the oxygen depletion in the core region downstream of the burner is more pronounced in the OF25 case than in the Air test. The CO_2 is, of course, much higher in the oxy case than in the Air case because of the high concentrations of CO_2 in the recycled flue gas. For the OF25 case, the CO exhibits stronger peak values in the near-nozzle region. The volatile fraction per unit mass of coal and the stoichiometric fraction of CO produced from the volatile decomposition are very similar between the OF25 case and the Air case. However, a higher percentage of the gas distribution is channeled through the inlet core, the inlet primary, Umluft-1, and Umluft-3 in the OF25 test than in the Air test, where the burning of the coal is directly impacted, so that correspondingly more of the char may be converted to CO in the near-nozzle region of OF25 than in the Air test, resulting in the higher computed CO peaks. However, because of the slightly higher overall excess oxygen in the OF25 case than in the Air test, the CO in the OF25 case burns out correspondingly faster in the OFA region.

The H_2 peak values in the near-nozzle region are significantly less in the OF25 case than in the Air test, and appear to burn out over a longer distance. H_2 originates only from the volatiles. The stoichiometric production of H_2 from the volatile decomposition in OF25 is about 3 percentage points less than in the Air case, which may account for the lesser near-nozzle values. That the H_2 persists longer through the main burner zone in the OF25 case may simply be because the oxygen appears to be more depleted, over

a wider span of the central core region, in the OF25 case than in the Air case. The Air case exhibits more pronounced instabilities in the core/flame region than the OF25 case, which may, in turn, produce an apparent enhanced mixing effect—bringing in surrounding oxygen where the eddy-like instabilities interrupt the shear layer trajectories—thus diminishing the radius of, or shortening the length of, the oxygen-starved core/flame downstream of the burner.

The velocity magnitude and longitudinal velocity appear to be similar for the OF25 and Air cases, except that the two centerline reverse flow zones in the OF25 case appear to be slightly larger and closer together. Again, the instabilities are apparent in both cases, but the OF25 case remains more symmetric, which in turn, promotes a truer bisection of the reverse flow zones on the x- and y-center planes in the OF25 case than in the Air case, thus making them more visible. Hence, the conclusion that the reverse flow zones are stronger in one case than another may simply be because the reverse flow zones in one case are more "out of plane" than in another case. A more quantitative and definitive evaluation of reverse flow zone shape and size was not performed. Recirculation zones first increase in length, with a slight increase in length, as the swirl number increases, and then begin to grow shorter and fatter beyond some threshold. In addition, recirculated mass flow rates scale with the increase in swirl number, along with gradients, entrainment, and mixing. Thus the proximity of the two reverse flow zones to the burner, and the magnitude of the reverse flow zone velocity, would tentatively indicate that the OF25 case has a larger swirl number than the Air case.

OF30 Test 334

The contour plot results for OF30 Test 334 are provided in Figure 4-18. OF30 has the lowest overall excess oxygen ratio (1.052), as well as the lowest excess oxygen in the main burner zone itself (0.87), than the other two tests. The coal flow rate for OF30 is intermediate between the other two cases, but the total inlet gas mass flow rate is significantly less (by 14 to 18%) than the other two test cases.

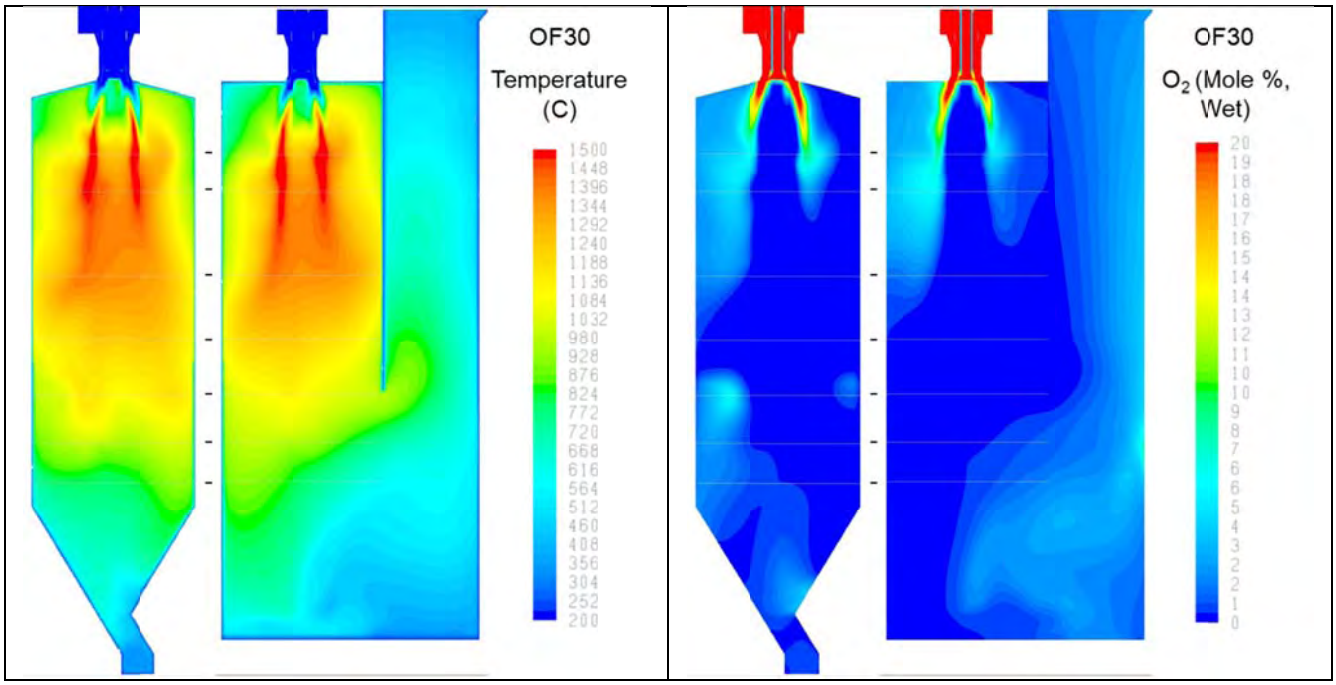

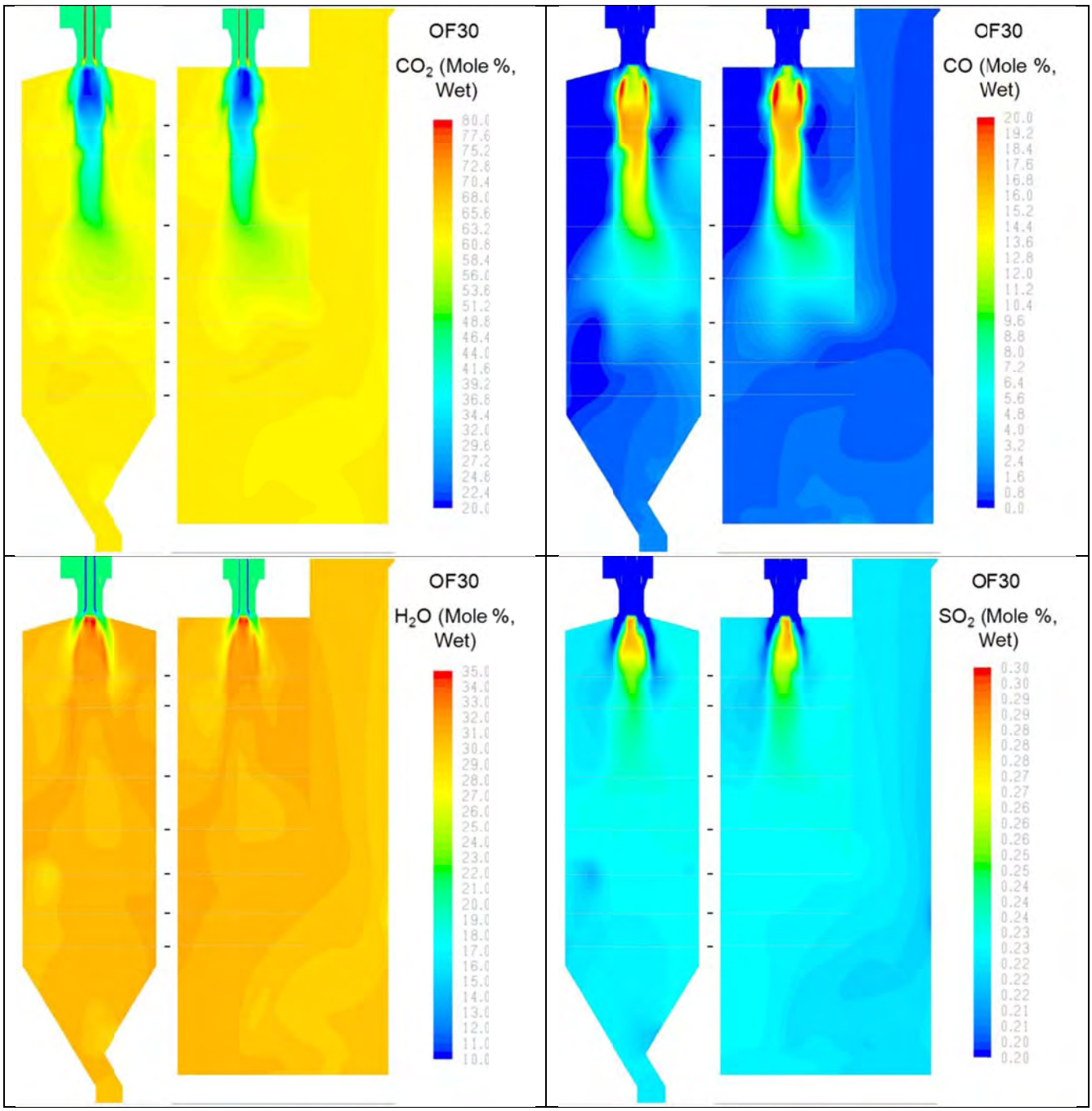
OF30
CO2 (Mole %, Wet)
OF30
CO (Mole %, Wet)
OF30
H2O (Mole %, Wet)
OF30
SO2 (Mole %, Wet)

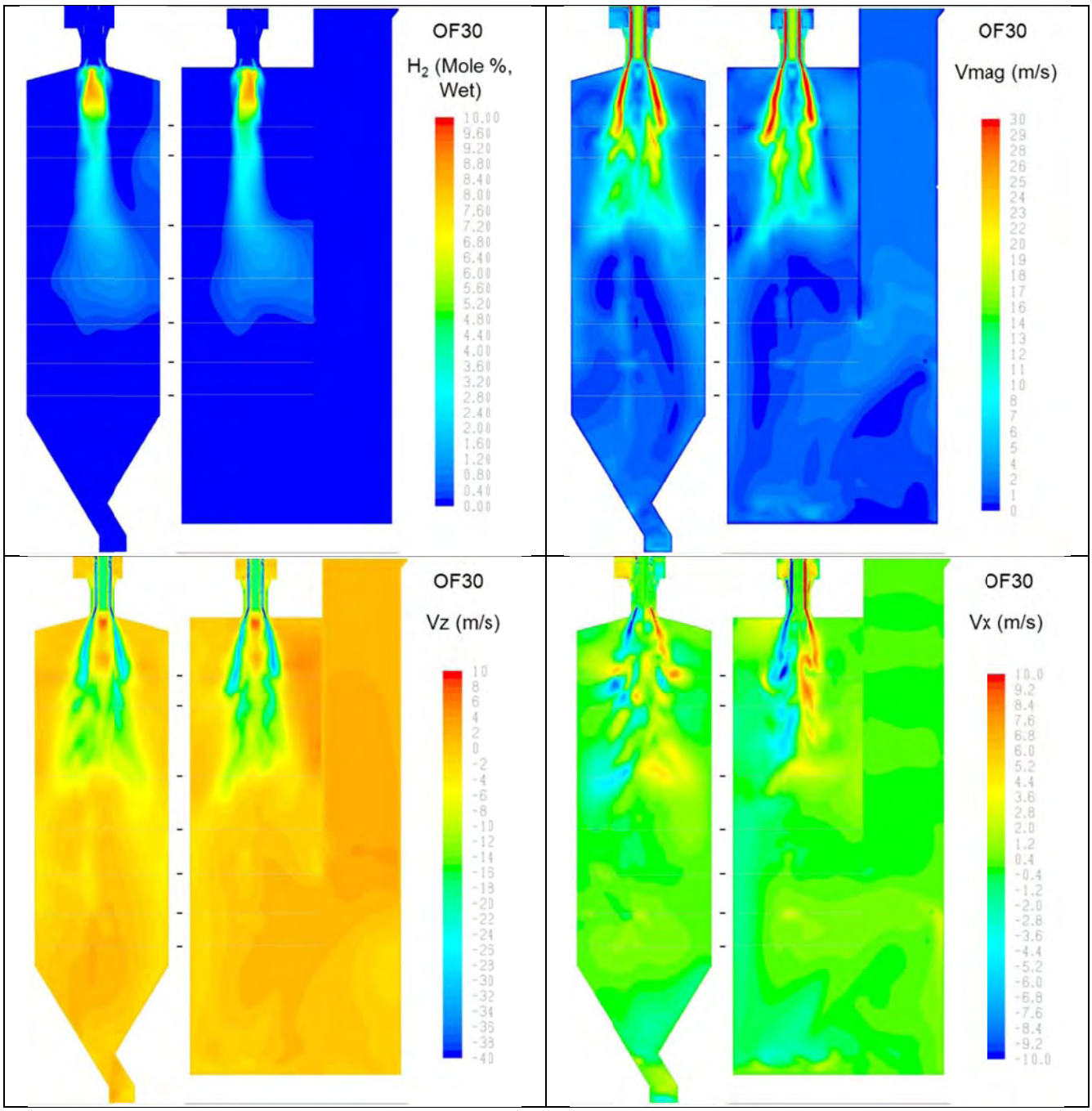

Figure 4-18. Contour Plots on Centerline Planes: OF30 Test 334

OF30 has the lowest swirl level. (The grid and prescribed vane settings were kept the same in each case, but the flow rates to the separate annuli were also changed from case to case which impacts the resulting swirl.) As seen from the longitudinal velocity, the first reverse flow zone is slightly weaker than that of OF25, and is comparable to that of the Air case. The second reverse flow zone is weaker than the corresponding reverse flow zones in either the OF25 or Air test cases, and is positioned farther downstream than in either of the other cases. Consequently, it is likely that the swirl number in the OF30 case is lower weaker than in the other two cases.

The length of a particular burner jet contour on the velocity magnitude plots, representing the expanding jet velocity emanating from the burner (and colored in red for the maximum velocity), appears to remain in its trajectory longer and in a more coherent fashion in the OF30 case, before it begins to break up due to the instabilities, than in the Air or OF25 cases. This observation is consistent with the hypothesis that the stronger the swirl and the more energetic the recirculation zone, the smaller the distance over which the jet remains coherent before it begins to break up.

The high (maximum) temperature region in the temperature contour plot shows a thickened flame sheet for the pulverized coal flame emanating from the nozzle, relative to either of the other cases. The temperature may be higher in the OF30 case because the overall inlet gas flow rate is 14% lower than the OF25 test and 18% lower than the Air case, so that the temperature dilution effect is much less in the OF30 case. The higher temperature may also be due to the higher oxygen mole fraction in the inlet streams of OF30 (in addition to alterations in the flow rate distribution to the annuli) which may increase the local stoichiometry in the vicinity of the burning particles. The overall extent of the flame zone (e.g., above 1000 °C) is somewhat shorter than in the other cases, presumably because the higher oxygen content in the inlet streams is countered by the lower overall excess oxygen in the main burner zone.

The depleted oxygen region in the OF30 case (in the core, furnace, and hopper zones) is more extensive than in the other cases. Residual oxygen from the OFA gas jets are apparent in a few locations, providing some oxygen for fuel consumption prior to the flue gas entering the convective pass. The CO_2-depleted region immediately downstream of the burner in the OF30, as well as the low-CO_2 region that extends for perhaps 5 to 6 nozzle diameters downstream of the burner, appears to be slightly longer than that of the OF25 case. The CO does not appear to be as strong in the near-burner region as the OF25 case, but appears to be more similar to that of the Air case; it does however, appear to require longer to burn out the CO in the low excess oxygen environment of the OF30 case, than in the other cases, and even produces residual CO at the exit. There is slightly more hydrogen and moisture in the OF30 coal than in the OF25 coal, so that both the near-burner values and the exit values for H_2O are higher for OF30 case.

The sulfur in the coal for the OF30 case is a little lower than that in the Air case or the OF25 case, so that its exhaust values of SO_2 are also lower. The region of high hydrogen immediately downstream of the burner in the OF30 case appears to be elongated relative to that of the OF25 case, due perhaps to the elongated reverse flow zone envelope in the OF30 case and the reduced oxygen. In addition, the hydrogen in the OF30 case persists farther downstream than in the OF25 case, before being consumed, probably because of the lower main burner zone excess oxygen and overall excess oxygen in the OF30 case.

4.9 Planar Averaged Plots as a Function of Elevation

Mass-weighted, planar averaged plots of temperature, oxygen, and CO mole fraction, as a function of elevation, were post-processed from the final FLUENT case and data files using an Alstom UDF. The plots reinforce the conclusions drawn previously with respect to the contour plots. The planar averaged plots for the 3 cases are provided in the following figures. The temperature history versus elevation is shown in Figure 4-19. The elevation of zero corresponds to the quarl effluence plane, while the elevation of approximately -15 m corresponds to the bottom of the computational hopper. The oxygen chart is shown in Figure 4-20. It should be noted that the oxygen scale on the abscissa of the second figure is reversed. The picture on the right of each plot shows the computational depth (or volume) that constituted the bounds for the planar averages; the volume in and below the convective pass was not included in the averages.

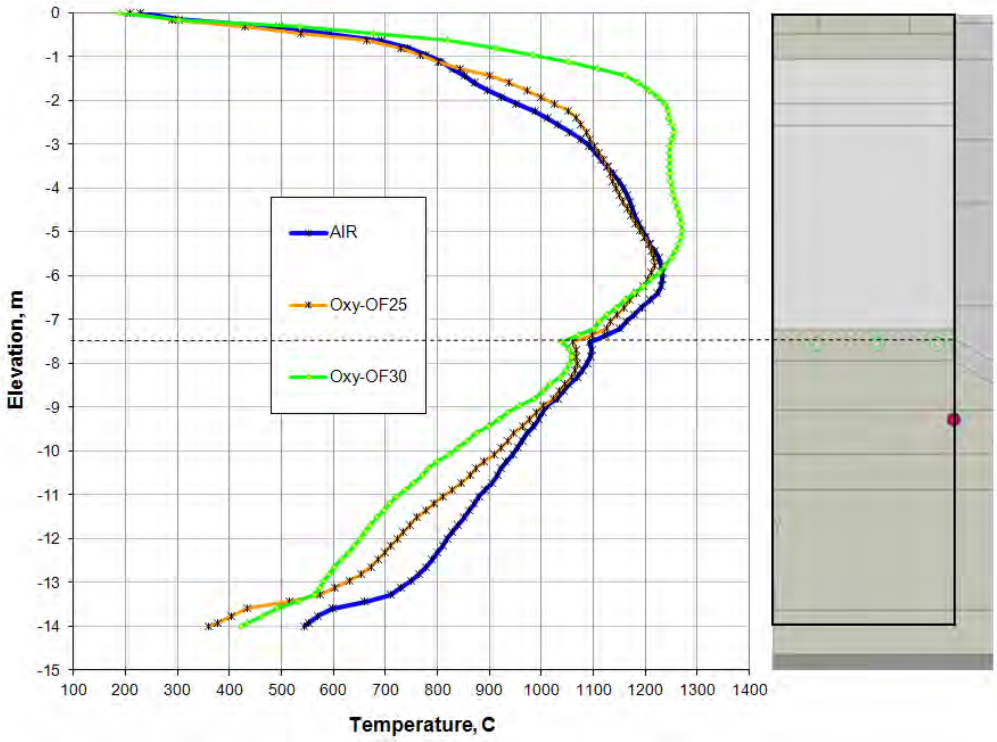

Figure 4-19. Planar Averaged Temperature vs. Elevation

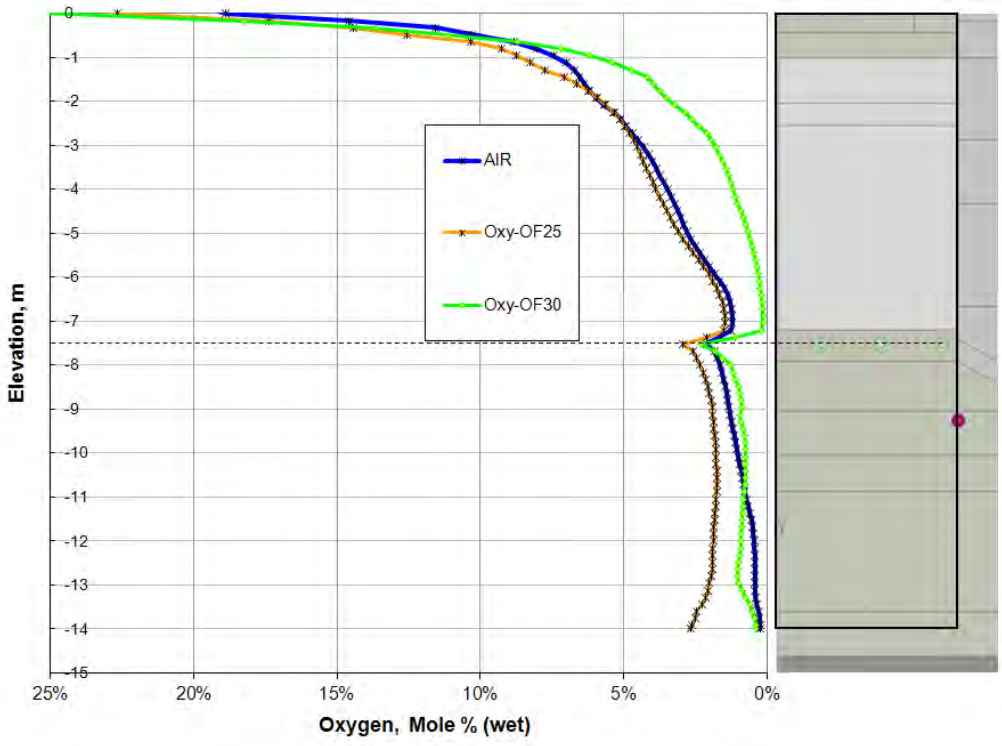

Figure 4-20. Planar Averaged Oxygen Mole Percent vs. Elevation

The temperatures for the OF30 case are higher in the upper portion of the main burner zone, presumably because of the higher oxygen content of the inlet gas, and a higher flow rate of some of the annular streams adjacent to the coal in the primary. However, the main burner zone excess oxygen for the OF30 case (0.87) is smaller than for the other cases (0.96 and 0.99), which subsequently causes the reaction to quench and the temperature to degrade by the time the OFA-1 elevation is reached. This scenario is reflected in the oxygen plot for OF30, showing how the oxygen content of the main burner zone almost reaches zero mole percent (note reversed scale) before the OFA-1 gas is added. This in turn causes the CO to be quite high in the same region, as indicated in the CO chart, Figure 4-21. The OF30 case has the lowest excess oxygen, both in the main burner zone and overall, so that CO is not completely burned out at the exit (not shown in the CO plot).

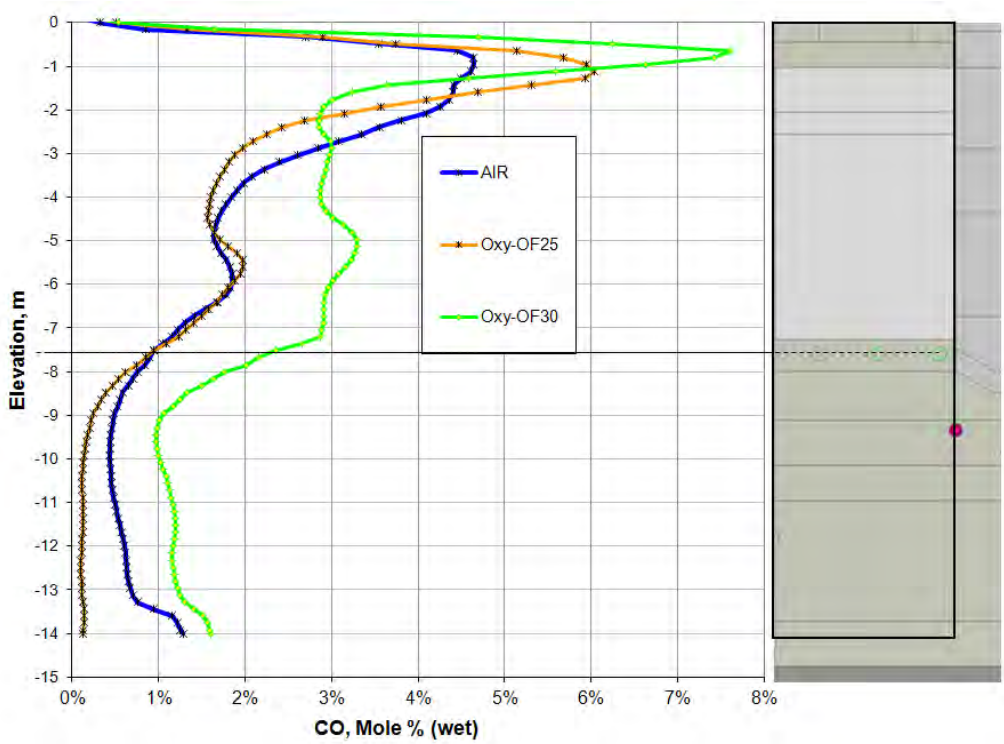

Figure 4-21. Planar Averaged CO Mole Percent vs. Elevation

The OF25 and the Air test case are not too dissimilar in the main burner zone, in terms of the planar averages, except that the CO profile in the near-burner region of the OF25 case has a higher peak CO value than the CO profile in the Air test. It was previously postulated that this is because a higher percentage of the gas distribution is channeled through the inlet core, the inlet primary, Umluft-1, and Umluft-3 in the OF25 test than in the Air test, where the burning of the coal is directly impacted, so that correspondingly more of the char may be converted to CO in the near-nozzle region of OF25 than in the Air test, resulting in the higher computed CO peaks. The greater propensity for gasification in the OF25 case may also play a role.

4.10 Comparisons with Experimental Data

Three cases were predicted with FLUENT CFD software – an air-fired test (Air Test 332) and two oxy-fired tests (OF25 Test 333 and OF30 Test 334). Detailed, two-dimensional line plots were prepared to compare these CFD calculations with the experimental data sets for three variables -- temperature,

oxygen mole percent (wet) and CO mole percent (wet), along a single traverse (connecting Ports 2 and 8) at six (6) different elevations.

Conclusions with respect to the predictions of the experimental data may be itemized as follows:

- The temperature predictions, for the Air test and the OF25 test, are generally aligned either with the DTU data or with the VPC data, or they lie somewhere in between the two data sets. The predictive accuracy appears to be reasonable and acceptable. For the OF30 test, the predictions were also acceptable, but the computations exhibited an excessive heat release in the upper furnace. This excessive computed heat release may be due to errors in the boundary conditions.
- For the Air test and the OF25 test, the calculations in the upper furnace exhibit an oxygen-starved core, near the burner symmetry axis, that is substantiated by the experimental data. The width of the core appears to be reasonably captured. However, the peak computed oxygen levels, on either side of the core, and extending to the walls, are higher than the experimental data. The calculated oxygen concentrations for OF30 Test 334 tend to underpredict the experimental oxygen concentrations in the main burner zone, which may be symptomatic of a feed stream boundary condition issue.
- The CO predictions for the Air test and the OF25 test are moderately good. The CO predictions for OF30 are somewhat excessive relative to the data in the upper furnace.
- The unburned carbon in the char appears to be reasonable.

5. References

1. DOE/NETL Cooperative Agreement.No. DE-NT0005290, "Recovery Act: Oxy-Combustion Technology Development for Industrial-Scale Boiler Applications," performed by Alstom Power Inc. for U.S. DOE National Energy Technology Laboratory.

Recovery Act: Oxy-Combustion Technology Development for Industrial-Scale Boiler Applications

DOE/NETL Cooperative Agreement No. DE-NT0005290

Volume III – Modeling and Validation

Chapter 3 – CFD Modeling of the 500 kW IFK Facility

Authors
Paul J. Chapman
David G. Sloan

Table of Contents

1. Executive Summary 4
2. Objectives 12
3. Description of KSVA 500 kW Test Facility 14
   3.1 Overall Geometric Description 14
   3.2 Measurement Ports and Probes 22
4. Technical Approach 28
   4.1 Computational Mesh 28
   4.2 Boundary Conditions 30
   4.3 Model Selections 34
5. Model Results 37
   5.1 Cold Flow Pitot Tube Results 37
   5.2 Contour Plots 45
   5.3 Heat Flux Predictions 50
6. References 55

List of Tables

Table 3-1. In-flame Measurement Variables and Locations 27
Table 4-1. Coal Composition and Heating Values 31
Table 4-2. Inlet Boundary Conditions 32
Table 4-3. Inlet Species Mass Fractions 33
Table 4-4. Inlet Boundary Conditions for Cold Flow Pitot Probe Runs 34
Table 4-5. Wall Thermal Boundary Conditions 34
Table 4-6. Reaction Expression Stoichiometries 35
Table 5-1. Case Outlet Concentrations and Energy Balance 45

List of Figures

Figure 1-1. Schematic of KSVA 500 kW Test Facility 5
Figure 1-2. Drawing of TW-1 Burner Configuration 6
Figure 1-3. Cold Flow Pitot Probe Predictions on Plane 1a 8
Figure 1-4. Temperature Contour Comparison 9
Figure 1-5. Oxygen Contour Plot Comparison (Mole %, Dry) 10
Figure 3-1. Schematic of KSVA 500 kW Test Facility 14
Figure 3-2. Drawing of Upper Furnace and Quarl 16
Figure 3-3. Exterior View of the Furnace Computational Domain 17
Figure 3-4. Drawing of TW-1 Burner Configuration 18
Figure 3-5. Drawing of TW-2 Burner Configuration 19
Figure 3-6. Solid Model Views of the Burner (TW-1) and Quarl 20
Figure 3-7. Lance or Probe for Air-Fired Staging 21
Figure 3-8. Lance or Probe for Oxy-Fired Staging 22
Figure 3-9. Process Measurements and Location 23
Figure 3-10. Measurement Traverse Levels or Elevations 24
Figure 3-11. Pressure-Tap Designations and Orientations for the 5-Hole, Pitot Probe 24
Figure 3-12. Locations of Pitot Probe Traverses 25
Figure 3-13. Experimental In-flame Probes 26
Figure 4-1. Grid in Selected Regions of the Domain. 30
Figure 4-2. Coal Fineness Rosin-Rammler Distributions 31
Figure 5-1. Cold Flow Cross-Sectional Contour Plots of Velocity Components 38
Figure 5-2. Cold Flow Velocity Magnitude Isosurface Plots 39

Figure 5-3. Cold Flow Contour Plots of Axial Velocity on Center Plane.....40
Figure 5-4. Cold Flow Pathline Plots Colored by Velocity Magnitude.....41
Figure 5-5. Cold Flow Pitot Probe Predictions.....43
Figure 5-6. Cold Flow Burner Profile Calculations to Assess Impact of Increased Swirl.....44
Figure 5-7. Temperature Contour Comparison.....46
Figure 5-8. Oxygen Contour Plot Comparison (Mole %, Dry).....47
Figure 5-9. CO Contour Plot Comparison (Mole %, Dry).....48
Figure 5-10. CO_2 Contour Plot Comparison (Mole %, Dry).....49
Figure 5-11. Wall Heat Flux Extraction Method.....51
Figure 5-12. Predictions of Ellipsoidal Radiometer Heat Flux Data.....52
Figure 5-13. Predictions of Total Heat Flux Probe Data.....53

1. Executive Summary

Alstom has worked with various corporate entities and universities in a number of broad, internal development programs that have been dedicated to oxy-fuel combustion research. One of the purposes of the programs has been to access world-class experts from around the world, and to gather detailed experimental data at various combustion test facilities, where air and oxy combustion tests were performed under controlled conditions. In conjunction with that effort, Alstom conducted computational fluid dynamics (CFD) modeling tasks to model the various pilot test facilities and to compare the calculations with the experimental data.

The objective of the present computational work was to support a portion of Subtask 6.1 (DOE/NETL Cooperative Agreement No. DE-NT0005290; see Ref. 1), in which "simulation results will … be compared with experimental validation data from small-scale facilities." One of those small-scale facilities is the KSVA 500 $kW_{thermal}$ test facility, which is part of the Institute of Combustion and Power Plant Technology or Institut für Feuerungs- und Kraftwerkstechnik (IFK) at the University of Stuttgart (Universität Stuttgart), located in Stuttgart, Germany. Other small-scale facilities include the 15 MW_{th} Boiler Simulation Facility (BSF) and the 30 MW_{th} Schwarze Pumpe oxy pilot plant, simulations of which have been reported in other sections of Volume III. This report specifically addresses the application and validation of the FLUENT® code with respect to the IFK 500 kW data.

The experimental work was conducted at IFK on their 500 kW 0.8 m diameter cylindrical test furnace. This included a series of air and oxy combustion firing tests using a down-fired lignite burner similar to that tested at Vattenfall AB's Schwarze-Pumpe 30 MW Oxy Combustion facility. The experimental tests conducted at IFK using the Vattenfall dried lignite included both staged and unstaged conditions. For the staged tests, a central OFA injection lance was used. Experimental measurements included probe traverses into the furnace at various elevations to measure gas temperatures, gas species and char burnout. The experimental data was collected by IFK ostensibly for the purpose of validating CFD models. To date, the validation has been performed separately by IFK, Vattenfall, and Alstom, using different codes. In an effort to be consistent with other oxy CFD studies reported under this DOE contract, tuning of the reaction models, rates and other factors were made consistent with the 30 MW pilot plant CFD modeling inputs described in a separate section of Volume III; ultimately, the same overall reaction coefficients and fuel reactivities were used in both studies. The CFD modeling and validation of several different IFK test conditions was conducted by Alstom at Windsor, CT, between the years 2010 and 2012. This written report provides a more comprehensive collection of all the important information, including geometry, experimental data, and predictions.

A schematic of the IFK facility and reactor are provided in Figure 1-1. The design of the IFK facility (Ref. 2) is based on the design of a conventional once-through pulverized fuel combustion boiler. The schematic depicts a "small-scale power plant" with a train of flue-gas cleaning unit operations, that includes a high-dust, selective catalytic reduction (SCR) unit, an electrostatic precipitator (ESP), and a bag-filter. Combustion air is provided by a forced draft (FD) fan, while an induced draft (ID) fan serves to transport the flue gases to the stack. The IFK test facility is optimized for investigation of pulverized fuel combustion processes and allows the characterization of different kinds of fuels at staged and un-staged conditions.

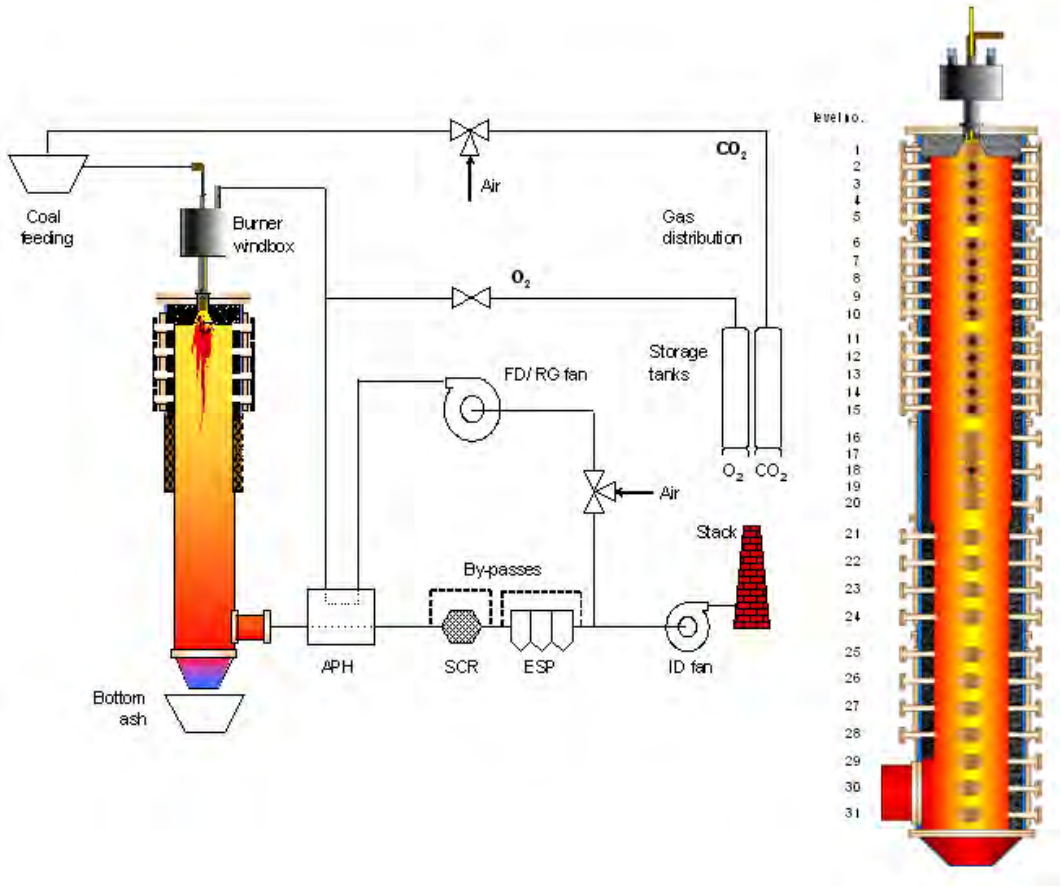

Figure 1-1. Schematic of KSVA 500 kW Test Facility

The reactor (see Ref. 2) is a vertical, down-fired combustion chamber that consists of several cylindrical segments with a total length of about 7 m and an inner diameter of 750 mm. The amount of pulverized fuel fed is gravimetrically controlled by a dosing system, and then the fuel is conveyed pneumatically to the burner. Combustion air is fed to the burner through a secondary line and mixes with the fuel and gas in the primary line at the burner quarl. Swirl can be imparted to the secondary gas stream.

Adjacent to the exterior wall is a water jacket, which has been integrated into the double wall arrangement which covers the length of the reactor. Adjacent to the water jacket, in the upper portion of the furnace (from Level 1 through Level 20, a distance of 4 m from the burner), is refractory. From 4 m downward, instead of the refractory, a type of blanket insulation is used, consisting of ceramic fibers (Levels 21 through 31).

Measurement openings or sampling ports are integrated into the reactor wall. The ports allow measurements of gas emissions, temperatures, and/or ash in both vertical and horizontal direction by means of specially designed probes. The hopper discharge at the bottom of the furnace is conical. An air pre-heater (APH) is installed downstream of the combustion chamber outlet and is used to pre-heat either air or recirculated flue gas.

A drawing of the burner and quarl region is provided in Figure 1-2. The central or core pipe is vacant except when natural gas flows through it during start-up mode. Coal is transported via a carrier gas in the thin (primary) annulus surrounding the central or core pipe. The secondary is split into inner (Secondary

1) and outer (Secondary 2) streams, each of which has swirl vanes at particular angles. The dotted red line denotes the zero elevation at the quarl bendline. For reference purposes, the distance from the zero line to the first measurement port (Port 2) is 180 mm. The inner diameter of the housing for the outer (Secondary 2) swirl vanes terminates in an angled or expanding deflector/trip.

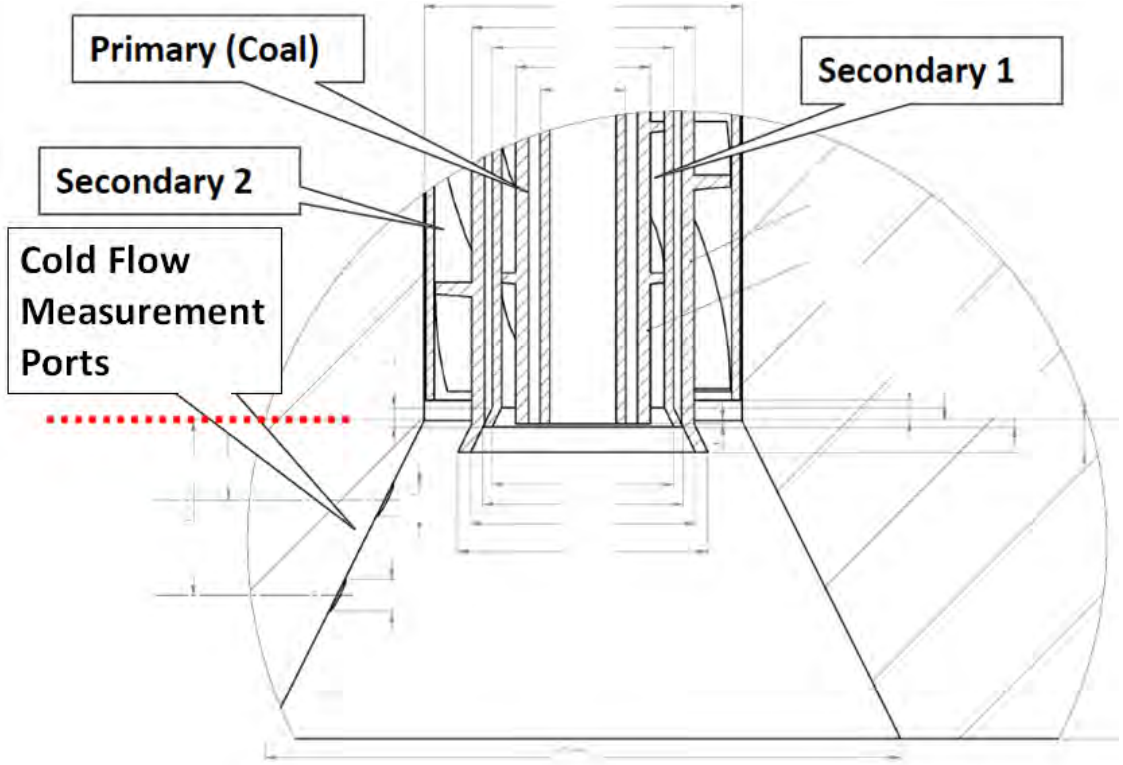

Figure 1-2. Drawing of TW-1 Burner Configuration

The final cases selected for modeling corresponded to two separate test campaigns or "test weeks":

- Test Week 1 (TW-1): unstaged condition: oxy and air test. The two data sets will be delineated simply as (a) "unstaged air" and (b) "unstaged oxy". In addition, cold-flow 5-hole pitot probe measurements in the near-burner region were also completed using the Test Week 1 burner configuration.

- Test Week 2 (TW-2): staged condition: oxy and air test. The two data sets will be delineated simply as (a) "staged air" and (b) "staged oxy".

The primary distinction between the TW-1 and TW-2 configurations is that the TW-2 configuration has a larger swirl magnitude associated with the Secondary-2 or SA-2 swirler (i.e., large vane angles) than the TW-1 configuration (which has moderate SA-2 vane angles). All of the hot cases were fired with lignite coal.

The cold-flow test and boundary conditions corresponded to the TW-1 Burner configuration, with a somewhat different air flow distribution than the unstaged air case. The cold flow measurements were performed with a 5-hole, spherical, pitot probe; the probe was inserted only into the ports corresponding to Levels 1a, 1b, and 2a, where Levels 1a and 1b are within the quarl region and Level 2a is slightly

downstream of the quarl exhaust plane. The gas temperature and gas species sampling probes are typical suction probes, with the gas temperature probe equipped with shielding to protect against radiation loss. Temperature and species measurements were taken at Levels 2 through 15, at various reactor radii. Total heat flux probes, as well as ellipsoidal radiometers (for total radiative heat flux measurements) were used at Levels 2 through 15, at a radial location relatively close to the insulated "wall".

For the staged tests, customized staging lances were used for the injection of overfire air or oxygen at Level 10 (air tests) or Level 11 (oxy tests) along the reactor symmetry axis. The lance exhaust tip was designed to direct the flow both radially away from the symmetry axis and in the downstream direction.

The meshing of the KSVA 500 kW Test Facility was accomplished by gridding the burner geometry as an integrated component with the reactor as part of a single computational domain. From drawings provided by IFK, a 3-D geometry of the computational domain was created using ANSYS Gambit® with about 2.7 million cells.

For the boundary condition specification, measured flow rates and compositions for the feed streams, as well as the experimental particle size distributions for the tests, were provided by IFK. To model the wall heat transfer in the hot cases, the reactor walls were given specified temperature boundary conditions. For the cold flow computational runs, specified inlet velocities and a constant fluid density were utilized.

For the gas-phase chemistry, 8 species were utilized – volatile, C-gas, CO, H_2, H_2O, O_2, SO_2, and N_2. The associated gas-phase reactions included volatile decomposition, CO oxidation, H_2 oxidation, and C-gas oxidation. The C-gas species was utilized as a surrogate soot species, but was not linked to the radiation submodel. For the main gas-phase combustion reactions in FLUENT®, the turbulence-chemistry interaction was modeled using the composite eddy-dissipation (mixing-limited / fast-chemistry) and Arrhenius rates (kinetically-limited) combustion submodel, in which the smaller of the two rates (eddy-dissipation or Arrhenius rates) takes local precedence.

The "wet combustion" model was also activated, to allow coal moisture to evaporate from the particle, prior to devolatilization. A single-rate model was used for devolatilization and the swelling factor was set to unity. The char particle was presumed to consist only of pure carbon (designated as C<s>), and ash. The heterogeneous char reactions were composed of one oxidation and two gasification reactions (for CO_2 and H_2O), using the multi-surface reaction model.

Alstom used the Realizable k-ε submodel, with standard wall functions, for turbulence closure. User-defined functions (UDFs) were used for the gas absorption coefficient and for the particle absorption efficiency. The Discrete Ordinates (DO) model was used for the radiation calculations. Second-order discretization was used for the pressure, and second-order upwind numerics was specified for all of the other transport equations except for the species.

As example of some of the 5-hole pitot probe predictions at a single plane is shown in Figure 1-3. Profile plots along the x- and y-coordinate directions are compared with experimental, 5-hole pitot probe data for the axial velocity, radial velocity, and tangential velocity at Plane 1a. The burner corresponds to the Test Week 1 configuration.

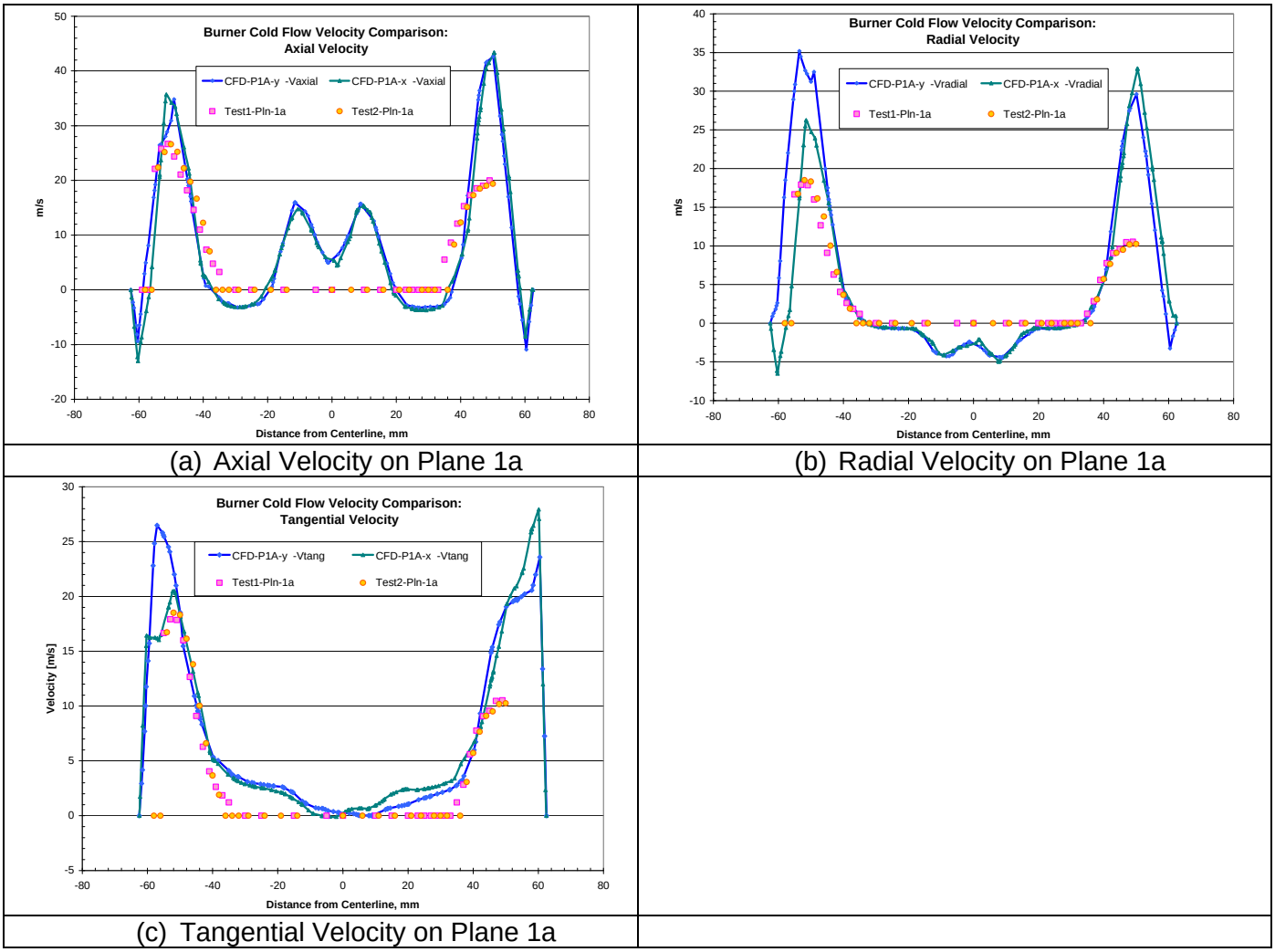

(a) Axial Velocity on Plane 1a

(b) Radial Velocity on Plane 1a

(c) Tangential Velocity on Plane 1a

Figure 1-3. Cold Flow Pitot Probe Predictions on Plane 1a

At Planes 1a and 1b, the external velocity component peaks near the quarl walls are reasonably captured, as they are at successive planes (shown in the body of the report). However, the experimental axial, radial and tangential velocities in the core region are all identically zero, which may indicate that rotation of the probe to coincide with the direction of flow may be required to pick up the velocity components below some threshold value (i.e., better calibration of the probe with a nulling method may be required).

Some examples of predictions for temperature and oxygen concentration in reacting flow are also provided in the following two plots. Contour plots of temperature on an x-plane, bisecting the reactor, for the four cases, are shown in Figure 1-4. Each contour plot is overlayed with experimental data in the form of discrete, colored dots that are referenced to the same legend as the contour plot itself. Only elevations through Level 10 are shown in the truncated plots; the OFA lance injection plugs are in the vicinity of Level 11 and are therefore downstream of what is displayed.

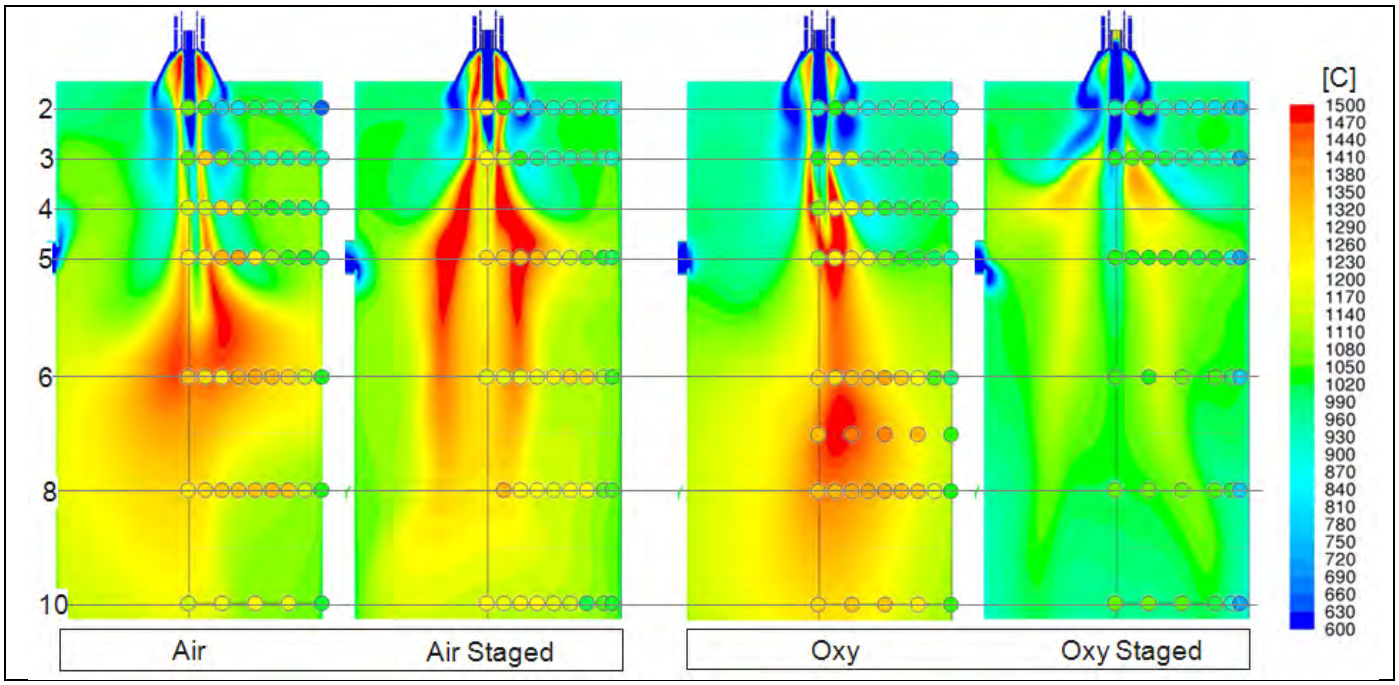

Figure 1-4. Temperature Contour Comparison

Differences exist between the computed contour plots. The unstaged cases appear to have corner recirculation zone reattachment points that are downstream of the Scan-2 port (the port on the left-hand side at Level 5), while the reattachment points in the staged cases appear to be positioned upstream of the Scan-2 port. This is probably due to the higher SA-2 swirl associated with the staged cases (i.e., higher swirl in TW-2 tests than in TW-1 tests), which helps to expand the flame beyond the quarl and mix out the flowfield more rapidly than in the unstaged case.

The experimental temperature data tends to follow the computed contours fairly well. For the air-unstaged case at Levels 1 through 5, for example, the suction pyrometry data appears to indicate that lower temperatures are on the symmetry axis and then temperatures increase with an increase of radius until a peak temperature is reached, after which temperatures decrease to the wall. The peak experimental temperature location is located at a radius which is slightly larger than the radius of the peak computed temperature. The computational jet or flame does not seem to expand as rapidly as the rate indicated by the experimental data, although downstream of Level 5, both the experimental and computed flame zone flare out or balloon out in shape at approximately the same level. The experimental data does not achieve the peak values of 1500 °C exhibited by the calculations, and the experimental flame high-temperature region appears to be somewhat more diffuse and spread out. This may indicate the necessity of having more intermediate species in the computed flame zone and perhaps slower reaction rates. Nevertheless, given the uncertainty in the temperature measurements, particularly in the high-temperature and high-gradient regions, the predictions are very reasonable and encouraging.

Similar statements regarding comparison between the predictions and data may be made for the other air-staged and oxy cases. Even in the oxy-staged case, where the computed temperatures are depressed relative to the other cases, the experimental data appear to follow suit and scale down in a corresponding manner.

The transition from air (unstaged or staged) to oxy (unstaged or staged) also appears to be captured reasonably well, indicating that the necessary physics for oxy combustion are encompassed within the FLUENT® property packages and the UDFs. The accuracy of the computed oxy results appears to be within error bands that are similar to the prediction error bands associated with the air-combustion results.

Contour plots of oxygen concentration (in units of mole %, dry) on an x-plane, bisecting the reactor, for the four cases, are shown in Figure 1-5.

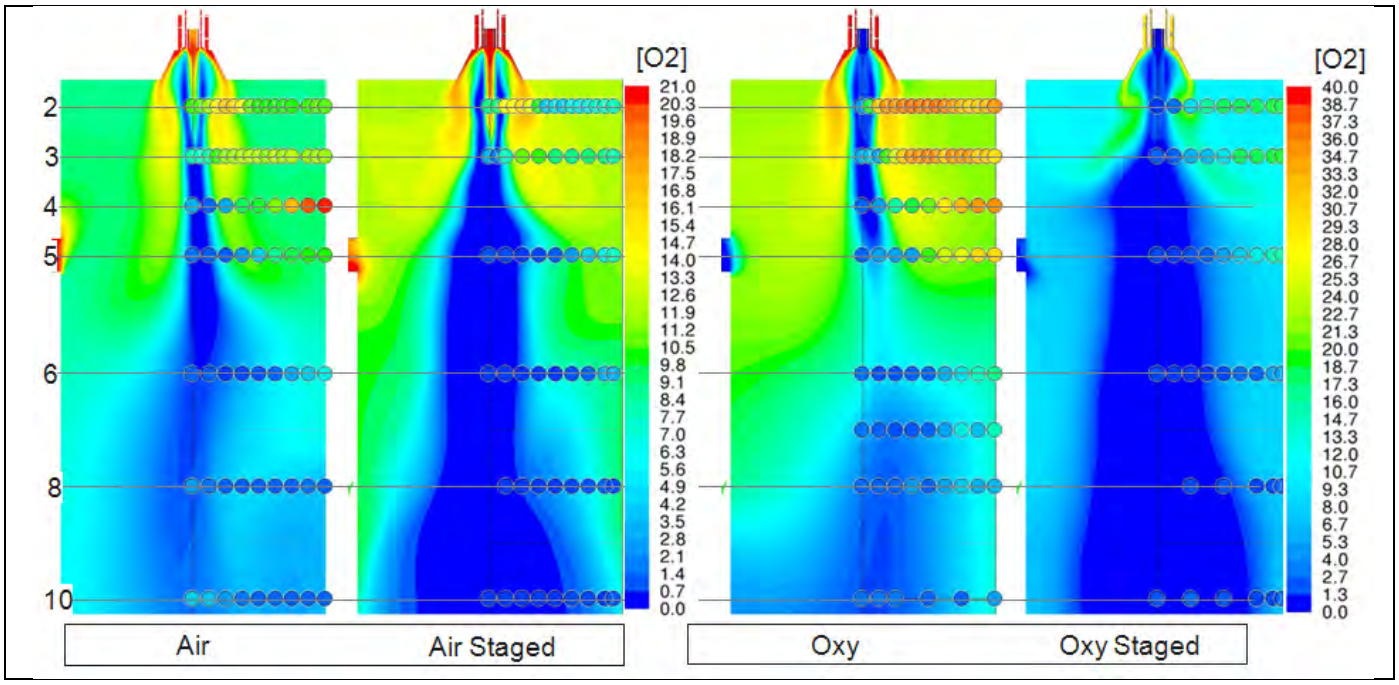

Figure 1-5. Oxygen Contour Plot Comparison (Mole %, Dry)

An oxygen-starved core is apparent in all of the computed contour plots. As expected, the staged cases exhibit a much larger or expanded oxygen-starved core than the unstaged cases (particularly since the OFA is introduced downstream at Level 11). The cases are qualitatively similar to each other in many respects, but they also have some quantitative differences.

Overall, the experimental data is similar to the computations. For the unstaged air case at Level 2 and 3, the experimental data indicate a peak oxygen mole fraction in the flame at a radius similar to that shown by the data. At Level 4, the oxygen seems to increase to high inlet values near the wall. The high oxygen value near the wall must be due to the in-leakage from the Scan-2 port which is swept upstream (again indicative of the reattachment point lying downstream of the Scan-2 port). At Level 5, the data appears to coincide with the computed contours. The oxygen data at Levels 6 through 10 are relatively low in magnitude from the symmetry axis to the wall, in a manner that is in reasonable agreement with the computations. Interestingly, at Levels 8 and 10, the highest experimental data value is on the symmetry axis, which may indicate asymmetry in the actual flame.

For the air-staged case, the experimental data at Level 2 are at about 5 or 6% (mole %, dry) near the wall, while the computations are at probably twice that value. Alternatively, for the oxy-unstaged case at Level 2, the experimental data shows values around 30%, while the computations are at concentration

magnitudes of around 20%. Therefore, the computation concentrations may depart from the data in the upstream corners of the reactor (and the departure may be positive or negative), but overall, the predictions appear to capture much of the expansion of the oxygen-starved core and appear to follow the trends through each Level. Again, the predictions appear to be reasonable and acceptable over most of the domain.

General conclusions and observations may be itemized as follows:

- Overall, given the large uncertainty bands in the probe data, the temperature predictions are reasonable and acceptable. Furthermore, the transition from air-combustion to oxy-combustion is adequately addressed by the FLUENT® property databases, coupled with the UDFs. The predictive error inherent in the air-combustion calculations does not seem to be exacerbated by changing the boundary conditions and performing oxy-combustion predictions.

  At Levels 1 through 5, the computational flame profile (as indicated by temperature) does not seem to expand as rapidly as the rate indicated by the experimental data, although it is difficult to know how much of that apparent expansion is due to the probe suction-volume characteristics. Experimental peak temperatures remain significantly below the computed peak temperature of 1500 °C and the experimental peak flame values at Levels 6 through 10 appear to be more spread out or diffuse than the computed flame.

- Overall, the comparison of the experimental species data with the predictions is very encouraging. The overall flame shapes and flame expansions as a function of staging appear to simulate the data trends. Major species, such as oxygen and CO_2, are predicted reasonably well, although some quantitative differences are apparent in certain regions. For example, for some tests, the experimental mole fraction for O_2 and CO_2 may be ±10 percentage points different from the computations in the upper corner regions of the reactor.

- The rate of experimental CO production is much slower than the calculations in the near-nozzle region, never reaching the high CO concentrations exhibited by the calculations, but then the measured CO continues to be produced over a wide radius through Levels 6 and 8 while the computational CO rapidly depletes. The slow, but sustained, CO production in the actual flame may point to CO production from soot or char conversion rather than to rapid volatile combustion. An examination of minor species, such as CO, indicates that some speciation and reaction rate studies are necessary to surface the underlying reasons for the differences between the experimental data and the calculations.

- With the exception of some flawed total heat flux probe data (noted by IFK), the trends exhibited by the wall heat flux data or the ellipsoidal radiometer data, and the associated predictions, appear to match each other reasonably well, with the difference in peak magnitudes between the data and predictions varying between 15 and 30%. Qualitatively, the trends are fairly similar. The relative scaling or difference in magnitude between the air and oxy experimental data is also fairly consistent with the difference in magnitude between the calculated air and oxy cases.

2. Objectives

Alstom has worked with various corporate entities and universities in a number of broad, internal development programs that have been dedicated to oxy-fuel combustion research. One of the purposes of the programs has been to access world-class experts from around the world, and to gather detailed experimental data at various combustion test facilities, where air and oxy combustion tests were performed under controlled conditions. In conjunction with that effort, Alstom conducted computational fluid dynamics (CFD) modeling tasks to model the various pilot test facilities and to compare the calculations with the experimental data.

This report summarizes computational fluid dynamics work that was done, in part, to support a portion of Subtask 6.1 (DOE/NETL Cooperative Agreement No. DE-NT0005290; see Ref. 1). This program has a number of different objectives.

Subtask 6.1 – CFD Oxy-Combustion Model

- The ANSYS FLUENT® code, with improved submodels for combustion and radiation under oxy-combustion conditions, will continue to be applied and validated.
- Application of large-eddy simulation (LES) modeling for oxy-boiler application will be assessed and compared with simplified steady-state simulation approaches (specifically FLUENT®). More rigorous analysis of experimental and simulation data will also be conducted to statistically quantify uncertainty of modeling/prediction at both submodel and model levels. This will help improve prediction capability and accuracy of the modeling tools. This work will be conducted in collaboration with the Institute of Clean and Secure Energy (ICSE) at the University of Utah (Professor Phil Smith).
- Simulation results will then be compared with experimental validation data from small-scale facilities, the 15-MWth BSF and from the 30-MWth Schwarze Pumpe oxy pilot plant. The CFD code evaluation will include predictions for combustion, heat flux distribution, corrosion, and pollutant control.

The present report only addresses the application and validation of the FLUENT® code to the third bullet – "Simulation results will then be compared with experimental validation data from small-scale facilities." – specifically the IFK facility (although none of the IFK reactors are specifically mentioned). Simulations of the 15-MW_{th} BSF and the 30-MW_{th} Schwarze Pumpe oxy pilot plant have been reported in other sections of Volume III. This report specifically addresses the application and validation of the FLUENT® code to the IFK 500 kW data.

Ultimately, the final cases selected for modeling corresponded to two separate test campaigns or "test weeks":

- Test Week 1: unstaged condition: oxy and air test. The two data sets will be delineated simply as (a) "unstaged air" and (b) "unstaged oxy". In addition, cold-flow 5-hole pitot probe measurements in the near-burner region were also made available for predictive comparisons using the Test Week 1 burner configuration.

- Test Week 2: staged condition: oxy and air test. The two data sets will be delineated simply as (a) "staged air" and (b) "staged oxy".

All of the hot cases were fired with lignite coal.

The objective of this CFD modeling task was to simulate the performance of the oxy-fired, swirl-burner configuration tests in the IFK 500 KW reactor, and to use the simulations to validate the CFD code, submodels, and physical/chemical properties for oxy-combustion. The FLUENT® code was used by Alstom to examine the apparent differences between air- and oxy-firing for a lignite coal. In addition, the accuracy of the CFD code and submodels were assessed and validated by comparing calculations with experimental data from the IFK test program. The overall aim of the simulation runs, as performed by Alstom, was to provide a more reliable and validated computational tool and methodology that could be used to bolster and supplement the design process for oxy-fired boilers.

3. Description of KSVA 500 kW Test Facility

3.1 Overall Geometric Description

The KSVA 500 $kW_{thermal}$ test facility is part of the Institute of Combustion and Power Plant Technology or Institut für Feuerungs- und Kraftwerkstechnik (IFK) at the University of Stuttgart (Universität Stuttgart), located in Stuttgart, Germany. Schematics of the facility and reactor are provided in Figure 3-1. The design of the IFK facility (Ref. 2) is based on the design of a conventional once-through pulverized fuel combustion boiler. The schematic depicts a "small-scale power plant" with a train of flue-gas cleaning unit operations, that includes a high-dust, selective catalytic reduction (SCR) unit, an electrostatic precipitator (ESP), and a bag-filter. Combustion air is provided by a forced draft (FD) fan, while an induced draft (ID) fan serves to transport the flue gases to the stack. The IFK test facility is optimized for investigation of pulverized fuel combustion processes and allows the characterization of different kinds of fuels at staged and un-staged conditions.

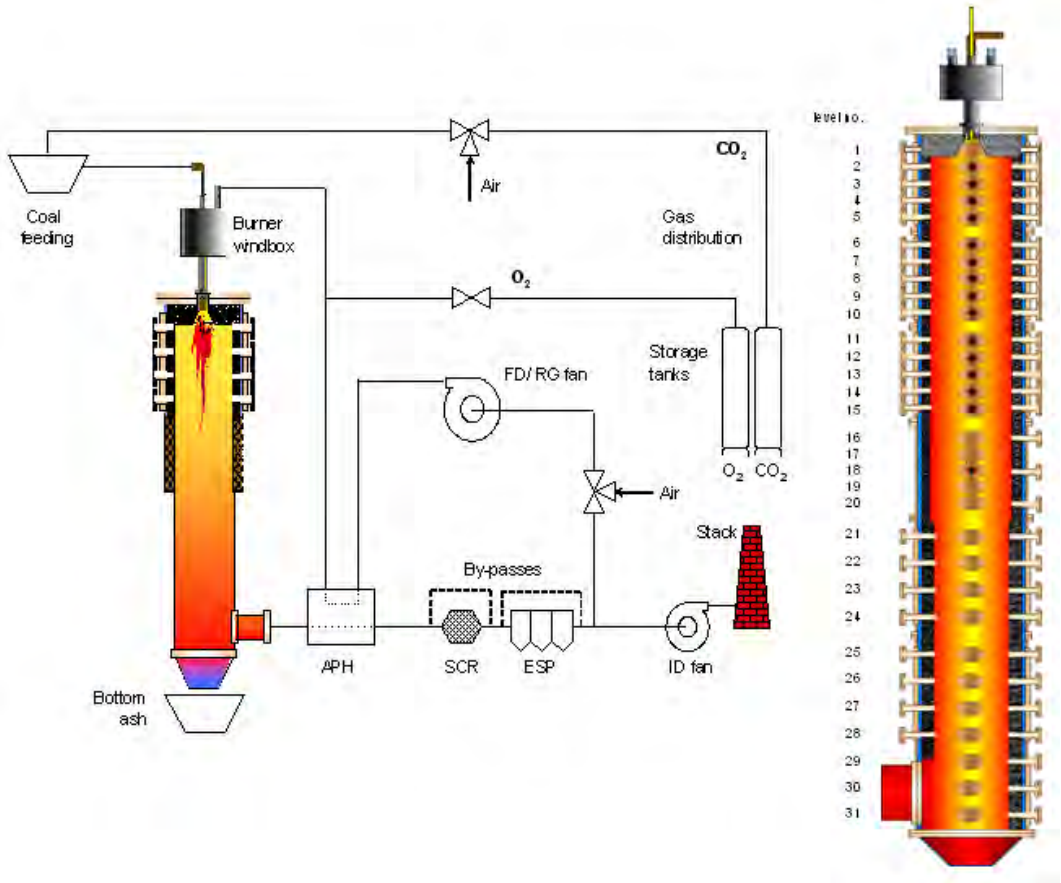

Figure 3-1. Schematic of KSVA 500 kW Test Facility

The reactor (see Ref. 2) is a vertical, down-fired combustion chamber that consists of several cylindrical segments with a total length of about 7 m and an inner diameter of 750 mm. The top-mounted burner is integrated into a centric opening of the burner plate, covering the combustion chamber. The amount of pulverized fuel fed is gravimetrically controlled by a dosing system. Fuel is conveyed pneumatically to the burner via a primary line with either (pressurized) air or CO_2 from storage tanks as the carrier medium.

The metered amounts of fuel vary between 35 and 50 kg/hr for hard coals and between 50 and 100 kg/hr for brown coals, which results in a maximum thermal performance of 0.5 MW. Combustion air is fed to the burner through a secondary line and mixes with the fuel and gas in the primary line at the burner quarl. Swirl can be imparted to the secondary gas stream.

Adjacent to the exterior wall is a water jacket, which has been integrated into the double wall arrangement which covers the length of the reactor. Adjacent to the water jacket, in the upper portion of the furnace (from Level 1 through Level 20, a distance of 4 m from the burner), is refractory, with a thickness of about 115 to 125 mm. The thermal conductivity of the refractory material is about 2.4 W/m-K. From 4 m downward, instead of the refractory, a type of blanket insulation is used, consisting of ceramic fibers with a thickness of 115 to 125 mm. A metal jacket of a thickness of 1.5 mm holds the ceramic fibers in place and constitutes the innermost surface exposed to the hot flue gas in the lower furnace (Levels 21 through 31).

Measurement openings or sampling ports are integrated into the reactor wall and are typically spaced about 150 to 170 mm apart. The ports allow measurements of gas emissions, temperatures, and/or ash in both vertical and horizontal direction by means of specially designed probes. The hopper discharge at the bottom of the furnace is conical.

An air pre-heater (APH) is installed downstream of the combustion chamber outlet and is used to pre-heat either air or recirculated flue gas. An opening in the APH permits the collection of ash samples during operation. The flue gas temperature exhausting from the APH is designed to be about 350 to 400 °C, the approximate temperature required for entrance into the SCR. Ammonia injection is also available. The flyash transported with the flue gas stream is removed in the ESP, which contains three collector fields. The flyash may be collected separately from each field during operation and subjected to laboratory analysis.

In oxy-fuel mode, ambient air is precluded from entering the process, and a portion of the flue gas is extracted downstream of the ESP and recycled to the reactor. Pure O_2 from an external storage tank may either be premixed with the wet recycled flue gas or directly injected into the furnace; flow rates are controlled by a mass flow controller unit. Bottled CO_2 is used as the carrier gas in the primary stream for oxy-coal operation.

A dimensioned drawing of the upper furnace section is provided in Figure 3-2. The figure shows the relative positions and dimensions of the burner nozzle, the quarl, and the sampling ports.

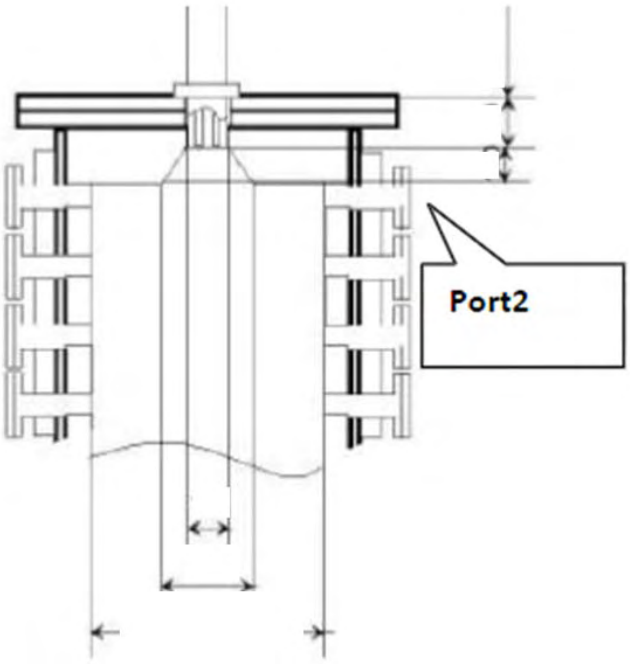

Figure 3-2. Drawing of Upper Furnace and Quarl

An exterior view of the computational domain of the furnace is provided in Figure 3-3. Two scanning portals are apparent in the picture, both of which are subject to a slight (but unknown) in-leakage during scanning or sampling procedures.

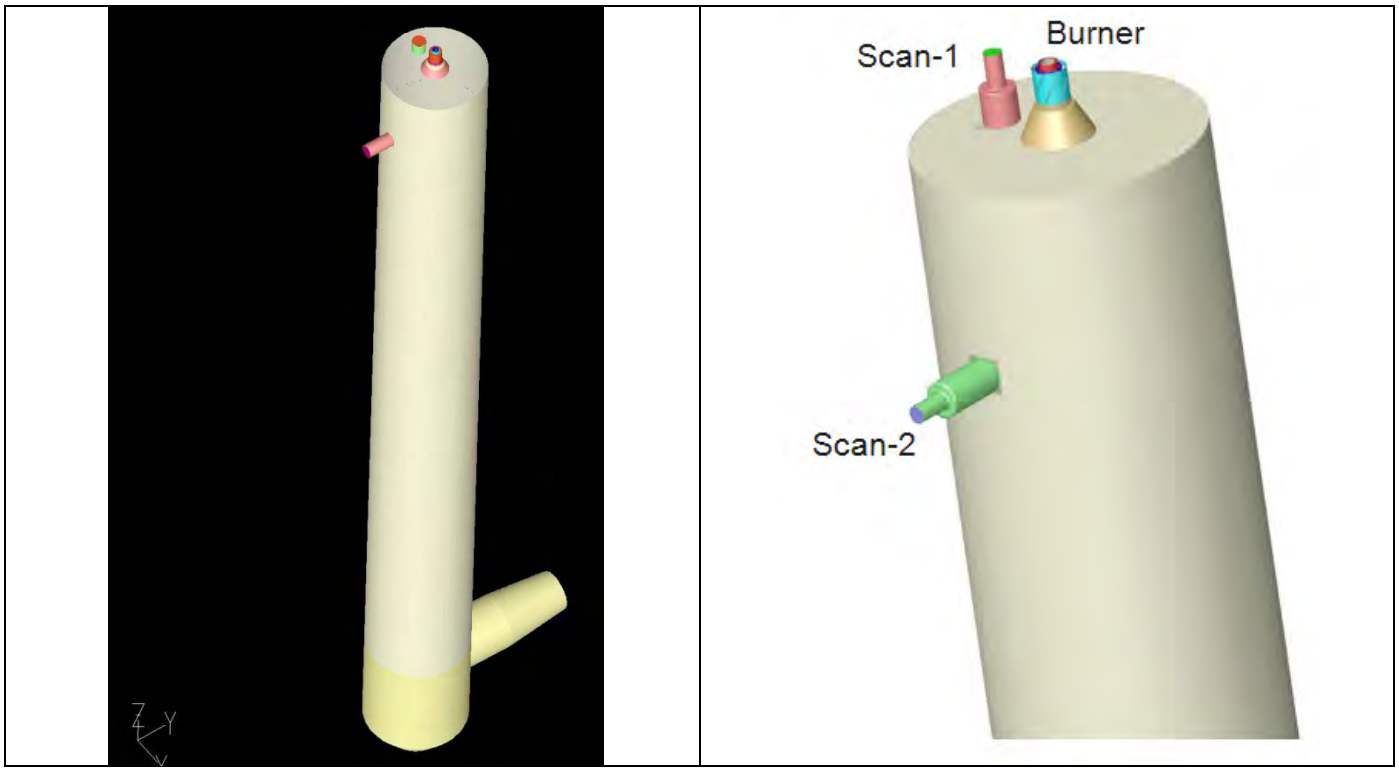

Figure 3-3. Exterior View of the Furnace Computational Domain

The experimental data was collected during two separate test campaigns or "test weeks":

- Test Week 1 (TW-1): unstaged condition: oxy and air test. The two data sets will be delineated simply as (a) "unstaged-air" and (b) "unstaged-oxy". In addition, cold-flow, 5-hole pitot probe measurements in the near-burner region were also made available for predictive comparisons using the Test Week 1 burner configuration.
- Test Week 2 (TW-2): staged condition: oxy and air test. The two data sets will be delineated simply as (a) "staged-air" and (b) "staged-oxy".

A slightly different burner configuration was used during Test Week 2 than was used during Test Week 1. The reason for the modification to the burner configuration was to enhance the flame attachment, which was observed to be less than optimal during Test Week 1. Each burner configuration will be discussed in turn.

Test Week 1 (TW-1) Burner Configuration

A drawing of the TW-1 Burner configuration, is provided in Figure 3-4. Coal is transported via a carrier gas in the thin (primary) annulus surrounding the central or core pipe. The secondary is split into inner (Secondary 1 or SA-1) and outer (Secondary 2 or SA-2) streams, each of which has swirl vanes at particular angles. The dotted red line denotes the zero elevation at the quarl bendline. For reference purposes, the distance from the zero line to the first measurement port (Port 2) is 180 mm. The inner diameter of the housing for the outer (Secondary 2) swirl vanes terminates in an angled or expanding deflector/trip.

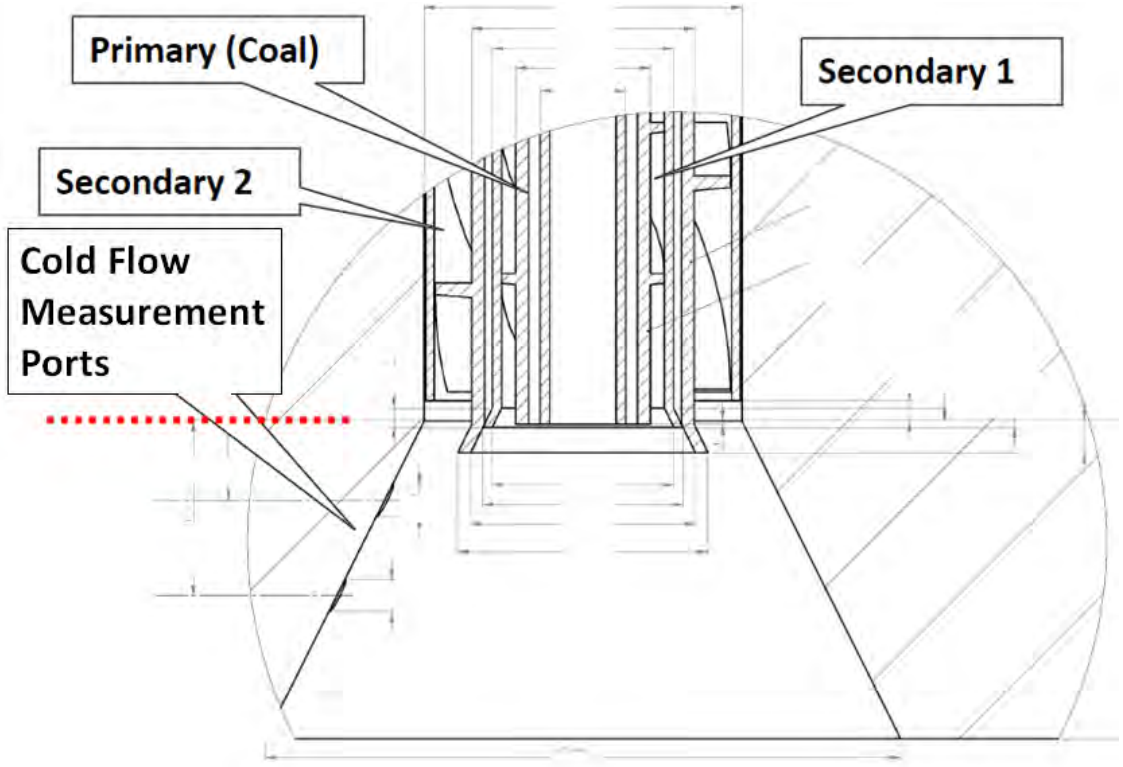

Figure 3-4. Drawing of TW-1 Burner Configuration

Test Week 2 (TW-2) Burner Configuration

A drawing of the TW-2 Burner configuration is provided in Figure 3-5. Coal is transported via a carrier gas in the thin (primary) annulus surrounding the central natural gas pipe. Again, the secondary is split into inner (Secondary 1 or SA-1) and outer (Secondary 2 or SA-2) streams. The dotted red line denotes the zero elevation at the quarl bendline. The inner diameter of the housing for the outer (Secondary 2) swirl vanes terminates in an angled or expanding deflector/trip.

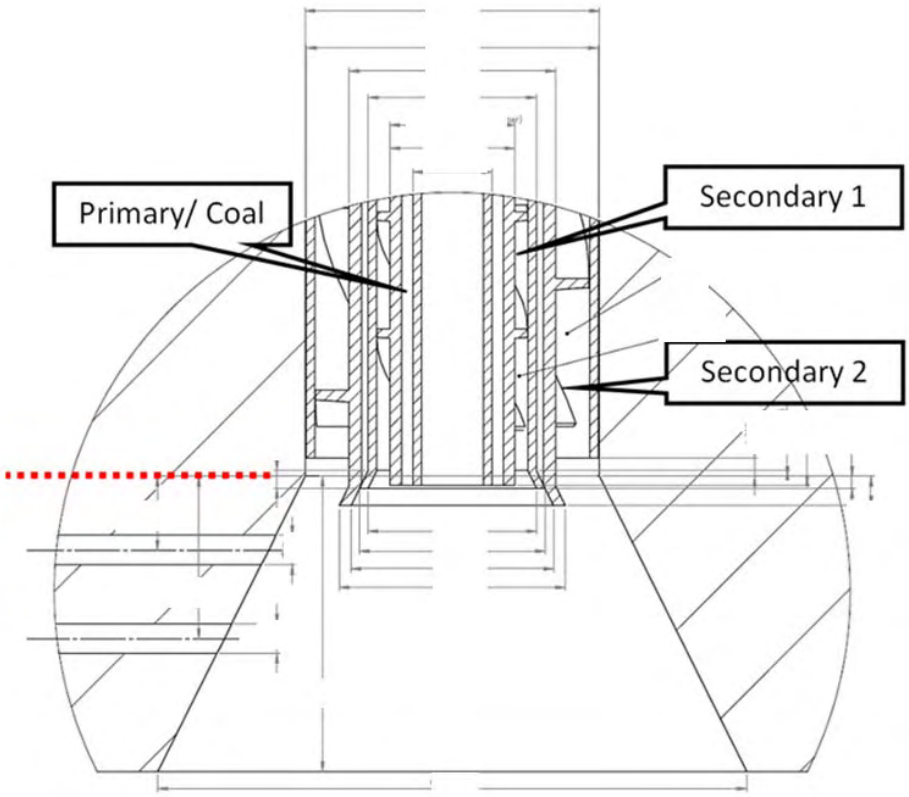

Figure 3-5. Drawing of TW-2 Burner Configuration

This Secondary-1 vane swirler is identical to the Secondary-1 vane swirler in the TW-1 configuration. However, this Secondary-2 swirler has a different number of vanes with a larger swirl angle, but a shorter length overall, than the Secondary-2 swirler used in the TW-1 burner configuration. Therefore, the primary distinction between the TW-1 and TW-2 configurations is the much larger swirl magnitude associated with the Secondary-2 swirler in the TW-2 configuration.

Solid model renderings of the burner (TW-1) and quarl are shown in Figure 3-6. Looking upstream from the interior of the furnace towards the burner, the swirl would be in a counter-clockwise direction.

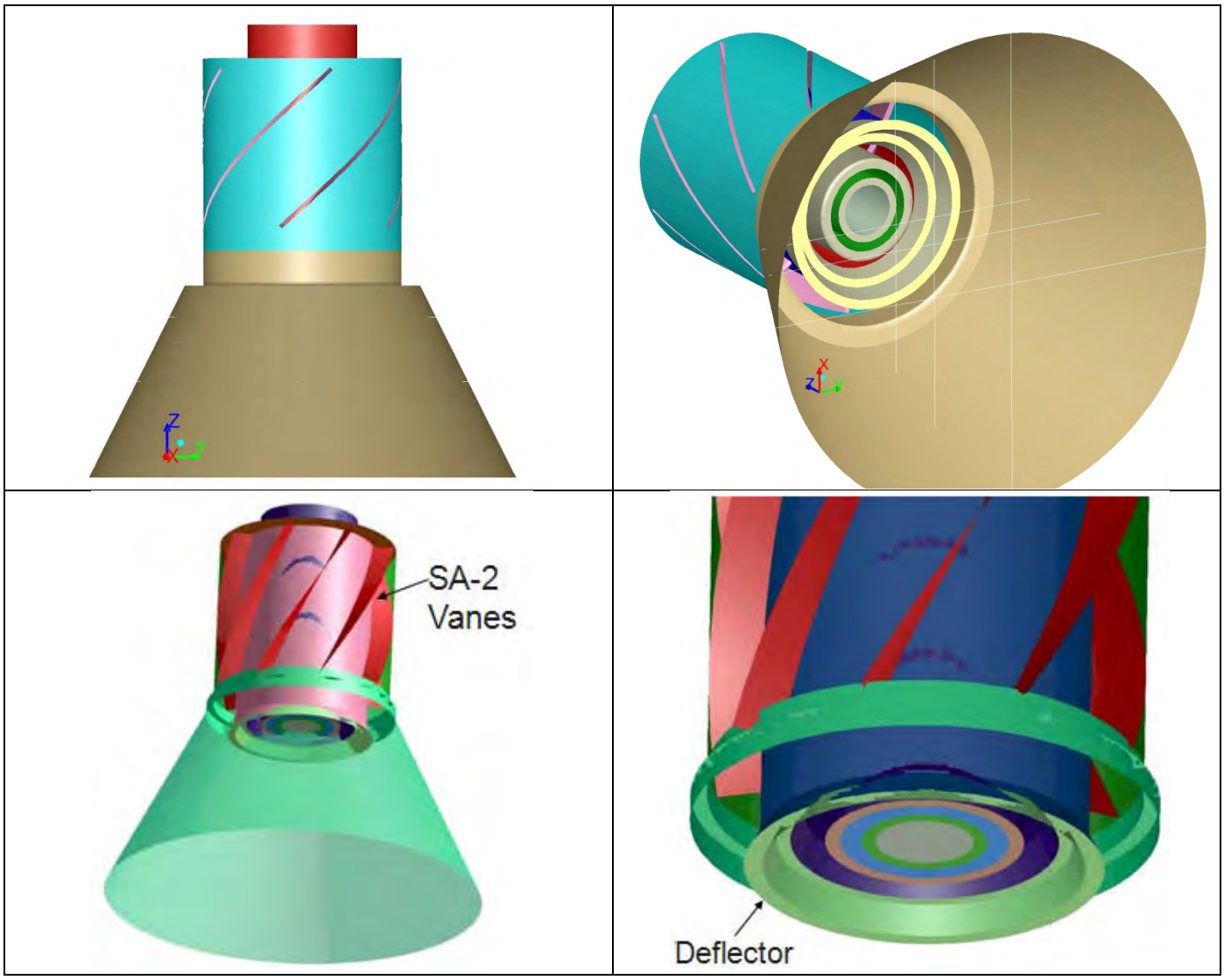

Figure 3-6. Solid Model Views of the Burner (TW-1) and Quarl

Staging Lances

For staging, customized lances or probes are used to feed the overfire air or oxygen to the reactor. Separate lances and lance injection elevations are used for staged air injection and for staged oxygen injection.

The lance used for air staging is shown in Figure 3-7. The air probe is a J-type lance. The support arm of the lance is horizontal at the furnace walls, but the probe curves gently downward as it approaches the symmetry axis, so that the lance exhaust tip is ultimately directed vertically downward (i.e., downstream) along the symmetry axis. The staging probe is inserted at Level 10 (1670 mm from the burner zero datum), but the end of the tip is at a longitudinal distance of 320 mm from the horizontal arm, so that the total distance from the burner datum is 1990 mm. The exhaust tip uses an opposed disk with radial curvature, so that the exhausting flow is directed radially away from the symmetry axis (and dispersed uniformly in the circumferential direction).

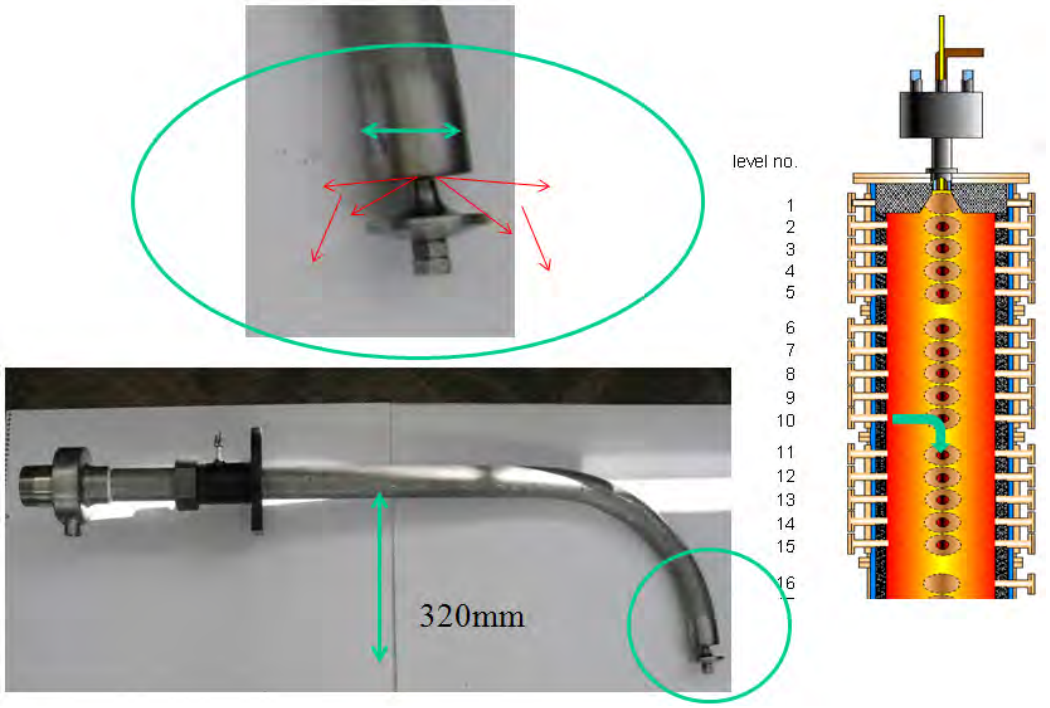

Figure 3-7. Lance or Probe for Air-Fired Staging

The corresponding lance or probe used for staging under oxy-firing conditions is shown in Figure 3-8. The lance is essentially horizontal, but the exhaust tip is directed vertically downwards, aligned with the symmetry axis. The staging probe for oxy-firing is inserted at Level 11 (1990 mm from the burner zero datum), one level below the elevation used for air-firing. The exhaust tip consists of a small plenum and bell-mouth opening, which expands the exhausting flow as a diffused jet. Although the staging probe for oxy-firing is inserted at a different level than the staging probe for air-firing, the exhaust tips for both probes are at about the same elevation.

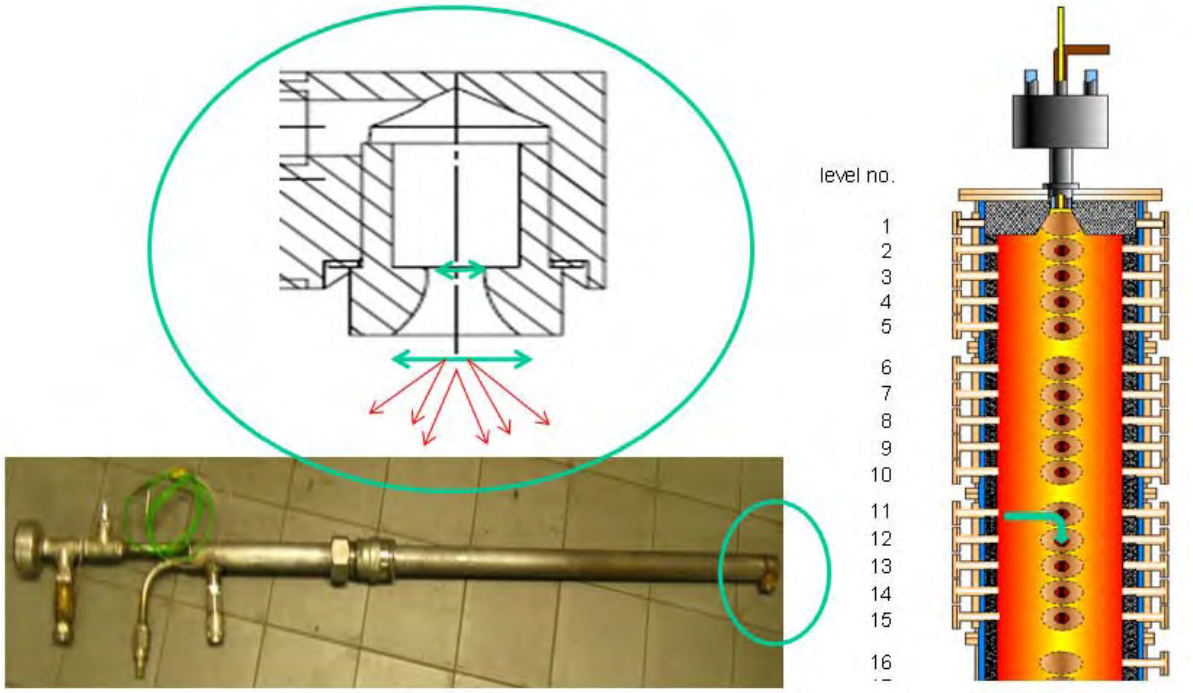

Figure 3-8. Lance or Probe for Oxy-Fired Staging

3.2 Measurement Ports and Probes

IFK provided the following information to Alstom and Vattenfall in order to permit construction of the CFD cases and to perform the validation against the experimental data:

- Descriptions of the test facility
- Burner geometry
- Measurement locations
- Lignite coal composition
- Particle size distribution
- Flow rates and operating conditions
- Continuous temperature and emissions measurements near the reactor outlet
- Measured SO_3 and HCl concentrations downstream of the air preheater
- Total heat flux and ellipsoidal radiometer probe measurements and a pictorial description of the probes
- In-flame gas temperature and species measurements (provided in EXCEL files)
- Ash analyses from the hopper, air preheater, and ESP
- Flyash analyses extracted along the centerline of the reactor at various elevations (or levels)
- Tabulation of the species analyzer equipment.
- Pitot (5-hole) probe measurements in the near-burner region (TW-1 configuration, cold flow only).

A pictorial representation of the location and type of measurements taken is shown in Figure 3-9. The in-flame gas species measurements include O_2, CO, CO_2, H_2S, SO_2, and NO. The SO_3 and HCl measurements were taken downstream of the air preheater where temperature levels were expected to be at approximately 400 °C. Ash samples were taken from the ash hopper, the air preheater, and the ESP.

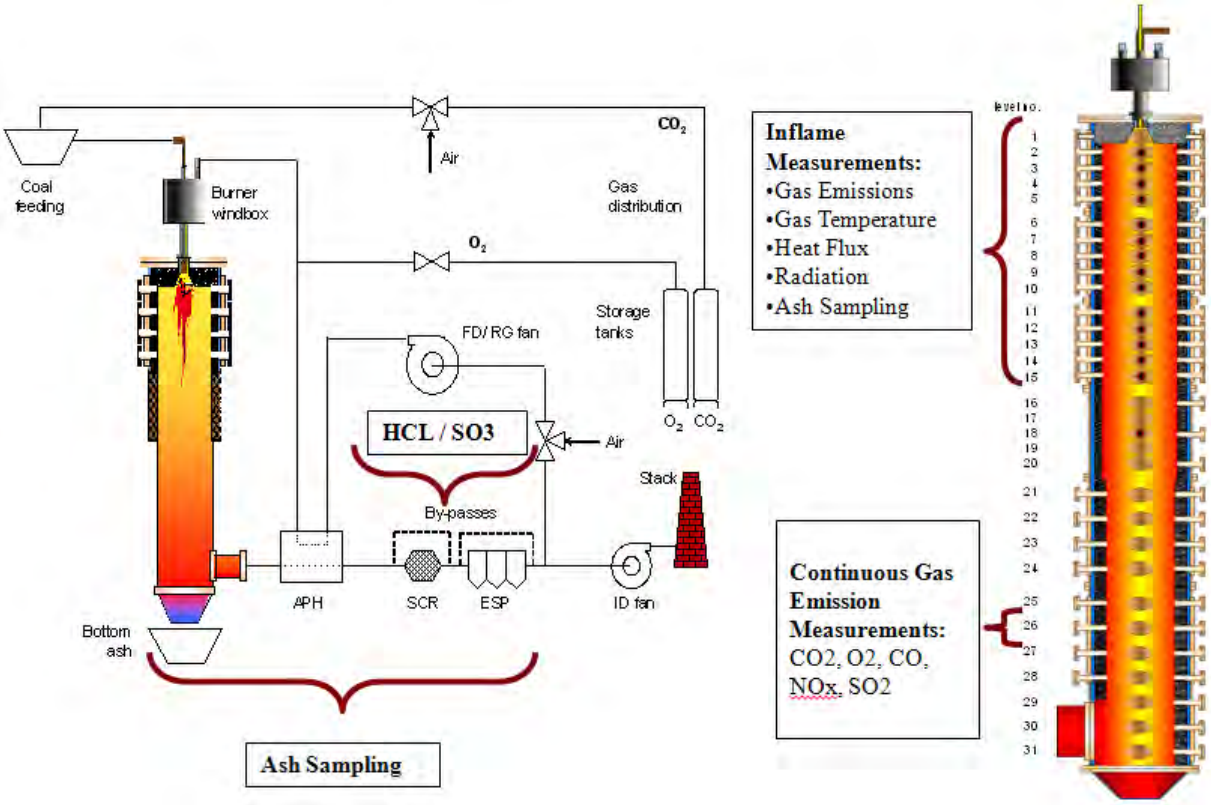

Figure 3-9. Process Measurements and Location

In-flame traverse measurements were taken at several elevations, as shown in Figure 3-10. The distances from the reference plane or zero datum (at the quarl bendline) are also provided. It should be noted that Levels 1a, 1b, and 2a apply only to the 5-hole pitot probe measurement traverses (cold flow). Levels 1a and 1b are within the quarl region and Level 2a is 15 mm downstream of the exhaust plane of the quarl.

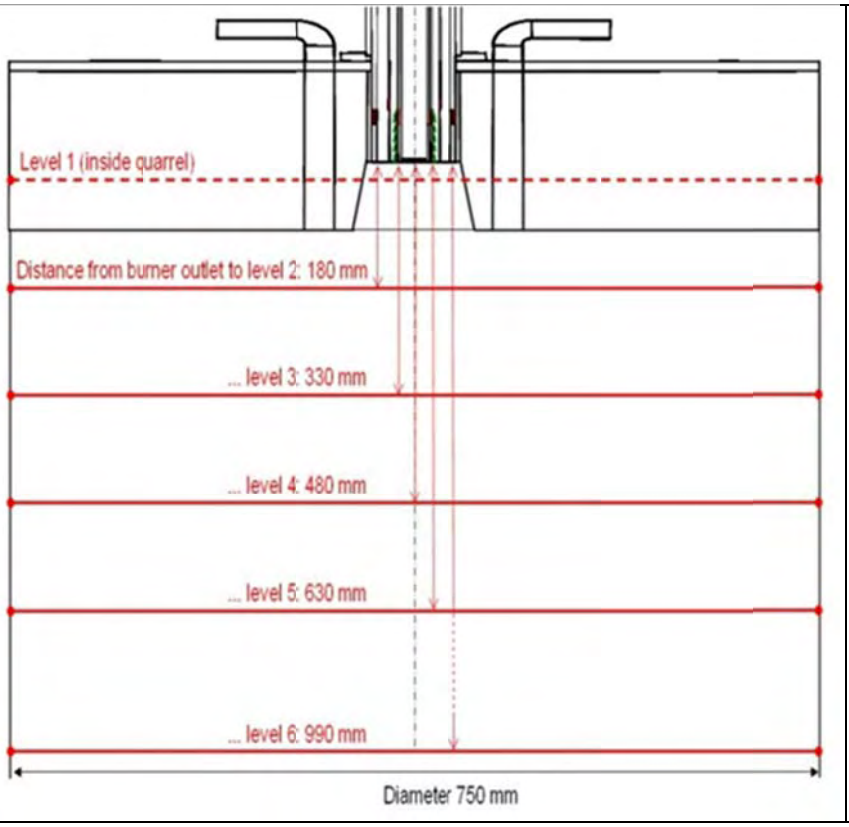

Level	Elevation (mm)	Experiment
Level 1a	25	Cold (Pitot)
Level 1b	55	Cold (Pitot)
Level 2a	115	Cold (Pitot)
Level 2	180	Reacting
Level 3	330	Reacting
Level 4	480	Reacting
Level 5	630	Reacting
Level 6	990	Reacting
Level 7	1,160	Reacting
Level 8	1,330	Reacting
Level 9	1,500	Reacting
Level 10	1,670	Reacting
Level 11	1,990	Reacting
Level 12	2,160	Reacting
Level 13	2,330	Reacting
Level 14	2,500	Reacting
Level 15	2,670	Reacting

Figure 3-10. Measurement Traverse Levels or Elevations

The cold flow measurements were performed with a 5-hole, spherical, pitot probe, shown in the figure below (Figure 3-11). The probe was inserted only into the Ports corresponding to Levels 1a, 1b, and 2a (as shown in Figure 3-12). The cold-flow test and boundary conditions corresponded to the TW-1 Burner configuration, with a somewhat different air flow distribution than the unstaged air case.

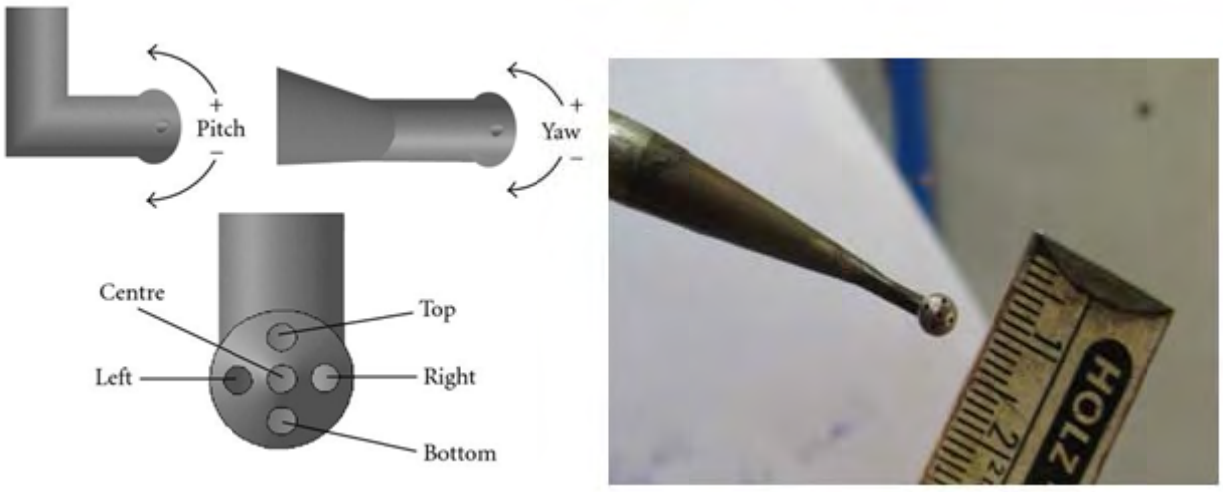

Figure 3-11. Pressure-Tap Designations and Orientations for the 5-Hole, Pitot Probe

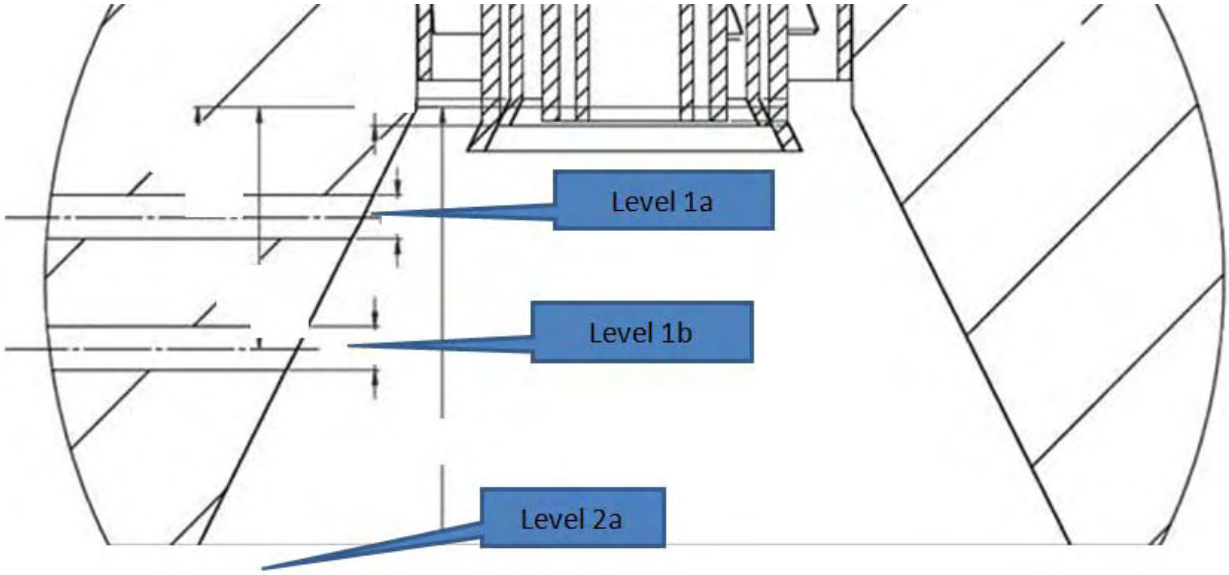

Figure 3-12. Locations of Pitot Probe Traverses

The probes used in the in-flame measurements are shown in Figure 3-13. The gas temperature and gas species sampling probes are typical suction probes, with the gas temperature probe equipped with shielding to protect against radiation loss. The total heat flux probe is designed to measure the total heat transfer (conduction + convection + radiation) from the combusting flow to its front surface. The ellipsoidal radiometer is used to measure the total radiative heat flux incoming from the medium, incident to the tip surface of the radiometer (kW/m^2). Heat flux and radiative flux measurements were taken at Levels 2 through 15, at a radial location relatively close to the insulated "wall".

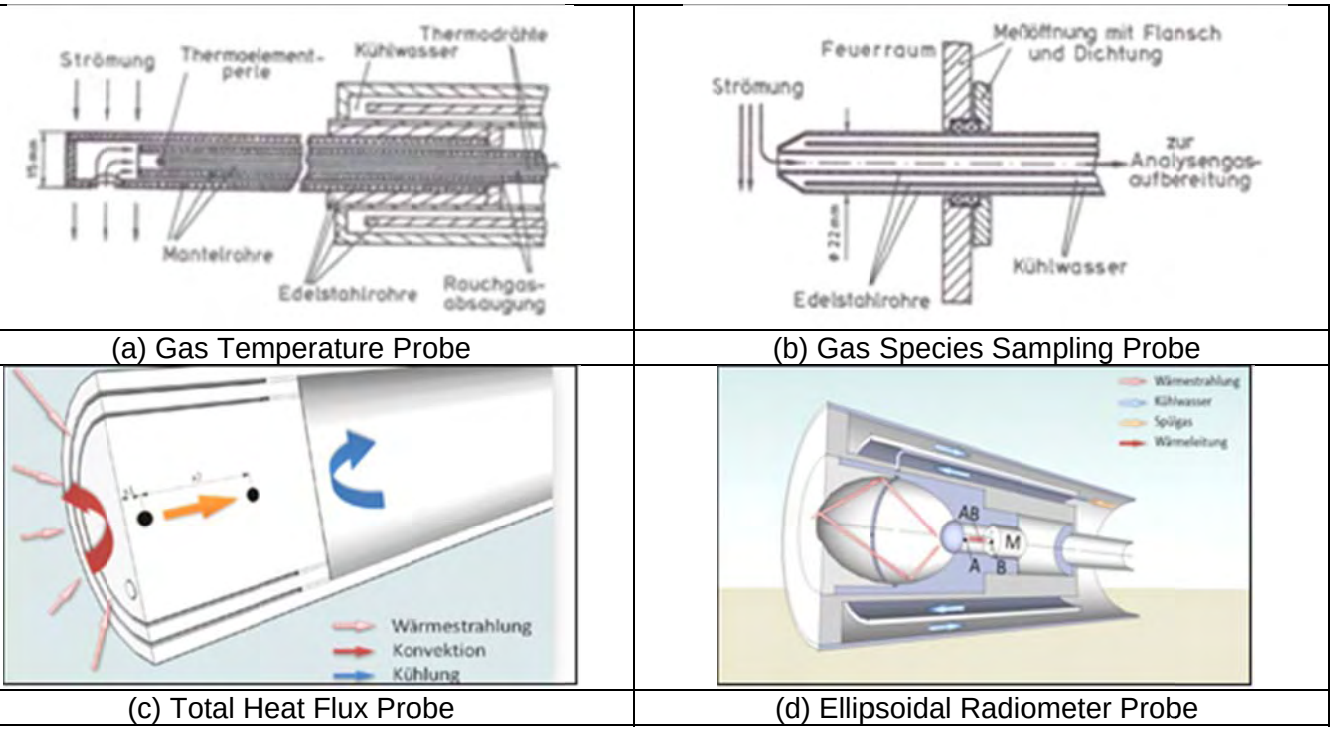

(a) Gas Temperature Probe | (b) Gas Species Sampling Probe

(c) Total Heat Flux Probe | (d) Ellipsoidal Radiometer Probe

Figure 3-13. Experimental In-flame Probes

The surface radiative heat flux at the probe tip surface is equal (according to the FLUENT® definition) to the sum of the absorbed, reflected, and transmitted (zero) heat fluxes at the control surface. If the metal surface of the probe is clean, or if slagging or ash deposits collect on the probe tip, then the reflectivity may be significant, so that the absorptivity = 1 – reflectivity. Alternatively, if a thin layer of soot collects on the probe surface, then the reflectivity may be rather low, so that almost all of the incident radiation is absorbed. In the present analysis, the absorptivity is presumed to be non-unity and equal to the wall emissivity (given to be 0.7). Since the total heat flux probe temperature is at a much lower temperature than the wall temperature, the amount of emitted radiation will be relatively low, compared to the surface incident radiation. Since most of the total heat flux measurement in the radiant region is due to the incident surface radiative heat flux (with minor contributions from the convective and conductive heat flux), it will be assumed that a direct comparison between the predicted absorbed radiation flux and the measured total heat flux is appropriate. The measurements associated with the ellipsoidal radiometer will be compared with the slightly higher surface incident radiation flux.

A synopsis of the in-flame temperature, species, flyash, and continuous monitoring measurements, as well as the associated port elevations and measurement locations across the furnace radius, are provided in Table 3-1.

Table 3-1. In-flame Measurement Variables and Locations

Temperature and Species Measurements				
Variables			**Level or**	
Measured	**Units**	**Tests**	**Radius**	**Measurement Locations**
Temperature	C°	Air	Levels:	Levels 2 through 15, with the exception of 7, 9, 12, and 14
O2	Vol % (dry)	Oxy	Levels:	Levels 2 through 15, with the exception of 9, 12, and 14
CO2	Vol % (dry)			
CO	Vol % (dry)	Air / Oxy	Radii (mm):	0 (axis), 50, 100, 150, 200, 250, 300, 350, 375 (wall)
NO	mg/Nm^3 (dry)		Additional Radii (mm) at Levels 2 and 3:	25, 75, 125, 175, 225, 275, 325
SO2	mg/Nm^3 (dry)	Note:	Increased sparsity of data for some variables downstream of Level 10	
H2S	mg/Nm^3 (dry)	Note:	SO3 (mg/m^3 (dry)) was measured at 810 °C at Level 26	
Flyash Measurements				
Variables				
Measured	**Analysis**	**Tests**	**Radius**	**Measurement Locations**
Flyash	Ultimate / Proximate	Air / Oxy	Centerline	Levels 3, 6, 8, 10, 11, 13, 15, 26
		Note:	Additional ash measurements in hopper, preheater, and ESP	
Total Heat Flux and Ellipsoidal Radiometer Measurements				
Variables				
Measured	**Units**	**Tests**	**Radius**	**Measurement Locations**
Total Heat Flux and Radiative Flux	kW/m^2	Air / Oxy	350 mm from Centerline	Levels 2, 3, 5, 6, 8, 10, 11, 13, 15
		Note:	The total heat flux measurements for TW-1 are too low (Ref. 1) and those for TW-2 are too high (Ref. 2). Error was not quantitatively resolved.	
Continuous Wall Temperature and Outlet Species Concentrations				
Variables				
Measured	**Units**	**Tests**	**Levels:**	**Measurement Locations**
Temperature	C°	Air / Oxy	Levels:	Levels 2, 3, 5, 6, 8, 10, 11, 13, 15
O2, CO2, CO2, SO2, NOx, [H2O]	Vol % (dry) or mg/Nm^3 (dry) or ppmv (dry)	Air / Oxy	Levels:	Level 26
		Note:	Temperature measurements are inside of wall, with two additional temperature measurements at Levels 4 and 8 that are inside of refractory (12 cm distance from the wall). The refractory thermocouples are exposed to much higher temperatures than the wall thermocouples.	

4. Technical Approach

4.1 Computational Mesh

The approach to the modeling of the KSVA 500 kW Test Facility was to simulate the burner geometry, with an appropriate level of detail, as an integrated component with the reactor as part of a single computational domain. The burner was modeled by defining inlet planes upstream of the swirl vanes, so that the fidelity of the calculated downstream flow field would be enhanced by direct passage through the swirlers and subsequent intermixing with adjacent annular flows.

The geometry for the burner, reactor, and discharge was provided previously in a series of dimensioned drawings. From these drawings, a 3-D geometry of the computational domain was created using ANSYS Gambit. Different values for the swirl settings, as well as the necessity of accommodating the nozzle tip openings for the overfire gas lances, forced each of the cases to have slightly different cell counts. The two unstaged cases each had 2,669,233 cells, while the staged air case had 2,680,666 cells, and the staged oxy case had 2,677,098 cells.

The lances themselves were not resolved; only the discharge openings were approximated. Since each of the air and oxy-fired overfire gas lances used for staging was constructed with a different exhaust configuration, a somewhat different approach was taken in modeling the air and oxy exhaust openings. Small, cylindrical, bluff bodies, in conjunction with an appropriate inlet surface, were used to represent the discharge openings at the tip of the lance.

Portrayals of selected portions of the grid, as shown on X- and Y-center planes, are provided in Sub-Figures or Panels (a) through (f) of Figure 4-1. The burner or nozzle region is shown in Panel (a). It can be seen that hexahedral cells are used predominantly throughout the upper nozzle region and in the annular passages, including the swirl vane regions. However, tetrahedral cells are used in the quarl region. The entire width of the reactor is not shown, but it can be seen that a core region of concentrated hexahedral cells is projected downstream from the quarl exhaust plane. The concentrated core region extends from the quarl exhaust plane to a tetrahedral transition region (shown in a later figure), and is expected to help resolve the larger gradients that are anticipated to exist in the core region. Hexahedral cells outside of the core region (e.g., in the corner dump region) have been expanded to help decrease and maintain the cell counts at a level that can be efficiently solved on Alstom computers.

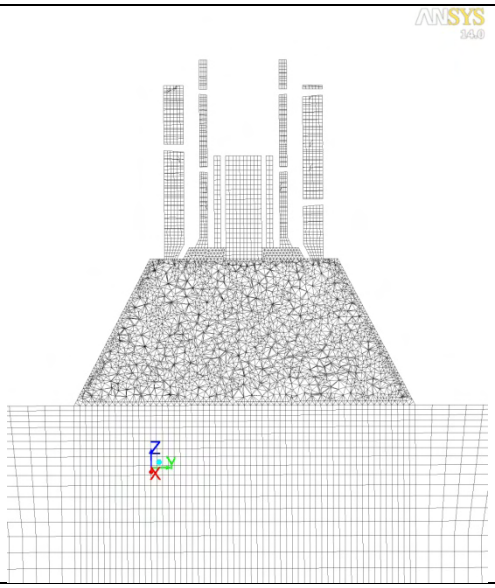

(a) Nozzle Region

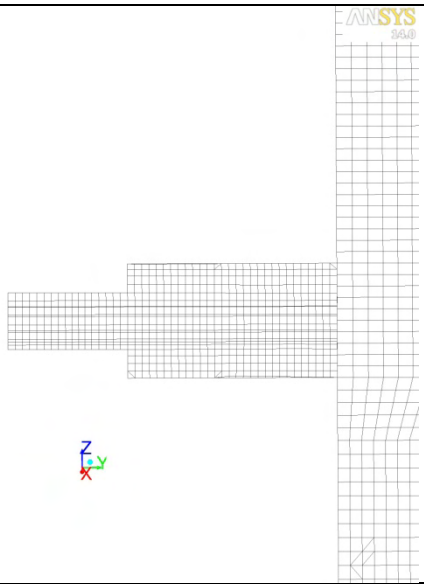

(b) Scanning Port on Vertical Wall

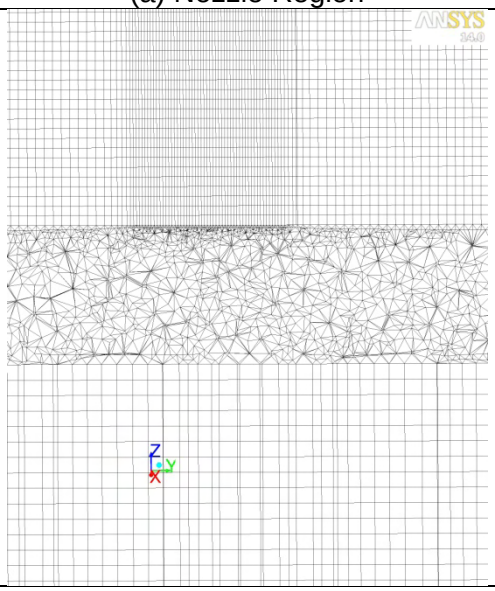

(c) Transition Region

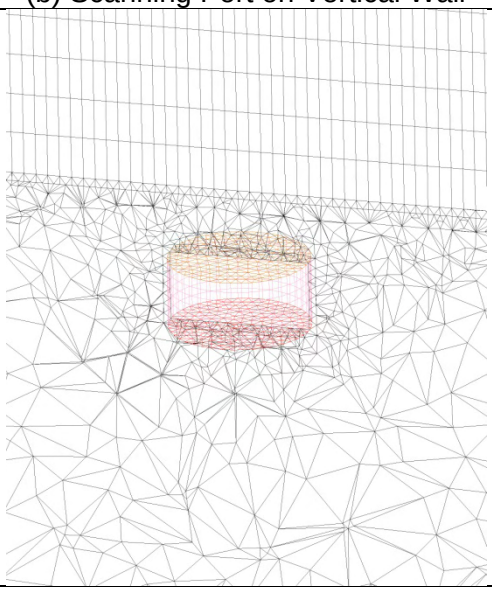

(d) Transition Region with Air Lance Exhaust

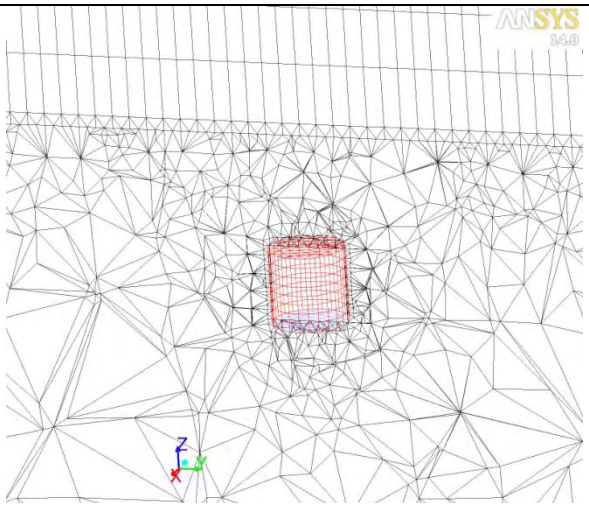

(e) Transition Region with Oxy Lance Exhaust

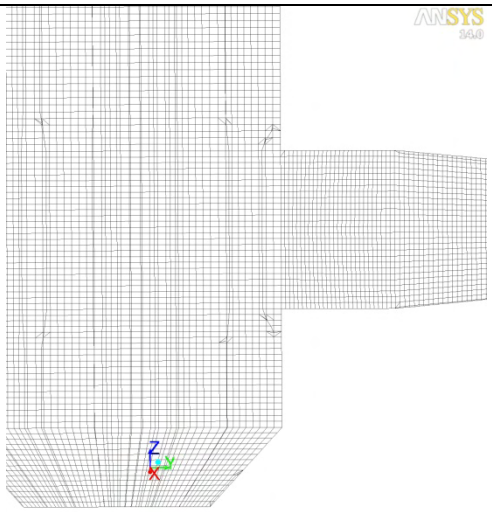

(f) Reactor Discharge and Outlet

Figure 4-1. Grid in Selected Regions of the Domain.

Panel (b) in the above figure shows the grid associated with a side-wall scanning port. It can be seen that the interface between the side-wall port and the reactor domain is non-conformal. Non-conformal interfaces were used to attach the grids for the two scanning ports (one on the side and one on top of the reactor), as well as for the outlet discharge or exhaust pipe for the reactor.

Panel (c) depicts a tetrahedral-cell transition region that is used to transition from the more concentrated cell pattern in the upper portion of the furnace to the much more coarse cell pattern in the lower portion of the furnace. As shown in Panels (d) and (e), the transition region is conveniently positioned to encapsulate the lance discharge openings. The lance arms are not resolved.

Panel (f) depicts the discharge or exhaust pipe for the reactor. A slight convergence has been designed into the actual discharge pipe in order to ensure that the flow accelerates as it exhausts in order to hinder any recirculation. A non-conformal interface was used to connect the discharge pipe grid to the main reactor mesh.

4.2 Boundary Conditions

Table 4-1 provides a summary of the coal composition and heating values used for the unstaged and staged tests. (Both the unstaged and staged tests consist of corresponding air and oxy tests). All of the tests summarized were fired with the (German) lignite coal. To determine the relative partitioning of the lignite coal into its computational constituents, the ultimate and proximate analyses were processed to determine the moisture, volatile, and char inputs. Alstom assigned a high-temperature volatile yield factor of 67.3% DAF for the coal associated with the unstaged runs (Test Week 1) and 68.58% DAF for the Test Week 2 staged runs. The impact of such a difference should be relatively minor. The initial char fraction was determined by difference, and prescribed in the corresponding input sections of the FLUENT® code.

Table 4-1. Coal Composition and Heating Values

Fuel Composition and Heating Values (As-Fired)		Unstaged Cases	Staged Cases
Ultimate Analysis			
	C	49.70%	52.93%
	H	3.89%	4.01%
	N	0.53%	0.46%
	S	1.69%	2.11%
	O	17.29%	20.97%
	Ash	16.75%	11.03%
	Water	10.15%	8.49%
	Total	100.00%	100.00%
Proximate			
	Volatile	41.65%	46.73%
	Char	31.45%	33.75%
	Total	73.10%	80.48%
HT-Yield			
	Volatile	49.20%	55.20%
	Char	23.90%	25.28%
	Total	73.10%	80.48%
Heating Values			
	HHV (J/g)	19,995	21,548
	LHV (J/g)	18,907	20,473

The particle size distribution (PSD) used in the FLUENT® cases was based on a Rosin-Rammler (logarithmic) distribution. The experimental particle size distribution was provided by IFK. The results are shown in Figure 4-2.

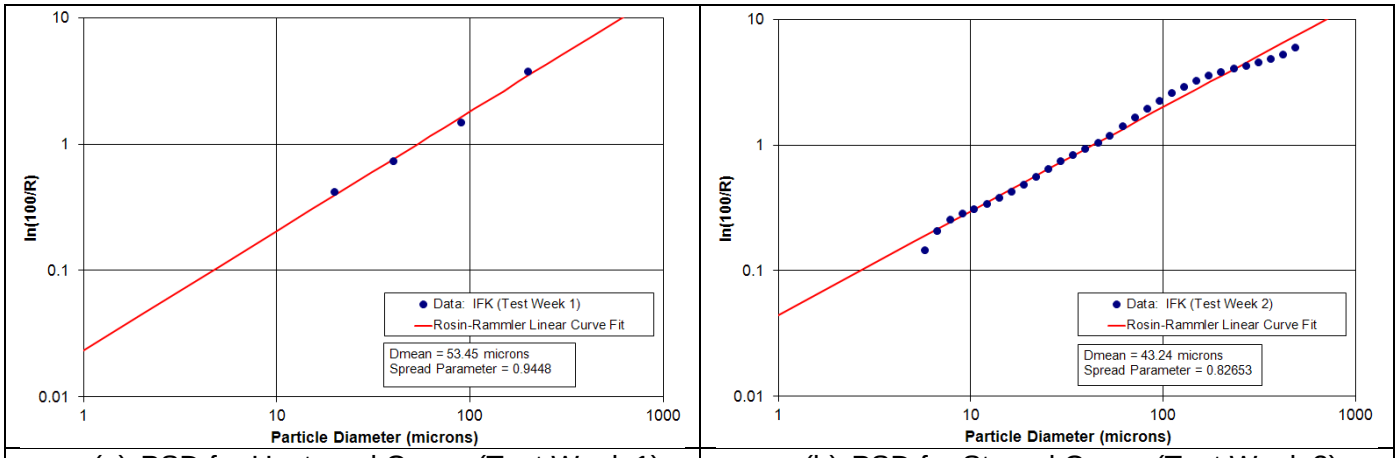

(a) PSD for Unstaged Cases (Test Week 1) (b) PSD for Staged Cases (Test Week 2)

Figure 4-2. Coal Fineness Rosin-Rammler Distributions

As shown in the figures, the mean diameter and spread parameter for each of the test coals are not too dissimilar – with a mean diameter of 53.5 and 43.2 microns for the unstaged and staged test PSD, respectively. The experimental PSD data for the unstaged tests are somewhat sparse, making it difficult to discern the difference between uncertainty in the data and the actual shape of the distribution, but the PSD

for the staged tests has a large number of points, making it easier to assess its characteristic shape. The PSD for the staged tests appears to be bi-modal, and may be tri-modal. In the present set of Alstom runs, the same Rosin-Rammler PSD was used for both the staged and unstaged tests, with a spread parameter of 0.9448 and a mean diameter of 71.37 microns. The larger mean diameter used in the present calculations (71.37 microns) was due to a minor linear fit (EXCEL) calculation error. Consequently, the particles should burn out somewhat faster in reality than they did in the calculations (for the same heterogeneous rates).

IFK has provided the flow rates and operating conditions for each of the inlet streams. Flow rates were typically provided in terms of volumetric flow or mass flow, and the species concentrations were given in volume percent (wet or dry). The boundary conditions were calculated in a form largely amenable with FLUENT® inputs and the results are provided in Table 4-2.

Table 4-2. Inlet Boundary Conditions

IFK TEST Summary		AIR Unstaged	OXY Unstaged	AIR Staged	OXY Staged
FUEL-Fired	kg/hr	60.60	61.10	54.80	55.30
HHV	MJ/kg	19.995	19.995	21.548	21.548
LHV	MJ/kg	18.909	18.909	20.476	20.476
Heat Input	KW	318.3	320.9	311.7	314.5
Stoich O2 Req'd	kg/kg	1.477	1.477	1.540	1.540
Primary	kg/hr	38.573	47.153	38.573	47.153
SA-1	kg/hr	79.717	74.477	52.716	65.100
SA-2	kg/hr	316.295	242.050	209.577	263.576
Scan-1	kg/hr	5.786	8.841	6.429	7.859
Scan-2	kg/hr	5.786	8.841	6.429	7.859
OFA	kg/hr	----	----	117.003	27.141
Total	kg/hr	446.156	381.362	430.727	418.687
Primary [O2]	Mass Fr	0.2315	0.0000	0.2315	0.0000
SA-1 [O2]	Mass Fr	0.2315	0.3198	0.2315	0.2253
SA-2 [O2]	Mass Fr	0.2315	0.3198	0.2315	0.2253
Scan-1 [O2]	Mass Fr	0.2315	0.0000	0.2315	0.0000
Scan-2 [O2]	Mass Fr	0.2315	0.0000	0.2315	0.0000
OFA [O2]	Mass Fr	----	----	0.2315	1.0000
Burner O2	kg/hr	103.301	101.237	72.638	74.043
Burner Stoich	-	1.154	1.122	0.861	0.870
Overall O2	kg/hr	103.301	101.237	99.729	101.184
Overall Stoich	-	1.154	1.122	1.182	1.188

Although the overall stoichiometries for each of the cases are similar (1.154 to 1.196), the staged cases are moderately sub-stoichiometric (~0.86) in the main burner zone (MBZ). It should be noted that the OFA gas is injected as pure oxygen in the oxy-staged case. Consequently, the OFA flow rate in the oxy-staged case is much lower than the OFA flow rate (air) in the air-staged case.

Although in-leakage through the scan ports is apparent in some of the near-wall experimental results, no scanner port in-leakage was explicitly accounted for in the above boundary condition formulations. Rather, any in-leakage would be observed as part of the overall experimental outlet oxygen concentration, and is therefore implicitly included as part of the flow rate scalings required to calculate the observed outlet oxygen concentration.

The corresponding inlet species mass fractions for each of the feed streams, as well as the burner splits, are shown in Table 4-3.

Table 4-3. Inlet Species Mass Fractions

AIR-Unstaged

Inlets	Temp (C)	O2	CO2	H2O (Mass Fr)	SO2	N2	Burner Splits (Mass Fr)
Primary	35	23.15%	0.06%	0.31%	0.00%	76.48%	8.87%
SA-1	188	23.15%	0.06%	0.31%	0.00%	76.48%	18.34%
SA-2	188	23.15%	0.06%	0.31%	0.00%	76.48%	72.79%
Scan-1	30	23.15%	0.06%	0.31%	0.00%	76.48%	
Scan-2	30	23.15%	0.06%	0.31%	0.00%	76.48%	

OXY-Unstaged

Inlets	Temp (C)	O2	CO2	H2O (Mass Fr)	SO2	N2	Burner Splits (Mass Fr)
Primary	35	0.00%	100.00%	0.00%	0.00%	0.00%	12.97%
SA-1	192	31.98%	55.69%	8.69%	0.00%	3.64%	20.48%
SA-2	192	31.98%	55.69%	8.69%	0.00%	3.64%	66.55%
Scan-1	30	0.00%	100.00%	0.00%	0.00%	0.00%	
Scan-2	30	0.00%	100.00%	0.00%	0.00%	0.00%	

AIR-Staged

Inlets	Temp (C)	O2	CO2	H2O (Mass Fr)	SO2	N2	Burner Splits (Mass Fr)
Primary	35	23.15%	0.06%	0.31%	0.00%	76.48%	12.82%
SA-1	195	23.15%	0.06%	0.31%	0.00%	76.48%	17.52%
SA-2	195	23.15%	0.06%	0.31%	0.00%	76.48%	69.67%
Scan-1	30	23.15%	0.06%	0.31%	0.00%	76.48%	
Scan-2	30	23.15%	0.06%	0.31%	0.00%	76.48%	
OFA	170	23.15%	0.06%	0.31%	0.00%	76.48%	

OXY-Staged

Inlets	Temp (C)	O2	CO2	H2O (Mass Fr)	SO2	N2	Burner Splits (Mass Fr)
Primary	35	0.00%	100.00%	0.00%	0.00%	0.00%	12.55%
SA-1	195	22.53%	65.04%	9.38%	0.00%	3.06%	17.32%
SA-2	195	22.53%	65.04%	9.38%	0.00%	3.06%	70.13%
Scan-1	30	0.00%	100.00%	0.00%	0.00%	0.00%	
Scan-2	30	0.00%	100.00%	0.00%	0.00%	0.00%	
OFA	30	100.00%	0.00%	0.00%	0.00%	0.00%	

CFD computations were also compared with cold flow pitot probe measurements. The cold flow measurements were associated only with the TW-1 burner configuration. The CFD inlet boundary conditions utilized for the cold flow calculations are provided in Table 4-4.

Table 4-4. Inlet Boundary Conditions for Cold Flow Pitot Probe Runs

CFD Computation of Cold Flow Pitot Probe Experiment			
Inlet	Inlet Velocity (m/s)	Temp (C)	Mass Flow Rate (kg/s)
Primary	26	12.767	0.01132
SA-1	26	12.767	0.02058
SA-2	37.4	12.767	0.13486
Core	0	---	0

Velocity boundary conditions were applied in the CFD (cold-flow) runs, along with a constant density of 1.225 kg/m^3.

To model the wall heat transfer in the hot cases, a specified temperature boundary condition was used in conjunction with the FLUENT® code's thin-wall thermal resistance formulation. The specified temperature is on the far side of a thin wall, away from the adjacent fluid zone. The thermal resistance is the ratio of the parameters $\Delta x/k$, where Δx is the thickness of the resistance material(s), and k is the thermal conductivity. It is usually necessary to adjust the thermal conductivity k of each zone (for a given inner surface temperature) to match the measured temperature data. For the present cases, the reactor walls were given the specified temperature boundary conditions shown in Table 4-5.

Table 4-5. Wall Thermal Boundary Conditions

Wall Thermal Boundary Conditions					
Elevation	Specified Temperature (K)	Wall Emissivity	Thickness (m)	Material Name	Thermal Conductivity (W/m-K)
Roof to Bottom of Wall Section 21 (Elevation = -4.11 m)	373	0.7	0.115	"insul"	3
Top of Wall Section 22 to Bottom of Hopper Plus Exhaust Discharge	373	0.7	0.115	"blanket"	0.01

The two sets of thermal boundary conditions are in rough accordance with the actual reactor construction, with refractory in the top portion of the reactor from the roof through Level 20, and with a ceramic fiber blanket (covered by a metal sheath) in the lower section of the reactor. Other entities in the domain, such as the plugs used for the lance tips, were made adiabatic (heat flux equal to 0).

4.3 Model Selections

All of the final IFK reactor simulations were completed using ANSYS FLUENT® Version 14.

For the main gas-phase combustion reactions, the turbulence-chemistry interaction was modeled using the composite Magnussen eddy-dissipation (mixing-limited / fast-chemistry) and Arrhenius rates (kinetically-limited) combustion submodel, in which the smaller of the two rates (eddy-dissipation or Arrhenius rates) takes local precedence. The Magnussen eddy-dissipation model is also commonly referred to as the "eddy-breakup" model in the open literature; over the years, this particular model has been used for almost all of the boiler computations at Alstom.

In the present runs, the char particle consists only of pure carbon (designated as C<s>), and ash. The heterogeneous reactions are composed of one (1) oxidation and two (2) gasification reactions, using the multi-surface reaction model. The char burning rate is a combination of a film-diffusion rate in series with a chemical reaction rate. The apparent chemical reaction rate actually includes the composite effects of pore diffusion and interior particle reaction, expressed on an external surface area basis. The overall rate therefore uses a combination of an Arrhenius based kinetic rate, as well as a diffusion rate of the reactant species through the film to the surface of the char particle. The char can be oxidized or gasified simultaneously, depending upon the local concentration levels, although, usually, the magnitude of the rates are such that oxidation will dominate whenever oxygen is present. The addition of heterogeneous char gasification reactions provides a mechanism to convert the char to CO and H_2 in an oxygen deficient environment.

The reaction stoichiometries are summarized in Table 4-6. The associated kinetic rates (not shown) were maintained for all of the IFK reactor cases. The stoichiometric coefficients for the chemical reaction expressions were also maintained for all cases, except for the fuel-specific thermal breakdown of the volatile species into a set of oxidized or partially oxidized products. The changes impacted only the thermal decomposition Reaction 1. Because the fuel composition was slightly different for each test coal, the composition of the volatile products was manipulated so that the reaction was neither endothermic nor exothermic. For example, a portion of the hydrogen and carbon were released as water or CO products so that the breakdown reaction had a heat of reaction equal to zero. All other general reaction coefficients in the 7-reaction mechanism were the same for all of the cases.

Table 4-6. Reaction Expression Stoichiometries

Reaction	General Stoichiometry
	Gas Phase Reactions
1 Decomposition	Volatile → C-gas , CO, H_2, H_20, O_2, SO_2, N_2
2 CO Oxidation	CO + ½ O_2 → CO_2
3 H_2 Oxidation	H_2 + ½ O_2 → H_2O
4 C-gas Oxidation	C-gas + ½ O_2 → CO
	Solid Surface Reactions
5 Char Oxidation	C<s> + ½ O_2 → CO
6 Char Gasification	C<s> + CO_2 → 2 CO
7 Char Gasification	C<s> + H_2O → H_2 + CO

It should be noted that Alstom's intent was to use the same kinetic parameters in both the Schwarze Pumpe Oxy Pilot Plant calculations (a separate section in Volume III) and the IFK calculations, since both experimental programs compared oxy- and air-fired scenarios, and both programs utilized the Schwarze Pumpe (German) lignite. The thermal decomposition stoichiometries are of course different because the coal analyses are slightly different. Other than the thermal decomposition stoichiometry difference, the only difference was that the activation energy in the thermal decomposition rate expression was 1.0E+07 in the IFK runs and 5.0E+04 in the Schwarze Pumpe Oxy Pilot Plant runs.

Alstom used the Realizable k-ε submodel for turbulence closure. Standard wall functions were also used. Some experimentation should be done with the more rigorous Reynolds Stress model (RSM).

Fifty particle diameters were defined for the Rosin-Rammler (logarithmic) distribution, but only one stochastic "try" was specified. The "discrete random walk" option was activated, but not the "random eddy lifetime" option. The "wet combustion" model was also activated, to allow coal moisture to evaporate from the particle, prior to devolatilization. A single-rate model was used for devolatilization and the swelling factor was set to unity.

User-defined functions (UDFs) were used for the gas absorption coefficient and for the particle absorption efficiency. The particle scattering factor was set to zero, but the mixture scattering coefficient was set to 0.1 (although the specification of a particle scattering factor is supposed to override the specification of the scattering coefficient in the FLUENT® code).

The SIMPLE algorithm was used for the pressure-velocity coupling, second-order discretization was used for the pressure, and second-order upwind numerics were used for momentum, turbulent kinetic energy, and the turbulent dissipation rate, energy and the Discrete Ordinates (DO) equations. First-order discretization was used for all of the species transport equations.

5. Model Results

5.1 Cold Flow Pitot Tube Results

Contour plots of the axial, radial, and tangential velocity components are provided at Planes 1a, 1b, and 2a in Figure 5-1. Planes 1a and 1b are within the quarl and Plane 2a is immediately downstream of the quarl exhaust plane. The plots show that the contours are not circumferentially uniform, but manifest some regions of non-homogeneity, which may in part be an apparent function of the grid structure (tetrahedral rather than polar) and the mesh resolution in the circumferential direction. In addition, some movement off the symmetry axis by the radial and tangential velocities is also apparent.

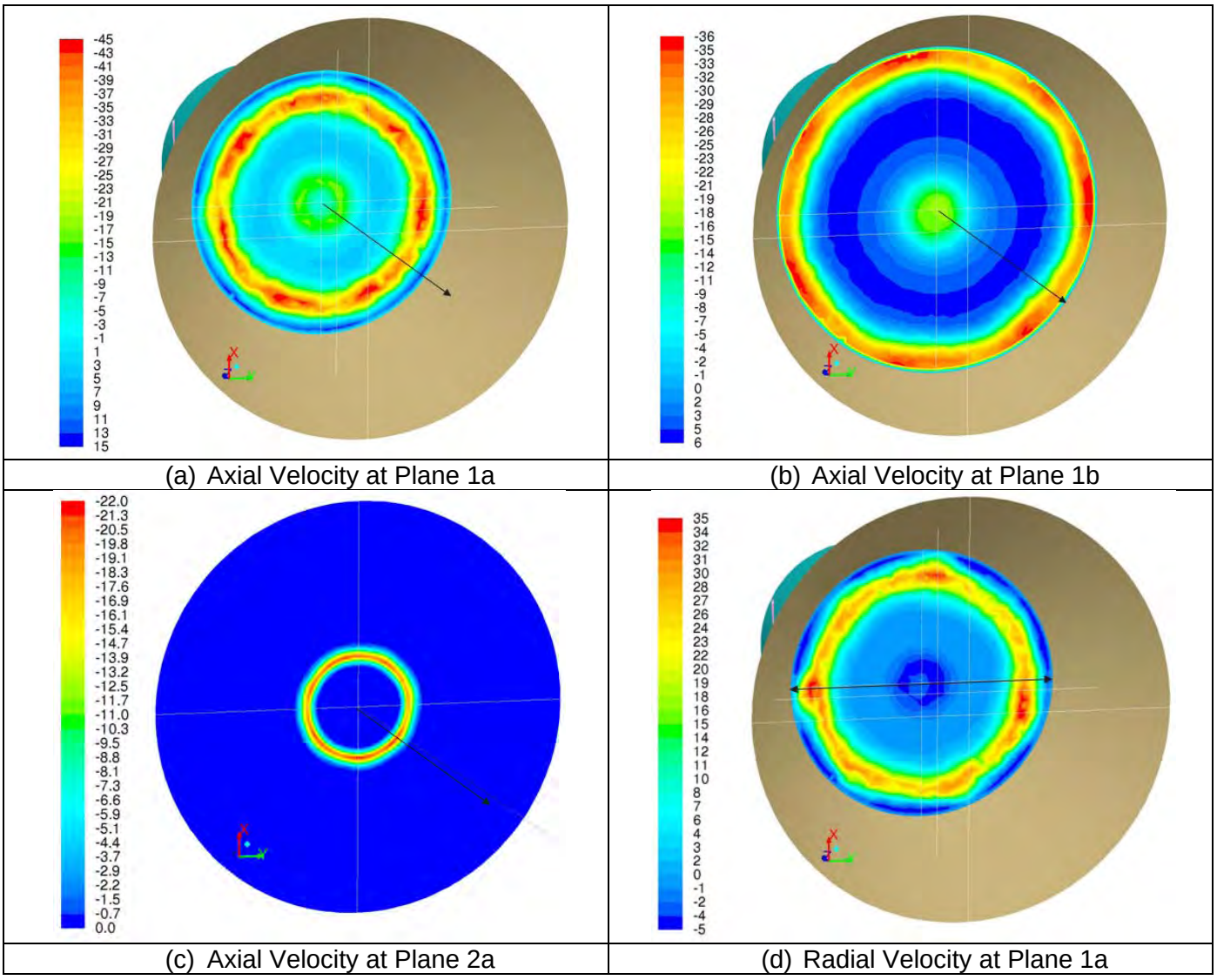

(a) Axial Velocity at Plane 1a

(b) Axial Velocity at Plane 1b

(c) Axial Velocity at Plane 2a

(d) Radial Velocity at Plane 1a

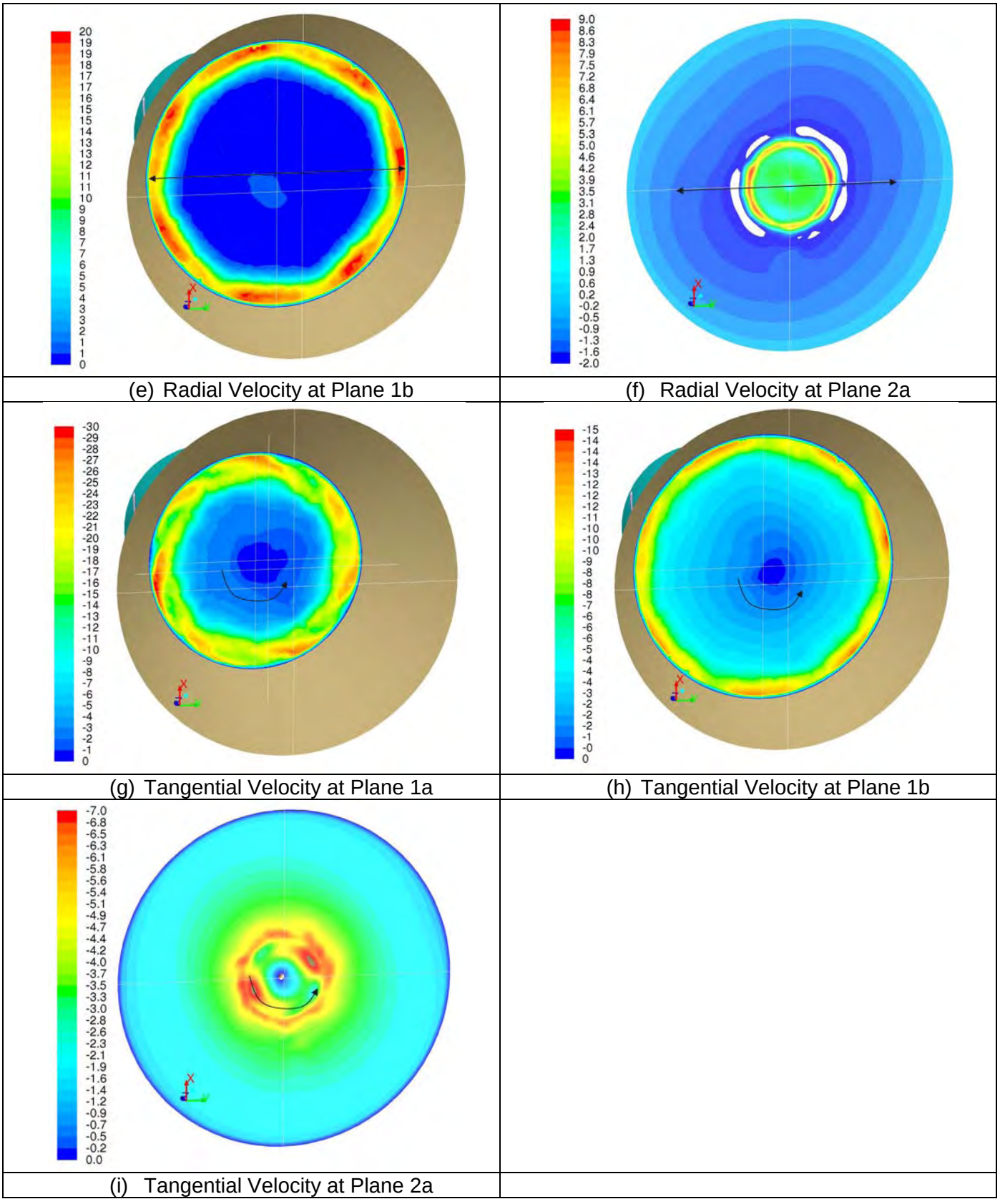

(e) Radial Velocity at Plane 1b

(f) Radial Velocity at Plane 2a

(g) Tangential Velocity at Plane 1a

(h) Tangential Velocity at Plane 1b

(i) Tangential Velocity at Plane 2a

Figure 5-1. Cold Flow Cross-Sectional Contour Plots of Velocity Components

Velocity magnitude isosurfaces emanating from the nozzle and quarl are presented in Figure 5-2. The isosurfaces are presented in an ordered sequence of decreasing values of velocity magnitude. The circumferential non-uniformity, with lobes or fingers around the periphery, as well as some indentations or folds in the surface, are clearly visible.

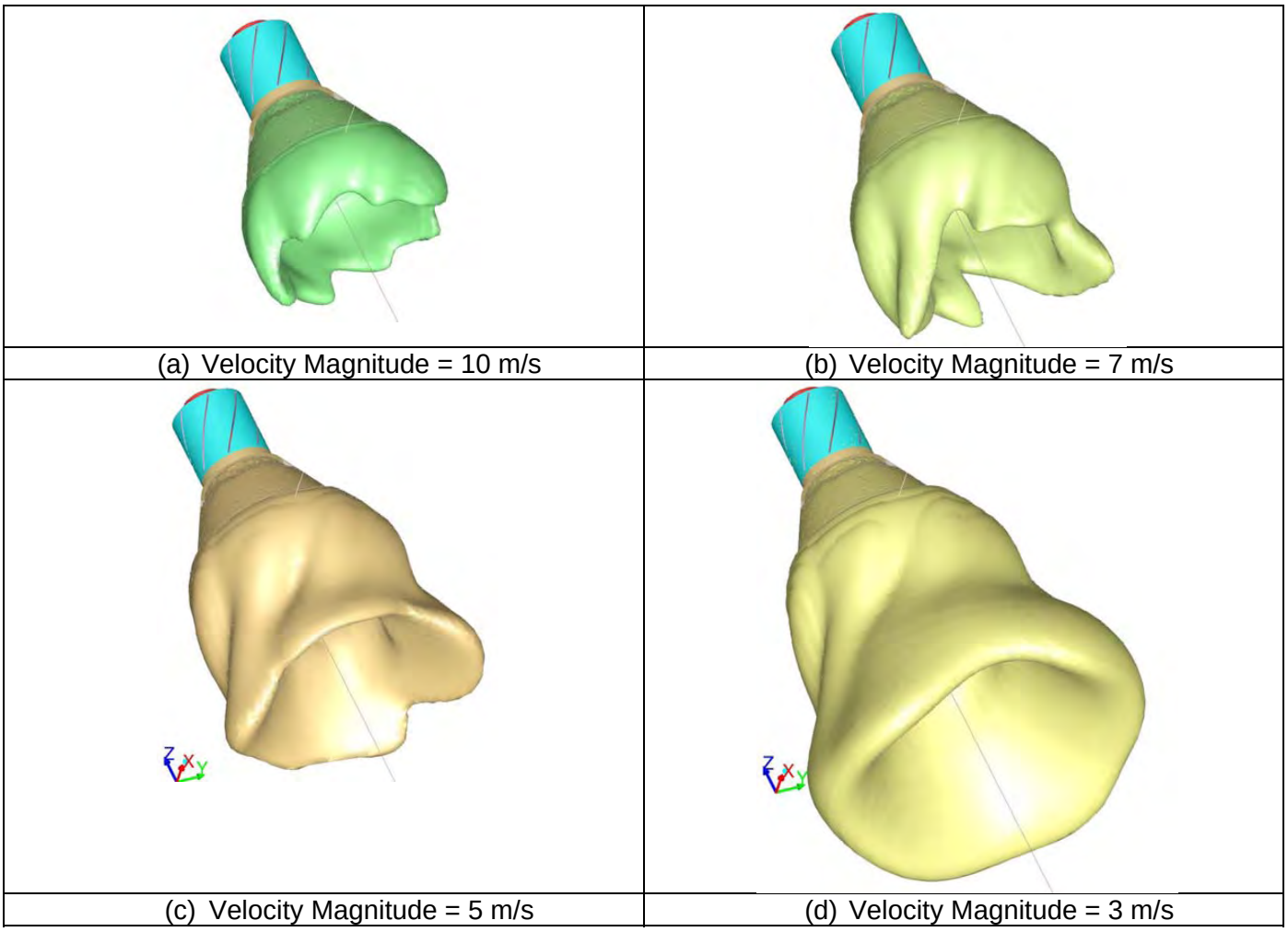

(a) Velocity Magnitude = 10 m/s

(b) Velocity Magnitude = 7 m/s

(c) Velocity Magnitude = 5 m/s

(d) Velocity Magnitude = 3 m/s

Figure 5-2. Cold Flow Velocity Magnitude Isosurface Plots

A contour plot of axial velocity on a longitudinal center-cut plane, as well as a separate plot of an enlargement of the upper reactor region, are provided in Figure 5-3. In the enlargement, a partially penetrated recirculation zone on the centerline is apparent. The centerline recirculation zone appears to consist of two conjoined reverse flow regions – one in the near nozzle region and one displaced farther downstream. The near-nozzle reverse flow zone is probably a function of the quarl expansion and the very low-flowrate core pipe acting as a hub, coupled with the swirl velocity, while the downstream reverse flow zone, may be more of a primary function of the overall expansion due to the swirl strength prevailing downstream. The corner recirculation zones in the dump region are also clearly visible.

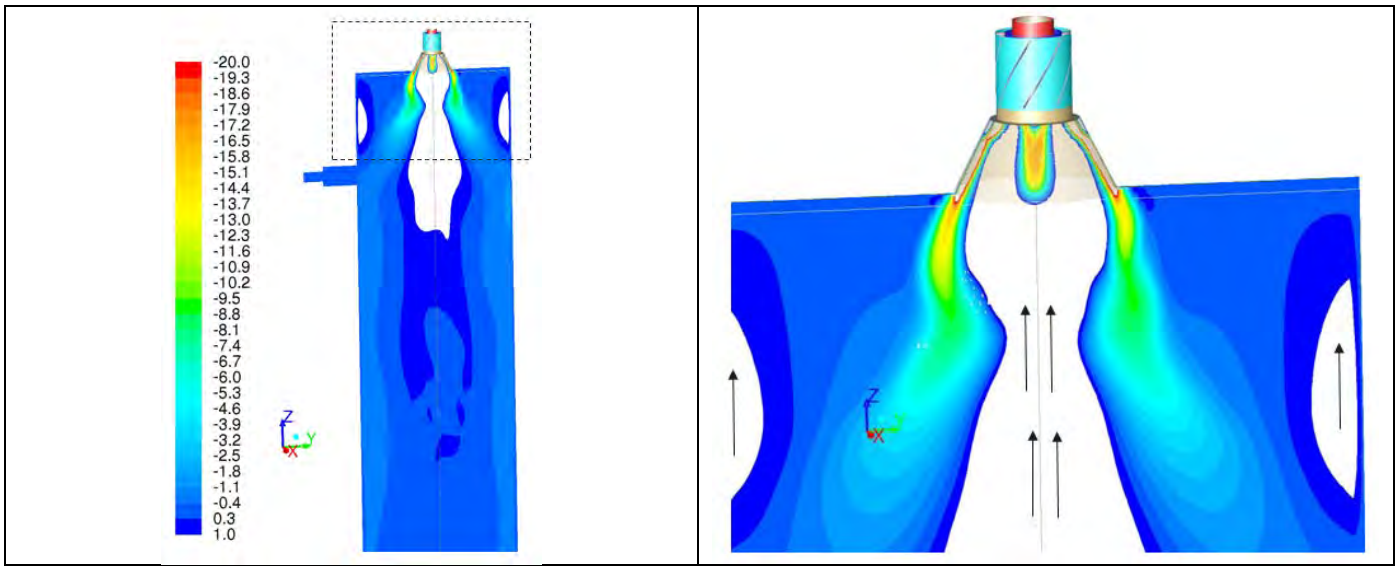

Figure 5-3. Cold Flow Contour Plots of Axial Velocity on Center Plane

The aerodynamics are displayed using the "pathlines" (essentially massless particles) capability in FLUENT®, where the pathlines are initiated at specified inlets. Pathlines emanating from the primary, SA-1 and SA-2 are displayed in Figure 5-4. The pathlines are colored by velocity magnitude.

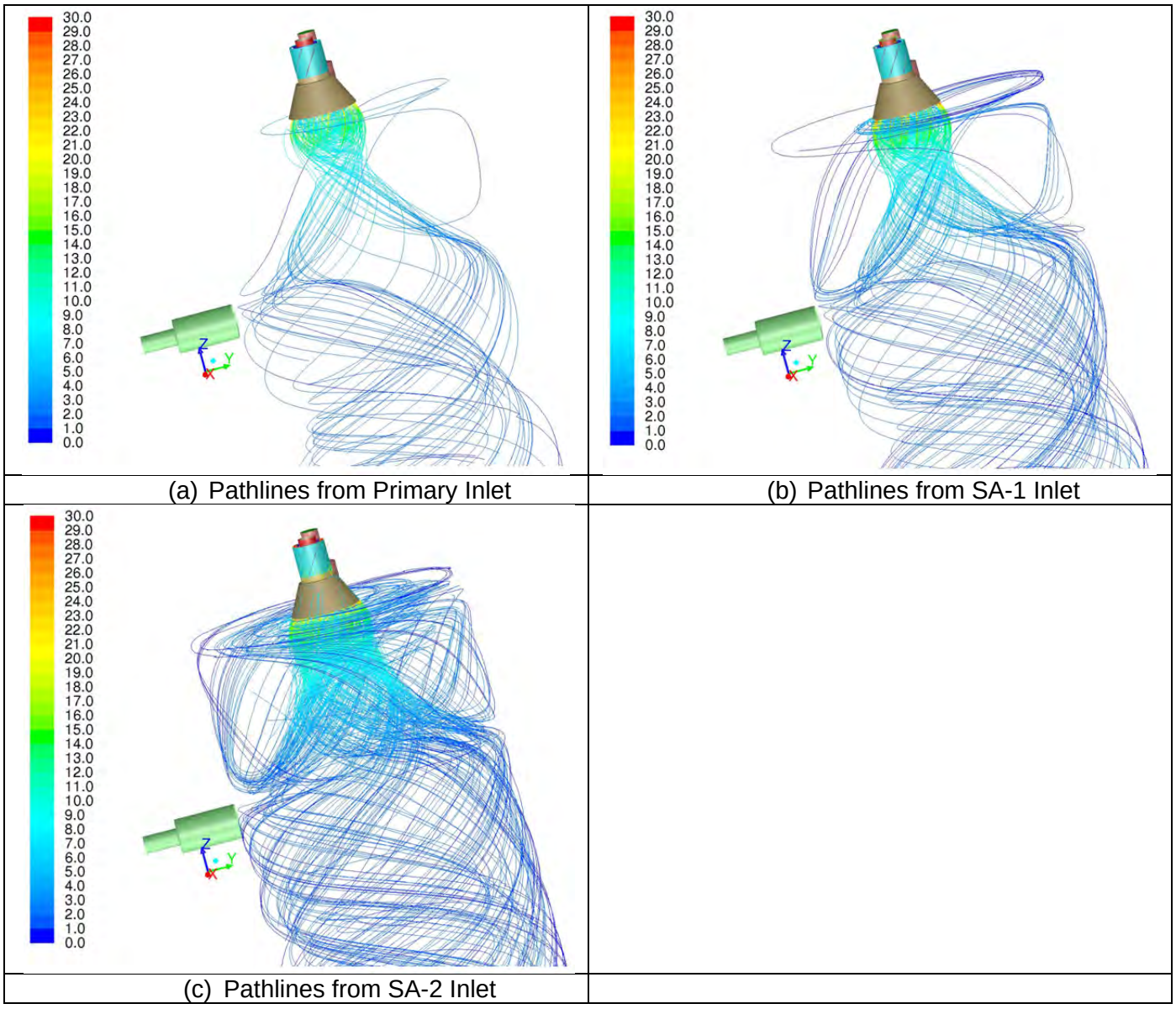

(a) Pathlines from Primary Inlet

(b) Pathlines from SA-1 Inlet

(c) Pathlines from SA-2 Inlet

Figure 5-4. Cold Flow Pathline Plots Colored by Velocity Magnitude

Pathlines emanating from the primary inlet appear to be constrained from expanding to the wall until they reach an elevation coincident with or downstream of the Scan-2 port elevation. Only a few of the pathlines emanating from the SA-1 inlet become part of the dump recirculation region. However, it can be seen that all or most of the pathlines emanating from the SA-2 inlet become part of the dump recirculation region. The pathlines indicate that the circumferential locus of reattachment points for the corner recirculation zones is very close to the Scan-2 port elevation. This begs the question as to whether air in-leakage through the Scan-2 port could be swept upstream, thus effectively modifying the stoichiometry in the upper reactor.

Profile plots along the x- and y-coordinate directions are compared with experimental, 5-hole pitot probe data in Figure 5-5. The burner corresponds to the Test Week 1 configuration. It can be seen that essentially a replicate set of data points was gathered for Plane 1a, while only a single set of data points

was gathered for Planes 1b and 2a. Typically, to measure both forward and reverse flow with a pitot probe, it is necessary to calibrate the probe with a nulling method. The nulling method requires the probe axis to be moved until the probe is consistent with the direction of flow, which occurs when the pressure of the four outer holes becomes equivalent. Since no negative velocities were measured, it is apparent that the probe was not turned or rotated to coincide with the direction of flow.

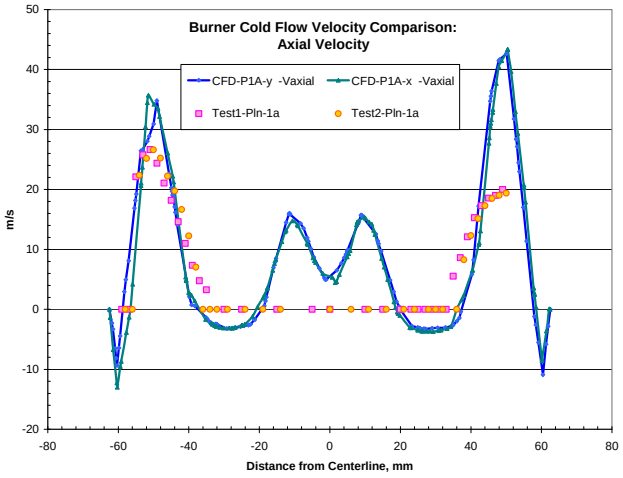

(d) Axial Velocity on Plane 1a

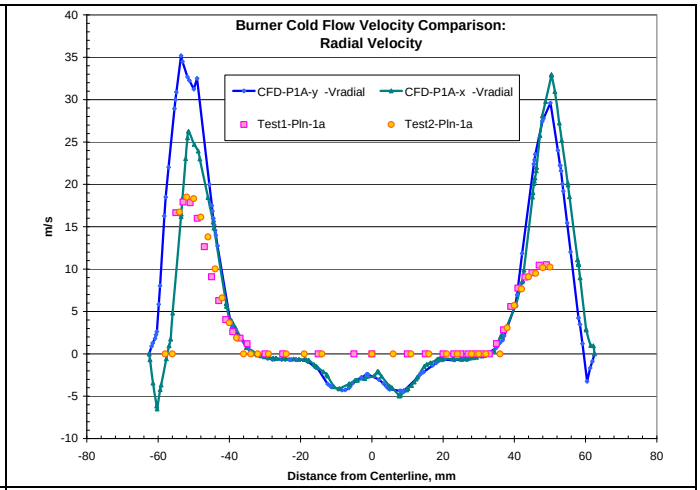

(e) Radial Velocity on Plane 1a

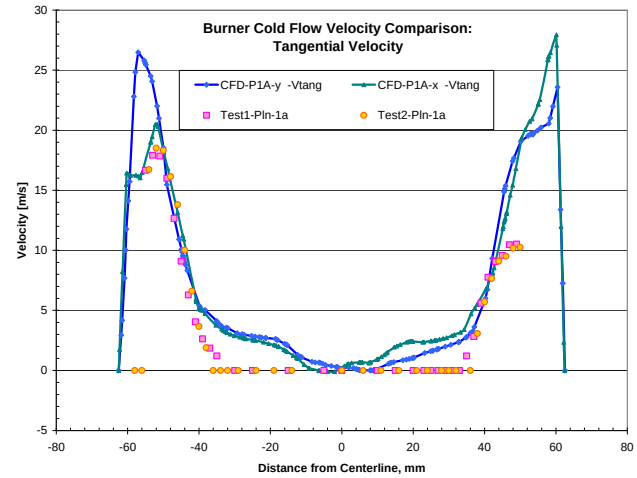

(f) Tangential Velocity on Plane 1a

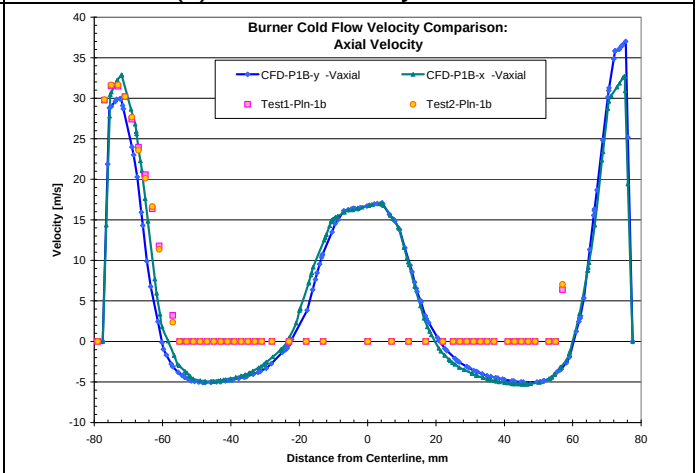

(g) Axial Velocity on Plane 1b

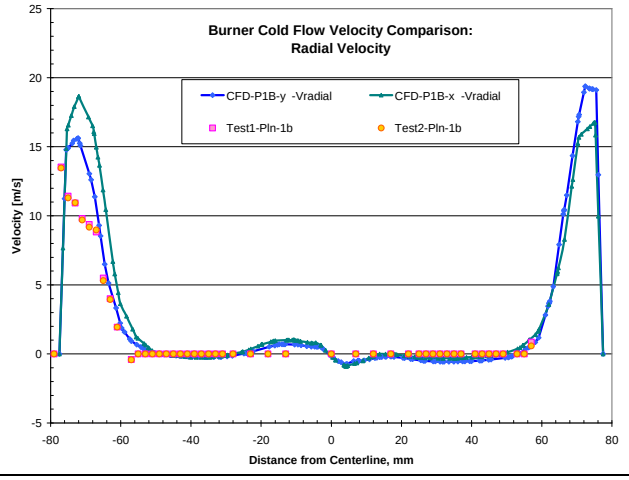

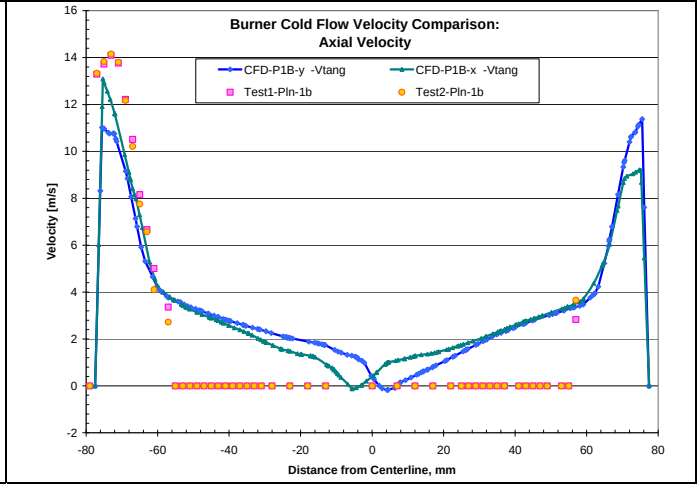

(h) Radial Velocity on Plane 1b

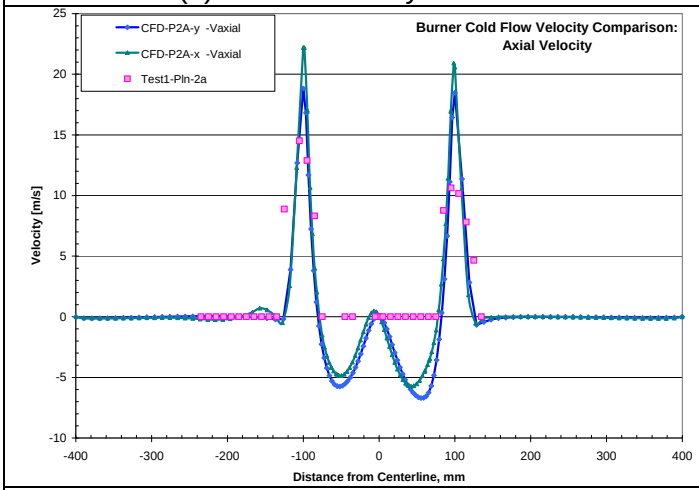

(i) Tangential Velocity on Plane 1b

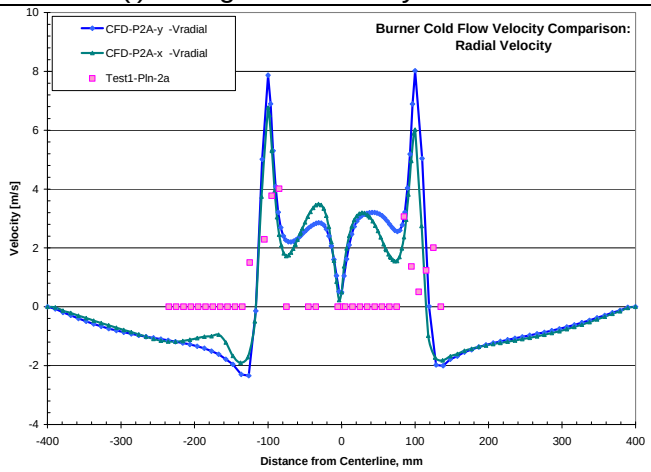

(j) Axial Velocity on Plane 2a

(k) Radial Velocity on Plane 2a

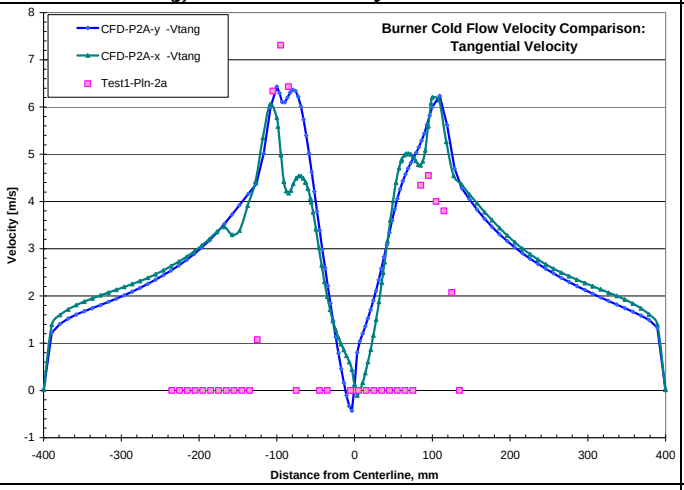

(l) Tangential Velocity on Plane 2a

Figure 5-5. Cold Flow Pitot Probe Predictions

At Planes 1a and 1b, the external axial velocity peaks near the quarl walls are reasonably captured. However, the single or dual axial velocity peaks near the centerline, predicted by the CFD code, are not exhibited by the experimental data. In addition, the solid-body rotation predicted in the core by the model is not exhibited by the data. In fact, the experimental axial, radial and tangential velocities in the core region are all identically zero. However, it is difficult to understand why the experimental tangential velocity is identically zero in the core region, since the nozzle is a co-swirled apparatus and the reverse flow velocities should have some finite tangential velocity component. Similarly, on Plane 2a, the calculated tangential velocity exhibits a Burger's vortex, while the experimental tangential velocity is zero both within the core and outside of the peak values. These observations may point to a problem with the measurements of the tangential velocity, and by association, all of the velocity measurements, both within the core and in the near wall region outside of the peak regions. Perhaps probe rotation is required to pick up tangential velocities below some threshold value.

If it is presumed that the experimental axial velocities in the core region are reliable, then this may infer that the partial penetration of the reverse flow zone did not occur. This may also imply that the experimental swirl strength may be stronger than that predicted by the model, since a larger swirl strength

(and a stronger reverse flow) would make it more difficult for any penetration to occur on the centerline against the adverse pressure gradient. Presuming that the inlet boundary conditions are properly duplicated, and that the axial velocity data is reliable, then a possible conclusion is that the k-ε model may not be adequate and that a more sophisticated Reynolds stress model should be investigated.

To qualitatively assess the impact of stronger swirl on the axial velocity profiles, a computational experiment was performed in which the SA-2 vane assembly was changed from a moderate vane angle to a higher vane angle (i.e., changed to produce a larger swirl magnitude). These results for Plane 1b are shown in Figure 5-6. As expected, the higher swirl level indicates that higher peak tangential velocities (and a higher swirl strength) are produced, although qualitatively, the shapes of the radial and tangential velocity profiles do not change very much. However, the higher swirl level completely eliminates the computed axial velocity penetration of the reverse flow zone on the symmetry axis. This is in accord with previous statements and strengthens the recommendation to investigate a more sophisticated turbulence model.

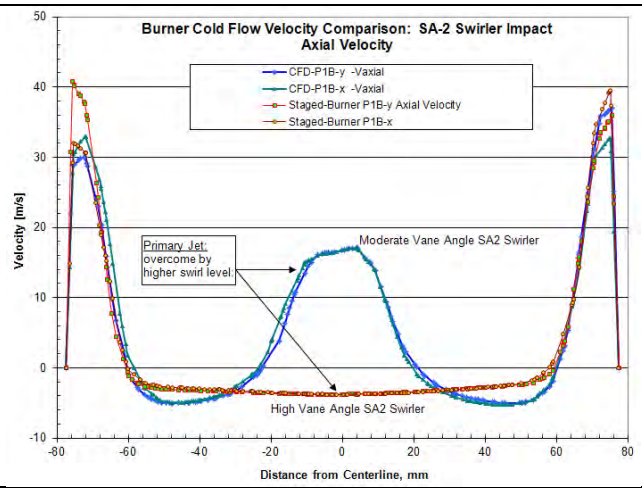

(a) Axial Velocity on Plane 1b

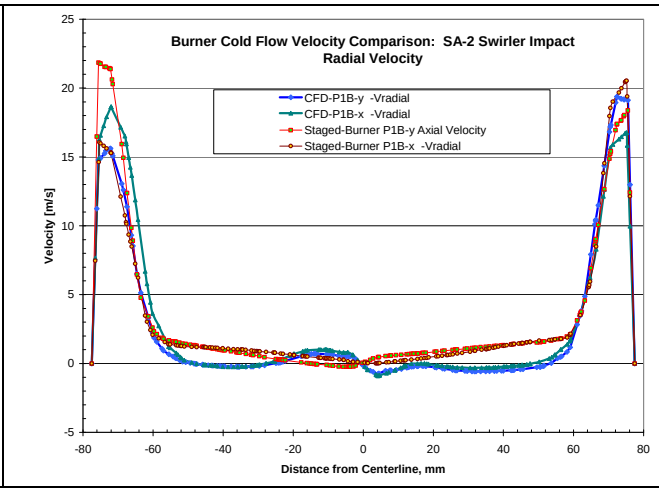

(b) Radial Velocity on Plane 1b

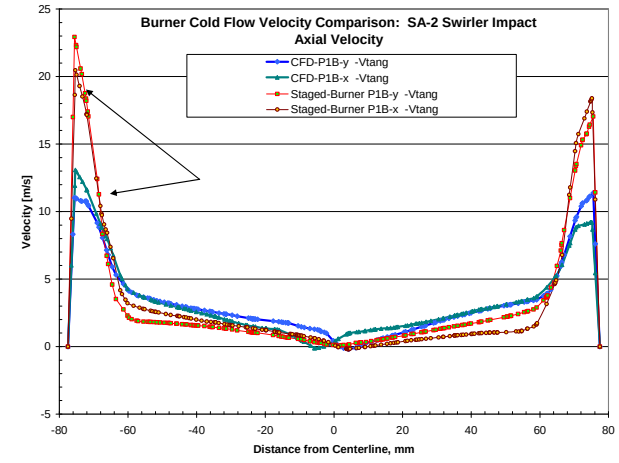

(c) Tangential Velocity on Plane 1b

Figure 5-6. Cold Flow Burner Profile Calculations to Assess Impact of Increased Swirl

The quantitative assessment of the differences in the profiles as a result of changing the SA-2 vane assembly from a moderate swirl magnitude to a higher swirl magnitude is also useful since this is the very

change that was made between the TW-1 and TW-2 burner configurations. A general assessment of the swirl patterns and the flow reattachment and recirculation zones are helpful in visualizing the flow.

Overall, the comparison of the cold-flow predictions to the pitot tube velocity data is perhaps satisfactory as far as the near-wall peak values are concerned, although a number of questions remain unanswered relative to the integrity of the data in the core (i.e., symmetry axis) or in the region near the reactor wall (for Plane 2a).

5.2 Contour Plots

Alstom completed 4 additional CFD runs and compared them with data from the following data sets:

- Test Week 1 (TW-1): unstaged condition: oxy and air test.
- Test Week 2 (TW-2): staged condition: oxy and air test.

A summary of the calculated outlet concentrations, residual carbon, and the overall energy balance at convergence are provided in Table 5-1. The column labeled "Complete Combustion" contains the outlet composition based on complete combustion of the reactant feeds. The domain outlet concentrations are in reasonable agreement with these expectations, given the relatively low unburned carbon.

Table 5-1. Case Outlet Concentrations and Energy Balance

	AIR_Unstaged		OXY Unstaged		AIR Staged		OXY Staged	
Outlet Composition Mole %	Complete Combustion	CFD Run	Complete Combustion	CFD Run	Complete Combustion	CFD Run	Complete Combustion	CFD Run
O2	2.58%	2.63%	2.90%	2.81%	2.97%	3.24%	3.95%	4.03%
CO2	15.00%	14.92%	67.54%	67.37%	15.01%	14.77%	68.68%	68.61%
H2O	0.09	0.09	25.73%	25.68%	8.82%	8.71%	24.19%	24.19%
CO	0.00%	0.03%	0.00%	0.10%	0.00%	0.03%	0.00%	0.00%
SO2	0.19%	0.19%	0.27%	0.45%	0.00	0.00	0.29%	0.29%
N2	72.76%	72.73%	3.56%	3.60%	72.97%	73.04%	2.89%	2.89%
Sum	100.00%	100.00%	100.00%	100.00%	100.00%	100.00%	100.00%	100.00%
Unburned Carbon % Carbon in Ash		0.85%		0.63%		0.75%		1.13%
Energy Balance		1.37%		1.88%		2.27%		0.79%

Contour plots of temperature on an x-plane, bisecting the reactor, for the four cases, are shown in Figure 5-7. In these plots, the air-unstaged results are placed adjacent to the air-staged results, and similarly, the oxy-unstaged results are positioned adjacent to the oxy-staged results. Each contour plot is overlayed with experimental data in the form of discrete, colored dots that are referenced to the same legend as the contour plot itself. Only elevations through Level 10 are shown in the truncated plots; the OFA lance injection plugs are in the vicinity of Level 11 and are therefore downstream of what is displayed.

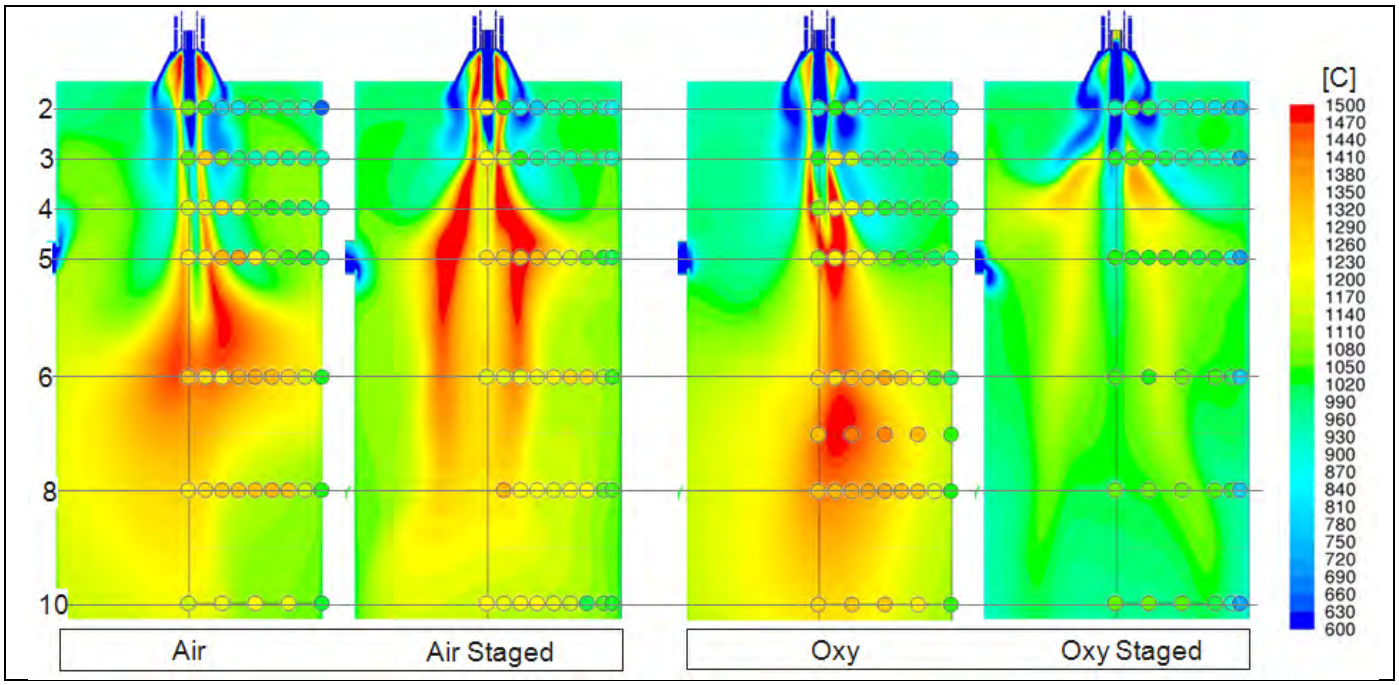

Figure 5-7. Temperature Contour Comparison

Differences exist between the computed contour plots. The unstaged cases appear to have corner recirculation zone reattachment points that are downstream of the Scan-2 port, so that the flame and mixing zone for the unstaged cases appear to be constrained to the core region for a longer distance than the equivalent zone for the staged cases. The reattachment points in the staged cases appear to be positioned upstream of the Scan-2 port. This observation is based on the position where the flame expansion occurs, and the visual extrapolation of the contours as they sweep toward the outer wall. However one visualizes the position of the reattachment points, it is very apparent that the central flame in the staged cases expands or balloons significantly upstream of the unstaged flame expansion. This is probably due to the higher SA-2 swirl associated with the staged cases (i.e., higher swirl in TW-2 tests than in TW-1 tests), which helps to expand the flame beyond the quarl and mix out the flow field more rapidly than in the unstaged case.

The experimental temperature data tends to follow the computed contours fairly well. For the air-unstaged case at Levels 1 through 5, for example, the suction pyrometer data appears to indicate that lower temperatures are on the symmetry axis and then temperatures increase with an increase of radius until a peak temperature is reached, after which temperatures decrease to the wall. The peak experimental temperature location is located at a radius which is slightly larger than the radius of the peak computed temperature. The computational jet or flame does not seem to expand as rapidly as the rate indicated by the experimental data, although it is difficult to know how much of that apparent expansion is due to the probe suction-volume characteristics. Downstream of Level 5, both the experimental and computed flame zone balloon out in shape and are in rough accord with each other. The computations may be asymmetric at some elevations, but the two sides (on each side of the symmetry axis) may be visually integrated by the reader when comparing with the data. Similar statements regarding comparison between the predictions and data may be made for the other cases. While there is not a perfect correspondence between the data and the computations, and the data may not achieve the peak values of 1500 °C exhibited by the calculations, the results are still very encouraging. Even in the oxy-staged case, where the computed

temperatures are depressed relative to the other cases, the experimental data appear to follow suit and scale down in a corresponding manner.

Contour plots of oxygen concentration (in units of mole %, dry) on an x-plane, bisecting the reactor, for the four cases, are shown in Figure 5-8.

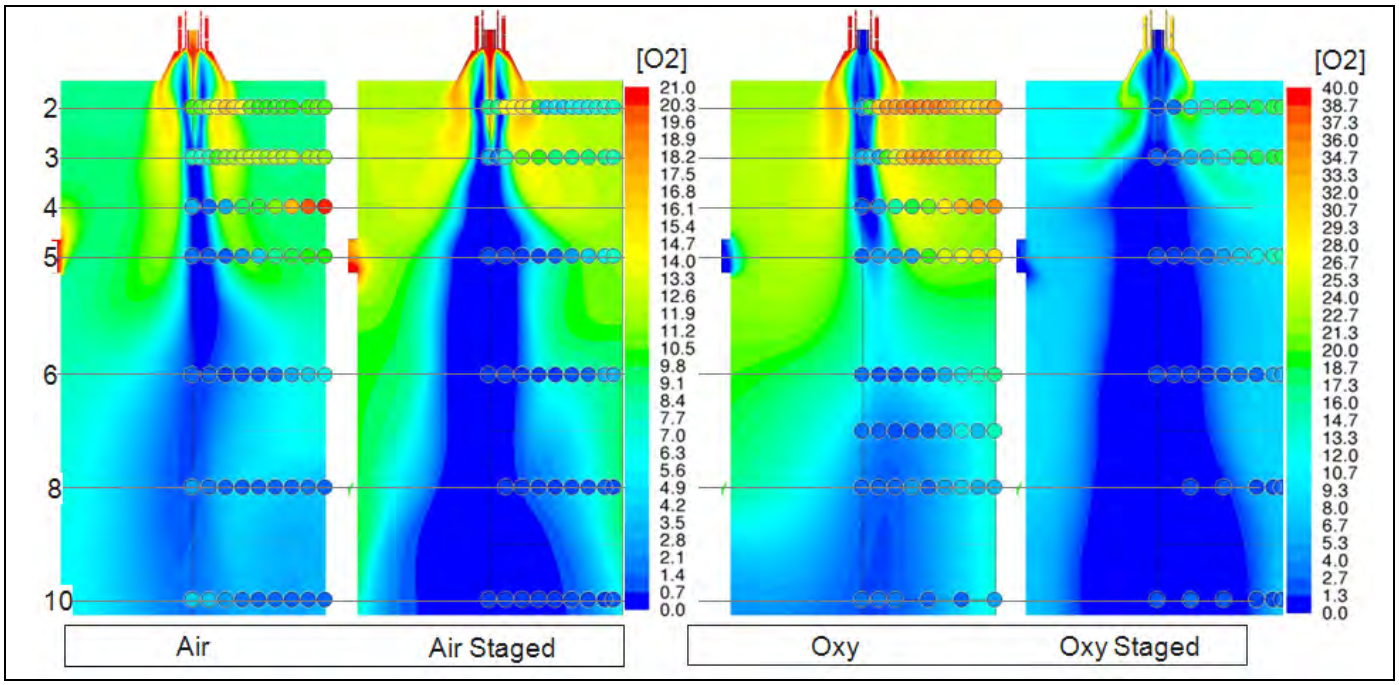

Figure 5-8. Oxygen Contour Plot Comparison (Mole %, Dry)

An oxygen-starved core is apparent in all of the computed contour plots. As expected, the staged cases exhibit a much larger or expanded oxygen-starved core than the unstaged cases (particularly since the OFA is introduced downstream at Level 11). The cases are qualitatively similar to each other in many respects, but they also have significant quantitative differences.

Overall, the experimental data is similar to the computations. For the unstaged air case at Levels 2 and 3, the experimental data indicate a peak oxygen mole fraction in the flame at a radius similar to that shown by the data. At Level 4, the oxygen seems to increase to high inlet values near the wall. The high oxygen value near the wall must be due to the in-leakage from the Scan-2 port which is swept upstream (again indicative of the reattachment point lying downstream of the Scan-2 port). At Level 5, the data appears to coincide with the computed contours. The oxygen data at Levels 6 through 10 are relatively low in magnitude from the symmetry axis to the wall, in a manner that is in reasonable agreement with the computations. Interestingly, at Levels 8 and 10, the highest experimental data value is on the symmetry axis, which may indicate asymmetry in the actual flame.

For the air-staged case, the experimental data at Level 2 are at about 5 or 6% (mole %, dry) near the wall, while the computations are at probably twice that value. Alternatively, for the oxy-unstaged case at Level 2, the experimental data shows values around 30%, while the computations are at concentration magnitudes of around 20%. Therefore, the computation concentrations may depart from the data in the upstream corners of the reactor (and the departure may be positive or negative), but overall, the

predictions appear to capture much of the expansion of the oxygen-starved core and appear to follow the trends through each Level.

Contour plots of CO concentration (in units of mole %, dry) on an x-plane, bisecting the reactor, for the four cases, are shown in Figure 5-9.

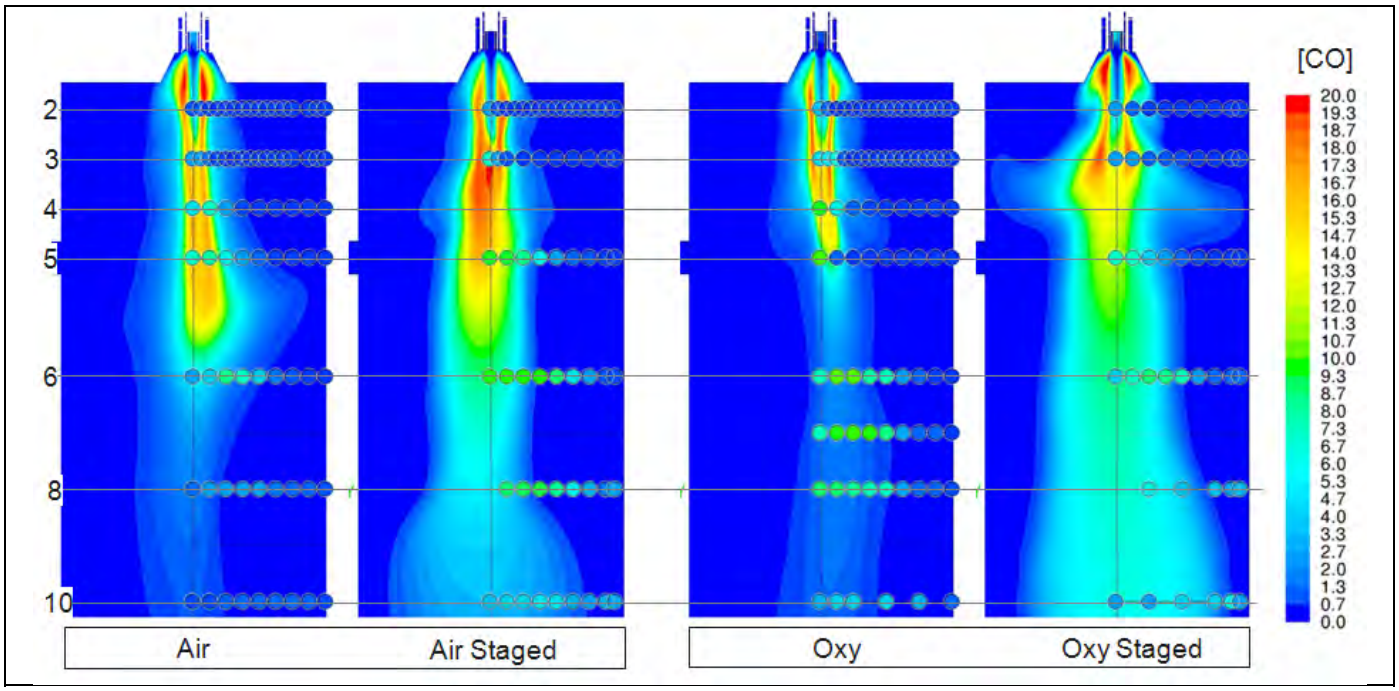

Figure 5-9. CO Contour Plot Comparison (Mole %, Dry)

Computationally, and as expected, the two staged cases appear to exhibit much more net CO production than the unstaged cases. The oxy-staged case exhibits the most CO (due in part to lower temperatures and lower oxygen magnitudes at every Level).

For the unstaged air case, the experimental data fail to indicate any high CO peaks at Levels 2 and 3, and only begins to exhibit CO values of around 5% (mole %, dry) in the vicinity of the symmetry axis at Levels 4 and 5. This may indicate that both the rate of CO formation, as well as the magnitude of the CO concentration is significantly diminished in the experimental flame compared to the computed flame. The CO peak moves off-axis at Level 6, and then CO values begin to diminish in magnitude at Levels 8 and 10. The measured CO never gets larger than perhaps 9% for any of the cases, despite high peak values (e.g., 20%) in the computations.

The staged air case shows one data point of 4 or 5% CO on the symmetry axis at Level 4, and then an expanding radius of CO at subsequent Levels, showing that finite magnitudes of CO expand rapidly and persist all the way to the wall. The staged oxy case is similar in many respects to the staged air case. The rate of experimental CO production is much slower than the calculations in the near-nozzle region, never reaching the high CO concentrations exhibited by the calculations, but then the CO continues to be produced over a wide radius through Levels 6 and 8 while the computational CO is rapidly depleting. The slow, but sustained, CO production in the actual flame may point to CO production from soot or char conversion rather than to rapid volatile combustion.

The oxy case shows the CO data with moderate concentration magnitudes at 3 points on Level 3, 2 points on Level 4, and 1 point on level 5, showing the reactions conceivably pinching off, but then showing a wide CO tail at subsequent Levels 6 through 10, as another CO producing reaction (perhaps soot or char oxidation) starts up downstream.

Contour plots of CO_2 concentration (in units of mole %, dry) on an x-plane, bisecting the reactor, for the four cases, are shown in Figure 5-10.

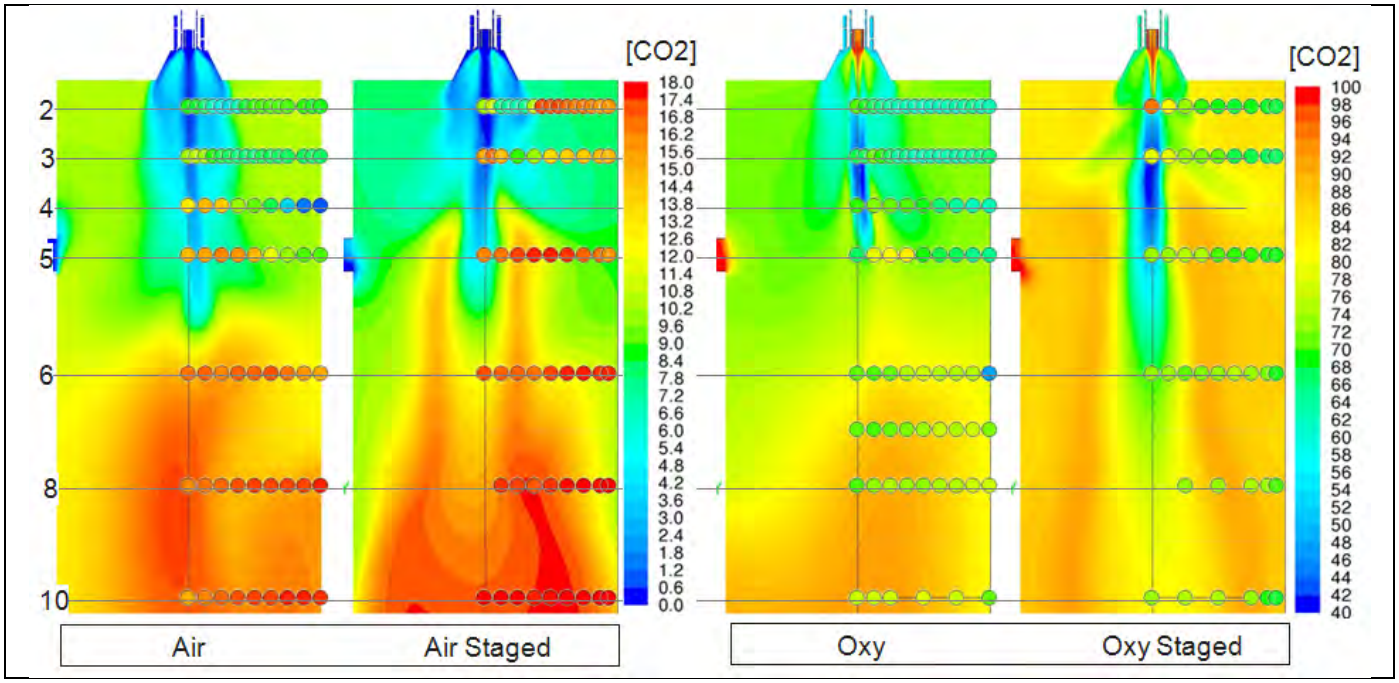

Figure 5-10. CO_2 Contour Plot Comparison (Mole %, Dry)

The two simulated staged cases exhibit much more CO_2 than the unstaged cases because of the effective "recycled" CO_2 in the feed streams (note the different scales). The simulations tend to have low CO_2 on the symmetry axis, at least from Level 2 through Level 5, and then the CO_2 begins to steadily build up past that point at downstream locations. The CO_2 concentration in the corners appears to be rather variable, and appears to have a trend opposite to that of the oxygen concentration.

The experimental data for the unstaged air case appears to have about an 8% (mole %, dry) concentration across the entire radius at Levels 2 and 3. At Levels 4 and 5, significant CO_2 builds up in the vicinity of the symmetry axis (with a low near-wall value at Level 4 due to the Scan-2 in-leakage). At subsequent downstream Levels, high CO_2 levels exist across the entire reactor radius.

The trend is similar for the staged air case, except that very high experimental CO_2 levels are apparent at Levels 2 and 3 in the corner (that are not reflected in the computations).

For the unstaged oxy case, the experimental CO_2 is probably about 60% (mole %, dry) in the corner, while the computations are over 70%. The experimental CO_2 starts to build up near the symmetry axis at Level 5, and begins to approach 80% at Level 10, but it is still almost 10 percentage points lower than the

computations. For the staged oxy case, the experimental CO_2 data remains almost constant over most of the radius at magnitudes between 70 and 80%, but again, the data remains at least 10 percentage points less than the computations over most of the domain displayed in the figure.

Although significant error should be attached to suction probes, if it is assumed that the experimental data is trending correctly, then it may be that predictive error is emanating from two different possibilities – (a) boundary condition error, where the feed compositions or flow rates in the computations are causing even the fully-mixed outlet values to disagree with the experimental outlet values, and (b) reaction speciation and rates. To address Point (1), additional work needs to be done to compare the experimental flue gas values with the simulated values to see if the overall material balance requires adjustment. Once Point (1) is addressed, then Point (2) can be attacked. To address Point (2), more effort needs to be put into comparing how the oxygen, CO, and CO_2 are changing locally relative to the data and whether the net production of the species (due to more than one reaction) should be reduced or increased to produce the correct quantitative results. It may be that uncertainty quantification can be used to good advantage to address the speciation and reaction rate issues.

Overall, the comparison of the experimental data with the predictions are very encouraging. Temperature and major species, such as oxygen and CO_2, are predicted reasonably well, although some quantitative differences are apparent. Minor species, such as CO, indicate that some speciation and reaction rate studies are necessary to surface the underlying reasons for the differences between the experimental data and the calculations.

5.3 Heat Flux Predictions

The heat flux on the reactor walls was extracted from the computations by creating four (4) longitudinal sample lines (see Figure 5-11), each separated circumferentially from an adjacent sample line by an angle of 90°. The four lines were then numerically averaged to provide a representative “average” for the circumferential heat flux profile. Despite the circumferential uniformity of the interior wall temperature and wall/deposit resistance assigned as a boundary condition to the wall, it can be seen that significant circumferential variation exists (e.g., ±15% in peak regions) in the wall heat flux. Although a more rigorously calculated circumferential average would have provided a more accurate averaged longitudinal profile, given the uncertainties in the experimental data along with the wall conditions and emissivities, the 4-line average is sufficient for present purposes.

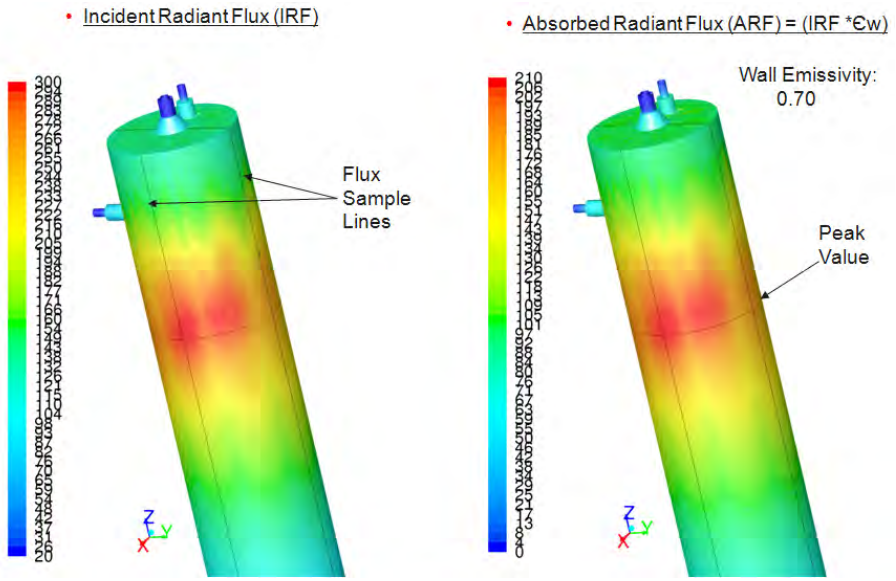

Figure 5-11. Wall Heat Flux Extraction Method

As mentioned previously, the computed absorbed radiant flux (ARF) is used to compare with the data from the total heat flux (TFH) probe, and the total surface incident radiant flux (SIRF or just IRF) is used to compare with the data from the ellipsoidal radiometer (ER). (Acronyms are supplied here in the text because they are used in subsequent figures.) The heat flux predictions using the ellipsoidal radiometer probe are shown in Figure 5-12, while the total heat flux probe predictions are shown in Figure 5-13.

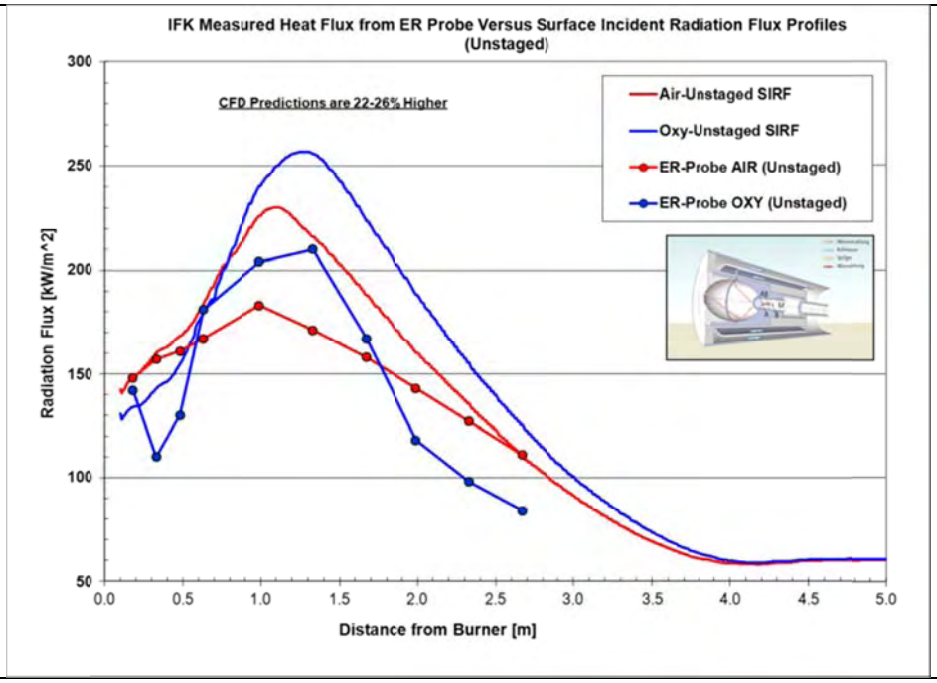

(a) ER Probe : Unstaged (TW-1)

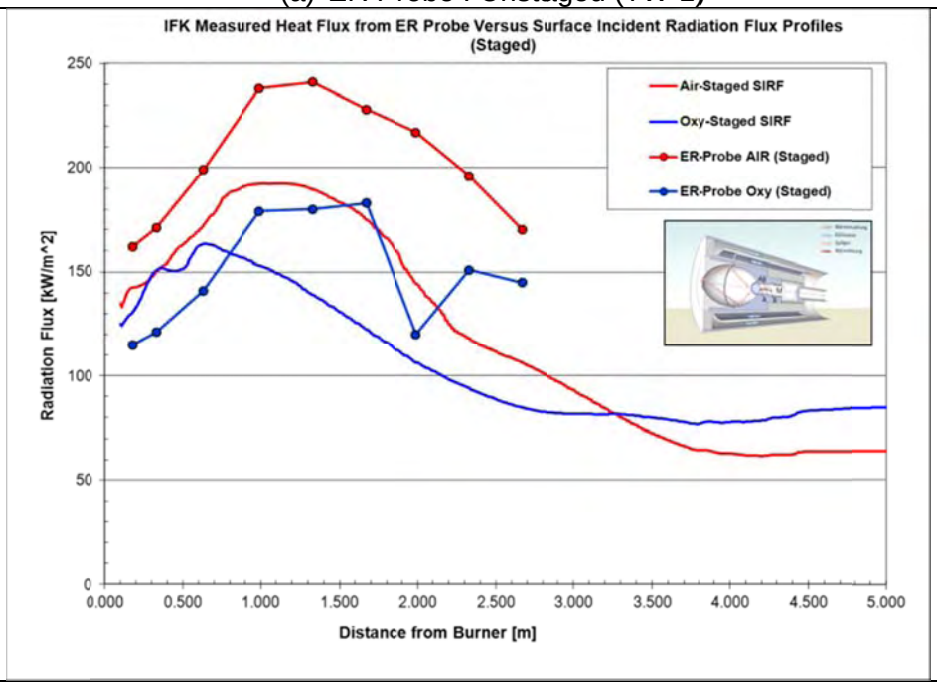

(b) ER Probe : Staged (TW-2)

Figure 5-12. Predictions of Ellipsoidal Radiometer Heat Flux Data

In the unstaged plot the oxy test has a higher peak value than the air test for both the experiment and the computations; similarly for the staged plot, the air test has a higher peak value than the oxy test for both the experiment and the computations. However, for the unstaged, TW-1 configuration, the predicted values are higher than the experimental ellipsoidal radiometer values by 22 to 26%. For the staged, TW-2 configuration, the opposite is true, and the predicted values are 21 to 30% lower than the ellipsoidal

radiometer data. Therefore, the computations reflect the experimental trend somewhat, although the magnitudes are in error.

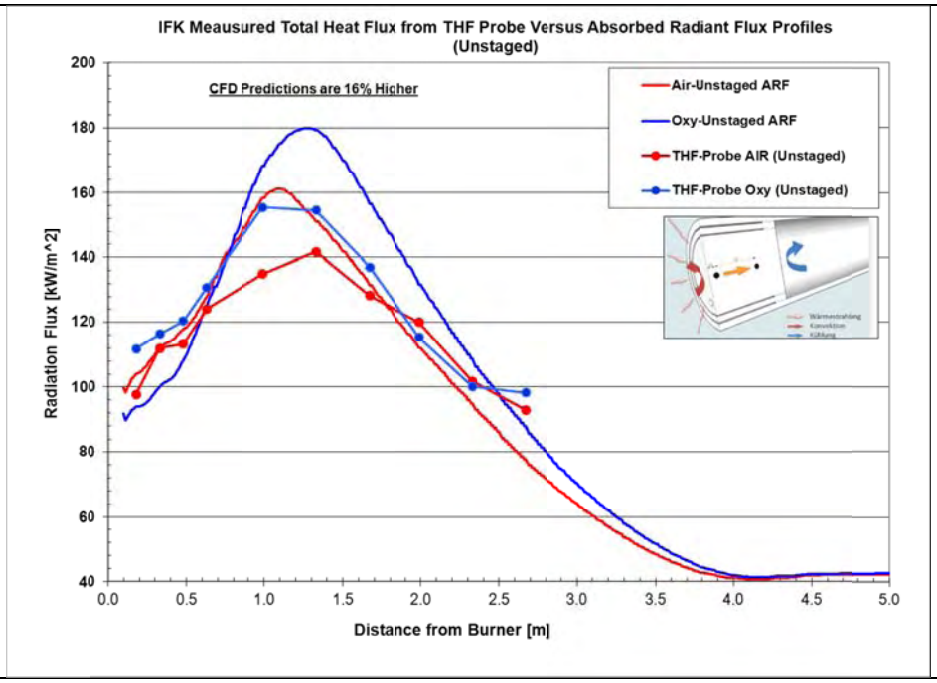

(a) THF Probe : Unstaged (TW-1)

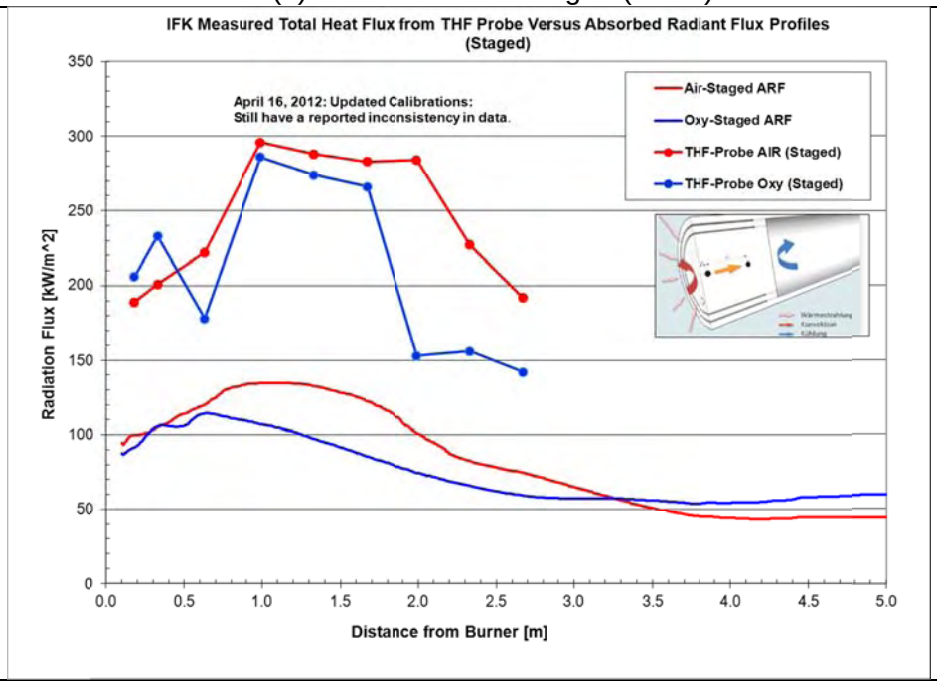

(b) THF Probe : Staged (TW-2)

Figure 5-13. Predictions of Total Heat Flux Probe Data

Qualitatively the trends exhibited by the total heat flux probe are similar to those of the ellipsoidal radiometer probe. In the unstaged plot the oxy test has a higher peak value than the air test for both the

experiment and the computations; for the staged plot, the air test has a higher peak value than the oxy test for both the experiment and the computations.

Quantitatively, the delta between the peak values of the computations and the experimental data for the total heat flux probe is in the same direction (i.e., positive or negative) as the ellipsoidal radiometer probe, although the magnitude of the delta is different. For the TW-1 (unstaged) configuration, the calculations are reported to be about 16% higher than the data at the peak, while for the TW-2 configuration, the calculations are much lower than the data (by a factor of two at the peak).

Some problems with the total heat flux probe were reported. Relative to the THF probe data for the unstaged configurations (Test Week 1), IFK reported that:

> ”Compared to the ellipsoidal measurement the values are too low. It looks like a negative systematic measuring off-set mistake. We think that this was a dirt or slagging problem. In this way the heat was additionally transferred to the outer gap of the water cooled probe.”

For the THF probe data for the staged configurations (Test Week 2), IFK reported that: “Total heat flux data are too high and have to be checked.” Even after a re-calibration and checking of the data, the data remained high relative to the predictions.

Considering the computations alone, the peak wall heat fluxes for the staged case is about 30% less than that of the unstaged case (for both the air and oxy feeds). Any trends exhibited by the experimental data are much more ambiguous because of uncertainties in the data.

The trends exhibited by the data and the predictions appear to match each other reasonably well, and the difference in magnitudes between the data and predictions are typically less than 30%, with the exception of some of the total heat flux probe data, some of which may simply reflect a problem with the probe.

6. References

1. DOE/NETL Cooperative Agreement.No. DE-NT0005290, "Recovery Act: Oxy-Combustion Technology Development for Industrial-Scale Boiler Applications," performed by Alstom Power Inc. for U.S. DOE National Energy Technology Laboratory.

2. Mönckert, P., D. Reber, J. Maier, G. Scheffknecht, "Operation of a Retrofited 0.5 MWth PF Combustion Facility under Oxyfuel Condtions – An Experience Report," Clearwater Clean Coal Conference (2007).

Recovery Act: Oxy-Combustion Technology Development for Industrial-Scale Boiler Applications

DOE/NETL Cooperative Agreement No. DE-NT0005290

Volume III – Modeling and Validation

Chapter 4 – Uncertainty Quantification of CFD Simulations

Authors
Paul J. Chapman
Yen-Ming Chen
David G. Sloan
David G. Turek

Table of Contents

1. Executive Summary 4
2. Objectives 9
3. Conclusions and Recommendations 12
4. Description of BSF 15
   4.1 Overall Geometric Description 15
   4.2 Measurement Ports and Heat Flux Panels 17
5. Technical Approach 20
   5.1 CFD Mesh 23
   5.2 Homogeneous and Heterogeneous Combustion Reaction Scheme 24
   5.3 Particle Combustion Model Description 26
   5.4 Boundary Conditions 28
   5.5 Convergence and Solution Considerations 34
   5.6 Validation Framework 35
   5.7 Data Collaboration and Consistency Analysis 38
6. Model Results for the V&UQ Analysis 42
   6.1 I/U Map and Parameter Prioritization 42
   6.2 Screening Trials 45
   6.3 Design of Experiments 51
   6.4 Data Collection 53
   6.5 Surrogate Model and Consistency Analysis 53
      6.5.1 Consistency Analysis I: C-3 (1, 4, 5), AV-1 (k_w), O-2 (Average Planar T, HF) 54
      6.5.2 Consistency Analysis II: C-3 (1, 4, 5), AV-1 (k_w), O-3 (T, HF, O_2) 59
      6.5.3 Consistency Analysis III: C-7 (1-7), AV-3 (k_w, CFR, DR), O-3 (T, HF, O_2) 68
7. Contour Plots and Visual Comparison 75
8. References 81

List of Tables

Table 5-1. Submodel and Parameter Differences 22
Table 5-2. Coal Analyses 25
Table 5-3. Reaction Stoichiometries Used in Alstom Runs 25
Table 5-4. PSD Parameters 27
Table 5-5. Mixture Fraction and Inert Boundary Condition Specification for ICSE Case 29
Table 5-6. Inlet Gas and Coal Flow Rates and Temperature for Baseline Case 29
Table 5-7. Windbox and Overfire Inlet Air/Gas Port Designations 32
Table 5-8. Wall Thermal Boundary Conditions 34
Table 6-1. I/U Map 43
Table 6-2. I/U Map (Condensed Version) 44
Table 6-3. Feed Stream Estimated Experimental Uncertainties 45
Table 6-4. Wall Thermal Conductivity Screening Runs Using FLUENT® 46
Table 6-5. Wall Thermal Conductivity Screening Runs Using ARCHES 49
Table 6-6. Model Parameter Scoping Runs Using FLUENT® 51
Table 6-7. V&UQ Run Matrix 53
Table 6-8. Results for Consistency Analysis II 60
Table 6-9. Results for Consistency Analysis III 69

List of Figures

Figure 1-1. Gas Temperature Field in BSF Using ARCHES (Ref. 16) 4
Figure 1-2. Particle Number Density as a f(Particle Size) Using ARCHES (Ref. 11) 5
Figure 4-1. Plan (or Top) View of Tangential Firing Pattern (Oil-Fired) in BSF 15
Figure 4-2. 15 MW Boiler Simulation Facility Model 16
Figure 4-3. Oxy Boiler Simulation Facility 17
Figure 4-4. BSF Furnace Probe Measurement Planes 18
Figure 5-1. BSF CFD Mesh 23
Figure 5-2. BSF Wall Insulations and Test Planes 33
Figure 6-1. Temperature Profile Predictions (FLUENT®) as a Function of Elevation and k_w. 47
Figure 6-2. Temperature Profile Predictions (ARCHES) as a Function of Elevation and k_w. 49
Figure 6-3. Three-dimensional Design of Experiments 52
Figure 6-4. RANS (a): T: Analysis I: C-3 (1, 4, 5), AV-1 (k_w), O-2 (Average Planar T, HF) 55
Figure 6-5. RANS (b): HF: Analysis I: C-3 (1, 4, 5), AV-1 (k_w), O-2 (Average Planar T, HF) 56
Figure 6-6. LES (a): T: Analysis I: C-3 (1, 4, 5), AV-1 (k_w), O-2 (Average Planar T, HF) 58
Figure 6-7. LES (b): HF: Analysis I: C-3 (1, 4, 5), AV-1 (k_w), O-2 (Average Planar T, HF) 59
Figure 6-8. LES (a): T: Analysis II: C-3 (1, 4, 5), AV-1 (k_w), O-3 (T, HF, O_2) 62
Figure 6-9. LES (b): HF: Analysis II: C-3 (1, 4, 5), AV-1 (k_w), O-3 (T, HF, O_2) 63
Figure 6-10. LES (c): O_2: Analysis II: C-3 (1, 4, 5), AV-1 (k_w), O-3 (T, HF, O_2) 64
Figure 6-11. RANS (a): T: Analysis II: C-3 (1, 4, 5), AV-1 (k_w), O-3 (T, HF, O_2) 65
Figure 6-12. RANS (b): HF: Analysis II: C-3 (1, 4, 5), AV-1 (k_w), O-3 (T, HF, O_2) 66
Figure 6-13. RANS (c): O_2: Analysis II: C-3 (1, 4, 5), AV-1 (k_w), O-3 (T, HF, O_2) 67
Figure 6-14. RANS (a): T: Analysis III: C-7 (1-7), AV-3 (k_w, CFR, DR), O-3 (T, HF, O_2) 70
Figure 6-15. RANS (b): HF: Analysis III: C-7 (1-7), AV-3 (k_w, CFR, DR), O-3 (T, HF, O_2) 70
Figure 6-16. RANS (c): O_2: Analysis III: C-7 (1-7), AV-3 (k_w, CFR, DR), O-3 (T, HF, O_2) 71
Figure 6-17. RANS (d): Consistent Sample Space for Analysis III 73
Figure 7-1. Gas Temperature Field in BSF Using ARCHES (Ref. 16) 75
Figure 7-2. Particle Number Density as a f(Particle Size) Using ARCHES (Ref. 11) 76
Figure 7-3. Comparison of Time-Averaged Temperature Using FLUENT® and ARCHES 78
Figure 7-4. Comparison of Time-Averaged Wall Heat Flux Using FLUENT® and ARCHES 79

1. Executive Summary

Computational fluid dynamic (CFD) coal-combustion simulations of Alstom's 15-MWth, tangentially-fired, Boiler Simulation Facility (BSF) were conducted using the ANSYS FLUENT® software and the large eddy simulation (LES) code ARCHES, developed at the Institute of Clean and Secure Energy (ICSE) at the University of Utah. The FLUENT® code contains both Reynolds-averaged Navier-Stokes (RANS) and LES capabilities, but the FLUENT® code was used only as a RANS simulator in the present project.

Accuracy and Fidelity of LES Codes

LES codes attempt to directly resolve a portion (e.g., 80%) of the turbulent kinetic energy spectrum, typically the larger length scales, and use modeling approximations to account for the smallest (dissipative) scales. The resolution of these turbulent eddies of varying spatial and temporal scales may be critical in correctly predicting the underlying physics that control boiler characteristics. Flame stability, particle drag effects, emissions, and other phenomena are strongly coupled to the turbulent eddies, which in turn, have an impact on the oxidant concentrations, local wall heat flux, etc. The LES codes are run in a time-accurate manner so that the majority of the turbulent kinetic energy spectrum is resolved, thus promoting much greater fidelity and predictive accuracy in the simulation than RANS computations.

An example of a volume-rendered gas temperature field at an arbitrary time step, using the ARCHES code, is provided in Figure **1-1**. The impact of the turbulent eddies on the flame structure is evident.

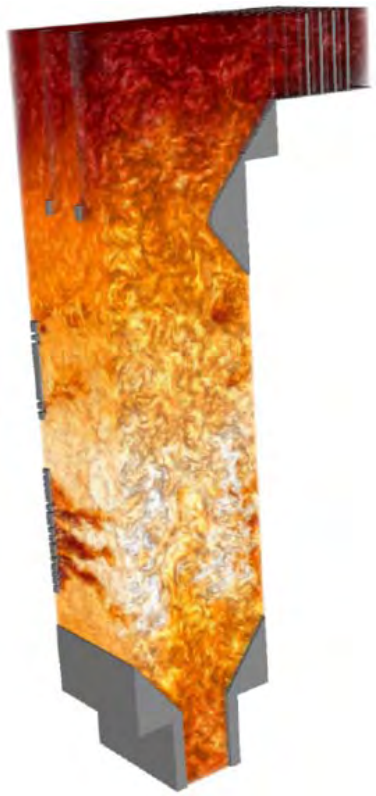

Figure 1-1. Gas Temperature Field in BSF Using ARCHES (Ref. 16)

Not all of the physics within the boiler are equally susceptible to the short time-scale phenomena. For example, the radiation flux to the walls responds instantaneously to the local temperatures, but since each ray must travel through a large volume of the domain, the integrated traces exhibit smoother results over time. The impact of the turbulent eddies on the particle number density depends on the particle size. This effect is shown in Figure 1-2. The particle number density is normalized to the inlet value, so that values greater than unity indicate local particle clustering.

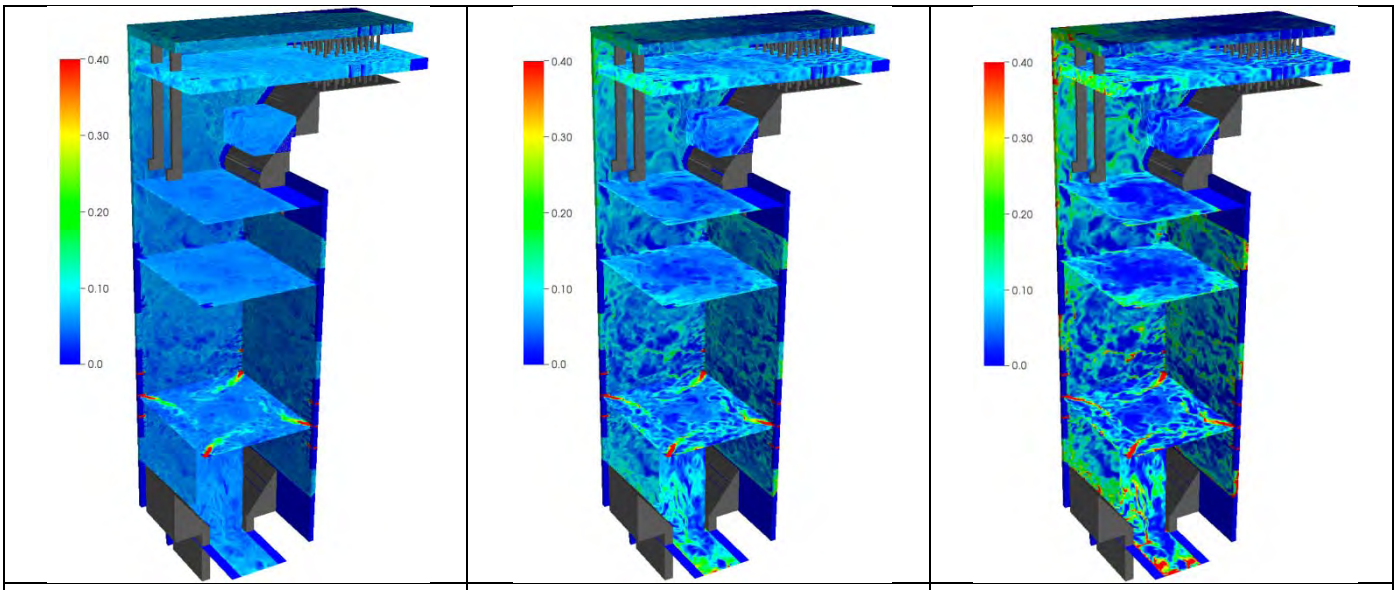

(a) d_p = 30 μm | (b) d_p = 60 μm | (c) d_p = 90 μm

Figure 1-2. Particle Number Density as a f(Particle Size) Using ARCHES (Ref. 11)

As the particle size changes, the particle inertia will change. This makes the particles with different sizes respond differently to the local turbulent eddies. The small particles have very little inertia and will be entrained by the small scale turbulent eddies, which enhances their diffusion. Thus, in Panel (a) the small particles are more evenly distributed within the furnace. As particle size increases, the particle inertia increases by the particle diameter to a power of 3. Consequently, as shown in Panel (c), the small-scale turbulent eddies have little effect on the ballistic motion of these larger particles. The larger particles concentrate along the edges of coherent structures, and the clusters are more segregated.

These examples indicate the predictive potential inherent in LES codes; the enhanced resolution of the turbulent spatial and temporal scales does have a beneficial impact on the underlying physics, which should produce predictions that are more accurate and that have greater congruence with the experimental data. The RANS computations attempt to represent a wide range of length scales with modeled approximations (rather than resolved physics) using "mean" parameters.

Background and Approach

A collaborative agreement between Alstom and the University of Utah was executed on August 30, 2011. The objective of the modeling simulations was to provide a more reliable computational tool and methodology through the validation and uncertainty quantification (V&UQ) process. The Alstom CFD simulations were performed as part of the "Recovery Act: Oxy-Combustion Technology Development for

Industrial-Scale Boiler Applications" program, under the DOE Agreement DE-NT0005290. The ICSE program is an independent, DOE-sponsored program with the long-term objective of (a) expanding high-performance simulation tools to quantitatively predict the temperature and heat flux in oxy-coal burners for retrofitting power boilers and industrial furnaces for CO_2 capture, and (b) to perform verification, validation and uncertainty quantification (V&V/UQ) of the numerical and modeling error associated with this intended use of the simulation tool. This report documents the results of the V&UQ process for both the FLUENT® (steady-state) and ARCHES LES (time-dependent) predictions, consistent with the project management plan and milestone log described in the Agreement.

The computational study focused on the application of the V&UQ process for BSF Oxy Test 134, which used the Schwarze Pumpe lignite coal for fuel. The intent of the V&UQ analysis was to study the impact of various parameters on observables such as wall heat flux, gas temperature, and species. An input/uncertainty (I/U) map was created in which selected model parameters and boundary conditions were ranked or prioritized with respect to their projected impact on the temperature and wall heat flux, based initially on prior knowledge. Screening or scoping runs were made with CFD, in conjunction with the construction of the I/U map, to better assess the sensitivity of the observables to selected parameters, such as the wall thermal conductivity, and to assign uncertainty bounds to those parameters. Utilizing a simple "design of experiments" (DoE) scheme, an initial V&UQ run or case matrix was constructed, with 13 runs and 4 active variables – inlet coal mass flow rate, inlet gas mass flow rate, wall thermal conductivity (in the main furnace section only), and the devolatilization rate. The 13 CFD runs were completed by Alstom, the calculations were post-processed by Alstom, and the results were sent to ICSE for the V&UQ analysis. The results consisted of (a) the experimental data at each measurement point, and (b) the calculated value at each measurement point for each of the 13 CFD runs. ICSE have collected (and are in the process of collecting) similar calculation results from their LES runs (using essentially the same run matrix). However, at the time of this writing, ICSE is still working on completing the first seven (7) runs, due principally to the immense computational burden involved, as well as to case corrections and re-runs. Consequently, only the first 7 of the 13 runs completed by Alstom have been utilized in the V&UQ analysis.

The V&UQ analysis is advancing in a progressive manner – from a more simplistic analysis (using only a few runs and a single independent variable), to a more complex analysis (involving several runs and multiple independent variables). Progressing from the simple to the more complex has been helpful in ensuring that the participants understand and digest both the methodology and the output from the analyses. Three separate V&UQ analyses have been performed by ICSE:

- Consistency Analysis I. An initial V&UQ analysis was conducted with only 3 of the computational cases (Cases 1, 4, and 5), in which a single active variable, the wall thermal conductivity, was independently varied. This analysis was performed for both the LES and RANS computations. The observables included only the mean temperature at 3 planes and the heat flux data.
- Consistency Analysis II. An initial V&UQ analysis was conducted with only 3 of the computational cases (Cases 1, 4, and 5), in which a single active variable, the wall thermal conductivity, was independently varied. This analysis was performed for both the LES and RANS computations. The difference between this analysis and the preceding analysis was that, in the present analysis, the number of observables was expanded to include all of the local point measurements of temperature, the heat flux data, and the oxygen concentrations.

- Consistency Analysis III. A second V&UQ analysis was conducted with 7 of the computational cases (Cases 1 through 7), in which 3 active variables – the wall thermal conductivity, the coal mass flow rate, and the devolatilization rate – were independently varied. This analysis was performed only for the RANS computations (since the LES computations were not yet completed). The observables included all of the local point measurements of temperature, the heat flux data, and the oxygen concentrations.

The run matrix was limited to the oxy-fired case (Test 134), although the baseline run of the companion air-fired case (Test 109) was also run for comparison purposes. In the run matrix, the fuel and air flow rates were varied by ±1.5%, while the main furnace wall thermal conductivity was varied by ±25%. The devolatilization rate was increased and diminished by a factor of 5 from the baseline value.

The V&UQ analysis was performed with the Frenklach, et al. (Ref. 13) "data collaboration" and "consistency analysis" approach, and the resulting constrained optimization problem was solved utilizing a quadratic surrogate model and a Monte-Carlo type sampling procedure.

Results

Consistency Analysis II. From the consistency analysis, the LES code is able to demonstrate slightly smaller error bars on temperature (+/- 85 K) and heat flux (+/- 2.0E+04 Btu/hr-ft^2) than the RANS calculations (+/- 100 K and +/- 3.0E+04 Btu/hr-ft^2, respectively), while the uncertainty on the oxygen concentration is somewhat larger for the LES code (+/- 3.0 mole % (wet)) than for the RANS code (+/- 2.5 mole % (wet)). However, the only statement of consistency that can be made, based on the application of the thermal conductivity as the single active variable, is that simultaneous consistency has been achieved for both the LES and RANS codes. One of ICSE's goals within their DOE project is to ultimately demonstrate the superiority of the LES code over RANS computations for some critical (as yet unidentified) facet of boiler physics. However, much more work needs to be done with the analysis before any conclusions about the superiority of a particular code or model can be claimed.

Consistency Analysis III. The consistency analysis was done only on the RANS results. Consistency was attained when the temperature error bars were expanded to +/- 125 K and the error bars on the oxygen concentration was limited to +/- 2 mole % (wet). The uncertainty bars on the wall heat flux varied as a function of the measurement port and took into account the replicates at each port. The error bars on temperature were adjusted to make the consistency region as narrow and small as possible. For the three active variables, the consistency region for the wall thermal conductivity ranged from 2.285 to 2.373 Btu/hr-ft-°F, and the consistency region for the coal flow rate ranged from 0.6046 to 0.6148 kg/s; the devolatilization rate multipliers appeared to have a very small impact on the results (even though the sampling ranged over an order of magnitude).

Simultaneous consistency has been achieved for both the LES and RANS codes. Differences in the upper and lower bounds of the observed variables between each code should not be used to infer that one code is more accurate than the other. Additional work needs to be done with the analysis before such a conclusion can be entertained: (a) First, the experimental uncertainties need to be determined for the active variables and observables, insofar as possible. This means that experimental uncertainties need to be determined for suction pyrometry, heat flux probes, sampling probes, and other instrumentation. The experimental uncertainty then becomes the "true" upper and lower bound to gauge the actual consistency region. (b) Secondly, additional active variables and observables (or parameters of interest) need to be

brought into the analysis. The analysis of additional active variables, particularly scenario (i.e., boundary condition) parameters, will provide a more comprehensive view of the influence of those parameters on the simulations. Once those are understood, then the relative influence or accuracy of selected models, or even of entire codes, can be bracketed and properly assessed.

The aim of the modeling simulations will be to provide a more reliable computational tool and methodology which can ultimately be used to provide commercially attractive CO2 capture solutions for both the retrofit of existing boilers and the installation of new boilers. The present task and report constitute only an initial foray into the realm of V&UQ analysis. A great deal more V&UQ work remains to be performed with the BSF data and the CFD models. This work will be carried out by ICSE (as they continue with their DOE funding). The V&UQ analysis is a formalized methodology which can highlight model or boundary condition weaknesses and inconsistencies; these weakness can then be subsequently addressed and improved, so that the goal of ultimately providing more reliable model predictions can be realized.

2. Objectives

Alstom Power Inc. (Alstom) has conducted a development program to provide the technical information needed for the next step of large-scale commercial demonstration of oxy combustion in tangentially fired boilers and to accelerate the commercialization of this technology. The development program was principally funded and administered through DOE/NETL Cooperative Agreement No. DE-NT0005290 (see Ref. 1), The main project objectives include:

- Design and develop an innovative oxyfuel system for existing tangentially-fired boiler units that minimizes overall capital investment and operating costs.
- Evaluate performance of oxyfuel tangentially fired boiler systems in pilot scale tests at Alstom's 15 MW_{th} tangentially fired Boiler Simulation Facility (BSF).
- Address technical gaps for the design of oxyfuel commercial utility boilers by focused testing and improvement of engineering and simulation tools.
- Develop the design, performance and costs for a demonstration scale oxyfuel boiler and auxiliary systems.
- Develop the design and costs for both industrial and utility commercial scale reference oxyfuel boilers and auxiliary systems that are optimized for overall plant performance and cost.
- Define key design considerations and develop general guidelines for application of results to utility and different industrial applications.

The DOE project was initiated in October 2008 and the scope was extended in 2010 under an American Resource and Recovery Act (ARRA) award. Comprehensive 15 MW_{th} oxy-fired test campaigns were completed with five different coals providing detailed data on combustion, emissions, and thermal behavior over a matrix of oxy-process variables and boiler design parameters. Contractual milestones and deliverables were achieved in the development of both oxy-boiler demonstration and large reference designs.

This report summarizes the computational fluid dynamics (CFD) and analysis work that was done to support the V&UQ portion of Subtask 6.1 (DOE/NETL Cooperative Agreement No. DE-NT0005290). Subtask 6.1 has three main components:

<u>Subtask 6.1 – CFD Oxy-Combustion Model</u>

- The ANSYS FLUENT® code, with improved submodels for combustion and radiation under oxy-combustion conditions, will continue to be applied and validated.
- Application of large-eddy simulation (LES) modeling for oxy-boiler application will be assessed and compared with simplified steady-state simulation approaches (specifically FLUENT®). More rigorous analysis of experimental and simulation data will also be conducted to statistically quantify uncertainty of modeling/prediction at both submodel and model levels. This will help improve prediction capability and accuracy of the modeling tools. This work will be conducted in collaboration with the Institute of Clean and Secure Energy (ICSE) at the University of Utah.
- Simulation results will then be compared with experimental validation data from small-scale facilities, the 15 MWth BSF and from the 30 MWth Schwarze Pumpe oxy pilot plant. The CFD code evaluation will include predictions for combustion, heat flux distribution, corrosion, and pollutant control.

The scope of the V&UQ effort is encompassed within the second bulleted item under Subtask 6.1. UQ analyses are oftentimes coupled with other analyses, such as verification (numerical error) and validation (physical submodel error) analyses, and may be referred to in combination with those analyses, as, e.g., V&V/UQ processes. The V&UQ effort, under this subtask, complements and is built upon a previous validation effort, associated with the third bulleted item under Subtask 6.1, which is also described as a separate section within Volume II. That validation effort consisted of the application and validation of the FLUENT® code to the 15 MWth BSF data. The test data used in the validation was collected for five (5) different test coals in test campaigns between the years 2009 and 2011. The five (5) test coals were: a Powder River Basin (PRB) (Black Thunder) sub-bituminous coal, a West Virginia (Fola) eastern (low-sulfur) bituminous coal, an Illinois No. 6 (Prairie Eagle) eastern (high-sulfur) bituminous coal, a North Dakota (Falkirk) lignite and a Schwarze Pumpe (Lusation) lignite. Other report sections in Volume II comprise the remaining workscope for the modeling task (Subtask 6.1).

Of the five different coals tested in the 15 MWth BSF test campaign, the tests with the Schwarze Pumpe lignite yielded the least fouling and the most reliable wall heat flux measurements. Consequently the oxy-fired Test 134, with Schwarze Pumpe lignite, was selected as the baseline test for the V&UQ study. The test included a set of detailed traverses, process data, and heat flux measurements with a set of replicate measurements tailored to the V&UQ process.

Under a collaboration agreement between Alstom and the Institute of Clean and Secure Energy (ICSE), as an entity of the University of Utah, ICSE provided the guidance and training during the tutorial process. As part of that process, joint discussions were conducted with ICSE to identify key model parameters that could be explored within a limited matrix of CFD runs. A decision was made to focus on the prediction of wall heat flux, gas temperatures, and species. The scope of the variables considered in the V&UQ process was limited to four (4) variables – the coal flow rate, oxidizer flow rate, the effective main furnace wall thermal conductivity, and the devolatilization rate. All other input parameters and boundary conditions remained unchanged.

The run matrix was limited to the oxy-fired case (Test 134), although the baseline run of the companion air-fired case (Test 109) was also run for comparison purposes. In the run matrix, the fuel and air flow rates were varied by ±1.5%, while the main furnace wall thermal conductivity was varied by ±25%. The devolatilization rate was increased and diminished by a factor of 5 from the baseline value. A total of 13 CFD simulations was conducted by Alstom using the commercial CFD code ANSYS FLUENT® that solves the steady-state Reynolds-averaged Navier-Stokes (RANS) equations. This matrix of cases was also simulated by ICSE at the University of Utah using the ARCHES code, a code designed to perform transient combustion simulations using the large eddy simulation (LES) model. The University of Utah performed an initial calibration of the wall thermal boundary conditions with the LES model in order to achieve a reasonable match with the planar temperature measurements, and Alstom utilized those same wall thermal boundary conditions for its baseline run.

This report details the calibration procedure for the baseline case as well as the Alstom results from the 13 CFD simulations. It discusses the validation framework or V&UQ process, including the input/uncertainty (I/U) map, the "design of experiments," the data collection, the application of the surrogate model, and the sampling procedure over the range of input variable combinations, as performed by both Alstom and ICSE. Any insights and ramifications that follow from the V&UQ consistency analysis are also discussed.

The aim of the modeling simulations will be to provide a more reliable computational tool and methodology which can ultimately be used to provide commercially attractive CO2 capture solutions for both the retrofit of existing boilers and the installation of new boilers. Indeed, the ultimate intent is to utilize the experimental test measurements and the simulation toolset to develop a basic design for a commercial-scale, oxy-boiler, demonstration project.

3. Conclusions and Recommendations

The computational study focused on the application of the V&UQ process to a single BSF test -- Oxy Test 134, which used the Schwarze Pumpe lignite coal as the fuel. The intent of the V&UQ analysis was to study the impact of various active variables on observables such as wall heat flux, gas temperature, and gas species. An input/uncertainty (I/U) map was created in which selected model parameters and boundary conditions were ranked or prioritized with respect to their projected impact on the temperature, wall heat flux, and oxygen concentration based initially on prior knowledge. Screening or scoping runs were made with CFD, in conjunction with the construction of the I/U map, to better assess the sensitivity of the observables to selected parameters, such as the wall thermal conductivity, and to assign uncertainty bounds to those parameters. Utilizing a simple "design of experiments" (DoE) scheme, an initial V&UQ run or case matrix was constructed, with 13 runs and 4 active variables – inlet coal mass flow rate, inlet gas mass flow rate, wall thermal conductivity (in the main furnace section only), and devolatilization rate. The 13 CFD runs were completed by Alstom, the calculations were post-processed, and the results were sent to ICSE for the V&UQ analysis. The results consisted of (a) the experimental data at each measurement point, and (b) the calculated value at each measurement point for each of the 13 CFD runs. ICSE has collected calculation results from their LES runs. However, at the time of this writing, ICSE is still working on completing the first seven (7) runs, due principally to the immense computational burden involved, as well as to case corrections and re-runs. Consequently, only the first 7 of the 13 runs completed by Alstom have been utilized in the V&UQ analysis.

The V&UQ analysis has advanced in a progressive manner – from a more simplistic analysis (using only a few runs and a single independent variable), to a more complex analysis (involving several runs and multiple independent variables). Progressing from the simple to the more complex has been helpful in ensuring that the participants understand and digest both the methodology and the output from the analyses. Three separate V&UQ analyses have been performed by ICSE:

- Consistency Analysis I. An initial V&UQ analysis was conducted with only 3 of the computational cases (Cases 1, 4, and 5), in which a single active variable, the wall thermal conductivity, was independently varied. This analysis was performed for both the LES and RANS computations. The observables included only the mean temperature at 3 planes and the heat flux data.
- Consistency Analysis II. An initial V&UQ analysis was conducted with only 3 of the computational cases (Cases 1, 4, and 5), in which a single active variable, the wall thermal conductivity, was independently varied. This analysis was performed for both the LES and RANS computations. The difference between this analysis and the preceding analysis was that, in the present analysis, the number of observables was expanded to include all of the local point measurements of temperature, the heat flux data, and the oxygen concentrations.
- Consistency Analysis III. A second V&UQ analysis was conducted with 7 of the computational cases (Cases 1 through 7), in which 3 active variables – the wall thermal conductivity, the coal mass flow rate, and the devolatilization rate – were independently varied. This analysis was performed only for the RANS computations (since the LES computations were not yet completed). The observables included all of the local point measurements of temperature, the heat flux data, and the oxygen concentrations.

The V&UQ analysis was performed with the Frenklach, et al. (Ref. 13) data collaboration and consistency analysis approach, and the resulting constrained optimization problem was solved with a MatLab script,

developed by ICSE. The script utilized a quadratic surrogate model and a Monte-Carlo type sampling procedure.

Conclusions and recommendations may be itemized as follows:

- Consistency Analysis II. From the consistency analysis, the LES code is able to demonstrate slightly smaller error bars on temperature (+/- 85 K) and heat flux (+/- 2.0E+04 Btu/hr-ft^2) than the RANS calculations (+/- 100 K and +/- 3.0E+04 Btu/hr-ft^2, respectively), while the uncertainty on the oxygen concentration is somewhat larger for the LES code (+/- 3.0 mole % (wet)) than for the RANS code (+/- 2.5 mole % (wet)). The uncertainty on the oxygen concentration is somewhat large overall, but the analysis has been performed only on a single active variable, the wall thermal conductivity, which has a very small effect on the oxygen concentration. Why the uncertainty on the oxygen concentration is so large, when the impact of the thermal conductivity is so small, is an open question that requires further analysis, but the analysis with additional active variables that impact stoichiometry should prove helpful.

- Consistency Analysis III. The consistency analysis was done only on the RANS results. Consistency was attained when the temperature error bars were expanded to +/- 125 K and the error bars on the oxygen concentration was limited to +/- 2 mole % (wet). The uncertainty bars on the wall heat flux varied as a function of the measurement port and took into account the replicates at each port. The error bars on temperature were adjusted to make the consistency region as narrow and small as possible. For the three active variables, the consistency region for the wall thermal conductivity ranged from 2.285 to 2.373 Btu/hr-ft-°F, and the consistency region for the coal flow rate ranged from 0.6046 to 0.6148 kg/s; the devolatilization rate multipliers appeared to have a very small impact on the results (even though the sampling ranged over an order of magnitude).

- Simultaneous consistency has been achieved for both the LES and RANS codes. It is evident that the calculated upper and lower bounds for the gas temperature, the wall heat flux, and the oxygen concentration are somewhat different for both codes. However, this fact should not be used to infer that one code is more accurate than the other. Such a conclusion cannot yet be drawn from the analysis. Additional work needs to be done with the analysis before such a conclusion can be entertained: (a) First, the experimental uncertainties need to be determined for the active variables and observables, insofar as possible. This means that experimental uncertainties need to be determined for suction pyrometry, heat flux probes, sampling probes, and other instrumentation. Replicates can be used to good advantage in determining the experimental uncertainty. The experimental uncertainty then becomes the “true” upper and lower bound to gauge the actual consistency region. (b) Secondly, additional active variables and observables (or parameters of interest) need to be brought into the analysis. The analysis of additional active variables, particularly scenario (i.e., boundary condition) parameters, will provide a more comprehensive view of the influence of those parameters on the simulations. Once those are understood, then the relative influence or accuracy of selected models, or even of entire codes, can be bracketed and properly assessed.

- The aim of the modeling simulations will be to provide a more reliable computational tool and methodology which can ultimately be used to provide commercially attractive CO_2 capture solutions for both the retrofit of existing boilers and the installation of new boilers. The present

task and report constitute only an initial foray into the realm of V&UQ analysis. A great deal more V&UQ work remains to be performed with the BSF data and the CFD models. This will be carried out by ICSE as they continue that work with their DOE/NETL funding. The V&UQ analysis is a formalized methodology which can highlight model or boundary condition weaknesses and inconsistencies; these weakness can then be subsequently addressed and improved, so that the goal of ultimately providing more reliable model predictions can be realized.

- Both the ICSE ARCHES code and the FLUENT® code were used in the V&UQ analysis. However, time and resources have not permitted additional checks to confirm that our heat inputs, regional total heat absorption, and overall energy balances are consistent between the codes. Additional checks need to be made to compare some of the submodels that impact wall heat transfer, as well as the parameters used in those submodels, and ensure that the submodels are as congruent between the two codes as possible. For example, it was observed that the FLUENT® code appears to produce temperature and wall heat flux deltas, for a given change in the wall thermal conductivity, that are almost twice as large as that observed in the ARCHES code. This issue needs to be resolved by carefully comparing the wall thermal heat transfer models in both codes.

- A number of other factors could be included in the uncertainty analysis of the experimental data, including (a) the uncertainty associated with the actual measurement or extraction volume around the tip of the sampling probe, (b) sagging of probe for long insertion lengths, (c) uncertainty in the time plots, (d) thermocouple uncertainty, (e) “instrument model” (e.g., equation or model to convert voltage from thermal conductivity to temperature) uncertainty, and (f) any inherent bias in the sampling probe measurements that becomes apparent when the measurements are compared to potentially more accurate diagnostics (e.g., optical) or references/standards.

4. Description of BSF

4.1 Overall Geometric Description

The BSF is part of the Alstom Power Inc. -- Power Plant Laboratories' (Alstom) Combustion Research Complex located in Windsor, Connecticut. This facility is an integral part of Alstom's worldwide corporate research network providing the key elements for successful power plant engineering and the development of new ideas and innovative designs for improved products and processes. The BSF is designed in such a way that it can be altered to test new design concepts, fire a wide variety of fuels, or to meet challenging project constraints stipulated by Alstom's clients.

The firing system includes a burner belt with three elevations of coal nozzles, a number of secondary air nozzles, including concentric firing system (CFS) tips and close-coupled overfire air (CCOFA) tips, and two elevations of separated overfire air (SOFA) nozzles. The firing system in the BSF incorporates corner-fired burners that have been configured to generate a tangential firing pattern, similar to that shown in the plan (or top) view provided in Figure 4-1. Considering a horizontal plane through an arbitrary nozzle, tangential firing is enabled by yawing the nozzle, in the direction of the fireball rotation, so that the firing angle of the nozzle is offset about 2.5 degrees from a hypothetical line connecting the corner with the center of the furnace. The air nozzles are positioned at the same offset angles as the coal nozzles; however, the CFS nozzles are offset an additional 22 degrees from the normal firing angle, as shown in Figure 4-2.

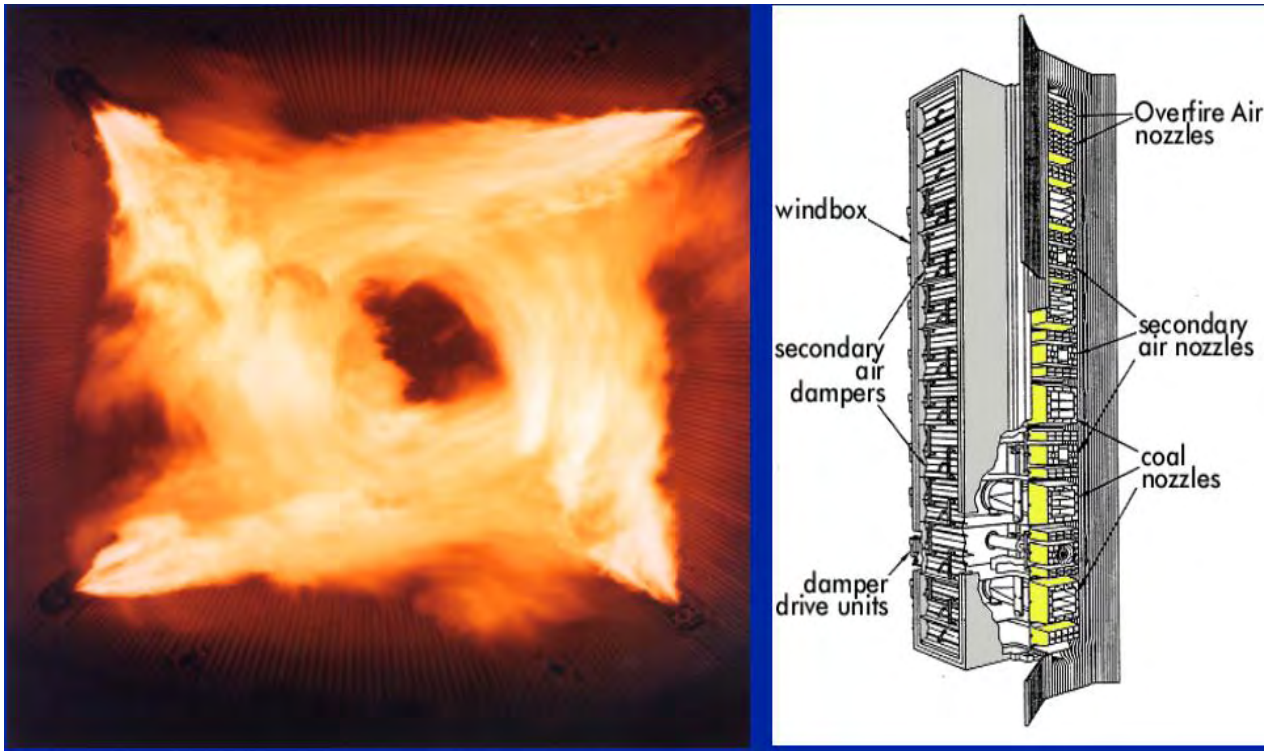

Top View **Windbox Elevation**

Figure 4-1. Plan (or Top) View of Tangential Firing Pattern (Oil-Fired) in BSF

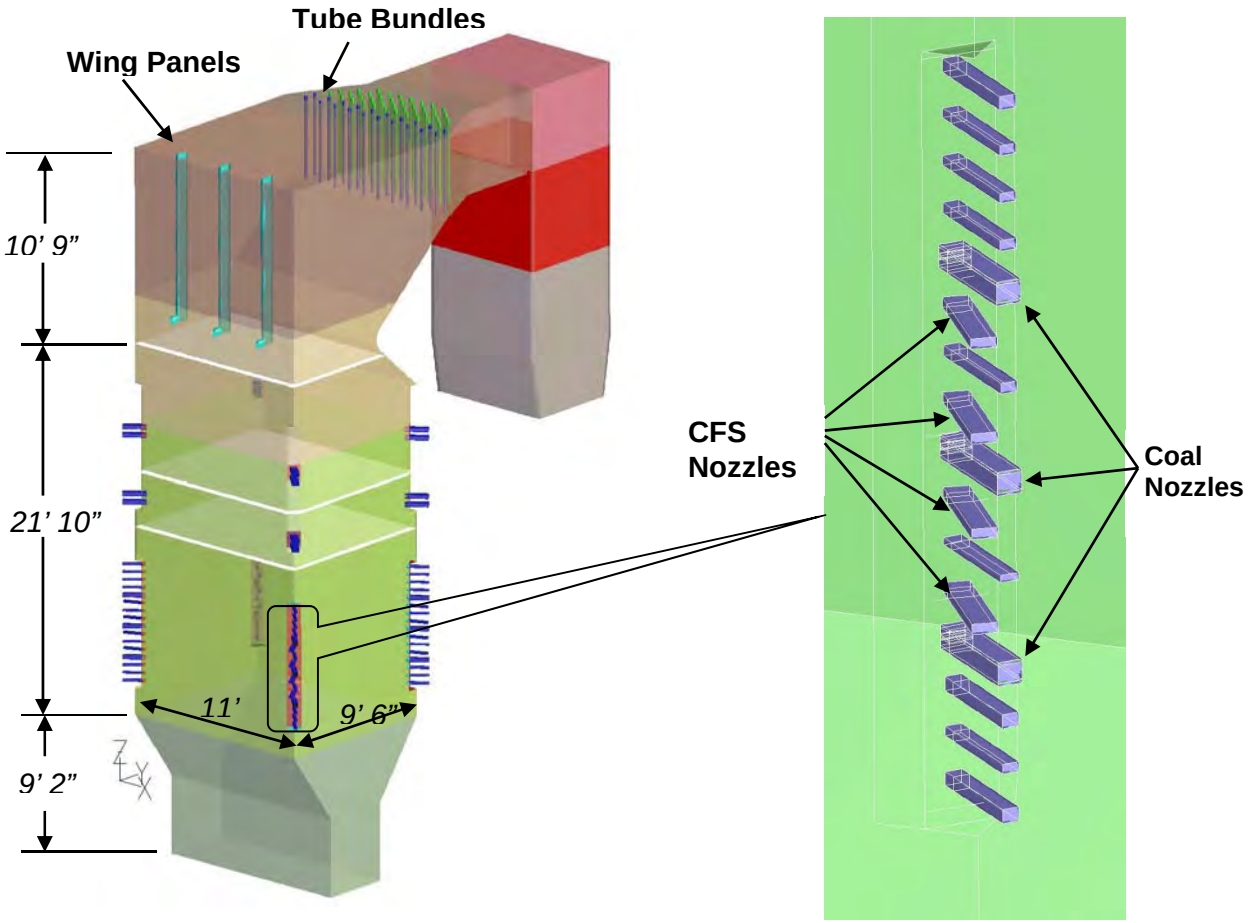

Figure 4-2. 15 MW Boiler Simulation Facility Model

The jacketed waterwalls and the interior insulation on the waterwalls are designed to provide the desired furnace absorption and furnace outlet temperatures. The wing panels and tube bundles, positioned in the upper furnace and convective pass, are intended to approximate additional superheat, reheat, or evaporative surface in a commercial furnace. The key dimensions of the BSF are shown in Figure 4-2.

To modify the BSF for oxy-combustion, several systems were added to the air-fired facility, including: oxygen supply tanks and injection system, flue gas recirculation ducting, dry scrubber fabric filter, and a CO2 supply system, some of which are shown in Figure 4-3. Only the boiler itself was modeled with CFD. A number of test campaigns have been completed with the designated testing coals. The data collected are used to compare with the CFD predictions and to validate and refine the CFD sub-models.

Figure 4-3. Oxy Boiler Simulation Facility

4.2 Measurement Ports and Heat Flux Panels

The BSF facility is instrumented to measure process flows, temperatures and pressures. Gas compositions are continuously measured at the economizer outlet, fabric filter inlet and fabric filter outlet. Oxygen concentrations are also continuously measured in the primary stream, windbox oxidant stream, and separated over-fire stream.

In addition to the data continuously logged by the Data Acquisition System (temperatures, pressures, flows, etc.) and the regular ash and fuel samples, several types of probes were used to map temperature, heat flux, and gas composition profiles in the furnace:

- Suction pyrometers were used to measure the gas temperature profile across a plane in the furnace
- Cooled gas extraction probes were used to measure the gas composition across a plane in the furnace. Species measured include O_2, CO, CO_2, H_2O, SO_2, and NO.
- Total heat flux and radiant heat flux probes were used to measure the incident radiation at the wall at various locations in the furnace.

Figure 4-4 shows the measurement planes and the relative position of the heat flux panel locations in the furnace. Measurement planes are labeled by their distance, in inches, from the bottom of the windbox. Additional details about the measurements, including information about the ports, the probes, and the data logging procedure, are discussed in Volume I.

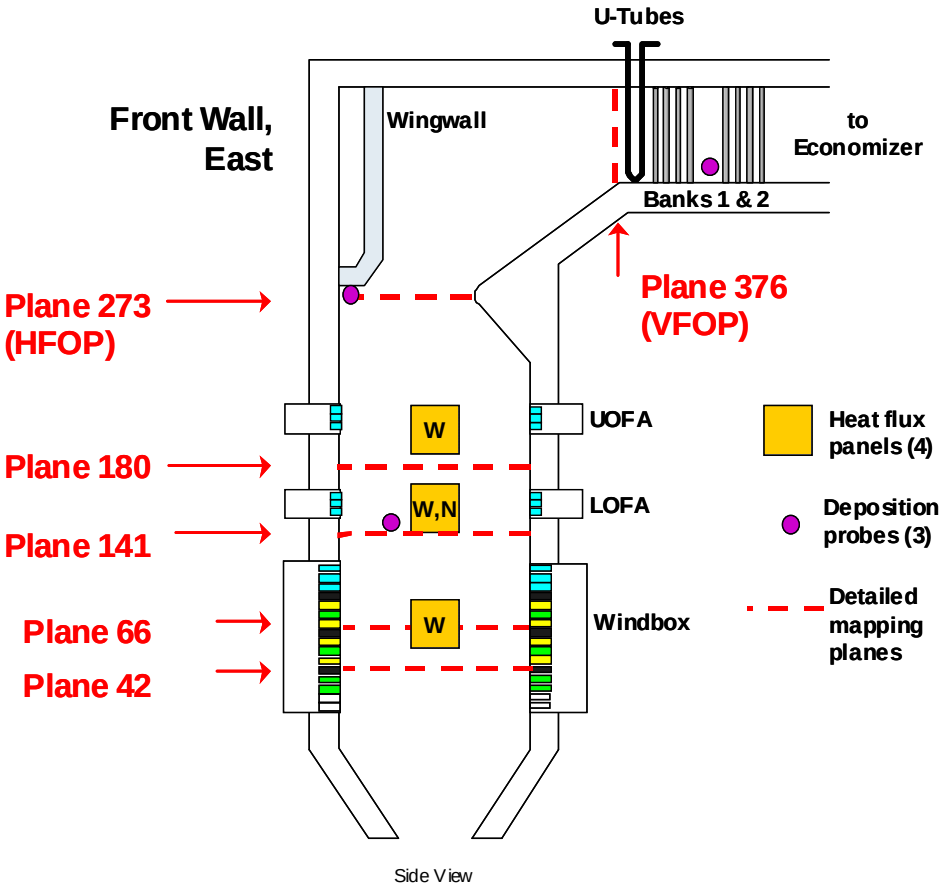

Figure 4-4. BSF Furnace Probe Measurement Planes

Planes 141, 180, and 273 are nominal planes. Plane 141 is at an approximate elevation of 141 in. above the hopper, depending upon which wall of the BSF the ports are on. Likewise, Plane 180 is at 180.0 in. above the hopper, and Plane 273 is at 273.0 in. above the hopper. The height of the hopper is 110 inches.

The total heat flux and radiant heat flux measurements are taken at a fixed traverse location (2 inches) into the furnace.

Gas sampling and suction pyrometer measurements are conducted on a grid pattern. Sample ports at Plane 141 are only located on the east and west wall, and due to access limitations imposed by the existing structural steel, short probes, which can only reach half-way into the furnace, are used. For a full grid, both the east and west wall must be probed with the short probe. Plane 141 ports include Ports 30, 31, 34, and 35 on the east wall, and Ports 42, 44, 47, and 48 along the west wall. Measurement distances are 4, 12, 30.5, and 49 inches beyond the refractory insulation into the furnace. The 4-inch (near-wall) sampling point was added after September 2009 testing.

Sampling at Planes 180 and 273 are conducted from the north wall of the facility using long probes. These probes are long enough to reach across the furnace, and are supported on probe racks. Plane 180

ports include Ports 62, 64, 65, and 67, and ports on Plane 273 include Ports 98, 100, 101, and 103. Measurement distances are 4, 19, 38, 57, 76, 95, 114, and 128 inches beyond the refractory insulation into the furnace. The 4-inch sampling point and 128-inch sampling point (4 inches from the far wall) were added after September 2009 testing.

5. Technical Approach

A commercial CFD code, ANSYS FLUENT® Version 14.0, was used by Alstom to model the Schwarze Pumpe lignite coal combustion in the 15 MW_{th}, tangentially-fired, Boiler Simulation Facility (BSF). Briefly, the code solves the conservation equations for mass, momentum and energy over the domain of interest by a finite volume method. The flow velocity components, static pressure and temperature at the center of each finite volume are obtained when the code converges to a steady state solution. The no-slip condition was imposed at solid surfaces. The flow field is assumed to be incompressible, but the physical properties such as density and specific heat are allowed to vary with temperature. The realizable k-ε turbulence model, with standard wall functions, was employed to model the turbulence, and the discrete ordinates model was used to model the radiation heat transfer. The computational domain of interest was decomposed and gridded using an ANSYS mesh generator. Additional details concerning the gridding approach, the FLUENT® submodels utilized, and the post-processed results and data comparisons will be discussed in turn.

In parallel with RANS simulations conducted by Alstom, large eddy simulations (LES) were conducted by the Institute of Clean and Secure Energy (ICSE) at the University of Utah (under the direction of Professor Phil Smith). The LES calculations are performed with a code called ARCHES. ARCHES is a massively parallel code that solves conserved quantities (mass, momentum, energy, and scalar) spatially and temporally in a turbulent flow field. The gas phase is solved in an Eulerian manner by a finite-volume method. A second-order central difference scheme is used to calculate the convection and diffusion terms of the transport equations. The RANS approach, as utilized in FLUENT®, relies on modeling the entire turbulent spectrum as a whole; consequently, many important physical processes are represented by fairly coarse modeling efforts. However, a wide range of physical length and timescales are present in boiler flow fields. Certain scales are controlling and require a sufficiently fine granularity to represent the physical process. The use of LES increases the fidelity of the resolved model while reducing the dependency on subgrid-scale (SGS) modeling. The subgrid scale stress tensor is calculated by the dynamic SGS model. The ARCHES code has coupled the LES turbulence submodel with other auxiliary submodels required for combustion systems, such as the 8-flux discrete ordinates (DO) method for radiation. The ARCHES code also contains the Direct Quadrature Method of Moments (DQMOM) to represent the solid coal phase. The DQMOM approach is utilized to represent moments of the particle number density function on the LES mesh. The ARCHES software code has been used for coal combustion in furnaces and boilers (Ref. 2 to 8), gas-fired furnaces and boilers, industrial flares, and pool fires.

To enable the University of Utah to construct CFD models of the BSF facility, a number of transmittals and information packages (with the appropriate confidentiality notations and limitations stipulated in the Alstom/University of Utah collaboration agreement) were sent to ICSE, including:

- Coal (or fuel) analyses
- Geometric details concerning the boiler walls, windbox and damper arrangements, firing angles, nozzle tips, wing walls, tube banks, wall thermal insulation, and roof blankets (for explosion protection).
- Inlet flow rates, temperatures, and gas compositions, as well as information about which tips were in or out of service, with their corresponding leakage.
- Information about the various probes (IFRF total heat flux probes, ellipsoidal radiometer probes, gas sampling probes, suction pyrometers, continuous heat transfer or heat flux panels, etc.), as well

as the probe and traverse locations, data acquisition system, board data, tag identifiers and descriptors.

- Photographs of the facility and equipment.

The University of Utah / ICSE analyzed the board data and constructed their own estimates of the inlet flow rates and compositions, which they subsequently used in their baseline run. They constructed a grid and prepared the baseline case very quickly in order to assess the feasibility of the grid and model, and to take advantage of computational windows of opportunity for CPU time on massively parallel clusters (e.g., Ember supercomputer at the University of Utah and the Titan supercomputer at Oak Ridge National Laboratory (ORNL)). Consequently, the ICSE effort was well underway in its baseline run calibration with the ARCHES LES code during the time frame that Alstom was preparing to calibrate its baseline run with FLUENT®. In discussions between the ICSE community and Alstom, it was agreed that in order to prevent parameter or submodel differences from masking more fundamental differences between the FLUENT® RANS and the ARCHES LES code, the LES and RANS calculations should be made as congruent as possible. Therefore the teams compared inlet boundary condition flow rates and compositions, as well as wall boundary conditions, etc., in order to ensure consistency between the two teams. Differences surfaced, but because the cost of correcting and repeating transient runs is so much larger for each LES calculation than for each RANS calculation, and because ICSE had already made a few runs, Alstom decided to concede some of its preferences and align its boundary conditions and model inputs with those that ICSE had already imposed. A summary of some of the changes are provided in Table 5-1.

Table 5-1. Submodel and Parameter Differences

Submodel or Parameter	Alstom	University of Utah / ICSE
Code	ANSYS FLUENT® (commercial)	ARCHES (open source)
Code Structure	Steady-state, Reynolds-averaged Navier Stokes (RANS)	Transient, large-eddy simulation (LES)
Grid	Conformal, body-fitted, hexahedral, pyramidal, and tetrahedral cells	Uniform (cubic), hexahedral cells, stair-stepped
Turbulence Model	Realizable k-ε with standard wall functions	LES
Particle Model	Discrete, Lagrangian particle model	Direct quadrature method of moments (DQMOM) model
Turbulent Combustion Model	Magnussen Eddy-Dissipation model (or eddy breakup) model	Presumed probability distribution function (PDF) model with equilibrium chemistry and inerts
Coal Moisture Evaporation	Wet-coal model (i.e., coal moisture evaporated as the first coal off-gas)	Coal moisture was given as a gas to the primary / transport stream
Char Oxidation	Preference: Surrogate rate from Alstom database Used: ICSE rate	Eastern Bituminous coal rate from Murphy and Shaddix (cited in Ref. 2)
Char Gasification	Preference: Rate from Goetz, et al. (Ref. 9) Used: Gasification not activated	Gasification not activated
Devolatilization	Preference: Single rate equation Used: Single rate equation that gives a devolatilization weight loss profile similar to that of the Yamamoto expression.	Yamamoto, et al. rate expression (cited in Ref. 2; Ref. 10)
High-Temperature Volatile Yield (DAF, %)	Preference: Value generated from PC Coal Lab software. Used: ICSE value	58%
Particle Radiation	Preference: UDFs for particle scattering and absorption efficiencies. Used: ICSE emissivity value	No particle scattering, particle emissivity = 0.8, soot radiation included (Ref. 8)
Particle Size Distribution (PSD)	Preference: Rosin-Rammler logarithmic distribution with 20 particle diameters, based on experimental PSD Used: [as above]	3 discrete sizes [First set of cases run with arbitrary distribution; cases are being re-run with the experimental PSD. Difference in PSD is being evaluated.]
Wall Thermal Boundary Conditions	Preference: Alstom-calibrated values Used: ICSE-calibrated values	Calibrated for the baseline run (oxy-fired Test 134) using the LES code

In an effort to accelerate their runs and take advantage of computational windows at the available supercomputer centers, ICSE ran their initial set of cases with an arbitrary PSD. The actual experimental PSD for the lignite coal was provided to the University of Utah some time later when Alstom constructed its CFD cases. As verbally reported by ICSE, all of the ICSE results presented in this report were unfortunately generated with the arbitrary PSD. ICSE are now in the process of re-running their cases with the experimental PSD; however, the cases have not yet run sufficiently to reach pseudo steady state, and will not be available by the delivery date of this report. All of the Alstom cases were run with the experimental PSD.

It should be noted that only a superficial comparison was made (by Alstom) between the two codes, and those differences that were highlighted were surfaced largely as a result of verbal communications

between the teams. Alstom did not thoroughly investigate the submodels within the LES code and make an exhaustive comparison with the FLUENT® counterparts. Consequently, there might be submodel and parameter differences between the two codes, beyond those tabulated here, that may have a controlling influence on the resultant differences calculated by the two codes.

A more complete description of some of the significant differences in the submodels between the FLUENT® and ARCHES computations will be provided in subsequent sections.

Rigorous analysis of experimental and simulation data was conducted to statistically quantify the uncertainty of the code/model predictions. This will help improve prediction capability and accuracy of the modeling tools as well as the experimental results. This uncertainty analysis was conducted in collaboration with ICSE. A description of the V&UQ analysis will also be presented in this report.

5.1 CFD Mesh

For the Alstom computations, the furnace geometry and computational mesh created for the BSF were generated using the ANSYS mesh program GAMBIT Version 2.2.30. The geometry and corresponding surface mesh for the BSF is pictured in Figure 5-1. The overall mesh contains over 4.135 million cells. The same mesh was used for all of the FLUENT® cases studied. The cases were run on local Alstom workstations and clusters.

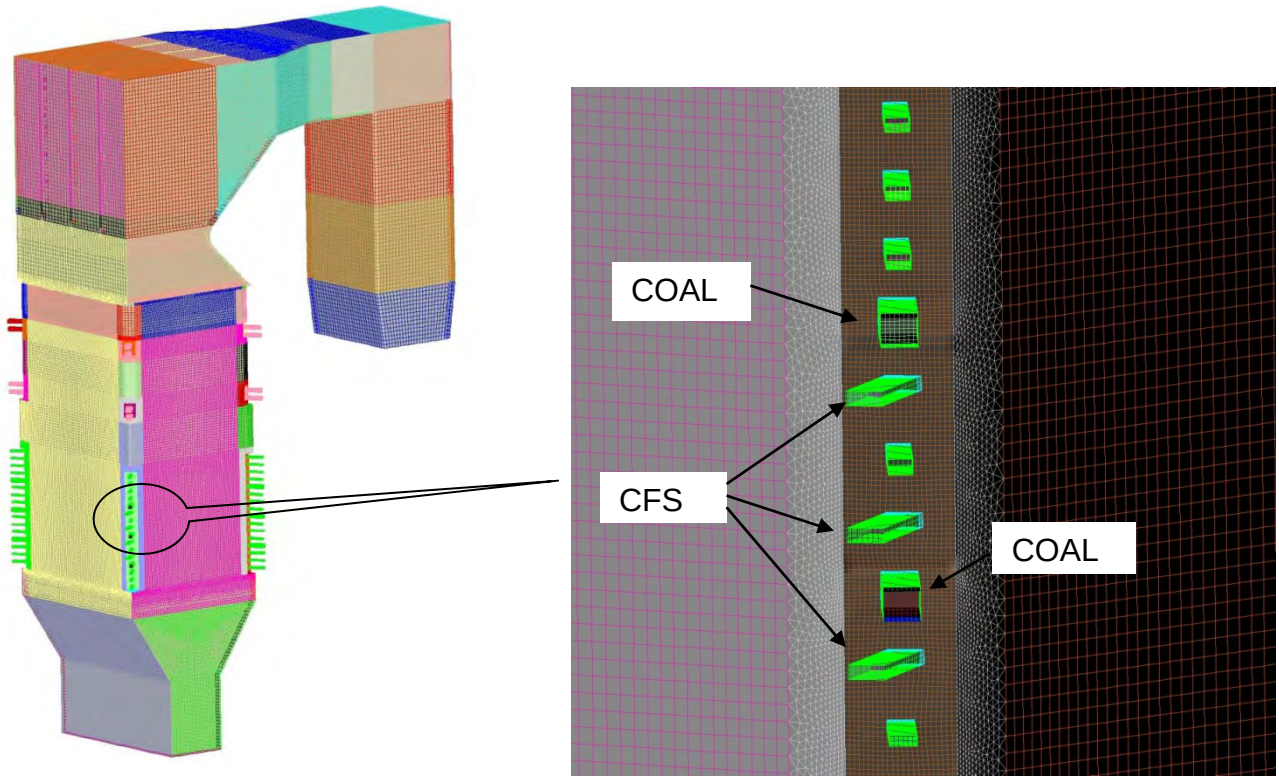

Figure 5-1. BSF CFD Mesh

For the LES runs, the cell size should (ideally) be small enough to resolve or capture 80% of the kinetic energy spectrum. Each of the ICSE cases was constructed with 2 cm (cell) resolution and has 17.414 million cells, although one (1) large case was run with a resolution of 1 cm, resulting in 137.216 million cells. For the case with 2 cm cell resolution, the cell size is such that the large-scale eddies can be calculated directly, so that the overall flame characteristics, as well as the particle dispersion, can be captured correctly. However, the cell size is not small enough to capture the detailed turbulent mixing near the burners (Ref. 8).

5.2 Homogeneous and Heterogeneous Combustion Reaction Scheme

Within the computational domain of the furnace, the gas phase reactions and particle surface reactions are coupled, with the coal particles providing mass sources of water vapor and volatiles to the gas phase, as well as mass sources of combustion products from the char surface reactions. For the main gas-phase combustion reactions, the turbulence-chemistry interaction was modeled in FLUENT® using the composite Magnussen eddy-dissipation (mixing-limited / fast-chemistry) and Arrhenius rates (kinetically-limited) combustion submodel, in which the smaller of the two rates (eddy-dissipation or Arrhenius rates) takes local precedence. The Magnussen eddy-dissipation model is also commonly referred to as the "eddy-breakup" model in the open literature.

For the Alstom cases, the gas-phase reaction mechanism was based upon four (4) single-step, irreversible, global reactions – volatile decomposition/reaction, CO oxidation, H_2 oxidation, and C-gas (surrogate soot species) oxidation. The global reaction mechanism includes nine (9) gaseous species: volatile, O_2, CO_2, CO, H_2O, SO_2, H_2, C-gas, and N_2. Species transport equations are converged for all of the species except for N_2, which is calculated by difference. The stoichiometry for the volatile decomposition reaction was calculated from a knowledge of the coal composition (see Table 5-2) and the high-temperature volatile yield value (prescribed in the University of Utah runs to be 58% (DAF basis)).

Table 5-2. Coal Analyses

	Schwarze Pumpe Lignite
Proximate/Ultimate:	(AF, Mass, %)
Moisture	13.70
Volatile Matter	31.67
Fixed Carbon	49.42
Ash	5.21
C	53.96
H	3.9
O	22.01
N	0.6
S	0.62
Heating Value:	
HHV (Btu/lb, AF)	9,008
Stoichiometric Mass of External O2 / Unit Mass of AF Coal	1.5332
Note: AF	As-Fired Basis

In the present Alstom runs, the char consists only of pure carbon (designated as C<s>), and ash. Gasification was omitted, in order to align the methodology with the University of Utah runs. The char burning rate is a combination of a film-diffusion rate in series with a chemical reaction rate. The apparent chemical reaction rate actually includes the composite effects of pore diffusion and interior particle reaction, expressed on an external surface area basis. The overall rate therefore uses a combination of an Arrhenius based kinetic rate, as well as a diffusion rate of the reactant species through the film to the surface of the char particle.

The gas phase and coal particle reaction stoichiometries that were used in the Alstom BSF cases are shown in Table 5-3. The gas-phase reaction constants are the same for all of the (Alstom) matrix runs.

Table 5-3. Reaction Stoichiometries Used in Alstom Runs

Reaction	Reaction Stoichiometry
1. Decomposition	Vol --> 1 C-gas + 1.167 H_2 + 0.403 O_2 + 0.012 SO_2 + 0.013 N_2
2. CO Oxidation	CO + 1/2 O_2 --> CO_2
3. H_2 Oxidation	H_2 + 1/2 O_2 --> H_2O
4. C-gas Oxidation	C-gas + 1/2 O_2 --> CO
5. Char Oxidation	C <s> + 1/2 O_2 --> 2 CO
Note on Reaction 5:	Murphy and Shaddix rate expression for Eastern bituminous coal (cited in Ref. 2)

In the University of Utah/ICSE runs, the presumed PDF model was used in which a single mixture fraction represented the coal off-gas, and a second mixture fraction was used to represent an oxidant mass fraction. When one mixture fraction represents the fuel, then two other gas streams (e.g., an oxidant and a "secondary" or "recycle" stream), each with a distinct composition, may be characterized with a second mixture fraction (called e.g., a secondary mixture fraction or a secondary partial mixture fraction in

FLUENT®). If necessary, an "inert" stream may also be defined. The inert stream may have its own species composition, but, while it participates thermally with the other species, it does not participate chemically. For the LES runs, the University of Utah elected to use equilibrium chemistry as the basis for the reactions.

5.3 Particle Combustion Model Description

The LES computations utilize the Direct Quadrature Method of Moments (DQMOM; see e.g., Ref. 2) for the particle model. The DQMOM approach solves the dispersed phase in an Eulerian manner, where a multivariate population balance equation (PBE) is tracked through its moments by integrating the internal coordinates. The PBE is based upon a transport equation for the particle number density function, which describes the number of particles per volume as a function of the spatial location and other independent variables (e.g., particle diameter, particle velocities, etc.). The independent variables are dependent upon space and time and constitute the internal coordinates for the integration of the PBE.

The coal particle combustion model in FLUENT® utilizes the Discrete Phase Model (DPM), which is a stochastic Lagrangian particle model. The model provides a means by which mass, momentum and energy, between the Lagrangian-based particle phase and the Eulerian-based gas phase, are coupled. In the present cases, surface injection was used for the particles at 3 elevations of 4 corners each (for a total of 12 injection inlets). Particles, injected at the burner inlets, sequentially pass through a series of discrete "laws" or stages that include heating, water vaporization, devolatilization, char combustion, and finally, inert (ash) heating/cooling. As the particles heat up, coal moisture is evaporated according to the moisture volume fraction specified in the "wet-combustion" model.

Following the moisture release, the particle continues to heat up until it reaches the devolatilization threshold or temperature. The University of Utah opted to use the Yamamoto, et al. single reaction rate model (Ref. 10), which is an empirical, computationally inexpensive rendition of the Distributed Activation Energy Model (DAEM). Since FLUENT® does not contain the Yamamoto, et al. model as a default expression, an effort was made to approximate the expression with a single reaction rate model in the format that FLUENT® allows. A time-temperature history was extracted from a wire-mesh run (20,000 °C/s to a temperature of 1350 °C) from the PC Coal Lab® software for the Schwarze Pumpe lignite coal. The devolatilization models were integrated over this time-temperature history and compared. Fortuitously, the integrations showed that the single reaction rate model used in FLUENT®, with the constants already being used in the Schwarze Pumpe case, was a reasonably close facsimile to the Yamamoto, et al. model, and that the single reaction rate expression could continue to be applied in the FLUENT® cases without adjustment.

In FLUENT®, the char burning process, based on the so-called multi-surface model, is limited to a constant-diameter, reducing-density model. The char oxidation rate was aligned with the Murphy and Shaddix rate (for an Eastern bituminous coal) selected by the University of Utah, as indicated in Table 5-3. Following the University of Utah practice for these runs, char gasification was not activated. It should be noted that the University of Utah used a single coal off-gas mixture fraction, so that the coal off-gas composition was uniform throughout the particle consumption process (i.e., the char had the same composition as the volatiles).

In the FLUENT® runs, 20 discrete particle sizes were used to represent the pulverized coal particle size distribution (PSD), based on the Rosin-Rammler (logarithmic) distribution option; the logarithmic

diameter characterization resolves the smaller particles and enhances accuracy because of the sensitivity of the particle radiation to the ensemble surface area of the smaller particles. The ICSE group selected 3 particle sizes to represent the PSD for use with the DQMOM model. A summary tabulation of the PSD parameters is provided in Table 5-4.

Table 5-4. PSD Parameters

Alstom PSD Parameters	
FLUENT® Rosin-Rammler (Logarithmic) Parameters	Schwarze Pumpe Lignite
Minimum Particle Size (microns)	3
Maximum Particle Size (microns)	200
Mean Particle Size (microns)	73
Spread Parameter	0.9
Number of Diameters	20

University of Utah PSD Parameters	
Original (Arbitrary) Distribution:	
Particle Size (microns)	Mass Fraction (%)
30	11.2
60	58.6
90	30.2
Sum:	100.0
Present Distribution Based on Experimental Data:	
Particle Size (microns)	Mass Fraction (%)
30	56.0
60	15.0
90	29.0
Sum:	100.0
Note 1: The original (arbitrary) distribution was used for the first set of ICSE runs in the run matrix; ICSE is presently re-running their cases with the actual experimental distribution.	

All of the Alstom cases were run with the experimental PSD. As previously mentioned, ICSE ran their initial set of cases with an arbitrary PSD. When they subsequently received the actual experimental distribution, they changed the particle mass fractions, used for the three (3) particle sizes in the LES runs, to reflect the experimental data. As seen in the above table, the actual PSD is somewhat bimodal, with a much larger fraction of small particles than specified in the arbitrary PSD. As verbally reported by ICSE, all of the ICSE results presented in this report were generated with the arbitrary PSD. ICSE is now in the process of re-running their cases with the experimental PSD; however, those cases have not yet been completed at the time of this writing.

Particle-radiation coupling was activated. Alstom followed the University of Utah specification by assigning a particle emissivity of 0.8 and neglecting particle scattering effects.

In the present set of Alstom runs, five (5) stochastic "tries" were specified, which ultimately produced approximately 67,200 total particle injections. Turbulent particle dispersion utilized both the "discrete random walk" model and the "random eddy lifetime" option. As an aside, in the equivalent air-fired case (Test 109), more of the larger particles appeared to congregate at the bottom of the hopper than occurred in the oxy-fired case (Test 134). It was found necessary to turn the bottom of the hopper into a trap in the air-fired case in order to prevent the apparent buildup of high particle concentrations at various points in the hopper region (which tends to produce some unnatural, locally high temperatures in those same regions).

5.4 Boundary Conditions

The University of Utah utilized the presumed PDF model, with one mixture fraction representing the coal off-gas, and a second mixture fraction representing an oxidizer stream. The coal off-gas mixture fraction is identically zero at the inlet boundaries. The calculation of the value of the second mixture fraction at each inlet boundary is dependent upon the partitioning of the gas species into two separate, artificial gas streams, with the constraint that all of the inlet feeds consist only of some combination of those artificial gas streams. The composition of a particular stream must be uniform among all of the gas feeds. For example, a case may have a large number of inlets or feeds, but the gases entering those inlets must be defined or constructed on the basis of the two artificially contrived streams. The use of inerts as a third stream provides an extra degree of flexibility and is beneficial in those circumstances where it is difficult to define the two gas streams without a redistribution of the gas species among the inlets. The inerts may be any particular combination of gas species; they participate in the thermal balances, but they are also treated as being chemically inert (i.e., they do not participate in the equilibrium chemistry).

The University of Utah has partitioned the gas species into three (3) separate streams, denoted Stream-1, Stream-2, and Stream-3 (or simply S1, S2, and S3). Stream-1 is designated as a pure oxygen stream and Stream-3 is designated as an inert stream containing only H_2O. Stream-2 contains the remaining mixture of gases (defined arbitrarily as the primary transport gas plus the coal moisture). The three streams, their respective compositions, and their distribution by flow rate among the various feeds are provided in Table 5-5. (The corresponding boundary condition or inlet values for the oxidant mixture fraction are provided subsequently as part of Table 5-6.)

Table 5-5. Mixture Fraction and Inert Boundary Condition Specification for ICSE Case

	Stream-1 [S1]	**Stream-2 [S2]**	**Stream-3 [S3] (Inerts = H2O)**
Species	Mass Frac (%)	Mass Frac (%)	Mass Frac (%)
O2	100	13.04476	0
CO2	0	70.84642	0
H2O	0	11.26106	100
SO2	0	0.04154	0
N2	0	4.80622	0
Total	100	100.00000	100
WB Primary Information			
Mass Flow (lbm/hr)	0.0	9,558.4	0.0
LOFA Information			
Mass Flow (lbm/hr)	330.9	2,476.1	96.7
UOFA Information			
Mass Flow (lbm/hr)	321.2	2,403.7	93.9
WB Secondary Information			
Mass Flow (lbm/hr)	4,099.3	14,504.4	566.3

For the Alstom runs, the inlet boundary conditions were prescribed through a mass-flow rate boundary specification. The inlet flow conditions for both the air- and oxy-combustion simulation cases (Tests 109 and 134, respectively) are shown in Table 5-6. This table includes the flow rates, temperatures, and species mass fractions (expressed as a percent) for the primary air (PA), windbox combustion air, lower overfire air (LOFA), and upper overfire air (UOFA) sections, as well as the coal feed rate. The stream compositions for the oxy cases are different from those of the air cases due to the flue gas recycle strategy used in oxy combustion.

Table 5-6. Inlet Gas and Coal Flow Rates and Temperature for Baseline Case

Case No.	1-Baseline		1-Baseline		
Firing Mode	**Air-Fired**		**Oxy-Fired**		
Coal	Schwarze Pumpe Lignite				
Test No.	**109**		**134**		
Source	**Alstom**		**Alstom**	**University of Utah / ICSE**	**Difference**
WB Primary Information					
Temperature [F]	106.90		137.53	136.80	-0.74
O2 [mass, %]	23.0623		14.0264	13.0448	-0.98
CO2 [mass, %]	0.0000		76.1882	70.8464	-5.34
H2O [mass, %]	0.9851		4.5726	11.2611	6.69
SO2 [mass, %]	0.0000		0.0448	0.0415	0.00
N2 [mass, %]	75.9526		5.1681	4.8062	-0.36
Mass Flow (lbm/hr)	7,554.8		8,888.4	9,558.4	670.02
G = S1/(S1+S2+S3)	-----		-----	0	-----
I = S3/(S1+S2+S3)	-----		-----	0	-----

LOFA Information					
Temperature [F]	296.75		329.58	328.50	-1.089
O2 [mass, %]	23.0623		20.8989	22.5196	1.621
CO2 [mass, %]	0.0000		63.2649	60.4141	-2.851
H2O [mass, %]	0.9851		12.0014	12.9324	0.931
SO2 [mass, %]	0.0000		0.0331	0.0354	0.002
N2 [mass, %]	75.9526		3.8018	4.0985	0.297
Mass Flow (lbm/hr)	4,596.2		3,128.8	2,861.2	-267.52
G = S1/(S1+S2+S3)	-----		-----	0.113957	-----
I = S3/(S1+S2+S3)	-----		-----	0.033295	-----

UOFA Information					
Temperature [F]	290.65		320.29	328.50	8.208
O2 [mass, %]	23.0623		20.8536	22.5196	1.666
CO2 [mass, %]	0.0000		63.3443	60.4141	-2.930
H2O [mass, %]	0.9851		11.9754	12.9324	0.957
SO2 [mass, %]	0.0000		0.0331	0.0354	0.002
N2 [mass, %]	75.9526		3.7936	4.0985	0.305
Mass Flow (lbm/hr)	4,628.9		3,043.8	2,861.2	-182.53
G = S1/(S1+S2+S3)	-----		-----	0.113957	-----
I = S3/(S1+S2+S3)	-----		-----	0.033295	-----

WB Secondary Information					
Temperature [F]	314.80		344.44	343.63	-0.810
O2 [mass, %]	23.0617		30.7755	31.2536	0.478
CO2 [mass, %]	0.0000		54.3216	53.6039	-0.718
H2O [mass, %]	0.9862		11.2967	11.4746	0.178
SO2 [mass, %]	0.0000		0.0281	0.0314	0.003
N2 [mass, %]	75.9521		3.5781	3.6365	0.058
Mass Flow (lbm/hr)	21,429.7		19,469.5	19,170.0	-299.51
G = S1/(S1+S2+S3)	-----		-----	0.213837	-----
I = S3/(S1+S2+S3)	-----		-----	0.029542	-----

Total Gas Flow Rate (lbm/hr)	38,209.6		34,530.4	34,450.9	-79.547
Coal Flow Rate (lbm/hr)	4,862.0		4,964.5	4,964.4	-0.065
Total Purge CO2 Included With Secondary (lbm/hr)	0.0		750.00	0.0	-----
Total Coal Moisture Added to Primary Stream (lbm/hr)	0.0		0.0	679.79	-----
Note 1:	G = Secondary mixture fraction based on oxidant				
Note 2:	I = Inert mass fraction				

The boundary condition values for the oxy-fired case used by ICSE are also shown in a side-by-side comparison with those used by Alstom. The ICSE extracted their boundary conditions from the

transmittals of the board data (sent to them by Alstom). Alstom subsequently garnered its boundary conditions from the same source, but the data was carefully scrutinized and checked from various vantage points and then rigorously balanced, based on selected tracers and an in-depth knowledge of the instrumentation and probes. The recommended boundary conditions were collated in an EXCEL spreadsheet, which was subsequently supplied to the University of Utah. Unfortunately, the spreadsheet was supplied to the University of Utah after ICSE had already begun to move through the baseline calibration and run matrix, but the two sets of boundary conditions are fairly close. The ICSE primary flow rate is higher than the corresponding Alstom feed principally because of the addition of coal moisture as a gas to the primary feed flow rate. In like manner, Alstom distributed the purge CO_2 for the flame scanner, cameras, and other equipment to the secondary windbox and OFA feeds, while the University of Utah did not account for the purge CO_2 streams.

Table 5-7 shows a mapping of the sixteen elevations of windbox air/coal ports plus the two levels each of the lower and upper overfire air ports. The port designations / names are also shown, as well as the port service status (i.e., in or out of service); "X" marks the ports with dampers in closed position. The flow rates through the air ports are proportional to the nozzle open area. A small amount of leakage air is allowed to pass through the small clearance (taken to be 0.5 square inches) of the closed ports. An EXCEL® spreadsheet is used to set up the FLUENT® inlet boundary conditions for all gas/fuel inlet ports.

Table 5-7. Windbox and Overfire Inlet Air/Gas Port Designations

	Schwarze Pumpe Lignite	
	Air Fired	Oxy Fired
Test No.	109	134
Port 20	UOFA	UOFA
Port 19	UOFA	UOFA
Port 18	LOFA	LOFA
Port 17	LOFA	LOFA
Port 16	X	X
Port 15	CCOFA	CCOFA
Port 14	X	X
Port 13	Top End	Top End
Port 12	**Coal**	**Coal**
Port 11	CFS	CFS
Port 10	Straight	X
Port 9	CFS	CFS
Port 8	**Coal**	**Coal**
Port 7	CFS	CFS
Port 6	Straight	X
Port 5	CFS	CFS
Port 4	**Coal**	**Coal**
Port 3	Bottom End	Bottom End
Port 2	Under Fire	Under Fire
Port 1	X	X

There are four (4) different wall-insulation zones as a function of vertical height in the BSF, with the upper furnace wall being un-insulated, bare steel, as shown in Figure 5-2. To model the effect of the insulation in the Alstom runs, a specified temperature boundary condition was used in conjunction with the FLUENT® code's thin-wall thermal resistance formulation. The specified temperature is on the far side of a thin wall, away from adjacent fluid zone and is fixed at 375 K for all simulations. The thermal resistance is the ratio of the parameters $\Delta x/kw$, where Δx is the thickness of the resistance material(s), and kw is the wall thermal conductivity. It was found necessary to adjust the thermal conductivity kw of each zone (for a given inner surface temperature) to match the measured temperature data taken from Planes 141, 180, and 273 shown in Figure 5-2. This calibration procedure is justified due to the lack of information about the degree and character of the fouling and slagging deposits on the wall surfaces in the different zones.

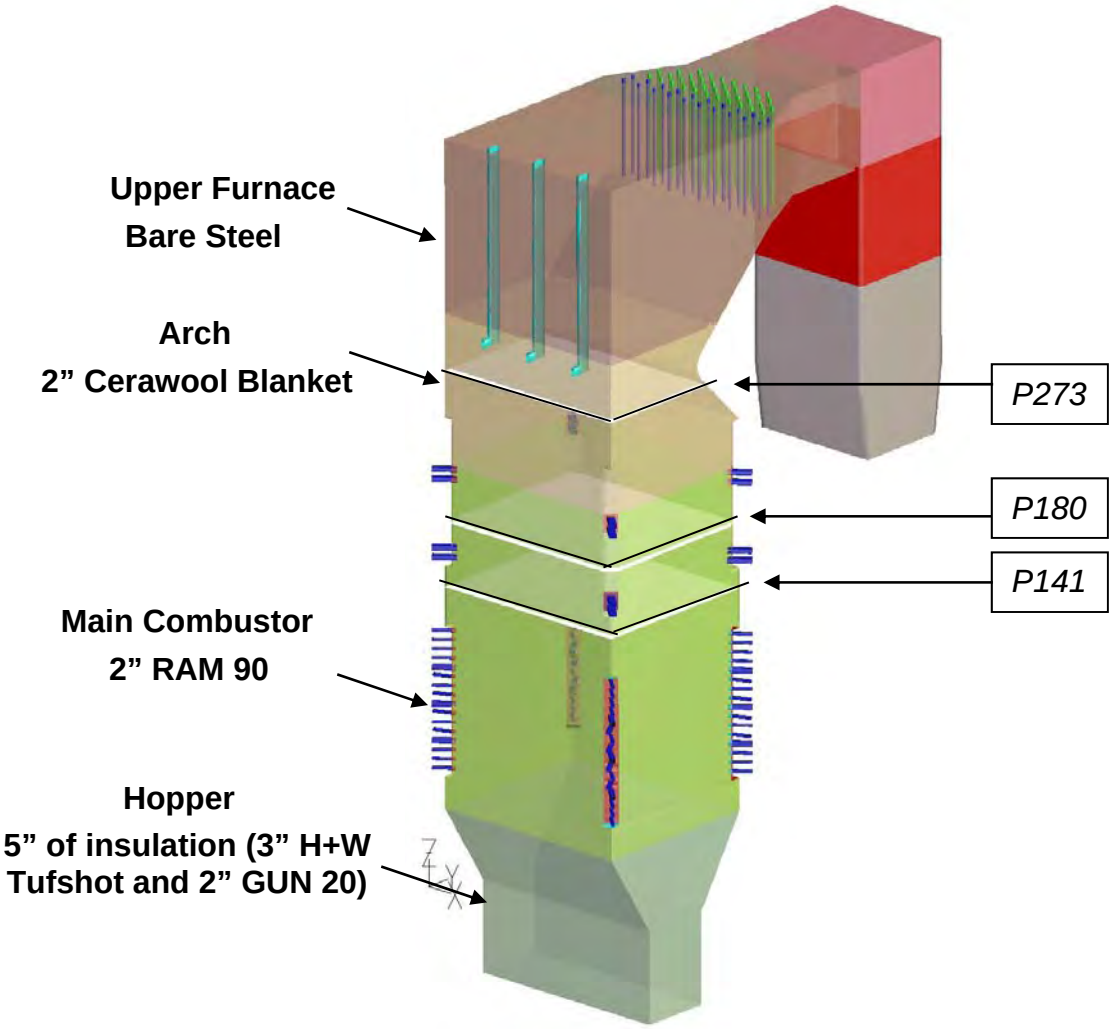

Figure 5-2. BSF Wall Insulations and Test Planes

When viewing or comparing lateral heat flux profiles in conjunction with locally sparse point measurements of the heat flux, it should be recognized that the fireball rotation in the BSF is in a counter-clockwise (from a view looking down on the top of the furnace), and the CFD predictions have presumed a uniform lateral deposit thickness all the way (circumferentially) around the furnace.

Table 5-8 lists the k_w, Δx, and inner surface temperature values used for all of the cases simulated. The thermal conductivity listed in the table for the main furnace pertains to the baseline case only; for the V&UQ study and run matrix, the main furnace thermal conductivity was varied. A few surfaces, such as the nozzles themselves and a portion of the corner plate through which the nozzles protrude, were prescribed with adiabatic thermal boundary conditions.

Table 5-8. Wall Thermal Boundary Conditions

Location	Thermal Conductivity k_w [W/m-°C (Btu/hr-ft-°F)]	Wall Material	Wall Thickness [m (in)]
Upper Furnace	5.1919 (3.0)	Bare Steel	0.018 (0.709)
Wing Walls	5.1919 (3.0)	Bare Steel	0.018 (0.709)
Tube Banks	5.1919 (3.0)	Bare Steel	0.018 (0.709)
Arch	0.5192 (0.3)	Cerawool Blanket	0.0529 (2.083)
Main Furnace	3.4613 (2.0)	RAM 90	0.0645 (2.54)
Hopper	1.3845 (0.8)	H+W Tufshot and GUN 20	0.1325 (5.217)
Panels [Note 3]	0.5192 (0.3)	Cerawool Blanket	0.1545 (6.083)
Note 1:	Specified temperature = 375 K and wall emissivity = 0.8 for all walls		
Note 2:	The main furnace thermal conductivity is for the baseline case only		
Note 3:	Insulated roof explosion panels (8 in number) above the main furnace		

The wall thermal boundary conditions should correspond to the values determined by the ICSE group from their calibration procedure with the LES code. In that calibration study, the ICSE community performed an initial calibration of the wall thermal boundary conditions with the LES model in order to achieve a reasonable match with the planar temperature measurements (e.g., Planes 141, 180, and 273). In the interest of congruity between the two codes, Alstom elected to utilize those same wall thermal boundary conditions for its baseline run, even though the calibration was performed with a different code and combustion submodel than those utilized by Alstom, leading perhaps to differences in heat release rates as a function of elevation.

Other tube banks, such as the economizer tube bank in the backpass, were modeled in FLUENT as porous media, with a characteristic inertial resistance in each of the coordinate directions, and a specified volumetric energy extraction.

5.5 Convergence and Solution Considerations

The solution algorithm used in FLUENT® for the run matrix was based upon the SIMPLE pressure-correction algorithm with first-order upwind differencing. The radiation submodel was the Discrete Ordinates radiation model (solved every 10 gas-phase iterations), with the control angle parameters (theta divisions and phi divisions) set to a value of 2. A proprietary UDF was used to extract the local gas-phase absorption coefficient, rather than the default weighted-sum-of-gray-gas model in FLUENT®. Such a UDF was deemed to be more reliable for systems which have high CO_2 or H_2O partial pressure than the default model. The UDF was compiled prior to run time.

The solution process for steady-state runs within FLUENT® is performed in a segregated fashion, where the DPM sources are updated by an injection sequence, and then the Eulerian transport equations are sequentially updated for 10 gas-phase iterations (in the present case), before a new sequence of injections is repeated. The cases converged well with a DPM under-relaxation factor of 0.2 on local platforms and clusters. Once the baseline case was converged, additional perturbations to the "restart" case (following the specifications in the run matrix) could be completed overnight on a 4-processor machine.

For the LES runs, a significant effort (see Ref. 11) was made by ICSE to improve the computational efficiency of the ARCHES code. A number of CPU-intensive tasks within the DQMOM, pressure-solver, char oxidation, and wall submodels were simplified or optimized in order to accelerate the convergence

process. For the large parallel cases, the final simulation efficiency was improved by a factor of two. Parallel scaling tests were also performed on simplified BSF computational domains in order to quantitatively assess how the CPU time per time step decreases as the number of processors increased.

Each of the ICSE cases in the run matrix was constructed with 2 cm resolution and has 17.414 million cells (see Ref. 8). Based on a preliminary investigation of the computing efficiency and associated wall clock time for the baseline case on a supercomputer cluster, about $(20.4)^3$ cells/processor was selected for the simulation runs. Each computation was run on 2,008 processors (approximately 126 nodes with each node containing 16 processors). One large case was constructed with a resolution of 1 cm, resulting in 137.216 million cells. This latter case required 9,920 processors (or 620 nodes) to run in parallel. After the code optimization analyses and several necessary initial tests, the final version of the baseline case was started in August of 2013 on the ORNL Titan machine. The typical time step in the LES simulations was about 3.0×10^{-5} seconds. It took 2,930,850 CPU hours to acquire a physical time of 22 seconds of simulation results. Accordingly, the estimated simulation cost is about 2.5~3 million hours for each of the V&UQ cases (to achieve the requisite 22 seconds of real time). The physical time of about 22 seconds is about 3 times longer than the boiler residence time. The initial testing showed that the evacuation time of the boiler was about 8 seconds (depending on the wall boundary conditions and the initial conditions). After each case was run, the results were time-averaged over the last 5 seconds of the simulation history, and then further post-processed for use in the V&UQ studies.

5.6 Validation Framework

In the evaluation of a computer model, the question is not whether a model is absolutely (quantitatively) accurate or whether it is only qualitatively correct (i.e., yes or no type questions), the real question (see Ref. 12) is:

> "To what degree is the model an effective surrogate for reality?" or, alternatively: "Does the model provide predictions accurate enough for intended use?"

"Data collaboration" is a formalized framework or approach, advanced by Frenklach and his associates (see e.g., Ref. 13), to assess, from a statistical viewpoint, the degree to which the data and the model are in agreement. The data collaboration approach accomplishes this assessment by quantifying the model uncertainty and by performing a consistency analysis on both the experimental data and the model predictions. In addition to the above, the analysis can be used to address the following (related and coupled) questions:

- "Do the experimental observations validate the theory (or model) to within acceptable limits? If the data and theory do not agree, where, within the model components or experimental variables, is the source of disagreement?"
- "Using the theory, do the experimental observations validate each other? Are the data mutually consistent? How does one recognize and pinpoint the data outliers?"
- "What is the relative prediction accuracy of one model (or code) versus another?"

The intent of the framework is to quantify the uncertainty and make a statement as to where the disagreement originates, but not necessarily to fix the problem. The V&UQ process integrates the simulations and experiments, and promotes predictions with uncertainty bounds, thus reducing risk.

The underlying philosophy of the proposed validation or V&UQ framework (Ref. 12) is based on the interpretation that there is a specified chance that the true value of any process lies within a specified range about the predicted value (i.e., within specified tolerance bounds). Tolerance bounds or limits are useful because:

- Models rarely give highly accurate predictions over the entire range of inputs of possible interest.
- The degree of accuracy needed can vary from one application of the model to another.
- The tolerance bounds account for model bias, the principal symptom of model inadequacy.

A rough validation framework or V&UQ process (Ref. 12 and 13), that encompasses the concept of data collaboration, consists of the following steps:

- Step 1. Create an Input/Uncertainty (I/U) Map.
  The analysts (and experimentalists), utilizing their "prior" knowledge and subject-matter expertise, specify the model inputs and parameters with their associated uncertainties or appropriate ranges. For example, an initial I/U map may be conceived as a spreadsheet tabulation with columns for (a) the parameter, (b) a reasonable range or uncertainty bounds for each parameter, and (c) a weighting or ranking factor based on prior knowledge. Other columns may provide parameter value preferences and commentary. Initial prioritization may be admittedly somewhat subjective. The number of model inputs listed on the I/U map may be arbitrarily large, but the intent of the investigators should be to study the input tabulation and assign relative priorities or ranking factors to those inputs that they believe have the greatest impact on the observables (or targets) identified for analysis. The top candidates in the list are selected for further evaluation and screening.

  The I/U map may be divided into three (3) different types of parameters:
  1. Verification or numerical parameters – e.g., mesh density, mesh topology, differencing schemes, solver types, etc. that impact the computational numerics.
  2. Model parameters – e.g., devolatilization submodel parameters, char consumption submodel parameters, turbulence model constants, radiation submodel constants, particle dispersion parameters, etc.
  3. Scenario parameters – e.g., inlet gas and fuel flow rates, wall thermal boundary conditions, leakages, flow maldistributions, etc. that constitute the boundary conditions for the computational problem. Oftentimes, scenario parameters may have a more dominant impact on the observables than either the model or numerical parameters.

  Where possible, an effort is made to assign an uncertainty range or a reasonable interval range with an upper or lower bounds to each parameter. Many of the computational parameters or observables may also correspond to an analogous measured quantity, such as an inlet flow rate. Each of the measured parameters will exhibit a specific experimental uncertainty associated with the operating conditions and the type of experimental apparatus. Random (epistemic) errors dominate in normal environments, and may be characterized through the statistical analysis of replicate data points. Bias (or systemic) errors may dominate in abnormal environments, often producing a significant one-sided uncertainty, that can only be captured with careful experimental verification. Experimental parameter uncertainty is the fourth type of uncertainty considered in this report, in addition to the simulation (i.e., verification, model, and scenario parameter) uncertainties already mentioned.

Where selection of the most sensitive parameters is ambiguous, or where the appropriate upper and lower bounds are unknown, additional screening of the candidate parameters may be beneficial. The screening may be performed with a few preliminary computational runs to gauge the parametric sensitivity of selected parameters. For example, the FLUENT® code could be judiciously exercised in order to determine the (input or inlet) variable values that bracket the targeted observables (or target parameters) within a reasonable interval range. In addition, these screening or scoping trials help to remove some of the uncertainty associated with the numerical (verification) parameters, by allowing the analyst to determine the optimal grid size, the best convergence parameters, etc. before the execution of the run matrix is initiated.

- Step 2. Determine Evaluation Criteria and Intended Use.
  From the prior knowledge and screening runs applied to the I/U maps parameters, the evaluation criteria are finalized. Consideration is given to the context and application in which the model is used, the feasibility of acquiring adequate computer runs and field data, given cost and resources, and the methodology used to complete the evaluation. The active parameters are selected with their upper and lower bounds, and the observables (or targets) are selected with their upper and lower bounds. In turn, the data collection and analyses will be critically affected by the range established for the parameter bounds. It may be prudent to start with a very low number (or dimensionality) of the active parameters initially (e.g., 1 or 2 parameters). After the consistency analysis is performed, and meaningful insight is gained from the analysis, then the I/U map can be revisited and updated, and the dimensionality of the active parameters list can be progressively increased with each successive round of the validation framework.

- Step 3. Develop the Design of Experiments and Complete Data Collection.
  Both computational runs and field experiments are part of the validation process. If the experimental data is not already available, then the experimental work will need to be designed in conjunction with the computer runs. The computational runs are a function of the evaluation criteria and are planned through any convenient design of experiments (DoE) methodology (e.g., factorial design, Latin Hypercube sampling, etc.). The application of the DoE leads to the construction of the run matrix; the runs are executed and the output information is post-processed and packaged in a form that can be utilized in the subsequent steps.

- Step 4. Construct Surrogate Model as Approximation to Computer Model Output.
  The data collaboration and consistency analysis requires frequent execution of the model. Since the model may be very CPU-intensive, it is more efficient to make a limited number of computational runs and then create a (fast) surrogate model or reduced-order model (ROM), based on the output from the computational runs. The surrogate model can be as simple as a polynomial curve-fit of the selected output. The surrogate model is used only for interpolation and sampling during the consistency analysis. The surrogate model, devised for each observable as a function of the active parameter(s), collectively constitutes a “response surface.”

- Step 5. Perform Consistency Analysis on Computer Output and Field Data.
  The uncertainty in the model inputs will propagate to uncertainty in the model output, and ascertaining which inputs most strongly affect outputs is required to refine the I/U map. Bayesian or related probabilistic methods can play an important role in determining this sensitivity. A more deterministic methodology is taken in this study, in the form of the so-called “data collaboration”

and "consistency analysis" approach advocated by Frenklach and his associates (Ref. 13). (The data collaboration approach has some similarities with facets of the Bayesian approach, but is also quite different (see Ref. 14)). The data collaboration approach will be discussed in the next sub-section. (A useful ICSE "tutorial" on the application of this approach, in comparing devolatilization models with high-temperature volatile yield data, is provided in Ref. 6.) If the data is not consistent with the predictions, then this consequence elicits a discovery process where new parameters are proposed and the steps are repeated.

- Step 6. Feed Back Information Gain to Validation Framework or Use in Predictions.
  The consistency analysis can potentially provide an analysis of the accuracy of the predictions (given the data), update the uncertainties for the active parameters, and gauge the mutual consistency of the experimental data. Such information can then be fed back to the validation framework so that the I/U map can be updated, and another round of the six-step procedure can be re-initiated. The feedback can be used to point to defects in the model, so that plans can be made to research solutions for those defects, or the feedback can be used to point to outlier data or to data with significant measurement bias, so that corrective action can be taken. Alternatively, if the model is validated to within acceptable tolerance limits, then the model can be applied to applications where field data are lacking.

5.7 Data Collaboration and Consistency Analysis

Details concerning the data collaboration approach and the consistency analysis are provided in Ref. 13. Uncertainty in the model or in the simulation has been linked to the error in the verification, model, and scenario parameters. Uncertainty in the measurements is linked to the experimental error in the validation data. Since the quantification of simulation error is achieved by comparing the simulation output to experimental observations, and since the experimental measurements themselves are inexact, the simulation accuracy cannot be known to any better degree of accuracy than the measurements themselves (Ref. 6). The data collaboration approach focuses on transferring the uncertainties of the experimental data into the model directly. Doing so allows one to harvest substantially more of the information content of the data and to determine more realistic bounds on model predictions (Ref. 13).

The approach is anchored in the concept of a "dataset," which is a construct that combines the experimental data and the simulation results, in a manner that lends itself to a structured analysis of the consistency between them. The numerical analysis allows one to explore more closely the true feasible or overlap region between the data and the model and to develop a numerical measure of the dataset consistency. The following descriptions of the equation sets are extracted piecemeal from Ref. 13 in an almost verbatim fashion.

In the data collaboration approach, E denotes a physical experiment and Y_e is a property of interest that is measured in the experiment. The value of Y_e is designated as (the estimate) y_e, and the experimentally measured value is d_e. The deviation of the measured value (d_e) from y_e has a lower and upper bounds, namely $l_e \le y_e - d_e \le u_e$.

A "dataset unit" (d_e, u_e, l_e, M_e) is associated with experiment E and consists of the measured value, the reported uncertainty in the measurement (upper and lower bound), and a mathematical model, respectively. A dataset is a collection of dataset units $\{(d_e, u_e, l_e, M_e)\}$. A dataset unit is denoted as U_e,

the dataset as *D*, and the set of indices *e* as $\mathcal{E}$; i.e., $U_e = (d_e, u_e, l_e, M_e)$, and $D = \{U_e\}_{e\in\mathcal{E}}$. The model M_e is defined as the functional relation between the model parameters and the prediction for Y_e.

It is presumed that the same model is common to all of the dataset units, and that the model is expected to predict Y_e when exercised at the conditions of experiment *E*. In other words, the mathematical structure of the model is presumed to be sufficient, in principle (with the "right" choice of parameter values), to predict all experimental observations included in the dataset. Any inadequacy associated with the model rests solely in the parameter values.

For an individual experiment *E*, only a small subset of all of the possible model parameters has a measureable influence on the property Y_e. The parameters within this subset are referred to as the "active variables" for experiment *E*. (From a practical viewpoint, the active variables may be considered to be those extracted from the I/U map and screening analysis as the most sensitive or impactful parameters on the observables.) The individual active variable is designated as X_j and the expression $x_j \in \boldsymbol{R}$ will be used to refer to a specific value of X_j. The total number of dataset active variables is denoted as "*n*" and vector $\boldsymbol{x} \in \boldsymbol{R}^n$ represents the dataset active variable values. In this context, the model M_e of the dataset unit U_e represents the relationship between values of the active variables of experiment *E* and model predictions for Y_e. In other words, $M_e(x_e)$ replaces y_e, yielding $l_e \le M_e(x_e) - d_e \le u_e$.

It is assumed that prior information is available on the possible values of the dataset active variables X_j that permits the analyst to assign an uncertainty to each variable. This prior information can be expressed as the confinement of possible values of the active variables to an *n*-dimensional "hypercube" $H = \{\boldsymbol{x} \in \boldsymbol{R}^n: \alpha_j \le x_j \le \beta_j\}$, where α_j and β_j are the lower and upper bounds on x_j for $j = 1,2,\ldots, n$. Each edge of the hypercube *H* represents the presumed interval of "physically allowed" values of the corresponding active variable, either the estimated uncertainty or a range containing the bounds.

Some parameter values drawn from *H* may result in model predictions that lie outside the experimentally determined ranges (l_e and u_e). In other words, not every $\boldsymbol{x} \in H$ predicts all experimental observations of the dataset within their specified uncertainties. The collection of parameter values that are both contained in the hypercube and satisfy $l_e \le M_e(x_e) - d_e \le u_e$ for every $e \in \mathcal{E}$ form the "feasible region" F_D. A point $\boldsymbol{x}$ that is not contained in F_D has, in essence, been eliminated from consideration as a possible value for the dataset active variables by either the prior information, through the α and β bounds of *H*, or by the experimental observations of the dataset, through the intervals $(d_e + l_e, d_e + u_e)$. It is in this manner that experimental observations increase our knowledge of the model parameters: an experiment may eliminate portions of the hypercube *H* from consideration, thus decreasing the uncertainty in the values of the model parameters.

In Ref. 13, the problem was cast as a constrained optimization over the feasible region. The authors first identified active parameters via sensitivity analysis. They subsequently configured or arranged the computational experiments according to factorial design (a DoE methodology). From the output of those experiments, the authors developed quadratic approximations as surrogate models for each dataset unit model M_e, which collectively enabled them to build a quadratic response surface. With the response surface, the authors then applied a consistency analysis, which will be described in the following paragraphs.

Given a dataset, the intent is to determine whether the data it contains are mutually consistent, establishing whether a given model is in agreement with the available experimental observations, recognizing data

outliers, or identifying the source of disagreement between the model and experiment. A dataset D (together with its corresponding prior information) is said to be "inconsistent" if there is no single point $\boldsymbol{x}$ in the hypercube H that satisfies $l_e \le M_e(x_e) - d_e \le u_e$ for all e in $\mathcal{E}$. Otherwise the dataset is "consistent." In other words, the dataset is inconsistent if the feasible region is empty.

The dataset constraints are represented by four sets of inequalities:

- from the prior information on H:

$$\begin{cases} -x_j \le -\alpha_j \ (for\ j = 1,2,\dots,n) \\ x_j \le \beta_j \end{cases}$$

- and from the data set units:

$$\begin{cases} -M_e(x_e) + d_e \le -l_e \ (for\ each\ e\ in\ \mathcal{E}) \\ M_e(x_e) - d_e \le u_e \end{cases} \quad (1)$$

The dataset is inconsistent if no single $\boldsymbol{x}$ satisfies all of these constraints. The values of $\boldsymbol{\alpha}$, $\boldsymbol{\beta}$, $\boldsymbol{l}$, and $\boldsymbol{u}$ affect the consistency of a dataset. A consistent dataset may become inconsistent with a decrease in the intervals of the active variables (affecting $\boldsymbol{\alpha}$ and $\boldsymbol{\beta}$) and/or in the levels of experimental error (affecting $\boldsymbol{l}$ and $\boldsymbol{u}$). The values of $\boldsymbol{\alpha}$, $\boldsymbol{\beta}$, $\boldsymbol{l}$, and $\boldsymbol{u}$ are not very well known and may be considered to be tentative. For example, by varying $\boldsymbol{l}$ and $\boldsymbol{u}$, questions can be answered such as, "at what level of the experimental error does the dataset become inconsistent?"

The dataset is defined to be consistent if there is at least one $\boldsymbol{x} \in H$, such that for each e, $M_e(x_e)$ is contained in the interval $[l_e + d_e, u_e + d_e]$. To determine if a dataset is consistent and quantify the degree of consistency, the analyst computes the smallest such intervals that contain $M_e(x_e)$ for some $\boldsymbol{x} \in H$. This is accomplished by introducing flexibility into the $\boldsymbol{l}$- and $\boldsymbol{u}$-constraints by adding to each l_e and subtracting from each u_e a "slack variable" γ. Let C_D denote the largest γ for which some value $\boldsymbol{x}$ satisfies both the $\boldsymbol{\alpha}$- and $\boldsymbol{\beta}$-constraints and the flexible $\boldsymbol{l}$- and $\boldsymbol{u}$-constraints:

$$C_D = maximum\ value\ of\ \gamma\ subject\ to\ the\ constraints:$$

$$\begin{cases} -x_j \le -\alpha_j \ (for\ j = 1,2,\dots,n) \\ x_j \le \beta_j \\ -M_e(x_e) + d_e \le -l_e - \gamma \ (for\ each\ e\ in\ \mathcal{E}) \\ M_e(x_e) - d_e \le u_e - \gamma \end{cases} \quad (2)$$

Defined in this way, C_D values greater than zero imply that the $\boldsymbol{\alpha}$-, $\boldsymbol{\beta}$-, $\boldsymbol{l}$-, and $\boldsymbol{u}$-constraints introduced in Eqn. (1) are satisfied, so the dataset is consistent. The magnitude of C_D provides a measure of the relative consistency (or inconsistency) of the dataset, with larger values of C_D indicating enhanced consistency. For this reason, C_D is referred to as the "consistency measure" of the dataset D.

ICSE has expressed Eqn. (2) in a more compact fashion:

$$C_D = maximum\ value\ of\ \gamma\ subject\ to\ the\ constraints:$$

$$\begin{cases} \beta_j \geq x_j \geq \alpha_j\ (for\ j = 1,2,\dots,n) \\ (1-\gamma)u_e \geq |M_e(x_e) - d_e| \geq l_e(1-\gamma)\ (for\ each\ e \in \mathcal{E}) \end{cases} \quad (3)$$

In the development of the dataset consistency measure, the uncertainty bounds ***l*** and ***u*** are viewed as fixed quantities (specified experimentally), and the question that is asked is whether the dataset is consistent at this uncertainty level. Alternatively, the analyst could consider the experimental uncertainties as variable quantities and compute the level at which the dataset switches from being consistent to inconsistent. This transition point is referred to as the "threshold uncertainty." Mathematically, for each experiment *E*, the threshold uncertainty is defined as $l_{thresh,e} = l_e + C_D$ and $u_{thres,e} = u_e - C_D$.

It should be noted that the threshold uncertainties, along with dataset consistency, may change with the variation in ***α*** and ***β***. One may repeat the uncertainty analysis with new values of ***α*** and ***β***, or perform a sensitivity analysis, to assess the possible effect.

Having developed a response surface using the surrogate model (e.g., quadratic surrogates), then a number of numerical methods may be used to solve the constrained optimization problem and find the consistency region. For the numerical method used to find the consistency space, ICSE appear to favor a Markov chain Monte Carlo (MCMC) sampling procedure, or simply a uniform random sampling approach for smaller problem sets (see Ref. 8).

6. Model Results for the V&UQ Analysis

Comparisons with temperature and species data are made primarily at three elevations, P141, P180 and P273 (shown in Figure 4-4), where most of the data were collected. The experimental temperature measurements were derived from water-cooled, suction pyrometers, and the species measurements were collected using water-cooled, heated, gas extraction sampling probes. It should be noted that the species concentrations measured in the experiments are on the dry molar basis.

Point measurements of the total (net) heat flux at the wall were derived from the use of "total heat flux" probes at various sampling locations and elevations around the furnace. Consistency analysis first requires that a calculated quantity be selected with which to compare with the experimental "total heat flux" measurement. Since the probe temperature is much lower than the wall temperature, the measured quantity is expected to be much closer to the incident radiation flux to the wall than to the net wall heat flux. Therefore, if most of the total (net) heat flux measurement in the radiant region is due to the net incident or incoming radiative heat flux (with minor contributions from the convective and conductive heat flux), a direct comparison between the predicted (surface) incident radiative flux and the measured total (net) heat flux should be acceptable. Consequently, the point measurements of total (net) heat flux were compared with computed (surface) incident radiant heat flux profiles across the span of each wall at those same elevations. However, any inherent error or bias introduced through the above interpretation or assertion should be considered as part of any discussion of the uncertainty in the heat flux prediction.

6.1 I/U Map and Parameter Prioritization

In this data collaboration effort, it was decided to focus initially on observables such as temperature and wall heat flux. Following the validation framework, a tabulation was made of the various numerical, modeling and scenario parameters that might impact the heat transfer. The tabulation was provided in the form of an I/U map (see Table 6-1), with estimated bounds or uncertainty intervals added for those parameters where prior knowledge was sufficient to provide such estimates. The parameters were ranked or prioritized based on their projected impact on temperature and wall heat flux.

Table 6-1. I/U Map

Parameter		Overall Priority	Range/Specification	Preference	Basis/Comments
Numerical / Verification Parameters					
Mesh Density /Number of Cells		11	200,000 - 8,000,000	3,000,000	
Fraction of cells in Windbox Zone			30%- 60%	50%	
Mesh topology - element types			Tetrahedral, Hexahedral	Hexahedral, with minimal Tets	
Mesh topology - transitions			Conformal, or Interfaces	Both - Geometry Dependent	
Mesh topology - cell expansion factors			1.02 - 1.10	lower	
Burner tip resolution # cells			min 4, max 100	10-20 cells	with protrusion into flow
Coal tip attachments/ deflectors			none to limited		
OFA Nozzle resolution/separation			Grouped or Separated	Separated	Mesh Size and Geometry Impacts
Differencing Scheme		12	1st, 2nd	2nd Order	First order OK for hex-meshes
Solver Type			Segregated, Coupled	Segregated	Memory Constraints
Convergence Parameters			Default values (except for URFs)	Default values (except for URFs)	
Model Parameters					
Gas Phase Reaction Mechanism - EBU/PDF/EDC...		7	EBU/PDF/EDC...	EBU	Presumed PDF with 2 coal mixture fractions has limitations
EBU - Number of Gas Phase Reactions			1 - 8	3 to 5	Extension of 2-step to include HC, H2, species
Volatile/Char Partitioning		8	ASTM Vol (1x) to 1.4	1.2 -1.3	Calculated from PC Coal Lab
Coal Moisture Evolution (wet coal)			Pre-Dried or Entering Furnace	Partially Pre-Dried + Wet Coal	Moisture Evolved in NBZ
Seconday / Primary Devolatilization Speciation			Elemental to Oxidized	Partially Oxidized	Ignition usually lags observed
Devolatilization Reaction Rate - # steps			1 - 2	2	local temperature heat-up limited
Devolatilization Pre-Exponential Factors		10	Kobayashi constants	Kobayashi constants	
Devolatilization Activation Energy		10	Modified Kobayashi values	Modified Kobayashi values	DG formula
Coal Swelling Factor Devolatilization			1.0 - 1.20	1.1	Experience
Gas Phase CO Oxidation Pre-Exponential		9	Literature: 1E8 to 1E14	Dryer-Glassman, etc. / Fast	Reaction orders, A, and E are not independent
Gas Phase CO Oxidation Activation Energy		9	Literature: 22 to 40 kcal/mole	Dryer-Glassman, etc. / Fast	
Gas Phase H2 Oxidation Pre-Exponential			Literature: 1E11 to 1E18	Marinov-Westbrook-Pitz, etc. / Fast	
Gas Phase H2 Oxidation Activation Energy			Literature: 30 to 41 kcal/mole	Marinov-Westbrook-Pitz, etc. / Fast	
Turbulence Model Selection			K-E, K-E Realizeable, RSM	K-E or K-E Realizable	Turbulence mixing may have high priority, but only different models are selected (model parameters are not varied).
Gas Properties - Thermal Conductivity			Pure Gas Polynomial Correlations		Database Functions, Polynomials
Gas Properties - Specific Heat Functions			Pure Gas Polynomial Correlations		Database Functions, Polynomials
Gas Properties - Diffusion Coefficients			Constant		
Char Oxidation Rate		6	Coal specific	"A" Calibrated to Outlet UBC	Rate extraced from Nsakala database
Char Diffusion coefficient			Constant (1600 K, O2 in N2)	Constant (1600 K, O2 in N2)	Calculated, consistent with char reaction expression
Char Gasification Rates (CO2 and H2O)			Coal specific	Coal specific	Estimated from Goetz, et al (1983) paper
Number of Particle Injections			Varies: e.g., 20,000 to 100,000	Varies	e.g, 10-20 diam; multiple stochastic tries
PSD Functions (Rosin-Ramler Distributions)			Logarithmic RR	Logarithmic RR	PSD size range: on the order of 1 to 200 microns
Number of Steps			10,000 - 30,000	10,000 or more	Monitor Statistics to minimize UBC, and Incompletes
Step length Factor			10 - 20	20	
Stochastic Tracking Parameters			Stochastic or Mean	Stochastic	
Particle Wall Properties - Restitution Coefficients			0 - 1.0 (Normal and Tangential)	0.3 - 0.5	Important to calibrate for ash collection devices
Radiation: Method - DO/P1			DO / P1	DO	Discrete Ordinates
Radiation Absorption Coefficient - Beam Length			domain or furnace: (0.9*4*Vol/Area)	domain or furnace: (0.9*4*Vol/Area)	Path length should represent upper and lower furnace
Radiation: DO Angular Descretization			2x2 to 4x4	2x2	4 per octant - for rectangular boxes.
Radiation Gas-Phase Absorption Coefficient			WSGG (or UDF for oxy-firing)	WSGG (or UDF for oxy-firing)	
Particle Absorption: Coal / Char / Ash		5	Absorption Efficiency Tables	Absorption Efficiency Tables	Custom UDFs built for specific component index of
Particle Scattering: Coal / Char / Ash			Scattering Efficiency Tables	Scattering Efficiency Tables	Custom UDFs built for specific component index of
Particle Radiation Coupling: Soot			Ignore or Include?	Coupled UDF	Experimentations show only local impact: increase of 10-15%
Fragmentation			------	------	No fragmentation model in current use.
Particle Dispersion			------	------	Particle dispersion may have high priority, but "discrete random walk" and "random eddy lifetime" are typically activated and time-scale constant is left at default value
Scenario Parameters					
Wall Thermal Resistance Hopper - 4" Cast	Kh=		0.8 - 1.6	0.8	BTU/hr-ft2-ft-R
Wall Thermal Resistance Main Furnace - 2" cast	Kw=	4	1.5 - 2.5	2	BTU/hr-ft2-ft-R
Wall Thermal Resistance SOFA-to-nose, 2" blanket	Kb=		0.1 - 0.5	0.3	BTU/hr-ft2-ft-R
Wall Thermal Resistance nose to backpass, steel	Ks=		3.0 - 9.4	3	BTU/hr-ft2-ft-R
Wall cold side temperature	F		200 - 230	212	Water at ~ atmospheric pressure
Convective Bank Surface Heat Transfer			Uniform Extraction, or UDF	Uniform Heat Extraction	Appropriate for areas without recirculation
Porous Media Inertial Pressure Drop Factors			Sectional Pressure Drop Match	Sectional Pressure Drop Match	Design Programs, Flow Handbooks, etc…
Porous Media Volumetric Heat Extraction					
Total Coal Flow Rate		1			
Windbox oxygen distribution		2			
Air Temperature					
Total Primary Air					
Primary Air Temperature					
Recycle Flow Rate		3			
Recycle Species Composition and H2O Content					
Recycle Temperature					
Leakage: Dampers / Valves					
Leakage: Hopper / Furnace Walls / Ports					
Maldistribution: Corner-to-Corner					
Maldistribution: Elevation-to-Elevation					
Misalignment of Tips					
Camera (CO2) Cooling Gas					
CCOFA-SOFA-WB Splits					

A more condensed version of the I/U map, with the high priority items only, is provided in Table 6-2.

Table 6-2. I/U Map (Condensed Version)

Parameter		Overall Priority	Range/Specification	Preference	Basis/Comments
Scenario Parameters					
Total Coal Flow Rate		1			
Windbox Oxygen Distribution		2			
Recycle Flow Rate		3			
Wall Thermal Resistance Main Furnace - 2" cast	Kw=	4	1.5 - 2.5	2	BTU/hr-ft2-ft-R
Model Parameters					
Particle Absorption: Coal / Char / Ash		5	Absorption Efficiency Tables	Absorption Efficiency Tables	Custom UDFs built for specific component index of refraction
Char Oxidation Rate		6	Coal specific	"A" Calibrated to Outlet UBC	Rate extraced from Nsakala database
Gas Phase Reaction Mechanism - EBU/PDF/EDC…		7	EBU/PDF/EDC…	EBU	Presumed PDF with 2 coal mixture fractions has limitations
Volatile/Char Partitioning		8	ASTM Vol (1x) to 1.4	1.2 -1.3	Calculated from PC Coal Lab
Gas Phase CO Oxidation Pre-Exponential		9	Literature: 1E8 to 1E14	Dryer-Glassman, etc. / Fast	Reaction orders, A, and E are not independent
Gas Phase CO Oxidation Activation Energy		9	Literature: 22 to 40 kcal/mole	Dryer-Glassman, etc. / Fast	
Devolatilization Pre-Exponential Factors		10	Kobayashi constants	Kobayashi constants	
Devolatilization Activation Energy		10	Modified Kobayashi values	Modified Kobayashi values	DG formula

The highest priority parameters are the scenario boundary conditions, and the scenario parameters selected that have the greatest impact on the wall heat flux are the flow rates -- the coal, oxygen and recycle flow rates. The wall thermal resistance in the main furnace was also selected as having a very high impact on the heat flux observable. Model parameters with lesser impacts are postulated to be radiation and homogeneous and heterogeneous reaction parameters.

For the present effort, it was decided to do an initial (introductory) assessment of consistency by focusing on the wall thermal conductivity as the single active variable (i.e., one-dimensional hypercube). The observables, or parameters of interest, are variables that are both experimentally determined and predicted with CFD, and in the present project, those parameters include local temperatures and heat fluxes; oxygen concentration was also added as a parameter later in the project.

The V&UQ cycle (or Bayesian analysis) requires prior estimates of interval bounds to perform the analyses, even though such estimates may be very approximate or rough. For this reason, ICSE analyzed the raw data associated with the pertinent BSF oxy test and extracted rough estimates of some of the experimental uncertainties associated with the feed stream mass flow rates and concentrations (see Table 6-3; Ref.15). It can be seen that the feed flow rate uncertainties are within 0.5 to 1.7%; the weighted uncertainty for the total gas feed flow rate is about 1.4%. The total uncertainty should encompass the experimental uncertainty. Consequently, when, for example, the active variables include any of the parameters tabulated below, then the upper and lower bounds for that variable should take into account the experimental uncertainty.

Table 6-3. Feed Stream Estimated Experimental Uncertainties

Items	Units	Value	Uncertainties (%)
Coal Transport			
Coal Mass Flow Rate	kg/s	0.63	-0.5 ~ 0.5
Primary (Windbox) Ports			
Mass Flow Rate	kg/s	1.12	-0.78 ~ 0.78
O_2	vol % (wet)	16.81	-1.2 ~ 1.5
CO_2	vol % (wet)	66.36	-1.4 ~ 2.8
SO_2	vol % (wet)	0.0267	------
H_2O	vol % (wet)	9.73	-2.3 ~ 2.3
N2	vol % (wet)	7.07	-30 ~ 10
Secondary (Windbox) Ports			
Mass Flow Rate	kg/s	2.42	-1.7 ~ 1.7
O_2	vol % (wet)	32.98	-1.5 ~ 2.3
CO_2	vol % (wet)	41.12	-2.5 ~ 2.4
SO_2	vol % (wet)	0.02	------
H_2O	vol % (wet)	21.5	-2.3 ~ 2.3
N_2	vol % (wet)	4.38	-24 ~ 10
Over-Fire Ports			
Mass Flow Rate	kg/s	0.72	-1.5 ~ 1.5
O_2	vol % (wet)	23.93	-1.8 ~ 3.0
CO_2	vol % (wet)	46.67	-2.5 ~ 2.8
SO_2	vol % (wet)	0.02	------
H_2O	vol % (wet)	24.41	-2.1 ~ 2.1
N_2	vol % (wet)	4.97	-29.7 ~ 12
Notes:	Uncertainties based on standard deviations from the noise in the raw data recordings.		

The experimental uncertainties associated with the measured/calculated properties of interest (or observables) are also very important when considering the interval bounds for the experimental data in the dataset unit. At present, the analysis to help determine the experimental uncertainty for properties of interest (e.g., temperature and heat flux) has not yet been performed.

6.2 Screening Trials

Alstom ran two sets of scoping or screening runs in order to determine e.g., how much the predicted planar temperatures changed, relative to the experimentally-averaged planar temperatures, at selected planes. A few selected model parameters were studied, as well as various observables. The screening runs were not meant to be extensive, but only to provide an indication of appropriate interval bounds.

The first set of screening runs was made to assess the sensitivity of the wall thermal conductivity on the observed temperatures. In these runs, the wall thermal conductivities associated with the hopper, main furnace, arch, and upper furnace were changed in a prescribed manner (see Table 6-4). The set of backside temperatures and wall thicknesses, used in the wall thermal boundary condition for the various

sections, were early values used by Alstom based on previous runs. At that time, Alstom was not aware of the corresponding values used by ICSE. Consequently, the results cannot be quantitatively or directly compared with later screening runs completed by either ICSE or Alstom, because a different set of wall thermal boundary conditions was used in later runs. However, lessons can still be learned from the relative differences in the results between the runs of the present scoping trial, as highlighted below.

Table 6-4. Wall Thermal Conductivity Screening Runs Using FLUENT®

Location	Backside Temperature	Wall Thickness
	[K (°F)]	[m (in)]
Upper Furnace: Steel	533.3 (500.3)	0.0127 (0.4992)
Arch/Nose: Blanket	422.2 (300.3)	0.0506 (1.992)
Main Furnace: RAM 90	422.2 (300.3)	0.0506 (1.992)
Hopper: Tufshot & GUN 2.0	422.2 (300.3)	0.1270 (4.9992)

Location	Run 0 (Baseline)	Run 6	Run 7	Run 8	Run 10	Run 12	Run 13
	Thermal Conductivity [W/(m-°C) (Btu/hr-ft-°F)]	Thermal Conductivity [W/(m-°C) (Btu/hr-ft-°F)]	Thermal Conductivity [W/(m-°C) (Btu/hr-ft-°F)]	Thermal Conductivity [W/(m-°C) (Btu/hr-ft-°F)]	Thermal Conductivity [W/(m-°C) (Btu/hr-ft-°F)]	Thermal Conductivity [W/(m-°C) (Btu/hr-ft-°F)]	Thermal Conductivity [W/(m-°C) (Btu/hr-ft-°F)]
Upper Furnace: Steel	5.192 (3.0)	unchanged	unchanged	unchanged	unchanged	1.731 (1.0)	unchanged
Arch/Nose: Blanket	0.519 (0.3)	unchanged	unchanged	unchanged	0.173 (0.1)	unchanged	unchanged
Main Furnace: RAM 90	3.461 (2.0)	unchanged	2.596 (1.5)	4.327 (2.5)	unchanged	unchanged	3.029 (1.75)
Hopper: Tufshot & GUN 2.0	1.385 (0.8)	2.596 (1.5)	unchanged	unchanged	unchanged	unchanged	unchanged
Note A:	The explosion (blanket) panels on the roof were not yet added to the geometry when these cases were run.						
Note B:	The wall thicknesses and backside temperatures are different in these runs than subsequent runs (i.e., later runs used the ICSE-proposed values)						

Computational Results Using FLUENT

Plane	Run 0 (Baseline)	Run 6	Run 7	Run 8	Run 10	Run 12	Run 13	Experimental Planar Average
	[°F]	[°F]	[°F]	[°F]	[°F]	[°F]	[°F]	[°F]
VFOP	1389	1384	1458	1342	1413	1535	1427	1536
Plane 273	2162	2138	2321	2038	2196	2172	2241	2264
Plane 180	2380	2353	2536	2256	2383	2381	2449	2398
Plane 141	2586	2556	2723	2479	2586	2588	2649	2566

Deviations between FLUENT Computational Results and the Experimental Planar Average

VFOP	-148	-152	-78	-195	-123	-2	-109
Plane 273	-102	-125	57	-226	-68	-92	-23
Plane 180	-18	-45	138	-142	-15	-17	51
Plane 141	20	-11	157	-87	19	21	82
Note 1:	VFOP = vertical furnace outlet plane (Plane 376)						

In the above table, the word "unchanged" in a table cell means that the given cell contains the same value as in the Baseline run. Between Run 0 and Run 6, the hopper thermal conductivity was increased by 88% (which should cause a corresponding temperature decrease due to increased heat loss). In Runs 7, 8, and 13, the wall thermal conductivity for the main furnace was changed from the baseline value by a maximum of +/- 25%. In Run 10, only the arch thermal conductivity was reduced by two-thirds, and in Run 12, the upper furnace thermal conductivity was reduced by two-thirds.

The changes in thermal conductivity induced corresponding changes in the temperature and wall absorption, although only the planar temperature results are provided in the above table. Run 6, in which the hopper thermal conductivity was almost doubled from that in Run 0, exhibited about a 30 °F decrease in temperatures for Planes 141 and 180. Runs 7, 8, and 13, in which the wall thermal conductivity of the main furnace is changed, experienced a temperature deviation from the baseline (Run 0) of about +156 °F (Run 7), -124 °F (Run 8), and +70 °F (Run 13), respectively, consistent with the change in the thermal conductivity. In Run 10, decreasing the arch/nose wall thermal conductivity by two-thirds from the baseline value did not change temperatures in the lower furnace very much, and only changed the temperatures in the upper furnace by about 30 °F. In Run 12, the wall thermal conductivity of the upper

furnace was decreased by two-thirds from the baseline value; the temperatures in the lower furnace hardly changed, but the temperature in the upper furnace increased by almost 150 °F. The main furnace section extends from the top of the hopper to the upper SOFA, encompassing the windbox fireball region, and most of the high-temperature SOFA region. Therefore, changing the wall thermal conductivity of the main windbox region by only 25% had as much or greater impact on the temperatures than changing (by 67 to 80%) the wall thermal conductivities of the other sections.

The FLUENT® temperature calculations, plotted against the experimental planar-averaged temperatures at Planes 141, 180, and 273 (in the form of profile plots as a function of elevation), are shown in Figure 6-1. Although the experimental measurements at the planes of interest can be considered to be somewhat sparse, if the average values of the experimental temperatures can be construed to be representative of the true average experimental temperature, then the predictions indicate that the data trendline, as a function of elevation, has a different slope than that of the predictions. The profile plots are all roughly parallel to each other above the main windbox, so that the data trendline would appear to intersect and cross over the nearest profile plots, making it more difficult for two closely-confining profiles to bracket the data. Two thermal conductivities that are sufficiently far apart, +/- 25% (Run 7 and Run 8), on either side of the baseline value (Run 0), do comfortably bracket the data, but tighter differences on the thermal conductivity would not. As will be seen, this difference in slope (temperature as a function of elevation) between the calculations and experimental data will have implications later on when consistency analysis is applied to the data. It may be difficult, e.g., to achieve consistency at both a lower and an upper plane simultaneously when a constant thermal conductivity is applied over a broad expanse of elevation.

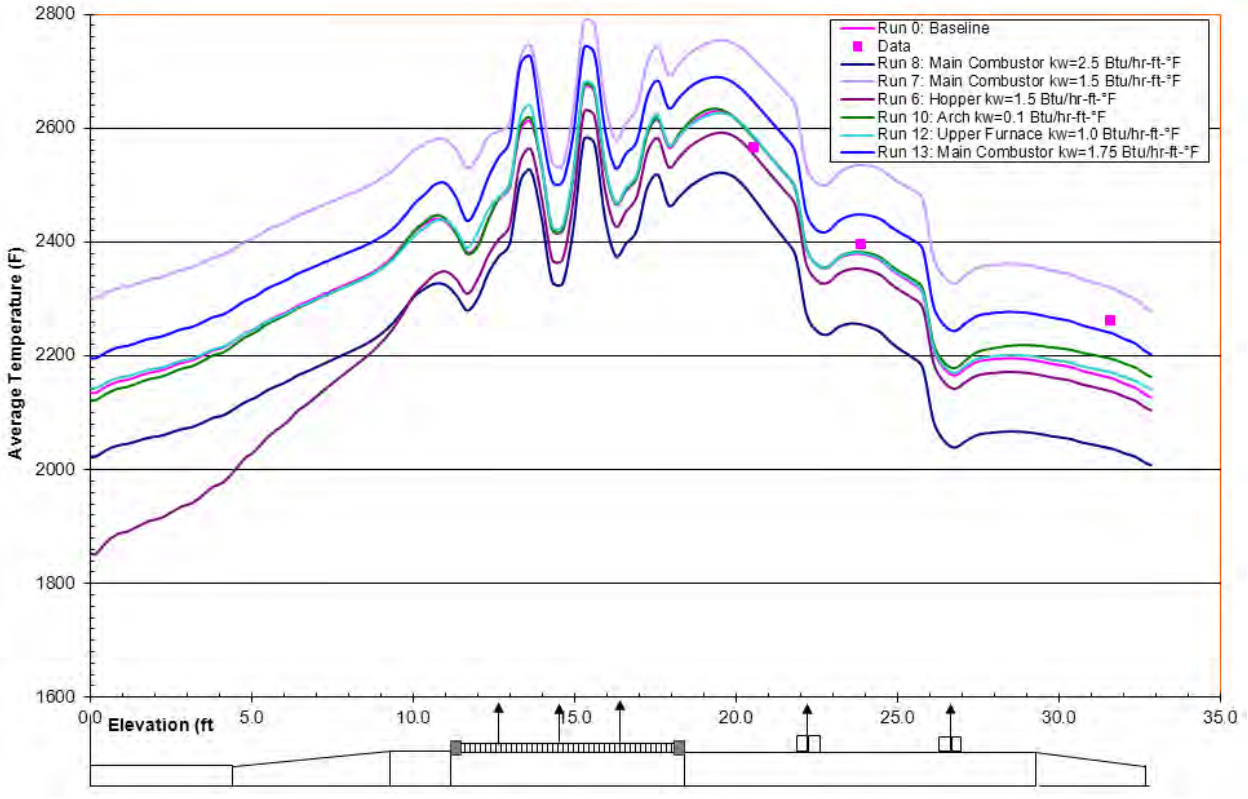

Figure 6-1. Temperature Profile Predictions (FLUENT®) as a Function of Elevation and k_w.

Again, if the data trendline is reliable (i.e., consistent with the "true" trendline), then the indication is that the model or model boundary conditions are not adequately representing the physics. If the data trendline is not reliable, then some (or all) of the data may be in error. Potential, contributing flaws in the model or data include:

- Unspecified error bars on the experimental data plus any apparent error due to data point sparsity in the construction of the averaged planar temperatures.
- A single wall thermal conductivity value for the main windbox, arch, and other sections. The main windbox and arch regions both cover elevations where substantial changes in deposition and surface temperature occur. Hence the windbox and arch regions should perhaps be broken up into smaller sections so that a more customized wall resistance profile can be specified. The appropriate question is: "Can a reasonable wall resistance profile be specified such that the computed temperature profile becomes congruent with the experimental profile?" Deposition and slagging maps would be helpful in these instances.
- Speciation and reaction rates associated with the homogeneous or heterogeneous combustion model. More extensive reaction rate expressions (with e.g., more species) and/or different reaction rates may impact the heat release profiles in the furnace.
- Particle dispersion and the location of the reacting particles relative to the local stoichiometry.
- Extent of turbulent mixing and the rapidity with which the reactants are mixed together to burn.
- Mutual consistency of the experimental temperature profile data with the experimental heat flux data. The heat flux data needs to be cross-checked with the temperature data to ensure that proper conclusions are being drawn.

The bulleted list can be made more extensive. As can be seen, a number of candidate models or boundary conditions in the furnace can contribute to the error. The quality of the data itself may also be uncertain. It is precisely this kind of ambiguity in the source of the error that data collaboration and consistency analysis attempts to resolve. Although the scope of UQ analysis is very challenging, the uncertainty of each source of modeling error can be addressed, in principle, by bringing it into the analysis as an active variable in a prioritized manner.

ICSE also made a number of screening runs in which the wall thermal conductivity of the main furnace section was changed. A few of those results are shown in Table 6-5 (Ref. 11). The height is given in meters instead of feet, but the plane locations for Planes 141, 180, and 273 are shown for reference. The "standard" case applied a baseline wall thermal conductivity value to the main windbox region, and then Cases 4 and 5 used thermal conductivity values that were about +/- 20% different from the baseline value.

Table 6-5. Wall Thermal Conductivity Screening Runs Using ARCHES

			Temperature			
			[°F]			
Plane	**Level**	**Height**	**Measurement**	**Standard**	**Case_4**	**Case_5**
		(m)		1.0 x k_w	1.2 x k_w	0.8 x k_w
Plane 141	Level_1	6.376	2566	2546	2609	2480
Plane 180	Level_2	7.367	2397	2368	2440	2293
Plane 273	Level_3	9.717	2264	2206	2273	2123
Plane 376 (VFOP)	Level_4	11.749	1819	1825	1879	1760
Plane 376 (VFOP)	Level_5	12.612	1749	1724	1810	1681

It can be seen that the maximum and minimum thermal conductivities, specified to be +/- 20% (Case 4 and Case 5), on either side of the "standard" case, bracket the data. The above results are plotted in Figure 6-2. Data may be more sparse at Levels 4 and 5, but the temperatures should also be more uniform across a given plane at the higher elevations, simply due to the longer accrued residence time during which more mixing has occurred.

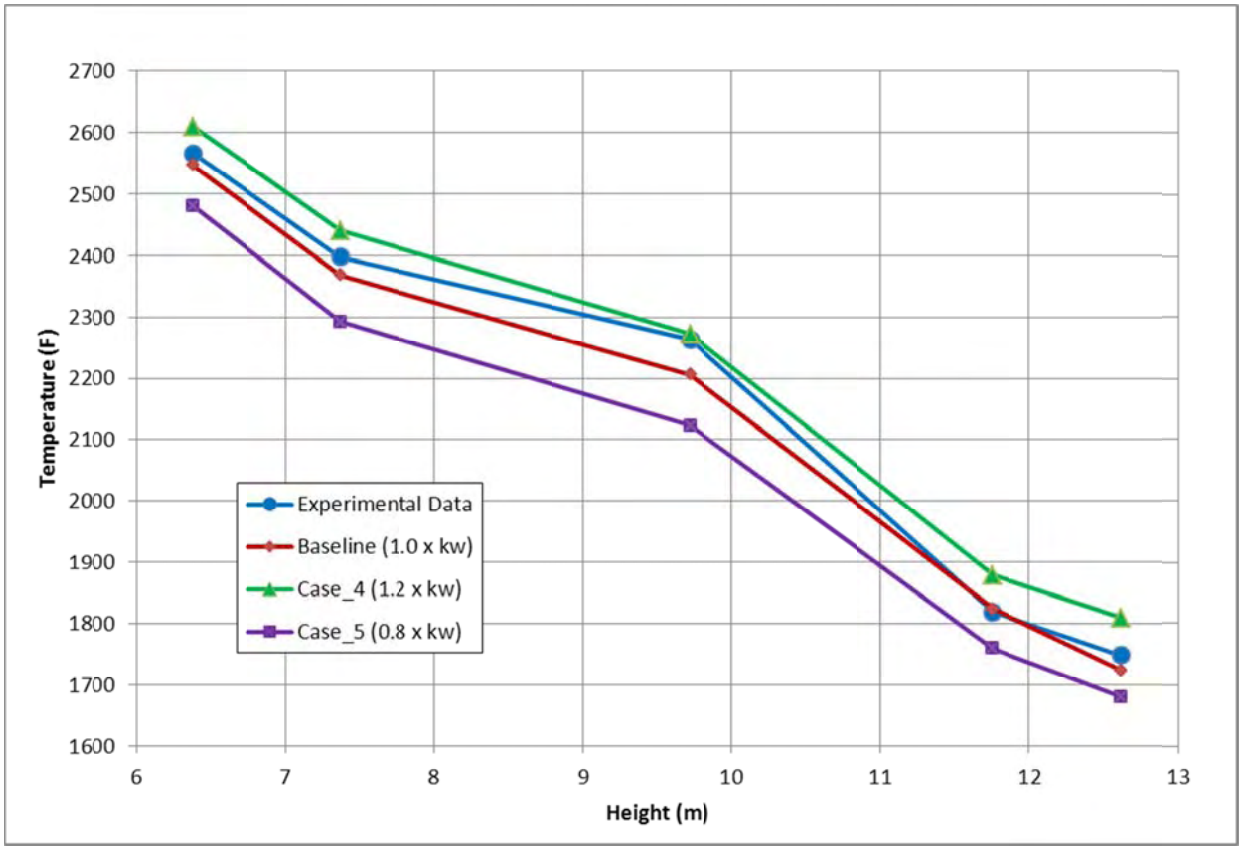

Figure 6-2. Temperature Profile Predictions (ARCHES) as a Function of Elevation and k_w.

It can be seen that the Case 4 and Case 5 calculations bracket the data over the entire height of the boiler and that the bracketing is somewhat symmetric except at the height 9.717 m (Plane 273), where the data

deviates from the calculation line for the standard or baseline case. This singular deviation is qualitatively similar to the Plane 273 deviation shown earlier in the FLUENT® screening runs. The bracketing is much tighter (by about a factor of 2) than in the FLUENT® runs, but again, the FLUENT® runs and the ICSE results cannot be directly compared because the wall thickness and backside temperatures are very different between these two sets of runs. A more careful study would need to be made to determine if both the ICSE and FLUENT® runs were inducing the same range of temperature changes for a given change in the thermal conductivity of the main wall section, and then to understand why that might occur. However, the ICSE and FLUENT® runs do indicate that, in order to bracket the data, thermal conductivity changes on the order of +/- 20% to 25% are appropriate as interval bounds on the wall thermal conductivity (as an active variable).

Alstom performed a second set of scoping runs, associated with changes in a number of different model parameters besides thermal conductivity, as shown in Table 6-6. In these runs the backside wall temperatures and the wall thicknesses were aligned with the values utilized by ICSE. As can be seen from the table, (a) the wall thermal conductivity was changed (only) between Case 0 and Case 1 (decreased by 20%), (b) the devolatilization rate was changed for Case 2, (c) in Case 3, some radiation parameters were changed, gasification was turned off, and the char oxidation rate was increased, (d) in Case 4, a severe change in the particle size distribution (PSD) was made, and (e) in Case 5, some of the gas-phase reaction rates are modified.

Table 6-6. Model Parameter Scoping Runs Using FLUENT®

Location	Case 0	Case 1	Case 2	Case 3	Case 4	Case 5	Wall Thickness
	Thermal Conductivity [W/(m-°C) (Btu/hr-ft-°F)]	Thermal Conductivity [W/(m-°C) (Btu/hr-ft-°F)]	Thermal Conductivity [W/(m-°C) (Btu/hr-ft-°F)]	Thermal Conductivity [W/(m-°C) (Btu/hr-ft-°F)]	Thermal Conductivity [W/(m-°C) (Btu/hr-ft-°F)]	Thermal Conductivity [W/(m-°C) (Btu/hr-ft-°F)]	[m (in)]
Upper Furnace: Steel	1.730 (1.0)	5.192 (3.0)	5.192 (3.0)	5.192 (3.0)	5.192 (3.0)	5.192 (3.0)	0.018 (0.709)
Arch/Nose: Blanket	0.5192 (0.3)	0.5192 (0.3)	0.5192 (0.3)	0.5192 (0.3)	0.5192 (0.3)	0.5192 (0.3)	0.0529 (2.083)
Main Furnace: RAM 90	4.327 (2.5)	3.461 (2.0)	3.461 (2.0)	3.461 (2.0)	3.461 (2.0)	3.461 (2.0)	0.0645 (2.54)
Hopper: Tufshot & GUN 2.0	1.385 (0.8)	1.385 (0.8)	1.385 (0.8)	1.385 (0.8)	1.385 (0.8)	1.385 (0.8)	0.1325 (5.217)
Panels: Explosion Blanket	0.5192 (0.3)	0.5192 (0.3)	0.5192 (0.3)	0.5192 (0.3)	0.5192 (0.3)	0.5192 (0.3)	0.1545 (6.083)
Note A:	Backside temperature = 375 K for all sections						

Model Parameters	Case 0	Case 1	Case 2	Case 3	Case 4	Case 5
Devolatilization Rate	A / E	A / E	(0.002)A/(0.3)E	A / E	A / E	A / E
Gasification	on	on	on	off	off	off
Particle Size Distribution	RR fit	RR fit	RR fit	RR fit	3 UOU sizes	RR fit
Gas Scattering	0.05	0.05	0.05	0	0	0
Particle Scattering	0.1	0.1	0.1	0	0	0
Particle Emissivity	UDF	UDF	UDF	0.8	0.8	0.8
CO + 1/2 O2 --> CO2	A / E	A / E	A / E	A / E	A / E	(0.36)A / E
H2+1/2 O2 --> H2O	A / E	A / E	A / E	A / E	A / E	(5e-7)A/(0.25)E
Cgas + 1/2 O2 --> CO	A / E	A / E	A / E	A / E	A / E	(7e-9)A/(0.5)E
C<s> + 1/2 O2 --> CO	A / E	A / E	A / E	(10.4)A/(0.46)E	(10.4)A/(0.46)E	(10.4)A/(0.46)E
Note 1:	"RR fit" = experimental Rosin-Rammler (logarithmic) fit					
Note 2:	"3 UOU sizes" = Initial (arbitrary) University of Utah PSD (see Table 4).					
Note 3:	"UDF" = user-defined function for particle absorption efficiency					
Note 4:	pairs of numbers for Arrhenius rates: pre-exponential rate factor (A) and activation energy (E)					

Computational Results Using FLUENT

Plane	Case 0	Case 1	Case 2	Case 3	Case 4	Case 5	Experimental Planar Average
	[°F]	[°F]	[°F]	[°F]	[°F]	[°F]	[°F]
VFOP	1579	1487	1486	1473	1486	1477	1536
Plane 273	2161	2282	2286	2274	2233	2283	2264
Plane 180	2386	2512	2508	2490	2454	2490	2398
Plane 141	2609	2712	2708	2701	2662	2689	2566

Deviations between FLUENT Computational Results and the Experimental Planar Average

VFOP	43	-49	-50	-63	-50	-59
Plane 273	-103	18	22	10	-31	19
Plane 180	-12	114	110	92	56	92
Plane 141	43	146	142	135	96	123
Note 5:	VFOP = vertical furnace outlet plane (Plane 376)					

By viewing the computational results and the deviations of the calculations from the experimental data at Plane 273, one can see that the change in thermal conductivity elicited a change of approximately 103 °F. The radiation and heterogeneous reaction rate modifications associated with Case 3 produced a change in the planar temperatures of only a few degrees. Changing the PSD in a severe fashion (comparing Cases 3 and 4) generated a change in planar temperatures of 30 to 40 °F. And in Case 5, changing the gas reaction rates induced a change in the planar temperatures of 12 °F or less. Consequently, the change in the wall thermal conductivity generated the greatest impact on the results, relative to the rest of the examined parameters (for the particular boundary condition and model variations given in the above tables).

6.3 Design of Experiments

As mentioned previously, it was decided to do an initial (introductory) assessment of consistency by focusing on the wall thermal resistance as the single active variable (i.e., one-dimensional hypercube *H*). From the screening runs, it was decided to allow the thermal conductivity to vary +/- 25%. Consequently with a baseline value for the thermal conductivity (k_w) of 3.46 W/m-K, the range of k_w was from ($k_{w,2}$ =)

2.6 W/m-K to ($k_{w,1}$ =) 4.3 W/m-K. The one-dimensional hypercube may be expressed as: $H = \{\boldsymbol{x} \in \boldsymbol{R}^1: k_{w,2} \leq k_w \leq k_{w,1}\}$, where the "vector" $\boldsymbol{x}$ retains only a single active variable $\boldsymbol{x} = (x_1 = k_w)$ over the range $[k_{w,2}, k_{w,1}]$.

The observables, or parameters of interest, are *y*-variables that are both experimentally determined and predicted with CFD, and in the present project, those parameters include local temperatures and heat fluxes; oxygen concentration was also added as a parameter later in the project.

The design of experiments (DoE) procedure initially produced a matrix of runs with 17 runs and 4 variables – inlet coal mass flow rate, inlet gas mass flow rate, wall thermal conductivity in the main furnace, and devolatilization rate. The inlet gas mass flow rate was not fully exercised in that DoE scheme. The matrix of 17 runs was subsequently collapsed to 11 runs and 3 variables – inlet coal mass flow rate, inlet gas mass flow rate, and wall thermal conductivity in the main furnace. A three-dimensional DoE may be pictorially represented by the diagram in Figure 6-3 (Ref. 15), where (a) the red star indicates the baseline case values, (b) the black dots represent the bounds of each of the 3 independent variables (where only one variable is realized at a time and the others are held at the baseline values), and (c) the yellow stars represent combinations of all three variables at their maximum or minimum values. Pictorially, 15 separate experiments are represented in the diagram. Since 11 runs were only specified in the present run matrix, one of the variables (i.e., inlet gas mass flow rate) was not fully exercised. However, this is not necessarily viewed as problematic, since DoE strategies vary and may range from structured approaches to more random approaches (e.g., Latin hypercube approach, etc.).

Figure 6-3. Three-dimensional Design of Experiments

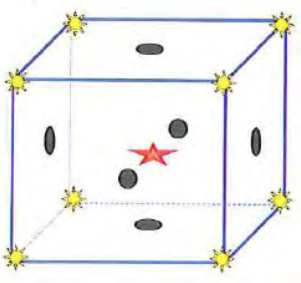

The present V&UQ run matrix is shown in Table 6-7. (The ICSE equivalent may appear to be somewhat different because of their use of slightly different flow rates.) The numbers in black indicate values that are different from those of the baseline case. The stoichiometric ratio column (based on external oxygen only) is included to help gauge the relative change in stoichiometry.

Table 6-7. V&UQ Run Matrix

Case Number	Inlet Coal Mass Flow Rate (kg/s)	Inlet Coal Mass Flow Rate (lbm/hr)	Inlet Coal Mass Flow Rate % Change from Baseline	Inlet Gas Mass Flow Rate (kg/s)	Inlet Gas Mass Flow Rate (lbm/hr)	Inlet Gas Mass Flow Rate % Change from Baseline	Stoichiometric Ratio [Note 1]	Thermal Boundary Conditions for Main Windbox [Note 2] (Btu/hr-ft-°F)	Thermal Boundary Conditions for Main Windbox [Note 2] (W/m-°C)	Thermal Boundary Conditions for Main Windbox [Note 2] % Change from Baseline	Devolatilization Rate [Note 3]
1-Baseline	0.62551	4,964.48	0.000	4.35076	34,530.43	0.000	1.1203	2.0	3.4615	0.0	Sv
2	0.63490	5,039.00	1.501	4.35076	34,530.43	0.000	1.1037	2.0	3.4615	0.0	Sv
3	0.61613	4,890.00	-1.500	4.35076	34,530.43	0.000	1.1373	2.0	3.4615	0.0	Sv
4	0.62551	4,964.48	0.000	4.35076	34,530.43	0.000	1.1203	1.5	2.5962	-25.0	Sv
5	0.62551	4,964.48	0.000	4.35076	34,530.43	0.000	1.1203	2.5	4.3269	25.0	Sv
6	0.62551	4,964.48	0.000	4.35076	34,530.43	0.000	1.1203	2.0	3.4615	0.0	0.2 Sv
7	0.62551	4,964.48	0.000	4.35076	34,530.43	0.000	1.1203	2.0	3.4615	0.0	5 Sv
8	0.61613	4,890.00	-1.500	4.35076	34,530.43	0.000	1.1373	1.5	2.5962	-25.0	Sv
9	0.61613	4,890.00	-1.500	4.35076	34,530.43	0.000	1.1373	2.5	4.3269	25.0	Sv
12	0.63490	5,039.00	1.501	4.35076	34,530.43	0.000	1.1037	1.5	2.5962	-25.0	Sv
13	0.63490	5,039.00	1.501	4.35076	34,530.43	0.000	1.1037	2.5	4.3269	25.0	Sv
16	0.62551	4,964.48	0.000	4.41471	35,038.00	1.470	1.1371	2.0	3.4615	0.0	Sv
17	0.62551	4,964.48	0.000	4.28683	34,023.00	-1.470	1.1034	2.0	3.4615	0.0	Sv
Note 1:	Stoichiometric mass of external O2 / unit mass of as-rec'd coal = 1.53315										
Note 2:	Backside temperature = 375 K and wall emissivity = 0.8										
Note 3:	Sv represents the baseline (single rate) devolatilization rate. Multipliers impact the pre-exponential factor.										

The inlet coal mass flow rate was allowed to change only by +/- 1.5%, and the inlet gas mass flow rate was allowed to change by a similar amount (+/- 1.47%). As mentioned previously, the wall thermal conductivity for the main furnace zone was allowed to change by +/- 25%. Variations to the devolatilization rate pre-exponential factor were made with a multiplier that changed by a factor of 5 from the baseline value. In the present run matrix, changes to the inlet gas mass flow rate and devolatilization rate were not made in conjunction with other parameter perturbations; it is expected that this would probably occur as the run matrix is expanded and the DoE becomes more sophisticated.

6.4 Data Collection

The "data collection" consists of both the experimental data and the simulation values, where the simulation values were extracted (via post-processing) at the same x, y, and z locations as the experimental data. The set of experimental and calculated oxygen concentration values was expressed on a wet basis. Some repeat measurements were available within the temperature data set. Experimental data replicates were also available in the measured wall heat flux data set. Where replicates of heat flux measurements were available, ICSE used the replicates to calculate a mean experimental value for a given probe location. The difference between the various replicates and the mean value was used to provide an initial estimate of an experimental uncertainty for the heat flux measurements, which was then utilized in the consistency analysis.

ICSE also constructed a similar simulation data set based on their LES computations.

6.5 Surrogate Model and Consistency Analysis

The ICSE group has performed two analyses – (a) the first analysis was performed with averaged (planar) temperature data and the heat flux data, and (b) the second, and more complicated analysis, was performed

with all of the individual temperature measurements, along with the heat flux data. ICSE performed the consistency analysis for the LES predictions, as well as for the Alstom RANS predictions. Each of these analyses will be described in turn. Alstom was not directly involved in performing these analyses but is simply reporting the results.

ICSE has also developed a MatLab script with which to perform the consistency analysis. The script is an evolving script to which more variables and statistical analyses and capabilities can be added. Alstom has received an early, primitive version of this script that was used by ICSE to perform the consistency analysis with the averaged (planar) temperature measurements.

A quadratic fit or interpolant was selected by the ICSE researchers for the surrogate model. A Monte Carlo method or random sampling method was used to sample the design space, to solve the constrained optimization problem, and to find the consistency region of k_w. In its most rudimentary form, the consistency region is found by solving:

$$\begin{cases} k_{w,1} \geq k_w \geq k_{w,2} \\ u_e \geq |M_e(k_w) - d_e| \geq l_e \ (for\ each\ e \in \mathcal{E}) \end{cases} \quad (4)$$

where k_w is the single active variable in the one-dimensional hypercube, with its upper and lower bounds; u_e and l_e are the upper and lower bounds for the experimental data; and the model prediction, $M_e(k_w)$, is acquired for each experiment through the surrogate model.

To be able to discriminate between the different analyses in the following headers and captions, "short-hand" notation and acronyms will be used to describe the content of the analyses:

- C-# : the number of CFD cases used in the analysis, with the actual cases delineated in parenthesis.
- AV-# : the number of independent or active variables used in the analysis, with the active variables listed in parenthesis as k_w = wall thermal conductivity, CFR = inlet coal mass flow rate, and DR = devolatilization rate.
- O-# : the number of observables, with the observables listed in parenthesis as T = temperature (K), HF = heat flux (Btu/ft^2-hr), and O_2 = oxygen molar concentration (mole %, wet).

6.5.1 Consistency Analysis I: C-3 (1, 4, 5), AV-1 (k_w), O-2 (Average Planar T, HF)

Incident heat flux is available at 26 ports, and temperature data are available at 116 measurement locations on three planes (Plane 141, 180, and 273). The experimental temperature data was averaged over each plane, so that the final set of measured data for the V&UQ analysis consisted of 29 points – 3 temperature points (one averaged temperature for each plane) and 26 heat flux data points.

Three (3) of the RANS and LES simulations were utilized from the set of cases simulated – (a) Case 1 (Baseline): the thermal conductivity (k_w) = 3.46 W/m-K, (b) Case 4: k_w = 2.60 W/m-K, and (c) Case 5: k_w = 4.33 W/m-K. All other boundary conditions remained unchanged. Based on the "prior information" available, the measurement error for temperature and heat flux were initially estimated to be +/- 50 K (based on a rough guess) and +/- 6.3x10^4 W/m^2 (based on the difference in replicate heat flux values). When all 29 data points satisfy Eq. (4) for the same region or values of k_w in the range [$k_{w,2}$, $k_{w,1}$], it can be said that the model and the measurements are consistent, given the experimental uncertainties in the range [l_e, u_e].

The consistency analysis for the Alstom RANS calculations is shown in Figure 6-4 and Figure 6-5. (These plots were sent to Alstom by the University of Utah/ICSE.) For Figure 6-4, the units on the abscissa for the thermal conductivity are in terms of Btu/hr-ft-°F. Each of the solid lines (blue, red, and green) represents a quadratic fit of the calculated temperature versus the thermal conductivity, at each of the three planes of interest (Level 1: Plane 141, Level 2: Plane 180, and Level 3: Plane 273). Since there were only 3 simulation cases in the analysis (i.e., 3 different thermal conductivities), the quadratic expression can fit the results perfectly. It can be seen that the fits are almost linear. There is a separate solid line or quadratic fit for each of the 3 planes. The dashed lines (of the same color) represent the average experimental temperature at each of the 3 planes, and the dotted lines represent uncertainty bands (+/- 30 K) on each side of the mean temperature. The consistency region (designated by the bold, black line segment) is that region of k_w (in the vicinity of 2.25 Btu/hr-ft-°F) that simultaneously satisfies each (average) temperature dataset unit, as well as each heat flux dataset unit (see next figure), given the assigned upper and lower experimental uncertainties.

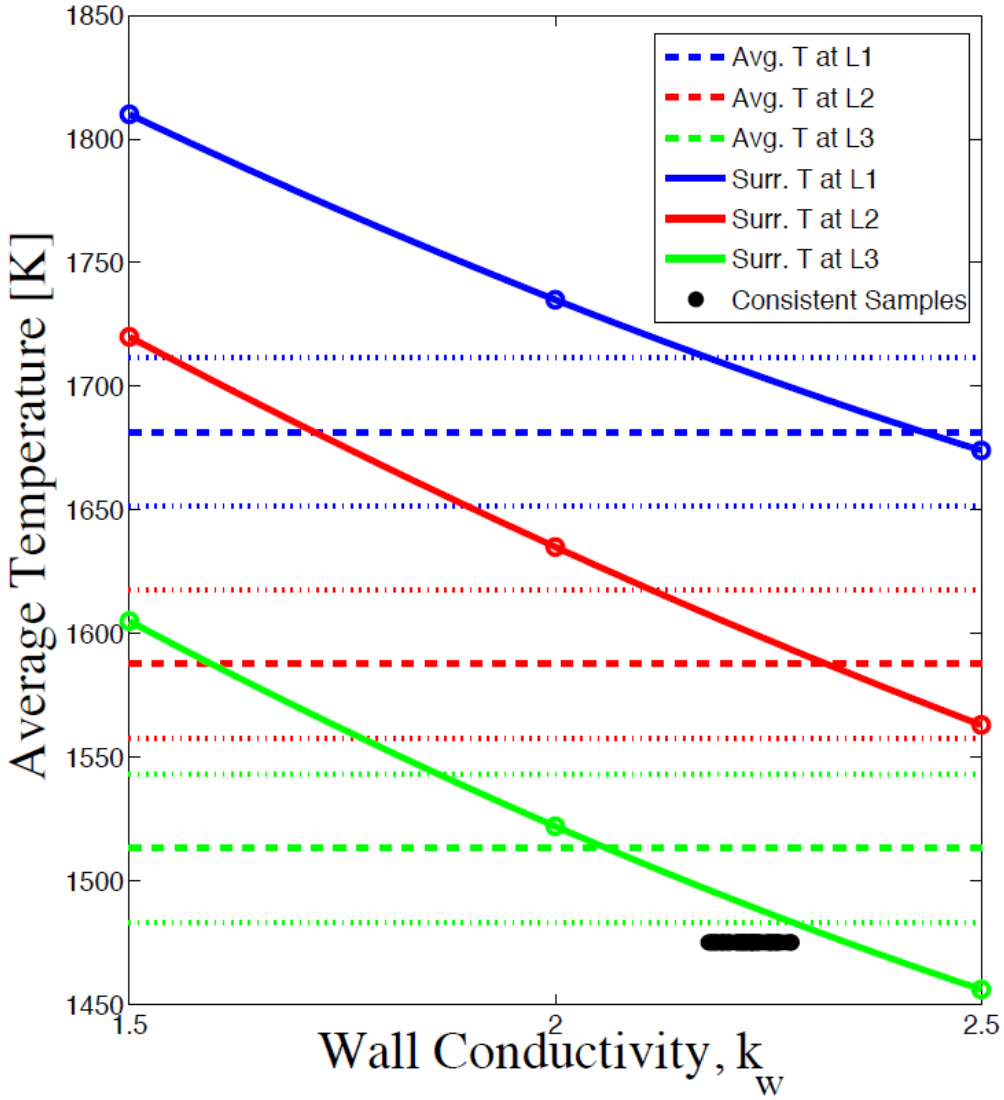

Figure 6-4. RANS (a): T: Analysis I: C-3 (1, 4, 5), AV-1 (k_w), O-2 (Average Planar T, HF)

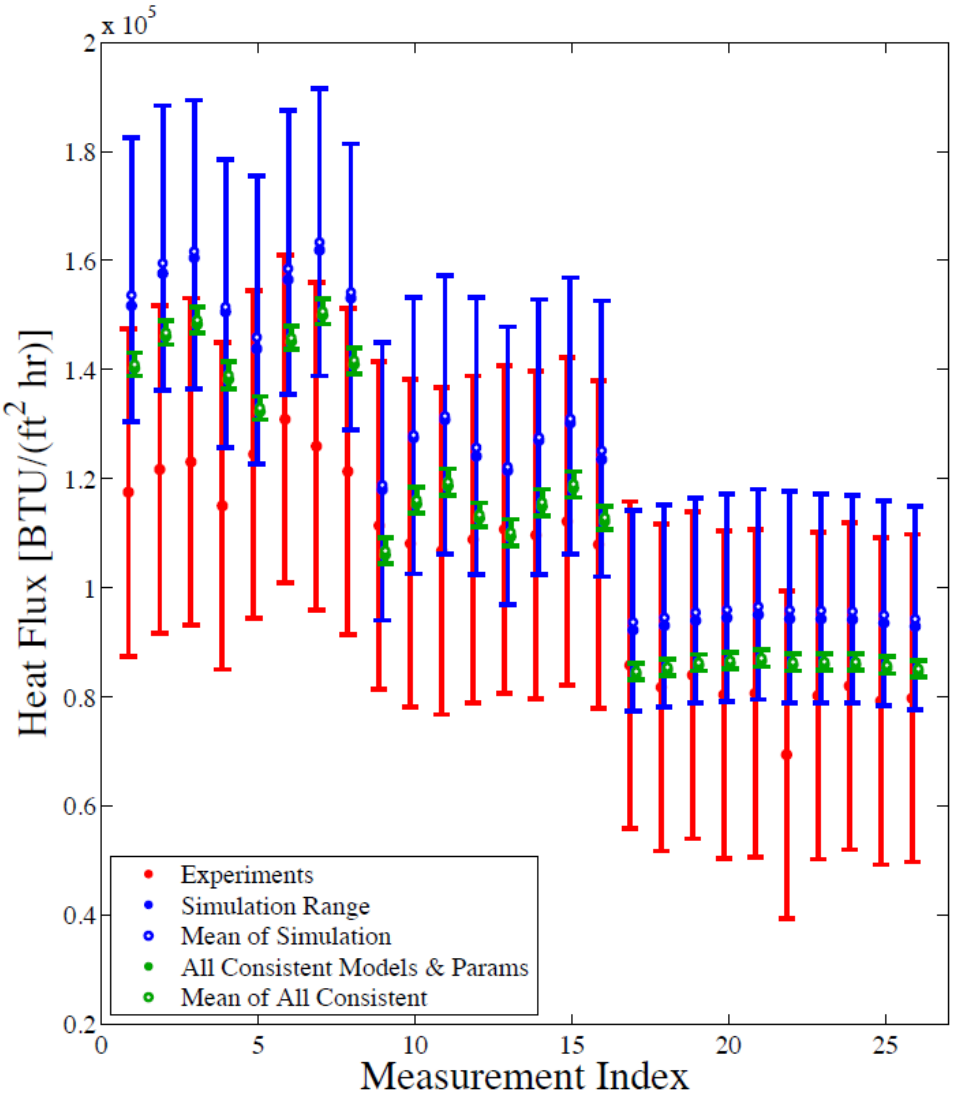

Figure 6-5. RANS (b): HF: Analysis I: C-3 (1, 4, 5), AV-1 (k_w), O-2 (Average Planar T, HF)

The actual experimental uncertainty in the BSF temperature measurements has not been estimated. In the absence of such an estimate, ICSE provided their own estimate of the "experimental uncertainty" averaged over each plane. In this instance, ICSE asked the question, "What do the experimental upper and lower limits have to be in order to ensure a modest consistency region?". The initial uncertainty bands for the average experimental temperature were estimated to be +/- 50 K; however, as a result of this analysis, the measurement error bands have been reduced to +/- 30 K. If it is subsequently determined that the "true" upper and lower experimental limits on the average temperature are, in actuality, much less than +/- 30 K, then the consistency region may be a null set.

In Figure 6-5, there are too many experimental data points to plot the heat flux analysis in the same way as the average temperature data. The abscissa is expressed as a "Measurement Index" that has discrete values from 1 to 26 (i.e., the number of experimental heat flux port locations). The error bars or uncertainty bands on the measured heat fluxes are indicated in red color, with the red dot representing the

actual value measured. The blue bars represent the simulated values of the heat flux at the three values of the thermal conductivity (associated with Cases 1, 4, and 5). The lower thermal conductivity (greater insulative capacity) yields a higher calculated gas temperature and a higher heat flux, as one would expect. The open blue circle is simply the mean (or average) value of all of the samples from the Monte-Carlo sampling of the surrogate model for each measurement port. The green bars constitute the mutual consistency region for each of the heat flux measurement ports, as well as for the 3 averaged temperatures. The open green circle is the mean of all of the consistent samples for each port (i.e., measurement index). It can be seen that the simulation (blue) error bars overlap with the upper region of the experimental (red) error bars, so that the consistency band (green) is very near the upper limit of the experimental error bars on the first eight heat flux measurement port locations.

As previously stated, the initial uncertainty for the heat flux was estimated to be +/- 6.3×10^4 W/m^2 (or +/- 2.0×10^4 Btu/hr-ft^2). This value is about +/- 15% of the highest measured heat flux value. To ensure a consistency region, the experimental uncertainty bands on the heat flux had to be extended to +/- 3.0×10^4 Btu/hr-ft^2.

The equivalent ICSE results with the LES model are found in Figure 6-6 and Figure 6-7. For Figure 6-6, the units on the abscissa for the thermal conductivity are again in terms of Btu/hr-ft-°F. It can be seen that the consistency region, centered at about 1.7 Btu/hr-ft-°F, is much larger than that for the RANS calculations. For the RANS calculations, it was possible to reduce the measurement error bands to a value of +/- 30 K and still maintain consistency, but in the LES calculations, it appears that it was possible to reduce the measurement error bands to a value of approximately +/- 20 K. In addition, for the RANS calculations, the temperature change over the range from 1.5 to 2.5 Btu/hr-ft-°F was about 150 K (270 °F), while the temperature change in the figure below, for the same range of k_w, was about 80 K (144 °F), almost a factor of two smaller. The reason why FLUENT® would exhibit a much greater sensitivity to a change in the thermal conductivity than the LES computations is unknown. It is presently believed that the thermal boundary condition formulation on the walls is similar in both codes, but the issue deserves further scrutiny.

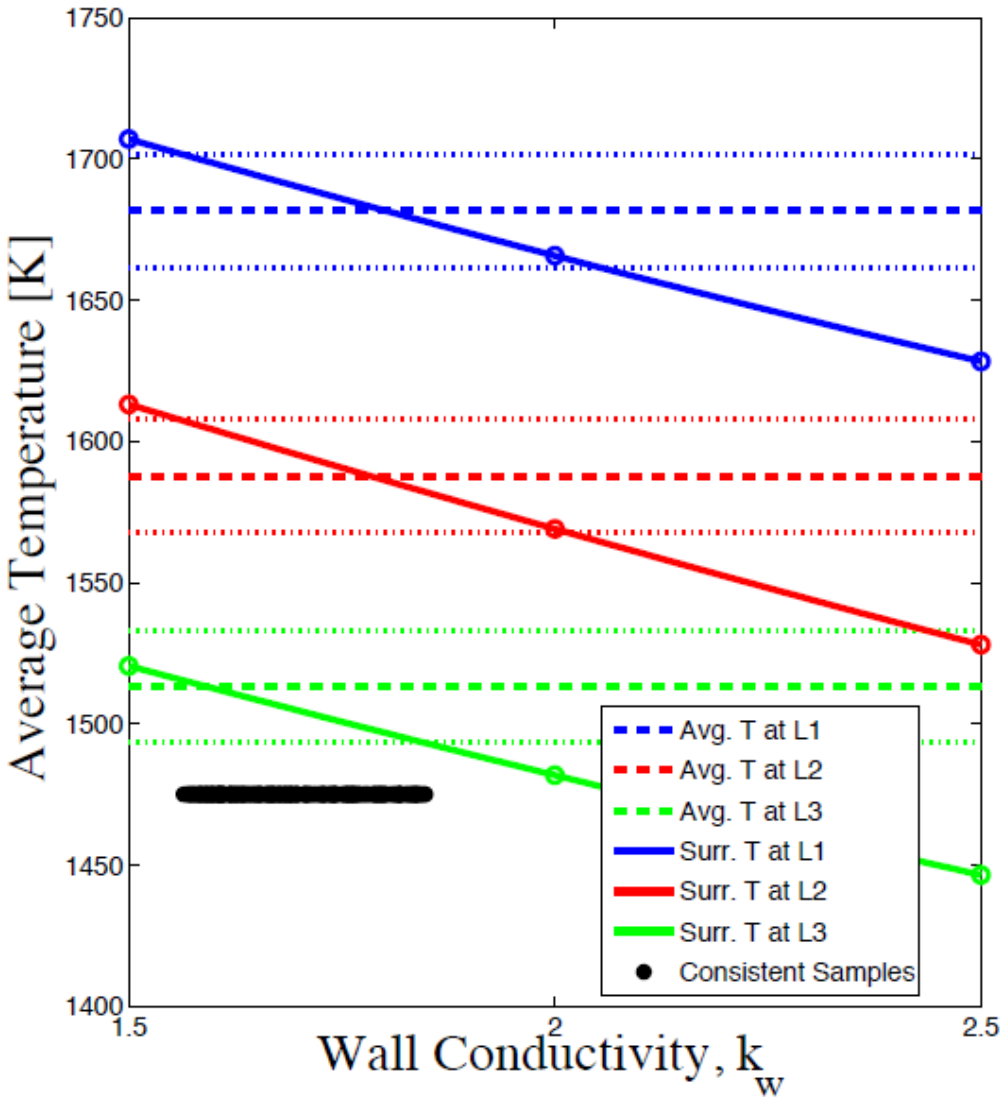

Figure 6-6. LES (a): T: Analysis I: C-3 (1, 4, 5), AV-1 (k_w), O-2 (Average Planar T, HF)

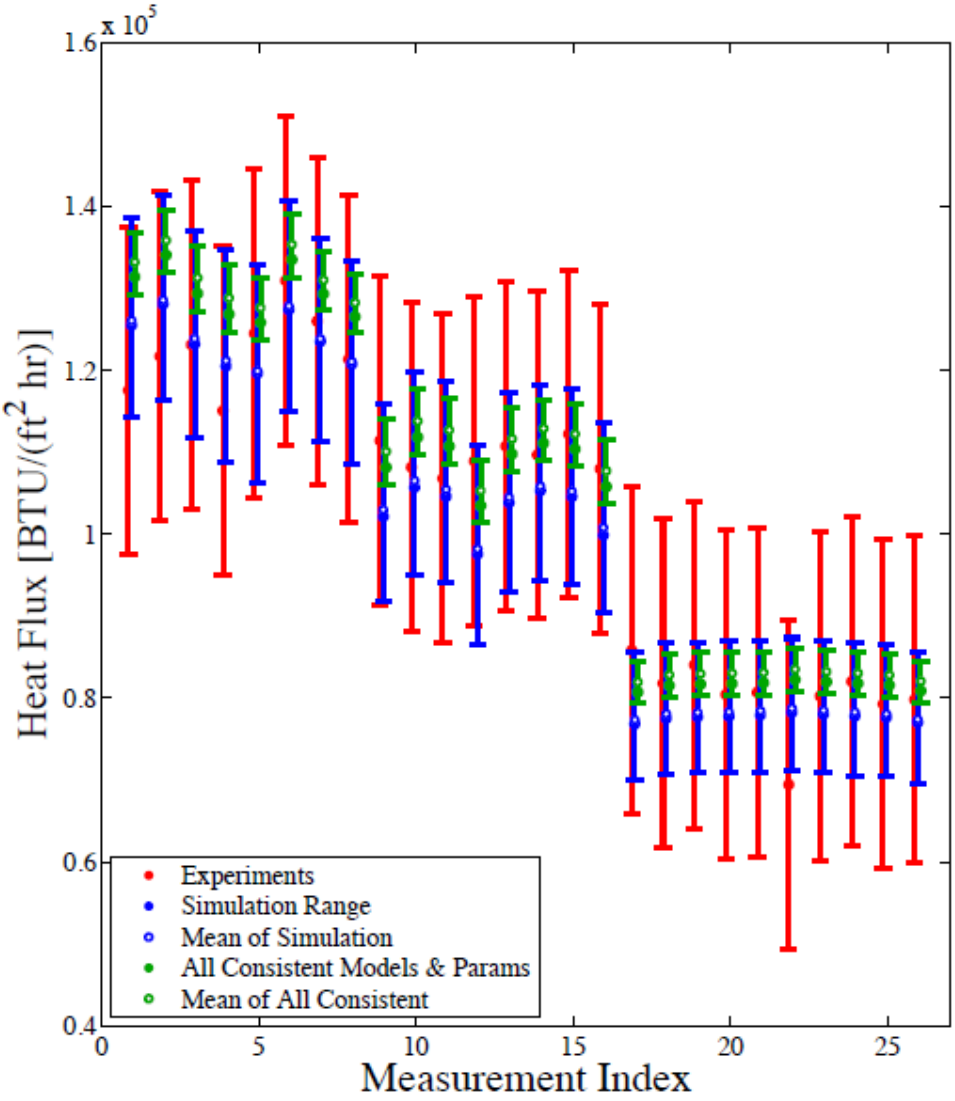

Figure 6-7. LES (b): HF: Analysis I: C-3 (1, 4, 5), AV-1 (k_w), O-2 (Average Planar T, HF)

For the heat flux measurements in Figure 6-7, the simulation (blue) error bars are largely encompassed within the experimental (red) error bars, so that the consistency band (green) is closer to the central portion of the experimental error bars for most of the measurement port locations. The initial experimental uncertainty for the heat flux was estimated to be +/- 6.3×10^4 W/m^2 (or +/- 2.0×10^4 Btu/hr-ft^2), and that value produced a modest consistency region without any adjustment.

6.5.2 Consistency Analysis II: C-3 (1, 4, 5), AV-1 (k_w), O-3 (T, HF, O_2)

The next step in complexity was to increase the number of y_e (or the equivalent d_e) values by using all of the local temperature data (available at 104 measurement locations on Planes 141, 180, and 273) instead of the averaged planar data. The incident heat flux data (available at 26 ports) was retained in the analysis. The mole % (wet) oxygen concentration data (available at 48 measurement points) were also ultimately added as additional y_e. A consistency analysis was performed on all of the point-wise data (simultaneously) for the three values of the thermal conductivity (associated with Cases 1, 4, and 5).

In the initial attempt to use all of the temperature data for Test 134, ICSE found that they had to extend the temperature error bars to +/- 600 K in order to achieve consistency. This degree of error was regarded as unreasonable. Examining the data, they first eliminated all data points that were at least 500 K lower than the body of the data. On Plane 141, there are 8 points near the front and rear walls that exhibit very low temperatures; this is presumably due to ambient cold air leaking through the measurement ports. These low-temperature data points were not mutually consistent with the rest of the data and were considered to be outliers or "bad" data. Apparently 3 other data points were also eliminated by ICSE, so that a total of 93 temperature points (out of the available 104 points) were retained.

A number of the oxygen data points were also problematic and made the consistency analysis struggle. On Plane 141 (between the windbox and lower OFA nozzles), 11 measurement points were removed. The 11 measurement points appeared to exhibit high oxygen levels (e.g., 3.5 to 5.5 mole % (wet)) in a region near the wall, which appeared to be incongruent with the simulations. It is uncertain where the high oxygen is coming from (at least in that particular region of the plane). Speculative reasons given may include: (a) CFS jets from a lower elevation, (b) ambient air leakage coming in with the probe, (c) the actual char burnout rate may be lower than the simulations, producing excess oxygen locally, or (d) unburned particles may be in the core, whereas the CFS gas is around the periphery of the boiler, etc. It may be warranted to examine the probe traces to see if there are any spikes on the oxygen trace that would make the average high. At any rate, the 11 measurement points were eliminated as bad points on a temporary basis, until more of the parameter space is studied. In other words, the thermal conductivity is the only active variable varied at the present time, but other active variables may also have a significant impact on the oxygen at Plane 141. The data deemed to be "bad" data in the present analysis may be found to be mutually consistent when other active variables are appropriately adjusted.

The consistency analysis was performed for both the RANS and LES calculations using the same experimental data points. The experimental error bars or bands that were required to achieve consistency, as well as the values of the wall thermal conductivity in the consistency region, are found in the following table:

Table 6-8. Results for Consistency Analysis II

Parameter	Units	LES	RANS
Upper and Lower Bounds:			
Wall Thermal Conductivity	[Btu/hr-ft-°F]	1.5 to 2.5	1.5 to 2.5
Gas Temperature	[K]	+/- 85	+/- 100
Wall Heat Flux	[Btu/hr-ft^2]	+/- 2.0E+04	+/- 3.0E+04
O_2 Concentration	[Mole % (wet)]	+/- 3.0	+/- 2.5
Consistency Region:			
Wall Thermal Conductivity	[Btu/hr-ft-°F]	1.7 to 1.8	2.3 to 2.5

The LES code is able to demonstrate slightly smaller error bars on temperature and heat flux than the RANS calculations, while the uncertainty on the oxygen concentration is somewhat larger for the LES code than for the RANS code. The uncertainty on the oxygen concentration is somewhat large overall, but the analysis has only been performed only on a single active variable, the wall thermal conductivity, which has a very small effect on the oxygen concentration. Consequently, the consistency analysis needs

to include other active variables (such as coal flow rate or stoichiometry) which will have a greater impact on the oxygen concentration.

The only statement of consistency that can be made at the present time is that simultaneous consistency has been achieved for both the LES and RANS codes. It is evident that the calculated upper and lower bounds for the gas temperature, the wall heat flux, and the oxygen concentration are somewhat different for both codes. However, this fact should not be used to infer that one code is more accurate than the other. Such a conclusion cannot yet be drawn from the analysis. Much more work needs to be done with the analysis before such a conclusion can be entertained:

- First, the experimental uncertainties need to be determined. ICSE (verbal communication) have stated that many published papers indicate that +/- 150 K is a very good uncertainty for suction pyrometry in a cold-walled furnace, due to radiative losses from the probe tip, etc. ICSE is also beginning to look at the experimental uncertainty associated with heat flux probes and sampling probes. Replicates can be used to assess experimental uncertainty, as well as other factors that are sensitive to changes in the observables and that can be independently confirmed. Assessing the experimental uncertainties is a very important "next step" in the data collaboration process. Once the "true" experimental uncertainties have been ascertained, then those "true" experimental uncertainties can be substituted for the "estimated" lower and upper bounds (shown in the above table), that were simply determined as the "incipient inconsistency" thresholds necessary to engender a consistency "region" in the analysis. Use of the "true" experimental uncertainties can then be used to infer whether one or both of the codes (or models within the codes) remains within consistency bounds. If, for example, the model predictions are found to be within the range of the "true" experimental uncertainty, then the model is consistent with the data.

- Secondly, additional active variables need to be studied and analyzed, and more observables (or parameters of interest) also need to be brought into the analysis. The most impactful active variables are supposedly the scenario (boundary condition) variables, such as coal flow rate, windbox oxygen flow rate, recycle gas flow rate, etc. In conjunction with the scenario parameters, the relative influence or accuracy of selected models can be bracketed and properly assessed.

The results for the LES temperature calculations are provided in Figure 6-8. The experiments and associated simulations appear to be in 3 temperature groupings: (a) Plane 141 (highest temperature group) with 23 measurement points out of the 32 available, (b) Plane 180 (intermediate temperature group) with 34 measurement points out of the 36 available, and (c) Plane 273 (lowest temperature group) with 36 measurement points (out of the 36 available). The simulation range (blue line) appears to be well within the experimental error bands (red line) for most of the points, although the simulation range appears to extend beyond the error bars of the red line for several points.

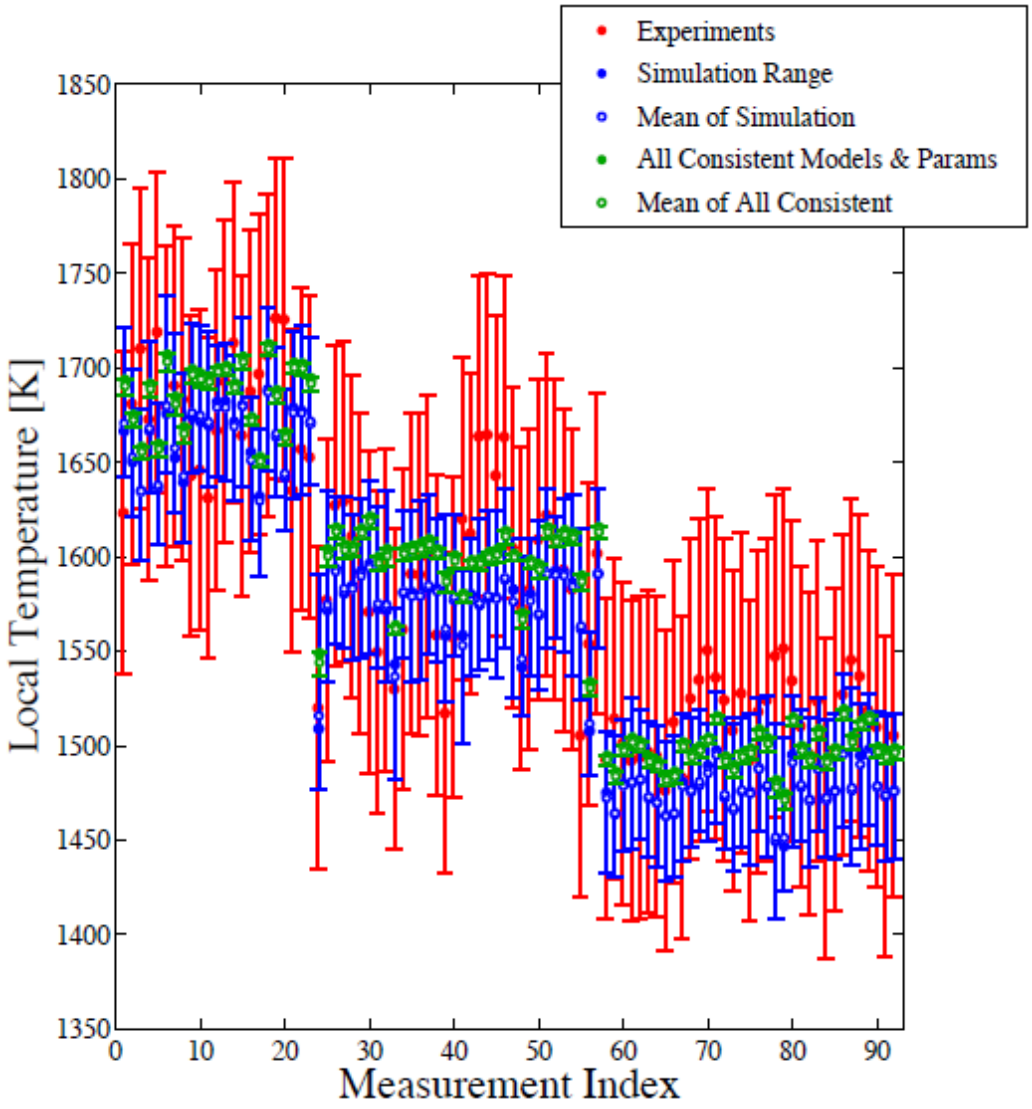

Figure 6-8. LES (a): T: Analysis II: C-3 (1, 4, 5), AV-1 (k_w), O-3 (T, HF, O_2)

The consistency range for the thermal conductivity in the LES calculations is from 1.7 to 1.8 Btu/hr-ft-°F, the lower end of the overall range of 1.5 to 2.5 Btu/hr-ft-°F. A lower thermal conductivity (corresponding a higher insulative capacity) will yield a higher calculated gaseous temperature and wall heat flux. Consequently, the green line segments are above the midpoint of the calculated temperature range. The same observation will be true for the heat flux in the following figure.

The results of the LES heat flux calculations are provided in Figure 6-9 and the oxygen concentration comparisons are shown in Figure 6-10. The heat flux results are very similar to those shown earlier, except that the consistency region (green line) is smaller, presumably because consistency must be ensured across all of the many temperature and oxygen concentration points, as well as the heat flux.

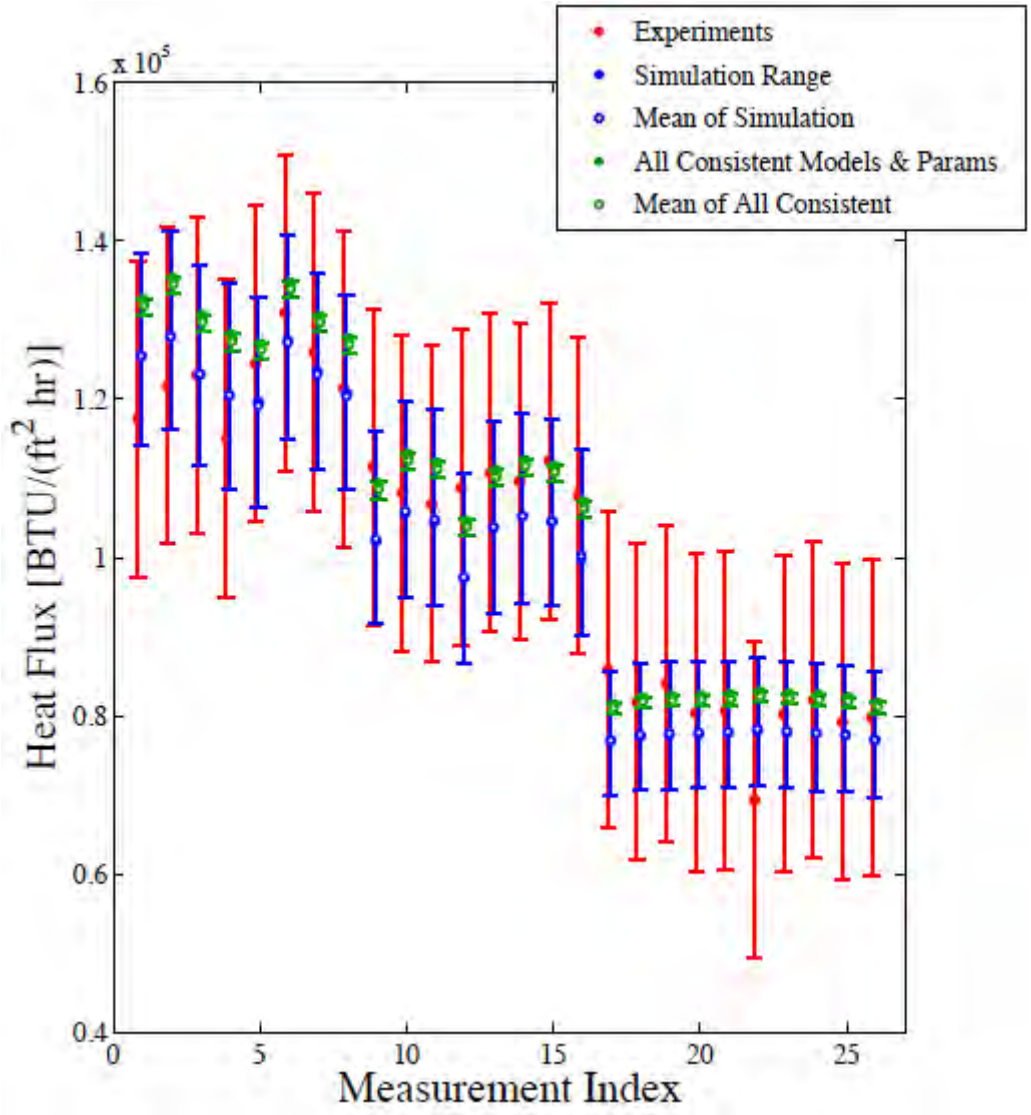

Figure 6-9. LES (b): HF: Analysis II: C-3 (1, 4, 5), AV-1 (k_w), O-3 (T, HF, O_2)

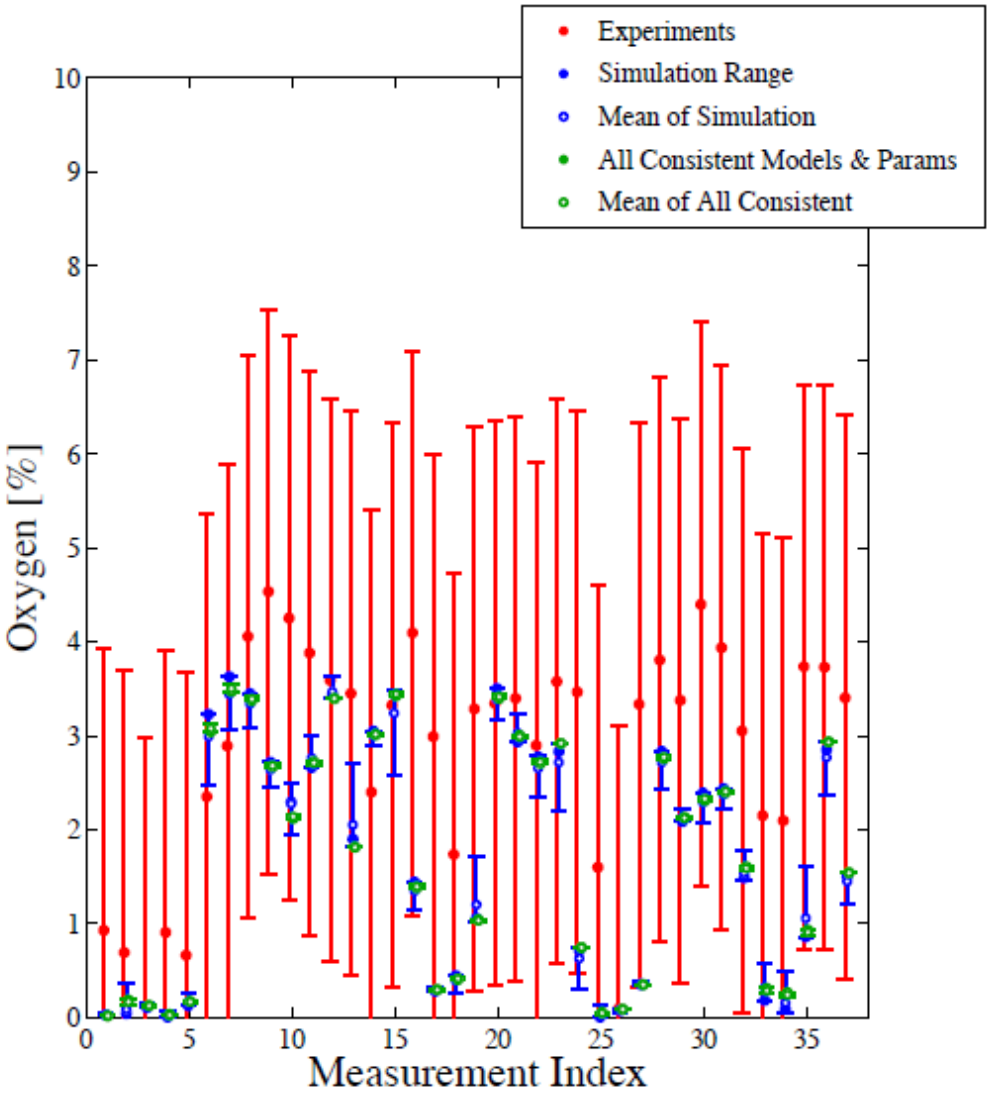

Figure 6-10. LES (c): O_2: Analysis II: C-3 (1, 4, 5), AV-1 (k_w), O-3 (T, HF, O_2)

It is apparent that the blue simulation bars are larger on the temperature and heat flux plots than they are on the oxygen plot, because the wall thermal conductivity has a correspondingly larger impact on the temperature and heat flux observables, but a much smaller impact on the oxygen concentration. In fact, the blue (simulation) lines and green (consistency) lines on plots associated with an analysis that consists solely of the temperature plus heat flux data should be almost identical to the blue and green lines on plots associated with an analysis that consists of temperature plus heat flux plus oxygen concentration data, simply because the oxygen concentration is so insensitive to the wall thermal conductivity. Although the impact of the thermal conductivity is small, it does vary a little at some of the point locations. For example, it has been observed that the green consistency region is at the bottom of the blue (calculated) line at Locations 13 and 19, but at the top of the blue (calculated) line at Locations 15 and 23. Perhaps this lack of ordered behavior is another indication of the insensitivity of the oxygen to the thermal conductivity and the points are simply responding to the inherent noise caused by the uncertainty in other factors in the calculations.

The results of the RANS temperature calculations are provided in Figure 6-11, the heat flux calculations are shown in Figure 6-12, and the oxygen concentration comparisons follow in Figure 6-13. As indicated in a previous table, the error bars on the temperature observables (+/- 100 K) are larger than those associated with the LES calculations. The simulation lines are consistently positioned towards the top half of the (red) experimental error bar lines. As mentioned earlier, the same delta in the wall thermal conductivity produces a simulation response range in the RANS calculation that is almost twice as large as the corresponding range in the LES calculations (for reasons that are presently unknown).

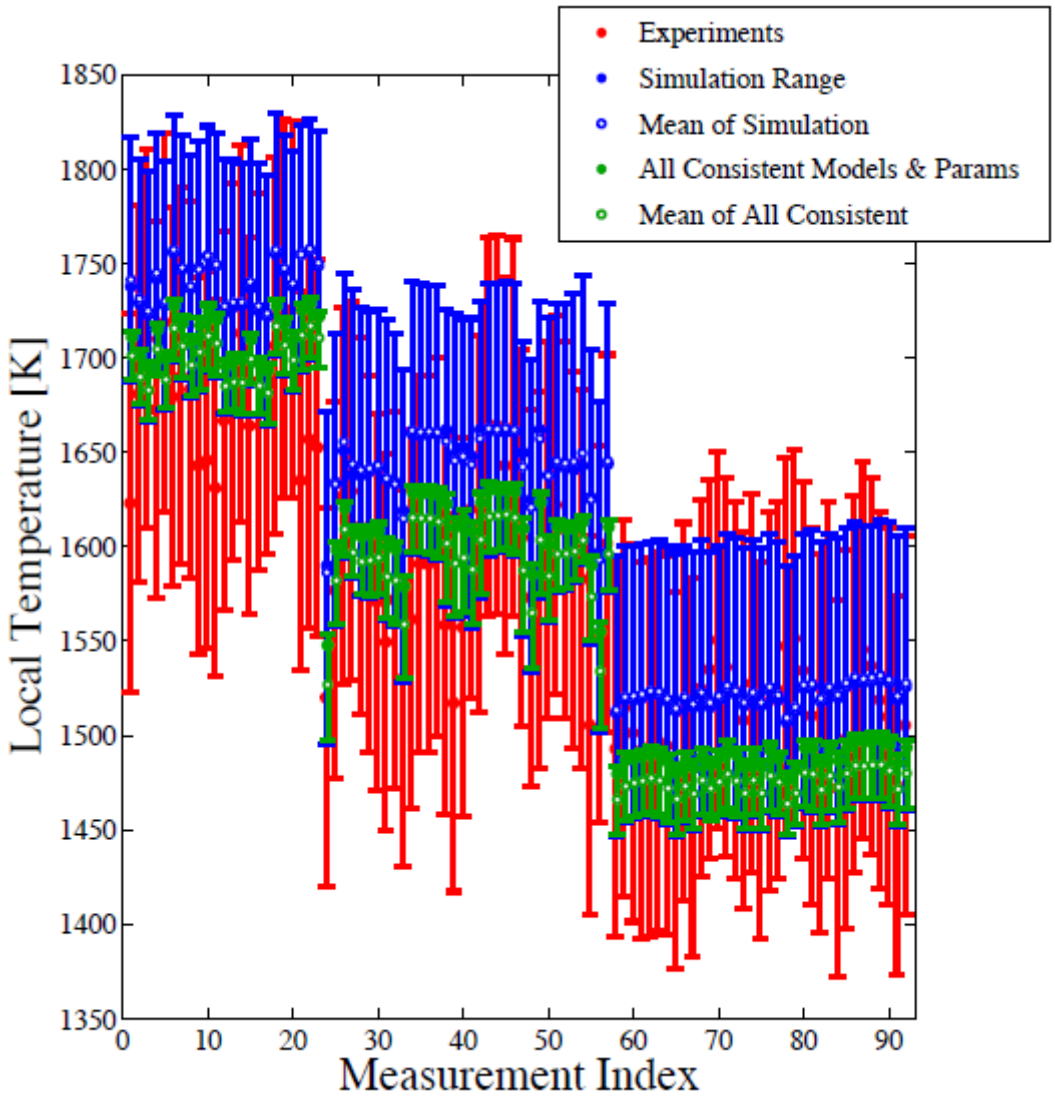

Figure 6-11. RANS (a): T: Analysis II: C-3 (1, 4, 5), AV-1 (k_w), O-3 (T, HF, O_2)

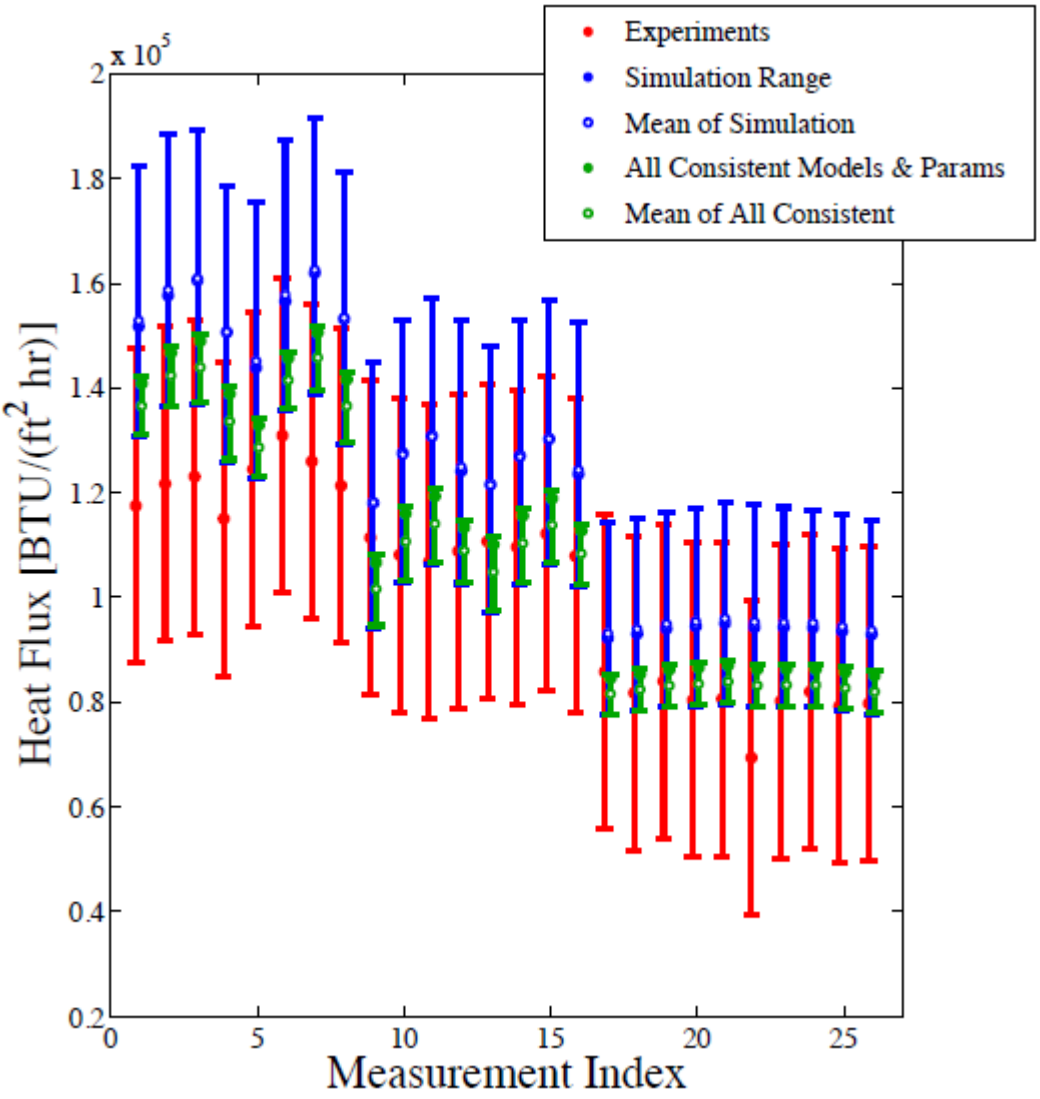

Figure 6-12. RANS (b): HF: Analysis II: C-3 (1, 4, 5), AV-1 (k_w), O-3 (T, HF, O_2)

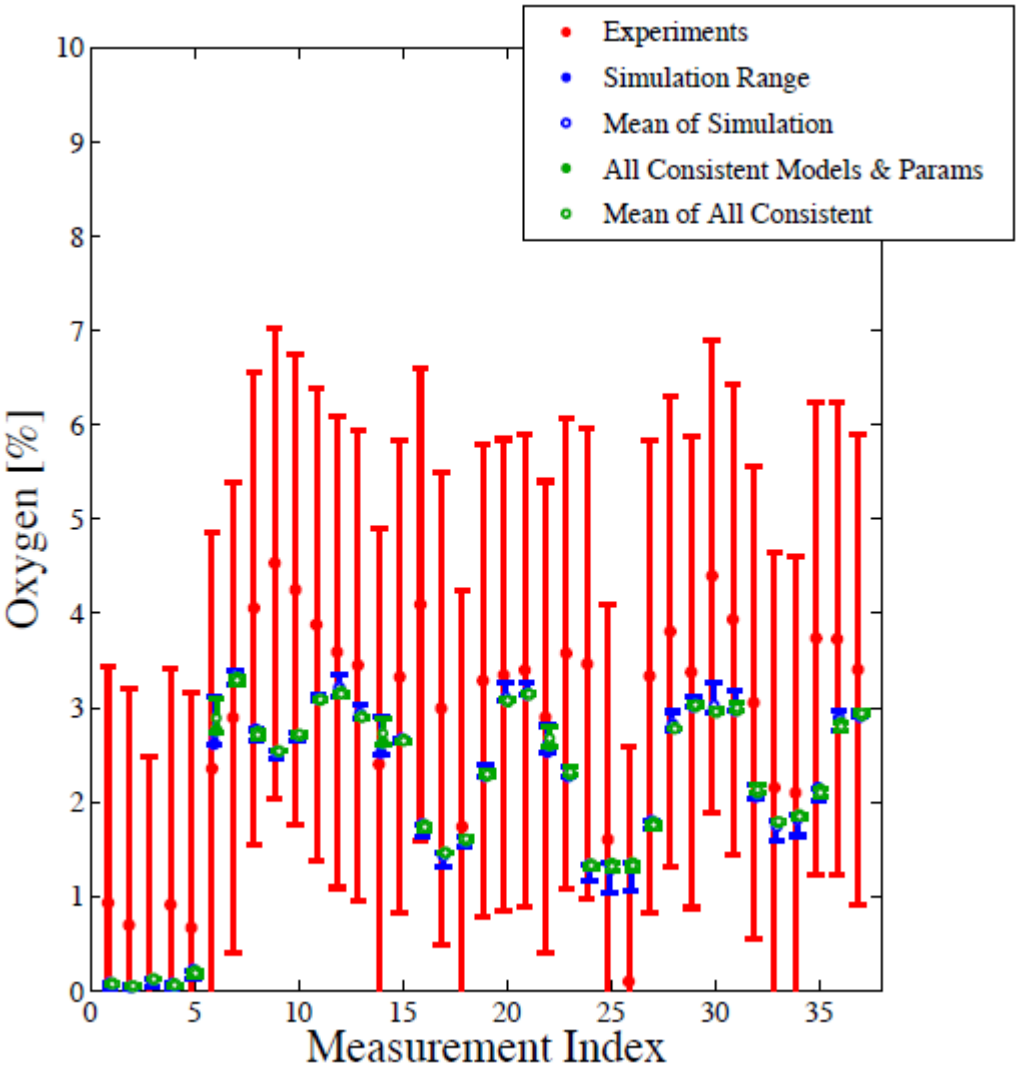

Figure 6-13. RANS (c): O_2: Analysis II: C-3 (1, 4, 5), AV-1 (k_w), O-3 (T, HF, O_2)

The consistency range for the thermal conductivity in the RANS calculations is from 2.3 to 2.5 Btu/hr-ft-°F, the upper end of the overall range of 1.5 to 2.5 Btu/hr-ft-°F. A higher thermal conductivity (corresponding to a lesser insulative capacity) will yield a lower calculated gaseous temperature and wall heat flux. Consequently, the green line segments in the temperature plot are below the midpoint of the calculated temperature range. The same observation is true for the heat flux.

The simulation heat fluxes for the RANS calculations, in a manner similar to the simulated temperatures, tend to overlap with the upper "half" of the experimental ranges. The RANS heat flux plot also is similar to that of the temperature plot, in that the change in the heat flux for a given delta in the wall thermal conductivity is much larger than the corresponding change in the LES heat flux.

The oxygen plot indicates very small simulation ranges (blue lines), again indicating that the wall thermal conductivity has very little effect on the oxygen. The effect is smaller than that exhibited in the LES results. Nevertheless, the consistency region appears to exist at both the top of the calculated (blue) line segments at some locations and at the bottom of the calculated (blue) line segments at other locations.

The inconsistent or "random" nature of this behavior is again indicative of the inherent noise or variability in the solution masking any underlying sensitivity.

In a similar manner, the observation that the change in the RANS temperature and heat flux values, for a given delta in the wall thermal conductivity, is almost a factor of two larger than the corresponding change in the LES observables, requires attention. This disparity in behavior between the codes has not been explained, and this issue needs to be resolved before too many LES computations are completed.

6.5.3 Consistency Analysis III: C-7 (1-7), AV-3 (k_w, CFR, DR), O-3 (T, HF, O_2)

For Consistency Analysis III, the complexity was augmented by increasing the number of independent or active variables from one to three. In addition to the wall thermal conductivity, the inlet coal mass flow rate and devolatilization rates were also added to the list of active variables. To accommodate the augmented list of active variables, the number of case simulations was also increased from three (3) to seven (7), where the pertinent cases correspond to cases in which the three active parameters were independently varied. The cases include (for additional details refer back to **Table 6-7**):

- Case 1 (Baseline): the thermal conductivity (k_w) = 3.46 W/m-K, the inlet coal mass flow rate (CFR) = 0.6255 kg/s, the devolatilization rate (DR) = baseline rate.
- Case 2: CFR = 0.635 kg/s, with other parameters at baseline values.
- Case 3: CFR = 0.616 kg/s, with other parameters at baseline values.
- Case 4: k_w = 2.60 W/m-K, with other parameters at baseline values.
- Case 5: k_w = 4.33 W/m-K. with other parameters at baseline values.
- Case 6: DR = 0.2 x baseline rate, with other parameters at baseline values.
- Case 7: DR = 5.0 x baseline rate, with other parameters at baseline values.

Cases 6 and 7 had not been run with the previous batch of runs that had been post-processed and sent to ICSE. Therefore, Cases 6 and 7 were run by Alstom, post-processed, and the requisite outputs were newly sent to ICSE for analysis. Only the RANS computations have been analyzed by ICSE to date.

A consistency analysis was performed by ICSE for the set of 7 cases, 3 active variables, and 3 observables (or targets). As before, in order to achieve consistency with reasonable error bounds or interval bounds on the experimental data, some of the data points were eliminated. The data points eliminated for the consistency analysis are itemized below (the entries or lines for the eliminated points are on data tables that are not shown):

- Temperature: points (or lines) 51, 55, 59, 63, 67, 71, 75, and 79 – These are 8 points (previously identified) on Plane 141 near the front and rear walls that exhibit very low temperatures; this is presumably due to ambient cold air leaking through the measurement ports.
- Temperature: points (or lines) 130 – This is a point (previously identified) that is a repeat simulation value.
- Temperature: points (or lines) 158, 160, 161, 162, and 165 – Reasonable temperature values, but they required that the experimental "error" bars on the temperature be about +/- 200 K. It was the desire of ICSE to make the error bars tighter in the present analysis, so those particular temperature points were eliminated from consideration.

- Oxygen: points (or lines) 3, 4, 5, 7, 8, and 13 – These are part of a set of points (previously identified) on Plane 141 (between the windbox and lower OFA nozzles), that exhibit high oxygen levels (e.g., 3.5 to 5.5 mole % (wet)) in a region near the wall, which appear to be incongruent with the simulations.

ICSE provided a spreadsheet that delineated each of the measurement points, along with a separate column with a logical parameter (e.g., "true") to indicate whether the point was eliminated from the analysis. Out of 116 temperature measurements, 15 were removed, leaving 101 measurements for the analysis. The final six (6) of those temperature measurements encompass Ports 123, 125, and 126, that are located in a vertical plane (essentially Plane 376 (VFOP)) in the upper furnace. Out of 48 oxygen measurements, 6 points were removed, leaving 42 points for the analysis. All of the heat flux measurements (26 points) were retained in the analysis (some of which had replicates).

The consistency analysis was performed for both the RANS and LES calculations using the same experimental data points. The experimental error bars or bands that were required to achieve consistency, as well as the values of the wall thermal conductivity in the consistency region, are found in the following table:

Table 6-9. Results for Consistency Analysis III

Parameter	Units	RANS
Upper and Lower Bounds:		
Gas Temperature	[K]	+/- 125
Wall Heat Flux	[Btu/hr-ft^2]	+/- [varies for each port]
O_2 Concentration	[Mole % (wet)]	+/- 2.0
Consistency Region:		
Wall Thermal Conductivity	[Btu/hr-ft-°F]	2.285 to 2.373
Coal Flow Rate (CFR)	[kg/s]	0.6046 to 0.6148
Devolatilization Rate (DR)	[Note 1]	-2.302 to 2.299
Note 1:	Range based on the ln(multiplier on pre-exponential factor). An upper limit of 2.3 corresponds to a multiplier of 10, and a lower limit of -2.3 corresponds to a multiplier of 0.1.	

The results of the RANS temperature calculations are provided in Figure 6-14, the heat flux calculations are shown in Figure 6-15, and the oxygen concentration comparisons follow in Figure 6-16. The term QOI on the ordinate labels refers to "quantity of interest."

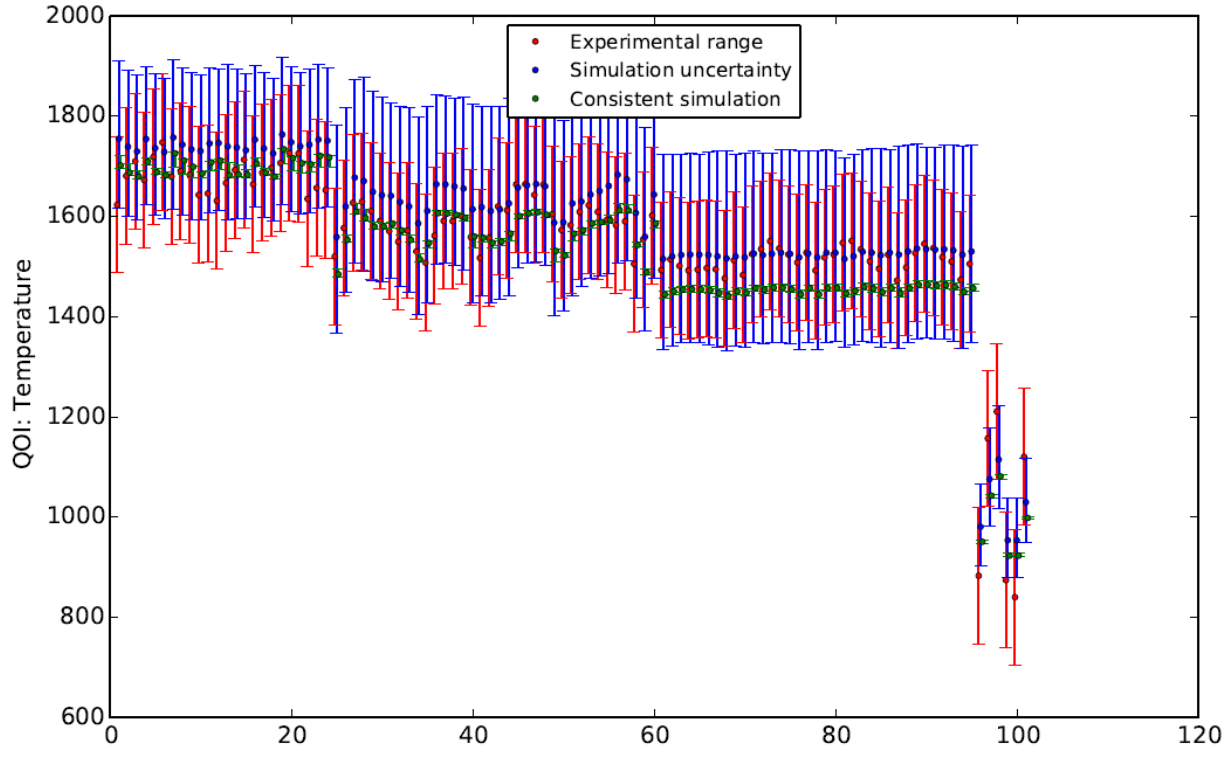

Figure 6-14. RANS (a): T: Analysis III: C-7 (1-7), AV-3 (k_w, CFR, DR), O-3 (T, HF, O_2)

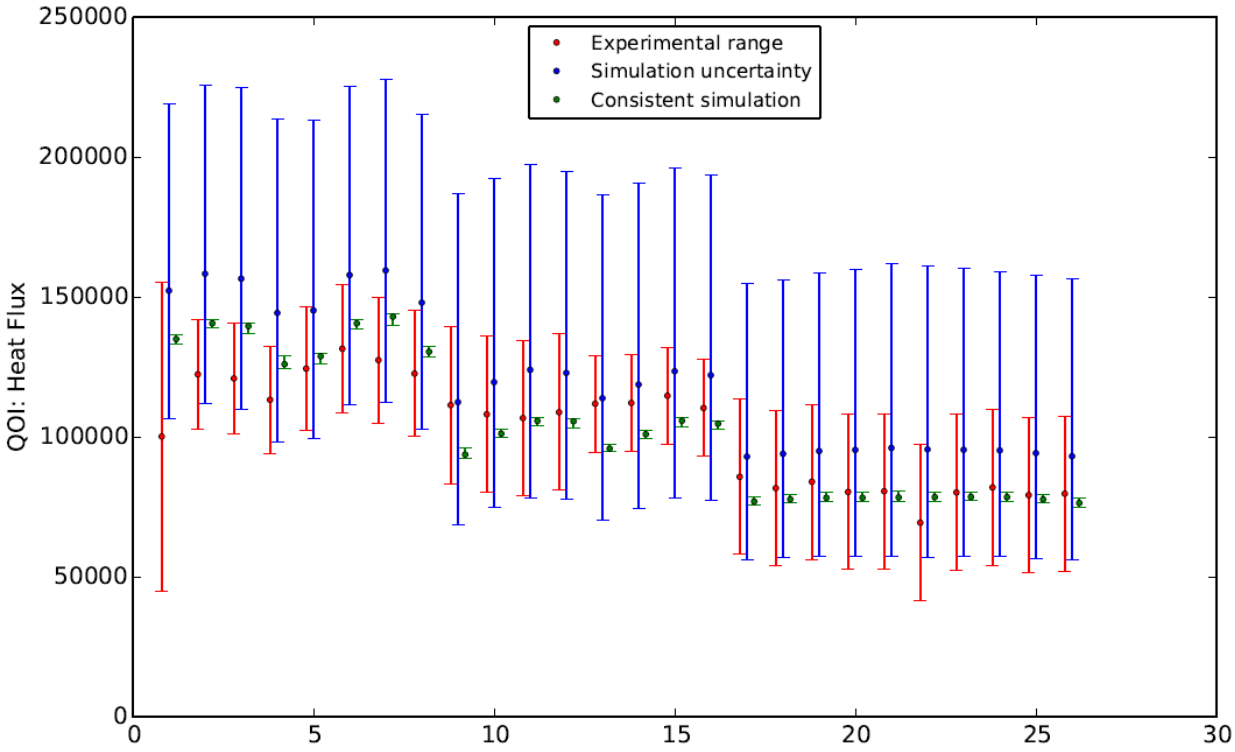

Figure 6-15. RANS (b): HF: Analysis III: C-7 (1-7), AV-3 (k_w, CFR, DR), O-3 (T, HF, O_2)

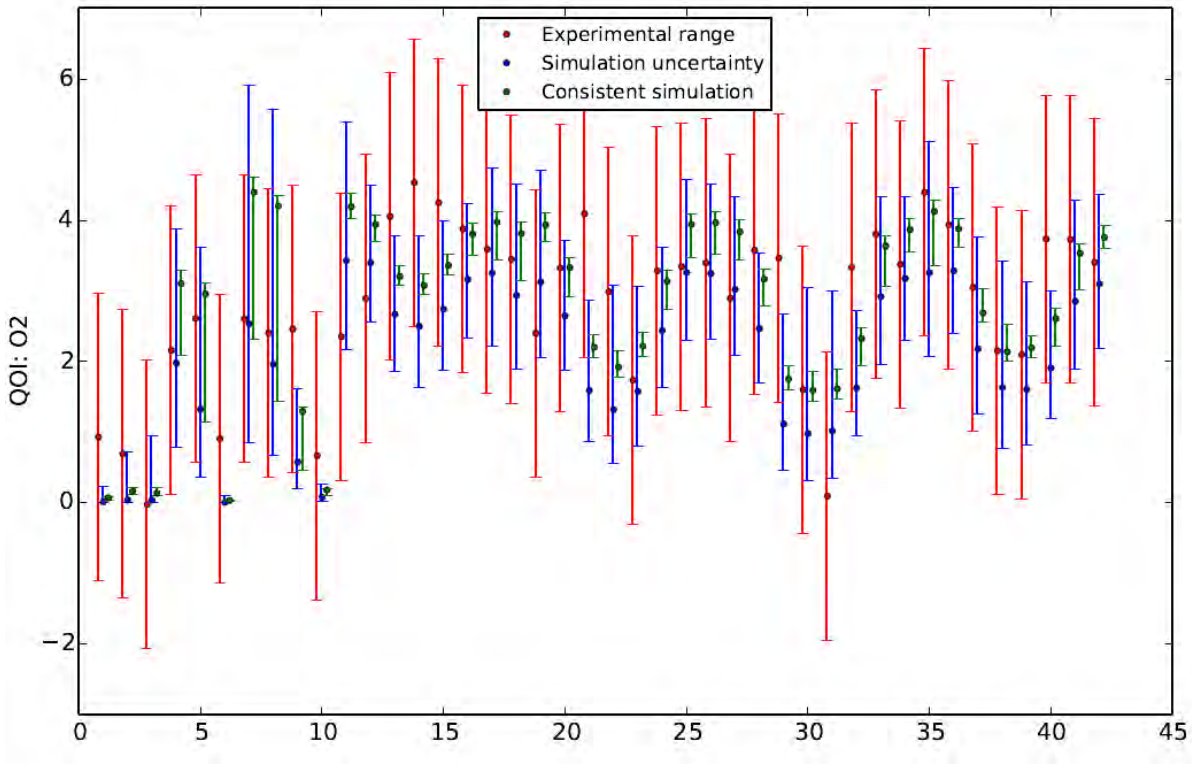

Figure 6-16. RANS (c): O_2: Analysis III: C-7 (1-7), AV-3 (k_w, CFR, DR), O-3 (T, HF, O_2)

ICSE used Bayesian data analysis to calculate an estimate of the experimental error bounds (red lines) based on a guessed prior. For the heat flux, the prior was equal to +/- 15,000 Btu/hr-ft^2; for the temperature, the prior was equal to +/- 50 K; and for the oxygen, the prior was equal to +/- 0.75 mole % (wet). However, because both the temperature and the oxygen concentration points only have 1 replicate, the Bayesian analysis gives a larger range for the error bars than the initial guessed priors – i.e., temperature: initial prior of +/- 50 K increased +/- 125 K, and oxygen concentration: initial prior of +/- 0.75 increased to +/- 2.0 mole % (wet). In addition, the error bars for the temperature and oxygen data are both self-consistent, since they all used the same priors and had the same number of replicates (1 in the present case). This result is consistent with what is observed in the Student's t-test, which gives a larger error with fewer observations (or replicates). For the heat flux, the prior for the experimental error bounds was equal to +/- 15,000 Btu/hr-ft^2, but after the Bayesian analysis with the replicates, the smallest bounds are on the order of +/- 18,000 Btu/hr-ft^2, while the largest bounds are perhaps +/- 55,000 Btu/hr-ft^2. The bound intervals appear to be grouped in the heat flux figure – each of the first four successive groups have a distinct number of replicates (each group having 4 data points each); the next point only has 1 replicate, and the final 9 points have 2 replicates per point. It can be seen that, except for the first point, each of those groups tends to have its own distinct set of error bars that appears to be a strong function of the number of replicates.

The bounds on the simulation lines (blue) are simply the largest and smallest values of the quantity of interest (QOI) predicted from the surrogate model over the range of model parameters selected. The solid blue circle shows an estimation of the observable or QOI from the surrogate model, where the model parameters are evaluated in the middle of their respective dimensions or ranges. For example, for the first heat flux point or observation, the blue circle or marker corresponds to a predicted heat flux of slightly over 150,000 W/m^2 (47,580 Btu/hr-ft^2). The marker was calculated by the surrogate model with a CFR of

0.6255 kg/s (midway between 0.616 and 0.635 kg/s), a thermal conductivity of 2.0 Btu/hr-ft-°F (midway between 1.5 and 2.5 Btu/hr-ft-°F), and a devolatilization rate multiplication factor of 1.0 (halfway between 0.2 and 5 on a logarithmic scale).

The green lines denote the consistency region. The green bounds are the interval of consistency between experiments and simulations over all of the model parameters. The green marker is the most consistent point within the consistency interval, calculated using the δ ("delta") parameter, defined as:

$$\delta = \frac{model\ value - mean\ experimental\ value}{confidence\ interval} \qquad (5)$$

Figure 6-14 shows the experimental range, the simulation range, and the consistency range for each temperature measurement point (with the exception of the excluded points), in units of K. The temperatures appear to be grouped (in four distinct groups) as a function of the planes they represent – Plane 141 (left-most group), Plane 180, Plane 273, and Plane 376 (right-most group). As indicated in the previous results table for Consistency Analysis III, the error bars on the temperature observables (approximately +/- 125 K) are slightly larger than those utilized in Consistency Analysis II (+/- 100 K). In accordance with the +/- prescription, the red solid dot/circle is located in the middle of the experimental "error" bars. The simulation (blue) lines are consistently positioned towards the top half of the (red) experimental error bar lines.

It can be seen that the consistency region on the temperature and heat flux plots (and on much of the oxygen plot) are mere "slivers." The intent in this analysis was to select an experimental uncertainty for the temperature that would make the consistency region as narrow or as small as possible. Since the experimental uncertainties are somewhat fabricated and not yet based on a more rigorous determination of the experimental error bounds, the consistency analysis does not produce a true or reliable posterior.

The heat flux plot is given in units of Btu/hr-ft^2. As mentioned previously, the upper and lower bounds for the experimental wall heat flux vary for each port. The simulation (blue) lines appear to be almost twice as long as the experimental (red) lines for most of the port measurements. However, the simulation markers (solid blue circles) calculated from the interval averages, appear to reside within the experimental bounds, with the exception of Plane 141.

The plot of the oxygen concentration is in units of mole % (wet). Its experimental error bars are at +/- 2%, which is somewhat large, but is still less than the +/- 2.5% associated with Consistency Analysis II. The simulation (blue) lines are much larger than those presented earlier in Consistency Analysis II, indicating that while the wall thermal conductivity does not impact the oxygen concentration (as learned from previous Analysis II plots), the coal feed flow rate and the devolatilization rates apparently do have an effect.

A three-dimensional plot, showing the consistency space (the black rectangle) for the three (3) active variables (wall thermal conductivity, coal flow rate (CFR), and devolatilization rate (DR)) is shown in Figure 6-17. The dimensions of the rectangle correspond to the consistency region bounds listed in Table 6-9. The colored dots or markers within the consistency rectangle are samples from the Monte Carlo or random sampling procedure that are evaluated through the surrogate models. The color of the markers corresponds to the δ or "delta" parameter shown earlier. Blue colored markers, corresponding to a near-zero delta, are the most consistent (meaning that they are closer to the experimental data), and the dark red

colors, corresponding to near-unity value, correspond to the least consistent values. The coal flow rate and the thermal conductivity exhibit rather narrow bounds for the consistency region, with a higher consistency (lower δ value) closer to a CFR of 0.61 and at the higher devolatilization rates. Nevertheless, the devolatilization rate exhibits consistency essentially over its entire range (corresponding to an order of magnitude change in the rate multiplier). Consequently, it can be concluded that the devolatilization rate actually has very little impact on the observables over the exercised range. In other words, the solution for an order of magnitude change in the rate multiplier is essentially identical to the solution where the rate multiplier is unity.

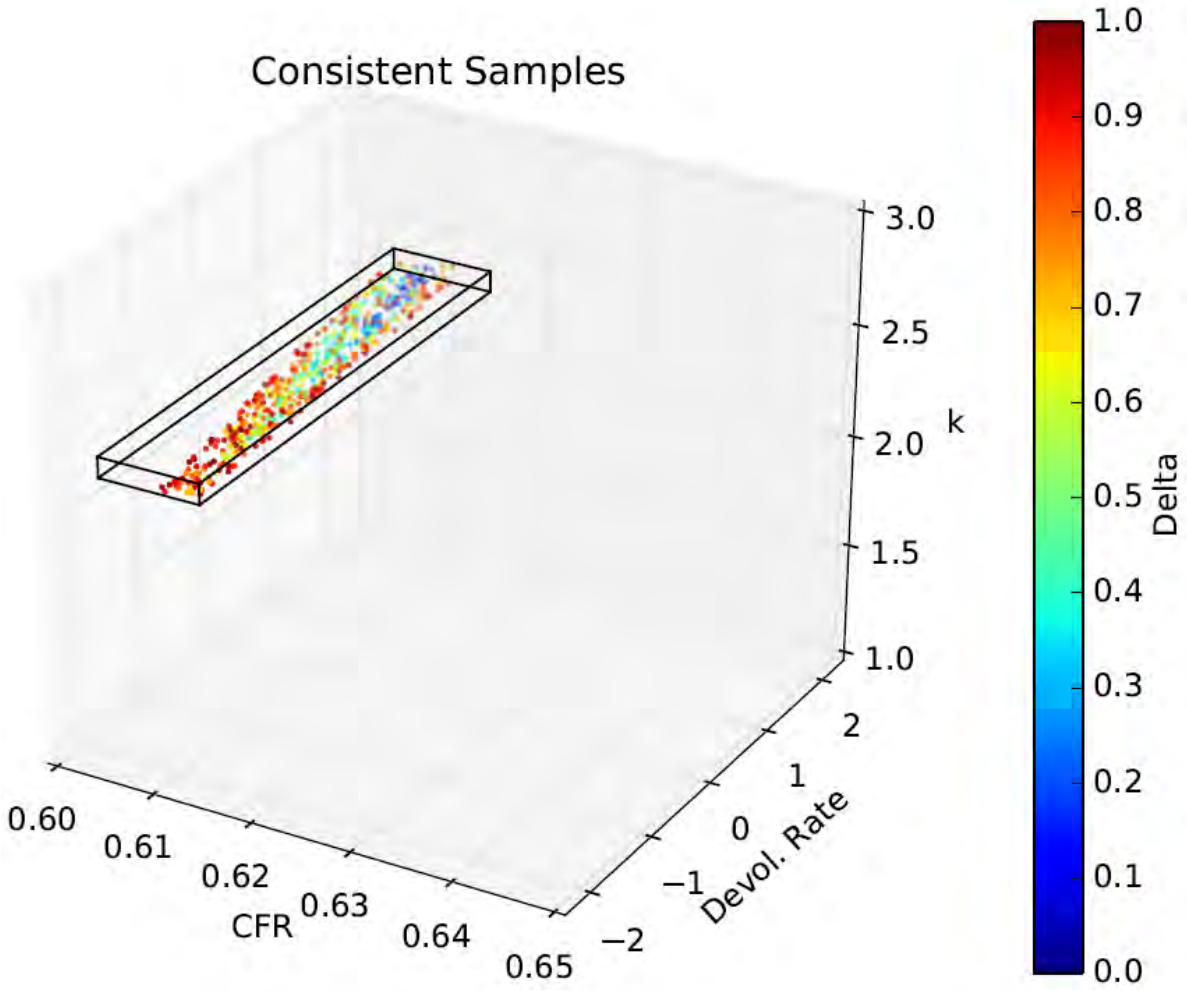

Figure 6-17. RANS (d): Consistent Sample Space for Analysis III

Closing Comments

The I/U map was constructed with the intent to prioritize factors that influence the heat transfer. Since a targeted quantity of interest in boiler design is the heat flux, then it is apparent that the thermal conductivity appears to be a very strong active variable. Given the sensitivity of the heat flux to the thermal conductivity from both the LES and RANS calculations, it is apparent that extrapolations to a commercial unit, based on the BSF experience alone, could not be accomplished with any reasonable degree of confidence. This was perhaps obvious from the outset, given the different fouling and slagging

characteristics of the various coals, and the change in deposit thickness as a function of elevation or proximity to certain nozzles. Nevertheless, the results indicate that (a) additional experiments must be performed that are closer to their intended use, or (b) fundamental deposition and slagging models must be developed with which to perform the predictive extrapolation.

When the consistency analysis becomes more complete, the resultant information can then be fed back to the validation framework so that the I/U map can be updated, and another round of the six-step procedure can be re-initiated. The feedback can be used to point to defects in the model, so that plans can be made to research solutions for those defects, or the feedback can be used to point to outlier data (which it has already done) or to data with significant measurement bias, so that corrective action can be taken.

7. Contour Plots and Visual Comparison

LES codes attempt to directly resolve a portion (e.g., 80%) of the turbulent kinetic energy spectrum, typically the larger length scales, and use modeling approximations to account for the smallest (dissipative) scales. The resolution of these turbulent eddies of varying spatial and temporal scales may be critical in correctly predicting the underlying physics that control boiler characteristics. Flame stability, particle drag effects, emissions, and other phenomena are strongly coupled to the turbulent eddies, which in turn, have an impact on the oxidant concentrations, local wall heat flux, etc. The LES codes are run in a time-accurate manner so that the majority of the turbulent kinetic energy spectrum is resolved, thus promoting much greater fidelity and reliability in the simulation than RANS computations.

An example of a volume-rendered gas temperature field at an arbitrary time step, using the ARCHES code, is provided in Figure 7-1. The impact of the turbulent eddies on the flame structure is evident.

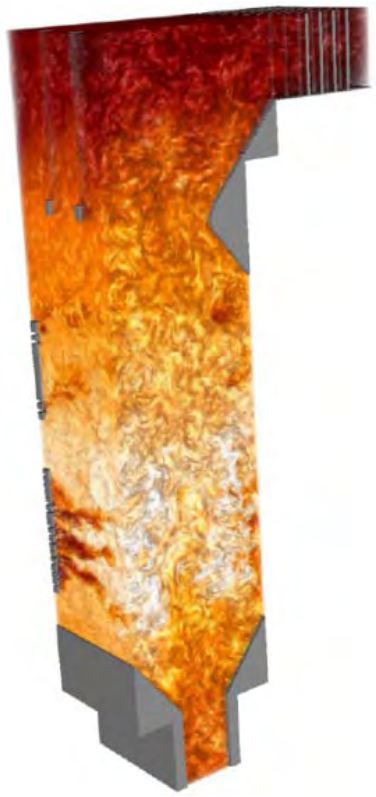

Figure 7-1. Gas Temperature Field in BSF Using ARCHES (Ref. 16)

Not all of the physics within the boiler are equally susceptible to the short time-scale phenomena. For example, the radiation flux to the walls responds instantaneously to the local temperatures, but since each ray must travel through a large volume of the domain, the integrated traces exhibit smoother results over time. The impact of the turbulent eddies on the particle number density depends on the particle size. This effect is shown in Figure 7-2. The particle number density is normalized to the inlet value, so that values greater than unity indicate particles clustering locally.

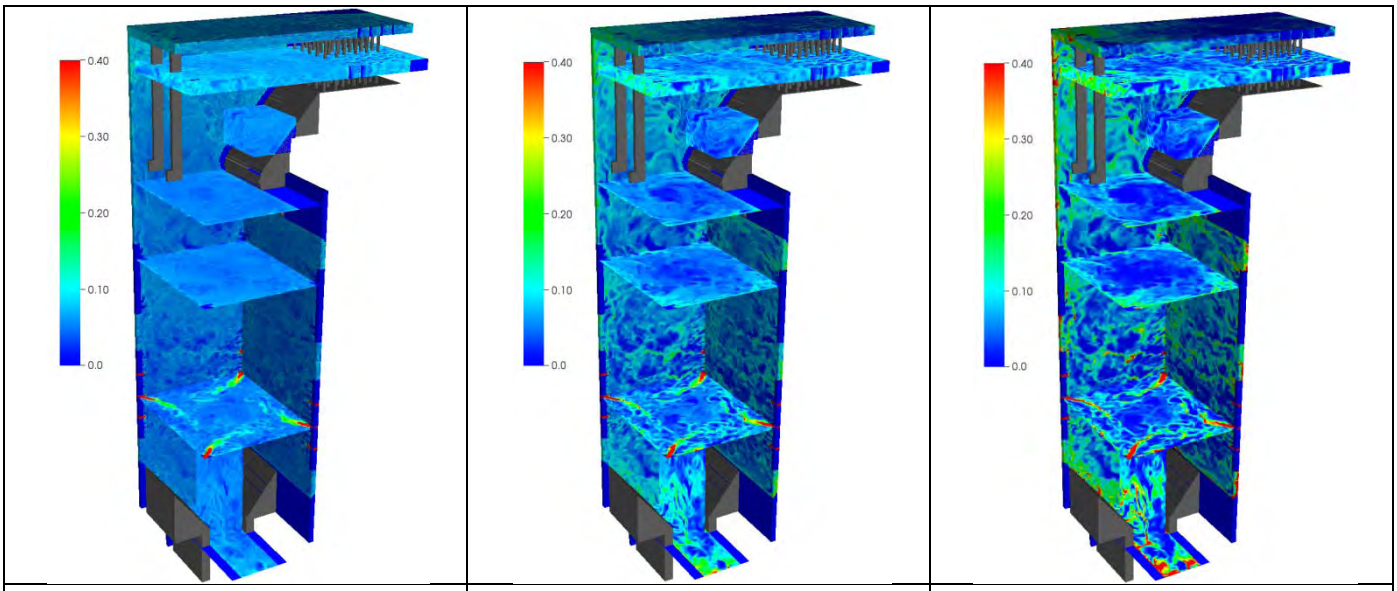

(a) d_p = 30 μm | (b) d_p = 60 μm | (c) d_p = 90 μm

Figure 7-2. Particle Number Density as a f(Particle Size) Using ARCHES (Ref. 11)

As the particle size changes, the particle inertia will change. This makes the particles with different sizes respond differently to the local turbulent eddies. The small particles have very little inertia and will be entrained by the small scale turbulent eddies, which enhances their diffusion. Thus, in Panel (a) the small particles are more evenly distributed within the furnace. As particle size increases, the particle inertia increases by the particle diameter to a power of 3. Consequently, the small-scale turbulent eddies have little effect on the ballistic motion of these larger particles. Therefore, in Panel (c), the larger particles concentrate along the edges of coherent structures, and the clusters are more segregated.

A comparison of gas temperature contour plots, in which steady-state FLUENT® calculations are compared with time-averaged ARCHES calculations, is provided at four different planar elevations in Figure 7-3. The temperature is in units of °F. In the time-averaging procedure, the time-mean temperature was computed by weighting the temperature by the mass flux. It should be stressed that the ARCHES results represent some intermediate (time-averaged) results achieved in 2013 (Ref. 11). ICSE has since changed the particle size distribution (and perhaps made other changes as well), all of which may require recalibration of the wall boundary condition. Therefore, the ARCHES results plotted here should be considered to be interim results and not final results.

Gas Temperature (°F)

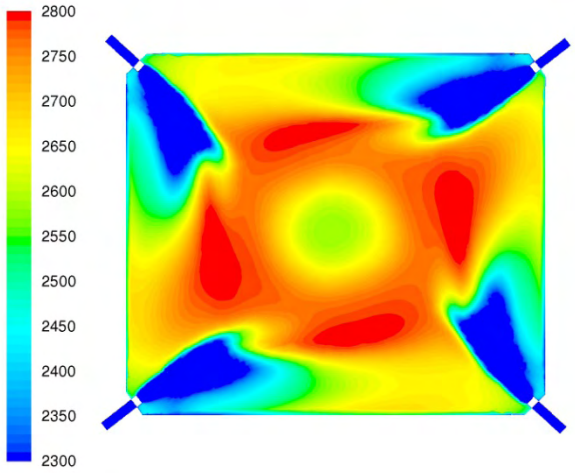

(a) FLUENT: Elevation = 3.86 m (Lower Coal)

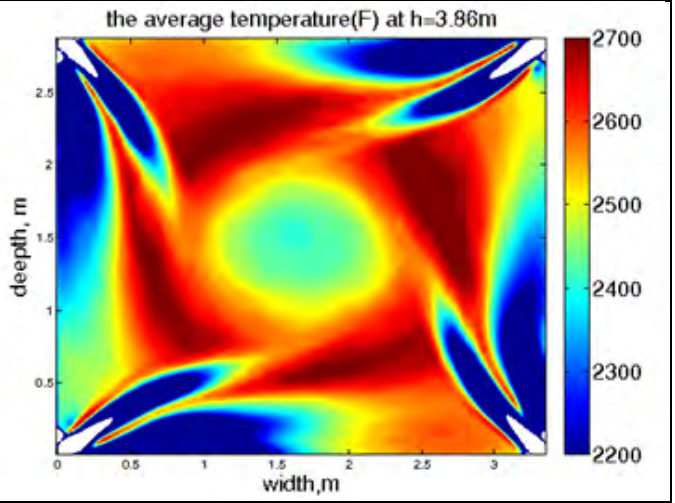

(b) ARCHES: Elevation = 3.86 m (Lower Coal)

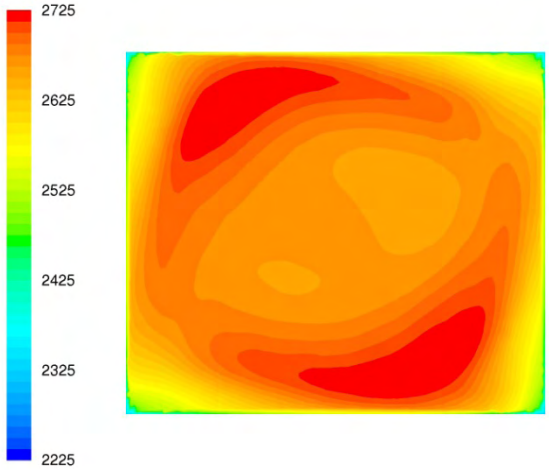

(c) FLUENT: Elevation = 6.38 m (Plane 141)

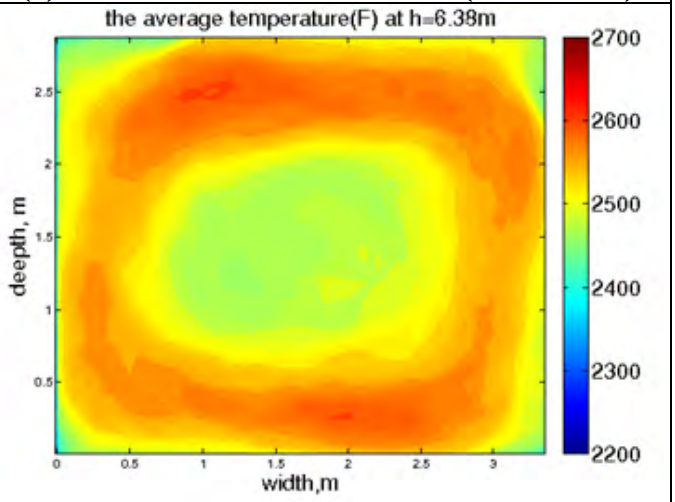

(d) ARCHES: Elevation = 6.38 m (Plane 141)

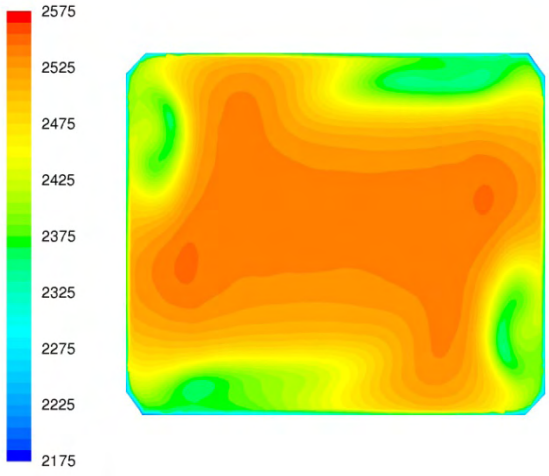

(e) FLUENT: Elevation = 7.37 m (Plane 180)

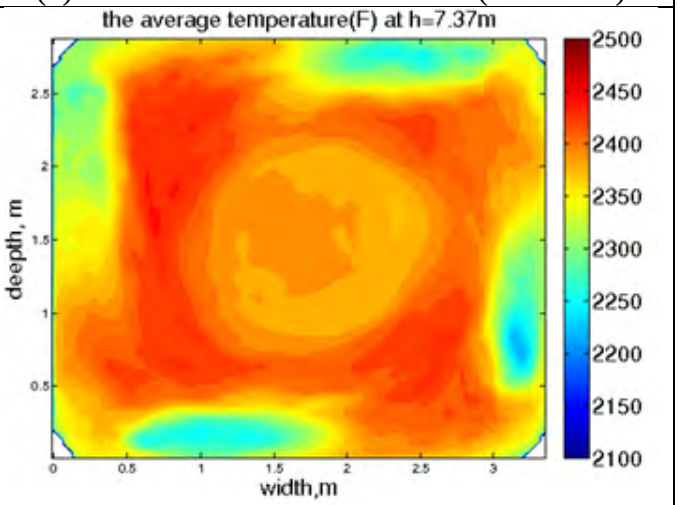

(f) ARCHES: Elevation = 7.37 m (Plane 180)

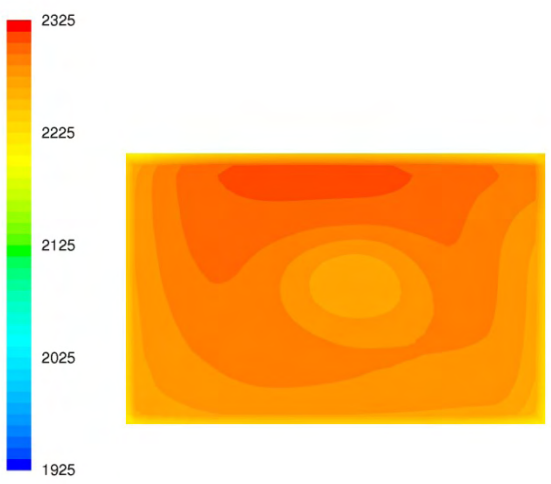

(g) FLUENT: Elevation = 9.72 m (Plane 273)

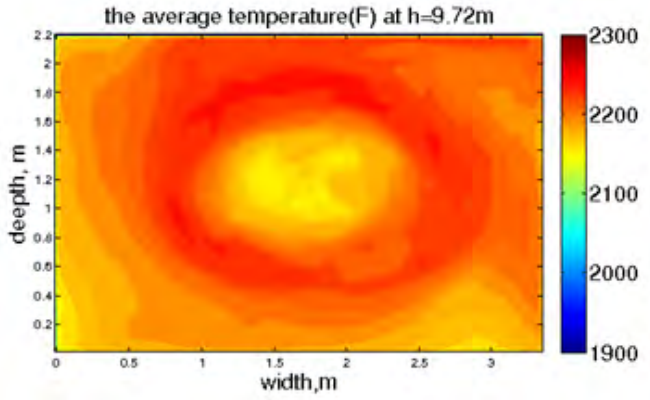

(h) ARCHES: Elevation = 9.72 m (Plane 273)

Figure 7-3. Comparison of Time-Averaged Temperature Using FLUENT® and ARCHES

It should be noted that the two cases have different temperatures at the same plane and are therefore plotted with different maxima and minima on the color scale; however, the same difference between the maximum and the minimum were preserved between the two cases for each pair of plots. Despite the attempt to keep the scales similar with respect to range, it should be noted that the colors are not necessarily in the same positions. For example, the maximum on the ARCHES plots is a brown color and the red is below it, whereas the red color on the FLUENT® plots is the maximum; the blue color is also displaced on the ARCHES plot relative to the FLUENT® plot.

In comparing Panels (a) and (b), it is apparent that the resolution of the jet and the integrity of the jet is much better in the ARCHES plot than in the FLUENT® plot. The jets in the FLUENT® plot do not appear to penetrate as far into the flowfield, and they diffuse or dissipate earlier than the jets in the ARCHES plot. Furthermore, a sheath of flame encompasses the ARCHES jets, creating a clear delineation between the coal jet and the residual cold gas between the jet and the wall. It is apparent that ignition on the outside of the coal jet is occurring early in the ARCHES case, while in the case of the FLUENT® jet, the jet may be igniting on one side of the jet, but a significant ignition on the other side is not visible (or resolved). The use of the presumed PDF combustion model (and equilibrium chemistry) by the ARCHES code may assist in the early onset and preservation of a stable flame around the coal jet.

Comparing Panels (c) and (d), the ARCHES plot has low temperature regions in the corner, with an annular high-temperature region, with a wide lower-temperature core region. The difference between the annular ring and the core region is perhaps 100 °F to 150 °F, depending on the location within the cross-section. The corresponding FLUENT® plot is more mixed out, varying form the core to the annular ring by about 100 °F. The same phenomena appear to be true at succeeding planes. At Plane 273, the ARCHES plot still shows a very significant difference between the core and the surrounding region (about 100 °F), while the FLUENT® manifests only about a 50 °F. For the temperature contour plots, in summary, the ARCHES calculations clearly show less diffusive tendencies in the results than the FLUENT® results.

Net wall heat flux contour plots, in which steady-state FLUENT® calculations are compared with time-averaged ARCHES calculations, is provided at two different longitudinal planar views in Figure 7-4. It should be noted that the FLUENT® scales are from 0 to -15 x 10^4 (in order to show that the absorption is non-zero), while the ARCHES scales are slightly different and range from 1 x 10^4 to 15 x 10^4. FLUENT® expresses net wall hat flux as a negative quantity. It should also be noted that the ARCHES computations have omitted the geometry below the windbox for the front-wall view and the lower portion of the hopper in the side-wall view. Again, the color matching on the color-map scales does not precisely match between the FLUENT® and the ARCHES plots.

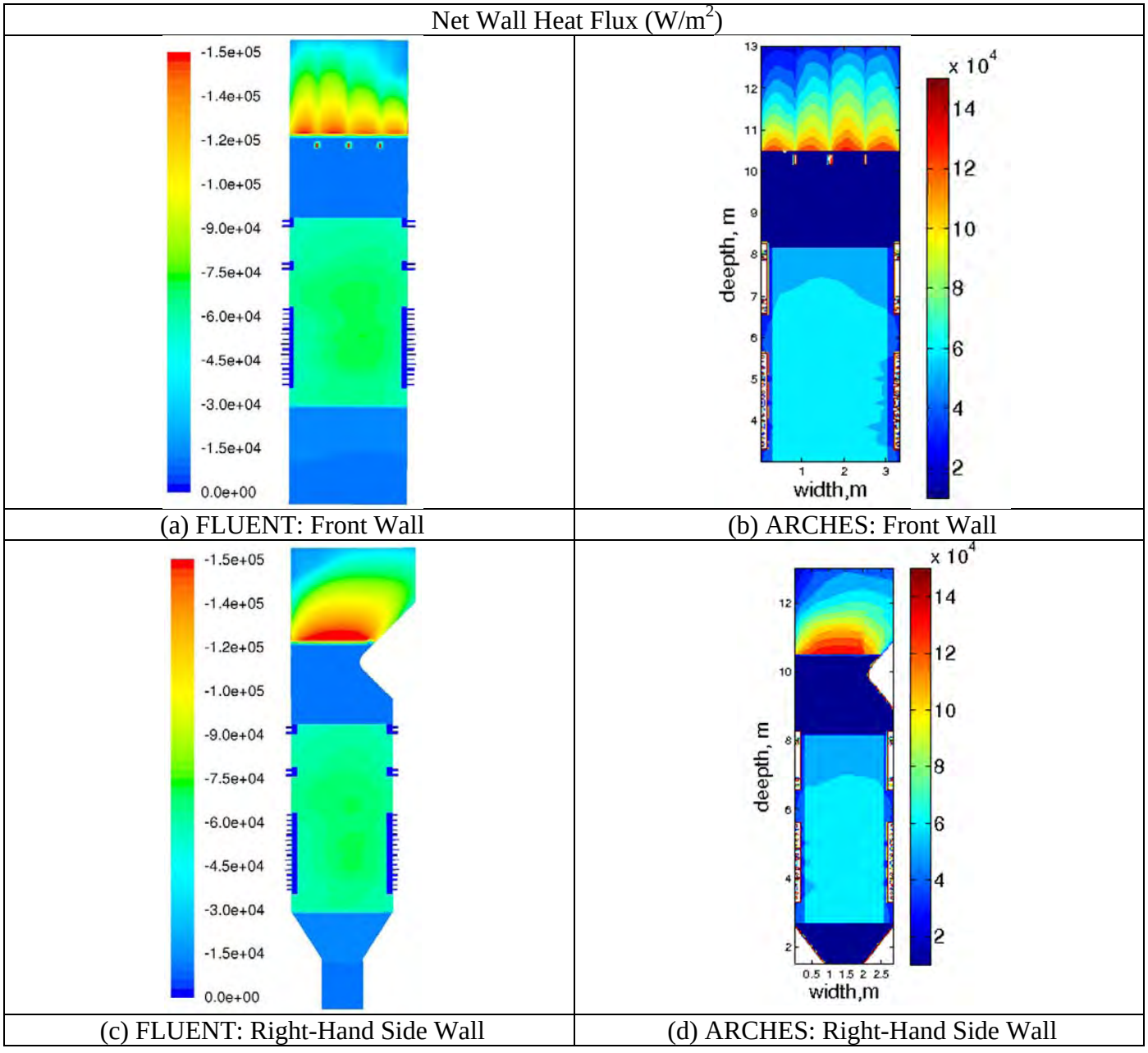

Figure 7-4. Comparison of Time-Averaged Wall Heat Flux Using FLUENT® and ARCHES

In the main windbox, the wall heat flux in the FLUENT® case appears to be about 6.5 x 10^4 or 7 x 10^4, whereas in the ARCHES case, it appears to be somewhat lower (about 6.0 x 10^4). This is in correspondence with the slightly higher peak temperatures that appear to prevail in the FLUENT® case.

8. References

1. DOE/NETL Cooperative Agreement.No. DE-NT0005290, "Recovery Act: Oxy-Combustion Technology Development for Industrial-Scale Boiler Applications," performed by Alstom Power Inc. for U.S. DOE National Energy Technology Laboratory.

2. Pedel, J., J. N. Thornock, and P. J. Smith, "Large Eddy Simulation of Pulverized Coal Jet Flame Ignition Using the Direct Quadrature Method of Moments," Energy and Fuels, 26(11), 6686-6694 (2012).

3. Pedel, J., J. N. Thornock, S. T. Smith, and P. J. Smith, "Large Eddy Simulation of Coal Particles in Turbulent Coaxial Jets Using the Direct Quadrature Method of Moments," Submitted to the Journal of Computational Physics (May, 2012).

4. Wu, Y., P. J. Smith, and J. Thornock, "Simulation of Oxy-Coal combustion in Subgrid Scale with One Dimensional Turbulence Model," The Clearwater Clean Coal Conference: The 34th International Technical Conference on Clean Coal & Fuel Systems, Clearwater, FL (May 31 to June 4, 2009).

5. Reid, C., J. Thornock, and P. Smith, "Temporally and Spatially Resolved Calculations of a Reacting Coal Jet Using Large Eddy Simulations (LES) and Direct Quadrature Method of Moments (DQMOM)," The Clearwater Clean Coal Conference: The 34th International Technical Conference on Clean Coal & Fuel Systems, Clearwater, FL (May 31 to June 4, 2009).

6. Pedel, J., J. Thornock, and P. Smith, "Validation and Uncertainty Quantification of Coal Devolatilization Models," The Clearwater Clean Coal Conference: The 34th International Technical Conference on Clean Coal & Fuel Systems, Clearwater, FL (May 31 to June 4, 2009).

7. Wu, Y., P. J. Smith, J. Zhang, J. N. Thornock, and G. Yue, "Effects of Turbulent Mixing and Controlling Mechanisms in an Entrained Flow Coal Gasifier," Energy Fuels, 24(2), pp. 1170-1175 (2010).

8. Wu, Y., P. J. Smith, J. N. Thornock, S. Smith, P. J. Chapman, and Y.-M. Chen, "LES simulation for a 15MW oxy coal-fired boiler and uncertainty quantification of temperature and heat flux," Prepared for submission to the 35th Symposium (International) on Combustion.

9. Goetz, G. J., N. Y. Nsakala, R. L. Patel, and G. H. Quentin, "Combustion and Gasification Kinetics of Chars from Four Commercially Significant Coals of Varying Rank," Presented at the International Conference on Coal Science, Pittsburgh, PA (August 15-19, 1983), see also Alstom publication C-E TIS-7290.

10. Yamamoto, K., T. Murota, T. Okazaki, M. Taniguchi, "Large eddy simulation of a pulverized coal jet flame ignited by a preheated gas flow," Proceedings of the Combustion Institute, 33, 1771-1778 (2011).

11. "Energy Application within the Uintah Framework: Simulation of the Alstom Boiler simulation Facility (BSF) – A simulation and experimental data collaboration," Draft of ALCC Report (September 27, 2013).

12. Bayarri, M. J., J. O. Berger, R. Paulo, J. Sacks, J. A. Cafeo, J. Cavendish, C. H. Lin, J. Tu, "A Framework for Validation of Computer Models," National Institute of Statistical Sciences (NISS) Technical Report Number 162 (April 2005).

13. Feeley, R., P. Seiler, A. Packard, and M. Frenklach, "Consistency of a Reaction Dataset," J. Phys. Chem. A, 108, pp. 9573-9583 (2004).

14. Russi, T., A. Packard, and M. Frenklach, "Uncertainty quantification: Making predictions of complex reaction systems reliable," Chemical Physics Letters, 499, pp. 1-8 (2010).

15. Wu, Y., P. J. Smith, K. Kelly, J. N. Thornock, "BSF-LES-Simulation-Progress-Report-April2013," University of Utah, Institute for Clean and Secure Energy, PowerPoint Presentation (April 4, 2013).

16. Smith, P., J. Thornock, Y. Wu, S. Smith, B. Isaac, P. Chapman, D. Sloan, D. Turek, Y-M. Chen, "Oxy-Coal Power Boiler simulation and Validation Through Extreme Computing," AFRC 2014 Industrial Combustion Symposium, Houston, Texas (September 7-10, 2014).

Recovery Act: Oxy-Combustion Technology Development for Industrial-Scale Boiler Applications

DOE/NETL Cooperative Agreement No. DE-NT0005290

Volume III – Modeling and Validation

Chapter 5 – Dynamic Process Modeling

Authors
Mahesh Mistry
Chuan Wang
Shizhong Yang
Xinsheng Lou

Table of Contents

1 EXECUTIVE SUMMARY 6

2 INTRODUCTION 10

3 OXY-FIRED PULVERIZED COAL BOILER ISLAND PROCESS 11

4 DYNAMIC MODEL 14

5 OXY BOILER ISLAND TRANSIENT ANALYSIS 18

5.1 TEST MATRIX 18
5.2 BOILER ISLAND NORMAL OPERATIONS 19
5.2.1 Transitions Between Air and Oxy-mode Operation 19
5.2.2 Load Ramp Operations 24
5.2.3 Load Step Change Operations 30
5.2.4 Oxy-Mode Minimum Load Operation 33
5.2.5 Start-up from Minimum Load Operation in Air Mode (25% MCR Air Mode to MCR in Oxy Mode) 36
5.3 BOILER ISLAND ABNORMAL OPERATIONS 39
5.3.1 Mill Trip 40
5.3.2 PA Fan Trip 43
5.3.3 FD Fan Trip 46
5.3.4 ID Fan Trip 49
5.3.5 Gas Processing Unit Trip 52

6 CONCLUSIONS 56

List of Figures

Figure 1-1 Load response to load ramp from 50% MCR to 100% MCR 7
Figure 1-2 Fuel/feedwater/oxidant/steam mass flow response to load ramp from 50% MCR to 100% MCR 7
Figure 1-3 Main/reheated steam temperature/pressure response to load ramp from 50% MCR to 100% MCR 7
Figure 1-4 Primary oxidant/secondary oxidant/supplementary O_2 flow response to FD fan trip 8
Figure 1-5 Fuel/feedwater/oxidant/steam mass flow response to FD fan trip 8
Figure 1-6 Main/reheated steam temperature/pressure response to FD fan trip 8
Figure 1-7 Furnace pressure response to FD fan trip 9
Figure 3-1 450 MWe dual-fired pulverized coal boiler island process flowsheet 13
Figure 4-1 Configuration of Aspen dynamic model for demonstration boiler 16
Figure 4-2 Integrated oxy CCS plant model 17
Figure 5-1 CO_2/O_2 concentration in flue gas response to transition from air mode to oxy mode at 40% MCR 19
Figure 5-2 Load response to transition from air mode to oxy mode at 40% MCR 20
Figure 5-3 Feedwater/steam mass flow response to transition from air mode to oxy mode at 40% MCR 20
Figure 5-4 Main/reheated steam temperature/pressure response to transition from air mode to oxy mode at 40% MCR 20
Figure 5-5 Desuperheater spray flow response to transition from air mode to oxy mode at 40% MCR 21
Figure 5-6 Furnace pressure response to transition from air mode to oxy mode at 40% MCR 21
Figure 5-7 CO_2/O_2 concentration in flue gas response to transition from oxy mode to air mode at 40% MCR 22
Figure 5-8 Load response to transition from oxy mode to air mode at 40% MCR 22
Figure 5-9 Feedwater/steam mass flow response to transition from oxy mode to air mode at 40% MCR 23
Figure 5-10 Main/reheated steam temperature/pressure response to transition from oxy mode to air mode at 40% MCR 23
Figure 5-11 Desuperheater spray flow response to transition from oxy mode to air mode at 40% MCR 23
Figure 5-12 Furnace pressure response to transition from oxy mode to air mode at 40% MCR 24
Figure 5-13 Load response to load ramp from 35% MCR to 50% MCR 24
Figure 5-14 Fuel/feedwater/oxidant/steam mass flow response to load ramp from 35%MCR to 50% MCR 26

Figure 5-15 Main/reheated steam temperature/pressure response to load ramp from 35% MCR to 50% MCR 26
Figure 5-16 Desuperheater spray flow response to load ramp from 35% MCR to 50% MCR....27
Figure 5-17 Furnace pressure response to load ramp from 35% MCR to 50% MCR....27
Figure 5-18 Load response to load ramp from 50% MCR to 100% MCR....28
Figure 5-19 Fuel/feedwater/oxidant/steam mass flow response to load ramp from 50% MCR to 100% MCR 29
Figure 5-20 Main/reheated steam temperature/pressure response to load ramp from 50% MCR to 100% MCR ..29
Figure 5-21 Desuperheater spray flow response to load ramp from 50% MCR to 100% MCR....29
Figure 5-22 Furnace pressure response to load ramp from 50% MCR to 100% MCR....30
Figure 5-23 Load response to load step from 50% MCR to 60% MCR 30
Figure 5-24 Fuel/feedwater/oxidant/steam mass flow response to load step from 50% MCR to 60% MCR....31
Figure 5-25 Main/reheated steam temperature/pressure response to load step from 50% MCR to 60% MCR....32
Figure 5-26 Desuperheater spray flow response to load step from 50% MCR to 60% MCR 32
Figure 5-27 Furnace pressure response to load step from 50% MCR to 60% MCR 32
Figure 5-28 Load response to oxy-mode minimum load operation....33
Figure 5-29 Fuel/feedwater/oxidant/steam mass flow response to oxy-mode minimum load operation 34
Figure 5-30 Main/reheated steam temperature/pressure response to oxy-mode minimum load operation 35
Figure 5-31 Desuperheater spray flow response to oxy-mode minimum load operation....35
Figure 5-32 Furnace pressure response to oxy-mode minimum load operation 35
Figure 5-33 Recirculation flow and separator level response to oxy-mode minimum load operation....36
Figure 5-34 Load response to start-up 37
Figure 5-35 Recirculation flow and separator level response to start-up....37
Figure 5-36 CO_2/O_2 concentration in flue gas response to start-up....37
Figure 5-37 Fuel/feedwater/oxidant/steam mass flow response to start-up 38
Figure 5-38 Main/reheated steam temperature/pressure response to start-up 38
Figure 5-39 Desuperheater spray flow response to start-up....38
Figure 5-40 Furnace pressure response to start-up....39
Figure 5-41 Load response to one mill trip....41
Figure 5-42 Fuel/feedwater/oxidant/steam mass flow response to one mill trip 42
Figure 5-43 Main/reheated steam temperature/pressure response to one mill trip 42
Figure 5-44 Desuperheater spray flow response to one mill trip....42
Figure 5-45 Furnace pressure response to one mill trip....43
Figure 5-46 Primary oxidant/secondary oxidant/supplementary O_2 flow response to PA fan trip....44
Figure 5-47 Load response to PA fan trip 45
Figure 5-48 Fuel/feedwater/oxidant/steam mass flow response to PA fan trip....45
Figure 5-49 Main/reheated steam temperature/pressure response to PA fan trip....45
Figure 5-50 Desuperheater spray flow response to PA fan trip 46
Figure 5-51 Furnace pressure response to PA fan trip 46
Figure 5-52 Primary oxidant/secondary oxidant/supplementary O_2 flow response to FD fan trip....47
Figure 5-53 Load response to FD fan trip 48
Figure 5-54 Fuel/feedwater/oxidant/steam mass flow response to FD fan trip....48
Figure 5-55 Main/reheated steam temperature/pressure response to FD fan trip....48
Figure 5-56 Desuperheater spray flow response to FD fan trip 49
Figure 5-57 Furnace pressure response to FD fan trip 49
Figure 5-58 Furnace pressure and ID mass flow response to ID fan trip....50
Figure 5-59 Load response to ID fan trip....51
Figure 5-60 Fuel/feedwater/oxidant/steam mass flow response to ID fan trip 51
Figure 5-61 Main/reheated steam temperature/pressure response to ID fan trip 51
Figure 5-62 Desuperheater spray flow response to ID fan trip 52
Figure 5-63 Primary oxidant/secondary oxidant/supplementary O_2 flow response to GPU trip....53
Figure 5-64 Load response to GPU trip 53
Figure 5-65 Fuel/feedwater/oxidant/steam mass flow response to GPU trip....54
Figure 5-66 Main/reheated steam temperature/pressure response to GPU trip....54
Figure 5-67 Desuperheater spray flow response to GPU trip 54
Figure 5-68 Furnace pressure response to GPU trip 55

List of Tables

Table 5-1 Statistical data of gross MW response to load ramp from 35% MCR to 50% MCR 25
Table 5-2 Statistical data of gross MW response to load ramp from 50% MCR to 100% MCR 28
Table 5-3 Statistical data of gross MW response to load step from 50% MCR to 60% MCR 31
Table 5-4 Statistical data of gross MW response to oxy-mode minimum load operation 34
Table 5-5 Major Equipment List for Referenced Oxy-PC Boiler Island 39
Table 5-6 Statistical data of gross MW response to one mill trip 41

List of Acronyms and Abbreviations

Air-Mode	Air-fired Combustion Mode
APH	Air Pre-heater
AQCS	Air Quality Control System
ASU	Air Separation Unit
BI	Boiler Island
BMCR	Boiler Maximum Continuous Rating
CCS	CO_2 Capture System
CGR	Concept Gate Review
DCC	Direct Contact Cooler
DMOL	Designed Minimum Operating Level
ECS	Environmental Control System
EOR	Enhanced Oil Recovery
ESP	Electrostatic Precipitator
FD	Forced Draft
FGC	Flue Gas Condenser
FGD	Flue Gas Desulfurization
FGR	Flue Gas Recirculation
GGH	Gas-Gas Heater (For oxy-fired Boiler)
GPU	Gas Processing Unit
LSOFA/LSOFO	Lower Separated Over-Fired Air/Oxidant (Zone)
ID	Induced Draft
HSOFA/HSOFO	Higher Separated Over-Fired Air/Oxidant (Zone)
MBZ	Main Burner Zones
MCR	Maximum Continuous Rating
MLP	Machine Load Point
OFA/OFO	Over-Fired Air/Oxidant (Zone)
Oxy-Mode	Oxygen-fired Combustion Mode
Oxy-PC	Oxygen-fired Pulverized Coal
PA/PO	Primary Air/Oxidant
PC	Pulverized Coal
PID	Proportional-Integral-Derivative
PFD	Process Flowsheet Diagram
P&ID	Piping & Instrumentation Diagram
RC	Registered Capacity
RH	Reheat
SOFA/SOFO	Separated Over-Fired Air/Oxidant (Zone)
SA/SO	Secondary Air/Oxidant
SCPC	Supercritical Pulverized Coal
SCR	Selective Catalytic Reduction
SH	Superheat
TI	Turbine Island
TMCR	Turbine Maximum Continuous Rating

1 Executive Summary

This chapter addresses project efforts for the development of oxy boiler dynamic modeling capabilities to assess and refine the design of controls and operation systems for oxy boilers. Discussed are the results of a control and operability investigation of the transient responses of critical process variables in the oxy boiler island for various plant event scenarios. Before the dynamic analysis work was done, the oxy boiler island dynamic model simulation tool was validated and calibrated with reference to recent air-fired utility boiler design performance data at different load operating conditions to ensure the representiveness of the dynamic model. Process control loops for the oxy boiler island process have been refined and incorporated after the validation of the dynamic model.

The control and operability dynamic analysis mainly focuses on the transient responses of the process under various pre-defined operating scenarios. For the purpose of this dynamic simulation study, most of the boiler island transient analyses were in the oxy-firing mode. Two main types of control and operability simulation were conducted:

- Boiler Island normal operations
    - Transitions between air and oxy-mode operation
    - Load ramp up with different rates
    - Load step change
    - Oxy-mode minimum load operation (40-25%, including startup system)
    - Start-up from minimum load operation in air mode
- Boiler Island abnormal operations
    - One mill trips (out of four)
    - Fan trips (PA/FD/ID fan trips)
    - Gas processing unit trip

During daily operation, the unit load demand of the power plant is generated based on the requirements from the electricity market, which requires the steam plant/boiler island to be able to adjust the operating load in a timely manner. Plant operating flexibility is increasingly important as the percentage of intermittent renewable power increases. Two simulation scenarios for load ramping were designed to study the oxy boiler island under the fast load change requirement: load ramping from 35% MCR to 50% MCR at 3% MCR/min, and load ramping from 50% MCR to 100% MCR at 5% MCR/min. Figure 1-1 to Figure 1-3 illustrate the reponse to load ramping from 50% MCR to 100% MCR at 5% MCR/min. In addition, a 10% MCR load step change from 50% MCR to 60% MCR was also investigated. Additionally, the capability to run under a very low load (about 25% TMCR with no supporting oil) in oxy mode was assessed to address scenarios during high renewable generation and no additional grid demand, when all the generated power is consumed by the ASU and the GPU. The dynamic model was used to examine the feasibility and stability of the plant, and specifically the boiler unit, running at such a low load condition.

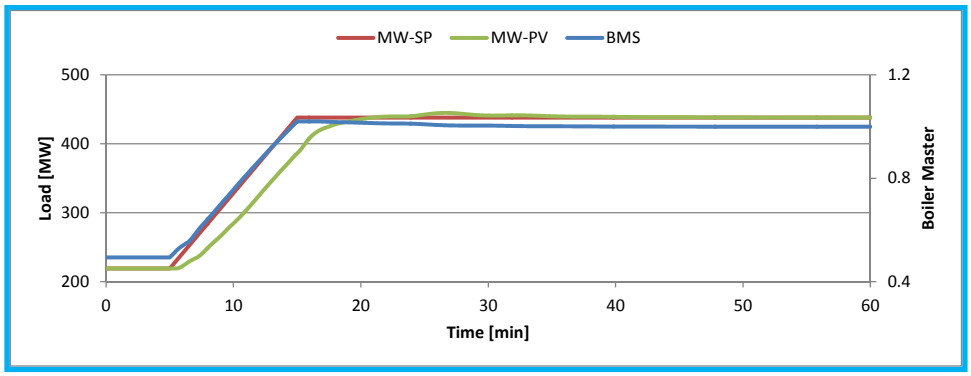

Figure 1-1 Load response to load ramp from 50% MCR to 100% MCR

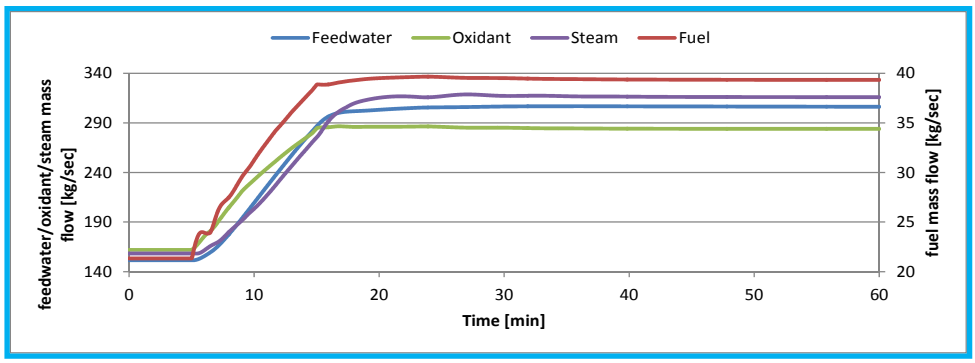

Figure 1-2 Fuel/feedwater/oxidant/steam mass flow response to load ramp from 50% MCR to 100% MCR

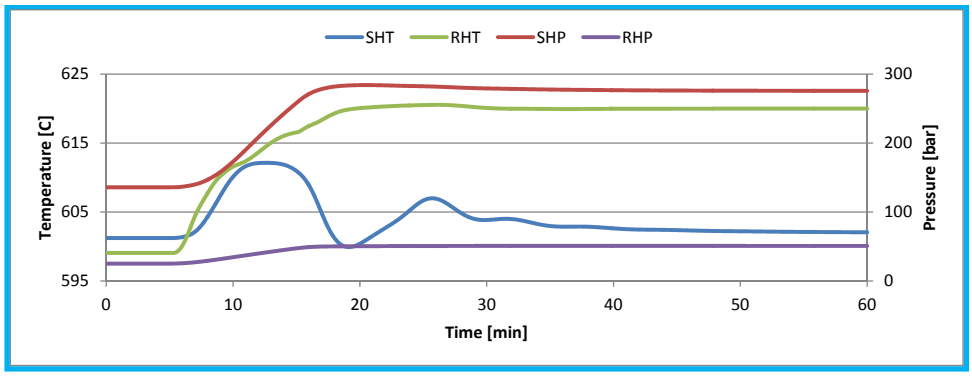

Figure 1-3 Main/reheated steam temperature/pressure response to load ramp from 50% MCR to 100% MCR

Abnormal operations, which refer to the unit's operations under unexpected disruptions, were also assessed. For the dual-fired pulverized coal boiler island process, typically these abnormal operating events require a fast and controlled response to various major equipment failures, including mill trips, fan trips, master fuel trip, as well as interface subsystem trips. In general, boiler island emergency operations under both air-firing mode and oxy-firing mode should be investigated. In this chapter, the emergency operations cases studied were limited and focused on oxy-mode operations. Responsive control actions for air-firing mode emergency operations can be designed based on conventional air-

fired boiler operation procedures. The emergency operations studied in this chapter include mill trip, PA fan trip, FD fan trip, and ID fan trip. The oxy-fired boiler island process is equipped with five coal mills, among which four are in use during full load normal operations with one coal mill as a spare. The mill trip will result in load run back to predetermined targets at specified run back rates. The oxy-fired boiler island process has one PA Fan, one ID Fan and one FD Fan. From the process design perspective, having a single fan may cost less compared to a pair of smaller fans, however, from the control and operation perspective, single fan design brings higher requirements of the fan performance for reliable plant control and operations, and any fan trip will cause the Master Fuel Trip (MFT) and the plant will go through an emergency plant shutdown sequence. The oxy boiler dynamic response to the forced draft fan trip resulting in a MFT are inllustrated in Figure 1-4 to Figure 1-7.

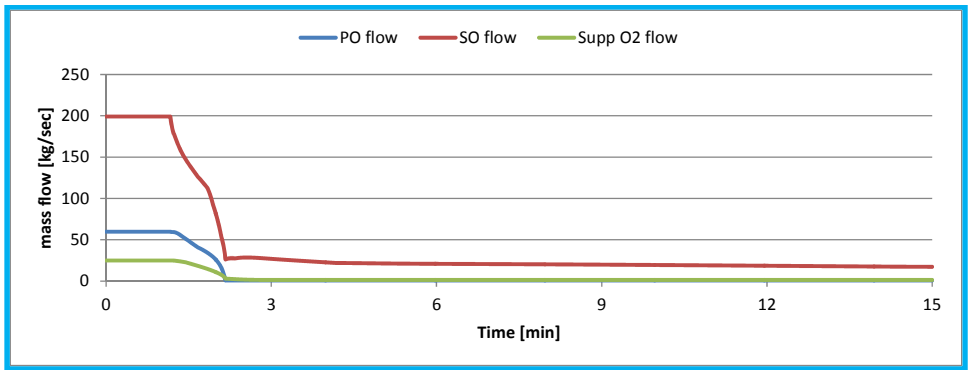

Figure 1-4 Primary oxidant/secondary oxidant/supplementary O_2 flow response to FD fan trip

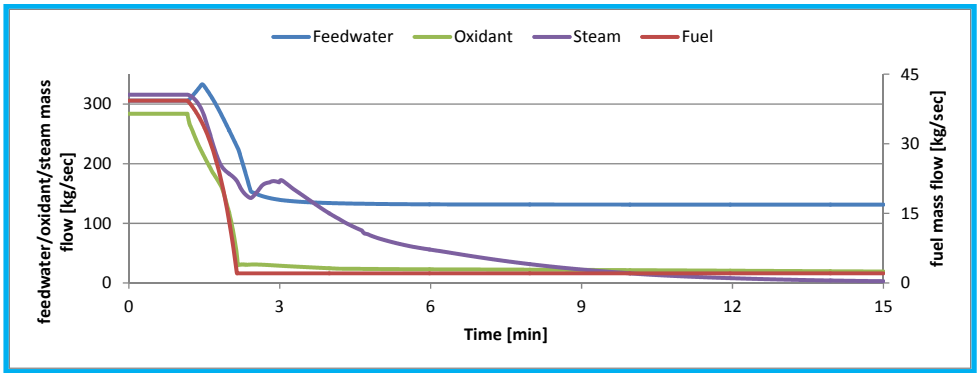

Figure 1-5 Fuel/feedwater/oxidant/steam mass flow response to FD fan trip

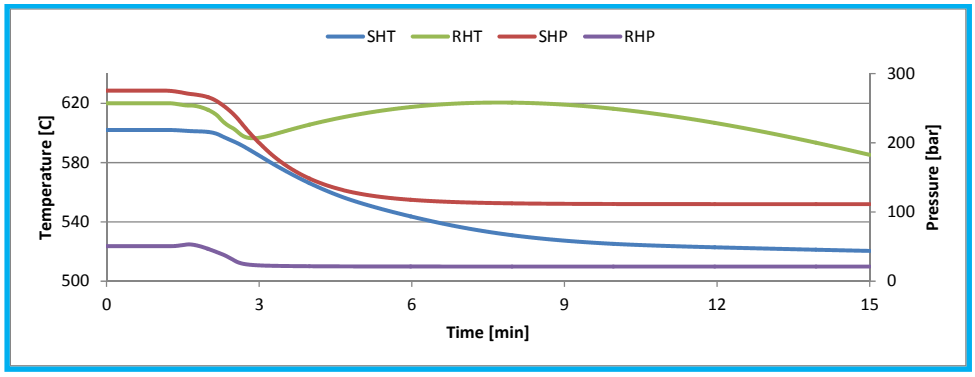

Figure 1-6 Main/reheated steam temperature/pressure response to FD fan trip

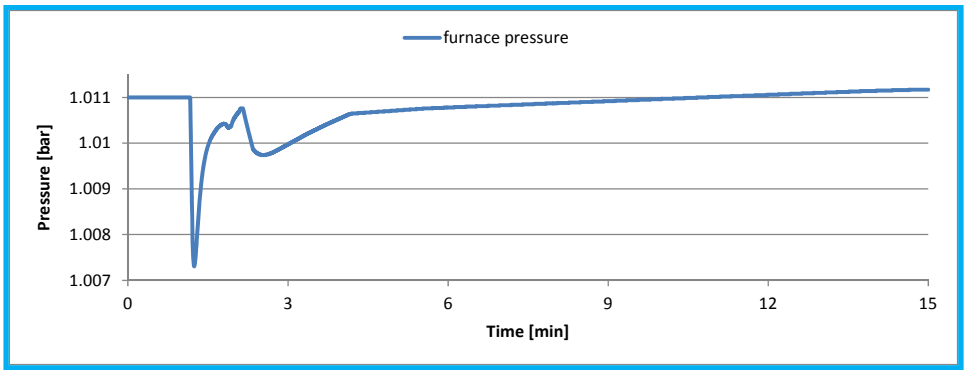

Figure 1-7 Furnace pressure response to FD fan trip

Overall, results of the transient analysis modeling for the oxy boiler island indicate that the dynamic response during normal operation such as load ramping during oxy-firing operation is generally similar to the behavior during traditional air-firing. The dynamic response of the oxy-boiler during abnormal events such as boiler equipment trips were also generally similar. The responses of the critical boiler process variables follow the same trends, however magnitudes and/or settling time may vary somewhat due to the differences in the design and greater complexity of some of the oxy-boiler subsytems.

2 Introduction

The purpose of this chapter is to present the results of control and operability simulation studies on the dynamic behaviors of the oxy-fired Supercritical Pulverized Coal (SCPC) Boiler Island (BI), when fast change of the unit load is strictly required and for certain equipment trip scenerios. The first principles based Oxy-Boiler and total plant based dynamic models and simulation tool were developed to support and evaluate the process control system design and boiler unit operational transient analyses for the new Oxy-Boiler plant. This 450 MWe oxy-fired SCPC boiler island model is a specific modeling example for the oxy-PC boiler process. However, the resulting Oxy-model and simulation tool can be re-configured with minimum re-work for any oxy-PC power plant engineering designs in the future.

A general oxy-fired PC power plant consists of the oxy-fired Boiler Island (BI), the Turbine Island (TI), the Air Separation Unit (ASU) and the Gas Processing Unit (GPU). A high fidelity dynamic model of the oxy-fired Boiler Island model first needed to be developed and validated before it could be integrated with other sub-system models of the plant, i.e. the AQCS units (e.g. ESP, FGD, FGC, etc.), Turbine Island, ASU and GPU and utilized for dynamic analysis.

Under this effort, the process simulation analysis focuses mainly on the oxy-fired Boiler Island process. The knowledge gained from the simulation studies will be used to support future product development and commercial demonstration of an oxy firing based CCUS (Carbon Capture, Utilization and Sequestration) plant. The scope of the process model for the dual-fired (air/oxy-fired) pulverized coal boiler island includes the dual-fired (air/oxy-fired) boiler unit and the backend air quality control system (AQCS). On the water/ steam side, the boiler is used to generate steam with certain quality and quantity requirements. On the flue gas side, the boiler combustion system produces a CO_2 enriched flue gas, which can be further purified by the Gas Processing Unit (GPU). This Alstom oxy-fired boiler island model was developed and validated using the input data generated from Alstom's "Reheat Boiler" design code. This model was also further validated using real plant data from a 830 MWe air-fired boiler unit and from Alstom's 15 MW_{th} Boiler Simulation Facility (BSF).

The scope of this transient analysis work includes the following:

- Transitions between air and oxy-mode operation
- Normal operations, including wide range load ramp up/down and small range load step changes
- Load ramp at design ramp rates, e.g. 5% MCR/min between 50% MCR to MCR
- Load step change operation to support requirements for grid code compliance analysis
- Low load operation with recirculation system running in oxy mode/air mode
- Impacts from emergency operations including mill and fan trips as well as GPU and ASU trip on the boiler unit operations

3 Oxy-Fired Pulverized Coal Boiler Island Process

The purpose of applying oxy-combustion technology to a pulverized coal power plant is to produce power while capturing the CO_2 from the combustion of coal and then cleaning and compressing it for subsequent transport and storage in saline aquifers or other utilization. An oxy-fired pulverized coal power plant generally consists of four major sub-systems:

- Air Separation Unit (ASU): it separates the oxygen from nitrogen, etc. in the air. In oxy fired steam plant design, the pure oxygen is mixed with recirculated flue gas to be used in the boiler for combustion.
- Dual-Fired (air/oxy-fired) Pulverized Coal Boiler Island: it includes the dual-fired boiler unit and the backend air quality control system (AQCS). On the water/steam side, the boiler is used to generate steam of specific quality and quantity. On the flue gas side, the boiler and its AQCS system produce a CO_2 enriched flue gas. Some of the flue gas is circulated back to the boiler and the remaining part is further purified by the gas processing unit (GPU).
- Gas Processing Unit (GPU): it compresses and dries the CO_2 enriched flue gas from the boiler island and then further purifies the CO_2 for sequestration or utilization, e.g. enhanced oil recovery (EOR).
- Turbine Island: it adopts conventional steam power plant design for the equipment, including steam turbines, generator, feedwater pre-heater train, main condenser, feedwater chemistry processing units, etc.

A simplified process flowsheet for the 450 MW_e demonstration oxy-boiler is shown in Figure 3-1. For oxy-firing, a mixture of recirculated flue gas and oxygen is used to make the primary and secondary "oxidant" streams ("oxidant" instead of air). Streams 3a (primary O_2) & 3b (secondary O_2) provide the oxygen for the primary and secondary streams respectively. The oxygen is provided from an ASU. The oxygen concentration of Stream 18b (i.e. the primary oxidant flow) and Stream 28 (the secondary oxidant flow) is controlled to a set point limited by the material selections of the duct and equipment with tolerance for incomplete mixing and appropriate control range redundancy. A third stream of pure oxygen (Stream 3c – supplemental O_2), which is the remaining oxygen required for combustion of the coal, is provided directly to the windbox where it mixes with the secondary oxidant stream just before entering the furnace. The flue gas oxygen content leaving the boiler (Stream 4) is maintained at a pre-determined value (typically for coal firing ~3% by volume-wet, same as with air firing with 20% excess air) under all operating conditions with oxygen firing by adjusting the Stream 3c flow rate. Minimizing the flue gas oxygen content under all operating conditions is very important with oxygen firing because the ASU has very high power requirements (typically 12~15% of generator output). Additionally, any excess oxygen contained in the flue gas will cause higher power requirements for the Gas Processing Unit (GPU) which is also a large power consumer in the plant (typically 8~10% of generator output).

The source for the recirculated flue gas for the primary stream is from the flue gas stream leaving the Flue Gas Condenser (FGC): Stream 18 – primary flue gas recirculation (PFGR). This location is selected because it contains the lowest water vapor content in the system and therefore it is better suited for coal drying. The flow quantity of the primary stream is dependent on the coal mill gas flow requirements for entrainment and transport of the pulverized coal to the furnace. In this design for the oxy-fired pulverized coal boiler island, the flue gas condenser is a direct contact cooler (DCC) and the primary FGR is extracted after the DCC with the remaining flue gas sent to the GPU.

Stream 27 – the secondary flue gas recirculation (SFGR) stream – is taken either from the outlet of the Flue Gas Desulphurization (FGD) System for relatively high sulfur content coals or before the FGD system for relatively low sulfur coals.

The oxygen-fired boiler unit is also capable of firing in the air-firing mode. Both the primary flue gas recirculation line and the secondary flue gas recirculation line have isolation dampers installed, which would be completely shut off in the air-firing mode. Ambient air will be supplied through the PA fan and the FD fan and the flue gas leaving the furnace will be processed by the air quality control system (AQCS) and released to atmosphere. The backend AQCS includes a fabric filter (FF) for removing the fly ash and a wet flue gas desulfurization (WFGD) unit for removing the acidic gases such as SO_2, SO_3 and HCl.

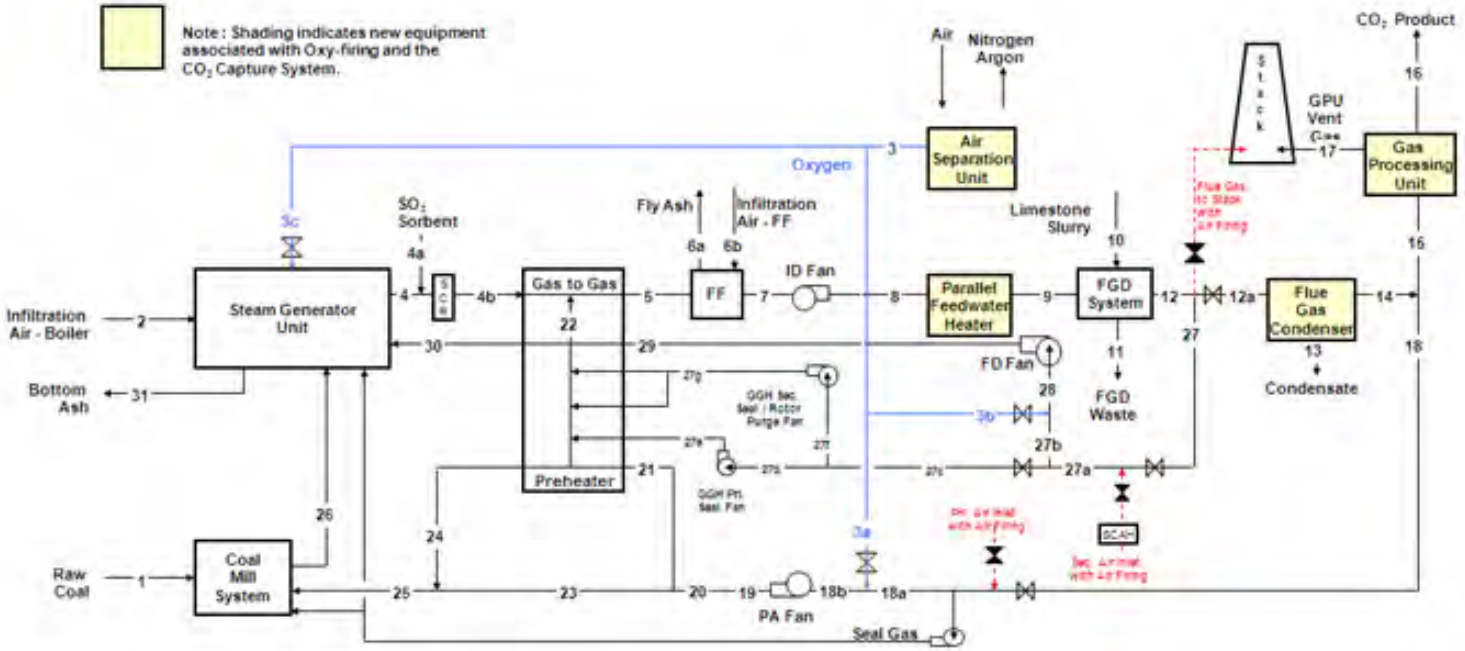

Figure 3-1 450 MWe dual-fired pulverized coal boiler island process flowsheet

4 Dynamic Model

Alstom has been working on dynamic modeling and simulation for conventional air fired boiler islands and steam plant systems to support product development and engineering design evaluations. This process dynamic model for the commercial scale oxy boiler island was developed based on Alstom's accumulated knowledge and experiences in boiler process and control design, field tuning and commissioning, etc. The dynamic process model for a 450 MWe oxy-fired SCPC Boiler Island was developed with the following scope and functionalities. To capture the operational characteristics of the oxy-fired Boiler Island process, a certain level of details of these sub-systems should be included in their process models:

- Oxy-Fired PC Boiler:
    - Fuel model: A fuel model is to match the elemental analysis and heat release of different fuels.
    - Combustion/Furnace model: Staged combustion, Combustion reactions, NO_x, CO and SO_x emission calculations, etc.
    - Firing system: Windboxes configuration, Ambient air / O_2 from ASU / Flue gas recirculation flows, etc.
    - Heat absorption surfaces: Economizer, Waterwall, Separator, SH radiant roof, SH cavity, SH panels, SH platens, SH finish, RHLT perpendicular, RHLT horizontal, RH finish, SH/RH desuperheaters, etc.
    - Selective Catalytic Reactor (SCR) for NO_x removal, required for Air-fired mode operation and/or Oxy-fired mode operation.
    - Coal Pulverizers.
    - Auxiliary equipment:, Air Pre-heater (APH) or Gas-Gas Heater (GGH), Damper/Valves, PA/FD/ID Fans, etc.
- Basic Regulatory Control System:
    - Regulatory control system for the Boiler Island including PID controllers, control function curves and other control logics.

The oxy boiler model was developed in Aspen Plus Dynamics. The steady state model for the oxy boiler model in Aspen Plus includes all the important subsystems in the boiler island, including a generic model to simulate various types of fuels, the combustor/furnace, the firing system, the heat absorption surfaces, the SCR, the auxiliary equipment, and etc. The steady state model was then converted into Aspen Dynamics. Simplified dynamic models for coal pulverizers, Particulate Collection (FF), Flue Gas Desulfurization (FGD) and Flue Gas Condenser (FGC) using Aspen Custom Modeler (ACM), which could characterize the basic functions and dynamic characteristics of such equipment. A preliminary control system has been added to the dynamic process simulator and tuned. The dynamic process model can ramp within the entire operating range with closed-loop controls. The dynamic process model could also run in the air-mode as well as the oxy-mode.

Such an oxy boiler process dynamic model is intended to support transient operation analysis as well as control system design and controls testing and evaluations. To support the simulation of the combustion process for dual firing modes (air and oxy), the combustion model has been refined with enhanced modeling features. Other modeling features also include the enhanced modeling capability for boiler tilts, the valve sizing and circulation systems, etc.

The real firing system is very complicated. However, it can be simplified for the purposes of the process dynamic modeling. For example, a single elevation model flowsheet in Aspen Dynamics was developed and tested to size the valves to give both the design pressure drop and or a reasonable pressure/flow response when operated. For example, the auxiliary air valves to the windbox change the pressure drop in the windbox when opened or closed and the valves for the oxygen lines to the furnace change the flow rate as the valve is opened or closed. Using 2 valves in a sequence allowed the pressure and flow to respond according to the ratio of valve size coefficients. When the Aspen Plus model is first simulated it calculates the valve flow coefficients which are then transferred when the flowsheet is converted to Aspen Dynamics. In Aspen Dynamics, the flow sheet is tested by changing the valve positions and observing the pressure drop/flow response when the valve position is changed manually in an open loop dynamic simulation. The hot and cold primary recirculation flue gas valves were tested to ensure that the changes in valve positions were sufficient to control mill outlet temperature and the flow of each primary air/secondary air line changed. Once the single elevation testing was completed the boiler model was updated and tested for the response again to ensure it worked with the rest of the flowsheet. The firing system model was also tested. The flowsheet also includes adding the CCOFA ports directly into the windbox.

Model validation is important in the development of a high fidelity dynamic process model. Generally, during the process model development, the model for each subsystem or a particular equipment/unit will be validated standalone before it is integrated into the complete process model. After each subsystem or equipment model is validated, the complete model can be achieved by integrating these pieces together. This oxy boiler combustion model has been validated using Alstom's pilot facility test data from Alstom's 15MW_{th} Boiler Simulation Test Facility (BSF). The model was also validated for air firing model using real unit operating data for an air fired boiler supplied by Alstom. The load ramping simulations for the oxy boiler design has been crossed checked against typical field unit operating characteristics for air fired boilers.

A schematic of the boiler model is shown in Figure 4-1. Load changes, firing mode transitions and low load operations were simulated using this enhanced oxy boiler dynamic model. A technical plan is developed for conducting systematic transient simulation analysis for assessing oxy boiler dynamic controls and operation performances. Meanwhile, the incorporation of interfaces and feedback loops with other capture plant components is conducted and tested in an integrated oxy-fired plant level dynamic simulation.

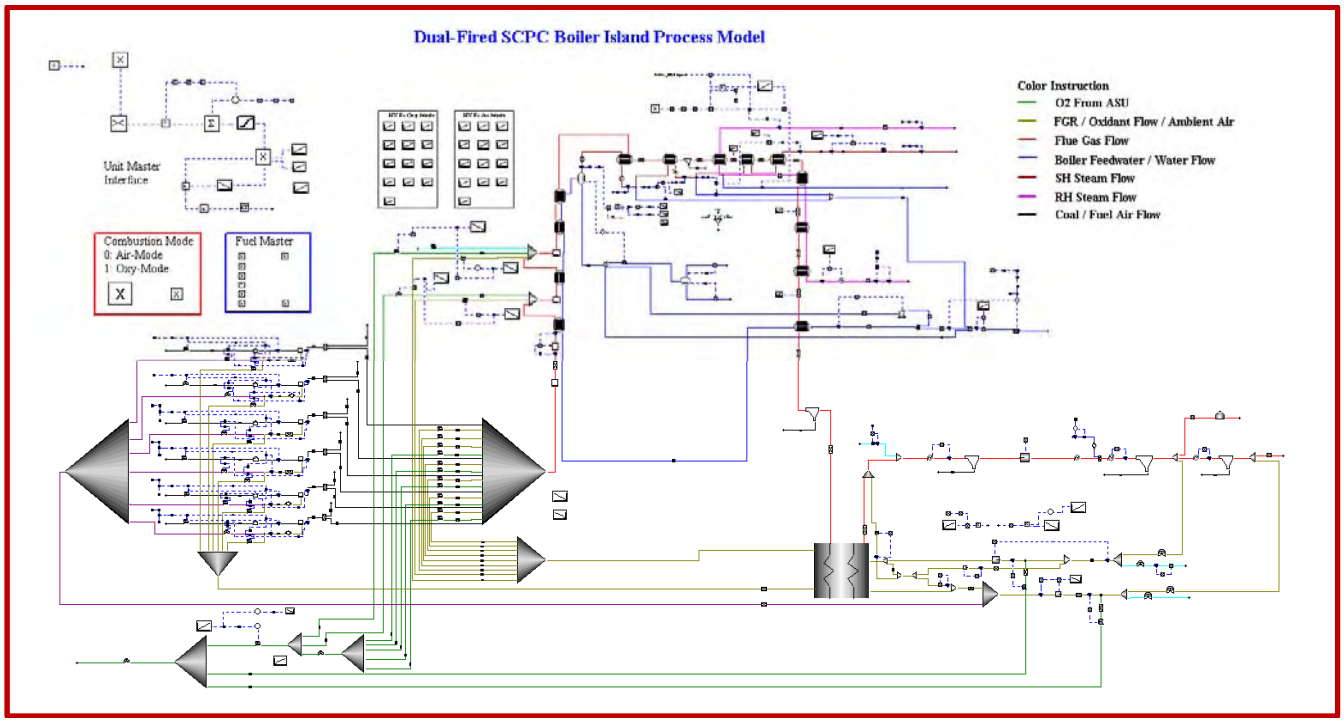

Figure 4-1 Configuration of Aspen dynamic model for demonstration boiler

Figure 4-2 illustrates the latest overall oxy-fired CO_2 capture plant model configuration. It is critical that dynamic modeling of the boiler island and other plant components consider the interactions within the entire plant. More comprehensive submodels of key components developed under other Alstom internal programs are being incorporated into the oxygen-fired plant model. The key component mainly include:

- Air Quality Control System (AQCS):
  - Ash removal unit: e.g. Fabric Filter (FF) or Electrostatic Precipitator (ESP).
  - Flue gas desulfurization (FGD) unit for SO_x removal: e.g. Wet FGD or Dry FGD.
  - Flue gas condenser (FGC) for flue gas drying: e.g. Direct contact cooler.
- Turbine Island Model
  - HP/IP/LP turbines and condensers
  - Feedwater pre-heater train & Feedwater tank
  - Feedwater pumps, control valves, etc.
- GPU Model:
  - Main Compressors and heat exchangers
- ASU Model:
  - Main compressors, turbines and heat exchangers

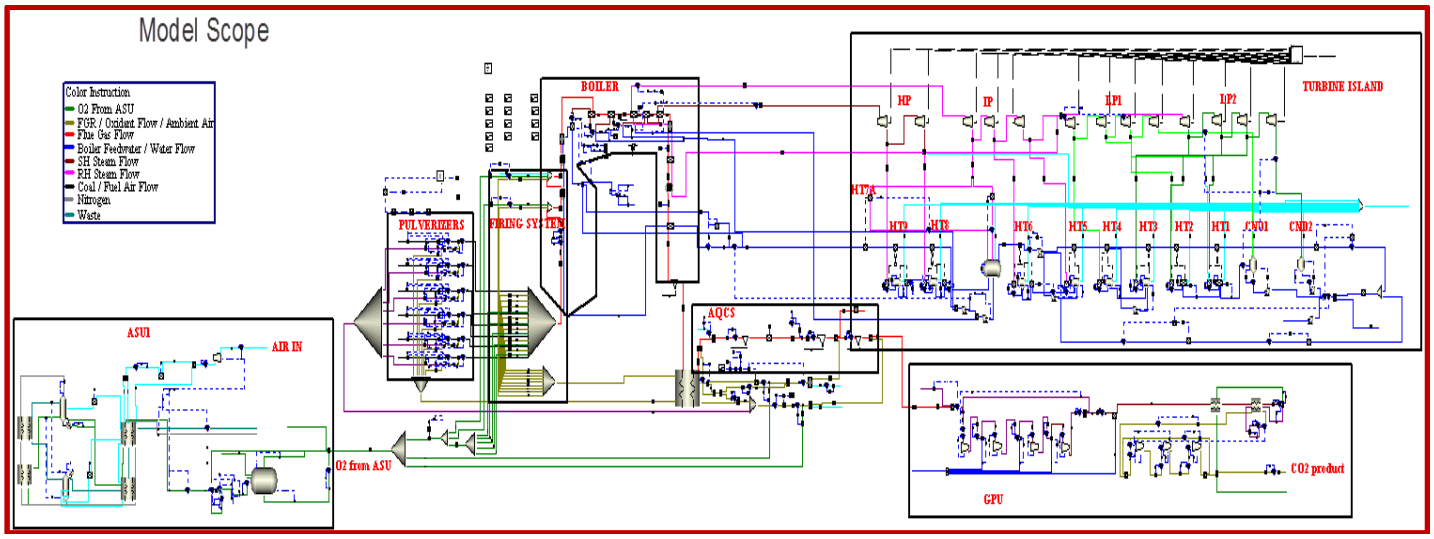

Figure 4-2 Integrated oxy CCS plant model

5 Oxy Boiler Island Transient Analysis

This section describes the major study in Oxy Boiler Island dynamic behavior in terms of specific operating conditions. Two catagories of simulation cases are defined, including air/oxy mode transition, normal load change operation, and abnormal operation when load runback is required in case of a main facility trip such as mill or fan. In order to present comparable results, some scenarios are further divided.

5.1 Test Matrix

The dynamic analysis for a dual-fired pulverized coal boiler island process mainly focuses on the transient responses of the process under various operating scenarios, which are summarized into 3 general categories. For the purpose of this dynamic simulation study, most of the transient analysis of the boiler island normal operations were in the oxy-firing mode.

- Boiler Island normal operations
    - Transitions between air and oxy-mode operations
    - Load ramp up with differenet rates
    - Load step change
    - Oxy-mode minimum load operation
    - Start-up from minimum load operation in air mode (25% MCR to 100% MCR)
- Boiler Island emergency operations
    - One mill trips (out of four)
    - Fan trips (PA/FD/ID fan trips)
    - Gas processing unit trip

5.2 Boiler Island Normal Operations

The boiler island normal operations refer to steady-state operation, load ramping, load step, and minimum load operation in oxy mode.

5.2.1 Transitions Between Air and Oxy-mode Operation

For a dual-fired boiler, the air-mode to oxy-mode transition will be performed at a predetermined transition load point (e.g., 40% TMCR). Since the transition may be carried out at any load it is important to study the flue gas side response during the transition phase such as furnace pressure, flue gas recirculation flow, ambient air flow and the oxygen supply transition, fan pressure drop variations, and other interactions between the fans in the boiler island and the compressors in the gas processing unit (GPU).

Air-Mode to Oxy-Mode Transition at 40% MCR

This scenario simulates the transition from air mode to oxy mode at a constant load condition of 40% MCR. As the flue gas is recirculated and mixed with the pure oxygen into the furnace, the concentration of CO_2 starts to increase from 13% at the air-firing mode to 61% at the oxy-firing mode, whereas the O_2 is maintained at nearly the same level during the transition as shown in Figure 5-1.

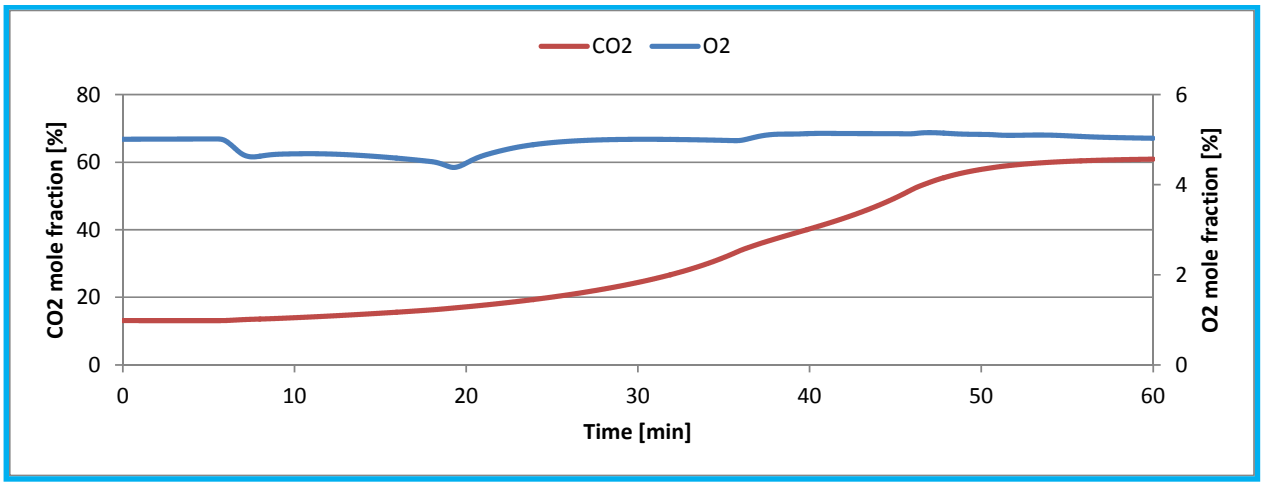

Figure 5-1 CO_2/O_2 concentration in flue gas response to transition from air mode to oxy mode at 40% MCR

The transition from air mode to oxy mode causes a little fluctuation in the response of unit load as indicated in Figure 5-2, whereas the supply of fuel and feedwater is controlled smoothly as shown in Figure 5-3. In Figure 5-4, the pressure and temperature of the main steam and reheated steam are well controlled. The responses of the desuperheater spray and the furnace pressure are given by Figure 5-5 and Figure 5-6.

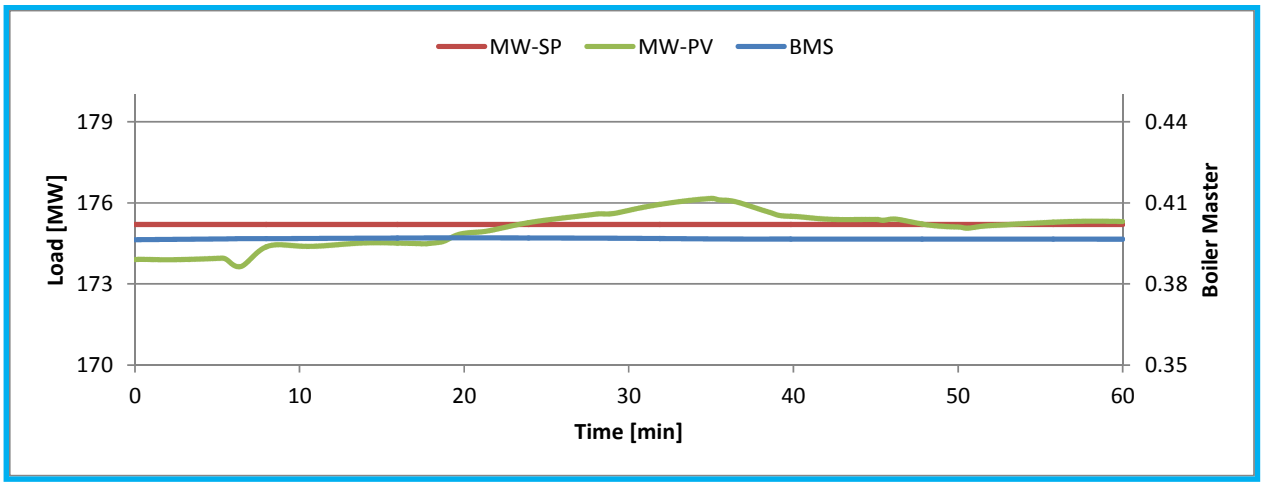

Figure 5-2 Load response to transition from air mode to oxy mode at 40% MCR

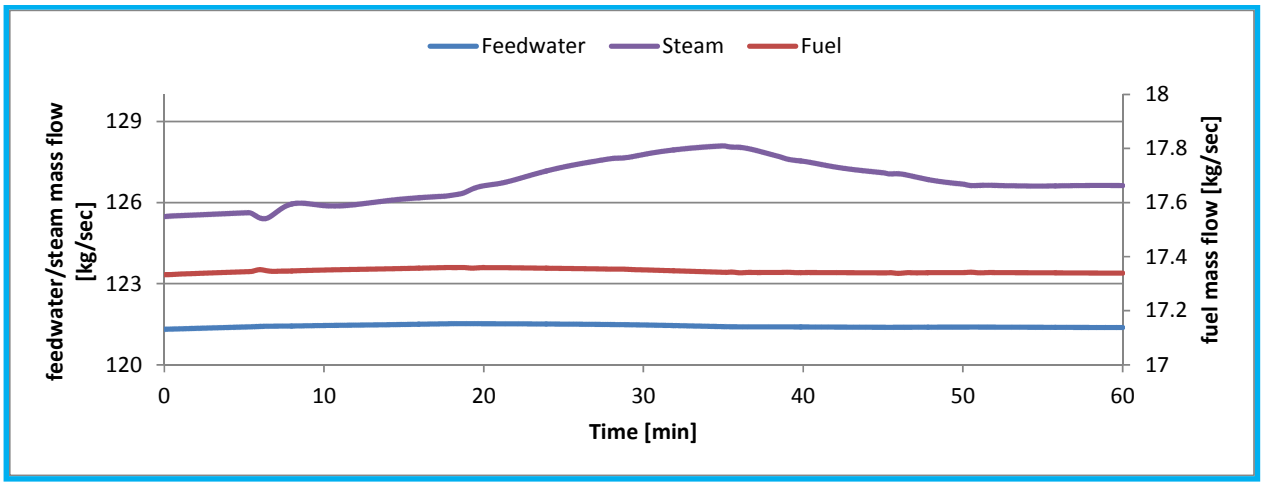

Figure 5-3 Feedwater/steam mass flow response to transition from air mode to oxy mode at 40% MCR

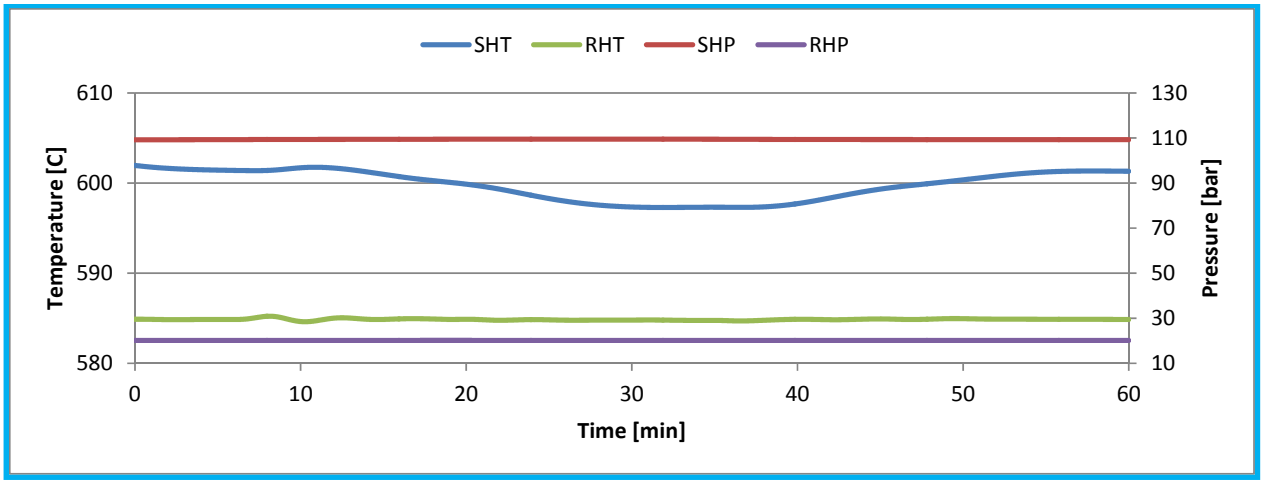

Figure 5-4 Main/reheated steam temperature/pressure response to transition from air mode to oxy mode at 40% MCR

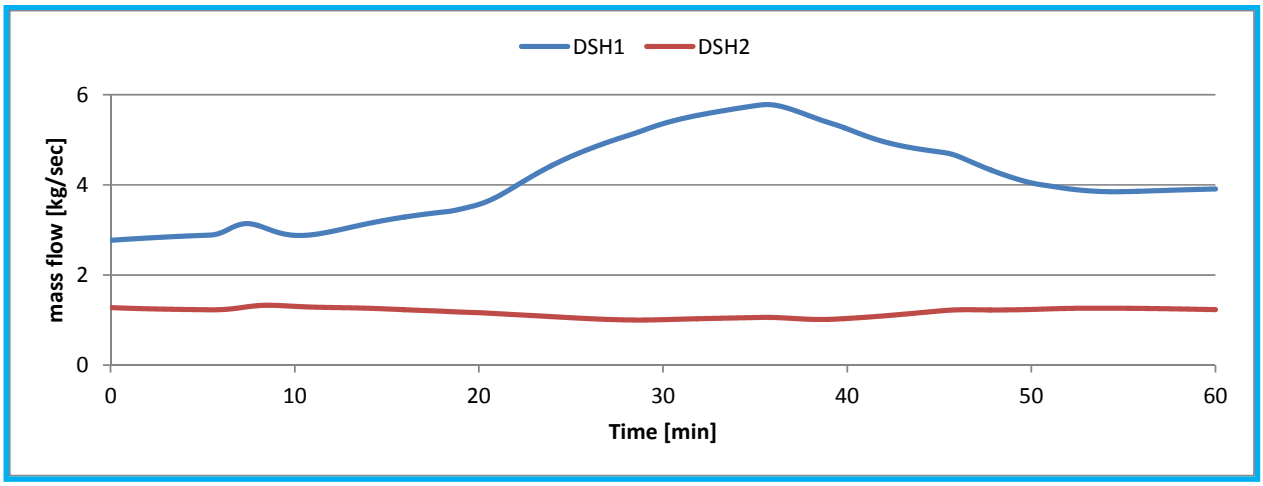

Figure 5-5 Desuperheater spray flow response to transition from air mode to oxy mode at 40% MCR

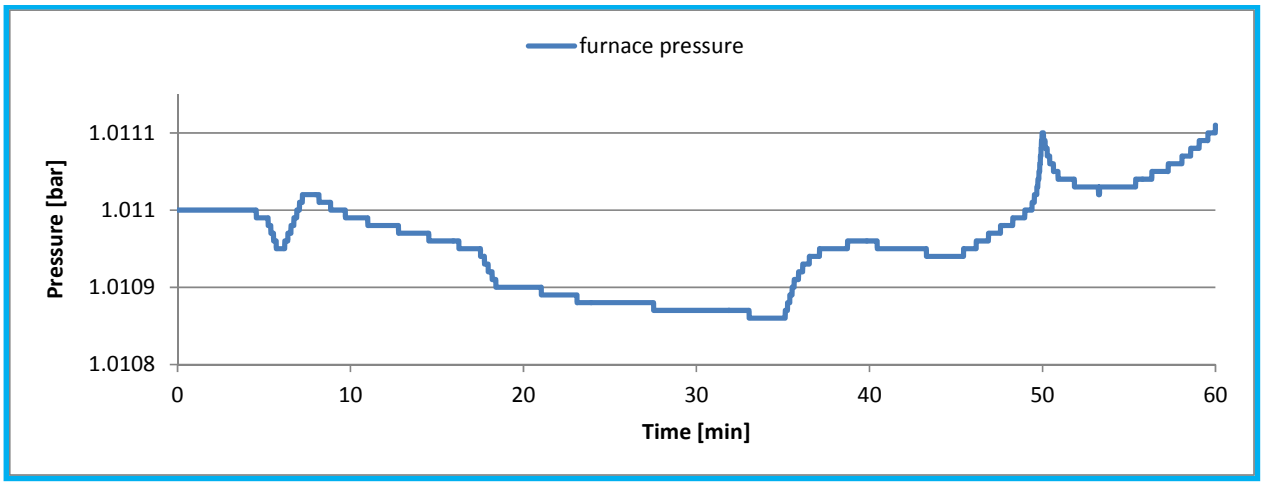

Figure 5-6 Furnace pressure response to transition from air mode to oxy mode at 40% MCR

Oxy-Mode to Air-Mode Transition at 40% MCR

Compared to the previous scenario, the boiler operation mode is switched back to the air mode from the oxy mode at the fixed load condition of 40% MCR. Figure 5-7 presents of the responses of CO_2 and O_2 concentration in the flue gas measured at the outlet of the economizer. The CO_2 mole fraction drops from from 60% to 13% when the transition is completed. Again, the O_2 concentration does not vary much during the transition.

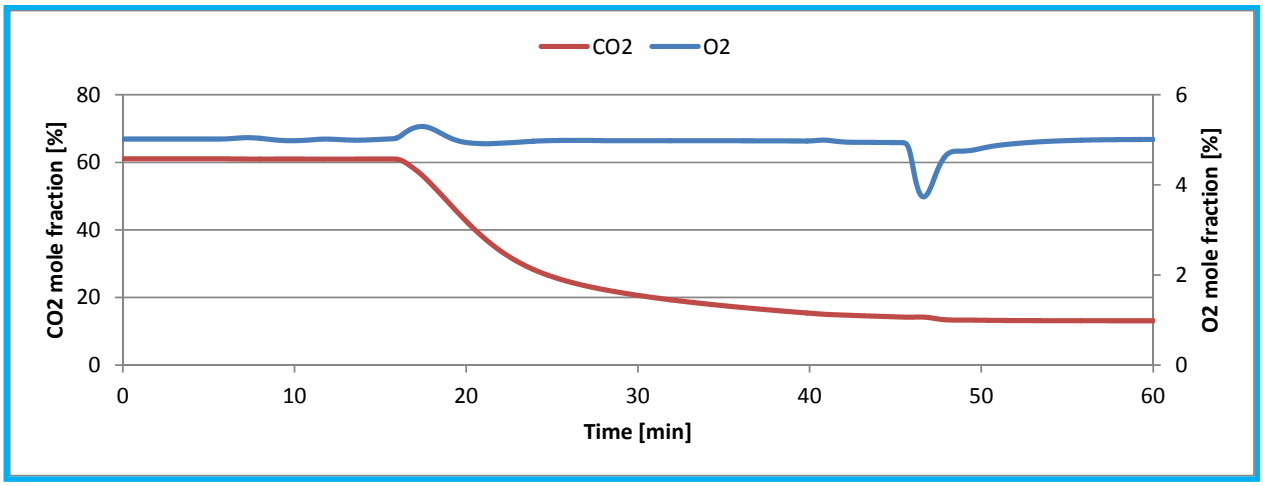

Figure 5-7 CO_2/O_2 concentration in flue gas response to transition from oxy mode to air mode at 40% MCR

The unit load demand is fixed during the transition of modes operation, whereas the load response fluctuates in a small range to the change of combustion as shown in Figure 5-8. Since the demand of fuel and feedwater flow is dominantly determined by the unit load demand, the flow of each process variable barely changes as indicated in Figure 5-9. In Figure 5-10, the temperature and pressure of main steam and reheated steam are well controlled during the transition. The responses of spray water and furnace pressure are given by Figure 5-11 and Figure 5-12 respectively.

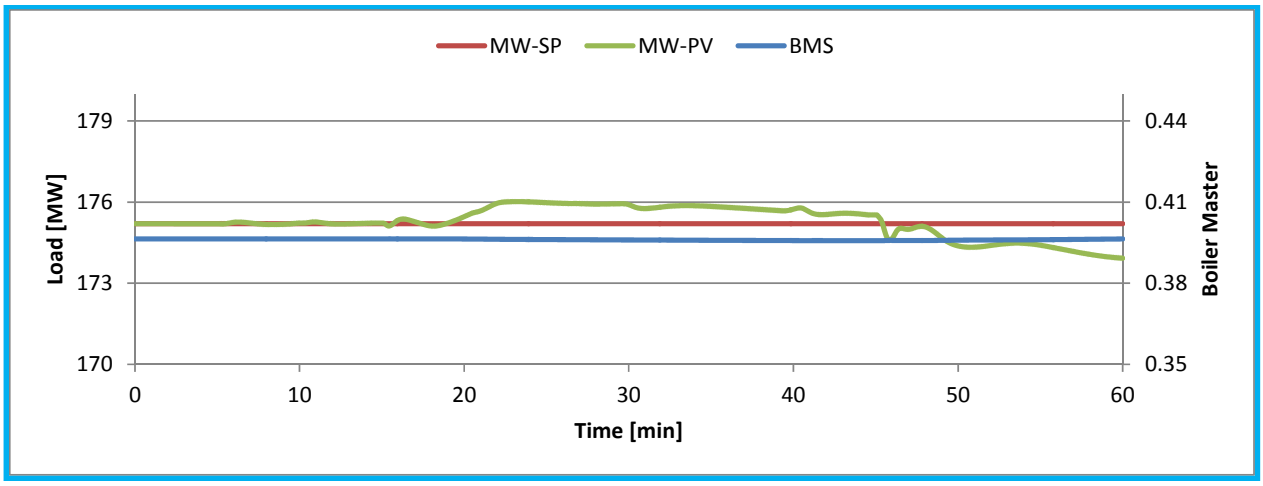

Figure 5-8 Load response to transition from oxy mode to air mode at 40% MCR

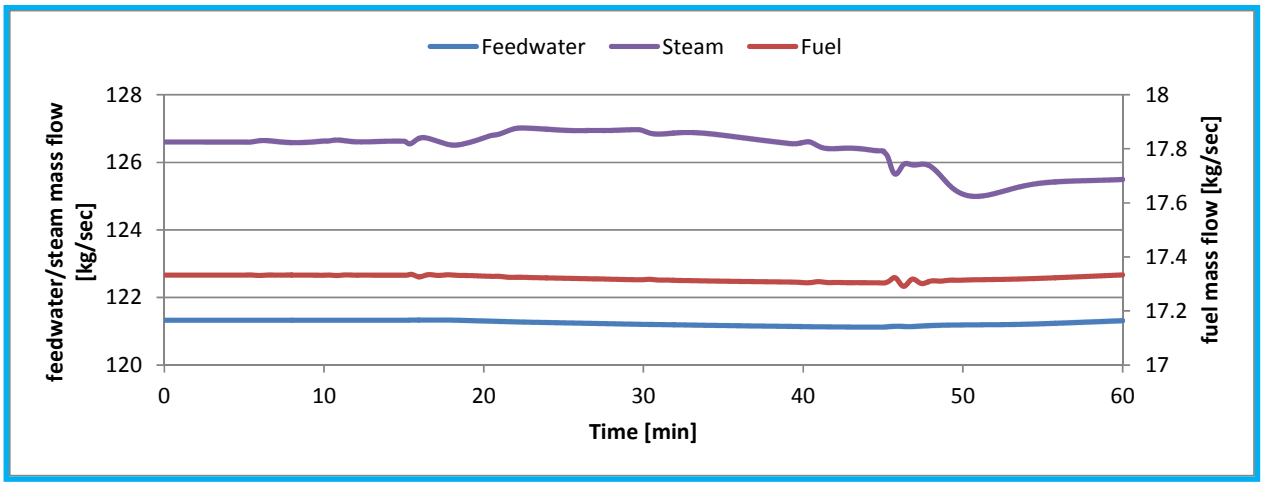

Figure 5-9 Feedwater/steam mass flow response to transition from oxy mode to air mode at 40% MCR

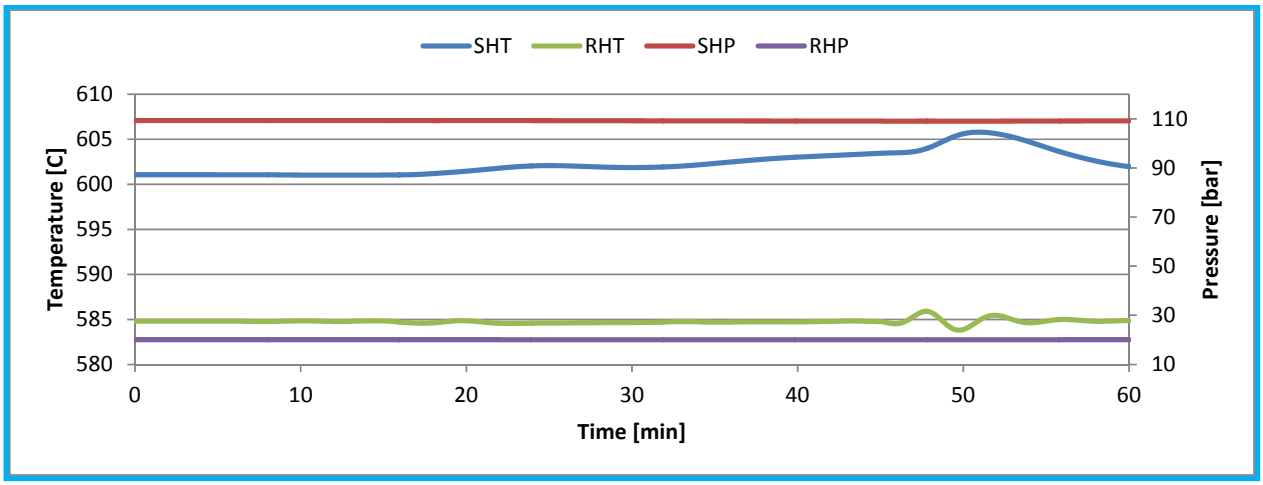

Figure 5-10 Main/reheated steam temperature/pressure response to transition from oxy mode to air mode at 40% MCR

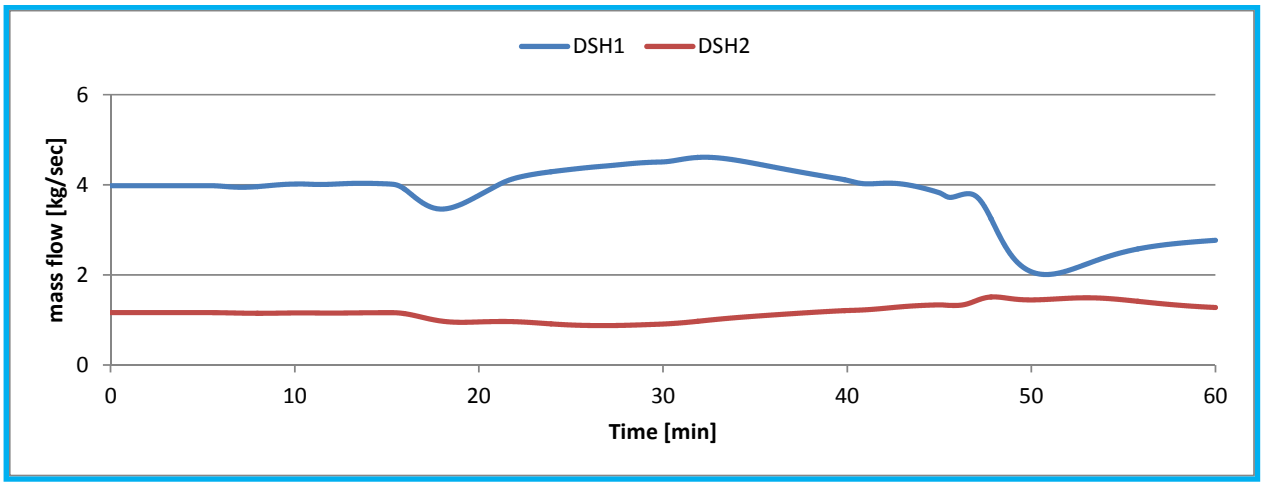

Figure 5-11 Desuperheater spray flow response to transition from oxy mode to air mode at 40% MCR

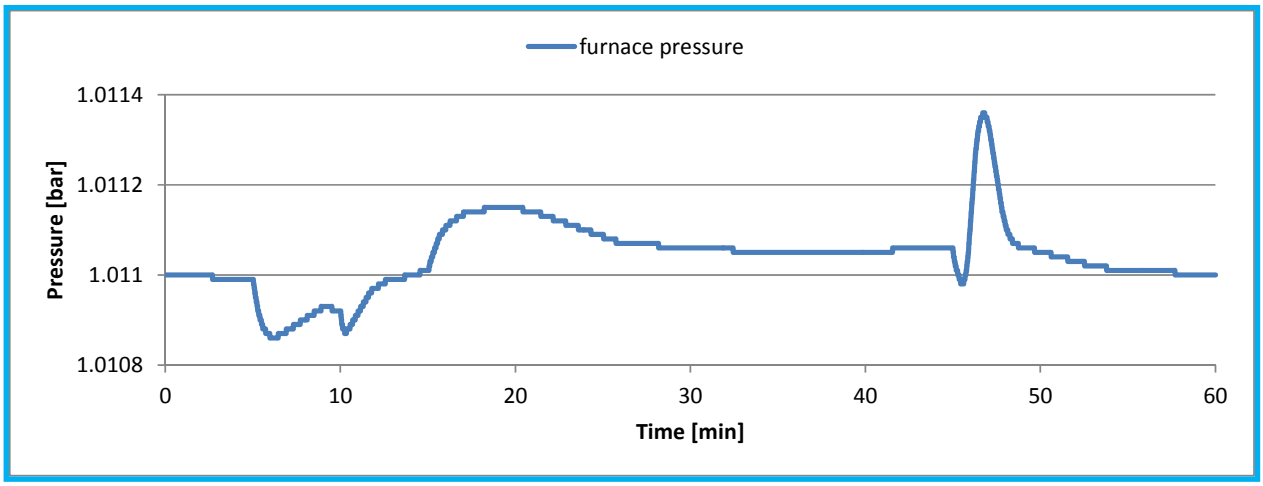

Figure 5-12 Furnace pressure response to transition from oxy mode to air mode at 40% MCR

5.2.2 Load Ramp Operations

Load ramp operation refers to unit load ramp at a specific ramping rate from the current MW load to the next MW load. Typical contractual load ramping rate requirements for a conventional air-fired boiler unit are 3% MCR/min between 35% MCR and 50% MCR and 5% MCR/min between 50% MCR and MCR.

Load ramp from 35%MCR to 50% MCR at 3% MCR/min

In this scenario, the Load demand is required to ramp from 35% MCR to 50% MCR at a rate of 3% MCR per minute. Figure 5-13 shows the response of the gross MW produced within the first 30 minutes. The Boiler Master signal that is dominantly dertermined by unit load demand and trimmed by the gross MW response is also provided in the same figure.

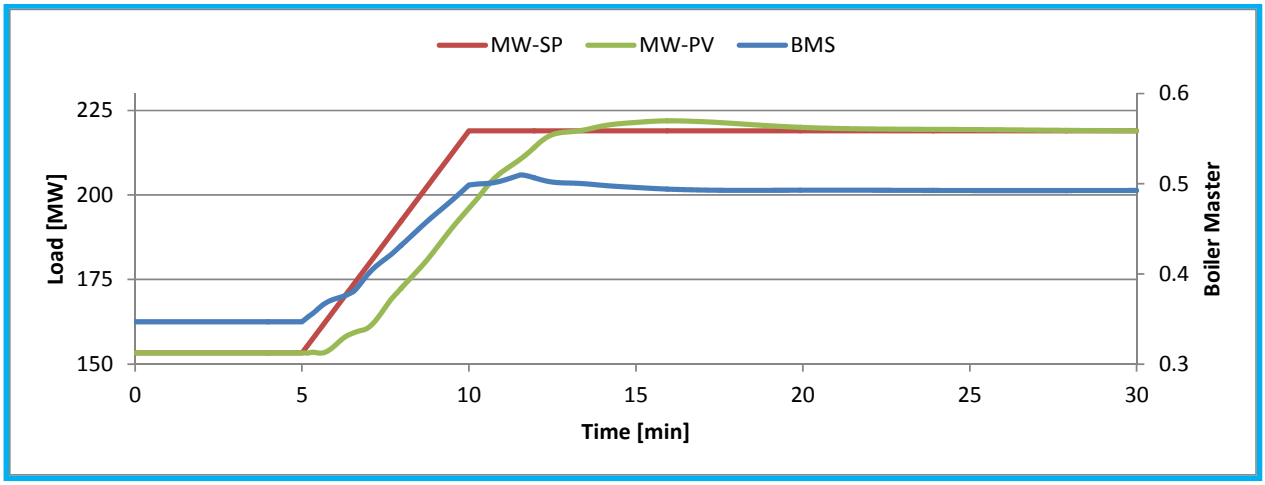

Figure 5-13 Load response to load ramp from 35% MCR to 50% MCR

As indicated in Table 5-1, the gross MW starts with an initial value of 153.3 MW (35% MCR), and stabilizes at 219 MW (50% MCR). The duration of the settling time is around 7 minutes, so the average value of changing rate is about 2.14% MCR/min. During the transient, the maximum value of the gross MW is about 222 MW, which presents an overshoot value of 4.5%.

*Note: the settling time is defined as the time at which the gross MW has entered and remained within a specified band of error. The size of the error band was calculated by 5% of the magnitude of the demand change. For example, in this scenario, the value of the MW increases from 153.3 to 219 with a magnitude of 65.7 MW. The size of the error band is about ±5%*65.7 = ±3.285 MW. Therefore if the gross MW entered and remained within the range between 215.715 MW and 222.285 MW, then it is considered to be in a steady state.*

The overshoot value of the response is calculated as follows [for load increase scenario].

$$Overshoot = \frac{Maximum\ value - Final\ value}{Final\ value - Initial\ value}$$

Table 5-1 Statistical data of gross MW response to load ramp from 35% MCR to 50% MCR

Load	Initial Value [MW]	Final Value [MW]	Rate of Change [%MCR/min]	Settling time [min]	Maximum value [MW]	Overshoot [%]
Demand	153.3	219	3			
Response	153.3	219	2.14	7	221.95	4.5

The coordination control of fuel, feedwater and the oxidant flow plays an important part in maintaining the unit load. To achieve this control objective, the flow demand for each component is set to be load dependant. Nevertheless, some of them are also trimmed by certain factors. For example, the feedwater flow is tuned by separator outlet temperature, and the secondary air flow is also affected by the excess O_2 level. Figure 5-14 indicates the fuel, feedwater, air, and main steam responses during the ramping up scenario, which show similar tendancies in transient process. The main steam flow is usually higher than the feedwater flow in that it also includes the desuperheater spray flows.

Note: The oxidant flow is the total flow of primary oxidant, secondary oxidant and supplementary oxygen into the windbox.

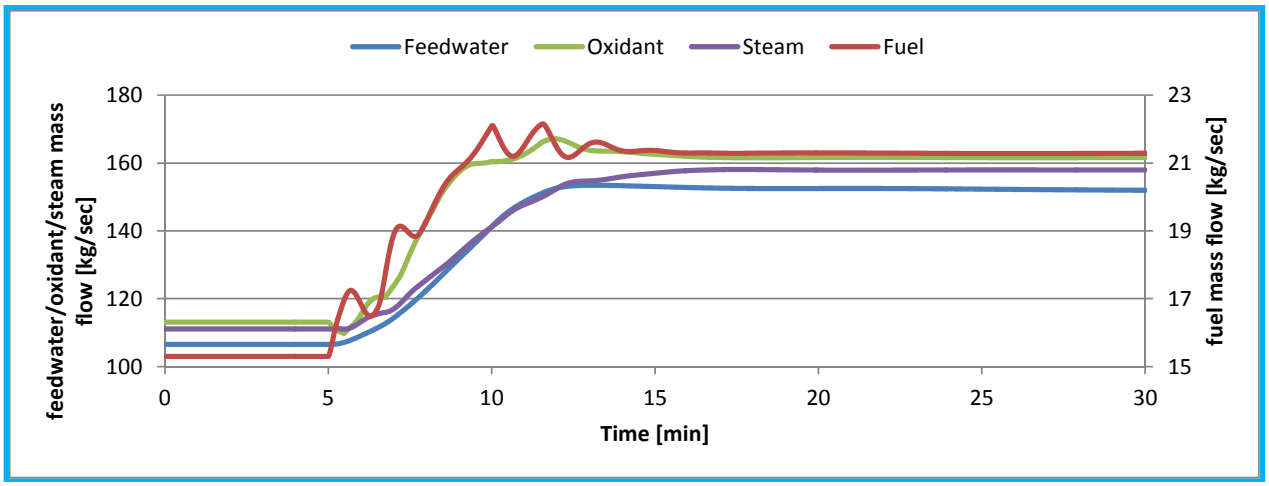

Figure 5-14 Fuel/feedwater/oxidant/steam mass flow response to load ramp from 35%MCR to 50% MCR

Steam pressure and temperature are other key components of the boiler control system. Figure 5-14 shows the pressure and temperature responses at the outlet of superheater, and reheater. The main steam temperature is aimed to be maintained at 600 °C, whereas the set point of reheated steam temperature is load dependent. The pressure of main steam and reheated steam are also determined by unit load demand. As shown in Figure 5-15, the maximum temperature of the main steam is 614 °C, which is 14 °C above its set point during the transient.

The responses of the two-stage desuperheater spray water mass flow rate are given by Figure 5-16, and furnace pressure reponse is presented in Figure 5-17.

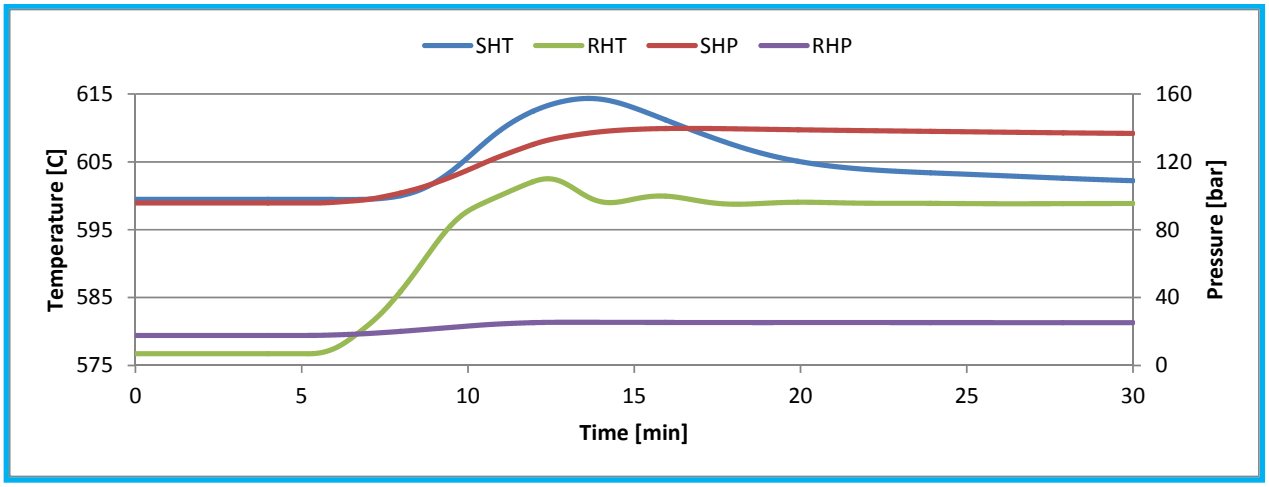

Figure 5-15 Main/reheated steam temperature/pressure response to load ramp from 35% MCR to 50% MCR

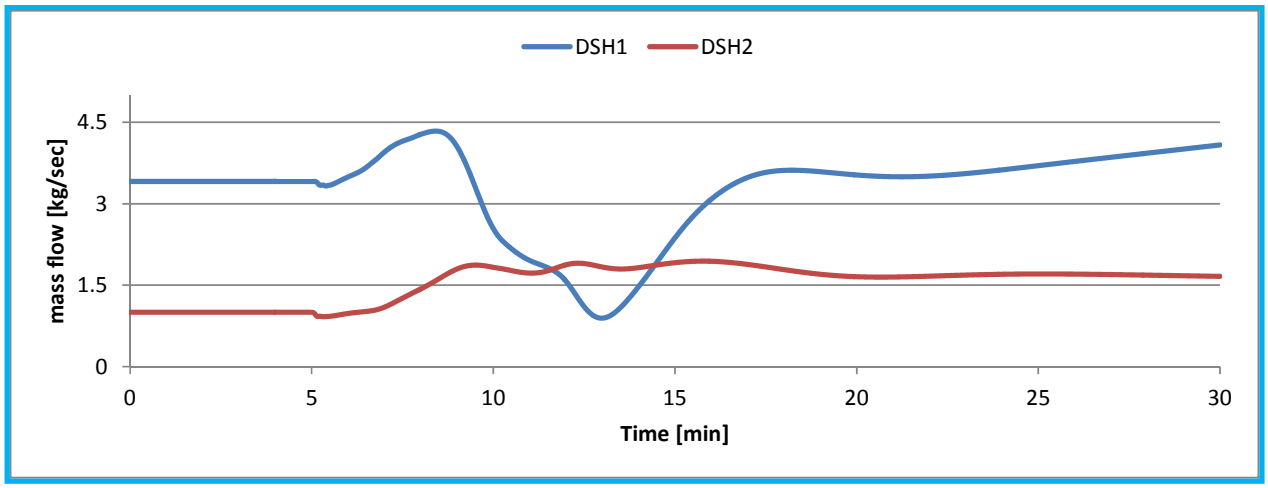

Figure 5-16 Desuperheater spray flow response to load ramp from 35% MCR to 50% MCR

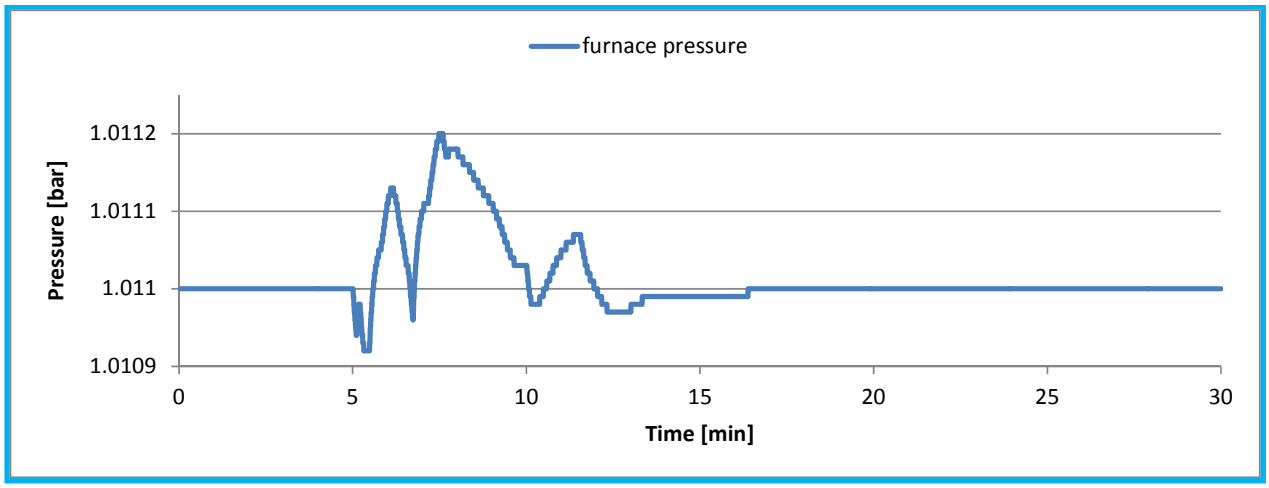

Figure 5-17 Furnace pressure response to load ramp from 35% MCR to 50% MCR

Load ramp from 50% MCR to 100% MCR at 5% MCR/min

In this scenario, the unit load demand keeps increasing from 50% MCR to MCR at a faster ramping rate of 5% MCR/min as indicated in Figure 5-18. The statistical results of gross MW response is given by Table 5-2. It takes 12 minutes for the gross MW to enter the steady state of MCR condition. During the transient, the maximum value of gross MW is about 445 MW, which delivers a slight overshoot of 0.78%. The response of the boiler master is also provided in Figure 5-18, which follows a similar trend of the MW demand signal.

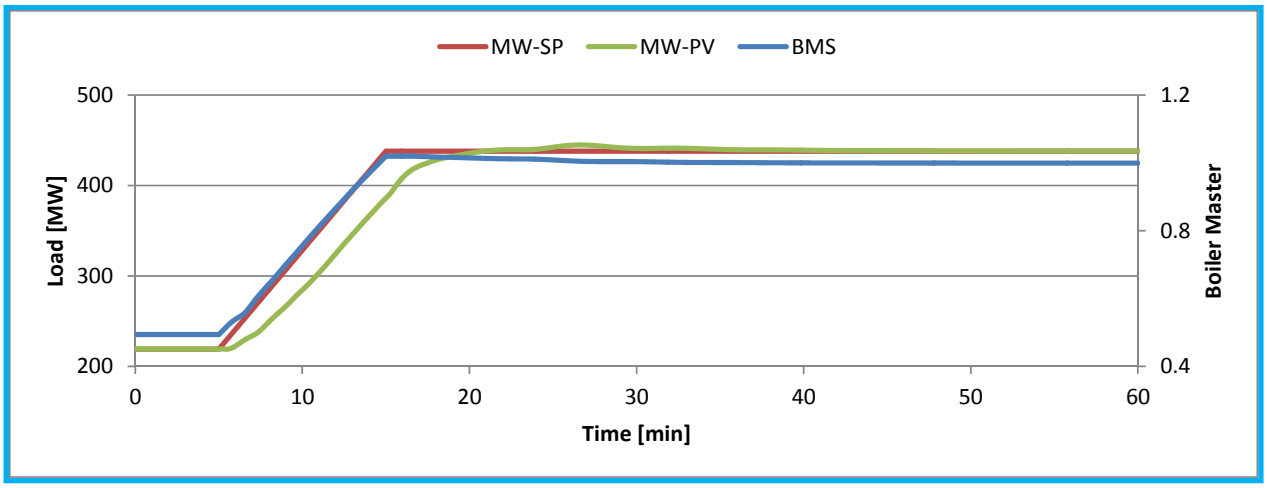

Figure 5-18 Load response to load ramp from 50% MCR to 100% MCR

Table 5-2 Statistical data of gross MW response to load ramp from 50% MCR to 100% MCR

Load	Initial Value [MW]	Final Value [MW]	Rate of Change [%MCR/min]	Settling time [min]	Maximum value [MW]	Overshoot [%]
Demand	219	438	5			
Response	219	438	4.17	12	444.85	0.78

The mass flow rate responses of fuel, feedwater, oxidant and main steam to load change from 50% MCR to MCR are presented in Figure 5-19. The control effect of the main steam temperature is influenced by the coordination between the feedwater flow and fuel combustion. The temperature and pressure responses of the main steam and reheated steam are shown in Figure 5-20, where the main steam temperature presents a maximum value of 612 °C during the transient. The spray actions of the two desuperheaters are indicated in Figure 5-21, and Figure 5-22 shows the response of furnace pressure.

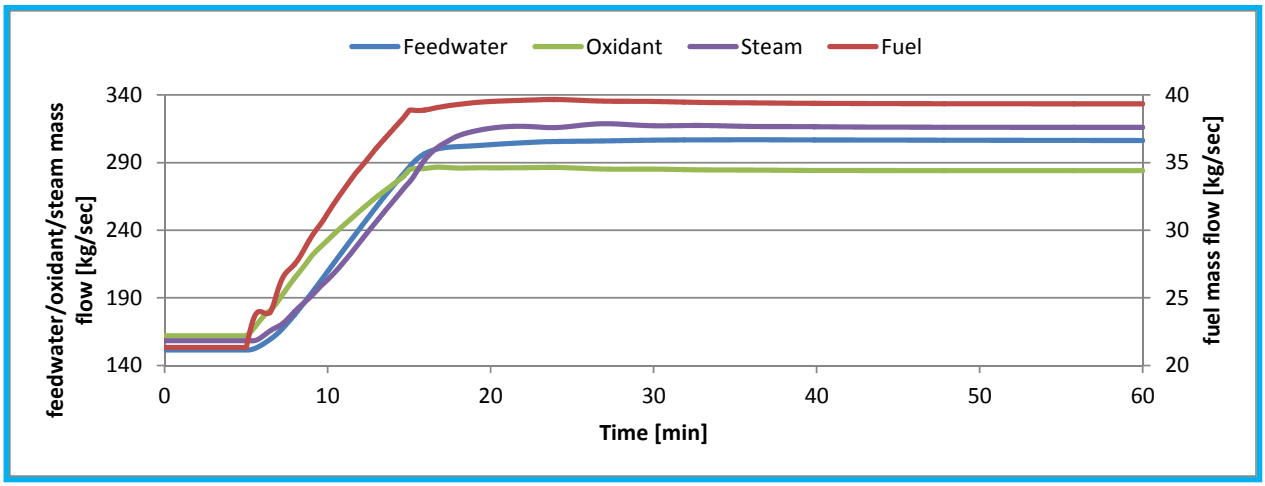

Figure 5-19 Fuel/feedwater/oxidant/steam mass flow response to load ramp from 50% MCR to 100% MCR

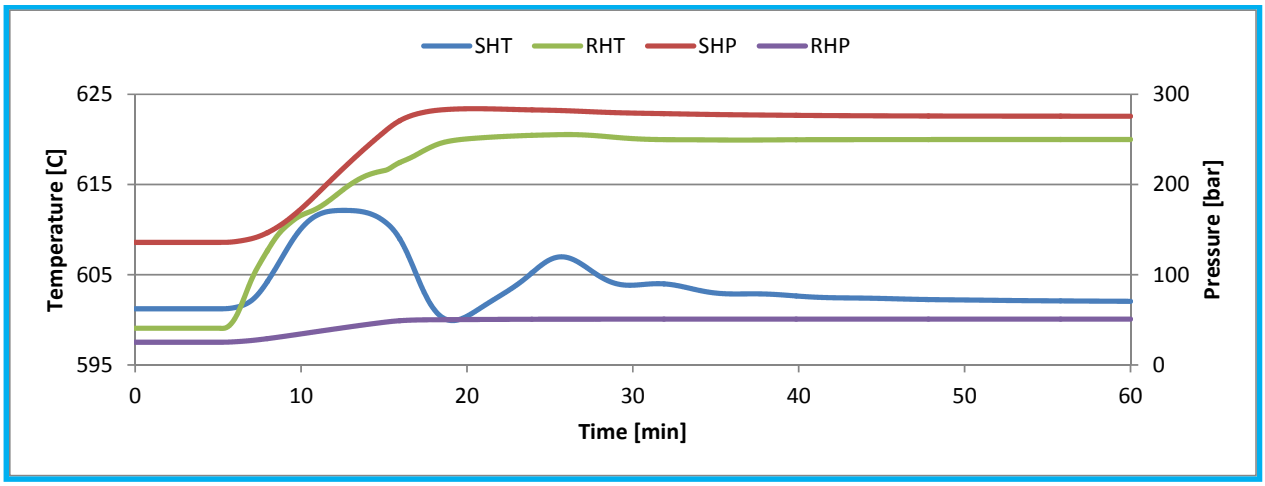

Figure 5-20 Main/reheated steam temperature/pressure response to load ramp from 50% MCR to 100% MCR

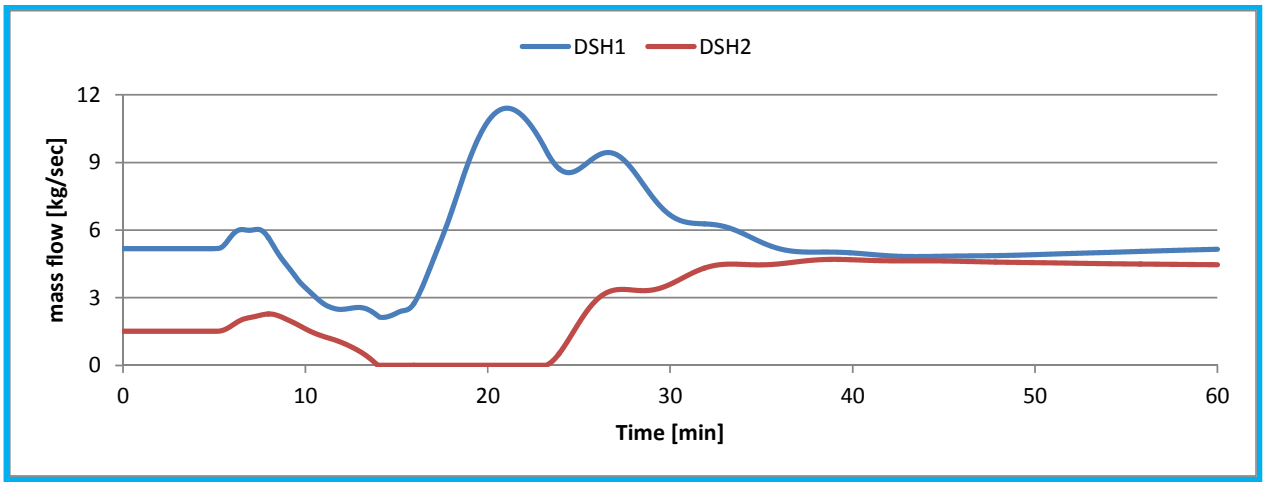

Figure 5-21 Desuperheater spray flow response to load ramp from 50% MCR to 100% MCR

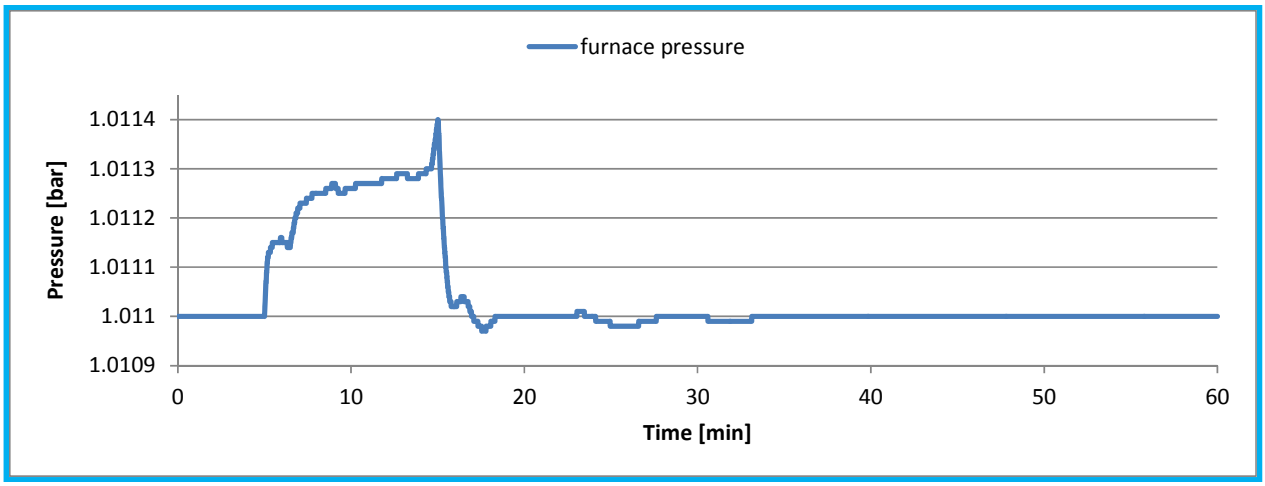

Figure 5-22 Furnace pressure response to load ramp from 50% MCR to 100% MCR

5.2.3 Load Step Change Operations

Load step change operation refers to an up to ±10% MCR step change on Unit Load Demand (ULD) when the unit is running between the boiler minimum stable load and full load. Step changes can be considered as the worst-case scenarios for boiler during normal operations because a step change introduces severe disturbances to the boiler operations. In order to test the control accuracy of the boiler island process under load step change scenarios, a ULD step from 50% MCR to 60% MCR was simulated.

Figure 5-23 presents the response of gross MW to the MW step reqirement from 50% MCR to 60% MCR. The step change in unit load demand will result in a step response of the boiler master simultaneously. As indicated in Table 5-3, the gross MW does not respond as fast as expected. The operation of the load step change requires the operation from the steam turbine side as well, such as reducing the amount of steam extraction to increase the total amount of steam through the steam turbine. This type of operation cannot be achieved due to the limitation of the current boiler island stand-alone model.

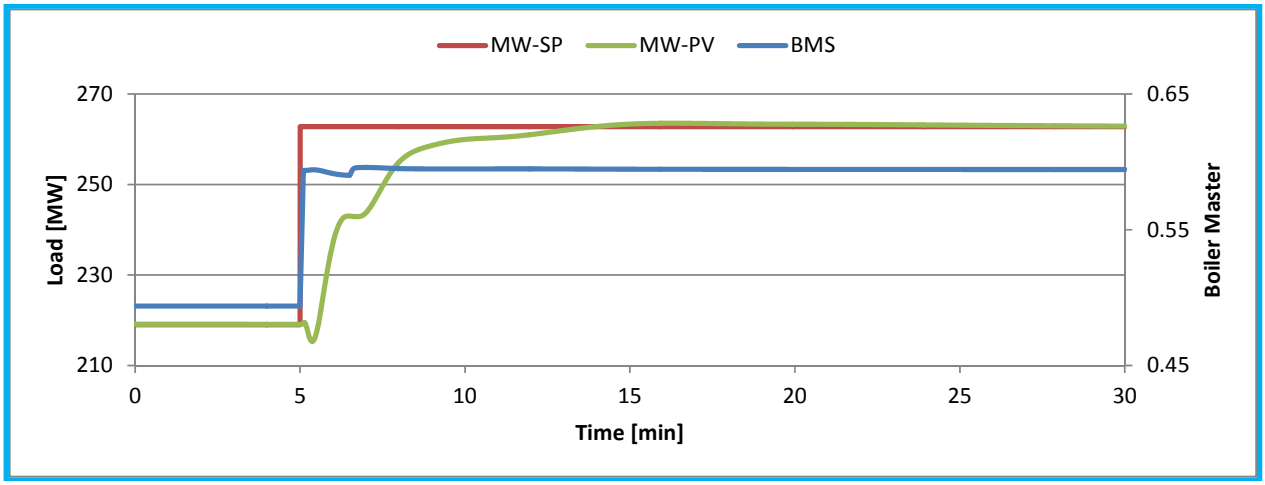

Figure 5-23 Load response to load step from 50% MCR to 60% MCR

Table 5-3 Statistical data of gross MW response to load step from 50% MCR to 60% MCR

Load	Initial Value [MW]	Final Value [MW]	Rate of Change [%MCR/min]	Settling time [min]	Maximum value [MW]	Overshoot [%]
Demand	219	262.8	inf			
Response	219	262.8	1.67	6	263.55	1.72

A step change in unit load demand will lead to step changes in the demands of fuel, air and feedwater. Considering the difference in the response of each component, the unit load demand cannot be distributed at the same speed into each local control loop. Some of them need to respond faster due to the dynamic inertia, and the others need to slow down to maintain the coordination. Figure 5-24 presents the mass flow rate responses of the feedwater, oxidant, steam and fuel. The temperature and pressure of the main steam and the reheated steam are shown in Figure 5-25, where the main steam temperature presents a maximum value of 607.7 °C, and Figure 5-26 shows the spray flow rate of the desuperheaters. The furnace pressure response is given by Figure 5-27.

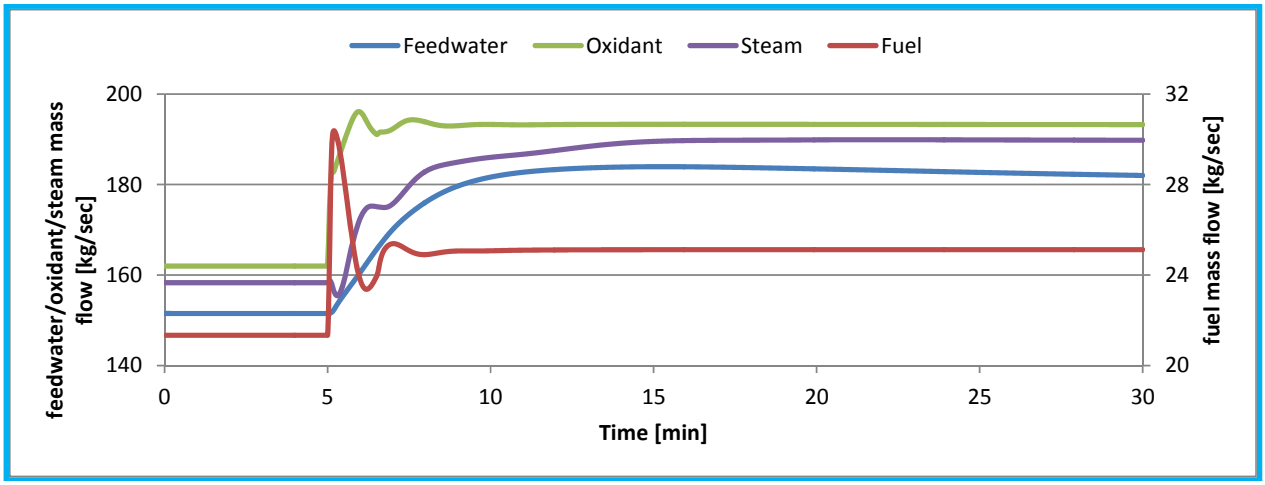

Figure 5-24 Fuel/feedwater/oxidant/steam mass flow response to load step from 50% MCR to 60% MCR

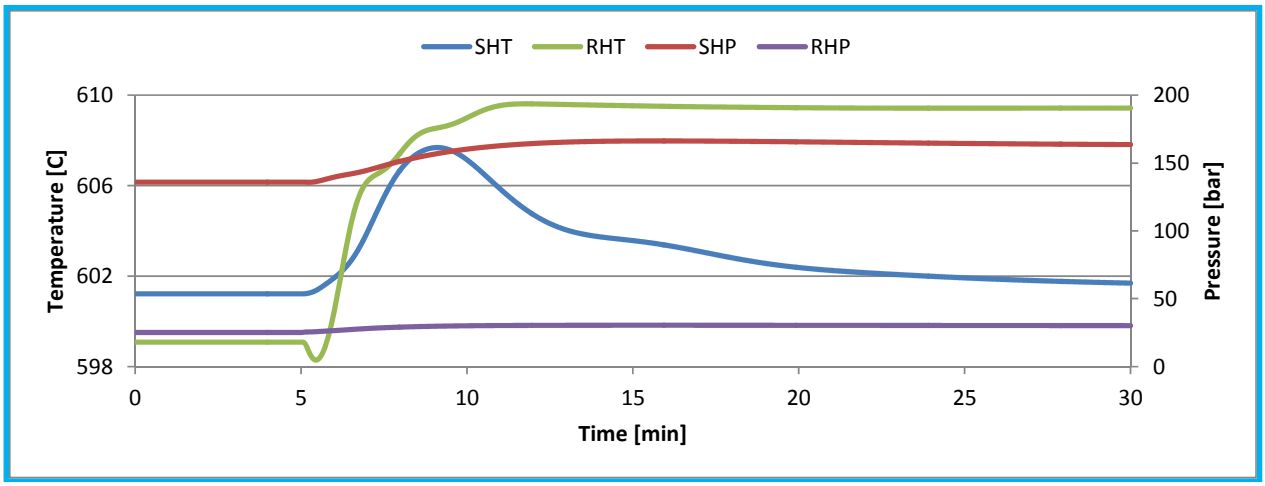

Figure 5-25 Main/reheated steam temperature/pressure response to load step from 50% MCR to 60% MCR

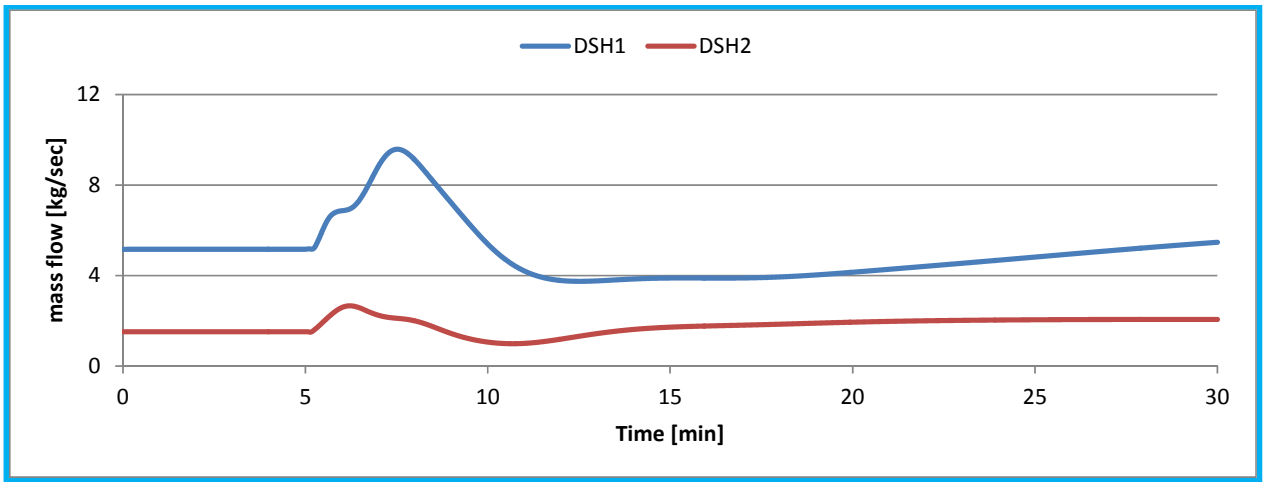

Figure 5-26 Desuperheater spray flow response to load step from 50% MCR to 60% MCR

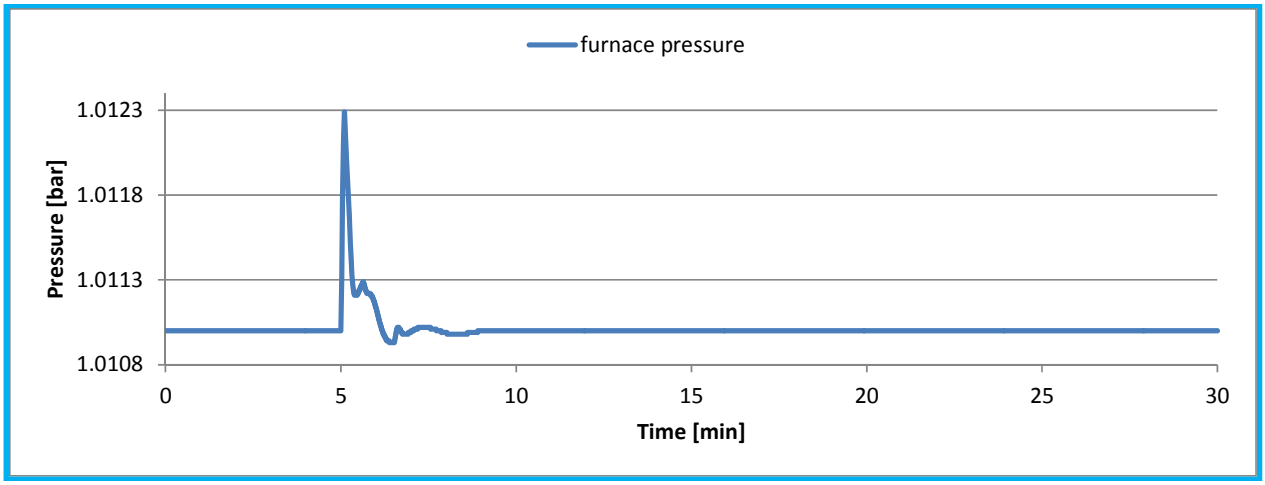

Figure 5-27 Furnace pressure response to load step from 50% MCR to 60% MCR

5.2.4 Oxy-Mode Minimum Load Operation

For such a commercial demo scale oxy-fired PC power plant design, Alstom proposes that the power plant shall have the capability to run under a low load condition (about 25% TMCR with no supporting oil) in oxy mode, when all the generated power is consumed by the ASU (to produce and store liquid oxygen for use when the electricity price is low or for fast transients) and the GPU. The power plant net output at this minimum load is expected to be close to zero.

The capability of running the power plant at the minimum load stably with little or no supporting oil can avoid the overnight shutdown and thus reduce the complexity of the plant operations. The dynamic model can be used to examine the feasibility and stability of the plant, especially the boiler unit, running at such a low load. The analysis should focus on the major auxiliary equipment of the boiler island, e.g. PA/ID/FD fans and the pulverizer system, etc. Information from the dynamic simulation can be fed to combustion system design engineers for further analysis.

The following results were generated as the boiler was turned down to 25% MCR from 40% MCR and at the same time the recirculation system pump was turned on when the feedwater flow rate is below a certain amount. The intention is to provide sufficient feedwater flow for cooling the economizer and water walls.

The response of gross MW to load ramping from 40% MCR to 25% MCR is shown in Figure 5-28. As indicated in Table 5-4, the gross MW settles down in 7 minutes with minimum value of 105 MW, and the overshoot is about 6.5%. The boiler master signal decreases from 40% to 25% gradually.

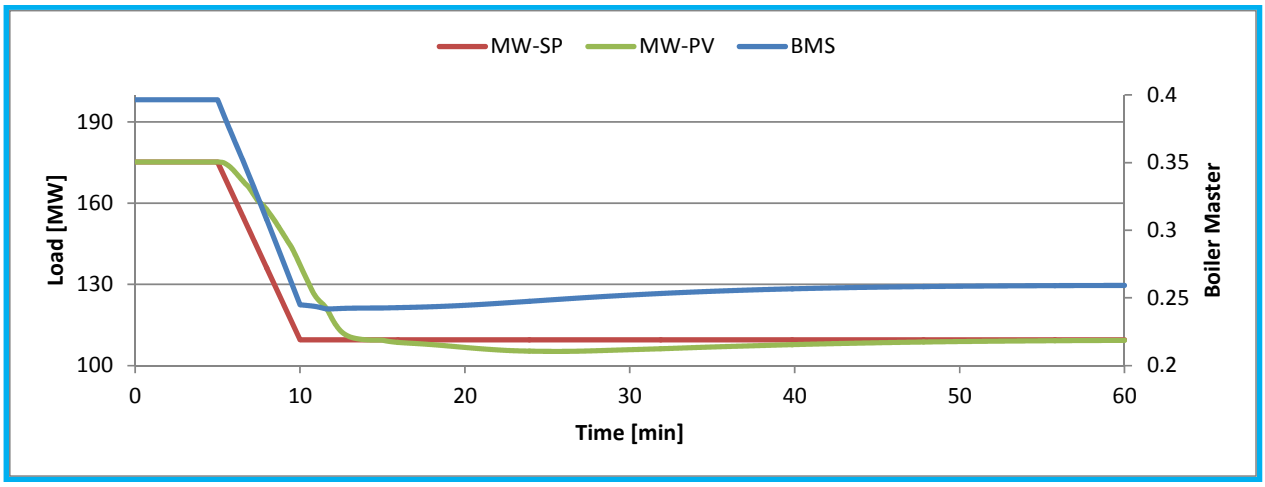

Figure 5-28 Load response to oxy-mode minimum load operation

Table 5-4 Statistical data of gross MW response to oxy-mode minimum load operation

Load	Initial Value [MW]	Final Value [MW]	Rate of Change [%MCR/min]	Settling time [min]	Minimum value [MW]	Overshoot [%]
Demand	175.2	109.5	3			
Response	175.2	109.5	2.14	7	105.223	6.51

The mass flow rates of feedwater/oxidant/main steam/fuel each reduce to their steady state value simultaneously as presented in Figure 5-29, while the pressures of the main steam and the reheated steam also decreases to lower values. At low load condition, the set point of the steam temperature is also defined at a low level as indicated in Figure 5-30. As shown in Figure 5-31, the valves in both desuperheaters are fully closed when the unit load approaches the steady state. The furnace pressure is well controlled by the FD fan as indicated in Figure 5-32. Figure 5-33 presents the responses of the recirculation flow and the separator level. The recirculation pump only starts to work when the feedwater flow is below a critical flow rate, and the recirculation of the feedwater aims to maintain the minimum flow rate through the economizer and the waterwall. When the separator level is above its set point, the liquid in the tank will be directly released into the flash tank.

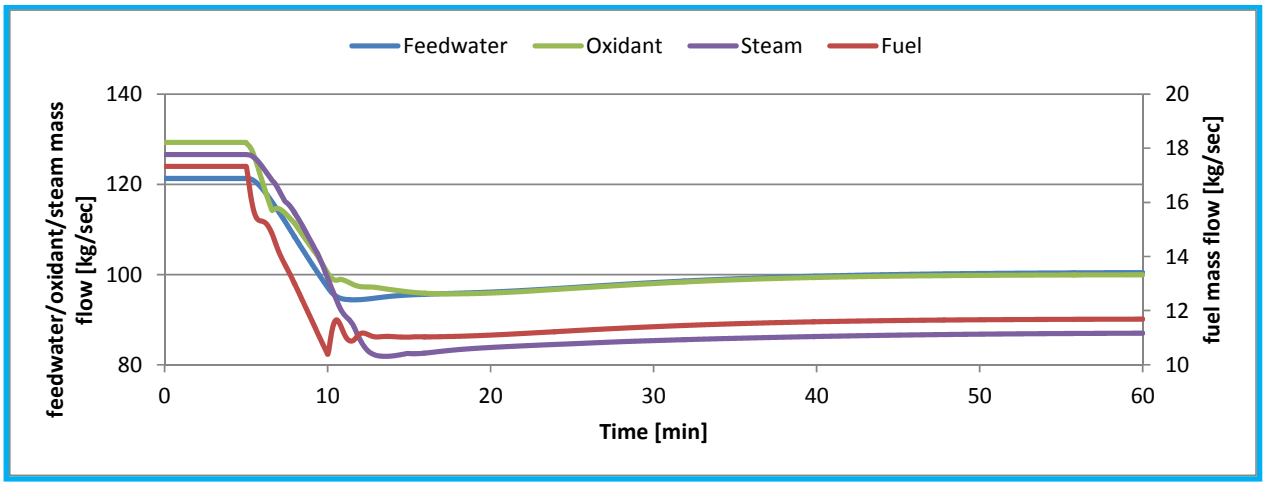

Figure 5-29 Fuel/feedwater/oxidant/steam mass flow response to oxy-mode minimum load operation

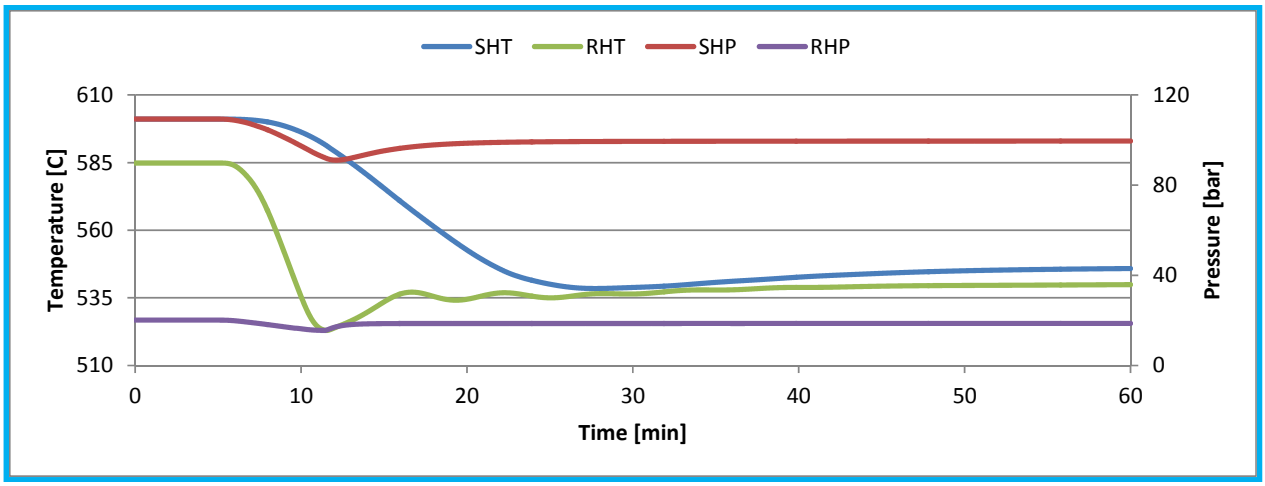

Figure 5-30 Main/reheated steam temperature/pressure response to oxy-mode minimum load operation

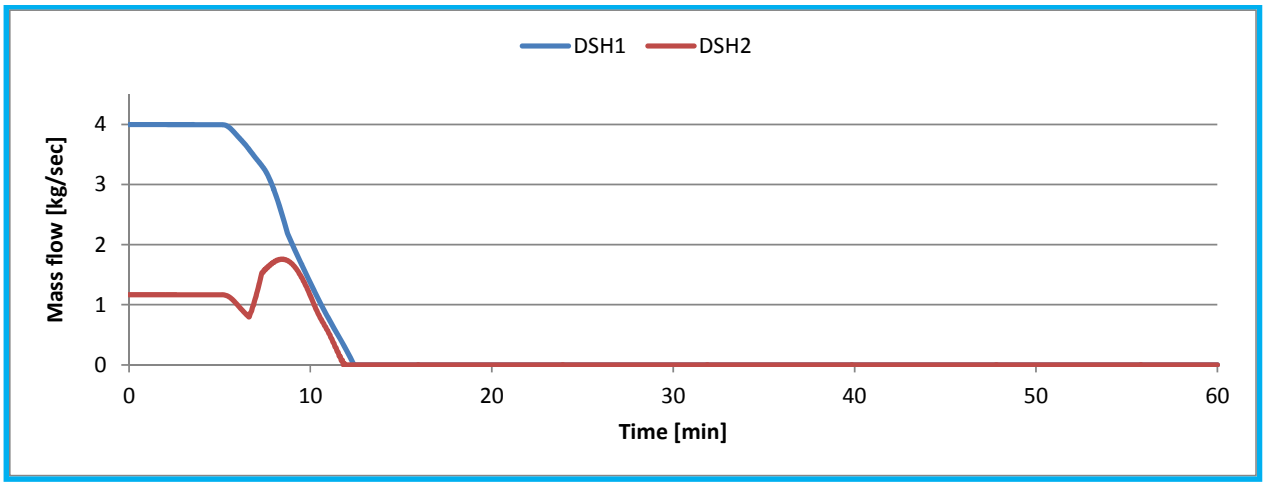

Figure 5-31 Desuperheater spray flow response to oxy-mode minimum load operation

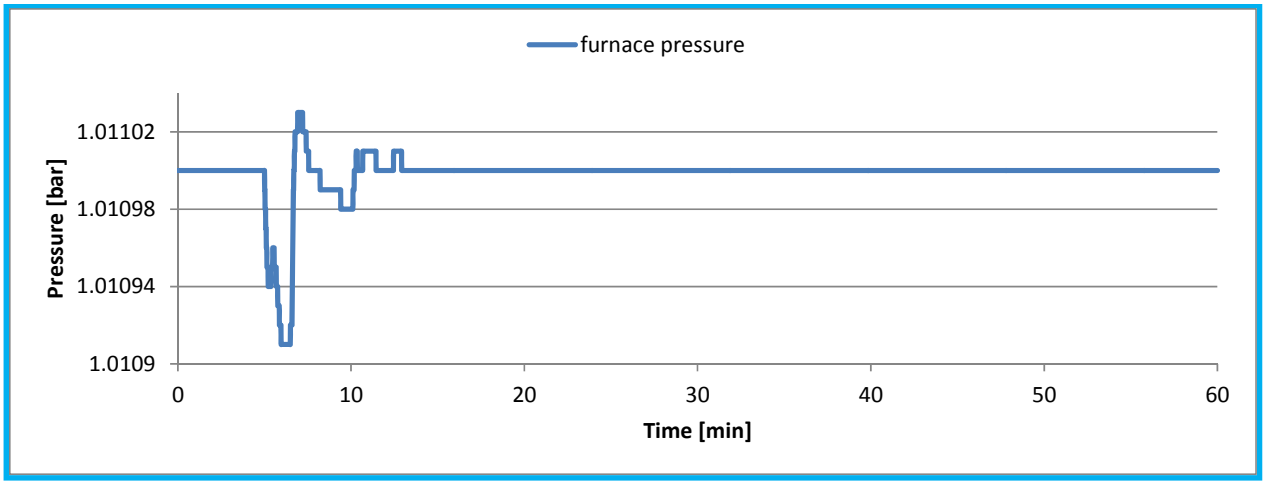

Figure 5-32 Furnace pressure response to oxy-mode minimum load operation

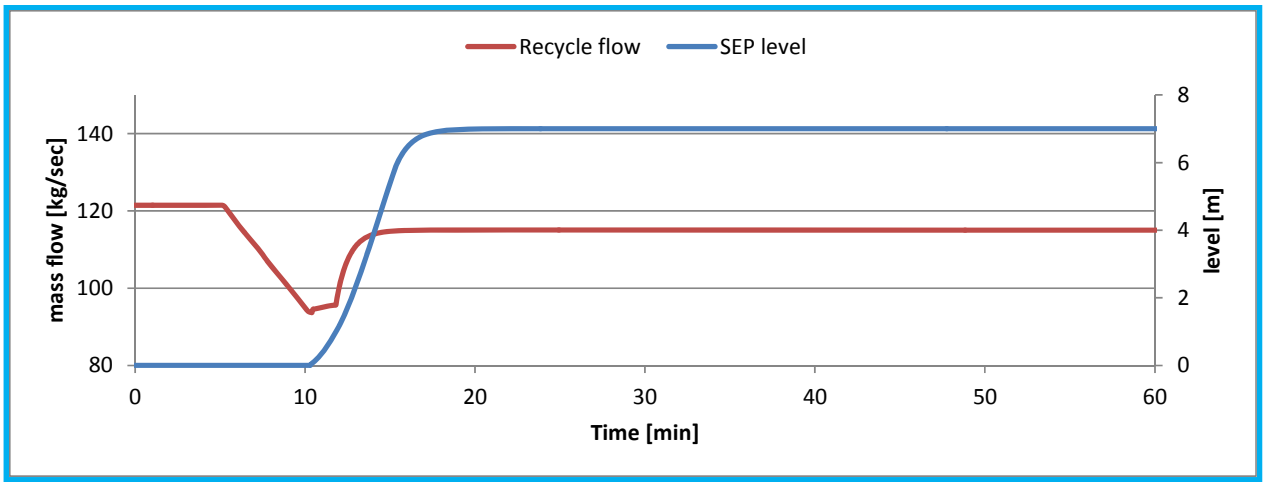

Figure 5-33 Recirculation flow and separator level response to oxy-mode minimum load operation

5.2.5 Start-up from Minimum Load Operation in Air Mode (25% MCR Air Mode to MCR in Oxy Mode)

The oxy-fired PC power plant will initially start up in air mode and then transition to oxy mode at a constant 40% MCR load and then ramp to full load.

In this simulation analysis, the initial condition for the boiler model is assumed to be running in steady state at 25% MCR in air mode. The analysis results show how the major auxiliary equipment of the boiler island, e.g. PA/ID/FD fans respond to the transition and the full load ramp up.

The following results were generated as the boiler went through the startup procedure as follows:

1. ramp from 25% MCR air mode to 40% MCR air mode,
2. switch to oxy-mode at constant 40% MCR
3. ramp to MCR in oxy mode.

Figure 5-34 presents the unit load response to the start-up sequence. As discussed above, the unit load demand increases at a rate of 3% MCR/min from 25% MCR to 40% MCR in air mode. During this time, the feedwater passes through the separator becoming superheated – as shown in Figure 5-35, the liquid level in the separator keeps decreasing. When the unit load approaches steady state, the transition from air mode to oxy mode starts at a constant load condition of 40% MCR. Figure 5-36 presents the responses of the CO_2 and O_2 concentration in the flue gas. The CO_2 mole fraction increases from below 20% to around 60%, while the O_2 concentration drops from 7% to about 3% at MCR. Figure 5-37 presents the mass flow responses of the feedwater, fuel, and oxidant, which are determined by the unit load demand. In

Figure 5-38, the temperature and pressure of the main steam and reheated steam are well maintained. Figure 5-39 and Figure 5-40 present the responses of the spray water actions and furnace pressure respectively.

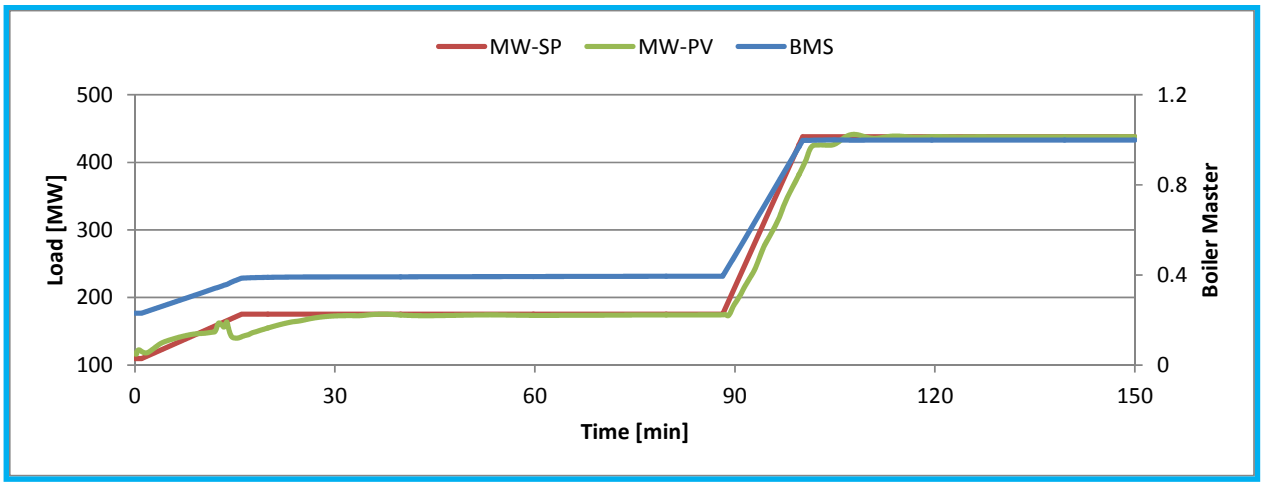

Figure 5-34 Load response to start-up

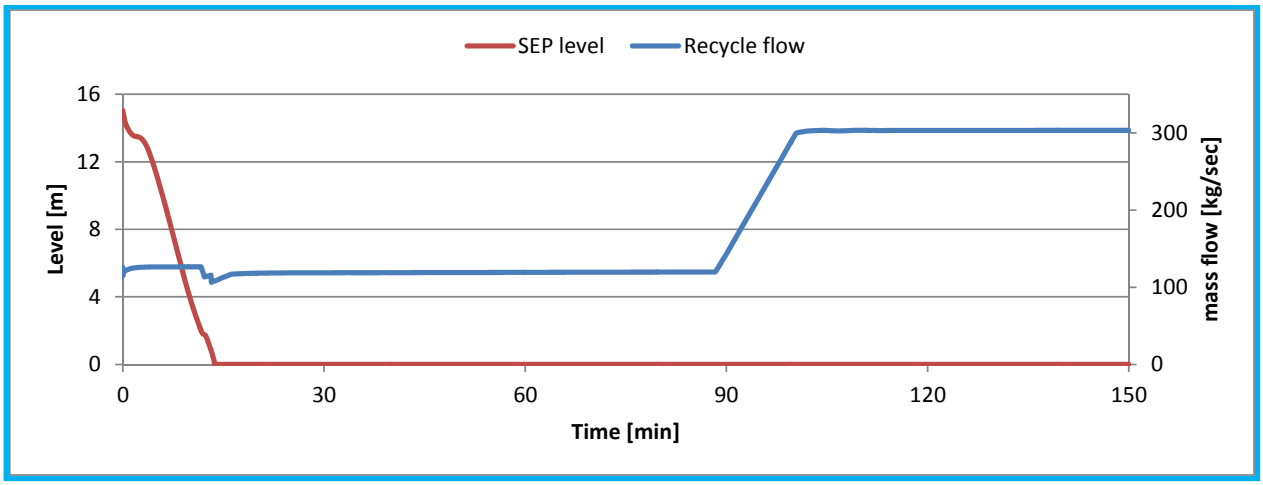

Figure 5-35 Recirculation flow and separator level response to start-up

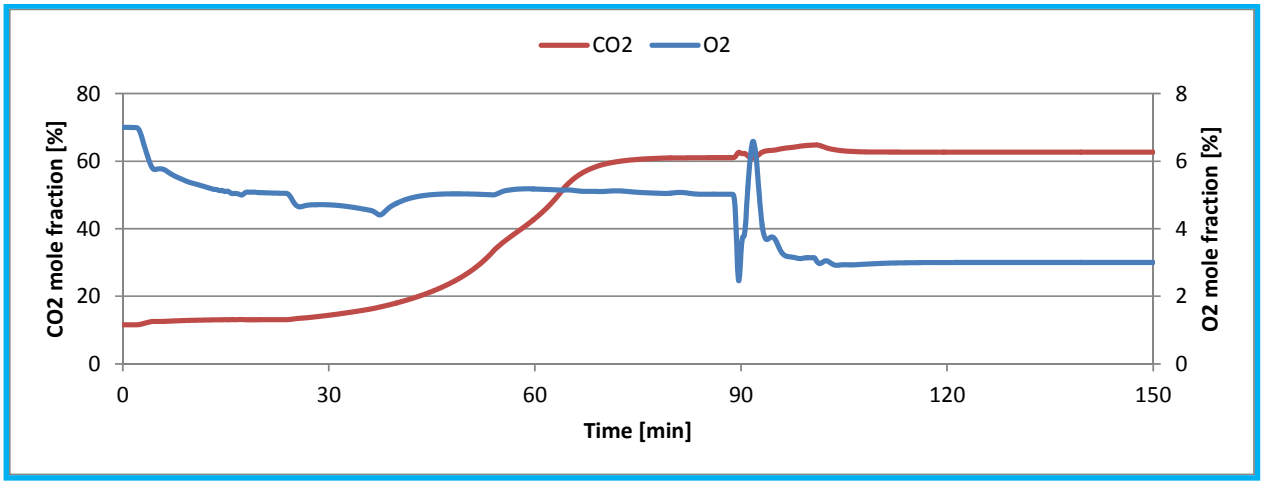

Figure 5-36 CO_2/O_2 concentration in flue gas response to start-up

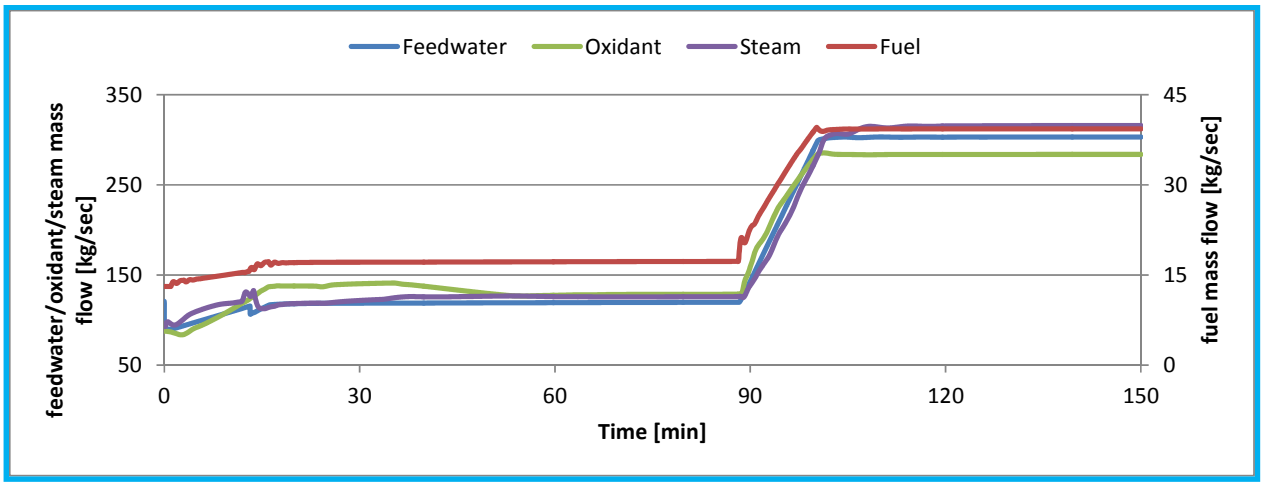

Figure 5-37 Fuel/feedwater/oxidant/steam mass flow response to start-up

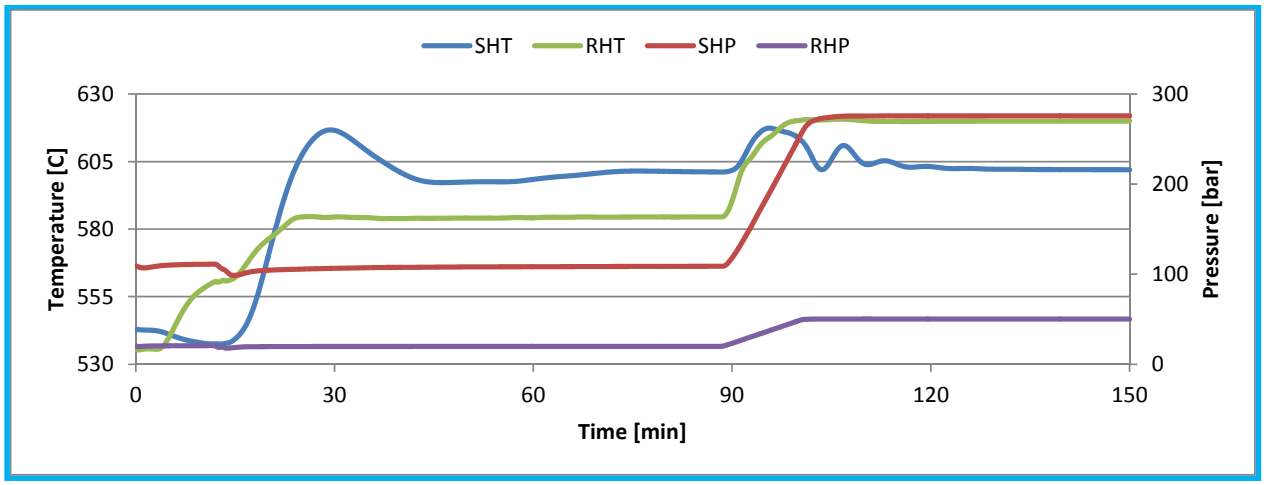

Figure 5-38 Main/reheated steam temperature/pressure response to start-up

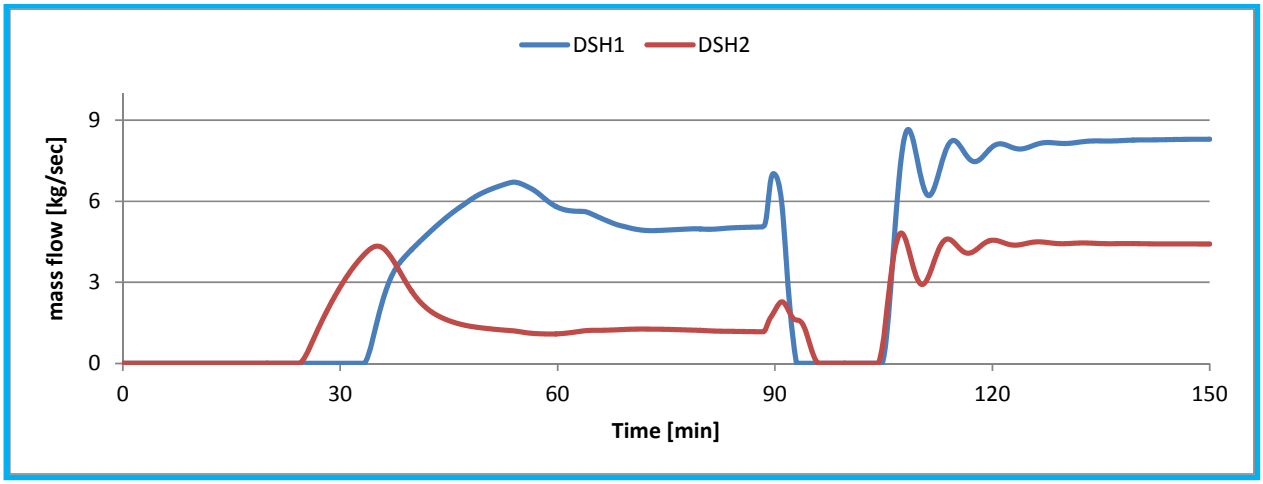

Figure 5-39 Desuperheater spray flow response to start-up

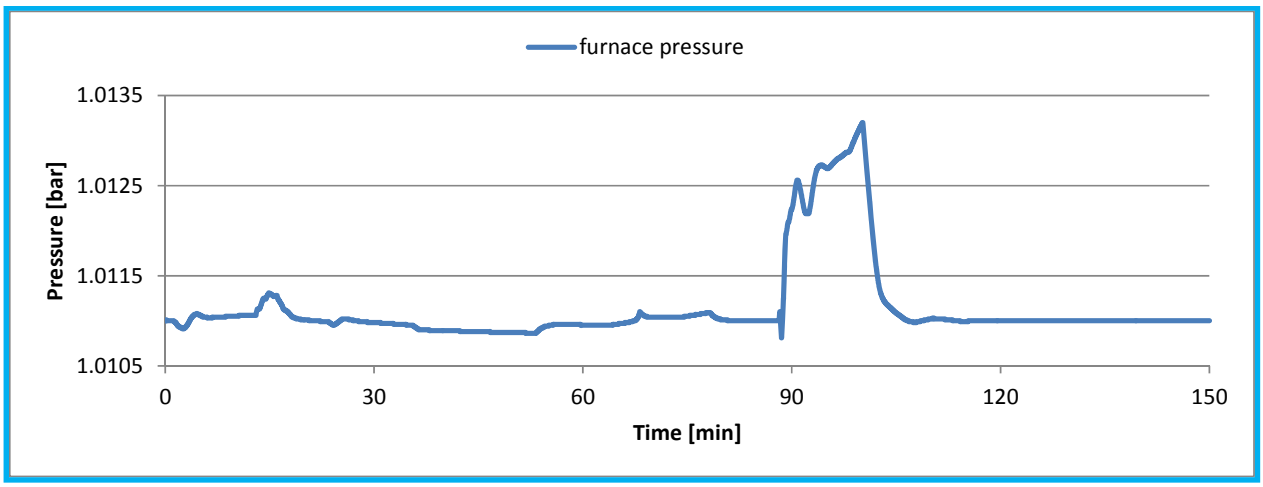

Figure 5-40 Furnace pressure response to start-up

5.3 Boiler Island Abnormal Operations

Abnormal operations refer to the unit's operations under unexpected disruptions. For the dual-fired pulverized coal boiler island process, these situations typically require a fast and controlled response to various major equipment failures, including mill trips, fan trips, master fuel trip, as well as interface subsystem trips.

For this work, the abnormal operations cases are focused on oxy-mode operation. Responsive control actions for air-firing operations can be designed based on conventional air-fired boiler operation procedures. The 450 MWe oxy-fired pulverized coal boiler island process model was developed building from Alstom air-fired model and incorporating features based on Alstom's current oxy-fired pulverized coal demo plant design. The major auxiliary equipment and their designed capacity for this Oxy-PC demo plant are summarized in Table 5-5.

Table 5-5 Major Equipment List for Referenced Oxy-PC Boiler Island

Major Equipment	Designed Capacity of Equipment	Sub-System
PA Fan	1 X 100%	Boiler Island
FD Fan	1 X 100%	Boiler Island
ID Fan	1 X 100%	Boiler Island
Coal Mills (Pulverizer)	5 X 25%	Boiler Island
Boiler Recirculation Water Pump	1 X 100%	Boiler Island
Feedwater Pumps	3 X 33%	Turbine Island
Condensate Booster Pump	1 X 100%	Turbine Island
HP Turbine	1	Turbine Island
IP Turbine	1	Turbine Island
LP Turbines	2	Turbine Island
HP Turbine Bypass	1 X 70%	Turbine Island
LP Turbine Bypass	2 X 35%	Turbine Island

For the power plant control logics, the load runback logic that ensures the overall unit load demand is constrained by the availability of major auxiliary equipment. Each piece of auxiliary equipment is

assigned a runback target load and a runback rate. The target load establishes the maximum permissible load. If an auxiliary equipment is lost, e.g. coal mill trip, feedwater pump trip, fan trips, etc., the unit load demand is reduced to the specified target load at the predetermined load runback rate.

Some equipment failures not only cause load runbacks, but activate the necessary bypass valves and other equipment will also have to be put into operation. For example, if the HP Turbine trips, the main steam is de-superheated and then bypassed to the cold reheat steam pipes. Meanwhile, since the main steam bypass line has a certain capacity limitation, the unit load has to be run back to a predetermined value. Responsive control actions defined for different trip scenarios might be different among different power plants. These responsive control actions for different equipment failure scenarios are summarized as guidelines for simulation configurations. These control actions serve as general examples for handling specific operating events, however, the details of each scenario should be further resolved.

Major equipment failures bring significant upsets to the overall process; therefore, the dynamic analysis of these test cases should include the entire process. However, the scope of this work focused on the boiler island, and only the responses of the boiler island equipment are discussed. The behavior of the other three subsystems, especially the turbine island subsystem and the gas processing unit also need to be investigated on an overall plant basis.

5.3.1 Mill Trip

As shown in Table 5-5, the oxy-fired boiler island process is equipped with five coal mills, among which four are in use during full load normal operations with one coal mill as a spare. The mill trip trigger conditions, responsive control actions, and simulation scenarios are summarized below:

Mill trip trigger conditions

- Pulverizer steam inerting system failure
- Loss of primary air
- Pulverizer lube oil system shutdown
- Wind box flame failure
- Master fuel trip
- Pulverizer discharge valve not open
- Pulverizer outlet temperature high, etc.

Mill trip responsive control actions

- Load run back to predetermined targets at specified run back rates

Simulation scenario

- 1 out of 4 mills trips (3 mills still in service)

One mill is tripped at a certain time and the assumed coasting down time is 10 seconds. At the same time, the demand for other three mills will ramp up close to the maximum capacity in 3 minutes, which make the unit load demand runback to a certain level which can be sustained with the remaining three mills.

Figure 5-41 presents the gross MW reponse due to the loss of one mill in operation. The unit load demand is designed to run back from MCR to 75% MCR in a minute. As shown in Table 5-6, the gross MW stabilizes in 7 minutes with a minimum value of 326 MW, and the overshoot is about 2.28%.

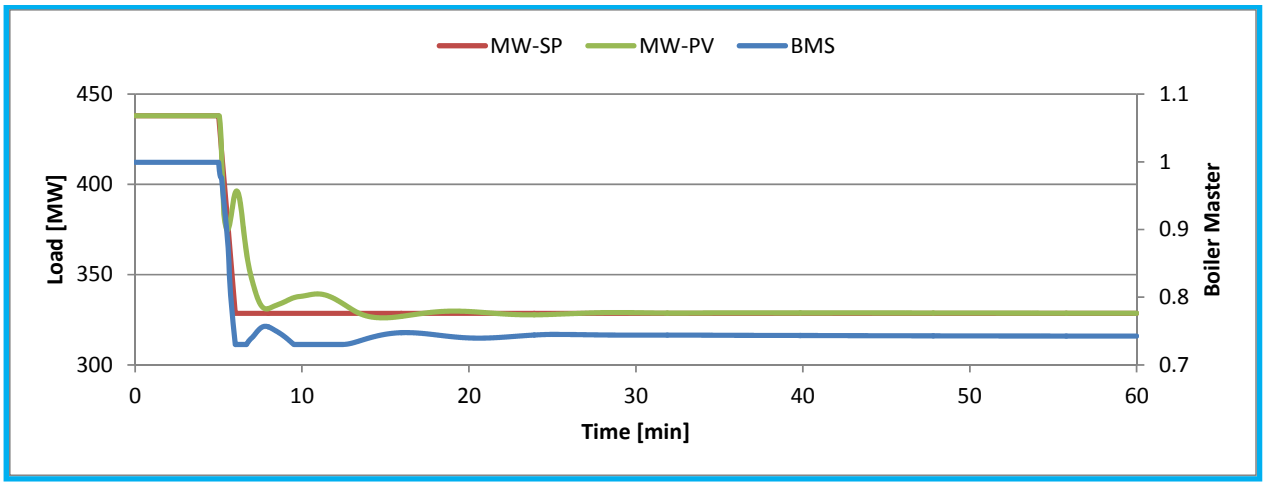

Figure 5-41 Load response to one mill trip

Table 5-6 Statistical data of gross MW response to one mill trip

Load	Initial Value [MW]	Final Value [MW]	Rate of Change [%MCR/min]	Settling time [min]	Minimum value [MW]	Overshoot [%]
Demand	438	328.5	25			
Response	438	328.5	3.57	7	326	2.28

As presented in Figure 5-42, the mass flow of the fuel drops down significantly when one of the mills is out of operation. All the other flows, such as feedwater, oxidant, will reduce accordingly once the unit load runback is active. In Figure 5-43, the main steam temperature drops dramatically during the transient with a minimum temperature of 587 °C due to the reduction of firing rate. The steam pressure also ramps down to a lower level of the new operating condition. The severe fluctuation of the main steam temperature results in the wide range operation of the spray valves as indicated in Figure 5-44. The loss of mill also leads to the disturbance in furnace pressure response as shown in Figure 5-45.

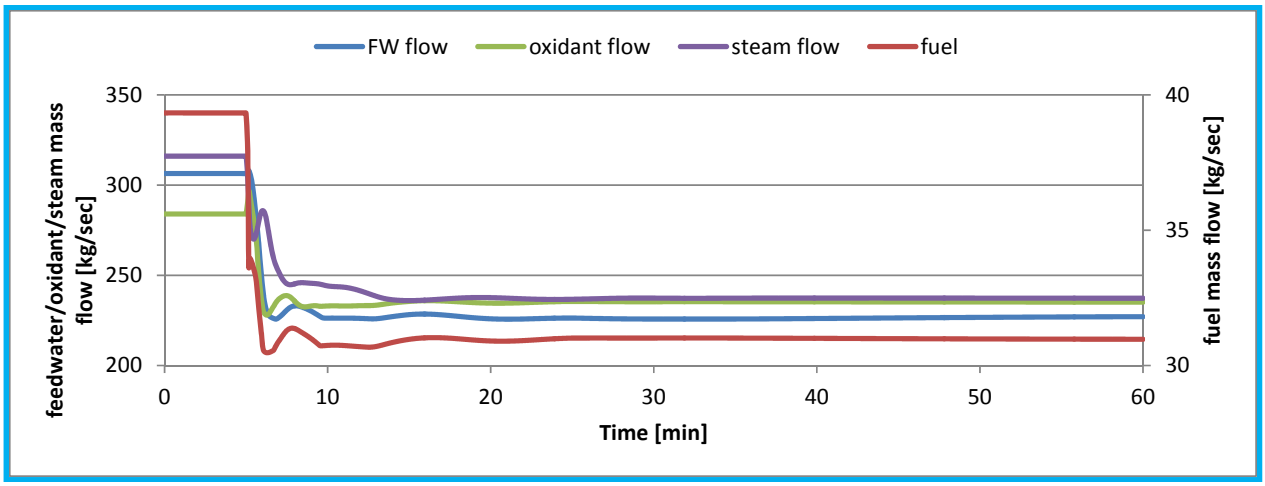

Figure 5-42 Fuel/feedwater/oxidant/steam mass flow response to one mill trip

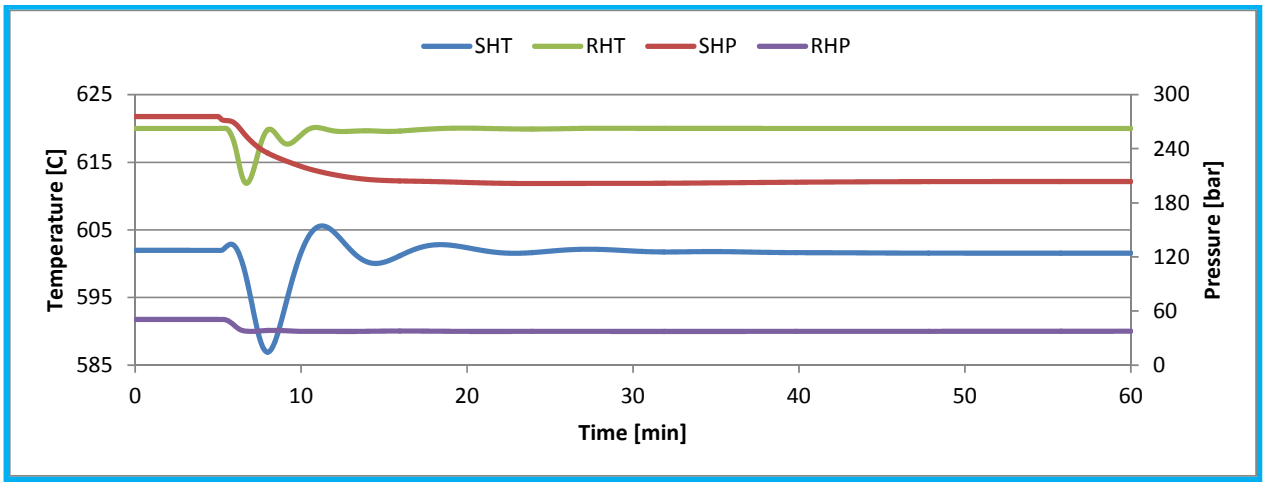

Figure 5-43 Main/reheated steam temperature/pressure response to one mill trip

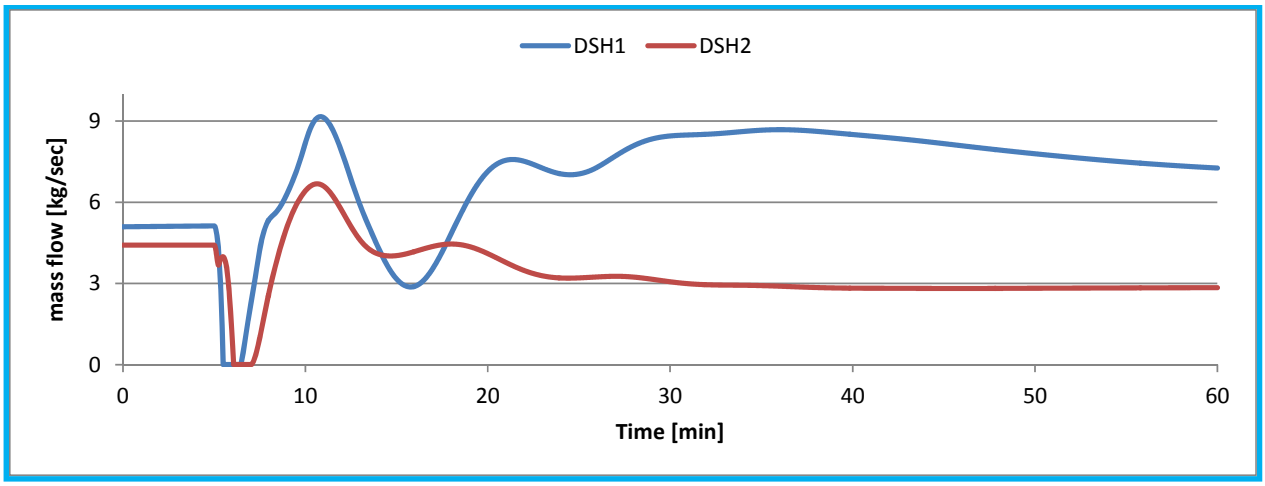

Figure 5-44 Desuperheater spray flow response to one mill trip

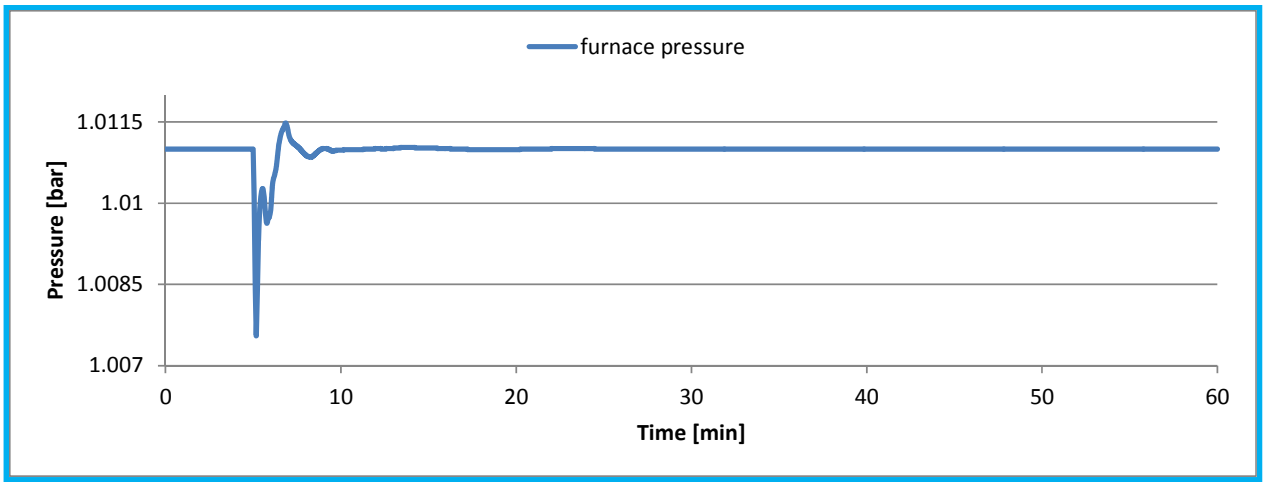

Figure 5-45 Furnace pressure response to one mill trip

5.3.2 PA Fan Trip

As shown in Table 5-5, the reference oxy-fired boiler island process has 1 PA Fan, 1 ID Fan and 1 FD Fan. From the process design perspective, having a single fan may cost less compared to a pair of smaller fans, however, from the control and operation perspective, single fan design brings higher requirements of the fan performance for reliable plant control and operations.

For example, if a boiler island process is designed with a pair of smaller fans (for PA/FD/ID fans), then 1 fan trip will generally cause the unit load to run back to 50% MCR at 55% MCR per minute. However, if the boiler island process is designed with single PA/FD/ID fans as in the reference plant design, then any fan trip will cause the Master Fuel Trip (MFT) and the plant will go through an emergency plant shutdown sequence.

In oxy-mode operations, one important responsive control action is to open the ambient air dampers and the stack dampers to quickly establish a complete air/flue gas path.

The cases for the fan trips are simulated and the resulting master fuel trip results are shown, as described below the specific fan in question will have a slightly different shutdown procedure since the working fans can reduce the catastrophic damage by allowing them to run as needed. It is assumed that the boiler feedwater is reduced to a 40% minimum load during any fan trip or master fuel trip scenario.

PA fan trip trigger conditions:

- PA fan bearing temperature high
- PA fan motor bearing temperature high
- PA fan motor bearing oil sump temperature high
- PA fan bearing vibration high
- PA fan motor bearing vibration high
- PA fan lube oil system failure
- Master fuel trip
- PA fan local trip, etc.

PA fan trip responsive control actions (Oxy-mode):

- Initiates master fuel trip (all mills should be taken out of service)
- Keep ID fan control in manual mode and ramp down its load quickly to balance furnace pressure
- Switch FD fan control to manual mode and keep steady and then ramp down steadily
- Switch all ASU oxygen controllers to manual mode and quickly shut off primary/secondary/supplemental oxygen flow control valves and ASU O_2 isolation valves
- Quickly open slightly secondary ambient air damper and stack isolation damper
- Quickly close primary and secondary flue gas recirculation dampers
- Boiler feedwater demand run back to predetermined minimum load (e.g. 40% MCR)

Figure 5-46 presents the responses of the major oxidant flow including the primary oxidant, the secondary oxidant and the supplementary oxygen to the PA fan trip. Since there is only one PA fan in the process, the PA fan trip will lead to the shutdown of the system. As indicated in Figure 5-47, the unit load demand is supposed to run back from MCR to 0% MCR in 2 minutes assuming the runback rate is 50% MCR/min during the PA fan trip scenario.

The PA fan trip will result in the fast drop in fuel flow as shown in Figure 5-48, while all the other process variables, including the total oxidant flow and feedwater flow, are expected to quickly reduce to target values. In this type of severe events, it is still important to make the steam pressure and temperature to reduce in anticipated trends as indicated in Figure 5-49 with the aid of desuperheater spray control shown in Figure 5-50. The furnace pressure control in Figure 5-51 is also critical to secure.

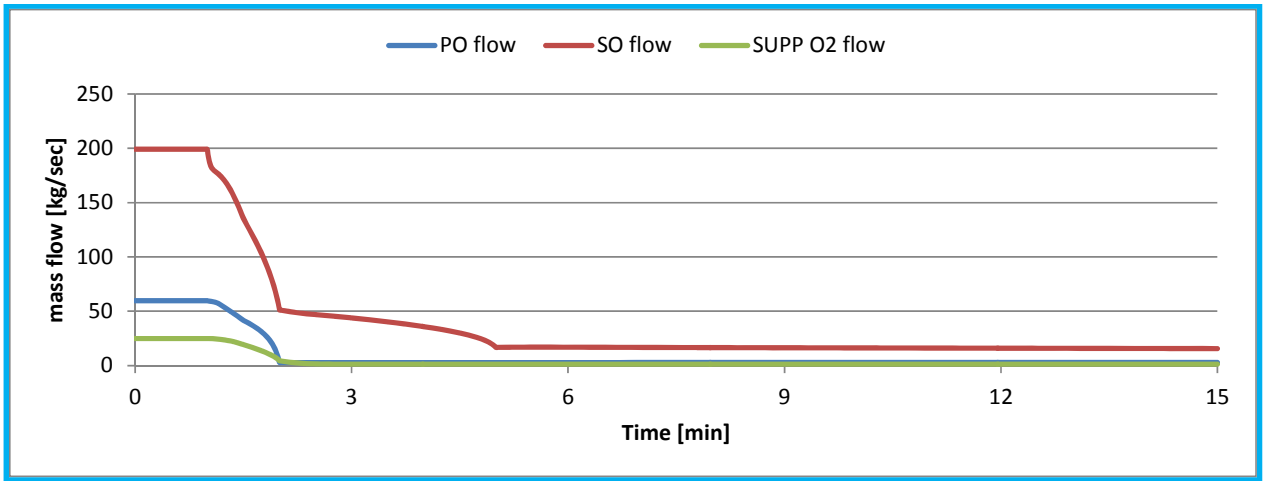

Figure 5-46 Primary oxidant/secondary oxidant/supplementary O_2 flow response to PA fan trip

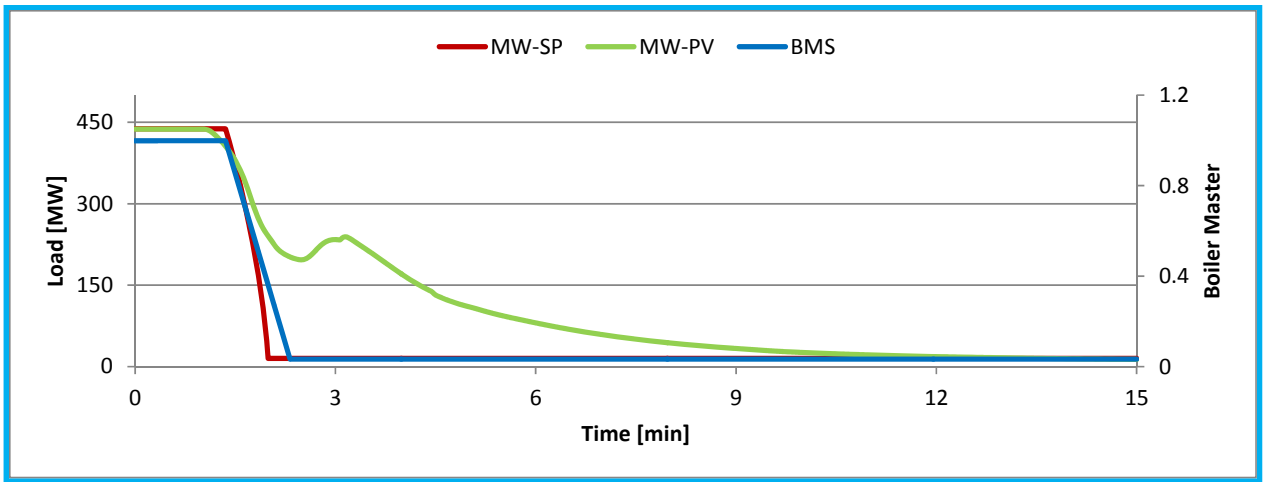

Figure 5-47 Load response to PA fan trip

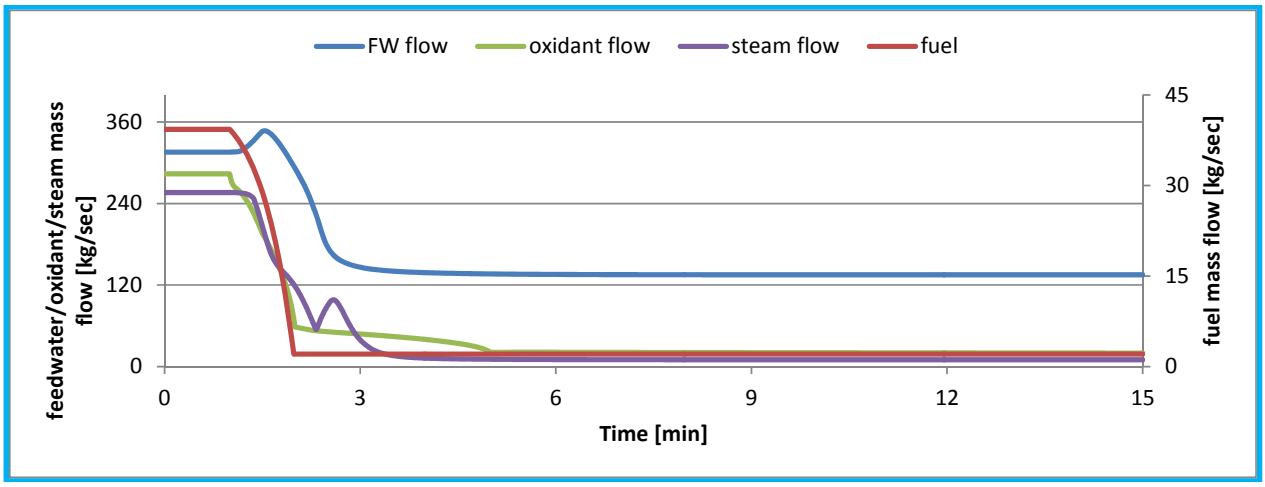

Figure 5-48 Fuel/feedwater/oxidant/steam mass flow response to PA fan trip

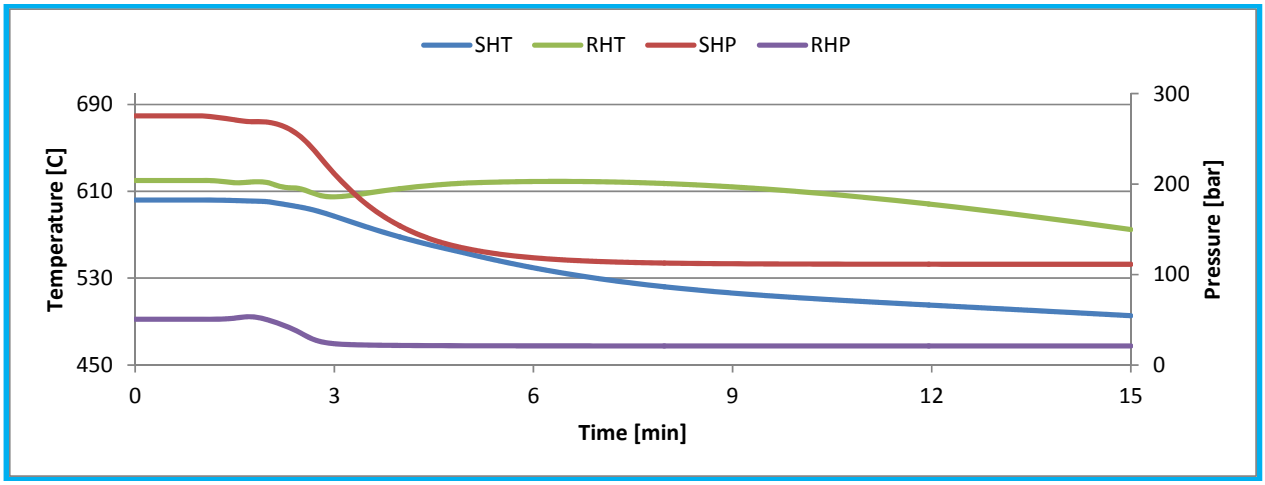

Figure 5-49 Main/reheated steam temperature/pressure response to PA fan trip

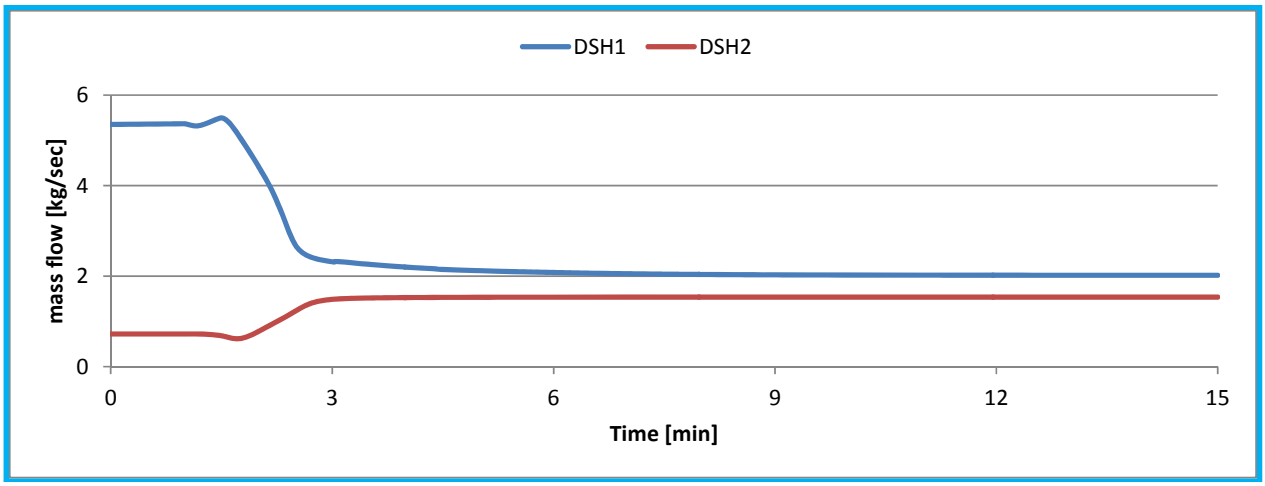

Figure 5-50 Desuperheater spray flow response to PA fan trip

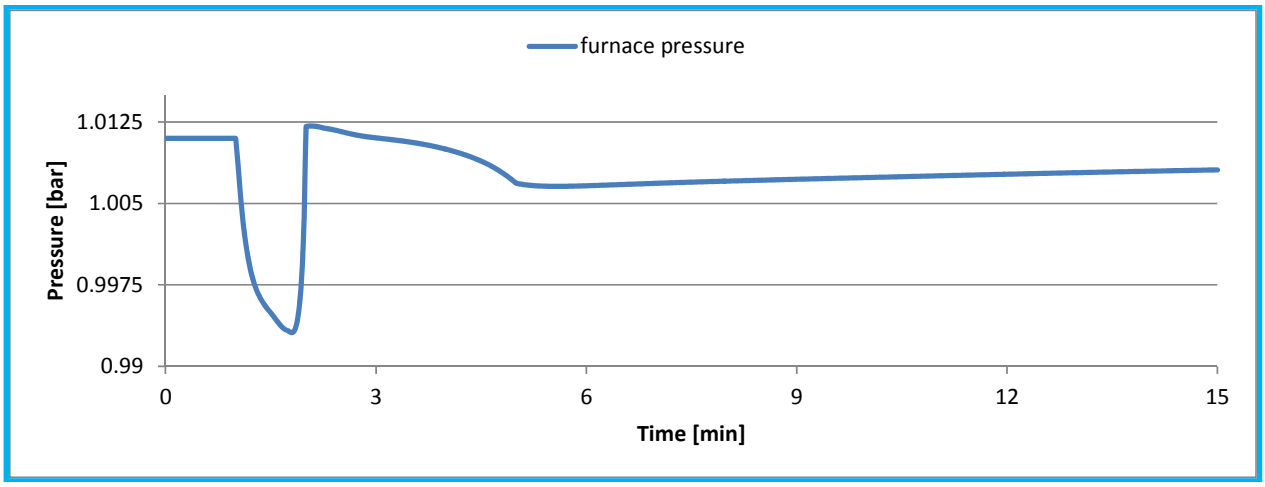

Figure 5-51 Furnace pressure response to PA fan trip

5.3.3 FD Fan Trip

FD fan trip trigger conditions:

- FD fan bearing temperature high
- FD fan motor bearing temperature high
- FD fan motor bearing oil sump temperature high
- FD fan bearing vibration high
- FD fan motor bearing vibration high
- FD fan lube oil system failure
- Furnace pressure high
- FD fan local trip, etc.

FD fan trip responsive control actions (Oxy-mode):

- Initiates master fuel trip (all mills should be taken out of service) and initiates PA fan trip

- Quickly open primary ambient air damper
- Quickly open secondary ambient air damper and stack isolation damper
- Quickly close primary and secondary flue gas recirculation dampers
- Switch all ASU oxygen controllers to manual mode and quickly shut off primary/secondary/supplemental oxygen flow control valves and ASU O_2 isolation valves
- Boiler feedwater demand run back to predetermined minimum load (e.g. 40% MCR)
- Keep ID fan control running in manual mode ramp down ID fan to prevent severe negative furnace pressure

Like the PA fan trip, the trip of the only FD fan in the process will also lead to the whole boiler unit shutdown. The primary oxidant, secondary oxidant and supplementary oxygen flow rate responses are shown in Figure 5-52. Once the FD fan trips, the unit load demand is designed to run back to zero in two minutes as presented in Figure 5-53. In Figure 5-54, all the critical process variables, such as fuel, oxidant and feedwater are required to decrease quickly due to the fast reduction of the unit load demand, while the temperature and pressure of the main steam and reheated decrease gradually as indicated in Figure 5-55 with the control of spray water in Figure 5-56. In terms of control, the secondary oxidant flow rate is used as a feed-forward signal for the ID fan control, therefore the FD fan trip will have a great impact on the furnace pressure reponse as shown in Figure 5-57.

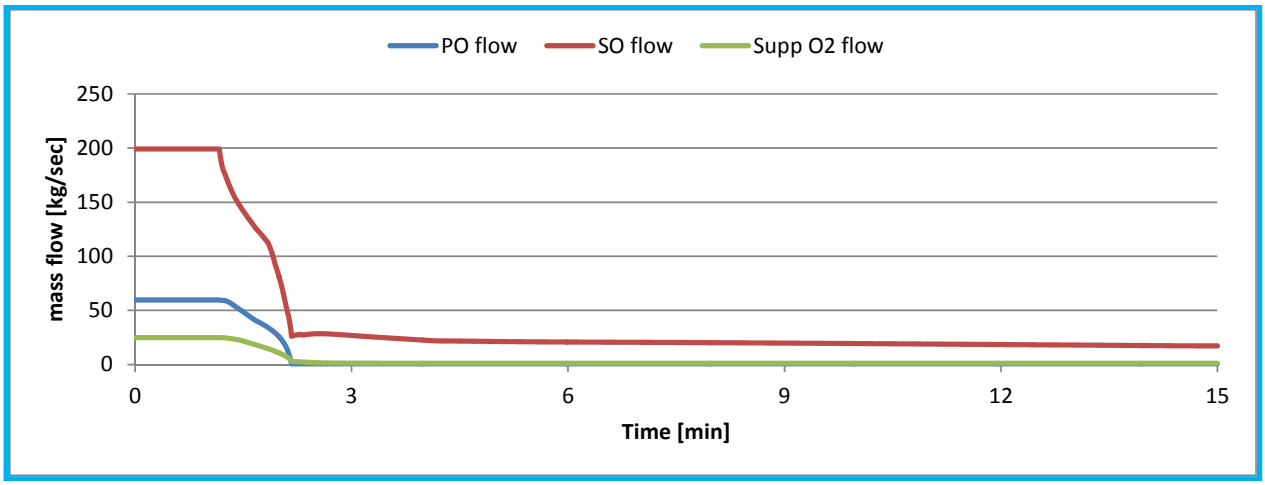

Figure 5-52 Primary oxidant/secondary oxidant/supplementary O_2 flow response to FD fan trip

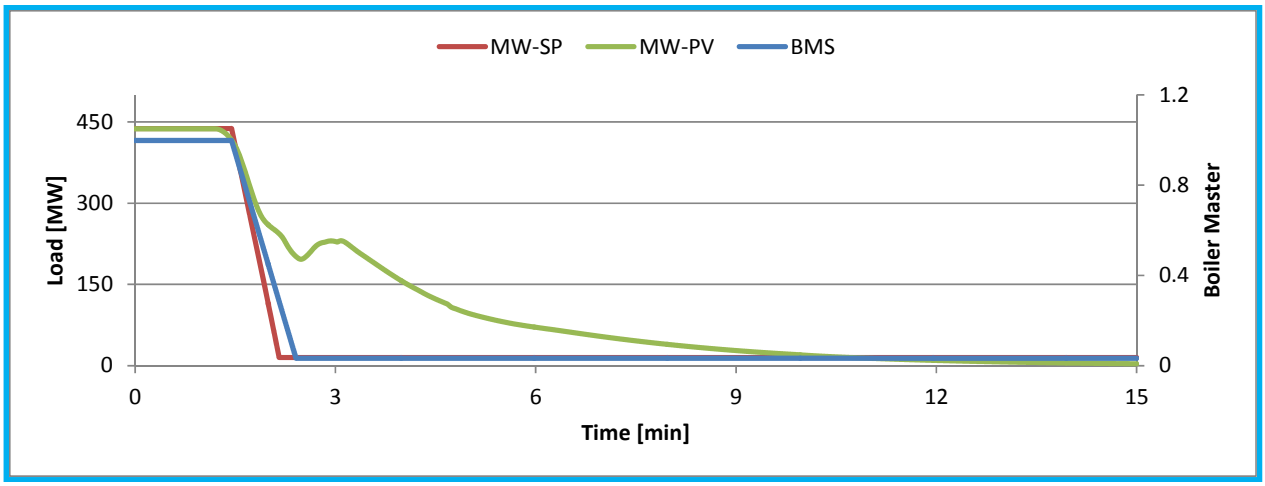

Figure 5-53 Load response to FD fan trip

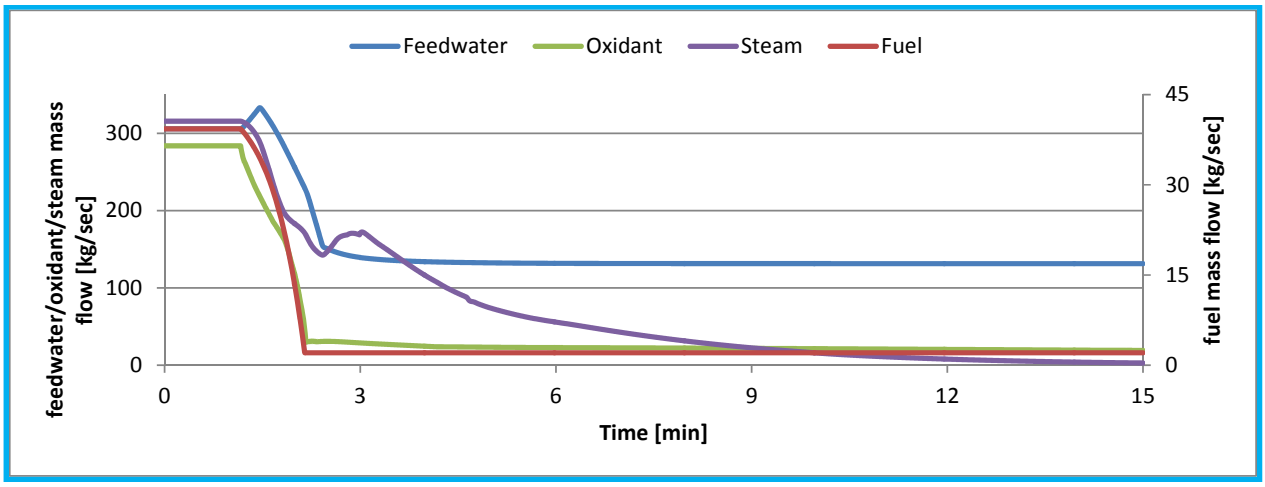

Figure 5-54 Fuel/feedwater/oxidant/steam mass flow response to FD fan trip

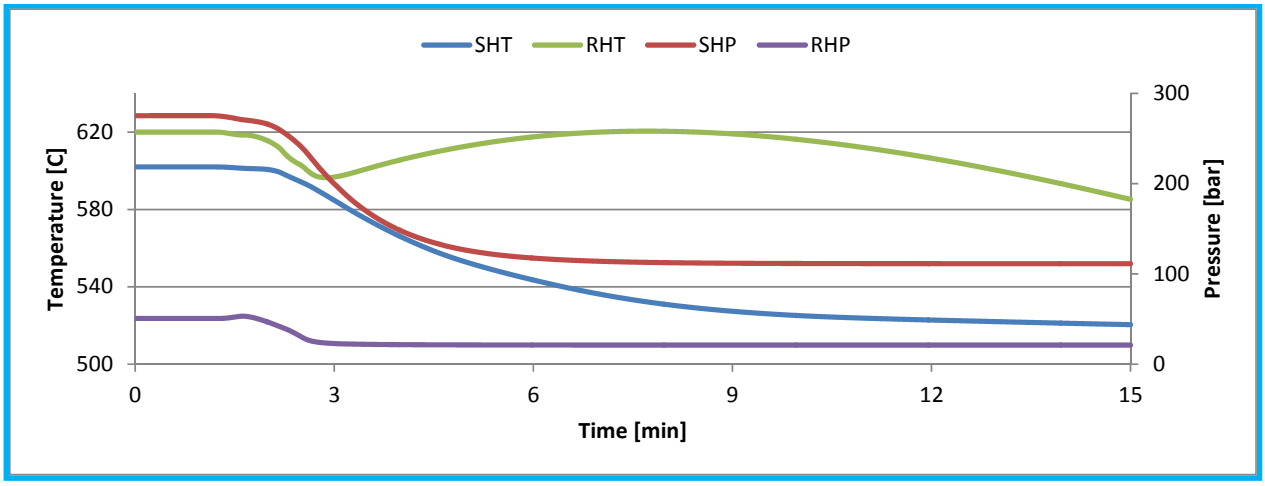

Figure 5-55 Main/reheated steam temperature/pressure response to FD fan trip

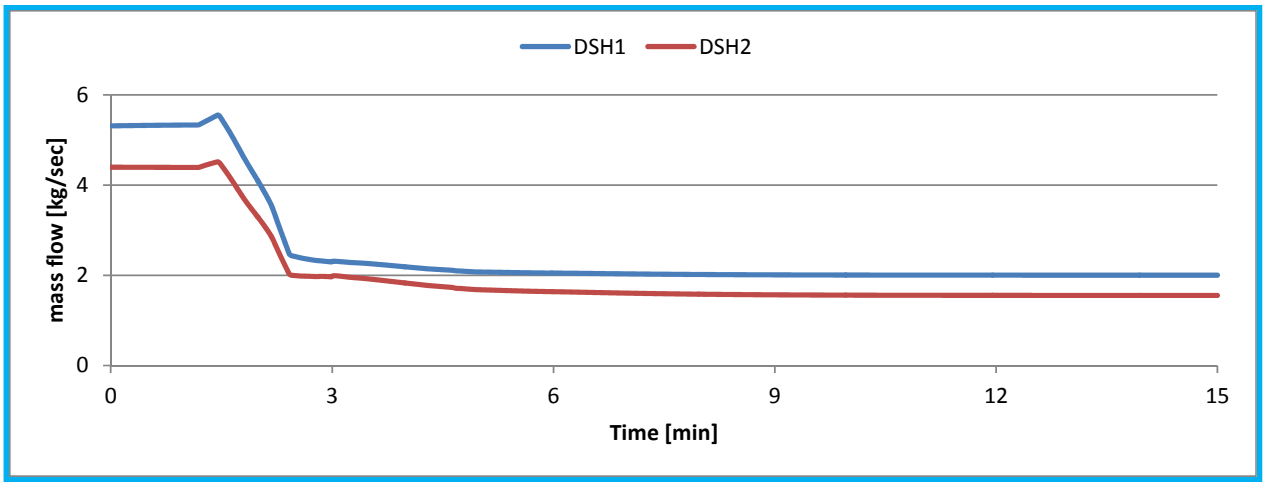

Figure 5-56 Desuperheater spray flow response to FD fan trip

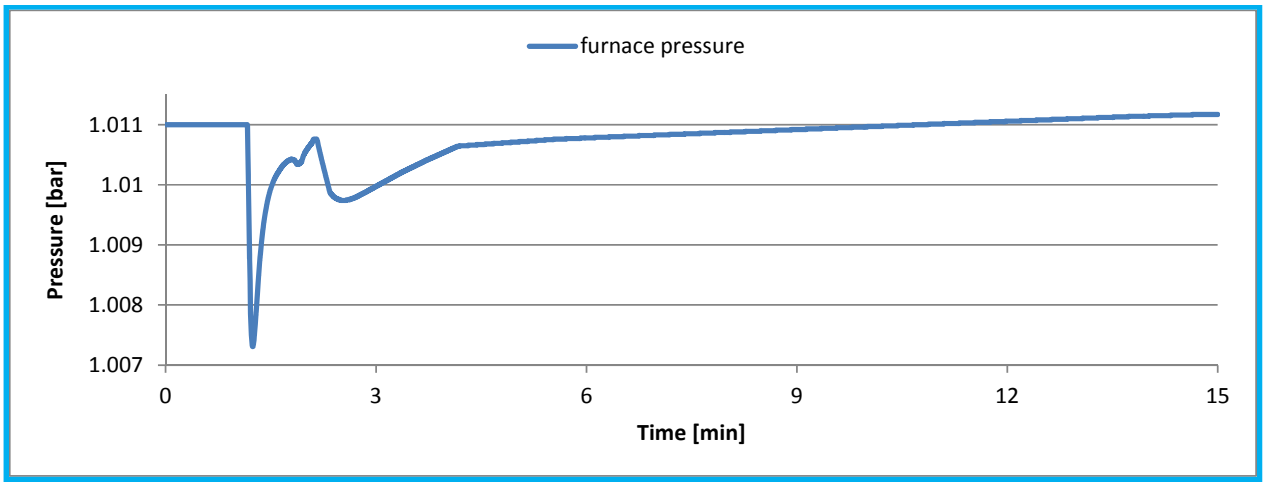

Figure 5-57 Furnace pressure response to FD fan trip

5.3.4 ID Fan Trip

ID fan trip trigger conditions

- ID fan bearing temperature high
- ID fan motor bearing temperature high
- ID fan motor bearing oil sump temperature high
- ID fan vibration high
- Furnace pressure low
- ID fan local trip, etc.

ID fan trip responsive control actions (Oxy-mode)

- Initiates master fuel trip (all mills should be taken out of service) and initiates PA fan trip
- Quickly open primary ambient air damper
- Quickly open secondary ambient air damper and stack isolation damper

- Quickly close primary and secondary flue gas recirculation dampers
- Switch FD fan control to manual mode and ramp down the load to maintain the same flow and then slowly ramp it down
- Switch all ASU oxygen controllers to manual mode and quickly shut off primary/secondary/supplemental oxygen flow control valves and ASU O_2 isolation valves
- Boiler feedwater demand run back to predetermined minimum load (e.g. 40% MCR)

In the control system of the boiler island, the furnace pressure is maintained by controlling the flow rate of the flue gas through the ID fan. As shown in Figure 5-58, the trip of ID fan will directly result in the significant drop of the flue gas flow through the ID fan. The furnace pressure rises up first during the transient and starts to reduce when the FD fan starts ramping down.

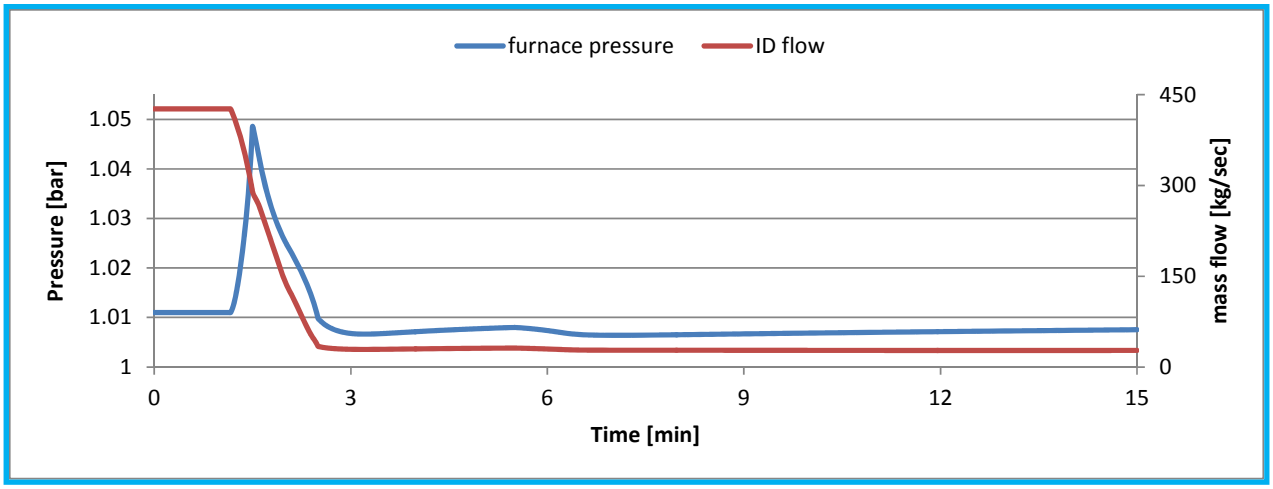

Figure 5-58 Furnace pressure and ID mass flow response to ID fan trip

Since there is only one ID fan in the oxy boiler island, the ID fan trip will also lead to the shutdown of the whole system. Figure 5-59 presents the load response to the ID fan trip for the first 15 minutes. Both unit load demand and boiler master signal is required to decrease from MCR to 0 in 2 minutes. The ID fan trip requires the FD fan to coast down as soon as possible for the safety concern of the furnace pressure, and meanwhile the fuel flow is also needed to reduce quickly as shown in Figure 5-60. As the fuel and oxidant decreases, the temperature of the superheated steam and reheated steam in Figure 5-61 decays gradually, while the pressure is also required to run back by following a load dependent curve. The reduction of the steam temperature will lead to the decrease of spray water flow in Figure 5-62.

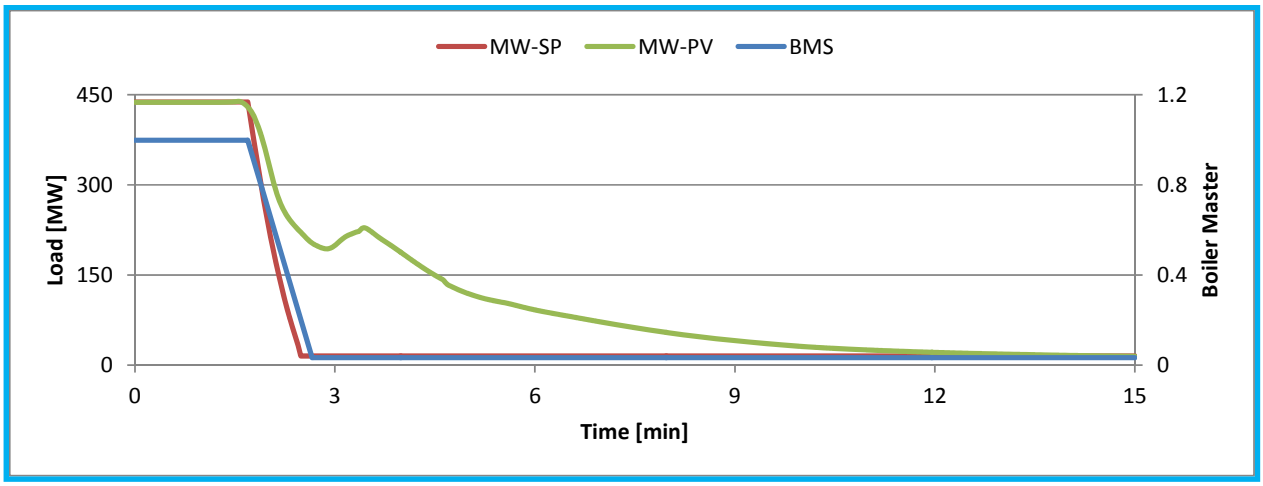

Figure 5-59 Load response to ID fan trip

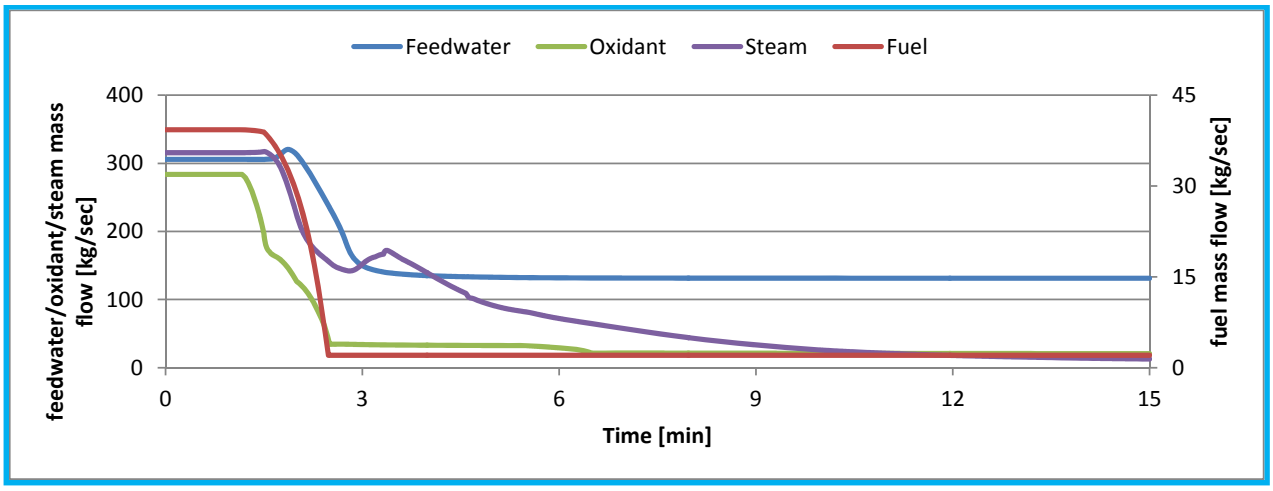

Figure 5-60 Fuel/feedwater/oxidant/steam mass flow response to ID fan trip

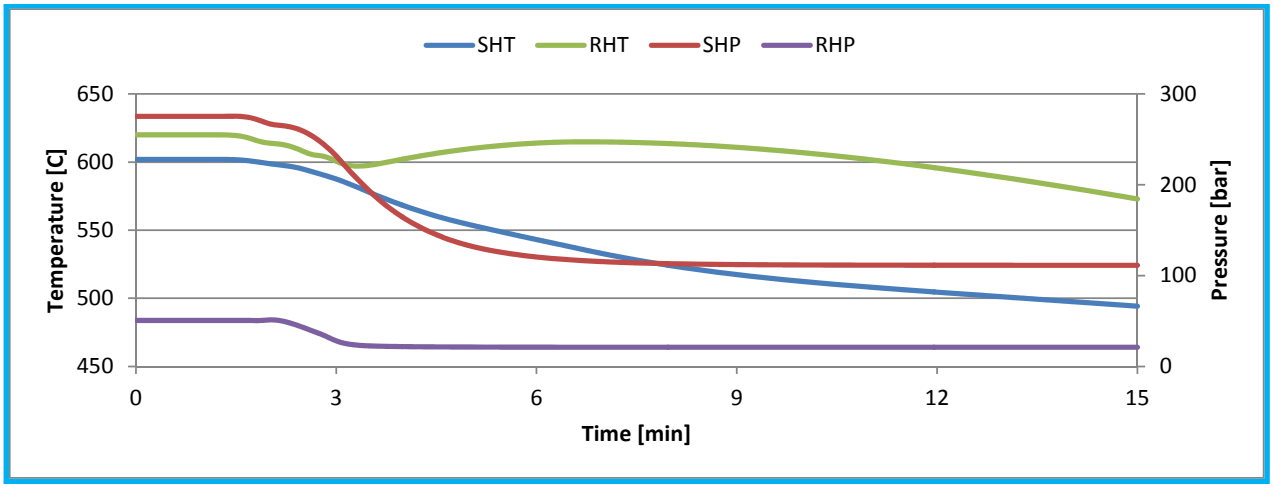

Figure 5-61 Main/reheated steam temperature/pressure response to ID fan trip

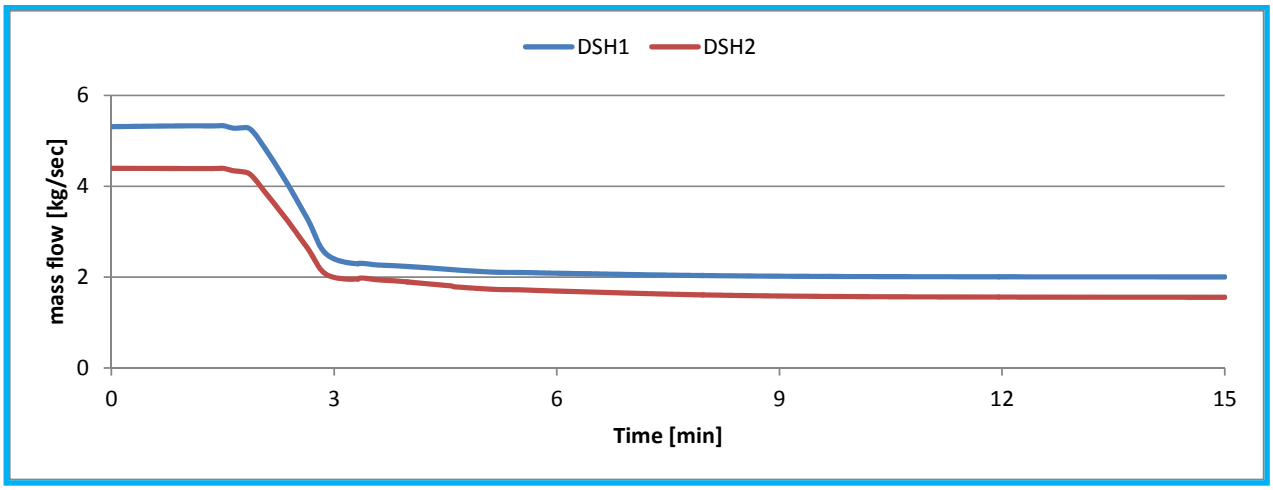

Figure 5-62 Desuperheater spray flow response to ID fan trip

5.3.5 Gas Processing Unit Trip

In an oxy-fired pulverized coal power plant, the CO_2 enriched flue gas leaves the boiler unit and enters the gas processing unit (GPU) for CO_2 purification. This flue gas is sucked into the gas processing unit through a multi-stage flue gas compressor. From this perspective, all boiler trips will affect the flow rate and compositions of the flue gas leaving the boiler unit and the pressure at the interface between the boiler island and the GPU. Thus major equipment failures of the boiler unit have a significant impact to the GPU operations. It is therefore recommended to include GPU in the boiler trip analysis.

On the other hand, if the flue gas compressor is tripped during normal oxy-mode operations, it may also affect the pressure at the interface between the boiler island and the GPU. The stack isolation damper has to be quickly opened to release the flue gas to stack, otherwise, the pressure at the interface between the boiler island and the GPU can increase or oscillate significantly.

Operating influences between the GPU and boiler island subsystems and the appropriate trip control logics have to be further analyzed based on the design and operation knowledge of both subsystems.

Responsive Control Actions

Assuming the GPU is not available completely:

- Open the stack valve in 1 minute
- Open the primary air and secondary air dampers over 1 minute
- Switch to air mode and close the flue gas recirculation dampers and the flow to the GPU in 1 minute
- Maintain excess O_2 concentration in the economizer outlet at 3%.

In this oxy boiler stand-alone model, a certain amount of flue gas is released to a boundary condition (with fixed pressure) to simulate the effect of flow distribution to the gas processing unit. In order to simulate the event of a GPU trip, the valve that controls the flow at the boundary condition is designed to fully close quickly, and its direct impact is the secondary oxidant mass flow as shown in Figure 5-63. The GPU trip results in the increase of secondary oxidant by almost 25%

in 5 minutes, while the mass flow the primary oxidant and supplementary oxgen need to reduce to certain level to maintain the balance of combustion.

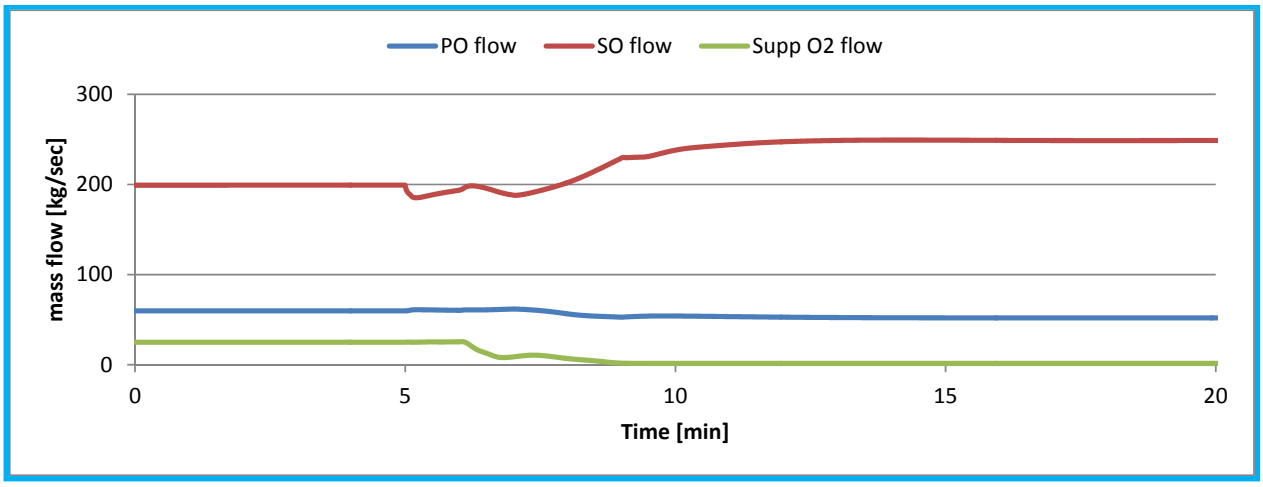

Figure 5-63 Primary oxidant/secondary oxidant/supplementary O_2 flow response to GPU trip

The disturbance of the secondary oxidant induced by the GPU trip results in the fluctuation of the unit load during the transient as indicated in Figure 5-64. In addition, the fuel flow is also slightly affected as shown in Figure 5-65. In Figure 5-66, the steam pressure is well maintained while the steam temperature fluctuates a little bit due to the oxidant flow disturbance. Figure 5-67 and Figure 5-68 present the responses of the desuperheater spray water flow and furnace pressure.

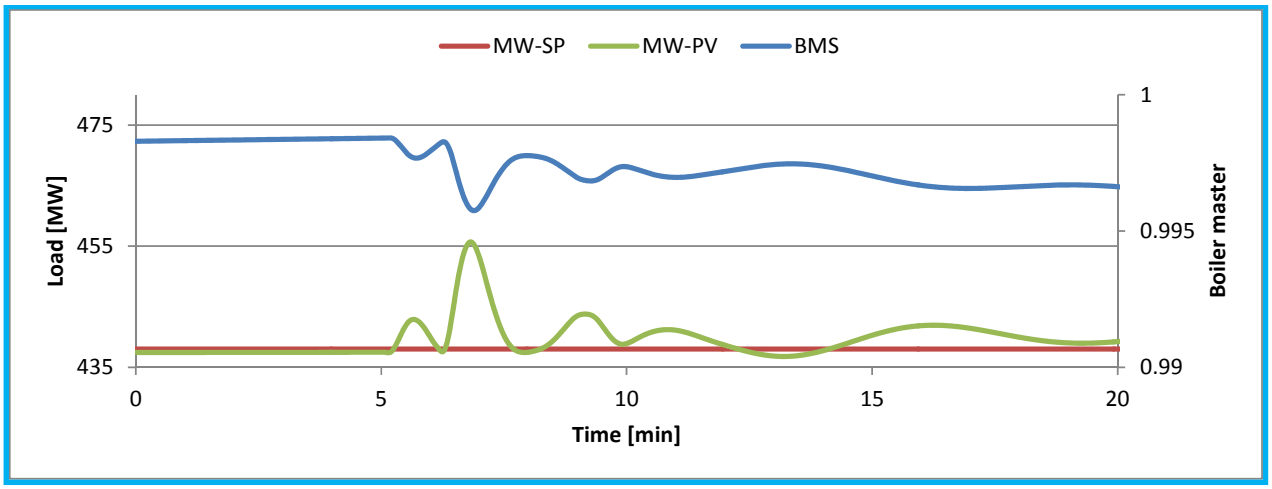

Figure 5-64 Load response to GPU trip

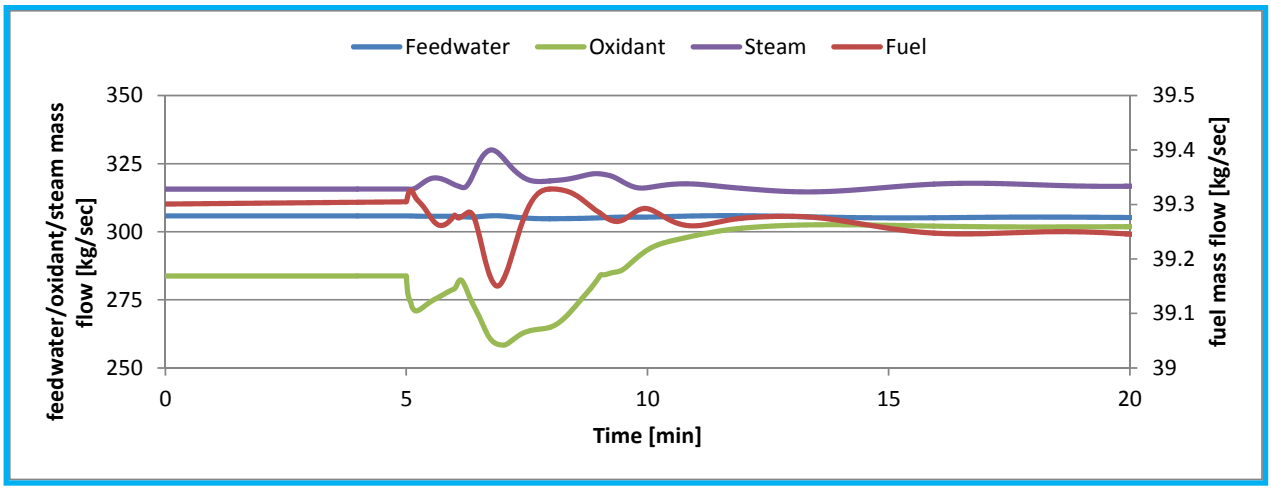

Figure 5-65 Fuel/feedwater/oxidant/steam mass flow response to GPU trip

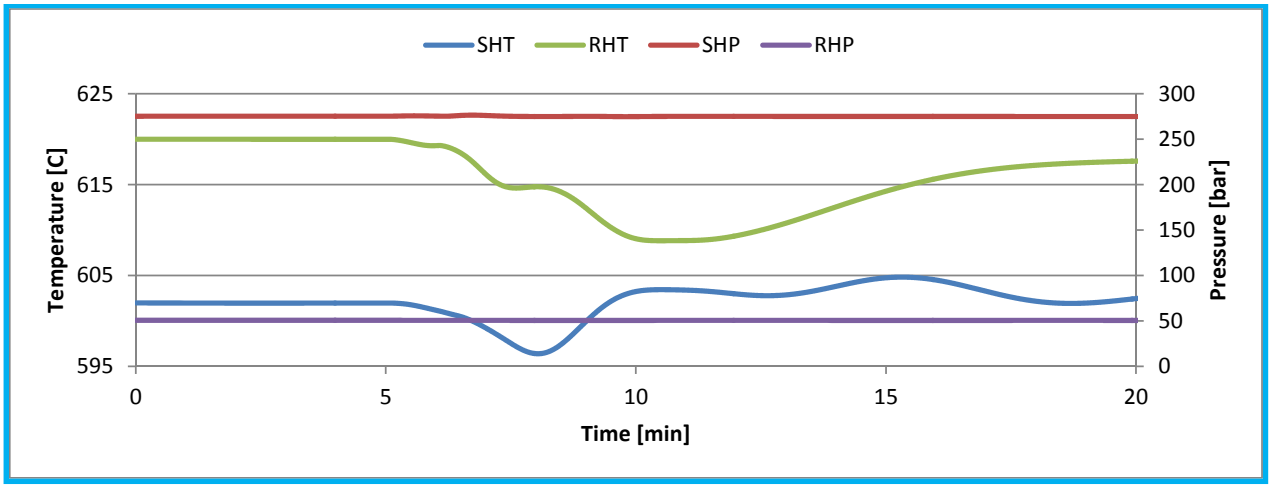

Figure 5-66 Main/reheated steam temperature/pressure response to GPU trip

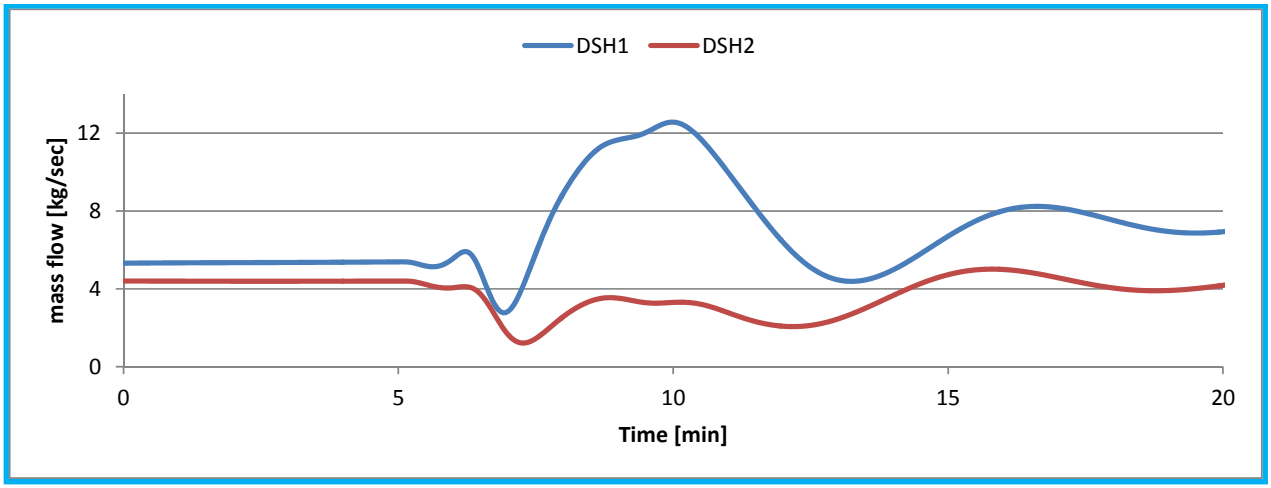

Figure 5-67 Desuperheater spray flow response to GPU trip

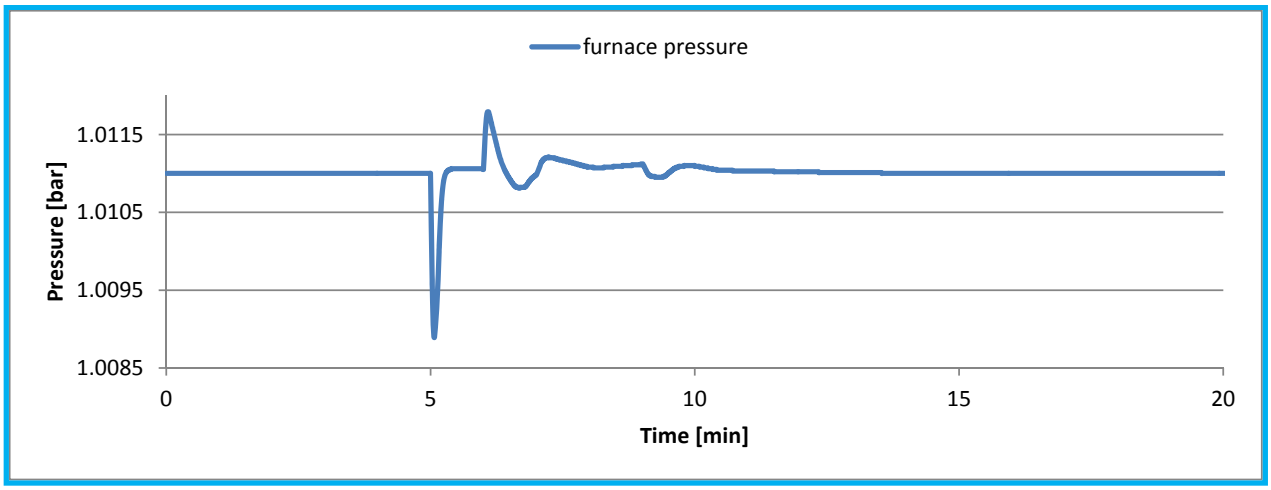

Figure 5-68 Furnace pressure response to GPU trip

6 Conclusions

The process dynamic model for the 450 MW_e oxy-fired Super Critical Pulverized Coal (SCPC) Boiler Island was used to perform the transient simulation analysis. The model was configured with the latest reference design data, tuned, and updated to support the analysis work.

The simulation analysis for normal daily operations include:

- Transition between air and oxy mode
- Load ramp at design ramp rates e.g. 5% per minute between 50%MCR to MCR
- Load step change operation to support grid code requirements
- Low load operation with recirculation system running in oxy mode/air mode
- Switching from air to oxy mode at constant load i.e. at 40% MCR
- Start up from 25%MCR in air mode and full feedwater recirculation mode, transition to oxy mode and ramp to MCR in oxy mode
- Abnormal operations including mill and fan trips as well GPU trip impacts on the boiler operation

The main conclusions of this simulator work is that the dynamic model is qualified for supporting transient operation and controls analysis for a new reference oxy boiler design. Based on the model based analysis, the oxy boiler design is evaluated and opportunities for parametric optimization have been identified. It is recognized that the process dynamic model can be further used to provide support in the evaluation of the oxy CCS flue gas train design and oxy CCS steam plant operation and controls performance in engineering and pre-commissioning stages. It can also be used to support the commissioning of the oxy boiler projects in the future.

By looking at each simulation case completed in this project work it was noted that:

During the ramp up cases:

- The FD Fan power exceeds its maximum MCR power requirements. The steam temperatures are within the specified range in the control requirements
- The furnace pressure is within the specified range in the control requirements
- The O_2 is outside the specified range in the control requirements
- The gross MW reaches its set point within 10 minutes

During the load step change case:

- The steam temperatures are within the specified range in the control requirements
- The O_2 is within the specified range in the requirements
- The gross MW jumps 20% within 2 minutes using SH throttle and shutting extraction valves simultaneously and steadies out with 10 minutes. This shows there is capacity for the boiler to quickly produce extra megawatts.

During ramping down to minimum load operation case:

- The PA Fan power increases to maintain the Furnace to PA duct pressure delta-P

- The steam temperatures are within control requirements
- The furnace pressure is within the specified range in the control requirements
- The O_2 is within the specified range in the control requirements
- The gross MW reaches its set point in about 10 minutes due to the 1% per minute load ramp
- The feedwater recirculation system will maintain the required feedwater flow rate and separator level

During ramping ramp up from minimum load to MCR case including transition to oxy mode:

- The FD Fan power increases
- The steam temperatures are within control requirements
- The furnace pressure is within control requirements
- The O_2 is within control requirements at MCR; it did not start near set point at minimum load
- The gross MW reaches its set point within 5 minutes
- The transition at 40% MCR load maintains the boiler within control requirements

During mill trip operation case:

- The steam temperatures exceed the specified range in the control requirements
- The furnace pressure exceed the specified range in the control requirements
- The O_2 is within the specified range in the control requirements
- The gross MW reaches its set point within 15 minutes

During FD fan trip operation case causing MFT:

- The furnace pressure exceeds the specified range in the control requirements
- The gross MW reaches goes to zero within 15 minutes due to master fuel trip

During PA fan trip operation case causing MFT:

- The furnace pressure is within the specified range in the control requirements
- The gross MW reaches goes to zero within 15 minutes due to master fuel trip

During ID fan trip operation case causing MFT:

- The furnace pressure is within the specified range in the control requirements
- The gross MW reaches goes to zero within 10 minutes due to master fuel trip

During GPU trip case:

- The steam temperatures are within control requirements
- The furnace pressure is within control requirements
- The O_2 is within control requirements and boiler is switched to air mode

Recovery Act: Oxy-Combustion Technology Development for Industrial-Scale Boiler Applications

DOE/NETL Cooperative Agreement No. DE-NT0005290

Volume IV – Reference Oxy Boiler Designs

Reporting Period
October 1, 2008 to April 30, 2014

Report Issued on July 29, 2014

Prepared for
U.S. Department of Energy
National Energy Technology Laboratory
Pittsburgh, Pennsylvania

Prepared by
Alstom Power Inc.
200 Great Pond Drive
Windsor, Connecticut 06095

Principal Investigator
Armand A. Levasseur

Volume IV – Reference Oxy Boiler Designs

Chapter 1 Oxy Boiler Design Guidelines

Chapter 2 Design, Performance, and Cost of 450MWe Demonstration, 900MWe Commercial, and Industrial Boilers

Chapter 3 Oxy Boiler Island Advanced Process Control

DISCLAIMER STATEMENT

This material is based upon work supported by the Department of Energy under Award Number DE-NT0005290.

This report was prepared as an account of work sponsored by an agency of the United States Government. Neither the United States Government nor any agency thereof, nor any of their employees, makes any warranty, express or implied, or assumes any legal liability or responsibility for the accuracy, completeness, or usefulness of any information, apparatus, product, or process disclosed, or represents that its use would not infringe privately owned rights. Reference herein to any specific commercial product, process, or service by trade name, trademark, manufacturer, or otherwise does not necessarily constitute or imply its endorsement, recommendation, or favoring by the United States Government or any agency thereof. The views and opinions of authors expressed herein do not necessarily state or reflect those of the United States Government or any agency thereof.

This report was prepared based on work conducted with support, in part, by grants made possible by the Illinois Department of Commerce and Economic Opportunity through the Office of Coal Development and the Illinois Clean Coal Institute as well as the Industrial Commission of North Dakota,. Neither the Illinois Department of Commerce and Economic Opportunity, Office of Coal Development, the Illinois Clean Coal Institute, nor the Industrial Commission of North Dakota, nor any person acting on behalf of either:

(A) Makes any warranty of representation, express or implied, with respect to the accuracy, completeness, or usefulness of the information contained in this report, or that the use of any information, apparatus, method, or process disclosed in this report may not infringe privately-owned rights; or

(B) Assumes any liabilities with respect to the use of, or for damages resulting from the use of, any information, apparatus, method or process disclosed in this report.

Information disclosed herein is furnished to the recipient solely for the use thereof as has been agreed upon with ALSTOM and all rights to such information are reserved by ALSTOM. The recipient of the information disclosed herein agrees, as a condition of its receipt of such information, that ALSTOM shall have no liability for any direct or indirect damages including special, punitive, incidental, or consequential damages caused by, or arising from, the recipient's use or non-use of the information.

Recovery Act: Oxy-Combustion Technology Development for Industrial-Scale Boiler Applications

DOE/NETL Cooperative Agreement No. DE-NT0005290

Volume IV – Reference Oxy Boiler Designs

Chapter 1 – Oxy Boiler Design Guidelines

Authors
David G. Turek
Armand A. Levasseur
Glen D. Jukkola

Table of Contents

1. Introduction 4
2. General Oxy-combustion Considerations 5
2.1 Basic concept 5
2.2 Oxy-firing configuration options 6
2.3 Global O_2 Concentration to Boiler 8
2.4 Oxygen requirement and combustion calculations guideline 9
2.5 Products of Combustion 10
3. Guidelines for General Arrangement of Oxy-Combustion Boiler 12
3.1 Boiler Surface Arrangement Considerations 12
3.2 Selection of Flue Gas Recycle Location 14
4. Fans – Design Considerations 17
5. Ducts and Dampers – Design Considerations 18
5.1 Oxygen Piping System Restrictions 18
5.2 Isolation Dampers 19
5.3 Other Duct Design Considerations 19
6. Guidelines for Thermal Design of Oxy-Combustion Boiler 20
6.1 Flue Gas Recycle Requirements 20
7. Guidelines for Firing System Design 23
7.1 Oxygen Injection Considerations 23
7.2 Oxygen Mixing Considerations 24
7.3 Burner / Windbox Design Considerations 26
8. Mill Design Considerations 30
9. Gas-Gas Heater 31
10. Guidelines for Operation and Controls of Oxy-Combustion Boiler 34
10.1 Continuous Operation at Full and Partial Loads 34
10.2 Start-Up and Shutdown 35
10.3 Air/Oxy Operating Transition Considerations 35
10.4 Boiler Loading Ramping 36
10.5 Steam Temperature Control Considerations 37
10.6 Combustion and Stoichiometry Control 38
11. Instrumentation and Measurement Considerations 40
12. Emission Considerations 41

12.1 Particulate Emissions 41
12.2 Carbon Monoxide Emissions (CO) 41
12.3 Nitrogen Oxides Emissions (NO_x) 41
12.4 Sulfur Emissions (SO_2 and SO_3) 43
12.5 Mercury and Other Trace Metal Emissions 44
13. Concluding Remarks 46

Table of Figures

Figure 2-1 – Schematic Of Oxy-Combustion Compared With Air Firing 6
Figure 2-2 – Simplified Boiler Island Process Flow Diagram for Oxygen-fired PC Boiler 7
Figure 2-3 – Typical Relationship Between Recycle Rate, Oxygen In Flue Gas, And Global O_2 8
Figure 2-4 – Typical Furnace Stoichiometry Vs. Global O_2 10
Figure 2-5 – Relationship between Flue Gas CO_2, H_2O, and O_2 content and Molecular Weight 11
Figure 3-1 – Oxy-Combustion CO_2 Capture Plant Layout (Example 900 MWe Design) 12
Figure 3-2 - Boiler General Arrangement Side Elevation View (Example 400 MWe Design) 13
Figure 3-3 – Boiler General Arrangement Plan View (Example 400 MWe Design) 13
Figure 3-4 –Example of Process Flow Diagram With Oxygen-fired PC Boiler 15
Figure 5-1 – Impingement Velocity Curve for Carbon Steel at 150 °C from European Industrial Gas Association IGC Doc 13/02/E 19
Figure 6-1-Furnace Heat Absorption versus Global Oxygen Content in the 15 MW_{th} BSF 21
Figure 6-2 – Effects of Oxy-fired Flue Gas Flow Rate on Furnace Performance for Study Boiler 22
Figure 7-1 – Example of a Static Mixer Installed in Ducting 25
Figure 7-2 – Example of CFD Simulation of Oxygen Mixing After a Grid-Type Mixer 26
Figure 7-3 – 15 MW_{th} BSF Furnace Heat Flux Profile (Furnace Height vs. Heat Flux) 28
Figure 7-4 – Examples of Tangential-Firing Burner/Windbox Assembly and Wall-firing Burner 29
Figure 8-1 – Example of Vertical Spindle Mill Typical for Pulverized Coal Applications 30
Figure 9-1 – Example of Ljungstrom® Preheater 31
Figure 9-2 – Ljungstrom® Purging and Pressurizing Sealing Systems 32
Figure 12-1 – BSF NO_x Emissions *vs.* MBZ Stoichiometry for Air- And Oxy-Firing 42
Figure 12-2 – Conversion of SO_2 to SO_3 43

1. Introduction

Alstom Power Inc. (Alstom), under U.S. DOE/NETL Cooperative Agreement No. DE-NT0005290, is conducting a development program to generate detailed technical information needed for application of oxy-combustion technology. The program is designed to provide the necessary information and understanding for the next step of large-scale commercial demonstration of oxy combustion in tangentially fired boilers and to accelerate the commercialization of this technology. The main project objectives include:

- Design and develop an innovative oxyfuel system for existing tangentially-fired boiler units that minimizes overall capital investment and operating costs.
- Evaluate performance of oxyfuel tangentially fired boiler systems in pilot scale tests at Alstom's 15 MW_{th} tangentially fired Boiler Simulation Facility (BSF).
- Address technical gaps for the design of oxyfuel commercial utility boilers by focused testing and improvement of engineering and simulation tools.
- Develop the design, performance and costs for a demonstration scale oxyfuel boiler and auxiliary systems.
- Develop the design and costs for both industrial and utility commercial scale reference oxyfuel boilers and auxiliary systems that are optimized for overall plant performance and cost.
- Define key design considerations and develop general guidelines for application of results to utility and different industrial applications.

The project was initiated in October 2008 and the scope extended in 2010 under an ARRA award. The project completion date was April 30, 2014. Eight comprehensive 15 MW_{th} oxy-fired test campaigns were performed with different coals, providing detailed data on combustion, emissions, and thermal behavior over a matrix of fuels, oxy-process variables and boiler design parameters. The 15 MW_{th} testing in the BSF provided in-depth understanding of oxy-combustion under boiler conditions, detailed data for improvement of design tools, and key information for application to commercial scale oxy-fired boiler design and design guidelines.

This chapter outlines guidelines and key considerations for design and operation of pulverized coal-fired boilers for oxy-combustion. The scope addressed includes only the boiler island, not the entire oxy-fired CO_2 capture plant. These guidelines are primarily developed for tangential-fired boilers and focus on designs capable of dual air and oxy-fired operation. The guidelines and considerations discussed are applicable to both new units and existing boiler retrofits. These guidelines are largely based on the findings from the extensive 15 MW_{th} pilot testing and design efforts conducted under this project. A summary level description is provided for each major aspect of boiler design impacted by oxy-combustion, and key considerations are discussed for broader application to different utility and industrial designs. Guidelines address the boiler system arrangement, firing system, boiler thermal design, ducting, materials, control system, and other key systems.

2. General Oxy-combustion Considerations

2.1 Basic concept

Oxy-combustion is a promising near-term technology for CO_2 capture and sequestration from coal-fired power plants. The basic concept of oxy-combustion (also referred to as 'oxyfuel' and 'oxy-firing') is illustrated in Figure 2-1.

The upper sketch in Figure 2-1 shows normal air firing of coal to produce a flue gas which contains mostly nitrogen from the air, approximately 15% CO_2 and about 3% oxygen. There are processes to remove the CO_2 from this flue gas for sequestration or use, but these processes have high energy consumption.

In oxy-combustion, the air is replaced by essentially pure oxygen from an air separation unit (ASU). With the nitrogen removed from the air, the combustion flue gas is now mostly CO_2 and moisture, and the volume of flue gas flow is reduced more than four-fold, as shown in the middle sketch in Figure 2-1. The advantage of oxy-firing is that it is easier to dry and purify this concentrated flue gas to produce a pure CO_2 stream for sequestration or use. The trade-off for the easier CO_2 processing is the additional energy and cost for the air separation step.

Burning the fuel with pure oxygen would produce flame temperatures too high for practical boiler materials and could also result in severe ash slagging and fouling. Therefore, most oxy-fired designs recycle a portion of the high-CO_2 concentration flue gas to dilute the oxygen and control the furnace temperature, as shown in the bottom sketch in Figure 2-1. Such an approach is mandatory for full dual air and oxy-fired operating capabilities and/or retrofit of an existing pulverized coal fired boiler.

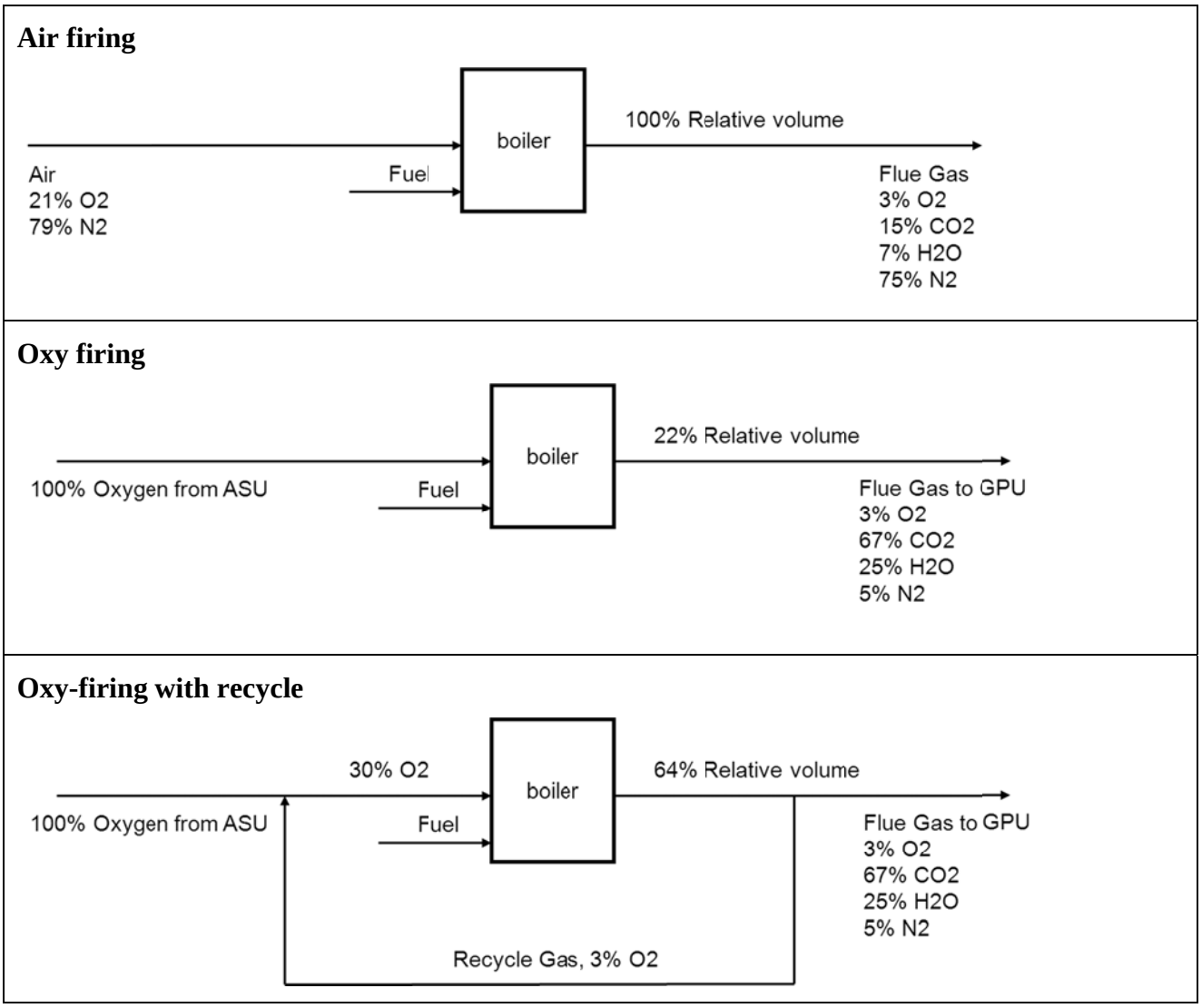

Figure 2-1 – Schematic Of Oxy-Combustion Compared With Air Firing

2.2 Oxy-firing configuration options

Figure 2-1 shows only the broad concepts of oxy-firing and flue gas recycle. Figure 2-2 is a more detailed schematic that shows some of the options for flue gas recycle take-off location.

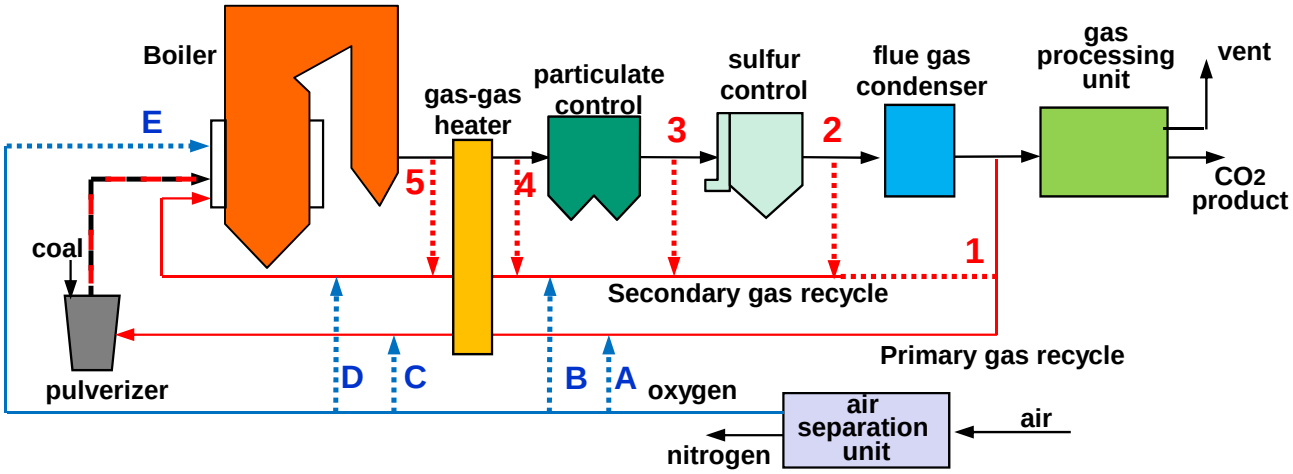

Figure 2-2 – Simplified Boiler Island Process Flow Diagram for Oxygen-fired PC Boiler

Typically two main recycle streams are used by the boiler system:

1. Primary gas recycle to provide coal drying for pulverization and to transport the pulverized fuel to the burners, and
2. Secondary gas recycle to mix with oxygen to provide the main oxidant gas for combustion.

There are several options for the location to take flue gas for recirculation back to the boiler. Figure 2-2 identifies possible flue gas recycle take-off locations with dotted arrows numbered 1 through 5. The primary gas recycle is generally taken from after the flue gas condenser (FGC) (location 1), where it has been dried and is suitable for coal pulverization and transport. The moisture content of the dried flue gas might typically be in the range of 3 to 7%, depending on the temperature of available cooling water.

Secondary recirculation could be taken from any of the five locations in Figure 2-2. The secondary recycle stream represents the bulk of the total recycle flow and has a strong impact on the composition of gas in the boiler. For high sulfur coals, recycle would typically be taken after flue gas desulfurization (FGD) and before the FGC (location 2); this gas is wet (20-30% water) but otherwise relatively clean, with a high percentage of particulate and sulfur dioxide removed. For low sulfur coal, it may be advantageous to recirculate from before the FGD (location 3). Recirculation from after the air heater (location 4) or even after the economizer (location 5) will contain particulates as well as sulfur dioxide. In general, recirculation taken from nearer the boiler would result in more buildup of particulate, sulfur, chlorides, alkali, etc., in the recirculation loop; on the other hand, the size of the downstream equipment can be reduced. These considerations are discussed in more detail in Section 3.2.

There are also several possibilities for adding the oxygen into the boiler system. Some or all of the oxygen can be mixed with the primary and/or secondary recycled flue gas. However, depending on the resultant oxygen concentration and the primary/secondary stream temperature, use of conventional materials such as carbon steel may not be suitable. Mixing a portion of the oxygen with the recycled flue gas before the gas-gas preheater provides an effective way of heating oxygen to improve boiler efficiency and also improve the performance of the gas-gas preheater. Trade-offs and considerations for the oxygen injection system will be discussed in more detail in Section 7.1.

2.3 Global O_2 Concentration to Boiler

The bottom sketch in Figure 2-1 shows a single oxidant stream with an oxidant concentration of 30%. Figure 2-2 shows that, in fact, there will be multiple streams, perhaps with different oxygen contents. It is convenient to calculate the average oxygen concentration of all the oxidant streams if they were mixed. This is called the global O_2 value. The global O_2 is an indication of the overall amount of flue gas recirculation – when more flue gas is recycled, the incoming nearly pure oxygen from the ASU is diluted to a lower value in the oxidant stream. The global O_2 value also depends on the amount of excess O_2 in the recycled flue gas.

This relationship between recycle ratio, O_2 concentration in the flue gas and global O_2 is shown in Figure 2-3. The recycle rate can be expressed as the ratio of recycle flow to net flue gas flow (recirculation ratio) or the ratio of recycle flow to total flue gas flow (recirculation fraction). With fixed O_2 input and a desired O_2 concentration in the flue gas leaving the furnace (i.e., furnace stoichiometry), global O_2 level decreases as the recycle rate increases.

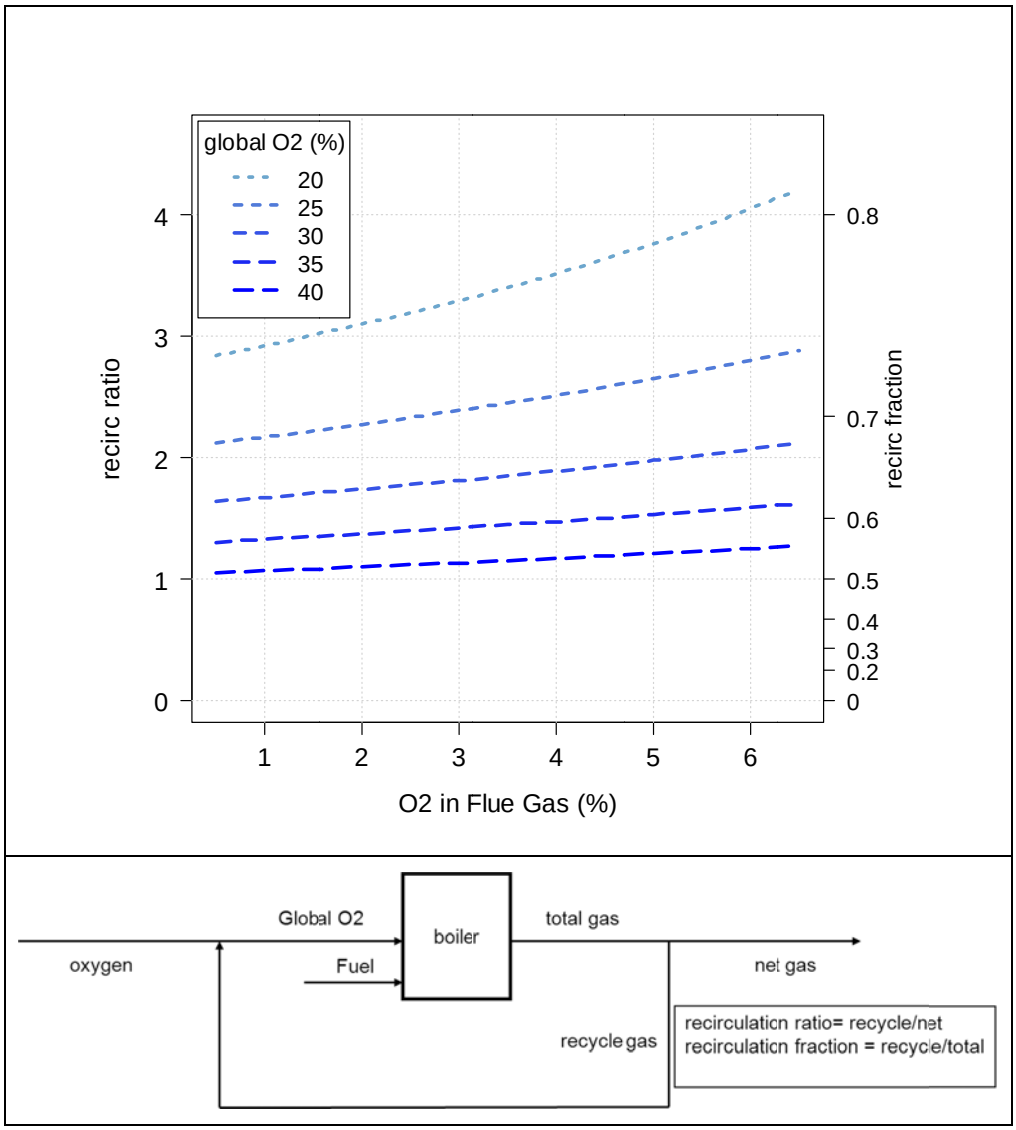

Figure 2-3 – Typical Relationship Between Recycle Rate, Oxygen In Flue Gas, And Global O_2

2.4 Oxygen requirement and combustion calculations guideline

The calculation of the amount of oxygen required for burning the coal is similar to that for air firing. For example, a simple equation based on the ultimate analysis of the fuel is

$$(C / 12 + H / 4 + S / 32 – O / 32) / 100 = \text{lb-mole } O_2 / \text{lb coal},$$

where C, H, S, O are the weight percents from the fuel ultimate analysis.

This gives the stoichiometric amount of oxygen required to combust the carbon, hydrogen, and sulfur in the fuel, correcting for the oxygen in the fuel.

One can multiply this value by the molecular weight of O_2 (32) to get the required lb O_2/lb coal for either air or oxy-firing. Multiplying the required lb O_2/lb coal by the lb air/lb O_2 gives the stoichiometric air requirement (lb air/lb coal).

For both air firing and oxy-firing, excess oxygen must be supplied to the furnace to insure the burnout of the fuel. For air firing, the excess air might be in the range of 15 to 22% of the stoichiometric amount of air or O_2. This results in a flue gas containing about 3 to 4% O_2.

For oxy-firing it is recommended to provide enough excess oxygen from the ASU (including any in-leakage to the furnace) to also produce a flue gas containing about the 3 to 4% O_2. This requires about 4 to 5% excess oxygen over the stoichiometric amount. Our guideline is to maintain the same oxygen concentration (wet, volume basis) in the flue gas for oxy-firing as would be designed for air firing with the same fuel under similar firing conditions. Maintaining the same oxygen concentration in the flue gas provides similar oxygen availability for fuel burnout.

Besides the excess oxygen requirement from the ASU, one can also consider the overall amount of oxygen entering the furnace, including the excess oxygen in the recycled flue gas. The upper sketch in Figure 2-4 shows an example with 3% excess O_2 in the flue gas and a global O_2 of 25%. The overall excess oxygen from the ASU is 4%, but by including the recirculated oxygen, the furnace stoichiometry is 1.15, or 15% excess oxygen.

The lower graph in Figure 2-4 shows the typical relationship between oxygen in flue gas, global O_2, and the furnace stoichiometry. As expected, the furnace stoichiometry increases with more excess oxygen in the flue gas and with more recycle (lower global O_2).

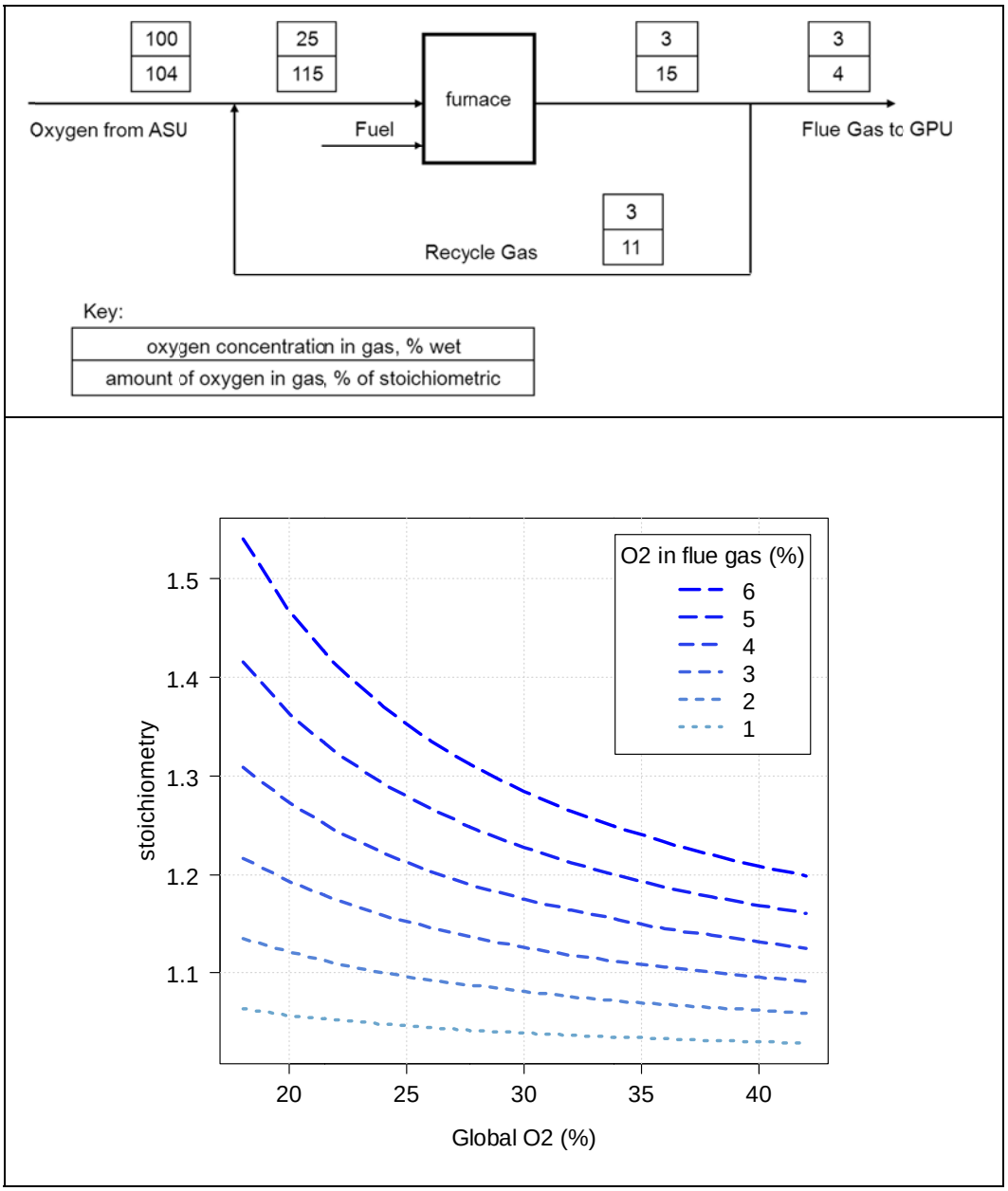

Figure 2-4 – Typical Furnace Stoichiometry Vs. Global O_2

2.5 Products of Combustion

Given the fuel analysis, the amount and purity of the added oxygen, and considering any air in-leakage, the resulting flue gas flow and composition can be calculated in a similar manner as for air firing. Carbon burns to form mostly CO_2; hydrogen burns to form water. The main difference is much less nitrogen. The molecular weight (and density) of the flue gas will be different than in air firing.

Figure 2-5 is a simplified nomogram showing the dry and wet molecular weights for flue gases of CO_2, O_2, N_2, and H_2O. The examples in Figure 2-5 include flue gas from air firing with a wet

molecular weight of about 30 and an oxy-fired flue gas with a wet molecular weight of about 36. If this flue gas is recycled and enriched with pure oxygen to a global O_2 of 25%, the wet molecular weight is reduced to about 35.

The concentration of minor constituents, such as SO_2, NO_x, and CO, is discussed in Section 12. These do not generally have a big impact on the molecular weight and gas density.

These different flue gas compositions have performance and design implications discussed in many of the later sections, including

- heat transfer coefficients in the furnace, backpass, and preheater,
- radiant properties of gases in the furnace,
- gas density for flow calculations through heat transfer surface, ducts, and other components,
- design of recirculation fans
- combustion and emissions
- corrosion potential of many components – for example from SO_2, SO_3, H_2O.

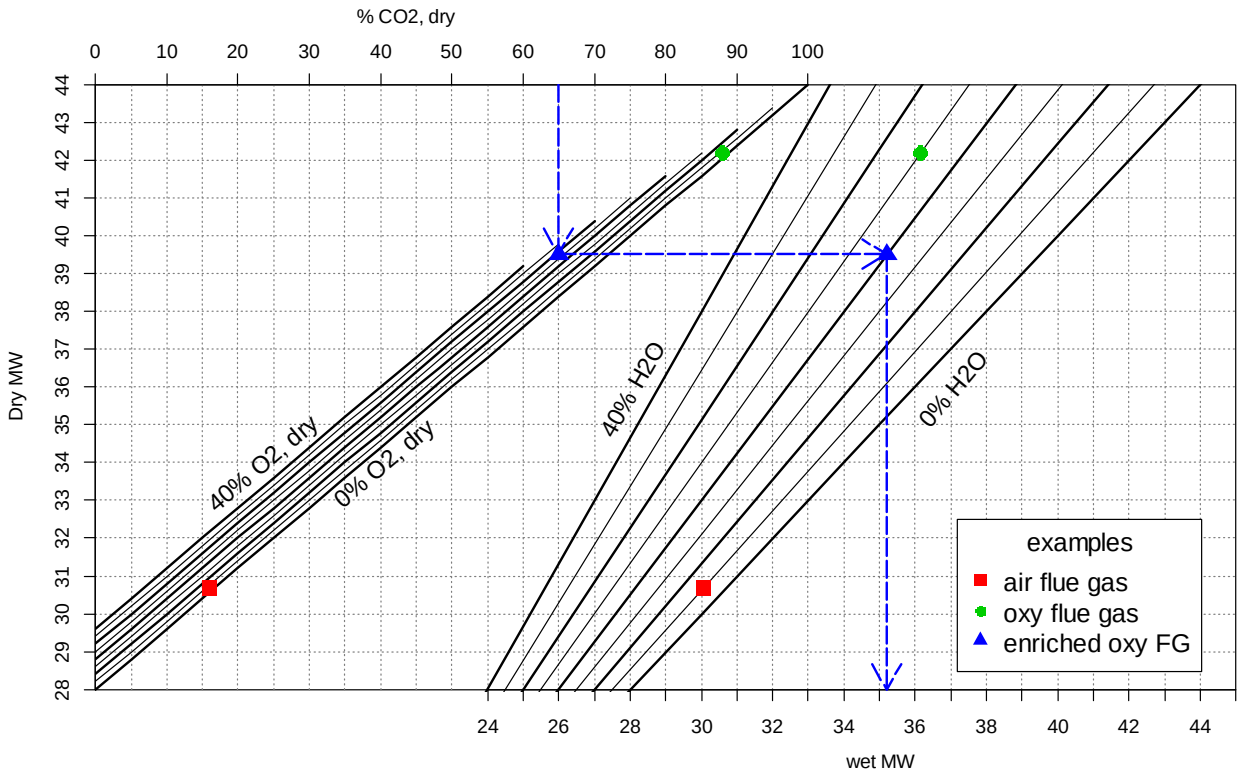

Figure 2-5 – Relationship between Flue Gas CO_2, H_2O, and O_2 content and Molecular Weight

3. Guidelines for General Arrangement of Oxy-Combustion Boiler

This section provides an overview of guidelines and considerations for oxy-boiler surfacing and its general arrangement as well as boiler island equipment layout. Figure 3-1 shows a possible layout of the major oxy-combustion CO_2 capture plant equipment. The basic layout for boiler island and pollution control systems is typical of conventional pulverized coal power plants as the primary considerations for arrangement of this equipment are the same for air and oxy-firing. Specific process and equipment design must be considered with the available site area to be space efficient and optimize arrangement with regards to equipment interfaces. The ASU would be typically located near the boiler and the flue gas condenser and GPU located close to the FGD system. Specific arrangements are strongly impacted by the site-specific factors.

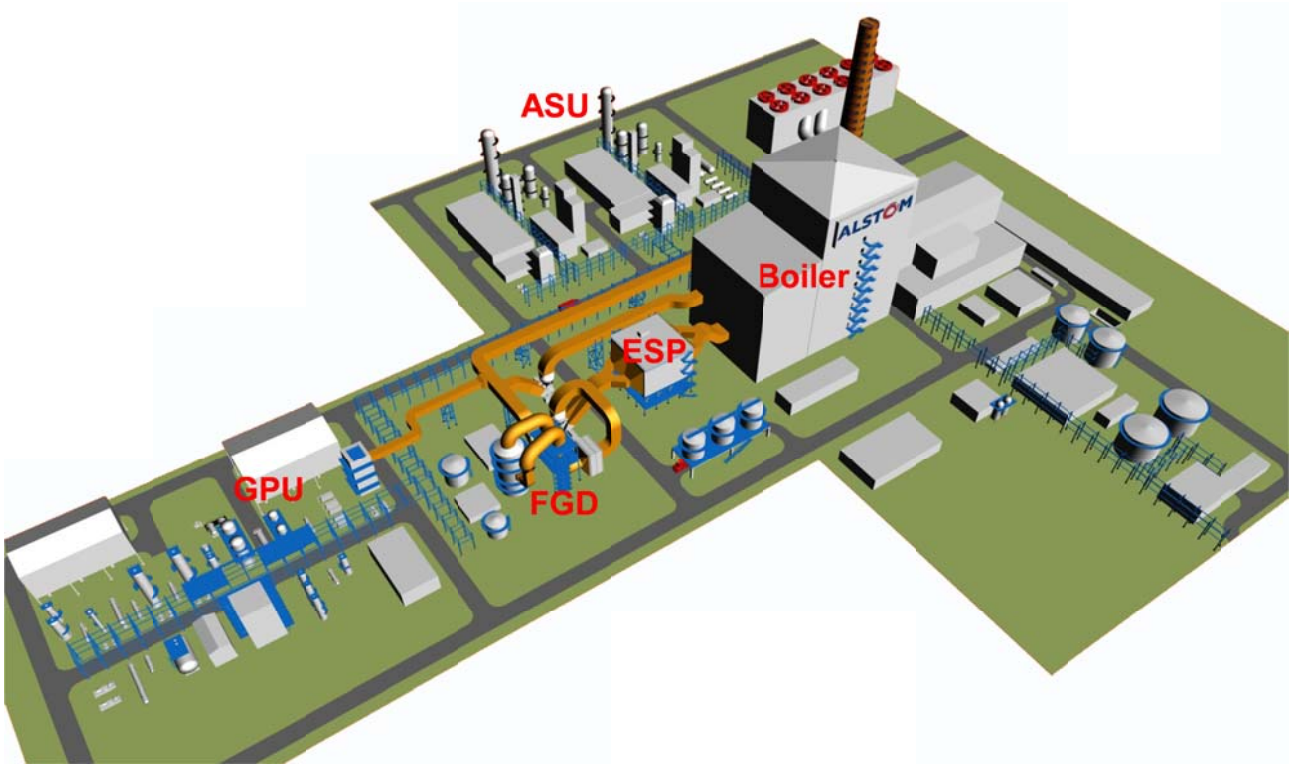

Figure 3-1 – Oxy-Combustion CO_2 Capture Plant Layout (Example 900 MWe Design)

3.1 Boiler Surface Arrangement Considerations

Changes in the general boiler arrangement are not necessary for oxy-firing with either an industrial, 2-pass or tower boiler configurations. An example of the possible general arrangement of an oxy-fired supercritical boiler is shown in Figure 3-2 (Side Elevation) and Figure 3-3 (Plan View).

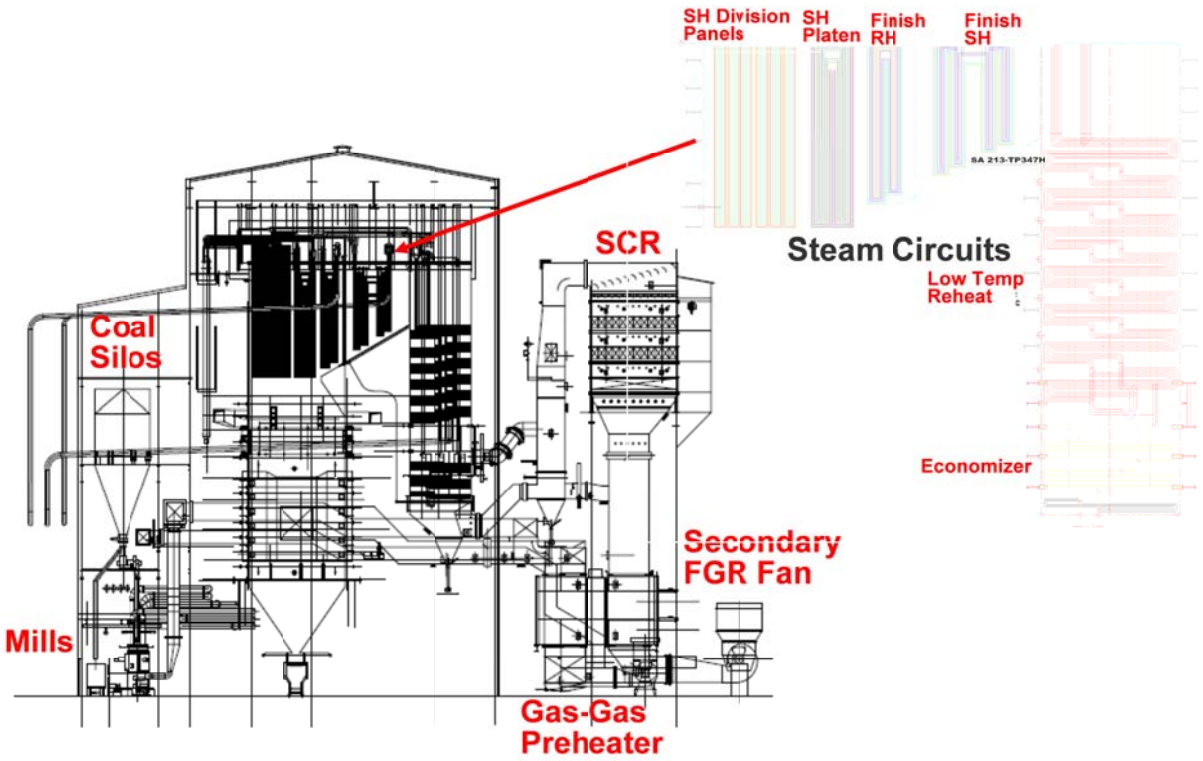

Figure 3-2 - Boiler General Arrangement Side Elevation View (Example 400 MWe Design)

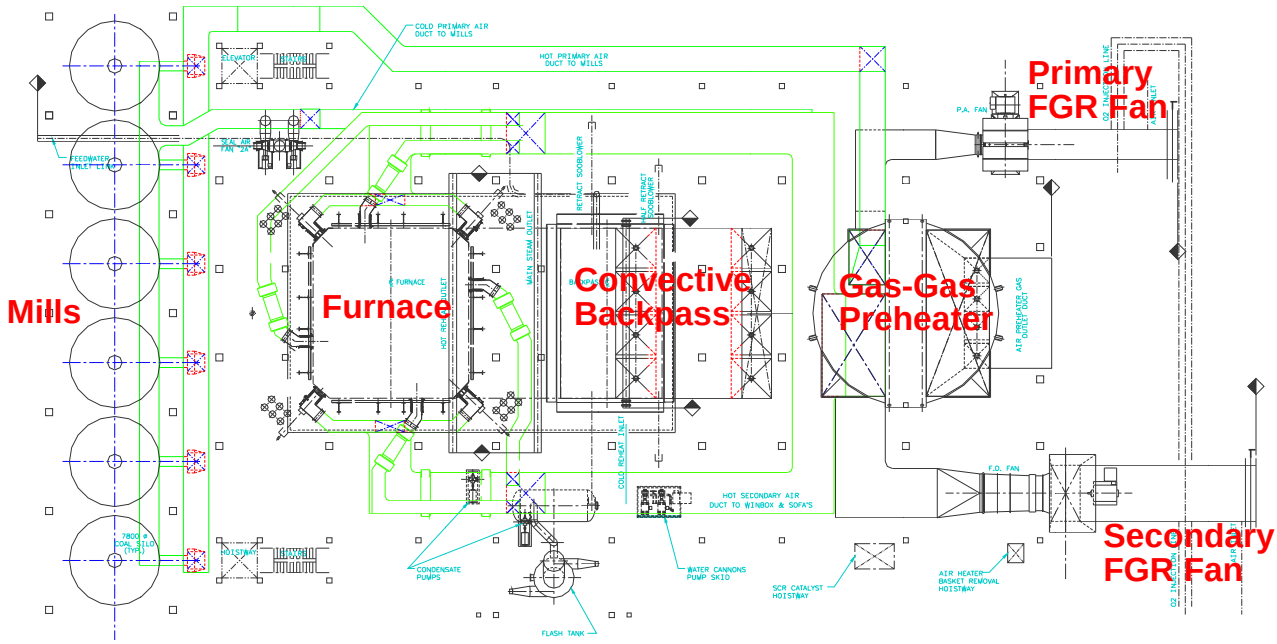

Figure 3-3 – Boiler General Arrangement Plan View (Example 400 MWe Design)

Selection of major heat transfer surfaces (Superheater, Reheater, and Economizer) and their locations can follow the same approach and procedures that are used for a traditional air fired boiler. Selection procedures are well established by boiler manufacturers for the commercial air fired pulverized coal fired designs and consider the properties of fuels burned, steam cycle requirements and other project specific requirements. The arrangement of heat exchanger sections are dependent on gas-side and steam-side temperatures and are optimized for surface area and the material requirements. The basic geometry of each section (surface area requirement, tube lengths, tube outside diameter, tube transverse spacing, and longitudinal spacing, etc.) is typically well defined based upon established design standards that consider several factors including ash fouling characteristics.

Since these selection procedures are usually proprietary and specific to manufacturers, they are not included in this document. However, key design considerations used in the procedures such as furnace slagging characteristics, ash fouling characteristics, and ash erosion characteristics do not change substantially between air and oxy-firing. These considerations remain primarily dependent on fuel properties and design/operating conditions such as thermal loadings, gas temperatures, gas velocities and thus can be treated similarly for air and oxy-firing. Other considerations such as changes in gas properties and radiation characteristics can change significantly with oxy-firing and need to be taken into account in the selection process. The amount of flue gas recirculated can be used to adjust for the differences in oxy-fired behavior and balance the boiler thermal performance. Additional discussion on thermal performance is provided in Section 6.

3.2 Selection of Flue Gas Recycle Location

Figure 3-4 shows a basic process flow diagram for a typical oxygen-fired capture plant. The diagram is for a direct-fired high sulfur coal case and shows two locations where flue recirculation is taken. New equipment within the boiler island (relative to the air-fired boiler scope) include oxygen supply lines and mixing devices, a low leakage gas-gas heater, and additional ductwork connecting to the inlets of the PA and FD fans for recirculated flue gas. The flue gas recirculation (FGR) ducts would also include isolation dampers and inlets for air, which are used during air firing (startup) as shown. Additionally, the fans and duct sizing would be different than for the air-fired design.

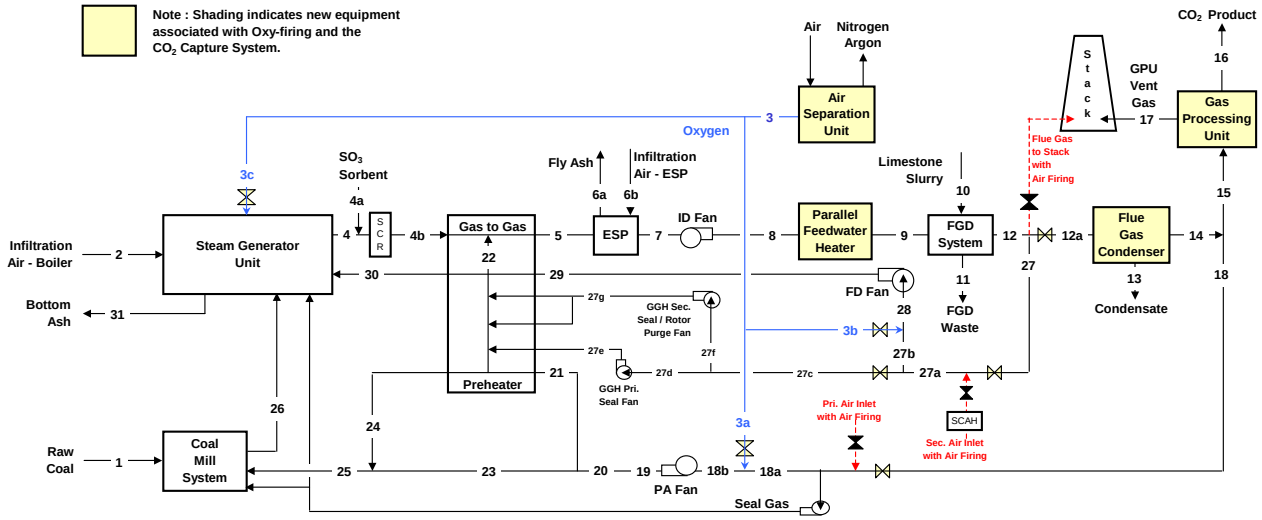

Figure 3-4 –Example of Process Flow Diagram With Oxygen-fired PC Boiler

As previously discussed, primary FGR is taken after the flue gas condenser (Stream 18) and serves to dry the coal during pulverization and transport it to the furnace for combustion. Primary FGR flow is also used as seal gas, which is needed to reduce air in-leakage. If primary FGR is taken before the condenser, it would contain higher moisture resulting in the need for much higher mill operating and outlet transport temperatures to maintain a reasonable approach to dewpoint for coal drying.

There are also trade-offs associated with selection of the location where secondary FGR is taken. The flow diagram shows the option of taking this FGR after the desulfurization system and before the condenser. The quantity of secondary FGR is established by furnace and convection pass heat transfer requirements to generate the specified steam flow and conditions.

The criteria for evaluation and selection of secondary FGR take-off location can be separated into three main areas:

- ***Technical Considerations***
  - SO_2 concentration in flue gas within the boiler and recirculation system. Sulfur concentrations impact fireside corrosion and gas acid dewpoint temperature.
  - Ash concentration in flue gas within the boiler and recirculation system. Ash levels impact deposition and erosion in the boiler and recirculation loop components, particularly fans.
  - Avoidance of new equipment that is commercially unproven.
  - Complexity of the process. Increased complexity typically increases risk of operational and reliability issues
- ***Efficiency and Performance Considerations***
  - Temperature of flue gas downstream of the gas-gas preheater. This temperature is commonly referred to as the boiler exit temperature and has a strong impact on the overall boiler efficiency.

  - Energy consumption. Power consumption of fans and other electrical motors as well as pressure requirements of oxygen supply, which impact ASU efficiency.

- ***CAPEX Considerations***
  - Flue gas volume at the flue gas desulfurization system. This is a main design parameter impacting desulfurization equipment size and cost.
  - Flue gas volume at the flue gas condenser. This is a main design parameter impacting the flue gas condenser size and cost.
  - Maximum load with air operation. Minimizing the size of equipment for only oxy-firing can limit the capacity with air-firing.

Secondary FGR is generally not taken downstream of the FGC because of the trade-offs associated with the higher condenser capital costs due to larger flue gas flow rate versus the benefits gained in boiler operating and performance from the reduced FGR moisture content. For an existing plant with a desulfurization system installed, it is generally advantageous to take the secondary FGR after the system in order to reduce SO_2 levels in the boiler systems. Lowering SO_2 concentrations in the flue gas decreases (improves) acid dewpoint allowing lower boiler exit temperatures and potentially improving efficiency. Lower SO_2 concentrations in the flue gas also reduce the potential for fireside corrosion allowing lower cost material selections. For new designs, the CAPEX versus performance benefit trade-offs associated with flue gas take-off location relative to the flue gas desulfurization system are largely dependent on the fuel sulfur content. Our general guideline limits the SO_2 concentrations in the boiler during oxy-firing to a maximum of 4000 ppm SO_2 by volume. This guideline is based upon commercial air-fired experience with high sulfur coal and acceptable SO_2 levels that do not required the use special materials. Results of corrosion studies under oxy-firing show similar behavior as with air firing forotherwise equivalent conditions. Corrosion attack is dependent primarily on gas sulfur and chlorine concentrations, ash impurities and metal surface temperature. Therefore, material selections procedures developed for air-firing can be used, but must consider in the environment (potential increased concentrations of corrosive constituents) oxy-firing conditions.

Another consideration that could be very important when evaluating whether to take FGR before or after the desulfurization system is the impact on air firing capacity. Since the desulfurization system is sized for the volume of gas flow to be treated, a size reduction decreases CAPEX, but also limits the gas flow rate thus restricting the capacity during air firing. For cases burning low sulfur coals or for oxy-fired only cases (air firing only for start-up and transition at low load to oxy-fired operation), then significant savings may be possible. These savings may be derived from reduced CAPEX and OPEX due to a smaller desulfurization system and ductwork downstream of the FGR location as well as gaining efficiency improvements associated with the return of higher temperature FGR.

4. Fans – Design Considerations

The use of FGR during oxy-combustion impacts the operation and requirements for all of the fans. During air firing, the FD, PA, and Seal Gas Fans supply ambient air for combustion, coal drying and transport, and for various sealing requirements. The ID Fan exhausts the combustion gas leaving the boiler and moves it through the downstream equipment and out the stack.

In oxy-fired mode, the FD fan now supplies FGR that is taken before/after the FGD, depending upon the fuel characteristics and overall system design. When in oxy-fired mode, rather than air-fired mode, this FD fan inlet stream has a higher gas temperature, lower mass flow rates (about 30% less, even with oxygen mixed into the stream), and gas composition that is much higher in CO_2 and H_2O but with little N_2. Since the secondary FGR stream can contain acid mist, a corrosive resistant design for the FD fan must be considered.

In oxy-fired mode, the PA fan supplies FGR that is taken after the flue gas condenser. When in oxy-fired mode rather than air-fired mode, this PA fan inlet stream has a slightly higher temperature (even after oxygen mixing), higher mass flow rates (about 20% more due to its higher molecular weight and density), and gas composition that has higher CO_2 and lower N_2 concentrations.

In oxy-fired mode, the ID fan now must exhaust the combustion gas through additional equipment, including a parallel feedwater heater (optional), flue gas condenser, and Gas Processing Unit (GPU). The gas temperature may be considerably hotter and the gas composition higher in CO_2 and H_2O and lower in N_2 than they are when in air-firing mode.

The Seal Gas fan also uses recirculated flue gas after the condenser to minimize the introduction of N_2 into the boiler system. The seal gas is typically used for mill and sootblower sealing, but it could be used in other locations. Additional fans might be used to pressurize and provide seal gas and sweep gas to minimize the leakage of oxygen between streams in the Gas-Gas Preheater. This system will be discussed in Section 10.

The fans are designed using normal air-fired design guidelines, but some unique aspects of oxy-firing need to be accommodated in the procedures. Modifications arise from the differences in physical properties of the recycled flue gas and from the need to avoid leakage of contaminants (N_2) into the flue gas or CO_2 into the surrounding environment. Further, requirements for corrosion resistance and condensate drainage may also be needed. For dual air-fired/oxy-fired applications, the maximum conditions (flow, fan head, temperature) should be based on whichever operating mode is higher.

5. Ducts and Dampers – Design Considerations

Ducts are used to convey air, flue gas, and FGR throughout the boiler island while isolation dampers are used to seal off the air inlets that are used for air-firing. There are a number of process differences between air-firing and oxy-firing that impact the selection of the ducts and isolation dampers.

The ducts used for the primary and secondary FGR and for the flue gas leaving the boiler are designed using normal design practices and use conventional materials (carbon steel). However, the secondary FGR ducts are exposed to acid mist following the FGD and require some corrosion protection such as either rubber lining or fiberglass reinforced plastic (FRP) lining. These linings are commonly used for transport of corrosive chemicals and have been commonly used to protect ducts after flue gas desulfurization systems.

5.1 Oxygen Piping System Restrictions

Although not within the boiler scope, the following information is provided for reference since the oxygen piping connects with ducts within the boiler island. The information is also relevant for those ducts following the oxygen mixers.

The oxygen piping must be designed within specified limits to ensure the safe transportation and distribution of oxygen. Guidelines have been published by the Compressed Gas Association, Inc.[1,2] and the European Industrial Gas Association[3], that indicate that carbon steel can be used for the oxygen pipeline system as long as the gas velocity is limited to a value below the impingement velocity curve. The impingement velocity is shown as a function of the absolute pressure in Figure 5-1. This curve is limited to design temperatures up to 302°F (150°C) for carbon steel pipes. For pressures less than 225 psia (1.5MPa), the impingement velocity is 100 ft/sec (30 m/sec). Thus, carbon steel pipelines can be used as long as the velocity throughout the piping system is maintained below this velocity limit. Dampers and valves are subject to high velocity when partially closed, and must be designed with appropriate materials.

[1] Industrial Practices for Gaseous Oxygen Transmission and Distribution Piping System, Third Edition, CGA G-4.4-1993, Compressed Gas Association, Inc., 1999
[2] Oxygen, Ninth Edition, CGA G-4-1996, Compressed Gas Association, Inc., 2002
[3] Oxygen Pipeline Systems,IGC Doc 13/02/E,European Industrial Gases Association,Brussels, 2002

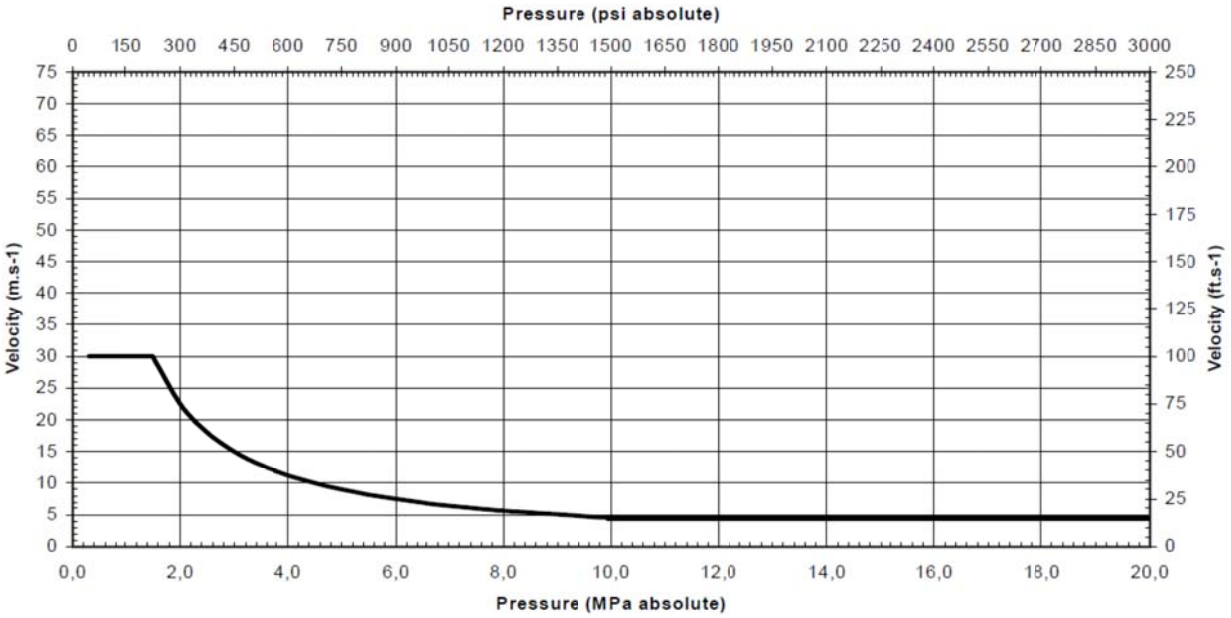

Figure 5-1 – Impingement Velocity Curve for Carbon Steel at 150 °C from European Industrial Gas Association IGC Doc 13/02/E

5.2 Isolation Dampers

The boiler island uses two isolation valves to isolate the air inlet used during air firing (for dual air/oxy firing or during an air-fired startup of an oxy-fired plant). The valves ensure that N_2 (from air) doesn't leak into the primary recirculation gas and prevent CO_2 in the secondary recirculation gas from leaking out. For example, double louver dampers are commonly used for 100% isolation of flue gas ducts. Isolation is accomplished by closing the two rows of blades and then pressurizing the space between the two rows with clean air (or gas) to a pressure greater than the upstream duct pressure. The air (or gas) barrier between the two rows prevents leakage of flue gas (into the surrounding environment) or air (into the recirculating flue gas).

5.3 Other Duct Design Considerations

The oxygen content of the primary and secondary FGR should be limited to a maximum of 21% by volume entering the gas-gas preheater for the oxy-firing. This minimizes the risk of carbon steel combustion in oxygen enriched atmospheres at temperatures exceeding 302°F (150°C). The Compressed Gas Association oxygen piping guidelines generally allows gas streams with oxygen concentrations up to 23.5% O_2 to be considered like air. A practical limit that is lower than this concentration should be used in system design to provide tolerance for incomplete mixing and control system variations. Our general guideline for maximum oxygen content for use of carbon steel with heated gas is 21%, which must be confirmed for adequate tolerance based upon the specific design conditions.

6. Guidelines for Thermal Design of Oxy-Combustion Boiler

This section provides a description of the primary considerations for boiler thermal performance under oxy-combustion. Generalized design approaches for furnace waterwalls and convective pass sections under oxy-firing conditions are discussed.

6.1 Flue Gas Recycle Requirements

Recirculated flue gas to the boiler is required in order to avoid slagging and/or fouling problems and to maintain thermal balance between the lower furnace region where steam is generated and the upper furnace and convective heat transfer sections where steam is superheated and reheated to the required temperature levels. For the boiler to operate in either an air- or an oxy-fired environment puts certain constraints on the boiler design and on the operation of the boiler in the oxy-fired mode. Air-fired boiler flue gas flow rates are defined to a large extent by the fuel analysis, excess air level, and fuel firing rate. Typically, specific flue gas flow rates with air-firing are about 1,000 lb flue gas/MMBtu (430 kg/GJ) fired. With oxygen-firing, theoretically flue gas flow rates could be much lower (as low as 300 lb flue gas/MMBtu, 130 kg/GJ) or could have even higher flue gas flow than with air-firing, depending on how much flue gas is recycled.

For conventional pulverized coal boilers that are directly fired from the mill, the use of some flue gas recirculation for fuel grinding and transport is unavoidable. The coal mills need to operate at specific gas flow rates for coal drying, grinding and transport of the pulverized coal out of the mills and to the furnace. Unless a different type of firing system is used, such as an indirect-fired system with pulverized coal storage and dense phase transport, use of flue gas recirculation will be needed at least for this primary stream.

The amount of primary recycle needed to match the equivalent volumetric air flow through the mills for air-firing is about 33% more on a mass basis due to its higher molecular weight. If oxygen were mixed into this primary recycle stream, the oxygen content in this stream would need to be limited to a maximum of about 21% to avoid safety issues, material upgrades, etc. This would reduce the primary recycle stream molecular weight and matching equivalent volumetric air flow through the mills for oxy-firing to about 20% more than air-firing on a mass basis. Even with oxygen enriched primary recycle, the amount of FGR needed for this stream is roughly 50% of the total amount of combustion gas generated when coal is burned in pure oxygen.

The amount of secondary FGR required will be dictated by the difference between the primary recycle flow and total amount of recycle needed based upon the boiler design, desired boiler thermal performance and long-term operability.

A boiler designed only for oxy-firing with minimal flue gas recirculation and without concern for air-firing capacity could look quite different than a comparable boiler designed for air-firing. Due to the lower gas flow rates and higher heat release, the furnace and convection pass size, heat transfer surfacing and materials requirements all change. Trade-offs involving design considerations to control ash deposition and material considerations associated with higher temperatures and increased corrosion rates are the main factors in establishing an optimum flue gas recirculation rate for oxy-fired only designs. However, if the boiler is required to operate in the air-fired mode over the entire load range, its basic boiler design cannot deviate too much from a traditional air-fired unit. For a dual air/oxy-fired requirement, operation in the oxy-fired mode is

controlled with flue gas recycle quantity, such that the boiler behaves thermally in a manner similar to that with air-firing.

In practice, if one tried to operate a boiler designed for air-firing with oxy-firing at too low a flue gas flow (i.e., low flue gas recirculation), combustion gas temperatures in the lower furnace and entering the upper furnace would be high as compared to air-firing. The higher resulting gas temperatures could cause significant issues with slagging and/or fouling in these regions and must be controlled at or below the maximum design temperatures acceptable for air-firing.

The higher combustion temperatures also increase the heat absorption in the lower furnace resulting in less thermal energy availability for downstream convection sections. Further, the convective heat transfer rates would be very low due to the lower gas velocities. Therefore, downstream superheat and reheat sections would not be absorbing very much heat as compared to the air-fired heat absorption values. This shift in heat absorption pattern as compared to air-firing is referred to as thermal unbalance.

The shift in heat absorption pattern between the lower radiant furnace sections and downstream convection section as the amount of FGR is changed was predicted in CFD simulations and demonstrated during 15 MWth BSF testing under this project. Figure 6-1 shows the change in furnace heat absorption measured as the FGR rate was varied firing different coals in the BSF. Although the percent of total heat input absorbed by the furnace varied with coal type, the recycle / global O_2 level that resulted in the same percentage of heat absorption in the furnace as during air-firing was about 26-28%.

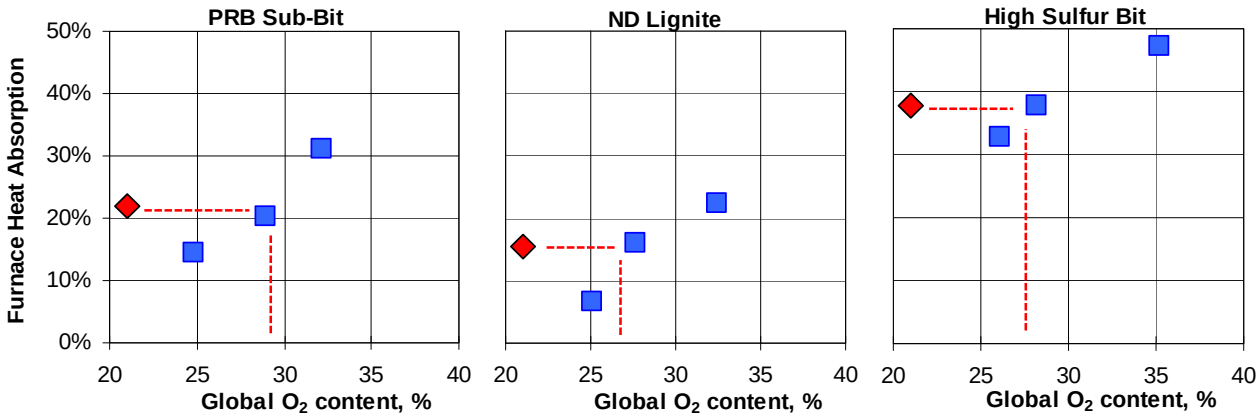

Figure 6-1-Furnace Heat Absorption versus Global Oxygen Content in the 15 MW_{th} BSF

Figure 6-2 provides an example of these FGR effects for a utility boiler design study. Relative flue gas flow (meaning the oxy-fired flue gas flow divided by the air-fired flow at the same firing rate) is plotted on the horizontal x-axis, furnace temperatures are shown on the left vertical axis and the Superheater/Platen heat absorption (at the top of the furnace) is shown on the right vertical axis. The plots in this figure were generated using Alstom boiler design programs modified for oxy-firing. Indicated by the dotted vertical line near the right axis is the relative flue gas flow (RFGF) value where a workable thermal balance was achieved (i.e., ~ 95% relative flue gas flow).

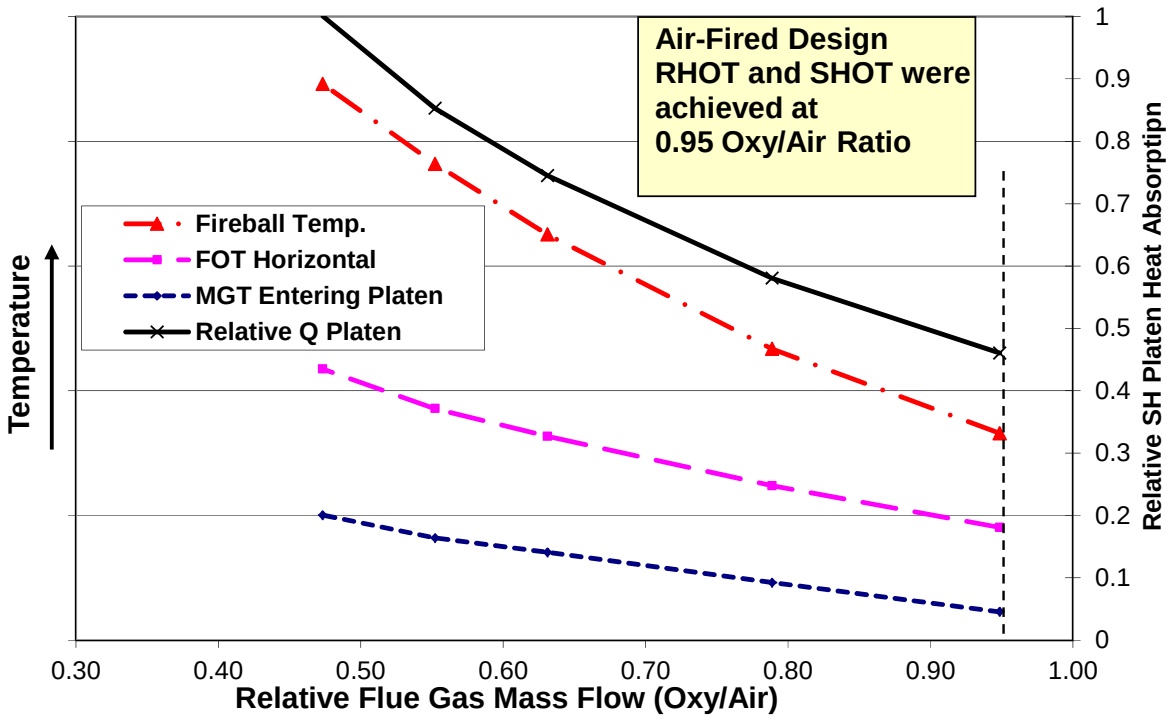

Figure 6-2 – Effects of Oxy-fired Flue Gas Flow Rate on Furnace Performance for Study Boiler

The furnace temperature values on the plots at the 95% RFGF value for oxy-firing are very close to the corresponding values for air-firing at 100% load with the same fuel. This is the relative flue gas flow value needed to obtain design superheat and reheat outlet temperatures (SHOT and RHOT) without reheat spray and with horizontal burner tilt.

In summary, the predictive results from CFD and boiler design programs consistently indicate that oxy-firing FGR rates are needed that provide only slightly less flue gas mass flow through the boiler than during air-firing to achieve similar thermal performance in an air-fired boiler design. The actual required gas flow rates are dependent upon the fuel properties and specific boiler design. Further reducing FGR flow results in increasing radiant furnace heat absorption and increased need for additional convection surfacing, and also includes potential changes in material selection to use additional high temperature (higher cost) alloys.

7. Guidelines for Firing System Design

This section discusses the primary considerations for design of an oxy-firing system. Included are discussion of a general design approach, typical ranges of combustion operating parameters, and design considerations for the oxygen injection system and the oxy burner/windbox system.

7.1 Oxygen Injection Considerations

The oxygen supplied by the ASU must be safely and effectively transported to the furnace for combustion. As noted in Section 2, there are several options for injection of oxygen from the ASU to the boiler firing system. Main criteria for selection of injection locations include:

- ***Technical Considerations***
  - Operating flexibility and/or performance of the boiler and overall plant
  - Safety risk associated with oxygen handling and use
  - Impact on existing equipment for retrofit or adaptation of proven equipment for new design
- ***Efficiency Considerations***
  - Oxygen preheating
  - Energy consumptions of fans
  - Oxygen pressure requirements / pressure loss
  - Flue gas exit temperature from Gas-Gas Heater
- ***CAPEX Considerations***
  - Cost of the oxygen injection system
  - Cost impact of other equipment

Oxygen from the ASU typically is delivered at about 70 - 100°F (20 – 40°C), and should be preheated prior to injection into the furnace to improve overall efficiency. The conventional gas-gas heater used to preheat air for air-fired boiler applications can be used to heat most of the oxygen if O_2 is premixed into the primary and secondary FGR streams prior to the preheater. Applying commonly used regenerative gas-gas heaters, such as a Ljungstrom® preheater, significantly reduces CAPEX compared to separate pure oxygen preheaters. The performance of the preheater for oxy-firing application is also improved due to the addition of oxygen that increases the cold-side FGR gas flow rate, resulting in a better match with the hot-side flue gas flow rate.

Although regenerative-type heaters have unavoidable leakage between streams, a commercial pressurized gas sealing system can be used to minimize oxygen loss from the oxygen enriched FGR to the flue gas. Alstom's Ljungstrom® has commercially available preheaters with pressurized sealing systems that reduce leakage between streams to less than 1%. Our evaluation indicates that maximizing the use of the Ljungstrom® gas-gas heater with a pressurized sealing system to heat oxygen is the most cost-effective overall solution. (Loss of oxygen from the boiler system increases capacity requirements and costs for both the ASU and GPU.) More detailed discussion of considerations for the gas-gas heater is provided in Section 9.

However, all of the oxygen needed for efficient combustion cannot be mixed and then heated with the FGR by the gas-gas heater. As previously discussed, in order to maintain similar thermal performance of an air-fired boiler design during oxy-firing, about 95% of the flue gas mass flow of air-firing is needed, which corresponds to about a 25% to 27% global oxygen content of the oxidant

to the boiler. Since the oxygen content of the gas stream must be limited to less than 23.5 % oxygen concentration to use conventional carbon steel construction, a significant amount (roughly 20-30%) of oxygen from the ASU cannot be premixed and heated by the gas-gas heater. This additional or supplemental oxygen necessary for combustion must be injected into the oxygen-rich secondary FGR after the preheater or injected directly into the furnace/windbox through lances.

The supplemental oxygen stream can be preheated by a separate heat exchanger (by either steam or flue gas) or can be injected at the temperature delivered by the ASU, based on plant specific trade-offs between the increased CAPEX for this oxygen heat exchanger and oxygen piping versus overall efficiency benefits. Main options for injection location of the supplemental oxygen include:

1. Injection and mixing of supplemental O_2 into the secondary FGR after the gas-gas heater before secondary FGR is divided into separate flows to burner and over-fire locations
2. Injection and mixing of supplemental O_2 separately into the secondary FGR streams after dividing the flows to the burners/windboxes and over-fire locations.
3. Injection of supplemental O_2 through lances separately into burner/windbox/overfire compartments or directly into the furnace.

The complexity of the supplementary oxygen injection system increases from Option 1 to 3. However, the flexibility of oxygen distribution into the furnace and control of combustion behavior also increases from Option 1 to 3. Since the oxygen concentration in the heated secondary FGR stream will be above the limit of 23.5%, appropriate materials such as stainless steels will be required for all components downstream of the oxygen injection. CAPEX trade-offs should be assessed between the high materials costs for stainless steel ducting and windboxes (including mixers and added ducting for required mixing lengths) versus the costs for additional oxygen piping and control values.

7.2 Oxygen Mixing Considerations

Injection and mixing is necessary for each of the three main oxygen streams into boiler system:

1. Injection into the primary recycle,
2. Injection into the secondary recycle, and
3. Supplemental injection into the windbox and overfire compartments.

Oxygen can be mixed with the primary and secondary FGR using various mixing approaches including static mixers and grid-type mixing systems. An example of a honeycomb-type static mixer installed in a duct is shown in Figure 7-1. Grid-type mixers are similar in concept to ammonia injection grids used in selective catalytic reduction (SCR) systems, but must address the much higher quantities of oxygen being injected through the grid.

Figure 7-1 – Example of a Static Mixer Installed in Ducting

Primary considerations for selection and design of the oxygen mixing system include:

- Ability to provide very good mixing that eliminates oxygen rich pockets within the main stream that could create local oxidation problems
- Required mixing length to provide desired mixing quality
- The gas draft loss associated with mixing
- The oxygen pressure loss associated with mixing
- CAPEX of the overall injection/ mixing system
- Complexity of the overall injection / mixing system

The purpose of the oxygen mixers for primary and secondary streams before the gas-gas heater is to allow the premixed oxygen-rich FGR streams to be handled in a similar manner as air. It is important that the oxygen in these premixed streams is nearly completely mixed to allow control of the oxygen concentration to approach the maximum limit, thus allowing the greatest amount of oxygen to be heated by the gas-gas heater. A common index used to define mixing quality is the Coefficient of Variation (CoV), which is a measure of the homogeneity (standard deviation in concentration / mean concentration). Streams with CoV of less than 0.05 are generally considered well mixed. The mixing system design should be simulated with CFD modeling over the range of operating conditions to evaluate performance. Figure 7-2 shows an illustration from a CFD simulation of oxygen mixing downstream of a grid-type mixing system. Our recommended guideline for mixing quality is based on achieving a CoV of less than 0.03 calculated from CFD simulations after the specified design mixing length.

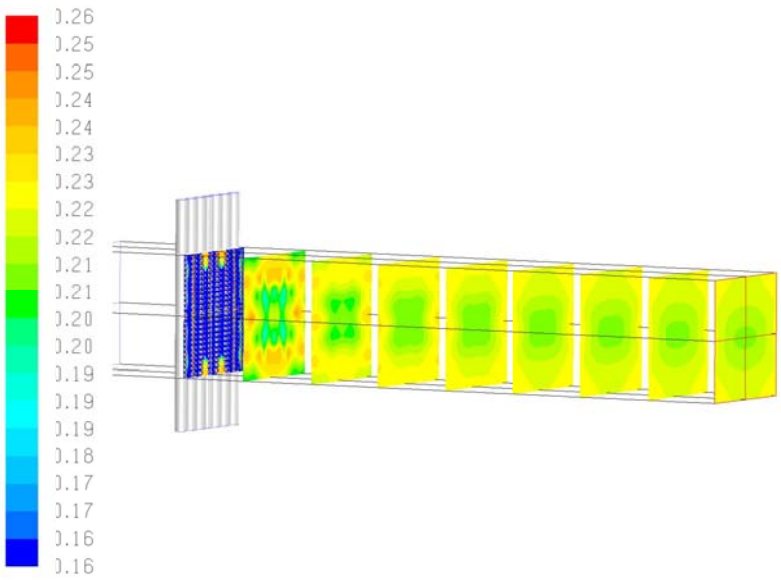

Figure 7-2 – Example of CFD Simulation of Oxygen Mixing After a Grid-Type Mixer

7.3 Burner / Windbox Design Considerations

As with air-firing, design of an oxy-firing system should be performed in coordination with the overall furnace sizing considering the design range in fuel properties to be burned and specific combustion and emission requirements. Selections of furnace and burner zone heat release rates, furnace residence times as well as the design of a separate over-fire injection system (as required) are strongly influenced by fuel characteristics for both air and oxy-firing.

The general approach and design principles for air-firing systems can be applied for oxy-firing systems while taking into consideration differences in gas properties. Some of the key differences for oxy-combustion compared to air-firing that should be considered include:

- Higher gas density due the reduction of nitrogen and increased CO_2 content
- Slower diffusion of oxygen through the CO_2-rich oxy-fired gas
- Higher heat capacity of oxy-fired gas
- Enhanced endothermic gasification reactions associated with high CO_2 and H_2O concentrations
- Increased gas radiation due to changes in gas radiant properties

In general, the typical ranges for burner/firing system design parameters such as gas velocities, flow splits, momentum ratios, and swirl numbers that have been developed for air-firing are still relevant for oxy-firing. Density differences between air and the recycle gas oxidant streams must be considered for sizing of ducting and burner compartment free-areas. As discussed in Section 3.5, the molecular weight of oxy combustion gas during coal firing is generally higher than for air-firing, resulting in lower volumetric flow rate. For dual air- and oxy-firing design requirements, the flexibility to block off selected burner compartments/flow areas to maintain desired velocities should be considered.

General air-firing principles applied for in-furnace NO_x control are still applicable for design of low NO_x oxy-firing systems. Extensive 15 MWth BSF tangential-fired testing shows the effectiveness of burner zone staging during both air- and oxy-firing. Further discussion on NO_x emissions is provided in Section 12. In general, NO_x generation on a mass basis is lower during oxy-firing than air-firing due to several factors including reduced thermal NO_x formation associated with low nitrogen content in the gas, reburning of the NO_x in the FGR from the recycle loop, and changes in NO_x chemistry associated with changes in gas composition.

Results from 15 MWth BSF oxy-fired testing as well as other investigators indicate the potential for delay of ignition and a decrease in early heat release during oxy-combustion compared with air-combustion. This is apparently due to a slower diffusion rate of oxygen through the CO_2-rich gas as well as the higher heat capacity of the oxy combustion gas. Additionally, there is a potential for the increase of endothermic gasification reactions due to higher CO_2 and H_2O concentration in oxy combustion gas, which would tend to reduce temperature and heat release. Therefore, firing system design features that promote ignition and early heat release should be considered. Design features such as lower fuel velocities, stronger burner internal recirculation zone, flame attachment hardware, enhance O_2 mixing and enrichment of O_2 concentration near the fuel admission location might be considered to help offset differences in heat release and potential impacts on furnace heat absorption.

Systematic control of oxygen injection is one method that can provide control of the oxy combustion process and heat release. The impact of changing the distribution and concentration of oxygen into a tangentially fired furnace is illustrated in plots in Figure 7-3. These plots show BSF furnace heat flux profiles (average incident heat flux at the furnace wall versus furnace height) for different operating cases. As shown in the left plot, the heat flux measured in the lower portion of the furnace for an oxy-firing case is less than that for comparative air-firing conditions when all of the oxygen was premixed with recycle to a uniform concentration before entering the windbox and over-fire compartments. The center plot shows changes to the furnace heat flux profile resulting from varying only the oxygen concentration at various locations into the furnace. The right plot in Figure 7-3 illustrates the capability to match air- and oxy-fired heat flux profiles by adjusting oxygen injection and gas recycle rate.

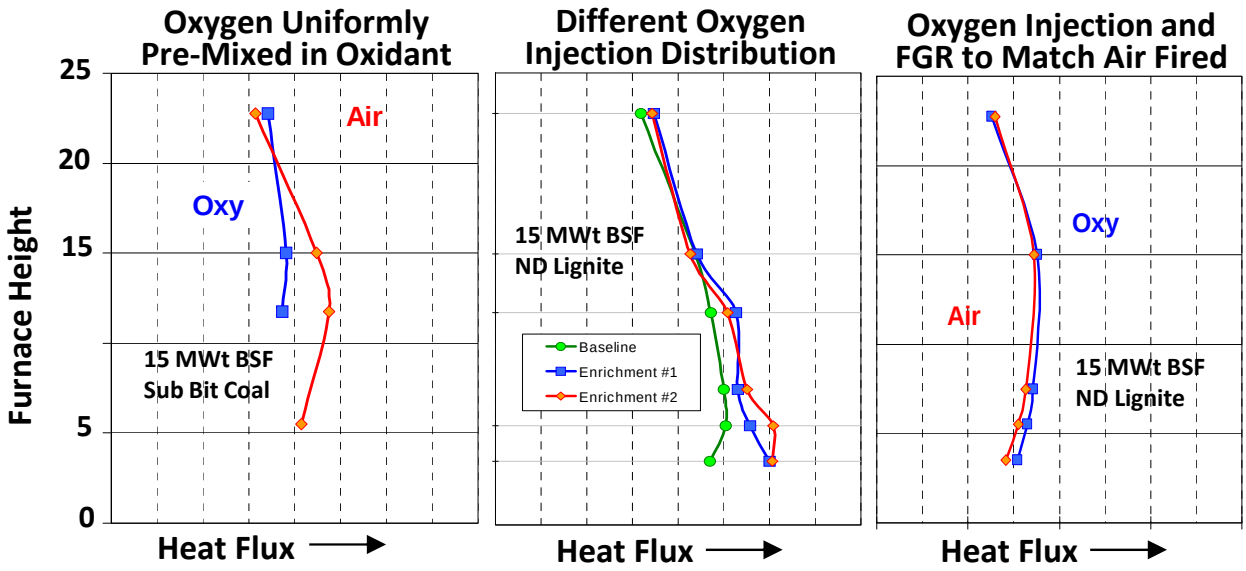

Figure 7-3 – 15 MW_{th} BSF Furnace Heat Flux Profile (Furnace Height vs. Heat Flux)

Oxygen injection and enrichment of oxygen concentrations above the global average oxygen concentration for specific oxidant streams to the burner is suggested to promote earlier heat release, particularly for dual air- and oxy-fired applications. An example of the burner/windbox compartments of a corner assembly for a tangential-fired system is shown in the left photo of Figure 7-4. Oxygen could be injected into specific compartments or to the entire burner/windbox assembly in addition to the premixed FGR oxidant flow. The photo on the right in Figure 7-4 is an example of a wall-firing burner. For a wall-fired burner design, oxygen could be added enriched to the inner oxidant annulus (typically referred to as secondary) or both the inner and the outer (tertiary) oxidants. The burner/windbox components and ducting downstream of oxygen injection locations where oxygen concentrations are greater than 23.5% must be fabricated with appropriate materials for heated oxygen service such as stainless steel.

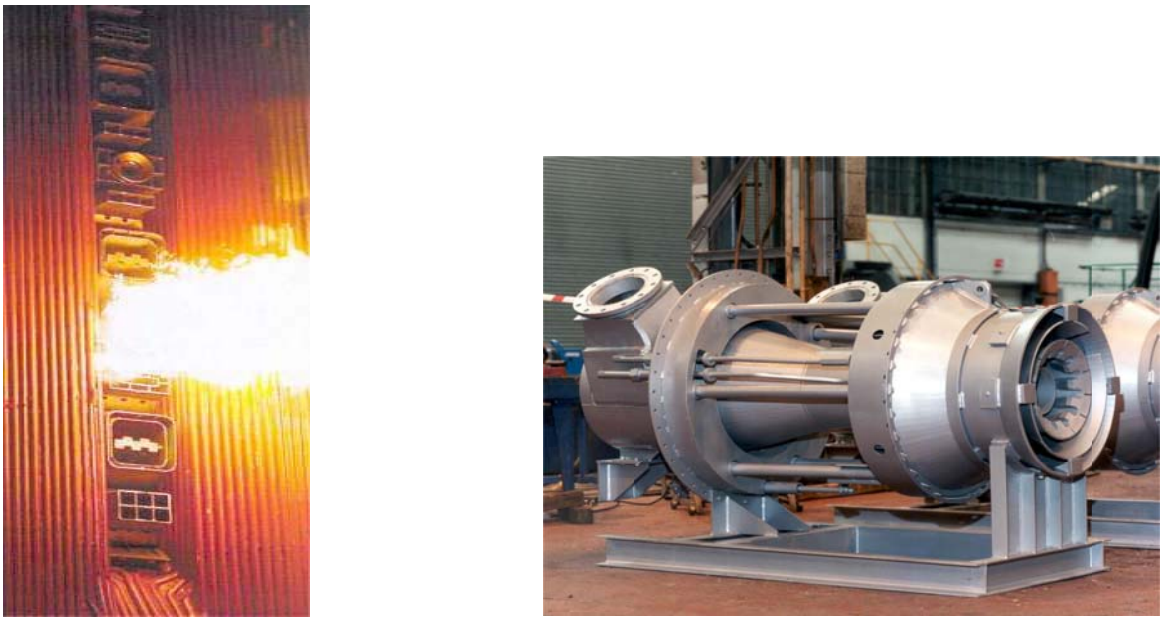

Figure 7-4 – Examples of Tangential-Firing Burner/Windbox Assembly and Wall-firing Burner

8. Mill Design Considerations

Vertical spindle mills are commonly used to grind fuel to the correct fineness for pulverized coal fired applications. Figure 8-1 shows an example of a vertical spindle mill such as Alstom's HP bowl mills. During conventional air-firing, these mills are air swept with heated primary air to facilitate drying and transport of the pulverized product through the mill. The mill can be designed and operated in a similar fashion for air- or oxy-firing. However, the difference in properties of the primary FGR oxidant to the mill must be considered for oxy-firing. Specific gas design velocities are critical to operation and must be maintained within tolerances. As previously discussed, the higher density of the primary oxidant stream during oxy-firing requires a higher mass flow rate to maintain the same volumetric flow rate and mill velocities as for air-firing. Our oxy-fired design guidelines recommend maintaining a minimum of 90% of the volumetric design flow rate as the air-fired design.

Differences in the primary oxidant gas properties also impact coal drying and grind performance. The higher moisture content in the oxy-fired primary stream and higher heat capacity must be considered in calculating the heat balance around the mill and establishing appropriate mill outlet temperatures for satisfactory drying. Mill manufacturers' procedures for selection of mill outlet design temperature typically consider fuel moisture and reactivity as well as approach to saturation temperature of outlet gas needed for drying.

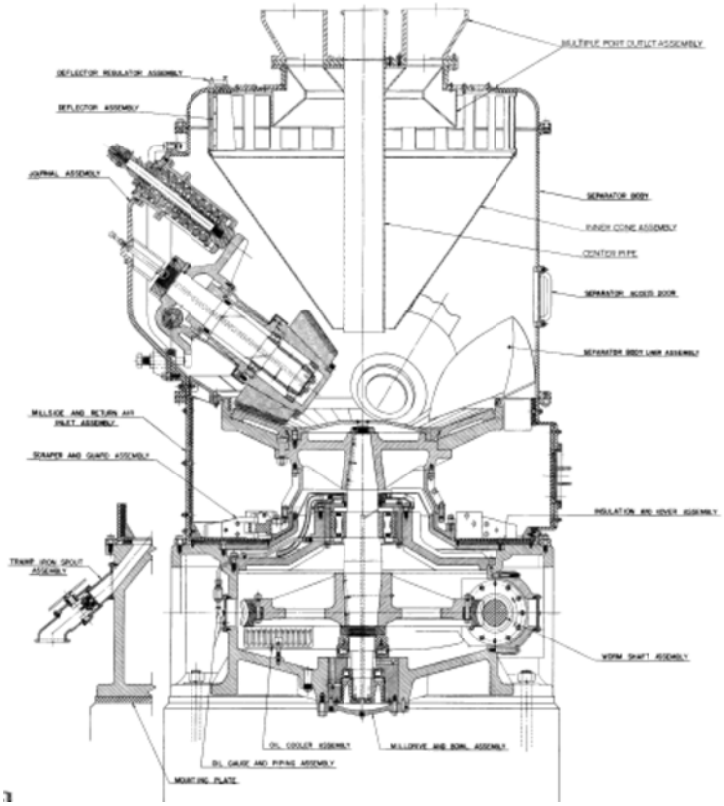

Figure 8-1 – Example of Vertical Spindle Mill Typical for Pulverized Coal Applications

9. Gas-Gas Heater

In convectional air fired boilers, air (gas-gas) heaters are used to recover the sensible energy from the flue gas leaving the boiler and transfer it to the combustion air. This process improves the boiler efficiency as the flue gas temperature leaving the air heater is reduced. In addition to preheating the secondary air (SA), the recovered energy can also be used to preheat the primary air (PA) that is used for coal drying and then for conveying the pulverized coal to the furnace.

There are a number of process differences between air- and oxy-firing that impact the design and selection of the preheater. For oxy-fired applications, typical process configurations premix oxygen from the ASU with the primary FGR to the pulverizers and with the secondary FGR to the furnace. Oxygen is mixed with these FGR streams before the gas-gas heater to improve preheater performance and to improve the boiler efficiency. The concentration of oxygen in the secondary FGR needs to be limited to 23.5% to allow fabrication with carbon steel material (and to avoid more costly stainless alloys). A 21% O_2 limit is more prudent to allow for O_2 concentration variations due to mixing, load variations, upset conditions, and control system response. Oxygen concentration in the primary FGR is also limited to 21% to maintain the same oxygen concentrations as are in air to the pulverizers to minimize potential hazards. The flow rates and physical properties (composition, molecular weights, density) of both primary and secondary streams to the preheater can vary significantly between air and oxy-firing and must be considered.

For convention air-fired boilers, often Ljungstrom® regenerative air preheaters are used. Figure 9-1 provides an illustration of a bi-sector Ljungstrom® air preheater, which has flue gas flowing downward and air flowing upward. The rotor is packed with heat transfer surface that is divided into radial compartments. The rotor compartments are closed with seal plates.

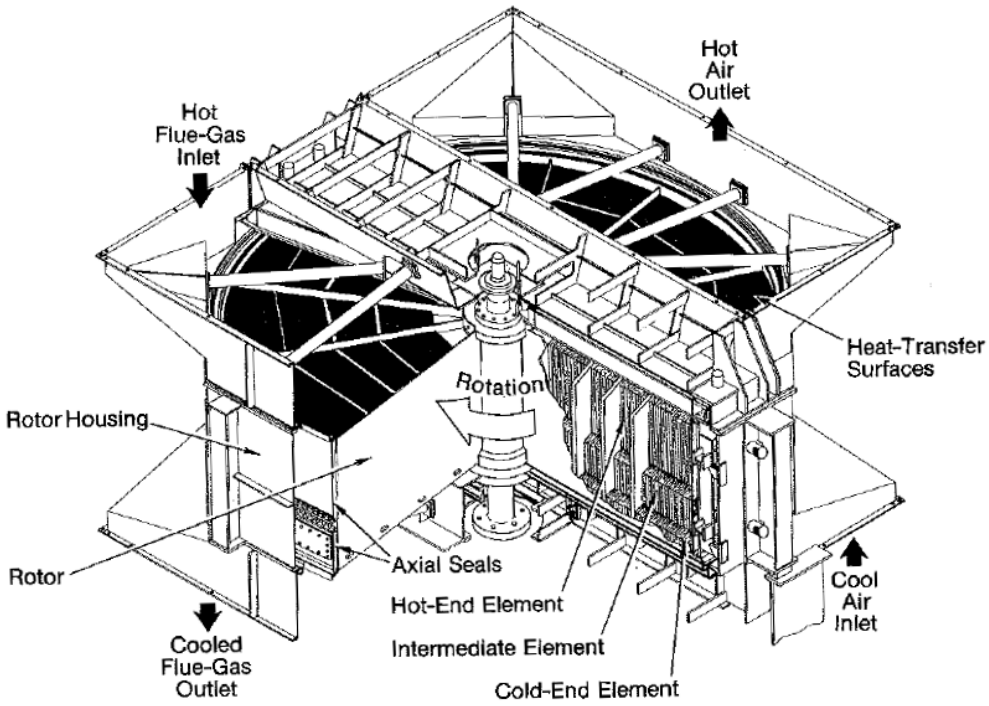

Figure 9-1 – Example of Ljungstrom® Preheater

Air leakage is an unavoidable aspect of regenerative type heaters. Leakage comes from two main sources:

- Direct leakage, which is the air from primary and secondary streams that passes into the flue gas stream between the radial and axial seals and sealing surfaces as a result of the static pressure differential between the air and gas streams.
- Entrained leakage, which is the air that is still contained in the rotor as it passes from the air side to the gas side.

For oxy-firing, oxygen leakage in the gas-gas heater is a major concern because of the high capital cost of the ASU and its high parasitic power consumption as well as the additional oxygen separation requirements for the GPU.

Alstom Air Preheater Company has developed sealing systems for their Ljungstrom® regenerative heaters that are commercially available to minimize the leakage between gas streams. Ljungstrom® gas-gas heaters (similar to an air preheater) are frequently used to recover sensible heat from the flue gas before the WFGD and then transfer it back to the flue gas after the WFGD, thus providing buoyancy to help the gas flow up the stack. Figure 9-2 provides an illustration of a gas-gas heater with an active leakage reduction system. Entrained leakage is reduced by blowing clean gas (secondary FGR) into the rotor as it passes between streams. Direct leakage is reduced by pressurizing the plenum between the sector plates and the rotor with the secondary FGR gas. With a fan assisted leakage reduction system, the leakage can be lower than 1%.

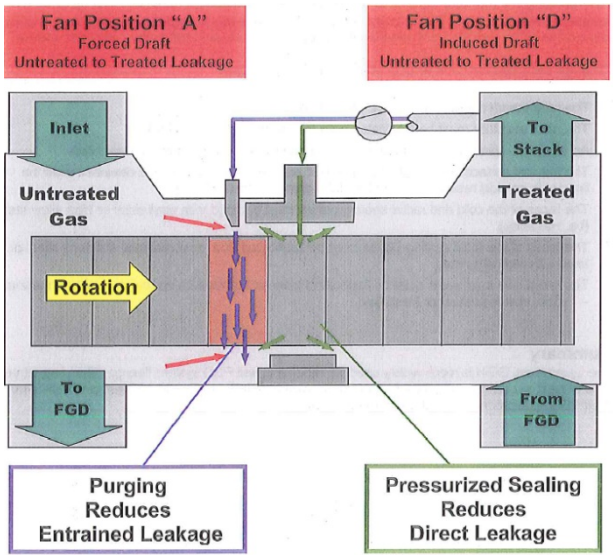

Figure 9-2 – Ljungstrom® Purging and Pressurizing Sealing Systems

Due to the importance for oxy-fired systems, where there is a steep cost associated with oxygen loss, a sensor-controlled system in conjunction with a pressurized sealing system is recommended in our guidelines for gas-gas heater design to control leakage to less than 1%.

It is common practice in air-fired power plants to provide a steam or hot water/glycol coil air heater ahead of the main regenerative air heater. The primary purpose of the steam or hot water coil is to preheat the incoming ambient air stream to raise the regenerative air heater cold-end temperature and thus reduce the potential for H_2SO_4 corrosion of the heating surfaces. The use of a steam coil is typically not required for oxy-firing because the temperature of recycle stream is sufficiently high (temperature of flue gas leaving the FGD system). Operation of oxygen-fired boilers in the air-fired mode will require the use of a steam coil air heater. However, the selected location of the coil may be different for dual air/oxygen-fired boilers than it is for traditional air-fired boilers.

Preheater performance is limited by the acid dewpoint, which is typically elevated for oxy-firing due to the higher moisture and SO_3 concentration as a result of flue gas recirculation. This limits the minimum flue gas temperature leaving the preheater to avoid corrosion of the heat transfer surfaces. Performance may be improved (if the heat transfer effectiveness is not already maximized) by reducing the SO_3 concentration entering the air heater. This can be achieved by injecting a sorbent (such as sodium carbonate or Trona) upstream of the air heater. Testing in the 15 MWth BSF has shown similar SO_3 capture performance of sodium- and calcium-based sorbents under air- and oxy-firing. The sorbent injection system should be designed to reduce the SO_3 concentration entering the air heater to 5 ppm or lower to maximize benefit.

10. Guidelines for Operation and Controls of Oxy-Combustion Boiler

The process design changes for the oxy-firing system present new operational and process control challenges. There are additional interfaces associated with new boiler equipment such as the oxygen injection system and flue gas recirculation streams. There is also a need to interface with additional plant equipment such as the ASU and GPU. The control system design for the oxy-firing process can build on the existing control design for the conventional air-firing process while considering the additional requirements.

The overall control structure for an oxy-fired boiler island process is generally consistent with that for a conventional air-fired boiler island process, which provides the following major control sub-systems:

- Boiler master: Boiler master is the interface to unit master (provided by plant coordination control system designer), which mainly includes the boiler related runbacks, load restrictions associated with loss of boiler auxiliaries.
- Combustion control: Overall control objectives for combustion control include coordinating fuel and oxidant flows according to the boiler master, maintaining combustion stability and boiler efficiency, and supporting combustion mode transitions between air-fired and oxy-fired modes, etc.
- Stoichiometry control: Stoichiometry control is designed to maintain the combustion stability and efficiency, and minimize the production of NO_x via staging the combustion appropriately. Stoichiometry control belongs to combustion control and will be significantly different compared to that of the conventional air-fired boiler island process.
- Combustion mode transition control: During combustion mode transition operation, the combustion control loops are used to assist the smooth transition of the air- and oxy-fired modes of combustion and minimize operators' manual operations.
- Water/Steam control: Overall control objectives for water/steam control include coordinating boiler feedwater flow according to the boiler master, controlling the SH steam and RH steam temperature, and maintaining the SH spray valves in the appropriate operating ranges, etc. No significant changes are made to the SH steam temperature control loops compared to a conventional air-fired unit. However, flue gas recirculation trim control loop has been added to the RH steam temperature control loops.
- SCR control: Although NO_x generation is lower in oxy-fired combustion, SCR may still be needed during air fired start up or for oxy-fired operation due to the specific NO_x emission requirements or CO_2 product requirements.

Several distinct modes of boiler operation that must be addressed by the operational and controls system including: air-fired start-up, transitions between air and oxy-firing modes, load ramping, continuous operation at full load oxy-fired operation and partial load, and shutdown. The basic requirements and considerations for each of these operating conditions are summarized below.

10.1 Continuous Operation at Full and Partial Loads

For continuous full load operation or partial load operating above the boiler minimum control load, the boiler control system responds automatically to meet the steam demand through signals from the plant master control and the boiler control systems. As with air-firing, fuel feed rate is varied

by the boiler control logic to control steam flow and follow load demand. Pulverizer operation and primary FGR flow rates are adjusted to meet the fuel demand. Secondary FGR flow rates are also adjusted by the boiler control logic to follow the change in demand. The total oxygen demand from the ASU and adjustment of specific oxygen flows is controlled to satisfy combustion requirements and to maintain specified ranges for material requirements. Combustion and furnace stoichiometry control consideration are discussed further in Section 10.6. Additional discussion of steam temperature control considerations is provided in Section 10.5.

10.2 Start-Up and Shutdown

Start-up and shutdown procedures are similar whether a hot or whether the boiler system is cold or has been cooled down for maintenance or inspection. The primary difference is the length of time required to come up in load. All start-up scenarios require beginning with normal air firing up to a minimum load before transitioning to oxy-firing. All of the precautions and operating sequences of systems and components of an equivalent air-fired unit should be followed.

The boiler should be transitioned from oxy-firing to air operation prior to shut down. Shutdown in the air-fired mode should follow the precautions and operating sequences of systems and components of an equivalent air-fired unit.

10.3 Air/Oxy Operating Transition Considerations

An oxy-fired pulverized coal boiler must be designed to operate under both air-fired and oxy-fired combustion modes. Typically, the boiler is started in air-mode and transitioned to oxy-mode at a certain load. It operates in oxy-fired mode for its normal operating range and is transitioned to air-fired mode before shutdown. The primary difference between these two modes of combustion is the method of supply of oxidant to the furnace and its composition. In air-fired mode ambient air acts as an oxidant whereas in oxy-fired mode a mixture of pure oxygen and recirculated flue gas is used as an oxidant. As such, transition of combustion modes involves activation of different systems, switching of control logic, control of the opening and closing of various valves and dampers, maintaining stable combustion, and balancing all the associated processes and equipment conditions. Among the additional systems that must be addressed during oxy-firing are the operation and controls of the FGR system, GPU, ASU, oxygen supply and storage systems, various isolation and control valves, instrumentation associated with oxy-fired operation, and dampers in specific ductworks and flow paths.

Before starting air-fired to oxy-fired mode transition, the status of the PC boiler and the rest of the capture plant equipment should be confirmed. Some of the key items to be confirmed include:

- Boiler running at desired load and operating conditions. Alstom's preliminary guideline recommends a minimum of approximately 40% BMCR in air-fired mode with a minimum of two pulverizers in service and in once-through operation. However, transition at lower operating load can be considered.
- ASU is in operation and is ready to support boiler oxygen requirements for load ramp-up.
- GPU is ready for operation
- Confirm instrumentation needed oxy-fired operation is in proper operating order. This may require calibration of gas analyzers for high CO_2 content gas and flow measurements set up for high density gas.

Transition from air-fired mode to oxy-fired mode can be initiated once the alignment of the equipment as required for the operation of the plant in oxy-combustion mode is accomplished. Among these are the stack damper, the valves in the oxygen supply system and the dampers in the oxidant supply system. In addition, the GPU unit must be in operation. Simplistically, the transition is accomplished by gradually opening the recycle dampers to the opening the recycle dampers to secondary and primary fans and gradually closing the inlet air isolation dampers to the fans to maintain desired flows rates. Simultaneously, the oxygen supply values must for opened and oxygen requirements for combustion controlled. Other systems associated with oxy-firing such as the seal gas system also must be placed in service and air fired systems not used including the stack damper should be secured. Once the transition is accomplished and the unit is in stable operation, the control system can be placed into control mode for continuous operation.

Similarly, for transition from oxy-fired to air fired mode, the status of the PC boiler and the rest of the plant equipment required for the air-fired mode should be confirmed and ready for operation. Alstom's preliminary guideline recommends transition with a minimum of approximately 40% BMCR in oxy-firing mode with a minimum of two pulverizers in service and in once-through operation. However, transition at lower operating load can be considered.

Transition from oxy-fired mode to air-fired mode can be initiated once the alignment of the proper dampers, control valves, fans in the oxygen/air supply system is made. The transition is accomplish by adjustment of stack isolation damper, primary and secondary inlet air isolation dampers, and oxygen injection flow control valves in a general reverse order as the air to oxy-fired mode transition. Primary and secondary flow requirements and oxygen requirements for combustion must be controlled over the transition process. Systems associated with the oxy-firing mode not in sue should be shut down and secured.

10.4 Boiler Loading Ramping

Load changes during oxy-fired operation can follow similar procedures and load ramping rates as for an equivalent air-fired unit, but must be integrated with all the ASU and GPU and conform with any limitations.

For load ramping in oxy mode, as with air-firing operational curves for the control system are used to accomplish the load change while maintaining key process and performance conditions. Some of the following process variables are critical and should be monitored:

-Boiler exit excess O_2

- Separator outlet steam temp

-SH/RH outlet steam temp

-SH/RH spray flow rate

- MBZ stoichiometry and SOFZ stoichiometry

-Furnace pressure

-Primary and secondary flow rates

-Oxygen concentrations in primary and secondary flows

-Windbox/furnace differential pressure

- Windbox burner tilt and SOFA tilt

10.5 Steam Temperature Control Considerations

Reheat outlet (RHO) steam temperature is controlled in order to protect the reheater (RH) circuit materials and components (RH tubing, RH piping, IP turbine) from being damaged by overheating as well as meet turbine requirements for high efficient. For a tangentially-fired boiler, reheat outlet steam temperature is controlled by adjusting one or more of the following variables, depending on boiler operating mode:

- De-superheating Spray Water Flow (air-firing or oxygen-firing)
- Burner Tilt Angle (air-firing or oxygen-firing)
- Excess Air Level or Flue Gas Recirculation Rate (air-firing or oxygen-firing)

The capability of burner tilt angle is generally not available for wall-fired boiler designs.

Among these different types of manipulated variables for the RHO steam temperature control, RH desuperheater spray water control responds immediately for fast control response. However, it is desired to minimize the use of RH desuperheater spray water flow via the other available manipulated variables, i.e. the fuel nozzle tilt positioning and the excess air level in Air-firing mode, or the fuel nozzle tilt positioning and the secondary flue gas recirculation (SFGR) flow demand in oxy-firing mode.

Reheater outlet steam temperature control with oxygen firing can be accomplished in a manner which is very similar to what is done with air firing. The ability to vary the secondary flue gas recirculation flow during oxy-firing is most notable and provides greater thermal control flexibility without significantly impacting combustion and emission performance (unlike changes to excess air, which can influence NO_x and unburned carbon emissions).

Low Reheat Outlet Temperature

For operating conditions with low reheat outlet steam temperature, burner tilt angle would be increased first to obtain the desired reheat outlet steam temperature. If the reheat outlet steam temperature were still low after the maximum burner tilt angle was reached, the secondary flue gas flow rate would be increased next. This would be done using FD fan controls (within pre-defined limits) to adjust flows within specified flow rate limits.

Increasing secondary flue gas flow rate after increasing burner tilt for low reheat outlet temperature situations improves plant efficiency by minimizing FD and ID Fan power requirements for this operating condition. Changing secondary flue gas flow rate with oxygen firing is analogous to changing excess air level in the air-fired mode. Both methods work by changing the relative flue gas flow rate throughout the boiler. An increase in flue gas flow at a given firing rate will reduce flue gas temperatures leaving the furnace. The reduced flue gas temperature will reduce radiant heat transfer whereas the increased flue gas flow increases convective heat transfer. The combined effect increases reheat outlet temperature. The opposite is true for a decrease in flue gas flow rate.

High Reheat Outlet Temperature

For operating conditions with high reheat outlet steam temperature the order of control variables changes as compared with low reheat outlet steam temperature situations. De-superheating spray

water flow would first be used for fast response followed by secondary flue gas flow reduction, to eliminate or minimize the de-superheating spray flow. The secondary flue gas flow rate would be decreased using FD fan controls (within pre-determined limits) to correct the situation. If secondary flue gas flow rate reaches the low secondary flow rate limit and de-superheating spray was still being used, burner tilt angle would then be decreased next to eliminate or minimize the spray.

Decreasing secondary flue gas flow rate before decreasing burner tilt for high reheat outlet temperature situations improves plant efficiency by minimizing FD and ID Fan power requirements for this operating condition.

10.6 Combustion and Stoichiometry Control

Most modern pulverized coal fired boilers have combustion systems designed to control NO_x emissions. This is typically accomplished by staging the amount of oxygen available, and thus the stoichiometry during the combustion process. For air-firing, stoichiometry control is directly related to the ambient air flow distribution control since the oxygen distribution and the ambient air flow distribution are controlled simultaneously. For oxygen-firing, however, the oxygen distribution and FGR flow distribution can be controlled independently. Therefore the stoichiometry control for oxygen-firing boilers has to coordinate the oxygen distribution with the FGR flow distribution.

With oxygen-firing, a mixture of recirculated flue gas and oxygen is typically used to make the primary and secondary "oxidant" streams ("oxidant" instead of air), and the oxygen is provided from an ASU. The oxygen concentration of the primary and secondary oxidant flow is controlled below 23.5% by volume (wet) prior to the gas-gas heater to allow the use of conventional materials. In addition to these oxidant streams, a third stream of relatively pure oxygen (supplemental O_2), which the remaining oxygen is required for combustion of the coal, is provided directly to the windbox compartments or added to the secondary oxidant stream closer to the furnace.

In order to optimize NO_x reduction while maintaining good combustion performance, the stoichiometry in various zones of the furnace needs to be controlled to predetermined values based on fuel flow and total oxygen supplied for each zone. Further, to ensure sufficient total oxygen for efficient combustion, the flue gas oxygen content leaving the boiler must be controlled by adjusting the supplemental O_2 flow rate to maintain a pre-determined value for flue gas O_2 concentration at the furnace exit (for coal firing typically ~2-3% O_2 by volume-wet, similar as with air firing at~15-20% excess air as discussed in Section 2.4).

In summary, the main functions of the combustion control system for an oxy-fired boiler are:

- To maximize the amount of pure oxygen pre-mixed with the flue gas recirculation flows while maintaining appropriate O_2% concentration in primary and secondary oxidant flows;
- To minimize the total oxygen supplied by the ASU and/or the oxygen storage equipment while maintaining sufficient oxygen for efficient combustion;
- To guarantee a proper combustion oxidant flow distribution in each burner zone in order to maintain combustion gas velocity in the windbox and over-fire compartments; and
- To reduce the production of NO_x by properly staging the oxygen distribution. The secondary oxidant flow and the supplemental O_2 flow distribution have to be controlled to achieve the predetermined combustion zone stoichiometry.

The most significant difference for the stoichiometry control between the oxygen-fired mode and the air-fired mode is that in the oxy-fired mode, the combustion oxidant flow distribution and the O_2 flow distribution (i.e. the stoichiometry) must be coordinated to meet the oxidant flow requirements and the stoichiometry set points for each combustion zone.

11. Instrumentation and Measurement Considerations

As with other components, instruments need to be selected to withstand the oxy-combustion flue gas environment. Flow measurement devices such as orifices and instruments such as thermocouples and pressure cells may be exposed to enriched or pure oxygen. High moisture, especially in the presence of high concentrations of SO_2 and other acid gases, may require careful selection of instruments.

Gas analyzers, to measure concentrations of O_2, SO_2, NO_x, etc., are not usually used in flue gases with up to 90% CO_2. Consideration must be given to possible interferences from the high CO_2 concentration. It may be necessary to use calibration gases made with a balance of CO_2 rather than N_2. For confirming that emission requirements are met, the measurement techniques – including calibration gases – may be set by regulations. Modifications for oxy-firing may need approval from regulators.

12. Emission Considerations

The emissions of particulate, CO, NO_x, SO_2, SO_3, mercury, and other trace metals are considered in this section. During air-firing, a certain level of each of these pollutants leaves the furnace, and may be further reduced – e. g., with a baghouse, scrubber, SCR – before entering the environment through the stack.

During oxy-firing, pollutants also leave the furnace and may be reduced in similar cleanup equipment. But from there, the flue gas is not just sent up the stack. A portion of the flue gas will be recycled to the furnace. Some of the pollutants will be removed in the GPU and some will be retained in the liquid CO_2 product and be sequestered. The vent gas from the GPU will be the main source of emissions. The amount of actual emissions to the atmosphere will depend on the required CO_2 product purity and the particular GPU design. This discussion will focus on the implications of oxy-firing on the emission levels both leaving the furnace and after gas cleanup and recycle, but before entering the GPU.

If coal were burned in pure oxygen and generated the same emission rate of a pollutant in lb/hr or lb/MMBtu fired as during air firing, the emission concentration will be higher due to the lack of nitrogen dilution. In oxy-firing with flue gas recycling, the pollutant concentration leaving the furnace depends on the concentration in the recycled flue gas. The emission rate (e.g., in lb/MMBtu) is usually more appropriate for comparisons between air- and oxy-firing.

12.1 Particulate Emissions

The amount of fly ash leaving the furnace depends on the amount of ash in the fuel and the split between bottom ash and fly ash. With oxy-firing, the bottom ash/fly ash might be slightly changed depending on the flue gas recycle rate, thermal environment and the velocity profile through the furnace. Results from 15 MWth BSF testing show that particulate characteristics do not change significantly between air- and oxy-firing. During both oxy-firing and air-firing, a high efficiency baghouse or ESP will be required and total emissions in the flue gas will be similar.

12.2 Carbon Monoxide Emissions (CO)

Good burnout of CO depends on sufficient oxygen in the gas and sufficient mixing and residence time, especially in the overfire air region. There is typically no downstream control of CO, so the use of low excess O_2 and deep staging of the O_2 for NO_x control is constrained by the CO emissions. Testing in the BSF has shown that for reasonable global O_2 levels and adequate overfire air velocities (i.e., good mixing), oxy-fired CO emission rates from the furnace (in lb/MMBtu) are comparable to those with air-firing.

12.3 Nitrogen Oxides Emissions (NO_x)

During conventional air-firing of pulverized coal, NO_x emissions leaving the boiler are primary generated from the nitrogen contained in the coal and from nitrogen present in the combustion air. The properties of the coal, fuel/air (oxygen) mixing and the availability of oxygen are the main factors controlling the net amount of fuel NO_x generated. These same factors also influence fuel NO_x generation during oxy-firing. The generation of NO_x from the molecular nitrogen present from the combustion air, typically called thermal NO_x, is mainly dependent on the intensity of combustion (temperature) and the availability of oxygen. Since the presence of nitrogen in the boiler is dramatically reduced during oxy-firing, thermal NO_x is not a significant contributor to the NO_x emissions.

Most modern boilers incorporate NO_x reduction systems that control the availability of oxygen to the fuel by staging the combustion air. Key factors that impact NO_x reduction include the fuel properties, the combustion stoichiometry of the staged zone and the residence time in staged zone. These same factors also impact the NO_x reduction during oxy-combustion. As with air firing, NO_x emissions drop as the main burner zone stoichiometry decreases during oxy-firing. Figure 12-1 shows one example from the BSF firing lignite. The NO_x concentration (ppm) is higher for oxy-firing without the nitrogen dilution, but the emission rate (lb/MMBtu) is typically lower.

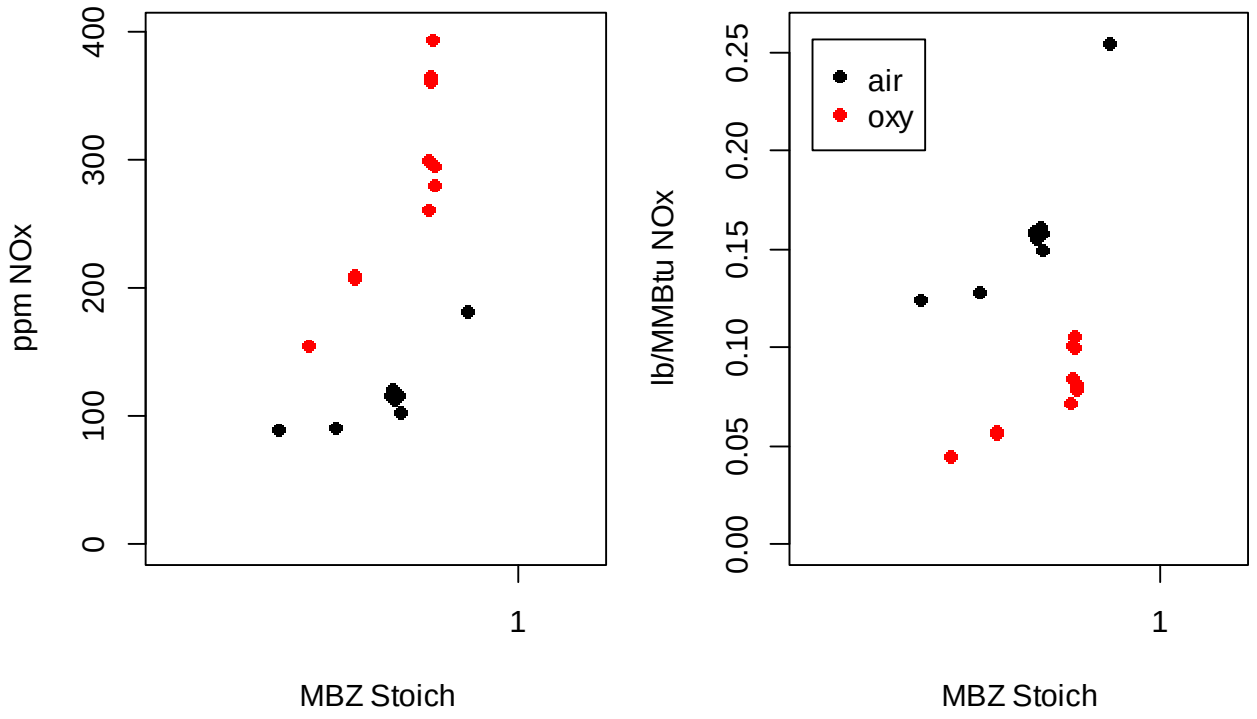

Figure 12-1 – BSF NO_x Emissions *vs.* MBZ Stoichiometry for Air- And Oxy-Firing

As mentioned above, one of reason for the lower emission rate with oxy-firing is reduced formation of thermal NO_x from atmospheric nitrogen. Another is that a portion of the NO_x formed is recycled to the furnace. The majority of the flue gas recycle is returned to the windbox region, where reburning will destroy a large portion of the recycled NO_x if the furnace is staged and has a sub-stoichiometry environment. Less of the NO_x recycled to the overfire region will be destroyed, since it does not see deeply staged conditions.

Based on the BSF data we expect that the oxy-fired NO_x emission rate (lb/MMBtu) leaving the boiler island (inlet to the GPU after gas recycle) will be about 25-40% of the air-fired rate for comparable staging and excess oxygen levels for bituminous coals and 35-50% for subbituminous coals and lignite.

A selective catalytic reduction (SCR) system can be installed if necessary to further reduce the NO_x emissions entering the gas processing unit (GPU). If the SCR is within the recycle loop, a portion of the NO_x leaving the SCR will make multiple passes through the SCR as well as through the

windbox region (for reburning). The prediction of the NO_x emission to the GPU needs to consider these combined effects.

12.4 Sulfur Emissions (SO_2 and SO_3)

Under both air- and oxy-firing, nearly all of the sulfur in the coal will be released in the furnace. If the sulfur is not removed from the recycled flue gas, the concentration will be higher in oxy-firing due to the lack of nitrogen dilution. If sulfur is removed, then the concentration is diluted by the recycled flue gas. In both air- and oxy-firing, the rate of SO_2 leaving depends on the extent of removal in the flue gas scrubber.

A portion of the sulfur in the flue gas is present as SO_3. In the presence of moisture in the flue gas, this can lead to acid deposition and corrosion on cooler surfaces, such as in the air heater. Here it is the flue gas concentration, not simply the emissions rate of SO_3 that is important.

The following figure shows the SO_2 and SO_3 concentrations at the economizer outlet for two fuels tested in the BSF. With air firing Illinois bituminous coal, the SO_2 was at about 2,000 ppm leaving the furnace with about 2% converted to SO_3. For oxy-firing without sulfur removal in the recycled gas, the SO_2 was concentrated to almost 10,000 ppm, again with about 2% conversion to SO_3. When sulfur was removed from the recycled flue gas, the SO_2 was diluted down to about 3,000 ppm and a similar percent conversion to SO_3.

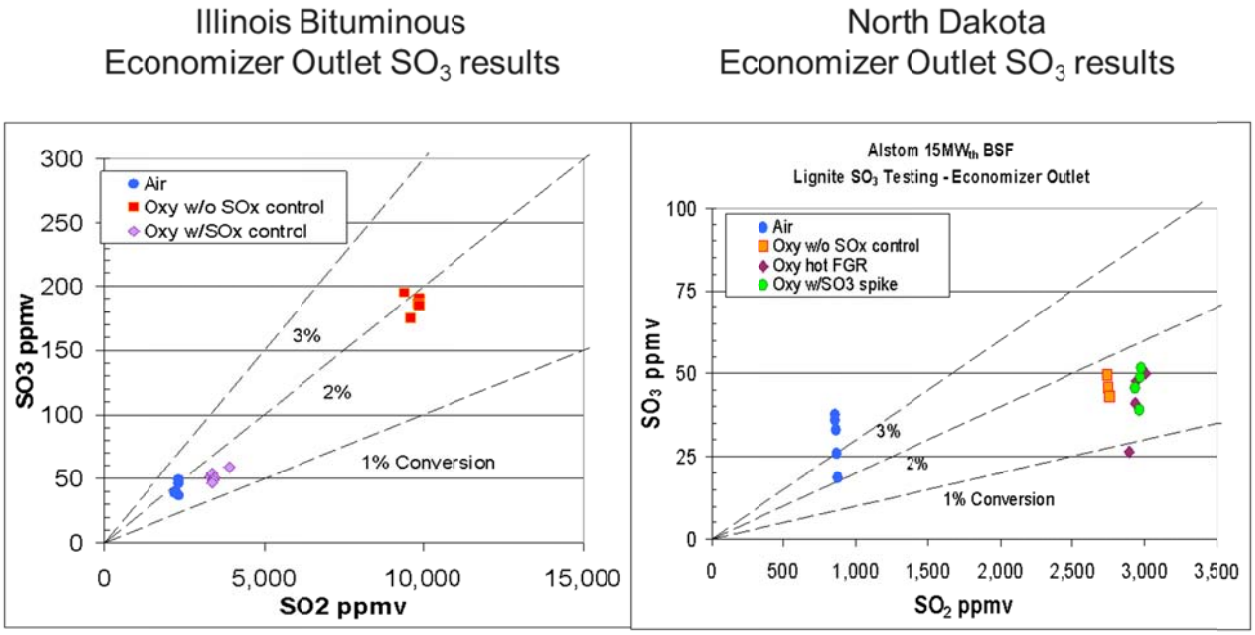

Figure 12-2 – Conversion of SO_2 to SO_3

For the North Dakota lignite shown in the figure, the conversion of SO_2 to SO_3 was slightly less for oxy-firing without sulfur removal in the flue gas.

Our guideline is to use the same percentage conversion of SO_2 to SO_3 for air- and oxy-firing. Note that the acid dewpoint also depends on the moisture concentration in the flue gas, which may also be more concentrated, depending on whether the recycled flue gas is dried.

Recognize that if an SCR is installed, the catalyst will enhance additional conversion of SO_2 to SO_3.

12.5 Mercury and Other Trace Metal Emissions

In air-firing, all of the mercury in the fuel is released into the flue gas as elemental mercury. The released elemental mercury is then transformed into oxidized mercury – a form that is more readily captured in existing air pollution control devices such as scrubbers, baghouses and flue gas condensers – as it is cooled down to a lower temperature while passing through the boiler backpass. The extent of its oxidation is significantly influenced by the concentration of halogen species (mostly chlorine and bromine) in the flue gas. Unburnt carbon provides catalytic surfaces for mercury oxidation. Unburnt carbon also captures some of the oxidized mercury in the flue gas. The extent of this native mercury capture by unburnt carbon in ash is, however, affected by the amount of SO_3 in the flue gas. Other site-specific parameters such as the SCR or ductwork design also affect the inherent mercury capture.

In general, US bituminous coals contain relatively high concentrations of chlorine (1,000 ppm to 3,000 ppm) and sulfur (up to 4%), and result in a relatively high unburnt carbon content in the flyash. As a result, 50 to 80% of the mercury in the coal is inherently captured; the mercury in the flue gas (at air heater inlet location) is found to be mostly in the oxidized form. In case of lower rank US coals, however, the inherent mercury capture tends to be low (<20%) as they contain relatively low chlorine (<500 ppm), and sulfur (<1%), and produce low (<0.5%) unburnt carbon in the ash. Most of the mercury in the flue gas is also found to be in elemental form.

In oxy-firing, mercury behaves the same way as in air firing. High concentrations of CO_2 in the flue gas in oxy-firing do not affect the mercury chemistry. In assessing the fate of mercury and its concentration in the flue gas, however, it is important to understand the effect of potentially higher concentrations of SOx and other species as a result of the absence of nitrogen in the flue gas. The effect of air pollution control devices (e.g., SCRs, scrubbers, baghouses, ESPs, flue gas condensers) on the fate of mercury needs to be properly assessed. In addition to these factors, flue gas recirculation scheme has to be taken into account.

SCRs would not be able to remove mercury but their catalysts oxidize a significant portion of the elemental mercury in the flue gas. Scrubbers, esp., wet scrubbers, if properly designed, absorb the majority of oxidized mercury, but may also reduce some of the oxidized mercury to elemental mercury ("re-emission"). Baghouses, in the presence of unburnt carbon or sorbent, are efficient in capturing the mercury. It is postulated that the carbon in the filter cake oxidizes elemental mercury, and then captures the oxidized mercury. ESPs are not as efficient as baghouses in oxidizing mercury or removing oxidized mercury. Finally, a properly designed FGC with sufficient contact between cooling liquid and flue gas is extremely effective in removing the oxidized mercury.

Consider an oxy-fired boiler configuration where the flue gas is taken off immediately downstream of the economizer (hot recycle). In this configuration, all of the oxidized mercury in the flue gas recycled into the furnace will be reduced back to elemental mercury. Immediately downstream of the flue gas take-off point, therefore, most of the mercury will be in elemental form. Mercury

speciation and concentration can then be predicted by assessing the effect of each of the air pollution control devices downstream of the take-off point.

In case of flue gas recirculation downstream of a scrubber, the mercury leaving the furnace will be all in elemental form. Some of it will be oxidized and captured as it passes through the air heater, ESPs or baghouses. The majority of the oxidized mercury entering the scrubber will be captured in the scrubber. The level of mercury in the recycled flue gas may be less than that for the previous hot recycle case as some of it would have been captured in the scrubber. Most of the recycled mercury is, however, expected to be elemental mercury.

In oxy-firing, mercury in the flue gas leaving the boiler island has to be controlled to a very low level in order to avoid any corrosion of aluminum surfaces in the cold circuit of GPUs. The required level is on the order of a few ng/Nm^3. The control strategy in achieving this level is to oxidize mercury as much as possible so that it could be removed in the air pollution control devices and the FGC. This may require injection of halogen additives into the furnace; or sorbents designed for maximal oxidation of incoming mercury. The remainder will have to be removed in an activated carbon bed usually installed before, or as part of a GPU system.

13. Concluding Remarks

There are significant differences between air-firing and oxy-firing with gas recycle that can impact the design and operation of the nearly all boiler systems. Combustion characteristics, gas properties, thermal characteristics and emission characteristics are different during air and oxy-firing. The general design guidelines and key considerations for oxy-firing have been developed for each of the major boiler systems. Many existing design procedures developed for air-firing can be applied for oxy-firing by taking into consideration the appropriate gas properties including changes in concentrations of trace constituents. Differences in combustion and thermal characteristics can be addressed by controlled by gas recycle rate and firing system design. In general, it is not necessary to make major changes in the boiler design, its size and arrangement, and the heat transfer surfacing for an oxy-firing. Guidelines and key design considerations to address the application of oxy-combustion to pulverized coal boiler design and operation have been discussed within this report and can be used assuming knowledge and understanding of air-fired boiler design.

Recovery Act: Oxy-Combustion Technology Development for Industrial-Scale Boiler Applications

DOE/NETL Cooperative Agreement No. DE-NT0005290

Volume IV – Reference Oxy Boiler Designs

Chapter 2 – Design, Performance, and Cost of 450MWe Demonstration, 900MWe Commercial, and Industrial Boilers

Authors
Glen D. Jukkola
Greg N. Liljedahl
Bhaumik Parikh
Wei D. Zhang

Abstract

Alstom Power Inc. is actively developing clean coal technologies which will enable the continued use of our nation's abundant coal reserves while contributing to domestic economic and energy security. Oxy-combustion is a promising CCS technology that has been under development for many years and is now ready for large scale demonstration. The objective of this study was to assess the design modifications and costs associated with applying oxy-combustion technology to coal-fired utility-scale power plants and to an industrial scale coal-fired steam plant.

Four utility scale power plants were designed and their costs developed under this study. A $450MW_{gross}$ oxy-fired SCPC plant was designed as representative of a demonstration plant for oxy-combustion technology. This was contrasted with a $450MW_{gross}$ air-fired SCPC plant. Similarly, a $900MW_{gross}$ oxy-fired SCPC plant was designed and costs were developed as representative of a first generation oxy-combustion commercial plant. A $900MW_{gross}$ air-fired plant was also included for comparison.

Finally, this study included an evaluation of the design modifications and costs necessary to retrofit an existing air-fired industrial steam plant equivalent to $150MW_{gross}$ to oxy-combustion. The design study focused on the necessary boiler modifications for this conversion, although the major cost items associated with the addition of an Air Separation Unit (ASU) and Gas Processing Unit (GPU) for the final CO_2 purification and compression were also considered.

Table of Contents

Table of Contents iii
List of Figures viii
List of Tables x
List of Acronyms xii
1. EXECUTIVE SUMMARY 1
1.1 Background 1
1.1 Equipment Design 2
1.2 Performance 4
1.2.1 Power Output 4
1.2.2 Net Plant Efficiency 7
1.3 Cost Results 9
1.3.1 Total Overnight Cost 9
1.3.2 Cost of Electricity (COE) 12
1.3.3 Variable Cost of Generation 18
1.3.4 Cost of CO_2 Avoided/Captured 20
1.4 Environmental Performance 21
1.4.1 CO_2 Emissions 21
1.4.2 Non-CO_2 Emissions 22
1.5 Sensitivity Study of FGR Location 23
1.6 Summary 25
2. Introduction 28
3. DESIGN AND EVALUATION BASIS 29
3.1 Site Description 29
3.2 Coal Characteristics 30
3.3 Limestone and Lime Characteristics 31
3.4 Environmental Targets 32
3.5 CO_2 Sequestration and CO_2 Purity 34
3.6 Plant Capacity Factor 36
3.7 Steam Conditions 37
3.8 Balance of Plant Assumptions 37
3.9 Cost Estimating Methodology 39
3.9.1 Capital Costs 39

3.9.2 Home Office, Process, and Project Contingencies 44
3.9.3 Estimation of Owner's Costs 45
3.9.4 Operations and Maintenance Costs 47
3.10 Economic Assumptions 48
3.10.1 Financial Structure Selection 48
3.10.2 Global Economic Assumptions 48
3.11 Cost of Electricity 50
3.12 Costs of CO_2 Captured (Removed) and Avoided 51
3.13 Costs of CO_2 Transport and Storage 52
3.14 Incremental Cost of Steam 52
4. Oxy-Fired Demonstration Unit Design and Costs (450MW) 53
4.1 Boiler Description (450MW) 53
4.2 Oxygen Firing Process Considerations 54
4.3 Steam Generator Design 59
4.3.1 Furnace 59
4.3.2 Economizer 61
4.3.3 Superheater and Reheater 61
4.3.4 Steam Temperature Control 62
4.3.5 Start-Up System 63
4.3.6 Mechanical Design Aspects 64
4.3.7 Boiler Pressure Parts 64
4.3.8 Boiler Steel Structure 65
4.3.9 Sootblower System 66
4.3.10 Coal Feeders 68
4.3.11 Coal Pulverizers 69
4.3.12 Firing System 70
4.3.13 Boiler Protection Burner Management System 80
4.3.14 Air/Oxidant and Flue Gas Systems 80
4.3.15 Ljungstrom® Regenerative Air/Oxidant Preheater 87
4.3.16 SCR System 93
4.3.17 SO_3 Removal System 96
4.3.18 Bottom Ash System 97
4.4 BOP Equipment (common to 450MW and 900MW) 97
4.4.1 Air Separation Unit (ASU) 97

4.4.2 Gas Processing Unit 99
4.4.3 Power Generation 100
4.4.4 Balance of Plant 101
4.5 Boiler General Arrangement Drawings 107
4.6 Boiler Island Process Description and Performance Data 111
4.7 450MW Plant Cost Estimating 124
4.7.1 Impact of Escalation on Cost Estimates 124
4.7.2 Total Plant and O&M Costs 124
5. Large Scale Oxy-Fired Utility Reference Unit Design and Cost (900MW) 138
5.1 Introduction 138
5.2 Oxygen Firing Process 138
5.3 Steam Generator Design 141
5.3.1 Furnace 141
5.3.2 Heating Surface Arrangement 141
5.3.3 Economizer 142
5.3.4 Superheater and Reheater 142
5.3.5 Steam Temperature Control 143
5.3.6 Start-Up System 143
5.3.7 Mechanical Design Aspects 143
5.3.8 Boiler Pressure Parts 143
5.3.9 Boiler Steel Structure 143
5.3.10 Sootblower System 143
5.3.11 Coal Feeders 145
5.3.12 Coal Pulverizers 145
5.3.13 Firing System 146
5.3.14 Air/Oxidant and Flue Gas Systems 147
5.3.15 Ljungstrom® Regenerative Air/Oxidant Preheater 149
5.3.16 SCR System 149
5.3.17 Bottom Ash System 149
5.3.18 Boiler Protection Burner Management System 149
5.3.19 Balance of Plant 149
5.3.20 Integration 149
5.4 Boiler General Arrangement Drawings 151
5.5 Boiler Island Process Description and Performance Data 154

5.6 900MW Plant Cost Estimating 165
5.6.1 Cost Adjustments 165
5.6.2 Total Plant and O&M Costs 165
6. Industrial Boiler 178
6.1 Introduction 178
6.2 Base Case Air-Fired Industrial Boiler Process Description 178
6.3 Oxygen Firing 181
6.4 Steam Generator Design 185
6.4.1 Furnace 185
6.4.2 Boiler Bank 188
6.4.3 Superheater and Desuperheater 188
6.4.4 Split Economizer 188
6.4.5 Circulation System 189
6.4.6 Tubular Heat Exchangers (Tubular Oxidant Heaters) 190
6.4.7 Mechanical Design Aspects 190
6.4.8 Boiler Pressure Parts 190
6.4.9 Boiler Steel Structure 190
6.4.10 Sootblower System 190
6.4.11 Coal Pulverizers 191
6.4.12 Coal Feeders 191
6.4.13 Firing System 191
6.4.14 Air/Oxidant and Flue Gas System 192
6.4.15 SCR System 194
6.4.16 Bottom Ash System 194
6.4.17 NID™/Baghouse 194
6.4.18 Boiler Island Performance Data 196
6.4.19 Total Industrial Boiler Capital and Operating Costs 200
7. SENSITIVITY STUDY ON FGR LOCATION 205
7.1 Boiler Efficiency 205
7.2 Case 1 - Base Case With Cold Recirculation 207
7.3 Case 2 - Warm Recirculation 207
7.4 Case 3 - Hot Recirculation Without Secondary O_2 Preheating 207
7.5 Case 4 - Hot Recirculation With Secondary O_2 Preheating 208
7.6 FGR Location Performance Summary 209

7.7 Cost Implications of FGR Location 210
8. PERFORMANCE AND COST SUMMARY 213
8.1 Performance 213
8.1.1 Power Output 213
8.1.2 Net Plant Efficiency 215
8.2 Cost Results 216
8.2.1 Total Overnight Cost 218
8.2.2 Cost of Electricity (COE) 219
8.2.3 Variable Cost of Generation 223
8.2.4 Cost of CO_2 Avoided/Captured 224
8.3 Environmental Performance 225
8.3.1 CO_2 Emissions 225
8.3.2 Non-CO_2 Emissions 226
8.4 Sensitivity Study on FGR Location 227
9. Summary 230
10. References 232

List of Figures

Figure 1-1: Simplified Process Flow Diagram for an Oxy-Fired Power Plant 1
Figure 1-2: Power Output Summary 6
Figure 1-3: Net Plant Efficiencies for all Air-Fired and Oxy-Fired Cases 8
Figure 1-4: Total Overnight Costs 12
Figure 1-5: COE and LCOE for All Cases 15
Figure 1-6: COE Breakdown by Cost Component 16
Figure 1-7: COE Sensitivity to CO_2 Allowance Price 17
Figure 1-8: COE Sensitivity to Coal Price 17
Figure 1-9: COE Sensitivity to Capacity Factor 18
Figure 1-10: Variable Cost of Generation vs. CO_2 Allowance Price 19
Figure 1-11: Cost of CO_2 Avoided and Captured 21
Figure 1-12: Summary of CO_2 Emissions for Air-Fired and Oxy-Fired Cases 22
Figure 4-1: Boiler Island Process Flow Diagram (Oxy-Fired Mode) 58
Figure 4-2: Furnace Design 60
Figure 4-3: Sectional Side View – HP Type Coal Pulverizer 69
Figure 4-4: Tangential Firing Flame Pattern 72
Figure 4-5: Typical LNTFS Tilting Tangential Windbox Arrangement 73
Figure 4-6: Lateral Heat Absorption Profile 74
Figure 4-7: Burner Tilt Impact on Fireball Position (horizontal, upward, downward) 75
Figure 4-8: Concentric Firing System 76
Figure 4-9: Stoichiometry vs. Elevation 78
Figure 4-10: Vertically and Horizontally Adjustable Air/Oxidant Nozzle 79
Figure 4-11: Example of a Static Mixer Installed in Ducting 82
Figure 4-12: Example of a Grid-Type Mixer Installed in Ducting 83
Figure 4-13: Example of CFD Simulation of Oxygen Mixing After a Grid-Type Mixer 84
Figure 4-14: Primary and Secondary Oxygen Mixer Design 85
Figure 4-15: Primary and Secondary Oxygen Mixers Arrangement 86
Figure 4-16: Ljungstrom® Quad-sector Air Preheater Vertical Shaft Arrangement 88
Figure 4-17: Duplex™ Sealing System 90
Figure 4-18: Thermal Deformations 90
Figure 4-19: Leakage Control System (LCS) 91
Figure 4-20: Pressurized Sealing and Purging System 93
Figure 4-21: SCR Process Chemistry 94
Figure 4-22: SCR System Components 95
Figure 4-23: SCR System Location 96
Figure 4-24: Typical Air Separation Process for Oxy-Firing Applications (source-Air Liquide) 98
Figure 4-25: Steam Generator General Arrangement Drawing – Side Elevation 108
Figure 4-26: Steam Generator General Arrangement Drawing – Plan View 109
Figure 4-27: Steam Generator General Arrangement Drawing – Front Elevation View 110
Figure 4-28: Simplified Process Flow Diagram – Air/Oxy-Fired Boiler (Oxygen Fired Mode) 115
Figure 4-29: Steam Turbine Heat Balance - Oxy-firing, TMCR Load 116
Figure 4-30: Simplified Process Flow Diagram – Air/Oxy-Fired Boiler (Air Fired Mode) 120
Figure 4-31: Steam Turbine Heat Balance - Air-firing, TMCR Load 121

Figure 4-32: IHS CERA Power Plant Capital Cost Index for North America Power Plants 124
Figure 5-1: Boiler Island Process Flow Diagram (Oxy-Fired Mode) 140
Figure 5-2: Heating Surface Arrangement Diagram 142
Figure 5-3: Furnace Water Lance Blower Arrangement 145
Figure 5-4: Tilting Tangential Windbox Arrangement 146
Figure 5-5: Flue Gas Heat Recovery System (HEX) 150
Figure 5-6: Steam Generator and Backend Equipment General Arrangement Drawing – Side Elevation 152
Figure 5-7: Steam Generator and Backend Equipment General Arrangement Drawing – Plan View 153
Figure 5-8: Simplified Process Flow Diagram – Air/Oxy-Fired Boiler (Oxygen Fired Mode) 157
Figure 5-9: Steam Turbine Heat Balance - Oxy-firing, 100% TMCR Load 158
Figure 5-10: Simplified Process Flow Diagram – Air-Fired Boiler 161
Figure 5-11: Steam Turbine Heat Balance - Air-firing, 100% TMCR Load 162
Figure 6-1: Industrial Boiler Island Process Flow Diagram for Air-Fired Base Case 180
Figure 6-2: Industrial Boiler Island Process Flow Diagram for Oxy-Fired PC Boiler 184
Figure 6-3: Side Elevation of Industrial Boiler 186
Figure 6-4: Plan View of Industrial Boiler 187
Figure 6-5: Alstom NID™ Concept for a Fossil Fuel Boiler Application 195
Figure 6-6: Industrial Boiler Process Flow Diagram – Oxygen Fired Mode 197
Figure 7-1: Boiler Efficiency Envelope Including Airheater 206
Figure 7-2: Boiler Efficiency Envelope Excluding Airheater 206
Figure 7-3: Warm Secondary FGR Before WFGD 207
Figure 7-4: Hot Secondary FGR Before GGH 208
Figure 7-5: Hot Secondary FGR Before GGH with Secondary O_2 Preheating 209
Figure 8-1: Power Output Summary 214
Figure 8-2: Net Plant Efficiencies for all Air-Fired and Oxy-Fired Cases 216
Figure 8-3: Total Overnight Costs 219
Figure 8-4: COE and LCOE for All Cases 220
Figure 8-5: COE Breakdown by Cost Component 221
Figure 8-6: COE Sensitivity to CO_2 Allowance Price 222
Figure 8-7: COE Sensitivity to Coal Price 222
Figure 8-8: COE Sensitivity to Capacity Factor 223
Figure 8-9: Variable Cost of Generation vs. CO_2 Allowance Price 224
Figure 8-10: CO_2 Avoided and Capture Costs 225
Figure 8-11: Summary of CO_2 Emissions for Air-Fired and Oxy-Fired Cases 226

List of Tables

Table 1-1: Summary of Case Configurations 2
Table 1-2: Summary of Thermal Performance and Auxiliary Loads 7
Table 1-3: Total Overnight and Total As Spent Capital Costs 11
Table 1-4: Summary of Emissions for all Air-Fired and Oxy-Fired Cases 23
Table 1-5: Cost Implications of FGR Location 24
Table 2-1: Summary of Case Configurations 28
Table 3-1: Site Characteristics 29
Table 3-2: Site Ambient Conditions 30
Table 3-3: Coal Proximate and Ultimate Analyses 30
Table 3-4: Other Coal Properties 31
Table 3-5: Greer Limestone Analysis 32
Table 3-6: Lime Analysis 32
Table 3-7: Environmental Targets for Oxy-Fired and Air-Fired PCs 34
Table 3-8: CO_2 Stream Compositions Recommended Limits 35
Table 3-9: Steam Cycle Conditions 37
Table 3-10: Balance of Plant Assumptions 38
Table 3-11: Cost Estimate Basis for Oxy-PC Plant Equipment 40
Table 3-12: Estimation Method for Owner's Costs 45
Table 3-13: Financial Structure for Investor Owned Utility High and Low Risk Projects 48
Table 3-14: Global Economic Assumptions 49
Table 4-1: GGH Leakage Levels 92
Table 4-2: Gas Side Material & Energy Balance (Oxy Firing, BMCR, High Sulfur Eastern Bituminous Coal) 117
Table 4-3: Gas Side Material & Energy Balance (Air Firing, BMCR, High Sulfur Eastern Bituminous Coal) 122
Table 4-4: Summary of Thermal Performance and Auxiliary Loads 123
Table 4-5: Capital Costs for 450MW Air-Fired Plant 126
Table 4-6: Capital Costs for 450MW Oxy-Fired Plant 131
Table 4-7: O&M Costs for 450MW_{gross} Air-Fired PC Steam Plant 136
Table 4-8: O&M Costs for 450MW_{gross} Oxy-Fired PC Steam Plant 137
Table 5-1: Material & Energy Balance - Oxy Firing 100% BMCR Loads 159
Table 5-2: Material & Energy Balance - Air Firing 100% BMCR Loads 163
Table 5-3: Summary of Thermal Performance and Auxiliary Loads 164
Table 5-4: Capital Costs for 900MW Air-Fired Plant 166
Table 5-5: Capital Costs for 900MW Oxy-Fired Plant 171
Table 5-6: O&M Costs for 900MW_{gross} Air-Fired PC Steam Plant 176
Table 5-7: O&M Costs for 900MW_{gross} Oxy-Fired PC Steam Plant 177
Table 6-1: Gas Side Material & Energy Balance SI Unit (Oxy Firing, BMCR) 198
Table 6-2: Gas Side Material & Energy Balance English Unit (Oxy Firing, BMCR Load) 199
Table 6-3: Incremental Capital Costs to Retrofit an Industrial Boiler to Oxy-Firing 201
Table 6-4: Incremental Auxiliary Power Requirements 201
Table 6-5: O&M Costs for Oxy-Fired Industrial Steam Plant 203
Table 6-6: Incremental Cost of Steam 204

Table 7-1: FGR Performance Characteristics 210
Table 7-2: Cost Implications of FGR Location 211
Table 8-1: Summary of Thermal Performance and Auxiliary Loads 215
Table 8-2: Total Overnight and Total As Spent Capital Costs 219
Table 8-3: Summary of Emissions for all Air-Fired and Oxy-Fired Cases 227
Table 8-4: Cost Implications of FGR Location 228

List of Acronyms

A&E	Architect and Engineers
AACE	Association for the Advancement of Cost Engineering
AFUDC	Allowance for Funds Used During Construction
AH	Air Heater
AISE	American Institute of Steel Construction
ASME	American Society for Mechanical Engineers
ASU	Air Separation Unit
A-USC	Advanced Ultrasupercritical
BACT	Best Available Control Technology
BEC	Bare Erected Costs
BFW	Boiler Feed Water
BMCR	Boiler Maximum Continuous Rating
BOP	Balance of Plant
BPS/BMS	Boiler Protection and Burner Management System
BSF	Boiler Simulation Facility
CCF	Capital Charge Factor
CCOFA	Close Coupled Overfire Air
CCS	Carbon Capture and Storage
CF	Capacity Factor
CFD	Computational Fluid Dynamics
CFS	Concentric Firing
COE	Cost of Electricity
CV	Coefficient of Variation
DCC	Direct Contact Condenser
DCS	Distributed Control System
DOE	Department of Energy
EOR	Enhanced Oil Recovery
EPA	Environmental Protection Agency
EPC	Engineering Procurement and Construction
EPCM	Engineering, Procurement, and Construction Management
EPRI	Electric Power Research Institute
FD	Forced Draft
FF	Fabric Filter
FGC	Flue Gas Condenser
FGD	Flue Gas Desulfurization
FGHR	Flue Gas Heat Recovery
FGR	Flue Gas Recirculation
FRP	Fiber Glass Reinforced Plastic
FW	Feed Water

GGH	Gas-Gas Heater
GJ	GigaJoule
GPU	Gas Processing Unit
HEA	High Energy Arc
HEX	Flue Gas Heat Exchanger
HGI	Hardgrove Grindability Index
HHV	Higher Heating Value
HP	High Pressure
I&C	Instrumentation & Controls
ID	Inner Diameter or Identified
IHS CERA	Cambridge Energy Research Associates
in Hg	Inches of Mercury
in w.g.	Inches of Water Gauge
IOU	Investor Owned Utility
IP	Intermediate Pressure
LCOE	Levelized Cost of Electricity
LCS	Leakage Control System
LHV	Lower Heating Value
LMTD	Log Mean Temperature Difference
LNB	Low NO_x Burner
LNTFS	Low NO_x Tangential Firing System
LP	Low Pressure
MCR	Maximum Continuous Rating
MM	Million
MPa	Megapascal unit of pressure
MW_e	MegaWatt Electrical
MW_{th}	MegaWatt Thermal
NEMA	National Electrical Manufacturers Association
NEPA	National Environmental Protection Act
NETL	National Energy Technology Laboratories
NFPA	National Fire Protection Association
NID™	Alstom's Novel Integrated Desulfurization Process
NSPS	New Source Performance Standards
O&M	Operations & Maintenance
O.J.	Operating Job
OC_{FIX}	Annual Fixed Operating Cost
OC_{VAR}	Annual Variable Operating Cost
OFA	Over-fire Air
Oxy	Oxygen-Fired
P&ID	Piping and Instrumentation Diagram

PA	Primary Air
PC	Pulverized Coal
PCCI	Power Capital Cost Index
PPS	Polyphenylensulfide
PPSL	Pressure part Support Level
PSFM	Power Systems Financial Model
PTFE	Polytetrafluorethylene
RFG	Recirculated Flue Gas
RH	Reheater
SC	Supercritical
SCAH	Steam Coil Air Heater
SCAPH	Steam Coal Air Pre-Heater
SCF	Standard Cubic Feet
SCOPH	Steam Coal Oxygen Pre-Heater
SCPC	Supercritical Pulverized Coal
SCR	Selective Catalytic Reduction process
SH	Superheater
SOFA	Separated Overfire Air
SPSC	Sliding Pressure Supercritical
SS	Stainless Steel
SSC	Submerged Scraper Conveyor
T	Trillion
T&S	Transport and Storage
TAG	Technical Assessment Guide
TASC	Total As-Spent Capital Costs
TFS	Tangential Firing System
TH	Tubular Heater
TMCR	Turbine maximum Continuous Rating
TOC	Total Overnight Capital Costs
Ton	2,000 pounds
Tonne	1,000 kilograms
TPC	Total Plant Costs
TPD	Tons Per Day
TPH	Tons Per Hour
USC	Ultra-Supercritical Steam Condition
WFGD	Wet Flue Gas Desulfurization

1. EXECUTIVE SUMMARY

1.1 Background

The objective of this design effort was to assess the modifications and costs associated with applying oxy-combustion technology to coal-fired utility-scale power plants and to an industrial scale coal-fired steam plant.

Four commercial scale power plants were designed and their costs developed under this work. A 450MW$_{gross}$ oxy-fired SCPC plant was designed as representative of a demonstration plant for oxy-combustion technology. Figure 1-1 shows a simplified process flow diagram for the 450MW oxy-fired power plant. This was contrasted with a 450MW$_{gross}$ air-fired SCPC plant. Similarly, a 900MW$_{gross}$ oxy-fired SCPC plant was designed and costs were developed as representative of a first generation oxy-combustion commercial plant. A 900MW$_{gross}$ air-fired plant was also included for comparison.

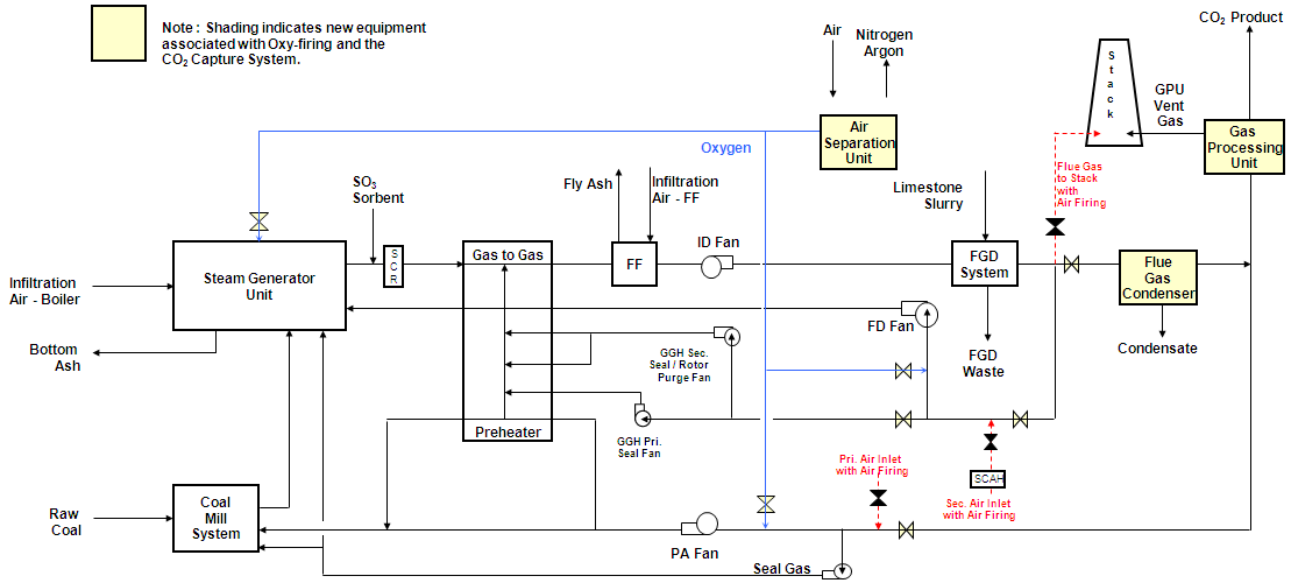

Figure 1-1: Simplified Process Flow Diagram for an Oxy-Fired Power Plant

Finally, this study included an evaluation of the design modifications and costs necessary to retrofit an existing air-fired industrial steam plant equivalent to 150MW$_{gross}$ to oxy-combustion. The design study focused on the necessary boiler modifications for this conversion, although the major cost items associated with the addition of an Air Separation Unit (ASU) and Gas Processing Unit (GPU) for the final CO_2 purification and compression were also considered.

Table 1-1 summarizes the five case configurations considered in this study.

Table 1-1: Summary of Case Configurations

Unit Cycle	Steam Cycle, psig/°F/°F	Boiler Technology	Steam Flow Rate lb/hr	Sulfur Removal	CO_2 Separation
450MW Air-Fired PC w/o CCS	3930/1116/1148	2-Pass Supercritical PC	2,811,000	Wet FGD, Gypsum	N/A
450MW Oxy-Fired PC	3930/1116/1148	2-Pass Supercritical PC	2,811,000	Wet FGD, Gypsum	GPU
900MW Air-Fired PC w/o CCS	3930/1116/1148	Tower Supercritical PC	5,703,000	Wet FGD, Gypsum	N/A
900MW Oxy-Fired PC	3930/1116/1148	Tower Supercritical PC	5,703,000	Wet FGD, Gypsum	GPU
Oxy-Fired Industrial Boiler	1175/1000	Industrial Boiler	980,000	NID™	GPU

Legend:
PC - Pulverized Coal
CCS - Carbon Capture and Storage
FGD - Flue Gas Desulfurization
GPU - Gas Processing Unit
NID™ - Alstom Dry FGD System

1.1 Equipment Design

A $450MW_{gross}$ oxy-fired SCPC plant was designed as representative of a demonstration plant for oxy-combustion technology. The boiler is designed for pulverized coal-firing with a nominal gross capacity of approximately 450 MW_e. It is designed for full load capability using either air or oxygen as the oxidant for combustion of the fuel. The boiler is a sliding pressure supercritical (SPSC), once-through design, utilizing a TFS 2000™ firing system and SCR for NO_X control. It is a single reheat unit designed for variable pressure operation, with a balanced draft furnace. The unit is capable of firing a range of pulverized coals, producing continuous steam flow to the turbine generator with nominal boiler maximum continuous rating (BMCR) outlet conditions of 2,550,680 lbm/hr (321.4 kg/s), 3,927 psig (270.8 bar), 1,117°F (602.5°C) at the superheater outlet, and 2,103,530 lbm/hr (265.0 kg/s), 726 psig (50.1 bar), 1,148°F (620.4°C) at the reheater outlet. Heavy fuel oil is used for start-up and as a support fuel during low load operation.

A $900MW_{gross}$ oxy-fired SCPC plant was designed and costs were developed as representative of a first generation oxy-combustion commercial plant. The boiler is a pulverized coal-fired unit, with a nominal capacity of approximately 900 $MW_{e\text{-}gross}$. It is designed for full load capability (100% TMCR) with oxygen firing and is limited to about 75% TMCR with air firing. It is a sliding pressure, supercritical, once-through design, utilizing a low-NO_x tangential firing system and SCR for NO_X control during air firing. It is a single reheat unit designed for variable pressure operation with a balanced draft furnace. The unit is capable of firing a range of pulverized coals and producing a continuous flow of steam to the turbine generator with nominal

boiler outlet conditions of 5,174,600 lbm/hr (652 kg/s), 4,130 psig (284.8 bar), 1,117°F (603°C) at the superheater outlet, and 4,280,100 lbm/hr (539.4 kg/s), 863 psig (59.5 bar), 1,150°F (621°C) at the reheater outlet. Light fuel oil is used for start-up and as a support fuel for low load operation. A $900MW_{gross}$ air-fired plant designed for the same steam conditions was also included for comparison.

This work also included an evaluation of the design modifications and costs necessary to retrofit an existing air-fired industrial steam plant equivalent to $150MW_{gross}$ to oxy-combustion. The base case air-fired industrial boiler is a coal-fired unit, with a nominal capacity of about 980,000 lbm/hr of superheated steam flow. It was retrofitted to operate at full load capability using recirculated flue gas as the oxidant for combustion of the fuel. The retrofit unit operates with base case TFS (Tangential Firing System) system, SCR for NO_x control, NID™ dry scrubber system for SO_2 and fly ash control, and two gas-to-gas tubular heaters (GGH). The retrofit unit is capable of firing the design pulverized coal, producing continuous steam flow at nominal boiler outlet conditions of 123.6 kg/s (980,000 lbm/hr), 108.5 bar (1600 psig), 538°C (1,000°F) at the superheater outlet. Heavy fuel oil is used for start-up.

Oxygen Firing Process Considerations

The approach taken to design a boiler capable of oxy-firing combustion was essentially the same for all oxy-fired cases in this study. Oxy-fired combustion replaces combustion air with a mixture of nearly pure oxygen and recycled flue gas. The resulting flue gas – primarily CO_2 and H_2O vapor along with some N_2, O_2, and trace gases like SO_2 and NO_x – is then dried, compressed, and purified for sequestration, or used for enhanced oil or gas recovery.

The primary impacts of oxy-firing on the boiler design are associated with the potentially reduced combustion gas flow due to the removal of nitrogen (present with air firing) and the differences in the thermal and radiant properties of the flue gas. Burning coal with pure oxygen would result in excessive furnace temperatures causing ash slagging issues, corrosion issues, fine ash aerosols, and damage to boiler waterwalls if steam-side circulation is insufficient. Recycling a portion of the flue gas can compensate for these impacts. Thus, the furnace temperature can be maintained low enough to avoid ash slagging, fouling and corrosion, and the heat flux to furnace walls can be maintained within the limits imposed to prevent overheating of the tubes.

The location of the flue gas recirculation take-off can have a significant impact on the design and operation of the boiler and ancillary equipment. As gas recycle is taken closer to the boiler outlet, more of the downstream equipment can be reduced in size and cost. However, the concentration of impurities returned to the boiler increases as the gas recycle takeoff point approaches the boiler outlet, which impacts ash deposition, corrosion and pollutant levels, and must be addressed in the boiler design. Trade-offs between boiler impacts and downstream equipment savings are generally controlled by fuel characteristics and site-specific factors.

The basic concept entails:

- Use oxygen instead of air for the combustion process in order to obtain a CO_2 rich flue gas mainly composed of CO_2 and H_2O (and some inert gases) "easily" cleaned and compressed
- Obtain the adequate purity of CO_2 in the flue gas in order to reach a composition suitable for transport under supercritical phase and then storage

This leads to the addition of two units to the conventional coal fired power plant:

- Air Separation Unit (ASU): An oxygen production unit
- Gas Processing Unit (GPU): A CO_2 purification unit to clean and compress under supercritical state the remaining CO_2 out of flue gas

In addition, some modifications of the power plant itself are necessary, mainly:

- Partial recirculation of the flue gas in order to maintain appropriate temperature and heat absorption in the furnace and convection pass
- Removal of the water from the flue gas before treatment in the GPU: Flue Gas Condenser
- Minimisation of leakage of air into the boiler
- Sizing of equipment, taking into account the additional needs of the ASU and GPU (mainly electrical energy, water…)
- Injection/Mixing of oxygen in the flue gas path

The basic oxy-firing concept uses a mixture of oxygen and recirculated flue gas as an oxidant to replace combustion air. Oxy-coal combustion produces a flue gas stream comprising mainly CO_2 and water vapor with much smaller amounts of oxygen, nitrogen, argon, sulfur dioxide, etc. The flue gas leaving the boiler is cooled and cleaned of ash and sulfur compounds in traditional boiler island equipment. It is then dried, compressed, and purified into a CO_2 product stream in the Gas Processing Unit (GPU). It can then be available as a product for usage or for sequestration. Some of the flue gas produced is recirculated and mixed with relatively pure oxygen to form the oxidant streams for combustion of the coal in the furnace as described below.

1.2 Performance

1.2.1 Power Output

Figure 1-2 summarizes the net power and auxiliary power requirements for the air and oxy-fired cases at 450MW and 900MW. The gross plant outputs (sum of net power and auxiliary power) for the 450MW air and oxy-fired cases were kept identical to each other. The same approach was applied for the 900MW cases. The net power varied for each 450MW and 900MW depending upon the total auxiliary power requirements for each case. This is different from the approach

used in the DOE Baseline Reports[1,2], where the SCPC w/o CCS and oxy-fired cases had a constant 550MW_{net} output, while the gross MW varied.

This difference in design approaches taken for the DOE cases required that the boiler size be increased for the oxy-fired case as the auxiliary power consumption increased considerably and the firing rate had to be increased. For the 450MW and 900MW cases under this study, the gross power output was fixed and the net power output was allowed to vary. Since the fuel firing rate remained constant, the boiler size remained essentially the same. Thus, the focus was on identifying the design changes and costs associated with redesigning an air-fired boiler for oxy-firing, rather than also accounting for an increased size boiler.

The auxiliary power requirements for all of the air-fired cases ranged from 5.0-5.2% of the gross power output. The auxiliary power requirement for the 450MW oxy-fired plant was 27.8% of the gross power output. This value decreased to 26.4% for the 900MW oxy-fired plant due to the improved thermal efficiency from integration of the ASU, GPU, and FGHR system. Although not shown here, the DOE Case 5C oxy-fired plant had an auxiliary power requirement of 30.2% of the gross power output. This is because this plant had a less efficient steam cycle than either the 450MW or 900MW plants in this study and did not have any integration.

Table 1-2 summarizes the performance results and auxiliary power requirements for the air and oxy-fired cases at 450MW and 900MW. The largest auxiliary power load for the oxy-fired cases was the ASU, which ranged from 64,550kW to 117,914kW for the 450MW and 900MW oxy-fired plants, respectively. The next largest auxiliary power load for the oxy-fired cases was the GPU CO_2 compressor, which was 37,683kW and 73,071kW for the 450MW and 900MW oxy-fired plants, respectively. In comparison, the boiler island auxiliary power decreased slightly to 22,647kW and 44,400kW for the 450MW and 900MW oxy-fired plants corresponding to a 3.7% and 0.5% decrease from air-firing. This is due to the higher gas density and lower volumetric gas flow rates in oxy-fired mode that resulted in reduced ID fan power consumptions.

The largest impact of the air-fired industrial steam plant retrofit to oxy-fired capability was the addition of the power intensive ASU and GPU. The ASU requires an additional 24.3MW and the GPU adds 14.1MW of auxiliary power. Since it was assumed that the power necessary to drive this equipment would be taken off the grid, the industrial boiler was therefore able to maintain its steam capacity output. It was also assumed that changes in the auxiliary power requirements for the remaining boiler and steam plant equipment were minor and could be ignored.

[1] Cost and Performance Baseline for Fossil Energy Plants Volume 1, DOE/NETL-2010/1397, November 2010
[2] Pulverized Coal Oxycombustion Power Plants Volume 1, DOE/NETL-2007/1291, August 2008

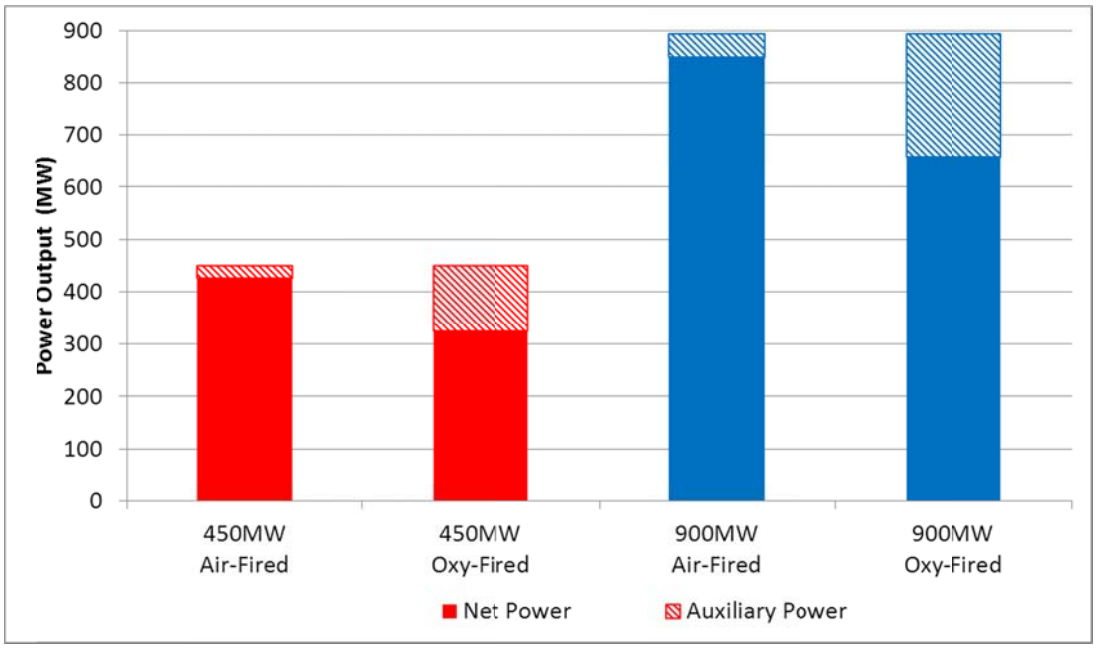

Figure 1-2: Power Output Summary

Table 1-2: Summary of Thermal Performance and Auxiliary Loads

		450MW	450MW	900MW	900MW
		Air-Fired	Oxy-Fired	Air-Fired	Oxy-Fired
Gross Power Output	MW	450.0	450.0	893.3	893.3
Net Power Output	MW	426.5	325.1	848.7	657.9
Coal Flow	lb/hr	295,086	296,543	598,606	601,529
Main Steam Flow	lb/hr	2,508,000	2,508,000	5,162,812	5,174,717
Fuel Heat Input (HHV)	MMBtu/	3,277	3,293	6,412	6,444
Net Plant Efficiency (HHV)	%	40.9%	31.5%	41.3%	32.5%
Boiler Efficiency	%	88.8%	88.8%	88.8%	88.8%

Auxiliary Load Summary

		450MW	450MW	900MW	900MW
		Air-Fired	Oxy-Fired	Air-Fired	Oxy-Fired
Coal Handling & Pulverizers	kW	2,319	2,331	4,705	4,728
Forced Draft Fans	kW	1,192	1,198	2,418	2,430
Primary Air Fans	kW	939	944	1,905	1,915
Induced Draft Fans	kW	5,423	4,413	11,001	10,811
SCR	kW	150	-	150	-
FF	kW	53	51	107	106
Wet FGD	kW	2,239	2,277	4,542	4,463
Power Plant Auxiliaries	kW	11,200	11,434	19,782	19,948
ASU Compressor/Auxiliaries	kW	-	64,550	-	117,914
GPU CO2 Compressor	kW	-	37,683	-	73,071
		-	-	-	-
Total Aux Power	kW	23,516	124,880	44,611	235,385
% Aux Power		5.2%	27.8%	5.0%	26.4%

1.2.2 Net Plant Efficiency

The net plant efficiency results in Table 1-2 are graphically presented in Figure 1-3. The net plant efficiency for the 450MW and 900MW air-fired cases are both about 41% HHV. This relatively high efficiency is attributed to the current state-of-the-art advanced steam conditions and efficient steam cycle arrangement. The net plant efficiency for the 450MW oxy-fired plant decreased by 9.4% points as compared to the 450MW air-fired case. This reduction is due to the increased auxiliary power requirements for the ASU and GPU. The net plant efficiency for the 900MW oxy-fired plant decreased by 8.8% points as compared to the 900MW air-fired case. The net plant efficiency for the 900MW oxy-fired plant was 0.6% points higher than the efficiency for the 450MW oxy-fired plant. This improvement is primarily due to the thermal integration of the ASU, GPU, and FGHR system. Further improvements can be expected in second generation

oxy-fired plants with more thermal integration and advances in ASU and GPU designs that reduce their power requirements.

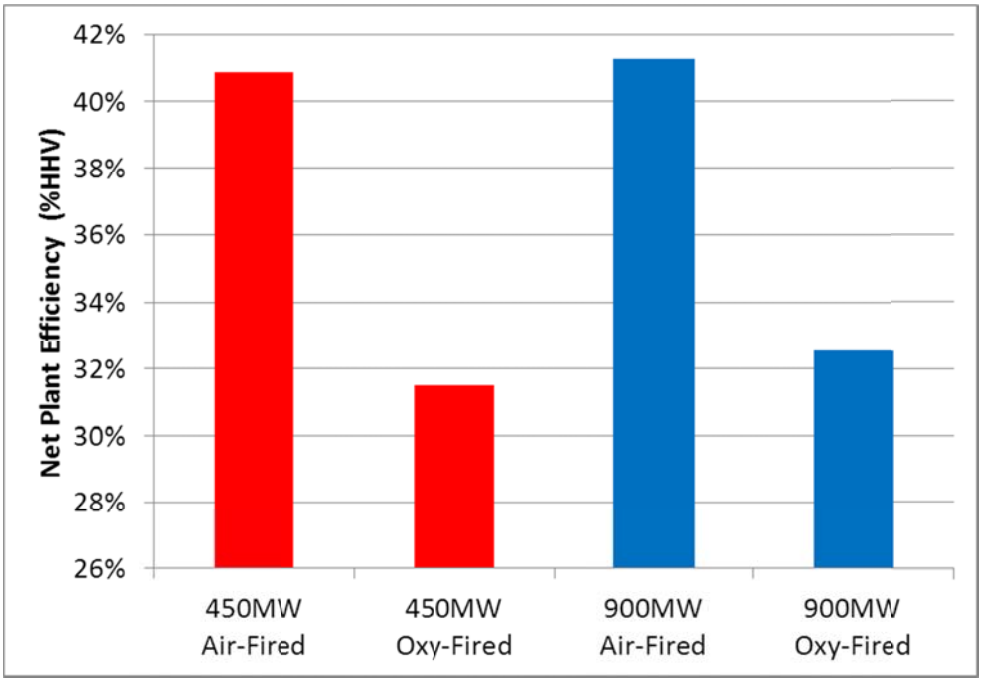

Figure 1-3: Net Plant Efficiencies for all Air-Fired and Oxy-Fired Cases

The energy penalty for the 450MW oxy-fired power plant (relative to the 450MW air-fired plant without CO_2 capture) is 23.0%. The energy penalty for the 900MW oxy-fired power plant (relative to the 900MW air-fired plant) decreased slightly to 21.3%. The Energy Penalty is defined here as:

$$\%\ \text{Energy Penalty} = \frac{-[\text{net plant efficiency(oxy-fired SCPC)} - \text{net plant efficiency(SCPC w/o CCS)}]}{\text{net plant efficiency(SCPC w/o CCS)}}$$

1.3 Cost Results

1.3.1 Total Overnight Cost

The capital costs for the 450MW and 900MW air-fired and oxy-fired plants and for the industrial steam plant retrofit to oxy-combustion were developed using the methodology described in the DOE's Cost Estimation Methodology guide.[3]

- Bare Erected Costs (BEC) were developed for all process equipment, facilities, and infrastructure – including materials and erection labor.
- Total Plant Costs (TPC) were developed by adding the cost of services by the engineering, procurement, and construction (EPC) contractor, along with process and project contingencies.
- The TPC is an overnight cost and is expressed in base year dollars (June 2011 dollars).
- Total Overnight Capital Cost (TOC) includes the TPC plus all other overnight costs, including owner's costs.
- The Total As-Spent Capital Costs (TASC) includes all capital expenditures during the capital expenditure period including their escalation and interest during construction. It is expressed in mixed, current-year dollars over the capital expenditure period.

Process contingencies were applied to selected capital cost estimates in the Total Plant Costs to compensate for performance uncertainties associated with the developmental status of the oxy-combustion technology. A 20% process contingency was applied to boiler island process area modifications associated with oxy-combustion that have not been demonstrated commercially and were thus designed using experimental data such as from Alstom's 15MW_{th} Boiler Simulation Facility. Process contingencies were applied to the following boiler equipment areas:

- Windbox and firing system modifications
- Ductwork modifications associated with oxy-firing
- Dampers and controls associated with oxy-firing

No process contingencies were taken for the ASU or GPU systems, consistent with the approach taken by the DOE for Case 5C and other DOE oxy-combustion cases.

The DOE developed detailed capital cost estimates of the Case 11 SCPC plant that are the basis for the many of the cost estimates for equipment outside of the boiler island used for the 450MW

[3] Cost Estimation Methodology for NETL Assessments of Power Plant Performance, NETL Quality Guidelines for Energy System Studies, DOE/NETL-2-11/1455, April 2011

and 900MW power plants in this study. The DOE subsequently updated the costs for this case to June 2011 dollars.[4] These updated costs were used in this study as a reference base and were adjusted by capacity factoring using the scaling parameters prescribed by the DOE[5] for those subsystems and components common to the 450MW and 900MW plants. Specifications for those components unique to these plants were based on heat and material balances. Costs were then developed by in-house cost-estimating, vendor quotes, or from quotes for similar equipment that were then adjusted for capacity and flow conditions. Costs for the major components included all items necessary to develop a complete cost, including items such as pressure parts, refractory, insulation, structural steel, casing, expansion joints, etc.

Table 1-3 summarizes the Total Overnight Costs (TOC) and the Total As Spent Capital Costs (TASC) for the 450MW and 900MW cases, without and with CCS. Also shown are the incremental capital costs to retrofit the $150MW_{gross}$ air-fired industrial steam plant to oxy-fired capability. All costs are based on June 2011 dollars. Figure 1-4 shows the Total Overnight Costs on a $/kW basis for the 450MW and 900MW cases. The following observations can be drawn from this study related to capital costs:

- The capital costs of these plants can't be compared directly since they are all designed with different net outputs. Normalizing the costs on a $/kW basis allows plants of different capacities to be fairly compared. On a $/kW basis, the total overnight capital cost for the 450MW oxy-fired plant increased by 78.1% relative to air-fired plant. The TOC cost increase for the 900MW oxy-fired plant was 78.5%. The added cost of integration of the ASU, GPU and FGHR for the 900MW offset some of specific cost decrease due to both scaleability and technology maturity (commercial vs. demonstration plant).
- Most of the capital cost increase for the oxy-fired plants and for the industrial steam plant retrofit is due to the addition of the ASU and GPU systems.
- The 450MW and 900MW boiler bare erected costs (materials and erection only) also increased by about 11% for the oxy-fired cases as compared to the air-fired cases. This increase accounts for the changes necessary to make the boiler oxy-capable, such as the addition of the flue gas recirculation system ducting, oxygen mixers, and windbox modifications.
- The Total As Spent Capital (TASC) shown in Table 1-3 can be derived by multiplying the Total Overnight Costs for the air-fired plants by a 1.134 factor (for low risk investor

[4] Updated Costs (June 2011 Basis) for Selection Bituminous Baseline Cases, DOE/NETL-341/082312, August 2012
[5] Capital Cost Scaling Methodology, Quality Guidelines for Energy System Studies, DOE/NETL-341/013113, January 2013

owned utilities) and by a 1.140 factor (for high risk investor owned utilities). The TASC includes all capital expenditures during the capital expenditure period including escalation and interest during construction. It is expressed in mixed, current-year dollars over the capital expenditure period.

- The incremental Total Overnight Capital Costs to retrofit a $150MW_{gross}$ air-fired industrial boiler to oxy-fired capability is approximately $200 million. The cost of the boiler modifications are relatively modest at only 7% of the total capital cost. About 34% of the boiler cost is to modify the windbox assembly and firing system. Another 25% of the boiler cost is to modify the ductwork system (FGR ducts, duct insulation, O_2 mixers, supports, and hangers). The remaining 41% of the boiler cost covers the necessary dampers, control valves, O_2 analyzer, flow elements, and instrumentation. The majority of the retrofit capital cost is for the addition of the ASU and GPU. The ASU is 58% of the total retrofit cost while the GPU is 35% of the total retrofit cost.

Table 1-3: Total Overnight and Total As Spent Capital Costs

Case	Total Overnight Cost		Total As Spent Capital	
	1000$	$/kW	1000$	$/kW
450MW Air-Fired w/o Capt	1,330,385	3119	1,508,657	3537
450MW Oxy-Fired	1,806,428	5556	2,059,328	6334
900MW Air-Fired' w/o Capt	1,780,293	2098	2,018,853	2379
900MW Oxy-Fired	2,468,813	3745	2,808,747	4269
$150MW_{gross}$ Industrial Retrofit	201,524		229,272	

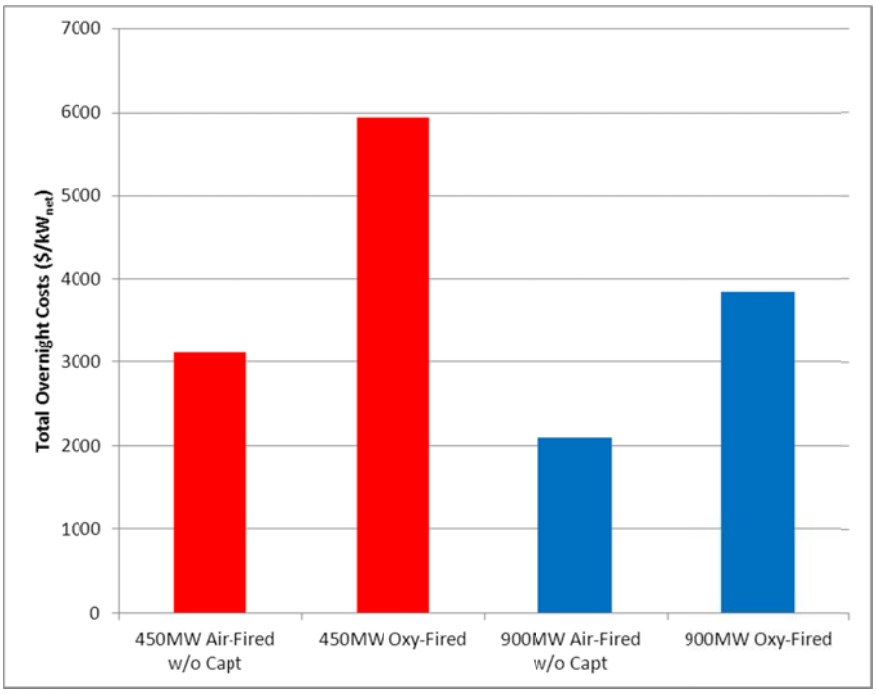

Figure 1-4: Total Overnight Costs

1.3.2 Cost of Electricity (COE)

The first year Cost of Electricity (COE) is the economic metric used in the analysis of the 450MW and 900MW power plant cases. It is the revenue received by the generator per net MWhr produced during the first year of operation assuming that the first year of operation COE escalates at a nominal annual rate equal to the general inflation rate (i.e. remains constant in real terms over the operational period of the plant). The levelized COE (LCOE) is the revenue received by the generator per net MWhr produced during the first year of operation assuming that the first year of operation COE escalates at a nominal annual rate of 0% (i.e. remains constant in nominal terms over the operation period of the plant).

The first year cost of electricity (COE) was developed using two different methodologies, consistent with the DOE guidelines.[6] The first method uses the NETL Power Systems Financial Model (PSFM). The model accepts all of the economic assumptions outlined in the DOE Cost Estimation Guidelines[7], along with specific information on the capital cost and fixed/variable

[6] Power Systems Financial Model Version 6.6 User's Guide, DOE/NETL-2011/1492, May 2011
[7] Cost Estimation Methodology for NETL Assessments of Power Plant Performance, DOE/NETL-2011/1455, April 2011

O&M costs for each case. An alternative approach is to use the simplified capital charge factor method to calculate the cost of electricity. This alternate approach is described below. Both COE methodologies provide similar results and both were used for analysis of the cases in this study.

Simplified Capital Charge Factor Methodology

A simplified method of calculating the first year cost of electricity is also provided in the DOE Financial Model User's Guide.[8] The PSFM calculates a first year capital charge factor (CCF) that can be used to calculate the COE with the simplified equation shown below. Based on the economic factors specified by the DOE, the CCF for the 450MW and 900MW air-fired power plants is 0.116 based on a Low Risk Investor Owned Utility (IOU) and five year capital expenditure period. The CCF for all of the 450MW and 900MW oxy-fired power plants is 0.124 based on a High Risk Investor Owned Utility (IOU) and five year capital expenditure period.

The simplified COE is calculated by the following equation:

$$COE = \frac{(CCF)(TOC) + OC_{FIX} + (CF)\,OC_{VAR}}{(CF)\,(MWh)}$$

where:

COE = revenue received by the generator ($/MWh) during the air-fired or oxy-fired power plant's first year of operation (expressed in 2011 dollars), assuming that the COE escalates at a nominal annual rate equal to the general inflation rate, i.e., that it remains constant in real terms over the operational period of the power plant.

CCF = is the first year Capital Charge Factor that matches the applicable finance structure and capital expenditure period

TOC = Total Overnight Capital in 2011 dollars

OC_{FIX} = the sum of all fixed annual operating costs in 2011 dollars

OC_{VAR} = the sum of all variable annual operating costs, including fuel at 100% capacity factor, in 2011 dollars

CF = plant capacity factor, assumed to be constant over the operational period

MWh = annual net megawatt-hours of power generated at 100% capacity factor

[8] Power Systems Financial Model Version 6.6 User's Guide, DOE/NETL-2011/1492, May 2011, pg. 14

Levelized COE

The Power Systems Financial Model provides the LCOE on a current dollar basis over a levelization period equal to the plants operational life – i.e., the LCOE is constant in current dollars over this period. The model provides a Levelization factor that can be multiplied by the COE to give the LCOE in base year dollars. The Levelization Factor for NETL defined economic inputs is 1.268.

Cost of CO_2 Transport and Storage

The cost of CO_2 transport and storage (T&S) needs to be included in the cost of electricity to derive the complete cost of capturing and storing CO_2. The updated DOE Baseline Report[9] specified the conditions and T&S costs to be used for DOE system studies. The costs are based on transporting high pressure (2200 psig) CO_2 from the 450MW or 900MW oxy-fired power plant through a 100km (62 mile) pipeline to the sequestration or EOR site. The CO_2 leaves the pipeline at a pressure of 1200 psig still in a supercritical state. For a Midwest plant location, the T&S value specified for DOE system studies is $10/tonne CO_2 in 2011 dollars. Note that the DOE's target of a COE Increase relative to the SCPC without CO_2 capture does not include T&S in the overall COE.

Summary of COE Results

Figure 1-5 compares the first year COE and the 30 year levelized LCOE for the 450MW and 900MW cases, without and with CCS. The COE (w/o T&S) for the 450MW oxy-fired plant increased by 72.9% relative to the 450MW air-fired plant. The COE increase for the 900MW oxy-fired plant increased by 68.5% relative to the 900MW air-fired plant. The COE increase for both oxy-fired plants is well above the DOE COE increase target of 35%, which is not surprising as these plants are first generation CCS technologies. The 450MW oxy-fired plant is a demonstration plant capable of 100% air firing capacity and has not been optimized for oxy-firing, thus accounting for the higher COE than the 900MW oxy-fired commercial plant.

Further reductions in the COE can be expected in second generation oxy-fired plants from continued reductions in the capital cost and power requirements for the ASU and GPU, along with further optimization and integration of the overall power plant.

[9] Updated Costs (June 2011 Basis) for Selection Bituminous Baseline Cases, DOE/NETL-341/082312, August 2012, pg. 5-6

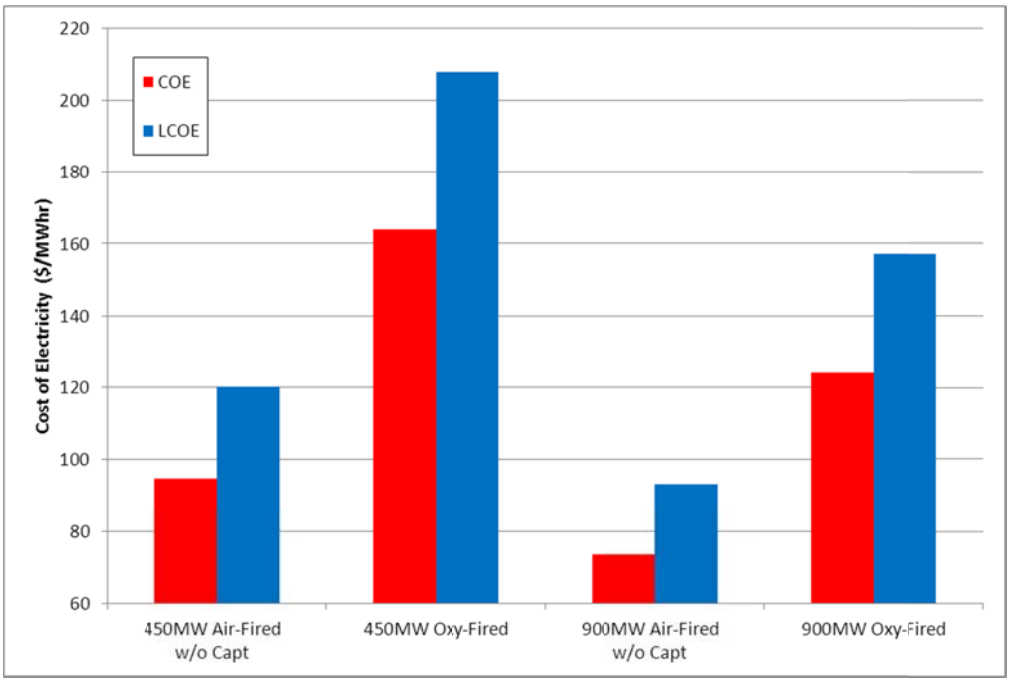

Figure 1-5: COE and LCOE for All Cases

Figure 1-6 again shows the COE for the 450MW and 900MW cases. The COE is broken down into its separate cost components of fuel, capital, fixed O&M, variable O&M, and T&S. The capital cost component shows the largest increase between the air-fired and oxy-fired cases due mostly to the additional ASU and GPU equipment. Fuel costs also increased due to the large parasitic power consumption of the ASU and GPU equipment.

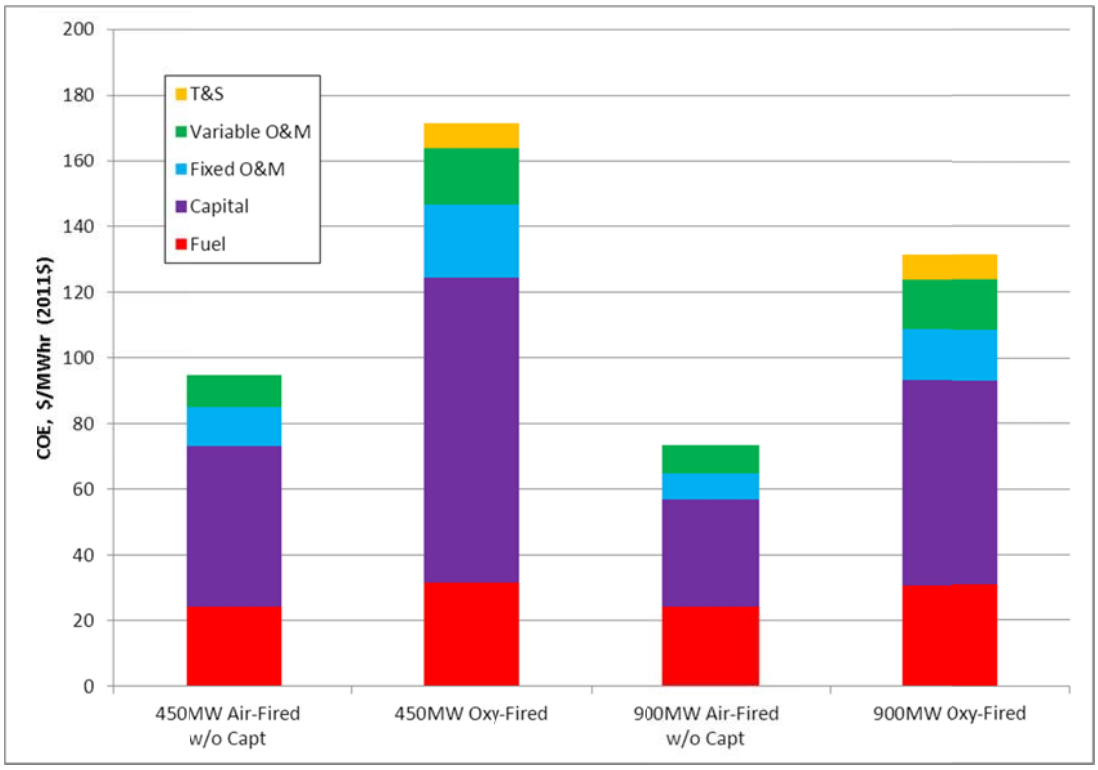

Figure 1-6: COE Breakdown by Cost Component

The economics of any technology can be heavily impacted by future legislation related to climate change. Figure 1-7 shows the COE sensitivity to a future CO_2 Allowance Price. The COE for the 450MW and 900MW oxy-fired cases show only modest COE increases since over 90% of the CO_2 is removed by the process. However, both air-fired plants without CO_2 capture show a significant increase in COE as the CO_2 Allowance Price is increased. The 900MW oxy-fired plant has economic parity (i.e. equal COEs) with the 900MW air-fired plant without CO_2 capture at a CO_2 allowance price 96 $/ton CO_2 before considering T&S costs. The 450MW oxy-fired plant has economic parity at a CO_2 allowance price of 120 $/ton CO_2

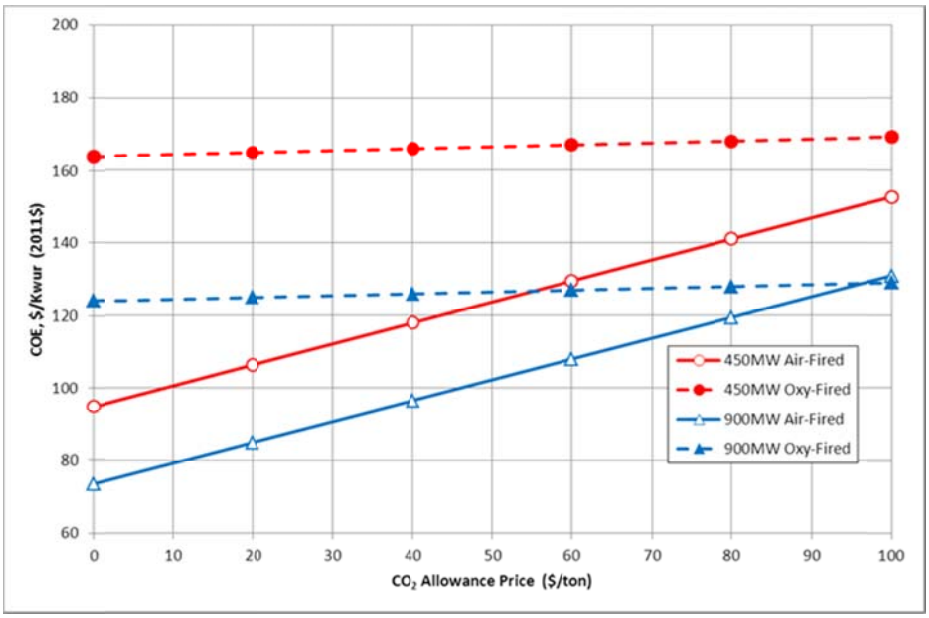

Figure 1-7: COE Sensitivity to CO_2 Allowance Price

Figure 1-8 shows the sensitivity of COE in $/MW-hr to coal price over the range from 1-5 $/MM-Btu for the 450MW and 900MW plants. The CO_2 capture plants are shown without the cost of CO_2 T&S included. Increasing fuel costs has a greater impact on the oxy-fired plants than on the air-fired plants because of its lower net plant efficiency due to the increased auxiliary power requirements of the ASU and GPU.

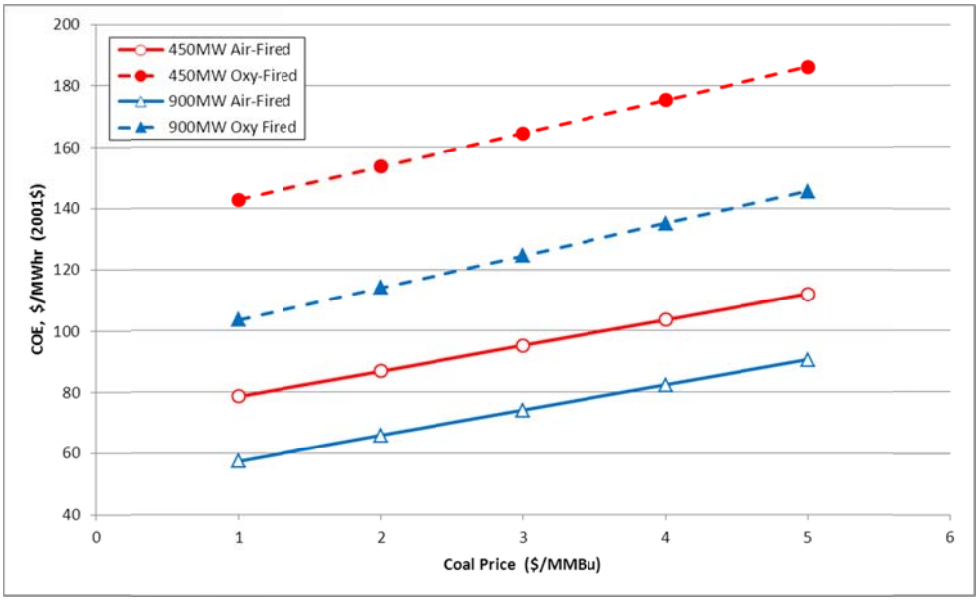

Figure 1-8: COE Sensitivity to Coal Price

Figure 1-9 shows the sensitivity of COE in $/MW-hr to capacity factor over the range from 30-90 percent for the 450MW and 900MW plants. The base capacity factor used in this study was 85 percent. All of the cases behave in a similar manner. As capacity factor is reduced, the COE increases exponentially. In general, for all of these plants as capacity factor is decreased from 90 percent to 30 percent, the COE is increased by about 250 percent.

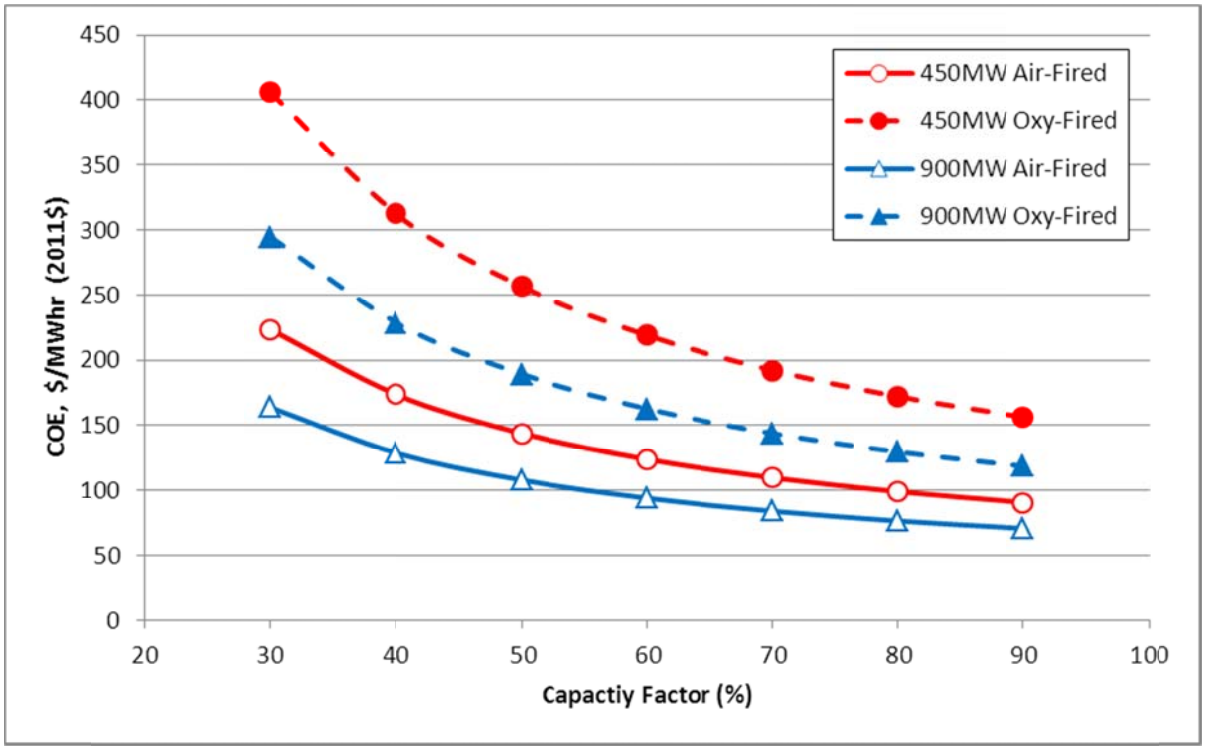

Figure 1-9: COE Sensitivity to Capacity Factor

1.3.3 Variable Cost of Generation

A key factor impacting the economics of a power generation technology is its variable cost of generation (or production cost). Technologies that have low variable costs of generation allow the units to dispatch to the highest capacity factors. It comprises those cost components that vary with the plants operation, including:

- Fuel
- Operating and maintenance
- CO_2 tax
- Transport and Storage

The fuel component depends on the cost of the fuel being consumed ($/10^6 Btu) and the efficiency of the plant (Btu/kWhr) utilizing the fuel. The operating and maintenance component includes the costs of all consumables and other variable costs, including water, sorbents, and ash disposal. The CO_2 tax component, which is not present in a non-carbon constrained world, depends on the tax level ($/Ton of CO_2 emitted), the carbon content of the fuel (lbm of carbon /10^6 Btu), and the fraction of CO_2 produced that is being captured. The transport and storage component depends upon the distance the CO_2 is being transported by pipeline and where it is being sequestered.

Figure 1-10 shows the variable cost of generation vs. the CO_2 Allowance Price for the 450MW and 900MW plants. The variable cost of generation includes all of the cost elements discussed above, including the T&S cost. With no CO_2 allowance price, the two air-fired plants without CCS (red and blue solid lines) would dispatch first. The 900MW oxy-fired plant will dispatch before the 900MW air-fired plant at CO_2 Allowance Prices above 26 $/ton. The 450MW oxy-fired plant will dispatch before the 450MW air-fired plant at CO_2 Allowance Prices above 29 $/ton CO_2.

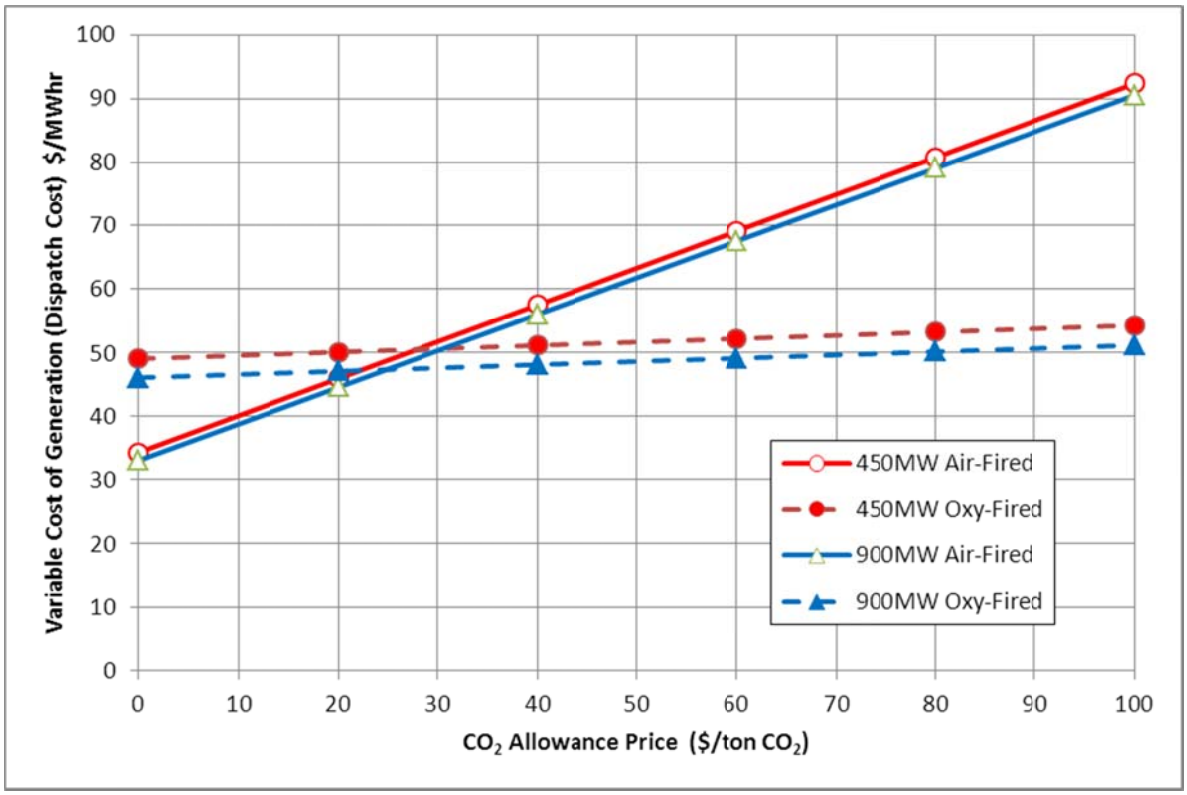

Figure 1-10: Variable Cost of Generation vs. CO_2 Allowance Price

1.3.4 Cost of CO_2 Avoided/Captured

The cost of CO_2 captured was calculated both from the standpoint of the cost of CO_2 removed and the cost of CO_2 avoided.

The Cost of CO_2 Captured or Removed is given by:

$$\text{Cost of } CO_2 \text{ Captured} = \frac{(\text{COE}_{\text{with removal}} - \text{COE}_{\text{w/o removal}})}{(CO_2 \text{ Captured})}$$

where

COE = cost of electricity ($/MWh$_{net}$)

CO_2 Captured = CO_2 captured for case (tonnes/MWh$_{net}$ or tons/MWh$_{net}$)

The equation used to calculate the Cost of CO_2 Avoided in $/tonnes or $/ton is as follows:

$$\text{Cost of } CO_2 \text{ Avoided} = \frac{(\text{COE}_{\text{with removal}} - \text{COE}_{\text{w/o removal}})}{(\text{Emissions}_{\text{w/o removal}} - \text{Emissions}_{\text{with removal}})}$$

where

COE = cost of electricity ($/MWh$_{net}$)

Emissions = CO_2 emissions for case (tonnes/MWh$_{net}$ or tons/MWh$_{net}$)

Figure 1-11 shows the CO_2 mitigation costs for the 450MW and 900MW oxy-fired plants. The costs are relative to the 450MW and 900MW air-fired plants, respectively, and do not include T&S. Including T&S will increase the CO_2 mitigation costs by 8-12 $/ton CO_2. The CO_2 Avoided Cost was 131 $/ton for the 450MW oxy-fired plant and decreased to 96 $/ton for the 900MW oxy-fired plant. The CO_2 Captured Cost was 99 $/ton for the 450MW oxy-fired plant and decreased to 75 $/ton for the 900MW oxy-fired plant.

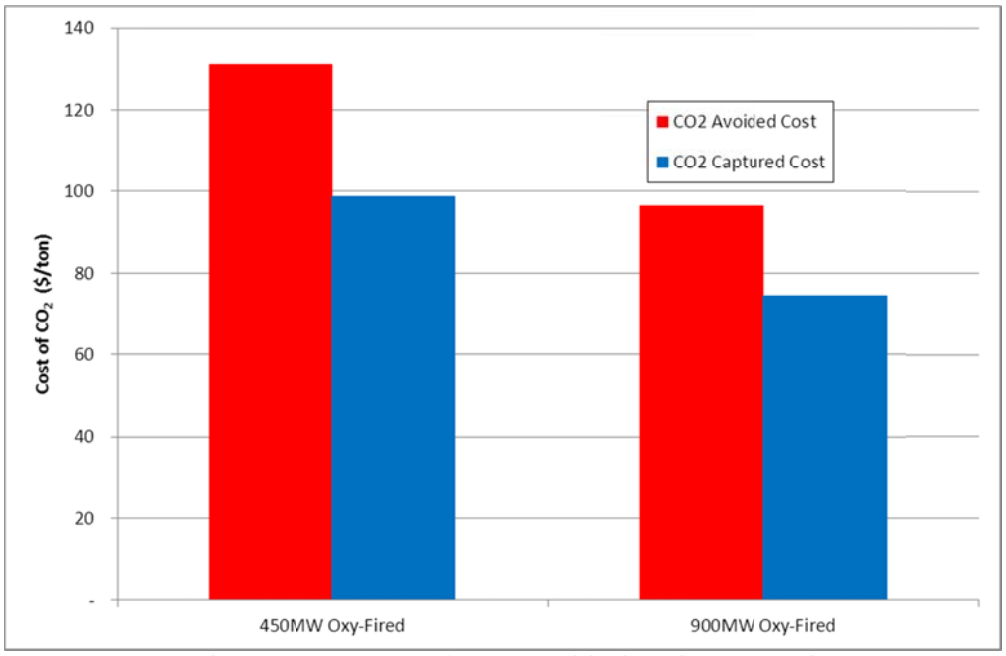

Figure 1-11: Cost of CO_2 Avoided and Captured

1.4 Environmental Performance

1.4.1 CO_2 Emissions

The carbon capture efficiency is a measure of the process effectiveness at capturing the carbon contained in the coal for sequestration or utilization. It is defined as:

$$\% \text{ Carbon Capture} = \frac{(CO_2\text{Coal} - CO_2\text{emitted})}{CO_2\text{Coal}}$$

The carbon capture efficiency for the oxy-fired 450MW Demonstration Plant, 900MW Commercial Plant, and Industrial Steam Plant was 93% for all cases. The carbon loss for each case was primarily from the GPU vent. The GPU design and performance for this techno-economic study was based on the GPU used in Case 5C of the DOE Baseline Study.[10] Since the carbon capture is largely controlled by the GPU performance, the % carbon capture for all of these cases was essentially the same as for the DOE Case 5C.

Figure 1-12 shows the actual carbon emissions in lb CO_2/MMBtu for the air-fired and oxy-fired Demonstration Plant, Commercial Plant, and Industrial Steam Plant cases.

[10] Pulverized Coal Oxycombustion Power Plants Volume 1, DOE/NETL-2007/1291, August 2008

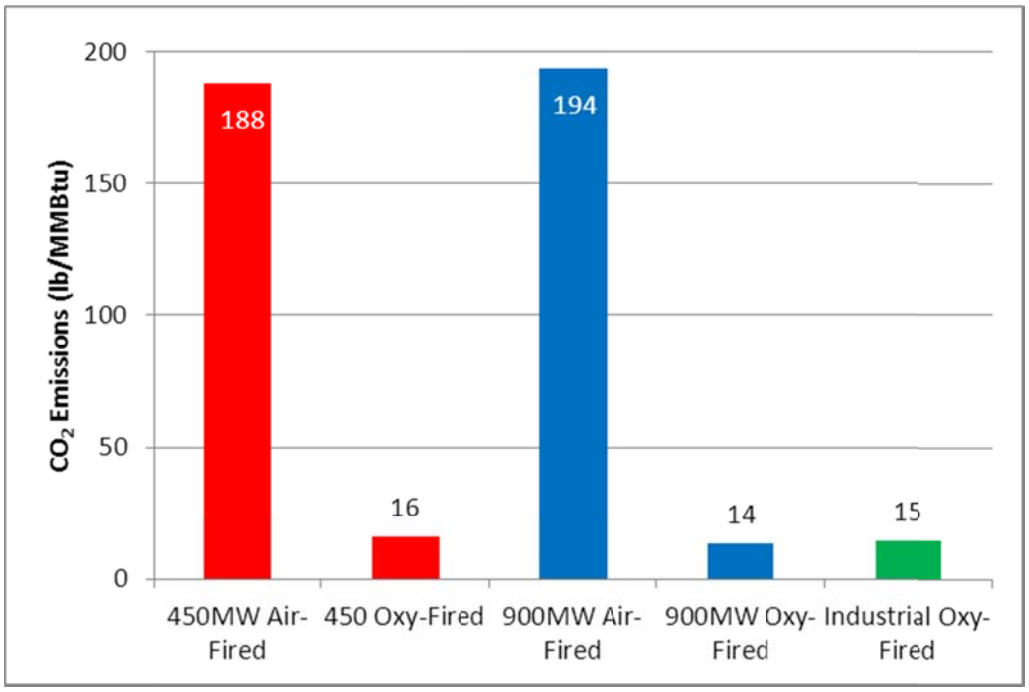

Figure 1-12: Summary of CO_2 Emissions for Air-Fired and Oxy-Fired Cases

1.4.2 Non-CO_2 Emissions

Table 1-4 summarizes the emissions from the air-fired and oxy-fired 450MW Demonstration Plant, 900MW Commercial Plant, and Industrial Steam Plant. The environmental targets selected for this study are identical to those chosen for the PC cases in the DOE Cost and Performance Baseline for Fossil Energy Plants[11] and are summarized in the first column of this table. This ensures that these cases can be compared fairly with plants evaluated in other DOE programs on a common basis. The targets established in the baseline report factored in existing environmental regulations and trends, recent permits, and the current BACT. This was compared with NSPS as of February 2006 which defined the minimum control level required for new fossil power plants. The BACT analysis was selected as the environmental target as shown in Table 1-4 since they exceeded the requirements for both NSPS and the average of recent permits.

The emissions for the air-fired cases shown in Table 1-4 match the environmental targets as the plants are designed and operated to meet these limits. NO_x emissions are controlled by the low NO_x firing system and SCR. SO_2 emissions are controlled by the WFGD for the 450MW and 900MW plants and by a NID™ for the industrial steam plant. Particulates are controlled by fabric filters for all cases. The fabric filter for the industrial steam plant is an integral part of the NID™ system. The mercury emission limits are met by co-benefit capture from the combined effects of the SCR, fabric filter, and FGD. The SCR promotes the oxidation of elemental

[11] Cost and Performance Baseline for Fossil Energy Plants Volume 1, DOE/NETL-2010/1397, November 2010

mercury. The oxidized mercury can then be more readily removed in the fabric filter and FGD. No activated carbon injection was necessary for these plants as the assumed 90% mercury co-benefit capture is sufficient to meet the mercury limits for this study.

The oxy-fired plants use the same environmental control equipment as for the air-fired plants. However, the emissions for the oxy-fired plants shown in Table 1-4 are significantly below emission targets used in this study. This is because additional removal takes place as the gas passes through the Flue Gas Condenser and GPU. A significant amount of the SO_2 remaining after the FGD is removed in the Flue Gas Condenser and then neutralized with NaOH. Most of the remaining SO_2 is further removed in the GPU. For NO_x emissions significantly lower (<50%) NO_x is generated from the oxy-boiler system due largely from reburning of the NO_x reciyced to the furnace. Additionally, much of the remaining NO_x is removed in the condensate when the flue gas is compressed in the GPU. A portion of the remaining NO_x is sequestered with the CO_2 product gas. Most of the oxidized mercury is removed in the FGD system and Flue Gas Condenser. The balance of the mercury is removed in an activated carbon bed in the GPU.

Table 1-4: Summary of Emissions for all Air-Fired and Oxy-Fired Cases

Power Plant Cases	Target	Air-Fired SCPC Power Plant 450MW	Oxy-Fired SCPC Power Plant 450MW	Air-Fired SCPC Power Plant 900MW	Oxy-Fired SCPC Power Plant 900MW	Oxy-Fired Steam Plant 150MW
SO_2 (lb/MMBtu)	0.085	0.085	< 0.01	0.085	< 0.01	< 0.01
NO_x (lb/MMBtu)	0.07	0.07	< 0.01	0.07	< 0.01	< 0.01
Particulates (lb/MMBtu)	0.013	0.013	< 0.01	0.013	< 0.01	< 0.01
Hg (lb/TBtu)	1.14	1.14	< 0.01	1.14	< 0.01	< 0.01
CO_2 (lb/MMBtu)		188	16	194	14	15

1.5 Sensitivity Study of FGR Location

A sensitivity study was conducted to evaluate the performance and cost impact of four different locations for the secondary flue gas recirculation duct take-off. The options considered included secondary FGR taken after the WFGD, before the WFGD, and before the Gas-Gas Heater. In this last scenario, an oxygen eductor is used to provide the motive force to convey the hot flue gas recycle back to the boiler. The last scenario had two options – one with the O_2 mixed directly with the secondary FGR and a second with the O_2 first preheated. The primary FGR ducts were taken after the Flue Gas Condenser for all cases to minimize the moisture concentration in the recirculation gas feeding the pulverizers. This study was focused on the performance and cost implications of the FGR location and did not consider the impact of increased SO_2 concentrations on the boiler design. However, the options that take recirculation gas before the WFGD would likely be limited to low sulfur fuels because of the potential impacts on boiler tube corrosion and additional costs associated with corrosion protection.

Model simulations showed that moving the secondary FGR duct before the WFGD slightly improved the boiler efficiency as compared to the base case with the secondary FGR after the WFGD. Moving the secondary FGR before the Gas-Gas Heater actually decreased the boiler

efficiency by 0.7% points due to the lower temperature of the FGR entering the furnace after cold O_2 is mixed with it. However, preheating the O_2 before mixing it with the secondary FGR improved the boiler efficiency for the case with FGR ducts located before the Gas-Gas Heater by 1% point relative to the base case.

Table 1-5 summarizes the qualitative cost impacts for the different FGR locations as compared to Case 1. Moving the FGR location from after the WFGD (Case 1) to before the WFGD (Case 2) results in a slightly larger fabric filter (due to a higher gas temperature and volumetric flow leaving the Gas-Gas Heater) and a smaller WFGD. Moving the FGR location before the Gas-Gas Heater (Cases 3 and 4) reduces the volumetric flow rate to all gas touched equipment downstream of the boiler and before the Flue Gas Condenser, including the Gas-Gas Heater, fabric filter, and WFGD. Case 4 also requires the addition of an O_2 heater.

A simple cost analysis was conducted to capture the cost impacts on a 900MW oxy-fired plant for some of the major pieces of equipment impacted by the choice of FGR location. Table 1-5 shows that moving the FGR upstream of the WFGD can have significant cost benefits. Of course, there are other considerations, such as the impact of increased SO_2 concentration on the boiler materials that may override any advantages of moving the FGR location. There was little cost benefit to moving the FGR location from before the WFGD to before the Gas-Gas Heater if there is no O_2 preheat before mixing with the secondary FGR. Although Case 3 has a lower cost fabric filter than Case 2 due to reduced volumetric gas flow, this savings is offset by a lower boiler efficiency due to the reduced secondary FGR gas temperature entering the furnace. Preheating the O_2 before mixing with the secondary FGR (Case 4) results in improved boiler efficiency and greater capital cost reduction relative to Case 1.

Table 1-5: Cost Implications of FGR Location

	Case 1 After WFGD	Case 2 Before WFGD	Case 3 Before GGH	Case 4 Before GGH O_2 Preheat
Gas-Gas Heater	Base	Similar	Smaller	Smaller
Fabric Filter	Base	Larger	Smaller	Smaller
WFGD	Base	Smaller	Smaller	Smaller
O_2 AH	N/A	N/A	N/A	New
Δ Total Overnight Capital Cost ($M)	Base	-66	-67	-85
Δ Total Overnight Capital Cost ($/Kw)	Base	-101	-101	-130

There are other costs that were not considered in this simple cost analysis. Cost additions include an increased ASU capital cost and higher ASU power requirements for Case 4 as the oxygen needs to be delivered at a higher pressure for the oxygen eductor to provide the motive force necessary to convey the hot FGR back to the boiler. There may be some windbox modifications

necessary for Cases 3 and 4 to deal with the hot, particulate laden FGR. Other costs may be necessary to cope with increase SO_2 concentrations in the boiler.

These cost adders are offset by various cost reductions that were not considered in this study. These include reduced capital costs for the ID Fan and gas ductwork, plus reduced auxiliary power requirements for the fabric filter, WFGD, and ID Fan. The impact on the flue gas heat exchanger (HEX) was also not considered, but the cost of this equipment would likely increase for Case 2 due to the increased sensible energy in the flue gas from the higher gas temperature. The HEX cost would likely decrease for Case 4 due to the significantly decreased volumetric flow rate relative to Case 1, which more than offsets an increase in flue gas temperature. The HEX cost for Case 3 would likely be just slightly less than for Case 1 as the increased flue gas temperature would almost offset the reduced volumetric flow rate.

Overall, the FGR location in Case 4 resulted in the most significant cost reduction as compared to the base case scenario. The capital cost reductions considered in this sensitivity study total 3.5% of the Total Overnight Costs of the 900MW oxy-fired plant that used the secondary FGR after the WFGD (Case 1). The additional costs and savings not considered in this study are expected to increase the overall savings.

1.6 Summary

- Four utility scale power plants were designed and costs were developed for them in this study. A $450MW_{gross}$ oxy-fired SCPC plant was designed as representative of a demonstration plant for oxy-combustion. A $900MW_{gross}$ oxy-fired SCPC plant was designed and costs were developed as representative of a first generation oxy-combustion commercial plant. These plants were contrasted with a $450MW_{gross}$ and a $900MW_{gross}$ air-fired SCPC plant. This study also included an evaluation of the design modifications and costs necessary to retrofit an existing air-fired industrial steam plant equivalent to $150MW_{gross}$ to oxy-combustion.

- The net plant efficiency for the 450MW oxy-fired plant was 31.5% HHV, or 9.4% points less than the 450MW air-fired case. The net plant efficiency for the 900MW oxy-fired plant was 32.5% HHV, or 8.8% points less than the 900MW air-fired case. The reduction in net plant efficiency for the oxy-fired cases is primarily due to the increased auxiliary power requirements for the ASU and GPU.

- The net plant efficiency for the 900MW oxy-fired plant was 0.6% points higher than the efficiency for the 450MW oxy-fired plant. This improvement is primarily due to the thermal integration of the ASU, GPU, and FGHR system that was used for the 900MW oxy-fired plant design.

- The Total Overnight Capital cost for the 450MW oxy-fired plant increased by 78.1% relative to the air-fired plant. The Total Overnight Capital cost increase for the 900MW

oxy-fired plant was 78.5% relative to the air-fired plant. The added cost of integration of the ASU, GPU, and FGHR for the 900MW offset some of the specific cost decrease due to both scalability and technology maturity (commercial vs. demonstration plant).

- Most of the capital cost increase for the oxy-fired utility plants is due to the addition of the ASU and GPU systems. The 450MW and 900MW boiler bare erected costs (materials and erection only) increased by about 11% for the oxy-fired cases as compared to the air-fired cases. This increase accounts for the changes necessary to make the boiler oxy-capable, such as the addition of the flue gas recirculation system ducting, oxygen mixers, and windbox modifications.
- The incremental Total Overnight Capital costs to retrofit the $150MW_{gross}$ air-fired industrial boiler to oxy-fired capability is approximately $200 million. The cost of the boiler modifications are only 7% of the total capital cost. The majority of the retrofit capital cost is for the addition of the ASU and GPU.
- The first year COE (w/o T&S) for the 450MW oxy-fired plant increased by 72.9% relative to the 450MW air-fired plant. The COE increase for the 900MW oxy-fired plant increased by 68.5% relative to the 900MW air-fired plant. The COE increase for both oxy-fired plants is well above the DOE COE increase target of 35%, which is not surprising as these plants are first generation CCS technologies. Further reductions in the COE can be expected in second generation oxy-fired plants from continued reductions in the capital cost and power requirements for the ASU and GPU, along with further optimization and integration of the overall power plant.
- The CO_2 Avoided Cost was 131 $/ton for the 450MW oxy-fired plant and decreased to 98 $/ton for the 900MW oxy-fired plant. The CO_2 Captured Cost was 99 $/ton for the 450MW oxy-fired plant and decreased to 75 $/ton for the 900MW oxy-fired plant.
- A sensitivity study evaluated the performance and cost impact of four different locations for the secondary flue gas recirculation duct take-off. Moving the FGR from after the WFGD to before the WFGD had little impact on the boiler efficiency. Moving the FGR before the Gas-Gas Heater actually decreased the boiler efficiency by 0.7% points due to the lower temperature of the FGR entering the furnace after cold O_2 is mixed with it. However, preheating the O_2 before mixing it with the secondary FGR improved the boiler efficiency for the case with FGR ducts located before the Gas-Gas Heater by 1% point relative to the case with the FGR location after the WFGD.
- A simple cost analysis identified the cost impacts on a 900MW oxy-fired plant for some of the major pieces of equipment impacted by the choice of FGR location. The results showed that moving the FGR upstream of the Gas-Gas Heater and preheating the O_2 before mixing with the secondary FGC can have significant cost benefits in terms of both

boiler efficiency improvement and capital cost reduction. These benefits need to be weighed against other considerations, such as the impact of increased SO_2 concentration on boiler materials.

2. Introduction

Alstom Power Inc. is actively developing clean coal technologies to enable the continued use of our nation's abundant coal reserves while contributing to domestic economic and energy security. Oxy-combustion is a promising CCS technology that has been under development for many years and is now ready for large scale demonstration. The objective of this design effort was to assess the design modifications and costs associated with applying oxy-combustion technology to coal-fired utility-scale power plants and to an industrial scale coal-fired steam plant.

Four commercial scale power plants were designed and costs were developed for them. A $450MW_{gross}$ oxy-fired SCPC plant was designed as representative of a demonstration plant for oxy-combustion technology. This was contrasted with a $450MW_{gross}$ air-fired SCPC plant. Similarly, a $900MW_{gross}$ oxy-fired SCPC plant was designed and costs were developed as representative of a first generation oxy-combustion commercial plant. A $900MW_{gross}$ air-fired plant was also included for comparison.

Finally, this study included an evaluation of the design modifications and costs necessary to retrofit an existing air-fired industrial steam plant equivalent to $150MW_{gross}$ to oxy-combustion. The design study focused on the necessary boiler modifications for this conversion, although the significant costs associated with the addition of an Air Separation Unit (ASU) and Gas Processing Unit (GPU) for the final CO_2 purification and compression were also considered.

Table 2-1 summarizes the five case configurations considered in this study.

Table 2-1: Summary of Case Configurations

Unit Cycle	Steam Cycle, psig/°F/°F	Boiler Technology	Steam Flow Rate lb/hr	Sulfur Removal	CO_2 Separation
450MW Air-Fired PC w/o CCS	3930/1116/1148	2-Pass Supercritical PC	2,811,000	Wet FGD, Gypsum	N/A
450MW Oxy-Fired PC	3930/1116/1148	2-Pass Supercritical PC	2,811,000	Wet FGD, Gypsum	GPU
900MW Air-Fired PC w/o CCS	3930/1116/1148	Tower Supercritical PC	5,703,000	Wet FGD, Gypsum	N/A
900MW Oxy-Fired PC	3930/1116/1148	Tower Supercritical PC	5,703,000	Wet FGD, Gypsum	GPU
Oxy-Fired Industrial Boiler	1175/1000	Industrial Boiler	980,000	NID™	GPU

Legend:
PC - Pulverized Coal
CCS - Carbon Capture and Storage
FGD - Flue Gas Desulfurization
GPU - Gas Processing Unit
NID™ - Alstom Dry FGD System

3. DESIGN AND EVALUATION BASIS

Alstom in-house design tools along with the Thermoflow cycle analysis program were used to design and model each of the oxy-fired plant configurations evaluated in this study. These models were used to develop mass and energy balances which became the design basis for the major equipment in each plant. The design basis in turn was used as the basis for developing both capital and operating cost estimates for each case. The capital costs were estimated from a combination of vendor quotes or scaled estimates from existing commercial contracts or from previous design studies. Wherever possible, costs were scaled off of existing DOE system studies for similar equipment. The Cost of Electricity (COE) was calculated for each case using the DOE's Power Systems Financial Model (PSFM) or a simplified COE model using a first year fixed charge rate derived from the PSFM model.

The balance of Section 3 describes the design basis used for the 450MW and 900MW air-fired and oxy-fired plants and for the industrial steam plant oxy-combustion retrofit, along with the environmental targets, costing assumptions, and economic criteria used in these studies.

3.1 Site Description

The 450MW and 900MW oxy-fired power plants, along with their companion air-fired plants, are all assumed to be located at a generic Midwestern U.S. plant site. The same apples to the oxy-fired industrial steam plant. Table 3-1 summarizes the characteristics for this site, while Table 3-2 describes the site's ambient conditions.[12]

Table 3-1: Site Characteristics

Location	Greenfield, Midwestern USA
Topography	Level
Size, acres	300
Transportation	Rail
Ash/Slag Disposal	Offsite
Water	50% Municipal / 50% Ground water
CO_2 Storage	Compressed to 15.3 MPa (2,215 psia, transported 100 kilometers (62 miles) and sequestered in a saline formation at a depth of 1,239 m (4,055 ft)

[12] Process Modeling Design Parameters – Site Description, DOE/NETL-341/081911, January 2012, pg. 2

Table 3-2: Site Ambient Conditions

Plant	450MW Demonstration Plant	900MW Commercial Plant	Industrial Boiler
Elevation ASL, m (ft)	100 (328)	100 (328)	60 (197)
Barometric Pressure, MPa (psia)	0.101 (14.7)	0.101 (14.7)	0.101 (14.7)
Nominal Ambient Temperature, °C (°F)	18 (64)	18 (64)	26.6 (80)
Relative Humidity Dry Bulb, %	65	65	60

3.2 Coal Characteristics

Table 3-3 summarizes the design coal analyses that were used in this study. The 450MW Demonstration Plant and the 900 MW Commercial Plant were both modelled using a high sulfur Illinois coal which was tested in Alstom's Boiler Simulation Facility as part of this DOE oxy-fired program. A medium sulfur bituminous coal was selected for the industrial boiler. Table 3-4 summarizes the coal ash composition, ash fusion temperatures, and Hardgrove Grindability Index for the coals used for this study.

Table 3-3: Coal Proximate and Ultimate Analyses

Plant	450MW Demonstration Plant	900MW Commercial Plant	Industrial Boiler
Coal Type	High Sulfur Bituminous	High Sulfur Bituminous	Medium Sulfur Eastern Bituminous
Proximate Analysis (weight %)	As-Received	As-Received	As-Received
Moisture	12.57	12.57	6.50
Ash	9.27	9.27	9.09
Volatile Matter	35.47	35.47	35.00
Fixed Carbon (BD)	42.69	42.69	49.41
HHV, Btu/lb	11,106	11,106	12,509
Ultimate Analysis (weight %)	As-Received	As-Received	As-Received
Moisture	12.57	12.57	6.50
Carbon	61.40	61.40	70.49
Hydrogen	4.13	4.13	4.74
Nitrogen	1.23	1.23	1.38
Chlorine	0.00	0.00	0.00
Sulfur	3.10	3.10	1.86
Ash	9.27	9.27	9.09
Oxygen	8.30	8.30	5.94

Table 3-4: Other Coal Properties

Plant	450MW Demonstration Plant	900MW Commercial Plant	Industrial Boiler
Coal Type	High Sulfur Bituminous	High Sulfur Bituminous	Medium Sulfur Eastern Bituminous
Ash Composition (weight %)	As-Received	As-Received	As-Received
SiO_2	50.85	50.85	48.48
Al_2O_3	20.53	20.53	21.67
Fe_2O_3	15.56	15.56	21.96
CaO	3.52	3.52	1.94
MgO	0.96	0.96	0.48
Na_2O	1.02	1.02	0.23
K_2O	2.11	2.11	1.52
TiO_2	0.94	0.94	1.0
MnO_2	0.04	0.04	0.5
P_2O_5	0.52	0.52	1.0
SO_3	2.81	2.81	0.95
Other	0.12	0.12	0.27
Ash Fusion Temperatures (°F)	Reducing	Reducing	Reducing
Initial – Limited Deformation	2020	2020	2020
Softening	2172	2172	2100
Hemispherical	2288	2288	2260
Fluid	2324	2324	2360
Hardgrove Grindability Index	50	50	50

3.3 Limestone and Lime Characteristics

Table 3-5 summarizes the design limestone characteristics that were used in this study for the WFGD used in the 450MW and 900MW oxy-fired and air-fired plant designs. All cases were modeled using Greer Limestone[13] from Morgantown, WV, as the feedstock to the air-fired and oxy-fired boilers.

[13] Quality Guidelines for Energy System Studies – Specification for Selected Feedstocks, DOE/NETL-341/011812, January 2012, pg. 4

Table 3-5: Greer Limestone Analysis

Component	Dry Basis wt %
Calcium Carbonate, $CaCO_3$	80.40
Magnesium Carbonate, $MgCO_3$	3.50
Silica, SiO_2	10.32
Aluminum Oxide, Al_2O_3	3.16
Iron Oxide, Fe_2O_3	1.24
Sodium Oxide, Na_2O	0.23
Potassium Oxide, K_2O	0.72
Balance	0.43
Total	100.00

Lime per DOE's specification[14] was also added to Alstom's NID™ desulfurization system used in the oxy-fired industrial boiler design.

Table 3-6: Lime Analysis

Component	Dry Basis wt %
Calcium Oxide, CaO	92.60
Magnesium Oxide, MgO	1.20
Silica, SiO_2	0.95
Aluminum Oxide, Al_2O_3	0.20
Iron Oxide, Fe_2O_3	0.34
Balance	4.71
Total	100.00

3.4 Environmental Targets

The environmental targets selected for this study are identical to those chosen for the PC cases in the DOE Cost and Performance Baseline for Fossil Energy Plants.[15] This ensures that the oxy-fired and air-fired cases can be compared fairly on a common basis. The targets established in

[14] Quality Guidelines for Energy System Studies – Specification for Selected Feedstocks, DOE/NETL-341/011812, January 2012, pg. 4

[15] Cost and Performance Baseline for Fossil Energy Plants Volume 1, DOE/NETL-2010/1397, November 2010, pg. 38

the baseline report factored in existing environmental regulations and trends, recent permits, and the current BACT. This was compared with NSPS as of February 2006 which defined the minimum control level required for new fossil power plants. The BACT analysis was selected as the environmental target as shown in Table 3-7 since they exceeded the requirements for both NSPS and the average of recent permits. Table 3-7 also shows the control technology used in this study for the oxy-fired and air-fired cases.

The environmental targets apply equally well to both oxy-fired and air-fired cases. NO_x emission requirements are met by the low NO_x firing system and SCR. The design of the low NO_x system is based on first maximizing in-furnace NO_x reduction to lower the overall design requirements of the backend SCR system. The extensive NO_x reduction capability of tangential firing systems allows the SCR to be optimized with respect to lower capital and operating costs. The significant in-furnace NO_x reduction results in lower catalyst volume, decreased ammonia flow requirements, and reduced draft losses across the catalyst.

Oxy-combustion results in lower NO_x generation than air-firing and may not require the use of a SCR to achieve the environmental targets shown in Table 3-7. SCRs were maintained in the oxy-fired plant designs as these plants may still operate in air-fired mode during startup and when the ASU is out of operation. Additionally, depending on the GPU design, a SCR could be required for some other oxy cases to achieve site specific emission limits or CO_2 product specifications.

SO_x emission requirements are met by limestone addition in the WFGD. A multi-stage approach is taken for mercury control. The combination of pollution control technologies used in the PC plants, SCR, fabric filters and FGD, result in significant co-benefit capture of mercury. The SCR promotes the oxidation of elemental mercury, which in turn enhances the mercury removal capability of the fabric filter and FGD unit. The mercury co-benefit capture is assumed to be 90 percent for this combination of control technologies. Co-benefit capture alone is sufficient to meet current NSPS mercury limits, so no activated carbon injection is included. Most of any remaining oxidized mercury is removed in the condenser. The balance of the mercury is removed in an activated carbon bed in the GPU.

A sodium-based SO_3 mitigation system was selected for the removal of SO_3 from the flue gas for the 450MW oxy-fired plant. The process uses a solution of sodium carbonate reagent that is injected and spray dried in the flue gas. The resulting dried product consists of extremely fine, reactive particulate matter that reacts with SO_3 to form a benign solid, sodium sulfate, which is subsequently removed from the flue gas in the fabric filter. This minimizes acid corrosion issues in the downstream equipment as the flue gas temperature approaches the acid dewpoint. This system may not be necessary if other appropriate measures are taken to minimize the impact of acid gas corrosion, such as duct protection and rubber-lined fans. This system was included in the 450MW plant as a conservative design approach that will also provide important design and performance information for future designs.

Table 3-7: Environmental Targets for Oxy-Fired and Air-Fired PCs

Pollutant	Environmental Target	NSPS Limit	Average of Recent Permits	Air-Fired & Oxy-Fired Power Plants	Oxy-Fired Industrial Boiler
NO_x	0.07 lb/MMBtu	1.0 lb/MWh (0.111 lb/MMBtu)	0.08 lb/MMBtu	low NOx burners, overfire air, and SCR	low NOx burners, overfire air, and SCR
SO_2	0.085 lb/MMBtu	1.4 lb/MWh (0.156 lb/MMBtu)	0.16 lb/MMBtu	Wet limestone scrubber	NID™
Particulate Matter (Filterable)	0.013 lb/MMBtu	0.015 lb/MMBtu	0.017 lb/MMBtu	Fabric filter	Fabric filter
Mercury	1.14 lb/Tbtu	$20x10^{-6}$ lb/MWh (2.2 lb/Tbtu)	2.49 lb/Tbtu	Co-benefit capture	Co-benefit capture

3.5 CO_2 Sequestration and CO_2 Purity

The CO_2 purity for the oxy-fired cases is shown in Table 3-8 as defined in the DOE's CO_2 Impurities Design Parameters report.[16] This table shows the recommended limits for CO_2 stream impurities for CO_2 transport by pipeline, along with the requirements for EOR applications and sequestration. The CO_2 purity specification for Enhanced Oil Recovery will guide the design of the oxy-fired cases. This specification exceeds the purity requirements for saline reservoir sequestration but enables the CO_2 use for EOR applications.

Despite the more stringent EOR purity specification, the CO_2 captured in the oxy-fired cases is assumed to be transported by pipeline and sequestered in a saline formation at a depth of 1,239 m (4,055 ft). This approach maintains consistency with the approach taken in the DOE Cost and Performance Baseline study[17] and facilitates comparison with other technologies being studied independently by the DOE. The CO_2 is supplied as a supercritical fluid to the pipeline at a pressure of 15.3 MPa (2,215 psia) and is transported 100 kilometers (62 miles) before it is sequestered in a saline formation.

[16] CO_2 Impurities Design Parameters, DOE/NETL-341/011212, January 2012, pg. 4
[17] Cost and Performance Baseline for Fossil Energy Plants Volume 1, DOE/NETL-2010/1397, November 2010, pg. 53

Table 3-8: CO_2 Stream Compositions Recommended Limits

Component	Unit (Max unless otherwise noted)	Carbon Steel Pipeline		Enhanced Oil Recovery		Saline Reservoir Sequestration		Venting Concerns
		Conceptual Design	Range in Literature	Conceptual Design	Range in Literature	Conceptual Design	Range in Literature	
CO_2	vol% (Min)	95	90-99.8	95	90-99.8	95	90-99.8	Yes-IDLH 40,000 ppmv
H_2O	ppm_{wt}	300	20 - 650	300	20 - 650	300	20 - 650	
N_2	vol%	4	0.01 - 7	1	0.01 - 2	4	0.01 - 7	
O_2	vol%	4	0.01 – 4	0.01	0.001 – 1.3	4	0.01 – 4	
Ar	vol%	4	0.01 – 4	1	0.01 – 1	4	0.01 – 4	
CH_4	vol%	4	0.01 – 4	1	0.01 – 2	4	0.01 – 4	Yes-Asphyxiate, Explosive
H_2	vol%	4	0.01 - 4	1	0.01 – 1	4	0.01 – 4	Yes-Asphyxiate, Explosive
CO	ppm_v	35	10 - 5000	35	10 - 5000	35	10 - 5000	Yes-IDLH 1,200 ppmv
H_2S	vol%	0.01	0.002 – 1.3	0.01	0.002 – 1.3	0.01	0.002 – 1.3	Yes-IDLH 100 ppmv
SO_2	ppm_v	100	10 - 50000	100	10 - 50000	100	10 - 50000	Yes-IDLH 100 ppmv
NO_X	ppm_v	100	20 - 2500	100	20 - 2500	100	20 - 2500	Yes-IDLH NO-100 ppmv, NO_2 - 200 ppmv

Component	Unit (Max unless otherwise noted)	Carbon Steel Pipeline		Enhanced Oil Recovery		Saline Reservoir Sequestration		Venting Concerns
		Conceptual Design	Range in Literature	Conceptual Design	Range in Literature	Conceptual Design	Range in Literature	
NH_3	ppm_v	50	0 - 50	50	0 - 50	50	0 - 50	Yes-IDLH 300 ppmv
COS	ppm_v	trace	trace	5	0 - 5	trace	trace	Lethal @ High Concentrations (>1,000 ppmv)
C_2H_6	vol%	1	0 - 1	1	0 - 1	1	0 - 1	Yes-Asphyxiant, Explosive
C_3+	vol%	<1	0 - 1	<1	0 - 1	<1	0 - 1	
Part.	ppm_v	1	0 - 1	1	0 - 1	1	0 - 1	
HCl	ppm_v	N.I.*	N.I.*	N.I.*	N.I.*	N.I.*	N.I.*	Yes-IDLH 50 ppmv
HF	ppm_v	N.I.*	N.I.*	N.I.*	N.I.*	N.I.*	N.I.*	Yes-IDLH 30 ppmv
HCN	ppm_v	trace	trace	trace	trace	trace	trace	Yes-IDLH 50 ppmv
Hg	ppm_v	N.I.*	N.I.*	N.I.*	N.I.*	N.I.*	N.I.*	Yes-IDLH 2 mg/m^3 (organo)
Glycol	ppb_v	46	0 - 174	46	0 - 174	46	0 - 174	
MEA	ppm_v	N.I.*	N.I.*	N.I.*	N.I.*	N.I.*	N.I.*	MSDS Exp. Limits 3 ppmv, 6 mg/m^3
Selexol	ppm_v	N.I.*	N.I.*	N.I.*	N.I.*	N.I.*	N.I.*	

**Not enough information is available to determine the maximum allowable amount*

3.6 Plant Capacity Factor

All of the oxy-fired and air-fired plants included in this study were designed for a capacity factor of 85%. This value is consistent with the approach taken by the DOE in their baseline reports for these technologies. PCs are a mature technology with proven high availabilities. Adding oxy-fired capability has only a minor impact on the boiler design. ASUs are also commercially available and a mature technology in industrial applications. GPUs are still in development, but many of their key components are standard equipment with proven performance. Use of multiple GPU trains will enable the oxy-fired plants to achieve the design capacity factor.

3.7 Steam Conditions

Two steam cycle conditions were selected for the cases to be evaluated in this study. Current state of the art steam conditions of 27.1MPa/603°C/620°C (3930psig/1117°F/1149°F) were selected for the 450MW air-fired and oxy-fired PC plants. The steam conditions for the 900MW air-fired and oxy-fired PC plants are slightly higher – see Table 3-9. The steam conditions for the oxy-fired industrial boiler were 11.1MPa/538°C (1609psig/1000°F).

Table 3-9: Steam Cycle Conditions

Plant	450MW Demonstration Plant	900MW Commercial Plant	Industrial Boiler
SH Steam Mass Flow, kg/hr	1,275,000	2,587,000	444,240
FW Inlet Pressure, MPa (psig)	30.1 (4364)	31.6 (4581)	11.9 (1725)
FW Inlet Temperature, °C (°F)	306.1	305.0	215.0
SH Outlet Pressure, MPa (psig)	27.1 (3930)	28.5 (4132)	11.1 (1609)
SH Outlet Temperature , °C (°F)	602.5 (1117)	603.0 (1117)	537.8 (1000)
RH Mass Flow , kg/hr	1,052,000	2,140,000	
RH Inlet Pressure, MPa (psig)	5.2 (754)	6.2 (899)	
RH Inlet Temperature , °C (°F)	347.3 (657)	360.0 (680)	
RH Outlet Pressure, MPa (psig)	5.1 (739)	6.0 (870)	
RH Outlet Temperature , °C (°F)	620.4 (1149)	621.0 (1150)	

3.8 Balance of Plant Assumptions

The assumptions for the balance of plant conditions will be maintained where appropriate to match the specifications established in the DOE Baseline Report.[18] Table 3-10 summarizes the BOP assumptions that will be used in this study for each case.

[18] Cost and Performance Baseline for Fossil Energy Plants Volume 1, DOE/NETL-2010/1397, November 2010, pg. 328

Table 3-10: Balance of Plant Assumptions

Cooling system	Recirculating Wet Cooling Tower
Fuel and Other storage	
Coal	30 days
Ash	30 days
Limestone	30 days
Plant Distribution Voltage	
Motors below 1 hp	110/220 volt
Motors between 1 hp and 250 hp	480 volt
Motors between 250 hp and 5,000 hp	4,160 volt
Motors above 5,000 hp	13,800 volt
Steam and GT generators	24,000 volt
Grid Interconnection voltage	345 kV
Water and Waste Water	
Makeup Water	The water supply is 50 percent from a local Publicly Owned Treatment Works (POTW) and 50 percent from groundwater, and is assumed to be in sufficient quantities to meet plant makeup requirements.
	Makeup for potable, process, and DI water is drawn from municipal sources.
Process Wastewater	Storm water that contacts equipment surfaces is collected and treated for discharge through a permitted discharge.
Sanitary Waste Disposal	Design includes a packaged domestic sewage treatment plant with effluent discharged to the industrial wastewater treatment system. Sludge is hauled off site. Packaged plant is sized for 5.68 cubic meters per day (1,500 gallons per day)
Water Discharge	Most of the process wastewater is recycled to the cooling tower basin. Blowdown will be treated for chloride and metals, and discharged.

3.9 Cost Estimating Methodology

The capital costs for the 450MW and 900MW oxy-fired plants were developed using the methodology described in the DOE's Cost Estimation Methodology guide.[19]

- Bare Erected Costs (BEC) were developed for all process equipment, facilities, and infrastructure – including materials and erection labor.
- The Total Plant Costs (TPC) were developed by adding the cost of services by the engineering, procurement, and construction (EPC) contractor, along with process and project contingencies.
- The TPC is an overnight cost and is expressed in base year dollars.
- The Total Overnight Capital Cost (TOC) includes the TPC plus all other overnight costs, including owner's costs – which are further described in section 3.9.3.
- The Total As-Spent Capital Costs (TASC) includes all capital expenditures during the capital expenditure period including their escalation and interest during construction. It is expressed in mixed, current-year dollars over the capital expenditure period.

3.9.1 Capital Costs

The DOE developed detailed capital cost estimates of the Case 11 SCPC plant that is the basis for the design and costs of much of the balance of plant equipment in this study. The DOE subsequently updated the costs for this case to June 2011 dollars.[20] These updated costs were used in this study as a reference base and were adjusted by capacity factoring using the scaling parameters prescribed by the DOE[21] for those subsystems and components common to the two oxy-fired plants. Specifications for those components unique to the oxy-fired plants were based on heat and material balances. Costs were then developed by in-house cost-estimating, vendor quotes, or from quotes for similar equipment that were then adjusted for capacity and flow conditions. Costs for the major components included all items necessary to develop a complete cost, including items such as pressure parts, refractory, insulation, structural steel, casing, expansion joints, etc. Table 3-11 shows the list of major oxy-fired equipment and the basis for adjusting the capital costs.

[19] Cost Estimation Methodology for NETL Assessments of Power Plant Performance, NETL Quality Guidelines for Energy System Studies, DOE/NETL-2-11/1455, April 2011
[20] Updated Costs (June 2011 Basis) for Selection Bituminous Baseline Cases, DOE/NETL-341/082312, August 2012
[21] Capital Cost Scaling Methodology, Quality Guidelines for Energy System Studies, DOE/NETL-341/013113, January 2013

Table 3-11: Cost Estimate Basis for Oxy-PC Plant Equipment

Account Number / Description	Cost Estimate Basis	Oxy-PC Cost Adjustment Rationale
1 COAL & SORBENT HANDLING		
1.1 Coal Receive & Unload	Factored estimate based on DOE Case 11	Coal Feed Rate, lb/hr
1.2 Coal Stackout & Reclaim	Factored estimate based on DOE Case 11	Coal Feed Rate, lb/hr
1.3 Coal Conveyors	Factored estimate based on DOE Case 11	Coal Feed Rate, lb/hr
1.4 Other Coal Handling	Factored estimate based on DOE Case 11	Coal Feed Rate, lb/hr
1.5 Sorbent Receive & Unload	Factored estimate based on DOE Case 11	Limestone Feed Rate, lb/hr
1.6 Sorbent Stackout & Reclaim	Factored estimate based on DOE Case 11	Limestone Feed Rate, lb/hr
1.7 Sorbent Conveyors	Factored estimate based on DOE Case 11	Limestone Feed Rate, lb/hr
1.8 Other Sorbent Handling	Factored estimate based on DOE Case 11	Limestone Feed Rate, lb/hr
1.9 Coal & Sorbent Hnd.Foundations	Factored estimate based on DOE Case 11	Coal and Limestone Feed Rate, lb/hr
2 COAL & SORBENT PREP & FEED		
2.1 Coal Crushing & Drying	Factored estimate based on DOE Case 11	Coal Feed Rate, lb/hr
2.2 Coal Conveyor to Storage	Factored estimate based on DOE Case 11	Coal Feed Rate, lb/hr
2.3 Coal Injection System	Factored estimate based on DOE Case 11	Coal Feed Rate, lb/hr
2.4 Misc.Coal Prep & Feed	Factored estimate based on DOE Case 11	Coal Feed Rate, lb/hr
2.5 Sorbent Prep Equipment	Factored estimate based on DOE Case 11	Limestone Feed Rate, lb/hr
2.6 Sorbent Storage & Feed	Factored estimate based on DOE Case 11	Limestone Feed Rate, lb/hr
2.7 Sorbent Injection System	Factored estimate based on DOE Case 11	Limestone Feed Rate, lb/hr
2.8 Booster Air Supply System	Factored estimate based on DOE Case 11	Same
2.9 Coal & Sorbent Feed Foundation	Factored estimate based on DOE Case 11	Coal and Limestone Feed Rate, lb/hr
3 FEEDWATER & MISC. BOP SYSTEMS		
3.1 FeedwaterSystem	Factored estimate based on DOE Case 11	HP BFW Flow Rate, lb/hr
3.2 Water Makeup & Pretreating	Factored estimate based on DOE Case 11	Raw Water Makeup, gpm
3.3 Other Feedwater Subsystems	Factored estimate based on DOE Case 11	HP BFW Flow Rate, lb/hr
3.4 Service Water Systems	Factored estimate based on DOE Case 11	Raw Water Makeup, gpm
3.5 Other Boiler Plant Systems	Factored estimate based on DOE Case 11	HP BFW Flow Rate, lb/hr
3.6 FO Supply Sys & Nat Gas	Factored estimate based on DOE Case 11	Total Fuel Feed Flow, lb/hr
3.7 Waste Treatment Equipment	Factored estimate based on DOE Case 11	Water to Treatment Flow, lb/hr
3.8 Misc. Equip.(cranes,AirComp.,Comm.)	Factored estimate based on DOE Case 11	Total Fuel Feed Flow, lb/hr

Account Number / Description	Cost Estimate Basis	Oxy-PC Cost Adjustment Rationale
4 OXY-PC BOILER		
4.1 Oxy-Fired Boiler		
Conventional boiler equipment	Vendor Cost Estimate	N/A
4.2 Oxy-Fired Boiler		
Flue gas recirc system, O_2 mixers	Vendor Cost Estimate	N/A
4.3 SCR (w/4.1)	Factored estimate based on DOE Case 11	Included in 4.1
4.4 ASU/Oxidant Compression	Factored estimate based on DOE Case S12F	O_2 Flow Rate, tpd
4.5 Boiler BoP (w/ ID Fans)	Factored estimate based on DOE Case 11	Included in 4.1
4.6 Primary Air System	Factored estimate based on DOE Case 11	Included in 4.1
4.7 Secondary Air System	Factored estimate based on DOE Case 11	Included in 4.1
4.8 Major Component Rigging	Factored estimate based on DOE Case 11	Included in 4.1
4.9 Boiler Foundations	Factored estimate based on DOE Case 11	Included in 4.1
5 FLUE GAS CLEANUP		
5.1 Absorber Vessels & Accessories	Factored estimate based on DOE Case 11	FGD Exit Flow, acfm
5.2 Baghouse & Accessories	Factored estimate based on DOE Case 11	Baghouse Flow, acfm
5.3 Other Particulate Removal Materials	Factored estimate based on DOE Case 11	N/A
5.4 Gypsum Dewatering System	Factored estimate based on DOE Case 11	Sypsum Flow, lb/hr
5.9 Mercury Removal System	Factored estimate based on DOE Case 11	N/A
5B CO2 REMOVAL & COMPRESSION (based on DOE Case S12F)		
5B.1 CO2 Condensing Heat Exchanger	Factored estimate based on DOE Case S12F	Heat Duty MMBtu/hr
5B.2 CO2 Compression & Drying	Factored estimate based on DOE Case S12F	CO2 Captured, lb/hr
6 COMBUSTION TURBINE/ACCESSORIES	N/A	
7 HRSG		
7.1 Flue Gas Heat Exchanger (Case 4 only)	N/A	
7.2 HRSG Accessories	N/A	Not present
7.3 Ductwork	Factored estimate based on DOE Case 11	Total Fuel Feed, lb/hr
7.4 Stack	Factored estimate based on DOE Case 11	Stack Flow, acfm
7.9 Duct & Stack Foundations	Factored estimate based on DOE Case 11	Total Fuel Feed, lb/hr
8 STEAM TURBINE GENERATOR		
8.1 Steam TG & Accessories	Factored estimate based on DOE Case 11	Turbine Capacity, MW
8.2 Turbine Plant Auxiliaries	Factored estimate based on DOE Case 11	Turbine Capacity, MW
8.3 Condenser & Auxiliaries	Factored estimate based on DOE Case 11	Condenser Duty, MMBtu/hr
8.4 Steam Piping	Factored estimate based on DOE Case 11	HP BFW Flow Rate, lb/hr
8.9 TG Foundations	Factored estimate based on DOE Case 11	Turbine Capacity, MW

Account Number / Description	Cost Estimate Basis	Oxy-PC Cost Adjustment Rationale
9 COOLING WATER SYSTEM		
9.1 Cooling Towers	Factored estimate based on DOE Case 11	Cooling Tower Duty, MMBtu/hr
9.2 Circulating Water Pumps	Factored estimate based on DOE Case 11	Circulating Water Flow Rate, gpm
9.3 Circ.Water System Auxiliaries	Factored estimate based on DOE Case 11	Circulating Water Flow Rate, gpm
9.4 Circ.Water Piping	Factored estimate based on DOE Case 11	Circulating Water Flow Rate, gpm
9.5 Make-up Water System	Factored estimate based on DOE Case 11	Raw Water makeup, gpm
9.6 Component Cooling Water Sys	Factored estimate based on DOE Case 11	Circulating Water Flow Rate, gpm
9.9 Circ.Water System Foundations& Structures	Factored estimate based on DOE Case 11	Circulating Water Flow Rate, gpm
10 ASH/SPENT SORBENT HANDLING SYS		
10.1 Rotary Ash Coolers	Vendor Cost Estimate	N/A
10.2 Cyclone Ash Letdown	Factored estimate based on DOE Case 11	Same
10.3 HGCU Ash Letdown	Factored estimate based on DOE Case 11	Not present
10.4 High Temperature Ash Piping	Factored estimate based on DOE Case 11	Same
10.5 Reducer Baghouse Ash Recycle System	Factored estimate based on DOE Case 11	Baghouse Ash Flow, lb/hr
10.6 Ash Storage Silos	Factored estimate based on DOE Case 11	Total Ash Flow, lb/hr
10.7 Ash Transport & Feed Equipment	Factored estimate based on DOE Case 11	Total Ash Flow, lb/hr
10.8 Misc. Ash Handling Equipment	Factored estimate based on DOE Case 11	Total Ash Flow, lb/hr
10.9 Ash/Spent Sorbent Foundation	Factored estimate based on DOE Case 11	Total Ash Flow, lb/hr
11 ACCESSORY ELECTRIC PLANT		
11.1 Generator Equipment	Factored estimate based on DOE Case 11	Turbine Capacity, MW
11.2 Station Service Equipment	Factored estimate based on DOE Case 11	Auxiliary Load, kW
11.3 Switchgear & Motor Control	Factored estimate based on DOE Case 11	Auxiliary Load, kW
11.4 Conduit & Cable Tray	Factored estimate based on DOE Case 11	Auxiliary Load, kW
11.5 Wire & Cable	Factored estimate based on DOE Case 11	Auxiliary Load, kW
11.6 Protective Equipment	Factored estimate based on DOE Case 11	Auxiliary Load, kW
11.7 Standby Equipment	Factored estimate based on DOE Case 11	Turbine Capacity, MW
11.8 Main Power Transformers	Factored estimate based on DOE Case 11	Turbine Capacity, MW
11.9 Electrical Foundations	Factored estimate based on DOE Case 11	Turbine Capacity, MW

Account Number / Description	Cost Estimate Basis	Oxy-PC Cost Adjustment Rationale
12 INSTRUMENTATION & CONTROL		
12.1 PC Control Equipment (w 12.7)	Factored estimate based on DOE Case 11	Same
12.2 Combustion Turbine Control	Factored estimate based on DOE Case 11	Same
12.3 Steam Turbine Control (w 8.1)	Factored estimate based on DOE Case 11	Same
12.4 Other Major Component Control	Factored estimate based on DOE Case 11	Same
12.5 Signal Processing Equipment (w12.7)	Factored estimate based on DOE Case 11	Same
12.6 Control Boards,Panels & Racks	Factored estimate based on DOE Case 11	Auxiliary Load, kW
12.7 Distributed Control System Equipment	Factored estimate based on DOE Case 11	Auxiliary Load, kW
12.8 Instrument Wiring & Tubing	Factored estimate based on DOE Case 11	Auxiliary Load, kW
12.9 Other I & C Equipment	Factored estimate based on DOE Case 11	Auxiliary Load, kW
13 IMPROVEMENTS TO SITE		
13.1 Site Preparation	Factored estimate based on DOE Case 11	BEC (minus Accounts 13 & 14)
13.2 Site Improvements	Factored estimate based on DOE Case 11	BEC (minus Accounts 13 & 14)
13.3 Site Facilities	Factored estimate based on DOE Case 11	BEC (minus Accounts 13 & 14)
14 BUILDINGS & STRUCTURES		
14.1 Boiler Building	Factored estimate based on DOE Case 11	BEC (minus Accounts 13 & 14)
14.2 Turbine Building	Factored estimate based on DOE Case 11	BEC (minus Accounts 13 & 14)
14.3 Administration Building	Factored estimate based on DOE Case 11	BEC (minus Accounts 13 & 14)
14.4 Circulation Water Pumphouse	Factored estimate based on DOE Case 11	Circulating Water Flow Rate, gpm
14.5 Water Treatment Buildings	Factored estimate based on DOE Case 11	BEC (minus Accounts 13 & 14)
14.6 Machine Shop	Factored estimate based on DOE Case 11	BEC (minus Accounts 13 & 14)
14.7 Warehouse	Factored estimate based on DOE Case 11	BEC (minus Accounts 13 & 14)
14.8 Other Buildings & Structures	Factored estimate based on DOE Case 11	BEC (minus Accounts 13 & 14)
14.9 Waste Treating Building & Str.	Factored estimate based on DOE Case 11	Raw Water Makeup, gpm

3.9.2 Home Office, Process, and Project Contingencies

The Bare Erected Cost (BEC) includes the cost of all oxy-fired and air-fired PC process equipment, on-site facilities, and infrastructure necessary to operate the plant. It also includes the labor required for construction and equipment installation. The Total Plant Cost (TPC) is derived by added Engineering, Procurement, and Construction Management (EPCM) costs, along with Process and Project Contingencies to the Bare Erected Cost.

EPCM

The EPCM contractor services include all home office engineering and procurement services as well as field construction management costs. These services typically range from 8-10% of the BEC. For this study, the EPCM costs were fixed at 9% of the BEC.

Process Contingencies

Process contingencies were applied to selected capital cost estimates to compensate for performance uncertainties associated with the developmental status of the oxy-fired technology. A process contingency was applied to oxy-fired process technology areas that are still under development. A 20% process contingency was applied to oxy-PC boiler process technology areas that have not been demonstrated commercially and were thus designed using experimental data such as from Alstom's Boiler Simulation Test Facility. Process contingencies were applied to the following equipment areas:

- Flue Gas Recirculation System
- Oxygen Mixers

No process contingencies were taken for the air separation unit nor the gas processing unit (CO_2 purification and compression), consistent with the approach taken by the DOE for Case 5C and other oxy-combustion cases.

Project Contingencies

Project contingencies were added to each capital account to cover project uncertainties and the cost of additional equipment that would be identified in a detailed design. The project contingencies represent costs that are expected to occur but were not identified in the individual cost accounts. The contingencies are applied to the BEC, EPCM, and Process Contingencies. For new equipment, the contingencies were either set to 15% or based on the contingency used in DOE Case 11 for similar equipment. The average Project Contingency for the oxy-fired cases was approximately 14%.

3.9.3 Estimation of Owner's Costs

Table 3-12 summarizes the procedure for estimating owner's costs. The methodology is defined by the DOE Cost Estimation Methodology[22] and mostly follows the guidelines from Sections 12.4.7 to 12.4.12 of AACE International Recommended Practice No. 16R-90.[23] This procedure is very similar to the guidelines established in EPRI's Technical Assessment Guide (TAG).

Table 3-12: Estimation Method for Owner's Costs

Owner's Cost	Estimate Basis
Prepaid Royalties	Any technology royalties are assumed to be included in the associated equipment cost, and thus are not included as an owner's cost.
Preproduction (Start-Up) Costs	• 6 months operating labor • 1 month maintenance materials at full capacity • 1 month non-fuel consumables at full capacity • 1 month waste disposal • 25% of one month's fuel cost at full capacity • 2% of TPC Compared to AACE 16R-90, this includes additional costs for operating labor (6 months versus 1 month) to cover the cost of training the plant operators, including their participation in startup, and involving them occasionally during the design and construction. AACE 16R-90 and EPRI TAG® differ on the amount of fuel cost to include; this estimate follows EPRI.
Working Capital	Although inventory capital (see below) is accounted for, no additional costs are included for working capital.
Inventory Capital	• 0.5% of TPC for spare parts • 60 day supply (at full capacity) of fuel. Not applicable for natural gas. • 60 day supply (at full capacity) of non-fuel consumables (e.g., chemicals and catalysts) that are stored on site. Does not include catalysts and adsorbents that are batch replacements such as WGS, COS, and SCR catalysts and activated carbon. AACE 16R-90 does not include an inventory cost for fuel, but EPRI TAG® does.
Land	• $3,000/acre (300 acres for PC and LCL-C™)

[22] Cost Estimation Methodology for NETL Assessments of Power Plant Performance, DOE/NETL-2011/1455, April 2011, pg. 5-6

[23] Conducting Technical and Economic Evaluations – As Applied for the Process and Utility Industries, AACE International Recommended Practice No. 16R-90.

Owner's Cost	Estimate Basis
Financing Cost	• 2.7% of TPC This financing cost (not included by AACE 16R-90) covers the cost of securing financing, including fees and closing costs but not including interest during construction (or AFUDC). The "rule of thumb" estimate (2.7% of TPC) is based on a 2008 private communication with a capital services firm.
Other Owner's Costs	• 15% of TPC This additional lumped cost is not included by AACE 16R-90 or EPRI TAG®. The "rule of thumb" estimate (15% of TPC) is based on a 2009 private communication with Worley-Parsons. The lumped cost includes: - Preliminary feasibility studies, including a Front-End Engineering Design (FEED) study - Economic development (costs for incentivizing local collaboration and support) - Construction and/or improvement of roads and/or railroad spurs outside of site boundary - Legal fees - Permitting costs - Owner's engineering (staff paid by owner to give third-party advice and to help the owner oversee/evaluate the work of the EPC contractor and other contractors) - Owner's contingency (Sometimes called "management reserve", these are funds to cover costs relating to delayed startup, fluctuations in equipment costs, unplanned labor incentives in excess of a five-day/ten-hour-per-day work week. Owner's contingency is NOT part of project contingency.) This lumped cost does NOT include: - EPC Risk Premiums (costs estimates are based on an Engineering Procurement Construction Management approach utilizing multiple subcontracts, in which the owner assumes project risks for performance, schedule and cost) - Transmission interconnection: the cost of interconnecting with power Transmission infrastructure beyond the plant busbar. - Taxes on capital costs: all capital costs are assumed to be exempt from state and local taxes. - Unusual site improvements: normal costs associated with improvements to the plant site are included in the bare erected cost, assuming that the site is level and requires no environmental remediation. Unusual costs associated with the following Design parameters are excluded: flood plain considerations, existing soil/site conditions, water discharges and reuse, rainfall/snowfall criteria, seismic Design, buildings/enclosures, fire protection, local code height requirements, noise

3.9.4 Operations and Maintenance Costs

The Operations and Maintenance (O&M) costs include all costs related to operating or maintaining the oxy-fired and air-fired plants over their expected life. These costs include the following items:

- Operating labor
- Maintenance – material and labor
- Administrative and support labor
- Consumables
- Fuel
- Waste disposal

The O&M has two components:

- Fixed O&M includes costs independent of power generation
- Variable O&M includes costs proportional to power generation

Fixed O&M Costs

The labor rates selected for this study were identical to those developed by WorleyParsons and used in the updated DOE Cost and Performance Baseline Report.[24] An independent check of labor rates was made by checking the prevailing wage rates for skilled crafts in Ohio. These rates were consistent with the rates used in the updated DOE Baseline report after correcting to a common dollar basis. Assumptions used to calculate the fixed O&M costs include:

- The labor rates used in this study were based on merit shop rates for a Midwest location. The rates are based on a 50 hour work week for a greenfield site.
- Operating Labor is based on a base labor rate of $39.70/hour.
- Labor burden is assumed to be 30 percent of the base labor rate.
- Administrative and support labor is 25% of the burdened O&M labor
- Taxes and insurance are considered as fixed O&M costs and are estimated as 2 percent of the Total Plant Cost (TPC).

[24] Updated Costs (June 2011 Basis) for Selection Bituminous Baseline Cases, DOE/NETL-341/082312, August 2012

Variable O&M Costs

Variable costs include the cost of all consumables, including fuel, sorbent, water, etc. The unit costs for consumables and waste disposal were based on the updated DOE Baseline Report.[22]

3.10 Economic Assumptions

This section summarizes the economic assumptions that were used in this study for the financial structure, estimation of owner's costs, global economic parameters, and labor rates. In addition, all costs developed in this study for the oxy-fired and air-fired cases were normalized to June 2011 dollars to facilitate comparison with other DOE system studies.

3.10.1 Financial Structure Selection

The financial structure for the cases in this study was based on an Investor Owned Utility (IOU) financial structure with a 5 year capital expenditure period, as specified in the DOE Cost Estimation Methodology report.[25] The financial structure for both low and high risk cases is shown in Table 3-13. The air-fired plants without capture are considered low risk, while all of the oxy-fired plants are considered high risk.

Table 3-13: Financial Structure for Investor Owned Utility High and Low Risk Projects

Type of Security	% of Total	Current (Nominal) Dollar Cost	Weighted Current (Nominal) Cost	After Tax Weighted Cost of Capital
		LOW RISK		
Debt	50	4.50%	2.25%	
Equity	50	12%	6%	
Total			8.25%	7.39%
		HIGH RISK		
Debt	45	5.50%	2.48%	
Equity	55	12%	6.60%	
Total			9.08%	8.13%

3.10.2 Global Economic Assumptions

Table 3-14 summarizes the global economic assumptions that were used for evaluating the economic performances of each case in this study. The assumptions are specified in the DOE Cost Estimation Methodology. [26]

[25] Cost Estimation Methodology for NETL Assessments of Power Plant Performance, DOE/NETL-2011/1455, April 2011, pg. 9
[26] Cost Estimation Methodology for NETL Assessments of Power Plant Performance, DOE/NETL-2011/1455, April 2011, pg. 8

Table 3-14: Global Economic Assumptions

Parameter	Value
TAXES	
Income Tax Rate	38% Effective (34% Federal, 6% State)
Capital Depreciation	20 years, 150% declining balance
Investment Tax Credit	0%
Tax Holiday	0 years
CONTRACTING AND FINANCING TERMS	
Contracting Strategy	Engineering Procurement Construction Management (owner assumes project risks for performance, schedule and cost)
Type of Debt Financing	Non-Recourse (collateral that secures debt is limited to the real assets of the project)
Repayment Term of Debt	15 years
Grace Period on Debt Repayment	0 years
Debt Reserve Fund	None
ANALYSIS TIME PERIODS	
Capital Expenditure Period	5 Years
Operational Period	30 years
Economic Analysis Period (used for IRROE)	35 Years (capital expenditure period plus operational period)
TREATMENT OF CAPITAL COSTS	
Capital Cost Escalation During Capital Expenditure Period (nominal annual rate)	3.6%[1]
Distribution of Total Overnight Capital over the Capital Expenditure Period (before escalation)	5-Year Period: 10%, 30%, 25%, 20%, 15%
Working Capital	zero for all parameters
% of Total Overnight Capital that is Depreciated	100% (this assumption introduces a very small error even if a substantial amount of TOC is actually non-depreciable)
ESCALATION OF OPERATING REVENUES AND COSTS	
Escalation of COE (revenue), O&M Costs, Fuel Costs (nominal annual rate)	3.0%[2]

[1] A nominal average annual rate of 3.6% is assumed for escalation of capital costs during construction. This rate is equivalent to the nominal average annual escalation rate for process plant construction costs between 1947 and 2008 according to the Chemical Engineering Plant Cost Index.

[2] An average annual inflation rate of 3.0% is assumed. This rate is equivalent to the average annual escalation rate between 1947 and 2008 for the U.S. Department of Labor's Producer Price Index for Finished Goods, the so-called "headline" index of the various Producer Price Indices. (The Producer Price Index for the Electric Power Generation Industry may be more applicable, but that data does not provide a long-term historical perspective since it only dates back to December 2003.)

3.11 Cost of Electricity

The first year Cost of Electricity (COE) is the revenue received by the generator per net MWhr during the first year of operation assuming that the first year of operation COE escalates at a nominal annual rate equal to the general inflation rate (i.e. remains constant in real terms over the operational period of the plant). The levelized COE (LCOE) is the revenue received by the generator per net MWhr during the first year of operation assuming that the first year of operation COE escalates at a nominal annual rate of 0% (i.e. remains constant in nominal terms over the operation period of the plant).

The first year COE was developed using two different methodologies, consistent with the DOE guidelines.[27] The first method uses the NETL Power Systems Financial Model (PSFM). The model accepts all of the economic assumptions outlined in Table 3-13 and Table 3-14, along with specific information on the capital cost and fixed/variable O&M costs for each case. An alternative approach is to use the simplified capital charge factor method to calculate the cost of electricity. This alternate approach is described below. Both COE methodologies provide similar results and both were used for analysis of the oxy-fired cases.

Simplified Capital Charge Factor Methodology

A simplified method of calculating the first year cost of electricity is also provided in the DOE Financial Model User's Guide.[28] The PSFM calculates a first year capital charge factor (CCF) that can be used to calculate the COE with the simplified equation shown below. Based on the economic factors specified by the DOE, the CCF for the air-fired cases is 0.116 based on a Low Risk Investor Owned Utility (IOU) and five year capital expenditure period. The CCF for the oxy-fired cases and for the DOE oxy-PC Case 5C is 0.124 based on a High Risk Investor Owned Utility (IOU) and five year capital expenditure period.

The simplified COE is calculated by the following equation:

$$COE = \frac{(CCF)(TOC) + OC_{FIX} + (CF)\,OC_{VAR}}{(CF)\,(MWh)}$$

where:

COE = revenue received by the generator ($/MWh) during the oxy-fired power plant's first year of operation (expressed in 2011 dollars), assuming that the COE escalates at a

[27] Power Systems Financial Model Version 6.6 User's Guide, DOE/NETL-2011/1492, May 2011
[28] Power Systems Financial Model Version 6.6 User's Guide, DOE/NETL-2011/1492, May 2011, pg. 14

nominal annual rate equal to the general inflation rate, i.e., that it remains constant in real terms over the operational period of the power plant.

CCF = is the first year Capital Charge Factor that matches the applicable finance structure and capital expenditure period

TOC = Total Overnight Capital in 2011 dollars

OC_{FIX} = the sum of all fixed annual operating costs in 2011 dollars

OC_{VAR} = the sum of all variable annual operating costs, including fuel at 100% capacity factor, in 2011 dollars

CF = plant capacity factor, assumed to be constant over the operational period

MWH = annual net megawatt-hours of power generated at 100% capacity factor

Levelized COE

The Power Systems Financial Model provides the LCOE on a current dollar basis over a levelization period equal to the plants operational life – i.e., the LCOE is constant in current dollars over this period. The model provides a Levelization factor that can be multiplied by the COE to give the LCOE in base year dollars. The Levelization Factor for NETL defined economic inputs is 1.268.

3.12 Costs of CO_2 Captured (Removed) and Avoided

The cost of CO_2 captured was calculated both from the standpoint of the cost of CO_2 removed and the cost of CO_2 avoided.

The Cost of CO_2 Captured or Removed in $/ton or $/tonne is given by:

$$\text{Cost of } CO_2 \text{ Captured} = \frac{(COE_{\text{with removal}} - COE_{\text{w/o removal}})}{(CO_2 \text{ Captured})}$$

where

COE = cost of electricity ($/$MWh_{net}$)

CO_2 Captured = CO_2 captured for case (tonnes/MWh_{net} or tons/MWh_{net})

The equation used to calculate the Cost of CO_2 Avoided in $/ton or $/tonne is as follows:

$$\text{Cost of } CO_2 \text{ Avoided} = \frac{(COE_{\text{with removal}} - COE_{\text{w/o removal}})}{(\text{Emissions}_{\text{w/o removal}} - \text{Emissions}_{\text{with removal}})}$$

where

COE = cost of electricity ($/MWh$_{net}$)

Emissions = CO_2 emissions for case (tonnes/MWh$_{net}$ or tons/MWh$_{net}$)

3.13 Costs of CO_2 Transport and Storage

The cost of CO_2 transport and storage (T&S) needs to be included in the cost of electricity to derive the complete cost of capturing and storing CO_2. The updated DOE Baseline Report[29] specified the conditions and T&S costs to be used for DOE system studies. The costs are based on transporting high pressure (2200 psig) CO_2 from the oxy-fired power plant through a 100km (62 mile) pipeline to the sequestration or EOR site. The CO_2 leaves the pipeline at a pressure of 1200 psig still in a supercritical state. For a Midwest plant location, the T&S value specified for DOE system studies is $10/tonne CO_2 in 2011 dollars.

3.14 Incremental Cost of Steam

The oxy-fired industrial steam plant included in this study is a retrofit of an existing air-fired industrial steam plant. The study focused solely on the costs to retrofit the air-fired boiler island to oxy-fired capability. Costs were therefore developed for the boiler island modifications and for the ASU and GPU. The economic metric for the industrial steam plant retrofit is the cost of steam generation, since the plant is used to generate process steam vs. power generation. The cost of steam developed in this study represents the incremental increase in the cost of steam of an oxy-fired industrial steam plant vs. an air-fired industrial steam plant.

[29] Updated Costs (June 2011 Basis) for Selection Bituminous Baseline Cases, DOE/NETL-341/082312, August 2012, pg. 5-6

4. Oxy-Fired Demonstration Unit Design and Costs (450MW)

This section describes a pulverized coal fired utility scale steam generator unit capable of using either air or oxygen for combustion of the fuel. It is part of a steam power plant that produces a nominal gross output of 450 MW_e. The plant was designed as an oxy-fired demonstration plant and thus has some degree of conservatism in its design. This plant, when operating in the oxy-fired mode, is designed to capture 93 percent of the CO_2 produced. The CO_2 product is purified to a level that is acceptable for EOR applications, although the intention is to sequester the CO_2 in a saline aquifer.

The section will concentrate on the description of the oxy-fired boiler itself, which was the focus of this study. It will also highlight where differences exist with the air-fired boiler and special features included in the design. A brief description is included for the ASU, GPU, AQCS system, steam turbine, and balance of plant equipment. This equipment is all based on similar equipment designed for the DOE Baseline Case 11 (air-fired SCPC w/o capture)[30] and Case 5C (oxy-fired SCPC)[31]. This equipment was resized for this study and the costs were re-estimated using scaling factors provided by the DOE[32].

The oxy-fired cases have process areas that are common to the 450MW and 900MW plant and the Industrial Boiler, such as coal receiving and storage, emissions control technologies, power generation, etc. As detailed descriptions of these process areas in each case section would be repetitious, they are presented in this section for general background information. The performance features of these sections are then presented in the case-specific sections.

4.1 Boiler Description (450MW)

The boiler is designed for pulverized coal-firing with a nominal gross capacity of approximately 450 MW_e. It is designed for full load capability using either air or oxygen as the oxidant for combustion of the fuel. The boiler is a sliding pressure supercritical (SPSC), once-through design, utilizing a TFS 2000™ firing system and SCR for NO_X control. It is a single reheat unit designed for variable pressure operation, with a balanced draft furnace. The unit is capable of firing a range of pulverized coals, producing continuous steam flow to the turbine generator with nominal boiler maximum continuous rating (BMCR) outlet conditions of 2,550,700 lbm/hr (321.4 kg/s), 3,927 psig (270.8 bar), 1,117°F (602.5 °C) at the superheater outlet, and 2,103,500 lbm/hr (265.0 kg/s), 726 psig (50.1 bar), 1,148°F (620.4°C) at the reheater outlet. Heavy fuel oil is used for start-up and as a support fuel during low load operation.

[30] Cost and Performance Baseline for Fossil Energy Plants Volume 1, DOE/NETL-2010/1397, November 2010 - Case 11
[31] Pulverized Coal Oxycombustion Power Plants Volume 1, DOE/NETL-2007/1291, August 2008 – Case 5C
[32] Capital Cost Scaling Methodology, Quality Guidelines for Energy System Studies, DOE/NETL-341/013113, January 2013

The once-through system is characterized by the arrangement of the evaporator sections in the main water/steam flow system and by the steam/water separator that is placed at the end of the evaporator sections. In a once-through system, the water flows only once through the evaporator circuit where it is converted into steam. At the outlet of the evaporator walls, or waterwalls, the steam produced is slightly superheated. In the load range between the minimum once-through load and the maximum load, the medium is always in a superheated condition and the steam/water separator operates in a dry mode. The advantage of the once-through system is that there is no fixed point at which the waterwall system ends and the superheater system starts. This system can operate with a very wide range of fuels and at different levels of furnace cleanliness.

Above the minimum once-through load, the separator is only a transit element. Below minimum once-through load, it performs its separation function. During start-up and low load operation, the steam/water mixture is separated in the separator. The steam goes to the superheater and the water to the start-up system. Above the minimum once-through load, the mass flow rate in the waterwalls is large enough to cool the waterwall tubes sufficiently, so that the start-up system is no longer needed in operation.

Below the minimum once through load (approximately thirty-five percent TMCR), the mass flow in the waterwalls is kept above a minimum value with water recirculation by the start-up system. At these low loads, a mixture of water and steam leaves the waterwalls and the steam/water separators operate in a wet condition. Care has been taken in selecting the location of the steam/water separators to ensure a smooth transition from the recirculating waterwall flow mode to the once-through flow mode. In addition, no significant steam temperature excursions occur at the superheater outlet.

The boiler is designed to operate in either the air mode or oxygen mode. The aspects of the oxy-fired process and the boiler island modifications required for oxygen firing are described below.

4.2 Oxygen Firing Process Considerations

Oxy-fired combustion replaces combustion air with a mixture of nearly pure oxygen and recycled flue gas. The resulting flue gas, – primarily CO_2 and H_2O vapor along with some N_2, O_2, and trace gases like SO_2 and NO_x – is then dried, compressed, and purified for sequestration, or used for enhanced oil or gas recovery.

The primary impacts of oxy-firing on the boiler design are associated with the potentially reduced combustion gas flow due to the removal of nitrogen (present with air firing) and the differences in the thermal and radiant properties of the flue gas. Burning coal with pure oxygen would result in excessive furnace temperatures causing ash slagging issues, corrosion issues, fine ash aerosols, and damage to boiler waterwalls if steam-side circulation is insufficient. Recycling a portion of the flue gas can compensate for these impacts. Thus, the furnace temperature can be maintained low enough to avoid ash slagging, fouling and corrosion, and the heat flux to furnace walls can be maintained within the limits imposed to prevent overheating of the tubes.

The location of the flue gas recirculation take-off can have a significant impact on the design and operation of the boiler and ancillary equipment. As gas recycle is taken closer to the boiler outlet, more of the downstream equipment can be reduced in size and cost. However, the concentration of impurities returned to the boiler increases as the gas recycle takeoff point approaches the boiler outlet, which impacts ash deposition, corrosion and pollutant levels, and must be addressed in the boiler design. Trade-offs between boiler impacts and downstream equipment savings are generally controlled by fuel characteristics and site-specific factors.

The basic concept entails:

- Use Oxygen instead of air for the combustion process in order to obtain a CO_2 rich flue gas mainly composed of CO_2 and H_2O (and some inert gases) "easily" cleaned and compressed
- Obtain the adequate purity of CO_2 in the flue gas in order to reach a composition suitable for transport under supercritical phase and then storage

This leads to the addition of two units to the conventional coal fired power plant:

- Air Separation Unit (ASU): An oxygen production unit
- Gas Processing Unit (GPU): A CO_2 purification unit to clean and compress under supercritical state the remaining CO_2 out of flue gas

In addition some modifications of the power plant itself are necessary, mainly:

- Partial recirculation of the flue gas in order to maintain appropriate temperature and heat absorption in the furnace and convection pass
- Removal of the water from the flue gas before treatment in the GPU: Flue Gas Condenser
- Minimisation of leakage of air into the boiler
- Sizing of equipment, taking into account the additional needs of ASU and GPU (mainly electrical energy, water…)
- Injection/Mixing of oxygen in the flue gas path

The basic oxy-firing concept uses a mixture of oxygen and recirculated flue gas as an oxidant to replace combustion air. Oxy-coal combustion produces a flue gas stream comprised of mainly CO_2 and water vapor with much smaller amounts of oxygen, nitrogen, argon, sulfur dioxide, etc. The flue gas leaving the boiler is cooled and cleaned of ash and sulfur compounds in traditional boiler island equipment. It is then dried, compressed, and purified into a CO_2 product stream in the Gas Processing Unit (GPU). It can then be available as a product for usage or for sequestration. Some of the flue gas produced is recirculated and mixed with relatively pure oxygen to form the oxidant streams for combustion of the coal in the furnace as described below.

Burning coal with nearly pure oxygen in existing boiler designs without flue gas recirculation would result in excessive furnace temperatures. This would cause ash slagging/fouling issues, corrosion issues, fine ash aerosols, and possible damage to boiler waterwalls if steam-side circulation was insufficient for the associated high heat fluxes. Therefore, flue gas is recirculated back to the furnace to moderate the furnace gas temperatures and to provide sufficient gas flow for effective convection section heat absorption. Relatively pure oxygen is mixed with the recirculated flue gas streams to provide the oxidant streams (primary and secondary) for combustion of the pulverized coal in the furnace.

Figure 4-1 shows the basic process flow diagram selected for the oxygen-fired boiler island. New equipment added within the boiler scope to allow oxy-firing capability is relatively modest (relative to a comparable air-fired boiler equipment scope). New equipment would include oxygen supply lines and control valves (Streams 3, 3a, 3b, 3c), oxygen mixing devices, a low leakage "air" heater or gas to gas heater (GGH), a SO_3 mitigation system, and additional ductwork and dampers to connect the inlets of the PA and FD fans to the recirculated flue gas sources (Streams 18 and 27). The flue gas recirculation (FGR) ducts also include isolation dampers and inlets for primary and secondary air, which are used during air firing, start-up, and during the transition between air and oxygen firing.

Additionally, sizing of the fans and ducts can be different than for an air-fired design due to the higher density of the recirculated flue gas as compared to air. The windbox is also modified in order to accommodate the use of a stream of nearly pure oxygen provided from the ASU. About 30% of the total oxygen produced in the ASU is introduced directly in the windbox (Stream 3c in Figure 4-1). This is done in order to keep oxygen content in the primary and secondary streams (Streams 25 and 30 in Figure 4-1) below a threshold value, above which would require the use of more costly alloys for the ducts and other equipment downstream of the oxygen mixing locations.

Other major new equipment/systems within the overall power plant scope to allow oxy-firing and CO_2 capture include a cryogenic distillation type Air Separation Unit (ASU) to produce the oxygen, a Flue Gas Condenser (FGC) to remove water vapor from the flue gas, and a Gas Processing Unit (GPU) to further purify the flue gas (mainly CO_2) to meet the CO_2 product specification.

There are several options available for the source of the flue gas for recirculation (FGR). The advantage of extracting the FGR nearer to the boiler is that the size of all downstream equipment can be reduced since it would be handling less flue gas flow. The disadvantage of taking FGR from locations nearer the boiler is the resulting higher concentrations of particulate, sulfur, chlorides, alkali, etc. in the recirculation loop, if the FGR source is located before the removal of these materials. This FGR location option is discussed further in the Sensitivity Study section.

Two flue gas recirculation locations were selected in this design as shown in Figure 4-1. Primary FGR is taken after the flue gas condenser (Stream 18) where most of the water vapor has been condensed (typically, about 4-6% by volume water vapor remains in the primary FGR stream). The primary FGR stream, after being mixed with oxygen, serves to dry the coal during pulverization and to transport the pulverized coal to the furnace for combustion. Primary FGR is also utilized for seal gas (instead of seal air) to reduce boiler air in-leakage. The seal gas is extracted from the primary FGR stream at a location just before the oxygen is mixed. The seal gas flow is kept as low as possible to minimize flow through the flue gas condenser equipment. Secondary FGR is taken downstream of flue gas desulphurization (FGD) system (Stream 27) to minimize the recycle of SO_2 within the boiler system. Oxygen is also mixed with the secondary FGR stream. The quantity of secondary FGR is established to provide conditions that meet the steam side heat requirements without causing excessive heat fluxes, slagging, fouling, or tube erosion problems.

Oxygen produced from the ASU is mixed with the recirculated flue gas streams in three locations. The first two mixing locations are just upstream of the PA and FD fans. Enough oxygen is added in these locations to provide oxygen content of 21 percent by volume in these streams. The mixers used are of the grid type design. The main advantages of mixing oxygen in these locations are to minimize ASU power requirements (lower O_2 pressure required by mixing before the fans) and to improve the GGH preheater performance (lower sink temperature and higher sink mass flow) thus providing a boiler efficiency improvement without the addition of a separate oxygen heater in the flue gas stream. Another requirement is to achieve a safe mixing of oxygen in the recirculated flue gas stream before the gas to gas preheater to avoid the risks associated with areas of high oxygen concentration in the presence of dust. The third oxygen stream, which represents the remaining oxygen required for complete combustion of the coal, is mixed with the heated secondary oxidant stream within the windbox.

Additionally, a low leakage Ljungstrom® gas-to-gas preheater design (total leakage of oxidant streams to flue gas stream < 1 percent) was specified to minimize the effects of oxygen leakage into the flue gas stream. Minimization of the GGH leakage reduces the ID and FD fan power and more importantly reduces the energy intensive ASU and GPU power requirements thus improving plant thermal efficiency.

Other changes include SO_3 mitigation, duct lining, fan protection, quad-sector vs. tri-sector air heater for leakage reduction, air heater enamelled section, O_2 control, and material selection depending on O_2 temperature.

.

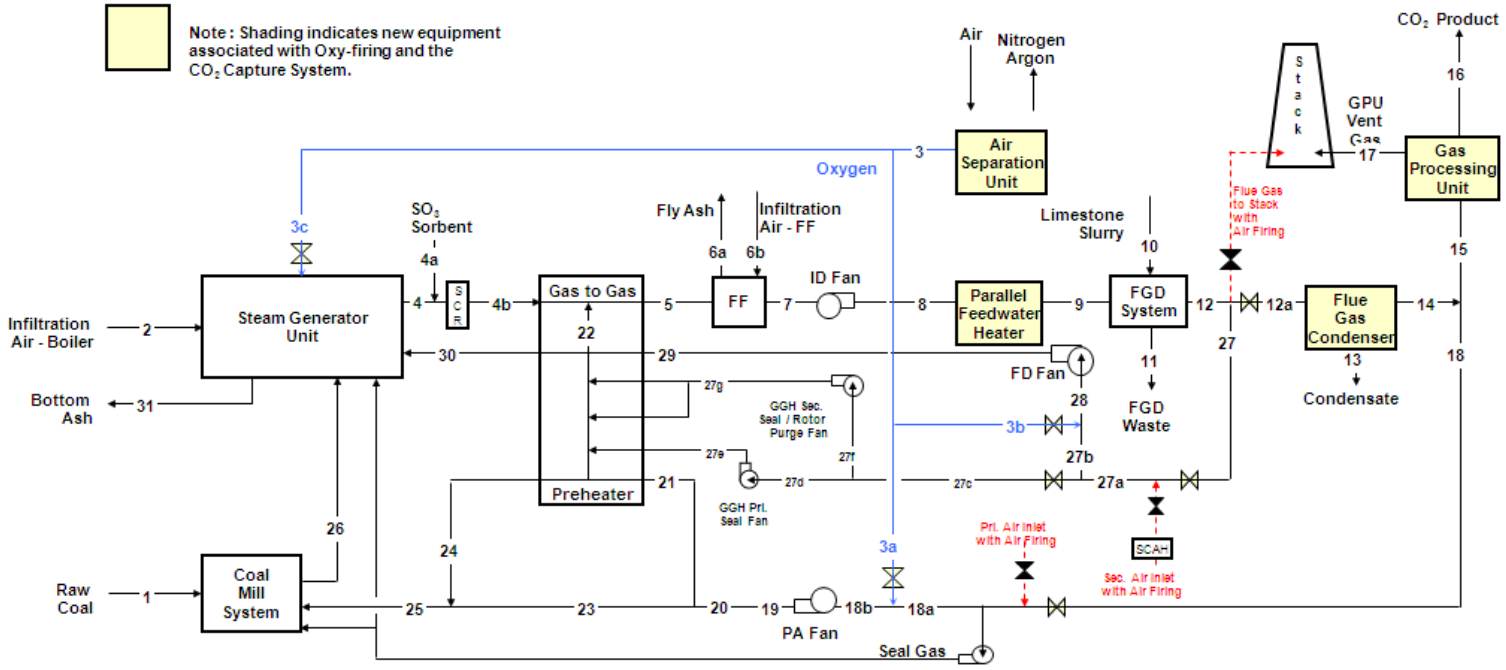

Material Flow Stream Identification

1	Raw Coal to Pulverizers	11	FGD System Waste to Disposal	24	Heated Primary "Air" from GGH
2	Boiler Infiltration Air	12	Fluegas leaving FGD	25	Tempered Primary "Air" to Pulverizers
3	Total Oxygen leaving ASU	12a	Fluegas Leaving FGD to Condenser	26	Pulverized Coal and Primary "Air" to Furnace
3a	Oxygen to Primary "Air" Stream	13	Condensed Water Stream from Fluegas	27	Recirc Secondary FG Stream from FGD
3b	Oxygen to Secondary "Air" Stream	14	Cooled Fluegas Stream	27a	Recirculated Secondary Fluegas
3c	Oxygen Stream to Windbox	15	Fluegas to Gas Processing Unit	27b	Recirculated Secondary Fluegas to O2 Mixer
4	Fluegas from Economizer to SCR	16	Compressed CO_2 Product	27c	GGH Seal and Purge Gas Stream (total)
4a	SO_3 Sorbent Injection	17	Vent from Gas Processing Unit	27d	GGH Primary Seal Gas to Fan
4b	Fluegas from SCR to Gas-Gas Heater (GGH)	18	Recirc Primary FG Stream from Condenser	27e	GGH Primary Seal Gas from Fan to GGH
5	Fluegas Leaving GGH to FF	18a	Recirc Primary FG Stream to O2 Mixer	27f	GGH Secondary Seal and Purge Gas to Fan
6a	Flyash Leaving FF	18b	Recirc Primary "Air" Stream to PA Fan	27g	GGH Sec. Seal and Purge Gas from Fan to GGH
6b	FF Infiltration Air	19	Pressurized Primary "Air" from PA Fan	28	Recirculated Secondary "Air" to FD Fan
7	Fluegas Leaving FF to ID Fan	20	Pressurized Primary "Air" to temp. split	29	Pressurized Secondary "Air" to GGH
8	Fluegas Leaving ID Fan to PFWH	21	Primary "Air" to GGH	30	Heated Secondary "Air" to Furnace
9	Fluegas Leaving PFWH to FGD	22	GGH Leakage Stream ("air" to flue gas)	31	Bottom Ash from Furnace to SSC
10	Limestone Slurry Feed to FGD System	23	Tempering Primary "Air"		

Figure 4-1: Boiler Island Process Flow Diagram (Oxy-Fired Mode)

4.3 Steam Generator Design

This section briefly describes several of the more important areas of the steam generator unit design.

4.3.1 Furnace

The boiler is arranged in a two-pass configuration with gas-tight welded-wall construction. The boiler is of the dry bottom type with spiral tubes enclosing the furnace from the coutant bottom to the approximate elevation of the nose arch. Vertical tubes form the remainder of the furnace enclosure, as shown in Figure 4-2 below. All furnace tubing is of the smooth bore type and is selected as required to meet the applicable code.

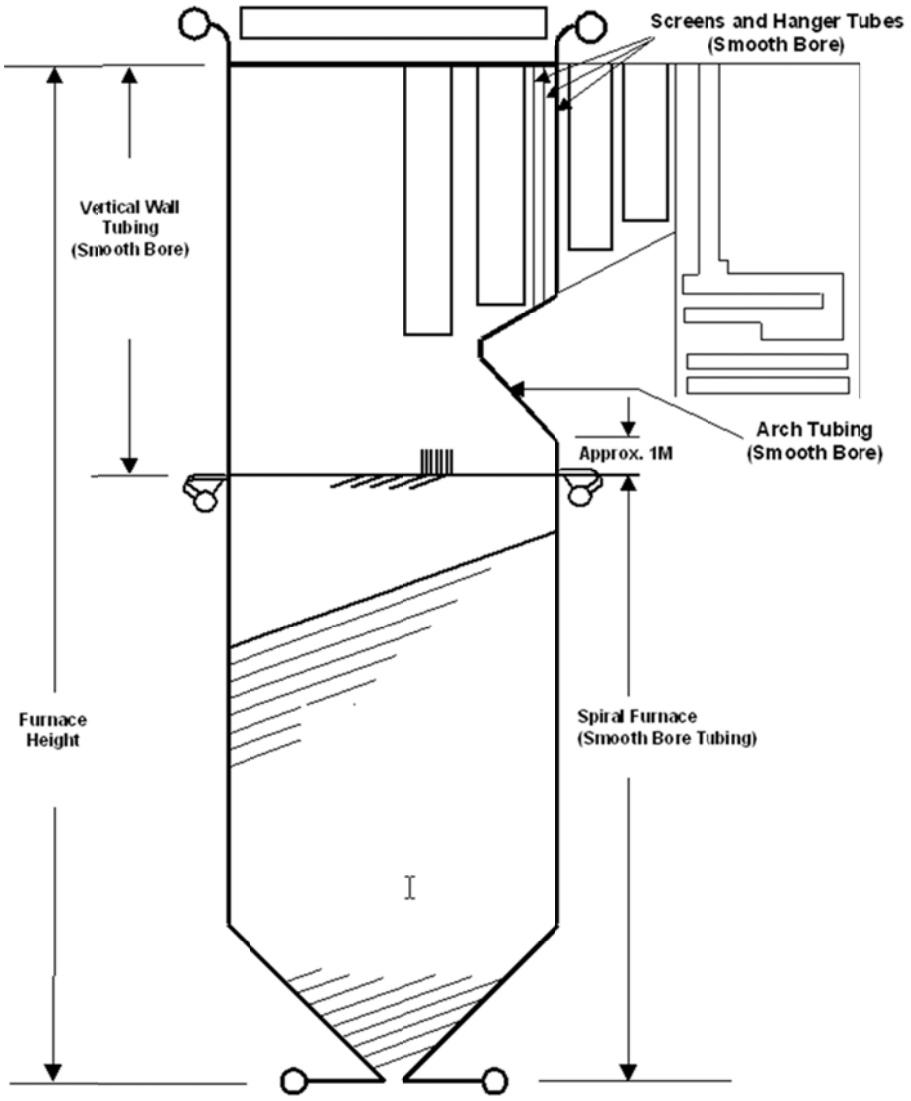

Figure 4-2: Furnace Design

The complex properties of coal and its ash have a major impact upon the design of the steam generator unit. The coal and ash must be carefully analysed, correctly interpreted, and appropriately applied to various aspects of the boiler design. It is the nature of the coal to be fired that ultimately determines the configuration and size of the furnace, convection pass, and air heater. The combustibility of the coal, the ash analysis and quantity, as well as the ash chemistry determines the slagging, fouling, and erosive properties to be considered under both air and oxy-firing conditions.

The furnace dimensions and the burner arrangement must reflect the resulting fuel ash slagging characteristics. While the ignition of coal particles and complete combustion must be achieved, sufficient radiant surfaces must be provided within the furnace to lower the gas temperature at the inlet to the convection heating surfaces to a level that eliminates sticky deposits from forming

on these surfaces. Based on experience with coal combustion in large furnaces and analytical investigations of coal ash behavior, characteristic parameters for the furnace have been derived to accurately determine furnace performance.

Considering the slagging characteristics associated with the coal ash, the furnace has been conservatively sized to reduce overall furnace temperatures and to minimize furnace slag accumulation. The furnace is designed to produce 100% BMCR steam flow for air or oxy-firing.

In addition, in order to minimize fouling in the superheater and reheater sections, the first three vertical heat transfer sections (superheater panels, superheater primary, and finishing reheater) are platenized.

4.3.2 Economizer

The economizer section is used to improve boiler efficiency by extracting heat from flue gas stream leaving the low temperature reheater section in the backpass of the unit. Heat is transferred from the flue gas to the feedwater, which enters the economizer at a temperature appreciably lower than that of saturated steam. The economizer is arranged for downward flow of flue gas and upward flow of water (counter-flow).

Feedwater and/or recirculated water enter from a lower header and flows through parallel rows of horizontal finned tubing, which comprises the heating surface. Return bends at the ends of the tubing provide continuous tube elements, with the upper ends connecting to junction headers located within the gas pass. The economizer terminal tubes act as hanger tubes for the horizontal low temperature reheater section. These tubes start at the junction headers and terminate at the economizer outlet header. The outlet header is connected to the lower waterwall inlet headers through connecting links.

Designing the economizer for counter-flow of flue gas and feedwater results in the maximum log mean temperature difference (LMTD) for efficient heat transfer. The selected economizer uses finned tubing arranged in a two-bank configuration. Only minor changes in surfacing are necessary to accommodate both air and oxy-firing. Upward flow of feedwater also helps to avoid water hammer, which may occur under the some operating conditions.

4.3.3 Superheater and Reheater

The superheater and reheater design depends on the specific duty to be performed. For relatively low final outlet steam temperatures, superheaters solely of the convection-type are generally used. For higher final temperatures, such as for this design, surface requirements are larger and, by necessity, superheater elements are located in higher gas temperature zones. Therefore, wide-spaced platen and/or panel superheaters and reheaters of the radiant type are used.

Convection sections are usually arranged for essentially pure counter-flow of steam and flue gas, with steam entering at the bottom and leaving at the top of the gas pass, while flue gas flow is the opposite. This arrangement allows for the maximum log mean temperature difference between

the gas and steam, which minimizes the heating surface requirements in the primary sections. Only minor changes in surfacing are necessary to accommodate both air and oxy-firing.

From the outlet headers of the vertical waterwalls, the fluid is led to a water separator. After the water separator, the steam is led to the steam-cooled roof. The subsequent steam path is through the backpass walls, into the superheater panels, platens, and finally to the finishing superheater pendant section located above the furnace arch. The superheater panels and platens have a wide pitch so that any ash deposits that may be formed on the elements can be easily removed.

The inlet to the reheater is in the rear pass of the boiler. Reheat steam passes through the horizontal and vertical sections in the rear pass and then to the reheater finishing platens located above the furnace arch.

The finishing superheater and reheater are arranged with a parallel flow of gas and steam in order to avoid very high metal temperatures at the outlets of these sections.

4.3.4 Steam Temperature Control

For both the fuel and auxiliary air/oxidant in the Tangential Firing System, vertically adjustable nozzle tips are designed within the windbox to direct the air/oxidant and fuel streams up or down (± 20 degrees). Simple lever arms within the windbox control the adjustable air/oxidant and fuel nozzle tips, and all are driven by a single drive outside the windbox. This mechanism gives tangential firing systems the capability of raising or lowering the flame pattern within the furnace. When tilted down, more radiant heat is absorbed in the furnace and the gas temperature available to the superheater and reheater is reduced. When tilted up, the reverse occurs.

The tilting feature of tangential firing gives the operator the ability to control outlet steam temperatures with the firing equipment (firing rate for SH, tilt position for RH) and the use of de-superheater spray water for trim or precision control. By using this technique, de-superheater spray water flow is minimized, resulting in significant improvements in steam turbine heat rate and plant thermal efficiency.

With the air-firing mode, the amount of reheat de-superheating spray water can be kept at minimal values over a wide range of furnace conditions and loads by placing the tilts in a mode that automatically controls the reheat outlet temperature. Thus, as firing rate is modulated to control superheat outlet temperature, the tilts are in constant movement, compensating for the continuously changing conditions of the furnace due to wall soot blower usage, load changes, and variations in ash composition.

With the oxy-firing mode, secondary flue gas recirculation flow rate is an additional control variable available for reheat outlet steam temperature control. For example, for operating conditions with low reheat outlet steam temperature, burner tilt angle would be increased first to obtain the desired reheat outlet steam temperature. If the reheat outlet steam temperature were still low after the maximum burner tilt angle was reached (typically +20°), the secondary flue gas

flow rate would be increased next (within pre-determined limits). Increasing secondary flue gas flow rate after increasing burner tilt for low reheat outlet temperature situations improves plant efficiency by minimizing FD and ID Fan power requirements for this operating condition.

For operating conditions with high reheat outlet steam temperature, de-superheating spray water flow would first be used for fast response followed by secondary flue gas flow reduction to eliminate or minimize the de-superheating spray flow. The secondary flue gas flow rate would be decreased using FD fan controls (within pre-determined limits) to correct the situation. If the low secondary flow limit was reached, in combination with the minimum burner tilt angle (typically -20°), and the reheat outlet steam temperature was still too high, de-superheating spray water flow would also be used in combination (similar to what is done in the air-fired mode of operation).

Superheater and Reheater De-superheaters

Two sets of superheater de-superheaters are used to control steam temperature. They are located in the links between the superheater division panels and the platens and in the links between the superheater platens and the superheat finishing section. One set of reheater de-superheaters is located in the reheat links between the low temperature reheater and finishing reheater sections. These de-superheaters, including the necessary spray-type internals, are used to control final steam temperatures over varying loads, fuels, furnace conditions, and transients.

4.3.5 Start-Up System

This sliding pressure supercritical once-through boiler has steam/water separators integrated into the main steam circuits. Above minimum once-through load (~35% TMCR), the separator is only a transit element. Below minimum once-through load, it performs its separation function. During start-up and at low loads, the steam/water mixture is separated in the separator. The steam is directed to the superheater circuit and the water to the start-up system. Above the minimum once-through load, the mass flow rate in the water walls is large enough to cool the water wall tubes sufficiently, and the start-up system is no longer needed in operation.

Below the minimum once-through load, the flow in the waterwalls is kept above a minimum value with the start-up system. At low loads, a mixture of water and steam leaves the waterwalls and the steam/water separator operates in a wet condition. Care has been taken in the location of the separators to ensure a smooth transition from the recirculating waterwall flow mode to the once-through flow mode. In addition, no significant steam temperature excursions occur at the superheater outlet.

For start-up, the boiler begins firing with air and ramps up to stabilize operation in the once through steam operating mode (>35% load) prior to the transition to oxy-firing.

Start-up Flash Tank and Condensate Receiver Tank

The boiler vent and drain system includes valves and motorized operators where required. The equipment includes one start-up flash tank and condensate receiver tank. The tanks are included

as a part of the boiler start-up system. The tanks are of welded construction and complete with external platforms and ladders.

4.3.6 Mechanical Design Aspects

The mechanical design of this boiler meets the demands of the specific loading such as pressure, temperature, and temperature transients during load changes. Only proven elements have been selected to create this design in order to assure its structural integrity. Careful material selections have been made, considering local temperatures, strength requirements, weld ability, and economical aspects.

Careful attention is given to the design of the boiler suspension system to facilitate an even loading distribution over the entire support rod system to the steel structure. High-strength materials are used for wall outlet, superheater outlet, and reheater outlet headers, to minimize wall thickness and, consequently, reduce thermal stresses.

4.3.7 Boiler Pressure Parts

The boiler has convection heat transfer sections located inside a rectangular enclosure formed by welded membrane walls. Within the membrane walls, wall openings are provided for windboxes, flue gas outlet, access, inspection doors, and soot blowers.

The boiler and its auxiliary equipment are designed and arranged in such a manner that all parts can be inspected with minimal effort. All the important parts are accessible by platforms.

The mechanical design of the pressure part components is performed in accordance with the ASME Boiler Pressure Vessel Code or other equivalent accepted code. No special mechanical design considerations are required for oxy-firing, although material selections must consider the environments under both air and oxy-firing.

Furnace

The furnace enclosure consists of tubes that are welded together along their lengths, by the fusion-welding process or the fin-welding process, to form a gas-tight envelope. The furnace is suspended at the top from a hanger rod suspension system that takes into account the transient temperature operating conditions that the boiler will experience. The furnace is guided at a number of elevations to keep it plumb during heat-up, cool-down, wind events, and seismic events. Buckstay structural members are employed to support the furnace walls for gas pressure excursions, winds and seismic loading, while allowing for the cubical expansion of a welded furnace. Four water cannons (one on each wall) are employed to clean the furnace heat-absorbing surface to maintain heat absorption efficiency.

Openings in the Membrane Walls

Inspection openings for fireball observation and slag accumulation assessment are provided. The convection heating surface and membrane walls are also accessible by openings in the walls at

all necessary locations. The observation door designs are based upon designs previously developed for pressurized furnaces to minimize possible air in-leakage.

4.3.8 Boiler Steel Structure

Structural steel framing and platforms are provided for the steam generator: All steel columns, beams, and bracing required to form a fully independent, simply supported, concentric, diagonally braced space frame are provided. The space frame provides vertical and horizontal support to all equipment provided within the contiguous boiler area. This includes all main columns and column bracing, all column-to-column girders, beams, and intermediate framing members. The design of the structural steel and connections are in accordance with the AISC "Manual of Steel Construction", Allowable Stress Design, GB Codes, or internationally accepted codes.

In general, the connections are field bolted utilizing bolts in bearing with threads excluded from the shear plane.

The structural steel is designed to accept the load imposed by equipment, piping, and electrical cable trays, which are located within the contiguous boiler area.

Boiler Buckstay Arrangement

The boiler walls are equipped with buckstays arranged with a suitable spacing. They are designed to take up forces due to positive and negative gas pressure excursions, wind, and seismic conditions. They are positioned outside of the boiler insulation and are connected to the boiler wall with stirrups. These stirrups permit a free relative movement between the cold buckstay and the hot boiler wall.

The fixed point of the horizontal displacement is set at the centerline of the wall. Corner retainer plates transfer the forces from the buckstays into tie channels on the adjacent membrane walls or directly into the adjacent membrane walls. Boiler guides connect the buckstays to the steel building structure.

Superheater, Reheater, and Economizer Assembly Supports

The horizontal economizer assembly tubes are supported by mechanical strap supports.

Water-cooled hanger tubes support the horizontal tube assemblies of the reheater. High crown seals above the boiler roof support these hanger tubes and the vertical tube assemblies of the superheater and reheater. These high crown seals support the assembly weight while also providing a gas tight boiler roof seal.

Boiler Suspension

Hanger rods from the steel structure grid at the pressure part support level (PPSL) suspend the boiler membrane walls. The upper end of each hanger rod is threaded and provided with a nut.

This allows an exact vertical positioning of each wall during erection and readjustment, if necessary, after initial operation.

The purpose of the furnace support system is to transfer the weight of the furnace to the structural steel frame in a manner that accommodates inherent movements, expansions, and contractions, occurring during operation, without imposing any life-limiting loads on the pressure parts.

Pressure Part Support Level (PPSL)

All membrane walls, tube assemblies, headers, and internal boiler piping are suspended from the PPSL, which consists of a grid of steel beams. This suspension principal allows free cubical expansion of the boiler. All load transfer points are located at the PPSL elevation, which facilitates easy access to the individual hanger.

Platforms, Walkways, and Stairs

A system of platforms and stairways, as required for the proper operation and maintenance of the boiler building components are included. Additionally, one industrial grade personnel elevator for the boiler area is provided.

Trolleys and Monorails

Included are provisions for overhead trolleys and/or monorail cranes as listed below:

- Boiler Maintenance Hoist & Trolley
- Primary Air Fan Rotor and Motor
- Forced Draft Fan Rotor and Motor
- Pulverizer Maintenance Hoist & Trolley
- Air Heater Maintenance
- ID Fan Hoist Supports

4.3.9 Sootblower System

One of the most important boiler auxiliary operations is the on-line, fireside cleaning of heat-absorbing surfaces. Not only is it important to maintain efficient heat transfer, but also to prevent sections of the boiler from becoming severely plugged. Plugged sections can restrict gas flow and cause load limitation, low steam temperatures, as well as tube erosion due to high local gas velocities. Of all the major fossil fuels, coal alone requires a large complement of permanently installed sootblowing equipment. Coals and coal ash resulting from combustion vary widely throughout the world, and even from region to region of the same country. Depending on certain properties, boilers burning various fuels require widely different sootblowing systems.

In the boiler furnace, the concentration of wall blowers or water cannons depends upon factors such as the ash-fusion temperatures. The lower these temperatures are, the more likely the ash will adhere to the furnace walls and accumulate. The percentage of ash in the coal is another factor considered in designing the furnace wall-blower system, with higher-ash coals requiring greater and more concentrated coverage. The Sootblower Control System controls the equipment used for this application. To minimize air infiltration into the boiler, the sootblower system was designed with a special sealing system, using recirculated flue gas as the seal gas.

Retractable Blowers

One hundred (100) retractable sootblowers are provided for this unit. These long retractable-type sootblowers are the most effective way to clean radiant and convective heating surface. They use two 180° opposed-cleaning nozzles at the tip which emit a high-pressure steam source perpendicular to the lance. While the lance traverses the boiler, it also rotates, forming a helical blowing pattern, which effectively cleans the tubes and spaces between tubes in a superheater, reheater, or economizer bank. In widely spaced platenized sections, these nozzles are angled slightly, leading and lagging the perpendicular to gain a longer dwell time on the tube surface. The effective cleaning range of retracts depends upon the gas temperature in the area to be cleaned, the ash characteristics of the particular fuel being fired, and the tube spacing of the particular section.

Each retractable blower includes the following:

- Electric motor drive
- Mechanically-operated valve
- Stainless-steel valve seats and discs
- Motor starters and limit switches

Due to the fuel properties specified for this study, comprehensive sootblower coverage is provided.

Furnace Wall Cleaning

In this furnace four (4) water cannons are specified (one on each furnace wall). Each water cannon directs a high-pressure jet of water through a furnace wall opening to clean surfaces on the opposite wall of the furnace. Each cannon can clean the entire wall from the nose arch to the bottom slope tubes and from one side to the other. The cleaning effect is based on the fact that the impacting water penetrates the topmost layer of the slag and expands into steam. In this way the slag is broken up and removed from the surface. The nozzle is at the leading tip of the lance tube and the lance tube is articulated by a horizontal and vertical axis drive system. The water cannons offer several advantages that make it an attractive cleaning option. The horizontal and

vertical axis capability can provide the cleaning coverage equivalent to many individual water lances, depending on the size and layout of the furnace. They are also more effective than steam wall blowers if the deposit is a dense slag type. Reducing the number of penetrations by using water cannons also decreases sealing requirements and reduces potential air in-leakage.

Each water cannon includes the following:

- Electric motor drive
- Mechanically-operated valve with adjustable pressure control
- Stellited valve seats and disc
- Motor starter and limit switches

Temperature Probes

Two (2) retractable furnace temperature probes are provided. The probes are inserted during the lighting-off period and remain in the furnace until reheater steam flow has been established. They come complete with totally enclosed motors, limit switches, position transmitters and position indicators, remote control switches, and local push-button stations. The design is based on that of the long retractable sootblower, but without the rotating feature. They traverse back and forth across the furnace and are driven by a single electric motor.

As a probe senses temperatures, it also transmits its position. A thermocouple, mounted on the end of the lance, measures gas temperatures. The standard thermocouple is suitable for temperatures up to 593°C (1,100°F). Two temperature probes are provided. Introduced into the travelling carriage, the cooling air/RFG passes through a small annular space between the lance wall and the inner liner. It then is discharged from a nozzle into the furnace. Located back from the end of the lance, the nozzle is slanted away from the thermocouple, such that the discharged air/RFG will have no effect on the temperature readings.

Electrical Accessories

Necessary starters will be shop mounted and wired to the terminal blocks in integral NEMA 4 or IP equivalent motor starter cabinets. Push buttons will be supplied, mounted, and wired on the sootblowers.

Pipes, Valves and Fittings

A complete piping system to the sootblower/water cannon heads will be provided.

4.3.10 Coal Feeders

Five (5) gravimetric feeders with acoustic-type coal monitors and microprocessor controls are provided to deliver the required mass flow rate of coal to the pulverizers.

4.3.11 Coal Pulverizers

The coal pulverizing system is designed to be flexible to meet a wide range of solid fuel preparation needs and to operate under both air and oxy-firing conditions. Five (5) HP-903 pulverizers with dynamic classifiers are used. The selected mills are capable of achieving BMCR conditions firing the range of fuels with one pulverizer out of service.

System Operation

The pulverizers are used to prepare and deliver fuel to the steam generator in a tangential fuel firing system. The pulverizer grinds, dries, and transports the coal to the furnace. Properly prepared coal insures complete combustion that results in high boiler efficiencies. Of primary importance in the coal pulverizing process is assuring the necessary coal product sizing. These pulverizers were selected to provide a fineness level of 80 percent through 200 mesh.

Coal is fed from a gravimetric coal feeder to the pulverizer through a center feed pipe onto a revolving bowl (see Figure 4-3). Centrifugal force causes the coal to travel outward toward the outer perimeter of the bowl. As the coal travels up the bowl, it passes through the grinding zone between the grinding ring and grinding rolls.

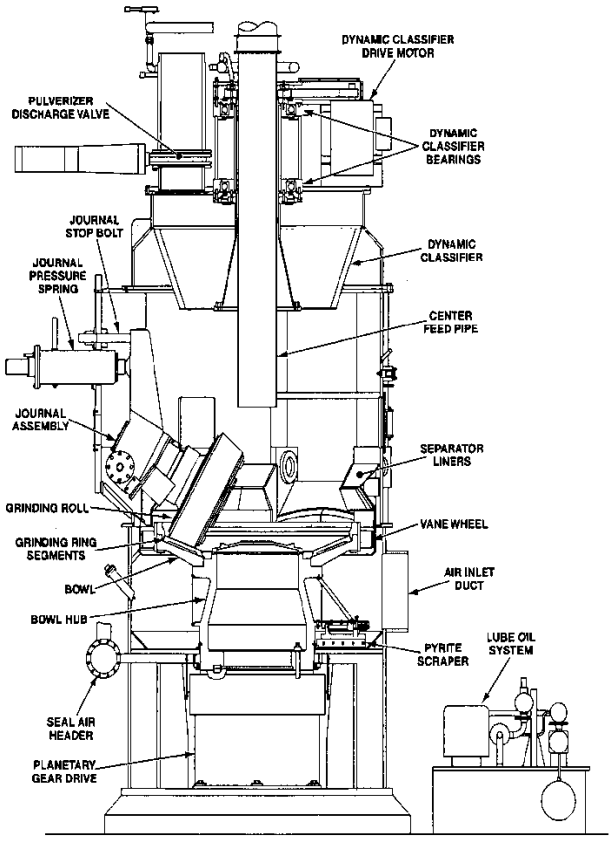

Figure 4-3: Sectional Side View – HP Type Coal Pulverizer

Grinding force is imparted on the coal bed through a pivoting roller journal assembly with the grinding force controlled by externally adjustable springs. As the partially pulverized coal passes beyond the roller the coal continues outward toward the edge of the bowl.

Oxygen is mixed into the primary flue gas recycle stream just before the primary recycle fan to a concentration of 21% by volume. The primary air/oxidant fan and preheater (GGH) are used to supply hot air/oxidant in the required quantities for the coal pulverizing process. The hot air/oxidant enters the mill-side housing below the bowl and is directed upward around the bowl through vanes attached to the circumference of the bowl. As the air/oxidant passes upward around the bowl, it entrains the partially pulverized coal and the drying and product sizing or classification process begins.

The coal/air/oxidant mixture then enters the primary classifier where heavier coal particles strike the deflector and intermediate liners and are returned to the bowl for further grinding. The lighter particles are carried up and through the deflector openings where secondary classification occurs.

Any tramp iron, or dense difficult-to-grind foreign material in the coal feed, is carried over the outer edge of the bowl where it drops through the air/oxidant stream to the mill bottom. Pivoted scrapers attached to the bowl hub sweep the tramp iron and other material to the tramp iron discharge opening and out of the pulverizer.

The main differentiation between bowl mills designed for air operation compared to those for oxy operation is the composition of the primary gas stream used for heat supply and for conveying of the pulverized coal out of the mill. The composition of air is well known and safe, proper operation of bowl mills using air as primary gas stream is well proven. With oxy-firing, due to the use of recirculated flue gas with increased CO_2 concentration and the near elimination of gaseous nitrogen, the primary gas stream in an oxy process has an increased density. In the current case, the density is increased approximately by a factor of 1.34. The effect on the primary gas system is an increase of pressure drop proportional to the difference in density.

If the conveying gas volumetric flow rate required for a comparable air-fired operation is applied for the oxy–fired operation, the result is an increased conveying gas mass flow in oxy operation. In fact, an improvement of mill performance compared to air-fired operation is expected. This is because there is an indication that the lifting capacity of the primary gas stream used in the oxy-fired operation might be higher. This is identified as an optimization potential since comparable pneumatic gas transport might be achieved in oxy-fired operation with a lower gas volumetric flow and a mass flow comparable to those for air-fired operation. Further investigations are required to verify and to demonstrate this optimized design approach.

4.3.12 Firing System

Alstom's state-of-the-art low NO_x tangential firing system was adapted and optimized for oxy-firing based on the extensive 15 MW_{th} testing conducted under Task 5 as well as other Alstom test programs such as the 30 MW_{th} Oxy Pilot at Vattenfall's Schwarze Pumpe facility. Alstom's

tangential firing system has proven to be one of the most efficient, reliable, and flexible firing systems available for utility boilers today. Its unique feature of tilting tangential nozzles allows for complete combustion of the fuel and for simple and reliable steam temperature control. In addition, the corner windbox firing method results in recognized low NO_x emissions with a variety of fuels, uniform furnace heat absorption patterns, and high boiler turndown capability.

The following section describes the firing system operation and equipment features as outlined below:

- System Operation
- Flexibility
- Steam Temperature Control
- Multi Compartment Auxiliary Air with Concentric Firing (CFS)
- Close Coupled and Separated Overfire Air
- Under-fire Air/Recycle Compartments
- Low NO_x Tangential Firing System
- Firing System Turndown
- Aerodynamics and Firing System Design
- HEA Ignition System
- Firing System Arrangement

System Operation

The left photo in Figure 4-4 shows a low NO_x tangential firing system with two levels for overfire air. Both the fuel and air are directed toward the tangent of an imaginary circle in the center of the furnace, thus, the name "Tangential Firing". A typical tangential firing flame pattern can be seen in the right photo in Figure 4-4. In operation, a horizontally swirling flame pattern is formed with a vortex in the center of the furnace. This unique mixing technique forms a large single flame envelope, forcing the fuel and air from each corner to take the maximum path length through the furnace before it exits at the furnace outlet. Both in theory and in practice, any imbalance between windboxes is quickly "averaged out" within the horizontal flame pattern providing for strong mixing not dependent on precision control of air and fuel admission assemblies.

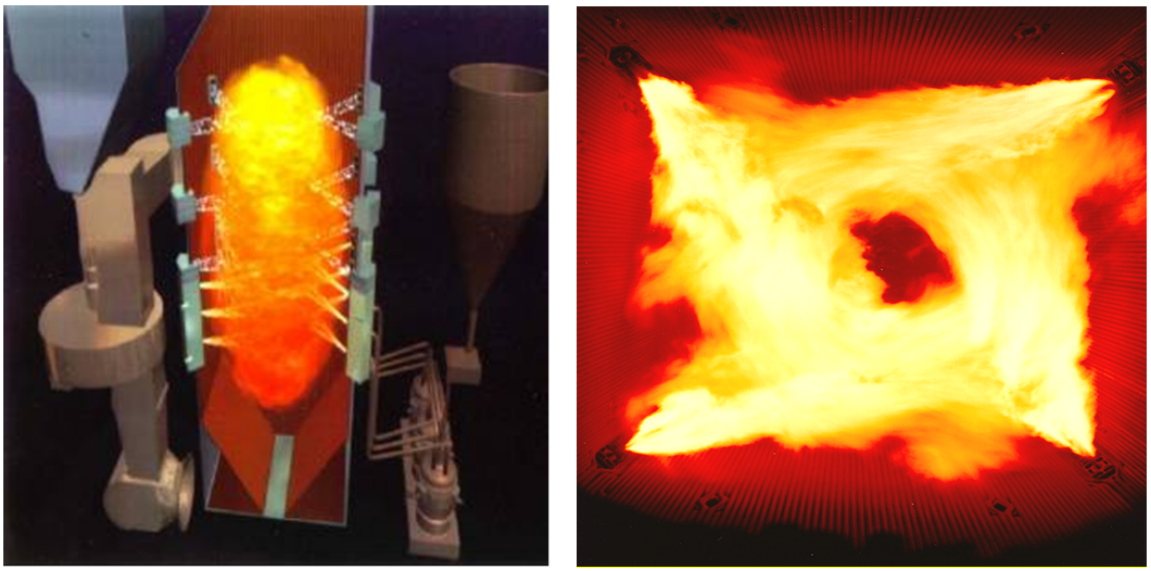

Figure 4-4: Tangential Firing Flame Pattern

The fuel and air/oxidant are introduced to the furnace through a device called a windbox assembly (see Figure 4-5). The windbox is a vertical stack of alternating fuel and air/oxidant compartments with dampers associated with each compartment. One windbox is located in each of the four corners of the furnace. A typical tilting tangential windbox design is shown in Figure 4-5. It is arranged vertically as alternating levels of air and fuel. The dampers at each compartment are controlled to vary the distribution of air over the height of the windbox, making it possible to change the velocities of the secondary air streams for ignition point adjustment.

The overall oxy-firing system design includes the flexibility to vary the quantity and location of oxygen supplied to the furnace for combustion. The design allows all of the oxygen to be injected and premixed into the recycle before being divided into overfire, windbox auxiliary and windbox fuel compartments flows. The design also allows the local addition of some of the oxygen through lances directly into the individual auxiliary and fuel compartments.

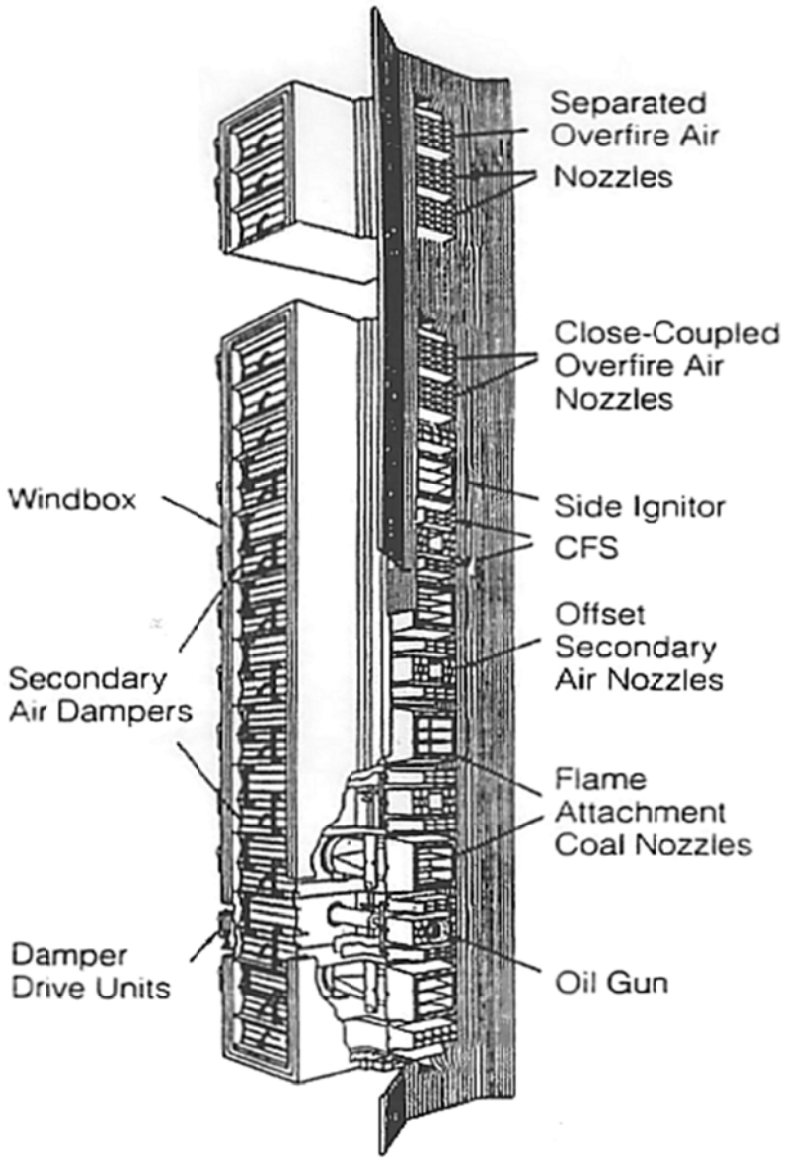

Figure 4-5: Typical LNTFS Tilting Tangential Windbox Arrangement

Flexibility

The concept of Tangential Firing is to form a single flame envelope within the furnace that is controlled by the windbox assemblies. Because there is one flame and four windboxes in the furnace, the windboxes are controlled on an "elevation basis". For example, the top coal nozzles in each of the four windboxes are physically identical and are operated as if they were one. The fuel piping is arranged such that the same pulverizer feeds all four coal nozzles of a given elevation.

As pulverizers are taken in and out of service, fuel is added or subtracted from the same elevation of each windbox. Thus, the symmetry of the flame is maintained regardless of the number of pulverizers or the unit load.

Because of flame pattern symmetry, each waterwall tube receives a predictable and repeatable percentage of the furnace radiant heat for all loads and combinations of pulverizers in service (see Figure 4-6).

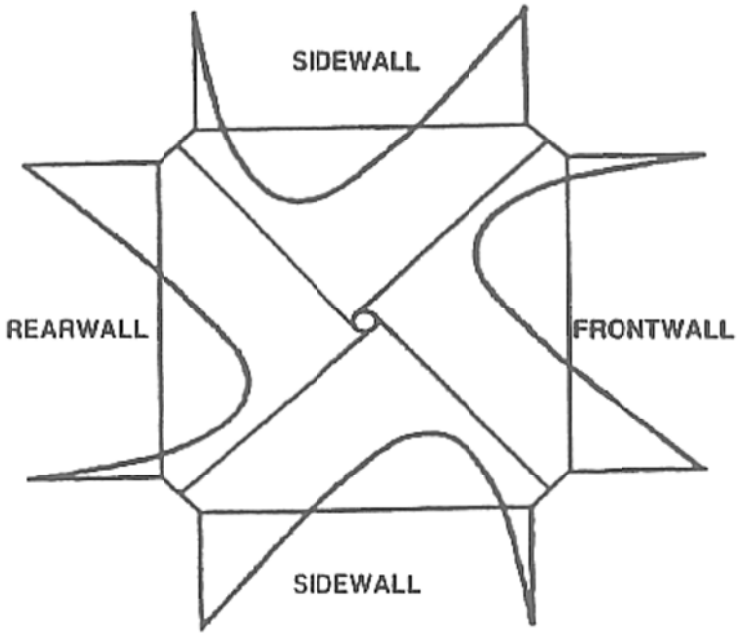

Figure 4-6: Lateral Heat Absorption Profile

Steam Temperature Control

Fuel and air nozzles tilt in unison to raise and lower the fireball in order to change total furnace heat absorption and thus heat available to the superheater and reheater circuits (see Figure 4-7). Tilts are automatically adjusted to maintain RH steam outlet temperature over the control load range. The tilts on coal-fired units automatically compensate for the effects of ash deposits on furnace wall heat absorption at any given load. In operation, furnace heat absorption decreases and exit gas temperature increases as ash deposits build up prior to sootblowing. The windbox tilts compensate by automatically lowering to increase heat absorption lower in the furnace. As the sootblowers clean ash from the upper walls, heat absorption is restored and the furnace exit gas temperature decreases, causing RH outlet steam temperature to decrease. The tilts automatically rise to reduce heat absorption in the lower furnace and to maintain RH outlet steam temperature at the set point value.

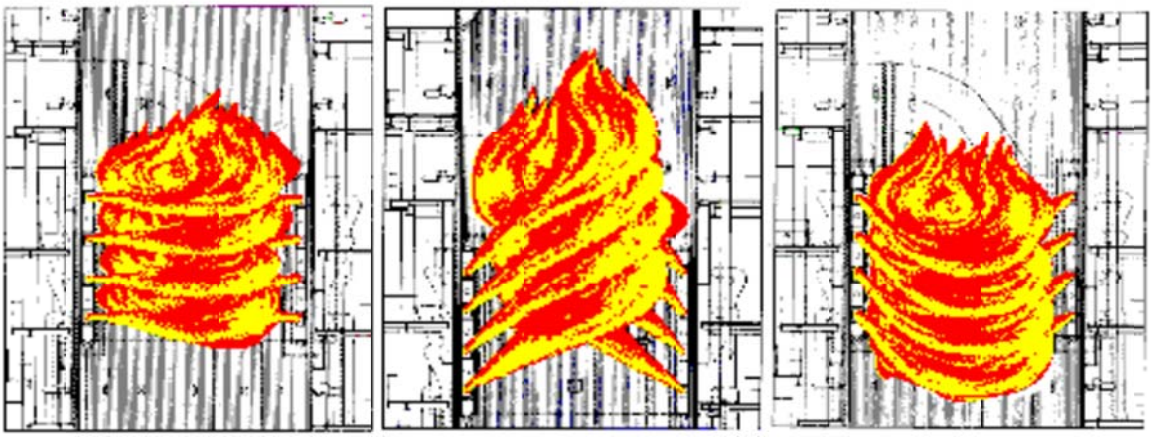

Figure 4-7: Burner Tilt Impact on Fireball Position (horizontal, upward, downward)

Multi-Compartment Auxiliary Air with Concentric Firing (CFS)

The windbox secondary air/oxidant is injected between the coal compartments through three (3) separate compartments and nozzle tips. The center compartment injects a portion of the auxiliary air/oxidant at the standard firing angle and contains the oil or gas firing equipment that is used for start-up and low loads. The upper and lower compartments contain CFS (Concentric Firing System) style nozzle tips that offset the secondary air/oxidant flow to a larger, concentric firing circle (Figure 4-8).

Horizontally offsetting (i.e. larger than standard firing angle) some of the auxiliary air/oxidant flow by CFS makes less air/oxidant available to the coal stream during the early stages of combustion. It also creates an oxidizing environment near the waterwalls in and above the firing zone. This reduces ash deposit quantity and tenacity, resulting in less wall blower usage and increased lower furnace heat absorption. Increased oxygen levels along the waterwalls also reduce the corrosion potential presented by certain coals.

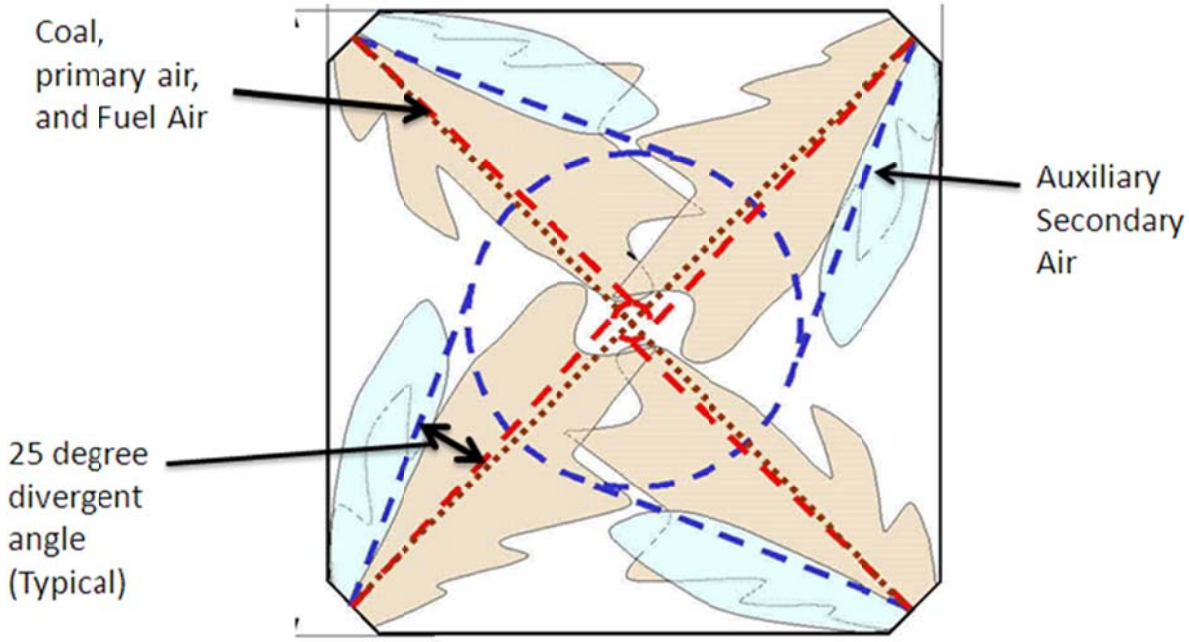

Figure 4-8: Concentric Firing System

When firing coals with low slagging and corrosion potential, the use of offset CFS style nozzle tips is not required and auxiliary airflow can be biased to the center (non-offset) tips by closing down the CFS compartment dampers. In this configuration, the auxiliary airflow is vertically offset from the coal stream, which also reduces the air available during the early stages of combustion. Thus, this multi-compartment design feature offers a great deal of flexibility to accommodate a wide range of coals while controlling NO_x formation in the primary combustion zone.

Low NO_x Tangential Firing System

Historically, tangentially fired boilers have demonstrated low NO_x production. There are two (2) basic reasons for this;

- The long diffusion flames emanating from each corner have moderate fuel and air mixing rates and low peak temperatures.
- The large amount of internal gas recirculation generated in the fireball by impingement of fresh fuel and air on hot products of combustion helps to reduce peak oxygen availability.

These attributes form the basis of an inherently low NO_x combustion system.

Global and local staging techniques have been progressively developed and designed to minimize O_2 availability during the critical early phases of combustion when the volatile nitrogen species are formed. Staged combustion minimizes NO_x emissions because the initial fuel-rich conditions promote the formation of N_2 from the volatile nitrogen species. Overfire air

(OFA) staging, which sets the global firing zone stoichiometry, has been used for over thirty years. Recent development efforts have advanced the original concept of "close coupled" overfire air (CCOFA) and separated overfire air (SOFA) to the next logical step in vertical staging of the OFA with a second, separated overfire air windbox. This was done in order to maximize the time at sub- or near-stoichiometric conditions. Coupling low NO_x staging principles with the tangential firing system results in the lowest NO_x emissions.[33]

Closed Coupled and Separated Overfire Air

Closed-coupled OFA (CCOFA) is a portion of the total combustion air (or oxidant) that is discharged through two (2) compartments at the top of each main windbox. Separated OFA (SOFA) is a portion of the total combustion air (or oxidant) which is discharged through two (2) discrete levels of windboxes (high and low level SOFA) located in the furnace corners between the top of the main windboxes and the furnace outlet plane. Each SOFA windbox contains OFA compartments with nozzle tips having adjustable yaw and tilt positioning capability.

The use of air staging, OFA, to control NO_x production in tangentially fired units has been extensively demonstrated. With the multiple-firing zone concept, OFA is injected to the furnace at several different levels. This, in effect, divides the furnace volume into three (3) discrete zones: the primary firing zone, the NO_x reduction zone, and the final burnout zone. The stoichiometric ratio in each zone is defined and controlled by the total OFA flow, the CCOFA vs. SOFA flow distribution, and the final excess air ratio. This advanced air staging approach provides better control of NO_x production through optimization of the stoichiometric ratio in each firing zone (Figure 4-9). These same principles also apply during oxy-firing by varying the amount of oxygen carried in the oxidant stream to each furnace zone to control the stoichiometric ratio.

[33] Enhanced Combustion Low NO_x Pulverized Coal Burner, Alstom Power, DOE Final Report, DE-FC26-04NT42300, March 2008

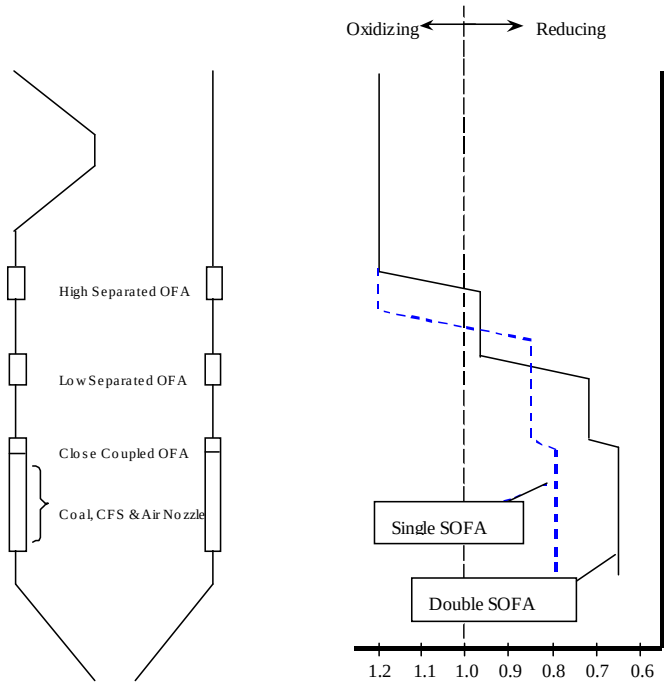

Figure 4-9: Stoichiometry vs. Elevation

Relative to single-level OFA injection, the multiple-level approach improves carbon burnout without increasing NO_x production. The use of SOFA windbox tilt and individual nozzle tip (horizontal) yaw adjustment provides a means for tuning the combustion air/oxidant and furnace gas mixing process and thereby minimizing combustible emissions such as carbon and CO.

Under-Fire Air/Recycle Compartments

A portion of the secondary air/recycle is discharged through compartments at the bottom of each main windbox to improve bottom ash carbon burnout without increasing NO_x production.

Firing System Turndown

Normal operating practice for large utility PC units is to remove mills from service as load is reduced in order to maintain the most favorable primary air/coal ratio possible. A minimum of two (2) mills feeding adjacent elevations are kept in service when operating at the lowest unit loads without supporting ignition energy. As previously discussed, an additional mill/firing elevation was included to improve turndown capability. Further, the global stabilization influence of the fireball (vortex), the modified mill characteristics with dynamic classifiers, the enhanced local flame stabilization achieved with specially designed coal nozzle tips, and a control strategy that includes coal feed biasing at minimum load allows maximum system turndown capability.

Aerodynamics and Firing System Design

Wall-fired and tangentially fired furnaces each produce a different, but typical, non-uniform gas flow distribution at the furnace outlet. To minimize this, the firing system design includes SOFA compartments that have both vertically and horizontally adjustable nozzle tips, which allows adjustment of SOFA flow direction to optimize mixing. Figure 4-10 shows a SOFA compartment with an oxygen lance.

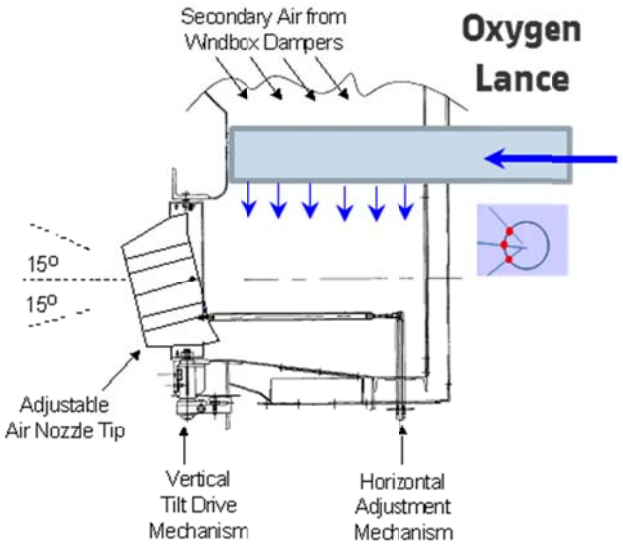

Figure 4-10: Vertically and Horizontally Adjustable Air/Oxidant Nozzle

This horizontal adjustment, known as yaw, has a range of +15° to -15° relative to the firing angle. By adjusting the yaw angle, the furnace aerodynamics can be changed and controlled to minimize non-uniform gas flow distribution at the furnace outlet. Also shown on this figure is the location of the oxygen lances.

HEA Ignition System

The High Energy Arc (HEA) igniter is engineered to light off fuel oils ranging from No. 2 to No. 6. The igniters are suitable for firing heavy oil. The igniter is a self-contained electrical capacitance discharge device for producing a discreet high intensity spark. A high-reactance transformer is used to produce a full-wave charging circuit and to control spark rate. This enables the sealed power supply to store maximum energy and deliver a greater percentage of this energy through insulated cables to the igniter spark tip. The surface shunned spark tip helps to initiate the low voltage, high amperage arcs that makes the design immune to oil or coke fouling.

Firing System Arrangement

The main windbox consists of five (5) coal nozzle elevations containing coal nozzle tips designed for enhanced ignition. Although four firing elevations would be typical for the capability of the demonstration unit, five elevations were selected to provide greater turndown. Between the coal nozzle elevations are located the concentric firing (CFS) air/oxidant nozzles,

and the normally oriented auxiliary nozzles. Three (3) of the auxiliary nozzles contain fuel oil burners, which provide the required oil-fired warm up capacity, and are situated such that coal elevations may be brought into service in any desired order or combination. HEA igniters are located next to each oil burner elevation. Two separated overfire air (SOFA) windboxes are located above the main windbox to optimize air/oxidant staging so as to minimize the required SCR NO_X removal efficiency. Each SOFA windbox contains four separate air/oxidant nozzles. All SOFA and CCOFA nozzles are both vertically and horizontally adjustable.

4.3.13 Boiler Protection Burner Management System

The Boiler Protection and Burner Management System (BPS/BMS) is provided to ensure the execution of a safe, orderly operating sequence in the start-up and shut-down of fuel firing equipment and to prevent errors of omission or commission in following such a safe operating procedure, as defined by NFPA 85. The design of the system incorporates protection against the malfunctioning of fuel firing equipment and associated air systems. The system is based on a state-of-the-art air-fired design modified to incorporate the oxygen injection and control systems.

4.3.14 Air/Oxidant and Flue Gas Systems

This section describes the primary and secondary air/oxidant systems as well as the flue gas system.

Primary Air/Oxidant System

This system supplies heated air/oxidant to the pulverizers for drying and pulverization of the coal and for conveying the pulverized coal to the windbox coal nozzles. The primary flue gas recirculation duct, primary air inlet duct, primary oxygen mixer, primary air/oxidant (PA) fan, primary oxidant ducts, and the required isolation dampers are all included in this system. Oxygen is injected and mixed with recirculated flue gas up-stream of the PA fan to a concentration of 21% by volume of oxygen. The recirculated flue gas for the primary stream is extracted from the main flue gas stream at the exit of the flue gas condenser (see Figure 4-1). Seal gas is extracted from this stream just before oxygen mixing.

A single, one hundred percent (100%), two-speed, centrifugal primary air/oxidant fan is provided to maintain the required air/oxidant flow for proper coal drying conditions in the pulverizers as well as proper velocities in the pulverizer and pulverized coal piping to the windbox nozzles. Primary air/oxidant fan inlet vanes control primary air/oxidant pressure.

Primary air/oxidant (PA) fans are sized to accommodate the most severe coal drying requirements within the specified fuel range. A minimum margin of twenty five percent (25%) on volumetric flow, thirty percent (30%) on pressure, and maximum ambient temperature are considered to size the PA fans relative to the boiler maximum continuous load condition. Both air and oxygen firing modes of operation are considered.

Secondary Air/Oxidant System

The secondary air/oxidant system supplies heated air/oxidant for combustion to the windboxes. The secondary flue gas recirculation duct, secondary air inlet duct, secondary oxygen mixer, secondary oxidant ducts, forced draft (FD) fan, and the required isolation dampers are all included in this system. Oxygen is mixed with recirculated flue gas just up-stream of the secondary air/oxidant fan to a concentration of 21% by volume of oxygen. The recirculated flue gas for the secondary stream is extracted from the main flue gas stream at the exit of the flue gas desulfurization system (see Figure 4-1). The extraction quantity of flue gas includes the flow required for the GGH pressurized seal and purge system.

The air/oxidant stream is delivered by a single, one hundred percent (100%), single-speed, axial flow FD fan. The secondary air/oxidant from the FD fan is raised to a higher temperature by the hot flue gases in the Ljungstrom® GGH. From the GGH, the heated secondary air/oxidant is fed to the windboxes through the hot secondary air/oxidant ducts. In the windboxes, individual compartment dampers distribute the air/oxidant. The secondary air/oxidant duct from the FGD outlet to the GGH is designed to be acid resistant to H_2SO_4.

The FD fan is sized to accommodate the maximum secondary air/oxidant flow corresponding to the requirements for the specified fuel range. A minimum margin of twenty percent (20%) on volumetric flow, forty percent (40%) on pressure, and maximum ambient temperature have been considered to size the FD fan relative to the boiler maximum continuous load condition. Both air and oxygen firing modes of operation are considered. The FD fan should be constructed to be resistant to the H_2SO_4 in the recycle flue gas.

Control of the boiler air/oxidant flow is provided by the forced draft fan inlet vanes, while the distribution of secondary air/oxidant to the individual windbox compartments will be controlled by the secondary air/oxidant dampers in the windbox compartments. These dampers are positioned by a sub-loop control system.

Steam Coil Air Heater (SCAH)

A steam coil air heater is provided to increase the air temperature prior to the GGH to minimize condensation/corrosion on GGH low temperature surfaces. The steam coil will be located in the secondary air inlet duct and will only be used during the air-firing mode of operation.

Oxygen Mixers

Oxygen is injected and mixed with recirculated flue gas in three locations in this design.

- Oxygen is mixed up-stream of the primary air/oxidant fan to a concentration of 21% by volume of oxygen.
- Oxygen is mixed up-stream of the secondary air/oxidant fan to a concentration of 21% by volume of oxygen.

- The remaining oxygen required for complete combustion of the coal is mixed with the secondary stream in the windbox just before entering the furnace.

The concentration of oxygen in the secondary stream needs to be limited to 23.5% to allow fabrication with carbon steel material (and to avoid more costly stainless alloys). A 21% O_2 limit is more prudent to allow for O_2 concentration variations due to mixing, load variations, upset conditions, and control system response. Oxygen concentration in the primary stream is also limited to 21% to maintain the same oxygen concentrations as are in air to the pulverizer to minimize potential hazards.

Oxygen can be mixed with the primary and secondary FGR using various mixing approaches including static mixers and grid-type mixing systems. An example of a honeycomb type static mixer installed in a duct is shown in

Figure 4-11. Grid-type mixers are similar in concept to ammonia injection grids for SCR, but must address the much higher quantities of oxygen being injected through the grid. An example of a grid type mixer installed in a duct is shown in Figure 4-12.

Figure 4-11: Example of a Static Mixer Installed in Ducting

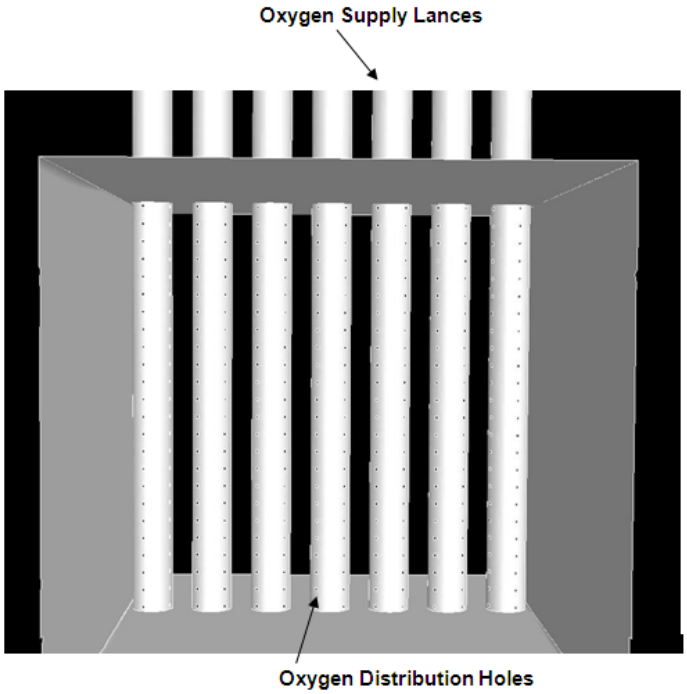

Figure 4-12: Example of a Grid-Type Mixer Installed in Ducting

Primary considerations for selection and design of an oxygen mixing system include:

- Ability to provide very good mixing that eliminates oxygen rich pockets within the main stream that could create local oxidation problems
- Required mixing length to provide desired mixing quality
- The gas draft loss associated with mixing
- The oxygen pressure loss associated with mixing
- CAPEX of the overall injection/mixing system
- Complexity of the overall injection/mixing system

The purpose of the oxygen mixers for primary and secondary streams before the Gas-Gas Heater (GGH) is to allow the premixed oxygen-rich FGR streams to be handled in a similar manner as air. It is important that the oxygen in these premixed streams is nearly completely mixed to allow control of the oxygen concentration to approach the maximum allowable limit dictated by erosion consideration, thus allowing the greatest amount of oxygen to be heated by the GGH. A common index used to define mixing quality is the Coefficient of Variation (CV), which is a measure of the homogeneity (standard deviation in concentration / mean concentration). Streams with a CV of less than 0.05 are generally considered well mixed. It is necessary that the mixing

system design be simulated with CFD modeling or physical flow modeling for the specific configuration over the range of operating conditions to evaluate the performance. Figure 4-13 shows an illustration from a CFD simulation of oxygen mixing downstream of a grid-type mixing system for the secondary flue gas recirculation system. The O_2 concentration varies from 20-24% 10 feet downstream of the mixer. By 30 feet, the O_2 concentration has tightened to between 21-23%. Similar CFD analysis was conducted for static mixers that indicated a substantially greater distance downstream was needed to provide equivalent oxygen mixing.

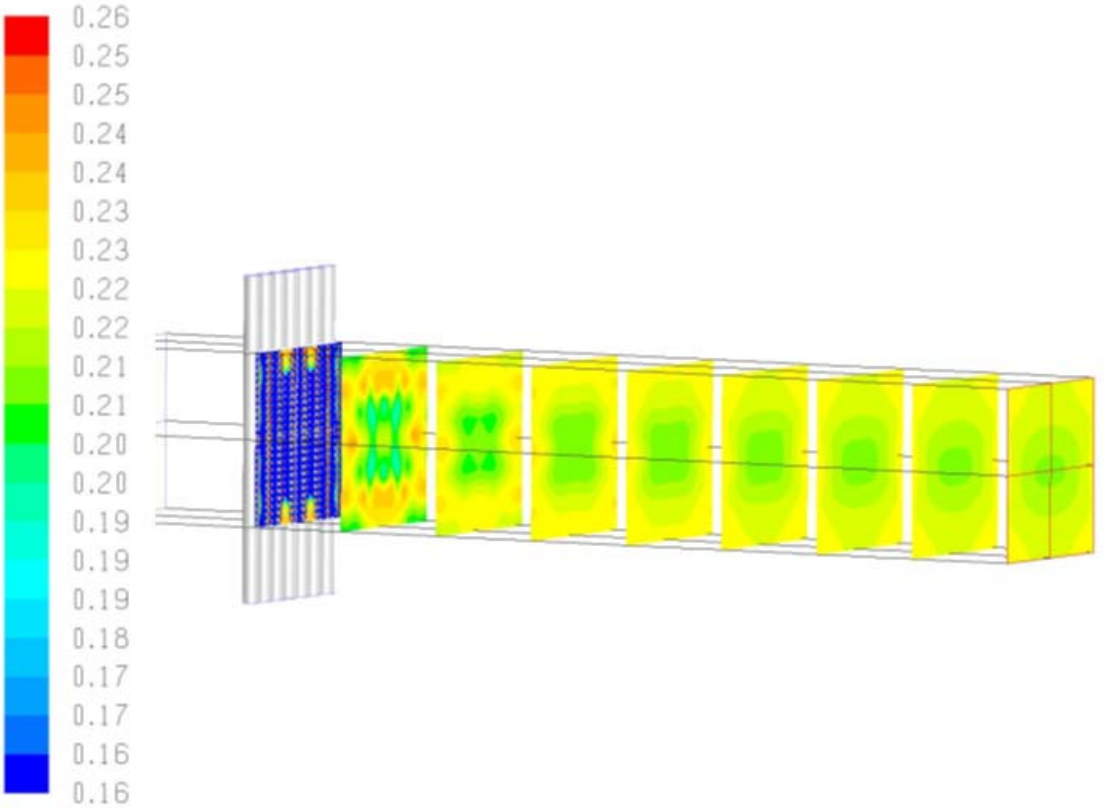

Figure 4-13: Example of CFD Simulation of Oxygen Mixing After a Grid-Type Mixer

For the 450MW design, grid type oxygen mixers are used for the primary and secondary mixers as shown in Figure 4-14. The arrangement of these mixers is shown in Figure 4-15.

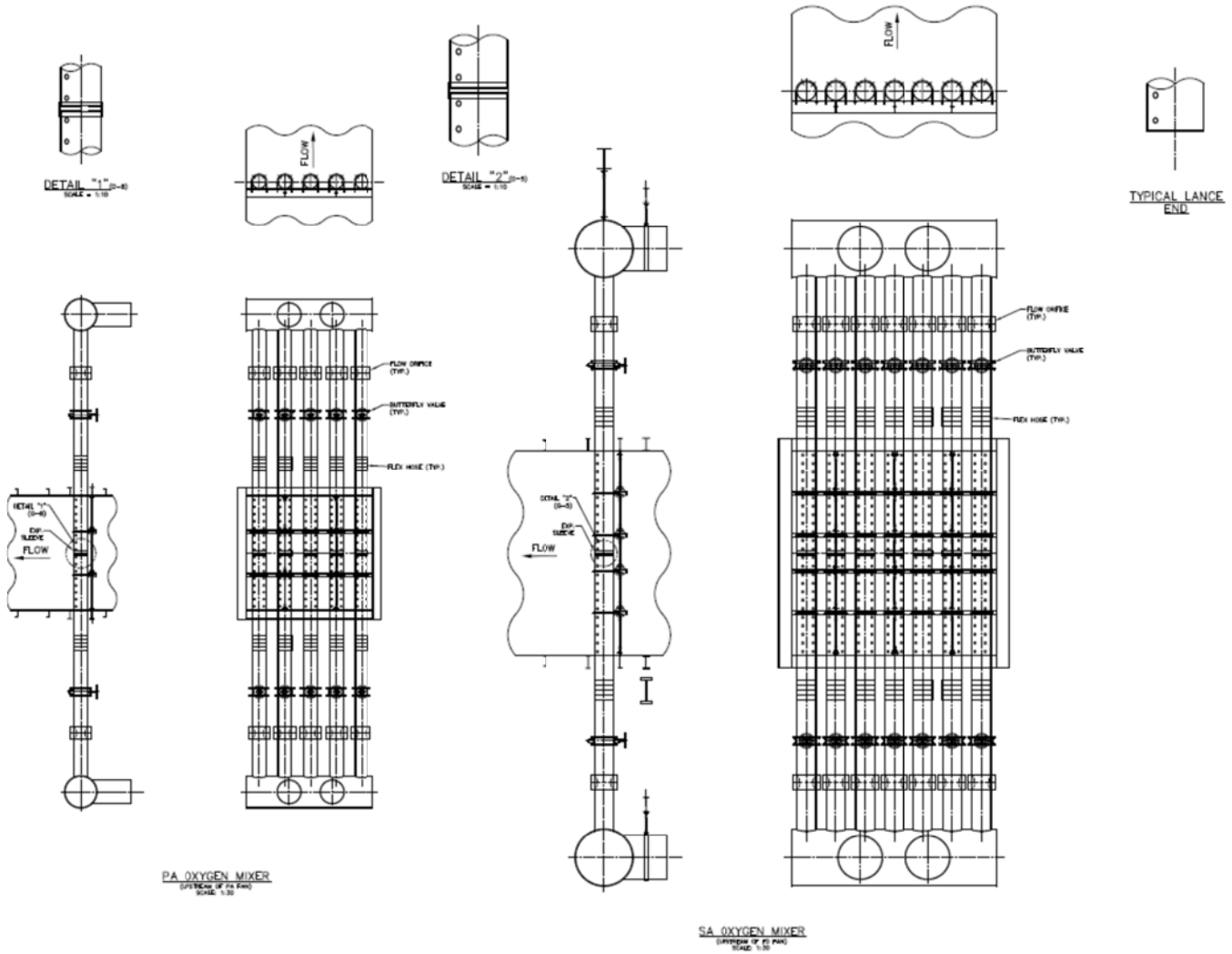

Figure 4-14: Primary and Secondary Oxygen Mixer Design

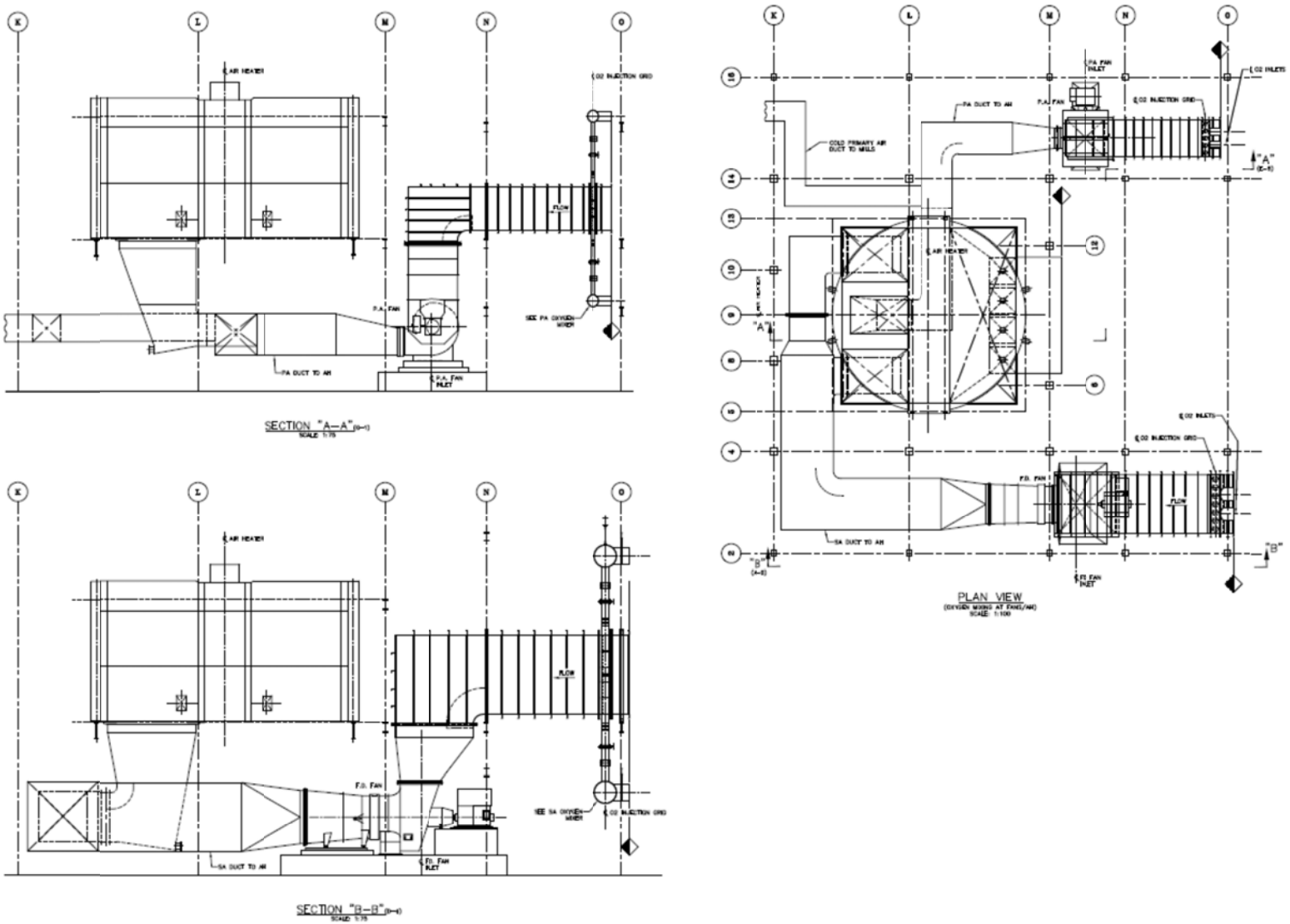

Figure 4-15: Primary and Secondary Oxygen Mixers Arrangement

Flue Gas System

The flue gas system includes the flue gas ductwork and the ID fan. The flue gas system provides a gas tight enclosure for the flue gas stream leaving the boiler. The flue gas system included with this oxy-fired steam generator includes the ductwork from the GGH to the fabric filter, ductwork from the fabric filter to the ID fan, the ID fan, ductwork from the ID fan to the FGD, ductwork from the FGD to the FGC, and ductwork from the FGC to the GPU. It also includes the ductwork from the FGD to the stack that is used during air-firing and during the transition between air and oxygen-firing. Also included are the various required isolation dampers (see Figure 4-1).

The oxy-fired boiler has been designed with a single, one hundred percent (100%), single-speed axial flow Induced Draft (ID) fan. It is located between the Fabric Filter outlet and the FGD system inlet. The ID fan is sized to accommodate the maximum gas flow predicted over the specified range of fuels. A minimum margin of twenty percent (20%) on volumetric flow, thirty percent (30%) on pressure, and maximum calculated temperature is considered to size the ID fan relative to the boiler maximum continuous load condition. Both air and oxy-firing are considered. The ID fan is controlled to maintain a flue gas pressure of 0.0 inches water gauge at the furnace exit.

4.3.15 Ljungstrom® Regenerative Air/Oxidant Preheater

A specially designed Ljungstrom® Regenerative Air/Oxidant Preheater is used for the oxy boiler design. The Ljungstrom® design has proven to be highly efficient, compact, and permits operation over extended periods without interruption.

Quad-Sector Design

A Quad-Sector Ljungstrom® air preheater was selected and is also referred to as a gas-to-gas heater (GGH) in this report. It permits a single heat exchanger to perform two functions:

- Coal drying (heat supply)
- Primary & Secondary air/oxidant heating.

Because only one flue gas duct is required, the need for ductwork, expansion joints, and insulation is greatly reduced, as compared to that required for separate primary and secondary air preheater arrangements. Equipment layout is also simplified. Less structural steel is needed to install the system and less cleaning equipment is required.

The quad-sector design has four separate sectors:

- One sector for flue gas
- One sector for primary air/oxidant
- Two sectors for secondary air/oxidant

In addition to reducing the cost of heating the air/oxidant for coal drying and reducing the overall gas-to-gas leakage, the Quad-Sector design permits simplified controls when compared with a separate primary and secondary air preheater system (see Figure 4-16).

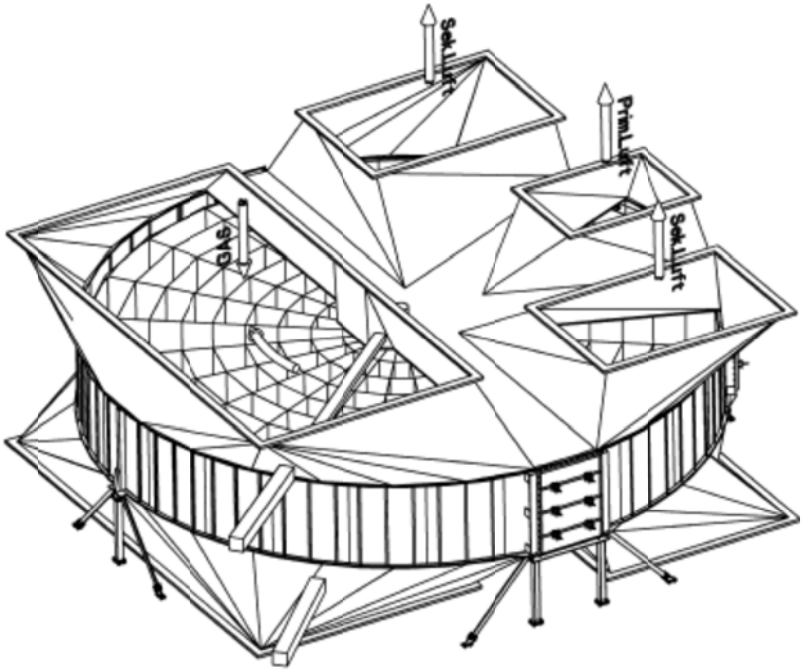

Figure 4-16: Ljungstrom® Quad-sector Air Preheater Vertical Shaft Arrangement

The Ljungstrom® regenerative air preheater design is one of the most efficient types of heat exchanger for utility applications available today. The design of rotating, modular elements coupled with highly efficient heat transfer surface make the Ljungstrom® extremely compact for a large amount of heat duty.

Ljungstrom® regenerative air preheaters are designed to safely operate at temperatures well below the flue gas acid dew point levels that are practically unattainable with other types of heat exchangers. For every 34 to 43°F (19 to 25°C) reduction in exit flue gas temperature (depending on fuel type), a boiler efficiency increase of one percent (1%) is realized.

Material Design

When the temperatures of cold end surfaces decline below acid dew points, increased cleaning and corrosion problems result. Precipitates, laden with acid, build-up and attack heat transfer surfaces resulting in increased maintenance and reduced heat transfer surface life when traditional materials are used.

These problems have been addressed in Ljungstrom® air preheaters. Enamel coated corrosion resistant steel is used for the fabrication of cold end heat transfer surfaces and rotor structural components. Enamel coated steel is also used for hot end elements.

Effective Cleanability

Power-operated sootblowers of oscillating or retractable types are used to clean Ljungstrom® air preheaters. Recommended blowing mediums are dry steam or compressed air. In all applications, the sootblower drive unit is located externally and can be serviced during operation. The cleaning equipment and blowing medium pressures and volumes are selected to achieve an optimum balance between duration of the cleaning cycle, energy consumption, and element life. In cases where residual deposit accumulations cannot be readily removed by sootblowing, water-washing equipment is used. The stationary washing device consists of a straight pipe with spray-type nozzles spaced to evenly distribute the wash water over the heat transfer surfaces.

Effective Leakage Control

Both the ASU and GPU are very energy intensive systems that are required with oxy-firing. Therefore, reducing flow requirements for these systems is important. Minimization of the GGH leakage is especially important with oxy-firing because it reduces ASU and GPU power requirements. The design of a Ljungstrom® GGH involves the continuous rotation of the heat transfer surfaces through the oxidant and flue gas streams. These gas streams normally operate at different pressures. Therefore a means of sealing against cross leakage between the gas streams is required to minimize oxygen leakage. Over many years of continuous operation, the Ljungstrom® sealing system has proven to be very effective with minimal maintenance. The design takes advantage of normal thermal growths to optimize the effectiveness of the sealing system.

The rotor is divided into sectors, each forming a separate pie-shaped gas passage. Fixed, leaf-type seals are attached radially and axially to the rotor structure between each sector. Sector-shaped radial sealing plates and axial sealing plates provide the sealing surfaces that divide the rotor into two equal gas passages. During operation the leaf seals rotate in close proximity to the sealing plates. The sealing plates are adjustable to allow for optimization of the operating clearance between the seals and sealing plates.

The angular size of the rotor sectors and sealing plates are such that, at any point in the rotational cycle, two seals will be adjacent to each sealing surface. This creates a plenum adjacent to each sealing plate that is at a static pressure approximately halfway between the higher-pressure side and the lower-pressure side. Therefore, the pressure differential that drives the leakage from the higher-pressure side to the lower-pressure side is reduced by half. Because pressure differential is a primary factor in the direct leakage rate, the use of Duplex™ sealing has a significant effect in reducing overall direct leakage. See Figure 4-17 below:

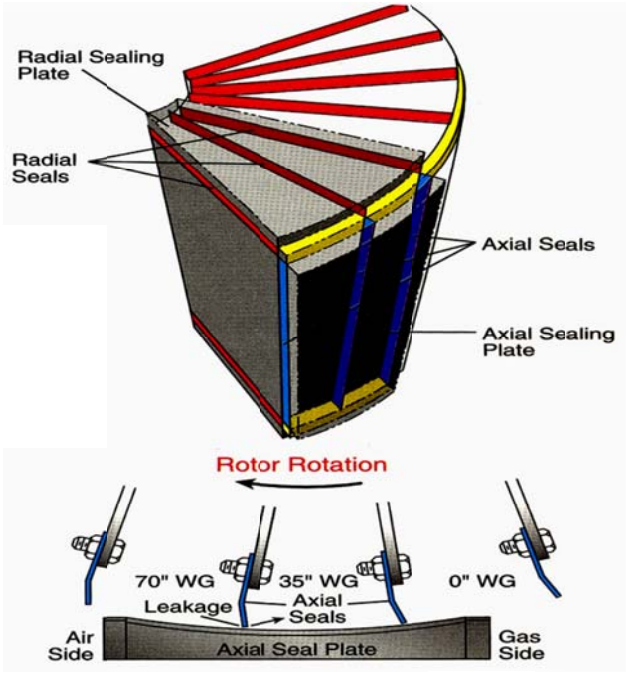

Figure 4-17: Duplex™ Sealing System

The continuous process of heat transfer results in a temperature gradient from the hot side to the cold side of the GGH, which leads to a predictable deformation of the cylindrical rotor. The hot end expands radially and becomes convex while the cold end remains smaller and becomes concave. To compensate for this thermal deformation the sealing system is set-up in the cold condition with pre-calculated gaps at the cold end radial and hot end axial sealing plates. (Shown below in yellow in Figure 4-18). During operation these gaps are reduced to zero by the thermal deformation of the rotor.

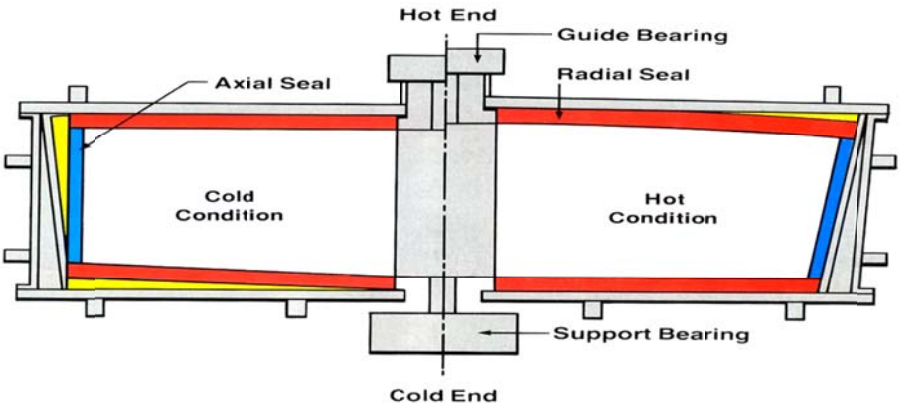

Figure 4-18: Thermal Deformations

As the cold radial and axial gaps are closed as the rotor approaches its operating temperature, an additional gap opens as the hot end radial seals move away from the sealing plates. In many

GGH's this additional gap is quite small and is therefore ignored. In certain applications, however, the GGH is equipped with an active Leakage Control System (LCS) shown in Figure 4-19 to minimize the direct leakage which occurs through this hot end radial seal clearance.

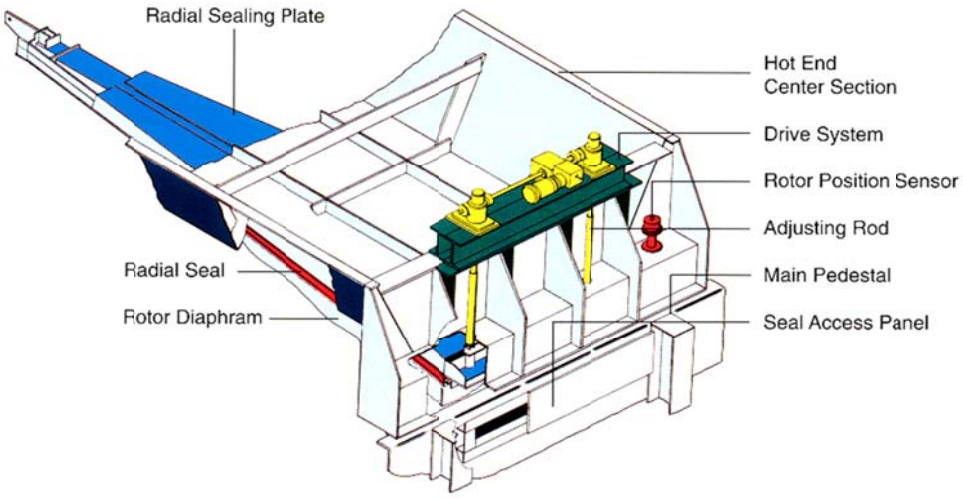

Figure 4-19: Leakage Control System (LCS)

Actively controlling the hot end radial seal clearance during operation is accomplished by physically moving the hot end sector plates. A small electro-mechanical drive system together with a sensing device is attached to each hot end sector plate. The sensor detects the position of the thermally deformed rotor and signals the electronic control panel, which commands the drive system to reposition the sector plate accordingly. With the system in the "auto" mode, the drives independently move the sector plates toward the rotor. Upon reaching the pre-specified clearance between the seals and sealing plate, the sensor signals the drive to stop, leaving a nominal clearance. If the seal clearance changes as a result of temperature changes in the rotor, the system will automatically reposition the sector plates to maintain the proper clearance. The Leakage Control System ensures that the hot end leakage is minimized across the operating load range.

The purpose of the Ljungstrom® sealing system is to minimize the amount of direct leakage that passes across the seals. Minimizing leakage is a prime consideration in the design of a GGH. A secondary type of leakage that occurs in a Ljungstrom® GGH is known as entrained leakage. As each sector of the rotor leaves the oxidant gas side and passes between the sealing plates, a volume of oxidant gas becomes trapped within the sector. As the sector rotates into the flue gas side the volume of trapped oxidant gas is released into the flue gas. Reducing this leakage is the function of the purging system. See Figure 4-20.

The purging system draws a volume of warm flue gas into a fan. Through connecting ductwork, the fan forces the flue gas into a plenum along the side of the radial sealing plate that is located on the trailing side of the oxidant gas inlet of the GGH. As the rotor rotates, each sector passes

under the plenum where the flue gas exiting the plenum purges the sector of entrained oxidant gas.

A further reduction in direct leakage can be achieved by installing pressurized sealing. Similar to purging, the pressurized sealing system draws a volume of warm flue gas into a fan. Through connecting ductwork, the fan forces the flue gas through openings in the sealing plates and into the rotor sectors as they rotate between the sealing plates. This causes each sector to become pressurized to a level that is higher than the oxidant gas stream, thereby precluding any leakage of oxidant gas into the flue gas. See Figure 4-20.

Table 4-1 shows the approximate levels of oxidant gas to flue gas leakage that can be achieved with the various leakage control features.

Table 4-1: GGH Leakage Levels

Leakage Reduction Features	Approximate Leakage Level
Standard sealing system	< 3%
with leakage control system	2 – 3%
with purging system	< 2%
with pressurized sealing system	< 1%

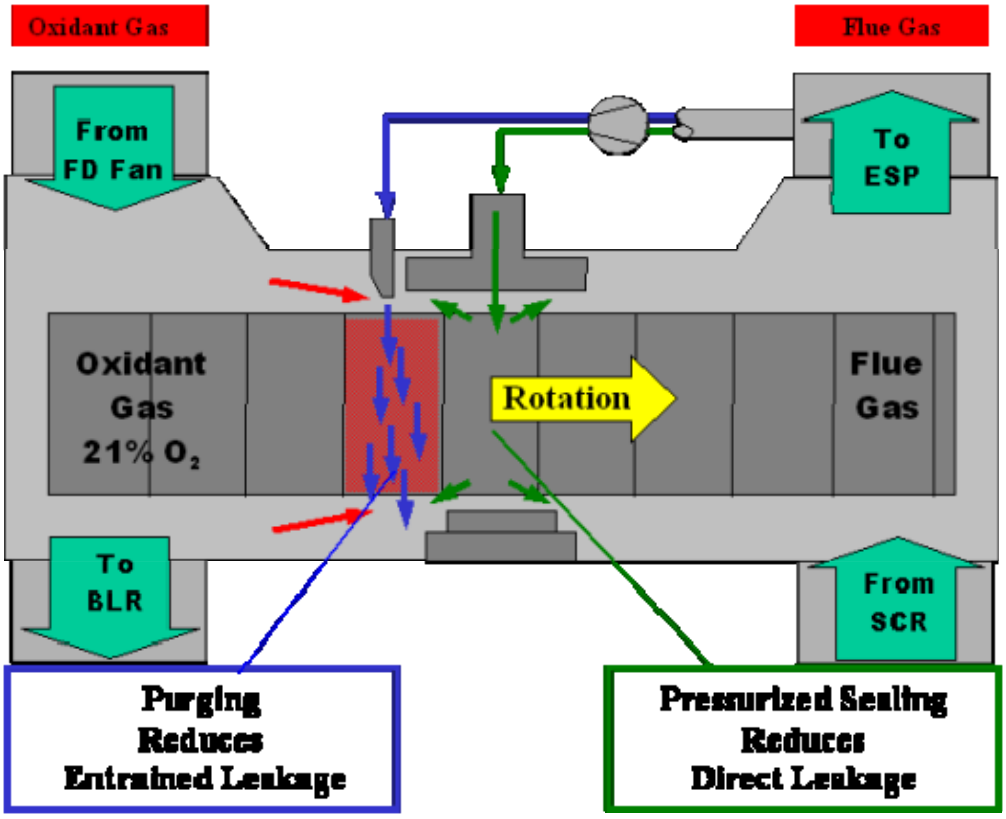

Figure 4-20: Pressurized Sealing and Purging System

4.3.16 SCR System

When designing a new tangentially fired steam generator, the SCR equipment can be effectively integrated with the low NO_x combustion system to achieve a specific outlet NO_x emission. The design of the low NO_x system for this project is based on first maximizing in-furnace NO_x reduction to lower the overall design requirements of the backend SCR system. The low NO_x produced by the TFS2000™ firing system allows the SCR to be optimized with respect to lower capital and operating costs. The significant in-furnace NO_x reduction results in lower catalyst volume, decreased ammonia flow requirements, and reduced draft losses across the catalyst.

The boiler includes a selective catalytic reduction system (SCR) located between the economizer outlet and air heater inlet. Reactor size, catalyst surface, ammonia injection, and sootblowing systems are designed to achieve the specified NO_x emissions requirements over the full range of specified coals.

The SCR system utilizes a catalyst and reductant (a diluted mixture of ammonia gas in air/RFG) to disassociate NO_x to nitrogen gas and water vapor. The primary catalytic process reactions are as follows:

$$4\ NO + 4\ NH_3 + O_2 \text{ catalyst} \rightarrow 4\ N_2 + 6\ H_2O$$

$$2\ NO_2 + 4\ NH_3 + O_2 \text{ catalyst} \rightarrow 3\ N_2 + 6\ H_2O$$

Since NO_x is about ninety-five percent (95%) NO in the flue gas stream, the first reaction dominates. Major critical variables that affect the percentage of NO_x removal are the reaction temperature, the flue gas volumetric flow rate, the inlet gas velocity, and the mole ratio of ammonia to inlet NO_x. See Figure 4-21.

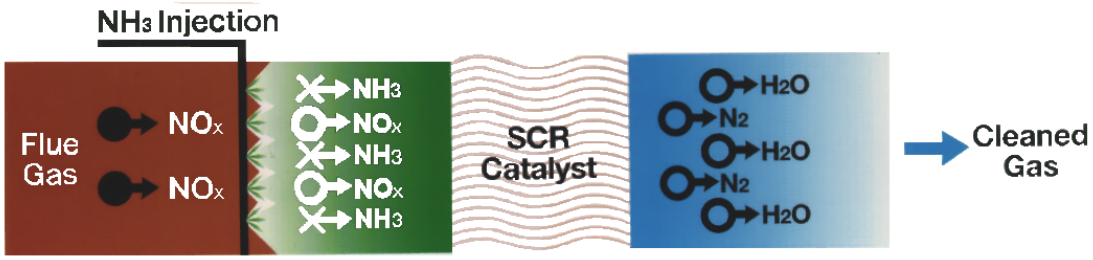

Figure 4-21: SCR Process Chemistry

SCR System Components

The SCR system consists of the following major components (see Figure 4-22).

- SCR reactor and catalyst modules
- NH_3 injection grid
- Ammonia System, Storage and Feed System
- SCR Instrumentation and Controls

SCR Reactor and Catalyst Modules

Each reactor chamber is composed of layers of catalyst modules. The number and size of the modules are based upon system design requirements such as NO_x removal efficiency, volumetric gas flow, unreacted ammonia, and catalyst life.

The SCR chamber is located between the economizer and the air heater. The flue gas exits the boiler economizer section and flows vertically down through various catalyst modules. Based on the removal rate required, two installed plus one future catalyst layers are provided.

The SCR reactor chamber internals are fabricated from carbon steel. The catalytic elements are packed in steel modular frames for ease of installation and removal through flanged duct openings at each layer in the reactor.

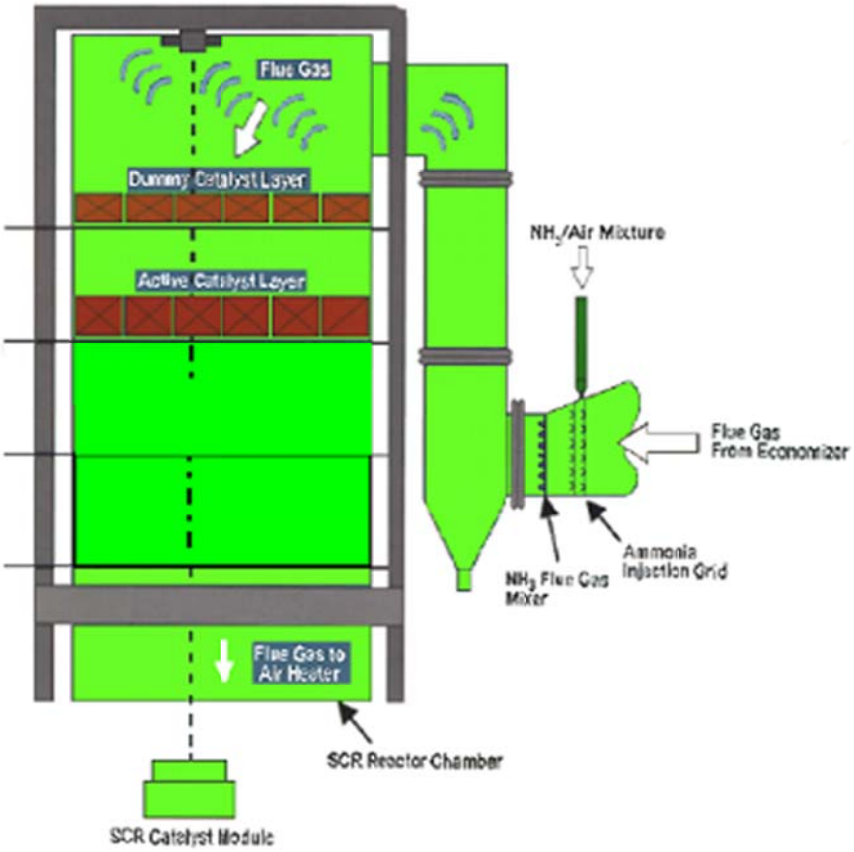

Figure 4-22: SCR System Components

NH_3 Injection Grid

Injection of the ammonia gas/air/RFG mixture into the flue gas upstream of the catalyst is accomplished with the injection grid. At this location (see Figure 4-23), a mixture of ammonia gas in air/RFG is injected into the flue gas stream. The grid consists of a network of pipes spaced uniformly across the flue gas path. Openings (i.e. multiple nozzles) in the injection pipes are oriented co-currently with gas flow at 45° angle from vertical to the direction of the flue gas flow to provide uniform ammonia distribution.

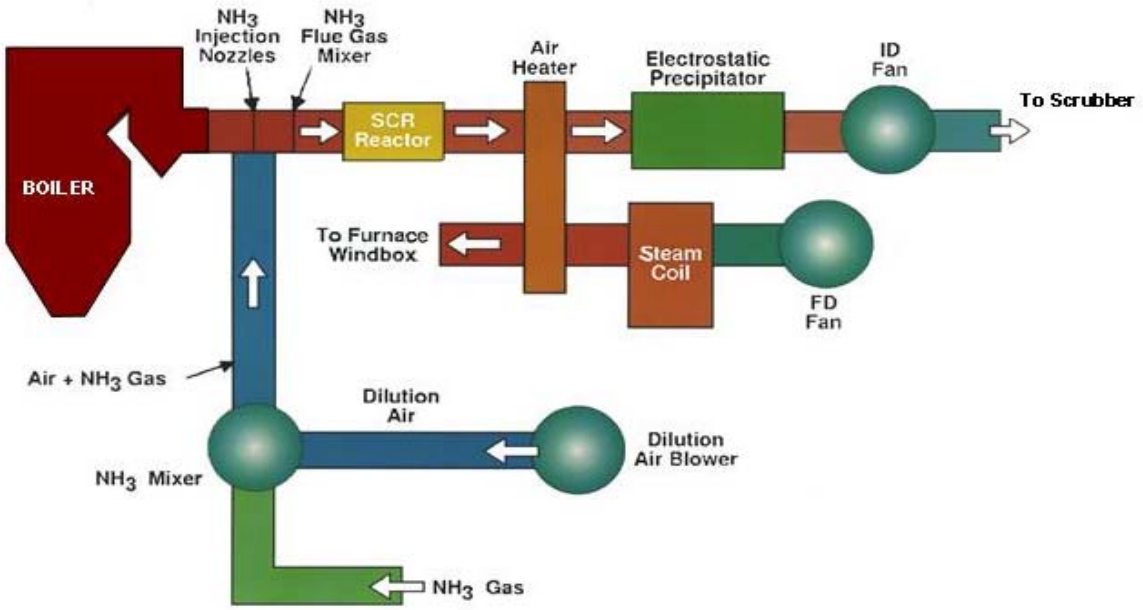

Figure 4-23: SCR System Location

4.3.17 SO_3 Removal System

A sodium based SO_3 mitigation system was selected for the removal of SO_3 from the flue gas. This minimizes acid corrosion issues in the downstream equipment as the flue gas temperature approaches the acid dewpoint. This system may not be necessary if other appropriate measures are taken to minimize the impact of acid gas corrosion, such as duct protection and rubber-lined fans. This system was included in the 450MW plant as a conservative design approach that will also provide important design and performance information for future designs.

The process uses a solution of sodium carbonate reagent that is injected and spray dried in the flue gas. The reagent is injected by an array of injection lances with atomizing nozzles located between the economizer outlet and the SCR inlet. The resulting dried product consists of extremely fine, reactive particulate matter that reacts with SO_3 to form a benign solid, sodium sulfate, which is subsequently removed from the flue gas in the fabric filter. Provisions are also made for injection after the SCR in case issues develop with SCR catalyst deactivation from the reagent.

The sodium carbonate powder is delivered by pneumatic hopper truck. It is wetted and stored as a 25% by weight solution in a storage tank. The concentrated solution is mixed with water before being sprayed into the flue gas duct through individual injection lances. Compressed air is supplied to each lance to atomize the reagent into fine droplets that quickly dry and promote effective reaction with the SO_3. The SO_3 mitigation system is designed to reduce the SO_3 concentration at the GHG inlet to no more than 5 ppm.

4.3.18 Bottom Ash System

Submerged Scraper Conveyor

A submerged scraper conveyor (SSC) is used to mechanically remove ash on a continuous basis so there is no long term storage in the water impoundment beneath the furnace. After discharge from the SSC in a dewatered condition, the ash is dumped into a bunker for removal.

Pulverizer Rejects System

The pyrites removal system is integrated into the bottom ash SSC system. Each pulverizer is provided with a water-impounded hopper at the pyrites discharge spout. Each pyrites hopper is equipped with a water seal overflow to prevent flow back into the pulverizer while maintaining the pressure seal, an observation port/access door, a sizing grate, and high level detector. Each pyrites hopper is fitted with a jet pump at its conical discharge. Periodically, the pyrites will be conveyed from each hopper by the sluicing system into the submerged scraper conveyor. An abrasion resistant centrifugal sluice pump takes water from the SSC and provides the motive water to the jet pumps under the pyrites hoppers on a sequential basis. Each pyrites hopper has its own dedicated abrasion resistant conveying line to transfer the pyrites from the hopper into the SSC.

4.4 BOP Equipment (common to 450MW and 900MW)

4.4.1 Air Separation Unit (ASU)

High purity oxygen that is fed to the oxy-fired boiler is produced by the Air Separation Unit. The only commercially available air separation technology of a sufficient scale is cryogenic air separation technology, which is illustrated in Figure 4-24.

Cryogenic Air Separation Units are already used in industrial applications and are a mature technology that offers extensive operating experience. This technology can be readily used in the 450MW boiler since ASU technology suppliers have been optimizing their designs for oxy-firing. Future ASU designs under development will provide further reductions in operating cost and energy demands of the Air Separation Unit which will provide additional benefits.

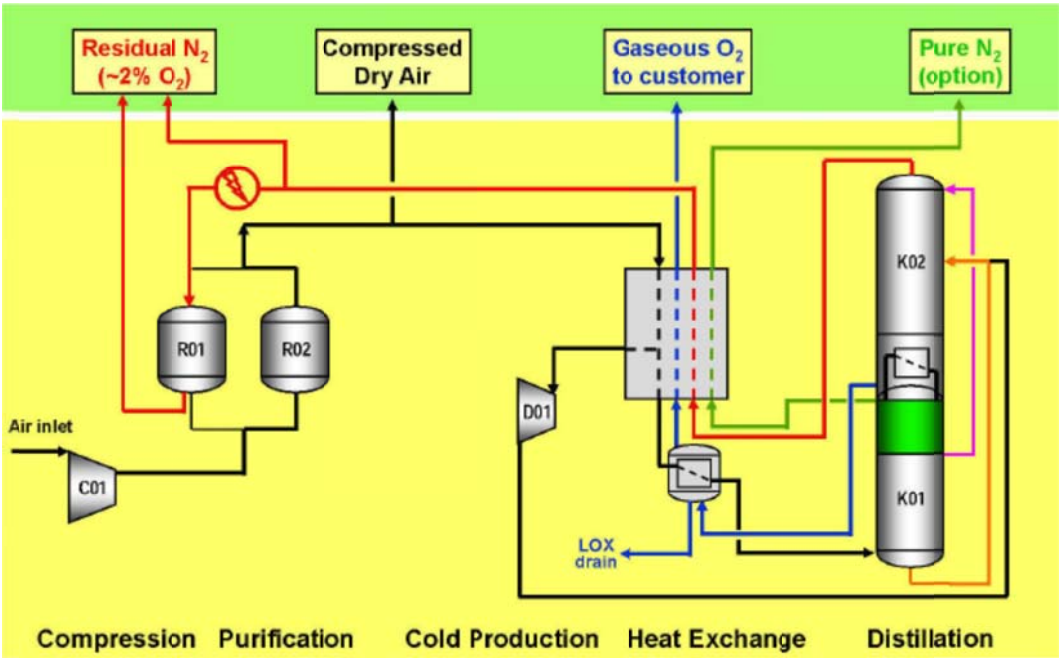

Figure 4-24: Typical Air Separation Process for Oxy-Firing Applications (source-Air Liquide)

The Air Separation Unit has three main systems: air compression, drying (molecular sieve), and cryogenic oxygen generation (cold box). The system has two separate process trains, each capable of delivering 50% of the total capacity of the unit.

The stages of cryogenic air separation are as follows:

- Atmospheric air is compressed, dried initially, and then passed through a molecular sieve for complete removal of water vapour
- Finally two stages of cryogenic distillation, around –190°C, separate oxygen and nitrogen

In normal operation, the load variation rate of the Air Separation Unit allows the system to match variations in consumption at the main power generating facility. Additionally, two intermediate storage systems for oxygen will be available:

- Gaseous storage at intermediate pressure allows for the matching of short-term fast increases in demand or other short-term variations
- A liquid storage vessel can be used as a buffer to store oxygen as a backup supply in the case of a shutdown in one of the Air Separation Unit trains. This storage vessel can be filled over an extended time when the Air Separation Unit is producing more oxygen than is required by a boiler. This stored liquid oxygen can also be used as a liquid assist for the start-up of the Air Separation Unit.

4.4.2 Gas Processing Unit

The primary purpose of the GPU is to purify and compress the CO_2 stream leaving the oxy-fired boiler so that the CO_2 product meets the specification for its particular use. For the purposes of this study, the treated CO_2 must meet the specification for use in Enhanced Oil Recovery (EOR), although its intended use will be sequestration. Accordingly, the GPU has several objectives. These include in the general order of occurrence:

1. Compression of CO_2
2. Removal of soluble species (e.g. moisture, SO_2, chlorines, ammonia)
3. Capture of mercury
4. Separation of O_2, and N_2 from CO_2
5. Vent O_2 and N_2 with some unavoidable loss of CO_2 (can be captured by other means, if necessary)
6. Exhaust CO_2 to meet the EOR composition specification

The gas stream leaving the oxy-fired boiler enters the GPU system. This stream contains mostly CO_2 and H_2O vapor with smaller amounts of N_2, O_2, and other trace gases. The GPU system starts with a direct contact condenser (DCC). The DCC is configured in a packed tower arrangement where the product gas is contacted with cold water in a countercurrent fashion. Here, the gas is cooled down to a temperature of 20 to 25°C and most of the H_2O vapor contained in the gas stream is condensed. Acid impurities like SO_x are removed here also.

The DCC, in addition to cooling, acts as a polishing device leaving the residual SO_x concentration in the low ppm levels. It is therefore advisable to remove as much SO_x as possible upstream of the DCC using a WFGD and thus minimizing the consumption of caustic for neutralization of the produced condensates. The DCC operates with an external water recirculation loop consisting of recycle pumps and heat exchangers for recycle loop water cooling. These heat exchangers are designed to remove both the sensible heat of the cooled gas as well as the latent heat of vaporization from the condensed water vapor.

After cooling the product gas in the DCC, the gas enters the multi-stage compressor station. Four stages are used to raise the pressure to approximately 36 atm. Each compression stage has an after-cooler followed by a water separator.

The next step is trace element removal. Mercury will lead to brittle corrosion in the aluminum heat exchangers. Therefore the residual Hg concentration has to be as low as 0.1 nanograms/Nm^3 to obtain vendor guarantees. This is accomplished by locating the Hg adsorber bed (activated carbon) upstream of the dryer.

Trace removal is followed by further cooling and removal of additional H_2O. This is required to avoid freezing in the cold section of the GPU system. Therefore a fixed bed dryer is installed

before the condensation and purification station. The gas stream is further cooled and partially condensed using the product and vent gas streams of the purification unit. To achieve a high recovery rate and high product purity, a distillation column is required.

The vent gas of the purification station is expanded in a staged expander system to recover some energy.

After the purification stage the pressure of the CO_2 product stream is raised. A compressor station and a pump are needed for this application. The pressure of the CO_2 product is typically more than 110 atm (above the critical pressure of CO_2). An associated valve at the line end controls the pressure.

The GPU design, which is modelled after the GPU used in Case 5C from the DOE Baseline Report[34], captures 93% of the CO_2 for each of the oxy-fired plants in this study.

4.4.3 Power Generation

The steam turbine for the 450MW plant has steam conditions of 27.1 MPa /603°C /620°C (3927 psig/1117°F/1148°F). It is a tandem compound type, consisting of HP-IP-two LP (double flow) sections enclosed in three casings, designed for condensing single reheat operation, and equipped with non-automatic extractions and four-flow exhaust. The turbine drives a hydrogen-cooled generator. The turbine has DC motor-operated lube oil pumps and main lube oil pumps, which are driven off the turbine shaft. The exhaust pressure is 50.8 cm (2 in) Hg in the single pressure condenser. There are eight extraction points. The condenser is two-shell, transverse, single pressure with divided waterbox for each shell.

Turbine bearings are lubricated by a closed-loop, water-cooled pressurized oil system. Turbine shafts are sealed against air in-leakage or steam blowout using a labyrinth gland arrangement connected to a LP steam seal system. The generator stator is cooled with a CL water system consisting of circulating pumps, shell and tube or plate and frame type heat exchangers, filters, and deionizers, all skid-mounted. The generator rotor is cooled with a hydrogen gas recirculation system using fans mounted on the generator rotor shaft.

Operation Description

Main steam from the boiler passes through the stop valves and control valves and enters the turbine at 27.1 MPa /603°C (3927 psig / 1117°F). The steam initially enters the high-pressure section of the turbine, flows through the turbine, and returns to the boiler for reheating. The reheat steam flows through the reheat stop valves and intercept valves and enters the double-flow IP section at 620°C (1148°F). After passing through the IP section, the steam enters crossover piping, which transports the steam to the two LP sections. The steam divides into two paths and flows through the LP sections, exhausting downward into the condenser.

[34] Pulverized Coal Oxycombustion Power Plants Volume 1, DOE/NETL-2007/1291, August 2008

4.4.4 Balance of Plant

Particulate Control

The fabric filter (or baghouse) consists of two separate single-stage, in-line, multi-compartment units. Each unit is of high (0.9-1.5 m/min [3-5 ft/min]) air-to-cloth ratio design with a pulse-jet on-line cleaning system. The ash is collected on the outside of the bags, which are supported by steel cages. The dust cake is removed by a pulse of compressed air. The bag material is polyphenylensulfide (PPS) with intrinsic Teflon Polytetrafluoroethylene (PTFE) coating. The bags are rated for a continuous temperature of 180°C (356°F) and a peak temperature of 210°C (410°F). Each compartment contains a number of gas passages with filter bags and heated ash hoppers supported by a rigid steel casing. The fabric filter is provided with necessary control devices, inlet gas distribution devices, insulators, inlet and outlet nozzles, expansion joints, and other items as required.

Mercury Removal

Mercury removal is based on a coal Hg content of 0.15 ppmd. The combination of pollution control technologies used in the PC boilers, SCR, fabric filters and FGD, result in significant co-benefit capture of mercury. The SCR promotes the oxidation of elemental mercury, which in turn enhances the mercury removal capability of the fabric filter and FGD unit. The mercury co-benefit capture is assumed to be 90 percent for this combination of control technologies, consistent with the assumptions used in the DOE Baseline Report. Co-benefit capture alone is sufficient to meet current NSPS mercury limits, so no activated carbon injection is included.

Flue Gas Desulfurization

The FGD system is a wet limestone forced oxidation positive pressure absorber non-reheat unit, with wet-stack and gypsum production. The function of the FGD system is to scrub the boiler exhaust gases to remove the SO_2 prior to release to the environment or entering into the GPU facility. Sulfur removal efficiency is 98 percent in the FGD unit. The scope of the FGD system is from the outlet of the ID fans to the GPU process inlet.

Reagent Preparation System

The function of the limestone reagent preparation system is to grind and slurry the limestone delivered to the plant. The scope of the system is from the day bin up to the limestone feed system. The system is designed to support continuous base load operation.

Operation Description – Each day bin supplies a 100% capacity ball mill via a weigh feeder. The wet ball mill accepts the limestone and grinds the limestone to 90 – 95% passing 325 mesh (44 microns). Water is added at the inlet to the ball mill to create limestone slurry. The reduced limestone slurry is then discharged into a mill slurry tank. Mill recycle pumps, two per tank,

pump the limestone water slurry to an assembly of hydrocyclones and distribution boxes. The slurry is classified into several streams, based on suspended solids content and size distribution.

The hydrocyclone underflow with oversized limestone is directed back to the mill for further grinding. The hydrocyclone overflow with correctly sized limestone is routed to a reagent storage tank. Reagent distribution pumps direct slurry from the tank to the absorber module.

FGD Scrubber

The flue gas exiting the GHG passes through a baghouse, then through the ID fans and into the 100% capacity absorber module. The absorber module is designed to operate with counter-current flow of gas and reagent. The gas stream enters the bottom of the absorber vessel and is subjected to an initial quenching spray of reagent. The gas flows upward through the spray zone, which provides enhanced contact between gas and reagent. Multiple spray elevations maintain a consistent reagent concentration in the spray zone. The reagent-laden gas passes up through several levels of chevron-shaped moisture separators that direct the gas flow through abrupt direction changes, separating the entrained droplets of liquid by inertial effects. The scrubbed flue gas exits at the top of the absorber vessel and is routed to the GPU.

The scrubbing slurry falls to the liquid inventory in the lower portion of the absorber vessel. Oxidation air is added to promote the oxidation of calcium sulphite contained in the slurry to calcium sulphate. Multiple agitators prevent settling of solids and enhance oxidation air and slurry mixing. Recirculation pumps recirculate the slurry from the lower portion of the absorber vessel to the spray level.

Byproduct Dewatering

The byproduct dewatering system acts to dewater the bleed slurry from the FGD absorber modules. The recirculating reagent in the FGD absorber vessel accumulates dissolved and suspended solids on a continuous basis as byproducts from the SO_2 absorption process. Maintenance of the quality of the recirculating slurry requires that a portion be withdrawn and replaced by fresh reagent. This is accomplished on a continuous basis by the bleed pumps pulling off byproduct solids and the reagent distribution pumps supplying fresh reagent to the absorber.

Gypsum (calcium sulfate) is produced by the injection of oxygen into the calcium sulphite produced in the absorber tower sump. The bleed from the absorber contains approximately 20 wt% gypsum. The absorber slurry is pumped to a primary dewatering hydrocyclone cluster. There it is dewatered from 20 wt% to 50 wt% solids and $CaCO_3$ is also separated from $CaSO_4$-$2H_2O$. This process ensures a limestone stoichiometry in the absorber vessel of 1.10 and an overall limestone stoichiometry of 1.05. The underflow from the hydrocyclone flows into the filter feed tank, from which it is pumped to a horizontal belt vacuum filter. Two 100% filter systems are provided for redundant capacity.

Hydrocyclones

The hydrocyclone is designed to increase the slurry concentration in one step to approximately 50 wt%. The hydrocyclone feed enters tangentially and experiences centrifugal motion so that the heavy particles move toward the wall and flow out the bottom. Some of the lighter particles collect at the center of the cyclone and flow out the top. The underflow is thus concentrated from 20 wt% at the feed to 50 wt%.

Multiple hydrocyclones are used to process the bleed stream from the absorber. The hydrocyclones are configured in a cluster with a common feed header. The system has two hydrocyclone clusters, each with 5 15 cm (6 inch) diameter units. Four cyclones are used to continuously process the bleed stream at design conditions, and once cyclone is spare.

Cyclone overflow and underflow are collected in separate launders. The overflow from the hydrocyclones still contains about 5 wt% solids, consisting of gypsum, flyash, and limestone residues, and is sent back to the absorber. The underflow of the hydrocyclones flows into the filter feed tank from where it is pumped to the horizontal belt vacuum filters.

Horizontal Vacuum Belt Filters

The secondary dewatering system consists of horizontal vacuum belt filters. The pre-concentrated gypsum slurry (50 wt%) is pumped to an overflow pan through which the slurry flows onto the vacuum belt. As the vacuum is pulled, a layer of cake is formed. The cake is dewatered to approximately 90 wt% solids as the belt travels to the discharge. At the discharge end of the filter, the filter cloth is turned over a roller where the solids are dislodged from the filter cloth. This cake falls through a chute onto the pile prior to the final byproduct uses. The filtrate is collected in a filtrate tank that provides surge volume for use of the filtrate in grinding the limestone. Filtrate that is not used for limestone slurry preparation is returned to the absorber.

Balance of Plant

The remaining balance of plant components consist of the condensate, feedwater, main and reheat steam, extraction steam, ash handling, ducting, stack, waste treatment, and miscellaneous systems. Most of this equipment is identical to that provided for the DOE SCPC Case 11 plant. The BOP description for that case is largely repeated below.

Condensate

The function of the condensate system is to pump condensate from the condenser hotwell to the deaerator, through the gland steam condenser, and the LP FW heaters. Each system consists of one main condenser; two variable speed electric motor-driven vertical condensate pumps each sized for 50 percent capacity; one gland steam condenser; four LP heaters (or five LP heaters for the A-USC cases); and one deaerator with storage tank.

Condensate is delivered to a common discharge header through two separate pump discharge lines, each with a check valve and a gate valve. A common minimum flow recirculation line

discharging to the condenser is provided downstream of the gland steam condenser to maintain minimum flow requirements for the gland steam condenser and the condensate pumps.

The LP FW heaters are 50 percent capacity, parallel flow, and are located in the condenser neck. All remaining FW heaters are 100 percent capacity shell and U-tube heat exchangers. Each LP FW heater is provided with inlet/outlet isolation valves and a full capacity bypass. LP FW heater drains cascade down to the next lowest extraction pressure heater and finally discharge into the condenser. Pneumatic level control valves control normal drain levels in the heaters. High heater level dump lines discharging to the condenser are provided for each heater for turbine water induction protection. Pneumatic level control valves control dump line flow.

Feedwater

The function of the FW system is to pump the FW from the deaerator storage tank through the HP FW heaters to the economizer. One turbine-driven BFW pump sized at 100 percent capacity is provided to pump FW through the HP FW heaters. One 25 percent motor-driven BFW pump is provided for startup. The pumps are provided with inlet and outlet isolation valves and individual minimum flow recirculation lines discharging back to the deaerator storage tank. The recirculation flow is controlled by automatic recirculation valves, which are a combination check valve in the main line and in the bypass, bypass control valve, and flow sensing element. The suction of the boiler feed pump is equipped with startup strainers, which are utilized during initial startup and following major outages or system maintenance.

Each HP FW heater is provided with inlet/outlet isolation valves and a full capacity bypass. FW heater drains cascade down to the next lowest extraction pressure heater and finally discharge into the deaerator. Pneumatic level control valves control normal drain level in the heaters. High heater level dump lines discharging to the condenser are provided for each heater for turbine water induction protection. Dump line flow is controlled by pneumatic level control valves.

The deaerator is a horizontal, spray tray type with internal direct contact stainless steel (SS) vent condenser and storage tank. The boiler feed pump turbine is driven by main steam up to 60 percent plant load. Above 60 percent load, extraction from the IP turbine exhaust (1.05 MPa/395°C [153 psig/743°F]) provides steam to the boiler feed pump steam turbine.

Main and Reheat Steam

The function of the main steam system is to convey main steam from the boiler superheater outlet to the HP turbine stop valves. The function of the reheat system is to convey steam from the HP turbine exhaust to the boiler reheater and from the boiler reheater outlet to the IP turbine stop valves.

Main steam exits the boiler superheater through a stop/check valve and gate valve and is routed in a single line feeding the HP turbine. Cold reheat steam exits the HP turbine, flows through an isolation gate valve and a flow control valve, and enters the boiler reheater. Hot reheat steam

exits the boiler reheater through a gate valve and is routed to the IP turbine. A branch line off the IP turbine exhaust feeds the boiler feed water pump turbine during unit operation starting at approximately 60 percent load. A branch connection from the cold reheat piping supplies steam to FW heater 7.

The turbine is protected from overspeed on turbine trip, from flash steam reverse flow from the heaters through the extraction piping to the turbine. This protection is provided by positive closing, balanced disc non-return valves located in all extraction lines except the lines to the LP FW heaters in the condenser neck. The extraction non-return valves are located only in horizontal runs of piping and as close to the turbine as possible.

The turbine trip signal automatically trips the non-return valves through relay dumps. The remote manual control for each heater level control system is used to release the non-return valves to normal check valve service when required to restart the system.

Circulating Water System

It is assumed that the plant is serviced by a public water facility and has access to groundwater for use as makeup cooling water with minimal pretreatment. All filtration and treatment of the circulating water are conducted on site. A mechanical draft, wood frame, counter-flow cooling tower is provided for the circulating water heat sink. Two 50 percent cooling water pumps are provided. The circulating water system provides cooling water to the condenser, the auxiliary cooling water system, and the gas processing unit.

The auxiliary cooling water system is a CL system. Plate and frame heat exchangers with circulating water as the cooling medium are provided. This system provides cooling water to the lube oil coolers, turbine generator, boiler feed pumps, etc. All pumps, vacuum breakers, air release valves, instruments, controls, etc. are included for a complete operable system.

Ash Handling System

The function of the ash handling system is to provide the equipment required for conveying, preparing, storing, and disposing of the fly ash and bottom ash produced on a daily basis by the boiler. The scope of the system is from the baghouse hoppers, air heater and economizer hopper collectors, and bottom ash hoppers to the hydrobins (for bottom ash) and truck filling stations (for fly ash). The system is designed to support short-term operation at the 5 percent over pressure/valves wide open condition (16 hours) and long-term operation at the 100 percent guarantee point (90 days or more).

The fly ash collected in the baghouse and the air heaters is conveyed to the fly ash storage silo. A pneumatic transport system using LP air from a blower provides the transport mechanism for the fly ash. Fly ash is discharged through a wet unloader, which conditions the fly ash and conveys it through a telescopic unloading chute into a truck for disposal.

Ducting and Stack

One stack is provided with a single fiberglass-reinforced plastic (FRP) liner. The stack is constructed of reinforced concrete. The stack is 152 m (500 ft) high for adequate particulate dispersion.

Waste Treatment/Miscellaneous Systems

An onsite waste treatment facility treats all runoff, cleaning wastes, blowdown, and backwash to within the U.S. EPA standards for suspended solids, oil and grease, pH, and miscellaneous metals. Waste treatment equipment is housed in a separate building. The waste treatment system consists of a water collection basin, three raw waste pumps, an acid neutralization system, an oxidation system, flocculation, clarification/thickening, and sludge dewatering. The water collection basin is a synthetic-membrane-lined earthen basin, which collects rainfall runoff, maintenance cleaning wastes, and backwash flows.

The raw waste is pumped to the treatment system at a controlled rate by the raw waste pumps. The neutralization system neutralizes the acidic wastewater with hydrated lime in a two-stage system, consisting of a lime storage silo/lime slurry makeup system, dry lime feeder, lime slurry tank, slurry tank mixer, and lime slurry feed pumps.

The oxidation system consists of an air compressor, which injects air through a sparger pipe into the second-stage neutralization tank. The flocculation tank is fiberglass with a variable speed agitator. A polymer dilution and feed system is also provided for flocculation. The clarifier is a plate-type, with the sludge pumped to the dewatering system. The sludge is dewatered in filter presses and disposed offsite. Trucking and disposal costs are included in the cost estimate. The filtrate from the sludge dewatering is returned to the raw waste sump.

Miscellaneous systems consisting of fuel oil, service air, instrument air, and service water are provided. A storage tank provides a supply of No. 2 fuel oil used for startup and for a small auxiliary boiler. Fuel oil is delivered by truck. All truck roadways and unloading stations inside the fence area are provided.

Buildings and Structures

Foundations are provided for the support structures, pumps, tanks, and other plant components. The following buildings are included in the design basis:

- Coal Crusher Building
- Boiler Building
- WFGD and GPU system buildings
- Continuous emissions monitor building

- Steam Turbine Building
- Industrial waste treatment building
- Makeup water and pretreatment building
- Pump house and electrical equipment building
- Runoff water pump house
- Fuel oil pump house
- Administration
- Guard house

Accessory Electric Plant

The accessory electric plant consists of switchgear and control equipment, generator equipment, station service equipment, conduit and cable trays, and wire and cable. It also includes the main power transformer, required foundations, and standby equipment.

Instrumentation and Control

An integrated plant-wide control and monitoring DCS is provided. The DCS is a redundant microprocessor-based, functionally distributed system. The control room houses an array of multiple video monitor and keyboard units. The monitor/keyboard units are the primary interface between the generating process and operations personnel. The DCS incorporates plant monitoring and control functions for all the major plant equipment. The DCS is designed to provide 99.5 percent availability. The plant equipment and the DCS are designed for automatic response to load changes from minimum load to 100 percent. Startup and shutdown routines are manually supervised, with operator selection of modular automation routines available.

Advanced controls were integrated into the design including adaptive control and model prediction control logic to improve response and optimize performance. Details on the advance control systems are discussed in Chapter 3.

4.5 Boiler General Arrangement Drawings

Figure 4-25 shows a Steam Generator General Arrangement Side View drawing, Figure 4-26 shows a Steam Generator General Arrangement Plan View drawing, and Figure 4-27 shows a Steam Generator General Arrangement Plan View drawing for the 450MW plant.

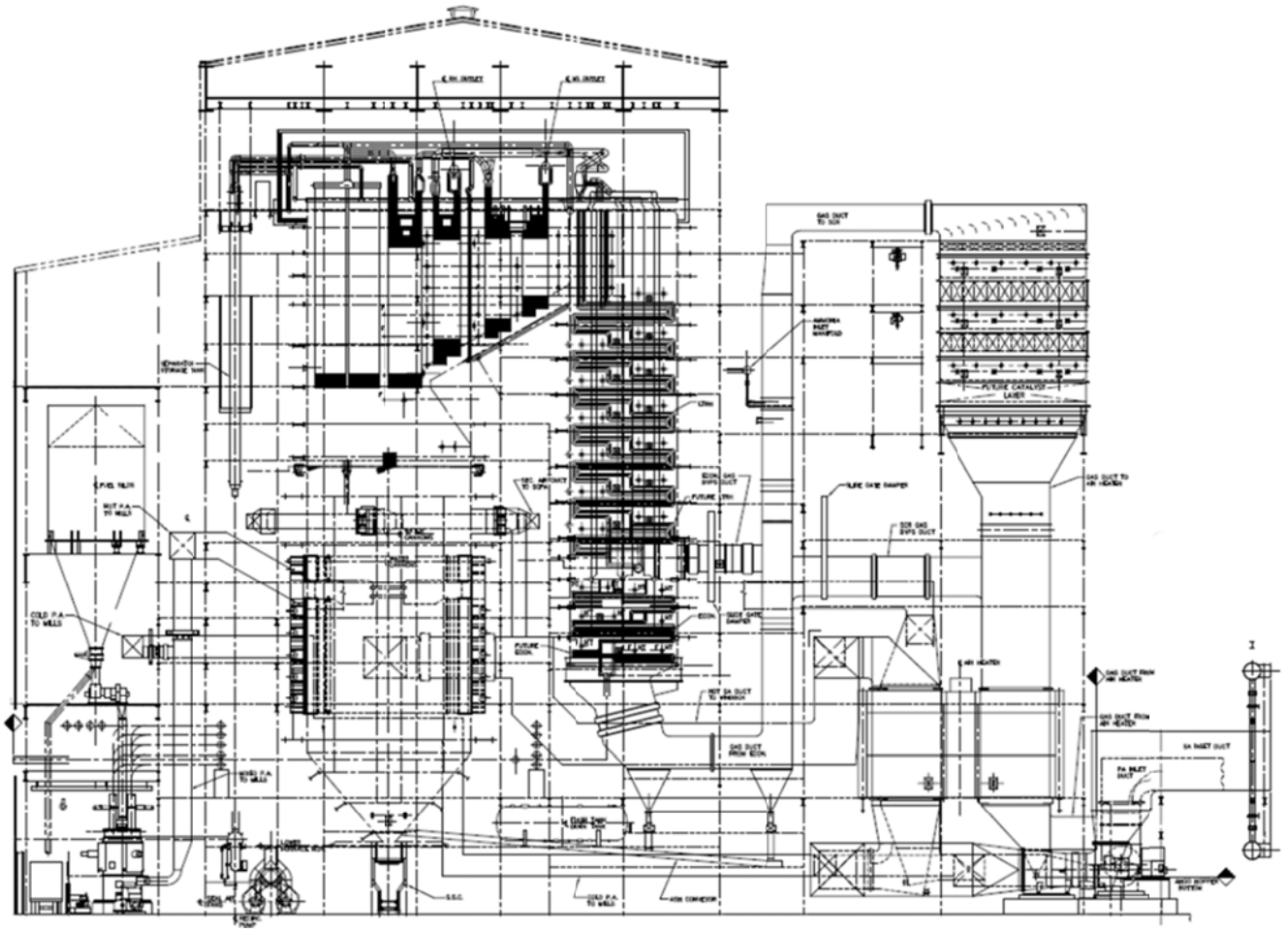

Figure 4-25: Steam Generator General Arrangement Drawing – Side Elevation

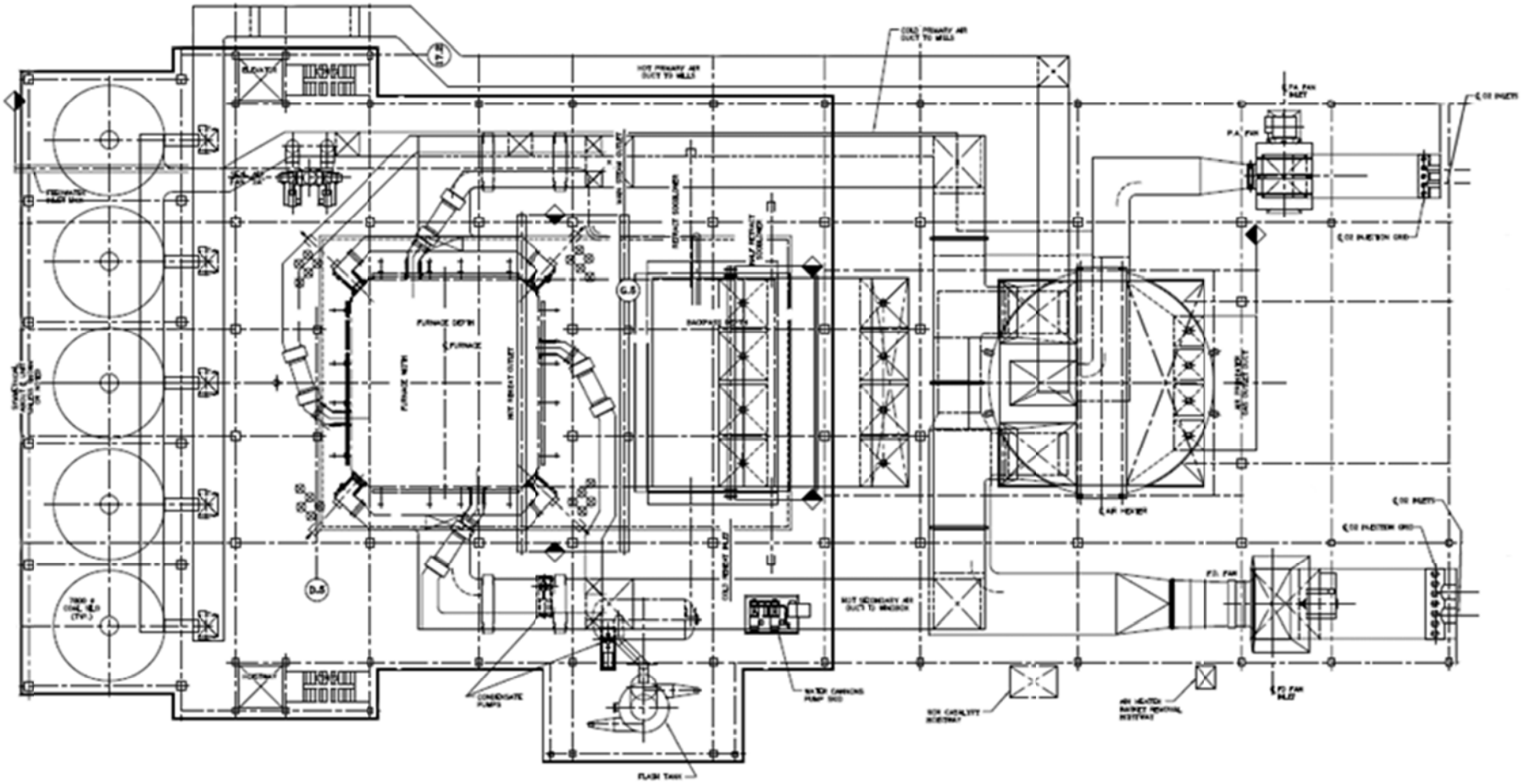

Figure 4-26: Steam Generator General Arrangement Drawing – Plan View

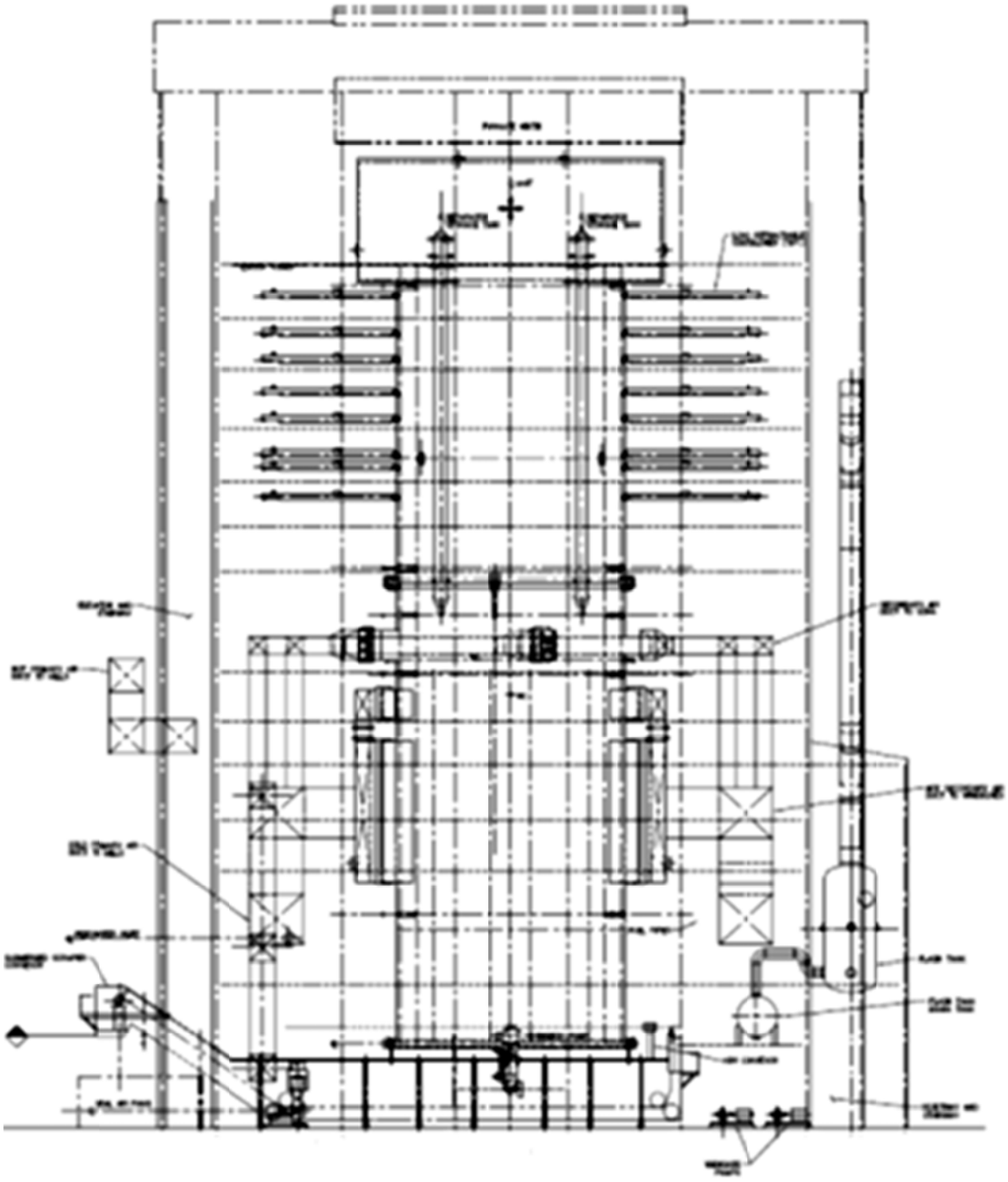

Figure 4-27: Steam Generator General Arrangement Drawing – Front Elevation View

4.6 Boiler Island Process Description and Performance Data

This section provides a description of the boiler island process and performance information for both the 450MW oxy-fired and air-fired steam plants. The following information is included:

- Process Flow Diagram
- Boiler island material and energy balances at BMCR load
- Steam turbine heat balance
- Auxiliary power requirements

Boiler Island Process Description – Oxygen Firing

Figure 4-28 shows a simplified process flow diagram for a pulverized coal fired, dual-air/oxygen capable, boiler island. This system is designed to permit full load (BMCR) operation with either air or oxygen firing. The damper configuration shown is for the oxy-fired mode of operation. In the oxygen-fired mode, the three streams shown in dashed red lines are not in use (i.e. primary air inlet, secondary air inlet, and flue gas outlet to stack).

Starting with the flue gas stream leaving the boiler economizer section (Stream 4), first a SO_3 sorbent is injected (Stream 4a) to remove more than 90 percent of the SO_3 in order to lower the acid dew point temperature throughout the flue gas system. The flue gas then flows through a Selective Catalytic Reduction system (SCR) for NO_x reduction. The flue gas leaving the SCR (Stream 4b) is then cooled in the gas side sector of the quad-sector Gas-to-Gas Heater (GGH). The cooled flue gas stream leaving the GGH (Stream 5) then enters a fabric filter (FF) where most of the particulate matter is removed (Stream 6a). The flue gas leaving the FF (Stream 7) flows through the Induced Draft (ID) fan (Stream 8) and then through the Flue Gas Desulfurization (FGD) system where most of the SO_2 is removed (Stream 11). The flue gas leaving the FGD system (Stream 12) is split into two streams (Stream 27 and Stream 12a).

Stream 27 represents the recirculated flue gas portion of the secondary oxidant stream. After Stream 27c is split off from Stream 27a (for use in the GGH), the remaining recirculated flue gas (Stream 27b) is mixed with oxygen (Stream 3b) to form Stream 28. The Stream 3b flow is controlled to provide an oxygen concentration of 21 percent by volume in Stream 28. Stream 28 is then increased to the required pressure with the Forced Draft (FD) fan, and heated in the secondary sectors of the GGH to form the hot secondary oxidant stream entering the furnace windbox (Stream 30). The portion of Stream 27 that was split off (Stream 27c) is a relatively small fraction of the total and is used within the GGH as purge and seal gas. The purge and seal gas is used to minimize GGH leakage (Stream 22) from the oxidant streams (Streams 21 & 29) to the flue gas stream (Stream 5). Minimizing this leakage quantity reduces ID and FD fan power requirements and more importantly reduces the energy intensive ASU and GPU power requirements thus improving overall plant thermal efficiency.

Stream 12a represents the remainder of the flue gas leaving the FGD system that is not used for the secondary recirculation stream (Stream 27). After leaving the FGD system, Stream 12a flows through a Flue Gas Condenser (FGC) where most of the water vapor contained in the flue gas is condensed out (Stream 13). The saturated flue gas leaving the FGC (Stream 14) is again split into two streams (Streams 15 and 18).

Stream 15 is the high CO_2 content raw product stream, which flows to the Gas Processing Unit (GPU) for further purification such that the final CO_2 product (Stream 16) is acceptable for usage or sequestration. Stream 17, leaving the GPU is the GPU vent stream, which contains non-condensable gases (i.e. O_2, N_2, Ar, etc.) and also a small fraction of the CO_2 contained in Stream 15.

Stream 18 represents the recirculated flue gas portion of the primary oxidant stream. This stream also provides the source for seal gas (instead of seal air) that is used with oxy-firing. After the seal gas extraction, the remainder (Stream 18a) is mixed with oxygen (Stream 3a) to provide an oxygen concentration of 21 percent by volume (Stream 18b). It is then increased to the required pressure with the Primary Air/Oxidant (PA) fan to form the primary oxidant stream. The primary oxidant stream leaving the PA fan (Stream 19) is split into a heated portion (Streams 21 and 24) and an un-heated portion (Stream 23). Stream 21 is heated in the primary sector of the GGH to form the hot primary oxidant stream (Stream 24). This hot stream is mixed with unheated Stream 23 to form Stream 25. The split between the heated and unheated streams is adjusted to control the temperature of the pulverized coal/oxidant mixture stream leaving the coal mills (Stream 26) to the desired value (typically about 180-200°F with this fuel).

The primary oxidant and pulverized coal mixture (Stream 26) leaving the coal mills is transported to the windbox fuel nozzles and combusted in the furnace. The total oxygen required for combustion is contained within three streams (Stream 26, Stream 30, and Stream 3c). Stream 30 is the hot secondary oxidant stream leaving the GGH and flowing to the furnace through the windbox. Stream 3c represents the remaining oxygen required for complete combustion of the coal, over and above that oxygen which is contained in Streams 26 and 30. The Stream 3c flow rate is controlled such that the oxygen content in the flue gas leaving the boiler (Stream 4) is about 3 percent by volume (i.e. similar to air firing). The products of combustion including flyash leave the lower furnace section and pass through radiant and convective heat exchangers located in the upper furnace, tunnel, and backpass areas of the boiler (Stream 4), which completes the cycle.

Selection of Location for Recirculated Flue Gas Streams

The location selected for the primary flue gas recirculation stream (Stream 18) was just downstream of the FGC. This location was selected in order to provide the coal mills with a primary oxidant stream that has low moisture content such that the coal drying process occurring inside the coal mills will be similar to air fired operation. For these cases, this stream contains

about 3 percent by volume water vapor content after the FGC. The location selected for the secondary flue gas recirculation stream (Stream 27) was just after the FGD system in order to provide SO_2 levels throughout the boiler island that are within our air-fired experience range.

Selection of Location for Oxygen Mixing

Oxygen produced from the ASU is mixed with the recirculated flue gas streams in three locations as described previously. The first two mixing locations (Streams 3a & 3b) are just upstream of the PA and FD fans. Enough oxygen is added in these locations to provide an oxygen content of 21 percent by volume in these streams. The mixers used are of the grid type design. The main advantages of mixing oxygen in these locations are to minimize ASU power requirements (lower O_2 pressure required by mixing before the fans) and to improve the GGH performance (lower sink temperature and higher sink mass flow) thus providing a boiler efficiency improvement. Another requirement is to achieve a safe mixing of oxygen in the recirculated flue gas streams before the GGH to avoid the risks associated with areas of high oxygen concentration in the presence of dust. The third oxygen stream (Stream 3c), which represents the remaining oxygen required for complete combustion of the coal, is mixed with the heated secondary oxidant stream within the windbox in the air/oxidant nozzles.

Bottom Ash Removal

Ash that is not entrained in the furnace with the flue gas (flyash) is called bottom ash. It is the ash that accumulates on the furnace walls, is removed with water cannons, and falls to the bottom of the furnace and into a trough containing water. The bottom ash (Stream 31) is removed continuously from the water trough, which is part of the submerged scraper conveyor (SSC) system.

Air Infiltration

With oxy-firing and carbon capture, it is important to minimize air infiltration in order to minimize the power requirements of the GPU and to keep overall plant thermal efficiency as high as possible. Infiltration air streams shown on Figure 4-28 include Stream 2 and Stream 6b. Stream 2 represents the infiltration air entering the boiler. This flow was assumed to be about 1 percent of the stoichiometric oxygen requirement of the boiler. This should be obtainable through the use of recirculated primary flue gas as a seal gas for the boiler (instead of seal air). Stream 6b represents infiltration air entering the fabric filter. This flow was assumed to be about 2 percent of the flue gas flow entering the fabric filter.

Boiler Island Performance – Oxygen Firing

Figure 4-29 shows the steam turbine heat balance associated with the BMCR load operating condition. The primary boiler/turbine interface locations are the feedwater stream to the boiler economizer, the superheater outlet stream, and the cold and hot reheat streams. The basic attributes of these streams (temperature, pressure, enthalpy, and mass flow) are shown on this

diagram. All boiler island performance tables shown in this section were developed to match this BMCR steam turbine heat balance load condition.

Table 4-2 shows the boiler island material and energy balance stream attributes for all the streams identified on Figure 4-28 when operating in the oxygen-fired mode, for the BMCR load condition and using the high sulfur eastern bituminous coal. The stream attributes in the table include mass flow rate, composition, temperature, pressure, and energy. The table includes both English and SI units.

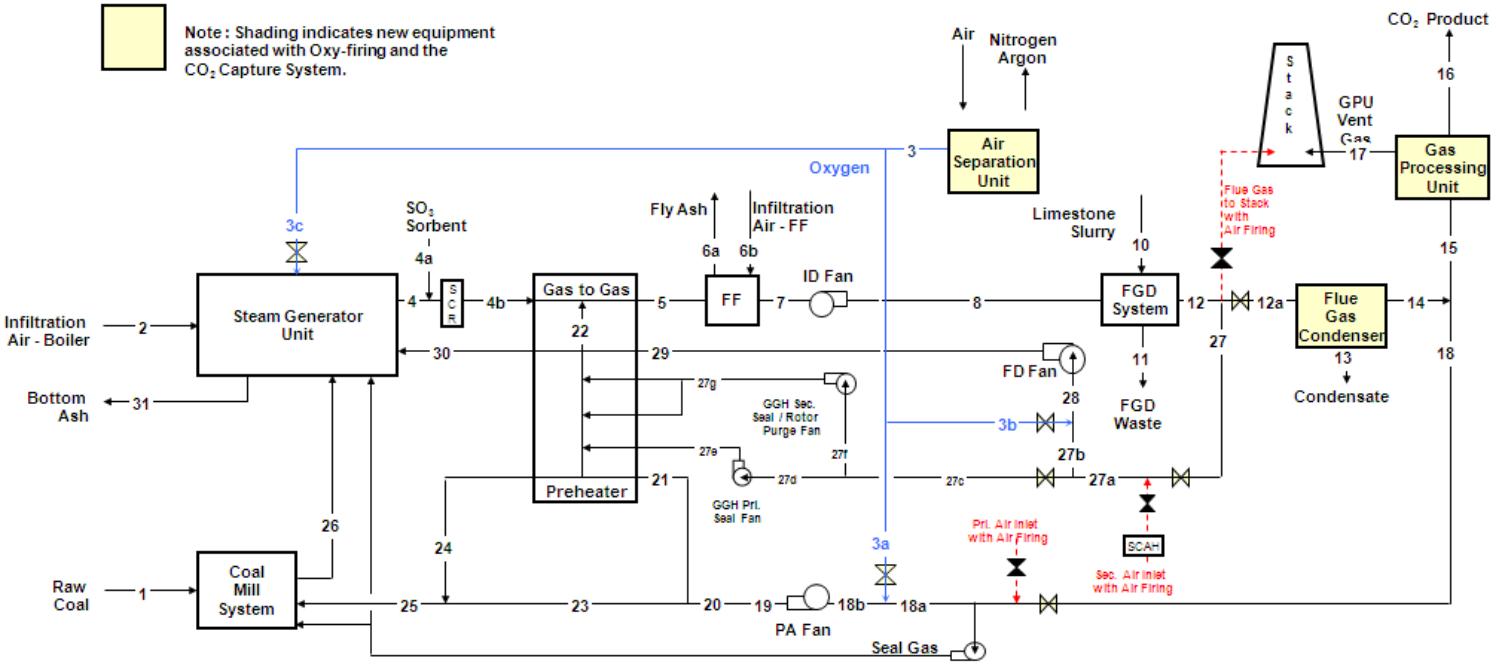

Material Flow Stream Identification

1	Raw Coal to Pulverizers	11	FGD System Waste to Disposal	24	Heated Primary "Air" from GGH
2	Boiler Infiltration Air	12	Fluegas leaving FGD	25	Tempered Primary "Air" to Pulverizers
3	Total Oxygen leaving ASU	12a	Fluegas Leaving FGD to Condenser	26	Pulverized Coal and Primary "Air" to Furnace
3a	Oxygen to Primary "Air" Stream	13	Condensed Water Stream from Fluegas	27	Recirc Secondary FG Stream from FGD
3b	Oxygen to Secondary "Air" Stream	14	Cooled Fluegas Stream	27a	Recirculated Secondary Fluegas
3c	Oxygen Stream to Windbox	15	Fluegas to Gas Processing Unit	27b	Recirculated Secondary Fluegas to O2 Mixer
4	Fluegas from Economizer to SCR	16	Compressed CO_2 Product	27c	GGH Seal and Purge Gas Stream (total)
4a	SO_3 Sorbent Injection	17	Vent from Gas Processing Unit	27d	GGH Primary Seal Gas to Fan
4b	Fluegas from SCR to Gas-Gas Heater (GGH)	18	Recirc Primary FG Stream from Condenser	27e	GGH Primary Seal Gas from Fan to GGH
5	Fluegas Leaving GGH to FF	18a	Recirc Primary FG Stream to O2 Mixer	27f	GGH Secondary Seal and Purge Gas to Fan
6a	Flyash Leaving FF	18b	Recirc Primary "Air" Stream to PA Fan	27g	GGH Sec. Seal and Purge Gas from Fan to GGH
6b	FF Infiltration Air	19	Pressurized Primary "Air" from PA Fan	28	Recirculated Secondary "Air" to FD Fan
7	Fluegas Leaving FF to ID Fan	20	Pressurized Primary "Air" to temp. split	29	Pressurized Secondary "Air" to GGH
8	Fluegas Leaving ID Fan	21	Primary "Air" to GGH	30	Heated Secondary "Air" to Furnace
10	Limestone Slurry Feed to FGD System	22	GGH Leakage Stream ("air" to flue gas)	31	Bottom Ash from Furnace to SSC
		23	Tempering Primary "Air"		

Figure 4-28: Simplified Process Flow Diagram – Air/Oxy-Fired Boiler (Oxygen Fired Mode)

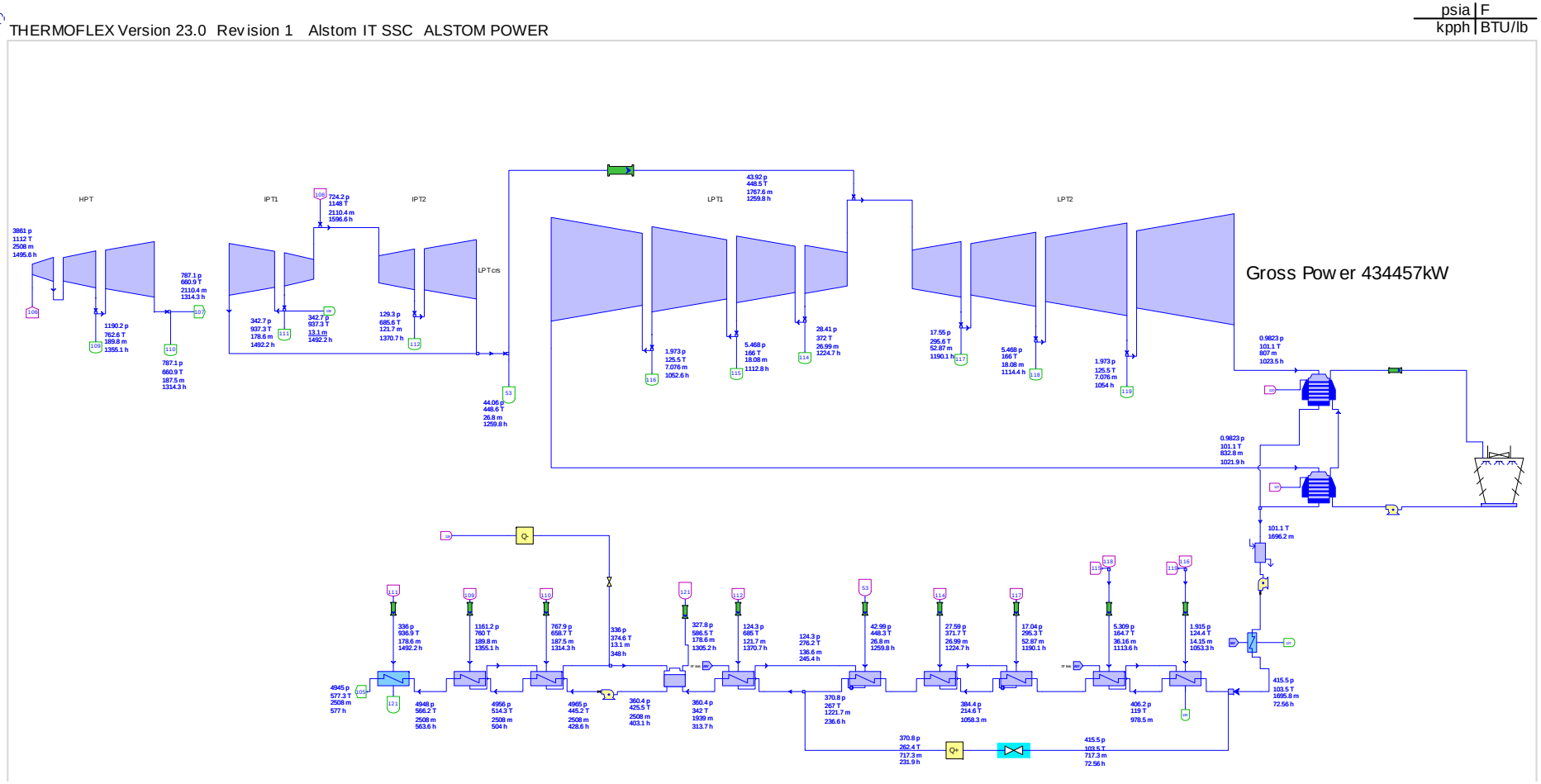

Figure 4-29: Steam Turbine Heat Balance - Oxy-firing, TMCR Load

Table 4-2: Gas Side Material & Energy Balance (Oxy Firing, BMCR, High Sulfur Eastern Bituminous Coal)

English Units

Constituent	(Units)	1	2	3	3a	3b	3c	4	4a	4b	5	6a	6b	7	8	10	11	12	12a	13	14	15	16	17	18
O_2	(Lbm/hr)	24,622	5,779	572,111	148,460	250,116	173,536	85,717		85,717	99,793		15,310	115,103	115,103	4,561		115,103	65,444		65,444	31,050			34,394
Ar	"		320	24,474	6,351	10,700	7,424	85,396		85,396	94,210		848	95,059	95,059			95,059	54,048		54,048	25,643			28,404
N_2	"	3,660	18,870	2,081	540	910	631	201,352		201,352	226,560		49,993	276,554	276,554			276,554	157,240		157,240	74,604			82,637
H_2O	"	37,265	208					336,712	5,905	342,618	389,137		552	389,688	389,688	169,150	40,875	517,963	294,499	270,068	24,430	11,591			12,839
CO_2	"							2,255,758		2,255,758	2,483,124			2,483,124	2,483,124			2,495,671	1,418,965		1,418,965	673,236			745,729
SOx as SO_2	"							18,431		18,431	18,447			18,447	18,447			184	105	95	10	5			5
H_2	"	12,248																							
Carbon	"	182,066						1,415		1,415	1,415	1,415													
Sulfur	"	9,190																							
CaO	"																								
MgO	"																								
$CaSO_3$	"																								
$CaSO_4$	"																38,812								
$MgSO_3$	"																								
$MgSO_4$	"																								
$CaCO_3$	"															29,364	830								
SO3 Sorbent	"								506																
Ash / Inerts	"	27,493						21,994		22,500	22,500	22,500				1,233	1,233								
		Raw Coal	Leakage Air Boiler	Oxygen from ASU	Primary O2	Secondary O2	Burner O2	Fluegas Ivg Econ.	SO3 Sorbent	Fluegas to SCR	Fluegas to FF	Fly Ash	Leakage Air AQCS	Fluegas to ID Fan	Fluegas from ID fan	Lime Slurry	FGD Byproduct	Fluegas from FGD	Fluegas to DCC	Condensate	Fluegas from DCC	Fluegas to GPU	CO2 Product	Vent to Stack	Pri Recirc FG
Total Gas	(Lbm/hr)		25,178	598,666	155,350	261,725	181,590	2,983,367		2,989,272	3,311,272		66,704	3,377,976	3,377,976			3,500,535	1,990,301	95	1,720,137	816,129	By Others	1,801,727	904,008
Total Solids	"	296,543						23,410	506	23,915	23,915	23,915				30,598	40,875								
Total Flow	"	296,543	25,178	598,666	155,350	261,725	181,590	3,006,776	6,411	3,013,187	3,335,187	23,915	66,704	3,377,976	3,377,976	204,309	81,751	3,500,535	1,990,301	270,164	1,720,137	816,129			904,008
Temperature	(Deg F)	64	64	72	72	72	72	690	64	682	331	331	64	313	329	64	155	155	155	72	78	78			78
Pressure	(Psia)	14.7	14.7	19.0	19.0	19.0	19.0	14.5	14.7	14.4	14.3	14.7	14.7	14.1	15.3	14.7	14.7	14.9	14.9	14.7	14.7	14.7			14.7
h-sensible	(Btu/lbm)	-4.680	-3.756	-1.812	-1.812	-1.812	-1.812	158.427	-3.900	156.312	61.300	62.750	-3.756	56.679	60.792	-3.900	18.833	18.282	18.282	-7.847	-0.507	-0.507			-0.507
Energy																									
Chemical	(10^6 Btu/hr)	3,293.372						19.952		19.952	19.952	19.952													
Sensible	(10^6 Btu/hr)	-1.794	-0.095	-1.085	-0.282	-0.474	-0.329	477.153	-0.094	470.858	204.481	1.501	-0.251	191.461	205.355	-2.825	3.845	63.996	36.386	-2.119	-0.872	-0.414			-0.458
Latent	(10^6 Btu/hr)	0.000	0.219	0.000	0.000	0.000	0.000	353.548	0.000	359.749	408.594	0.000	0.579	409.173	409.173	0.000	0.000	543.861	309.224	0.000	25.652	12.171			13.481
Total Energy(1)	(10^6 Btu/hr)	3,291.578	0.124	-1.085	-0.282	-0.474	-0.329	850.653	-0.094	850.559	633.026	21.452	0.329	600.634	614.528	-2.825	3.845	607.858	345.610	-2.119	24.780	11.757			13.023
O2	(wt percent)	8.30	22.95	95.56	95.56	95.56	95.56	2.87		2.87	3.01		22.95	3.41	3.41			3.29	3.29		3.80	3.80			3.80
H_2O	(wt percent)	12.57	0.83	0.00	0.00	0.00	0.00	11.29		11.46	11.75		0.83	11.54	11.54			14.80	14.80		1.42	1.42			1.42

Note:
(1) Energy Basis; Chemical based on Higher Heating Value (HHV); Sensible energy above 80F; Latent based on 1,050 Btu/Lbm of water vapor

SI Units

Constituent	(Units)	1	2	3	3a	3b	3c	4	4a	4b	5	6a	6b	7	8	10	11	12	12a	13	14	15	16	17	18
O2	(kg/hr)	11,168	2,621	259,504	67,340	113,450	78,714	38,881		38,881	45,265		6,945	52,210	52,210	2,069		52,210	29,685		29,685	14,084			15,601
Ar	"		145	11,101	2,881	4,853	3,367	38,735		38,735	42,733		385	43,118	43,118			43,118	24,515		24,515	11,631			12,884
N2	"	1,660	8,559	944	245	413	286	91,331		91,331	102,766		22,676	125,442	125,442			125,442	71,323		71,323	33,839			37,483
H2O	"	16,903	94					152,729	2,679	155,408	176,509		250	176,759	176,759	76,725	18,541	234,943	133,582	122,500	11,081	5,258			5,824
CO2	"							1,023,189		1,023,189	1,126,320			1,126,320	1,126,320			1,132,011	643,628		643,628	305,373			338,255
SO2	"							8,360		8,360	8,368			8,368	8,368			84	48	43	4	2			2
H2	"	5,556																							
Carbon	"	82,583						642		642	642	642													
Sulfur	"	4,169																							
CaO	"																								
MgO	"																								
CaSO3	"																								
CaSO4	"																17,605								
MgSO3	"																								
MgSO4	"																								
CaCO3	"															13,319	376								
SO3 Sorbent									229																
Ash / Inerts	"	12,470						9,976		10,206	10,206	10,206				559	559								
		Raw Coal	Leakage Air Boiler	Oxygen from ASU	Primary O2	Secondary O2	Burner O2	Fluegas Ivg Econ.	SO3 Sorbent	Fluegas to SCR	Fluegas to FF	Fly Ash	Leakage Air AQCS	Fluegas to ID Fan	Fluegas to PFWH	Lime Slurry	FGD Byproduct	Fluegas from FGD	Fluegas to DCC	Condensate	Fluegas from DCC	Fluegas to GPU	CO2 Product	Vent to Stack	Pri Recirc FG
Total Gas	(kg/hr)		11,420	271,549	70,465	118,716	82,368	1,353,225	0	1,355,904	1,501,960		30,256	1,532,216	1,532,216			1,587,807	902,781	43	780,237	370,188	By Others	1,801,727	410,049
Total Solids	"	134,509						10,618	229	10,848	10,848	10,848				13,879	18,541								
Total Flow	"	134,509	11,420	271,549	70,465	118,716	82,368	1,363,844	2,908	1,366,752	1,512,808	10,848	30,256	1,532,216	1,532,216	92,673	37,081	1,587,807	902,781	122,544	780,237	370,188			410,049
Temperature	(Deg C)	18.0	18.0	22.0	22.0	22.0	22.0	365.7	18.0	361.1	166.1	166.1	18.0	156.1	165.0	18.0	68.5	68.5	68.5	22.3	25.3	25.3			25.3
Pressure	(mbar)	1,013.0	1,013.0	1,311.8	1,311.8	1,311.8	1,311.8	1,002.1	1,013.0	991.2	983.8	1,013.0	1,013.0	975.8	1,054.7	1,013.0	1,013.0	1,029.8	1,029.8	1,013.0	1,013.0	1,013.0			1,013.0
h-sensible	(kJ/kg)	-10.886	-8.737	-4.215	-4.215	-4.215	-4.215	368.505	-9.071	363.586	142.585	145.958	-8.737	131.837	141.404	-9.071	43.805	42.524	42.524	-18.252	-1.179	-1.179			-1.179
Energy																									
Chemical	(10^6 kJ/hr)	3,474.705						21.050		21.050	21.050	21.050													
Sensible	(10^6 kJ/hr)	-1.893	-0.100	-1.145	-0.297	-0.500	-0.347	503.425	-0.099	496.784	215.740	1.583	-0.264	202.003	216.662	-2.981	4.057	67.520	38.390	-2.236	-0.920	-0.437			-0.484
Latent	(10^6 kJ/hr)	0.000	0.231	0.000	0.000	0.000	0.000	373.014	0.000	379.556	431.091	0.000	0.611	431.702	431.702	0.000	0.000	573.806	326.249	0.000	27.064	12.841			14.223
Total Energy(1)	(10^6 kJ/hr)	3,472.812	0.131	-1.145	-0.297	-0.500	-0.347	897.490	-0.099	897.390	667.881	22.633	0.347	633.705	648.364	-2.981	4.057	641.326	364.639	-2.236	26.144	12.404			13.740

Notes:
(1) Energy Basis; Chemical based on Higher Heating Value (HHV); Sensible energy above 26.7C; Latent based on 2,194 kJ/kg of water vapor

English Units

Constituent	(Units)	18a	18b	19	20	21	22	23	24	25	26	27	27a	27b	27c	27d	27e	27f	27g	28	29	30	31
O_2	(Lbm/hr)	34,394	182,853	182,853	182,853	109,442	14,076	73,412	84,414	157,825	182,447	49,659	49,659	39,794	9,864	3,436	3,436	6,428	6,428	289,910	289,910	310,727	
Ar	"	28,404	34,755	34,755	34,755	20,802	8,814	13,953	16,045	29,998	29,998	41,011	41,011	32,864	8,147	2,838	2,838	5,309	5,309	43,564	43,564	47,654	
N_2	"	82,637	83,177	83,177	83,177	49,783	25,208	33,394	38,398	71,792	75,451	119,313	119,313	95,612	23,701	8,256	8,256	15,445	15,445	96,522	96,522	106,400	
H_2O	"	12,839	12,839	12,839	12,839	7,685	46,519	5,155	5,927	11,082	48,346	223,465	223,465	179,075	44,390	15,463	15,463	28,928	28,928	179,075	179,075	178,703	
CO_2	"	745,729	745,729	745,729	745,729	446,335	227,367	299,394	344,264	643,657	643,657	1,076,706	1,076,706	862,824	213,882	74,502	74,502	139,380	139,380	862,824	862,824	951,411	
SOx as SO_2	"	5	5	5	5	3	17	2	2	4	4	80	80	64	16	6	6	10	10	64	64	64	
H_2	"										12,248												
Carbon	"										182,066												354
Sulfur	"										9,190												
CaO	"																						
MgO	"																						
$CaSO_3$	"																						
$CaSO_4$	"																						
$MgSO_3$	"																						
$MgSO_4$	"																						
$CaCO_3$	"																						
SO3 Sorbent	"																						
Ash / Inerts	"										27,493												5,499

		Pri SC Outlet	Mixed Pri "Air"	PA Fan Outlet	Primary "Air"	PA to Air Htr	AH leakage gas	Temp. Flue gas	Hot Pri Air	Tempered Pri Air	Cool+PA Mix	Scc Air to SCAH	Scc Air to FD	Scc Air from FD	GGH Seal & Purge	GGH Pri Seal	GGH Pri Seal	GGH Scc Seal & Purge	GGH Scc Seal & Purge	Scc Air to SCAH	Scc Air to AH	Scc Air to Furn	Bottom Ash
Total Gas	(Lbm/hr)	904,008	1,059,359	1,059,359	1,059,359	634,050	322,000	425,309	489,050	914,359	914,359	1,510,234	1,510,234	1,210,234	300,000	104,500	104,500	195,500	195,500	1,471,959	1,471,959	1,594,959	
Total Solids	"										296,543												5,852
Total Flow	"	904,008	1,059,359	1,059,359	1,059,359	634,050	322,000	425,309	489,050	914,359	1,210,902	1,510,234	1,510,234	1,210,234	300,000	104,500	104,500	195,500	195,500	1,471,959	1,471,959	1,594,959	5,852
Temperature	(Deg F)	78	77	91	91	91	160	91	639	397		155	155	155	155	155	170	155	158	142	143	635	2000
Pressure	(Psia)	14.6	14.5	15.8	15.8	15.8	15.8	15.8	15.7	15.7	15.2	14.9	14.8	14.9	14.9	14.8	16.0	14.8	15.1	14.8	14.9	14.8	14.7
h-sensible	(Btu/lbm)	-0.507	-0.698	2.278	2.278	2.278	19.463	2.278	130.861	71.051		18.282	18.282	18.282	18.282	18.282	21.863	18.282	19.004	14.709	15.035	142.415	480.000
Energy																							
Chemical	(10^6 Btu/hr)										3293.372												4.988
Sensible	(10^6 Btu/hr)	-0.458	-0.740	2.413	2.413	1.444	6.267	0.969	63.998	64.966		27.610	27.610	22.125	5.485	1.910	2.285	3.574	3.715	21.651	22.131	227.146	2.809
Latent	(10^6 Btu/hr)	13.481	13.481	13.481	13.481	8.069	48.845	5.412	6.224	11.636		234.638	234.638	188.028	46.610	16.236	16.236	30.374	30.374	188.028	188.028	187.638	0.000
Total Energy(1)	(10^6 Btu/hr)	13.023	12.741	15.894	15.894	9.513	55.112	6.381	70.221	76.602	3,365.628	262.248	262.248	210.154	52.094	18.146	18.520	33.948	34.089	209.679	210.160	414.784	7.797

Note:
(1) Energy Basis; Chemical based on Higher Heating Value (HHV); Sensible energy above 80F; Latent based on 1,050 Btu/Lbm of water vapor

SI Units

Constituent	(Units)	18a	18b	19	20	21	22	23	24	25	26	27	27a	27b	27c	27d	27e	27f	27g	28	29	30	31
O2	(kg/hr)	15,601	82,940	82,940	82,940	49,642	6,385	33,299	38,289	71,588	82,756	22,525	22,525	18,050	4,474	1,559	1,559	2,916	2,916	131,500	131,500	140,943	
Ar	"	12,884	15,765	15,765	15,765	9,436	3,998	6,329	7,278	13,607	13,607	18,602	18,602	14,907	3,695	1,287	1,287	2,408	2,408	19,760	19,760	21,615	
N2	"	37,483	37,728	37,728	37,728	22,581	11,434	15,147	17,417	32,564	34,224	54,119	54,119	43,369	10,751	3,745	3,745	7,006	7,006	43,781	43,781	48,262	
H2O	"	5,824	5,824	5,824	5,824	3,486	21,100	2,338	2,688	5,027	21,929	101,361	101,361	81,226	20,135	7,014	7,014	13,121	13,121	81,226	81,226	81,058	
CO2	"	338,255	338,255	338,255	338,255	202,453	103,131	135,802	156,155	291,956	291,956	488,383	488,383	391,368	97,015	33,793	33,793	63,221	63,221	391,368	391,368	431,551	
SO2	"	2	2	2	2	1	8	1	1	2	2	36	36	29	7	2	2	5	5	29	29	29	
H2	"										5,556												
Carbon	"										82,583												161
Sulfur	"										4,169												
CaO	"																						
MgO	"																						
CaSO3	"																						
CaSO4	"																						
MgSO3	"																						
MgSO4	"																						
CaCO3	"																						
SO3 Sorbent																							
Ash / Inerts	"										12,470												2,494

		Pri SC Outlet	Mixed Pri "Air"	PA Fan Outlet	Primary "Air"	PA to Air Htr	AH leakage gas	Temp. Flue gas	Hot Pri Air	Tempered Pri Air	Cool+PA Mix	Scc Air to SCAH	Scc Air to FD	Scc Air from FD	GGH Seal & Purge	GGH Pri Seal	GGH Pri Seal	GGH Scc Seal & Purge	GGH Scc Seal & Purge	Scc Air to SCAH	Scc Air to AH	Scc Air to Furn	Bottom Ash
Total Gas	(kg/hr)	410,049	480,514	480,514	480,514	287,599	146,056	192,916	221,828	414,744	414,744	685,027	685,027	548,950	136,077	47,400	47,400	88,677	88,677	667,666	667,666	723,457	0
Total Solids	"										134,509												2,655
Total Flow	"	410,049	480,514	480,514	480,514	287,599	146,056	192,916	221,828	414,744	549,253	685,027	685,027	548,950	136,077	47,400	47,400	88,677	88,677	667,666	667,666	723,457	2,655
Temperature	(Deg C)	25.3	24.8	32.7	32.7	32.7	71.3	32.7	337.2	202.9	-17.8	68.5	68.5	68.5	68.5	68.5	76.5	68.5	70.1	61.1	61.8	334.9	1093.3
Pressure	(mbar)	1,010.2	999.8	1,089.6	1,089.6	1,089.1	1,089.1	1,089.1	1,084.5	1,080.8	1,047.9	1,029.8	1,022.9	1,029.0	1,029.0	1,022.9	1,104.1	1,022.9	1,038.9	1,021.6	1,029.0	1,024.0	1,013.0
h-sensible	(kJ/kg)	-1.179	-1.624	5.298	5.298	5.298	45.271	5.298	304.386	165.267	0.000	42.524	42.524	42.524	42.524	42.524	50.853	42.524	44.204	34.213	34.973	331.260	1116.490
Energy																							
Chemical	(10^6 kJ/hr)										3474.705												5.263
Sensible	(10^6 kJ/hr)	-0.484	-0.781	2.546	2.546	1.524	6.612	1.022	67.521	68.543	0.000	29.130	29.130	23.344	5.787	2.016	2.410	3.771	3.920	22.843	23.350	239.653	2.964
Latent	(10^6 kJ/hr)	14.223	14.223	14.223	14.223	8.513	51.534	5.710	6.566	12.277	0.000	247.557	247.557	198.381	49.176	17.130	17.130	32.046	32.046	198.381	198.381	197.970	0.000
Total Energy(1)	(10^6 kJ/hr)	13.740	13.443	16.769	16.769	10.037	58.146	6.732	74.088	80.820	3,550.939	276.687	276.687	221.725	54.962	19.145	19.540	35.817	35.966	221.224	221.731	437.623	8.226

Notes:
(1) Energy Basis; Chemical based on Higher Heating Value (HHV); Sensible energy above 26.7C; Latent based on 2,194 kJ/kg of water vapor

Boiler Island Process Description – Air Firing

Figure 4-30 shows a simplified process flow diagram for a dual-Air/Oxygen fired boiler island. The damper configuration shown is for the air-fired mode of operation. In the air-fired mode, the three streams shown in dashed red lines are now in use (i.e. primary air inlet, secondary air inlet, and flue gas outlet to stack). In the air-fired mode of operation, several major systems are not used and are therefore isolated as indicated by the damper configuration shown in Figure 4-30 (i.e. the ASU, FGC, and GPU). Additionally, primary and secondary flue gas recirculation streams (Streams 18 & 27) are not used, oxygen mixing is not used (Streams 3, 3a, 3b, and 3c), and the GGH pressurized seal and purge system is not used (Streams 27c, 27d, 27e, 27f, and 27g). With the damper configuration shown, this air-fired process uses the primary and secondary air inlets and the flue gas to stack duct. This configuration is the same as many air fired pulverized coal fired plants in use today and therefore it is not further described here.

Boiler Island Performance – Air Firing

Figure 4-31 shows the steam turbine heat balance associated with the air-fired BMCR load operating condition. The primary boiler/turbine interface locations are the feedwater stream to the boiler economizer, the superheater outlet stream, and the cold and hot reheat streams. The basic attributes of these streams (temperature, pressure, enthalpy, and mass flow) are shown on this diagram. All boiler island performance tables shown in this section were developed to match this BMCR steam turbine heat balance.

Table 4-3 shows the stream attributes for all the streams identified on Figure 4-30 when operating in the air-fired mode for the BMCR load condition and using the high sulfur eastern bituminous coal. The stream attributes in the table include mass flow rate, composition, temperature, pressure, and energy. The table includes both English and SI units.

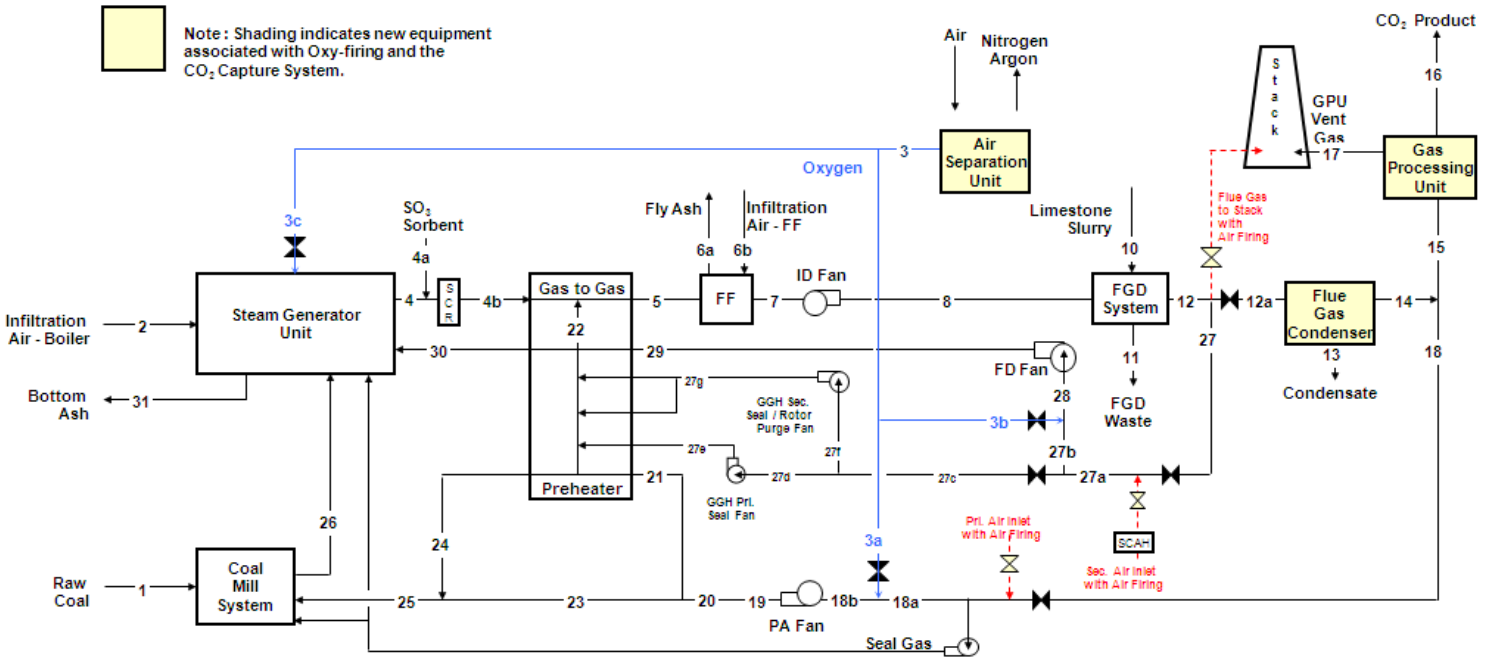

Material Flow Stream Identification

1	Raw Coal to Pulverizers	11	FGD System Waste to Disposal	24	Heated Primary "Air" from GGH
2	Boiler Infiltration Air	12	Fluegas leaving FGD	25	Tempered Primary "Air" to Pulverizers
3	Total Oxygen leaving ASU	12a	Fluegas Leaving FGD to Condenser	26	Pulverized Coal and Primary "Air" to Furnace
3a	Oxygen to Primary "Air" Stream	13	Condensed Water Stream from Fluegas	27	Recirc Secondary FG Stream from FGD
3b	Oxygen to Secondary "Air" Stream	14	Cooled Fluegas Stream	27a	Recirculated Secondary Fluegas
3c	Oxygen Stream to Windbox	15	Fluegas to Gas Processing Unit	27b	Recirculated Secondary Fluegas to O2 Mixer
4	Fluegas from Economizer to SCR	16	Compressed CO_2 Product	27c	GGH Seal and Purge Gas Stream (total)
4a	SO_3 Sorbent Injection	17	Vent from Gas Processing Unit	27d	GGH Primary Seal Gas to Fan
4b	Fluegas from SCR to Gas-Gas Heater (GGH)	18	Recirc Primary FG Stream from Condenser	27e	GGH Primary Seal Gas from Fan to GGH
5	Fluegas Leaving GGH to FF	18a	Recirc Primary FG Stream to O2 Mixer	27f	GGH Secondary Seal and Purge Gas to Fan
6a	Flyash Leaving FF	18b	Recirc Primary "Air" Stream to PA Fan	27g	GGH Sec. Seal and Purge Gas from Fan to GGH
6b	FF Infiltration Air	19	Pressurized Primary "Air" from PA Fan	28	Recirculated Secondary "Air" to FD Fan
7	Fluegas Leaving FF to ID Fan	20	Pressurized Primary "Air" to temp. split	29	Pressurized Secondary "Air" to GGH
8	Fluegas Leaving ID Fan	21	Primary "Air" to GGH	30	Heated Secondary "Air" to Furnace
10	Limestone Slurry Feed to FGD System	22	GGH Leakage Stream ("air" to flue gas)	31	Bottom Ash from Furnace to SSC
		23	Tempering Primary "Air"		

Figure 4-30: Simplified Process Flow Diagram – Air/Oxy-Fired Boiler (Air Fired Mode)

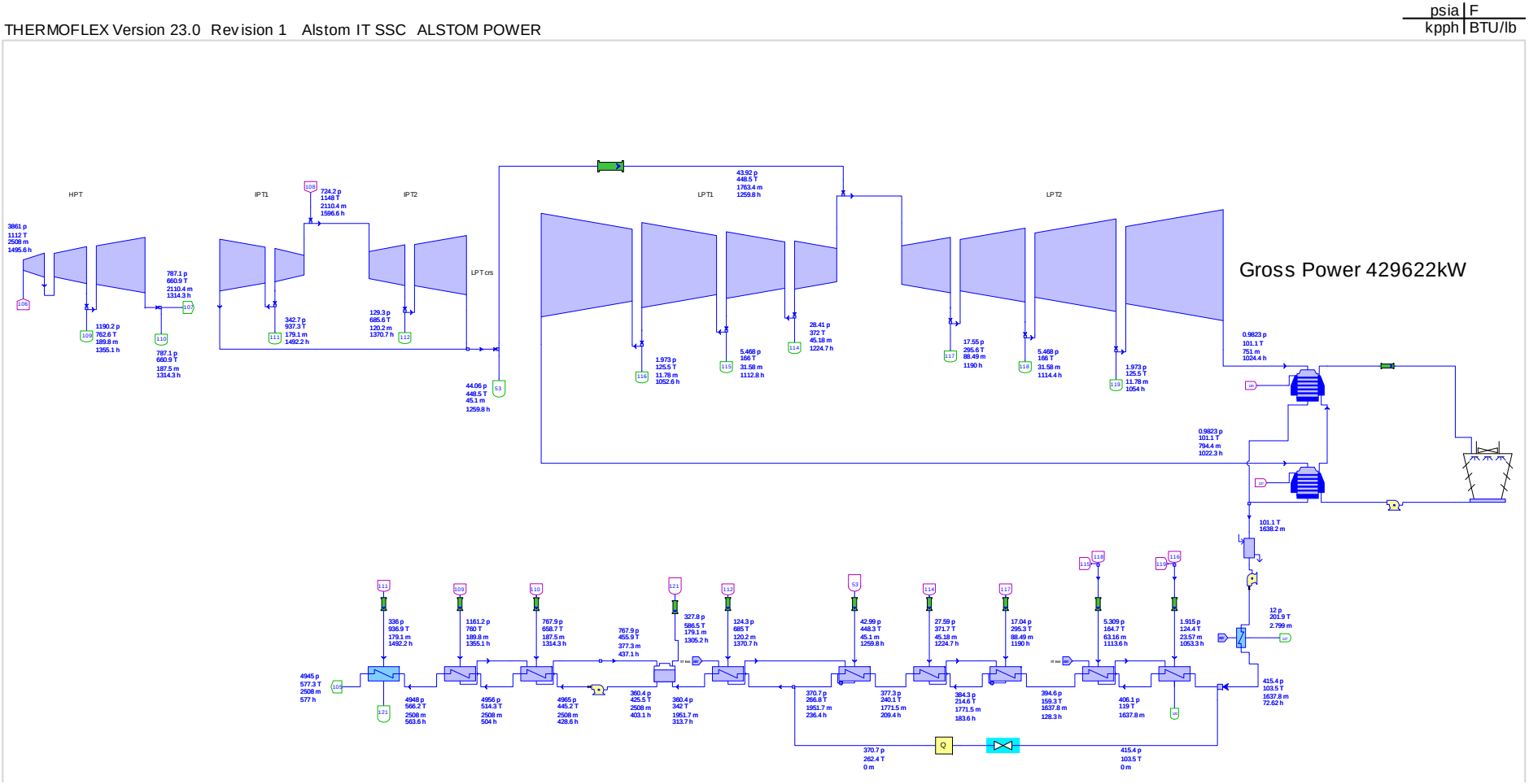

Figure 4-31: Steam Turbine Heat Balance - Air-firing, TMCR Load

Table 4-3: Gas Side Material & Energy Balance (Air Firing, BMCR, High Sulfur Eastern Bituminous Coal)

English Units

Constituent	(Units)	1	2	4	4a	4b	5	6a	6b	7	8	10	11	12	18a	18b	19	21	22	23	24	25	26	27a	27b	28	29	30	31
O2	(Lbm/hr)	24,501	33,687	113,700		113,700	151,572		15,467	167,039	167,039	4,427		167,039	196,696	196,696	196,696	135,288	37,872	61,408	93,973	155,381	179,882	480,576	480,576	480,576	480,576	484,019	
N2	"	3,642	111,868	2,238,807		2,238,807	2,364,570		51,362	2,415,932	2,415,932			2,415,932	653,180	653,180	653,180	449,260	125,763	203,921	312,063	515,984	519,625	1,595,881	1,595,881	1,595,881	1,595,881	1,607,314	
H2O	"	37,082	1,214	170,254	5,855	176,108	177,473		557	178,030	178,030	144,564	39,670	282,925	7,088	7,088	7,088	4,875	1,365	2,213	3,386	5,599	42,681	17,318	17,318	17,318	17,318	17,442	
CO2	"			657,442		657,442	657,442			657,442	657,442			669,619															
SOx as SO2	"			18,273		18,273	18,273			18,273	18,273			548															
H2	"	12,188																					12,188						
Carbon	"	181,172		1,408		1,408	1,408	1,408															181,172						352
Sulfur	"	9,145																					9,145						
Ca	"																												
Mg	"																												
MgO	"																												
MgSO3	"																												
MgSO4	"																												
CaSO3	"																												
CaSO4	"												37,668																
CaCO3	"											28,499	805																
SO3 Sorbent	"				501																								
Ash / Inerts	"	27,358		21,886		22,387	22,387	22,387				1,197	1,197										27,358						5,472

		Raw Coal	Leakage Air	Fluegas Ivg Ec	SO3 Sorbent	Fluegas to SC	Fluegas to ESP	Flyash	AQCS infiltratio	Fluegas to ID F	Fluegas from I	Lime Slurry	FGD Disposal	Fgas to Stack	Pri Air to PA Fan	Pri Air to PA Fan	PA from PA F	Pri Air to AH	Air Htr Lkg Ai	Tempering Air	Hot Pri Air	Mixed Pri Air	Coal-Pri Air Mix	Sec Air to FD	Sec Air to SCA	Sec Air to SCA	Sec Air to AH	Hot Sec Air	Bottom Ash
Total Gas	(Lbm/hr)		146,769	3,198,476		3,204,330	3,369,330		67,387	3,436,717	3,436,717			3,536,063	856,964	856,964	856,964	589,423	165,000	267,541	409,423	676,964	676,964	2,093,775	2,093,775	2,093,775	2,093,775	2,108,775	
Total Solids	"	295,086		23,294	501	23,796	23,796	23,796				34,122	39,670																5,824
Total Flow	"	295,086	146,769	3,221,770	6,356	3,228,126	3,393,126	23,796	67,387	3,436,717	3,436,717	178,687	79,340	3,536,063	856,964	856,964	856,964	589,423	165,000	267,541	409,423	676,964	972,050	2,093,775	2,093,775	2,093,775	2,093,775	2,108,775	5,824
Temperature	(Deg F)	64.4	64.4	706.7	64.4	697.5	259.0	259.0	64.4	241.0	259.9	64.4	124.0	124.0	64.4	64.4	83.9	83.9	83.9	83.9	660.0	435.5	0.0	64.4	64.4	64.4	71.4	641.0	2000.0
Pressure	(Psia)	14.7	14.7	14.5	14.7	14.2	14.1	14.7	14.7	14.0	15.1	14.7	14.7	14.7	14.6	14.6	15.8	15.8	15.8	15.8	15.8	15.7	15.2	14.5	14.5	14.5	15.0	14.9	14.7
h-sensible	(Btu/lbm)	-4.680	-3.781	161.441	-14.657	159.191	44.648	44.750	-3.781	40.090	44.848	-3.900	11.007	11.150	-3.781	-3.781	0.955	0.955	0.955	0.955	143.155	86.954		-3.781	-3.781	-3.781	-2.079	138.347	480.000
Energy																													
Chemical	(10^6 Btu/hr)	3,277.188				19.853	19.853	19.853															3,277.188						
Sensible	(10^6 Btu/hr)	-1.785	-0.555	520.015	-0.093	513.775	151.500	1.065	-0.255	137.779	154.130	-2.385	2.180	39.426	-3.240	-3.240	0.818	0.563	0.158	0.255	58.611	58.864		-7.916	-7.916	-7.916	-4.353	291.743	2.795
Latent	(10^6 Btu/hr)		1.275	178.766	0.000	184.914	186.347		0.585	186.932	186.932	0.000	0.000	297.071	7.442	7.442	7.442	5.119	1.433	2.324	3.556	5.879		18.184	18.184	18.184	18.184	18.314	
Total Energy(1)	(10^6 Btu/hr)	3,275.403	0.720	718.635	-0.093	718.542	357.700	20.918	0.330	324.711	341.062	-2.385	2.180	336.497	4.203	4.203	8.261	5.682	1.590	2.579	62.167	64.744	3,340.146	10.268	10.268	10.268	13.831	310.057	7.759

Notes:
(1) Energy Basis; Chemical based on Higher Heating Value (HHV); Sensible energy above 80F; Latent based on 1,050 Btu/Lbm of water

SI Units

Constituent	(Units)	1	2	4	4a	4b	5	6a	6b	7	8	10	11	12	18a	18b	19	21	22	23	24	25	26	27a	27b	28	29	30	31
O2	(kg/hr)	11,113	15,280	51,573		51,573	68,752		7,016	75,767	75,767	2,008		75,767	89,219	89,219	89,219	61,365	17,178	27,854	42,625	70,479	81,593	217,985	217,985	217,985	217,985	219,546	
N2	"	1,652	50,742	1,015,500		1,015,500	1,072,545		23,297	1,095,843	1,095,843			1,095,843	296,276	296,276	296,276	203,780	57,045	92,496	141,549	234,045	235,697	723,875	723,875	723,875	723,875	729,061	
H2O	"	16,820	551	77,225	2,656	79,881	80,500		253	80,753	80,753	65,573	17,994	128,332	3,215	3,215	3,215	2,211	619	1,004	1,536	2,540	19,360	7,855	7,855	7,855	7,855	7,912	
CO2	"			298,209		298,209	298,209			298,209	298,209			303,733															
SOx as SO2	"			8,288		8,288	8,288			8,288	8,288			249															
H2	"	5,528																					5,528						
Carbon	"	82,178		639		639	639	639															82,178						160
Sulfur	"	4,148																					4,148						
Ca	"																												
Mg	"																												
MgO	"																												
MgSO3	"																												
MgSO4	"																												
CaSO3	"																												
CaSO4	"												17,096																
CaCO3	"											12,927	365																
SO3 Sorbent	"				227																								
Ash / Inerts	"	12,409		9,927		10,155	10,155	10,155				543	543										12,409						2,482

		Raw Coal	Leakage Air	luegas Ivg Ecor	SO3 Sorbent	luegas to SCR	luegas to ESP	Flyash	AQCS infiltration	luegas to ID Fa	egas from ID F	Lime Slurry	FGD Disposal	Fgas to Stack	Pri Air to PA Fan	Pri Air to PA Fan	A from PA Fa	Pri Air to AH	Air Htr Lkg Air	Tempering Air	Hot Pri Air	Mixed Pri Air	Coal-Pri Air Mix	Sec Air to FD	Sec Air to SCAI	Sec Air to SCAI	Sec Air to AH	Hot Sec Air	Bottom Ash
Total Gas	(kg/hr)		66,573	1,450,797		1,453,452	1,528,294		30,566	1,558,860	1,558,860			1,603,923	388,710	388,710	388,710	267,356	74,842	121,354	185,710	307,064	307,064	949,715	949,715	949,715	949,715	956,519	
Total Solids	"	133,848		10,566	227	10,794	10,794	10,794				15,478	17,994																2,642
Total Flow	"	133,848	66,573	1,461,363	2,883	1,464,246	1,539,088	10,794	30,566	1,558,860	1,558,860	81,050	35,988	1,603,923	388,710	388,710	388,710	267,356	74,842	121,354	185,710	307,064	440,912	949,715	949,715	949,715	949,715	956,519	2,642
Temperature	(Deg C)	18.0	18.0	374.8	18.0	369.7	126.1	126.1	18.0	116.1	126.6	18.0	51.1	51.1	18.0	18.0	28.9	28.9	28.9	28.9	348.9	224.2	-17.8	18.0	18.0	18.0	21.9	338.3	1093.3
Pressure	(mbar)	1,013.0	1,013.0	1,000.0	1,013.0	982.0	972.8	1,013.0	1,013.0	962.3	1,040.7	1,013.0	1,013.0	1,016.6	1010.1	1,010.1	1,091.6	1,091.6	1,091.6	1,091.6	1,087.2	1,082.5	1,047.9	999.7	999.7	999.7	1,033.0	1,025.3	1013.0
h-sensible	(kJ/kg)	-10.886	-8.794	375.516	-34.091	370.282	103.853	104.089	-8.794	93.251	104.317	-9.071	25.603	25.934	-8.794	-8.794	2.220	2.220	2.220	2.220	332.981	202.256	0.000	-8.794	-8.794	-8.794	-4.836	321.798	1116.490
Energy																													
Chemical	(10^6 kJ/hr)	3,457.630				20.947	20.947	20.947															3,457.630						
Sensible	(10^6 kJ/hr)	-1.883	-0.585	548.647	-0.098	542.063	159.842	1.123	-0.269	145.365	162.616	-2.516	2.300	41.597	-3.418	-3.418	0.863	0.594	0.166	0.269	61.838	62.106		-8.352	-8.352	-8.352	-4.593	307.806	2.949
Latent	(10^6 kJ/hr)	0.000	1.345	188.609	0.000	195.095	196.607	0.000	0.617	197.224	197.224	0.000	0.000	313.427	7.852	7.852	7.852	5.401	1.512	2.451	3.751	6.203		19.185	19.185	19.185	19.185	19.322	0.000
Total Energy(1)	(10^6 kJ/hr)	3,455.746	0.759	758.203	-0.098	758.105	377.395	22.070	0.349	342.589	359.841	-2.516	2.300	355.024	4.434	4.434	8.715	5.994	1.678	2.721	65.589	68.308	3,524.055	10.833	10.833	10.833	14.592	327.128	8.186

Notes:
(1) Energy Basis; Chemical based on Higher Heating Value (HHV); Sensible energy above 26.7C; Latent based on 2,194 kJ/kg of water vapor

Table 4-4 summarizes the thermal performance and auxiliary loads for the 450MW air and oxy-fired plants. Both plants were designed for 450MW gross power, while the net power decreased to 427MW for the air-fired case and to 320MW for the oxy-fired case. This approach allowed the fuel heat input to remain the same for both cases. The oxy-fired boiler design thus did not require major revisions from the air-fired case.

The auxiliary power requirements for the oxy-fired plant increased from 5.1% of the gross power output for the air-fired plant to 26.7% of the gross power output. Most of this increase was due to the addition of the ASU and GPU, which added 64,550 kW and 37,683 kW, respectively, to the oxy-fired plant's power consumption.

Table 4-4: Summary of Thermal Performance and Auxiliary Loads

		450MW	450MW
		Air-Fired	Oxy-Fired
Gross Power Output	MW	450.0	450.0
Net Power Output	MW	426.5	325.1
Coal Flow	lb/hr	295,086	296,543
Main Steam Flow	lb/hr	2,508,000	2,508,000
Fuel Heat Input (HHV)	MMBtu/	3,277	3,293
Net Plant Efficiency (HHV)	%	40.9%	31.5%
Boiler Efficiency	%	88.8%	88.8%

Auxiliary Load Summary

		450MW	450MW
		Air-Fired	Oxy-Fired
Coal Handling & Pulverizers	kW	2,319	2,331
Forced Draft Fans	kW	1,192	1,198
Primary Air Fans	kW	939	944
Induced Draft Fans	kW	5,423	4,413
SCR	kW	150	-
FF	kW	53	51
Wet FGD	kW	2,239	2,277
Power Plant Auxiliaries	kW	11,200	11,434
ASU Compressor/Auxiliaries	kW	-	64,550
GPU CO2 Compressor	kW	-	37,683
		-	-
Total Aux Power	kW	23,516	124,880
% Aux Power		5.2%	27.8%

4.7 450MW Plant Cost Estimating

4.7.1 Impact of Escalation on Cost Estimates

Many of the vendor quotes and cost estimates developed for the 450MW boiler equipment were based on current pricing in 2013 dollars. However, the costs developed in the DOE Baseline report were based on June 2011 dollars. To facilitate comparison with prior DOE studies, all cost estimates in this techno-economic study were therefore de-escalated back to June 2011 dollars using the IHS CERA Power Capital Cost Index (PCCI) for North America[35]. This index tracks the costs associated with constructing a portfolio of 30 different power plants in North America, indexed to year 2000. Figure 4-32 shows the PCCI index for North American power plants (excluding nuclear) from Q2 2011 through Q3 2012. A linear trend line was used to extrapolate the PCCI index to the present. The results show a modest 3.3% increase in the cost of power plant construction from June 2011 to today. This factor was used to de-escalate present day 450MW boiler cost estimates to the June 2011 dollars cost basis used in this study.

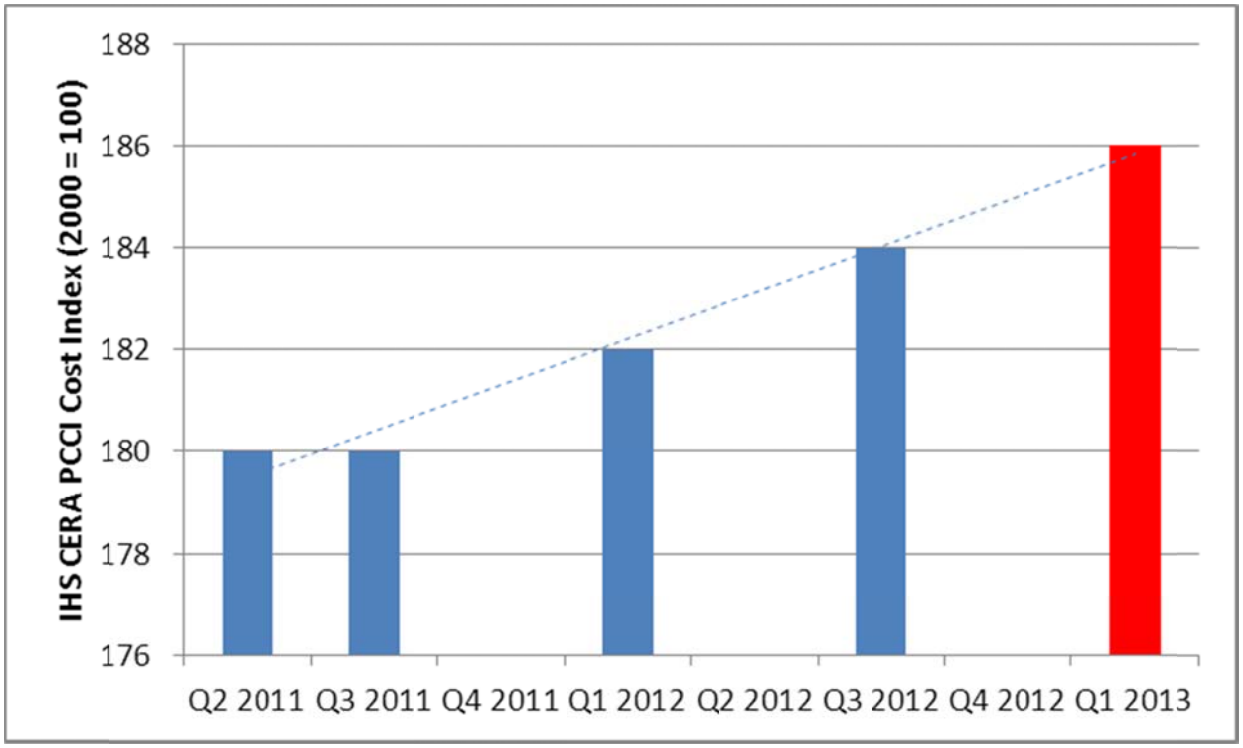

Figure 4-32: IHS CERA Power Plant Capital Cost Index for North America Power Plants

4.7.2 Total Plant and O&M Costs

Table 4-5 and Table 4-6 show the total plant capital cost summary organized by cost account for the 450MW$_{gross}$ air-fired and oxy-fired plants, respectively. These tables include a detailed

[35] IHS Website - http://www.ihs.com/info/cera/ihsindexes/index.aspx

breakdown of the capital costs, owner's costs, Total Overnight Costs (TOC), and Total As Spent Costs (TASC). Table 4-7 and Table 4-8 show the fixed and variable O&M costs for the $450MW_{gross}$ air-fired and oxy-fired power plants, respectively.

Table 4-5: Capital Costs for 450MW Air-Fired Plant

Client: USDOE/NETL
Project: Bituminous Baseline Study
TOTAL PLANT COST SUMMARY
Case: 450 MW Air-Fired Plant
Estimate Type: Conceptual
Cost Base: June 2011 ($x1000)

Report Date: May 30, 2014

Acct No.	Item/Description	Equipment Cost	Material Cost	Labor Direct	Labor Indirect	Bare Erected Cost $	Eng'g CM H.O.& Fee %	Eng'g CM H.O.& Fee Total	Process Contingency %	Process Contingency Total	Project Contingency %	Project Contingency Total	TOTAL 450MW AIR PLANT Cost	450MW AIR COST $/kW
	1 COAL & SORBENT HANDLING													
	SUBTOTAL 1.	$16,531	$4,205	$9,723	$0	$30,459		$2,741		$0		$4,980	$38,183	$89.5
	2 COAL & SORBENT PREP & FEED													
	SUBTOTAL 2.	$11,889	$448	$2,956	$0	$15,292		$1,376		$0		$2,500	$19,170	$45.0
	3 FEEDWATER & MISC. BOP SYSTEMS													
	SUBTOTAL 3.	$39,872	$0	$18,371	$0	$58,243		$5,242		$0		$10,324	$73,811	$173.1
	4 PC BOILER													
	SUBTOTAL 4.	$228,600	$0	$115,200	$0	$343,800		$30,942		$0		$56,211	$430,954	$1,010.5
	5 FLUE GAS CLEANUP													
	SUBTOTAL 5.	$71,840	$0	$36,203	$0	$108,042		$9,724		$0		$11,777	$129,544	$303.7
	5B CO2 REMOVAL & COMPRESSION (based on DOE Case S12F)													
	SUBTOTAL 5B.	$0	$0	$0	$0	$0		$0		$0		$0	$0	$0.0
	6 COMBUSTION TURBINE/ACCESSORIES													
	SUBTOTAL 6.	$0	$0	$0	$0	$0		$0		$0		$0	$0	$0.0
	7 HRSG													
	SUBTOTAL 7.	$18,991	$1,095	$12,804	$0	$32,890		$2,960		$0		$4,675	$40,526	$95.0
	8 STEAM TURBINE GENERATOR													
	SUBTOTAL 8.	$88,234	$1,042	$22,088	$0	$111,364		$10,023		$0		$13,830	$135,218	$317.1
	9 COOLING WATER SYSTEM													
	SUBTOTAL 9.	$10,955	$6,220	$10,774	$0	$27,949		$2,515		$0		$4,188	$34,654	$81.3
	10 ASH/SPENT SORBENT HANDLING SYS													
	SUBTOTAL 10.	$7,049	$209	$9,152	$0	$16,410		$1,477		$0		$1,839	$19,727	$46.3
	11 ACCESSORY ELECTRIC PLANT													
	SUBTOTAL 11.	$18,494	$7,082	$19,391	$0	$44,967		$4,047		$0		$6,071	$55,088	$129.2
	12 INSTRUMENTATION & CONTROL													
	SUBTOTAL 12.	$10,231	$0	$10,262	$0	$20,493		$1,844		$0		$2,757	$25,096	$58.8
	13 IMPROVEMENTS TO SITE													
	SUBTOTAL 13.	$3,328	$1,913	$7,136	$0	$12,378		$1,114		$0		$2,699	$16,192	$38.0
	14 BUILDINGS & STRUCTURES													
	SUBTOTAL 14.	$0	$27,094	$25,641	$0	$52,735		$4,746		$0		$8,622	$66,105	$155.0
	TOTAL COST	$526,015	$49,307	$299,701	$0	$875,023		$78,752		$0		$130,474	$1,084,249	$2,542.3

Client: USDOE/NETL
Project: Bituminous Baseline Study
TOTAL PLANT COST SUMMARY
Case: 450 MW Air-Fired Plant
Estimate Type: Conceptual
Cost Base: June 2011 ($x1000)

Report Date: May 30, 2014

Acct No.	Item/Description	Equipment Cost	Material Cost	Labor Direct	Labor Indirect	Bare Erected Cost $	Eng'g CM H.O.& Fee %	Eng'g CM H.O.& Fee Total	Process Contingency %	Process Contingency Total	Project Contingency %	Project Contingency Total	TOTAL 450MW AIR PLANT Cost	450MW AIR COST $/kW
	1 COAL & SORBENT HANDLING													
1.1	Coal Receive & Unload	$3,304	$0	$1,503	$0	$4,807	9.0%	$433	0%	$0	15%	$786	$6,026	$14.1
1.2	Coal Stackout & Reclaim	$4,312	$0	$964	$0	$5,275	9.0%	$475	0%	$0	15%	$863	$6,613	$15.5
1.3	Coal Conveyors	$4,009	$0	$953	$0	$4,962	9.0%	$447	0%	$0	15%	$811	$6,220	$14.6
1.4	Other Coal Handling	$1,049	$0	$220	$0	$1,269	9.0%	$114	0%	$0	15%	$207	$1,591	$3.7
1.5	Sorbent Receive & Unload	$147	$0	$44	$0	$190	9.0%	$17	0%	$0	15%	$31	$239	$0.6
1.6	Sorbent Stackout & Reclaim	$2,361	$0	$426	$0	$2,787	9.0%	$251	0%	$0	15%	$456	$3,494	$8.2
1.7	Sorbent Conveyors	$842	$183	$204	$0	$1,229	9.0%	$111	0%	$0	15%	$201	$1,541	$3.6
1.8	Other Sorbent Handling	$509	$120	$263	$0	$891	9.0%	$80	0%	$0	15%	$146	$1,117	$2.6
1.9	Coal & Sorbent Hnd.Foundations	$0	$3,902	$5,145	$0	$9,048	9.0%	$814	0%	$0	15%	$1,479	$11,341	$26.6
	SUBTOTAL 1.	$16,531	$4,205	$9,723	$0	$30,459		$2,741		$0		$4,980	$38,183	$89.5
	2 COAL & SORBENT PREP & FEED													
2.1	Coal Crushing & Drying	$620	$0	$119	$0	$739	9.0%	$67	0%	$0	15%	$121	$927	$2.2
2.2	Coal Conveyor to Storage	$4,829	$0	$1,040	$0	$5,869	9.0%	$528	0%	$0	15%	$960	$7,357	$17.2
2.3	Coal Injection System	$0	$0	$0	$0	$0	9.0%	$0	0%	$0	0%	$0	$0	$0.0
2.4	Misc.Coal Prep & Feed	$0	$0	$0	$0	$0	9.0%	$0	0%	$0	0%	$0	$0	$0.0
2.5	Sorbent Prep Equipment	$6,240	$0	$1,344	$0	$7,584	9.0%	$683	0%	$0	15%	$1,240	$9,506	$22.3
2.6	Sorbent Storage & Feed	$200	$0	$60	$0	$260	9.0%	$23	0%	$0	15%	$43	$326	$0.8
2.7	Sorbent Injection System	$0	$0	$0	$0	$0	9.0%	$0	0%	$0	0%	$0	$0	$0.0
2.8	Booster Air Supply System	$0	$0	$0	$0	$0	9.0%	$0	0%	$0	0%	$0	$0	$0.0
2.9	Coal & Sorbent Feed Foundation	$0	$448	$393	$0	$841	9.0%	$76	0%	$0	15%	$137	$1,054	$2.5
	SUBTOTAL 2.	$11,889	$448	$2,956	$0	$15,292		$1,376		$0		$2,500	$19,170	$45.0
	3 FEEDWATER & MISC. BOP SYSTEMS													
3.1	FeedwaterSystem	$17,245	$0	$5,560	$0	$22,805	9.0%	$2,052	0%	$0	15%	$3,729	$28,587	$67.0
3.2	Water Makeup & Pretreating	$4,025	$0	$1,273	$0	$5,299	9.0%	$477	0%	$0	20%	$1,155	$6,931	$16.3
3.3	Other Feedwater Subsystems	$5,425	$0	$2,227	$0	$7,652	9.0%	$689	0%	$0	15%	$1,251	$9,592	$22.5
3.4	Service Water Systems	$806	$0	$421	$0	$1,227	9.0%	$110	0%	$0	20%	$267	$1,606	$3.8
3.5	Other Boiler Plant Systems	$6,398	$0	$6,048	$0	$12,446	9.0%	$1,120	0%	$0	15%	$2,035	$15,602	$36.6
3.6	FO Supply Sys & Nat Gas	$301	$0	$352	$0	$653	9.0%	$59	0%	$0	15%	$107	$819	$1.9
3.7	Waste Treatment Equipment	$2,721	$0	$1,575	$0	$4,296	9.0%	$387	0%	$0	20%	$936	$5,620	$13.2
3.8	Misc. Equip.(cranes,AirComp.,Comm.)	$2,951	$0	$913	$0	$3,864	9.0%	$348	0%	$0	20%	$843	$5,055	$11.9
	SUBTOTAL 3.	$39,872	$0	$18,371	$0	$58,243		$5,242		$0		$10,324	$73,811	$173.1

Acct No. Item/Description	Equipment Cost	Material	Labor		Bare Erected Cost $	Eng'g CM H.O.& Fee		Process Contingency		Project Contingency		TOTAL 450MW AIR PLANT Cost	450MW AIR COST $/kW
		Cost	Direct	Indirect		%	Total	%	Total	%	Total		
4 PC BOILER													
4.1 PC Boiler & Accessories	$228,600	$0	$115,200.00	$0	$343,800	9.0%	$30,942	0%	$0	15%	$56,211	$430,954	$1,010.5
4.1 PC Boiler & Accessories	$0	$0	$0	$0	$0	9.0%	$0	20%	$0	15%	$0	$0	$0.0
4.2 SCR (w/4.1)	$0	$0	$0	$0	$0	9.0%	$0	0%	$0	15%	$0	$0	$0.0
4.3 ASU/Oxidant Compression	$0	$0	$0	$0	$0	0.0%	$0		$0	0%	$0	$0	$0.0
4.4 Boiler BoP (w/ ID Fans)	$0	$0	$0	$0	$0	0.0%	$0		$0	0%	$0	$0	$0.0
4.5 Primary Air System	$0	$0	$0	$0	$0	0.0%	$0		$0	0%	$0	$0	$0.0
4.6 Secondary Air System	$0	$0	$0	$0	$0	0.0%	$0		$0	0%	$0	$0	$0.0
4.8 Major Component Rigging	$0	$0	$0	$0	$0	0.0%	$0		$0	0%	$0	$0	$0.0
4.9 Boiler Foundations	$0	$0	$0	$0	$0	0.0%	$0		$0	0%	$0	$0	$0.0
SUBTOTAL 4.	$228,600	$0	$115,200	$0	$343,800		$30,942		$0		$56,211	$430,954	$1,010.5
5 FLUE GAS CLEANUP													
5.1 Absorber Vessels & Accessories	$46,830	$0	$23,599	$0	$70,429	9.0%	$6,339	0%	$0	10%	$7,677	$84,445	$198.0
5.2 Other FGD	$0	$0	$0	$0	$0	9.0%	$0	0%	$0	10%	$0	$0	$0.0
5.3 Bag House & Accessories	$9,370	$0	$4,722	$0	$14,092	9.0%	$1,268	0%	$0	10%	$1,536	$16,896	$39.6
5.4 Other Particulate Removal Materials	$0	$0	$0	$0	$0	9.0%	$0	0%	$0	10%	$0	$0	$0.0
5.5 Gypsum Dewatering System	$9,870	$0	$4,974	$0	$14,844	9.0%	$1,336	0%	$0	10%	$1,618	$17,798	$41.7
5.6 Mercury Removal System	$4,690	$0	$2,363	$0	$7,053	9.0%	$635	0%	$0	10%	$769	$8,457	$19.8
5.9 Open	$1,080	$0	$544	$0	$1,624	9.0%	$146	0%	$0	10%	$177	$1,948	$4.6
SUBTOTAL 5.	$71,840	$0	$36,203	$0	$108,042		$9,724		$0		$11,777	$129,544	$303.7
5B CO2 REMOVAL & COMPRESSION (based on DOE Case S12F)													
5B.1 CO2 Condensing Heat Exchanger	$0	$0	$0	$0	$0	9.0%	$0	0%	$0	0%	$0	$0	$0.0
5B.2 CO2 Compression & Drying	$0	$0	$0	$0	$0	9.0%	$0	0%	$0	0%	$0	$0	$0.0
SUBTOTAL 5B.	$0	$0	$0	$0	$0		$0		$0		$0	$0	$0.0
6 COMBUSTION TURBINE/ACCESSORIES													
SUBTOTAL 6.	$0	$0	$0	$0	$0		$0		$0		$0	$0	$0.0
7 HRSG													
7.1 Flue Gas Recycle Heat Exchanger	$0	$0	$0	$0	$0	9.0%	$0	0%	$0	0%	$0	$0	$0.0
7.2 HRSG Accessories	$0	$0	$0	$0	$0	9.0%	$0	0%	$0	0%	$0	$0	$0.0
7.3 Ductwork	$9,334	$0	$5,892	$0	$15,226	9.0%	$1,370	0%	$0	15%	$2,489	$19,085	$44.8
7.4 Stack	$9,657	$0	$5,613	$0	$15,270	9.0%	$1,374	0%	$0	10%	$1,664	$18,309	$42.9
7.9 Duct & Stack Foundations	$0	$1,095	$1,300	$0	$2,395	9.0%	$216	0%	$0	20%	$522	$3,132	$7.3
SUBTOTAL 7.	$18,991	$1,095	$12,804	$0	$32,890		$2,960		$0		$4,675	$40,526	$95.0
8 STEAM TURBINE GENERATOR													
8.1 Steam TG & Accessories	$55,766	$0	$6,880	$0	$62,646	9.0%	$5,638	0%	$0	10%	$6,828	$75,112	$176.1
8.2 Turbine Plant Auxiliaries	$350	$0	$745	$0	$1,095	9.0%	$99	0%	$0	10%	$119	$1,312	$3.1
8.3 Condenser & Auxiliaries	$14,446	$0	$4,892	$0	$19,338	9.0%	$1,740	0%	$0	10%	$2,108	$23,186	$54.4
8.4 Steam Piping	$17,673	$0	$7,852	$0	$25,525	9.0%	$2,297	0%	$0	15%	$4,173	$31,996	$75.0
8.9 TG Foundations	$0	$1,042	$1,719	$0	$2,761	9.0%	$249	0%	$0	20%	$602	$3,612	$8.5
SUBTOTAL 8.	$88,234	$1,042	$22,088	$0	$111,364		$10,023		$0		$13,830	$135,218	$317.1

Acct No.	Item/Description	Equipment Cost	Material Cost	Labor Direct	Labor Indirect	Bare Erected Cost $	Eng'g CM H.O.& Fee %	Eng'g CM H.O.& Fee Total	Process Contingency %	Process Contingency Total	Project Contingency %	Project Contingency Total	TOTAL 450MW AIR PLANT Cost	450MW AIR COST $/kW
9	COOLING WATER SYSTEM													
9.1	Cooling Towers	$8,063	$0	$2,494	$0	$10,556	9.0%	$950	0%	$0	10%	$1,150	$12,657	$29.7
9.2	Circulating Water Pumps	$1,606	$0	$101	$0	$1,708	9.0%	$154	0%	$0	10%	$186	$2,047	$4.8
9.3	Circ.Water System Auxiliaries	$479	$0	$64	$0	$543	9.0%	$49	0%	$0	10%	$59	$651	$1.5
9.4	Circ.Water Piping	$0	$4,038	$3,656	$0	$7,694	9.0%	$692	0%	$0	15%	$1,258	$9,645	$22.6
9.5	Make-up Water System	$416	$0	$535	$0	$951	9.0%	$86	0%	$0	15%	$155	$1,192	$2.8
9.6	Component Cooling Water Sys	$391	$0	$300	$0	$691	9.0%	$62	0%	$0	15%	$113	$866	$2.0
9.9	Circ.Water System Foundations& Structures	$0	$2,182	$3,624	$0	$5,806	9.0%	$523	0%	$0	20%	$1,266	$7,595	$17.8
	SUBTOTAL 9.	$10,955	$6,220	$10,774	$0	$27,949		$2,515		$0		$4,188	$34,654	$81.3
10	ASH/SPENT SORBENT HANDLING SYS													
10.1	Rotary Ash Coolers	$620	$0	$312	$0	$932	9.0%	$84	0%	$0	10%	$102	$1,118	$2.6
10.2	Cyclone Ash Letdown	$0	$0	$0	$0	$0	9.0%	$0	0%	$0	0%	$0	$0	$0.0
10.3	HGCU Ash Letdown	$0	$0	$0	$0	$0	9.0%	$0	0%	$0	0%	$0	$0	$0.0
10.4	High Temperature Ash Piping	$0	$0	$0	$0	$0	9.0%	$0	0%	$0	0%	$0	$0	$0.0
10.5	Reducer Baghouse Ash Recycle System	$0	$0	$0	$0	$0	9.0%	$0	0%	$0	10%	$0	$0	$0.0
10.6	Ash Storage Silos	$922	$0	$2,822	$0	$3,744	9.0%	$337	0%	$0	10%	$408	$4,489	$10.5
10.7	Ash Transport & Feed Equipment	$6,127	$0	$6,074	$0	$12,201	9.0%	$1,098	0%	$0	10%	$1,330	$14,629	$34.3
10.8	Misc. Ash Handling Equipment	$0	$0	$0	$0	$0	9.0%	$0	0%	$0	0%	$0	$0	$0.0
10.9	Ash/Spent Sorbent Foundation	$0	$209	$257	$0	$466	9.0%	$42	0%	$0	20%	$101	$608	$1.4
	SUBTOTAL 10.	$7,049	$209	$9,152	$0	$16,410		$1,477		$0		$1,839	$19,727	$46.3
11	ACCESSORY ELECTRIC PLANT													
11.1	Generator Equipment	$1,681	$0	$269	$0	$1,950	9.0%	$175	0%	$0	7%	$159	$2,284	$5.4
11.2	Station Service Equipment	$2,967	$0	$995	$0	$3,962	9.0%	$357	0%	$0	8%	$324	$4,643	$10.9
11.3	Switchgear & Motor Control	$3,405	$0	$592	$0	$3,997	9.0%	$360	0%	$0	10%	$436	$4,793	$11.2
11.4	Conduit & Cable Tray	$0	$2,335	$7,544	$0	$9,879	9.0%	$889	0%	$0	15%	$1,616	$12,384	$29.0
11.5	Wire & Cable	$0	$4,446	$7,948	$0	$12,394	9.0%	$1,115	0%	$0	15%	$2,026	$15,536	$36.4
11.6	Protective Equipment	$306	$0	$1,063	$0	$1,369	9.0%	$123	0%	$0	10%	$149	$1,642	$3.8
11.7	Standby Equipment	$1,333	$0	$31	$0	$1,364	9.0%	$123	0%	$0	10%	$148	$1,635	$3.8
11.8	Main Power Transformers	$8,803	$0	$183	$0	$8,986	9.0%	$809	0%	$0	10%	$980	$10,775	$25.3
11.9	Electrical Foundations	$0	$301	$766	$0	$1,067	9.0%	$96	0%	$0	20%	$233	$1,397	$3.3
	SUBTOTAL 11.	$18,494	$7,082	$19,391	$0	$44,967		$4,047		$0		$6,071	$55,088	$129.2
12	INSTRUMENTATION & CONTROL													
12.1	PC Control Equipment (w 12.7)	$0	$0	$0	$0	$0	9.0%	$0	0%	$0	0%	$0	$0	$0.0
12.2	Combustion Turbine Control	$0	$0	$0	$0	$0	9.0%	$0	0%	$0	0%	$0	$0	$0.0
12.3	Steam Turbine Control (w 8.1)	$0	$0	$0	$0	$0	9.0%	$0	0%	$0	0%	$0	$0	$0.0
12.4	Other Major Component Control	$0	$0	$0	$0	$0	9.0%	$0	0%	$0	0%	$0	$0	$0.0
12.5	Signal Processing Equipment (w12.7)	$0	$0	$0	$0	$0	9.0%	$0	0%	$0	0%	$0	$0	$0.0
12.6	Control Boards,Panels & Racks	$511	$0	$312	$0	$823	9.0%	$74	0%	$0	15%	$135	$1,032	$2.4
12.7	Distributed Control System Equipment	$5,156	$0	$920	$0	$6,076	9.0%	$547	0%	$0	10%	$662	$7,285	$17.1
12.8	Instrument Wiring & Tubing	$3,108	$0	$5,657	$0	$8,765	9.0%	$789	0%	$0	15%	$1,434	$10,988	$25.8
12.9	Other I & C Equipment	$1,456	$0	$3,373	$0	$4,830	9.0%	$435	0%	$0	10%	$526	$5,791	$13.6
	SUBTOTAL 12.	$10,231	$0	$10,262	$0	$20,493		$1,844		$0		$2,757	$25,096	$58.8

Acct No.	Item/Description	Equipment Cost	Material Cost	Labor Direct	Labor Indirect	Bare Erected Cost $	Eng'g CM H.O.& Fee %	Eng'g CM H.O.& Fee Total	Process Contingency %	Process Contingency Total	Project Contingency %	Project Contingency Total	TOTAL 450MW AIR PLANT Cost	450MW AIR COST $/kW
13	IMPROVEMENTS TO SITE													
13.1	Site Preparation	$0	$56	$1,190	$0	$1,246	9.0%	$112	0%	$0	20%	$272	$1,630	$3.8
13.2	Site Improvements	$0	$1,857	$2,454	$0	$4,311	9.0%	$388	0%	$0	20%	$940	$5,640	$13.2
13.3	Site Facilities	$3,328	$0	$3,492	$0	$6,820	9.0%	$614	0%	$0	20%	$1,487	$8,921	$20.9
	SUBTOTAL 13.	$3,328	$1,913	$7,136	$0	$12,378		$1,114		$0		$2,699	$16,192	$38.0
14	BUILDINGS & STRUCTURES													
14.1	Boiler Building	$0	$9,904	$8,703	$0	$18,607	9.0%	$1,675	0%	$0	15%	$3,042.10	$23,324	$54.7
14.2	Turbine Building	$0	$14,137	$13,166	$0	$27,303	9.0%	$2,457	0%	$0	15%	$4,464	$34,224	$80.2
14.3	Administration Building	$0	$702	$740	$0	$1,442	9.0%	$130	0%	$0	15%	$236	$1,808	$4.2
14.4	Circulation Water Pumphouse	$0	$162	$129	$0	$291	9.0%	$26	0%	$0	15%	$48	$365	$0.9
14.5	Water Treatment Buildings	$0	$669	$610	$0	$1,279	9.0%	$115	0%	$0	15%	$209	$1,603	$3.8
14.6	Machine Shop	$0	$469	$314	$0	$783	9.0%	$71	0%	$0	15%	$128	$982	$2.3
14.7	Warehouse	$0	$317	$318	$0	$636	9.0%	$57	0%	$0	15%	$104	$797	$1.9
14.8	Other Buildings & Structures	$0	$259	$221	$0	$480	9.0%	$43	0%	$0	15%	$79	$603	$1.4
14.9	Waste Treating Building & Str.	$0	$474	$1,439	$0	$1,914	9.0%	$172	0%	$0	15%	$313	$2,399	$5.6
	SUBTOTAL 14.	$0	$27,094	$25,641	$0	$52,735		$4,746		$0		$8,622	$66,105	$155.0
	TOTAL COST	$526,015	$49,307	$299,701	$0	$875,023		$78,752		$0		$130,474	$1,084,249	$2,542.3

Owner's Costs		
Pre production Costs		
6 months all labor	$7,914	$18.6
1 month maintenance materials	$905	$2.1
1 Month non-fuel consumables	$1,117	$2.6
1 Month Waste Disposal	$579	$1.4
25% of 1 Months Fuel Cost at 100% CF	$1,495	$3.5
2% of TPC	$21,685	$50.8
Total Pre-production costs	$33,694	$79.0
Inventory Capital		
60 day supply of fuel and consumables at 100% CF	$14,191	$33.3
0.5% of TPC (Spare parts)	$5,421	$12.7
Total Inventory Capital	$19,612	$46.0
Initial Cost for Catalyst and Chemicals	$0	$0.0
Land	$900	$2.1
Other Owners' Costs	$162,637	$381.3
Financing Costs	$29,275	$68.6
Total Overnight Costs (TOC)	$1,330,367	$3,119.4
TASC Multiplier (IOU, high-risk, 35 year)	1.140	
Total As-Spent Cost (TASC)	$1,516,619	$3,556.1

Table 4-6: Capital Costs for 450MW Oxy-Fired Plant

Client: USDOE/NETL
Project: Bituminous Baseline Study
TOTAL PLANT COST SUMMARY
Case: 450 MW Oxy Plant
Estimate Type: Conceptual
Cost Base: June 2011 ($x1000)

Report Date: May 30, 2014

Acct No.	Item/Description	Equipment Cost	Material Cost	Labor Direct	Labor Indirect	Bare Erected Cost $	Eng'g CM H.O.& Fee %	Eng'g CM H.O.& Fee Total	Process Contingency %	Process Contingency Total	Project Contingency %	Project Contingency Total	TOTAL 450MW Oxy PLANT Cost	450MW Oxy COST $/kW
1	COAL & SORBENT HANDLING													
	SUBTOTAL 1.	$16,310	$4,170	$9,651	$0	$30,130		$2,712	$0		$4,926		$37,770	$116.2
2	COAL & SORBENT PREP & FEED													
	SUBTOTAL 2.	$11,905	$446	$2,958	$0	$15,308		$1,378	$0		$2,503		$19,190	$59.0
3	FEEDWATER & MISC. BOP SYSTEMS													
	SUBTOTAL 3.	$40,068	$0	$18,439	$0	$58,507		$5,266	$0		$10,382		$74,156	$228.1
4	PC BOILER													
	SUBTOTAL 4.	$360,851	$0	$208,227	$0	$569,079		$34,857	$9,357		$64,727		$678,021	$2,085.4
5	FLUE GAS CLEANUP													
	SUBTOTAL 5.	$71,840	$0	$41,455	$0	$113,294		$10,196	$0		$12,349		$135,842	$417.8
5B	CO2 REMOVAL & COMPRESSION (based on DOE Case S12F)													
	SUBTOTAL 5B.	$45,103	$0	$23,872	$0	$68,975		$6,208	$0		$14,101		$89,284	$274.6
6	COMBUSTION TURBINE/ACCESSORIES													
	SUBTOTAL 6.	$0	$0	$0	$0	$0		$0	$0		$0		$0	$0.0
7	HRSG													
	SUBTOTAL 7.	$19,410	$1,095	$13,049	$0	$33,555		$3,020	$0		$4,749		$41,324	$127.1
8	STEAM TURBINE GENERATOR													
	SUBTOTAL 8.	$88,895	$1,042	$22,311	$0	$112,248		$10,102	$0		$13,926		$136,278	$419.2
9	COOLING WATER SYSTEM													
	SUBTOTAL 9.	$11,375	$6,220	$10,919	$0	$28,513		$2,566	$0		$4,251		$35,332	$108.7
10	ASH/SPENT SORBENT HANDLING SYS													
	SUBTOTAL 10.	$7,068	$209	$9,177	$0	$16,455		$1,481	$0		$1,844		$19,781	$60.8
11	ACCESSORY ELECTRIC PLANT													
	SUBTOTAL 11.	$25,186	$14,205	$37,328	$0	$76,719		$6,905	$0		$10,694		$94,320	$290.1
12	INSTRUMENTATION & CONTROL													
	SUBTOTAL 12.	$12,711	$0	$12,750	$0	$25,461		$2,292	$0		$3,425		$31,179	$95.9
13	IMPROVEMENTS TO SITE													
	SUBTOTAL 13.	$3,569	$2,052	$7,652	$0	$13,273		$1,195	$0		$2,894		$17,362	$53.4
14	BUILDINGS & STRUCTURES													
	SUBTOTAL 14.	$0	$28,247	$26,694	$0	$54,941		$4,945	$0		$8,983		$68,871	$211.8
	TOTAL COST	$714,291	$57,685	$444,482	$0	$1,216,458		$93,121	$9,357		$159,755		$1,478,692	$4,548.2

Client: USDOE/NETL
Project: Bituminous Baseline Study
TOTAL PLANT COST SUMMARY
Case: 450 MW Oxy Plant
Estimate Type: Conceptual
Cost Base: June 2011 ($x1000)

Report Date: May 30, 2014

Acct No.	Item/Description	Equipment Cost	Material Cost	Labor Direct	Labor Indirect	Bare Erected Cost $	Eng'g CM H.O.& Fee %	Eng'g CM H.O.& Fee Total	Process Contingency %	Process Contingency Total	Project Contingency %	Project Contingency Total	TOTAL 450MW Oxy PLANT Cost	450MW Oxy COST $/kW
1	COAL & SORBENT HANDLING													
1.1	Coal Receive & Unload	$3,314	$0	$1,508	$0	$4,822	9.0%	$434	0%	$0	15%	$788	$6,044	$18.6
1.2	Coal Stackout & Reclaim	$4,325	$0	$967	$0	$5,292	9.0%	$476	0%	$0	15%	$865	$6,633	$20.4
1.3	Coal Conveyors	$4,021	$0	$956	$0	$4,977	9.0%	$448	0%	$0	15%	$814	$6,239	$19.2
1.4	Other Coal Handling	$1,052	$0	$221	$0	$1,273	9.0%	$115	0%	$0	15%	$208	$1,596	$4.9
1.5	Sorbent Receive & Unload	$137	$0	$41	$0	$178	9.0%	$16	0%	$0	15%	$29	$223	$0.7
1.6	Sorbent Stackout & Reclaim	$2,202	$0	$398	$0	$2,600	9.0%	$234	0%	$0	15%	$425	$3,259	$10.0
1.7	Sorbent Conveyors	$785	$171	$190	$0	$1,146	9.0%	$103	0%	$0	15%	$187	$1,437	$4.4
1.8	Other Sorbent Handling	$474	$112	$245	$0	$831	9.0%	$75	0%	$0	15%	$136	$1,042	$3.2
1.9	Coal & Sorbent Hnd.Foundations	$0	$3,887	$5,125	$0	$9,012	9.0%	$811	0%	$0	15%	$1,474	$11,297	$34.7
	SUBTOTAL 1.	$16,310	$4,170	$9,651	$0	$30,130		$2,712		$0		$4,926	$37,770	$116.2
2	COAL & SORBENT PREP & FEED													
2.1	Coal Crushing & Drying	$620	$0	$119	$0	$739	9.0%	$67	0%	$0	15%	$121	$927	$2.9
2.2	Coal Conveyor to Storage	$4,845	$0	$1,043	$0	$5,888	9.0%	$530	0%	$0	15%	$963	$7,381	$22.7
2.3	Coal Injection System	$0	$0	$0	$0	$0	9.0%	$0	0%	$0	0%	$0	$0	$0.0
2.4	Misc.Coal Prep & Feed	$0	$0	$0	$0	$0	9.0%	$0	0%	$0	0%	$0	$0	$0.0
2.5	Sorbent Prep Equipment	$6,240	$0	$1,344	$0	$7,584	9.0%	$683	0%	$0	15%	$1,240	$9,506	$29.2
2.6	Sorbent Storage & Feed	$200	$0	$60	$0	$260	9.0%	$23	0%	$0	15%	$43	$326	$1.0
2.7	Sorbent Injection System	$0	$0	$0	$0	$0	9.0%	$0	0%	$0	0%	$0	$0	$0.0
2.8	Booster Air Supply System	$0	$0	$0	$0	$0	9.0%	$0	0%	$0	0%	$0	$0	$0.0
2.9	Coal & Sorbent Feed Foundation	$0	$446	$391	$0	$837	9.0%	$75	0%	$0	15%	$137	$1,050	$3.2
	SUBTOTAL 2.	$11,905	$446	$2,958	$0	$15,308		$1,378		$0		$2,503	$19,190	$59.0
3	FEEDWATER & MISC. BOP SYSTEMS													
3.1	FeedwaterSystem	$17,245	$0	$5,560	$0	$22,805	9.0%	$2,052	0%	$0	15%	$3,729	$28,587	$87.9
3.2	Water Makeup & Pretreating	$4,185	$0	$1,324	$0	$5,509	9.0%	$496	0%	$0	20%	$1,201	$7,206	$22.2
3.3	Other Feedwater Subsystems	$5,425	$0	$2,227	$0	$7,652	9.0%	$689	0%	$0	15%	$1,251	$9,592	$29.5
3.4	Service Water Systems	$838	$0	$438	$0	$1,276	9.0%	$115	0%	$0	20%	$278	$1,669	$5.1
3.5	Other Boiler Plant Systems	$6,398	$0	$6,048	$0	$12,446	9.0%	$1,120	0%	$0	15%	$2,035	$15,602	$48.0
3.6	FO Supply Sys & Nat Gas	$302	$0	$352	$0	$654	9.0%	$59	0%	$0	15%	$107	$820	$2.5
3.7	Waste Treatment Equipment	$2,721	$0	$1,575	$0	$4,296	9.0%	$387	0%	$0	20%	$936	$5,620	$17.3
3.8	Misc. Equip.(cranes,AirComp.,Comm.)	$2,955	$0	$914	$0	$3,869	9.0%	$348	0%	$0	20%	$844	$5,061	$15.6
	SUBTOTAL 3.	$40,068	$0	$18,439	$0	$58,507		$5,266		$0		$10,382	$74,156	$228.1

Acct No. Item/Description	Equipment Cost	Material	Labor		Bare Erected Cost $	Eng'g CM H.O.& Fee		Process Contingency		Project Contingency		TOTAL 450MW Oxy PLANT Cost	450MW Oxy COST $/kW
		Cost	Direct	Indirect		%	Total	%	Total	%	Total		
4 PC BOILER													
4.1 PC Boiler & Accessories	$226,414	$0	$114,098	$0	$340,512	9.0%	$30,646	0%	$0	15%	$55,674	$426,833	$1,312.8
4.1 PC Boiler & Accessories	$27,586	$0	$19,200	$0	$46,786	9.0%	$4,211	20%	$9,357	15%	$9,053	$69,407	$213.5
4.2 SCR (w/4.1)	$0	$0	$0	$0	$0	9.0%	$0	0%	$0	15%	$0	$0	$0.0
4.3 ASU/Oxidant Compression	$106,851	$0	$74,929	$0	$181,780	0.0%	$0		$0	0%	$0	$181,780	$559.1
4.4 Boiler BoP (w/ ID Fans)	$0	$0	$0	$0	$0	0.0%	$0		$0	0%	$0	$0	$0.0
4.5 Primary Air System	$0	$0	$0	$0	$0	0.0%	$0		$0	0%	$0	$0	$0.0
4.6 Secondary Air System	$0	$0	$0	$0	$0	0.0%	$0		$0	0%	$0	$0	$0.0
4.8 Major Component Rigging	$0	$0	$0	$0	$0	0.0%	$0		$0	0%	$0	$0	$0.0
4.9 Boiler Foundations	$0	$0	$0	$0	$0	0.0%	$0		$0	0%	$0	$0	$0.0
SUBTOTAL 4.	$360,851	$0	$208,227	$0	$569,079		$34,857		$9,357		$64,727	$678,021	$2,085.4
5 FLUE GAS CLEANUP													
5.1 Absorber Vessels & Accessories	$46,830	$0	$27,023	$0	$73,853	9.0%	$6,647	0%	$0	10%	$8,050	$88,550	$272.4
5.2 Other FGD	$0	$0	$0	$0	$0	9.0%	$0	0%	$0	10%	$0	$0	$0.0
5.3 Bag House & Accessories	$9,370	$0	$5,407	$0	$14,777	9.0%	$1,330	0%	$0	10%	$1,611	$17,718	$54.5
5.4 Other Particulate Removal Materials	$0	$0	$0	$0	$0	9.0%	$0	0%	$0	10%	$0	$0	$0.0
5.5 Gypsum Dewatering System	$9,870	$0	$5,695	$0	$15,565	9.0%	$1,401	0%	$0	10%	$1,697	$18,664	$57.4
5.6 Mercury Removal System	$4,690	$0	$2,706	$0	$7,396	9.0%	$666	0%	$0	10%	$806	$8,868	$27.3
5.9 Open	$1,080	$0	$623	$0	$1,703	9.0%	$153	0%	$0	10%	$186	$2,042	$6.3
SUBTOTAL 5.	$71,840	$0	$41,455	$0	$113,294		$10,196		$0		$12,349	$135,842	$417.8
5B CO2 REMOVAL & COMPRESSION (based on DOE Case S12F)													
5B.1 CO2 Condensing Heat Exchanger	$16,607	$0	$556	$0	$17,163	9.0%	$1,545	0%	$0	15%	$2,806	$21,515	$66.2
5B.2 CO2 Compression & Drying	$28,496	$0	$23,315	$0	$51,811	9.0%	$4,663	0%	$0	20%	$11,295	$67,769	$208.4
SUBTOTAL 5B.	$45,103	$0	$23,872	$0	$68,975		$6,208		$0		$14,101	$89,284	$274.6
6 COMBUSTION TURBINE/ACCESSORIES													
SUBTOTAL 6.	$0	$0	$0	$0	$0		$0		$0		$0	$0	$0.0
7 HRSG													
7.1 Flue Gas Recycle Heat Exchanger	$0	$0	$0	$0	$0	9.0%	$0	0%	$0	0%	$0	$0	$0.0
7.2 HRSG Accessories	$0	$0	$0	$0	$0	9.0%	$0	0%	$0	0%	$0	$0	$0.0
7.3 Ductwork	$9,352	$0	$5,903	$0	$15,254	9.0%	$1,373	0%	$0	15%	$2,494	$19,121	$58.8
7.4 Stack	$10,058	$0	$5,846	$0	$15,904	9.0%	$1,431	0%	$0	10%	$1,733	$19,069	$58.7
7.9 Duct & Stack Foundations	$0	$1,095	$1,301	$0	$2,396	9.0%	$216	0%	$0	20%	$522	$3,134	$9.6
SUBTOTAL 7.	$19,410	$1,095	$13,049	$0	$33,555		$3,020		$0		$4,749	$41,324	$127.1
8 STEAM TURBINE GENERATOR													
8.1 Steam TG & Accessories	$55,766	$0	$6,880	$0	$62,646	9.0%	$5,638	0%	$0	10%	$6,828	$75,112	$231.0
8.2 Turbine Plant Auxiliaries	$350	$0	$745	$0	$1,095	9.0%	$99	0%	$0	10%	$119	$1,312	$4.0
8.3 Condenser & Auxiliaries	$15,106	$0	$5,116	$0	$20,222	9.0%	$1,820	0%	$0	10%	$2,204	$24,246	$74.6
8.4 Steam Piping	$17,673	$0	$7,852	$0	$25,525	9.0%	$2,297	0%	$0	15%	$4,173	$31,996	$98.4
8.9 TG Foundations	$0	$1,042	$1,719	$0	$2,761	9.0%	$249	0%	$0	20%	$602	$3,612	$11.1
SUBTOTAL 8.	$88,895	$1,042	$22,311	$0	$112,248		$10,102		$0		$13,926	$136,278	$419.2

Acct No. Item/Description	Equipment Cost	Material	Labor		Bare Erected Cost $	Eng'g CM H.O.& Fee		Process Contingency		Project Contingency		TOTAL 450MW Oxy PLANT Cost	450MW Oxy COST $/kW
		Cost	Direct	Indirect		%	Total	%	Total	%	Total		
9 COOLING WATER SYSTEM													
9.1 Cooling Towers	$8,468	$0	$2,619	$0	$11,087	9.0%	$998	0%	$0	10%	$1,208	$13,293	$40.9
9.2 Circulating Water Pumps	$1,606	$0	$101	$0	$1,708	9.0%	$154	0%	$0	10%	$186	$2,047	$6.3
9.3 Circ.Water System Auxiliaries	$479	$0	$64	$0	$543	9.0%	$49	0%	$0	10%	$59	$651	$2.0
9.4 Circ.Water Piping	$0	$4,038	$3,656	$0	$7,694	9.0%	$692	0%	$0	15%	$1,258	$9,645	$29.7
9.5 Make-up Water System	$431	$0	$554	$0	$985	9.0%	$89	0%	$0	15%	$161	$1,234	$3.8
9.6 Component Cooling Water Sys	$391	$0	$300	$0	$691	9.0%	$62	0%	$0	15%	$113	$866	$2.7
9.9 Circ.Water System Foundations & Structures	$0	$2,182	$3,624	$0	$5,806	9.0%	$523	0%	$0	20%	$1,266	$7,595	$23.4
SUBTOTAL 9.	$11,375	$6,220	$10,919	$0	$28,513		$2,566		$0		$4,251	$35,332	$108.7
10 ASH/SPENT SORBENT HANDLING SYS													
10.1 Rotary Ash Coolers	$620	$0	$358	$0	$978	9.0%	$88	0%	$0	10%	$107	$1,173	$3.6
10.2 Cyclone Ash Letdown	$0	$0	$0	$0	$0	9.0%	$0	0%	$0	0%	$0	$0	$0.0
10.3 HGCU Ash Letdown	$0	$0	$0	$0	$0	9.0%	$0	0%	$0	0%	$0	$0	$0.0
10.4 High Temperature Ash Piping	$0	$0	$0	$0	$0	9.0%	$0	0%	$0	0%	$0	$0	$0.0
10.5 Reducer Baghouse Ash Recycle System	$0	$0	$0	$0	$0	9.0%	$0	0%	$0	10%	$0	$0	$0.0
10.6 Ash Storage Silos	$925	$0	$2,829	$0	$3,754	9.0%	$338	0%	$0	10%	$409	$4,501	$13.8
10.7 Ash Transport & Feed Equipment	$6,144	$0	$6,091	$0	$12,234	9.0%	$1,101	0%	$0	10%	$1,334	$14,670	$45.1
10.8 Misc. Ash Handling Equipment	$0	$0	$0	$0	$0	9.0%	$0	0%	$0	0%	$0	$0	$0.0
10.9 Ash/Spent Sorbent Foundation	$0	$209	$257	$0	$467	9.0%	$42	0%	$0	20%	$101	$610	$1.9
SUBTOTAL 10.	$7,068	$209	$9,177	$0	$16,455		$1,481		$0		$1,844	$19,781	$60.8
11 ACCESSORY ELECTRIC PLANT													
11.1 Generator Equipment	$1,681	$0	$269	$0	$1,950	9.0%	$175	0%	$0	7%	$159	$2,284	$7.0
11.2 Station Service Equipment	$6,083	$0	$2,039	$0	$8,123	9.0%	$731	0%	$0	8%	$665	$9,519	$29.3
11.3 Switchgear & Motor Control	$6,981	$0	$1,213	$0	$8,194	9.0%	$737	0%	$0	10%	$894	$9,826	$30.2
11.4 Conduit & Cable Tray	$0	$4,787	$15,467	$0	$20,255	9.0%	$1,823	0%	$0	15%	$3,312	$25,390	$78.1
11.5 Wire & Cable	$0	$9,116	$16,295	$0	$25,411	9.0%	$2,287	0%	$0	15%	$4,154	$31,853	$98.0
11.6 Protective Equipment	$306	$0	$1,063	$0	$1,369	9.0%	$123	0%	$0	10%	$149	$1,642	$5.0
11.7 Standby Equipment	$1,333	$0	$31	$0	$1,364	9.0%	$123	0%	$0	10%	$148	$1,635	$5.0
11.8 Main Power Transformers	$8,803	$0	$183	$0	$8,986	9.0%	$809	0%	$0	10%	$980	$10,775	$33.1
11.9 Electrical Foundations	$0	$301	$766	$0	$1,067	9.0%	$96	0%	$0	20%	$233	$1,397	$4.3
SUBTOTAL 11.	$25,186	$14,205	$37,328	$0	$76,719		$6,905		$0		$10,694	$94,320	$290.1
12 INSTRUMENTATION & CONTROL													
12.1 PC Control Equipment (w 12.7)	$0	$0	$0	$0	$0	9.0%	$0	0%	$0	0%	$0	$0	$0.0
12.2 Combustion Turbine Control	$0	$0	$0	$0	$0	9.0%	$0	0%	$0	0%	$0	$0	$0.0
12.3 Steam Turbine Control (w 8.1)	$0	$0	$0	$0	$0	9.0%	$0	0%	$0	0%	$0	$0	$0.0
12.4 Other Major Component Control	$0	$0	$0	$0	$0	9.0%	$0	0%	$0	0%	$0	$0	$0.0
12.5 Signal Processing Equipment (w12.7)	$0	$0	$0	$0	$0	9.0%	$0	0%	$0	0%	$0	$0	$0.0
12.6 Control Boards,Panels & Racks	$634	$0	$388	$0	$1,023	9.0%	$92	0%	$0	15%	$168	$1,282	$3.9
12.7 Distributed Control System Equipment	$6,406	$0	$1,143	$0	$7,548	9.0%	$679	0%	$0	10%	$823	$9,050	$27.8
12.8 Instrument Wiring & Tubing	$3,862	$0	$7,028	$0	$10,890	9.0%	$980	0%	$0	15%	$1,781	$13,651	$42.0
12.9 Other I & C Equipment	$1,810	$0	$4,191	$0	$6,001	9.0%	$540	0%	$0	10%	$654	$7,195	$22.1
SUBTOTAL 12.	$12,711	$0	$12,750	$0	$25,461		$2,292		$0		$3,425	$31,179	$95.9

Acct No.	Item/Description	Equipment Cost	Material Cost	Labor Direct	Labor Indirect	Bare Erected Cost $	Eng'g CM H.O.& Fee %	Eng'g CM H.O.& Fee Total	Process Contingency %	Process Contingency Total	Project Contingency %	Project Contingency Total	TOTAL 450MW Oxy PLANT Cost	450MW Oxy COST $/kW
13	IMPROVEMENTS TO SITE													
13.1	Site Preparation	$0	$60	$1,276	$0	$1,336	9.0%	$120	0%	$0	20%	$292	$1,748	$5.4
13.2	Site Improvements	$0	$1,992	$2,631	$0	$4,623	9.0%	$416	0%	$0	20%	$1,008	$6,048	$18.6
13.3	Site Facilities	$3,569	$0	$3,744	$0	$7,313	9.0%	$658	0%	$0	20%	$1,595	$9,567	$29.4
	SUBTOTAL 13.	$3,569	$2,052	$7,652	$0	$13,273		$1,195		$0		$2,894	$17,362	$53.4
14	BUILDINGS & STRUCTURES													
14.1	Boiler Building	$0	$10,220	$8,981	$0	$19,201	9.0%	$1,728	0%	$0	15%	$3,139.19	$24,068	$74.0
14.2	Turbine Building	$0	$14,741	$13,729	$0	$28,470	9.0%	$2,562	0%	$0	15%	$4,655	$35,688	$109.8
14.3	Administration Building	$0	$726	$767	$0	$1,493	9.0%	$134	0%	$0	15%	$244	$1,872	$5.8
14.4	Circulation Water Pumphouse	$0	$162	$129	$0	$291	9.0%	$26	0%	$0	15%	$48	$365	$1.1
14.5	Water Treatment Buildings	$0	$840	$765	$0	$1,605	9.0%	$144	0%	$0	15%	$262	$2,011	$6.2
14.6	Machine Shop	$0	$486	$326	$0	$811	9.0%	$73	0%	$0	15%	$133	$1,017	$3.1
14.7	Warehouse	$0	$329	$330	$0	$658	9.0%	$59	0%	$0	15%	$108	$825	$2.5
14.8	Other Buildings & Structures	$0	$269	$228	$0	$497	9.0%	$45	0%	$0	15%	$82	$624	$1.9
14.9	Waste Treating Building & Str.	$0	$474	$1,439	$0	$1,914	9.0%	$172	0%	$0	15%	$313	$2,399	$7.4
	SUBTOTAL 14.	$0	$28,247	$26,694	$0	$54,941		$4,945		$0		$8,983	$68,871	$211.8
	TOTAL COST	$714,291	$57,685	$444,482	$0	$1,216,458		$93,121		$9,357		$159,755	$1,478,692	$4,548.2

Owner's Costs		
Pre production Costs		
6 months all labor	$9,533	$29.3
1 month maintenance materials	$1,228	$3.8
1 Month non-fuel consumables	$1,087	$3.3
1 Month Waste Disposal	$582	$1.8
25% of 1 Months Fuel Cost at 100% CF	$1,502	$4.6
2% of TPC	$29,574	$91.0
Total Pre-production costs	$43,506	$133.8
Inventory Capital		
60 day supply of fuel and consumables at 100% CF	$14,190	$43.6
0.5% of TPC (Spare parts)	$7,393	$22.7
Total Inventory Capital	$21,584	$66.4
Initial Cost for Catalyst and Chemicals	$0	$0.0
Land	$900	$2.8
Other Owners' Costs	$221,804	$682.2
Financing Costs	$39,925	$122.8
Total Overnight Costs (TOC)	$1,806,410	$5,556.2
TASC Multiplier (IOU, high-risk, 35 year)	1.140	
Total As-Spent Cost (TASC)	$2,059,307	$6,334.1

Table 4-7: O&M Costs for 450MW$_{gross}$ Air-Fired PC Steam Plant

BOILER ISLAND AND BALANCE OF PLANT O&M COSTS

Client: DOE - NETL — **INITIAL & ANNUAL O&M EXPENSES** — Cost Base: Jun-11

Project: ALSTOM Oxy-firing Study — **Case 1** - 1 x 450 MW-gross Air-fired PC SuperCritical Steam Plant

Net Plant Heat Rate (Btu/kWh): 7,684
Net Power Output (kW): 426,484
Capacity Factor (%): 85

FIXED OPERATING COSTS

OPERATING & MAINTENANCE LABOR

Operating Labor Requirements (O.J.) per shift	1 unit/mod.	Total Plant
Skilled Operator	2.0	2.0
Operator	7.0	7.0
Foreman	1.0	1.0
Lab Tech's, etc.	2.0	2.0
TOTAL O.J.'s	12.0	12.0

Operating Labor	
Operating Labor Rate (base):	39.70 $/hour
Operating Labor Burden:	30.00 % of base
Labor O-H change Rate:	25.00 % of labor

	Annual Cost $ / year	Annual Unit Cost $/kW-net
Annual Operating Labor Costs (calc'd)	5,425,243	12.72
Maintenance Labor Costs (calc'd)	7,237,532	16.97
Administrative & Support Labor (calc'd)	3,165,694	7.42
Property Taxes ans Insurance	21,617,020	50.69
TOTAL FIXED OPERATING COSTS	**37,445,489**	**87.80**

VARIABLE OPERATING COSTS

						$/kWh-net
Maintenance Material Cost					10,856,297	0.00342
Consumables	Consumption Initial Fill	Consumption Per Day	Unit Cost ($/unit)	Initial Fill Cost ($)		
Water (1,000 gallons)		2,770	1.67		1,438,499	0.00045
Chemicals						
MU & WT Chem. (lbs.)		14,575	0.27	0	1,211,203	0.00038
Limestone (tons)		409	33.48	0	4,253,172	0.00134
Ammonia (19% NH_3) (tons)		57.01	330.00	0	5,836,332	0.00184
Subtotal Chemicals				0	11,300,707	0.00356
Other Consumables						
Supplemental Fuel (10^6 Btu)						
SCR Catalyst Replacement (m^3)	w/equip.	0.24	8,938.80		664,497	0.00021
Emissions Penalties						
Subtotal Other Consumables					664,497	0.00021
Waste Disposal						
Fly Ash (ton)		713	25.11		5,555,374	0.00175
Bottom Ash (ton)		178	25.11		1,388,844	0.00044
Subtotal Waste Disposal					6,944,218	0.00219
TOTAL VARIABLE OPERATING COSTS					**31,204,219**	**0.00983**
Fuel (ton)		3541	65.30		**71,742,522**	**0.02259**

Table 4-8: O&M Costs for 450MW$_{gross}$ Oxy-Fired PC Steam Plant

BOILER ISLAND AND BALANCE OF PLANT O&M COSTS								
Client: DOE - NETL	**INITIAL & ANNUAL O&M EXPENSES**						Cost Base:	Jun-11
Project: ALSTOM Oxy-firing Study	**Case 1** - 1 x 450 MW-gross Oxy-fired PC SuperCritical Steam Plant							
						Net Plant Heat Rate (Btu/kWh):		10,130
						Net Power Output (kW):		325,120
						Capacity Factor (%):		85
FIXED OPERATING COSTS								
OPERATING & MAINTENANCE LABOR								
Operating Labor								
Operating Labor Rate (base):	39.70	$/hour		Operating La	1 unit/mod.	Total Plant		
Operating Labor Burden:	30.00	% of base		Skilled Opera	2.0	2.0		
Labor O-H change Rate:	25.00	% of labor		Operator	7.0	7.0		
				Foreman	1.0	1.0		
				Lab Tech's, e	2.0	2.0		
Operating Labor Requirements (O.J.) per shift	1 unit/mod.	Total Plant		TOTAL O.J.'s	12.0	12.0		
Skilled Operator	2.0	2.0						
Operator	7.0	7.0						
Foreman	1.0	1.0						
Lab Tech's, etc.	2.0	2.0						
TOTAL O.J.'s	12.0	12.0						
							Annual Cost	**Annual Unit Cost**
							$ / year	**$/kW-net**
Annual Operating Labor Costs (calc'd)							5,425,243	16.69
Maintenance Labor Costs (calc'd)							9,827,321	30.23
Administrative & Support Labor (calc'd)							3,813,141	11.73
Property Taxes ans Insurance							29,352,190	90.28
TOTAL FIXED OPERATING COSTS							**48,417,895**	**148.92**
VARIABLE OPERATING COSTS								
								$/kWh-net
Maintenance Material Cost							14,740,982	0.00609
Consumables		Consumption		Unit Cost	Initial Fill			
		Initial Fill	Per Day	($/unit)	Cost ($)			
Water (1,000 gallons)			2,926	1.67			1,519,512	0.00063
Chemicals								
MU & WT Chem. (lbs.)			14,575	0.27	0		1,211,203	0.00050
Limestone (tons)			367	33.48	0		3,813,920	0.00158
Ammonia (19% NH_3) (tons)			57.01	330.00	0		5,836,332	0.00241
Subtotal Chemicals					0		10,861,455	0.00449
Other Consumables								
Supplemental Fuel (10^6 Btu)								
SCR Catalyst Replacement (m^3)		w/equip.	0.24	8,938.80			664,497	0.00027
Emissions Penalties								
Subtotal Other Consumables							664,497	0.00027
Waste Disposal								
Fly Ash (ton)			717	25.11			5,582,804	0.00231
Bottom Ash (ton)			179	25.11			1,395,701	0.00058
Subtotal Waste Disposal							6,978,505	0.00288
TOTAL VARIABLE OPERATING COSTS							**34,764,951**	**0.01436**
Fuel (ton)			3559	65.30			**72,096,753**	**0.02978**

Client: DOE - NETL	**ANNUAL O&M EXPENSES SUMMARY**	Cost Base:	Jun-11
		Annual Cost	**Annual Unit Cost**
BOILER ISLAND AND BALANCE OF PLANT O&M COSTS			
		$/Year	$/kW
TOTAL FIXED O&M COSTS		48,417,895	148.92
TOTAL VARIABLE O&M COSTS		34,764,951	0.0144
AIR SEPARATION UNIT (ASU)			
TOTAL FIXED O&M COSTS		4,761,881	14.65
TOTAL VARIABLE O&M COSTS		895,960	0.0004
GAS PROCESSING UNIT (GPU)			
TOTAL FIXED O&M COSTS		693,588	2.13
TOTAL VARIABLE OPERATING COST		6,029,495	0.0025
TOTAL PLANT O&M COSTS			
TOTAL FIXED OPERATING COSTS		53,873,365	**165.70**
TOTAL VARIABLE OPERATING COST		41,690,406	**0.01722**

5. Large Scale Oxy-Fired Utility Reference Unit Design and Cost (900MW)

This section describes the design of an oxy-fired boiler, which is part of a steam power plant that produces a nominal gross output of approximately 900 MW_e and the capability to capture more than 90 percent of the CO_2 produced. The plant is started up with air firing and can also operate in air mode when the ASU is not in operation up to a maximum of 75% TMCR. The CO_2 product is purified to a level that is acceptable for sequestration.

The design basis for the 900MW oxy-boiler and plant were discussed in Section 3. Much of the 900MW steam generator design and description is nearly identical to the 450MW boiler and is not repeated here. The 450MW plant is an oxy-demonstration plant, while the 900MW is designed as a commercial oxy CO_2 capture plant.

5.1 Introduction

The boiler is a pulverized coal-fired unit, with a nominal capacity of approximately 900 MWe-gross. It is designed for full load capability (100% TMCR) with oxygen firing and is limited to about 75% TMCR with air firing. It is a sliding pressure, supercritical, once-through design, utilizing a low-NO_x tangential firing system and SCR for NO_X control during air firing. It is a single reheat unit designed for variable pressure operation with a balanced draft furnace. The unit is capable of firing the full range of pulverized coals specified and producing a continuous flow of steam to the turbine generator with nominal boiler outlet conditions of 5,174,600 lbm/hr (652 kg/s), 4,130 psig (284.8 bar), 1,117°F (603°C) at the superheater outlet, and 4,280,100 lbm/hr (539.4 kg/s), 863 psig (59.5 bar), 1,150°F (621°C) at the reheater outlet. Light fuel oil is used for start-up and as a support fuel for low load operation.

As discussed in Section 4, sliding pressure supercritical once-through boilers have steam/water separators integrated into their water/steam circuits. Above minimum loads, the separator is only a transit element. Below minimum once-through load, it performs its separation function. During start-up and low load operation, the steam/water mixture is separated in the separator. The steam goes to the superheater and the water to the start-up system. Above the minimum once-through load, the mass flow rate in the waterwalls is large enough to cool the waterwall tubes sufficiently so that the start-up system is no longer needed in operation.

The boiler is capable of operating under either the air-fired mode or oxy-fired mode. However, the boiler design is optimized for oxy-firing which consequently restricts operating capacity for air-firing. The aspects of the oxy-fired process and the boiler island modifications for oxygen firing are described below.

5.2 Oxygen Firing Process

The basic oxy-firing concept is the same as for the 450MW oxy-fired boiler and is thus not repeated here. Figure 5-1 shows the basic process flow diagram selected for the oxygen-fired

boiler island. New equipment to allow oxy firing capability within the boiler scope is relatively modest (relative to a comparable air-fired boiler scope). Included would be oxygen supply lines (shown in blue), oxygen mixing devices, a low leakage "air" heater or gas to gas heater (GGH), and additional ductwork to connect the inlets of the PA and FD fans to the recirculated flue gas sources (Streams 18 and 27). The flue gas recirculation (FGR) ducts also include isolation dampers and an inlet for primary and secondary air, which is used during air firing, start-up, and during the transition between air and oxygen firing.

As previously discussed, there are design changes that must be considered including sizing of the fans and ducts due to the higher density of the recirculated flue gas as compared to air. The design of the hot secondary air duct is also modified in order to accommodate the mixture of a stream of nearly pure oxygen provided from the ASU. About 30% of the total oxygen produced in the ASU is introduced in the hot secondary air duct. This is done in order to keep oxygen content in the primary and most of the secondary ducts below a threshold value, above which would require the use of more costly alloys for the ducts and other equipment downstream of the oxygen mixing locations.

Other major new equipment/systems within the plant include a cryogenic distillation type Air Separation Unit (ASU), a Direct Contact Cooler (DCC), and a Gas Processing Unit (GPU). The plant includes a fabric filter (FF) for particulate and a wet flue gas desulfurization system (WFGD). For this 900MW design, an additional flue gas heat exchanger (HEX) was included between the ID fan and the WFGD to further reduce the gas temperature entering the WFGD and to extract additional heat to improve efficiency.

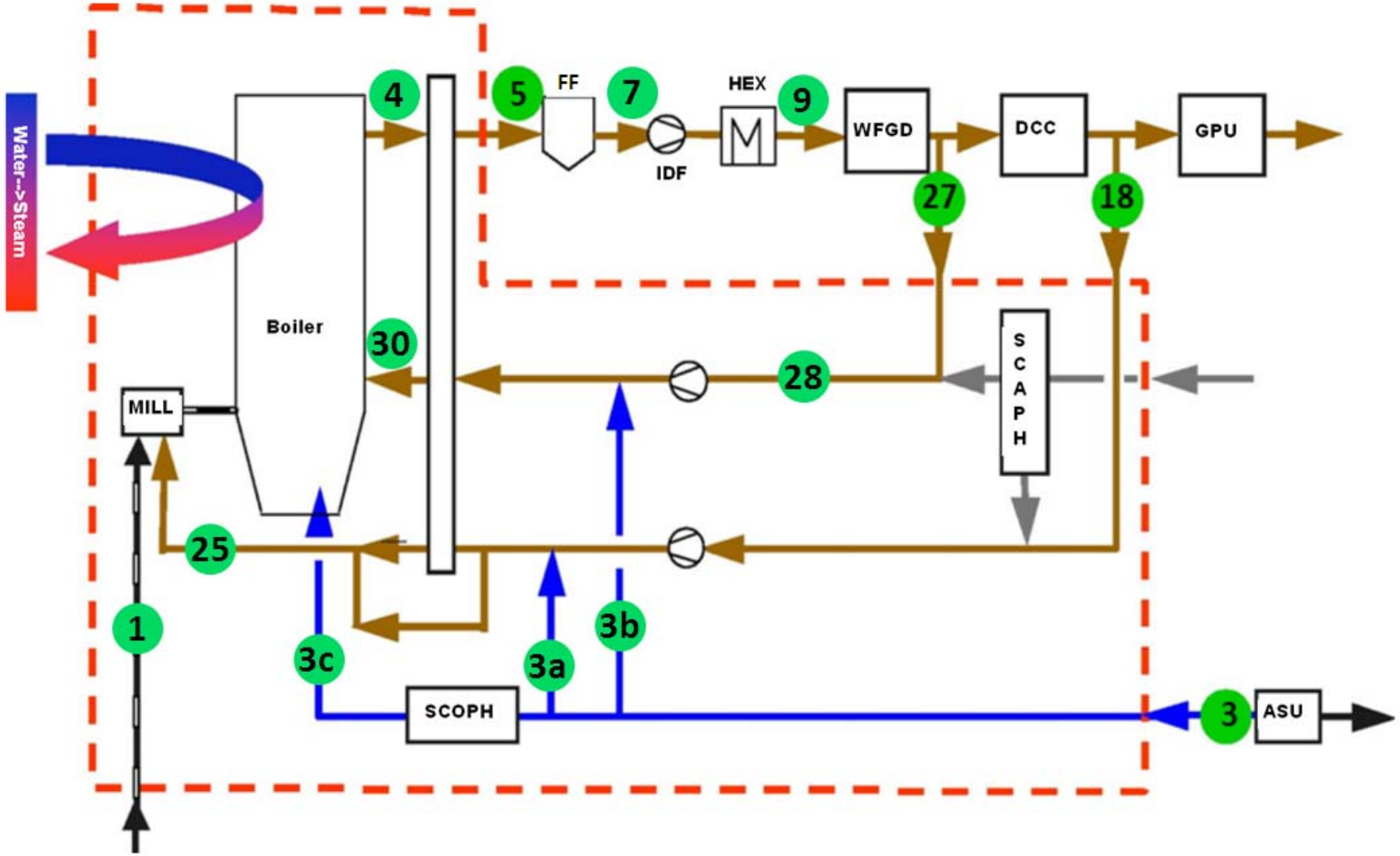

Figure 5-1: Boiler Island Process Flow Diagram (Oxy-Fired Mode)

5.3 Steam Generator Design

This section briefly describes several of the more important areas of the steam generator unit design.

5.3.1 Furnace

The boiler is a tower type design with gas-tight welded-wall construction. The boiler is of the dry bottom type with spiral tubes enclosing the furnace from the coutant bottom to the approximate elevation of the start of the horizontal heat exchanger sections (i.e. superheater, reheater, and economizer). Vertical tubes form the remainder of the furnace enclosure. All furnace tubing is of the smooth bore type and is selected as required to meet the applicable code.

Considering the slagging characteristics associated with the coal ash, the furnace has been conservatively sized to reduce overall furnace temperatures and minimize furnace slag accumulation. The furnace is designed to produce 100% TMCR steam flow with oxy-firing for all coals.

5.3.2 Heating Surface Arrangement

The following heating surfaces are arranged above the furnace in the direction of the flue gas flow as shown in Figure 5-2.

- Superheater 2 – Support tube grid–low temperature superheater (SH 2)
- SH final stage – Superheater 4 (SH 4)
- RH final stage – Reheater 2 (RH 2)
- Superheater 3– intermediate temperature superheater (SH 3)
- Reheater 1– low temperature reheater (RH 1)
- Economizer – (Eco)

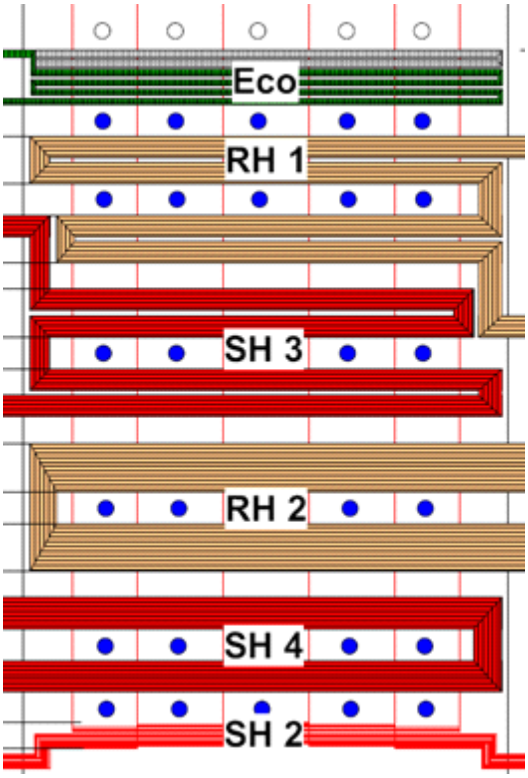

Figure 5-2: Heating Surface Arrangement Diagram

5.3.3 Economizer

The economizer section is used to help improve boiler efficiency by extracting heat from flue gases discharged from the low temperature reheater section of a boiler. Heat is transferred to the feedwater, which enters the economizer at a temperature appreciably lower than that of saturated steam. Economizers in tower boilers are arranged for upward flow of gas and upward flow of water (parallel flow). Upward flow of water helps avoid water hammer, which may occur under the some operating conditions.

Feedwater and/or recirculated water enter the economizer from the inlet header and flows through horizontal tubing comprising the heating surface. Return bends at the ends of the tubing provide continuous tube elements that terminate at the economizer outlet header. This header is connected to the lower waterwall inlet headers through connecting links.

The selected economizer is a finned tube arrangement, constructed of carbon steel tubing.

5.3.4 Superheater and Reheater

From the outlet headers of the spiral waterwalls, the fluid flows to a water separator. After the water separator, the steam flows to the vertical walls (SH-1) that enclose the horizontal heating surface. The subsequent steam path is into the SH2, SH3, and finally to the finishing superheater

SH4. The SH2, SH4, and RH2 banks have a wide pitch so that any ash deposits, which may be formed on the elements, can be easily removed.

Cold reheat steam from the HP turbine exhaust flows to the inlet of the low temperature reheater section (RH1) of the boiler. Reheat steam passes through this first horizontal section and then to the reheater finishing section, RH2. The high temperature steam leaving the RH2 section flows back to the IP turbine inlet for power generation.

5.3.5 Steam Temperature Control

Steam temperature control is the same as described for the 450MW boiler.

Superheater and Reheater De-superheaters

Spraywater attemperators are also provided for superheater steam temperature control. Reheat steam temperature control is also provided by means of spraywater attemperators. Reheat spray flow is automatically minimized by the steam temperature control system as described in the previous section. These de-superheaters, including the necessary spray-type internals, are used as one means for control of final steam temperatures over varying loads, fouling levels, and fuels.

5.3.6 Start-Up System

The start-up system is the same as described for the 450MW boiler.

5.3.7 Mechanical Design Aspects

The mechanical design of this boiler meets the demands of the specific loading such as pressure, temperature, and temperature transients during load changes. Its design is the same as described for the 450MW boiler.

5.3.8 Boiler Pressure Parts

The boiler has superheater, reheater and economizer heat exchanger sections located inside a rectangular enclosure formed by welded membrane walls. The pressure parts are similar to that for the 450MW boiler.

Twelve water cannons (three on each wall) are employed to clean the furnace heat-absorbing surface to maintain heat absorption efficiency.

5.3.9 Boiler Steel Structure

The boiler steel structure is similar to that for the 450MW boiler.

5.3.10 Sootblower System

Retractable Blowers

Retractable sootblowers are provided for cleaning the superheater, reheater, and economizer sections of the boiler. Long retractable sootblowers (fully retractable sootblowers) are installed in the steam generator sidewalls. During operation, the long retractable blowers advance a rotating lance for half the boiler's width. They normally use two 180° opposed-cleaning nozzles

at the tip which emit a high-pressure steam source perpendicular to the lance. The rotating lance enters between heating surfaces while two nozzles at the lance tip clean the surfaces with steam. In the off position the lance tube is fully retracted. Partially retractable (helical) sootblowers are installed to clean the economizer. The lance for the partially retractable sootblower is supported with element bearings. The helical movement of the blowing tube or lance tube is effected by the chain drive at the sootblower carriage, which is driven by a geared motor. In the off position the lance tube will remain partially in the boiler.

For cleaning of SCR catalyst and dummy modules, rake type sootblowers are installed above the modules.

The rake type blower consists of the main tube, which is movable in longitudinal direction and has several cross arms attached depending on the length of travel. The lance tubes are provided with nozzles that are vertically directed onto the modules. The sootblower is held in place by sliding supports and it remains in the flue gas flow path.

Steam operated multi nozzle jet blowers are used for the cleaning of the air heater or gas – gas heat exchanger (GGH).

Furnace Wall Cleaning

In the boiler furnace, the concentration of wall blowers or water cannons depends upon factors such as the ash fusion temperatures. The lower these temperatures are, the more likely the ash will adhere to the furnace walls and accumulate. The percentage of ash in the coal is another factor considered in designing the furnace cleaning system, with higher ash coals requiring greater and more concentrated coverage. The Sootblower Control System controls the equipment used for this application. With oxy-fired boilers, the sootblower systems use a special sealing system, using recirculated flue gas as the seal gas to minimize any air infiltration into the boiler.

In this furnace, twelve (12) water cannons are specified (three on each furnace wall) as shown by the red dots in Figure 5-3. Each water cannon directs a high-pressure jet of water through a furnace wall opening to clean surfaces on the opposite wall of the furnace. Each cannon can clean about one third of the entire opposite wall.

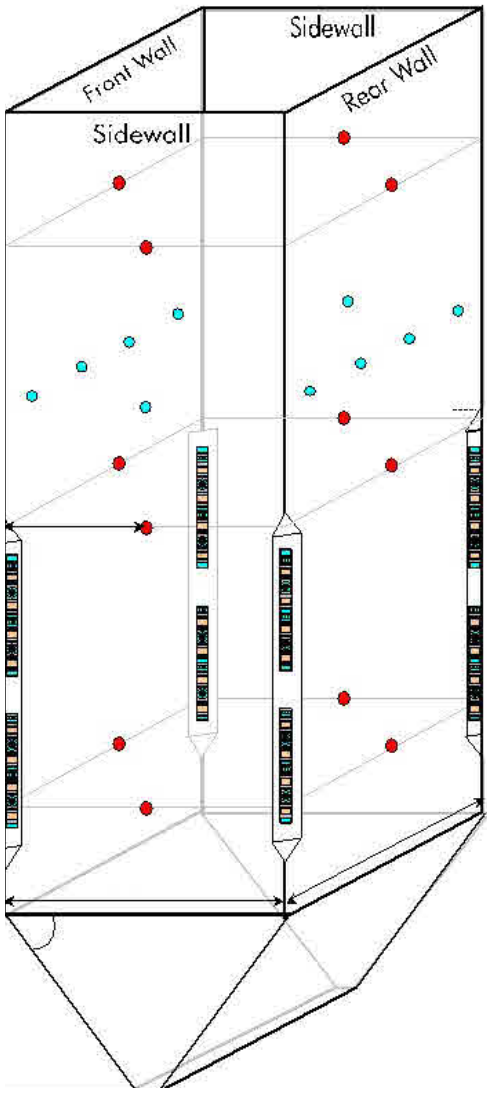

Figure 5-3: Furnace Water Lance Blower Arrangement

5.3.11 Coal Feeders

Eight (8) gravimetric feeders (2 per mill) with a control are suitable in all aspects for continuous operation. The control system will regulate the flow of coal in proportion to the demand signal from the boiler control system or remotely by the operator. The design of the feed system is similar to that described for the 450MW boiler.

5.3.12 Coal Pulverizers

The coal pulverizing system is a flexible system designed to meet a wide range of solid fuel preparation needs and to operate under both air and oxy-fired conditions. Four (4) vertical bowl mill pulverizers with dynamic classifiers are used. The selected mills are capable of achieving 100% TMCR conditions firing the range of fuels with one pulverizer out of service. The pulverizer design is similar to that for the 450MW boiler described in Section 4.3.11.

5.3.13 Firing System

The firing system is the similar to that for the 450MW boiler.

A schematic diagram of the tilting tangential windbox arrangement for this unit is shown in Figure 5-4. The right side of Figure 5-4 shows the lower section of the windbox and the left shows the upper. It is arranged vertically as alternating levels of air and fuel. The dampers at each compartment are controlled to vary the distribution of air/oxidant over the height of the windbox, making it possible to change the velocities of the secondary air/oxidant streams for ignition point adjustment.

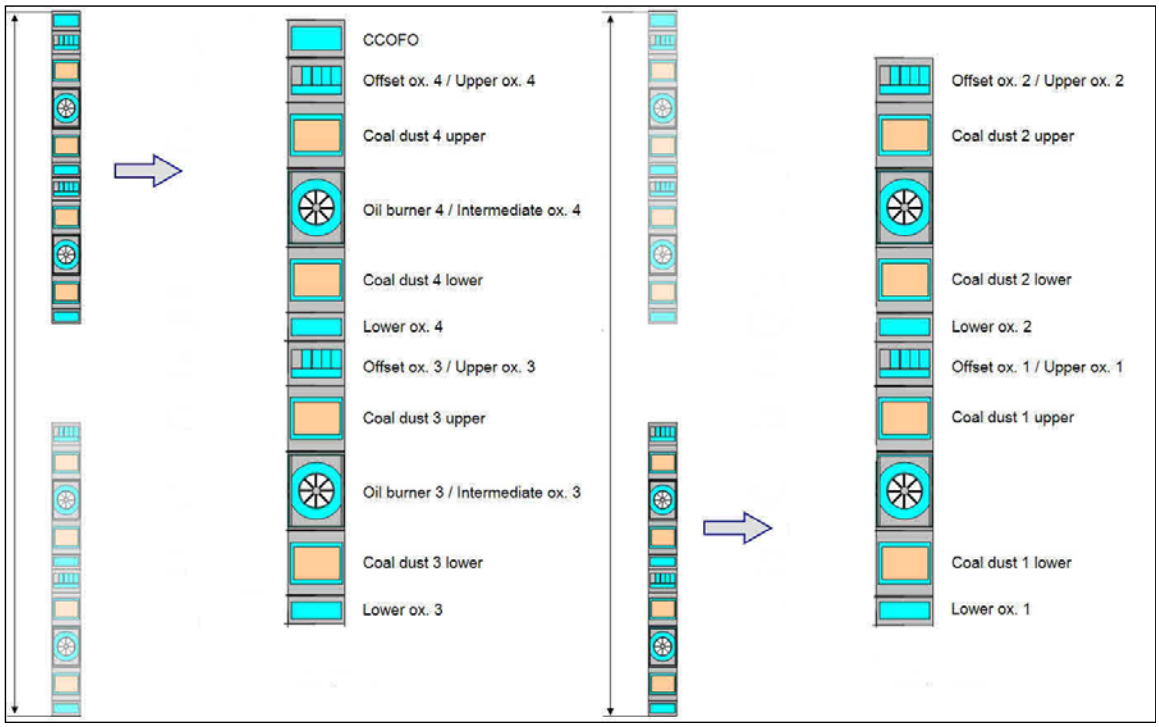

Figure 5-4: Tilting Tangential Windbox Arrangement

Firing System Arrangement

The main windbox arrangement consists of eight (8) coal nozzle elevations containing enhanced ignition coal nozzle tips as shown previously in Figure 5-4. Each mill feeds two elevations. Fuel oil burners are located between each of the four paired coal nozzle elevations. HEA igniters are located next to each oil burner elevation.

Two separated overfire air (SOFA) windboxes are located above the main windbox to optimize air staging so as to minimize the required SCR NO_X removal efficiency. Each SOFA windbox contains four separate air/oxidant nozzles. All SOFA and CCOFA nozzles are both vertically and horizontally adjustable.

5.3.14 Air/Oxidant and Flue Gas Systems

This section describes the primary and secondary air/oxidant system and the flue gas system.

Primary Air/Oxidant System

The primary air/oxidant system supplies heated air/oxidant to the pulverizers for drying the pulverized coal and for conveying it to the windbox coal nozzles. Oxygen is mixed with recirculated flue gas downstream of the primary air/oxidant fan to a concentration of 21% by volume of oxygen. The oxygen mixers are described in a separate subsection later. The recirculated flue gas for the primary stream is extracted from the main flue gas stream at the exit of the flue gas condenser (see Figure 5-1).

A single, one hundred percent (100%) radial primary air/oxidant fan is provided to maintain the required air/oxidant flow for proper coal drying conditions in the pulverizers and proper velocities in the pulverized coal piping to the windbox nozzles for the entire specified fuel range. Primary air/oxidant fan inlet vanes control primary air/oxidant pressure.

The primary air/oxidant (PA) fan is sized to accommodate the most severe coal drying requirements within the specified fuel range. Tolerances similar to air firing for flow and pressure have been considered to size the PA fan for oxy-firing relative to the boiler maximum continuous load condition. The primary flue gas recirculation duct, primary air inlet duct, primary oxygen mixer, PA fan, primary oxidant ducts, and the required isolation dampers are all included in this system.

Secondary Air/Oxidant System

The secondary air/oxidant system supplies heated air/oxidant for combustion to the windboxes. Oxygen is mixed with recirculated flue gas downstream of the secondary air/oxidant fan (forced draft or FD fan) to a concentration of 21% by volume of oxygen. The oxygen mixers are described in a separate subsection later. The recirculated flue gas for the secondary stream is extracted from the main flue gas stream at the exit of the flue gas desulfurization system (see Figure 5-1).

The secondary recirculation fan conveys recirculated flue gas extracted downstream of the WFGD. Up to 20 mg/Nm³ of liquid droplets and aerosols in the secondary recirculation gas are considered at the inlet of the fan. The liquid phase consists of condensed water and acid traced back to sulfur components in the flue gas. Furthermore, traces of gypsum and ash are suspended in the liquid phase. To operate under wet conditions, a single-flow radial fan is chosen.

The secondary air/oxidant from the forced draft fan is raised to a higher temperature by the hot flue gases in the Ljungstrom® GGH. From the GGH, the heated secondary air/oxidant is mixed with the remaining oxygen and fed to the windboxes through the hot secondary air/oxidant ducts. In the windboxes, individual compartment dampers distribute the air/oxidant. The secondary air/oxidant duct from the FGD outlet to the GGH is designed to be acid resistant to H_2SO_4.

The forced draft fan is sized to accommodate the minimum primary air/oxidant flow corresponding to the specified fuel range. Control of the boiler air/oxidant flow is provided by the forced draft fan inlet vanes, while the distribution of secondary air/oxidant to the individual windbox compartments will be controlled by the secondary air/oxidant dampers in the windbox compartments.

Oxygen Mixers

Oxygen is mixed with recirculated flue gas in three locations in this plant as shown in Figure 5-1.

- Oxygen is mixed downstream of the primary air/oxidant fan to a concentration of 21% by volume of oxygen.
- Oxygen is mixed downstream of the secondary air/oxidant fan to a concentration of 21% by volume of oxygen.
- The remaining oxygen required for complete combustion of the coal is mixed with the secondary stream in the hot secondary air/oxidant ducts just before the oxidant streams enter the windbox.

These streams provide the primary and secondary oxidant streams for combustion of the coal. In the first two mixing locations, it is important to produce well-mixed streams at 21% oxygen. Limiting the oxygen concentration avoids the use of special alloys in downstream equipment.

The oxygen mixer design is similar to that described for the 450MW boiler and is discussed in Section 4.3.14.

Steam Coil Air Pre-Heater (SCAPH)

One steam coil air heater is provided. This steam coil will be located in the air inlet duct upstream of the PA and FD fans. Extraction steam from the steam turbine is used as the heat source with the condensate returning to the appropriate location in the feedwater cycle.

The steam coil air heater is used to preheat the air entering the air heater, under certain operating conditions, such that the average cold end metal temperature of the rotary air heater elements is sufficiently higher than the acid dew point temperature in order to prevent excessive corrosion.

Steam Coil Oxygen Pre-Heater (SCOPH)

One steam coil oxygen heater is provided. This steam coil preheats the pure oxygen stream that after heating is mixed with the secondary stream downstream of the GGH. This oxygen stream is heated to 140°C. Extraction steam from the steam turbine is used as the heat source with the condensate returning to the appropriate location in the feedwater cycle. The steam coil is located near the oxygen mixing point, which is close to the boiler.

Flue Gas System

The flue gas system includes ductwork, the ID fan, and the flue gas heat recovery system. The flue gas system provides a gas tight enclosure for the flue gas stream leaving the boiler. The flue gas system included with this oxy-fired steam generator includes the ductwork from the economizer to the SCR, from the SCR to the GGH, from the GGH to the fabric filter, from the fabric filter to the ID fan, the ID fan, ductwork from the ID fan to the flue gas heat exchanger (HEX), the HEX, ductwork from the HEX to the FGD, ductwork from the FGD to the FGC, and ductwork from the FGC to the GPU. It also includes the ductwork from the FGD to the stack that is used during air firing and during the transition between air and oxygen firing. Also included are the various required isolation dampers (see Figure 5-1).

A single, one hundred percent (100%) axial flow induced draft (ID) fan is supplied. It is located between the fabric filter outlet and the HEX inlet. The ID fan is sized to accommodate the maximum gas flow predicted over the specified range of fuels. Tolerances similar to air firing for flow and pressure have been considered to size the ID fan for oxy-firing relative to the boiler maximum continuous load condition. Both air and oxy-firing are also considered. The ID fan is controlled to maintain a flue gas pressure of 0.0 inches water gauge at the furnace exit.

5.3.15 Ljungstrom® Regenerative Air/Oxidant Preheater

The Ljungstrom® Regenerative Air Preheater is the same design as that described for the 450MW boiler.

5.3.16 SCR System

The SCR is the same design as that described for the 450MW boiler.

5.3.17 Bottom Ash System

The bottom ash system is the same design as that described for the 450MW boiler.

5.3.18 Boiler Protection Burner Management System

The Boiler Protection and Burner Management System is the same design as that described for the 450MW boiler.

5.3.19 Balance of Plant

The balance of plant equipment is the same basic equipment and design as that described for the 450MW boiler.

5.3.20 Integration

The 900MW oxy-fired plant is designed to utilize the waste heat available in the cycle to preheat the feedwater and to improve the overall net plant efficiency. Multiple waste heat sources are utilized for heat integration, including from the ASU compressor, from the flue gas leaving the GGH, and from the GPU compressor. This integration provides a significant efficiency improvement (about 1% point) for the 900MW oxy-fired plant compared to the 450MW oxy-fired plant.

The waste heat discharged from the main ASU air compressor is recovered in an air/water heat exchanger that preheats the feedwater. The heat exchanger is designed to handle a high volume of low pressure air (about 3 bara) with a minimum of pressure drop to minimize the power consumption of the ASU air compressors. The heat exchanger is also designed for a low water flow rate at high velocity through the heat exchanger, resulting in the water being heated up from 23°C to 120°C at MCR design conditions.

Some of the sensible heat in the flue gas leaving the GGH is also recovered in a flue gas heat recovery system (FGHRS). The FGHRS transfers heat recovered from the flue gas into the low-pressure condensate system of the steam cycle. The main effect is to increase the gross output and overall efficiency of the plant. The FGHRS shown in Figure 5-5 includes a flue gas/water heat exchanger (HEX), a water/water heat exchanger, and an intermediate piping circuit in between those heat exchangers.

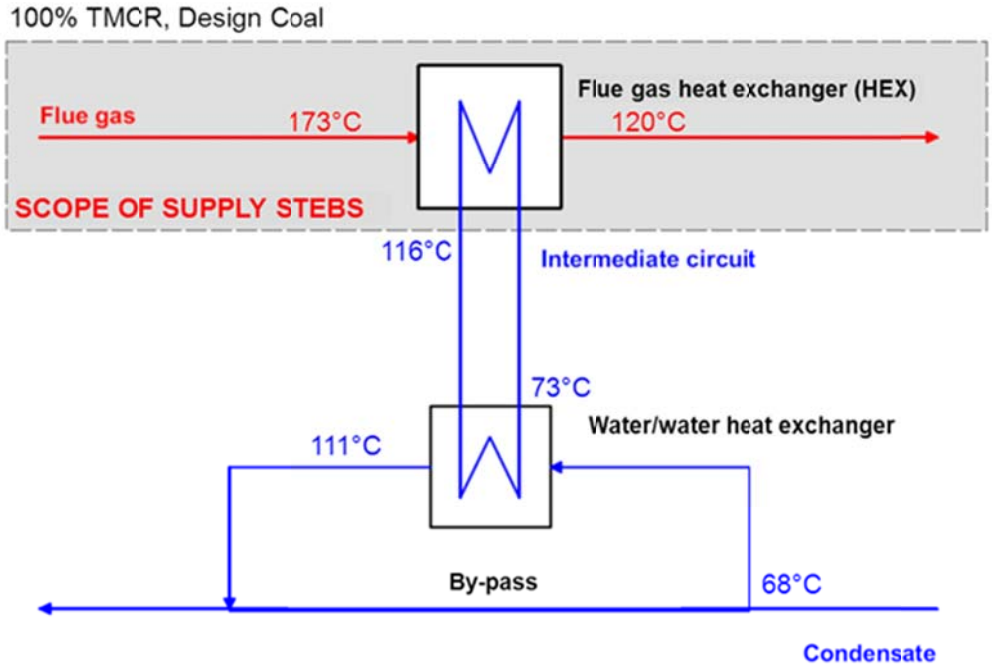

Figure 5-5: Flue Gas Heat Recovery System (HEX)

Within the flue gas HEX (single flue gas duct arrangement), the flue gas leaving the ID fan is cooled by water from the intermediate circuit. This water serves as an intermediate heat transfer media, which circulates between the two heat exchangers. Within the water/water heat exchanger, the heat is transferred to the cold LP condensate stream of the steam cycle. At the design point of the HEX, the flue gas is cooled from approximately 173°C down to 120°C, while the water in the intermediate circuit is heated up from 73°C to 116°C. The condensate temperature is increased from 68°C to 111°C.

The HEX lowers the temperature of the flue gases below the acid dew point. Therefore the HEX is a designed as a corrosion resistant heat exchanger that cools the flue gas before entering the FGD process. Because of the condensation due to the SO_3 and moisture content in the flue gas, the HEX tubes are made from a plastic material to avoid corrosion. Furthermore, the U-shaped design of the modules allows free expansion of the tubes. An automatic cleaning system is used to remove any ash deposition from the tubes.

The waste heat discharged from the GPU compressor is also recovered in a gas/water tubular heat exchanger that preheats the feedwater. The flue gas is compressed in the first compressor stage up to about 6 bara. The heat from this compression is recovered by heating the condensates downstream of the compressor. Additional heat recovery after the next compression stages allows the heat to be recovered at much higher temperatures. Feedwater temperatures can be heated up to 150°C at MCR design conditions.

5.4 Boiler General Arrangement Drawings

Figure 5-6 shows the Steam Generator and Backend Equipment General Arrangement Side Elevation Drawing and Figure 5-7 shows the Steam Generator and Backend Equipment General Arrangement Side Plan Drawing for the 900MW plant.

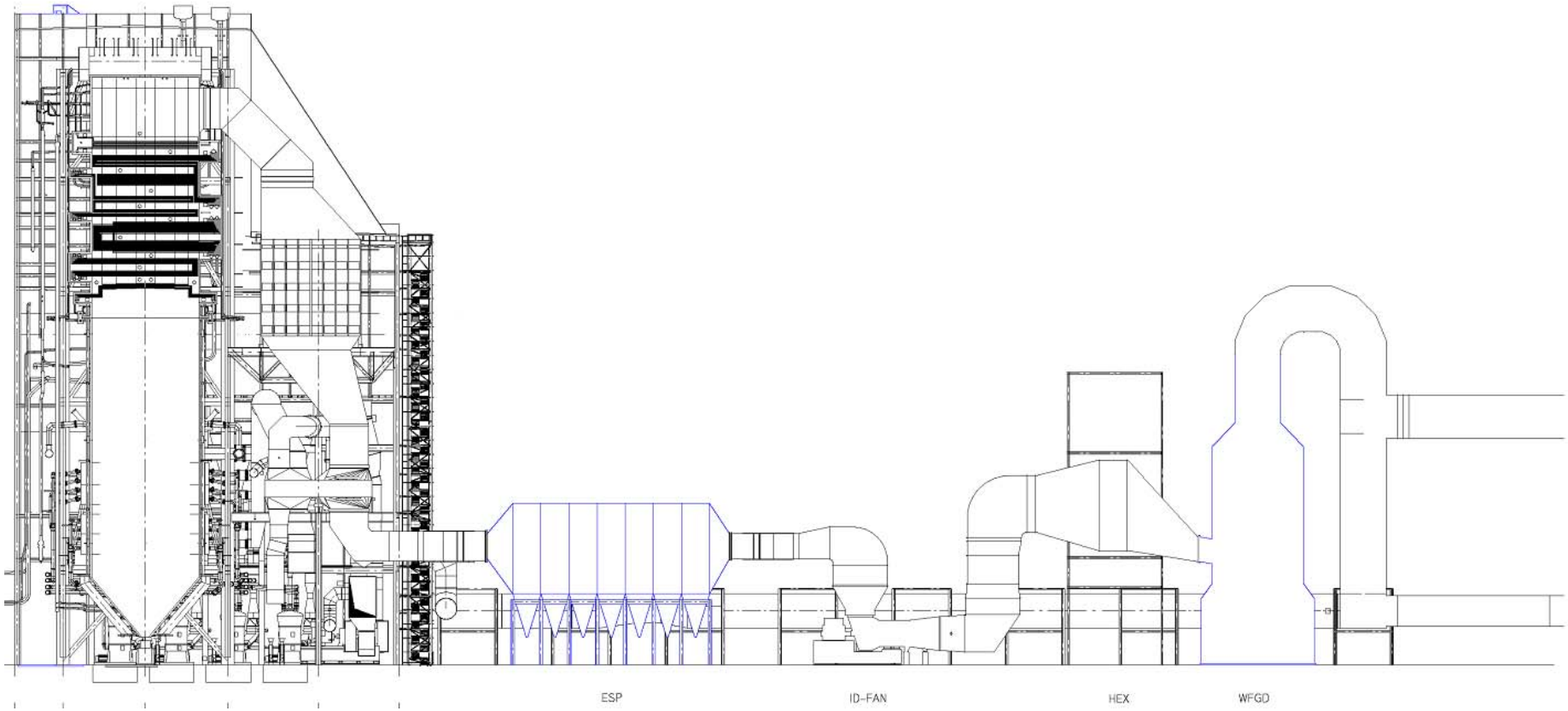

Figure 5-6: Steam Generator and Backend Equipment General Arrangement Drawing – Side Elevation

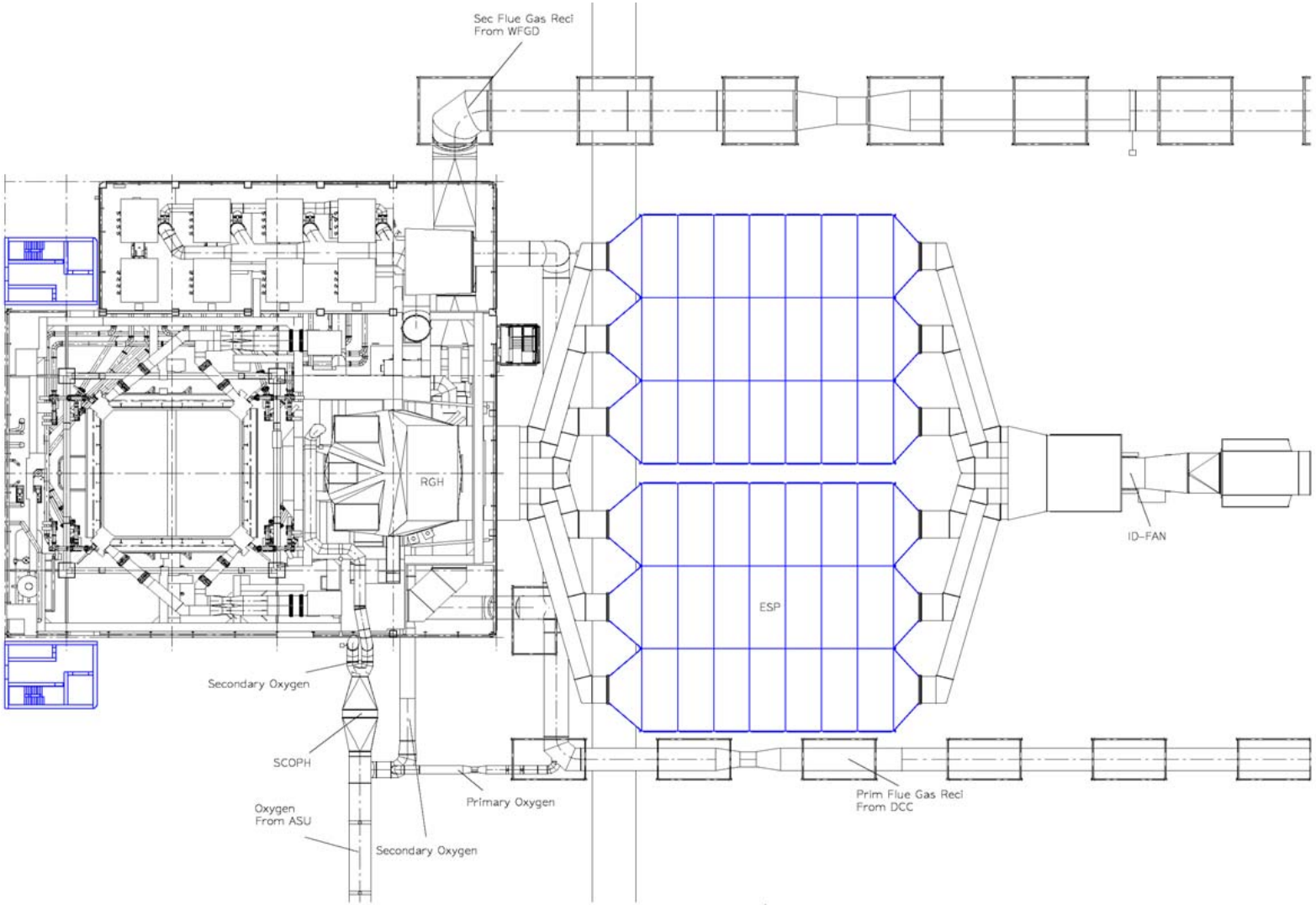

Figure 5-7: Steam Generator and Backend Equipment General Arrangement Drawing – Plan View

5.5 Boiler Island Process Description and Performance Data

This section provides a description of the boiler island process and performance information for both the 900MW oxy-fired and air-fired steam plants. The following information is included:

- Process Flow Diagram
- Boiler island material and energy balances at BMCR load
- Steam turbine heat balance
- Auxiliary power requirements

Boiler Island Process Description – Oxygen Firing

Figure 5-8 shows a simplified process flow diagram for the 900MW Boiler Island, which is similar to that previously described for the 450MW Boiler Island. This design permits full load (100% TMCR) operation with oxygen firing and 75% TMCR with air firing.

Starting with the flue gas stream leaving the boiler economizer section, the flue gas first flows through a Selective Catalytic Reduction (SCR) system for NO_x reduction. The flue gas leaving the SCR is then cooled in the gas side sector of the quad-sector Gas-to-Gas Heater (GGH). The cooled flue gas stream leaving the GGH (Stream 5) then enters a fabric filter (FF) where most of the particulate matter is removed. The flue gas stream leaving the FF flows through the Induced Draft (ID) Fan and then through the flue gas heat recovery system heat exchanger (HEX). The flue gas leaving the HEX flows through the Flue Gas Desulfurization (FGD) system where most of the SO_2 is removed. The flue gas leaving the FGD system is split into two streams.

Stream 27 represents the recirculated flue gas portion of the secondary oxidant stream. It is mixed with oxygen to form the secondary oxidant stream. The oxygen flow is controlled to provide an oxygen concentration of 21 percent by volume in this stream. The secondary oxidant is increased to the required pressure with the Forced Draft (FD) fan and heated in the secondary sectors of the GGH to form the heated secondary oxidant stream. This stream is then combined with the remaining oxygen required for combustion of the coal in the hot secondary oxidant ducts just before entering the windbox and furnace. The location selected for the secondary flue gas recirculation stream (Stream 27) is just after the FGD system in order to provide SO_2 levels throughout the boiler island that are within our air fired experience range.

The remainder of the flue gas leaving the FGD system that is not used for the secondary recirculation stream, after leaving the FGD system, flows through a Direct Contact Cooler (DCC) where most of the moisture contained in the flue gas is condensed out. The saturated flue gas leaving the DCC is split into two streams.

One stream is the high CO_2 content product stream, which flows to the Gas Processing Unit (GPU) for further purification such that the final CO_2 product is acceptable for usage or

sequestration. There is also a vent stream leaving the GPU, which contains non-condensable gases (i.e.O_2, N_2, Ar, etc.) and also a small fraction of the CO_2.

The remaining flue gas leaving the DCC (Stream 18) represents the recirculated flue gas portion of the primary oxidant stream. It is mixed with oxygen to provide an oxygen concentration of 21 percent by volume. It is increased to the required pressure by the Primary Air (PA) fan to form the primary oxidant stream. The primary oxidant stream leaving the PA fan is split into a heated portion and an un-heated portion. The heated stream is heated in the primary sector of the GGH to form the hot primary oxidant stream. The hot stream is mixed with the unheated stream that bypasses the GGH to form the total primary oxidant stream. The split between the heated and unheated streams is adjusted to control the temperature of the pulverized coal/oxidant mixture leaving the coal mills to the desired value.

The location selected for the primary flue gas recirculation stream (Stream 18) is just downstream of the DCC. This location was selected in order to provide the coal mills with a primary oxidant stream that has low moisture content such that coal drying inside the mills will be similar to air fired operation.

The primary oxidant and pulverized coal mixture leaving the coal mills is combusted in the furnace together with the heated secondary oxidant stream and also with a pure oxygen stream. The pure oxygen stream is heated with steam from the steam cycle and is mixed with the secondary oxidant stream after the GGH. This stream represents the remaining oxygen required for complete combustion of the coal, over and above that oxygen which is contained in the primary and secondary streams. The pure oxygen stream flow rate is controlled such that the oxygen content in the flue gas leaving the boiler is about 3 percent by volume (i.e. similar to air firing). The products of combustion along with fly ash leave the furnace section and pass through radiant and convective heat exchangers in the boiler, which completes the cycle.

Ash that is not entrained in the furnace with the flue gas is called bottom ash. It is the ash that accumulates on the furnace walls, is removed with wall blowers, and falls to the bottom of the furnace and into a trough containing water. The bottom ash is removed continuously from the water trough, which is part of the submerged scraper conveyor (SSC) system.

It is important to minimize air infiltration for an oxy-fired system with carbon capture in order to minimize the power requirement of the GPU and to keep plant thermal efficiency as high as possible. Infiltration air streams include infiltration air entering the boiler and infiltration air entering the fabric filter. The infiltration air entering the boiler was assumed to be about 1 percent of the stoichiometric oxygen requirement of the boiler. This should be obtainable through the use of recirculated flue gas instead of air as a seal gas for the boiler. Infiltration air entering the fabric filter was assumed to be about 2 percent of the flue gas flow entering the fabric.

Boiler Island Performance – Oxygen Firing

Figure 5-9 shows the steam turbine heat balance associated with the BMCR load operating condition. The primary boiler/turbine interface locations are the feedwater stream to the boiler economizer, the superheater outlet stream, and the cold and hot reheat streams. The basic attributes of these streams (temperature, pressure, enthalpy, and mass flow) are shown on this diagram. All boiler island performance tables shown in this section were developed to match this BMCR steam turbine heat balance load condition.

Table 5-1 shows the boiler island material and energy balance stream attributes for all the streams identified on Figure 30 when operating in the oxygen-fired mode, for the BMCR load condition and using high sulfur eastern bituminous coal. The stream attributes in the table include mass flow rate, composition, temperature, pressure, and energy. The table includes both English and SI units.

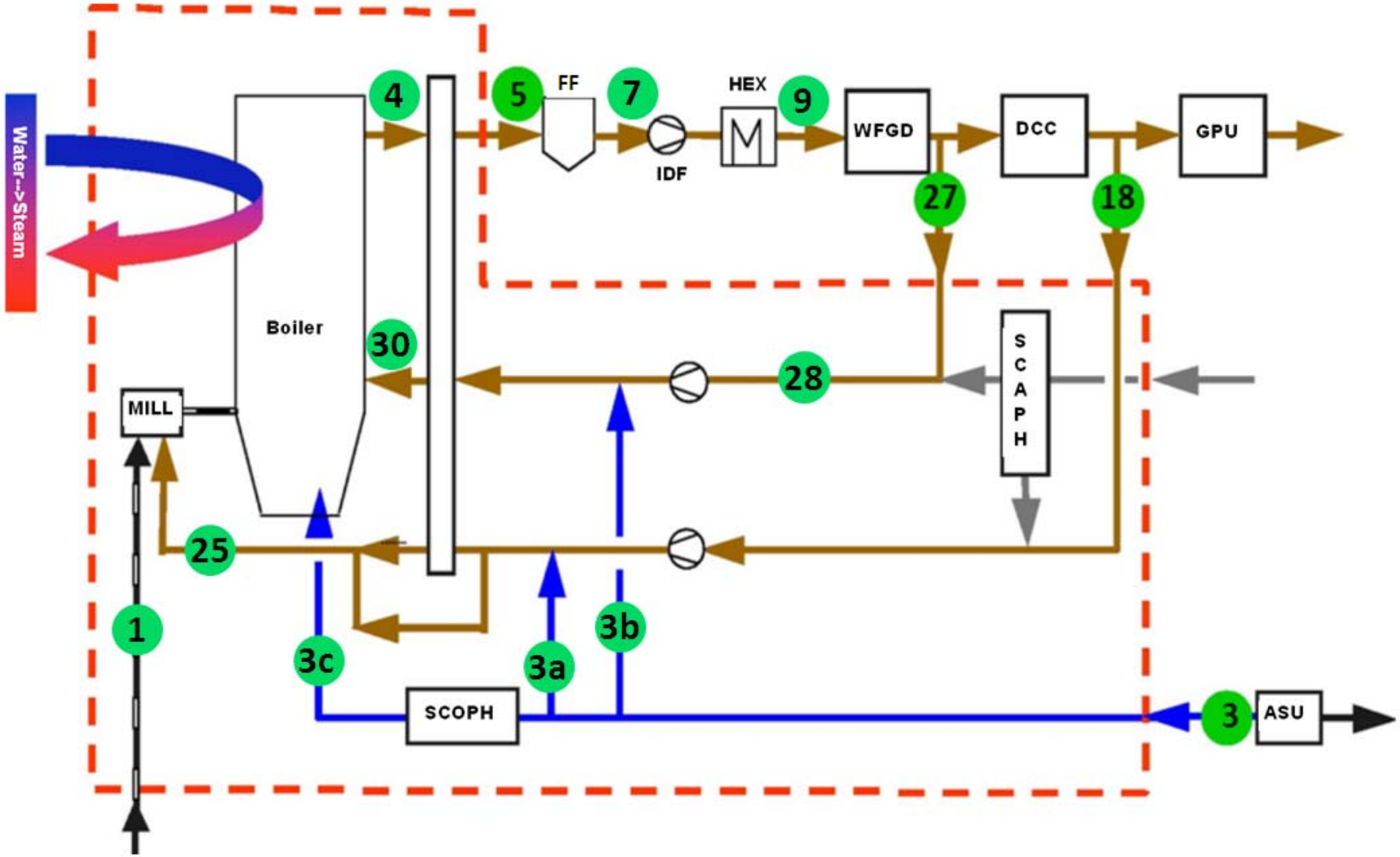

Figure 5-8: Simplified Process Flow Diagram – Air/Oxy-Fired Boiler (Oxygen Fired Mode)

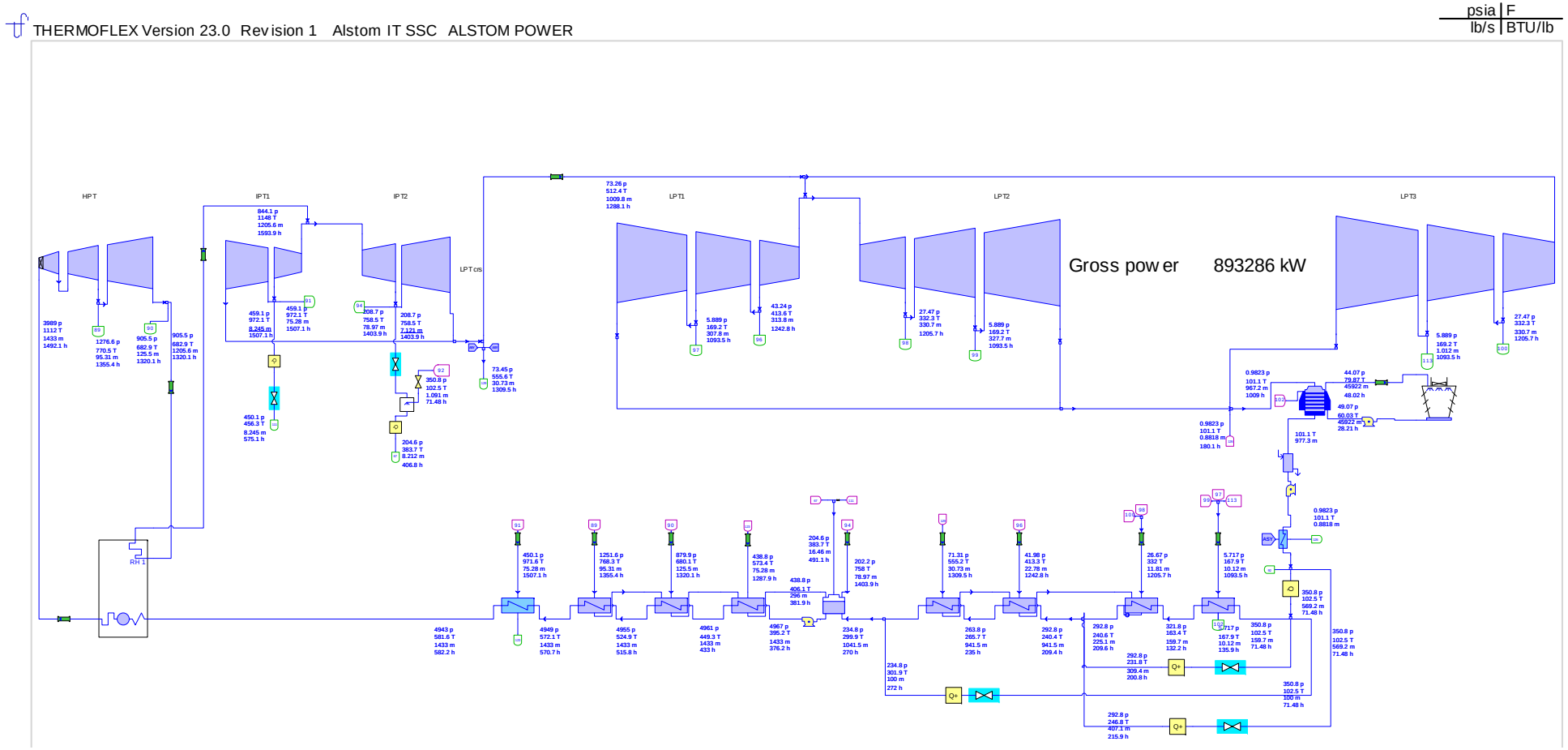

Figure 5-9: Steam Turbine Heat Balance - Oxy-firing, 100% TMCR Load

Table 5-1: Material & Energy Balance - Oxy Firing 100% BMCR Loads

English Units

Constituent	(Units)	1	3	3a	3b	3c	4	5	7	9	18	25	27	28	30
O_2	(Lbm/hr)	49,945	1,160,510	301,146	507,352	352,012	173,875	202,427	233,484	233,484	69,767	320,144	100,732	588,074	630,300
Ar	"	0	49,646	12,883	21,704	15,059	173,224	191,102	192,823	192,823	57,617	60,850	83,190	88,369	96,665
N_2	"	7,423	4,220	1,095	1,845	1,280	408,437	459,571	560,981	560,981	167,626	145,628	242,024	195,792	215,828
H_2O	"	75,590					683,011	789,352	790,471	790,471	26,044	22,479	453,291	363,247	362,494
CO_2	"	0					4,575,737	5,036,943	5,036,943	5,036,943	1,512,689	1,305,639	2,184,066	1,750,213	1,929,909
SOx as SO_2	"	0					37,387	37,420	37,420	37,420	10	9	161	129	129
H_2	"	24,845													
Carbon	"	369,316					2,871	2,871							
Sulfur	"	18,642													
Ash / Inerts	"	55,768					44,614	45,640							
		Raw Coal	Oxygen from ASU	Primary O2	Secondary O2	Burner O2	Fluegas lvg Econ.	Fluegas to FF	Fluegas to ID Fan	Fluegas lvg PFWH	Pri Recirc FG	Tempered Pri Air	Sec Air to SCAH	Sec Air to SCAH	Sec Air to Furn
Total Gas	(Lbm/hr)		1,214,376	315,124	530,901	368,351	6,051,670	6,716,816	6,852,123	6,852,123	1,833,754	1,854,749	3,063,464	2,985,824	3,235,326
Total Solids	"	601,529					47,486	48,511							
Total Flow	"	601,529	1,214,376	315,124	530,901	368,351	6,099,155	6,765,327	6,852,123	6,852,123	1,833,754	1,854,749	3,063,464	2,985,824	3,235,326
Temperature	(Deg F)	64	72	72	72	72	690	331	313	247	78	397	155	142	635
Pressure	(Psia)	14.7	19.0	19.0	19.0	19.0	14.5	14.3	14.1	15.3	14.7	15.7	14.9	14.8	14.8
h-sensible	(Btu/lbm)	-4.680	-1.812	-1.812	-1.812	-1.812	158.427	61.300	56.679	56.679	-0.507	71.051	18.282	14.709	142.415
Energy															
Chemical	(10^6 Btu/hr)	6,680.506					40.471	40.471							
Sensible	(10^6 Btu/hr)	-3.639	-2.201	-0.571	-0.962	-0.668	967.891	414.784	388.374	388.374	-0.930	131.782	56.006	43.918	460.759
Latent	(10^6 Btu/hr)						717.162	828.820	829.995	829.995	27.346	23.603	475.956	381.410	380.619
Total Energy(1)	(10^6 Btu/hr)	6,676.867	-2.201	-0.571	-0.962	-0.668	1,725.524	1,284.075	1,218.369	1,246.552	26.416	155.385	531.962	425.328	841.378

Note:
(1) Energy Basis; Chemical based on Higher Heating Value (HHV); Sensible energy above 80F; Latent based on 1,050 Btu/Lbm of water vapor

O2	(wt percent)	8.30	95.56	95.56	95.56	95.56	2.87	3.01	3.41	3.41	3.80	17.26	3.29	19.70	19.48
H_2O	(wt percent)	12.57	0.00	0.00	0.00	0.00	11.29	11.75	11.54	11.54	1.42	1.21	14.80	12.17	11.20

SI Units

Constituent	(Units)	1	3	3a	3b	3c	4	5	7	9	18	25	27	28	30
O2	(kg/hr)	22,654	526,396	136,597	230,130	159,669	78,868	91,819	105,906	105,906	31,646	145,214	45,691	266,745	285,898
Ar	"		22,519	5,843	9,845	6,831	78,573	86,682	87,463	87,463	26,135	27,601	37,734	40,083	43,846
N2	"	3,367	1,914	497	837	581	185,263	208,457	254,455	254,455	76,034	66,055	109,780	88,809	97,898
H2O	"	34,287					309,807	358,042	358,550	358,550	11,813	10,196	205,608	164,765	164,424
CO2	"						2,075,508	2,284,707	2,284,707	2,284,707	686,141	592,225	990,671	793,879	875,388
SO2	"						16,958	16,973	16,973	16,973	5	4	73	59	59
H2	"	11,269													
Carbon	"	167,518					1,302	1,302							
Sulfur	"	8,456													
Ash / Inerts	"	25,296					20,237	20,702							
		Raw Coal	Oxygen from ASU	Primary O2	Secondary O2	Burner O2	Fluegas lvg Econ.	Fluegas to FF	Fluegas to ID Fan	Fluegas lvg PFWH	Pri Recirc FG	Tempered Pri Air	Sec Air to SCAH	Sec Air to SCAH	Sec Air to Furn
Total Gas	(kg/hr)		550,829	142,937	240,812	167,080	2,744,977	3,046,681	3,108,054	3,108,054	831,772	841,296	1,389,557	1,354,340	1,467,512
Total Solids	"	272,848					21,539	22,004							
Total Flow	"	272,848	550,829	142,937	240,812	167,080	2,766,516	3,068,685	3,108,054	3,108,054	831,772	841,296	1,389,557	1,354,340	1,467,512
Temperature	(Deg C)	18.0	22.0	22.0	22.0	22.0	365.7	166.1	156.1	165.0	25.3	202.9	68.5	61.1	334.9
Pressure	(mbar)	1,013.0	1,311.8	1,311.8	1,311.8	1,311.8	1,002.1	983.8	975.8	1,053.2	1,013.0	1,080.8	1,029.8	1,021.6	1,024.0
h-sensible	(kJ/kg)	-10.886	-4.215	-4.215	-4.215	-4.215	368.505	142.585	131.837	141.404	-1.179	165.267	42.524	34.213	331.260
Energy															
Chemical	(10^6 kJ/hr)	7,048.335	0.000	0.000	0.000	0.000	42.699	42.699							
Sensible	(10^6 kJ/hr)	-3.839	-2.322	-0.603	-1.015	-0.704	1,021.183	437.622	409.758	439.493	-0.981	139.038	59.090	46.337	486.129
Latent	(10^6 kJ/hr)	0.000	0.000	0.000	0.000	0.000	756.649	874.454	875.694	875.694	28.852	24.903	502.162	402.410	401.575
Total Energy(1)	(10^6 kJ/hr)	7,044.496	-2.322	-0.603	-1.015	-0.704	1,820.531	1,354.776	1,285.452	1,315.187	27.871	163.941	561.252	448.747	887.704

Notes:
(1) Energy Basis; Chemical based on Higher Heating Value (HHV); Sensible energy above 26.7C; Latent based on 2,194 kJ/kg of water vapor

Boiler Island Process Description – Air Firing

Figure 5-10 shows a simplified process flow diagram for a 900MW boiler island designed to be operated in air-fired mode only. In this mode, the primary and secondary air inlet, and flue gas outlet to stack streams are used. In the air-fired mode of operation, several systems are not required (i.e. the ASU, DCC, and GPU). Additionally, primary and secondary flue gas recirculation streams (Streams 18 & 27) are not required and oxygen mixing is not used. With air firing, this process uses the primary and secondary air inlet and the flue gas to stack ducts. This configuration is the same as many coal fired plants in use today and therefore it is not further described here.

Boiler Island Performance – Air Firing

Figure 5-11 shows the steam turbine heat balance associated with the BMCR load operating condition in air-fired mode. The primary boiler/turbine interface locations are the feedwater stream to the boiler economizer, the superheater outlet stream, and the cold and hot reheat streams. The basic attributes of these streams (temperature, pressure, enthalpy, and mass flow) are shown on this diagram. All boiler island performance tables shown in this section were developed to match this BMCR steam turbine heat balance load condition

Table 5-2 shows the boiler island material and energy balance stream attributes for all the streams identified on Figure 30 when operating in the air-fired mode, for the BMCR load condition and using high sulfur eastern bituminous coal. The stream attributes in the table include mass flow rate, composition, temperature, pressure, and energy. The table includes both English and SI units.

Table 5-3 summarizes the thermal performance and auxiliary loads for the nominal 900MW air and oxy-fired plants. Both plants were designed for 893MW gross power, while the net power decreased from 847MW for the air-fired case to 655MW for the oxy-fired case. This design approach allowed the fuel heat input to remain the same for both cases. The oxy-fired boiler design thus did not require major revisions from the air-fired case.

The auxiliary power requirements for the oxy-fired plant increased from 5.1% of the gross power output for the air-fired plant to 26.7% of the gross power output. Most of this increase was due to the addition of the ASU and GPU, which added 117,914 kW and 77,277 kW, respectively, to the oxy-fired plant’s power consumption.

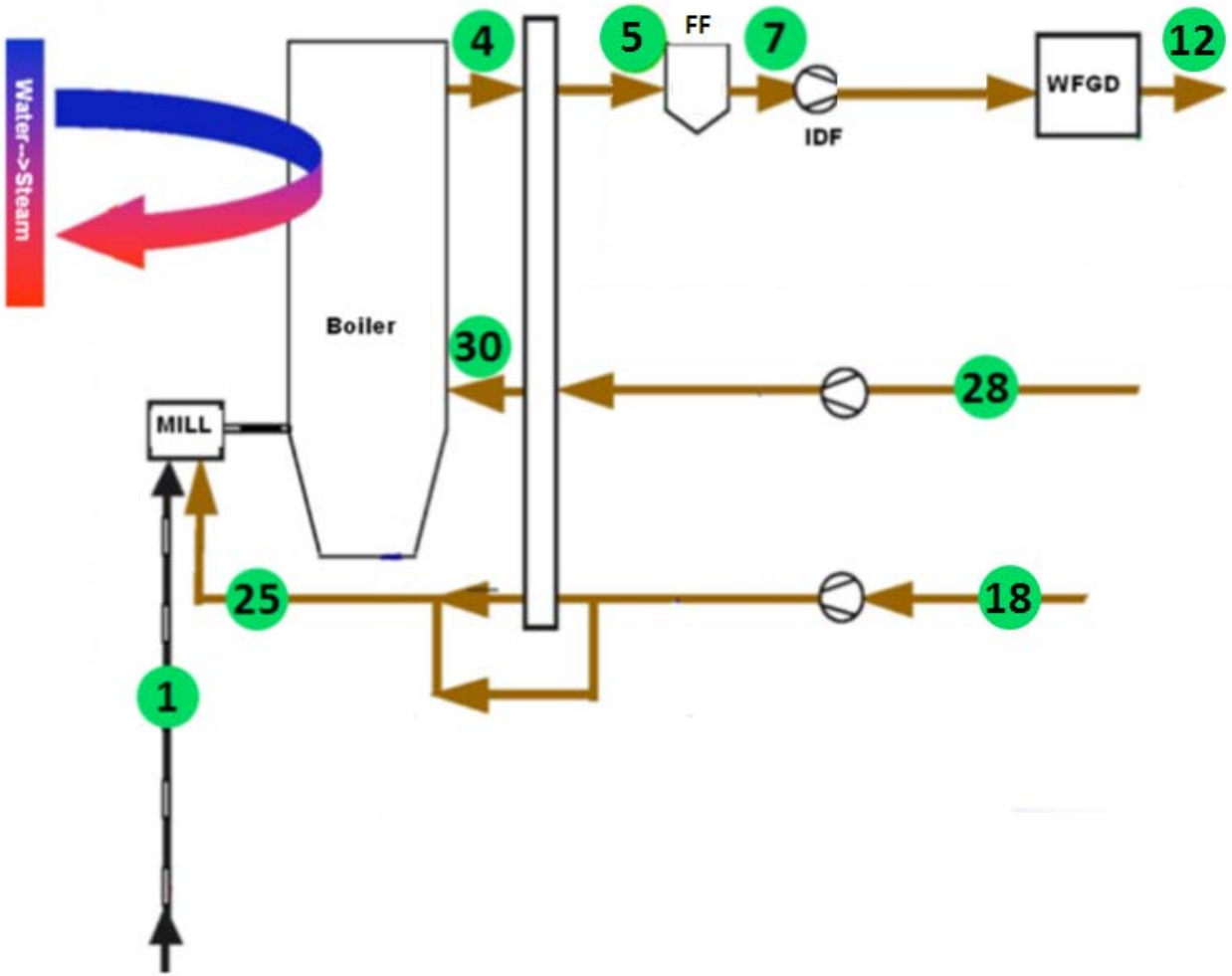

Figure 5-10: Simplified Process Flow Diagram – Air-Fired Boiler

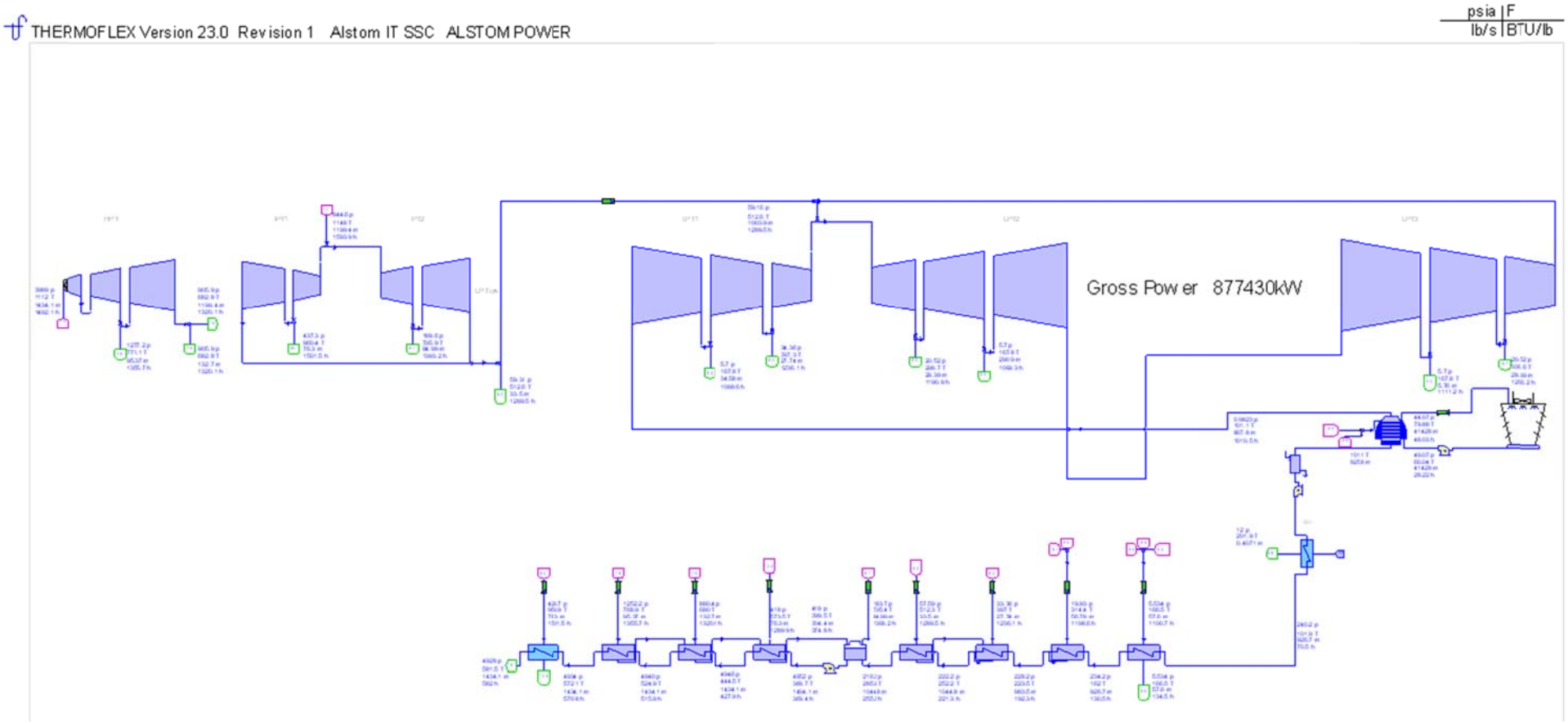

Figure 5-11: Steam Turbine Heat Balance - Air-firing, 100% TMCR Load

Table 5-2: Material & Energy Balance - Air Firing 100% BMCR Loads

English Units

Constituent	(Units)	1	4	5	7	10	12	18	25	28	30
O2	(Lbm/hr)	49,702	113,700	151,572	167,039	4,427	167,039	196,696	155,381	480,576	484,019
N2	"	7,387	4,541,599	4,796,720	4,900,912		4,900,912	1,325,028	1,046,714	3,237,371	3,260,564
H2O	"	75,223	345,373	360,018	361,149	293,260	573,935	14,379	11,359	35,131	35,382
CO2	"		1,333,674	1,333,674	1,333,674		1,358,376				
SOx as SO2	"		37,067	37,067	37,067		1,112				
H2	"	24,724									
Carbon	"	367,521	2,857	2,857							
Sulfur	"	18,551									
Ash / Inerts	"	55,497	44,398	45,414		2,428					
		Raw Coal	Fluegas Ivg Ec	Fluegas to FF	Fluegas to ID F	Lime Slurry	Fgas to Stack	Pri Air to PA Fan	Mixed Pri Air	Sec Air to SCA	Hot Sec Air
Total Gas	(Lbm/hr)		6,488,363	6,834,956	6,971,655		7,173,188	1,738,420	1,373,276	4,247,389	4,277,818
Total Solids	"	598,606	47,255	48,272		69,220					
Total Flow	"	598,606	6,535,618	6,883,227	6,971,655	362,480	7,173,188	1,738,420	1,373,276	4,247,389	4,277,818
Temperature	(Deg F)	64.4	706.7	259.0	241.0	64.4	124.0	64.4	435.5	64.4	641.0
Pressure	(Psia)	14.7	14.5	14.1	14.0	14.7	14.7	14.6	15.7	14.5	14.9
h-sensible	(Btu/lbm)	-4.680	161.441	44.648	40.090	-3.900	11.150	-3.781	86.954	-3.781	138.347
Energy											
Chemical	(10^6 Btu/hr	6,648.037		40.274							
Sensible	(10^6 Btu/hr	-3.621	1,054.892	307.330	279.496	-4.838	79.979	-6.572	119.411	-16.058	591.823
Latent	(10^6 Btu/hr)		362.642	378.019	379.206		602.632	15.098	11.926	36.887	37.152
Total Energy(1)	(10^6 Btu/hr	6,644.416	1,457.808	725.623	658.702	-4.838	682.610	8.525	131.338	20.829	628.975

Notes:
(1) Energy Basis; Chemical based on Higher Heating Value (HHV); Sensible energy above 80F; Latent based on 1,050 Btu/Lbm of water vapor

O2	(wt percen	8.30	3.55	4.50	4.86		4.72	22.95	22.95	22.95	22.95
H_2O	(wt percen	12.57	5.32	5.27	5.18		8.00	0.83	0.83	0.83	0.83

SI Units

Constituent	(Units)	1	4	5	7	10	12	18a	25	28	30
O2	(kg/hr)	22,544	104,621	139,468	153,700	4,073	153,700	180,988	142,973	442,199	445,367
N2	"	3,351	2,060,024	2,175,744	2,223,005		2,223,005	601,020	474,779	1,468,439	1,478,959
H2O	"	34,120	156,658	163,301	163,813	133,020	260,331	6,522	5,152	15,935	16,049
CO2	"		604,941	604,941	604,941		616,146				
SOx as SO2	"		16,813	16,813	16,813		504				
H2	"	11,215									
Carbon	"	166,704	1,296	1,296							
Sulfur	"	8,415									
Ash / Inerts	"	25,173	20,138	20,600		1,101					
		Raw Coal	luegas Ivg Eco	Fluegas to FF	luegas to ID Fa	Lime Slurry	Fgas to Stack	Pri Air to PA Fan	Mixed Pri Air	Sec Air to SCAI	Hot Sec Air
Total Gas	(kg/hr)		2,943,057	3,100,268	3,162,273		3,253,686	788,530	622,904	1,926,573	1,940,375
Total Solids	"	271,521	21,434	21,895		31,398					
Total Flow	"	271,521	2,964,491	3,122,163	3,162,273	164,417	3,253,686	788,530	622,904	1,926,573	1,940,375
Temperature	(Deg C)	18.0	374.8	126.1	116.1	18.0	51.1	18.0	224.2	18.0	338.3
Pressure	(mbar)	1,013.0	1,000.0	972.8	962.3	1,013.0	1,016.6	1010.1	1,082.5	999.7	1,025.3
h-sensible	(kJ/kg)	-10.886	375.516	103.853	93.251	-9.071	25.934	-8.794	202.256	-8.794	321.798
Energy											
Chemical	(10^6 kJ/hr)	7,014.078		42.492							
Sensible	(10^6 kJ/hr)	-3.821	1,112.975	324.252	294.885	-5.105	84.382	-6.934	125.986	-16.942	624.409
Latent	(10^6 kJ/hr)		382.609	398.833	400.085		635.813	15.929	12.583	38.918	39.197
Total Energy(1)	(10^6 kJ/hr)	7,010.258	1,538.075	765.576	694.970	-5.105	720.195	8.995	138.569	21.976	663.606

Notes:
(1) Energy Basis; Chemical based on Higher Heating Value (HHV); Sensible energy above 26.7C; Latent based on 2,194 kJ/kg of water vapor

Table 5-3: Summary of Thermal Performance and Auxiliary Loads

		900MW	900MW
		Air-Fired	Oxy-Fired
Gross Power Output	MW	893.3	893.3
Net Power Output	MW	848.7	657.9
Coal Flow	lb/hr	598,606	601,529
Main Steam Flow	lb/hr	5,162,812	5,174,717
Fuel Heat Input (HHV)	MMBtu/	6,412	6,444
Net Plant Efficiency (HHV)	%	41.3%	32.5%
Boiler Efficiency	%	88.8%	88.8%

Auxiliary Load Summary

		900MW	900MW
		Air-Fired	Oxy-Fired
Coal Handling & Pulverizers	kW	4,705	4,728
Forced Draft Fans	kW	2,418	2,430
Primary Air Fans	kW	1,905	1,915
Induced Draft Fans	kW	11,001	10,811
SCR	kW	150	-
FF	kW	107	106
Wet FGD	kW	4,542	4,463
Power Plant Auxiliaries	kW	19,782	19,948
ASU Compressor/Auxiliaries	kW	-	117,914
GPU CO2 Compressor	kW	-	73,071
		-	-
Total Aux Power	kW	44,611	235,385
% Aux Power		5.0%	26.4%

5.6 900MW Plant Cost Estimating

5.6.1 Cost Adjustments

The 900MW tower oxy-fired tower boiler was adopted from a European-based design. The boiler design and performance was updated to reflect a mid-western US location. Boiler materials were globally sourced, costs were adjusted for the US location, and costs were also de-escalated slightly from 2012 to June 2011 dollars. The IHS CERA Power Capital Cost Index (PCCI) for North America (see Figure 4-32) was used to de-escalate the costs.

5.6.2 Total Plant and O&M Costs

Table 5-4 and Table 5-5 show the total plant capital cost summary organized by cost account for the $900MW_{gross}$ air-fired and oxy-fired plants, respectively. These tables include a detailed breakdown of the capital costs, owner's costs, Total Overnight Costs (TOC), and Total As Spent Costs (TASC). The TOC for the 900MW oxy-fired power plant with CO_2 capture is $2,469M or 3745 $/kW. The TASC for this plant is $2,808M or 4269 $/kW. These capital costs are about 79% higher than the baseline air-fired case. Table 5-6 and Table 5-7 show the fixed and variable O&M costs for the $900MW_{gross}$ air-fired and oxy-fired power plants, respectively. Additional discussion on the plant performance and costs is provided in Section 8.

Table 5-4: Capital Costs for 900MW Air-Fired Plant

Client: USDOE/NETL
Project: Bituminous Baseline Study
TOTAL PLANT COST SUMMARY
Case: 900 MW Air Plant
Estimate Type: Conceptual
Cost Base: June 2011 ($x1000)

Plant Size **848.7** Mwnet

Report Date: Jun 12, 2012

Acct No.	Item/Description	Equipment Cost	Material Cost	Labor Direct	Labor Indirect	Bare Erected Cost $	% by DOE	Eng'g CM H.O.& Fee	Contingencies Process %	Contingencies Process	Contingencies Project %	Contingencies Project	TOTAL 900MW Air PLANT Cost	900MW Air COST $/kW
1	COAL & SORBENT HANDLING													
	SUBTOTAL 1.	$19,844	$5,077	$11,756	$0	$36,677		$3,221		$0		$5,985	$45,885	$54.1
2	COAL & SORBENT PREP & FEED													
	SUBTOTAL 2.	$10,595	$547	$2,288	$0	$13,430		$1,145		$0		$2,186	$16,763	$19.8
3	FEEDWATER & MISC. BOP SYSTEMS													
	SUBTOTAL 3.	$51,493	$0	$23,858	$0	$75,351		$6,690		$0		$13,326	$95,369	$112.4
4	PC BOILER													
	SUBTOTAL 4.	$139,000	$0	$81,791	$0	$220,791		$19,871		$22,632		$39,494	$302,790	$356.8
5	FLUE GAS CLEANUP													
	SUBTOTAL 5.	$87,244	$0	$45,031	$0	$132,275		$12,321		$0		$14,462	$159,059	$187.4
5B	CO2 REMOVAL & COMPRESSION (based on DOE Case S12F)													
	SUBTOTAL 5B.	$46,721	$0	$35,341	$0	$82,062		$8,206		$0		$17,820	$108,088	$127.4
6	COMBUSTION TURBINE/ACCESSORIES													
	SUBTOTAL 6.	$0	$0	$0	$0	$0		$0		$0		$0	$0	$0.0
7	HRSG													
	SUBTOTAL 7.	$21,085	$1,146	$14,144	$0	$36,375		$3,252		$0		$5,171	$44,798	$52.8
8	STEAM TURBINE GENERATOR													
	SUBTOTAL 8.	$96,268	$1,248	$23,294	$0	$120,810		$10,357		$0		$15,120	$146,288	$172.4
9	COOLING WATER SYSTEM													
	SUBTOTAL 9.	$14,774	$7,749	$13,729	$0	$36,252		$3,319		$0		$5,379	$44,952	$53.0
10	ASH/SPENT SORBENT HANDLING SYS													
	SUBTOTAL 10.	$5,436	$161	$7,058	$0	$12,655		$1,178		$0		$1,422	$15,256	$18.0
11	ACCESSORY ELECTRIC PLANT													
	SUBTOTAL 11.	$20,760	$7,933	$21,603	$0	$50,296		$4,326		$0		$6,771	$61,395	$72.3
12	INSTRUMENTATION & CONTROL													
	SUBTOTAL 12.	$10,579	$0	$10,611	$0	$21,190		$1,871		$0		$2,843	$25,905	$30.5
13	IMPROVEMENTS TO SITE													
	SUBTOTAL 13.	$3,342	$1,921	$7,165	$0	$12,428		$1,233		$0		$2,733	$16,395	$19.3
14	BUILDINGS & STRUCTURES													
	SUBTOTAL 14.	$0	$27,221	$25,803	$0	$53,024		$4,682		$0		$8,656	$66,364	$78.2
	TOTAL COST	$527,141	$53,003	$323,472	$0	$903,616		$81,672		$22,632		$141,368	$1,149,307	$1,354.2

Client: USDOE/NETL
Project: Bituminous Baseline Study
TOTAL PLANT COST SUMMARY
Case: 900 MW Air Plant
Estimate Type: Conceptual
Cost Base: June 2011 ($x1000)

Plant Size **848.7** Mwnet

Report Date: Jun 12, 2012

Acct No.	Item/Description	Equipment Cost	Material Cost	Labor Direct	Labor Indirect	Bare Erected Cost $	% by DOE	Eng'g CM H.O.& Fee	Contingencies Process %	Contingencies Process	Contingencies Project %	Contingencies Project	TOTAL 900MW Air PLANT Cost	900MW Air COST $/kW
1	COAL & SORBENT HANDLING													
1.1	Coal Receive & Unload	$4,048	$0	$1,842	$0	$5,890	8.7%	$514	0%	$0	15.0%	$961	$7,365	$8.7
1.2	Coal Stackout & Reclaim	$5,283	$0	$1,181	$0	$6,464	8.5%	$548	0%	$0	15.0%	$1,052	$8,064	$9.5
1.3	Coal Conveyors	$4,912	$0	$1,168	$0	$6,080	8.5%	$516	0%	$0	15.0%	$989	$7,586	$8.9
1.4	Other Coal Handling	$1,285	$0	$270	$0	$1,555	8.5%	$132	0%	$0	15.0%	$253	$1,940	$2.3
1.5	Sorbent Receive & Unload	$164	$0	$49	$0	$213	8.5%	$18	0%	$0	15.0%	$35	$266	$0.3
1.6	Sorbent Stackout & Reclaim	$2,641	$0	$477	$0	$3,118	8.4%	$263	0%	$0	15.0%	$507	$3,888	$4.6
1.7	Sorbent Conveyors	$942	$205	$228	$0	$1,375	8.4%	$115	0%	$0	15.0%	$224	$1,714	$2.0
1.8	Other Sorbent Handling	$569	$134	$294	$0	$997	8.5%	$85	0%	$0	15.0%	$162	$1,245	$1.5
1.9	Coal & Sorbent Hnd.Foundations	$0	$4,738	$6,247	$0	$10,985	9.4%	$1,030	0%	$0	15.0%	$1,802	$13,817	$16.3
	SUBTOTAL 1.	$19,844	$5,077	$11,756	$0	$36,677		$3,221		$0		$5,985	$45,885	$54.1
2	COAL & SORBENT PREP & FEED													
2.1	Coal Crushing & Drying	$400	$0	$77	$0	$477	8.5%	$40	0%	$0	15.0%	$78	$595	$0.7
2.2	Coal Conveyor to Storage	$5,995	$0	$1,291	$0	$7,286	8.5%	$617	0%	$0	15.0%	$1,185	$9,089	$10.7
2.3	Coal Injection System	$0	$0	$0	$0	$0	9.0%	$0	0%	$0	15.0%	$0	$0	$0.0
2.4	Misc.Coal Prep & Feed	$0	$0	$0	$0	$0	9.0%	$0	0%	$0	15.0%	$0	$0	$0.0
2.5	Sorbent Prep Equipment	$4,000	$0	$380	$0	$4,380	8.4%	$369	0%	$0	15.0%	$712	$5,462	$6.4
2.6	Sorbent Storage & Feed	$200	$0	$60	$0	$260	8.6%	$22	0%	$0	15.0%	$42	$325	$0.4
2.7	Sorbent Injection System	$0	$0	$0	$0	$0	9.0%	$0	0%	$0	15.0%	$0	$0	$0.0
2.8	Booster Air Supply System	$0	$0	$0	$0	$0	9.0%	$0	0%	$0	15.0%	$0	$0	$0.0
2.9	Coal & Sorbent Feed Foundation	$0	$547	$480	$0	$1,027	9.3%	$96	0%	$0	15.0%	$168	$1,292	$1.5
	SUBTOTAL 2.	$10,595	$547	$2,288	$0	$13,430		$1,145		$0		$2,186	$16,763	$19.8
3	FEEDWATER & MISC. BOP SYSTEMS													
3.1	FeedwaterSystem	$22,338	$0	$7,202	$0	$29,540	8.5%	$2,524	0%	$0	15.0%	$4,810	$36,874	$43.4
3.2	Water Makeup & Pretreating	$5,434	$0	$1,719	$0	$7,153	9.1%	$654	0%	$0	20.0%	$1,561	$9,368	$11.0
3.3	Other Feedwater Subsystems	$7,027	$0	$2,885	$0	$9,912	8.6%	$852	0%	$0	15.0%	$1,615	$12,379	$14.6
3.4	Service Water Systems	$1,088	$0	$569	$0	$1,657	9.0%	$149	0%	$0	20.0%	$361	$2,167	$2.6
3.5	Other Boiler Plant Systems	$8,511	$0	$8,046	$0	$16,557	9.1%	$1,507	0%	$0	15.0%	$2,710	$20,774	$24.5
3.6	FO Supply Sys & Nat Gas	$327	$0	$382	$0	$709	8.9%	$63	0%	$0	15.0%	$116	$888	$1.0
3.7	Waste Treatment Equipment	$3,565	$0	$2,064	$0	$5,629	9.6%	$542	0%	$0	20.0%	$1,234	$7,405	$8.7
3.8	Misc. Equip.(cranes,AirComp.,Comm.)	$3,203	$0	$991	$0	$4,194	9.5%	$399	0%	$0	20.0%	$919	$5,512	$6.5
	SUBTOTAL 3.	$51,493	$0	$23,858	$0	$75,351		$6,690		$0		$13,326	$95,369	$112.4

Acct No. Item/Description	Equipment Cost	Material	Labor		Bare Erected Cost $		Eng'g CM H.O.& Fee	Contingencies				TOTAL 900MW Air PLANT Cost	900MW Air COST $/kW
		Cost	Direct	Indirect		% by DOE		Process %	Process	Project %	Project		
4 PC BOILER													
4.1 PC Boiler & Accessories	$66,200	$0	$46,960	$0	$113,160	9.0%	$10,184	20%	$22,632	15.0%	$21,896	$167,873	$197.8
4.2 SCR (w/4.1)	$72,800	$0	$34,831	$0	$107,631	9.0%	$9,687	0%	$0	15.0%	$17,598	$134,916	$159.0
4.3 Open	$0	$0	$0	$0	$0	9.0%	$0	0%	$0	10.0%	$0	$0	$0.0
4.4 Boiler BoP (w/ ID Fans)	$0	$0	$0	$0	$0	9.0%	$0	0%	$0	10.0%	$0	$0	$0.0
4.5 Primary Air System	w/4.1	$0	w/4.1	$0	$0	9.0%	$0	0%	$0	10.0%	$0	$0	$0.0
4.6 Secondary Air System	w/4.1	$0	w/4.1	$0	$0	9.0%	$0	0%	$0	10.0%	$0	$0	$0.0
4.8 Major Component Rigging	$0	w/4.1	w/4.1	$0	$0	9.0%	$0	0%	$0	10.0%	$0	$0	$0.0
4.9 Boiler Foundations	$0	w/14.1	w/14.1	$0	$0	9.0%	$0		$0	10.0%	$0	$0	$0.0
SUBTOTAL 4.	$139,000	$0	$81,791	$0	$220,791		$19,871		$22,632		$39,494	$302,790	$356.8
5 FLUE GAS CLEANUP													
5.1 Absorber Vessels & Accessories	$30,000	$0	$6,414	$0	$36,414	9.3%	$3,380	0%	$0	10.0%	$3,979	$43,774	$51.6
5.2 Other FGD	$3,490	$0	$3,927	$0	$7,417	9.5%	$703	0%	$0	10.0%	$812	$8,932	$10.5
5.3 Bag House & Accessories	$20,000	$0	$12,606	$0	$32,606	9.4%	$3,064	0%	$0	10.0%	$3,567	$39,237	$46.2
5.4 Other Particulate Removal Materials	$1,274	$0	$1,354	$0	$2,628	9.5%	$249	0%	$0	10.0%	$288	$3,165	$3.7
5.5 Gypsum Dewatering System	$31,780	$0	$20,030	$0	$51,810	9.3%	$4,799	0%	$0	10.0%	$5,662	$62,272	$73.4
5.6 Mercury Removal System		$0	$0	$0	$0	9.0%	$0	0%	$0	10.0%	$0	$0	$0.0
5.9 Open	$700	$0	$700	$0	$1,400	9.0%	$126	0%	$0	10.0%	$153	$1,679	$2.0
SUBTOTAL 5.	$87,244	$0	$45,031	$0	$132,275		$12,321		$0		$14,462	$159,059	$187.4
5B CO2 REMOVAL & COMPRESSION (based on DOE Case S12F)													
5B.1 CO2 Condensing Heat Exchanger	$3,928	$0	$328	$0	$4,256	10.0%	$426	0%	$0	15.0%	$702	$5,384	$6.3
5B.2 CO2 Compression & Drying	$42,793	$0	$35,013	$0	$77,806	10.0%	$7,781	0%	$0	20.0%	$17,117	$102,704	$121.0
SUBTOTAL 5B.	$46,721	$0	$35,341	$0	$82,062		$8,206		$0		$17,820	$108,088	$127.4
6 COMBUSTION TURBINE/ACCESSORIES													
SUBTOTAL 6.	$0	$0	$0	$0	$0		$0		$0		$0	$0	$0.0
7 HRSG													
7.1 Flue Gas Recycle Heat Exchanger	$0	$0	$0	$0	$0	9.0%	$0	0%	$0	15.0%	$0	$0	$0.0
7.2 HRSG Accessories	$0	$0	$0	$0	$0	9.0%	$0	0%	$0	15.0%	$0	$0	$0.0
7.3 Ductwork	$10,572	$0	$6,673	$0	$17,245	8.4%	$1,457	0%	$0	15.0%	$2,805	$21,507	$25.3
7.4 Stack	$10,513	$0	$6,110	$0	$16,623	9.4%	$1,560	0%	$0	10.0%	$1,818	$20,001	$23.6
7.9 Duct & Stack Foundations	$0	$1,146	$1,361	$0	$2,507	9.4%	$235	0%	$0	20.0%	$548	$3,290	$3.9
SUBTOTAL 7.	$21,085	$1,146	$14,144	$0	$36,375		$3,252		$0		$5,171	$44,798	$52.8
8 STEAM TURBINE GENERATOR													
8.1 Steam TG & Accessories	$66,640	$0	$8,221	$0	$74,861	8.8%	$6,572	0%	$0	10.0%	$8,143	$89,576	$105.5
8.2 Turbine Plant Auxiliaries (incl in 8.1)	$418	$0	$890	$0	$1,308	9.6%	$125	0%	$0	10.0%	$143	$1,576	$1.9
8.3 Condenser & Auxiliaries	$8,091	$0	$2,740	$0	$10,831	9.3%	$1,010	0%	$0	10.0%	$1,184	$13,025	$15.3
8.4 Steam Piping	$21,119	$0	$9,383	$0	$30,502	7.7%	$2,338	0%	$0	15.0%	$4,926	$37,766	$44.5
8.9 TG Foundations	$0	$1,248	$2,060	$0	$3,308	9.4%	$312	0%	$0	20.0%	$724	$4,344	$5.1
SUBTOTAL 8.	$96,268	$1,248	$23,294	$0	$120,810		$10,357		$0		$15,120	$146,288	$172.4

Acct No. Item/Description	Equipment Cost	Material	Labor		Bare Erected Cost $		Eng'g CM H.O.& Fee	Contingencies				TOTAL 900MW Air PLANT Cost	900MW Air COST $/kW
		Cost	Direct	Indirect		% by DOE		Process %	Process	Project %	Project		
9 COOLING WATER SYSTEM													
9.1 Cooling Towers	$10,951	$0	$3,387	$0	$14,338	9.3%	$1,336	0%	$0	10.0%	$1,567	$17,241	$20.3
9.2 Circulating Water Pumps	$2,187	$0	$138	$0	$2,325	8.5%	$198	0%	$0	10.0%	$252	$2,775	$3.3
9.3 Circ.Water System Auxiliaries	$601	$0	$80	$0	$681	9.3%	$63	0%	$0	9.9%	$74	$818	$1.0
9.4 Circ.Water Piping	$0	$5,062	$4,584	$0	$9,646	8.9%	$854	0%	$0	15.0%	$1,575	$12,075	$14.2
9.5 Make-up Water System	$545	$0	$701	$0	$1,246	9.2%	$115	0%	$0	15.0%	$204	$1,565	$1.8
9.6 Component Cooling Water Sys	$490	$0	$376	$0	$866	9.1%	$79	0%	$0	15.0%	$142	$1,087	$1.3
9.9 Circ.Water System Foundations& Structures	$0	$2,687	$4,463	$0	$7,150	9.4%	$674	0%	$0	20.0%	$1,565	$9,389	$11.1
SUBTOTAL 9.	$14,774	$7,749	$13,729	$0	$36,252		$3,319		$0		$5,379	$44,952	$53.0
10 ASH/SPENT SORBENT HANDLING SYS													
10.1 Rotary Ash Coolers	$400	$0	$774	$0	$1,174	9.0%	$106	0%	$0	10.0%	$128	$1,408	$1.7
10.2 Cyclone Ash Letdown	$0	$0	$0	$0	$0	9.0%	$0	0%	$0	10.0%	$0	$0	$0.0
10.3 HGCU Ash Letdown	$0	$0	$0	$0	$0	9.0%	$0	0%	$0	10.0%	$0	$0	$0.0
10.4 High Temperature Ash Piping	$0	$0	$0	$0	$0	9.0%	$0	0%	$0	10.0%	$0	$0	$0.0
10.5 Reducer Baghouse Ash Recycle System	$0	$0	$0	$0	$0	9.0%	$0	0%	$0	10.0%	$0	$0	$0.0
10.6 Ash Storage Silos	$711	$0	$2,176	$0	$2,887	9.6%	$277	0%	$0	10.0%	$316	$3,481	$4.1
10.7 Ash Transport & Feed Equipment	$4,725	$0	$4,684	$0	$9,409	9.2%	$867	0%	$0	10.0%	$1,028	$11,304	$13.3
10.8 Misc. Ash Handling Equipment	$0	$0	$0	$0	$0	9.0%	$0	0%	$0	10.0%	$0	$0	$0.0
10.9 Ash/Spent Sorbent Foundation	$0	$161	$198	$0	$359	9.5%	$34	0%	$0	19.8%	$78	$471	$0.6
SUBTOTAL 10.	$5,436	$161	$7,058	$0	$12,655		$1,178		$0		$1,422	$15,256	$18.0
11 ACCESSORY ELECTRIC PLANT													
11.1 Generator Equipment	$1,943	$0	$311	$0	$2,254	9.0%	$202	0%	$0	7.5%	$184	$2,640	$3.1
11.2 Station Service Equipment	$3,314	$0	$1,111	$0	$4,425	9.3%	$411	0%	$0	7.5%	$363	$5,199	$6.1
11.3 Switchgear & Motor Control	$3,803	$0	$661	$0	$4,464	9.3%	$413	0%	$0	10.0%	$488	$5,365	$6.3
11.4 Conduit & Cable Tray	$0	$2,608	$8,426	$0	$11,034	9.3%	$1,030	0%	$0	15.0%	$1,810	$13,874	$16.3
11.5 Wire & Cable	$0	$4,966	$8,877	$0	$13,843	8.0%	$1,112	0%	$0	15.0%	$2,243	$17,198	$20.3
11.6 Protective Equipment	$306	$0	$1,063	$0	$1,369	9.6%	$131	0%	$0	10.0%	$150	$1,650	$1.9
11.7 Standby Equipment	$1,498	$0	$35	$0	$1,533	9.1%	$140	0%	$0	10.0%	$167	$1,840	$2.2
11.8 Main Power Transformers	$9,896	$0	$206	$0	$10,102	7.6%	$767	0%	$0	10.0%	$1,087	$11,956	$14.1
11.9 Electrical Foundations	$0	$359	$913	$0	$1,272	9.4%	$120	0%	$0	20.0%	$279	$1,671	$2.0
SUBTOTAL 11.	$20,760	$7,933	$21,603	$0	$50,296		$4,326		$0		$6,771	$61,395	$72.3
12 INSTRUMENTATION & CONTROL													
12.1 PC Control Equipment (w 12.7)	w/12.7	$0	w/12.7	$0	$0	9.0%	$0	0%	$0	15.0%	$0	$0	$0.0
12.2 Combustion Turbine Control	N/A	$0	N/A	$0	$0	9.0%	$0	0%	$0	15.0%	$0	$0	$0.0
12.3 Steam Turbine Control (w 8.1)	w/8.1	$0	w/8.1	$0	$0	9.0%	$0	0%	$0	15.0%	$0	$0	$0.0
12.4 Other Major Component Control	$0	$0	$0	$0	$0	9.0%	$0	0%	$0	15.0%	$0	$0	$0.0
12.5 Signal Processing Equipment (w12.7)	w/12.7	$0	w/12.7	$0	$0	9.0%	$0	0%	$0	15.0%	$0	$0	$0.0
12.6 Control Boards,Panels & Racks	$528	$0	$323	$0	$851	9.4%	$80	0%	$0	15.0%	$140	$1,071	$1.3
12.7 Distributed Control System Equipment	$5,331	$0	$951	$0	$6,282	9.2%	$580	0%	$0	10.0%	$686	$7,548	$8.9
12.8 Instrument Wiring & Tubing	$3,214	$0	$5,849	$0	$9,063	8.1%	$734	0%	$0	15.0%	$1,470	$11,267	$13.3
12.9 Other I & C Equipment	$1,506	$0	$3,488	$0	$4,994	9.6%	$477	0%	$0	10.0%	$547	$6,018	$7.1
SUBTOTAL 12.	$10,579	$0	$10,611	$0	$21,190		$1,871		$0		$2,843	$25,905	$30.5

Acct No.	Item/Description	Equipment Cost	Material Cost	Labor Direct	Labor Indirect	Bare Erected Cost $	% by DOE	Eng'g CM H.O.& Fee	Contingencies Process %	Contingencies Process	Contingencies Project %	Contingencies Project	TOTAL 900MW Air PLANT Cost	900MW Air COST $/kW
13	IMPROVEMENTS TO SITE													
13.1	Site Preparation	$0	$56	$1,195	$0	$1,251	9.8%	$122	0%	$0	20.0%	$275	$1,648	$1.9
13.2	Site Improvements	$0	$1,865	$2,464	$0	$4,329	9.9%	$430	0%	$0	20.0%	$952	$5,711	$6.7
13.3	Site Facilities	$3,342	$0	$3,506	$0	$6,848	9.9%	$681	0%	$0	20.0%	$1,506	$9,035	$10.6
	SUBTOTAL 13.	$3,342	$1,921	$7,165	$0	$12,428		$1,233		$0		$2,733	$16,395	$19.3
14	BUILDINGS & STRUCTURES													
14.1	Boiler Building	$0	$9,922	$8,719	$0	$18,641	8.8%	$1,640	0%	$0	15.0%	$3,042	$23,323	$27.5
14.2	Turbine Building	$0	$14,171	$13,198	$0	$27,369	8.8%	$2,415	0%	$0	15.0%	$4,468	$34,252	$40.4
14.3	Administration Building	$0	$703	$742	$0	$1,445	8.9%	$128	0%	$0	15.0%	$236	$1,809	$2.1
14.4	Circulation Water Pumphouse	$0	$201	$160	$0	$361	8.9%	$32	0%	$0	15.0%	$59	$452	$0.5
14.5	Water Treatment Buildings	$0	$678	$618	$0	$1,296	8.8%	$114	0%	$0	15.0%	$211	$1,621	$1.9
14.6	Machine Shop	$0	$470	$315	$0	$785	8.7%	$68	0%	$0	15.0%	$128	$981	$1.2
14.7	Warehouse	$0	$318	$319	$0	$637	8.8%	$56	0%	$0	15.0%	$104	$797	$0.9
14.8	Other Buildings & Structures	$0	$260	$221	$0	$481	8.7%	$42	0%	$0	15.1%	$79	$602	$0.7
14.9	Waste Treating Building & Str.	$0	$498	$1,511	$0	$2,009	9.3%	$187	0%	$0	15.0%	$329	$2,525	$3.0
	SUBTOTAL 14.	$0	$27,221	$25,803	$0	$53,024		$4,682		$0		$8,656	$66,364	$78.2
	TOTAL COST	$527,141	$53,003	$323,472	$0	$903,616		$81,672		$22,632		$141,368	$1,149,307	$1,354.2

Owner's Costs		
Pre production Costs		
6 months all labor	$8,517	$10.0
1 month maintenance materials	$1,073	$1.3
1 Month non-fuel consumables	$1,670	$2.0
1 Month Waste Disposal	$364	$0.4
25% of 1 Months Fuel Cost at 100% CF	$2,564	$3.0
2% of TPC	$22,986	$27.1
Total Pre-production costs	$37,174	$43.8
Inventory Capital		
60 day supply of fuel and consumables at 100% CF	$23,454	$27.6
0.5% of TPC (Spare parts)	$5,747	$6.8
Total Inventory Capital	$29,201	$34.4
Initial Cost for Catalyst and Chemicals	$0	$0.0
Land	$900	$1.1
Other Owners' Costs	$172,396	$203.1
Financing Costs	$31,031	$36.6
Total Overnight Costs (TOC)	$1,420,009	$1,673.2
TASC Multiplier (IOU, high-risk, 35 year)	1.14	
Total As-Spent Cost (TASC)	$1,618,810	$1,907.5

Table 5-5: Capital Costs for 900MW Oxy-Fired Plant

Client: USDOE/NETL
Project: Bituminous Baseline Study
TOTAL PLANT COST SUMMARY
Case: 900 MW Oxy Plant
Estimate Type: Conceptual
Cost Base: June 2011 ($x1000)

Report Date: May 30, 2014

Acct No.	Item/Description	Equipment Cost	Material Cost	Labor Direct	Labor Indirect	Bare Erected Cost $	Eng'g CM H.O.& Fee %	Eng'g CM H.O.& Fee Total	Process Contingency %	Process Contingency Total	Project Contingency %	Project Contingency Total	TOTAL 900MW Oxy PLANT Cost	900MW Oxy COST $/kW
1	COAL & SORBENT HANDLING													
	SUBTOTAL 1.	$25,366	$6,471	$14,982	$0	$46,819		$4,214	$0	$7,655			$58,690	$89.2
2	COAL & SORBENT PREP & FEED													
	SUBTOTAL 2.	$14,787	$701	$3,802	$0	$19,290		$1,736	$0	$3,154			$24,182	$36.8
3	FEEDWATER & MISC. BOP SYSTEMS													
	SUBTOTAL 3.	$65,305	$0	$30,374	$0	$95,679		$8,611	$0	$16,932			$121,224	$184.3
4	PC BOILER													
	SUBTOTAL 4.	$535,332	$0	$272,742	$0	$808,073		$48,445	$11,692	$89,761			$957,972	$1,456.1
5	FLUE GAS CLEANUP													
	SUBTOTAL 5.	$71,840	$0	$36,601	$0	$108,441		$9,760	$0	$11,820			$130,022	$197.6
5B	CO2 REMOVAL & COMPRESSION (based on DOE Case S12F)													
	SUBTOTAL 5B.	$60,596	$0	$36,547	$0	$97,143		$8,743	$0	$20,241			$126,128	$191.7
6	COMBUSTION TURBINE/ACCESSORIES													
	SUBTOTAL 6.	$0	$0	$0	$0	$0		$0	$0	$0			$0	$0.0
7	HRSG													
	SUBTOTAL 7.	$26,373	$1,209	$17,376	$0	$44,958		$4,046	$0	$6,275			$55,281	$84.0
8	STEAM TURBINE GENERATOR													
	SUBTOTAL 8.	$120,349	$1,789	$39,724	$0	$161,832		$14,565	$0	$20,480			$196,879	$299.3
9	COOLING WATER SYSTEM													
	SUBTOTAL 9.	$20,034	$9,991	$17,905	$0	$47,930		$4,314	$0	$7,047			$59,292	$90.1
10	ASH/SPENT SORBENT HANDLING SYS													
	SUBTOTAL 10.	$10,503	$311	$13,638	$0	$24,452		$2,201	$0	$2,740			$29,394	$44.7
11	ACCESSORY ELECTRIC PLANT													
	SUBTOTAL 11.	$33,842	$18,743	$48,971	$0	$101,555		$9,140	$0	$14,158			$124,855	$189.8
12	INSTRUMENTATION & CONTROL													
	SUBTOTAL 12.	$13,803	$0	$13,845	$0	$27,648		$2,488	$0	$3,719			$33,857	$51.5
13	IMPROVEMENTS TO SITE													
	SUBTOTAL 13.	$3,806	$2,188	$8,160	$0	$14,155		$1,274	$0	$3,087			$18,516	$28.1
14	BUILDINGS & STRUCTURES													
	SUBTOTAL 14.	$0	$29,477	$27,806	$0	$57,283		$5,155	$0	$9,366			$71,807	$109.1
	TOTAL COST	$1,001,936	$70,850	$582,473	$0	$1,655,259		$124,691	$11,692	$216,437			$2,008,079	$3,052.3

Client: USDOE/NETL
Project: Bituminous Baseline Study
TOTAL PLANT COST SUMMARY
Case: 900 MW Oxy Plant
Estimate Type: Conceptual
Cost Base: June 2011 ($x1000)

Report Date: May 30. 2014

Acct No.	Item/Description	Equipment Cost	Material Cost	Labor Direct	Labor Indirect	Bare Erected Cost $	Eng'g CM H.O.& Fee %	Eng'g CM H.O.& Fee Total	Process Contingency %	Process Contingency Total	Project Contingency %	Project Contingency Total	TOTAL 900MW Oxy PLANT Cost	900MW Oxy COST $/kW
	1 COAL & SORBENT HANDLING													
1.1	Coal Receive & Unload	$5,138	$0	$2,338	$0	$7,475	9.0%	$673	0%	$0	15%	$1,222	$9,371	$14.2
1.2	Coal Stackout & Reclaim	$6,705	$0	$1,499	$0	$8,204	9.0%	$738	0%	$0	15%	$1,341	$10,284	$15.6
1.3	Coal Conveyors	$6,234	$0	$1,482	$0	$7,717	9.0%	$694	0%	$0	15%	$1,262	$9,673	$14.7
1.4	Other Coal Handling	$1,631	$0	$343	$0	$1,974	9.0%	$178	0%	$0	15%	$323	$2,474	$3.8
1.5	Sorbent Receive & Unload	$215	$0	$64	$0	$279	9.0%	$25	0%	$0	15%	$46	$350	$0.5
1.6	Sorbent Stackout & Reclaim	$3,462	$0	$625	$0	$4,088	9.0%	$368	0%	$0	15%	$668	$5,124	$7.8
1.7	Sorbent Conveyors	$1,235	$269	$299	$0	$1,803	9.0%	$162	0%	$0	15%	$295	$2,260	$3.4
1.8	Other Sorbent Handling	$746	$176	$385	$0	$1,307	9.0%	$118	0%	$0	15%	$214	$1,639	$2.5
1.9	Coal & Sorbent Hnd.Foundations	$0	$6,027	$7,946	$0	$13,973	9.0%	$1,258	0%	$0	15%	$2,285	$17,515	$26.6
	SUBTOTAL 1.	$25,366	$6,471	$14,982	$0	$46,819		$4,214		$0		$7,655	$58,690	$89.2
	2 COAL & SORBENT PREP & FEED													
2.1	Coal Crushing & Drying	$620	$0	$119	$0	$739	9.0%	$67	0%	$0	15%	$121	$927	$1.4
2.2	Coal Conveyor to Storage	$7,727	$0	$1,664	$0	$9,391	9.0%	$845	0%	$0	15%	$1,535	$11,771	$17.9
2.3	Coal Injection System	$0	$0	$0	$0	$0	9.0%	$0	0%	$0	0%	$0	$0	$0.0
2.4	Misc.Coal Prep & Feed	$0	$0	$0	$0	$0	9.0%	$0	0%	$0	0%	$0	$0	$0.0
2.5	Sorbent Prep Equipment	$6,240	$0	$1,344	$0	$7,584	9.0%	$683	0%	$0	15%	$1,240	$9,506	$14.4
2.6	Sorbent Storage & Feed	$200	$0	$60	$0	$260	9.0%	$23	0%	$0	15%	$43	$326	$0.5
2.7	Sorbent Injection System	$0	$0	$0	$0	$0	9.0%	$0	0%	$0	0%	$0	$0	$0.0
2.8	Booster Air Supply System	$0	$0	$0	$0	$0	9.0%	$0	0%	$0	0%	$0	$0	$0.0
2.9	Coal & Sorbent Feed Foundation	$0	$701	$615	$0	$1,316	9.0%	$118	0%	$0	15%	$215	$1,650	$2.5
	SUBTOTAL 2.	$14,787	$701	$3,802	$0	$19,290		$1,736		$0		$3,154	$24,182	$36.8
	3 FEEDWATER & MISC. BOP SYSTEMS													
3.1	FeedwaterSystem	$28,220	$0	$9,099	$0	$37,319	9.0%	$3,359	0%	$0	15%	$6,102	$46,780	$71.1
3.2	Water Makeup & Pretreating	$7,296	$0	$2,308	$0	$9,604	9.0%	$864	0%	$0	20%	$2,093	$12,561	$19.1
3.3	Other Feedwater Subsystems	$8,877	$0	$3,645	$0	$12,522	9.0%	$1,127	0%	$0	15%	$2,048	$15,697	$23.9
3.4	Service Water Systems	$1,461	$0	$764	$0	$2,225	9.0%	$200	0%	$0	20%	$485	$2,910	$4.4
3.5	Other Boiler Plant Systems	$11,014	$0	$10,412	$0	$21,426	9.0%	$1,928	0%	$0	15%	$3,504	$26,859	$40.8
3.6	FO Supply Sys & Nat Gas	$360	$0	$421	$0	$781	9.0%	$70	0%	$0	15%	$128	$979	$1.5
3.7	Waste Treatment Equipment	$4,550	$0	$2,635	$0	$7,185	9.0%	$647	0%	$0	20%	$1,566	$9,398	$14.3
3.8	Misc. Equip.(cranes,AirComp.,Comm.)	$3,526	$0	$1,091	$0	$4,617	9.0%	$416	0%	$0	20%	$1,007	$6,040	$9.2
	SUBTOTAL 3.	$65,305	$0	$30,374	$0	$95,679		$8,611		$0		$16,932	$121,224	$184.3

Acct No. Item/Description	Equipment Cost	Material	Labor		Bare Erected Cost $	Eng'g CM H.O.& Fee		Process Contingency		Project Contingency		TOTAL 900MW Oxy PLANT Cost	900MW Oxy COST $/kW
		Cost	Direct	Indirect		%	Total	%	Total	%	Total		
4 PC BOILER													
4.1 PC Boiler & Accessories	$338,791	$0	$141,022	$0	$479,813	9.0%	$43,183	0%	$0	15%	$78,449	$601,446	$914.2
4.1 PC Boiler & Accessories	$41,278	$0	$17,182	$0	$58,460	9.0%	$5,261	**20%**	$11,692	15%	$11,312	$86,725	$131.8
4.2 SCR (w/4.1)	$0	$0	$0	$0	$0	9.0%	$0	0%	$0	15%	$0	$0	$0.0
4.3 ASU/Oxidant Compression	$155,263	$0	$114,538	$0	$269,801	0.0%	$0		$0	0%	$0	$269,801	$410.1
4.4 Boiler BoP (w/ ID Fans)	$0	$0	$0	$0	$0	0.0%	$0		$0	0%	$0	$0	$0.0
4.5 Primary Air System	$0	$0	$0	$0	$0	0.0%	$0		$0	0%	$0	$0	$0.0
4.6 Secondary Air System	$0	$0	$0	$0	$0	0.0%	$0		$0	0%	$0	$0	$0.0
4.8 Major Component Rigging	$0	$0	$0	$0	$0	0.0%	$0		$0	0%	$0	$0	$0.0
4.9 Boiler Foundations	$0	$0	$0	$0	$0	0.0%	$0		$0	0%	$0	$0	$0.0
SUBTOTAL 4.	$535,332	$0	$272,742	$0	$808,073		$48,445		$11,692		$89,761	$957,972	$1,456.1
5 FLUE GAS CLEANUP													
5.1 Absorber Vessels & Accessories	$46,830	$0	$23,859	$0	$70,689	9.0%	$6,362	0%	$0	10%	$7,705	$84,756	$128.8
5.2 Other FGD	$0	$0	$0	$0	$0	9.0%	$0	0%	$0	10%	$0	$0	$0.0
5.3 Bag House & Accessories	$9,370	$0	$4,774	$0	$14,144	9.0%	$1,273	0%	$0	10%	$1,542	$16,959	$25.8
5.4 Other Particulate Removal Materials	$0	$0	$0	$0	$0	9.0%	$0	0%	$0	10%	$0	$0	$0.0
5.5 Gypsum Dewatering System	$9,870	$0	$5,029	$0	$14,899	9.0%	$1,341	0%	$0	10%	$1,624	$17,864	$27.2
5.6 Mercury Removal System	$4,690	$0	$2,389	$0	$7,079	9.0%	$637	0%	$0	10%	$772	$8,488	$12.9
5.9 Open	$1,080	$0	$550	$0	$1,630	9.0%	$147	0%	$0	10%	$178	$1,955	$3.0
SUBTOTAL 5.	$71,840	$0	$36,601	$0	$108,441		$9,760		$0		$11,820	$130,022	$197.6
5B CO2 REMOVAL & COMPRESSION (based on DOE Case S12F)													
5B.1 CO2 Condensing Heat Exchanger	$16,607	$0	$556	$0	$17,163	9.0%	$1,545	0%	$0	15%	$2,806	$21,515	$32.7
5B.2 CO2 Compression & Drying	$43,988	$0	$35,991	$0	$79,980	9.0%	$7,198	0%	$0	20%	$17,436	$104,614	$159.0
SUBTOTAL 5B.	$60,596	$0	$36,547	$0	$97,143		$8,743		$0		$20,242	$126,128	$191.7
6 COMBUSTION TURBINE/ACCESSORIES													
SUBTOTAL 6.	$0	$0	$0	$0	$0		$0		$0		$0	$0	$0.0
7 HRSG													
7.1 Flue Gas Recycle Heat Exchanger	$0	$0	$0	$0	$0	9.0%	$0	0%	$0	0%	$0	$0	$0.0
7.2 HRSG Accessories	$0	$0	$0	$0	$0	9.0%	$0	0%	$0	0%	$0	$0	$0.0
7.3 Ductwork	$12,235	$0	$7,723	$0	$19,958	9.0%	$1,796	0%	$0	15%	$3,263	$25,017	$38.0
7.4 Stack	$14,138	$0	$8,217	$0	$22,355	9.0%	$2,012	0%	$0	10%	$2,436	$26,803	$40.7
7.9 Duct & Stack Foundations	$0	$1,209	$1,436	$0	$2,646	9.0%	$238	0%	$0	20%	$576	$3,460	$5.3
SUBTOTAL 7.	$26,373	$1,209	$17,376	$0	$44,958		$4,046		$0		$6,275	$55,281	$84.0
8 STEAM TURBINE GENERATOR													
8.1 Steam TG & Accessories	$79,702	$0	$19,925	$0	$99,627	9.0%	$8,966	0%	$0	10%	$10,859	$119,453	$181.6
8.2 Turbine Plant Auxiliaries (incl in 8.1)		$0		$0	$0	9.0%	$0	0%	$0	10%	$0	$0	$0.0
8.3 Condenser & Auxiliaries	$11,013	$0	$3,730	$0	$14,742	9.0%	$1,327	0%	$0	10%	$1,607	$17,676	$26.9
8.4 Steam Piping	$29,635	$0	$13,166	$0	$42,801	9.0%	$3,852	0%	$0	15%	$6,998	$53,651	$81.5
8.9 TG Foundations	$0	$1,759	$2,903	$0	$4,662	9.0%	$420	0%	$0	20%	$1,016	$6,098	$9.3
SUBTOTAL 8.	$120,349	$1,759	$39,724	$0	$161,832		$14,565		$0		$20,480	$196,879	$299.3

Acct No. Item/Description	Equipment Cost	Material	Labor		Bare Erected Cost $	Eng'g CM H.O.& Fee		Process Contingency		Project Contingency		TOTAL 900MW Oxy PLANT Cost	900MW Oxy COST $/kW
		Cost	Direct	Indirect		%	Total	%	Total	%	Total		
9 COOLING WATER SYSTEM													
9.1 Cooling Towers	$14,783	$0	$4,572	$0	$19,355	9.0%	$1,742	0%	$0	10%	$2,109	$23,206	$35.3
9.2 Circulating Water Pumps	$3,124	$0	$197	$0	$3,321	9.0%	$299	0%	$0	10%	$362	$3,982	$6.1
9.3 Circ.Water System Auxiliaries	$780	$0	$104	$0	$884	9.0%	$80	0%	$0	10%	$96	$1,060	$1.6
9.4 Circ.Water Piping	$0	$6,573	$5,953	$0	$12,526	9.0%	$1,127	0%	$0	15%	$2,048	$15,701	$23.9
9.5 Make-up Water System	$711	$0	$914	$0	$1,625	9.0%	$146	0%	$0	15%	$265	$2,037	$3.1
9.6 Component Cooling Water Sys	$636	$0	$488	$0	$1,125	9.0%	$101	0%	$0	15%	$184	$1,410	$2.1
9.9 Circ.Water System Foundations & Structures	$0	$3,418	$5,677	$0	$9,094	9.0%	$818	0%	$0	20%	$1,983	$11,896	$18.1
SUBTOTAL 9.	$20,034	$9,991	$17,905	$0	$47,930		$4,314		$0		$7,047	$59,292	$90.1
10 ASH/SPENT SORBENT HANDLING SYS													
10.1 Rotary Ash Coolers	$620	$0	$316	$0	$936	9.0%	$84	0%	$0	10%	$102	$1,122	$1.7
10.2 Cyclone Ash Letdown	$0	$0	$0	$0	$0	9.0%	$0	0%	$0	0%	$0	$0	$0.0
10.3 HGCU Ash Letdown	$0	$0	$0	$0	$0	9.0%	$0	0%	$0	0%	$0	$0	$0.0
10.4 High Temperature Ash Piping	$0	$0	$0	$0	$0	9.0%	$0	0%	$0	0%	$0	$0	$0.0
10.5 Reducer Baghouse Ash Recycle System	$0	$0	$0	$0	$0	9.0%	$0	0%	$0	10%	$0	$0	$0.0
10.6 Ash Storage Silos	$1,374	$0	$4,204	$0	$5,578	9.0%	$502	0%	$0	10%	$608	$6,689	$10.2
10.7 Ash Transport & Feed Equipment	$9,130	$0	$9,050	$0	$18,180	9.0%	$1,636	0%	$0	10%	$1,982	$21,799	$33.1
10.8 Misc. Ash Handling Equipment	$0	$0	$0	$0	$0	9.0%	$0	0%	$0	0%	$0	$0	$0.0
10.9 Ash/Spent Sorbent Foundation	$0	$311	$383	$0	$694	9.0%	$62	0%	$0	20%	$150	$906	$1.4
SUBTOTAL 10.	$10,503	$311	$13,638	$0	$24,452		$2,201		$0		$2,740	$29,394	$44.7
11 ACCESSORY ELECTRIC PLANT													
11.1 Generator Equipment	$2,484	$0	$398	$0	$2,882	9.0%	$259	0%	$0	7%	$235	$3,377	$5.1
11.2 Station Service Equipment	$7,990	$0	$2,678	$0	$10,668	9.0%	$960	0%	$0	8%	$873	$12,501	$19.0
11.3 Switchgear & Motor Control	$9,168	$0	$1,594	$0	$10,762	9.0%	$969	0%	$0	10%	$1,174	$12,905	$19.6
11.4 Conduit & Cable Tray	$0	$6,287	$20,314	$0	$26,601	9.0%	$2,394	0%	$0	15%	$4,350	$33,346	$50.7
11.5 Wire & Cable	$0	$11,972	$21,401	$0	$33,373	9.0%	$3,004	0%	$0	15%	$5,456	$41,833	$63.6
11.6 Protective Equipment	$306	$0	$1,063	$0	$1,369	9.0%	$123	0%	$0	10%	$149	$1,642	$2.5
11.7 Standby Equipment	$1,827	$0	$43	$0	$1,869	9.0%	$168	0%	$0	10%	$203	$2,241	$3.4
11.8 Main Power Transformers	$12,067	$0	$251	$0	$12,318	9.0%	$1,109	0%	$0	10%	$1,343	$14,770	$22.4
11.9 Electrical Foundations	$0	$483	$1,229	$0	$1,713	9.0%	$154	0%	$0	20%	$374	$2,241	$3.4
SUBTOTAL 11.	$33,842	$18,743	$48,971	$0	$101,555		$9,140		$0		$14,158	$124,855	$189.8
12 INSTRUMENTATION & CONTROL													
12.1 PC Control Equipment (w 12.7)	$0	$0	$0	$0	$0	9.0%	$0	0%	$0	0%	$0	$0	$0.0
12.2 Combustion Turbine Control	$0	$0	$0	$0	$0	9.0%	$0	0%	$0	0%	$0	$0	$0.0
12.3 Steam Turbine Control (w 8.1)	$0	$0	$0	$0	$0	9.0%	$0	0%	$0	0%	$0	$0	$0.0
12.4 Other Major Component Control	$0	$0	$0	$0	$0	9.0%	$0	0%	$0	0%	$0	$0	$0.0
12.5 Signal Processing Equipment (w12.7)	$0	$0	$0	$0	$0	9.0%	$0	0%	$0	0%	$0	$0	$0.0
12.6 Control Boards,Panels & Racks	$689	$0	$421	$0	$1,110	9.0%	$100	0%	$0	15%	$182	$1,393	$2.1
12.7 Distributed Control System Equipment	$6,956	$0	$1,241	$0	$8,197	9.0%	$738	0%	$0	10%	$893	$9,828	$14.9
12.8 Instrument Wiring & Tubing	$4,194	$0	$7,632	$0	$11,825	9.0%	$1,064	0%	$0	15%	$1,934	$14,824	$22.5
12.9 Other I & C Equipment	$1,965	$0	$4,551	$0	$6,516	9.0%	$586	0%	$0	10%	$710	$7,813	$11.9
SUBTOTAL 12.	$13,803	$0	$13,845	$0	$27,648		$2,488		$0		$3,719	$33,857	$51.5

Acct No.	Item/Description	Equipment Cost	Material Cost	Labor Direct	Labor Indirect	Bare Erected Cost $	Eng'g CM H.O.& Fee %	Eng'g CM H.O.& Fee Total	Process Contingency %	Process Contingency Total	Project Contingency %	Project Contingency Total	TOTAL 900MW Oxy PLANT Cost	900MW Oxy COST $/kW
13	IMPROVEMENTS TO SITE													
13.1	Site Preparation	$0	$64	$1,361	$0	$1,425	9.0%	$128	0%	$0	20%	$311	$1,864	$2.8
13.2	Site Improvements	$0	$2,124	$2,806	$0	$4,930	9.0%	$444	0%	$0	20%	$1,075	$6,449	$9.8
13.3	Site Facilities	$3,806	$0	$3,993	$0	$7,799	9.0%	$702	0%	$0	20%	$1,700	$10,202	$15.5
	SUBTOTAL 13.	$3,806	$2,188	$8,160	$0	$14,155		$1,274		$0		$3,087	$18,516	$28.1
14	BUILDINGS & STRUCTURES													
14.1	Boiler Building	$0	$10,520	$9,245	$0	$19,765	9.0%	$1,779	0%	$0	15%	$3,231.38	$24,775	$37.7
14.2	Turbine Building	$0	$15,321	$14,269	$0	$29,591	9.0%	$2,663	0%	$0	15%	$4,839	$37,093	$56.4
14.3	Administration Building	$0	$750	$792	$0	$1,542	9.0%	$139	0%	$0	15%	$252	$1,933	$2.9
14.4	Circulation Water Pumphouse	$0	$258	$205	$0	$463	9.0%	$42	0%	$0	15%	$76	$581	$0.9
14.5	Water Treatment Buildings	$0	$1,035	$943	$0	$1,978	9.0%	$178	0%	$0	15%	$323	$2,479	$3.8
14.6	Machine Shop	$0	$502	$336	$0	$838	9.0%	$75	0%	$0	15%	$137	$1,050	$1.6
14.7	Warehouse	$0	$339	$340	$0	$680	9.0%	$61	0%	$0	15%	$111	$852	$1.3
14.8	Other Buildings & Structures	$0	$277	$236	$0	$513	9.0%	$46	0%	$0	15%	$85	$644	$1.0
14.9	Waste Treating Building & Str.	$0	$474	$1,439	$0	$1,914	9.0%	$172	0%	$0	15%	$313	$2,399	$3.6
	SUBTOTAL 14.	$0	$29,477	$27,806	$0	$57,283		$5,155		$0		$9,366	$71,807	$109.1
	TOTAL COST	$1,001,936	$70,850	$582,473	$0	$1,655,259		$124,691		$11,692		$216,437	$2,008,079	$3,052.3

Owner's Costs		
Pre production Costs		
6 months all labor	$12,333	$18.7
1 month maintenance materials	$1,675	$2.5
1 Month non-fuel consumables	$2,197	$3.3
1 Month Waste Disposal	$1,180	$1.8
25% of 1 Months Fuel Cost at 100% CF	$3,047	$4.6
2% of TPC	$40,162	$61.0
Total Pre-production costs	$60,594	$92.1
Inventory Capital		
60 day supply of fuel and consumables at 100% CF	$28,769	$43.7
0.5% of TPC (Spare parts)	$10,040	$15.3
Total Inventory Capital	$38,810	$59.0
Initial Cost for Catalyst and Chemicals	$0	$0.0
Land	$900	$1.4
Other Owners' Costs	$301,212	$457.8
Financing Costs	$54,218	$82.4
Total Overnight Costs (TOC)	$2,463,813	$3,745.0
TASC Multiplier (IOU, high-risk, 35 year)	1.140	
Total As-Spent Cost (TASC)	$2,808,747	$4,269.3

Table 5-6: O&M Costs for 900MW$_{gross}$ Air-Fired PC Steam Plant

BOILER ISLAND AND BALANCE OF PLANT O&M COSTS

Client: DOE - NETL — **INITIAL & ANNUAL O&M EXPENSES** — Cost Base: Jun-11

Project: 900MW Air-Fired Plant

Net Plant Heat Rate (Btu/kWh): 8,273

Net Power Output (kW): 848,675

Capacity Factor (%): 85

FIXED OPERATING COSTS

OPERATING & MAINTENANCE LABOR

Operating Labor

Operating Labor Rate (base):	39.70 $/hour
Operating Labor Burden:	30.00 % of base
Labor O-H change Rate:	25.00 % of labor

Operating Labor Requirements (O.J.) per shift	1 unit/mod.	Total Plant
Skilled Operator	2.0	2.0
Operator	9.0	9.0
Foreman	1.0	1.0
Lab Tech's, etc.	2.0	2.0
TOTAL O.J.'s	14.0	14.0

	Annual Cost $ / year	Annual Unit Cost $/kW-net
Annual Operating Labor Costs (calc'd)	6,329,450	7.46
Maintenance Labor Costs (calc'd)	9,685,187	11.41
Administrative & Support Labor (calc'd)	4,003,659	4.72
Property Taxes ans Insurance	28,927,663	34.09
TOTAL FIXED OPERATING COSTS	**48,945,960**	**57.67**

VARIABLE OPERATING COSTS

		Consumption		Unit Cost	Initial Fill		
		Initial Fill	Per Day	($/unit)	Cost ($)		$/kWh-net
Maintenance Material Cost						14,527,780	0.00230
Consumables							
Water (1,000 gallons)			5,783	1.67		3,003,192	0.00048
Chemicals							
MU & WT Chem. (lbs.)			28,933	0.27	0	2,404,335	0.00038
Limestone (tons)			831	33.48	0	8,627,900	0.00137
Ammonia (19% NH_3) (tons)			113	330.00	0	11,585,585	0.00183
Subtotal Chemicals					0	22,617,821	0.00358
Other Consumables							
Supplemental Fuel (10^6 Btu)							
SCR Catalyst Replacement (m^3)		w/equip.	0.48	8,938.80		1,319,080	0.00021
Emissions Penalties							
Subtotal Other Consumables						1,319,080	0.00021
Waste Disposal							
Fly Ash (tons)			1,447	25.11		11,269,521	0.00178
Bottom Ash (tons)			362	25.11		2,817,380	0.00045
Subtotal Waste Disposal						14,086,901	0.00223
TOTAL VARIABLE OPERATING COSTS						**55,554,774**	**0.00879**
Fuel (tons)			7183	65.30		**145,535,444**	**0.02303**

Table 5-7: O&M Costs for 900MW$_{gross}$ Oxy-Fired PC Steam Plant

BOILER ISLAND AND BALANCE OF PLANT O&M COSTS

Client: DOE - NETL — **INITIAL & ANNUAL O&M EXPENSES** — Cost Base: Jun-11

Project: Alstom Oxy-Firing Study — **Case 2 - 1 x 930 MW-gross Oxy-fired SCPC Steam Plant**

Net Plant Heat Rate (Btu/kWh): 10,486
Net Power Output (kW): 657,901
Capacity Factor (%): 85

FIXED OPERATING COSTS

OPERATING & MAINTENANCE LABOR

Operating Labor Requirements (O.J.) per shift	1 unit/mod.	Total Plant
Skilled Operator	2.0	2.0
Operator	9.0	**9.0**
Foreman	1.0	**1.0**
Lab Tech's, etc.	2.0	2.0
TOTAL O.J.'s	14.0	14.0

Operating Labor	
Operating Labor Rate (base):	39.70 $/hour
Operating Labor Burden:	30.00 % of base
Labor O-H change Rate:	25.00 % of labor

	Annual Cost $ / year	Annual Unit Cost $/kW-net
Annual Operating Labor Costs (calc'd)	6,329,450	9.62
Maintenance Labor Costs (calc'd)	13,403,762	20.37
Administrative & Support Labor (calc'd)	4,933,303	7.50
Property Taxes ans Insurance	40,034,285	60.85
TOTAL FIXED OPERATING COSTS	**64,700,801**	**98.34**

VARIABLE OPERATING COSTS

		Consumption		Unit Cost	Initial Fill		$/kWh-net
		Initial Fill	Per Day	($/unit)	Cost ($)		
Maintenance Material Cost						20,105,643	0.00410
Consumables							
Water (1,000 gallons)			6,401	1.67		3,324,128	0.00068
Chemicals							
MU & WT Chem. (lbs.)			28,933	0.27	0	2,404,335	0.00049
Limestone (tons)			745	33.48	0	7,736,421	0.00158
Ammonia (19% NH_3) (tons)			113	330.00	0	11,585,585	0.00237
Subtotal Chemicals					0	21,726,342	0.00444
Other Consumables							
Supplemental Fuel (10^6 Btu)							
SCR Catalyst Replacement (m^3)		w/equip.	0.48	8,938.80		1,319,080	0.00027
Emissions Penalties							
Subtotal Other Consumables						1,319,080	0.00027
Waste Disposal							
Fly Ash (tons)			1,454	25.11		11,324,551	0.00231
Bottom Ash (tons)			363	25.11		2,831,138	0.00058
Subtotal Waste Disposal						14,155,688	0.00289
TOTAL VARIABLE OPERATING COSTS						**60,630,882**	**0.01238**
Fuel (tons)			7218	65.30		**146,246,101**	**0.02985**

Client: DOE - NETL — **ANNUAL O&M EXPENSES SUMMARY** — Cost Base: Jun-11

	Annual Cost $/Year	Annual Unit Cost $/kW
BOILER ISLAND AND BALANCE OF PLANT O&M COSTS		
TOTAL FIXED O&M COSTS	64,700,801	98.34
TOTAL VARIABLE O&M COSTS	60,630,882	0.0124
AIR SEPARATION UNIT (ASU)		
TOTAL FIXED O&M COSTS	9,601,686	0.00
TOTAL VARIABLE O&M COSTS	1,806,581	0.000000
GAS PROCESSING UNIT (GPU)		
TOTAL FIXED O&M COSTS	1,427,607	2.17
TOTAL VARIABLE OPERATING COST	12,410,459	0.0025
TOTAL PLANT O&M COSTS	**$/Year**	**$/kW**
TOTAL FIXED OPERATING COSTS	75,730,093	**100.51**
TOTAL VARIABLE OPERATING COST	74,847,923	**0.01491**

6. Industrial Boiler

This section describes the retrofit design of an existing air-fired industrial size steam generator equivalent to $150MW_{gross}$ to oxy-firing capability. This power plant is designed to capture 93 percent of the CO_2 produced. The design study focused on the necessary boiler modifications for this conversion, although the major cost items associated with the addition of an Air Separation Unit (ASU) and Gas Processing Unit (GPU) for the final CO_2 purification and compression were also considered.

6.1 Introduction

The base case air-fired industrial boiler is a coal-fired unit, with a nominal capacity of about 980,000 lbm/hr of superheated steam flow. It is retrofitted to operate at full load capability using recirculated flue gas as the oxidant for combustion of the fuel. The retrofit unit operates with a TFS (Tangential Firing System) system, SCR for NO_x control, NID^{TM} dry scrubber system for SO_2 and fly ash control, and two gas to gas tubular heaters (GGH). The retrofit unit is capable of firing the design pulverized coal, producing continuous steam flow at nominal boiler outlet conditions of 123.6 kg/s (980,000 lbm/hr), 108.5 bar (1600 psig), 538°C (1,000°F) at the superheater outlet. Heavy fuel oil is used for start-up.

The process flow diagram and a brief overview of the base case air fired industrial boiler design is described below. The aspects of the oxy-fired process and the boiler island modifications for oxygen firing are also discussed in the oxygen firing section.

6.2 Base Case Air-Fired Industrial Boiler Process Description

Figure 6-1 shows a simplified process flow diagram for a base case air fired boiler island. This arrangement permits full load operation with air firing.

The flue gas leaving the boiler upper economizer section (Stream 50) flows through a Selective Catalytic Reduction (SCR) system for NO_x reduction. The flue gas leaving the SCR (Stream 48) is then goes to the lower economizer for feedwater heating. The flue gas from the lower economizer goes into Tubular Air Preheaters (Primary Air Heater and Secondary Air Heater). The Tubular Heaters (TH) are connected in series for the flue gas side flow. The cooled flue gas leaving the secondary TH (Stream 22) then enters a NID^{TM} where most of the particulate and SO_2 is removed. The particulate free flue gas leaving the NID^{TM} (Stream 20) then flows through the induced draft (ID) fan. The flue gas from the ID fan goes into the exhaust stack (Stream 46).

Stream 28 represents the secondary air stream entering the forced draft fan at ambient condition. Stream 28 is then increased to the required pressure by the forced draft (FD) fan and heated in the secondary tubular air heater. The secondary air from air preheater enters the furnace through the wind-box (see Stream 42).

Stream 27 represents the primary air stream to the primary air fan. The primary air at ambient condition flows into the PA fan where the air is raised to the required pressure (Stream 30). The

primary air stream leaving the PA fan (Stream 30) is split into a heated portion (Stream 18) and an un-heated tempering air (Stream 34). Stream 33 is heated in the primary tubular air heater to form the hot primary air (Stream 18). The hot primary air is mixed with unheated tempering air before it goes to the coal mill. The split between the heated and unheated streams is adjusted to control the temperature of the solids/gas mixture leaving the coal mills (Stream 31) to the desired value (typically about 180°F with this fuel).

The primary air and pulverized coal mixture (Stream 31) leaving the coal mills is combusted in the furnace together with the heated secondary air stream (Stream 42). The secondary stream (Stream 42) flow rate is controlled such that the flue gas oxygen content in the flue gas leaving the boiler (Stream 49) is about 3 percent by volume. The products of combustion along with flyash leave the lower furnace section and pass through radiant and convective heat exchangers located in the upper furnace, tunnel, and backpass areas of the boiler.

Ash that is not entrained in the furnace with the flue gas is called bottom ash. It is the ash that accumulates on the furnace walls, is removed with wall blowers, and falls to the bottom of the furnace, and into a trough containing water. The bottom ash is removed continuously from the water trough, which is part of the submerged scraper conveyor (SSC) system.

It is important to minimize air infiltration to keep plant thermal efficiency as high as possible. Infiltration air streams shown on Figure 14 include Stream 12 and Stream 23. Stream 12 represents the infiltration air entering the boiler. Stream 23 represents infiltration air entering the NID™.

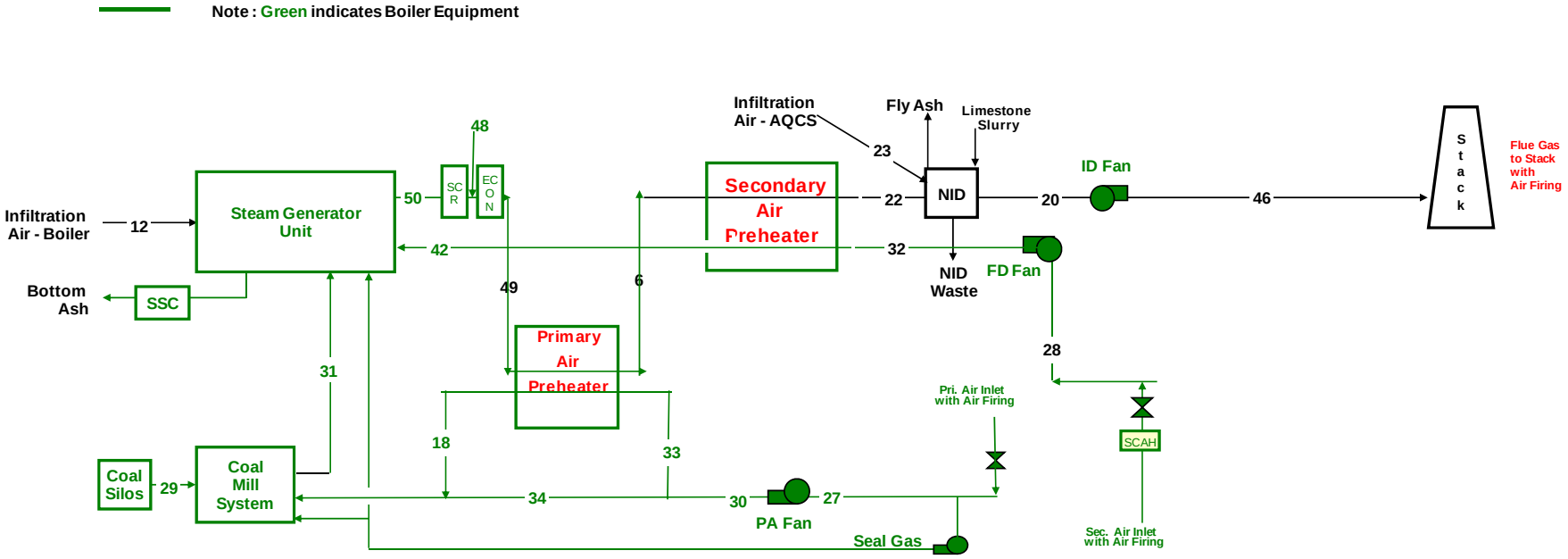

29	Raw Coal to Pulverizers	46	Fluegas to Stake
12	Boiler Infiltration Air	27	Primary Air to PA Fan
50	Fluegas from Upper Economizer to SCR	30	Pressurized Primary Air to spliter
48	Fluegas from SCR to lower Economizer	34	Tempered Primary air to Pulverizer
49	Fluegas to Primary Air Preheater	33	Primary air to Primery Air Preheater
6	Flue Gas to Secondary Air Preheater	18	Hot Primary air to Pulverizer
23	AQCS Infiltration Air	31	Pulverized Coal and Primary "Air" to Furnace
22	Fluegas to NID	28	Secondary air to FD Fan
20	Fluegas to ID Fan	32	Pressurized Secondary air to Secondary Air Preheater
	Limestone Slurry Feed to NID System	42	Heated Secondary air to Furnace
	NID System Waste to Disposal		Bottom Ash from Furnace to SSC
			Seal Gas Flow

Figure 6-1: Industrial Boiler Island Process Flow Diagram for Air-Fired Base Case

6.3 Oxygen Firing

Figure 6-2 shows the basic process flow diagram selected for the oxygen-fired boiler island. New equipment within the boiler scope (relative to a comparable air-fired boiler scope) would include oxygen supply lines, oxygen mixing devices, redesigned secondary tubular heater to preheat recirculated flue gas, and additional ductwork to connect the inlets of the PA and FD fans to the recirculated flue gas sources. The flue gas recirculation (FGR) ducts would also include isolation dampers and inlets for air, which are used during start-up and transition from air to oxygen-firing. Additionally, the sizing of the fans and ducts will be different than for an air-fired design due to the higher density of the recirculated flue gas as compared to air. The windbox would also be slightly different than for an air-fired design in order to accommodate the use of nearly pure oxygen provided from the Air Separation Unit (ASU). About 25% of the total oxygen produced in the ASU is introduced directly in the windbox (Stream 39 in Figure 6-2). This is done in order to keep the oxygen content in the primary and secondary streams (Streams 34 and 42 in Figure 6-2) below a threshold value above which would require the use of more costly alloys for the ducts and other equipment downstream of the oxygen mixing location.

Primary flue gas is taken after the flue gas condenser where most of the water has been condensed (typically, about 4% by volume water remains in the primary FGR stream). The primary recirculated flue gas serves to dry the coal during pulverization and transport the pulverized coal to the furnace for combustion. Its flow rate, which also contains seal gas to reduce boiler air in-leakage, is kept as low as possible to minimize flow through the flue gas condenser equipment. Secondary flue gas is taken downstream of flue gas desulfurization (NID^{TM}) system to minimize the recycle of SO_2. The quantity of secondary FGR is established by superheat circuit heat transfer requirements. The secondary FGR flow rate is adjusted to provide the specified superheat outlet steam temperature leaving the boiler. Slagging and fouling considerations also can influence the minimum amount of secondary FGR.

Oxygen produced from a cryogenic distillation type air separation unit (ASU) is mixed with the recirculated flue gas streams upstream of the PA and FD fans. The Primary and Secondary Gas to Gas heaters are arranged in series (flue gas connected in series between primary and secondary tubular air heaters). The main advantages of mixing oxygen in these locations are to minimize ASU power requirements (lower O_2 pressure required by mixing before the fans) and to improve the GGH preheater performance (lower sink temperature and higher sink mass flow) thus providing a boiler efficiency improvement without the use of a separate oxygen heater.

Boiler Island Process Description– Oxygen Firing

Figure 6-2 shows a simplified process flow diagram for an Oxygen fired boiler island. This arrangement permits full load operation with either air or oxygen-firing. The damper configuration shown in this figure is for the oxy-fired mode of operation. In the oxygen-fired mode, the streams shown in dashed red lines are not in use (i.e. primary air inlet, secondary air inlet, and flue gas outlet to stack).

The flue gas leaving the boiler upper economizer section (Stream 50) flows through a Selective Catalyst Reduction (SCR) system for NO_x reduction. The flue gas leaving the SCR (Stream 48) then goes to the lower economizer for feedwater heating. The flue gas from the lower economizer (stream 49) goes into two Gas to Gas Tubular Heaters (Primary Heater and Secondary Heater). The Tubular Heaters are connected in series for the flue Gas side flow. The cooled flue gas leaving the secondary GGH (Stream 22) then enters a NID^{TM} where most of the particulate and SO_2 is removed. The particulate free flue gas leaving the NID^{TM} (Stream 20) then flows through the induced draft (ID) Fan. The flue gas leaving the ID Fan (Stream 46) is split into two streams (Stream 24 and Stream 3).

Stream 24 represents the recirculated flue gas portion of the secondary stream. The secondary recirculated flue gas stream (Stream 24) is mixed with oxygen (Stream 25) to form Stream 28, which has an oxygen concentration of 21 percent by volume. Stream 28 is then increased to the required pressure with the forced draft (FD) fan and heated in the secondary sector of the GGH to form the heated secondary oxidant stream entering the furnace (Stream 42).

Stream 3 represents the remainder of the flue gas leaving the ID Fan that is not used for the secondary recirculation stream (Stream 24). After leaving the ID Fan, Stream 3 flows through a flue gas condenser (FGC) where most of the moisture contained in the flue gas is condensed out (Stream 13). The saturated flue gas leaving the FGC (Stream 3) is split into two streams (2 and 26).

Stream 2 is the high CO_2 content product stream, which flows to the Gas Processing Unit (GPU) for further purification such that the final CO_2 product is acceptable for usage or sequestration. The GPU vent stream leaving the GPU contains non-condensable gases (i.e.O_2, N_2, Ar, etc) and also a small fraction of the CO_2.

Stream 26 represents the recirculated flue gas portion of the primary stream. It is mixed with oxygen (Stream 14) to an oxygen concentration of 21 percent by volume and is increased to the necessary pressure with the primary air (PA) fan to form the primary oxygen enriched recirculated flue gas stream. The primary FGR stream leaving the PA fan (Stream 30) is split into a heated portion (Stream 18) and an un-heated portion (Stream 34). Stream 33 is heated in the primary GGH to form the hot primary FGR (Stream 18). The hot stream is mixed with unheated Stream 34. The split between the heated and unheated streams is adjusted to control the temperature of the solids/gas mixture leaving the coal mills (Stream 31) to the desired value (typically about 180°F with these fuels).

The location selected for the primary flue gas recirculation stream (stream 26) is just downstream of the FGC. This location was selected in order to provide the coal mills with a primary oxidant stream that has low moisture content such that coal drying inside the mills will be similar to air-fired operation. The location selected for the secondary flue gas recirculation stream (Stream 27) is just after the NID^{TM} system in order to provide SO_2 levels throughout the boiler island that are within our air fired experience range.

The primary oxidant and pulverized coal mixture (Stream 31) leaving the coal mills is combusted in the furnace together with the heated secondary oxidant stream (Stream 42) and also with a pure oxygen stream (Stream 39). Stream 39 represents the additional oxygen required for combustion of the coal over and above already contained in streams 29 and 42. Stream 39 flow rate is controlled such that the flue gas oxygen content in the flue gas leaving the boiler (Stream 49) is about 3 percent by volume. The products of combustion along with flyash leave the lower furnace section and pass through radiant and convective heat exchangers located in the upper furnace, tunnel, and backpass areas of the boiler (Stream 49).

It is important to minimize air infiltration for an oxy-fired system with carbon capture in order to minimize the power requirement of the GPU and to keep plant thermal efficiency as high as possible. Infiltration air streams shown on Figure 14 include Stream 12 and Stream 23. Stream 12 represents the infiltration air entering the boiler. This flow was assumed to be about 1 percent of the stoichiometric oxygen requirement of the boiler. This should be obtainable through the use of recirculated flue gas instead of air as a seal gas for the boiler. Stream 23 represents infiltration air entering the NID^{TM}. This flow was assumed to be about 2 percent of the flue gas flow entering the NID^{TM}.

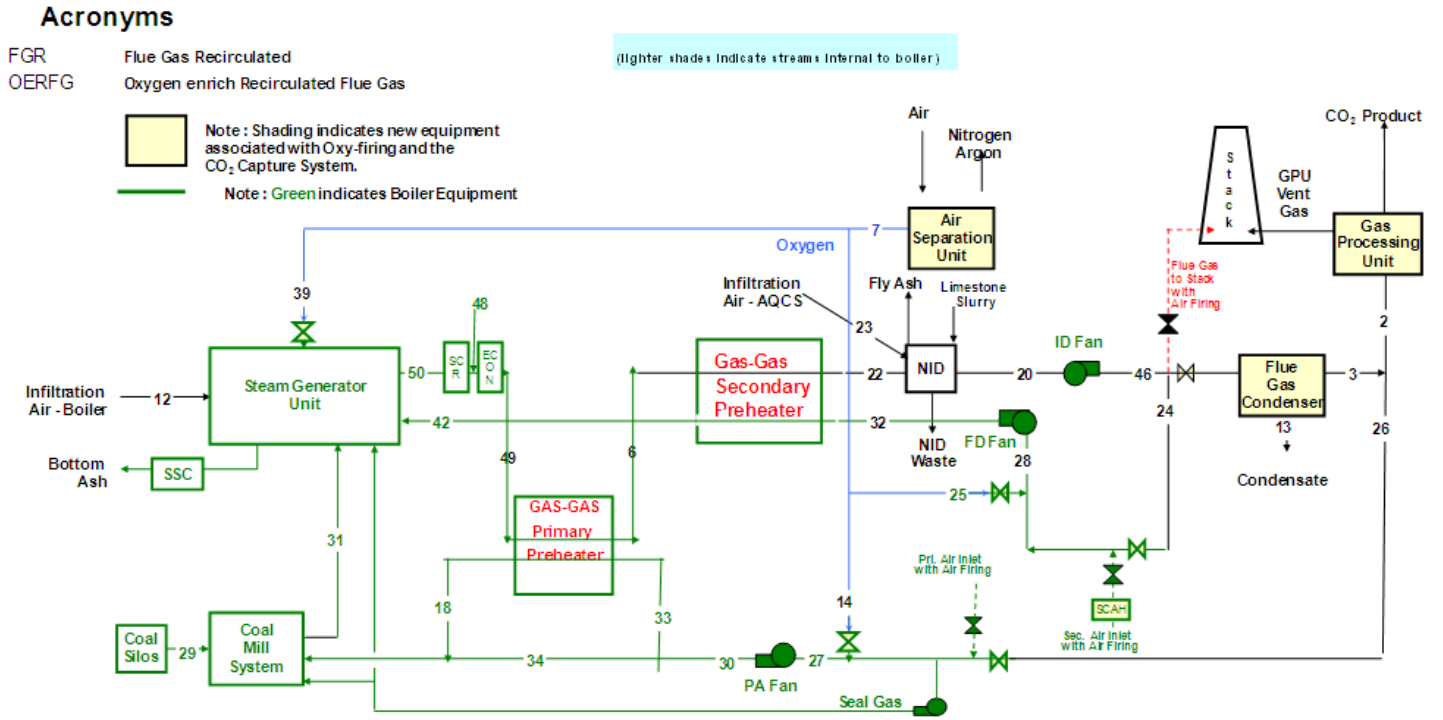

ThermoFlow Stream #	Material Flow Stream Identification
29	Raw Coal to Pulverizers
12	Boiler Infiltration Air
7	Total Oxygen leaving ASU
14	Oxygen to Primary FGR Stream
25	Oxygen to Secondary FGR Stream
39	Oxygen Stream to Furnace
50	Fluegas from Upper Economizer to SCR
48	Fluegas from SCR to lower Economizer
49	Fluegas to Primary Gas-Gas Heater
6	Flue Gas to Secondary Gas - Gas Heater
23	AQCS Infiltration Air
22	Fluegas to NID
20	Fluegas to ID Fan
	Limestone Slurry Feed to NID System
	NID System Waste to Disposal
46	Fluegas leaving ID Fan
3	Fluegas to Condenser
2	Fluegas to Gas Processing Unit
	Condensed Water Stream from Fluegas
26	Cooled Fluegas Stream
27	Primary Oxygen Enrich Recirculated Flue G
30	Pressurized Primary OERFG
	Pressurized Primary OERFG to temp. split
34	Tempered Primary OERFG to Pulverizer
33	Primary OERFG to Gas-Gas Primery Heater
18	Hot Primary OERFG from Primary GGH to Pulverizer
31	Pulverized Coal and Primary OERFG to Furnace
24	Recirc Secondary FG Stream from ID Fan
	Recirculated Secondary FG to O2 Mixer
28	Secondary OERFG to FD Fan
32	Pressurized Secondary OERFG to Secondary GGH
42	Heated Secondary OERFG to Furnace
13	Liquid water from FG Condensor
	Bottom Ash from Furnace to SSC
	Vent Gas from GPU to Stack
	Seal Gas

Figure 6-2: Industrial Boiler Island Process Flow Diagram for Oxy-Fired PC Boiler

6.4 Steam Generator Design

6.4.1 Furnace

The furnace is constructed with welded waterwall tubes, which provides structural rigidity to the construction and a positive seal from leaking furnace gases. This eliminates casing hot spots, the need for an inner casing, and air infiltration. The furnace wall tubing has a built-in thickness tolerance for longer tube life and greater unit availability. Figure 6-3 and Figure 6-4 show side view and plan view general arrangement drawings of the industrial boiler.

The furnace volume and projected surface are sized to yield conservative heat release rates. Conservative heat release rates yield lower emissions, maximize carbon burnout, and minimize the potential for burning in the superheater or flame impingement on the waterwalls.

The slagging characteristics associated with the coal ash had been considered in the base case air-fired furnace design. The Furnace had been conservatively sized to reduce overall furnace temperatures and minimize furnace slag accumulation. Based on the pilot plant testing at Alstom's $15MW_{th}$ boiler, it was determined that the slagging and fouling characteristic during the oxy-fired are similar to air-firing. Therefore, no changes are required for the furnace, superheater, and boiler bank. In addition, in order to minimize fouling in the superheater sections, the first vertical heat transfer section (primary superheater) is platenized.

The furnace is designed for balanced draft operation and a pressure tap is provided at the furnace outlet. This pressure tap is linked to the ID fan to maintain a constant -0.1" w.g. under all firing conditions. This design prevents the escape of hot flue gases from the combustion chamber and also dampens the effect of a furnace "puff" or excursion to positive pressure. The furnace buckstay system is designed in accordance with NFPA.

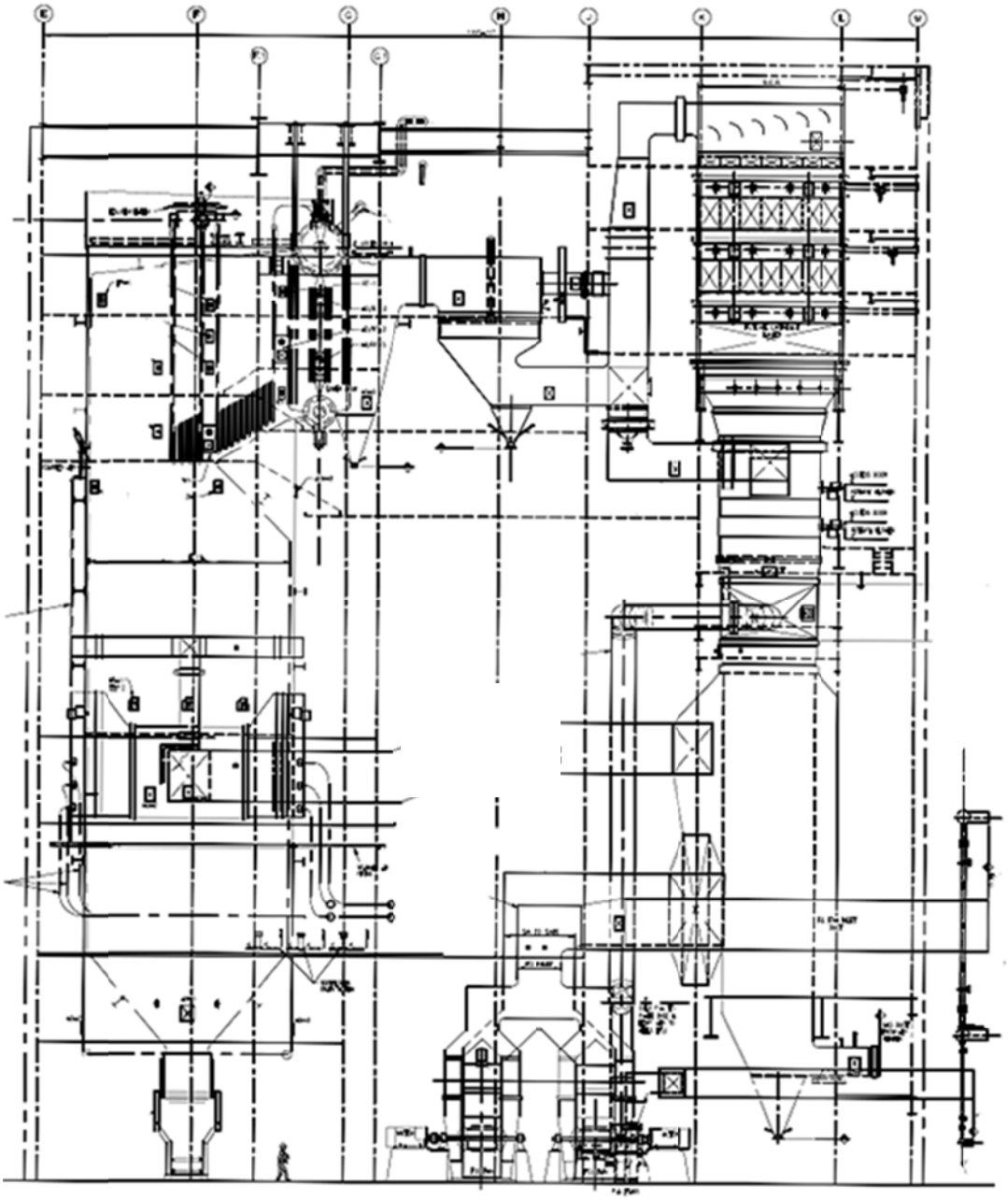

Figure 6-3: Side Elevation of Industrial Boiler

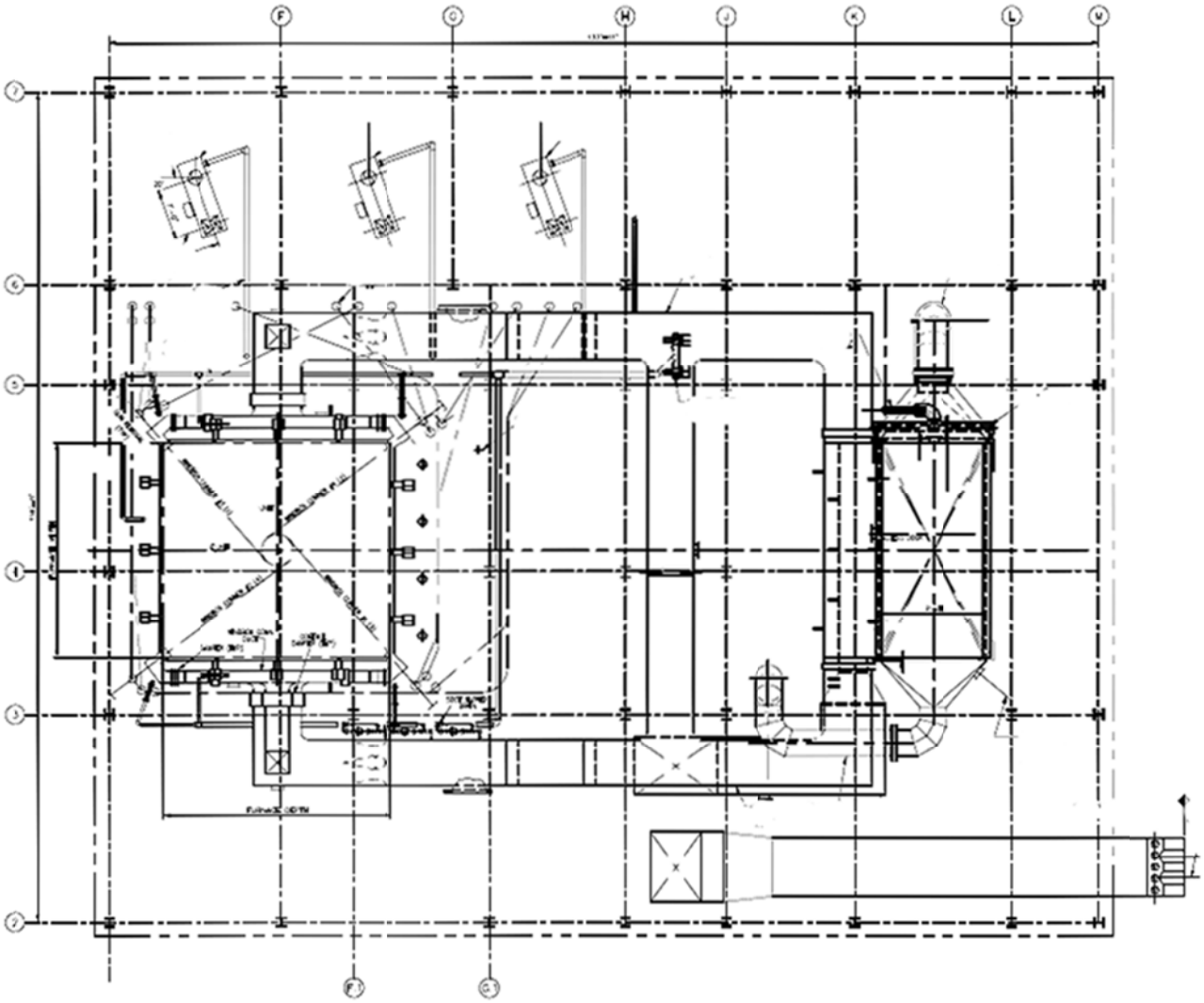

Figure 6-4: Plan View of Industrial Boiler

6.4.2 Boiler Bank

The boiler bank is a single pass, cross flow heat exchanger located after the superheater. The boiler bank consists of vertical, in-line carbon steel tubes arranged in two sections. The sections are separated by a cavity which allows installation of sootblowers and facilitates maintenance and inspection.

Retractable sootblowers are used in this area, not so much due to the temperature constraint as to a better job of cleaning that is done compared to rotary blowers. All boiler bank tubes are rolled into the upper and lower drums.

The flue gas makes a single pass across the boiler bank tubes which contain saturated water or a steam/water mixture. The most active steam generating circuits are located in the front bank where the hottest gas temperatures exist. The final few tube rows primarily act as downcomers since insufficient thermal head exists to generate steam. The boiler bank acts as a heat sink to absorb any system thermal transients.

6.4.3 Superheater and Desuperheater

A two stage superheater arrangement is provided for the proposed steam generator. The arrangement employs a parallel flow platen section followed by a counterflow pendent spaced section. Maximum heat transfer is achieved in the superheater by exposing the lowest temperature steam to the hottest flue gases as well as radiant heat from the furnace. A dual crossover interstage desuperheater is provided for steam temperature control.

To provide a gas tight seal in the penthouse, the superheater assemblies are supplied with shop installed high crown seals at the point where the tubes penetrate the furnace roof.

A steam-cooled spacer serves to maintain the lateral or transverse alignment of the superheater tubes. Front to rear longitudinal spacing of the tubes is maintained by flex ties.

In order to facilitate inspection and maintenance, the superheater tube assemblies are arranged in-line with sootblower/access cavities located between the two sections and within the spaced section. Observation ports are provided at the superheater elevation and two access doors are located in the penthouse.

6.4.4 Split Economizer

From the boiler bank, the flue gas flows to the final pressure part heat transfer surface, the split economizer. In the economizer the incoming feedwater is heated in order to increase overall unit efficiency. The economizer tube surface is arranged for counterflow, with the hot flue gas flowing down over the tubes and the feedwater flowing up inside the tubes. The economizer section is split into upper and lower parts to accommodate flue gas temperature requirement for the SCR. The SCR requires the inlet flue gas temperature between 700°F - 725°F. The gas exit temperature at the upper economizer falls within the 700°F - 725°F range. The upper economizer tubes are arranged in a single bank with access/sootblower cavities below the bank. The flue gas

from the upper economizer flows into the SCR for NO_x removal. The flue gas from the SCR enters into the lower economizer at around 700°F.

The lower economizer tubes are arranged in two banks with access/sootblower cavities between the banks. Rotary sootblowers are used in this area because of the low flue gas temperature and the dry, sintered ash deposits that accumulate.

6.4.5 Circulation System

The steam generator design employs a natural circulation system. The feedwater passes through the lower and upper economizers respectively and then enters the water side of the steam drum where it is distributed along the entire length of the drum via a distribution pipe.

The steam drum has an internal diameter sized to separate the maximum quantity of steam to be generated. It is supplied with primary and secondary screen type internals to meet steam purity requirements.

The boiler bank acts as a heat sink and buffer between the superheater and economizer. The first half of the boiler bank generates the bulk of the steam due to the high gas temperatures. These tubes are essentially riser circuits between the upper and lower drums. The rear half of the boiler bank acts as heated downcomers feeding water to the lower drum.

The lower drum is sized based on the number of tubes deep in the boiler bank and provides the source of water supplied to the waterwalls. From the lower drum, the preheated water is fed through four unheated downcomers to the four corners of the lower furnace. The lower furnace headers are connected forming a ring which supplies water to all four waterwalls. In the waterwall tubes, the water flows at a velocity low enough so as not to inhibit the natural circulation, but high enough to prohibit departure from nucleate boiling.

The waterwall tubes generate a steam/water mixture which is carried into the steam drum as follows:

- The front wall tubes form the roof and relieve directly into the steam drum.
- The rear wall tubes relieve into the lower drum where the steam/water mixture is baffled into the first three boiler bank rows and passed to the steam drum.
- The sidewall tubes relieve into upper headers which are in turn relieved by a series of riser tubes that feed into the steam drum.

6.4.6 Tubular Heat Exchangers (Tubular Oxidant Heaters)

Downstream of the lower economizer are the two tubular heat exchangers for preheating the oxidant streams. The first tubular heater is for preheating the primary oxidant stream. The primary tubular heater has oxidant flow inside the tubes and flue gas over the tubes. The primary heater design for the oxy-fired case is kept the same as the air-fired base case.

The flue gas leaving the primary tubular heater goes into the secondary tubular heater. The secondary tubular is preheating the high moisture oxidant stream. It is the final means of heat recovery and is sized to reduce the exiting flue gas temperature. The exit flue gas temperature from the secondary tubular heater is higher by about 20°F from the base case air-fired mode. The higher exit gas temperature is due to about 80°F higher inlet secondary oxidant temperature in the oxy-fired case than base case. The secondary heater has three gas passes compared to two passes required in the air-fired base case. An extra pass (higher surface area) is required due to the lower LMTD. The surface area is increased by about 50% in the oxy-fired secondary heat exchanger. In the secondary heater, gas flows through the tubes counterflow to the oxidant flowing over the tubes. This arrangement maximizes the heat transfer and reduces the plugging potential.

Access has been left for maintenance and cold-end tube removal if required. A steam coil air heater is provided in the oxidant stream duct leading to the tubular preheater to protect against cold-end corrosion.

6.4.7 Mechanical Design Aspects

Same as the design that was described for the 450MW boiler.

6.4.8 Boiler Pressure Parts

Similar to the design that was described for the 450MW boiler.

6.4.9 Boiler Steel Structure

Same as the design that was described for the 450MW boiler.

6.4.10 Sootblower System

Rotary blowers

The rotary type blower is designed to clean convection surfaces of the economizer or air heater where the temperatures do not exceed 1800°F. The blowers are placed between the tube banks to clean the ash on the convective surface. Steam or air is used as cleaning fluid in the blower. The blower element lengths are limited to approximately 20ft. The element contains multiple nozzles for air or steam cleaning. The element rotates at 1.5rpm.

Each Rotary blower includes the following:

- Electric motor
- Valve stem and plunger

- Switch box, push button, and limit switches
- Elements

Wall Blowers

This short, single-nozzle retractable blower removes ash deposited on the walls of furnace chambers. It is a short stroke lance, which penetrates the furnace wall. Supported by wall boxes welded to the furnace tubes, it moves with the tubes as they heat and cool. The single nozzle at the tip directs a jet of high-pressure steam tangent to the furnace face of the water wall tubes, dislodging the slag deposits. The lance rotates through 360° and cleans approximately a 2-meter (6.6 ft) radius. The effective radius depends upon how tenacious the deposit is. Blowing frequency depends on the rate of slag build up.

Each blower includes the following:

- Electric motor drive
- Mechanically-operated valve with adjustable pressure control
- Stellited valve seats and disc
- Motor starter and limit switches

6.4.11 Coal Pulverizers

The coal pulverization system is similar to that described for the 450MW design in Section 4.3.11. The pulverizing system for the base air-firing case includes three (3) Alstom HP-643 pulverizers with dynamic classifiers. This system is adequate for both air and oxy-firing for a range of coals at 100% BMCR providing appropriate primary oxidant flow, and temperature and moisture levels are maintained.

6.4.12 Coal Feeders

Gravimetric feeders with acoustic-type coal monitors and microprocessor controls are used in the base design and do not need modification for oxy-firing.

6.4.13 Firing System

Overview

The base case firing system for the air case is a four corner tangential firing design with three coal firing elevations and one elevation for separate overfire air. This system is retrofitted to comply with oxy-firing requirements. The modified firing system design for oxy-firing is similar to that described for the 450MW design. The oxy-firing system allows a portion of the oxygen to be distributed directly to windbox compartments to avoid oxygen concentration in the oxidant streams higher than 23%.

The requirements are listed below.

- The remaining oxygen from ASU (Stream 39, Figure 6-2) is injected into the Windbox.
- Oxygen injected into the Windbox AUX and CFS Damper compartments using Lances downstream of the dP control dampers.
- Oxygen injected into the High and Lower OFA Damper Compartments using lances downstream of the dP control dampers.
- Windbox oxygen flow on/off to compartment with dP control dampers.
- All materials stainless steel (>13% Chromium) downstream of oxygen injection.

6.4.14 Air/Oxidant and Flue Gas System

Primary Oxidant System

The primary oxidant system is specifically designed for the oxy-fired industrial boiler case. The primary oxidant system supplies the flue gas/oxygen mixture to the pulverizers for drying the pulverized coal and for conveying it to the windbox coal nozzles. Oxygen is mixed upsteam of the primary air/oxidant fan to a concentration of 21% by volume of oxygen.

For the retrofit oxy-fired case, the fans are maintained at the same size as for the air-fired base case. Two fifty percent (50% flow per fan) two-speed centrifugal fans are provided to maintain the required primary oxidant flow for proper coal drying conditions in the pulverizers and proper velocities in the pulverized coal piping to the windbox nozzles for the entire specified fuel range. Primary fans inlet vanes control primary oxidant stream pressure.

Primary fans are sized to accommodate the most severe coal drying requirements within the specified fuel range. The margins on volumetric flow, pressure, and maximum ambient temperature have been considered to size the primary fans relative to the boiler maximum continuous load condition.

The primary oxidant ducts are also supplied.

Secondary Oxidant System

The secondary FGR/oxidant system supplies oxygen enriched recirculated flue gas for combustion to the windboxes. It is delivered by two fifty percent (50% flow per fan) centrifugal forced draft fans. The fans are maintained at same size as the air-fired base case. The secondary oxidant from the forced draft fan is raised to a higher temperature by the flue gases in the Tubular Heat Exchanger (Gas to Gas Heat Exchanger). From the GGH, secondary oxidant is fed to the windboxes through the hot secondary FGR ducts. In the windboxes, individual compartment dampers distribute the oxygen enriched recirculated flue gas. The secondary oxidant duct from the NID^{TM} outlet to the GGH inlet is designed to be acid resistant to H_2SO_4.

Forced draft fans require upgrading and are sized to accommodate the maximum primary recirculated flue gas flow corresponding to the specified fuel range during both air and oxy-firing. The margins on volumetric flow, pressure, and maximum oxidant temperature have been considered to size the FD fans relative to the boiler maximum continuous load condition. The FD fan is constructed to be resistant to the H_2SO_4 in the recycle flue gas.

Control of the boiler secondary oxidant flow is by the forced draft fan inlet vanes, while the distribution of secondary oxidant to the individual windbox compartments is controlled by the secondary oxidant dampers in the windbox compartments. These dampers are positioned by a sub-loop control system.

Flue Gas System

The flue gas system provides a gas tight enclosure for the flue gas stream leaving the boiler. The flue gas system included with this oxy-fired steam generator includes the ductwork from the GGH to the NID™, ductwork from the NID™ to the ID fan, the ID fan, ductwork from the ID fan to the FGC, and ductwork from the FGC to the GPU. It also includes the ductwork from the FGD to the stack that is used during air-firing and during the transition between air and oxygen-firing. Also included are the various required isolation dampers.

A single one hundred percent (100%) single-speed centrifugal induced draft fan is supplied. It is located between the NID™ and the flue gas dondenser. The existing ID fan sized to accommodate the maximum gas flow predicted over the specified range of fuels during air-firing is also adequate for oxy-firing. The margins on volumetric flow, pressure, and maximum calculated temperature have been considered to size the ID fan relative to the boiler maximum continuous load conditions during both air and oxy-firing.

Steam Coil Air Heater (SCAH)

The existing steam coil is located in the secondary air inlet duct and will only be used during the air-firing mode of operation.

Oxygen Mixers

Oxygen is mixed with recirculated flue gas in three locations in this plant.

- Oxygen is mixed up-stream of the primary air fans to a concentration of 21% by volume of oxygen.
- Oxygen is mixed up-stream of the FD fans to a concentration of 21% by volume of oxygen.
- The remaining oxygen required for complete combustion of the coal is mixed with the secondary stream in the windbox just before the oxidant streams enter the furnace.

These streams provide the primary and secondary oxidant streams for combustion of the coal. In the first two mixing locations, it is important to produce well-mixed streams at 21% oxygen. Limiting the oxygen concentration avoids the use of special alloys in downstream equipment.

6.4.15 SCR System

The existing SCR is similar to the design that was described for the 450MW boiler. It is assumed that the SCR system is only used in the air-fired mode of operation.

6.4.16 Bottom Ash System

The existing system is similar to the design that was described for the 450MW boiler and is adequate for both air and oxy-fired operation.

6.4.17 NID^{TM}/Baghouse

A NID^{TM}/baghouse system is used for sulfur removal from the flue gas leaving the oxy-fired industrial boiler. It is of Alstom design and supply as commonly used in the electric power industry on coal-fired boilers. Based upon extensive testing in Alstom's 15MW$_{th}$ oxy pilot facility, the existing NID^{TM} system is adequate for the necessary sulfur removal.

The NID^{TM} System is a Dry Flue Gas Desulfurization (DFGD) process that is based on the reaction between SO_2 and $Ca(OH)_2$ in humid conditions. A humidified mixture of hydrated lime and reaction product is injected into the NID^{TM} system absorber where it cools the inlet flue gas by evaporation of water. The cooled flue gas then flows to the dust collector (fabric filter), where the particulate matter in the flue gas is removed and recycled back through the NID^{TM} FGD system.

Hot untreated flue gas from the oxy-fired boiler, when introduced into the NID^{TM} absorber via a gas disperser, contacts a free flowing, humidified powder of fly ash and lime. The lime is supplied from the lime feed system to the mixer where it is slaked with water to become $Ca(OH)_2$. The mixer blends recycled flyash and water in controlled ratios to achieve the desired gas outlet temperature. The acidic components of the flue gas are rapidly absorbed into the moist alkaline dust particles, which become a dry powder. Liquid water is simultaneously evaporated to obtain the flue gas temperature and humidity required for efficient collection of acidic components, such as SO_2. The control of gas distribution, recycled dry powder flow rate, and distribution and the amount of humidifying water ensures the optimum conditions for SO_2 removal are maintained.

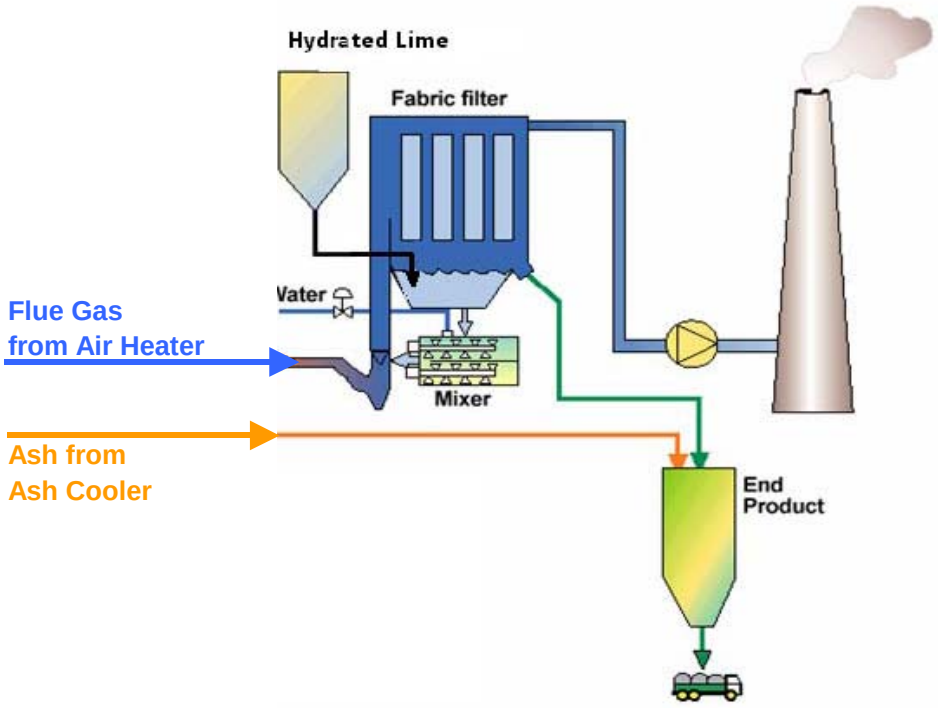

Figure 6-5: Alstom NID™ Concept for a Fossil Fuel Boiler Application

The treated flue gas flows to a particulate collector (in this case a fabric filter), where particulates in the flue gas are removed. Outlet gases from the particulate collector are transported to a stack by means of an induced draft fan. The solids collected in the fabric filter are recycled to the NID™ mixer(s) via a fluidized trough where the recycled solids are humidified and returned to the NID™ reactor(s). The trough level controls the blow-down of solids to the by-product silo for disposal.

Lime is added via a backpack hydrator to the dust mixer of the NID™ FGD system. The addition of lime into the NID™ system enables SO_2 removal in the NID™. The lime bin of the lime feed system is designed to receive quick lime by unloading trucks. A variable speed live bottom screw feeder, located in the discharge section of the day bin, promotes mass flow out of the flanged discharge connections. Lime is fed from the discharge feeder to a screw conveyor. The lime is conveyed by the screw conveyor to the NID™ hydrator. The hydrator uses a controlled amount of water, in proportion to the lime feed rate, to convert the CaO to $Ca(OH)_2$ powder. The hydrator is mounted directly to the side of the recycle ash mixer and discharges the powdered $Ca(OH)_2$ by gravity into the ash mixer. The amount of lime discharged to the day bin is a manual set point by the operator.

6.4.18 Boiler Island Performance Data

Figure 6-6 shows a simplified process flow diagram for an oxygen-fired boiler island. This arrangement permits full load operation with either air or oxygen-firing. The damper configuration shown in this figure is for the oxy-fired mode of operation. In the oxygen-fired mode, the streams shown in dashed red lines are not in use (i.e. primary air inlet, secondary air inlet, and flue gas outlet to stack). The process description is the same as provided in Section 6.3.

Heat and mass balances (SI and English units) for the oxy-fired plant are shown in Table 6-1 and Table 6-2.

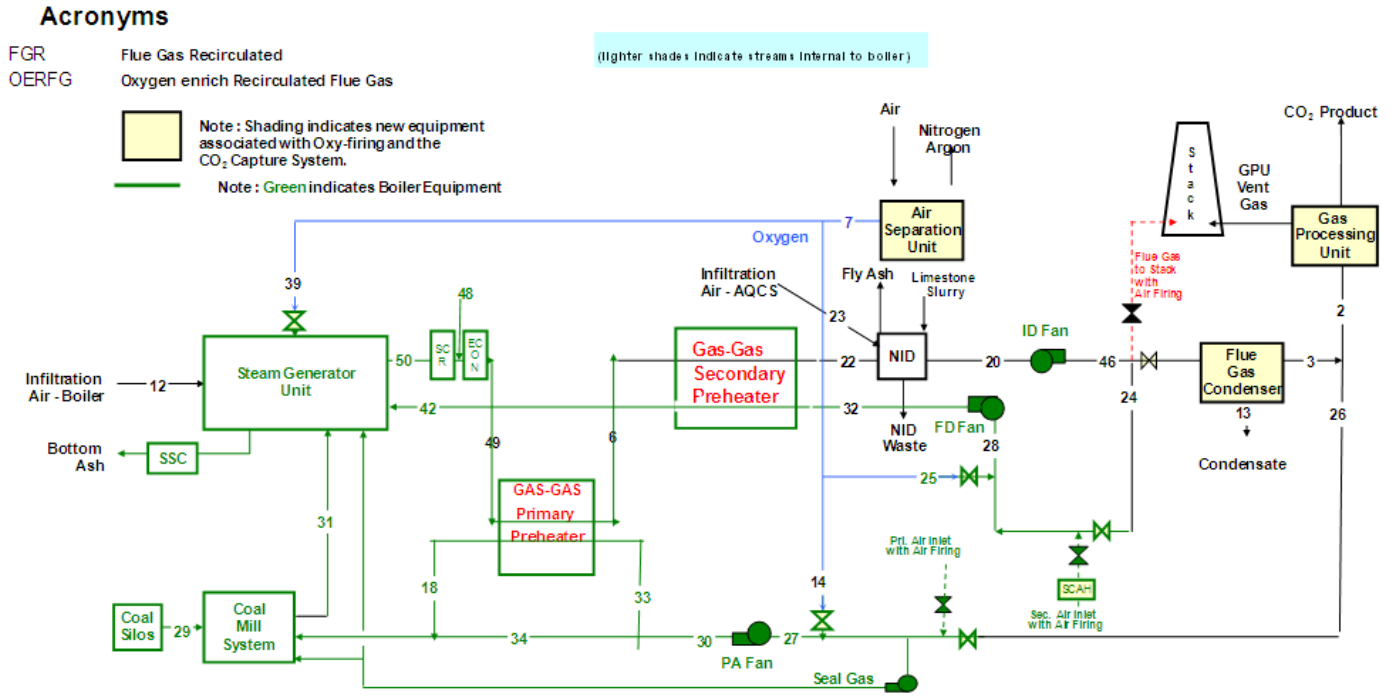

ThermoFlow Stream #	Material Flow Stream Identification
29	Raw Coal to Pulverizers
12	Boiler Infiltration Air
7	Total Oxygen leaving ASU
14	Oxygen to Primary FGR Stream
25	Oxygen to Secondary FGR Stream
39	Oxygen Stream to Furnace
50	Fluegas from Upper Economizer to SCR
48	Fluegas from SCR to lower Economizer
49	Fluegas to Primary Gas-Gas Heater
6	Flue Gas to Secondary Gas - Gas Heater
23	AQCS Infiltration Air
22	Fluegas to NID
20	Fluegas to ID Fan
	Limestone Slurry Feed to NID System
	NID System Waste to Disposal
46	Fluegas leaving ID Fan
3	Fluegas to Condenser
2	Fluegas to Gas Processing Unit
	Condensed Water Stream from Fluegas
26	Cooled Fluegas Stream
27	Primary Oxygen Enrich Recirculated Flue G
30	Pressurized Primary OERFG
	Pressurized Primary OERFG to temp. split
34	Tempered Primary OERFG to Pulverizer
33	Primary OERFG to Gas-Gas Primery Heater
18	Hot Primary OERFG from Primary GGH to Pulverizer
31	Pulverized Coal and Primary OERFG to Furnace
24	Recirc Secondary FG Stream from ID Fan
	Recirculated Secondary FG to O2 Mixer
28	Secondary OERFG to FD Fan
32	Pressurized Secondary OERFG to Secondary GGH
42	Heated Secondary OERFG to Furnace
13	Liquid water from FG Condensor
	Bottom Ash from Furnace to SSC
	Vent Gas from GPU to Stack
	Seal Gas

Figure 6-6: Industrial Boiler Process Flow Diagram – Oxygen Fired Mode

Table 6-1: Gas Side Material & Energy Balance SI Unit (Oxy Firing, BMCR)

Stream #	Stream Location	P	T	Mgas	Mash	Mole Composition %							H*	V	M.W.
		[bar]	[C]	[kg/s]	[kg/s]	N2	O2	CO2	H2Ov	H2Ol	Ar	SO2	[kJ/kg]	[m^3/s]	
2	Flue Gas to GPU	1.01	29.31	38.25	0.00	12.51	4.68	75.55	4.02	0	3.23	110	3.79	23.6	40.27
3	Flue Gas leaving FGD	1.02	76.69	73.22	0.00	8.87	3.32	53.58	31.93	0	2.29	80	53.74	61.5	33.80
4	Flug Gas for SH2 to ECON1	1.01	436.70	141.40	0.89	7.98	3.01	59.31	27.00	0	2.51	1820	464.28	234.1	35.29
6	Flue Gas to Secondary GGH	0.99	290.14	141.40	0.89	7.98	3.01	59.31	27.00	0	2.51	1820	287.72	189.7	35.29
7	Total Oxygen leaving ASU	1.04	26.67	28.32	0.00	0.40	96.30	0.00	0.00	0	3.30	0	1.50	21.1	32.25
12	Boiler infiltration air	1.01	26.67	1.30	0.00	76.47	20.52	0.03	2.07	0	0.92	0	1.70	1.1	28.74
14	Oxygen to Primary FGR Stream	1.01	26.67	4.14	0.00	0.40	96.30	0.00	0.00	0	3.30	0	1.50	3.2	32.25
18	Hot Primary OERFG to Pulverizers	1.08	260.00	12.49	0.00	10.34	21.12	61.99	3.30	0	3.24	90	224.96	13.2	38.83
20	Flue Gas to ID Fan	0.95	69.44	150.40	0.00	8.87	3.32	53.58	31.93	0	2.29	80	45.69	132.8	33.80
21	Flue Gas to FGD	0.98	175.03	144.20	0.00	9.61	3.43	57.90	26.41	0	2.47	1780	157.18	156.6	35.13
22	Flue Gas to Baghouse	0.98	175.03	144.20	0.89	9.61	3.43	57.90	26.41	0	2.47	1780	157.18	156.2	35.13
23	BagHouse infiltration air	0.98	26.67	2.81	0.00	76.41	20.50	0.03	2.14	0	0.92	0	1.70	2.5	28.73
24	FG Splitter (15) to Oxygen Mixter(24)	1.02	76.69	77.19	0.00	8.87	3.32	53.58	31.93	0	2.29	80	53.74	64.8	33.80
25	Oxygen to Secondary Oxygen Mixter(24)	1.02	26.67	17.40	0.00	0.40	96.30	0.00	0.00	0	3.30	0	1.50	13.1	32.25
26	Cooled FG from Condenser	1.01	29.31	23.62	0.00	12.51	4.68	75.55	4.02	0	3.23	110	3.79	14.5	40.27
27	Primary Oxygen enrich Recirculated FG to ID Fan	1.01	28.90	27.75	0.00	10.34	21.12	61.99	3.30	0	3.24	90	3.45	17.7	38.83
28	Secondary OERFG to FD Fan	1.02	68.58	94.59	0.00	7.25	21.09	43.34	25.83	0	2.48	70	44.13	78.3	33.50
30	Pressurized Primary OERFG	1.10	36.67	27.75	0.00	10.34	21.12	61.99	3.30	0	3.24	90	10.34	16.7	38.83
32	Pressurized Secondary OERFG to Secondary GGH	1.05	70.76	94.59	0.00	7.25	21.09	43.34	25.83	0	2.48	70	46.47	77.1	33.50
33	Primary OERFG to primary GGH	1.10	36.67	12.49	0.00	10.34	21.12	61.99	3.30	0	3.24	90	10.34	7.5	38.83
34	Tempered Primary OERFG to Pulverizers	1.08	36.67	15.26	0.00	10.34	21.12	61.99	3.30	0	3.24	90	10.34	9.4	38.83
35	Flue Gas from Condensor to PA Spliter (8)	1.01	29.31	61.87	0.00	12.51	4.68	75.55	4.02	0	3.23	110	3.79	38.1	40.27
38	Oxygen to FGD	1.01	26.67	0.35	0.00	0.40	96.30	0.00	0.00	0	3.30	0	1.50	0.3	32.25
39	Oxygen stream to Furnace	1.03	26.67	6.78	0.00	0.40	96.30	0.00	0.00	0	3.30	0	1.50	5.1	32.25
42	Heated Secondary OERFG to Furnace	1.03	244.27	94.59	0.00	7.25	21.09	43.34	25.83	0	2.48	70	235.12	118.5	33.50
45	Flue Gas from Furnace to SH2	1.01	927.78	141.40	0.89	7.98	3.01	59.31	27.00	0	2.51	1820	1118.36	395.1	35.29
46	Flue Gas Leaving ID Fan	1.02	76.69	150.40	0.00	8.87	3.32	53.58	31.93	0	2.29	80	53.74	126.3	33.80
48	Flue Gas from SCR to Lower Economizer	1.00	379.54	141.40	0.89	7.98	3.01	59.31	27.00	0	2.51	1820	394.15	217.4	35.29
49	Flue Gas to Primary Gas-Gas heater	1.00	306.48	141.40	0.89	7.98	3.01	59.31	27.00	0	2.51	1820	306.86	193.3	35.29
50	Flue Gas from Upper Economizer to SCR	1.01	379.54	141.40	0.89	7.98	3.01	59.31	27.00	0	2.51	1820	394.15	215.7	35.29
111	Flue Gas from SH2 to SH1	1.01	742.78	141.40	0.89	7.98	3.01	59.31	27.00	0	2.51	1820	862.73	334.5	35.29
148	Flue Gas from GPU to CO2 sink	151.68	35.00	37.57	0.00	13.03	4.87	78.69	0.04	0	3.36	120	-188.62	0.0	41.20

Table 6-2: Gas Side Material & Energy Balance English Unit (Oxy Firing, BMCR Load)

Stream #	Stream Location	P	T	Mgas	Mash	Mole Composition %							H*	V	M.W.
		[psia]	[F]	[lb/s]	[lb/s]	N2	O2	CO2	H2Ov	H2Ol	Ar	SO2 (PPM)	[BTU/lb]	[ft^3/s]	
2	Flue Gas to GPU	14.70	84.75	84.32	0.00	12.51	4.68	75.55	4.02	0	3.23	110	1.63	832.0	40.3
3	Flue Gas leaving FGD	14.85	170.05	161.40	0.00	8.87	3.32	53.58	31.93	0	2.29	80	23.11	2170.4	33.8
4	Flug Gas for SH2 to ECON1	14.66	818.05	311.80	1.95	7.98	3.01	59.31	27.00	0	2.51	1820	199.62	8265.8	35.3
6	Flue Gas to Secondary GGH	14.35	554.25	311.80	1.95	7.98	3.01	59.31	27.00	0	2.51	1820	123.71	6699.7	35.3
7	Total Oxygen leaving ASU	15.03	80.00	62.44	0.00	0.40	96.30	0.00	0.00	0	3.30	0	0.65	746.1	32.2
12	Boiler infiltration air	14.70	80.00	2.86	0.00	76.47	20.52	0.03	2.07	0	0.92	0	0.73	39.2	28.7
14	Oxygen to Primary FGR Stream	14.70	80.00	9.12	0.00	0.40	96.30	0.00	0.00	0	3.30	0	0.65	111.4	32.2
18	Hot Primary OERFG to Pulverizers	15.68	500.00	27.53	0.00	10.34	21.12	61.99	3.30	0	3.24	90	96.72	465.6	38.8
20	Flue Gas to ID Fan	13.81	156.98	331.60	0.00	8.87	3.32	53.58	31.93	0	2.29	80	19.64	4690.1	33.8
21	Flue Gas to FGD	14.17	347.05	318.00	0.002	9.61	3.43	57.90	26.41	0	2.47	1780	67.58	5529.4	35.1
22	Flue Gas to Baghouse	14.21	347.05	318.00	1.95	9.61	3.43	57.90	26.41	0	2.47	1780	67.58	5515.4	35.1
23	BagHouse infiltration air	14.21	80.00	6.20	0.00	76.41	20.50	0.03	2.14	0	0.92	0	0.73	88.0	28.7
24	FG Splitter (15) to Oxygen Mixter(24)	14.85	170.05	170.20	0.00	8.87	3.32	53.58	31.93	0	2.29	80	23.11	2288.1	33.8
25	Oxygen to Secondary Oxygen Mixter(24)	14.85	80.00	38.37	0.00	0.40	96.30	0.00	0.00	0	3.30	0	0.65	464.1	32.2
26	Cooled FG from Condenser	14.70	84.75	52.07	0.00	12.51	4.68	75.55	4.02	0	3.23	110	1.63	513.7	40.3
27	Primary Oxygen enrich Recirculated FG to ID Fan	14.70	84.03	61.18	0.00	10.34	21.12	61.99	3.30	0	3.24	90	1.48	625.3	38.8
28	Secondary OERFG to FD Fan	14.85	155.45	208.50	0.00	7.25	21.09	43.34	25.83	0	2.48	70	18.97	2764.3	33.5
30	Pressurized Primary OERFG	16.00	98.00	61.18	0.00	10.34	21.12	61.99	3.30	0	3.24	90	4.44	589.4	38.8
32	Pressurized Secondary OERFG to Secondary GGH	15.17	159.37	208.50	0.00	7.25	21.09	43.34	25.83	0	2.48	70	19.98	2724.1	33.5
33	Primary OERFG to primary GGH	16.00	98.00	27.53	0.00	10.34	21.12	61.99	3.30	0	3.24	90	4.44	265.2	38.8
34	Tempered Primary OERFG to Pulverizers	15.68	98.00	33.65	0.00	10.34	21.12	61.99	3.30	0	3.24	90	4.44	330.7	38.8
35	Flue Gas from Condensor to PA Spliter (8)	14.70	84.75	136.40	0.00	12.51	4.68	75.55	4.02	0	3.23	110	1.63	1345.8	40.3
38	Oxygen to FGD	14.70	80.00	0.77	0.00	0.40	96.30	0.00	0.00	0	3.30	0	0.65	9.4	32.2
39	Oxygen stream to Furnace	14.87	80.00	14.95	0.00	0.40	96.30	0.00	0.00	0	3.30	0	0.65	180.5	32.2
42	Heated Secondary OERFG to Furnace	14.87	471.69	208.50	0.00	7.25	21.09	43.34	25.83	0	2.48	70	101.09	4183.4	33.5
45	Flue Gas from Furnace to SH2	14.69	1702.00	311.80	1.95	7.98	3.01	59.31	27.00	0	2.51	1820	480.84	13953.0	35.3
46	Flue Gas Leaving ID Fan	14.85	170.05	331.60	0.00	8.87	3.32	53.58	31.93	0	2.29	80	23.11	4458.5	33.8
48	Flue Gas from SCR to Lower Economizer	14.51	715.17	311.80	1.95	7.98	3.01	59.31	27.00	0	2.51	1820	169.47	7676.0	35.3
49	Flue Gas to Primary Gas-Gas heater	14.49	583.67	311.80	1.95	7.98	3.01	59.31	27.00	0	2.51	1820	131.94	6825.8	35.3
50	Flue Gas from Upper Economizer to SCR	14.62	715.17	311.80	1.95	7.98	3.01	59.31	27.00	0	2.51	1820	169.47	7619.0	35.3
111	Flue Gas from SH2 to SH1	14.68	1369.01	311.80	1.95	7.98	3.01	59.31	27.00	0	2.51	1820	370.93	11813.7	35.3
148	Flue Gas from GPU to CO2 sink	2199.97	95.00	82.82	0.00	13.03	4.87	78.69	0.04	0	3.36	120	-81.10	1.7	41.2

6.4.19 Total Industrial Boiler Capital and Operating Costs

This study evaluated the changes necessary to retrofit a 150MW gross air-fired industrial boiler to oxy-fired capability. Since this is a retrofit study, the cost analysis only focused on incremental cost changes rather than the total cost of both the air-fired and oxy-fired plant.

Table 6-3 shows the incremental capital costs to retrofit a $150MW_{gross}$ air-fired industrial boiler to oxy-fired capability. The cost of the boiler modifications are relatively modest (only 7% of the total capital cost), with a bare erected cost of $9.8 million. About 34% of the boiler cost is to modify the windbox assembly and firing system. Another 25% of the boiler cost is to modify the ductwork system (FGR ducts, duct insulation, O_2 mixers, supports, and hangers). The remaining 41% of the boiler cost covers the necessary dampers, control valves, O_2 analyzer, flow elements, and instrumentation.

The majority of the retrofit capital cost is for the addition of the ASU and GPU. The ASU is 58% of the total retrofit cost at $79 million. The GPU is 35% of the total retrofit cost at $47 million. The total bare erected retrofit cost is $135 million. Adding in EPCM contractor services, Process and Project Contingencies, and Owners Costs increase the total retrofit cost to $202 million.

Table 6-4 shows the incremental auxiliary power requirements for the oxy-fired boiler retrofit. The primary impact of this retrofit is the addition of the auxiliary power requirements for the power intensive ASU and GPU. The ASU requires an additional 24.3MW and the GPU adds 14.1MW of auxiliary power. For the economic analysis, the assumption was made that the power necessary to drive this equipment would be taken off the grid, thus allowing the industrial boiler to maintain its steam capacity output. It was also assumed that changes in the auxiliary power requirements for the remaining boiler and steam plant equipment were minor and could be ignored.

Table 6-5 summarizes the fixed and variable O&M costs and fuel costs for the oxy-fired industrial steam plant. Most of these costs remain the same as for the air-fired industrial steam plant as the steam capacity remained the same. However, there were increases in both the fixed and variable costs due to the addition of the ASU and GPU. The fixed O&M costs increased by 11% to $19.5 million and the variable O&M costs increased by 21% to 13.1 million. The fuel costs remained essentially the same as the steam capacity was unchanged after the retrofit.

Table 6-3: Incremental Capital Costs to Retrofit an Industrial Boiler to Oxy-Firing

Incremental Capital Costs		$K
Boiler		**9,800**
Windbox Assembly		3,322
Ductwork		2,489
Dampers and Controls		3,989
ASU		**79,040**
GPU		**46,549**
Total Incremental Capital Cost (Bare Erected)		**135,389**
Incremental Overnight Capital Cost (with Owner's C		**201,524**

Table 6-4: Incremental Auxiliary Power Requirements

Incremental Auxiliary Power Requirements		kW
ASU		24,270
GPU		14,089
Total		38,359

Table 6-6 summarizes the incremental costs of retrofitting the air-fired industrial steam plant to oxy-firing. The cost summary is shown as both an annual cost and also a cost to generate steam ($/1000 lb steam). Only the incremental capital and operating costs are considered in the retrofit cost of steam generation.

The first (yellow highlighted) box in this table summarizes the O&M and fuel costs that are common to both the air-fired and oxy-fired steam plant and remain unchanged by the retrofit. These costs total $54.5 million/yr or $7.47/1000 lb steam, with 48% of the cost due to fuel.

The second box in Table 6-6 summarizes the incremental fixed and variable O&M costs associated with the addition of the ASU and GPU. The incremental O&M adds only $2.3 million/yr or $0.58/1000lb steam to the cost of steam generation.

The third box in Table 6-6 summarizes the incremental capital costs to modify the boiler and to add the ASU and GPU. Assuming the same fixed charge capital rate used for the 450MW and 900MW oxy-fired plants, the capital modifications add $25.0 million/yr or $3.42/1000 lb steam to the cost of steam generation.

The fourth box in Table 6-6 summarizes the incremental costs associated with the additional auxiliary power requirements for the ASU and GPU. Assuming the power to operate this equipment is taken off the grid at $0.05/kwh, the incremental auxiliary power requirement adds another $14.3 million/yr or $1.96/1000 lb steam to the cost of steam generation.

The final box in Table 6-6 summarizes all of the incremental costs to retrofit the industrial steam plant to oxy-firing. The retrofit adds a total of $43.5 million/yr or $5.97/1000 lb steam to the cost of steam generation. The cost is in addition to costs common to the air-fired steam plant, which adds another $54.5 million/yr or $7.47/1000 lb steam to the costs of steam generation for fixed and variable O&M costs and fuels costs. This brings the cost of steam generation for the oxy-fired plant to $98 million or $13.44/1000 lb steam. Not included (as it was not part of this study) is the capital cost contribution of the air-fired plant to the cost of steam generation.

Table 6-5: O&M Costs for Oxy-Fired Industrial Steam Plant

BOILER ISLAND AND BALANCE OF PLANT O&M COSTS

Client: DOE - NETL — **INITIAL & ANNUAL O&M EXPENSES** — Cost Base: Jun-11 — Jun-11

Project: ALSTOM Oxy-firing Study — **Case 3** - 1 x 150 MW-gross Oxy-fired PC SubCritical Steam Plant

Boiler Efficiency (frac HHV):	11,276	0.8932
Net Heat Output (MM-Btu/hr):	106,000	**1,067.6**
Capacity Factor (%):	85	85

FIXED OPERATING COSTS

OPERATING & MAINTENANCE LABOR

Operating Labor Requirements (O.J.) per shift	1 unit/mod.	Total Plant
Skilled Operator	1.0	1.0
Operator	4.0	4.0
Foreman	1.0	1.0
Lab Tech's, etc.	1.0	1.0
TOTAL O.J.'s	7.0	7.0

Operating Labor		
Operating Labor Rate (base):	39.70	$/hour
Operating Labor Burden:	30.00	% of base
Labor O-H change Rate:	25.00	% of labor

	Annual Cost $ / year	Annual Unit Cost $/kW-net	Annual Unit Cost $/MM-Btu/hr
Annual Operating Labor Costs (calc'd)	3,164,725	29.86	2,964
Maintenance Labor Costs (calc'd)	3,201,208	30.20	2,999
Administrative & Support Labor (calc'd)	1,591,483	15.01	1,491
Property Taxes ans Insurance	9,561,350	90.20	8,956
TOTAL FIXED OPERATING COSTS	**17,518,766**	**165.27**	**16,409**

VARIABLE OPERATING COSTS

		Consumption		Unit Cost	Initial Fill			
		Initial Fill	Per Day	($/unit)	Cost ($)		$/kWh-net	$/MM-Btu
Maintenance Material Cost						4,801,812	0.00608	0.60405
Consumables								
Water (1,000 gallons)			984	1.67		510,857	0.00065	0.06426
Chemicals								
MU & WT Chem. (lbs.)			4,761	0.27	0	395,660	0.00050	0.04977
Limestone (tons)			122	33.48	0	1,264,975	0.00160	0.15913
Ammonia (19% NH_3) (tons)			18.62	330.00	0	1,906,535	0.00242	0.23984
Subtotal Chemicals					0	3,567,170	0.00452	0.44874
Other Consumables								
Supplemental Fuel (10^6 Btu)								
SCR Catalyst Replacement (m^3)		w/equip.	0.059	8,938.80		163,622	0.00021	0.02058
Emissions Penalties								
Subtotal Other Consumables						163,622	0.00021	0.02058
Waste Disposal								
Fly Ash (ton)			183	25.11		1,422,462	0.00180	0.17894
Bottom Ash (ton)			46	25.11		355,616	0.00045	0.04474
Subtotal Waste Disposal						1,778,078	0.00225	0.22368
TOTAL VARIABLE OPERATING COSTS						**10,821,539**	**0.01371**	**1.36131**
Fuel (ton)			1147	73.55		**26,166,270**	**0.03315**	**3.29162**

Client: DOE - NETL — **ANNUAL O&M EXPENSES SUMMARY** — Cost Base: Jun-11

		Annual Cost $/Year	Annual Unit Cost $/kW	Annual Unit Cost $/MM-Btu/hr
	BOILER ISLAND AND BALANCE OF PLANT O&M COSTS			
TOTAL FIXED O&M COSTS		17,518,766	165.27	16409.49
TOTAL VARIABLE O&M COSTS		10,821,539	0.0137	1.3613
TOTAL FIXED O&M COSTS	**AIR SEPARATION UNIT (ASU)**	1,766,124	16.66	1654.29
TOTAL VARIABLE O&M COSTS		332,301	0.0004	0.0418
TOTAL FIXED O&M COSTS	**GAS PROCESSING UNIT (GPU)**	223,492	2.11	209.34
TOTAL VARIABLE OPERATING COST		1,942,863	0.0025	0.2444
TOTAL FIXED OPERATING COSTS	**TOTAL PLANT O&M COSTS**	19,508,383	**184.04**	**18273.12**
TOTAL VARIABLE OPERATING COST		13,096,702	**0.01659**	**1.64752**

Table 6-6: Incremental Cost of Steam

O&M AND FUEL COSTS (Common to oxy and air firing)	Annual Cost $/Year	Steam $/1000lb
BOILER ISLAND AND BALANCE OF PLANT O&M COSTS		
TOTAL FIXED O&M COSTS	17,518,766	2.40
TOTAL VARIABLE O&M COSTS	10,821,539	1.48
FUEL COSTS	26,166,270	3.59
TOTAL O&M AND FUEL COSTS (Common to oxy and air firing)	54,506,575	7.47

INCREMENTAL O&M COSTS	Annual Cost $/Year	Cost of Steam $/1000lb
AIR SEPARATION UNIT (ASU)		
TOTAL FIXED O&M COSTS	1,766,124	0.24
TOTAL VARIABLE O&M COSTS	332,301	0.05
GAS PROCESSING UNIT (GPU)		
TOTAL FIXED O&M COSTS	223,492	0.03
TOTAL VARIABLE OPERATING COST	1,942,863	0.27
TOTAL INCREMENTAL FIXED AND VARIABLE O&M		
TOTAL INCREMENTAL FIXED O&M COSTS	1,989,617	**0.27**
TOTAL INCREMENTAL VARIABLE OPERATING COST	2,275,164	**0.31**

INCREMENTAL CAPITAL COSTS	Annual Cost $/Year	Cost of Steam $/1000lb
Incremental Capital Cost (Bare Erected)	135,389,210	
Incremental Overnight Capital Cost (with Owner's Cost)	201,523,563	
Fixed Charge Rate	0.124	
Annual Incremental Capital Cost	24,988,922	**3.42**

INCREMENTAL AUX POWER COSTS	Annual Cost $/Year	Cost of Steam $/1000lb
Incremental Power for ASU and GPU	14,281,002	**1.96**

TOTAL INCREMENTAL O&M AND CAPITAL	Annual Cost $/Year	Cost of Steam $/1000lb
	43,534,704	**5.97**

7. SENSITIVITY STUDY ON FGR LOCATION

A sensitivity study was conducted to evaluate the performance and cost impact of four different locations for the flue gas recirculation duct take-off. The primary FGR ducts are commonly taken after the Flue Gas Condenser to minimize the moisture concentration in the recirculation gas feeding the pulverizers. The secondary FGR ducts are normally taken either before or after the WFGD depending upon the coal sulfur concentration. Flue gas recirculation increases the SO_2 concentration in the recycled flue gas and increases the SO_2 levels beyond normal boiler operating experience for moderate to high sulphur coals if the FGR is taken before the FGD system. Taking the FGR after the FGD system reduces the SO_2 concentration in the boiler and flue gas at the expense of a larger and more costly FGD system. The impact of higher SO_2 concentrations on the boiler design was not considered as part of this study.

An alternative approach is to employ a hot FGR system where the flue gas recycle is extracted before the Gas to Gas Heater. An oxygen eductor is used to provide the motive force to convey the hot flue gas recycle back to the boiler. The primary FGR is still taken from after the FGC.

7.1 Boiler Efficiency

The sensitivity study evaluated the impact of the FGR location on the boiler efficiency. The boiler efficiency is calculated from the following equation:

$$(Q_{FUEL} + Q_{CREDIT} - Q_{LOSS})/ Q_{FUEL}$$

Boiler efficiency can be improved by either increasing Q_{CREDIT} or reducing Q_{LOSS}. The boiler efficiency is normally calculated by drawing a boundary around the boiler and airheater (or Gas-Gas Heater for oxy-fired boilers) as shown by the dashed red line in Figure 7-1.

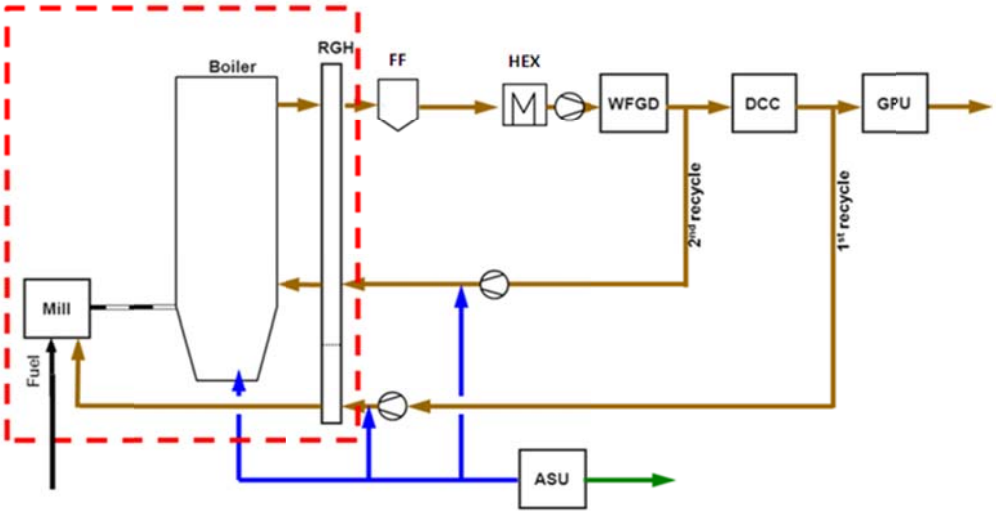

Figure 7-1: Boiler Efficiency Envelope Including Airheater

The boiler efficiency boundary can also be drawn excluding the airheater (RGH) as shown by the dashed red line in Figure 7-2. If the heat loss in the airheater is neglected, then the boiler efficiency calculated by either method should be the same. This second approach for calculating boiler efficiency was used in this sensitivity study to assess the impact of secondary gas recirculation locations as it properly captures the impacts of using hot FGR.

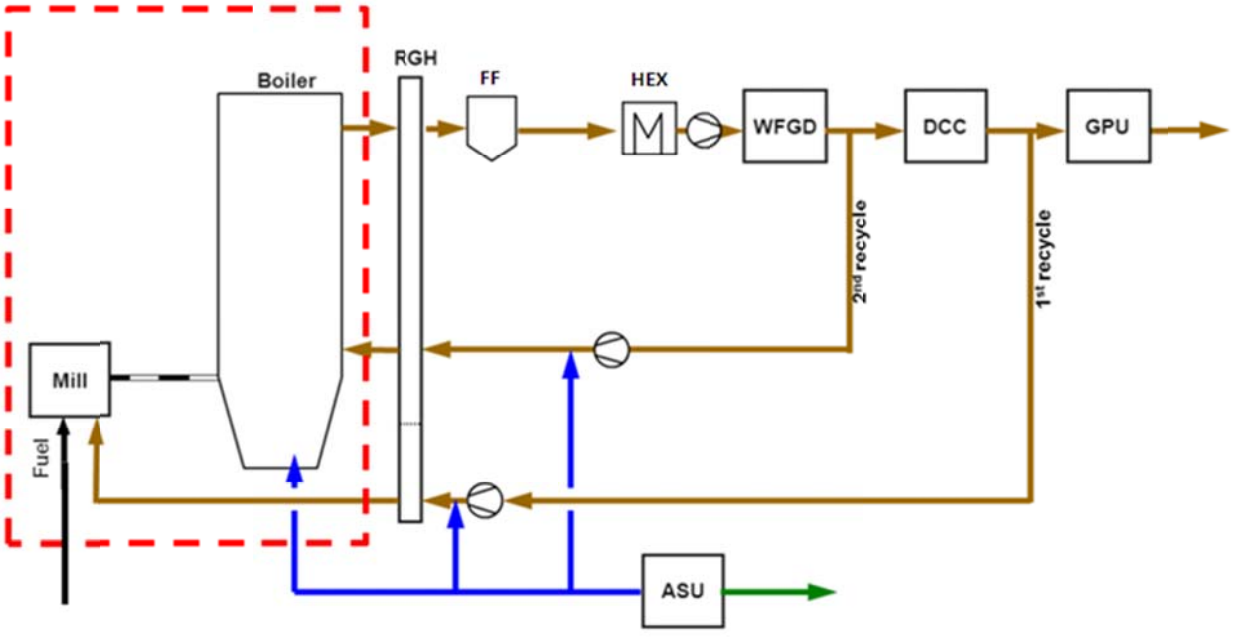

Figure 7-2: Boiler Efficiency Envelope Excluding Airheater

The following sections describe four different secondary recirculation arrangements as applied to a 900MW oxy-fired plant. In each case, the hot primary recirculation stream leaving the Gas-Gas Heater is always kept at the same temperature to meet coal pulverizing requirements. Both the synthetic primary and secondary "air" O_2 concentrations are kept the same, as is the flue gas O_2 concentration.

7.2 Case 1 - Base Case With Cold Recirculation

The base case scenario in this sensitivity study is the same as was used for the 900MW oxy-fired power plant in this techno-economic study. As shown previously in Figure 7-2, the primary flue gas recirculation is taken from downstream of the direct contact cooler (DCC) at the entrance of GPU. The secondary flue gas recirculation is taken from downstream of the WFGD and before the DCC.

7.3 Case 2 - Warm Recirculation

In this case, the secondary flue gas recirculation is taken from upstream of the WFGD and downstream of the flue gas heat recovery system (HEX), as shown in Figure 7-3. The secondary flue gas recirculation into the Gas-Gas Heater is warmer than the base case. This makes the secondary recirculation into the boiler efficiency boundary hotter and brings in more heat credit, resulting in improved boiler efficiency.

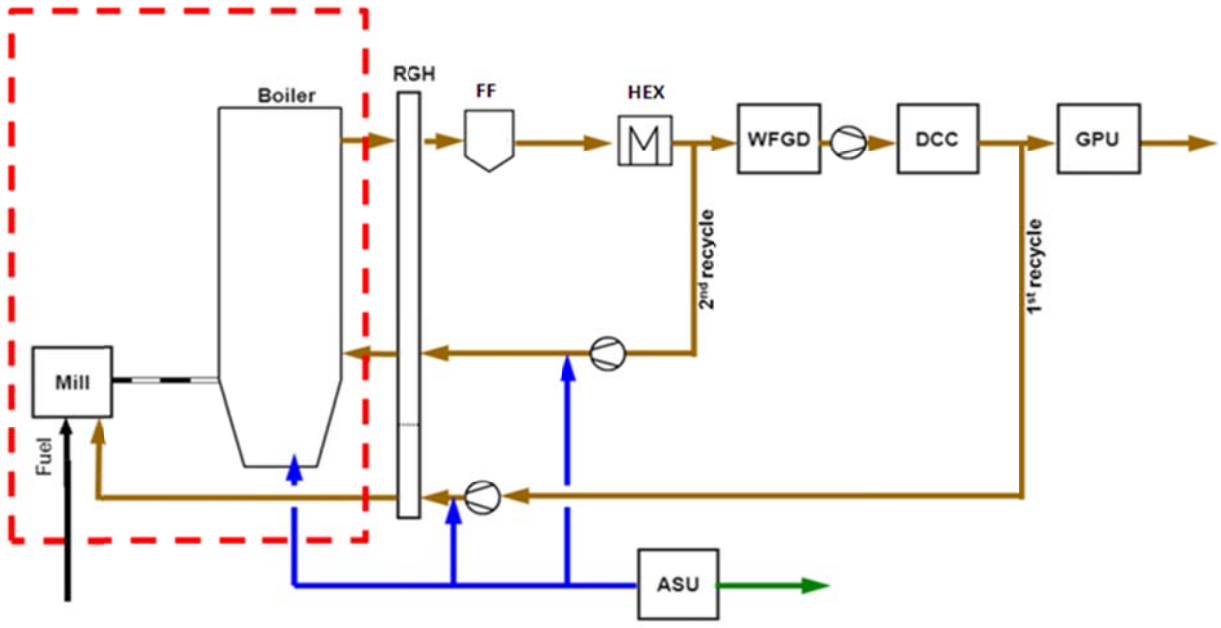

Figure 7-3: Warm Secondary FGR Before WFGD

7.4 Case 3 - Hot Recirculation Without Secondary O_2 Preheating

In this case, the secondary flue gas recirculation is taken from downstream of the economizer and before the Gas-Gas Heater, as shown in Figure 7-4. Oxygen from the ASU is not preheated

before it is mixed with the recycled hot flue gas. As a result, the mixed temperature of the secondary flue gas recirculation and oxygen as it crosses the boiler efficiency envelope (dashed red line) is less than in the base case, thus resulting in a lower heat credit. Without a redesign of the boiler and an increase in heating surfaces, there is almost no change in the exhaust loss leaving the boiler efficiency envelope. Therefore, the Case 3 boiler efficiency is lower than in the base case.

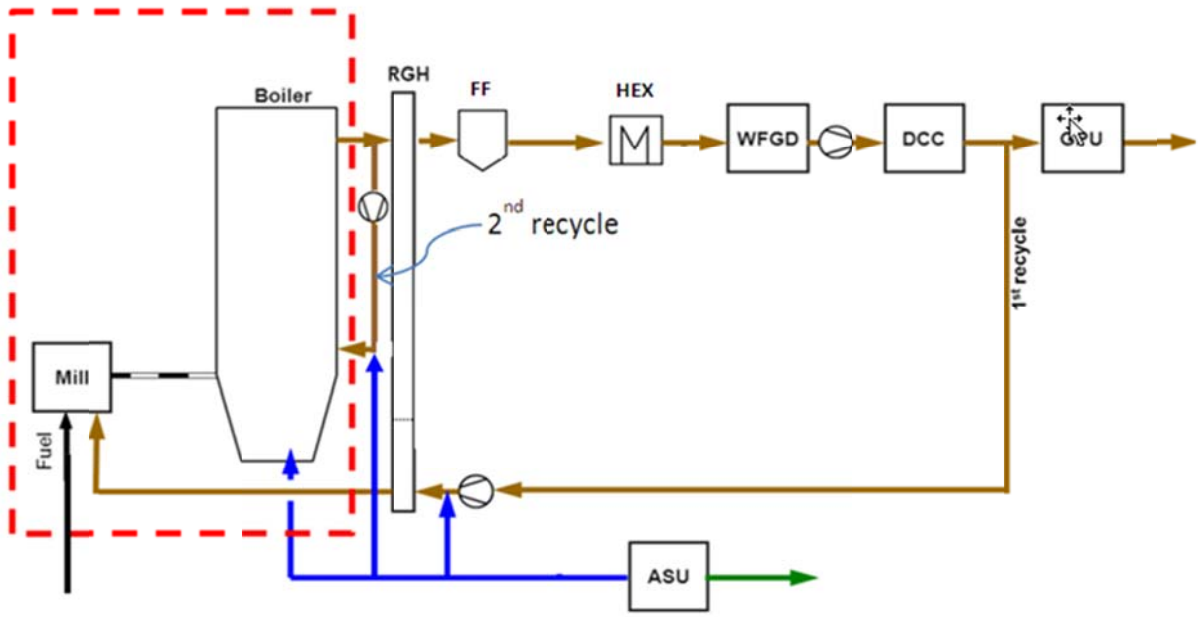

Figure 7-4: Hot Secondary FGR Before GGH

7.5 Case 4 - Hot Recirculation With Secondary O_2 Preheating

This case is similar to Case 3 where secondary flue gas recirculation is taken from downstream of the economizer and before the Gas-Gas Heater. However in this case, the secondary O_2 from ASU is preheated before it is mixed with the recycled hot flue gas, as shown in Figure 7-5. The heat for O_2 preheating comes from flue gas downstream of the economizer. For simplicity, Figure 7-5 secondary O_2 preheating is shown in Figure 7-5 through the same Gas-Gas Heater used for primary recirculation preheating. But in reality, the secondary O_2 preheating requires a separate tubular air preheater in parallel with the main Ljungstrom regenerative Gas-Gas Heater. The boiler efficiency is improved when the secondary O_2 is heated to a temperature level such that the secondary mixture temperature into the boiler efficiency boundary is no lower than that in the base case (> 663°F). For Case 4, the tubular O_2 preheater must be made with stainless steel heat transfer tubes when preheating O_2 to such a high temperature.

With this arrangement, more heat credit can be conveyed into the boiler efficiency boundary than in the base case (Case 1). The higher the secondary O_2 preheat temperature, the higher the efficiency gain. In the as-modeled case, the secondary O_2 is preheated to the same temperature of

the hot secondary recirculation gas as in Case 2 (675°F**)**. This approach results in approximately a 1% point (HHV) boiler efficiency improvement as compared to Case 1.

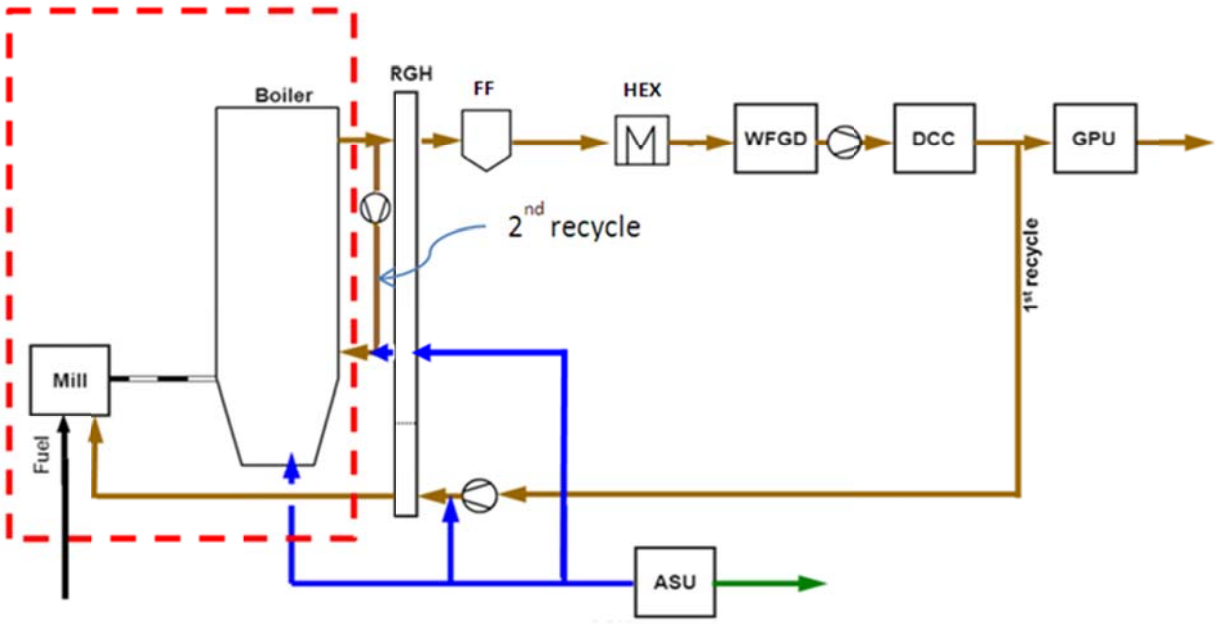

Figure 7-5: Hot Secondary FGR Before GGH with Secondary O_2 Preheating

7.6 FGR Location Performance Summary

Each of the four cases was modelled using ALPRO 4.6, an Alstom performance and design program. Selected results from the four simulations are shown in Table 7-1. Performance values that changed significantly from Case 1 are highlighted in red.

Table 7-1: FGR Performance Characteristics

		Case 1 After WFGD	Case 2 Before WFGD	Case 3 Before GGH	Case 4 Before GGH O_2 Preheat
Gas Flow Leaving Economizer	lb/hr	6,324,941	6,373,915	6,378,290	6,378,008
Gas Flow to ESP	lb/hr	6,451,440	6,501,395	2,721,125	2,699,190
Gas Flow to WFGD	lb/hr	6,451,440	2,725,649	2,721,125	2,699,190
Secondary FGR Flow	lb/hr	3,714,659	3,775,751	3,684,107	3,731,739
Primary FGR Flow	lb/hr	906,749	903,464	886,288	879,608
Gas Temp leaving Econ	°F	719	720	720	720
Gas Temp to ESP	°F	287	370	541	384
Hot Primary FGR Temp into Furnace	°F	601	601	601	601
Hot Secondary FGR Temp into Furnace	°F	663	675	627	714
O_2 Temp into Secondary FGR Recirc Mixer	°F	86	86	86	675
Secondary FGR Temp into Gas-Gas Heater	°F	141	276	N/A	N/A
Boiler Efficiency (HHV)	%	91.8	92.0	91.1	92.8
Boiler Efficiency (LHV)	%	95.2	95.5	94.5	96.3

7.7 Cost Implications of FGR Location

Table 7-2 summarizes the qualitative cost impacts for the different FGR locations as compared to Case 1. Moving the FGR location from after the WFGD (Case 1) to before the WFGD (Case 2) results in a slightly larger fabric filter (due to a higher gas temperature and volumetric flow leaving the Gas-Gas Heater) and a smaller WFGD. Moving the FGR location before the Gas-Gas Heater (Cases 3 and 4) reduces the volumetric flow rate to all gas touched equipment downstream of the boiler and before the Flue Gas Condenser, including the Gas-Gas Heater, fabric filter, and WFGD. Case 4 also requires the addition of an O_2 heater.

A simple cost analysis was conducted to capture the cost impacts for some of the major pieces of equipment impacted by the choice of FGR location. The capital costs of the Gas-Gas Heater, fabric filter, and WFGD were adjusted based on the change in volumetric gas flow and using the DOE capital cost scaling methodology[36]. The cost of a tubular O_2 heater with stainless steel tubes was also estimated and added to the costs for Case 4. Minor cost adjustments were made to other equipment (such as coal preparation, handling, and feeding) based on the revised boiler efficiency. Revised Total Overnight Capital Costs were then calculated for each case. The change in the Total Overnight Capital Cost relative to Case 1 is shown in Table 7-2.

[36] Capital Cost Scaling Methodology, Quality Guidelines for Energy System Studies, DOE/NETL-341/013113, January 2013

Table 7-2: Cost Implications of FGR Location

	Case 1 After WFGD	Case 2 Before WFGD	Case 3 Before GGH	Case 4 Before GGH O_2 Preheat
Gas-Gas Heater	Base	Similar	Smaller	Smaller
Fabric Filter	Base	Larger	Smaller	Smaller
WFGD	Base	Smaller	Smaller	Smaller
O_2 AH	N/A	N/A	N/A	New
Δ Total Overnight Capital Cost ($M)	Base	-66	-67	-85
Δ Total Overnight Capital Cost ($/Kw)	Base	-101	-101	-130

Focusing on just these capital costs, it shows that moving the FGR upstream of the WFGD can have significant cost benefits. Of course, there are other considerations, such as the impact of increased SO_2 concentration on the boiler materials that may override any advantages of moving the FGR location. There was little additional cost benefit of moving the FGR location from before the WFGD to before the Gas-Gas Heater if the O_2 is not preheated before mixing with the secondary FGR. Although Case 3 has a lower cost fabric filter than Case 2 due to reduced volumetric gas flow, this savings is offset by a lower boiler efficiency due to the reduced secondary FGR gas temperature entering the furnace. Preheating the O_2 before mixing with the secondary FGR (Case 4) results in improved boiler efficiency and the greater capital cost reduction relative to Case 1.

There are other costs that were not considered in this simple cost analysis. Cost additions include an increased ASU capital cost and higher ASU power requirements for Case 4 as the oxygen needs to be delivered at a higher pressure for the oxygen eductor to provide the motive force necessary to convey the hot FGR back to the boiler. There may be some windbox modifications necessary for Cases 3 and 4 to deal with the hot, particulate laden FGR. Other costs may be necessary to cope with increased SO_2 emissions in the boiler.

These cost adders are offset by various cost reductions that were not considered in this study. These include reduced capital costs for the ID Fan and gas ductwork, plus reduced auxiliary power requirements for the fabric filter, WFGD, and ID Fan. The impact on the flue gas heat exchanger (HEX) was also not considered, but the cost of this equipment would likely increase for Case 2 due to the increased sensible energy in the flue gas from the higher gas temperature. The HEX cost would likely decrease for Case 4 due to the significantly decreased volumetric flow rate relative to Case 1, which more than offsets an increase in flue gas temperature. The HEX cost for Case 3 would likely be just slightly less than for Case 1 as the increased flue gas temperature would almost offset the reduced volumetric flow rate.

Overall, the FGR location in Case 4 resulted in the most significant cost reduction as compared to the base case scenario. The capital cost reductions considered in this sensitivity study total

3.5% of the Total Overnight Costs of the 900MW oxy-fired plant that used the secondary FGR after the WFGD (Case 1). The additional costs and savings not considered in this study are expected to increase the overall savings.

8. PERFORMANCE AND COST SUMMARY

8.1 Performance

8.1.1 Power Output

Figure 8-1 summarizes the net power and auxiliary power requirements for the air and oxy-fired cases at 450 and 900MW. The gross plant outputs (sum of net power and auxiliary power) for the 450MW air and oxy-fired cases were identical to each other. The same applied to the 900MW case. The net power varied for each case depending upon the total auxiliary power requirements for each case. This is different from the approach used in the DOE Baseline Reports, where the SCPC w/o CCS and oxy-fired cases had a constant $550MW_{net}$ output, while the gross MW varied.

This difference is due to the different design approaches taken. The DOE cases were designed for a constant net power output. This required that the boiler size be increased for the oxy-fired case as the auxiliary power consumption increased considerably and the firing rate had to be increased. For the 450MW and 900MW cases, the gross power output was fixed and the net power output was allowed to vary. Since the fuel firing rate remained constant, the boiler size remained essentially the same. Thus, the focus was on identifying the design changes and costs associated with redesigning an air-fired boiler for oxy-firing, rather than also accounting for an increased size boiler.

The auxiliary power requirements for all of the air-fired cases ranged from 5.0-5.2%. The auxiliary power requirement for the 450MW oxy-fired plant was 27.8%. This value decreased to 26.4% for the 900MW oxy-fired plant due to the improved thermal efficiency from integration of the ASU, GPU, and FGHR system. Although not shown here, the DOE Case 5C oxy-fired plant had an auxiliary power requirement of 30.2%. This is because this plant had a less efficient steam cycle than either the 450MW or 900MW plants and did not have any integration.

Table 8-1 summarizes the performance results and auxiliary power requirements for the air and oxy-fired cases at 450MW and 900MW. The largest auxiliary power load for the oxy-fired cases was the ASU, which ranged from 64,550kW to 117,914kW for the 450 and 900MW oxy-fired plants, respectively. The next largest auxiliary power load for the oxy-fired cases was the GPU CO_2 compressor, which ranged from 37,683kW to 73,071kW for the 450MW and 900MW oxy-fired plants, respectively. In comparison, the boiler island auxiliary power decreased slightly to 22,647kW and 44,400kW for the 450MW and 900MW oxy-fired plants corresponding to a 3.7% and 0.5% decrease from air-firing. This is due to the higher gas density and lower volumetric gas flow rates in oxy-fired mode that resulted in reduced ID fan power consumptions.

The largest impact of the air-fired industrial steam plant retrofit to oxy-fired capability was the addition of the power intensive ASU and GPU. The ASU requires an additional 24.3MW and the GPU adds 14.1MW of auxiliary power. Since it was assumed that the power necessary to drive this equipment would be taken off the grid, the industrial boiler was therefore able to maintain its

steam capacity output. It was also assumed that changes in the auxiliary power requirements for the remaining boiler and steam plant equipment were minor and could be ignored.

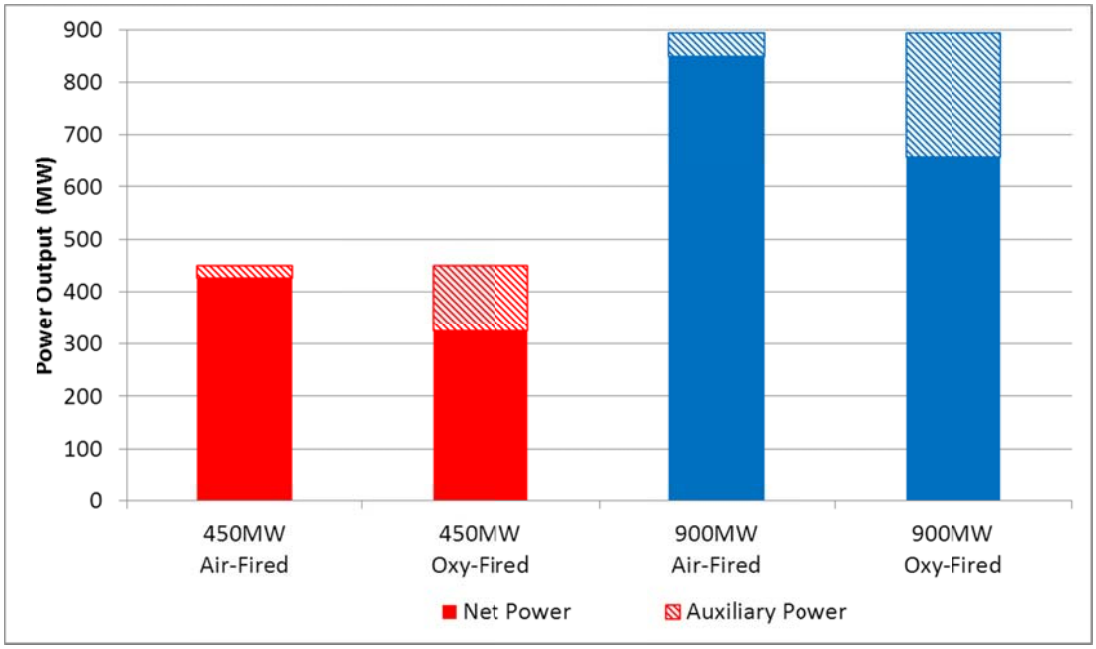

Figure 8-1: Power Output Summary

Table 8-1: Summary of Thermal Performance and Auxiliary Loads

		450MW	450MW	900MW	900MW
		Air-Fired	Oxy-Fired	Air-Fired	Oxy-Fired
Gross Power Output	MW	450.0	450.0	893.3	893.3
Net Power Output	MW	426.5	325.1	848.7	657.9
Coal Flow	lb/hr	295,086	296,543	598,606	601,529
Main Steam Flow	lb/hr	2,508,000	2,508,000	5,162,812	5,174,717
Fuel Heat Input (HHV)	MMBtu/	3,277	3,293	6,412	6,444
Net Plant Efficiency (HHV)	%	40.9%	31.5%	41.3%	32.5%
Boiler Efficiency	%	88.8%	88.8%	88.8%	88.8%

Auxiliary Load Summary

		450MW	450MW	900MW	900MW
		Air-Fired	Oxy-Fired	Air-Fired	Oxy-Fired
Coal Handling & Pulverizers	kW	2,319	2,331	4,705	4,728
Forced Draft Fans	kW	1,192	1,198	2,418	2,430
Primary Air Fans	kW	939	944	1,905	1,915
Induced Draft Fans	kW	5,423	4,413	11,001	10,811
SCR	kW	150	-	150	-
FF	kW	53	51	107	106
Wet FGD	kW	2,239	2,277	4,542	4,463
Power Plant Auxiliaries	kW	11,200	11,434	19,782	19,948
ASU Compressor/Auxiliaries	kW	-	64,550	-	117,914
GPU CO2 Compressor	kW	-	37,683	-	73,071
		-	-	-	-
Total Aux Power	kW	23,516	124,880	44,611	235,385
% Aux Power		5.2%	27.8%	5.0%	26.4%

8.1.2 Net Plant Efficiency

The net plant efficiency results in Table 8-1 are graphically presented in Figure 8-2. The net plant efficiency for the 450MW and 900MW air-fired cases are both about 41% HHV. This relatively high efficiency is attributed to the advanced steam conditions and efficient steam cycle arrangement The net plant efficiency for the 450MW oxy-fired decreased by 9.4% points as compared to the 450MW air-fired case. This reduction is due to the increased auxiliary power requirements for the ASU and GPU. The net plant efficiency for the 900MW oxy-fired plant decreased by 8.8% points as compared to the 900MW air-fired case. The net plant efficiency for the 900MW oxy-fired plant was 0.6% points higher than the efficiency for the 450MW oxy-fired plant. This improvement is primarily due to the thermal integration of the ASU, GPU, and FGHR

system. Further improvements can be expected in second generation oxy-fired plants with more thermal integration and advances in ASU and GPU designs that reduce their power requirements.

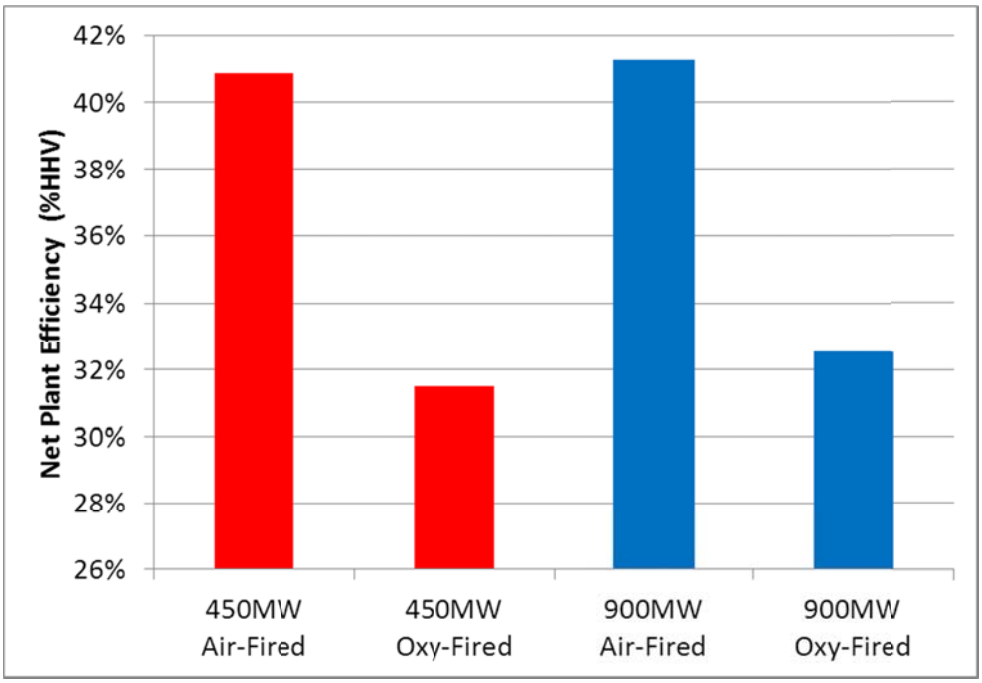

Figure 8-2: Net Plant Efficiencies for all Air-Fired and Oxy-Fired Cases

The energy penalty for the 450MW oxy-fired power plant (relative to the 450MW air-fired plant without CO_2 capture) is 23.0%. The energy penalty for the 900MW oxy-fired power plant (relative to the 900MW air-fired plant) decreased slightly to 21.3%. The Energy Penalty is defined here as:

$$\%\ \text{Energy Penalty} = \frac{\text{net plant efficiency(SCPC w/o CCS)} - \text{net plant efficiency(oxy-fired SCPC)}}{\text{net plant efficiency(SCPC w/o CCS)}}$$

8.2 Cost Results

The capital costs for the 450MW and 900MW air-fired and oxy-fired plants and for the industrial steam plant retrofit to oxy-combustion were developed using the methodology described in the DOE's Cost Estimation Methodology guide.[37]

- Bare Erected Costs (BEC) were developed for all process equipment, facilities and infrastructure – including materials and erection labor.

[37] Cost Estimation Methodology for NETL Assessments of Power Plant Performance, NETL Quality Guidelines for Energy System Studies, DOE/NETL-2-11/1455, April 2011

- Total Plant Costs (TPC) were developed by adding the cost of services by the engineering, procurement, and construction (EPC) contractor, along with process and project contingencies.
- The TPC is an overnight cost and is expressed in base year dollars (June 2011 dollars).
- Total Overnight Capital Cost (TOC) includes the TPC plus all other overnight costs, including owner's costs.
- The Total As-Spent Capital Costs (TASC) includes all capital expenditures during the capital expenditure period including their escalation and interest during construction. It is expressed in mixed, current-year dollars over the capital expenditure period.

Process contingencies were applied to selected capital cost estimates in the Total Plant Costs to compensate for performance uncertainties associated with the developmental status of the oxy-combustion technology. A 20% process contingency was applied to boiler island process areas modifications associated with oxy-combustion that have not been demonstrated commercially and were thus designed using experimental data such as from Alstom's $15MW_{th}$ Boiler Simulation Facility. Process contingencies were applied to the following boiler equipment areas:

- Windbox and firing system modifications
- Ductwork modifications associated with oxy-firing
- Dampers and controls associated with oxy-firing

No process contingencies were taken for the ASU or GPU systems, consistent with the approach taken by the DOE for Case 5C and other DOE oxy-combustion cases.

The DOE developed detailed capital cost estimates of the Case 11 SCPC plant that are the basis for the many of the cost estimates used for the 450MW and 900MW power plants in this study. The DOE subsequently updated the costs for this case to June 2011 dollars.[38] These updated costs were used in this study as a reference base and were adjusted by capacity factoring using the scaling parameters prescribed by the DOE[39] for those subsystems and components common to the 450MW and 900MW plants. Specifications for those components unique to these plants were based on the heat and material balances. Costs were then developed by in-house cost-estimating, vendor quotes, or from quotes for similar equipment that were then adjusted for capacity and flow conditions. Costs for the major components included all items necessary to develop a complete cost, including items such as pressure parts, refractory, insulation, structural steel, casing, expansion joints, etc.

[38] Updated Costs (June 2011 Basis) for Selection Bituminous Baseline Cases, DOE/NETL-341/082312, August 2012
[39] Capital Cost Scaling Methodology, Quality Guidelines for Energy System Studies, DOE/NETL-341/013113, January 2013

8.2.1 Total Overnight Cost

Table 8-2 summarizes the Total Overnight Costs (TOC) and the Total As Spent Capital Costs (TASC) for the 450MW and 900MW cases, without and with CCS. Also shown are the incremental capital costs to retrofit the $150MW_{gross}$ air-fired industrial steam plant to oxy-fired capability. All costs are based on June 2011 dollars. Figure 8-3 shows the Total Overnight Costs on a $/kW basis for the 450MW and 900MW cases. The following observations can be drawn from this study related to capital costs:

- The capital costs of these plants can't be compared directly since they are all designed with different net outputs. Normalizing the costs on a $/kW basis allows plants of different capacities to be fairly compared. On a $/kW basis, the total overnight capital cost for the oxy-fired plant increased by 78.1% relative to air-fired plant. The TOC cost increase for the 900MW oxy-fired plant was 78.5%. The added cost of integration of the ASU, GPU, and FGHR for the 900MW offset some of specific cost decrease due to both scalability and technology maturity (commercial vs. demonstration plant).
- Most of the capital cost increase for the oxy-fired plants and for the industrial steam plant retrofit is due to the addition of the ASU and GPU systems.
- The 450MW and 900MW boiler bare erected costs (materials and erection only) also increased by about 11% for the oxy-fired cases as compared to the air-fired cases. This increase accounts for the changes necessary to make the boiler oxy-capable, such as the addition of the flue gas recirculation system ducting, oxygen mixers, and windbox modifications.
- The Total As Spent Capital (TASC) shown in Table 8-2 can be derived by multiplying the Total Overnight Costs air the air-fired plants by a 1.134 factor (for low risk investor owned utilities) and by a 1.140 factor (for high risk investor owned utilities). The TASC includes all capital expenditures during the capital expenditure period including their escalation and interest during construction. It is expressed in mixed, current-year dollars over the capital expenditure period.
- The incremental Total Overnight Capital Costs to retrofit a $150MW_{gross}$ air-fired industrial boiler to oxy-fired capability is approximately $200 million. The cost of the boiler modifications are relatively modest at only 7% of the total capital cost. About 34% of the boiler cost is to modify the windbox assembly and firing system. Another 25% of the boiler cost is to modify the ductwork system (FGR ducts, duct insulation, O2 mixers, supports, and hangers). The remaining 41% of the boiler cost covers the necessary dampers, control valves, O_2 analyzer, flow elements, and instrumentation. The majority of the retrofit capital cost is for the addition of the ASU and GPU. The ASU is 58% of the total retrofit cost while the GPU is 35% of the total retrofit cost.

Table 8-2: Total Overnight and Total As Spent Capital Costs

Case	Total Overnight Cost		Total As Spent Capital	
	1000$	$/kW	1000$	$/kW
450MW Air-Fired w/o Capt	1,330,385	3119	1,508,657	3537
450MW Oxy-Fired	1,806,428	5556	2,059,328	6334
900MW Air-Fired' w/o Capt	1,780,293	2098	2,018,853	2379
900MW Oxy-Fired	2,468,813	3745	2,808,747	4269
150MW$_{gross}$ Industrial Retrofit	201,524		229,272	

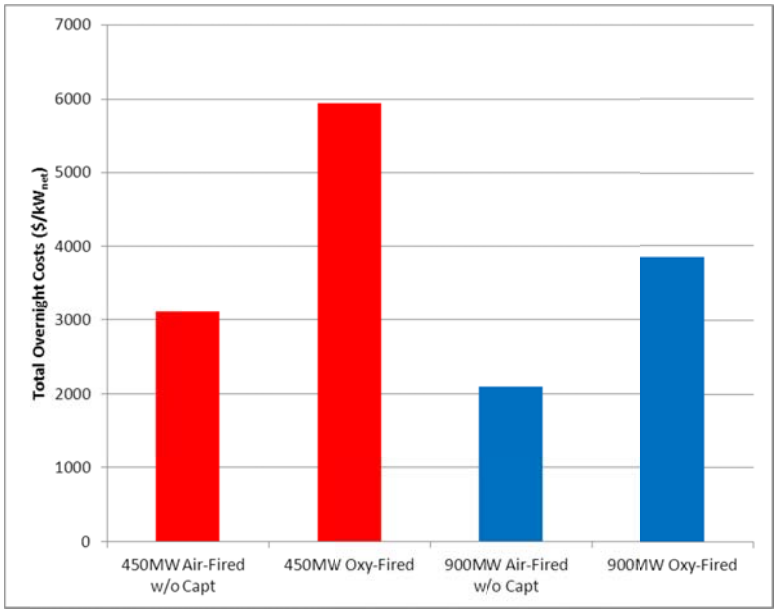

Figure 8-3: Total Overnight Costs

8.2.2 Cost of Electricity (COE)

The first year Cost of Electricity (COE) is the economic metric used in the analysis of the 450MW and 900MW air-fired and oxy-fired cases. It is the revenue received by the generator per net MWhr during the first year of operation, assuming that the first year of operation COE escalates at a nominal annual rate equal to the general inflation rate (i.e. remains constant in real terms over the operational period of the plant). The levelized COE (LCOE) is the revenue received by the generator per net MWhr during the first year of operation, assuming that the first

year of operation COE escalates at a nominal annual rate of 0% (i.e. remains constant in nominal terms over the operation period of the plant).

The Power Systems Financial Model provides the LCOE on a current dollar basis over a levelization period equal to the plants operational life – i.e., the LCOE is constant in current dollars over this period. The model provides a Levelization factor that can be multiplied by the COE to give the LCOE in base year dollars. The Levelization Factor for the NETL defined economic inputs is 1.268.

Figure 8-4 compares the first year COE and the 30 year levelized LCOE for the 450MW and 900MW cases, without and with CCS. The COE (w/o T&S) for the 450MW oxy-fired plant increased by 72.9% relative to the 450MW air-fired plant. The COE increase for the 900MW oxy-fired plant increased by 68.5% relative to the 900MW air-fired plant. The COE increase for both oxy-fired plants is well above the DOE COE increase target of 35%, which is not surprising as these plants are first generation CCS technologies. The 450MW oxy-fired plant is a demonstration plant capable of 100% air firing capacity and has not been optimized for oxy-firing, thus accounting for the higher COE than the 900MW oxy-fired commercial plant.

Further reductions in the COE can be expected in second generation oxy-fired plants from continued reductions in the capital cost and power requirements for the ASU and GPU, along with further optimization and integration of the overall power plant.

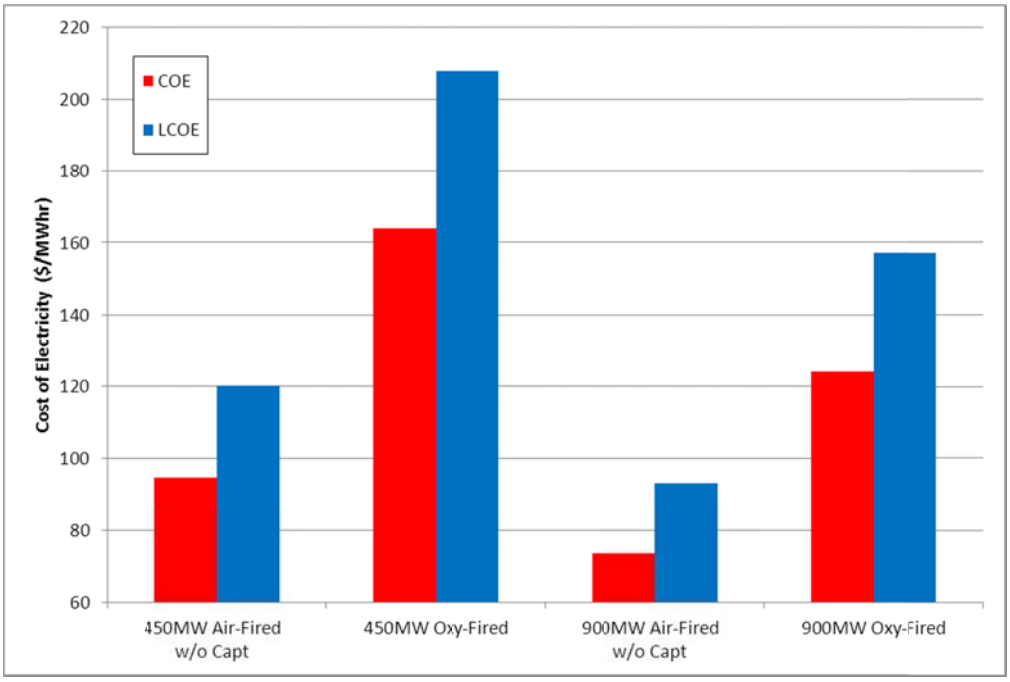

Figure 8-4: COE and LCOE for All Cases

Figure 8-5 again shows the COE for the 450MW and 900MW cases. The COE is broken down into its separate cost components of fuel, capital, fixed O&M, variable O&M, and T&S. The capital cost component shows the largest increase between the air-fired and oxy-fired cases due mostly to the additional ASU and GPU equipment. Fuel costs also increased due to the large parasitic power consumption of the ASU and GPU equipment.

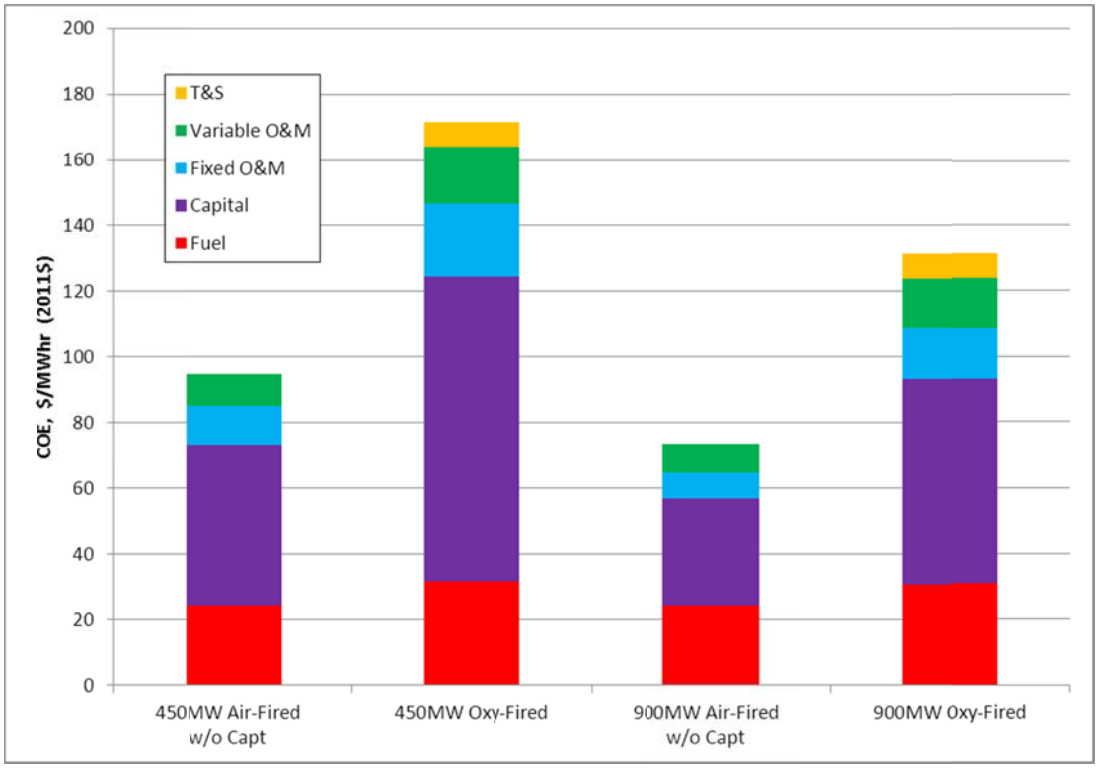

Figure 8-5: COE Breakdown by Cost Component

The economics of any technology can be heavily impacted by future legislation related to climate change. Figure 8-6 shows the COE sensitivity to a future CO_2 Allowance Price. The COE for the 450MW and 900MW oxy-fired cases show only modest COE increases since over 90% of the CO_2 is removed by the process. However, both air-fired plants without CO_2 capture show a significant increase in COE as the CO_2 Allowance Price is increased. The 900MW oxy-fired plant has economic parity (i.e. equal COEs) with the 900MW air-fired plant without CO_2 capture at a CO_2 allowance price of 96 $/ton CO_2 before considering T&S costs. The 450MW oxy-fired plant has economic parity at a CO_2 allowance price of 120 $/ton CO_2.

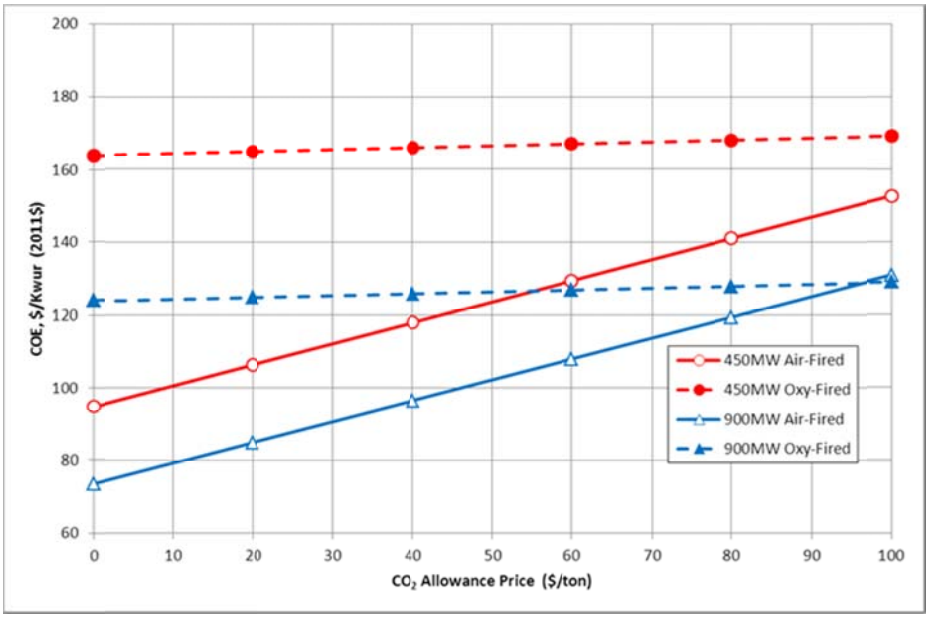

Figure 8-6: COE Sensitivity to CO_2 Allowance Price

Figure 8-7 shows the sensitivity of COE in $/MW-hr to coal price over the range from 1-5 $/MM-Btu for the 450MW and 900MW plants. The CO_2 capture plants are shown without the cost of CO_2 T&S included. Increasing fuel costs has a greater impact on the oxy-fired plants than on the air-fired plants because of its lower net plant efficiency due to the increased auxiliary power requirements of the ASU and GPU.

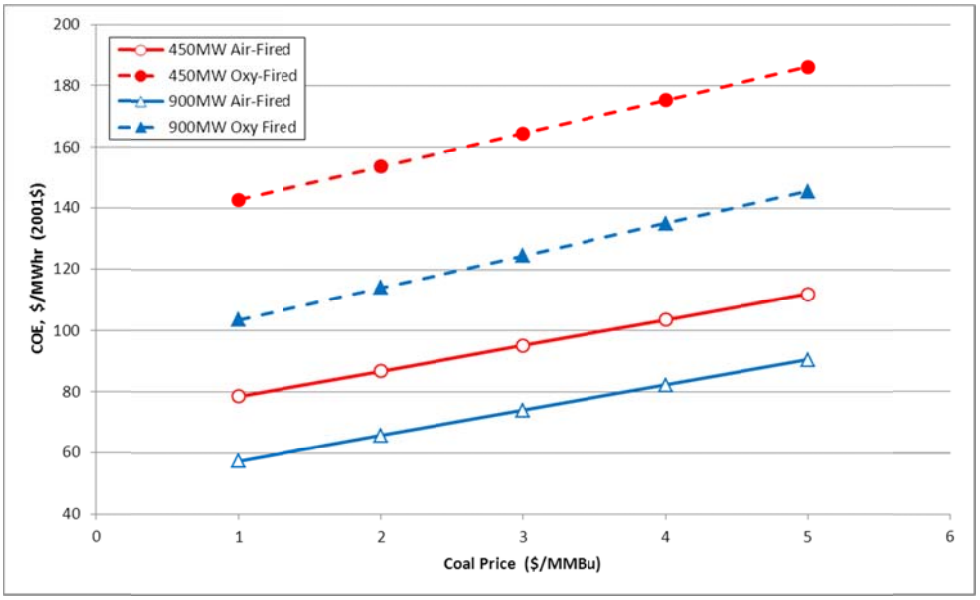

Figure 8-7: COE Sensitivity to Coal Price

Figure 8-8 shows the sensitivity of COE in $/MW-hr to capacity factor over the range from 30-90 percent for the 450MW and 900MW plants. The base capacity factor used in this study was 85 percent. All of the cases behave in a similar manner. As capacity factor is reduced the COE

increases exponentially. In general, for all of these plants as capacity factor is decreased from 90 percent to 30 percent, the COE is increased by about 250 percent.

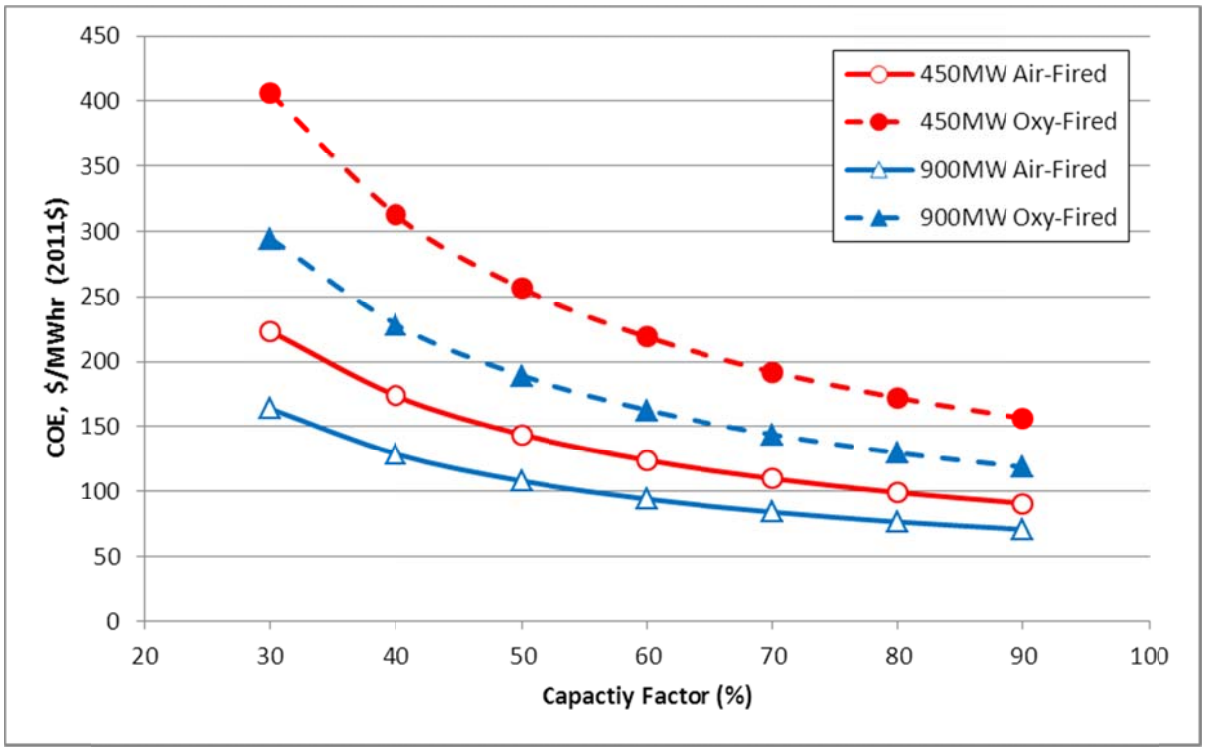

Figure 8-8: COE Sensitivity to Capacity Factor

8.2.3 Variable Cost of Generation

A key factor impacting the economics of a power generation technology is its variable cost of generation (or production cost). Technologies that have low variable costs of generation allow the units to dispatch to the highest capacity factors. It is comprised by those cost components that vary with the plants operation, including:

- Fuel
- Operating and maintenance
- CO_2 tax
- Transport and Storage

The fuel component depends on the cost of the fuel being consumed ($/10^6 Btu) and the efficiency of the plant (Btu/kWhr) utilizing the fuel. The operating and maintenance component includes the costs of all consumables and other variable costs, including water, sorbents, and ash disposal. The CO_2 tax component, which is not present in a non-carbon constrained world, depends on the tax level ($/Ton of CO_2 emitted), the carbon content of the fuel (lbm of carbon /10^6 Btu), and the fraction of CO_2 produced that is being captured. The transport and storage

component depends upon the distance the CO_2 is being transported by pipeline and where it is being sequestered.

Figure 8-9 shows the variable cost of generation vs. the CO_2 Allowance Price for the 450MW and 900MW plants. The variable cost of generation includes all of the cost elements discussed above, including the T&S cost. With no CO_2 allowance price, the two air-fired plants without CCS (red and blue solid lines) would dispatch first. The 900MW oxy-fired plant will dispatch before the 900MW air-fired plant at CO_2 Allowance Prices above 26 $/ton. The 450MW oxy-fired plant will dispatch before the 450MW air-fired plant at CO_2 Allowance Prices above 29 $/ton CO_2.

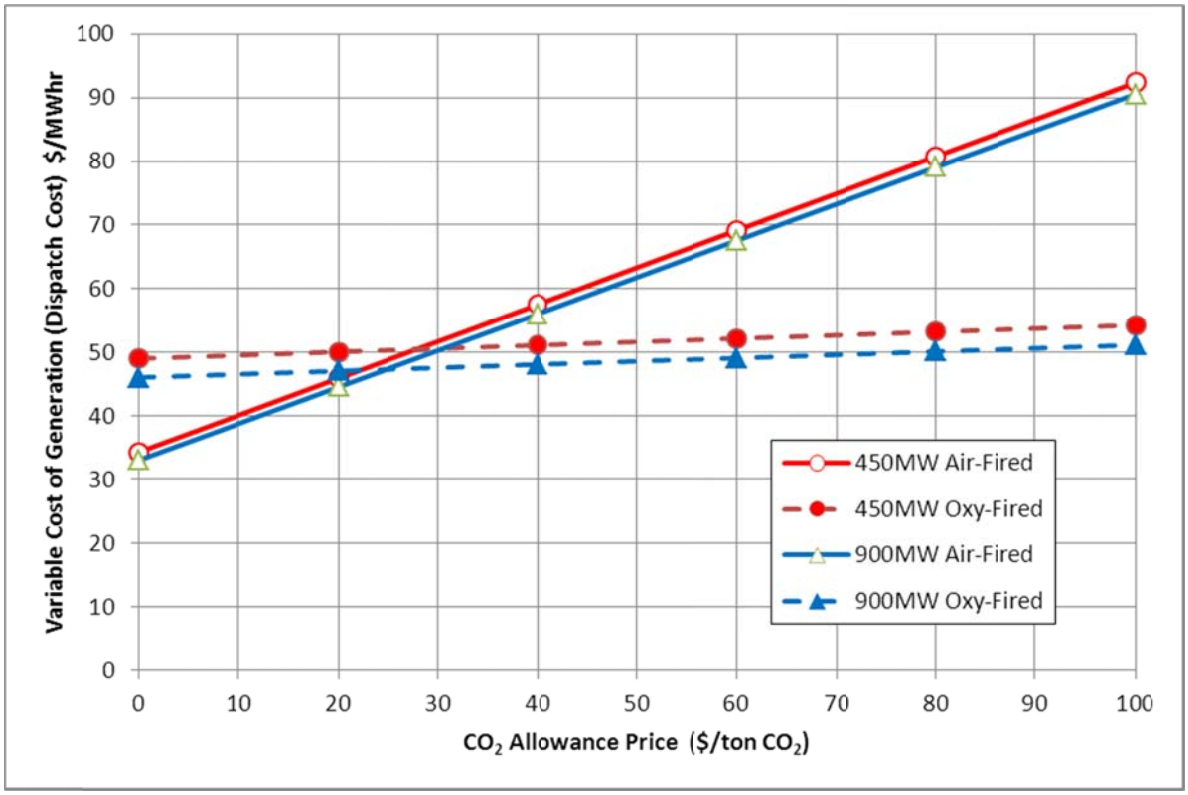

Figure 8-9: Variable Cost of Generation vs. CO_2 Allowance Price

8.2.4 Cost of CO_2 Avoided/Captured

Figure 8-10 shows the CO_2 mitigation costs for the 450MW and 900MW oxy-fired plants. The costs are relative to the 450MW and 900MW air-fired plants, respectively, and do not include T&S. Including T&S will increase the CO_2 mitigation costs by 8-12 $/ton CO_2. The CO_2 Avoided Cost was 131 $/ton for the 450MW oxy-fired plant and decreased to 96 $/ton for the 900MW oxy-fired plant. The CO_2 Captured Cost was 99 $/ton for the 450MW oxy-fired plant and decreased to 75 $/ton for the 900MW oxy-fired plant.

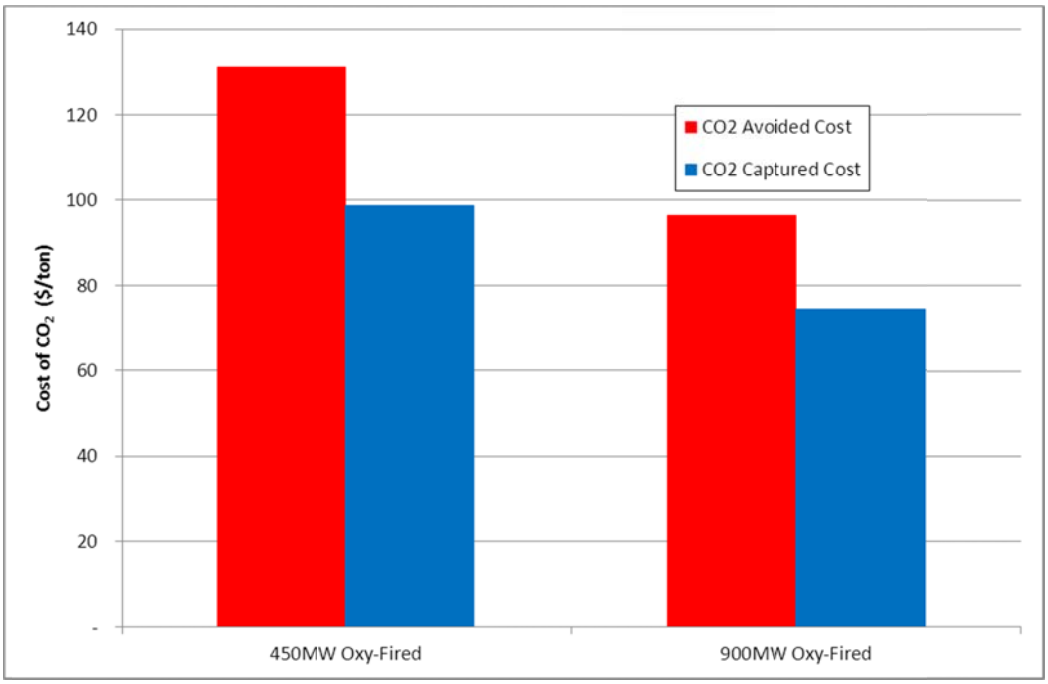

Figure 8-10: CO_2 Avoided and Capture Costs

8.3 Environmental Performance

8.3.1 CO_2 Emissions

The carbon capture efficiency is a measure of the process effectiveness at capturing the carbon contained in the coal for sequestration or utilization. It is defined as:

$$\%\ \text{Carbon Capture} = \frac{(CO_2\text{Coal} - CO_2\text{emitted})}{CO_2\text{Coal}}$$

The carbon capture efficiency for the oxy-fired 450MW Demonstration Plant, 900MW Commercial Plant, and Industrial Steam Plant was 93% for all cases. The carbon loss for each case was primarily from the GPU vent. The GPU design and performance for this techno-economic study was based on the GPU used in Case 5C of the DOE Baseline Study.[40] Since the carbon capture is largely controlled by the GPU performance, the % carbon capture for all of these cases was essentially the same as for the DOE Case 5C.

Figure 8-11 shows the actual carbon emissions in lb CO_2/MMBtu for the air-fired and oxy-fired Demonstration Plant, Commercial Plant, and Industrial Steam Plant cases.

[40] Pulverized Coal Oxycombustion Power Plants Volume 1, DOE/NETL-2007/1291, August 2008

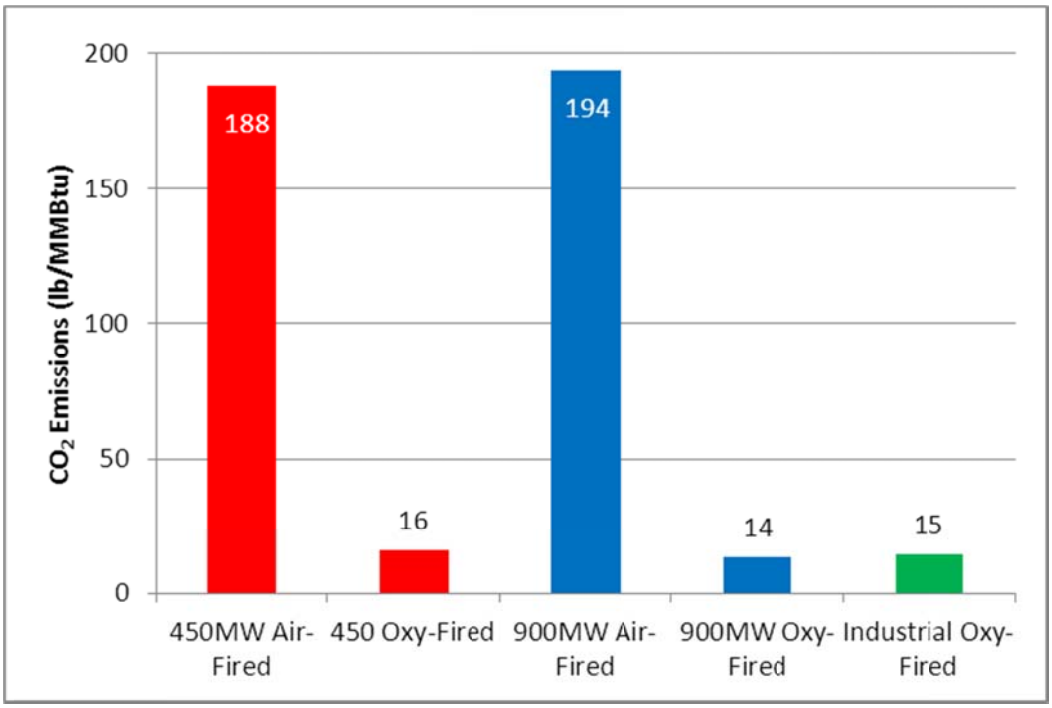

Figure 8-11: Summary of CO_2 Emissions for Air-Fired and Oxy-Fired Cases

8.3.2 Non-CO_2 Emissions

Table 8-3 summarizes the emissions from the air-fired and oxy-fired 450MW Demonstration Plant, 900MW Commercial Plant, and Industrial Steam Plant. The environmental targets selected for this study are identical to those chosen for the PC cases in the DOE Cost and Performance Baseline for Fossil Energy Plants[41] and are summarized in the first column of this table. This ensures that these cases can be compared fairly with plants evaluated in other DOE programs on a common basis. The targets established in the baseline report factored in existing environmental regulations and trends, recent permits, and the current BACT. This was compared with NSPS as of February 2006 which defined the minimum control level required for new fossil power plants. The BACT analysis was selected as the environmental target as shown in Table 1-4 since they exceeded the requirements for both NSPS and the average of recent permits.

The emissions for the air-fired cases shown in Table 8-3 match the environmental targets as the plants are designed and operated to meet these limits. NO_x emissions are controlled by the low NO_x firing system and SCR. SO_2 emissions are controlled by the WFGD for the 450MW and 900MW plants and by a NID™ for the industrial steam plant. Particulates are controlled by fabric filters for all cases. The fabric filter for the industrial steam plant is an integral part of the NID™ system. The mercury emission limits are met by co-benefit capture from the combined effects of the SCR, fabric filter, and FGD. The SCR promotes the oxidation of elemental

[41] Cost and Performance Baseline for Fossil Energy Plants Volume 1, DOE/NETL-2010/1397, November 2010

mercury. The oxidized mercury can then be more readily removed in the fabric filter and FGD. No activated carbon injection was necessary for these plants as the assumed 90% mercury co-benefit capture is sufficient to meet the mercury limits for this study.

The oxy-fired plants use the same environmental control equipment as for the air-fired plants. However, the emissions for the oxy-fired plants shown in Table 8-3 are significantly below emission targets used in this study. This is because additional removal takes place as the gas passes through the Flue Gas Condenser and GPU. A significant amount of the SO_2 is removed in the Flue Gas Condenser and is then neutralized with NaOH. Most of the remaining SO_2 is removed in the GPU. Similarly, most of the remaining NO_x is removed in the condensate when the flue gas is compressed. The remaining NO_x is sequestered with the CO_2 product gas. Most of the oxidized mercury is removed in the Flue Gas Condenser. The balance of the mercury is removed in an activated carbon bed in the GPU.

Table 8-3: Summary of Emissions for all Air-Fired and Oxy-Fired Cases

Power Plant Cases	Target	Air-Fired SCPC Power Plant 450MW	Oxy-Fired SCPC Power Plant 450MW	Air-Fired SCPC Power Plant 900MW	Oxy-Fired SCPC Power Plant 900MW	Oxy-Fired Steam Plant 150MW
SO_2 (lb/MMBtu)	0.085	0.085	< 0.01	0.085	< 0.01	< 0.01
NO_x (lb/MMBtu)	0.07	0.07	< 0.01	0.07	< 0.01	< 0.01
Particulates (lb/MMBtu)	0.013	0.013	< 0.01	0.013	< 0.01	< 0.01
Hg (lb/TBtu)	1.14	1.14	< 0.01	1.14	< 0.01	< 0.01
CO_2 (lb/MMBtu)		188	16	194	14	15

8.4 Sensitivity Study on FGR Location

A sensitivity study was conducted to evaluate the performance and cost impact of four different locations for the secondary flue gas recirculation duct take-off. The options considered included secondary FGR taken after the WFGD, before the WFGD, and before the Gas-Gas Heater. In this last scenario, an oxygen eductor is used to provide the motive force to convey the hot flue gas recycle back to the boiler. The last scenario had two options – one with the O_2 mixed directly with the secondary FGR and a second with the O_2 first preheated. The primary FGR ducts were taken after the Flue Gas Condenser for all cases to minimize the moisture concentration in the recirculation gas feeding the pulverizers. This study was focused on the performance and cost implications of the FGR location and did not consider the impact of increased SO_2 concentrations on the boiler design. However, the options that take recirculation gas before the WFGD would likely be limited to low sulfur fuels because of the potential impacts on boiler tube corrosion and additional costs associated with corrosion protection.

Model simulations showed that moving the secondary FGR duct before the WFGD slightly improved the boiler efficiency as compared to the base case with the secondary FGR after the WFGD. Moving the secondary FGR before the Gas-Gas Heater actually decreased the boiler efficiency by 0.7% points due to the lower temperature of the FGR entering the furnace after cold O_2 is mixed with it. However, preheating the O_2 before mixing it with the secondary FGR

improved the boiler efficiency for the case with FGR ducts located before the Gas-Gas Heater by 1% point relative to the base case.

Table 8-4 summarizes the qualitative cost impacts for the different FGR locations as compared to Case 1. Moving the FGR location from after the WFGD (Case 1) to before the WFGD (Case 2) results in a slightly larger fabric filter (due to a higher gas temperature and volumetric flow leaving the Gas-Gas Heater) and a smaller WFGD. Moving the FGR location before the Gas-Gas Heater (Cases 3 and 4) reduces the volumetric flow rate to all gas touched equipment downstream of the boiler and before the Flue Gas Condenser, including the Gas-Gas Heater, fabric filter, and WFGD. Case 4 also requires the addition of an O_2 heater.

A simple cost analysis was conducted to capture the cost impacts on a 900MW oxy-fired plant for some of the major pieces of equipment impacted by the choice of FGR location. Table 8-4 shows that moving the FGR upstream of the WFGD can have significant cost benefits. Of course, there are other considerations, such as the impact of increased SO_2 concentration on the boiler materials that may override any advantages of moving the FGR location. There was little additional cost benefit from moving the FGR location from before the WFGD to before the Gas-Gas Heater if the O_2 was not preheated before mixing with the secondary FGR. Although Case 3 has a lower cost fabric filter than Case 2 due to reduce volumetric gas flow, this savings is offset by a lower boiler efficiency due to the reduced secondary FGR gas temperature entering the furnace. Preheating the O_2 before mixing with the secondary FGR (Case 4) results in improved boiler efficiency and greater capital cost reduction relative to Case 1.

Table 8-4: Cost Implications of FGR Location

	Case 1 After WFGD	Case 2 Before WFGD	Case 3 Before GGH	Case 4 Before GGH O_2 Preheat
Gas-Gas Heater	Base	Similar	Smaller	Smaller
Fabric Filter	Base	Larger	Smaller	Smaller
WFGD	Base	Smaller	Smaller	Smaller
O_2 AH	N/A	N/A	N/A	New
Δ Total Overnight Capital Cost ($M)	Base	-66	-67	-85
Δ Total Overnight Capital Cost ($/Kw)	Base	-101	-101	-130

There are other costs that were not considered in this simple cost analysis. Cost additions include an increased ASU capital cost and higher ASU power requirements for Case 4 as the oxygen needs to be delivered at a higher pressure for the oxygen eductor to provide the motive force necessary to convey the hot FGR back to the boiler. There may be some windbox modifications necessary for Cases 3 and 4 to deal with the hot, particulate laden FGR. Other costs may be necessary to cope with increase SO_2 emissions in the boiler.

These cost adders are offset by various cost reductions that were not considered in this study. These include reduced capital costs for the ID Fan and gas ductwork, plus reduced auxiliary power requirements for the fabric filter, WFGD, and ID Fan. The impact on the flue gas heat exchanger (HEX) was also not considered, but the cost of this equipment would likely increase for Case 2 due to the increased sensible energy in the flue gas from the higher gas temperature. The HEX cost would likely decrease for Case 4 due to the significantly decreased volumetric flow rate relative to Case 1, which more than offsets an increase in flue gas temperature. The HEX cost for Case 3 would likely be just slightly less than for Case 1 as the increased flue gas temperature would almost offset the reduced volumetric flow rate.

Overall, the FGR location in Case 4 resulted in the most significant cost reduction as compared to the base case scenario. The capital cost reductions considered in this sensitivity study total 3.5% of the Total Overnight Costs of the 900MW oxy-fired plant that used the secondary FGR after the WFGD (Case 1). The additional costs and savings not considered in this study are expected to increase the overall savings.

9. Summary

- Four utility scale power plants were designed and costs were developed for them in this study. A $450MW_{gross}$ oxy-fired SCPC plant was designed as representative of a demonstration plant for oxy-combustion. A $900MW_{gross}$ oxy-fired SCPC plant was designed and costs were developed as representative of a first generation oxy-combustion commercial plant. These plants were contrasted with a $450MW_{gross}$ and a $900MW_{gross}$ air-fired SCPC plant. This study also included an evaluation of the design modifications and costs necessary to retrofit an existing air-fired industrial steam plant equivalent to $150MW_{gross}$ to oxy-combustion.

- The net plant efficiency for the 450MW oxy-fired plant was 31.5% HHV, or 9.4% points less than the 450MW air-fired case. The net plant efficiency for the 900MW oxy-fired plant was 32.5% HHV, or 8.8% points less than the 900MW air-fired case. The reduction in net plant efficiency for the oxy-fired cases is primarily due to the increased auxiliary power requirements for the ASU and GPU.

- The net plant efficiency for the 900MW oxy-fired plant was 0.6% points higher than the efficiency for the 450MW oxy-fired plant. This improvement is primarily due to the thermal integration of the ASU, GPU, and FGHR system that was used for the 900MW oxy-fired plant design.

- The Total Overnight Capital cost for the 450MW oxy-fired plant increased by 78.1% relative to the air-fired plant. The Total Overnight Capital cost increase for the 900MW oxy-fired plant was 78.5% relative to the air-fired plant. The added cost of integration of the ASU, GPU, and FGHR for the 900MW offset some of the specific cost decrease due to both scalability and technology maturity (commercial vs. demonstration plant).

- Most of the capital cost increase for the oxy-fired utility plants is due to the addition of the ASU and GPU systems. The 450MW and 900MW boiler bare erected costs (materials and erection only) increased by about 11% for the oxy-fired cases as compared to the air-fired cases. This increase accounts for the changes necessary to make the boiler oxy-capable, such as the addition of the flue gas recirculation system ducting, oxygen mixers, and windbox modifications.

- The incremental Total Overnight Capital costs to retrofit the $150MW_{gross}$ air-fired industrial boiler to oxy-fired capability is approximately $200 million. The cost of the boiler modifications are only 7% of the total capital cost. The majority of the retrofit capital cost is for the addition of the ASU and GPU.

- The first year COE (w/o T&S) for the 450MW oxy-fired plant increased by 72.9% relative to the 450MW air-fired plant. The COE increase for the 900MW oxy-fired plant increased by 68.5% relative to the 900MW air-fired plant. The COE increase for both

oxy-fired plants is well above the DOE COE increase target of 35%, which is not surprising as these plants are first generation CCS technologies. Further reductions in the COE can be expected in second generation oxy-fired plants from continued reductions in the capital cost and power requirements for the ASU and GPU, along with further optimization and integration of the overall power plant.

- The CO_2 Avoided Cost was 131 $/ton for the 450MW oxy-fired plant and decreased to 98 $/ton for the 900MW oxy-fired plant. The CO_2 Capture Cost was 99 $/ton for the 450MW oxy-fired plant and decreased to 75 $/ton for the 900MW oxy-fired plant.
- A sensitivity study evaluated the performance and cost impact of four different locations for the secondary flue gas recirculation duct take-off. Moving the FGR from after the WFGD to before the WFGD had little impact on the boiler efficiency. Moving the FGR before the Gas-Gas Heater actually decreased the boiler efficiency by 0.7% points due to the lower temperature of the FGR entering the furnace after cold O_2 is mixed with it. However, preheating the O_2 before mixing it with the secondary FGR improved the boiler efficiency for the case with FGR ducts located before the Gas-Gas Heater by 1% point relative to the case with the FGR location after the WFGD.
- A simple cost analysis identified the cost impacts on a 900MW oxy-fired plant for some of the major pieces of equipment impacted by the choice of FGR location. The results showed that moving the FGR upstream of the Gas-Gas Heater and preheating the O_2 before mixing with the secondary FGC can have significant cost benefits in terms of both boiler efficiency improvement and capital cost reduction. These benefits need to be weighed against other considerations, such as the impact of increased SO_2 concentration on boiler materials.

10. References

1. Cost and Performance Baseline for Fossil Energy Plants Volume 1, DOE/NETL-2010/1397, November 2010

2. Pulverized Coal Oxycombustion Power Plants Volume 1, DOE/NETL-2007/1291, August 2008

3. Cost Estimation Methodology for NETL Assessments of Power Plant Performance, NETL Quality Guidelines for Energy System Studies, DOE/NETL-2-11/1455, April 2011

4. Updated Costs (June 2011 Basis) for Selection Bituminous Baseline Cases, DOE/NETL-341/082312, August 2012

5. Capital Cost Scaling Methodology, Quality Guidelines for Energy System Studies, DOE/NETL-341/013113, January 2013

6. Power Systems Financial Model Version 6.6 User's Guide, DOE/NETL-2011/1492, May 2011

7. Cost Estimation Methodology for NETL Assessments of Power Plant Performance, DOE/NETL-2011/1455, April 2011

8. Power Systems Financial Model Version 6.6 User's Guide, DOE/NETL-2011/1492, May 2011, pg. 14

9. Updated Costs (June 2011 Basis) for Selection Bituminous Baseline Cases, DOE/NETL-341/082312, August 2012, pg. 5-6

10. Pulverized Coal Oxycombustion Power Plants Volume 1, DOE/NETL-2007/1291, August 2008

11. Cost and Performance Baseline for Fossil Energy Plants Volume 1, DOE/NETL-2010/1397, November 2010

12. Process Modeling Design Parameters – Site Description, DOE/NETL-341/081911, January 2012, pg. 2

13. Quality Guidelines for Energy System Studies – Specification for Selected Feedstocks, DOE/NETL-341/011812, January 2012, pg. 4

14. Quality Guidelines for Energy System Studies – Specification for Selected Feedstocks, DOE/NETL-341/011812, January 2012, pg. 4

15. Cost and Performance Baseline for Fossil Energy Plants Volume 1, DOE/NETL-2010/1397, November 2010, pg. 38

16. CO_2 Impurities Design Parameters, DOE/NETL-341/011212, January 2012, pg. 4

17. Cost and Performance Baseline for Fossil Energy Plants Volume 1, DOE/NETL-2010/1397, November 2010, pg. 53

18. Cost and Performance Baseline for Fossil Energy Plants Volume 1, DOE/NETL-2010/1397, November 2010, pg. 328

19. Cost Estimation Methodology for NETL Assessments of Power Plant Performance, NETL Quality Guidelines for Energy System Studies, DOE/NETL-2-11/1455, April 2011

20. Updated Costs (June 2011 Basis) for Selection Bituminous Baseline Cases, DOE/NETL-341/082312, August 2012

21. Capital Cost Scaling Methodology, Quality Guidelines for Energy System Studies, DOE/NETL-341/013113, January 2013

22. Cost Estimation Methodology for NETL Assessments of Power Plant Performance, DOE/NETL-2011/1455, April 2011, pg. 5-6

23. Conducting Technical and Economic Evaluations – As Applied for the Process and Utility Industries, AACE International Recommended Practice No. 16R-90.

24. Updated Costs (June 2011 Basis) for Selection Bituminous Baseline Cases, DOE/NETL-341/082312, August 2012

25. Cost Estimation Methodology for NETL Assessments of Power Plant Performance, DOE/NETL-2011/1455, April 2011, pg. 9

26. Cost Estimation Methodology for NETL Assessments of Power Plant Performance, DOE/NETL-2011/1455, April 2011, pg. 8

27. Power Systems Financial Model Version 6.6 User's Guide, DOE/NETL-2011/1492, May 2011

28. Power Systems Financial Model Version 6.6 User's Guide, DOE/NETL-2011/1492, May 2011, pg. 14

29. Updated Costs (June 2011 Basis) for Selection Bituminous Baseline Cases, DOE/NETL-341/082312, August 2012, pg. 5-6

30. Cost and Performance Baseline for Fossil Energy Plants Volume 1, DOE/NETL-2010/1397, November 2010 – Case 11

31. Pulverized Coal Oxycombustion Power Plants Volume 1, DOE/NETL-2007/1291, August 2008 – Case 5C

32. Capital Cost Scaling Methodology, Quality Guidelines for Energy System Studies, DOE/NETL-341/013113, January 2013

33. Enhanced Combustion Low NO_x Pulverized Coal Burner, Alstom Power, DOE Final Report, DE-FC26-04NT42300, March 2008

34. Pulverized Coal Oxycombustion Power Plants Volume 1, DOE/NETL-2007/1291, August 2008

35. IHS Website - http://www.ihs.com/info/cera/ihsindexes/index.aspx

36. Capital Cost Scaling Methodology, Quality Guidelines for Energy System Studies, DOE/NETL-341/013113, January 2013

37. Cost Estimation Methodology for NETL Assessments of Power Plant Performance, NETL Quality Guidelines for Energy System Studies, DOE/NETL-2-11/1455, April 2011

38. Updated Costs (June 2011 Basis) for Selection Bituminous Baseline Cases, DOE/NETL-341/082312, August 2012

39. Capital Cost Scaling Methodology, Quality Guidelines for Energy System Studies, DOE/NETL-341/013113, January 2013

40. Pulverized Coal Oxycombustion Power Plants Volume 1, DOE/NETL-2007/1291, August 2008

41. Cost and Performance Baseline for Fossil Energy Plants Volume 1, DOE/NETL-2010/1397, November 2010

Recovery Act: Oxy-Combustion Technology Development for Industrial-Scale Boiler Applications

DOE/NETL Cooperative Agreement No. DE-NT0005290

Volume IV – Reference Oxy Boiler Designs

Chapter 3 – Oxy Boiler Island Advanced Process Control

Authors
Chuan Wang
Xinsheng Lou

Table of Contents

1 EXECUTIVE SUMMARY 4

2 INTRODUCTION 6

2.1 OXY-FIRED PULVERIZED COAL POWER PLANT OVERVIEW 6

3 OXY BOILER ISLAND REGULATORY CONTROL 9

3.1 COMBUSTION CONTROL 9
3.1.1 Fuel Flow Control 9
3.1.2 Flue Gas Recirculation Flow Control 9
3.1.3 Pulverizer System Control 10
3.1.4 Furnace Pressure Control 10
3.2 STOICHIOMETRY CONTROL 10
3.2.1 Secondary Oxidant O_2 Concentration Control 11
3.2.2 Secondary Oxidant Flow Distribution Control 11
3.2.3 Combustion Zone Stoichiometry Control 11
3.3 WATER/STEAM CONTROL 12
3.3.1 Feedwater Control 12
3.3.2 SH Steam Temperature Control 12
3.3.3 RH Steam Temperature Control 13

4 OXY BOILER ISLAND ADAPTIVE CONTROL 15

4.1 L1 ADAPTIVE CONTROL FUNDAMENTAL THEORY 15
4.2 L1 ADAPTIVE CONTROL DESIGN AND VALIDATION FOR OXY BOILER ISLAND 17

5 OXY BOILER ISLAND MODEL PREDICTIVE CONTROL 20

5.1 INTRODUCTION TO MODEL PREDICTIVE CONTROL 21
5.1.1 Model Predictive Control Fundamental Theory 21
5.1.2 Model Identification 22
5.1.3 Off-line Configuration and Validation 24
5.1.4 On-line Deployment 25
5.2 MODEL PREDICTIVE CONTROL FOR THE OXY BOILER ISLAND 25
5.2.1 Oxy Boiler Island MPC Structure 26
5.2.2 Oxy Boiler Island MPC Model Identification 30
5.2.3 Oxy Boiler Island MPC Data Communication Configuration 31
5.3 MODEL PREDICTIVE CONTROL SIMULATION VALIDATION 33
5.3.1 NO_x Emission Reduction 33
5.3.2 Reheat Spray Reduction 35

6 OXY BOILER ISLAND REAL-TIME OPTIMIZATION 39

6.1 REAL TIME OPTIMIZATION OVERVIEW 39
6.1.1 General 39
6.1.2 RTO Calculation Cycle 40
6.2 REAL-TIME OPTIMIZATION FOR THE OXY BOILER ISLAND 41
6.3 OPTIMIZATION OBJECTIVES 42

BIBLIOGRAPHY 44

List of Figures

Figure 2-1. PFD of the Dual-Fired Boiler Island of Oxy-PC Demo Plant 8
Figure 4-1. Block diagram of an adaptive system 15
Figure 4-2. Schematic representation of L1 adaptive controller 16
Figure 4-3. Main steam temperature responses 18
Figure 4-4. Reheated steam temperature responses 19
Figure 5-1. Control hierarchy of oxy-fired power plant 20
Figure 5-2. Principle of model predictive control 21
Figure 5-3. Model predictive control structure for Oxy Boiler Island 27
Figure 5-4. Oxy Boiler Island MPC modeling results grid overview 31
Figure 5-5. Oxy Boiler Island Aspen Plus Dynamic Model 32
Figure 5-6. Oxy Boiler Island MPC Control Panel 32
Figure 5-7. OBI MPC Analysis case 1: NO_x emission response 34
Figure 5-8. OBI MPC Analysis case 1: SHO steam temperature response 34
Figure 5-9. OBI MPC Analysis case 1: MBZ stoichiometry response 34
Figure 5-10. OBI MPC Analysis case 1: Burner tilts position response 35
Figure 5-11. OBI MPC Analysis case 2: RH spray water flow rate response 35
Figure 5-12. OBI MPC Analysis case 2: RHO steam temperature response 36
Figure 5-13. OBI MPC Analysis case 2: MBZ stoichiometry response 36
Figure 5-14. OBI MPC Analysis case 2: Burner tilts position response 36
Figure 6-1. General hierarchical control optimization 39
Figure 6-2. RTO calculation cycle 41

List of Tables

Table 4-1. Variable description of L1 adaptive controller 17
Table 4-2. Comparative simulation results of main steam temperature between PID and L1AC 18
Table 4-3. Comparative simulation results of reheated steam temperature between PID and L1AC 19

1 Executive Summary

Advanced control development is an integral part of the oxy boiler development design effort. Advanced control techniques have been widely used in the process industry to enhance the control quality and optimize the system performance. This chapter discusses results of the project effort to explore advanced control strategies to improve the control and hence overall process operational performance of the oxy-fired boiler island. Several types of advanced control methods are addressed, namely, L1 adaptive control, model predictive control and Real-Time optimization. The L1 adaptive control is a relatively new control approach, which is considered as an alternative to conventional PID (Proportional-Integral-Derivative) controllers, to provide a fast response with guaranteed robustness. At the same time, model predictive control (MPC) and RTO concepts are designed for the Oxy Boiler Island to optimize its control and operation. This chapter includes the following technical aspects:

- the regulatory controls of Oxy-Fired Boiler Island, including major control sub-systems, such as combustion control, water/steam control, etc.
- the fundamental theory of L1 adaptive control and its design and implementation for Oxy Boiler Island steam temperature controls.
- the reduction of NO_x emission as well as reheat spray by utilizing the technology of model predictive control.
- the concept of real-time optimization and its optimization objective to oxy boiler island application.

An adaptive controller is a controller that can modify its behavior in response to changes in the dynamics of the process and the character of the disturbances. The adaptive controller becomes nonlinear because of the parameter adjustment mechanism, and the essence of the adaptive controller is how its parameters are adjusted to meet the requirement of the changing control environment. The L1 adaptive control is a new type of adaptive control, which emerged in recent years. It can be viewed as a modified MRAC (Model Reference Adaptive Control) scheme where the basic structure is based on internal model principle. The key feature of the L1 adaptive control architecture is its guaranteed robustness in the presence of fast adaptation. Compared to conventional PID controllers, the L1 adaptive controller provides a better control performance in considering these complicated conditions of the thermal plant. The L1 adaptive controller technique has been proved to provide fast adaptation of transient response in a large variety of systems due to its basic control architecture that the state predictor offers a model estimation of the dynamics of the system, while the adaptive law deals with the mismatch of the model. Some of the model-based control methods usually need to obtain the model of the plant at the beginning and depend on the accuracy of the model, while there is no such requirement in the L1 adaptive controller, which simplifies the process of controller design. In addition, some model-based controllers may not work properly if the dynamics of the system change. The robustness of the L1 adaptive controller guarantees that a good control performance can also be achieved in such conditions. Due to its robustness and fast adaptation, the L1 adaptive controller is demonstrated to obtain a better transient performance than the PID controller in controlling the temperature of the superheated and reheated steam in the oxy boiler simulator. Further, the adaptive controller is shown to reduce the process transients caused by disturbances of changing MW and thermal load in the simulation studies.

Model-based predictive control provides a very competent solution to this type of multivariable process control issue. Model Predictive Control (MPC) is an advanced method of process control that

has been used in the process industries such as chemical plants and oil refineries for decades. The essence of MPC technology is a dynamic model which is used to capture the internal relationship between dependent variables and independent variables of the modeled process. In industrial processes, independent variables often appear in the form of set points in regulatory controllers that govern valve movement, while dependent variables are most often constraints in the process. Based on current plant measurements and the predictive model, the model predictive controller can calculate future independent variable control moves that satisfy an optimization objective and also ensure all independent and dependent variables remain within constraints. The MPC will function as a supervisory controller in that the set of independent variable control moves will be sent as biases to the corresponding regulatory controller set points to be implemented in the process control. In this study, an MPC design was implemented on the commercial scale dynamic simulator for the oxy boiler island. The process model and cost functions for optimization involve process variables from both flue gas side and water-steam side of the oxy boiler process. Simulation testing of the model predictive controllers for NO_x emissions and reheat spray water consumption was conducted to demonstrate the benefits, e.g. a) Reduce NO_x emissions and b) Reduce reheat spray water consumption. More studies can be done to evaluate the enhanced control performance to improve the operating flexibility of the oxy boiler and integrated plant.

The potential of advanced process control to optimize the oxy-fired boiler island control and operation was illustrated by examples demonstrating L1 adaptive control and the model predictive control design concepts applying dynamic simulation software platform of the oxy-fired boiler island process. The preliminary test cases demonstrated process improvement in multiple aspects, including NO_x emission reduction, spray water consumption reduction, and steam temperature deviation suppression. The full potential of a model predictive controller has not yet been fully investigated and requires optimization through the future field unit implementation. Provided is a basic guideline to the design concept of advanced process control and the procedure to develop and validate such a system for the oxy-fired pulverized coal power plant with the CO_2 capture system.

The use of Real-Time Optimization (RTO) for an oxy boiler island is also discussed. A preliminary RTO specification for oxy-fired boiler island was developed. The basic RTO architecture is depicted and economic objectives for optimization carbon capture plant are outlined.

2 Introduction

This chapter addresses development work to improve the control performance of the Oxy-Fired Boiler Island by applying two types of advanced control technologies: L1 Adaptive Control (L1AC) and Model Predictive Control (MPC). Compared to conventional Proportional-Integral-Derivative (PID) controllers, these two controllers are working at different control levels. The L1AC is working at the same level as a PID controller, and it is treated as an alternative method for the PID to provide a fast process response with guaranteed robustness. The MPC is positioned above the regulatory control level to provide optimum set points for the control system. As a typical advanced process control method, the model predictive control aims to optimize the control and operation of the Oxy-fired Boiler Island. In addition, Real-time Optimization is also presented to achieve economic optimization for the oxy boiler island.

The following control approaches will discuss:

- the regulatory controls of Oxy-Fired Boiler Island including major control sub-systems, such as combustion control, water/steam control, etc.
- the fundamental theory of L1 adaptive control and its design and implementation for Oxy Boiler Island steam temperature controls.
- the reduction of NO_x emission as well as reheat spray by utilizing the technology of model predictive control.
- the concept of real-time optimization and its optimization objective to oxy boiler island application.

2.1 Oxy-Fired Pulverized Coal Power Plant Overview

Compared with conventional air-fired combustion, the essential difference of oxy-fired combustion is the use of relatively pure oxygen (O_2) provided by an Air Separation Unit in combination with the recycled flue gas, which replaces ambient air for combustion. Due to the removal of nitrogen (N_2) in the Air Separation Unit, the flue gas leaving the furnace consists of mainly carbon dioxide and water vapor, the latter of which is condensed through cooling. The result is that a carbon dioxide rich stream that only needs purification before it can be transported and either stored or used.

An oxy-fired pulverized coal power plant generally consists of 4 major sub-systems:

- Air Separation Unit (ASU): separates the oxygen from ambient air and supplies the pure oxygen to the boiler for combustion.
- Dual-Fired (Air/Oxy-Fired) Pulverized Coal Boiler Island: includes the dual-fired (air/oxy-fired) boiler unit and the backend Air Quality Control System (AQCS). On the water/steam side, the boiler is used to generate steam with certain quality and quantity requirements. On the flue gas side, the boiler and its AQCS system produce a CO_2 enriched flue gas, which can be further purified by the gas process unit.
- Gas Processing Unit (GPU): compresses the CO_2 enriched flue gas from the boiler island and further purifies the CO_2 for sequestration or utilization.

- Turbine Island (TI): utilizes a conventional steam power plant design for the equipment, including steam turbines, generator, feedwater pre-heater train, main condenser, feedwater chemistry processing units, etc.

Figure 2-1 shows the Process Flow Diagram (PFD) for the 450 MW_e oxy-fired demonstration design. A mixture of recirculated flue gas and oxygen is used to make the primary and secondary "oxidant" streams ("oxidant" instead of air). Streams 3a (primary O_2) & 3b (secondary O_2) provide the oxygen for the primary and secondary streams respectively. The oxygen is provided by the Air Separation Unit (ASU). The oxygen concentration of Stream 18b (i.e. the primary oxidant flow) and Stream 28 (the secondary oxidant flow) is controlled to a set point limited by the material selections of the duct and equipment with tolerance for incomplete mixing and appropriate control range redundancy. A third stream of relatively pure oxygen (Stream 3c – supplemental O_2), which is the remaining oxygen required for combustion of the coal, is provided directly to the wind-box where it mixes with the secondary oxidant stream just before entering the furnace. Flue gas oxygen content leaving the boiler (Stream 4) is maintained at a pre-determined value (typically for coal firing ~3% by volume-wet – similar to air firing with ~20% excess air) under all operating conditions with oxygen firing by adjusting the Stream 3c flow rate. Minimizing the flue gas oxygen content under all operating conditions is very important with oxygen firing because the ASU has very high power requirements (typically 12~15% of generator output). Additionally, the increase of oxygen concentration in the flue gas will also result in the reduction of the product quality in the Gas Processing Unit (GPU).

The source for the recirculated flue gas for the primary stream is selected at the outlet of the Flue Gas Condenser (FGC), namely, Stream 18 – Primary Flue Gas Recirculation (PFGR) in that the flue gas stream contains the lowest water vapor content at this location and therefore it is well suited for coal drying. The flow quantity of the primary stream is dependent on the coal mill gas flow requirements for entrainment, drying and transport of the pulverized coal to the furnace. The primary FGR is extracted after the direct contact cooler. The rest of flue gas (stream 15) at the outlet of DCC flows through the GPU where the CO_2 enriched flue gas gets compressed and further purified for CO_2 storage or utilization. The turbine island stays the same as in a conventional air-fired power plant.

For this design, the source of the recirculated flue gas for the secondary stream (Stream 27 – secondary flue gas recirculation (SFGR) is from the outlet of the Flue Gas Desulphurization (FGD) System; however it could be from before the FGD system for designs for lower sulfur coals.

The oxygen-fired boiler unit is also capable of firing in air-fired mode. Both the primary flue gas recirculation line and the secondary flue gas recirculation line have isolation dampers installed, which would be completely shut off in air-fired mode. Ambient air will be supplied through the Primary Air (PA) fan and the Forced Draft (FD) fan, and all the flue gas leaving the furnace will be processed by the air quality control system before being released to the atmosphere.

The backend Air Quality Control System (AQCS) mainly includes an Electrostatic Precipitator (ESP) and a Wet Flue Gas Desulfurization (WFGD) unit. The flue gas leaving the boiler enters the ESP where the fly ash is removed, and then the WFGD where the acidic gases such as SO_2 can be captured.

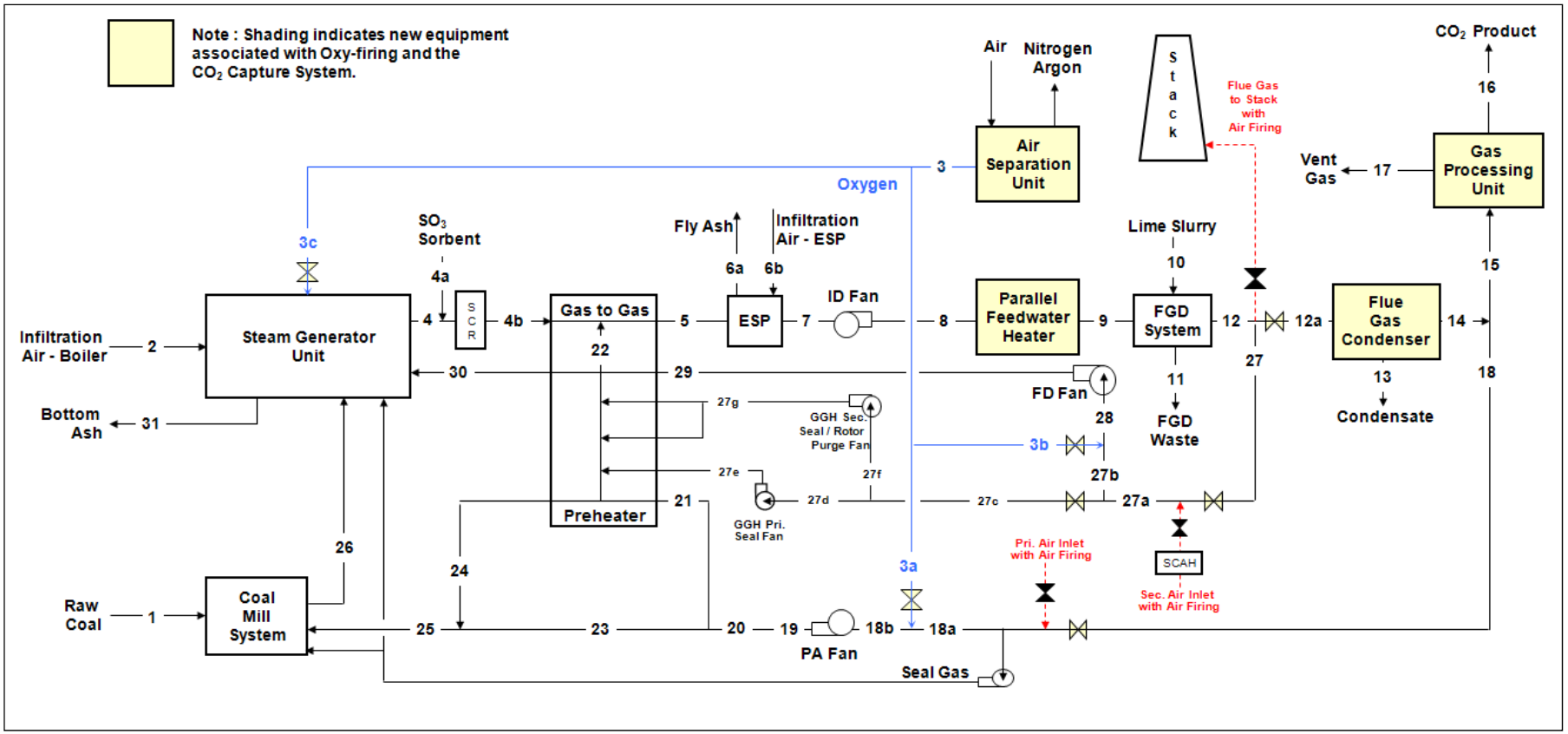

Figure 2-1. PFD of the Dual-Fired Boiler Island of Oxy-PC Demo Plant

3 Oxy Boiler Island Regulatory Control

The overall control structure for the Oxy-Fired Boiler Island process is generally consistent with the control system of a conventional air-fired boiler island process with some additional features to address oxy-firing. The major control loops consist of the following:

- Combustion Control The main control objectives of combustion control loops include 1) the coordination of fuel and oxidant flows, 2) maintenance of combustion stability and boiler efficiency, and 3) combustion mode transitions between air-fired mode and oxy-fired mode. Significant changes have been made to the combustion controls for the oxy-fired boiler process compared to conventional air-fired boiler process.
- Stoichiometry Control Stoichiometry control is designed to maintain the combustion stability and efficiency, and minimize the production of NO_x via staging the combustion appropriately. Stoichiometry control belongs to combustion control; however, it has significant difference compared with that of the conventional air-fired boiler process.
- Water/Steam Control Overall control objectives for water/steam control include coordinating boiler feedwater flow according to the boiler master, controlling the SH steam and RH steam temperature, and maintaining the SH spray valves in the appropriate operating ranges, etc. No significant changes are made to the SH steam temperature control loops compared to conventional Air-fired unit. However, flue gas recirculation trim control loop has been added to the RH steam temperature control loops.

3.1 Combustion Control

The basic closed-loop control logics of the oxy boiler island combustion system including the following subsections: Fuel Flow Control, Flue Gas Recirculation Flow Control, Pulverizer System Control, and Furnace Pressure Control.

3.1.1 Fuel Flow Control

It is essential to maintain tight control of the ratio between the fuel and the oxidant in the combustion process to maintain high combustion efficiency as well as low emissions. For the fuel flow side, the Boiler Master Demand, limited by actual measured total oxygen flow (trimmed by furnace exit flue gas O_2% controller output), provides the total unit fuel demand. Total coal flow is calculated by the sum of individual feeder speeds processed through a “mill model” modifying the speed signal to reflect the actual fuel feed dynamics and corresponding furnace heat release. The resulting total coal flow signal is corrected by the output of a PI controller comparing main steam flow to total corrected fuel flow. This controller provides an automatic adjustment of the fuel signal to minimize the effects of varying fuel characteristics on the overall control response.

3.1.2 Flue Gas Recirculation Flow Control

To maintain sufficient combustion gas flow through the furnace, flue gas recirculation flow must be controlled based on the unit load. A unit load dependent control curve is used to determine the total flue gas recirculation flow with appropriate settings of lower and upper limits. This flow demand is the sum of the primary and the secondary flue gas recirculation flow. The total flue gas recirculation flow guarantees sufficient combustion gas flow to the furnace, thus maintaining the combustion stability and the convective heat transfer efficiency in the boiler back pass section.

In oxygen-fired mode, the mixture of the primary oxygen and primary flue gas recirculation is used for the primary oxidant. The primary oxidant (PO) flow takes the place of primary air for coal transportation, and the demand of primary oxidant flow is set based on the coal feeder speed. Since the primary flue gas recirculation (PFGR) flow is controlled, the secondary flue gas recirculation (SFGR) flow demand can be calculated by subtracting the measured PFGR flow from the total FGR flow demand. The secondary flue gas recirculation flow demand is fulfilled by manipulating the forced draft fan (FD fan).

3.1.3 Pulverizer System Control

The controls of the pulverizing system mainly contain the primary oxidant O_2 concentration control, the primary oxidant (PO) flow control, and the pulverizer outlet temperature control.

The primary oxidant flow is supplied by mixing the primary oxygen with the primary flue gas recirculation (PFGR) flow. The O_2 concentration of the primary oxidant flow has to be tightly controlled under the safety limit of material and equipment for the operation of the coal pulverizer system. In oxy-fired mode, the primary oxidant flow is an oxygen enriched flue gas recirculation flow and its O_2 concentration is controlled by manipulating the primary oxygen supply control valves.

The demand of the primary oxidant flow determines both the primary flue gas recirculation flow and the primary oxygen flow provided that the furnace exit flue gas O_2 level is maintained. The primary oxidant flow demand is fulfilled by the coordination of the primary air fan (PA fan) and the cold/hot primary oxidant dampers. PA fan boosts the pressure of primary oxidant to a set pressure by the coal delivery system. By bypassing part of the primary oxidant flow to the Gas-Gas Heater (GGH), the primary oxidant is divided into hot PO flow and cold PO flow. Due to the reactivity of the coal, the mill temperatures should not exceed a safe limit in order to reduce the risk of mill fires. The cold primary oxidant flow is controlled to maintain mill temperatures.

3.1.4 Furnace Pressure Control

The furnace pressure must be tightly controlled under all conditions for the safety of boiler operation. As with a conventional air-fired boiler unit, the furnace pressure of an oxy-fired boiler unit is also controlled through the induced draft fan with a feed forward signal from the forced draft fan.

3.2 Stoichiometry Control

The stoichiometry control is important for coal fired boiler operation and controls since it is designed to maintain the combustion stability and efficiency, and minimize the production of NO_x via staging the combustion appropriately. Stoichiometry for a coal-fired boiler is generally controlled based on the three combustion zones: the Main Burner Zone (MBZ), the Lower Separated Over-Fired oxidant Zone (LSOFZ) and the Higher Separated Over-Fired oxidant Zone (HSOFZ). For an oxygen-fired PC boiler unit, pure oxygen flow and flue gas recirculation flow are supplied to the furnace independently, which need to be coordinated to maintain appropriate combustion gas flow and oxygen flow distribution into the furnace wind-boxes.

The control logic for oxy-fired boiler island stoichiometry includes the following three major loops: Secondary Oxidant O_2 Concentration Control, Secondary Oxidant Flow Distribution Control, and Combustion Zone Stoichiometry Control.

3.2.1 Secondary Oxidant O_2 Concentration Control

A majority of the pure O_2 from ASU and/or the oxygen storage equipment is pre-mixed with flue gas recirculation flow, and then supplied to the furnace. The O_2 concentrations in the Primary Oxidant (PO) flow and the Secondary Oxidant (SO) flow have to be maintained below a safe limit for material and safety considerations. For example, for carbon steel duct work, the material limitation for oxygen concentration is 23.5%; the set point for the oxygen concentration of the primary and secondary oxidant flows can be set around 20.0% to have certain tolerance for incomplete mixing and control response/performance. The primary and secondary oxidant O_2 concentration is controlled by manipulating the secondary O_2 flow control valves.

3.2.2 Secondary Oxidant Flow Distribution Control

The total requirement of Flue Gas Recirculation (FGR) flow is determined by a control function curve dependent on unit load demand. The total flue gas recirculation flow guarantees sufficient combustion gas flow to the furnace, thus maintaining the combustion stability and the convective heat transfer efficiency in the boiler back pass section. While the primary oxidant flow is supplied to the main burner zone with the pulverized coal, the secondary oxidant flow is usually distributed to the MBZ, LSOFZ and HSOFZ for staged combustion. In air-fired mode, the distribution of the secondary air flow is based on the load dependent MBZ and LSOFZ stoichiometry set point control function curves. In oxygen-fired mode, the combustion zone stoichiometry cannot be controlled solely by staging the secondary oxidant flow because the oxygen to each combustion zone can come from two sources: the oxidant flow to the burner zone as well as the supplemental oxygen to the burner zone.

Therefore, the distributions of the secondary oxidant flow and supplemental oxygen flow have to be coordinately controlled based on predetermined relationships with unit load. The distribution of the secondary oxidant flow is first determined (established) because the secondary oxidant flow provides the majority of combustion gas flow and oxygen to the furnace, thus is more effective for maintaining the desired gas flow rates and combustion stoichiometry to each burner zone. Once the secondary oxidant flow distribution is determined, the supplemental oxygen flow distribution to each burner zone can be calculated accordingly.

3.2.3 Combustion Zone Stoichiometry Control

The total unit O_2 flow demand is generated from a predetermined control function curve based on unit load demand. This total unit O_2 demand will be corrected by the furnace exit flue gas O_2% level control, which guarantees a sufficient amount of total O_2 to furnace. Unlike the excess O_2% level control for air-fired boiler, in which the furnace excess O_2% set point will increase significantly as the unit load decreases; for oxygen-fired boiler, the furnace excess O_2% set point can be held relatively constant (e.g. 3.0%) for the entire operating range. The corrected total unit O_2 demand will be fulfilled by manipulating the total supplemental O_2 flow control valve and adjustments in boiler gas flow for thermal performance are made by adjusting the secondary recycle rate.

Based on the fuel properties and the measured fuel flow, the total stoichiometric required O_2 flow at a given load can be calculated. The unit stoichiometry S_{unit} is defined as the ratio between the measured total unit O_2 flow and the calculated total stoichiometric required O_2 flow. Note that since coal flow measurements have limited accuracy in field implementation, the stoichiometric required O_2 flow calculation must be checked with the measurements of the total O_2 to furnace and the total O_2 leaving furnace. It is worthwhile to point out that for a given unit stoichiometry, the amount of flue gas recirculation flow can be different. Assuming the furnace exit flue gas O_2% is controlled at the same

level, different flue gas recirculation flow rate give different amounts of oxygen recycled back to the furnace, which in turn varies the demand of pure O_2 flow from ASU. Therefore, for a given load, the demand for the total unit O_2 flow and the demand for the total flue gas recirculation flow must be set coordinately to provide sufficient oxygen flow and combustion gas flow.

3.3 Water/Steam Control

The basic closed-loop control logics of the oxy boiler island water/steam system including the following subsections: Feedwater Control, SHO steam temperature control, and RHO steam temperature control.

3.3.1 Feedwater Control

The set point for feedwater is established predominately by the Boiler Master demand, which is processed though a "boiler transfer function". The "boiler transfer function" is a tunable dynamic element providing a means to dynamically match the feedwater set point demand to actual evaporator heat transfer. Optimization of the feedwater set point in this manner minimizes temperature fluctuations that may otherwise result from varying dynamic response between the firing and feedwater control systems, thereby lessening the dependence on feedback correction.

Feedwater set point is corrected by two PI controllers in a cascade arrangement. The first controller acts on a load dependent average superheat platen spray differential temperature. Its output represents the required adjustment to evaporator heat transfer/steam generation to maintain both the steam conditions and flue gas temperatures entering the platen superheat section to ensure adequate platen superheat spray in a desired range. The second controller acts on a load dependent separator outlet temperature set point corrected by the superheat platen spray differential temperature controller's output. This controller aims to adjust feedwater in response to firing system disturbances and the relatively fast effect they have on separator outlet steam temperatures. The overall combined feedwater set point control action is such that feedwater demand is responsive to changes in the overall unit heat transfer profile.

3.3.2 SH Steam Temperature Control

Overall SH steam temperature control is accomplished with adjustment of spray water flow and manipulation of feedwater flow. Two spray-type superheater desuperheaters are installed at the superheater platen outlet headers and superheat finishing inlet headers. The basic control objective is to maintain superheater outlet steam temperature by adjusting spray water control valves and simultaneously adjust feedwater flow in response to average superheat desuperheater differential temperatures.

The control structure is a cascade arrangement where the first PID controller acts on the superheater outlet temperature as compared to the set point dependent to the main steam flow. The controller output is modified by a feed forward signal, which is calculated with the difference between the rates of change of the main stream flow and the total corrected fuel flow. This action compensates the tendency beforehand for variant steam temperatures resulting from a temporary imbalance between the steam flow and the firing rate. The resulting corrected master output provides the set point to a slave controller. The controller acts on this set point as compared to steam temperature measured at the superheater desuperheater outlet. The slave controller output, subject to an overriding "saturation" protection circuit provides the spray valve position demand.

3.3.3 RH Steam Temperature Control

The reheat outlet (RHO) steam temperature is controlled by a combination of RH desuperheater spray water, fuel nozzle tilt positioning, and excess air level in air-firing mode or secondary flue gas recirculation (SFGR) flow demand in oxy-firing mode.

3.3.3.1 Reheat Desuperheater Spray Water Control Loop

The reheat desuperheater spray water control loop is a cascade arrangement where the first PID controller acts on RHO steam temperature as compared to the set point dependent on the main steam flow. The controller output is modified by a feed-forward signal, which is calculated with the difference between rate of change of main steam flow and total corrected fuel flow. The resulting corrected master output provides the set point to a slave controller – the RH desuperheater outlet temperature set point. The inner loop PID controller acts on this set point as compared to steam temperature measured at the RH desuperheater outlet. The slave controller output provides the RH spray valve position demand. The design of this control loop allows the RH desuperheater spray water control valve to respond to the RHO steam temperature deviation promptly.

3.3.3.2 Fuel Nozzle Tilts Control Loop

Demand for fuel nozzle tilts is developed by a PID controller acting on the biased RHO temperature set point and the measured steam temperature at the RH outlet. The RHO steam temperature set point is a load-dependent signal indexed from the main stream flow. This RHO temperature set point is biased down by the RH desuperheater differential temperature, limited by a constant RHO temperature set point maximum bias for the purpose of forcing the reheat spray water control valves to close in the long term.

The selector logic is designed to arrange the control priority of the fuel nozzle tilts versus the SFGR flow demand to minimize the RH spray water flow as well as the fan power consumption. When the RHO steam temperature is higher than the set point and the SFGR flow has not reached its low limit, the selector logic forces the fuel nozzle tilts PID controller to select the measured RHO steam temperature as its set point. As the set point of this PID controller is tracking the measured process variable, the tilts will not react to the RHO steam temperature difference. This logic allows the SFGR flow demand control to saturate before the fuel nozzle tilts start to respond in the high RHO steam temperature situation. Once the SFGR low limit is reached, the selector logic selects the biased RHO steam temperature set point as the set point for the fuel nozzle tilts PID controller. The fuel nozzle tilts demand controller controls the main tilts, the LSOFO tilts and the HSOFO tilts. The fuel nozzle tilts position will keep decreasing and consequently the RHO temperature will decrease. In response, the RH spray water control valves will be closing to maintain RHO temperature. The fuel nozzle tilts controller will keep forcing the closing of the spray valve until the fuel nozzle tilts saturate or the RH spray water control valves are fully closed.

3.3.3.3 Secondary Flue Gas Recirculation Flow Control Loop

The SFGR flow control loop is designed similarly as the fuel nozzle tilts control loop. The first PID controller acts on the difference between the biased RHO temperature set point and the measured steam temperature at RH outlet, and generates a SFGR flow demand bias. The RHO temperature set point is biased down by the RH desuperheater differential temperature limited by a constant RHO temperature set point maximum bias for the purpose of forcing the reheat spray water control valves to close.

The selector logic is designed to arrange the control priority of the fuel nozzle tilts versus the SFGR flow demand to minimize fan power consumption. If the RHO steam temperature is higher than the set

point, the SFGR flow demand bias controller will select the biased RHO temperature set point and force the SFGR flow demand to decrease. In the meantime, the fuel nozzle tilts will not respond until the SFGR flow reaches its low limit.

In addition, if the RHO steam temperature is lower than the set point, the fuel nozzle tilt will be raised up immediately and consequently the RHO steam temperature increases. At this moment, the measured RHO temperature is lower than its set point and the fuel nozzle tilts have not reached their high limits. The set point of the SFGR flow demand bias controller will track the RHO steam temperature and the SFGR flow demand will be kept constant. Once the fuel nozzle tilts reach their high limit, the SFGR flow demand bias controller will select the biased RHO temperature set point. Since the RH spray valves are closed with low RHO steam temperature, the RH desuperheater differential temperature is zero. And the biased RHO temperature set point is the true RHO steam temperature set point. Therefore, the SFGR flow demand bias will be increased and the final SFGR flow demand will be increased accordingly. This final SFGR flow demand is limited by a high/low limit and is fulfilled by the local control of the FD fans. This control priority arrangement allows the fuel nozzle tilts to saturate before the SFGR flow demand is increased under low RHO temperature situation and thus fulfills the purpose of minimizing the FD/ID fan power consumption.

4 Oxy Boiler Island Adaptive Control

More than 90% of all control loops in industry are controlled by Proportional-Integral-Derivative (PID) controllers, which by far play a dominant role in the feedback control domain. Most of the existing PID controllers are PI, in that the derivative part is not used very often. Most power plant operations also depend on the PID-based control systems, which make direct regulations of flows, pressures, temperatures, etc. The wide use of PID results from its simple control strategy that only three control parameters need to be configured.

For power plant control, the first priority is to meet the basic requirement of stability, which can be achieved by reasonable design of the control loops and appropriate tuning of controller parameters. In general, a PID controller is essentially an error based controller that only responds when the process variable deviates from its set point. The PID controller is also a Single-Input-Single-Output (SISO) controller, which means it merely concentrates on the process variable in the control loop, and does not care about how other process variables behave in other control loops. However, complicated interactions and coupling effect do exist among certain process variables in the power plant, which cannot simply be handled by conventional PID controllers.

An adaptive controller is a controller that can modify its behavior in response to changes in the dynamics of the process and the character of the disturbances. The adaptive controller becomes nonlinear because of the parameter adjustment mechanism, and the essence of the adaptive controller is how its parameters are adjusted to meet the requirement of the changing control environment. As shown in Figure 4-1, there are normally two loops in the structure of an adaptive controller: one loop is a normal feedback with the process and the controller. The other loop is the parameter adjustment loop.

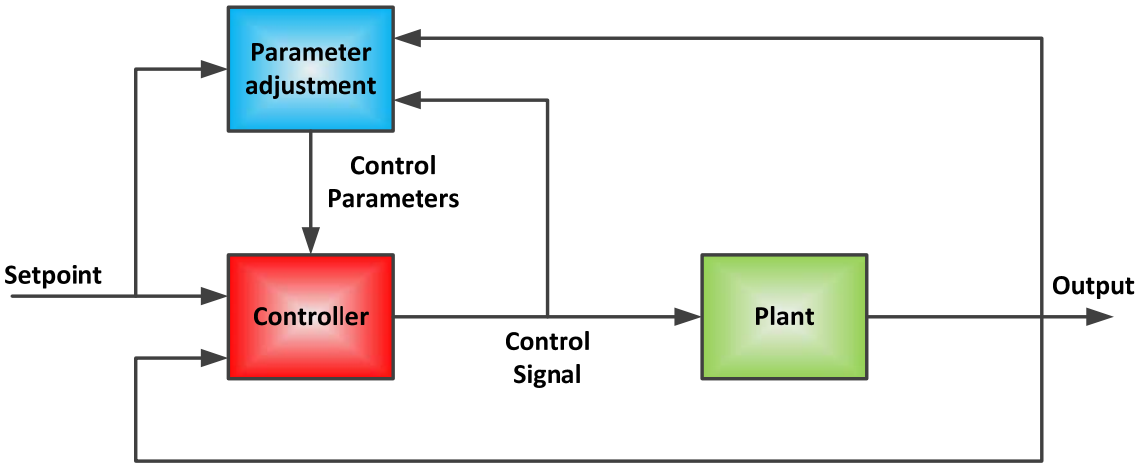

Figure 4-1. Block diagram of an adaptive system

4.1 L1 Adaptive Control Fundamental Theory

The L1 adaptive control is a new type of adaptive control, which emerged in recent years. It can be viewed as a modified MRAC (Model Reference Adaptive Control) scheme where the basic structure is based on internal model principle. The key feature of the L1 adaptive control architecture is its guaranteed robustness in the presence of fast adaptation.

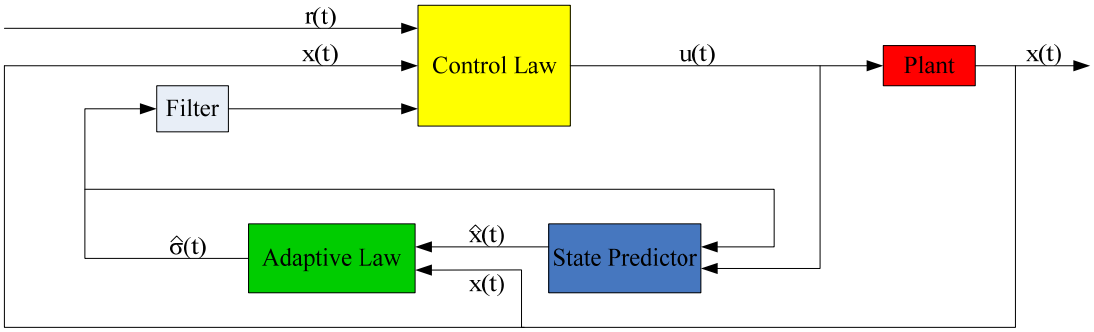

Figure 4-2. Schematic representation of L1 adaptive controller

Figure 4-2 presents the basic architecture of the L1 adaptive controller which includes three main components: a) adaptive law, b) state predictor, and c) control law. The state predictor is used to perform an estimate of each measurable state/variable in the process by using the control signal and the output of the adaptive law. The adaptive law mostly focuses on estimating the uncertain part or mismatch part by the deviation between the measured states and the estimated states. The control signal is eventually generated by the control law which uses the reference signal, the measurable states, and the adaptive law output as its input. Thereby, the three components in L1 adaptive controller are firmly connected and interact with each other. The design of each part in an L1 adaptive controller is given as follows.

State predictor design

$$\dot{\hat{x}}(t) = A_m\hat{x}(t) + B_m u(t) + \hat{\sigma}(t),$$

Adaptive law design

$$\tilde{x}(t) = x(t) - \hat{x}(t),$$

$$\hat{\sigma}(t) = \hat{\sigma}(iT), t \in [iT, (i+1)T),$$

$$\hat{\sigma}(iT) = -\Phi^{-1}(T)\mu(iT), i = 0,1,2 \ldots,$$

$$\Phi(T) = \int_0^T e^{A_m(T-\tau)}\, d\tau,$$

$$\mu(iT) = e^{A_m T}\tilde{x}(iT), i = 0,1,2 \ldots.$$

Control law design

$$u(s) = k_g r(s) + C(s)B_m^{-1}\hat{\sigma}(s).$$

The description of each variable is listed in Table 4-1.

Table 4-1. Variable description of L1 adaptive controller

Name	Description
$x(t)$	Measurable states
$\hat{x}(t)$	Estimated states
$\tilde{x}(t)$	Mismatch between $x(t)$ and $\hat{x}(t)$
$u(t)$	Control signal
$u(s)$	Laplace transform of $u(t)$
$\hat{\sigma}(t)$	Model mismatch/uncertainty
$\hat{\sigma}(s)$	Laplace transform of $\hat{\sigma}(t)$
k_g	DC gain of the internal model
$C(s)$	Laplace transform of a low pass filter
A_m	Model parameter of the state predictor
B_m	Model parameter of the state predictor
T	Sampling time

Once the L1 adaptive controller is set up, parameters A_m, B_m and the bandwidth of the low pass filter $C(s)$ need to be well tuned to achieve the required control performance.

4.2 L1 Adaptive Control Design and Validation for Oxy Boiler Island

Compared to conventional PID controllers, the L1 adaptive controller provides a better control performance in considering these complicated conditions of the power plant. The L1 adaptive controller technique has been proven to provide fast adaptation of transient response in a large variety of systems due to its basic control architecture that the state predictor offers a model estimation of the dynamics of the system, while the adaptive law deals with the mismatch of the model to the real process. Some of the model based control methods usually need to obtain the model of the plant at the beginning and depend on the accuracy of the model, while there is no such requirement in the L1 adaptive controller, which simplifies the process of controller design. In addition, some model-based controllers may not work properly if the dynamics of the system changes. The robustness of the L1 adaptive controller guarantees that a good control performance can also be achieved in such conditions. Due to its robustness and fast adaptation, the L1 adaptive controller is demonstrated to obtain a better transient performance than the PID controller. Further, the adaptive controller is shown to reduce the process transients caused by disturbances of changing unit load.

This section discusses the advantage of L1 adaptive controller over conventional PID controller by implementing a simulation scenario on an Oxy Boiler Island dynamic simulator. In the simulation, the boiler island is assumed to be operating at the steady state of 100% load as an initial condition, and the unit load is designed to ramp down to 70% at a rate of 5% MCR/min. The set point of the main steam temperature control loop maintains at a constant value of 602 °C all through the simulation time.

Figure 4-3 presents the main steam temperature responses of both the PID controller and the L1 adaptive controller with the statistical results listed in Table 4-2. The simulation results show that L1 adaptive control provides a better control performance in terms of maximum temperature, minimum temperature, as well as main steam temperature standard deviation. It is worthwhile to point out that the main steam temperature response is related to many factors: fuel flow, feedwater flow, air flow,

spray flow, fuel nozzle tilt positioning, etc. The coordination among fuel, feedwater, and air is absolutely dominant. That's why in regular control design, those flow demands are all generated by load dependent curves. In the simulation result presented, only the PID control loops of the main steam temperature control have been replaced by the L1 adaptive control to indicate the improvement of local control, while all the other control logics remain the same.

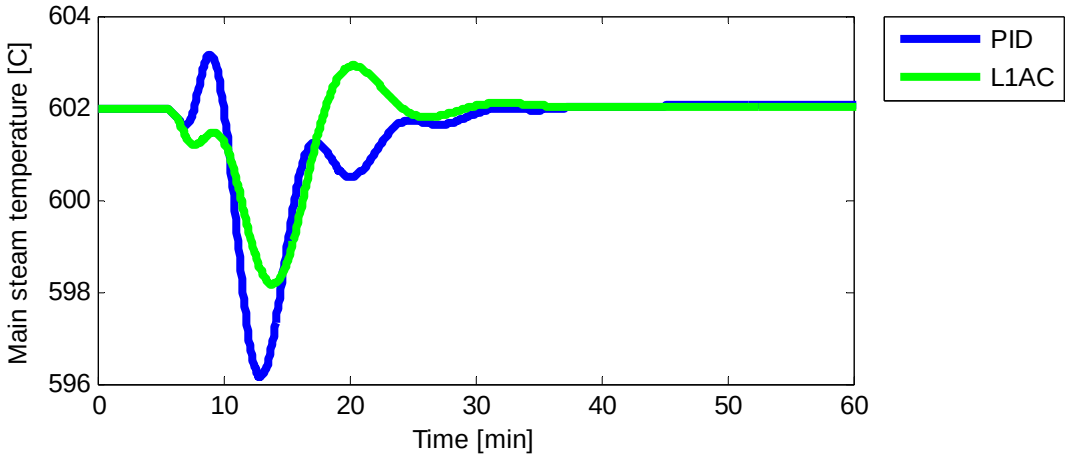

Figure 4-3. Main steam temperature responses

Table 4-2. Comparative simulation results of main steam temperature between PID and L1AC

Controller name	Max [C]	Min [C]	Std [C]
PID	603.2	596.1	1.27
L1AC	602.9	598.1	0.95

Reheat steam temperature controls for Oxy Boiler Island must address additional challenges from a conventional air fired system. Unlike the main steam temperature, the set point value of the reheated steam temperature is dependent on unit load rather than a fixed value. The reheated steam temperature is controlled by a combination of RH desuperheater spray water control valves, fuel nozzle tilt positioning, and excess air level in Air-firing mode or secondary flue gas recirculation (SFGR) flow demand in Oxy-firing mode to achieve minimum deviations from the reheat steam temperature set point and maximum plant efficiency. It is worthwhile to point out that the burner tilts and flue gas recirculation also affect the combustion emissions at the flue gas side. Figure 4-4 and Table 4-3 present the simulation results of reheated steam temperature responses in the load ramping down scenario under the conventional PID controllers and the L1 adaptive controllers, respectively. Statistical results in Table 4-3 show that the L1 adaptive controller provides a better control performance than the PID controller in terms of reducing reheated steam temperature deviation.

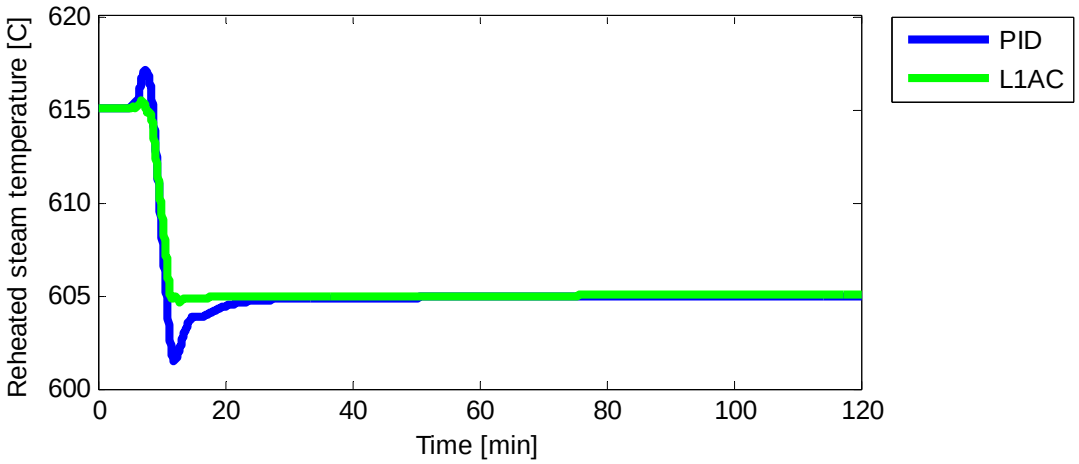

Figure 4-4. Reheated steam temperature responses

Table 4-3. Comparative simulation results of reheated steam temperature between PID and L1AC

Controller name	Dev Max [C]	Dev Min [C]	Dev Std [C]
PID	2.7	-3.3	0.59
L1AC	1.9	-0.2	0.28

5 Oxy Boiler Island Model Predictive Control

Model Predictive Control (MPC) is an advanced method of process control that has been used in the process industries such as chemical plants and oil refineries for decades. The essence of MPC technology is a dynamic model which is used to capture the internal relationships between dependent and independent variables of the modeled process. In industrial processes, independent variables often appear in the form of set points in regulatory controllers that govern valve movement, while dependent variables are most often constraints in the process. Based on current plant measurements and the predictive model, the model predictive controller can calculate future independent variable control moves that satisfy an optimization objective and also ensure all independent and dependent variables remain within constraints. The MPC will function as a supervisory controller in that the set of independent variable control moves will be sent as biases to the corresponding regulatory controller set points to be implemented in the process control.

Figure 5-1 shows the hierarchical control configuration proposed for the oxy-fired power plant. The control hierarchy is divided into four levels from bottom to top, i.e. the Distributed Control System (DCS) regulatory control layer, Model Predictive Control (MPC) layer, Real-Time Optimization (RTO) layer and Planning and Scheduling. The MPC is located in between the RTO and the regulatory controls in the existing DCS, and it provides an optimal constraint-based control to find the solutions to the real-time optimization control problem. The solutions, usually set points and/or biases, will be sent to the regulatory control system for implementation. Currently, planning and scheduling tend to be based on off-line economic optimization at the plant or corporate level.

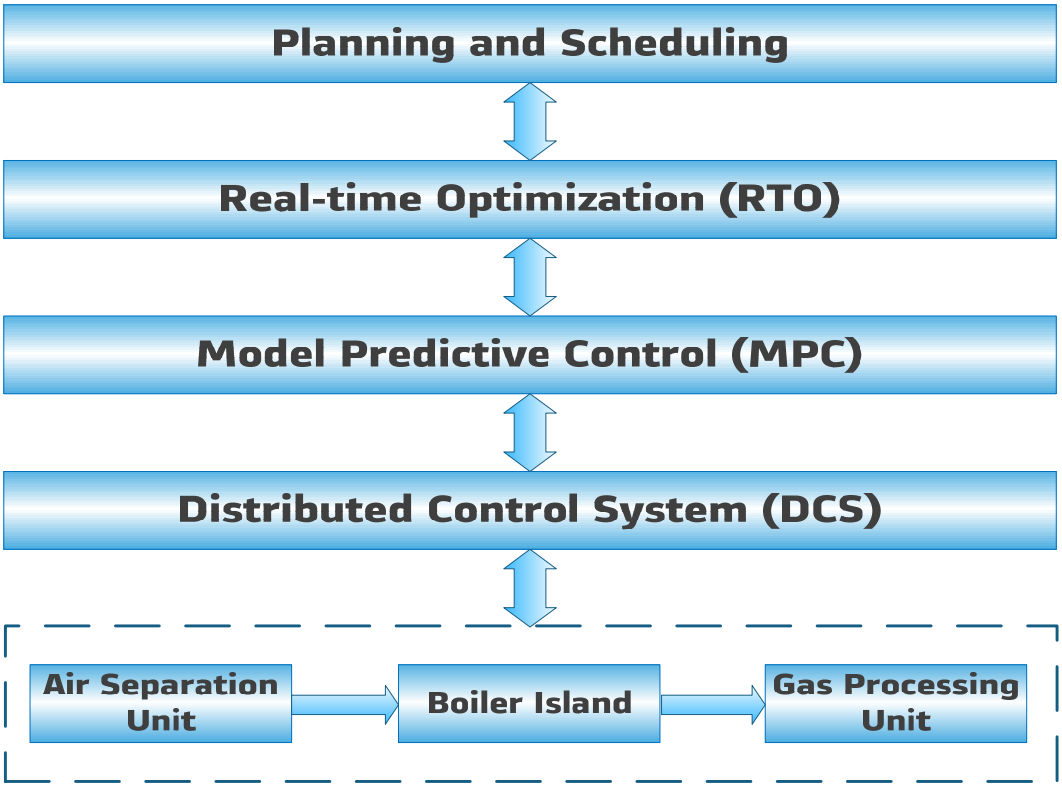

Figure 5-1. Control hierarchy of oxy-fired power plant

5.1 Introduction to Model Predictive Control

5.1.1 Model Predictive Control Fundamental Theory

The Model Predictive Control aims to solve an on-line finite horizon open-loop optimal control problem subject to system dynamics and constraints including both states and controls. Figure 5-2 shows the basic principle of model predictive control. Based on measurements obtained at time t, the controller predicts the future dynamic behavior of the system over a prediction horizon N and determines the inputs such that a predetermined open-loop performance objective functional is optimized. Ideally, one could apply the optimal control solution found at current time t to the system for all the time afterwards. Nevertheless, due to disturbances and model-plant mismatch, the practical system behavior is different from the predicted behavior based on the dynamic model. Therefore the open-loop optimal control solution will be only implemented until the next measurements are available so as to incorporate the feedback mechanism. Based upon this type of mechanism, the operation of prediction and optimization keep repeating to find a new optimal control solution at each sampling time with the control and prediction horizons moving forward.

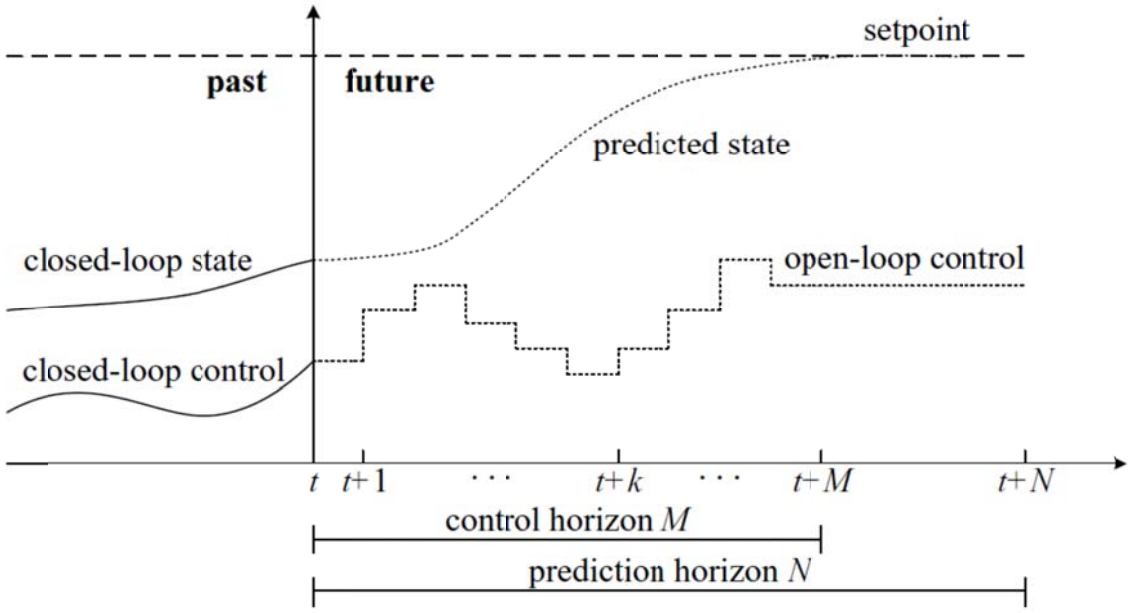

Figure 5-2. Principle of model predictive control

In terms of controller structure, the MPC is a multivariable control algorithm that uses

- an internal dynamic model of the process,
- a history of past control moves, and
- an optimization cost function J over the receding prediction horizon

to calculate the optimum control moves.

The optimization cost function is given by:

without violating constraints (low/high limits), where

x_i: i -th controlled variable (e.g. measured temperature)

r_i: i -th reference variable (e.g. required temperature)

u_i: i -th manipulated variable (e.g. control valve)

w_{x_i}: weighting coefficient reflecting the relative importance of x_i

w_{u_i}: weighting coefficient penalizing relative big changes in u_i

5.1.2 Model Identification

The process knowledge is captured by a model predictive controller through the process models between the process inputs and process outputs. There are generally two types of models that can be incorporated by the model predictive controller: parametric model and non-parametric model. In this document, the MPC algorithm used for the implementation is based on parametric models (i.e. process transfer function). The non-parametric models, such as time domain step or impulse response, are also widely used in industrial MPC application in that it is a simple and easy approach to capture the dynamic feature of the process.

For the applications of linear model based MPC, the dynamic process models are usually identified from process test data. To collect the appropriate process data for developing MPC models, the first step is to define an appropriate dynamic test matrix. The design of the dynamic test matrix requires a certain amount of process control and operation knowledge to include the major process dynamics between the process inputs and outputs. After the dynamic test matrix is defined, it has to be implemented on the process and then the process test data can be collected and processed for future model identification.

The dynamic test matrix is implemented by a series of step changes of the process inputs or the manipulated variables of the model predictive controller. The process responses, therefore, refer to the responses of the process outputs, i.e., the controlled variables and constraint variables, when the process is subjected to the step changes. The feed-forward variables and disturbance variables are also considered as process inputs. Although they cannot be directly manipulated by the MPC, the responses between the feed-forward variables/disturbance variables and the process outputs also need to be captured by historical data or specifically designed dynamic plant tests.

For the selection of testing signals, there are multiple types of input signals generally used to conduct the dynamic tests required for model identification. Two commonly used signals are: a) step tests of the manipulated variable using a Pseudo Random Binary Signal (PRBS) or PRBS-like stepping signal; and b) a kind of binary signal optimized for dynamic plant testing purpose. Most MPC packages test one manipulated variable at a time with other manipulated variables at fixed values; a few MPC packages could step change a number of manipulated variables at the same time with uncorrelated signals. The choice of the testing signals can be determined by various factors, including the complexity of the process dynamics and correlations, the model identification method, the desired time duration, etc.

For MPC development based on a process dynamic simulator, to conduct step testing of the manipulated variables, one at a time is the preferred option simply because the process model is deterministic and noise free. An appropriately designed step test of one manipulated variable (with appropriate magnitude and duration) can generally capture the process dynamics under the influence of this particular process input.

The magnitude of the step tests should be large enough to make sure the Signal to Noise Ratio (SNR) is sufficient. The MPC design is also affected by the signal type of the dynamic test, sampling time, step change, shortest and longest time duration, step change magnitude and direction, one manipulated variable at a time versus simultaneous step changes on all manipulated variables, etc. Unlike the process simulator, in real plant testing, process test data can be corrupted by process noises or unexpected disturbances during tests. Various reasons can cause the test data to not represent the true dynamics of the process, and thus these data have to be removed before they are used for model identification.

Once the process testing data are collected and processed, these data can be used to build the linear process models to be incorporated in a model predictive controller. The model predictive control software used in this MPC application uses empirical, dynamic and linear models of the process. The modeling tool is used for linear model identification from process data and the model output at the current time depends on input from current and all previous times. Both non-parametric (e.g. FIR) and parametric models (e.g. ARX and Box-Jenkins) can be used for model identification.

The Finite Impulse Response (FIR) model is set as the standard model in the modeling tool, which has several advantages over other modeling techniques. For instance, the identification problem can be easily solved using least squares regression; the model requires only independent variables as inputs to predict future CVs; FIR can easily fit/capture high-order process dynamics. Both ARX and Box-Jenkins models are developed by estimating the parameters of the polynomials using the least-squares method, while the Box-Jenkins model can identify the noise characteristics from the system dynamics separately. A general procedure for model identification task is summarized as follows.

Data Importing

Once the raw data are generated from step tests via the process dynamic simulator, they can be processed and transformed into a spreadsheet, which can be imported into the model development tool for further processing.

Data Selection

All the data are derived from the process dynamic simulator, but the most appropriate data for model identification must still be determined. In order to obtain an accurate model, those bad data segments must be removed from the raw data. It is of great importance to exclude the bad data segments for all variables during the modeling to guarantee the accuracy of the estimated dynamic model.

Model Identification

The model is developed for each pair between manipulated variable (i.e. process input) and control variable (i.e. process output) for either a parametric or non-parametric model. Some commercial modeling tools include a built-in statistics calculator for checking the quality of an identified process model.

By repeating the above steps for all possible pairs of the manipulated variables, disturbance variables and feed-forward variables (i.e. process inputs) and the control/constraint variables (i.e. process outputs), the complete process model grid for the model predictive controller is developed. It is worthwhile to point out that not all pairs of process inputs and process outputs have significant correlations, the process model grid for the model predictive controller should be accurate and representative of all the dynamic system behaviors in a given operating range.

The models developed for a model predictive controller should be examined regularly to make sure they are still representative of the process dynamics. Minor changes in the process equipment and/or the control systems should not bring significant changes to the process dynamics. Nevertheless, gradual and/or significant changes to the process or its control system can affect the process dynamics and therefore the original MPC models will deviate further away from the process and eventually the model predictive controller will not be able to provide reasonable control moves.

5.1.3 Off-line Configuration and Validation

Once the process model grid development for the model predictive controller is completed, the MPC needs to be well tuned and validated before on-line implementation. Some advanced control software also provides the tools for off-line configuration.

General Settings

Before configuring each variable within the MPC scope, some general settings should be done. The control interval should be specified to determine the runtime frequency of the online controller. Usually the time interval is specified in seconds. In addition, it is also needed to specify the proper projection horizon. Too long or too short projection horizon may make the control performance even worse. In order to check the communications between the MPC platform and the dynamic process simulator, a watchdog tag should be specified to check the real time data communication status continuously.

Process Model Variables Configuration

In this step, process variables (all process inputs and outputs) within the MPC scope should be configured. The tag names with their descriptions should be configured appropriately. For all MVs, their initial values should be given. In addition, the constraints on the MVs, such as the high and low limits and the rate limit should be also specified. For all the CVs, both the initial values and targets should be given. For constraint variables (CTs), one should be able to choose the high limit and/or the low limit. The feed-forward variables (FFs) or disturbance variables (DVs) should also be given an initial value. All the variables except the feed-forward variables and disturbance variables should have a tuning weight factor to represent its importance in the model predictive controller cost function. A preliminary value can be specified based on experience and it should be further tuned based on the off-line simulation results.

Dynamic Off-line Simulation

The dynamic off-line simulations are able to help us complete the initial controller tuning in an off-line environment. During the off-line simulations, the process model identified from the process test data serves as the virtual plant while the model predictive controller can be tuned for different optimization scenarios. Notice there is no mismatch between the process and the models used by the MPC during the off-line simulations. By validating the MPC design in this off-line simulation tool, the MPC engineer can tune the MPC based on the assumption that the model used in the MPC is a perfect representation of the process dynamics and provides process control engineers a good starting point for the MPC on-line tuning.

Tag Configuration

For the closed-loop simulation with the process dynamic simulator, the tag names should be configured to enable the real-time communications between the MPC platform and the process dynamic simulator. For each of the MVs, both the local set point and the remote set point should be

read by the MPC. The local set point is the current set point read from DCS (here from the process simulator). New set points are calculated by the MPC based on current operation conditions and the optimization objects. The newly calculated set points will then be sent to the process simulator through the remote set point of this PID controller. For the control variables, constraint variables, and feed-forward variables, the current measured process values should be sent to the MPC from the process simulator. A tag name for Watchdog should also be configured. Its purpose is to verify that communications are still intact by resetting the timer each execution so it does not time out.

5.1.4 On-line Deployment

After the model predictive controller is designed, configured, tuned and tested via the off-line MPC design tool, it is ready to be deployed to the field for on-line configuration. For field implementation, many important issues have to be solved before the model predictive controller can be connected with the local DCS.

Data communication between the MPC platform and the DCS

The MPC is often implemented using a standalone work station or a laptop PC in the field, and MPC platform is required to continuously communicate with the DCS through a common data communication protocol. The standard OPC connection is a common option for data communications. Current generations of DCS and data historians, etc. all have the capability for standard OPC communication. While this common data communication protocol makes the connection between the MPC platform and the DCS straightforward, careful design and configurations have to be done to make sure reliable data communications can be performed at all times. Usually a watchdog tag is created just for testing the data connection in real time. Exceptions and data connection failings have to be handled explicitly by the DCS.

Interface between MPC and DCS

The model predictive controller is designed as a supervisory control to optimize the performances of the unit equipped with local PID controllers. If not well configured, there is no guarantee that the MPC can always perform more superiorly than the existing PID controllers in real field implementations. As an operational backup for the unit operators, a convenient interface that is aimed to monitor/switch on/switch off the model predictive controller and revert to PID control only or manual control should be designed.

DCS configurations

To accommodate the changes made by a model predictive controller, the local DCS may need to be configured to accept the calculated manipulated variables from the MPC. The DCS should also be configured for bump-less transfer when a model predictive controller is switched on or off.

In order for communication between MPC and other systems, it is essential to incorporate software interfaces for linking the MPC controller with the process controls. It should include a standard, supported network-aware, multiple-device connection layer which works consistently with a large set of DCS's and information system environments. Each interface should be a standard, fully-supported, and product-quality software package.

5.2 Model Predictive Control for the Oxy Boiler Island

Development and implementation of a model predictive controller carries a certain amount of cost, which needs to be justified by its potential benefits before it is implemented. The confidence that a

properly designed and implemented MPC system can generally be beneficial is based on the fact that the set points and tuning of a regulatory control system are usually determined based upon conservative approaches. A model predictive control system, therefore, can be used to push the process and its control system to their maximum limits under all control and operation constraints. As the initial step of an MPC application, the design/operations/controls of the process have to be analyzed and potential benefits from an MPC system should be estimated first.

5.2.1 Oxy Boiler Island MPC Structure

This section details the design of a model predictive controller (MPC) for an oxy-fired boiler island process. The design, development and implementation of a model predictive controller for the oxy-fired boiler island process follow the general procedure for an industrial MPC application:

- Analyze process operations/issues and identify the potential tradeoffs for MPC optimization
- Define the MPC model structure (determination of MVs, CVs, CTs, and DVs/FFs)
- Design and carry out plant step tests, and gather/process the plant test data for MPC model development
- Develop MPC models using the process test data via various model identification methods
- Off-line designing, tuning and validating the model predictive controller
- On-line tuning and validating the model predictive controller

The integration of a model predictive controller into an advanced plant level distributed control system (DCS) for the oxy-fired pulverized coal boiler island process will provide the decision support layer to achieve economically optimized Boiler Island operational performance. The following summarizes the potential benefits of a model predictive controller for an oxy-fired pulverized coal boiler island process.

- Improve heat rate and reducing raw material cost

  Minimizing the amount of CO emission and unburned carbon (UBC) in ash, or reducing the amount of RH spray water usage, or reducing the dry gas energy lost could improve heat rate and thus the boiler efficiency; minimizing the raw material consumptions under given power demand and emission regulations results in a reduction in raw material cost, including the raw coal consumption, the usage of limestone/lime in FGD, and the usage of ammonia in SCR, etc.

- Reduce boiler island auxiliary power consumption

  Minimizing the auxiliary power consumption of various boiler island auxiliary equipment; potential power consumption reductions for an MPC mainly include ID fans, FGR fans (FD fans in Air-fired mode), FGD recycle pumps, etc.

- Reduce NO_x emissions and assisting CO_2 capture in GPU

  NO_x generation is significantly lower in oxy-fired combustion compared to air-fired combustion due to the elimination of nitrogen from air. However, it still has a potential to be further reduced by proper staging for reduction of ammonia usage in SCR. NO_x regulation for oxy-fired power plants is still an uncertainty and NO_x removal should still be considered at the early stage of the project.

The separation of CO_2 from other impurities in the GPU is directly correlated with original CO_2 concentration of the flue gas to the GPU, optimization can be considered to maintain the CO_2 concentration. Although so far no legislation has been created for CO_2 production, captured CO_2 has the potential to become profits/credits for the integrated oxy-fired power plant.

- Minimize oxygen consumption

  Minimizing the total O_2 usage by tightly controlling and minimizing the furnace exit flue gas O_2% concentration becomes even more beneficial than conventional air-fired boiler units since an energy intensive air separation unit consumes a significant power to produce pure oxygen. For Oxy-fired boiler island controls, fresh O_2 supply and combustion gas flow can be controlled independently, which suggests the potential to minimize the fresh O_2 from the ASU over the entire load range, especially in the low load range.

- Minimize the SH/RH steam temperature deviations

  A model predictive controller can be used to improve the control of SH/RH steam temperatures by optimally adjusting available and relevant manipulated variables. The minimization of the SH/RH steam temperature deviations is indirectly correlated with the heat rate and may also improve the overall plant's responses.

- Enhance operating flexibility and power plant load change capability

  A model predictive controller can be used to more tightly control the main process variables (steam temperatures and pressures, furnace pressure, etc.) within the appropriate ranges and thus the load change capability and the flexibility of an oxy plant can be fully pushed to the design limits.

The MPC model structure plays an important role in the MPC design and implementation. Since the MPC will be interacting with the PID layer, it is very important to make sure that the regulatory PID control loops are well tuned. Also understanding this PID layer is a key ingredient to decide the MPC structure. Before the MPC validation via the process or a process simulator, step tests need to be conducted to obtain data for dynamic MPC model identification. Based on the current process design and operation knowledge and the optimization objectives for an oxy-fired boiler island process, the Oxy Boiler Island model predictive control structure is presented in Figure 5-3.

Figure 5-3. Model predictive control structure for Oxy Boiler Island

Control variables and/or constraint variables are the process outputs that should be controlled to their pre-defined targets or maintained within appropriate operating ranges by the MPC system. For example, NO_x emission level at the stack generally has a high limit based on environmental regulations and power plant operation capability and requirements; thus it can be used as a constraint variable with a high limit for the MPC. On the other hand, if a NO_x minimization optimization scenario is carried out by the model predictive controller, a NO_x emission target can be assigned to the MPC and it becomes a control variable. It is common for a process output to be used as both a control variable and a constraint variable at the same time in an MPC application. The following summarizes the list of the control variables (CVs) and constraint variables (CTs) in the oxy-fired pulverized coal boiler island process:

Furnace exit gas temperature, pressure, flow and composition

Energy loss in the hot flue gas exiting the furnace can be calculated based on the temperature, pressure, flow rate, and compositions of the flue gas stream. Minimizing the energy loss through this flue gas stream can improve the overall boiler efficiency and the heat rate. For conventional air-fired combustion optimization, the furnace exit gas temperature is usually used as an indirect measure for the energy loss; for oxy-fired combustion, however, the temperature/pressure/flow/compositions have to be considered in the energy loss calculation..

Furnace exit gas O_2% composition

Furnace exit gas O_2% composition has to be controlled to a certain level for complete combustion of fuel. Minimizing the furnace exit gas O_2% composition under restrictions of CO emission regulation and unburned carbon in ash amount can reduce the oxygen consumption. Since fresh oxygen is provided by an energy-intensive cryogenic air separation unit, reduction in oxygen consumption can lead to a reduction in ASU power consumption, which in turn improves the overall plant efficiency.

Furnace exit gas CO emission

CO emission is usually used as a constraint variable with a high limit predetermined by the environmental regulation and the plant operation conditions. The model predictive controller should use the available control handle to minimize CO emissions.

Unburned carbon in ash (UBC)

UBC is a direct indicator of the completeness of coal combustion and thus should be minimized by the model predictive controller. A difficulty of using UBC as a control variable or constraint variable in an MPC application is the reliability and accuracy of this measurement. If no reliable measurement is available, this process out should be turned off when the model predictive controller is in closed-loop control mode.

SH steam temperature deviation and RH steam temperature deviation

SH/RH steam temperatures are usually controlled to their respective referenced temperature set points by the underlying regulatory PID controllers. A model predictive controller can be used to simultaneously adjust multiple control handles for tighter control of the steam temperatures. Then it becomes feasible and reliable to raise the steam temperature set points to be closer to the designed values for an improvement of the overall plant efficiency.

RH spray water flow

In a boiler island process, SH/RH spray water flows are used as major control handles for fast SH/RH steam temperature controls. The usages of the SH and RH spray water flows can both decrease the overall plant efficiency; however, the influence of SH spray is minimal and it is designed for better SH steam temperature control which is more effective for plant efficiency. The usage of RH spray water flow, on the other hand, should be minimized under restrictions of RH steam temperature controls since the usage of RH spray correlates to a significant loss in the overall plant efficiency.

NO_x emission before SCR

NO_x emission before SCR can be optimized using available handles on staged combustion. Reduction in NO_x generation can lead to a reduction in ammonia usage; however, too deep staging can cause incomplete combustion and result in a loss of boiler efficiency.

Manipulated variables are the inputs to the process that the model predictive controller can manipulate based on the current operation conditions and the optimization objectives. For industrial model predictive control implementation, the MPC system is generally integrated with the regulatory PID based control system and its manipulated variable is the set point or set point bias of the PID controllers. For example, the furnace exit flue gas O_2% set point is usually based on a load dependent control function curve in the regulatory control system design. A furnace exit flue gas O_2% set point bias can be added to the original indexed set point and this bias can be derived by a model predictive controller. The following summarizes the list of the manipulated variables (MVs) in the oxy-fired pulverized coal boiler island process:

Furnace exit flue gas O_2% set point bias

Final furnace exit flue gas O_2% set point is directly related to the completeness of the fuel combustion, the amount of NO_x, CO and UBC generations.

Total SFGR flow set point bias

Total SFGR flow has a significant influence on furnace back pass convection heat transfer rate. Therefore it affects the RH steam temperature and the RH spray flow significantly.

MBZ stoichiometry set point bias and LSOFZ stoichiometry set point bias

MBZ and LSOFZ stoichiometry set point bias mainly affects the combustion regarding the boiler combustion efficiency and the NO_x/CO generations.

Burner tilts (main burner tilts and SOFA burner tilts)

Burner tilts have multiple effects: firstly it shifts the fire ball elevation and thus affects the heat distribution particularly in the radiant zone and therefore the SH/RH steam temperatures; secondly, it also affects the NO_x generation as has been observed in many coal fired power plants.

A disturbance variable (DV) can be a process input, which could affect the process significantly but the model predictive controller has no control over. For example, the ambient temperature, etc. can affect the boiler operations but it cannot be directly manipulated. A feed-forward variable (FF) can also be a process input, which is able to affect the process significantly but is controlled by another control system and is not available for the model predictive controller. For example, the unit load demand is usually based on grid dispatch or set by the operator manually and is not available for the MPC to change. However, the unit load demand can bring significant influences to the process and it would be beneficial for the MPC to know its effects in advance. Therefore the unit load demand can be used a

feed-forward variable and its effects can be captured by models between the feed-forward variable and the control variables or constraint variables.

5.2.2 Oxy Boiler Island MPC Model Identification

The process knowledge is captured by a model predictive controller through the process models between the process inputs and process outputs. In this document, the MPC algorithm used for the implementation is based on linear dynamic process models. A simple and easy to understand form of linear process models can be expressed in time domain step or impulse models. It is widely used in industrial MPC applications because of the ease of understanding and developing such models.

The dynamic process models are usually identified from process data. To gather the appropriate process data for developing MPC models, the first step is to define an appropriate dynamic test matrix. The design of the dynamic test matrix requires a certain amount of process control and operation knowledge to cover the major process dynamics between the process inputs and outputs. After the dynamic test matrix is defined, it has to be implemented on the process and then the process test data can be collected and processed for future model identification.

The dynamic test matrix can be implemented by a series of step changes of the process inputs, i.e., the manipulated variables of the model predictive controller. The process responses, therefore, refer to the responses of the process outputs, i.e., the control variables and constraint variables, when the process is subjected to the step changes. The feed-forward variables and disturbance variables are also considered as process inputs. Although they cannot be directly manipulated by the MPC, the responses between the feed-forward variables/disturbance variables and the process outputs should also be captured by historical data or specifically designed dynamic plant tests.

It is worthwhile to point out that the models developed for a model predictive controller should be examined regularly to make sure they are still representative of the process dynamics. Generally, minor changes in the process equipment and/or control systems should not bring significant changes to the process dynamics. However, gradual and/or significant changes to the process or its control system can affect the process dynamics and therefore the original MPC models will deviate further away from the process and eventually the model predictive controller will not be able to provide reasonable control moves. The example model grid shown in Figure 5-4 is a preliminary model grid based on the current process simulator; as the dynamic oxy-fired boiler island process model is further updated and tuned, the dynamic MPC test should be re-implemented through the process simulator and the MPC model grid should be updated using the newly generated data.

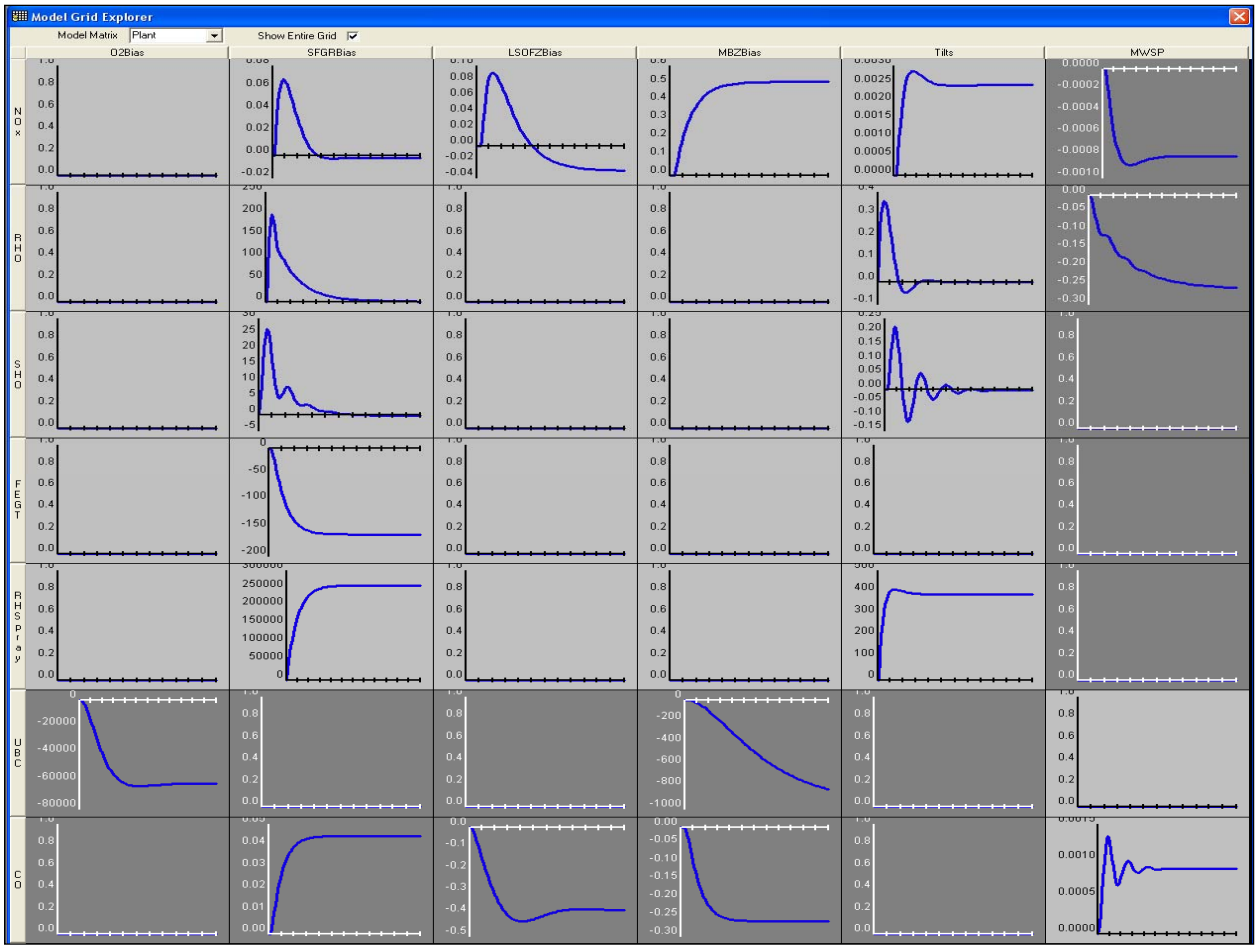

Figure 5-4. Oxy Boiler Island MPC modeling results grid overview

5.2.3 Oxy Boiler Island MPC Data Communication Configuration

After the model predictive controller is designed, tuned and tested; it is then ready to be deployed to the field by the on-line implementation tool: MACSRuntime. For field implementation, many important issues have to be solved before the model predictive controller can be connected with the local DCS.

An Excel interface is created as the data connection link between the Aspen based process simulator and the MPC controller. Aspen (see Figure 5-5) has developed Aspen Simulation Workbook (ASW), a data connection program between Aspen based models and Excel. ASW is an add-in for Excel which can enable the Excel spreadsheet to be connected with process variables within the Aspen models. On the other hand, Excel can also serve as an OPC server and communicate with MPC controller (see Figure 5-6) through standard OPC connections.

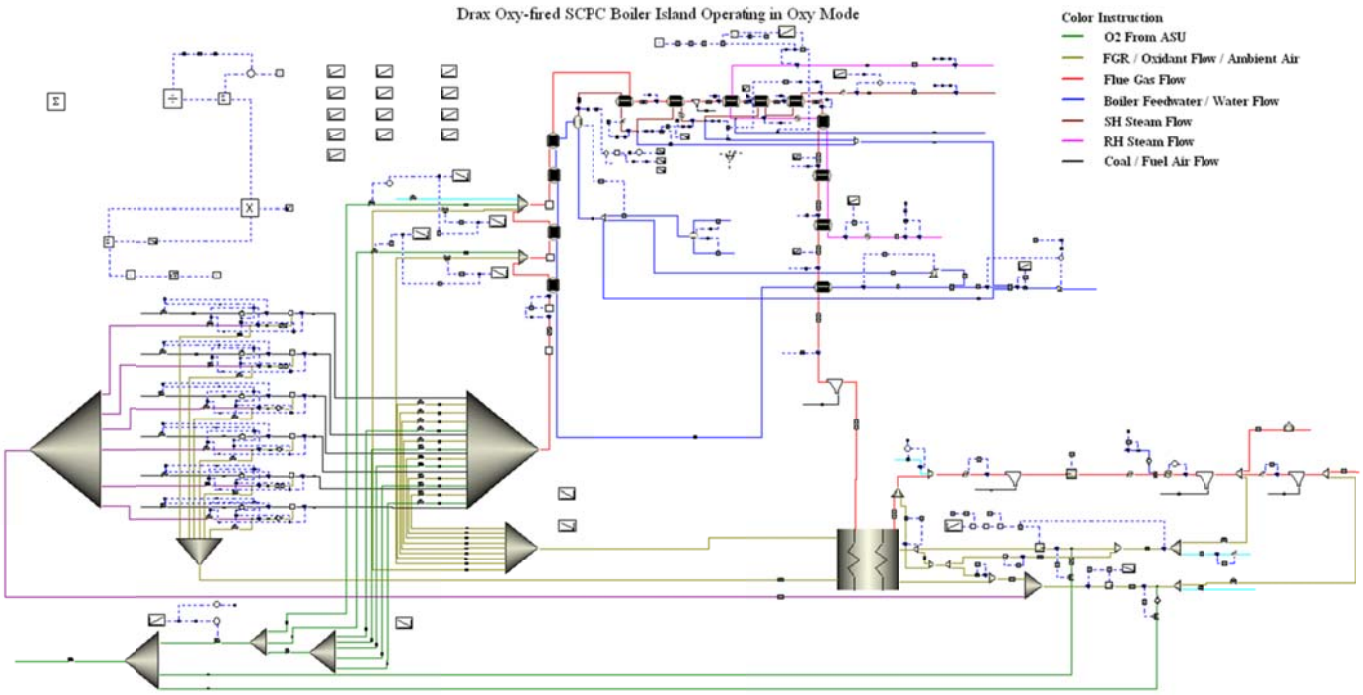

Figure 5-5. Oxy Boiler Island Aspen Plus Dynamic Model

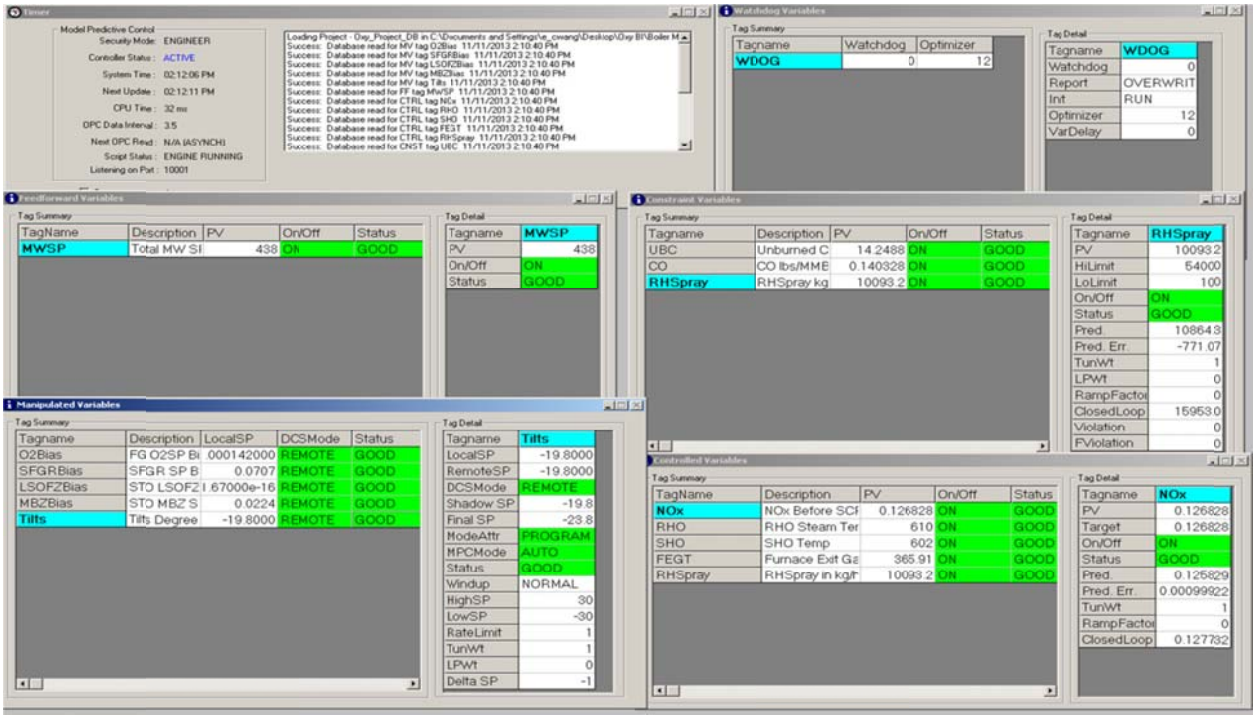

Figure 5-6. Oxy Boiler Island MPC Control Panel

5.3 Model Predictive Control Simulation Validation

This section discusses the potential benefits that can be brought by model predictive control to the Oxy Boiler Island process. Three closed-loop dynamic simulation case studies are presented to show the validation results of the model predictive controller. The simulation studies mainly concentrates on NO_x emission reduction and reheat spray water flow reduction.

5.3.1 NO_x Emission Reduction

Most of NO_x contained in the flue gas is removed by the Selective Catalyst Reduction section before the flue gas is sent for compression or recirculation. It is still of great benefit if the NO_x concentration level in the flue gas can be reduced at the combustion section while all the other control objectives are maintained. Based on the modeling results presented in Figure 5-4, only MBZ stoichiometry has a dominant impact on the NO_x level in terms of steady state response. For all the other manipulated variables, their influences on the NO_x level are relatively small.

Figure 5-7 shows the response of NO_x emission before SCR. The initial value of the NO_x emission before SCR is at 0.127 Lbs/MMBtu and a target of 0.100 Lbs/MMBtu is given to this control variable. Based on the process model grid, 4 out of the 5 manipulated variables have significant correlations with NO_x emission before SCR. However, we can see only 2 out of the 4 manipulated variables are responded to this NO_x target: the MBZ stoichiometry set point bias (see Figure 5-9) and the burner tilts set point (see Figure 5-10). This is because in the model predictive controller configuration, we selected the MBZ stoichiometry set point bias and the burner tilts set point as the control handles for NO_x optimization and the other 2 manipulated variables, the LOSFZ stoichiometry set point bias and SFGR flow set point bias are left out because their relative gains on NO_x emission are too small. Clearly, the MBZ stoichiometry is reduced and the burners tilted down to achieve the NO_x target. It is also worthwhile to point out that the manipulation of MBZ stoichiometry and burner tilts also disturbs other process variables including the main steam temperature. Figure 5-8 presents the steam temperature response at the outlet of Superheater. The main steam temperature is tightly controlled, and the maximum temperature deviation is 1 °C. With the aid of MPC, the NO_x concentration is decreased by more than 20%, while other control requirements are still maintained.

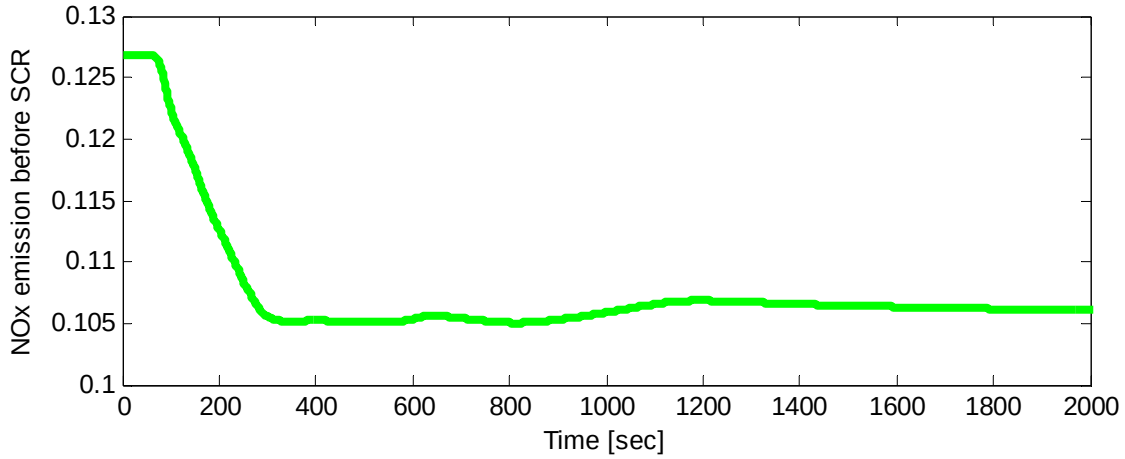

Figure 5-7. OBI MPC Analysis case 1: NO_x emission response

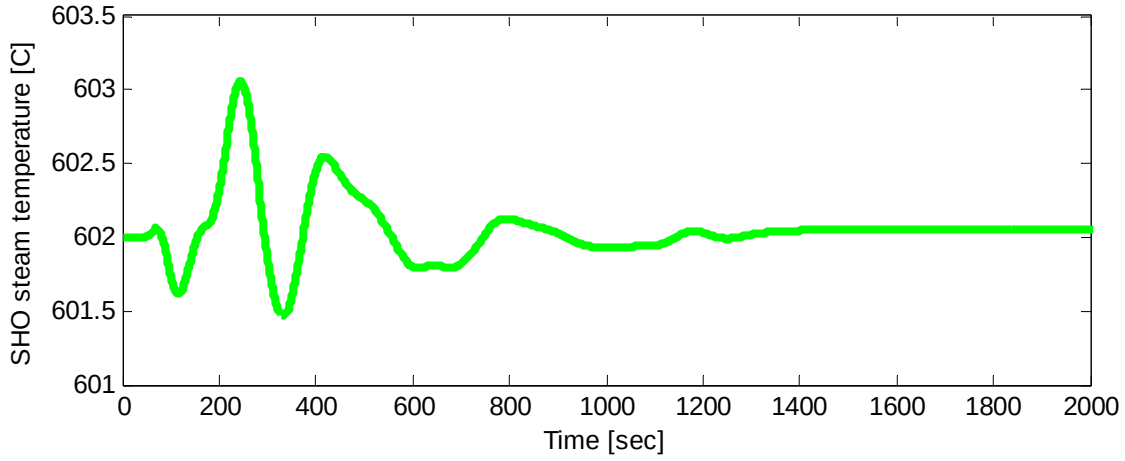

Figure 5-8. OBI MPC Analysis case 1: SHO steam temperature response

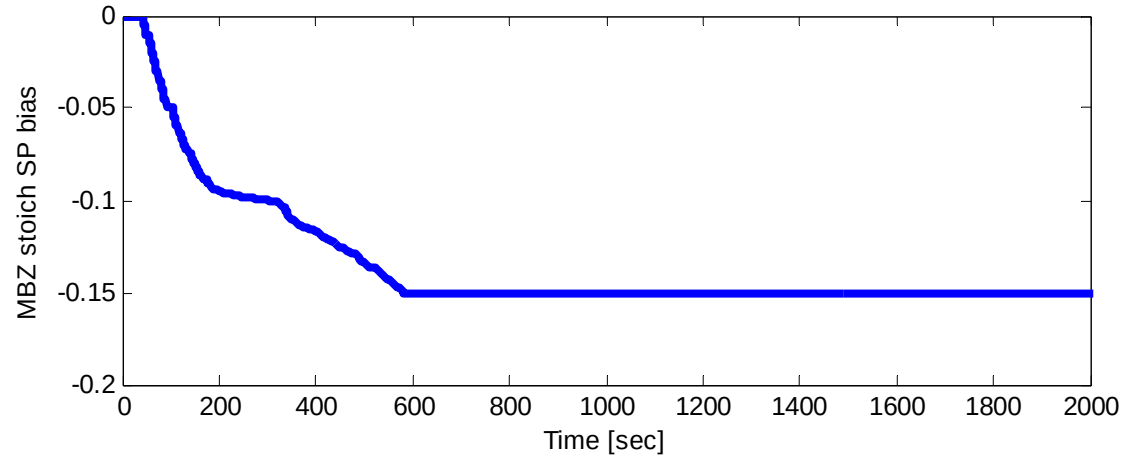

Figure 5-9. OBI MPC Analysis case 1: MBZ stoichiometry response

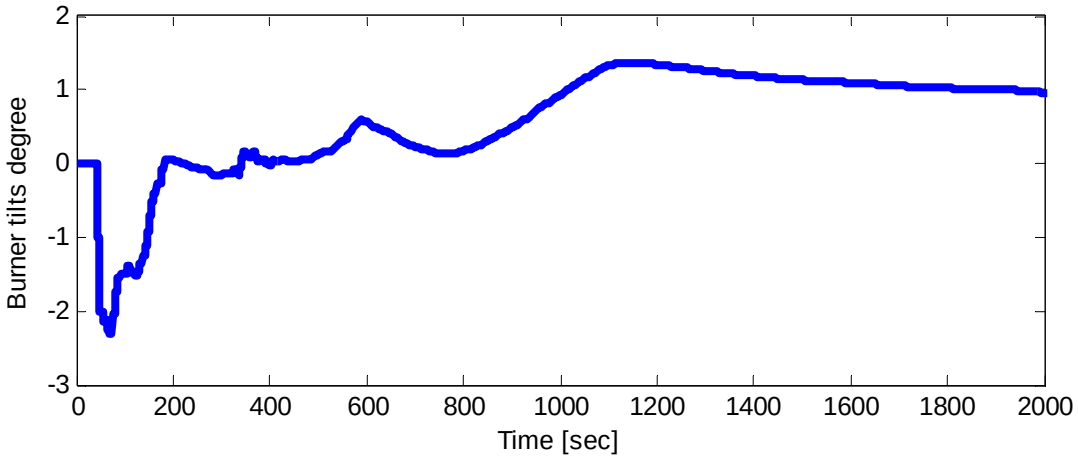

Figure 5-10. OBI MPC Analysis case 1: Burner tilts position response

5.3.2 Reheat Spray Reduction

The reheat spray water flow is directly related to the economic performance of the boiler island operation. As previously stated, there are three individual approaches that are able to affect the reheat steam temperature, i.e., reheat spray water, burner tilts position, and recirculation flow rate. The reheat spray water flow reduction will result in the increase of RHO steam temperature instantly. To maintain the reheat steam temperature at the set point value, other control loops need to function properly to achieve the target.

The second MPC optimization validation case is an optimization case to reduce the RH spray water usage given the same SH/RH outlet steam temperature set point. The reheat spray water flow rate reduces from 10095 lbs/hr to 7048 lbs/hr as shown in Figure 5-11, while the reheat steam temperature is still maintained at 610 °C with a maximum deviation of 2 °C during the transient. The responses of MBZ stoichiometry and burner tilts are given by Figure 5-13 and Figure 5-14.

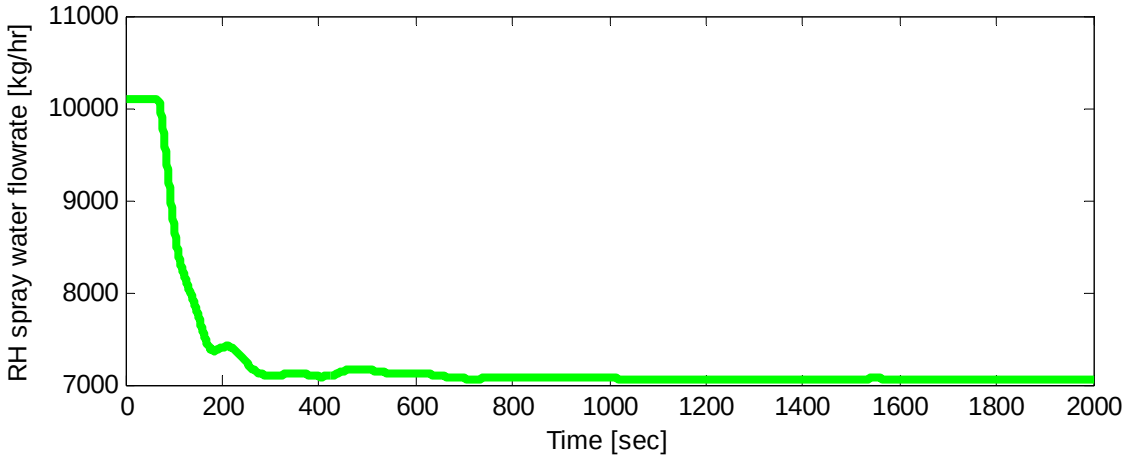

Figure 5-11. OBI MPC Analysis case 2: RH spray water flow rate response

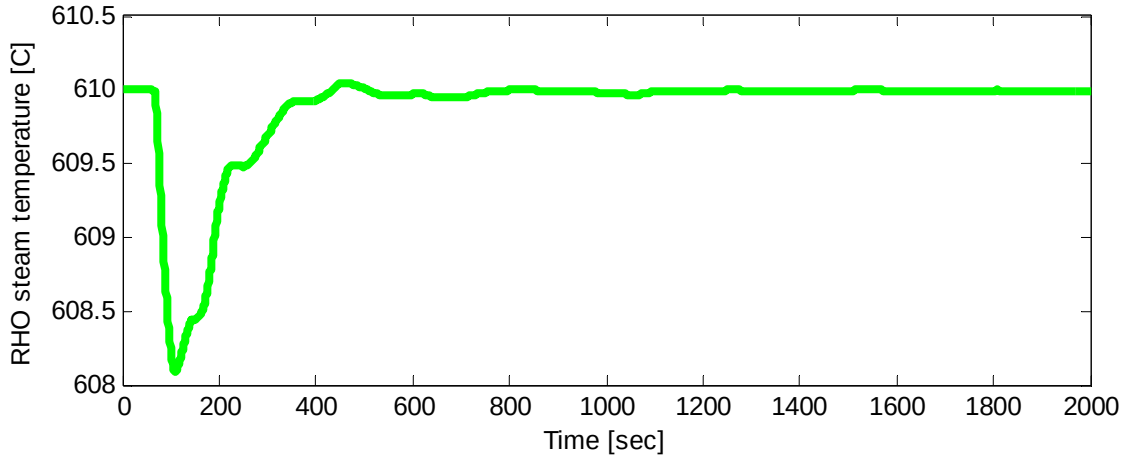

Figure 5-12. OBI MPC Analysis case 2: RHO steam temperature response

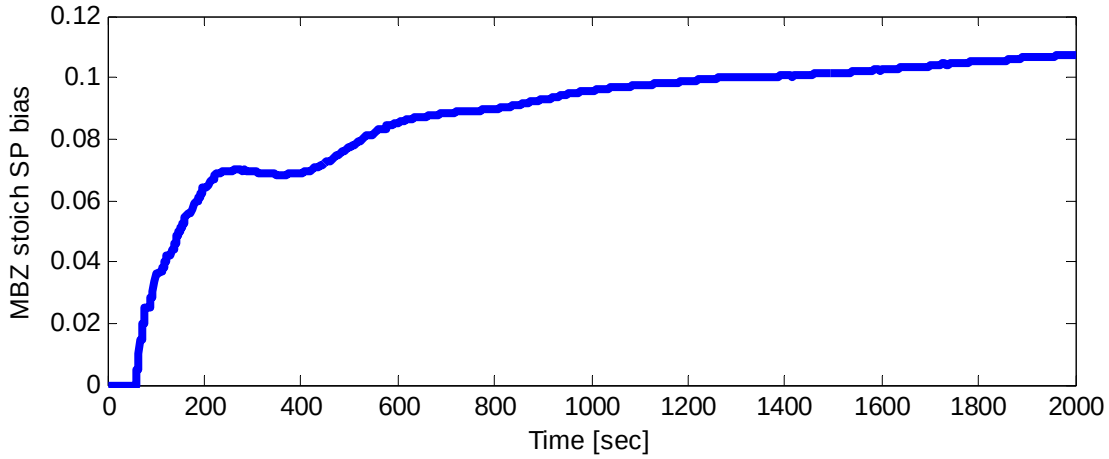

Figure 5-13. OBI MPC Analysis case 2: MBZ stoichiometry response

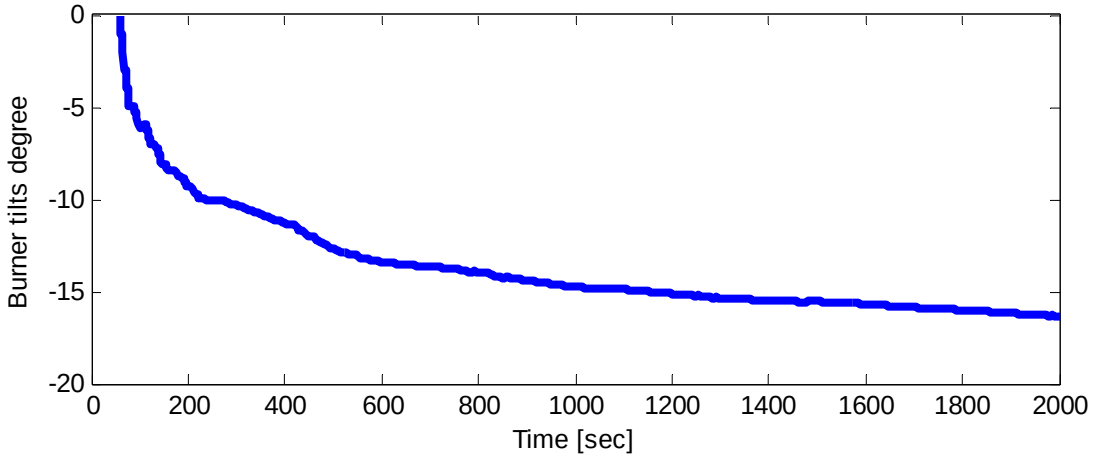

Figure 5-14. OBI MPC Analysis case 2: Burner tilts position response

In summary, a model predictive controller for the oxy-fired boiler island process has been developed to optimize performance. Preliminary testing of the model predictive controllers for NO_x emissions and reheat spray water consumption was conducted to provide examples of potential performance benefits:

Reduce NO_x emissions

NO_x reduction is an important objective for boiler combustion optimization. The first simulation scenario shows that the NO_x concentration in the flue gas can be reduced by more than 20% by optimizing the main burner zone stoichiometry and other control variables. The NO_x reduction in the combustion section is also able to reduce the consumption of ammonia in the SCR.

Reduce reheat spray water consumption

The potential of the model predictive controller to improve boiler island operation has also been illustrated in the second MPC optimization case. For Oxy-fired boiler island controls, the reheat water spray can suppress the reheat steam temperature deviation promptly. Nevertheless, from the long term operation viewpoint, the reheat spray water flow reduces the economic performance of unit operation. Model predictive control provides an alternative way to control the reheat steam temperature at its set point while maintaining the reheat spray water flow at a low level.

There are several additional key benefits that are feasible applying a model predictive controller for the oxy-fired boiler island including:

Improve heat rate and reducing raw materials cost

The heat rate improvement and reduction of fresh O_2 from ASU consumption have been demonstrated in the second MPC optimization case. The MPC also has the potential to improve a wider range of raw materials for different sub-systems within the boiler island process. However, limited by the model fidelity of the process simulator, not all possible savings can be demonstrated.

Minimize the SH/RH steam temperature deviations

As discussed, both MPC optimization cases are implemented at a fixed unit load demand and thus the SH/RH steam temperature disturbances are minimal. A model predictive controller has the potential to improve the control of the SH/RH steam temperatures by optimally adjusting available and relevant manipulated variables.

Maintain CO_2 concentration in flue gas and assisting CO_2 capture in GPU

The separation of CO_2 from other impurities in the GPU is directly correlated with original CO_2 concentration of the flue gas to GPU stream. A model predictive controller can be used to maintain CO_2 concentration of the flue gas to GPU stream and assist GPU's operation.

Reduce boiler island auxiliary power consumption

The potential for an MPC to minimize the auxiliary power consumption of various boiler island auxiliary equipment, including the ID fans, FGR fans (FD fans in Air-fired mode), FGD recycle pumps, etc. has yet to be demonstrated through more simulations.

Enhance operating flexibility and power plant load change capability

The potential of using a model predictive controller to enhance the load change capability and the flexibility of an oxy plant comes from a tighter control of the main process variables (steam temperatures and pressures, furnace pressure, etc.) within appropriate operation ranges. Firstly, the closed-loop control performances of the regulatory control system with and without the model

predictive controller have to be compared through dynamic simulations of fast load change scenarios. Then the oxy plant has to be tested against more aggressive ramp rates with the model predictive controller.

The full potential of a model predictive controller is yet to be demonstrated through further simulations and finally in the field implementation. As the scope of the process increases, the opportunity for optimizing such an integrated process increases and the complexity of the model predictive control system also grows. However, the fundamental concept and procedure to design and implement such multivariable model based control system remain consistent with the methodologies discussed here. .

6 Oxy Boiler Island Real-Time Optimization

6.1 Real Time Optimization Overview

6.1.1 General

One of the key challenges in the process industry is how to best operate the plant under different conditions such as feed compositions, production rates, energy availability, feed and product prices that change all the time. To meet the requirement of optimum process control and operation, a supervisory control technique is needed. One such technique that has received considerable attention in the process industry is Real Time Optimization.

Real Time Optimization (RTO), or on-line operations optimization, has a wide appeal in the process industries because of its promise for improving process profitability. The optimization of process operations is of considerable interest in industry due to increasing global competition and tightening product requirements. RTO is a model-based process control approach that uses current process information (i.e. process model and economic data) to predict the optimal operating policy for a process unit during the next RTO interval. RTO is also used to indicate the continuous re-evaluation and alteration of operating conditions of a process so that the economic productivity of the process is maximized subject to certain operational constraints. Real Time Optimization is an appealing concept in that it is at the level of the control hierarchy where business decisions are integrated into the operations. Meanwhile, the advances in the speed and power of computer at lower costs are making on-line optimization a more cost effective method of improving plant performance. Processes that experience a wide range of operating conditions due to variability in product prices and material costs, large variations in ambient conditions or economic trade-offs and constraints will benefit the most from Real Time Optimization.

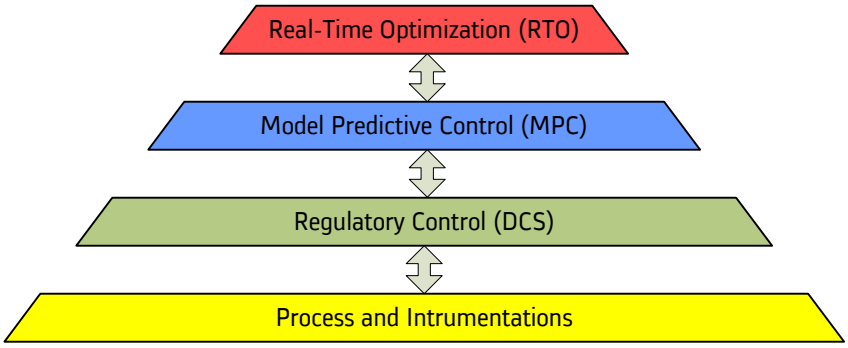

Figure 6-1. General hierarchical control optimization

Figure 6-1 presents the general hierarchical control optimization where the RTO system is essentially the economic optimization layer that is integrated into Advanced Process Control and/or Regulatory Control to provide updated process targets for the control system in real time. The Real Time Optimization does not directly interact or manipulate the processes. Instead, the RTO system guides the process operations by updating the targets within the Model Predictive Controllers (MPC). This hierarchical structure enables the RTO to drive the process operations towards the optimal operating point on condition that the basic requirements of process safety and controllability criteria at the lower layer of controls are satisfied.

6.1.2 RTO Calculation Cycle

The RTO is based on the assumption that model and disturbance transients can be neglected if the optimization execution time interval is long enough to allow the process to reach and maintain steady-state. Figure 6-2 provides a calculation cycle for model based Real Time Optimization, which includes the following key steps:

- Steady State Detection

  This detects when the process is close enough to steady state to allow the real time optimizer to model the process with reasonable accuracy. When the plant is determined to be at steady state, data from the process is passed onto the optimizer. If unsteady or transient data is used, the reconciled results may not accurately reflect the operation of the plant, and therefore the subsequent optimization of the plant may not yield a realistic optimum for the current operating conditions.

- Data Reconciliation & Gross Error Detection

  Data reconciliation adjusts the measured variables (e.g. temperature, pressure, mass flow rate, etc.) and, if possible, estimates any unmeasured variables for the process so that they satisfy the balance constraints. Gross errors are caused by non-random events such as instrument biases, malfunctioning measuring devices, inaccurate or incomplete process models and process leaks. Gross Error Detection aims to take appropriate corrective actions to rectify the gross errors found in the process data. The adjusted data from the plant is then used to proceed to the next step.

- Parameter Estimation

  Parameter estimation, or model parameter updating, involves updating of any process parameter in the model that changes slowly over time, perhaps due to wear and tear or fouling of the equipment. Process parameters include heat transfer coefficients, loading factors, and equipment efficiencies, etc. The Real Time updating of a model's parameters permits realistic models to be provided for an optimization system. Another benefit of parameter estimation is the ability to track the condition of equipment in the plant with time. Given the adjusted data available, the parameters of the process model are estimated and updated, which are then used in the process model for the calculation of optimal set points.

- Process Model

  The process model used in Real Time Optimization must represent changes in the manipulated variables of the process given the updated set points calculated by the optimization algorithm. The model approximates the effect of these variables on the dependent variables, which are usually process constraints or that have a significant economic impact on process operation. The complexity of the process model also determines the sophistication of the maintenance required. Not all variables and constraints can be included in the process model. The art of optimization modeling is to select the variables that have the most significant effect on the economics and important constraints, while eliminating those of less significance.

- Optimization

  The optimization component contains the objective function and the optimization algorithm. The objective function is derived from the plant model, and is to be either maximized or minimized through changes in the process variables. The objective function for Real Time

Optimization normally represents the economic model of the process. The optimization algorithm uses the process model and the objective function to solve for the new optimum set points for the plant. The important considerations in choosing an optimizing algorithm are computational requirements, number of objective function evaluations, and robustness.

- Updating of Process Set Points

  The optimum set points for the process found by the optimizer are returned to the process. Once the plant has returned to steady state, another circle of Real Time Optimization is performed to keep the plant operate at its optimum. It is worthwhile to point out that bounds must be placed on certain variables during the optimization to prevent the solution from moving to far from the starting point. This is because it takes a finite amount of time to move to a new operating point; therefore the set points should not be moved a great deal on each run of the optimizer.

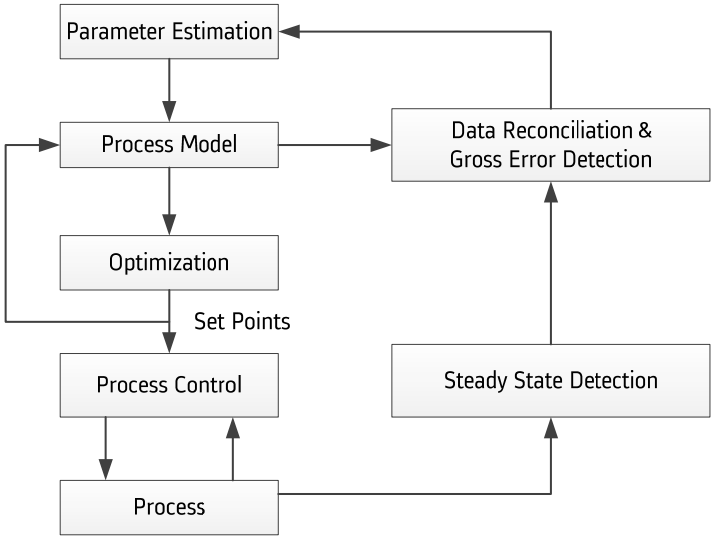

Figure 6-2. RTO calculation cycle

All process models are only approximations of real process behavior, and therefore as operating conditions in the plant shift with time, the model coefficients will require updating. New constraints may also need to be added or old ones deleted at some point. Whether some model maintenance should be carried out manually or automatically is an important decision to be made in the implementation of the optimizer. Ongoing long term maintenance of the on-line optimizer must be carried out after implementation as well.

6.2 Real-Time Optimization for the Oxy Boiler Island

The target of the Real Time Optimization is to achieve the maximum profit of the process by pushing the operating condition at steady state towards the optimum point. There is no exception for the RTO application to the oxy-fired power plant. As previously stated, the oxy-fired power plant is quite different from the conventional coal-fired power plant in that two more components (i.e. Air Separation Unit and Gas Processing Unit) have been added into the process. The oxy-fired power plant is essentially designed to significantly reduce the CO_2 concentration in the released flue gas. However, the cost of the power product has been increased in that the air separation and CO_2 capture consumes significant amount of energy.

RTO shall consider the overall economic trade-offs among all the sub-systems in the oxy-fired steam plant by taking the current available equipment and the current line-up of that equipment into consideration. The RTO model shall have the resolution not only to predict the changes in conversion and emissions caused by small changes in stoichiometry and classifier speed, but also to predict how much of the improvement in combustion efficiency can be captured by the process. Thus, some sections of the RTO model shall be more detailed than the engineering design model for the plant.

The fundamental engineering/science principles approach can also help configure the underlying model to match field operational conditions. The underlying model is a set of equations; to model a piece of equipment out of service, one must only turn off the equations associated with that piece of equipment. For example, the logic can be used to configure which coal elevations are out of service or to take a feed water heater out of service. The same set of equations shall be able to model the degradation of process performance with time, provided that the cause of the degradation is known. For example, as slag builds up on the boiler surfaces, higher temperatures are required to provide the necessary heat transfer to produce steam and air is shifted into the over-fired registers to offset the increased emissions. After a soot blow, the heat transfer coefficients immediately improve, the exhaust temperatures fall and air can be diverted back into the lower registers for efficiency. The RTO model shall track changes in process efficiency and report that estimated performance.

As for the data requirements, the RTO model does not require a large set of process data over a wide range of operations to tune the correlations. The RTO system can be built on a single data point which can be a snapshot of data at a base condition or the design basis. However, the data point does require a much richer set of data. Once the RTO model is built and parameterized to a single point, the rate-dependent terms, such as heat transfer, shall be adjusted to match the process response identified during the MPC development.

6.3 Optimization Objectives

Real Time Optimization (RTO) is a supervisory system to optimize stable plant operations. These systems calculate the targets for the supervisory control system, and the control system calculates the trajectory to achieve the optimization targets. As a system in the supervisory layer, a RTO system must run without an operator's intervention.

The RTO system continuously monitors plant operations, and it does not perform its calculation at a fixed frequency, which is quite different from a supervisory control such as model predictive control. The main reason relies on the steady state detection as a primary step for RTO. Once the system detects steady operations, it starts to proceed with the rest of sequences including parameters estimation, process optimization, and set points calculation.

The power utility industry generates a single product, electricity. Though cogeneration plants produce both electricity and steam, the cogeneration plant typically cannot buy or sell excess steam production. Over-production of steam must be vented, costing both fuel and water; under-production of steam is a failure to meet a contract. Therefore, cogeneration plants can be considered to have a single (saleable) product.

From the power system view, the total generated power must equal demand. Excess power typically must be avoided or dissipated. Combustion byproducts, such as ash, may have a value, but the power plant will not change its production (of electricity) to produce more or less of a byproduct. However, the power plant may change operations to affect the quality of the byproduct.

The operational costs include not only the expected costs for fuel, ammonia/urea for the SCR and lime/limestone for an FGD unit, but also include any costs for ash removal. The power plant process for the purposes of RTO has been defined so that all ancillary power demands are provided internal to this scope. These ancillary power demands are both generated and consumed within the scope, hence, the ancillary power demands have zero effective cost and zero net value.

Costs associated with emissions are another major factor in power plant economics. CO_2 emissions are becoming regulated in an effort to reduce worldwide production. Rather than arbitrarily assigning limits on the total CO_2 that can be produced at a given site, two mechanisms are being implemented to give an economic incentive to reduce emissions while not shutting down inefficient facilities. Both mechanisms effectively assign a cost to CO_2 production. Taxation of CO_2 emissions, one mechanism proposed in the United States, puts a direct cost on CO_2 production. In a cap and trade system, currently in effect with the European Economic Community, each site is assigned a base allowable CO_2 production rate or cap. In order to produce emissions above the cap, production credits must be purchased from a plant in the amount that the latter plant is operating below its cap. In cap and trade, CO_2 has a direct cost; a power plant must either purchase CO_2 credits or the plant can convert CO_2 production below its cap into credits. A major difference between these two systems is the frequency of price changes. A taxation system will change costs at the frequency of budget cycle; a cap and trade system will see costs based on current industrial demand. NO_x and SO_x are already regulated with limitations on production at each source. In an effort to limit total production, the emissions of NO_x and SO_x are also starting to be regulated with economic mechanisms. The RTO system is being designed for the future economics where emissions – whether NO_x, SO_x or CO_2 – have an economic cost.

The power produced must equal the power demand and the power demand is set by external systems. Therefore, the power exported from the plant is a fixed quantity. Given that profit equals product value minus costs, maximizing profit for a fixed product is equivalent to minimizing costs. Cost minimization is the standard objective function for power applications.

- Minimize total cost = cost of {operations + emissions} - value of {additional capacity + byproducts}
    - cost of operations = Cost of {fuel + ammonia/urea + lime/limestone + imported power (under production)};
    - cost of emissions = Cost of {CO_2 emissions + NO_x emissions + SO_x emissions}; and
    - value of byproducts = Value of {saleable ash+ gypsum (WFGD w/forced oxidation)}.

The introduction of additional capacity into the objective function allows the RTO model to be used to perform a second set of calculations. The first set of calculations is the cost minimization described above, which is essentially the cost tradeoff between efficiency and emission costs. After calculating the minimum cost to generate the desired power, a second optimization case could be run to estimate remaining power generation capacity which could be offered above base.

Bibliography

1. S. J. Qin, T. A. Badgwell, A Survey of Industrial Model Predictive Control Technology, Control Engineering Practice, 11, pp: 733 – 764, 2003.
2. J. Rawlings, Tutorial: Model Predictive Control Technology, Proceedings of the American Control Conference, pp: 662 – 676, 1999.
3. N. Hovakimyan and C. Cao, L1 Adaptive Control Theory: Guaranteed Robustness with Fast Adaptation (Advances in Design and Control): Society for Industrial & Applied Mathematics, 2010.
4. C. Wang, I. Gregory, and C. Cao, "L1 Adaptive Control with Output Constraints Applied to Flight Envelope Limiting," AIAA Guidance, Navigation, and Control Conference, 2012.
5. C. Wang, S. Yang, X. Lou, C. Neuschaefer, and C. Cao, "L1 adaptive controller and its application to main steam temperature process control," 54th Annual ISA POWID Symposium, Charlotte, NC, 2011.
6. C. Wang, R. Sharifi, and C. Cao, "L1 Adaptive Control of Uncertain Nonlinear Systems in the Presence of Output Limits," Proceedings of the AIAA Infotech@Aerospace, St. Louis, Missouri, Paper No. -2011-1400, March 2011.
7. X. Lou, C. Neuschaefer, A. Herb Andrus, I. Abdulally, Model Predictive Control and Real-Time Optimization for Chemical Looping Process, 57th ISA POWID Symposium, Scottsdale, Arizona, 1-6 June 2014